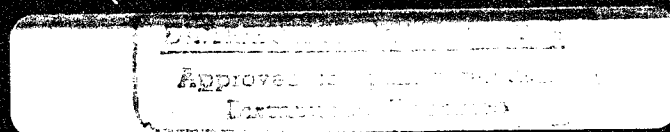


Proceedings of

ION GPS-95

*The 8th International Technical Meeting of
The Satellite Division of The Institute of Navigation*

Part 2 of 2



September 12-15, 1995
Palm Springs Convention Center
Palm Springs, California



Accession For	
NTIS	ORAS!
DTIC	TAB
Unannounced	
Justification	
By	
Distribution!	
Availability Codes	
Dist	Avail and/or Special
A-1	

Proceedings of

ION GPS-95

*The 8th International Technical Meeting of
The Satellite Division of The Institute of Navigation*

Part 2 of 2

19951219 058

September 12-15, 1995

Palm Springs Convention Center

Palm Springs, California

DISCLAIMER NOTICE



**THIS DOCUMENT IS BEST
QUALITY AVAILABLE. THE
COPY FURNISHED TO DTIC
CONTAINED A SIGNIFICANT
NUMBER OF PAGES WHICH DO
NOT REPRODUCE LEGIBLY.**



Session A4

DGPS Algorithms

Chair:

Dr. Gerard Lachapelle
The University of Calgary

Co-Chair:

Dr. Paul Cross
University of Newcastle

Computation and Quality Control of Differential GPS Corrections

Xin-Xiang, Hans van der Marel, and Cees de Jong
Delft University of Technology

Biography

Xin-Xiang Jin is currently a project staff member with the Faculty of Geodetic Engineering of Delft University of Technology, The Netherlands. He holds B.Sc. and M.Sc. degrees, both in geodesy, from Wuhan Technical University of Surveying and Mapping, China. Hans van der Marel is an academic staff member with the Faculty of Geodetic Engineering of Delft University of Technology, where he received his Ir. and PhD. degrees, both in geodesy. Cees D. de Jong was a project staff member with the Faculty of Geodetic Engineering of Delft University of Technology, where he received his Ir. degree in geodesy. In April 1995, he joined Philips Electronics N.V., The Netherlands.

Abstract

The DGPS technique can considerably improve the accuracy of stand-alone GPS positioning, but the improvement depends on the distance between the user and the reference station (spatial correlation), the latency of differential corrections (temporal correlation), and the quality of differential corrections. Therefore, how to correctly generate differential corrections as well as their precision is one of the keys to the DGPS positioning technique. This paper presents a new algorithm for generating differential GPS corrections. This algorithm directly uses code and carrier observations in the measurement model of a Kalman filter, so that it is possible to use a simple stochastic observation model and to use the standard algorithm of the Kalman filter. The algorithm accounts for biases like multipath errors and instrumental delays in code observations and it clearly shows how differential corrections are differently affected by code biases when dual or single frequency data are used. In addition, the algorithm can be integrated with a recursive quality control procedure. As a consequence, the quality of differential corrections can be guaranteed with certain probability.

1. Introduction

The DGPS technique can considerably improve the accuracy of stand-alone GPS positioning, since biases inherent in the latter technique are greatly reduced or even eliminated. But the improvement depends on the distance between the user and the reference station (spatial correlation), the latency of differential corrections (temporal correlation), and the quality of differential corrections. Therefore, how to correctly generate differential corrections as well as their precision is one of the keys to the DGPS positioning technique. Currently, there already exist several algorithms for the generation of differential corrections, for instance, the algorithm based on carrier filtered code observations [van Dierendonck 1993], [Landau 1993] and the algorithm based on code observations and sequential differences of carrier observations [Loomis 1986], [Loomis et al. 1989]. But all these algorithms have at least difficulties to correctly specify stochastic models, since the input measurements of them are either correlated in time or correlated with dynamic noises of states.

This paper derives a new algorithm for generating differential corrections along with a recursive quality control procedure. The derivation of the algorithm is followed by a discussion on how the recursive quality control procedure, as detailed in [Teunissen 1990a, 1990b], can be applied for this particular case.

2. Measurement model and dynamic model

At time t_k , a general form of GPS code and carrier observation equations are used as follows

$$P_k = \rho_k + c(dT_k - dt_k) + E_k + I_k + T_k + b_k + \epsilon_k \quad (1)$$

$$\lambda \phi_k = \rho_k + c(dT_k - dt_k) + E_k - I_k + T_k - \lambda N + \eta_k \quad (2)$$

where

P_k : code observation (m)

- ϕ_k : carrier observation (cycles)
- ρ_k : satellite-receiver range computed from ephemeris data and station coordinates (m)
- c : speed of light (m/s)
- dT_k : receiver clock bias (s)
- dt_k : satellite clock bias (including SA clock error) (s)
- E_k : effect of ephemeris error (including SA orbit error) plus a priori coordinate error of station (m)
- I_k : ionospheric effect (m)
- T_k : tropospheric delay (m)
- b_k : code observation bias (m)
- ϵ_k : code observation noise (m)
- λ : wave length corresponding to one of the GPS carriers (m)
- N : carrier ambiguity (cycles), which does not have to be an integer.
- η_k : carrier observation noise (m)

Note that the parameter b_k in the code observation equation is new. It has been shown in [Jin 1995a] that without introducing this parameter, code observation noises are biased and their time series appear to have linear and/or periodic behaviour. Whereas after introducing the bias parameter b_k in the code observation equation, code observation noises become unbiased random noises of zero mean. The code bias b_k is a combination of all systematic errors in the code observation, which could have resulted from, for example, multipath and instrumental delay. For the same satellite, the sizes and behaviours of code biases on different frequencies may not be the same. For different channel or different observation environment, the bias behaves also differently. It has been found that in quite good observation environments the variation of the bias can be about 0.5 metres or more for a period of one hour and it appears more clearly in Trimble 4000 SSE receivers than in TurboRogue SNR-8000 receivers. With the improvement of GPS receiver and antenna designs, this bias may become less and less significant in the future. For more details on the behaviour of the code bias, one can refer to [Jin 1995a].

By using the broadcast navigation data, the approximate value dt_k^0 for dt_k can be computed. Let us denote the correction to dt_k^0 by δt_k and represent the combination of receiver-clock bias, correction to the approximate value of satellite-clock bias, tropospheric delay and ephemeris error by S_k ,

$$S_k = c(dT_k - \delta t_k) + T_k + E_k \quad (3)$$

Consider the case that four types of observables, L1 and L2 code and carrier, are available. In the following, we use P_k , b_k , ϵ_k , λ_1 , ϕ_k and N to represent the quantities related to the L1 frequency and \tilde{P}_k , \tilde{b}_k , $\tilde{\epsilon}_k$, λ_2 , $\tilde{\phi}_k$ and \tilde{N} for those related to the L2 frequency. In the GPS observation equations, the ionospheric effect depends on the frequency of the transmitted signal. Generally, when dual frequency data are processed, only the first-order ionospheric effect is accounted for. The first-order L2 ionospheric effect is equal to the first-order L1 effect multiplied by the squared ratio of the L1 and L2 frequencies. Therefore, if I_k denotes the first order ionospheric effect for the L1 frequency and r the squared ratio of the L1 and L2 frequencies ($r \approx 1.647$), we arrive at the following system of code and carrier observation equations

$$\begin{bmatrix} P_k - \rho_k + c dt_k^0 \\ \lambda_1 \phi_k - \rho_k + c dt_k^0 \\ \lambda_2 \tilde{\phi}_k - \rho_k + c dt_k^0 \\ \tilde{P}_k - \rho_k + c dt_k^0 \end{bmatrix} = \begin{bmatrix} 1 & 1 & & 1 \\ 1 & -1 & -1 & \\ 1 & -r & & -1 \\ 1 & r & & 1 \end{bmatrix} \begin{bmatrix} S_k \\ I_k \\ \lambda_1 N \\ \lambda_2 \tilde{N} \\ b_k \\ \tilde{b}_k \end{bmatrix} + \begin{bmatrix} \epsilon_k \\ \eta_k \\ \tilde{\epsilon}_k \end{bmatrix} \quad (4)$$

The ambiguities N and \tilde{N} are constant in time, provided that no cycle slips occur in the L1 and L2 observations, respectively. All other parameters generally are changing in time and have to be solved for every epoch. Equation (4) cannot be used directly because the number of unknowns is larger than the number of observations, regardless of the number of epochs for which data are available. It is, however, possible to estimate the variations of b_k and \tilde{b}_k with respect to b_0 and \tilde{b}_0 , respectively. This can be achieved by the following parameter transformation

$$\begin{bmatrix} S_k + \frac{r}{r-1}b_0 - \frac{1}{r-1}\tilde{b}_0 \\ I_k - \frac{1}{r-1}b_0 + \frac{1}{r-1}\tilde{b}_0 \\ \lambda_1 N + \frac{r+1}{r-1}b_0 - \frac{2}{r-1}\tilde{b}_0 \\ \lambda_2 \tilde{N} + \frac{2r}{r-1}b_0 - \frac{r+1}{r-1}\tilde{b}_0 \\ b_k - b_0 \\ \tilde{b}_k - \tilde{b}_0 \end{bmatrix} = \begin{bmatrix} 1 & & & & & \\ & 1 & & & & \\ & & 1 & & & \\ & & & 1 & & \\ & & & & 1 & \\ & & & & & 1 \end{bmatrix} \begin{bmatrix} \frac{r}{r-1} & -\frac{1}{r-1} \\ -\frac{1}{r-1} & \frac{1}{r-1} \\ \frac{r+1}{r-1} & -\frac{2}{r-1} \\ \frac{2r}{r-1} & -\frac{r+1}{r-1} \\ -1 & \\ -1 & \end{bmatrix} \begin{bmatrix} S_k \\ I_k \\ \lambda_1 N \\ \lambda_2 \tilde{N} \\ b_k \\ \tilde{b}_k \\ b_0 \\ \tilde{b}_0 \end{bmatrix} \quad (5)$$

which results in

$$\begin{bmatrix} P_k - \rho_k + c dt_k^0 \\ \lambda_1 \Phi_k - \rho_k + c dt_k^0 \\ \lambda_2 \tilde{\Phi}_k - \rho_k + c dt_k^0 \\ \tilde{P}_k - \rho_k + c dt_k^0 \end{bmatrix} = \begin{bmatrix} 1 & 1 & & \\ 1 & -1 & -1 & \\ 1 & -r & & -1 \\ 1 & r & & \end{bmatrix} \begin{bmatrix} S_k + \frac{r}{r-1}b_0 - \frac{1}{r-1}\tilde{b}_0 \\ I_k - \frac{1}{r-1}b_0 + \frac{1}{r-1}\tilde{b}_0 \\ \lambda_1 N + \frac{r+1}{r-1}b_0 - \frac{2}{r-1}\tilde{b}_0 \\ \lambda_2 \tilde{N} + \frac{2r}{r-1}b_0 - \frac{r+1}{r-1}\tilde{b}_0 \\ b_k - b_0 \\ \tilde{b}_k - \tilde{b}_0 \end{bmatrix} + \begin{bmatrix} e_k \\ \eta_k \\ \tilde{\eta}_k \\ \tilde{e}_k \end{bmatrix} \quad (6)$$

This system can be solved for every epoch. For epoch $k=0$, the first four parameters are computed, and for the remaining epochs parameters 1, 2, 5 and 6 are solved, while parameters 3 and 4 are constant.

In order to improve the precision of the estimates of the parameters and to estimate the rate of change of the differential corrections as well as the corrections themselves and to provide redundancy for quality control, we introduce dynamic models for S_k , I_k , b_k and \tilde{b}_k . It has been shown in [Jin 1995a] that the third order time derivative of S_k and the second order time derivative of I_k , denoted by \dot{S}_k and \dot{I}_k , respectively, can be modelled as zero-mean white noise processes with constant spectral densities q_s (m^2/s^5) and q_I (m^2/s^3). The second order time derivatives of b_k and \tilde{b}_k , denoted by \ddot{b}_k and $\ddot{\tilde{b}}_k$, can be modelled as zero-mean white noise processes with the same constant spectral density q_b (m^2/s^3). Therefore, it follows from (6) that the estimable state vector related to epoch k ($k>0$) reads

$$\left(S_k + \frac{r}{r-1}b_0 - \frac{1}{r-1}\tilde{b}_0, \dot{S}_k, \ddot{S}_k, I_k - \frac{1}{r-1}b_0 + \frac{1}{r-1}\tilde{b}_0, \dot{I}_k, \ddot{I}_k, \lambda_1 N + \frac{r+1}{r-1}b_0 - \frac{2}{r-1}\tilde{b}_0, \lambda_2 \tilde{N} + \frac{2r}{r-1}b_0 - \frac{r+1}{r-1}\tilde{b}_0, b_k - b_0, \dot{b}_k, \ddot{b}_k, \tilde{b}_k - \tilde{b}_0, \dot{\tilde{b}}_k, \ddot{\tilde{b}}_k \right)^* \quad (7)$$

The corresponding original non-estimable state vector is

$$(S_k, \dot{S}_k, \ddot{S}_k, I_k, \dot{I}_k, \ddot{I}_k, \lambda_1 N, \lambda_2 \tilde{N}, b_k, \dot{b}_k, \ddot{b}_k, \tilde{b}_k, \dot{\tilde{b}}_k, \ddot{\tilde{b}}_k, b_0, \tilde{b}_0)^* \quad (8)$$

Our goal is to compute differential corrections. Additionally it is preferred to build up a model that links the L2 code bias \tilde{b}_k only with the L2 code observable so that it can also be easily adapted to situations when L2 code observable is missing or L2 and/or L1 carrier is missing. For these purposes, a transformation has to be applied to (7) or (8). For reasons of convenience, we transform (8) as follows

(9)

It follows from (9) and (4) that the measurement model for the Kalman filter we use reads

(10)

$$E\{\mathbf{e}_k\} = \mathbf{0} \quad (11)$$

(12)

To derive the dynamic model for x_k , we need to note that N and \tilde{N} are constants just like b_0 and \tilde{b}_1 , unless a

cycle slip occurs. The second order time derivative of differential correction \ddot{v}_k is equal to that of ionosphere-free differential correction \ddot{s}_k , because the I_k is white noise and is included in the dynamic noise term. The three ionospheric-delay related states in the transformed

state vector, i.e. $I_k + \frac{\lambda_1 N + b_0}{2}$, $I_k + \frac{\lambda_2 N + b_0}{r+1}$ and $I_k - \frac{b_0 - b_0}{r-1}$, have the same rate I_k . In addition, it follows from (9) that the dynamic noise of the state vector x_k from epoch $k-1$ to k is that of the original non-estimable vector (8) premultiplied by the transformation matrix T of (9). Thus the dynamic model reads

$$x_k = \underbrace{\begin{bmatrix} 1 & \Delta t_k & \frac{1}{2}\Delta t_k^2 & & & & & & \\ & 1 & \Delta t_k & & & & & & \\ & & 1 & & & & & & \\ & & & 1 & \Delta t_k & & & & \\ & & & & 1 & & & & \\ & & & & \Delta t_k & 1 & & & \\ & & & & \Delta t_k & & 1 & & \\ & & & & & & & 1 & \Delta t_k \\ & & & & & & & & 1 \\ & & & & & & & & & 1 \end{bmatrix}}_{\Phi_{k,k-1}} x_{k-1} + T \int_{t_{k-1}}^{t_k} \underbrace{\begin{bmatrix} \frac{1}{2}(t_k-t)^2 \ddot{S}(t) \\ (t_k-t) \ddot{S}(t) \\ \ddot{S}(t) \\ (t_k-t) \ddot{I}(t) \\ \ddot{I}(t) \\ 0 \\ 0 \\ (t_k-t) \ddot{b}_k \\ \ddot{b}_k \\ (t_k-t) \ddot{b}_k \\ \ddot{b}_k \\ 0 \\ 0 \end{bmatrix}}_{d_k} dt \quad (13)$$

with

$$E\{d_k\} = 0 \quad (14)$$

$$E\{d_k d_k^*\} = \delta_{kl} T \begin{bmatrix} q_s Q_{11} & & & & & & & & \\ & q_f Q_{22} & & & & & & & \\ & & 0_{2 \times 2} & & & & & & \\ & & & q_b Q_{22} & & & & & \\ & & & & q_b Q_{22} & & & & \\ & & & & & q_b Q_{22} & & & \\ & & & & & & 0_{2 \times 2} & & \end{bmatrix} T^* \quad (15)$$

where

$$Q_{11} = \begin{bmatrix} \frac{\Delta t_k^5}{20} & & & & & & & & \\ & \text{SYM.} & & & & & & & \\ \frac{\Delta t_k^4}{8} & \frac{\Delta t_k^3}{3} & & & & & & & \\ & & & & & & & & \\ \frac{\Delta t_k^3}{6} & \frac{\Delta t_k^2}{2} & \Delta t_k & & & & & & \end{bmatrix}, \quad Q_{22} = \begin{bmatrix} \frac{\Delta t_k^3}{3} & & & & & & & & \\ & \text{SYM.} & & & & & & & \\ \frac{\Delta t_k^2}{2} & & \Delta t_k & & & & & & \end{bmatrix} \quad (16)$$

On the basis of the above dynamic and measurement models, the recursive prediction and estimation

equations for the states read

$$\hat{x}_{k|k-1} = \Phi_{k,k-1} \hat{x}_{k-1|k-1} \quad (17)$$

$$\hat{x}_{k|k} = \hat{x}_{k|k-1} + K_k [y_k - A \hat{x}_{k|k-1}] \quad (18)$$

with corresponding covariance matrices for $\hat{x}_{k|k-1}$ and $\hat{x}_{k|k}$ respectively

$$P_{k|k-1} = \Phi_{k,k-1} P_{k-1|k-1} \Phi_{k,k-1}^* + Q_{d_k} \quad (19)$$

$$P_{k|k} = [I - K_k A] P_{k|k-1} \quad (20)$$

where

$$K_k = P_{k|k-1} A^* [Q_y + A P_{k|k-1} A^*]^{-1} \quad (21)$$

is the so-called Kalman gain matrix. It will be shown later that the predicted residual vector, defined as

$$v_k = y_k - A \hat{x}_{k|k-1} \quad (22)$$

can play an important role in the process of model testing. Its covariance matrix reads

$$E\{v_k v_k^*\} = \delta_{kl} Q_{v_k}, \quad Q_{v_k} = Q_y + A P_{k|k-1} A^* \quad (23)$$

[Kailath 1968], [Teunissen and Salzmann 1989]. The initial values of the filter state and its covariance matrix can be determined by solving the first three epochs simultaneously by least squares.

As can be seen from the dynamic and measurement models, when L2 code is not available, this algorithm can still be applied by simply removing the columns and rows related to \dot{P}_k , \dot{b}_k , \dot{b}_0 , or \dot{b}_k from the models.

Most reference stations are probably equipped with dual frequency receivers, when differential corrections need to be generated. But there may be cases when differential corrections have to be generated by using only single frequency data. Since in the case of only L1 code and carrier observables available it is no longer possible to individually estimate the rates \dot{v}_k , \dot{t}_k and \dot{b}_k , the above dynamic and measurement models should be adapted by combining the code bias b_k with the differential correction ∇_k . More specifically, if the types of observables available are L1 code and carrier, the equations (9), (10), (12), (13) and (15) should be replaced by the following ones, respectively

$$\begin{bmatrix} \nabla_k + b_k \\ \dot{\nabla}_k + \dot{b}_k \\ \ddot{S}_k \\ I_k + \frac{b_k + \lambda_1 N}{2} \\ \dot{I}_k + \frac{1}{2} \dot{b}_k \end{bmatrix} = \underbrace{\begin{bmatrix} 1 & 1 & 1 & 1 \\ & 1 & 1 & 1 \\ & & 1 & \\ & & & 1 \\ & & 1 & \frac{1}{2} \\ & & & 1 \\ & & & & \frac{1}{2} \end{bmatrix}}_T \begin{bmatrix} S_k \\ \dot{S}_k \\ \ddot{S}_k \\ I_k \\ \dot{I}_k \\ \lambda_1 N \\ b_k \\ \dot{b}_k \end{bmatrix} \quad (9')$$

$$\underbrace{\begin{bmatrix} P_k - \rho_k + c \, dt_k^0 \\ \lambda_1 \Phi_k - \rho_k + c \, dt_k^0 \end{bmatrix}}_{y_k} = \underbrace{\begin{bmatrix} 1 & 0 & 0 & 0 & 0 \\ 1 & 0 & 0 & -2 & 0 \end{bmatrix}}_A \underbrace{\begin{bmatrix} \nabla_k + b_k \\ \dot{\nabla}_k + \dot{b}_k \\ \ddot{S}_k \\ I_k + \frac{b_k + \lambda_1 N}{2} \\ \dot{I}_k + \frac{1}{2} \dot{b}_k \end{bmatrix}}_{x_k} + \underbrace{\begin{bmatrix} e_k \\ \eta_k \end{bmatrix}}_{e_k} \quad (10')$$

$$E\{e_k e_k^*\} = \delta_{ki} Q_y, \quad Q_y = \begin{bmatrix} \sigma_e^2 \\ \sigma_\eta^2 \end{bmatrix} \quad (12')$$

$$x_k = \underbrace{\begin{bmatrix} 1 & \Delta t_k & \frac{1}{2} \Delta t_k^2 \\ & 1 & \Delta t_k \\ & & 1 \\ & & & 1 & \Delta t_k \\ & & & & 1 \end{bmatrix}}_{\Phi_{k,k-1}} x_{k-1} + T \int_{t_{k-1}}^{t_k} \underbrace{\begin{bmatrix} \frac{1}{2} (t_k - t)^2 \ddot{S}(t) \\ (t_k - t) \ddot{S}(t) \\ \ddot{S}(t) \\ (t_k - t) \ddot{I}(t) \\ \ddot{I}(t) \\ 0 \\ (t_k - t) \ddot{b}_k \\ \ddot{b}_k \end{bmatrix}}_{d_k} dt \quad (13')$$

$$E\{d_k d_k^*\} = \delta_{ki} T \begin{bmatrix} q_s Q_{11} & & & \\ & q_f Q_{22} & & \\ & & 0 & \\ & & & q_b Q_{22} \end{bmatrix} T^*, \quad (15')$$

As is easy to see, this algorithm is also applicable, when only L1 code is available. Therefore, the type of observable used in the algorithm can be L1 code alone or along with other code and carrier observables.

3. Quality control

The Kalman filter produces recursively optimal estimators of the state vector with well defined statistical properties. When the input data of the filter are normally distributed, the state estimators are unbiased, are Gaussian distributed and have minimum variance within the class of linear unbiased estimators. It is important to realize, however, that optimality is only guaranteed as long as the assumptions underlying the mathematical model hold. Misspecifications in the model will invalidate the results of the estimation and thus also any conclusions based on them. It is therefore of importance to have ways to verify the validity of the working hypothesis, denoted by H_0 , made for the dynamic model and measurement model.

The testing procedure of [Teunissen 1990a] consists of three steps:

- i) Detection: An overall model test is carried out to detect if an unspecified model error has occurred.
- ii) Identification: In case an unspecified model error is detected, various alternative hypotheses are evaluated to identify the most likely error source.
- iii) Adaptation: After identification of the most likely error source, the filter is adapted.

3.1 Detection of model errors

Assume that the observation noises are normally distributed and the validation of the null hypothesis H_0

has been verified up to time $k-1$. What we need to detect at time k is whether an unspecified model error has occurred at the present time. Therefore, the null and alternative hypotheses are

$$\left. \begin{aligned} H_0^k: & \begin{aligned} E\{y_k\} &= A_k x_k \\ E\{d_k\} &= x_k - \Phi_{k|k-1} x_{k-1} \end{aligned} \\ H_a^k: & \begin{aligned} E\{y_k\} &= A_k x_k + \nabla y_k \\ E\{d_k\} &= x_k - \Phi_{k|k-1} x_{k-1} + \nabla d_k \end{aligned} \end{aligned} \right\} \quad (24)$$

or, when expressed in terms of the predicted residuals

$$H_0^k: v_k \sim N(0, Q_{v_k}) \text{ and } H_a^k: v_k \sim N(\nabla v_k, Q_{v_k}) \quad (25)$$

with $\nabla v_k = \nabla y_k$ in the case of model errors in the measurement model or $\nabla v_k = A_k \nabla d_k$ in the case of model errors in the dynamic model.

Assume that the m_k -dimensional vector ∇v_k can be written as

$$\nabla v_k = C_{v_k} \nabla \quad (26)$$

where C_{v_k} is a known $m_k \times l$ matrix of full rank l and ∇ is an unknown model error vector of dimension l . The appropriate test statistic for testing H_0 against H_a reads then [Teunissen and Salzmann 1989]

$$T^k = v_k^* Q_{v_k}^{-1} C_{v_k} [C_{v_k}^* Q_{v_k}^{-1} C_{v_k}]^{-1} C_{v_k}^* Q_{v_k}^{-1} v_k \quad (27)$$

which is distributed under H_0 and H_a as

$$H_0: T^k \sim \chi^2(l, 0) \text{ and } H_a: T^k \sim \chi^2(l, \lambda) \quad (28)$$

with noncentrality parameter

$$\lambda = \nabla^* C_{v_k}^* Q_{v_k}^{-1} C_{v_k} \nabla \quad (29)$$

In most cases, it is impossible to be sure if the class of the alternative hypotheses specified by C_{v_k} indeed contains the true hypothesis. In order to test the overall validity of the local hypothesis H_0^k , the mean $\nabla v_k = C_{v_k} \nabla$ of v_k under H_a^k should remain completely unspecified. This implies mathematically that the matrix C_{v_k} should be chosen to be a square and regular matrix. Thus C_{v_k} can be eliminated from (27), which results in the local overall model test statistic

$$T^k = v_k^* Q_{v_k}^{-1} v_k \quad (30)$$

In case

$$T^k \geq \chi_{\alpha}^2(m_k, 0) \quad (31)$$

we may at the confidence level of $1-\alpha$ reject the null hypothesis H_0 of (24) and consider that an unspecified local model error is present at time k .

3.2 Identification of model errors

The next step after detection is the identification of the most likely alternative hypothesis. As with detection,

identification is based on the test statistic (27). For identification, however, candidate alternative hypotheses need to be specified explicitly. In the following, the discussion is restricted to model errors in the measurement model. The theory is, however, applicable for the case of model errors in the dynamic model as well. For the case that the local alternative hypothesis H_a^k of (24) is restricted to the measurement model, we denote C_{v_k} by C_k . It follows from (24) that the local alternative hypothesis reads

$$H_a^k: E\{y_k\} = A_k x_k + C_k \nabla \quad (32)$$

This class of alternative hypotheses can be considered to model a slip in the mean of the vector of observables at time k . The dimension of the l -dimensional vector ∇ in (32) depends on the alternative hypotheses considered and can range from 1 to m_k for identification purposes. Here we consider the case $l = 1$, that is, the case of a single model error. But the theory is also applicable to the case of multiple model errors [Teunissen 1990b].

With $l = 1$, the model error vector ∇ reduces to a scalar and the matrix C_k reduces to an m_k -dimensional vector. Choose

$$c_i = (0 \dots 0 \ 1 \ 0 \dots 0)^* \quad (33)$$

\uparrow element i

It follows from taking the square-root of (27) that

$$t^i = \frac{c_i^* Q_{v_k}^{-1} v_k}{(c_i^* Q_{v_k}^{-1} c_i)^{1/2}} \quad i = 1, \dots, m_k \quad (34)$$

This is the local slippage test statistic for the identification of a single local model error. The identification step is based on the so-called conventional alternative hypothesis or data snooping [Baarda 1968] in combination with the local slippage test statistic. The model error which is tested is

$$\nabla_i = c_i \nabla \quad (35)$$

For m_k predicted residuals, we have m_k local slippage test statistics (34). The alternative hypothesis for which $|t^j|$ is at a maximum is then considered as the one that contains the most likely model error. Determine j that

$$j = \{i \mid |t^i| = \max\{|t^1|, \dots, |t^{m_k}|\}\} \quad (36)$$

and note that t^j has the following distribution

$$t^j \sim \begin{cases} N(0, 1) & \text{under } H_0 \\ N(\nabla_j^* \sqrt{c_j^* Q_{v_k}^{-1} c_j}, 1) & \text{under } H_a \end{cases} \quad (37)$$

In case

$$|t^j| \geq N_{\frac{\alpha}{2}}(0, 1) \quad (38)$$

where $N_{\frac{\alpha}{2}}(0,1)$ is the upper $\frac{\alpha}{2}$ -percentage point of the standard normal distribution, one may accept the alternative hypothesis H_a of (32) at confidence level of $1-\alpha$ and consider predicted residual j in v_k to be the most likely predicted residual containing the detected model error. Since other residuals may also contain unspecified model errors, remove predicted residual j and corresponding covariances from v_k and Q_k , respectively, and repeat the same procedure as above until (38) is not fulfilled for any of the remaining predicted residuals any more.

3.3 Adaptation

After identification of the most likely alternative hypotheses, the recursive filter needs to be adapted. Consider the general case that L1 and L2 code and carrier observables are available, i.e. $m_k=4$. It will be shown later that the adaptation procedure can be applied to any case, as long as L1 code observable is available alone or along with other observables.

Depending on the accepted alternative hypotheses, see (37), the adaptation can be carried out as follows.

- $j=1$ or $j=4$ This is most likely corresponding to the situation that the L1 and/or L2 code measurement contains an outlier. In this case one can simply eliminate predicted residual j from the residual vector v_k and then continue the measurement update by using the remaining residuals.

- $j=2$ or $j=3$ This case happens most likely due to the occurrence of a cycle slip or an outlier in the L1 and/or L2 carrier measurement. When a cycle slip occurs in a carrier measurement, a new ambiguity is introduced. As can be seen from the measurement model, the L1-carrier and L2-carrier related states are $I_k + \frac{\lambda_1 N + b_0}{2}$ and $I_k + \frac{\lambda_2 \tilde{N} + b_0}{r-1}$, which contain their own ambiguities respectively. In this case the L1-carrier or L2-carrier related states should be reinitialized and the filter can continue the measurement update by using the other unbiased predicted residuals. It can be expected that if the unspecified model error is an outlier instead of a cycle slip, this adaptation will be repeated in the following epoch.

- $j=1, j=2, j=3$, and $j=4$ Since all predicted residuals are considered to have an unspecified model error in this case, it is probably caused by a slip in the state of the differential correction ∇_k . In this case, the states $\nabla_k + b_0$, $I_k + \frac{\lambda_1 N + b_0}{2}$, $I_k + \frac{\lambda_2 \tilde{N} + b_0}{r-1}$, $b_k - b_0$ and $\xi_k - \xi_0$ should be reinitialized.

We have discussed how to adapt the recursive filter in

such three cases that an unspecified model error occurs in the code measurement, in the carrier measurement, and in all measurements. Apparently if unspecified model errors occur in some of code and carrier measurements, the adaptation of the recursive filter can still be done in the same way. In short, if an unspecified model error is identified in a code predicted residual, then exclude the residual in the measurement update; if an unspecified model error is identified in a carrier predicted residual, then initialize its carrier ambiguity related state; but if an unspecified model error is identified in all measurements, then reinitialize all states related to the measurements.

4. Discussions

Compared with other published algorithms for generating differential corrections, this new algorithm has some distinct features. First of all, this algorithm directly uses code and carrier observations in the measurement model of a Kalman filter, so that the measurements do not become correlated in time, as is the case when differences of observations at subsequent epochs are formed or when carrier filtered code observations are used. This makes it possible to use a simple stochastic observation model and to use the standard algorithm of the Kalman filter. Secondly, the algorithm accounts for biases like multipath errors and instrumental delays in code observations. It can be applied in the case that code biases are significantly present or absent. In the former case, the effect of a time-independent code bias at the initial epoch on the estimates of differential corrections can clearly be shown, whereas in the latter case, the algorithm can generate unbiased estimates of differential corrections. Thirdly, the algorithm can be integrated with a quality control procedure. Therefore, the quality of the estimated states including differential corrections can be guaranteed with certain probability. Finally, all of its state estimates are not affected by the opposite influence of the ionosphere on code and carrier observations.

The three ionospheric delay related states $I_k + \frac{\lambda_1 N + b_0}{2}$, $I_k + \frac{\lambda_2 \tilde{N} + b_0}{r+1}$ and $I_k - \frac{b_0 - \xi_0}{r-1}$ in the state vector x_k can be used to analyze the variation of ionospheric delays. Often dual-frequency GPS code observations are used to estimate the first order ionospheric delay. Strictly speaking, it should only be done in the case that L1 and L2 code biases are absent or the same or negligible. In general, by using dual frequency GPS code observations, one can only estimate the ionospheric delay contaminated by code biases b_k and ξ_k (or b_0 and ξ_0), like the state $I_k - \frac{b_0 - \xi_0}{r-1}$.

The time-varying states S_k , I_k , b_k and ϵ_k are affected by different factors. The ionosphere-free differential correction S_k is related with receiver and satellite clock biases, ephemeris error and tropospheric condition. The ionospheric delay I_k is related with the condition of the ionosphere. The code biases b_k and ϵ_k are related with receiver, antenna and the observation environment.

The greater the number of observables available, the better the other information like the variations of ionospheric delays and code biases can be obtained along with differential corrections. There are some essential differences in the estimation of differential corrections and their rates of changes when using dual frequency data and using single frequency data. In the former case, the estimates of differential corrections at all epochs are biased by a constant which is the initial value of L1 code bias (see (10)); those of the rates of change of differential corrections are not biased. In the latter case, the estimates of differential corrections and their rates of changes are biased by L1 code biases and their rates of changes at the same epochs (see (10')), respectively. Thus, the quality of the estimates of rates of change of differential corrections based on dual frequency data is much better than that based on single frequency data. It should be noted that when code biases become negligible, this algorithm is still usable after simply removing the columns and rows related to code biases and their rates of changes. The estimates of both differential corrections and their rates of change are then no longer biased.

Acknowledgement

Prof. P.J.G. Teunissen has critically read the manuscript of this paper and his improvements are acknowledged.

References

- Baarda W (1968) *A Testing Procedure for Use in Geodetic Networks*. Netherlands Geodetic Commission, Publications on Geodesy, New Series, Vol. 2(5), Delft, The Netherlands
- van Dierendonck AJ (1993) *Receiver Technology, Developments and Performance, and RTCM Data Link Standards for Precision Differential Operation*. In: Navtech Seminars Inc., Dynamic Real Time DSNS (Part I), Navtech Seminars Inc., USA
- Jin XX (1995a) *A Recursive Procedure of Computation and Quality Control of GPS Differential Corrections*. Publications of the Delft Geodetic Computing Centre, LGR-Series No. 8, Delft University of Technology
- Jin XX (1995b) *The Change of GPS Code Accuracy with Satellite elevation*. In: Proceedings of DSNS-95, The Nordic Institute of Navigation, Norway
- Kailath T (1968) *An Innovations Approach to Least-Squares Estimation, Part I: Linear Filtering in Additive White Noise*. IEEE Transactions on Automatic Control, Vol. AC-13(6): 646-655
- Landau H (1993) *Differential System Design, Error Analysis and Performance*. In: Navtech Seminars Inc., Fundamentals of Differential Satellite Navigation Systems, Navtech Seminars Inc. USA
- Loomis P (1986) *Design Document for Differential GPS Ground Reference Station Pseudorange Correction Generation Algorithm*. DOT-CG-N-03-86, US Department of Transportation
- Loomis P, Kremer G, Reynolds J (1989) *Correction Algorithm for Differential GPS Reference Stations*. Navigation, Journal of The Institute of Navigation, Vol. 36(2): 179-193
- RTCM SC-104 (1990) *RTCM Recommended Standards for Differential NAVSTAR GPS Service*. Radio Technical Commission for Maritime Services, Washington, D.C., USA
- Teunissen PJG, Salzmann MA (1989) *A Recursive Slippage Test for Use in State-Space Filtering*. Manuscripta geodetica Vol. 14(6): 383-390
- Teunissen PJG (1990a) *Quality Control in Integrated Navigation Systems*. In: Proceedings of the IEEE PLANS '90 Position Location and Navigation Symposium, Las Vegas, pp. 158-165
- Teunissen PJG (1990b) *An Integrity and Quality Control Procedure for Use in Multi Sensor Integration*. In: Proceedings of ION'90, Colorado Springs, pp. 513-522

Effects of the Ionosphere and Cycle-Slips in Long Baseline Dynamic Positioning

George Dedes and Angela Mallett
The Ohio State University

BIOGRAPHY

George C. Dedes received his M.S. and Ph.D. degrees from the Dept. of Geodetic Science and Surveying at The Ohio State University. Dr. Dedes is a Research Scientist at the Center for Mapping where he supervises and conducts research and development for high accuracy dynamic positioning using the Global Positioning Systems Satellites (GPS), in combination with Inertial Navigation and Dead Reckoning Systems. He has over 10 years of experience in high accuracy dynamic positioning, orbital dynamics, and system and software engineering. Dr. Dedes has published more than 15 papers in his area of expertise and he is a member of the IAG working group on high accuracy GPS dynamic positioning.

Angela Mallett received her BA and MA degrees in Physics from Oxford University, Oxford, England. She is a Senior Research Associate at the Center for Mapping, working on the design, code and test of object-oriented software in C++ used for high-accuracy GPS positioning. She has over 10 years of software engineering experience in the following areas; image processing/ pattern recognition; mathematical modeling/ simulation; robotics.

ABSTRACT

High accuracy positioning using GPS over long baselines requires On-The-Fly ambiguity resolution with simultaneous estimation of ionospheric effects. The GPS signals are dispersed by the ionosphere causing a group delay to pseudorange and a phase advance to carrier phase measurements. Proper modeling of ionospheric effects is very important for high accuracy positioning over long baselines for which the effects are significant.

The Center for Mapping GPS positioning system uses a four measurement filter to estimate the widelane ambiguities and ionospheric effects. Positioning is

performed using smoothed widelane pseudoranges. With this approach, horizontal positioning accuracies at the 0.05-0.10m level and vertical positioning accuracies at the 0.10-0.15m level have been achieved over baselines of 60 km. These accuracies can be increased to the few cm-level when the ionosphere and the pseudorange and carrier phase multipath are properly modeled.

Cycle-slip detection is very important since undetected cycle-slips will introduce systematic errors to the estimated positions. Cycle-slips are detected using the geometry-free carrier phase observables together with the epoch-to-epoch widelane estimates. The epoch-to-epoch widelane estimates detect cycle-slips resulting from those combinations to which the geometry-free carrier phase observables are not sensitive.

INTRODUCTION

The GPS positioning system discussed in this paper is currently used for high accuracy dynamic positioning by The Ohio State University GPSVan™. The General Railway Signal Corp. (GRS) is using the GPSVan™ to map the infrastructure of several thousand miles of railroad. Data collected in a survey of railway tracks from two base stations is used to evaluate the accuracy of the dynamic positioning using widelane pseudoranges.

To increase the accuracy of GPS dynamic positioning, the ionosphere and multipath effects should be properly modeled. For this purpose, the initial ionospheric delays and the epoch-to-epoch variations of the ionosphere were analyzed to identify proper stochastic modeling of the ionosphere and multipath.

MATHEMATICAL MODEL

In the presence of Anti-Spoofing, the mathematical model for double difference dual frequency GPS observations takes the following form:

$$DD(R_1) = DD(\rho) + DD(I) / f_1^2 + DD(\epsilon_{R1}) \quad (1)$$

$$DD(R_2 - R_1) = (DD(I) / f_1^2) (f_1^2 / f_2^2 - 1) + DD(\epsilon_{R2-R1}) \quad (2)$$

$$\lambda_1 DD(\Phi_1) = DD(\rho) - DD(I) / f_1^2 + \lambda_1 DD(N_1) + DD(\epsilon_{\Phi1}) \quad (3)$$

$$\lambda_2 DD(\Phi_2) = DD(\rho) - DD(I) / f_2^2 + \lambda_2 DD(N_2) + DD(\epsilon_{\Phi2}) \quad (4)$$

By dividing equation 4 by λ_2 and equation 3 by λ_1 and subsequently subtracting these two equations, one obtains the expression for the widelane phase observable:

$$\lambda_w DD(\Phi_w) = DD(\rho) + (DD(I) / f_1^2) (f_1 / f_2) + \lambda_w DD(N_1 - N_2) + DD(\epsilon_{\Phi w}) \quad (5)$$

or,

$$\lambda_w DD(\Phi_w) - \lambda_w DD(N_1 - N_2) = DD(\rho) + (DD(I) / f_1^2) (f_1 / f_2) + DD(\epsilon_{\Phi w}) \quad (6)$$

Equation 6 has the same form as equation 1 with the ionospheric effects amplified by the factor f_1 / f_2 ($=77/60$). In the context of this paper, this observable will be referred to as the "widelane pseudorange."

The geometry-free carrier phase observable is obtained by subtracting equation 4 from equation 3.

$$\begin{aligned} DD(\Phi_{gf}) &= \lambda_1 DD(\Phi_1) - \lambda_2 DD(\Phi_2) \\ &= (DD(I) / f_1^2) (f_1^2 / f_2^2 - 1) + \lambda_1 DD(N_1) - \lambda_2 DD(N_2) + DD(\epsilon_{gf}) \end{aligned} \quad (7)$$

In the above equations, DD specifies the double difference operator, R_1 is the C/A pseudorange measurement, $(R_2 - R_1)$ is the (Y2-Y1) cross-correlation pseudorange measurement, Φ_1 is the L1 carrier phase measurement, Φ_w is the (Y1-Y2) cross-correlation carrier phase measurement, and Φ_2 is the L2 carrier phase measurement as derived from the Φ_1 and Φ_w measurements.

The quantity I is proportional to the total electron content along the path of the satellite signal, f_1 ($=1575.42$ MHz) and f_2 ($=1227.60$ MHz) are the L1 and L2 carrier phase frequencies, N_1 and N_2 are the L1 and L2 carrier phase ambiguities and λ_w is the wavelength of the widelane phase observable:

$$\lambda_w = \lambda_1 \lambda_2 / (\lambda_2 - \lambda_1) \quad (8)$$

The quantity ρ is the pseudorange affected only by tropospheric effects and has the following form:

$$\rho = \rho_{geom} + c \epsilon_{ts} - c \epsilon_{tr} + \tau \quad (9)$$

where ρ_{geom} is the geometric range from the receiver to the satellite, c is the speed of light, ϵ_{ts} and ϵ_{tr} are the satellite and receiver clock errors respectively, and τ is the effect of the troposphere.

In all of the above equations the units of pseudoranges are in meters, and the units of the carrier phases are in cycles.

Substituting $I / f_1^2 = I_{R1}$, $(f_1^2 / f_2^2 - 1) = \alpha$, and $f_1 / f_2 = \beta$, the above equations take the following form: where $\alpha = \beta^2 - 1$

$$DD(R_1) = DD(\rho) + DD(I_{R1}) + DD(\epsilon_{R1}) \quad (10)$$

$$DD(R_2 - R_1) = DD(I_{R1}) \alpha + DD(\epsilon_{R2-R1}) \quad (11)$$

$$\lambda_1 DD(\Phi_1) = DD(\rho) - DD(I_{R1}) + \lambda_1 DD(N_1) + DD(\epsilon_{\Phi1}) \quad (12)$$

$$\lambda_2 DD(\Phi_2) = DD(\rho) - DD(I_{R1}) \beta^2 + \lambda_2 DD(N_2) + DD(\epsilon_{\Phi2}) \quad (13)$$

$$\lambda_w DD(\Phi_w) = DD(\rho) + DD(I_{R1}) \beta + \lambda_w DD(N_1 - N_2) + DD(\epsilon_{\Phi w}) \quad (14)$$

$$\begin{aligned} \lambda_w (DD(\Phi_w) - DD(N_1 - N_2)) \\ = DD(\rho) + DD(I_{R1}) \beta + DD(\epsilon_{\Phi w}) \end{aligned} \quad (15)$$

$$DD(\Phi_{gf}) = DD(I_{R1}) \alpha + \lambda_1 DD(N_1) - \lambda_2 DD(N_2) + DD(\epsilon_{\Phi gf}) \quad (16)$$

ESTIMATION OF WIDELANE AMBIGUITIES AND CYCLE-SLIP DETECTION

Estimation of Widelane Ambiguities

The equations 10, 11, 12 and 14 of the previous section are used to estimate $DD(\rho)$, $DD(I_{R1})$, $DD(N_1)$, and $DD(N_1 - N_2)$, using separate four measurement Kalman filters for each satellite. Figures 1, 2 and 3 show the filtered widelane ambiguity as a function of time for high and low elevation satellites. It is clear from these figures that the widelane ambiguities converge to their correct values after 4, 3, and 1 minutes of continuous tracking for elevation angles of 15, 30, and 70 degrees respectively. Therefore, if tracking to at least four satellites is maintained for 2- 4 minutes, widelane pseudorange positioning is possible.

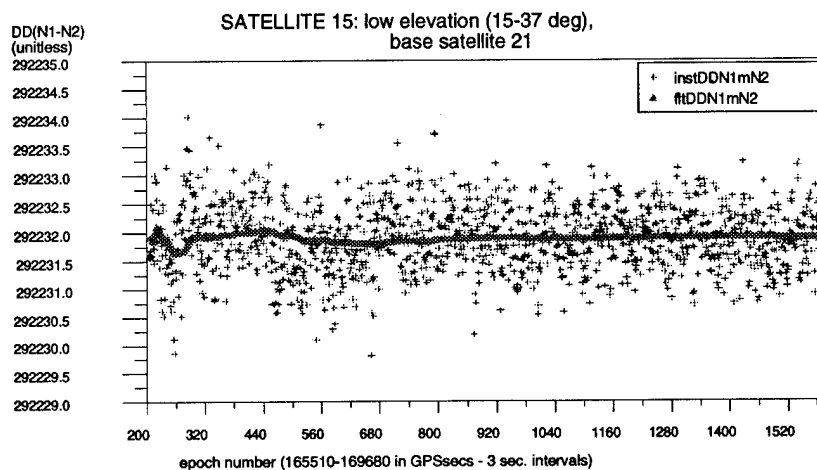


Figure 1. Filtered DD Widelane Ambiguity for Satellite 15 (low elevation satellite)

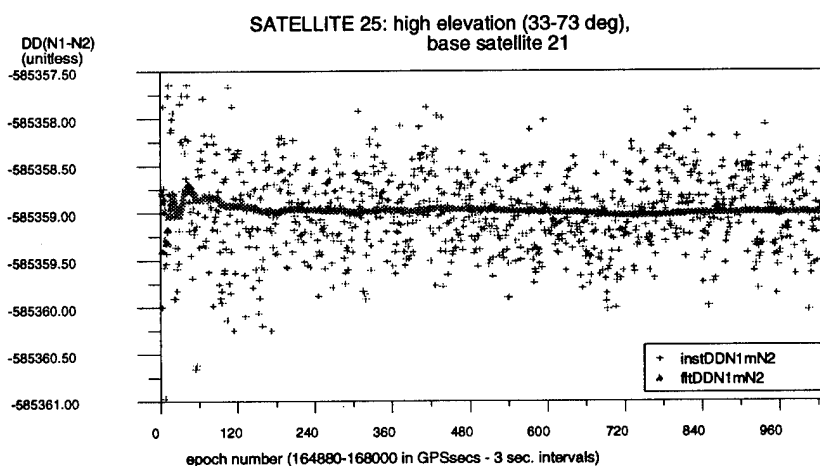


Figure 2. Filtered DD Widelane Ambiguity for Satellite 25 (high elevation satellite)

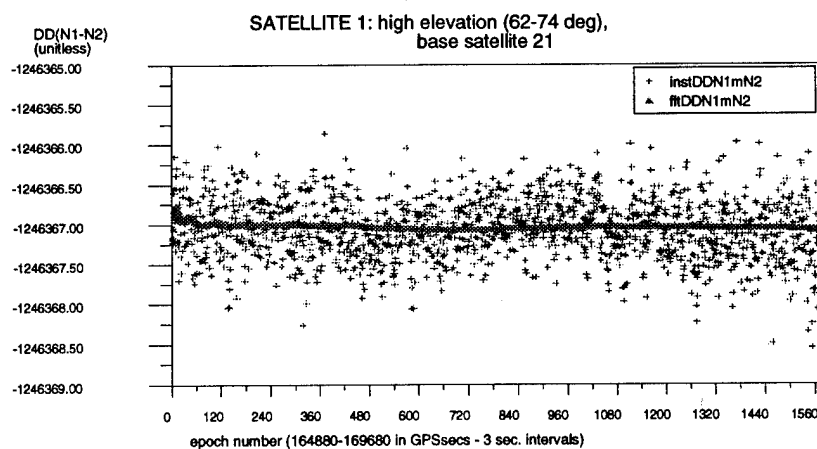


Figure 3. Filtered DD Widelane Ambiguity for Satellite 1 (high elevation satellite)

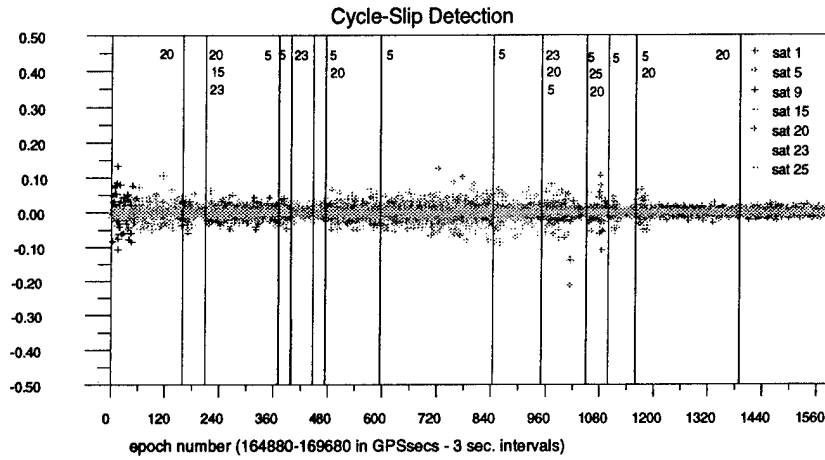


Figure 4. $V_{\Phi_{gf}}$ used for Cycle-Slip Detection

The estimated widelane double difference ambiguities are used to form the widelane pseudoranges as shown in equation 15. A widelane ambiguity is fixed to an integer value if its standard deviation is less than a certain value (~ 0.1 cycles) and if the difference of this ambiguity from the nearest integer is less than a certain value (~ 0.1 cycles). If these two conditions are not satisfied, the widelane ambiguities maintain their floating values. Subsequently, if the widelane ambiguities for three or more double differences have been fixed, and if the PDOP of the corresponding satellites is less than 20, then a position is estimated using the fixed widelane ambiguities. Using this position and equation 15, the rest of the widelane ambiguities are estimated using the widelane phase observables.

The widelane pseudoranges computed with equation 15 are affected by ionospheric effects; therefore, the estimated positions will also be affected by those effects amplified by the corresponding PDOP. However, the estimated widelane ambiguities are not affected by ionospheric effects since the ionospheric effects are estimated as part of the state in the four measurement filter.

Cycle-Slip Detection

In the approach described above, it is very important to detect cycle-slips since any undetected cycle-slips will bias the filter systematically from the epoch of the undetected cycle-slip to the epoch of the next cycle-slip. Therefore, during this time period any undetected cycle-slip will introduce systematic errors into the estimated positions.

The detection of cycle-slips is based on the time variations of the geometry-free carrier phase. Differencing in time the geometry-free carrier phases and assuming no cycle-slips, equation 16 yields:

$$\begin{aligned} & DD(\Phi_{gf}(t)) - DD(\Phi_{gf}(t-1)) \\ &= (DD(I_{R1}(t)) - DD(I_{R1}(t-1))) \alpha + DD(\epsilon_{\Phi_{gf}}) \end{aligned} \quad (17)$$

Taking the running average of both sides of equation 17 and assuming that the average value $DD(\epsilon_{\Phi_{gf}})$ converges to zero, one obtains:

$$\begin{aligned} & Ave(DD(\Phi_{gf}(t)) - DD(\Phi_{gf}(t-1))) \\ &= Ave(DD(I_{R1}(t)) - DD(I_{R1}(t-1))) \alpha \end{aligned} \quad (18)$$

The residual of the geometry-free carrier phase change in time is obtained with the following equation:

$$\begin{aligned} V_{\Phi_{gf}} / \alpha &= DD(\Phi_{gf}(t)) - DD(\Phi_{gf}(t-1)) \\ &\quad - (Ave(DD(\Phi_{gf}(t)) - DD(\Phi_{gf}(t-1)))) \end{aligned} \quad (19)$$

A cycle-slip is detected if $V_{\Phi_{gf}} > 0.20$. Figure 4 shows $V_{\Phi_{gf}}$ as a function of time.

The cycle-slip detection described above is based on the assumption that the epoch-to-epoch ionospheric variations are very small, and the combination $(\lambda_1 N_1 - \lambda_2 N_2)$ is sensitive to all possible cycle-slips. For very short time intervals of a few seconds, the ionospheric variations are at the subcentimeter level (Figures 11-14). However, there exist k_1 slips on the L1 channel and k_2 slips on the L2 channel which leave the $(\lambda_1 N_1 - \lambda_2 N_2)$ combination unchanged. These slips are those satisfying the following ratio:

$$k1/k2 = 77/60 \quad (20)$$

This equation is satisfied exactly for values of $k1$ and $k2$ that are the same multiples of 77 and 60. These slips result in widelane changes that are multiples of 17 widelanes. These cycle-slips are detected very easily using the epoch-to-epoch widelane estimates, which are accurate to 2 or 3 widelanes which is much smaller than 17 widelanes. As shown in table 1, there exist combinations of $k1$ and $k2$ that are very close to the ratio 77/60.

k1	k2	77/60 k2	k1 - 77/60 k2	k1 - k2 widelane change
	1	1.2833		
	2	2.5666		
4	3	3.8500	0.1500	1
5	4	5.1333	-0.1333	1
	5	6.4166		
	6	7.7000		
9	7	8.9833	0.0167	2
	8	10.2666		
	9	11.5500		
	10	12.8333		
14	11	14.1166	-0.1166	3

Table 1. Combinations of $k1$ and $k2$

It is obvious from the above table that the $k1=9$, $k2=7$ cycle-slip combination is practically undetectable through the geometry-free carrier phase due to noise in the carrier phases. This cycle-slip introduces a step of two widelanes that can be detected from the epoch-to-epoch widelane estimates, if sub-meter accuracy pseudoranges are available. If the noise in the double difference geometry-free carrier phase is in the order of 0.15 cycles, then the $k1=4$, $k2=3$ and $k1=5$, $k2=4$ cycle-slips are also very difficult to detect, either through the geometry-free or the widelane estimates, because they introduce a step of only one widelane. Any other cycle-slip combination that can not be detected from the geometry-free carrier phases will introduce a step of three widelanes or more. These combinations will be detected by the epoch-to-epoch widelane estimates if pseudoranges with 1.0-2.0m accuracies are available.

POSITIONING ACCURACY USING WIDELANE PSEUDORANGES

The dynamic positioning with widelane pseudoranges is performed with two passes through the data. In the first pass, the four measurement filter is used for each satellite to estimate the widelane ambiguities between cycle-slips.

In a second pass through the data, the estimated widelane ambiguities are fixed, as described in the previous section, and then used to form the widelane pseudoranges that are subsequently employed to perform pseudorange differential positioning. The accuracy of dynamic positioning with widelane pseudoranges was evaluated using data collected in a survey of railroad tracks by The Ohio State University GPSVanTM.

The GPSVanTM was positioned simultaneously from two base stations approximately 50km apart. The positions of the GPSVanTM were estimated independently using the GPS data collected from each of these base stations and the method described above. One of the base stations was a control station. The geodetic coordinates of the other station were computed using the GPS vector, which was estimated from the static GPS data collected during the survey by the two base stations.

Figures 5, 6 and 7 show the difference in east, north and up directions of the GPSVanTM coordinates computed independently from the two base stations.

The trace of the variance-covariance matrix of the estimated coordinates is shown on the same figures. It is evident from these figures that the differences in the east and north directions are in the order of 0.05m-0.10m, and the differences in the up direction are in the order of 0.10m-0.15m. Furthermore, there are a few epochs in the neighborhood of epochs 165500 and 168000, where these differences are much larger. The trace of the variance-covariance matrix of the estimated positions is also large at the same epochs. An examination of the GPS data of the rover receiver shows missing epochs and missing L2 data in the neighborhood of these epochs.

The positioning accuracy seems to be very good even without correcting the widelane pseudoranges for ionospheric effects. Figure 8 shows the number of satellites used in positioning. The average number of satellites used for positioning is between 5 and 6. Since the ionospheric effects are different for each satellite, and since several satellites were tracked during that period, the ionospheric effects tend to average out. However, with fewer satellites tracked and for longer baselines, the ionospheric effects on the positioning will tend to be larger. Therefore, it is important during the second pass through the data to estimate ionospheric effects and positions simultaneously using ionospheric modeling similar to that proposed in Klobuchar 1987, Goad & Yang 1994 and Oiu et. al 1995.

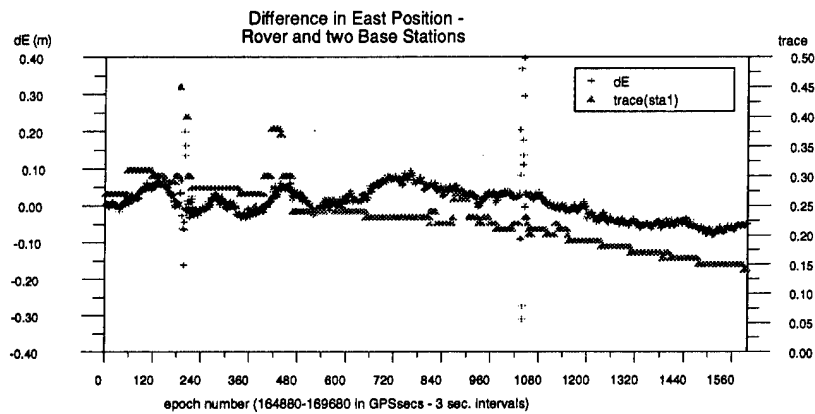


Figure 5. Difference in East Position between GPSVan™ and two Base Stations

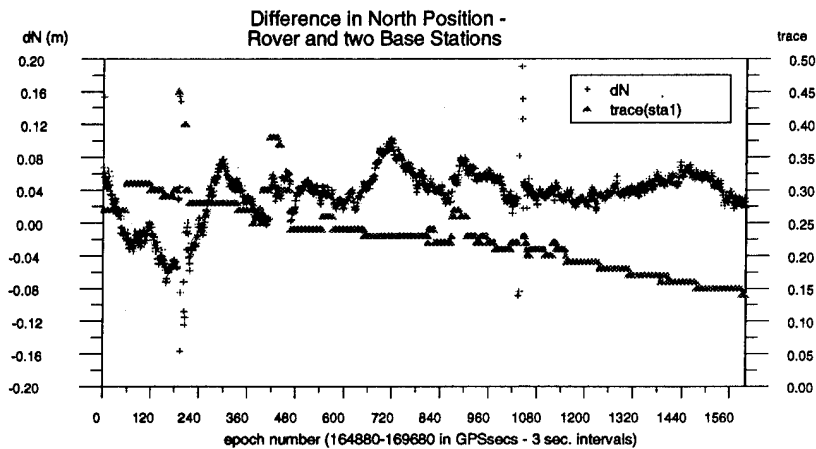


Figure 6. Difference in North Position between GPSVan™ and two Base Stations

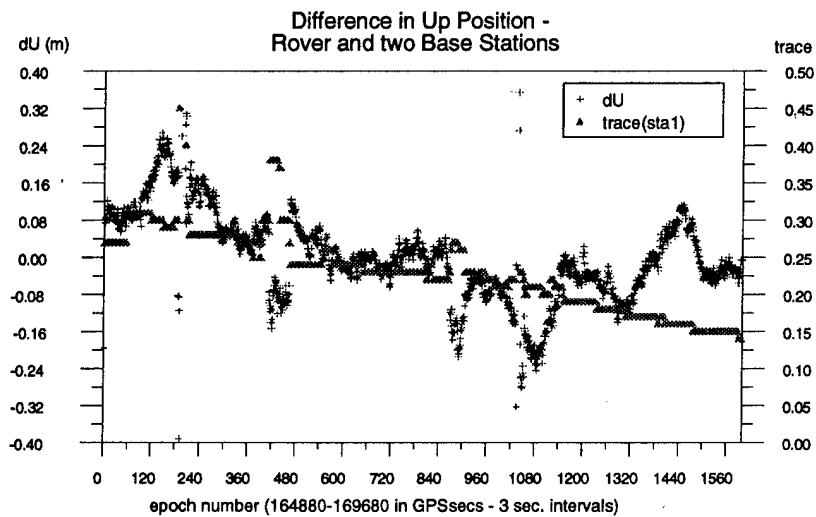


Figure 7. Difference in Up Position between GPSVan™ and two Base Stations

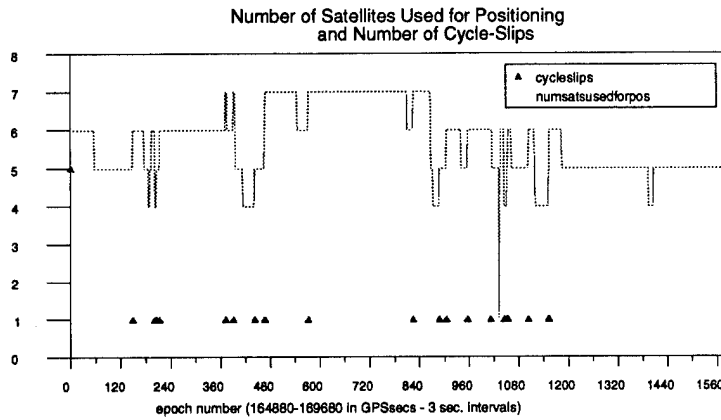


Figure 8. Number of Satellites used in Positioning and Cycle-Slips

STOCHASTIC MODELING OF THE IONOSPHERE

Before determining the stochastic model for the ionosphere, it is important to consider that the initial offset of the ionospheric effects is obtained from the pseudoranges and the epoch-to-epoch variations of the ionosphere are obtained from the carrier phases. The pseudoranges are very likely to have long wavelength multipath errors caused by nearby reflecting surfaces. Therefore, the multipath errors affecting the pseudoranges should be modeled properly using a different stochastic model than the one used to model the ionospheric effects. If the multipath errors are not modeled properly or not modeled at all, then the pseudorange information should be incorporated into the solution through weighted widelane constraints. These constraints are determined in the first pass through the data as described in the previous section.

The ionospheric effects at an epoch t can be described as the sum of the ionospheric offset at an epoch t_0 , plus the ionospheric variation from epoch t_0 to epoch t :

$$DD(I_{R1}(t)) = DD(I_{R1}(t_0)) + DD(\Delta I_{R1}(t_0, t)) \quad (21)$$

where $I_{R1}(t)$ is the ionospheric refraction in the L1 channel at epoch t (group delay for pseudoranges, phase advance for carrier phases), $I_{R1}(t_0)$ is the ionospheric refraction at epoch t_0 , and $\Delta I_{R1}(t_0, t)$ is the difference of the ionospheric effects from epoch t to epoch t_0 . Substituting equation 21 into equations 11 and 16, and assuming no cycle-slips between epochs t_0 and t , yields:

$$DD(I_{R1}(t_0)) = DD(R_2 - R_1)(t) / \alpha - DD(\Delta I_{R1}(t_0, t)) \quad (22)$$

$$DD(\Delta I_{R1}(t_0, t)) = (DD(\Phi_g(t)) - DD(\Phi_g(t_0))) / \alpha \quad (23)$$

Equations 22 and 23 show that the initial ionospheric delay is obtained from the (Y2-Y1) pseudorange measurement, and the differential ionospheric delay from epoch t_0 to epoch t is obtained from the carrier phase measurements.

Figures 9 and 10 show the instantaneous and weighted average of initial ionospheric delay for one low elevation and one high elevation satellite. It is evident from these two figures that the initial double difference ionospheric delay converges to 0.10m for the high elevation satellite and to 1.2m for the lower elevation satellite. This offset for the lower elevation satellite is probably caused by multipath affecting the (Y2-Y1) cross-correlation measurements. Therefore, the initial ionospheric delay should be modeled as a stochastic process able to absorb the multipath effects and not just as a random constant attempting to model the initial ionospheric delay.

Figures 11, 12, 13 and 14 show the epoch-to-epoch variations of the ionospheric refraction. These variations have a range of about 0.05m for the high elevation satellites and a range of about 0.10m for the low elevation satellites over a time period of about 1.3 hours. These epoch-to-epoch variations could be modeled effectively with a first order Gauss-Markov process with long correlation times. The effect of the baseline length should also be taken into consideration as proposed by Schaffrin & Bock 1988 or by Goad & Yang 1994, supplemented with proper modeling of the pseudorange and carrier phase multipath.

The research on ionospheric modeling for long baseline dynamic positioning is not completed at this time.

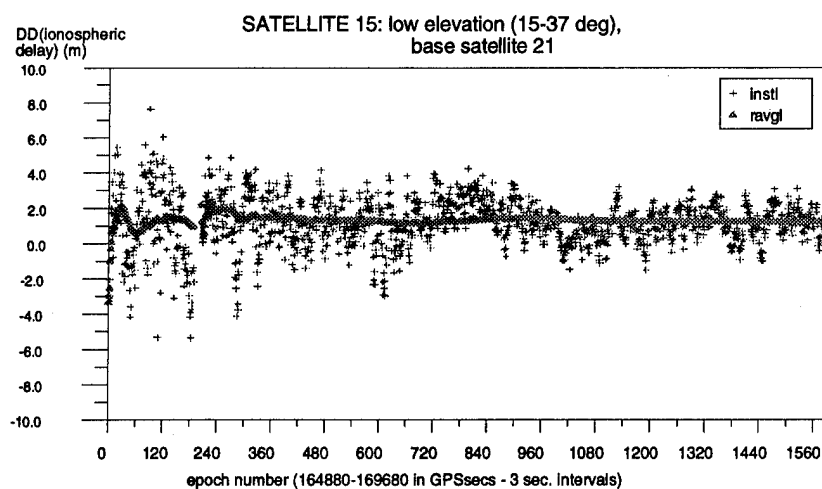


Figure 9. Instantaneous DD Ionosphere Delay for Satellite 15 (low elevation satellite)

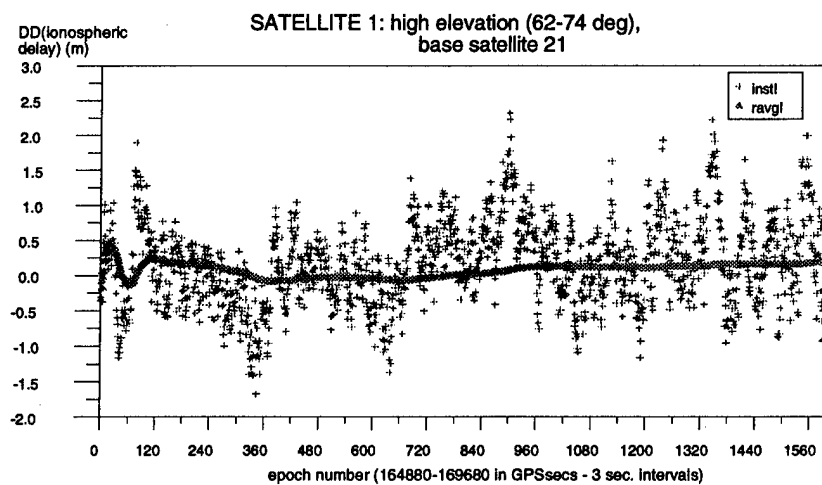


Figure 10. Instantaneous DD Ionosphere Delay for Satellite 1 (high elevation satellite)

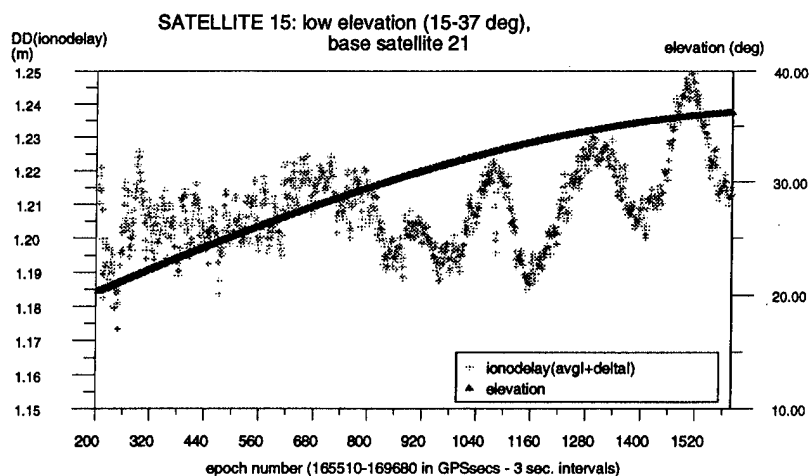


Figure 11. DD Ionosphere Delay for Satellite 15 (low elevation satellite)

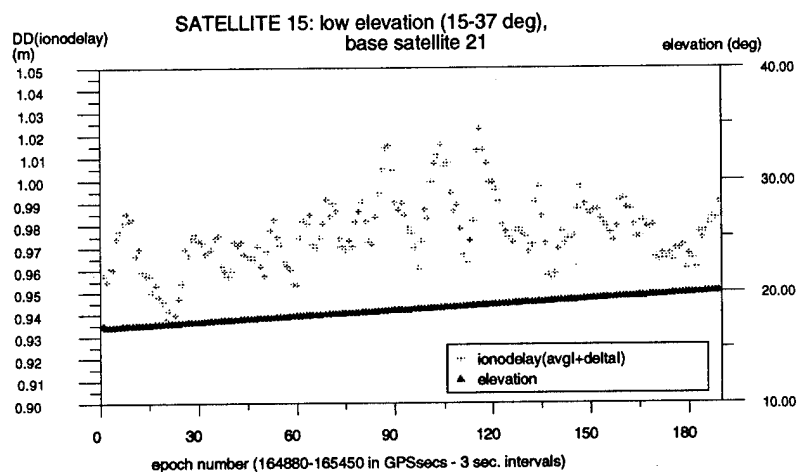


Figure 12. DD Ionosphere Delay for Satellite 15 (low elevation satellite)

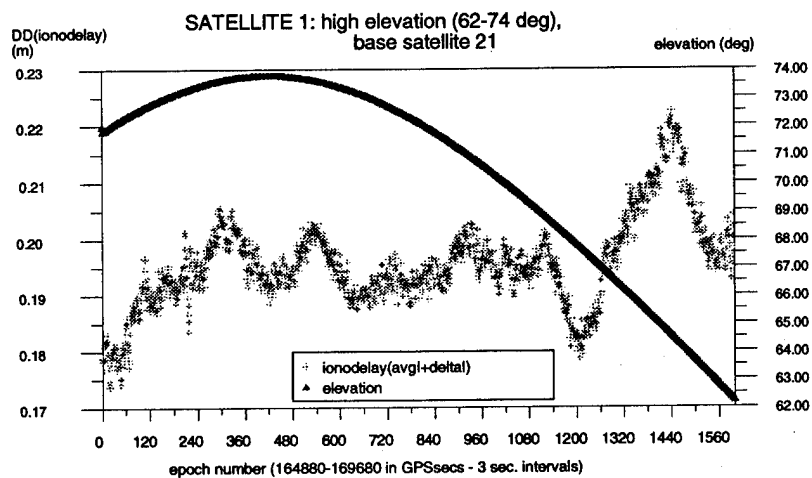


Figure 13. DD Ionosphere Delay for Satellite 1 (high elevation satellite)

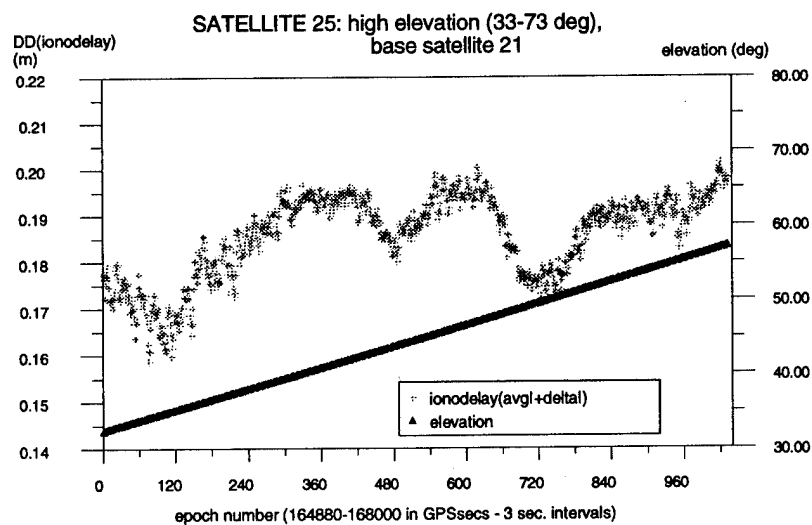


Figure 14. DD Ionosphere Delay for Satellite 25 (high elevation satellite)

CONCLUSION

In this paper, horizontal positioning accuracies at the 0.05-0.10m level and vertical positioning accuracies at the 0.10-0.15m level (with good satellite geometries) have been achieved using widelane pseudoranges not corrected for ionospheric effects for baselines of up to 60 km.

An attempt was made to model the ionospheric effects as a first order Gauss-Markov process. It was determined that the pseudorange multipath dominates the estimation of the ionospheric random bias. Therefore, proper modeling of the ionosphere requires modeling of pseudorange and carrier phase multipath.

REFERENCES

Goad, C., Yang, M. 1994, On Automatic Precision Airborne GPS Positioning: Proceedings of the International Symposium on Kinematic Systems in Geodesy, Geomatics and Navigation, Banff, Canada, Aug.30-Sept.2 1994, pp. 131-138.

Klobuchar, J.A. 1987, Ionospheric Time-Delay Algorithm for Single-Frequency GPS Users: IEEE Transactions on Aerospace and Electronic Systems, AES-23, pp. 325-331.

Oiu, W., Lachapelle, G., Cannon, M.E. 1995, Ionospheric Effect Modelling for Single-Frequency GPS Users: Manuscripta Geodaetica (1995), Vol.20, No.2, pp. 96-109.

Schaffrin, B., Bock, Y. 1988, A unified scheme for processing GPS dual-band phase observations: Bulletin Geodesique, The Journal of the International Association of Geodesy, Vol.62, No.2, pp. 142-160.

Using the Ionosphere for DGPS Measurement Error Control

Gregory Bishop
USAF Phillips Laboratory

Andrew Mazzella and Elizabeth Holland
NorthWest Research Associates

BIOGRAPHIES

Gregory Bishop is a Project Engineer in the Ionospheric Effects Division of the USAF Phillips Laboratory. He is a consultant to Sacramento Air Logistics Center, Air Weather Service, and Air Force Space Command, in the areas of: application of GPS to ionospheric monitoring, and mitigation of ionospheric effects on Air Force surveillance and communication systems.

Andrew Mazzella is a Senior Physics Analyst with NorthWest Research Associates (NWRA), a small research and development firm that specializes in geophysical fluid dynamics. He is involved in development and evaluation of parametric representations of physical systems and phenomena, with special emphasis on the design of algorithms and systems for ionospheric measurement.

Elizabeth Holland is a Research Engineer with NWRA. She studies ionospheric morphology and model performance for application to error correction for AF systems.

ABSTRACT

The ionosphere can be used to monitor and control measurement errors in DGPS base stations. The Self-Calibration Of pseudoRange Errors (SCORE) technique [1] can calibrate an installed GPS two-frequency receiver system for the combination of all system components' contributions to pseudorange error, and detect changes in these errors. With this ability to calibrate and monitor the integrity of pseudorange measurements, SCORE algorithms can contribute to ionosphere error measurement/modeling for DGPS and WAAS. Recently, an improved algorithm has been developed that permits calibrations to be generated in minutes instead of hours, making it possible to perform near-real-time system monitoring. Technical details of

these SCORE algorithms' evolution and operation will be presented. Test results comparing algorithm performance and examining stability of the calibration results and system drift monitoring will be reviewed. Initial results from improvements to the SCORE algorithms to accelerate real-time applications, and to permit single-frequency receivers some capability to monitor ionospheric pseudorange error will also be discussed. If sufficiently capable, these enhancements may enable single-frequency systems to contribute to ionospheric error monitoring, possibly simplifying WAAS error modeling.

DGPS PSEUDORANGE ERRORS

DGPS pseudorange measurement errors have their source in the same major contributors both at the base station and in mobile receivers. If the base station is chosen to be a (codeless) dual-frequency receiver, more error mitigation and calibration can be performed. Mobile receivers are usually single-frequency, but some potential exists for improved error correction in this case as well. The major pseudorange error contributors, in addition to Selective Availability (S/A), are: the *ionosphere*, *multipath* in the receive antenna environment, *satellite group delay errors*, and errors in the *receiver system* [2]. The *ionosphere* is considered the greatest error source but two-frequency receivers can measure and remove ionospheric error, subject to control of other error sources. The ionosphere is a major issue being addressed for the single-frequency mobile receivers in WAAS studies [3]. The integrated ionospheric "total electron content" (TEC) along the raypath is usually measured in "TEC units". (One TEC unit corresponds to 1×10^{16} electrons/m² on the raypath to the satellite. Also, 1 ns of differential delay = 2.852 TEC units, and 1 ns of pseudorange delay at L1 = 1.845 TEC units). *Multipath* errors can be as important as the ionospheric errors, but methods have recently been developed for autonomous correction. For example, the Phillips Laboratory (PL) "multipath template" technique [4] in stationary GPS applications, corrects multipath with

accuracies on the order of 1 TEC unit. *Satellite group delay (T_{GD}) errors* were formerly believed to be an important factor due to feared high/rapid variability, but recent improved measurements have minimized this concern and recent results suggest that 1 ns of differential delay (3 TEC units) would be a bound on the typical T_{GD} change for a given satellite over a period of years [1]. *Receiver system pseudorange errors* may originate in the receiver, pre-amp, antenna, and possibly in dispersive (poor) cabling connections. These errors may be subject to drift due to temperature variations or ageing.

THE "SCORE" CONCEPT

The SCORE concept is to use a self-consistency constraint on the receiver's own measurements of ionospheric delay to calibrate the receiver system for the sum of satellite- and ground-based pseudorange (group delay) errors. The self-consistency concept is illustrated by considering a "conjunction" occurring between two satellites, i.e. an event where both satellites arrive at the same moment at a point where their observed paths cross. In such an event the same ionospheric pseudorange error (TEC value) should be seen on each satellite. We must employ a coordinate transformation from UT to ionospheric local time (or "ionospheric penetration point" local time: IPP LT) before requiring satellites' observations to "see the same TEC". Using this transformation assumes the diurnal behavior of ionospheric TEC in a local latitude region is consistent over 1 to 2 hours. SCORE works by requiring maximum agreement in ionospheric measurements at IPP LT - latitude "conjunctions". SCORE derives the *sum of the receiver system and satellite error* for each satellite without using any test signal or assuming any model ionosphere. This "sum" in addition to the ionospheric error, is what is required for pseudorange error correction [1]. Monitoring changes in this sum provides integrity checks. For example, a uniform change in summed error for all satellites implies a change in station bias error has occurred. Likewise, a change in just one satellite sum implies a change in that satellite's bias has occurred.

PSEUDORANGE ERROR CONTROL

When SCORE is applied to monitor and correct hardware pseudorange errors as described above, and multipath is mitigated [4], the ionospheric error can be more accurately measured [5] and modeled for DGPS and WAAS applications. The accuracy of the ionospheric measurement can be confirmed graphically by the self-consistency of 1-degree latitude bands of data plotted vs IPP LT over 24 hours. Figure 1 shows a full 24 hours of data, calibrated by SCORE, from all satellites visible at Otis ANGB, MA, observed down to about 10 degrees

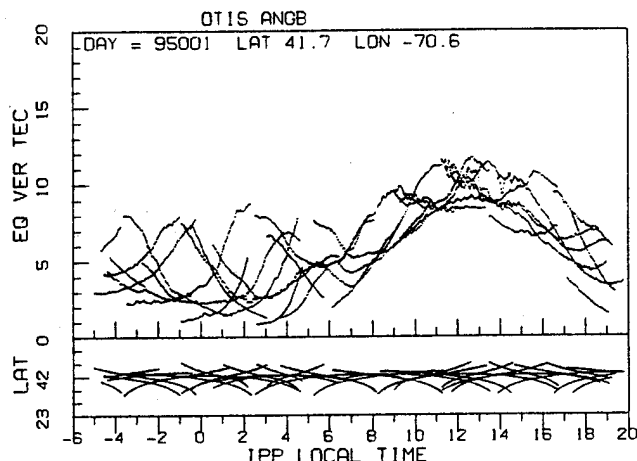


Figure 1. A full 24 hours of data calibrated by SCORE, from all satellites visible at Otis ANGB, MA, 01Jan95, observed down to about 10 degrees elevation.

elevation. The data appear not to show a clear diurnal cycle, but this is deceptive. Figure 2a shows a 3-degrees-of-latitude subset from Figure 1, centered directly overhead the station, and revealing a much clearer diurnal cycle, but still somewhat "hairy". This effect results from the latitudinal gradients in TEC. This may be seen in Figures 2b-2d, which divide Figure 2a into three one-degree bands of latitude. Here clear diurnal cycles and a steady decrease in TEC with greater latitude may be easily seen. Figure 2 includes all observations down to 10 degrees elevation within the 1-degree of latitude overhead the station. However, looking this low in elevation actually produces more opportunity for the profile to be affected by the slight changes that occur in the diurnal TEC behavior over a few degrees of longitude, and the assumptions made in converting slant TEC observations to equivalent vertical. Figure 3 repeats Figure 2c, but limits the observations to 35 degrees elevation and above, resulting in reduction of these effects, and an even tighter diurnal TEC curve. These data resolve TEC changes of ≤ 1 TEC unit, or about 1/3 ns of differential delay.

"SCORE" ALGORITHM EVOLUTION

The SCORE *minimization search algorithm* was originally developed to mathematically implement a technique of correlating the equivalent vertical TEC for overlapping satellite tracks in the ionosphere [6]. The utilized segments of the satellite tracks were those within a relatively narrow (3 degree) band of the station latitude, and the tolerance of local time differences between the segments was moderately large (120 minutes), establishing only a general local time continuity among the satellite

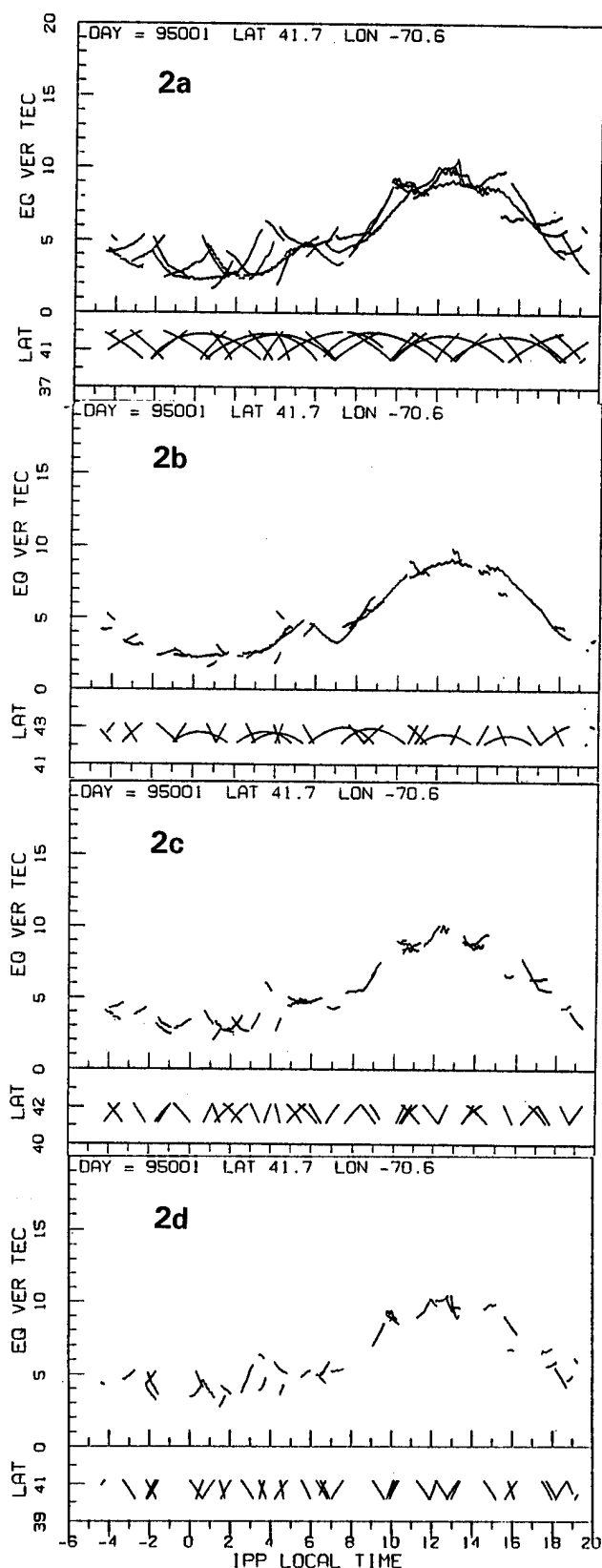


Figure 2. 2a: A 3°-latitude "overhead" subset of Fig. 1, "hairy" diurnal cycle, due to latitudinal TEC gradients; 2bcd: Divide 2a into three 1° bands, sharp diurnal curves.

track segments. For mid-latitude stations, this mode was generally adequate, but it did not appropriately accommodate latitudinal variations in vertical TEC. Narrowing the selection band of latitude could ameliorate this deficiency, but usually at the expense of losing the local time proximity of the satellite track segments or even losing all segments for some satellites.

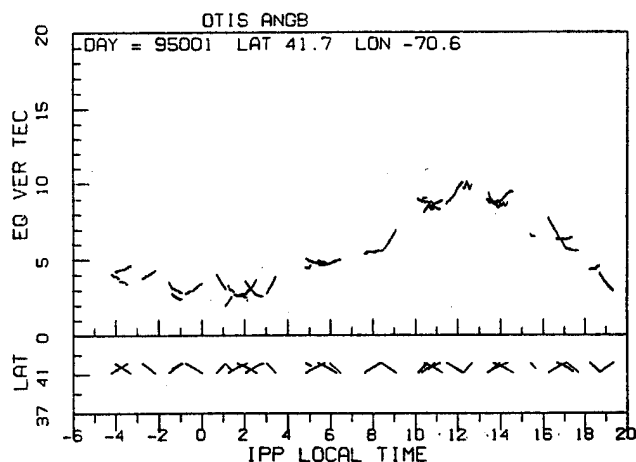


Figure 3. Same data as Figure 2c, limited to $\geq 35^\circ$ elevation, reducing low elevation effects, and giving a tighter diurnal TEC curve.

A number of adjustable values were incorporated into the original algorithm for the selection of latitude bands and weighting parameters, as well as for threshold elevation and longitude domains, and it was expected that a suitable assignment for these values could be determined in order to address the latitudinal TEC variation. In particular, a wider latitude selection band together with a tighter tolerance in both latitude and local time for the allowed segment correlations was expected to provide a significant improvement in the performance of the algorithm. It was not until the *matrix solution method* was developed to succeed the *minimization search algorithm*, and dramatically reduce processing requirements, that the necessary experiments could be performed to determine an appropriate set of selection and weighting parameters.

The matrix solution method follows directly from the same minimization condition as the original algorithm, but additionally exploits the fact that the minimization condition is a pure quadratic form in the unknown bias values. Thus, the minimization condition can be expressed in an alternative form using the derivatives of the total vertical TEC discrepancy, and these derivative expressions are linear in the biases. An exact solution can therefore be obtained in one step, provided the

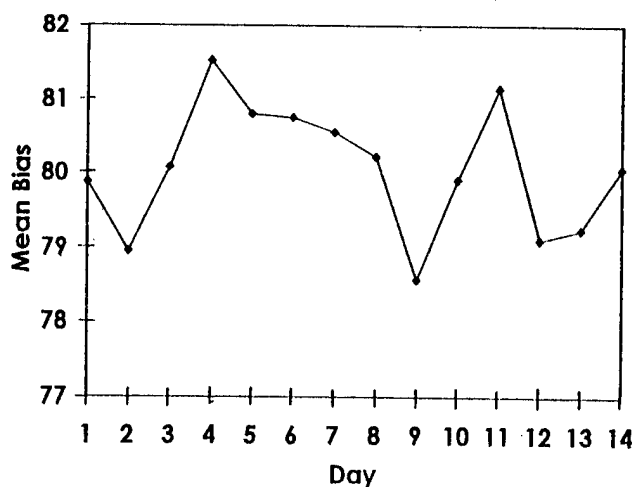


Figure 4. SCORE monitoring of a two-frequency ground receiver station error drift over a 14-day period in January 1995.

coefficient matrix is not singular. Some circumstances in which this matrix is singular have already been determined, and further investigations of this matter are in progress.

A restriction on the width or latitudinal offset of the latitude band which can be designated for use in the SCORE algorithm arises from the slant factor formula used to convert slant TEC measurements into equivalent vertical TEC. This formula has been derived on the basis of an infinitesimally thin ionosphere, which is not an appropriate assumption. Preliminary investigations have indicated errors in excess of 5% for this formula, when compared to a simple Chapman ionosphere profile. This error decreases at higher elevation angles, so the current parameters utilized for the SCORE algorithm include a threshold elevation of 35 degrees for satellite track segments which will be correlated. A beneficial secondary effect of this assignment is that the correlated segments cannot then differ in real-time occurrence by more than 32 minutes, reducing the possibility of intrinsic ionospheric variations adversely affecting the correlations.

The original SCORE algorithm required more than 6 hours [6] to run a single calibration. The matrix method permits calibrations in minutes making near-real-time applications feasible. The matrix method's TEC bias products are also essentially identical to those from the original algorithm.

The third evolution of the SCORE process, now in development, will apply the SCORE constraints in real time on a continuous basis. Several additional considerations are involved in applying SCORE in real

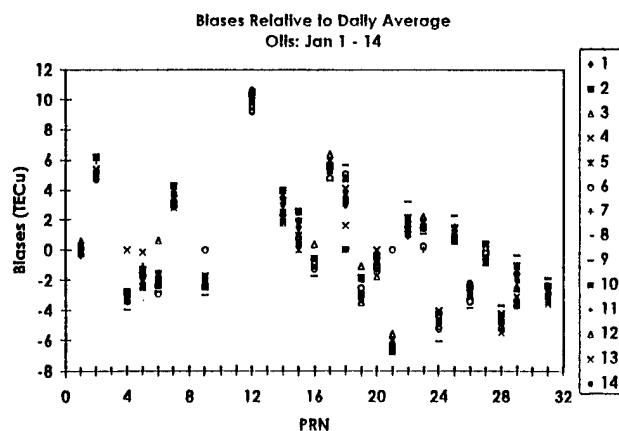


Figure 5. Zero-mean satellite bias values calculated daily over the period of Figure 4.

time, for example, a real time process to detect and correct signal dropouts or discontinuities.

TESTS OF "SCORE"

Figure 4 plots SCORE monitoring of a two-frequency ground receiver station error drift over a 14-day period in January 1995. The station's error may be seen to drift within a 3 TEC unit band over this period. Figure 5 plots the zero-mean [6] satellite bias values calculated daily over this period. The variation in each of these values is within about 2 TEC units, in most cases. The drifts observed in this station, and the variability of the satellite biases are reasonably consistent with other observations, [7,8].

Tests were also conducted of the stability of SCORE products vs loss of input from 1 or more satellites. The variation in the station bias from loss of 1 or 2 satellites is less than half a TEC unit. Even with loss of up to 8 of 25 satellites individual satellites' biases varied less than 1 TEC unit, Figure 6.

Sensitivity of the SCORE results to the sampling interval was also investigated. Station and satellite biases from full sampling of once/30 sec., were contrasted with results from data decimated down to as seldom as once per half hour. With the data decimated to as seldom as one point per 20 minutes there was only 0.3 TEC unit loss in accuracy. Since the run time is directly affected by the quantity of points to be processed, a significant speed increase is possible as the data is decimated, Figure 7. These test results indicate that run time on a Pentium 90 can be reduced to minutes or even seconds, with errors less than 0.3 TEC unit vs "all-data" results. Figure 8

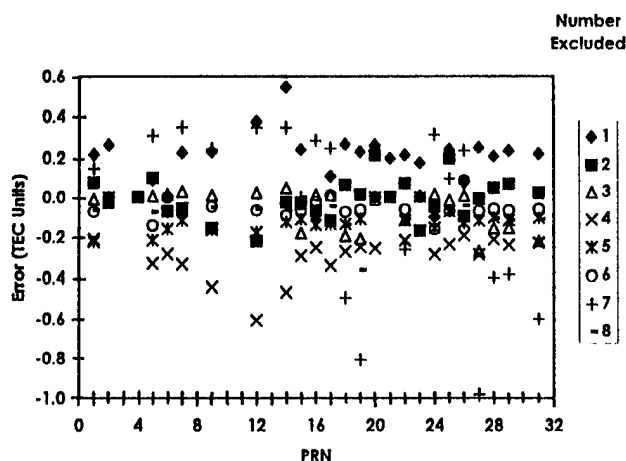


Figure 6. The variation in individual satellites' biases resulting from satellites' removal SCORE inputs, up to 8 of 25 available.

shows these errors as a function of the decimation factor. This robustness is somewhat unexpected, and certainly exciting for real-time application prospects.

The run time decrease can be understood from the details of the matrix process. The two distinct steps in performing the bias calculation are the calculation of the matrix coefficients and inhomogeneous terms, and the inversion of the resulting matrix. The duration for the matrix inversion process depends only on the number of elements in the matrix, which is determined by the number of satellites observed. This number is nearly constant from day to day, but can decrease significantly for shorter observation periods of only a few hours. However, the calculation of the matrix coefficients and inhomogeneous terms involves a sample-by-sample comparison for all satellite pairs, and this requires a processing duration roughly proportional to the square of the typical number of samples recorded for a satellite. This number is effectively reduced if only a subset of the data samples is used, as with a decimation selection. The execution times displayed in Figure 7 demonstrate the decrease in the required time as the number of samples is reduced, and also imply a generally negligible inversion execution time. A strict variation according to the inverse square dependence shown is not achieved because the processing requires some additional bookkeeping overhead, but also because the number of samples recorded for each satellite was not the same, accounting for some of the fluctuations from the expected dependence. It should also be noted that the execution time measurements were quantized at the one-minute level.

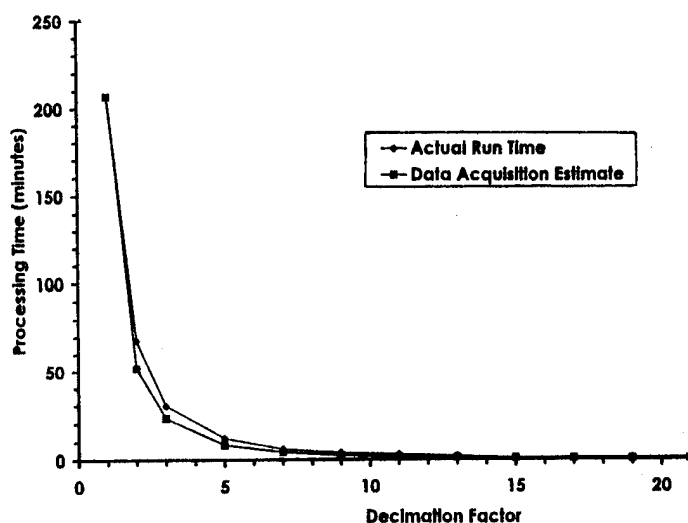


Figure 7. Execution time for the bias calculation, using a full day of data (sampling interval 30 seconds), then decimated down to 1 sample in 20, performed on a 90 MHz Pentium.

Because the differential phase delay data are relatively smoothly varying with time, the decimation process does not introduce significant error into the bias calculation until a relatively severe decimation is invoked. Figure 8 shows the maximum bias error for any of the 25 satellites at each decimation level. It is noteworthy that the error performance degrades rapidly at exactly the point (decimation factor: 40) corresponding to the allowed time separation between data samples from different satellites in a "conjunction". This circumstance suggests that a fundamental data sampling interval less than the maximum

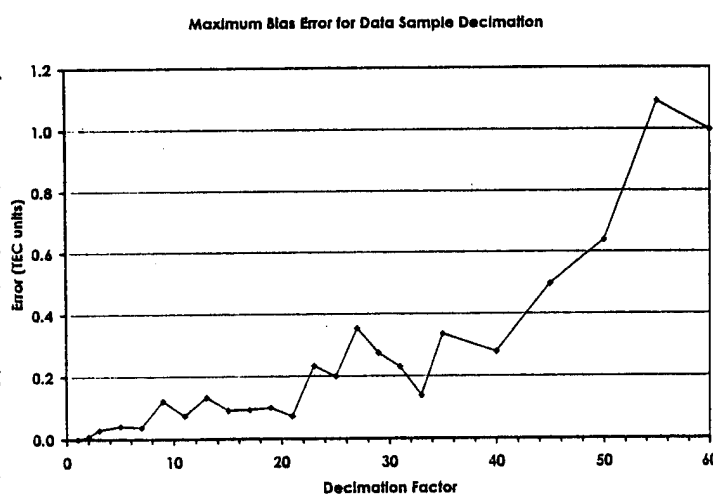


Figure 8. Maximum error in all satellite biases as decimation level increases, with respect to bias values determined from undecimated data.

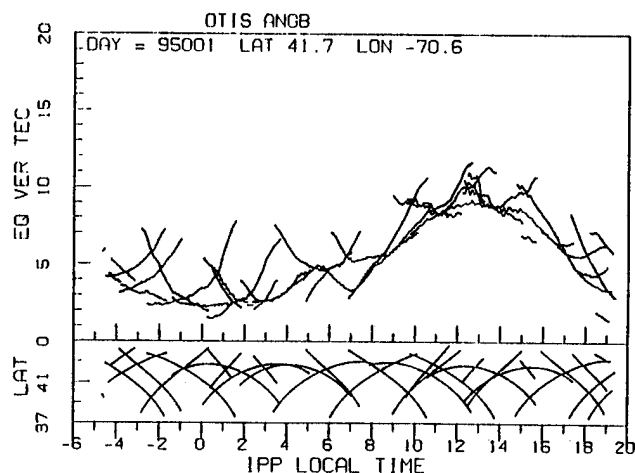


Figure 9. The same day as Figure 1, limited to observations at or above 35 degrees elevation.

time envelope in the "conjunction" definition will produce good error results.

Tests of the effect of reduced data intervals were also conducted. Earlier tests [1], showed products from the initial algorithm (station and zero-mean satellite biases) for four consecutive days at Hanscom AFB. Each day's set of products was independent. The algorithm was run individually for each day, using all available satellites over 24 hours, then re-run using a an eight-hour subset of observations from a handful of satellites between 0900 and 1700 LT. (Products are also derived from reduced satellite subsets of the 24-hour run.) The result was that the day-to-day variation in the overall bias derived from 24 hours of data could also be seen in examining a reduced quantity of satellites over the whole day, and in a set limited to only eight hours.

Tests were also conducted with 6-hour data periods. As a baseline, Figure 9 shows the same day as Figure 1, here limited to observations at or above 35 degrees elevation. Figure 10 shows results from 6-hour subsets of the data of the same day as Figures 1 & 9, subsets processed independently, using just those 6 hours. The data was clipped in UT and only passes with 2 to 3 hours or more of data were used. Comparing Figures 9 and 10 shows a systematic level change in some of the Figure 10 data, indicating the 6-hour process is less accurate in its present implementation. Some changes in the shape of individual satellites' TEC profiles is also evident. Station bias changes are reflected in Figure 11 (expected since each satellite set has a different mean bias), where the station bias level derived from the complete 24-hour data set for each day is plotted as a level dotted line, and the

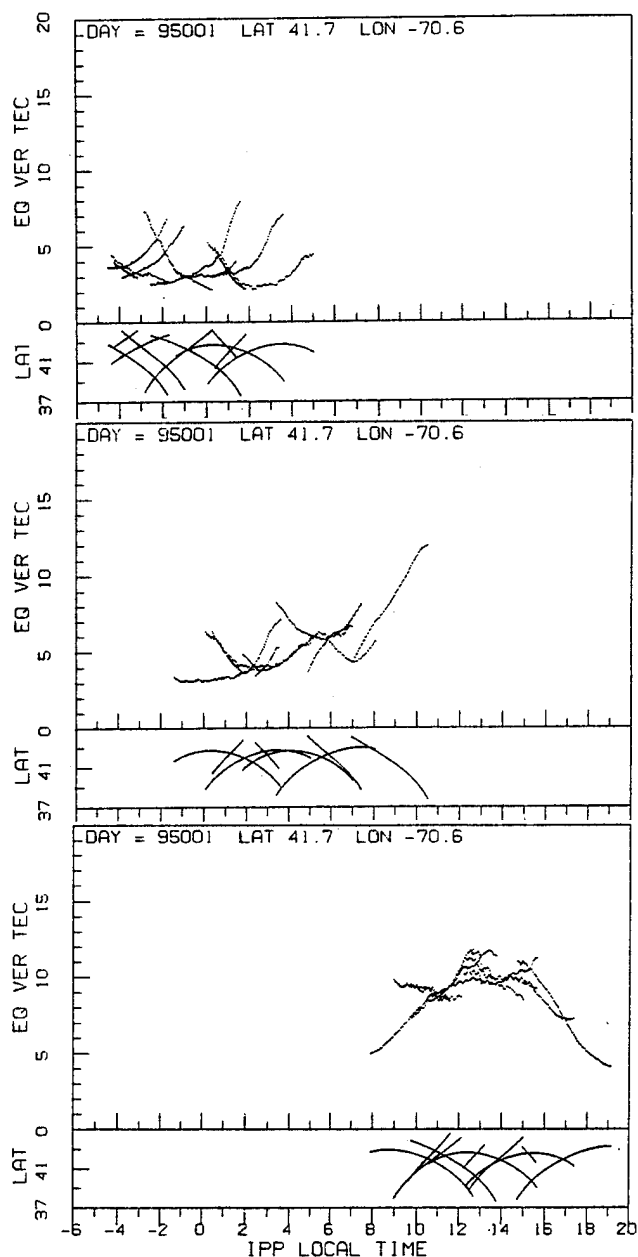


Figure 10. 6-hour subsets of data, same day as Figs 1 & 9, subset clipped in IPP-LT, and only passes with ≥ 2 hours of data were used. Expected station bias changes present but the TEC profiles agree well with Figure 9.

overlying curve tracks the (3-hour overlapping) 6-hour station biases for that day. The four days' curves show reasonable consistency as expected, but significant day-to-day variability. These test results indicate that the SCORE process may be applicable to short time periods for day-to-day or semi-continuous integrity monitoring for DGPS base stations. Ongoing work is examining accuracy improvement, how short these periods can be and how often the process should be updated.

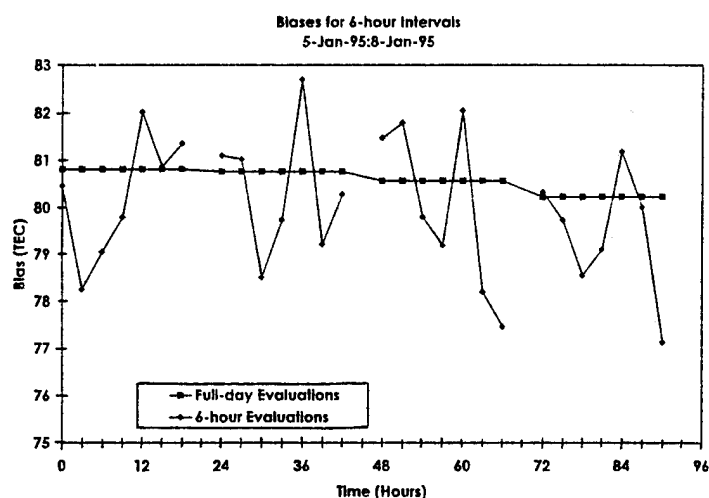


Figure 11. Station biases derived from overlapping 6-hour data sets plotted vs 24-hour bias for same day, four successive days.

SINGLE-FREQUENCY TEC: "SCORE-1"

Initial tests have indicated that the SCORE technique can also be applied to single-frequency data, to obtain absolute TEC measurements without the need for the second frequency. Techniques for extracting *relative* TEC from single frequency data are well established, but assumptions, such as an ionospheric obliquity model, had to be made in order to estimate absolute TEC [9]. The SCORE process is applicable to single frequency because SCORE actually works with *relative* TEC data, it is only the process of "phase-averaging" or pre-fitting the relative TEC (differential phase) data to absolute TEC obtained from the differential group delay, that allows the SCORE corrections to the data to be valid as measures of station and satellite biases. With single-frequency relative TEC as input to SCORE the corrections produced by SCORE have no meaning as system biases, (since each satellite pass is given to SCORE with an effectively random, relative, overall level), but once the corrections are applied to the relative data the result is absolute ionospheric TEC, within the accuracy of the process. With this capability, single-frequency SCORE (SCORE-1) will aid single frequency systems' ionospheric error monitoring. Thus a single frequency ground station may now obtain direct absolute TEC, and a mobile station may also be able to do this, since the SCORE process is dependent on the ionospheric penetration points, and not on the exact receiver location. Studies of this application must deal with ionospheric spatial decorrelation [10].

There are several detail aspects of SCORE-1 that differ from SCORE. Firstly, each satellite is corrected at each appearance, up until a loss-of-lock that cannot be

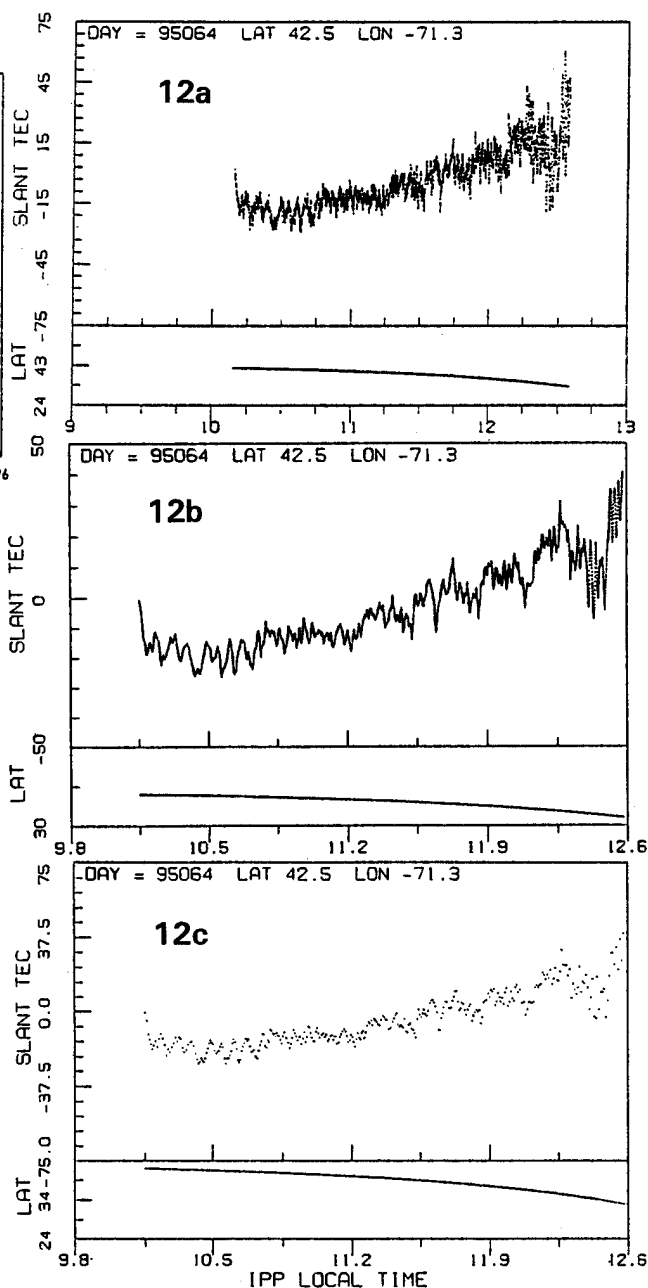


Figure 12. a: Half-pass of unprocessed 1-frequency *relative* TEC data, sampled at ≈ 1 Hz; b: Same data as "a", averaged over 30 seconds; c: Same data as "c" reduced to one sample per 20 seconds.

bridged. This means that the second observation of a satellite in any given day operates as if it were a completely different satellite. This is likewise true for any segment of a pass that is interrupted by a loss-of-lock. As noted above, SCORE-1 produces no bias products for either the receiver system or the satellites. (SCORE, on the other hand, since it produces bias products, links multiple appearances of satellites, as well as fragments of passes.) Overall, single-frequency absolute TEC will be less accurate than two-frequency TEC. The issues are:

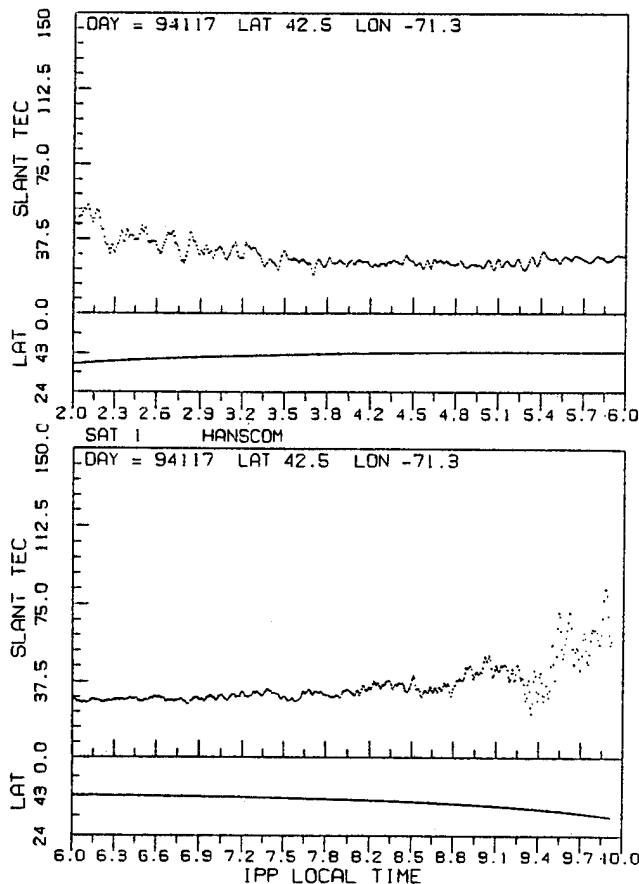


Figure 13. A pass of uncalibrated dual-frequency data sampled at 1 sample per 20 seconds, shown to same scale as Figure 12.

how accurate can we make it, and how fast can we update it? Multipath and noise will be a major limiting factor for SCORE-1 (see figures above) since these are higher for single frequency. Since short passes will suffer from significant multipath effects, data processing requirements include data continuity maintenance, and smoothing for noise and multipath. An hour or so of observation may need to be accumulated for multipath to damp down before a satellite's data should be used. Once calibrated, each satellite pass produces absolute TEC continually. Several approaches are being investigated elsewhere in the GPS community which promise to reduce multipath *within* single-frequency GPS receivers, [11]. If successful, such techniques would greatly improve SCORE-1 products' quality.

SIMULATION TESTS OF "SCORE-1"

Because accurate timing information is required in single frequency GPS data, to support extraction of relative TEC, much of our single-frequency test data was very difficult to analyze due to timing variations in the

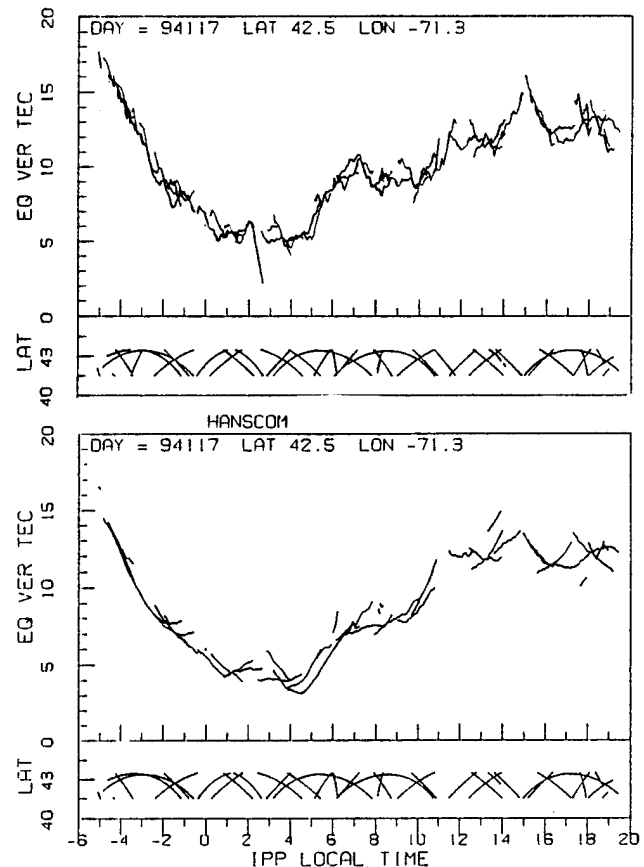


Figure 14. Initial result simulating SCORE producing absolute TEC from 1-frequency GPS; 30-minute smoothing on simulated 1-freq. data, and phase-averaging on the 2-freq. GPS data, 35° elev. cutoff.

equipment/software we had available. To obtain enough data from a 24-hour observation to use for SCORE-1 tests, we employed *uncalibrated* dual-frequency differential delay data, taken on our laboratory rooftop - a "worst-case" multipath environment. Figure 12a gives a half-pass sample of typical single-frequency *relative* TEC from our data. This is unprocessed data, sampled at a rate of about 1 Hz. Figure 12b shows the same data, averaged over 30 seconds, and Figure 12c reduces the product in Figure 12b to one sample/20 seconds. In comparison, Figure 13 shows, to the same scale, a pass of uncalibrated dual-frequency data sampled at 1 sample/20 seconds. Comparison of Figures 12 and 13 show that the multipath levels are approximately comparable, thus the dual-frequency data is not unreasonable to use for an initial test. Figure 14 shows an initial SCORE-1 simulation result using a 35 degree elevation cutoff for the SCORE correlation area and 30-minute smoothing on the simulated single-frequency data. The 2-frequency GPS data uses phase-averaging and links appearances of the same satellite. The SCORE-1 result,

even with the severe multipath, agrees with the SCORE calibration within about 3 TEC units ($\approx 0.3\text{m}$), or better. This is consistent with required accuracies cited for WAAS, [2].

SUMMARY AND CONCLUSIONS

The Self-Calibration Of pseudoRange Errors (SCORE) technique can use ionospheric measurements to monitor and control pseudorange errors in two-frequency DGPS base stations. SCORE produces a measure of the sum of satellite and ground-based pseudorange biases. By frequent updates SCORE can detect and provide correction for drift or changes in this total error. SCORE can monitor/detect a change in station bias error, or a change in one satellite's bias, thus improving the integrity of system's pseudorange measurements. As a result the ionospheric error can be more accurately measured and modeled for DGPS and WAAS applications. Recent improvements in the SCORE technique permit calibrations in minutes, making near-real-time applications feasible. Initial tests have shown SCORE to be robust against loss of input from 1 or more satellites - with variation in the station bias of less than half a TEC unit from loss of 2 satellites, and less than 1 unit from loss of 8 of 25 satellites. Test results also show that SCORE data input may be decimated to as seldom as one point per 20 minutes with only 0.3 TEC unit loss in accuracy. Initial applications of the SCORE process to 8 and 6-hour data periods have been made, with useful but less accurate results. Initial tests have shown that the SCORE technique can also be applied to single-frequency data (SCORE-1), allowing the extraction of absolute TEC measurements without the need for the second frequency. Thus a single frequency ground station may now obtain direct absolute TEC (albeit less accurate than 2-frequency due to multipath), and a mobile station may also be able to do this and aid ionospheric error monitoring, since the SCORE process is dependent on the ionospheric penetration points, and not on the exact receiver location. *With appropriate development to include integrity checks, full autonomous operation, and data compression, both SCORE and SCORE-1 may be feasible for integration in GPS receiver firmware.* For WAAS, these SCORE capabilities open potential to improve accuracies between reference stations impacted by ionospheric decorrelation, and possibly, to reduce the number of grid points or monitor stations required and/or reduce the ionospheric modeling requirement.

ACKNOWLEDGEMENTS

The authors wish to thank Mr. Charley Andreasen, SSgt Carlton Curtis, Dr. Susan Rao, and Mr. Jonathan Copp

for their contributions to equipment test/deployment and data analysis.

REFERENCES

- [1] Bishop, G.J., A.J. Mazzella and E.A. Holland, "Self-Calibration of Pseudorange Errors by GPS Two-Frequency Receivers", in Proceedings of 1995 National Technical Meeting, The Institute of Navigation, Washington, D.C., Jan. 1995.
- [2] Bishop, G.J., D.S. Coco, P.H. Kappler, and E.H. Holland, "A Review of Some Issues in Analysis of GPS Data for Extraction of Accurate Ionospheric Measurements", Proceedings of 11th Symposium, URSI Beacon Satellite Group, University of Wales, Aberystwyth, July, 1994.
- [3] Pullen, S., P. Enge, and B. Parkinson, "Simulation-Based Evaluation of WAAS Performance: Risk and Integrity Factors", Proceedings of ION GPS-94, The Institute of Navigation, Washington, DC, September, 1994.
- [4] Bishop, G.J., D.S. Coco, P.H. Kappler, and E.A. Holland, "Studies and Performance of a New Technique for Mitigation of Multipath Effects in GPS Ground Stations", Proceedings of 1994 National Technical Meeting, The Institute of Navigation, Washington, D.C., Jan. 1994.
- [5] Bishop, G.J., A.J. Mazzella, and E. H. Holland, "Application of SCORE Techniques to Improve Ionospheric Observations", Proceedings of ION GPS-95, The Institute of Navigation, Washington, DC, September, 1995.
- [6] Bishop, G., D. Walsh, P. Daly, A.J. Mazzella, and E.A. Holland, "Analysis of Temporal Stability of GPS and GLONASS Group Delay Correction Terms Seen in Various Sets of Ionospheric Delay Data", Proceedings of ION GPS-94, The Institute of Navigation, Washington, DC, September, 1994.
- [7] Wilson, B., and A. Mannucci, "Extracting Ionospheric Measurements from GPS in the Presence of Anti-Spoofing", Proceedings of ION GPS-94, The Institute of Navigation, Washington, DC, September, 1994.
- [8] Sardon, E., A. Ruis, and N. Zarraoa, "Estimation of the Transmitter and Receiver Differential Biases and the Ionospheric TEC from GPS Observations", Rad. Sci., Vol 29, No. 3, 577-586, May-June 1994.

[9] Cohen, C.E., B. Perven, and B.W. Parkinson, "Estimation of Absolute Ionospheric Delay Exclusively through Single-Frequency GPS Measurements", Proceedings of ION GPS-92, The Institute of Navigation, Washington, DC, September, 1992.

[10] Klobuchar, J.A., P.H. Doherty, and M.B. El-Arini, "Potential Ionospheric Limitations to Wide-Area Differential GPS", Proceedings of ION GPS-93, The Institute of Navigation, Washington, DC, September, 1993.

[11] Townsend, B.R., D.J.R. van Nee, P.C. Fenton, and K.J. Van Dierendonk, "Performance Evaluation of the Multipath Estimating Delay Lock Loop", Proceedings of 1995 National Technical Meeting, The Institute of Navigation, Washington, D.C., Jan. 1995.

Fast Ambiguity Resolution Using an Integer Nonlinear Programming Method

Dr. Ming Wei and Dr. Klaus-Peter Schwarz
The University of Calgary

BIOGRAPHIES

Dr. Ming Wei is research associate at the University of Calgary specializing in GPS/INS integration, advanced filtering methods, and airborne gravity systems. He is chairman of Special Study Group for Airborne Gravimetry Instrumentation and Methods of the International Association of Geodesy. He has a B. Sc. degree from China and a Ph. D. degree from the Technical University of Graz, Austria.

Dr. Klaus-Peter Schwarz is professor of the Department of Geomatics Engineering at the University of Calgary, and President of the International Association of Geodesy. He holds degrees from universities in Germany, Canada, Austria, and a honorary degree from China. His area of expertise is geodesy with special emphasis on the use of inertial systems in Geomatics and the integration of satellite and inertial techniques for precise aircraft positioning, attitude determination, and gravity field modelling.

ABSTRACT

This paper presents a new and efficient strategy for ambiguity resolution on the fly. The new approach is based on the method of Integer Nonlinear Programming (INLP). After discussing some typical methods for INLP, ambiguity resolution of GPS phase measurements based on the Integer Least-Squares Method (ILSM) is formulated as a problem of INLP. A new ambiguity search method is then presented based on a combination of different INLP methods. The new ambiguity search method performs the search for the optimal integer ambiguities of 7 to 8 satellites within 0.1 - 0.2 seconds. It thus, can be used for real-time applications. Based on this search method, ambiguity resolution on the fly is carried out using a sequential approach which estimates the optimal integer ambiguities at each epoch by using all GPS observations available at that epoch. This approach is very robust because it avoids the critical issue of erroneously rejecting the optimal ambiguities. To validate the estimated integer

ambiguities at each epoch, a number of criteria are discussed and tested to ensure the correctness of the estimated integer ambiguities. The method has been successfully tested and has shown robustness as well as reliability.

INTRODUCTION

Without the exact determination of the integer ambiguity precise positioning at the cm level using GPS phase observations cannot be achieved. Thus, ambiguity resolution plays a key role for precise positioning and navigation when using GPS carrier phase observations in either the static or kinematic mode. The review paper by Hatch and Euler (1994) summarizes many different techniques for ambiguity resolution on the fly (AROF) developed over last decade. They are, for example, the ambiguity function method (Counselman and Courevitch, 1981; Remondi, 1991; Madar, 1992), the least squares ambiguity search technique (Hatch, 1989 & 1991; Lachapelle et al, 1992), the fast ambiguity resolution approach (Frei and Beutler, 1990, Frei, 1991), the optimized Cholesky decomposition algorithm (Euler and Landau, 1992), the fast ambiguity search filter (Chen and Lachapelle, 1994), and the ambiguity transform method (Teunissen, 1993 & 1994). There are many different methods of ambiguity resolution using dual frequency data (Hatch, 1989; Wübbena, 1989; Abidin, 1991; Goad 1992). In the following the investigation mainly focuses on single frequency data. The method developed in this paper can also be applied to dual frequency data, e.g. wide-lane observations. The principle for both single frequency data and dual frequency data is the same.

The difficulty in ambiguity resolution on the fly is the integer constraint on the ambiguity parameters. Due to this constraint, there is no unique analytical solution for the integer ambiguities. Unless very precise code observations are available, the principle of integer ambiguity resolution is mainly based on geometrical constraints which require a significant geometrical change of the GPS constellation. Uncertainties and errors, such as

orbital errors, atmospheric effects, multipath effects and measurement noise of the carrier phase also affect the solution of the integer ambiguity. In this paper, the double differencing technique is applied and the integer ambiguities to be determined are the double differenced integer ambiguities. In this case, the total observation error is smaller than one cycle of the integer ambiguity for baselines shorter than about 15 km.

Most methods for ambiguity resolution on the fly are based on the concept of the search space for potential ambiguities. The definition and construction of the search space are different for different search methods. At each epoch the potential ambiguities are tested and identified using various test and validation techniques. The ambiguities which do not pass the test and validation procedure are rejected and the search space is reconstructed for the next epoch. This procedure continues until the optimal integer ambiguities are identified and fixed. In this paper a direct integer ambiguity search (DIAS) method is developed. One major characteristics of this algorithm is that the optimal integer ambiguities are directly searched for without counting the potential solutions, using a quadratic integer programming (QIP) algorithm. Another feature is that the mathematical model used for the direct integer ambiguity search algorithm is based on all GPS data available. Thus, the optimal solution for the integer ambiguities at each epoch is the global solution for all GPS data available at that epoch which is equivalent to including all geometric constraints of the GPS constellation in the integer ambiguity solution. The most critical issue for integer ambiguity resolution on the fly is to validate whether the optimal solution is the true solution for the integer ambiguities. Based on the information on the global optimal solution and the second best solution, some very reliable test and validation procedures are applied to the direct ambiguity search algorithm.

In chapter 2, the general model for integer ambiguity resolution using a mixed integer least-squares estimation method is discussed. Using the separation principle, integer ambiguity resolution is formulated as the minimization problem of quadratic integer programming (QIP). In the third chapter 3, different methods for quadratic integer programming are introduced. The implementation of quadratic integer programming algorithms to integer ambiguity resolution is described in Chapter 4. The validation procedure of the optimal solution of the integer ambiguity is also given in Chapter 4. In Chapter 5, the direct integer ambiguity search method is tested using kinematic data and the validation procedure is analyzed using the test data.

MIXED INTEGER LEAST-SQUARES ESTIMATION

The concept of integer and non-integer least-squares estimation is found in Teunissen (1993, 1994). At the

epoch k , the double differenced GPS carrier phase observation is generally modelled by the following linear system of equations

$$\mathbf{l}_k = \mathbf{A}_k \bar{\mathbf{x}} + \mathbf{B}_k \mathbf{y}_k + \mathbf{n}_k \quad \text{with } \bar{\mathbf{x}} \in \mathbf{Z}^n, \mathbf{y}_k \in \mathbf{R}^m \quad (1)$$

where \mathbf{l}_k is the vector of double differenced GPS observation at epoch k , $\bar{\mathbf{x}}$ is the vector of double differenced integer ambiguity parameters, \mathbf{y}_k contains the parameters of geometric or time unknowns, \mathbf{n}_k is the vector of observation errors; \mathbf{Z}^n is the n -dimensional space of integer numbers and \mathbf{R}^m is the m -dimensional space of real variables.

To estimate the parameters in the linear equations (1) the following least-squares criterion is applied

$$\Omega_k = (\mathbf{l}_k - \mathbf{A}_k \tilde{\mathbf{x}} - \mathbf{B}_k \tilde{\mathbf{y}}_k)^T \mathbf{Q}(k)^{-1}_{11} (\mathbf{l}_k - \mathbf{A}_k \tilde{\mathbf{x}} - \mathbf{B}_k \tilde{\mathbf{y}}_k) = \min \quad (2)$$

where $\tilde{\mathbf{x}}$ is an integer estimate of the ambiguity parameter $\bar{\mathbf{x}}$, $\tilde{\mathbf{y}}_k$ is the real-valued estimate of \mathbf{y} , and $\mathbf{Q}(k)^{-1}_{11}$ the variance-covariance matrix of the observations \mathbf{l}_k .

Due to the integer constraint on the ambiguity parameter \mathbf{x} in the linear model (1), equation (2) is not the conventional least-squares problem. Equation (2) is a mixed minimization problem. The solution of equation (2) cannot be obtained in analytical form. One common approach for the solution of (2) is to decompose the mixed minimization problem (2) into the continuous minimization problem and the integer minimization problem. Using the constraint on the ambiguity parameters \mathbf{x} , the linear model (1) is reformulated as

$$\mathbf{l}_k = \mathbf{A}_k \mathbf{x} + \mathbf{B}_k \mathbf{y}_k + \mathbf{n}_k \quad (3)$$

$$\text{with} \quad \mathbf{D} \mathbf{x} = \bar{\mathbf{x}} \quad (4)$$

$$\text{where} \quad \mathbf{x} \in \mathbf{R}^n, \mathbf{y}_k \in \mathbf{R}^m, \text{ and } \bar{\mathbf{x}} \in \mathbf{Z}^n \quad (5)$$

This is the Gauss-Markoff model with constraint conditions (Koch, 1987). In equations (3) to (5) the ambiguity parameters \mathbf{x} are estimated as real variables, but will be fixed to integer numbers by the constraint condition (4). To solve the linear model (3) with constraints (4) and (5), the following minimum criterion is applied

$$\Omega_k = (\mathbf{l}_k - \mathbf{A}_k \tilde{\mathbf{x}} - \mathbf{B}_k \tilde{\mathbf{y}}_k)^T \mathbf{Q}(k)^{-1}_{11} (\mathbf{l}_k - \mathbf{A}_k \tilde{\mathbf{x}} - \mathbf{B}_k \tilde{\mathbf{y}}_k) + (\mathbf{D} \tilde{\mathbf{x}} - \bar{\mathbf{x}})^T \mathbf{Q}(k)^{-1}_{\bar{\mathbf{x}}\bar{\mathbf{x}}} (\mathbf{D} \tilde{\mathbf{x}} - \bar{\mathbf{x}}) = \min \quad (6)$$

or for $\mathbf{D} = \mathbf{I}$

$$\Omega_k = (I_k - A_k \tilde{x} - B_k \tilde{y}_k)^T Q(k)_{\tilde{x}\tilde{x}}^{-1} (I_k - A_k \tilde{x} - B_k \tilde{y}_k) + (\tilde{x} - \bar{x})^T Q(k)_{\tilde{x}\bar{x}}^{-1} (\tilde{x} - \bar{x}) = \min \quad (7)$$

where \tilde{x} is the real-valued estimate of the linear model (3) without the constraints (4) and $Q(k)_{\tilde{x}\bar{x}}^{-1}$ is the covariance matrix of the estimate \tilde{x} .

The least-squares criterion (7) for the linear model (3) to (5) is equivalent to the least-squares criterion (2) for the linear model (1). The two solutions of the least-squares estimation (2) and (7) are the same. Using equation (7), the mixed minimization problem (2) can be decomposed into two parts. The first part is the continuous minimization problem, while the second part is the integer minimization problem. Equation (7) implies that an integer search for the integer number \bar{x} with the minimum criterion is applied instead of a direct integer estimation using equation (2). Using the separation principle of (7), the estimation of the parameters x and y in equation (1) can be solved in two steps. In the first step, the minimum criterion applied to equation (3) without using the integer constraint of x is of the form

$$\Omega_k' = (I_k - A_k \tilde{x} - B_k \tilde{y}_k)^T Q(k)_{\tilde{x}\tilde{x}}^{-1} (I_k - A_k \tilde{x} - B_k \tilde{y}_k) = \min, \quad (8)$$

with $\tilde{x} \in R^n, \tilde{y}_k \in R^m$.

In the second step the integer number of the ambiguity parameters \bar{x} is sought by using the following minimum criterion

$$\Omega_k'' = (\tilde{x} - \bar{x})^T Q(k)_{\tilde{x}\bar{x}}^{-1} (\tilde{x} - \bar{x}) = \min, \quad (9)$$

where $\tilde{x} \in R^n, \bar{x} \in Z^n$.

Up to now, the estimation has been done only using the observation I_k at epoch k . The estimate \tilde{x} and its covariance matrix $Q(k)_{\tilde{x}\tilde{x}}^{-1}$ are based on the information at epoch k . Thus, the solution using equations (8) and (9) is a local solution. If only GPS phase observations are used for ambiguity resolution, the integer ambiguities cannot be determined by only using one epoch of data, due to the rank deficiency of the design matrix. Even with a few data over a short period the solution of the integer ambiguities is not stable because the phase observation equations over short periods are highly correlated due to the small geometric change.

The integer ambiguity \bar{x} can be reliably estimated using all observation I_i available at epoch k . The general linear

model for the global solution of the integer ambiguities \bar{x} is of the form

$$I_i = A_i x + B_i y_i + n_i \quad \text{for } i = 1, \dots, k \quad (10)$$

with $x = \bar{x} \quad (11)$

where $x \in R^n, y_i \in R^m$, and $\bar{x} \in Z^n. \quad (12)$

To estimate the parameters in the linear model (10) to (12), the following minimum criterion is applied

$$\Omega_{k/k} = \Omega'_{k/k} + \Omega''_{k/k} = \min \quad (13)$$

with

$$\Omega'_{k/k} = \sum_{i=1}^k \{ (I_i - A_i \tilde{x} - B_i \tilde{y}_i)^T Q(i)_{\tilde{x}\tilde{x}}^{-1} (I_i - A_i \tilde{x} - B_i \tilde{y}_i) \}$$

and

$$\Omega''_{k/k} = (\tilde{x} - \bar{x})^T Q(k/k)_{\tilde{x}\bar{x}}^{-1} (\tilde{x} - \bar{x}),$$

where \tilde{x} and \bar{x} are the float and integer estimates of the ambiguity parameter x based on all observations I_i ($i=1, \dots, k$), and $Q(k/k)_{\tilde{x}\bar{x}}^{-1}$ is the covariance of the global float estimate \tilde{x} .

Solving equation (13) can be implemented in two steps. In the first step, the float ambiguities x and the parameters y are estimated using the following minimum criterion for linear models

$$\Omega'_{k/k} = \sum_{i=1}^k \{ (I_i - A_i \tilde{x} - B_i \tilde{y}_i)^T Q(i)_{\tilde{x}\tilde{x}}^{-1} (I_i - A_i \tilde{x} - B_i \tilde{y}_i) \} = \min, \quad (14)$$

with $x \in R^n, y_i \in R^m$.

Equation (14) can be solved using the standard recursive least-squares method. In the second step, using the estimated float ambiguities \tilde{x} , the global solution for the integer ambiguities \bar{x} is obtained by solving the following minimum equation

$$\Omega''_{k/k} = (\tilde{x} - \bar{x})^T Q(k/k)_{\tilde{x}\bar{x}}^{-1} (\tilde{x} - \bar{x}) = \min, \quad (15)$$

with $\bar{x} \in Z^n$.

The difference between the minimization problem (9) and (15) is that the estimate \bar{x} in equation (15) is the global estimate based on all observations I_i available at the

epoch k and its covariance matrix $\mathbf{Q}(k/k)_{\bar{x}\bar{x}}^{-1}$ contains the covariance information of all observations \mathbf{l}_i while equation (9) only yields a local solution based on the information at one epoch. The integer ambiguity \bar{x} obtained using equation (15) is thus the global solution of the linear model (10) to (12). Unfortunately, there is no analytic solution available for the minimization problem (15). Many different integer ambiguity search methods (Frei and Beutler, 1990, Euler and Landau, 1992, Teunissen, 1993 & 1994) have been developed for the minimization problem (15). Determining the integer ambiguities \bar{x} using the minimum criterion (15) is a typical quadratic integer programming problem. One can use the quadratic integer programming technique to directly search for the optimal integer ambiguity \bar{x} which is also the global optimal estimate of all GPS data. The minimization problem (15) is rewritten in the standard form of quadratic integer programming as

$$\min \Omega = \bar{x}^T \mathbf{Q}(k/k)_{\bar{x}\bar{x}}^{-1} \bar{x} - 2 \bar{x}^T \mathbf{Q}(k/k)_{\bar{x}\bar{x}}^{-1} \bar{x} + \bar{x}^T \mathbf{Q}(k/k)_{\bar{x}\bar{x}}^{-1} \bar{x} \quad (16)$$

where $\bar{x} \in \mathbf{Z}^n$.

QUADRATIC INTEGER PROGRAMMING

Quadratic integer programming is of the general form

$$\min f(\mathbf{x}) = -2\mathbf{c}^T \mathbf{x} + \mathbf{x}^T \mathbf{Q} \mathbf{x} \quad \text{with } \mathbf{x} \in S \quad (17)$$

where $f(\mathbf{x})$ is the objective function, \mathbf{Q} is a $n \times n$ symmetric positive matrix and S is the solution space of all feasible solutions defined as

$$S = \{ \mathbf{x} \mid |\mathbf{x}_i| < b, \mathbf{x} \in \mathbf{Z}^n \}. \quad (18)$$

In equation (18), $|\mathbf{x}_i| < b$ defines the search cube.

Equations (17) and (18) describe a constrained integer nonlinear minimization problem. If b is selected large enough, the minimization problem (17) and (18) can be considered as an unconstrained minimization problem. There are two difficulties to solve the integer nonlinear minimization problem (17). First, there is no analytical solution for quadratic integer programming. All methods to solve the problem (17) are numerically based algorithm. The second difficulty is the convexity of the objective function at the discrete integer points. For the real variables the objective function (17) is convex, but for the objective function (17) defined on the discrete space S , the convex condition is usually not satisfied. In this case the local optimum is sometimes not the global optimum on the discrete solution space S . Compared to continuing nonlinear programming, integer nonlinear programming has the advantage that the space S of all feasible solutions is a finite space. Thus, the numerical

search method can be very efficient in the discrete finite space and the exact solution of the integer nonlinear minimization problem (17) can be obtained using a numerical algorithm.

The branch and bound method

The basic concept of the branch and bound method is to divide and discard. Since the original problem is too difficult to be solved directly, an efficient search can be accomplished by successively dividing the solution space into smaller subsets of feasible solutions. The dividing is done by partitioning the entire space of all feasible solutions into smaller and smaller subsets. The discard (fathoming) is done by evaluating how good the best solution in the subset is to determine whether it should be searched further or discarded. It involves calculating lower bounds f_i^* and upper bound \bar{f} of the objective function. More details can be found in Garfinkel and Nemhauser (1972).

In general, the branch-and-bound algorithm has three basic steps - branching, bounding and fathoming:

(1) **Branching:** Branching involves selecting one remaining subsets, and partitioning it into two or more new solution subsets. Let S be a given set of feasible solutions. The set S is divided into two or more subsets S_i with the following conditions:

- (i) Every feasible solution of S is a feasible solution of exactly one of the subsets,
- (ii) A feasible solution of any of the subsets S_1, S_2, \dots, S_i is a feasible solution of S .

(2) **Bounding:** For each newly defined subset S_i , determine the lower bound for the objective value f_i^* by solving the problem

$$\min f(\mathbf{x}), \text{ for } \mathbf{x} \in S_i, \quad (19)$$

i.e. the lower bound f_i^* is the best feasible solution on the subset S_i

$$f_i^* = \min f(\mathbf{x}), \text{ for } \mathbf{x} \in S_i. \quad (20)$$

(3) **Fathoming:** Fathoming is used to rapidly discard many of the possible solutions without analyzing them. If a subset does not contain a feasible integer solution or the lower bound f_i^* of the subset is larger than the current upper bound \bar{f} of the optimal solution:

- (i) $S_i = \emptyset$,

$$(ii) f_i^* > \bar{f},$$

this subset will be fathomed (discarded). If the lower bound f_i^* of the subset S_i is smaller than the current upper bound \bar{f} , it becomes the new upper bound of the entire solution on S :

$$\bar{f} = f_i^* \quad (21)$$

After the third step, the current upper bound \bar{f} is the best feasible solution so far. Repeat the above three steps to the subsets which can still be partitioned until no unfathomed subsets remaining. Then stop the procedure. The best solution defined by the upper bound \bar{f} is the optimal solution.

If the branching and bounding operations are implemented intelligently, subsets containing many possible integer solutions can be discarded at early stages. This is equivalent to the principle of implicit enumeration. The difficult part of the algorithm is to determine the lower bound f_i^* of a subset S_i . Another important task is to guarantee that the lower bound f_i^* is the global optimum on each subset S_i , in particular, if the numerical method can only find the local optimum. However, if the objective function $f(x)$ on the subset S_i satisfies the condition of discrete convexity, so that a local optimum is the global optimum on the subset S_i , one can obtain the global optimum solution of the subset S_i . In Miller (1971), a sufficient condition, called discrete convexity, for a local optimum to be the global optimum is given. For the objective function $f(x)$ that satisfies the discrete convex condition on the subset S_i , some direct discrete search methods are discussed in the following to find the lower bound f_i^* defined on the subset S_i .

Integer gradient direction method

At the k -th step, the direct search can be described as

$$x_{k+1} = x_k + \lambda \cdot n \quad (22)$$

where x_k is the base point to start the search at the k -th step, x_{k+1} is the new point to be searched and n is a unit direction vector and usually determined by the direction of steepest descent of the objective function $f(x_k)$ at the base point x_k . If the search direction n is determined, the increment scale λ along the direction n can be determined using a one-dimensional search algorithm.

The integer gradient direction method is a gradient-based direct search method. The gradient of the objective function $f(x)$ at the point x_k is used to generate the search direction. In order to search over a set of discrete points on

S_j , the integer gradient is introduced and used as a discrete search direction. Similar to the continuous variable case, the unit direction vector n in (22) is defined by the gradient vector of the objective function $f(x)$ at point x_k

$$n = \{ n_1, n_2, \dots, n_k \} = -\text{grad } f(x_k) / |\text{grad } f(x_k)|. \quad (23)$$

Using the non-zero minimum element of n

$$d = \min \{ n_1, n_2, \dots, n_k \} \quad (24)$$

a new vector called relative direction vector \bar{n} is given by

$$\bar{n} = \{ \bar{n}_1, \bar{n}_2, \dots, \bar{n}_k \} = \{ n_1/d, n_2/d, \dots, n_k/d \}. \quad (25)$$

Based on the relative direction vector \bar{n} , the integer direction m is defined as

$$m = \{ m_1, m_2, \dots, m_k \}, \quad (26)$$

where m_i is the nearest integer value of \bar{n}_i .

Using the integer gradient direction m the new point x_{k+1} is searched along the direction m using the following equation

$$x_{k+1} = x_k + \lambda \cdot m. \quad (27)$$

To find the new point x_{k+1} , the increment scale λ along the given integer direction m is determined such that at the point x_{k+1} , the objective function $f(x)$ has a minimum value along the direction m . The most efficient discrete one-dimensional search technique to determine the increment scale λ is the discrete Fibonacci search procedure described by Nemhauser (1966). Details about implementation of the integer gradient search method can be found in Glankwahnadee (1976) and Glankwahnadee et al. (1979).

Due to the second-order effects of the objective function $f(x)$ on the subset S_j , the discrete search procedure sometimes oscillates and even stalls at a false optimum point. To avoid such problems, the regeneration technique is required to restart from the false local optimum. Many effective regeneration techniques have been developed by Glankwahnadee (1976) and Cheng (1989).

In general, the integer gradient direction represent a direction of descent. Because of the transformation of the unit gradient direction into the integer direction, the integer gradient direction m will not represent the real direction of steepest descent of the objective function $f(x)$ at point x_k . Thus, some discrete points could be missed. To avoid this problem the direct enumeration technique is applied around the approximate point x_{k+1} . The neighborhood search algorithm introduced by Reiter and Sherman (1965) is the most reliable method. Particularly, if the subset S_j is discrete convex, the best solution

among the neighborhood points is the optimal solution of the subset S_i . Combining the integer gradient direction method and the neighborhood search algorithm, the optimal solution of the subset S_i can be efficiently and reliably found.

Discrete modified complex method

In equation (22) the search direction can also be determined without computing the gradient of the objective function. Based on the complex method, a modified simplex method, by Box (1965), the discrete modified complex (DMC) method was developed for the integer variable by Beveridge and Schechter (1970) and Fox (1981). The basic idea is to create a complex figure with $2N+1$ vertices, with each vertex at a discrete point of the n -dimensional space of points \mathbf{x} . Starting from the $2N+1$ vertices, the principle of the DMC method is to discard the vertex with the worst objective function value and locate a new vertex along the direction of the line between the poorest vertex and the centroid of the remaining vertices. For the k -th step search, the poorest vertex is selected as the base point in equation (22). The unit search direction \mathbf{n} is determined as follows

$$\mathbf{n}_b = (\mathbf{x}_c - \mathbf{x}_b) / \|\mathbf{x}_c - \mathbf{x}_b\| \quad (28)$$

where \mathbf{x}_b is the vertex with the worst objective function value, \mathbf{x}_c is the centroid of all vertices except the poorest vertex \mathbf{x}_b .

Starting from the base point \mathbf{x}_b which is the poorest vertex, the new point \mathbf{x}_n is searched along the search direction \mathbf{n}_b as follows

$$\mathbf{x}_n = \mathbf{x}_b + \lambda \mathbf{n}_b. \quad (29)$$

Again the increment scale λ is determined by the unidimensional search method. Once the new point \mathbf{x}_n is selected, the discrete point is located to be nearest to the new point \mathbf{x}_n in each coordinate

$$\mathbf{x}_d = \langle \mathbf{x}_n \rangle. \quad (30)$$

To avoid oscillation of the search algorithm and stalling at the false optimum point, Fox (1981) and Cheng (1989) suggested some effective regeneration techniques to continue the successful search. At the end of the search, the neighborhood search algorithm is also applied to find the best integer solution \mathbf{f}_i^* defined on the subset S_i .

IMPLEMENTATION AND VALIDATION

Combining the branch and bound method and the direct discrete search algorithms discussed above, a very efficient direct integer ambiguity search (DIAS) algorithm has been developed at the University of Calgary and implemented in the GPS/INS processing software KINGSPAD (Kinematic

Geodetic System for Position and Attitude Determination). The software KINGSPAD can be used to process either GPS observations or INS data and integrate GPS/INS data in both static and kinematic modes for different applications. Figure 1 shows the DIAS procedure for ambiguity resolution on the fly.

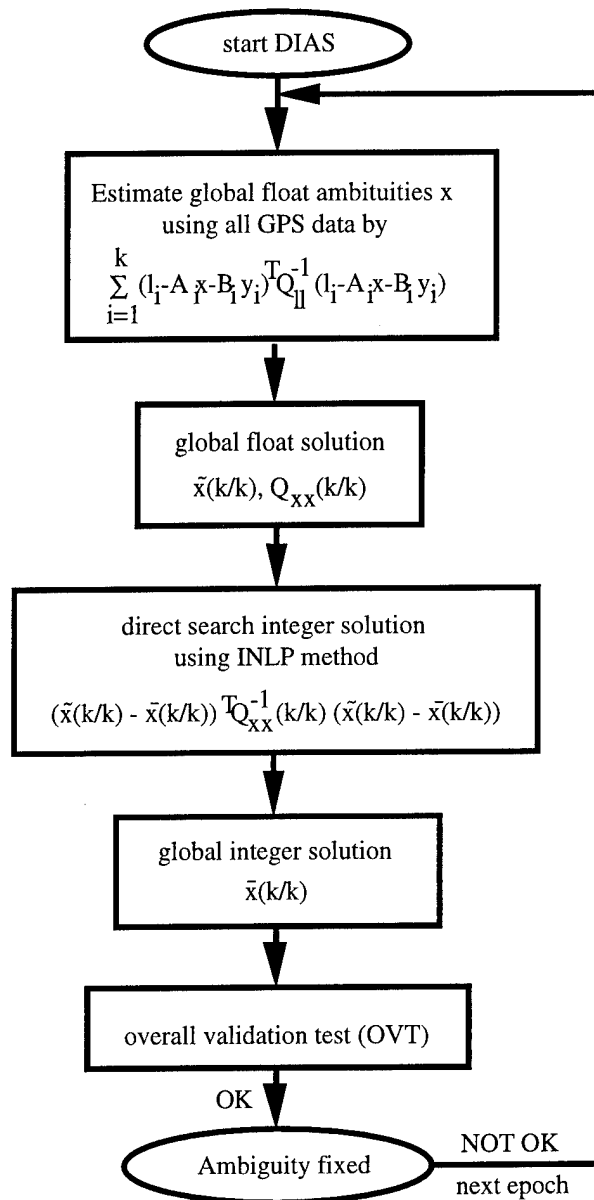


Figure 1: Flowchart of DIAS procedure

For static and kinematic GPS applications the DIAS algorithm has the following features:

(i) The DIAS algorithm is a direct integer search method, which directly yields the optimal solution for the integer ambiguities without counting potential solutions at each epoch. The approach is very robust because it does not have to deal with the critical issue of erroneously

rejecting the optimal ambiguities which is possible when using the concept of potential solutions;

(ii) The DIAS algorithm guarantees the best feasible solution to be the global optimum of the minimization problem (15);

(iii) The optimal integer ambiguity obtained by the DIAS algorithm is the global solution based on all GPS observations, if the least-squares estimation method is applied to equation (14);

(iv) The search algorithm is very efficient. At each epoch it typically takes only 0.1 to 0.2 seconds for 7 to 8 satellites. It thus can be used for real-time applications;

(v) The search algorithm also gives the second best solution for the integer ambiguities.

(vi) DIAS includes an overall validation test (OVT) procedure to validate the optimal integer ambiguities as the true solution.

Validation test procedure

As mentioned above, the solution using the DIAS algorithm directly gives the global optimal solution for the integer ambiguities based on all GPS observations available. Now the question is whether the global optimal integer ambiguities are the true solution for the integer ambiguities. This step is called validation. For kinematic or real-time applications, a solution for the integer ambiguities without a reliable validation procedure is not useful in practice. One major merit of the DIAS algorithm is that it can simultaneously yield the second best solution. Using the optimal and second best solutions one can form very reliable test criteria to validate the obtained optimal solution. Once the optimal and second best solutions for the integer ambiguities are obtained, the quadratic form (15) is computed for both solutions by using

$$\Omega_1'' = (\bar{x} - \bar{x}_1)^T Q(k/k)_{\bar{x}\bar{x}}^{-1} (\bar{x} - \bar{x}_1) \quad (31)$$

$$\Omega_2'' = (\bar{x} - \bar{x}_2)^T Q(k/k)_{\bar{x}\bar{x}}^{-1} (\bar{x} - \bar{x}_2). \quad (32)$$

Given a prior number χ as the threshold of the quadratic form Ω'' , the threshold test for the optimal and second best solution is given by

$$\text{i) } \Omega_1'' < \chi, \Omega_2'' < \chi, \quad (33)$$

$$\text{ii) } \Omega_1'' < \chi, \Omega_2'' > \chi, \quad (34)$$

$$\text{iii) } \Omega_1'' > \chi, \Omega_2'' > \chi, \quad (35)$$

There are three possible outcomes of the threshold test. In the first case the difference between the optimal solution and the second best solution is not significant. The integer ambiguity cannot be fixed because there is more than one solution which could be accepted. This most often happens in case of poor satellite geometry. In the second case the quadratic form of the optimal solution is very small and significantly different from the second best solution. In the third case both quadratic forms are very large. This happens at the beginning of the integer ambiguity search or when some observations have large biases. It is clear that in the first and third cases the optimal solution cannot be considered as the true solution of the integer ambiguities. The search for the integer ambiguity solution should be continued until the second case is obtained. In that case the optimal solution is considered as the true solution of the integer ambiguities. The validation procedure using the three conditions (33) to (35) has a rigorous statistical background (Koch, 1987). Practically, the threshold value χ cannot always be determined using statistical test theory, because the GPS observation errors really do not always satisfy the assumptions for the statistical test. The difficulty in using the threshold test is in the determination of a reasonable threshold value χ . Usually, it will vary from case to case depending on satellite geometry and observation error behavior.

Another criterion uses the ratio between the second best solution and the optimal solution. The test criterion of the ratio test is given by

$$\frac{\Omega_2''}{\Omega_1''} < F \quad (36)$$

$$\frac{\Omega_2''}{\Omega_1''} > F \quad (37)$$

where F is a priori given number. Using the ratio test, the optimal solution is accepted as the true solution if the quadratic form Ω_1'' of the optimal solution is much smaller than that of the second best solution.

In general, equation (36) is almost equivalent to cases (33) and (35) of the threshold test and equation (37) is equivalent to case (34) of the threshold test. For most cases the number F can be chosen to be the same value.

The threshold test and ratio test for the optimal and second best solution can be applied to the quadratic sum of the observation residues (13). Using equations (14) and (15) the quadratic sum of the observation residues of the optimal and second best solutions is computed from

$$\Omega_1 = \Omega' + \Omega''_1 \quad (38)$$

$$\Omega_2 = \Omega' + \Omega''_2 \quad (39)$$

In principle, using the threshold test and the ratio test, one can decide whether the optimal solution is the true solution of the integer ambiguity. Practically, it is still risky to apply these tests to an individual epoch, particularly, if the satellite geometry is quite poor and the observations are noisy. A reliable validation procedure must apply the threshold test and the ratio test to a certain time period, say 30 to 60 seconds. If all epochs during this period pass the above tests with the same optimal solution, the optimal solution can be considered as the solution of the true integer ambiguities. This validation procedure is called overall validation test (OVT).

There are three important steps in the overall validation test (OVT) procedure: detection, confirmation and decision (fixing). Usually, the true integer ambiguities can be detected by the optimal solution at an early stage. The obtained optimal solution must be tested and validated. Therefore, the validation test is applied at every epoch. Only after the optimal solution passes the validation test, it is considered as the solution for the true integer ambiguities. The period between the first detection of the true integer ambiguity and the time when it is considered to be reliably detected, is called the detection period. During the detection period the optimal solution must always be the same. For the ratio test, the time when the true integer ambiguities are considered to be detected is that epoch when the ratio between the second best solution and the optimal solution is larger than the threshold F . The detected integer ambiguities must be confirmed using the validation procedure. The ratio test is continuously applied for a certain fixed period, say 30 to 60 seconds, which is called the confirmation period. During this period, the ratio between the second best solution and the optimal solution is always larger than the threshold F and the optimal solution is always the same. Otherwise, the confirmation period will start again. This procedure is called the confirmation procedure. After the confirmation procedure is completed, it is assumed that the optimal solution is the solution of the true integer ambiguities. At this epoch, the integer ambiguities are fixed using DIAS and validated by the overall validation test (OVT). If the optimal solution is the solution of the true integer ambiguities, the optimal solution is always the same during the entire overall validation test procedure and the ratio between the second best solution and optimal solution gradually increases. At the epoch when the true integer ambiguities are considered to be detected, the ratio is larger than the confirmation level ($\Omega_2/\Omega_1 > F$). The confirmation level has been chosen as $F=2$. At the time when the integer ambiguities are fixed using the optimal

solution, the ratio is relatively large. To illustrate the behavior of the optimal solution during the validation procedure, the ratio between the second best solution and the optimal solution are plotted in Figure 2.

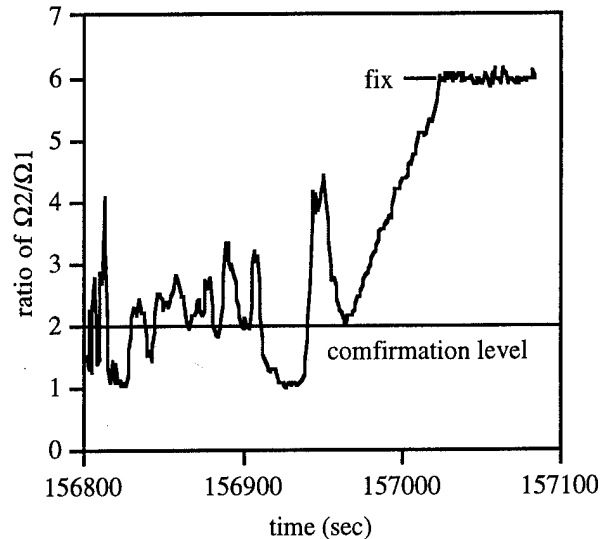


Figure 2: Ratio between the best and the second best optimal solution,

kinematic test, May 8, 1995

RESULTS AND ANALYSIS

The DIAS technique as implemented in KINGSPAD was tested both in static and kinematic mode. Four data sets obtained in land and airborne tests are used to analyze the performance of the integer ambiguity resolution using DIAS. All test data consist of about 15 to 20 minutes of static data and another period of kinematic data. Using 20 minutes of static data, the initial integer ambiguities can be reliably determined. They are used as reference for ambiguity resolution on the fly. The static data of the airborne tests were collected when the engine of the aircraft was on. Due to long baselines between the master station and the aircraft, with distances of 50 to 100 km, the wide-laning is used for airborne data.

Results when using DIAS for ambiguity resolution on the fly are shown in Table 1 to Table 4. The first column gives the start time of the DIAS procedure. The second column gives the epoch when the correct solution is detected by the optimal solution. The third column gives the time when the ratio between the second best solution and the optimal solution is larger than the confirmation level $F=2$. At this time the correct integer ambiguities are considered to be detected. The fourth column is the time when the integer ambiguities are fixed as the true integer ambiguities. The fifth column is the ratio between the

second best solution and the optimal solution at the time when the integer ambiguities are fixed.

start time	time of det.	$\Omega_2/\Omega_1 \geq 2$	time of fixed	Ω_2/Ω_1
594800	594954	595178	595298	2.8
595680	595693	595700	595819	3.0
595950	595962	596054	596173	4.1

Table 1: DIAS results of the land test on March 11, 1995

start time	time of det.	$\Omega_2/\Omega_1 \geq 2$	time of fixed	Ω_2/Ω_1
155350	155389	155418	155537	3.9
156800	156935	156965	157084	6.0
157600	158157	158951	159070	2.6

Table 2: DIAS results of the land test on May 8, 1995

start time	time of det.	$\Omega_2/\Omega_1 \geq 2$	time of fixed	Ω_2/Ω_1
163800	163924	163936	164055	4.0
166030	166492	166912	167032	2.6
167000	167095	167270	167389	4.1

Table 3: DIAS results of the land test on May 8, 1995

start time	time of det.	$\Omega_2/\Omega_1 \geq 2$	time of fixed	Ω_2/Ω_1
405240	405240	405308	405427	4.2
406500	406500	406864	406983	2.5

Table 4: DIAS results of the airborne test on April 28, 1994

As shown in Tables 1 to 4, the true integer ambiguities are found by the DIAS algorithm at a very early stage. The time span between the time to start the validation

procedure and the time when the true integer ambiguities are fixed varies in each case. It depends largely on satellite geometry and size of observation errors. As shown in Tables 1 to 4, the average time span is about 100 to 300 seconds under normal condition of 6 to 7 satellites. However, large deviations from the average are possible, see e.g. the third row in Table 2 where 1200 seconds are needed. This is due to two satellites dropping and arising over a period of time, which cause unstable geometric conditions for integer ambiguity resolution on the fly. The confirmation period for these test is 120 seconds. As shown in Tables 1 to 4, during the confirmation period the ratio between the second best solution and the optimal solution rapidly increases. Depending on the satellite geometry and the behavior of GPS observation errors, the increase rates are different in each case.

CONCLUSIONS

In this paper the direct integer ambiguity search (DIAS) algorithm has been introduced for ambiguity resolution on the fly. The basic principle is the direct search for the global optimal solution of the integer ambiguities using integer nonlinear programming methods.

The major merit of the DIAS method is its robustness, because it always searches for the optimal global solution based on all GPS data available at each epoch. The concept of a potential solution is not necessary. The problem of rejecting the true integer ambiguity can thus be avoided. The critical issue here is to use all GPS data and their covariance information properly. Test results indicate that the DIAS algorithm implemented in KINGSPAD is very efficient. It only takes about 0.1 to 0.2 second for 7 to 8 satellites. The total computation time for the GPS processor in KINGSPAD, including ephemeris computation, navigation algorithm and the DIAS method, is less than 0.3 second using a 486/50 PC computer. Thus, real-time applications can be processed.

The question of validating optimal integer ambiguities is the most critical issue for integer ambiguity resolution procedures. The DIAS method compares the optimal solution to the second best solution and applies threshold and ratio tests to determine the validity of the solution. The overall validation test (OVT) using different test algorithms has been developed and tested. Test results show that these algorithms are reliable.

REFERENCES

- Abidin, H.Z. (1991), New strategy for on-the-fly ambiguity resolution. *Proc. of ION GPS-91*, The Institute of Navigation, Albuquerque, New Mexico, Sept. 11-13, 1991.
- Beveridge G.S. and R.S. Schechter (1970), *Optimization: Theory and Practice*. McGraw-Hill.

- Box, M.J. (1965), A new method of constrained optimization and a comparison with other methods, *Comp. J.*, 8, (1), pp. 42-52, 1965.
- Cheng, D.S. and G. Lachapelle (1994), A comparison of the FASF and least-squares search algorithms for ambiguity resolution on-the-fly. *Proc. of KIS94 Symposium*, Banff, Aug. 30 - Sept. 2 1994.
- Cheng, L.Z. et al. (1989), *Discrete Optimization in Engineering: Theory and Applications*. (in Chinese).
- Counselman, C.C., III, and S.A. Gourevitch (1981), Miniature interferometer terminals for earth surveying: ambiguity and multipath with Global Positioning System. *IEEE Transactions on Geoscience and Remote Sensing*, Vol. GE-19, No. 4, October, pp. 244-252.
- Euler, H.-J. and H. Landau (1992), Fast GPS ambiguity resolution on-the-fly for real-time applications. *Proc. of the 6th International Symposium on Satellite Positioning*, Columbus, Ohio, March 17-20, 1992.
- Fox, D.B. and J.S. Liebman (1981), A discrete nonlinear simplex method for optimized engineering design. *Engineering Optimization*, Vol. 5, pp. 129-149, 1979.
- Frei, E. (1991), *Rapid Differential Positioning with the Global Positioning System*. Schwarzerische Geodätischen Kommission, Band 44.
- Frei, E. and G. Beutler (1990), Rapid static positioning based on the fast ambiguity resolution approach FARA: Theory and first results. *Manuscripta Geodaetica*, Vol. 15, No. 6.
- Garfinkel, R. and G. Nemhauser (1976), *Integer Programming*. John Wiley & Sons.
- Glankwahmdee, A. (1976), Unconstrained Nonlinear Discrete Search. Ph.D. Dissertation, Department of Mechanical and Industrial Engineering, University of Illinois.
- Glankwahmdee, A. and J.S. Liebman, and G.L. Hogg (1979), Unconstrained discrete nonlinear programming. *Engineering Optimization*, Vol. 4, (2), pp. 95-107, 1979.
- Goad, C. (1992), Robust Techniques for determining GPS phase ambiguities. *Proc. of 6th international Geodetic Symposium on Satellite positioning*, Columbus, Ohio, March 17-20.
- Hatch, R. (1989), Ambiguity resolution in the fast lane. *Proc. of ION GPS-89*, The Institute of Navigation, Colorado Springs, Sept. 27-29, 1989.
- Hatch, R. (1990), Instantaneous ambiguity resolution. *Proc. of IAG international Symposium on Kinematic Systems in Geodesy, Surveying and Remote Sensing*, Sept. 10-13, 1990, Springer Verlag.
- Hatch, R. and H.-J. Euler (1994), Comparison of several AROF kinematic techniques. *Proc. of ION GPS-94*, The Institute of Navigation, Sept., 1994.
- Koch, (1987), *Parameter Estimation and Hypothesis Testing in Linear Models*. Springer Verlag, New York.
- Lachapelle G., M.E. Cannon and G. Lu (1992), High-precision GPS navigation with emphasis on carrier-phase ambiguity resolution. *Marine Geodesy*, Vol. 15 No. 4, 1992.
- Mader G.L. (1992), Kinematic GPS phase initialization using ambiguity function. *Proc. of the sixth International Symposium on Satellite Positioning*, Columbus, Ohio, March 17-20.
- Miller, B.L. (1971), On minimizing nonseparable functions defined on the integers with an inventory application. *SIAM J. Appl. Math.*, Vol. 21, No. 1, July 1971.
- Nemhauser, G.L. (1966), *Introduction to Dynamic Programming*. John Wiley & Sons.
- Remondi, B.W. (1991), Pseudo-kinematic GPS results using the ambiguity function method. *Navigation*, Vol. 38, No. 1, Spring, 1991.
- Reiter, S. and G. Sherman (1965), Discrete optimizing. *Journal of SIAM*, Vol. 13, 1965.
- Teunissen, P.J.G. (1993), Least-squares estimation of the integer GPS ambiguities. Invited Lecture, Section IV Theory and Methodology, IAG General Meeting, Beijing, August 1993.
- Teunissen, P.J.G. (1994), A new method for fast carrier phase ambiguity estimation. *Proc. of IEEE PLANS-94*, Las Vegas, Nevada, April 11-15.
- Wübbena, G. (1989), The GPS adjustment software package GEONAP, concept and models. *Proc. of the 5th International Geodetic Symposium on Satellite Positioning*, Las Cruces, New Mexico, March 13-17.

Improving the Reliability of OTF Ambiguity Resolution with Dual Frequency GPS Observations

Gang Lu*, M. Elizabeth Cannon, and Gerard Lachapelle
The University of Calgary

** Now with Trimble Navigation Ltd.*

BIOGRAPHY

Gang Lu graduated from the University of Calgary, Canada, with a M.Sc. and Ph.D. in Geomatics Engineering in 1991 and 1995 respectively. He has been involved in GPS research and applications since 1989. He is now a Member Technical Staff with Trimble Navigation Ltd., Sunnyvale.

M. Elizabeth Cannon is an Associate Professor in the Department of Geomatics Engineering where she conducts research into GPS static and kinematic positioning. She has a B.Sc., M.Sc. and Ph.D. in Surveying Engineering from The University of Calgary.

Gerard Lachapelle is a professor and the chairman of the Department of Geomatics Engineering at The University of Calgary. He is responsible for teaching and research related to positioning, navigation and hydrography. He has been involved with GPS developments and applications since 1980.

ABSTRACT

Full wavelength carrier phase observations on L1 and L2 frequencies are available nowadays from high precision dual frequency GPS receivers. In the presence of Anti-Spoofing, the L2 carrier phase measurement is more noisy and more likely to have cycle slips. This paper presents a fast and reliable on-the-fly ambiguity resolution method based on dual frequency GPS measurements. This method is not affected by L2 carrier phase cycle slips and uses full observation information provided by the two frequencies. The information content of various combinations of carrier phase observations is examined. Kinematic test results using dual frequency receivers have shown that carrier phase integer ambiguities can be very reliably resolved quickly over short distances with the method presented.

1. INTRODUCTION

The use of dual frequency GPS sensors and receivers is likely to increase in the future due to the continuous

improvement of GPS signal tracking technologies and the reduced receiver cost. Under Anti-Spoofing, however, pseudorange measurements on both frequencies are noisy and do not provide enough accuracy to directly resolve the carrier phase ambiguities (Yang and Goad, 1994). Most of the current techniques employ a single wide-lane processing or combined L1 and L2 phase processing, in which the integer lane constraint and the geometry constraint between the two frequencies have not been fully exploited.

This paper presents a method which uses information offered by full wavelength L1 and L2 carrier phase measurements for OTF ambiguity resolution over relatively short distances. The main purpose is to increase the reliability of OTF ambiguity resolution while keeping the observation time span as short as possible.

To reliably resolve the carrier phase integer ambiguities on the fly, all the information contained in the GPS measurements should be utilized. Generally speaking, this information includes

- (a) lane combinations between L1 and L2 carrier phase observations,
- (b) geometry constraints from redundant satellites,
- (c) accumulation of geometry change of satellite constellation and
- (d) systematic bias levels in the observations.

Various combinations between L1 and L2 carrier phase observations are widely used in GPS data processing for ionospheric correction, cycle slip detection and ambiguity resolution. Our focus in this paper is on ambiguity resolution. Instead of using a single combination of L1 and L2 carrier phase observations, an approach to use a pair of combinations to replace L1 and L2 observations for ambiguity resolution is presented. A similar idea for pairing ambiguities between L1 and L2 is also described in Teunissen (1994), where the purpose is to find compatible (integer to integer) transformations between the derived carrier phase combinations and the original measurements. For ambiguity resolution, however, it is the incompatibility of the integer ambiguities between

different lanes that significantly improves the reliability and speed of ambiguity resolution.

Geometry constraints from redundant satellites play an important role in ambiguity resolution. If more than four satellites are available at one epoch, integer ambiguities from any sub-group of satellites should be compatible and give a unique position solution. The geometry constraints among the satellites are usually measured by the sum of squared carrier phase residuals and the uncertainty range of the estimated floating ambiguities from a least squares adjustment procedure. Unfortunately, these selection criteria are affected by systematic errors such as multipath and thus, are not very reliable. As pointed out by Martin-Neira et al (1994) as well as Borge and Forsell (1994), the correct integer ambiguity vector may not minimize the instantaneous carrier phase residuals, but it does minimize the time average of residuals. This implies that by accumulating the geometry change information within the observations, one should be able to significantly increase the reliability of integer ambiguity resolution.

Different approaches have been proposed to utilize the accumulated geometry information in carrier phase observations. Remondi (1991) presented a method to project the potential ambiguity candidates to each observation epoch in order to check the compatibleness between carrier phase observations and the selected ambiguity vector. A recent method given by Borge and Forsell (1994) uses the polynomials to fit the adjusted residuals. For dual frequency GPS data, the time average of residuals may not significantly increase the reliability of integer ambiguity resolution due to a small number of potential ambiguity sets, relatively large degrees of freedom and stronger geometry constraints. For single frequency GPS data, however, it is probably the most robust criterion to select the correct integer ambiguities.

2. COMBINATIONS OF PHASE OBSERVABLES AND THEIR AMBIGUITIES

Instead of combining L1 and L2 phase data into a single phase observable, the more general form is to transform dual frequency carrier phase observations L_1 and L_2 into a corresponding pair of combinations, as expressed by

$$\begin{pmatrix} L_a \\ L_b \end{pmatrix} = \begin{pmatrix} t_{11} & t_{12} \\ t_{21} & t_{22} \end{pmatrix} \begin{pmatrix} L_1 \\ L_2 \end{pmatrix} \quad (1)$$

where L_a and L_b denote two derived phase observables, i.e. combinations of L_1 and L_2 . t_{11} , t_{12} , t_{21} and t_{22} are

transformation coefficients. This type of transformation was first proposed by Teunissen (1994) to investigate the invertible carrier phase combinations, i.e. the combinations that lead to a set of integer ambiguities of L_a and L_b from a set of integer ambiguities of L_1 and L_2 or vice versa. The advantage of this transformation is to retain all the information in L_1 and L_2 if the coefficient matrix is properly chosen and full rank.

According to (1), a single wide-lane transformation corresponds to $t_{11} = 1$, $t_{12} = -1$, $t_{21} = 0$ and $t_{22} = 0$. This transformation from L_1 and L_2 to wide-lane ($L_1 - L_2$) will lose information because the inverse transformation, i.e. from wide-lane to L_1 and L_2 is impossible. This implies that L_1 or L_2 or any other linear combination independent from the wide-lane will provide additional complimentary information for data processing.

For integer ambiguity resolution, the transformation matrix (t_{11} , t_{12} , t_{21} , t_{22}) in Eqn. (1) has to be composed of integers in order to let L_a and L_b possess integer ambiguities. As we know, at the correct position both ambiguities from L_a and L_b have to be integers. This is the fact that we can use for our integer ambiguity resolution and we call it *integer lane constraint* between two frequencies.

For relatively short baseline applications, the ionospheric and tropospheric effects are assumed to be canceled by double differencing. The derivations in the following are therefore concentrated on potential ambiguity selections.

If L1 and L2 carrier phase observations are used directly, the corresponding pair of observation equations is

$$\nabla\Delta\Phi_1 = \nabla\Delta\rho / \lambda_1 + \nabla\Delta N_1 \quad (2)$$

$$\nabla\Delta\Phi_2 = \nabla\Delta\rho / \lambda_2 + \nabla\Delta N_2 \quad (3)$$

Eliminating $\nabla\Delta\rho$ term in (2) and (3), we obtain

$$\nabla\Delta N_2 = \nabla\Delta\Phi_2 - \lambda_1 / \lambda_2 (\nabla\Delta\Phi_1 - \nabla\Delta N_1) \quad (4)$$

$$\sigma_{\nabla\Delta N_2}^2 = \sigma_{\nabla\Delta\Phi_2}^2 + (\lambda_1 / \lambda_2)^2 \sigma_{\nabla\Delta\Phi_1}^2 \quad (5)$$

For every potential integer $\nabla\Delta N_1$ in equation (4), if the computed $\nabla\Delta N_2$ is not an integer within the error limit of (5), $\nabla\Delta N_1$ is not the right choice and can be rejected right away. For a 0.1 cycle phase noise on both $\nabla\Delta\Phi_1$ and $\nabla\Delta\Phi_2$, $\sigma_{\nabla\Delta N_2}$ is at 0.127 cycle level. Test results show that if $\nabla\Delta N_1$ varies from -15 to +15 cycles, there

are only about nine to ten potential integers for $\nabla\Delta N_2$ within the 0.127 cycle level limit.

Based on the same principle, we may form other pairs of observations, such as wide-lane and L_1 observables. The equations similar to (4) and (5) are

$$\nabla\Delta N_w = \nabla\Delta\Phi_w - \lambda_1 / \lambda_w (\nabla\Delta\Phi_1 - \nabla\Delta N_1) \quad (6)$$

$$\sigma_{\nabla\Delta N_w}^2 = \sigma_{\nabla\Delta\Phi_2}^2 + (1 - \lambda_1 / \lambda_w)^2 \sigma_{\nabla\Delta\Phi_1}^2 \quad (7)$$

However, a close examination reveals that equations (6) and (7) have exactly the same effect as those given by equations (4) and (5) regarding the selection of potential ambiguities.

One might think that equations (6) and (7) could be used in reverse form, namely using $\nabla\Delta N_1$ to check $\nabla\Delta N_w$. If it works, it would be beneficial to help wide-lane ambiguity resolution for long baseline applications. For this case, the formulas are

$$\nabla\Delta N_1 = \nabla\Delta\Phi_1 - \lambda_w / \lambda_1 (\nabla\Delta\Phi_w - \nabla\Delta N_w) \quad (8)$$

$$\sigma_{\nabla\Delta N_1}^2 = (\lambda_w / \lambda_1)^2 \sigma_{\nabla\Delta\Phi_2}^2 + (1 - \lambda_w / \lambda_1)^2 \sigma_{\nabla\Delta\Phi_1}^2 \quad (9)$$

The problem is that the computed $\nabla\Delta N_1$ from equation (8) is very noisy, as seen from (9). The standard deviation for $\sigma_{\nabla\Delta N_1}$ is 0.57 L_1 -cycles for a 0.1 cycle phase accuracy, which makes equation (8) useless. This means that one can not use the nature of L_1 integers to check the wide-lane ambiguities by the above method.

3. AMBIGUITY SEARCH STRATEGY

The integer ambiguity search strategy developed here utilizes all the information available from carrier phase data, which includes lane constraints between two frequencies, satellite geometry constraints and time averages of phase residuals. As pointed out by Hatch (1992), only three primary double difference ambiguities need to be tested. The ambiguities and their uncertainty ranges from the secondary satellites can be used to further test the potential primary ambiguities. To avoid strong multipath influence at low elevation angles and signal obstruction, the four primary satellites selected usually are highest satellites so long as their PDOP is not so poor (such as less than 10). In fact, by using *integer lane constraint* between the two frequencies, the PDOP of the four primary satellites can be relaxed a little bit because the two nearest integers around the rounded

secondary integer ambiguity can be quickly checked. And only the one fits the integer lane constraint is the potential one.

Potential Ambiguity Selection

The initial ambiguity search ranges can be defined by (smoothed) pseudorange solution or sequential code and carrier floating ambiguity solution. The L_1 phase integer ambiguities $\nabla\Delta N_1$ for three primary double difference observables are checked using Eqns. (4) and (5) or Eqns (6) and (7) immediately. Only the L_1 ambiguities that produce integer L_2 or wide-lane ambiguities within the error limit of Eqn. (5) or (7) are potential ambiguities. Test computations show that within a ± 3 meter search cube, there are about nine to ten potential integer ambiguities that could pass the integer lane constraint test for each satellite. Since the L_2 or wide-lane ambiguities are computed and checked at each epoch separately, cycle slips or discontinuity on L_2 phase measurements will not affect the results.

Correct Ambiguity Selection and Validation

The ambiguity selection and validation is composed of two steps. The first step is to use secondary satellite information to eliminate the incorrect potential ambiguity sets related to the primary satellites. Only the potential ambiguity sets which produce integer L_2 or wide-lane ambiguities for all the secondary satellites are saved for further testing. The second step is to test the carrier phase residuals from a least squares adjustment based on all the satellites available. Both of the estimated a posterior carrier phase variance and the polynomial fitting pattern of individual carrier phase residuals are checked against their pre-set thresholds. A given or specified bias level in carrier phase measurements is usually used as a threshold for polynomial testing. The ambiguity sets that pass all the above tests are carried forward to the next epoch until one set of ambiguities is left and meets all the assurance criterion.

4. TEST RESULTS AND ANALYSIS

Data sets from two kinematic tests using Trimble 4000SSE dual frequency receivers were processed to verify the proposed OTF ambiguity resolution method. The first test is a land kinematic test within 2 km distances, while the second is an airborne flight test with baseline lengths ranging from 200 m to some 60 km.

4.1 Land Kinematic Test and Results

This test was carried out on December 28, 1992. P-code GPS signals were available during that time. Two Trimble 4000SSE dual frequency receivers were used to collect the data. The monitor receiver and its antenna were set up on the roof of the Engineering Building. The rover receiver antenna was mounted on the car roof and driven along a road from the campus to a nearby shopping mall. Two kinematic test runs were made. In the first run, both receivers were operating in P-code mode and collecting P-code pseudoranges and carrier phases. In the second run, both receivers were forced to operate in cross-correlation mode by setting the appropriate receiver control parameters. C/A code pseudoranges and cross-correlation L2 carrier phases were collected for the second run. Data collection interval was 1 second. At the beginning of both runs, about 10 minutes static data were collected while the rover antenna was placed on a tripod on a parking lot. The distance between the monitor receiver and the tripod was 412 metres. The first run lasted about 40 minutes in time and the second run lasted about one hour.

During the test, the air temperature was below -31° Celsius and the road was covered with some 0.3 m depth of snow. The moving antenna was passing nearby trees, buildings and traffic lights which caused frequent cycle slips on lower elevation ($<25^{\circ}$) satellites due to their shadowing effects. The test environment was considered very harsh. The vehicle trajectory for the test is shown in Figure 1.

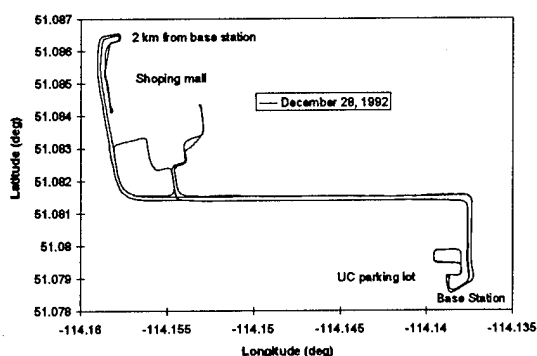


Fig. 1 Trajectory for land kinematic test

P-Code Run Results

The PDOP for the first run with P-code tracking was changing from 3.14 to 2.89. Five to seven satellites were tracked above 15° elevation, as shown in Figure 2.

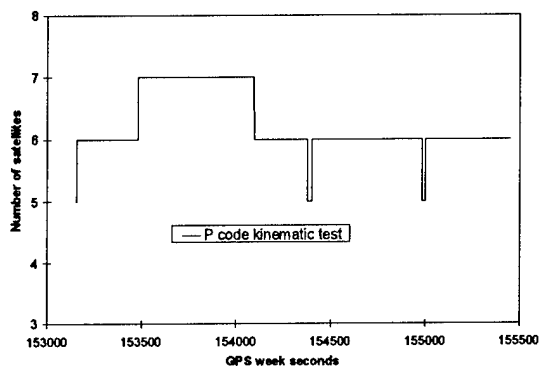


Fig. 2: Number of satellites observed

The on-the-fly ambiguity resolution using L1 and L2 P-code observations based on the proposed search method was performed numerous times, each one shifted in time by 10 seconds, along the whole 40 minutes data set. Such an OTF testing scheme by shifting the starting time along the data set was used before by the authors, such as Lachapelle, et al (1992). In this processing, the double difference pseudorange noise was set to 0.4 m and the double difference carrier phase noise was set to 1 cm. The number of epochs required for ambiguity resolution corresponding to each separate OTF trial is shown in Figure 3.

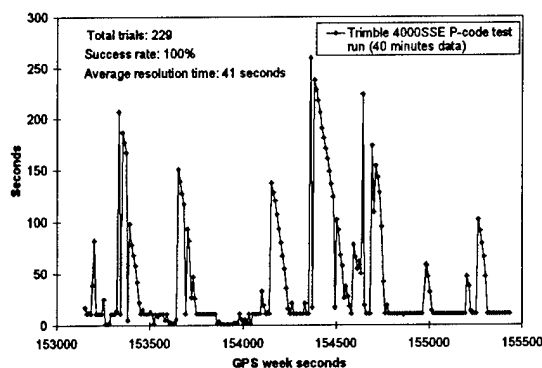


Fig. 3: Time to ambiguity resolution

With total of 229 trials along the 40 minutes data, the successful rate was 100%. The average time required is about 41 seconds. If seven satellites are available, the observation time to ambiguity resolution is normally less than 10 seconds, with a few occasions reaching about 3 minutes in this case.

Cross-correlation Run Results

The PDOP for the second run with cross-correlation tracking mode was changing from 2.86 to 1.56. Five

satellites are tracked during most of the test period. In this run, the vehicle was driven a little bit further on the road than it did for the P-code test run, passing under a big overhead traffic sign which caused a complete loss of lock on all the satellites. Due to the shadowing of a container moving truck at an intersection, the satellites observed were dropped to two during the middle of the test. Furthermore, the lower elevation satellites SV 15 and SV 24 had numerous cycles slips due to the shadowing of trees and surroundings. In this regard, this data set was a good test for the method. Shown in Figure 4 was the satellite number observed during the test.

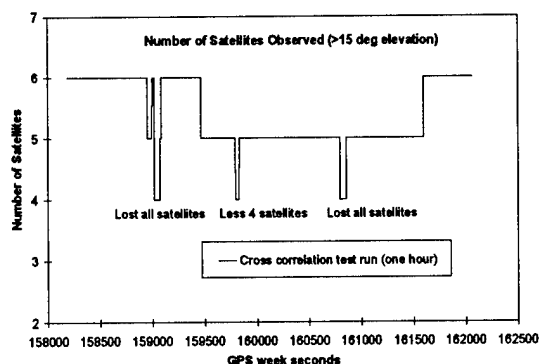


Fig. 4: Number of satellites observed

Again, the OTF ambiguity resolution using L1 C/A code carrier phase and cross-correlation L2 carrier phase was started every 10 seconds along the whole one hour data set. The double difference pseudorange noise was set to 0.6 m and double difference phase noise was set to 1 cm. The number of epochs required for ambiguity resolution for each trial is shown in Figure 5.

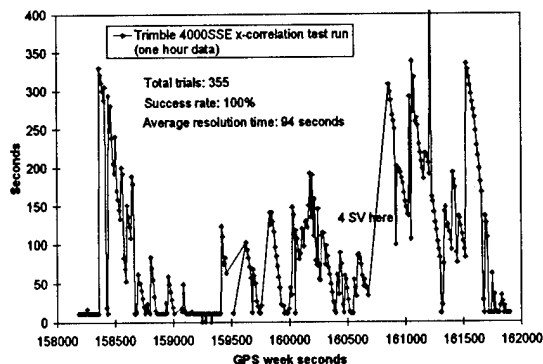


Fig. 5: Time to ambiguity resolution

Of total of 355 trials, the successful rate was 100%. None of the resolved ambiguity set was wrong. The average observation time was 94 seconds. Considering a harsh testing environments and only five satellites

available for more than half of the time, this result was satisfactory.

4.2 Airborne Test and Results

The airborne GPS data was provided by GeoSurv Inc. Ottawa, and was collected in the Muskoka area of Ontario on April 9, 1993. Two Trimble 4000SSE receivers were used. One receiver was installed on a small airplane and the other was set up as a differential base station at the airport. P-code L1 and L2 data were collected at an 1 Hz rate. During the test, the distances between the base station and the aircraft changed from 110 m to some 60 km. The satellites observed above 15° elevation were dropped from seven at the beginning to five at the middle of the test. The aircraft speed ranged from 60 to 100 m/s and the flight height reached about 2500 m. The flight trajectory is shown in Figure 6.

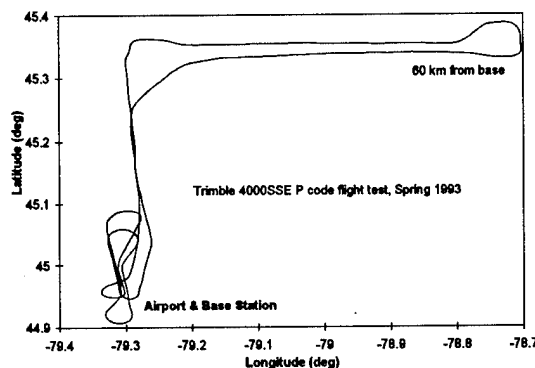


Fig. 6: Flight trajectory for airborne test

The purpose using this data set is to test how far the proposed OTF ambiguity resolution method can be applied directly without any ionospheric error correction and modeling, which is the major limiting factor for long distance OTF ambiguity resolution. The standard tropospheric model was used to correct the pseudorange and carrier phase measurements between the base station and aircraft.

Shown in Figures 7 and 8 were the number of satellites tracked during the test and the time to ambiguity resolution for OTF trials starting at different time. Numerous OTF trials were executed independently along the whole data set. Each new trial was started by shifting the beginning time 10 second forward within the data set. A positive time to ambiguity resolution (the dots above 0 along the vertical axis) means that a correct ambiguity set was obtained by the OTF processing starting at the corresponding time marked on the horizontal (time) axis. A negative time to ambiguity resolution (the dot below 0

along the vertical axis) mean the corresponding OTF processing starting at that time failed to obtain the correct ambiguities.

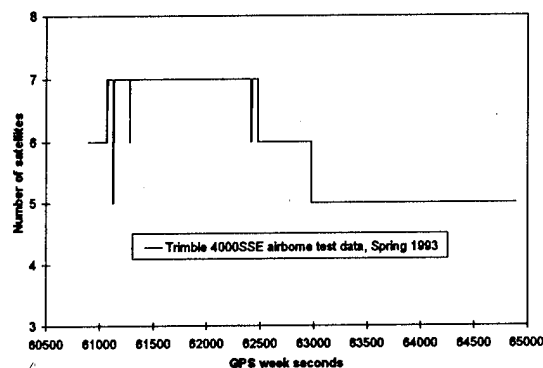


Fig. 7: Number of satellites observed (>15°)

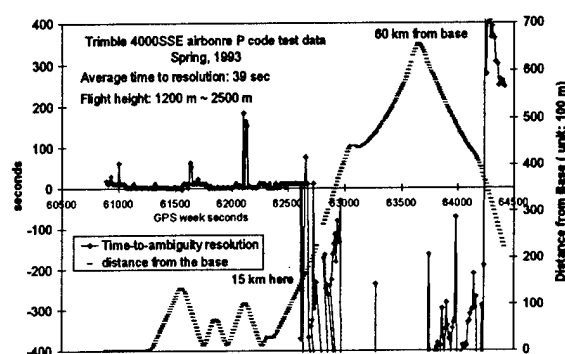


Fig. 8: Time to ambiguity resolution

It can be seen from Figure 8 that the OTF ambiguity resolution works very well when the distance between the base station and the aircraft was within 15 km without any ionospheric corrections and modeling. The average time to ambiguity resolution was 39 seconds (epochs) for this airborne test. For dual frequency receivers, it should be able to compute the ionospheric changes and apply them to OTF algorithm when the aircraft flew away from the base station which located at the airport. This would be a topic for further investigation.

5. CONCLUSIONS

OTF ambiguity resolution using a pair of observables from dual frequency GPS measurements is investigated with the emphasis on integer lane constraints between the observables. Test computations have shown that the integer lane constraint between two appropriately chosen observables, together with the geometry constraints from

the redundant satellites and the residual monitoring, can provide a very reliable and fast OTF ambiguity resolution strategy over short baselines (<15 km). The application of this method to longer baselines, however, is very much affected by the atmospheric errors and requires further investigations into the ionospheric correction methods and the possible use of alternative pairs of observables.

ACKNOWLEDGMENTS

The authors wish to thank Dr. Timo Allison from Trimble Navigation Ltd. for his critical comments on the first draft of this paper. GeoSurv Inc., Ottawa, is also thanked for providing the airborne Trimble GPS data used in this paper.

REFERENCES

- Borge, T. and B. Forssell (1994): A New Real-time Ambiguity Resolution Strategy Based on Polynomial Identification. Proceedings of the International Symposium on Kinematic Systems in Geodesy, Geomatics and Navigation, Banff, Canada, August 1994.
- Hatch, R. (1991): Instantaneous Ambiguity Resolution. Proceedings of Kinematic System in Geodesy, Surveying and Remote Sensing, IAG Symposium No. 107, Banff, Canada, 299-308.
- Lachapelle, G., M.E. Cannon and g. Lu (1992): Ambiguity Resolution On-the-Fly - A comparison of P-code and High Performance C/A Code Receiver Technologies. Proceedings of ION GPS-92, The Institute of Navigation, Alexandria, VA, pp. 1025-1032.
- Martin-Neira, M., R. Lucas, J. Legido (1993): The Null Space Method for GPS Ambiguity Resolution. Paper distributed by the European Space Agency -ESTEC, G.M.V. Madrid, Spain
- Remondi, B. (1991): Kinematic GPS Results without Static Initialization. NOAA Technical Memorandum NOS NGS - 55, May 1991.
- Teunissen, P.J.G. (1994): The Invertable GPS Ambiguity Transformation. manuscript geodaetica, Vol. 19, No. 6, 1994.
- Yang, M., C. Goad and B. Schaffrin (1994): Real-time On-the-Fly Ambiguity Resolution over Short Baselines in the Presence of Anti-Spoofing. Proceedings of ION GPS-94 Seventh International Meetings, Salt Lake City, Sept. 1994.

Ambiguity Resolution Over Long Baselines for Airborne Differential GPS Positioning

J. G. Sonntag and C. F. Martin
EG&G Washington Analytical Services Center, Inc.

W. B. Krabill
NASA Goddard Space Flight Center

BIOGRAPHIES

J.G. Sonntag is a Senior Analyst at EG&G Washington Analytical Services Center, Inc., where he has been employed for two years. He currently supports NASA's Arctic Ice Mapping Project as a GPS analyst. He received his M.S. in Aerospace Engineering at the University of Texas at Austin in 1993.

C.F. Martin is a Principal Scientist at EG&G Washington Analytical Services Center, Inc. He currently supports the AIM project in the analysis of attitude errors of the Airborne Terrain Mapper as well as in GPS trajectory analysis and software development. Dr. Martin holds a Ph. D in Applied Physics from North Carolina State University.

W.B. Krabill is the Principal Investigator for the Arctic Ice Mapping Project at NASA's Goddard Space Flight Center / Wallops Flight Facility. He is currently Principal Investigator for the AIM Project at NASA's Wallops Flight Facility. Mr. Krabill has a B.S. degree in Mathematics from Salisbury State University.

ABSTRACT

A technique has been developed for reliably resolving GPS carrier phase ambiguities over long baselines in an airborne kinematic application. The technique has been used to compute aircraft trajectories accurate to the sub-decimeter level in support of NASA's Arctic Ice Mapping (AIM) Program. A total of 25 missions from the 1993 and 1994 field seasons, as well as several missions from the 1995 field season, have been successfully processed using this method. During these missions, the aircraft routinely flew 1000 km or more from the fixed reference receiver, although it began and ended the missions within 2-3 km of it. The long baselines and prolonged duration of the missions, often seven hours or more of flying time, complicated the ambiguity resolution problem in two key ways. First, L1 and L2 ambiguities had to be resolved for satellites tracked solely in-flight using ionosphere-free dual frequency data. Second, since no single satellite could be tracked for the entire duration of the long missions, it was necessary to reconcile the otherwise independent pre- and post-flight ambiguity solutions using the

overlap provided by the in-flight data. To deal with these complications, the technique utilizes a combination of information from pre-flight static solutions, in-flight ambiguity and trajectory estimation, and post-flight static solutions in order to determine a consistent set of integer ambiguities for the entire mission. Dual-frequency carrier phase measurements are supplemented with dual-frequency pseudoranges in order to resolve the ambiguities of the satellites tracked only in flight, as well as to reconcile and merge the pre- and post-flight solutions with each other and with the in-flight solution.

INTRODUCTION

In the summer of 1993, NASA's Mission to Planet Earth Program began a series of annual campaigns aimed at studying the time-varying topography of the world's Arctic ice sheets. Now known as the Arctic Ice Mapping, or AIM, Project, this initiative utilizes an extremely accurate and productive airborne surveying system to sample the surface topography of the ice sheets with an absolute accuracy of 10 centimeters or better. By repeating these airborne surveys over a period of several years, NASA expects to produce an extensive data set from which scientists can extract geophysical signals from the changing topography of the ice sheets. Such information should enable global climate change researchers to gain a better understanding of the nature of global climate changes, and of how the world's polar ice masses both affect, and are affected by, such changes. Since 1993, 34 missions with flight lines totaling over 50,000 kilometers have been flown over Greenland and the ice sheets of northern Canada. Figure 1 shows these flight lines.

The airborne surveying system used in the AIM Project consists of a NASA P-3B Orion aircraft, a number of remote sensors carried on board the aircraft, and a GPS system which provides post-flight positioning for the aircraft, as well as real-time navigation and precise timing for the remote sensing equipment. The primary remote sensing instrument carried on the P-3 is the Airborne Terrain Mapper (ATM), a scanning laser altimeter whose predecessor was the Airborne Oceanographic Lidar, or AOL. In typical Arctic operations, the ATM takes 2000 range measurements every second, while scanning an oval-shaped pattern 135 meters wide directly

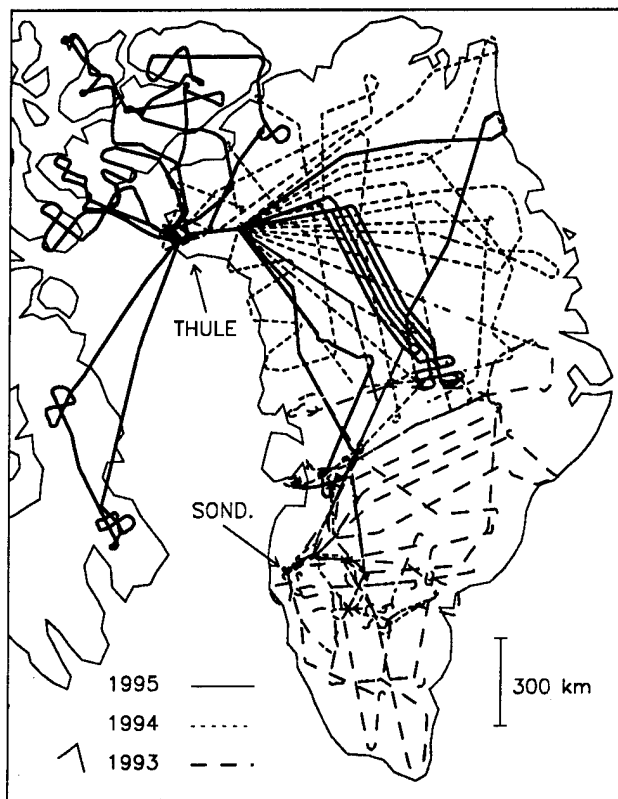


Figure 1. Flight lines of ice-mapping missions conducted over Greenland and northern Canada in 1993, 1994 and 1995.

under the aircraft's flight path 10 times each second. The aircraft also carries a profiling laser altimeter and a radar depth sounder capable of measuring the thickness of the ice sheet. More information about the AIM Project may be found in Refs. [6] and [7], and on the World-Wide-Web at <http://aol16.wff.nasa.gov/>.

If the trajectory of the aircraft is known with sufficient accuracy, it can be merged with the laser altimetry data and with knowledge of the aircraft's orientation (provided by an inertial navigation system) to assign a latitude, longitude and altitude to each laser range measurement. The problem, then, is to compute the position of the aircraft throughout each flight with an accuracy of 10 centimeters or better.

Well-known kinematic differential GPS techniques are capable of positioning a moving vehicle with this level of accuracy, provided the integer cycle ambiguities in the carrier phase measurements can be resolved. Most of the relevant work in this field, however, has been concerned with positioning a moving receiver within a few tens of kilometers of a fixed reference receiver, where single-frequency code and carrier measurements are useful (Refs. [4], [5], [8] and [9]). Since the AIM Project aircraft begins and ends its ice mapping missions at the air base and within a few hundred meters of the

fixed reference receivers, these techniques can be, and are, applied to parts of the missions. However, the aircraft spends most of each mission hundreds of kilometers away from the base, where dual-frequency observations are required to remove ionospheric effects and the established single-frequency techniques for resolving cycle ambiguities do not apply. Furthermore, the long duration of the ice mapping missions, usually 6-8 hours, means that no single satellite can be tracked throughout most missions. This introduces complications in obtaining a consistent set of cycle ambiguities across the entire mission, which is required to take full advantage of the short-baseline solutions at the beginning and end.

This paper documents the approach developed for the AIM Project to overcome these difficulties and compute decimeter-level trajectories for long duration, long baseline flights using dual-frequency kinematic GPS techniques. First, the overall configuration of the ice mapping missions is described, in relation to the operation of the GPS receivers and analysis of the data. Next, the methods by which carrier phase cycle ambiguities are resolved for each phase of the missions is described. After this, the method used to combine the ambiguity information from each mission phase into a consistent set of integer L1 and L2 ambiguities for an entire mission is presented. This is followed by experimental results from analyses of several missions which validate certain assumptions made about the ability to identify integer ambiguities in the data. A comparison of two trajectories computed from different data sets for the same mission is also given, which verifies the repeatability of the ambiguity resolution method.

MISSION CONFIGURATION

Since the scientific value of each ice mapping flight is dependent on the availability and quality of the precise GPS trajectory, the missions are designed with the requirements of the positioning system in mind. During the missions, survey-grade GPS receivers are operated at a sampling rate of 2 Hz, both aboard the aircraft and at a fixed site near the airfield where the P-3 is based. The simultaneous operation of the receivers on the aircraft and on the ground allows the data to be processed with a double-differencing scheme. A real-time precise trajectory is not required, so the data is simply logged by each receiver and no data link between the aircraft and the fixed site is needed. The twice-per-second sampling frequency is chosen to minimize errors introduced when the position of the aircraft is interpolated between points in the precise trajectory, which are computed only for the times at which the receivers record raw observations.

For redundancy, at least two receivers are operated at the fixed site during each mission. These receivers are connected to

survey-type antennas which are not moved at any time during the deployment to that base. While missions are not being flown, these receivers record data once every 30 seconds. This data is eventually used to compute the position of the fixed site relative to the GPS Global Tracking Network, which in turn ties the aircraft trajectories and ice topography to the International Terrestrial Reference Frame.

Aboard the P-3 aircraft, at least three receivers are operated during each flight. These receivers are connected to avionics-style antennas mounted at the top of the fuselage near the aircraft's center of gravity. During the flights, the pilots are asked to keep the aircraft's roll angle less than 10 degrees at all times, in order to avoid problems with satellite tracking associated with satellites falling below the horizon of the antennas.

The primary receiver type used in the project is the Ashtech P-12 (1993) and Z-12 (1994 and after). Both are 12-channel survey grade receivers, and the Z-12 is capable of tracking dual-frequency code and carrier signals in the presence of Anti-Spoofing (A/S). Eight-channel Turbo-Rogue receivers were also operated in 1993 and 1994 as backup equipment.

After the missions are completed, the raw receiver data is translated into Rinx format and analyzed for cycle slips and other data problems. The most trouble-free data sets from the fixed site and from the aircraft are then selected to be used in computing the precise trajectory, and this data is carefully edited. In practice, it is usually necessary to examine observation residuals in order to completely correct all data problems. This makes the data editing and trajectory computation process iterative in nature. The ambiguity resolution procedure described below, however, can achieve its best reliability and accuracy only when all cycle slips are repaired and most other data problems have been corrected.

The computation of the precise trajectory, along with the ambiguity resolution process, is done using the dual-frequency carrier phase data in a purely geometric, double-differencing approach. Pseudorange data is used only to help resolve the cycle ambiguities, as discussed below. Precise orbits for the GPS satellites provided by JPL are used in the analysis. Meteorological data recorded at the reference site and on board the aircraft are used to correct for tropospheric delays using a modified Hopfield model.

AMBIGUITIES AND BIASES

The pseudorange and carrier phase observables are modeled as shown in Equations (1a) through (1d). For the purposes of this discussion, the effects of multipath and noise are neglected.

$$P_1 = P + kf_1^2 \quad (1a)$$

$$P_2 = P + kf_2^2 \quad (1b)$$

$$L_1 = P - kf_1^2 + \lambda_1 n_1 \quad (1c)$$

$$L_2 = P - kf_2^2 + \lambda_2 n_2 \quad (1d)$$

In these equations, P_1 and P_2 are the measured pseudoranges and L_1 and L_2 are the measured carrier phases (converted to range units by multiplying by the appropriate wavelength). P is the non-dispersive delay, which includes geometric delay, tropospheric delay, clock errors, and any other effects which influence all the observables equally. The parameter k is an ionospheric delay multiplier (proportional to the integrated electron density along the signal path), f_1 and f_2 are the two carrier signal frequencies, λ_1 and λ_2 are the corresponding wavelengths, and n_1 and n_2 are the undifferenced integer cycle ambiguities. The quantities $\lambda_1 n_1$ and $\lambda_2 n_2$ are referred to as the undifferenced L1 and L2 biases.

When a double-differencing scheme is used over short baselines, the quantity k is nearly the same for each leg of the difference, and the ionosphere term cancels. Over longer baselines, k differs significantly between legs and must be removed from the formulation using a linear combination of the L_1 and L_2 observables given by

$$P = k_1 L_1 - k_2 L_2 - k_1 \lambda_1 n_1 + k_2 \lambda_2 n_2 \quad (2)$$

where the constants k_1 and k_2 are defined as

$$k_1 = f_1^2 / (f_1^2 - f_2^2) \quad (2a)$$

$$k_2 = f_2^2 / (f_1^2 - f_2^2) \quad (2b)$$

The first two terms on the right-hand side of (2) are collectively referred to as the L3 observable, while the last two terms together are known as the L3 bias, or b_3 . The L3 bias is a constant for a satellite-receiver pair over one complete pass, as long as all cycle slips are removed. Equation (2) can be rewritten as the sum of the L3 observable and bias,

$$P = L_3 + b_3 \quad (3)$$

A single-difference observable may now be formed between two receivers. In the following development, subscripts 1 and 2 refer to different receivers, and superscripts A and B refer to different satellites. A single difference for satellite A between receivers 1 and 2 is given by

$$SD_{12}^A = L_{31}^A - L_{32}^A = P_{11}^A - P_{12}^A - b_{31}^A + b_{32}^A \quad (4)$$

When the two biases are combined to form a single-difference L3 bias, (4) may be rewritten as

$$SD_{12}^A = P_{11}^A - P_{12}^A + b_{312}^A \quad (5)$$

When another single-difference is formed between receivers

1 and 2 and satellite B, and the result is differenced from (5), the double-difference is obtained.

$$DD_{12}^{AB} = P_{11}^A - P_{12}^A - P_{11}^B + P_{12}^B + b_{312}^A - b_{312}^B \quad (6)$$

Equation (6) is the fundamental relationship used for computing the trajectories of the AIM Project aircraft. The two single-difference biases in (6) are not separable, and only their difference can be estimated along with the receiver position. However, if one of the single-difference L3 biases is held fixed at some arbitrary value, the other bias can be estimated. Since only the difference in the biases appears in the observation relation, this approach is equivalent to estimating the double-difference bias.

The single-difference biases are linear combinations of the single-difference ambiguities. Using Equations (2) through (5) for satellite A,

$$b_{312}^A = -k_1 \lambda_1 n_{112}^A + k_2 \lambda_2 n_{212}^A \quad (7)$$

where n_{112}^A and n_{212}^A are the single-difference L1 and L2 ambiguities. If the integer values of these ambiguities can be found, the bias terms are known exactly. When dual-frequency phase data is used, only the real-valued biases can be estimated simultaneously with the aircraft's trajectory. The integer L1 and L2 ambiguities can be resolved by combining the estimated biases with information from the dual-frequency pseudoranges. Ideally, the pseudoranges would be combined with the phase data to resolve the L1 and L2 ambiguities directly, without the estimated L3 biases. In practice, however, only the difference between the L1 and L2 ambiguities can be resolved with sufficient accuracy (about 1 cycle) to be useful for ambiguity resolution. The difference between the L1 and L2 ambiguities is known as the widelane ambiguity, or n_{wl} . The widelane formulation removes all geometry as well as the effects of the ionosphere, and therefore is unaffected by baseline length (Refs. [1] and [2]).

From Eqns. (1a)-(1d), the undifferenced widelane ambiguity is given by

$$n_{wl} = L_1/\lambda_1 - L_2/\lambda_2 + k_3(P_1/\lambda_1 + P_2/\lambda_2) \quad (8)$$

where

$$n_{wl} = n_1 - n_2 \quad (8a)$$

$$k_3 = (f_2 - f_1)/(f_1 + f_2) \quad (8b)$$

The widelane ambiguity can be computed for each satellite-receiver pair at every time point when the receiver tracks the satellite. Single-difference widelane ambiguities can also be computed by differencing these quantities.

$$n_{wl12}^A = n_{112}^A - n_{212}^A \quad (9)$$

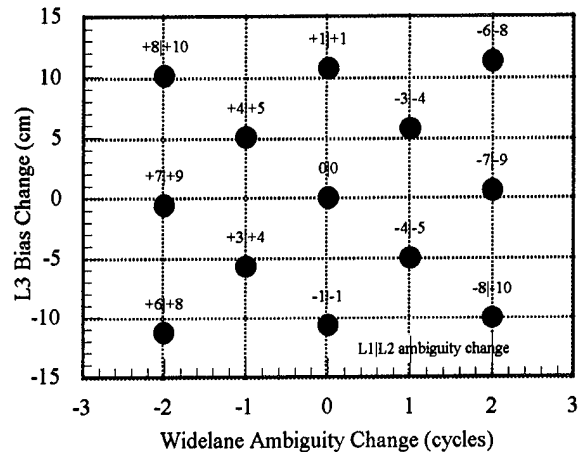


Figure 2. Relationship between widelane ambiguities, L3 biases, and integer L1 and L2 ambiguities.

If the single-difference L3 bias for each satellite is known from a simultaneously trajectory and bias solution, and the single-difference widelane ambiguities are known from some application of Equation (8), Equations (7) and (9) together yield two equations in two unknowns for each satellite, which can be readily solved for the single-difference L1 and L2 ambiguities. The difficulty lies in computing the L3 biases and widelane ambiguities with sufficient accuracy so that the integer L1 and L2 ambiguities can be identified.

For any given pair of L1 and L2 integer ambiguities, a corresponding widelane ambiguity and an L3 bias exist. Therefore it is possible to plot integer ambiguity pairs as discrete points in L3 bias / widelane space. This is shown in Figure 2. The center of the plot, the 0/0 point, represents the true pair of L1 and L2 ambiguities for a single-difference satellite pass. The plot shows all other ambiguity pairs which are nearby in L3 bias / widelane space. Given real-valued estimates of the L3 bias and widelane ambiguity for a satellite pass, it is necessary to reliably select the corresponding pair of integer L1 and L2 ambiguities. For this to be possible, the point representing the estimated widelane ambiguity and L3 bias must be closer to the 0/0 point on Figure 2 than to any nearby point. This condition will be satisfied if the L3 bias estimates are accurate to 2.5 cm or better and the widelane ambiguity estimates are accurate to 1 cycle or better, as can be seen by examining Figure 2.

MISSION PHASES

For the purposes of ambiguity resolution and trajectory computation, each ice-mapping mission is divided into three distinct phases. These are the pre-flight calibration, the in-flight phase, and the post-flight calibration. In order to take full advantage of the information present in each of these

phases, the three phases are processed sequentially. The overall strategy for resolving a consistent set of ambiguities for the entire mission is as follows. The kinematic solution is initialized by performing a static solution prior to takeoff. Then a dual-frequency kinematic solution is performed beginning at takeoff, starting with the known ambiguities from the pre-flight static solution. This kinematic solution yields estimates of L3 biases for each satellite tracked after takeoff, which are combined with estimates of the widelane ambiguities to produce preliminary L1 and L2 integer ambiguities. A post-flight static solution is then performed, and the additional information thus obtained is used to constrain the kinematic estimates of L3 biases and widelane ambiguities. This constrained solution improves the estimates of the L3 biases and widelane ambiguities, which allows the correct integer pair of L1 and L2 ambiguities for each satellite to be reliably selected.

Pre-Flight Calibration

Approximately one hour prior to the scheduled takeoff of every mission, the GPS receivers aboard the aircraft and at the reference site begin recording high-rate (2 Hz) data. The fact that the aircraft is stationary for about an hour at this time allows ample time for a static position solution between the fixed site and the aircraft. Since the aircraft is parked within a few hundred meters of the reference site at this time, ionospheric delay in the carrier phase measurements at both receivers are nearly identical, so independent, single-frequency L1 and L2 solutions can be performed. These independent static solutions yield the position of the aircraft's GPS antenna as well as the L1 and L2 integer cycle ambiguities for each satellite tracked by both receivers during this pre-cal period.

As pointed out in the previous section, single-difference biases (and ambiguities in the single-frequency solution) cannot be independently estimated using double-difference observations. In a solution involving several satellites tracked over many observation epochs, this means that if n satellites are tracked during a session, there are only $n-1$ independent single-difference biases. This problem is easily solved, at this point, by simply fixing one of the single-difference biases at an arbitrary value. The remaining biases are then independent and can be estimated along with the position of the receiver. They are also tied to the bias that was held fixed. The fact that the single-difference biases are known only relative to each other, and not in an absolute sense, becomes a significant issue later in the analysis when information from the post-flight calibration is included.

In-Flight Phase

Once the pre-cal is completed, a reliable set of integer L1 and L2 single-difference ambiguities is obtained for the satellites

tracked at the beginning of the mission. These ambiguities are used to compute single-difference L3 biases, which are held fixed while a dual-frequency, kinematic solution is performed for the entire mission, including the post-flight calibration period. For the early part of the mission, the known L3 biases from the pre-cal solution are used in the observation relationship, Equation (6). During the mission, however, the pre-cal satellites begin to set and new satellites are tracked by the receivers as they rise. However, there is considerable overlap in the tracking of the pre-cal satellites and the new satellites. Also, since seven or more satellites are typically being tracked at any one time at the high latitudes flown during AIM missions, more than enough redundancy exists to compute both the position of the aircraft and a preliminary estimate of the L3 bias for the new satellites. So each time a new satellite is acquired, its single-difference L3 bias is estimated by taking advantage of the redundancy in the observations, and this preliminary estimate is used for processing all subsequent observations from that satellite. If the mission is long enough, and most are, all of the pre-cal satellites eventually set and only satellites acquired in-flight remain in the solution.

Throughout the trajectory, normal equations are formed for solution of the aircraft's instantaneous position and for the L3 biases. While the position parameters are partitioned out at each time point, the normal equations for the biases are accumulated and solved at the end of the trajectory. This yields least-squares estimates of the L3 biases for each satellite. Again, the biases of the pre-cal satellites, which are known exactly, are held fixed in this adjustment.

After the L3 biases are computed, the single-difference widelane ambiguities for all of the satellites are estimated using the following procedure. At each time point, the undifferenced widelane ambiguities for each satellite tracked by each receiver are computed using Equation (8). For satellites which are tracked by both the aircraft and reference receivers, these ambiguities are differenced between the two receivers to form single-difference widelane ambiguities. Next, double differences are formed between satellites, and partial derivatives of these double-difference widelane ambiguities with respect to the single-difference widelane ambiguities are computed. The results are accumulated in normal equations, and after the entire mission has been processed in this way, single difference widelane ambiguities are estimated by holding at least one of them fixed to a predetermined value. This value is a widelane ambiguity from the pre-cal L1 and L2 ambiguity solutions - the difference between the L1 and L2 ambiguities for one of the pre-cal satellites. By holding at least one of the widelane ambiguities fixed to the pre-cal reference in this way, the estimated widelane ambiguities are tied to, and compatible with, the pre-cal solution. This is analogous to the situation for the L3 biases, where when n satellites are tracked during a mission,

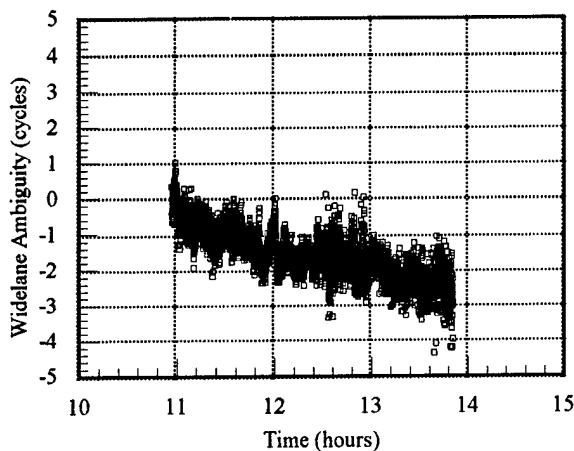


Figure 3. Undifferenced widelane ambiguities for SV29 tracked by mobile receiver P324 on 18 May 1995 (large integer removed).

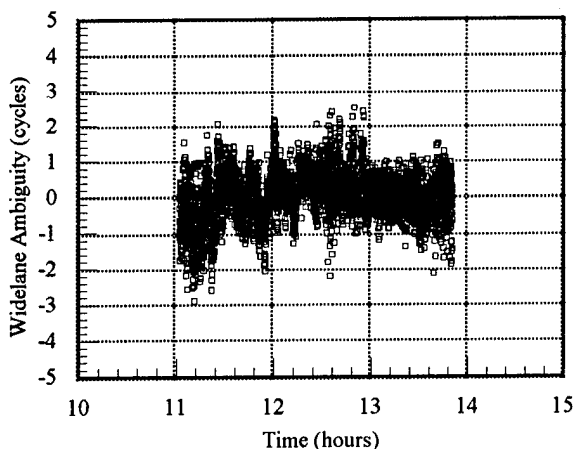


Figure 4. Widelane ambiguities differenced between SV29 and SV18 tracked by mobile receiver P324 on 18 May 1995 (large integer removed).

only $n-1$ of the single-difference L3 biases are independent. The same is true for the widelane ambiguities, since they were estimated from double-differenced data.

The reason the single-difference widelane-ambiguities were estimated from double-differences is illustrated in Figures 3 and 4. Figure 3 shows the time history of the undifferenced widelane ambiguity for a satellite-receiver pair. Although the widelane ambiguity is theoretically a constant, the figure shows a marked linear trend amounting to several cycles of change in the widelane ambiguity over the satellite's pass. With Ashtech data, this is not an unusual occurrence, particularly with mobile receiver data. Gourevitch [3] attributes such "drifts" to the filters used internally in the Ashtech receivers, and states that this is a common mode

effect and therefore should be eliminated by double-differencing. This appears to be the case, as Figure 4 illustrates. Figure 4 shows the difference in widelane ambiguities between the satellite shown in Figure 3 and another satellite tracked by the same receiver at about the same time. The trend which was apparent in the undifferenced widelane ambiguities is not present in the differenced ambiguities. In order for differencing to remove the effects of the trends in the estimated single-difference widelane ambiguities, the differencing must be done point-by-point. In other words, the data must first be differenced, then averaged, not the other way around, to completely remove the effects of these drifts. This is accomplished by estimating the single-difference widelane ambiguities from double-differenced data.

With single-difference L3 biases and widelane ambiguities estimated for each satellite tracked after the pre-cal, it is possible to select the pair of L1 and L2 ambiguities which is nearest the estimated values in L3 bias / widelane space for each satellite. Conceptually, this can be accomplished by plotting the estimated bias and widelane on a chart similar to the one shown in Figure 2, and selecting the integer ambiguity pair which is within 1 widelane cycle and 2.5 cm in L3 bias of the estimate. This can also be accomplished by the following procedure. For each satellite, the real-valued widelane estimate is rounded to the nearest integer. Using this integer widelane ambiguity and the estimated L3 bias, the system of two linear equations in two unknowns formed by Equations (7) and (9) is solved for real-valued L1 and L2 ambiguities n_1 and n_2 . These ambiguities are then rounded to the nearest integers.

This rounding process does not guarantee that the resulting pair of integer L1 and L2 ambiguities is the closest pair to the estimated L3 bias and widelane ambiguity. Since the widelane ambiguity was rounded prior to the solution of the simultaneous equations, the difference in the rounded L1 and L2 ambiguities is guaranteed to be within 0.5 cycles of the widelane estimate. However, the L3 bias corresponding to the integerized ambiguities can be as far as 10.7 cm away from the L3 bias estimate, which can be seen by using Equation (7) with a maximum change due to rounding in both n_1 and n_2 of 0.5 cycles. Therefore it is possible to search a limited number of ambiguity pairs which are near the integerized pair for the unique ambiguity pair which corresponds to an L3 bias within 2.5 cm of the estimate and a widelane ambiguity within 1 cycle of its estimate. Counting the original integerized ambiguities, Figure 2 shows that seven ambiguity pairs exist which are within these maximum limits of ± 1 widelane cycle and ± 10.7 cm in L3 bias. In terms of changes to L1/L2 ambiguities, these are $+1/+1$, $+4/+5$, $-3/-4$, $0/0$, $+3/+4$, $-4/-5$, and $-1/-1$. By searching through the seven pairs of ambiguities obtained by perturbing the original integerized numbers obtained from Equations (7) and (9) by these pairs and computing the resulting L3 bias and widelane ambiguity,

one (and only one) ambiguity pair will be found for which the corresponding L3 bias and widelane ambiguity agree with the estimated values to 2.5 cm and 1 cycle, respectively. This pair is selected as the best estimate of the ambiguities for one satellite obtained up to this point. However, the estimates of the widelane ambiguities and particularly the L3 biases may not be sufficiently accurate at this point to correctly resolve the ambiguities for all the satellites. The estimates can be improved, however, by taking advantage of the post-flight static solution, and these improved estimates will be accurate enough to correctly resolve the ambiguities.

Post-Flight Calibration

When the aircraft lands and taxis to a stop after each mission, the receivers aboard the aircraft and at the reference site continue to record data for about one more hour. This period is known as the post-flight calibration, or post-cal. As in the case of the pre-cal, the observation data recorded during the post-cal is used in independent L1 and L2 static solutions. These solutions provide the position of the aircraft as well as the integer L1 and L2 ambiguities for the satellites tracked during the post-cal. As in the pre-cal, only $n-1$ of n single-difference ambiguities of satellites tracked during the post-cal are independent, so the ambiguities for one satellite are arbitrary. If the mission is very short, one of the pre-cal satellites may still be present during the post-cal. If this is the case, this satellite's ambiguities are fixed to their pre-cal values for the post-cal solution. Otherwise, any post-cal satellite is selected, and its ambiguities are fixed to the ambiguities obtained from the L3 bias / widelane solution.

COMBINED AMBIGUITY RESOLUTION

Three distinct sets of single-difference, L1 and L2 integer ambiguities have been obtained up to this point. The ambiguities for the satellites tracked during pre-cal are known exactly from the independent L1 and L2 static solutions. Since these are single-difference ambiguities they are actually known only relative to each other, but by simply holding one of them fixed an absolute reference is established for all the satellites tracked during the mission. Ambiguities for the satellites tracked only in-flight have also been computed, but these ambiguities are subject to possible inaccuracies in the estimation of the L3 biases and widelane ambiguities, which can be reduced by taking advantage of the post-cal solution. The post-cal ambiguities are known exactly, relative to each other. If one of the post-cal satellites was tracked during the same pass in the pre-cal, the post-cal ambiguities are also known exactly relative to the pre-cal ambiguities, since they are tied to the same absolute reference. For most missions, though, the post-cal ambiguities are tied to the ambiguities of the satellites tracked only in-flight, and so, as a group, are subject to the same errors as the in-flight ambiguities.

The trajectory / bias solution, as well as the widelane ambiguity solution, can be constrained in a way that takes advantage of what is known about the three sets of ambiguities. These constrained solutions will then produce estimates of the L3 biases and widelane ambiguities which are sufficiently accurate to allow integer L1 and L2 ambiguities to be reliably resolved. To accomplish this, the trajectory solution is re-run using the L3 biases obtained from the known pre-cal ambiguities, the estimated in-flight ambiguities, and the known but potentially offset post-cal ambiguities as starting values. The biases of the pre-cal satellites are held fixed, the biases of the satellites tracked only in-flight are adjusted independently, and the biases of the post-cal satellites are held fixed relative to each other and adjusted as a group. An analogous set of starting values and constraints is used for the widelane ambiguity estimation. These two constrained solutions yield real-valued adjustments to the L3 biases and widelane ambiguities for each satellite tracked in-flight and the group of post-cal satellites. These real-valued adjustments are interpreted in terms of integer L1 and L2 ambiguity adjustments in exactly the same way as was done for the in-flight kinematic solution earlier. If the L3 bias and widelane ambiguity adjustments using this full set of constraints are accurate to 2.5 cm and 1 cycle respectively, the L1 and L2 ambiguities resolved using this method are correct. The next section will show that for a sample of several AIM Project missions, this is indeed the case.

OPERATIONAL RESULTS

It remains to be shown that actual mission data can be used to reliably resolve the cycle ambiguities. First it must be shown that the widelane ambiguities for the satellites tracked in-flight can be estimated, using the pseudorange data, with an accuracy of ± 1 cycle or better. In addition, the L3 bias estimates for these satellites must be shown to be accurate to 2.5 cm or better. It must also be demonstrated that the addition of the post-cal information improves the accuracy of the estimates and reliably identifies the correct pair of integer L1 and L2 ambiguities for each satellite. Four separate ambiguity solutions for three ice-mapping missions from the 1995 field season are included in the results presented below, providing a large and diverse data set which shows that correct L1 and L2 ambiguities can be reliably chosen. Finally, since two independent data sets were available for one of these missions, the two trajectories for this mission can be directly compared, yielding further evidence that the ambiguity resolution method is repeatable.

Widelane Ambiguity Assessment

The quality of the single-difference widelane ambiguities may be assessed directly by comparing the estimates from the

pseudorange data with the difference between the L1 and L2 ambiguities for the post-cal satellites. The post-cal ambiguities are exactly known integers, so their difference provides a truth to which the pseudorange estimates can be compared. Such a comparison is shown in Figure 5. This comparison includes every post-cal satellite from the four data sets processed from the 1995 season. The figure shows that for every post-cal satellite from these four missions, the estimated widelane ambiguities are within 1 cycle of the known values.

From this, it can be inferred that the widelane estimates for the satellites tracked only in-flight are also accurate to the 1 cycle level. Since the widelane formulation is independent of geometry and non-dispersive delay, the fact that the widelane estimates were estimated in part from data taken over a short baseline with the aircraft sitting still should provide no advantage. Thus the widelane estimates for the satellites tracked in-flight should be accurate to the same level as those shown in Figure 5.

L3 Bias Assessment

The accuracy of the L3 biases estimated from the kinematic solution may also be assessed by a comparison with the biases obtained from the known post-cal ambiguities. Unlike the widelane estimates, however, the L3 bias estimates could potentially benefit from data taken over short baselines after the aircraft has landed. Satellite orbit error and poorly-modeled tropospheric delay could degrade the L3 bias estimates made using long-baseline data, where estimates made on short baselines would minimize these effects. For this reason, the comparison was made by running the kinematic solutions from takeoff up to the time that the aircraft approaches the airfield near the end of its missions. Thus,

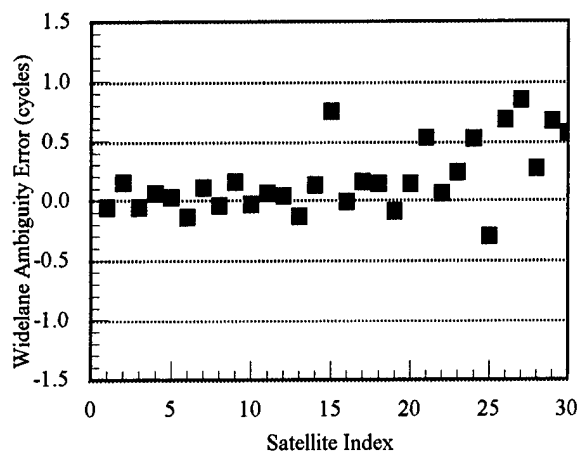


Figure 5. Difference between estimated widelane ambiguities and widelane obtained from post-cal solution, for all post-cal satellites tracked during four 1995 missions.

these L3 bias estimates for the post-cal satellites use mostly long-baseline data, as do the estimates for the satellites tracked only in-flight.

In fact, the quality of these estimates should be pessimistic, compared to the final estimates used to resolve the ambiguities for satellites tracked in-flight. The L3 bias estimates for these satellites benefit from having the full span of data from the satellites' entire pass, while the estimates for this post-cal comparison use artificially shortened data spans. The final bias estimates for the in-flight satellites also benefit from the constraints applied to the post-cal biases, while the estimates made for this comparison do not.

The comparison is presented in Figure 6, which shows the differences between the estimated L3 biases and the known biases obtained from the post-cal ambiguities. Again, all of the post-cal satellites for the four 1995 data sets are shown. The figure shows that all of the bias estimates are accurate to 2.5 cm, although some of them approach that limit.

Integer Ambiguity Identification Assessment

The widelane and L3 bias assessments showed that for the four missions from 1995, all of the widelane ambiguities tested were accurate to ± 1 cycle and all of the L3 biases were accurate to ± 2.5 cm. However, the fact that some of the estimates were close to these limits suggests that it might still be possible to occasionally select an incorrect pair of integer ambiguities which is near the correct pair in L3 bias / widelane space. The post-cal information was not taken advantage of in the accuracy assessments presented above, though, and this additional information significantly improves the accuracy of the L3 bias estimates, and to a lesser extent the widelane estimates, when incorporated into the solution.

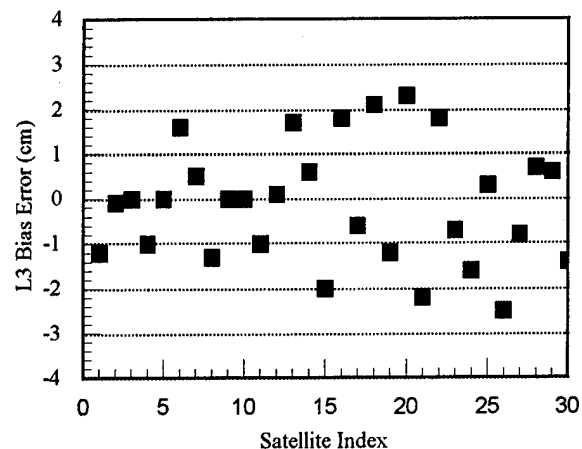


Figure 6. Difference between estimated L3 biases and biases obtained from post-cal solution, for all post-cal satellites tracked during four 1995 missions.

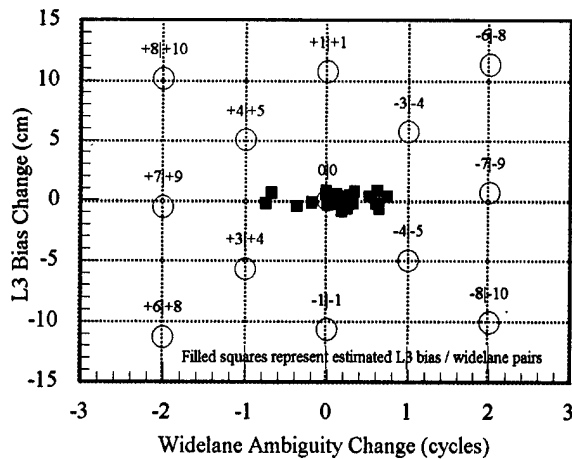


Figure 7. Differences between resolved ambiguities and constrained L3 bias and widelane estimates for all satellites from four 1995 missions.

This is shown in Figure 7. For each satellite tracked in-flight, and for the group of post-cal satellites for each of four missions from the 1995 season, the differences between the real-valued bias and widelane estimates and the corresponding values from the resolved ambiguities are plotted in L3 bias / widelane space. The plot shows that in every case, the L3 biases fell very much closer to the bias corresponding to one ambiguity pair than to those corresponding to nearby pairs. The widelane estimates show more scatter, although most are still close enough to clearly identify one ambiguity pair. The figure suggests that the most likely mistake to be made in integer ambiguity selection would be to choose a pair which is incorrect by ± 7 L1 cycles and ± 9 L2 cycles, due to the uncertainty in some of the widelane estimates. Even if this mistake is made, however, the resulting L3 bias, which is the only quantity that matters for the trajectory computation, can only be incorrect by 6 millimeters. With a PDOP of 4, which is the average PDOP for the AIM missions, an L3 bias error of 6 mm would cause a trajectory error of less than 2.5 cm. While this would be undesirable, it could be tolerated occasionally since the trajectories are only expected to be accurate to 10 cm.

Trajectory Repeatability

Since multiple receivers with different firmware versions were connected to common antennas aboard the aircraft and at the fixed site during the 1995 season, it was possible to compute two trajectories independently, one using the data from the version 1E00 receivers and the other using the 1E24 data. As long as the ambiguities for both trajectories are correctly resolved, the only difference between the two trajectories is due to receiver noise. Since the receivers share antennas, effects such as multipath, media delays, orbit error and

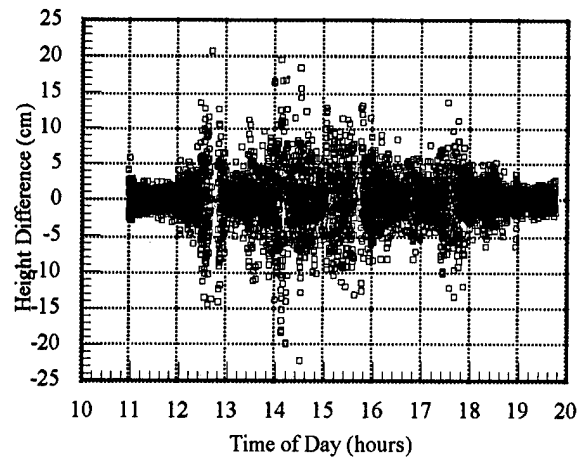


Figure 8. Trajectory height differences between 1E24 and 1E00 solutions for 18 May 1995 mission.

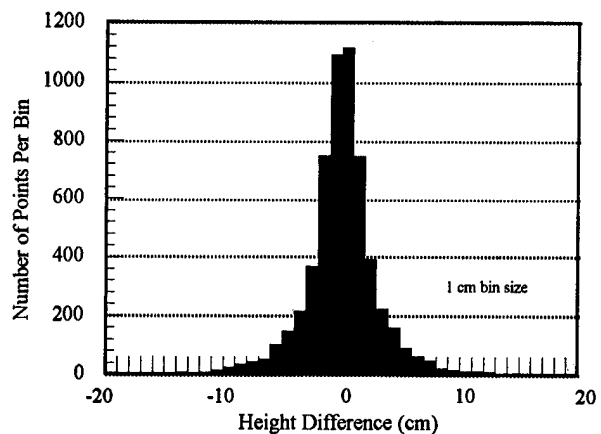


Figure 9. Distribution of trajectory height differences for the 18 May 1995 comparison.

Selective Availability are common to the two trajectory solutions. Receiver clock error is almost entirely canceled through double-differencing. Thus, a direct comparison of two trajectories computed in this way is an optimistic assessment of absolute accuracy, but is a very good indicator of the repeatability of the ambiguity resolution method.

The differences in geodetic height between the two trajectories computed for the 18 May 1995 mission are shown in Figure 8. Figure 9 illustrates the distribution of the differences. Figure 8 shows that the height differences are noise-like, with no apparent systematic characteristics, which would be expected if one of the trajectories had an incorrectly determined ambiguity. Figure 9 shows that 99% of the trajectory points agree to within 10 cm in height, and 95% agree to within 5 cm. The largest excursions in the height differences correlate very well with ionospheric disturbances which one or more of the receivers had problems tracking

through. For this mission, then, the ambiguity resolution technique produced repeatable results.

CONCLUSION

This technique provides a way to reliably determine integer L1 and L2 ambiguities using dual-frequency carrier phase and pseudorange data for long baseline kinematic applications. The ambiguities for the first part of the mission are determined from pre-flight L1 and L2 static short-baseline solutions, while the ambiguities for the satellites tracked in-flight are determined using redundancy of observations and dual-frequency pseudorange data. Static L1 and L2 solutions using data recorded after landing is used to improve the ambiguity solution for the satellites tracked in-flight. The method has been successfully applied to missions from three field seasons, yielding trajectories accurate to the 10 cm level.

Integer ambiguities are correctly resolved when the estimates of the L3 biases are accurate to 2.5 cm and the estimates of the widelane ambiguities are accurate to one cycle. These accuracies are readily achievable with Ashtech Z-12 receivers under normal conditions, particularly once the post-cal constraints have been applied. However, the phase data must be free of cycle slips, and both phase and code data should be free of large outliers for the method to correctly identify integer ambiguities. In practice, cycle slips are often difficult to identify and correct properly without examining residuals, so some iteration between data editing and trajectory computation is usually required before all data problems can be corrected and the ambiguities successfully resolved.

ACKNOWLEDGMENTS

This work was supported by NASA contract NASS-32169. The authors would like to thank Serdar Manizade for providing one of the illustrations in this paper.

REFERENCES

- [1] Blewitt, G., An Automatic Editing Algorithm for GPS Data, *Geophysical Research Letters*, Vol. 15, No. 3, 1990, pp. 199-202.
- [2] Blewitt, G., Carrier Phase Ambiguity Resolution for the Global Positioning System Applied to Geodetic Baselines up to 2000 km, *Journal of Geophysical Research*, Vol. 94, No. B8, pp. 10,187-10,203, 1989
- [3] Gourevitch, S., Implications of "Z" Technology for Civilian Positioning, *ION GPS-94 Proceedings*, 1994.
- [4] Krabill, W.B., C.L. Lennon, and E.B. Frederick, GPS Differential Carrier Phase Applications to the Space Shuttle Landing System, *Proceedings of the 5th International Symposium on Satellite Positioning*, Las Cruces, N.M., New Mexico State University, 660-667, 1989.
- [5] Krabill, W.B., and Martin, C.F., Aircraft Positioning Using Global Positioning System Carrier Phase Data, *Navigation: Journal of the Institute of Navigation*, Vol. 34, No. 1, Spring 1987.
- [6] Krabill, W.B., R.H. Thomas, K. Jezek, K. Kuivinen, and S. Manizade, Greenland Ice Sheet Thickness Changes Measured by Laser Altimetry, *Geophysical Research Letters*, (in press).
- [7] Krabill, W.B., R.H. Thomas, C.F. Martin, R.N. Swift, and E.B. Frederick, Accuracy of Airborne Laser Altimetry over the Greenland Ice Sheet, *International Journal of Remote Sensing*, (in press).
- [8] Mader, G.L., Ambiguity Function Techniques for GPS Phase Initialization and Kinematic Solutions, *Proceedings of the Second International Symposium on Precise Positioning with the Global Positioning System*, 1990.
- [9] Remondi, B.W., Kinematic and Pseudo-Kinematic GPS, *Proceedings of the Satellite Division's International Technical Meeting*, Institute of Navigation, Colorado Springs, CO., September 19-23, 115-121, 1988.

Adaptive Modeling of Receiver Clock for Meter-Level DGPS Vertical Positioning*

P. Misra, M. Pratt, B. Burke, and R. Ferranti
Massachusetts Institute of Technology

ABSTRACT

A significant improvement in the quality of GPS-derived vertical position estimates has been demonstrated with an approach requiring predictable behavior from the receiver clock. The approach is based on a structure inherent in the GPS measurements: errors in the estimates of vertical position and clock bias obtained from a snapshot of pseudorange measurements are highly correlated. This correlation allows us to compute improved vertical position estimates, and provides a basis for integrity monitoring. The practicality of this approach currently rests on our ability to model the receiver clock behavior accurately using the past GPS measurements.

Results are presented on receiver clock modeling from laboratory and field tests for a range of commercial products. Several oven-controlled crystal oscillators and rubidium oscillators have been found to offer the requisite stability, and have provided superior vertical position estimates in field trials, including flight tests. Clock-aided navigation cuts the rms vertical position error by a third to a half, and provides vertical position estimates of a quality comparable with that of the horizontal estimates.

1. INTRODUCTION

It is widely believed that GPS provides better accuracy horizontally than vertically. Reports on experiences with GPS and differential GPS have invariably confirmed this view. The GPS performance specifications, according to which 95% of the time the horizontal error in a user's

position shall not exceed 100 m and vertical error shall not exceed 156 m, also implicitly support this view. According to an intuitive argument, the horizontal accuracy is better because the satellites are on all sides of a user; the vertical accuracy is poorer because the satellites are all above the user, and none below. Fortunately, the argument is specious, and the premise false.

As is well known, clocks are at the heart of satellite navigation. While the satellites carry very precise and ultra stable clocks costing several tens of thousands of dollars, most users can get by with an inexpensive clock (\$50-200) in their receivers. This benefit, however, has a price: there is an additional unknown, namely, instantaneous receiver clock bias relative to the GPS time, the estimation of which requires an additional satellite measurement. This approach, which we refer to as 4-D estimation, actually makes satellite navigation practical. We explore below the penalty paid for this fourth unknown in terms of positioning accuracy, and propose a practical scheme to minimize the loss.

The proposed approach, called clock-aided navigation, is based on the following premise [1]. When navigating with GPS, in general a user wouldn't know what his position would be in, say, one, five, or fifteen minutes in the future, but the receiver clock bias can be predictable. How well and how far ahead such clock behavior can be predicted depends upon the stability characteristics of the clock. Insofar as the clock behavior is to be 'learned' from the past GPS measurements, the quality of the prediction would also depend upon the quality of the measurements. The basic idea is to take advantage of the verifiable stability characteristics of a receiver clock. As shown below, this approach effectively restores a

* This work is sponsored by the Federal Aviation Administration. Opinions, interpretations, conclusions, and recommendations are those of the authors and are not necessarily endorsed by the FAA.

degree of freedom to position estimation, with significant gain in vertical accuracy.

The previous work on exploiting the receiver clock stability for navigation and receiver autonomous integrity monitoring (RAIM) [2-5] has dealt with 'clock coasting' over relatively short periods while the satellite coverage is sparse, or satellite geometry poor. If the number of satellites in view falls to three, the only way to continue navigation is to skip estimation of the clock bias. In the schemes proposed, the clock bias is held fixed at the last estimated value [5], or propagated using the values of the clock model parameters estimated before the period of poor coverage began [4]. As the satellite coverage and geometry improve, the receiver returns to 4-D estimation mode. We propose instead to take advantage of the estimated clock stability characteristics regularly and continuously to improve the navigation and RAIM performance.

In the next section, we discuss GPS positioning with a perfect receiver clock. A perfect clock being impractical, the focus is on the potential for improving the quality of the position estimates by using a 'right clock' and by using a 'clock right'. In Section 3, the issue is reexamined in terms of correlations observed among of the 4-D estimates obtained from GPS measurements. The results of Sections 2 and 3 are used to define an approach to navigation in Sections 4 and 5 based on clock aiding. The approach consists of verifying in real-time the clock stability characteristics, exploiting them to improve the position estimate, and obtaining a measure of the quality of this estimate.

2. NAVIGATION WITH A PERFECT CLOCK

Given a snapshot of n GPS pseudorange measurements ($n \geq 4$), we can estimate the three coordinates of user position (x, y, z), and the instantaneous receiver clock bias (b). We referred earlier to this approach as 4-D estimation. On the other hand, if the receiver clock were known to be perfectly stable, and its bias relative to the GPS system time known precisely, GPS-based navigation can proceed by estimating only the position coordinates (x, y, z). This special case will be referred to as one of 3-D estimation. We know *a priori* that

having one fewer parameter to estimate from the measurements should improve the quality of the remaining estimates. The question is: by how much? The perfect clock is, clearly, hypothetical, but the idealization offers an upper bound on the performance which may be achievable with practical clocks.

We examine first the quality of the position estimates in the two cases (i. e., with and without a perfect clock, or 3-D versus 4-D estimation) at an rms level. The idea is to base the comparison on the following well-known relationship [6]:

$$\text{rms position error} = \sigma_{\text{URE}} \cdot \text{DOP},$$

where σ_{URE} is the rms value of the error in the user's range measurements (user range error, or URE), and DOP is a characterization of satellite geometry. Since URE is the same in both 4-D and 3-D estimations, we need only compare the distributions of the DOP parameters in the two cases. The definitions of HDOP and VDOP in terms of the observation matrix ($4 \times n$) for the linearized problem of 4-D estimation are well known [6]. For 3-D estimation, these parameters are redefined appropriately on the basis of the revised observation matrix ($3 \times n$) so that the relationship above remains valid. We will refer to the DOPs for 3-D estimation as HDOP3 and VDOP3 to distinguish them from the notation in the 4-D case.

Figure 1 gives the cumulative probability distribution functions (cdf's) of the HDOP, VDOP, HDOP3 and VDOP3 for the 24-satellite constellation of GPS. The VDOPs indeed tend to be larger than the HDOPs and, in view of the relationship given, this leads to the conclusion that in 4-D estimation the rms vertical error would be larger than the rms horizontal error. But the cdf's of HDOP3 and VDOP3 tell a different story for 3-D estimation: (i) VDOP3 shows little variability, and its values are significantly smaller than those of VDOP and somewhat smaller than those of HDOP, and (ii) the distributions of HDOP3 and HDOP are substantially similar. In other words, a GPS user equipped with a perfect receiver clock would obtain much-improved vertical position estimates via 3-D estimation because

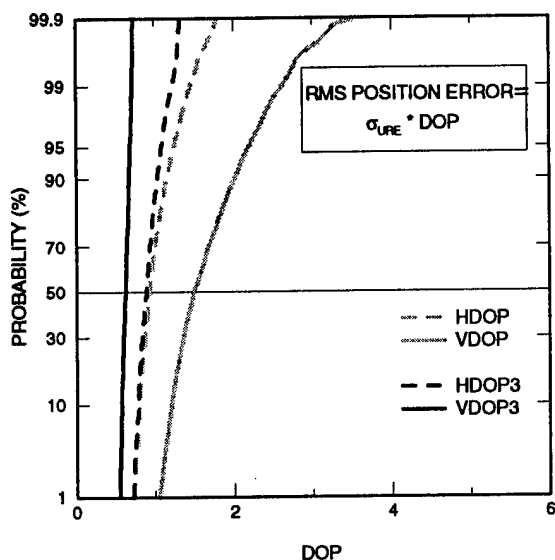


Figure 1.

of the much-improved DOPs. By contrast, a perfect clock gains little in horizontal accuracy.

Clearly, the price for estimation of the clock bias is being paid by loss of accuracy in the vertical dimension. Stated another way, there is a large potential for improvement in the quality of the vertical position estimates, but not in the horizontal estimates. The next question, then, is: How much of this potential for improvement can be realized with a practical receiver clock? This question is addressed in Section 4.

3. CORRELATIONS AMONG THE 4-D ESTIMATES FROM GPS

We examine next the relationships among the GPS-based estimates of position (x, y, z) and clock bias (b) obtained via 4-D estimation. Figure 2 shows scatter plots of errors in the horizontal and vertical position estimates versus the error in the corresponding clock bias estimates computed from GPS pseudorange measurement snapshots taken 10 seconds apart over a day. Computation of the error in a position estimate is straightforward, given the surveyed location of the antenna. Computation of error in clock bias estimates also takes advantage of the known antenna location. As in time-transfer mode, we post-process a batch of GPS measurements, fitting a smooth curve to the observed differences between the

pseudorange measurements and the computed ranges from the antenna to each satellite. This fitted curve serves as the 'truth' for computation of the error in clock bias as estimated from each snapshot.

Figure 2a is a scatter plot of the error in a horizontal position estimate versus that in the corresponding clock bias estimate, shown in units of length. The scatter shows no apparent correlation between the two errors. By contrast, Figure 2b, a scatter plot of the error in the vertical position estimate and that in clock bias estimate, shows a strong linear correlation. The proposed schemes for clock-aided navigation and RAIM are based on this correlation: the error in the clock bias estimate from a snapshot of pseudorange measurements is a good predictor of the error in the corresponding vertical position estimate. Actually, this relationship remains true even if one or more of the range measurements had arbitrary biases. That's the basis of RAIM.

The correlation between the errors in the estimates of clock bias and the vertical position is not a surprise. A change in the user clock bias changes all pseudoranges equally: *all* increase, or decrease, by a common amount. The net effect of a change in the user altitude is similar: *all* pseudoranges increase, or decrease, though not equally in general. Hence the correlation. Note, however, that if all the satellites were at the same elevation, a change in user altitude would indeed change all pseudoranges equally, and we wouldn't be able to distinguish between the user altitude and the clock bias. In the terminology of experiment design, the effects of altitude and clock bias in this situation would be *confounded*.

Obviously, if we were to obtain somehow an accurate estimate of the receiver clock bias, we would know the error in the current snapshot-based estimate of the receiver clock bias, and would be able to correct the corresponding vertical position estimate. Actually, if we were to know the current receiver clock bias accurately, there would be no need to solve for it. The knowledge of receiver clock bias reduces the problem to 3-D with the accompanying improvement in the vertical position estimate, as discussed in

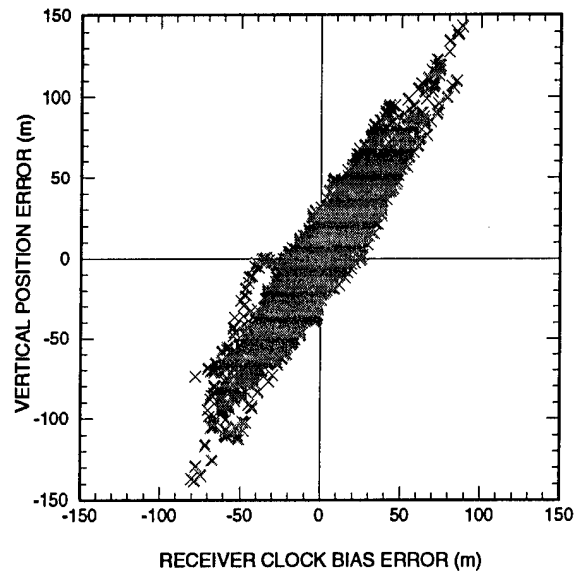
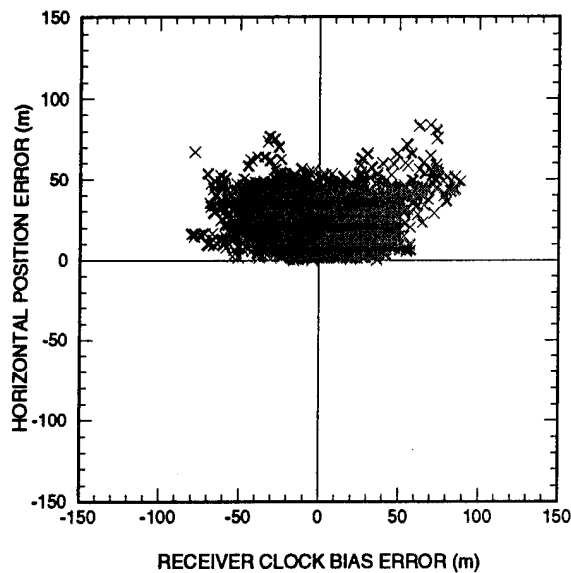


Figure 2.

Section 2. The results of this section are basically a confirmation of those in Section 2; the difference is that we have gone from an rms level characterization to snapshot-by-snapshot results.

In general, we cannot expect to know the true receiver clock bias. But we can estimate it from GPS measurements over a time period consistent with the stability characteristics of a given clock. From Figure 2, the extent of the improvement in the vertical position estimate would depend upon the quality of clock bias prediction. The horizontal position estimate is expected to be substantially unaffected. The obvious questions are: (i) how do we estimate the receiver clock bias from the measurements so as to transform the 4-D problem into a 3-D problem? and (ii) what is required of the clock in order for this approach to work? These issues are addressed in the next section.

4. CLOCK MODELING AND BIAS ESTIMATION

It is well known that the rms error in clock bias estimate (in units of length) based upon a single snapshot of pseudorange measurements is [6]:

$$\sigma_b = \sigma_{URE} \cdot TDOP,$$

where σ_{URE} , introduced previously, is the rms error in the GPS pseudorange measurements, and TDOP is the time dilution of precision parameter reflecting the satellite geometry. In the presence of Selective Availability (SA), σ_{URE} has been estimated conservatively as 33 m (observed value: 25 m). For the constellations of interest, TDOP typically ranges between 0.75 and 1.25. Taking a typical value of 1 for TDOP in our simple calculations below, the rms error in clock bias estimated from a single snapshot of the range measurements, $\sigma_b \approx \sigma_{URE} \approx 33$ m. Our focus in this report, however, is on differential GPS, where TDOP is unchanged but the measurement error is significantly lower, say, $\sigma_{UDRE} \approx 2$ m, where UDRE denotes the user differential range error. The rms error in clock bias estimated from a single snapshot of the differentially-corrected range measurements, $\sigma_b \approx \sigma_{UDRE} \approx 2$ m.

If we had available GPS measurements over a time period (t_0, t) during which the frequency drift rate of the receiver clock is stable, we could model the clock bias at time t simply as a quadratic function

$$b(t) = b_0 + b_1 (t - t_0) + b_2 (t - t_0)^2,$$

and estimate parameters b_0 , b_1 , and b_2 from the available measurements. Given k

statistically independent measurement snapshots, the rms error in the clock bias estimate will be $\sigma_b \approx \sigma_{UDRE} / \sqrt{k-3}$. Given, say, snapshots of differentially-corrected pseudorange measurements over 30 minutes (correlation time ≈ 3 minutes),

$$\sigma_b \approx \sigma_{UDRE} / \sqrt{(k-3)} \approx 2 / \sqrt{7} \approx 0.8 \text{ m.}$$

If the model were valid for a receiver clock, we expect to be able to predict clock bias with an rms error of about 3 ns or 1 m. We see next how well these simple calculations check out with actual measurements.

Figure 3 shows the behavior of several receiver clocks as observed in our laboratory over a 12-hour period. Included are a cesium standard, a rubidium oscillator, an oven-controlled crystal oscillator (OCXO) and a temperature-compensated crystal oscillator (TCXO). The figure shows 3-second samples of clock bias estimates in units of meters for each clock based on GPS measurement with differential corrections. The clock bias estimates are computed via the usual 4-D estimation from the DGPS data snapshot by snapshot. The plots are intended as typical examples for each of the clocks, and our purpose is draw attention to certain qualitative features.

In Figure 3, frequency stability of the cesium standard (FTS 4040, price > \$10K) is obvious: no frequency offset or drift is apparent. The rubidium oscillator (Ball Efratom FRS-C, \$2-4K) also shows no significant frequency offset, but signs of slight drift are clear. Such drift, however, appears constant over 30-60 minutes. The OCXO (HP 10811E, \$1K) has accumulated a small frequency offset (about 1 part in 10^8) so that the clock bias actually changes by about 2 m/s on average. We have taken out the effect of this offset via a linear regression, and have plotted the residuals, which show a clear quadratic trend. The behavior of both atomic clocks and the OCXO appears consistent with the proposed model: clock bias is indeed predictable, given recent data. The quality of such prediction is discussed below.

The TCXO (price \approx \$100) has accumulated a frequency offset of about 1 part in 10^6 , and its bias changes by about 200 m/s on average. Again, the residuals from linear regression are plotted. These residuals, however, are two orders of magnitude larger than those for the OCXO, and swing widely and wildly. It's clear that the TCXO does not exhibit stability of frequency drift rate for the length of time required, and the proposed model doesn't fit. Experience with other TCXOs was similar.

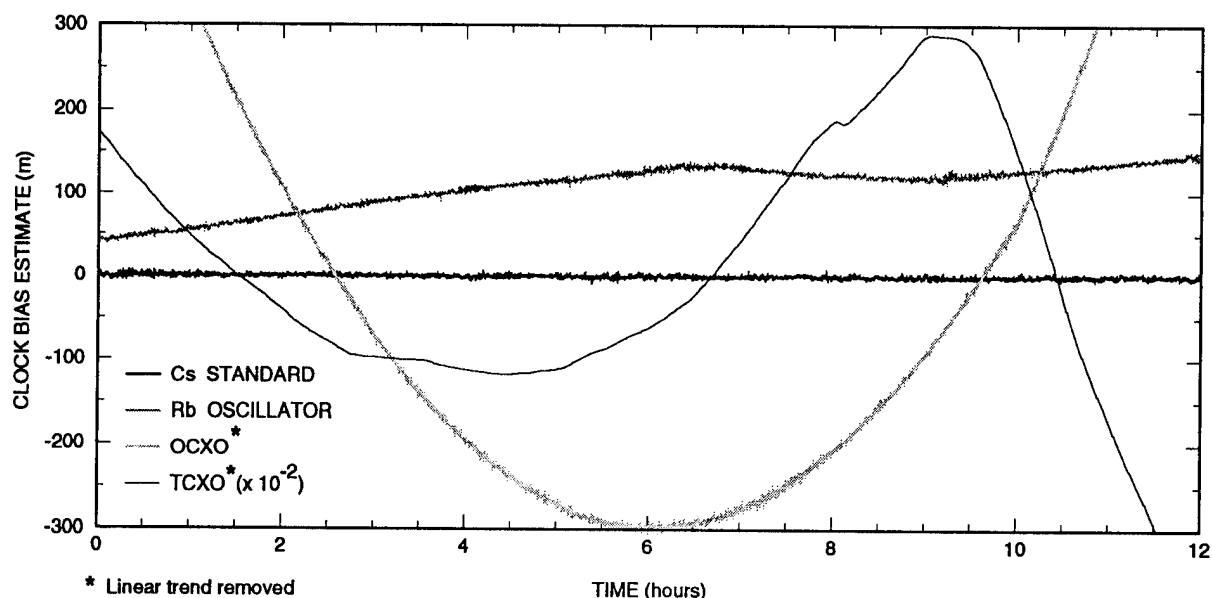


Figure 3.

How well does the proposed clock model fit our measurements for the atomic clocks and the OCXO? For the OCXO, the answer is given in Figure 4; the atomic clocks did better. Figure 4 gives the post-fit residuals for the OCXO bias estimates shown in Figure 3. At each point, a quadratic model is fitted to data over the previous 30 minutes, and clock parameters b_0 , b_1 , and b_2 estimated. The residual at each point is defined as the discrepancy between the predicted value of clock bias based on the fitted model, and the actual measurement. The parameter estimation process begins in each case at $t = 0$ with no prior knowledge assumed, and for the first 10-15 minutes, there aren't enough measurements on which to base a model, and the discrepancy between the predicted and actual values tend to be large. The rms error in the snapshot-based clock bias estimates is 1.6 m; the rms error in model-based clock bias predictions is under 1 m. Both rms values are consistent with the results of our simple calculations earlier in this Section. The model, clearly, fits the data. Both the OCXO and the rubidium oscillator have been found to exhibit the requisite stability for periods of 1-2 hours. (Results on clock modeling without the benefit of GPS

differential corrections are given in a companion paper [7]).

The measurements shown in Figure 3 were taken under typical laboratory conditions. The clocks did not have to contend with any serious temperature gradients or vibrations, which would be encountered by a receiver installed in an aircraft. Representative data from several field tests are shown in Figure 4 for the rubidium oscillator and the OCXO. These tests consisted of data collection using a mobile GPS receiver (a NovAtel GPS Card installed in a PC, with provision for external clock input). This demonstration unit was driven in a utility van and flown in an aircraft. No attempt was made to coddle the clock: no special shock mounting or temperature regulation. The results, shown in Figure 5, show no significant change in clock behavior from that observed in the laboratory: for both clocks tested, the clock bias remains predictable, given recent data. The main purpose of the field tests was to see if the requirements of the proposed clock model could be met reasonably under real-world conditions. The clocks appear robust, but more tests are needed to observe their behavior in carefully controlled environments, as specified in RTCA DO-160C [8].

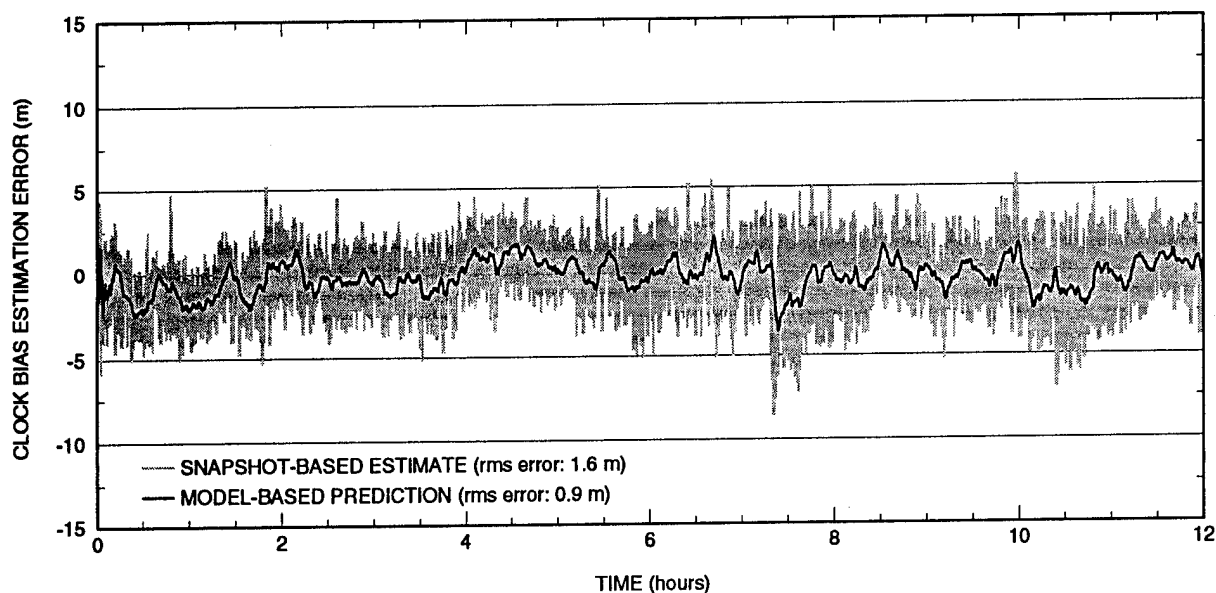


Figure 4.

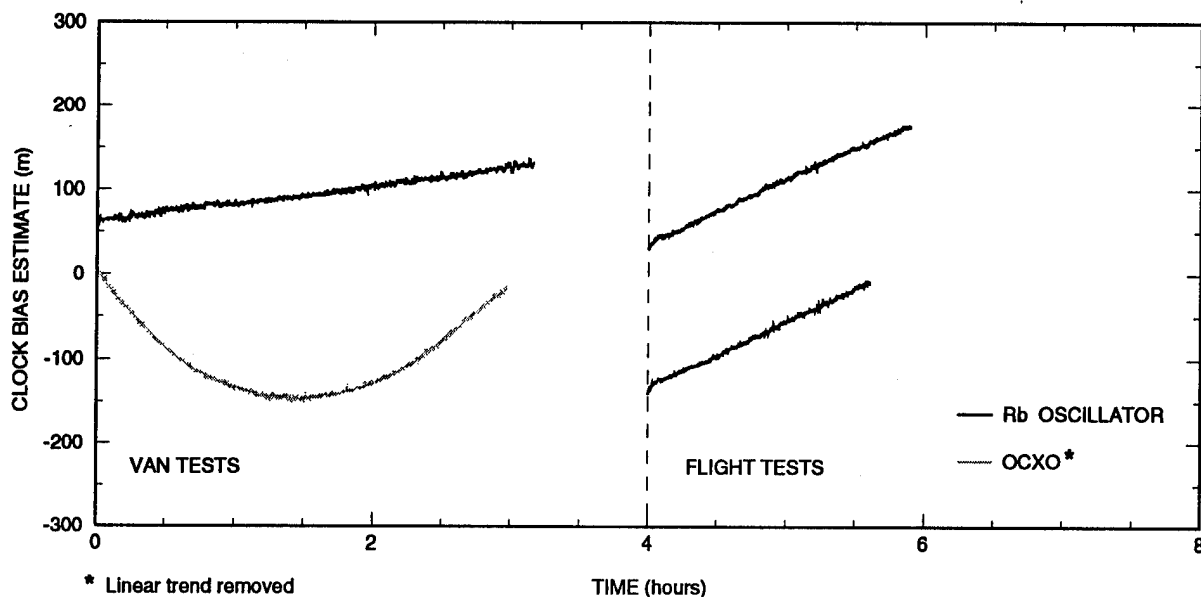


Figure 5.

5. CLOCK-AIDED NAVIGATION

Clock aiding approach requires that the frequency drift rate of the receiver clock be stable over long enough a period to allow its model parameters to be estimated adaptively from the GPS measurements. If this condition is met, the current user position can be obtained from a snapshot of the GPS range measurements via 3-D estimation, as discussed earlier. If the adaptively derived clock bias estimates are reasonably accurate, the vertical position estimate would improve substantially, as seen in Sections 2 and 3. We examine below the quality of clock-aided position estimates corresponding to the clock modeling results of the previous section.

Figure 6 shows the vertical position estimates obtained from GPS measurements in differential mode in our laboratory over a 12-hour period with and without clock aiding. The figure shows the error in vertical position estimates obtained from 4-D estimation snapshot by snapshot. These are to be compared with the vertical position estimates obtained from 3-D estimation where we have used the estimate of clock bias derived adaptively from the measurements over the previous half-hour, as discussed in the previous section. Clearly, clock modeling offers a distinct improvement: The clock-aided

navigation cuts the rms error nearly by a third (2.2 m versus 1.5 m). Another noteworthy factor is that clock aiding consistently avoids the peak errors obtained with 4-D estimation. This is important in view of typical integrity monitoring requirements in civil aviation where a large, undetected excursion from the defined flight path due to navigation error may create a hazard.

Results from two of the flight tests conducted at the FAA Technical Center (FAATC), Atlantic City, NJ, are given in Figure 7. In these tests, the mobile data collection system was placed in a rack in a Beechcraft 200. The clock sat next to the receiver, with no provision to isolate it from any environmental stresses. The GPS measurements were recorded as the aircraft executed a set of approaches and missed approaches as part of a broad plan related to development of Terminal Instrument Procedures (TERPS) for satellite-based navigation. Data were also recorded simultaneously at a local, ground-based reference station with another NovAtel receiver. Both data sets were processed post-flight to generate position estimates in both 4 D (snapshot based) and 3-D (clock aided) mode. The 'ground truth' in each flight was generated by the FAATC personnel

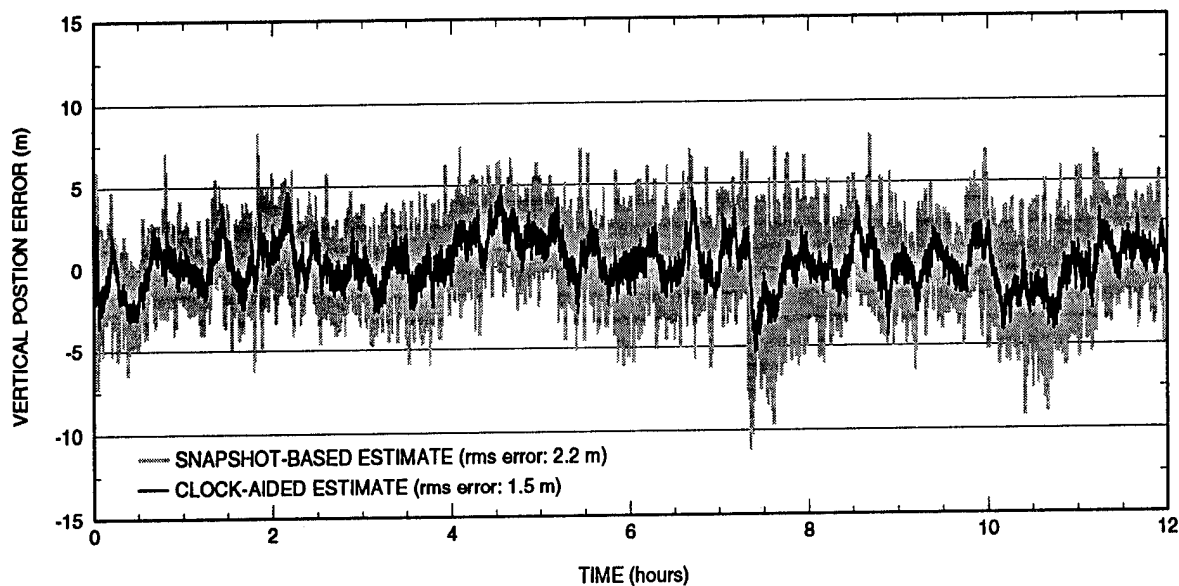


Figure 6.

independently by post-processing the carrier phase measurements recorded by a pair of Ashtech Z-12 receivers, one aboard the airplane, the other at a surveyed location on the ground, using Ashtech PNAV software with typical centimeter-level accuracy.

The flight test results are similar to those based on laboratory data. Clock aiding improves the quality of vertical position estimates significantly. The snapshot-based DGPS vertical position estimates in both flight tests show a bias of 0.6 m, attributed to problems in tropospheric modeling. As expected, this bias carries over to clock-aided estimates. The standard deviation of the error for the snapshot-based vertical position estimates is 1.6 m in each test; the corresponding value for clock-aided navigation is 0.9 m. Again, note that clock aiding avoids large excursions from true value as seen in the snapshot-based estimates.

In practice, the navigation filter would generally be implemented as a Kalman filter [9], with clock model parameters estimated adaptively, and the quality of their estimates checked continuously via the residual errors. If the clock were known to be extremely stable, the clock parameters may only be verified adaptively. The stringent integrity monitoring requirements of precision approaches essentially preclude the

acceptance of even an atomic standard on faith. In estimation of the clock parameters, the filter is to be implemented so as to down-weight the older measurements. The details of implementation will be discussed in a future report.

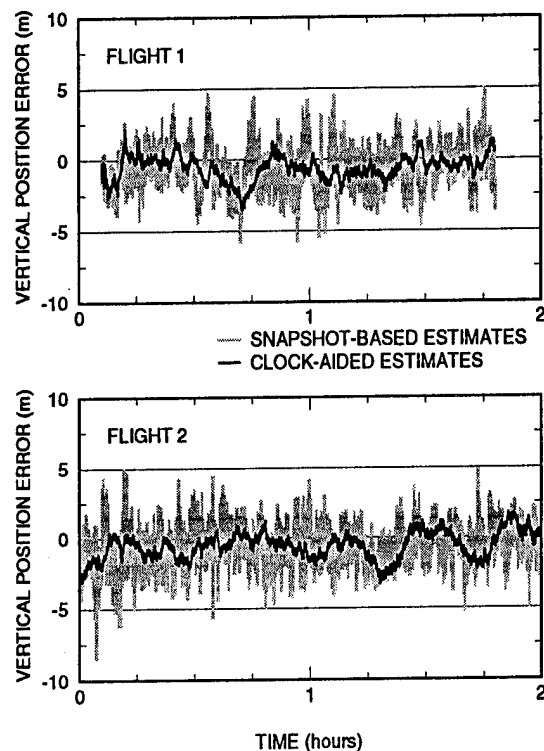


Figure 7.

7. CONCLUSIONS

We have analyzed an approach to GPS navigation based on receiver clock modeling to predict its bias. Such modeling requires that the frequency drift rate of the clock be stable for long enough to allow accurate estimation of its parameters from GPS measurements. This approach, referred to as clock aiding, has been shown to offer a significant improvement in the accuracy of the vertical position estimates. Clock modeling also provides a basis for RAIM.

Laboratory and field tests have shown the approach to be practical. Clock-aided navigation with several commercial receiver clocks has been shown to offer a significant improvement in vertical accuracy, reducing the rms vertical error by a third to a half. Such improvement can make a large difference in the availability of precision approaches. In order for clock aiding to be practical for general aviation, however, robust clocks have to be available at lower prices. It's noteworthy that there are encouraging developments in the time reference industry with a trend toward higher stability at lower prices.

ACKNOWLEDGMENTS

This work was sponsored by the Federal Aviation Administration under Interagency Agreement DTFA01-95-Z-02046. The authors are grateful to Joseph F. Dorfler, Program Manager, FAA Satellite Program, for his support. A debt of gratitude is owed to Simon Newby and Pat Fenton of NovAtel for being responsive to our unique requirements. Thanks are due to Cliff Mackin, John Warburton, Steve Malick, and Tom D'Ottavi for their support in overseeing the flight tests at the FAA Technical Center, Atlantic City, NJ. Thanks are also due to James Hungerford, GFI Technologies; Dr. Tom McLelland, Frequency Electronics; and Andrew Snow, FTS, for loaning us promising candidates for GPS receiver clocks for testing.

REFERENCES

- [1]. P. Misra, "Clock-aided GPS Navigation and RAIM," talk delivered at ION National Technical Meeting, San Diego, CA, 22-24 January 1994.
- [2]. M. A. Sturza, "GPS Navigation Using Three Satellites and a Precise Clock," *Global Positioning System*, Vol. II, Washington, DC: The Institute of Navigation, 1984, pp. 122-132.
- [3]. N. Knable and R. Kalafus, "Clock Coasting and Altimeter Error Analysis for GPS," Proc. ION Technical Meeting, 1984.
- [4]. P. W. McBurney and R. G. Brown, "Receiver Clock Stability: An Important Aid in GPS Integrity Problem," Proc. ION National Technical Meeting, Santa Barbara, CA, 1988.
- [5]. Y. C. Lee, "RAIM Availability for GPS Augmented with Barometric Altimeter aiding and Clock Coasting," *NAVIGATION, The Journal of the Institute of Navigation*, Vol. 40, No. 2, Summer 1993, pp. 179-198.
- [6]. R. J. Milliken and C. J. Zoller, "Principle of operation of NAVSTAR and System Characteristics," *Global Positioning System*, Vol. I, Washington, DC: The Institute of Navigation, 1980, pp. 3-14.
- [7]. P. Misra, M. Pratt, R. Muchnik and B. Manganis, "A General RAIM Algorithm Based on Receiver Clock," Proc. ION GPS-95, Palm Springs, CA, 12-15 September 1995.
- [8]. *Environmental Conditions and Test Procedures for Airborne Equipment*, RTCA/DO-160C, RTCA, Washington, D.C., December 1989.
- [9]. R. G. Brown and P. Y. Hwang, *Introduction to Random Signals and Applied Kalman Filtering*, New York: John Wiley and Sons, 1992, Chapter 10.

Comparison of Different On-The-Fly Ambiguity Resolution Techniques

Dr. Günter Hein and Wolfgang Werner
University FAF Munich

BIOGRAPHIES

Dr. Günter W. Hein is Full Professor and Director of the Institute of Geodesy and Navigation at the University of Federal Armed Forces Munich. He is responsible for research and teaching in the field of high-precision GPS/GLONASS positioning, navigation, physical geodesy, gravimetry and satellite geodesy. He works in the field of GPS since 1984 and is the author of numerous papers on static and kinematic positioning and navigation.

Wolfgang Werner is Research Associate at the Institute of Geodesy and Navigation at the University FAF Forces Munich. He studied computer sciences at the Technical University of Munich. Since 1993 he is concerned with research in GPS ambiguity resolution mainly for a project for high-precision differential GPS navigation.

ABSTRACT

On-the-fly carrier phase ambiguity resolution is a key element for high-precision centimeter-level kinematic DGPS positioning in real-time. Different techniques have been developed and investigated within the last years. Sequential square root information filtering combined with Bayesian statistics turned out to be one of the most promising approaches. Due to its achievable computational speed it is well suited for kinematic real-time applications, where a measurement update rate of at least 1 Hz is needed. At IfEN (Institute of Geodesy and Navigation) different ambiguity resolution techniques have been developed and implemented. A combination of Teunissen's LAMBDA (Least-squares AMBiguity Decorrelation Adjustment) method and the time-optimized search proposed by Euler and Landau using different search-tree algorithms have been investigated. Extensive kinematic real-time tests have been conducted by car using the high-precision DGPS navigation system PHARAO (PHase Ambiguity

Resolution Applications On-the-fly) developed at IfEN.

This paper describes some ambiguity resolution techniques in detail. Furthermore, the used algorithms, software and hardware design of PHARAO are outlined. The results of the tests and a comparison of the algorithms' performance are given.

INTRODUCTION

The key to high precision kinematic GPS navigation is the determination of the number of full phase cycles between receivers and satellites, the so-called integer ambiguities. Having determined these ambiguities once, continuous precise positioning is possible in the range of a few centimeters even for moving vehicles as long as no cycle slips occur. Considerable research has been done within the last few years, to find a fast and reliable strategy for determining the GPS carrier phase ambiguities in kinematic cases on-the-fly.

Generally there are two possible spaces, where the search can be conducted: the physical three-dimensional position space and the multidimensional mathematical integer ambiguity space.

But as the search in the position space (see e.g. the ambiguity function method in Counselman and Gourevitch (1981) is very time-consuming and highly dependent on the initial precision of the position, its application for kinematic positioning in realtime is hardly possible.

Therefore more recent approaches are performing the search in the ambiguity space. Normally some kind of square root information filtering is used. Assuming a bias-free noise distribution, the integer ambiguities are determined by minimizing the a posteriori error variance. As the resulting problem is a minimum integer problem, no closed solution is available. Therefore the influence of individual integer combinations on the total error residual have to be computed separately.

Double-differencing of the phase observations eliminates most common error sources, but has the

disadvantage that the ambiguities are statistically correlated. Thus some search strategies apply some kind of transformation in the ambiguity space before carrying out the search (see Teunissen (1994a) or Ober (1993)). Others, e.g. Knight (1994) simply avoid double-differencing.

In this paper we are focussing on double-differenced ambiguities, as the implemented Kalman filter seemed to be more stable in this case than in case of single differences. The choice of a reference satellite is no problem, because a smooth transition in the filter covariance matrix is possible in case of changing satellite geometry.

PHASE OBSERVATIONS AND LEAST SQUARES

In simplified form the GPS carrier phase observation equation can be written as:

$$D\Phi = D\frac{1}{\lambda}\rho + DN + D\delta + D\epsilon \quad (1)$$

where	Φ	phase observable
	λ	wavelength
	ρ	satellite receiver distance (from receiver position estimation)
	N	integer ambiguity
	δ	receiver clock error term
	ϵ	measurement noise
	D	single or double difference operator (' Δ ' or ' $\nabla\Delta$ ')

Linearizing and Kalman filtering of these observation equations leads to an a posteriori covariance matrix of the unknowns (at least with receiver position and ambiguities as filter states). Restricted to the ambiguity states we get the ambiguity covariance matrix Q_a , and the float estimates \hat{a} for the integer ambiguities a . We will omit an exact derivation of the matrix Q_a here, and refer the reader instead e.g. to Xu, Cannon, Lachapelle (1995).

The problem now is to find the integer combination, that minimizes the error variance. This can be done by finding the integer least-squares solution in:

$$\min_{a \in \mathbb{Z}^n} (\hat{a} - a)^T Q_a^{-1} (\hat{a} - a), \quad (2)$$

where n is the number of ambiguities.

This problem is the common starting point for the algorithms described in the next chapter. Because of the integreress of a , no closed solution can be hoped for. Based on Q_a , search windows for the individual ambiguities around the float estimates are chosen and the search is carried out. The difference between the searches lies in the strategy of how to exploit partial knowledge of the structure of Q_a and of the partial computed residuals of incomplete integer combinations. As the set of possible integer ambiguity

candidates is usually huge, it is necessary to reject false candidates as early as possible in the search process.

Remind, that this paper only refers to the mathematical solution of problem (2). Due to system noise behavior this may be not the correct integer vector of the physical problem. For the validation of the solution a ratio test between the best and second best solution is usually performed. As this test assumes a Gaussian noise distribution and certainly unmodelled systematic effects are present in the measurements (e.g. receiver interchannel biases or multipath effects), we consider the validation problem as still unsolved.

In this paper, however, we will concentrate on finding the minimizer in (2) as our primary goal.

AMBIGUITY SEARCH ELEMENTS

The ambiguity search techniques tested in this paper are combinations of one or more of the following elements, that are described below:

- the time-optimized search of Euler and Landau using a Cholesky factorization of Q_a ,
- the pre-search LAMBDA-transformation proposed by Teunissen (1994a), and
- a best-first or depth-first tree search algorithm.

Different combinations of these elements have been tested against each other in post-processing, thus guaranteeing working on the same sets of data. The tests and results are described below.

THE TIME-OPTIMIZED SEARCH OF EULER / LANDAU

The time optimized search algorithm proposed by Euler and Landau (1992) uses the symmetry of Q_a for the Cholesky factorization

$$Q_a^{-1} = CC^T. \quad (3)$$

The residual for each combination can then be computed via

$$\Omega = f^T f, \quad (4)$$

with

$$f = C^T (\hat{a} - a). \quad (5)$$

The advantage of this matrix decomposition is, that the computations of (4) and (5) can be mixed very efficiently, because C is triangular. Equation (4) shows, that Ω can be computed as sum of quadratic (non-negative) terms. That means, the evaluation of a group of integer combination candidates can be stopped, as soon as a partial residual is computed, that

is bigger than the best residual computed so far. For a more detailed consideration on how to evaluate equations (4) and (5) see Hatch and Euler (1994).

TEUNISSEN'S LAMBDA-TRANSFORMATION

The GPS double-difference ambiguities are highly correlated - especially in the case of a short observation time span. Therefore Teunissen proposes in Teunissen (1994b) proposes a linear multi-channel transformation in the ambiguity space to decorrelate the ambiguities, called LAMBDA (Least-squares AMBiguity Decorrelation Adjustment), prior to the search. This multi-channel transformation consists of consecutive two-dimensional Gauss transformations of the type

$$\begin{pmatrix} a_1 \\ a_2 \end{pmatrix} = \begin{pmatrix} 1 & 0 \\ \alpha & 1 \end{pmatrix} \cdot \begin{pmatrix} a_1 \\ a_2 \end{pmatrix} \quad (6)$$

where a_1 and a_2 are two ambiguities and α is an integer. To decorrelate the ambiguities as far as possible, the value for α should be chosen as

$$\alpha = - \left[\frac{\sigma_{12}}{\sigma_{11}} \right] \quad (7)$$

where σ_{12} is the covariance of a_1 and a_2 , σ_{11} is the variance of a_1 and $[.]$ means rounding to the next integer. Using this value for α and exchanging the roles of the two ambiguities a correlation coefficient smaller than 0.5 can be achieved (see Teunissen

(1994b)). Iterating this process with adequate renumbering of the unknowns leads to nearly decorrelated ambiguities. The problem can now be formulated as

$$\min_{z \in Z^n} (\hat{z} - z)^T Q_z^{-1} (\hat{z} - z) \quad (8)$$

with

$$z = Z^{-1} a, \quad \hat{z} = Z^{-1} \hat{a}, \quad Q_z = Z^{-1} Q_a Z \quad (9)$$

where Z is the composed transformation matrix.

TWO DIFFERENT TREE SEARCH ALGORITHMS

Even after the mathematical part of the problem is chosen, there are different evaluation algorithms that can be used to improve the ambiguity search times further. At IFEN two different tree search algorithms have been implemented and tested, a depth-first and a best-first tree search algorithm.

Depth-First Tree Search Algorithm

The depth-first tree search algorithm is easily implemented recursively or with an iterative loop, that generates successively partial integer combinations and evaluates the corresponding residuals. If this computed residual exceeds the optimal residual, that has been found so far, the search tree for that particular partial combination can be cut off. The disadvantage with this search strategy is, that it does

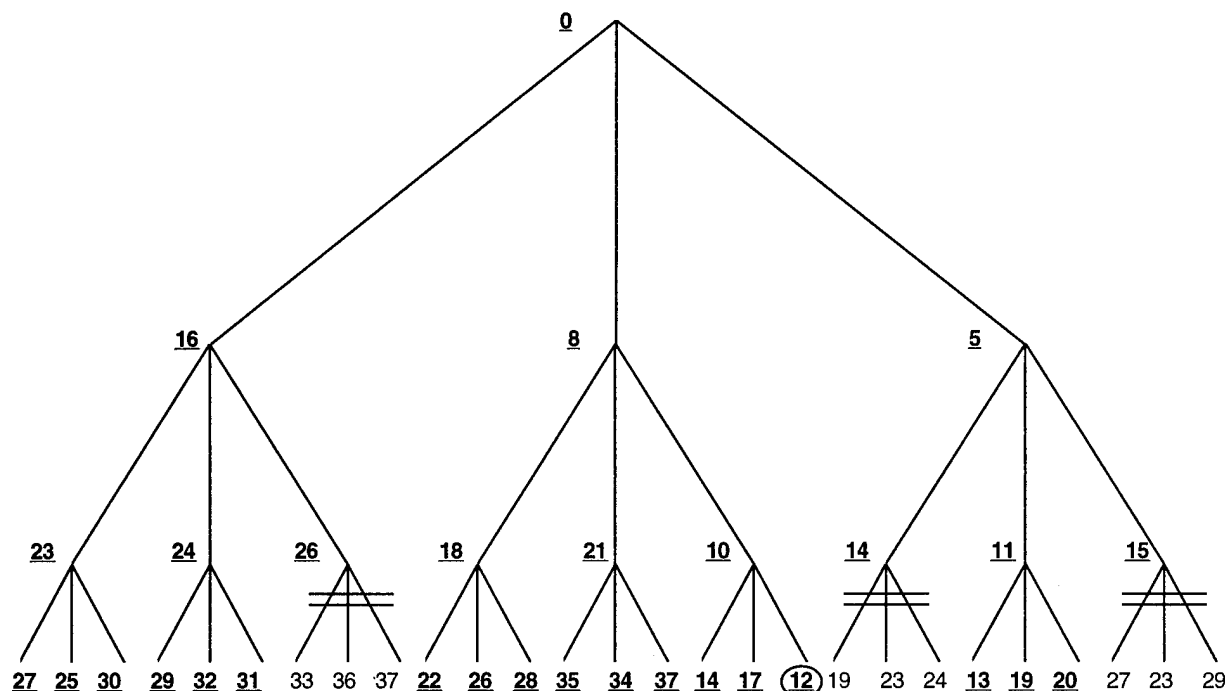


Fig.1: Depth-First Search in the Ambiguity Tree
Search order of nodes: 0-16-23-27-25-30-24-29-32-31-26-8-18-22-26-28-...

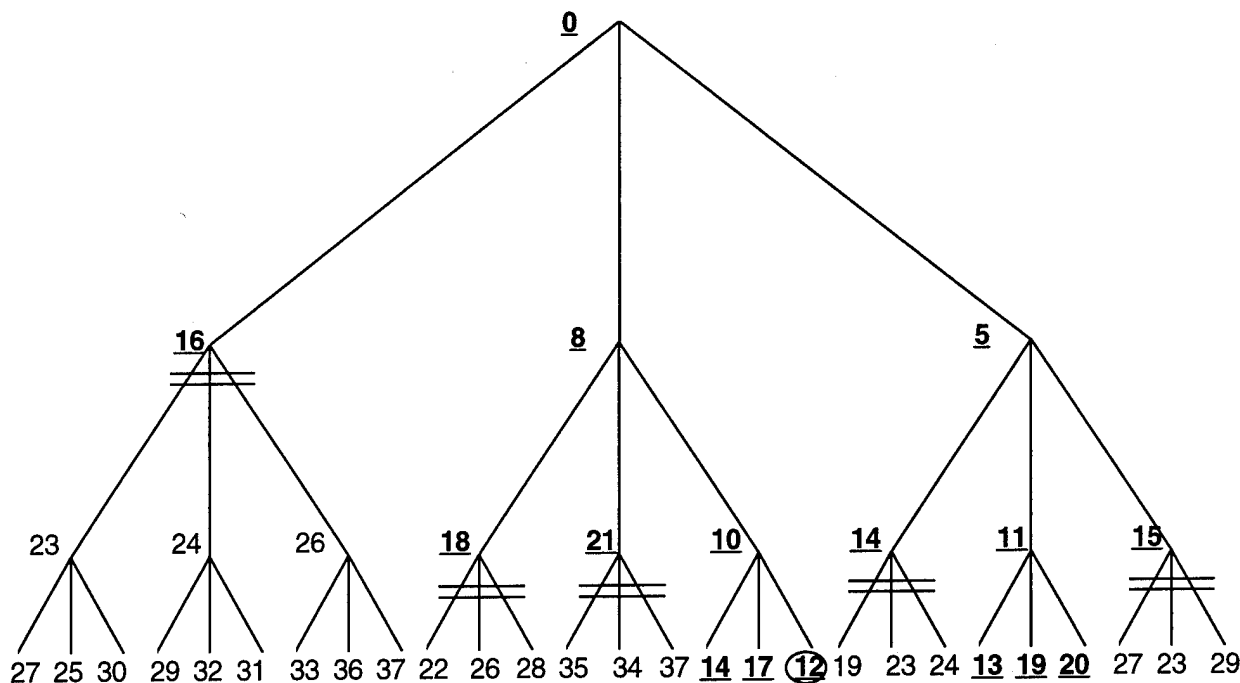


Fig.2: Best-First Search in the Ambiguity Tree
Search order of nodes: 16-8-5-14-11-15-18-21-10-14-17-12-13-19-20

not make full use of the cut-off potential of the search tree. Even if the initial "optimal" residual is set to that of the rounded float solution, there may be many combinations that are to be checked further than necessary before the right optimum is found. Consider the small example for the search strategy based on the depth-first search shown in Fig.1.

Each level represents the fixing of one ambiguity. The numbers next to the nodes are examples of partial residuals that result from fixings of the ambiguities at this and higher levels. For easy comprehension integer values are chosen for the partial residuals in the example. It is assumed, that the search space only contains three possibilities for each ambiguity, so the branching factor for each node in the tree is three. Note the increasing residual values along the branches from the top, where no ambiguity has been fixed, to the leaves, where all three ambiguities are fixed. The search order of the nodes is given in Figure 1. All nodes with underlined bold partial residuals have to be evaluated by the algorithm. Double horizontal lines mean cutting points in the search. Note for example, that the algorithm has to expand the node with residual 16, although the optimal solution only has a residual of 12, because the algorithm has not found the minimum of 12 yet as it works "from left to right" in the tree. This means, that some unnecessary computations have to be done. The amount depends primarily on the statistical distribution of residuals and partial residuals in the search tree and on the number of ambiguities (number of levels in the search tree). In case of many ambiguities - that means many levels in the search tree- early cutting is important, because the

search space increases exponentially with the number of tree levels.

Best-First Tree Search Algorithm

The search order used by the best-first algorithm is depicted in Fig.2. In comparison to the depth-first search, it needs the management of an internal sorted list (called "open"-list) of partial ambiguity combinations with their partial residuals.

At the beginning the list of open nodes only contains one node with the value 0, for no ambiguities are fixed yet and the residual thus is 0. In each step the algorithm takes the first node of the open-list and generates all successor nodes by fixing the next ambiguity to all values in the search window. All these new partial combinations are sorted into the list with their corresponding residual. Any combination, which residual exceeds the residual of the rounded float solution can be excluded from the search. If the first node with all ambiguities fixed is taken from the open-list, the search is complete. To validate the solution with a ratio test of the second best residual against the best residual the algorithm may proceed until the next solution has been found. This algorithm evaluates every combination only as far as necessary, and therefore needs less computation than the depth-first tree search. The disadvantage in this kind of search comes with the overhead of list management and the necessary storage requirements. Compared to unnecessary time consuming multiplications with double-float numbers, the time that is needed for

maintaining an ordered list is small. In case of big search windows and many ambiguities, however, the storage space can be crucial.

OVERVIEW OF THE NAVIGATION SYSTEM PHARAO

IfEN has developed a high-precision navigation

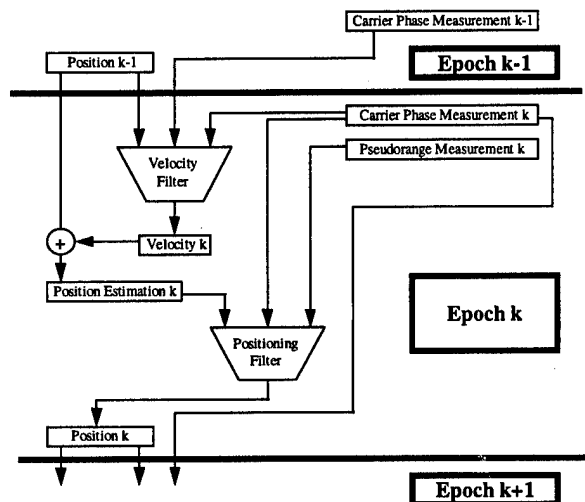


Fig. 3: PHARAO filtering algorithm

system called PHARAO. It is a real-time and post-processing capable positioning system for kinematic applications with update rates of at least 1 Hz. The hardware components of the system are at least two

GPS receivers, a telemetry link (consisting of sender and receiver unit) and a laptop or other IBM-compatible PC with at least 486DX-33 processor, to run the software.

The PHARAO system is designed very flexible thus allowing the usage of different receiver types like the NovAtel GPS OEM board, Trimble 4000SSE or others.

The PHARAO software is written in C++. There are different source code modules which contain classes for data acquisition, data decoding, Kalman filtering, ambiguity solving etc. The object-oriented style of C++ makes it easier to expand and debug the system. Modules can easily be exchanged or extended to fit new purposes.

The system can be configured either for reading data from files in post-processing mode or to read data from two serial ports in real-time mode. In either case the system additionally respects user commands that come from the keyboard. So the system configuration can be changed interactively while the system is running, e.g. changing the positioning mode from single-difference positioning to double-difference positioning. The system can even be paused at any time, and different ambiguity search algorithms can be tested in the same data epoch, using the same filter and observation data. Pausing the system in real-time mode surely means loss of some data.

The decoder module is able to process data of various receiver formats like the Trimble 4000SSE compact measurement data format, ASCII or binary data format, NovAtel data format or (for postprocessing

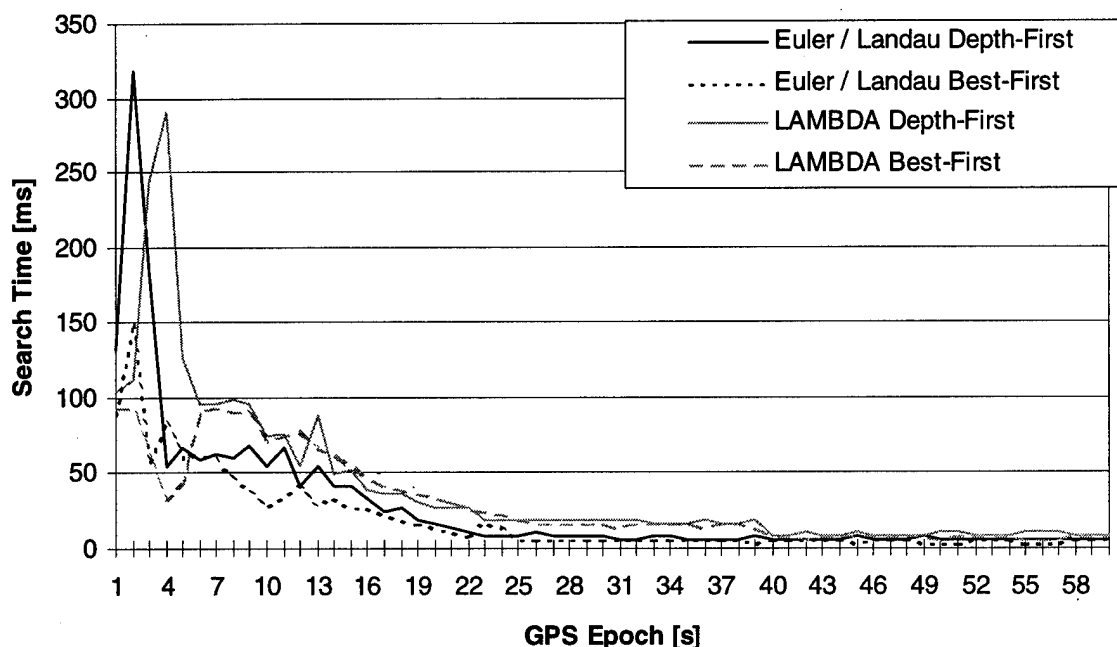


Fig. 4: Comparison of ambiguity search times (kinematic case, 5 double difference ambiguities)

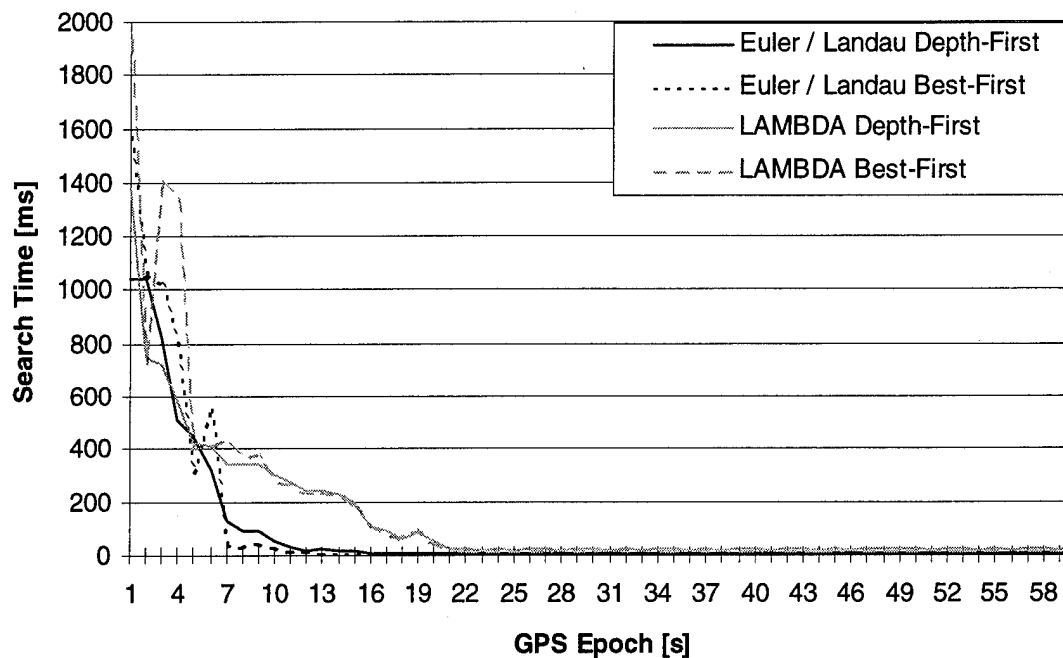


Fig. 5: Comparison of ambiguity search times (kinematic case, 6 double difference ambiguities)

purposes) RINEX 2 format data.

The positioning module can be configured for single or double-difference positioning mode using ranges, phases or both simultaneously. L1 and/or L2 usage may be configured. The user can choose, which ambiguity resolution technique should be applied.

The positioning is done via Kalman filtering. The velocity determination is made by triple-differencing

carrier phase measurements, thus providing an ideal time-update to the Kalman filter (see Fig.3).

TESTS AND RESULTS

Tests of the system have been conducted in real-time and post-processing modes. To check the efficiency of

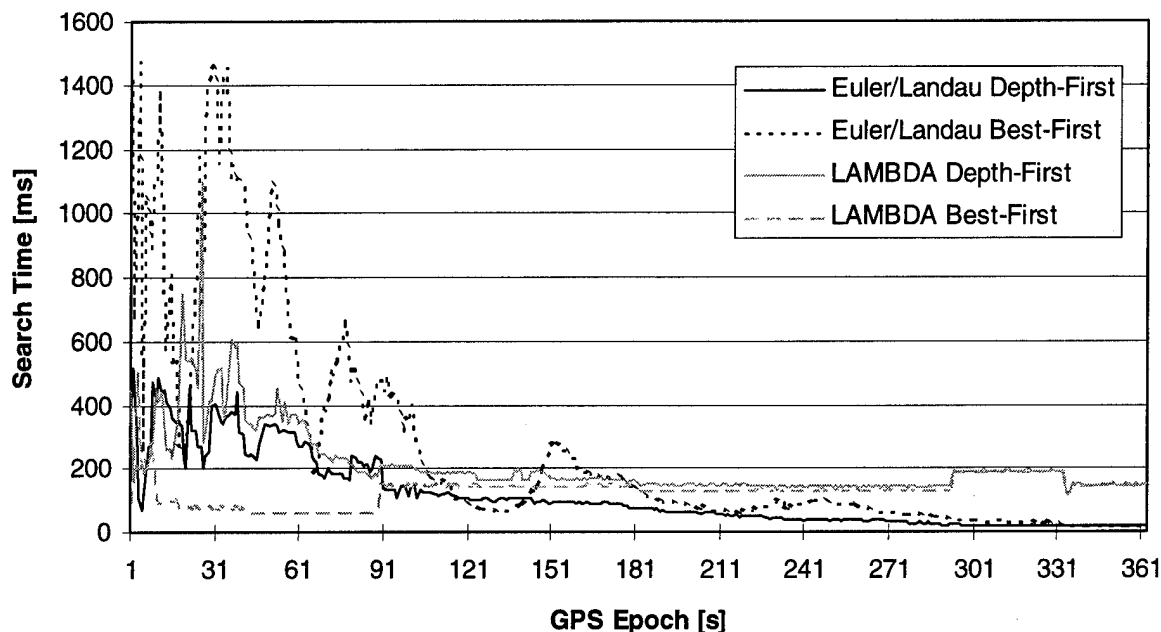


Fig. 6: Comparison of ambiguity search times (static case, 5 double difference ambiguities)

the ambiguity search algorithms, the system was configured to post-process kinematic data with on-the-fly algorithms. The data rate was set to 1 Hz. After each measurement epoch, the algorithms have been run working on an identical set of filter data.

The data in Figures 4 and 5 have been taken from a kinematic test by car with an approximate velocity of 50 km/h (about 31 mph), where five and six L1-ambiguities had to be solved for. The distance between reference station and rover was about 1 to 2 km. Figure 6 shows a set of static data on a short baseline of 6 m, where the L1 code solution has been far of the correct solution. Six ambiguities were unknown. Here the search times are considerably longer.

There are some points worth considering in the figures.

First of all, it can be stated, that all ambiguity search techniques succeeded in solving the minimum problem given by (2) well within one epoch after a few epochs of data.

Secondly, for long observational times the simple Euler/Landau depth-first search is best. This can be seen in Figure 6, where the ambiguity search times over the first few minutes are given. There are two obvious reasons therefore. The first reason is, that after long observation times the float values for the ambiguities are close to the correct solution. Therefore it is highly probable, that the rounded float solution is the correct solution. As the Euler/Landau search begins with the rounded float solution, optimal cutting in the search tree is possible. The second reason is, that in comparison to the other algorithms the depth-first algorithm has very low computational overhead.

The best-first search performs nearly as good as the depth-first search at long observational time spans, because its computational overhead is low, if the search windows are not too big. The LAMBDA method, however, still needs time for performing the transformation to decorrelate the ambiguities prior to the search.

The tested methods for fast integer ambiguity solving are thought to be used for short observational time spans.

The time optimized depth-first Euler/Landau search performs very well, but the computation time depends largely on the distribution of residuals among the ambiguity combinations. Therefore it may happen that the algorithm has to expand many partial integer combinations further than necessary. The number of unnecessarily computed residuals increases considerably with the number of ambiguities involved.

The time-optimized best-first Euler/Landau search performs similar to the depth-first search when few ambiguities are involved. Due to the large discontinuity in the spectrum of the conditional covariances of the double difference ambiguities shown by Teunissen (1994b), it is most likely that the algorithm will have to expand many partial integer combinations for the first three ambiguities. As the number of ambiguities exceeds three, however, the search tree will be cut more often. This suggests, that the best-first Euler/Landau algorithm will perform better in comparison to the depth-first, when quite a lot of ambiguities are involved.

Figure 7 shows another example of kinematic data, where a cycle slip occurs. As can be seen clearly both

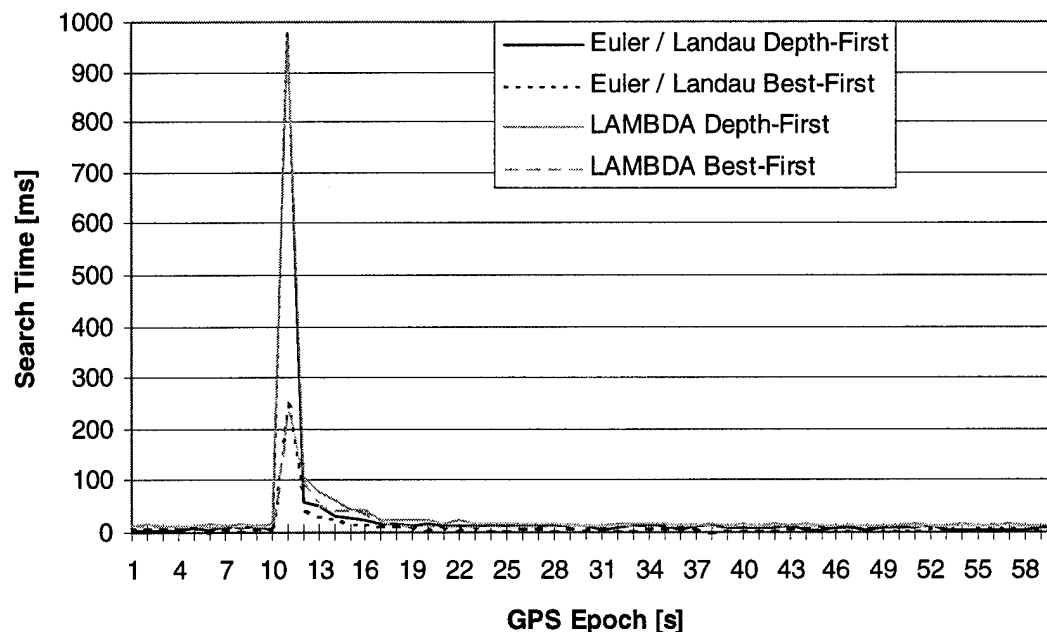


Fig. 7: Comparison of ambiguity search times after cycle slip (6 double difference ambiguities)

best-first tree searches perform better than the depth-first approaches in that case.

The properties of the ambiguity searches discussed so far, suggest a combination of the LAMBDA method with the time optimized best-first Euler/Landau search approach. This combination first deletes the correlation of the ambiguities as far as possible and performs an efficient search for the transformed ambiguities. How well the symbiosis of these two algorithms works in short observational time spans can be seen in Figure 6. Due to the decorrelation of the ambiguities the search tree can be cut very early.

CONCLUSION

All of the above ambiguity search techniques succeed in solving the minimum problem given in (2) well within one epoch after few epochs of data. From the results of the field tests it can be said, that the best approach to solve for the ambiguities in short observational time spans seems to be a LAMBDA transformation followed by a best-first Euler/Landau search.

However, one important problem, that still remains, concerns the physical aspects. Especially unmodelled systematic noise may bias the acceptance test.

ACKNOWLEDGEMENT

This project is funded by the German Space Agency (Deutsche Agentur für Raumfahrtangelegenheiten GmbH, DARA, Bonn) within a national demonstration project on Differential GPS.

REFERENCES

Counselman, C.C., Gourevitch, S.A. (1981): Miniature Interferometer Terminals for Earth Surveying: Ambiguity and Multipath for the Global Positioning System, IEEE Transactions on Geoscience and Remote Sensing, Vol. GE-19, No.4, pp.244-252, October 1981.

Euler, H.-J., Landau, H. (1992): Fast GPS Ambiguity Resolution On-The-Fly for Real-Time Applications, Proceedings of the Sixth International Geodetic Symposium on Satellite Positioning, Columbus, Ohio, Vol.2, pp. 650-659, March 1992.

Hatch, R., Euler, H.-J. (1994): Comparison of Several AROF Kinematic Techniques, ION GPS-94, Salt Lake City, September 1994.

Knight, D. (1994): A New Method of Instantaneous Ambiguity Resolution, ION GPS-94, Salt Lake City, September 1994.

Ober, P.B. (1993): Split-Second Ambiguity Resolution For GPS Using The Basis-Reduction Method, TU Delft, report-nr. A-565, November 1993.

Teunissen, P. (1994a): A New Method for Fast Carrier Phase Ambiguity Estimation, IEEE Position Location and Navigation Symposium (PLANS-94), Las Vegas, April 1994.

Teunissen, P. (1994b): On the Spectrum of the GPS DD-Ambiguities, ION GPS-94, Salt Lake City, September 1994.

Xu, P., Cannon, E., Lachapelle, G. (1995): Mixed Integer Programming for the Resolution of GPS Carrier Phase Ambiguities, IUGG 95, Boulder, Colorado, July 1995.

A New Method for Constructing Multi-satellite Ambiguity Combinations for Improved Ambiguity Resolution

Chris Rizos and Shaowei Han
The University of New South Wales

BIOGRAPHY

Chris Rizos received a B.Surv. in 1975, and a PhD in 1980, both from the School of Surveying, The University of New South Wales. In 1984 he joined the research group at UNSW working on the application of GPS to geodetic problems such as crustal motion determination. He has been involved in software development over the last ten years. In 1987 he was appointed as lecturer and in 1989 was promoted to senior lecturer. His interests now range over all GPS applications from geodesy to vehicle navigation.

Shaowei Han received a B.Sc. and M.Sc. in Geodesy in 1986 and 1989, respectively, from the Wuhan Technical University of Surveying and Mapping. He then joined the academic staff in the same university and was involved in several projects in GPS rapid static and kinematic positioning, orbit determination and deformation analysis. From 1994, he has been studying at the School of Geomatic Engineering, The University of New South Wales, as a full-time PhD student under the supervision of Dr. Chris Rizos. His research focus is on the use of GPS for precise long range kinematic positioning.

ABSTRACT

Single-satellite ambiguity combinations constructed from L1 and L2 observations can create long wavelength ambiguities, a technique widely used in ambiguity resolution procedures. However, such combinations do not consider the geometric relations between all channel or satellite ambiguities and cannot be formed using single frequency data. Certain multi-satellite ambiguity combinations (sometimes referred to as "multi-channel" combinations) have useful properties, such as resulting in their real estimated ambiguities having minimal uncertainties and minimal correlations. This property has been successfully exploited by the LAMBDA approach (Teunissen, 1994). The conditions for the admissible

class of linear combinations are that the combination ambiguities have integer values and that the original integer ambiguities can then be recovered. However, at present there is no consistent method for constructing multi-satellite ambiguity combinations. In this paper, the authors describe a new method for creating the transformation matrix to construct multi-satellite ambiguity combinations. The standard deviations of the real-valued ambiguity estimations are significantly smaller than the original and the computation of the transformation matrix is very efficient. This method has been implemented in a number of ambiguity search procedures, such as FARA, LSAST, the Cholesky decomposition method, FASF, and the LDL^T decomposition method. Based on a comparison of these search methods the most efficient procedures are suggested.

INTRODUCTION

High precision relative GPS positioning requires the analysis of very precise carrier phase measurements. If enough data are collected, the estimated ambiguities will have very small uncertainties and can be rounded to the nearest integer. This requirement for a long observation session would at best make GPS an inefficient technique for many static positioning applications, or impossible for kinematic positioning applications. In order to make GPS phase positioning more efficient (that is short observation time) and able to be used for high precise kinematic positioning, techniques for rapid ambiguity resolution (in the case of GPS static positioning) and ambiguity resolution on-the-fly (for GPS kinematic positioning) have been developed over the past few years.

There are three general classes of techniques: search techniques in the measurement domain (orbit free techniques); search techniques in the coordinate domain (particularly suitable when good approximate initial coordinates are available), and; search techniques in the estimated ambiguity domain using

least-squares estimation. The search techniques in the estimated ambiguity domain, widely used in short range GPS positioning applications, will be discussed in this paper. The search can be implemented for the original ambiguity parameters, as well as the combinations of the original parameters. In the case of the former the search is made of the integer ambiguities directly, using techniques such as: the Fast Ambiguity Resolution Approach (FARA) (Frei & Beutler, 1990); the Least Squares Ambiguity Search Technique (LSAST) (Hatch, 1990); the Cholesky decomposition method (Euler & Landau, 1992); the Fast Ambiguity Search Filter (FASF) (Chen, 1993), and; the LDL^T decomposition method, which all use the variance-covariance matrix to construct the initial integer ambiguity candidates. On the other hand, the LAMBDA method performs the search using transformed integer ambiguities (Teunissen, 1994). The transformed integer ambiguities are constructed from the original ambiguities, and can be used to recover the original integer ambiguities. The advantage of this procedure is that the transformed real-valued ambiguities have much smaller standard deviations and that there is a much smaller number of integer candidate sets. Consequently the computation time will be significantly reduced.

The key to the LAMBDA method is the computation of the transformation matrix for constructing the multi-satellite ambiguity combinations. At present there is no consistent method to determine the transformation matrix. In this paper a new method for constructing multi-satellite ambiguity combinations is suggested and employed in the standard search procedures (FARA, LSAST, Cholesky decomposition method, FASF, and LDL^T decomposition method). A comparison of these search methods, based on the integer least squares estimation before and after the ambiguity transformation, is discussed and the most efficient procedures identified.

INTEGER LEAST-SQUARES ESTIMATION

Linearization of the double differenced carrier phase observations can be represented by the following system of equations:

$$V = AX - L \quad (1a)$$

where

$$A = [A_C \quad A_N] \quad (1b)$$

$$X = \begin{bmatrix} X_C \\ X_N \end{bmatrix} \quad (1c)$$

and the weight matrix of the observations P with respect to the unit weight variance factor σ_0^2 . The integer least-squares criteria for solving the linearized system of observation equations are:

$$V^T P V = \min \quad (2a)$$

$$X_C \in R^t \quad (2b)$$

$$X_N \in Z^m \quad (2c)$$

where X_C is the $t \times 1$ real value parameter vector which includes coordinate parameters (and any other real type parameter that may be included); X_N is the $m \times 1$ integer value parameter vector; L is the $n \times 1$ residual vector between the double differenced carrier phase and/or pseudorange observations and their computed value vectors; R^t refers to t -dimensional real space and Z^m refers to m -dimensional integer space.

The above integer least-squares problem may be solved in two steps. The first step consists of solving the problem with R^m replacing Z^m using the traditional least-squares theory. That is:

$$\hat{X} = (A^T P A)^{-1} A^T P L \quad (3)$$

$$Q_{\hat{X}} = (A^T P A)^{-1} = \begin{bmatrix} Q_{\hat{X}_C} & Q_{\hat{X}_C \hat{X}_N} \\ Q_{\hat{X}_N \hat{X}_C} & Q_{\hat{X}_N} \end{bmatrix} \quad (4)$$

$$\Omega = V_0^T P V_0 \quad (5)$$

$$m_0^2 = \frac{\Omega}{n - t - m} \quad (6)$$

In this step, the accuracy estimation is always over-optimistic. In order to obtain more reliable accuracy estimations, the observation correlations between epochs should be considered (El-Rabbany, 1994), or the standardization procedure of the co-factor matrix and *a posteriori* unit weight variance factor should be employed (Han & Rizos, 1995). On the other hand, the following test should be employed in order to check the fidelity of the stochastic and functional models.

The null hypothesis H_0 and the alternative hypothesis H_1 are:

$$H_0: m_0^2 = \sigma_0^2 \quad (7a)$$

$$H_1: m_0^2 \neq \sigma_0^2 \quad (7b)$$

and the corresponding test statistic is:

$$\frac{\Omega}{\sigma_0^2} = \frac{m_0^2}{(n-t-m) \cdot \sigma_0^2} \sim \chi_{n-t-m}^2 \quad (8)$$

The rejection regions of H_0 are:

$$\frac{m_0^2}{(n-t-m) \cdot \sigma_0^2} > \xi_{\chi_{n-t-m}^2; 1-\alpha/2} \quad (9a)$$

$$\frac{m_0^2}{(n-t-m) \cdot \sigma_0^2} < \xi_{\chi_{n-t-m}^2; \alpha/2} \quad (9b)$$

where $\xi_{\chi_{n-t-m}^2; \alpha/2}$ and $\xi_{\chi_{n-t-m}^2; 1-\alpha/2}$ are the lower and upper boundary of the $1-\alpha$ confidence interval for χ^2 -distribution statistic with $n-t-m$ degrees of freedom.

If the *a posteriori* unit weight variance factor is rejected by eqn (9a), a check should be made for outliers in the observations, such as cycle slips, multipath, system biases (eg., the ionospheric or tropospheric delay effects not eliminated in double differencing), or the *a priori* standard deviations of the observations do not reflect the accuracies of these observations. If the *a posteriori* unit weight variance factor is rejected by eqn (9b), a check should be made as to whether there are too many parameters (eg., the ionospheric or tropospheric delay parameters are included in the functional model, though the ionospheric/tropospheric delay effects are not significant), or the *a priori* standard deviations of the observations do not reflect the accuracies of these observations.

The second step requires a constraint to be added:

$$X_N = N_k \quad (10)$$

where N_k is an integer vector. The results can then be obtained as follows:

$$\tilde{X}_{C,k} = \hat{X}_C - Q_{\hat{X}_C \hat{X}_N} Q_{\hat{X}_N}^{-1} (\hat{X}_N - N_k) \quad (11)$$

$$Q_{\tilde{X}_{C,k}} = Q_{\hat{X}_C} - Q_{\hat{X}_C \hat{X}_N} Q_{\hat{X}_N}^{-1} Q_{\hat{X}_N \hat{X}_C} \quad (12)$$

$$V_k^T P V_k = \Omega + R_k \quad (13)$$

where

$$R_k = (\hat{X}_N - N_k)^T Q_{\hat{X}_N}^{-1} (\hat{X}_N - N_k) \quad (14)$$

and the standard deviation m_{0k} can be represented as:

$$m_{0k} = \sqrt{\frac{V_k^T P V_k}{n-t}} \quad (15)$$

The equivalent relations can be obtained:

$$V_k^T P V_k = \min \quad (16)$$

$$(\hat{X}_N - N_k)^T Q_{\hat{X}_N}^{-1} (\hat{X}_N - N_k) = \min \quad (17)$$

For a different integer set N_k , a different value of R_k and associated $V_k^T P V_k$, m_{0k} will be obtained. Then the optimal integer set, which satisfies the following validation and rejection criteria, should be searched.

VALIDATION AND REJECTION CRITERIA

The correct integer vector N_k in the constraint equation (10) should satisfy the following conditions:

N_k should be within the confident region of \hat{X}_N

This condition for the integer vector N_k can be expressed as:

$$\frac{(\hat{X}_N - N_k)^T Q_{\hat{X}_N}^{-1} (\hat{X}_N - N_k)}{m \cdot m_0^2} \leq \xi_{F_{m,n-t-m}; 1-\alpha} \quad (18)$$

where $\xi_{F_{m,n-t-m}; 1-\alpha}$ is the one-tailed boundary of the $1-\alpha$ confidence interval for the Fisher's distribution statistic with m and $n-t-m$ degrees of freedom.

This condition for each element $(n_i)_k$ ($i=1,2, \dots, m$) in the integer vector N_k can be represented as:

$$\frac{|\hat{x}_{n_i} - (n_i)_k|}{m_0 \cdot Q_{\hat{x}_{n_i}}^{1/2}} \leq \xi_{t_{n-t-m}; 1-\alpha/2} \quad (19)$$

where \hat{x}_{n_i} and $m_0 \cdot Q_{\hat{x}_{n_i}}^{1/2}$ are the i -th element of the vector \hat{X}_N and its standard deviation; $(n_i)_k$ is the i -th element of the integer vector N_k ; $i=1,2,\dots,m$; $\xi_{t_{n-t-m}; 1-\alpha/2}$ is the upper and lower range-width of the two-tailed confidence range $1-\alpha$ based on the Student's distribution statistic with $n-t-m$ degrees of freedom.

This condition for a linear combination $f((n_1)_k, \dots, (n_m)_k)$ of the elements in the integer vector N_k can be represented as:

$$\frac{|f(\hat{x}_{n_1}, \dots, \hat{x}_{n_m}) - f((n_1)_k, \dots, (n_m)_k)|}{m_0 \cdot Q_f^{1/2}} \leq \xi_{t_{n-t-m}; 1-\alpha/2} \quad (20)$$

where $m_0 \cdot Q_f^{1/2}$ is the standard deviation of the linear combination $f(\hat{x}_{n_1}, \dots, \hat{x}_{n_m})$.

$\tilde{X}_{C,k}$ should be within the confident region of \hat{X}_C

This condition for the vector $\tilde{X}_{C,k}$ can be expressed as:

$$\frac{(\hat{X}_C - \tilde{X}_{C,k})^T Q_{\hat{X}_C}^{-1} (\hat{X}_C - \tilde{X}_{C,k})}{t \cdot m_0^2} \leq \xi_{F_{t,n-t-m}; 1-\alpha} \quad (21)$$

and for each element in the vector can be represented as:

$$\frac{|(\hat{x}_i)_C - (\tilde{x}_i)_{C,k}|}{m_0 \cdot Q_{(\hat{x}_i)_C}^{1/2}} \leq \xi_{t_{n-t-m}; 1-\alpha/2} \quad (22)$$

where $(\hat{x}_i)_C$ and $m_0 \cdot Q_{(\hat{x}_i)_C}^{1/2}$ are the i -th element of the vector \hat{X}_C and its standard deviation; $(\tilde{x}_i)_{C,k}$ is the i -th element of the vector $\tilde{X}_{C,k}$; $i=1,2,\dots,t$; $\xi_{F_{t,n-t-m}; 1-\alpha}$ is the one-tailed boundary of the $1-\alpha$ confidence interval for the Fisher's distribution statistic with t and $n-t-m$ degrees of freedom.

m_{0k}^2 should be compatible with σ_0^2

This condition can be expressed as:

$$\xi_{\chi_{n-t}^2; \alpha/2} \leq \frac{m_{0k}^2}{(n-t) \cdot \sigma_0^2} \leq \xi_{\chi_{n-t}^2; 1-\alpha/2} \quad (23)$$

where $\xi_{\chi_{n-t}^2; \alpha/2}$ and $\xi_{\chi_{n-t}^2; 1-\alpha/2}$ are the lower and upper boundary of the $1-\alpha$ confidence interval for the χ^2 -distribution statistic with $n-t$ degrees of freedom.

If m_{0k}^2 is rejected, the corresponding integer vector will be rejected.

$R_k = \min$ in order to obtain $V_k^T P V_k = \min$

All integer vectors which are consistent with the above conditions should be selected as integer vector candidates and the two integer vectors which make

R_k a minimum and the second minimum should be found.

Contrast test between $\sec(R_k)$ and $\min(R_k)$

All other candidates, especially the second smallest $\sec(R_k)$ should be significantly larger than the $\min(R_k)$ to ensure that the unique result can be obtained. This condition can be expressed as the test:

$$\frac{\sec(m_{0k}^2)}{\min(m_{0k}^2)} > \xi_{F_{n-t,n-t}; 1-\alpha} \quad (24)$$

where $\xi_{F_{n-t,n-t}; 1-\alpha}$ is the boundary of the $1-\alpha$ confidence interval for the Fisher's distribution statistic with degrees of freedom $n-t$ and $n-t$.

Several search procedures based on all or some of the above mentioned validation and rejection criteria have been developed in the past few years, such as the Fast Ambiguity Resolution Approach (FARA) (Frei & Beutler, 1990), the Least Squares Ambiguity Search Technique (LSAST) (Hatch, 1990), the Cholesky decomposition method (Euler & Landau, 1992; Landau & Euler, 1992), the Fast Ambiguity Search Filter (FASF) (Chen, 1993; Chen & Lachapelle, 1994), and the LDL^T decomposition method (Teunissen et al, 1994). As an alternative, Teunissen (1994) suggested the Least-squares AMBiguity Decorrelation Adjustment (LAMBDA) which searches the transformed ambiguities.

LAMBDA METHOD

All search procedures are directly or indirectly dependent on the diagonal elements of the variance-covariance matrix of the real-valued ambiguity estimation. If the invertible integer transformation matrix can be obtained and the diagonal elements of the variance-covariance matrix of the transformed integer parameters are much smaller than the original ones, the search methods will become much more efficient. This idea was first suggested by Ibid (1994) as the Least-squares AMBiguity Decorrelation Adjustment (LAMBDA) method, which uses an ambiguity transformation matrix Z that reformulates the original ambiguity vector \hat{X}_N as the transformed ambiguity vector \hat{Z}_N whose variance-covariance matrix has much smaller diagonal elements:

$$\hat{Z}_N = Z \cdot \hat{X}_N \quad (25)$$

$$Q_{\hat{Z}_N} = Z Q_{\hat{X}_N} Z^T \quad (26)$$

and eqn (14) can be re-written as:

$$R_k = (\hat{Z}_N - N_k^Z)^T Q_{\hat{Z}_N}^{-1} (\hat{Z}_N - N_k^Z) \quad (27)$$

The original ambiguity estimation problem has therefore been changed. The new problem is to search N_k^Z for an integer set that makes $R_k = \min$ and passes the validation and rejection criteria test.

In order to ensure that the transformed ambiguity has integer characteristics, the transformation matrix Z has to have integer entries. In order to ensure that the original ambiguity can be determined from the transformed ambiguity, the inverse of the transformation matrix has also to have integer entries. Therefore, *matrix Z is an admissible ambiguity transformation if and only if matrix Z has integer entries and its determinant equals ± 1* . The original ambiguities are transformed:

$$N_k = Z^{-1} \cdot N_k^Z \quad (28)$$

The key to the LAMBDA method is to find the admissible ambiguity transformation which makes $Q_{\hat{Z}_N}$ have almost the same and minimum diagonal values, and then search the optimal integer solution.

A SUGGESTED METHOD FOR CONSTRUCTING MULTI-SATELLITE AMBIGUITY COMBINATIONS

The number of integer ambiguity candidate sets is dependent on the variance-covariance matrix, especially the determinant of the diagonal matrix of the variance-covariance matrix of real-valued ambiguity estimations ($\det(R_{\hat{X}_N})$). The transformation matrix, which has integer entries and determinant equal to ± 1 , should make the diagonal elements as small as possible. In order to quantify the extent of the decorrelation, the correlation matrix and decorrelation number are introduced.

The correlation matrix for the co-factor matrix $Q_{\hat{X}_N}$ is defined as:

$$R_{\hat{X}_N} = \left[\text{diag}(Q_{\hat{X}_N}) \right]^{-1/2} Q_{\hat{X}_N} \left[\text{diag}(Q_{\hat{X}_N}) \right]^{-1/2} \quad (29)$$

and its determinant is defined as the decorrelation number (Teunissen, 1994):

$$r_{\hat{X}_N} = \sqrt{\det(R_{\hat{X}_N})} \quad (30)$$

Due to the fact that $Q_{\hat{X}_N}$ and $Q_{\hat{Z}_N}$ have the same determinant, the following relation can be obtained:

$$r_{\hat{Z}_N}^2 \cdot \det[\text{diag}(Q_{\hat{Z}_N})] = r_{\hat{X}_N}^2 \cdot \det[\text{diag}(Q_{\hat{X}_N})] = \text{const.} \quad (31)$$

In order to make $\det[\text{diag}(Q_{\hat{Z}_N})]$ as small as possible, $r_{\hat{Z}_N}$ should be made as large as possible. This can be easily achieved using the following procedure to compute the integer transformation matrix Z .

The first step is the unit upper triangular factorisation (UDU^T) for $Q_{\hat{X}_N}$:

$$Q_{\hat{X}_N} = U_1 D_{U_1} U_1^T \quad (32)$$

and compute the integer matrix Z_{U_1} :

$$Z_{U_1} = [\text{Int}(U_1)]^{-1} \quad (33)$$

where Int is an operator to round all elements in U_1 to the nearest integers, and then

$$Q_{\hat{Z}_{N,U_1}} = Z_{U_1} Q_{\hat{X}_N} Z_{U_1}^T \quad (34)$$

The second step is the unit lower triangular factorisation (LDL^T) for $Q_{\hat{Z}_{N,U_1}}$:

$$Q_{\hat{Z}_{N,U_1}} = L_1 D_{L_1} L_1^T \quad (35)$$

and compute the integer matrix Z_{L_1} :

$$Z_{L_1} = [\text{Int}(L_1)]^{-1} \quad (36)$$

and

$$Q_{\hat{Z}_{N,L_1}} = Z_{L_1} Q_{\hat{Z}_{N,U_1}} Z_{L_1}^T \quad (37)$$

An iterative procedure is used for the first and second steps to create Z_{U_i} from $Q_{\hat{Z}_{N,L_{i-1}}}$ (or $Q_{\hat{X}_N}$ when $i=1$) and Z_{L_i} from $Q_{\hat{Z}_{N,U_i}}$ until both integer matrices $\text{Int}(U_k)$ and $\text{Int}(L_k)$ become unit matrices. The integer transformation matrix can be obtained using the following relation:

$$Z = Z_{L_{k-1}} \cdot Z_{U_{k-1}} \cdots Z_{L_1} \cdot Z_{U_1} \quad (38)$$

Z can be used to transform the original ambiguities to the transformed ambiguities and to cause the variance-covariance matrix to have a large decorrelation number in order to carry out the search in an efficient way. The suggested procedure provides an easy way to implement the LAMBDA approach.

Four examples are given in Table 1 to compare the original variance-covariance (VCV) matrix and the transformed VCV matrix. $e_{\hat{x}_N}$ and $e_{\hat{z}_N}$ are the ratios of the length of the largest principal axis with respect to the length of the smallest principal axis of the confidence ellipsoids for the original VCV matrix and

the transformed VCV matrix, respectively; $\min(\sigma_{\hat{x}_N})$ and $\max(\sigma_{\hat{x}_N})$ are the minimum and maximum values of the standard deviations of the original ambiguity estimates; $\min(\sigma_{\hat{z}_N})$ and $\max(\sigma_{\hat{z}_N})$ are the minimum and maximum values of the standard deviations of the transformed ambiguities. Comparing the original and transformed ellipsoid it is obvious that the transformed ellipsoid is much more like a sphere, the decorrelation number is much larger and the maximum value of the standard deviation of the transformed ambiguities is much smaller. The transformation time is from a few milliseconds to a few tens of milliseconds using a 486 DX4-100MHz PC. Note that the variance-covariance matrices in the examples have been standardized using the Han & Rizos (1995) procedure.

Table 1. Comparison between the Original VCV Matrix and the Transformed VCV Matrix

	Original VCV Matrix				Transformed VCV Matrix				Time (ms)
	$r_{\hat{x}_N}$	$e_{\hat{x}_N}$	$\min(\sigma_{\hat{x}_N})$	$\max(\sigma_{\hat{x}_N})$	$r_{\hat{z}_N}$	$e_{\hat{z}_N}$	$\min(\sigma_{\hat{z}_N})$	$\max(\sigma_{\hat{z}_N})$	
Example 1	5.26×10^{-14}	2069.07	5.88	14.11	0.33	3.86	0.18	0.26	58.8
Example 2	1.14×10^{-10}	468.54	0.88	2.39	0.29	3.92	0.08	0.12	32.5
Example 3	6.99×10^{-7}	2936.38	2.02	21.93	0.80	3.65	0.26	0.81	11.5
Example 4	2.16×10^{-5}	448.19	0.04	3.65	0.72	3.08	0.12	0.31	9.3

Example 1: Dual frequency phase data, 5 satellites, 30 second session with 1 second data rate.

Example 2: Dual frequency phase data, 5 satellites, 4 minute session with 1 second data rate.

Example 3: Single frequency phase data, 6 satellites, 1 minute session with 1 second data rate.

Example 4: Single frequency phase data, 6 satellites, 5 minute session with 1 second data rate.

COMPARISON OF THE SEARCH METHODS

The search problem has been investigated during the past few years. The earliest and simplest method is to round the real-valued ambiguities to the nearest integer. A long observation session is normally required in order to ensure even one integer is in the confidence region of the real-valued ambiguities.

Frei & Beutler (1990) have suggested the Fast Ambiguity Resolution Approach (FARA), which uses eqn (19) to define the initial search region and then reduce the number of candidate sets by making use of the correlations through all combinations of the difference between two ambiguities and the relations between two ambiguities on L1 and L2 to create the candidates (eqn (20)). The linear functions in eqn (20) are selected as:

$$f(\hat{x}_{n_1}, \dots, \hat{x}_{n_m}) = \hat{x}_{n_i} - \hat{x}_{n_j} \quad (39)$$

for any combinations of $i=1,2,\dots,m-1$ and $j=i+1,\dots,m$ and

$$f(\hat{x}_{n_1}, \dots, \hat{x}_{n_m}) = \hat{x}_{n_i} - \frac{\lambda_2}{\lambda_1} \cdot \hat{x}_{n_j} \quad (40)$$

for dual frequency observations, where \hat{x}_{n_i} and \hat{x}_{n_j} are the real-valued ambiguities for L1 and L2 carrier phase observations for the same pair of satellites.

The tests of eqns (22), (23) and (24) can be used to determine the final unique solution from the candidate sets.

The number of candidates in Tables 2 and 3 refers to the number of candidates after test of eqn (20) using the combinations of eqns (39) and (40). The search time for the transformed ambiguities is much shorter than the search time for the original ambiguities. Note

that the test of eqn (20) using the combination of eqn (40) is not applied in the search for the transformed ambiguities using dual frequency data.

Hatch (1990) has suggested the Least Squares Ambiguity Search Technique (LSAST), which makes use of the feature that four satellites are sufficient for positioning and for determining the other satellites' ambiguities if the three double-differenced ambiguities for these four satellites have been resolved. This technique separates the satellites into two groups. The first or primary group consists of a set of four satellites which are used to generate a set of potential solutions that lie within some uncertainty region. After one set of three ambiguities is fixed, the remaining ambiguities can be estimated (real values) and then rounded to the nearest integer to form the ambiguity candidate sets. The search results for the original ambiguities are given in Tables 2 and 3. If three transformed ambiguities are fixed, the other transformed ambiguities, in general, cannot be rounded to the nearest integer. Therefore, the LSAST method is not used to search the transformed ambiguities.

Euler & Landau (1992) have suggested the Cholesky decomposition for $Q_{\hat{x}_N}^{-1}$ (the computation of R_k will be very efficient). The candidates are constructed using eqn (19). From the results in Tables 2 and 3, it can be seen that the Cholesky decomposition method has been improved significantly using the suggested transformation procedure.

Chen (1993) and Chen & Lachapelle (1994) have suggested the Fast Ambiguity Search Filter (FASF), which uses a Kalman filter and a recursive computation of the search range for the ambiguities (RCSR). The concept of RCSR is described as follows. Assuming the ambiguity series as n_1, n_2, \dots, n_m , the search range of the ambiguities is computed from n_1 to n_m . The search range of the possible integers for ambiguity parameter n_i are computed for each specific integer set of the ambiguities on the left of n_i , ie., n_1, n_2, \dots, n_{i-1} , which is treated as being known, while n_i, n_{i+1}, \dots, n_m are the estimated parameters. The search range for n_i can be expressed as:

$$|\hat{x}_{n_i/n_1, n_2, \dots, n_{i-1}} - n_i| \leq \xi_{t_{f_i}; 1-\alpha/2} \cdot m_0 \cdot \sqrt{q_i} \quad (41)$$

where $m_0 \cdot \sqrt{q_i}$ is the standard deviation of $\hat{x}_{n_i/n_1, n_2, \dots, n_{i-1}}$ for the fixed n_1, n_2, \dots, n_{i-1} ; $\hat{x}_{n_i/n_1, n_2, \dots, n_{i-1}}$ is the float estimation of n_i corresponding to a specific integer set for

n_1, n_2, \dots, n_{i-1} ; $\xi_{t_{f_i}; 1-\alpha/2}$ has the same meaning as in eqn (19) but with f_i degrees of freedom. The results in Tables 2 and 3 are given for searching the original ambiguities and the transformed ambiguities. The computation time has been improved by using the suggested transformation procedure.

Teunissen (1994) has suggested the LDL^T decomposition search method to search the transformed ambiguities (sometimes also generally referred to as the LAMBDA method). But it can be used to search the original ambiguities as well. $Q_{\hat{x}_N}$ can be decomposed as:

$$Q_{\hat{x}_N} = LDL^T \quad (42)$$

where

$$L = \begin{bmatrix} 1 & 0 & 0 & \dots & 0 \\ L_{21} & 1 & 0 & \dots & 0 \\ L_{31} & L_{32} & 1 & \dots & 0 \\ \vdots & \vdots & \vdots & \ddots & \vdots \\ L_{m1} & L_{m2} & L_{m3} & \dots & 1 \end{bmatrix} \quad (43)$$

$$D = \text{diag}(q_1, q_2, \dots, q_m) \quad (44)$$

\hat{x}_{n_i} is not changed and $\hat{x}_{n_i/n_1, n_2, \dots, n_{i-1}}$ can be represented as the following for $i > 1$:

$$\hat{x}_{n_i/n_1, n_2, \dots, n_{i-1}} = \hat{x}_{n_i} - \sum_{j=1}^{i-1} [L_{ij} (\hat{x}_{n_j/n_1, n_2, \dots, n_{j-1}} - n_j)] \quad (45)$$

Eqns (42-45) define the other computation method of $\hat{x}_{n_i/n_1, n_2, \dots, n_{i-1}}$ and q_i for the FASF method. The following relation should hold from eqns (18):

$$\sum_{i=1}^m \left[\frac{(\hat{x}_{n_i/n_1, n_2, \dots, n_{i-1}} - n_i)^2}{q_i} \right] < m \cdot m_0^2 \cdot \xi_{F_{m, n-t-m}; 1-\alpha} \quad (46)$$

The search region is defined as:

$$|\hat{x}_{n_i/n_1, n_2, \dots, n_{i-1}} - n_i| < m \cdot m_0^2 \cdot \xi_{F_{m, n-t-m}; 1-\alpha} - \sum_{j=1}^{i-1} \left[\frac{(\hat{x}_{n_j/n_1, n_2, \dots, n_{j-1}} - n_j)^2}{q_j} \right] \quad (47)$$

The LDL^T decomposition method is used to search the original ambiguities and the transformed ambiguities and the results are given in Tables 2 and 3.

Using the suggested method for constructing the multi-satellite ambiguity combinations and searching the transformed ambiguities, all search methods, such as FARA, LSAST, Cholesky, FASF and LDL^T , will be significantly improved.

All these search methods can also be compared. Although FARA is not efficient for single frequency data, it is comparatively efficient for use with dual

frequency data, and is implemented within the SKI commercial GPS software. LSAST and FASF are quite good for single frequency data. The Cholesky decomposition method has been significantly improved by searching the transformed ambiguities and appears to be one of the best methods when combined with the LAMBDA transformation procedure. Although the LDL^T decomposition search method is suggested for searching the transformed ambiguities (Teunissen, 1994), it is also one of the most efficient methods to search the original ambiguities, especially for a huge search region.

Table 2. Comparison of the Different Methods for Searching the Original Ambiguities and for Searching the Transformed Ambiguities

Search Methods	Searching the Original Ambiguities		Searching the Transformed Ambiguities	
	Number of Candidates	Time (sec)	Number of Candidates	Time (ms)
FARA	24095934	1195.46	956	35.37
LSAST	83720	2.91	N/A	N/A
Cholesky	6.85×10^8	3.41	2250	4.23
FASF	24637	1.15	1906	60.20
LDL^T	978	1.54	977	49.76

Note: Single frequency phase data from 6 satellites, 1 minute session and 1 second data rate are used. The variance-covariance matrix has been standardized using the Han & Rizos (1995) procedure. The confidence level is selected as 0.997. The volume of the ellipsoid determined by eqn (18) is 987.44 cycle⁵. The search time for the transformed ambiguities does not include the transformation time. A 486 DX4-100MHz PC and Fortran code written by the present authors (not the original authors) has been used.

Table 3. Comparison of the Different Methods for Searching the Original Ambiguities and for Searching the Transformed Ambiguities

Search Methods	Searching the Original Ambiguities		Searching the Transformed Ambiguities	
	Number of Candidates	Time (sec)	Number of Candidates	Time (ms)
FARA	788	2.08	88	9.45
LSAST	370175	28.29	N/A	N/A
Cholesky	5.55×10^{13}	5.22	1296	8.68
FASF	85227	7.80	624	44.98
LDL^T	10	0.27	10	4.34

Note: Dual frequency phase data from 5 satellites, 30 second session and 1 second data rate are used. The variance-covariance matrix has been standardized using the Han & Rizos (1995) procedure. The confidence level is selected as 0.997. The volume of the ellipsoid determined by eqn (18) is 10.573 cycle⁸. The search time for the transformed ambiguities does not include the transformation time. A 486 DX4-100MHz PC and Fortran code written by the present authors (not the original authors) has been used.

CONCLUSIONS

A new method for constructing multi-satellite ambiguity combinations to implement LAMBDA is suggested which can make the variance-covariance matrix significantly decorrelated. The transformation time is very short, typically between a few milliseconds and a few tens of milliseconds. The search methods, such as FARA, LSAST, the Cholesky decomposition method, FASF and the LDL^T decomposition method, are employed to search the transformed ambiguities and the results are shown to have been significantly improved. Hence, if the existing software packages employing such search methods were modified to implement the suggested transformation method, the data processing will become much more efficient.

The suggested transformation method can be easily combined with the Cholesky decomposition search procedure or the LDL^T decomposition search procedure, resulting in a procedure that is highly efficient in terms of computation time.

ACKNOWLEDGEMENTS

The first author is supported by Australian Research Council funding.

REFERENCES

- Chen D. (1993), "Fast Ambiguity Search Filter (FASF): A Novel Concept for GPS Ambiguity Resolution", proceedings of the ION GPS-93, Salt Lake City, Utah, 22-24 September, 781-787.
- Chen D. and G. Lachapelle (1994), "A Comparison of the FASF and Least-Squares Search Algorithms for Ambiguity Resolution On The Fly", proceedings of the International Symposium on Kinematic Systems in Geodesy, Geomatics and Navigation, Banff, Canada, 30 August - 2 September, 241-253.
- El-Rabbany, A. E-S. (1994), "The Effect of Physical Correlations on the Ambiguity Resolution and Accuracy Estimation in GPS Differential Positioning. Ph.D. dissertation, Department of Geodesy and Geomatics Engineering Technical Report No. 170, University of New Brunswick, Fredericton, New Brunswick, Canada, 161pp.
- Euler, H-J. and H. Landau (1992), "Fast GPS Ambiguity Resolution On-The-Fly for Real-time Applications", proceedings of the 6th International Geodetic Symposium on Satellite Positioning, Columbus, Ohio, 17-20 March, 650-659.
- Frei, E. and G. Beutler (1990), "Rapid Static Positioning Based on the Fast Ambiguity Resolution Approach FARA: Theory and First Results", *Manuscripta Geodaetica*, 15:325-356.
- Han, S. (1994), "Validation and Rejection Criteria for Integer Least-Squares Estimation", presented at 1994 UNSW Annual Research Seminars, (abstract), *Australian Journal of Geodesy, Photogrammetry and Surveying*, No. 61, December, 1994.
- Han, S. and C. Rizos (1995), "Standardization of the Variance-Covariance Matrix for GPS Rapid Static Positioning", *Australian Journal of Geodesy, Photogrammetry and Surveying*, No. 62, June, 1995.
- Hatch, R. R. (1990), "Instantaneous Ambiguity Resolution", *Kinematic Systems in Geodesy, Surveying and Remote Sensing*, IAG Symposia 107, Springer Verlag, New York, 299-308.
- Landau, H. and H. J. Euler (1992), "On-The-Fly Ambiguity Resolution for Precise Differential Positioning", proceedings of ION GPS-92, Albuquerque, New Mexico, 16-18 September, 607-613.
- Teunissen, P. J. G. (1994), "A New Method for Fast Carrier Phase Ambiguity Estimation", proceedings IEEE Position Location and Navigation Symposium PLANS94, Las Vegas, 11-15 April, 562-573.
- Teunissen, P. J. G., P. J. de Jonge and C. C. J. M. Tiberius (1994), "On the Spectrum of the GPS DD-Ambiguities", proceedings of ION GPS-94, Salt Lake City, Utah, 20-23 September, 115-124.

Long Period Systematic Errors in GPS Measurements

Shane Nelson

Applied Research Laboratory, University of Texas

Biography

Shane Nelson is a Research Scientist Associate at the Applied Research Laboratories, The University of Texas at Austin, ARL:UT, where he is involved in GPS research. He received a BS in physics and a BA in the Plan II liberal arts program at the University of Texas at Austin.

Abstract

Improvements in the quality of GPS receivers in recent years have significantly reduced the "random" component of GPS measurement error. This has allowed more detailed analysis of the systematic errors manifested in GPS measurements. Applied Research Laboratories, The University of Texas, ARL:UT, has investigated long period (>1 hour) systematic trends in the two frequency corrected range minus phase combination formed with data from modern commercial geodetic GPS receivers. Specifically, these trends represent a slowly changing, non-ionospheric, difference between the range and phase measurements. These trends are shown to be sensitive to antenna design and are attributed primarily to code multipath manifested in very long periods. It is shown that trends in measurement error can also be induced by receiver temperature gradients but that these trends, common to all satellites in track, do not affect double difference observables and can be mitigated through simple temperature stabilization.

Introduction

In characterizing GPS receiver performance for precise positioning applications, great emphasis is placed on assessing measurement data quality and integrity. While the observables of interest will vary for different applications, it is assumed that the measurement characteristics are well understood, in general. The goal, then, of receiver performance analysis is to ensure that the actual measurement characteristics of a particular receiver

type or class can be quantified and shown to behave in a predictable manner.

During such performance analysis of geodetic GPS receivers at ARL:UT, a previously unaddressed phenomenon was identified. Systematic trends in the two frequency corrected range minus phase were observed with periods as long as a satellite pass and magnitudes of up to three meters. The author was unable to find references to this phenomenon in literature or in speaking with other researchers. Tests were therefore conducted to determine the cause of the trends. The results of those tests are reported below as well as the recommended mitigation strategies and possible effects on the user community.

Background

The difference between the GPS pseudorange and phase measurements is a useful tool for investigating pseudorange measurement noise, pseudorange multipath, and ionospheric effects, since other effects of the same or greater magnitude are canceled out in this difference (satellite and receiver clocks, tropospheric delay, Selective Availability). Moreover, the availability of two GPS frequencies allows for the creation of well known linear combinations of observables in which the effects of the dispersive ionosphere are removed to first order[10]. The equations for these ionosphere corrected observables are reprinted below:

$$R_{cor} = R_{L1} - \alpha^2 \times R_{L2}$$

$$\varphi_{cor} = \varphi_{L1} - \alpha \times \varphi_{L2}$$

where:

$$\alpha = \frac{f_{L2}}{f_{L1}}$$

The difference between the ionosphere corrected pseudorange and the ionosphere corrected phase is known as the two frequency corrected range minus phase, TFC RMP, allows an estimate of pseudorange measurement noise and pseudorange multipath[6].

$$TFC RMP = R_{cor} - \phi_{cor}$$

The magnitude of the noise resulting from this linear combination of four observables is approximately 4 times that on the L1 pseudorange measurement.[9] Since this relationship is known, however, receiver pseudorange noise (with multipath) can be isolated and examined using this combination. It can therefore be used as an indicator of code measurement precision.

Characterization of the Phenomenon

In the absence of signal multipath, the TFC RMP would appear as a constant with added noise. Typically, code multipath is present and is readily observable in the TFC RMP as sawtooth periodic variations with periods on the order of minutes. Investigators at ARL:UT, however, in conducting performance tests on geodetic GPS receivers, discovered systematic trends in the TFC RMP, with periods much longer than this, as shown in Fig. 1. The shorter period multipath is still evident, but is superimposed on a longer period systematic trend. These systematic trends were found to exhibit a number of consistent characteristics:

Periodicity: The trends in the TFC RMP can have periods as long as a satellite pass (3-6 hours) Fig. 1, for instance, represents a period of 5 hours. In this paper "long period" will be used to characterize systematic trends of period greater than an hour and "short period" will be used to characterize trends of period less than an hour.

Amplitude: The long period trends in the data collected from a given satellite can reach peak to peak magnitudes of up to three meters. More typical magnitudes of one to two meters are evident in Fig. 2.

Non Common Mode: For a given tracking interval, the long period trends neither occur for all satellites nor are they common to all satellites on which they do occur. Fig. 2 is a plot of the TFC RMP for PRN 7 during the same interval that the TFC RMP is shown for PRN 2 in Fig. 1. The long period components are obviously dissimilar.

Day to Day Repeatability: The long period trends remain very similar from day to day. Figs. 3-5 are plots of the TFC RMP for PRN 12 tracked on three consecutive days at the same antenna location.

Because the noise and multipath levels are amplified in the TFC RMP combination, the magnitude of observed trends in this combination is greater than that of the error in the raw measurements. Amplitudes, then, of 1-3 meters in the TFC RMP imply decimeter to meter level differences between the range and phase measurements.

It must be assumed that the observed difference between the pseudorange and phase measurements, at least to first order, represents an error in the pseudorange measurement. Were it an error in the phase measurement, not common to all satellites, millimeter level surveying with the carrier phase observable would not be possible; However, the L1 carrier phase observable and the ionosphere corrected carrier phase are now routinely used in geodetic surveys to produce millimeter level repeatabilities on a variety of baseline lengths and millimeter level verifiable accuracies on short baselines[5],[11].

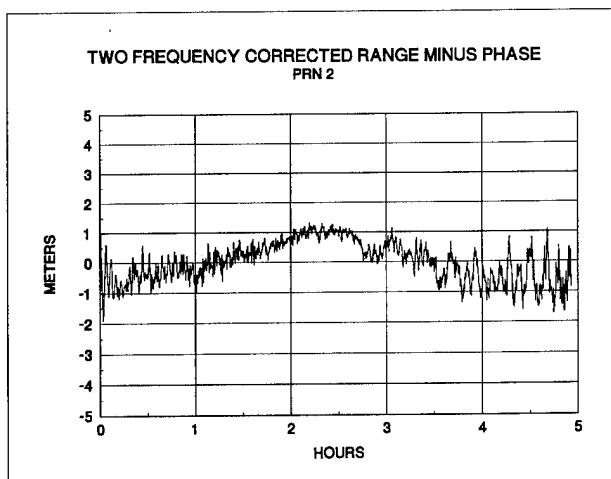


Fig. 1: Ashtech Z(Y)-12 receiver; Y-code; Ashtech groundplane antenna.

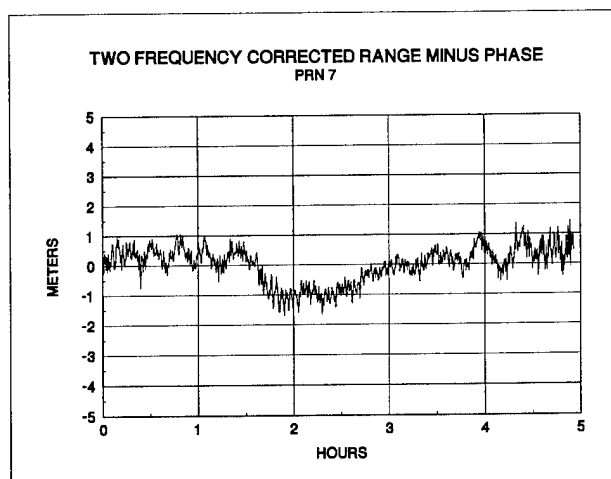


Fig. 2: Ashtech Z(Y)-12 receiver; Y-code; Ashtech ground plane antenna.

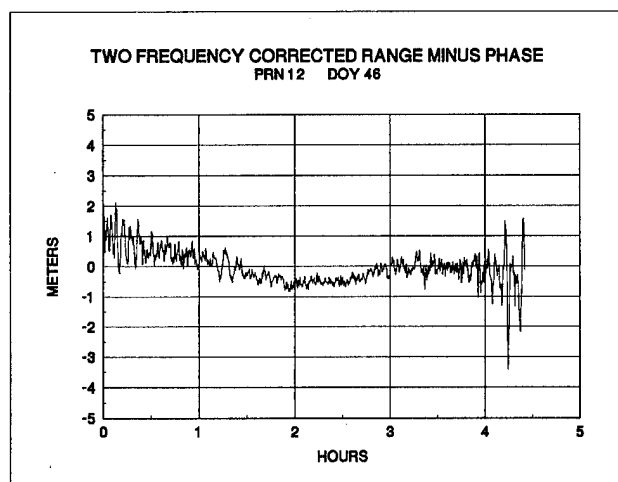


Fig. 3: Ashtech Z-12 receiver; Z-codeless tracking mode; Ashtech ground plane antenna

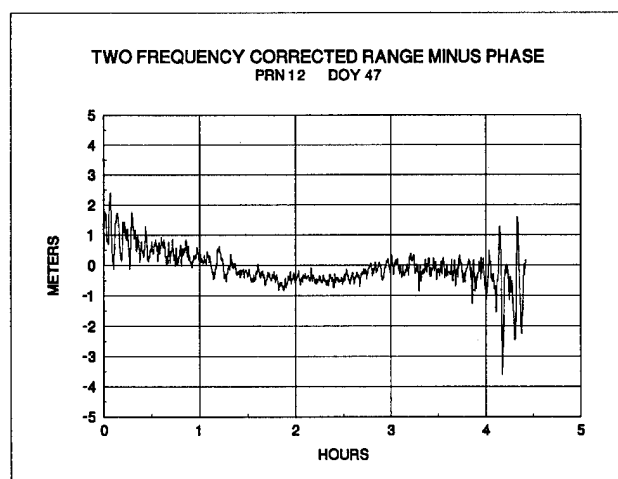


Fig. 4: Ashtech Z-12 receiver; Z-codeless tracking mode; Ashtech ground plane antenna

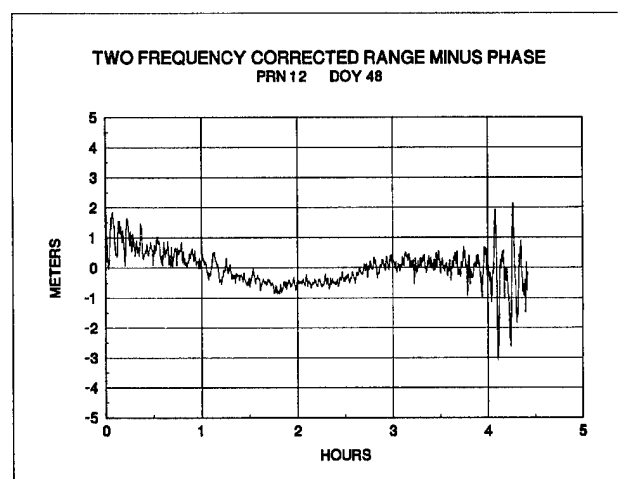


Fig. 5: Ashtech Z-12 receiver; Z-codeless tracking mode; Ashtech ground plane antenna

Potential user concerns

Long period errors in the pseudorange measurement are of concern to that portion of the GPS community which requires the highest accuracy possible in the undifferenced pseudorange. e.g.: users interested in determining absolute ionospheric delay, users who require precise knowledge of the satellite clocks, users of the pseudorange for precise satellite orbit determination and realtime DGPS users requiring the highest possible accuracy.

It is also clear that the effectiveness of smoothing or filtering the TFC RMP to obtain a carrier smoothed pseudorange will be degraded in the presence of such long period multipath. Typically a smoothing interval is chosen to be as long as, or longer than, the period of the dominant systematic error. Errors then with periods as long as the satellite pass cannot be effectively smoothed.

It should also be noted that the observations reported in this paper do not reflect the observed double difference measurement noise of the geodetic receivers tested. **Appendix 1** reports the receiver measurement noise, as determined at ARL:UT, of the Ashtech Z(Y)-12 receiver which was used for much of the analysis reported in this paper. The results indicate that there are no channel specific systematic errors above the level of the measurement noise occurring inside that receiver.

The satellite specific signature of this error, as well as the day to day repeatability indicate that it is attributable to pseudorange multipath. However, because the long period is not consistent with the common conception of multipath, analysis was conducted to confirm that the observed error was, in fact, multipath and to determine its nature. Antenna testing was conducted to confirm that the error originated outside the receiver. When this was confirmed, tests of the receivers themselves were conducted to determine if any receiver features make measurements more or less susceptible to long period multipath.

Antenna tests

Various antenna configurations were tested to determine the effectiveness of standard multipath mitigation strategies on this particular type of multipath. Receiver conditions suspected as error sources, such as receiver firmware, tracking mode, and temperature, were held constant for all receivers. Differences in the data can then be attributed to sources external to the receiver.

Multipath mitigation strategies included several ground plane antenna assemblies, a commercial choke ring

antenna assembly, a fabricated (hand constructed) choke ring antenna assembly, and an antenna imbedded in microwave absorbent foam. Antennas were mounted on tripods approximately 1.5 meters above the ground -- except when this height was varied as a parameter -- and passed signals to Ashtech Z(Y)-12 receivers operating in direct Y tracking mode and held at the same stable external temperature. These antenna configurations were set near to one another in an open environment free from obstructions or above ground reflectors for a radius of more than 30 meters.

Choke Rings

The results of tests with these various antenna assemblies and configurations, while showing conclusively that the long period trends in the TFC RMP are antenna dependent and can be virtually eliminated by using a choke ring/antenna assembly, also showed that *some* proven multipath mitigation strategies are not effective at eliminating long period multipath. The results of the tests with the Ashtech choke ring assembly are illustrated in Fig. 6 which is a plot of the TFC RMP for PRN 2. This is to be compared with Fig. 1, showing data collected simultaneously on a receiver using a commercial ground plane in the same environment. Both receivers were temperature stabilized.

In the case of the data collected on the choke ring/ antenna assembly, the trends are absent. The improvement is typical of satellites tracked on the two receivers, and illustrates the strong antenna dependence of long period multipath. This result also rules out signal propagation effects which would be common to proximate antennas.

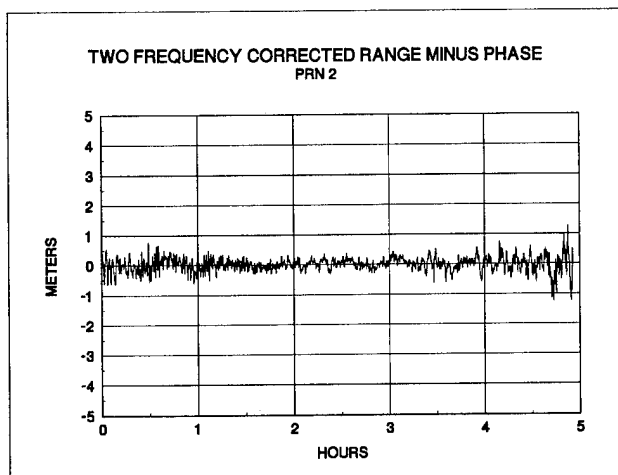


Fig. 6: Ashtech Z(Y)-12 receiver; Y-code; Ashtech choke ring antenna

Conversations with Fred Solheim at Radiometrics Inc., who reported very effective pseudorange multipath reduction through the use of easily constructed choke rings,[12] led ARL:UT to construct several of these choke

rings for testing. These fabricated choke ring/antennas were found to eliminate the long period multipath in all collected data sets as well as, and for some elevation angles better than, the commercial choke rings tested. Shown in Fig. 7 is the fabricated choke ring made with inexpensive building materials and aluminum tape.

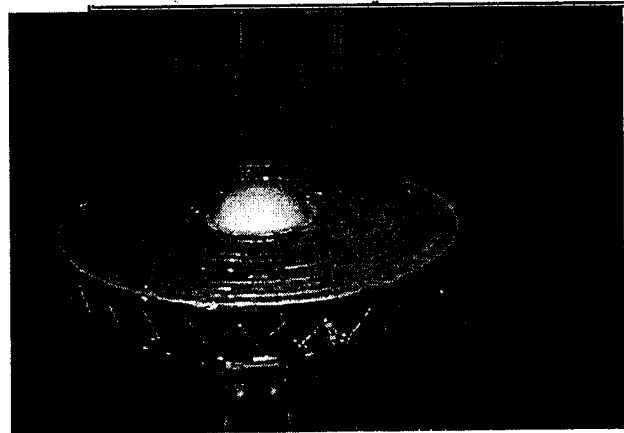


Fig. 7: Fabricated choke ring assembly with Dorne & Margollan antenna

Fabrication of this simple choke ring assembly also enabled us to equip the antenna with the same preamp being used in a commercial ground plane antenna and thereby diagnose any pre-amp dependence. The fact that the long period multipath can be eliminated using a choke ring with the same preamp as the more susceptible ground plane antenna, indicates that the preamp is not the source of this error.

Other Mitigation Strategies

Other various multipath mitigation strategies were not as effective as the choke rings. It was found that this multipath is not sensitive to antenna height. The long period trends remain evident even when the antenna is placed directly on the ground, a technique which is effective at reducing some short period multipath. This same result was obtained when the ground antenna was embedded in microwave absorbent foam. Further, testing with various ground plane dimensions up to a 24" radius, indicated that many ground planes are ineffective at eliminating long period multipath effects. In each of these tests, the short period trends due to multipath were reduced, as has been previously reported, indicating that overall multipath can be reduced while this unique long period manifestation is undiminished.

Statistics computed with the data collected on several ground planes (including the Ashtech ground plane), an Ashtech choke ring, and the fabricated choke ring are given in Table 1 below. Note that averaging over 300 s. intervals is intended to reduce the effect of short period multipath and "random" noise. Hence, the statistics are more representative of the long period errors.

Also note that the greatest improvement in measurement performance resulting from the use of the choke rings is in the highest satellite elevation angle bin, 40-90 degrees, where high SNR's and low angles of signal incidence result in a minimum of short period measurement error. This is indicative of the fact that the error characteristics (noise and multipath) of the pseudorange measurement can be dominated by the systematic long period multipath, a fact which is also obvious in Figs. 1-5.

Table 1. Standard Deviation of TFC RMP observable (after 300 second averaging) Y-code data

Satellite Elevation Angle (deg)	Ashtech Commercial and Fabricated Ground Planes	Ashtech Choke Ring	Fabricated Choke Ring
10 - 30	25-30 cm	25 cm	15 cm
20 - 40	25-45 cm	12 cm	11 cm
40 - 90	30-75 cm	11 cm	12 cm

Receiver Tests

Three commercial geodetic GPS receivers were tested to determine whether this particular long period multipath corruption is receiver unique. The Ashtech Z(Y)-12, The Allen Osbourne and Associates TurboRogue, and the Trimble 4000SSE were tested.

Receiver Type

An Ashtech Z(Y)-12 and an Allen Osbourne and Associates TurboRogue receiver were operated in a zero baseline configuration. In such a configuration, two receivers track virtually the same signal. This allows the investigator to observe differences in the data which can only have occurred in the receiver itself.[3] Both receivers were held at the same external temperature and tracked in codeless mode (each receiver does employ a different codeless tracking technique.) As expected, the "random" noise characteristics of the Ashtech and AOA data were dissimilar due to the different codeless tracking techniques employed. However, the long period trend of the TFC RMP for a given satellite is common to both receivers. Figs. 8-11 are plots of the TFC RMP for PRNs 12 and 24 tracked on the Ashtech Z(Y)-12 and AOA TurboRogue receivers.

Though extensive testing was not carried out with the Trimble 4000SSE receiver, the one data set that was examined indicated that the Trimble receiver is also

susceptible to this manifestation of multipath corruption, though not necessarily the Trimble antenna. Fig. 12 shows PRN 7 being tracked in codeless mode by a temperature stabilized Trimble 4000SSE receiver and an Ashtech ground plane antenna.

Tracking Mode

To determine the effects of receiver tracking mode on long period multipath, two Ashtech Z(Y)-12's were operated in a zero baseline configuration. Both receivers were held at a constant external temperature. One receiver tracked in Z-codeless mode while the other receiver, which was keyed, directly tracked the Y code. Although, as expected, the "random" noise of the data were dependent on the tracking mode in which the receiver operated, the long period multipath is clearly not dependent on the tracking mode. Figs. 13-14 are plots of the TFC RMP for PRN's 2 and 7 being tracked, in codeless mode, on a receiver in zero baseline configuration with the receiver of Figs. 1 and 2. The long period components of the signal are common to both receivers for a given satellite.

Receiver Temperature

To evaluate the effect of receiver temperature on the measurements, data was provided by Ashtech Inc. taken on two Ashtech Z-12 receivers in a zero baseline configuration. The signals were simulated in a Stanford Telecomm GPS simulator. One control receiver was operated at the ambient lab temperature while the other was placed in a temperature chamber. Two hours into the four hour data set, the chamber temperature was raised by 10 degrees centigrade. Fig. 15 shows the TFC RMP for PRN 10 tracked on the heated receiver. The long period trend, beginning at the onset of the receiver temperature change, is obvious. This trend is not evident in the control receiver, but is evident in all SV's tracked on the heated receiver.

To illustrate the common mode character of this temperature effect, the TFC RMP for PRN 10 was differenced with that of PRN 2. Fig. 16, a plot of this difference, shows that the zero-mean, random error characteristics are recovered in this difference. Changes in receiver temperature affect all tracking channels equally, at least to the level of the random measurement noise. This substantiates the claim that receiver temperature induced errors will not affect carrier phase based GPS surveying.

Conclusions of Receiver Testing

The results of these antenna and receiver tests imply that the long period trends are a manifestation of code multipath which is not unique to a single receiver type or to a particular codeless tracking method. While each of the receivers tested employs some multipath mitigating

signal processing, it is apparent that this signal processing does not eliminate the long period multipath. Finally, while temporal temperature gradients do cause errors in the raw observables, these errors are common across all tracking channels and are independent of the satellite specific long period multipath.

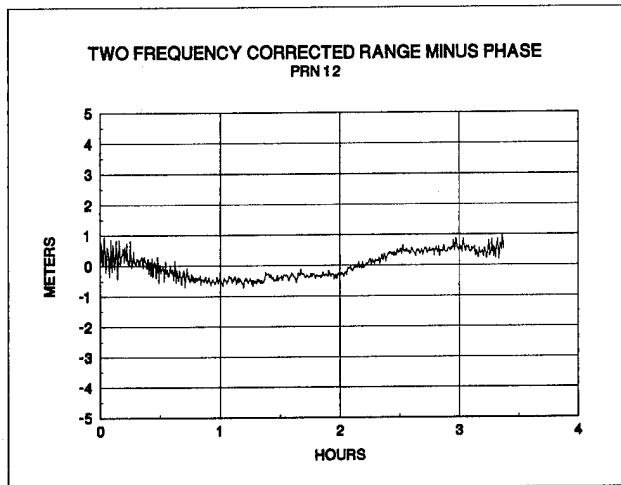


Fig. 8: Ashtech Z-12 receiver; P-code tracking; Ashtech ground plane antenna

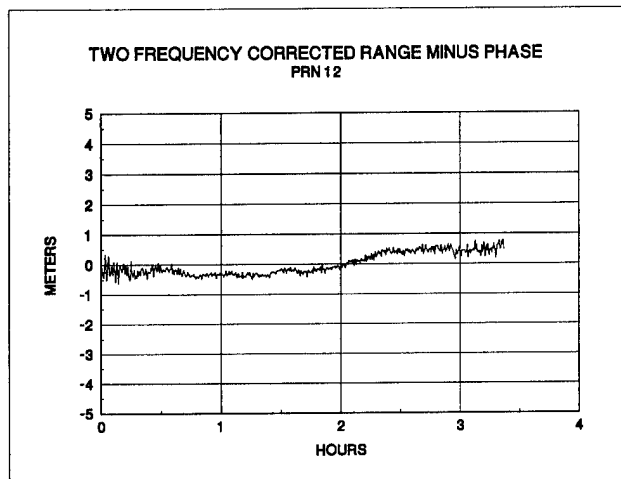


Fig. 9: AOA TurboRogue receiver; P-code tracking; Ashtech ground plane antenna

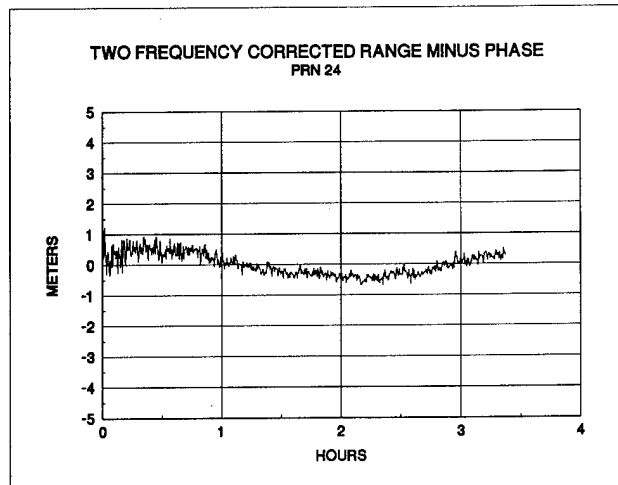


Fig. 10: Ashtech Z-12 receiver; Z-codeless tracking mode; Ashtech ground plane antenna

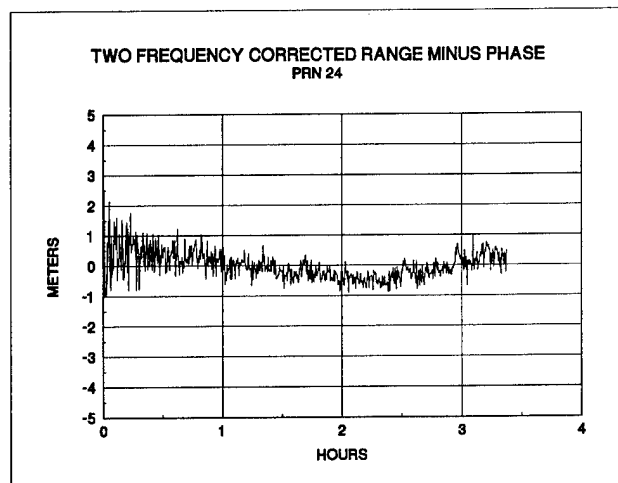


Fig. 11: AOA TurboRogue receiver; codeless tracking mode; Ashtech ground plane antenna

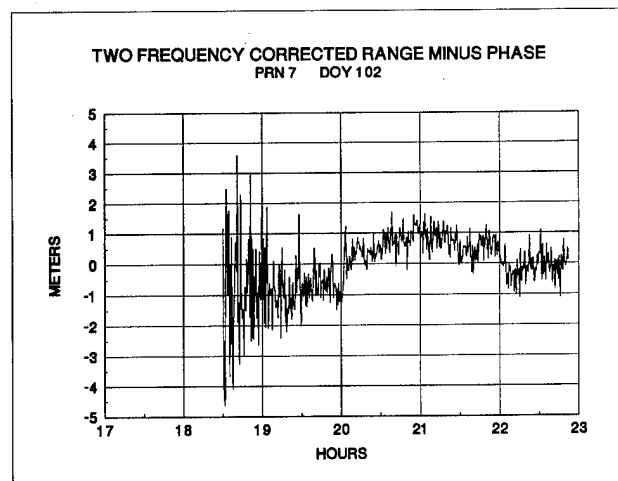


Fig. 12: Trimble 4000SSE receiver; codeless tracking mode; Ashtech ground plane antenna

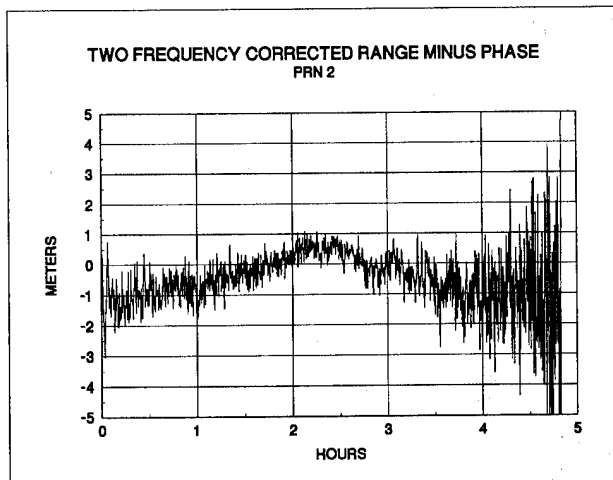


Fig. 13: Ashtech Z(Y)-12 receiver; Z-codeless tracking mode; Ashtech ground plane antenna

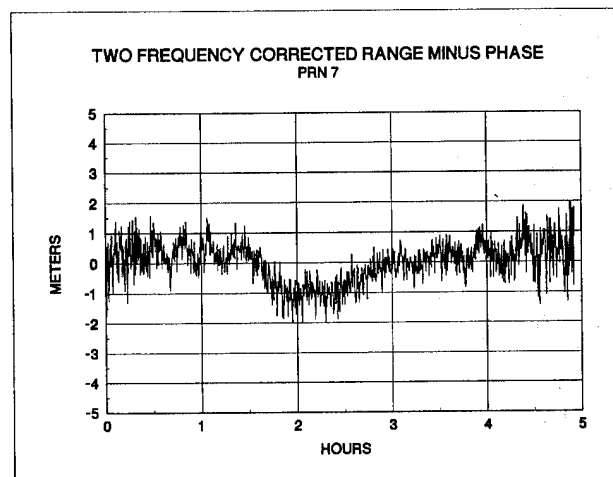


Fig. 14: Ashtech Z(Y)-12 receiver; Z-codeless tracking mode; Ashtech ground plane antenna

Speculation on long period multipath

Code multipath has been traditionally thought of as being manifested in sinusoidal oscillations of period about 1-30 minutes[8],[15]. Multipath oscillations with periods on the order of an hour have been noted[14], and have been theoretically described elsewhere.[15] The observed multipath, described in this paper, has periods as long as a satellite pass, and thus requires a specific explanation.

The existence of long period multipath in an environment free from any discrete reflectors above the level of the antenna indicates that it cannot be attributed to various small reflectors. Nor can it easily be attributed to backlobe gain of the antenna, as it remains evident even when an antenna is embedded in microwave absorbent foam resting on the ground.

Signal diffraction at the edge of a GPS antenna is a known phenomenon and a likely candidate for the source of long

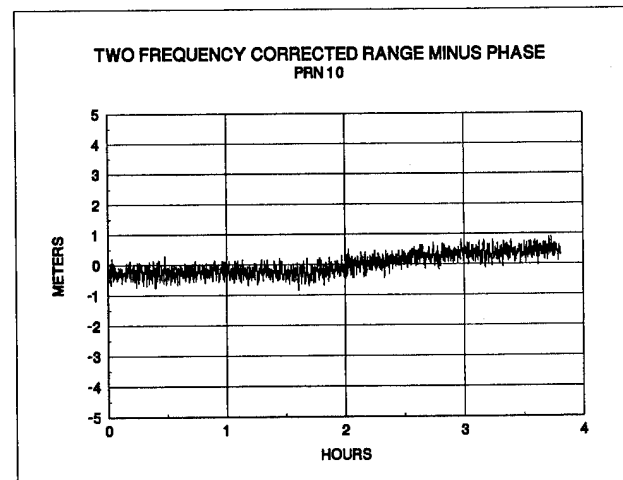


Fig. 15: Simulator data; external receiver temperature increased by 10 degrees centigrade at the two hour mark.

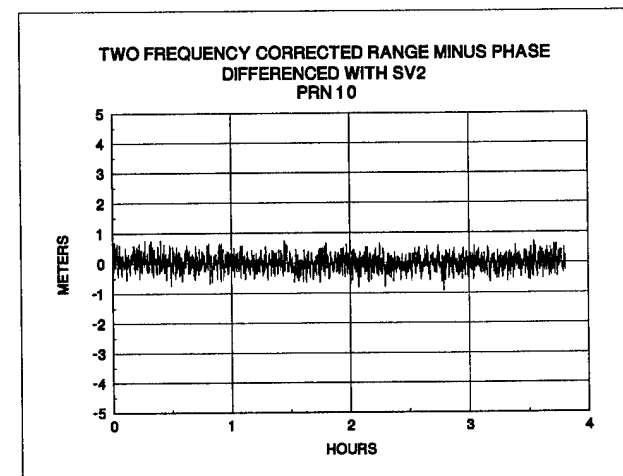


Fig. 16: Simulator data; TFC RMP difference between PRN's 2 and 10.

period multipath. It is known that the effectiveness of some ground planes at reducing short period multipath is a function of signal interference from an edge diffracted signal[13] Also, researchers have reported that multipath is not eliminated by placing an antenna high above all reflecting objects and imbedding it in microwave absorbent foam. These results led them to the conclusion that diffraction at the edge of the absorbent foam and into the antenna element, was responsible for significant residual multipath.[12]

It is the author's speculation, then, that the long period trends in the TFC RMP, evident in various antenna configurations, are a result of a continuous, or nearly continuous signal being diffracted at the edge of the antenna assembly (antenna edge, ground plane, foam) and into the antenna element. The amplitude of the diffracted signal is a function of the satellite elevation angle but varies slowly with the changes in this angle. It is not yet clear whether ground reflected signals being diffracted at

the edge of the antenna or signals directly striking this edge are responsible for the signal corruption. Conversations with Fred Solheim, who suggested the fabrication of inexpensive choke rings, suggest that the choke ring design is specifically intended to reduce such edge diffracted signals. This accounts for the effectiveness of the choke ring at eliminating long period multipath if it is fact caused by an edge diffracted signal.

15. Conclusions

The observed long period systematic trends in the TFC RMP of the receivers studied are believed to be primarily due to long period code multipath. Like shorter period multipath, this manifestation is not common to all satellites and is repeatable day to day. Susceptibility to such multipath (>1 hour) is not unique to one receiver type or to receiver tracking mode.

Long period multipath can be virtually eliminated (reduced at least to below the level of random measurement noise and short period multipath) by using an appropriate choke ring antenna assembly. Other multipath mitigation techniques tested were not effective at eliminating long period multipath. These included several sizes of ground planes, the use of microwave absorbent foam, and placing the antenna directly on the ground.

The long period nature of such multipath makes traditional filtering techniques less useful. Standard pseudorange carrier smoothing, for instance, operates on the assumption that the averaging window is larger than the period of the noise or dominant multipath. This is difficult to accomplish, if the period of the multipath is as long as the satellite pass.

Realtime DGPS users can obviously be affected by this long period multipath at either the reference station or the mobile station. Because traditional filtering techniques can be ineffective at mitigating such multipath, this is true whether the raw pseudorange observable is being used or the carrier smoothed pseudorange. This problem, then, will not be obviated by including the phase observable in the updated RTCM message. Similarly, due to the potential ineffectiveness of smoothing, determination of the absolute ionospheric delay is detrimentally affected by long period multipath corruption and can therefore be improved by using an effective multipath mitigation strategy. The same is true for GPS satellite orbit determination techniques using the pseudorange.

Temperature effects, in a controlled environment are typically manifested in drifts on the centimeter to decimeter level in the TFC RMP. These can be larger under conditions of intense temperature gradients.

However, they are common to all satellites in track, as expected, and therefore do not affect a double difference application.

It is the author's speculation that signal diffraction at the edge of the antenna assembly (absorbent foam, when surrounding the antenna, can be considered a part of the assembly) is responsible for long period multipath. This may be in one of two forms 1) ground reflections diffracting over the edge of the antenna assembly or to 2) a direct signal striking and diffracting off of the edge of the antenna assembly. Testing to date has not separated these two possibilities.

ACKNOWLEDGMENTS

Credit for this work and paper is due primarily to researchers in the Geomatics Systems Division at ARL:UT, especially Mark Leach, Mike Hyzak, Mike Cardoza, Annabelle Colestock, Allison Floyd, Peter Kappler, Henry Harya, and Linda Martinez. For suggestions and recommendations, thanks goes to Sergei Gourevitch (Ashtech), Ben Roth, Steve Malys, Fred Solheim (Radiometrics), A.J. Van Dierendonck, Tom Meehan (JPL), Ron Hatch, James Clynych (NPS), and Bob Schutz (CSR:UT).

REFERENCES

- [1] Bishop G.J., Klobuchar J.A.; Multipath Effects on the Determination of Absolute Ionospheric Time Delay from GPS Signals; *Radio Science* 20(3), p. 388; 1985.
- [2] Bishop, Greg; Multipath Impact on Ground-based Global Positioning System Range Measurements: Aspects of Measurement, Modeling, and Mitigation; *Proceedings of AGARD EEP, 53rd Symposium*.
- [3] Coco, David; Clynych, James; System Performance Tests for the TI 4100 Geodetic Receiver; *Proceedings of the 4th International Geodetic Symposium on Satellite Doppler Positioning*; Austin, TX; 1986.
- [4] Cohen C.; Pervan B., Parkinson B.W.; Estimation of Absolute Ionospheric Delay Exclusively through Single Frequency GPS Measurements; *Proceedings of ION-GPS 92*; Albuquerque, NM; Sept. 1992.
- [5] Emerle R, Leach M, Hyzak M; Sub-Centimeter Level Surveying with GPS: An Initial Assessment; *Proceedings of the International Symposium on Kinematic Systems in Geodesy, Geomatics and Navigation*; Banff, Canada; 1994.
- [6] Evans, Al; Comparison of GPS Pseudorange and Biased Doppler Range Measurements to Demonstrate

Signal Multipath Effects; Proceedings 4th International Symposium on Satellite Positioning; Austin, TX; 1986.

[7] Furgason, S; Ashtech Z(Y)-12 Measurement Precision; Interoffice Memorandum; Applied Research Laboratories; University of Texas; March, 1995.

[8] General Dynamics, Electronics Division; Final user field test report for the NAVSTAR GPS system phase I, major field test objective no. 17: Environmental effects, multipath rejection, Rep. GPS-GD-025-C-US-7008, sect. II; San Diego, CA; 1979.

[9] Hatch, Ron; The Synergism of GPS Code and Carrier Measurements; 3rd International Geodetic Symposium on Satellite Doppler Positioning; Las Cruces, NM; Feb. 1982.

[10] Hofman-Wellenhof B., Lichtenegger H., Collins J.; GPS Theory and Practice; Springer-Verlag Wien; New York; 1992.

[11] Hyzak, M; GSTSS Choke Ring Evaluation; Interoffice Memorandum Applied Research Laboratories; University of Texas; July, 1995.

[12] Rocken C., Solheim F., Meertens M., Johnson J.; Development of Multipath Reduction Hardware and Software; Phillips Laboratory Report PL-TR-94-2008; 13 January, 1994.

[13] Tranquilla J.M., Colpitts B.G.; GPS Antenna Design Characteristics for High Precision Applications; Proceedings ASCE Specialty Conference GPS-88 Engineering Applications of GPS Satellite Survey Technology; Nashville, TN; 1988.

[14] Tranquilla, J.M. ; Carr, J.P.; GPS Multipath Field Observations at Land and Water Sites; Navigation, 37, 4, 393, Winter 1990-91

[15] van Nee R.; Multipath Effects on GPS Code Phase Measurements; Proceedings of the ION-GPS 91; Washington D.C.; Sept. 1991.

APPENDIX 1

Much of the analysis reported in this paper was done on data collected on Ashtech geodetic GPS receivers. To illustrate that the reported pseudorange measurement error originates outside the receiver, the average values for the P1, P2, L1, and L2 measurement noise in the Ashtech Z(Y)-12, as calculated at ARL:UT from a double difference, are shown below. [7] These numbers represent the receiver measurement noise independent of all other error sources. They are within expected values.

Ashtech Z(Y)-12 Receiver Measurement Noise (1 sigma) Direct Y code tracking

P1	7.17 cm
P2	8.59 cm
L1	0.36 mm
L2	0.38 mm



Session B4

Earth Observation and Timing

Chair:

Mr. David Allan

Allan's TIME

Co-Chair:

Mr. Greg Bishop

Phillips Laboratory

Sensing the Atmosphere From a Low-Earth Orbiter

Tracking GPS: Early Results and Lessons

From the GPS/MET Experiment

George Hajj, E. Rob Kursinski, Willy Bertiger, Stephen Leroy,
Larry Romans, and J. Tim Schofield
Jet Propulsion Laboratory

BIOGRAPHIES

Dr. George Hajj is a Member of the Technical Staff at the Jet Propulsion Laboratory in the Tracking Systems and Applications Section. He received his Ph.D. in physics from Rice University in 1988. His research experience and interests are in the areas of radio propagation and scattering, tomographic imaging, and GPS radio occultation techniques and applications.

E. Rob Kursinski is a member of the Technical Staff in the Earth and Space Sciences Division. He is pursuing a Ph.D. in Planetary Science at the California Institute of Technology and has an extensive background in the application of radio occultation instrumentation and techniques to the remote sounding of planetary atmospheres. His current interests are in applying the GPS radio occultation techniques to study the Earth's atmosphere.

Dr. Willy Bertiger received his Ph.D. in Mathematics from the University of California, Berkeley, in 1976 specializing in Partial Differential Equations. He is currently a Member of the Technical Staff at the Jet Propulsion Laboratory in the Tracking Systems and Applications Section. His work at JPL has been focused on the use of GPS for high precision orbit determination.

Dr. Stephen Leroy is a postdoctoral associate in the Earth and Space Sciences Division at the Jet Propulsion Laboratory. He received his Ph.D. in planetary science from the California Institute of Technology and his primary interests are in atmospheric waves and the climatology of the middle and lower atmosphere.

Dr. Larry Romans received his Ph.D. in theoretical physics from Caltech in 1985. He is currently a Member of the Technical Staff in the Space Geodesy and Geodynamics Group at JPL, where his work has focused on geodetic applications of GPS.

Dr. Tim Schofield is a Member of Technical Staff in the Earth and Space Sciences Division. He received his D. Phil. in atmospheric physics at the University of Oxford and his primary interest is the remote sounding of atmospheres.

ABSTRACT

The radio occultation technique, which has been repeatedly proven for planetary atmospheres, was first utilized to observe Earth's atmosphere by the GPS-MET experiment (launched in April 1995), in which a high performance GPS receiver was placed into a low-Earth orbit. During certain phases of the mission, more than 100 occultations per day are acquired. A subset of this occultation data is analyzed and temperature in the neutral atmosphere and electron profiles in the ionosphere are obtained. Comparing about 100 GPS-MET retrievals to accurate meteorological analyses obtained from the European Center for Medium-range Weather Forecasting at heights between 5-30 km, temperature differences display biases of less than 0.5K and standard deviations of 1-2K in the northern hemisphere, where the model is expected to be most accurate. Furthermore, electron density profiles obtained for different geodetic locations and times show the main features that are expected in the ionosphere.

1-INTRODUCTION

When a signal transmitted by the global positioning system (GPS) and received by a low-Earth orbiter (LEO) passes through the Earth's atmosphere [Fig. 1] its phase and amplitude are affected in ways that are characteristic of the index of refraction of the propagating medium. By applying certain assumptions on the variability of the index of refraction of the propagating media (e.g. spherical symmetry in the locality of the occultation), phase change measurements between the transmitter and the receiver yield refractivity profiles in the ionosphere (~60-1000 km) and neutral atmosphere (0-50 km). The refractivity, in turn, yields electron density in the ionosphere, and temperature and pressure in the neutral atmosphere. In the

lower troposphere, where water vapor contribution to refractivity is appreciable, independent knowledge of the temperature can be used to solve for water vapor abundance.

The radio occultation technique has a 30 year tradition in NASA's planetary program and has been a part of the planetary exploration programs to Venus, Mars and the outer planets [see, for example, Tyler, 1987]. However, the application of the technique to sense the Earth's atmosphere using GPS, first suggested by Melbourne et al. [1988] and Yunck et al. [1988], was tested for the first time with the launch of the GPS-MET mission on April 3, 1995. GPS-MET is an experiment managed by the University Corporation of Atmospheric Research (UCAR) [Ware et al., 1995] and it consists of a 2 kg GPS receiver piggybacked on the MicroLab I satellite which has a circular orbit of 730 km altitude and 60° inclination. The GPS receiver is a space qualified TurboRogue [Meehan et al., 1992] capable of tracking up to 8 GPS satellites simultaneously at both frequencies transmitted by GPS. Under an optimal mode of operation, the GPS receiving antenna boresight is pointed in the negative velocity direction of the LEO and provides 100-120 globally distributed setting occultations per day. By the end of the mission (nominal life time of 6 months), thousands of occultations will have been collected and can be used to assess the accuracy and potential benefit of the GPS radio occultations.

To date, a relatively small fraction of all recorded occultations have been analyzed using the Abel transform approach (presented below). This paper discusses how the GPS-MET data are analyzed and presents some results of temperature retrievals compared to radiosonde measurements and atmospheric analyses obtained from the European Center for Medium-range Weather Forecast (ECMWF). It also presents some preliminary results of electron density profiles obtained in the ionosphere. The paper is structured as follows: Section 2 gives a brief background on the radio occultation technique. The basic features of the technique are presented in section 3. The manner in which the GPS-MET phase data are calibrated to isolate the atmospheric excess phase is described in section 4. Section 5 presents an individual temperature profile and statistics obtained for all occultations available from 2 days during the experiment. These retrievals are compared to atmospheric analysis from ECMWF. In section 6, we show retrievals of ionospheric profiles obtained at different times of day and geographical locations. A conclusion is given in section 7.

2-THE RADIO OCCULTATION TECHNIQUE

The basic observable for each occultation is the phase change between the transmitter and the receiver as the signal descends through the ionosphere and the neutral atmosphere. After removal of geometrical effects due to the motion of the satellites and proper calibration of the transmitter and receiver clocks, the extra phase change

induced by the atmosphere can be isolated. Excess atmospheric Doppler shift is then derived. This extra Doppler shift can be used to derive the atmospheric induced bending, α , as a function of the asymptote miss distance, a , [Fig. 1]. Assuming a spherically symmetric atmosphere, the relation between the bending and excess Doppler shift, Δf , is given by

$$\Delta f = \frac{f}{c} \left[\vec{v}_t \cdot \hat{k}_t - \vec{v}_r \cdot \hat{k}_r + (\vec{v}_t - \vec{v}_r) \cdot \hat{k} \right], \quad (1)$$

where f is the operating frequency, c is the speed of light, \vec{v}_t and \vec{v}_r are the transmitter and receiver's velocity respectively, \hat{k}_t and \hat{k}_r are the unit vectors in the direction of the transmitted and received signal respectively, \hat{k} is the unit vector in the direction of the straight line connecting the transmitter to the receiver.

The spherical symmetry assumption can also be used to relate the signal's bending to the medium's index of refraction, n , via the relation

$$\alpha(a) = 2a \int_a^\infty \frac{1}{\sqrt{a'^2 - a^2}} \frac{d \ln(n)}{da'} da', \quad (2)$$

where $a = nr$ and r is the radius at the tangent point [Fig. 1]. This integral equation can then be inverted by using an Abel integral transform given by

$$\ln(n(a)) = \frac{1}{\pi} \int_a^\infty \frac{\alpha(a')}{\sqrt{a'^2 - a^2}} da' \quad (3)$$

The refractivity, N , is related to atmospheric quantities via

$$N = (n-1) \times 10^6 = 77.6 \frac{P}{T} + 3.73 \times 10^5 \frac{P_W}{T^2} - 40.3 \times 10^6 \frac{n_e}{f^2}, \quad (4)$$

$$P = \frac{\rho R T}{m}, \quad (5)$$

$$\frac{\partial P}{\partial h} = -g\rho, \quad (6)$$

where P is total pressure (mbar), T is temperature (K), P_W is water vapor partial pressure (mbar), n_e is electron density (m^{-3}), f is operating frequency (Hz), ρ is density, R is the gas constant, m is the gas effective molecular weight, h is height, g is gravitational acceleration.

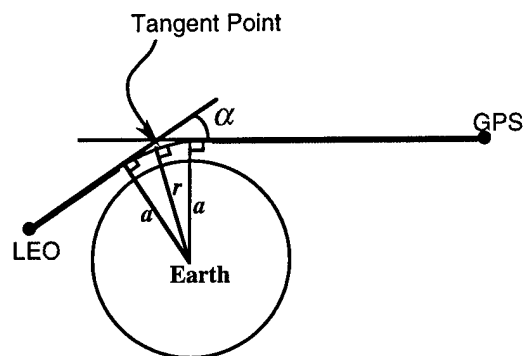


Fig. 1: Occultation geometry defining a , r , α and the tangent point.

When the signal is passing through the ionosphere (tangent point height > 60 km), use of a single GPS frequency is sufficient to estimate α to be used in Eq. (3). Moreover, the first two terms on the right hand side of Eq. (3) are negligible, therefore, knowledge of the index of refraction leads directly to electron density.

When the signal is going through both the neutral atmosphere and the ionosphere (tangent point height < 60 km), a linear combination of the two bending angles, associated with the two GPS frequencies, is used to isolate the *neutral* atmospheric bending and its refractivity profile is derived by use of Eq. (3) [Vorob'ev and Krasil'nikova, 1993]. In the stratosphere and the region of the troposphere where temperature is colder than ~250K, the water vapor term in Eq. (4) is negligible. Therefore, knowledge of refractivity yields the density of the medium by use of the ideal gas law (Eq. 5). The density in turn yields the pressure by assuming hydrostatic equilibrium (Eq. 6) and a boundary condition at some height. Applying the gas law once more, knowledge of density and pressure yields the temperature. In the troposphere, at height where the temperature is larger than 250K, the water vapor term in Eq. (4) becomes significant and it is more efficient to solve for water vapor given some independent knowledge of temperature [Kursinski et al., 1995a].

3-GPS RADIO OCCULTATION FEATURES

Details about vertical and horizontal resolution of the technique, and refractivity, temperature, pressure, water vapor or electron density accuracies as a function of height, are given elsewhere in the literature [Hardy et al., 1993, Kursinski et al., 1993; Hajj et al., 1994]. In this section we quickly summarize the results of these studies.

Due to the nature of the measurement, which is a pencil-like beam of the electromagnetic signal probing the atmosphere, the technique has a much higher vertical and across-beam resolution than horizontal (i.e. along the beam). The vertical resolution of the technique is essentially set by the physical width of the beam where geometrical optics is applicable. This scale is set by the Fresnel diameter which, in vacuum, is given by

$$D_{\text{vacuum}} = 2 \sqrt{\frac{\lambda R_{\text{GPS}} R_{\text{LEO}}}{(R_{\text{GPS}} + R_{\text{LEO}})}}, \quad (7)$$

where λ is the signal's wavelength, R_{GPS} and R_{LEO} are the distances of the tangent point (see Fig. 1) to the GPS and LEO respectively. For a LEO, D_{vacuum} is ~1.5 km. In the presence of a medium, due to bending induced on the signal, the Fresnel diameter is ~0.5 near the surface and approaches 1.5 km above 20 km altitude where bending becomes small. When the signal encounters sharp gradients in refractivity due to either water vapor layers near the surface or sharp electron density changes at the bottom of the ionosphere, the Fresnel diameter shrinks to ~200 meters.

A horizontal resolution scale is set by the length of the beam inside a layer with a Fresnel diameter thickness. This length is 160-280 km for a Fresnel diameter of 0.5-1.5 km.

In the ionosphere, the vertical scale is still set by the Fresnel diameter; however, the horizontal scale can extend several thousands of kilometers due to the large vertical extent and scale height of the ionosphere. These features of the ionosphere allow one to use tomographic approaches in order to combine information from neighboring occultations to solve for horizontal and vertical structure [Hajj et al., 1994].

Under ideal conditions, when a LEO tracking GPS has a 360° field of view of the Earth's horizon, about 750 occultations per LEO per day can be obtained. However, side-looking occultations (GPS-LEO link > 45° from velocity or anti-velocity of LEO) sweep across a large horizontal region, and the spherical symmetry assumption described in Sec. 2 becomes inaccurate. Discarding side-looking occultations, one LEO provides up to 500 occultations per day.

In the case of GPS-MET, only an aft-looking antenna was mounted on the satellite, which reduces the viewing geometry to 1/2 the Earth's limb ($\pm 90^\circ$ from boresight). In addition, in order to calibrate the clocks of the occulting transmitter and receiver, one other GPS transmitter and one ground GPS receiver are required (see Fig. 2; the technique of calibration is described in more detail in the next section). This requirement, in addition to some memory limitations inside the flight receiver, limits the number of occultations to about 100 per day.

A high inclination LEO provides a set of occultations that covers the globe fairly uniformly. This feature is particularly advantageous when comparing LEO-GPS occultation coverage to that obtained from balloon launched radiosondes. A total of about 800 radiosondes are launched each 12 hours from sites around the world. The vast majority of these sites are over the northern hemisphere continents, particularly Europe and North America. This creates the need for high resolution temperature/pressure/water vapor profiles in the southern hemisphere and over the oceans. The contribution of radio occultation retrievals to climate and weather modeling should be particularly important in these regions. (Global data provided by spaceborne nadir sounders average over large—3-7 km—vertical distances.)

When compared to infrared spaceborne sounders, the radio occultation technique has the advantage of being an "all-weather" system. Namely, it is insensitive to aerosols, cloud or rain due to the relatively large GPS wavelengths. Unlike other techniques such as radiosonde or microwave sounders, where instruments need constant calibration, the GPS radio occultation provides a self calibrating system, as will be discussed in more detail below. The long term

stability inherent in radio occultation make this an excellent system to keep an accurate record of climate changes.

4-CALIBRATING THE GPS SIGNALS/ISOLATING ATMOSPHERIC EXCESS DELAY

The main observable used in an occultation geometry is the phase change between the transmitter and the receiver as the occulting signal descends through the atmosphere. This phase change is due to (1) the relative motion of the LEO with respect to the GPS, (2) clock drifts of the GPS and LEO and (3) delay induced by the atmosphere. In order to derive the excess atmospheric Doppler shift, one must remove the contribution of the first two effects.

Accurate knowledge of the GPS orbits comes from an overall solution involving all 24 GPS satellites and a global network of ground receivers. The LEO orbit is determined by use of other links tracking the non-occulting GPS satellites.

When the occultation is mostly radial (i.e. GPS-LEO link has no horizontal motion out of the occultation plane), the occultation link descends through the ionosphere and stratosphere at a rate of about 3 km/sec; thus, crossing a Fresnel diameter (see Sec. 3) in about 0.5 seconds. However, in order to investigate sub-Fresnel structure (by examining the diffraction pattern of the received signal's phase and amplitude) and for other purposes (such as eliminating different signals caused by atmospheric multipath in the lower troposphere) the occulting data is taken at a rate of 50 Hz. In order to calibrate the LEO clock, one more GPS transmitter is tracked by the LEO at the same high rate (link 2 in Fig. 2). In addition, in order to calibrate the GPS clocks, a ground receiver tracks both GPS satellites at 1 Hz (links 3 and 4 in Fig. 2). One can interpolate the lower rate GPS clock solutions to 50 Hz, due to the greater clock stability (of order 10^{-12} sec/sec, as opposed to 10^{-9} sec/sec for the LEO clock), and the smoothness of the DoD Selective Availability dithering.

Knowing the position of all four participants (i.e. two GPS satellites, one LEO and one ground receiver), and modeling various physical effects such as light travel time, the three spaceborne clocks can be solved for w.r.t. to the ground clock. The net result of the calibration is the excess phase due to the atmosphere as a function of time (see Fig. 3.a).

5-DATA ANALYSIS AND TEMPERATURE PROFILES

In this section we show the various steps of processing for a single retrieval in order to understand the basic characteristics of the atmospheric effects on the signal. We then look at statistical differences between two days'

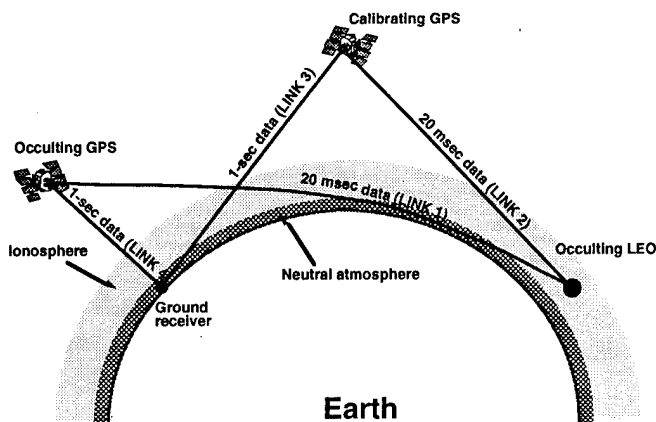


Fig. 2: The occultation geometry involving two GPS transmitters, one ground receiver and one space receiver.

worth of occultations and a numerical weather prediction model.

An Individual Retrieval

After applying the calibration described in the previous section, we obtain the atmospherically induced phase delay (up to a constant bias). Fig. 3 shows the L1 delay, Doppler shift and instrumental signal-to-noise ratio for an occultation near Pago Pago, -14 N and 190 E near midnight UT of April 25, 1995. The following features can be observed from these two plots: 1- The phase has a constant bias of about 20 m; this bias is irrelevant for consequent processing since it is the phase time derivative that is used. 2- Near the bottom of the ionosphere, there is a sharp fluctuation of the SNR due to the sharp gradient in refractivity which causes more bending and therefore defocusing. This is suggestive of the sensitivity of GPS radio occultation to sense the sharp structure of the bottom of the E-layer in the ionosphere. 3- The rapid increase in excess phase and Doppler shift and the decrease in SNR starting at the lower stratosphere is due to the fact that atmospheric bending is becoming significant. This bending causes the SNR to drop from ~130 volt/volt at the top to ~35 v/v at the bottom (averaged over 1 sec.), corresponding to about 11 dB of signal loss, and finally to lose the signal. 4- The SNR shows a clear oscillation near the tropopause which is indicative of a diffraction pattern caused by the sharp change in temperature lapse rate. 5- The SNR shows a peak (~150 v/v) in the middle-troposphere which can be caused by signals coming from a large region (relative to a Fresnel zone) and focusing near the receiver. The corresponding L1 and L2 bending for the same occultation are shown in Fig. 4. Again the sharp feature around 90 km is caused by the sharp curtailing of electron density. The L2 bending as a function of asymptote miss distance, $\alpha_2(a_2)$, is interpolated to the L1 asymptote miss distance and the following relation is used to calculate the neutral atmosphere's contribution to bending [procedure suggested by Vorob'ev and Krasil'nikova, 1993]

$$\alpha(a) = 2.54 \alpha_1(a_1) - 1.54 \alpha_2(a_1), \quad (8)$$

where the first and second coefficients of Eq. 8 corresponds to $f_1^2/(f_1^2-f_2^2)$ and $f_2^2/(f_1^2-f_2^2)$ respectively, and f_1, f_2 are the operating frequencies for L1 and L2 respectively. The difference in bending in L1 and L2 frequencies is due to the dispersive nature of the ionosphere (which leads to Eq. 8). Above 40 km, bending due to the ionosphere dominates.

Using the ionosphere free bending, $\alpha(a)$ and Eqs. (3)-(6), temperature is derived in the neutral atmosphere and is shown as a function of pressure in Fig. 5. Also shown on the same figure are temperature profiles obtained from a nearby radiosonde and a stratospheric numerical weather prediction model obtained from the National Meteorological Center (NMC). The GPS-MET profile agrees with the radiosonde and the NMC analysis to about 2K between 450-10 mbar and to the NMC analysis to about 10 K between 10-1 mbar. The only auxiliary information used in deriving the GPS-MET temperature is an initial condition of temperature at 50 km altitude equal to the NMC analysis temperature. Given the measured density at that height, this initial condition can be translated into a pressure boundary condition which is

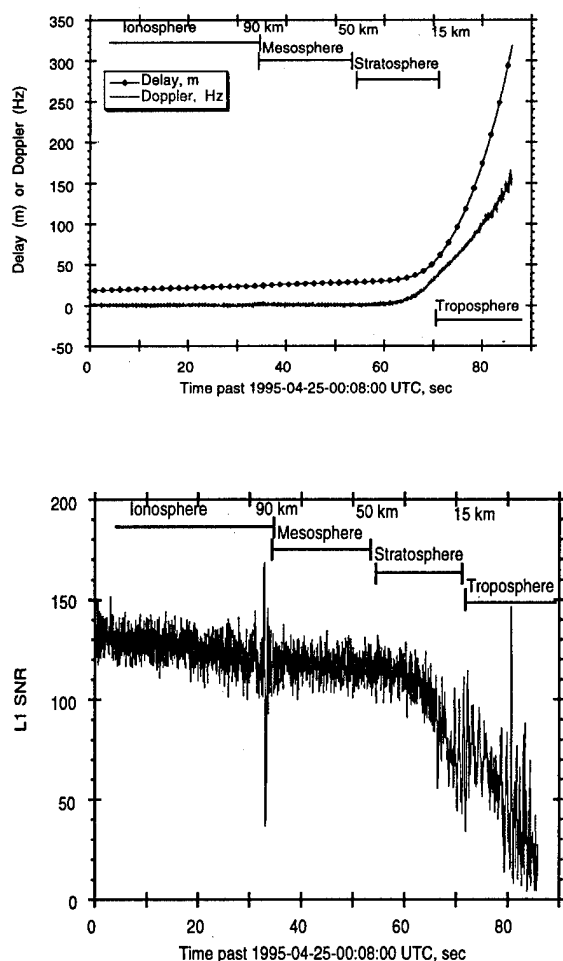


Fig. 3: (a) top: excess atmospheric phase and doppler as a function of time; (b) bottom: receiver's signal-to-noise ratio as a function of time

needed in order to integrate Eq. 6. The oscillation of the GPS-MET temperature above 10 mbar can be attributed to thermal noise in the GPS phase measurement and residual ionospheric effects. The lowest point in the GPS-MET profile corresponds to about 7 km where the signal is lost. This loss of the signal is due to signal defocusing which is exacerbated by the presence of water vapor layers in the lower troposphere.

More individual temperature retrievals as well as statistical differences between numerical weather prediction analyses obtained from the European Center for Medium-range Weather Forecasting (ECMWF) and GPS-MET are also discussed by Kursinski et al. [1995b].

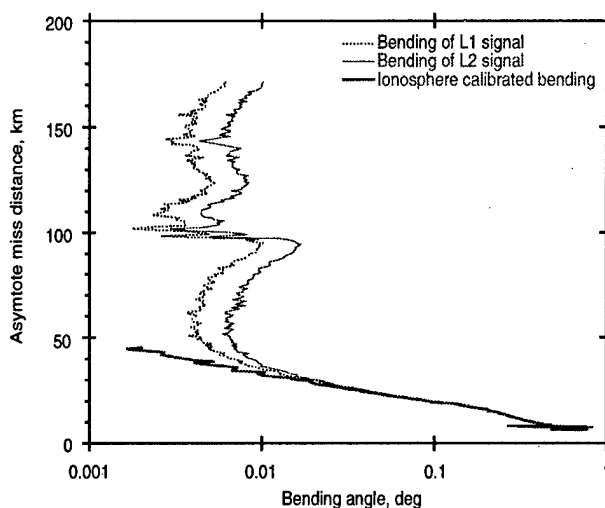


Fig. 4: Bending of GPS-L1 and L2 signals and ionospheric free bending as a function of asymptote miss distance

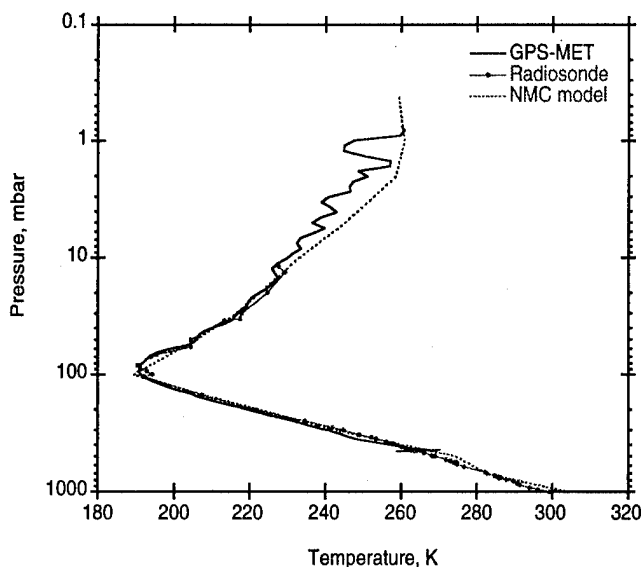


Fig. 5: Temperature profile from GPS-MET radiosonde and NMC stratospheric model

Statistical Comparisons

GPS-MET, which is a secondary instrument on MicroLab I, is configured in a favorable geometry (antenna boresight in the anti-velocity direction) only for about two weeks out of each repeat cycle of the satellite (55 days). Thus far, this has happened twice: once between April 22-May 6, 1995, and again between June 17-July 11, 1995. (These periods were interrupted by times of non-ideal viewing geometry, due to attitude control problems.) AS was off during these periods and data for April 24, 25 and May 4, 5 were analyzed. On each of these days respectively, 98, 119, 98 and 69 occultations were recorded, with about half of these successfully inverted, while the rest were automatically discarded, normally due to a data gap in one of the four links discussed above (see Fig. 2). The number of occultations for these four days as a function of the lowest height that an occultation reaches is shown in Fig. 6.

In order to assess the accuracies of retrieved temperature profiles from GPS occultations, we compare with the 6-hour ECMWF analyses. These are among the best available global analyses of atmospheric temperature structure below 10 mbar, and comparison against them has become a standard method for evaluating the accuracy and resolution of observational results [Flobert et al., 1991]. Fig. 7 shows temperature difference statistics for all successfully retrieved profiles for May 4 and 5, 1995. In order to eliminate temperature retrieval errors due to water vapor, tropospheric temperatures exceeding 250 K have been excluded from the comparisons. The three panels in Fig. 7 display temperature difference statistics

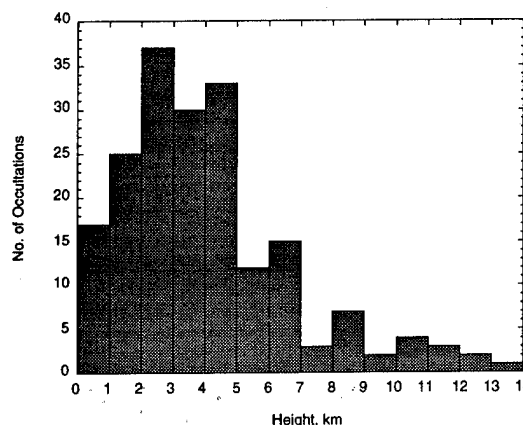


Fig. 6: Lowest height of occulting signal for days April 24,25 and May 4,5 of 1995.

for the northern high latitudes (30N-90N), the tropics (30S-30N), and the southern high latitudes (30S-90S). Within each latitude zone, retrieved profiles are widely scattered in both location and time.

It is clear from Fig. 7 that agreement between the two data sets in the northern hemisphere is impressive with mean differences of generally less than 0.5 K and difference standard deviations of typically 1 to 2 K. It should also be remembered that these differences include retrieved vertical structure that is not resolved by the ECMWF analysis, especially above 100 mbar. This agreement is particularly significant because the ECMWF analyses are expected to be most accurate in the northern hemisphere. Although both radiosonde and TOVS (TIROS Operational Vertical

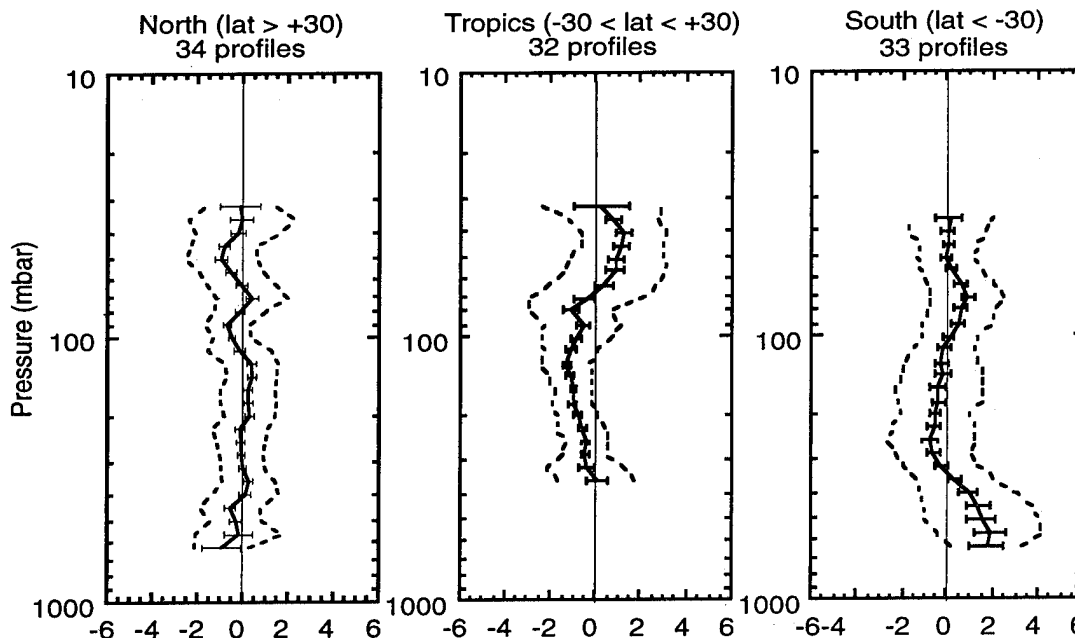


Fig. 7: GPS occultation retrievals from 95/05/04 and 95/05/05 vs. ECMWF analyses. Mean temperature difference with standard error bars (K) (solid lines); One standard deviation about mean difference (shaded lines).

Sounder, a space-based sensors with typical 3-7 km vertical resolution) data are assimilated into the ECMWF model, the analyses are expected to be less accurate in some regions of the southern hemisphere due to the sparse distribution of radiosondes. Southern hemisphere radiosondes cluster over a few land masses whereas the occultations fall mostly over the ocean. Fig. 7 shows that in the southern hemisphere, both mean temperature differences and standard deviations increase at lower altitudes. As the occultation retrieval process has little dependence on latitude, the good agreement in the northern hemisphere suggests that the larger systematic and random differences at southern latitudes originate in the analyses rather than in the retrieved profiles. Further inspection of the data shows that this difference feature is produced by a small sub-set of 8 occultation profiles concentrated far from radiosonde ascents in the southern hemisphere storm track and close to the ice edge, where problems in the assimilation of TOVS data are known to arise [Eyre et al., 1993]. Agreement with the remaining 25 profiles is comparable with that achieved in the northern hemisphere.

Temperature differences at tropical latitudes also display distinctive structure in Fig. 7. On average, retrieved profiles are about 1 K colder than the analyses between 300 and 100 mbar whereas above 70 mbar, they are warmer by a similar amount. A statistical comparison between tropical radiosondes and the ECMWF analysis revealed a qualitatively similar temperature difference structure, although the radiosonde temperatures in the upper troposphere are generally not quite as cold as the retrievals. Retrieved temperature gradients are systematically larger than analysis gradients just above the tropopause. These gradients are associated with wave-like structure often seen in the retrievals just above the tropical tropopause, and not resolved in the ECMWF analyses. While tropospheric standard deviations are similar to those

in the northern hemisphere, stratospheric values are somewhat larger due, perhaps, to waves above the tropopause. Accurate temperature measurements near the tropical tropopause are needed to understand convection and energy transfer within the atmosphere, troposphere-stratosphere exchange processes, and future climatic variations. Although the temperature retrievals are preliminary, and in spite of the clear need for more data, the tropical results are felt to be reliable because of the excellent agreement achieved in the northern hemisphere.

6-IONOSPHERIC PROFILES

Although the purpose of the GPS-MET experiment was mainly to demonstrate the usefulness of the GPS radio occultation for sensing the neutral atmosphere, the same technique can be used to obtain profiles of electron density in the ionosphere. In the ionosphere, the spherical symmetry assumption is not as accurate as in the neutral atmosphere, for reasons that are described in Sec. 3. Nevertheless, in this section we show some representative profiles of electron densities obtained from GPS-MET with the spherical assumption. A first order, but significant, improvement of the spherical symmetry has been proposed elsewhere [Hajj et al., 1994] where global maps of integrated zenith electron density [Mannucci et al., 1994] can be used in order to constrain the horizontal variability.

The nominal design of the GPS-MET receiver was to collect data at three different rates depending on the geometry of the GPS-LEO link. When the link is at positive elevation (i.e. looking above the LEO local horizontal at 730 km) the rate is 0.1 Hz. When the link has a negative elevation (i.e. its tangent point is below the LEO altitude), data is taken at 1 Hz rate. When the tangent point gets as low as ~120 km altitude (30 km

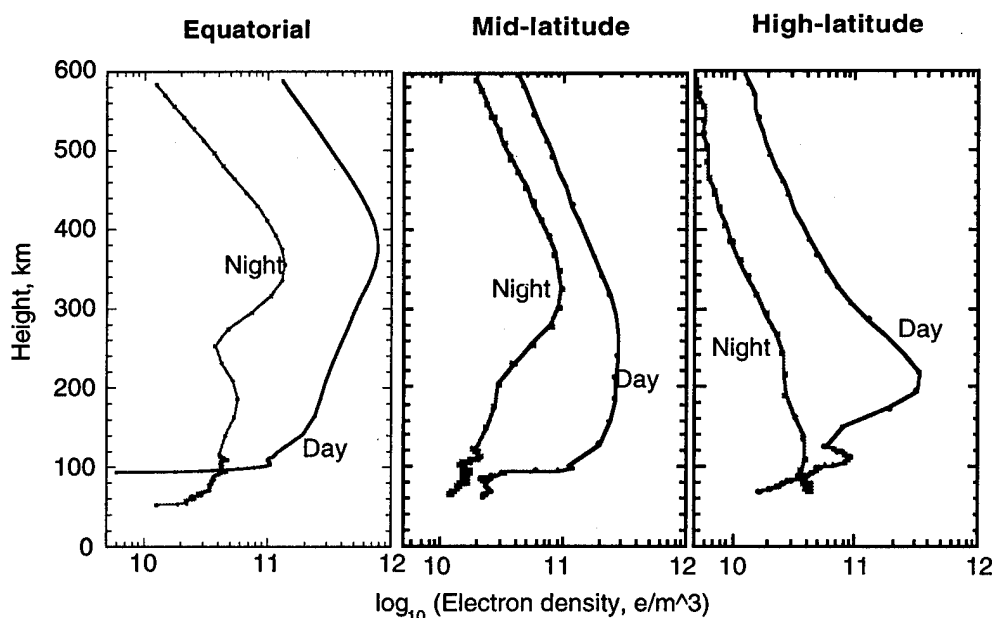


Fig. 9: Ionospheric electron density profiles for three different geographical regions for night and day time obtained with the assumption of spherical symmetry.

above which the neutral atmospheric effect starts to be detectable) the data is taken at 50 Hz. (Data used in deriving Fig. 5, had a high rate starting at 180 km.) Due to complications with the receiver software, however, one second data has not been collected. Instead, 0.1 Hz data was available through the ionosphere down to 120 km below which 50 Hz was taken. The inversions shown below are based on connecting these two data rates which explains the higher density of points below 120 km.

One can readily distinguish numerous prominent features of the ionosphere at day and night time and for different geodetic latitudes. These profiles are obtained around midnight (night-time profiles) and noon (day-time profiles) of May 4, 1995. The main features that are readily observed are the presence of the three distinct layers, E, F1 and F2 in the mid-latitude and equatorial day-time profiles, the higher electron density during the day, the sharp drop of the F1 region at night, the higher F2 peak near the equator and the very low peak at high-latitude night. Normally, one would expect the electron density to drop down to effectively zero around 60 km. The fact that they do not can be attributed to the spherical symmetry assumption used in the retrieval which can create an overall bias in the E-layer electron density, although the point-to-point structure can be accurate. Ways of improving these retrievals are now underway and will be presented in a future work.

7-CONCLUSION

Based on theoretical estimations and simulations [Hardy et al., 1993] atmospheric temperature profiles are expected to be accurate to the sub-Kelvin level between 5-30 km heights. Initial results of GPS-MET are consistent with these predictions. The GPS radio occultation measurements combine accuracy with the vertical resolution necessary to resolve tropopause structure in a way that is well beyond the capabilities of current space-based atmospheric sounders. A single orbiting GPS receiver provides up to 500 globally distributed soundings daily. The density of these measurements exceeds that of high vertical resolution radiosonde soundings by several factors in the southern hemisphere. The coverage, robustness, accuracy, vertical resolution, and insensitivity to cloud inherent to GPS radio occultation suggest that it will have a major contribution to global change and weather prediction programs around the globe.

In the ionosphere, GPS radio occultations provide electron density profiles. Spherical symmetry is accurate enough to see the prominent structures in the ionosphere, but improvements over this assumption, such as using information from ground data and/or nearby occultations, can be applied to get more accurate profiles.

ACKNOWLEDGMENTS

We thank M. Exner and R. Ware of UCAR for providing the GPS-MET flight data and Y. Bar-Sever, T. Lockhart, R. Muellerschoen and S. Wu of JPL for their significant contributions. This research was performed at the Jet Propulsion Laboratory, California Institute of Technology, under contract with the National Aeronautics and Space Administration.

REFERENCES

- Eyer et al., *Quart. J. R. Met. Soc.*, 119:1427-1463, 1993.
- Flobert, J. F. et al., *Mon. Weath. Rev.*, 119:1881-1914, 1991.
- Hajj G. A. et al., *Int. J. of Imaging Sys. and Tech.*, Vol. 5, 174-184, 1994.
- Hardy K. R. et al., *Proc. of the ION-GPS 93 Conf.*, Salt Lake City, pp. 1545-1557, 1993.
- Kursinski E. R. et al., *Proc. of the 8th Symp. on Meteorological Observations and Instrumentation*, pp. J153-J158, American Meteorological Society, Anaheim, 1993.
- Kursinski E. R. et al., *Geophy. Res. Lett.*, 1995a.
- Kursinski E. R. et al., in press, 1995b.
- Mannucci, A. J. et al., *Proc. of the Int. Beacon Satellite Symp.*, L. Kersley ed., University of Wales, Aberystwyth, pp 338-341, July 1994.
- Meehan et al, *6th Int. Geodetic Symp. on Satellite Positioning*, Columbus Ohio, 1992.
- Melbourne W.G. et al., *GPS geoscience instrument for EOS and Space Station*, GGI proposal to NASA, July 15, 1988.
- Tyler G. L., *Proc. IEEE*, 75:1404-1431, 1987.
- Vorob'ev V.V. and T.G. Krasil'nikova, *Fizika Atmosfery i Okeana*, 29, 626-633, 1993.
- Ware R. M. et al, in press, 1995.
- Yunck T. P. et al., *Proc. of IEEE position location and navigation symposium*, Orlando, 1988.

Time Calibration Using the INMARSAT Geostationary Overlay Signal From the AOR-W Satellite

James LaMance and Alison Brown
NAVSYS Corporation

Bruce Haines, Willy Bertiger, and Sien Wu
Jet Propulsion Laboratory

JAMES LAMANCE

James LaMance is a Senior Engineer at NAVSYS Corporation, in Colorado Springs, CO, where he is involved with GPS navigation systems design and analysis. Dr. LaMance has worked in the areas GPS, remote sensing, and orbit determination for the past six years. Dr. LaMance holds a PhD and MS in Aerospace Engineering from the University of Colorado at Boulder, and a BS in Aerospace Engineering from Auburn University, Auburn, AL.

ALISON BROWN

Alison Brown is the President of NAVSYS Corporation, which specializes in developing GPS customized products and services. Dr. Brown has over 15 years experience in GPS receiver design and has seven GPS related patents. She has published numerous papers on GPS applications and is on the editorial board for GPS World and GIS World magazines. She is currently the Space Representative for the ION Council. Dr. Brown received her BA and MA in Engineering from Cambridge University, an MS from MIT, and a PhD from UCLA.

BRUCE HAINES

Bruce Haines received his PhD in Aerospace Engineering from the University of Colorado at Boulder specializing in satellite altimetry applications with an emphasis in precise orbit determination. Following his PhD, he began work at JPL as a Member of the Technical Staff in the Earth Orbiter Systems Group. His work at JPL has been focused on the use of GPS for high precision orbit determination.

WILLY BERTIGER

Willy Bertiger received his PhD in Mathematics from the University of California, Berkeley, in 1976, specializing in Partial Differential Equations. In 1985, he began work at JPL as a Member of the Technical Staff in the Earth Orbiter Systems Group. His work at JPL has been focused on the use of GPS for high precision orbit determination. GPS studies have included: high precision geodetic baseline determination, software development and analysis for the Topex/Poseidon-GPS orbit determination

experiment, and filter software and algorithm development for gravity field determination.

SIEN WU

Sien Wu received his BSEE degree from the National Taiwan University, Taipei, Taiwan, and PhD degree from the University of Waterloo, Ontario, Canada. He joined the Jet Propulsion Laboratory in 1975 and is currently a Technical Group Leader in the Tracking Systems and Applications Section. Dr. Wu has been involved with the development of various tracking systems for deep-space as well as near-earth space vehicles, and their applications to precision geodesy. His current interest is in precision GPS applications.

ABSTRACT

INMARSAT has designed a GPS (L1) transponder that will be carried on their third generation satellites. This transponder will broadcast a pseudo-GPS signal that can be used for navigation and timing, and also for disseminating integrity data or differential corrections for the GPS satellites. Use of this INMARSAT Geostationary Overlay (IGO) broadcast service will require accurate knowledge of the satellite positions. Orbit accuracies on the order of 1 m or less are achievable, and would support nanosecond level precise time transfer and dissemination over the INMARSAT area of coverage.

NAVSYS has built a ground station test-bed to generate the pseudo-GPS signal that is relayed via the IGO satellite transponder. The ground station includes a closed-loop control mechanism that precisely synchronizes the IGO broadcast signal to an external UTC time reference. This provides the capability for using the IGO signal to disseminate precise time on a global basis. Synchronizing the IGO signal to UTC and providing GPS differential corrections also improves the performance of the IGO service for aircraft navigation, as this technique eliminates signal degradation due to GPS selective availability.

The INMARSAT-2 AOR-West geostationary satellite, which is presently stationed over the Western Hemisphere, carries a transponder that was used for testing the IGO. Data were collected at two ground monitoring stations during system tests to measure the L-band signal transmitted by the satellite transponder. Specially modified receivers, synchronized to UTC (NIST) time, were set up at the National Institute of Standards and Technology (NIST) in Boulder, CO, and at the COMSAT Earth Station (ESTA) in Southbury, CT, to measure pseudo-range and carrier phase to the satellite.

A preliminary orbit adjustment based on the pseudo-range measurements demonstrates an orbit accuracy which is presently at the level of 4 m radial, 9 m cross-track, and 9 m along-track. With appropriate monitoring station distribution, group and atmospheric delay calibrations, and use of carrier phase measurements, orbit accuracies at the few meter level is anticipated, supporting time transfer at the few nano-second level.

INTRODUCTION

The INMARSAT-3 constellation of four geo-stationary communications satellites will provide redundant coverage over most of the earth. In addition to the communications payload, the INMARSAT-3 satellites will also carry a specialized navigation transponder that will be used to broadcast simulated GPS-like signals at the GPS L1 (1575.42 MHz) frequency.

This simulated GPS broadcast can be received by GPS receivers with only slight hardware and software modifications. The IGO service will provide an additional satellite signal that can be used for navigation, thereby improving the available GPS and GLONASS satellite coverage. Another major motivation for the IGO is the requirement expressed by the aviation community for a GPS Integrity Channel (GIC) to monitor the health and status of the constellation. The GIC integrity data will be broadcast through the IGO in the form of a navigation message modulated on the simulated GPS signal.

The IGO signal will be generated at specifically established satellite earth stations. It will be controlled so that the IGO signal broadcast by each satellite will appear to be synchronized with the GPS satellite signals. It is also possible to use this architecture to precisely synchronize the IGO signal to a time reference. Since only a single satellite signal is required for precise time dissemination at fixed installations, the four INMARSAT-3 satellites can also provide redundant worldwide coverage for precise time dissemination.

Key to the effective use of the IGO are the calibration of the signal timing to a standard time reference such as UTC and accurate knowledge of the INMARSAT satellite orbits. Applications using the signals for navigation and precise time transfer require the orbital position be known to an accuracy consistent with the known accuracy of the

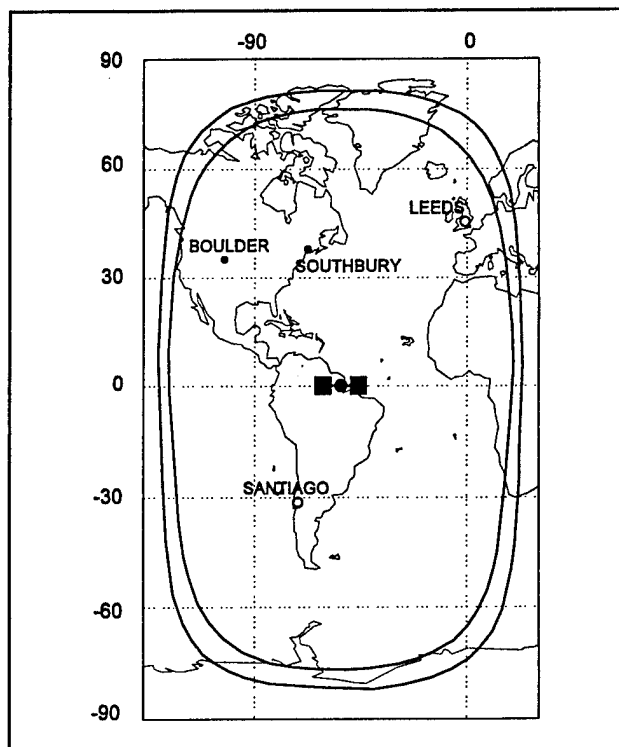


Figure 1 AOR-West Footprint and Monitor Sites

GPS satellites. The goal is to eventually be able to determine the INMARSAT orbital positions to meter level or better.

Ranging data resulting from the signal generated at the IGO test-bed were collected over a two-week period and used to estimate improved INMARSAT orbits. The L-band GPS-like signal generated at the COMSAT ESTA in Southbury, CT, was broadcast by the AOR-West satellite and monitored from two receivers modified to track the signal. The signal monitoring sites were located at NIST in Boulder, CO, and at the Southbury ESTA. The tracking site geometry and AOR-West footprint are shown in **Figure 1**, where Leeds and Santiago are indicated as additional planned tracking sites for orbit improvement.

TEST-BED EQUIPMENT

The system architecture for the equipment used at the monitor sites is depicted in **Figure 1**. The IGO SIGGEN system was designed and built by NAVSYS to provide precise synchronization of the IGO signal to an external time reference. The system components include a Communication Server, a Precision Time and Frequency Reference, SIGGEN Controller, and SIGGEN Monitor.

SIGGEN Communication Server

The FAA is developing a network of ground-based reference stations, the Wide Area Augmentation System (WAAS), which will be used to continuously monitor the status of the GPS satellites and generate differential

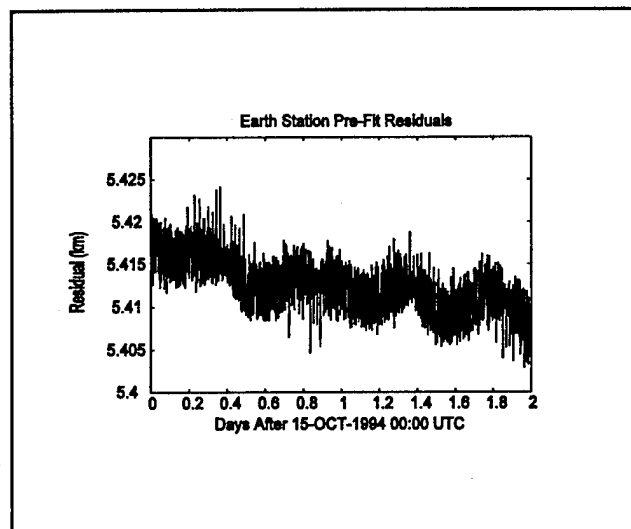


Figure 2 Southbury Pre-Fit Residuals: First and Second Days

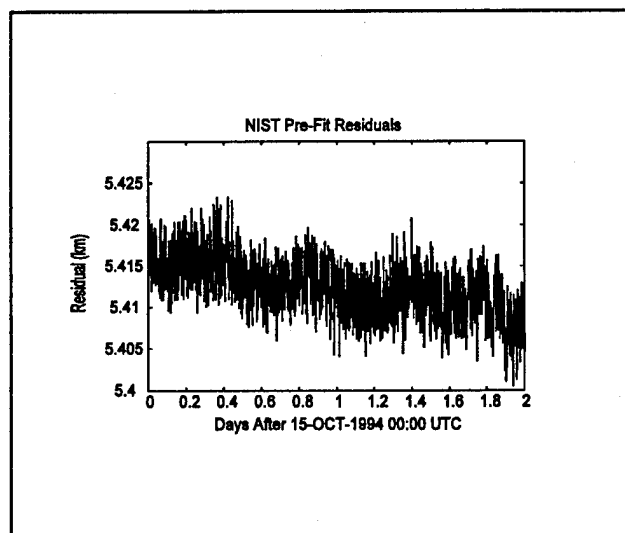


Figure 3 NIST Pre-Fit Residuals: First and Second Days

corrections for the observed range errors. These data are processed at a central facility to generate a GPS Integrity Broadcast (GIB) message for transmission by the IGO. The function of the communication server is to continuously receive the GIB message from the FAA central facility and pass the data to the SIGGEN controller for modulation on the IGO signal.

SIGGEN Precision Time and Frequency Reference

The SIGGEN time and frequency reference provides the time standard to which the IGO signal is synchronized. In the initial test phase, an HP 5071A primary frequency standard was provided on loan by Hewlett Packard. The HP 5071A clock includes an improved cesium beam tube design that results in an accuracy of $\pm 2 \times 10^{-12}$. The HP clock was operated during the calibration phase under

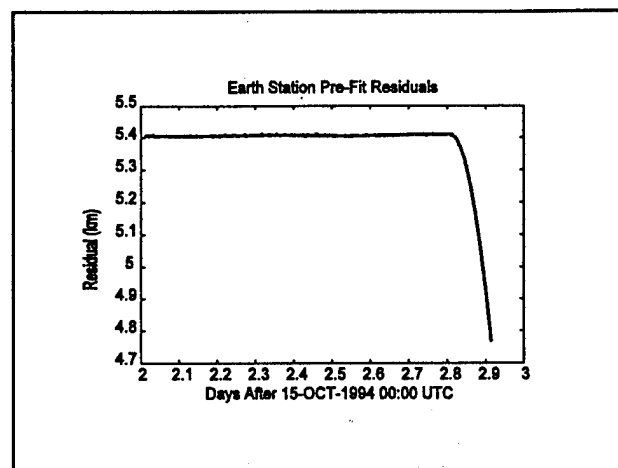


Figure 5 Southbury Pre-Fit Residuals: Third Day

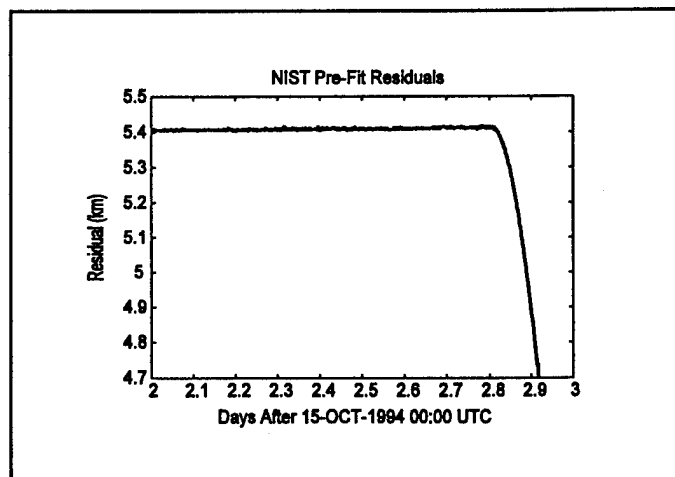


Figure 4 NIST Pre-Fit Residuals: Third Day

remote control from NAVSYS using monitor data collected at NIST to adjust the reference for time offset and synchronize it with the NIST UTC time standard. The INMARSAT-2 orbital elements at the time of the calibration allowed synchronization to about 1 μ sec [1]. The HP clock at the ESTA was synchronized just prior to the two week data collection interval used in this analysis.

SIGGEN Controller

The purpose of the SIGGEN controller is to generate the IGO signal and control its timing relative to the SIGGEN precision time reference. The IGO signal is

steered so that the timing elements of the signal (the C/A code and data epochs) appear to be synchronous with the SIGGEN time reference when they are transmitted by the INMARSAT satellite. In order to achieve this, the signal output by the SIGGEN controller must be advanced in time to compensate for the delays on the up-link path through the satellite transponder. Uncalibrated group delays will result in an apparent timing error in the SIGGEN signal transmit time [2]. These show that the group delay can be calibrated

are subsequently used to offset the SIGGEN signal time-tags to synchronize them with a transmission time.

RANGE DATA

The range data used for this analysis was collected simultaneously at the Southbury ES and the NIST MS over the three days of October 15, 16 and 17, 1994. The a-priori modeled ranges and range-rates were computed from the Keplerian orbital elements for AOR-West to determine the a-priori measurement residuals needed for estimating the initial clock offset and for examining possible orbit errors. The average range from NIST to AOR-West is about 39,500 km and varies by about ± 182.5 km from the mean. At Southbury, the average range to the satellite is about 37,900 km and varies by about ± 195 km from the mean. The range-rate at both sites is about ± 13 m/s. The C/A code PRs have a noise level of about 2-3 m.

The range residuals were computed by taking the differences between the measured C/A code PRs and the ranges computed from the Keplerian elements provided by INMARSAT Operations in London. PR measurements were collected at 1-minute intervals at each site. Figure 2 shows the pre-fit residuals for the data collected at Southbury for the first and second days and Figure 3 shows the pre-fit residuals for the data collected at NIST over the first and second days. A satellite maneuver was initiated at 19:28:24 (UTC) on the third day, 10/17/94, and is apparent toward the end of that day in Figures 4 and 5. For this reason, only the first two days and the first part of the third day were used for the ranging and orbit analysis. These residuals have a mean offset of 5.408 km and a standard deviation of 2.5 m. Obvious diurnal and longer scale features can be seen in the residuals shown in Figure 3 and Figure 4, strongly indicating the presence of orbit errors.

INMARSAT PRECISE ORBIT DETERMINATION PROCEDURE

The INMARSAT orbit was adjusted using the range data which was collected from NIST and Southbury. The processing software used was the GIPSY-OASIS II software system developed at JPL for precise processing of radiometric data. This software has been used in positioning the TOPEX/Poseidon spacecraft with GPS data to radial accuracy of 3 cm [12] and in monitoring positions on the earth to centimeter level [13]. A Bent model [11] was used to compensate the measurements for ionospheric delay. The tropospheric delay is expected to be small compared to the other error sources [17]. A nominal zenith delay was applied at both receivers (2 m dry and 10 cm wet).

Table 1 Data Arcs

	Start Time	Stop Time	# Data Points
Clock Soln	10/15/94 0 hr	10/17 19 hr	4020
Arc A	10/15/94 0 hr	10/16 10 hr	2040
Arc B	10/15/94 17 hr	10/17 3 hr	2040
Arc C	10/16/94 10 hr	10/17 20 hr	2040

during the orbit determination process to better than one

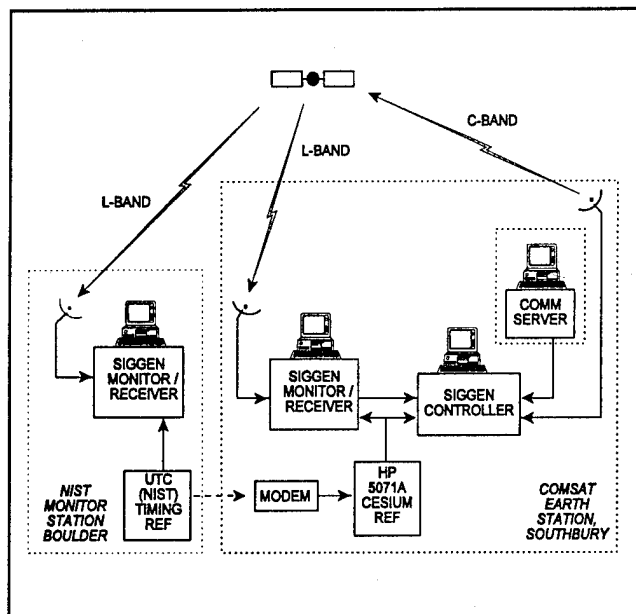


Figure 6 Test-Bed Configuration

meter.

SIGGEN Monitor/Receiver

In order to dynamically compensate for the group delays and frequency offsets, the SIGGEN monitor is used to measure the time and frequency offsets of the received signal relative to the SIGGEN time and frequency reference. It also serves as the receiver for measuring the range data. The SIGGEN control loop estimates the range and range-rate to the satellite from the two-way range measurements [2]. These

Clock solutions were computed using a quadratic model fit over the 67 hours of data spanning the three days. These results indicate a clock bias of -18 microsec, a drift of 24.7 nsec/day, and an acceleration of -3.8 nsec/day². The -18 microsec bias corresponds to about -5.4 km and likely the result of the combination of errors in the INMARSAT ephemeris used to slew the HP 5071A time reference to UTC-NIST, and the ES group delays.

A good indication of orbit accuracy is obtained by comparing the orbits between the three data arcs integrated to a common time. The start and stop times for the three arcs (A, B, and C) are given in Table 1. Note that there is no overlap in data used to fit the arcs between arcs A and C. The RMS orbit differences between arcs in the radial, cross-track, and along-track components are shown in Figure 7. These differences indicate orbit accuracies at the level of 2-4 m radial, 4-9 m cross-track, and 6-9 m along-track. The RMS formal errors (errors due to the data noise determined by the covariance matrix resulting from the data fit) are shown in Table 2. The largest formal errors are in cross-track (-C) at about 30 m. This is the result of using only observation stations located north of the equator (one side of the satellite orbit). The along-track (-L) error is at the 10 m level. The smallest formal error is in the radial component (-H), having values at the 3 m level. Larger C and L due to lack of tracking geometry could be improved through the addition of other tracking stations.

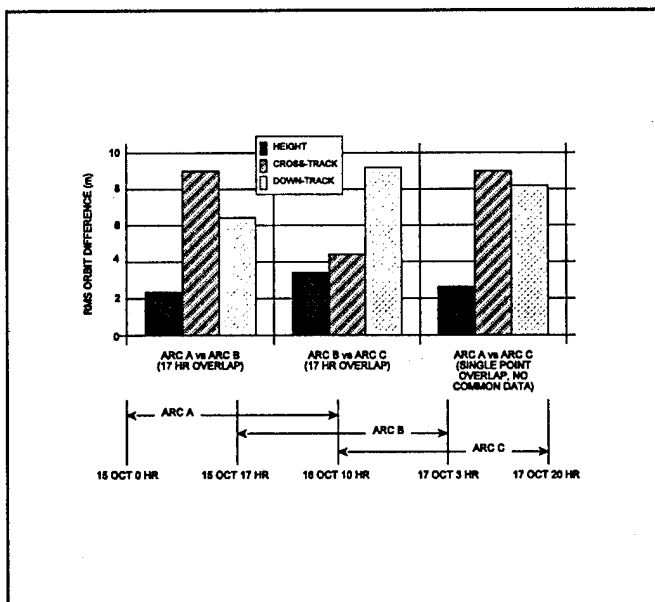


Figure 7 RMS Orbit Differences - Arcs A, B, and C

The post-fit residuals for the Southbury and NIST data are shown in Figures 8 and 9. Since some systematic effects were not modeled, those effects should appear in the post-fit range residuals. A slight systematic signature with a 24 hour period can be seen in the residuals. Further analysis is required to isolate this effect.

Table 2 Formal Errors

	Clock Soln	Arc A	Arc B	Arc C
RMS-H (m)	2.174	3.157	3.057	3.112
RMS-C (m)	20.29	29.26	27.97	28.98
RMC-L (m)	5.199	7.937	8.162	7.873

IMPROVEMENTS WITH THE CURRENT DATA SET

Several improvements are possible with the current data set. Other approaches could utilize global or regional

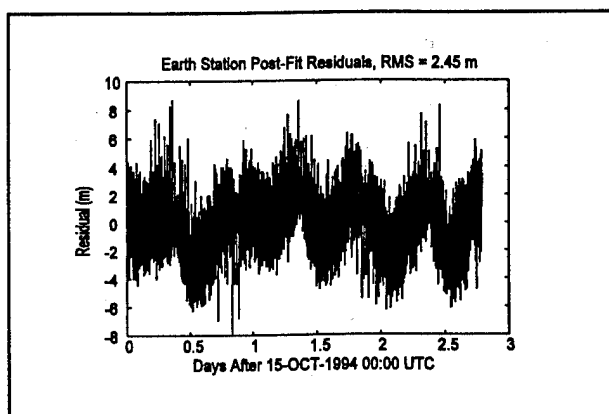


Figure 8 Southbury Post-Fit Range Residuals

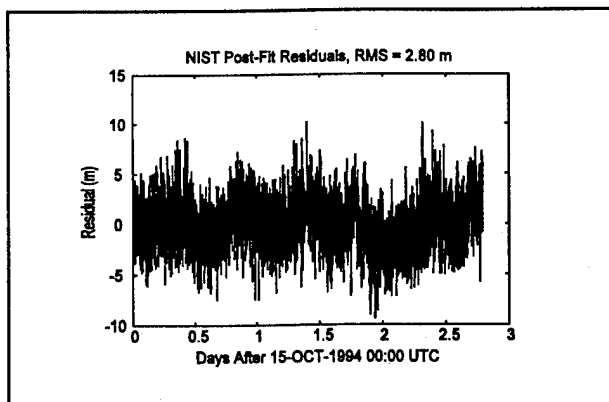


Figure 9 NIST Post-Fit Range Residuals

ionospheric maps, incorporating GPS dual-band ground data when available [6-8]. Software changes in the data preprocessing can allow the use of the phase and range data to correct for the ionosphere by adding the phase data to the range data [9]. Data from the control loop of the uplink can be used to process the data as true three-way range and phase.

FUTURE ACCURACY

In order to improve INMARSAT orbit accuracies, a number of enhancements to the experimental configuration should be implemented. Among them is the addition of one or two

stations to improve the tracking geometry, and the use of carrier phase from INMARSAT in addition to C/A range. Also critical is the use of GPS receivers at the monitor stations. Clock errors, as well as atmospheric delays from the ionosphere and troposphere, can be calibrated by receiving the IGO signal in a dual-frequency GPS receiver that is simultaneously tracking the GPS constellation. The ionosphere calibration is important for the L-band IGO signal (1.57542 Ghz). Dual-frequency GPS signals from the constellation are routinely used to calibrate ionosphere delays for tracking of deep space probes. The software for performing this function could be adapted to compute the delay along the line of site to INMARSAT from each of the IGO monitor stations. We note that the third generation INMARSAT spacecraft will broadcast at two frequencies (C and L Band), implying the ionosphere delay can be computed to first order directly from the IGO signal.

To determine whether 1-m orbit accuracies can be approached with the proposed system, we conducted a covariance study. Two ground stations—one at Leeds, UK, and a second in Santiago, Chile—were added to improve the observability. Other assumptions are given in Table 3. Note that INMARSAT carrier phase measurements were included in the analysis, in addition to the C/A code range. Two parameters were treated as “consider” parameters: the solar radiation pressure coefficient for INMARSAT and the a scale parameter to account for residual errors in the ionosphere calibration along the line of site to INMARSAT. Earth orientation and rotation parameters were not considered, since the errors have little impact on the orbit error in the terrestrial (i.e., Earth-fixed) reference frame.

Depicted in Table 4 are the statistics of the mapped orbit errors for a 34-hr solution. Under the assumptions in Table 3, the total position error (1 s) for INMARSAT is about 4 m. Most of this error is in the along-track component of the orbit. More important for IGO time transfer applications is the radial component, which in this case has an RMS magnitude of 1.4 m. This level of accuracy is adequate to support time transfer at the few-ns level. Recent results from an experiment conducted for the European Complement to GPS (CE-GPS) seem to corroborate that this level of orbit accuracy is achievable. Using an experimental system with stations in Toulouse, France; Hartebeesthoek, South Africa and Kourou, French Guiana, *Barbier et al.* report orbit overlap differences of less than 4 m in total position for INMARSAT-2 AOR-East.

What can be done to further improve the orbit accuracy? In practice, the impact of mismodeling the solar radiation pressure will be mitigated by estimating the scale coefficient. Additional improvement could be gained by developing a custom force model, as was done for the GPS and Topex/Poseidon spacecraft. Concerning the ionosphere correction, the 10% estimate for residual delays is somewhat pessimistic for typical conditions (A. Mannucci, private communication, 1995). Moreover, for the third-generation INMARSAT, the impact of the ionosphere delay will be

reduced to negligible levels by using a dual-frequency formulation. With careful treatment and control of these systematic error sources, it is reasonable to conclude that

Table 3 Estimation Strategy for INMARSAT Covariance Analysis

Data Type	Data Weight
INMARSAT PR (C/A)	5 m
INMARSAT CPH	1 cm
GPS PR	1 m
GPS CPH	1 cm

Consider Parameters	Uncertainty
INMARSAT Sol. Rad. Pressure Coeff.	2%
INMARSAT Iono.	10% Bent Model (L1)

Estimated Parameters	Constraint
INMARSAT Epoch State (3-D Pos. & Vel.)	100 km 1 m/s
GPS Epoch State (3-D Pos. & Vel.)	100 km 1 m/s
Troposphere (random-walk zenith delay)	40 cm 5 cm/hr ^{1/2}
GPS, INMARSAT, and receiver clocks (white noise)	1s
INMARSAT Solar Radiation	100%

Table 4 RSS 3-D Position Error (m)

Formal	2.23
Solar Rad. Press.	2.61
Iono.	2.58
Total Error	4.29

orbit accuracy consistent with the formal errors (2 m, 1 s) can be approached. We expect that further improvement (to the 1-m level) is contingent on the addition of ground stations, and to a lesser extent on the improvement of the range quality. Fixing the GPS orbits and clocks to precise values determined a priori should also result in reduction of the INMARSAT orbit error. This is corroborated to some extent by the results of an earlier covariance analysis which predicted sub 1-m position errors for INMARSAT using the same 4 tracking stations. The earlier analysis assumed perfect knowledge of station clocks and tropospheric delays, thus circumventing the need for common view of multiple GPS spacecraft from each of the stations. The current analysis directly uses the GPS data to estimate these contributions, along with the GPS and INMARSAT orbital states, boosting the formal errors. Further covariance analysis is required to separately quantify the effects of the various enhancements.

CONCLUSION

Orbit accuracy is presently achievable using PR measurements at the level of 4 m RMS radial, 9 m RMS cross-track, and 9 m along-track, as demonstrated by the two-station orbit prediction comparison and error analysis. This level of accuracy meets the current requirements for navigation and integrity monitoring. In the future, with enhancement to the tracking system, it will be possible to obtain orbit accuracies of a few meters, with the radial component of 1.4m, which would support time transfer at the nanosecond level with the appropriate ionospheric and tropospheric calibrations.

REFERENCES

- [1] A. Brown, T. Kelecy, D. Davis, R. Walton, "Time Transfer Test Results Using the INMARSAT Geostationary Overlay," ION Nat'l Tech Mtg, San Diego, CA, Jan 1994.
- [2] A. Brown, D. Davis, R. Walton, "Precise Time Dissemination through INMARSAT— Preliminary Results," ION Sat Div Int'l Tech Mtg, Salt Lake City, UT, Sept 1993.
- [3] W.I. Bertiger et al., "GPS Precise Tracking Of Topex/Poseidon: Results and Implications," *JGR Oceans Topex/Poseidon Special Issue*, accepted for publication 1/94.
- [4] G. Blewitt et al, "Absolute Far-field Displacements from the 28 June 1992 Landers Earthquake Sequence," *Nature*, 361, 340-342, 1993.
- [5] R.B. Bent et al., "The Development of a Highly Successful World-wide Empirical Ionospheric Model and Its Use in Certain Aspects of Space Communications and World-wide Total Electron Content Investigations," in J. Goodman, ed, *Effect of the Ionosphere on Space Systems and Communications*, Springfield, VA, 1976.
- [6] B.D. Wilson, A.J. Mannucci, C.D. Edwards, "Sub-Daily Northern Hemisphere Ionospheric Maps Using an Extensive Network of GPS Receivers," 7th International Ionospheric Effects Symposium, Alexandria, VA, May 1993 (updated version to appear in a special issue of Radio Science, in press).
- [7] A.J. Mannucci, B.D. Wilson, C.D. Edwards, "A New Method for Monitoring the Earth's Ionospheric Total Electron Content Using the GPS Global Network," ION Sat Div Int'l Tech Mtg, Salt Lake City, UT, Sept 1993.
- [8] B.D. Wilson, A.J. Mannucci, "Instrumental Biases in Ionospheric Measurements Derived from GPS Data," ION Sat Div Int'l Tech Mtg, Salt Lake City, UT, Sept 1993.
- [9] K. Gold et al., "GPS Orbit Determination for the Extreme Ultraviolet Explorer (EUVE)," ION Sat Div Int'l Tech Mtg, Salt Lake City UT, Sept 1993.
- [10] S.M. Lichten et al., "New Ground and Space-Based GPS Tracking Techniques for High-Earth and Deep-Space Orbit Determination Applications," ION National Technical Meeting, San Diego, CA, Jan 1994.
- [11] Barbier, J. et al., "European Complement to GPS: Main Experimental Results", proceedings of the 7-th Intl. Tech. Mtg. of the Inst. of Navigation (GPS '94), pp 995-1005, Salt Lake City, September 1994.

Real Time Estimation of Ionospheric Delays

Dr. Evelin Engler, Dr. Esther Sardón, and Dr. Dietmar Klähn
DLR Remote Sensing Ground Station

BIOGRAPHY

The authors work at the Remote Sensing Ground Station Neustrelitz, part of the German Aerospace Research Establishment. Mrs. E. Engler holds a Ph.D degree in Electronics from the Technical University of Dresden and has long experiences in communication theory, GPS algorithms for real-time error separation, quality control, and design of GPS reference and monitoring stations. Mrs. E. Sardón holds a Ph.D. degree in mathematics from the Universidad Complutense de Madrid, and worked in several areas of Space Geodesy, including VLBI, GPS and GLONASS. D. Klähn holds his Ph.D. degree in physics from the University of Rostock. His experiences are in the fields of theoretical physics, numerical mathematics, communication theory, microwave network theory and design, GPS algorithms, and quality control and design of GPS reference and monitoring stations.

ABSTRACT

The estimation of the ionospheric delay in real time with GPS can be very useful, especially for high precision navigation applications. To estimate TEC in real time it is necessary to separate the ionospheric delay from the total error budget. Therefore, the reachable accuracy of the derived real time absolute values of slant TEC is determined by several parameters: number of epochs before the first ambiguity fixing, elevation cut-off, predicted or estimated satellite and receiver instrumental delays, and the multipath and its handling.

Our method for real time TEC estimation will be described and demonstrated with real observations, using two independently working GPS receivers. The influence of selected processing parameters on the reachable accuracy of the real time TEC will be shown. The evaluation of the quality will be obtained by comparison of the real time with the

postprocessed TEC, using our reference receiver, and with the postprocessed TEC obtained using our station plus a subset of IGS stations.

These comparisons will permit the determination of an optimized setup of real time estimation algorithms.

INTRODUCTION

The presence of electrically charged particles in the propagation space of GPS signals introduces propagation errors to the observations of GPS navigation measurements. The main error contributions are due to free electrons in the ionosphere, so the error is often termed ionospheric propagation error (IPE). It is well known that it is possible to separate for the propagation errors by using two frequency GPS code and phase measurements [1] and by taking advantage of the dispersive nature of the effect. On the other hand, due to the fact that the dispersion effect is opposite in sign for code and phase measurements, a single frequency approach can be made also [2,3,4]. To take advantage of the complete observations set of two frequency measurements the present study restricts to two frequency GPS measurement only. This way, additional errors that may be introduced by ionospheric modelling approaches like mapping functions and TEC models can be avoided and the maximum potential of real time IPE estimation methods may be shown as an upper limit for other methods. To validate for the accuracy of the method, the results achieved by the real time method will be compared to high precision postprocessed results derived by using two frequency GPS data from the IGS network [6] for the same times of observation. The postprocessing method allows for the computation of the receivers and satellites instrumental differential code delays

(instrumental biases) as an useful prerequisite for the real time algorithm.

The main sources of errors in the IPE estimation algorithms by using GPS observations are the individual instrumental biases of the satellites and the receivers, and the effects of multipath propagation on differential code delay measurements. It is important to notice that in general IPE estimation algorithms depends on the individual sums of the receiver bias and the satellite bias only. These combined receiver and satellite instrumental biases can reach up to some nanoseconds. Both, postprocessing and real-time algorithms becomes significant simplified under the condition that the instrumental biases are slowly varying in time. For the satellites some prelaunch calibration is made and transmitted to the user in the GPS ephemeris t_{gd} information. Estimations of actual satellite biases by present methods [5,6,9] show a poor agreement with this t_{gd} values. For this reason, the sum of receiver and satellite instrumental biases is usually estimated simultaneously with the IPEs.

Due to the increased number of observations, the best estimation of the instrumental biases can be obtained by combining data from GPS stations located in some wide spread network, like the IGS network. Only for some IGS network reference receivers bias values are available from hardware calibration measurements. The main advantage of the network postprocessing method is in the possibility, that by combining the observations for different time and stations all error effects can be reduced up to a higher accuracy compared to the single station postprocessing or real time approaches. The main drawback of the network postprocessing approach is that the estimation of TEC in real time, as needed in various applications, is impossible due to the time needed to acquire all the measurements from the network (in case of the IGS at least two days).

The real time handling of an equivalent network with full receiver data rate is a tricky task, so the basic idea of a network linking real time IPE monitoring stations arose. At our institution, there are two single-station approaches under consideration to solve for the problems. The first one is in attempting to estimate the instrumental biases simultaneously with the IPE, the second is to use predicted biases, as estimated by the postprocessing of data from the IGS network.

For the present, we have choosen the latter approach, but in this case we have to check for the stability of the instrumental biases in time to know about the range of applicability of the postprocessed instrumental biases. The second, autonomous approach, is in its verification phase, so first results will be given in some follow up publication.

STABILITY OF INSTRUMENTAL BIASES

In [6] Sardón et al. found that the variation in time of the GPS satellite instrumental biases (relative to its mean) was below 1 ns, using different epochs during an 1-year period (September 1990 to September 1991). In [7] a study on the stability of the GPS satellite biases over some long time periods was presented, demonstrating that the variation of the satellite biases in different epochs during about 1.5 years (Jan. 1993 to Sept. 1994) was below 1.5 ns. Results of other authors in this field can be found in [5] and [9].

Next we have to discuss the variation of the combined receiver and satellite instrumental biases in periods of consecutive days, because this combination enters into the real-time IPE monitoring algorithm. Since February 1995 we are processing GPS data from several IGS stations and two additional receivers at Neustrelitz in a daily routine analysis. All stations are equipped with Rogue or Turbo-Rogue¹ receivers. For each day we produce, in post-processing, the IPEs and hourly maps of

PRN	1	2	4	5	6	7	9	12	14	15	16	17
rms [ns]	0.16	0.14	0.12	0.11	0.12	0.11	0.10	0.11	0.12	0.15	0.15	0.18
PRN	19	20	21	22	23	24	25	26	27	28	29	31
rms [ns]	0.14	0.13	0.16	0.18	0.16	0.13	0.16	0.12	0.13	0.22	0.14	0.17

Tab. 1 RMS of combined biases (Ref. ds60)

¹ The Investigations on the bias stability of other qualified GPS receivers are not completed at present.

station	ds10	ds42	brus	bor1	mate	nzre	nzmo	onsa	pots	trom	wtz1
rms [ns]	0.25	0.37	0.29	0.29	0.31	0.40	0.23	0.98	0.45	0.58	0.28

Tab. 2 RMS of combined receiver biases (Ref. ds 60)

the vertical TEC over the central European region, and also a set of instrumental biases. Referring to the algorithm and results as given in [8] we found for the rms of the sum of the satellite biases plus the bias of the reference receiver (IGS station ds60, Madrid) during a period of two months (1.Feb. 95 to 31.Mar. 1995) the behaviour as shown in Table 1. For the same period, Table 2 shows the rms of the difference of station bias minus reference station bias for each station of the network.

The large rms for satellite PRN 28 could be explained by taking into account the changes from A/S to P code mode and some satellites maintenance during the time of observation. The largest receiver rms corresponds to Onsala, and as can be seen by a closer inspection of the data, is due to a jump in the bias of that station in doy 80. In fact, the receiver at Onsala had some problems and it was replaced by another one [8].

In all cases, the rms error of the combinations of satellite bias plus receiver bias is small enough, usually less than 0.2 ns, to allow for using predictions of this combination for the real time estimation of TEC. It is worth noting, that the daily variations may be up to 0.5 ns, so we have to count for this uncertainty if using this biases in the real time algorithms. At present at DLR Neustrelitz all receiver and satellite combined biases are processed with a delay of three days.

Resuming the considerations on the bias stability we arrive at the conclusions:

- The stability of combined instrumental biases as needed in an external fed IPE estimation algorithm is about 0.5 ns.
- The combined instrumental biases can be postprocessed from IGS network data with a delay of about two days.
- Satellite bias and receiver bias stability allows for setting up a real time algorithm that is fed by external bias informations.
- If faulty satellites are excluded and Turbo Rogue GPS receiver are used for the monitoring station, the absolute accuracy limit of the real time algorithm is limited to about 0.5 ns on principle.

REAL TIME ESTIMATION OF THE IONOSPHERIC PROPAGATION ERROR

If using GPS L_1 , L_2 code and phase measurements, the basic equations for the estimation of the IPE for a measurement at satellite k may be written:

$$P_{1k} = A_k + \frac{40.3 \text{ TEC}_k}{f_1^2} + E_{1k} \quad (1)$$

$$P_{2k} = A_k + \frac{40.3 \text{ TEC}_k}{f_2^2} + E_{2k} \quad (2)$$

$$\phi_{1k} = A_k - \frac{40.3 \text{ TEC}_k}{f_1^2} - \lambda_1 N_1 - \zeta_{1k} \quad (3)$$

$$\phi_{2k} = A_k - \frac{40.3 \text{ TEC}_k}{f_2^2} - \lambda_2 N_2 - \zeta_{2k} \quad (4)$$

and:

- P_{1k}, P_{2k} measured code ranges [m],
 A_k sum of geometric range, tropospheric error, and clock error [m],
 TEC_k total electron content in the path of observation [electrons/m²],
 E_{1k}, E_{2k} sum of all errors [m] due to instrumental delays, multipath, and random noise for L_1 , and L_2 code measurements,
 ζ_{1k}, ζ_{2k} sum of all errors [m] due to instrumental delays, multipath, and random noise for L_1 and L_2 phase measurements,
 N_1, N_2 phase ambiguities for L_1 and L_2 signal,
 $f_1, f_2, \lambda_1, \lambda_2$ frequency and wavelength of L_1 and L_2 GPS signals.

TEC_k , the ionospheric propagation error, and the range measure A_k are the unknown quantities, that we are interested in. It proves helpful to define two quantities Ar_k and Tr_k that can be calculated from the code measurements:

$$Ar_k = \frac{f_1^2 P_{1k} - f_2^2 P_{2k}}{f_1^2 - f_2^2} \quad (5)$$

$$Tr_k \equiv \frac{P_{2k} - P_{1k}}{CT} \quad (6)$$

and

$$CT \equiv 40.3 \frac{f_1^2 - f_2^2}{f_1^2 f_2^2} \quad (7)$$

Inserting (2) and (3) into (6) and (7) we will get

$$Ar_k = A_k + \frac{f_1^2 E_{1k} - f_2^2 E_{2k}}{f_1^2 - f_2^2} \quad (8)$$

$$Tr_k = TEC_k + \frac{E_{2k} - E_{1k}}{CT} \quad (9)$$

Next, as done for the code measurements, we define two quantities $A\phi_k$ and $T\phi_k$, that can be calculated from the phase measurements:

$$A\phi_k \equiv \frac{f_1^2 \phi_{1k} - f_2^2 \phi_{2k}}{f_1^2 - f_2^2} \quad (10)$$

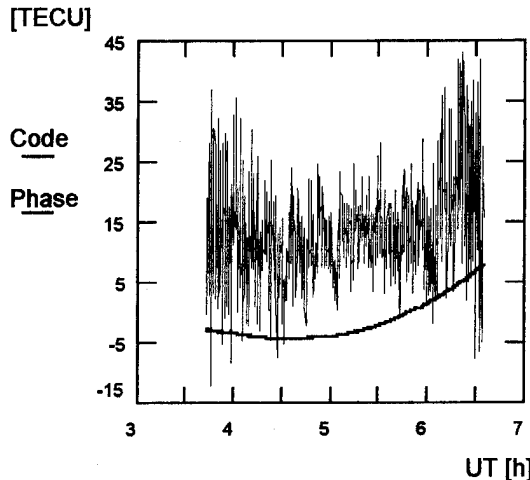
$$T\phi_k \equiv \frac{\phi_{1k} - \phi_{2k}}{CT} \quad (11)$$

By inserting (4) and (5) into (11) and (12) we get

$$A\phi_k + \frac{f_1^2 \lambda_1 N_{1k} - f_2^2 \lambda_2 N_{2k}}{f_1^2 - f_2^2} = A_k - \frac{f_1^2 \zeta_{1k} - f_2^2 \zeta_{2k}}{f_1^2 - f_2^2} \quad (12)$$

$$T\phi_k + \frac{\lambda_1 N_{1k} - \lambda_2 N_{2k}}{CT} = TEC_k - \frac{\zeta_{1k} - \zeta_{2k}}{CT} \quad (13)$$

It is seen that all the error effects are now in the last terms of equation (8), (9), (12), and (13).



Splitting up the contributions to E_{ik} , we can write for the error term of (8)

$$f_1^2 E_{1k} - f_2^2 E_{2k} = f_1^2 b_{1k} - f_2^2 b_{2k} + f_1^2 m_{1k} - f_2^2 m_{2k} + f_1^2 n_{1k} - f_2^2 n_{2k} \quad (14)$$

with b_{ik} , m_{ik} , and n_{ik} instrumental (combined) biases, multipath errors, and random noise for frequency i and satellite k respectively.

The same way, from the error term of equation (9) we get

$$E_{2k} - E_{1k} \equiv b_{2k} - b_{1k} + m_{2k} - m_{1k} + n_{2k} - n_{1k} \quad (15)$$

showing, how the different measurement errors are splitted up.

The basic idea of the algorithm for the estimation of the IPE, TEC_k is to take advantage of the statistical properties of the differential multipath and random code and phase noise errors, that is to assume in first

$$\overline{f_1^2 \zeta_{1k} - f_2^2 \zeta_{2k}} = 0 \quad (16)$$

$$\overline{\zeta_{1k} - \zeta_{2k}} = 0 \quad (17)$$

$$\overline{f_1^2 n_{1k} - f_2^2 n_{2k}} = 0 \quad (18)$$

$$\overline{n_{2k} - n_{1k}} = 0 \quad (19)$$

if the average is taken for a sufficient long time interval.

Obviously, the terms due to (16) and (17) are in the millimeter range, and (18) and (19) holds if the code noise may be considered to be white noise. The only suspicious terms to be consider in more detail are the differential multipath errors. Fig. 1 gives an impression about the

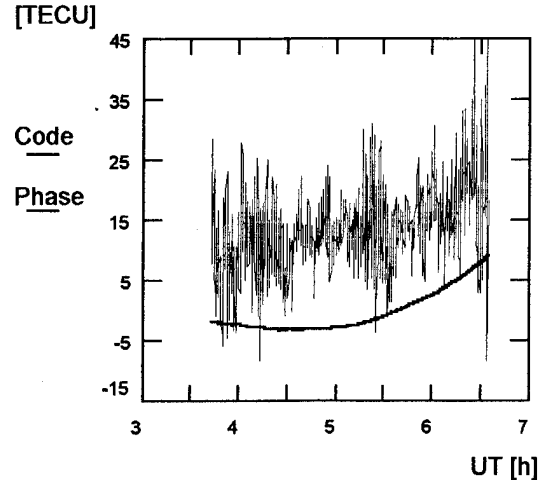


Fig. 1 Ionospheric propagation errors Tr_k , $T\phi_k$ for 15. Jul. 1995, station: nzmo, SV #1, station2: nzfi, SV #1

stat	date	CH1	CH2	CH3	CH4	CH5	CH6	CH7	CH8	Sum
nzre	261194	0	1	0	0	0	0	0	0	1
nzmo	261194	0	0	0	0	0	0	1	0	1
nzfi	150795	0	15	13	2	0	0	0	4	34
nzmo	150795	1	0	0	0	0	10	0	0	11
nzfi	160795	14	11	0	8	1	3	0	6	43
nzmo	160795	0	0	0	0	1	0	0	0	1
nzfi	170795	10	20	0	0	0	17	0	11	58
nzmo	170795	0	0	0	0	0	0	2	0	2

Tab. 3 Observed Cycle Slips at several stations

correlation of code multipath measurements at two locations differing in position by about 4 m.

Inspecting the phase measurements in Fig. 1 it is obvious, that equations (16) and (17) holds. Besides, Fig. 1 shows the offset between Tr_k and $T\phi_k$, as given by equation (13).

To calculate the IPE we have to consider $Tr_k - T\phi_k$ and $Ar_k - A\phi_k$. Taking into account all approximations made up to now, we get

$$\overline{Ar_k - A\phi_k} = \frac{f_1^2 \lambda_1 N_{1k} - f_2^2 \lambda_2 N_{2k}}{f_1^2 - f_2^2} + \frac{f_1^2 b_{1k} - f_2^2 b_{2k}}{f_1^2 - f_2^2} + \frac{f_1^2 m_{1k} - f_2^2 m_{2k}}{f_1^2 - f_2^2} \quad (20)$$

$$\overline{Tr_k - T\phi_k} = \frac{\lambda_1 N_{1k} - \lambda_2 N_{2k} + b_{2k} - b_{1k} + m_{2k} - m_{1k}}{CT} \quad (21)$$

By replacing the b_{ik} biases by the bias predicted from postprocessing, we can solve

equations (20) and (21) for the ambiguities N_1 and N_2 .

If done so, the real time TEC may be computed continuously from the measurement using

$$TEC_k = \frac{(\phi_{1k} - \phi_{2k}) + (\lambda_1 N_{1k} - \lambda_2 N_{2k})}{CT} \quad (22)$$

It is desirable to be able to detect and to remove cycle slips. At least cycle slips must be detected to recalculate the ambiguities. Some representative number of cycle slip events are given in Tab. 3 for three receivers at our location.

In (22) we are left with an uncertainty of some millimetres, due to equation (13) and some error in N_1 and N_2 due to the assumption that $\overline{f_1^2 m_{1k} - f_2^2 m_{2k}}$ and $\overline{m_{1k} - m_{2k}}$ becomes small if the observation time until the N_1 and N_2 are estimated are chosen to be sufficient long. In praxis a time to first fixing in the range from 10 to 20 minutes is choosen, depending on A/S on or off condition. If the average multipath errors are small, we have a good chance to hit the true

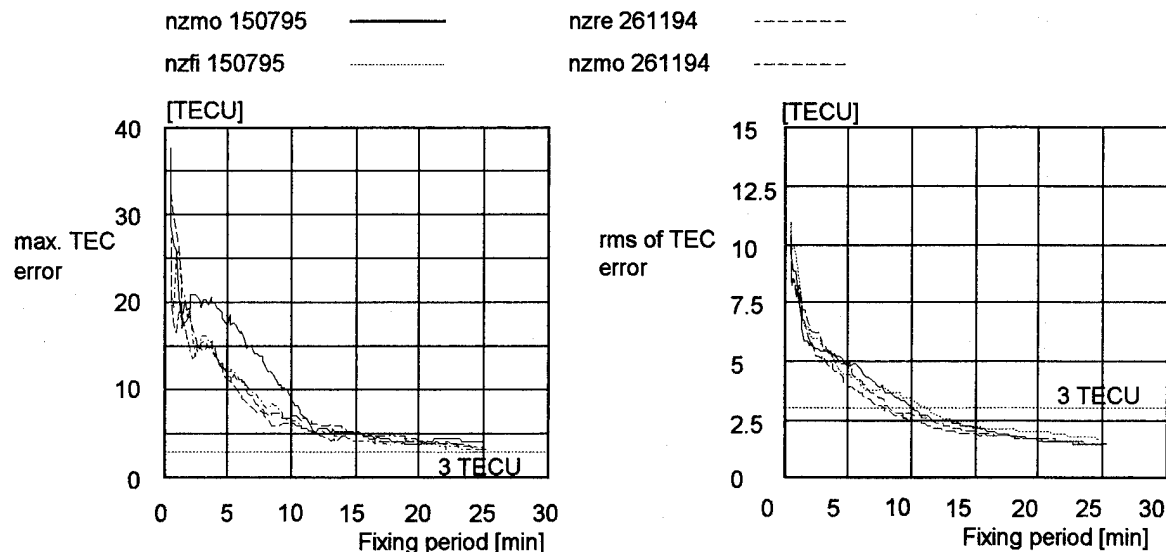


Fig. 2 Influence of the fixing period on the real time ionospheric propagation error at several days

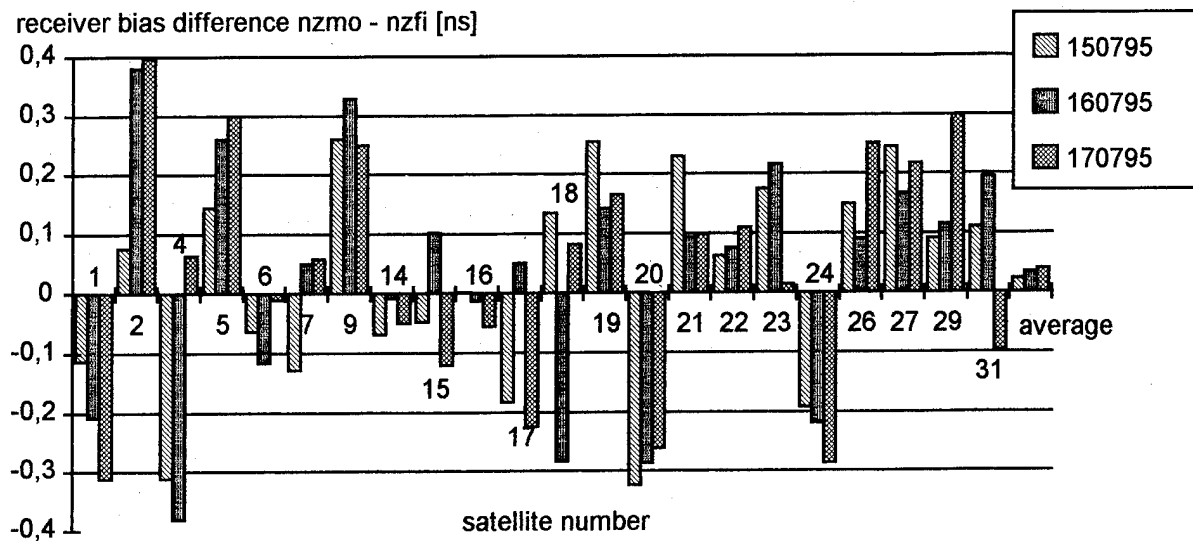


Fig. 3 Estimated receiver bias difference relative to postprocessed value of the 15 July 1995

values of N_1 and N_2 and to remove the multipath error. This way we have some kind of quantized error in the IPE. Besides the introduction of an elevation cutoff mask proves to be necessary (Fig. 1).

ERROR CONSIDERATIONS

By our opinion, only in the outlined way full advantage of the potential of two frequency measurements may be taken. The accuracy of the real time algorithm, besides the error included in the postprocessed biases, is limited by the individual multipath environment of the IPE monitoring station only. In Fig. 2 the influence of the length of observation time before fixing the ambiguities on the maximum and rms IPE error is illustrated.

An impression on the residual error on the method may be gained from Fig. 3, where the differenced IPE of all visible satellites due to

$$Tr_k(rec_i) = TEC_k + b(rec_i) + b_k + m_k(rec_i) \quad (23)$$

of two receivers operated at locations spaced about 4 meters is represented for three successive days. In this case the satellite biases and the ionospheric propagation error cancels due to

$$\Delta Tr_k(rec_{1,2}) \equiv Tr_k(rec_1) - Tr_k(rec_2) \quad (24)$$

If taking the postprocessed receiver biases of the first day and applying the average of all common views of satellite k of the complete data set using

$$\Delta Tr_k(rec_{1,2}) = b(rec_1) - b(rec_2) + \overline{m_k(rec_1) - m_k(rec_2)} \quad (25)$$

we get a maximum error of about 0.4 ns. Up to now, is not quite clear how this error has to be partitioned into receiver bias variations and multipath effects.

Besides of the ΔTr_k , also the ensemble average taken over all satellites is shown in the last column of Fig. 3. According to the post-processing algorithm, this average minimizes.

To verify the real time algorithm a measurement campaign was organized with three Turbo Rogue receivers situated at a straight N-S line and located at Neustrelitz

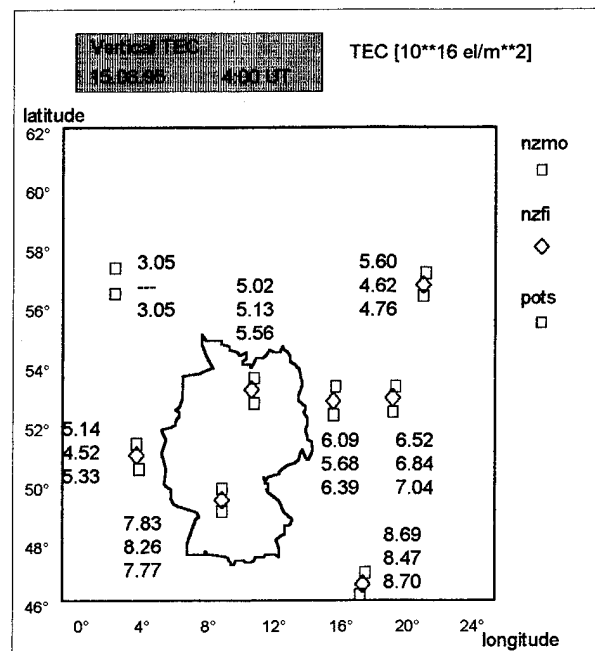


Fig. 4 Vertical TEC estimated in postprocessing for stations nzmo, nzfi and pots

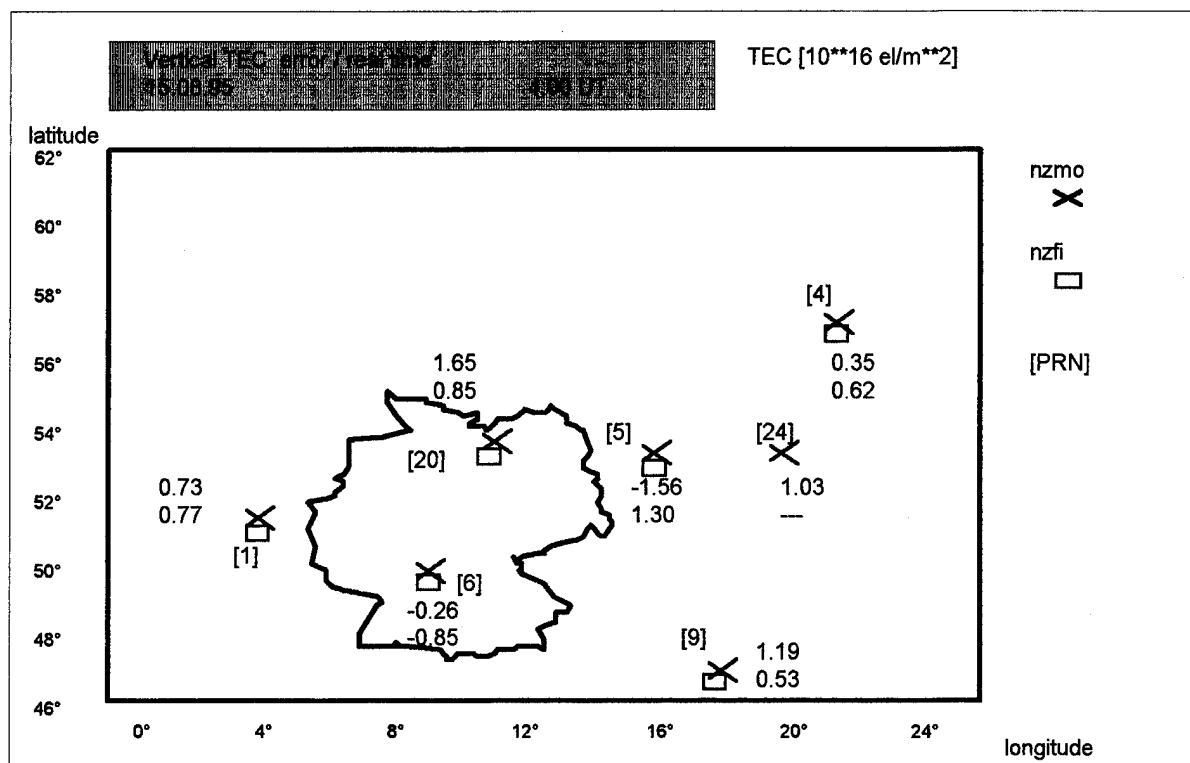


Fig.5 Real time vertical TEC errors referred to postprocessed results at stations nzmo and nzfi (4h UT)

(nzmo), Gransee (nzfi) and Potsdam (pots). The spacing of the stations is about 50km. Besides to check for the accuracy of the real time algorithm, the campaign was aimed to decide if TEC local decorrelation measurements may be performed in real time or if postprocessing methods have to be used.

Fig. 4 shows the vertical TEC values resulting from the postprocessing method for all visible

satellites with an elevation mask of 20° at 4h UT.

As may be seen, due to the small spacing of the stations, there is only a small variation in the TEC values. The variation is in the range of the error of the method, so no significant conclusions about ionospheric decorrelation may be drawn, but on the other hand, the accuracy of the postprocessing method is

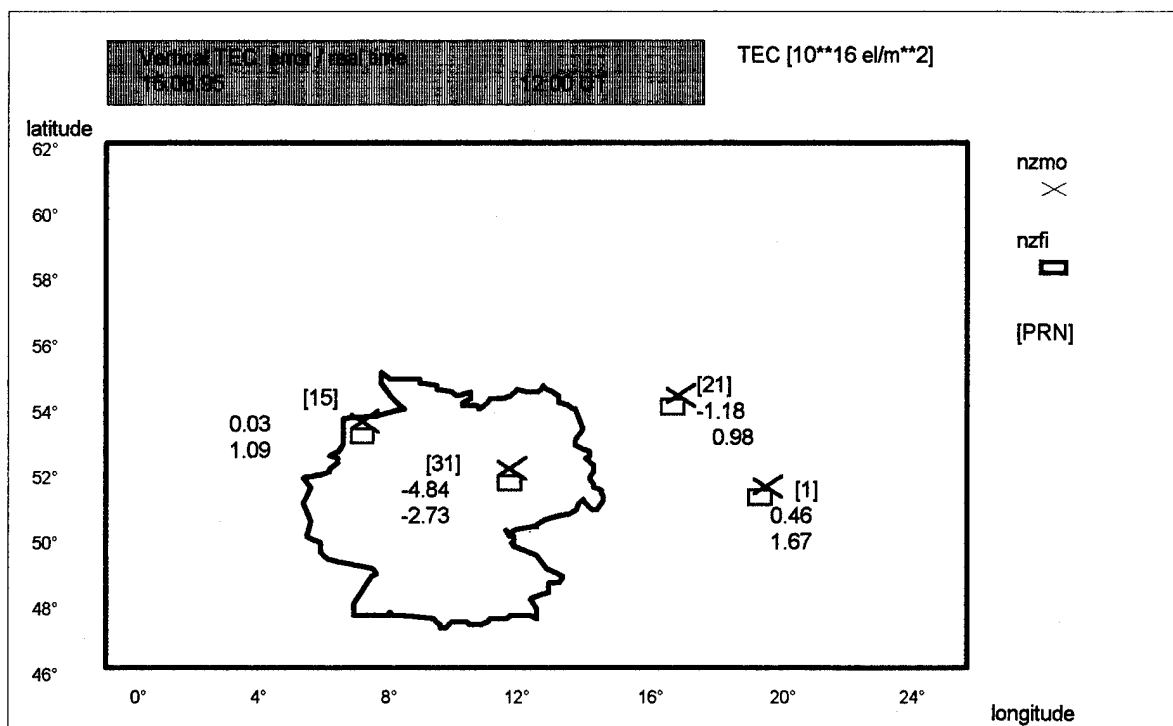


Fig. 6 Real time vertical TEC errors referred to postprocessed results at stations nzmo and nzfi (12h UT)

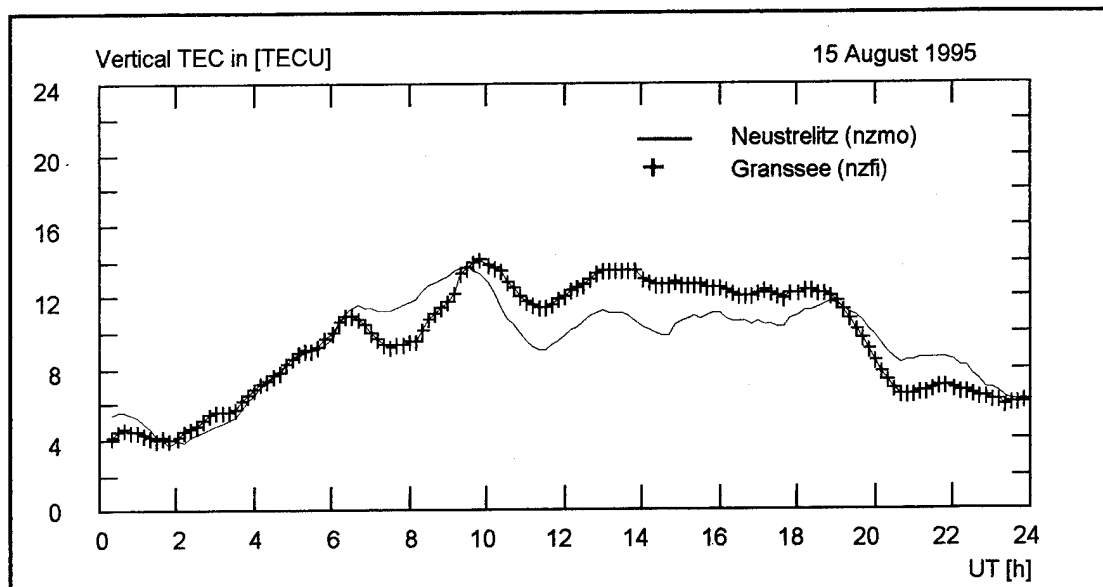


Fig. 7 Vertical TEC for a complete day for stations nzmo and nzfi

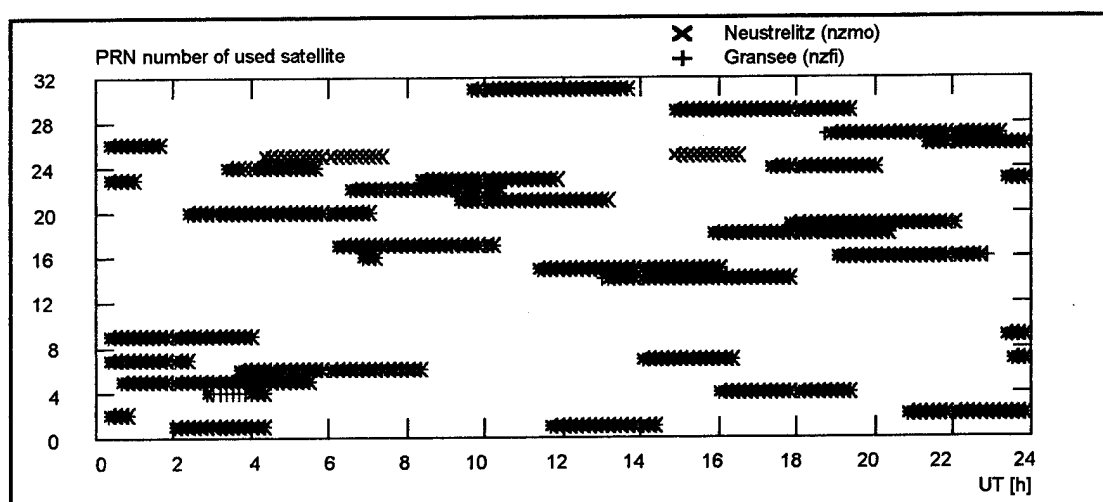


Fig. 8 Satellite visibility for nzmo and nzfi (elevation cutoff is 20°)

prooven.

Next step was to process the nzmo and nzfi stations in the real time algorithm. Examples for the differences between the results of the real time algorithm and the postprocessing method are given in Fig. 5 and Fig. 6. A time span of 20 minutes was chosen for the interval from tracking the first epoch to ambiguity fixing.

As may be seen, the results of the real time algorithm are quite satisfactory, on the other hand, the limitations in the accuracy due mainly to the multipath effects are demonstrated. The influence of the multipath effect is verified again by Fig. 7 and Fig. 8, where the complete vertical TEC slopes of the two stations under consideration are shown. Though the postprocessing results indicate no significant differences in the TEC behaviour, for the real

time TEC significant differences can be seen starting at about 6:30UT. Checking the visibility plot we notice that at this time station nzmo tracks an additional satellite (#26), and besides of this, most of the satellites are rising or just going down, so the multipath situation is very poor, giving the maximum TEC error of about 4 TECU.

SUMMARY

A real time algorithm on the basis of instrumental bias predictions was developed and implemented into the software of a Real Time IPE Monitoring Station. The algorithm independently processes all channels of a L1/L2 GPS P-code receiver. It was shown that the main error contribution in the estimation of the IPE is due to the individual multipath

environment of the monitoring station. For the examples given, the maximum error was about 5 TECU. Due to the multipath characteristic of the examples chosen, we consider this error to be an upper limit. A principal lower error limit of 1 TECU was estimated for the method. This limit is due to the accuracy of the variations of the instrumental receiver-satellite bias combinations as estimated by postprocessing, to the delay of the postprocessing of at least 3 days and due to the intrinsic variation of the receiver and satellite biases themselves. The Real Time IPE Monitoring Station is capable of being a component in a real time network for TEC monitoring and modeling.

ACKNOWLEDGEMENTS

Our thanks are due to the German Space Agency (DARA) for the financial support of our investigations through several projects in the last years. We want to acknowledge for the contributions from A. Jungstand and N. Jakowski to special topics and scientific discussions. Besides, we are grateful to H.-G. Kugland and K. Hiersche for performing the campaigns.

LITERATURE

- [1] Lanyi, G.E., Roth, T., A comparison of mapped and measured total ionospheric electron content using Global Positioning System and beacon satellite observations", 1988, Radio Science, Vol. 83 (4), 483-492
- [2] Klobuchar, J.A., Ionospheric Time-Delay Algorithm for Single Frequency GPS Users, IEEE Transactions on Aerospace and Electronic Systems, Vol. AES-23, No. 3, May 1987, pp.325-31
- [3] Cohen C.E., Pervan B., Parkinson B.W., Estimation of absolute Ionospheric delay Exclusively through Single-Frequency GPS measurements, ION GPS-92 Proc., September 1992, 325 - 330
- [4] Xia R., Determination of Absolute ionospheric Error Using a Single-Frequency GPS Receiver, ION GPS-92 Proc., September 1992, 483 - 490
- [5] Coco, D.S., Cocker, C., Dahlke, S.R., Clynych, J.R., Variability of GPS satellite differential group delay biases, IEEE Transactions on Aerospace and Electronic Systems, 1991, 27(6), 931 - 938
- [6] Sardón, E., Rius, A., Zarraoa, N., Estimation of transmitter and receiver differential biases and the ionospheric total electron content from GPS observations, Radio Science, 1994, 29(3), 577 - 586
- [7] Jungstand, A., Engler, E., Sardon, E., Klähn D., Error Separation Concept in Experimental TEC Monitoring Network, ION Technical Meeting 1995, Anaheim (CA), USA
- [8] Engler, E., Sardon, E., N. Jakowski, Jungstand, A., Klähn, D. Real-Time monitoring of the ionosphere, IGS-Workshop 1995, Potsdam
- [9] Wilson, D., Mannuchi, A.J., Instrumental Biases in Ionospheric Measurements Derived from GPS Data, ION GPS-93 Proc., September 1992, 1343-1351

Real-Time TEC Determination for Ionospheric Modeling in WADGPS

José Fraile-Ordóñez
Kayser-Threde GmbH

BIOGRAPHY

Mr. José M. Fraile-Ordóñez studied Mathematics at the Complutense University of Madrid in 1989. After working for two years at the University FAF in Munich as research associate, he joined the Navigation Group of Kayser-Threde GmbH in October 1992. He has been deeply involved in the development of a number of GPS-based systems, e.g. DGPS Reference and Mobile Stations for Geodesy and Navigation, a GPS/GIS Data Collection System, an Ionosphere Monitoring System and a Train Tracking System.

Mr. Fraile-Ordóñez is currently mainly involved in space applications of GPS including e.g. autonomous navigation and control of satellites, accurate DGPS positioning of spacecrafts, GPS/INS navigation during atmospheric re-entries, use of GPS at high altitude orbiting satellites and relative navigation with GPS.

ABSTRACT

In this paper, an algorithm for the real-time computation of Ionospheric Total Electron Content (TEC) will be presented. The computation is based on a sequential least-squares algorithm applied to dual frequency GPS pseudorange and carrier phase measurements. It will be shown that this combination enables a strong reduction of noise on the TEC determination as compared to TEC values computed from simple frequency differenced pseudoranges.

Thanks to its real-time processing capability, this algorithm is mainly expected to be implemented in Wide Area Differential GPS Reference Stations or in Ionosphere Monitoring Stations.

1 INTRODUCTION

Signals transmitted by artificial satellites travel through the ionosphere before being received at the earth's surface. They are affected by the non-linear dispersion characteristics of the ionosphere and as a result they experience a path delay which depends on the signal frequency and on the electrons density of the ionosphere (the so-called Ionospheric Total Electron Content or TEC). Since the GPS satellites broadcast signals in two frequencies, TEC determination is possible by simply

analyzing the difference in path delays experienced by each of the signals.

Accurate real-time TEC determination for ionospheric modeling in Wide Area Differential GPS (WADGPS) is currently a topic of great international interest (e.g. [1]). The reason for this is that the ionospheric delay is a significant source of error in GPS navigation, only surpassed by Selective Availability. In local DGPS, the ionospheric delay can be nearly entirely removed as long as the baseline between user and reference station remains relatively short. In WADGPS on the contrary, those baselines can reach up to several thousand kilometers and the ionospheric effects within those larger areas are not automatically eliminated by the differential approach. Therefore, the ionospheric delay component must be explicitly determined from a spatial model of the ionosphere.

In a WADGPS system the reference stations obtain local TEC data for all satellites in view and transfer these data to the Master Station. There, the TEC information is processed and an ionospheric model is generated. The quality of the local TEC information will be one of the key issues to generate accurate ionospheric models.

Unfortunately, TEC determination with GPS relies heavily on dual-frequency pseudorange (or group-delay) measurements which can show high noise levels caused by Anti-Spoofing (AS) and its encryption of the P-code into the secret Y-code. Low pass filtering techniques and combination of pseudorange and carrier phase data are two potential methods to overcome those limitations.

In this article an algorithm for real-time TEC determination based on a least-squares processing of dual-frequency pseudorange and carrier phase data will be presented. It will be shown that the TEC information obtained with this technique is affected by very low noise levels since errors associated to code-less tracking and multipath are strongly eliminated (specially at low elevation angles).

2 DETERMINATION OF IONOSPHERIC TEC IN THE PRESENCE OF ANTI-SPOOFING

The ionospheric delay on GPS pseudoranges is often formulated in first order as follows (unmodeled higher

order effects amount only to some very few centimeters):

$$\delta\rho_i^{ion} = \frac{40.3}{f_i^2} TEC,$$

where i is the L1 or L2 frequency, f is the carrier frequency and TEC is the line-of-sight Total Electron Content in electrons/meter².

If this equation is written for pseudoranges in L1 and L2, ρ_1 and ρ_2 , and simple math is used, then the instantaneous and absolute line-of-sight TEC can be determined through the difference between the GPS pseudorange measurements at both frequencies in the following way:

$$TEC = \frac{\rho_1 - \rho_2}{40.3} \frac{f_1^2 f_2^2}{f_2^2 - f_1^2}$$

It can be noticed that the absolute value of individual pseudorange measurements at each of the GPS frequencies is not necessary for TEC determination but only the difference between both. This is of great importance as the P-codes are not normally available to civil users; they are encrypted into the secret Y-codes when Anti-Spoofing is on. In this way, receivers capable of tracking GPS signals on both frequencies with code-less (cross-correlation) techniques are able to compute slant TEC with this very simple and robust method.

Unfortunately, when Anti-Spoofing is on and the GPS receiver tracks in code-less mode, the precision of the pseudorange data is severely degraded, specially at low elevations. Very high cut-off angles (30 degrees with AS on, 20 degrees with AS off) are sometimes applied in order to avoid such problems ([3]).

Smoothing with a low pass filter can greatly reduce the noise level of the TEC obtained with this method. On the other hand, implementing efficient low pass filters in real-time is not an easy task since only information about the past is available.

3 ALGORITHM FOR REAL-TIME COMPUTATION OF PHASE-SMOOTHED TEC

A new algorithm has been developed at Kayser-Threde GmbH for the efficient determination of TEC. This algorithm takes advantage of the high accuracy and very low noise level of the GPS carrier phase measurements. It combines pseudoranges and carrier phases in a least squares adjustment which can be implemented in both a batch and a recursive formulation. The recursive formulation is specially well suited for real-time TEC determination.

In order to describe the mathematical formulation of this algorithm, we need to define now the following two new terms $\Delta\rho$ and $\Delta\Phi$ as follows:

$$\Delta\rho = \rho_2 - \rho_1 = 40.3 TEC \frac{f_1^2 - f_2^2}{f_1^2 f_2^2} + \Delta n^p$$

$$\Delta\Phi = \Phi_2 - \Phi_1 = -40.3 TEC \frac{f_1^2 - f_2^2}{f_1^2 f_2^2} + \lambda_2 N_2 - \lambda_1 N_1 + \Delta n^\Phi$$

where Φ_i , λ_i and N_i are the L1 and L2 GPS carrier phase measurements, wavelengths and phase ambiguities respectively. Δn^p and Δn^Φ represent measurement errors associated to sources other than the ionosphere. In order to obtain those expressions we have made use of the known fact that the ionospheric effects on pseudorange and carrier phase measurements have the same magnitude but opposite signs.

If a GPS data set with n measurement epochs is available, $\Delta\rho$ and $\Delta\Phi$ terms can be computed for every epoch t_k ($k=1, \dots, n$). When doing so, the following equation system can be created:

$$\begin{pmatrix} \Delta\rho \\ \Delta\Phi \end{pmatrix} = \begin{pmatrix} I & \underline{0} \\ -I & \underline{i} \end{pmatrix} \begin{pmatrix} x \\ b \end{pmatrix} + \begin{pmatrix} \Delta n^p \\ \Delta n^\Phi \end{pmatrix}$$

where:

$$\underline{\Delta\rho} = (\Delta\rho(t_1), \Delta\rho(t_2), \dots, \Delta\rho(t_n)),$$

$$\underline{\Delta\Phi} = (\Delta\Phi(t_1), \Delta\Phi(t_2), \dots, \Delta\Phi(t_n)),$$

I is a diagonal unit matrix,

$\underline{0}$ is a null vector,

\underline{i} is a unit vector,

$$b = \lambda_2 N_2 - \lambda_1 N_1,$$

$$\underline{\Delta n^p} = (\Delta n^p(t_1), \Delta n^p(t_2), \dots, \Delta n^p(t_n)),$$

$$\underline{\Delta n^\Phi} = (\Delta n^\Phi(t_1), \Delta n^\Phi(t_2), \dots, \Delta n^\Phi(t_n)),$$

and x is a new vector which accounts for the ionospheric effects in every epoch. Its elements are:

$$x(t_k) = 40.3 \frac{f_1^2 - f_2^2}{f_1^2 f_2^2} TEC(t_k).$$

If a diagonal weight matrix accounting for the pseudorange and carrier phase measurement accuracy is defined as follows:

$$W = \begin{pmatrix} \varpi_{\Delta\rho} & & & 0 \\ & \ddots & & \\ & & \varpi_{\Delta\Phi} & \\ 0 & & & \ddots \end{pmatrix}$$

then the equation system can be easily solved with a batch least squares adjustment to obtain:

$$\hat{b} = \frac{i'(\Delta\rho + \Delta\Phi)}{n}$$

$$\hat{x} = \frac{\varpi_{\Delta\rho}\Delta\rho - \varpi_{\Delta\Phi}\Delta\Phi}{\varpi_{\Delta\rho} + \varpi_{\Delta\Phi}} + \frac{\varpi_{\Delta\Phi}\hat{b}_i}{\varpi_{\Delta\rho} + \varpi_{\Delta\Phi}}.$$

The least squares adjustment can be easily implemented in a recursive form which allows real-time estimation of the unknowns in the following way:

$$\hat{b}_{k+1} = \frac{k}{k+1} \hat{b}_k + \frac{\Delta\rho(t_{k+1}) + \Delta\Phi(t_{k+1})}{k+1}$$

$$\hat{x}_{k+1}(t_{k+1}) = \frac{\varpi_{\Delta\rho}\Delta\rho(t_{k+1}) - \varpi_{\Delta\Phi}(\Delta\Phi(t_{k+1}) - \hat{b}_{k+1})}{\varpi_{\Delta\rho} + \varpi_{\Delta\Phi}}.$$

The interested reader can find a much more detailed description of this algorithm in [2].

5 SLANT AND VERTICAL TEC

GPS measurements are taken from satellites which are tracked at various elevation angles. This causes the GPS signals to cross largely different portions of the ionosphere (the lower the elevation angle, the larger the portion). The TEC values computed with the algorithms described above, correspond to the so-called "slant" or "line-of-sight" TEC. For ionospheric modeling purposes however, "vertical" TEC is required (see e.g. [1]).

It is usually assumed that slant TEC is related to vertical TEC at the ionospheric intersection point (at 350km height) by an elevation mapping function which enables the computation of an obliquity correction factor.

We used in our investigations the following obliquity factor for the conversion of slant to vertical TEC ([3]):

$$M(e) = \frac{1}{\sqrt{1 - \left(\frac{\cos e}{1 + (h/R_E)} \right)^2}}$$

where R_E is the mean earth radius, e is the satellite elevation angle and h is the height of the "ionospheric shell" used to determine the interception point (we have here considered $h = 350\text{km}$).

The resulting obliquity factor as a function of the elevation angle is shown in Figure 1.

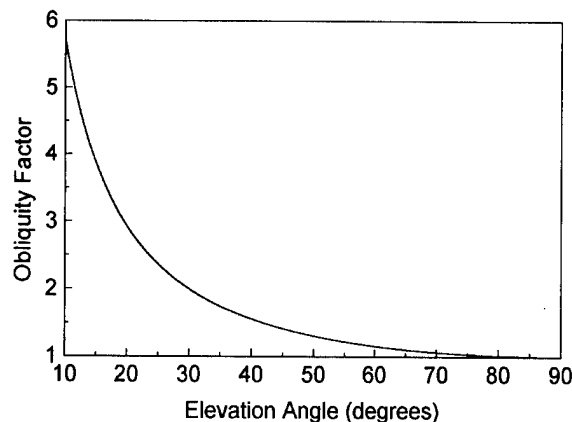


Fig. 1: Obliquity factor vs. elevation angle

4 DIFFERENTIAL INSTRUMENTAL DELAYS

Actually, the frequency differenced GPS measurements contain both the delays induced by the ionosphere and by the satellite and receiver hardwares (the latter ones are called differential instrumental delays). The differential instrumental delays are caused by the different paths that the GPS signals at L1 and L2 travel within the GPS satellites and receiver hardwares.

The receiver's differential delay affects all measurements from different satellites in much the same way. A periodic receiver calibration can help overcome the effects of this delay.

GPS satellite differential instrumental delays are more difficult to handle with. Each satellite's differential delay has been calibrated in laboratory previously to launch and the obtained value is transmitted in the navigation message's parameter T_{gd} . However, it has been observed that these pre-launch values have very little to do with the actual delays once the satellite was in orbit. Therefore, very much effort has been invested in order to estimate the actual satellite instrumental delays ([3, 4]).

In our investigations, we corrected the TEC values with the satellite differential instrumental delays estimated by the Institut für Erdmessung of the University of Hannover ([4]). [3] showed that satellite differential delays do not experience large variations in time and that they did not change significantly after AS was switched on in January 1994.

5 DATA PROCESSING, RESULTS AND DISCUSSION

We have extensively processed dual frequency GPS data in order to validate the described new algorithm and to compare its performance with other techniques.

We obtained GPS data from the IGS network tracking station Wettzell in Germany for the day July 26, 1995 ([5,6]). Wettzell is equipped with a Turbo Rogue receiver connected to a H-Maser external frequency standard. This receiver can operate in code-less mode (cross-correlation) when AS is on which was the case on July 26.

The IGS data consist of 30 seconds values of GPS carrier phase and pseudoranges at both the L1 and L2 frequencies in RINEX format ([7]). We have selected the data from PRNs #28, #15 and #29 since these satellites were visible during long and consecutive periods of time. The observed satellites elevation angles at Wettzell are shown in Figure 2. It can be noticed that we used a 30 degrees cut-off angle for our analyses.

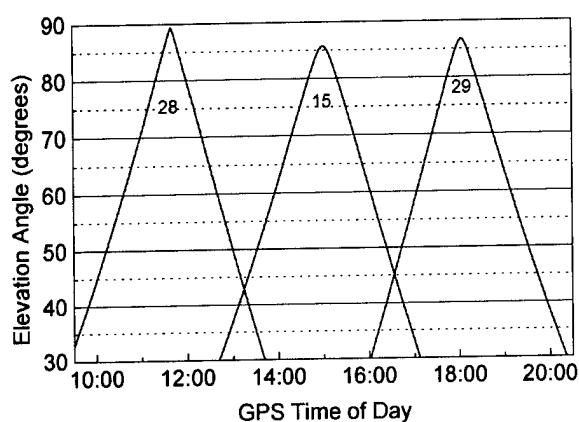


Fig. 2: Elevation angles

We first processed the data with the simple method described in Section 2 using frequency differenced pseudoranges. The results are shown in Figure 3 (please remember that 1 TEC Unit = 10^{16} electrons/meter² = 0.35 nanoseconds of differential delay).

The predicted high noise level caused by measurement errors associated to code-less tracking and multipath can be clearly observed. Additionally and fortunately for comparison purposes, AS was off for PRN #28 on that day. Please observe that the scatter of the code-less data (PRNs #15 and #29) is much larger than that of the code data (PRN #28).

In an attempt to reduce the noise of the data, we re-processed the data with the same algorithm but performing a smoothing of the obtained TEC values over periods of 300 seconds (10 measurement epochs which were equivalent to 5 minutes with the IGS data). For this smoothing we assumed that the ionospheric conditions don't change severely over such a short period of time and we computed for every epoch the average of TEC obtained in the ten last available epochs (including the current one). No averaging was accomplished making use of posterior data to the actual processing epoch since we tried to simulate real-time processing.

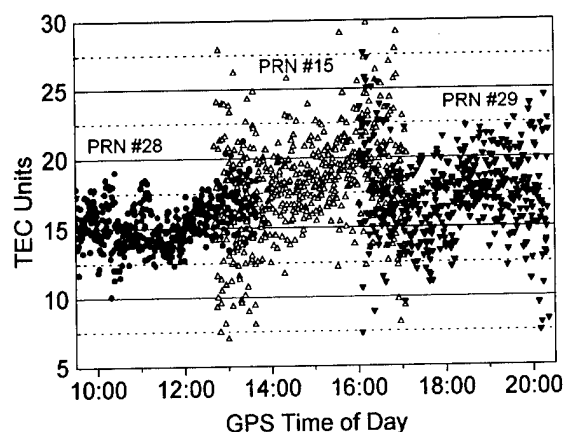


Fig. 3: TEC from group-delays

The results of this real-time averaged TEC are plotted in Figure 4. It can be clearly seen that although the noise level has been greatly reduced, the results are still unsatisfactory.

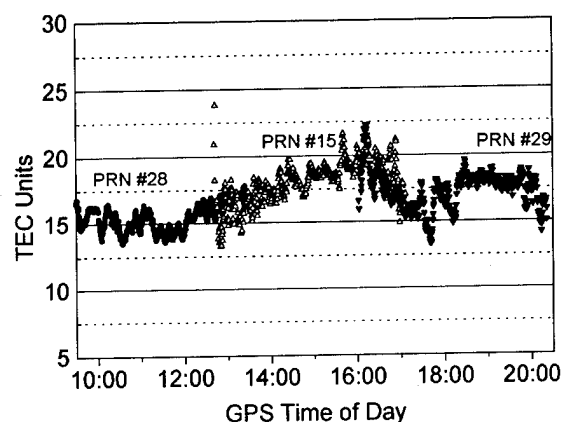


Fig. 4: Averaged TEC from group-delays

Finally, we processed the data using the recursive formulation of the carrier phase-smoothing algorithm described in Section 3. This algorithm has the disadvantage of being sensitive to cycle slips, i.e. it needs to be re-initialized whenever a slip occurs. In normal conditions however, a cycle slip will only occur when the GPS satellite is tracked at low elevations. In our data we did not have any cycle slip above the cut-off angle and all data were processed very successfully. The results are shown in Figure 5.

The improvement achieved processing the data with this algorithm are obvious. Only at the beginning of the satellite signal tracking the noise level is relatively high (specially for code-less data), but after a short while the smoothing effect of the low-noise carrier phase measurements is clear.

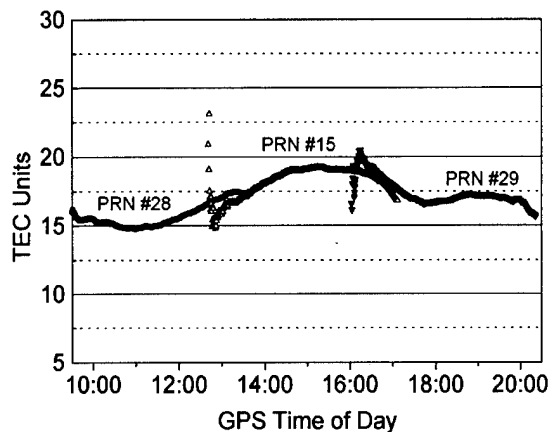


Fig. 5: Carrier phase smoothed TEC

6 CONCLUSIONS

The determination of reliable TEC data to be processed at a WADGPS Master Station for ionospheric modeling is one the key issues influencing the final accuracy of the ionosphere spatial model to be generated. Such TEC data has to be determined in real-time at the reference stations.

Obtaining low noise TEC information in real-time is a challenging task due to the large pseudorange measurement errors originated by code-less tracking and multipath.

In this paper an algorithm for TEC determination which combines dual frequency pseudorange and carrier phase measurements has been presented. It has been shown that this algorithm greatly reduces the noise level of the obtained TEC thanks to the smoothing effect that the high accuracy carrier phase measurements have on the pseudoranges.

Finally, this algorithm can be easily implemented in a recursive formulation which allows for efficient real-time processing. This is one of the reasons why it is very well suited to be used in future WADGPS reference stations.

7 ACKNOWLEDGEMENTS

Dr. Bernd Eissfeller's efforts developing the carrier phase smoothing algorithm described in this paper are hereby truly acknowledged.

I would also like to thank the International GPS Service for Geodynamics for providing the GPS data.

8 REFERENCES

- [1] Bakry El-Arini, M.; et. al.: *Comparison of Real-Time Ionospheric Algorithms for a GPS Wide-Area Augmentation System (WAAS)*. NAVIGATION, Journal of the Institute of Navigation, Vol. 41, No. 4, Winter; 1994-95.
- [2] Fraile-Ordóñez, J.M.: *Ionospheric Total Electron Content Determination from Dual-Frequency GPS Measurements for Real-Time Applications in Satellite Navigation*. To be published in SPN, Journal for Satellite-Based Positioning, Navigation and Communication, October; 1995.
- [3] Wilson, B. and A. Mannucci: *Extracting Ionospheric Measurements from GPS in the Presence of Anti-Spoofing*. Proceedings of the 7th International Technical Meeting of The Satellite Division of The Institute of Navigation, ION Salt Lake City, Utah, GPS-94, September 20-23; 1994.
- [4] Wanninger, L. and E. Sardón: *Improved Data Sets of the Differential Instrumental Delays of GPS Satellites*. IfE-MEMO WA-09/93, September; 1993.
- [5] Zumberge, J.; R. Neilan; G. Beutler and W. Gurtner: *International GPS Service for Geodynamics-Benefits to Users*. Proceedings of the 7th International Technical Meeting of The Satellite Division of The Institute of Navigation, ION Salt Lake City, Utah, GPS-94, September 20-23; 1994.
- [6] International GPS Service for Geodynamics: *Resource Information*. International Association of Geodesy, International Union of Geodesy and Geophysics, September; 1994.
- [7] Gurtner, W.: *RINEX-The Receiver Independent Exchange Format*. GPS World, Vol. 5, No. 7, July; 1994.

An Improved Ionospheric Correction Method for Wide-Area Augmentation Systems

Anthony Mannucci, Brian Wilson, and Dah-Ning Yuan
Jet Propulsion Laboratory

Biographies

Anthony J. Mannucci is a member of the technical staff in the GPS Networks and Operations Group at the Jet Propulsion Laboratory in Pasadena, CA. He has played a principal role in development of the global ionospheric mapping technique, and has spent the last four years developing and characterizing ionospheric calibration systems for deep space tracking and Earth-based satellite applications. He has over ten years of experience developing high accuracy measurement techniques in a variety of technical areas. Currently, he is focusing on increasing the accuracy of GPS-based global ionospheric maps by improving the models and estimation strategy. Dr. Mannucci received a Ph.D. degree in physics from the University of California at Berkeley in 1989.

Brian Wilson, a member of the GPS Networks and Operations Group at the Jet Propulsion Laboratory in Pasadena, CA, has been studying the ionosphere using GPS for five years. He is the Cognizant Design Engineer of the operational ionosphere calibration software for the Deep Space Network, which is used to correct navigation radiometric data for ionospheric delay effects. Brian is a co-developer of the global ionospheric mapping (GIM) technique, which assimilates GPS data from 60+ globally distributed sites to produce sub-hourly maps of total electron content. Currently, he is working to improve the accuracy of GIM by incorporating an improved physical ionosphere model, and validate its accuracy by comparisons with independent ionosphere measurements from Very Long Baseline Interferometry and the TOPEX dual-frequency altimeter.

Dah-Ning Yuan is a member of the technical staff in the Tracking Systems and Applications section at the Jet Propulsion Laboratory (JPL) in Pasadena, California. He has been studying the ionospheric data assimilation problem for the past 2 years using total electron content (TEC) data derived from a world-wide network of dual-frequency GPS receivers. Prior to devoting his time to research in physical ionosphere modeling, he was involved in implementing SLR (satellite laser range) and DORIS (Doppler Orbitography and Radio Positioning Integrated by Satellite) data processing techniques for the

TOPEX/Poseidon project in the Navigation Systems Section at JPL. He obtained his Ph.D. in Aerospace Engineering from the University of Texas at Austin in 1991. His graduate research concentrated on development of an Earth gravity field model for TOPEX/Poseidon precision orbit determination using satellite tracking, satellite altimeter, and surface gravity anomaly data.

Abstract

A powerful approach for generating ionospheric corrections in wide area differential GPS applications has been developed, that can be applied to the Federal Aviation Administration's Wide Area Augmentation System (WAAS). This approach has been used to support ionospheric calibration for NASA's Deep Space Network and will be supporting real-time operations for global ionospheric specification and, possibly, single-frequency satellite altimeter calibration. It is a real-time, grid-based technique relying on a computationally efficient Kalman-type filter to produce accurate, smoothly varying ionospheric correction maps over the coverage area. Formal error maps are also computed, providing vertical delay errors over the WAAS grid, which are useful in integrity monitoring. This solution to the ionospheric correction problem is self-calibrating, since GPS transmitter inter-frequency biases are obtained as a by-product of the mapping procedure. This contrasts with other techniques in which bias values must be provided from some additional source.

Simulated data were generated for the proposed configuration of 24 WAAS reference GPS stations, using a well-tested climatological ionosphere model (Bent) to compute ionospheric total electron content (TEC) during conditions typical near the peak of the solar cycle. Slant TEC delays often exceed 30 meters over the continental US (CONUS) during solar maximum, but the simulations indicate that the corrections are accurate to 0.25-0.5 meter over the CONUS, Alaska and Hawaii (this includes any errors in estimating the transmitter biases). Our technique is therefore useful for en-route navigation and precision approach, the latter requiring 1.5 meter correction accuracy.

Introduction

We have developed a powerful and accurate method of exploiting data from a dense GPS receiver network to generate high resolution "snapshot" images of the ionospheric vertical delays anywhere within the coverage area. The mapping technique has been used to support operational ionospheric calibrations for NASA's Deep Space Network and will support real-time operations for a global network of GPS receivers that monitor ionospheric total electron content (TEC). The correction method relies on a Kalman filter implementation and can automatically produce formal error maps. It is therefore ideally suited for incorporation into a real-time correction system such as the Federal Aviation Administration's wide area augmentation system (FAA WAAS). It is a grid-based algorithm with a built-in interpolation scheme to provide corrections at any point within the continuous coverage area, and is well adapted to provide a real-time estimate of both the ionosphere and the errors at the specified set of WAAS grid points.

In this paper, we will summarize our wide-area ionospheric correction technique, which is based on the Jet Propulsion Laboratory's GPS Inferred Positioning System software (GPSY), extended to include the triangular interpolation technique for ionospheric corrections (TRIN). This method has been described in a previous Institute of Navigation Proceedings paper (Mannucci *et al.*, 1993, hereafter known as Paper I). We will summarize the specific advantages of our method, in particular the use of a grid that is fixed with respect to the Sun rather than co-rotating with the Earth. We will present simulation results that demonstrate the GPSY/TRIN method is capable of 0.25-0.5 meter correction accuracy over the continental US (CONUS) during conditions typical of solar maximum. Finally, we will indicate how the GPSY/TRIN software could be incorporated into the FAA's real-time WAAS.

The GPSY/TRIN Method for Computing the Real-Time Ionospheric Correction

The GPSY/TRIN ionospheric correction algorithms have been described in a previous Institute of Navigation Proceedings (Paper I), and only features of particular relevance to WAAS will be summarized here. We will discuss several unique features of the GPSY/TRIN method: 1) the use of a Sun-fixed, rather than Earth-fixed grid for the initial interpolation step; 2) the use of a triangular grid, not a rectangular one and 3) the instrumental inter-frequency bias estimation capability.

Ionospheric total electron content is extracted from GPS by computing the difference between satellite-receiver range measured at the two GPS frequencies, L1 and L2 (see Paper I). The line-of-sight measurements of ionospheric delay are interpolated to form a wide-area correction map that applies to the entire coverage area.

The GPSY/TRIN method employs a "shell" model of the ionosphere: the ionospheric electrons are assumed to be concentrated in a thin shell at a fixed height of about 350 km. The delay due to this shell is parametrized in terms of a set of vertex values uniformly distributed over a spherical surface, in a triangular tiling scheme. The grid is Sun-fixed so that it does not rotate with respect to the basic structure of the ionosphere.

Each ionospheric measurement from a GPS receiver in the network is modeled as a simple linear combination of the grid vertex parameters in the following form:

$$I_{rs}(t_i) = M(E) \sum_{i=1}^3 W_i(\phi_{pp}, \lambda_{pp}) V_i + b_r + b_s \quad (1)$$

where $I_{rs}(t_i)$ is the real-time measurement from receiver r and satellite s at time t_i , V_i is the value of the TEC at vertex i (i.e. parameter i) and $M(E)$ is the obliquity factor relating slant delay to vertical for elevation angle E . The factor $W_i(\phi_{pp}, \lambda_{pp})$ is a distance-weighting function that relates the TEC at the ionospheric pierce point location $(\phi_{pp}, \lambda_{pp})$ to the TEC at the three vertices of the intersected tile. This function is based on a simple bilinear interpolation scheme (see Paper I). This "measurement model" is used in the GPSY Kalman filter for estimating the vertex parameters V_i from the real-time data. The final two terms, b_r and b_s , refer to the instrumental inter-frequency (L1/L2) bias in the ground receiver and satellite transmitter respectively. These biases can be estimated simultaneously with the ionosphere delays or held fixed to a priori values.

The ionospheric mapping process makes extensive use of the stochastic estimation features of the GPSY Kalman filter. As measurements become available, the zenith ionospheric delay at every point of the triangular grid over the coverage area is re-estimated. (For current NASA operations where GPSY/TRIN is used, this coverage area is the entire globe.) The vertex parameters are modeled as Gauss-Markov stochastic processes, so that the updated values at each grid point are correlated with their values at the previous time step (i.e., they are not estimated entirely independently at each step, so that the recent history of measurements contributes to the current estimate). Since a distance weighting function is used in equation 1, the vertex TEC values are also correlated spatially with the values at adjacent grid points. This results in stable and smoothly varying ionospheric maps.

Sun-Fixed Grid

The FAA WAAS specification requires that the ionosphere delay be specified over an Earth-fixed grid covering the CONUS coverage area (the grid spacing varies between 5 and 10 degrees). Most correction techniques interpolate the TEC measurements from the GPS receivers in the WAAS network in an Earth-fixed coordinate system (e.g. Brown, 1989; Kee *et al.*, 1991).

However, the ionosphere varies much more slowly in a Sun-fixed reference frame, so interpolation over a grid fixed with respect to the Sun produces more accurate correction maps. In a final step, translation to the Earth-fixed WAAS grid can be performed rapidly with no loss of precision since the Sun-fixed correction map overlaps the Earth-fixed grid.

The temporal stability of the ionosphere in a Sun-fixed reference frame is demonstrated in Figures 1 and 2, which are plots of the diurnal variation of TEC over three widely separated sites in the North American continent sharing similar geomagnetic latitudes: Goddard (49.97 geomagnetic latitude, -76.83 geographic longitude), North Liberty (51.93, -91.57) and Quincy (46.44, -120.94). The zenith delay over each site was determined by evaluating the GIPSY/TRIN global map solution directly overhead each station for a relatively active day in March 1993 (solar sunspot number = 67.1, F10.7 flux = 140). The usual diurnal variation in the ionosphere causes the TEC above each station to be markedly different at the same universal time (figures 1a and 1b). This causes large changes in successive Earth-fixed correction maps. However, when zenith TEC is plotted in terms of local time (equivalent to using Sun-fixed coordinates), the differences between the stations is significantly reduced (figures 2a and 2b), showing that all three stations undergo similar diurnal variations. Therefore, correction map variations are much smaller in Sun-fixed coordinates, and the correlation time between successive maps is longer. This leads to more accurate wide-area corrections when Kalman-filter updating is used.

In addition to reduced variability, the ionospheric pierce points of the TEC measurements cover a larger portion of the ionospheric shell when a Sun-fixed grid is used, as shown in figure 3a and 3b. These are plots of ionospheric penetration points for the WAAS reference stations during a three-hour period using an elevation cutoff of 20 degrees. A higher density of ionospheric pierce points is evident for the Sun-fixed grid. The Earth rotates underneath the Sun-fixed grid, so the Sun-fixed longitude of each station changes with time, allowing a single station to cover an additional 15 degrees of longitude per hour. Since the Earth-fixed grid rotates with the stations, gaps in the coverage may persist indefinitely, potentially leading to large inaccuracies.

Triangular Grid

The WAAS specification requires that the ionospheric corrections are computed for a set of fixed points over a rectangular grid, that covers the CONUS region and extends into southern latitudes. Most proposed correction methods also use a rectangular grid for interpolation between the measurements, which is disadvantageous for two reasons. First, the distance between the grid points determines the spatial correlation scales that can be reproduced in the TEC map. For a rectangular grid, this will be latitude-dependent in a manner which does not

match the correlation scales in the ionosphere. Second, a scheme based on rectangular grids cannot be expanded to cover the entire globe and therefore is naturally limited in extent. If the WAAS correction algorithms are based on Earth-fixed grids, and the coverage region is expanded in the future, the basic interpolation algorithms may require significant modification. In contrast, a triangular grid covers the sphere uniformly and is used in GIPSY/TRIN since it is a global mapping technique. A triangular grid can be used to form corrections over a limited region as well, and the correction map can of course be evaluated at a set of rectangular grid points that overlap the coverage area.

Self-Calibration

Ionospheric measurements using dual-frequency GPS receivers are affected by inter-frequency biases which, if left uncalibrated, can corrupt the measurements by as much as 5 meters. These biases, which affect both the receivers and the satellite transmitters, can be accurately estimated using the GIPSY/TRIN technique. Numerous comparisons between global map solutions and independent measurements of TEC show that the biases are determined to better than 0.5 meter accuracy, even for periods when the solar sunspot numbers were a factor of 3-5 larger than current values (see Wilson *et al.*, 1994; Mannucci *et al.*, 1994). Therefore, in contrast to other proposed ionospheric correction methods, the GIPSY/TRIN method is self-calibrating, and does not require that biases be provided from an external source. However, should more accurate bias values be available, they can be used to directly calibrate the data.

Even if receiver and satellite calibrations are available from an independent source, it is still useful to estimate these biases off-line (i.e. not in real-time) on a regular basis. A frequently-updated database of bias values can be used to detect anomalous changes in the receiver and satellite hardware. Therefore, we would recommend that bias estimation be performed frequently for the WAAS network for the purpose of integrity monitoring.

Simulation Results

To assess the suitability of GIPSY/TRIN for applications such as the FAA's wide area augmentation system, a simulation using the proposed configuration of 24 WAAS remote stations was performed for conditions typical of solar maximum, when slant ionosphere delays over CONUS frequently exceed 30 meters. Line-of-sight TEC measurements were synthesized every 5 minutes, based on the proposed WAAS station geometry and assuming a full GPS constellation of 24 satellites. The Bent ionospheric model (Bent *et al.*, 1976) was used for generating realistic ionospheric delays for each satellite-receiver line of sight. The GIPSY/TRIN method was applied to the simulated data and a correction map was formed over an extended region covering the CONUS, Alaska and Hawaii. Comparing the correction map with

the model, the simulation results show that the GIPSY/TRIN global mapping technique is accurate to 0.25-0.5 meters over the CONUS and in the vicinity of the Alaskan and Hawaiian GPS stations. This indicates that GIPSY/TRIN is suitable for en-route navigation and precision approach. For the latter case, 1.5 meter correction accuracy is required near land (WAAS Specification, 1994). Greater accuracy will generally be achieved away from the peak of the solar cycle.

For each slant measurement, the vertical TEC values predicted by the Bent model were multiplied by the elevation-dependent slant range factor, assuming the usual cosecant (thin shell) obliquity factor $M(E)$:

$$M(E) = \{1 - [\cos E / (1 + h / R_E)]^2\}^{-1/2} \quad (2)$$

where E is the elevation angle, h is the height of the shell and R_E is the radius of the Earth. For the simulated data, the shell height was not held constant, but was set equal to the height of peak electron density predicted by the Bent model. Using varying heights h in the mapping function is realistic, since in practice the exact equivalent shell height or mapping function is not known. When forming the correction map, however, the standard fixed shell height of 350 km was used.

The Bent model was run for a day representative of solar maximum conditions, in this case February 15, 1991. For this day, the model predicted daytime vertical delays exceeding 14 meters over the US and slant delays exceeding 30 meters. Solar activity inputs were: solar sun spot number of 176.5; F10.7 flux value of 243.0. These numbers are factors of 3-10 above current solar minimum values.

A new grid solution was produced every 30 minutes rather than every 5 minutes as would be done in an actual WAAS implementation, in order to reduce the disk storage requirements for the comparison. Accuracy of the corrections will generally improve with more frequent solutions. The station and satellite biases were assumed to be unknown and were estimated using the self-calibration capability of GIPSY/TRIN. Each data point was given the same data weight and an elevation cutoff of 20 degrees was used.

Figure 4 is a contour plot of the residual difference between the Bent model and the correction map, for the interval 20:00-20:30 UT. This figure is a typical case of a daytime residual plot. The GIPSY/TRIN ionospheric correction method produces an accurate representation of the simulated data set over North America and in the vicinity of Hawaii and Alaska. The maps are completely data driven and an a priori ionospheric value of zero was assumed to initialize the mapping procedure. This accounts for the fall-off in accuracy in the extreme Northern and Southern areas of the map, where no data was collected (see the coverage maps in Figure 3). In practice, a more realistic a priori ionosphere available

from a climatological model would be used to smoothly continue the maps outside the area directly covered by the measurements. However, to avoid confusion in interpreting the results, we did not use any a priori information from an ionosphere model in this work.

Figure 5 is a plot of the residual root mean square (RMS) difference between the correction maps and the Bent model, computed over two rectangular-shaped regions for all 48 maps generated at 30-minute intervals. The extended region covers the same area shown in figure 4, and includes areas not covered by GPS data (primarily in the northern and southern edges of the region). The RMS residual for this region is an overestimate of the expected error for a WAAS implementation since it covers regions where no GPS data were available. To determine more realistic errors for the FAA's WAAS, the RMS has also been computed for a rectangular-shaped region restricted to the CONUS where data coverage is more complete (this area is outlined in figure 3a). For both regions, the accuracy of the GIPSY/TRIN method is generally better than 1 meter. Over the smaller region where there is more complete data coverage, the agreement is better than 0.4 meter for all the maps. Note that the residuals were computed using the inter-frequency bias values estimated by the GIPSY/TRIN method itself and did not rely on external calibration values. Smaller residuals can be expected if these biases are fixed to values determined off-line from several days of data, which would be possible in an actual WAAS implementation.

Applying GIPSY/TRIN to the FAA's WAAS Implementation

A real-time implementation of the GIPSY/TRIN method could be applied directly to the ionospheric correction component of WAAS. The formation of an ionospheric correction for the WAAS user is essentially a two-step process. First, a selected set of delays and errors at the grid points must be generated as part of the slow correction (every 5 minutes would be sufficient). This is the critical task which can be performed by GIPSY/TRIN with high accuracy. Second, the updated grid values are broadcast to a user who will convert them to a line-of-sight correction at the user's location. Interpolation between the grid values to form the user correction is a less demanding task which can be executed with standard interpolation techniques and is not addressed here.

The data flow for producing the ionospheric correction and errors at the grid locations is shown in figure 6. The data are input to the real-time implementation of the GIPSY filter along with an estimate of the receiver and satellite L1/L2 delay biases. (These biases can be obtained from an independent source or estimated off-line with the GIPSY filter.) Filtering is a recursive estimation process in which a previously estimated ionospheric delay map is incrementally adjusted with new data at regular intervals, nominally every 5 minutes for WAAS. The updates take only a few seconds of CPU time. The

process is initialized with the Bent ionospheric model (other models can also be used) so that when it is started up for the first time, adjustments are made to reasonable a priori values rather than to arbitrary or zero values. After a few update intervals, the great data strength of the WAAS GPS receiver network will cause the estimated maps to be fully determined by the data, with no further dependence on the a priori model.

At each step, the updated map and associated errors are stored for use at the next time update. The GIPSY/TRIN vertex points are not in general collocated with the WAAS grid, and the maps must be evaluated at the Earth-fixed WAAS grid locations. Since the GIPSY/TRIN correction map overlaps the WAAS grid, this can be accomplished in a few milliseconds with no loss of precision. Finally, a selection criterion is applied to determine which updated grid point values should be sent to the user. The selection should be based on a comparison between each of the latest updated grid values and an average of the prior set of values.

Summary

A wide area ionospheric correction method used to support operational ionospheric calibrations for NASA's Deep Space Network has been applied to the FAA's proposed wide area augmentation system (WAAS). Simulation results show that, even under conditions typical of solar maximum, the GIPSY/TRIN ionospheric correction method is accurate to 0.25-0.5 meter and therefore meets the WAAS specification calling for 0.5 meter accuracy in the slow ionospheric correction. This accuracy was obtained using the inter-frequency biases estimates produced in the fit. In an actual WAAS implementation, the bias values would be estimated off-line using data from several days, resulting in even better accuracy.

It should be emphasized that the solar flux, which drives the formation of the ionosphere, is currently near the minimum of the solar cycle, or a factor of 3-10 less than maximum. Simulations were performed for this study since tests using current data from a network similar to WAAS are not indicative of performance during more challenging periods. Further work should be performed to test the system under conditions characteristic of major ionospheric storms, which occur infrequently but cause instabilities in the ionosphere that can degrade correction performance.

The GIPSY/TRIN technique can be readily incorporated into a real-time correction scheme for the WAAS. Since the algorithm is grid-based and has a built-in interpolation scheme, vertical ionospheric delays and errors can be evaluated at each of the fixed WAAS grid points in real-time.

Acknowledgments

We would like to thank Sien Wu of Jet Propulsion Laboratory (JPL) for his help in setting up the simulation appropriate for the proposed network of WAAS reference stations. Thanks also goes to Tom Yunck of JPL for providing information about the FAA's WAAS specifications, and for suggestions on portions of the manuscript. We also wish to express our appreciation to Ulf Lindqwister and Tom Runge for helpful discussions and suggestions related to the GIPSY/TRIN ionospheric correction method. The research described in this paper was performed by the Jet Propulsion Laboratory, California Institute of Technology, under contract with the National Aeronautics and Space Administration.

References

- Brown A. (1989), Extended Differential GPS, *Navigation, Journal of the Institute of Navigation*, **36**, #3, pp. 265-286.
- Bent, R. B., Llewellyn, S. K., Nesterczuk, G., Schmid, P. E., (1976) The development of a highly successful world-wide empirical ionospheric model and its use in certain aspects of space communications and world-wide total electron content investigations, *Effect of the Ionosphere on Space Systems and Communications*, J. Goodman, ed., Springfield, VA, 1976.
- Kee, C., B. W. Parkinson, A. Axelrad (1991), Wide Area Differential GPS, *Navigation, Journal of the Institute of Navigation*, **38**, #2, pp. 123-146.
- Mannucci, A. J., B. D. Wilson, and C. D. Edwards (1993) A New Method for Monitoring the Earth's Ionospheric Total Electron Content using the GPS Global Network, *Proceedings of the Institute of Navigation GPS-93*, Salt Lake City, Utah, September, 1993.
- Mannucci, A. J., B. D. Wilson and D. N. Yuan (1994) Monitoring Ionospheric Total Electron Content Using the GPS Global Network and TOPEX/POSEIDON Altimeter Data, *Proceedings of the International Beacon Satellite Symposium*, L. Kersley, ed., Aberystwyth, Wales, 1994.
- Wide Area Augmentation System (WAAS) Specification (1994), U. S. Department of Transportation, Federal Aviation Administration, May 9.
- Wilson, B. D. and A. J. Mannucci (1994), Extracting Ionospheric Measurements from GPS in the Presence of Anti-Spoofing, *Proceedings of the Institute of Navigation GPS-94*, Salt Lake City, Utah, September, 1994.

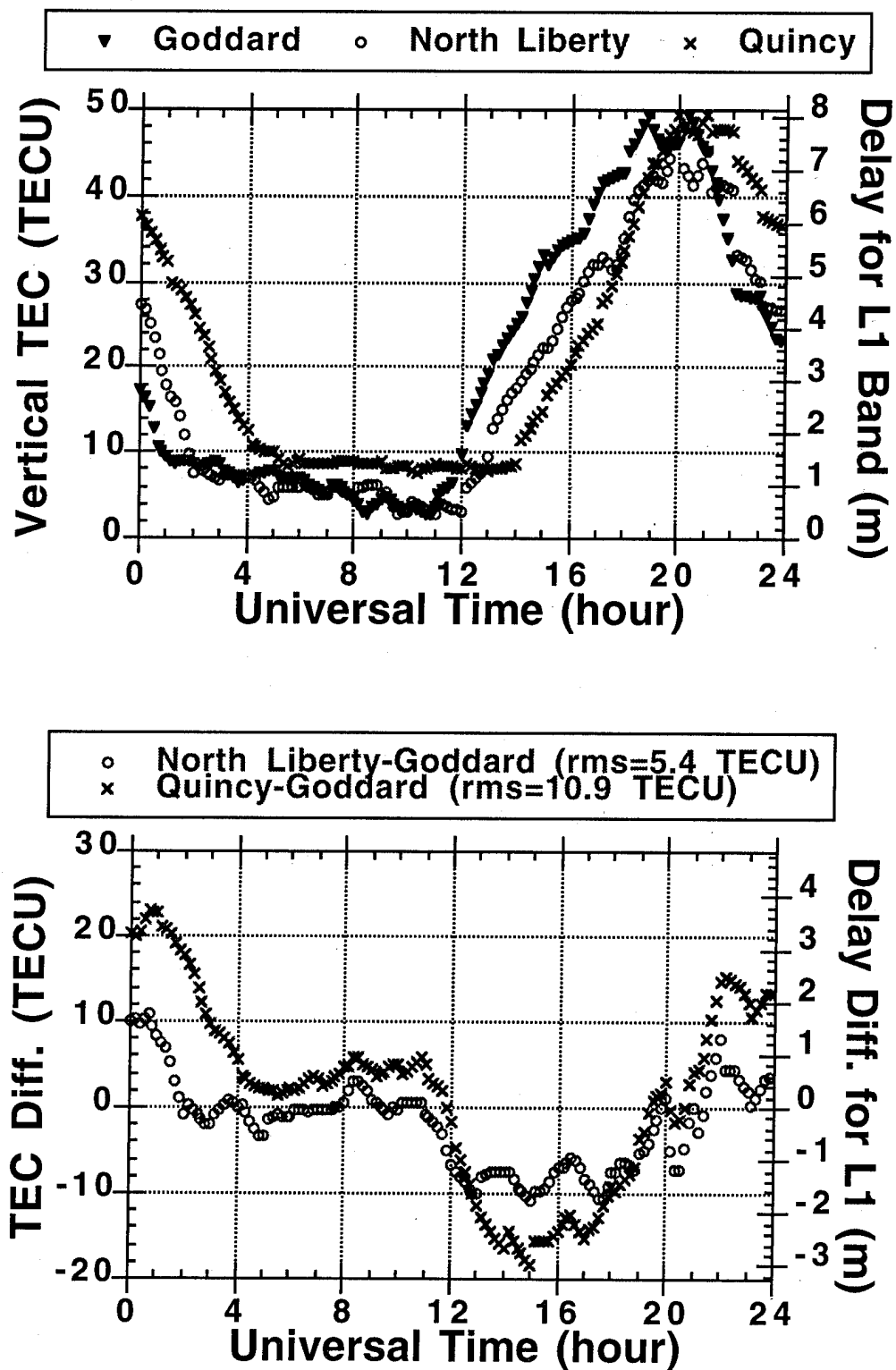


Figure 1. This figure is a plot of the diurnal TEC variation over three North American receivers in the GPS global network, plotted as a function of universal time, for March 13, 1993. Each receiver shares similar geomagnetic latitude (Goddard geomagnetic latitude 49.97, geographic longitude -76.83; North Liberty 51.93, -91.57 and Quincy 46.44, -120.94). In (a), the total TEC is plotted; in (b), the difference with Goddard is plotted. Earth-fixed correction maps over the WAAS coverage area must follow these large diurnal variations.

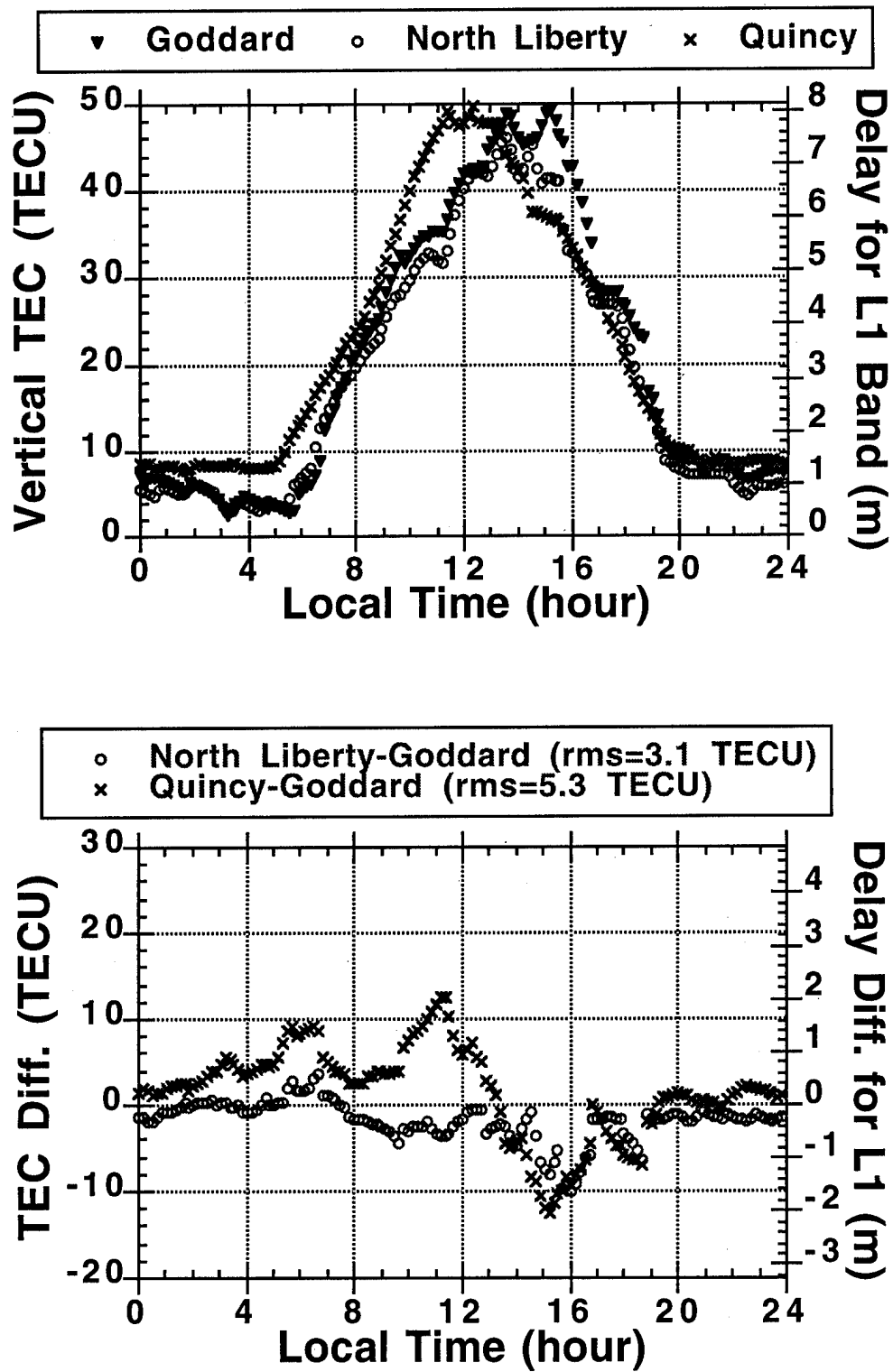


Figure 2. This plot is similar to figure 1, but the diurnal TEC variation is plotted as a function of local time. Comparison with figure 1 indicates that Sun-fixed (local time) correction maps have smaller gradients than the Earth-fixed maps.

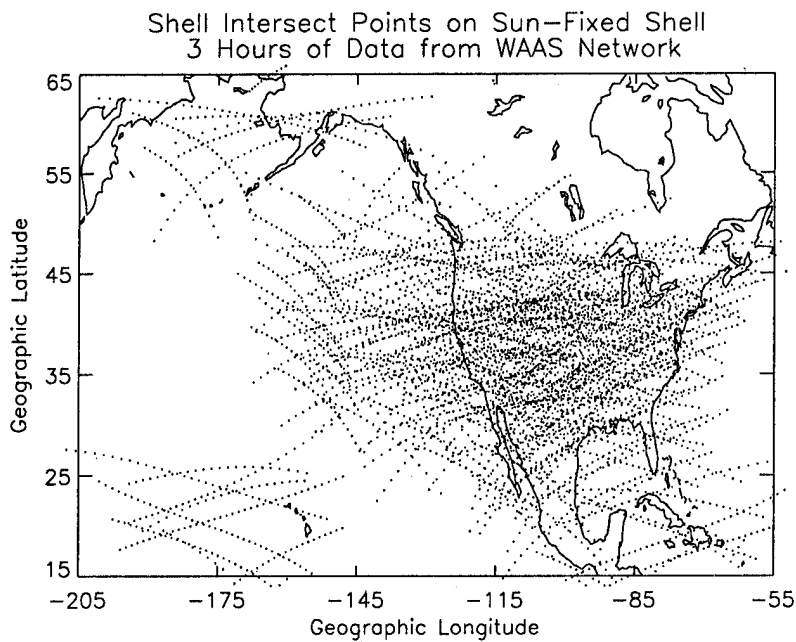
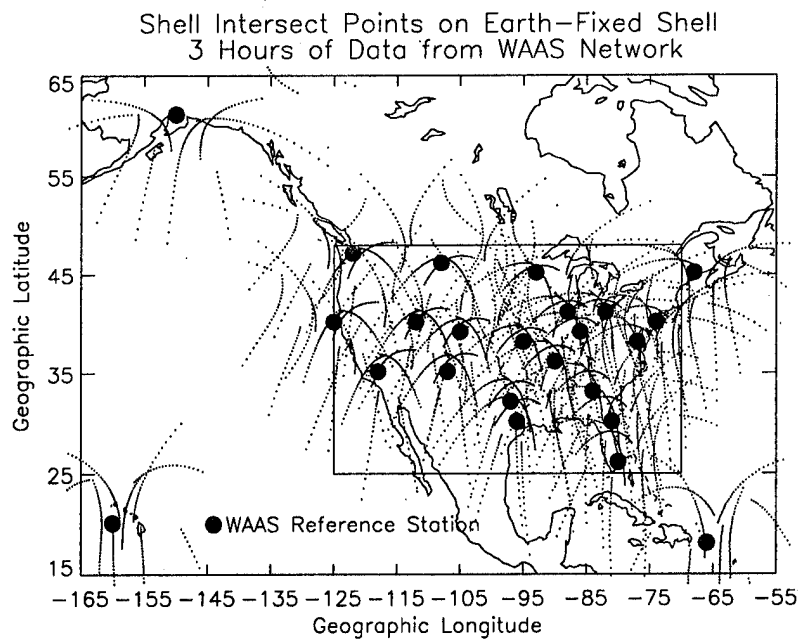


Figure 3. These plots show the locations of the shell intersect points for a 3 hour span of data simulated for March 21, 1997 using the proposed configuration of 24 WAAS reference receivers. In (a), the coverage is shown of for an Earth-fixed shell. In (b), coverage is shown over a Sun-fixed shell. The shell height was assumed to be 350 km, and the elevation cutoff was 20 degrees. The continent map is placed to reflect the position of the Earth after an elapsed time of 2.5 hours.

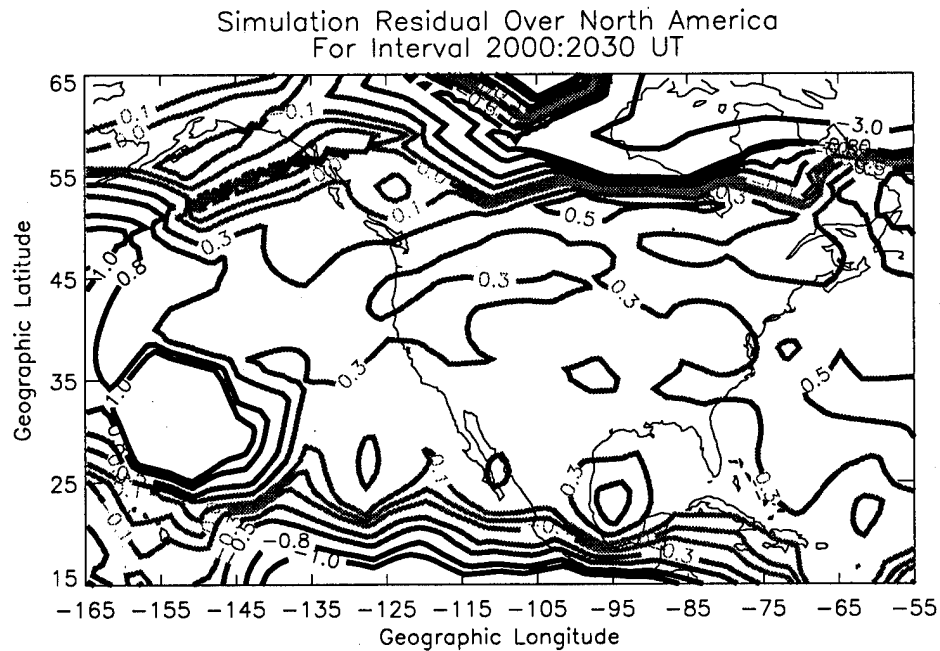


Figure 4. This is a plot of the residual difference between the Bent model TEC used in the simulations and the correction map produced by the GIPSY/TRIN technique. This typical daytime residual map covers the period 20:00-20:30 universal time. The correction maps are generally accurate to 0.3 meter or better, except in regions where no measurements were available (see the coverage maps in Figure 3).

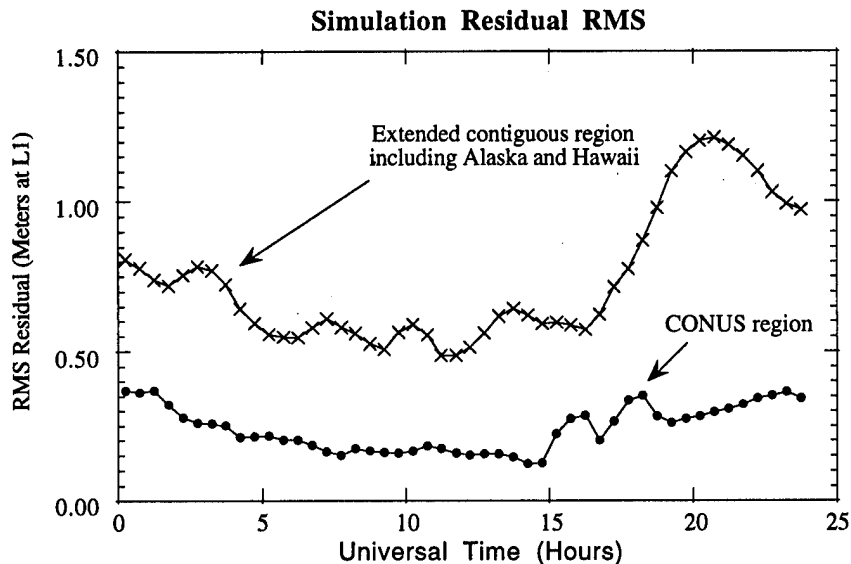


Figure 5. This is a plot of the root mean square residual between the Bent model TEC and the correction map, for each of the 48 correction maps generated in the simulation. The RMS was computed for 1x1 degree grids over two regions: an extended region covering the CONUS and Alaska and Hawaii, defined by the southwest corner at (15.0, -165.0) and the northeast corner at (65.0, -55.0), geographic latitude and longitude. The other rectangular-shaped region was restricted to cover the CONUS, where ionospheric measurements are always available: SW corner at (25.0, -125.0) and NE corner at (48.0, -70.0).

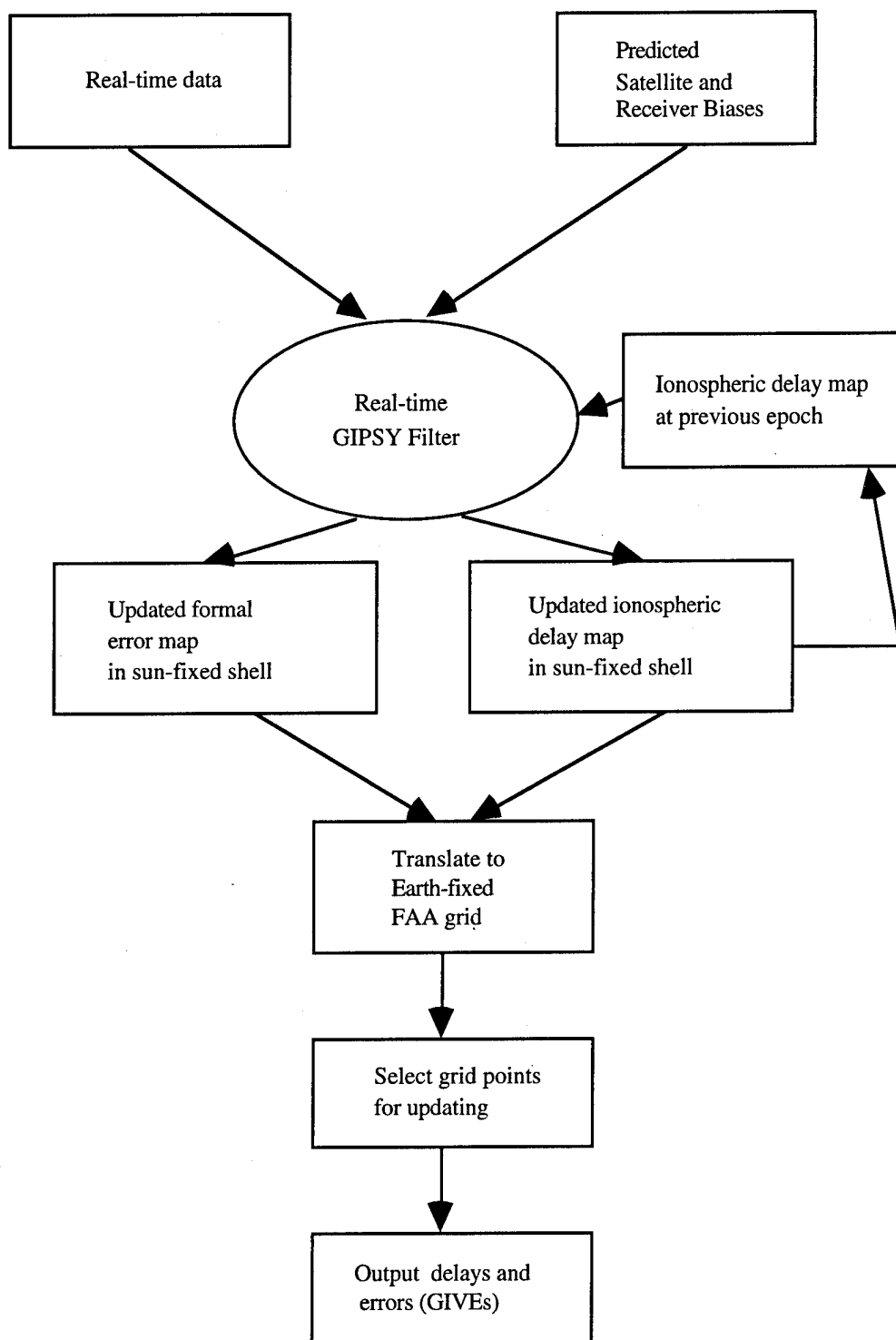


Figure 6: Data flow diagram showing the process involved for forming the grid delay corrections and errors for the FAA's proposed WAAS.

Application of SCORE Techniques to Improve Ionospheric Observations

Gregory Bishop
USAF Phillips Laboratory

Andrew Mazzella and Elizabeth Holland
NorthWest Research Associates

BIOGRAPHIES

Gregory Bishop is a Project Engineer in the Ionospheric Effects Division of the USAF Phillips Laboratory. He is a consultant to Sacramento Air Logistics Center, Air Weather Service, and Air Force Space Command, in the areas of: application of GPS to ionospheric monitoring, and mitigation of ionospheric effects on Air Force surveillance and communication systems.

Andrew Mazzella is a Research Scientist with NorthWest Research Associates (NWRA), a small research and development firm that specializes in geophysical fluid dynamics. He is involved in development and evaluation of parametric representations of physical systems and phenomena, with special emphasis on the design of algorithms and systems for ionospheric measurement.

Elizabeth Holland is a Research Engineer with NWRA, studying ionospheric morphology and model performance for application to error correction for AF systems.

ABSTRACT

Self-Calibration Of pseudoRange Error (SCORE) techniques [1] can improve accuracy of ionospheric total electron content (TEC) covering 10 degrees of latitude from one station. SCORE uses self-consistency constraints on the TEC data to calibrate a two-frequency GPS receiver system for the sum of system contributions to pseudorange error. These errors come from components such as receiver, pre-amp, antenna and satellite transmitters. Frequent application of SCORE can thus reduce system component drift contributions to TEC measurement error and improve long-term measurement accuracy. SCORE was first developed out of data presentation techniques that permitted a single GPS station to simulate zenith TEC monitoring from stations spaced over 10 degrees of latitude, along the same longitude [2]. Applying these presentation techniques in conjunction with

SCORE allows accurate parallel monitoring of the diurnal TEC behavior over this wide latitude region from a single station. Typically, in well-calibrated data, latitudinal TEC gradients of less than 1 TEC unit per degree may be identified. We will present results of SCORE application studies showing variation in TEC accuracy with the time interval and the number of satellites used in the process, and the effects of improved calibration on the observable TEC morphology in widely-spaced latitude regions. We will also examine how these results differ in high-latitude and equatorial regions, where the diurnal behavior of the ionosphere can be radically different from over CONUS. We will also present results from an initial application of the SCORE process to single-frequency measurements, compared with simultaneous two-frequency TEC data. These initial tests show potential for useful single-frequency ionospheric TEC observation.

INTRODUCTION

The SCORE process converts the ionosphere from an error source into a constraint on the GPS measurement calibration, by requiring maximum agreement between measurements at satellite near-conjunctions. Before requiring agreement, a coordinate transformation to ionospheric penetration point local time (IPP-LT) is necessary, else we would at times be requiring observations from different ionospheric times to agree. Figure 1 illustrates the stages between uncalibrated and SCORE-calibrated GPS TEC data. Recently, an improved algorithm has been developed that permits calibrations to be generated in minutes instead of hours [3]. Using SCORE to maintain a very accurate receiver system error calibration will enable 2-frequency GPS receivers to more accurately measure absolute ionospheric TEC. (TEC is usually measured in "TEC units". One TEC unit corresponds to 1×10^{16} electrons/m² on the raypath. Also, 1 ns of differential delay = 2.852 TECu, and 1 ns of pseudorange delay at L1 = 1.845 TECu).

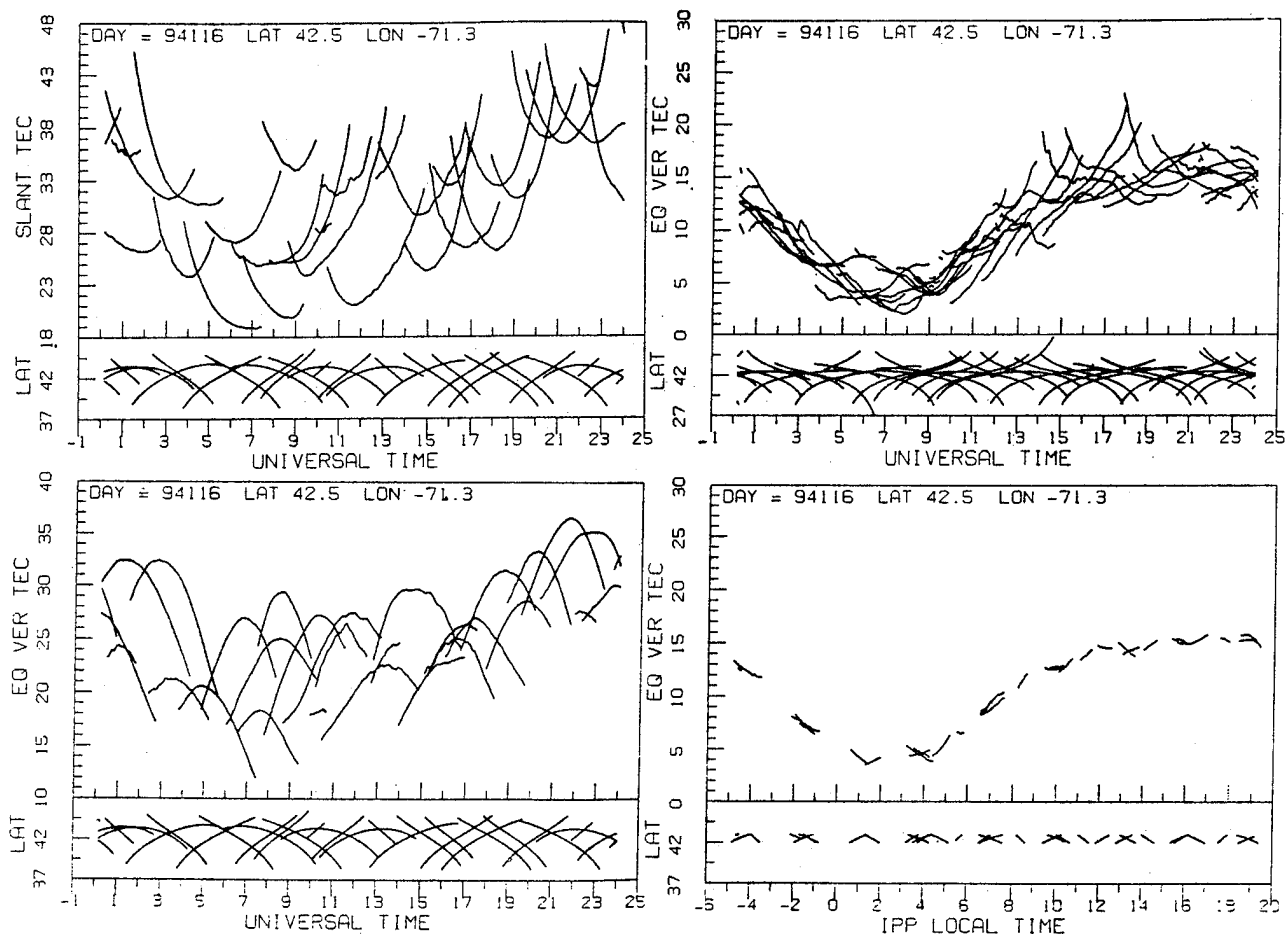


Figure 1. Comparison of uncalibrated GPS slant TEC data vs UT, with stages in the transition to narrow latitude diurnal curve produced by SCORE calibration.

BENEFITS TO IONOSPHERIC OBSERVATIONS

Use of SCORE improves GPS TEC monitoring capability, both in terms of its accuracy and the ability to display readily evaluated data over a wide region from one station. It is important to emphasize that the SCORE process does *not* require multiple stations, or external parameter input. SCORE may be run solely by a single station. In effect, the station is doing parallel monitoring of diurnal zenith TEC in adjacent latitude bands. Figures 2,3,4, and 5 (from [4]) show examples of these bands, as observed from central and lower mid-latitude stations respectively. One plot in each figure shows all observed data and the other plots break-out fairly narrow bands of latitude. Particularly overhead the station a very well-defined diurnal curve may be observed. (Outliers from these curves are normally due to inclusion of data from elevations $< 35^\circ$, which is subject to inaccuracy due to equivalent vertical TEC conversion assumptions, and to temporal changes in the east/west diurnal behavior.)

The validity and accuracy of the SCORE process may be graphically affirmed by the tightness and consistency of

these narrow-latitude-band diurnal curves. Earlier studies [5] have shown that consistent, smooth diurnal behavior in narrow latitude bands would only be obtained if satellite or station biases were well-calibrated. It is also possible to show that we can resolve latitudinal TEC gradients of < 1 TEC unit per degree from the data. Figure 6 plots the latitudinal gradients extracted from 01-04Jan95 at Otis ANGB, MA, for 0000 IPP-LT. These curves show smooth latitude variation and good resolution, often to better than a TEC unit. The effect of changing geomagnetic activity in the period is also evident, with the highest TEC on the most active day, and the lowest on the day following. (High daily Kp values were approximately: 2, 5, 7, and 3, respectively).

SCORE APPLICATION STUDY RESULTS

GPS receiver systems can have drift in their contribution to ionospheric TEC (pseudorange error). Such drift may have its source in the receiver itself, or in an antenna pre-amp (particularly likely in the case of narrow bandpass filters situated outdoors with no temperature control), or other component. Figure 7 shows low level drift

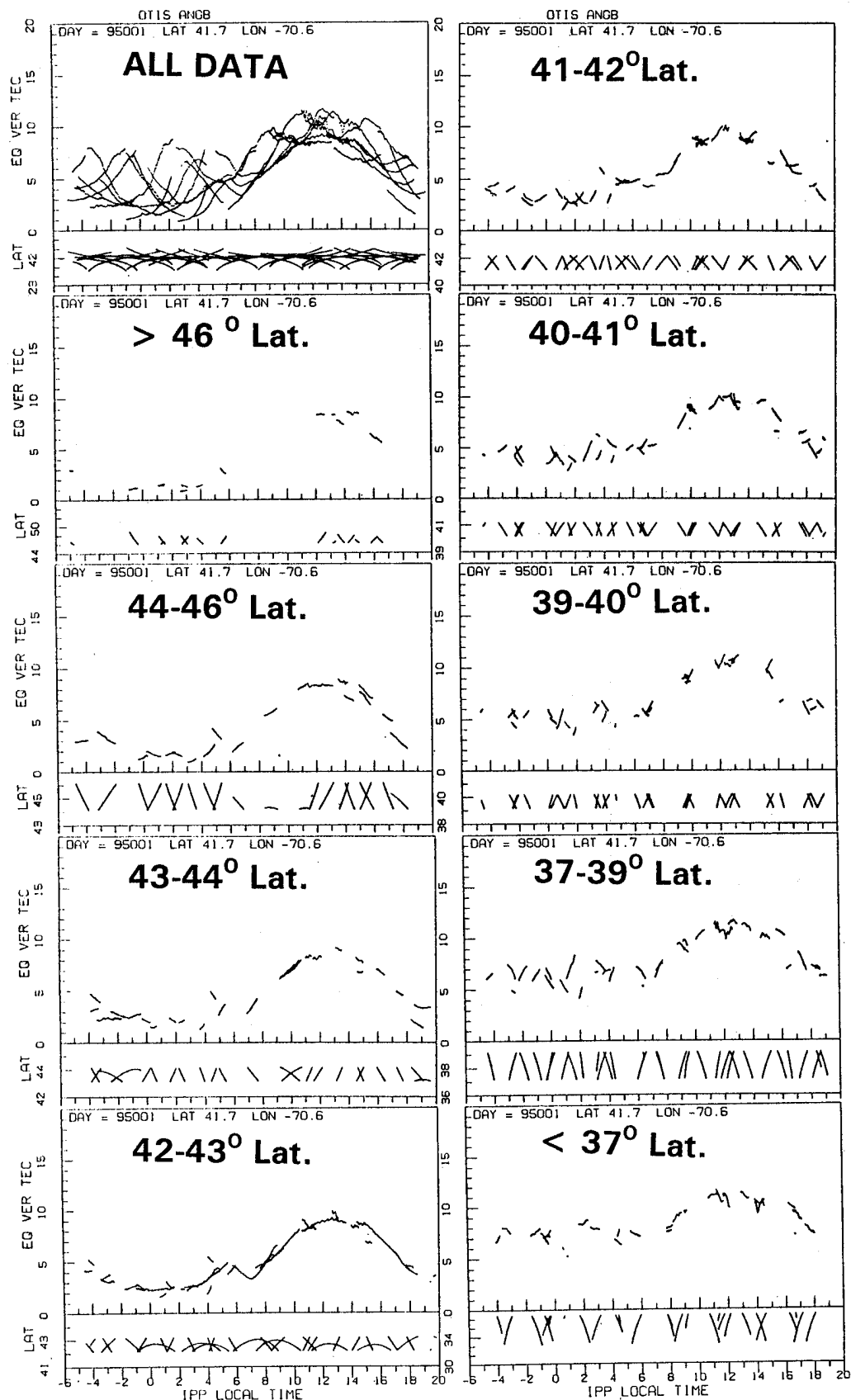


Figure 2. Latitude separation of SCORE-calibrated single-station GPS TEC data from Otis ANGB, MA, day 001, 1995.

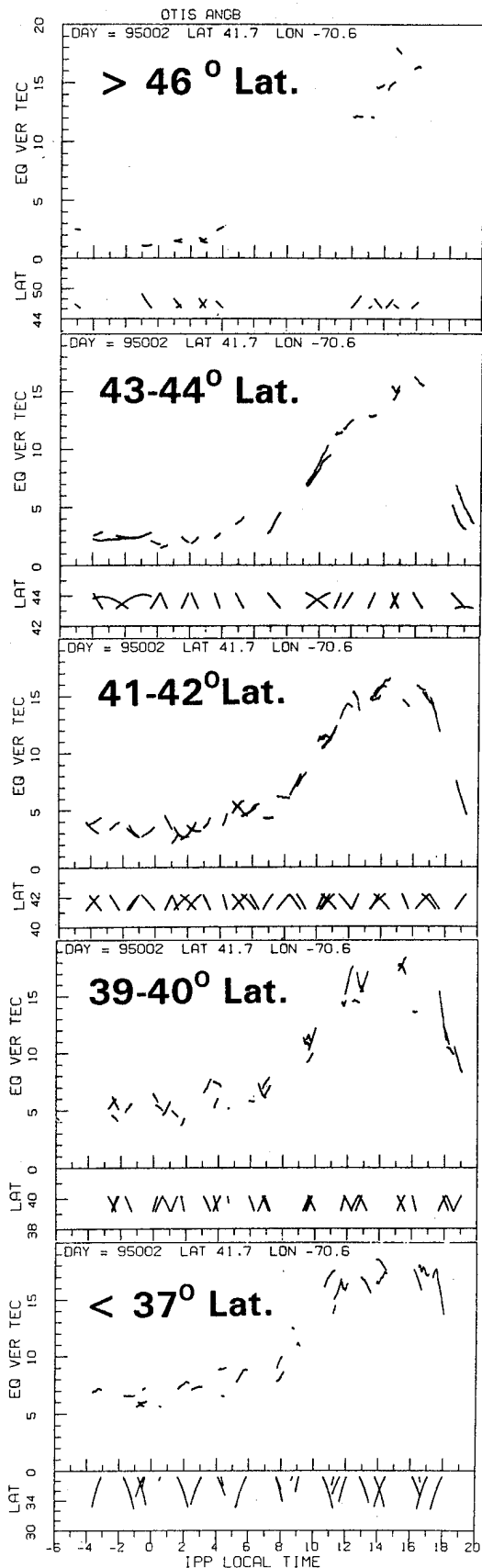


Figure 3. SCORE-GPS TEC, Otis, day 002, 1995.

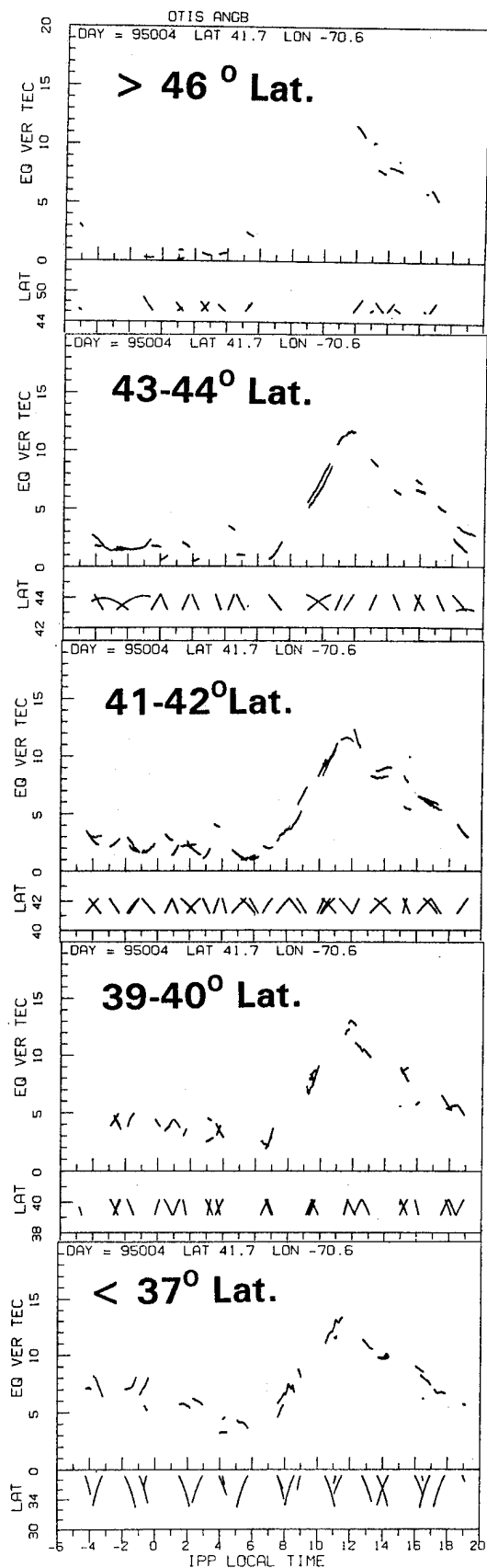


Figure 4. SCORE-GPS TEC, Otis, day 004, 1995.

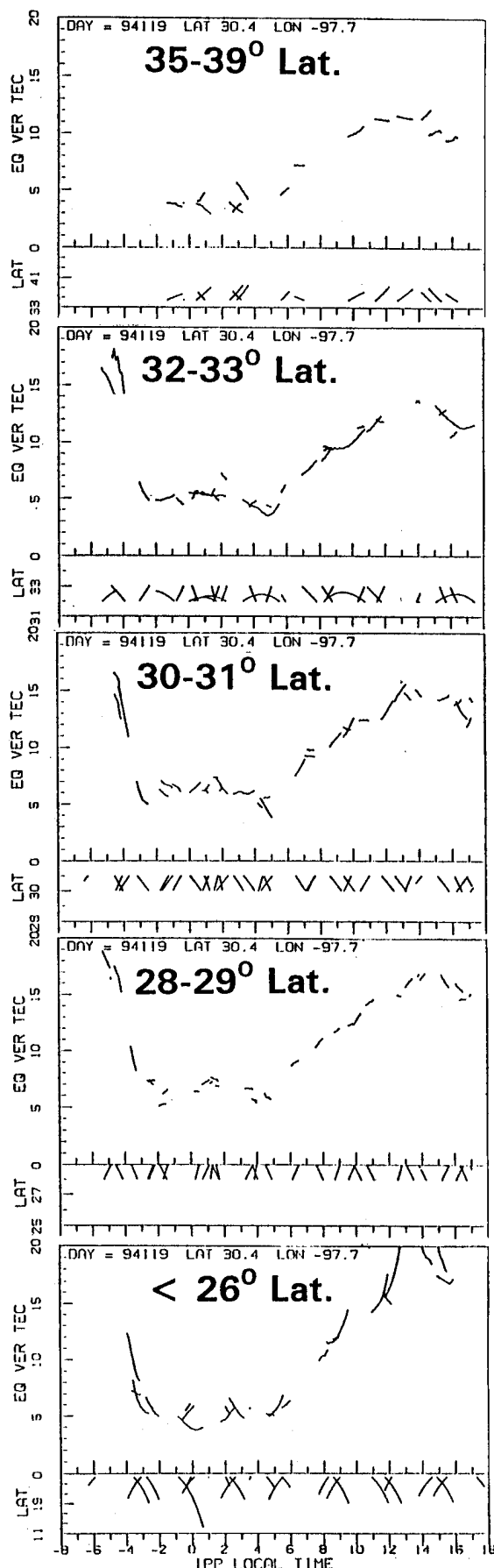


Figure 5. SCORE-GPS TEC, Austin, day 119, 1994 [4].

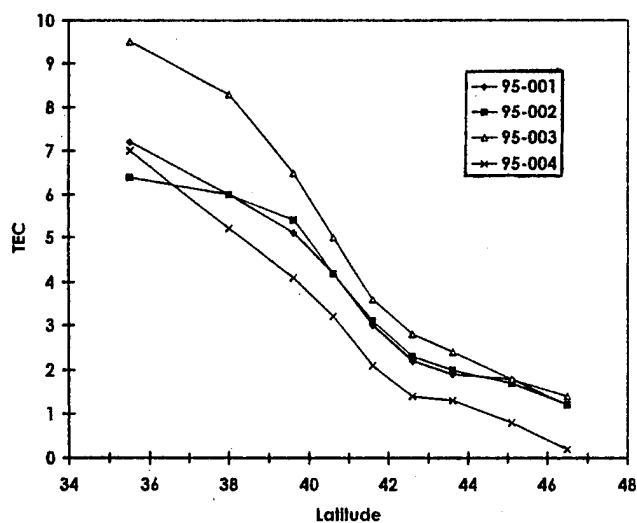


Figure 6. Latitudinal TEC gradients extracted from SCORE-calibrated data, days 001-004, 1995; Otis ANGB, MA; for 0000 IPP-LT.

occurring in one GPS system over a 14-day period. These system bias values were derived by applying SCORE to each day's data independently. Figure 8 shows the 1-degree latitude band overhead the station for 2 days from this period, two plots for each day: one calibrated by SCORE for that day, and the other calibrated using the SCORE products from day 1 of the sequence. In these two examples, the diurnal curve self-calibrated with "today's" data is seen to be much "tighter". In effect the curves calibrated with products from day 1 have inserted station bias errors of about 1 and 1.5 TEC units, respectively. Yet even at this low error level the increase in "noisiness" of the product curve is evident. Day 14 yielded a fairly tight curve using the day 1 calibration. This is reasonable as Figure 7 shows that day 14 had almost the same station bias as day 1.

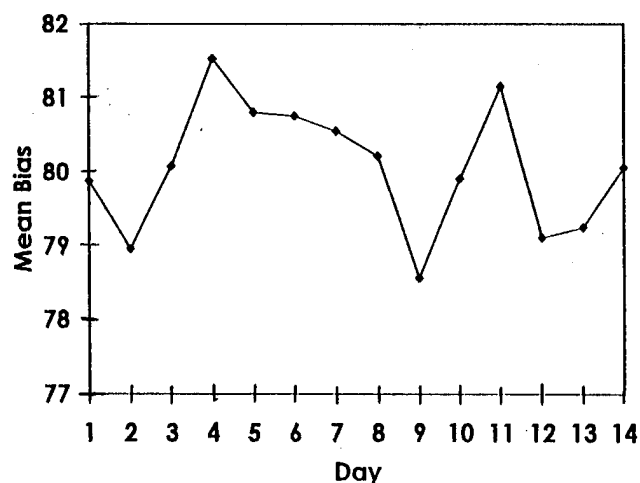


Figure 7. SCORE monitoring of a two-frequency ground receiver station error drift over a 14-day period in January 1995, [3].

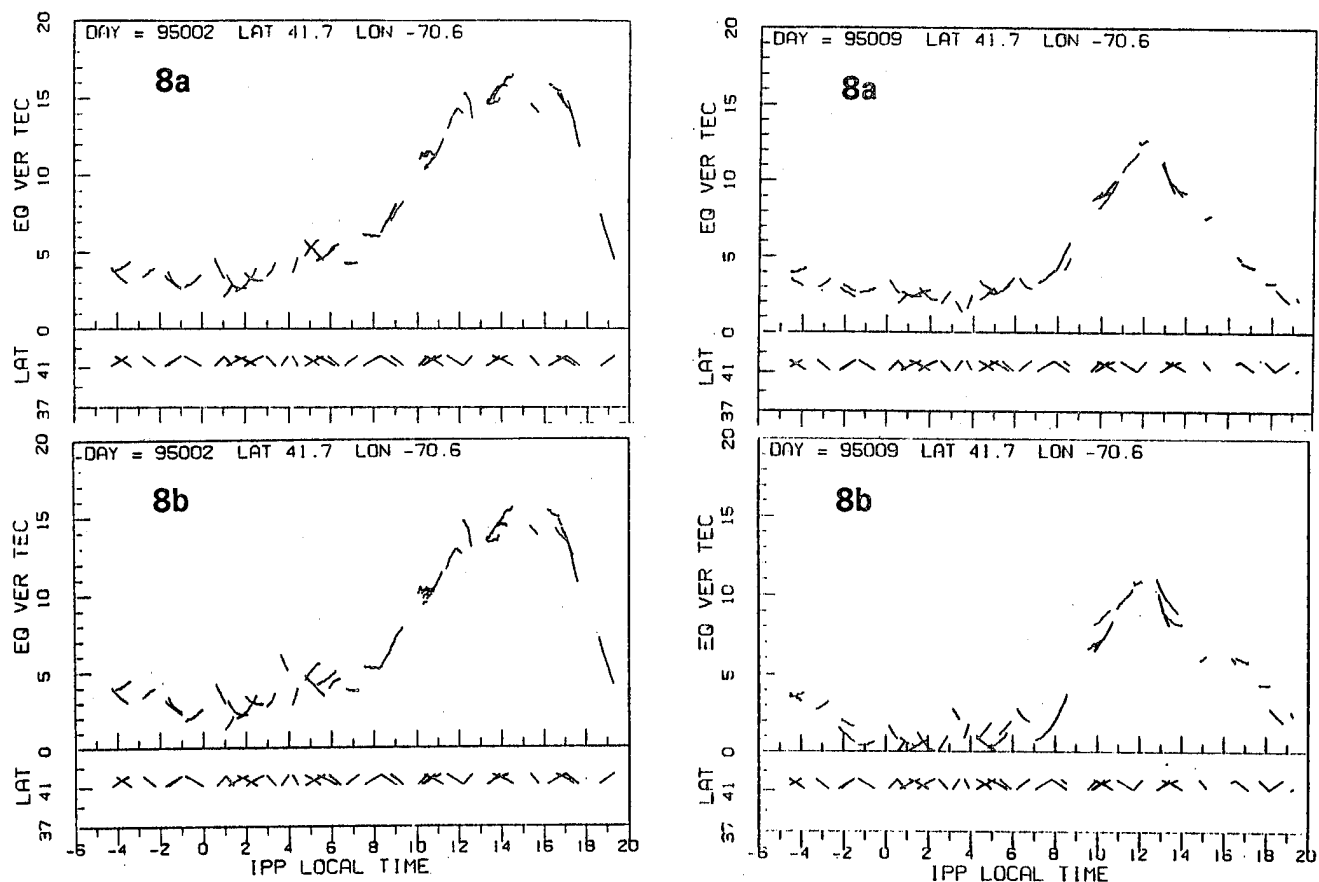


Figure 8. 1-degree latitude band overhead the station, two plots for each day: calibrated by SCORE for that day (8a), and calibrated using the SCORE products from day 1 of the sequence (8b).

The above results suggest that there would be benefit at least for some receiver systems, in running the SCORE process often, if not in near-real-time. One approach to doing this would be to run SCORE on a short subset of the day's data. An initial study of this has been done for 6-hour intervals [3]. The system biases derived from this study were compared with the results from 6-hour equivalent subsets of the full 24-hour data set for each day. Figure 9 plots the differences between the 6-hour-derived biases and the biases from 6-hour subsets calibrated from 24-hours of data. It may be seen that these differences are greater than the maximum variation in the system biases over 14 days, as shown in Figure 7. Therefore, updates using a period as short as 6 hours are less accurate at present. However, Figure 7 indicates that updates using a 24-hour period should hold high accuracy. Further efforts are being directed at using a sliding 24-hour update process, to provide near-continuous updates.

Tests were also conducted of the stability of SCORE products vs loss of input from 1 or more satellites [3]. Results of these tests showed that loss of 1 or 2 satellites had only a fraction of a TEC unit impact. Loss of up to 8 of 25 satellites caused at most a 1 TEC unit change in

a satellite bias result. Variation in station bias, from loss of 1 or 2 satellites, was less than half a TEC unit.

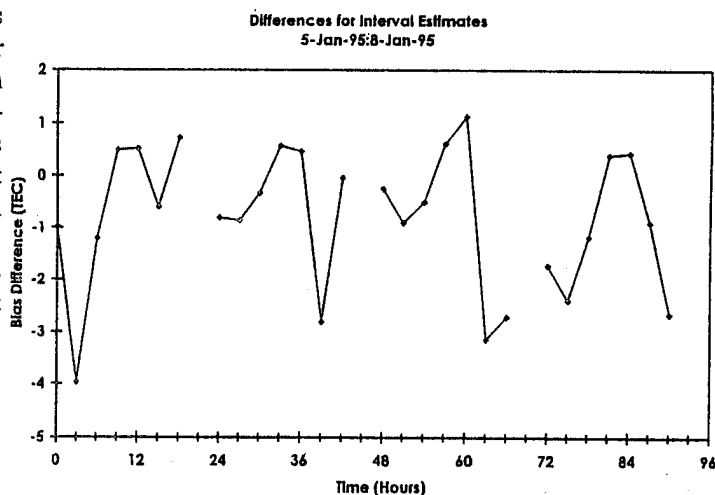


Figure 9. Differences between receiver station biases derived by running SCORE on 6-hour subsets of the day's data, and the biases derived from 6-hour equivalent subsets of the full 24-hour data set for each day.

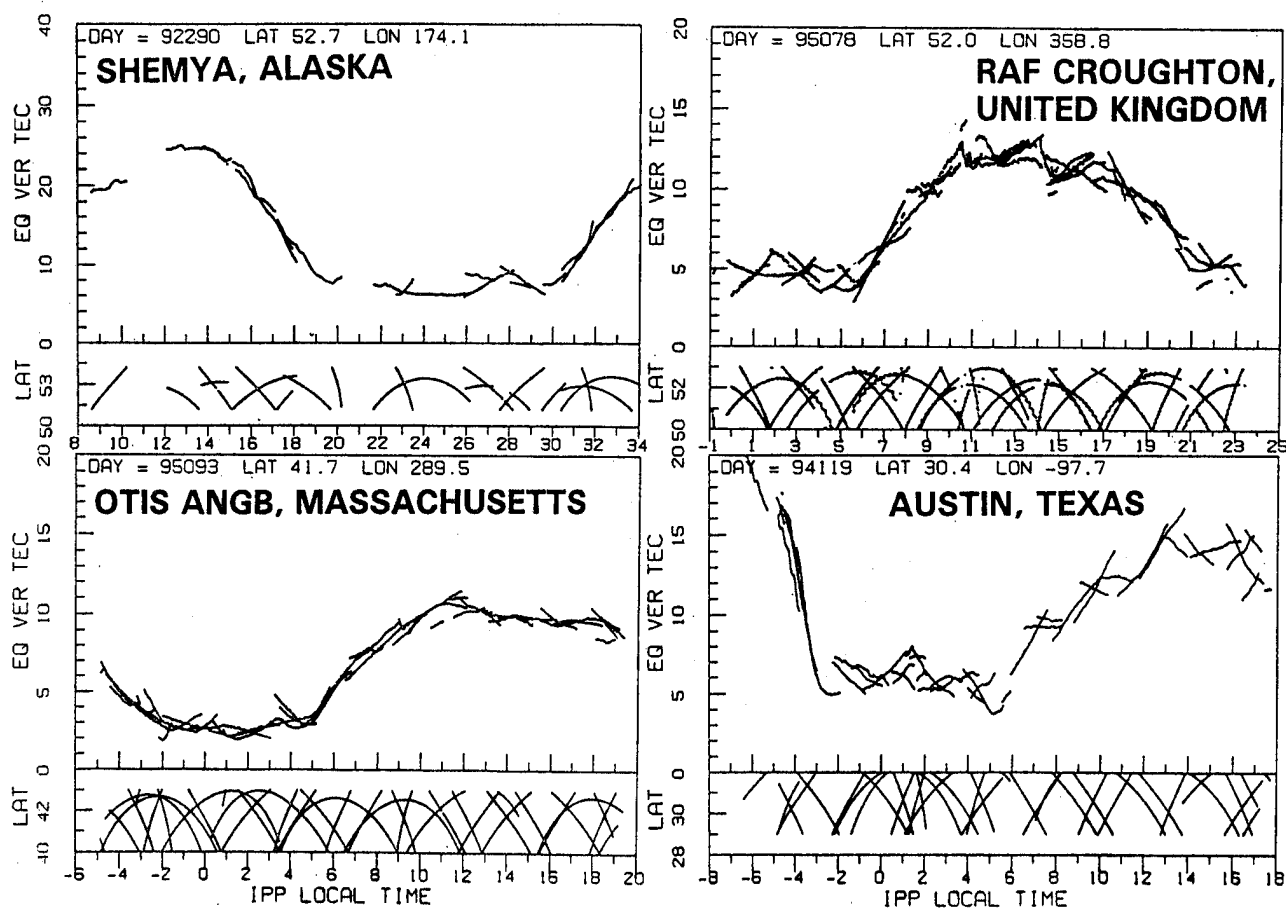


Figure 10. Example profiles derived from SCORE at widely varied mid-latitude sites.

SCORE RESULTS FOR DIFFERENT REGIONS

The SCORE algorithm has been applied at sites with a significant geographic distribution, and over all seasons at some of these regions. The method is regularly applied to calibrate the Ionospheric Measuring System [6] currently deployed at Otis ANGB, MA; RAF Croughton, UK; and Thule, Greenland. Figure 10 gives example profiles derived from SCORE at widely varied mid-latitude sites. Tight diurnal curves covering 3 degrees of latitude are obtained at each site, despite wide differences in diurnal profiles and data quantity. Figure 11 shows results from SCORE applied at Santiago, Chile. This site observes the equatorial ionosphere which has much higher TEC values and steeper gradients. Higher TEC and reasonably tight curves were obtained. Some of the observed data irregularities are attributable to the fact that this day is from a magnetically active period, and has a Kp value of about 7. Figure 12 plots the latitudinal TEC variation for this and the following day at 0000 IPP-LT. These curves also show smooth latitude gradients with good resolution. Figure 13 shows recent results from Thule, Greenland. It may be noted that diurnal variation is evident both over Thule and at lower latitudes. To the north, however, little such variation is seen. This is as

expected since this perspective is viewing nearly over the geographic pole and the polar ionosphere is in nearly constant illumination during this season.

POTENTIAL 1-FREQUENCY ABSOLUTE TEC

Initial tests have indicated that the SCORE technique can also be applied to single-frequency data (SCORE-1), allowing extraction of absolute TEC measurements without the need for the second frequency [3]. Results from this simulation test are shown in Figure 14 which uses a 35 degree elevation cutoff for the SCORE correlation area and 30-minute smoothing on the simulated single-frequency data. The 2-frequency GPS data uses phase-averaging and links appearances of the same satellite. The SCORE-1 result, even with the severe multipath, agrees with the SCORE calibration within about 3 TEC units ($\approx 0.3\text{m}$), or better. This is consistent with required accuracies cited for WAAS, [7]. The simulation was conducted due to difficulties in processing our single-frequency data. However, Figure 5 shows a SCORE-1 product from a small data set (mostly half-passes) of single-frequency data (1000 second filtered), compared with dual-frequency results. In the 1400-2000 LT interval, where the data availability is

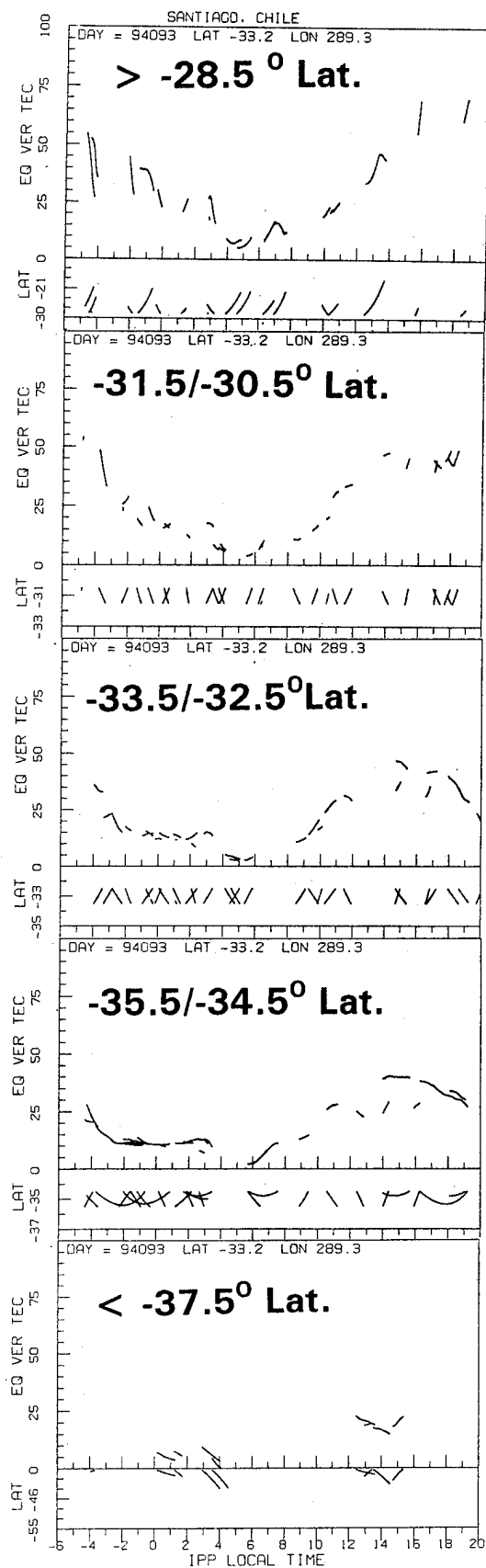


Figure 11. SCORE-GPS TEC, Santiago, day 093, 1995.

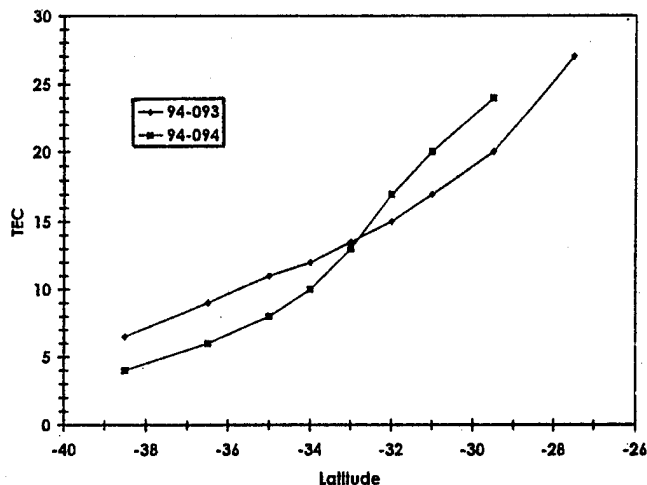


Figure 12. Latitudinal TEC variation at 0000 IPP-LT, for Santiago, Chile data of Figures 17 and 18.

fairly good, the agreement with dual-frequency is approaching that of the simulation. These results indicate that single frequency receivers may be able to yield useful absolute TEC, without assuming a model or profile.

SUMMARY AND CONCLUSIONS

Self-Calibration Of pseudoRange Error (SCORE) correction techniques and product geometry allow a single station to effectively perform parallel monitoring of diurnal zenith TEC in adjacent latitude bands over 10 degrees of latitude. Test results suggest that many receiver systems would benefit from running the SCORE process often, if not in near-real-time. Calibration updates based on a 24-hour period have been shown to maintain high accuracy. Data presented here shows resolution of latitudinal TEC gradients of < 1 TEC unit per degree from well-calibrated data. TEC products of successful SCORE applications have been presented from widely varied mid-latitude sites, as well as polar and equatorial regions. Initial tests have indicated that the SCORE technique can also be applied to single-frequency data, allowing the extraction of absolute TEC measurements without the need for the second frequency, although with less accuracy, due to multipath.

ACKNOWLEDGEMENTS

The authors wish to thank the Danish Commission on Scientific Research in Greenland for permission to conduct experiments at Thule AB, Greenland. The authors also wish to thank Mr. Charley Andreasen, Ssgt Carlton Curtis, Dr. Susan Rao, and Mr. Jonathan Copp for their contributions to equipment test/deployment and data analysis. Thanks to Dr. David Coco for use of the Austin data. Santiago data is from the IGS network.

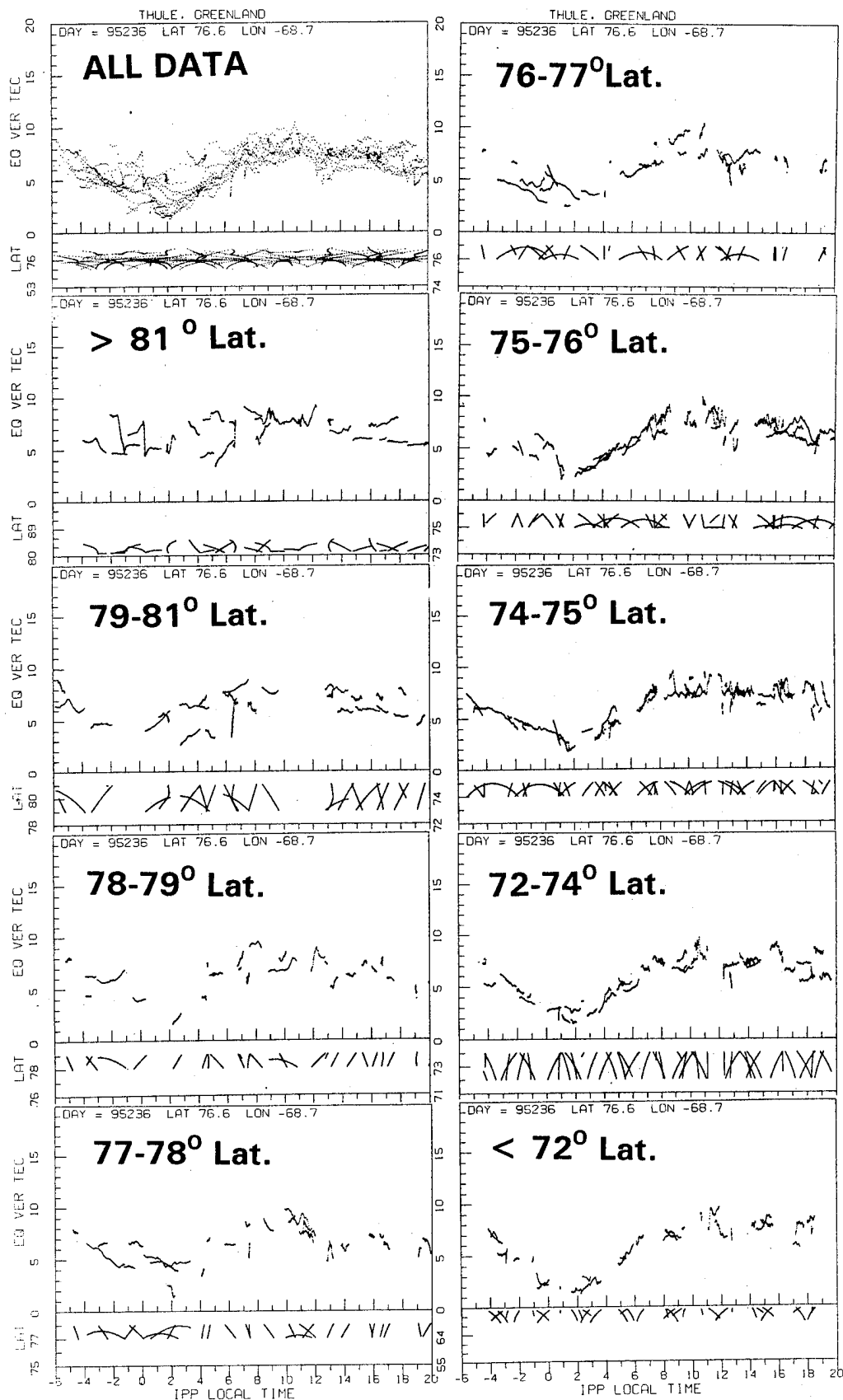


Figure 13. Latitude separation of single-station GPS TEC data from Thule, Greenland, day 236, 1995.

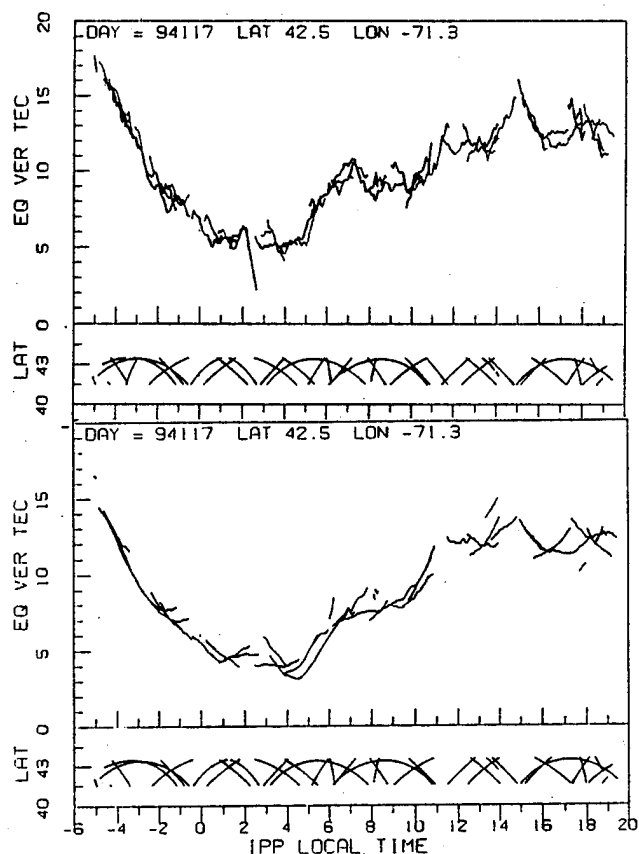


Figure 14. SCORE-1 product using a 35 degree elevation cutoff for the SCORE correlation area and 30 minute smoothing, compared with 2-frequency results [3].

REFERENCES

- [1] Bishop, G.J., A.J. Mazzella and E.A. Holland, "Self-Calibration of Pseudorange Errors by GPS Two-Frequency Receivers", in Proc. 1995 National Tech. Mtg., Institute of Navigation, Washington, D.C., Jan. 1995.
- [2] Bishop, G. J., I. K. Walker, C. D. Russell, and L. Kersley, "Total Electron Content and Scintillation Over Northern Europe", in "Proc. of the 1993 Ionospheric Effects Symposium", Alexandria, VA, May, 1993.
- [3] Bishop, G.J., A.J. Mazzella, and E.H. Holland, "Using the Ionosphere for DGPS Measurement Error Control", Proceedings of ION GPS-95, The Institute of Navigation, Washington, DC, September, 1995.
- [4] Bishop, G.J., A.J. Mazzella, and E.A. Holland, "The Ionospheric Factor: Effects and Mitigation in RF Navigation, Surveillance, and Communication", Proceedings of AGARD SPP 3rd Symposium, May 1995.
- [5] Bishop, G.J., D.S. Coco, P.H. Kappler, and E.A. Holland, "Studies and Performance of a New Technique for Mitigation of Multipath Effects in GPS Ground Stations", Proc. of 1994 National Technical Meeting, The Institute of Navigation, Washington, D.C., Jan. 1994.
- [6] Bishop, G.J., D.O. Eyring, K.D. Scro, S. Deissner, D.J. Della-Rose, W. Cade, N. Ceaglio, and M. Colloello, "Air Force Ionospheric Measuring System Supports Global Monitoring and Mitigation of Effects on AF Systems", Proceedings of ION GPS-94, The Institute of Navigation, Washington, DC, September, 1994.
- [7] Pullen, S., P. Enge, and B. W. Parkinson, "Simulation-Based Evaluation of WAAS Performance: Risk and Integrity Factors", Proceedings of ION GPS-94, The Institute of Navigation, Washington, DC, Sept. 1994.

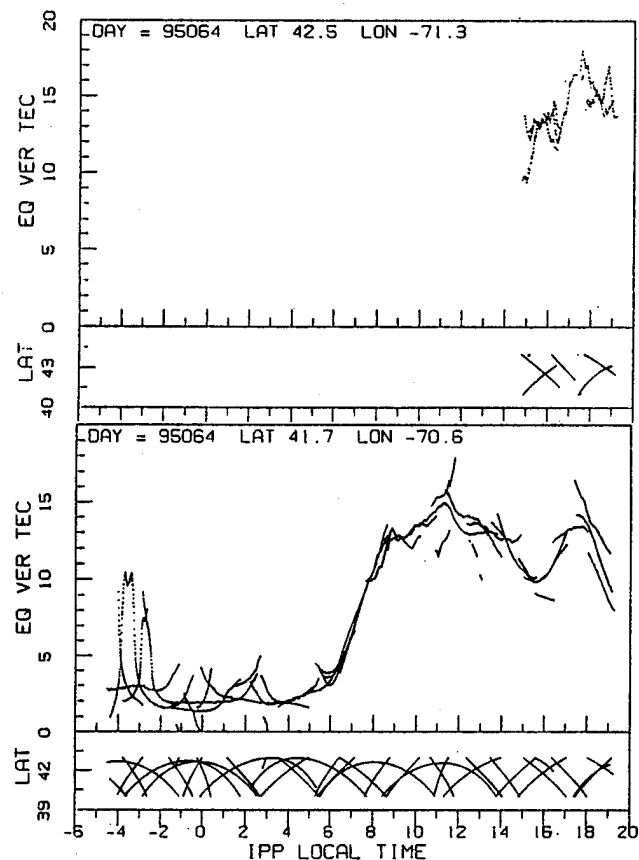


Figure 15. The SCORE-1 product from the limited set of real 1-frequency data we had available (1000 second filtered), compared with 2-frequency results.

Test Results of Wilcox Electric's Ionospheric Monitoring Network

Craig Stull
Wilcox Electric

A. J. Van Dierendonck
AJ Systems

BIOGRAPHY

Craig Stull received his BA in Physics from Fort Hays State University and his BSEE from Kansas State University. He currently works as a senior software engineer at Wilcox Electric. Craig specializes in software specification and design and has spent the last 4 years developing CAT II/III ILS and MLS systems. He is currently involved in the development of WAAS software and algorithms.

Dr. A. J. Van Dierendonck received his BSEE from South Dakota State University and MSEE and PhD from Iowa State University. Currently, he is self-employed, as AJ Systems. He is also a general partner of GPS Silicon Valley, a subcontractor to Wilcox on the WAAS development. Dr. Van Dierendonck recently was awarded the Johannes Kepler Award by the Institute of Navigation Satellite Navigation Division for outstanding contributions to satellite navigation. A. J. has over 21 years of GPS experience.

ABSTRACT

The ionosphere delay as an error source in GPS ranging is second only in magnitude to Selective Availability (SA). The delay is inversely proportional to the square of the frequency and can thus be measured using dual frequency L1/L2 GPS receivers.

In order to meet CAT I landing requirements the Wide Area Augmentation System (WAAS) solution to this error source is to broadcast ionosphere corrections at specified ionospheric grid points (IGPs) over the WAAS coverage area. These ionosphere corrections are computed from data gathered from L1/L2 receiving reference stations located about the coverage region.

This paper provides the test results of Wilcox Electric's ionosphere monitoring network experiment. This experiment consisted of using three ionospheric reference stations set up to measure the ionosphere delay of the GPS signals. A Rover receiver was also used to perform delay measurements at various locations in the coverage region.

A description of the implementation of an adaptive Kalman filter to estimate the vertical delays and their rate of change is also given in the paper. This estimation process uses the dual frequency measurements collected at the reference locations. Experimental results using a prototype of this process are presented that provide a preliminary value for the ionospheric delay error for the overall WAAS error budget. Finally, enhancements and improvements to the algorithm are discussed.

INTRODUCTION

The Wilcox ionosphere monitoring experiment was setup to verify the validity and performance of Wilcox's WAAS ionospheric delay estimation algorithms and to gain experience with the process of ionospheric delay estimation. The performance of the algorithms was evaluated against a truth source. The experiment consisted of setting up three reference stations located in Lake Dallas, TX, Crested Butte, CO, and Kansas City, MO as shown in Figure 1. A Rover receiver was used as the truth source for measuring the ionospheric delay at various locations in the coverage region.

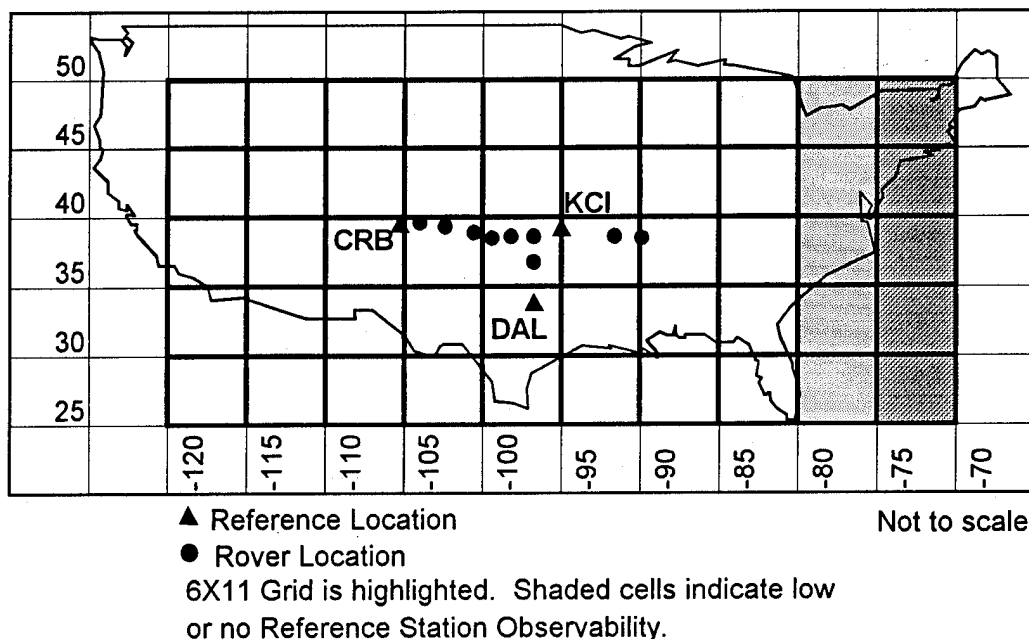


Figure 1. Experiment Reference and Rover Locations and the Corresponding Ionospheric Pierce Point Grid

The model for estimating the ionospheric delays follows the model given in Appendix A of the RTCA SC159 WAAS Minimum Operational Performance Standard (MOPS) [1]. That is, vertical ionospheric delays are represented at a grid of ionospheric pierce points at the mean height of the ionosphere (≈ 400 km), spaced in terms of latitude and longitude, such as is shown in Figure 1. A set of these ionospheric grid point (IGP) vertical delays, as well as an estimate of the 99.9% errors in the delays -- Grid Ionospheric Vertical Errors (GIVEs) -- are broadcast via a geostationary satellite (GEO) link. The user can interpolate these vertical delays and corresponding GIVEs to the ionospheric pierce point (IPP) along the line-of-sight to the chosen satellite. The purpose of the estimation process is to estimate the delays and GIVEs at these IGPs. Before presenting the results of the experiment, the estimation process algorithms are presented.

THE ESTIMATION PROCESS

The estimation process uses an adaptive Kalman filter to estimate the vertical delays and their change between estimation epochs at the selected IGPs. It also estimates the GIVEs based upon reference station observations. These GIVEs are also augmented with an estimate of decorrelation error at potential user locations, which is not part of the estimation process. The model for this Kalman filter takes advantage of the interpolation algorithm given in [1], and in Appendix A of this paper, effectively doing the inverse of what the user would be doing. (This is not exactly true since there could be many IPPs affecting a given IGP.) This fits well in the

context of a Kalman Filter. A least-squares algorithm could have been used as well. However, because some IGP delays may not always be observable, the state vector of the least-squares algorithm would have to change dynamically. This unobservability can be handled much easier in a Kalman Filter, as can sequentially available measurements and adaptivity.

Kalman Filter Implementation The Kalman Filter is implemented as shown in Figure 2 [2]. It starts with an initial estimate of the state vector and a corresponding initial error covariance matrix. When a set of measurements is available at time t_k , the inner loop of Figure 2 is exercised until all measurements at that time are processed. Then the outer loop is exercised to update to the time of the next set of measurements, at which time the inner loop is again exercised. The equations are described below.

GIVE Estimation The advantage of using the adaptive Kalman Filter for estimation of the IGP delays is that it also estimates the GIVEs. The diagonal elements of the predicted error covariance matrix of the Kalman Filter are proportional to the square of the GIVEs at the IGP. The adaptivity ensures that the line-of-sight projection of the covariance matches the statistics of the measurement residuals. More details of this GIVE estimation will be provided below.

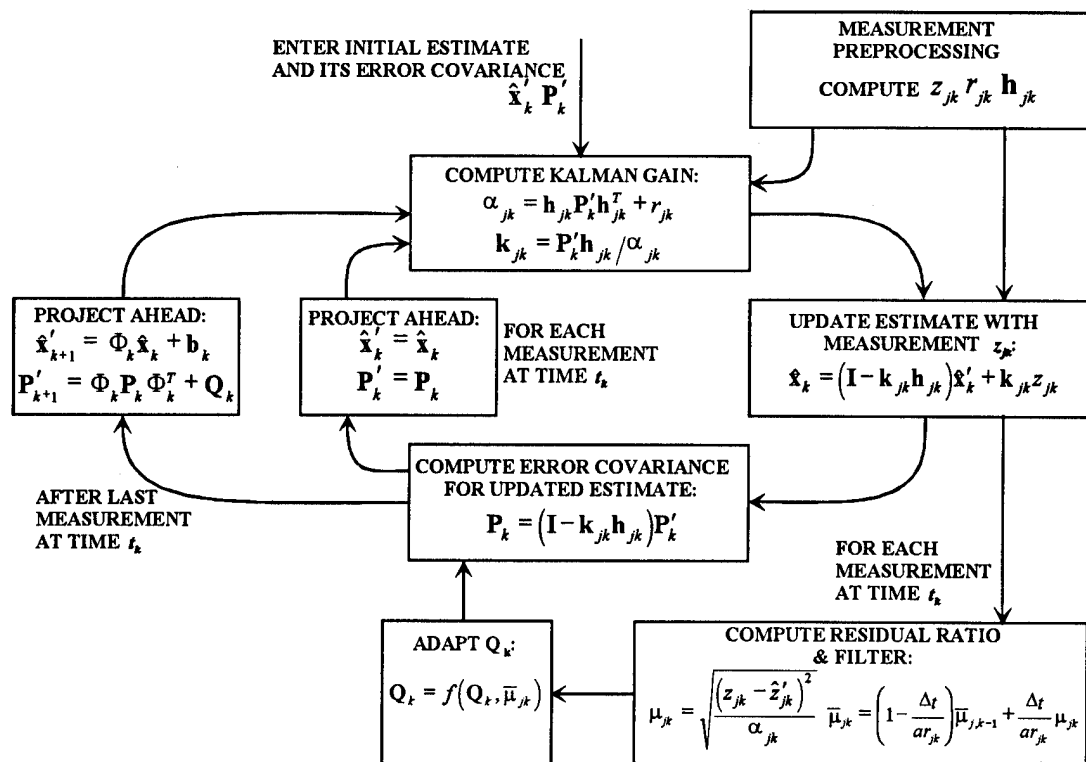


Figure 2. Kalman Filter Implementation

Table 1. States and Measurements Used in the Estimation Process

$\mathbf{x}_k = [\tau_{1k} \quad \dots \quad \tau_{Nk} \quad (\dot{\tau}\Delta t)_{1k} \quad \dots \quad (\dot{\tau}\Delta t)_{Nk}]^T$	1.1)
$\mathbf{z}_k = \left[\frac{\tau_{L1-L2,1k}}{F_1} \quad \dots \quad \frac{\tau_{L1-L2,Mk}}{F_M} \quad \frac{\Delta\tau_{car,1k}}{F_1} \quad \dots \quad \frac{\Delta\tau_{car,Mk}}{F_M} \right]^T$	1.2)
$\mathbf{z}_k = \left[\frac{\tau_{L1-L2,1k}}{F_1} \quad \dots \quad \frac{\tau_{L1-L2,Mk}}{F_M} \quad \frac{\Delta\tau_{div,1k}}{2F_1} \quad \dots \quad \frac{\Delta\tau_{div,Mk}}{2F_M} \right]^T$	1.3)
$\frac{\tau_{L1-L2,jk}}{F_j} = \sum_{n=1}^4 W_n(x_{pp,jk}, y_{pp,jk}) \tau_{i(n)k} + \frac{w_{L1-L2,jk}}{F_j} + \frac{bias_{L1-L2,j}}{F_j}$	1.4)
$\frac{\Delta\tau_{car,jk}}{F_j} = \left\{ \sum_{n=1}^4 [W_n(x_{pp,jk}, y_{pp,jk}) - W_n(x_{pp,j,k-1}, y_{pp,j-1,k})] \right\} \tau_{i(n)k} + \sum_{n=1}^4 W_n(x_{pp,jk}, y_{pp,jk}) (\dot{\tau}\Delta t)_{i(n)k} + \frac{w_{car,jk}}{F_j}$	1.5)
$\frac{\Delta\tau_{div,jk}}{2F_j} = \left\{ \sum_{n=1}^4 [W_n(x_{pp,jk}, y_{pp,jk}) - W_n(x_{pp,j,k-1}, y_{pp,j-1,k})] \right\} \tau_{i(n)k} + \sum_{n=1}^4 W_n(x_{pp,jk}, y_{pp,jk}) (\dot{\tau}\Delta t)_{i(n)k} + \frac{w_{div,jk}}{2F_j}$	1.6)

Delay Estimation Measurements In the WAAS being developed by Wilcox Electric for the FAA, the ionospheric delay estimation process will use dual frequency GPS semi-codeless P code pseudorange and carrier phase measurements collected at the Wide-Area Reference Station (WRS) locations. Semi-codeless P code is as defined in Reference 3. Because these semi-codeless measurements can be noisy with possible drop-outs due to low signal-to-noise conditions or scintillation, C/A code

code/carrier divergence measurements will also be used as a backup to the L1-L2 carrier phase measurements. These much-more-robust divergence measurements are the difference between the C/A code pseudorange measured from code correlation and pseudorange measured from the carrier phase. Because the ionosphere is a dispersive media that acts like a wave guide, the code is delayed (group delay) while the carrier phase advances.

This is because, for such a media, the group and phase velocity of the signal are related as

$$v_g v_\phi = c^2 \quad 1)$$

This difference measures twice the ionospheric delay, but with a carrier cycle ambiguity, making it somewhat useless as a delay measurement. However, it can be used to measure twice the rate-of-change of the ionosphere. Since the C/A code is used for this measurement, the signal-to-noise ratio is much higher than that of the semi-codeless measurements and much more robust in a scintillating environment.

Measurement Preprocessing Prior to applying the measurements to the estimation filter, 10-second L1-L2 pseudorange measurements will be smoothed against the L1-L2 carrier to support the filter update rate of once per 30 seconds. This is sufficient for tracking the rate-of-change of the group delay during ionospheric storms.¹ In the WAAS, the IGP delays are broadcast every 2 to 5 minutes so that there is no reason to update the filter at any higher rate. C/A carrier/code divergence measurements will be collected every second, and then smoothed to the same once per 30 second rate.

Estimation Model The estimation model consists of a state vector comprising of the vertical IGP delays and their changes. The state vector is as shown in Table 1, Equation 1.1, where τ_{ik} is the vertical delay at IGP i at time t_k , $(\dot{\tau}\Delta t)_{ik}$ is the change in that vertical delay (at IGP i between time updates) and N is the number of pre-established IGPs. The measurement vector is either that of Equation 1.2, if L1-L2 carrier phase measurements are available, or that of Equation 1.3 if the C/A code divergence measurements are being used, where $\tau_{L1-L2,jk}$ is the slant L1-L2 delay through IPP j at time t_k , M is the maximum number of IPPs (that is, the total number of GPS satellites times the total number of WRSs), F_j is the obliquity factor for IPP j as defined in Appendix A,

¹ During magnetic storms, the Total Electron Content (TEC) can vary over 1 TECu per 30 seconds, which is equivalent to 0.165 meters per 30 seconds at L1 [4]. This effect is much different from scintillation effects more prevalent in the magnetic equator region. Scintillation causes very short term rapid signal phase and amplitude variations that can cause problems with receiver tracking, but does not usually cause ranging errors [5]. Both effects are caused by magnetic storms and mostly occur in the local evening hours. The TEC variation that causes ranging errors is more prevalent in the polar regions, but occasional extends to the mid-latitudes.

$\Delta\tau_{car,jk}$ is the carrier phase change since the last time update and $\Delta\tau_{div,jk}$ is the C/A code code/carrier divergence change since the last time update, all at time t_k . Not all of these $2M$ measurements are available at each time step. The ones not available are simply not processed (that is, nothing has to be done). Since the measurement errors are independent, they can be processed one at a time as scalars. Note that they have all been transformed to vertical delay or change in vertical delay measurements using the obliquity factor in the denominator.

The Kalman Filter is partitioned into two processes -- the Time Update and the Measurement Update. The Time Update is processed after the completion of all measurement processing at time t_k .

Time Update The state vector \mathbf{x}_k in the Kalman Filter includes all of the estimated IGP delays and their changes, including those that are not currently observable, but will be at some time. The delay change estimates of the non-observable states are allowed to "coast" when the IGP is no longer observable, and declare it as *not-monitored* in the WAAS messages. The time update of the process is given in the "PROJECT AHEAD" block of Figure 2, where \mathbf{x}_k is the state vector made up of N IGP vertical delays and N IGP vertical delay changes. The last N elements of the vector \mathbf{b}_k are made up of *a priori* second differences of vertical delay at the IGPs over the time update interval. That is, the last N elements of the vector are made up of

$$b_{i+N,k} = \tau_{Bent,i,k+1} - 2\tau_{Bent,i,k} + \tau_{Bent,i,k-1} \quad 2)$$

where $\tau_{Bent,i,k}$ is the vertical delay at IGP i at time t_k as predicted by the Bent Model [6]. The first N elements of \mathbf{b}_k are always zero. This vector varies with solar activity (sun-spot number, solar flux), IGP location, time of year and time of day.

The state transition matrix is

$$\Phi_k = \begin{bmatrix} \mathbf{I}_N & \mathbf{I}_N \\ \mathbf{0} & \mathbf{I}_N \end{bmatrix} \quad 3)$$

where \mathbf{I}_N is an $N \times N$ identity matrix for N IGPs. The associated covariance update is also given in the "PROJECT AHEAD" block of Figure 2. \mathbf{P}_k is the estimation error covariance matrix prior to the time update and \mathbf{P}'_{k+1} is the same after the time update.

A Priori Delay Model As stated above, the Bent Model is used to update the delay changes. This model has been in existence for quite some time, but has been determined

to still be the best overall model of the ionosphere available [7]. This process takes advantage of the knowledge of the dynamics of the ionosphere. The \mathbf{b}_k is mainly used to keep the changes in ionospheric delay states close between updates to minimize the update uncertainty, and when not observed for better reinitialization after they again become observable. Its use here is analogous to aiding a GPS navigation solution with velocities from an inertial reference system.

The \mathbf{Q}_k is also defined as a percentage of the square of Equation 2 to account for the uncertainty of the *a priori* model. This percentage adapts to filter measurement residuals as described below.

GIVE Evaluation The diagonal elements of the upper $N \times N$ matrix of \mathbf{P}'_k are the squares of the estimated *GIVES* divided by 3.29. However, the broadcast *GIVES* will be increased by an amount that is a function of distance to the nearest IPP and the sun-spot number to account for spatial decorrelation. That is,

$$GIVE_{ik} \geq 3.29 \sqrt{P'_{iik} + \sigma_{sd,ik}^2} \quad 4)$$

where the inequality indicates that the *GIVE* is the least upper bound selected from Table A-9 of [1]. Since \mathbf{P}'_k is altered by the \mathbf{Q}_k adaptation based upon measurement residuals, it will adapt to an unmodeled changing ionosphere.

Measurement Update The measurement process for the Kalman Filter is as illustrated in Figure 1, which describes the plane view of the grid used in the experiment. A measurement is modeled as a linear combination of the four (4) IGP's surrounding the IPP of the measurement. It includes measurement noise and known WRS and satellite biases. All are divided by the appropriate obliquity factor to convert them to vertical delays. Equation 1.4 represents the L1-L2 pseudorange measurements, Equation 1.5 represents the L1-L2 carrier phase measurements and Equation 1.6 represents the C/A code divergence measurements. The W_n 's are the weighting functions defined in Appendix A and $i(n)$ denotes the IGP number related to IGP n surrounding the IPP. $w_{L1-L2,jk}$ is the L1-L2 measurement noise, $bias_{L1-L2,j}$ is the sum of the known WRS and satellite L1-L2 biases, $w_{car,jk}$ is the carrier phase measurement noise and $w_{div,jk}$ is the divergence measurement noise. These measurement models map the prediction of the IGP delays into a predicted IPP vertical delay for the purpose of defining measurement residuals when differenced from the actual measurement. The $\Delta\tau_{div,jk}/2$ and $w_{div,jk}/2$ quantities can be replaced with change in L1-L2 carrier phase and its noise, if it is available.

The measurement vectors \mathbf{h}_{jk} of the "MEASUREMENT PROCESSING" block of Figure 2 are made up of the coefficients of the IGP states given in Equations 1.4 through 1.6 of Table 1. They map the vertical IGP delay states into the slant range IPP delay measurements. Note that the equation for each measurement in a cell surrounded by IGP's is identical to the interpolation model for the user given in Appendix A.

The associated measurement uncertainties are represented in

$$\mathbf{R}_k = \begin{bmatrix} \mathbf{R}_{L1-L2,k} & \mathbf{0} \\ \mathbf{0} & \mathbf{R}_{div,k} \text{ or } \mathbf{R}_{car,k} \end{bmatrix} \quad 5)$$

which is made-up of diagonal elements representing the variances of the individual smoothed L1-L2 measurements (first M) and the individual divergence or carrier phase measurements (second M). Both are converted to variances of vertical delay measurements. The first M variances will be dominated by the noise of the semi-codeless measurements. The second M variances will have an additive multipath component, if divergence measurements are used, weighted by the inverse of the \tan^2 of elevation angle, as well as a small measurement noise component. If the L1-L2 carrier phase measurements are available, the delay change measurement variances will be reduced significantly. The noise variances will be estimated using C/N_0 measurements accompanying the data from the WRSs, which will effectively de-weight noisy measurements coupled with low elevation angle satellites. This will have the effect of influencing IGP delays that are already established very little, while also providing IGP delays that have not been established, but with a larger uncertainty.

One of the features of a Kalman Filter processing independent measurements is that the measurements can be processed sequentially. Thus, if a measurement is missing because of a drop-out, it is simply skipped in the processing. Measurements are de-weighted in the filter gain computation by the expected variance of the residual α_{jk} evaluated as shown in the "COMPUTE KALMAN GAIN" block of Figure 2, where r_{jk} is the j th diagonal element of \mathbf{R}_k . The gain matrix for this j th measurement is also shown in that block.

The updated covariance and state vector are shown in the next two blocks of the inner loop of Figure 2, where

$$z_{jk} = \frac{\tau_{L1-L2,jk} - bias_{L1-L2,j}}{F_j} \quad 6)$$

for L1-L2 measurement $z_{L1-L2,jk}$, and

$$z_{jk} = \frac{\Delta\tau_{\text{car},jk}}{F_j} \text{ or } z_{jk} = \frac{\Delta\tau_{\text{div},jk}}{2F_j} \quad (7)$$

for carrier phase change and divergence change measurements, respectively. The equations in the "UPDATE ESTIMATE WITH MEASUREMENT z_{jk} " block of Figure 2 can be rewritten as

$$\begin{aligned} \hat{\mathbf{x}}_k &= \hat{\mathbf{x}}'_k + \mathbf{k}_{jk} (z_{jk} - \mathbf{h}_{jk} \hat{\mathbf{x}}'_k) \\ &= \hat{\mathbf{x}}'_k + \mathbf{k}_{jk} (z_{jk} - \hat{z}'_{jk}) \end{aligned} \quad (8)$$

where the terms within the brackets are known as "measurement residuals" or "innovations." Their associated variances are the α_{jk} 's. These quantities will be saved and used in the adaptation process. The L1-L2 versions will be archived for non-real-time use in WRS and satellite L1-L2 bias error estimation described below.

The covariance and state vector are updated as updated as shown in the inner loop "PROJECT AHEAD" block in-between each measurement update, which is the same as a zero-second time update. The inner loop computations are repeated until all measurements collected at time t_k are processed.

Edge of Coverage Considerations Not all IGP delays are observable at the time slice of definition. However, if the WRS IPPs cover the same grid that all users would observe at some time, unobserved IGP delays are of no consequence. The measurement vectors would eventually fill in when they become observable to the WRSs (and the users). In the case that the WRSs do not provide full coverage at any given time, the grid spacing should be increased so that there are always IPPs among four IGP delays at all times. That is, the spacing should be commensurate with the WRS IPP density in that region.

Bias Determination L1-L2 biases can exist in both the WRS receivers and GPS satellites. Since the biases are essentially constant (except for configuration changes), they will appear as biases in the innovations, since they will not agree with the innovation model. The residuals will be used in a separate Kalman filter to estimate these biases similar to the techniques used in References 8 and 9. The authors of these references included these biases in the ionospheric delay state vector. However, the large difference between the time constants of these biases and the ionosphere allows the state vector to be partitioned into two state vectors, and thus, two Kalman filters. Both

estimation filters will be initialized with known calibration numbers.

Adaptive Q Determination The \mathbf{Q}_k are part of the adaptive process that adjusts the statistics of the filter to respond to ionospheric model deficiencies and measured anomalies, where

$$\mathbf{Q}_k = \begin{bmatrix} \mathbf{Q}_{11k} & \mathbf{Q}_{12k} \\ \mathbf{Q}_{21k} & \mathbf{Q}_{22k} \end{bmatrix} \quad (9)$$

where the \mathbf{Q}_{ijk} are defined as follows:

$$\mathbf{Q}_{22k} = \mathbf{D}_k \mathbf{Q}_{\text{Bent},k} \mathbf{D}_k \quad (10)$$

$$\mathbf{Q}_{12k} = \mathbf{Q}_{21k}^T = \mathbf{C}_k \mathbf{Q}_{22k} \quad (11)$$

$$\mathbf{Q}_{11k} = \mathbf{C}_k \mathbf{Q}_{22k} \mathbf{C}_k \quad (12)$$

where

$$\mathbf{Q}_{\text{Bent},k} = \left(\frac{p}{100} \right)^2 \mathbf{b}_{2k} \mathbf{b}_{2k}^T + \mathbf{Q}_{\min} \quad (13)$$

where \mathbf{b}_{2k} is the second half of the \mathbf{b}_k vector with elements defined in Equation 2 and p is a percentage error expected in the Bent Model (~25%). \mathbf{C}_k and \mathbf{D}_k are diagonal matrices used to adapt the \mathbf{Q}_k described below and \mathbf{Q}_{\min} is a minimum diagonal matrix that prevents zero elements when the Bent Model has no dynamics.

The α_{jk} 's and the corresponding innovations are also used in the filter adaptation process. The α_{jk} 's represent the *a priori* variances of the innovations that, if the process is modeled correctly, are the variances of the innovations. If not, the \mathbf{Q}_k can be adjusted to make the match occur. The innovation variances are used to adjust the \mathbf{Q} values for IGP delays adjacent to the cell of the j th measured IPP based upon a measurement residual ratio given by

$$\mu_{jk} = \sqrt{\frac{(z_{jk} - \hat{z}'_{jk})^2}{\alpha_{jk}}} \quad (14)$$

These μ_{jk} are low-passed filtered to reduce the effects of the measurement noise and are used to build up the diagonal matrices \mathbf{C}_k and \mathbf{D}_k used in Equations 10 through 12. Since the details of this process are quite involved, and since the process was not used in the experiment, the details are not covered in this paper.

Filter Initialization The initial IGP delay and its uncertainty is determined from the Bent model. That is, the initial states i are

$$\hat{x}'_{i,0} = \tau_{Bent,i,0} \quad (15)$$

$$\hat{x}'_{i+N,k} = \tau_{Bent,i,k+1} - \tau_{Bent,i,k} \quad (16)$$

and the initial error covariance matrix is

$$\mathbf{P}'_0 = \left(\frac{P}{100} \right)^2 \hat{\mathbf{x}}'_0 \hat{\mathbf{x}}'^T_0 \quad (17)$$

EXPERIMENT RESULTS

Experiment Description

The experiment consisted of setting up three reference stations located in Lake Dallas TX, Crested Butte CO, and Kansas City, MO. A Rover receiver was used to measure the ionospheric delay at various locations in the coverage region (see Figure 1) that were used as truth sources. The reference receiver data was processed using IGP vertical delay estimation algorithms similar to those described above. The Rover receiver L1-L2 delay data was then converted to vertical delays and compared to vertical delays interpolated from the estimated IGP delays.

Processing Differences The experiment processing implemented the basic Kalman filter equations described above. However, only L1-L2 delay measurements were processed. The Bent Model and adaptive processing described above also were not implemented. The \mathbf{Q}_k were set to a constant value determined experimentally. The data was processed at a 15 second sampling interval with no smoothing of samples.

Experiment Equipment and Measurements For the experiment described herein, semi-codeless receivers were not readily available, so codeless receivers (the Trimble 4000SSE) were used instead. In this receiver, the L1-L2 measurements are actually C/A code L1 minus P code L2 measurements, available for both code and carrier. Because the C/A code was used, the measurements were susceptible to C/A code multipath errors. The divergence measurements could have been derived, but, because the pseudorange measurements were corrected with a receiver clock solution, while the carrier phase measurements were not, these divergence measurements were useless. There also tended to be discontinuities in the carrier phase measurements, so they were not used.

L1-L2 Bias Calibration The Kansas City receiver was calibrated with a calibrated L1/L2 GPS signal generator. The biases of the other receivers were then determined by comparing measurements at co-located pierce points for all three stations and the Rover receiver. The co-location factor was 0.3 degrees within 15 seconds of the co-located pierce points. A fit was then performed by converting the Kansas City slant delay to a vertical delay with respect to the co-located pierce point. The difference was then weighted by the signal to noise ratio of each measurement and the average of the difference was used to determine the biases for the other stations. The satellite biases were taken from Reference 9. No bias estimation using the processed data was attempted.

Rover Location Accuracy Results

Figure 3 shows an example of a comparison of the measured and interpolated vertical delays and those delays \pm UIVE (99.9%) at the Wichita Rover site for three satellites. (UIVE -- User Ionospheric Vertical Error -- is interpolated from the GIVEs computed as 3.29 times the square root of the diagonal elements of the error covariance matrix corresponding to the IGP.) The measured data are the L1-L2 vertical delays obtained using the Rover receiver at the Wichita site for the three satellites shown on the chart. The interpolated vertical delay is the delay obtained for the Rover's pierce point interpolated from the Kalman filter output IGP vertical delay estimates (using the interpolation algorithm of Appendix A). The measured delays compared to the interpolated delays to within the UIVE bound at all times except during right after initialization on the PRN 26 satellite. The adaptive implementation would have likely provide the necessary UIVE bound.

Figure 4 shows the rms differences between the measured and interpolated vertical ionospheric delay at various Rover locations for all satellites tracked for periods of 0.3 to 13.4 hours. Of course, these rms errors include measurement errors such as receiver noise and multipath errors. In fact, the standard deviation of the measurements (converted to vertical delays) was 0.675 meters for the reference stations and 0.476 meters for the Rover. Mostly, the rms vertical errors hovered around 0.6 meters except for at the St. Louis location and one Denver location that had rms errors of over a meter. The St. Louis location IPPs lacked good reference receiver IPP density and measurement quality, and the Denver data had some periods of high multipath.

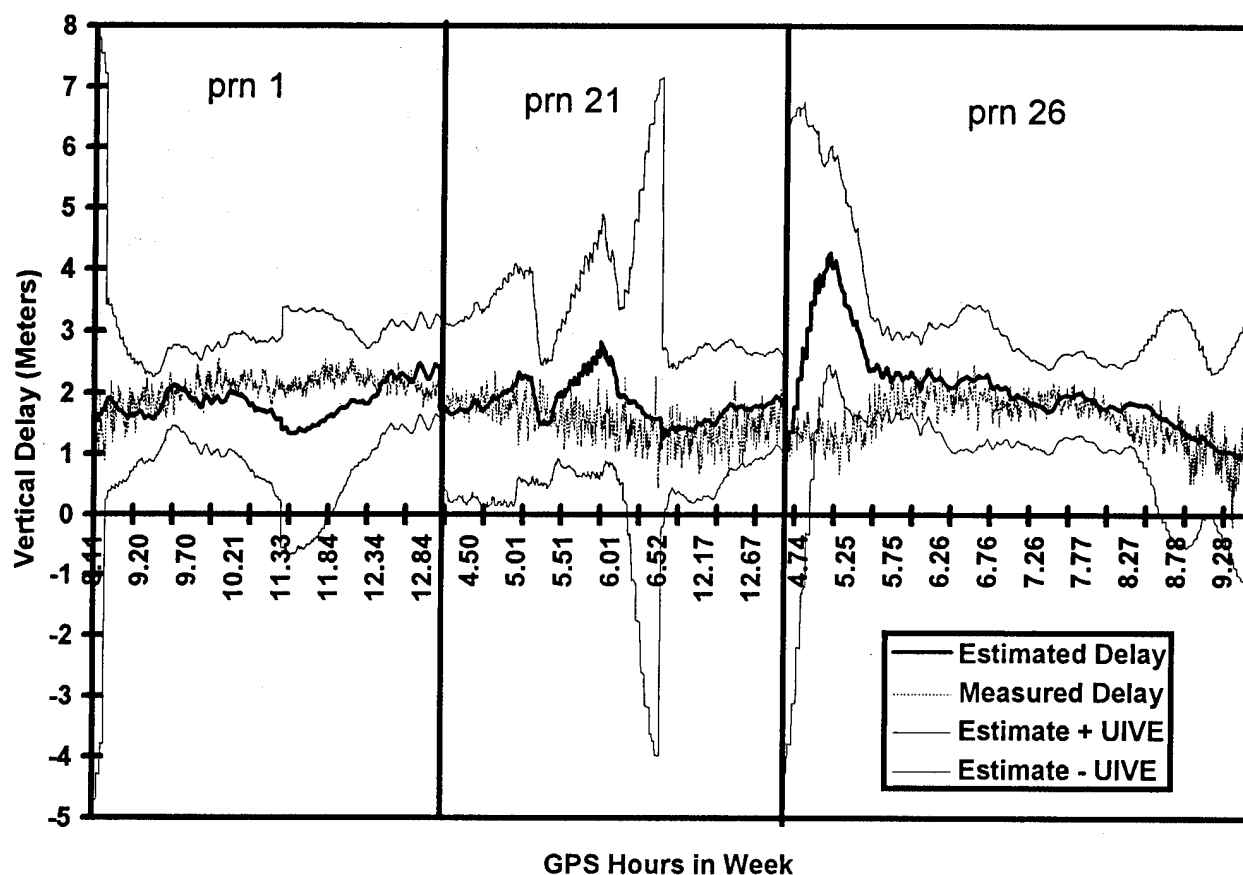


Figure 3. Rover Results at Wichita -- Measured Versus Estimated Vertical Delays

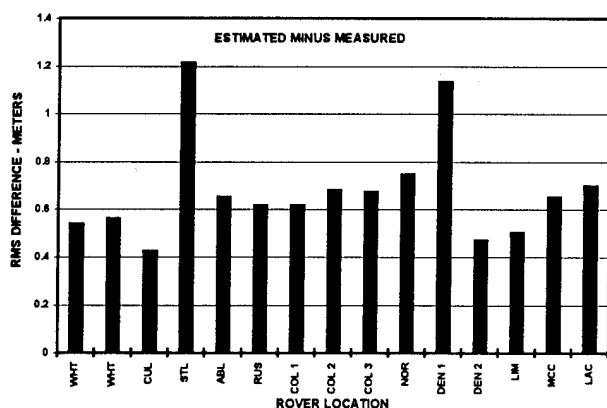


Figure 4. Test results for selected Rover locations.

Problems Encountered and Extrapolation to Future Performance

Receiver Problems Problems with the receivers used in the experiment were alluded to above -- data discontinuities, multipath susceptibility and noisy measurements. These problems were compounded with the fact that the receiver exhibited inter-channel biases that further degraded performance of the estimation. Common measured pierce point delays from two satellites would

differ because of an unknown inter-channel bias. If this would have been known before the data were collected, channel calibration could have been performed and channel information could have been extracted. Unfortunately, this was not the case and these biases resulted in some degradation of performance.

The receiver to be used in the actual WAAS implementation will be the new NovAtel Millennium L1/L2 receiver coupled with the NovAtel Multipath Elimination Delay Lock Loop (MEDLL) receiver. The L1-L2 delay measurements will still be C/A code L1 minus P code L2 measurements. However, the C/A code measurements will be realized using the MEDLL technology, which has multipath performance equal to that of P code tracking [10]. In addition, the P code L2 tracking is multi-bit semi-codeless, providing 12 - 15 dB better performance than the receiver used in the experiment [3]. There are no inter-channel biases in these new receivers.

Prior to the actual WAAS implementation, the algorithms will continue to be tested using data from the FAA's WAAS Test Bed. The four years experience gained by the FAA in using that data has allowed them to

overcome most of the problems encountered here. This data is expected to have much higher quality.

Processing Enhancements As stated above, no L1-L2 carrier phase or divergence measurements were used in the experiment, the *a priori* model was not used and Kalman filter adaptation was not implemented. Because of this, the experimentally determined constant Q_k values had to be set to handle the worst case situations and to prevent excessive multipath contamination. These factors caused the vertical delay estimates to be much noisier and much more influenced by multipath than would be if the full processing capability could have been realized. All of these processing enhancements will be implemented on the future processing of the WAAS Test Bed data and in the actual WAAS implementation. In addition, L1-L2 bias estimation will be added to further enhance performance.

CONCLUSIONS

Even though the data collected in the Wilcox ionospheric monitoring network had marginal quality, the objectives of the experiment were met -- to verify the validity and performance of the ionospheric delay estimation algorithms and to gain experience with the process of ionospheric delay estimation. Even with the marginal data, estimation errors that were also contaminated with Rover receiver measurement errors, the performance of the algorithms was usually within expectations and within the desired error budget. Certainly, based upon lessons learned, the objective of gaining experience with the process was met.

ACKNOWLEDGMENTS

The authors wish to acknowledge the efforts of Fred Gerken for acquiring and setting up the equipment, Todd Skoog for developing receiver interface software and setting up equipment, Stephen Peck (Hughes Aircraft Company) and Steven Bauer for data analysis and Cindy Liu for developing data processing and formatting software.

REFERENCES

1) Minimum Operational Performance Standard for Global Positioning System/Wide Area Augmentation System Airborne Equipment, Draft 6, RTCA Paper No. 396-95/SC159-661, July 24, 1995.

2) R. G. Brown and P. Y. C. Hwang, Introduction to Random Signals and Applied Kalman Filtering, Second Edition, J. Wiley & Sons, Inc., 1983.

3) A. J. Van Dierendonck, "Innovation: Understanding GPS Receiver Technology -- A Tutorial," GPS World, Volume 6, Number 1, January 1995, pp. 34 - 44.

4) G. J. Bishop and J. A. Klobuchar, "Ranging Errors Due to Disturbances in the Polar Ionosphere," *Proceedings of ION GPS-90*, The Third International Technical Meeting of the Satellite Division of The Institute of Navigation, Colorado Springs, CO, September 19 - 21, 1990, pp. 175 - 179.

5) J. A. Klobuchar, "Ionospheric Effects on GPS," GPS World, Volume 2, Number 4, April 1991, pp. 48 - 51.

6) S. K. Llewellyn and R. B. Bent, "Documentation and Description of the Bent Ionospheric Model," AFCRL-TR-73-0657, AD 772733, 1973.

7) L. D. Brown, R. E. Daniell, Jr., M. W. Fox, J. A. Klobuchar and P. H. Doherty, "Evaluation of Six Ionospheric Models as Predictors of Total Electron Content," Radio Science, Vol. 26, No. 4, July-August 1991, pp. 1007 - 1015.

8) B. D. Wilson and A. J. Mannucci, "Instrument Biases in Ionospheric Measurements Derived from GPS Data," *Proceedings of ION GPS-93*, Salt Lake City, UT, September 22 - 24, 1993, pp. 1343 - 1351.

9) B. Wilson and A. Mannucci, "Extracting Ionospheric Measurements from GPS in the Presence of Anti-Spoofing," *Proceedings of ION GPS-94*, Salt Lake City, UT, September 21 - 23, 1994, pp. 1599 - 1608.

10) B. Townsend, P. Fenton, K. Van Dierendonck and D. J. R. van Nee, "Performance Evaluation of the Multipath Estimating Delay Lock Loop," *Proceedings of the National Technical Meeting*, The Institute of Navigation, Anaheim, CA, January 18 - 20, 1995, pp. 277 - 283.

11) J. L. Junkins, G. W. Miller and J. R. Jancaitis, "A Weighting Function Approach to Modeling of Irregular Surfaces," Journal of Geophysical Research, Volume 78, No. 110, April 1973.

APPENDIX A: DEFINITION OF TERMS IN THE MEASUREMENT EQUATIONS

The following defines the terms of the measurements of Equations 1.4 through 1.6 of Table 1:

A.1 Pierce Point Location Determination

Considering the satellite and user locations, the user must first determine the location of the IPP of the signal path from satellite. These equations are given in [1].

A.2 Ionospheric Pierce Point Delay Interpolation [1]

Although the data base broadcast to the user is as vertical IGP delays, these points do not generally correspond with his computed IPP locations. Thus, it is necessary for the user to interpolate from the broadcast IGP delays to that at his computed IPP locations. Given four nodes of a cell of the IGP grid described above that surround the user's IPP to a satellite, the user can interpolate from the nodes to his pierce point using the following algorithm.

A weighting function approach for modeling irregular surfaces provides a simple procedure for approximating an irregular surface from regularly spaced ionospheric grid point vertical delay data [11]. The mathematical formulation for interpolated vertical IPP delay $\tau_{vpp}(\phi_{pp}, \lambda_{pp})$ as a function of IPP latitude ϕ_{pp} and longitude λ_{pp} is

$$\tau_{vpp}(\phi_{pp}, \lambda_{pp}) = \sum_{i=1}^4 W_i(x_{pp}, y_{pp}) \tau_{vi} \quad A-1$$

where the general equation for the weighting function is

$$W(x, y) = x^2 y^2 (9 - 6x - 6y + 4xy) \quad A-2$$

and τ_{vi} are the broadcast grid point vertical delay values at four corners of the IGP grid, as shown in Figure A-1. In particular, τ_{vpp} is the output value at desired pierce point pp , whose geographical coordinates are ϕ_{pp}, λ_{pp} ,

$$W_1(x, y) = W(x, y) \quad A-3$$

$$W_2(x, y) = W(1-x, y) \quad A-4$$

$$W_3(x, y) = W(1-x, 1-y) \quad A-5$$

$$W_4(x, y) = W(x, 1-y) \quad A-6$$

$$\Delta\lambda_{pp} = \lambda_{pp} - \lambda_1 \quad A-7$$

$$\Delta\phi_{pp} = \phi_{pp} - \phi_1 \quad A-8$$

$$x_{pp} = \frac{\Delta\lambda_{pp}}{\lambda_2 - \lambda_1} = \frac{\Delta\lambda_{pp}}{\text{longitude grid interval}} \quad A-9$$

$$y_{pp} = \frac{\Delta\phi_{pp}}{\phi_2 - \phi_1} = \frac{\Delta\phi_{pp}}{\text{latitude grid interval}} \quad A-10$$

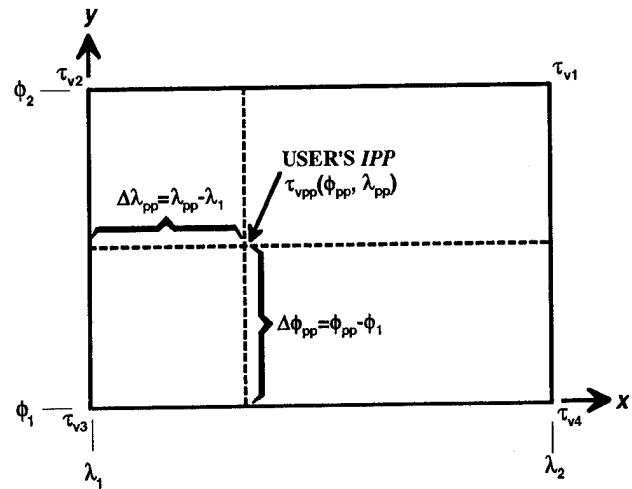


Figure A-1. Interpolation Algorithm Definitions

As can be seen from Equations A-1 and A-2, this interpolation technique involves only simple algebra, and provides a continuous surface. It does not matter that the grids are not square. They can also be rectangles.

The evaluated UIVE can be interpolated from the GIVEs to the IPP in a similar manner.

A.3 Computing Slant Ionospheric Delay

The vertical delay at a grid point or pierce point can be converted to a slant line-of-sight delay by multiplying that vertical delay by the obliquity factor F_{pp} as

$$\tau_{spp}(\lambda_{pp}, \phi_{pp}) = F_{pp} \cdot \tau_{vpp}(\lambda_{pp}, \phi_{pp}) \quad A-11$$

where τ_{vpp} is the interpolated vertical delay at the user-to-satellite IPP derived as described above, and

$$F_{pp} = \left[1 - \left(\frac{R_e \cos E}{R_e + h_I} \right)^2 \right]^{-\frac{1}{2}} \quad A-12$$

Precise GPS Time Transfer to a Moving Vehicle

Tor Egil Melgård and David Last
University of Wales

Bernard Thomas
DCN Brest (DGA)

BIOGRAPHY

Tor Egil Melgård holds a Master's degree in Electrical Engineering from the Norwegian Institute of Technology, University of Trondheim. For the last two years he has been involved in GPS research and the development of GPS applications. He is currently working at the University of Wales in Bangor on the development of a methodology for mapping the ASFs of the North-West European Loran system (NELS).

Professor David Last is Head of the Radio-Navigation Group at the University of Wales, Bangor. He was awarded the degrees of BSc(Eng) by the University of Bristol, England, in 1961, PhD by the University of Sheffield, England, in 1966 and DSc by the University of Wales in 1985. Prof. Last is a Fellow and former Council Member of the Royal Institute of Navigation, a Board Member of the Wild Goose Association, a Fellow of the Institution of Electrical Engineers and a Chartered Engineer. He has published many papers on navigation systems, including Loran-C, Decca Navigator, Radiobeacons and GPS. He acts as a Consultant on radio-navigation and communications to companies and government organisations. He is an instrument-rated pilot and user of terrestrial and satellite navigation systems.

Bernard Thomas is an engineer of the Direction des Constructions Navales (DCN) Brest, France, a division of the Délégation Générale de l'Armement (DGA) of the French Department of Defence. Since 1991 he has worked on the Loran-C and GPS radio-navigation systems, especially on navigation and time applications.

ABSTRACT

GPS time transfers normally employ the common-view method and take place between pairs of stationary receivers at precisely-known locations. This paper focuses on techniques for time transfer to a

GPS navigation receiver on a moving ship, a land vehicle or aircraft. The accuracy requirement is 20 ns (1σ) and, preferably, the system should work anywhere on earth.

Single point precise orbit and clock positioning emerges as the best way of achieving extremely high timing accuracy when computation is performed post-mission. Its key advantage is its global coverage without reference stations or communications links. DGPS time transfer using a calibrated time standard at the reference station is a viable alternative. It may be employed in real time, although its performance may also benefit from post-mission processing using precise orbit data. Both these techniques will be presented in detail and their performance evaluated.

The context of this study is the measurement on a moving ship, a land vehicle or aircraft of the arrival times of Loran-C pulses. The arrival times are required in order to calibrate the Additional Secondary Factors (ASFs) caused by the propagation of the signal over land paths. In this application all processing may be carried out post-mission.

Our experiments show that both timing methods can meet the 20 ns accuracy requirement. The paper compares the two with one another and with more conventional timing techniques, including time transfer via a common-view satellite and geodetic positioning. The specifications of the GPS receivers required to implement the methods are set out. The techniques presented are, of course, also applicable to GPS time transfers between stationary locations.

INTRODUCTION

A GPS signal propagates through the earth's atmosphere on its way from the satellite to the user. The signal's propagation in the atmosphere is slower than in a vacuum and its arrival is delayed in consequence. We must take this delay into account when calculating the distance from the satellite to the user.

Loran-C (LONg RANGE Navigation) is the world's most widely-used terrestrial aid to navigation. Its mode of operation may be considered comparable to that of GPS in that transmitters at known locations radiate signals and a receiver calculates its distances from them by timing their arrivals and from knowledge of their speed of propagation. Loran-C signals suffer propagation delays when they cross land masses which are analogous to the delays of GPS signals passing through the atmosphere. However, unlike GPS atmospheric delays which change constantly, the land-mass delays of Loran-C are virtually constant. We can measure and record these 'Additional Secondary Factors (ASFs)' and so incorporate them into the range measurements made by receivers [1,2].

We determine ASF values by measuring on a survey ship, a land vehicle or aircraft the arrival times of Loran-C signals at known locations. These positions must be known with 1σ accuracies of approximately 7 m and the time measurements made with an accuracy of better than 20 ns. GPS is a candidate to provide both the position and time references. This paper focuses on ways of obtaining precise time with GPS on a moving vehicle. Our objective is a low-cost technique which may be employed as part of a fully automatic, unattended, measuring unit to be installed on a ship and left to record Loran-C information throughout a voyage. The recorded data will be processed at the end of the voyage to reveal the ASF values. The equipment may be used anywhere throughout the sea areas of North-Western Europe.

This an unusual and very demanding application of GPS for time measurement. Without being GPS timing experts, we sat down and evaluated the following standard GPS timing techniques: 'common-view', 'Enhanced GPS' and 'geodetic positioning' to see whether any of them could fulfil our requirements.

STANDARD GPS TIMING TECHNIQUES

In the 'common-view method', two very accurate and stable clocks are used as the time references for two GPS receivers, and compared against the clock of a pre-selected GPS satellite which is visible to both receivers [3,4,5]. Conventionally the time measurements are averaged over a period of 13 minutes. The two receivers are stationary, in precisely-known locations. Corrections are applied to account for the differences between the distances travelled by the signals from the satellite to the locations of the two receivers.

This time transfer method is unsuitable for our purpose: our receiver will be in an unknown location, and moving, and we do not have a relatively-

expensive atomic standard as part of the mobile equipment to use in the averaging process.

'Enhanced GPS' was the second technique evaluated. Most of the effects of Selective Availability (SA) may be averaged out by using a stable reference clock, for instance a rubidium standard [6]. The rubidium clock is stable in the short term and the effects of SA are minimised by adjusting it to match GPS via a control loop of very long time constant. The performance of this technique is not as good as that of the common-view method. Besides, it requires a rubidium standard as part of the mobile equipment which is costly and would need several hours of SA averaging time before use.

Geodetic positioning used for precise time transfer can provide very high accuracy [7]. The method employs GPS carrier phase measurements. It is, of course, necessary to solve for the phase ambiguities on the fly in our application. This is very demanding to do when the mobile is a considerable distance from the reference station. It is made even more difficult if the receiver experiences cycle slips because of short periods of signal blockage. We judged this otherwise very accurate method inadequately robust for unattended use on a vessel.

Having found none of these standard GPS timing techniques suitable for our application, we identified two less conventional options: 'Precise Single Point (PSP)' and 'DGPS' time transfer. PSP is a new technique for timing applications; it employs *precise orbit and clock values* post-mission. DGPS time transfer is essentially the same as conventional DGPS. However, the reference station is equipped with an accurate clock and generates *range corrections* instead of the usual *pseudorange corrections*. We will now describe and demonstrate these two options in further detail.

PRECISE SINGLE POINT TIME TRANSFER

Stand-alone GPS has a timing accuracy of only some 300 ns. This is limited mainly by the component of SA which dithers the satellites' clocks and, to a lesser extent, by the component which introduces errors in the ephemeris values they broadcast. The principle of PSP is simply to replace the broadcast clock and orbit parameters with so-called 'precise orbit and clock' values. The European Space Agency (ESA), *inter alia*, calculate such values post-mission, using data from the stations of the International GPS Service (IGS).

PSP has been used for positioning [8,9], achieving an accuracy comparable to that of DGPS. However, not only are the three position coordinates, latitude, longitude and height, determined in the GPS solution,

but also the receiver's clock offset; 4 unknowns and at least 4 satellites are needed to do this. Our assumption was that the timing accuracy obtainable should be comparable to the position accuracy. Specifically, a 1σ 3D position accuracy of 7 m, for example, would correspond to a 1σ timing accuracy of 10 ns (applying the 'TDOP is half the PDOP' rule of thumb and assuming that 1 m is the distance travelled by signals in 3 ns).

Essentially PSP may be thought of as wide-area, post-processed, DGPS. It has the great advantage of complete global coverage while not requiring the user to provide any reference stations. In addition, not only does it give precise time values, but also the precise position values which we also need.

However, there are complications! We must ask: what time does PSP provide? It appears that time values derived using the ESA PSP data use a time scale, re-computed independently each day, which is referenced to GPS time (including the instantaneous effects of SA) at the epoch of the start of that day.

Our objective in making Loran-C time-of-arrival measurements is to compare the arrival times of Loran-C signals with their transmission times. These are known very precisely with respect to a timescale generated in France: the so-called 'UTC (Brest)'. The solution to the problem of the time scale is therefore straightforward: we simply observe the difference between PSP time and UTC (Brest) by means of a GPS receiver located at the Brest Loran-C control centre. Because this means we are now employing a single GPS time reference station, we have chosen to regard PSP as a time transfer technique.

This method of time measurement is very attractive since it requires neither reference stations, nor rubidium standards, but simply the logging of pseudorange measurements at the mobile and at Brest.

Computing PSP solutions

The 'precise orbit' files from ESA give the satellite position every 15 minutes using the earth-fixed International Terrestrial Reference Frame (ITRF). The consistency of this system with the World Geodetic System (WGS) 1984 is believed to be within approximately 1 m. We have used a 9th-order Lagrange polynomial to interpolate the satellite coordinates to any epoch, transformed the coordinates from ITRF to WGS84, and corrected the pseudoranges for the phase-versus-mass-centre offset. The latter adjustment is required because the precise orbit coordinates calculated are those for the satellite's mass centre, while the pseudoranges are measured with respect to its antenna phase centre. The difference is

85.4 cm for Block I satellites and 95.2 cm for Block II satellites; this offset must be added to the observed pseudorange [8]. Finally the satellite coordinates were corrected for the Sagnac effect, i.e. the rotation of the earth-fixed reference frame during the travel time of the signal from the satellite to the receiver.

The ESA clock data, in contrast to standard 15-minute precise ephemeris data, contains precise clock values at 1 minute intervals. For PSP use, this shorter interval is essential, given the relatively rapid SA dithering of the satellites' clocks. We used a 5th-order Lagrange polynomial to interpolate the clock values to any epoch and corrected the observed pseudoranges for the satellite clock offsets. The clock values from ESA come already corrected for the periodic relativistic effects caused by the slightly eccentric orbits of the satellites.

For the results presented in this paper we have simply ignored the existence of the ionosphere. We are currently close to the low point of the 11 year solar cycle and so the solar activity causes relatively little ionospheric delay. We believe that in the future, as solar activity increases again, it would be valuable if the IGS computing centres published additional parameters which single-frequency GPS users could employ for calculating ionospheric delays.

We estimated tropospheric delays by means of Black's model [10], assuming a surface temperature of 15 °C and a pressure of 980.0 mbar.

DGPS TIME TRANSFER

Standard DGPS pseudorange corrections improve the accuracy of positions over that of non-differential GPS, but not the accuracy of timing. This is because the reference station does not have a precise clock. 'DGPS time transfer' employs a reference station equipped with an accurate clock - normally an atomic standard. Thus it is able to generate true range corrections and not simply pseudo-range corrections. The mobile adds these range corrections to its measured ranges, and then calculates its position and also its receiver clock offset. This clock offset is with respect to the clock at the reference station and, as with PSP, the timing accuracy should be commensurate with the position accuracy. This method may also be used over longer base lines and also when there are fewer than 4 satellites in common view, provided that the position of the mobile is then provided by other means. DGPS time transfer may be carried out in real-time, which is essentially what happens when using the RTCM SC-104 type 9 message [11]. Alternatively, it can be computed post-mission; in that case a further improvement in accuracy may be achieved by replacing the broadcast parameters with precise orbital data. We favour the latter solution

because it involves no real-time data links.

DGPS time transfer is not unlike the common-view method, but it involves no averaging and also it may be used if the receiver's position is unknown (as long as there are 4 or more satellites in common view). If both receivers' positions are fixed it has the advantage that the measurement is made against all possible satellites, rather than just a single satellite. This increases the accuracy of the measurement and gives greater redundancy than does the common-view method. The disadvantage of post-mission DGPS time transfer over the common-view method is that pseudorange records must be stored, but this is acceptable in our application.

RECEIVER HARDWARE REQUIREMENTS

A GPS receiver has two internal clocks: a so-called 'hardware clock' and 'software clock'. The hardware clock is the externally accessible, physical, clock which provides, for instance, 1 PPS output and higher-frequency outputs. It is the internal clock against which input strobes are used to time-tag external events or it may be a higher frequency external clock fed into the receiver. The software clock is the internal clock against which the receiver measures the arrivals of the satellite signals and so calculates pseudorange values. If the GPS receiver is used in a precise timing application, it is essential that the hardware clock be accurately synchronized to the software clock, or that, if not, the discrepancy between them is recorded. Not all GPS receivers fulfil this essential requirement.

Further, the signal delay from GPS antenna, through the antenna cable and the front-end of the receiver to the point at which time measurements are made, must have been calibrated and must remain constant. These specialised timing requirements mean that the GPS receiver to be used must be chosen with care if good timing performance, as well as accurate position measurements, are to be obtained. And both timing and position measurement functions must work well when the receiver is in motion.

PSP VERSUS DGPS TIME TRANSFER

DGPS time transfer has the advantage compared to PSP that it may be implemented in real-time, but for our application this is of no great benefit. The two techniques are expected to give comparable timing accuracies, and both methods output an accurate position as well as accurate time. DGPS time transfer suffers from baseline limitations, and several reference stations would be required to cover all of North-West Europe. If we are to use the DGPS time

transfer technique to get both time and position information on the mobile, we will need to install several DGPS reference stations because of the large operating area.

An advantage of DGPS time transfer is that, to the extent that the ionospheric and tropospheric delays experienced at the reference station are the same as those at the mobile, their effects will cancel out; this will generally be the case for separations of up to several hundred kilometres. Moreover DGPS does not need precise clock values. PSP, on the other hand, offers global coverage.

From a theoretical point of view both methods appeared feasible for our application. To establish whether that would be the case in practice we set up an experiment to demonstrate and evaluate the performance of the two techniques. We also wished to confirm that the specific GPS receiver model we planned to use, a NovAtel GPSCard 3951R Narrow Correlator receiver, was suitable for precise time transfers. We knew from previous experiences that this receiver had a satisfactory navigational performance [12,13,14].

RESULTS AND ANALYSES

Measurements and computations

The measurements were conducted at Direction des Constructions Navales (DCN) at Brest, France, the location of the UTC (Brest) time standard. UTC (Brest) is a time scale realized by a system based on a minimum of two HP 5071 high performance cesium beam tubes. It is used for Loran-C synchronisation. Our measurement setup compared the 1 PPS's hardware clock signal from the NovAtel receiver with that of the UTC (Brest) standard, using an HP 5345 time interval counter with a resolution of 2 ns. We could have employed the option provided by the NovAtel receiver to time-tag incoming pulses. However, this function has a resolution of only 49 ns approximately. For the same reason it will not be used in the final ASF measurement system.

The antenna of the GPS receiver was mounted without a choke ring above a metal roof which gave noticeable multipath reflections of the satellite signals but is probably more typical of a mobile installation. A 45 m antenna cable with two connectors was used, attenuating the satellite signal by some 4-6 dB and resulting in a poor signal-to-noise ratio (SNR).

We allowed the NovAtel receiver's hardware and software clocks to drift freely and recorded the timing of the hardware clock (1 PPS) against UTC (Brest) once per second. We also stored the pseudoranges measured and the difference between the receiver's

Position	Latitude	Longitude	Height
Mean (m)	0.85	-0.23	1.85
RMS (m)	2.51	1.55	4.77

Table 1: PSP position solutions for a 17-hour-long session compared against the position of the antenna at Brest which was recorded in WGS84.

hardware and software clocks. The measurements took place 5 and 6 April 1995 and SA was in operation.

At the subsequent data-processing stage we calculated the receiver's software clock error and used it, together with the recorded differences between the hardware and software clocks, to compute the hardware clock errors. We then tested both the PSP and DGPS time transfer techniques, using the same raw data. We adopted a cut-off elevation mask of 10° and a maximum GDOP of 5.

As reference stations for the DGPS time transfer measurements we selected the two IGS reference stations at Ny-Ålesund (79° north and 12° east) on the Arctic island of Svalbard and Herstmonceux (51° north 0° east) in the United Kingdom. Ny-Ålesund is 3477 km, and Herstmonceux 451 km, from Brest (48° north and 5° west). As reference clocks Ny-Ålesund employs a Hydrogen Maser time standard and Herstmonceux only a Rubidium standard.

Results

The results to be presented should be compared with our accuracy requirements of 7 m in position and 20 ns in time.

The PSP position solutions for a 17 hour-long data set are shown in Table 1. The results are slightly poorer than had been achieved using similar measurements by Lachapelle [8]; this is very much to be expected in view of the relatively-high multipath environment and the low SNR as described above.

The timing performance from the same data is displayed in Figure 1. The time jump at GPS time 345600 occurs at mid-night and is due to the change of daily time reference by ESA (see Section 'Precise single point time transfer' above). When this step is removed (by calculating the mean offsets of the data sets from the two days), the time data has a 1σ variation of 11.6 ns. We also calculated PSP solutions using the known, fixed, position: this reduced the 1σ variation to 4.2 ns. The mean difference between the time solutions with unknown and fixed positions was 3.8 ns.

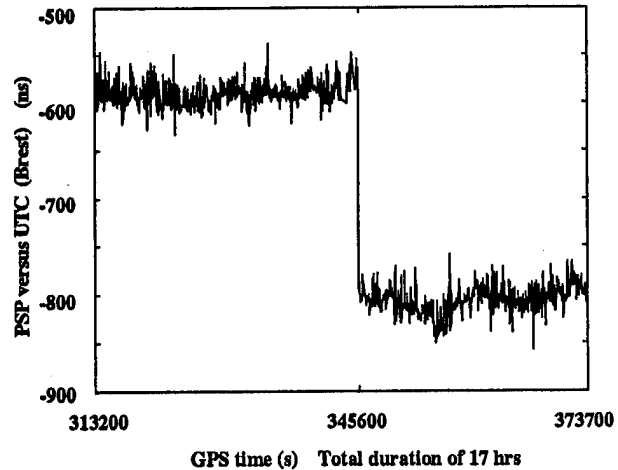


Figure 1: PSP time versus UTC (Brest) when the antenna position is assumed to be unknown. The shift at GPS time 345600 is because of the daily change of reference time of the ESA clock data.

Position	Latitude	Longitude	Height
Mean (m)	0.03	-0.04	-1.96
RMS (m)	3.68	2.24	7.31

Table 2: Brest positions determined using the DGPS time transfer technique, employing precise orbit data, from Herstmonceux. The results from a 17-hour-long session compared against the position of the antenna at Brest which was recorded in WGS84.

DGPS time transfer using Herstmonceux as the reference station gave the position results shown in Table 2. The mean offset is a little less than that of the PSP solutions in latitude and longitude (and better than one would normally expect from DGPS over a 451 km distance) and the height components are similar. The RMS variations of the DGPS solution are slightly greater than those from PSP.

The accuracy achieved using DGPS time transfer from Herstmonceux is a little difficult to establish because the reference clock there drifts relatively quickly. We, therefore, did the calculation as a two-step process: at every epoch we first calibrated the Herstmonceux clock by computing a PSP solution there, assuming its fixed position; then we calculated the results of the DGPS time transfer from Herstmonceux to Brest, assuming that the position of the receiver in Brest was unknown but using precise orbit data. The result was a 1σ variation of 15.8 ns when compared with UTC (Brest). This is a very satisfactory performance, bearing in mind that allowance must be made for the errors in the PSP time

Time	Precise orbits	Broadcast Orbits
1σ (ns)	3.7	4.1

Table 3: DGPS time transfer from Ny-Ålesund to Brest. Because of the exceptional 3477 km separation of the two stations, relatively-few common-view satellites were available and so the known locations of the stations were employed.

calibration of the Herstmonceux clock to which no smoothing was applied.

Finally, we also went one step further, and closed the Herstmonceux-Brest loop, to check that we had no residual offset values: first we calculated PSP solutions for Herstmonceux assuming that its position was unknown; then we did a DGPS time transfer to Brest, with the position of Herstmonceux fixed and Brest unknown and using precise orbit data; and finally we compared this result with the PSP solutions for Brest assuming its position unknown. We got a mean offset of 0.024 ns for the 17 hours long session. This tiny residual value shows conclusively that the residual offsets over a period of 17 hours are negligible.

Finally, we set out to evaluate the performance of DGPS time transfer over longer base lines. We also wished to check the difference in performance if we used broadcast orbit data rather than precise orbit data. For this experiment we used data from Ny-Ålesund, comparing its very accurate Hydrogen Maser clock against UTC (Brest). We employed the known positions of the two stations since they were so far apart that they could only see the required common-view satellites (four or more, above 10° elevation, with a $\text{GDOP} \leq 5$) for about 50% of the time. There were hour-long gaps with fewer than four common-view satellites.

The standard deviations obtained with both precise orbits and broadcast orbits are shown in Table 3. The 1σ variation using broadcast orbit data was 4.1 ns. When the precise orbit data was employed this fell to 3.7 ns. These results are so good that the 2 ns resolution of the time interval counter used becomes a significant factor! The mean difference between the precise orbit solutions and the broadcast orbit solutions is 0.4 ns. And the improvement between them due to using precise orbit data is less than 1 ns; this suggests that SA was having little effect on the satellites' broadcast orbit data during our measurements. (It has been reported that the principal component of SA recently has been clock dither and that the orbital component has been relatively weak.) Figure 2 shows the time transfer results when using the poorer, broadcast, orbit data.

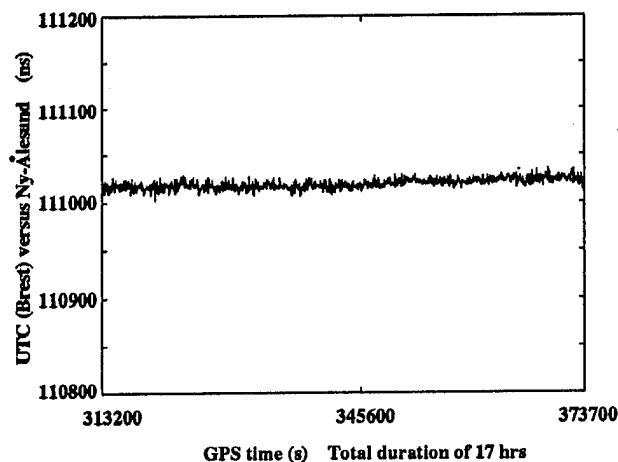


Figure 2: DGPS time transfer from Ny-Ålesund to Brest using broadcast orbit data. The positions of both stations are assumed to be fixed. The 1σ variation is only 4.1 ns.

Summary of the results

We have demonstrated that both the PSP and DGPS time transfer methods satisfy the requirements set out in the introduction to this paper (7 m in position and 20 ns in time, 1σ), with some margin in hand. Thus we consider both methods to be excellent candidates for our application.

We have ignored the existence of ionospheric delays in our PSP solutions, and got away with this because of the favourable conditions at the current point in the solar cycle. We will certainly develop a satisfactory way of estimating the ionospheric delays if we conduct further PSP time transfers in the future. DGPS time transfer is much less affected by atmospheric delays.

The NovAtel receiver we used performed very satisfactory. We still have left to assess its long-term timing stability.

Our next objective is to demonstrate time transfer, using these techniques, on a ship. We chose to conduct the experiment in two stages, employing a stationary receiver for the first because it makes the measurements much simpler. However, there are strong reasons for arguing that the results are also valid for time transfer to a moving vehicle: we have demonstrated that we can achieve timing accuracies commensurate with the positioning accuracies of our GPS receiver. The navigation performance of the receiver when in motion is known to be similar to its static performance [12,13]. In addition, the long term position performance of PSP [8,9] and of DGPS are well known and satisfactory which indicates that the results are reproducible. In addition, apart from being at a fixed location, our stationary measure-

ments were conducted under very realistic conditions, with no antenna choke ring, a poor multipath receiving environment and low SNR.

This paper focuses principally on the stability of time transfers, rather than on absolute accuracy. Achieving absolute timing is a matter of calibrating offsets and thereafter ensuring that receiver delays do not change significantly with time and temperature - by more than some 5 ns in our application. GPS receivers especially designed for time transfer necessarily fulfil this requirement.

CONCLUSIONS

The objective of this investigation was to identify low-cost time transfer techniques suitable for eventual use on a moving ship, a land vehicle or aircraft. The demanding accuracy requirement set was 20 ns, and the technique had to be capable of being implemented in an automatic, unattended, measuring system, and, preferably, offering global coverage. This is a very unusual timing application of GPS.

Two possible techniques have been identified and evaluated: the use of precise orbit and clock values to calculate the accurate time and position post-mission, and DGPS time transfer with an accurate clock at the DGPS reference station.

The results reported here demonstrate that both techniques offer time stability of the order of 10 ns (1σ). A NovAtel GPS receiver was used for the measurements, and its position was assumed to be unknown and was calculated together with the precise time as will be the case in the eventual application. Even better results were achieved when the receiver's position was assumed to be known and fixed. It is anticipated that both techniques are suitable for our application.

Precise orbit and clock solutions give global coverage, and may be used for precise time transfer between GPS receivers at opposite sides of the world, stationary or mobile, in known or unknown locations.

ACKNOWLEDGEMENTS

The authors would like to thank: the Orbit and Attitude Division of the European Space Agency at the European Space Operations Centre, Darmstadt, Germany, for generously providing us with precise clock values; personnel of DCN Brest, France, for providing the facilities and giving helpful assistance during the measurements; and Pat Fenton and Bryan Townsend of NovAtel Communications Ltd., Calgary, Canada, for providing the GPS receiver used for the measurements.

REFERENCES

- [1] Melgård, T.E., Forssell, B., Kjerstad, N. and Lachapelle, G. *Loran-C TD distortion measurements at the Norwegian coast*. WGA, Newport, Rhode Island, 1-4 Nov. 1994.
- [2] Sennedot, D., Minguy, Y., Elies, D. and Carreau, L. *New european prospects for time frequency applications with Loran-C waves*. 8th European Frequency and Time Forum Munic, 9-11 March 1994.
- [3] Lewandowski, W. and Thomas, C. *GPS Time Transfer*. IEEE, Vol. 79, No. 7, July 1991.
- [4] Allan, D.W., Davis, D.D., Weiss, M., Clements, A., Guinot, B., Granveaud, M., Dorenwendt, K., Fisher, B., Hetzel, P., Aoki, S. Fujimoto, M.-K., Charron, L. and Ashby, N. *Accuracy of International Time and Frequency Comparisons Via Global Positioning System Satellites in Common-View*. IEEE Transactions on Instrumentation and Measurement, Vol. IM-34, No. 2, June 1985.
- [5] Allan, D.W. and Thomas, C. *Technical Directives for Standardization of GPS Time Receiver Software*. Metrologia, 31, pp. 69-70, 1994.
- [6] Efratom Time & Frequency Products. *Precision Time and Frequency handbook*. Ball Corporation, 3 Parker, Irvine, California 92718-1605, 1993.
- [7] Schildknecht, T., Beutler, G., Gurtner, W. and Rothacher, M. *Nanosecond GPS Time Transfer using Precise Geodetic Processing Techniques*. Astronomical Institute, University of Berne, Switzerland.
- [8] Lachapelle, G., Klukas, R., Qiu, W., and Melgård, T.E. *Single Point Satellite Navigation Accuracy - What the Future May Bring*. IEEE PLANS'94, Las Vegas, 11-15 April 1994.
- [9] Lachapelle, G., Klukas, R., Roberts, D., Qui, W. and McMillan, C. *One-Meter Level Point Positioning Using Precise Orbit and Timing Information*. ION GPS-94, Salt Lake City, 21-23 September 1994.
- [10] Black, H.D., *An Easy Implemented Algorithm for the Tropospheric Range Correction*. Journal of Geophysical Research, Vol. 83, No. B4, pp. 1825-1828, April 1978.
- [11] RTCM Special Committee No. 104. *RTCM Recommended Standards for Differential Navstar GPS Service, Version 2.1*. Radio Technical Commission For Maritime Services, 655 Fifteenth Street, NW, Suite 300 Washington, D.C. 20005 U.S.A. 3 January 1994.

- [12] Melgård, T.E., Lachapelle, G., and Gehue, H. *GPS Signal Availability in an Urban Area - Receiver Performance Analysis*. IEEE PLANS'94, Las Vegas, 11-15 April 1994.
- [13] Cannon, M.E. and Lachapelle, G. *Analysis of a High Performance C/A Code GPS Receiver in Kinematic Mode*. Navigation, 39, 3, The Institute of Navigation, Alexandria VA, 285-299, 1992.
- [14] Lachapelle, G., Henriksen, J., and Melgård, T.E. *Seasonal Effect of Tree Foliage on GPS Signal Availability and Multipath for Vehicular Navigation*. GPS-94, ION, Salt Lake City, 21-23 Sept. 1994.

WADGPS Ionospheric Correction Model Performance Simulation

Tysen Mueller
Seagull Technology, Inc.

Bob Hamry and Andrew Johnson
Rockwell International

BIOGRAPHY

Mr. Mueller received his BS degree in Physics from Purdue University and his MA degree in Physics from the California State University at Long Beach. He has over 25 years of experience in guidance, navigation, and optimal estimation, specializing in Wide Area DGPS (WADGPS) network design and Automatic Vehicle Location System (AVLS) technology applications. At Seagull Technology, Mr. Mueller is a program manager involved with the development of aircraft collision avoidance technologies under a NASA contract in support of the FAA's 'Free-Flight' program. As president of Teal Consulting, which he founded in 1992, Mr. Mueller designed and evaluated WADGPS network architectures for the US Coast Guard, under a contract through the Volpe National Transportation Systems Center. While at Trimble Navigation, he was program manager for the NASA Phase II SBIR Worldwide DGPS network contract and co-authored a patent for a global ionospheric delay algorithm as well as a WADGPS network algorithm.

Mr. Bob Hamry received his BS degree in Mechanical Engineering from the University of Washington and his MS degree in Applied Mathematics from West Coast University. He has 22 years of experience in aerospace technologies including mathematical modeling of dynamic systems and real time software for hardware-in-the-loop simulations. At Rockwell's System Development Center, he most recently helped design the WADGPS performance simulation. While at Northrop, he was involved with onboard real time applications such as a fighter aircraft control system and Kalman filter mechanization.

Mr. Johnson received his BS degree in Mathematics from California Polytechnic State University, San Luis Obispo, and his MA degree in Applied Mathematics from the University of Maryland. He has over 10 years experience in the development and application of large-scale architecture

performance simulations. He established and continues to manage Rockwell's System Analysis Laboratory, where object-oriented distributed simulation is combined with graphical visualization techniques to improve the credibility and timeliness of the advanced systems engineering trades. He is currently Director, Systems Requirements, at Rockwell's System Development Center, with technical oversight responsibility for Rockwell's System Development Center.

ABSTRACT

A Monte Carlo performance simulation was developed to predict the performance of a Wide Area DGPS ionospheric correction model - the Jet Propulsion Laboratory (JPL) GIPSY/TRIN ionospheric correction software. WADGPS network architectures, such as for the FAA's Wide Area Augmentation System (WAAS), require that ionospheric corrections be computed for a geographic matrix of grid points using dual-frequency (code-less) GPS measurements obtained from a network of reference stations. The output from this performance simulation is the WADGPS Grid Ionospheric Vertical Error (GIVE) and the corresponding User Ionospheric Vertical Error (UIVE).

INTRODUCTION

A performance simulation was developed to predict the performance of a Wide Area DGPS ionospheric correction model. WADGPS ionospheric correction software, such as is required for the FAA's Wide Area Augmentation System (WAAS), computes ionospheric corrections for a geographic matrix of grid points using dual-frequency (code-less) GPS measurements obtained from a network of reference stations. The performance simulation developed by the authors selected the Jet Propulsion Laboratory GIPSY/TRIN ionospheric correction software [1] as a baseline. The output from this performance

simulation is the WADGPS Grid Ionospheric Vertical Error (GIVE) and the corresponding User Ionospheric Vertical Error (UIVE).

The intent of this study was to model and evaluate the performance of a WAAS user operating with a WAAS network computed ionospheric grid, to evaluate the performance of the underlying ionospheric delay model which estimates this grid, and to incorporate this performance model into the WADGPS performance simulation [2]. In addition, the optimality of both the user mapping algorithms and the ionospheric grid model was also determined.

DERIVATION OF THE GRID IONOSPHERIC VERTICAL ESTIMATION (GIVE) ERROR

Due to the limited space available in this paper only a few of the derivations will be presented. The remainder can be found in [3].

Single Measurement for a Single Grid Point

To estimate the ionospheric vertical delay at a grid point based on a dual-frequency GPS slant range ionospheric delay measurement the following equations must be evaluated:

$$\hat{\delta l}_G = w \delta l_m$$

where, $\delta l_m = Q^{-1} \delta r_m = \delta l + Q^{-1} \xi = \delta l + \eta$
 δr_m = measured ionospheric slant range delay
 $Q = \frac{1}{\sqrt{1 - \left(\frac{R_e \cos(EL)}{R_e + h_i} \right)^2}}$, Obliquity Factor

R_e, h_i, EL = Earth radius, ionospheric shell altitude, and elevation angle
 δl = actual ionospheric delay
 $\hat{\delta l}_G$ = Grid point ionospheric vertical estimate
 ξ, η = direct and effective measurement noise
 w = measurement weighting coefficients

The Grid Ionospheric Vertical Error (GIVE) is then obtained as:

$$\varepsilon_G = (\hat{\delta l}_G - \delta l_G) = (w(\delta l + \eta) - \delta l_G)$$

The GIVE variance, σ_ε^2 , is:
 $\sigma_\varepsilon^2 = \text{Var}\{\varepsilon_G\} = E\{\varepsilon_G^2\}$

Let: $\sigma_l^2 = E\{\delta l^2\}$, $\sigma_G^2 = E\{\delta l_G^2\}$, $\sigma_\eta^2 = E\{\eta^2\}$,
and $\rho_{lG} \sigma_l \sigma_G = E\{\delta l \delta l_G\}$,

then: $\sigma_\varepsilon^2 = w^2(\sigma_l^2 + \sigma_\eta^2) - 2w(\rho_{lG} \sigma_l \sigma_G) + \sigma_G^2$

If we select $w = 1$, we obtain the differential GPS ionospheric delay (single-difference) error:

$$\sigma_\varepsilon^2 = (\sigma_l^2 + \sigma_\eta^2) - 2(\rho_{lG} \sigma_l \sigma_G) + \sigma_G^2$$

$$\approx 2\sigma_G^2(1 - \rho_{lG}) + \sigma_\eta^2, \quad \text{if } \sigma_l^2 \approx \sigma_G^2$$

If the former equation is solved for the ionospheric spatial decorrelation function then,

$$\rho_{lG} \approx \left(1 - \frac{(\sigma_\varepsilon^2 - \sigma_\eta^2)}{2\sigma_G^2} \right)$$

Hence, a way to estimate the ionospheric spatial decorrelation function has been derived, based on field data measurements of the standalone GPS (absolute) ionospheric delay grid sigma, σ_G , the differential ion delay sigma, σ_ε , and the measurement noise sigma, σ_η .

Multiple Measurements for Multiple Grid Points

For the general case of multiple measurements used to estimate the grid delays for multiple grid points, the general GIVE covariance matrix is obtained as follows:

$$\hat{\delta l}_G = W \delta l_m = W(\delta l + \eta)$$

which is the estimate of grid iono delays, δl_G

The GIVE error and the GIVE covariance matrix are: $\varepsilon_G = (\hat{\delta l}_G - \delta l_G)$, and $P_G \equiv \text{Cov}\{\varepsilon_G\}$

Then with: $\hat{\delta l}_G = W(\delta l + \eta)$, $C_l \equiv E\{\delta l \delta l^T\}$,
 $C_{lG} \equiv E\{\delta l \delta l_G^T\}$, $C_G \equiv E\{\delta l_G \delta l_G^T\}$, and $R_l \equiv E\{\eta \eta^T\}$

$$P_G = C_G - [W C_{lG} + C_{lG}^T W^T] + W[C_l + R_l]W^T$$

This is the GIVE covariance matrix. The first covariance matrix in this expression is the unknown absolute ionospheric delay grid covariance matrix. The last term is the weighted measured absolute ionospheric delay covariance matrix. Finally, the middle expression consists of the measured-to-grid weighted ionospheric delay covariance matrices.

An optimum choice for the weighting matrix, W , is to choose it such that the GIVE covariance matrix, P_G , is minimized. This leads to the Minimum Variance weighting matrix and corresponding minimum variance GIVE covariance matrix [3]:

$$W = C_{IG}^T [C_I + R_I]^{-1}$$

$$P_G = C_G - C_{IG}^T [C_I + R_I]^{-1} C_{IG}$$

GIPSY/TRIN IONOSPHERIC DELAY KALMAN FILTER

The ionospheric delay problem can be formulated in a slightly different form, as was the case for the GIPSY/TRIN model, developed by the Jet Propulsion Laboratory. Specifically, the measured dual frequency ionospheric delays for the lines-of-sight to the visible GPS satellites are assumed to be direct measurements of the ionospheric grid values in the presence of noise.

$$\delta l_m = H \delta l_G + \eta$$

The state equation is assumed to be:

$$\delta \dot{l}_G = v$$

GIPSY/TRIN uses a distance weighting scheme which is based on relative direct distance weighting using a triangular (not rectangular) sun-fixed grid, to compute the measurement matrix, H . In the ionospheric performance simulation of this paper a rectangular sun-fixed grid was used, without loss of generality.

GIPSY/TRIN Mapping Coefficients

Consider an ionospheric triangular grid 'tile' with vertices: $(0,0)$, (x,y) , and $(2x,0)$ and with an imbedded measurement at: (x_m, y_m) , as illustrated in Figure 1. The GIPSY/TRIN software computes the grid-to-measurement mapping coefficients as follows:

$$\text{or } \delta l_m = h_{GA} \delta l_A + h_{GB} \delta l_B + h_{GC} \delta l_C,$$

$$\text{with, } h_{GA} = \sqrt{\frac{(x_m - x_D)^2 + y_m^2}{(x - x_D)^2 + y^2}}$$

$$h_{GB} = \left(\sqrt{\frac{(x - x_m)^2 + (y - y_m)^2}{(x - x_D)^2 + y^2}} \right) \left(\frac{2x - x_D}{2x} \right),$$

$$h_{GC} = \left(\sqrt{\frac{(x - x_m)^2 + (y - y_m)^2}{(x - x_D)^2 + y^2}} \right) \left(\frac{x_D}{2x} \right)$$

$$\text{and } x_D = x - \left(\frac{x - x_m}{y - y_m} \right) y = \left(\frac{yx_m - xy_m}{y - y_m} \right)$$

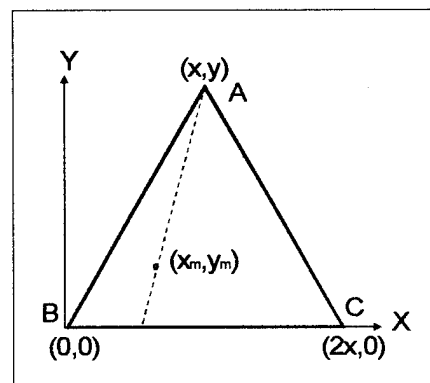


FIGURE 1 GIPSY/TRIN TRIANGULAR GRID

Optimum Mapping Coefficient:

An alternate possibility to the direct distance weighting used in the GIPSY/TRIN code measurement matrix is to derive the 'optimum' measurement matrix, H , as follows:

For a single measurement and 4 grid points:

$$\delta l_{m1} = \hat{h}_{IG}^T \delta l_G + \eta_1 = \delta l_1 + \eta_1$$

$$\text{or defining, } \delta \hat{l}_1 = \hat{h}_{IG}^T \delta l_G$$

then the estimation error:

$$\epsilon_1 \equiv (\delta \hat{l}_1 - \delta l_1) = (\hat{h}_{IG}^T \delta l_G - \delta l_1)$$

or with:

$$C_G = E\{\delta l_G \delta l_G^T\}, \quad C_{IG} = E\{\delta l_G \delta l_1\}, \quad E\{\delta l_1^2\} = \sigma_1^2$$

$$\sigma_{\epsilon_1}^2 = \hat{h}_{IG}^T C_G \hat{h}_{IG} - 2 \hat{h}_{IG}^T C_{IG} + \sigma_1^2$$

Hence, minimizing the estimation error variance, $\sigma_{\varepsilon_1}^2$, leads to the Minimum Variance Measurement Vector:

$$\hat{h}_{1G} = C_G^{-1} C_{1G}$$

If this is then extended to the general case of multiple measurements and multiple grid points:

$$\hat{H} = C_{1G} C_G^{-1}$$

which is the Minimum Variance measurement matrix

Hence, the optimum measurement matrix is shown to be a direct function of the measured-to-grid covariance matrix and inversely dependent on the grid point covariance matrix.

Let us check how the TRIN weighting coefficients compare to the optimum measurement matrix weighting coefficients and the inverse distance weighting coefficients. Consider a single ionospheric delay measurement located anywhere on a vertical line between: (x,0) and (x,y) of a (7° x 7°) equilateral triangle. Then using the three alternate algorithms, we obtain the weighting coefficient for the three grid points shown in the two plots of Figure 2.

What these two sets of curves show is that the GIPSY/TRIN and the optimum measurement matrix weighting coefficients are nearly identical. The inverse distance weighting coefficient, however, is not as optimum. Hence the GIPSY/TRIN weighting coefficients are nearly optimum for a triangular grid.

Kalman Filter Implementation

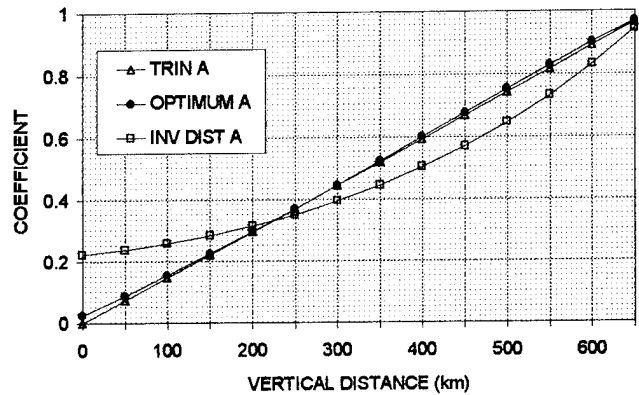
The general state and covariance propagation equations for the GIVE error are given by:

$$\begin{aligned} \varepsilon_n &= \varepsilon_{n-1} + u_{n-1} n \\ P_n^- &= P_{n-1}^- + Q_{n-1} \end{aligned}$$

The general error measurement and covariance update equations are given by:

$$\begin{aligned} \varepsilon_k^+ &= \varepsilon_k^- + K_k [H_k \varepsilon_k^- + v_k] \\ K_k &= P_k^- H_k^T [H_k P_k^- H_k^T + R_k]^{-1} \\ P_k^+ &= [I - K_k H_k] P_k^- = \left[(P_k^-)^{-1} + H_k^T R_k^{-1} H_k \right]^{-1} \end{aligned}$$

GRID A WEIGHTING COEFFICIENT



GRID B & C WEIGHTING COEFFICIENTS

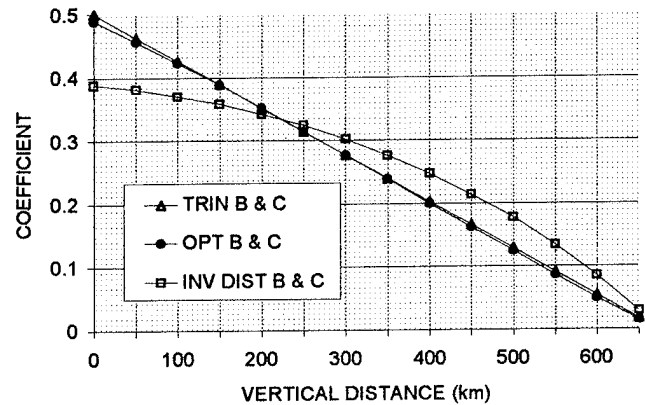


FIGURE 2 TRIANGULAR GRID WEIGHTING COEFFICIENT COMPARISON

When the optimum measurement matrix is used:

$$\begin{aligned} P_{G,k}^+ &= [1 - K_k H_k] P_{G,k}^- = \left[1 - K_k [C_{1G,k} C_{G,k}^{-1}] \right] P_{G,k}^- \\ \text{or, } P_{G,k}^+ &= \left[P_{G,k}^{(-1)} + [C_{G,k}^{-1} C_{1G,k}^T] R_k^{-1} [C_{1G,k} C_{G,k}^{-1}] \right]^{-1} \end{aligned}$$

The grid estimation error covariance matrix can be initialized as: $P_{G,0}^- = C_G$, since at $t = t_0$ there is no grid estimate.

USER IONOSPHERIC VERTICAL ERROR (UIVE) DERIVATION

A complete derivation of the following equations is found in [4].

Single Satellite Calculation

For a user who obtains an ionospheric delay estimate for a single satellite line-of-sight based on the nearest four grid point ionospheric delay estimates:

$$\begin{aligned}\delta \hat{U}_k &= \underline{v}_k^T \delta \hat{I}_{G,k} = \underline{v}_k^T (\delta I_{G,k} + \varepsilon_{G,k}) \\ \text{or with } \varepsilon_{G,k} &\equiv (\delta \hat{I}_{G,k} - \delta I_{G,k}) \\ \text{then } \delta \hat{I}_{G,k} &= \delta I_{G,k} + \varepsilon_{G,k}\end{aligned}$$

The user k'th correction estimation error (UIVE) is:

$$\varepsilon_{U,k} = (\delta \hat{U}_k - \delta I_{U,k}) = \underline{v}_k^T (\delta I_{G,k} + \varepsilon_{G,k}) - \delta I_{U,k}$$

The UIVE variance is:

$$\sigma_{\varepsilon,k}^2 = E\{\varepsilon_{U,k}^2\} = E\left\{\left(\underline{v}_k^T \delta \hat{I}_{G,k} - \delta I_{U,k}\right)\left(\underline{v}_k^T \delta \hat{I}_{G,k} - \delta I_{U,k}\right)^T\right\}$$

$$\begin{aligned}\text{Hence with: } \sigma_{U,k}^2 &\equiv E\{\delta I_{U,k}^2\}, \quad C_{G,k} \equiv E\{\delta I_{G,k} \delta I_{G,k}^T\}, \\ P_{G,k} &\equiv E\{\varepsilon_{G,k} \varepsilon_{G,k}^T\}, \text{ and } C_{UG,k} \equiv E\{\delta I_{G,k} \delta I_{U,k}\}\end{aligned}$$

$$\sigma_{\varepsilon,k}^2 \approx \left(\sigma_{U,k}^2 - 2\underline{v}_k^T C_{UG,k} + \underline{v}_k^T C_{G,k} \underline{v}_k\right) + \underline{v}_k^T P_{G,k} \underline{v}_k$$

$$\text{Now for: } \sigma_{U,k}^2 \approx \sigma_{G,k}^2,$$

$$\sigma_{\varepsilon,k}^2 = \sigma_{U,k}^2 \left[1 - 2\underline{v}_k^T \underline{P}_{UG,k} + \underline{v}_k^T [\underline{P}_{GG}]_k \underline{v}_k\right] + \underline{v}_k^T P_{G,k} \underline{v}_k$$

$$\text{where } \underline{P}_{UG,k} \equiv \begin{pmatrix} \rho_{G1,U} \\ \rho_{G2,U} \\ \rho_{G3,U} \\ \rho_{G4,U} \end{pmatrix}_k$$

$$\text{and } [\underline{P}_{GG}]_k \equiv \begin{bmatrix} 1 & \rho_{G1,G2} & \rho_{G1,G3} & \rho_{G1,G4} \\ \rho_{G1,G2} & 1 & \rho_{G2,G3} & \rho_{G2,G4} \\ \rho_{G1,G3} & \rho_{G2,G3} & 1 & \rho_{G3,G4} \\ \rho_{G1,G4} & \rho_{G2,G4} & \rho_{G3,G4} & 1 \end{bmatrix}_k$$

Hence, the user's k'th ionospheric vertical error (UIVE) variance is approximately equal to the spatial decorrelation error between the user's k'th ionospheric delay and the surrounding four grid point ion delays, plus the GIVE covariance matrix for those grid points.

User Optimum Grid Weighting Coefficients

The user weighting coefficient vector, \underline{v}_k , can be selected in a number of ways for a rectangular ionospheric grid. For a user ionospheric pierce-point

located at (x,y) relative to the rectangular grid, illustrated in the Figure 3 below.

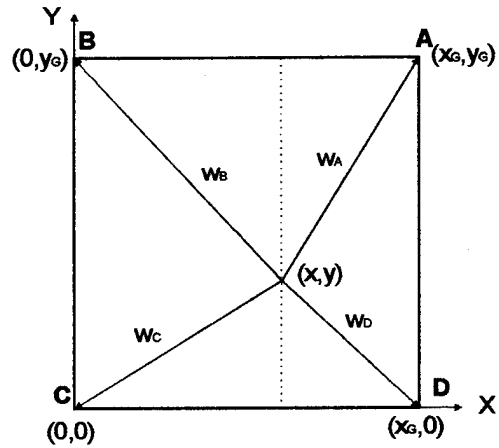


FIGURE 3 RECTANGULAR IONOSPHERIC GRID

The direct distance weighting coefficients for a rectangular grid are obtained as follows:

$$\begin{aligned}w_{DD,A} &= \left(\frac{\hat{w}_A}{w}\right), \quad w_{DD,B} = \left(\frac{\hat{w}_B}{w}\right), \quad w_{DD,C} = \left(\frac{\hat{w}_C}{w}\right), \\ \text{and } w_{DD,D} &= \left(\frac{\hat{w}_D}{w}\right), \text{ with } w = (\hat{w}_A + \hat{w}_B + \hat{w}_C + \hat{w}_D) \\ \text{and, } \hat{w}_A &= xy, \quad \hat{w}_B = (x_G - x)y, \quad \hat{w}_C = (x_G - x)(y_G - y), \\ \text{and, } \hat{w}_D &= x(y_G - y)\end{aligned}$$

Let us compare these direct distance weighting coefficients relative to the optimum, inverse distance, and the WAAS Specification suggested grid weighting coefficients [5]. Assume that the user pierce-point (x,y) is located on the dotted vertical line, which is itself located half-way between lines BC and AD.

As (x,y) varies between (280 km, 0) and (280 km, 560 km) we obtain the Grid Point C weighting coefficient curves of Figure 4 below. The grid coordinates are assumed to be $(x_G, y_G) = (560 \text{ km}, 560 \text{ km})$ which correspond to a $5^\circ \times 5^\circ$ grid at the equator. This figure shows that the direct distance weighting coefficients are nearly identical to the optimum coefficients. The inverse distance and WAAS Specification weighting coefficients, in turn, appear less optimum.

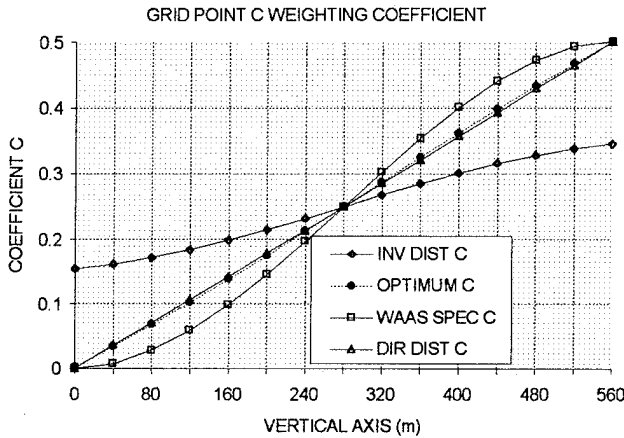


FIGURE 4 RECTANGULAR GRID WEIGHTING COEFFICIENT COMPARISON

Multiple Satellite Tracking

If the user tracks k satellites and, hence, obtains k pseudorange measurements, he has to compute and apply k pierce-point ionospheric estimates to his raw measurements.

Stacking the k correction estimates into a vector:

$$\hat{\underline{\delta l}}_U = \begin{pmatrix} \underline{v}_1^T (\underline{\delta l}_{G,1} + \underline{\varepsilon}_{G,1}) \\ \vdots \\ \underline{v}_k^T (\underline{\delta l}_{G,k} + \underline{\varepsilon}_{G,k}) \end{pmatrix} = \underline{V} (\underline{\delta l}_G + \underline{\varepsilon}_G)$$

The user correction error (UIVE) vector, $\underline{\varepsilon}_U$, is:

$$\underline{\varepsilon}_U = (\hat{\underline{\delta l}}_U - \underline{\delta l}_U) = [\underline{V} (\underline{\delta l}_G + \underline{\varepsilon}_G) - \underline{\delta l}_U]$$

where,

$\underline{\delta l}_G$ = the iono delay vector for all grid points

$\underline{\delta l}_U$ = the iono delay vector for the user's k pierce-points

$\underline{\varepsilon}_G$ = the GIVE vector for all grid points

\underline{V} = generalized user weighting matrix which relates all the grid points to the user's k pierce-points

For non-overlapping grid rectangles:

$$\underline{V} = \begin{bmatrix} \underline{v}_1^T, 0^T, \dots, 0^T \\ 0^T, \underline{v}_2^T, \dots, 0^T \\ \vdots \\ 0^T, 0^T, \dots, \underline{v}_k^T \end{bmatrix}$$

The user iono correction estimation error (UIVE) covariance matrix, \underline{P}_U , is:

$$\begin{aligned} \underline{P}_U &= \text{Cov}\{\underline{\varepsilon}_U\} \\ &= E\left\{(\underline{V}(\underline{\delta l}_G + \underline{\varepsilon}_G) - \underline{\delta l}_U)(\underline{V}(\underline{\delta l}_G + \underline{\varepsilon}_G) - \underline{\delta l}_U)^T\right\} \\ \text{or,} \\ \underline{P}_U &\approx [\underline{C}_U - (\underline{V}\underline{C}_{GU} + \underline{C}_{GU}^T \underline{V}^T) + \underline{V}\underline{C}_G \underline{V}^T] + \underline{V}\underline{P}_G \underline{V}^T \end{aligned}$$

where

$$\begin{aligned} E\{\underline{\delta l}_G \underline{\delta l}_U^T\} &= \underline{C}_{GU} = \underline{C}_{UG}^T, & E\{\underline{\delta l}_G \underline{\delta l}_G^T\} &= \underline{C}_G, \\ \text{and, } E\{\underline{\varepsilon}_G \underline{\varepsilon}_G^T\} &= \underline{P}_G \end{aligned}$$

The UIVE covariance matrix is seen to be a function of the stand-alone user ionospheric delay covariance matrix, the weighted stand-alone grid ionospheric delay covariance matrix, a weighted two-term grid-to-user covariance matrix expression plus the weighted GIVE covariance matrix. If the user and grid points are the same, and the weighting coefficients become zero or unity, as is appropriate, the expression within the brackets becomes zero.

PERFORMANCE SIMULATION RESULTS

This section presents the WADGPS GIVE calculation results from the performance simulation for a $(5^0 \times 5^0)$ grid spanning the continental United States. The grid is initialized with ionospheric delay estimates from the Bent model which leads to an initial delay GIVE sigma of one meter, based on the statistics presented in Appendix A. The spatial decorrelation error function used is the annual function, also presented in Appendix A.

A WAAS network of 23 GPS reference stations, 20 of which are located in the 48 contiguous states, was assumed. These perform dual-frequency slant range ionospheric delay measurements to all GPS satellites which have a local elevation angle greater than five degrees. These slant range ionospheric delays are converted to an equivalent vertical delay and each measurement is used to update the nearest four surrounding grid points.

Between measurement updates, every 5 minutes, the Kalman filter propagates the last measurements forward in time to the next measurement time point with process noise. Hence, if at the next measurement time point, a grid point does not obtain a nearby measurement, its GIVE error continues to increase due to the process noise. The

Kalman filter operates in a sun-fixed coordinate system which moves westward at the rate of fifteen degrees of geodetic longitude per hour.

The measurement errors are summarized in Table 1:

TABLE 1: MEASUREMENT ERRORS

ERROR	MAGNITUDE (1σ)
Net Inter-Frequency Bias	0.16 m
Measurement Noise	0.10 m
Process Noise	$0.67 \text{ m/hr}^{0.5}$

The inter-frequency bias error is the combined error from the satellite and receiver dual-frequency bias errors. It is the net error following periodic (daily) estimates of the inter-frequency bias using the GIPSY/TRIN code with data collected during the previous day. The measurement noise statistics, which are assumed to vary inversely to the sine of the elevation angle, are representative for a network of dual-frequency Rogue receivers. The process noise estimate, obtained from JPL, is based on the observed field data.

The performance simulation was run for eight hours. A typical contour plot of the GIVE sigmas every $5^\circ \times 5^\circ$ is presented in Figure 5. The continental US (CONUS) is loosely contained within the rectangular region between -125° and -70° longitude and 25° and 50° latitude. The ionospheric horizon, however, extends out by approximately 14° from a reference station with a 5° mask angle if it is located at the equator. Hence, the CONUS region would need to be extended by 14° along the geographic boundaries to account for any users who are located within the CONUS region but may be tracking low elevation satellites outside of this region.

Figure 5 shows the best GIVE statistics for the CONUS region and the regions to the west and south. Both regions benefit from the westward motion of the sun-fixed grid.

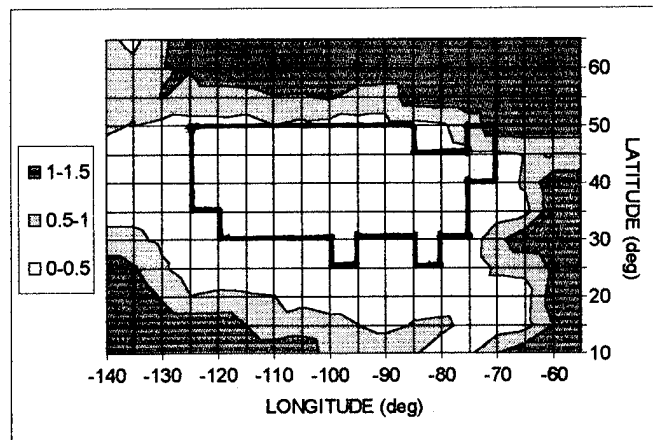


FIGURE 5 GRID IONOSPHERIC VERTICAL ERROR (GIVE) SIGMA (2 Hours)

Another way to look at the Kalman filter GIVE sigma's, is by examining their time history for selected cities. This is shown in the three figures comprising Figure 6 - 8, which present eight hour time histories for three different latitude regions. Figure 6 presents three northern latitude cities, Figure 7 presents three mid-latitude cities, and finally, Figure 8 presents three southern latitude cities. As can be seen, the northern latitude cities have more dynamic and larger GIVE sigmas than do the other cities.

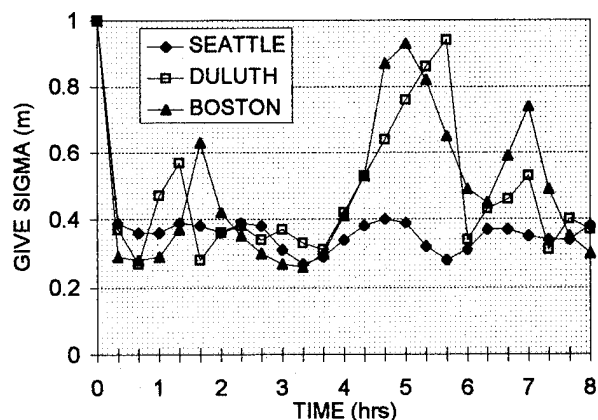


FIGURE 6 GIVE SIGMA HISTORIES FOR NORTHERN LATITUDE CITIES

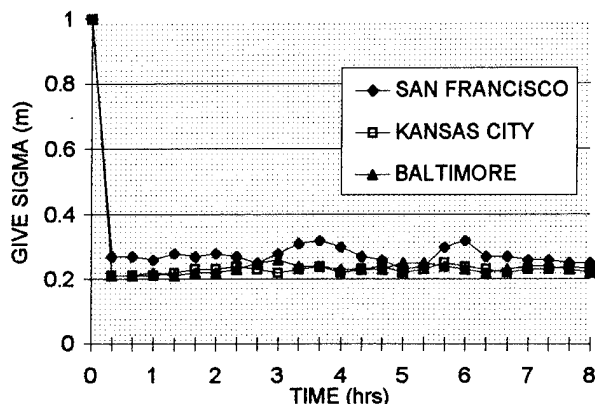


FIGURE 7 GIVE SIGMA HISTORIES FOR MID-LATITUDE CITIES

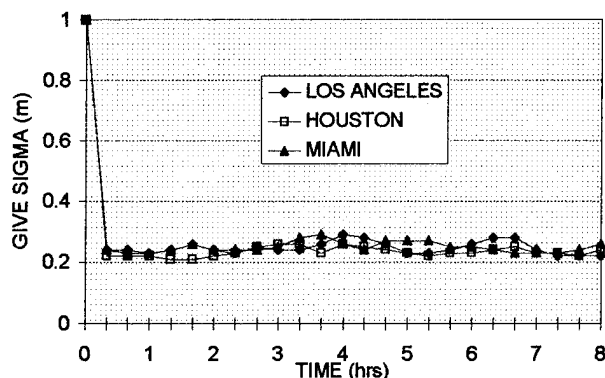


FIGURE 8 GIVE SIGMA HISTORIES FOR SOUTHERN LATITUDE CITIES

CONCLUSIONS

A detailed ionospheric delay performance simulation has been derived which takes into account the standard dual-frequency GPS receiver measurement errors. It also formally includes the spatial decorrelation errors between the measurement point, the grid point, and the user line-of-sight. Using the JPL GIPSY/TRIN global ionospheric delay model as an example, the merits of using a Kalman filter have been examined. In addition to the GIPSY/TRIN direct distance measurement weighting, an optimal measurement matrix has been derived. This optimal measurement matrix is found to be a function of the ionospheric spatial decorrelation function.

Separately, an optimum user grid weighting algorithm was obtained and compared to the direct distance, inverse distance, and FAA WAAS

specification weighting algorithm. It was found that the direct distance weighting was nearly identical to the optimum weighting.

The benefits of using a Kalman filter which operates in a sun-fixed grid, were explored. Using the ionospheric performance simulation, the GIVE statistics were computed for a CONUS earth-fixed rectangular grid. Simulated measurements were obtained from a WAAS network consisting of 23 reference stations, of which 20 were assumed to be located within CONUS. It was concluded that stable GIVE statistics can be expected for most of the CONUS grid points, except for some of the northern locations. This was illustrated using eight hour time histories for selected cities within the CONUS region.

ACKNOWLEDGMENTS

The authors wish to acknowledge the management of Rockwell International for the funding provided to perform the majority of this research.

REFERENCES

1. Mannucci, A.J., et al, "A New Method for Monitoring the Earth's Ionospheric Total Electron Content Using the GPS Global Network," ION GPS-93, Salt Lake City, UT, September 1993.
2. Johnson, A., et al, "Space-Based Navigational System Accuracy Performance Model," Proceedings of the National Technical Meeting, The Institute of Navigation, Anaheim, CA, January 1995.
3. Mueller, T., "WADGPS Network Ionospheric Performance Model Derivation," Teal Consulting, March 1995.
4. Mueller, T., "User Ionospheric Estimation Error (UIE) Performance Model," Teal Consulting, March 1995.
5. "Wide Area Augmentation System (WAAS) Specification," Federal Aviation Administration, June 1994.
6. Klobuchar, J.A., et al, "Potential Ionospheric Limitations to Wide-Area Differential GPS," Proceedings of ION GPS-93, Salt Lake City, UT, September 1993.
7. Coco, D.S., et al, "Mitigation of Ionospheric Effects for Single Frequency GPS Users," Applied Research Laboratories, The University of Texas at Austin

8. Newby, S.P., et al, "Ionospheric Modeling for Single Frequency Users of the Global Positioning System, A Status Report," The Institute of Navigation Conference: GPS-90, September 1990

APPENDIX A: DIFFERENTIAL IONOSPHERIC DELAY FIELD DATA

The DGPS ionospheric delay estimation error can be obtained from field data measurements, such as performed by Klobuchar [6], as summarized in Table A-1:

TABLE A-1 IONOSPHERIC RANGE DELAY DIFFERENCES
(Daytime Hours: 1100-1700 hrs, 1992-93, Meters)

CUMULATIVE PROBABILITY [6]				Equivalent
Distance	Quarter	1 %	99 %	One Sigma*
434 km	Winter	-1.3	1.6	0.62
	Summer	-1.3	1.0	0.49
	Equinox	-1.5	1.3	0.60
	Annual			0.57
805 km	Winter	-2.3	2.4	1.01
	Summer	-1.2	1.2	0.52
	Equinox	-3.0	1.9	1.05
	Annual			0.89
1,238 km	Winter	-3.1	2.8	1.27
	Summer	-1.9	1.7	0.77
	Equinox	-4.8	2.4	1.54
	Annual			1.24
1,586 km	Winter	-3.9	4.4	1.78
	Summer	-1.9	2.1	0.86
	Equinox	-5.1	3.5	1.85
	Annual			1.56

The equivalent one sigma ionospheric delay can be derived from the difference between the 99% and the 1% cumulative probability data. This corresponds to data between -2.326σ and $+2.326 \sigma$, if the statistics are normally distributed. When this one sigma data is fit to the following curve for σ_e , the coefficients of Table A-2 are obtained.

$$\sigma_e(d) = \left(\frac{|d|}{D} \right)^\gamma$$

TABLE A-2 DIFFERENTIAL IONOSPHERIC DELAY

CURVE PARAMETER ESTIMATES
(Based on Table A-1 data)

SEASON	DISTANCE, D (km)	EXPONENT, γ
Winter	816	0.772
Equinox	770	0.876
Summer	2380	0.460
Annual	916	0.769

The ionospheric spatial decorrelation function, ρ_{IG} , was previously derived in the main body of this paper and found to be:

$$\rho_{IG}(d) \approx \left(1 - \frac{\sigma_e^2(d) - \sigma_e^2(0)}{2\sigma_G^2} \right)$$

where $\sigma_e \approx \sigma_e(0)$

The differential ionospheric delay is obtained from Table A-2 while the stand-alone ionospheric delay statistics, σ_G , are summarized in Tables A-3:

TABLE A-3: CUMULATIVE RANGE IONOSPHERIC DELAY STATISTICS AT HANSCOM, MA
(Daylight Hours: 1100-1700 hrs, 1992-1993, Meters)

CUMULATIVE PROBABILITY [6]				Equivalent	
Season	1%	50%	99%	Sigma*	RMS.
Winter	1.8	6.0	17.6	3.4	6.9
Equinox	1.0	5.3	18.0	3.6	6.4
Summer	1.4	5.0	14.7	2.9	5.8
Annual		5.4		3.3	6.3

* $(99\% - 1\%)/(4.65 \sigma)$

With the statistics of Tables A-3, and the curve fit parameters of Table A-2, we can obtain the following ionospheric spatial decorrelation function curve:

$$\rho_{IG}(d) \approx \left[1 - \frac{1}{2\sigma_G^2} \left(\frac{|d|}{D} \right)^{2\gamma} \right]$$

Hence, if we select the annual statistics (eg: $\sigma_G = 6.3$ m (rms), $D = 916$ km, and $\gamma = 0.769$), we obtain:

$$\rho_{IG}(d) \approx \left[1 - \left(\frac{1}{79} \right) \left(\frac{|d|}{916 \text{ km}} \right)^{1.54} \right],$$

The GIPSY/TRIN code initializes the ionospheric grid estimates, prior to any measurement updates, using the Bent Ionospheric Model. Hence, statistics on the accuracy of the Bent model are also of interest and are summarized in Table A-4 [8]:

TABLE A-4 BENT MODEL vs. ACTUAL
IONOSPHERIC DELAYS*(rms.)

LATITUDE (deg)	SUNSPOT CYCLE		
	High (January 1980)	Medium (November 1982)	Low (June 1986)
47	1.23 m	1.35 m	0.19 m
38	1.12 m	1.38 m	0.24 m
26	1.08 m	1.27 m	0.41 m

* Hourly measurements for month differenced with
Bent monthly average

Development of Real-Time Algorithms to Estimate the Ionospheric Error Bounds for WAAS*

Robert Conker, M. Bakry El-Arini, and Thomas Albertson
The MITRE Corporation

John Klobuchar
USAF Phillips Laboratory

Patricia Doherty
Boston College

BIOGRAPHIES

Robert S. Conker is a Member of the Technical Staff of the MITRE Corporation. His recent work is on estimating errors of ionospheric delays related to the WAAS. Other work has included modeling and simulation of automated air traffic control systems, and work on computer vision and pattern recognition problems. He received a Ph.D. and M.S. in Computer Science from the Iowa State University and an A.B. in Mathematics from Duke University.

M. Bakry El-Arini is a Lead Engineer at the MITRE Corporation. He has contributed to a number of studies involving GPS, MLS, and LORAN-C navigation and landing systems for the FAA. He received his Ph.D.EE and M.S.EE from the University of Manitoba, Canada, and B.S.EE from Ain Shams University, Cairo, Egypt.

Thomas W. Albertson is a Technical Aide for the MITRE Corporation. His major concentration is software engineering with a focus on GUI (graphical user interface) development and Client/Server issues. He is currently working toward a masters degree in Computer Science and Information Systems at American University.

John A. Klobuchar is a senior Physical Scientist at the Ionospheric Effects Division of the Air Force Phillips Laboratory. He is an international expert on ionospheric total electron content, and ionospheric effects on Air

Force systems. He is a Fellow of the IEEE and a consultant to numerous Air Force and DOD programs.

Patricia H. Doherty is a Research Analyst at the Institute for Space Research at Boston College. She has extensive experience in analysis of total electron content from world-wide stations. She uses analytical models of the earth's ionosphere to perform scientific studies of the variability of electron content. She has a BS in Mathematics from the University of Massachusetts, Amherst.

ABSTRACT

The Federal Aviation Administration (FAA) Satellite Program Office, AND-510, is developing a Wide Area Augmentation System (WAAS) based on the Global Positioning System (GPS) and intended to support enroute through precision approach flight operations down to the lowest Category I (CAT I) decision height (DH) of 200 feet. In the WAAS, a vector of corrections to the GPS signal-in-space, including components for ionosphere, clock, and ephemeris errors, is sent to the user via geostationary earth orbiting (GEO) communications satellites (e.g., INMARSAT). Also sent to the user is a bound on the post-correction ionospheric vertical error at each point of an ionospheric delay correction grid covering the service area. Using these bounds, the user then calculates a vertical error bound on his own ionospheric pierce points. This paper presents

* This paper is based on system analysis studies performed by the Center for Advanced Aviation System Development (CAASD), the MITRE Corporation and the Air Force Phillips Laboratory for the FAA Satellite Program Office (AND-510). This paper reflects the views of the authors, who are responsible for the accuracy of the facts, analyses and suggestions presented herein, and does not reflect the official views or policy of the FAA.

© 1995 The MITRE Corporation

This work contains technical data that is the copyright work of The MITRE Corporation. All rights reserved. The technical data was produced for the U. S. Government under Contract Number DTFA01-93-C-00001, and is subject to Federal Acquisition Regulation Clauses 52.227-14, Rights in Data-General, and 52.227-17, Rights in Data-Special Works. Use or distribution of this technical data is strictly limited to the U. S. Government or those contractors in performance of a contract on behalf of the U. S. Government.

real-time algorithms developed to estimate these bounds and associated service areas based on assumptions regarding the proposed WAAS ground system configuration and GPS/GEO constellation. The ionospheric error bounds and their methods of determination are important elements in the development of an overall integrity algorithm for the WAAS.

INTRODUCTION

The Federal Aviation Administration (FAA) Satellite Program Office, AND-510, is developing a Wide Area Augmentation System (WAAS) based on the Global Positioning System (GPS) and intended to support enroute through precision approach flight operations down to the lowest Category I (CAT I) decision height (DH) of 200 feet. In the WAAS, a vector of corrections to the GPS signal-in-space, including components for ionosphere, clock, and ephemeris errors, is sent to the user via geostationary earth orbiting (GEO) communications satellites (e.g., INMARSAT). Also sent to the user is a bound on the post-correction ionospheric vertical error at each of the ionospheric grid points (IGPs) of an ionospheric delay correction grid covering the service area. The ionospheric error bound at each IGP is called the grid ionospheric vertical error (GIVE). Using the ionospheric delay values at each IGP, the user interpolates to determine the estimate of ionospheric delay at his ionospheric pierce point (IPP). Using the appropriate GIVE values, the user also calculates a vertical error bound on his own IPPs. This error bound is called the user ionospheric vertical error (UIVE). According to the WAAS Specification [1], service availability is dependent upon GIVE values being ≤ 2.0 m for the initial WAAS and ≤ 1.5 m for the end-state WAAS. Any UIVE calculated from the GIVEs must bound the user's post-correction vertical ionospheric error with a probability of 0.999. Finally the user calculates a conservative bound of his vertical position error (VPE) using his calculated UIVE. The requirement for this bound is $VPE \leq 19.2$ m¹.

This paper presents real-time algorithms developed to: 1) estimate the GIVE value to be included in the WAAS broadcast, and 2) determine the resultant UIVEs expected to be calculated at the user receiver, based on actual ionospheric data collected at key points in the Conterminous US (CONUS) over a period of months. The GIVE and UIVE bounds and their methods of determination are important elements in the development of an overall integrity algorithm for the WAAS.

The GIVE and UIVE algorithms have been developed and tested using P-code data measured from five mini-rogue L1/L2 dual-frequency GPS receivers on the East Coast of CONUS over a nine month period. This period is characterized by a generally "quiet" ionosphere with periodic, major and severe geomagnetic storm activity.

L1/L2 receiver and satellite biases [2] are included in the estimation. Based on the availability of in-tolerance UIVE and GIVE values and assumptions regarding the proposed WAAS ground system topography and GPS/GEO constellation, a service volume for ionospheric corrections for the initial WAAS is defined.

PURPOSE

The purpose of this analysis is to develop real-time algorithms to estimate GIVE and UIVE values such that they meet the requirements for the WAAS. Data from five sites is used to construct an ionospheric grid with estimates of ionospheric vertical delay along with GIVE values. One of the sites is selectively employed as a user and its dual-frequency measurements at each of its IPPs are used as truth for determining how effective the numerical estimates are. The results are then extrapolated to the proposed WAAS architecture in order to determine if the WAAS availability requirements can be met.

A SIMPLIFIED ARCHITECTURE FOR WAAS IONOSPHERIC FUNCTIONS

Figure 1 shows a simplified architecture for WAAS ionospheric functions. In this figure there are three groups of receivers with their associated antennas and weather stations, one WAAS master station (WMS), one ground earth station (GES), GPS and GEO satellites. The three groups of receivers do not have to be co-located; in fact, it is preferable that they are separated such that greater diversity in viewing the ionosphere is provided. The first group consists of n_1 ($=24$ for initial WAAS) wide-area reference stations (WRSs). Each WRS consists of one L1/L2 dual-frequency codeless GPS receiver, L1/C² GEO receivers, and weather stations. The main function of these receivers is to collect the pseudorange (PR) and carrier phase data for each visible GPS and GEO satellite at L1, L2, and C frequency bands and send this data to the WMS. In addition, weather data collected by the sensors is sent to the WMS. The WMS will use this data to calculate the carrier smoothed vertical ionospheric delays for each GPS and GEO satellite IPP using a Kalman filter. Then the WMS uses the calculated vertical ionospheric delays at the WRS IPPs to calculate the vertical ionospheric delays for each IGP of the ionospheric

¹ The WAAS Specification was recently changed to eliminate the 2 m initial WAAS and 1.5 m end-state WAAS GIVE bounds. This allows greater flexibility in meeting the VPE requirement. Nevertheless, some initial analysis has shown that in order to satisfy the VPE requirement, GIVE values on the order of 2 m or less are needed.

² The C-band receiver for GEO satellites is optional. It could be used with the L1 receiver to estimate the ionospheric delay for the GEO's IPPs.

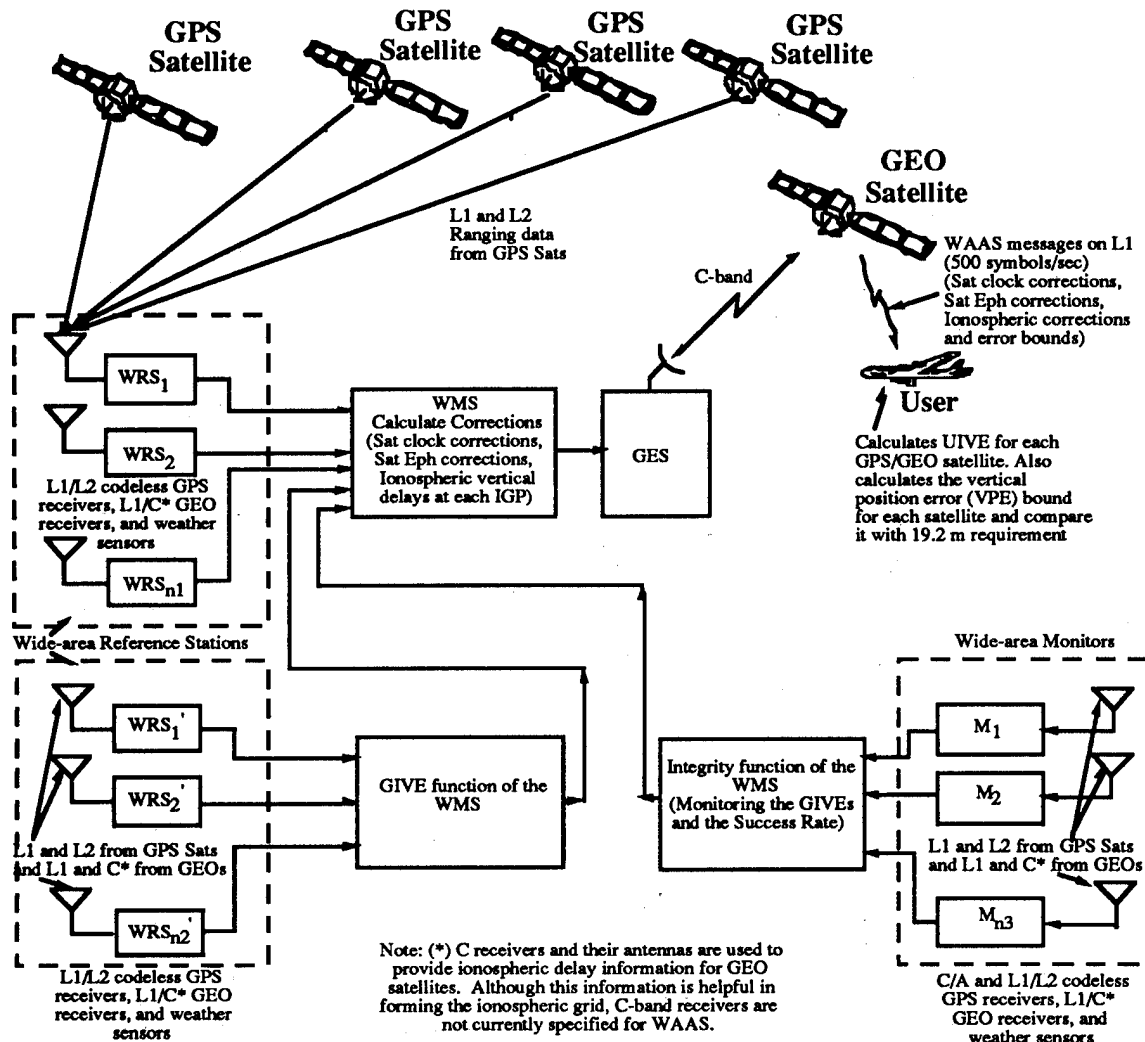


Figure 1. A simplified architecture for WAAS ionospheric functions.

grid. The weather information is used to calculate the tropospheric delay at each WRS location. The slant ionospheric and tropospheric delays for each satellite are subtracted from the PR measurement for the same satellite. The residual PRs will be used to calculate the satellite clock and ephemeris correction. The latter two corrections are not discussed in this paper. The second group of receivers consists of n_2 stations. For initial WAAS $n_2 = n_1 = 24$, and this group of receivers will be co-located with the WRSs. Each station consists of L1/L2 dual-frequency codeless GPS receivers, and L1/C GEO receivers in addition to the weather sensors. These receivers send their measurements to the WMS in a similar manner to the first group. The WMS will use this data and the already calculated vertical delays of the ionospheric grid to calculate the GIVE for each of the IGP of the ionospheric grid. The methodology of the GIVE calculation is shown in a separate section in this paper.

The GIVEs will be used by the users to calculate UIVEs which are specified to bound vertical ionospheric errors with a probability of 0.999. A third group of n_3 ($\leq n_1$) receivers monitors the success rate of this error bound. Each station consists of an L1-C/A code GPS receiver, an L1/L2 dual-frequency codeless GPS receiver, an L1-C/A code GEO receiver, an optional C-band GEO receiver, and weather sensors. These monitors essentially act as users. Their measurements will be sent to the WMS. The WMS compares the vertical ionospheric errors from the measured data of these monitors to the calculated UIVEs. If the errors at any monitor exceed the UIVE, the maximum excess above UIVE will be added to each GIVE. During the next update period, the WMS will add the maximum excess of monitor errors above UIVE to each GIVE of the region which contains that monitor. This is referred to as a closed-loop system. As will be seen in the results in this paper, this closed-loop

monitoring system is expected to only rarely increase the GIVEs (and nominally by a few centimeters) to increase the success rate. Just as the second group of receivers determined how well the grid was representing ionospheric delay, this third group of receivers determines how effective the error bounds are.

DEVELOPMENT CONSTRAINTS

The development of the initial WAAS must take place within the limits of the physical resources available as well as the performance and availability requirements which have been established.

WAAS Physical Environment

The initial WAAS will employ a satellite constellation consisting of 24 GPS satellites and 3 GEO satellites. The ground station architecture will consist of 24 WAAS reference stations (WRSs) (21 in CONUS, one in Alaska, one in Hawaii, and one in Puerto Rico), and two master stations. For the end-state WAAS, additional WRSs and GEOs may be required. Each WRS will have GPS dual-frequency receivers which periodically collect ionospheric data from the visible constellation. Currently this period is 10 seconds. The raw data will be sent to the WMS which will estimate ionospheric delays and error bounds at grid points and broadcast these to the users approximately every 5 minutes via geostationary communications satellites. The grid size has been fixed at 5 degrees in CONUS, 10 degrees between 55 and 75 degrees latitude, and 15 degrees above 75 degrees latitude. These GIVE and UIVE algorithms were designed and tested for 5-degree grid squares (at mid latitudes) and may require modification beyond 55 degrees latitude.

WAAS Requirements

For the initial WAAS, the system is defined as available if UIVEs calculated from GIVEs bound the post-correction user-interpolated ionospheric error with a probability of 0.999 and GIVEs are ≤ 2.0 m (1.5 m for end-state WAAS). The system is required to be available 95% of the time over 50% of the CONUS [1]. Because of WAAS message size restrictions, the grid delay broadcast to the user must be quantized by q_u (0.0625 m) such that $\text{mod}(IGP_delay, q_u) = 0$. In addition GIVE values on the grid must be given as an index to a table of maximum GIVE values as shown in Table 1. Therefore for each IGP, the WMS broadcasts the quantized vertical ionospheric delay and the GIVE indicator (GIVEI) corresponding to the GIVE values shown in Table 1 as required in the WAAS specification [1]. The user will use these broadcast values to calculate his vertical ionospheric delay and UIVE for each of his IPPs.

DESCRIPTION OF ALGORITHMS

Periodically (every 10 seconds) the WMS receives, for each satellite, PR and carrier-phase measured data (on L1 and L2) from each WRS. A Kalman filter similar to the

Table 1: GIVE Table

GIVEI	GIVE(m)
0	0.80
1	1.00
2	1.10
3	1.20
4	1.30
5	1.40
6	1.50
7	1.75
8	2.00
9	2.25
10	2.50
11	2.75
12	3.00
13	5.00
14	10.00
15	50.00

filter developed by Goad [3,4] and designed and implemented by STel [5] for the FAA National Satellite Test Bed (NSTB) uses this measured data to estimate (and smooth) the vertical ionospheric delays at the ionospheric pierce points (IPPs) for each WRS. This information is used to estimate ionospheric delays at ionospheric grid points (IGPs) on a 5x5 degree imaginary grid located 350 km above the Earth.

A slightly modified version of the WAAS ionospheric grid algorithm [6] uses equation (1) to estimate the vertical ionospheric delays at each IGP. This ionospheric grid algorithm is a simple interpolation scheme which weights directly according to the sine of the elevation angle and inversely according to distance. All IPPs farther than 600 nm from the interpolated position are ignored in order to increase local fidelity while at the same time gathering enough points to produce a useful average. At the beginning of each data collection interval, the maximum gradient in the 16 grid squares surrounding each grid node is determined. If the gradient exceeds the equivalent of 1.6 m/5 degrees of earth centered angle, the distance limit is reduced to 425 nm for averaging at that grid node. (The selection of the 600 nm distance and the 1.6 m/5 degree gradient limits are based on extensive testing of the FAA ionospheric data.) This operation sacrifices pierce point density in favor of locality when the ionospheric gradient is large. This latter distance restriction was chosen since it is approximately the maximum diagonal distance of a grid square and ensures inclusion of all points in the 4 grid squares surrounding a grid node. For any set of n points ($i = 1, \dots, n$), the

vertical ionospheric delay can be estimated at a point p through the following interpolation formula [6]:

$$\hat{D}_{vp} = \begin{cases} \sum_{i=1}^n \left(\frac{\tau_i}{\tau_p} \right) \frac{\left(\frac{\sin(\theta_i)}{d_{ip}} \right)}{\sum_{k=1}^n \frac{\sin(\theta_k)}{d_{kp}}} D_{vi} & d_{ip} \neq 0 \\ D_{vj} & d_{ip} = 0; \\ & j \in \{1, 2, \dots, n\} \end{cases} \quad (1)$$

where

D_{vi} = vertical ionospheric delay at the i th point

\hat{D}_{vp} = estimated vertical ionospheric delay at point p

d_{ip} = distance between the i th given point and point p

τ_i = predicted vertical ionospheric delay at the i th point as estimated by an ionospheric model [7]

τ_p = predicted vertical ionospheric delay at point p from ionospheric model

θ_i = elevation angle from monitor station to satellite.

At each IPP of the second group of receivers $WRS_1', WRS_2', \dots, WRS_n'$ shown in Figure 1, the WMS estimates the value of vertical delay using (1) where the n given points refer to the values of vertical ionospheric delay at the 4 surrounding grid nodes. The truth values supplied by each remote station are used to determine the vertical errors at the i th IPP at time t :

$$e_{vi}(t) = \hat{D}_{vi}(t) - D_{vi}(t)$$

where

$\hat{D}_{vi}(t)$ = predicted delay at time t at the monitor's IPP based on the surrounding 4 grid nodes,

$D_{vi}(t)$ = measured value of delay at time t at the monitor's IPP.

At the end of the update period (currently 5 minutes), the WMS will broadcast the latest delay values to users. These delay values are required to be quantized with a scale factor of q_u ($= 0.0625$ m) such that the value of delay at row r and column c of the grid (IGP_{rc}) is:

$$\hat{D}_v^q(IGP_{rc}) = \begin{cases} \hat{D}_v(IGP_{rc}) - h + q_u, & h \geq \frac{q_u}{2} \\ \hat{D}_v(IGP_{rc}) - h, & h < \frac{q_u}{2} \end{cases}$$

where $h = \text{mod}(\hat{D}_v(IGP_{rc}), q_u)$.

Because of this requirement, the user may receive a delay value which is up to $q_u/2$ ($= 0.03125$ m) removed from that of the WMS. This can be somewhat mitigated by adding the exact quantization error at each grid node to the GIVE at that grid node. We have chosen to add the maximum quantization error $q_u/2$ m to the GIVE estimates at all IGPs.

Calculation of GIVEs

Since the broadcasting of vertical delays/GIVEs to the user will occur approximately every 5 minutes, the data collection interval has been set to 5 minutes (although this is not required). Consequently, the WMS will collect $m = 30$ error values (1 every 10s) for each IPP sequence of the monitor.

A GIVE will be calculated for every IGP on condition that there are at least 3 surrounding grid squares each with at least 1 IPP sequence; otherwise, the GIVE is marked unavailable which means it cannot be used in any subsequent UIVE calculation for that period.

This restrictive condition guarantees that GIVEs will only be calculated when the local pierce point density is sufficiently high and will be related to a subsequent discussion on service volume availability.

Where this condition is met, a conservative tolerance bound is constructed with error bound E_{vi} for every monitor IPP sequence in the 4 grid squares surrounding node IGP_{rc} . This bound is derived from a two-sided 100% statistical tolerance interval which contains at least a proportion p of a normally distributed population and is given by [8,9]:

$$E_{vi} = |\bar{e}_{vi}| + g_{(\gamma; p; m)} s_{vi}$$

with

$$\bar{e}_{vi} = \frac{1}{m} \sum_{k=1}^m e_{vi}(t_k)$$

$$s_{vi} = \sqrt{\frac{1}{m-1} \sum_{k=1}^m (\bar{e}_{vi} - e_{vi}(t_k))^2}$$

and where $g_{(\gamma; p; m)} = 5.43$ for confidence level $\gamma = 0.999$, $p = 0.999$, and sample size $m = 30$. Of course $g_{(\gamma; p; m)}$ will have a different value if any of the three parameters γ , p , or m is changed. The value $g_{(\gamma; p; m)} = 5.43$ was calculated using the method described in reference [9].

The WMS then determines the grid vertical absolute error bias \hat{e}_v at node IGP_{rc} by using the interpolation scheme described earlier except without the ionospheric model values:

$$\hat{e}_v(IGP_{rc}) = \sum_{i=1}^n \frac{\left(\frac{\sin(\theta_i)}{d_{ip}} \right)}{\sum_{k=1}^n \frac{\sin(\theta_k)}{d_{kp}}} |e_{vi}(t_m)|$$

Finally, the GIVE is computed as the sum of the absolute error bias at the node, the maximum tolerance error bound in the 4 surrounding grid squares, and an allowance for the vertical ionospheric delay quantization requirement at the IGP:

$$GIVE(IGP_{rc}) = \hat{e}_v(IGP_{rc}) + \max_k \{E_{vk}\} + q_v/2$$

where E_{vk} is the tolerance bound for the k th monitor IPP sequence in one of the surrounding squares.

Because the GIVE sent to the user is required to come from a table value, the calculated GIVE is raised to the next highest value in Table 1.

Calculation of UIVEs

As mentioned previously, the GIVEs and vertical delay estimates at each IGP are broadcast to the user approximately every 5 minutes. With this information and its pierce point, the user receiver calculates the predicted vertical delay at the IPP and the UIVE at that IPP. The UIVE is the maximum of the surrounding IGP GIVEs with the condition that there be at least 3 GIVEs marked available:

$$UIVE_p = \max_{k=0,1} \{GIVE(IGP_{r+k,c+k})\}$$

where IGP_{rc} indicates the grid node at the southwest corner of the square which contains the user's IPP.

Closed Loop Monitoring

Experiments have been conducted (by the authors of this paper) to increase the percentage of user errors bounded by the UIVEs. These techniques either increase the size of the GIVEs unacceptably or require an even higher amount of pierce point density than is reasonably practical. In order to strike a balance between the often competing requirements of low GIVEs and high error bound rates, a system of independent regional monitors (Monitors M_1, M_2, \dots, M_{n3} in Figure 1) at locations other than WRSs is proposed that will act as users in the sense of determining predicted delay and UIVEs for its IPPs from

the grid. However the monitor's truth values will be compared to the predicted delay from the grid in order to determine the actual error. A monitor will determine the maximum amount (if any) that its actual vertical error exceeded any UIVE at any time in the 5 minute data collection period. At the next grid update time, this amount will be used to increase the GIVEs in the region with the monitor that detects the excess. The excess error will be added to the newly calculated GIVEs sent to the user, but will not be added to the GIVEs sent to the monitor. This group of closed-loop monitors have minor effects on the results as will be seen in the next section. The concept itself may be important, however, in cases where the ionosphere changes faster than normal (e.g., during severe geomagnetic storms).

RESULTS

In order to determine if the ionospheric requirements for an initial WAAS are met with these algorithms, it is necessary to:

- (1.) Examine the numerical results of applying the algorithms to a 52-day set of ionospheric data in order to assess whether the 2m limit on GIVE can be attained while UIVEs bound the residual errors at a consistently high rate.
- (2.) Examine the feasibility of bounding the ionospheric errors during a disturbed ionosphere (e.g., during a severe geomagnetic storm.). Do the algorithms work during these severe storms? One would expect the GIVEs to be greater than 2.0 m in such cases, but can the errors be consistently bounded?
- (3.) Examine what effect the real-time requirement for high data density has on the size of the service volume in order to assess whether this algorithm supports daily availability of 95% over 50% of the CONUS.

Numerical Results

In order to assess the effectiveness of these algorithms, actual user errors were compared to the calculated UIVEs at each user IPP where all previously mentioned conditions have been met. In this way the percentage of time the UIVE actually bounded the user's error was measured.

The condition that there be at least 1 IPP in each of at least 3 surrounding grid squares at all times when GIVEs were calculated eliminated several sets of data. The resulting sets of data which met this criterion at least some time during the day consisted of 50 days of quiet

Table 2. Test Period

Quiet Ionospheric and Major Storms Data ($A_p \leq 100$)		Disturbed Ionospheric Data (Severe Geomagnetic Storm) ($A_p > 100$)	
November 1992:	6 to 7, 10 to 13, 16 to 21, 25 to 30	April 1993:	4* to 5
December 1992:	8, 10 to 13		
April 1993:	4*, 7 to 18, 21		
June 1993:	21, 23		
July 1993:	2 to 5, 7-12, 14		

*The morning part of April 4 was quiet and the afternoon part was stormy.

ionosphere and 2 days of severe stormy geomagnetic conditions. (See Table 2.)

Figures 2, 3, and 4 depict the results for all periods of geomagnetic activity. Figure 2 shows the mean, standard deviation (sigma), 95th and 99th percentiles for GIVEs. On 04/04/93, the 95th percentile derived from the calculated GIVEs before translation into table values was approximately 4m. Since there is no 4 m table value, 5 m is chosen. Also, on 04/08/93, the 99th percentile before translation into table values is approximately 3.6m. Again the next highest table value is 5. These two examples suggest that several more gradations in the table above 3m would lessen excessive overestimation of GIVEs. It is seen from this figure that the 95th percentiles of GIVEs are below 2.0m most of the time.

Figure 3 shows the percentage of GIVEs below 2m. This percentage is between 95% and 100% for all except four days. The percentages for these days are: 90.2% on 11/19/92, 91.9% on 12/8/92, 93% on 7/2/93, and 60.8% on 4/4/93. In the first two days (11/19/92 and 12/8/92), the ionosphere was quiet ($A_p \leq 50$). The 95th percentiles of GIVE for both days are 2.25 m. On the third day (7/2/93) there is a major (not severe) geomagnetic storm ($50 < A_p \leq 100$) which caused a large gradient in the ionosphere. The 95th percentile of the GIVE for that day is also 2.25 m. On the 4th day (4/4/93) there is a severe geomagnetic storm ($A_p > 100$) which causes a large ionospheric gradient. The 95th percentile of the GIVE for that day is 5.0 m.

Figure 4 shows the percentage of time that calculated errors (using truth values) are below the predicted UIVE value for the closed-loop monitor and for the user. The monitor and the user results are almost identical for the majority of days. The monitor helps to improve the success rate of the user when the rate is relatively low. For example on 11/16/92, the success rate for the user is increased from 97.8% to 98.6%, and from 98.97% to 99.46% on 11/19/92.

Table 3 depicts combined results for the several kinds of geomagnetic conditions. During a quiet ionosphere ($A_p \leq$

50) and major (not severe) storms ($50 < A_p \leq 100$), the 95th and 99th percentiles of GIVE are 1.75m and 2.25m, respectively. The combined success rate in bounding GIVE for the user is 99.95%. During severe geomagnetic storms ($A_p > 100$), the 95th and 99th percentiles of GIVE are both 5.0m. The combined success rate for the user is 99.91%.

Table 4 shows statistical parameters, maximum, and minimum of the distributions of vertical error exceeding UIVE at the monitor (per 5 minute update period). The table shows the same parameters for user errors after the maximum monitor error above UIVE for one grid update period has been added to the GIVEs for the next grid update period. It can be seen from this table that when the user error exceeds the UIVEs, the maximum value of the difference between the user error and UIVE is about 0.48m, and the $|\text{mean}| + 2 \text{ sigma} = 0.19 \text{ m}$.

Figure 5 shows the 95th percentile of GIVEs mapped against the solar flux density (F10.7). The graph indicates the absence of a clear relationship or correlation between solar flux density and ionospheric grid error bounds. The results of [10] also show no correlation between short-term F10.7 and the total electron content (TEC) which is proportional to ionospheric delay. Typical values for F10.7 during solar maximum are between 300 and 350, and about 75 during solar minimum. The reader should be cautioned not to extrapolate the results of Figure 5 to the peak of the solar cycle. Extrapolation is not a substitute for examining data during the peak of the solar cycle.

Service Volume Implications

The results in the previous section were conditioned on the existence of at least 1 IPP in each of at least 3 grid squares surrounding the IGP in real time. Whenever this condition is not met, the IGP is marked "unavailable.". This restriction maintains a high degree of pierce point density which favors the calculations in the algorithm. In order to determine if this degree of pierce point density could be maintained in the initial WAAS, a map of pierce point density was constructed using the 24 known sites,

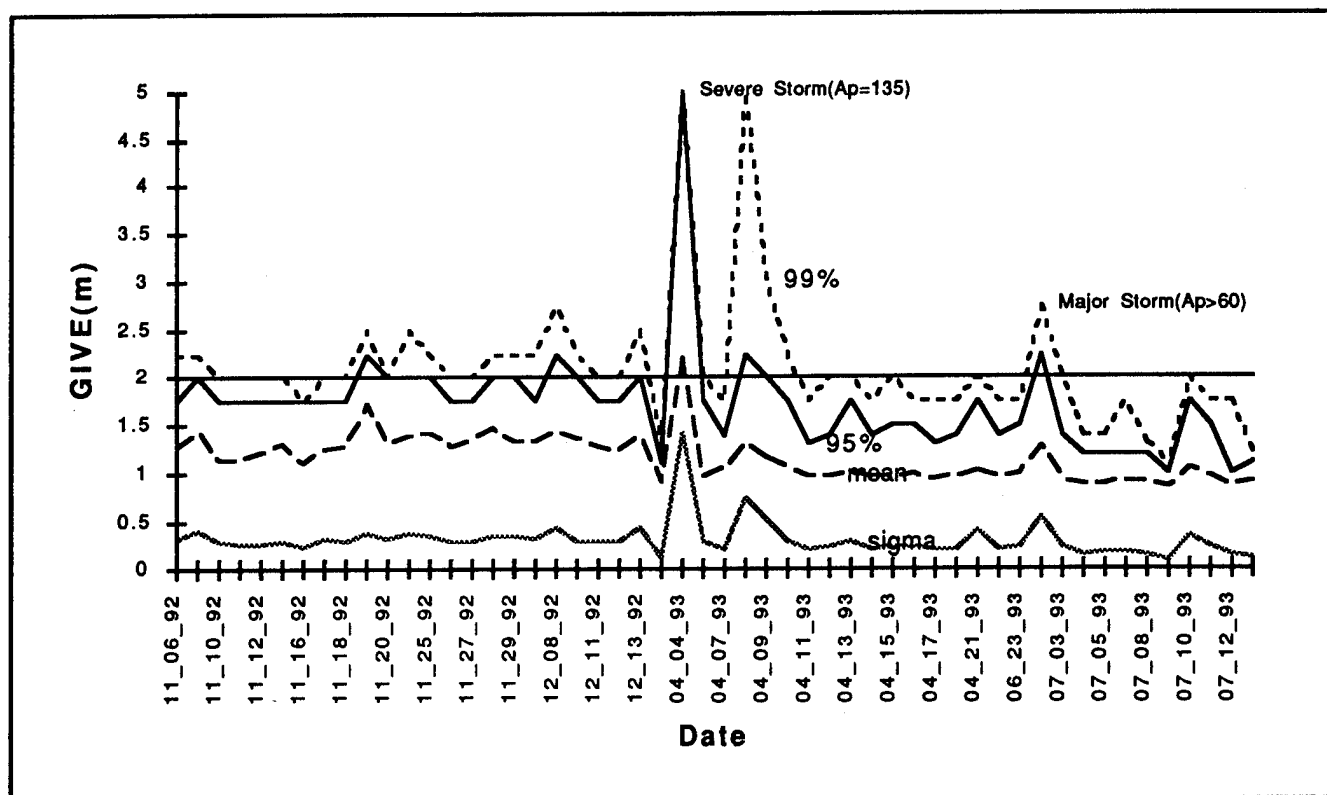


Figure 2: Magnitude of GIVE

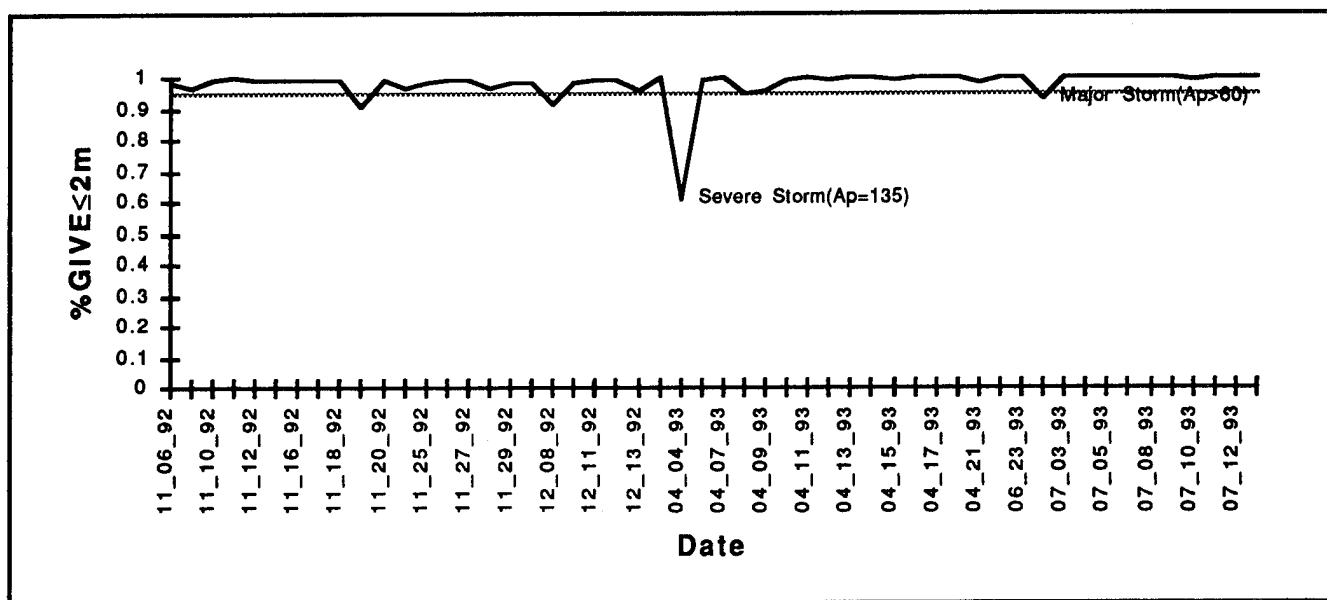


Figure 3: Percentage GIVEs ≤ 2m

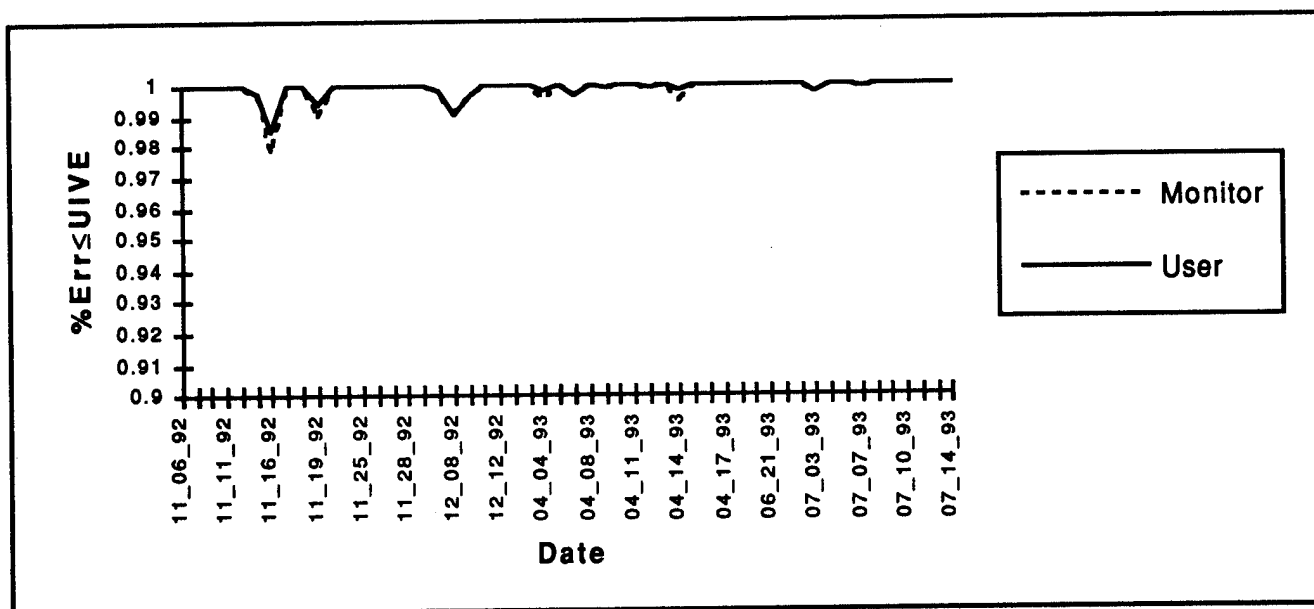


Figure 4: % Monitor and User Errors \leq UIVE

Table 3: Combined Results

	Ap Index	GIVE Mean	GIVE Sigma	GIVE 95%	GIVE 99%	% \leq UIVE (monitor)	% \leq UIVE (user)	% GIVE \leq 2.0 m
Quiet Ionosphere and Major Storms	≤ 100	1.13m	.36m	1.75m	2.25m	99.92%	99.95%	98.80%
Severe Storms	> 100	1.6m	1.2m	5m	5m	99.74%	99.91%	80.00%

Table 4: Error Distribution Above UIVE for Monitor and User

Errors at:	Min	Max	Mean	Sigma
Monitor(max)	.0011m	.4815m	.0728m	.0964m
User	.0001m	.4815m	.0511m	.0640m

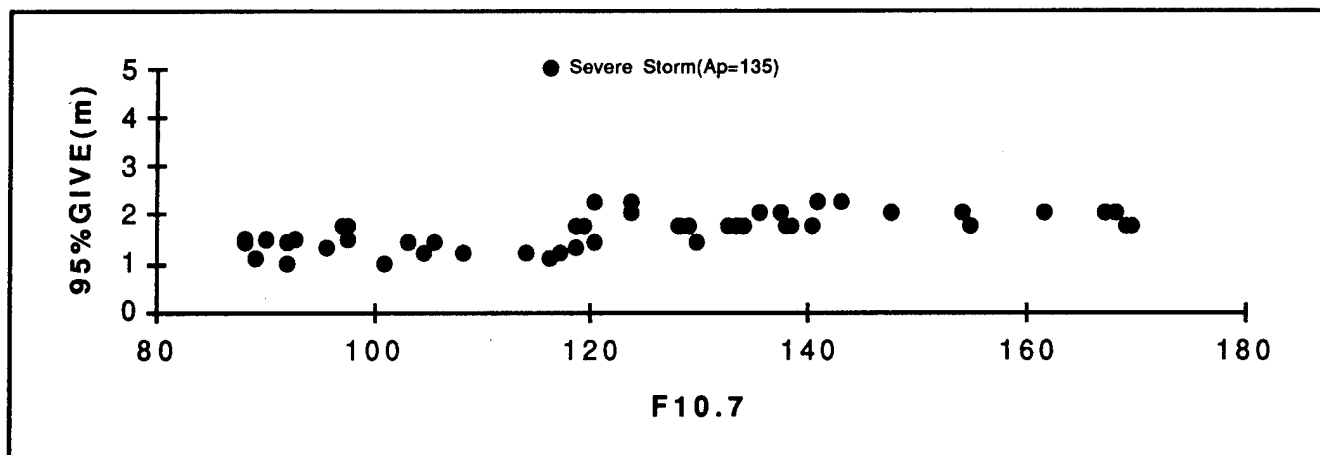


Figure 5: Mapping of 95% of GIVE to Solar Flux Density (F10.7)

the 24 GPS satellites, and the 3 GEO satellites (located at 15.5W, 55.5W, 180) all projected to be in operation for the initial WAAS. A modified version of the NAVSTAR program [11] was employed to determine how many pierce points would be available every minute in every grid square throughout the day. Next, for each grid node, the percentage of the day that the condition of at least 1 IPP in each of at least 3 grid squares surrounding an IGP was determined.

For the purposes of this analysis, we considered the following conditional probability relationship:

$$\begin{aligned} \Pr[\text{Ionospheric WAAS function available}] = \\ \Pr[\text{overall GIVE} \leq 2 \text{ m} | \\ \text{IPP density requirement satisfied}] \\ \times \Pr[\text{IPP density requirement satisfied}] = .95 \end{aligned}$$

Since $\Pr[\text{overall GIVE} \leq 2 \text{ m} | \text{IPP density requirement satisfied}] = .988$ for non-severe ionospheric conditions (from Table 3), then $\Pr[\text{IPP density requirement satisfied}]$ must be at least .96 for a grid node to be marked as satisfying the density requirement.

Figure 6 depicts this condition over the defined service area. Dark circles indicate nodes where the IPP density requirement is satisfied at least 96% of the day, and clear circles indicate where the condition is not satisfied at least 96% of the day. Figure 7 depicts the grid squares (dark) which would be operational based on this condition and the requirement that there be at least 3 surrounding grid nodes with GIVEs in order to calculate UIVEs.

CONCLUSIONS

Based on the results of this paper, the following conclusions are given:

1. GIVE and UIVE real-time algorithms have been developed in this paper and tested on static data. The

final test of these algorithms will be the implementation in a user receiver while conducting many flight tests during different ionospheric conditions.

2. Under non-severe geomagnetic conditions ($A_p \leq 100$), more than 50% of the CONUS has a pierce point density which can sustain GIVEs ≤ 2 m 95% of the time, and the subsequent UIVEs calculated from these GIVEs bound the residual user errors an average of 99.95% of the time (and never get below 97.84% for any day).
3. For one severe geomagnetic storm ($A_p > 100$), the 95th percentile of the GIVEs is 5.0 m, and the user's success rate is 99.91%. This result means that the algorithms were able to detect the change of the ionospheric conditions and bound the ionospheric errors with a very high success rate. The impact of such large values of the ionospheric error bounds on the integrity and continuity of WAAS service must be further evaluated.
4. During the few cases where the user errors exceeded the UIVEs, the maximum value of the difference between the user error and UIVE was about 0.48 m, and the $|\text{mean}| + 2 \text{ sigma}$ was 0.19 m.
5. There is no apparent correlation between solar flux density (F10.7) and ionospheric grid error bounds. Typical values for F10.7 during solar maximum are between 300 to 350, and about 75 during solar minimum.
6. The percentage of the GIVEs below 2.0 m is 98.8% for quiet and major (not severe) geomagnetic storm conditions. During the one severe geomagnetic storm for which data was available, this percentage drops to 80.00%.

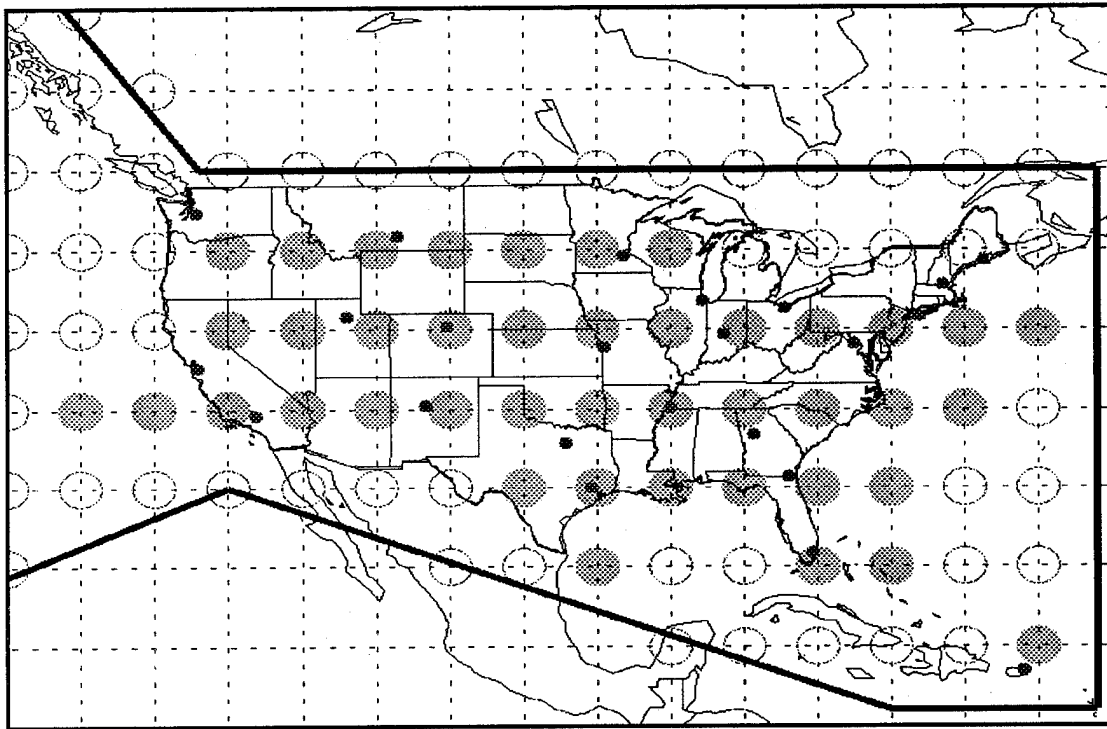


Figure 6: Grid Nodes with Required Surrounding IPP Density

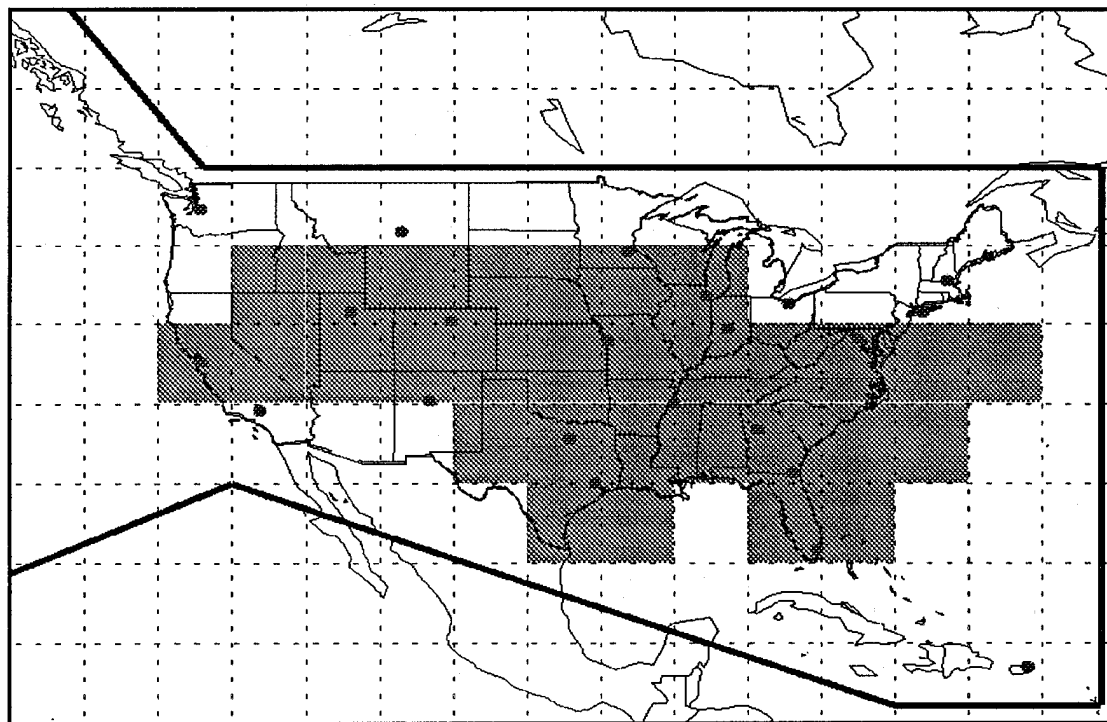


Figure 7: Grid Squares with at Least 3 Surrounding Grid Nodes with Required IPP Density

ACKNOWLEDGEMENTS

The authors would like to acknowledge James K. Reagan and J. P. Fernow from the MITRE Corporation/Center for Advanced Aviation System Development (CAASD) for their review. The authors would also like to acknowledge Joseph Dorfler, the manager of the FAA Satellite Program Office (AND-510), who is the sponsor of this work.

REFERENCES:

1. Specification for Wide Area Augmentation System (WAAS), U.S. Department of Transportation, Federal Aviation Administration, FAA-E-2892, 9 May 1994.
2. Wilson, B. D., and A. J. Mannucci, *Extracting Ionospheric Measurements from GPS in the Presence of Anti-Spoofing*, National Technical Meeting of the Institute of Navigation, 23 September, 1994.
3. Goad C. C., *Optimal Filtering of Pseudoranges and Phases from Single-Frequency GPS Receivers*, Navigation: Journal of The Institute of Navigation, Vol. 37, No. 3, Fall 1990.
4. Eucler, H., and Goad, C. C., *On Optimal Filtering of GPS Dual Frequency Observations Without Using Orbit Information*, Bulletin Geodesique, Vol. 65, No. 2, pp 130-43, 1991.
5. "NSTB Software Requirements Specification - Appendix A: Baseline Algorithms," Report No. TR-92072, Stanford Telecommunication Inc., Reston, VA, August 1992..
6. El-Arini, M. B., P. A. O'Donnell, P. Kellam, J. A. Klobuchar, T. Wisser, P. H. Doherty, *The FAA Wide Area Differential GPS (WADGPS) Static Ionospheric Experiment*, National Technical Meeting of the Institute of Navigation, 20-22 January 1993, San Francisco, California.
7. Klobuchar, J. A., *Ionospheric Time-Delay Algorithm for Single-Frequency GPS Users*, IEEE Transactions on Aerospace and Electronic Systems, Vol. AES-23, No. 3, pp. 325-331, May 1987.
8. Hahn, G. J., and W. Q. Meeker, *Statistical Intervals A Guide for Practioners*, John Wiley & Sons, Inc., New York, 1991.
9. Odeh, R. E., and D.B. Owen, *Tables for Normal Tolerance Limit, Sampling Plans, and Screening*, New York: Marcel Dekker, Inc., 1980.

10. Klobuchar, J. A., and P. H. Doherty, "The Correlation of Daily Solar Flux Values with Total Electron Content," *Proceedings of International Beacon Satellite symposium*, pp. 192-195, MIT, Cambridge, MA, July 6-10, 1992.
11. Livingston, R., NAVSTAR program, Stanford Research Institute, February, 1977.

LIST OF ACRONYMS

CAT I	Category I
CONUS	Conterminous US
DH	Decision Height
GEO	Geostationary Earth Orbiting
GIVE	Grid Ionospheric Vertical Error
GIVEI	Grid Ionospheric Vertical Error Indicator
GPS	Global Positioning System
IGP	Ionospheric Grid Point
IPP	Ionospheric Pierce Point
NSTB	National Satellite Test Bed
PR	Pseudorange
TEC	Total Electron Content
UDRE	User Differential Range Error
UIVE	User Ionospheric Vertical Error
VPE	Vertical Position Error
WAAS	Wide Area Augmentation System
WMS	Wide-area Master Station
WRS	Wide-area Reference Station



Session C4

Land Vehicular Applications

Chair:

Mr. Robert Denaro
Motorola

Co-Chair:

Mr. Jim Arnold
FHWA

Kinematic GPS for Closed-Loop Control of Farm and Construction Vehicles

Michael O'Connor, Gabriel Elkaim, and Dr. Bradford Parkinson
Stanford University

BIOGRAPHY

Michael L. O'Connor is a Ph.D. candidate in Aeronautics and Astronautics at Stanford University. He received his S.B. in Aeronautics and Astronautics from MIT in 1992 and his M.S. from Stanford in 1993. He has worked on communication satellites for Hughes Aircraft Company in El Segundo, California.

Gabriel H. Elkaim is a Ph.D. candidate in Aeronautics and Astronautics at Stanford University. He received his BSE in Aerospace Engineering from Princeton University in 1990 and his M.S. from Stanford in 1995. He has worked for Schlumberger Wireline Logging and Testing in Montrouge, France.

Bradford W. Parkinson, Ph.D., is professor of Aeronautics and Astronautics at Stanford University, and Program Manager of the Relativity Gyroscope Experiment (Gravity Probe B). He served for six years as the first Program Director of the GPS Joint Program Office, and has been instrumental in GPS program development. Dr. Parkinson heads the NASA advisory council and is a Fellow of the AIAA and a member of the National Academy of Engineering.

ABSTRACT

Operating heavy equipment can be a difficult and very tedious task; control of an agricultural tractor requires the continuous attention of the driver, and farmers often work long hours during the critical times of planting and harvesting. Loaders and other ground vehicles are frequently used in situations which are unpleasant or even hazardous for the human operator. In the past, some efforts have been made to automate agricultural vehicles, but they have been largely unsuccessful due to sensor limitations.

This paper explores the use of kinematic GPS as the primary sensor in closed loop control of farm and construction vehicles. A single, low-cost GPS receiver can measure position to within a few centimeters and

attitude to within 0.1° , and does not drift with time. The ability to provide accurate information about multiple vehicle states makes GPS ideal for system identification and control of dynamic systems. In this work, a ground vehicle control system was designed and simulated using realistic plant, sensor, and disturbance models. Optimal control methods were examined to deal with non-linear and time-varying vehicle dynamics. To validate this simulation, experimental data was taken at Stanford using a GPS-equipped electric golf cart.

This research builds upon previous work in developing GPS-based aircraft autopilots. It is significant because it is the first step towards a safe, low-cost system for adaptive, highly accurate control of a ground vehicle. It is anticipated that the implementation of these ideas will take place in three steps: (1) driver-in-the-loop control using a graphical display; (2) driver assisted automatic control, with an on-board operator making only high-level decisions; and (3) vehicle autonomous guidance and control with on-line parameter identification and adaptive control that will operate for several hours without human intervention.

INTRODUCTION

Ground vehicle automatic control has been a goal for many years. Superior control for individual vehicles and cooperative efforts for multiple vehicles have myriad applications. Smart roads in which the driver merely programs the destination, construction vehicles that automatically build roads, agricultural vehicles which allow full resource utilization, and vehicles operating in hazardous environments are some examples. In the short term, the largest application of autonomous vehicle control would be farm vehicles in which only high level decisions are made by a human operator.

Farming vehicle operation can be a trying and tedious task; speeds are very slow across large fields, and often fog, dust, or darkness limit visibility. Operating heavy

equipment requires the full attention of the driver in a high noise and vibration environment. Further, farming operations during critical times such as harvest require long hours and are usually limited to daylight hours. Autonomous control has many potential benefits; such as allowing operation with limited visibility, more accurate control of row spacing, removal of a human operator from a chemically hazardous environment, and an increased efficiency in farming techniques.

Autonomous guidance of agricultural vehicles is not a new idea. However, previous attempts to navigate and control ground vehicles for farming applications have been largely unsuccessful due to sensor limitations. Some require cumbersome auxiliary guidance mechanisms in or around the field of interest [1,2]. Others rely on a camera system requiring clear daytime weather and field cues that can be deciphered by visual pattern recognition [3,4].

The ground vehicles described above typically operate in environments with good sky visibility. With the recent arrival of GPS, engineers now have access to a low cost sensor that is well suited for use in vehicle navigation. GPS is already being used in a number of ground vehicle applications, including agriculture. *Code differential* techniques are being used for geographic information systems [5-7] driver assisted control [8] and even automatic control of ground vehicles [9].

Using *precise differential carrier phase measurements* of the satellite signals, GPS navigation systems have demonstrated accuracy's of a few centimeters in vehicle positioning [10], and better than 0.1° in attitude [11]. This ability to accurately measure multiple states makes GPS ideal for system identification, state estimation, and automatic control of dynamic systems. Also, with aiding from a Pseudo-Satellite Integrity Beacon, navigation system integrity is impeccable [12].

This paper specifically focuses on the automatic



Figure 1 - Golf Cart

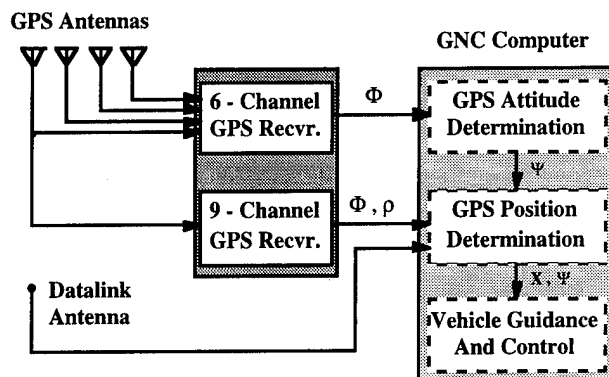


Figure 2 - GPS Hardware Architecture

control of ground vehicles using carrier-phase differential GPS as a sensor. A ground vehicle automatic control system using GPS was developed and simulated in software. This control system was implemented and tested experimentally on an electric golf cart. Experimental data was used to study a recursive system identification algorithm to determine if important, time-varying vehicle parameters could be ascertained from sensor data in real time.

EXPERIMENTAL SETUP

The platform used for initial ground vehicle testing was a 1984 model Yamaha Fleetmaster electric golf cart pictured in Figure 1. The vehicle has a 1.55 meter wheel base, and is just under 2 meters tall with the canopy attached. Four single-frequency GPS antennas are mounted to the top of the canopy. The top speed of the golf cart is around 5 meters per second, and is controlled manually by the driver. Experiments took place on a grass field, and the vehicle was driven at a nominal speed of 2 m/s.

The GPS system used for vehicle position and attitude determination was identical to the one used by the Integrity Beacon Landing System (IBLS) [10], as shown in Figure 2. A 4-antenna, 6-channel Trimble Quadrex receiver produced 4 hertz carrier phase measurements for attitude determination. Measurements from a single-antenna 9-channel Trimble TANS receiver were used to determine vehicle position. An on-board Dolch computer with a Pentium-90 running under LYNX-OS real time operating system performed attitude, position, and control signal computations.

The ground reference station consisted of a Dolch computer with a 9-channel TANS receiver generating carrier phase measurements, and a Trimble 4000ST receiver generating RTCM code differential corrections. Data was transmitted from the ground station to the vehicle through Pacific Crest 450-470

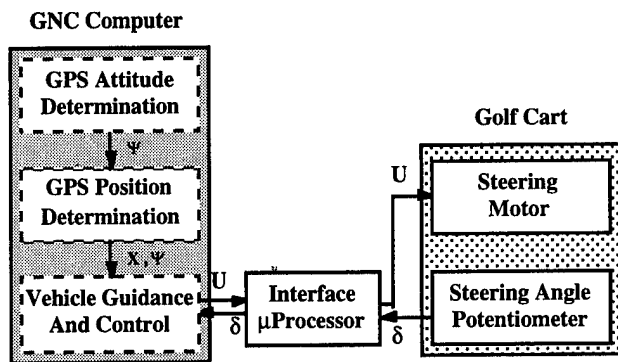


Figure 3 - Control Hardware Setup

MHz. radio modems over a range of less than one kilometer.

Vehicle steering angle was sensed and actuated by a modified Navico WP5000 boat autopilot. A Motorola MC68HC11 microprocessor board performed the communications between the computer serial port and the autopilot as shown in Figure 3. Analog steering angle was encoded from a potentiometer attached to the front wheels, and a pulse width modulated signal was sent to the steering motor. The maximum steering angle was $\pm 30^\circ$, and the motor commanded rate was limited to $\pm 2.3^\circ/\text{sec}$.

To achieve centimeter level accuracy quickly and reliably, a pre-defined location was surveyed using the IBLIS software. To begin testing, the vehicle was taken to this location and its navigation solution was initialized. The integer residuals were checked after the initialization to help verify that the correct integers were obtained. A final system for safe, reliable ground vehicle navigation and control will probably require a better method of integer cycle ambiguity resolution. Using an Integrity Beacon near the field of operation would allow rapid integer determination, provide an additional ranging signal for navigation system accuracy and integrity, and would still allow the user to operate with less expensive, more reliable single-frequency SPS equipment.

VEHICLE MODEL IDENTIFICATION

The most difficult aspect of performing a meaningful ground vehicle simulation is arriving at a good model of vehicle dynamics and disturbances. Ground vehicle dynamic models range from very simple to overwhelmingly complex, and there is no single model that is widely accepted in the literature [13]. The most complex mathematical model of a dynamic system is not always appropriate to use [14], especially since controller and estimator design requires a simple (typically linear) model of plant dynamics.

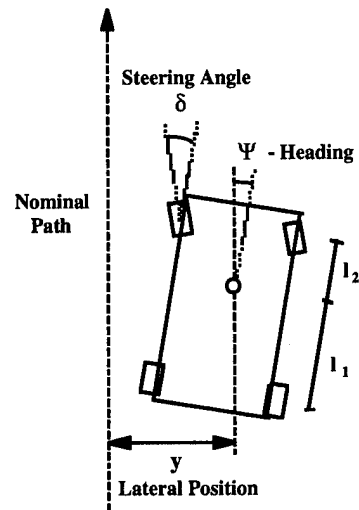


Figure 4 - Simple Vehicle Model

Before performing experiments to identify golf cart dynamics, initial calibration tests were run to linearize the steering angle sensor and the steering actuator. The calibration produced look-up tables which were implemented in software on the navigation and control computer.

Open-loop tests using sinusoidal or random control inputs (standard system identification techniques [15]) posed a problem. Only a limited amount of data could be taken before the vehicle traveled to the end of the field of operation. For this reason, a controller was designed for closed-loop straight line and U-turn driving based on a simple kinematic vehicle model with no estimator. The vehicle model used assumed no wheel

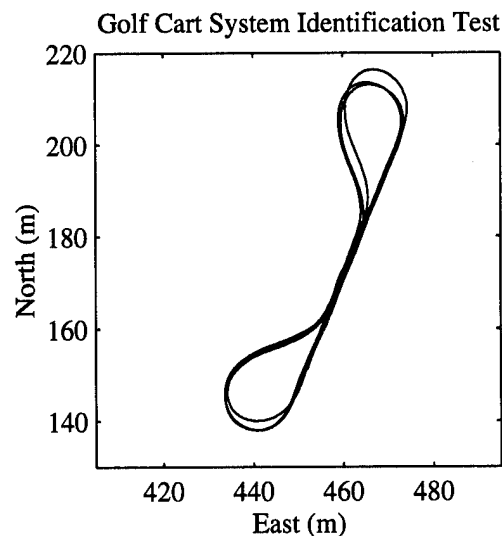


Figure 5 - Golf Cart Identification Passes

$$\begin{bmatrix} \dot{y} \\ \dot{\psi} \\ \dot{\delta} \end{bmatrix} = \begin{bmatrix} 0 & V_{x0} & -\frac{V_{x0}l_1}{(l_1+l_2)} \\ 0 & 0 & -\frac{V_{x0}}{(l_1+l_2)} \\ 0 & 0 & 0 \end{bmatrix} \begin{bmatrix} y \\ \psi \\ \delta \end{bmatrix} + \begin{bmatrix} 0 \\ 0 \\ 1 \end{bmatrix} u$$

Figure 6 - State-Space Equations

slip, small steering and heading angles, constant velocity of the rear wheels, actuation through a single front tire, and no roll or pitch motion (see Figure 4.).

This original controller was intentionally designed with no filtering of sensor data so the control signal would be noisy in response to noisy sensor measurements. Feed-forward U-turn trajectories were also designed to require large positive and negative control signals. Both of these were done to sufficiently excite the golf cart dynamics, providing rich data for identification of an appropriate vehicle model in post-processing.

After some problems with instability due to actuator hard limiting, the controller succeeded in guiding the golf cart for a five-minute trial, complete with 6 U-turns as seen in figure 5. Recursive transfer function system identification techniques based on the LMS algorithm [16] were used on the golf cart data to determine the appropriate discrete model order to use for control system design. By performing identification on increasing model orders until pole-zero near-cancellations occurred, it was found that only 1 state was needed to describe the control to steering angle transfer function, and 2 states were needed to describe the control to heading transfer function. Furthermore, the transfer functions found were consistent with the simple kinematic vehicle model described above. The

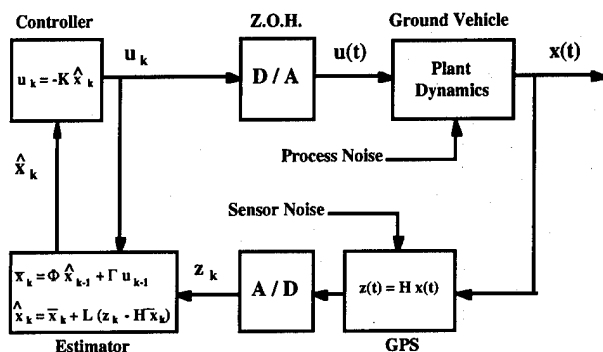


Figure 7 - Control Block Diagram

equations describing this model are shown in figure 6.

GROUND VEHICLE SIMULATION

Because the simple kinematic model described above matched the golf cart experimental data, it was used for the vehicle simulation and control system design in this work. Using this model, the controllable vehicle states are lateral deviation from desired position (y), heading (ψ), and steering angle (δ). The steering angle rate (u) was commanded by the control computer, and was physically limited by the motor to $\pm 2.3^\circ/\text{sec}$.

The technique used for vehicle automatic control was a discrete Linear Quadratic Regulator / Estimator, as shown in figure 7. The control gains (K) were chosen to minimize a quadratic cost function based on control inputs and state deviations from nominal [17]. The full vehicle state was appended to include the observable sensor biases ψ -bias and δ -bias for estimation purposes. The optimal estimator gains (L) were found using the assumed vehicle dynamic model and a model of disturbances based on the experimental data [18].

The ground vehicle simulation and estimator design both assumed random, uncorrelated measurement noise with normal distribution. The $1\text{-}\sigma$ measurement and discrete disturbance errors that were assumed are shown in Table 1.

Table 1 - Simulated Measurements and Disturbances

	$1\text{-}\sigma(\text{noise})$	$1\text{-}\sigma(\text{dist})$
Position y (cm)	2.0	0.1
Heading ψ (deg)	0.3	0.06
Steering δ (deg)	0.3	0.3
Heading Bias (deg)	-	0.006
Steering Bias (deg)	-	0.006

Two cases were explored in the simulation. In one case, the control signal sent to the vehicle was a linear combination of the *optimally estimated state* described above (Estimator Case). In the second case, the control signal was a linear combination of the *measured state* with sensor biases approximated and no filtering (No Estimator Case). The same controller gains, sensor noise, and measurement noise were used in both cases.

Figure 8 shows the simulation results for both cases simulated with an initial lateral position error of 30 cm. Cross track position error (y), actuator control effort (u), and estimated sensor biases are plotted for a typical 100 meter path. The initial errors on steering and heading biases were 0.2° .

An extended simulation was run for a 10 kilometer path to gather statistical data. The results for true vehicle

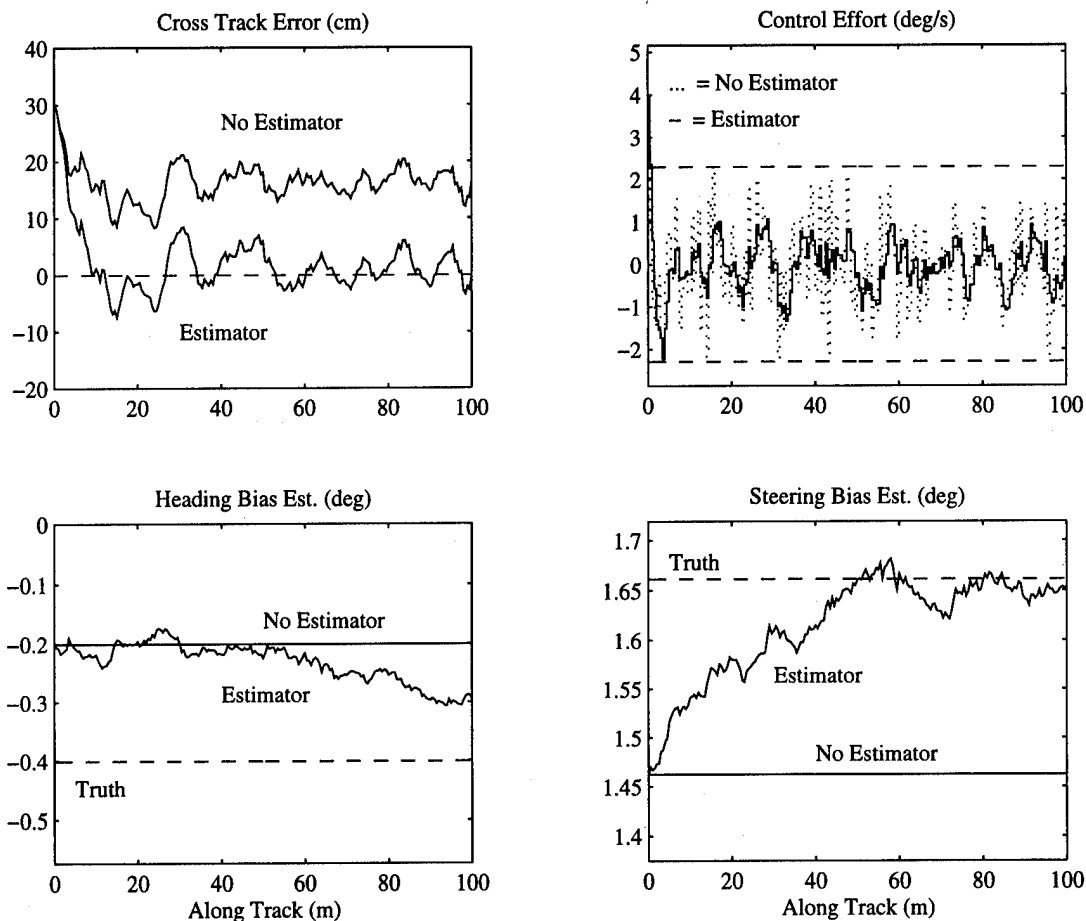


Figure 8 - Simulation Results

position error (y), control signal (u), and sensor bias estimate errors are shown in Table 2.

Table 2. - Simulation Statistical Results

	Estimator (Mean \pm 1- σ)	No Estimator (Mean \pm 1- σ)
Position y (cm)	0.0 \pm 3.1	16.3 \pm 2.7
Control u (deg/s)	.00 \pm .43	.00 \pm .92
ψ -Bias Error (deg)	.00 \pm .06	.20 \pm .00
δ -Bias Error (deg)	.00 \pm .03	.20 \pm .00

The simulation shows that a fairly small sensor bias error can significantly affect the lateral position accuracy of the ground vehicle. This is especially true because the level of control being sought is so precise. A 0.2° bias in two sensors caused a 16.3 centimeter bias in the lateral position, which was held to a precision of around 3 centimeters. Estimating sensor biases in real time eliminated the lateral position bias.

The amount of control used in the simulation was also quite different between the two cases. The control signal standard deviation in the Estimator case was

half the size of the No Estimator case. During controller design, lateral position accuracy was traded-off for control effort because of the physical limit of the steering motor. Based on this, an estimator should allow more aggressive control design, since less control was required for the same system accuracy.

GOLF CART TEST RESULTS

The controller and observer gains from the simulation were used to perform closed-loop tests on the actual golf cart. The vehicle attempted to follow the same straight line for 12 separate trials. Hard limits on actuator authority caused instability in 2 of the 12 trials, but the golf cart successfully followed the line for 100 meters in the other 10. The raw measurements from the 10 successful runs are shown in Figure 9. Note that no "truth" was available for lateral position error since the only position sensor in use was GPS.

The measured lateral position was *zero mean* with standard deviation of 5.0 centimeters. The control effort was mean of -0.01 degrees/second with standard deviation of 1.26 degrees/second.

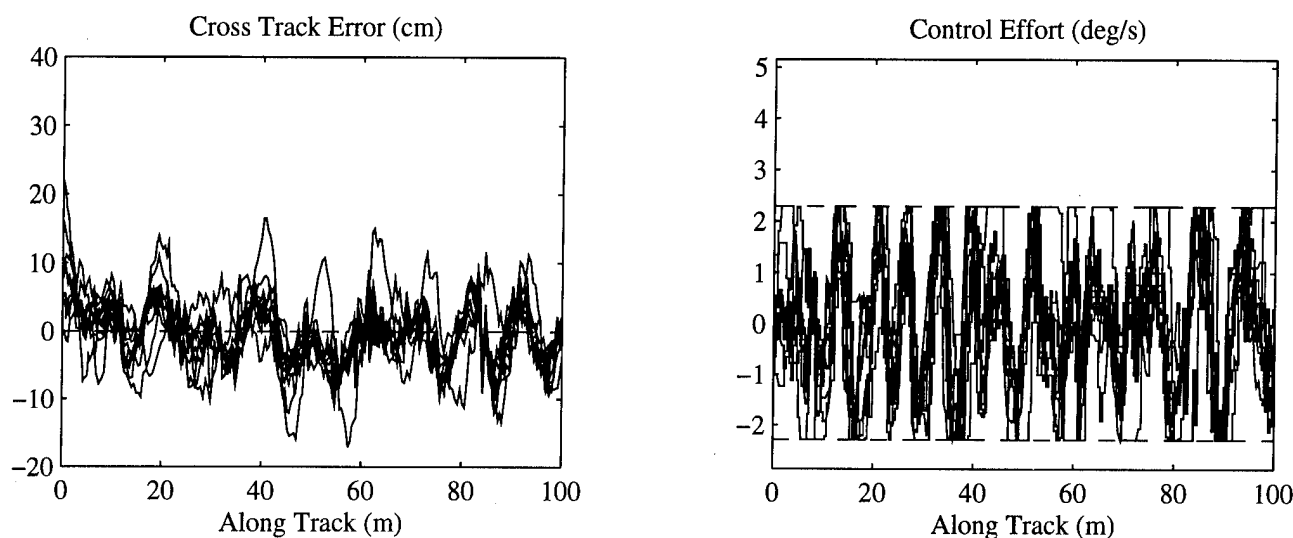


Figure 9 - Golf Cart Experimental Results

The experimental results show that more control effort was required and accuracy was poorer than predicted by the simulation. This is most likely due to an inexact disturbance model in the simulation, since the measurement performance of GPS is fairly well understood.

One likely cause of the disturbance noise was the roll motion of the golf cart. Although the roll angle of the vehicle was measured, the resulting motion of the 2 meter high positioning antenna relative to the wheel base was not corrected for. The data shows that the roll motion was on the order of ± 1 degree over a few seconds, which corresponds to a lateral disturbance motion of about 4 centimeters.

PARAMETER IDENTIFICATION

In order to determine the feasibility of real-time parameter identification using GPS, the data taken during the first closed-loop control trial (Figure 5) was run through an Extended Kalman Filter [19]. The vehicle state included ψ , δ , and δ -bias. In addition, the state transition matrix parameter $-V_{x0}/(l_1+l_2)$ was appended to the state vector and estimated along with the state.

The parameter and steering bias values were initially set to zero to see how the filter would converge. The results of the identification are shown in Figure 10. The time history of these values are plotted along with their "expected" values based on previous identification and golf cart dimensions. The parameter estimate

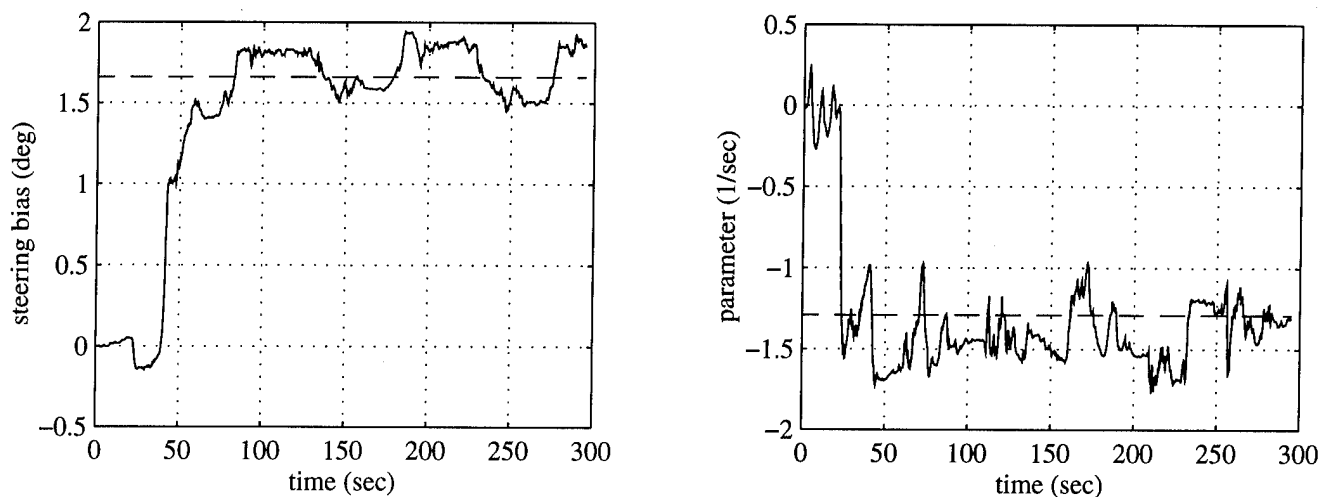


Figure 10 - Extended Kalman Filter Results

converged within about 25 seconds, and the steering bias within around 60 seconds.

CONCLUSION

The Results presented in this paper are promising for a number of reasons.

- (1) A ground vehicle control system was simulated and demonstrated using GPS as the *only* sensor for position and heading. One additional sensor—a potentiometer—was used to measure steering angle.
- (2) A constant gain controller based on a *very* simple vehicle model successfully stabilized and guided a golf cart along a straight, pre-determined path.
- (3) Using a slow actuator and sensors with significant biases, a vehicle was controlled along a path *with no steady lateral position bias and a 5 centimeter lateral position standard deviation*.
- (4) The ability to estimate vehicle dynamic parameters *in real-time* has been demonstrated using an Extended Kalman Filter on experimental data. This suggests that adaptive control may be feasible to deal with changing vehicle dynamics in more complex field settings.

The structure and repeatability in the experimental path-following data suggests that we could improve performance significantly by correcting for the positioning antenna moment arm. Also, we feel the experimental results presented here could be improved with a stronger actuator.

The dynamic model used to represent the electric golf cart will almost certainly be inadequate for simulation and testing of farm and construction vehicles in realistic settings. It is the authors' hope that the control methodology discussed here can be extended to more complicated dynamic systems. Once an accurate vehicle model is developed, and reduction of that model to one sufficiently linear for control system design is achieved, optimal control methods can be applied to implement autonomous control.

The implication is that GPS could be used with a real-time parameter identification algorithm to create a control system that is able to adapt to changing vehicle conditions. Future research is intended to further explore this possibility in the automatic control of ground vehicles.

ACKNOWLEDGMENTS

The authors would like to thank several groups and individuals who made this research possible. At Stanford, Dave Lawrence, Stu Cobb, Boris Pervan,

Clark Cohen, Chris Shaw, Konstantin Gromov, Andy Barrows, and Jock Christie were all extremely helpful. Trimble Navigation provided the GPS equipment used to conduct the experiments. Funding was provided by the FAA for research related to GPS, and by Deere and Company.

REFERENCES

1. Young, S.C., Johnson, C. E., and Schafer, R. L. *A Vehicle Guidance Controller*, Transactions of the American Society of Agricultural Engineers, Vol. 26, No. 5, 1983, pp. 1340-1345.
2. Palmer, R. J. *Test Results of a Precise, Short Range, RF Navigational / Positional System*, First Vehicle Navigation and Information Systems Conference - VNIS '89, Toronto, Ont., Canada, Sept. 1989.
3. Brown, N. H., Wood, H. C., and Wilson, J. N. *Image Analysis for Vision-Based Agricultural Vehicle Guidance*, Optics in Agriculture, Vol. 1379, 1990, pp. 54-68.
4. Brandon, J. R., and Searcy, S. W. *Vision Assisted Tractor Guidance for Agricultural Vehicles*, International Off-Highway and Powerplant Congress and Exposition, Milwaukee, WI, Sept. 1992. Publ by SAE, Warrendale, PA, pp. 1-17 921650.
5. Lachapelle, G., Cannon, M. E., Gehue, H., Goddard, T. W., and Penney, D. C. *GPS Systems Integration and Field Approaches in Precision Farming*, Navigation, Vol. 41, No. 3, Fall 1994, pp. 323-335.
6. Pounton, J., and Babu, K. LANDNAV: A Highly Accurate Land Navigation System for Agricultural Applications, Proceedings of ION GPS-94, Salt Lake City, UT, Sept. 1994, pp. 1077-1080.
7. Lawton, Kurt. GPS System in a Box, Farm Industry News, Vol. 28, No. 8, July/August 1995, p. 10.
8. Vetter, A. A. *Quantitative Evaluation of DGPS Guidance for Ground-Based Agricultural Applications*, Transactions of the American Society of Agricultural Engineers, Vol. 11, No. 3, 1995, pp. 459-464.
9. Crow, S. C. and Manning, F. L. *Differential GPS Control of Starcar 2*, Navigation, Vol. 39, No. 4, Winter 1992-93, pp. 383-405.
10. Lawrence, D., Pervan, B., Cohen, C., Cobb, H. S., Powell, J. D., and Parkinson, B.W. *A Real-Time Architecture for Kinematic GPS Applied to the Integrity Beacon Landing System*, Proceedings of the 51st Annual Meeting - Institute of Navigation, Colorado Springs, CO, June 1995, pp. 271-280.
11. Cohen, C. E., McNally, B. D., and Parkinson, B. W. *Flight Tests of Attitude Determination Using GPS Compared Against an Inertial Navigation Unit*, National Technical Meeting -

- Institute of Navigation, San Francisco, CA, Jan 1993.
12. Pervan, B., Cohen, C., Lawrence, D., Cobb, H. S., Powell, J. D., and Parkinson, B.W. *Autonomous Integrity Monitoring for GPS-Based Precision Landing Using Ground-Based Integrity Beacon Pseudolites*, Proceedings of ION - GPS '94, Salt Lake City, UT, Sept. 1994, pp. 609-618.
 13. Owen, G. M. *A Tractor Handling Study*. Vehicle System Dynamics, Vol. 11, 1982, pp. 215-240.
 14. El-Gindy, M. and Wong, J. Y. *A Comparison of Various Computer Simulation Models for Predicting the Directional Responses of Articulated Vehicles*. Vehicle System Dynamics, Vol. 16, 1987, pp. 249-268.
 15. Norton, J. P. An Introduction to Identification, Academic Press, 1986.
 16. Widrow, B., and Stearns, S. D. Adaptive Signal Processing, Practice-Hall Signal Processing Series, 1985.
 17. Bryson, A.E., and Ho, Y.C., Applied Optimal Estimation, Hemisphere Publishing Corp., 1975.
 18. Kalman, R.E., *A New Approach to Linear Filtering and Prediction*, Trans. ASME. Ser. D.J. Basic Eng. Vol. 82, pp. 35-45
 19. Gelb, A., Applied Optimal Estimation, Analytic Sciences Corp., 1989.

An Examination of the Relative Merits of Various Sensors for Vehicle Navigation

Eric Abbott and Prof. David Powell
Stanford University

BIOGRAPHIES

Eric Abbott is a student at Stanford University. He received a Bachelor's degree in mechanical engineering from the University of Illinois in 1990 and a Master's degree in the same field from Stanford in 1993. He is currently nearing the completion of a PhD in mechanical engineering with a minor in electrical engineering.

Prof. J. David Powell has been on the Stanford faculty for 24 years. His research has dealt with land, air, and space vehicle navigation and control. He is a co-author of two control system textbooks.

ABSTRACT

The research described in this paper is aimed at providing a quantitative measure and a qualitative understanding of the contribution that each sensor in a land-vehicle navigation system makes to the system's overall performance. This includes a quantitative evaluation of the relative merits of various sensors typically used in existing land-vehicle navigation systems.

The results presented in this paper are based on data obtained from analytical studies and simulations. An analytical error model was derived for each sensor that was examined. These error models were subsequently used in a Kalman filter whose purpose was to generate an estimate of the vehicle's position. The Kalman filter was used in several Monte Carlo simulation studies of various system architectures. In addition, experimental data has been obtained from a prototype navigation system that has been installed in a test vehicle. These experimental data have been used to verify the analytical error models for several sensors.

Results show that the accurate calibration of a navigation system's heading and heading rate sensors to be of prime importance. It has been found that a rate gyro's scale

factor exhibits poor observability characteristics, and the use of differential GPS fixes do not substantially improve the estimate of this quantity. In addition, it has been found that a rate gyro's bias error contributes more to positioning error than other rate gyro errors. Finally, we have found that, in the absence of absolute position measurements, the presence of a compass in the navigation system plays a significant role in reducing positioning errors.

INTRODUCTION

Various designs for land-vehicle navigation systems can be found in the patent literature [33-39] and the technical literature [1-14]. While the details of each system's design usually vary from system to system, a group of navigation sensors, a subset of which is typically found in many land-vehicle navigation systems, were identified. Table 1 shows a list of such sensors.

Table 1 - Example Navigation Sensors and Aids

Sensor	Measurement/Aid
GPS	Absolute position
Rate gyro	Heading rate
Compass	Absolute heading
Odometer	Position change
Map-matching	Position and heading aid

While the list in Table 1 is not necessarily exhaustive, 138 of the 160 land-vehicle navigation systems identified in [45] make use of some subset of these sensors.

The variety of sensors in Table 1 leads one to wonder what criteria navigation system designers have used when selecting sensors for use in their vehicle navigation system. One could probably say with some certainty that the set of sensors selected by a design team is heavily influenced by the team's dual goals of maximizing the system's performance while minimizing its total cost. Unfortunately for system designers, however, system cost

and performance are usually directly, rather than inversely, related--very accurate sensors may improve the performance of a system, but they tend to cost more than similar, less accurate sensors. Designers of land-vehicle navigation systems are therefore faced with trading off system cost and performance and must judiciously select that set of sensors deemed to be most cost-effective. The purpose of this paper is to provide information that can aid designers in this selection process.

This paper presents a quantitative examination of the contributions that various sensors make to the performance of a land-vehicle navigation system. The results presented in this paper were obtained principally by means of analytical studies and simulations. Analyses of various sensors were performed in order to arrive at error models for those sensors. Based on these error models, an extended Kalman filter was designed to combine information from the sensors and to arrive at an estimate of the vehicle's position. Once this filter was designed, the performance of several sets of navigation sensors was evaluated using the Kalman filter to combine the sensor data. Because the filter equations are nonlinear, Monte Carlo simulations, rather than covariance analyses, were used to evaluate the performance of each system of interest. The accuracy of the Kalman filter's estimate of the vehicle's position was the metric used to evaluate each system's performance. The relative performance of each navigation system was then attributed to differences between the systems.

Many automotive navigation systems use map-matching to improve positioning accuracy. As long as there is enough variation in a vehicle's path to allow the map-matching algorithm to identify the vehicle's correct path, the error in the estimate of a vehicle's position is primarily that of the map database. The dead-reckoning sensors have virtually no effect on the errors. However, the presence of GPS and the quality of the dead-reckoning sensors do affect the speed and reliability of a map-matching algorithm's convergence. As a measure of the degree of usefulness of the various sensors, we have chosen to evaluate various navigation systems without map-matching. The resulting positioning accuracy should correlate directly with the sensors' ability to aid a map-matching algorithm's convergence.

SECTION 1 - PREVIOUS RESEARCH

Many land-vehicle navigation systems have been designed and presented in the literature. Previous work presenting land-vehicle navigation system designs and analyses includes navigation systems for automobiles [1-14,21,22,23,33-39] and other types of land-based vehicles, including mobile robots [15,17-20,26], planetary rovers [29], and exploratory vehicles [25].

While much attention has been given to the algorithms used to combine the information obtained from various sensors and navigation aids [1-14,33-39,40-43], relatively little analytical or quantitative work seems to have been done to establish rationales for sensor selection. Nor has much work been done to quantify the relative merits of various navigation sensors. In [28], the authors discuss the effects of inertial sensor quality on the performance of a navigation system; however, this work focuses on military-grade navigation systems, which are generally far too expensive to be practicable for commercial land-vehicle use. In [29], the author presents a simulation study in which the relative merits of two inertial navigation systems for use in a Mars rover are examined. While the spirit of the work in [29] is similar to that of this research, there are important differences. First, the author sought to evaluate two navigation *systems*, not individual sensor contributions. Second, one of the systems, composed of 3 accelerometers and 3 gyroscopes, is generally not found in existing automobile navigation systems. Finally, the author assumed that the vehicle moved over level terrain at a maximum speed of 1.0 meters per second, a speed that is much lower than is typical of an automobile. In an earlier work, [27], the author enumerates various error sources in a particular vehicle navigation system. However, the navigation system examined used only LORAN-C to position the vehicle; dead-reckoning sensors were not examined. Finally, in [30], the author presents a methodology for evaluating a land-vehicle navigation system by assigning it a "score" based on a host of criteria. The purpose of the scoring method is to provide an objective basis by which to compare systems. However, the author's scoring system considers a wide variety of evaluation criteria, including functional features, cost, power consumption, reliability, and so on. The author does not address the relative merits of various navigation sensors.

SECTION 2 - ERROR ANALYSIS AND KALMAN FILTER IMPLEMENTATION

This section includes an examination of several of the sensors in Table 1. For each sensor, a mathematical model that describes the errors in that sensor's output is included. For some of the sensors, the error models are derived, while for others, the error models are simply taken from other sources. Each sensor will be examined in turn; following this, the error equations will be incorporated into a Kalman filter.

2.1 - Odometer Error Model

An odometer measures the curvilinear distance traveled by a vehicle. This section includes an analysis of the errors that appear in an odometer's output. Equations

describing the use of odometer data in particular navigation systems appear in [15,17,18,22]; a particularly detailed analysis is given in [17]. In [21] and [4], the authors discuss various error sources in odometry and actual data is presented in [4], but no formal analyses are presented. The following analysis is slightly different from other analyses in the literature.

For the analysis that follows, we first consider Figure 1, which is meant to be a functional representation of any one of a number of odometer implementations. This figure shows a cross-section of a rotating shaft or gear in the vehicle. Upon the rotating shaft are several evenly-spaced "trigger points" which pass a "pick-up sensor" that is mounted to the body of the vehicle. The odometer operates in such a way that the pick-up sensor generates a single digital pulse when any one of the trigger points passes it.

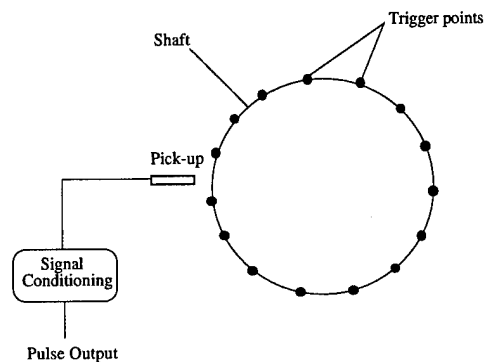


Figure 1. A schematic representation of an odometer

For an odometer comprised of an optical shaft encoder, as in [3], the trigger points represent the slots in the encoder wheel and the pick-up sensor represents an opto-electric device that generates a digital pulse when a slot passes through its field of vision. For an odometer comprised of a series of magnets and a pick-up coil, as in [4] and [12], the trigger points represent the magnets, and the pick-up sensor represents the coil and any necessary signal-conditioning circuitry.

However the odometer is physically implemented, it will be assumed in the following analysis that the odometer is any sensor that generates a constant integer number of digital pulses for each revolution of a rotating shaft on the vehicle. It is further assumed that the rotation rate of the shaft is (approximately) linearly proportional to the forward speed of the vehicle, and that this rotation rate is independent of whether the vehicle is turning. (An odometer on a vehicle's drive shaft would satisfy these assumptions.) Finally, it will be assumed that the odometer readings are taken at points in time separated by a constant sampling period, T , and that, between sampling points, the cumulative number of odometer

pulses, N , is stored. In the following analysis, k is an integer that refers to the sample taken at time $t = kT$.

By way of definition, we first define the *true odometer scale factor*, S_{true} , to be the curvilinear distance traveled by the vehicle between two consecutive pulse outputs of the odometer. The value of S_{true} depends on the radii of the vehicle's tires and is therefore not necessarily constant because the radii of the vehicle's tires may vary with the vehicle's speed, the tires' air pressure, or the progressive wear of the vehicle's tires [4]. Despite this fact, we will, for this analysis, assume that significant variations in S_{true} take place over a time period that is much longer than one sampling period. Therefore, we will consider S_{true} to be constant over one sampling period and treat it as an unknown quantity. We next define the *nominal odometer scale factor*, $S_{nominal}$, to be a known *constant* that is approximately equal to the true odometer scale factor, S_{true} . Finally, we define the odometer scale factor bias, δS , to be the difference between S_{true} and $S_{nominal}$:

$$\delta S \equiv S_{true} - S_{nominal} \quad (1)$$

Note that δS is not necessarily constant, nor is it known exactly. Note also that S_{true} , $S_{nominal}$, and δS all have dimensions of distance traveled per pulse.

We now seek to derive an expression for the error in the odometer measurement. We begin our analysis by assuming that, when the k^{th} sample is taken, the pick-up sensor is located randomly, with uniform distribution, between any two trigger points on the shaft. Let us next define d_k as the forward distance that the vehicle must travel in order to cause the next trigger point to pass the pick-up sensor. The quantity d_k is a random variable with a uniform distribution from 0 to S_{true} , denoted

$$d_k = U(0, S_{true}) \quad (2)$$

If the vehicle subsequently moves forward by some arbitrary distance D_{true} over the next T seconds, then the odometer will generate N pulses. At the start of the $k+1^{th}$ sampling time, the pick-up sensor can be located anywhere between two trigger points. Let us define d_{k+1} as the forward distance that the vehicle must travel in order to cause the next trigger point to pass the pick-up sensor. The forward distance traveled from timestep k to timestep $k+1$, D_{true} , is therefore related to N and S_{true} by

$$D_{true} = S_{true}(N-1) + d_k + (S_{true} - d_{k+1}) \quad (3)$$

or

$$D_{true} = S_{true}N + d_k - d_{k+1} \quad (4)$$

On the right-hand side of Equation (4), we see the difference of two random variables, d_k and d_{k+1} , both of which are uniformly distributed from 0 to S_{true} . This difference is also a random variable, which shall be denoted $d_{k,k+1}$, whose distribution is the convolution of $U(0, S_{true})$ with $U(0, -S_{true})$ and is shown in Figure 2.

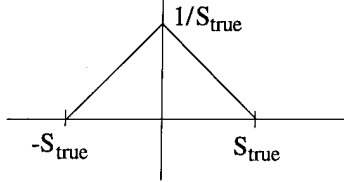


Figure 2. - Probability density function of $d_{k,k+1}$

Therefore,

$$D_{true} = S_{true} N + d_{k,k+1} \quad (5)$$

Note that $d_{k,k+1}$ is a quantization error that arises because the odometer discretizes the distance traveled by the vehicle into pieces that are S_{true} in length.

We now turn our attention to the measurement that is made by the odometer. The measurement that is actually made with the odometer is the distance D_{meas} , the product of $S_{nominal}$ and N :

$$D_{meas} = S_{nominal} N \quad (6)$$

In general, D_{meas} will not be equal to D_{true} , not only because $S_{nominal}$ is not generally equal to S_{true} , but also because D_{true} contains the random quantity $d_{k,k+1}$. We seek, as the result of this analysis, a mathematical expression for the difference between D_{meas} and D_{true} . To that end, we next define the error in the measurement, D_{error} , such that

$$D_{meas} = D_{true} + D_{error} \quad (7)$$

then, substituting from (1) and (6) into (7), we arrive at

$$D_{meas} = (S_{true} - \delta S) N \quad (8)$$

So, substituting from (5) into (8) for S_{true} ,

$$D_{meas} = D_{true} - d_{k,k+1} - N\delta S \quad (9)$$

Finally, setting the right-hand sides of (7) and (9) equal to each other, we arrive at an expression for the error in the distance measured by the odometer:

$$D_{error} = -N\delta S - d_{k,k+1} \quad (10)$$

Equation (10) shows that the error in the measured distance has two components: a non-random component that is proportional to the distance traveled and a random component that is distributed as shown in Figure 2. Equation (10) is the basic error equation for the odometer that will be used in the Kalman filter developed in Section 2.5.

2.2 - Rate Gyro Error Model

A rate gyro measures the vehicle's rotation rate about a vertical axis. Obviously, such an instrument can be used to obtain information about the vehicle's change in heading. In this section, an error model for a typical rate gyro is developed. In other work, a particularly thorough analysis of two low-cost rate gyros can be found in [26]; in this research, the authors develop error models for the rate gyros and then evaluate them on real gyro data. Perhaps one drawback of the work in [26] is that the authors' error models appear to compensate only for bias errors in the gyro's output, but not for scale factor errors.

The output of a rate gyro (V_{RG}) is usually an analog voltage that varies (nominally) linearly with the rotation rate (ω) of the gyro. The quantity measured from a rate gyro includes three sources of error--scale factor error, bias error, and white noise error [46-48]. The relationship between V_{RG} and ω is given by

$$V_{RG} = (K + \delta K)\omega + V_{nominal} + \delta V + v \quad (11)$$

where δK (the scale factor error) is the deviation from $K_{nominal}$ of the slope of the line that relates ω to V_{RG} , δV (the bias error) is the deviation from $V_{nominal}$ of the zero-angular-speed output of the rate gyro, and v is uncorrelated white noise that appears in the output signal of the gyro. Equation (11) is the measurement equation used in the authors' Kalman filter. The models for the bias and scale factor errors are first-order Gauss-Markov processes given by

$$\delta \dot{V} = -\beta_{\delta V} \delta V + u_{\delta V} \quad (12)$$

$$\delta \dot{K} = -\beta_{\delta K} \delta K + u_{\delta K} \quad (13)$$

where $\beta_{\delta V}$ and $\beta_{\delta K}$ are constants and $u_{\delta V}$ and $u_{\delta K}$ are zero-mean Gaussian white noise.

It should be noted that, for various reasons, several sources of error that may appear in the output of a rate gyro have been ignored in the preceding derivation. Each of these error sources will now be briefly defined and an explanation will be given as to why they were ignored. The error sources that were ignored are g-sensitivity, cross-axis sensitivity, and nonlinearity.

The g-sensitivity of a rate gyro causes errors to be introduced into the gyro's output as a result of linear acceleration. The output of an ideal rate gyro would be entirely insensitive to acceleration. This quantity has been ignored because the authors have found that most manufacturers of low-cost rate gyros do not include this error source in their specification; also, the authors have not tested a real rate gyro to measure its g-sensitivity. A "typical" size for this error source could not, therefore, be substantiated for the low-cost rate gyros that were examined.

Cross-axis sensitivity causes errors to be introduced into the gyro's output as a result of rotations about an axis perpendicular to the axis of sensitivity. This error has been ignored because a land vehicle typically rotates about a vertical axis only.

Finally, nonlinearity errors are introduced into the gyro's output because the relationship between angular speed and the gyro's output is not truly linear. This error source has been ignored because it has been the author's experience that rate gyro manufacturers generally do not provide an analytical model for this error. Furthermore, simulation results have shown that specified nonlinearity errors are generally small enough that they can be lumped with other error sources in the Kalman filter implementation.

2.3 - Magnetic Compass Error Model

A magnetic compass is an electronic device that measures its heading relative to magnetic North. These devices measure the direction of the Earth's magnetic field locally, using any one of several physical implementations, including magnetometers, a Hall effect sensor, or a set of orthogonal coils referred to as a "fluxgate".

It seems generally true that, of the existing compass implementations, the fluxgate compass is most commonly used in existing land-vehicle navigation systems [45]. Therefore, in the following section, an error model for the fluxgate compass only is presented, and the derivation of error models for other implementations is left to future work.

Error compensation schemes for the fluxgate compass have received significant attention. Some error compensation methods depend on having other sensors available, such as an angular velocity sensor [32] or GPS [31]. Other approaches involve calibrating the compass errors by generating a lookup table of the errors as a function of heading [12,13,23] or involve some type of basic prefiltering technique [22,15]. Still other approaches involve gimbaling the compass to prevent

the compass from tilting relative to the local horizontal, thereby avoiding tilt-induced errors in the compass' output [24].

An analytical study of fluxgate compass errors has shown that the errors that appear in a compass' output can be mathematically modeled as a function of magnetic heading [16]. In [16], the authors derive the following mathematical expression for the fluxgate compass errors that arise from various error sources :

$$\delta\Theta = A + B \sin(\Theta) + C \cos(\Theta) + D \sin(2\Theta) + E \cos(2\Theta) \quad (14)$$

where A, B, C, D, and E are constants and Θ is the true magnetic heading of the compass. It has been the authors' experience that this model is difficult to use because of the relatively large number of parameters that must be estimated. The estimates of the parameters A, B, C, D, and E were unstable when the authors mechanized this model in a Kalman filter. In [21], this model was also rejected, but for other reasons. Also, in [15], this model was cited but apparently not used.

Some fluxgate compass manufacturers specify a method by which the user can calibrate the errors in the compass. Usually, this involves rotating the compass through at least a 360-degree turn. The calibration process is designed to eliminate systematic measurement errors that are a function of heading. The authors have therefore assumed that the compass used in their simulated navigation systems has been calibrated. The residual errors (i.e. after calibration) have been modeled as a random walk :

$$\delta\dot{\Theta} = u \quad (15)$$

The quantity $\delta\dot{\Theta}$ is the residual error and u is zero-mean Gaussian white noise.

2.4 - GPS Discussion and Error Model

For the simulation work in this paper, the authors have explored the use of both unaided GPS and differential GPS. The main source of error in the authors' error model for unaided GPS is Selective Availability (SA), an intentional performance degradation that causes the system's horizontal positioning accuracy to fall to approximately 100 meters (2dRMS) [49]. For unaided GPS positioning, the model used to simulate SA-induced positioning errors is a second-order Gauss-Markov process presented in [44]. This model has been shown to accurately simulate positioning errors induced by Selective Availability [44].

Because DGPS may be used in a navigation system, the authors have also explored various effects of using DGPS positioning. Unlike unaided GPS, the use of DGPS requires a source of differential corrections. One source of differential corrections includes commercial services to which users can subscribe. For a fee, subscribers are given access to differential corrections that are broadcast on a radio frequency in their locale [50,51].

Two other sources of differential corrections may be available to navigation systems for land-based vehicles, although both are not yet widely available. The U.S. Coast Guard (USCG) is in the process of building differential GPS correction stations scattered around the U.S. coasts. When complete, the system will provide differential GPS corrections to the marine community free of charge [52]. The radiobeacons broadcasting the corrections transmit nondirectionally at a frequency of 285-325 kHz with enough power to reach a user 10 to 175 miles away [53]. Therefore, although not designed primarily for land-based GPS users, the corrections may be receivable by land-based GPS users in the vicinity of the U.S. coast.

A second potential source of differential corrections for users of land-vehicle navigation systems comes from the Wide Area Augmentation System (WAAS), a system currently under development by the Federal Aviation Administration. The WAAS is a GPS-based navigation system being developed for the aviation community. According to current plans, differential GPS corrections would be broadcast free of charge over the entire U.S. by a set of geosynchronous communications satellites [49].

Although DGPS positioning can improve the positioning accuracy of a navigation system substantially, accessing DGPS corrections is generally not without some cost. Commercial differential correction services, for example, add to system cost through the subscription costs and the cost of the equipment required to access the broadcast corrections. The USCG DGPS system would require equipment (in addition to a GPS receiver) to receive the broadcast corrections. In contrast, current indications are that WAAS corrections will be broadcast in such a way that an ordinary GPS receiver with an internal software modification will be able to receive them--no external RF receivers will be required [49].

Because these and other differential correction services are appearing, the authors believe that DGPS may play an important role in the evolution of land-vehicle navigation systems. In addition, the authors believe that the use of DGPS positioning (as opposed to unaided GPS positioning) in a vehicle navigation system may affect the relative importance of various dead-reckoning sensors.

Furthermore, the additional costs associated with accessing DGPS corrections present a tradeoff to navigation system designers--is the improvement in positioning accuracy worth the added cost? For these reasons, the authors believe that it is justifiable to include in our research the examination of navigation systems that use DGPS positioning.

Errors in DGPS position fixes were simulated simply as additive white noise with an RMS value of 1.0 meter. This is probably the smallest that DGPS positioning errors would reasonably be in practice. The authors chose this value so that our results will reveal the best performance that could reasonably be expected using DGPS. Some commercial differential correction services advertise their best positioning accuracy to be on the order of 1.0 meter. Whether the WAAS and USCG differential correction services will be this accurate is unknown.

2.5 - Kalman Filter Design

Details of the Kalman filter algorithm and the development of the extended Kalman filter will not be given here. For such details, the reader is referred to [54]. Equations for the Kalman filter algorithm are given only to acquaint the reader with the authors' notation. The principle feature of this section is the set of model and measurement equations of the Kalman filter used for this research.

With regard to notation, column matrices, or vectors, will be shown in lowercase bold type, scalars will be shown with lowercase non-bold type, and matrices of general dimensions will be shown with uppercase letters. Also, the symbols used to denote various quantities are defined as follows :

p_x	: x-location of the vehicle in a local x-y-z frame defined with its origin at an arbitrary location
p_y	: y-location of the vehicle in a local x-y-z frame defined with its origin at an arbitrary location
V	: the speed of the vehicle
a	: the acceleration of the vehicle
τ_a	: the time constant of the vehicle's acceleration
β_a	: $1/\tau_a$
Θ	: the heading of the vehicle defined from 0 to 2π relative to true North
ω	: the heading rate of the vehicle
τ_ω	: the time constant of the vehicle's angular speed
β_ω	: $1/\tau_\omega$
$\delta\Theta$: the bias error in the fluxgate compass' heading measurement
K_{nominal}	: the rate gyro's nominal scale factor
δK	: the deviation of the rate gyro's true scale factor from K_{nominal}

$\tau_{\delta K}$: the time constant of δK
 $\beta_{\delta K}$: $1/\tau_{\delta K}$
 V_{RG} : the voltage output by the rate gyro
 $V_{nominal}$: the voltage nominally output by the rate gyro at zero angular speed
 δV : the deviation of the rate gyro's true zero-angular-speed output from $V_{nominal}$
 δS : the odometer's scale factor bias
 $S_{nominal}$: the nominal odometer scale factor
 $\tau_{\delta S}$: the time constant on the variations in the odometer's scale factor bias
 $\beta_{\delta S}$: $1/\tau_{\delta S}$
 ϵ_x : the x-component of Selective Availability
 v_x : the x-component of Selective Availability's rate of change
 ϵ_y : the y-component of Selective Availability
 v_y : the y-component of Selective Availability's rate of change
 λ : a constant used in the model for Selective Availability
 ζ : a constant used in the model for Selective Availability
 N : the number of pulses output by the vehicle's odometer between samples k and $k+1$
 T : the time between measurements
 u_a : white noise driving the model equation for the vehicle's acceleration
 u_ω : white noise driving the model equation for the vehicle's heading rate
 $u_{\delta S}$: white noise driving the model equation for the odometer's scale factor bias
 $u_{\delta \Theta}$: white noise driving the model equation for the fluxgate compass' bias
 $u_{\delta K}$: white noise driving the model equation for the rate gyro's scale factor bias
 $u_{\delta V}$: white noise driving the model equation for the rate gyro's zero output bias
 u_{vx} : white noise driving the model equation for the x-component of Selective Availability's rate of change
 u_{vy} : white noise driving the model equation for the y-component of Selective Availability's rate of change
 $p_{x,GPS}$: the vehicle's x-location measured by GPS
 $p_{y,GPS}$: the vehicle's y-location measured by GPS
 $\Theta_{compass}$: heading measurement from the compass
 v_{px} : white noise in the measurement of the vehicle's x-location
 v_{py} : white noise in the measurement of the vehicle's y-location
 $v_{\Delta d,od}$: white noise in the measurement of the vehicle's change in location by the odometer
 v_Θ : white noise in the measurement of heading by the compass

v_{RG} : white noise in the rate gyro measurement

According to [54], the evolution of the state vector, \mathbf{x} , of a nonlinear Kalman filter may be described by the nonlinear differential equations

$$\dot{\mathbf{x}} = \mathbf{f}(\mathbf{x}, t) + \mathbf{u} \quad (16)$$

where \mathbf{u} is a vector of zero-mean Gaussian white noise, and t is time. This set of differential equations will henceforth be referred to as the filter's *model equations*.

The measurement vector, \mathbf{z} , bears the following relationship to the filter's states :

$$\mathbf{z} = \mathbf{h}(\mathbf{x}) + \mathbf{v} \quad (17)$$

where \mathbf{h} is a nonlinear function, and \mathbf{v} is a vector whose elements are Gaussian white noise. The right-hand side of Equation (17) will henceforth be referred to as the filter's *measurement equations*.

Because we seek to evaluate navigation systems that have various sensor combinations, the number of model equations used in the filter will vary depending on which sensors are present to provide measurement information. The following equations model the vehicle's kinematic motion and are present in the filter regardless of which sensors are present :

$$\dot{p}_x = V \sin(\theta) \quad (18)$$

$$\dot{p}_y = V \cos(\theta) \quad (19)$$

$$\dot{\theta} = \omega \quad (20)$$

$$\dot{\omega} = -\beta_\omega \omega + u_\omega \quad (21)$$

$$\dot{V} = a \quad (22)$$

$$\dot{a} = -\beta_a a + u_a \quad (23)$$

The following equations model sensor errors and are present in the filter only if the corresponding sensor is also present to provide measurement information :

$$\dot{\delta \Theta} = u_{\delta \Theta} \quad (24)$$

$$\dot{\delta V} = -\beta_{\delta V} \delta V + u_{\delta V} \quad (25)$$

$$\dot{\delta K} = -\beta_{\delta K} \delta K + u_{\delta K} \quad (26)$$

$$\dot{\delta S} = -\beta_{\delta S} \delta S + u_{\delta S} \quad (27)$$

$$\dot{\epsilon}_x = v_x \quad (28)$$

$$\dot{v}_x = -\lambda^2 \epsilon_x - 2\lambda \zeta v_x + u_{vx} \quad (29)$$

$$\dot{\epsilon}_y = v_y \quad (30)$$

$$\dot{v}_y = -\lambda^2 \epsilon_y - 2\lambda \zeta v_y + u_{vy} \quad (31)$$

The model equations (18)-(31) are continuous-time differential equations. The derivative of the elements of

the filter's state vector, \mathbf{x} , are the quantities on the left-hand sides of these equations. Before these equations can be mechanized in a discrete-time Kalman filter, they must first be discretized. However, the discretized equations will not be given here.

The Kalman filter's measurement equations will now be presented. In the following measurement equations, the left-hand side of the equation represents the actual quantity that is put into the measurement vector \mathbf{z} ; this quantity is usually measured directly from a sensor. The right-hand side represents $h(\mathbf{x})$, the combination of states that is equal to the measured quantity. First, if GPS measurements are available, we have

$$P_{x,GPS} = P_x + \varepsilon_x + v_{px} \quad (32)$$

$$P_{y,GPS} = P_y + \varepsilon_y + v_{py} \quad (33)$$

If DGPS measurements are available, then

$$P_{x,GPS} = P_x + v_{px} \quad (34)$$

$$P_{y,GPS} = P_y + v_{py} \quad (35)$$

If an odometer is available, then

$$S_{\text{nominal}} N = \frac{1}{2} a T^2 + VT - \delta S N + v_{\Delta d, od} \quad (36)$$

If the fluxgate compass is available, then

$$\Theta_{\text{compass}} = \Theta + \delta\Theta + v_{\Theta} \quad (37)$$

If the rate gyro is available, then

$$V_{RG} - V_{\text{nominal}} = (K_{\text{nominal}} + \delta K) \omega + \delta V + v_{RG} \quad (38)$$

Note that model equations (18) and (19) and measurement equation (38) are nonlinear. The presence of these nonlinear equations require the use of an extended Kalman filter or some other nonlinear filtering algorithm. Also, all of the white noise variables are assumed to have a mean of zero and a Gaussian distribution. The particular values chosen for each variable's variance will not be given here.

2.6 Intuitive and Analytical Observations

2.6.1 Poor observability of the rate gyro's scale factor

If a Kalman filter is to correctly estimate any particular element of its state vector, information about that element must be obtainable from the sensor measurements. If it is possible to establish an estimate of a state from the measurement sequence, then, loosely speaking, that state is said to be *observable* [54]. While there exist formal

observability tests which may be applied to optimal linear Kalman filters [54], the authors know of no observability tests which may be applied to a nonlinear filter. The intuitive arguments which follow are therefore provided to support, not prove, the following hypothesis.

The hypothesis we wish to examine is this : the rate gyro's scale factor is observable only when the vehicle's heading rate is nonzero (i.e. when the vehicle is turning). An argument in support of this hypothesis can be made if the measurement equation for the rate gyro is examined. Recall equation (38) from Section 2.5 :

$$V_{RG} - V_{\text{nominal}} = (K_{\text{nominal}} + \delta K) \omega + \delta V + v_{RG} \quad (38)$$

The quantities in this equation that are relevant to this discussion are δK , the rate gyro's scale factor bias, and ω , the heading rate of the vehicle. If the heading rate of the vehicle is identically zero, then

$$V_{RG} - V_{\text{nominal}} = \delta V + v_{RG} \quad (39)$$

The absence of K_{nominal} and δK in equation (39) suggests that no information about the scale factor is available in the rate gyro's output, V_{RG} . In other words, if the heading rate of the vehicle is zero, then the rate gyro's output contains no data from which the gyro's scale factor can be deduced. Because this is the *only* measurement that contains *any* information about the rate gyro's scale factor, we are led to believe that the scale factor is unobservable when the vehicle's heading rate is zero.

The significance of the scale factor's poor observability will become more apparent in the Results section. Suffice it to say here that, because a vehicle traveling on a road network probably spends most of its time traveling in straight lines, its heading rate is probably nearly zero most of the time. Therefore, one might expect that the rate gyro's scale factor would not be observable most of the time, and, consequently, that the Kalman filter would generally do a poor job of estimating this quantity.

It is worth noting that, while this result may be interesting, it will be shown later that bias error (for the rate gyro we simulated) contributes much more to positioning errors than does scale factor error. The fact that the rate gyro's scale factor exhibits poor observability characteristics may be more important if a navigation system uses a rate gyro with a widely-varying scale factor.

2.6.2 The role of heading estimates

In this section we wish to discuss the impact that errors in heading and heading rate estimates have on the error

in a position estimate. These results will be relevant when we examine the roles that a compass and a rate gyro play in limiting position errors for a navigation system in which absolute position measurements are absent.

It can be shown that a heading bias ($\Delta\Theta$) causes position errors to grow linearly with time, while a heading rate bias ($\Delta\omega$) causes position errors to grow with the square of time. The amount of time it takes for positioning errors that result from a heading rate bias error to exceed those that result from a heading bias error is given by

$$t = \frac{2\Delta\Theta}{\Delta\omega} \quad (45)$$

Our results have shown heading bias errors to typically be on the order of 2 to 5 degrees and heading rate biases to be on the order of 0.1 degrees per second. Equation (45) then implies that a heading bias of 3 degrees and a heading rate bias of 0.1 degrees per second will produce the same positioning error in 60 seconds; beyond 60 seconds, the error caused by the heading rate bias will exceed that caused by the heading bias. The relevance of this result will become more apparent in the discussion of our simulation results. Suffice it to say here that this result underscores the importance of the accurate calibration of a navigation system's heading rate sensor(s) and the importance of a stable rate gyro bias.

SECTION 3 - ANALYSIS METHOD

In order to understand the analysis method used in this research, it is first necessary to recognize that the contribution that a sensor makes to the performance of a system as a whole must be evaluated in the context of that system. In other words, the impact that a particular sensor has on a system's performance will vary according to which *other* sensors are used in the system; the contribution of a particular sensor is not independent of the other sensors in the system. This is true because a Kalman filter makes use of *all* available information to estimate its states, implying that the errors in certain sensor readings may be estimated more or less accurately depending on what other sensor information is available to the filter. Armed with this insight, it becomes clear that the value of a particular sensor cannot be quantified by examining the performance of only a single system. Furthermore, it is not possible to accurately quantify the relative merits of two different sensors unless both sensors are examined with the same complement of other sensors.

Another realization that had an impact on our analysis methodology is that, when GPS is in use, errors in the GPS position fix dominate the errors in the position

estimate. When DGPS is used in a navigation system, the position fix is so accurate that information from the dead-reckoning sensors do not figure prominently into the position estimate. When stand-alone GPS (with Selective Availability errors) is used in a system, the dead-reckoning sensors are not sufficiently accurate to reduce Selective Availability errors significantly. Evidence for this is given by Figure 3.

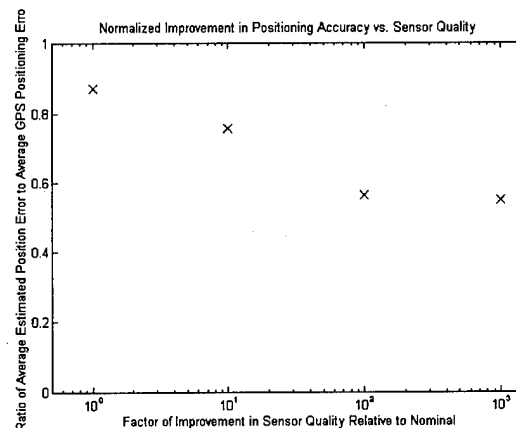


Figure 3. - This figure shows positioning error versus dead-reckoning sensor quality for four systems. The positioning error has been normalized by the mean error in the GPS position fixes.

Figure 3 shows a plot of average normalized positioning error versus dead-reckoning sensor quality for 4 navigation systems. Although the same dead-reckoning sensors were used in all four systems that were simulated, the *quality* of those sensors was different. The leftmost point represents a system that used dead-reckoning sensors with errors of "typical" magnitude. Moving from left to right, each successive system used sensors whose RMS errors are lower by approximately a factor of 10.

To generate the data shown in Figure 3, a vehicle driving on a road network for 40 minutes was simulated and corresponding sensor data were generated. The sensor data were generated using stochastic error models similar to those described in Section 2. The sensor data were then filtered using the Kalman filter whose equations are given in Section 2. This process of generating and filtering sensor data was done 50 times, and the ensemble average of the error in the position estimate was computed over all 50 simulations. The time average of this ensemble average was then computed. The points plotted in Figure 3 are the ratio of this time average to the average error in the GPS position fixes.

Figure 3 suggests that the quality of dead-reckoning sensors must be substantially greater than "typical" to reduce SA-induced positioning errors significantly. Even with very accurate dead-reckoning sensors, the

positioning errors due to SA are only halved. This result suggests that if GPS position fixes are used by the Kalman filter to aid in the position estimation, then it will be very difficult to detect significant changes in positioning accuracy that result from changes in the dead-reckoning sensors. Therefore it will be very difficult to detect the individual contributions that sensor make to the performance of the a given navigation system.

Because GPS position fixes veil the contribution that individual dead-reckoning sensors make to the accuracy of the Kalman filter's position estimate, the authors chose to evaluate the impact of individual dead-reckoning sensors by examining the trends in positioning error that appeared when GPS was not available. A similar procedure was followed in [28], in which the authors examined the effects of inertial sensor quality on system performance during a GPS outage. Unlike the work here, however, the inertial sensors examined in [28] were limited to accelerometers and rate gyroscopes, and the navigation system at hand was designed for tactical missile applications. This procedure is further justified by the fact that land-vehicle navigation systems which use GPS suffer from GPS outages whenever the number or quality of received satellite signals falls below a certain point. During a GPS outage, a land-vehicle navigation system must rely solely on its dead-reckoning sensors (and possibly map-matching) for navigation information, and an understanding of the contributions that individual sensors make to the system's performance under these circumstances is particularly useful.

To evaluate several navigation systems, the authors followed the procedure schematically shown in Figure 4 and described in the following paragraph.

First, a "driving simulator" was used to simulate a vehicle moving along an arbitrary path on a road network represented by a digital map. The driving simulator generated a set of "truth data" that contained the "true" location, heading, and heading rate of the vehicle. This "truth data" was then used as input to a second simulator. The second simulator could be thought of as a "sensor simulator," because it generated data that could reasonably be obtained from a specified set of sensors inside the vehicle. The sensor simulator generated sensor data that contained errors that were computed using stochastic error models, some of which are similar to those discussed in Section 2. The sensor data that was generated was subsequently used as measurement data for the Kalman filter. For each navigation system of interest, 50 Monte Carlo simulations were run; each simulation involved generating a new set of sensor data and filtering the new data with the Kalman filter. For

each system of interest, the error in the Kalman filter's estimated position was then computed for all 50 simulations, and the ensemble average of this error was considered to be a measure of the "average" performance of that system.

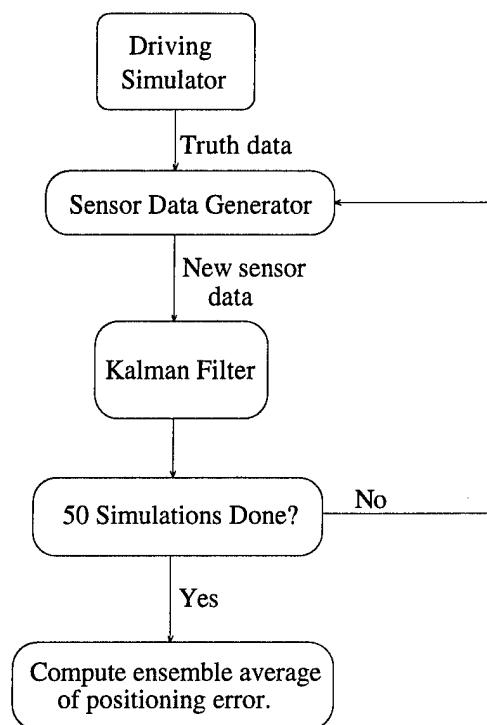


Figure 4. - A diagram schematically showing the procedure followed to evaluate various navigation systems.

To obtain information about the contribution that each dead-reckoning sensor made to a particular system's performance, the trends in positioning error that appeared when GPS was not available were examined. The driving simulator was therefore used to simulate the vehicle moving on the road network for a total of 3000 seconds*. For the first 2400 seconds, GPS location measurements were used by the Kalman filter to aid in the position estimation and to calibrate the dead-reckoning sensors. For the last 600 seconds, the GPS location measurements were ignored by the Kalman filter. The subsequent performance of the filter was then examined.

As mentioned in the Introduction, it is important to note that no map-matching algorithm was used to aid in the positioning of the vehicle. The authors are aware that if map-matching were used, some key results of this

* The authors felt that 3000 seconds was long enough to allow the Kalman filter's initial transients to die out.

research might change. The authors intend to examine the effects of map-matching in future work.

SECTION 4 - RESULTS

Simulation results for 4 navigation systems will be presented. The sensors used in each of the systems that were examined are listed in Table 2. Note that, for System 3, 4 different variations of the rate gyro error parameters were examined; unaided GPS and the odometer were used in all 4 variations.

Table 2 - Systems Evaluated

System	Sensors
1	Rate gyro, unaided GPS, fluxgate, odometer
2	Rate gyro, DGPS, fluxgate, odometer
3a	Typical rate gyro, unaided GPS, odometer
3b	Low noise and stable scale factor rate gyro
3c	Low noise and stable bias rate gyro
3d	Stable scale factor and stable bias rate gyro
4	Rate gyro, DGPS, odometer

Some values for the key parameters in the Kalman filter are given in Table 3. Definitions of the symbols in Table 3 are given in Section 2. The symbol $\sigma^2(x)$ signifies the variance of the random quantity x . Also, the values shown for the rate gyro parameters are "typical" values.

Table 3 - Values For Several Key Parameters

Parameter	Value
$\beta_{\delta K}$	$1.4 \times 10^{-4} \text{ sec}^{-1}$
$\beta_{\delta V}$	$1.0 \times 10^{-4} \text{ sec}^{-1}$
$\sigma^2(u_{\delta K})$	$1.25 \times 10^{-7} (\text{volts/rad/sec})^2$
$\sigma^2(u_{\delta V})$	$2.22 \times 10^{-7} (\text{volts/sec})^2$
$\sigma^2(v_{RG})$	$1.11 \times 10^{-5} \text{ volts}^2$
$\sigma^2(v_{\Theta})$	$3.046 \times 10^{-2} \text{ rad}^2$

We first compare System 1 with System 3a. Because System 1 contains a fluxgate compass and System 3a does not, one can probably attribute differences between the performance of the systems to the fluxgate compass. Figure 5 shows the ensemble average of the error in the Kalman filter's position estimate during the GPS outage for Systems 1 and 3a.

Note that the sudden increase in the curve's slope occurs at a point at which the vehicle turned. During the turn, the error in the heading estimate increased. After the turn, the positioning error grew more rapidly because of this increase in heading error.

As Figure 5 shows, the differences between the average performances of Systems 1 and 3a are significant. By the end of the 600-second GPS outage, the error in the estimated position for System 3a was more than 10 times

greater than that for System 1. This evidence leads us to conclude that, in the presence of long GPS outages, the fluxgate compass plays an important role in reducing the growth rate of the error in the filter's estimate of position.

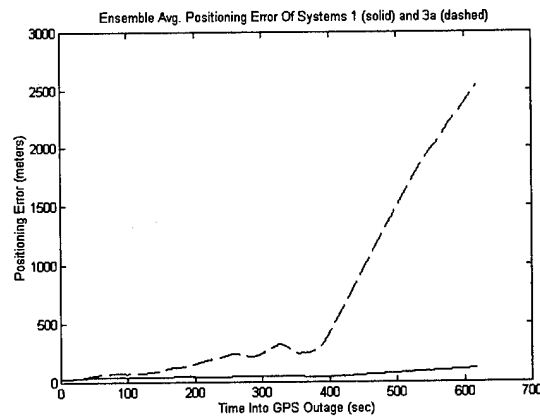


Figure 5. - This figure shows the ensemble average of the position error of Systems 1 and 3a during the GPS outage. The positioning error for System 1 is shown with the solid line, and that for System 3a is shown with the dashed line.

Analytical evidence for this conclusion is given in Section 2.6. In Section 2.6.2, it was shown that errors in position grow roughly linearly with time in the presence of a heading bias, but grow with the square of time in the presence of a heading rate bias. This conclusion leads us to speculate that a navigation system without an absolute measurement of heading will exhibit rapid position error growth. Because System 1 has both a heading and heading rate sensor, the growth rate of its positioning error is much lower than that of System 3a, which has only a heading rate sensor.

We next compare System 1 with System 2. Figure 6 shows the ensemble average of the error in the Kalman filter's position estimate for Systems 1 and 2 after the GPS outage occurred.

Notice that, when the GPS outage occurred (at $t = 0$ in Figure 6), the error in the position estimate was about 20 meters for System 1 and less than 1 meter for System 2. This difference is explained by the fact that the GPS position fixes for System 1 were corrupted by Selective Availability errors while those for System 2 were not. As Figure 6 shows, the error growth rate during the GPS outage is nearly the same for both System 1 and System 2. This may seem surprising—one might expect System 2 to have a lower error growth rate because the Kalman filter had DGPS position fixes at its disposal, while System 1 had only stand-alone GPS position fixes. One might guess that, with DGPS position fixes, the filter could calibrate the errors in all of the dead-reckoning

sensors more accurately than it could using stand-alone GPS position fixes.

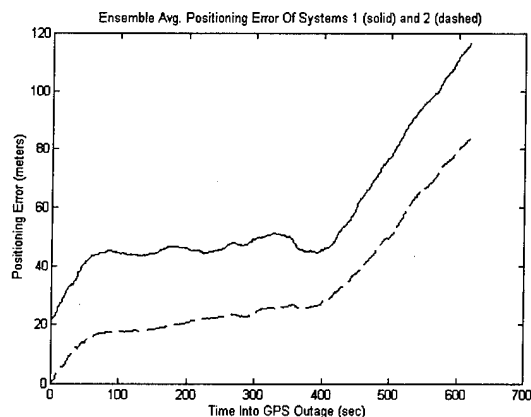


Figure 6. - This figure shows the ensemble average of the position error of Systems 1 and 2 during the GPS outage. The positioning error for System 1 is shown with the solid line, and that for System 2 is shown with the dashed line.

Our results show, however, that this conclusion is only partially true. While it is true that the Kalman filter *does* calibrate the errors in *certain* sensors more accurately when DGPS measurements are used, it appears that the Kalman filter, when using DGPS measurements, is not able to better calibrate the errors in those sensors that *dominate* the error growth rate after a GPS outage occurs. The following evidence explains why this is so.

After the GPS outage begins, only the fluxgate compass, the odometer, and the rate gyro remain. As Figure 7 shows, before the GPS outage occurred, the estimate of the odometer scale factor was accurate to approximately 1.1% for System 1 and 0.5% for System 2. The total distance traveled during the GPS outage was 3727 meters; therefore, the error in the estimated position due to error in the odometer scale factor estimate would be less than 40 meters for both systems.

From Figure 7, it appears that, on the average, the Kalman filter was better able to estimate the odometer error when DGPS measurements were available. Notice also that the Kalman filter was able to converge on an accurate estimate of the odometer scale factor *faster* when DGPS measurements were available.

For both Systems 1 and 2, the positioning error that is *not* attributable to the error in the odometer scale factor estimate must be due to error in the heading estimate. Therefore, because only a *fraction* of the total positioning error is attributable to the error in the estimate of the odometer scale factor, it seems that the majority of

positioning error must be attributed to error in the heading estimate.

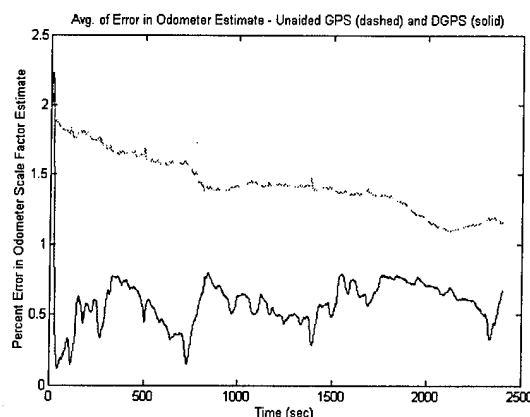


Figure 7. - This figure shows the ensemble average of the percent error in the odometer scale factor estimate for Systems 1 and 2. The data for System 1 is shown with the dashed line, and that for System 2 is shown with the solid line.

Hence, in order for a DGPS-based system to have a significantly smaller error growth rate during a GPS outage, it must successfully calibrate the system's *heading* sensors more accurately than a system that uses unaided GPS. Furthermore, the random variations in the heading sensors' errors must be sufficiently small that the accurate calibration makes a difference during the whole GPS outage. However, because the positioning error grows at nearly the same rate for both Systems 1 and 2, we conclude that, after the GPS outage begins, the random errors in the heading sensors' outputs are overriding any improvements in calibration accuracy afforded by DGPS.

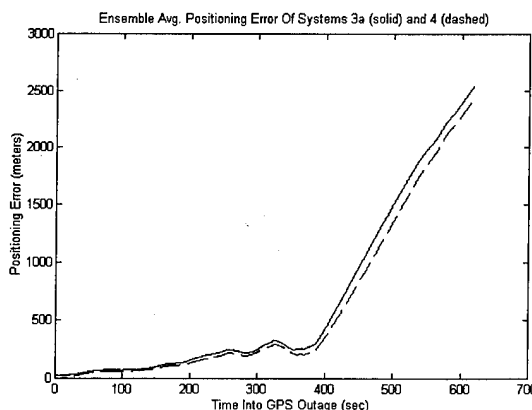


Figure 8. - This figure shows the ensemble average of the position error of Systems 3a and 4 during the GPS outage. The positioning error for System 3a is shown with the solid line, and that for System 4 is shown with the dashed line.

Similar results are shown in Figure 8. Figure 8 shows the average positioning error for Systems 3a and 4. Systems 3a and 4 are identical except that System 3a uses unaided GPS, while System 4 uses DGPS. As Figure 8 shows, the positioning error grows at nearly the same rate for both systems. This result seems to support the hypothesis that random errors in the rate gyro parameters are large enough that any improvement in calibration accuracy resulting from the use of DGPS becomes irrelevant during a GPS outage.

Our results further show that using DGPS fixes will not substantially improve the Kalman filter's ability estimate the rate gyro's scale factor. Evidence for this provided in Figure 9, which shows the ensemble average of the error in the estimate of the rate gyro scale factor for both Systems 1 and 2.

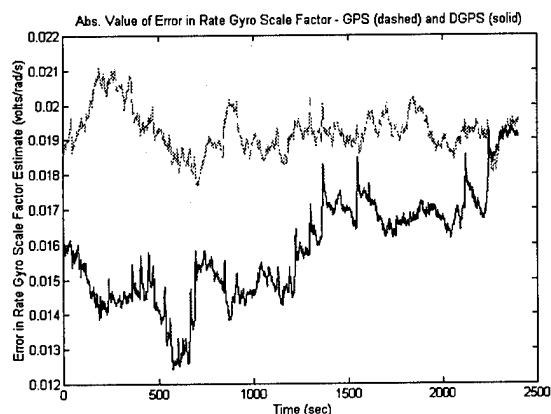


Figure 9 - This plot shows the ensemble average of the error in the estimate of the rate gyro scale factor for both Systems 1 and 2. The data for System 1 is shown with the dashed line, and that for System 2 is shown with the solid line.

As Figure 9 shows, when the Kalman filter used DGPS measurements, it did not estimate the rate gyro's scale factor much more accurately than when it used stand-alone GPS measurements. The following simple calculations show that the error in the estimate of the rate gyro scale factor was almost the same for both systems. The nominal rate gyro scale factor used for these simulations is 1.273 volts/rad/s. By examining Figure 9, then, we can roughly estimate that the error in the scale factor estimate for Systems 1 and 2 to be

$$\text{Error for System 1} = \frac{0.019}{1.273} = 1.5\% \quad (53)$$

$$\text{Error for System 2} = \frac{0.016}{1.273} = 1.3\% \quad (54)$$

In addition to these simulation results, analytical evidence was given in Section 2.6.1. In Section 2.6.1, an examination of the Kalman filter's measurement equation for the rate gyro suggested that the rate gyro's scale factor is observable only when the vehicle is turning. Consequently, the accurate positioning measurements obtained with DGPS figure into the estimation of the rate gyro's scale factor only when the vehicle is turning. However, because a vehicle that travels on a road network probably spends most of the time traveling in straight lines, one may speculate that, when it comes to estimating the rate gyro's scale factor, using DGPS would not be substantially more beneficial than using stand-alone GPS. However, while the fact that the rate gyro's scale factor is difficult to estimate is an interesting result, it will be shown next that scale factor errors do not contribute as significantly to positioning errors as do bias errors.

Because such large positioning errors accrue in the absence of a compass measurement, the authors decided to investigate System 3 in more detail. We sought to determine which of the rate gyro's error parameters--scale factor error, bias error, or white noise error--were responsible for the rapid growth of positioning error. In order to identify the contribution that each of these three error parameters make to the errors in the heading (and therefore position) estimate, 3 variations of the error parameters for the rate gyro were investigated.

As Table 2 suggests, each of the 3 parameters that govern the rate gyro error--the scale factor, bias, and white noise--were examined in turn. First, the scale factor error and noise were both lowered (a factor of 100 below typical) while a "typical" bias model was maintained. Then, the bias variations and noise error were lowered (a factor of 100 below typical) while a typical scale factor model was used. Finally, the bias and the scale factor variations were lowered (a factor of 100 below typical) and a typical level of additive white noise was used.

Simulation results are shown in Figure 10. Figure 10 shows 4 curves, each representing the average performance of System 3a (curve 1), 3b (curve 2), 3c and 3d (curves 3 and 4). As Figure 10 shows, the error in the estimate of the rate gyro bias contributes most substantially to the overall positioning error. This result is consistent with the analytical finding in Section 2.6.2, which showed that a heading rate bias can cause large positioning errors.

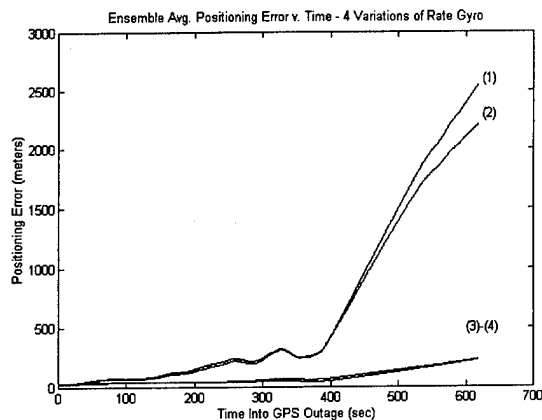


Figure 10. - The average performance of System 3a (curve 1), 3b (curve 2), 3c and 3d (curves 3 and 4).

SECTION 5 - CONCLUSIONS

An examination of the performance of several land-vehicle navigation systems has been presented. Error models for several sensors have been given and used in a Kalman filter design. The Kalman filter has been used to study the performance of navigation systems that use a variety of sensors. In addition, some analytical work has been done to support simulation results.

For a system that uses map-matching and for which there is sufficient vehicle motion for the map-matching algorithm to converge, the system's positioning accuracy is that of the map database. Navigation sensor accuracy affects only the probability and speed of the map-matching algorithm's convergence. For a system that uses unaided GPS, but does not use map-matching, the positioning accuracy of the system is approximately that of the GPS position fixes. Dead-reckoning sensors that are practicable for commercial automotive use do not improve that accuracy significantly. Even significantly increasing the accuracy (and therefore cost) of dead-reckoning sensors will not cause a navigation system's positioning accuracy to be substantially better than that of unaided GPS.

Analytical and simulation results show that the accurate calibration of a navigation system's heading rate sensor(s) to be of prime importance. It has been found that a rate gyro's scale factor exhibits poor observability characteristics, and that use of differential GPS fixes (as opposed to unaided GPS fixes) do not substantially improve the estimate of this quantity. This result is not necessarily of great consequence, however, because, for the rate gyro simulated in this research, scale factor errors were not found to contribute substantially to positioning errors. This result would be more important for a rate gyro that suffers from large, randomly-driven scale factor errors.

It has also been shown that the rate gyro's bias error contributes much more to positioning errors than either white noise error or scale factor errors. Furthermore, in the absence of absolute position measurements, the presence of a compass in the navigation system plays a significant role in reducing positioning errors.

Furthermore, it has been shown that the growth rate of positioning error during a GPS outage is nearly the same for systems that use either unaided GPS or DGPS. Results have shown that errors in the heading estimate (and not errors in the odometer scale factor estimate) dominate the growth rate of positioning errors during a GPS outage. Results have further shown that, during a GPS outage, the random errors in a system's heading sensors dominate any improvements in calibration afforded by DGPS fixes before the outage occurred.

Finally, results show that the Kalman filter can calibrate the odometer scale factor more rapidly and accurately with DGPS measurements than it can with unaided GPS measurements.

ACKNOWLEDGMENTS

The authors are also grateful to Etak, Inc. for the use of its digital map database of the San Francisco Bay Area, and to Gyration, Inc. for its partial financial support of this research.

REFERENCES

1. French, R. L., and G. M. Lang, *Automatic Route Control System*, IEEE Transaction on Vehicular Technology, Vol. VT-22, No. 2, 1973, pp. 36-41.
2. Thoone, M. L. G., *CARIN, A Car Information and Navigation System*, Philips Technical Review, Vol. 43, No. 11/12, 1987, pp. 317-327.
3. King, D., *LANDFALL, A High Resolution Automatic Vehicle-Location System*, GEC Journal of Science and Technology, Vol. 45, No. 1, 1978, pp. 34-44.
4. Lezniak, T., R. Lewis, and R. McMillen, *A Dead Reckoning/Map Correlation System for Automatic Vehicle Tracking*, IEEE Transactions on Vehicular Technology, Vol. VT-26, No. 1, 1977, pp. 47-60.
5. Oshizawa, H., and C. Collier, *Description and Performance of Navmate, an In-Vehicle Route Guidance System*, Proceedings of the 1990 American Control Conference, pp. 782-787.
6. Ishikawa, K., M. Ogawa, S. Azuma, and T. Ito, *Map Navigation Software of the Electro-Multivision of the '91 Toyota Soarer*, Proceedings of the 1991 Vehicle Navigation and Information Systems Conference, Vol. 1, pp. 463-473.
7. Ikeda, H., Y. Kobayashi, S. Kawamura, and H. Nobuta, *Sumitomo Electric's Navigation Systems for Private Automobiles*, 1991 Vehicle Navigation and

- Information Systems Conference, Vol. 1, pp. 451-462.
8. Harris, C., E. Krakiwsky, *AVLN 2000 Automatic Vehicle Location and Navigation System*, 1989 Vehicle Navigation and Information Systems Conference, pp. 126-130.
 9. Hunter, T. and J. Ashjaee, *Land Navigation and Fleet Management With GPS, LORAN, and Dead Reckoning Sensors*, IEEE 1988 Position, Location and Navigation Symposium, pp. 54-60.
 10. Oki, N., Y. Hosokawa, E. Sugimoto, Y. Abe, and T. Taniguchi, *Portable Vehicle Navigation System (NV-1): Its Features and Operability*, 1993 Vehicle Navigation and Information Systems Conference, pp. 482-485.
 11. Collier, W.C., *In-Vehicle Route Guidance Systems Using Map Matched Dead Reckoning*, IEEE 1990 Position, Location and Navigation Symposium, pp. 359-363.
 12. Muraszko, J., *Pathfinder--An Automatic Vehicle Location and Status monitoring System*, Second International Symposium on Land Vehicle Navigation, Munster, Germany, 1989, pp. 8.1-8.12.
 13. Last, J. and C. Scholefield, *The Combined Use of Low Frequency Radio and Dead Reckoning for Automatic Vehicle Location*, First International Symposium on Land Vehicle Navigation, Munster, Germany, 1984, pp. 14.1-14.19.
 14. Harris, C., *Prototype For a Land Based Automatic Vehicle Location and Navigation System*, Master's thesis, Report No. 20033, Department of Surveying Engineering, University of Calgary, Calgary, Alberta, Canada, 1989.
 15. von der Hardt, H., P. Arnould, D. Wolf, and M. Dufaut, *A Method of Mobile Robot Localisation by Fusion of Odometric and Magnetometric Data*, International Journal of Advanced Manufacturing Technology, Vol. 9, 1994, pp. 65-69.
 16. Liu, S., Z. Zhang, and J. Hung, *A High Accuracy Magnetic Heading System Composed of Fluxgate Magnetometers and a Microcomputer*, Proceedings of the 1989 IEEE National Aerospace and Electronics Conference, Vol. 1, pp. 148-152.
 17. Wang, C., *Location Estimation and Uncertainty Analysis For Mobile Robots*, Proceedings of the 1988 IEEE International Conference on Robotics and Automation, pp. 1230-1235.
 18. Chenavier, F. and J. Crowley, *Position Estimation for a Mobile Robot Using Vision and Odometry*, Proceedings of the 1992 IEEE International Conference on Robotics and Automation, pp. 2588-2593.
 19. Kleeman, L., *Optimal Estimation of Position and Heading for Mobile Robots Using Ultrasonic Beacons and Dead-reckoning*, Proceedings of the 1992 IEEE International Conference on Robotics and Automation, pp. 2582-2587.
 20. Watanabe, Y. and S. Yuta, *Position Estimation of Mobile Robots With Internal and External Sensors Using Uncertainty Evolution Technique*, Proceedings of the 1990 IEEE International Conference on Robotics and Automation, pp. 2011-2016.
 21. Zickel, R., N. Nehemia, *GPS Aided Dead Reckoning Navigation*, Proceedings of the 1994 ION National Technical Meeting, pp. 577-586.
 22. Ostertag, M., *Improved Localisation For Traffic Flow Control*, Submitted to Periodica Polytechnica in 1994 for publication.
 23. Beatty, C., *Land Vehicle Navigation--From Concept To Production*, First International Symposium on Land Vehicle Navigation, Munster, Germany, 1984, pp. 9.1-9.17.
 24. Whitcomb, L., *Using Low Cost Magnetic Sensors on Magnetically Hostile Land Vehicles*, IEEE 1988 Position, Location and Navigation Symposium, pp. 34-38.
 25. McMillan, J., *An Integrated Land Navigation System*, IEEE Position Location and Navigation Symposium, 1988, pp. 221-229.
 26. Barshan, B. and H. Durrant-Whyte, *Inertial Navigation Systems For Mobile Robots*, IEEE Transactions On Robotics and Automation, Vol. 11, No. 3, 1995, pp. 328-342.
 27. Janc, R., *Consideration of the Various Error Sources In a Practical Automatic Vehicle Location System*, Proceedings of the 1984 IEEE Vehicular Technology Conference, pp. 277-284.
 28. Ritland, J. and K. Spalding, *Impact of Inertial System Quality on GPS-Inertial Performance in a Jamming Environment*, AIAA Paper 87-2594, 1987, pp. 1459-1467.
 29. Leber, D., *A Systems Analysis Of the Impact Of Navigation Instrumentation On-Board a Mars Rover, Based On a Covariance Analysis of Navigation Performance*, Master's thesis, Department of Aeronautics and Astronautics, MIT, 1992.
 30. Klimmek, D., *Valuation of Land Vehicle Navigation Systems*, First International Symposium on Land Vehicle Navigation, Munster, Germany, 1984, pp. 21.1-21.14.
 31. Koa, Wei-Wen, *Apparatus for Correcting Vehicular Compass Heading With the Aid of the Global Positioning System*, U.S. Patent 5,339,246, Aug. 16, 1994.
 32. Matsuzaki, S., *Apparatus For Estimating Current Heading Using Magnetic and Angular Velocity Sensors*, U.S. Patent 5,235,514, Aug. 10, 1993.

33. Tamai, H. and T. Abe, *Navigation System*, U.S. Patent 5,291,412, Mar. 1, 1994.
34. Zeevi, E., *Vehicle Navigation System*, U.S. Patent 4,878,170, Oct. 31, 1989.
35. Yokoyama, S. and A. Nanba, *Vehicular Navigation Apparatus*, U.S. Patent 5,043,902, Aug. 27, 1991.
36. Komura, F. et. al., *Navigation System and Method Using Map Data*, U.S. Patent 5,311,173, May 10, 1994.
37. Ueyama, Y. and Yasui, N., *Vehicle In-situ Locating Apparatus*, U.S. Patent 5,060,162, Oct. 22, 1991.
38. Honey, S. et. al, *Vehicle Navigational System and Method*, U.S. Patent 4,796,191, Jan. 3, 1989.
39. Nishikawa, K., M. Fujimoto, and A. Yoshikazu, *Land Vehicle Navigation System*, U.S. Patent 4,949,268.
40. Krakiwsky, E., C. Harris, and R. Wong, *A Kalman Filter For Integrating Dead Reckoning, Map Matching and GPS Positioning*, 1988 IEEE Position, Location and Navigation Symposium, pp. 39-46.
41. Tsuji, H., et. al., *Evaluation of Location System Combining a GPS Receiver With Inertial Sensor*, 1991 Vehicle Navigation and Information Systems Conference, pp. 645-649.
42. Neculescu, D., J. Sasiadek, and D. Green, *Fusion of Inertial and Kinematic Navigation Systems for Autonomous Vehicles*, Proceedings of the 1993 IEEE Vehicle Navigation and Information Systems Conference, pp. 462-465.
43. Sausen, F., *Position Location Methods For Road Bound Mobiles By Dead Reckoning With Support of Stored Digital City-Map Information*, First International Symposium on Land Vehicle Navigation, Munster, Germany, 1984, pp. 6.1-6.18.
44. Gazit, R., *Aircraft Tracking Using GPS Position and Velocity Reports*, Awaiting publication in the Proceedings of the 1995 ION-GPS International Technical Meeting, Palm Springs, CA.
45. Krakiwsky, E. et. al., *The Intelligent Vehicle-Highway Navigation Systems Database*, Intelligent Databases International Ltd., Software Program, Version 4.6.
46. Specification sheets for the Gyrostar piezoelectric vibrating gyroscope, Part no. ENX-0011, Murata Erie North America, 1993.
47. Specification sheets for the Gyrochip II solid state rate gyroscope, Part no. QRS14-00100-102, Systron Donner, 1994.
48. Specification sheets for the Micropulse rate gyroscope, British Aerospace Systems and Equipment.
49. Parkinson, B.W. et. al., *The Global Positioning System--Theory and Applications*, Vols. 1 and 2., Chapters 2, 11, and 24, Publication pending.
50. New Release, ACCQPOINT Communications Corp., Salt Lake City, Utah, Sept. 21, 1994.
51. Marketing brochure, Differential Corrections, Inc., Cupertino, CA, 1995.
52. U.S. Coast Guard, *U.S. Coast Guard Differential GPS*, Brochure, 1993.
53. U.S. Coast Guard, *Radiobeacon Facts and Figures*, Brochure, 1993.
54. Gelb, A. et. al., *Applied Optimal Estimation*, M.I.T. Press, 1974.

Nonlinear Smoothing of Dead Reckoning Data With GPS Measurements

Ren Da and George Dedes
The Ohio State University

BIOGRAPHY

Dr. Ren Da is a research specialist at the Center for Mapping, The Ohio State University. He received his B.S., M.S., and Ph.D. degrees in Automatic Control Engineering from Northwestern Polytechnical University. His research interests are in robust estimation, inertial system and integrated navigation fields, especially the design of fault-tolerant integrated GPS/INS systems. He has published 14 journal papers in these research areas.

George C. Dedes received his M.S. and Ph.D. degrees from the Department of Geodetic Science and Surveying at The Ohio State University. Dr. Dedes is a Research Scientist at the Center for Mapping where he supervises and conducts research and development for high accuracy dynamic positioning using the Global Positioning Systems Satellites (GPS) in combination with Inertial Navigation and Dead Reckoning Systems. He has over 10 years of experience in high accuracy dynamic positioning, orbital dynamics, and system and software engineering. Dr. Dedes has published more than 15 papers in his area of expertise and he is a member of the IAG working group on high accuracy GPS dynamic positioning.

ABSTRACT

This paper presents a low cost and high accuracy integrated Global Positioning System (GPS)/dead reckoning system (DRS). The integrated GPS/DRS system is capable of proving highly accurate position data in real-time or in post processing. Based on the analysis of the main error sources affecting the DRS measurements, an eight-state mathematical model has been developed to represent these errors. This eight-state model has been used to build a nonlinear smoother for the estimation of the state vector at every epoch when DRS measurements are available. The accuracy of the system has been evaluated using 10Hz DRS

measurements and 3sec continuous GPS positions estimated using On-The-Fly ambiguity resolution techniques. The system performance during periods with GPS outages has been further investigated by deleting GPS positions for various time intervals. Investigation results have shown that the navigation system is capable of providing cm-level accuracy using low cost gyros and wheel counter sensors.

1. INTRODUCTION

The Center for Mapping at The Ohio State University, has built a prototype vehicle, named the GPSVanTM for mobile digital data acquisition [1]. The GPSVanTM has enormous potential for a variety of applications [2, 3]. The obvious examples include roadway feature inventory and status, e.g., positioning and describing signs, bridges, guardrails, media strip dimensions and many more. The powerful feature of the GPSVan is that everything within the view of the stereo cameras can be positioned to an accuracy of five to ten centimeters using advanced differential GPS and optimal estimation techniques.

The positioning module of the GPSVanTM consists of a base GPS receiver, a rover GPS receiver and a dead reckoning system (DRS) that contains a Three Axis Reference System (TARS) and wheel sensors (Figure 1). The TARS consists of a vertical gyro and a directional gyro in a self-contained gyro package, providing heading and attitude data. The wheel sensors 60 indentations in the brake drum that are sensed by digital magnetic proximity sensors as the wheel rotates yield the distance traveled. The purpose of the DRS is to account for the van's travel between GPS updates or if the satellite signal is lost. Loss-of-lock occurs when obstacles such as trees, tunnels, buildings, and others are encountered combining the GPS observations with data from the DRS solves this problem.

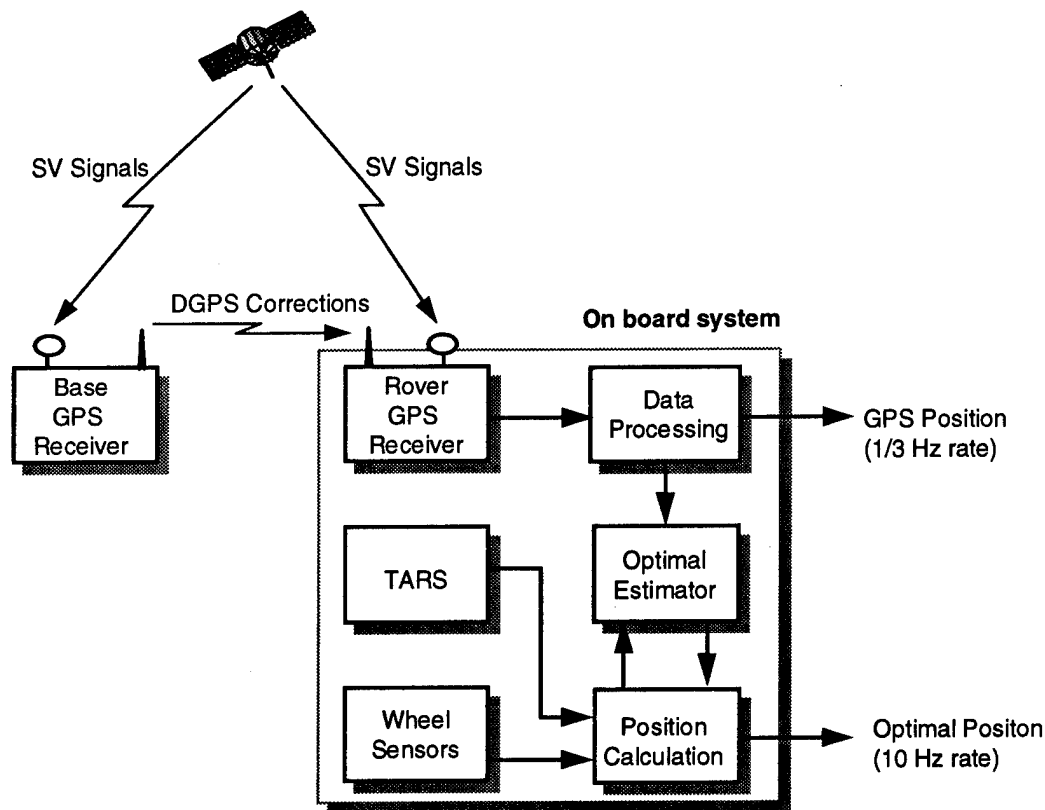


Figure 1. The Integrated GPS/DRS System Structure

The DRS calculates the vehicle's position based on the measurements from the gyros and wheel counters. These measurements, however, are unavoidably erroneous. In order to get accurate vehicle positions, effective approaches must be adopted to minimize the effect of these errors. A sequential least squares estimation procedure, in which the error terms are modeled as polynomial functions of time, has been applied to estimate the orientation unknowns and drifts using GPS derived absolute position data. Our experience has shown that position accuracy of better than 1 meter is achievable using this approach. There exists, however, a fundamental problem that prevents us from the further improvements in position determination accuracy. The problem is that the positional accuracy depends mainly on the estimation accuracy of the polynomial model parameters, which is unfortunately sensitive to the data processing time.

Application of optimal estimation theory to the integration of GPS and inertial systems has drawn much attention in recent years. The most widely accepted estimation theory in use today is the Kalman filtering/smoothing technique. In a Kalman filtering/smoothing system, the errors are modeled by stochastic state equations, and optimal estimation

algorithms are applied to estimate these error states. The main difference between a filter and a smoother is that the former uses only the past system measurements $y(k)$ ($0 \leq k \leq t$) to estimate the state vector $x(t)$ at the time t in real-time, while the latter uses both past and future measurements $y(k)$ ($0 \leq k \leq T$) to estimate the state vector. Since the smoothed state vector estimate is obtained based on all the measurements available, its accuracy is normally higher than that of a filtered estimate.

This paper presents the design approach of the integrated GPS/DRS system, in which the extended Kalman filter and the nonlinear smoother are applied that have evident advantages over the previously used least squares estimator. The estimation algorithms of the extended Kalman filter and the nonlinear smoother are described in Section 2. The differential GPS system is presented in Section 3. The dead reckoning formulation of the DRS is given in Sections 4, while an eight-state mathematical model developed for the estimators is provided in Section 5. More system design considerations are discussed in Section 6. The effectiveness of the estimators is evaluated in Section 7, using the data collected by the GPSVanTM. Finally, a conclusion is provided in Section 8 that summarizes the main results of the paper.

2. ESTIMATION ALGORITHM

Consider a discrete-time dynamic system described by the following nonlinear stochastic difference equations

$$x(k+1) = f(x(k), k) + w(k) \quad (1)$$

$$y(k) = h(x(k)) + v(k) \quad (2)$$

where both the vector f and h are nonlinear functions of the state vector $x(k)$; $w(k)$ and $v(k)$ are white random sequences of zero mean Gaussian random variables with associated covariance matrices $Q(k)$ and $R(k)$ respectively; and $y(k)$ ($0 \leq k \leq T$) is the system measurement vector.

2.1 EXTENDED KALMAN FILTERING ALGORITHM

Given the dynamic and measurement equations in Equation (1), the extended Kalman filtering algorithm (a simple nonlinear filtering algorithm) may be applied to calculate the estimate of $x(k)$ as a function of time and the measurement data. The algorithm includes the following time-update and measurement-update equations [4]:

Time-update equation:

$$\hat{x}(k+1|k) = f(\hat{x}(k|k), k) \quad (3)$$

$$P(k+1|k) = F(\hat{x}(k|k), k)P(k|k)F^T(\hat{x}(k|k), k) + Q(k) \quad (4)$$

Measurement Equation:

$$\begin{aligned} \hat{x}(k+1|k+1) &= \hat{x}(k+1|k) + K(k+1) \\ &\times [y(k+1) - h(\hat{x}(k+1|k))] \end{aligned} \quad (5)$$

$$\begin{aligned} K(k+1) &= P(k+1|k)H(\hat{x}(k+1|k)) \\ &\times [H(\hat{x}(k+1|k))P(k+1|k) \\ &\times H^T(\hat{x}(k+1|k)) + R(k)]^{-1} \end{aligned} \quad (6)$$

$$\begin{aligned} P(k+1|k+1) &= [I - K(k+1)H(\hat{x}(k+1|k))] \\ &\times P(k+1|k) \end{aligned} \quad (7)$$

where $\hat{x}(k|k)$ and $P(k|k)$ denote, respectively, the estimated state vector and its covariance matrix at time $t=k$, based on measurements up to and including $y(k)$. $\hat{x}(k+1|k)$ and $P(k+1|k)$ represent, respectively, the estimated state vector and its covariance matrix predicted to time $t=k+1$, based on $\hat{x}(k|k)$ and $P(k|k)$. The

Jacobian matrices $F(\hat{x}(k|k), k)$ and $H(\hat{x}(k+1|k))$ are given by

$$F(\hat{x}(k|k), k) = \left. \frac{\partial f(x(k), k)}{\partial x(k)} \right|_{x(k) = \hat{x}(k|k)} \quad (8)$$

$$H(\hat{x}(k+1|k)) = \left. \frac{\partial h(x(k))}{\partial x(k)} \right|_{x(k) = \hat{x}(k+1|k)} \quad (9)$$

Equations 2-5 provide the extended Kalman filter algorithm, which utilizes all of the past data to estimate the system state vector. For a post data processing case, it is desirable to use not only the past measurements but also the future measurement data to estimate the system state vector in order to achieve better estimation accuracy. In this case, a smoothing technique, which uses all measurements between time $t=0$ to $t=T$ to estimate the states of a system at a certain time $t=k$ ($0 \leq k \leq T$), may be applied.

2.2 SMOOTHING ALGORITHM

The smoothed estimate of $x(k)$ based on all the measurements between 0 and T is denoted by $\hat{x}(k|T)$. The smoothing algorithm applied in this paper is a combination of two extended Kalman filters (One of the filters, called a "forward filter," operates on all the measurements up to and including time k and produces the estimate $\hat{x}_f(k|k)$; the other filter, called a "backward filter," operates on all the data after time k and produces the estimates $\hat{x}_b(k|k+1)$. Together these two filters utilize all the available information to get the state vector estimate $\hat{x}(k|T)$ [4,5]:

$$\hat{x}(k|T) = P(k|T)[P_f^{-1}(k|k)\hat{x}_f(k|k) + P_b^{-1}(k|k+1)\hat{x}_b(k|k+1)] \quad (10)$$

$$P(k|T) = [P_f^{-1}(k|k) + P_b^{-1}(k|k+1)]^{-1} \quad (11)$$

where $P_f(k|k)$ and $P_b(k|k+1)$ are, respectively, the covariance matrices of the state vector estimates $\hat{x}_f(k|k)$ and $\hat{x}_b(k|k+1)$. Although in equation (10), $\hat{x}(k|T)$ is a linear combination of estimates $\hat{x}_f(k|k)$ and $\hat{x}_b(k|k+1)$, the smoothing algorithm is nonlinear, simply because the estimates $\hat{x}_f(k|k)$ and $\hat{x}_b(k|k+1)$, and, thereby $\hat{x}(k|T)$, are nonlinear functions of the filtering measurements.

3. DEAD RECKONING SYSTEM

This section contains a description of how the DRS determines the position of the GPSVanTM. Assume the position of the GPSVanTM at time $t=k$ is $[r_E(k), r_N(k), r_U(k)]$, where the subscripts (E, N, U) represent the East-North-Up navigation frame (n-frame). Then the position of the GPSVanTM at time $t=k+1$ is reckoned by using the following equation:

$$\begin{bmatrix} r_E(k+1) \\ r_N(k+1) \\ r_U(k+1) \end{bmatrix} = \begin{bmatrix} r_E(k) \\ r_N(k) \\ r_U(k) \end{bmatrix} + f(k)\Delta w(k) \begin{bmatrix} \sin\alpha(k)\cos p(k) \\ \cos\alpha(k)\cos p(k) \\ \sin p(k) \end{bmatrix} \quad (12)$$

where Δw is the wheel count difference between measured wheel counts at $t=k$ and $t=k+1$, $f(k)$ is the wheel count scale factor, α the direction (azimuth) angle, and p the pitch angle.

When equation 8 is converted into the earth-fixed Cartesian coordinate frame (e-frame), the vehicle's position (x, y, z) is determined recursively by

$$\begin{bmatrix} x(k+1) \\ y(k+1) \\ z(k+1) \end{bmatrix} = \begin{bmatrix} x(k) \\ y(k) \\ z(k) \end{bmatrix} + f(k)\Delta w(k)C_n^e(k) \begin{bmatrix} \sin\alpha(k)\cos p(k) \\ \cos\alpha(k)\cos p(k) \\ \sin p(k) \end{bmatrix} \quad (13)$$

where C_n^e is the Direction Cosine Matrix (DCM) from the n-frame to the e-frame

$$C_n^e = \begin{bmatrix} -\sin\lambda & -\sin\phi\cos\lambda & \cos\phi\cos\lambda \\ \cos\lambda & -\sin\phi\sin\lambda & \cos\phi\sin\lambda \\ 0 & \cos\phi & \sin\phi \end{bmatrix} \quad (14)$$

where ϕ and λ denote, respectively, the geographic latitude and longitude of the reference point.

4. ERROR ANALYSIS AND MODELING

The DRS calculates the vehicle's position based on the measurements from the gyros and wheel counters, which are affected by systematic errors. To estimate these errors through nonlinear smoothing techniques, appropriate mathematical models must be established. After investigating a variety of error models, a simplified eight state model was adopted for calibrating the DRS measurement. This error model is capable of providing accuracy at the .40m (1 σ) level, as shown in Section 7,

when GPS positions are not available for about 60 seconds.

4.1 WHEEL COUNTER MODEL

The main factor that degrades the accuracy of the wheel counters is the inaccuracy of its scale factor, which is influenced by many sources, such as road surface conditions. In order to describe uncertainty in the scale factor, the following model was developed:

$$f(k) = f^* + \Delta f(k) \quad (15)$$

$$\Delta f(k+1) = \tau_f \Delta f(k) + w_f(k) \quad (16)$$

where f^* is the nominal wheel counter scale factor, and Δf the random scale factor uncertainty, which was modeled by a first-order Markov process. τ_f is a constant representing the correlation between $\Delta f(k)$ and $\Delta f(k+1)$, and w_f the Gaussian white noise.

4.2 DIRECTION GYRO MODEL

The azimuth measurement α_m from the direction gyro includes not only the information of the true azimuth angle α , but also the initial orientation bias α_0 , the effects of the rotation of the earth, and the gyro drift, e.g.,

$$\alpha_m(k) = \alpha(k) + \alpha_0 + \Omega \sin\phi(k)\Delta T + \Delta\alpha_1(k) \quad (17)$$

where Ω is the constant earth rotation rate and ΔT the data sampling time interval of the gyro. $\Delta\alpha_1$ represents the gyro measurement error and the uncertainty of the direction gyro's initial orientation. The investigation showed that a good model for the $\Delta\alpha_1$ is:

$$\Delta\alpha_1(k+1) = \Delta\alpha_1(k) + \Delta\alpha_2(k)\Delta T + w_{\alpha 1}(k) \quad (18)$$

$$\Delta\alpha_2(k+1) = \tau_\alpha \Delta\alpha_2(k) + w_{\alpha 2}(k) \quad (19)$$

where $\Delta\alpha_2$ is a first order Markov process with the time constant τ_α . $w_{\alpha 1}$ and $w_{\alpha 2}$ are the Gaussian white noise.

4.3 VERTICAL GYRO MODEL

The measurement p_m from the vertical gyro also includes the true pitch angle p , the initial orientation bias p_0 , the influence of the earth rotation, and random errors:

$$p_m(k) = p(k) + p_0 - \Omega \cos \phi(k) \cos \alpha(k) \Delta T + \Delta p_1(k) \quad (20)$$

where Δp_1 , which represents the gyro measurement error and the uncertainty of the gyro's initial orientation, was modeled as

$$\Delta p_1(k+1) = \Delta p_1(k) + \Delta p_2(k) \Delta T + w_{p1}(k) \quad (21)$$

$$\Delta p_2(k+1) = \tau_\alpha \Delta p_2(k) + w_{p2}(k) \quad (22)$$

where τ_p is the time constant for the first order Markov process Δp_2 . w_{p1} and w_{p2} are the Gaussian white noise.

4.4 STATE EQUATION

Based on equations 8-15, an eight-state mathematical model was developed for the smoother. The state vector $\mathbf{x}(k)$ is expressed as:

$$\mathbf{x}(k) = [x(k), y(k), z(k), \Delta f(k), \Delta \alpha_1(k), \Delta \alpha_2(k), \Delta p_1(k), \Delta p_2(k)]^T \quad (23)$$

The nonlinear function \mathbf{f} and noise vector \mathbf{w} in the state equation 1 are described by the following functions:

$$\mathbf{f}(\mathbf{x}(k), k) = \begin{bmatrix} f_1(\mathbf{x}(k), k) \\ f_2(\mathbf{x}(k), k) \end{bmatrix} \quad (24)$$

$$\mathbf{f}_2(\mathbf{x}(k), k) = \begin{bmatrix} \tau_f \Delta f(k) \\ \Delta \alpha_1(k) + \Delta \alpha_2(k) \Delta T \\ \tau_\alpha \Delta \alpha_2(k) \\ \Delta p_1(k) + \Delta p_2(k) \Delta T \\ \tau_p \Delta p_2(k) \end{bmatrix} \quad (25)$$

$$\alpha(k) = \alpha_m(k) - \alpha_0 - \Omega \sin \phi(k) \Delta T - \Delta \alpha_1(k) \quad (26)$$

$$p(k) = p_m(k) - p_0 + \Omega \cos \phi(k) \cos \alpha(k) \Delta T - \Delta p_1(k) \quad (27)$$

$$\mathbf{w}(k) = [0, 0, 0, w_f(k), w_{\alpha 1}(k), w_{\alpha 2}(k), w_{p1}(k), w_{p2}(k)]^T \quad (28)$$

The Jacobian matrix $F(k)$, derived by using equation 4, has the following form:

$$F(k) = \begin{bmatrix} I_{3 \times 3} & C_n^e(k) A(k)_{3 \times 5} \\ 0_{5 \times 3} & B_{5 \times 5} \end{bmatrix} \quad (22)$$

with

$$A = \begin{bmatrix} c_1 \sin \hat{\alpha}(k|k) \cos \hat{p}(k|k) & c_2 \cos \hat{\alpha}(k|k) \cos \hat{p}(k|k) \\ c_1 \cos \hat{\alpha}(k|k) \cos \hat{p}(k|k) & -c_2 \sin \hat{\alpha}(k|k) \cos \hat{p}(k|k) \\ c_1 \sin \hat{p}(k|k) & 0 \\ 0 & -c_2 \sin \hat{\alpha}(k|k) \sin \hat{p}(k|k) & 0 \\ 0 & -c_2 \cos \hat{\alpha}(k|k) \sin \hat{p}(k|k) & 0 \\ 0 & c_2 \cos \hat{p}(k|k) & 0 \end{bmatrix} \quad (29)$$

$$c_1 = \Delta W(k) C_n^e(k), \quad c_2 = c_1 \hat{f}(k|k) \quad (30)$$

$$B(k) = \begin{bmatrix} \tau_f & 0 & 0 & 0 & 0 \\ 0 & 1 & \Delta T & 0 & 0 \\ 0 & 0 & \tau_\alpha & 0 & 0 \\ 0 & 0 & 0 & 1 & \Delta T \\ 0 & 0 & 0 & 0 & \tau_p \end{bmatrix} \quad (31)$$

4.5 MEASUREMENT EQUATION

When the GPS position measurement $\mathbf{y}(k) = [y_x(k), y_y(k), y_z(k)]^T$ is obtained, they are used by the smoother to update system state vector estimate. Since the GPS position data, estimated by using On-The-Fly ambiguity resolution techniques [6], is very accurate, the GPS measurement errors can be simply modeled as white noise in our system. Therefore, the measurement equation is written as:

$$\mathbf{y}(k) = H(k) \mathbf{x}(k) + \mathbf{v}(k) \quad (32)$$

with

$$H(k) = [I_{3 \times 3} \quad 0_{3 \times 5}] \quad (33)$$

and $\mathbf{v}(k)$ being the GPS measurement white noise with covariance $R(k)$.

5. OTHER SYSTEM DESIGN CONSIDERATIONS

5.1 GPS MEASUREMENT TEST

In order to maintain a high level of system performance, it is necessary to detect and isolate bad GPS measurements promptly. Over the past decades, a number of approaches have been developed to detect and isolate of bad measurements. As a statistical hypothesis testing method for examining if a random Gaussian vector has the assumed mean and covariance, the chi-square test is

widely applied. Assume that $r(k)$ is a p -dimensional measurement residual from the Kalman filter. Under normal working status, r is a zero-mean random Gaussian white vector with a covariance $V(k)=[H(k)P(k|k-1)H^T(k)+R(k)]$. Then the variable $\zeta(k)=r(k)V^{-1}(k)r^T(k)$ is a chi-square random variable with p degrees of freedom, and the following rule is considered for the detection of bad GPS measurements:

if $\zeta(k) \geq \mu$, then the measurement is bad
if $\zeta(k) < \mu$, then the measurement is good

where μ is a chosen decision threshold. With the aid of a chi-square distribution table, the probability of false alarm can be calculated as a function of the decision threshold μ . The chi-square test has been applied in monitoring the Kalman filter residual to detect failures in dynamic systems and to monitor the health of GPS satellites [7, 8].

5.2 WHEEL SENSOR MEASUREMENT TEST

Occasionally, it might happen that one of the wheel sensors does not work properly. In this case, it is required to give the user a warning signal, so that he can check the wheel sensor and fix the problem. Based on the physical relationship between the wheel sensor measurements, a test rule is implemented in the program to detect the health of the wheel sensors. As shown in Figure 2, the relationship between the measurements of the two wheel sensors can be written as:

$$f[\Delta w_{left}(k+1) - \Delta w_{right}(k+1)] = [\alpha(k+1) - \alpha(k)]d \quad (34)$$

where Δw_{left} and Δw_{right} are, respectively, the measurements from the left and right wheel sensors; d is the distance between the two wheels.

Let

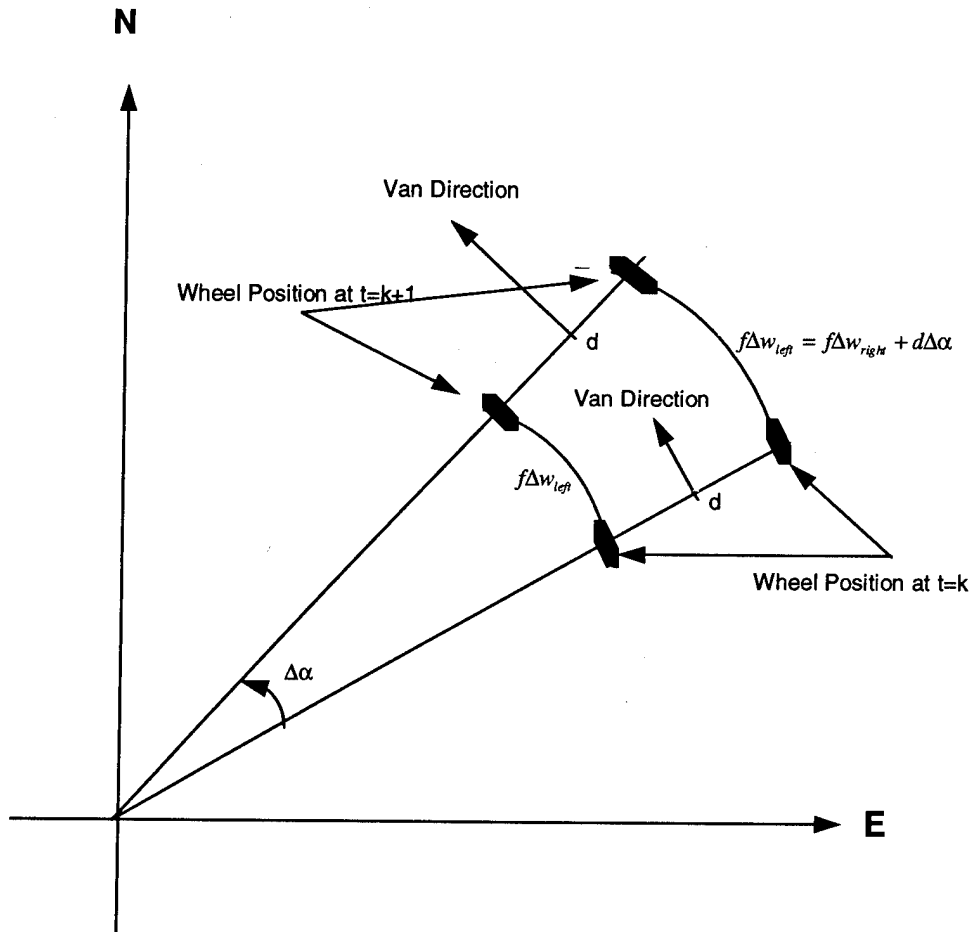


Figure 2. The Relationship Between Wheel Sensor Measurements

$$\zeta_w(k) = |f[\Delta w_{left}(k+1) - \Delta w_{right}(k+1)] - [\alpha(k+1) - \alpha(k)]d| \quad (35)$$

The following rule is implemented to check the consistency between the measurements of the wheel sensors and provide us the information about their working status

If $\zeta_w > \mu_w$,
then there is a failure in one of the wheel sensors;
If $\zeta_w \leq \mu_w$,
then there is no failure in the wheel sensors.

where $\mu_w > 0$ is a chosen constant. Once a failure is detected, a warning signal is given to the user, who will then check the wheel sensors and to locate the problem.

5.3 U-D FACTORIZATION ALGORITHM

The standard Kalman filter algorithm given in equations 2 and 3 is sensitive to computer roundoff and the numerical accuracy might degrade to the point where the results cease to be meaningful. The effects of numerical errors are generally manifested in the appearance of computed covariance matrices that fail to retain nonnegative values (i.e., with nonnegative eigenvalues). Several methods have been applied to improve accuracy and to maintain nonnegativity and symmetry of the computed covariance. One common practice is to replace the Kalman measurement update equation

$$P(k+1|k+1) = [I - K(k+1)H(\hat{x}(k+1|k))] \times P(k+1|k) \quad (36)$$

with the so called stabilized Kalman filtering algorithm

$$\begin{aligned} P(k+1|k+1) = & [I - K(k+1)H(\hat{x}(k+1|k))] \\ & \times P(k+1|k)[I - K(k+1)H(\hat{x}(k+1|k))]^T \\ & + K(k+1)R(k+1)K^T(k+1) \end{aligned} \quad (37)$$

Although this algorithm has greater numerical accuracy than the standard Kalman filtering algorithm, the main drawback of equation 37 is that it needs much more arithmetic operation than equation 7. Even so, the

stabilized Kalman mechanization may still lose numerical stability and give negative diagonal computed results [9].

Another way is to adopt square root filtering algorithms that have coherently better stability and numerical accuracy than does the standard Kalman filter. The improved numerical behavior of square root algorithms is due in large part to a reduction of the numerical ranges of the variables. Loosely speaking, one can say that computations which involve numbers ranging between 10^{-N} and 10^N are reduced to ranges between 10^{-N} and 10^N . Thus the square root algorithms achieve accuracies that are comparable with a Kalman filter that uses twice their numerical precision.

In our system, the Bierman's U-D factorization algorithm was implemented ($P=UDU^T$, with U being upper triangular and D diagonal matrices) [9]. The algorithm is considered to be of the square root type since $UD^{1/2}$ is a covariance square root of P . The U-D factorization algorithm has the accuracy characteristic of square root algorithms and not involve scalar square roots. Thus it qualifies for use in real-time applications. The U-D algorithm is considerably more efficient than most of the square root covariance algorithms and is in fact almost as efficient as the standard Kalman algorithm.

6. PERFORMANCE EVALUATION

Given the state and measurement equations described by equations 23-33, the optimal algorithms presented in above sections can now readily be applied to estimate the DRS error states. The position estimation capability of the optimal estimators was investigated by using 10Hz DRS measurements and 3sec continuous GPS positions estimated using On-The-Fly ambiguity resolution techniques. Because of the high accuracy of the GPS measurements, the performance of the estimators can be evaluated by comparing their position estimates with those given by the GPS. Plots of the differences between the estimated position data with those given by the GPS measurements provide graphic evidence of the estimators' capability to estimate the vehicle position in the presence of process and measurement noise.

Evaluation of the optimal estimators was conducted in two steps. First, all of the GPS measurements available in 3 second rates were used to update the state vector estimate. A representative set of such plots is shown in Figures 3-5, where the solid lines show the position differences between the smoothed estimates and those given by the GPS measurements, while the dashed lines give the differences between the estimates of the forward Kalman filter and those of the GPS measurements. It is shown in these graphs that:

1. The position estimates of the Kalman filter are usually quite accurate, except in the first 30 seconds. Larger estimation errors occur in the first 30 seconds because the Kalman filtering needs to process a certain quantity of measurement data to get rid of the initial state estimation errors;
2. The estimation accuracy is evidently further improved when the optimal smoother is applied, especially for the first estimation period. Using all the GPS measurements to update the state vector estimate, the smoother is capable of providing very accurate positioning for the GPSVan™. The differences between the estimated position of the smoother and that given by GPS are less than 0.1m (1σ) when GPS positions are available at 3s rate.

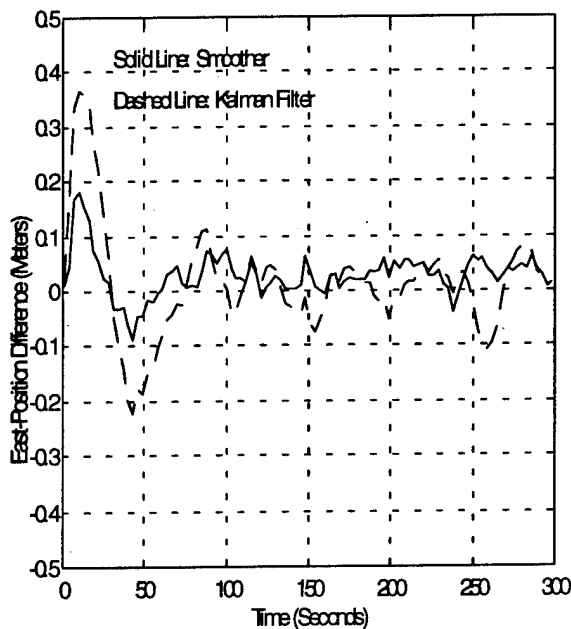


Figure 3. The East Position Difference between the GPS and the DRS (GPS Position Update in Every 3 Seconds)

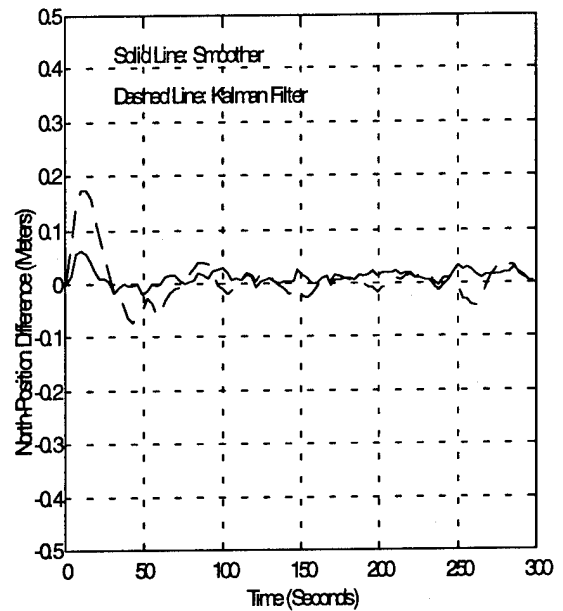


Figure 4. The North Position Difference between the GPS and the DRS (GPS Position Update in Every 3 Seconds)

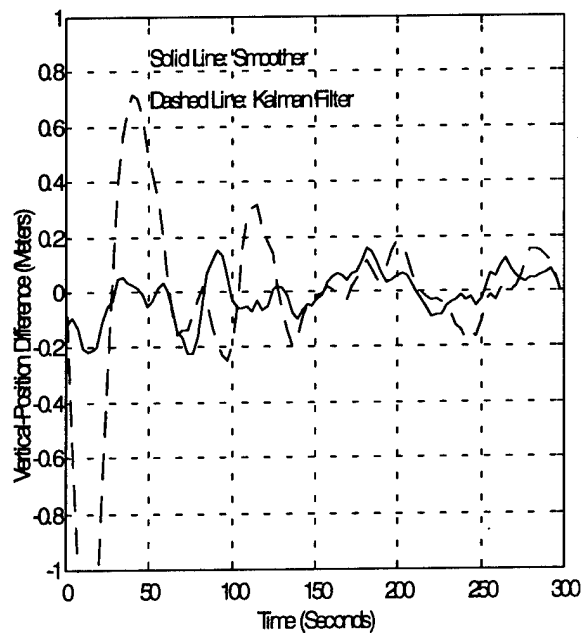


Figure5. The Vertical-Position Difference between the GPS and the DRS (GPS Position Update in Every 3 Seconds)

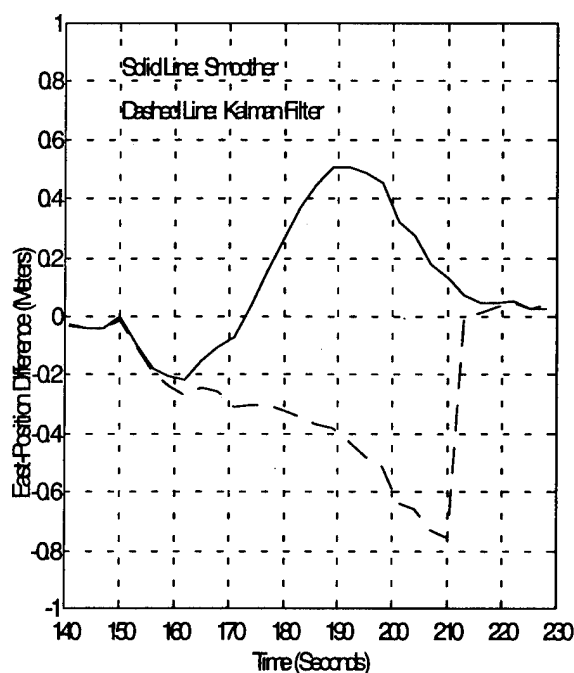


Figure 6. The East Position Difference between the GPS and the DRS (GPS Outage for 60 Seconds)

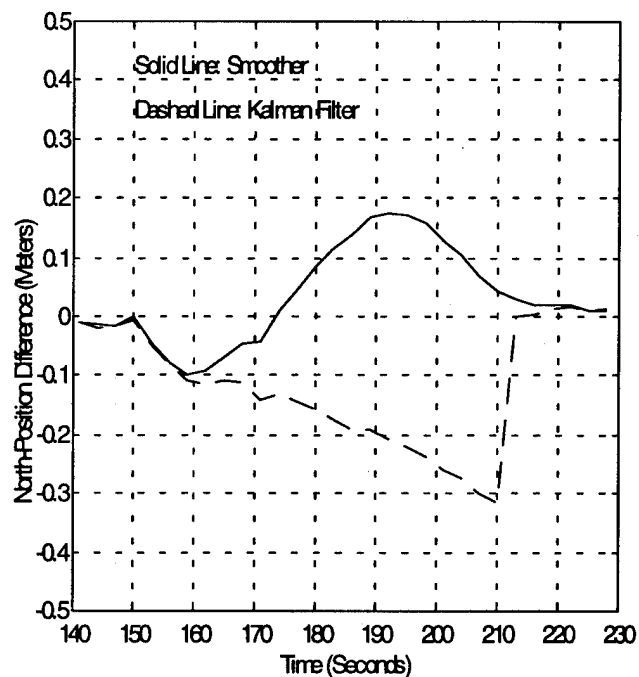


Figure 8. The Vertical-Position Difference between the GPS and the DRS (GPS Outage for 60 Seconds)

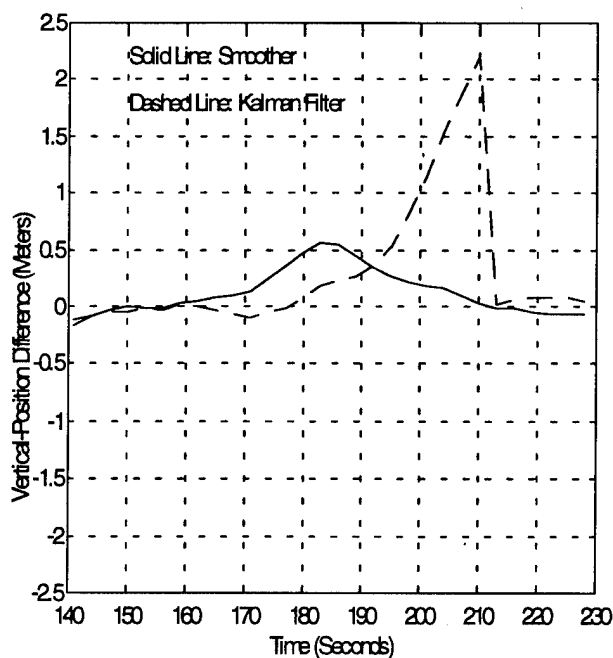


Figure 7. The North-Position Difference between the GPS and the DRS (GPS Outage for 60 Seconds)

In the second step of the performance evaluation, GPS position data were purposely deleted for 30sec, 60sec and 120sec respectively. This evaluation provides a measure of how accurate the filter and the smoother position data will be during periods with GPS outages. The data processing results showed that when GPS positions were not available for 30sec, 60sec and 120sec, the positioning accuracy deteriorates to 0.20m, 0.40m and 1.0m (1σ) respectively for the smoother. A representative set of such plots for GPS positions being deleted for 60sec is presented in Figures 6-8. It is shown in the figures that the maximum position differences in the east and north direction are, respectively, 0.75m and 0.32m for the Kalman filter, while the maximum position differences are only 0.5m and 0.18m in east and north directions respectively for the smoother.

7. CONCLUSIONS

In this paper a low cost and high accuracy integrated Global Positioning System/dead reckoning system (DRS) was investigated. This system is capable of providing highly accurate position data in real-time or in post processing. A number of issues involved in designing the integrated GPS/DRS were discussed,

including the application of optimal estimation algorithms, development of the estimator mathematical model, and GPS and wheel sensor measurements test, etc. The performance of the optimal estimator was evaluated in two steps by comparing the GPS position data with that given by the estimators. First, all of the GPS measurements available every 3 seconds were used to update the state vector estimates. This result gives us the position estimation effectiveness of the estimators in normal conditions. Second, GPS position data were deleted for 30sec, 60sec and 120sec respectively to investigate the estimation ability of the system during periods with GPS outages. The investigation results show that a positioning accuracy of 10 cm (1σ) is possible in the first case, while the positioning accuracy deteriorates only to 0.20m, 0.40m and 1.0 m (1σ) respectively in the second case.

REFERENCES

1. Center for Mapping, "GPS/Imaging/GIS Project: An Application of the Global Positioning System for Transportation Planning," Center for Mapping, The Ohio State University, December 1991.
2. Bossler, J. D., Goad, C. C., Johnson, P. and Novak, K., "GPS and GIS Map the Nation's Highways," *GeoInfo Systems*, March 1991.
3. Bossler J. D., "GPSVan-Input to GIS," *Proceedings of ION GPS-92*, fifth international technical meeting of the satellite division of the Institute of Navigation, Albuquerque, New Mexico, September 1992.
4. Sage, A. P. and Melsa, J. L., *Estimation Theory with Applications to Communications and Control*, McGraw-Hill Book Company, New York, 1971.
5. Gelb, A. (ed.), *Applied Optimal Estimation*, The M.I.T. Press, Massachusetts Institute of Technology, Cambridge, Massachusetts, 1979.
6. Dedes, G. and Mallett, A., "Effects of the Ionosphere and Cycle Slips in Long Baseline Dynamic Positioning," Center for Mapping, The Ohio State University, May 1995.
7. Willsky, A. S., "A Survey of Design Methods for Failure Detection in Dynamic Systems," *Automatica*, Vol.12, 1976, pp.601-611.
8. Da, R. and Lin, C. F., "Failure Detection and Isolation Structure for Global Positioning System Autonomous Integrity Monitoring", *AIAA Journal of Guidance, Control, and Dynamics*, Vol.17, No.2, 1995.
9. Bierman, G. J., *Factorization Methods for Discrete Sequential Estimation*. Academic Press, New York, 1977.

Next Generation Fiber Optic Gyroscopes for Use with GPS in Vehicle Navigation and Location Systems

Vincent Martinelli
Corning Incorporated

Ray Ikeda
Hitachi Cable America

BIOGRAPHY

Mr. Vincent P. Martinelli is Supervisor of Applications Engineering for Corning Incorporated's Industrial/Government Fiber & Components group. He has been working in the field of optical gyroscopes for past 8 years. He has an S.M. degree in Electronic Materials and a S.B. degree in Materials Science and Engineering, both from the Massachusetts Institute of Technology.

Mr. Ray Ikeda is a Sales Engineer for Hitachi Cable America. Prior to this position, he was a member of Hitachi Cable Ltd.'s fiber-optic gyroscope development group in Japan. Mr. Ikeda has Bachelor's and Master's degrees in Electrical and Electronic Engineering from Toyohashi University of Technology.

ABSTRACT

Fiber-optic gyroscope (FOG) technology has proven to be a suitable candidate for many applications where it is desirable to integrate GPS with a dead reckoning sensor. Open-loop, all-fiber type FOGs have been available commercially for several years for this purpose. Progress in minimizing size and reducing cost for these FOGs has been reported in several conferences previously.

As application areas grow and commercial markets materialize, FOG technology is being pushed further to reduce dead reckoning sensor cost and size. In this paper we report the latest progress in the development of a low-cost FOG using an integrated optical circuit. The advantage of this design approach is that several functional devices can be integrated onto one small chip. Hitachi Cable's approach has been to develop the chip design and the manufacturing technology simultaneously in order to achieve short product development cycle time and low cost in manufacturing.

In this paper we will report on several engineering tradeoffs for this new gyro design, with consideration for the perspective of a systems designer who is trying to integrate the FOG with GPS into vehicle navigation and location systems. The FOG design will be reviewed and the development program status will be summarized. We will present FOG data relevant for dead reckoning sensor use in an integrated system. We will discuss existing and potential uses for this new technical approach to low-cost FOG design.

Introduction

Fiber-optic gyroscopes (FOGs) are finding increasing application in a variety of navigation and stabilization systems.^{1,2} One of the most interesting application areas, from a commercial viewpoint, is the use of a FOG as a dead reckoning sensor in conjunction with a GPS receiver as part of a vehicle navigation system. This type of system is being offered as a factory-installed option on luxury sedan models in Japan. Tens of thousands of FOGs have been manufactured for use in these systems and have been operating in the field without failure. Similar systems have been developed for fleet tracking and vehicle location, such as for delivery trucks and emergency vehicles.

As the FOG technology has matured, improvements have been made to simplify the design while maintaining the inherent FOG benefits, e.g. compactness, light weight, quick start up, long, maintenance-free operating life, and stability in the automotive environment. One such improvement is the integration of several of the optical functions onto one integrated optical circuit (IOC).

We will review the basic FOG operating principles and the open loop all-fiber FOG design briefly before introducing the IOC FOG approach. We will consider

designs. We will also discuss future possibilities for using the IOC FOG approach in FOG/GPS systems.

Basic FOG operating principle

The operating principle of the FOG is based on the Sagnac effect, which describes the relative difference in pathlength traveled by counter-propagating beams of light in a rotating reference frame. Figure 1 shows counter-propagating light beams launched into a closed path, such as an optical fiber coil, from a beamsplitter, which is at the point BS. When the fiber coil is not rotating, the two beams of light travel exactly the same path before being recombined at BS. In the case where the coil is rotating, the beamsplitter moves from BS to BS' (for a counter-clockwise rotation) during the time that it takes for the light to transit the coil. The two beams arrive at the beamsplitter at different times since they have traveled different distances through the coil. The path length difference, ΔL , is given by:

$$\Delta L = \frac{RL}{c} \Omega, \quad (1)$$

where R is the radius of the coil, L is the length of fiber in the coil, c is the speed of light in a vacuum, and Ω is the rotation rate. Note that the pathlength difference is directly proportional to the rotation rate.

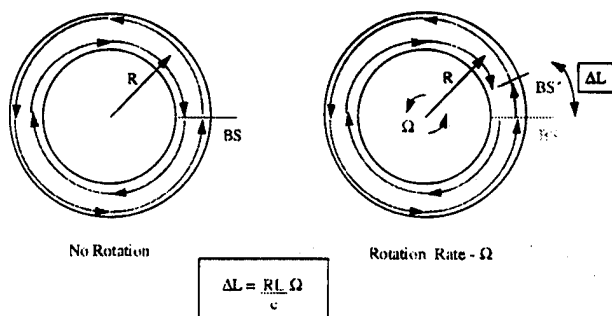


Figure 1. The principle of the Sagnac effect. When viewed from a rotating reference frame, two counter-propagating beams of light travel different distances through a closed path.

In general the pathlength difference is quite small. For example, if we choose parameters such as,

$$R = 25 \text{ mm}$$

$$L = 100 \text{ m}$$

$$\Omega = 0.1 \text{ deg/sec}$$

then the length, ΔL , is about $1.5 \times 10^{-11} \text{ m}$.

An interferometric technique, which involves detecting the change in output intensity for the interference between the two counter-propagating beams, is used to measure the pathlength difference. The intensity of the interference depends upon the relative phase difference, $\Delta\phi$, which can be written from (1) as,

$$\Delta\phi = \frac{4\pi RL}{\lambda c} \Omega, \quad (2)$$

where λ is the wavelength of light in vacuum. Given (2), the intensity of the interference is

$$I = I_0 (1 + \cos \Delta\phi), \quad (3)$$

where I is the detected intensity of the interference and I_0 is the intensity at zero rotation. From (3) it can be seen that the intensity of the interference signal depends upon the phase difference which is directly related to the rotation rate.

In order to detect such a small length difference it is necessary to carefully control the optical path through which the beams travel. Apparent changes in pathlength can be created by reflections, polarization effects and thermal transients. The minimum reciprocal configuration FOG includes components such as polarization-maintaining (PM) fiber to reduce these extraneous effects. Details on FOG design aspects relative to reciprocity may be found in the literature.³

The output characteristic of the interferometer described by (3) suffers from two flaws that must be addressed in order to make practical FOGs. First, for low rotation rates, the output of the interferometer is relatively insensitive to changes in rate (the slope of the cosine curve is flat). This shortcoming has been overcome by using a phase modulation technique.⁴ Second, unambiguous determination of $\Delta\phi$ is only possible for a range of $\pm \pi/2$. For applications requiring large dynamic range, this problem can be solved using closed loop signal processing techniques.³

Open loop all-fiber FOG

Figure 2 is a schematic representation of a Hitachi Cable open loop, all-fiber FOG. The term "all-fiber" refers to the fact that the beamsplitters, polarization control elements and modulator are all built from optical fiber. The beamsplitters in this case are fiber-optic couplers. The polarization control elements include a polarizer, made from elliptical jacket fiber, and a sensing coil made from elliptical core PM fiber. Elliptical core fiber meets

the technical requirements for the FOG design at a much lower cost than traditional stress-rod type PM fibers. The phase modulator uses a length of fiber wound on a PZT cylinder. Details on these components and on the signal processing scheme used have been published previously.³

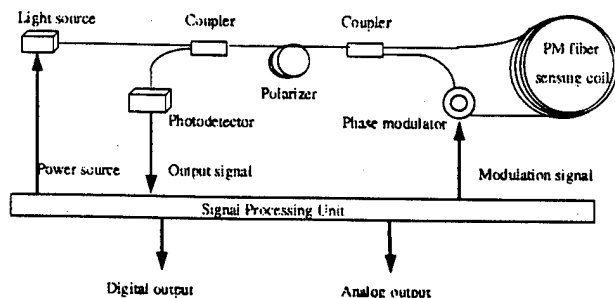


Figure 2. The open loop all-fiber FOG configuration. This type of FOG is in mass production for FOG/GPS vehicle navigation systems.

The open loop all-fiber FOG has been in mass production since 1992. It has met all of the technical requirements for navigation and location systems, including environmental performance. Table 1 summarizes the environmental requirements for automotive applications along with the results for the latest generation production FOG.

Table 1. Environmental test conditions for FOGs in automotive navigation and location systems.

Test	Condition	Result
High temperature operation	75° C, 500 hr.	Pass
Low temperature operation	-30°C, 250 hr.	Pass
Heat shock	-40 to +85°C, 2 hr./cycle 1500 cycles	Pass
Vibration	8 to 200 Hz, 2.5 G x, y, and z axes, 17 hr. each	Pass
Shock	80 G x, y and z axes, 3 times each	Pass

FOG requirements for FOG/GPS navigation systems

Almost all commercially available vehicle location and navigation systems rely in part on GPS receivers for position information. Most systems that provide

navigation functions use a combination of GPS and some type of dead reckoning sensor, such as the FOG. The dead reckoning sensor serves two functions in the system. During normal operation, when the GPS signal is accessible, the dead reckoning sensor input can be used in combination with the GPS input, odometer input and map-matching algorithms to improve the overall position solution. Improved position information is necessary for systems that deliver high levels of user functionality, such as dynamic route guidance. During operating periods when the GPS signal is blocked by tall buildings, tunnels, mountainous areas, etc., the dead reckoning sensor can operate with the odometer input and map-matching software to meet most road navigation needs.¹ In either case, the use of a dead reckoning sensor improves the overall system performance.

Several dead reckoning technologies are being considered for use in navigation systems. The FOG delivers high reliability and consistent, high performance allowing system designers to develop products with high levels of functionality. In addition to those systems already in production, designers continue to evaluate navigation system configurations combining FOG with GPS. Although the exact technical requirements depend in part on the details of the system design, Table 2 summarizes the FOG performance specification for a typical system.

Table 2. Technical requirements for FOG in FOG/GPS navigation systems

Input rate range	± 60 deg/s
Scale factor error	$< 2\%$
Zero bias	± 0.2 deg/s
Random walk	< 5 deg/ $\sqrt{\text{hr}}$
Warm up time	< 10 s
Frequency response	10 Hz
Operating temperature	-30 to +75° C
Power supply	8-16 V DC
Output	Digital

FOG design considerations

FOG technology can be used to make a wide performance range of rotation sensors: from inertial navigation grade devices for commercial aircraft and spacecraft to rate gyroscopes for chassis control systems in cars. The performance range is achieved by adjusting one of several variables, including the length of fiber and radius of the fiber coil, the operating wavelength and type of light source, and the signal processing scheme. Detailed discussion of these design tradeoffs can be found in the literature.³

The main design choices for Hitachi Cable FOGs are summarized in Table 3 for the application requirements of a FOG/GPS navigation system.

Table 3. FOG design guidelines for FOG/GPS automotive navigation systems.

Operating wavelength	780 nm
Light source type	CD laser diode
Fiber length	50-150 m
Fiber type	elliptical core PM fiber
Coil radius	20-50 mm

FOG with integrated optical circuit

Navigation system designers continue to request higher performance sensors even as they strive to reduce system cost. Hitachi Cable has been working on the development of a FOG using an IOC in order to address this market need.

Figure 3 shows the basic IOC FOG design. In comparison to the all-fiber design, the IOC approach eliminates the need for several optical components and the additional step of splicing those components together.

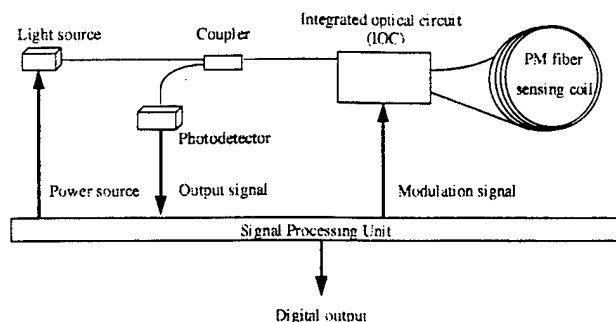


Figure 3. The IOC FOG design. The number of components has been reduced as compared to the all-fiber FOG.

A detailed description of the IOC is given in Figure 4. The IOC is fabricated by titanium diffusion in x-cut lithium niobate crystal. The polarizer, coupler and phase modulator functions can all be integrated on this chip using standard processing techniques. The fiber is attached, or pigtailed, to the IOC using a v-grooved assembly. Angle polishing of the fiber and the lithium niobate is used to minimize any backreflections.

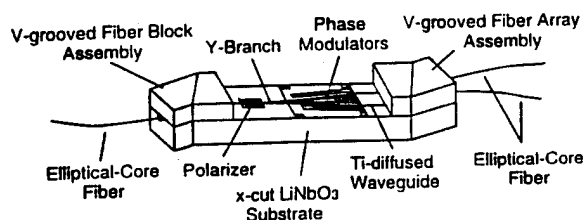


Figure 4. Detailed configuration of the IOC.

The IOC has been tested for the expected environmental conditions of the automotive environment. Figure 5 shows the change in output power of the pigtailed IOC for 100 cycles of -30 to +80° C. These test results are within the operating specification for the IOC in the FOG. Based on this data and the fact that the IOC FOG uses a subset of the components required for the field-proven open loop design, the environmental performance and reliability for the IOC FOG is expected to be excellent.

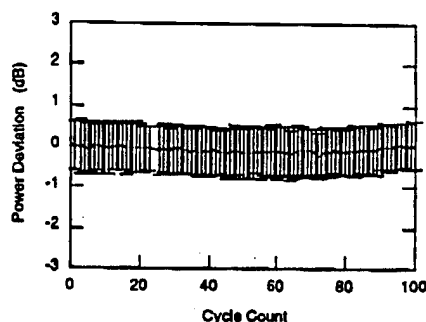


Figure 5. Environmental test results for IOC.

One of the parameters used to judge the FOG performance is the stability of the scale factor with changing temperature. Figure 6 gives the result of scale factor testing at 25° C, 40° C, 0° C and upon return to 25° C. In all cases, the scale factor error has remained less than 1 %.

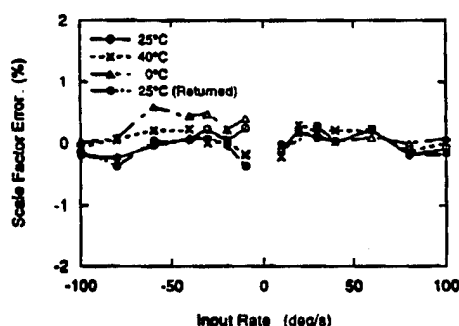


Figure 6. Scale factor performance of IOC FOG at several temperatures.

Complete qualification testing for the IOC FOG for use in FOG/GPS vehicle navigation systems is ongoing.

Status of IOC FOG development

Hitachi Cable is developing an IOC FOG using a digital signal processing technique for use in vehicle navigation systems. This FOG may also find use in other industrial applications where the performance requirements are similar to those presented in Table 2. In addition to reducing the number of components in the FOG and simplifying the assembly process, the IOC FOG with digital signal processing has higher performance than the all-fiber FOG currently in production.

The development program has focused on producing a manufacturable IOC FOG. The IOC can be mass-

produced using semiconductor compatible processing technology. A project to develop an automated pigtail station based on a side-view image processing fiber alignment technique has been completed. Subsequent environmental testing has confirmed the reliability of the fiber pigtail joining technique.

Summary

FOGs are in mass production for use in FOG/GPS vehicle navigation and location systems. The first generation production design is based on an all-fiber open loop approach. The IOC FOG approach is being developed for the next generation FOG/GPS systems. The new design offers better performance while reducing the number of components and simplifying the assembly process.

ACKNOWLEDGMENTS

The authors would like to thank Dr. H. Kajioka and Dr. T. Yuhara of Hitachi Cable Ltd. for their support.

REFERENCES

1. T. Kumagai, H. Kajioka, S. Oho, and H. Sonobe, "Development of open-loop fiber optic gyroscopes for industrial and consumer use," *Proc. SPIE 1795 Fiber Optic and Laser Sensors X*, Boston, USA, 1992, pp. 74-86.
2. T. Kumagai, H. Soekawa, T. Yuhara, H. Kajioka, S. Oho, and H. Sonobe, "Fiber optic gyroscopes for vehicle navigation systems," *Proc. SPIE 2070 Fiber Optic and Laser Sensors XI*, Boston, USA, 1993, pp. 181-191.
3. Lefèvre, H., *The Fiber-Optic Gyroscope*, Artech House, Boston, USA, 1993
4. T. Yuhara, T. Kumagai, H. Soekawa and H. Kajioka, "Fiber-optic gyroscopes for automotive applications," *Journal of Circuits, Systems and Computers*, Vol. 5, No. 1, 1995, pp. 17-36.

Hybrid GPS for Land Vehicle

S. Ishikawa, Y. Suwa, N. Nakahara, T. Ito,
T. Yamamoto, Y. Murakami, and T. Yasuda
AISIN SEIKI Co., Ltd.

Biographies

Mr. Ishikawa is a graduate of Okayama University with B. S. in Physics in 1987 and a graduate of Osaka University with M. S. in Engineering in 1989. He has 3 years experience in designing GPS receivers and has been engaged in designing software for integration of GPS and DR sensors for the last 3 years.

Mr. Suwa is a graduate of Nagoya Institute of Technology with B. S. in Engineering in 1991 and M. S. in Engineering in 1993. He has been engaged in designing software for integration of GPS and DR sensors for the last 2 years.

Mr. Nakahara has over 12 years experience in designing plant and ship control unit. For the last 8 years, he has been engaged in designing software for many products including GPS receivers.

Mr. Ito is a graduate of Doshisha University with B. S in 1984. He has 5 years experience in designing external memory device for computers. For the last 5 years, he has been engaged in designing GPS receivers.

Mr. Yamamoto is a graduate of Nagoya Institute of Technology with B. S. in Engineering in 1984. He has been engaged in designing GPS receivers for the last 10 years.

Mr. Murakami is a graduate of Miyazaki University with B. S. in Engineering in 1982. He has been engaged in designing GPS antenna and GPS receivers for the last 11 years.

Mr. Yasuda is a graduate of Tokyo Denki University with B. S. in Engineering in 1974. He has been engaged in designing GPS receivers and car navigation systems for the last 9 years.

Abstract

Simple Kalman filter model is described for the hybrid GPS system which includes GPS receiver, strapdown vibration gyro and conventional speed sensor for the speed meter of the vehicle.

4 dimensional state vector of Kalman filter,

$$\mathbf{X} = [\Delta x \ \Delta y \ \Delta z \ c \ \Delta t]^T$$

enable us to consider the effects of constellation of satellites, SVACC and DR (dead reckoning) sensors' error.

To prevent covariance matrix from becoming too small during iteration, multiplied factor k has been introduced in our hybrid GPS system.

All in view operation is easily available by using this Kalman filter model.

As the result, the effect of constellation of satellites, SVACC and DR sensors' error can be practically calculated by our basic navigation equations for land vehicle, which can be easily modified for various types of GPS receivers and DR sensors.

One of the significant features of this development is that our Kalman filter model is able to calculate fix position every second on commercial CPU (Central Processing Unit).

Simulation results and some of the field data are shown.

1. Background

For the purpose of obtaining higher precision and fix rate, integration of GPS and DR has been suggested. ⁽²⁾ GPS provides absolute position ⁽¹⁾ with a variance, while DR sensors provide precise relative position with a cumulative position error.

Although Kalman filter has been often used as optimal filter for the integration, large dimension of state vector makes it difficult to solve the equations in reasonable time by commercial CPU.

Moreover, theoretical covariance matrix elements rapidly become small during the iteration, which will not be suitable for many applications.

In our development, the employment of 4 dimensional state vector and additional factor k have solved above two problems of long calculation time and small covariance matrix elements.

2. Kalman filter equations ^{(2) (3)}

2.1. System configuration

Fig. 1 shows the construction of the hybrid GPS system that has been integrated. DR sensors are consisted of vibration gyro and speed sensor of vehicle speed meter. Both sensors are corrected by GPS direction and speed data under the pre-determined condition. For example, the initial DR direction is given by direction data of GPS.

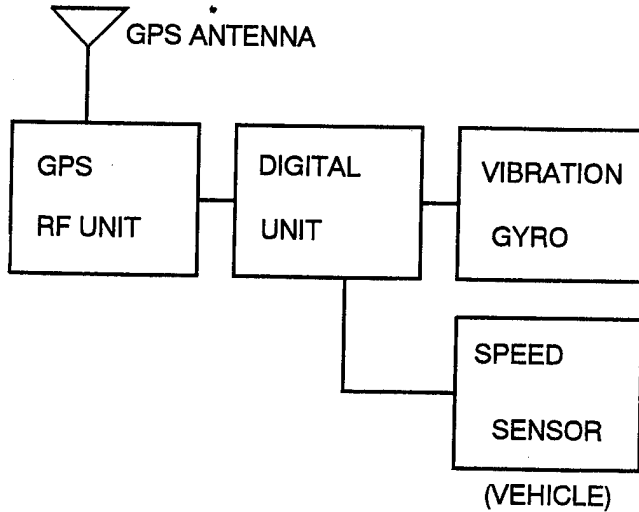


Fig. 1 hybrid GPS system

2.2. Navigation equations

First, the equation for the fixed position is described below.

$$\mathbf{X}_{HGPS} = \mathbf{X}_{DR} + \mathbf{G}(\mathbf{L} - \mathbf{H}\mathbf{X}_{DR}) \quad (1)$$

Equation(1) gives fixed position as the displacement from previous fixed position. where

$$\mathbf{G} = \mathbf{E}_{DR} \mathbf{H}^T (\mathbf{E}_L + \mathbf{H} \mathbf{E}_{DR} \mathbf{H}^T)^{-1}$$

is Kalman gain, \mathbf{X}_{DR} is DR position vector, \mathbf{E}_{DR} is covariance matrix of \mathbf{X}_{DR} , \mathbf{H} is GPS navigation matrix that is comprised of satellite-user line-of sight direction cosines, \mathbf{L} is the vector that is comprised of pseudorange differences between measured and predicted, \mathbf{E}_L is covariance matrix of \mathbf{L} and \mathbf{X}_{HGPS} is fixed position vector, the solution of this equation.

Because of using \mathbf{H} and \mathbf{E}_L , All in view operation is available, the effect of constellation of satellites is included, pseudorange error differences between satellites, like SVACC, can be handled, and it is easy to modify our equations for various types of GPS receivers.

By using \mathbf{H} and \mathbf{E}_L , covariance matrix of GPS fixed position is

$$\mathbf{E}_{GPS} = (\mathbf{H}^T \mathbf{E}_L^{-1} \mathbf{H})^{-1}$$

Position vector

$$\mathbf{X} = [\Delta x \Delta y \Delta z c \Delta t]^T$$

is 4 dimensional state vector of our Kalman filter.

Next, covariance matrix of fixed position is

$$\mathbf{E}_{HGPS} = \mathbf{k} (\mathbf{I} - \mathbf{G} \mathbf{H}) \mathbf{E}_{DR} \quad (2)$$

where \mathbf{I} is 4 dimensional unit matrix and first term of right-hand side of (2), \mathbf{k} is additional factor introduced in our hybrid GPS system, which can make covariance matrix suitable for many applications. Without factor \mathbf{k} , \mathbf{E}_{HGPS} is always smaller than both of \mathbf{E}_{GPS} and \mathbf{E}_{DR} , so \mathbf{E}_{HGPS} becomes smaller and smaller during iteration. In this situation, even if GPS fixed position that has relatively good accuracy is obtained, the equation *without* factor \mathbf{k} gives small Kalman gain that means very low sensitivity for variation of GPS accuracy and no advantage of GPS existence in the system. If the system does not have extremely precise DR system, the equation *without* factor \mathbf{k} will not suitable for the system. This discrepancy between theory and actual system may occur because \mathbf{E}_{DR} of actual DR sensors should have been handled as the offset along with constant direction, not as variance.

The additional factor \mathbf{k} is determined to make \mathbf{E}_{HGPS} nearly equal to \mathbf{E}_{GPS} under the condition of that \mathbf{E}_{GPS} is almost constant because of same constellation of satellites. The \mathbf{k} gives the system high sensitivity for variation of GPS accuracy.

\mathbf{E}_{DR} is

$$\mathbf{E}_{DR} = \mathbf{E}_{HGPS-1} + \mathbf{D} \quad (3)$$

where \mathbf{E}_{HGPS-1} is covariance matrix of previous fixed position and \mathbf{D} is the covariance matrix of relative displacement. There is no limitation in the determination of the elements of \mathbf{D} , so it is easy to modify our equations for various types of DR sensors. As \mathbf{X}_{DR} is the displacement from previous fixed position, \mathbf{E}_{DR} , covariance matrix of \mathbf{X}_{DR} , is sum of \mathbf{E}_{HGPS-1} and \mathbf{D} .

In case of every second fix, \mathbf{D} is much smaller than \mathbf{E}_{HGPS-1} . Because initial value of \mathbf{E}_{HGPS-1} is \mathbf{E}_{GPS} , neglecting \mathbf{D}

$$\mathbf{E}_{DR} \approx \mathbf{E}_{GPS}$$

The additional factor \mathbf{k} can be determined to attain $\mathbf{E}_{HGPS} \approx \mathbf{E}_{GPS}$ at $\mathbf{E}_{DR} \approx \mathbf{E}_{GPS}$.

3. Simulation based on measured data in the field

3.1. Field data gathering apparatus

By using PC (Personal Computer) for data gathering apparatus, GPS receiver data come into PC through the RS232-C communication port and DR sensors' data which were converted from analog to 12 bits digital signal come into PC through the extension port. Data sampling intervals are 1 second for GPS and 10 milli second for DR sensors.

The data are integrated on PC every second as hybrid GPS fixed position by our Kalman filter program which is the same as the program for commercial CPU.

3.2. Condition of the simulation

To confirm the effect of the additional factor k , the data that make E_{GPS} almost constant are used for the simulation. The constellation of satellites and E_{GPS} are shown in table 1.

TABLE 1 simulation data

No.	azimuth[deg]	elevation[deg]	range error[m]
1	8.44	63.58	33.8
2	271.41	45.70	33.8
3	196.88	45.00	11.6
4	50.62	37.97	11.6
5	306.56	25.31	33.8
6	68.91	16.88	33.8
7	119.53	15.47	33.8

$$E_{GPSxx} = 268[m^2], 16.4[m]$$

$$E_{GPSyy} = 384[m^2], 19.6[m]$$

$$(E_{GPSxx} + E_{GPSyy})^{1/2} = 25.5[m]$$

3.3. Results of simulation of the factor k effect

Figs. 2, 3 and 4 show the effect of additional factor k of eq. (2). The lateral axes of Fig. 2, 3 and 4 are longitude subtracted by $E. 137$ deg of fixed position in unit of second. The perpendicular axes of Figs. 2 and 3 are latitude subtracted by $N. 35$ deg of fixed position in unit of second. The vehicle trajectory is from upper right to lower left.

HGPS means hybrid GPS fixed position that is result of integration of GPS and DR sensors.

Point A is initial position of HGPS by GPS fixed position. DR sensors are initialized by GPS direction data before reaching this point A.

The results of the equation *without* factor k are shown in Fig. 2. The HGPS fixed positions have asymptotic behavior to DR positions. Because small values of E_{HGPS} keep HGPS fixed positions around DR positions, GPS fixed position is no

longer meaningful in this case.

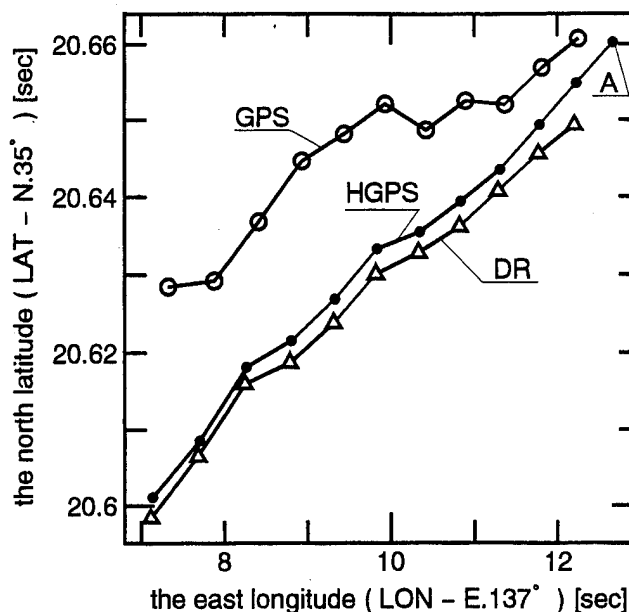


Fig. 2 conventional result(no factor k)

Fig. 3 shows the results of eq. (2), the additional factor k in it. The condition of $E_{HGPS} \approx E_{GPS} (\approx E_{DR})$ that is shown in Fig. 4 as horizontal error, $(E_{HGPSxx} + E_{HGPSyy})^{1/2}$ leads this trajectory. HGPS fixed position maintain high sensitivity for variation of GPS fixed position accuracy. So, if GPS fixed position that has relatively good accuracy (small E_{GPS}) is obtained in the trajectory beyond Fig. 3, larger Kalman gain put HGPS fixed position around GPS fixed position.

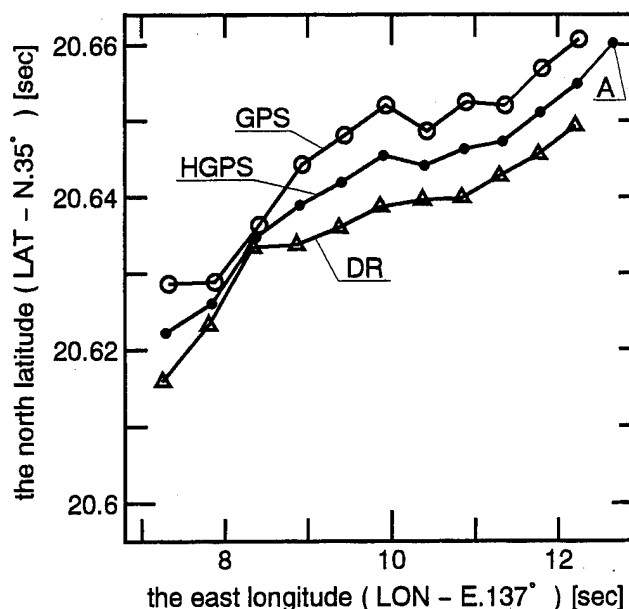


Fig. 3 result of the new equations

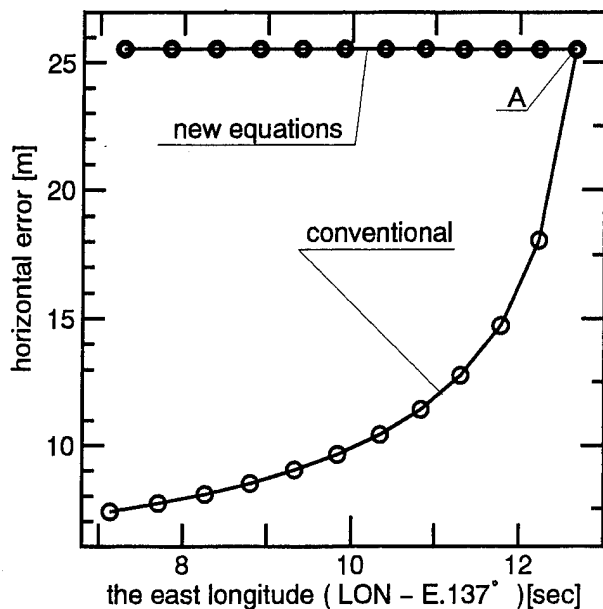


Fig. 4 horizontal error of HGPS

3. 4. Results of simulation of the DR sensors' error effect

Figs. 5, 6, 7 and 8 show the effects of E_{DR} in eq. (1) and eq. (2) by using first 4 point including point A in Fig. 3. Note that GPS fixed position was slightly moved to east to easily understand how the effect is, while E_L is intact.

The numerical values divided by slash are elements of covariance matrix. The values of Left side of slash are variance corresponding to North-South direction and the value of right side of slash are variance corresponding to East-West direction.

If E_{DR} is intact, HGPS fixed position is HGPS (basic), center of GPS and DR positions, in Figs. 5, 6, 7 and 8.

Figs. 5 and 6 show the effect of larger element of covariance matrix E_{DR} (16.4 → 17.9 etc.) corresponding to North-South and East-West direction, respectively. HGPS fixed position is given large Kalman gain of specified direction.

Figs. 7 and 8 show the effect of smaller element of E_{DR} (16.4 → 15.3 etc.) corresponding to North-South and East-West direction, respectively. HGPS fixed position is given small Kalman gain of specified direction.

According to eq. (3), it is impossible to realize E_{DR} that is smaller than E_{HGPS-1} , but external data for E_{DR} will make it possible to determine E_{DR} without E_{HGPS-1} .

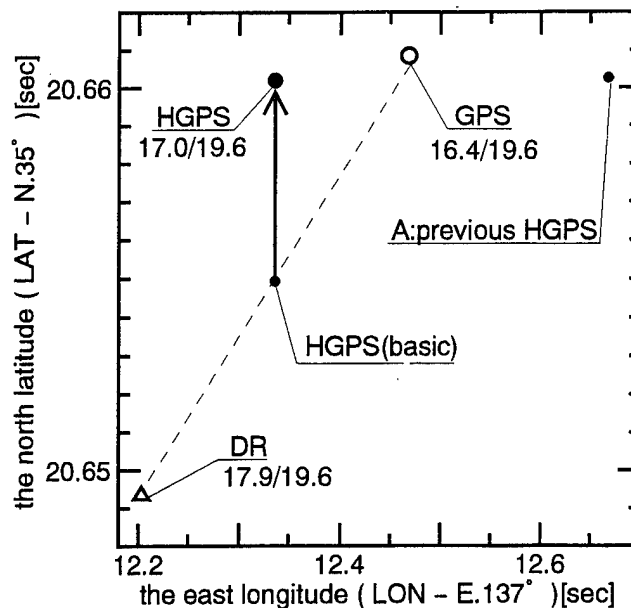


Fig. 5 "small" GPS error (north - south)

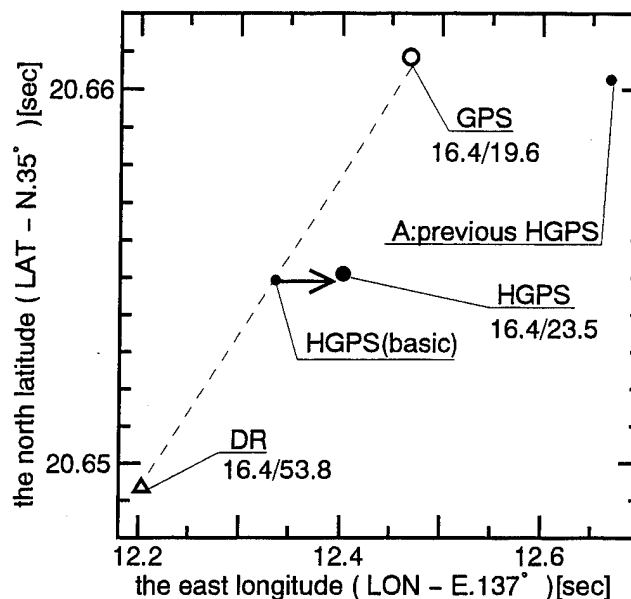


Fig. 6 "small" GPS error (east - west)

4. Results of field experiments

The field experiments by using commercial CPU have been done to confirm that our Kalman filter model has reasonable performance. Fig. 9 shows rough trajectory of experiments at Broadway, downtown of Los Angeles, about 1 km width North-South and 1.3 km width East-West.

GPS fixed positions that are discontinuous and disturbed are shown in Fig. 10. It is hard to recognize upper, North, trajectory from Fig. 10.

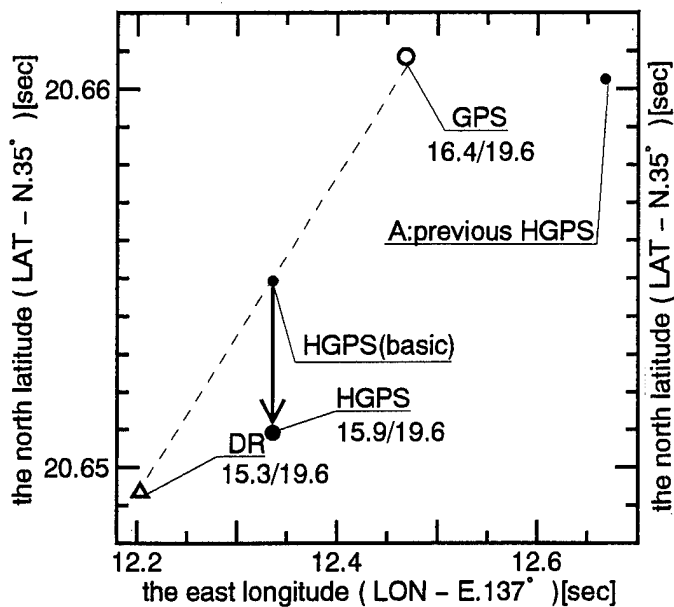


Fig. 7 "small" DR error (north - south)

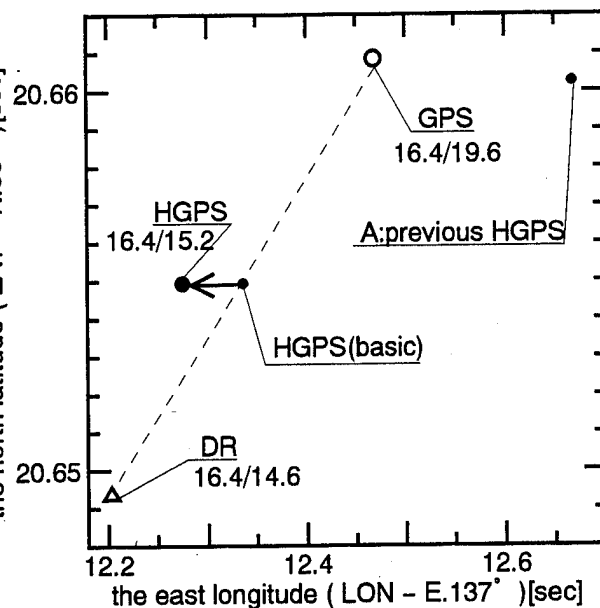


Fig. 8 "small" DR error (east - west)

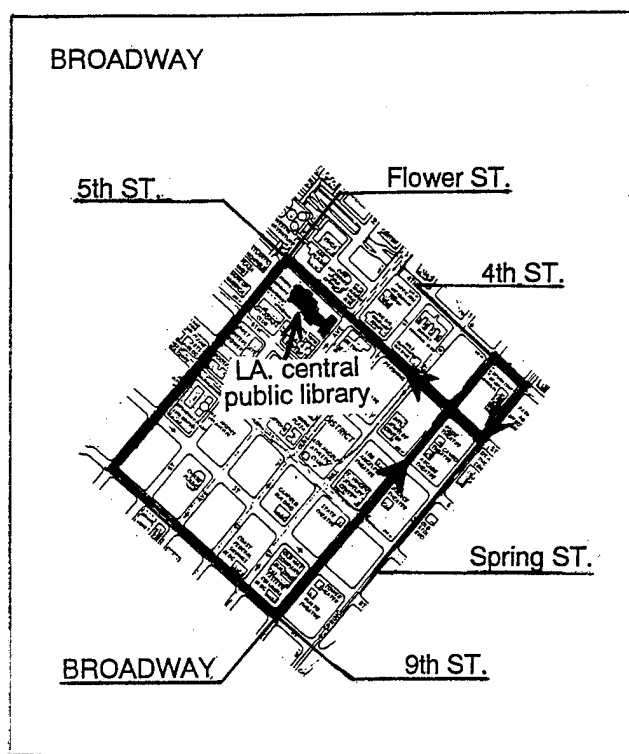


Fig. 9 BROADWAY trajectory

Fig. 11 shows HGPS fixed positions that are calculated in every second on commercial CPU. It is easy to recognize whole trajectory from Fig. 11 because of little discontinuance and disturbance.

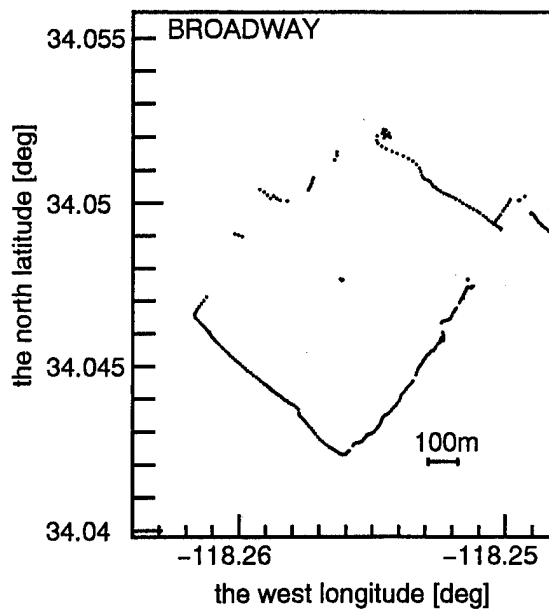


Fig. 10 field data(GPS)

5. Conclusions

Simple Kalman filter model by 4 dimensional state vector with the additional factor k has been developed to be easily modified for various types of GPS receivers and DR sensors.

The simulation based on measured data and field experiment have been done to confirm reasonable performance of our Kalman filter.

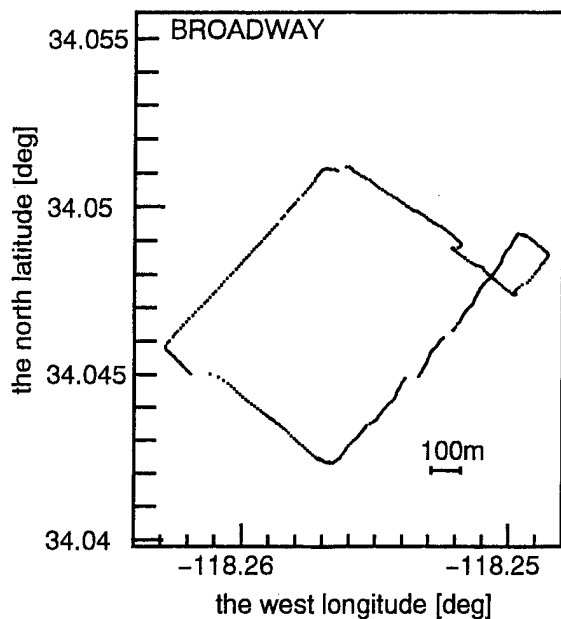


Fig.11 field data(HGPS)

6. References

- (1)GLOBAL POSITIONING SYSTEM:
SIGNAL STRUCTURE AND PERFORMANCE
CHARACTERISTICS 1978
James J. Spilker, Jr.
STANFORD TELECOMMUNICATIONS INC.
STI-TM-8802
- (2)DATA PROCESSING FOR GPS / INS
INTEGRATION 1988
Michael Napier Nottingham University
International Workshop on 'High Precision
Navigation', May 17th-20th, 1988, Stuttgart
and Altensteig-Wart, West Germany
- (3)GEOMETRIC PERFORMANCE OF THE
GLOBAL POSITIONING SYSTEM 1974
A. H. Bogen Aerospace Corporation
Prepared for Air Force System Command
NTIS, SAMSO-TR-74-169

VISAT: A Mobile City Survey System of High Accuracy

Naser El-Sheimy, Klaus-Peter Schwarz, and Ming Wei
The University of Calgary

Martin Lavigne
GEOFIT Inc.

BIOGRAPHIES

Mr. El-Sheimy is a Ph.D. Candidate at the University of Calgary specializing in GPS/INS integration, photogrammetry, and multi-sensor systems. These areas are components of his research thesis, integration of GPS/INS/CCD cameras for GIS applications. He holds a B.Sc. and M.Sc. from Egypt, and two post-graduate Diplomas in Photogrammetry and Remote Sensing from ITC, the Netherlands. Mr. El-Sheimy is currently employed by Geofit Inc. while finishing his thesis work.

Dr. Klaus-Peter Schwarz is Professor at the Department of Geomatics Engineering at the University of Calgary, and the President of the International Association of Geodesy (IAG). He holds degrees from universities in Germany, Canada, Austria and an honorary degree from China. His area of expertise is geodesy with special emphasis on the use of inertial systems in geomatics and the integration of satellite and inertial techniques for precise aircraft positioning, attitude determination, and gravity field modeling.

Dr. Ming Wei is a research associate at The University of Calgary specializing in GPS/INS integration, advanced filtering methods, and airborne gravity systems. He holds a B.Sc. degree from China and a Ph.D. degree from the Technical University of Graz, Austria. He is the chairman of the (IAG) special study group on airborne gravimetry.

Mr. Martin Lavigne is the Vice President of Research and Development at Geofit Inc. He has 10 years experience in software development and hardware integration.

ABSTRACT

This paper assesses the performance of VISAT, a mobile city survey system, for Geographic Information System (GIS) applications in urban centers. In this system, jointly developed by the University of Calgary and Geofit

Inc., GPS and INS provide the position and attitude, while a cluster of video cameras produce a set of 8 images at each exposure. The three sensors are mounted on a road vehicle moving with a velocity of 50-60 Km/h. The overall objective of the system is to reach object coordinates with an accuracy of 30 cm for objects within 30m from the van. The GPS position and velocity will control the INS error propagation, and the high frequency INS position output bridges GPS outages, corrects cycle slips, and gives precise interpolation between GPS updates. The updated GPS/INS information is used to georeference the video images. The system is synchronized by the clock Pulse Per Second (PPS) of the GPS receiver and the logging PC real-time-clock chip.

In this paper a brief description of the production system sensor integration and the essential features of the system design is given. Data collected in test networks in Calgary and Laval City will be used to assess the system performance in terms of accuracy and reliability. The concept of using INS positions to detect and fix GPS cycle slips will be investigated using data collected in the Laval city test network where frequent cycle slips occur due to tree coverage. Special emphasis is given to GPS performance in urban areas and the effectiveness of INS bridging in this case.

1. INTRODUCTION

With the continuing growth of urban centers on a worldwide scale, the demand of city planners for up-to-date information is increasing at a rapid rate. This has led to the establishment of spatially referenced GIS for a variety of applications. The information needed is expensive to establish by conventional methods and is therefore not well suited for rapid updating. In addition, conventional methods often supply only pointwise information and are therefore not suited to answer the increasingly complex questions concerning the interaction of different factors in urban centers and their time dependencies.

In order to address these problems, the University of Calgary and GEOFIT Inc., Laval, Quebec, have developed a precise mobile survey system for road inventory and general cadastral GIS applications. The total system consists of a data acquisition system, called VISAT (Video, Inertial, and SATellite GPS), and a measuring and processing system, called GEOSTATION (Li et. al., 1994). It implements the idea of storing georeferenced digital images as the basic unit and of combining an arbitrary number of such units, which may be from different time periods, to obtain the specific information required. The system can be used to selectively update GIS data bases very quickly and inexpensively. The system integrates a cluster of video cameras, an Inertial Navigation System (INS), and satellite receivers of the Global Positioning System (GPS). The system carrier is currently a van, but airborne or marine applications can be realized in a similar way.

The overall objective of the VISAT development was to design a precise mobile survey system that could be operated at speeds of up to 60 km per hour and would achieve an accuracy of 0.3 m (RMS) with respect to the given control and a relative accuracy of 0.1 m (RMS) for points within a 30 m radius. This accuracy is required in all environments including inner cities, where a stand-alone GPS is not reliable. Sensor integration has been optimized to reach the requirements of the survey market. The data flow has been streamlined to facilitate the subsequent feature extraction process and transfer into a GIS system. For further details on the design of the VISAT system, see Schwarz et al (1993a) and El-Sheimy and Schwarz (1993). A similar system has been developed by the Ohio State University's Center of Mapping (Bossler et al 1993), for use with minimal GPS signal blockage.

2. SYSTEM CONCEPT

Figure 1 shows the conceptual design and data flow of the VISAT system in schematic form. The system components are a strap-down INS system, two L1/L2 GPS receiver, a cluster of video cameras, an Anti-Braking-System (ABS) pick-up, image control unit, and two SVHS cameras. In the vehicle, all sensors are interfaced to a Pentium PC which controls the different data streams through programmed interrupt processes. The hardware is housed in three 30 inch rack mounts inside the van.

The function of each component can be subdivided into primary and secondary tasks. In terms of primary functions, the camera cluster provides three-dimensional positioning with respect to the VISAT reference which in most cases is the perspective center of one of the cameras. The position of this reference with respect to the existing control is determined by differential GPS, while the

camera orientation in three-dimensional space is given by the INS. The ABS system will trigger the cameras at constant distance intervals using the VISAT controller trigger channel. In terms of secondary functions, the camera cluster provides redundancy, i.e. more than two images of the same object, the GPS controls the INS error propagation, and the INS, when used in positioning mode, bridges GPS outages, corrects GPS cycle slips, and gives precise interpolation between GPS fixes. The ABS data can be used to update the INS data if the GPS signal is blocked for periods longer than the INS bridging level required to fix the GPS ambiguities (half a cycle).

Surveying by VISAT, therefore, consists essentially of two parts. Position and orientation of the moving VISAT reference is obtained from GPS and INS. Positioning of objects in the road corridor with respect to the VISAT reference is done using two or more oriented camera images. A brief description of each component is given in subsequent paragraphs.

3. THE NAVIGATION COMPONENT

The navigation component of the VISAT prototype system consists of two ASTECH Z12 GPS receivers and a Honeywell Laser-ReflIII strapdown INS. The GPS, when operated in differential mode, is capable of providing very accurate position and velocity information when the carrier phase observable is used. Under ideal conditions, the GPS measurements are consistent in accuracy throughout the survey mission. However, such conditions do not often exist. Independent GPS navigation requires at least four satellites with good geometry. The major drawback of GPS is the accuracy degradation due to poor satellite geometry, cycle slips, satellite outages, and dynamic lag during maneuvers. This is especially prevalent in urban centers and when encountering highway overpasses or tunnels.

The INS measures linear acceleration and angular rates very accurately and with minimum time delay. For short time intervals, the integration of acceleration and angular rate results in extremely accurate velocity, position, and attitude with almost no noise or time lags. However, because the INS outputs are obtained by integration, they

drift at low frequencies. To obtain very accurate outputs at all frequencies, the INS should be updated periodically using external measurements. For this purpose, GPS velocities and positions are update measurements which complement the INS output in an ideal way.

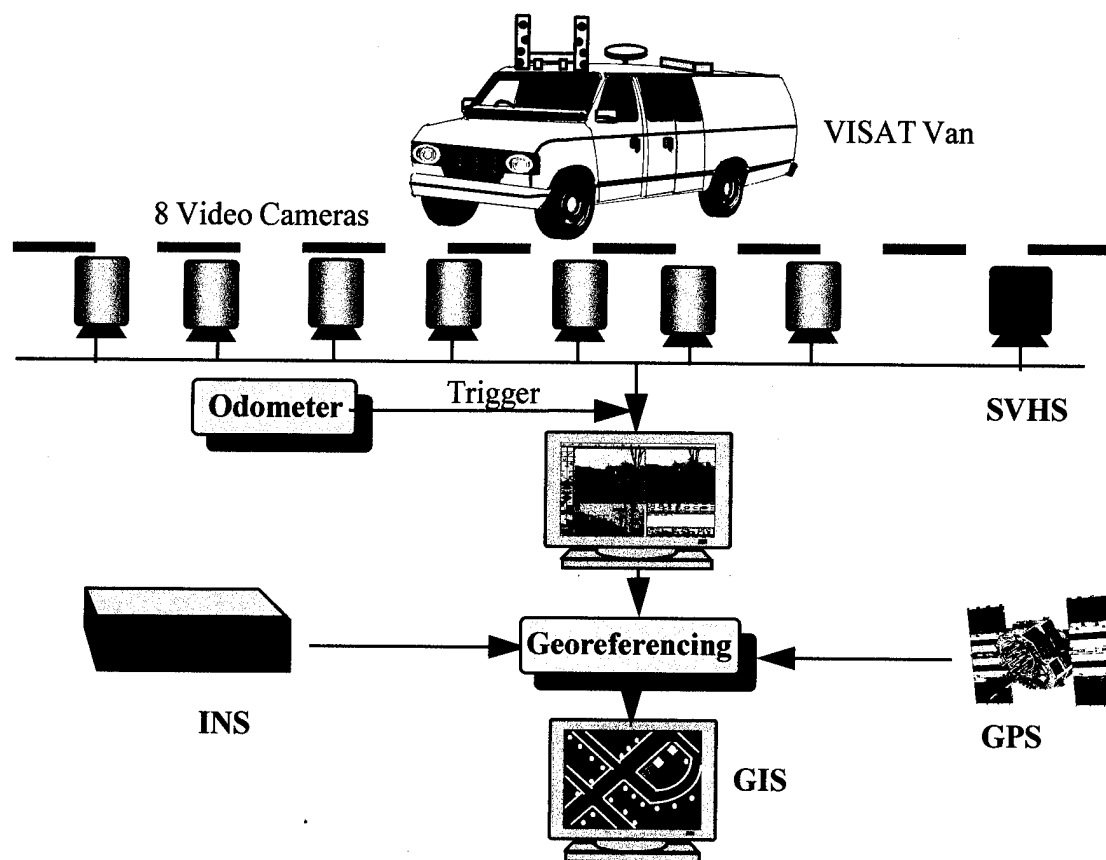


Figure (1) : The VISAT System Concept.

The integration of GPS and INS, therefore, provides a survey system that has superior performance in comparison with either a GPS or an INS stand-alone system. For instance, GPS derived positions have approximately white noise characteristics over the whole frequency range. The GPS-derived positions and velocities are therefore excellent external measurements for updating the INS, thus improving its long term accuracy. Similarly, the INS can provide precise position and velocity data for GPS signal acquisition and reacquisition after outages. This reduces the time and the search domain required for detecting and correcting cycle slips.

4. IMAGING COMPONENT

The imaging component of the VISAT system consists of 8 video cameras with a resolution 640 x 480 pixels. The cameras are housed in a pressurized case and mounted inside two towers which are attached to a fixed base on top of the VISAT-Van, thus eliminating any chance for the cameras to move during the survey. Six of these

cameras are arranged in such away that they provide 270 degree horizontal field of view (FOV) and 40 degrees vertical FOV. The other two cameras are dedicated to image special high features, e.g. power lines. All cameras are externally synchronized so that any image record (8 images) is related to one position of the van. The images grabbed from these cameras are compressed in real-time and then stored to a RAID (Redundant Array of Independent Hardisks). The RAID can store up to 20 Gbyte of data, which correspond to 102000 images (about 100 Km of data). Each image record is stamped with the GPS time indicating the time of grabbing the images. This time is used in post-mission to georeference the video images using the GPS/INS position and attitude data as described in section 7.

5. VISAT CONTROLLER

The controller, developed at Geofit, can handle up to 16 cameras and redirect 8 of them in real-time according to a predefined user configuration. This will allow the addition of more cameras in the future. The controller also includes two dedicated input channels for the ABS data and the

GPS receiver PPS pulse. With these data the controller can perform the following functions:

- trigger the cameras at a certain predefined user distance, thus all the images within the survey mission are equally spaced,
- switch off/on the cameras if the van stops at traffic signal,
- stamp any distance dependent events (e.g. start/end of INS ZUPTs (Zero Velocity Update), start/end of GPS static periods etc.) automatically with the GPS time,
- provide the sync signal required for synchronizing the 8 output images,
- send a warning message to the driver to stop the system for INS ZUPT in case of frequent GPS signal blockage.

6. SUPER VHS MODULE

The VISAT-Van include two SVHS video cameras. The cameras can be oriented in real-time in any direction using a control unit inside the van. The images will be coded with the GPS position and time on the audio track of the video tape. The colored images will be used in applications which do not require metric measurement.

7. GEOREFERENCING OF VIDEO IMAGES

The problem of georeferencing video images can be defined as the problem of transforming the 3-D coordinate vector \mathbf{r}^c of the camera frame (c-frame) to the 3-D coordinate vector \mathbf{r}^m of the mapping frame (m-frame) in which the results are required. The m-frame can be a system of curvilinear geodetic coordinates (latitude, longitude, height), a system of UTM or 3TM coordinates, or any other earth-fixed coordinate system. For more details on georeferencing of remotely sensed images using INS/GPS data see Schwarz et al (1993b) and El-Sheimy and Schwarz, 1994.

The georeferencing process can be described by the following formula :

$$\mathbf{r}_i^m = \mathbf{r}_{INS}^m(t) + \mathbf{S}_i \cdot \mathbf{R}_b^m(t) (\mathbf{R}_c^b \cdot \mathbf{r}^c + \mathbf{a}^b) \quad (1)$$

where,

- \mathbf{r}_i^m the coordinate vector of point (i) in the mapping frame (m-frame),
- $\mathbf{r}_{INS}^m(t)$ is the interpolated coordinate vector of the INS (or the GPS) in the m-frame,

- $\mathbf{R}_b^m(t)$ is the interpolated rotation matrix between the INS body frame (b-frame) and the m-frame,
- (t) is the time of exposure, i.e. the time of capturing the images,
- \mathbf{R}_c^b is the differential rotation between the camera coordinate frame (c-frame) and the b-frame,
- \mathbf{a}^b is the offset between the INS and the cameras.

The georeferencing formula implies that in order to perform precise positioning, it is necessary to calibrate the entire system. As part of the calibration, the camera geometry, the relative orientation between the cameras and the INS b-frame (\mathbf{R}_c^b), the offset between the cameras

and the INS center (\mathbf{a}^b) must be determined. The calibration process is accomplished using a bundle adjustment and a test field of control points, for more details about system calibration see El-Sheimy et. al., 1995.

8. POSITIONING OF THE VISAT SYSTEM

Determining the position and orientation of the VISAT reference in three-dimensional space is in principle a problem of trajectory determination. The general motion of a vehicle in space can be described by six parameters (3 position and 3 rotation). They are typically the output of the GPS and INS. To optimally combine the GPS and the INS data, a Kalman filtering scheme is used (Schwarz et. al., 1990). The University of Calgary has developed a software package for centralized and decentralized Kalman filtering called **KINGSPAD** (**KINematic Geodetic System for Position and Attitude Determination**) for processing INS/GPS data. In the centralized case, a common state vector is used to model both the INS and the GPS errors. In this case, the INS measurements are used to determine the reference trajectory and GPS measurements to update the solution and estimate the state vector components. In the second approach, different filters are run simultaneously and interact only occasionally. The GPS data are Kalman filtered to obtain estimates of position and velocity which are then used as quasi-observations to update the INS Kalman filter. At the same time, the GPS data are continuously checked for cycle slips. For more details on the mathematical formulation and Kalman filtering alternatives, see Wei and Schwarz (1990).

The KINGSPAD software can perform the following functions:

- processing the data in three different modes, that is, pure GPS, pure INS, and hybrid INS/GPS,
- processing static, semi-kinematic, and kinematic data,
- defining which GPS data will be used to update the INS, namely, position, velocity, and position/velocity,
- viewing individual space vehicle (SV) data, thus allowing the rejection of specific SV in the GPS processor,
- selecting the GPS update rate according to a specific application (airborne, land application),
- computing the updated INS position, velocity, and attitude at 1-64 Hz to suit different applications,
- applying rapid static integer ambiguity resolution techniques for short baselines (under 7 km),
- applying 'on-the-fly' ambiguity techniques for kinematic processing of GPS data,
- providing a suite of bridging procedures in case of GPS outages.

The output from the KINGSPAD program is used to georeference (position and orient) the video images as described in section 7.

9. CYCLE SLIP DETECTION AND CORRECTION

The basic idea of using the INS in cycle slip detection is to use the predicted INS coordinates in computing the triple difference phase $\delta\nabla\Delta\phi$. By computing the cycle slip difference v between the predicted and measured value of the triple difference, it is possible to detect cycle slips. The formula for cycle slip detection is of the:

$$v = \delta\nabla\Delta\phi_{\text{predicted}} - \delta\nabla\Delta\phi_{\text{measured}}, \text{ and} \\ \delta\nabla\Delta\phi_{\text{predicted}} = (\delta\nabla\Delta\rho + \nabla\Delta N) \quad (2)$$

where,

$\delta\nabla\Delta\rho$ is the triple difference range obtained from the predicted INS coordinates,

$\delta\nabla\Delta N$ are the triple difference ambiguities.

The noise in v is due to the estimation error of the integrated INS and the measurement noise from the GPS. However, since v is a relative change of the double difference from one epoch to the next, the noise from common error sources will be removed or greatly reduced.

For precise positioning with GPS/INS the v values, expressed in cycles, will be close to zero and continuous with respect to time. A simple method of fixing cycle slips can therefore be obtained by monitoring the v continuously in time and compute the effect of cycle slips

on the triple differences by equation (2). This method will provide cycle slip recovery for the phase triple difference with high accuracy. To reduce the influence of noise, the v function can be modeled through the use of all available information before and after the cycle slip. The function v can be used without differencing with respect to time. In this case, the double differenced observation at time t will be obtained. For some further discussion, see Schwarz et. al., 1994.

10. INS BRIDGING

The basic idea behind INS bridging is the use of the INS predicted coordinates to reset the position of the GPS antenna after loss of lock and signal re-acquisition. The bottom line, in INS bridging, is that any errors incurred during unaided INS operation should be below half a cycle in order to prevent a bias in the GPS computation following re-acquisition of lock. The reason for such a bias is that the inertially derived position is used in re-computing the phase ambiguities. Since they are considered as constant biases, until the next loss of lock, errors in the ambiguity determination, due to errors in the INS coordinates, will show up as a constant bias. Should there be a large number of satellites available, the GPS filter will attempt to re-establish precise ambiguity terms in kinematic mode. Although this is not uniformly reliable, since it is geometry dependent, it works well if there is a longer period of uninterrupted GPS observations with at least 4 satellites.

In general, INS bridging is used as a prediction method only, i.e., current filter estimates are used to predict position from INS observations. Due to errors in the Kalman filter states and the data, the length of the bridging interval is limited depending on the quality of the INS. For navigation grade systems, typical intervals are 20 - 30 seconds (Cannon, 1990). These intervals can be considerably extended if prediction is combined with smoothing after signal re-acquisition. The principle is shown in Figure 2.

In the forward prediction process, GPS information up to the time epoch t_1 , at which the GPS signal is lost, is used to predict the trajectory during the period t_1 to t_2 in which no GPS data is available. This results in the error curve E1. Due to the double integration of errors at time t_1 , the error curve E1 increases rapidly. Using the information in time sections t_2 to t_3 after GPS signal re-acquisition, a backward prediction can be used for the t_1 - t_2 section, resulting in the error curve E2. It is the mirror image of the error behavior of E1. A smoothing procedure combines both the forward prediction and the backward prediction optimally and gives the improved estimation of

the trajectory with error curve E3. As can be seen, the bridging interval is greatly extended by using this procedure.

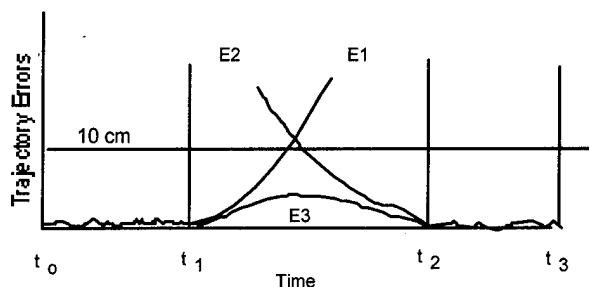


Figure 2: INS bridging with forward - backward predictions and smoothing

It should be noted that INS bridging by prediction can be used as a real-time method, while bridging by prediction and smoothing is clearly a post-mission method. In geomatics applications, this is usually not a problem because post-mission processing is the norm.

A further extension of the bridging interval can be achieved if dual frequency GPS receivers are used. By using wide-laning techniques, the accuracy required from the INS stand-alone solution is 43 cm instead of 10 cm. Thus the bridging interval for which the INS solution is valid is much longer. For more details about INS bridging accuracy and results see Schwarz et. al., 1994.

11. SYSTEM TESTING

Field tests of the VISAT navigation component were carried out on May, 1995 along a L-Shape baseline in Calgary, while full system testing took place in August 1995 along a test field of ground control points in Laval using the Van shown in Figure 3. The objective of the first test was to calibrate the INS sensors and estimate the sensor performance in INS stand-alone mode (ZUPT mode). The second test was mainly for checking the system repeatability and final accuracy as well as system performance after frequent signal blockage when driving through underpasses.



Figure 3: The VISAT Van.

11.1 INS Bridging Accuracy

Figure 4 depicts the error behavior of the INS in stand-alone mode during the May test. During the 80 second period, GPS observations were removed from the data and the INS data was processed in stand-alone mode. The truth model of this diagram was obtained using the trajectory computed from the original GPS/INS measurements. The INS stand-alone positioning results stay below the half cycle level (10 cm for L1 and 43 cm for wide-lane) for about 42 seconds for L1 and 52 sec for the wide-lane. Thus, bridging by INS results would have been correct in this case for up to 40 seconds. It should be noted that this is valid only for this class of inertial hardware, the Honeywell LaserRef III strap-down system, i.e. an INS rated at one nautical mile per hour at 95% CEP in unaided navigation mode. It also should be mentioned that the accuracy shown in Figure 4 is not consistently achieved in all runs; a more typical time interval for reaching the half a cycle level is 20 seconds for L1 and 30 seconds for wide-lane.

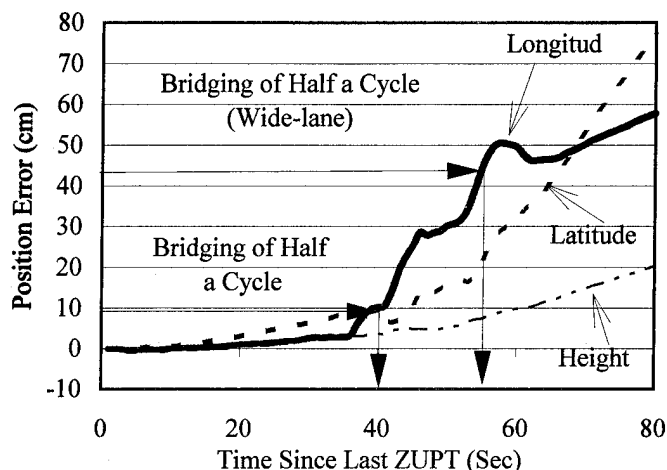


Figure 4: INS Error Behavior in Stand-alone Mode

11.2 INS ACCURACY FOR CYCLE SLIP DETECTION AND CORRECTION

There are a number of ways to assess the use of the INS predicted coordinates for cycle slip detection and. Table 1 gives the statistical summary of the difference between the GPS and the one second predicted INS solutions for a sample of eight hundred seconds for the two runs of the August test. The mean values are close to zero which indicate that the Kalman filter correctly models the vehicle dynamics and systematic errors. The values for the standard deviation (σ) are within the three centimetre range. These results indicate the effectiveness of using the high data rate (50 Hz) of the INS in interpolating the camera coordinates at the time of exposure.

Another method of assessing the INS predicted accuracy is by monitoring the values of ∇ , i.e. the difference between the INS predicted double difference phase $\nabla\Delta\phi_{\text{predicted}}$ and the measured double difference phase, $\nabla\Delta\phi_{\text{measured}}$. Table 2 lists the mean and standard deviation of ∇ values for different satellites and sample sizes during the August test. The listed standard deviation values indicate the level of cycle slip that can be detected. In these tests, the level of cycle slip detection is less than quarter of a cycle, when using 1 Hz GPS data.

Table 1: GPS Versus INS Prediction In Kinematic Mode
(Sample size = 800 sec)

Run No.	Coord.	Mean (cm)	St. dev. (σ) (cm)	Max diff. (cm)
1	ϕ	1.2	2.1	3.1
	λ	1.4	2.0	-2.4
	h	-3.3	2.7	-5.1
2	ϕ	-2.2	1.9	3.1
	λ	1.1	2.2	4.2
	h	-2.1	1.7	-2.6

Another method for the assessment of INS cycle slip fixing capability is the prediction of the ambiguities of emergine satellites by INS and the comparison with the measured GPS results (using the computed position from tracked satellites). Table 4 list the ambiguities for a number of satellites in one of the August runs as determined from GPS and as estimated from the INS predicted coordinates. The maximum difference in cycles agrees with the standard deviation values of Tables (1) and (2). This confirms that both solutions are more or less

identical and Kalman filter results correctly model the dynamics of the van.

Table 2: Difference between $\nabla\Delta\phi_{\text{predicted}}$ using the INS predicted coordinates and $\nabla\Delta\phi_{\text{measured}}$ using GPS (Sample 800 sec).

SV Number	Mean (cm)	St. dev. (σ) (cm)
26	-1.9	1.5
6	2.1	2.9
16	1.4	1.4
17	3.0	1.9
9	2.9	2.3
23	-1.8	2.1
12	2.7	2.5

Table (4) : Difference between estimated $\nabla\Delta N$ from GPS and INS

SV Number	$\nabla\Delta N$ INS	$\nabla\Delta N$ INS	Diff. in Cycles
6	-1748369	-1748369.1	0.1
16	-1938404	-1938403.8	0.2
17	833425	8344425.1	-0.1
27	-802652	-802651.7	0.3
23	879599	879598.8	0.2

11.3 INS Supporting OTF

In order to test the accuracy of using the INS predicted coordinates in fixing the GPS coordinate after signal blockage, a test along a highway with a number of bridges was performed. In this test the van was stopped for about 600 sec after passing under the bridge. This is not necessary for GPS/INS integration, but the static period can be used to fix the ambiguities which are then a good indication of the accuracy of the INS bridging accuracy after GPS blockage of about 10-30 sec. In this periods the INS filter will proceed in prediction mode only. Table (5) shows some of the wide-lane ambiguity values as estimated from the INS predicted coordinates, and compare them to the one fixed by the OTF technique.

Table (5) : Ambiguity Estimation Using INS Predicted Coordinates.

SV Number	Blockage Interval (Sec)	$\nabla \Delta N$ GPS	$\nabla \Delta N$ INS	Diff. in cm
6	13	-2804419	-2804419.1	-8.62
16	16	-2423079	-2423079.1	-8.62
17	17	833425	833424.85	12.9
23	18	2351363	2351362.9	8.62
12	23	272884	272884.2	-17.2

In this case, the actual coordinates difference are larger than before, although still well within the half cycle range of 43 cm for wide laning. This can be explained by the higher noise level in wide lanning and by satellite geometry.

The reliability of the INS bridging depends on the accumulation of errors in each subsystem and on the effectiveness of the updating procedure in reducing these errors. The largest accumulation of errors occurs during periods of unaided INS operation, that is, upon loss of satellite lock or absence of sufficient zero velocity updates. During these periods, the inertial system is used as a stand-alone positioning system. After re-acquisition of the satellites, its results are used to fix the phase ambiguities. In general the ambiguities fixed by the INS are float. Following that, the GPS filter will attempt to re-establish fixed ambiguity terms while in kinematic mode. This, however, is not uniformly reliable since it is geometry dependent. But in general, the INS predicted coordinates will reduce the time required to fix the ambiguities due to the good approximate coordinates after the bridging process.

Figure (5) shows the ambiguity fixing interval as a function of the number of satellites, once by using OTF technique only, second by using the INS predicted coordinates as approximation in the OTF procedure, and finally by using the INS predicted coordinates after 10 seconds of ZUPT. The results indicate that by using the INS predicted coordinates, the time required to fix the ambiguities is reduced by 80% to 95% for poor satellite geometry and by 20% to 60% in good satellite geometry. This indicates that the INS constant bias terms (mainly accelerometer biases) are well estimated and the two systems are perfectly synchronized. Similar results were obtained for L1 ambiguities where more time for ambiguity fixing is needed when using the GPS only. This highlight an efficient operational procedure to deal with the bridging problem. By switching the processing of the GPS data to the wide-lane after passing under a bridge and then rewinding the GPS and INS files to start at the

epoch of signal re-acquisition. This would eliminate the errors in the trajectory after signal re-acquisition and ambiguity fixing. The same principle can be used for back smoothing the INS trajectory during the periods of signal blockage.

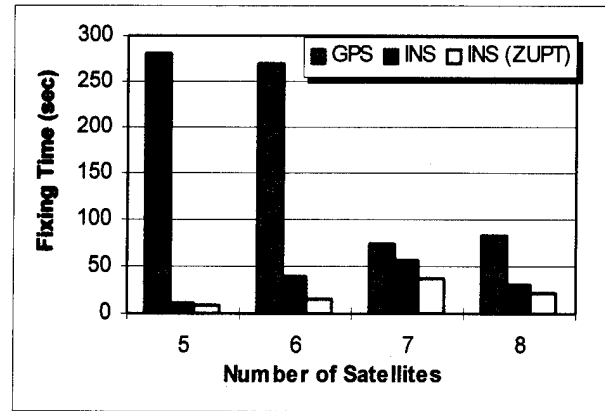


Figure (5) : Effect of using the INS predicted coordinates in speeding up the ambiguity fixing

These results indicate the importance of frequent ZUPTs, when the system alert for loss of lock is on, and of static re-initialization of the system in case of long satellite blockage in urban centers. This static re-initialization will give the GPS filter time to converge after the reset by the INS filter.

11.4 SYSTEM ACCURACY

The main objective of the VISAT system is the determination of 3-D coordinates for all objects within the FOV of the video cameras. The final accuracy of the 3-D coordinates is a function of the complete processing chain which involves GPS positions, INS position/attitude, target localization in the images, system calibration, the distance between the object and the cameras, and the geometry (the cameras used in the 3-D computation).

To check the system absolute accuracy, some well-defined Ground Control Points (GCP) along the August test runs were used for comparison. Figure 6 shows the difference between the GCP coordinates and the coordinates obtained from the VISAT system. They were obtained by deriving GPS-based measured by the VISAT system and transforming them to 3TM coordinates. These coordinates were then compared to the completely independent GCP coordinates. The GCP were about 10-30 m away from the van. The figure combines the results of two runs on two different days for the same test area.

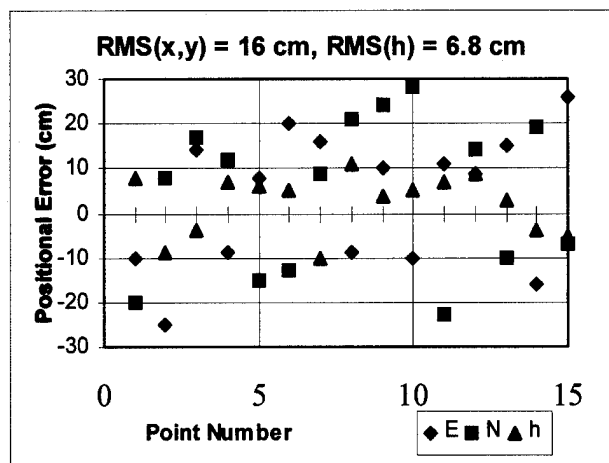


Figure (6) : The VISAT Absolute Accuracy

Results shows clearly that an RMS of 0.16 m in the horizontal coordinates and a few centimeters in height are achievable for distances up to 30 m under normal conditions. The results in height indicate that the GPS/INS positioning component is working at the centimeter level. Since the height component in GPS is the weakest, it can be expected that the X and Y components are at least of the same accuracy. The increase in errors for the horizontal components must therefore be due to the image pointing errors, because an error of one pixel error in the x image coordinate will introduce about 40 cm for objects 30 m away from the van.

CONCLUSION

The VISAT system presented in this paper is a kinematic survey system which can be operated continuously under diverse operational conditions. In particular, the complementary features of the integrated INS/GPS positioning and orientation subsystem permit the resolution of cycle slips and outages as well as INS drift control. System testing indicate that highway velocities of 60 km/h can be maintained with adequate data transfer. Target positioning is done in a post-processing mode at a workstation. Day-to-day system accuracy achieved in the first system testing is about 16 cm (RMS) in horizontal and about 6.7 cm (RMS) in height.

ACKNOWLEDGMENTS

The VISAT system represents the combined effort of a research team at The University of Calgary and Geofit Inc., Laval, Quebec. Besides the authors, the following persons are thanked for their contribution to the system testing: Skaloud, J., Mohamed, A., Argensu, V., Li, Z., Gascon, M.

9. REFERENCES

- [1] Bossler, J.D. and Novak, K., Mobile Mapping System: New Tools for the Fast Collection of GIS Information, GIS'93, Ottawa, Canada, March 23-25, 1993, pp. 306-315.
- [2] Cannon, E., Airborne GPS/INS with an Application to Aerotriangulation, Report No. 20040, Department of Geomatics Engineering, The U of C, 1991.
- [3] El-Sheimy, N. and Schwarz K.P., Kinematic Positioning In Three Dimension Using CCD Technology, VNIS93 Conference, Ottawa, October 12-15 1993, pp. 472-475.
- [4] El-Sheimy, N. and Schwarz K.P., Integrating Differential GPS Receivers with an Inertial Navigation System (INS) and CCD Cameras for a Mobile GIS Data Collection System, ISPRS94, Ottawa, Canada, October, 1994, pp. 241-248.
- [5] El-Sheimy, N., Schwarz, K.P., and Gravel, M., Mobile 3-D Positioning Using GPS/INS/Video Cameras, The Mobile Mapping Symposium, Ohio State, USA, May 24-26, 1995, pp. 236-249.
- [6] Li, R., M. A. Chapman, Qian, L., Xin, Y., and K. P. Schwarz, Rapid GIS Database Generation Using GPS/INS Controlled CCD Images, ISPRS 94 GIS/SIG, Ottawa, Canada, June 6-10, 1994, pp. 465-477.
- [7] Schwarz, K. P., Martell, H., El-Sheimy, N., Li, R., Chapman, M., Cosandier, D. (1993a): VISAT- A Mobile Highway Survey System of High Accuracy, VNIS Conference '93 Conference, Ottawa, October 12-15, 1993, pp. 476-481.
- [8] Schwarz, K.P., Chapman, M.A, Cannon, M. W., Gong, P. (1993b): An Integrated INS/GPS Approach to the Georeferencing of Remotely Sensed Data, PE&RS Vol. 59, No. 11, November 1993, pp. 1667-1674.
- [9] Schwarz, K. P., Wei, M. and Gelderen, M.V., Aided Versus Embedded - a Comparison of Two Approaches to GPS/INS Integration, Proceedings of IEEE Position Location and Navigation Symposium, 1994, pp. 314-322
- [10] Schwarz, K. P., El-Sheimy, N., Liu, Z. (1994): Fixing GPS cycle Slips By INS/GPS: Methods and Experience, KIS94, Banff, Canada, September 1-2, 1994, pp. 265-275.
- [11] Wei, M. and K.P. Schwarz: A Strapdown Inertial Algorithm Using an Earth-Fixed Cartesian Frame, Navigation, Vol. 37, No. 2, 1990, pp.153-167

Field test Results of an Enhanced GPS Coverage Through Map Aiding in Urban and Canyon Environments

James LaMance and Alison Brown
NAVSYS Corporation

James LaMance

James LaMance is a Senior Engineer at NAVSYS Corporation, in Colorado Springs, CO, where he is involved with GPS navigation systems design and analysis. Dr. LaMance has worked in the areas of GPS, remote sensing, and orbit determination for the past six years. Dr. LaMance holds a PhD and MS in Aerospace Engineering from the University of Colorado at Boulder, and a BS in Aerospace Engineering from Auburn University, Auburn, AL.

Alison Brown

Alison Brown is the President of NAVSYS Corporation, which specializes in developing GPS technology. She has 15 years experience in GPS receiver design and has seven GPS related patents. She has published numerous technical papers on GPS applications and is on the editorial board for GPS World and GIS World magazines. Dr. Brown is currently the Space Representative for the ION Council and Vice Chair for the IEEE Pikes Peak Section.

Abstract

The development of an effective motorist Mayday system for travelers in rural and urban parts of the United States and Canada has been hampered by the lack of an infrastructure to receive and process emergency requests and by the inability of most motorists to precisely define the location of their vehicle. The development of intelligent vehicle-highway systems and an expanded network of computer-switched radio systems will greatly improve the ability of highway agencies, both public and private, to respond to emergency requests. The missing element is still an inexpensive and reliable means of determining the location of vehicles in distress. The requirements for a viable motorist Mayday service are: low cost, reliable response, and automatic linking to a two-way radio service.

GPS has been proposed as a potential method of providing location in support of a Mayday service. However, the expense of a conventional GPS receiver will prohibit widespread installation on vehicles. One market source has indicated that the total cost to the user must be less than \$100 before the system would be widely used. Also,

the time-to-first-fix of a GPS receiver is unacceptable for use in an emergency situation unless the receiver is continually operating. Finally, the inability of a receiver to compute a navigation fix except when four satellites are in view makes this a poor system design for operation in mountainous or urban regions where there is poor satellite visibility.

NAVSYS has developed a low cost GPS sensor, the TIDGET™, which solves these problems for a GPS Mayday service. The TIDGET sensor does not track the GPS signals, but instead captures a brief "snapshot" of raw GPS sampled data. This "snapshot" is transmitted to the emergency dispatch facility where it is processed to compute the location of the motorist. The processing also includes aiding data from a map database to allow the vehicle's location to be determined when fewer than four satellites are in view of the sensor. In large quantities, the TIDGET sensor cost is reduced to \$50 a unit (not including the communications link). The TIDGET requires no initialization or warm up time, since the data processing functions are not performed at the vehicle. The sophisticated software used to process this message at the dispatch center allows a three-dimensional position solution to be derived in many cases when only two GPS satellites are in view. This paper includes a description of the TIDGET Mayday system and presents test results demonstrating the ability to locate a stranded motorist even in areas of decreased GPS coverage.

Introduction

Applications for global positioning systems (GPS) have expanded to many unique areas that were unthought of only a few years ago. One that is still not given wide credibility is the potential for equipping every vehicle on the roadway, both commercial and non-commercial, with a GPS receiver for Mayday and automatic vehicle location (AVL) applications. However, in order to address this market, significant enhancements are needed to improve the receiver performance when operating in an urban environment.

In an urban or canyon environment, satellite visibility is generally obstructed which significantly limits the number

of satellites that can be tracked. The classic method of solving the GPS visibility problem, adopted by many receiver manufacturers, is to aid the GPS solution with data from other in-vehicle sensors.

In the conventional AVL system, the vehicle installation includes heading and distance sensors to allow dead-reckoning, and a digital map to provide altitude aiding. These additional components significantly increase the cost of the equipment and complicate the vehicle installation.

NAVSYS has developed an alternative system architecture designed specifically for AVL applications. This innovative design provides improved navigation accuracy and performance in an urban environment without requiring additional on-board sensors to aid the GPS navigation solution. This results in a highly cost-competitive AVL system without compromising performance.

Test data results will be presented that show the 3-dimensional positioning capability of this system architecture. The GPS data was collected with a state-of-the-art Novatel receiver and truth data was provided by the NAVSYS GPS Inertial Mapping (GIM) system. The results demonstrate the situations when conventional GPS will fail, but the Mayday architecture will still provide position information.

TIDGET Mayday System Architecture

The TIDGET Mayday system architecture is illustrated in Figure 1. The system includes the following elements:

TIDGET Sensor The TIDGET sensor is used to provide the GPS data from which the vehicle location can be derived.

Mayday Terminal The Mayday terminal installed on the vehicle provides the two-way data link from the vehicle to the Operations Center. This terminal is integrated with the TIDGET sensor to access the location data. The terminal is also used to call for help and display messages to the motorist from the Operations Center.

Operations Center The Mayday Operations Center includes the TIDGET processing system which determines the vehicle location from the TIDGET data. The Operations Center also places priorities on the calls, routes call for assistance to the appropriate agency (e.g., state police, AAA, towing service, or medical facility), and

notifies the motorist of the action taken and the anticipated response time.

TIDGET Tracking Sensor

The TIDGET sensor was developed by NAVSYS specifically for tracking applications [1,4]. It uses GPS satellite signals to provide data to the Mayday Operations Center on the location of the vehicle. Because the sensor employs a much simpler architecture than that of a classic GPS receiver, it achieves a significantly lower cost and better performance for emergency location.

A number of manufacturers, such as Rockwell, Motorola, and Trimble, offer OEM GPS card products that adopt the digital architecture illustrated in Figure 2. These cards include the hardware to receive the GPS satellite signals and convert them to a digital data stream through a down-conversion and sampling process. The satellite signals are then processed digitally using a custom ASIC, and the measurements of the pseudo-range and carrier frequency are used in a microprocessor to derive the navigation solution. In an emergency location application, the OEM card would output the vehicle coordinates (latitude, longitude, altitude) across an RS-232 interface for transmission back to the Operations Center.

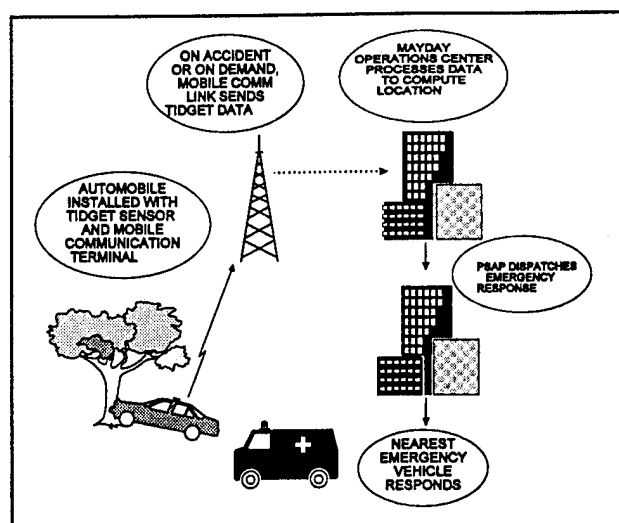


Figure 1 TIDGET Mayday System Architecture

As illustrated in Figure 2, the TIDGET sensor architecture is significantly simpler than a conventional GPS receiver. Instead of processing the GPS data on the vehicle, the TIDGET simply converts the GPS satellite signals into a digital data stream. When the device is triggered (e.g., by an air-bag sensor or keypad), the TIDGET captures a short (~1 kbyte) "snapshot" of the GPS data in a digital data

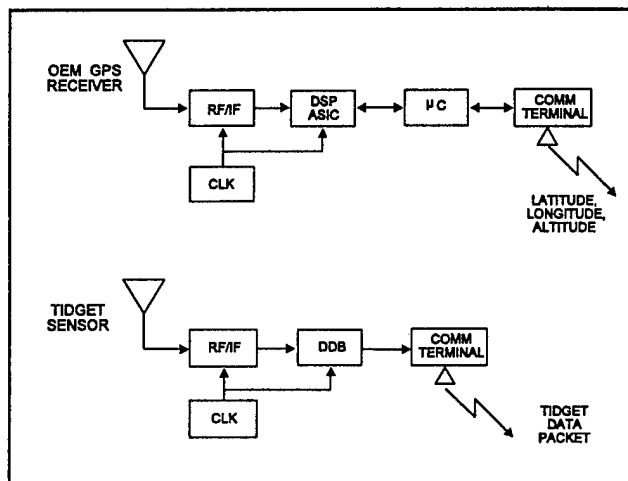


Figure 2 TIDGET and GPS Receiver Architectures

buffer (DDB), and transmits the raw data back to the Operations Center for processing.

When an emergency message is received, the TIDGET data in the message is processed to extract the satellite code phase and carrier frequency observations. A reference GPS receiver at the Operations Center is used to provide data on the visible GPS satellites and compute the TIDGET location from the satellite observations. A digital map is also maintained at the Operations Center. Data from this map is used to "aid" the TIDGET navigation solution, allowing the vehicle location to be determined in most cases using only two satellite observations [2,3,4].

The TIDGET has the following advantages over a conventional GPS receiver for emergency vehicle location:

Sensor Cost The simple design adopted by the TIDGET reduces the sensor component count to almost one-third that of a conventional receiver. This results in a similar savings in cost. The TIDGET currently costs less than \$100 per unit—one third the cost of an OEM GPS receiver. TIDGET sensor prices are projected to drop to less than \$50 within a year for large quantity purchases. The TIDGET is ideally suited for applications such as emergency location that are highly cost-sensitive.

No Initialization A conventional GPS receiver must go through an extensive initialization procedure before a navigation solution can be computed. The receiver must first search for the visible GPS satellites, lock onto their signals, and then demodulate the navigation message broadcast by the satellites. This procedure takes a minimum of 30 seconds to perform and can take 15 minutes or longer if the current location of either the

vehicle or the satellite is not known. The time-to-first-fix (TTFF) can be a significant obstacle for an emergency service where it is imperative that the location data is available immediately to allow prompt dispatching of assistance.

The TIDGET takes less than 1 second to turn on, capture a snapshot of data, and send this data back to the Operations Center. The TIDGET processing workstation developed by NAVSYS can process the TIDGET data to determine a solution for the vehicle within a few seconds. This rapid acquisition is achieved by using timing data from the communication link and satellite data from the Operations Center's reference GPS receiver to reduce the search and acquisition process. The TIDGET architecture therefore minimizes the delay time in determining the current vehicle location from the GPS satellite measurements.

Reliable Operation The emergency location sensor will not be used frequently, but when it is used, it is critical that the sensor operates reliably. GPS receivers have made significant advances in recent years to improve their reliability and ease of operation. However, tracking and processing the GPS satellite signals is a complicated process, and there are a lot of factors that can cause a receiver to have difficulties computing a navigation solution. If the receiver is slow to acquire and track the satellites, the emergency response could be delayed. If the accident happens in a location where four GPS satellites are not visible, a standard GPS receiver might never be able to provide the vehicle location.

The TIDGET design provides significantly more reliable operation than a conventional receiver for the following reasons:

- The simplicity of the TIDGET sensor design (fewer parts, no processing) means that there is less potential for failure.
- The TIDGET data is processed at the Operations Center, so that no acquisition or tracking is performed at the vehicle.
- By taking advantage of aiding data from digital maps, a navigation solution can be computed from the TIDGET data even when four satellites are not visible. This increases the reliability of the emergency service when operating in a city or in mountainous regions where the satellite signals might be blocked.

TIDGET Workstation

The NAVSYS tracking workstation is designed to process

data from many different vehicles simultaneously. The workstation also provides altitude and map-aiding data to allow a three-dimensional solution to be computed for a vehicle even when only two GPS satellites are being tracked by using map aiding.

The NAVSYS PC-based workstation is used to process the measurements received from the different vehicles being tracked. A highly efficient navigation algorithm has been developed at NAVSYS that allows solutions to be computed in parallel for more than 100 vehicles simultaneously, using a 486 PC.

The workstation is integrated with a GPS reference receiver which performs a dual function. First, it provides the workstation with the satellite ephemeris data needed to compute the vehicle navigation solutions. Second, it also provides differential GPS corrections to improve the accuracy of the data provided.

The workstation serves as the operator interface. A digital map database is integrated with the workstation, which allows the vehicle locations to be displayed to the operator superimposed on a city map. The map database also provides the capability of aiding the navigation solution.

Obstructions in an urban environment can often reduce the satellite visibility to two observations. The workstation must be able to reliably track vehicles even under these conditions. When three satellites are visible, the workstation can compute a navigation solution by "looking up" the vehicle altitude from the digital map. This can be iteratively applied to compute a navigation solution with only three satellite measurements. A more sophisticated "road-aiding" algorithm is applied to derive a solution when only two satellites are visible. The algorithm works on the principle that the two satellite measurements define a line-of-position. The digital map data reduces the possible GPS solutions to one of the points where the two-satellite line-of-position and the city roads intersect.

The design adopted for the TIDGET workstation with the superior tracking performance provided by the TIDGET sensor allows a navigation solution to be reliably determined even in dense urban and canyon environments.

Two Satellite Tests Results

Test Results

To demonstrate the ability of the altitude aiding in the recovery of 2 satellite positioning, tests were conducted using a state-of-the-art Novatel receiver to collect data in an urban environment and the NAVSYS GIM System as the truth reference. The advantage to this data collection configuration is the accuracy of the position solution provided by the GIM system during GPS drop-out and

time tagged video provided by the GIM system. The video provided the opportunity to view the obstructions that decreased the satellite visibility. The data were collected on September 9, 1995 in residential portion downtown Colorado Springs. A total of about 15 minutes of data were analyzed for this paper.

GIM System Description

The NAVSYS GIM system incorporates an innovative optimal processing algorithm that enhances the performance of the inertial/GPS system enabling a low cost Inertial Measurement Unit (IMU) to be employed in combination with a GPS receiver, and a differential GPS correction system to provide an accurate, real time position and attitude reference. The overall process is controlled by an intelligent data management system capable of recording feature and attribute information in real time, with associated time tagging for exact location. The GIM system is packaged into a portable, modular architecture that is suited for various vehicles such as cars, four wheel drives, watercraft, or railroad cars, allowing quick and accurate surveys to be performed in a wide variety of geographies.

Recent results obtained from roadway surveys demonstrate that the system is capable of maintaining 1-2 meter accuracy while driving over several different types of terrain with varying degrees of GPS coverages, and while operating at highway speeds [5].

Data Analysis

The first step of the analysis was to determine the satellite coverage and the times that had only 2 satellites visible in the one-per-second data. Table 1 shows the number of satellites visible to the Novatel receiver as a percentage of the total data set. From this table, it is clearly seen that more than 12% of the time there are either 2 or 3 satellites visible. For emergency location applications, this represents an unacceptably large portion of the time to not have GPS positioning.

Based on solely pseudorange measurements from the Novatel receiver, solutions were computed for each occurrence of only 2 satellites in view. This solution produces a very thin ellipse, or a thick line, encompassing the set of possible positions. The true solution can then be derived by searching for the intersection of this thick line described by the 2 GPS satellites in view and a road.

The geometry of the solution ellipse is determined by three factors: the uncertainty on the initial position, the uncertainty on the pseudorange measurements, and the

Table 1 Satellite Coverage

# SVs	Percentage
0	.44%
1	.89%
2	3.77%
3	8.66%
4	14.87%
5	20.87%
6	14.43%
7	32.30%
8	3.77%

satellite geometry. The uncertainty on the initial position defines the length of the ellipse. The uncertainty on the pseudorange defines the width of the ellipse. The smaller the uncertainty on the pseudorange, the thinner the ellipse will be and thus more closely resemble a line. Typical dimensions on this ellipse are about 50 meters thick and a few kilometers in length. The satellite geometry will determine the northeast rotation of the ellipse.

Figure 3 shows the satellite visibility for one of the 2 satellite cases observed. The outage in this case was caused by trees bordering the road (observed in the video). The full error ellipse is shown in **Figure 4**. At this scale, the error ellipse appears as a thick line as discussed above. The true location is represented by the circle. It is clear that the line of possible positions passes through the true position. By observing the satellite geometry in **Figure 3**, the line of positions shown in **Figure 4** can be seen to be perpendicular to the line between the satellites. A blow up of the area around the truth solution of **Figure 4** is shown in **Figure 5**. The dashed line is the road traveled by the GIM system. The circle is the true position at the time only 2 satellites were visible. The straight parallel lines are the sides of the error ellipse. The scale on the plot is 1 kilometer in the north and east direction. Based on this information, we know the vehicle is located in the ellipse along the road in a segment about 100m long.

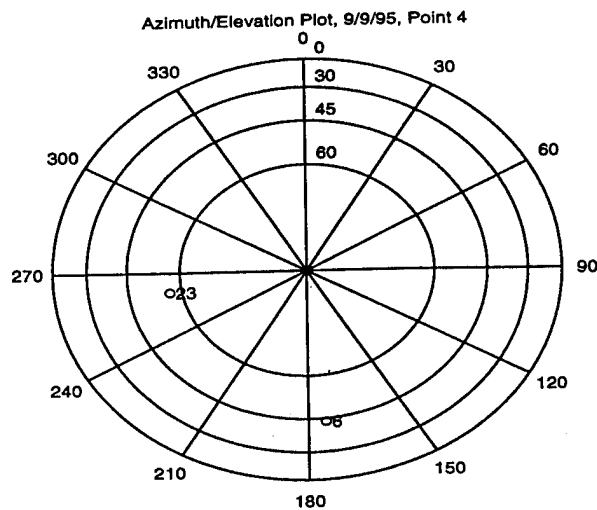


Figure 3 Sample Azimuth/Elevation Plot

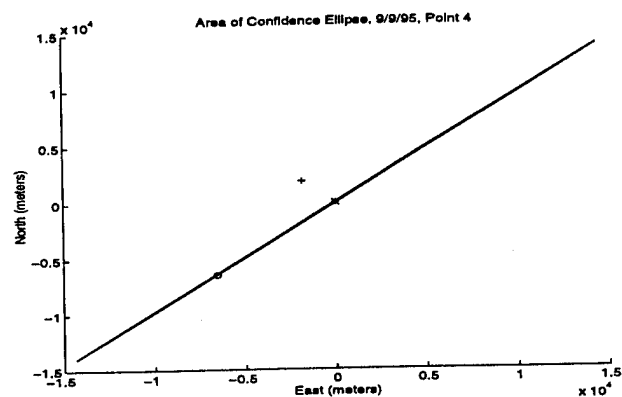


Figure 4 Sample Full Error Ellipse

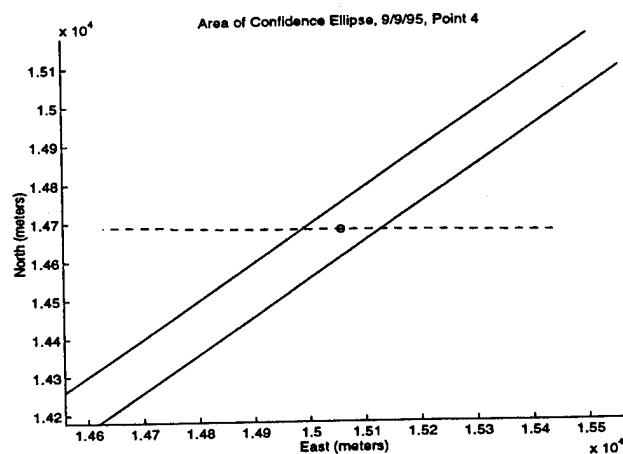


Figure 5 Blow-up of Sample Error Ellipse

Although only 1 sample is given of these ellipses, a total of 34 epochs with only 2 satellites were processed to account for the 3.77% of the epochs. All 34 of the processed points fall within the bounds of the ellipse.

Conclusions

This paper demonstrates that 3 dimensional navigation solutions are reliably provided with 2 GPS satellites in view through the use of map aiding. We've shown that even in normal city driving in a residential section of downtown Colorado Springs, even the Novatel receiver experiences tracking of only 2 and 3 satellites more than 12% of the time. At these locations, conventional GPS receivers would fail to produce a current navigation solution. This also reveals that the largest error source in emergency vehicle location and AVL may be satellite visibility and not multipath.

REFERENCES

- [1] A. Brown, "The TIDGET™—A Low Cost GPS Sensor for Tracking Applications," *Proceedings of GPS-92, ION Satellite Division 5th International Technical Meeting*, Albuquerque, Sept 1992.
- [2] A. Brown, "Low Cost Vehicle Location and Tracking using GPS," *Proceedings of ION 48th Annual Meeting*, Washington, D.C., June 1992.
- [3] A. Brown, "A Low-Cost Vehicle Location and Tracking System," *Proceedings of IEEE PLANS '92 Conference*, CA, March 1992.
- [4] A.K. Brown, M.A. Sturza, "Vehicle Tracking System Employing Global Positioning System (GPS) Satellites," US patent 1993, European patent 1992.
- [5] Timothy Ash, Josef Coetsee, Randy Silva, and Alison Brown, "Test Results of the NAVSYS GPS/Inertial Mapping (GIM) System," *Proceedings of ION 50th Annual Meeting*, Colorado Springs, CO, June 1995.

GPS Receiver Structures for the Urban Canyon

Capt. Benjamin Peterson, Cdr. Richard Hartnett, and Ens. Geoffrey Ottman
U.S. Coast Guard Academy

BIOGRAPHIES

CAPT Benjamin Peterson and CDR Richard Hartnett are Academy electrical engineering faculty. CAPT Peterson earned the PhD from Yale University in 1983 and is Eastern Region Vice President of the ION. CDR Hartnett earned the PhD from University of Rhode Island in 1992. ENS Geoffrey Ottman is a 1995 BSEE Academy graduate and is presently aboard the USCGC Bramble in Honolulu HI. For his contribution to this study he received the annual ION Award at the Academy.

ABSTRACT

Conventional GPS receivers typically have limited capabilities for continuous tracking of satellite signals in deep urban canyons. In such environments we find that receivers obtain brief glimpses of satellites, but rarely see three or more satellites simultaneously, resulting in poor fix availability. This would suggest that a GPS receiver that can obtain useful pseudorange information from brief glimpses of satellites, or one which can obtain fixes from as few as two satellites, may enhance fix availability in urban canyons.

Here we present interim results of an ongoing effort to address these issues. More specifically, we present several software and hardware modifications to GPS Builder™, a 12 channel GPS development system from GEC Plessey Semiconductors. The hardware has been modified to use either a Cesium or ovenized quartz oscillator as an external frequency reference, thereby allowing a position solution from as few as two satellites. As the number of tracked satellites decreases from three to two, the clock is assumed to drift at its last known frequency, a pseudolite is placed at the earth's center, and the fix is calculated. Results on effects of clock accuracy on initial acquisition times and the ability of a receiver to coast through periods when a satellite is in the shadow of a structure are presented.

We also present results on obtaining fixes based on as little as one millisecond of data. The cross correlation of "Doppler shifted PRN templates" and one millisecond of digitized RF are calculated using Fast Fourier Transform (FFT) techniques. The peaks in absolute values of these

cross correlation functions are then further processed to obtain a Time of Arrival (TOA) resolution of 10 ns. These TOA's (modulo 1 millisecond) have typical one sigma code phase noise of 30-50 ns.

Finally, we present an interesting method whereby these TOA's can be processed to obtain a fix, even if time is only known to several minutes (and hence satellite positions are not known).

INTRODUCTION

In [1], the results of a comprehensive study of radionavigation systems in an urban environment were presented. While the basic conclusions regarding GPS reached in that study will be repeated here for completeness, we refer the reader to [1] for more details or for data on LORAN availability and accuracy. The approach used in [1] to determine GPS signal and thus fix availability was to use the binary information provided by commercially available GPS receivers on whether they were tracking particular satellites. Then using the known azimuths and elevations of the satellites, the PDOP's were calculated for a number of fix categories and compared to a threshold. The category showing use of a precise clock assumes that any clock bias had been determined in an open area with redundant signals and had been stored. Table 1 summarizes the fix availabilities of GPS.

After completion of the 1994 data collection phase in New York City, it was decided that all future effort would be focused on GPS receiver issues, because of the uncertain future of LORAN in the U. S. [2] Based on the data from [1] summarized in Table I, a few areas looked promising. First, implementation of a GPS receiver that would produce two dimensional fixes with only two satellites would improve fix availability. Second, it was clear that improvements in initial acquisition and reacquisition after blockages would be needed. Finally, we felt that a receiver needed to be able to process short glimpses of data in order to improve fix availability.

	PDOP less than 3	PDOP less than 6	No limit
Wall St. 3D	0.4%	1.0%	6.9%
Wall St. 2D	8.0%	11.2%	21.8%
Wall St. 2D w/clock	11.8%	34.9%	57.1%
Bronx 3D	43.0%	71.1%	81.1%
Bronx 2D	76.5%	85.2%	89.3%
Bronx 2D w/clock	87.1%	91.1%	97.4%
Third Ave. 3D	1.3%	33.1%	55.3%
Third Ave. 2D	47.0%	60.0%	84.2%
Third Ave. 2D w/clock	65.4%	77.3%	96.0%
GW Bridge 3D	59.3%	83.3%	88.7%
GW Bridge 2D	89.8%	92.1%	93.5%
GW Bridge 2D w/clock	92.8%	94.7%	95.0%
Foliage 3D	3.9%	9.5%	16.5%
Foliage 2D	39.5%	44.2%	53.2%
Foliage 2D w/clock	53.1%	77.5%	82.4%

Table 1. GPS Fix availabilities.

It is clear that the accuracy and stability of the receiver's oscillator is critical to implementing some of these proposals. The issue of clock stability in GPS receivers has been addressed by several research groups [3-5]. When [3] was written in 1983, plans were for an 18 satellite constellation to be operational in 1988. That 18 satellite constellation would have experienced extensive outage periods for conventional 3D (4 satellite) navigation, and the authors analyzed accuracy as function of outage duration and clock stability [3]. Researchers in [4] develop analytic solutions for the steady state optimal estimate (Kalman filter) covariance, and in particular look at the improved performance in situations with bad geometry. It is well known that because the satellites used (by receivers on the earth's surface) all must lie within a cone starting at some (elevation mask) angle above the horizon, there is high correlation between altitude and clock errors. In [5], the authors find that by using very stable clocks, the altitude error on aircraft precision approaches can be substantially reduced.

To study these issues in GPS receivers we use a modified GPS Builder™ Kit [6] from GEC Plessey Semiconductors (Figure 1). With this kit, the researcher has control of all aspects of the receiver, from the acquisition to the final position solution. We modified the hardware to allow an external frequency reference, and made software changes to 'C' source code provided with the GPS Builder™ Kit as documented below.

ACQUISITION TIMES FOR RECEIVERS

The first consideration of navigation in an urban environment is that only short duration, periodic looks

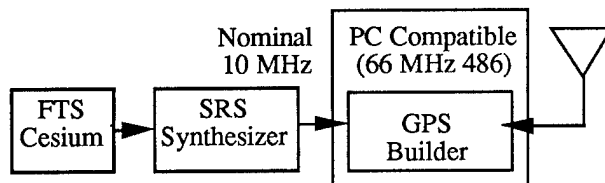


Figure 1. Block diagram of GPS Builder Kit system.

at the satellite constellation will be available to the receiver. To improve availability the satellites have to be acquired more quickly. An actual example of this process for one satellite is shown in Figure 2. Each stage is represented on the horizontal axis as an increasing value with the maximum value, corresponding to the satellite signal being usable in the solution.

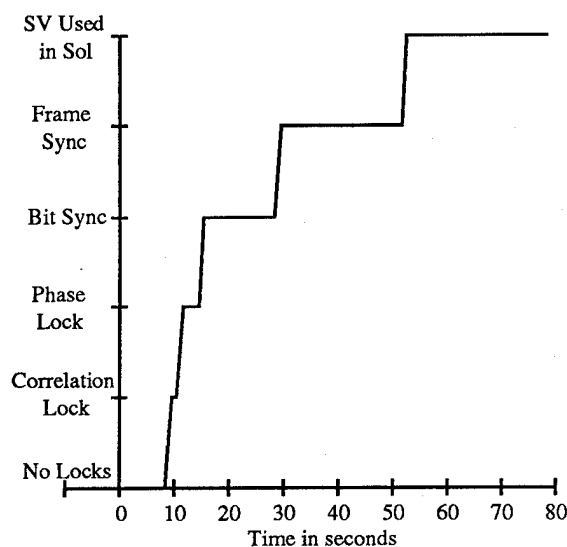


Figure 2. Typical Acquisition Stages versus time

The effects of using a Cesium oscillator were examined to determine if the acquisition time could be lowered. In the initial acquisition stage the receiver estimates Doppler based on a stored almanac and assumed position, and then searches in Doppler bins spaced 500 Hz (or 3.2×10^{-7}) apart starting with the assumption of a perfect clock. Since the standard TCXO was within this tolerance, the standard receiver performed as well as the Cesium in the initial tests. To illustrate the effects of the clock on acquisition, several tests were conducted with the Cesium referenced synthesizer operating at different offsets from 10 MHz. As the offset increases the receiver has to search over more Doppler for the satellite signal. This causes the position fix to be delayed greatly. These results are summarized below.

Offset	Time to 3-D Fix
0 Hz	~45 seconds
±20 Hz	~1.5 minutes
±30 Hz	~2 minutes
±40 Hz	~3 minutes
±50 Hz	No fix obtained

The pattern of increasing time to fix as a function of the oscillator error is evident. It is cut off at ± 50 Hz due to the maximum oscillator error of 4 ppm (parts per million) being exceeded. Indeed initial acquisition time is a function of clock accuracy, but only to a point. More specifically, there is little to be gained in improved acquisition time by improving oscillator accuracies beyond 0.2 to 0.3 ppm.

COAST TIME IMPROVEMENTS

Coasting allows for short intervals of signal loss. By propagating the satellite's tracking state forward, the time before a loss-of-lock condition can be controlled. This enables the receiver to lock onto the satellite's signal immediately when it returns to view [6]. During this time the receiver will determine if the satellite is still a valid addition to the position solution. With high buildings blocking large sections of the horizon, the only feasible time to receive satellite information is at the short times available at the intersections of streets. If the receiver can maintain these signals from city block to city block, it becomes possible to have continuous coverage by the satellite.

Because the receiver propagates the correlation and phase lock forward to allow for coasting, a stable clock is important. The receiver can coast for minutes, but if upon the signal's return to view the locks are not synched, the locks will be lost, requiring complete signal reacquisition. This would then invalidate all position solutions during this coast time due to error. The effects of the improved coasting runs were studied with the standard receiver and the receiver with an external Cesium reference. In addition, the software for the coasting time in the modified version was extended from 5 seconds to 20 seconds. Blockages were simulated by masking sections of the horizon with a large metal sheet. Blockages of 3, 7, 17, and 23 seconds were conducted to the east, west, and south. The plot of satellite state versus time into the scenario shows the effects of the Cesium reference on the coast time (Figure 3).

Both receivers entered the coast mode as expected for the shorter blockages at 2.5 and 3 minutes into the scenario and immediately returned to a usable signal when the satellite returned to view. When the 17 second blockage occurred at 3.5 minutes into the scenario, the standard receiver lost all locks after a short coast period. It then attempted to reacquire the satellite, but was unable to do so due to the later blockage at 4.5 minutes into the scenario. Note that it took about two minutes before the satellite signal was fully recovered and usable in the position solution. The Cesium enhanced receiver entered the coast mode for the duration of the 17 second blockage. When the satellite returned to view, the frame sync had been lost but was almost immediately recovered. In this case the effect due to the signal loss was minor since the receiver was able to "coast" through the signal outage, and there were no ill effects on the position solution.

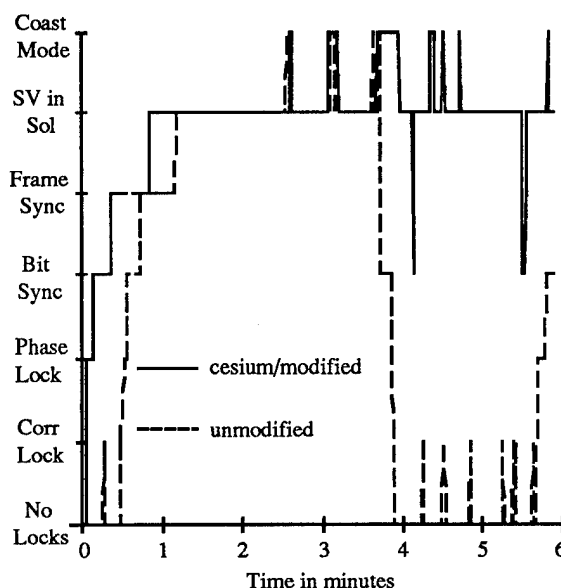


Figure 3. Satellite State versus time, with blockages of 3, 7, 17, and 23 seconds.

TWO DIMENSIONAL FIXES FROM TWO SATELLITES

The solution for a three satellite, two dimensional (2-D) fix has long been implemented by conventional GPS receivers. This is accomplished by constraining the altitude. For the GPS Builder™, this entails using the known radius of the earth to act as a pseudorange from an imaginary satellite at the center of the earth.

For a two satellite fix, the receiver is assumed to be already in the 2-D mode due to imposition of an altitude constraint. With an extremely stable clock, the clock frequency drift can be assumed to be zero. This eliminates the time correction component of the solution and leaves three unknowns. With the two satellites and the third augmented satellite, position can again be fixed. If the clock is in error the effects should be readily apparent as the position walks along a straight line bisecting the azimuths of the satellites used. When the clock moves ahead of true GPS time the pseudoranges of the satellites will be increased at each solution increment. This will cause the position to move away from the satellites and the true position. The same holds true for slower clocks, except the position will move towards the satellites as the pseudoranges are decreased (Figure 4).

To test this, the receiver was operated with modified software (to support a two satellite fix with altitude constraint), but with the standard TCXO frequency reference. Satellites were de-selected until two satellites (SV 25 and SV 28) remained. The position scatter plot for a 27 minute period is shown in Figure 5.

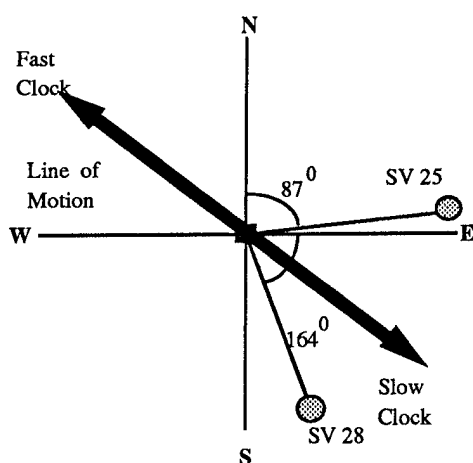


Figure 4. Two Satellite Position - Effects of Clock Error.

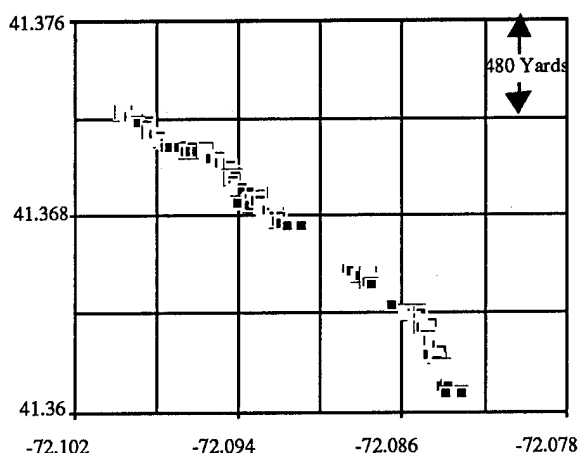


Figure 5. Movement of two satellite fix over 27 minutes, standard (TCXO) oscillator.

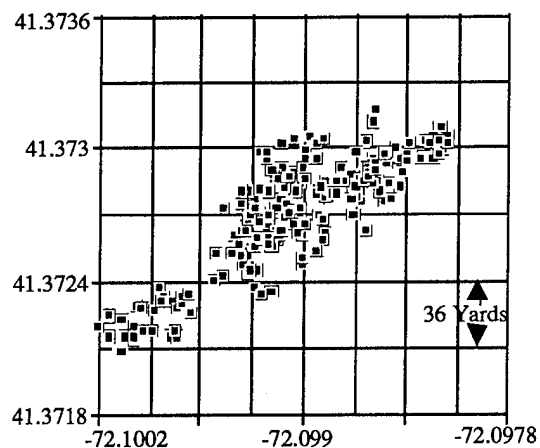


Figure 6. Movement of two satellite fix, Cesium reference.

The final test for determining the accuracy of a two satellite fix was the application of the Cesium reference with the oscillator error entered as zero in the GPS software. The same process of de-selecting satellites was followed, leaving two satellites separated by 78° . When plotted over 40 minutes (Figure 6), the receiver using the two satellites and the Cesium reference has accuracy comparable to that of SPS (100 meters, 2DRMS).

BLOCK PROCESSING OF ONE MILLISECOND TIME RECORDS

In an extension of the FFT techniques presented in [7], we look at position solutions based on block processing of 1 msec long time records once satellite ephemeris and clock offset data has been obtained and stored. This will allow for GPS navigation with only very brief glimpses of satellites. In law enforcement applications, the difference between getting position information immediately upon a tracked vehicle exiting a building and several minutes later may be extremely important.

In addition to rapid signal acquisition in the urban environment, this concept may have application elsewhere. In [8] the Committee on the Future of the Global Positioning System of the National Research Council recommended that in war, the US DoD deny use of all GPS signals to an opponent including the jamming of C/A code, and focus effort on the development of direct Y code receivers. Depending on the original error in the receiver's clock, this could require searching through vast amounts of code space. We feel direct calculation of the cross correlation of the signal and the code template will make this search several orders of magnitude more efficient than a sliding replica code search.

The present/near term future hardware configuration for this study is shown in Figure 7. As discussed later in the Future Directions section, over the next year we will be attempting to substantially reduce the weight, power, and cost of this system. The RF signal from an active antenna is bandlimited to 7 MHz bandwidth, down-converted to 6 MHz and digitized at 25.6 MHz and 14 bits. The signal is then digitally mixed with the sine and cosine of effectively the L1 frequency. The resulting I and Q mixer outputs are low pass filtered for a final combined bandwidth of 2.5 MHz, and sampled at 3.2 MHz.

Unlike [7] where the center frequency of the vector signal analyzer was adjusted for Doppler and the cross correlation of the signal and PRN templates calculated within the analyzer, the same digitized RF is correlated with Doppler shifted templates of all visible SV's within the host computer. Figure 8 illustrates this processing. For standard C/A code the code templates do not change and neither they nor their FFT's need be calculated in real time. We envision storing the FFT's with 0 and 500 Hz Doppler and wrapping around for Doppler shifts of 1 kHz or more. A standard result is that an N

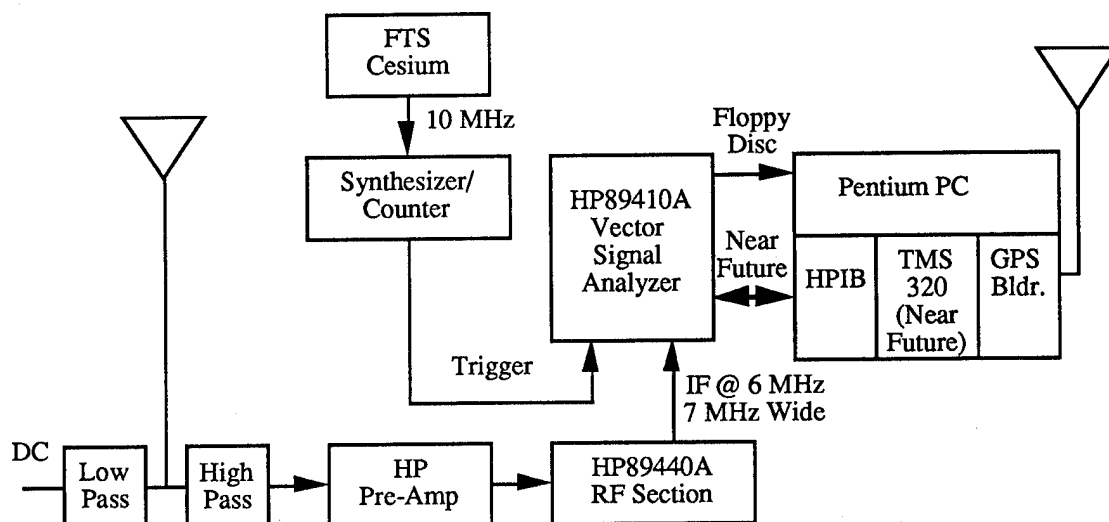


Figure 7. Present/Near Future Hardware Block Diagram.

point FFT or IFFT takes $N \log_2(N)$ complex adds and $N/2 \log_2(N)$ complex multiplies. Therefore for C/A code and 4096 point complex FFT's, (4.096 MHz complex sampling and 3.2 MHz bandwidth) $49152 + 49152 N_{ch}$ complex adds and $24576 + 28672 N_{ch}$ complex multiplies are required where N_{ch} is the number of channels. For direct L2 acquisition, the codes and their FFT's do not repeat, so these need to be calculated in real time resulting in one additional FFT per channel. Table II summarizes the computations required for 6 and 10 channel C/A and Y code receivers.

	6 channel		10 channel	
	C/A	Y	C/A	Y
Complex Adds	344K	6.39M	541K	10.32M
Complex Multiplies	197K	3.62M	311K	5.85M

Table II. Computations to process 1 ms of RF data.

Although beyond our present plans, the possibility of real time processing of all data in a C/A code receiver is well within present technology. For Y code, real time processing of 10 ms or more of data per second is feasible at reasonable cost. If one assumes a sliding replica correlator can search a quarter chip per millisecond, and if the initial clock uncertainty is 100 ms, searches could require in excess of an hour. With FFT processing this search could be reduced to several seconds.

Because the spectrum of the RF is explicitly calculated, this structure naturally lends itself to detecting and eliminating narrow band interference. Future efforts will focus on accomplishing this in the frequency domain. While one might initially think that interference elimination is most easily accomplished by "zeroing out" (a few) corrupted bins in the frequency domain, that method inherently assumes that an interfering sinusoid falls on one or more integer bin numbers. Instead, if

energy falls between bins, one must estimate amplitude, phase, and frequency of the interfering sinusoid (in the frequency domain), and subtract that complete spectrum from the FFT of the incoming RF.

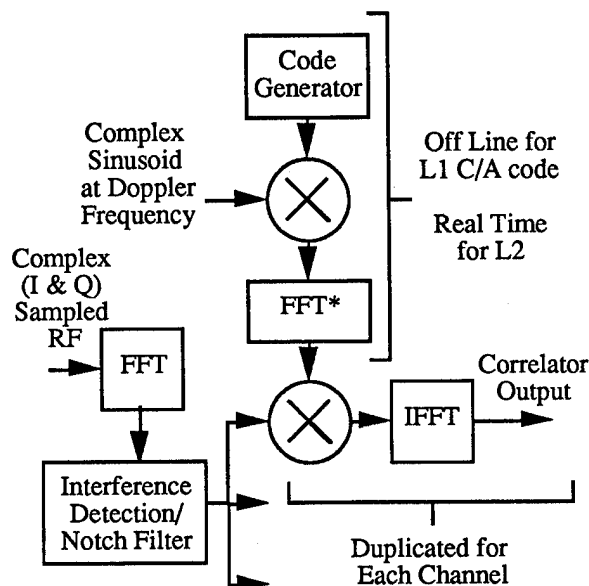


Figure 8. FFT Processing of GPS signals

Figure 9 shows an example of this correlation with the peak measured to 312.5 usec resolution. Figure 10 illustrates how this resolution is improved to 10 ns. The FFT of the absolute value of the 16 bins in the vicinity of the correlation peak is calculated, zero padded in the frequency domain, and correlated with a triangular model of a correlation peak at an effective sampling frequency of 102.4 MHz. Figure 11 shows the results of processing 54 consecutive 1 ms blocks of data resulting in a standard deviation of 30 ns. Comparable blocks of data on numerous satellites result in a standard deviation ranging from 30 to 60 ns. While this is significantly worse than carrier phase aided sliding replica correlators

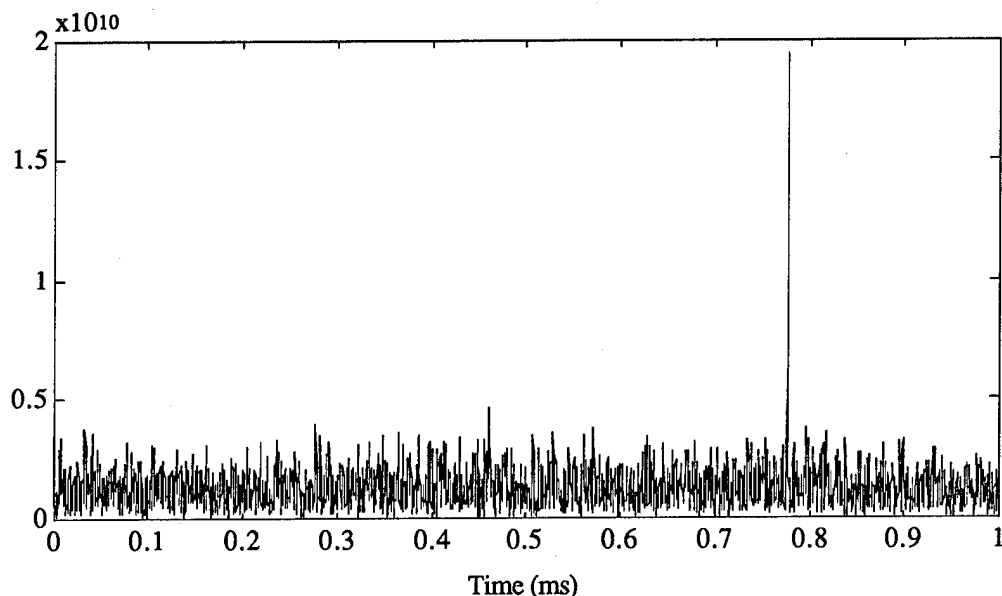


Figure 9. Coarse resolution measured TOA from 1 ms sample, SVN 16, 25 AUG 95.

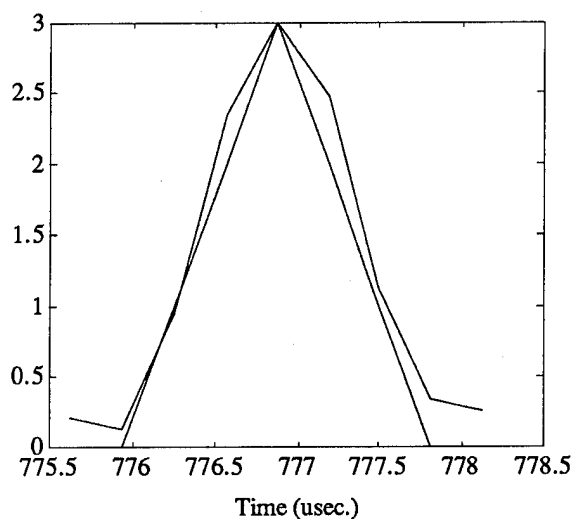


Figure 10. Fine resolution measured TOA from 1 ms sample, SVN 16, 25 AUG 95

in current C/A code receivers, with SA on, SA remains the dominant source of error. With software fixes added to deal with the additional complication of data bit transitions, longer samples could be processed with improvements in both code phase noise and detection threshold.

Figure 12 shows a plot of the short term (54 ms) repeatable accuracy of 2D fixes obtained with this method. Since the period is less than the time constants of selective availability, the variations are due mostly to receiver noise.

We did explore the potential of cancelling the (interfering) signals from other satellites in order to reduce code phase noise, but only noted marginal (10-15%) improvements at substantially increased processor loading. The method involved least squares estimates of

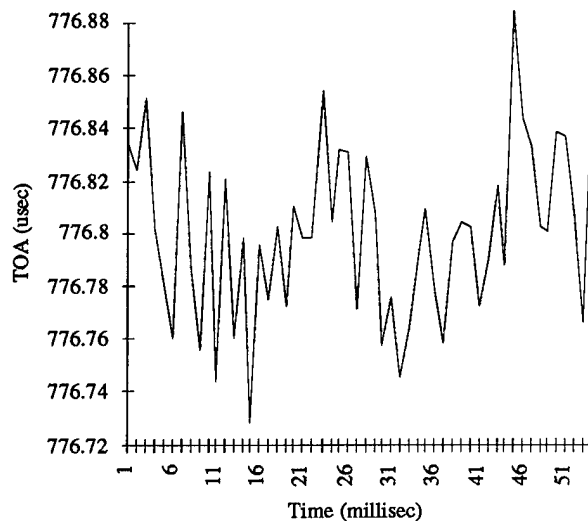


Figure 11. Measured TOA from 1 ms samples, SVN 16, 25 AUG 95

each satellite's amplitude and phase based on the original correlation calculations being subtracted from the original data. The second pass through, the signal subtracted for each satellite would be added back in and the correlation calculated a second time. For some satellites that could only be marginally detected, our cancellation procedure did increase the number of

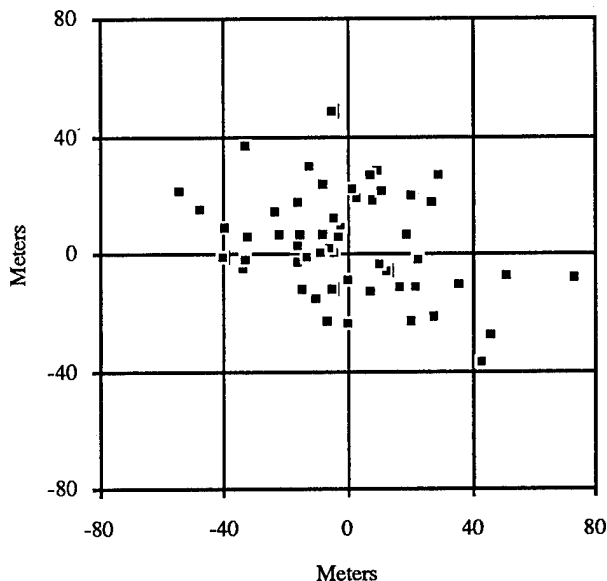


Figure 12. Repeatable accuracy of 2D fixes obtained by processing 54 ms of data in 1 ms blocks.

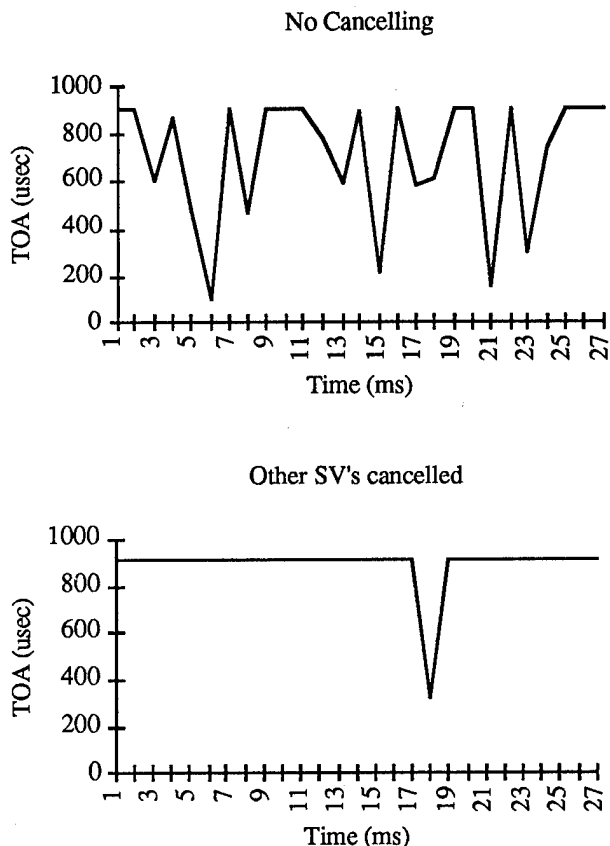


Figure 13. Example of Cancelling Signals from Other Satellites

samples successfully detected. Figure 13 is shown for a particular case, showing some improvement from interference cancellation.

OBTAINING FIXES WITHOUT TIME FROM SATELLITES

Since the technique presented above does not find frame sync, etc., exact knowledge of when the signals received were transmitted from the satellites is not necessarily available. Under normal circumstances, we envision the technique would be used in parallel with a conventional receiver to aid in rapid reacquisition after loss of signal. The clock uncertainty would then be a function of clock stability and the duration of signal outage. If this uncertainty is less than 100 nsec, then a 2D fix with two signals becomes possible, and if less than 500 usec., then the inherent 1 ms ambiguity can be resolved and a conventional 2D fix with three signals is possible.

Even if this 1 ms ambiguity cannot be resolved, it is still possible to obtain a fix provided sufficient signals are available to solve for one additional unknown, which we will call 'coarse time.' This means in general four signals (with good geometry) for a 2D fix and five for a 3D fix. We assume we have ephemeris information, an assumed position accurate to approximately 100 km, and coarse time to within a minute or two. (The issue of ephemeris will be discussed in more detail later.) This accuracy of assumed position and coarse time is such as to allow the receiver to know satellite Doppler shifts and to resolve the 1 ms ambiguities in the time differences among the satellite TOA's. Just as in conventional GPS position solutions, we have measurements of relative ranges to satellites, but unlike those solutions, we do not have the satellite positions that produced those relative ranges. The basic principle in the solution is that there exists a unique solution in both space and time for which the set of time differences could have been observed.

POSITION SOLUTION

Starting with assumed positions and time, (x_o, y_o, z_o, t_o) , and n (> 4) TOA's modulo 1 ms, we solve for satellite positions (x_i, y_i, z_i) and relative velocities (v_i) at:

$$t_o - r_i/c, \quad i = 1, 2, \dots, n,$$

where r_i is the range from the assumed position to the i^{th} satellite and c represents the propagation velocity. We can now calculate $\text{TOA}_o(i)$ (for $i=1$ to n) and the pseudorange equations can be written as

$$\begin{aligned} [\text{TOA}(i) - \text{TOA}_o(i)] c = & \\ & - (x - x_o)c_x(i) - (y - y_o)c_y(i) - (z - z_o)c_z(i) \\ & - (t_g - t_o)v(i) - (t_f - t_o)c \end{aligned}$$

where c_x, c_y, c_z are direction cosines, t_g is gross estimate of time to calculate satellite positions, and t_f is fine time which will be carried along as a variable but will only be accurate when considered modulo 1 ms. In matrix form these equations are

$$\begin{bmatrix} c_x(1) & c_y(1) & c_z(1) & v(1)/c & 1 \\ c_x(2) & c_y(2) & c_z(2) & v(2)/c & 1 \\ c_x(3) & c_y(3) & c_z(3) & v(3)/c & 1 \\ c_x(4) & c_y(4) & c_z(4) & v(4)/c & 1 \\ \dots & \dots & \dots & \dots & \dots \\ c_x(n) & c_y(n) & c_z(n) & v(n)/c & 1 \end{bmatrix} \begin{bmatrix} \Delta x \\ \Delta y \\ \Delta z \\ c\Delta t_g \\ c\Delta t_f \end{bmatrix} = \begin{bmatrix} c\Delta TOA(1) \\ c\Delta TOA(2) \\ c\Delta TOA(3) \\ c\Delta TOA(4) \\ \dots \\ c\Delta TOA(n) \end{bmatrix}$$

(Note: The fourth column has the speed of light in the denominator so the entire matrix and the DOP's calculated from it remain dimensionless, even though this results in an ill-conditioned matrix. All calculations including DOP need to be done in double precision.)

Figure 14 illustrates this solution for position using the same data as was used in Figure 13. Figure 15 shows the solution for coarse time as a function of time for the same data set. The position solution is slightly degraded and the solution for coarse time deviates from actual time with $\sigma = 25$ ms.

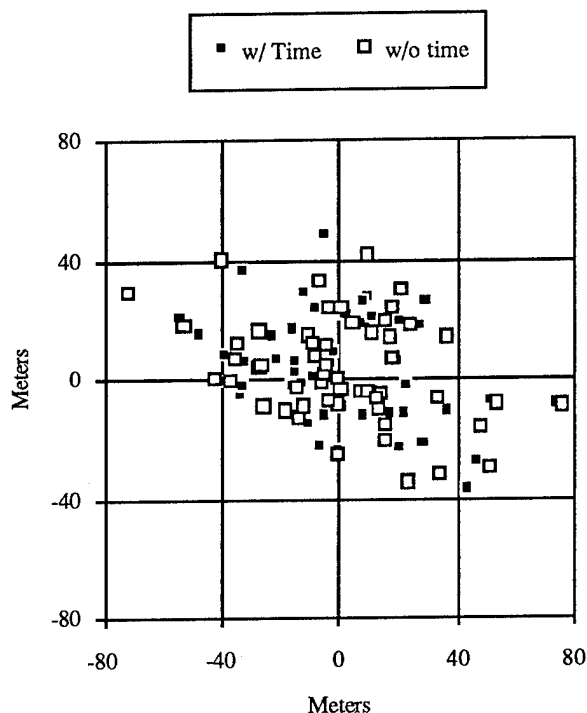


Figure 14. Comparison of conventional position solution with positions requiring solution for time.

We can calculate various types of Dilution of Precision (DOP's). Figures 16 and 17 show the Horizontal Dilution of Precision (HDOP) for 2D and 3D fixes respectively and compares them to conventional HDOP. The data points are based on a recent day in New London, five minute intervals, satellites actually tracked, and an elevation mask of 7° . The HDOP's in cases for which time must be solved are slightly worse and have peak values of 2.2 and 2.7 for 2D and 3D fixes respectively. Even though we were initially

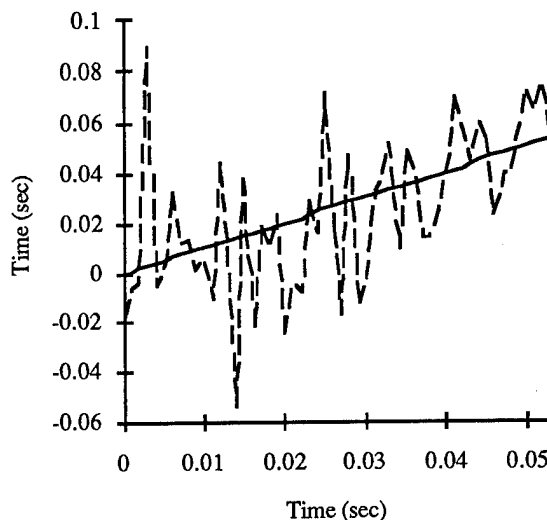


Figure 15. Solution for coarse time as a function of time.

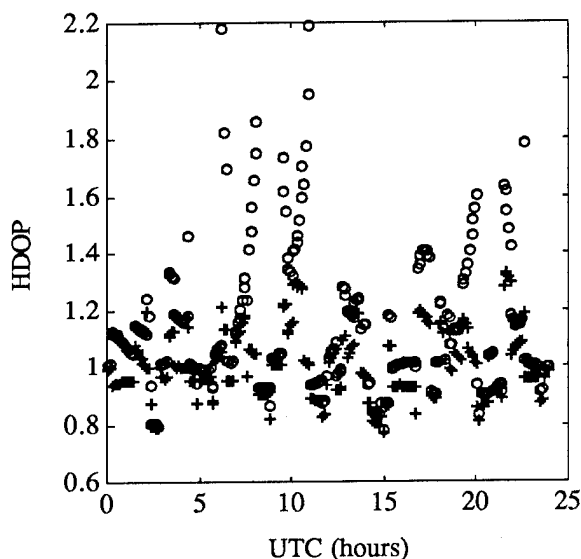


Figure 16. HDOP for 2D fix with (+) and without (o) transmission time from satellites.

unsure, these results do make sense intuitively. The GPS constellation is designed so that at any one location and time, some satellites are rising and some are setting, i.e. they have different Doppler shifts or relative velocities. Figure 18 shows Dilution of Precision in the solution for coarse time using the same data and shows most points in the range of 2 to 8×10^5 . If the standard deviation of a TOA measurement is 100 nsec, this would imply standard deviations in coarse time of 20 to 80 msec.

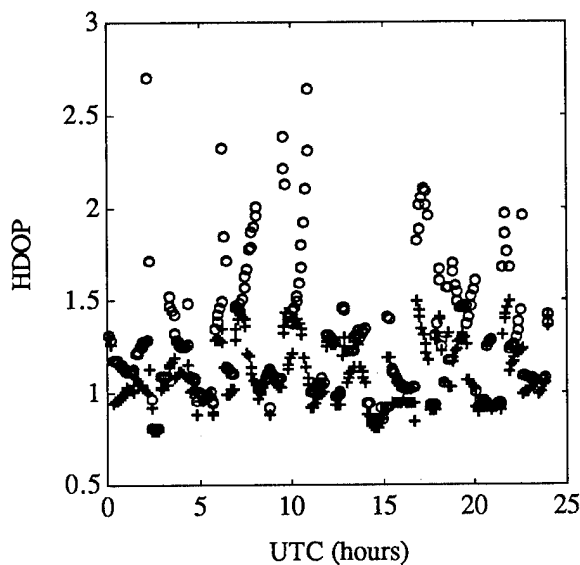


Figure 17. HDOP for 3D fix with (+) and without (o) transmission time from satellites.

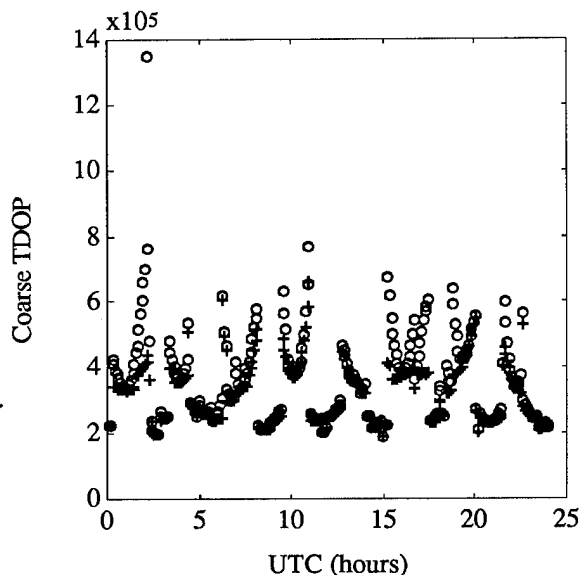


Figure 18. Coarse TDOP for 2D (+) and 3D (o) fixes.

The techniques presented above do not provide for demodulation of the transmitted data, but rather assume satellite clock and ephemeris data will be obtained by other means. For vehicle tracking applications, the on board receiver need only have almanac data so that it can know what satellites to look for and at which Dopplers. In vehicle tracking, TOA information vice position information would be transmitted to a base station which would have current ephemeris data, and the position solutions would be done there. For vehicle navigation, a conventional receiver would run in parallel, and would need to have several contiguous minutes of tracking each satellite every few hours in order to obtain a reasonably current ephemeris. In [9] it states the data is valid over a

four hour curve fit interval (assuming daily uploads), and that the start of the transmission interval corresponds to the beginning of this fit interval. Based on our limited observations, it appears that practice is to in fact begin transmission at the start of the fit interval as in [9], and then to frequently (sometimes hourly) change to a new data set such that a transmitted ephemeris will be valid for three to four hours after it has been received.

Figure 19 shows the accuracy in meters of transmitted ephemeris data as a function of time relative to Issue of Data, Ephemeris (IODE) for ten separate satellites. Actual satellite positions used were precise post fit data available over the Internet from the National Geodetic Service. The fit interval in practice is seen to extend from approximately 2 hours before to 3.5 hours after IODE. In our limited observations, IODE has always been from 0 to 2 hours after the data has been received which implies one can go 3 to 4 hours without successfully demodulating a complete message.

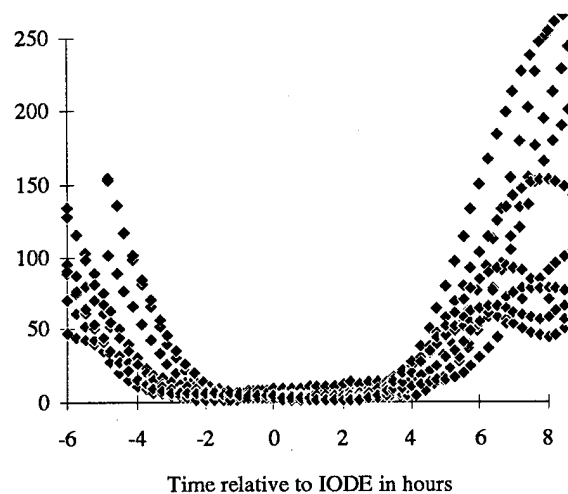


Figure 19. Accuracy in meters of transmitted ephemeris data as a function of time relative to IODE for ten separate satellites.

CONCLUSIONS AND FUTURE DIRECTIONS

Improving GPS fix availability in an urban environment was examined with several objectives: improving acquisition times for satellites, extending the time period the receiver can coast, and obtaining position fixes with only two satellites. These were shown to be powerful extensions to the standard receiver when used with a precise time reference such as a Cesium oscillator.

We also presented results on obtaining fixes based on as little as one millisecond of data. This technique allows for GPS navigation with only very brief glimpses of satellites. For example, in law enforcement applications, this will allow for an immediate fix of tracked vehicle upon exiting a building. It could also permit several orders of magnitude faster code search for direct Y code acquisition in a battlefield environment where L1 had

been intentionally jammed by the US DoD to deny its use to all parties.

In the technique, the cross correlation of "Doppler shifted PRN templates" and one millisecond of digitized RF were calculated using Fast Fourier Transform (FFT) techniques. The peaks in absolute values of these cross correlation functions were then further processed to obtain a Time of Arrival (TOA) resolution of 10 ns. These TOA's (modulo 1 millisecond) have typical one sigma code phase noise of 30-50 ns.

Finally, we presented an interesting method whereby these TOA's can be processed to obtain a fix, even if time has not been obtained by demodulation of satellite signals and is only known to several minutes.

Future goals will be to continue further analysis in all three areas. With two receivers operating at the same time with the same conditions, acquisition time and coasting effects can be further examined and improved. The further expansion of the code to include a Kalman filter will enable the receiver to use signals acquired at various times to perform an electronic "running fix".

We will also be working to substantially reduce the cost, weight, and power consumption of the system in Figure 7 by using the the 2 bit digitized RF that already exists in the GPS Bulider™ as shown in Figure 20.

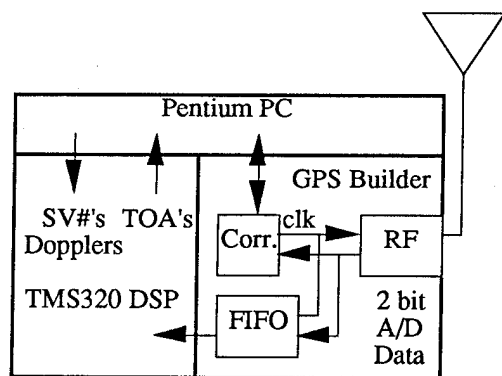


Figure 20. Proposed future system.

ACKNOWLEDGEMENT

This project was sponsored by the USCG Navigation Center.

REFERENCES

- [1] Benjamin Peterson, Michael McKaughan, Lance Miller and Steven Bartlett, "Evaluation of Radionavigation Systems in an Urban Environment," Condensed version in **Proceedings of Institute of Navigation National Technical Meeting**, Anaheim, CA, January 1995. Long version available as NTIS report number PB95-129391.
- [2] 1994 Federal Radionavigation Plan, U. S. Departments of Defense and Transportation, NTIS Report DOT-VNTSC-RSPA-95-1/DOD-4650.5, 1995.
- [3] M. A. Sturza, "GPS Navigation Using Three Satellites and a Precise Clock," GLOBAL POSITIONING SYSTEM, Vol. II, pp. 122-132, Institute of Navigation, 1984.
- [4] E. M. Copps, "An Aspect of the Role of the Clock in a GPS Receiver," GLOBAL POSITIONING SYSTEM, Vol. III, pp. 44-53, Institute of Navigation, 1986.
- [5] P. N. Misra, and R. L. Ferranti, Clock Aided Satellite Navigation for Precision Approaches, presented at IEEE International Frequency Control Symposium, San Francisco, June 1995.
- [6] GPS Builder™ Designer's Guide, GEC Plessey Semiconductors, GPS Group, Swindon, Wiltshire, UK, 1994.
- [7] Benjamin B. Peterson, Eric A. Chamberlin, Terry R. Vogler, Peter Daly and Stuart Riley, "GPS/GLONASS Time Difference Measurements and Test Bed Development," **Proceedings of Institute of Navigation GPS-94**, Salt Lake City, September, 1994, also NTIS report number PB95-130019.
- [8] "The Global Positioning System, A Shared National Asset, Recommendations for Technical Improvements and Enhancements," Committee on the Future of the Global Positioning System, Commission on Engineering and Technical Systems, National Research Council, National Academy Press, Washington, 1995.
- [9] "Technical Characteristics of the Navstar GPS," NATO Navstar GPS Technical Support Group, June 1991.

Autonomous Vehicle Using WADGPS

Daljit (Dave) Singh
Naval Air Warfare Center

Harkirat (Helen) Grewal
American GNC

BIOGRAPHY

Daljit (Dave) Singh, MS (Aerospace), PE, Lead Cruise Missile Simulation Engineer, Naval Air Warfare Center, China Lake, CA. Dave has 25 years of US experience, and the last 7 years are in Tomahawk cruise missile simulation work. The work described in this paper is independent of his work with the US Navy.

Harkirat (Helen) Grewal, PhD (Electrical Engineering), GPS Scientist, American GNC, Chatsworth, CA. Helen has 25 years of experience in Electrical Engineering, and her last one year was dedicated to GPS applications, in particular towards the autonomous vehicles. The work described in this paper is independent of her work with American GNC.

ABSTRACT

Global positioning System (GPS) has proven to be an extremely accurate positioning sensor for a wide variety of applications. However, in ground vehicle automation, still higher accuracy is required. Wide Area Differential GPS (WADGPS) offers a robust system that readily deals with Selective Availability (SA) errors, Ephemeris errors and Satellite Clock errors. An error level of decimeter/centimeter is guaranteed by WADGPS which satisfies the ground vehicle control algorithm. This paper deals with a highly responsive digital computer control system application algorithms for fully automatic ground vehicles. These algorithms are tested using a six degree of freedom (6DOF) simulation. The 6DOF simulation includes the Autonomous Vehicle Embedded Software (AVES) and the Vehicle Environment Model (VEM). AVES includes Guidance, Navigation, Kalman Filter and Mission handling algorithms. Whereas as VEM includes the GPS, Road, Atmospheric, Engine and Actuator models.

The human intervention is completely eliminated by implementing reliable sensors and actuators. The concept of WADGPS is incorporated, thereby, making the overall performance of transportation system to be both congestion-free as well as collision-free and cost-effective. The models for GPS aiding sensors Dead Reckoning, Radar and Camera are included. A commuter is simply required to feed his/her destination into a dash-board computer. Highly sensitive actuators simulate human driver completely, and direct the vehicle on to the road. The car transmitter broadcasts its position and velocity to other cars for collision avoidance and lane changing maneuvers. Both, forward and reverse motions, and U-turns are achieved as per requirements. Furthermore, an accurate steering control is obtained using pulse code modulation technique, and acceleration/braking control is successfully implemented using learning-adaptive system.

INTRODUCTION

GPS assisted land navigation is only a small part of the total spectrum of the several uses of the GPS [1-3]. The perspective of nonmilitary GPS augmented users remains incomplete until professionals have had the opportunity to experience GPS and to unleash all of its innovative uses. A GPS reference receiver at a known and well-surveyed location measures the range to all satellites in view [4-8]. The Differential GPS (DGPS) reference receiver operates from an optimally placed antenna, and common-mode bias errors are eliminated easily. Several DGPS networks have been reported which are ideal for ground navigation purposes. WADGPS network algorithms have also been tested which guarantee an error level of decimeter/centimeter, and in conjunction with map matching, a perfect faster-than-real-time maneuvering can be envisaged.

The well-known partial derivative algorithm offers low performance especially in coastal regions, therefore a minimum variance algorithm is reported in this paper. The algorithm solves for the minimum variance weighting coefficients which are applied by the user to the corrections received from multiple DGPS reference stations [9].

The simplest form of vehicle navigation employs a heading sensor, velocity sensor and a processor. Typically, a navigation system requires an input of an initial position and self-initialize the heading sensor with respect to north. The processor then integrates the velocity sensor output to determine distance traveled and resolves the heading sensor data to calculate a new position. This dead reckoning navigation requires additional vision sensors, route guidance and map matching algorithms for making the driving task fully automatic. The high cost inertial systems are used primarily on vehicles, aircraft, and missiles which require high performance in all three axes: azimuth, pitch, and roll. A full-up inertial system consists of 3 accelerometers and 3 gyros to provide 3 axes of linear acceleration and 3 axes of angular rate, respectively. However, for autonomous road navigation, one directional gyro with heading indicator, fluxgate magnetic sensor as the north reference, distance transmitting unit and a computer display unit suffice.

VEHICLE REQUIREMENTS

The reliability, efficiency, and cost-effectiveness of an autonomous vehicle depend mainly on how judiciously its navigation sensors, perception unit, and computer control are incorporated, and how well their performance match today's transportation needs [10-14]. More often, a human driver is forced to maintain attention for long periods of time and commit to unpredictable contingencies on the freeways together with objectionable traffic jams. All this leads to fatigue and hypovigilance at the wheel, and consequently leads to more frequent collisions and congestion. The driver's activity is influenced by several factors that depend on the driver himself and his environment such as traffic density, traffic status, time of travel, and weather. Thus, the driving activity deals with a combined driver-vehicle-environment system shown in Figure 1 [15].

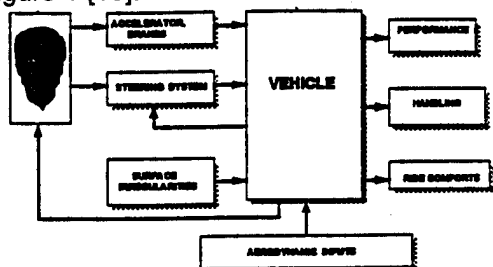


Fig.1 - The driver-vehicle system [15]

The vehicle is required to blend its environmental perception capabilities with its intelligent control in order to effect optimal path-planning strategies that not only avoid obstacles, but also minimize criteria such as time of travel, fuel consumption, exposure to pollution/danger. However, basic driving function consists of lane keeping, safe (positive) distance maintenance, timely lane changing and overtaking. The key to all these driving tasks is collision avoidance. Table 2.1 indicates the various accuracy levels required for 1-15 seconds time alarm and 99.7% availability.

Table 1- Positioning Requirements

Land Application	Accuracy (2 drms)	Coverage Area
Navigation and Route Guidance	5-20 meters	nationwide
Mayday/Incident Alert	5-30 meters	nationwide
Vehicle Command and Control	30-50 meters	nationwide
Collision Avoidance: Control	1 meter	critical locations
Collision Avoidance: Hazardous Situation	5 meters	critical locations
Accident Data Collection	30 meters	nationwide
Infrastructure Management	10 meters	nationwide
Automated Bus Stop Announcement	5-30 meters	nationwide

SENSORS

The remarkable advances in microelectronics and data processing technology have made possible the miniaturization of sensors, integration, and the combination of data (fusion) from a number of sensors. The signals from individual sensors are processed to obtain a robust intelligent sensor system [11,14]. The sensors for autonomous vehicles are required to exhibit the following properties:

- Non-interference.
- High sensitivity
- Small measurement pressure
- High speed
- Low noise
- Robustness.

In practice, a sensor scarcely satisfies all these requirements, and it is necessary to evolve a synergistic combination with suitable integration. As large portion of the outside world information is acquired by visual senses, more emphasis is laid on the perception unit [16-18]. The vision sensors (imaging sensors), most widely used in television

cameras, can detect brightness data using several photoelectric semiconductor elements arranged in regular vertical and horizontal lines, and scan these signals in sequel. The Charge-Coupled Device (CCD) type sensor is more sensitive than the human eye, small in size and highly responsive. For spatial measurements, 3-D stereoscopic recognition is utilized. Additionally, the visual perception generates reactions with the use of knowledge about the behavior of traffic participants. For a robust visual perception, laser radar and infrared sensors are also installed on the autonomous vehicle.

GPS RECEIVER

The GPS can provide extremely accurate positioning information, and proves to be a versatile all-time all-weather radionavigation system. The Commercial Off-the Shelf (COTS) equipment lends itself to cost-effective GPS receivers suitable for manpack as well as vehicular applications. The ground vehicles are categorized as low dynamic systems, and the COTS GPS-instrumented Position Location System (PLS) derives its accurate positioning location by employing WADGPS concept. The Master Control Station (MCS) substation is the center of the autonomous vehicle PLS. The Data Link Subsystem (DLS) links the GPS receiver, reference station subsystems, and the MCS together in order to disseminate data throughout the PLS. The DLS can use either Very High Frequency (VHF) band ranging from 100 to 300 MHz, Ultra High Frequency (UHF) band (300 MHz to 1 GHz), or L-band (i.e., 1-2 GHz) [19]. The UHF is assumed for the present application incorporating Time Division Multiple Access (TDMA) protocol to handle variants of dynamic vehicular network on the roads. A block forward error correction code is employed to protect and maintain the message integrity, and the update rate (< 0.1 s) can be readily achieved.

In the absence of measurement errors, a GPS pseudorange for the k^{th} satellite is given by

$$\rho_k = r_k + cb + cd_k$$

where r_k is the actual range to the k^{th} satellite, b is the receiver clock offset, and d_k is the delay due to total ionosphere electron content. In perturbed form, the above equation can be expressed in matrix notation as

$$\Delta \rho = A \Delta x$$

where ρ is a K-dimensional vector $[\rho_1 \ \rho_2 \dots \rho_K]^T$, A is determined by user-satellite geometry, and x denotes the 4-dimensional user position. If the pseudorange measurements suffer from random

errors with zero mean and P_p is the error covariance matrix of these measurements, then the estimate of Δx which minimizes the mean square error is obtained by iterating

$$\Delta x = [A^T P_p^{-1} A]^{-1} A^T P_p^{-1} \Delta \rho$$

and the resulting error covariance matrix for Δx is given by

$$P_x = [A^T P_p^{-1} A]^{-1}$$

In case the pseudorange errors are uncorrelated, and exhibit zero mean and equal variance, then

$$P_p = I \sigma_p^2$$

and
$$P_x = [A^T A]^{-1} \sigma_p^2$$

where σ_p^2 is the variance of the GPS pseudorange error. With these assumptions, a reasonably good horizontal dilution of precision (HDOP) can be obtained for successful autonomous navigation of the road vehicle. In navigation applications, the key to success in real-time Kalman filtering is to generate a filter model of adequate size to predict the actual system performance and at the same time operate within the processor throughput constraints [20,21]. For autonomous navigation, the filter must be robust enough to operate in more than one dynamical environment. In case the dynamics change drastically, or a sensor failure occurs, the filter must contain some mechanism to detect and rectify the situation. A robust filter has the characteristic that it caters for near-optimum performance over a large class of process and measurement models. A Schmidt-Kalman filter is used which allows certain states to be considered without being estimated, and other partially updated depending on the event. Figure 2 illustrates the evolution of an autonomous vehicle.

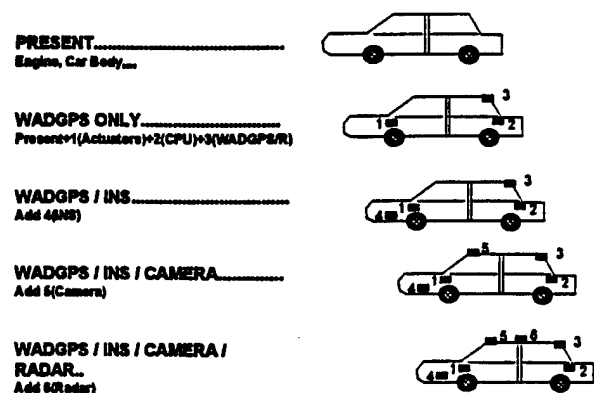


Fig. 2 - Multi-sensor Autonomous Vehicle.

GUIDANCE SYSTEM

The in-vehicle Route Guidance Systems have matured to the point of practical usefulness as well as cost-effectiveness [22]. Such a system is responsible for selecting optimum routes in a given road network (available on CD-ROM) and providing digitized directions to a human driver and/or an autonomous system. The Dijkstra algorithm emphasizing the path of least resistance is utilized, and different weighting factors are attached for minimum fuel or minimum exposure to pollution/danger criteria. Figure 3 displays a series of interconnected functional subsystems of hardware/software components. The desired destination and the starting position of the vehicle together with the time of travel manifest an optimal route on the road network. Once the vehicle commences the journey, sensors continuously keep track of the direction and displacement of the vehicle. Initial calibration is little crucial for dead reckoning performance, however, a feedback calibration indicated in Figure 3 is suggested to obtain distance accuracy better than 99.9% using efficient map matching algorithm [12,22]. Both segmentation and feature extraction are used as an initial step in map matching. The process concatenates co-linear vectors, and creates phase angle difference whenever the vehicle takes a turn.

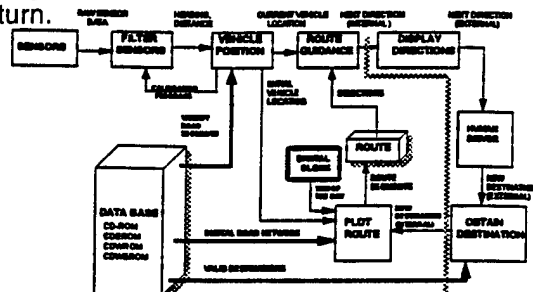


Fig. 3 - Overall Setup for Autonomous Vehicles.

LONGITUDINAL CONTROL

For brevity reasons, only the longitudinal control is illustrated in Figure 4 [16]. Let d_0 be the relative distance between two vehicles at standstill, and V_a represent the controlled vehicle speed. Then, the transfer function relating V_a to V_d is given by the expression

$$\frac{V_a}{V_d} = \frac{C_v + C_p}{\tau s^3 + s^2 + (C_v + h C_p) s + C_p}$$

where a first-order model is used for the propulsion system exhibiting the lag time constant τ . This time constant is chosen to be 0.1s. The throttle input u leads to acceleration a of the vehicle. A negative feedback on both position as well as velocity is incorporated as depicted in the figure.

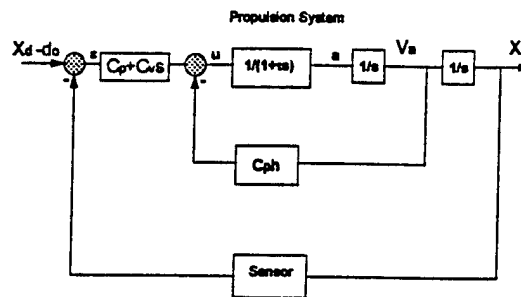


Fig. 4 - Block Diagram for Longitudinal Control.

In order to have a robust and fast controlling action, the poles of the transfer function must have negative real part. Moreover, the overshoot is avoided by forcing one of the poles to be equal to the zero, i.e., $\frac{-C_p}{C_v}$, resulting in a second order

system

$$\frac{V_a}{V_d} = \frac{\omega^2}{s^2 + 2\xi\omega s + \omega^2}$$

A choice of $C_p = 3.2s^{-2}$, $C_v = 1.6s^{-1}$, and $h = 0.5s$ yields double poles $p_{1,2} = -4$. A slight tuning in these parameters, i.e., $C_p = 3.0s^{-2}$ and $C_v = 1.5s^{-1}$ gives a better location of the poles, that is, $p_1 = -3$ and $p_2 = -5$. The damping ratio ξ also contributes towards more stable response.

Digital control algorithms are established by applying a combination of controller design for a desirable closed loop response and finite difference approximations. However, the anticipated degree of stability for an autonomous system is reduced by sampling process, and the filtering process takes care of maintaining the robust performance of the system. Furthermore, the redundant data is used to corroborate the final estimates for throttle, heading angular change and braking. A processor controller is composed of proportional, integral, and derivative control actions (PID)

$$\frac{M(s)}{E(s)} = K_p + \frac{K_i}{s} + K_d s$$

The control algorithm is given by

$$m_n = \frac{1}{1 + \lambda T} [m_{n-1} + \lambda T m_{n-1} + \lambda T e_n]$$

where Γ is the number of sample intervals of length T in the dead time D . The control is thus function of the previous value of the manipulated variable and the present error e_n . The pulse modulation technique can guarantee absence of oscillations and instability by incorporating a check on the error estimate of the concerning variables.

AUTONOMOUS VEHICLE INTERFACE

The new generation of microprocessors promises further increase in system capabilities, while simultaneously shrinking both volume and power consumption of the Autonomous Vehicle embedded system. The spectrum of vehicular technology has expanded far beyond the classically recognized role of stability and control, autopilot, and control linkages. The spectrum now includes integration of technologies spanning functional, physical and man-machine features. The integration critically impacts the vehicle design options, operation effectiveness, and safety measures. The Digital Road Maps, available on a CD-ROM, have substantially increased the safety of automobiles. These maps along with the GPS navigation provide a feasible solution to the Autonomous Vehicle System (AVS). Figure 6 illustrates a functional block diagram for the AVS. The expert system technologies are integrated with the digital maps, the radar, CCD camera images, magnetic compass, together with the GPS system for obtaining a real-time intelligent decision support navigation package. This package has three primary objectives, namely, processing/fusion of navigation data, display/operation of digital road maps, and analysis/decision making of navigation operations.

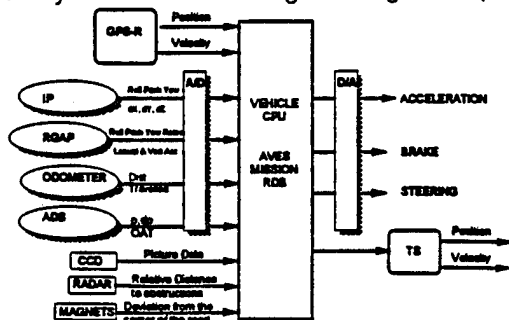


Fig. 5 - The Integrated Autonomous Vehicle.

The integration of GPS and communications suggests an efficient transportation system for increasing the road traffic safety, smooth driving without traffic jams, and a comfortable driving environment. Furthermore, the autonomous vehicles rely on such an intelligent system integration which leads to a complete collision avoidance in any type of real-time situation. The vehicle Transmitting System (TS) continuously provides information about its position and velocity to its participants. A safe distance with respect to its immediate surroundings is maintained by the acceleration/brake and steering controls. The Inertial Platform (IP) and Rate Gyro and Accelerometer Package (RGAP) keep the vehicle Central Processing Unit (CPU) well-informed with the incremental changes in the vehicle's parameters. The wheel odometers provide the

vehicle traveling distances by multiplying the number of electronically generated pulses by a constant depending on the wheel perimeter. As the actual tire size is influenced by vehicle speed, tire pressure, vehicle payload, and atmospheric conditions, appropriate corrections are applied by the CPU. The Atmospheric Data System (ADS) keeps a continuous record of the Outside Atmospheric Temperature (OAT), pressure p and differential pressure dp . The information concerning deviation from the road center is obtained by magnetic as well as optical sensors and fed to the CPU. The digital road maps in the form of a road data base (RDB) are already stored on the CD-ROM. The GPS receiver updates the vehicle's position (and velocity) to centimeter/decimeter levels as required for the lateral or longitudinal control actions. The Autonomous Vehicle Embedded Software (AVES) mission finally yields the estimates for throttle and heading angle increments for a safe and accident-free maneuver, and can be readily incorporated.

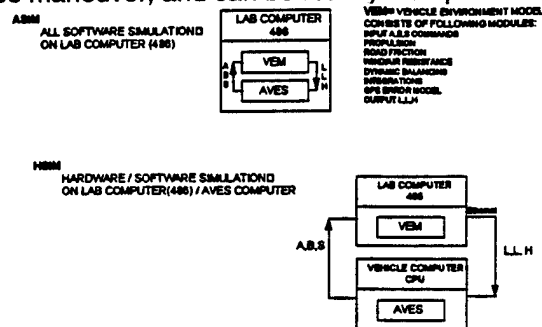


Fig. 6 - Two-stage Strategy for AVES.

CONCLUDING REMARKS

The actual placement of the sensors for autonomous navigation is expected to improve the system performance. The cost of augmenting GPS can be further reduced by employing cots equipment, and this will encourage more users to opt for autonomous vehicles. This in turn would lead to intelligent transportation system with substantial share of electronically controlled next generation vehicles. Authors feel at this juncture that hybrid electric vehicles shall be accepted by our information-based society. A synergistic combination of heat engine, electric drives, electronic controls and in-vehicle computer with inter-vehicle communications shall soon be in the automobile market.

REFERENCES

- [1] Robert P. Denaro, NAVSTAR: The All-purpose Satellite, IEEE Spectrum May 1981.
- [2] Bradford W. Parkinson, and Stephen W. Gilbert, NAVSTAR: Global Positioning System - Ten years later, Proceedings IEEE, October 1983.

- [3] Andrew Silverman, Concepts and Technology for Navigation Equipment, IEEE PLANS 1988.
- [4] A. Van Dierendonck, Understanding GPS Receiver Terminology: A Tutorial, GPS World, Jan. 1995.
- [5] A. Brown, Extended Differential GPS, NAVIGATION, vol. 36, No. 3, Fall 1989.
- [6] H. Blomenhofer, G.W. Hein, E.T. Blomenhofer and W. Werner, Development of a Real-time DGPS system in the Centimeter range, IEEE PLANS 1994.
- [7] Tom Hunter, Wojciech Kosmalski, Phan Traong, Vehicle Navigation using Differential GPS, IEEE PLANS 1990.
- [8] Changdon Kee, Bradford W. Parkinson, and Penina Axelrad, Wide Area Differential GPS, NAVIGATION, Journal of The Institute of Navigation, vol. 4, 1993.
- [9] T. Mueller, Minimum Variance Network DGPS Algorithm, IEEE PLANS, 1994.
- [10] A. White and D.A. Sofge, Handbook of Intelligent Control: Neural, Fuzzy, and Adaptive Approaches. Van Nostrand Reinhold, N.Y., 1992.
- [11] R. Ohba, Intelligent Sensor Technology. New York: John Wiley 1992.
- [12] R. Jurgen, Electronic Motorist, IEEE Spectrum, March 1995.
- [13] K. M. Passino, Intelligent Control of Autonomous Systems, IEEE Spectrum, June 1995.
- [14] Ramon Pallas-Areny and John G. Webster, Sensors and Signal Processing. New York: John Wiley 1991.
- [15] J. Y. Wong, Theory of Ground Vehicles. New York: John Wiley 1992, Figure 1.
- [16] M. Parent, P. Daviet, J. C. Denis and T. M'Saada, Automatic Driving in Stop and Go Traffic, Intelligent Vehicles 1994.
- [17] E.D. Dickmanns, R. Behringer, D. Dickmanns, T. Hildebrandt, M. Maurer, F. Thomanek, J. Schiehlen, The Seeing Passenger Car VaMoRs-P, Intelligent Vehicles 1994.
- [18] Keiji Saneyoshi, 3-D Image Recognition System by Means of Stereoscopy Combined with Ordinary Image Processing, Intelligent Vehicles 1994.
- [19] Simon Haykin, Communication Systems. New York: John Wiley, 1994 (Third Edition).
- [20] Ching-Fang Lin, Modern Navigation, Guidance, and Control Processing. Englewood Cliffs, NJ: Prentice-Hall 1991.
- [21] Ching-Fang Lin, Advanced Control System Design. Englewood Cliffs, NJ: Prentice-Hall, 1994.
- [22] Robert L. French, Navigation Aids and Intelligent Vehicle-Highway Systems, Chapter 29, Automotive Electronics Handbook, Ronald K. Jurgen, Editor-in-Chief, 1995.
- [23] Hayashi, K., Shimizu, Y., Takayama, A., and Hirako, A., Neural Fuzzy Transmission Control for Automobile with Variable Loads, IEEE Trans. Control Systems Technology, vol. 3, no.1, March 1995.
- [24] Kevin M. Passino, Intelligent Control for autonomous Systems, IEEE Spectrum June 1995.



Session D4

GNSS Policy and Technology Issues

Chair:

Mr. Keith McDonald
Sat Tech Systems

Co-Chair:

Maj. Gen. Ralph Jacobson, USAF, Ret.
Draper Laboratory

GPS: A Shared National Asset – A Summary of the National Research Council Report

Laurence Adams
Chair of the National Research Council Committee

Allison Sandlin and Dave Turner
National Research Council

Keith McDonald
Sat Tech Systems

BIOGRAPHY

Laurence Adams chaired the National Research Council's Committee on the Future of the Global Positioning System and is the retired president of the Martin Marietta Corporation.

Allison Sandlin is a Senior Program Officer at the National Research Council and was the GPS study director.

Keith McDonald is president of Sat Tech Systems, Arlington, VA, and served as a member of the National Research Council's Committee on the Future of the Global Positioning System.

Dave Turner is a Program Officer at the National Research Council and was a consultant to the GPS study.

ABSTRACT

At the request of Congress, the National Research Council (NRC) and the National Academy of Public Administration (NAPA) conducted a joint study to examine the management, funding, and technical improvement issues related to the Global Positioning System (GPS). The NRC was specifically asked to recommend improvements that would enhance the use of GPS for civil, commercial, and military users. In addition, the NRC was asked to determine if Selective Availability and Anti-Spoofing were meeting their intended purpose. This summary paper contains the findings of the NRC study.

INTRODUCTION

At the request of Congress, the National Research Council (NRC) and the National Academy of Public Administration (NAPA) conducted a joint study to examine the Department of Defense's Global Positioning System (GPS). The NRC was asked to

determine if Selective Availability (SA)¹ and Anti-Spoofing (A-S)² were meeting their intended purpose and to recommend technical improvements and augmentations that could enhance GPS for all users--military and civilian. NAPA was asked to address GPS management and funding issues, including commercialization, governance, and international participation. This paper discusses the major findings and recommendations made by the NRC. The complete findings and recommendations of both study groups can be found in the joint report, *The Global Positioning System-Charting the Future*.

SELECTIVE AVAILABILITY

The most controversial issue in the report is the recommendation to turn SA to zero immediately. Although naturally embraced by most civilian users, this recommendation is being strongly contested by many DOD officials. From the onset of the study, both the NAPA panel and the NRC committee agreed that national security was of paramount importance and that, without exception, the U.S. military advantage should be maintained. During the year-long study, both the NRC and NAPA groups heard extensive briefings of the military utility of GPS by DOD, including its interest in retaining SA. After substantial evaluation of DOD and civilian inputs over many months, the groups unanimously concluded that SA

¹ SA is a purposeful degradation in GPS navigation and timing accuracy that is accomplished by intentionally transmitting erroneous information on ephemeris and precise time of the clocks on board the satellites, which introduces errors into the GPS signal. With SA, the civilian C/A-code signal is limited to a specified accuracy of 100 meters, (95%). Military receivers with the appropriate decryption keys can eliminate the effects of SA and obtain an accuracy of approximately 21 meters, 2 drms, or better.

² Anti-Spoofing (A-S) is the encryption process used to deny unauthorized access to the military Y-code. It also improves the performance of a receiver in the presence of GPS mimicked or spoofing signals, which could potentially provide incorrect information to a GPS user.

is not providing a meaningful denial of accuracy and is no longer meeting its intended military purpose. This determination was made after intense discussion and careful deliberation. Outside the two study groups, however, the debate is still ongoing and the outcome unknown at this point.

Table 1 summarizes the case for and against the continuation of SA. DOD officials have stated that SA is an important security feature because it limits the accuracy obtainable directly from the C/A-code to 100 meters, 2 drms (42 meters, CEP).³ Because the military has access to a position accuracy of 21 meters, 2 drms (8 meters, CEP) and undegraded velocity as well, DOD believes that U.S. forces have a distinct tactical and strategic advantage. The DOD believes that obtaining accuracies better than 42 meters CEP requires a substantial amount of effort. DOD representatives have expressed their belief that our adversaries are much more likely to exploit the GPS C/A-code, rather than DGPS, because its use requires less effort and technical sophistication than is required to use DGPS. In addition, some DOD

officials contend that local-area DGPS broadcasts do not diminish the military advantage of SA because they could be rendered inoperative, if warranted, through detection and destruction or by jamming. This appears to imply that adversaries are either precluded from obtaining GPS navigation accuracies better than 100 meters and a few tenths of a meter per second in velocity, or that a significant amount of effort is required to achieve this.

It was the opinion of the NRC committee that meter-level accuracies are readily obtainable, even in the presence of SA set at its current level or even at higher levels. As shown in Figure 1, several commercial and government DGPS systems routinely provide position accuracies approaching the meter level (2 drms) and velocities equal to or superior to that of the undegraded (no SA) GPS signal, in the United States and in most of the populated areas of the world. Within the U.S. government, agencies such as the Federal Aviation Administration, the Coast Guard, and the Army Corp of Engineers are implementing and planning to operate systems that

TABLE 1. Arguments for and Against Leaving SA at its Current Level

ISSUE: TURNING SELECTIVE AVAILABILITY TO ZERO IMMEDIATELY.	
ARGUMENTS FOR MAINTAINING SA AT IT'S CURRENT LEVEL OR HIGHER LEVELS	ARGUMENTS FOR REMOVING SA
SA provides protection.	100 meters, 2 drms, is still more than adequate to deliver chemical, biological, or explosive weapons.
DGPS signals are not readily obtainable and adversaries are much more likely to exploit the GPS C/A code rather than DGPS because it requires less effort and technical sophistication.	DGPS services with accuracies approaching 1 m are available in the United States and in most of the populated areas of the world through commercial vendors and government agencies. Local-area DGPS stations are: <ul style="list-style-type: none"> • inexpensive, • can be set-up in less than an hour.
If an adversary does use local-area DGPS broadcasts, they could be detected and destroyed or jammed.	Local-area DGPS stations are difficult to detect because they are small and the signals can be broadcast at: <ul style="list-style-type: none"> • low power and spread spectrum frequencies or • rapid on/off cycles with very short transmission times. <p>Further, it would be politically difficult to destroy DGPS stations in noncombative countries, especially if they were used for transportation and public safety, such as civil aviation.</p>
SA can be turned to a higher level.	DGPS methods can still be used to defeat SA.
	The United States has publically announced that the accuracy will be at least 100 meters, 95% of the time for the foreseeable future.
If SA was removed, denial of accurate C/A-code on L1 to enemy forces through jamming would interfere with friendly force acquisition of the encrypted Y-code.	Direct L2 Y-code acquisition and/or alternative operating procedures could be used.
GLONASS is unreliable.	80 % of GLONASS constellation is complete and is providing free signals with accuracies comparable to undegraded GPS performance.

³ The Coarse Acquisition (C/A) code is broadcast on the L-band carrier signal known as L1, which is centered at 1575.42 MHz.



Figure 1. DGPS coverage provided by commercially available systems, including Skyfix and Sercel. (Courtesy of the National Air Intelligence Center)

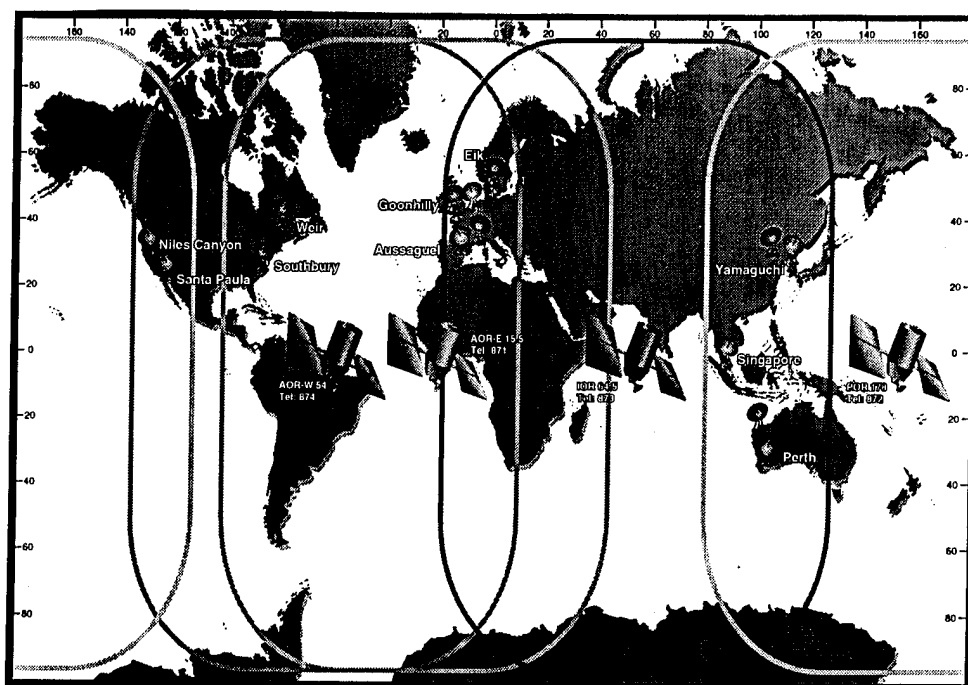


Figure 2. DGPS coverage provided by the planned FAA WAAS (Wide-Area Augmentation System). Source: Innovative Solutions International, Inc., presentation at the National Technical Meeting of the Institute of Navigation Meeting, Anaheim, California, January 1995.

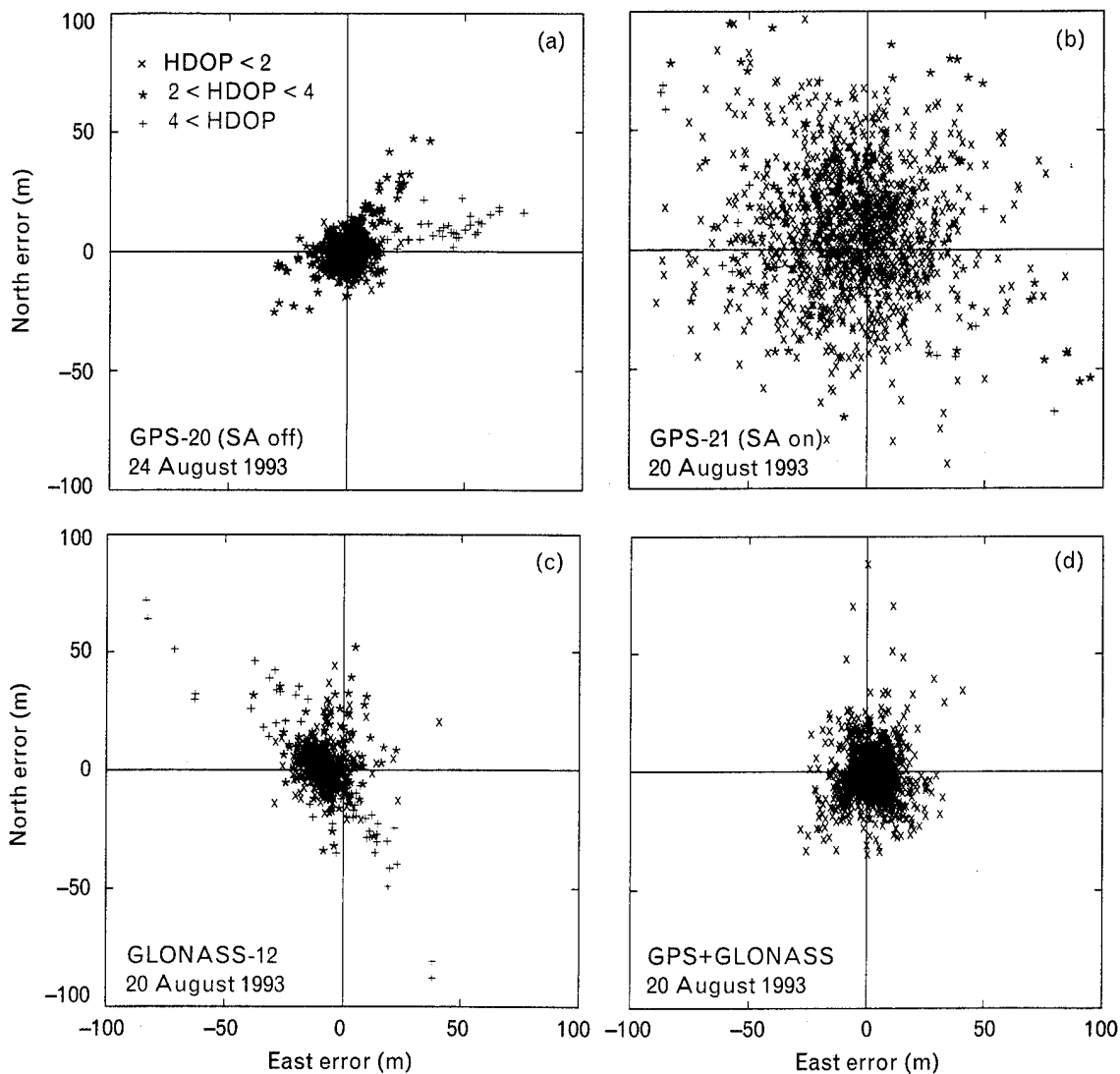


Figure 3. Position estimates from GPS and GLONASS obtained from measurement snapshots taken 1 minute apart over an entire day. Position from (a) GPS with SA off, (b) GPS with SA on, (c) GLONASS, and (d) GPS plus GLONASS. (Courtesy of MIT Lincoln Laboratory)

will, in combination, cover the entire United States and beyond, as shown in Figure 2. Furthermore, if the full GLONASS constellation is completed in 1995 as planned, this system also will provide properly equipped users with an additional source of highly accurate positioning data, as shown in Figure 3.

Even if potential adversaries are not taking advantage of DGPS at this time, the NRC committee believed that it would be prudent for the DOD to

recognize the potential capability that exists with currently available systems. In addition, the establishment of a low-cost, militarily controlled local-area DGPS network for use by an adversary in a theater of conflict also is a possibility. Local-area differential systems are easy to build or buy and are not expensive. Reference stations for local-area DGPS operations are small and can be typically installed in less than an hour. Signals from such systems may be

difficult to detect because they can be broadcast at low power and as spread-spectrum signals or in rapid on/off cycles, with very short transmission times, minimizing the chance of being detected.

Some DoD officials contend that the level of SA could be increased substantially in times of serious enemy threat. This would further degrade accuracy and would act to discourage deployment of GPS-guided munitions by potential adversaries. However, even if the level of SA is increased, DGPS methods could still be used to provide an enemy with accurate signals. Additionally, the United States has declared its intention not to degrade the C/A-code signal to more than 100 meters, 2 drms. A violation of this declaration could have a serious impact on numerous civil users.

The NRC committee expected that any enemy of the United States sophisticated enough to operate GPS-guided weapons will be sophisticated enough to acquire and operate differential systems. Adversaries could potentially take advantage of the existing, commercial systems available worldwide or install local-area DGPS stations, as described earlier. As has been pointed out, these systems can have the capability to provide velocity and position corrections to cruise and ballistic missiles with accuracies that are equal to or superior to those available from an undegraded C/A-code.

Regardless of the level of SA, GPS, DGPS, and GLONASS signals can be used against us today. The unencrypted C/A-code, which is degraded by SA, still provides our adversaries with an accuracy of 100 meters, 2 drms, which would still be more than adequate to deliver chemical, biological, or explosive weapons. With SA set at zero, the stand-alone accuracy improves to better than 30 meters, 2 drms.⁴ While this improvement enhances the ability of an adversary to successfully attack high-value point targets, significant damage also can be inflicted with use of the GPS signal. With even 100-meter accuracy, the NRC Committee believes that the risk is sufficiently high to justify denial of the L1 signal by jamming. The jamming strategy has the additional benefit of denying an adversary all radionavigation capability, including the even more accurate DGPS threat.

The NRC committee recognized that the principal shortcoming of a denial strategy is the difficulty that military GPS receivers currently have in acquiring the Y-code during periods when the C/A-code is unavailable due to jamming of the L1 signal. The implementation of direct Y-code acquisition capability would provide the optimal solution to this problem. Although the technology for developing advanced, direct Y-code receivers is available today,

unfortunately, such capabilities are not currently fielded by the military. The NRC committee believed that a focused, high-priority effort by the DOD to develop and deploy advanced, direct Y-code user equipment, backed by forceful political will from both the legislative and executive branches, can bring about the desired result in a relatively short period of time. In the interim, alternative operating procedures can be used to mitigate the problem. These will be discussed later.

In summary, the NRC committee strongly believed that preservation of our military advantage with regard to radionavigation systems should focus on electronic *denial* of all useful signals to an opponent, for example, by jamming and spoofing, while improving the ability of civil and friendly military users to employ GPS in a jamming and spoofing environment. Continued effort to deny the accuracy of GPS to all users except those authorized by the military via SA appears to be a strategy that ultimately will fail. Thus, the NRC committee stated that the military employ denial techniques in a theater of conflict to prevent enemy use of GPS or other radionavigation systems. Both the NRC and the NAPA study groups unanimously made the following recommendation.

Selective Availability should be turned to zero immediately and deactivated after three years. In the interim, the prerogative to reintroduce SA at its current level should be retained by the National Command Authority.

ANTI-SPOOFING

Although many civil users could benefit if A-S is turned off, the NRC committee found that A-S remains critically important to the military because it forces potential adversaries to use the C/A-code on L1, which can be jammed if necessary without inhibiting the U.S. military's use of the encrypted Y-code on L2. Further, encryption provides resistance to spoofing of the military code. The NRC committee determined, however, that the current method of manual distribution of Y-code decryption keys is laborious and time consuming. The DOD has recognized this problem and has ongoing efforts to distribute keys electronically. The NRC committee believed that an electronic key distribution capability

⁴ Recent measurements with SA turned to zero have ranged from 5 meters to 10 meters, 2 drms. However, the accuracy without SA greatly depends on the condition of the ionosphere at the time of observation and user equipment capabilities.

would greatly enhance the use of the encrypted Y-code on L2. The committee also believed that technology is available to upgrade the current encryption method and suggests that the Air Force should explore the necessity of utilizing this technology. Modifications to the Block IIR satellites and the Block IIF request for proposal may be required if upgraded encryption methods are necessary. Changes to military receivers also will be required. The committee recommended that

A-S should remain on and the electronic distribution of keys should be implemented at the earliest possible date. In addition, the Air Force should explore the necessity of upgrading the current encryption method. Required receiver enhancements should be incorporated in future planned upgrades.

TECHNICAL ENHANCEMENTS TO IMPROVE GPS PERFORMANCE FOR MILITARY USERS

As stated previously, the committee believes that the military usefulness of SA is severely diminished and that it is urgent that the DOD focus its attention on *denial* of all useful signals to an opponent, for example, through jamming and spoofing techniques, including jamming of the unencrypted C/A-code, rather than relying on SA. Several technical enhancements that would improve the overall performance of military receivers operating in the presence of spoofing, jamming and interference were identified by the committee and are listed below. The greatest improvement in user equipment performance will result from the combined implementation of all five recommended enhancements in a single integrated system.

The development of receivers that can rapidly lock onto the Y-coded signals in the absence of the C/A-code should be completed. The deployment of direct Y-code receivers should be given high priority by the DOD.

Nulling antennas and antenna electronics should be employed whenever feasible and cost effective. Research and development focused on reducing the size and cost of this hardware should actively be supported.

The development of low-cost, solid-state, tightly-coupled integrated inertial navigation system/GPS receivers to improve immunity to jamming and spoofing should be accelerated.

The development and operational use of GPS receivers with improved integration of signal processing and navigation functions for enhanced performance in jamming and spoofing should be accelerated.

Military receivers should be developed that compensate for ionospheric errors when L1 is jammed, by improved software modeling and use of local-area ionospheric corrections.

GPS receivers are especially vulnerable during their signal acquisition phase. Also, most military GPS receivers cannot acquire the Y-code during periods when the C/A-code is being jammed. Future receivers capable of direct Y-code acquisition will correct this operational deficiency. In any event, tactics must be developed and put in place to facilitate acquisition and tracking during jamming. In the interim, before advanced, direct Y-code receivers can be fielded by the military, various operating disciplines can be used to minimize the impact of L1 C/A-code jamming on the ability to acquire the Y-code directly.

For example, as with existing plans to destroy radars in a hostile area, plans and procedures could be developed to remove jammers and DGPS stations. In addition, prior to entering the jamming area, the C/A-code can be used to acquire the Y-code. Once the Y-code is obtained, and while still within the active jamming area, PPS receivers could be operated continuously or be repowered every few hours in order to maintain accurate time, which will aid in faster, direct reacquisition of the Y-code. This technique can be extended to aircraft-based GPS-guided munitions using low-powered C/A-code retransmissions aboard, or by the inclusion of time-transfer circuits.

Ground forces also can make use of natural terrain and man-made obstructions to obtain some shielding from ground-based jammers. From a tactical standpoint, the U.S. military can interrupt denial jamming/spoofing for short time periods, typically 2 to 3 minutes hourly, to assist those friendly forces in need of C/A-code to reacquire the Y-code. These scheduled times should be short and random to prevent hostile troops from taking advantage of interrupted jamming. Finally, C/A-code selective denial techniques could be developed and utilized that minimize impact upon friendly L1-only military receivers, such as the Plugger receiver.

IMPROVING GPS PERFORMANCE FOR CIVIL AND COMMERCIAL USERS

Although GPS was originally designed to provide a military advantage for U.S. forces, the number of civilian users now far exceeds the number of military users. The NRC committee found that the most prominent need for commercial and civil users is greater stand-alone accuracy, availability, and integrity. With improved performance of the basic GPS signal, many users would no longer require augmentations to obtain the data they require. Any additional system enhancements and modifications to improve stand-alone positioning accuracy for civilian users are relatively ineffective in the presence of SA. However, with SA removed, the major enhancement that would greatly increase accuracy for civilian users is the addition of a new, unencrypted signal. Civilian access to an additional frequency would enable improved accuracy through ionospheric corrections, multipath rejection, and single-frequency operation when interference jams one of the two civilian frequencies.

In studying possible options for the addition of another civilian frequency, the committee developed the following guidelines:

- *The signal must not interfere with the military's jamming techniques for denial of GPS signals.* Any signal enhancement should preserve and maximize the ability of the military to deny the GPS signal to adversaries through local jamming without adversely impacting the L2 Y-code signal.
- *The signal must be backward compatible.* A significant investment has been made in receiver purchases and existing receiver performance must not be degraded. However, existing receivers may not be able to take advantage of the new signal.
- *The frequency allocation for the signal must be considered.* The signal should be assigned a frequency in the L-band spectrum that has a reasonable chance of receiving an official allocation from the Federal Communications Commission and, if appropriate, the International Telecommunications Union as well.⁵

⁵ A preliminary analysis of the L-band spectrum allocation was conducted by Mr. Melvin Barmat, Jansky/Barmat Telecommunications Inc., Washington D.C.

- *The signal should optimally be spaced for ionospheric correction and wide lane ambiguity resolution.* Ideally, the new GPS signal should be on an L-band frequency sufficiently offset from L1 to permit user correction of ionospheric delay, which would improve user accuracy yet be close enough to L1 to allow fast, wide-lane cycle ambiguity resolution, also termed wide-laning. For adequate ionospheric correction, the separation between L1 and a new frequency should be at least 200 MHz. For optimal wide-lane ambiguity resolution, the frequency difference between L1 should be no greater than 350 MHz.

- *The signal should optimally occupy a wide (at least 10 MHz) frequency band.* A wide-band signal has two main advantages over a narrow-band (2 MHz) signal. First, use of a wide-band signal allows about a 10-dB improvement in interference rejection over a narrow-band signal. This is significant for both stand-alone and differential users needing improved availability in the presence of wide-band or continuous wave interference. The second advantage is that upon signal reacquisition, a wide-band signal can recover submeter pseudorange accuracy faster than a narrow-band signal in both low- and high-multipath environments.

Based on these guidelines, the NRC committee determined that the optimal scenario for an enhanced civilian GPS signal would entail the provision of a new wide-band frequency, termed L4, that would be broadcast unencrypted to allow for universal access. If a wide-band frequency allocation proves impossible to obtain for L4, a narrow-band signal should be considered as a desirable option. Table 2 below compares estimated achievable accuracies for five potential frequencies.

Although the selection of a specific frequency would require additional analysis, the NRC committee believed that a new L4 signal could be added to several Block IIR spacecraft using existing volume and power. Based on cost information for the current Block IIR L-band navigation package provided by the ITT Corporation, the committee estimated that the cost would be approximately \$1.3 million per Block IIR satellite. The committee recommended that

Immediate steps should be taken to obtain authorization to use an L-band frequency for an additional GPS signal, and the new signal should be added to GPS Block IIR satellites at the earliest opportunity.

Table 2. Effect of an Additional L-Band Frequency for Reduction of Ionospheric Error on Civil GPS Accuracy

Error Source	Typical Range Error Magnitude (meters, 1 σ): Improved Standard Positioning Service (no SA, additional L-Band Signal)				
	1237.83	1258.29	1841.40	1258.29	1841.40
	Narrow-band, C/A-type code	Narrow-band, C/A-type code	Narrow-band, C/A-type code	Wide-band, P-type code	Wide-band, P-type code
Atmospheric Error					
Ionospheric	0.01	0.01	0.01	0.01	0.01
Tropospheric	0.2	0.2	0.2	0.2	0.2
Clock and Ephemeris Error	3.6	3.6	3.6	3.6	3.6
Receiver Noise	0.6	0.7	0.9	0.5	0.8
Multipath	1.5	1.6	2.3	1.0	1.9
Total User Equivalent Range Error (UERE)	3.9	4.0	4.3	3.8	4.2
Typical Horizontal DOP (HDOP)	1.5	1.5	1.5	1.5	1.5
Total Stand-Alone Horizontal Accuracy (2 drms)	11.9	12.0	13.1	11.3	12.5

RECOMMENDATIONS TO ENHANCE GPS PERFORMANCE FOR ALL USERS

In view of the rapidly expanding use of GPS by commercial, civilian, and military users, the NRC committee believed that GPS must be capable of continuous operation in all foreseeable contingencies. This capability is critical. The one area where the NRC committee found limited system redundancy was in the operational control segment (OCS). Although the NRC committee determined that the Air Force has several experiments planned to improve the system, it believed there are some additional improvements that can be made to the OCS that would increase stand-alone accuracy, availability, and integrity; improve the overall reliability of the system; or simplify day-to-day operations.

There are three recommendations that would result in greater stand-alone GPS accuracy and integrity. These include (1) uploading more current clock and orbit information to all satellites, (2) increasing the number of monitor sites, and (3) improving the operational control software to reduce the clock and ephemeris errors.

By uploading pseudorange corrections for all satellites with each scheduled, individual satellite upload, the Air Force predicts a 50 percent reduction in the combined clock and ephemeris errors to PPS users. See Table 3. The Air Force has experiments

underway to validate this assumption. Furthermore, if the number of monitor station sites can be increased, the Air Force expects an additional 15 percent improvement in the combined clock and ephemeris accuracy. Tests in a simulated Kalman Filter currently are underway by the Air Force. A final 20 percent improvement in the combined clock and ephemeris error can be obtained by software improvements to the Kalman Filter and dynamic models used in predicting the state of the GPS satellites. The specific NRC recommendations relating to the above improvements are as follows:

The DOD's more frequent satellite navigation correction update strategy should be fully implemented as soon as possible following the successful test demonstration of its effectiveness. In addition, the current security classification policy should be examined to determine the feasibility of relaxing the 48-hour embargo on the clock and ephemeris parameters to civilian users.

Additional GPS monitoring stations should be added to the existing operational control segment. Comparison studies between cost and location should be completed to determine if Defense Mapping Agency or Air Force sites should be used.

The operational control segment Kalman Filter should be improved to solve for all GPS satellites' clock and ephemeris errors simultaneously through the elimination of partitioning, and the inclusion of more accurate dynamic models. These changes should be implemented in the 1995 OCS upgrade request for proposal.

If all three of the above recommendations are implemented, the combined clock and ephemeris error is expected to be approximately 1.2 meters (1σ). As shown in Table 4 and Figure 4, if: (1) SA is turned to zero; (2) an additional GPS L-band signal is added; (3) more advanced receivers are utilized; and (4) each

of the clock and ephemeris accuracy improvements are implemented, then a stand-alone GPS SPS accuracy of 5.4 meters (2 drms) with a narrow, L-band signal should be obtainable, and a stand-alone GPS SPS accuracy of 4.9 meters (2 drms) with a wide-band signal should be obtainable.⁶ In addition, a PPS accuracy of 4.2 meters (2 drms) (1.8 meters CEP) also would be obtainable.

In addition to the above recommendations, the NRC committee found a need for (1) a simulator to test software and train personnel, (2) modern receivers at the monitor stations, and (3) a permanent, backup master control station. The committee believed that these improvements would enhance the overall reliability of the system.

Table 3. Reduction of Combined Clock and Ephemeris Errors

Enhancement	Anticipated Combined Clock and Ephemeris Error Improvement over Existing Combined Error of 3.6 meters (1σ)
Correction Updates (50% reduction)	1.8 meters
Additional Monitor Stations (additional 15% reduction)	1.5 meters
Non-partitioned Kalman Filter (additional 15% reduction)	1.3 meters
Improved Dynamic Model (additional 5% reduction)	1.2 meters

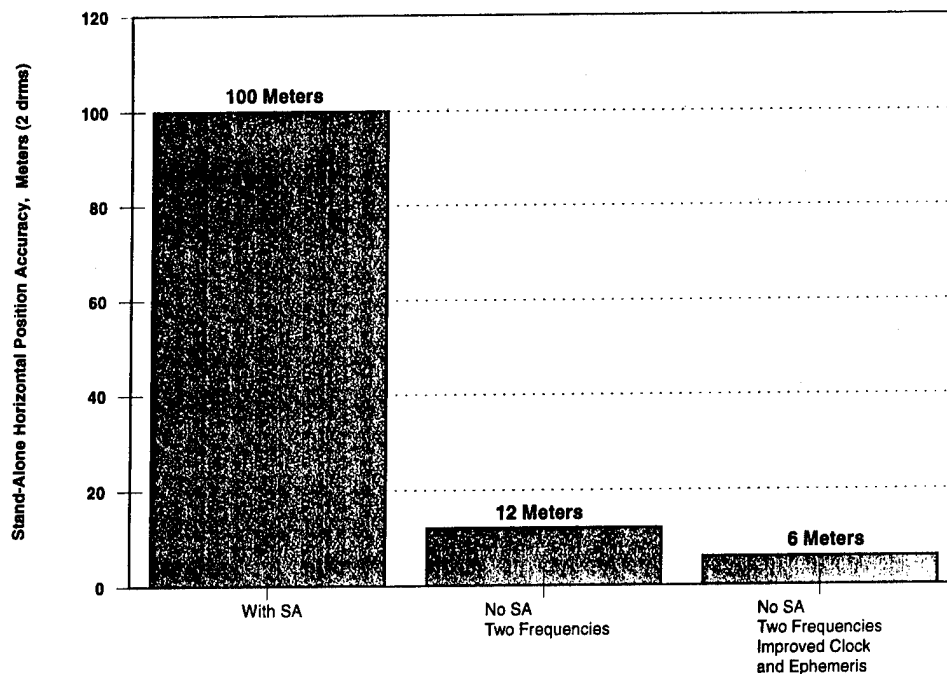


Figure 4. Approximate stand-alone horizontal SPS accuracy, 2 drms, resulting from recommended improvements.

⁶ Civil users would have access to this level of accuracy only if the 48-hour embargo on clock and ephemeris parameters is lifted.

Table 4. Impact of Reduced Clock and Ephemeris Error on SPS Stand-Alone Accuracy

Error Source	Typical Range Error Magnitude (meters, 1σ): Improved Standard Positioning Service (no SA, additional L-Band Signal)				
	1237.83 Narrow-band, C/A-type code	1258.29 Narrow-band, C/A-type code	1841.40 Narrow-band, C/A-type code	1258.29 Wide-band, P-type code	1841.40 Wide-band, P-type code
Selective Availability	0.0	0.0	0.0	0.0	0.0
Atmospheric Error					
Ionospheric	0.01	0.01	0.01	0.01	0.01
Tropospheric	0.2	0.2	0.2	0.2	0.2
Clock and Ephemeris Error	1.2	1.2	1.2	1.2	1.2
Receiver Noise	0.6	0.7	0.9	0.5	0.8
Multipath	1.2	1.6	2.3	1.0	1.9
Total User Equivalent Range Error (UERE)	1.8	2.1	2.8	1.7	2.4
Typical Horizontal DOP (HDOP)	1.5	1.5	1.5	1.5	1.5
Total Stand-Alone Horizontal Accuracy (2 drms)	5.4	6.4	8.3	4.9	7.1

CONCLUSION

Because of its widespread utilization by both military and civilian users, GPS has truly emerged as a dual-use system. The tasking placed upon both the NRC and NAPA study groups by Congress recognized this indisputable fact. As a result, the NRC committee endeavored to balance the features that would enhance civil applications against the clear requirement to maintain the military integrity of the system. Taken as a whole, the recommendations discussed in this paper were intended to meet this criterion.

ACKNOWLEDGEMENTS

The authors would like to acknowledge the other members of the National Research Council Committee on the Future of the Global Positioning System.

Dr. Penina Axelrad
University of Colorado
at Boulder

Dr. John D. Bossler
Ohio State University

Mr. Ronald Braff
MITRE Corporation

Dr. A. Ray Chamberlain
American Trucking Association, Inc.

Dr. Ruth M. Davis
Pymatuning Group, Inc.

Dr. John V. Evans
COMSAT Laboratories

Dr. John S. Foster, Jr.
TRW Inc. (Ret.)

Mr. Emanuel J. Fthenakis
Fairchild Industries (Ret)

Dr. J. Freeman Gilbert
University of California,
San Diego

Mr. Ralph H. Jacobson
The Charles Stark Draper
Laboratory, Inc.

Dr. Irene C. Peden
Univ. of Washington (Ret)

Dr. James W. Sennott
Bradley University

Mr. Joseph Spalding
U.S. Coast Guard Research
and Development Center

Dr. Lawrence E. Young
Jet Propulsion Laboratory

The authors also would like to acknowledge and thank the many individuals from government and industry who participated in this study.

GPS: CHARTING THE FUTURE

A Summary of the Report by the GPS Panel of the National Academy of Public Administration

Arnold Donahue and Roger Sperry
Co-Directors of the NAPA Study

BIOGRAPHIES

Arnold E. Donahue served as Project Director for the National Academy of Public Administration's (NAPA) portion of the joint NAPA/NRC study of GPS. He is currently Executive Vice President of Pacific Trade Associates. He formerly served as Chief, Command, Control, Communications and Intelligence (C³I) in the Office of Management and Budget, Executive Office of the President and as intelligence officer and economist in the Central Intelligence Agency.

Roger L. Sperry served as Co-Project Director for NAPA's portion of the joint study and is NAPA's Director of Management Studies. He formerly served as a professional staff member of the Committee on Governmental Affairs, U.S. Senate, and as Senior Group Director and Special Assistant to the Comptroller General, U.S. General Accounting Office.

ABSTRACT

Congress directed that the National Academy of Public Administration (NAPA) and the National Academy of Sciences to provide guidance on the future of GPS. Congress wanted to know how GPS should be governed, managed, and funded in the future and how its technology could be improved. To conduct its portion of the study, NAPA formed a panel of experts in defense management, government organization, intelligence and security, international trade and finance, science and policy management, technology assessment, and telecommunications. The NAPA panel¹ addressed policy, management, and funding issues. The National Research Council (NRC) acted on behalf of the National Academy of Sciences to review the technical issues.

The NAPA panel assigned the highest priority to maintaining the military advantages associated with GPS. Its initial preference was to isolate this dominant influence and then address the commercial, international,

management, and funding issues. The panel's deliberations, however, led to the conclusion that national security and other issues could not be treated separately. National security could only be addressed simultaneously with consideration of the commercial and international aspects of GPS in assessing appropriately the available options. The panel found that the best approach for preserving national security is one that also adapts to the rapidly evolving commercial and international dimensions shaping the future of GPS.

The NAPA panel concluded that GPS is an invaluable asset that is rapidly becoming a *de facto* "global utility."² To maintain U.S. leadership in satellite radionavigation, the NAPA panel recommended that:

- The President adopt explicit national goals to guide GPS policy making and implementation.
- The United States underscore its commitment to make GPS available free of direct charges to all users.
- To sustain its military advantage, DOD develop the capability to counter adverse use of GPS and other radionavigation signals. Selective Availability (SA),³ which degrades the civilian GPS signal, is not fulfilling the purpose for which it was created. It should be turned down to zero immediately and deactivated after three years.
- The United States develop a more effective mechanism of governance by broadening civil agency participation in U.S. policy making and providing a greater voice for civilian, commercial, and international interests in the future evolution of GPS. A GPS Executive Board that represents these diverse interests should be created.
- Stable federal funding of GPS for national security and public safety be continued, while pursuing contributions from other nations as international participation grows.

NAPA's TASKS AND PROJECT APPROACH

Under the tasks that Congress directed be reviewed and in coordination with the DOD and the NRC, NAPA was assigned the following specific tasks:

1. How should the GPS program be structured and managed to maximize its dual utility for civilian and military purposes?
2. How should the GPS program infrastructure be funded to assure consistent, sustainable, and reliable services to civilian and military users around the world? In consideration of its worldwide user community, are there equitable cost recovery mechanisms that may be implemented to make the GPS program partially or fully self-supporting without compromising U.S. security or international competitive interests?
3. Is commercialization or privatization of all or parts of the GPS consistent with U.S. security, safety, and economic interests?
4. Is international participation in the management, operation, and financing of GPS consistent with U.S. security and economic interests?

The NRC reviewed the technical issues described in their separate paper, though both panels and staffs worked closely and harmoniously on crosscutting questions, such as selective availability.

Forces Driving Change

Early on in its deliberation, the NAPA panel identified a set of powerful forces that it felt were shaping the future of GPS. Such forces would affect the ways the United States maintains the military advantage inherent in GPS, which the NAPA panel believed was paramount. These forces included:

- **GPS as a potential weapon of war and terrorism.** The United States, having developed GPS, rightly wants to retain the military advantages of this technology for its own and allied forces and to deny these advantages to enemies. Consequently, the United States must devote greater energy to achieving countermeasures. As with other technologies, other nations will acquire GPS-like capabilities. How fast this happens depends, in part, on policies and actions of the U.S. government. In the longer term, the increased availability of accurate positioning capabilities will undoubtedly pose an increased threat to U.S. and allied military interests.
- **Rapidly growing commercial markets.** Sales of GPS-related products and services are expected to grow to more than \$30 billion annually by early in the next century. GPS capability will be integrated

into many other widely used technologies throughout the world. There is great potential for still other uses of GPS.

- **Use by much larger segments of the general public.** GPS is still relatively unknown to the general public; users number only in the hundreds of thousands. As GPS becomes a key part of vehicular navigation systems and mobile communications, millions of people will come to know and depend on it.
- **Further potential technological improvements.** Technical improvements can and are being made to the basic satellite system to provide higher levels of accuracy, integrity, and availability.⁴ Other improvements are possible in user equipment and in enhancements and augmentations to the basic system.
- **International markets and influences.** A rapid expansion is occurring in international markets as well. Foreign manufacturers and service providers interested in capturing these markets are pressing their governments for a strong U.S. assurance of continued GPS signal availability and for increased international participation in system governance and management. Foreign unease with reliance on a U.S. military-controlled system provides incentive for international development of a competing global navigation system under multilateral control.

Thus, the NAPA panel organized its work quite logically around the forces driving change - the commercial marketplace, the international sector, national security interests, and management - as well as funding, while the NRC took on the technical questions. But because these forces operate in concert, not independently, and policy makers do not enjoy the luxury of developing categorical responses, the panel found that comprehensive policies to address interrelated challenges were necessary. The United States must not only stay at the leading edge of technological development but also must establish a governance and management framework capable of balancing the various national goals set for GPS. The key was to design a flexible framework for reconciling the competing demands on the system in ways that respond to the national interest.

National Strategy and Goals For GPS

Early on, the NAPA panel also recognized the need for a clearly articulated national strategy to guide U.S. efforts and serve as the basis for both protecting national security and providing a position, velocity, and timing capability acceptable and usable worldwide. Therefore, the panel

recommended the following national goals for GPS, including augmentations funded by the U.S. government, and urged that they be adopted. The goals are:

- Protect the security of the United States and its allies and seek to counter or limit the hostile use of the system by others.
- Maintain an efficient, effective, dual-use geopositioning capability providing responsive, highly accurate, and reliable positioning, velocity, and timing information worldwide.
- Maintain U.S. leadership in GPS technology by encouraging its evolution, growth, and commercial applications.
- Maintain GPS as a global resource by considering international interests and concerns in GPS governance and management.
- Establish policies governing the availability, use, and funding of GPS that are – and are seen to be – stable, consistent, and workable for all major users of the system.
- Provide a flexible management structure capable of adapting rapidly to changing technical and international circumstances.
- Consistent with the other national goals, limit the overall burden on the U.S. taxpayer.

In short, GPS goals should aim to protect national security, encourage commercial growth, and foster international acceptance and continued U.S. leadership in this field.

EVOLVING GPS GOVERNANCE

Two fundamental questions confront U.S. policy makers responsible for GPS: Who governs and manages it? Who pays for it?

The Department of Defense has successfully developed and fielded this highly useful satellite-based system. DOD deserves both public gratitude and congratulations for this impressive technological achievement. DOD's governance and management structure worked well during two decades of development. But demands on the system are widening and becoming far more complex than before, and rival systems may emerge. The Department of Transportation (DOT) has been given a stronger role as representative of civil interests but is still a relatively weak partner to DOD. Governance and management will need to evolve further to meet effectively the challenges of the future. Proliferating

civilian users – domestic and foreign – will need to be better represented in federal policy making on GPS.

As to funding, the NAPA panel concluded that the value of GPS is extraordinarily high, both as a vital and proven military system and as a stimulus to the national and international economies. GPS constitutes a national asset that the nation should continue to own, support financially, and offer as a global utility. To date, DOD has borne the costs of providing a national program benefiting the entire world. In the future, where possible, those who benefit from availability of the GPS signals should contribute toward the cost of providing them. In the panel's view, system enhancements and augmentations that benefit national security or public safety should receive federal support; those that benefit primarily the private sector should be paid for, insofar as possible, by the beneficiaries. If other nations agree to contribute, DOD's financial burden should be reduced.

GPS is fast becoming a global information resource. Few technical obstacles to international diffusion remain, and great advantages accrue to other nations in adopting a system that provides accurate timing and location data at no direct cost. As GPS becomes an invaluable global information utility, foreign governments will, nevertheless, increasingly wish to have a voice in setting policy for the system and will likely become more unhappy with the current *ad hoc* approach to international consultation. Some foreign governments already express a preference that an international organization be responsible for GPS governance and policy making, even though ownership and operation of the GPS satellites would remain in the hands of the U.S. government. U.S. willingness to provide a meaningful voice in GPS governance to the international community might well be accompanied by foreign financial support for maintaining and augmenting the system.

BURGEONING GPS MARKETS

At earlier stages in the development of GPS, military requirements drove the evolution of the satellite system; civilian and commercial needs were subordinate. Final management responsibility for GPS still resides with DOD. Nonetheless, as with computers, microelectronics, and other technologies, commercial applications and technologies are increasingly leading their military counterparts, and commercial developments are setting the terms for many of the debates over the future of GPS. The commercial demand for GPS products and services now overshadows military demand, with nine out of ten receivers being sold to civilian or commercial users. Many in the private sector wonder how DOD will accept and manage the growing dependence of civil users on the system's continued availability, a

dependence which increasingly circumscribes the military's freedom to control the application of GPS.

The markets for GPS applications are diverse, dynamic, and expanding rapidly in the United States and abroad. Opportunities for U.S. GPS product and service vendors of all sizes are growing. Considered from a larger perspective, the growth of civilian use means that people are increasingly enjoying the considerable peacetime benefits of GPS technologies in the areas of increased productivity and cost savings, public safety, and convenience.

NAPA's project team surveyed seventy companies in an effort to achieve a clear understanding of GPS markets. Responses obtained from forty-nine of those companies indicated that the estimated size of global GPS markets is currently about \$2 billion (Figure 1 below). These markets are growing at an annual rate of about 38 percent and are expected to grow to at least \$11 billion by 2000. By 2005, the world market is expected to reach \$31 billion, 55 percent of which will be outside of the United States. Other studies by the European Commission and a major U.S. consulting firm support the conclusion that GPS markets will grow rapidly.

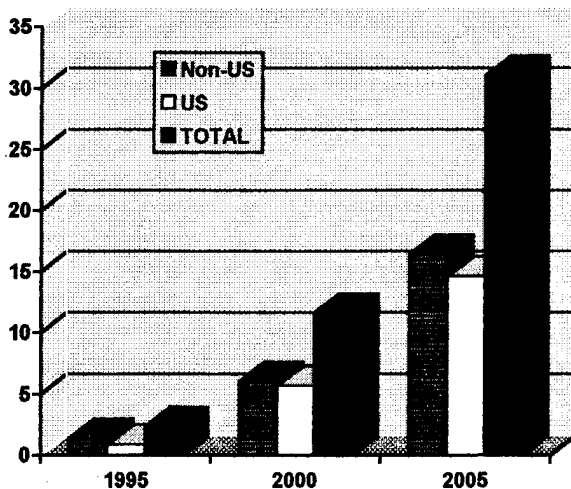


Figure 1: World GPS Market (\$ Billion)

Why is the use of GPS growing so rapidly? One key reason is that the price of basic GPS user equipment is dropping as a result of technological progress, increasing scale economies, and competition among vendors. Another reason is that qualitative improvements in GPS-based technologies are bringing greater accuracy and reliability to traditional users of positioning and navigation data. The NAPA survey confirmed that prospects for GPS in air navigation are particularly bright because alternative systems

generally pale in comparison when all relevant factors are taken into account.

The synergistic combination of lower prices and improved performance characteristics is creating entirely new GPS applications. As noted earlier, the explosive growth of GPS is already impacting the automobile industry. America's leading automobile companies are anticipating a huge market for GPS in the area of automobile navigation, an application that is already catching on among Japanese consumers. Consumer recreational use is another growth market; as prices drop and inexpensive personal positioning technologies become accessible to the public, GPS receivers may become ubiquitous among hikers, boaters, tourists, and other recreational users. (Figure 2 on the following page projects GPS market growth by major segment.)

Future growth in the use of GPS will be accompanied by the integration of GPS with other technologies, such as telecommunications, remote sensors, data storage technologies, and liquid crystal displays. The combination of GPS with communications technologies, for example, has led to automatic vehicle location software that provides a central dispatcher with the exact location of each vehicle in a fleet. It also holds out the prospect for reducing auto theft through automatic tracking of stolen vehicles.

Both U.S. and foreign governments continue to wield considerable influence over the pace and direction of GPS market development. U.S. businesses are largely satisfied with the current management of the GPS satellite system at the moment but are concerned about future policy stability and international acceptance. As entire industries and essential civil government services become dependent on GPS, these questions will become increasingly important.

The willingness or reluctance of foreign governments to embrace GPS as a central component of a future global navigational satellite system could greatly affect the fortunes of U.S. GPS vendors in the long term. Currently, some foreign governments maintain a cautious attitude toward the system out of concern for the DOD-dominated management arrangements and for the political leverage and economic benefits that would accrue to the United States as the owner and operator of a *de facto* global satellite radionavigation system.

Similarly, U.S. civilian government agencies such as the Federal Aviation Administration (FAA) and the U.S. Coast Guard have a powerful impact on GPS markets as a result of their role in providing augmentations called "differential services" for air transportation and maritime use, augmentations that improve the accuracy of the basic GPS signal.⁵ Constructing and maintaining such systems

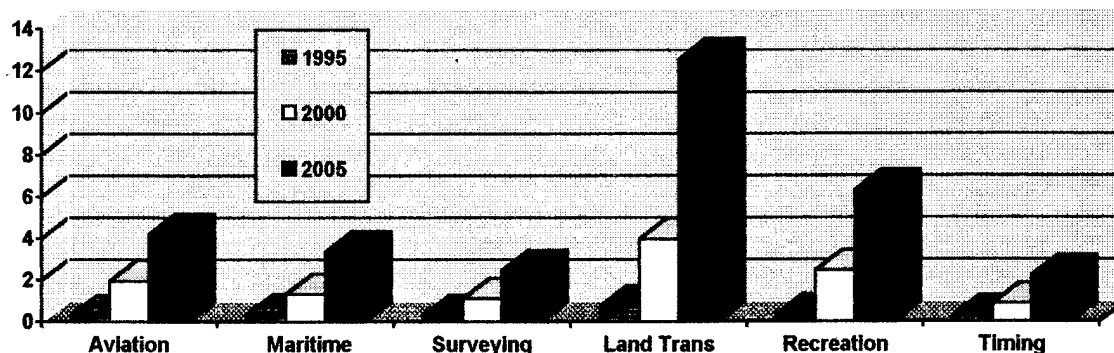


Figure 2: World Market Growth by Segment (\$ Billion)

translates into large hardware, software, and service contracts for U.S. firms, and the commercial sector generally welcomes the proactive approach that government agencies have taken toward differential services. Equipment manufacturers cite the incorporation of GPS into public infrastructure as the second most important measure that the government could take to promote GPS-based industries (the first is to ensure policy stability). Still, U.S. private companies that provide differential services, while supportive of government use, oppose government competition. Freely available government-provided augmentations to GPS will impinge upon markets otherwise open to private providers.

Finally, the military has a strong effect on GPS markets. First, it has the lead role in setting policy for the system. Second, at least for the moment, it is a major purchaser of GPS equipment for its own use. However, as shown in Table 1 below, the military's policy of degrading the civilian GPS signal through SA tends to constrain the growth of commercial applications. Research conducted for the NRC, as well as the NAPA survey, indicate that the market impact of eliminating SA would be favorable and could be quite substantial in some product categories.

TABLE 1

North American GPS Market: Cumulative 1994-2003		
(\$ Billion)	SA On	SA Off
GPS Products	19.8	30.1
Network Services	7.1	13.1
Data Commun.	10.5	12.5
Software & Integ.	4.8	8.3
TOTAL	42.3	64.0

MAKING GPS THE CORE OF A GLOBAL POSITIONING AND NAVIGATION NETWORK

Despite the rapid international diffusion of GPS technologies and the apparent willingness of many foreign users to rely upon the system, concerns continue to be expressed. The NAPA panel believed that such concerns should be addressed, consistent with U.S. national security interests, if GPS is to gain universal acceptance as the system at the core of a future international navigation system. These concerns include control of the system, participation in governance and funding of the system, and standards setting.

While some take U.S. dominance for granted, unresolved issues and concerns about control and national sovereignty nonetheless could lead to the development of a competing navigation satellite system similar to GPS, notwithstanding the worldwide availability of the GPS civil signal free of direct charge. A Russian system, GLONASS, has been partially fielded; Inmarsat, the International Marine Satellite Organization, may include a navigation capability in a future satellite network. The International Civil Aviation Organization is working on a Global Navigation Satellite System, with GPS and GLONASS as components. Whether these systems become complementary to or competitive with GPS depends on U.S. government actions.

GPS is becoming a *de facto* international utility, and it is in the U.S. interest to encourage the further diffusion and acceptance of GPS in this capacity. To the extent that the United States neglects the concerns and requirements of international GPS users, other nations would be more inclined to press on with plans to create alternative, stand-alone systems. Such a development would have a number of negative implications for the United States, in both the economic and the national security areas. It would be more difficult to maintain the military advantage accruing to the

United States as the technological leader. It could also diminish the commercial advantages and the prospect of international contributions to GPS as well as impede the formation of an international navigation network.

The NAPA panel concluded that the United States needs to pay close attention to other countries and relevant international bodies. The panel found that:

- Foreign interest and involvement in GPS are increasing rapidly as the system gains greater international acceptance as the navigation and positioning system of choice, despite some concerns among foreign governments and other users about the future reliability and availability of GPS, concerns that are heightened by the continued use of SA.
- Current, largely *ad hoc*, channels for foreign participation in GPS will, over time, likely be insufficient to meet other nations' demands for a stronger international voice in any global navigation system.
- Participation by international institutions, regional organizations, and foreign countries is appropriate in defining GPS requirements, monitoring the system's performance, and establishing compatible differential services, and this participation promotes GPS expansion worldwide.
- Foreign contributions to a worldwide navigation and positioning system based on GPS could reduce the costs of the system to the American taxpayer. However, such contributions would presumably be contingent upon greater international participation in the policy-making aspects of the system.

Opportunities exist for increased international involvement in GPS, including participation in both the definition of future requirements and financing of the system. The panel's recommendations aimed at seeing that GPS was the basis for a truly global positioning and navigation system. They included the following:

- *The United States should issue a clear and concise policy statement at the highest level that reasserts the U.S. commitment to provide permanent international access to the GPS signal and that states the U.S. intention to consider foreign interests in the future evolution of GPS.*
- *The United States should formulate an explicit strategy to increase international acceptance and use of GPS that reassures foreign users of the*

reliability, credibility, and consistency of the United States as a provider.

- *The U.S. government should encourage and participate in developing and organizing a global navigation network with GPS as its foundation, and with appropriate arrangements for governance, management, and funding.*

MEETING NATIONAL SECURITY INTERESTS AND CONCERNS

GPS is an essential element of the U.S. national security posture. Already widely deployed in military units and systems, GPS is programmed, over the next decade, to become an integral part of all major weapon platforms (planes, ships, and land vehicles); a mainstay of troop and equipment maneuvering; and an embedded subsystem in an increasing number of so-called "smart" precision-guided munitions.

Balancing the commercial and societal advantages of widespread civilian access to reliable, accurate GPS positioning data and the national security interests has been a long-standing concern. The realization that a military adversary could use GPS technology against its creators led DOD first to separate military and civilian GPS signals and then intentionally to degrade the latter using SA when it proved more accurate than had been expected. The advantages and disadvantages of SA have been subjected to extensive debate as the importance of GPS to military and civilian users grows.

Military thinking about GPS has focused on securing the precision military GPS signal through encryption and on denying a highly accurate civilian signal to potential adversaries through SA. The security of the military signal is intact, but the difficulties with SA include:

- First, as the demand for and use of GPS grow, the military utility of using the civilian signal in wartime also grows. Many U.S. troops carried commercial receivers during the Gulf War and the 1994-1995 military operation in Haiti. In both cases, U.S. military commanders opted to turn SA to zero to improve signal accuracy for troops using such receivers. The anomalous situation thus exists of having SA to protect national security, yet turning it off in the very circumstances it was designed to serve.
- Second, DOD's reliance on SA to degrade the civilian signal is quickly being undermined by the proliferation of inexpensive and robust differential systems.

- Finally, the political feasibility of denying or further degrading the civilian signal in response to military imperatives is eroding rapidly. The increasing integration of GPS technologies into the commercial and civil sectors ensures that denial or degradation would imperil public safety, adversely impact the economy, and impede the delivery of an increasing array of public and private services. Military commanders know that SA can be turned up to confound the enemy but may ignore the substantial commercial and international costs associated with such an action.

In addition, since most military receivers require the acquisition of the civilian signal prior to gaining access to the more accurate military signal, jamming of the civilian signal can currently affect the military's access adversely. Techniques to prevent this effect were discussed in the NRC portion of the report.

The current level of SA (100 meters) is an inconvenience, an obstacle relatively easily overcome, rather than a significant deterrent to those who seek greater accuracy. But SA cuts both ways – a fact often forgotten in DOD – by encouraging ways such as differential GPS to around it and leading to speculation on alternative stand-alone systems. The global diffusion of differential GPS, including to potential adversaries, is already well underway and accelerating rapidly. The United States cannot prevent the growth of such systems, aside from recourse to the politically untenable and economically ill-advised option of discontinuing or encrypting the civilian signal.

DOD is rightly concerned about the military implications of the increasing worldwide availability of high-quality, GPS-derived radionavigation data. But the existence of SA has distracted DOD from confronting this incipient problem head-on. For many in military commands, SA is a mental crutch that has slowed and inhibited the development of the capabilities required to address the problem directly: the ability to decrease accuracy to levels worse than 100 meters provides a superficially appealing, if unrealistic, answer to concerns about the availability of accurate navigation data.

SA will no longer be effective in denying potential adversaries the accuracies inherent in GPS and its augmentations; the NRC portion of the report addressed the technical considerations supporting this conclusion. The use of SA, and the uncertainty surrounding U.S. policy toward GPS, may be a temporary deterrent to foreign military (as well as civilian) users. But it is rapidly eroding as differential systems spread. In the longer term, the continuation of SA will be ineffective and could be counterproductive.

Nonetheless, the greater accuracy provided by GPS – with or without SA – and other augmentations of the civil signal poses an increased threat to U.S. and allied military forces. Even if, on balance, U.S. forces benefit more from GPS than do their adversaries, the advances in targeting and positioning that will arise from the increased availability of GPS signals pose an increasing threat and must be taken seriously. Memories of SCUD attacks on Riyadh and Tel Aviv are too recent to ignore the implications of this threat.

The most obvious tactical change required to respond to these threats is to develop the capability to counter adverse use of GPS signals and other radionavigation signals, to acquire the necessary electronic warfare hardware, and to train U.S. military forces to use them. Military research and development should focus more on developing options to both deny the availability of accurate positioning from GPS should the need arise and to protect the availability of the military signal to U.S. and allied forces. U.S. military planning, doctrine, and operations should emphasize the denial of precision radionavigation data to adversaries in wartime. Technical approaches to limiting the availability of differential signals should also be investigated.

Accordingly, the NAPA panel recommended:

- *U.S. military planning, research and development, doctrine, training, and operations should focus on denying the advantages of accurate positioning and navigation signals to adversaries in wartime through methods other than Selective Availability (SA), including jamming.*
- *The administration and the Congress should provide the resources required to develop and procure needed countermeasures and equipment as soon as possible.*
- *Selective Availability should be turned to zero immediately and deactivated after three years. In the interim, the prerogative to reintroduce SA at its current level should be retained by the National Command Authority.*

GOVERNANCE AND MANAGEMENT: THE NEED FOR EVOLUTION

For the first two decades of GPS development, DOD carried out both the governance and management functions. DOD deserves great credit for its accomplishments. The Air Force, as DOD's executive agent, successfully developed and fielded the system and brought it to initial operational

capability in December 1993. DOD also cooperated with civil agencies and the commercial sector as they explored and developed applications for a wide variety of civil government and private-sector users.

Recently, the DOT has become more involved, and through it, the civil government sector. In the absence of clear and comprehensive policy guidance, participating organizations have been free to pursue their own agendas. Not surprisingly, DOD focuses on the attributes that best serve military needs; DOT's attention is focused on proposed differential systems for civil air and marine uses. This arrangement has led to conflicts, such as that between DOD and the Federal Aviation Administration (FAA) over the accuracy of FAA's proposed wide-area augmentation system (WAAS), which reflect the sometimes competing interests, in this case, civil air navigation needs versus concerns about national security. While not surprising, given the conflicting goals and viewpoints, such conflicts affect program implementation and costs, and slow realization of GPS's potential benefits to broad segments of society.

Although not an equal partner, DOT has taken some useful first steps to improve its interactions with DOD. The NAPA panel was concerned, however, that DOT has been slow in taking other needed actions, such as appointing a senior official with clear and continuing authority to oversee departmental initiatives, as well as coordinate all civil activities, on GPS. In addition, DOT is only minimally represented at the DOD operating levels and is only modestly representative of other civil users. With a DOT departmentwide reorganization in the offing, further delay is likely.

The NAPA panel was also concerned about the requirements-setting process and its implementation in DOD. Civil agency, commercial, and international input into the system is occurring in a more organized fashion but is still limited. This situation exists in large part as a reflection of the military requirements-setting process, which was not crafted to embrace the needs of civilian agencies or the private sector. In addition, various military commands have only recently become more aware of their own requirements for GPS as they continue to research and examine the potential applications of GPS.

The Air Force is limited by DOD guidance and funding to maintaining the system and responding only to defined military requirements. If a military command has requirements that exceed DOD guidance, the command is expected to provide the funds for meeting more demanding requirements. Any civil agency, private-sector, or international requirements in excess of military requirements are to be financed with non-DOD funds. The panel believed DOD needed to reexamine its procedures for identifying and

funding research and development requirements for GPS improvements to better take into account the overall demands for GPS.

Several models of governance structures potentially relevant to GPS were explored during this study, including possible privatization. No alternative governance and management arrangement emerged as fundamentally superior to the current arrangement at this time. The panel believed that governance and management of GPS must evolve over time if they are to meet a rapidly changing and growing user environment. GPS must provide a quality of service second to none, and its governance must remain flexible, responsive, and able to accommodate international and commercial interests. A rigid or unresponsive governance and management structure would, in and of itself, provide an incentive for others to establish competing systems or technologies. A flexible structure is especially desirable in view of the likelihood that technological advances, and increasing international, commercial, and consumer applications, will continue to drive the evolution of GPS.

The panel took special note of the privatization option as requested in NAPA's charter for the study. Privatization is receiving increased attention in both the executive and legislative branches as they consider fundamental changes in the role, scope, and size of the federal government. Although this focus is not new, its intensity is.

GPS is essential to national security and, thus, its availability must be assured. Current arrangements provide for this access. As for civil use, GPS is user-passive and free. Its civil signal is unencrypted, making it readily available to anyone anywhere with a GPS receiver. Therefore, anyone can acquire and use the basic GPS signal with an off-the-shelf receiver. How then would a private firm offering the civil signal as a service cover its costs? Unlike a sovereign government, a private company cannot place a tax on receivers. Such a firm would have to market an encrypted signal; only then could it restrict and control the use of the signal and charge a fee for it. If the civilian signal were to be encrypted, the hundreds of thousands of civil receivers already in use would no longer work, violating a basic tenet of GPS operations that all system changes be "backward compatible."

For this and other reasons, the NAPA panel concluded that privatizing GPS is not a satisfactory option. As interesting and provocative as the idea might be, outright sale of GPS would create serious problems and should be avoided. Greater private-sector involvement could be achieved if the Air Force gave the GPS satellite contractor responsibility for future systems integration and operations, an approach proposed by one Air Force office. This approach also could improve system performance, economy, and efficiency.

The panel's recommendations for governance and management took cognizance first and foremost of national security considerations. The best way to preserve the control needed for national security is for DOD to continue to manage and operate the basic system. Within this framework, the panel believed the United States should move toward a governance and management structure that pays greater attention to other nations and international bodies. People and governments all over the world are increasingly dependent on GPS for many and varied uses; some relate directly to saving lives. The U.S. government has a primary responsibility to protect national security; it is also obligated to ensure the availability of this important and valuable resource to U.S. and international civilian users, consistent with national security.

The most important factor driving a decision by others to establish a competing system is the lack of confidence in a U.S.-provided basic GPS service perceived primarily as military-controlled and dominated. It follows that the most important actions the United States can take to enhance its position are to:

- Keep the civil GPS signal free of direct user charges and available to all;
- Turn Selective Availability to zero immediately and deactivate it after three years;
- Broaden civil agency participation in GPS governance; and
- Provide a forum for international parties to voice their needs, interests, and concerns.

These actions should increase international acceptance of GPS and forestall the day when competing satellite navigation systems are circling overhead. These actions are fully compatible and mutually reinforcing. Increased international cooperation provides the best opportunity for cost-sharing for GPS.

The panel recommended that *the President promulgate an executive order to set forth a national strategy and guidelines for GPS, establish a GPS Executive Board, reassert the policy of the United States to provide the civil GPS signal free of direct user charges worldwide, and announce that Selective Availability will be turned to zero immediately and deactivated after three years.*

Governance and policy leadership of GPS need a broader base and perspective. To achieve the national goals for GPS, the current governance and policy-making arrangement must be strengthened. Therefore, *the GPS Executive Board should be created as soon as practicable.*

- *The board, to be co-chaired by high-level designees of the secretaries of defense and transportation, should be responsible for governance oversight, highest level policy setting and policy guidance, and overall coordination for the entire GPS program, including augmentations.*
- *The board's membership should extend beyond DOD and DOT to the Departments of Commerce, Interior, and State, so as to be more inclusive and representative of the broad spectrum of the domestic and worldwide GPS user.*
- *The board should be directed to prepare an annual report for the President who, in turn, should forward it to the Congress.*
- *The board also should be responsible for formulating a comprehensive strategy to increase international acceptance and use of GPS that reassures foreign users of the reliability and consistency of the United States as a provider.*
- *The board should ensure that DOD's and the Air Force's requirements processes effectively accommodate military and civilian GPS requirements and that appropriate means are established to fund non-military requirements.*
- *The board, acting through its co-chairs, should be responsible for resolving disputes arising over GPS program management, operations, and funding.*

The NAPA panel also recommended that:

- *DOD retain responsibility for operation and maintenance of the basic GPS, and the Air Force continue to act as executive agent; DOD also should continue to be responsible for international military cooperative arrangements.*
- *DOT should be strengthened and become a more assertive executive agent for all U.S. civil systems, oversee U.S. participation in international organizations and GPS-related systems, and make arrangements with DOD to satisfy civil requirements for positioning and navigation using the civil GPS signal.*

The executive order recommended above should provide a stronger charter for DOT's role, but effective leadership will be needed to carry it out. In this role, DOT should:

- *Coordinate civil agency requirements for and use of GPS and actively represent the civilian GPS community (including private and commercial interests, both domestic and international).*
- *Institutionalize its consolidated requirements identification process for all civil requirements for GPS and work with DOD to formalize the mechanisms for incorporating them, where appropriate, into the current military operational requirements process for GPS.*
- *Work with DOD to better coordinate military and civilian research and development efforts.*
- *Cooperate with the Air Force to monitor and report on the integrity of the civil GPS signal.*

Regarding use of the private sector for GPS differential services, the panel recommended that:

- *As a general policy, the federal government should make use of the private sector for GPS augmentations beyond those specifically designed or required for public safety and national security.*

MAINTAINING STABLE FUNDING SOURCES

Based on available economic and financial evidence, the panel proposed a financing structure that relies on federal funds for maintenance of the basic system and augmentations vital to national security and public safety. In thinking about funding, it should be kept in mind that increasing private-sector activity will produce taxable income resulting in substantial revenue to the Treasury and foreign exchange from exports. With SA turned to zero, that income would increase. Indeed, continued federal support for GPS is essential to maintaining the system as a U.S.-operated military asset and is a good investment for the American taxpayer in that it stimulates economic growth. The panel reached six general conclusions about funding GPS.

First, any policy change in the funding structure for GPS must take into account the fact that the United States has a profound stake in maintaining GPS for military use alone, quite independent of any other uses or developments. As a vital military asset, GPS needs a solid and reliable funding base; its funding should not be placed in any jeopardy through experiments with other funding structures and mechanisms.

Second, the basic GPS program is a public good.⁶ The investment of public funds for its primarily military purposes

has already been made. The system is currently available, no charge is made for its commercial use, and it is not feasible to charge directly for individual use of the signal. In addition, the last three administrations have committed to making the civil signal available free of direct charges to users. Those who want accuracy beyond that available from the basic civil signal can purchase differential services or use augmentations provided by the federal government.

Third, the existing GPS program, even without augmentation, is already stimulating significant growth in important industries, especially those that have high potential for generating jobs and raising standards of living, such as the knowledge and electronics industries. Imposing user fees or taxes could slow that growth and delay important new uses of GPS. Fees and taxes could also reduce the taxable income from GPS-related activities. Furthermore, it is impossible to calculate the amount of an "equitable" user charge, given current and likely available data; it is not even technically possible to determine who uses the GPS signal or how much they use it. It would be possible to tax individual users or impose user charges in the United States in some fashion, but it would not be possible to tax users overseas in the same fashion or on the same basis, if at all.

Fourth, the greatest economic effect of GPS, and thus the program's most likely method of paying for itself, is reflected in the revenues generated through the existing tax structure. This revenue can be enhanced by turning SA to zero, which will stimulate additional revenue-producing activity in the private sector. The benefits that GPS provides the economy, and the national policy of encouraging the growth of the information and communications infrastructure, outweigh the potential revenue that might be generated by a direct tax on vendors or users.

Fifth, many augmentations of GPS now in operation or in the planning stage are privately funded and will generate economic growth and additional revenue at no direct cost to the federal government. Federally funded augmentations of GPS, such as the FAA's WAAS and the Coast Guard's differential system, support traditional functions of the federal government that serve vital public safety purposes; as such, it would be inappropriate to charge additional user fees or impose taxes for them.

Sixth, the United States should be prepared to seek cash and in-kind contributions to maintain and enhance a global navigation network with GPS at its heart. This approach also supports the panel's earlier recommendations that the United States explore international funding in support of GPS and that a forum be provided for international voice in GPS as a global navigation network based on it evolves.

Therefore, the NAPA panel recommended that:

- *Congress and the administration treat the current basic GPS as a public good, paid for through general revenues.*
- *Congress and the administration refrain from imposing a receiver tax and impose no special fee or tax on private differential systems.*
- *The costs of the Coast Guard's and FAA's augmentations of GPS and related systems should be covered by the appropriate trust funds without raising fees.*

SUMMING UP

GPS is much more than a satellite system for positioning and navigation. It represents a stunning technological achievement that is becoming a global utility with immense benefits for the U.S. military, civil government, and commercial users and consumers worldwide.

Civilian navigational applications were expected from the outset of GPS. Unanticipated innovative applications have grown exponentially in recent years, going far beyond the basic uses originally envisaged for the system. GPS technologies have been applied in fields such as aircraft approach and landing, surveying and mapping, oil prospecting, geological research, telecommunications network synchronization, and even automobile navigation, thus replacing older, inferior, and more expensive technologies and providing capabilities where none previously existed.

Management and funding challenges exist, but they do not raise serious questions about the established management and funding of the basic GPS system. In part, they are symptomatic of the complexities involved in any dual-governance arrangement involving organizations with different cultures and missions. More fundamentally, they represent the clash between the demands for improved accuracy and integrity by civil users, both domestic and international, and DOD concerns about the impact of these trends on the U.S. national security posture.

Evolution, rather than revolution, in governance, management, and funding is needed for the United States to maintain its leadership in this vital technology and to encourage commercial and international reliance on GPS.

ENDNOTES

¹ The NAPA Panel was chaired by James R. Schlesinger and included as member Carl O. Bostrom, Charles W. Cook, Harold B. Fingers, Edwin L. Harper, Ray Kline, William Y. Smith, Milton J. Socolar, John G. Stewart, and Terence A. Todman.

² GPS provides an internationally available service, similar in many respects to a public utility. The system requires a substantial up-front capital investment, has decreasing average costs, is generally available to anyone, and therefore is a natural monopoly; that is, it is more efficient to have one instead of many providers.

³ Selective Availability is a feature of current GPS satellites that purposefully degrades the civilian (SPS) signal from approximately 30 meters to 100 meters. It operates like a rheostat and can be set from zero to well above 100 meters. The satellites also broadcast an encrypted military signal that is not affected by SA.

⁴ *Accuracy* is the degree of conformity between the estimated or measured position or velocity of a platform at a given time and its true position and velocity. *Integrity* is the ability of a system to provide timely warnings to users when the system should not be used for navigation. *Availability* of a navigation system is the percentage of time that the services are usable, for example, an indication of the ability of the system to provide usable service within the specified coverage area.

⁵ Differential service enhances the accuracy (and often other characteristics) of GPS signals by employing ground facilities of known location to determine positioning error in GPS signals and transmitting corrections to users.

⁶ A public good has two major characteristics: first, once the public good has been paid for and is available, an additional user imposes no cost on the system and does not diminish its availability to others; second, it is impossible or very expensive to prevent anyone from using it. In addition, a public good usually benefits a large segment of the citizenry.

GPS Performance Characteristics and Trends

Rob Conley, Mark Fryt, and Sean Scott
Overlook Systems Technologies, Inc.

BIOGRAPHY

Rob Conley is a Senior Engineer with Overlook Systems Technologies, Inc. He graduated from the Air Force Academy in 1981, with a Bachelor's degree in astronautical engineering, and has worked in various capacities in the GPS program for over 14 years. His most significant efforts to date include managing the GPS Block II satellite control software development and the GPS control/space development test program, and developing the GPS SPS Signal Specification. Mr. Conley is currently responsible for managing the reengineering of navigation mission control algorithms, as part of the larger effort to develop a next-generation GPS OCS. He is also currently serving as the chairman of the IEEE's satellite navigation Technical Panel.

Mark Fryt is also with Overlook Systems Technologies, Inc. He is currently the Program Manager for the FAA's GPS Performance Analysis Network (PAN). Mr. Fryt graduated from the University of Colorado in 1983, with a Bachelor's degree in engineering physics. He has spent a significant portion of his career developing and maintaining software for GPS applications and satellite operations. Mr. Fryt's most significant efforts to date include the development of a distributed system for gathering and displaying tactical data for the army, and the GPS PAN development effort.

Sean Scott is a Technical Analyst with Overlook Systems Technologies, Inc. Mr. Scott spent several years as a crew member of the Air Force Space Command squadron responsible for operating the GPS constellation. He is currently responsible for routine PAN operations and maintenance, to include data editing, data reduction and product generation.

ABSTRACT

This paper provides up-to-date information regarding a wide range of GPS performance characteristics, based upon

observations from the Federal Aviation Administration's GPS Performance Analysis Network (GPS PAN).[1] GPS provides a service with a broad range of application, so performance must be examined from several perspectives to understand its implications for any given user group. GPS performance is also changing slowly over time. These time-varying dynamics are important to the identification of potential trends in performance, and in an assessment of GPS stability and maturity. The specific topics the paper addresses are listed below:

- Coverage and service availability patterns and trends.
- Two year trends in predictable positioning accuracy.
- Self-surveying accuracy with averaging times up to 24 hours, measured against DMA surveyed locations.
- Post-processed ionosphere-corrected, common-view time transfer performance across all GPS PAN monitor stations.
- Range-domain performance, to include range, rate and acceleration error characteristics and trends.
- Satellite outage patterns and trends.

The paper concludes with an assessment of performance implications for several key user applications. The information provided in this paper builds upon the body of work already established within the community regarding GPS performance, and adds long-term, continuous observations from several different perspectives.

Identification of performance characteristics and trends, and the overall stability of the service, is important to all user groups. The paper provides information that is important particularly to differential applications, surveying, time transfer and synchronization (particularly of wide area differential reference station networks), and aviation operations using GPS.

1. INTRODUCTION

GPS is a complex system with many degrees of freedom. Its current measures of performance provide a well defined, but narrow perspective upon which to judge how the system is performing at a system level. The fundamental error behaviors of the system -- orbit error, clock error and individual satellite outage patterns -- are the common root of all perspectives on system performance. These behaviors however do not lend themselves well to specifications that are easily translated into specific expectations for any given user group. The ultimate objective of a "universal" GPS specification is to be able to define a multitude of user requirements based upon these common roots. In this paper, we start such a process by first examining performance from a service provider's perspective, and then by exploring alternative views of system performance. As we describe each alternative measurement, we provide some insights into why that measurement and its behavior are important to the user community.

2. GPS PAN OVERVIEW

The data used in the development of this paper was gathered primarily using the GPS Performance Analysis Network (PAN). The GPS PAN is an FAA initiative begun

several years ago. The FAA's objective in establishing the GPS PAN was to support a sustained evaluation of GPS performance on a long-term basis, through an independent network of monitor stations. Three monitor stations are currently deployed, in Los Angeles CA, Colorado Springs CO and Vienna VA. Each monitor station consists of a six-channel receiver (capable of tracking up to eight satellites), a processor and a rubidium frequency standard. The monitor station processor is responsible for receiver control, time scale management, data storage and detection of service failures. Data is transferred on a regular basis to the GPS PAN's central processing location in Colorado Springs. We began archiving GPS performance data in April 1993. We now have a continuous 29 month history of GPS performance characteristics.

3. GPS PERFORMANCE STANDARDS

Until GPS Initial Operational Capability (IOC) was declared in December 1993, the civil community's expectations of GPS performance were driven primarily by the experiences of its user constituency. Department of Defense (DoD) guarantees of performance were limited, open to interpretation and of little applicability to the majority of civil users. Upon declaration of IOC, the DoD provided the Department of Transportation (DOT) with a Standard Posi-

Table 1. GPS Standard Positioning Service Performance Standards

<i>Performance Parameter</i>	<i>Values from SPS Signal Specification</i>	<i>Measurement Sampling</i>
Coverage	99.9% global average 96.9% worst-case site	24 hour sample period, 30 second sample interval (each site) 24 hour sample period, 30 second sample interval
Service Availability	99.85% global average 99.16% average location 95.87% worst-case day 83.92% at worst-case point on worst-case day	30 day sample period, 30 second sample interval 24 hour sample period, 30 second sample interval
Service Reliability	99.97% global average 99.79% average location	12 month sample period, 4 second sample interval
Positioning Domain Accuracy		
Predictable Horizontal Error	100 meters 95% 300 meters 99.99%	24 hour sample period, 60 second sample interval 24 hour sample period, 4 second sample interval
Predictable Vertical Error	156 meters 95% 500 meters 99.99%	24 hour sample period, 60 second sample interval 24 hour sample period, 4 second sample interval
Repeatable Horizontal Error	141 meters 95%	24 hour sample period, 60 second sample interval
Repeatable Vertical Error	221 meters 95%	24 hour sample period, 60 second sample interval
Relative Horizontal Error	1.0 meters 95%	24 hour sample period, 60 second sample interval
Relative Vertical Error	1.5 meters 95%	24 hour sample period, 60 second sample interval
Range Domain Accuracy		
Range Error	150 meters Not To Exceed	24 hour sample period, 1 second sample interval
Range Rate Error	2 meters/second Not To Exceed	24 hour sample period, 1 second sample interval
Range Acceleration Error	8 millimeters/second ² 95% 19 millimeters/second ² Not To Exceed	24 hour sample period, 60 second sample interval 24 hour sample period, 1 second sample interval
Time Transfer Accuracy		
4 Satellite Solution Time Error with respect to UTC	340 nanoseconds 95%	24 hour sample period, 60 second sample interval

tioning Service (SPS) Signal Specification. This document provided for the first time a quantitative definition of performance the civil community could expect from GPS. A summary of GPS performance standards identified in the SPS Signal Specification is provided in Table 1.[2]

Along with these performance standards, the SPS Signal Specification provides performance measurement algorithms that serve to quantify precisely the definition of the performance standard.[3] This is important, because of the need to minimize ambiguity among the user community. In Table 1, we define sample periods and rates required to assess performance for each of the performance standards.

Although the SPS Signal Specification does define quantifiable performance standards, note that they are rather generic in nature. Generic performance standards reflect a deliberate effort by the DoD to define performance from a minimally equipped positioning user's perspective. The intent of the approach was to limit the scope of DoD involvement in civil usage, by finding the lowest possible common denominator across all civil users. Although this approach is justifiable from a service provider's perspective, it does not answer a need to better define the service a diverse body of users can expect to receive from GPS. We will pursue this line of thought further once we have described GPS performance trends from an SPS Signal Specification point of view.

4. SPS PERFORMANCE TRENDS

Our primary interests in performance trends are usually broken down into three areas:

- Coverage & Service Availability
- Service Reliability
- Positioning Accuracy

We discuss each in the following sections, in terms of Continental United States (CONUS) performance. These discussions are relatively brief, since we described generic SPS performance in great detail in a paper presented at GPS ION-94.[4]

4.1 Coverage and Service Availability

GPS four-satellite coverage has been essentially continuous since the early 1990's, even considering a Position Dilution of Precision (PDOP) cap of 6. On a few days a year, PDOP values as high as 12 have been detected for as long as 20 minutes. These transient conditions have been associated each time with reported satellite outages.

Service availability values are generally over 99%. Service availability performance is highly sensitive to not only satellite downtime, but the specific pattern of downtime. Removal of two satellites from service can have absolutely no effect on one area, but be devastating to another region. A case that is illustrative of this point occurred in January 1995, when Colorado Springs experienced a significant degradation in service availability due to multiple satellite being removed from service. At the same time, Vienna and Los Angeles experienced no degradation in performance. We discuss this event more in Section 4.3. We have also had transient availability problems in our Vienna monitor station, due to anomalous levels of signal interference.

In Figure 1, we combine coverage and service availability to indicate a stable trend since April 1993, of the percentage of time that a navigation solution is available and usable by positioning users. The service availability requirement without consideration of coverage is provided to highlight the combined performance of coverage and service availability.

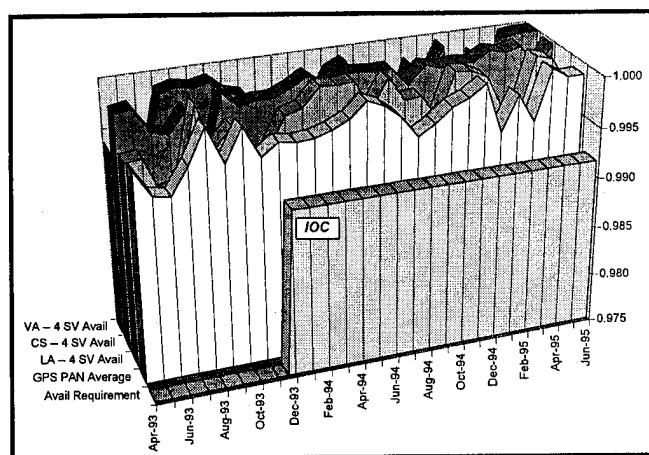


Figure 1. Trends in GPS Availability

4.2 Service Reliability

At ION GPS-94, we reported that relatively few service failures had occurred since IOC (December 1993), and that most of those had been Block I satellites.[5] Since June 1994, we have detected no major service failures (as of August 1995).

Prior to GPS becoming an operational system, integrity concerns centered around the expectations of catastrophic clock failures and their effect on the navigation solution. At least to date, the satellite clock has not been a significant failure mode. We believe this lack of clock failures is due primarily to the Air Force Space Command operational practice of anticipating a clock failure based upon ion beam

tube current measurements, and switching the clock prior to a failure.

Service failures experienced to date fall into three general categories:

- 1) Instantaneous phase jumps due to clock register hits (Block I satellites only)
- 2) Instantaneous phase jumps, cause not known (Block II satellites)
- 3) Slow orbit error growth over several days (OCS Kalman filter)

The first failure type has been catastrophic from a user perspective since Block I satellites were first launched. The last Block I satellite (SVN10/PRN12) is at the end of its operational life, so these failures will not plague users for much longer. The second failure type is unique to Block II satellites, but its behavior is similar to the Block I clock register hit in that it instantaneously induces a phase jump. It is different from the Block I failures in that no error observed to date has exceeded approximately 200 meters. The third failure type has occurred only once, in the spring of 1993. This failure was markedly different than the first two types, because it originated with the Master Control Station (MCS) Kalman filter. Problems within the MCS caused partitions within the filter to diverge, which led gradually to erroneous uploads over a week's time. Although the MCS considered this to be a catastrophic failure, most civil users were not sensitive to the up to 70 meter range errors the failure induced. Modifications to system software have since removed that particular failure mechanism. A new system capability, the L-Band State of Health system, also supports very quick detection of Kalman filter estimate divergence using monitor station ground truths.[6]

One other type of service failure requires mention here. Over the past year, it was observed that receivers sometimes lose lock on Block II satellites, for between 6 and 24 seconds. This problem is due to a satellite processor idiosyncrasy that sometimes causes the satellite to transmit non-standard code during upload. During non-standard code transmission, the user is unable to track the satellite. This problem appears to occur about every third upload, so the problem will occur three times per day somewhere around the globe. Since no range errors are experienced by the user during a non-standard code event, this service failure is considered an impact on availability, not reliability.

4.3 Positioning Accuracy

Positioning accuracy for stand-alone SPS users has followed some interesting trends over the past few years. We

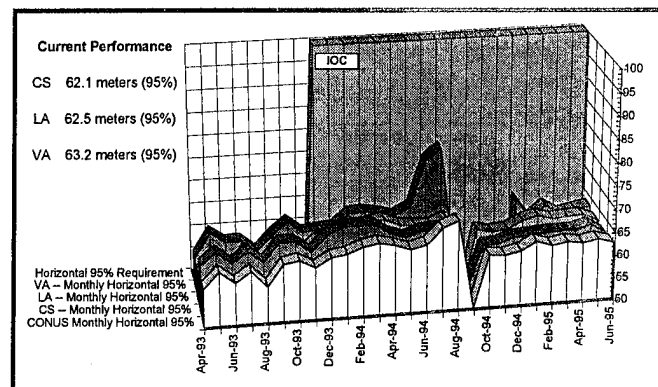


Figure 2. GPS SPS Horizontal Error Trends

show the predictable horizontal error trend since April 1993 in Figure 2. When we first began our monitoring program, GPS was providing a civil horizontal predictable error of between 55 and 60 meters (95%), and a civil vertical predictable error of approximately 80 meters (95%). These errors gradually grew over the next 15 months, until they were at 70 meters (horizontal) and 105 meters (vertical). This slight upward trend was due to Block I satellites without Selective Availability (SA) gradually leaving the constellation, and Block II satellites with SA filling the constellation. Then in September 1994, SA was turned off for almost a week. This served to skew the error statistics downward. The next month, October, showed the error statistics had decreased to 63 meters (horizontal) and 102 meters (vertical), values at which the constellation has since seemed to have stabilized for the CONUS. We have no explanation for the slight reduction in error after September 1994.

The worst position errors we have observed since April 1993 (without a service failure or anomalous signal interference) occurred on 13 January 1995, at the Colorado Springs monitor station. On this day several satellites had been removed temporarily from service for maintenance. For approximately 30 minutes, the position solution provided a PDOP in excess of 9, horizontal errors exceeding 450 meters, and vertical errors exceeding 300 meters. We mention this occurrence only to highlight the fact that behavior such as this is very rare. GPS position errors are relatively well behaved and seldom even approach their specified 99.99% values as defined in Table 1. Typically, 99.99% horizontal error is on the order of 185 meters and 99.99% vertical error is on the order of 250 meters.

5. DIFFERENT PERSPECTIVES ON GPS PERFORMANCE

An examination of different perspectives concerning GPS performance is a lengthy task if it is to be thoroughly accomplished. Our objective in this paper is much more lim-

ited. The following discussion serves only to identify the differences that exist between the service provider and the user community, and within the user community itself. Over the next few years, we believe that a mechanism will come into being to bring the diversity represented by these different perspectives into a consensus on the future of satellite navigation. Our purpose in this paper is to begin the dialogue.

It is a truism that GPS performance is in the eye of the beholder, the user of the service. The widespread appeal that is GPS' strength also makes it difficult to define performance parameters in a way that ties all users to a common set of requirements. Another difficulty is a dichotomy of culture between the military operators of a satellite control system and the civil users of the resulting signal.

So, what is the user's perspective on GPS performance? The real question should be, which user? Each user group has a separate set of needs, usage priorities and cultural characteristics. For example, a surveyor is not going to have a lot in common with an aircraft avionics integrator other than the fact that they both make use GPS. This situation creates a "Tower of Babel" effect that makes the task of communicating requirements to policy makers very difficult.

The service provider, on the other hand, has a different set of problems. As we mentioned before, GPS SPS performance standards are generic in nature. The DoD has had to reconcile the needs of military and civil users for a positioning/navigation/timing service with the very different requirements for flying a complex satellite constellation. We also need to keep in mind that the system was originally built as a military force enhancement system, so its performance parameters are defined in terms of the system's ability to support military objectives. The SPS performance standards are a result of a best compromise between these varying points of view, and the need to serve the civil community.

In this paper, we will examine four different alternative GPS behaviors that have a direct bearing on three different user groups: surveyors, differential users and time transfer users. The four behaviors are:

- Individual Satellite Availability
- Self-Surveying
- Range Rate and Range Acceleration Error
- Common-View Time Transfer

As we discuss each behavior, we examine the implications of that particular behavior on the three user groups defined above.

5.1 Satellite Availability

Most users are content to know when they have sufficient satellites to support their navigation solution. Some user groups however deal with individual satellites. Common-view time transfer users are the best example of such a user group. Other user groups concern themselves with individual satellite availability patterns to assure themselves that instantaneous coverage for an area of interest will be available. An example of such a user group are aviation users, particularly augmented service users performing critical maneuvers such as precision approach.

We track individual satellite availability from the GPS PAN. However, we are limited to CONUS coverage. So, our current methodology is to gather Air Force Space Command notices of satellite outages (NANUs), and check them as best we can with our CONUS coverage. Based upon our assessment, Air Force Space Command on average publishes outage times that are 20 minutes in excess of the actual outage time. The results of our complete analysis since 1 July 1994 are provided in Figure 3.

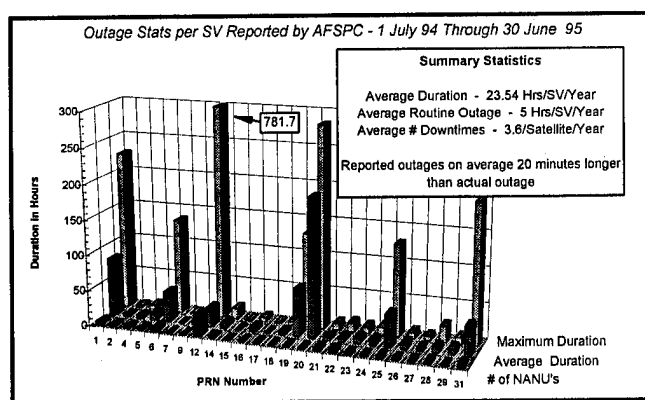


Figure 3. Individual Satellite Availability

In general, most satellites experience very little downtime on a yearly basis. If we discount the Block I satellite and the five Block II satellites that clearly had some sort of problem, the constellation averaged approximately 5 hours of downtime per satellite over the year we examined. This translates into an average satellite availability of 99.94%. The five Block II satellites that experienced significant downtime averaged 288 hours of downtime apiece, for an average satellite availability of 96.7%. The average satellite availability across all but the Block I satellite is 98.8%. These downtime-per-satellite values are particularly impor-

tant to aviation users of differential services, since their availability requirements are extremely stringent.

5.2 Self-Surveying

Surveyors are typically interested in establishing a very precise baseline relative to a benchmark that has already been surveyed in "absolute" coordinates. These users rely upon carrier aiding and differential corrections to provide them with the utmost accuracy and consistency in their surveys. Many users however require precise "absolute" knowledge of their coordinates but do not wish to invest in a professional survey. What kind of performance can such a user expect, particularly if the user is standalone without the benefit of differential corrections? We examined this question over the past year and found an interesting answer.

Our first step was to evaluate self-survey error as a function of increasing averaging time. We accomplished our self-surveys relative to Defense Mapping Agency (DMA) benchmarks. Figure 4 shows an example result for March 1995, of self-survey accuracy as a function of increasing averaging time. The minimum, maximum and average lines indicate values for each minute increase in averaging time across all 30 days of the evaluation period.

As shown in Figure 4, performance can be expected to vary over any given 24 hour interval. After a four hour averaging period, a user can expect to see between one and nine meter horizontal error in the user's self survey. After a 24 hour averaging period, a user can expect between 0.5 and four meter error in the self-survey. For an average 24 hour period, our analysis indicates that a user should be able to achieve five meter horizontal accuracy after four hours, and approach two meter horizontal accuracy after 14 to 24 hours. These results were consistent across all three of our monitor stations. Obviously, this indicates that the longer the averaging period (even beyond 24 hours), the more confidence the user will have in the resulting survey.

The second step in our self-survey analysis was to assess long-term stability of a 24 hour averaging period. As shown in Figure 5, we did get some variation over the year we evaluated our self-survey performance. The maximum horizontal error over 24 hours was 11 meters, but we only saw two days over the year where the error was above six meters. The horizontal Root-Mean-Square (RMS) was 2.3 meters, in keeping with the results shown in Figure 4. Our average East and North errors were both 0.5 meters, indicating a satisfactory level of consistency with the survey accomplished by DMA for our monitor station benchmark.

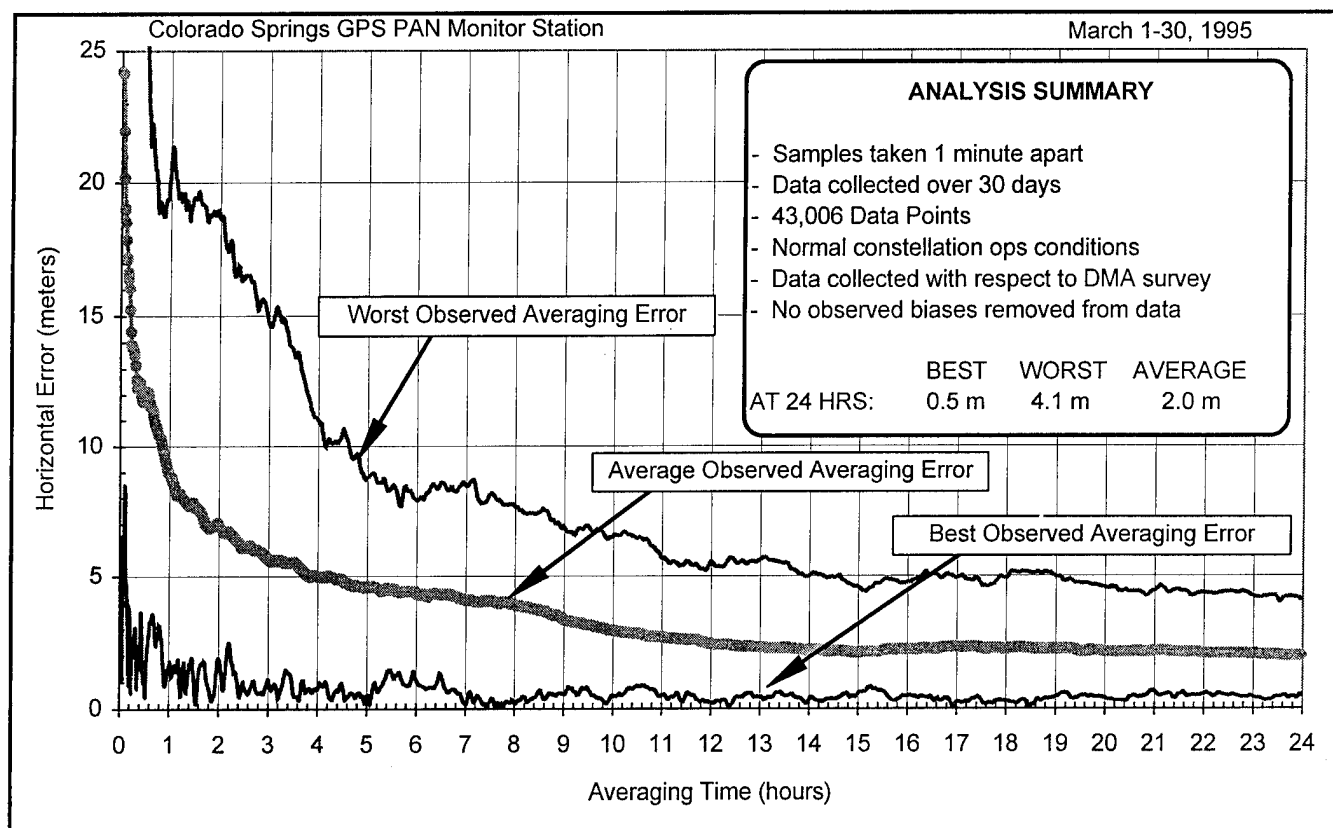


Figure 4. Self-Survey Error as Function of Averaging Time

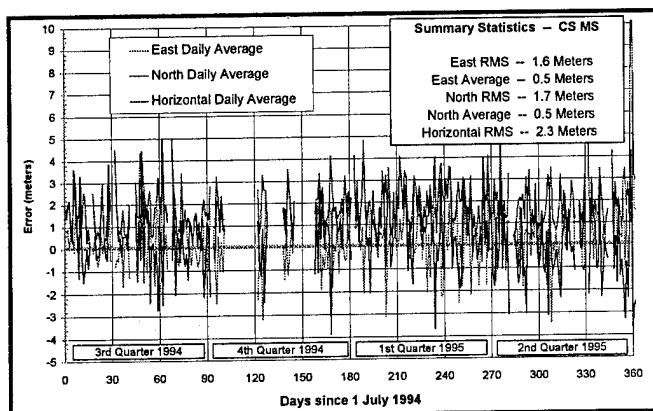


Figure 5. 24-Hour Self-Survey Errors - 1 July 94 to 30 June 95

5.3 Range Domain Error Behavior

The objective in measuring range domain performance is to isolate to the greatest degree possible the errors associated with the signal-in-space. This is necessary due to the types of statistical measures required by users of range domain parameters, primarily differential and time transfer users. Differential users require very precise range rate values in order to properly project differential corrections to the next update, and an accurate assessment of range acceleration error in order to develop differential error statistics. Time transfer users require very accurate measures of range residuals in order to generate common-view measurements. We have examined range domain behavior since April 1994. We currently use a single frequency receiver, a rubidium frequency standard, an ensemble time algorithm and our own ionosphere correction model to maintain close monitor station synchronization with the GPS time scale. We will discuss time management in more detail in Section 5.4. In this section we focus on the range domain measurements that are output from our monitor stations.

Ionosphere-corrected range error behavior across the constellation is consistent over time. The range error standard deviation for those satellites with SA is approximately 24 meters, with maximum values seldom exceeding 100 meters. Satellites without SA (PRNs 12, 15 and 28) provide range error standard deviations of between 2.5 and 3.5 meters, with maximum values usually less than 15 meters.

Range rate error behavior has changed somewhat over the past year. Range rate standard deviations for those satellites with SA were approximately 0.22 to 0.23 meters/second in April of 1994. As of June 1994, the standard deviation dropped to 0.19 meters/second. We examined maximum values very closely over the past year, due to their importance to differential applications. Maximum values, as shown in Figure 6, are generally below one me-

ter/second. Values can be as high as two meters/second on rare occasions.

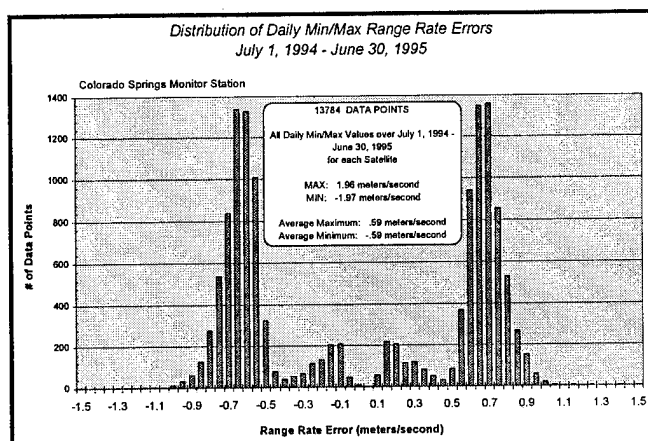


Figure 6. Range Rate Error Min/Max Values

Range acceleration error behavior has also shown a slight reduction in its statistical behavior. Range acceleration error 95% values for those satellites with SA were approximately 8 millimeters/second² in April of 1994. As of June 1994, the 95% value dropped to 5.4 millimeters/second². Range acceleration error is somewhat more difficult to quantify when we examine the outer boundaries of its behavior, due to significant levels of noise in the measurement. We examined maximum values very closely over the past year, due to their importance to differential applications. Maximum values, as shown in Figure 7, are on average 12 millimeters/second². We have measured values as high as 30 millimeters/second², but we believe these values to be the product largely of noise. In examining Figure 7, note the cutoff of values at approximately 20 millimeters/second². This cutoff is due to a mask angle we have placed on range acceleration error measurements of 20 degrees. This tells us that the majority of these large range acceleration error values occur below a 20 degree elevation angle, which leads us to conclude that residual noise causes these excursions. We believe that the "true" signal-in-space

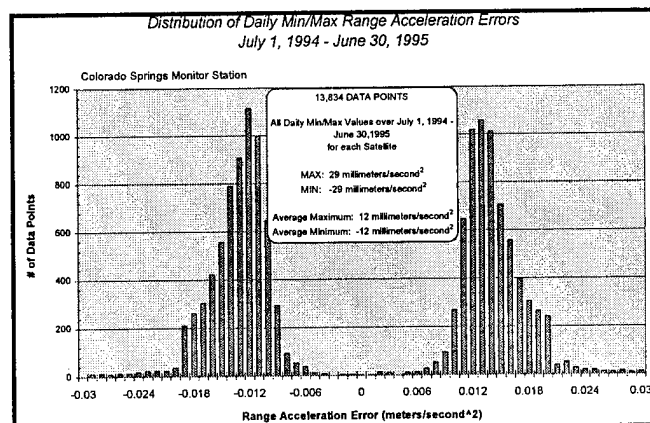


Figure 7. Range Acceleration Error Min/Max Values

maximum value falls in the 15 to 17 millimeter/second² range.

5.4 Common-View Time Transfer

Common-view time transfer is becoming an increasingly important capability provided by GPS. Once the province primarily of laboratories with predominantly scientific applications, common-view time transfer is now being used by power companies, communications networks and differential networks to name just a few user groups. Although users such as power companies and communications networks have not yet pushed the envelope of GPS time transfer capabilities, these users will do so as phase and frequency synchronization requirements become more stringent. Differential networks on the other hand are stressing GPS time transfer capabilities. Since one meter equates to 3.3356 nanoseconds in time, it is easy to see that synchronization of time across several differential stations is essential to the generation of consistent range corrections.

Our objective in time scale management was to tie our monitor stations as closely as possible to GPS time. This was important for two reasons. First we wanted to measure "true" range error behavior, with minimal time scale aliasing of the measurement. Second, we wanted to investigate how closely a wide area differential system can tie itself to GPS time. Local differential systems can manage their timescales with significant bias and bias rates with respect to GPS time, because their message structures can accommodate large bias values. The current Wide Area Augmentation System (WAAS) can not tolerate such biases.

In our pursuit of common-view time difference measurements, we did experience some operational problems. Our primary problem was the effect of residual propagation path errors on our common-view time difference algorithm. We solved this problem by restricting our measurements to those satellites with a common elevation angle above 20 degrees. As can be seen in Figure 8, this approach did impose limits on common view visibility even over a relatively short baseline between Colorado Springs and Vienna, but the outages were of no consequence since they were short enough to coast through with our frequency standards. Our other major problem was synchronizing measurement time tags, and assuring ourselves that each measurement was within the ± 0.5 second resolution provided by our receivers. This problem occurred primarily when a monitor station experienced significant interference levels, which disrupted our time ensemble algorithm.

Figure 8 provides an example of a daily plot of time differences between two of our monitor stations. As can be seen, the average across all satellites in view is generally within \pm

5 nanoseconds, with a few excursions as large as 16 nanoseconds.

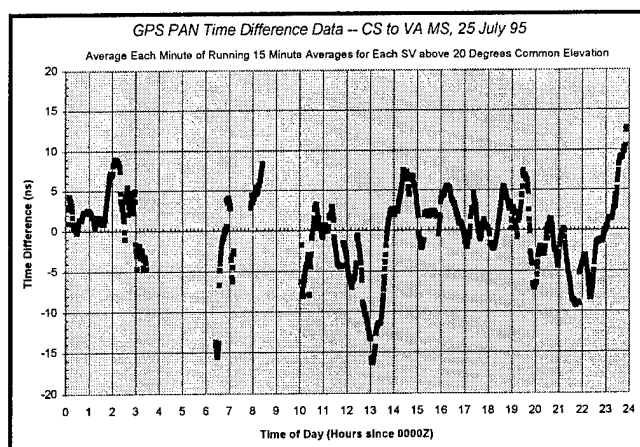


Figure 8. Time Difference Values over a Typical Day

Figure 9 provides a summary of our initial time transfer experiments to date. Time transfers between Colorado Springs and Vienna were the most consistent, with a minimal bias between the two and excellent consistency with a 5 nanosecond standard deviation. Time transfer between Los Angeles and the other two monitor stations did not fair quite so well. We believe the problem was due to extreme thermal variations in the Los Angeles monitor station. We can isolate the problem to the Los Angeles monitor station because of the consistency of results between Los Angeles and the other two sites.

Common-view time transfer users and surveyors are very sensitive to orbit errors. We have made no attempt to date to isolate clock and orbit errors in our range domain measurements. Our common-view time difference measurements however would reflect any obvious orbit problems as they are transmitted via each satellite's navigation message, since we do not make use of "precise" ephemeris in our monitor stations. The fact that our time difference performance was as good as represented by our analysis is an indirect indication that users are currently receiving quality orbit data via the navigation message.

7. CONCLUSION

In this paper we have described a number of GPS performance characteristics and trends, within a context of how GPS performance is viewed from a number of perspectives. We can draw several conclusions from our data:

- From a service provider's point of view, GPS is maturing and providing a stable, consistent service

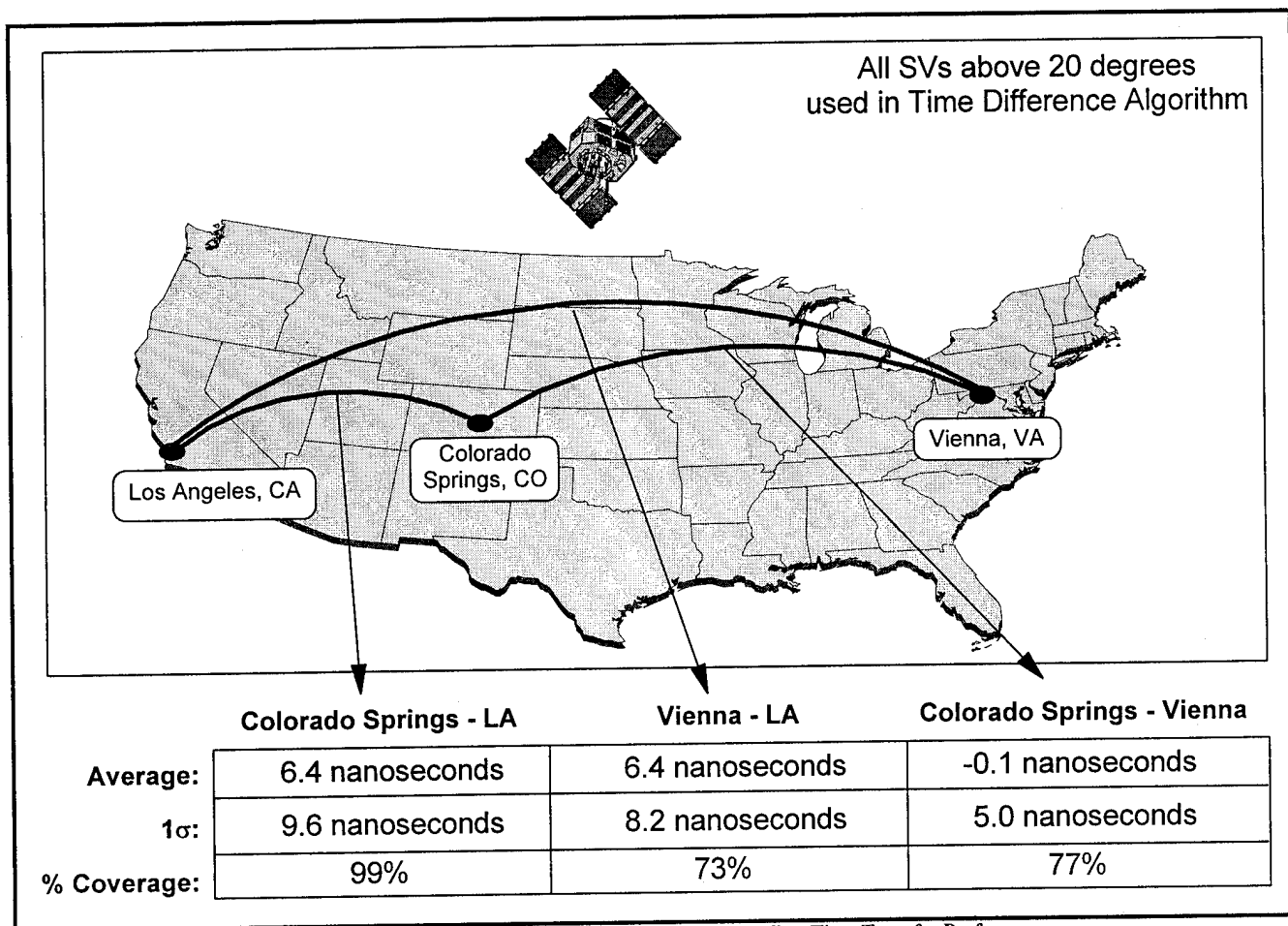


Figure 9. Preliminary GPS PAN Assessment of Common-View Time Transfer Performance

- GPS performance is in the eye of the beholder -- what is promised by the service provider is not necessarily what the user wants
- Understanding each major user group's perspective is essential to a successful assessment of GPS adequacy to support that user group's needs

The DoD is doing an exemplary job of providing a satellite navigation service. But GPS or its successor has the promise of providing more than what we currently specify as the Standard Positioning Service. Keeping in mind a necessary balance between security interests, economics, safety and user interests, it is time for the user community to develop a common grounds for understanding its requirements. This common ground can help to define the nature of satellite navigation for a long time to come.

REFERENCES

- [1] As documented in *GPS Performance Analysis Report, Volumes 1-10*, published quarterly for the FAA.
- [2] *GPS SPS Signal Specification*, 2nd Edition, June 2, 1995, Annex A.
- [3] *GPS SPS Signal Specification*, 2nd Edition, June 2, 1995, Annex C.
- [4] *A Summary of GPS SPS Performance as Observed by the FAA's GPS Performance Analysis Network*, Proceedings of ION GPS-94, September 20-23, 1994, pp. 1117-1125.
- [5] Johns, J.C. and Conley, Rob., *A Summary of GPS SPS Performance as Observed by the FAA's GPS Performance Analysis Network*, Proceedings of ION GPS-94, September 20-23, 1994, pg. 1121.
- [6] Brown, K. Jr., Chien, M.K., Mathon, W., Hutsell, S., and Shank, C., *L-Band Anomaly Detection in GPS*, Proceedings of the 51st Annual Meeting of the ION, June 5-7, 1994, pp. 107-117.

Practical Measurements of Radio Frequency Interference to GPS Receivers and an Assessment of Interference Levels by Flight Trials in the European Regions

Paul Nisner
National Air Traffic Services

John Owen
Defence Research Agency

BIOGRAPHIES

Paul Nisner is a Principal Engineer employed by the United Kingdom Civil Aviation Authority (CAA) and is responsible for the R&D projects relating to operational applications of the Global Navigation Satellite System (GNSS). He won an industrial university sponsorship from Marconi Avionic Systems graduating with honours in 1976. He is a member of the Royal Institute of Navigation and a Chartered Engineer. Mr. Nisner has represented his country on various ICAO groups addressing GNSS issues.

John Owen is technical research manager for navigation systems, investigating GPS for the United Kingdoms Defence Research Agency (DRA). He has an Honours degree in Electrical Engineering and is a Chartered Engineer. He is the UK Technical representative to the NATO GPS Technical Support and Working Group and has also acted as UK adviser to various ICAO groups addressing GNSS issues. John is the author of STANAG 4392 - Data Interchange Format for Navstar GPS (PPS Differential).

ABSTRACT

Augmented GPS satisfies the accuracy requirements of the Required Navigation Performance (RNP), for many of the phases of flight, particularly en-route navigation. However it has been previously shown (Ref 1) that Radio Frequency Interference (RFI) poses a significant threat to GPS and all other GNSS currently under consideration, requiring practical spectrum management policy issues to be addressed. This paper describes the work which was undertaken to determine the effects of RFI on GPS and measure the spectrum content within Europe. The work was carried out by the Defence Research Agency (DRA) for the CAAs National Air Traffic Services (NATS),

as part of a study of global navigation satellite systems (GNSS).

INTRODUCTION

There are increasing demands for the use of GNSS to provide onboard aircraft guidance, including critical functions such as precision approach. It is therefore vital that an analysis of susceptibility to RFI and a measurement of the electromagnetic environment is performed as is common with other aids such as ILS, DME etc. This is especially important following reports of problems with GPS signal reception due to interference. Some examples of these reports are:

- (a) in Germany fixed point-to-point military communications links and radar systems have been identified as a significant problem;
- (b) the United States and NATO Navies have reported problems in the central Mediterranean, near Venice, and in Brindisi near the Straits of Otranto which is thought to be due to Italian communication links;
- (c) the Norwegian hydrographic services have identified Stavanger harbour region as a problem area for GPS reception;
- (d) in Switzerland, flight trials at Lugano Airport had to be re-arranged due to interference from unknown sources but believed to be from TV transmitters; and
- (e) GPS reception problems have been reported in the Boston area, believed to be due to interference from TV transmitters.

Due to these incidents the UK CAA decided to investigate both the theoretical and practical magnitude of the problem. Following some initial results (indicated below) further equipment tests, specifically on equipment certified to a TSO standard

were performed. In addition a survey of potential interfering sources was undertaken and practical measurements of the interference environment of some areas of Europe was performed.

INITIAL GPS SUSCEPTIBILITY FROM RFI

Previous work carried out by Johanesen Ref 1, Owen Ref 2, identified the potential vulnerability of GPS to RFI. The CAA commissioned Booz-Allen and Hamilton to investigate this further. Theoretical work in this study by Moelker Ref 3 showed that different signal processing technologies would have corresponding different levels of immunity to RFI. This was confirmed to some extent by Stevens Ref 4 performing practical laboratory and flight trials on five GPS receivers representing five different technologies examined by Moelker. These receiver technologies are identified in Table 1.

Table 1: GPS Receiver Technologies Tested

System	GPS Technology Description
GPS No 1	Standard Correlator; Carrier Phase Tracking; Single Level ADC; Coherent System; Dual Frequency Capability.
GPS No 2	Standard Correlator; Single Level ADC; Non-Coherent System; Designed for General Aviation.
GPS No 3	Standard Correlator; Single Level ADC; Non-Coherent System; DGPS Reference Station.
GPS No 4	Narrow Correlator; Multi-Level ADC, Non-Coherent System, In-Built RFI Detector.
GPS No 5	Standard Correlator; Multi-Level ADC; Coherent System.

INITIAL LABORATORY TRIALS

The laboratory trials suggested that interference of 1 Watt (EIRP) being radiated from an isotropic antenna could interfere with GPS with ranges of up to 180 km depending on the technology used. The results were as shown in table 2.

To study this in an operational environment further trials were performed using a medium size commercial jet aircraft, a British Aircraft Corporation One-Eleven (BAC 1-11). This aircraft is similar in size and construction to the McDonald Douglas DC-9. The GPS antennas were installed on top of the fuselage, towards the front and along the aircraft's

centre line. The aircraft was flown in both orbit patterns and ILS 3° glide path approach situations.

A summary of these results are presented in Table 3. The apparent anomalies are believed to be due to the varying geometry of the aircraft GPS antennas in relation to the ground transmitter.

In addition to the receivers losing lock, it was also found possible to cause positional errors of many 10's of metres in the calculated navigation solution for two of the receivers. However the magnitude of these errors was not constant and varied depending on the frequency of the interference and the space vehicles (SV) being used for the navigation solution.

Table 2: Theoretical Range of Interferer with 1 W (EIRP)

GPS Under Test	Theoretical Range of 1 W Interference	
	6 dB CNO	Loss of Lock
GPS No 1	275 km	183 km
GPS No 2	69 km	55 km
GPS No 3	44 km	20 km
GPS No 4	39 km	11 km
GPS No 5	54 km	10 km

Table 3: Calculated Loss of Lock from a 1 W (EIRP) Interference Source for the Various Tested Operational Scenarios.

TEST INFO	GPS 1	GPS 2	GPS 4	GPS 5
1000ft	20	44	24	20
5000ft	7.7	14	no meas	no meas
50 nm 8000ft	9.7	27	12	14
ILS 1	2.7	6.7	5.5	14

"no meas" means no measurements made.

Following these initial results, the CAA commissioned work to further assess receiver characteristics, list and measure the RFI levels throughout Europe.

GPS SENSOR VULNERABILITY

As shown previously, there are numerous receiver designs each with its own particular characteristics, however a generic analysis can be made by considering the four primary components of the receiver:

- (1) The antenna;
- (2) RF and IF rejection;
- (3) Code and Carrier Signal Processing;
- (4) Demodulation of the navigation message.

AIRCRAFT ANTENNA

The relative attenuation provided by the aircraft antenna against ground interference sources is significantly less than the attenuation due to distance (r^2), which is approximately 95 dB for the first kilometre. An aircraft GPS antenna is designed to achieve optimum signal reception over as much of the upper hemisphere as possible; however, as the GPS signal is circularly polarised, a compromise is needed between reception performance for low elevation satellites and a low profile to maintain efficient aerodynamic performance. It is important to maintain antenna gain at low elevation levels to ensure satellite near the horizon can be acquired and tracked to provide optimum satellite visibility for navigation and RAIM.

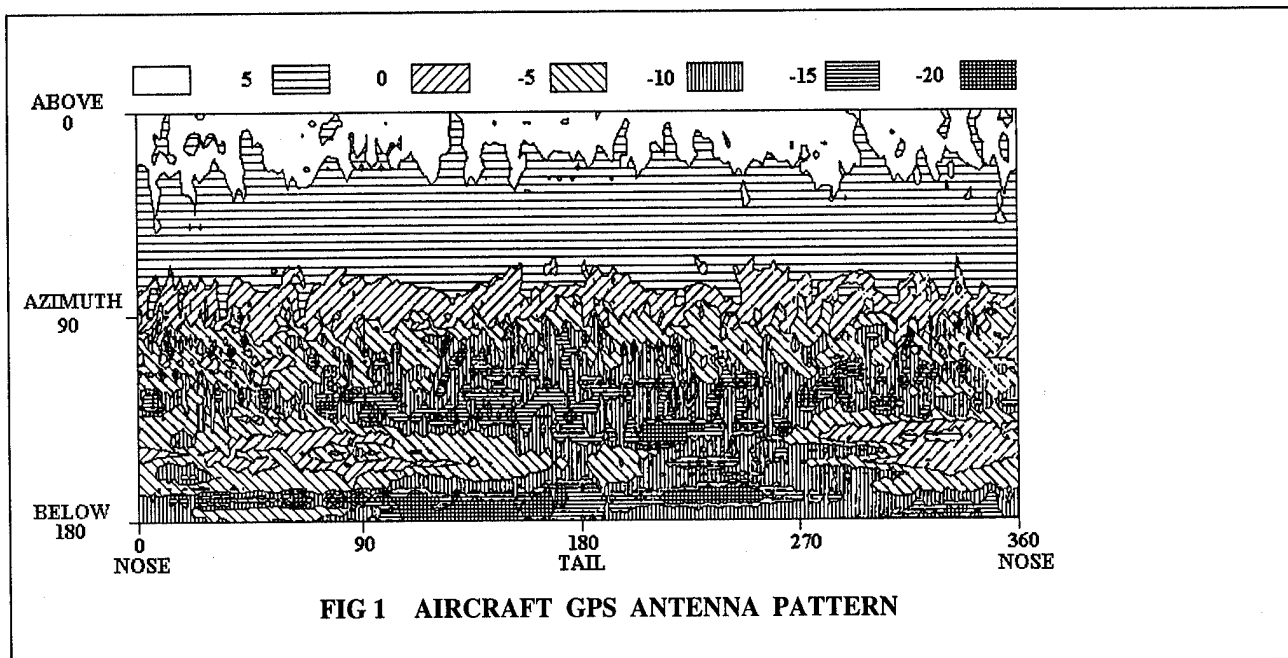
A typical aircraft (BAC 1-11) GPS antenna radiation pattern is illustrated in Fig 1. To maintain lock with the aircraft banked by up to 40° during turns, the antenna gain must not fall below approximately -10

dBic. As is illustrated by Fig 1, the gain below the azimuth plane is typically very broken but does not fall significantly below -10 dBic until elevation angles exceed -30°. Roll angles above 30° may cause obscuration of the satellite by the aircraft wings reducing the gain to <-20 dBi over small sectors. Further problems result from the rapid variation in gain of the radiation pattern with a resultant high rate of phase change which is detrimental to carrier tracking. It is also observed that the gain at the azimuth plane is approximately -5 dB falling to typically -10 to -15 dB under the aircraft, although several areas of relatively high gain, -5 dB are present. These results indicate that very little protection against ground interference is provided by the airframe.

RF AND IF REGULATION

The post correlation noise density is generated by convolving the interference (in terms of its noise density) with the spectral density of the C/A code. However the receiver's down converter and A/D converter cause near band interference to be aliased into the detection filter's response. A narrow band high order filter is required to reject near band interference, and the RTCA MOPS (Ref 5) specifies a response defined in Fig 2. Antenna bandwidth is usually very wide, perhaps 100 MHz or more for a single frequency L1 antenna and therefore does not provide significant attenuation to near band signals.

High power emitters, radars and broadcast transmitters, can drive the low noise amplifier in the receiver's front end into a non linear region. The RTCA MOPS requires a 1 dB compression point that



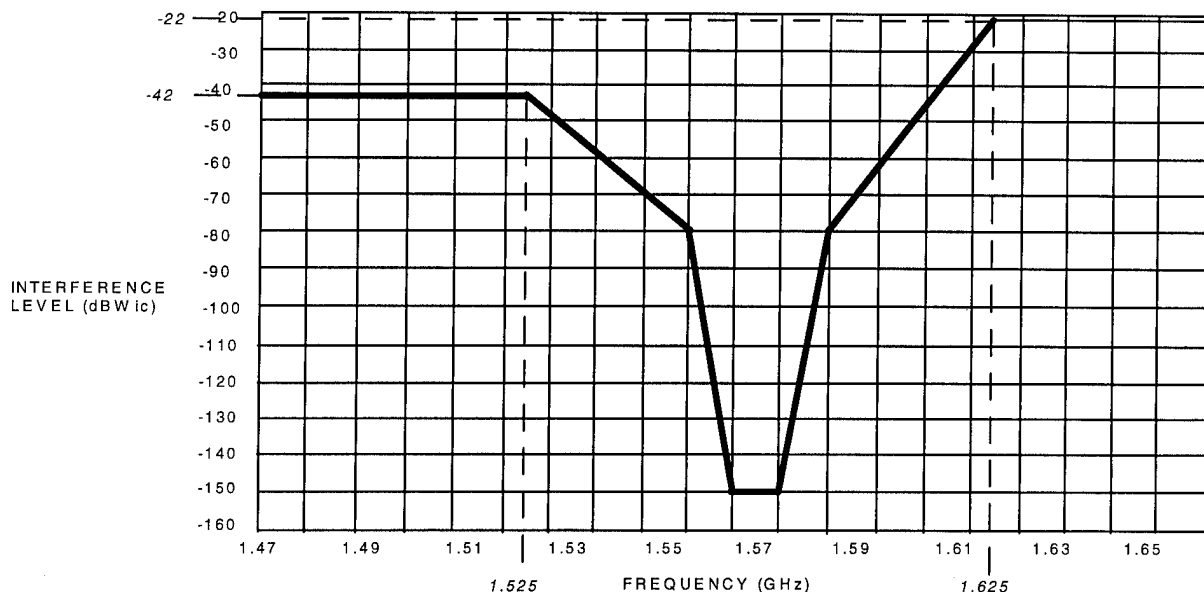


FIG 2 MOPS INTERFERENCE REJECTION CRITERIA

is approximately -20 dBW high near-band and -40 dBW low near-band. A burn out limit of 1w continuous input power is specified.

Interference outside the GPS band will be attenuated by the filter; however, near-band interference or very strong out of band interference will reach the correlator. The high rejection in the near band frequencies is required to protect the receiver from SATCOM interference in the band 1625 to 1659 MHz that may be operating on the same aircraft. Whatever the filter response, no protection can be provided against wide band noise generated by frequency synthesis in collocated transmission systems if it falls within the receiver's pass-band. The only jamming resistance against such noise is provided by the GPS processing gain.

GPS CODE AND CARRIER SIGNAL PROCESSING

Satellite signal power is -20 dB, compared with the receiver's noise floor of -137 dBW in the signal bandwidth. Only after the spread spectrum modulation produced by the C/A code is removed by the correlator is a positive S/N ratio is produced. Assuming a typical received signal level of -160 dBW from the antenna and a noise floor of -202.5 dBW/Hz, the theoretical maximum signal level of 42.5 dBHz CNo is available in the carrier tracking loop. RTCA have defined receiver levels of 32 dBHz as a minimum requirement for approach and landing systems, 29 dBHz to decode the navigation and WAAS data and a minimum of 22 dBHz for code measurements.

These levels allow for a maximum increase in the noise level of 10.5 dB before significant degradation is observed in the receivers performance. If the noise is of the same spectral density as the receiver's thermal noise this is equivalent to a power of -129.5 dBW in the signal bandwidth. However several interference sources contain spectral components with significant peaks. The CW characteristics of these signals correlate with the C/A code significantly increasing the effect of the interference. It is suggested by RTCA that power levels as low as -150 dBW are detrimental to GPS receiver performance.

MEASURED RECEIVER PERFORMANCE

The interference resistance of several receivers was tested using a high performance GPS signal simulator. Power levels that generated a decrease of 1 dB and 3 dB in the reported CNo figure and loss of code tracking were recorded. Fig 3, 4 and 5 illustrates the results from three units. Fig 3 indicates a C-129 Commercial aviation receiver of a type installed on a British Airways Boeing 767 undergoing trials at Heathrow airport. The unit demonstrates performance close to the MOPS and TSO-129 requirement, and in terms of interference rejection. Fig 4 shows a general aviation C-129 approved receiver and Fig 5 shows the results from a non certified receiver using the narrow correlation technology. Such receivers are significantly degraded by a 1 Watt interference if it is in band even at ranges in excess of 30 km, a result confirmed in DRA flight trials.

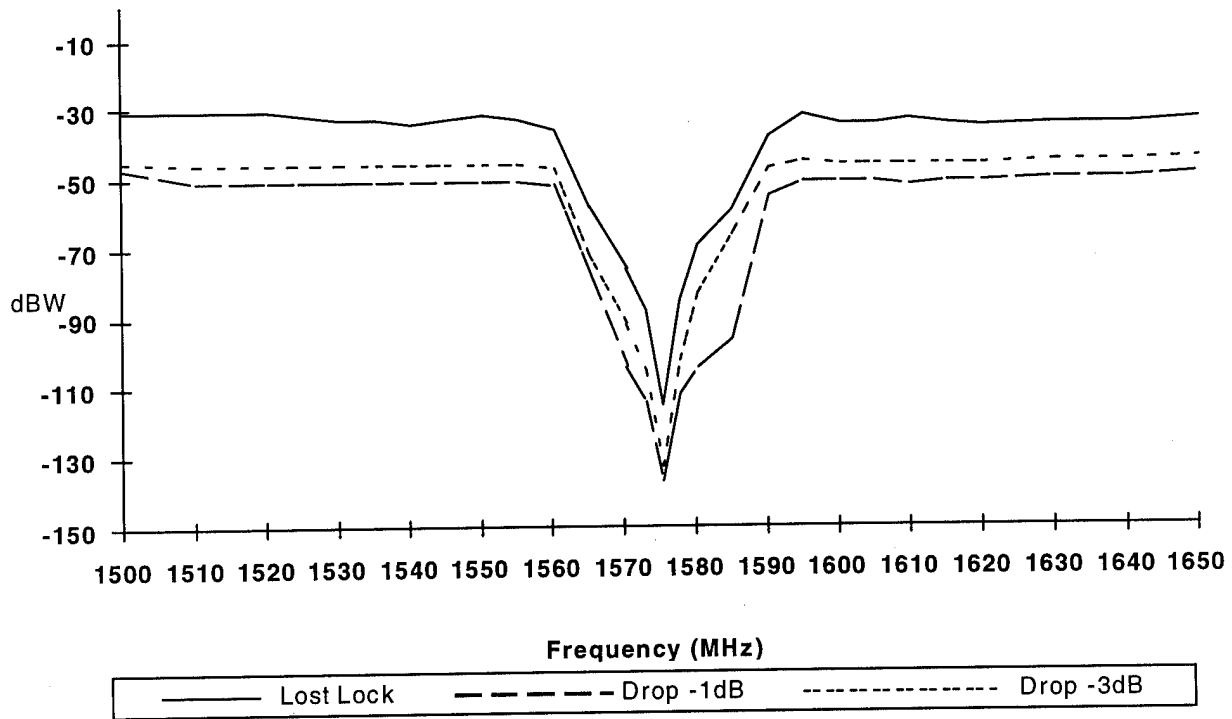


FIG 3 TSO-129 COMMERCIAL AVIATION INTERFERENCE PERFORMANCE



FIG 4 TSO C-129 GENERAL AVIATION RECEIVER TRACKING PERFORMANCE

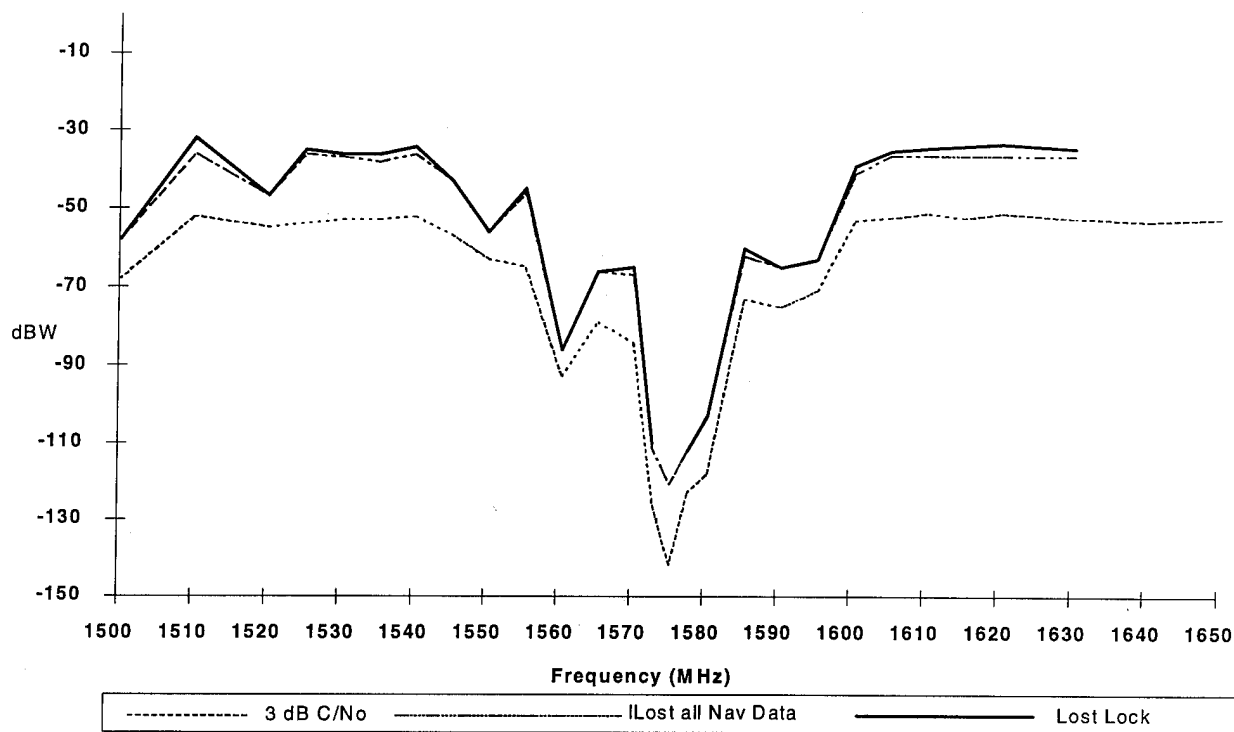


FIG 5 NARROW CORRELATOR INTERFERENCE PERFORMANCE

INTERFERENCE SURVEY

Radio frequency transmitters that were identified during the study as primary sources of interference into GNSS are indicated in Table 4. The results of the European licensed transmitter survey indicates the number of potential interference sources into GPS to be in excess of one hundred thousand; the numbers of mobile transmitters in one state alone are in excess of 30000. Such transmitters are difficult to characterise but Johannesen shown, Ref 6, that a high probability existed of high order harmonics (11th, 13th etc) being generated. The likely cause of these harmonics was old cables and RF joints particularly the antenna to body bonding. Although the problem can be mitigated by maintenance, the costs of such corrective action may be very high.

The survey demonstrated how difficult it is to obtain data on transmitters from national authorities although an extensive list of broadcast transmitters was obtained from the International Telecommunications Union. In most countries a central institute or authority is responsible for the coordination of frequency use. However, within agreed limits, several organisations (military, aviation, police, civil etc.) may be responsible for the implementation of the national frequency plans. Provision of information may also be restricted for security reasons.

Interference from SATCOM equipment presents the largest threat to GNSS operation. Although receiver performance specifications are being established to reduce interference from Aeronautical SATCOM the advent of Mobile Satellite Systems MSS transmissions in the 1610 to 1625 MHz band will be more difficult to mitigate. Masking (filtering) the transmitted spectrum may enable GPS to operate without significant problems but it will be far more difficult and expensive to achieve the same level of rejection in a Glonass receiver. Spurious transmissions are a fundamental problem that can only be solved by reducing the harmonics generation within the transmission terminals.

The survey was confined to licensed transmitters. During the survey it became apparent that many unlicensed transmitters were operating, for example 'FLASH TV' and neighbourhood radio stations which contained spectra with high harmonic content. Due to the low satellite signal levels these broadcasts are likely to cause operational problems for GNSS. Although ITU regulations specify a level of -60 dBc or a maximum radiated power of 100 mW for spurious emissions, the enforcement of these recommendations is the prerogative of the national authorities. Similarly deliberate interference will always remain a problem, the likelihood of its occurrence is beyond the scope of this paper.

Source and Baseband Centre Frequency	Harmonic, Interference Type, licensed power level in GNSS band
Aeronautical SATCOM spurious emissions and inter modulation products	Near Band and In-Band -55 dBW/1 MHz (1 565 - 1 585 MHz & 1 602 - 1 616 MHz) otherwise /4 MHz.
MSS Transmissions and Spurious emissions. 1 610 - 1 620 MHz	Near Band and In band -70 dBW/MHz (1 574 - 1 576 MHz) -60 dBW/MHz (1 550 - 1585 MHz) rising to -10dBW/MHz at 1 610 MHz
UHF TV Broadcasting 787.21 - 788.24 MHz 524.80 - 525.48 MHz	2nd and 3rd Harmonics In Band, Desensitisation of receiver front end, burn out if close. 100 mW
U/VHF (Coms and VOR) 394, 315, 262.5 MHz, 197, 175, 143.2, 131.3, 121.1 MHz	4, 5, 6, 7, 8, 9, 10, 11, 12 & 13 th Harmonics In Band 100 mW

Table 4: Primary Sources of Interference Threat to GPS L1.

INTERFERENCE MEASUREMENTS

To investigate the interference levels present a short series of measurement flights, using a DRA BAC 1-11 was performed. A total of five flight sorties were flown on the BAC 1-11 aircraft, the first of which was a shakedown sortie to prove the receiving equipment and data logging capability. During January, four sorties were flown over two days across several European countries as shown in Fig 6. The sorties were flown at 20,000 feet (flight level 200). All the on-board GPS (GPS Type No 2, 3 & 5) receivers continued to navigate throughout the flight; however, at times, the carrier to noise ratio was degraded to 30 - 31dBHz, and if a lower altitude route had been flown, (i.e. 5000 feet, characteristic of a terminal approach pattern), the receivers would have lost satellite signals.

DISCUSSION OF MEASUREMENT RESULTS

Sortie 1

No interference was detected in the GPS L band for all logged data in the UK. The second and third harmonics of the broadcast television band lie in the GPS band. It should be noted that no second or third harmonics of these TV transmissions were detected in the GPS L band plots over the UK. However it is also notable that unexpected frequencies in this band did occur.

Sortie 2

It was noted that there were no significant areas of GPS interference was recorded during the initial leg

of the European Flight Programme. During the flight however, increased amounts of interference in the GPS/GNSS band were detected as the flight approached southern France. As the aircraft crossed the coastline above Nice in France, significant levels of interference to GNSS were detected, Fig 7.

The island of Elba to the east of Italy was also a source of interference into GPS and high levels of power occurred in the logged bands.

Although the interference does not appear at the 1575MHz GPS carrier, it is near-band and, therefore, would not be totally removed by the RF/IF filtering. Narrow correlation receivers would be potentially vulnerable to this type of interference.

Sortie 3

High levels of interference in the GNSS band were measured on this sortie, Fig 8, and show the highest values of interference recorded. The comparison with the results from the shakedown flight over the UK in Figure 9 show that there are a large number of interference sources in this area each of which could potentially cause a degradation in GPS and or GLONASS navigation performance, especially if the aircraft was at a lower altitude.

Sortie 4

The sortie again demonstrated high levels of interference in the GPS L band. Fig 10 shows the signals detected over a three minute period which indicates several transmissions appearing over a wide band from 1556MHz to 1611MHz with a potentially powerful 3MHz signal at 1580MHz.

Sortie 5

Over Germany, more interference was noted in the Aeronautical band, particularly over Stuttgart and then over the Ruhr.

Several reports of severe interference into GPS have been made from Southern Germany. The cause was a military fixed communications link operating in the 1 500 - 1 600 band. It is presumed that the link has been moved to 1558 MHz where it is far enough away from GPS not to cause a problem with a well engineered receiver.

CONCLUSIONS

Stand-alone GPS navigation, is extremely vulnerable to interference. Several areas where high levels of interference to GNSS exist in Europe were identified by a the DRA. Potential sources of interference are TV transmissions and mobile communications equipment. In this respect an allocation granted by WARC-92 for Mobile Satellite Services, MSS as a co-primary user of the frequency band 1610 - 1626.5 MHz is the most serious threat to GNSS operation.

It is therefore a recommendation arising out of this

work that experts from all States interested in the use of GNSS should participate in a co-operative manner in the ITU radiocommunications sector activities to ensure that ITU-R recommendations are established and enforced to protect GNSS. There should be world-wide encouragement to develop suitable radio system performance standards using ITU-R recommendations and other available criteria to ensure protection to GNSS.

REFERENCES

- 1 R Johanesen, Support To CAA for ICAO FANS, CAA Contract No 7D/S/457, 1988.
- 2 J Owen, A Review of the Interference and Jamming Resistance of SPS GPS Receivers for Aviation. Navigation (USA), Volume 40, Nr. 3, Fall 1993, pp 249-259.
- 3 D J Moelker, GPS Interference Evaluation Assessments, Final Report, Delft University of Technology, 8th November 1994.
- 4 E G Stevens, Practical Measurements of Interference to GPS Receivers in Laboratory and Aircraft Environments, ISPA 95, Braunschweig, 21-24, February 1995.

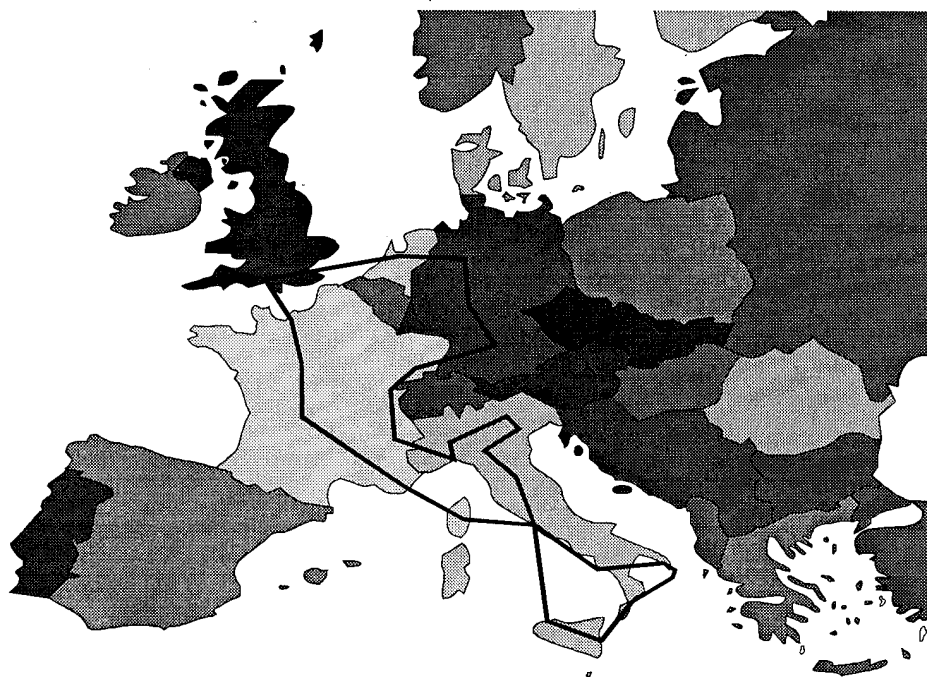
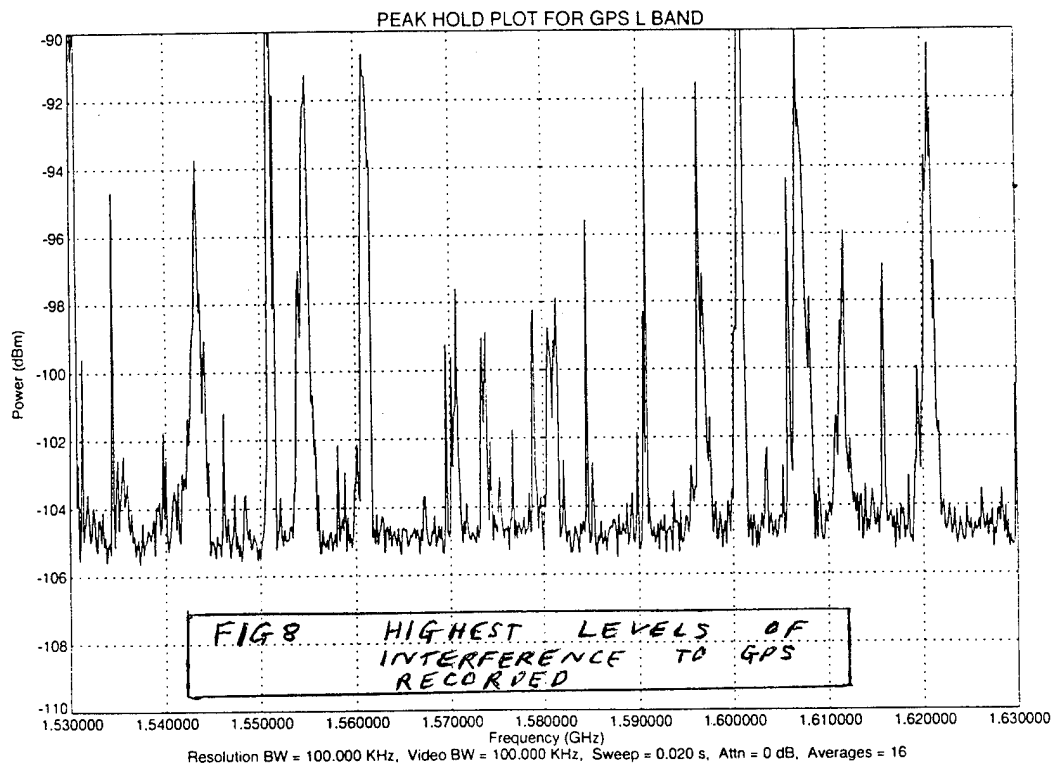
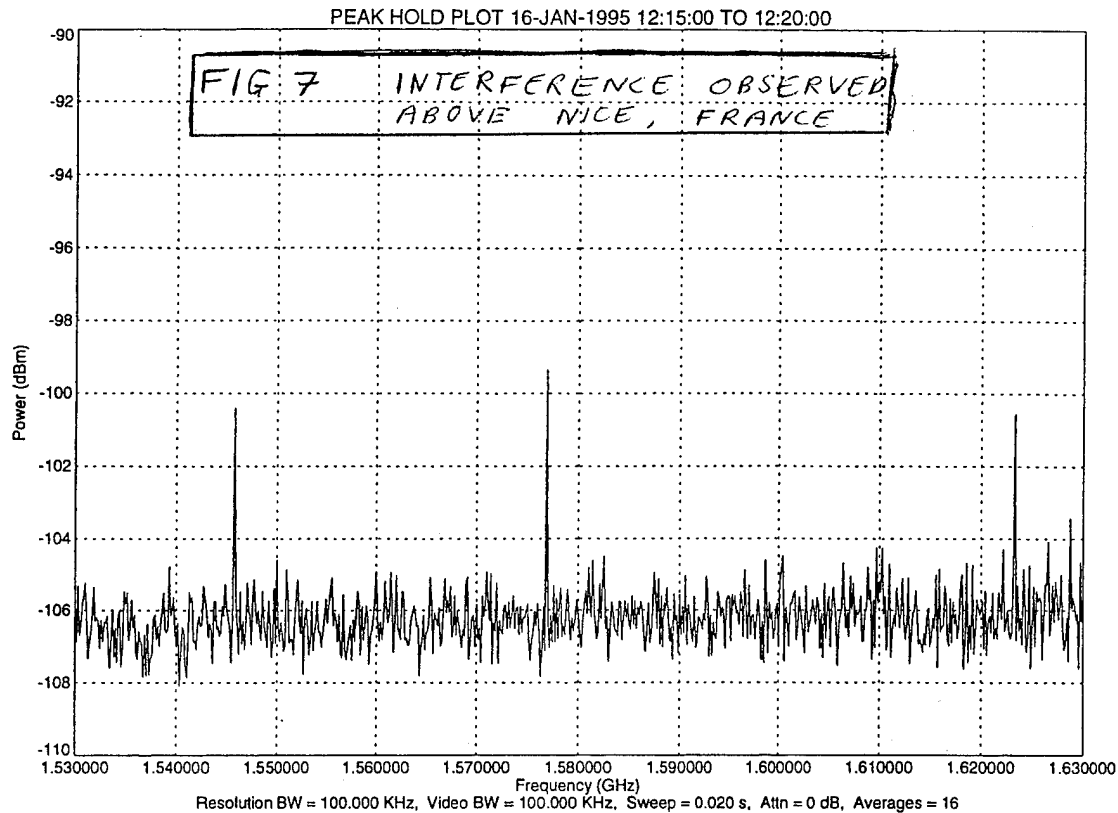
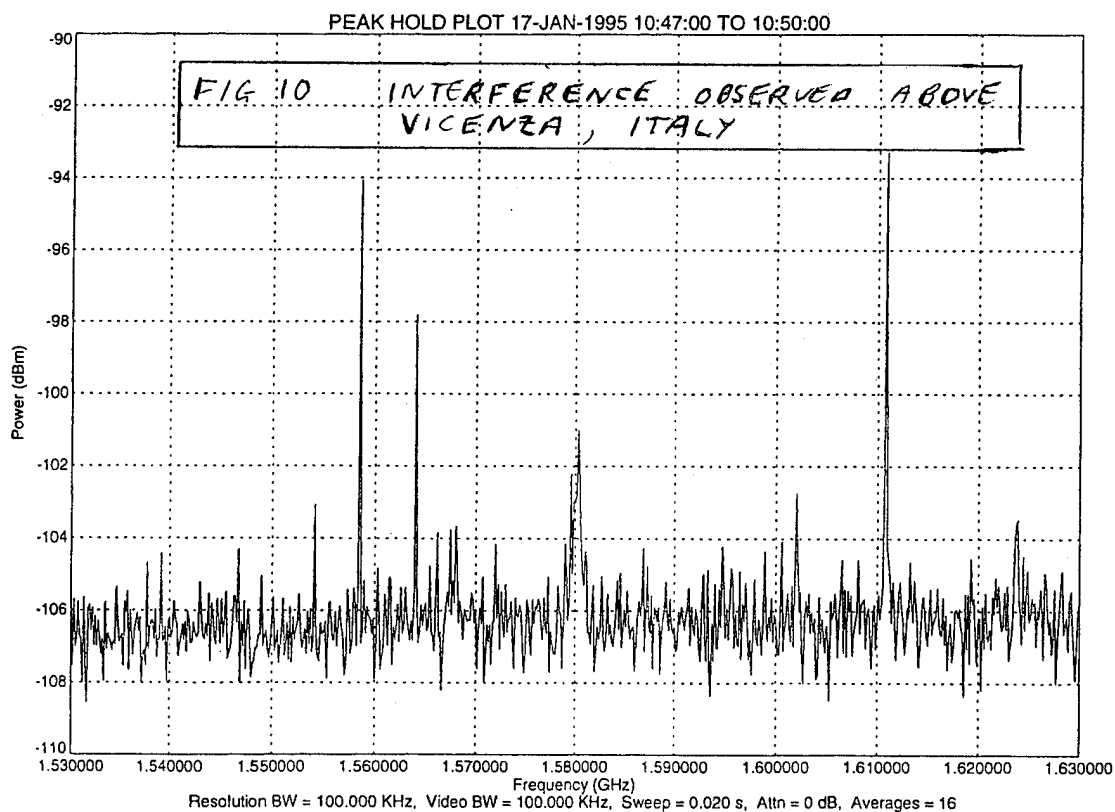
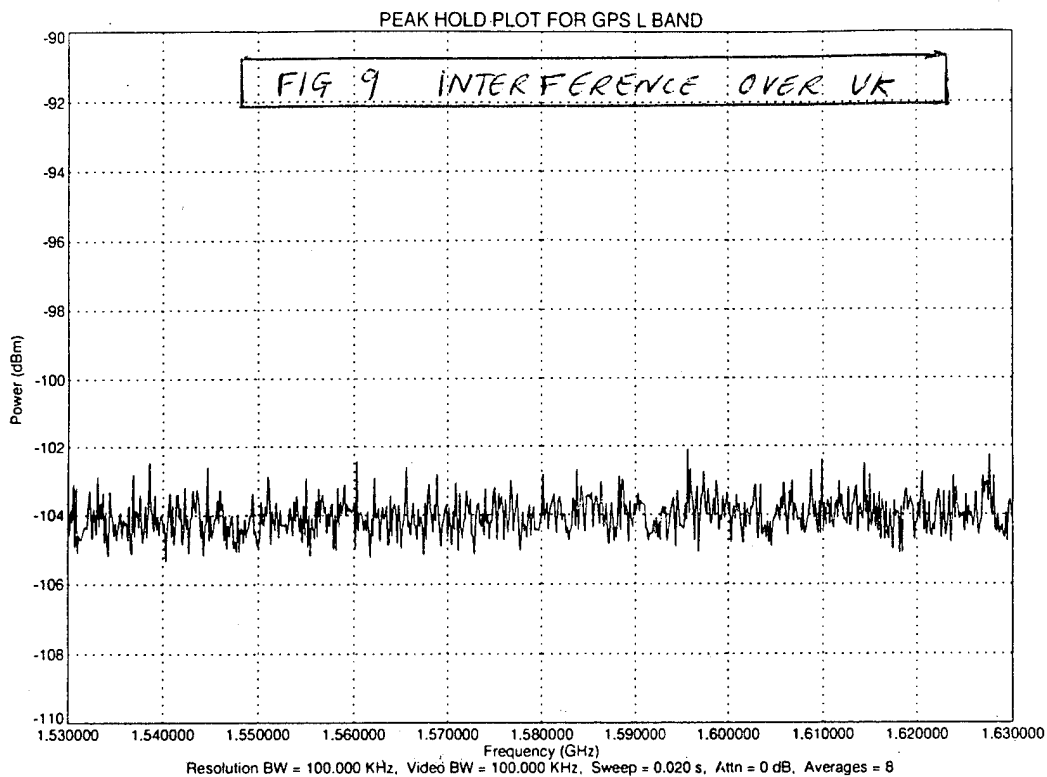


FIG 6 MEASUREMENT FLIGHT EUROPEAN ROUTING





The Role of GPS in Automatic Dependent Surveillance (ADS) and a Methodology for the Formulation of Requirements in That Role

Michael Ashbury
Civil Aviation Authority

Rolf Johannessen
Lambourne Navigation Ltd.

BIOGRAPHY

Michael Asbury joined the Civil Aviation Authority in 1977 after twenty years as a long range transport aircraft navigator, and having taken a BA in Mathematics and Technology. Among his projects have been the development of MNPS in North Atlantic operations and long term ATM matters including satellite studies. Mike was chairman of the GNSS technical subgroup within the ICAO FANS. He is currently head of INT7 in the Directorate of International Policy and Coordination within National Air Traffic Services (NATS) in London, where he is responsible for the implementation of ADS. Mike is a Fellow of the London based RIN.

Rolf Johannessen obtained his PhD from London University. A period developing ILS was followed by several years developing computer systems. In 1969 he joined the research laboratory which is now known as BNR Europe Limited in Harlow where for many years he was manager of the navigation department. In 1994 he left to form his own company, Lambourne Navigation Limited, where as Director he now undertakes consultancy work in Communication, Navigation and Surveillance. Rolf is a Fellow of the London based IEE, a Fellow of the RIN in London and a Member of the ION.

ABSTRACT

In Automatic Dependent Surveillance (ADS) the air traffic controller is presented with data on the aircraft position based on the aircraft's own navigation instruments. This form of surveillance differs considerably from that of radar. The paper discusses these differences and considers in particular how GPS fits into the overall system. A methodology is then developed for determining the requirements from ADS in terms of availability and service continuity.

INTRODUCTION

To achieve efficient use of air space Air Traffic Management (ATM) uses a number of tools. These include Communication, Navigation and Surveillance, generally known as the CNS of ATM.

In over-land airspace with a high traffic density, as is generally the case in continental USA and in Europe, communication is effected by voice modulation using the frequency band around 125 MHz. Navigation is by distance measuring equipment (DME) operating around 1,000 MHz and by the bearing based system known as VHF omnidirectional radio range (VOR). This uses frequencies around 115 MHz. Larger aircraft also use some form of inertial navigation which in many cases is updated using multiple DME, subject to a good fix. Surveillance is currently by secondary surveillance radar (SSR) where the ground interrogates on 1,030 MHz and the aircraft responds on 1,090 MHz.

In over-sea and remote airspace, like the greater part of the North Atlantic Oceanic Airspace, communication is at High Frequency, generally between 2 MHz and 10 MHz. Navigation relies on inertial systems with a few cases of Omega, and surveillance is by voice reports from the pilot who informs air traffic control (ATC) of the position he obtains from his on-board instruments.

The differences between the systems used over land and those used in oceanic airspace as described above result from the basic propagation characteristics of radio transmissions at frequencies of VHF and above. At these frequencies there is very little refraction or reflection by the atmosphere and ionosphere such that reliable propagation is line-of-sight limited. For an aircraft at 30,000 feet this implies a range of approximately 200 to 250 n miles only. Beyond these ranges neither VHF communication, nor VOR/DME navigation, nor SSR offers reliable performance. The universality of the Global Positioning System (GPS) to provide accurate navigation is therefore an important asset. Since an aircraft has direct line-of-sight to these satellites, whether

the aircraft is over land or over sea, it follows that such systems can be used seamlessly during an entire flight, though there may need to be different safeguards depending upon the phase of flight. In this respect GPS represents a navigational leap forward for aviation.

This consequence of radio propagation characteristics affects not only GPS, but also GLONASS and any other likely Global Navigation Satellite System. However, in this paper it is GPS which is the main focus.

STRENGTHS OF SSR AS A SURVEILLANCE TOOL WITHIN AN INTEGRATED CNS ENVIRONMENT

The two main components of secondary radar are the interrogator, which is the ground system, and the transponder, which is the airborne system.

In its most elementary form the interrogator transmits a group of pulses in the direction in which its antenna points. Any aircraft within the main beam of the radar senses this interrogation and the transponder replies by transmitting a different group of pulses. From this reply group, it is generally possible to determine the aircraft call sign and height. The interrogator determines the range to the aircraft from the two-way propagation time, and the bearing by the direction in which the antenna is pointing at the time the reply is received. The estimate of aircraft position is therefore made by the ground component, independent of any reference to the aircraft's 2-D or 3-D navigation system.

In an industry where safety is paramount this independence is valuable, since a malfunction in the airborne navigation system generally can be compensated for by reliance on the surveillance system. While surveillance can also fail, the probability that the aircraft's navigation system has a failure at the same time as the surveillance system, is generally the product of the probabilities of their individual system failure probabilities. That probability will be very small indeed, and well below other probabilities that will dominate the situation.

LIMITATIONS OF SSR

Secondary radar has some limitations as well. These are:

- 1 As indicated in the introduction, the range is line-of-sight limited. Oceanic surveillance cannot therefore depend upon SSR.
- 2 The same limitations restrict the extent to which SSR can be relied upon for low level flights in regions like the North Sea where considerable

helicopter operations take place, much of it at 2,000 - 3,000 feet above sea level [1].

- 3 In terminal areas also, the need to monitor aircraft at all stages of airport approach using SSR requires that the SSR interrogator be placed in the terminal area, thus the number of interrogators required grows with the number of airports.
- 4 Being an angular system, the resolution in terms of distance is range dependent.

AUTOMATIC DEPENDENT SURVEILLANCE

The term Automatic Dependent Surveillance is defined [2] as *"A surveillance technique in which aircraft automatically provide, via a data link, data derived from on-board navigation and position-fixing systems, including aircraft identification, four-dimensional position, and additional data as appropriate."*

The key point here is that the surveillance function derives its position information from the aircraft's on-board navigation sensors, and the ADS function can be accomplished by any data-link system which meets the communications criteria; HF, VHF, satellite or Mode-S are all candidates.

Two consequences flow from this, one good and one bad.

- 1 Beneficially ADS allows surveillance to be provided in any airspace where navigation is possible. In particular it allows ATC surveillance in oceanic and remote airspace as well as at low levels in other regions where, up to now, only procedural control was possible. Procedural control in this context is a method of control in which the pilot reports his position and intent, where ATC issues a clearance (subject to other traffic) on the assumption that the stated position is correct and that the pilot will adhere to the clearance. ADS when properly used is therefore a major step forward which can allow more optimised traffic control leading to reduced separation and direct routing.
- 2 However, against this, since ADS relies on the on-board navigation instruments and any associated signals-in-space, it follows that if those instruments or their required signals-in-space malfunction, then the surveillance will also malfunction. In particular, if the signals-in-space that are used by many aircraft fail, or behave correctly but cause the receivers to fail as appear to be suggested by [3], then many aircraft may simultaneously lose both navigation and surveillance. The amount of separation reduction and other ATC benefits which could be made possible by the introduction of ADS are

therefore limited by the probability of such common failures.

GPS IN ADS

The ICAO definition of ADS as given above clearly allows ADS to be operated with any navigation system. There is no need to use GPS. Indeed the current capacity limitations on the North Atlantic stem principally from the need to protect against erroneous way-point insertion by the flight-deck crew and not by a lack of performance of navigational equipment. Such protection will be provided by any form of ADS, and it is therefore anticipated that all requirements for capacity on the North Atlantic foreseen for the near term could be fully realised by ADS used in conjunction with the current state of inertial systems. Nevertheless GPS has a number of strengths that are relevant to ADS. These are enumerated below.

- 1 A GPS receiver is considerably cheaper than an inertial platform. A basic GPS receiver fully approved to the relevant Technical Standards Order costs around \$3,000 whereas a Ring Laser Gyro (RLG) is around \$100,000. This allows all aircraft to derive the benefit of ADS, from wide-bodied transport aircraft to single engine general aviation aircraft.
- 2 With GPS the 2-D surveillance information is with respect to a common grid reference, WGS-84.
- 3 With GPS the 2-D surveillance information has a precision controlled by the GPS control segment, currently 300 metres at 99.99 % for a non-differentially corrected solution. With inertial systems the precision is controlled by crew initialisation and inertial sensor drift rates and will therefore vary from aircraft to aircraft. Given a typical 0.5 n miles per hour drift rate an inertially-navigated aircraft could have an error of 2 n miles when making land-fall after a 4 hour oceanic crossing. A GPS-navigated aircraft would be expected to be within 0.15 n miles of cleared track independent of the length of oceanic crossing.
- 4 GPS provides time to a precision better than a micro second. For surveillance purposes a one second resolution would be a considerable improvement on the current one minute resolution. GPS time precision is therefore over-performing relative to the operational requirements. Nevertheless the automatic provision of time in GPS (which does not rely on the crew setting a clock, as does the current systems), and the common reference it provides for time, is an attractive adjunct for ADS. Indeed a day might come when ADS transmissions are timed relative to UTC derived

from GPS, thus optimising the use of the ADS transmission channel.

ADS AS A REPLACEMENT OR AS AN AUGMENTATION TO SSR

The best possible surveillance performance would be achieved if SSR was retained in those places where it currently gives good service, and if ADS was provided where SSR can never be implemented for the reasons of propagation characteristics as identified above. Thus a degree of co-existence of SSR and ADS is envisaged as outlined at ICAO's 10th Air Navigation Conference (ANC) [4]. It may however be expected that the pressures on cost will question the retention of some SSR stations as ADS improves in maturity. The question is then how one quantifies the surveillance performance that is considered operationally cost effective. This might be expected to lead to a gradual increase in the types of airspace where implementation of ADS takes place, and some phasing out of SSR becomes possible.

Before any such phasing out takes place the operational requirements of future surveillance systems need to be developed, particularly in terms of availability, continuity of service, integrity and accuracy. The first two of these are examined in detail below.

BACKGROUND DATA IMPORTANT FOR ESTABLISHING REQUIREMENTS

It is envisaged the three most common tasks for a surveillance system will continue to be the following:

- 1 To predict conflicts between aircraft tracks and to seek their most efficient resolution,
- 2 To detect ATC loop errors,
- 3 To maintain safety when there are malfunctions for the navigation system either in ground or airborne installations.

Items 1 and 3 are self explanatory. Item 2 is a term to cover any of the following events:

- (a) the ATC controller intends to issue one clearance but speaks another, for instance he means to say 'turn right' but says 'turn left'.
- (b) the ATC controller says what he means, but the pilot mis-hears and does not read back the instruction, or reads it back in error, which is not picked up by the controller; he then executes what he thought was the intention.
- (c) the pilot heard correctly, but through carelessness or distractions executes a different manoeuvre.

While item 1 may occur more frequently, items 2 and 3 are rare but important. For items 1 and 2 ADS and SSR are equally powerful; for item 3 there are important limitations in ADS, whether the positional information comes from IRS or GPS, but particularly if GPS is used.

FREQUENCY OF ATC LOOP ERRORS

To determine the probable rate at which such loop errors arise staff from 4 different control centres were asked to make an estimate of the rate at which there was an ATC loop error which the surveillance system detected in time for the error to be overcome.

Their estimates varied, depending on the complexity of clearances used in their sector, and on the pilots' familiarity with English and with the procedures that were common in the relevant airspace.

The typical rate was one ATC loop error per 1,000 flight hours.

OPERATIONAL RELIABILITY OF CURRENT AVIONICS

To establish the reliabilities achieved in operational airline use a number of airlines were asked to provide details of the Mean Time Between Failures (MTBF) achieved for avionics. Five airlines provided useful data. They were;

American Airlines, USA
United Airlines, USA
KLM, the Netherlands
Britannia, UK
British Midland Airways, UK

Ring Laser Gyro based Inertial Reference Systems (IRS) had MTBFs ranging from 63,000 hours in the best case to 11,352 in the worst case. The Flight Management Computer (FMC) ranged from 15,688 hours to 3,800 hours. The SSR Tx/Rx boxes had MTBFs ranging from 60,000 hours in the best case to 3,200 hours in the worst case.

If a precise system failure rate were required it would be necessary to consider the degree of cross-switching possible between RLG and FMC. That has not been done here: indeed it may differ between aircraft types. However the above figures suggest it is realistic to use a MTBF of 10,000 hours as typical for the failure rate of both a combined RLG/FMC, and also for a typical transponder.

If the typical flying time is taken to be two hours, the probability of simultaneous loss of two transponders is

then p_{2t} where

$$p_{2t} = (2/10,000)^2 = 4 \times 10^{-8}$$

since the two transponders are assumed to be independent of each other.

The probability of simultaneous loss of two inertial platforms will be the same, given the above assumptions, though it should be noted that many aircraft carry three inertial platforms rather than two.

GPS RECEIVER RELIABILITIES

There is only minimal documented data on the performance of GPS receivers. In any case performance will vary considerably between receiver models. Reference [3] suggested an MTBF of 874 hours was achieved on an early GPS receiver design in use in a transport aircraft flying today. The reference postulated that an improvement of at least 10 times might be achievable. It might be appropriate therefore to use a figure of some 10,000 flying hours, which would make it similar to that used for the inertial reference and transponder systems referred to elsewhere in this paper.

The work reported on in reference [3] suggested that the symptoms indicated software problems. While it is stressed that the following postulations are assumptions only, it is suggested the 10,000 hours MTBF should be split into different categories along the following lines:

- (a) Failures leading to no receiver output, or to an output of position which is so obviously wrong that the crew will recognise the failure and disconnect or disregard the receiver.
- (b) Failures that are significant in ATM terms, but less obvious, such that they will not be recognised, and will lead the aircraft to deviate from cleared track.

The 10,000 hours is split equally giving 20,000 hours each. (a) and (b) are then further sub divided between three groups:

- (i) software failures that are common between all identical receivers using those signals in space (60,000 hours),
- (ii) software failures that are random between identical receivers using the same signals in space (60,000 hours),
- (iii) hardware failures that are random between identical receivers (60,000 hours).

Given a failure tree like this the consequence can be evaluated in ATM terms, and the requirements placed upon surveillance, in order to preserve the integrity of the

airspace, can be determined.

It is clear that, in particular, the possibility of common failures is a matter which requires very careful scrutiny. UK NATS has put in place a programme which seeks to establish more fully what the probabilities might be.

METHODOLOGY USED TO DETERMINE THE REQUIREMENTS OF AVAILABILITY OF A FUTURE ADS/SSR MIX FOR SURVEILLANCE FOR EN-ROUTE HIGH LEVEL OPERATIONS

"Availability" of surveillance is here taken to be the proportion of time and space that the surveillance system provides both 2-D and altitude data from and about an aircraft to the air traffic control centre, and which data appears to the user to be correct, so that he can be expected to act upon it.

The UK London and Scottish flight information regions (FIR) have a total of 16 SSR stations covering some 350,000 square nautical miles. At most en-route flight levels there is therefore considerable redundancy in that each aircraft is covered by several radars. The current availability of surveillance by SSR is a function of two parameters:

- (a) the rate at which a surveillance station fails to deliver surveillance information to the air traffic control centres (due to a break-down) and,
- (b) the number of surveillance stations within range and which offer redundancy.

The former can be ascertained from the comprehensive maintenance data maintained by NATS. The latter was determined by superimposing on a map of the FIRs a grid of 50 n mile separation and counting the number of radars in range at each grid intersection. Since range for a SSR depends upon the altitude of the aircraft, this grid was scrutinised at heights of 15,000, 25,000 and 35,000 feet. With 148 grid points per level this yielded 444 points for the evaluation. It was also necessary to take into account that for some radars there were obstructions like high level terrain which reduced the range in certain directions. There were also some operational range limitations within the radars.

The following symbols are now used:

- n_3 = the number of grid points with 3 or more SSRs in range
- n_2 = the number of grid points with 2 SSRs in range
- n_1 = the number of grid points with only one SSR in range
- n_0 = the number of grid points outside SSR cover.

p_1 = the probability that one single average SSR station fails to provide SSR information to the ATCC.

Since the radar stations and their links to the ATCCs may be taken to be independent of each other one can assume that the probability that all n radars simultaneously fail to deliver information to the ATCC, where n radars are in range of an aircraft, will be $(p_1)^n$.

The current availability of SSR for these flight levels is then A where

$$A = (1-f)$$

and where in turn

$$f = \frac{n_0}{444} + \frac{(n_1/444)*p_1}{1} + \frac{(n_2/444)*p_1^2}{1} + \frac{(n_3/444)*p_1^3}{1}$$

This worked out to an availability of

$$A = \frac{(1-2.96*10^{-2})}{(1-3*10^{-2})} \text{ rounded to}$$

A first estimate for the requirement of availability is therefore that as ADS is introduced and SSR possibly partly withdrawn, the overall surveillance availability must not be allowed to fall below this level.

However, to take into account the growing use of GPS for navigation and in ADS, and the consequent possibility of common failures, additional, more stringent requirements were also demanded. The draft requirements are as follows.

Concise requirements

- (a) Averaged between 35,000 and 15,000 feet and averaged over the London and Scottish airspace the availability of surveillance shall be equal to or better than $1-3*10^{-2}$.
- (b) At all levels from the cruising heights for supersonic aircraft down to the landing pad of any off-shore rig in the London and Scottish regions the availability shall, at a date to be determined, be better than $1-4*10^{-3}$.
- (c) At all levels above UK land from cruising heights for supersonic transports down to the levels where a different system of surveillance is installed to safe-guard an approach and landing the availability shall, at a date to be determined, be better than $1-4*10^{-3}$.
- (d) Where there is currently SSR coverage, the

availability of ADS and, in the transition period, the availability in the mixed SSR/ADS environment must be so arranged that the probability that there simultaneously exists loss of surveillance to two or more aircraft within a range of 5 n miles of each other (ie for situations where radar separation is currently utilised) must be less than 1.5×10^{-5} .

- (e) In designing the ground system to meet these requirements it shall be assumed that for each aircraft the avionics include a duplicate system each with MTBF 10,000 flying hours, and that those two systems fail independently of each other and of the similar units in other aircraft.
- (f) For the purpose of meeting these requirements, the averaging period shall be any calendar year.

METHODOLOGY USED TO DETERMINE THE CONTINUITY OF SERVICE REQUIREMENTS FOR ADS

Attachment C to Part I section 2.8 of [5] introduces the concept of service continuity in the context of ILS by saying that "Continuity of service is needed to ensure that an aircraft in the final stages of approach will have a low probability of being deprived of a guidance signal". That reference does not use the concept in connection with either surveillance or long range navigation.

FANS defined GNSS continuity as "the probability that the GNSS will continue to provide GNSS performance for the period required, in this case for the time period of a typical phase of flight in the region of interest" [6].

In [7] the All Weather Operations Panel (AWOP) said "Continuity is the ability of the total system to perform its function without interruption during the intended operation".

Both for the ILS and the GNSS definitions there are three elements to the quantity:

- (a) there is the stress on *continuous* information,
- (b) there is the permitted *probability* that the information is not continuous,
- (c) there is a *time* element (in the case of ILS 30 seconds, in the case of GNSS the duration of the phase of flight).

For both ILS and GNSS the information has to be continuous since the lack of continuity deprives the aircraft of track guidance information. In the case of ILS the signal as received at the intended beneficiary (the aircraft) is present as a continuous carrier.

In surveillance the signal is not continuous. The radar beam (for SSR) sweeps through the aircraft and excites the transponder. The carrier then disappears while the radar antenna continues its rotation and re-appears some seconds later. Thus the signal at the aircraft is intermittent but regular. The reply at the intended beneficiary (the radar station) is likewise intermittent but regular, as far as a particular aircraft is concerned.

It is therefore apparent that there is a short-term signal absence which in surveillance is perfectly normal, but a long term absence which is not so.

As far as the surveillance continuity requirement is concerned, the importance is that continuous information *is not* needed, but a minimal information rate *is*.

With this understanding of the background the following definition is used:

The "Continuity of service" for surveillance is the probability that a specified minimum information rate remains available for the duration of a phase of flight, given that it was available at the commencement of that phase of flight.

Discussion of requirements

Assume that:

- (a) Based on the discussions with air traffic control staff referred to above 1 ATC instruction in 10^3 flying hours is associated with an ATC loop error,
- (b) 80% of these instructions lead an aircraft to descend or climb to a wrong flight level with the rest turning to a wrong heading. Half of these turn away and half turn into the parallel track,
- (c) aircraft follow common tracks with traffic at multiple levels such that the order of probabilities can be estimated by assuming that if an aircraft climbs too high or descends too low it will move to a flight level full of other traffic,
- (d) In a future environment most of the aircraft perform their azimuthal navigation to some extent by GPS, and therefore have common errors, rather than from a system like IRS which will lead to a random azimuthal positioning error, (it should however be noted that at present and in the foreseeable future, a large portion of aircraft will use IRS),
- (e) the precision available from the navigation system is of the order of 300 metres 99.99 %,
- (f) the average aircraft wingspan is $\lambda_y = 0.033$ nm (=200 feet) [8].

The consequence of (d), (e) and (f) is that, an aircraft which climbs or descends wrongly will do so in the path of another aircraft. This would be different for an aircraft

with 200 feet wing span in a 100 m random navigation system which could be considered to place many of the aircraft tracks offset relative to each other. However, in GPS common satellites are used and probably common satellite selection algorithms like minimum PDOP, therefore one must assume that the aircraft on a common nominal track in fact do follow the same ground track.

Now make the following additional assumptions:

- (g) the average aircraft length is $\lambda_x = 0.033$ n.m (=200 feet) [8],
- (h) the longitudinal separation is $S = 5$ n.m [9],
- (i) all aircraft on the track under consideration have the same horizontal velocity,
- (j) the unauthorised climb or descent rate is 1,000 feet per minute,
- (k) the vertical separation is 1,000 feet in the worst possible case,
- (l) there is a tolerance of + or - 150 feet on the assigned level before the surveillance system will recognise an incursion. This is a value $C = 2A + B$ where;

"A" is the value taken from [10] which assumes "an automatic altitude-keeping device shall be required and will be capable of controlling altitude within a tolerance band of +/- 50 feet about commanded altitude when operated in the altitude-hold mode in straight and level flight under non-turbulent, non-gust conditions". This is doubled to deal with the turbulent and gusting, hence $2*A$.

"B" is the +/- 50 feet tolerance associated with the altitude transmission code for SSR [11].

Taking these factors it is clear that an alarm in the surveillance system could not be raised until an aircraft indicates it has deviated more than $2*50+50 = 150$ feet from its assigned level.

From (g) and (h) it follows that if the unauthorised level change is not detected, there is then a maximum probability of $2*0.033/5 = 1.32*10^{-2}$ of a collision. However, by (a) and (b) above, the rate of such unauthorised level changes is $0.8*10^{-3}$. The rate of collisions from this cause, assuming the deviation from cleared track is not detected, is then R_1 where;

$$\begin{aligned} R_1 &= 0.8*10^{-3}*1.32*10^{-2} \\ &= 1.06*10^{-5} \end{aligned}$$

The quality of the surveillance system will allow most of these excursions to be detected, but there will be a small proportion which is not detected. Let P_v be this rate at

which such vertical deviations are not detected early enough for an accident to be avoided. This leads to a rate of accidents R_2 , where

$$R_2 = 1.06*10^{-5}*P_v$$

In Appendix B to the Report on Agenda Item 3 of [7] the Tunnel Concept Target Level of Safety (TLS) for oceanic or en-route risk is set to $5*10^{-8}$ per hour.

This TLS is now assumed to be divided between three components;

Loss of vertical separation	$0.8*5*10^{-8}$
Loss of horizontal separation	$0.1*5*10^{-8}$
Loss of longitudinal separation	$0.1*5*10^{-8}$
Total	$1.0*5*10^{-8}$

The 10% value assigned to the horizontal component is supported by the discussions with ATC staff referred to above. The required probability of failure to detect vertical errors in a timely manner is then determined by setting $R_2 = 0.8*5*10^{-8}$ and solving for P_v . This gives

$$\begin{aligned} P_v &= 0.8*5*10^{-8}/1.06*10^{-5} \\ &= 3.77*10^{-3} \end{aligned}$$

rounded to $4*10^{-3}$.

The time available from when the stray aircraft leaves the upper boundary of the cleared altitude and until it conflicts with the aircraft one level above is T_1 , where

$$T_1 = \delta H/v$$

and

$$\begin{aligned} \delta H &= 1000-150*2 = 700 \text{ feet} \\ v &= 1,000 \text{ feet/minute} \end{aligned}$$

giving a time $T_1 = 0.70$ minute (42 seconds). A time budget would be:

T_r	=	time for the SSR antenna to complete the current rotation and get to the aircraft causing the problem: this will be in the range 0 to 6 seconds.
T_c	=	time for the controller to register the problem, assuming that the system will itself recognise an intrusion and cause some indicator to flash in front of the controller: let this be 1 second.
T_a	=	time for the controller to gain access to the VHF channel which may already be used by another aircraft: let this be 0 to 4 seconds.
T_s	=	time for the controller to speak a message requesting the aircraft to level

immediately or to reverse its climb or descent: let this be 4 seconds.

T_p = time for the pilot to realise he needs to take immediate action and to instruct the aircraft to alter its climb: let this be 1 second.

T_i = time for the aircraft to overcome its inertia and to respond to his command: let this be 3 seconds.

Adding these times algebraically gives a worst case of 19 seconds and a best case of 9 seconds. But the term T_r is part of the SSR system and may be different for a different surveillance system. The time available for the system to cover (continuity + access time) is therefore $42 - 13 = 29$ seconds. However, it will also be necessary to consider the processing times involved, this could impose an additional 3 seconds delay.

The above considerations focused on detection by surveillance of an un-authorised climb or descent. Similar considerations apply to detection by surveillance of an un-authorised heading. However, space does not allow inclusion of the detailed analysis here.

The current draft requirements are as follows.

Concise requirement for continuity of service

The surveillance system protecting a particular volume of airspace must have a continuity of service such that once an aircraft has entered that volume of airspace, then for the duration of that flight in that airspace:

- (a) there must be a probability better than $(1-4*10^{-3})$ that if the aircraft climbs through a level 150 feet above cleared level (or descends through a level 150 feet below cleared level), the surveillance system detects it and raises an alarm for the controller within 29 seconds of the aircraft passing the upper (lower) tolerance level of the cleared level.
- (b) there must be a probability better than $(1-3*10^{-2})$ that if the aircraft changes to an un-cleared heading, and as a consequence moves off track, the surveillance system detects it and raises an alarm within 47 seconds of the deviation exceeding 1 n mile.
- (c) there must be a much higher probability "P" that the errors are detected within the longer timedelay "T" where "P" and "T" are as follows:

Vertical errors:

$$P = (1-4*10^{-4}) \text{ for } T=29*2 \text{ seconds}$$

$$P = (1-4*10^{-6}) \text{ for } T=29*10 \text{ seconds}$$

Horizontal errors:

$$P = (1-3*10^{-3}) \text{ for } T=47*2 \text{ seconds}$$

$$P = (1-3*10^{-5}) \text{ for } T=47*10 \text{ seconds}$$

- (d) If the surveillance system suffers an outage, then the time limits under (a) to (c) must cover both the outage itself and the time for the system to recover after that outage.
- (e) This performance shall be achieved by averaging over any calendar year.

OTHER PERFORMANCE ASPECTS

It is the availability and continuity of service that have been focused on here. However, a comprehensive requirement specification must also consider accuracy and integrity aspects in a manner similar to the way they have been studied in detail within the GPS navigation field. The use of GPS for ADS requires particular attention to these requirements, but space for this paper does not allow inclusion here.

Even for the availability and continuity requirements there are other matters to consider. The greater use of direct routing, for instance, will affect the probability that a level change will take place through the track of a different aircraft. Furthermore, when intent is included in the ADS through the extended projected profile down-link messages, this will itself lower the probability that there will be an uncleared level change.

These and other considerations show that a study of requirements for ADS, and particularly for the role of GPS in ADS, will be a subject of greatly increased interest in the years to come. It will be necessary to examine the extent to which it is valid to draw on current figures from a variety of airspace types. Also it may be appropriate to have several ADS specifications, one for each type of airspace, depending upon current radar separations.

CONCLUSIONS

The introduction of the two technologies of GPS and ADS represent major milestones. Surveillance with increased confidence will be possible worldwide to a standard which is much better than the surveillance relied upon in many regions today. The difference in characteristics between ADS and SSR does however demand a careful scrutiny before firm operational requirements can be formulated.

ACKNOWLEDGEMENTS

The authors wish to acknowledge the encouragement and input of many colleagues, particularly operational ATCOs in the UK National Air Traffic Services. They also wish to acknowledge the valuable maintenance data provided by several international airlines referred to in the paper.

REFERENCES

- [1] Johannessen R and Howson D; The application of differential GPS to the conduct of helicopter off-shore approaches in the North Sea. Proceedings of the 51st Annual meeting of the ION, June 5-7, 1995, pps 475-480.
- [2] ICAO Automatic Dependent Surveillance Panel (ADSP), Third meeting, Montreal 9-20 May 1994, Report on Agenda Item 5, ADSP/3-WP/77 Appendix B, section 1.3.
- [3] Asbury MJA and Johannessen R; Single Points of failures in complex aviation systems for communication, navigation and surveillance. Proceedings of NAV94, organised by the Royal Institute of Navigation, London 8-10.11.1994.
- [4] Report of the tenth Air Navigation Conference, Montreal 5-20 September 1991, ICAO Doc 9583, AN-CONF/10, CNS System Evolution, Table 1 in Appendix A to the Report on Agenda Item 7.
- [5] Aeronautical Telecommunications, Annex 10 to the Convention on International Civil Aviation, ICAO, Fourth edition of Volume 1 - April 1985, Amendment 69, applicable 11 November 1993.
- [6] FANS(II)/3-WP/87 Appendix D to the Report on Agenda Item 4, Attachment I.
- [7] AWOP/15-WP/718 section 1.3.4.
- [8] ICAO Doc9426-AN/924 Air Traffic Services Planning Manual, First Edition, Part II, section 2, Chapter 4 p17.
- [9] Manual of Air Traffic Services, Part 1, Chapter 3, Section 10 "Radar Separation". The value quoted there for when both returns are within a range of 80 n miles from the radar station.
- [10] ICAO Doc 9574-AN/934, Manual on Implementation of a 300 metre vertical separation between FL290 and FL410 inclusive, 1st edition dated 1992.
- [11] Aeronautical Telecommunications, Annex 10 to the Convention on International Civil Aviation, ICAO, 4th edition to Volume 1, Part I, Equipment and Systems, Table B.

ACRONYMS

ADS	Automatic Dependent Surveillance
ANC	Air Navigation Conference
ATC	Air Traffic Control
ATCC	Air Traffic Control Centre
ATCO	Air Traffic Control Officer
ATM	Air Traffic Management
AWOP	All Weather Operations Panel
CNS	Communication Navigation and Surveillance
DME	Distance Measuring Equipment
FANS	Future Air Navigation Systems committee
FIR	Flight Information Region
FMC	Flight Management Computer
GNSS	Global Navigation Satellite System
HF	High Frequency
ICAO	International Civil Aviation Organisation
ILS	Instrument Landing System
IRS	Inertial Reference System
MTBF	Mean Time Between Failures
NATS	National Air Traffic Services
n.m	nautical miles
PDOP	Positional Dilution Of Precision
RLG	Ring Laser Gyro
SSR	Secondary Surveillance Radar
TLS	Target Level of Safety
UK	United Kingdom
UTC	Universal Time Coordinated
VHF	Very High Frequency
VOR	VHF Omnidirectional Radio range

Aircraft Approach and Landing Studies with the Global Positioning System

Douglas Hardwick and Jeffrey Liu
National Research Council of Canada

BIOGRAPHY

Douglas Hardwick is Manager of Resource Geoscience at the Flight Research Laboratory, Institute for Aerospace Research, of the National Research Council of Canada. His projects in navigation include the development of one of the first fully automatic VLF Communication Station processors and the integration of VLF, Loran-C and GPS with an inertial navigation system. Current projects include the development of precise differential GPS for airborne gravity.

Mr. Hardwick graduated from the Royal Military College of Canada in 1955 as a navy pilot and obtained a B.Sc. in Electrical Engineering from the University of Toronto. He worked on the design of advanced flight control systems in Canada, the US and Germany before joining the National Research Council in 1971.

Jeffrey Liu received his M.Sc. in Geomatics Engineering from the University of Calgary in 1993. He also holds a B.Sc. and M.Sc. in Geodesy from Tongji University, Shanghai, China. He is currently doing research in the areas of GPS development for airborne gravity and precise GPS landing studies at National Research Council of Canada.

ABSTRACT

The National Research Council of Canada (NRC) is conducting a study of the accuracy of C/A code Differential GPS (DGPS) for Category I landings. In order to strengthen the existing landing data base, DGPS approach and landing data were collected at Resolute and Inuvik in the Canadian Arctic and at St. John's, Newfoundland, using the NRC Convair 580 aircraft. Data were collected for a total of 56 landings, 21 of which were flown on full DGPS guidance. These tests were carried out over a period of 2½ years, during which time

the DGPS receiver suite evolved from C/A code only, to single frequency NovAtel GPSCardTM with C/A code and carrier phase and in the Saint John's tests, dual frequency Ashtech Z-12 receivers were flown with the NovAtels. Kinematic carrier phase with ambiguity initialization was used as the basic ground truth to estimate the accuracy of real time C/A code DGPS, which was the system under test. Several C/A code data processing techniques, namely C/A code differential positioning, carrier phase smoothing of code positioning and single point positioning with precise orbits and clocks, were compared. Carrier phase solutions from the Novatel and Ashtech receivers were also compared.

INTRODUCTION

In a collaborative program with the Canadian Ministry of Transport (MOT) and the FAA, the National Research Council of Canada (NRC) has carried out flight tests to assess the suitability of local DGPS C/A Code for Category I (Cat I) approach and landing guidance. There is particular interest in collecting data at the higher geographical latitudes to show that although the GPS satellites do not attain high elevations at these latitudes, the accuracy of the height solution is nevertheless sufficient for Cat I operations. The MOT also wished to compare local DGPS performance with that of the Wide Area Augmentation System (WAAS). Using the NRC Convair 580 research aircraft as the test vehicle, high latitude tests were flown at Resolute Bay and Inuvik in the Canadian Arctic, and another series of tests was flown at St. John's, Nfld. All of these tests were flown in conjunction with atmospheric data collection and aeromagnetic survey projects, and in many cases, approaches were made in instrument flight conditions, whereby conventional ILS had to be used for guidance, with DGPS data being recorded for post-flight analysis. However, out of the total of 56 landings, 21 were flown using DGPS guidance. "Ground truth" at Inuvik and St.

John's was provided by post-flight processed DGPS carrier phase data, while at Resolute, because carrier phase was not available, conventional ILS and radar altimeter were used, after the spatially-correlated errors in these systems had been determined by comparison with the ensemble of the DGPS C/A code data.

The specific objectives of this program were as follows:

For all flight trials,

- To assess the accuracy of C/A code guidance for landings, using local DGPS.

For the Saint John's trials,

- To compare the guidance accuracy of local DGPS with WAAS, in this case, using data from the Canadian Active Control System (CACS).
- To compare the carrier phase accuracy of the Novatel 3951R receiver with that of the Ashtech Z-12 as position reference systems.
- During atmospheric flights, to collect carrier phase data that can be correlated with data from the Convair's atmospheric sensors for a study to improve the modelling of GPS tropospheric errors.

This report shows the results for all but the last of the above items, the study for which is on-going and reported in these proceedings (Langley *et al*, 1995).

EQUIPMENT

The NRC Convair 580 is a multi-purpose flying laboratory, equipped to carry out atmospheric sensing studies, advanced radar experiments and aeromagnetic research. The DGPS receivers were, for the Resolute trials, Trimble 4000RL II's, providing C/A code only, while for the later trials at Inuvik and Saint John's, Novatel 3951R receivers were used, providing both narrow correlator spacing C/A code and L1 carrier phase data. In the aircraft, C/A code DGPS position and speed solutions were sent to the aircraft's main computer at 5 Hz, where they were resampled at 8 Hz, the basic data rate of the main computer. From this stream, guidance signals were generated to exactly mimic the ILS localizer and glide slope. For the approaches that were flown in DGPS mode, the guidance signals were displayed as course deviations on the pilots' CDI and HSI instruments.

The data link to the aircraft was a Data Radio packet modem, operating at 4800 baud to give an update rate of 1 Hz. The modem fed a VHF transmitter with an effective radiated power of 25 watts. For the Saint John's trials, where carrier phase solutions were being compared, Ashtech Z-12 receivers were also used in the aircraft and in the ground station.

METHODOLOGY AND DATA PROCESSING

For the Inuvik and Saint John's trials, where carrier phase DGPS was used for ground-truth, the processing algorithm was developed at NRC especially for this project, with certain routines adapted from public domain GPS software. It does standard static ambiguity resolution for the carrier phase and processes all satellite pseudoranges as double differences, using the highest-elevation satellite as a reference. Once initial cycle ambiguities have been solved, the recorded data are processed in kinematic mode with cycle integrity monitored as a function of satellite residuals. C/A code and carrier phase latitude, longitude and height are transformed into a runway-oriented frame whose origin is the runway threshold and whose X-axis is aligned with the runway bearing. This transformation produces cross-track position (Y) and a height (Z) positions relative to the runway threshold and bearing. CA code accuracy is measured in terms of System Error (SE) (VanDierendonck, A.J. *et al*, 1992), i.e.

$$\text{C/A code (Y,Z) minus Carrier phase (Y,Z)}$$

The on-line DGPS algorithm in the aircraft uses the same transformation to generate "look-alike" ILS signals for DGPS guidance.

Accurate location in WGS-84 coordinates of the DGPS ground station antennas and of the various runway thresholds was of prime importance. At Resolute, when no carrier phase was available, these positions were determined by averaging C/A code solutions over extended periods to remove most of the selective availability (SA) effects. For example, for the antenna, five sessions were recorded for a total of 18,500 samples and a cumulative time of 20 hours. At Inuvik, the position of the ground station antenna was surveyed, using a TurboRogueTM SNR 8000 receiver, from a Geodetic Survey monument, classified as first order vertical and second order horizontal, located near the airport. Inuvik has only one runway, and its threshold was surveyed in a similar manner, with reference to the monument and the ground station. At Saint John's, where three different runways were used, the threshold coordinates were already available from a project in which the MOT is accurately surveying the thresholds at all major airports in Canada. The ground station antennas for the NovAtel and Ashtech receivers were each located over surveyed monuments that are part of a CACS site at Saint John's, at a distance of 5 km from the airport. At Resolute and Inuvik, the ground stations were slightly less than 1 km from the airport.

RESULTS

C/A Code Sensor Errors

The SE accuracy figures at 95% probability that follow, are calculated as

$$| \text{mean error} | + 2 \times (\text{Standard Deviation})$$

The data samples cover 10 km from the runway threshold to touchdown point on the runway.

The accuracy specification for CAT I as defined by the USA Federal Radio Navigation Plan at a decision height of 200 feet is:

Vertical sensor error 4.1 metres

Cross-track sensor error 17.1 metres

Resolute Bay results for 13 landings:

Vertical error 4.6 metres

Cross-track error 8.8 metres

Inuvik results for 19 landings:

Vertical sensor error 1.565 metres

Cross-track sensor error 0.814 metres

Saint John's results for 27 landings:

Vertical sensor error 1.810 metres

Cross-track sensor error 1.207 metres

Typical SE errors are shown in Figures 1 and 2, for height and cross-track, for the Saint John's landings. The NovAtel receivers used do not produce carrier-smoothed C/A code solutions, but these solutions were computed post-flight and from the Inuvik and Saint John's statistics shown below, it can be seen that considerably quieter guidance is available if this processing method is used. The corresponding error plots are shown in Figures 3 and 4.

Inuvik carrier-smoothed C/A code:

Vertical sensor error 0.554 metres

Cross-track sensor error 0.369 metres

Saint John's carrier-smoothed C/A code:

Vertical sensor error 0.922 metres

Cross-track sensor error 0.637 metres

C/A Code Flight Technical Errors (FTE)

Flight Technical Error is a measure of how closely the pilot (or autopilot) follows the guidance signal as presented. (Perfect tracking of the guidance would represent zero FTE). For the methodology of this project, it can be shown that FTE is simply the Y or Z C/A code position (Hardwick *et al*, 1995 A). DGPS is capable of providing smoother and more accurate guidance than a conventional ILS and it was hoped that approaches flown

with DGPS guidance would show less FTE than those flown on ILS, especially since, on dedicated DGPS, the pilots' concentration was definitely focused on the approach task. However, there was only a slight trend towards a lower FTE for the DGPS approaches. More tests will be required in order to establish a realistic relationship between FTE and DGPS.

DGPS vs CACS "Single Point" Solutions

The Canadian Active Control System data can be used to test the potential of this system, in its present non-real time form, to replace a local DGPS station for approach guidance. (This technique is sometimes referred to as "single point" because no differential data are needed). The CACS data consisted of precise ephemerides at a sampling interval of 15 minutes and of satellite clock corrections at a 30 second sampling interval. These were network-downloaded from the Geodetic Survey Division of Natural Resources Canada (NRCan). The program GPSPACE, also from NRCan, was used to interpolate these data to 1 Hz to replace the broadcast ephemerides and to correct the satellite clock data as recorded from the Novatel and Ashtech airborne receivers. This comparison was only made in the Saint John's trials and to date, not all the flights have been processed using Canadian Active Control System data. However, the trends in the one-landing example shown in this section can be considered typical.

Figures 5 and 6 show the respective height and cross-track CACS and DGPS solution errors for the sample landing and their statistics are tabulated further down. The following observations can be made with respect to each of these solutions:

- NovAtel DGPS C/A -- The results are consistent with those already presented for this type of positioning.
- Ashtech DGPS C/A -- These results are surprisingly noisy. However, note the next item...
- Ashtech DGPS P1 Code -- In the Z-12 receiver, the L1 P-Code is generated by a cross-correlation process. It shows the least error of all the solutions. One suspects that that with such accuracy, no great care has been taken in the processing of the C/A code solution.
- Novatel Single Point C/A -- See next item.
- Ashtech Single Point C/A -- Both these solutions exhibit biases of up to -6 m. This is attributable to non-uniform ionosphere on the satellite-to-receiver paths. The CACS does not at this time incorporate an ionospheric correction model.
- Ashtech Single Point L3 -- This solution, derived from the L1 and L2 frequencies, shows the advantage of a two-frequency receiver in effectively calculating and removing the ionospheric errors.

	HEIGHT		CROSS-TRACK	
	Mean	Std. Dev.	Mean	Std. Dev.
Novatel Differential C/A	-0.43	0.45	-0.62	0.43
Ashtech Differential C/A	-0.90	3.00	-0.42	1.21
Ashtech Differential P1	-0.29	0.40	0.02	0.27
Novatel Single Point C/A	-4.72	0.41	-2.09	0.12
Ashtech Single Point C/A	-6.09	0.47	-2.68	0.21
Ashtech Single Point L3	0.52	0.20	-0.69	0.06

Comparison of Ashtech Z-12 and NovAtel 3951R Carrier Phase Accuracies

Within the FAA, the Ashtech Z-12 is currently used as a "Time Space Position Information (TSPI)" System, to be used as a "truth" reference for the evaluation of other positioning systems. Since for the Inuvik and St John's trials, the NovAtel has been used for this purpose, a comparison of the two systems was seen as desirable to compare their respective performances in carrier phase positioning for the landing phase of some of the flights, where the differential baseline would be reasonably short. Over longer baselines than about 20 km, one would expect better performance from the Ashtech, since it is a dual-frequency receiver and is able to correct for differential ionospheric effects, something that is not possible with the single frequency NovAtel.

A simple method of comparing the carrier-phase accuracy of the two receivers was to compute the magnitude of the difference of their horizontal positions, which should be 1.78 m, the longitudinal separation of the two antennas on the roof of the aircraft. The height solutions were also compared; their mean errors should agree, since the average pitch attitude of the aircraft was close to zero and with the short lever arm between the two antennas, the attitude errors should average out. The results that follow can be considered as representative.

Measurement of Antenna Baseline Ashtech minus NovAtel

	Mean	Std. Dev.
Flight 7, 8 & 22 landings	1.780 m	0.018 m
Flight 13, landings 1, 2 & 3	1.671 m	0.022 m

Height Solution - Ashtech minus NovAtel

	Mean	Std. Dev.
Flight 7, 8 & 22 landings	0.029 m	0.066 m
Flight 13, landings 1, 2 & 3	0.015 m	0.071 m

For the Flight 13 baseline measurement, there is a 10 cm difference from the nominal 1.78 m, indicating cycle slip

in one of the systems or possibly, a small amount of differential ionosphere. (The latter could be in either system, because the software only processed the L1 phase data from the Ashtech). The height comparisons are slightly noisier than for the horizontal, which can be expected in GPS, but a contributing factor could be that the solutions were not corrected for pitch attitude. Figure 7 is a typical plot of the antenna baseline measurement for one landing, while Figure 8 is the corresponding height difference.

DISCUSSION OF RESULTS

C/A Code System Error Results

The composite results from Inuvik are slightly better than those from St. John's. We attribute the slightly poorer results at St. John's to:

a) The slightly longer differential baseline, 5 km vs. about 1 km at Inuvik. With a single frequency (L1) receiver such as the NovAtel, differential ionosphere errors over even short baselines, can be a problem. Furthermore, from the stand-alone CACS results, it is clear that the ionosphere was active during the St. John's trials.

b) Poor satellite availability, leading to poorer geometry than was the case at Inuvik. For example, at St. John's, for one flight on which 13 dedicated DGPS-guided landings were carried out, there were at times only five satellites usable and the PDOP was as high as 3.25. By contrast, at Inuvik, there were always 8 to 10 satellites at usable elevations, giving PDOP's of 1.6 to 1.8 on the average.

The difference in results is most apparent in the carrier-smoothed C/A code, where it is almost a factor of two.

The Resolute results are much poorer than those of the later trials. We attribute this to the use of the narrow-correlator C/A code techniques used in the two later trials, a proprietary technique used by NovAtel that significantly reduces the short-term receiver noise. The considerable bias error in the Resolute statistics is mostly due to bias

uncertainty in determination of the reference antenna and runway positions. The worst-case example is the 95% confidence limit for the reference antenna height, namely 6.6 m (Onno *et al*, 1993).

DGPS vs CACS Solutions

In DGPS, with short baselines of up to about 20 metres, the satellite paths to the two receivers pass through roughly the same ionospheric anomalies and the attendant ionospheric errors tend to cancel. At St. John's, all the "single point" (i.e. non-DGPS) solutions, both static and kinematic, showed bias errors of a few metres. An accurate, wide-area, position-based ionospheric model for the CACS may take considerable time to implement and until such time, it would appear that two-frequency receivers should be used in wide-area experiments such as this one.

CONCLUSIONS

These tests show that C/A code DGPS can easily meet the FAA specification of 4.1 and 17.1 metres (95% probability), for height and cross track respectively, for Category I approaches. The Resolute height results are slightly outside this specification, but the result can be qualified by the consideration that the GPS equipment and the truth methods were less refined than was the case for the two later trials. It would appear that decreased height accuracy at high latitudes is not a problem; the increase in the number of satellites in view would seem to offset the fact that they do not, on the average, attain as high elevation angles as they do at lower latitudes.

WAAS definitely requires a geographic-based ionospheric correction model, unless two-frequency receivers are used. The Canadian Active Control System (CACS) appears to produce good single point positioning, provided that it is used with two-frequency receivers.

Processed approach and landing data showed that the NovAtel 3951R and Ashtech Z-12 receivers offer about the same accuracy of L1 carrier phase positioning under static and kinematic operation. Both receivers have sophisticated techniques for producing very low-noise code positioning.

REFERENCES

Hardwick, C.D., Starcevic, D. and Liu, J. (1995A), DGPS Landing Tests at Inuvik, N.T., NRC-IAR Flight Research Laboratory Technical Report LTR-FR-125.

Hardwick, C.D., Starcevic, D. and Liu, J. (1995B), DGPS Tests with the NRC Convair 580 at St. John's, Nfld., NRC-IAR Flight Research Laboratory Technical Report LTR-FR-126.

Langley, R., Mendes, V., Brown, A., Collins, P. (1995), The Effect of Tropospheric Errors on a Kinematic GPS Precision Approach and Landing System, Proceedings of ION GPS-95, Palm Springs, CA.

Onno, T., Hardwick, C.D., Marcotte, D.L. (1994), Differential GPS Testing During Landing Approaches in the High Arctic, NRC Lab Technical Report LTR-FR-123.

VanDierendonck, A.J., Fenton, P., Ford, T. (1992), Theory and Performance of Narrow Correlator Spacing in a GPS Receiver, NAVIGATION, Journal of The Institute of Navigation, Vol. 39.

Youngdall, G. (1995), Flight Test of Ashtech GPS Receiver For Use as Time Space Position Information System (TSPI) To Verify Specific Performance Standards, FAA Technical Center Report ACD-330, Atlantic City, NJ., March, 1995.

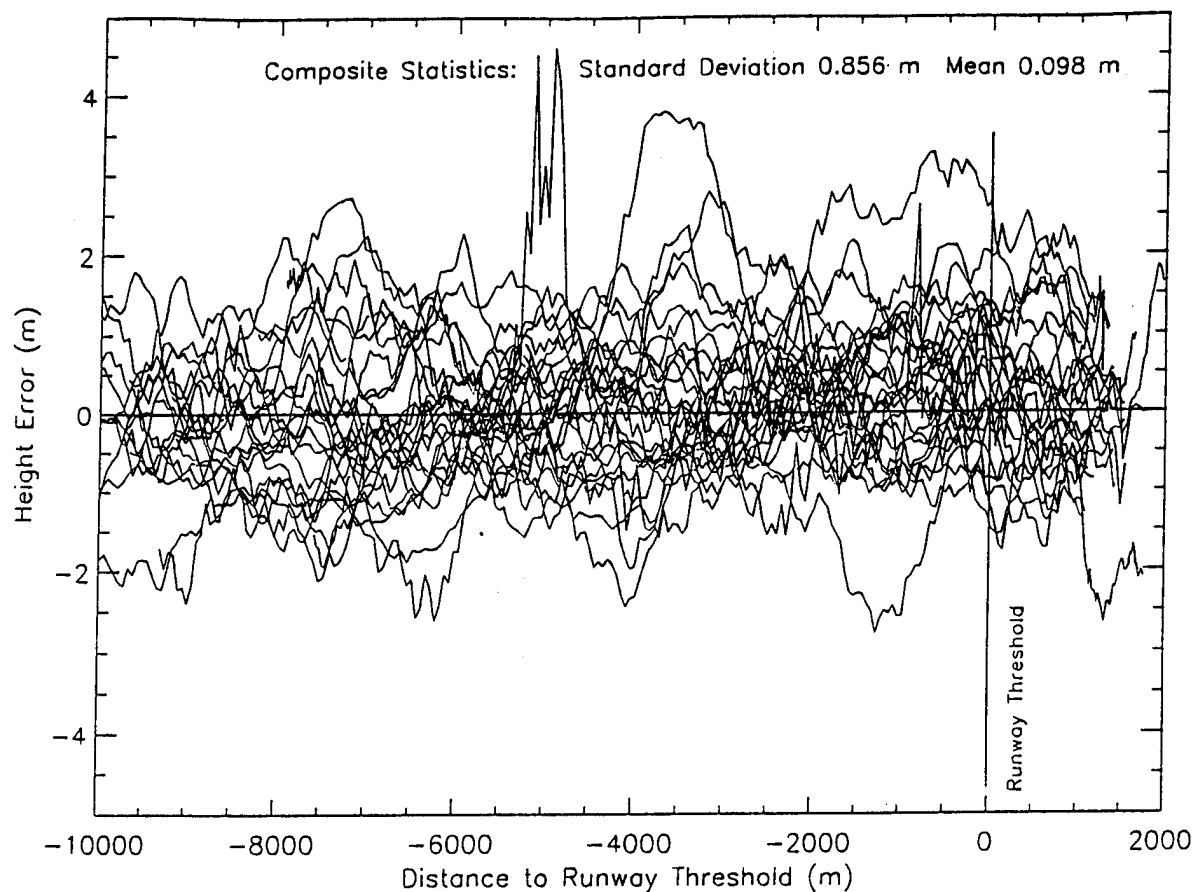


Figure 1: Sensor Height Error, ST John's - 27 DGPS Landing, C/A Code

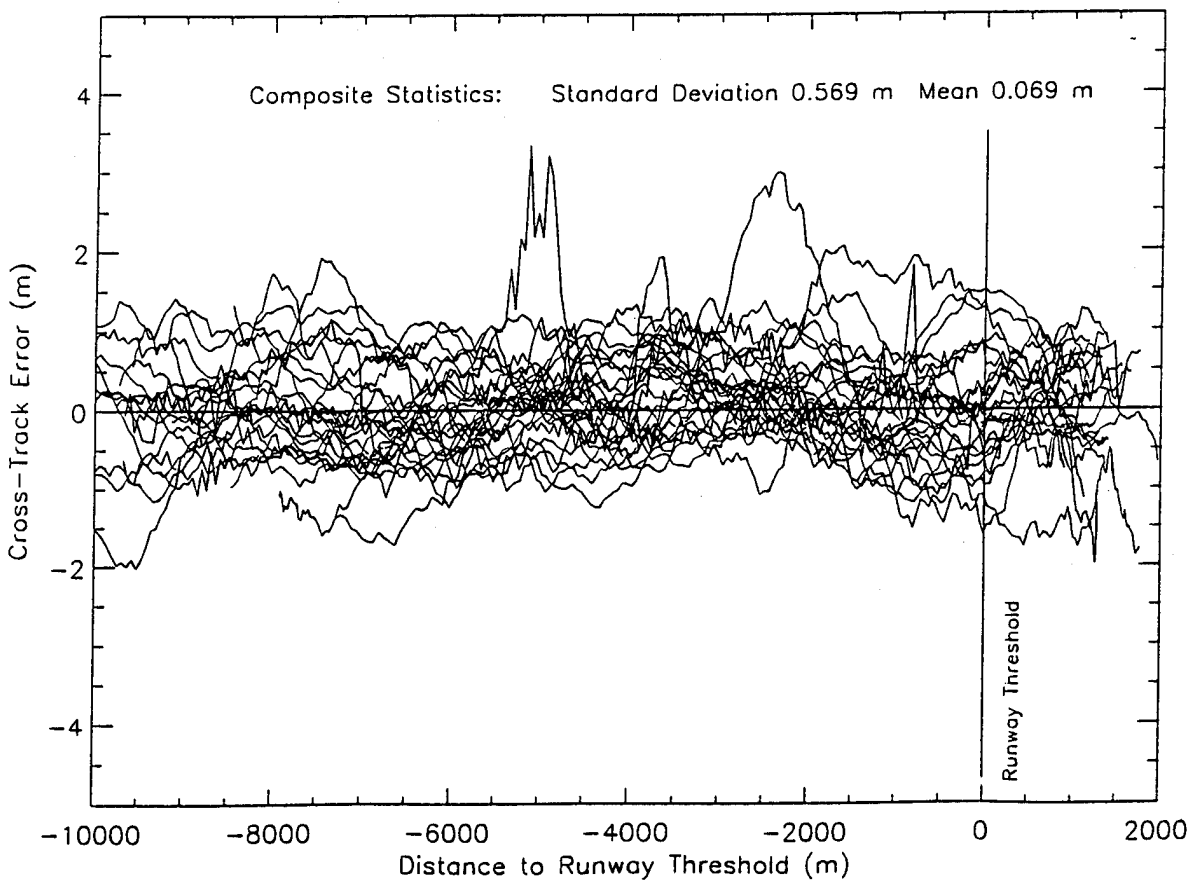


Figure 2: Sensor Cross-Track Error, ST John's - 27 DGPS Landing, C/A Code

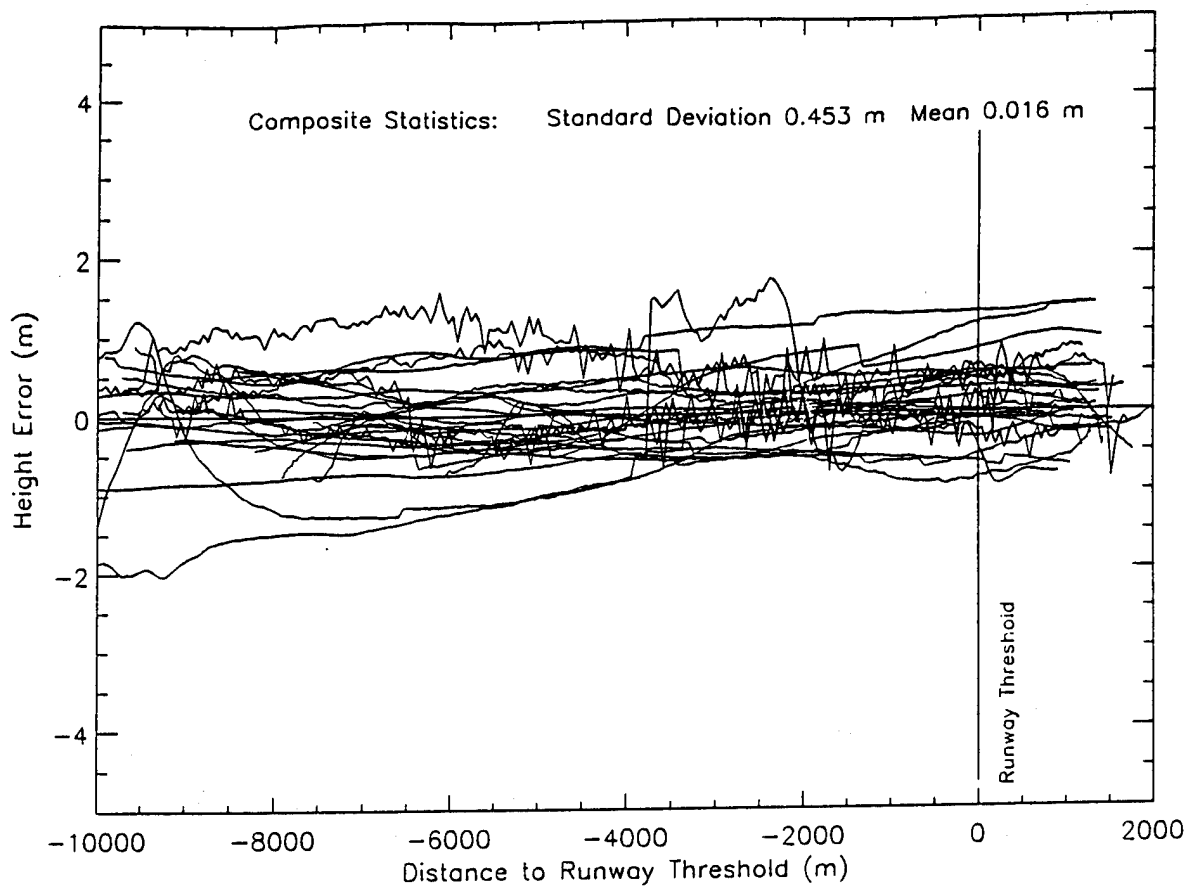


Figure 3: Sensor Height Error, ST John's - 27 DGPS Landing, Carrier-Smoothed C/A Code

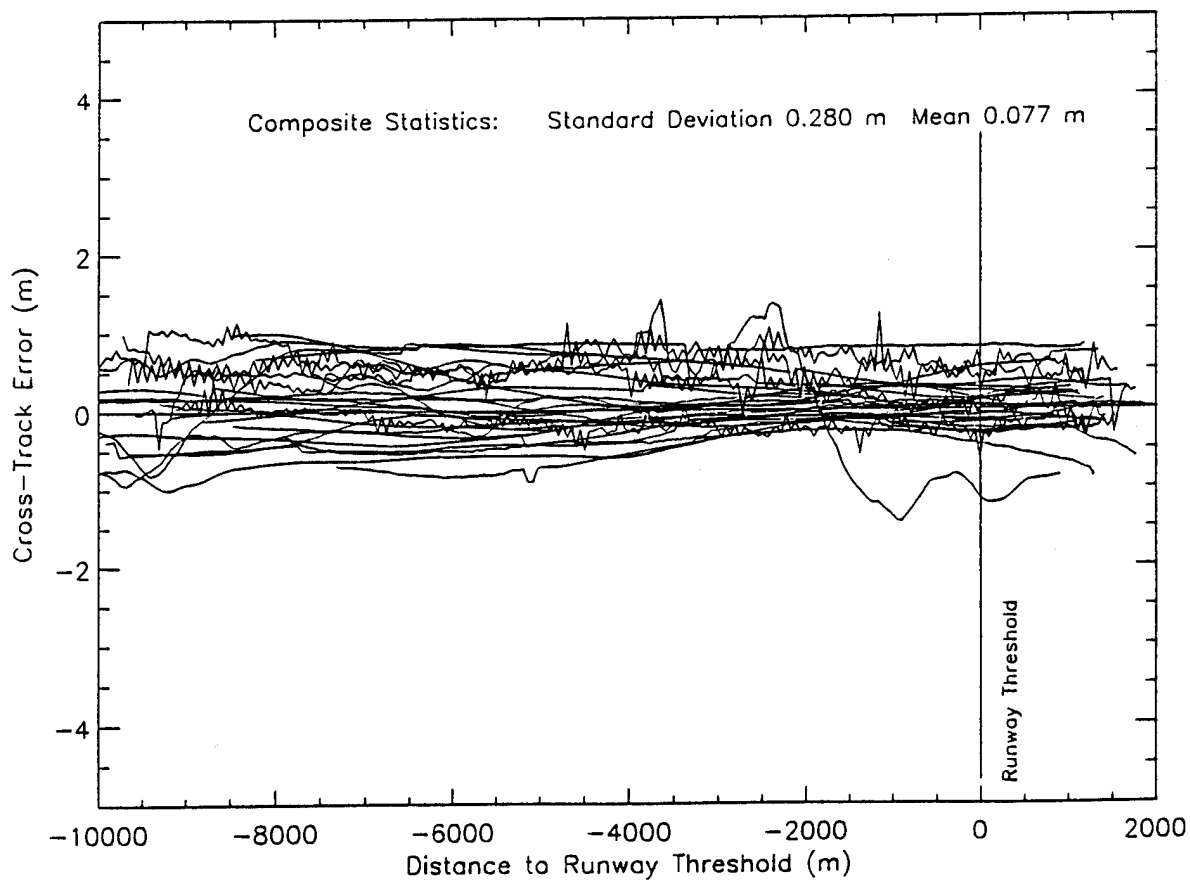


Figure 4: Sensor Cross-Track Error, ST John's - 27 DGPS Landing, Carrier-Smoothed C/A Code

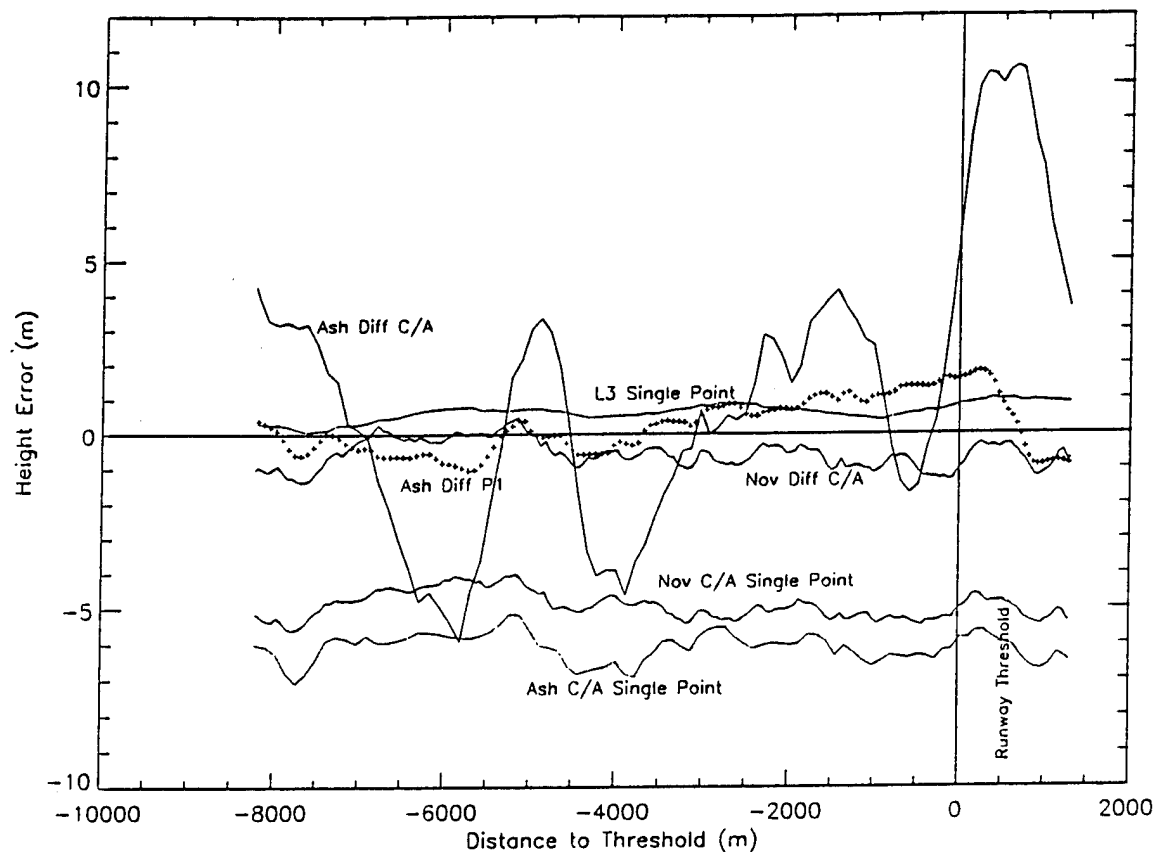


Figure 5: CACS and DGPS Solution Error in Height for One Sample Landing

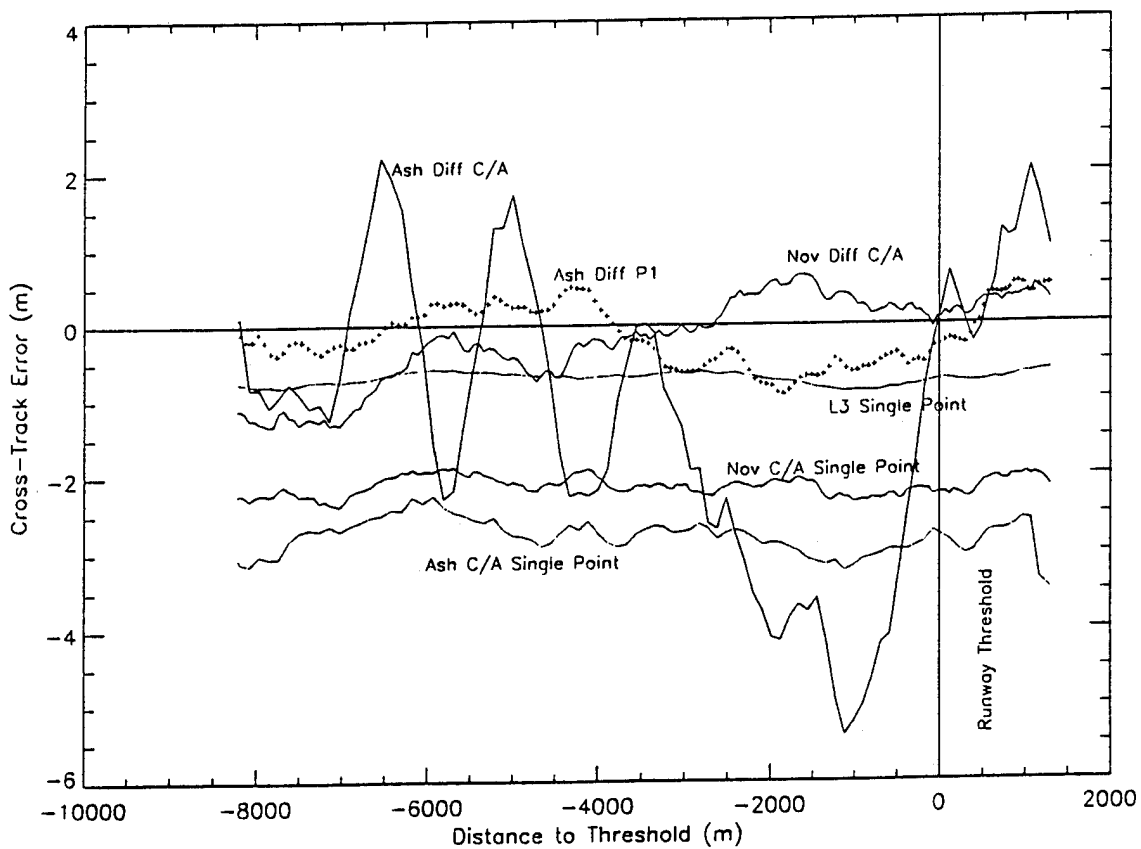


Figure 6: CACS and DGPS Solution Error in Cross-Track for One Sample Landing

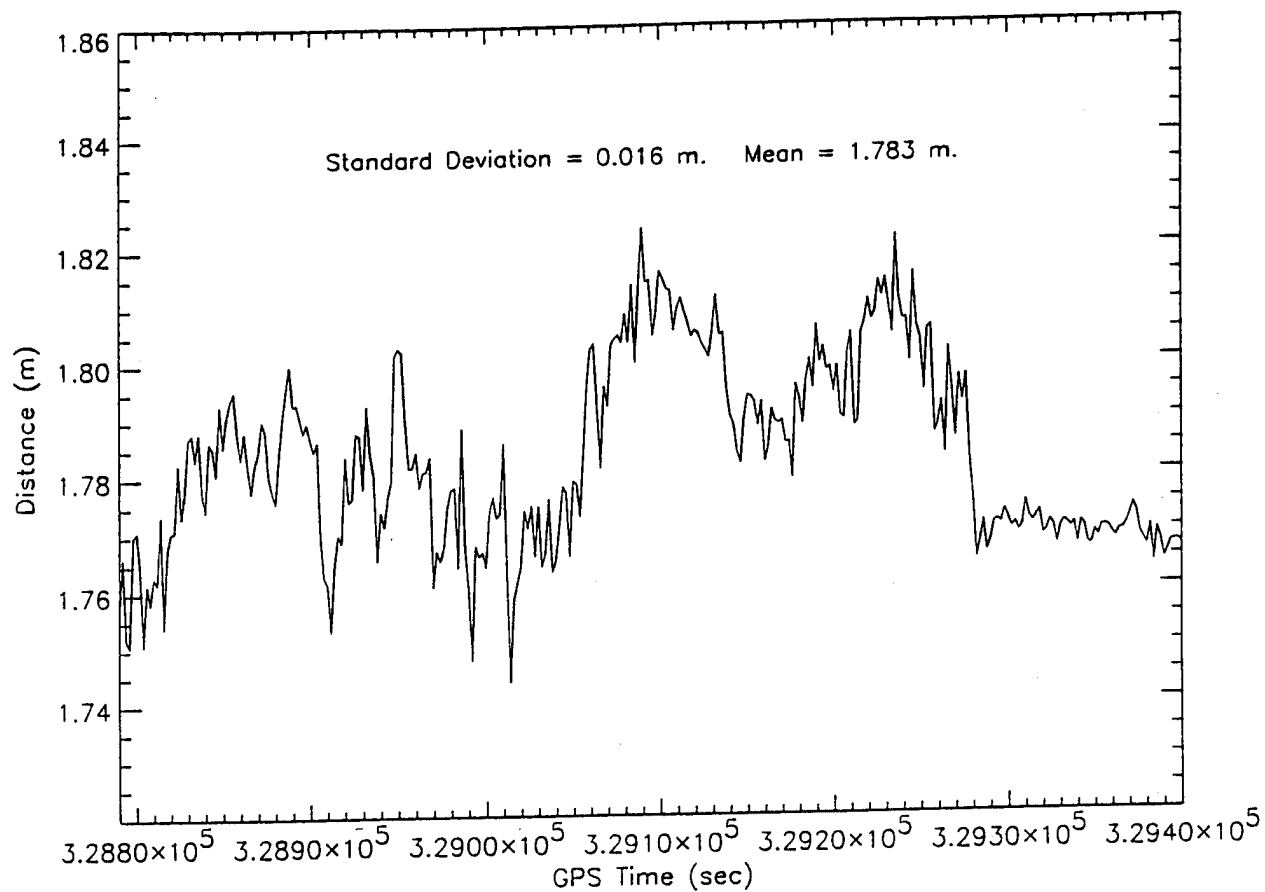


Figure 7: Novatel and Ashtech Aircraft antenna's Separation (Carrier Phase Solutions)

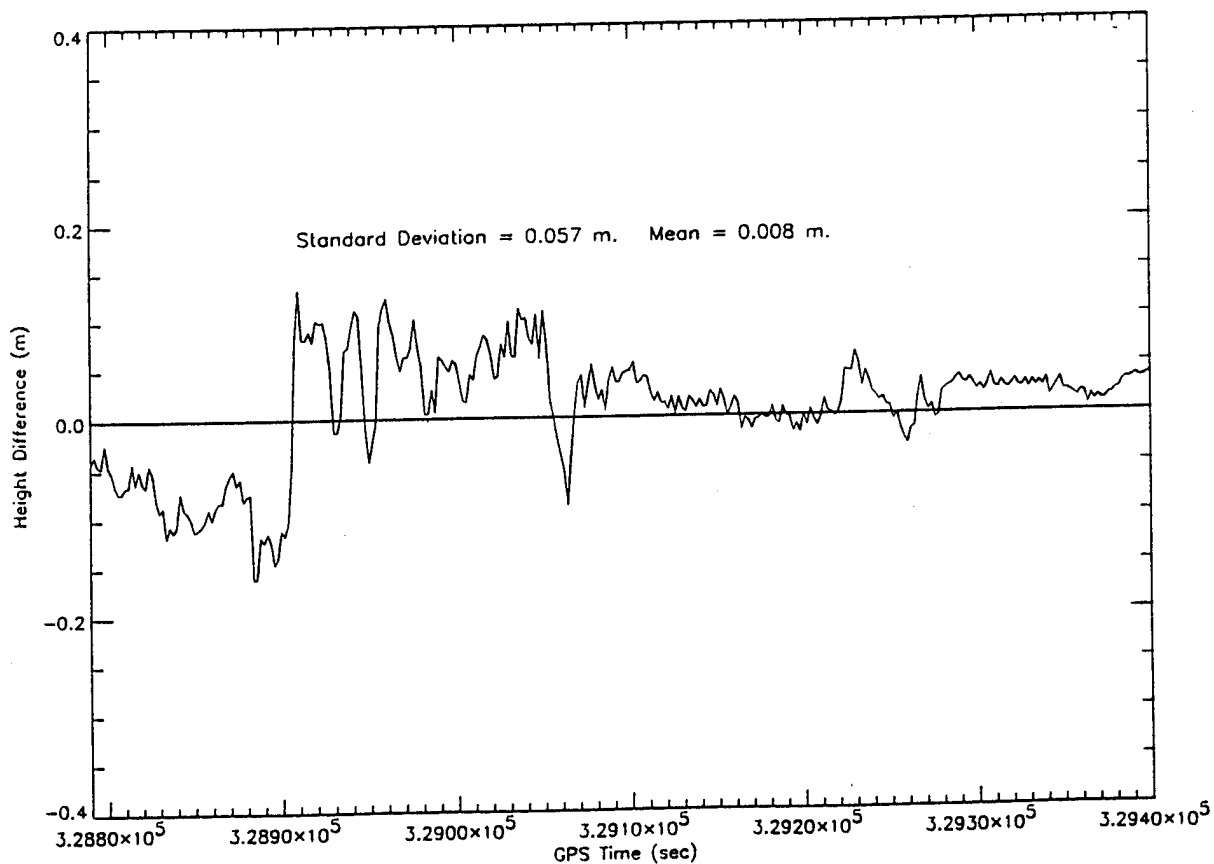


Figure 8: Height Difference Between Novatel and Ashtech Aircraft antennas (Carrier Phase Solutions)

Global Optimization of GPS Augmentation Architectures Using Genetic Algorithms

Samual Pullen, Per Enge, and Bradford Parkinson
Stanford University

BIOGRAPHIES

Sam Pullen is finishing his Ph.D. thesis as a Research Assistant in the Gravity Probe-B project at Stanford University. An S.B. Graduate of MIT, he conducts research on spacecraft design for reliability and robust control design along with studies of DGPS performance.

Per Enge is a Research Professor of Aeronautics and Astronautics at Stanford University. A Ph.D. graduate of the University of Illinois, his research focuses on DGPS aircraft landing applications. He previously taught at WPI and is an ION Satellite Division ex-Chairman.

Brad Parkinson is a Professor of Aeronautics and Astronautics at Stanford University and is the program manager for the Gravity Probe B spacecraft. He served as the first Program Director of the GPS Joint Program Office and was instrumental in the system's development.

ABSTRACT

The prediction of augmented GPS performance for spread-out user locations requires analyses of both accuracy under normal conditions and integrity in the case of system failures. Methods that combine covariance propagation and Monte Carlo simulation for the Wide Area Augmentation System (WAAS) have been developed, allowing system designers to study performance, risk, and cost tradeoffs. This process can be automated into computer search techniques that make WAAS network optimization possible

Revisions to our previously published accuracy and integrity algorithms have been made, including more detailed WAAS accuracy models and probability models for spacecraft, ionosphere, and ground errors. Updated results are given for the FAA testbed (NSTB) network and for an example WAAS system for Europe.

Next, a framework for network optimization is constructed from two bases. A top-level *user value model* expresses the relative quality of the combined

accuracy and integrity evaluations for a given network. Global optimization is carried out using a *genetic algorithm* which maintains a population of possible network designs and "evolves" the next generation using operators derived from the Theory of Natural Selection. The optimization process is computer-intensive but has the potential to converge to the best possible network for a given application. A complete model for European WAAS network optimization is presented, and the prospects for improved computer speed using parallelized code are discussed.

1.0 Introduction

Networks of ground stations and geosynchronous satellites designed to augment civilian GPS navigation performance have been shown to provide corrected pseudorange accuracies of 1-2 meters, making aircraft precision approach using augmented GPS possible. Local Area Augmentation Systems (LAAS) broadcast corrections from a single site to nearby users. Wide Area Augmentation Systems (WAAS) instead use a network of spread-out reference stations (WRS's) which transmit their observations to a master station (WMS). This master site computes coordinated corrections for all GPS satellites in view of any WRS and uplinks them to communications satellites for downlink to any user within a very large geographic region [1].

While the augmented-GPS performance demonstrated to date in flight tests is very promising, the prediction of overall system performance for the entire user population is difficult. Previous studies conducted at Stanford have described new methods to predict normal-condition WAAS navigation *accuracy* over a large user area [2]. In addition, Monte Carlo simulation of specific WAAS failure modes allows a prediction of post-RAIM *integrity* risk, or the risk of being placed in a dangerous situation due to not being warned of a GPS/WAAS system failure [4]. Combining these two separate evaluations gives a comprehensive picture of the overall performance and acceptability of a given WAAS network.

This paper expands and extends our previous work in several respects. In Section 2.0, the WAAS coverage prediction model is summarized, and new results for the FAA WAAS testbed are shown which incorporate improved ranging error models. In addition, new results for a proposed European WAAS network are presented. Section 3.0 describes the integrity evaluation model, which uses Monte Carlo sampling to optimize RAIM thresholds in the presence of various rare-event errors. Integrity results of this evaluation for the WAAS networks studied in Section 2.0 are given there.

Section 4.0 summarizes the use of *genetic algorithms* (GA's) to provide a very flexible global optimization capability. The evolutionary search operators used in standard GA's are explained, and the encoding of a GPS augmentation network into a GA-compatible form is demonstrated. Section 5.0 outlines our proposed WAAS network objective function or value model which is used to combine DGPS performance analyses with a user cost/benefit assessment into a single top-level measure. This function goes a step beyond current requirements to suggest, at a policy level, what the basic goals of augmented-GPS navigation systems should be.

Section 6.0 demonstrates the potential of top-level GA optimization by showing the improvement obtained for the European WAAS network in the first few GA generations. Finally, Section 7.0 discusses the software improvements needed to allow optimization of GPS networks on a national and international scale. A set of conclusions from the latest augmented-GPS performance studies and optimization runs are then given. In particular, WAAS is shown to be a cost-effective approach to wide-area precision navigation, and further developments should provide the capacity to tailor future systems to specific user needs in a very efficient manner.

2.0 WAAS Coverage Prediction Methodology

While it is already apparent that WAAS has the potential to provide Category I accuracy for aircraft landing and that baselines of hundreds of kilometers are possible, a coverage prediction model is needed to predict accuracy across the entire geographic spread of users and to help determine just how many wide-area reference stations (WRS's) are needed to meet the RTCA MOPS accuracy requirements [1]. Our method is summarized here, and revisions to the WAAS error models are also explained along with new WAAS network results.

2.1 Summary of Coverage Prediction Method

The coverage prediction approach used here is based on the solution of least-squares covariance equations for

given GPS and WRS geometries. This is a summary of the detailed explanation of the method contained in [2].

Accuracy predictions for large geographic areas are generated by a computer program which simulates a large number (between 1440 and 10,000) GPS and geosynchronous satellite geometries using a GPS orbit model. For each geometry, the matrix of direction cosines to each visible satellite G_w^i is computed for each WRS location i (using a 5° mask angle). At this stage, the ranging observation errors for each satellite visible at each WRS are computed from the RMTSA model given in Table 1. The large WRS ionosphere covariance matrix P^p can then be computed element-by-element.

Noise Source	WRS Error (m)	User Error (m)
receiver noise	0.33	0.50
SA latency	not applicable	0.20
multipath	$0.20 / \tan(\epsilon)$	$0.30 / \tan(\epsilon)$
troposphere*	$0.07 / \sin(\epsilon)$	$0.20 / \sin(\epsilon)$

*changed since publication in [2]

Table 1: One-Sigma RMTSA Errors

The program then cycles through a grid of user locations separated by 1-4 degrees in latitude and longitude. For each user, the geometry matrix G_u is computed, and two separate processes of covariance propagation are carried out in parallel. The first is for *clock/ephemeris* error for satellites in view of the user (using a 7.5° mask angle) based on the WRS's that can also see the satellite in question and can provide clock/ephemeris corrections. The second is for *ionospheric* spatial decorrelation projected from the pierce points observed by each WRS to the WMS, which fits a set of predictions to a grid, and finally to each user.

Covariance projections from these two error sources are brought together into a single pseudorange error covariance matrix P_v^* for each user which includes user-specific RMTSA errors. The weighted least-squares position error covariance \hat{P}_x is then computed, and the (Gaussian) vertical position error variance is given by the [3,3] entry of this final matrix. The vertical error for each geometry is stored in a histogram for that user, as is the Vertical DOP for the satellite geometry visible to that user [2]. "Availability" in this case is defined as the percentage of geometries for which a given user's vertical one-sigma error (given by $\sqrt{\hat{P}_x[3,3]}$) is within either the ILS or RNP Category I one-sigma requirements of 2.05 and 3.6 meters respectively. Geometries for which this requirement is exceeded are deemed "non-available", and if this state persists over time, an "outage period" for Category I landings results.

Figure 1 gives a conceptual flow chart for this covariance propagation method. Note that propagation of error covariance follows two separate, parallel paths. The *clock/ephemeris* process results in a 4×4 matrix \mathbf{P}_k^{SV} of error covariances for each satellite k (this is equal to the SPS covariance if no WRS's can see this satellite). For each user, the covariances for all the satellites he or she can see are arranged into \mathbf{P}^{SV} , which acts as the "plant" matrix for computation of the user position error covariance as follows:

$$\mathbf{P}_{\hat{x}} = \mathbf{G}_u^* \tilde{\mathbf{G}}_u \mathbf{P}^{SV} \tilde{\mathbf{G}}_u^T (\mathbf{G}_u^*)^T + \mathbf{G}_u^* \mathbf{P}_v^* (\mathbf{G}_u^*)^T \quad (1)$$

Note that the User Differential Range Error (UDRE) for each satellite in view is given by the diagonal elements of the matrix $\tilde{\mathbf{G}}_u \mathbf{P}^{SV} \tilde{\mathbf{G}}_u^T$, which maps the clock/ephemeris error from the WMS correction through the user's satellite geometry (expressed by $\tilde{\mathbf{G}}_u$) [2].

The process of *ionosphere* covariance propagation instead fits the vector of combined WRS ionosphere pierce-point measurements to the WMS ionosphere grid of 5-15 degrees in latitude and longitude. A model for estimating the decorrelation between ionospheric delays at points that are far apart has been fitted to data in [3] and is detailed in [2]. The covariance of this fit, \mathbf{P}^G , is then propagated to each pierce point of each user in the user grid. The resulting ionosphere fit error covariance, \mathbf{P}_e^U , is propagated to the overall position error as part of the "noise" term on the far right-hand-side of (1). The diagonal elements of \mathbf{P}_e^U also give the User Ionosphere Vertical Error (UIVE) variances.

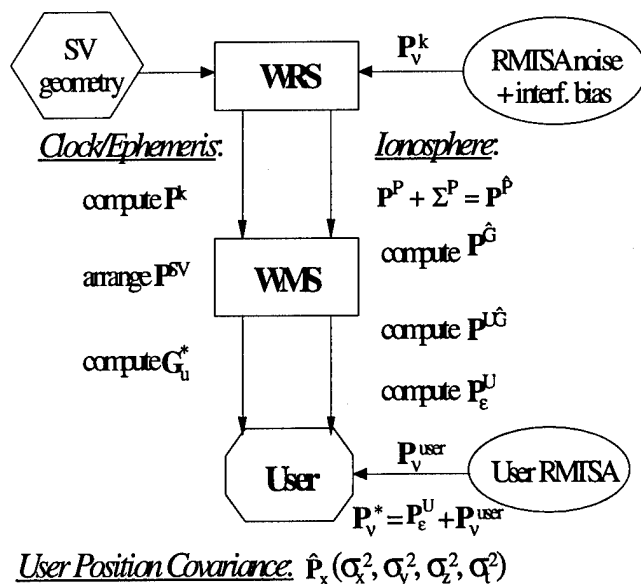


Figure 1: WAAS Covariance Overview

2.2 Revised Error Models

An ongoing effort is being made to update the error modes used for WRS and user observations. These revisions are based on the latest research on real-time algorithms at Stanford and the results from the experimental Stanford WAAS, which has three WRS's at Arcata and San Diego, California, and Elko, Nevada [9].

The Stanford WAAS implements *carrier smoothing* to reduce WRS observation errors. A Hatch/Eshenbach filter is used to average code pseudorange observations with much more precise carrier information (which has only 1-2 mm of noise) [11]. When a WRS first sees a given GPS satellite, the averaging process begins, leading to a reduction in the magnitude of receiver and multipath noise as a function of the time that satellite has been observed (without a cycle slip). Receiver noise has a short correlation time, but multipath takes much longer to average out. We now use an abstract exponential-decay model which gives a combined noise reduction factor *NRF* defined as follows:

$$NRF = \exp\left(-\frac{t_{obs}}{\tau_{cs}}\right) \quad (2)$$

where the generic carrier smoothing time constant τ_{cs} is conservatively estimated to be 60 minutes. In the code, the cumulative time t_{obs} is tallied as the satellite geometry is updated. The receiver and (elevation-dependent) multipath standard deviations (from the RMTSA) are then reduced by multiplying by *NRF* from (2).

In addition, the assumption of a *bivariate Normal* distribution among ionospheric pierce-point observations has been relaxed. In [2], the variance ($\sigma^2(d)$) of the true ionosphere delay relative to an observed point a distance d away is given by a linear/exponential function of d . This variance is converted to a covariance entry $\bar{\sigma}^2$ between two points using the bivariate Normal equation:

$$\bar{\sigma}_{i,j}^2 = \sigma_b^2 \left[1 - (\sigma_{i,j}(d)/\sigma_b)^2 \right]^{0.5} \quad (3)$$

where σ_b is a base deviation at a given point, assumed to be about 2.8 meters. The exponent 0.5 in the bivariate formulation results in closely correlated ionosphere measurements, even when separated by hundreds of kilometers. As a result, this exponent has been increased to 1.0 for our current studies, introducing more spatial decorrelation into the ionosphere correction process.

2.3 Ionosphere Observation Model Variants

Research on improving the calibration of satellite and receiver *interfrequency bias* suggests that this prevailing

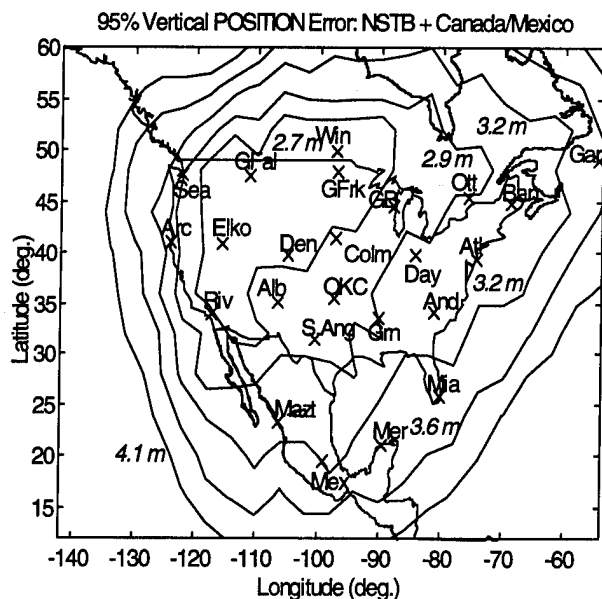


Figure 2: FAA NSTB 95% Vertical Accuracy

bias error (which affects WRS ionospheric delay observations) can be cut almost in half from what is observed today. Currently, the ionosphere model in [2] assumes a 0.75-meter additional noise (1σ) term to model uncorrected interfrequency bias. Estimates of the slowly-changing bias parameters are possible over several hours of data-taking, making it possible to improve this to about 0.4 meters [12]. This has not yet been demonstrated in an end-to-end sense; thus this adjustment is considered a provisional improvement.

A more radical change to the WAAS network would be to assume only *single-frequency* WRS ionosphere observations. It is possible to extract a measurement of ionospheric delay from the code-carrier divergence on a single broadcast frequency, as described in [8,13]. Because dual-frequency measurements by definition require the use of L2, which is not part of the SPS service guaranteed to civilian users, WAAS networks deployed by non-U.S. agencies may choose to restrict themselves to the use of L1 measurements only [14].

From comparisons of single-frequency measurements to more accurate dual-frequency ones, our best current estimate is that the use of single-frequency observations would add a one-sigma *vertical* error of around 0.8 meters to the WRS ionosphere delay measurement. However, since single-frequency receivers cannot directly separate ionosphere from other error sources, the covariance propagation method used here must be re-worked to combine the clock/ephemeris and ionosphere into one larger estimator for this case. We now expect this change to reduce 95% accuracy by about 15-20%, but the effect on integrity could be much worse.

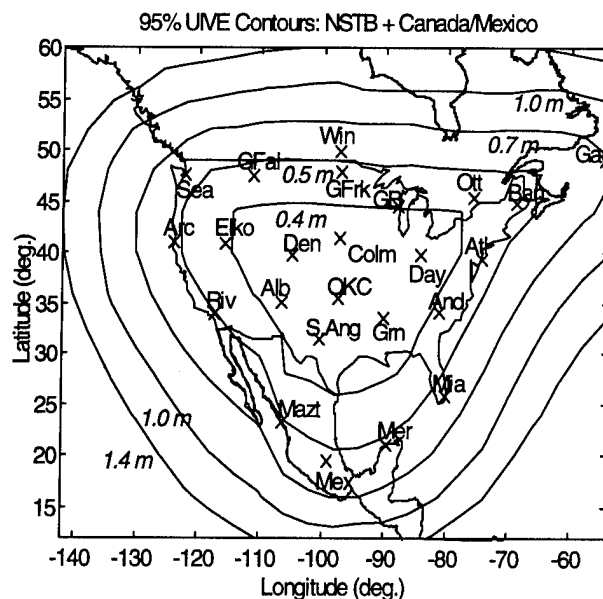


Figure 3: FAA NSTB 95% UIVE

2.4 Results of Improved Models

All of the following results incorporate carrier smoothing (2) and revised ionosphere decorrelations (3). The effects of further changes are cited where applicable.

Figures 2-4 show 95% vertical error, 95% UIVE, and 95% UDRE, respectively, for the revised FAA WAAS testbed, or NSTB, which will precede the operational WAAS into service on an experimental basis. It now includes six additional WRS's, three in Canada and three in Mexico, giving a total of 24. From Figure 2, the best accuracy is obtained in the Western plains states and southern Manitoba, where users can see both the 180° and 55° W geosynchronous satellites. Overall accuracy, compared to the 18-WRS all-CONUS NSTB [2], has improved to the point that all of CONUS is within $2\sigma_v = 3.5$ m under normal conditions. Improvement is most noticeable over the Eastern seaboard. The three WRS's in Mexico provide improved coverage to the Southwestern U.S. and provide better than 3.6 m accuracy over almost all of Mexico.

In Figures 3 and 4, both UIVE and UDRE contours tend to follow the outline of the outermost WRS's in the network. Ranging errors from both sources are comparable, and both are very small near the center of the network. It is a little surprising that UDRE degrades more rapidly as one moves away from the center, as fewer WRS's provide data to correct pseudoranges of satellites visible to these more distant users.

One problem with the proposed WRS layout is that, while the Gander WRS is in a very useful location, the Canadian WRS's in Ottawa and Winnipeg are too far

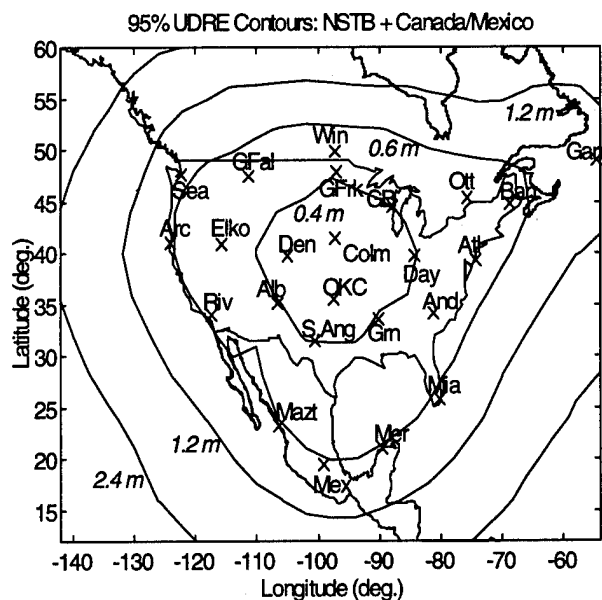


Figure 4: FAA NSTB 95% UDRE

East and are too close to the northern border of the U.S. to add significantly to coverage over most of Canada. Figure 5, which plots 95% vertical accuracy in 3-D, shows that accuracy degrades most rapidly in the Northwest corner of the user grid, over British Columbia. This may not be a significant drawback, since the network will be used as an experimental testbed only, but it is possible to achieve significantly better coverage of the Canadian provinces by moving the Ottawa and Winnipeg stations westward and northward.

Figure 6 shows 95% vertical position error results for a WAAS that could provide precision GPS corrections to Europe. It has a "four corner" arrangement of WRS's in Scotland, Spain, Northern Russia, and Turkey. Note that this minimal WRS arrangement provides sufficient accuracy to exceed the 4.1-meter vertical 95% ILS Category I precision approach requirement over almost all of Europe. This shows the potential of WAAS to provide high accuracy in a very cost-effective way, but the next question is whether such an arrangement also provides sufficient integrity, or user safety.

3.0 WAAS Integrity Simulations

3.1 Background and User Cost Model

Unlike the "normal conditions" assumed by the WAAS coverage prediction model, integrity threats are hazardous events that are presumed to occur rarely but have the potential to put the user in serious danger if he or she is not promptly warned. Since WAAS includes both ground-station and user elements, detecting these events is a shared responsibility of the augmentation network and of each user. Individual users can use Receiver Autonomous Integrity Monitoring (RAIM) to

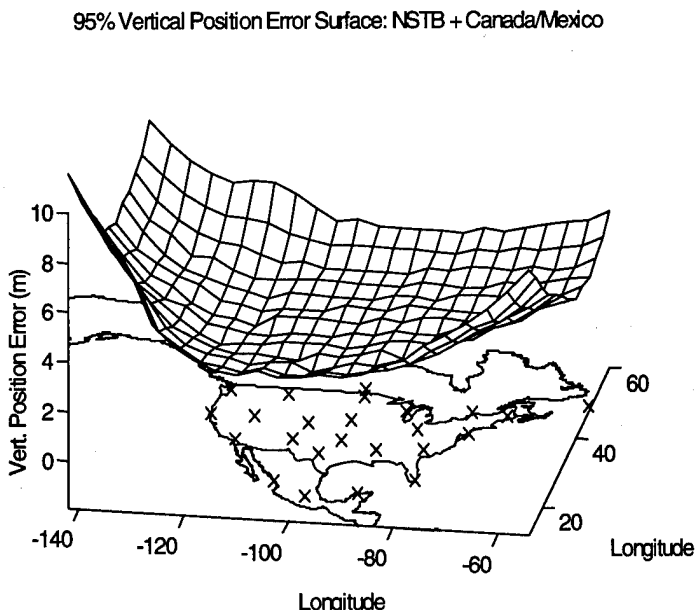


Figure 5: FAA NSTB 95% Vertical Accuracy Surface

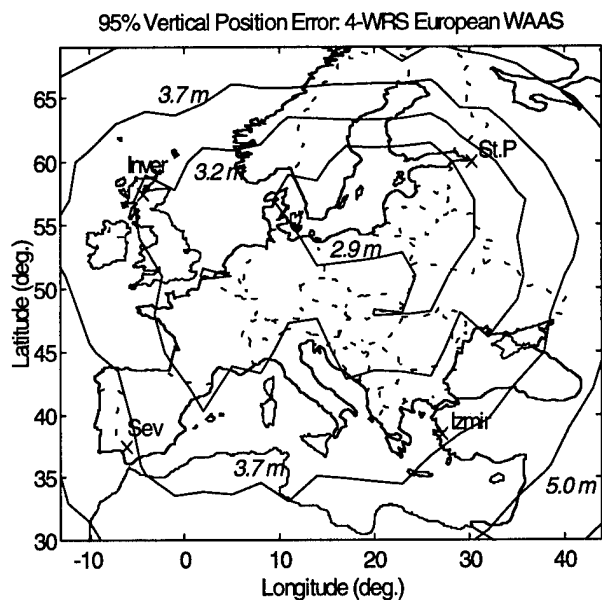


Figure 6: European WAAS 95% Vertical Accuracy

provide a warning from his overdetermined set of ranging measurements if he can see more than four satellites. This process uses the magnitude of a residual vector as the decision statistic; when it exceeds a pre-set threshold, the user is warned that conditions are unsafe. The ground stations can also monitor statistics that compare primary and redundant system measurements to each other. Warnings of unreliable satellites or corrections can then be included in the WAAS message to warn all affected users [5,6].

In [4], a method of setting WAAS RAIM residual thresholds based on a *user cost model* was developed and demonstrated. The cost model measures the likelihood of a fatal aircraft accident if certain outcomes, such as

missed detections and false alarms, occur. Table 2 gives this model expressed in terms of consequent user risks from various RAIM outcomes (also see Section 5.4). This relative measure of RAIM event costs allows us to optimize the detection thresholds rather than relying on the chi-square probability assumption used in [6].

RAIM Result	Base Cost	Variable Cost
good position	0	0
detected error	1	0
missed detect.	200	5
false alarm	1.012	0
non-available	0.012	0

Table 2: User RAIM Cost Parameters

3.2 WAAS Rare-Event Probability Models

The RAIM analyses in [4] focus on worse-than-Gaussian ionospheric spatial decorrelations, which are assumed to be possible in the worst 10% of cases based on previously published experimental data [3]. More severe decorrelations are possible in the worst 2% of cases. The effects of these “non-Normal” decorrelations must be analyzed by Monte Carlo simulation.

The approach taken here is based on [4] but uses the coverage prediction UIVE results. It samples ionospheric delay using the Normal distribution implied by the UIVE for a given site. If a sampled standard normal variable $|z| \leq 1.645$, the vertical ionosphere ranging error is simply the sample z times one-half of the assumed 2σ 95% UIVE result. If the sample exceeds 1.645 (the 90% cutoff), the UIVE-based standard deviation is *multiplied* by an expansion factor TM which accounts for the abnormal spatial decorrelation possibility:

$$\begin{aligned}
 1.645 \leq |z| \leq 2.33 &\Rightarrow TM = 1.13 \pm 0.11 \\
 |z| \geq 2.33 &\Rightarrow TM = 1.40 \pm 0.25 \\
 \text{otherwise} &\Rightarrow TM = 1.0
 \end{aligned} \quad (4)$$

This inflated deviation is multiplied by the already-large sample z to give the vertical delay in this case. Finally, the vertical error is multiplied by the appropriate obliquity factor (a function of the satellite elevation angle ϵ) to provide the slant pseudorange error [4].

For dual-frequency WRS receivers (the base case), the actual TM is periodically sampled from the Normal distribution in (3), where $TM = 1.13 \pm 0.11$ becomes Normal ($\mu=1.13$, $\sigma=0.11$). In the case of single-frequency WRS ionosphere observations (Section 2.3), rare-event spatial decorrelation uncertainty is much worse; thus the sampled TM from (3) is at least doubled.

In [4], N_s satellite geometries are updated in the same way as in Section 2.0, but each satellite is sampled to determine if it is “out of service” and is thus not usable. These failure probabilities, derived from [4,10], are:

$$\begin{aligned}
 \Pr(\text{GPS satellite unhealthy}) &= 0.014 \\
 \Pr(\text{GEO satellite unhealthy}) &= 0.010
 \end{aligned}$$

In addition, it is assumed that a failure of the WAAS ground network could lead to errors in the broadcast clock/ephemeris corrections that are much larger than UDRE. This could result from database or computation errors that are not caught by the WRS and WMS monitor systems. Because we are interested in sampling failure cases, the probability of having an increased UDRE is taken to be 0.001, which is at least 10 times higher than expected of an operational WAAS [5]. If a given satellite experiences this type of failure, its effective UDRE is increased by one plus a factor sampled from an *exponential* distribution with a mean $\mu = 2.0$.

3.3 Integrity Simulation Procedure

For each of N_s satellite geometries, N_k failure states are sampled. In each failure trial, each satellite is sampled to see if it is functioning normally, and unhealthy ones are removed from the user geometries. Each satellite next has the state of its ground correction sampled. The overall ionosphere decorrelation state, which applies to all users, is then sampled. A failure *bias* $|z| = 1.645$ is applied to this sample to insure that all cases at least have this amount of non-standard conditions.

Rather than attempting to run simulations for each user in the coverage prediction grid of Section 2.0, the user population is melded into a much smaller number N_u of user locations. For each sampled failure state, a weighted position fix is carried out for each user location. This position fix is based on the normal UIVE and UDRE for that location given by the coverage prediction method. Each user constructs a diagonal weighting matrix \mathbf{W} from the RSS of his RMTSA, UIVE, and UDRE variances (from Section 2.0), but a 25% random factor is applied to prevent the use of perfect weighting information. The true pseudorange error vector dx and the weighted residual statistic D are given by [4,6]:

$$dx = \mathbf{G}^* z = (\mathbf{G}^T \mathbf{W}^{-1} \mathbf{G})^{-1} \mathbf{G}^T \mathbf{W}^{-1} z \quad (5)$$

$$D^2 = z^T \mathbf{W}^{-1} (\mathbf{I}_m - \mathbf{G} \mathbf{G}^*) z \quad (6)$$

where \mathbf{I}_m is a $m \times m$ identity matrix (m is the number of functioning satellites in view), \mathbf{G} is the $(m \times 4)$ user geometry matrix, and z is the $(m \times 1)$ vector of pseudo-range measurements.

After all failure simulations are completed, the 90% of cases that would exist under normal DGPS conditions are added to the dx vs. D matrix stored for each discrete VDOP bin. Under normal conditions, dx and D are independent, with (vector) dx being Normally distributed with a covariance given by the vertical position error result from coverage prediction and D^2 having a chi-square distribution with variance parameter D^2/σ_z^2 and $m-4$ degrees of freedom [7]. The revised matrix is then searched to find the RAIM detection threshold T that minimizes the overall weighted RAIM cost (see Table 2) over all N_u user locations (each with a separate dx vs. D matrix). Note that only one set of thresholds is chosen for all users. If this optimal threshold T^* gives a cost that is lower than the non-availability cost in Table 2, RAIM is *available* for that VDOP and the system is usable. Otherwise, RAIM is *unavailable*, and the system incurs the non-availability inconvenience cost for those trials [4].

3.4 Integrity Results for 4-WRS European WAAS

Integrity evaluation for the European WAAS is done at 11 user locations shown as 'o' in Figure 7 (discussed in Section 4.1). These locations receive different weights as explained in Section 5.0. For these locations and the basic 4-WRS network of Figure 6, 1 million failure states and position fixes were simulated from 1000 satellite geometries for each of the 11 user locations. Table 3 contains the results in terms of the overall weighted RAIM cost and also probabilities of various hazardous events. For WAAS Category I approaches, the RPE or "required (vertical) protected error" is 19 meters at the 200-foot decision height.

Overall RAIM user cost	0.0019
Prob(RAIM available)	0.983
VDOP limit for availability	2.9
Prob(position error > RPE)	3.3×10^{-5}
Prob(missed detect. error > RPE)	0.109
Prob(false alarm)	0.0007
Fatal Accident Prob. per approach	6.8×10^{-7}

Table 3: 4-WRS European WAAS User Integrity

Although it is clear from Figure 6 (Section 2.4) that this 4-WRS network meets the WAAS Cat. I accuracy requirements at all 11 user locations, it is equally clear here that this network does not provide adequate integrity given the failure uncertainty models from Section 3.2. Availability is not bad at 98.3%, but the probability of exceeding the RPE is too high. RAIM catches 90% of these events, but the remaining 10% that become "missed detections" translate into an unacceptably high fatal accident risk, which is computed by dividing the

part of the RAIM cost due to integrity risk (0.0017) by the value of a single fatal accident in this cost model (2500). Note from this value that it implies that 10% of all missed detections (average cost of about 250) lead to fatal crashes. While current Cat. I requirements do not specify a maximum acceptable fatal accident risk, the implied requirement from the RNP and the Cat. III requirements is 10^{-9} . This network has considerably higher risk; so additional augmentations will be required.

4.0 Genetic Algorithm Optimization Model

By combining the coverage prediction model and integrity simulations, it is possible to generate overall evaluations for any GPS augmentation architecture. If the user population (or government agency) can derive a function that computes a top-level "figure of merit" based on the predicted geographic spread of accuracy and integrity performance, optimization of entire networks becomes possible. However, the use of complex covariance and simulation models to generate these evaluations requires a flexible optimal-search approach that does not require well-defined, deterministic problem formulations.

Evolutionary algorithms, a recent development of research in Artificial Intelligence (AI), now provide this capability. Several specific methods, including Simulated Annealing and Genetic Algorithms, have been used to solve a wide variety of problems. In general, they attempt to "evolve" better solutions over time by perturbing the best solutions found up to that point using semi-random operators that can avoid being "trapped" by local maxima or minima. They can also tolerate the noisy evaluations given by complex simulation models.

4.1 WAAS Network Design Encoding

Much of the work in designing an evolutionary search method for a specific application lies in tailoring the search to fit a natural encoding of the design space. For WAAS network optimization, the design variables can be expressed in a vector of binary (0/1) elements, or *genes*, which makes it possible to apply a standard *genetic algorithm* (GA) to evolve toward the optimal solution.

A computer search alone cannot design an optimal network -- the input of design engineers is crucial. In this case, we rely on human designers to provide a list of possible WAAS augmentation elements for the GA to consider. This list may include reference station sites, provision for independent monitor sites, and additional geosynchronous spacecraft to broadcast corrections and add redundant ranging measurements. Essentially, it can include any option that can be modeled in the GPS/WAAS accuracy and safety prediction algorithms.

Pop. Multipliers in Italics

Latitude (deg.)

Longitude (deg.)

0.1

1.0

1.2

2.0

2.5

1.0

2.0

1.0

1.4

1.0

1.0

1.0

GEO SV

Table 4 below gives a list of 12 augmentation options for the European WAAS application that we shall consider in this paper. Ten of these are potential WRS locations, which are shown as ‘x’ in Figure 7. Next is the use of single-frequency ionosphere corrections (see Section 2.3) instead of dual-frequency ones, and the last is a third geosynchronous satellite placed over Central Europe at 15° E longitude (shown by a dashed line in Figure 7). Given this list of options, a design solution is simply a vector of $N_d = 12$ 0-1 entries, where a 1 represents the presence of the relevant option and a 0 represents its absence. Note that the addition of new options thought up by the human designers can be handled simply by increasing the length of the design vector. This flexibility is important, as the results of early evaluations and optimization runs may motivate the designers to think of new augmentation options.

No.	Augmentation	Inc. Cost (\$ K)
1	Inverness WRS (UK)	2000
2	Seville WRS (SP)	2000
3	St. Petersburg WRS (RU)	2000
4	Izmir WRS (TU)	2000
5	Padua WRS (IT)	2000
6	Trondheim WRS (NO)	2000
7	Saratov WRS (RU)	2000
8	Nantes WRS (FR)	2000
9	Frankfurt WRS (GE)	2000
10	Kracow WRS (PO)	2000
11	Single-Freq. WRS RCR's.	- 90 N _{WRS}
12	add'l. GEO SV at 15° E	25,000

4.2 GA Population Evolution Operators

The canonical GA used here evolves the next-generation design solutions based on the current-generation members and objective values. Three operators are used. The first is *reproduction*, in which a percentage $P_R = 60\%$ of the current solution members are chosen as parents of the next generation according to their objective value, or *fitness*. This is done by a variant of *roulette-wheel selection*, in which the parents are randomly chosen with probabilities that are proportional to their linearly normalized fitnesses. In addition, the best solution is automatically copied directly into the next generation (*elitism*) [15].

one-point crossover

Mutation is the final canonical GA operator. Once the N_n solutions that make up the next generation have been chosen by reproduction and crossover, a Uniform random sample is made for each gene in each solution. If this sample is lower than a chosen mutation probability P_M , that gene (bit) is flipped to its binary complement (e.g., 0 \rightarrow 1, 1 \rightarrow 0). This process, akin to rare genetic mutations in biological organisms, helps maintain the genetic diversity of the solution population, preventing a small set of apparently good solutions from achieving

premature dominance (i.e., a local optimum). Normally, P_m is chosen to be ≤ 0.01 (we have chosen 0.01), but higher mutation rates (inducing more diversity) have been successful for other problems [15].

001100111001 \Rightarrow 001101111001
one-bit mutation

4.3 GA Optimization Procedure

Figure 8 gives a flow chart of the procedure by which the GA “breeds” new generations of solutions and evaluates their fitnesses. Generation 0 is initialized as mentioned in Section 4.1, then a loop of generations begins. Given a generation n , the fitnesses of each of its N_p solution members are evaluated using both coverage (Section 2.0) and integrity (Section 3.0) analyses fed into the cost model of Section 5.0. Reproduction, crossover, and mutation are then applied to generate the new generation $n+1$. The GA evolution can be stopped when the population (or the value of its best solution) stops improving, or it can be ended after a set number of generations. Each re-evaluation of a given network is added to those conducted previously; thus statistical significance increases with each new evaluation. Once a given network evaluation converges to within an uncertainty tolerance, no further accuracy/integrity evaluations are needed. Therefore, later GA generations will run faster on the computer than earlier ones.

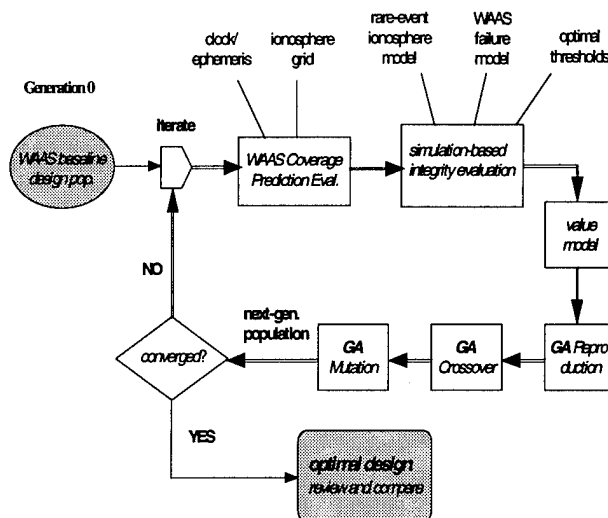


Figure 8: GA Optimization Procedure

5.0 WAAS Network Objective Function

Each of the possible solutions generated by GA evolution needs a *fitness* evaluation, or a measure of its relative “goodness”. Because GA optimization is very flexible, there are no mathematical constraints on the form of this system objective function. We can thus

construct a “value model” that attempts to express the system’s top-level utility for the total user population. This is a key driver of the optimization process, as the GA evolution will tend to exploit any inconsistency or “hole” in the fitness model. For this reason, the elements of the objective function should be carefully considered, and the results of early GA runs may motivate changes in the value model.

The value model developed here is a provisional attempt to weigh user benefits and system costs in as wide a framework as possible, knowing that substantial revisions may be necessary as more designer and user input is received. The overall objective function $F(n)$ to be maximized is given by:

$$F_{\text{WAAS}}(n) = \sum_{u=1}^{11} PM_u [B_{\text{air}}^u f_{\text{acc}}^u - f_{\text{integ}}^u] - LCost_n \quad (7)$$

where f_{acc}^u and f_{integ}^u represent evaluations of coverage and integrity performance respectively for user location u , B_{air}^u is the Cat. I user benefit for a given user location, PM_u is a “population multiplier” which measures the size of the user population near that location, and $LCost_n$ is the acquisition cost of a given WAAS network solution n , which includes the procurement cost and four years of OEM (operations and maintenance).

5.1 Population Multiplier

The basic definition for the population multiplier is:

$$PM_i = \begin{cases} \sqrt{p_i / p_c} & \text{where } p_i > p_c \\ 1 & \text{otherwise} \end{cases} \quad (8)$$

where p_i is the user population (which could be total population, number of air passengers, etc.) and p_c is a “critical value” which insures that all areas covered by WAAS get a minimum base priority. Locations which exceed this critical value do get a higher priority, but it does not scale linearly. The values of PM for the 11 user locations selected for the European WAAS is shown in Figure 7. Note that the location over the North Sea is valued at 10% of the overland site values since precision approaches cannot be done there. The maximum value of 2.5 given to the Leipzig, Ger. user location implies a critical value for overall population of about 8 million.

5.2 Network Acquisition Costs

The system acquisition cost for all WAAS networks assumes a well-equipped triply-redundant hardware setup at all ground stations. It includes a WMS procurement cost estimated at \$6 million and four years of OEM at \$2 million/year, giving a WMS acquisition cost of around \$14 million. The incremental WRS cost

estimated to be \$1.1 million, includes a \$0.5 million procurement cost and \$150 thousand per-year OEM cost. The cost savings obtained by using single-frequency receivers in the WRS's is estimated at 75% of the cost of a dual-frequency receiver set multiplied by the number of WRS's in a given solution. For all ground augmentations, an 80% administrative and indirect cost factor is added, giving conservative final life cycle costs of \$25 million for a WMS and \$2 million for each WRS (as shown in Table 4). This is based on the high overall cost estimates for the FAA WAAS given in [16]. Finally, the cost of providing an additional geosynchronous satellite is assumed to be \$25 million, the estimated cost of an inexpensive satellite designed for just this purpose. As in the Inmarsat case, leasing a GEO transponder may be an option, but the high value of the 15° E location suggests even a lease cost will be much higher than the \$2 million/year paid by the FAA. The sensitivity of the optimal result to this cost should be examined further.

5.3 User Benefit Estimates

The calculation of benefits provided by Category I to precision approach users requires making significant assumptions. According to [17], WAAS is expected to increase the number of Category I approaches in the U.S. from 765 (in 1994) to over 5,000. It also suggests an overall user benefit for WAAS Cat. I to be \$992 million, or about \$200,000 per approach. In Europe, we estimate that this life-cycle per-approach benefit will be doubled due to the poorer weather there. In [18], Europe is estimated to have 326 Cat. I ILS facilities (1994), and we conservatively assume that WAAS will allow this to grow to 1200, giving a total user benefit of \$480 million.

An estimate of the per-approach benefit of having Cat. I available is estimated by [18] as saving 2 minutes. Converted to aircraft per-hour fuel and direct operating costs of a weighted mix of passenger aircraft (about \$4800), the benefit (conservatively) becomes an average of \$160 per approach. Given 1200 Cat. I approaches each providing benefits of \$400,000 on average over a four-year life cycle, approximately 3 million Cat. I approaches in Europe are expected in during this time.

A second user benefit to WAAS is removing the need to support and maintain the 326 current ILS facilities that now provide Cat. I capability. This cost is estimated by [18] to be \$400,000 per ILS facility (per life cycle), which, multiplied by 326, gives an added benefit to WAAS of \$130 million. While it can be argued [14] that the current ILS network has been recently upgraded and represents a "sunk cost," the continual maintenance of it would no longer be necessary after WAAS becomes operational. Under this model, the total life-cycle benefit of WAAS Cat. I is \$610 million.

5.4 Accuracy and Integrity Evaluation

The WAAS accuracy evaluation f_{acc}^u is simply a percentage of the benefit for each user location, which is broken down from the \$610 million total based on the population multiplier for that site. Perfect navigation gets 100% credit, a 2σ vertical error of 2.1 m gets 99%, 4.1 m (the ILS requirement) gets 90%, and 7.6 m (the WAAS RNP requirement) gets only 20% (since it is at the outermost limit of acceptability). A cubic polynomial fit gives, for a resulting 2σ vertical accuracy a (m):

$$f_{acc}^u = 1 - 0.005a + 0.0052a^2 - 0.0024a^3 \quad (9)$$

where f_{acc}^u is in decimal terms (i.e. from 0 to 1).

Converting the RAIM user cost of Section 3.1 to this value framework requires two further assumptions. In Probabilistic Risk Assessment (PRA), it is considered valid to assign cost values to fatalities if the underlying risk is sufficiently small (below 10^{-4}) [19], which it is for GPS integrity. Assuming an average (based on the breakdown of aircraft sizes for Cat. I approaches) of 100 fatalities per fatal incident and a conservative "value per life" of \$10 million, each fatal accident incurs a loss of about \$1 billion. Since 3 million approaches are foreseen over the 4-year life cycle, and a fatal accident implies a cost of 2500 in the RAIM cost model, we can convert from RAIM cost (R_c) to overall value (f_{integ}^{tot}):

$$f_{integ}^{tot} = \frac{(\$1 \times 10^9)(3 \times 10^6)}{2500} R_c = 1.2 \times 10^{12} R_c \quad (10)$$

Note that this calculation is also broken down by user location and population multiplier within the RAIM user cost optimization (Section 3.3). Also note that the non-availability cost per approach (0.012) from Table 2, which is included in the integrity evaluation, implies a nuisance cost equivalent to an average of an hour of added aircraft cost, including all consequent delays.

5.5 Value of 4-WRS Baseline European WAAS

The accuracy of the baseline 4-WRS European WAAS network (shown in Figure 6) translates into a accuracy multiplier (weighted by PM) of 0.958, giving an overall user benefit of \$584 million. However, the RAIM user cost of 0.0019 from Table 3 translates (using (10)) into an integrity cost of \$1.73 billion, or 3 times the user benefit. Clearly, this network is insufficient. Note that the acquisition cost of \$33 million is dwarfed by the benefits and costs that result, indicating that additional augmentations would be very cheap relative to the possible performance improvement. Also, the fact that a 4-WRS WAAS network cannot provide sufficient integrity suggests that proposed augmented-GPS systems

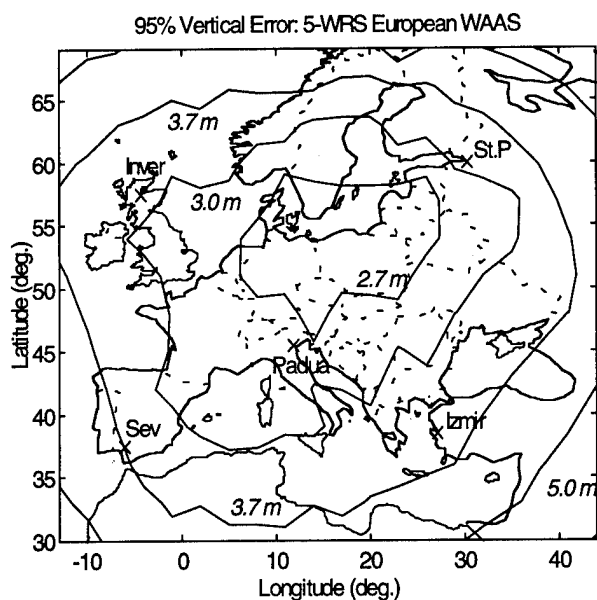


Figure 9: 95% Position Error for 5-WRS Network

for large regions of Europe that are based on one or two DGPS sites would be insufficient as well, even though they may meet the Cat. I accuracy requirements [20].

6.0 "First-Generation" WAAS Results

In our efforts to run the GA optimization code on the European WAAS problem, we have discovered that the software needs to be re-written for parallel processing and that a computer with sufficient available processors will be needed to evolve a population of networks toward optimal convergence. However, we can conduct a first-generation evolution using the GA operators and manually investigate some of the networks that result. Results for two of these variants are shown here.

Figure 9 shows 95% vertical accuracy contours for a network coded [111110000000], which is simply the base 4-WRS network plus a 5th WRS in Padua, Italy, in south-central Europe. Compared to Figure 6, accuracy over highly-populated central Europe is significantly better, resulting in an accuracy benefit of \$590.5 million. More importantly, integrity risk has decreased by a factor of 5.6 to give a total cost of \$403.6 million. The acquisition cost is still only \$35 million, giving a final value of about \$152 million. The addition of a single WRS in a beneficial location thus has resulted in a feasible design.

Figure 10 shows vertical accuracy for a network coded [111110000101]. This adds a 6th WRS in Cracow, Poland, and it also uses the additional GEO at 15° E, giving an acquisition cost of \$62 million. Although the accuracy contours continue to improve, the benefit has only slightly increased to \$593 million. However, the

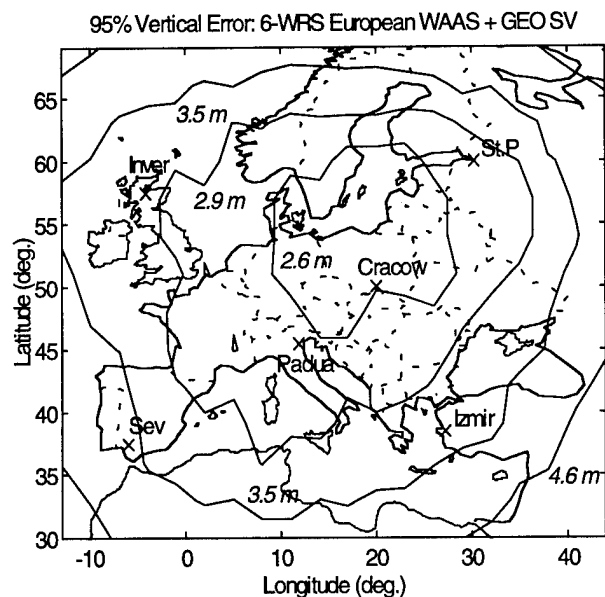


Figure 10: Pos. Error for 6-WRS + GEO Network

addition of the GEO satellite has made a further substantial improvement to integrity. All failure trials were available, and the integrity cost has fallen to just \$73 million. The total value for this network is \$458 million, demonstrating that the addition of the 15° E GEO satellite is desirable even if its acquisition cost is much higher than \$25 million.

Table 5 gives the relevant integrity parameters for both of these networks. We are continuing to run evaluations of the first and second-generation GA designs as well as manually-designed alternatives, but we have not yet found the point of "diminishing returns" beyond which further augmentations are not cost-effective.

Category	5-WRS	6-WRS+GEO
<i>RAIM user cost</i>	0.000336	0.000061
Prob(available)	0.9998	1.0
VDOP avail. limit	4.6	N/A
Pr(error > RPE)	1.4×10^{-5}	6×10^{-6}
Pr(MDlerror > RPE)	0.055	0.020
Pr(false alarm)	0.0002	3.2×10^{-5}
Fatal Acc. Prob/app.	1.3×10^{-7}	2.4×10^{-8}

Table 5: Integrity for European WAAS Varaints

7.0 Conclusions and Further Work

Given the current state of information about augmented DGPS systems (WAAS in particular), it is difficult to make predictions regarding WAAS system-level performance from which network design decisions can be made. We have succeeded in doing so by

developing algorithms that combine covariance propagation to determine position accuracy for large areas of potential users with failure-case simulations that incorporate the best available current knowledge. Further improvements in these prediction methods are possible, including fitting more detailed error models to the rapidly-growing Stanford WAAS database. Better models of ground integrity can also be developed, allowing us to add detailed ground integrity monitor optimization to our current optimal-RAIM algorithm. Finally, the wealth of data to be collected by the FAA's NSTB starting in 1997 should dramatically reduce our uncertainty about potential failure sources, most notably including ionospheric spatial decorrelation.

The augmented-GPS network optimization results we have achieved to date are impressive. We have demonstrated the policy-level feasibility and desirability of using WAAS to provide Category I precision approach capability to Europe with the network designs of Section 6.0, and we are continuing to search for the best possible combination of WRS's and geosynchronous satellites to accomplish this. The 6-WRS + GEO SV combination looks very promising, as it meets all implied Cat. I requirements and provides a value benefit of over \$450 million, depending on the cost of the GEO. We plan to expand the applicability of our optimization approach by revising the assumptions of European value model for networks in North America and the rest of the world.

As noted before, our ability to make this vision of augmented-GPS evolutionary optimization a reality requires implementing the coverage prediction and integrity simulation software on a multi-processor computer. This is intuitively easy because the evaluation of accuracy or integrity for each user location is a similar process that can be done simultaneously for as many locations as there are available processors. Stanford's GPS research groups plan to acquire a workstation with at least 16 fast processors by early next year. This computer will be used for extensive simulations of both LAAS and WAAS architectures, as Stanford is contracted by the FAA to evaluate the cost-benefit performance and certifiability of various competing LAAS systems. This work will utilize and further develop the GPS evaluation and optimization techniques reported in this paper.

ACKNOWLEDGEMENTS

The authors would like to thank the following people for their help with this research and the software on which it is based: Y.C. Chao, Dave Lawrence, Dr. Changdon Kee, Boris Pervan, Y.J. Tsai, and Dr. Todd Walter. The advice and interest of many other people in

the Stanford GPS research group is appreciated, as is funding support from NASA, the FAA, and Boeing Commercial Airplane Group.

REFERENCES

- [1] P. Enge and A.J. Van Dierendonck, "The Wide Area Augmentation System", *Proc. 8th Int'l. Flight Inspection Symposium*, Denver, CO., June 1994.
- [2] S. Pullen, P. Enge, B. Parkinson, "A New Method for Coverage Analysis for the Wide Area Augmentation System (WAAS)", *Proc. of ION 51st Annual Meeting*, Colorado Springs, CO., June 5-7, 1995, pp. 501-513.
- [3] J.A. Klobuchar, P.H. Doherty, and M.B. El-Arini, "Potential Ionospheric Limitations to Wide-Area Differential GPS", *Proceedings of ION GPS-93*, Salt Lake City, UT., Sept. 22-24, 1993, pp. 1245-1254.
- [4] S. Pullen, P. Enge, B. Parkinson, "Simulation-Based Evaluation of WAAS Performance: Risk and Integrity Factors", *Proceedings of ION GPS-94*, Salt Lake City, UT., Sept. 20-23, 1994, pp. 975-983.
- [5] R. Loh and J.P. Fernald, "Integrity Concepts for a GPS Wide-Area Augmentation System (WAAS)", *Proceedings of ION NTM-94*, San Diego, CA., Jan. 24-26, 1994, pp. 127-134.
- [6] T. Walter, P. Enge, F. Van Graas, "Integrity for the Wide Area Augmentation System", *Proceedings of DSNS-95*, Bergen, Norway, April 24-28, 1995, No. 38.
- [7] S. Pullen and B. Parkinson, "A New Approach to GPS Integrity Monitoring using Prior Probabilities and Optimal Threshold Search", *Proceedings of IEEE PLANS '94*, Las Vegas, NV., April 11-15, 1994, pp. 739-746.
- [8] V. Ashkenazi, C.J. Hill, J. Nagel, "Wide Area Differential GPS: A Performance Study", *Proc. of ION GPS-92*, Albuquerque, NM., Sept. 16-18, 1992, pp. 589-598.
- [9] T. Walter, C. Kee, *et.al.*, "Flight Trials of the Wide Area Augmentation System (WAAS)", *Proc. of ION GPS-94*, Salt Lake City, UT., Sept. 20-23, 1994, pp. 1537-1546.
- [10] W. Phlong, B. Elrod, "Availability Characteristics of GPS and Augmentation Alternatives", *Navigation*, Vol. 40, No. 4, Winter 1993-94, pp. 409-428.
- [11] R. Hatch, "The Synergism of GPS Code and Carrier Measurements", *Proc. 3rd Int'l. Geodetic Symposium on*

Satellite Doppler Positioning, Las Cruces, NM., Feb. 1982, pp. 1213-1232.

[12] Y.C. Chao, Y.J. Tsai, *et.al.*, "An Algorithm for Inter-Frequency Bias Calibration and Application to WAAS Ionosphere Modeling", *Proc. of ION GPS-95*, Palm Springs, CA., Sept. 12-15, 1995.

[13] C. Cohen, B. Pervan, B. Parkinson, "Estimation of Absolute Ionospheric Delay Exclusively through Single-Frequency GPS Measurements", *Proc. of ION GPS-92*, Albuquerque, NM., Sept. 16-18, 1992, pp. 325-330.

[14] W. Lechner, private conversation, Stanford GPS Research presentation, August 11, 1995.

[15] L. Davis, Ed., *Handbook of Genetic Algorithms*. New York: Van Nostrand Reinhold, 1991.

[16] *A Technical Report to the Secretary of Transportation on a National Approach to Augmented GPS Services*. U.S. Department of Commerce, NTIA Special Publication 94-30, December 1994.

[17] FAA HDQTRS - APO, "Projected GNSS Cat I/II/III Precision Landing Operations", *Proc. of ICAO Comm./Ops. Meeting*. Montreal: Mar. 27-Apr. 7, 1995. Item 1.

[18] ICAO Secretariat, "Economic Evaluations of the Main Options for Precision Approach and Landing Systems", *Proc. of ICAO Comm./Ops. Meeting*. Montreal: Mar. 27-Apr. 7, 1995, Item 2-3, WP/23.

[19] J.D. Graham and J.W. Vaupel, "Value of a Life: What Difference Does It Make?", *Risk Analysis*, Vol. 1, No. 1, 1981, pp. 89-95.

[20] G. Schanzer, "Satellite Navigation for Precision Approach: Technological and Political Benefits and Risks", *Proceedings of ISPA '95*. Braunschweig, Ger., Feb. 21-24, 1995, pp. 25-30.

G.N.S.S. Combined with Head-Up Display for Precision Landing

Jean-François Jehl and Luc Baron
SEXTANT Avionique

BIOGRAPHY

- J.F. JEHL is an engineer in Mathematics graduate from ENSIMAG School in France (1971).

Specialist of digital computer techniques and software design, he joined the Aeronautical Industry in 1974 within CROUZET Company for the design of airborne navigation equipment.

From 1974, working for SEXTANT Avionique, he has got more than 20 years expertise in the design and marketing of avionics equipment. Specialist in navigation, he has been the Product Manager for the OMEGA/VLF, RNAV computer and G.P.S. activity.

Since 1994, he is the Marketing Manager in the Commercial Avionics Division of SEXTANT Avionique for the G.N.S.S. Navigation Activity.

- Luc G. BARON is an engineer in Aeronautics. He graduated from Ecole Supérieure de l'Aéronautique et de l'Espace in France, in 1976.

He joined THOMSON-CSF General Avionics Division (now merged into SEXTANT Avionique) in 1977, where he worked for 4 years on advanced electro-optical infrared and laser weapon systems.

Still in the same division, he moved to the civil activities, first on EFIS/ECAM for the Airbus A 310 program, then appointed as program manager for the primary fly-by-wire flight control computer of the Airbus A 320.

After 4 years as marketing manager for Head-Up Displays for the Commercial Avionics Division of SEXTANT Avionique, he was appointed in May 1995 as Program Manager for the Alitalia MD-82 Upgrade Program (H.U.D. and G.N.S.S.).

He was a member of a NATO/AGARD working group on Validation of Flight Critical Control Systems.

ABSTRACT

With the growing interest in the airline community for G.N.S.S. and its contemplated precision performances, new avionics sub-systems combining the G.N.S.S. and Head-Up Display equipment can be designed. They offer cost-effective solutions for improving the landing function of an aircraft.

Systems including G.N.S.S. can efficiently upgrade aircraft to achieve CAT2 and ultimately CAT3 weather conditions landing operational minimums thanks to HUD, without modification of the existing aircraft avionics and autopilot/autoland, to runways that currently can basically support non-precision approaches only.

Examples may be given where the basic avionics (e.g. AHRS) have not, without G.P.S., the level of performance and precision that may be required for a HUD and, for some parameters, do not even compute them. The G.P.S. then provides additional inputs that allow to compute or enhance those data in the H.U.D. system. The resulting system, using hybrid algorithms, can be used for global operational improvement of the aircraft as SEXTANT Avionique successfully proposed it to Alitalia to gain CAT3B certification on their MD-82 aircraft initially CAT3A.

The paper presents the architectures suitable for coupling the G.N.S.S. equipment to HUD and the achievable performances. The Alitalia's MD-82 installation is described to emphasize the operational and economical advantages of such an "hybrid landing system" and summarize the main certification issues.

1. INTRODUCTION

One of the most demanding function of an aircraft is precision approach and landing for operation in all weather conditions. The profitability of an airline operator, particularly in those countries where bad weather conditions are frequent, may be strongly dependant on the landing equipment of its fleet.

Until now, the lowest CAT3 minima capability could only be reached with complex and quite expensive equipment involving on board redundant CAT3 Instrument Landing System, Autopilot and triple inertial installation plus a CAT3 ILS installation on the ground. For that reason, many aircraft that would need CAT3 System are not equipped and are operating within CAT1 or CAT2 minima only.

With the new Global Navigation Satellite System (G.N.S.S.) presenting unequaled performances and the Head-Up Display (HUD) modern technology, it becomes possible to increase the landing performance in an aircraft originally designed for a given category by reducing the minima with acceptable cost impact.

Separately, the two techniques are able to bring improvement in the precision approach system in two different ways : G.N.S.S. as a very performant and low-cost positioning system, HUD as a complementary instrumentation. When installed jointly H.U.D. and G.N.S.S. can be combined advantageously ; each technique being able to enhance or complete the performance of the other one.

On the basis of the GNSS/HUD combination principles, SEXTANT Avionique is designing integrated landing subsystems that include a core HUD/GNSS equipment, adaptable to different landing requirements.

The following paragraphs present the basic principles for H.U.D. and G.N.S.S. combination and system architectures that can be adopted for different applications including enhancement to CAT3b of a CAT3a system, as installed on the MD82 Alitalia's fleet.

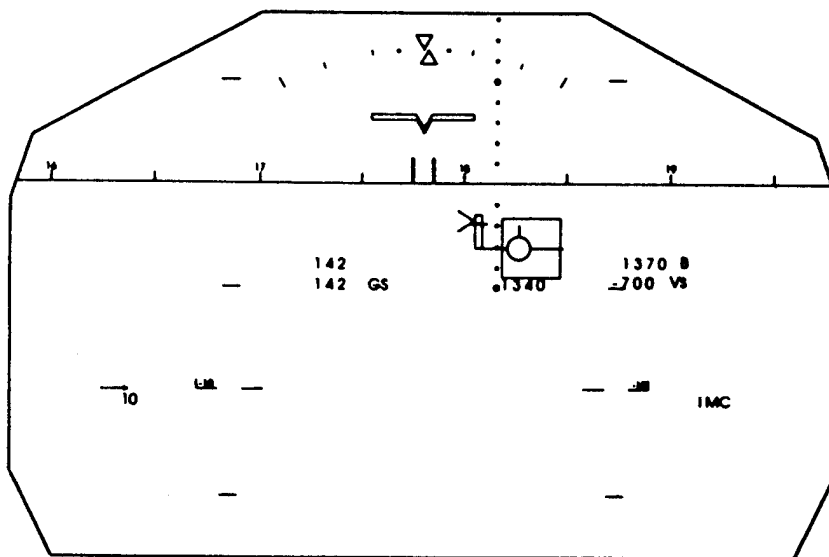


Fig 1 - HUD SYMBOLOGY EXAMPLE

2. HUD : Piloting Instrumentation

2.1 Principle

The HUD, designed for enhancing pilot monitoring and reaction time during the critical phases of flight (landing, roll-out, take-off) displays in the field of view of the pilot (superimposed with external view of the environment) the parameters used for controlling the aircraft.

Basically during the landing phase, it displays (as shown on figure 1) a synthetic image of the runway and of the flight path vector of the aircraft that enables the pilot to perform immediate transition from instrument flight without visibility to visual conditions and to control the trajectory of the aircraft in poor visibility with reduced stress. This pilot monitoring and reaction time improvement enable to qualify the system for shorter R.V.R. (minimum Runway Visual Range) and lower D.H. (Decision Height for missed approach).

2.2 H.U.D. Interfaces with the Avionic System

As shown in the diagram in figure 2, the H.U.D. receives from various sources Inertial System, radioalt, ILS data to calculate and present the symbol on the display.

The most significant data are :

- Attitude (roll and pitch) and Heading
- Horizontal and vertical deviations (LOC, GLIDE)
- Radioaltitude
- Flight Path Vector (3-D).

2.3 The H.U.D. Performance issues

The efficiency of the monitoring function ensured by the pilot using the H.U.D. depends on the accuracy of the picture calculated by the H.U.D. computer with these data. On aircraft equipped with VG/DG or A.H.R.S., the FLIGHT PATH VECTOR is not computed by the system and the installation of an additional Inertial Reference System (I.R.S.) is necessary to obtain the desired symbology.

Accuracy of ATTITUDE & HEADING data is also significant for the performance of the H.U.D. installation and may be a limitation that can also require the installation of additional I.R.S. when the basic system is not accurate enough.

The following GNSS/HUD coupling considerations show how these issues can be solved.

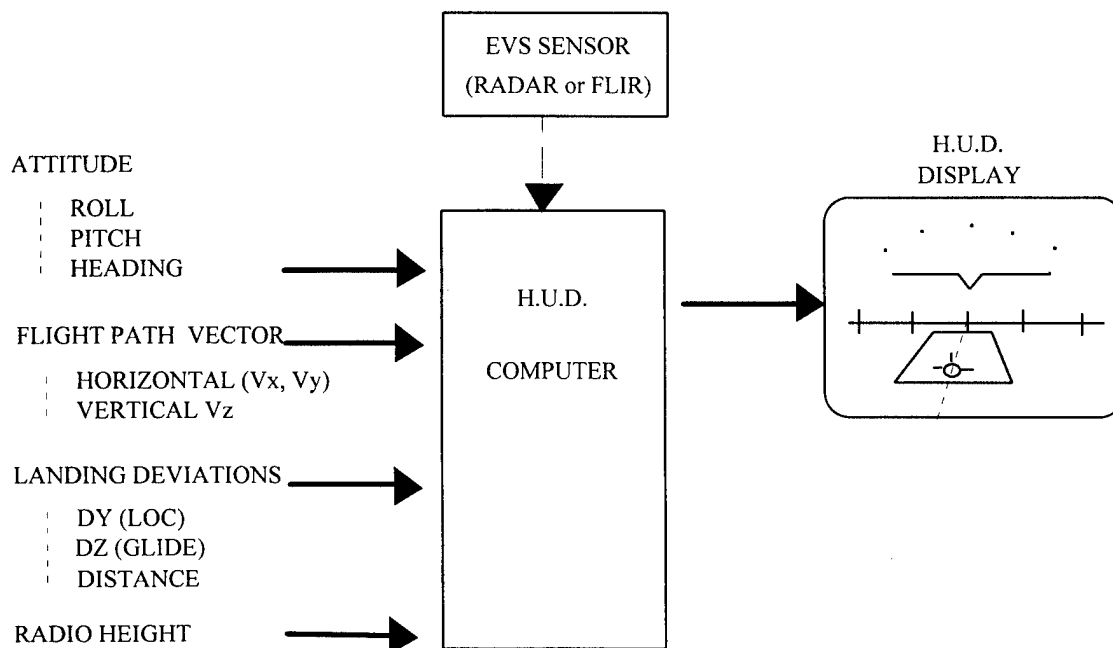


Fig 2 - HUD INTERFACE BLOCK DIAGRAM

3.4 Differential G.N.S.S. Landing Function (G.L.S.)

This G.N.S.S. function includes :

- Ground G.N.S.S. reference receiver to calculate differential corrections and monitor the space segment
- Data link for transmission to the users (local LAD or wide WAD)
- Differential processing in the user receiver to obtain better accuracy and integrity
- Precision approach navigator, that delivers lateral and horizontal deviations on the approach flight path.

It is designed to be "interchangeable" with current I.L.S. equipment and to interface with the piloting displays and autopilot as an I.L.S. does.

4. G.N.S.S./H.U.D. Combined System

Figure 4 gives the general block diagram of the GNSS/HUD system onboard. It represents where the G.N.S.S. data can potentially be used in place of or combined with the data used currently without G.N.S.S.

The 3 main changes brought by G.N.S.S. are :

- A ground speed vector with remarkable accuracy and integrity, and availability acceptable for landing operation.
This data is combined in the H.U.D. computer with the inertial data to obtain the best hybrid velocity vector to monitor the approach and is compliant with a H.U.D. CAT3b monitoring.
- D.G.N.S.S. "ILS-like" guidance deviations compliant with CAT1 requirement that could enable CAT3 Head-Up monitored approach on non-ILS equipped runway.
- Positioning Data (and attitude data when a multi-antenna attitude option is installed) that enable attitude and heading improvement in those installations where the basic CAT1/CAT2 system do not reach the requirements for CAT3 landing.

The improvements can be performed in a H.U.D. computer that develops Inertial/G.N.S.S. hybrid filters adapted to the avionics configuration.

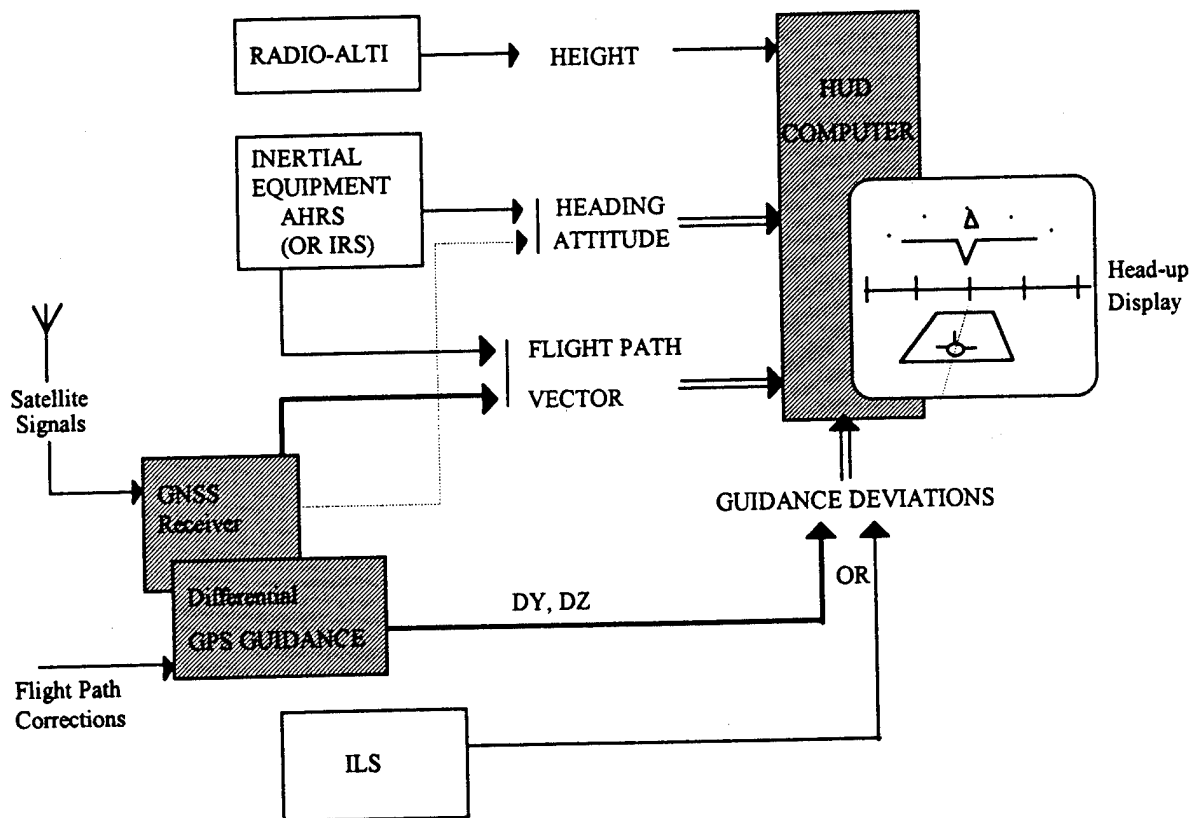


Fig 4 - HUD/GNSS : GENERAL BLOCK DIAGRAM

5. G.N.S.S. - H.U.D. INSTALLATION ON ALITALIA MD-82

5.1 Brief description of the context

The Italian flag carrier, Alitalia, is the largest operator of McDonnell Douglas MD-80 family in Europe and one of the largest in the world, with 85 MD-82s. Those aircraft, which are capable of CAT3a operations, are used on their domestic routes, and, as such, also feed their overseas connections out of Milan and Rome. They also fly from Milan, Torino and Rome to most of the European capitals (in particular, Paris and London) and major cities, where they compete head to head with the local carriers which all have direct flights to Italy.

Milan and, at a lower extent, Torino, are two important cities in Northern Italy, often affected by fog, which significantly impacts the fluent operations on their airports. Even though those airports are well equipped with ILS capable of CAT3 operations, it happens often enough that Alitalia cannot successfully and consistently operate their MD-82s to or out of those airports, when the competition, with more recent airplanes capable of CAT3b operations, can. On the contrary, Alitalia position is balanced when they operate their Airbus A321s, which are CAT3b capable.

The lack of competitiveness is three-fold :

- for European international flights to Italy : other European carriers can land in Milan under CAT3b weather conditions when Alitalia MD-82s cannot,
- for European international flights out of Italy : Alitalia MD-82s cannot perform flights to other major European cities where CAT3b conditions are likely to happen as consistently as some other carriers,
- for overseas long-range flights out of Italy : Alitalia MD-82s face some efficiency problems in feeding the long-range flights or allowing timely connections from those flights.

This lack of competitiveness led Alitalia to seek for remedies, the basic needs being to lower operational minima of the MD-82s. This goal could not be achieved with an improvement of the autoland only, as this autoland is fail-passive only.

Within Alitalia, a reference was made to former certifications and operational approvals obtained by Swissair and Australian Airlines on MD-80s with the addition of Head-Up-Display, and even earlier, in the mid-70s by the French domestic carrier Air Inter on the Dassault Mercure with the installation of a THOMSON (now SEXTANT Avionique) system. In parallel,

SEXTANT Avionique had already applied for a Supplemental Type Certificate in order to get CAT3b operations for the Boeing 737-300s of the French mail and package carrier L'AEROPOSTALE.

5.2 System description

When comparing the L'AEROPOSTALE B737-300s and the Alitalia MD-82s from an avionic standpoint, regardless of the performance and the detailed characteristics of the aircraft and their systems, the major discrepancy that one can immediately point out is that :

- B 737-300s have two Inertial Reference Systems (I.R.S.)
- MD-82s have three Attitude Heading Reference Systems (A.H.R.S.).

The requirements of FARs and JARs, as far as criticality and hazard assessment are concerned, lead to install a third source for critical parameters (namely, in the case of the system proposed : pitch, roll and heading), which means that the installation of a third I.R.S. was needed for the L'AEROPOSTALE program, when the three sources are already there on the Alitalia aircraft.

In terms of signal accuracy and long-term performance, I.R.S. is the reference when A.H.R.S. is considered to be less accurate. In addition, some information which are processed by an I.R.S. are not available with an A.H.R.S. In particular, inertial speeds are not and cannot be computed accurately. Those data are the primary information needed to display the flight path vector in the Head-Up Display.

The Return-On-Investment computations showed that the addition of an I.R.S. to the avionic system could not be considered. However, the installation of G.N.S.S. receivers would be extremely efficient, as those receivers provide the velocity information. Indeed, not only had Alitalia to improve the landing capabilities of the aircraft, but also the need to cope with the new European regulations in terms of precision navigation. The navigation benefits to be expected from G.N.S.S. receivers fully justified their installation.

The Head-Up-Display does not use the navigation capabilities of the G.N.S.S., but only the velocity information to compute the flight path vector, and the position in order to be able to compensate for the magnetic variation. It is important to remind here that a G.N.S.S. receiver computes geographic (true) data, when the convention wants that instruments be referenced to magnetic North. As a consequence, and as A.H.R.S. measures a magnetic heading, magnetic

variation needs to be taken care of in the Head-Up-Display computer.

The precision landing performances expected (and already demonstrated) from the differential G.P.S. are not used in the Head-Up-Display. The G.N.S.S. receiver is used strictly to elaborate the flight path vector symbol with respect to attitudes of the aircraft, which makes it a real monitoring tool of the autopilot, with a totally independant source.

The landing system to be certified on the MD-82 is a CAT3b hybrid system. It consists of a primary fail-passive automatic landing system, which is the existing autopilot of the aircraft, of a backup Head-Up Flight Display System (H.F.D.S.) developed and certified by SEXTANT Avionique, which will be installed on the pilot's side (left), and two "TOPSTAR 200A" G.N.S.S. receivers recently developed by SEXTANT Avionique according to ARINC 743-A standard. These receivers contain the specific 3D velocity processing and the associated Velocity Autonomous Integrity Monitoring (VAIM) algorithm. They are operating in absolute mode during all phases of flight : for navigation connected to FMS computer and for landing combined with the HFDS.

The H.F.D.S. is an independant fail-passive system that enables the pilot to complete a landing, or go-around, manually after failure of the primary system. It provides the pilot with relevant information and symbology to monitor an automatic approach and landing, to satisfactorily take over control of the aircraft in case of failure, and to guide the aircraft during roll-out.

5.3 New operational capabilities

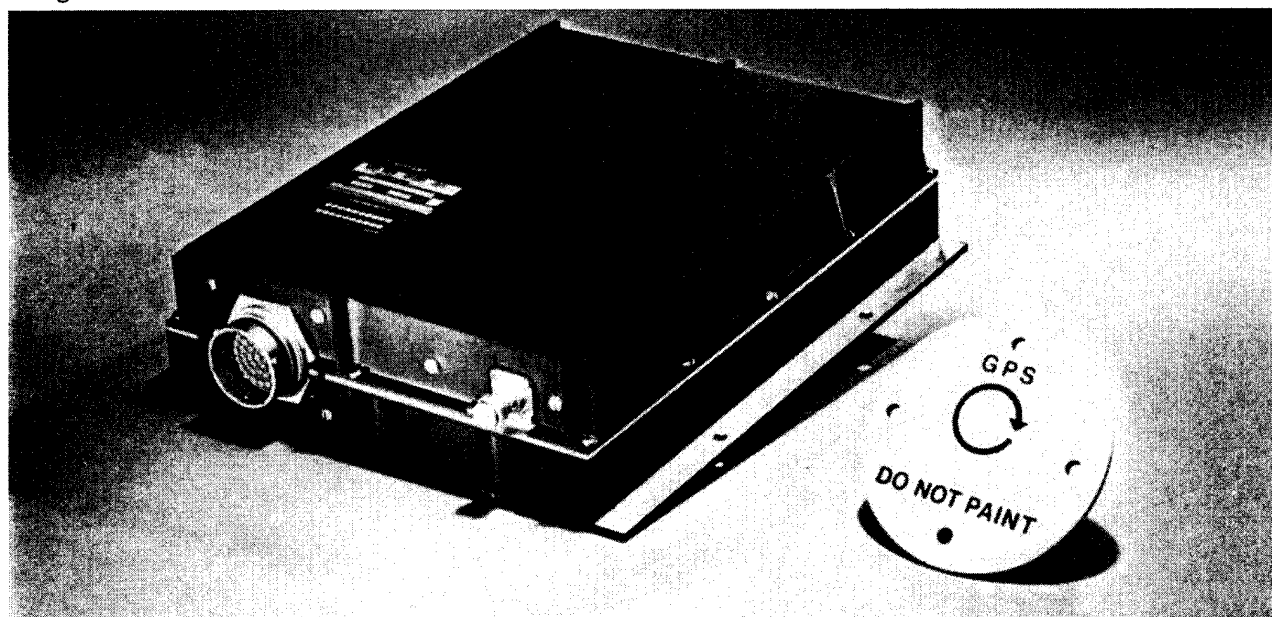
The current MD-82s are capable of CAT3a operations, which means that, on runways equipped with appropriate I.L.S. beam, the autopilot allows to perform landing with a decision height of 50 ft, and a runway visual range of 200 m. Takeoff is forbidden with runway visual range less than 150 m.

The operational minima pursued today by Alitalia and SEXTANT Avionique, for the same aircraft equiped with a Head-Up Display driven mainly by A.H.R.S. and G.N.S.S. (see the picture of the equipment attached), are as follows :

- landing :
decision height : 20 ft.
runway visual range : 100 m
- takeoff :
runway visual range : 75 m.

The contract was awarded by Alitalia to SEXTANT Avionique in March 1995, and the system is intended to be certified in August 1996.

Because of lack of Type Certificate granted for this aircraft by the European J.A.A. as a whole, no J.A.A. certification can be sought at this time. Consequently, SEXTANT Avionique had to apply for an R.A.I. (Registro Aeronautico Italiano) S.T.C., and intend to get J.A.A. certification after this initial Italian approval.



TOPSTAR 200A

ARINC 743-A GNSS Sensor of SEXTANT Avionique equipped with specific "VAIM" algorithm

6. CONCLUSION

As a general statement, it is to be emphasized that even though G.N.S.S. promises to offer "CAT3-like" landing capabilities for the near future, it will never do it as a stand-alone equipment, but associated with the autopilot and flight instrumentation of the aircraft.

CAT3 operations can only be achieved, from a regulatory and safety standpoint, if the proper level of redundancy is met in the global autopilot and autoland system.

The certification of the HUD/GNSS system for ALITALIA MD82 program will confirm that G.N.S.S. can efficiently complement A.H.R.S., and that the resulting data, when well mitigated, can rival those of an I.R.S for a CAT3b HUD operation.

For the future, as briefly described in this document, the possible combinations between HUD, GNSS and AHRS/IRS equipment promise to enable installation of HUD/GNSS landing equipment in a cost-effective manner for various airline customers.

Specific HUD/GNSS functions must be present in the GNSS receiver and in the HUD computer, to properly address the landing requirements. For the ALITALIA MD82 application, they have been implemented in SEXTANT Avionique HUD/GNSS product (TOPSTAR 200 GNSS sensor and HFDS Head-Up Display) and many provisions have been made to support the foreseen evolutions of this function.

With the first ALITALIA MD82 program, it clearly appears that SEXTANT Avionique becomes a leader in the field of diversified usages of G.P.S. and G.N.S.S., based on a unique G.P.S. sensor technology that allows extremely precise measurements and autonomous monitoring of data which were not initially intended to be a direct result of this satellite positioning system.



HEAD-UP DISPLAY EQUIPMENT
"HFDS" OF SEXTANT AVIONIQUE

Implementation of a GPS-Based Oceanic Air Traffic Control System

Joseph Fee
Federal Aviation Administration

Theodore Simpson
Adsys tech Inc.

BIOGRAPHY

Joseph J. Fee is the leader of the Oceanic and Offshore Integrated Product Team at FAA Headquarters. Mr. Fee joined the FAA in 1980 and, in addition to his Oceanic ATC work, has managed several FAA satellite, data link, and collision avoidance programs. Overall, he has more than 30 years experience in systems engineering and applied research in navigation, surveillance and communications. Mr. Fee received both a B.E.E. and an M.S.E.E. from the University of Kansas and is a pilot with instrument and seaplane ratings.

Theodore R. Simpson is a senior member of the technical staff at Adsys tech Inc. At the present time he is providing technical support to FAA Headquarters in the areas of long-range planning and policy, primarily on the use of satellites for communications, navigation and surveillance. Mr. Simpson has over 30 years experience in the aerospace industry, both as an engineer and as a manager, on a variety of aeronautics and space programs. He received a B.E.E. from Manhattan College and has two masters degrees from the Polytechnic Institute of Brooklyn -- the first in Electrical Engineering and the other in System Science.

ABSTRACT

When Charles Lindbergh flew from New York to Paris in May 1927 he was literally on his own. The *Lone Eagle* spoke to no one during the entire 33 hours that he was aloft. Today, voice messages relayed via high frequency (HF) radio and teletype allow pilots to stay in touch with a rudimentary Oceanic Air Traffic Control (ATC) System as they cross the Atlantic and Pacific.

To keep pace with the anticipated growth in air traffic during the next two decades, the Oceanic ATC System will increase in sophistication. Satellites will begin to be used for communications, navigation and surveil-

lance, and new hardware and software will be installed both in the cockpit and on the ground. These advances will allow each aircraft to further improve the efficiency of its flight trajectory, thereby reducing both the amount of fuel consumed and the time aloft during its journey.

This paper describes the FAA's plans to use GPS in its Oceanic ATC System, both for navigation and surveillance, as well as the additional contributions of weather and communications satellites.

PRESENT OCEANIC ATC SYSTEM

Besides managing air traffic over the U.S. mainland, the FAA also supervises the flow of aircraft in a large portion of the international airspace over the Atlantic and Pacific Oceans, as well as the Gulf of Mexico and the Caribbean (see Figure 1). Personnel at ATC facilities in New York, California and Alaska control oceanic air traffic using:

- Non-radar ATC procedures,
- Pilot reports of their position transmitted about once an hour,
- Each aircraft's flight plan, and
- Some knowledge of the weather an aircraft will encounter along the way to its destination.

As shown in Figure 2, air traffic control is done without surveillance information, and minimal automation is available to help the controllers perform their tasks. In addition, the HF voice communication link between the pilots and the controllers is noisy and congested. Due to these limitations, aircraft flying in trail along the same oceanic route at the same altitude are separated longitudinally by at least 10 minutes (80 nautical miles [nm]) to prevent them from colliding with each other. Similarly, aircraft flying along parallel tracks at the same altitude are separated laterally from each other by at least 100 nm. These separation distances are an order of magnitude greater than those used over the U.S.

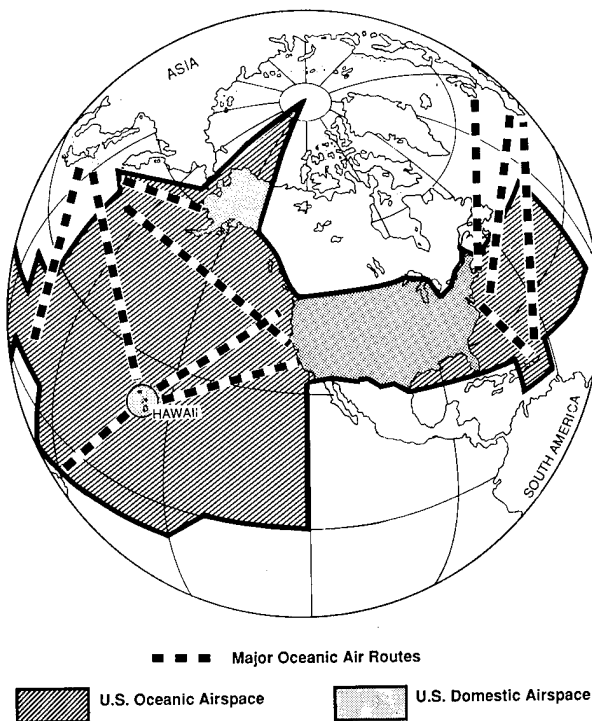


Figure 1
U.S.-Managed Airspace

mainland, where radar and reliable voice communications are available to aid the controllers.

Most of the air traffic across the Atlantic and Pacific flows along a few major routes, e.g., from the East Coast to Great Britain, and from California to Hawaii. There are four such routes in the North Atlantic controlled by New York, one in the North Pacific controlled by Anchorage, and six in the North Pacific controlled by Oakland. The precise locations of most of these routes are adjusted daily based upon the forecasted winds aloft, however some of them do remain fixed. Some of the routes have a peak time for the flow of traffic in each direction, e.g., south from New York to Puerto Rico in the morning, and north in the late afternoon; and along some major routes there may be several parallel tracks along which a number of aircraft are flying.

Most air carrier aircraft would like to fly between 31,000' and 39,000' mean sea level (MSL) over the Atlantic and Pacific. As an aircraft burns fuel and becomes lighter, less fuel would be consumed if the aircraft could fly at a higher altitude. Thus, if permitted, they would start their journey at a lower altitude and

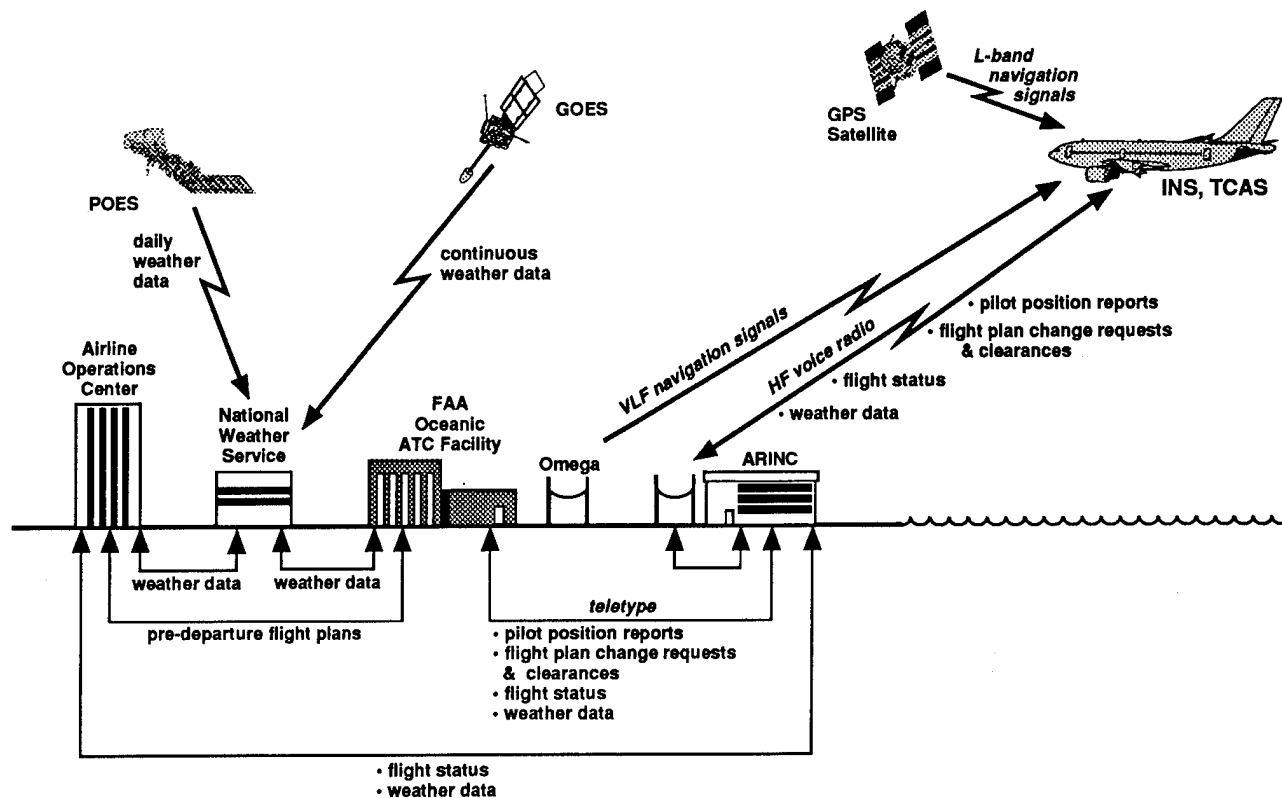


Figure 2
Present Oceanic ATC System

gradually rise in 2000' increments during the course of the flight, e.g., from 31,000' to 33,000' to 35,000' MSL on a unidirectional track. And if there are significant head winds aloft, the great circle route might not be the best route either in terms of minimum flight time or fuel consumed, even though it is the shortest in distance.

Due to the limitations of the current Oceanic ATC System, aircraft are frequently unable to fly in this manner to achieve maximum fuel efficiency and minimum travel time, or to select a preferred takeoff time or a flight path that is free of severe turbulence. And as oceanic traffic levels increase in the future, producing ever more airspace congestion and more demand on the ATC System, it will become even more difficult for each aircraft to achieve these goals.

FUTURE OCEANIC ATC SYSTEM

During the next decade, from 1996 to 2005, the FAA estimates that the number of air carrier flights over both

the Atlantic and Pacific Oceans will approximately double. By the start of the next century, through the use of satellite-based communications, navigation and surveillance, plus additional hardware and software both in the aircraft and on the ground:

- The vertical separation distance on oceanic routes will be reduced from 2,000' to 1,000',
- The in-trail separation distance will be shortened from 10-15 minutes (80-120 nm) to 4 minutes (30 nm),
- The lateral separation distance on parallel tracks will be reduced from 100 nm to 30 nm, and
- Properly equipped aircraft will no longer have to fly along standard routes.

Communications

Currently, the number of aircraft operating in a given airspace can be so great at times that the HF voice link becomes congested. When this media limitation is coupled with the need for a manual conversion of the

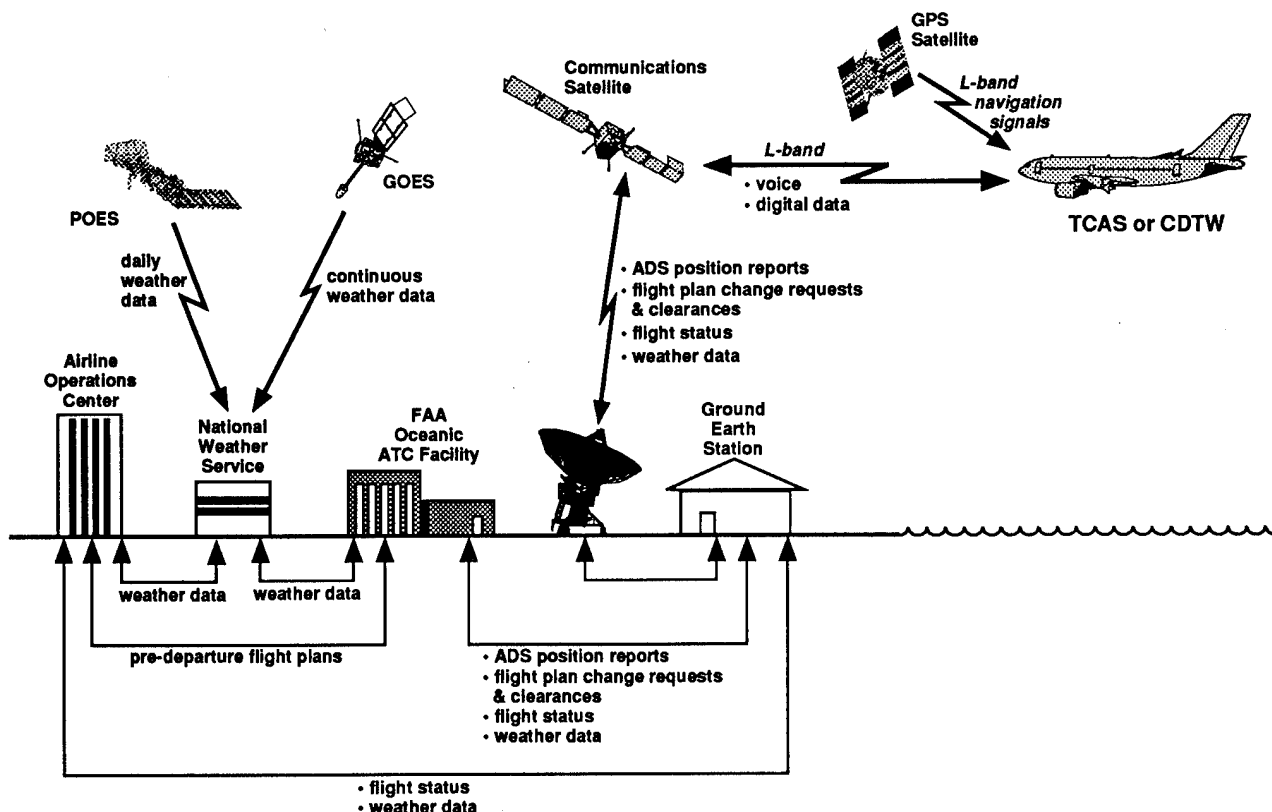


Figure 3
Future Oceanic ATC System

voice messages into digital data and transmission by teletype through a third-party service provider (ARINC), as is presently the case, the message delays can be even greater.

To improve this situation, by the year 2000 air-to-ground communications will primarily be made directly between the pilots and the controllers via digital data links that use communications satellites (see Figures 3 and 4). This will allow clearance requests and other vital messages to be routinely expedited by being transmitted as digital data. By 2010 the use of the HF voice communications link will become a rarity.

Similarly, starting in 1996, when an aircraft is about to leave U.S.-managed oceanic airspace, ground-based digital communications between an FAA Oceanic ATC Facility and other adjacent ATC facilities that it interfaces with will allow computer-to-computer transfer of flight plan data and current flight status, plus the automatic handoff of control between the two ATC facilities.

Navigation

The FAA has already approved the use of GPS as a primary means of navigation in U.S.-managed oceanic en route airspace, and it is planning to withdraw its support for the Omega ground-based navigation system in 1997.

Built by the Department of Defense, GPS is a constellation of 24 navigation satellites, each of which is in a 12-hour Earth orbit. GPS was initially conceived of as a military system, but has since become the first phase of an international satellite constellation known as the Global Navigation Satellite System (GNSS). As such, it is a universal standard both for navigation and time for all aircraft, both inside and outside U.S.-managed airspace.

Inertial Navigation Systems (INSs) onboard most air carrier aircraft will continue to be used as a back-up for GPS during the next 5 to 10 years.

Surveillance

Starting in 1996 over the Pacific and in 1998 over the Atlantic, aircraft position reports derived from GPS navigation data will begin to be sent automatically to the appropriate Oceanic ATC Facility via a communications satellite. Using a concept called Automatic Dependent Surveillance (ADS), each aircraft's GPS-derived position will be known with an accuracy of at least 100 m horizontally and 156 m vertically, 95% of the time. Its position, along with such other information as winds

aloft, will be sent periodically as digital data at an agreed-upon time interval. Due to the high cost of using a communications satellite, the rate of reporting will vary depending upon each aircraft's phase of flight and its proximity to other aircraft.

The improved accuracy of the aircraft's navigation system, plus the shortened time interval needed for a pilot to communicate with a controller, will allow long intervals between position reports if an aircraft is not near another aircraft, and it is not changing either its altitude or direction. Each position report will contain both the present location of the aircraft and its planned future trajectory.

Besides data on the location of aircraft, the FAA is currently also receiving information on the weather in oceanic airspace both from pilots aloft and the National Weather Service (NWS). The NWS data includes remote sensing information from two types of weather satellites -- one type is in geostationary orbit and the other

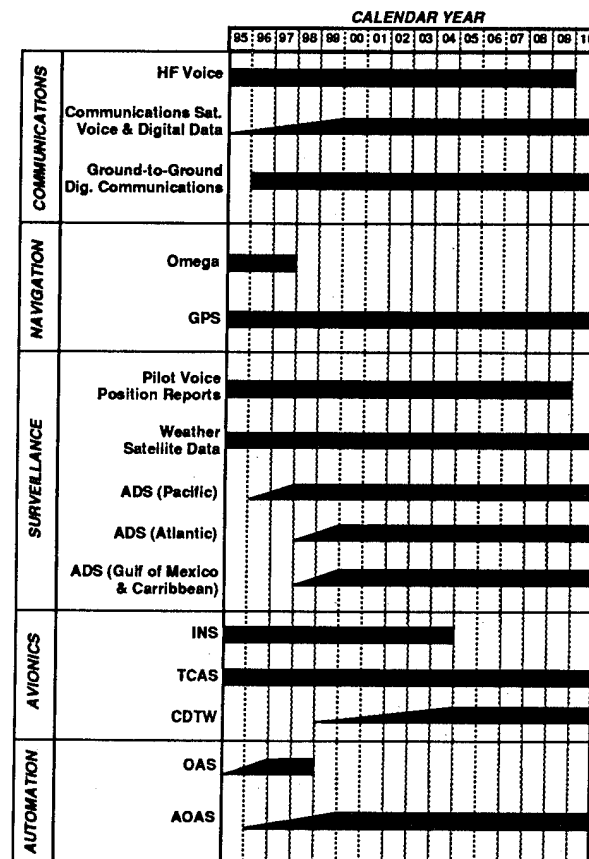


Figure 4
Improving Oceanic ATC

is in low Earth orbit.

In geostationary orbit, 22,300 statute miles (sm) above the equator, there are two satellites that continuously observe the weather over various portions of U.S.-managed airspace. Built by NASA and operated by NOAA, each of them are referred to as a Geostationary Operational Environmental Satellite (GOES). One of the satellites is located over the East Coast, and the other over the West Coast. Both of them observe the U.S. mainland plus a portion of either the Atlantic or Pacific Oceans.

In low Earth orbit there are several weather satellites that periodically observe the weather over the entire globe. Among these are two in near-polar, sun-synchronous orbits about 530 sm above the Earth that were built by NASA and are operated by NOAA. Each of these is referred to as a Polar Operational Environmental

Satellite (POES). One POES scans the U.S. mainland every day in the morning, and the other POES observes it every afternoon.

Avionics

Aircraft equipped with either a Traffic Alert and Collision Avoidance System (TCAS) or a Cockpit Display of Traffic & Weather (CDTW) system will provide visual and audio cues to the pilot about other air traffic in the vicinity. TCAS is already mandatory on all air carrier aircraft, and CDTW will probably be required to allow the separation distance between aircraft over the ocean to be reduced.

In addition, weather information could be sent to the aircraft via a digital data link that uses a communications satellite. This data would be shown graphically either

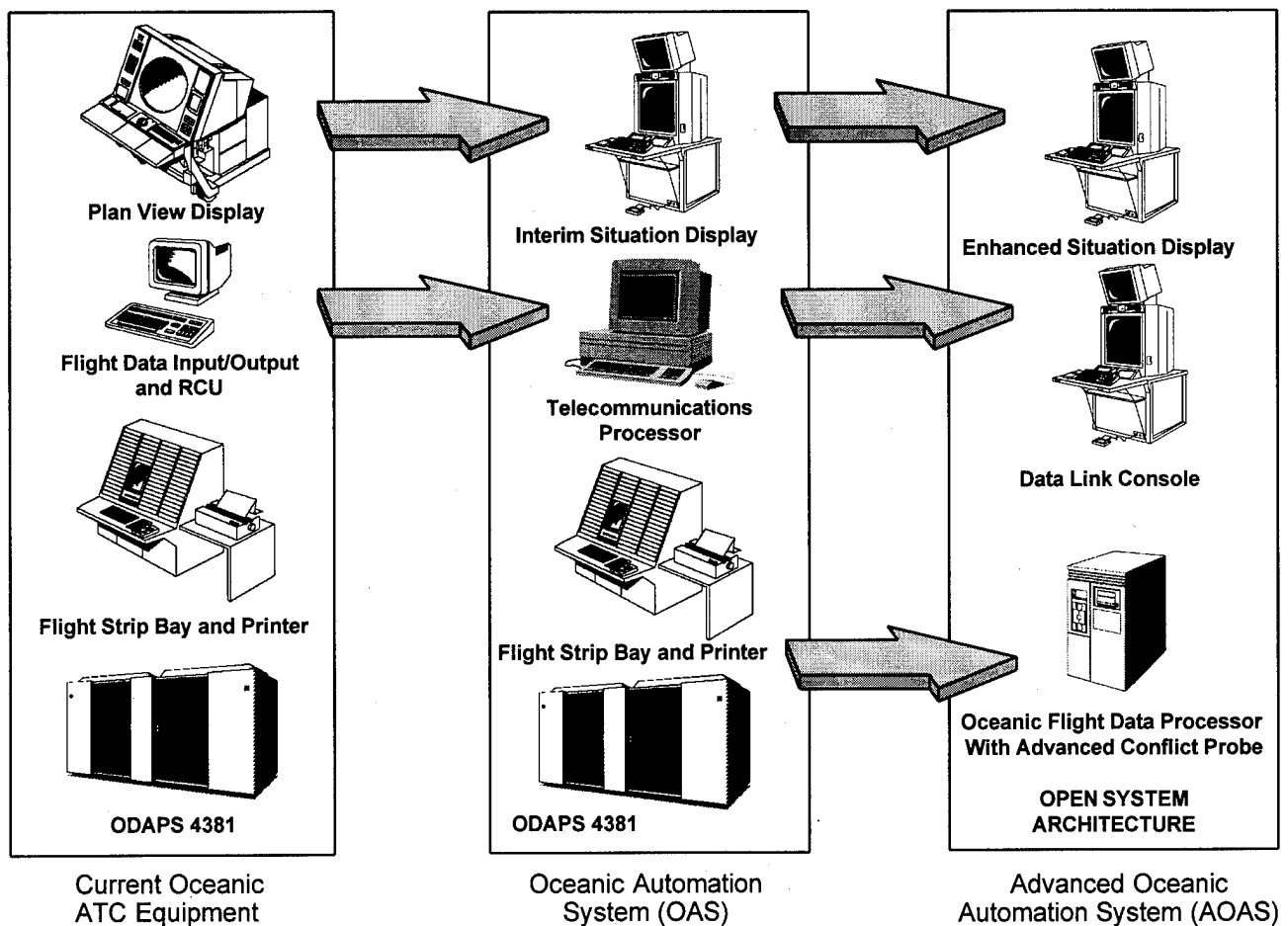


Figure 5
Evolution of Oceanic ATC Automation

on the CDTW or another display.

Due to the high-cost of obtaining ADS surveillance data through communications satellites, sometime beyond the year 2000, TCAS and CDTW are likely to become the primary means of separating aircraft on a tactical basis. The Oceanic ATC System would then be used primarily for strategic planning to optimize the overall flow of air traffic under its supervision.

Oceanic ATC Automation

In 1996 the FAA will complete the installation of Oceanic Automation Systems (OASs) at its Oceanic ATC Facilities (see Figure 5). OAS will provide the initial capability to automatically transfer digital data between an Oceanic ATC Facility and both the Ground Earth Station (GES) of a communications satellite, and adjacent ATC facilities that the Oceanic ATC Facility interfaces with.

From 1996 to 1999, the FAA will install various parts of its Advanced Oceanic Automation Systems (AOASs) at its Oceanic ATC Facilities. AOAS will build upon the initial capabilities of OAS, including providing enhanced situation displays for the controllers, and installing software to:

- Detect potential conflicts between aircraft,
- Optimize the flow of oceanic air traffic, and
- Display refined weather data.

BENEFITS

Once these improvements have been completed on the ground, in the air, and in space, the FAA will be able to keep pace with the anticipated increased growth in air traffic; and equipped aircraft will be able to fly when and where they want across the ocean, thereby saving a significant amount of time and fuel.

For example, it is estimated that an air carrier aircraft can save on the average about \$200K per year if it is used solely for flights over the Pacific Ocean. These savings are due to fuel not consumed and shorter flight times. Similarly, the average annual saving for an air carrier aircraft used in flights over the Atlantic is estimated to be almost \$100K per year.



Session A5

Precise Real-Time Positioning

Chair:

Ms. Sally Frodge
DOT

Co-Chair:

Mr. Richard Barker
John E. Chance & Associates

High Precision Real-Time Positioning Using Low Cost OEM Sensors

Adel Tabsh and Hugh Martell
Premier GPS Inc.

Darren Cosandier
The University of Calgary

Biographies

Adel Tabsh

Mr. Tabsh is the President and CEO of Premier GPS Inc. He is the inventor of numerous GPS products and systems and has been involved with GPS systems for the past six years. His background is in Electrical Engineering and he has focused his research efforts for the last few years at producing accurate, robust and affordable high accuracy, centimetric RTP real time positioning systems.

Hugh Martell

Hugh Martell is the Senior Software Engineer at Premier GPS Inc. He has some seven years experience in software development for inertial and GPS systems. Mr. Martell completed his education at the University of Calgary where he received an M.Sc.

Darren Cosandier

Darren Cosandier is completing his Ph.D. in the Department of Geomatics Engineering at the University of Calgary. His area of research includes photogrammetry, GPS, image processing and precise image georeferencing by GPS/INS. He is one of the co-authors of the GPS software described in this document.

Abstract

This paper describes a real-time kinematic GPS system which is capable of accuracies up to the level of a few centimetres utilizing various phase-capable low cost GPS sensors. Typical real-time kinematic applications currently involve the use of relatively high cost GPS sensors. Users who require high accuracy in real-time may find that existing conventional systems are not always cost-effective for their particular task. In fact, for some applications the cost of a real-time GPS system may approach the cost of the equipment on which it is installed.

Applications where low cost may be desirable or necessary in some instances, include agriculture, hydrography, military testing, construction, and surveying.

Described in this paper are the results of various real-time tests conducted under typical field conditions, to accuracies ranging from 2 cm - 30 cm depending on the type of application for which the survey was performed. Tests varied from parallel tracking for high precision site specific farming, to moving baseline surveys, as well as typical land & geodetic work. These showed conclusively that low cost code-phase

sensors are capable of cost-effective high precision survey work for many tasks.

Introduction

Real-Time Kinematic Positioning (RTP) is currently defined by GPS systems which provide centimetre level accuracy at virtually the same moment that data is received at both a base and remote station. To date, such systems have been exclusively in the domain of a handful of high end GPS manufacturers.

The justification for the cost of these units has been attributed to the quality of the sensors utilized. DGPS, on the other hand, has been traditionally an area where low cost GPS OEM sensors have dominated. While these units have proven their worth in such market regions as the automotive industry, the precision achieved has not been acceptable to the surveying industry. Nor have these sensors been utilized effectively in the area of very high precision navigation.

This paper describes the implementation of a generic real time

high precision GPS system developed by Premier GPS of Calgary, Canada. This RTP system uses a number of low cost readily available phase capable OEM GPS receivers from manufacturers traditionally associated with the DGPS market. The following sections outline a number of production level tests illustrating the high precision capability of inexpensive OEM units from such manufacturers as Motorola, Navsymm and Canadian Marconi. These tests include examples of high precision farm guidance, geodetic level GPS surveys and high accuracy surveys for real time relative positioning of a moving baseline.

System Configuration

The RTP system presented here consists of a hardware/software configuration developed by Premier GPS currently supporting a variety of GPS engines. All hardware and software design and implementation, with the exception of the GPS engine have been developed in-house.

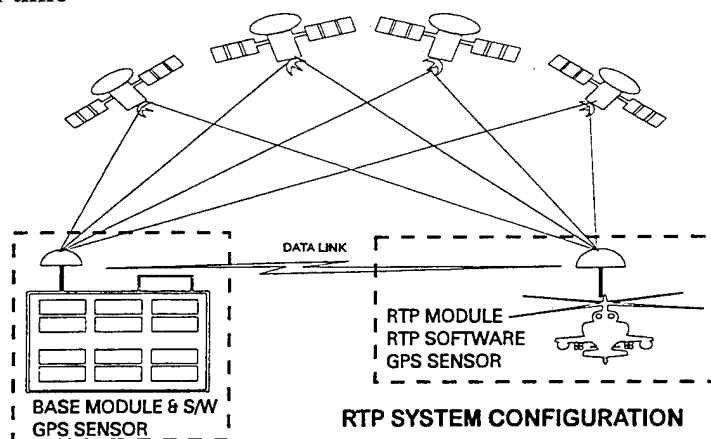


Figure 1 Typical RTP System

System Description

The base station shown in Figure 2 consists of an Intel based CPU, 270 megabyte hard disk, LCD display and base station software. The units may be configured as 8 or 12 channels depending on the requirement. The base station CPU is utilized in collecting raw GPS time, pseudorange and phase data from the embedded GPS receiver. This data is reformatted in a proprietary compact message and broadcast via radio modem to the remote RTP station. Raw data broadcast from the base station is received via the data link and processed with one of Premier's proprietary real-time software modules at the remote station. The raw GPS binary records may be optionally stored to the internal hard disk for centimetric level post-processing with Premier's GRAFNAV™ or GRAFNET™ post mission modules.

The RTP remote unit is available in 6, 8, 10 or 12 channel models. Once again, system configuration is largely dependent on the task to which the unit is being assigned. In the case of high precision agriculture for instance, 6 channel units may be sufficient. Geodetic, and high dynamic airborne users may require a greater number of satellites in view, although it should be noted that all RTP units regardless of structure are ultimately capable of centimetric precision.

The major difference in the remote unit is the optional 640 x 480 LCD VGA display which may be used in place of the standard 4-line display. Once again

data may be stored to a 270 Mb hard disk if the user wished to post-process the binary GPS records.

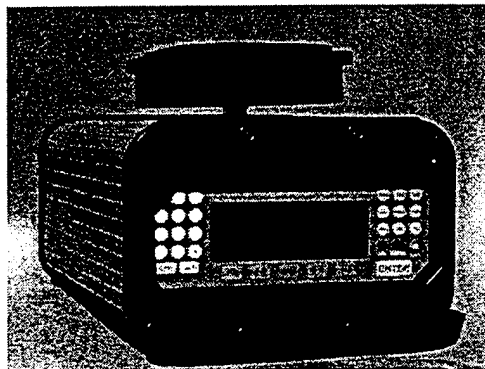


Figure 2: RTP Unit

Data broadcast in generic form from the base station can be processed in real-time with a number of RTP software modules written for a variety of purposes. All these modules employ double difference carrier phase techniques. Ambiguity resolution can be accomplished in a number of modes, including quick static, KAR (kinematic ambiguity resolution) or basic floating ambiguity resolution for tasks which demand slightly less accuracy.

While the processing engine is similar in all cases, Premier has implemented a number of different RTP routines depending on the requirement. High precision swath guidance and real-time mapping displays are available for the agricultural industry. A geodetic engine is available for standard surveying and hydrographic applications, such as waypoint guidance and setting out, while specialized modules are available for such tasks as airplane to airplane tracking. Many other implementations of RTP including azimuth and attitude

modules are in the prototyping and field testing stages.

The following paragraphs detail a number of actual real-time high accuracy surveys performed under production level circumstances. Described is a swath guidance agricultural survey undertaken with two 6 channel GPS receivers, a relative antenna survey where two 12 channel receivers were placed on a moving baseline, as well as several high precision kinematic geodetic surveys utilizing 8 channel systems.

Precision Agriculture Guidance

A number of farming applications require vehicle guidance at a higher level than is currently available utilizing wide area differential corrections. These agricultural tasks include spraying of some herbicides and pesticides, as well as precision seeding and soil testing techniques.

The accuracy required by these applications is typically determined by the ability of a human or robotic system to force the vehicle to respond to the guidance data in real time. This is typically on the level of 10 - 30 centimetres at best. At this level, RTP is still required. Wide area differential is not acceptable.

However, at present the high precision user in the GPS farm market is confronted with the high cost of current L1/L2 and narrow correlator receivers. For instance, real-time kinematic systems produced with these units may approach 50-100% of the cost of an

agricultural spraying unit. The challenge here is to make use of a GPS engine priced in the range usually designed for low accuracy vehicle guidance and produce via phase information, real time guidance at the level of centimetres or decimetres. The 6 channel Motorola Oncore with the phase option was chosen for this particular application.

In a typical parallel swath application, the farm operator will perform one pass around the entire perimeter of the field in order to allow room for vehicle turns at the end of each swath line. For this reason, the Premier parallel guidance module allows the user to first map the perimeter of the field area as the farmer drives it. The real time software automatically closes the polygon formed and saves the exterior of the field. The operators next step is to define a strike line which will order all the subsequent lines to be driven by the vehicle operator throughout the field. Upon marking the two endpoints of this first swath line, the RTP routine then plots a series of lines parallel to the original strike line. The spacing of these driving lines is an input option dependent on the width of the boom array being towed by the application vehicle.

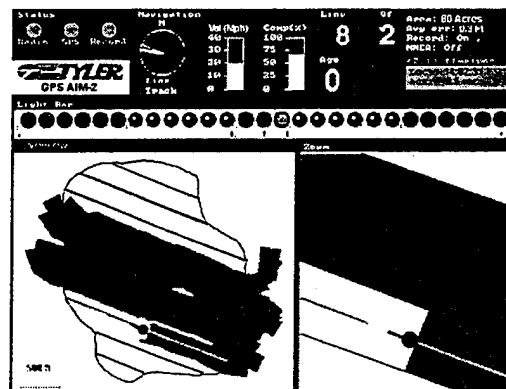


Figure 3: RTP Ag-Guidance GUI

The image below is a bitmap collected in the RTP Ag system during a real-time agriculture survey performed by a major U.S. distributor of farm implements.

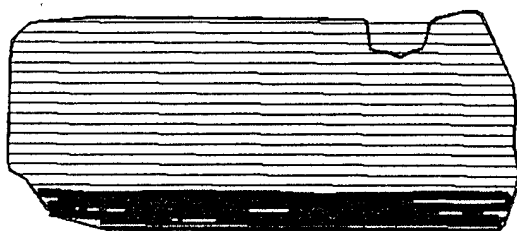


Figure 4: Bitmap displaying Parallel Lines and Swath area completed in a typical field

Numerous systems based on these 6 channel receivers are already in the field and results from independent operators have confirmed that centimetre/decimetre accuracies are easily achievable in this application.

Costwise these systems are virtually on par with turn-key systems built around wide area differential. Accuracies on the other hand are significantly better and are sufficient for vehicle guidance generally above the driving abilities of the equipment operator. An RTP based automatic steering system is currently being implemented by Premier for a large US farm equipment manufacturer and will be onboard tractors in the spring of 1996.

Relative Moving Base Antenna Survey

A specialized GPS application is dynamic vehicle to vehicle tracking. This is an instance where the base station resides on one moving vehicle while the remote station is mounted on another moving target. One major application for this is real-time air to air tracking of

one aircraft with respect to another on a moving baseline of one kilometre or less.

In the survey presented in this section a pre-production dynamic tracking system was tested utilizing a road vehicle. Two 12 channel GPS receivers were connected to two antennae mounted at a fixed distance of 0.64 m on the roof of a car. One antenna was designated as the reference station, while the other antenna acted as the remote. Instead of a radio modem link, a serial cable was simply stretched from one RTP system to the other.

After a static initialization of some 1500 seconds, the vehicle was driven at an average velocity of approximately 60 Km/hr for 40 minutes. At each epoch a pseudorange solution was used to provide a new set of master coordinates and the relative baseline to the remote antenna was computed.

Two different GPS OEM engines were employed in this test. One was a 12 channel Navsymm XR5 receiver and the other a prototype GPS OEM recently developed by Canadian Marconi.

The purpose of this particular test was to demonstrate the ability of the two RTP systems to reconstruct the 64 cm baseline between their antennas to an accuracy of ± 5 cm. The absolute coordinates of the antennae were of no consequence, only the relative vector across the roof of the car was of interest.

To add an extra element of ground truth to the survey, a 12 channel Navsymm base station was also set up at a fixed point on the roof of the Premier offices.

This was designed to provide an independent post mission check on the precision of the moving baseline. The primary analysis of the accuracy of this test would be the comparison of the known baseline distance against that computed from the moving base to the remote antenna in real-time. A secondary analysis was conducted post mission, as it was possible to compute the baseline vectors from the fixed antenna on the Premier roof to the roving antennas positioned on the moving car. Similarly, the post mission computed baseline distance between the two roving antennas could be compared against the real-time processed inter station antenna vector.

The graphs below show the results of the moving baseline survey. It can be readily seen in Figure 5 that the real time computed distance from the Navsymm antenna to the Marconi antenna is consistently within 5 centimetres of the nominal baseline distance of 0.64 m. Note that the graph begins at about the 1500 second mark. This is the beginning of the kinematic portion of the moving baseline survey. The static period was used to resolve the phase ambiguities at both receivers.

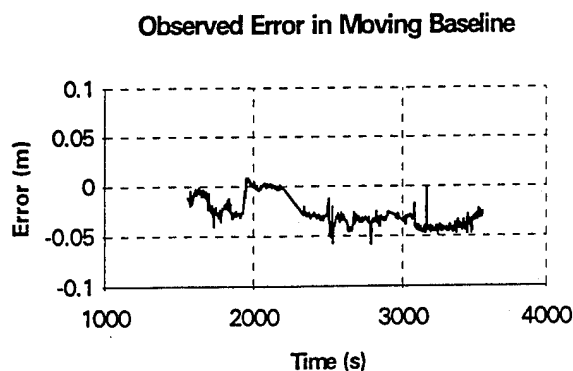


Figure 5: Computed real time moving baseline distance minus actual baseline length

Figure 6 depicts the results of the antenna difference vector computed in post-processing mode. This was processed by taking the baseline vectors from the Premier roof to each of the car antennas and computing post-mission the coordinate differences between fixed base solution and the real-time moving base solution. Note that the large differences at the beginning of the survey are due to convergence of the

solution during static initialization. At approximately the 1500 second mark, the phase ambiguities were resolved and the 2000 second kinematic portion of the survey was performed. The spikes are due to noise on very low satellites popping in and out of view. Once more it can be seen, that there is a typical error of less than 5 cm., consistent with the observed real time results

Comparison of moving base processing (antenna difference vector)

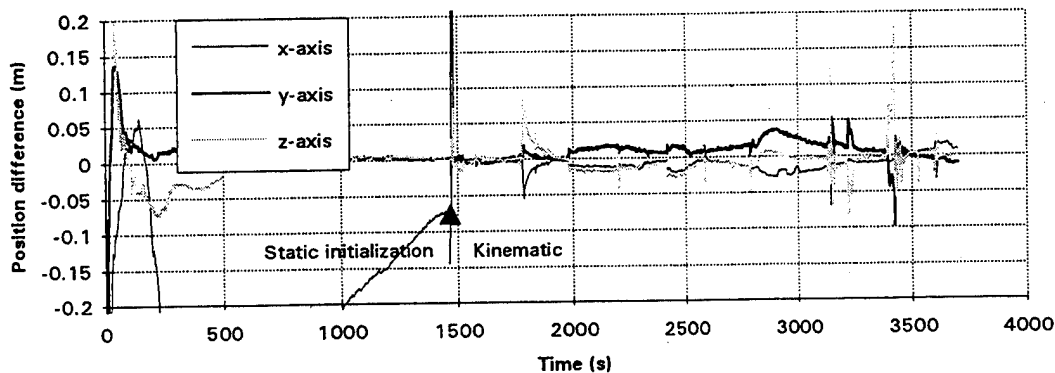


Figure 6: Post Mission Vector minus Vector computed in Real Time

Both of the GPS OEM engines embedded in the RTP systems used here have normally been employed in DGPS applications. High precision dynamic surveys have traditionally been performed only with top end systems with corresponding price tags. The success of this test illustrates once more the capability of low cost sensors when embedded in Premier's RTP systems to perform at high levels in an area where expensive units have to date dominated the market.

Conventional Real-Time Kinematic Surveys

The final section is devoted to the results from several conventional real-time kinematic surveys. The object of these surveys was to demonstrate the ability of a typical low end code/phase sensor to carry out tasks for which users have to date paid a premium. The GPS receivers used in the RTP systems developed for these surveys were 8 channel Motorola Oncore engines. Although these units were originally developed for the vehicle tracking market, they are used here for

kinematic surveys at the level of precision generally reserved for systems at the highest end of the Geodetic market.

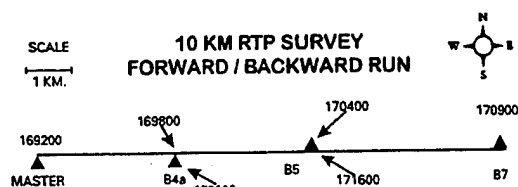


Figure 7: 10 km Real Time Traverse

In the 10 km RTP survey displayed above, a 10 minute static session was performed to resolve phase ambiguities. Following this, the antenna was placed on the roof of a vehicle and the vehicle driven for a total of 20 kilometres.

Points B4a, B5 and B7 are pre-surveyed control monuments at a distance of up to 10 km from the base station. At these points, the antenna was removed from the vehicle and placed on a range pole over the control point for approximately 10 seconds. The position was marked and recorded. Total time for the kinematic portion of the survey was 45 minutes

Errors in 10 Km RTP Survey			
Station	Northing	Easting	Height
B4a	-0.006	0.008	-0.003
B5	0.019	0.019	0.050
B7	0.009	0.010	-0.012
B5	0.031	0.021	0.012
B4a	0.028	0.015	0.018

Table 1: Real Time Errors observed in 10 km forward/backward run

The results seen in Table 1 are typical of many production level surveys performed by Premier utilizing this RTP system.

The next survey shown in Figure 8 below was originally performed as a conventional land survey using total station technology. In conjunction with a Calgary land surveying firm, a real time kinematic GPS survey was performed in order to check the consistency of the conventional work. Once again, this survey was accomplished using the 8-channel ONCORE engine embedded in Premier's RTP system.

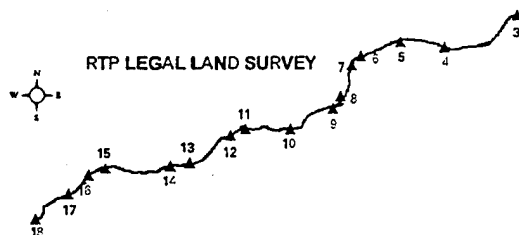


Figure 8: 17-Station Legal Land Survey

Following a 10 minute static initialization, a kinematic survey was performed forward and backward over the points seen in the diagram above. Total distance for the survey is about 1 Km. At walking speed, the forward/backward run took about 1.5 hours. Given the many courses on this traverse, considerably more time would have been

spent to complete this project using angles and distances.

Figures 9 and 10 illustrate the differences between the GPS derived coordinates and the conventionally computed positions. The consistent trend seen in the graph presenting the differences in northings is not actually an error. Instead, it is due to an azimuth rotation with the original land survey. The constant increase in the northing difference is consistent with the angular convergence from ellipsoidal north to grid north on a line having a general east/west orientation.

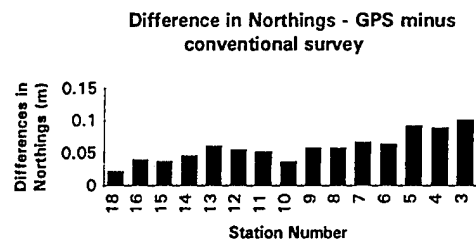


Figure 9: Comparison of GPS Derived Coordinates and Total Station Coordinates

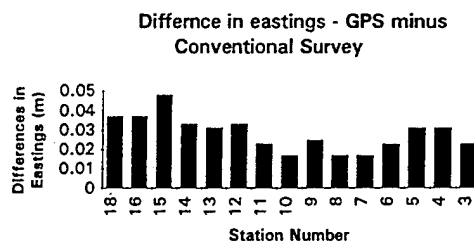


Figure 10: Comparison of GPS Derived Coordinates and Total Station Coordinates

While the differences between the GPS and the conventional survey range up to 10 cm at the maximum distance of 1 km, the real-time GPS computed coordinates of the forward and backward runs generally agree in the one centimetre range. The internal consistency of the

GPS survey is depicted in the graphs below.

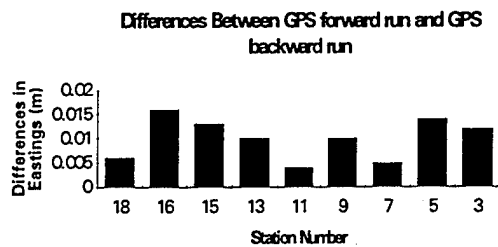


Figure 11: Internal Consistency of the East GPS Coordinate on the Forward and Backward Run

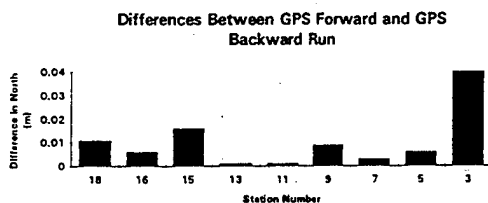


Figure 12: Internal Consistency of the GPS North Coordinate on the Forward and Backward Run

The figures above clearly show the high internal precision of this system. In fact, it can be seen from both the examples presented in this section that this low cost sensor, when coupled with the Premier RTP system, is capable of accuracy at and above the level required for general geodetic or land surveying purposes.

Conclusion

Low cost GPS sensors from a number of manufacturers were utilized in a generic real time centimetric positioning system developed by Premier GPS Inc. of Calgary, Alberta, Canada. A number of tests have been presented here illustrating the ability of these low end code/phase units to perform tasks generally reserved for sensors at the highest end of the cost

scale, when coupled with Premier's RTP technology. These tasks include precision agriculture guidance, high dynamic moving baseline surveys, and typical high precision real time kinematic land surveys.

Acknowledgements

Acknowledgements are due to Ms. Carol LaFlamme for her help in data processing and to Mr. Paul Masters of Tyler Inc. for his aid in collecting data for the precision agricultural tests.

Bibliography

Lapucha, D., Barker, R., *Two Methods of Multiple Reference Station DGPS Performance Comparison*, KIS 94, Banff, Alberta, Canada, 1994.

Szabo, D, Tubman, T., *DPPS Positioning in Regions of Multiple Reference Coverage*", 10th Symposium on Navigation, Canadian Aeronautics and Space Institute, Winnipeg, Manitoba, Canada, 1994

Tyler Inc, *Connecting the Pieces of Precision Farming*", Internal Tyler Corporation Document, 1995.

High-Rate Precise Real-Time Positioning Using Differential Carrier Phase

Dr. Dariusz Lapucha, Richard Barker, and Ziwen Liu
John E. Chance & Associates, Inc.

BIOGRAPHY

Dr. Dariusz Lapucha is a Senior Geodesist with John E. Chance & Associates, Inc. (JECA). He holds a Ph.D. from the Warsaw Technical University in Poland and a M.S. from The University of Calgary, Canada, both in Surveying Engineering. He has been with JECA since 1991 in the area of development of real-time GPS systems.

Richard Barker is Manager of Systems Engineering with JECA. He holds a B.S. from the California State Polytechnic University, Pomona, California. He has been with JECA since 1979 in the area of integration and development of navigation and positioning systems.

Ziwen Liu joined JECA in 1995 as a Geodesist. He holds a M.S. in Geomatics Engineering from the University of Calgary, Canada and both a M.S and B.S. in Electrical Engineering from Harbin Engineering University, China. His previous experience includes five years of research work in GPS/INS integration at the University of Calgary.

ABSTRACT

Differential Carrier Phase positioning overcomes some of the operational limitations of the carrier phase kinematic positioning in the real-time environment. Unlike kinematic positioning, differential carrier phase positioning does not require time-matching of reference and remote station data. The observation time-matching adds the data link delay to the position latency and prevents positioning when the reference data transmission is interrupted. The differential carrier phase algorithm is based on determining and then applying the GPS carrier phase errors instead of direct observation differencing. Differential Carrier Phase method enables several centimeter positioning at a high-rate dependent only on the remote receiver observation rate but independent on the data link transmission rate. This paper discusses the design, successful implementation and test results of the real-time differential carrier phase system developed by John E. Chance and Associates Inc.

INTRODUCTION

Real-Time Kinematic GPS using carrier phase observations enables centimeter level real-time positioning of a moving platform. The major breakthrough in the application of carrier phase observations for real-time positioning has been the development of rapid and reliable methods of On-The-Fly (OTF) carrier phase ambiguity resolution without static initialization. However, the carrier phase positioning has still some operational limitations in the real-time environment. The major challenge is to overcome these limitations to approach the level of versatility of code based Differential GPS (DGPS).

The first real-time On-The-Fly kinematic system, for instance the one developed by John E. Chance & Associates in conjunction with the US Army Corps of Engineers and Dr. B. Remondi (Frodge et al 1994), typically used the same kinematic GPS algorithms as in the post-processing. The real-time systems architecture was based on the same premise of time-matching of the reference and remote station data as in the post-processing case. The reference station data pseudorange and carrier phase data were sent to the remote station where they were time-matched and processed with the remote station data using double differencing techniques. This design had the advantage of relatively simple implementation of the post-processing algorithms for real-time application.

The time-matching of the observation data unfortunately adds data link delay to the kinematic position latency. The data link delay may be as much as a few seconds depending on the type of the data link. Several seconds position latency severely limits some of the real-time kinematic GPS applications. Moreover, the requirement of time-matching limits the position output rate to the data link transmission rate. In addition, any interruption in the data link transmission would stop remote station positioning. Therefore the real-time GPS observation time-matching prevents continuous high-rate positioning.

The drawbacks of time-matching are overcome in the real-time differential carrier phase system that was

recently developed by John E. Chance & Associates. This system applies the predicted GPS carrier phase corrections instead of direct differencing of the observation data. Using the differential carrier phase method enables uninterrupted remote station positioning with slightly degraded accuracy for a limited period of time. With this approach, the position update rate is limited only by the rover receiver observation rate.

The differential carrier phase processing model is introduced in the first segment of the paper. It is preceded by discussion of the influence of the major error source on the positioning accuracy. Finally, the differential carrier phase system test results are presented and discussed.

CARRIER PHASE DIFFERENTIAL MODEL

The main objective of Differential Carrier Phase positioning is to combine the remote station observations that relate to the current time t_i with the reference station observations that relate in general to the past time t_0 . The time-matched observation differencing commonly used in other carrier phase relative positioning techniques cannot be applied. The observation differencing is being used to cancel some of the unmodelled GPS errors. This canceling of unmodelled errors has to be achieved by other means in differential carrier phase positioning.

The differential carrier phase model is derived from the fundamental observation equation of carrier phase Φ :

$$\Phi = \rho + c(dt - dT) + \lambda N + d\rho \quad (1)$$

Where:

- ρ - receiver to satellite range
- dt, dT - satellite & receiver clock errors respectively
- N - carrier phase ambiguity
- $d\rho$ - orbit and atmospheric errors

Equation (1) shows that all information about unknown remote station position and dynamics is contained in the station to satellite range. The other terms, are also in general, unknown and need to be accounted for in the processing. The composite of the unknown error terms, called further carrier phase correction Φ_c can be determined from the reference station data by subtracting the station to satellite range satellite and station dock offsets, as:

$$\Phi_c = \Phi - (\rho + c \cdot dt_B - c \cdot dT) \quad (2)$$

where dt_B is approximate satellite clock offset computed from the satellite broadcast message. The approximate receiver clock offset is computed using the algorithm described in (Gloeckler et al 1992). The carrier phase correction Φ_c is thus equivalent to:

$$\Phi_c = c \cdot dt_{SA} + \lambda N + d\rho \quad (3)$$

where dt_{SA} represents unknown satellite clock dithering error due to Selective Availability.

The carrier phase corrections as defined by the equations (2) and (3) refer to the past time t_0 . These corrections have to be extrapolated to the current user time t_i . The extrapolation leads to the inevitable error. The size of the extrapolation error is dependent on the actual dynamics of the extrapolated quantity. The sample carrier phase correction rates and their accelerations are shown in Figures 1 and 2 respectively. The observed carrier phase correction changes are mainly driven by the Selective Availability satellite clock dithering dt_{SA} . The term $d\rho$ due to orbit and atmosphere, errors vary slowly when compared with clock dithering term.

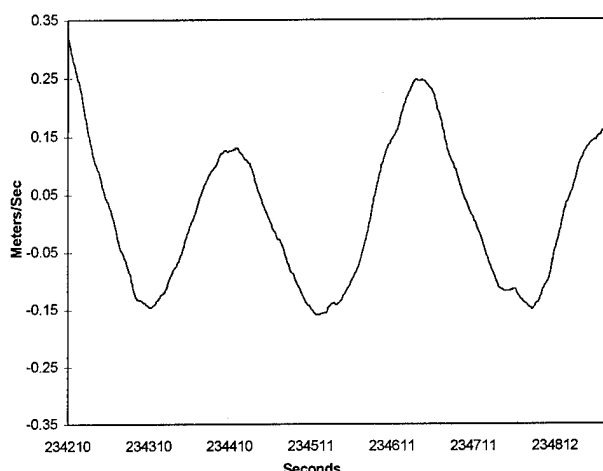


Figure 1. Correction Rate

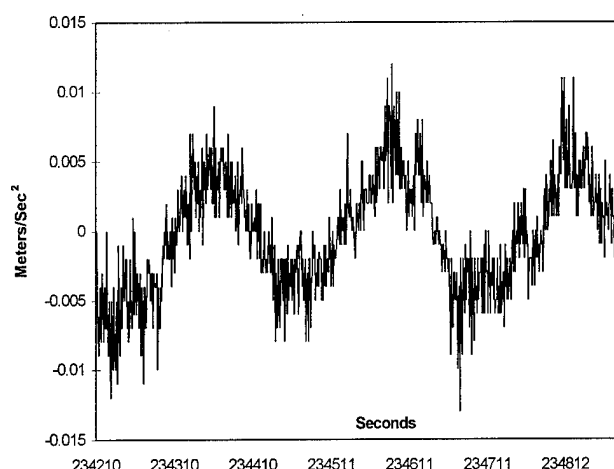


Figure 2. Correction Acceleration

Figure 2 shows that the correction accelerations can reach up to 0.01m/s/s. Unlike the case of meter level DGPS where only range correction rates are used, these acceleration terms are significant for centimeter level carrier phase positioning. Neglecting these accelerations would cause an error of several centimeters in the phase correction extrapolation. Therefore, the second order terms have been included in the extrapolation model, as follows:

$$\Phi_c(t_i) = \Phi_c(t_o) + \dot{\Phi}_c(t_o)(t_i - t_o) + \ddot{\Phi}_c(t_o) \cdot \frac{(t_i - t_o)^2}{2} \quad (4)$$

where carrier phase rate $\dot{\Phi}_c$ and acceleration $\ddot{\Phi}_c$ are estimated in the carrier phase correction filter based on the past reference station observations.

The user applies extrapolated carrier phase corrections to its carrier phase observations, as:

$$\tilde{\Phi}_u(t_i) = \Phi_u(t_i) - \Phi_c(t_i) \quad (5)$$

The actual observable used in the user differential carrier phase positioning filter is the difference of the corrected carrier phase observations with respect to reference satellite. The user observation model is thus derived by combining equations 1, 2 and 5, as:

$$\tilde{\Phi}_u^{jk} = \rho_u^{jk} + N_{bu}^{jk} \quad (6)$$

where superscript jk represents the differencing operator between satellite j and reference satellite k , and subscript bu between remote and reference station differencing. The time argument was dropped in the equation (6) for

the purpose of better clarity. The N_{bu}^{jk} represents carrier phase double difference ambiguity. It is assumed that carrier phase double difference integer ambiguities have been established using On-The-Fly ambiguity resolution techniques. The description of the employed OTF algorithm can be found in (Frodge et al 1994).

It can be shown that if the reference correction time t_o is equal to user time t_i the above formulation is equivalent to double difference kinematic model:

$$\Phi_{bu}^{jk} = \rho_{bu}^{jk} + N_{bu}^{jk} \quad (7)$$

Differential Carrier Phase and Kinematic GPS are affected by the same error sources and therefore provide similar accuracies. These error sources are well known and are not discussed here. The additional error source in Differential Carrier Phase is the prediction error in extrapolation of carrier phase correction using equation (4). This error increases when the correction update interval increases.

CARRIER PHASE CORRECTION PREDICTION ERROR

Minimizing the error of carrier phase extrapolation is critical for maintaining several centimeter accuracy of the differential carrier phase positioning. The previous section stated the need to refine the extrapolation model with the second order terms because of the range of carrier phase correction accelerations. The need to include second order terms is further validated by determining the errors of extrapolated carrier phase corrections based on linear and second order extrapolation models. These errors were determined by comparing predicted corrections at the predefined interval and their observed values. In the linear model only rate terms were used. In the second order model both rate and acceleration terms were used according equation (4). Results of the computations for five second prediction intervals are presented below.

Figure 3 presents the prediction errors for the simple linear model with no accelerations. Figure 4 shows these errors for the extrapolation model with accelerations. The linear model shows prediction errors of more than five centimeters with some systematic error pattern. These errors are significantly reduced and the systematic pattern is removed when the second order extrapolation model is used. This proves the usefulness of applying accelerations in the extrapolation model.

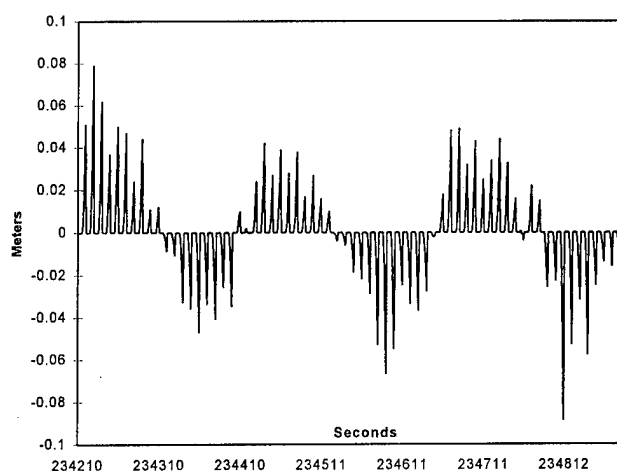


Figure 3. Prediction Error with no Acceleration - 5 Seconds

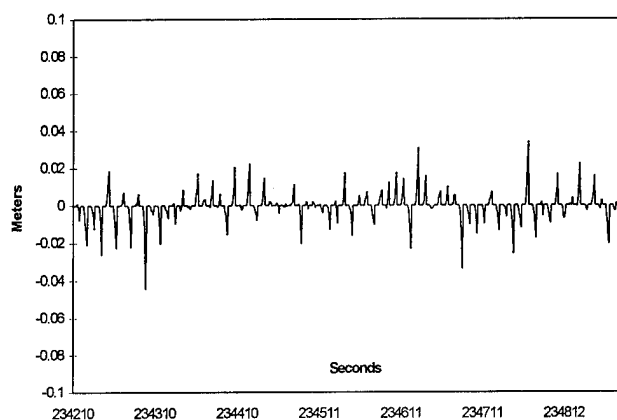


Figure 4. Prediction Error with Acceleration - 5 Seconds

The results presented in Figure 4 also show that the carrier phase prediction error is on average below five centimeters at a five seconds correction update interval. Therefore, if the update correction update interval stays below five seconds then the positioning accuracy should be maintained at several centimeter level. This opens the possibility of using slower data links than of these required for real-time kinematic positioning to maintain the same position output rate.

DIFFERENTIAL CARRIER PHASE IMPLEMENTATION

The real-time differential carrier phase positioning system has been developed from the existing real-time OTF Kinematic GPS system. This former system was developed by John E. Chance & Associates in

conjunction with the US Army Corps of Engineers and Dr. B. Remondi within the framework of the Dredging Research Program (Frodge et al 1994). The new system offers differential carrier phase positioning capability while relying on the key feature of the old system such as On-The-Fly Ambiguity Resolution. The old system provided simultaneously meter level code DGPS positioning output for navigation purposes and centimeter level kinematic output based on observation time-matching. In the upgraded system the kinematic output has been retained while more accurate several centimeter level differential carrier phase GPS supersedes the code based DGPS after OTF ambiguity resolution.

The system uses two dual frequency receivers, one at the reference station and one at the remote station. The system currently can use two types of the GPS receivers, Trimble 4000 SSE or SSI and Ashtech Z12. The work is under way to add the interface to the Leica 399 series receivers. The reference station GPS observations data, L1/L2 code and carrier are transmitted to the remote stations. All real-time computations i.e. OTF ambiguity resolution, kinematic and DGPS positioning computations are carried out at the remote station. The 9600 UHF (460 MHz) radio links are typically used with the system. These data links can operate at line-of-sight distances up to 25 km. The typical OTF resolution time varies between 15 to 30 seconds.

The high-precision carrier phase based differential positioning has been added within the JECA OTF system architecture. One of the main design features of the old system was transmitting the raw GPS observations from the reference station to the remote station. The main implication of that for the new system is that the carrier phase corrections, their rates and accelerations are computed at the remote station from the reference station carrier phase data. They are computed parallel to DGPS code corrections and their rates. The several centimeter differential carrier phase positioning output is available after successful OTF ambiguity resolution. Code DGPS meter accuracy position output is now only active prior to OTF ambiguity resolution or if age of carrier phase corrections exceeds predefined limit (e.g. 5 seconds). Differential Carrier Phase output has the same characteristics as the code DGPS output which is continuous output with minimum latency. The continuous high-precision positioning or DGPS positioning is maintained without interruption even in the case of intermittent data link transmission.

The kinematic output rate is limited by the rate of the data link because of the requirement of observation time-matching. In the present system, the raw data packet is

comprised of about 200 to 300 bytes of data. This implies the limitation of raw GPS data packet transmission rate and corresponding kinematic output rate to 2 Hz at 9600 baud rate. On the other hand, the differential carrier phase output is not limited by the GPS data transmission rate. Its output rate is only limited by the observation rate of the remote GPS receiver. The processing power is not an issue as the differential fix computations take several milliseconds. Therefore the differential carrier phase output can be as high as 10 Hz provided the remote receiver can output observation data at such a rate. It has to be emphasized that this high-rate positioning can be achieved with the present data links that transmit data at a slower rate e.g. 1 Hz.

Real-time kinematic and differential carrier phase positioning methods are complimentary. The real-time kinematic provides the ultimate in terms of accuracy. It is used mainly in surveying applications where its operational limitations in terms of positioning output continuity and latency are not relevant. Differential carrier phase addresses the applications that require not only high positioning accuracy but also continuous output with minimum latency. The applications of the differential carrier phase positioning include construction

machine guidance and high-resolution hydrographic surveying.

REAL-TIME RESULTS

The real-time differential carrier phase system has been tested in different operating environments. Presented below, there are real-time positioning results from testing on the static 140 meters baseline. In this test, the reference station was set to transmit GPS raw data every two seconds. The remote station was set on the known point. The remote station was simultaneously performing differential carrier phase and kinematic positioning. The positioning results were logged and then compared with the coordinates of the known point. The differential carrier phase positioning was carried out at the rate of 2 Hz, corresponding to the maximum GPS observation output rate of the remote GPS receiver used (Trimble 4000 SSE). The resulting age of carrier phase corrections varied between 0.5 and 2.5 seconds. The kinematic positioning was carried out at a slower rate of 0.5 Hz, that is every two seconds. A two seconds rate was the maximum kinematic positioning rate in this case because the data transmission interval was two seconds.

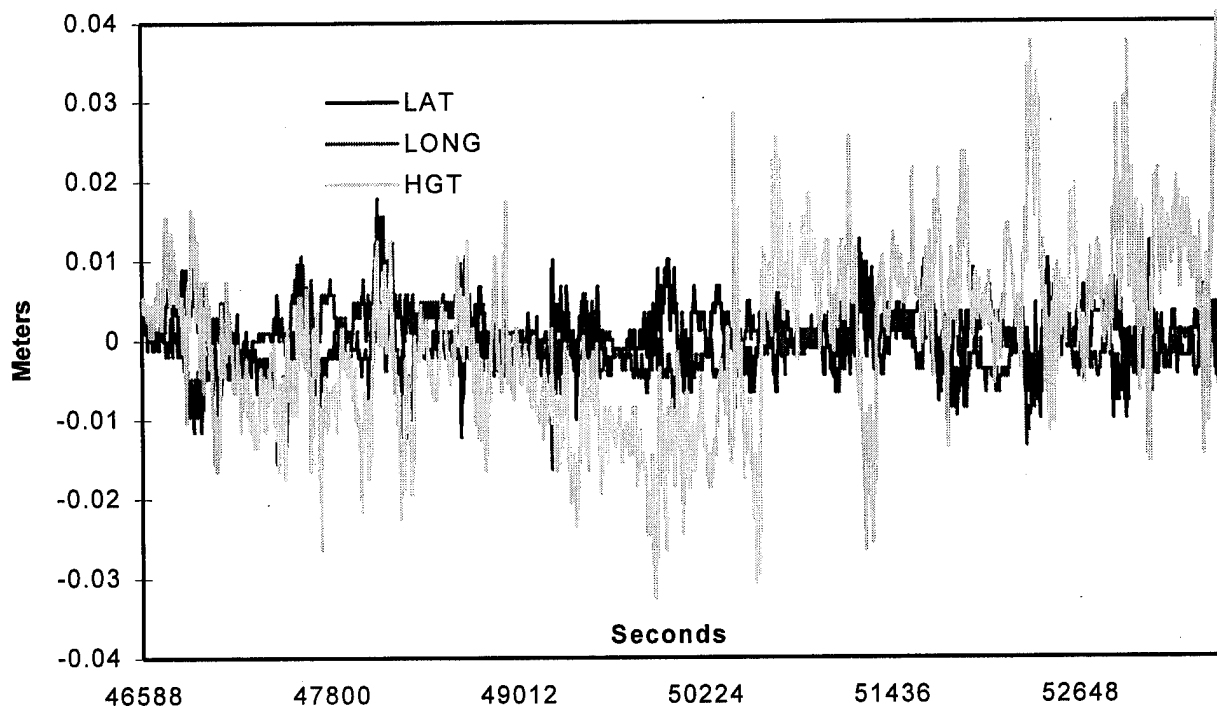


Figure 5. Differential Carrier Phase Results

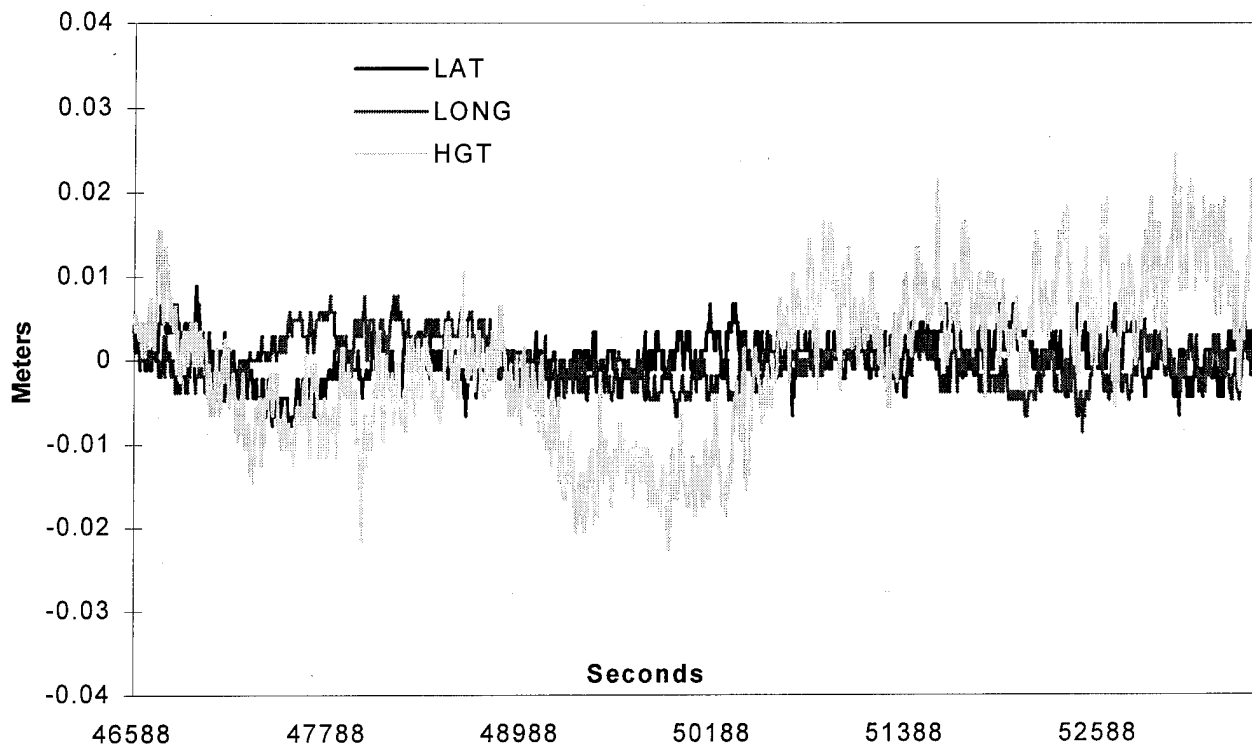


Figure 6. Kinematic Results

Differential carrier phase and corresponding kinematic results are shown in Figures 5 and 6, respectively. The differential carrier phase results in terms of standard deviation are 0.010 m in latitude, 0.009 m in longitude and 0.018 m in height. The respective kinematic results are 0.006 m in latitude, 0.005 m in longitude and 0.010 m in height. The differential carrier phase and kinematic results exhibit the same error pattern which is mainly due to the GPS receiver carrier phase noise and multipath. The differential carrier phase results have a slightly higher noise level, as expected, due to carrier phase prediction errors. These results are at the several centimeter level and are considered very satisfactory. The differential carrier phase results demonstrate that continuous high-precision navigation at centimeter level is possible.

POSITION LATENCY

Differential carrier phase and kinematic position outputs have different latencies. Differential carrier phase latency comprises mainly of the remote station GPS receiver observation data latency. The observation data latency varies from 0.3 to 1.5 second depending on the GPS receiver and data output baud rate. Kinematic position

output latency comprises of remote or reference station GPS receiver raw data packet latency, whichever is greater, and data link transmission delay. Because of this additional data link transmission delay the kinematic output latency is greater than the differential carrier phase output latency.

The real-time position output latencies were determined using special setup synchronized to UTC time scale. This setup comprised of customized PC clock card that uses WWV signals to synchronize PC clock to UTC reference time. The incoming position record was time-tagged with the external reference driven PC time and then compared with the nominal time.

The real-time system setup was comprised of the same setup that was described in the previous section. The GPS receivers at reference and remote stations were outputting the raw GPS observation data at 38400 baud rate. The data link rate was 9600 baud. Both differential carrier phase and kinematic records were output at 9600 baud rate. The Dataradio data link was used in this experiment. The differential carrier phase and kinematic output latencies were measured using the external time reference.

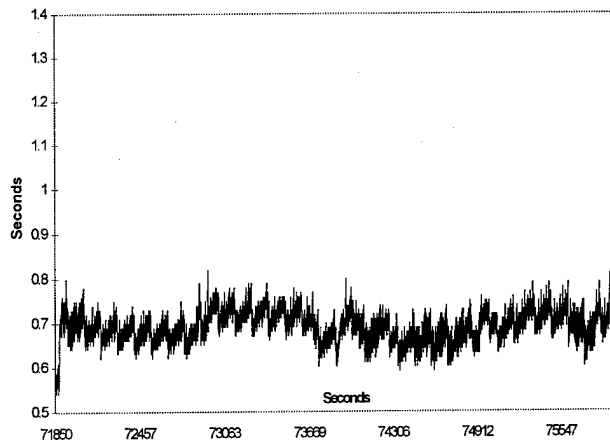


Figure 7. Differential Carrier Phase Output Latency

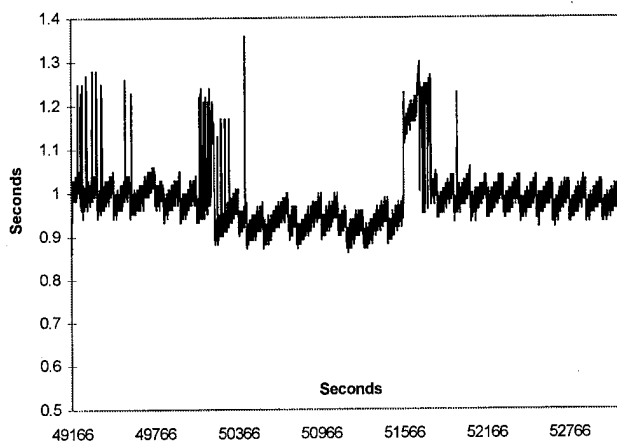


Figure 8. Kinematic Output Latency

The typical differential carrier phase and kinematic position output latencies are shown in Figures 7 and 8, respectively. These plots show relatively stable differential carrier phase latency and more erratic kinematic output latency. The differential carrier phase

output latency is about 0.7 seconds. The differential carrier phase latency results also correspond to the standard Trimble receiver position (NMEA GGA record) latency results at the same output rate. The kinematic latency is on average about one second but with the deviations that reach 0.4 second. The kinematic latency is more erratic because of variations in the amount of transmitted data and random like behavior of the data modem.

CONCLUSIONS

The results presented in this paper show that the differential carrier phase method enables several centimeter precise real-time positioning. Unlike kinematic positioning, the differential carrier phase positioning can be carried out with the high-rate independent on the transmission rate and delays of the data link. This is achieved by using the extrapolated carrier phase correction instead of the direct differencing of the GPS data. The differential carrier phase positioning rate is only limited by the GPS observation rate of the remote GPS receiver. The differential carrier phase positioning addresses the needs of these applications that require high precision, high-rate, continuous positioning output with minimum latency.

REFERENCES

- Frodge, S.L., DeLoach, S.R., Remondi, B.W., Lapucha, D., Barker, R.A., "Real-Time On-The-Fly Kinematic GPS System Results," NAVIGATION, Journal of The Institute of Navigation, Vol. 41, No 2, Summer 1994.
- Gloeckler F., Van Dierendonck A.J., Hatch R.R., "Proposed Revisions to RTCM SC-104, Recommended Standards for Differential NAVSTAR/GPS Service for Carrier Phase Application", Proceedings of ION GPS-92, Fifth International Technical Meeting of the Satellite Division of The Institute of Navigation, Albuquerque, New Mexico, 1992.

Maintaining GPS Positioning in Steep Turns Using Two Antennas

David Lawrence, H. Stewart Cobb, Clark Cohen, Jock Christie,
J. David Powell, and Bradford Parkinson
Stanford University

ABSTRACT

Satellite availability studies commonly assume a fixed elevation mask angle. However, as an aircraft banks, relatively high satellites can be masked from the field of view of the GPS antenna. Not only are fewer satellites visible, but those that are in view are clustered in one section of the sky. This geometry typically leads to high PDOP. During steep turns, this effect can limit the availability of GPS and WAAS satellites, especially at high latitudes. However, if a second GPS antenna is installed on the aircraft, satellites masked from the main antenna may still be used. This paper presents experimental results of kinematic GPS positioning using two antennas.

The Integrity Beacon Landing System (IBLS) developed at Stanford uses a bottom GPS antenna to acquire pseudolite signals. Attitude is provided to account for the moment arm from the top antenna to the bottom antenna. With a bottom antenna and attitude already available, the IBLS test aircraft required few changes to demonstrate GPS positioning using multiple antennas.

A nine channel Trimble receiver with an RF section dedicated to each of the two antennas was used for these tests. Each channel could switch between the top and bottom antennas as required to track the desired satellite. The switches were performed using attitude information provided by a separate GPS attitude receiver. Satellites were handed off from one antenna to the other in real time as the aircraft attitude changed.

Experiments were first performed using a model aircraft on the ground. Flight tests were then performed on a Piper Dakota already equipped for IBLS testing. The results of these tests show that multiple GPS antennas can be used effectively to improve the availability of GPS positioning.

1.0 INTRODUCTION

Satellite masking due to aircraft roll maneuvers is often neglected in availability and continuity studies. Kinal [1] started to address this issue for the Wide Area Augmentation System (WAAS). He showed that satellites can be tracked below the local horizon of the GPS antenna, allowing the aircraft to maintain satellite tracking continuity in most maneuvers associated with final approach. This research focused on non-precision and Category I precision approaches. For the extreme Required Navigation Performance (RNP) of a Category III approach, it is useful to explore the feasibility of using two antennas for GPS positioning.

Two antennas offer an obvious increase in satellite visibility during roll maneuvers; if one antenna cannot receive a satellite, the other one often can. This point raises the question of antenna placement. Ideally, there should be some overlap in the fields of view of the two antennas. That way, the second antenna can acquire the signal *before* the first antenna loses it. If this hand-off procedure from one antenna from another is robust, continuous tracking of most satellites can be guaranteed. To maximize the total coverage of the two antennas, this overlap region should be minimized. The results of [1], which show that the "field of view" of an antenna may comfortably extend 10 degrees below the antenna's horizon, imply that the optimal antenna placement is for the antennas to be pointed in opposite directions. Due to a combination of antenna patterns and receiver signal detection thresholds, the overlap region for diametrically opposed antennas could not be consistently demonstrated here. However, positioning with diametrically opposed antennas was demonstrated as was satellite hand-offs between antennas pointed 120 degrees apart. With the appropriate hardware and software modifications, robust hand-offs should be possible with diametrically opposed antennas.

IBLS [2-4] uses diametrically opposed antennas, one on top to receive satellite signals, and one on the bottom to

receive signals from ground-based pseudolites. This bottom antenna can also be used to track satellites, providing nearly 4π steradian visibility. Section 4.2 presents experimental results for flight tests of a Piper Dakota equipped for IBLIS. Experimental results using a model aircraft are also presented in Section 4.1.

2.0 EXPERIMENTAL SETUP

2.1 RECEIVERS

A nine channel Trimble receiver was used in this research. To accept inputs from two antennas, it was modified to include a second RF section. Both RF sections run off a common local oscillator. Each channel has a switch to allow it to accept inputs from either RF section; in real time, the flight software can select antennas on a channel-by-channel basis.

To maximize continuity, satellites must be tracked by one antenna before they are lost by the other. Therefore, the same satellite must be tracked on two channels at the same time. The receiver firmware was modified to accommodate this requirement. To track a satellite on two channels, that satellite's PRN code is copied over an unused PRN code (PRN's 3, 8, 10, 11, 13, 30, and 32 are currently unused) and the "aliased" satellite is tracked on one of the channels.

A similar nine channel receiver was used as the differential reference station receiver. However, the reference receiver did not require the above modifications.

The phase measurements for GPS attitude were provided by a Trimble TANS Quadrex, a six-channel multiplexing receiver. In application, one receiver could be used for both positioning and attitude; two receivers were used here for convenience. The attitude solutions were performed in the flight computer (a Pentium PC).

2.2 AIRCRAFT

MODEL

Figure 2.1 shows a one meter wingspan model aircraft used in the first experiments. Antennas on the nose, wings, and tail are used for attitude determination. Two additional antennas mounted behind the nose are used for positioning. Several configurations were tried for the positioning antennas; in the figure, they are placed on the starboard and port, with 120 degrees between boresights. The model is mounted on a tripod which allows any heading and ± 90 degrees of roll.

PIPER DAKOTA

A Piper Dakota was also used to test two antenna positioning in flight. The aircraft was already equipped

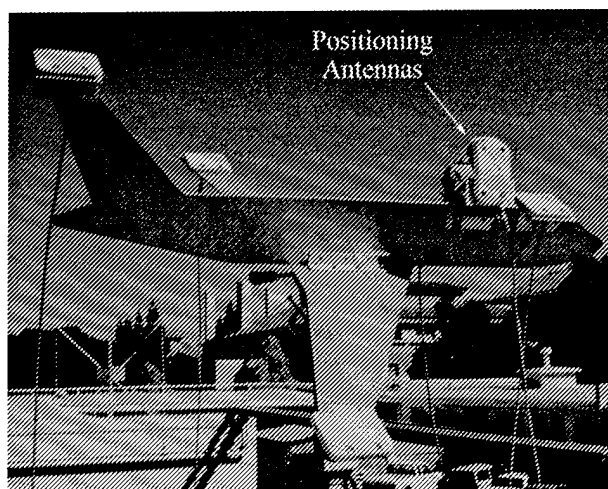


Figure 2.1: Model Aircraft

with four attitude antennas and a belly antenna to receive pseudolite signals for testing IBLIS. One of the attitude antennas and the belly antenna were used for the two antenna positioning experiments.

2.3 SOFTWARE

The flight software executes on a Pentium PC running the Lynx Real-Time operating system. Two processes are run simultaneously, an attitude process and a positioning process. The attitude process sends attitude solutions to the positioning process. To calculate position fixes using two antennas, attitude is required to account for the lever arm between those antennas.

REAL-TIME CHANNEL SELECTION

As part of the positioning process, a simple algorithm is used to select the satellites and antennas for each channel. The highest seven satellites are selected and tracked on the antenna whose boresight is closest to the line-of-sight to each satellite. This selection is made in real-time at 4 Hz using GPS attitude to determine which antenna is closest. The two satellites closest to the borderline between antennas are aliased to unused PRN's and tracked a second time. These channels are used to provide tracking continuity in the event that a borderline satellite switches antennas.

ATTITUDE SOFTWARE

The software developed by Cohen [5] was used to solve for attitude. The attitude accuracy is sufficient to account for the lever arm correction with errors on the millimeter level.

POSITIONING SOFTWARE

The positioning software for this two antenna research evolved from the software described in detail in [6]. That software performs kinematic position fixes in real-time using estimates of the integer cycle ambiguities associated with the carrier phase. The integer estimator also

provides a mechanism for handing off integer estimates as constellations change. Only a few changes were required to modify this software to accommodate positioning with two antennas:

- The antenna selection algorithm described above.
- A correction for the lever arm between the two antennas.
- A correction for the orientation of the antennas. This correction results from the circular polarization of the incoming signal and is described in detail in Section 3. It is now required because the two antennas may point in significantly different directions than the reference station antenna.

To apply the lever arm correction, the phases measured at the second antenna are simply projected to the first antenna:

$$\phi_{\text{projected}} = \phi + \hat{e} \cdot R_{AC}^{ENU} \bar{a}$$

where:

\hat{e} is the unit line-of-sight vector to the satellite expressed in East, North, Up.

R_{AC}^{ENU} is the rotation matrix from the aircraft coordinate frame to East, North, Up.

\bar{a} is the vector from antenna 1 to antenna 2 expressed in the aircraft coordinate frame.

After applying these corrections, all phase measurements appear to have come from one antenna; the remainder of the software is identical to the single antenna software.

The aliased satellites are treated as if they were separate satellites with identical line-of-sight vectors to the true satellite. The aliases do not switch antennas when the true satellites switch, so the satellites can be continuously tracked. Using the phase measurement of the aliased satellite, the estimator will implicitly hand off the integer estimate when the true satellite switches antennas.

3.0 CIRCULAR POLARIZATION CORRECTION

As specified in [7], the transmitted GPS signal is right-hand circularly polarized (RHCP). Therefore, GPS receive antennas are designed to receive RHCP signals. The measured carrier phase of a circularly polarized signal is a function not only of the distance between the transmit and receive phase centers, but also of the relative orientation of the antennas.

Traditionally, kinematic GPS applications do not correct for this effect. When the boresights of all of the receive antennas are parallel, the correction is common to all satellites. It therefore affects only the differential clock error or line bias, not the position or attitude solution. However, if the angle between receive antenna boresights becomes large, a RHCP correction should be applied.

This section develops two different, yet equivalent strategies for finding a RHCP correction.

3.1 ABSOLUTE RHCP CORRECTION

One strategy is to find a correction for each transmit and receive antenna pair. The receive antennas are assumed to be flat patch antennas; the results can be generalized for other types of antennas given their off-boresight phase characteristics. To first order, the phase characteristics of a patch antenna can be approximated by assuming the antenna is made up of two dipoles 90 degrees out of phase.

In general, the incoming signal will be elliptically polarized if the transmit antenna boresight does not point directly at the receive antenna. For terrestrial users receiving satellite signals, the ellipticity is guaranteed not to exceed 1.2 dB [7], so the incoming signal can be assumed to be circularly polarized. However, for applications involving pseudolites, the boresight of the transmit antenna may not point toward the receive antenna; in this case, the ellipticity should be modeled. Therefore, the RHCP correction is a function of the orientation of the receive antenna, the line-of-sight to the transmit antenna, and the ellipticity and orientation of the incoming signal. To develop a correction for a transmit/receive pair, two coordinate frames are defined. A right handed orthogonal coordinate frame is attached to the receive antenna with the z direction aligned with the boresight. The y direction can be arbitrarily chosen normal to z ; the x direction is then constrained. The second coordinate frame will be called the transmit frame. The transmit frame is defined such that the z axis points *opposite* the line-of-sight to the transmit antenna and the y axis points in the major axis direction of the incoming elliptically polarized signal. If the incoming signal is circularly polarized, this direction may be chosen arbitrarily. The arbitrary terms in the absolute correction will cancel when single and double differences are performed.

The output of a RHCP patch antenna can be simply modeled as the E-field component in the x direction plus the component in the y direction delayed by 90 degrees:

$$r(t) = x_r(t) + y_r \left(t - \frac{1}{4L_1} \right)$$

where:

$r(t)$ is the antenna output as a function of time.

$x_r(t)$ is the E-field component in the receive antenna x direction.

$y_r(t)$ is the E-field in the receive antenna y direction.

L_1 is the carrier frequency.

This model accurately approximates the phase, but not the gain of a RHCP patch antenna.

Similarly, the incoming signal can be expressed in the transmit frame:

$$x_{tx}(t) = \cos(2\pi L_1 t)$$

$$y_{tx}(t) = e \sin(2\pi L_1 t)$$

$$\vec{E}(t) = x_{tx}(t)\hat{i}_{tx} + y_{tx}(t)\hat{j}_{tx}$$

where:

$\vec{E}(t)$ is the vector E-field at the receive antenna.

e is the ellipticity of the incoming signal.

\hat{i} is a unit vector in the x direction.

\hat{j} is a unit vector in the y direction.

The received signal is then:

$$\begin{aligned} r(t) &= \hat{i}_r \cdot (\hat{i}_{tx} x_{tx}(t) + \hat{j}_{tx} y_{tx}(t)) \\ &+ \hat{j}_r \cdot \left(\hat{i}_{tx} x_{tx}\left(t - \frac{1}{4L_1}\right) + \hat{j}_{tx} y_{tx}\left(t - \frac{1}{4L_1}\right) \right) \\ &= \cos(2\pi L_1 t) (\hat{i}_r \cdot \hat{i}_{tx} - \hat{j}_r \cdot \hat{j}_{tx}) + \sin(2\pi L_1 t) (\hat{e} \hat{i}_r \cdot \hat{j}_{tx} + \hat{i}_{tx} \cdot \hat{j}_r) \\ &= \cos(2\pi L_1 t) (R_{11} - eR_{22}) + \sin(2\pi L_1 t) (eR_{12} + R_{21}) \\ &= \langle R_{11} - eR_{22}, eR_{12} + R_{21} \rangle \cos\left(2\pi L_1 t + \arctan\left(\frac{eR_{12} + R_{21}}{R_{11} - eR_{22}}\right)\right) \end{aligned}$$

where:

R_{ij} is the (i,j) element of the rotation matrix from the transmit coordinate system to the receive coordinate system.

The phase term, $\arctan\left(\frac{eR_{12} + R_{21}}{R_{11} - eR_{22}}\right)$, represents

additional delay of the received signal due to orientation. If the sign convention is such that additional delay increases phase (moving away from the spacecraft increases phase), this correction should be subtracted from the phase measurement. Care should be taken to "unwrap" the arc-tangent function. The corrected phase, expressed in cycles can be written:

$$\phi_{corrected} = \phi - \frac{1}{2\pi} \arctan\left(\frac{eR_{12} + R_{21}}{R_{11} - eR_{22}}\right)$$

3.2 RELATIVE RHCP CORRECTION

In kinematic GPS applications, the phase measured from one antenna is always subtracted from that measured at another antenna. For kinematic positioning, the phase measured at the reference station is subtracted from that measured at the roving antenna. For attitude

determination, the phase measured at a master antenna is subtracted from those measured at slave antennas. Another method for applying a RHCP correction is to apply a correction to the single differenced phases. This correction is a function of the two receive antenna orientations and the line-of-sight to the transmit antenna. The incoming signal is assumed to be circularly polarized in the derivation of this correction. Although less general than the previous one, this correction is sufficient for most applications.

Referring to Figure 3.1, a simple graphical interpretation for this relative correction can be developed. The figure shows a unit sphere with a spherical triangle. The corner of the spherical triangle labeled A is at the tip of a unit vector in the direction toward the line-of-sight to the transmit antenna. The corners labeled B and C are at the tips of unit vectors in the reference antenna boresight direction and the roving antenna boresight direction respectively. The correction to the single differenced phase is simply the sum of the interior angles of the spherical triangle:

$$(\phi_C - \phi_B)_{corrected} = (\phi_C - \phi_B) - \frac{1}{2\pi} (\alpha + \beta + \gamma)$$

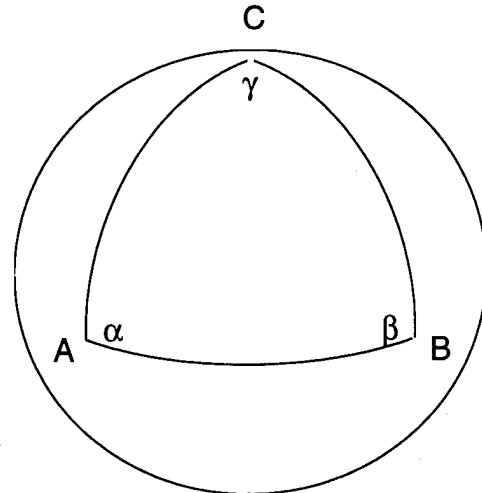


Figure 3.1: Relative RHCP Correction Geometry

To derive this correction, the reference antenna is rotated until its orientation is parallel to the roving antenna, keeping track of the phase changes due to rotation. The y directions of the receive antennas have been arbitrarily chosen to point along a great circle toward each other. To keep track of the phase changes, two facts must be understood:

- Rotating an antenna counterclockwise about its boresight increases the phase of all satellites by the angle through which it is rotated.
- Rotating an antenna about an axis perpendicular to both its boresight and the transmit antenna boresight does not

affect the phase. The E-field component on the antenna parallel to the rotation direction remains unchanged, while the other component changes in magnitude only.

First, rotate the reference antenna counterclockwise through an angle β . This will increase the phase by β and the y direction of will point along a great circle toward point A. Next, rotate the boresight direction up to point A. No phase change occurs, because the rotation axis is normal to both boresights. Next, rotate the reference antenna counterclockwise through an angle α , increasing the phase by the same amount. The y direction will now point along a great circle away from point C. Now rotate the boresight down to point C; the phase does not change. Finally, rotate counterclockwise about the boresight through an angle γ . Now the reference antenna is parallel to the roving antenna. The total phase change rotating from the reference antenna coordinate system to the roving antenna coordinate system is $\alpha + \beta + \gamma$, so this amount should be subtracted from the single differenced phase.

4.0 EXPERIMENTAL RESULTS

4.1 GROUND TESTS

The model aircraft shown in Figure 2.1 was used to validate the software and demonstrate satellite hand-offs from one antenna to the other. Several antenna configurations were used, including diametrically opposed antennas. For the hardware used in these tests, the greatest continuity improvement was with the antenna configuration shown in the picture. One antenna pointed up to the left and one pointed up to the right; the angle between boresights was 120 degrees.

To demonstrate the effectiveness of dual antenna positioning, the model was placed in exaggerated attitudes. Roll reversals from 90 degrees to -90 degrees were performed; kinematic positioning was maintained throughout these extreme maneuvers. Figure 4.1 plots the roll for one such maneuver. The model started level with a southward heading and remained there for about 15 minutes. During this time, satellites were tracked on both the starboard and port antennas. The model was then rolled left to a roll of nearly -90 degrees, where it remained for several minutes.

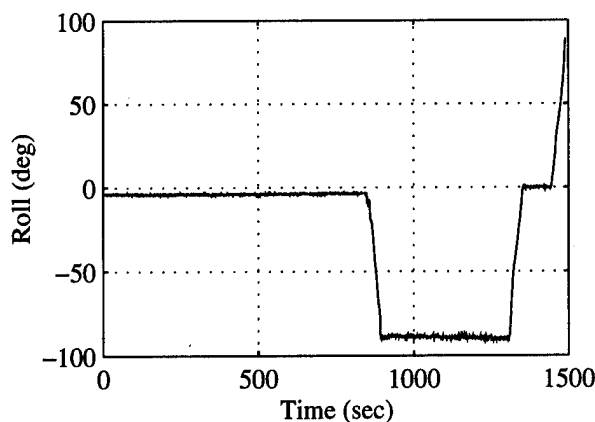


Figure 4.1: Model Aircraft Roll Reversal

The satellite tracking status for this roll to the left is shown in Figures 4.2. These figures are traditional azimuth, elevation polar plots. The radial direction represents elevation (90 degrees at the center to 0 degrees at the outside); the azimuth varies in the clockwise direction as shown. The x's and o's denote satellite positions. An 'x' means the satellite is tracked on the port antenna while an 'o' means it is tracked on the starboard antenna. Both an 'o' and an 'x' means it is simultaneously tracked on both antennas. The solid arc represents the boundary between those satellites closer to one antenna and those closer to the other. For the antenna configuration of the model aircraft, this borderline separates satellites with line-of-sight vectors having components in the starboard direction from those having components in the port direction.

In Figure 4.2a the aircraft is in its initial level configuration. Two satellites are tracked by the starboard antenna, three by the port antenna and two are tracked by both. The borderline between antennas runs north to south. In Figure 4.2b, the aircraft has started its bank to its left (east). Four satellites are now tracked on the starboard antenna, two on the port antenna and one on both antennas. Note that one satellite has been acquired by the port antenna before being lost by the starboard antenna. This process continues until the roll reaches about -90 degrees in Figure 4.2f. At this time, all seven satellites in view are tracked only by the starboard antenna. During this bank to the left, all of those satellites were continuously tracked by a single or both antennas. The cycles ambiguity estimates were therefore maintained throughout the bank.

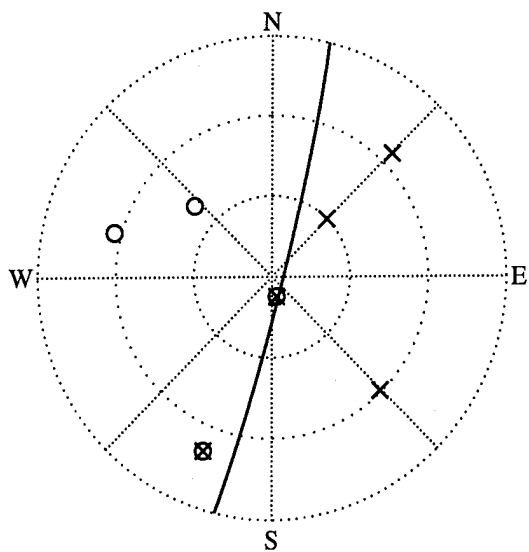


Figure 4.2a

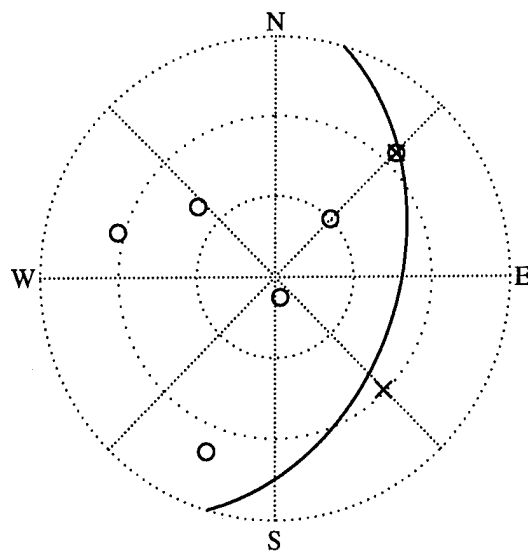


Figure 4.2d

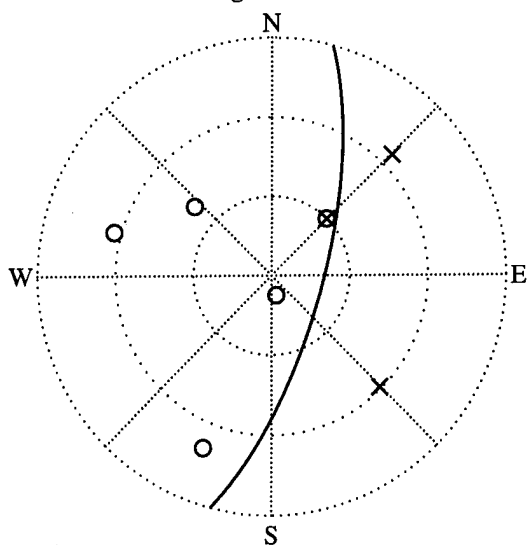


Figure 4.2b

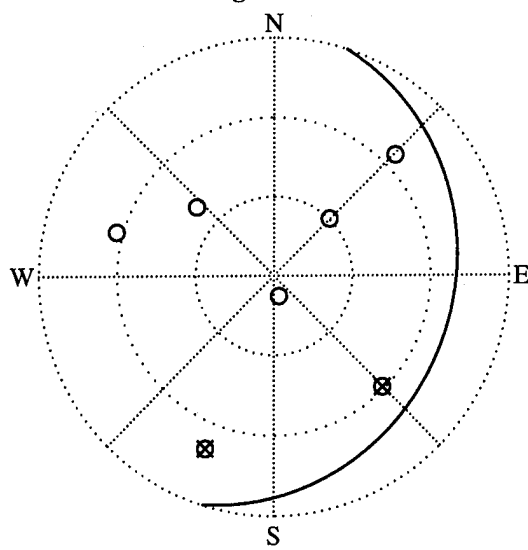


Figure 4.2e

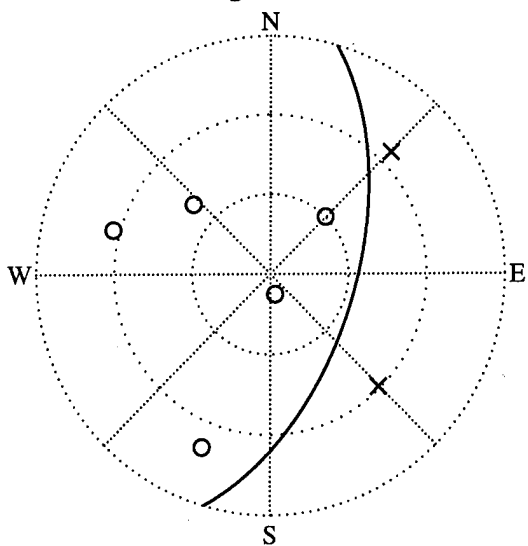


Figure 4.2c

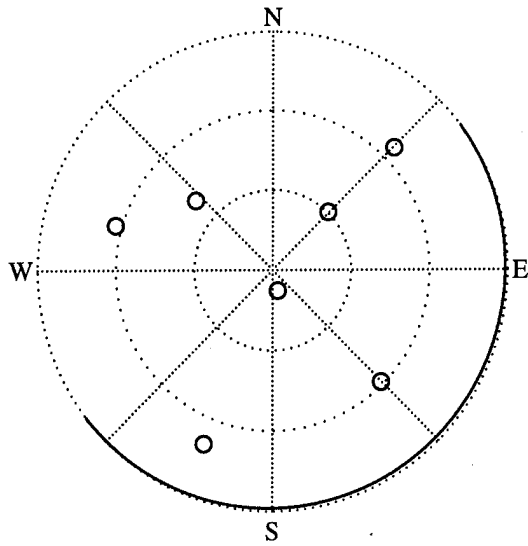


Figure 4.2f

x:port antenna, o:starboard antenna

The model was then returned to level "flight" and then rolled 90 degrees to the right. For the duration of this test, kinematic positioning was maintained. Interestingly, at a roll of 90 degrees, the GPS attitude solution was lost. Typically, GPS attitude is more robust than GPS positioning, because fewer satellites are required. However, due to the dual positioning antennas, the position solution was maintained and attitude was lost.

As the aircraft rolled about the tripod pivot, the positioning antennas traced out a nearly semi-circular arc. The kinematic position solutions for the starboard antenna are plotted in Figure 4.3. This north-looking view clearly shows the arc traced out by the antenna. A nearly independent measure of position can be derived from the attitude if the tripod pivot position and the lever arm from the pivot to the antenna are known. These positions were compared, and agreed to within 6 cm. The 1σ position error is estimated to be about 2 cm.

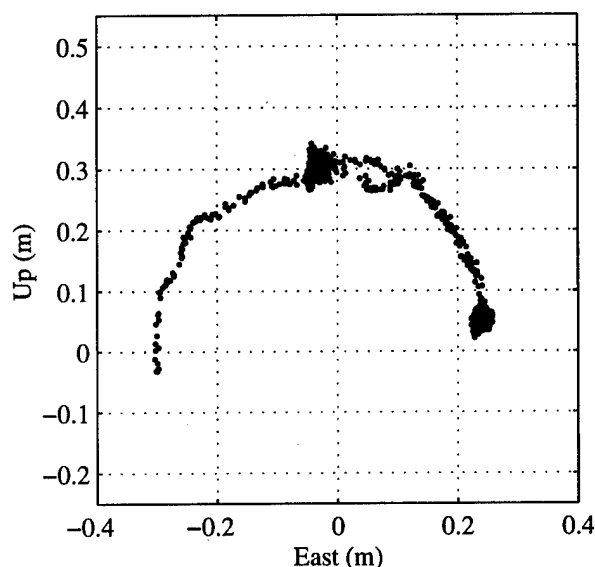


Figure 4.3: Starboard Antenna Position

4.2 FLIGHT TESTS

After validating the dual antenna positioning system on the model aircraft, the system was flight tested on the Piper Dakota. The two antennas used for positioning were on the top and bottom of the piper instead of the starboard and port.

The first flight test was conducted in the traffic pattern at Palo Alto Airport. During the crosswind and base turns, satellites were acquired on the bottom antenna. However, the dual antenna positioning solution was inconsistent. Occasionally, the Receiver Autonomous Integrity Monitoring (RAIM) software detected a high residual soon after incorporating the bottom antenna into the

solution. Phase errors greater than 5 meters were discovered. Errors of that size are extremely rare for kinematic GPS; the carrier phase error is typically less than a centimeter. In post processing, it was discovered that the error was due to a reflected signal dominating the signal received by the bottom antenna. Palo Alto Airport is situated next to the San Francisco Bay; the downwind leg of the standard closed pattern is over water. Water is a good reflector, and satellite signals can reflect off the bay and into the bottom antenna. This reflected signal can enter the antenna at small angles from the boresight, while the direct signal may enter at a less favorable angle or be blocked by part of the aircraft. The phase error due to this extreme multipath scales with the altitude above the reflecting surface. The error profile can therefore be predicted from the altitude profile. Figure 4.4 shows a comparison between the predicted multipath profile and the observed phase error profile. The correlation of the two profiles strongly suggests that the bottom antenna was receiving a reflection from the bay.

This phenomenon does not preclude using a bottom antenna for acquiring satellite signals. Care must be taken to ensure that the direct signal is dominant before using the satellite. These precautions can be taken both at the signal processing level and in the positioning software.

To reduce the impact of multipath on the remaining dual antenna flight tests, the trials were conducted over land. Similar multipath problems were not encountered.

For the next flight test, a series of steep turns were performed over the Stanford campus. The cycle ambiguities were initialized using the IBLIS software. One Autonomous Integrity Beacon [8] was placed on campus for this purpose. After solving for the cycle ambiguities, the aircraft position was known to the centimeter level. The steep turns then commenced, and satellites were acquired through the bottom antenna on several occasions. During one turn, a satellite was continuously tracked for 8 seconds through the bottom antenna. Figure 4.5 shows the geometry at one time during that period. Note that the borderline between antennas now separates satellites with line-of-sight components toward the top of the plane from those with line-of-sight components toward the bottom of the plane; an 'o' means the satellite is tracked on the top antenna and an 'x' means it is tracked on the bottom antenna. In the figure, the aircraft heading is northwest and its roll is -32 degrees. Six satellites were tracked on the top antenna and one was tracked on the bottom. To quantify the dual antenna positioning performance, this 8 second period was post-processed and single antenna position solutions were compared with dual antenna solutions. The traditional single antenna software used the six satellites tracked on the top antenna to generate a centimeter-level trajectory. The dual antenna software

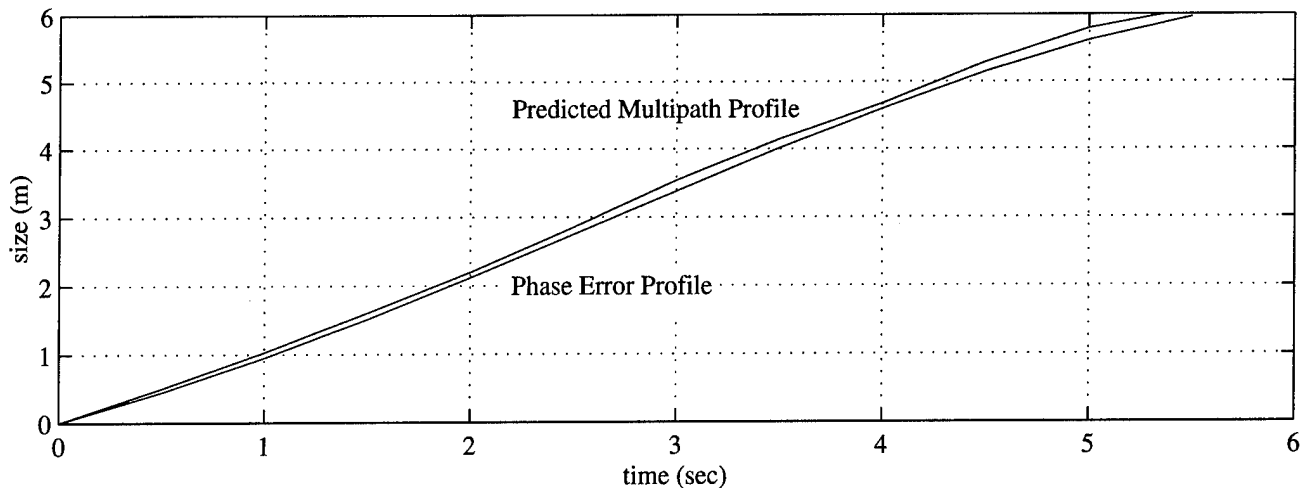


Figure 4.4: Evidence of Reflection Dominating Received Signal

was then used to calculate the same trajectory using carrier phases measured from both antennas. To simulate poor satellite geometry, three of the top satellites were removed from the dual antenna solution. Therefore, the dual antenna trajectory used three top satellites and the bottom satellite. Before the bottom satellite was lost, the three top satellites were reintroduced. Figure 4.6 shows the difference between the single and dual antenna trajectories. From this comparison, it can be seen that the bottom antenna can be used to provide centimeter-level accuracy in the event that the top antenna satellite geometry is poor.

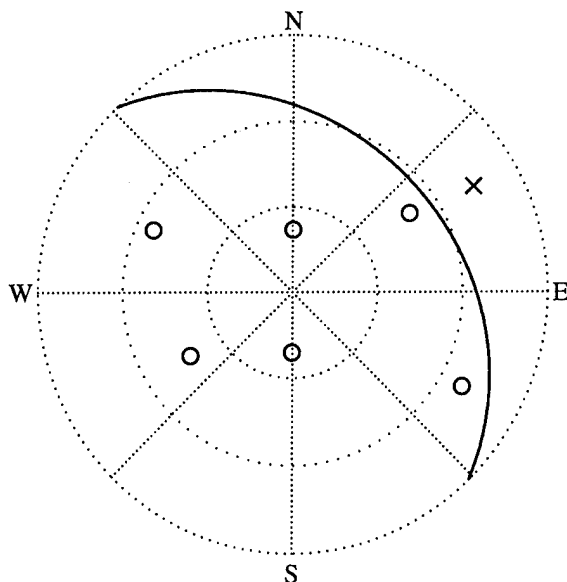


Figure 4.5: Az/EI Plot of Satellite Tracking Status

x:bottom antenna, o:top antenna

5.0 CONCLUSIONS

- Centimeter-level kinematic positioning was demonstrated in flight using two opposing antennas. With the appropriate hardware, nearly 4π steradian visibility should be attainable using opposing antennas.
- Multiple antennas can greatly improve the availability and continuity of GPS positioning in banked turns without a large increase in expense. This improvement may be significant for applications such as curved approaches.
- Navigation in mountainous areas, at high latitudes, and during times of satellite failures is particularly reliant on maintaining continuous lock on all satellites in view. It is under these conditions that aircraft can benefit the most from multiple antenna positioning.
- Ideal applications for multiple antenna positioning are systems that already have multiple antennas:
 - Integrated positioning and attitude for spacecraft [9] and aircraft.
 - The Integrity Beacon Landing System.
- Multipath from the ground can be more severe when antennas are not oriented vertically. Care should be taken to ensure that the direct signal dominates the received signal.

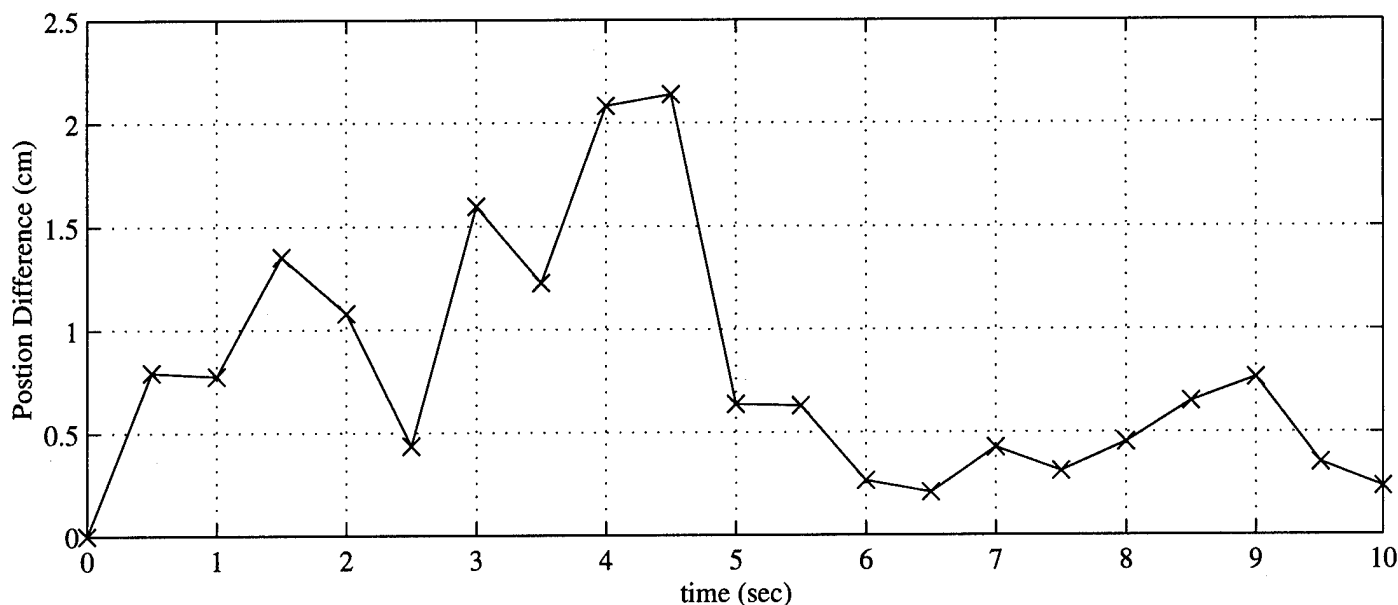


Figure 4.6: Comparison of Single and Dual Antenna Positioning

6.0 ACKNOWLEDGMENTS

The authors wish to thank several individuals and organizations who made this research possible. At Stanford, Boris Pervan, Konstantin Gromov, Ping-Ya Ko, Mike O'Connor, Andy Barrows, Gabe Elkaim and Denise Nunes provided generous assistance. Trimble Navigation provided the GPS equipment used to conduct the experiments. This research was sponsored by the FAA.

7.0 REFERENCES

1. G. Kinal, "Consideration of Practical Visibility of Geostationary Augmentation Satellites from Aircraft", ION National Technical Meeting, Anaheim, CA, January, 1995.
2. C.E. Cohen, B. Pervan, H.S. Cobb, D. Lawrence, J.D. Powell, B.W. Parkinson, "Real-Time Flight Test Evaluation of the GPS Marker Beacon Concept for Category III Kinematic GPS Precision Landing", ION GPS-93, Salt Lake City, UT, September, 1993.
3. C.E. Cohen, D. Lawrence, B. Pervan, H.S. Cobb, A. Barrows, J.D. Powell, B.W. Parkinson, "Flight Test Results of Autocoupled Approaches Using GPS and Integrity Beacons", ION GPS-94, Salt Lake City, UT, September, 1994.
4. C.E. Cohen et. al., "Automatic Landing of a 737 using GNSS Integrity Beacons", ISPA '95, Braunschweig, Germany, February, 1995.
5. C. E. Cohen, "Attitude Determination Using GPS", Ph.D. Thesis, Department of Aeronautics and Astronautics, Stanford University, December, 1992.
6. D. Lawrence, B. Pervan, C.E. Cohen, H.S. Cobb, J.D. Powell, B.W. Parkinson, "A Real-Time Architecture for Kinematic GPS Applied to the Integrity Beacon Landing System", ION 51st Annual Meeting, Colorado Springs, Colorado, June 5-7, 1995.
7. "Global Positioning System Standard Positioning Service Signal Specification", Second Edition, June 2, 1995.
8. S. Cobb, D. Lawrence, B. Pervan, C. Cohen, J. Powell, B. Parkinson, "Precision Landing Tests with Improved Integrity Beacons", ION GPS-95, Palm Springs, CA, September, 1995.
9. H. Uematsu, B. Parkinson, E.G. Lightsey, "GPS Receiver Design and Requirement Analysis for the Stanford Gravity Probe B Relativity Mission", ION GPS-95, Palm Springs, CA, September, 1995.

Precise RTK Positioning Using the New RTCM-104 V2.1 Standard

J.P. Thomas Goguen and Timo Allison
Trimble Navigation

BIOGRAPHY

Thomas Goguen graduated from the University of New Brunswick in 1986 with a B.Sc.E. and from the University of Ottawa in 1988 with a M.A.Sc. in Electrical Engineering. Prior to joining Trimble in 1994 he worked with the Department of National Defence in Canada. At Trimble he has been responsible for GPS receiver firmware development.

Timo Allison graduated from the University of Leeds, England, with a B.Sc. and Ph.D. in Electrical & Electronic Engineering in 1982 and 1985 respectively. He has been active in the field of satellite navigation since 1981, and has been with Trimble Navigation since 1985. He is currently responsible for survey receiver firmware development, with an emphasis on Real-time Kinematic systems. He was treasurer of the Satellite Division of the Institute of Navigation from its inception in 1987 until 1993.

ABSTRACT

Real-time Kinematic (RTK) surveying is now established as a reliable field technique, and has been commercially available since 1993. Combining both GPS and radio modem technologies, processing to yield baseline vectors can occur in real-time. This results in substantial increases in productivity when compared with traditional Kinematic and Static GPS techniques which require the downloading of stored GPS observables from two or more receivers and time consuming post-processing. Accuracies at the centimeter level are typical.

Differential GPS (DGPS) achieves accuracies at the sub-meter level with high performance receivers. Although less accurate than RTK, there is no requirement to *initialize* the system (resolve integer wavelength ambiguities), allowing operation over longer baselines. In fact, both RTK and DGPS are differential systems with

different levels of accuracy and operational constraints. However, DGPS has one big advantage from a customer viewpoint—the communication link provides differential corrections based on the RTCM-104 standard. This allows equipment from different manufacturers to be combined in a network comprising reference and rover receivers. The first RTK systems had to use proprietary data formats to allow double-difference carrier phase processing. These proprietary formats can be very efficient from a data communications standpoint, but are inherently manufacturer dependent.

A system is described which achieves similar positioning performance to an existing RTK product, the **GPS Total Station™**, while using Version 2.1 of the RTCM-104 standard. While adhering to this industry standard, some new and interesting possibilities unfold. The system is capable of transmitting traditional RTCM DGPS corrections together with RTK-style messages on the same RTCM radio link. This provides a service for both RTCM DGPS and RTK users. Of course, if radio modem bandwidth (baud rate) restrictions are a problem, only those RTCM messages required for RTK operation should be selected for survey applications. As compared to DGPS, the effects of Selective Availability (SA) are reduced for RTK by time-synchronized double-differenced processing.

The implementation of RTCM-104 Version 2.1 is discussed in an enhanced version of the **GPS Total Station™**. Problems in Version 2.1 which affect RTK are highlighted, together with proven methods to alleviate these limitations. An application is described in which the system is being successfully used to provide both an RTCM DGPS and RTK service with a single communication link.

INTRODUCTION

™ Denotes a Trade Mark of Trimble Navigation Ltd.

A simple illustration of a differential (RTCM or RTK) system is shown in Figure 1. Note that the system consists of a reference (or base) station, a rover, and a data link between the two. Typically the data link is one way: raw measurements, or measurement corrections, are sent from the reference station to the rover.

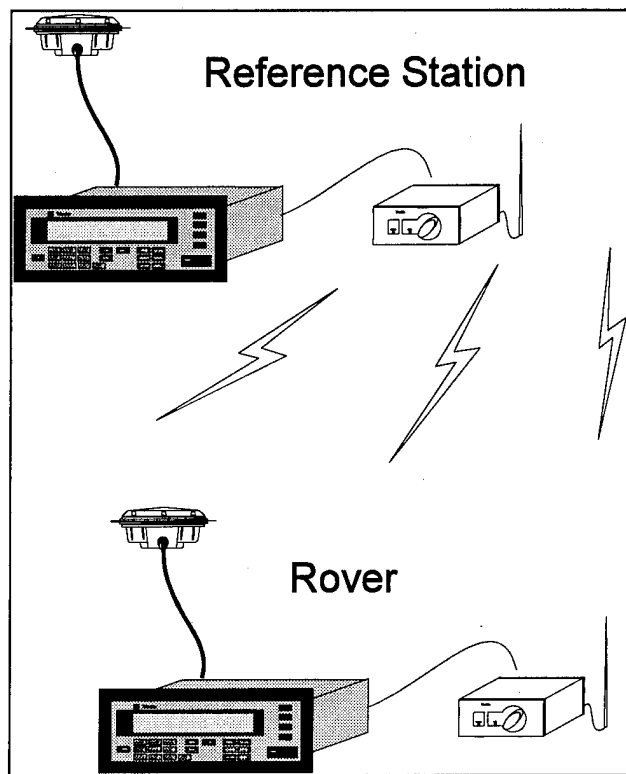


Figure 1: RTCM System

Until recently the application of RTK techniques to navigation and survey required the use of proprietary communications protocols developed by individual manufacturers. The new standard will accentuate the growth of RTK especially for navigation. Users will have the potential to take advantage of the economies derived from using a single reference station and a single communications channel in a combined differential and RTK network.

The RTCM SC-104 committee has described a set of messages to support RTK solutions at the Rover. These are Types 18, 19, 20, and 21. Types 18 and 19 provide uncorrected carrier phase and uncorrected pseudorange measurements respectively. Types 20 and 21 provide carrier phase and pseudorange corrections respectively. A typical Reference Station transmits 18 and 19 or 20 and 21 at the discretion of the service provider. In addition, an RTK solution requires the transmission of a Type 3 (Reference Station Coordinates). The original intent of

the duplicate message sets was to allow for smaller messages by using corrections as delineated in Types 20 and 21. Unfortunately these messages are identical in size per satellite as Types 18 and 19. So no reduction in communications channel bandwidth is available through the use of these messages.

Until now neither set of these messages has been used by a commercial manufacturer of GPS equipment for the provision of RTK services. Trimble has chosen to implement Types 18 and 19 in their RTCM V2.1 compatible Reference Stations. The format of these message types is provided in Appendix 1. Types 18 and 19 are used by Trimble's 4000SSi Rover to produce RTK solutions with cm accuracy with 1 or 2 updates per second (1 or 2 Hz).

There are several drawbacks to the RTCM RTK system. Messages 18 through 21 require extensive bandwidth in the communications channel. Furthermore, assumptions relating to the base station's capabilities must be made in order to minimize the latency of the solution in the rover. There has been no provision for the extended precision of these RTK solutions in the base station position message. This means that the computed vector between the rover and the base is more precise than the transmitted base station position. Thus, using RTCM V2.1 the rover's position cannot be fixed as accurately as provided by RTK when using Trimble's proprietary format. RTK using RTCM V2.1 provides opportunities for commercial navigation. However extensions in the communications protocol are required to provide this utility to the surveyor. Finally, it is worth noting that no work has been published regarding the use of different manufacturer's equipment at the base and rover. Despite the existence of a common and workable communications protocol there still exists the need for some investigation of the effects of inter-receiver and antenna biases on the computation of RTK solutions.

IMPLEMENTATION

Since 1993, Trimble has provided a reliable RTK product in the survey market. The core RTK software in the 4000SSi, the RTK processor, relies on phase and pseudorange observables transmitted from a base station each measurement epoch. Using this information in concert with similar measurements made locally at the rover the RTK processor generates solutions once or twice per second. These observables are transmitted in a Trimble proprietary format which is similar in content to that found in the RTCM Type 18 and 19 messages. Thus a combination of Types 18 and 19 is used in Trimble RTCM compatible RTK systems. RTK performance using

RTCM is similar to that using Trimble's proprietary data format since both protocols feed the same RTK engine. For a detailed description of the RTK system performance the reader is referred to [2] and [3].

Recently released firmware for Trimble base stations supporting RTK using the RTCM V2.1 format provides for two modes of operation: *RTK Only* and *RTK+RTCM*. The *RTK Only* mode allows the RTCM base station to work with bandwidth limited data communications channels by transmitting only the RTCM Type 3, Type 18 and Type 19 messages. This provides enough data for the RTCM RTK solution but does not allow for the DGPS solution. In *RTK+RTCM* mode the RTCM base station will generate all of the messages used for both the RTCM DGPS and the RTCM RTK solutions.

The RTCM RTK system includes most of the features which are currently available within the **GPS Total StationTM** including Fully Automatic Ambiguity Resolution, often known as initialization On-The-Fly (OTF). This relies on the reference station providing high quality dual frequency observables. Alternatively, ambiguity resolution requires the use of an initializer plate or occupation of a known position. These two methods do not require L2 information but may be inconvenient in the typical RTCM system where the reference station's GPS antenna or a known survey mark may be inaccessible. Within the rover Trimble has implemented two modes of RTK support using the RTCM format: *RTK-L1* or *L1/L2*. In *L1* mode the rover uses only the *L1* messages in the RTK solution. In *L1/L2* mode the data from all four messages are fed into the RTK solution providing rapid and reliable OTF initialization. The rover in each of the RTCM RTK modes generates solutions with the same level of accuracy and precision as that provided when using Trimble's proprietary format from a similarly equipped base station.

Although not contained within the current specification, every Trimble 4000SSi RTCM base station will transmit a complete set of two Type 18 messages (*L1* and *L2*) and two Type 19 messages (*L1* and *L2*) each measurement epoch. In the event that no data is available for a given message, the header is still transmitted for that measurement epoch. As explained later, the specification should require this. Trimble's base stations broadcast these messages first in any measurement epoch.

Because of the accuracy limitation in the base station position message, Type 3, additional precision is needed for high precision RTK. Trimble has supplemented the Type 3 message with a Type 59 message. The Type 59 is a provider specific message. A single Type 59 is used to extend the precision of the Type 3 to 0.1 mm in the belief

that the 1 cm resolution of the Type 3 is insufficient for survey applications. The RTCM SC-104 committee should address this issue with the adoption of a message type providing similar information. The format of the Trimble Type 59 used for this purpose is provided in Appendix 2.

DATA LINK CONSIDERATIONS

RTCM uses byte lengths of 6 bits combined to form words of 30 bits including 6 bits of parity information. Each message requires a two-word header. The RTK messages use another word as a sub-header and use two words for each satellite. These messages, type 18 and type 19 or type 20 and type 21, must be transmitted twice each measurement epoch, once with *L1* data and once with *L2* data, for dual frequency base stations. Thus 8 RTCM words (240 bits total) must be transmitted for each satellite. In a typical RS-232 link each word is transmitted as five 8 bit bytes. Thus for each satellite RTCM requires 40 bytes of data plus supporting structure in order to transmit the RTK information alone. The Trimble proprietary format requires much less bandwidth as it does not suffer from this overhead.

It is worth noting that the RTCM differential service can run over relatively slow links e.g., 200 bits per second, using Type 9 messages in place of Type 1. The rover suffers only a slight degradation in position accuracy due to the need to propagate the differential corrections over a short time (up to 10 seconds). The same cannot be said for RTK. It is imperative to send the RTK data each solution epoch as reference/rover measurements must be synchronized to eliminate Selective Availability (SA) errors and maximize position accuracy.

Tables 1, 2, and 3 below illustrate the bandwidth requirements on a standard RS-232 link for RTCM and RTCM with the RTK messages. Tables 1 and 2 provide the number of bytes transmitted in an epoch. Peak refers to the total number of bytes transmitted in the epoch which would include all of the messages in the table. The epoch following a peak epoch is likely to require fewer bytes. (e.g., Type 3's are never transmitted in consecutive epochs unless specified by the user.) Thus some radio solutions may be able to contain the peak with a lower baud rate than that indicated. The data in Table 3 assumes 10 bits transmitted per 8 bit data byte (1 start bit, 1 stop bit, no parity) and a 1 Hz update rate. The brackets indicate the minimum available baud rates for operation.

Table 1: RTCM V2.0 Bandwidth Requirements
(bytes/epoch)

Message	4 SV's	8 SV's	9 SV's	12 SV's
Type 1	45	80	85	110
Type 2	45	80	85	110
Type 3	30	30	30	30
Peak	120	190	200	250

Table 2: RTCM V2.1 Bandwidth Requirements
(bytes/epoch)

Message	4	8	9	12
Type 18 L1	55	95	105	135
Type 19 L1	55	95	105	135
Type 18 L2	55	95	105	135
Type 19 L2	55	95	105	135
Type 3	30	30	30	30
Peak (RTK ONLY)	250	410	450	570
Peak (RTCM+RTK)	340	570	620	790

Table 3: RTCM Minimum Baud Rates

RTCM Mode	4	8	9	12
Version 2	1200	2400	2400	2400 ¹
RTK ONLY	2400 ¹	4800	4800	4800 ¹
RTCM+RTK	4800	4800 ¹	9600	9600

The amount of data sent each epoch creates another problem over more compact formats. A one bit error anywhere in the link forces a failure for the word being sent. This effectively nullifies the particular message in which the error occurred. If it is one of the four RTK messages then a solution may be missed for that epoch. The length of the RTK data using RTCM is nominally 3 times as large as Trimble's proprietary format for observables alone, therefore the RTCM format is more susceptible to burst interference in the RTK application. Note that for 9 satellites the *RTCM+RTK* format requires a data link capable of 9600 baud.

SOLUTION LATENCY CONCERNS

¹ Actual peak bit rates exceed the indicated baud rate. However some messages are not normally transmitted in successive measurement epochs. A radio link with suitable buffering may operate successfully at this rate. Latency may increase during peak periods.

RTCM leaves much of the implementation to the service provider. One difficulty with this lies in the use of the RTK messages. Measurements from the reference station must be synchronized with those in the rover for double differencing processing. In any given measurement epoch the rover cannot know a priori which of the four RTK RTCM messages (18-L1, 18-L2, 19-L1, 19-L2) will be sent from the base. Thus the rover must wait until all four messages have been received or until the first of the next epoch's messages is received in order to be certain that it has all available information from the base. At the rover, solutions may be attempted in the absence of some of the information contained within these messages. Nothing in the specification dictates that all 4 messages must be transmitted each epoch. From the rover's standpoint this may increase the latency in the solution by nearly 1 measurement epoch.

To alleviate this problem all Trimble base stations transmit all four messages in sequence in each solution epoch. This occurs even when the base is not tracking satellites on L2. Also these messages are transmitted ahead of any other messages in the epoch. Because RTCM has not specified the use of these messages in the absence of L2 information at the base, the rover employs a more general scheme which will work with both Trimble and non-Trimble base stations. If the rover is in L1 mode an RTK solution will be attempted after the L1 messages have been received. In L1/L2 mode the rover will attempt a solution only after all four messages have been received from the base otherwise it will compute the DGPS solution for that measurement epoch. Since all Trimble Base Stations transmit all four messages, RTK rovers may determine the data available (L1 and/or L2) and generate solutions accordingly, for each measurement epoch with the lowest possible latency.

BASE STATION COORDINATES

The RTCM standard has been designed as a navigation and positioning service. It leaves much to be desired by the professional surveyor. Very little information about the RTCM base station is supported in the broadcast standard aside from its position. This position information is limited to a resolution of 1 cm in WGS-84 Cartesian X, Y, and Z. In attempting to support RTK applications which can provide sub-cm vectors from the base it needs to be extended. As stated, a Type 59 message is used to extend the precision of the Type 3 data to 0.1 mm.

For RTK operation it would be useful to know if the base was capable of L2 operation. This would help the processor decide whether to wait for L2 information from

the base and would simplify the mechanisms described above to overcome latency concerns.

For survey applications user-controlled RTCM base stations are supplemented with the provider specific Type 59 messages. Trimble's 4000SSi receivers enhance the base station information in the RTK mode to aid in survey applications. This information includes some basic status information, L2 capability, and the Base Station antenna height.

GRACEFUL DEGRADATION

Given enough radio link bandwidth the service provider can transmit both the RTK message set and the DGPS support on the same link. One benefit of using RTCM with the RTK messages is the potential for a more graceful degradation in the position solution when there are interruptions in the data link. The RTK processor only provides a 3D solution since an altitude hold solution does not satisfy centimeter level survey accuracies. It is possible for an RTCM rover to provide a DGPS solution in the absence of sufficient information for RTK solutions. For example when tracking only 3 SV's or when the radio link is interrupted for a brief period (less than 10 seconds), the RTK rover can still generate an RTCM differential solution.

In particular, this may be exploited in navigation applications. If an RTK solution cannot be computed, the rover reverts automatically to DGPS (1m) positioning. Of course if the base station corrections are not received for an extended period of time then the rover will operate in an autonomous mode providing the C/A code position with an accuracy dependent upon Selective Availability (SA) levels.

BASE STATION – Kobe, Japan

The first commercially available RTCM V2.1 base station providing RTK services has been established near Kobe, Japan. This station employs a dual frequency 4000 series receiver. It transmits the full set of RTCM messages for differential and RTK applications described above as *RTCM+RTK* mode. A TrimTalk 450 radio is combined with a 10 watt amplifier to broadcast the RTCM V2.1 messages.

The base station receiver was set up to log data continuously providing the opportunity for post-processed kinematic and fast static surveys. Routes out to 10 Km from the base were surveyed by crews from Trimble using RTCM DGPS and RTCM RTK capable rovers. The routes were covered at least twice on different days and

data was logged for post-processing. The RTCM RTK solutions were logged using the same station points. After processing the logged data it was determined that the station to station vectors using RTCM V2.1 RTK were comparable to the post-processed values at the cm level.

Finally note that Trimble has tested RTCM V2.1 with RTK in Toronto, Canada using a FM sub-carrier link. This communications channel is capable of 9600 baud and extended range.

APPENDIX 1

Outlined below are the RTCM Type 18 and Type 19 messages used for RTK. These are described extensively in [1]. Note that each message is preceded by a two word header also described in [1].

Message Type 18 - Uncorrected Carrier Phase Measurements

1 2 3 4 5 6 7 8 9 10 11 12 13 14 15 16 17 18 19 20 21 22 23 24 25 26 27 28 29 30

F	SP	GPS TIME OF MEASUREMENT																										PARITY
---	----	-------------------------	--	--	--	--	--	--	--	--	--	--	--	--	--	--	--	--	--	--	--	--	--	--	--	--	--	--------

2 Words For Each Satellite

1 2 3 4 5 6 7 8 9 10 11 12 13 14 15 16 17 18 19 20 21 22 23 24 25 26 27 28 29 30

H	P	R	SATELLITE ID	DATA QUAL.	CUMULATIVE LOSS OF CONTINUITY	CARRIER PHASE UPPER BYTE	PARITY
---	---	---	--------------	------------	-------------------------------	--------------------------	--------

CARRIER PHASE LOWER THREE BYTES																										PARITY
---------------------------------	--	--	--	--	--	--	--	--	--	--	--	--	--	--	--	--	--	--	--	--	--	--	--	--	--	--------

Where: F indicates the frequency.

SP are spare bit.

H/P indicates half or full phase data.

P/C indicates C/A or P Code data.

R is reserved.

Message Type 19 - Uncorrected Pseudorange Measurements

1 2 3 4 5 6 7 8 9 10 11 12 13 14 15 16 17 18 19 20 21 22 23 24 25 26 27 28 29 30

F	SM	GPS TIME OF MEASUREMENT																								PARITY
---	----	-------------------------	--	--	--	--	--	--	--	--	--	--	--	--	--	--	--	--	--	--	--	--	--	--	--	--------

2 Words For Each Satellite

1 2 3 4 5 6 7 8 9 10 11 12 13 14 15 16 17 18 19 20 21 22 23 24 25 26 27 28 29 30

S	P	R	SATELLITE ID	DATA QUAL.	MULTIPATH ERROR	PSEUDORANGE UPPER BYTE	PARITY
---	---	---	--------------	------------	-----------------	------------------------	--------

PSEUDORANGE LOWER THREE BYTES																										PARITY
-------------------------------	--	--	--	--	--	--	--	--	--	--	--	--	--	--	--	--	--	--	--	--	--	--	--	--	--	--------

Where: F indicates the frequency.

SM indicates the smoothing interval.

S is a spare bit.

P/C indicates C/A or P code data.

R is reserved.

APPENDIX 2

Illustrated below is the Type 59 message used to extend the precision of the RTCM Type 3 message. DELTA X is computed by taking the absolute reference station coordinate in WGS-84 Cartesian, X, and subtracting the X coordinate transmitted in the RTCM Type 3. The result to 0.1 mm is transmitted as a 16 bit integer. DELTA Y and DELTA Z are computed in a similar manner using their respective vectors. As with all RTCM messages the Type 59 is preceded by a 2 word RTCM header described in [1].

Message Type 59 - Trimble Type 3 Precision Extension

1 2 3 4 5 6 7 8 9 10 11 12 13 14 15 16 17 18 19 20 21 22 23 24 25 26 27 28 29 30

54 ₍₁₆₎	4E ₍₁₆₎	03 ₍₁₆₎	PARITY
DELTA X		DELTA Y UPPER BYTE	PARITY
DELTA Y LOWER BYTE	DELTA Z		PARITY

ACKNOWLEDGMENTS

The authors would like to thank their numerous co-workers and in particular acknowledge the support of Nick Talbot, Scott Dreier, Pete Raby, Tom Morris, and Geoffrey Kirk.

REFERENCES

- [1] RTCM Recommended Standards For Differential Navstar GPS Service, V2.1, RTCM Paper 194-93/SC104-STD, January 3, 1994.
- [2] Timo Allison, Peter Griffioen, Nicholas Talbot, "Acceptance of Real-Time Kinematic by the Professional Surveyor", *Proceedings of the ION GPS-94*, Salt Lake City, Utah, September 1994.
- [3] P. Griffioen, T. Allison, S. Dreier, "Real-time Kinematic: The Next Surveying Tool", *Proceedings of the 1993 ION Technical Meeting*, San Francisco, January 1993.

First Results Using the New DGPS Real-Time Deformation Monitoring System "DREAMS"

Dr. Günter Hein and Bernhard Riedl
University FAF Munich

BIOGRAPHIES

Dr. Günter W. Hein is Full Professor and Director of the Institute of Geodesy and Navigation at the University FAF Munich. He is responsible for research and teaching in the field of high-precision GPS/GLONASS positioning, navigation, physical geodesy, gravimetry and satellite geodesy. He works in the field of GPS since 1984 and is the author of numerous papers on static and kinematic positioning and navigation.

Bernhard Riedl is Research Associate at the Institute of Geodesy and Navigation at the University FAF Munich. He studied Electrical Engineering and Information Technology at the Technical University of Munich. Since 1993 he has been concerned with research in the field of real-time GPS applications for deformation monitoring purposes.

ABSTRACT

At the Institute of Geodesy and Navigation (IfEN) a high-precision DGPS based deformation monitoring system has been built-up. It is called DREAMS (*Differential REAL-time Monitoring System*) and has the capability to monitor continuously all kinds of man-made and natural structures where the early detection of possible movements may prevent disasters. Its main objective is not only to allow the user to watch the time-line updated in real-time on the screen, but more important, it gives him a tool at hand that supports him in deciding in or near real-time whether the monitored object has moved significantly or not.

The software is currently available as a standard DOS application. Due to DOS memory limitations the software has been ported to LINUX (a PC UNIX) using the same hardware as for the DOS version and it will be soon available for Windows NT and the upcoming Windows 95. So there are no limitations for future applications or larger networks that may need more memory or computing power. Also the use of multiprocessor systems is possible.

First results obtained with this new system have proven its high precision. Initial tests were carried out using two stations. In order to generate a vertical deformation, the receiver of the monitor station was fixed on a slide for precise 3D movements. The collected and evaluated data show that the system is capable of reaching the millimeter level accuracy and better.

This new system overcomes the disadvantages of the post-mission static GPS analysis concept commonly used and might gain more insights into the short-time behaviour of deformation objects. This is especially due to its real-time capabilities, the high portability and the high update rates (up to 20 Hz).

This paper presents this new sophisticated system, outlines the algorithms, the software and hardware architecture as well as reports from first experiences in the field.

INTRODUCTION

In surveying and geodesy we are trying to measure the exact position of a point in the field or of an object that is moving. Nowadays this is usually done using GPS space techniques. For most applications it is not necessary to evaluate the conducted measurements in real-time. This is of course not the case if we think about the use in navigation on land, water or in the air. For these tasks real-time systems clearly have to be used since it is necessary to determine the exact position and velocity of a vehicle immediately after the measurements are conducted by the sensors.

So it is not surprising that a real-time system is employed in fields where man, nature, buildings or structures are in danger. It is even possible to use it in areas where the collapse of manmade engineering objects could lead to destruction or natural disasters. But also the application of such a system in conjunction with the observation of volcanoes and earthquake areas comes to mind. The range of applications is wide and this new monitoring system has great advantages compared to traditional systems like surveying robots, theodolite and levelling instruments or terrestrial photogrammetry, since it overcomes the disadvantages all these systems have in common. These disadvantages are:

- the long time intervals between the measurements (days or months)
- averaging of data over too long time spans (often some hours are smoothed which leads to smoothing effects that could hide real movements of the stations)
- batch mode analysis (data is collected, transmitted to a computer center and evaluated a few hours later).

It is mainly due to the first point that the International Commission for Large Dams [ICOLD, 1988] considered those contemporary surveying techniques to be of only limited importance for monitoring purposes.

It should be mentioned that the reasons for the displacement of most objects can be divided in three categories,

- long term changes (depending on the season)
- short time changes (influenced through environmental effects like temperature or wind, etc.)
- the modifications in the load and changes of the material of the building and respectively in the structure of rocks or the earth around the observed point.

The third point is of our main interest since changes there can lead to permanent changes in the position of the object under investigation.

SYSTEM DESIGN

The overall goals of the system are to be flexible in applications, easy to install and maintain, and to be highly variable in configuring the system. In order to fulfill these objectives for a deformation monitoring system like DREAMS a lot of integration work of standard hardware components together with a custom-made design was undertaken. This is also true for the development cycle of the software. Originally based on MS-DOS it is now running under the standard GUI MS-Windows and already under Windows 95 utilizing features as its 32-bit capability.

System Overview

In order to design the system to be as flexible as possible we have developed two different types of stations. This is important for applications where fast installation and independence from data connections by wire are main goals. The prediction of volcano eruptions is one of these applications.

The stations that are placed at the observed points are the so-called **monitor stations**. The major advantage is their compact design and ease in use. Fig. 1 and Fig. 2 show the monitor station and its hardware components.

At the central control point a **network master station** is installed (see Fig. 3). It serves as DGPS reference station and is responsible for computing the position deviations and the visualization of the results. There the computing load is high since the stations of the whole network are



Fig. 1 Monitor station on top of a pillar

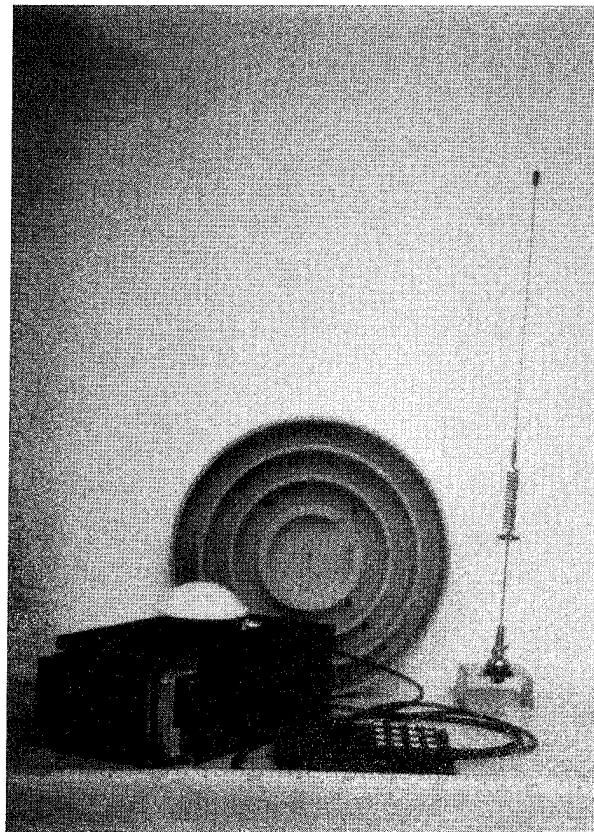


Fig. 2 Monitor station (details)



Fig. 3 Network master station

processed. As a rule of thumb you need ten times more time for processing 10 stations compared to 2 stations.

Hardware Architecture

Common to both type of stations is the housing for the GPS receiver and the telemetry. It is a so-called „black box“, which has some connectors on its back and all

other components are hidden inside. Its size is about 10 cm x 20 cm x 30 cm. Fig. 1 and Fig. 2 show the box together with some other components including the telemetry antenna. The box is sealed against dust and water using a sealing ring. This protects it against harsh environmental conditions. To make sure that the plugs are also sealed, MIL-connectors are used. The connectors are as follows:

- serial port 1 (connection line to PC)
- serial port 2 (connection to telemetry)
- telemetry antenna
- GPS antenna
- power supply (12V)

Inside the box are the GPS receiver card, the telemetry, a backplane connecting these two components and a power conversion module. In detail these parts are

- GPS receiver card, at present NovAtel GPSCard (OEM Performance series), L₁ only, 12 channels
- telemetry, 10 W HF output, halfduplex
- power conversion (input: 12V, output: $\pm 12V$, +5V)

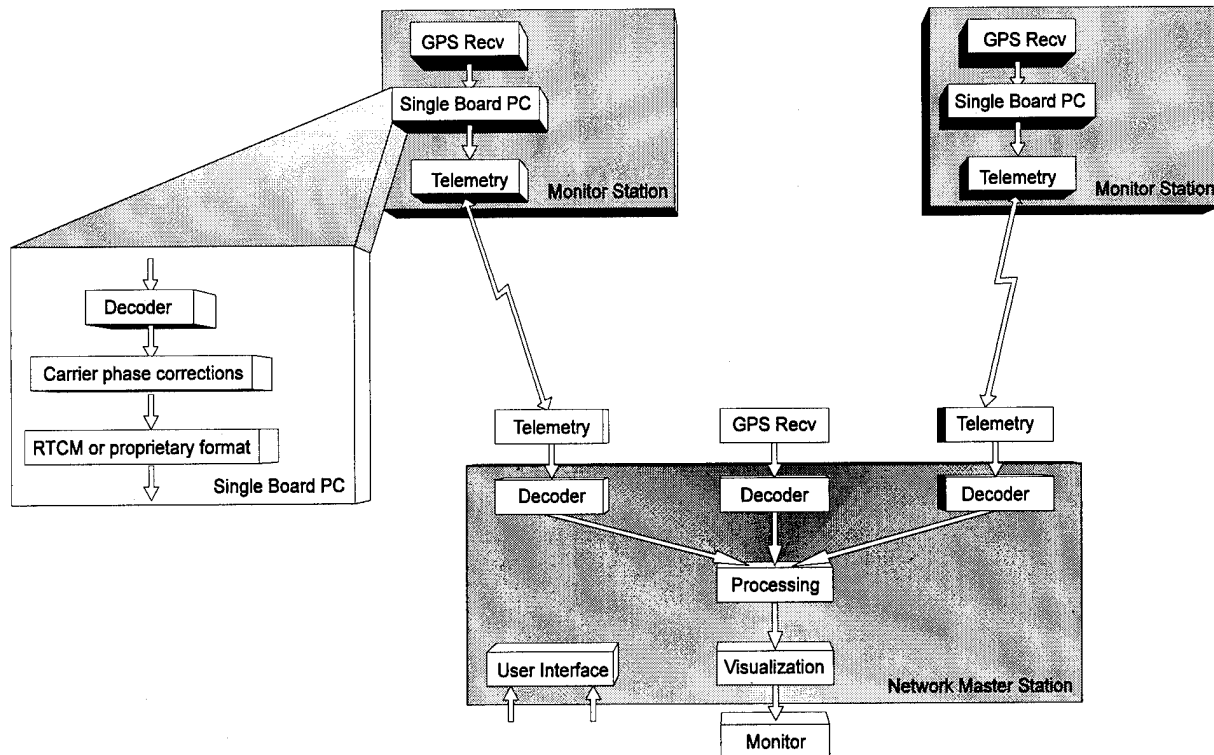


Fig. 4 Overview system modules and data flow

Network master station

At the network master station (which, of course, can be also in a different location as the reference station) a powerful PC is necessary in addition to the black box. Therefore a 80486 PC is currently used. It may be replaced by a Pentium system to take into account the amount of data that has to be processed and evaluated with higher data rates of 10 or 20 Hz.

Monitor station

The black box of the monitor station includes in addition to the above-mentioned parts an industrial single-board computer of type 80486 (low power version) in conjunction with a 2.5" fixed disk. The disk is used to store the collected data temporarily.

Software Architecture

Since some effort has been undertaken in developing the software system it was fairly simple to adapt it for the MS-Windows operating system (see below). Its structure is based on an object-oriented design. The system is divided in three specialised groups utilizing one common data interface:

- I/O modules (hardware and operating system dependent)
- processing and data management
- visualization and user interface.

This concept is supported utilizing the object-oriented programming language C++. This is especially useful when developing large software systems as it is the case with DREAMS. It is therefore easy to write extensions to the software without changing anything within other code modules and classes.

Fig. 4 depicts the main system components and shows the data flow from the monitor stations to the master station and within the modules itself.

Network master station

As mentioned above the software at the network master station was originally developed for MS-DOS. Since the software was planned to be easy to use, to be configurable and to be unlimited in possible extensions it was decided to move towards developments for the family of MS-Windows operating systems.

Fig. 5 shows the main computing cycle. It is incorporated into the main processing module that is responsible for Kalman-filtering, smoothing of the raw data and ambiguity fixing.

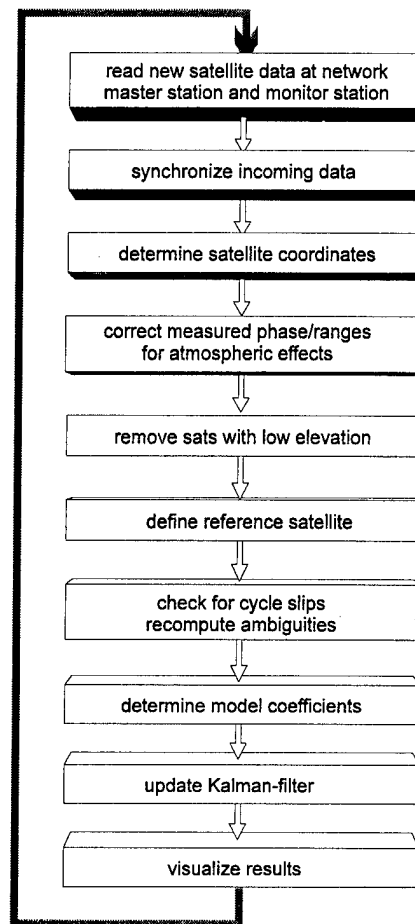


Fig. 5 Main computing cycle at network master station

The system can be run in real-time as well as in post-processing mode. To achieve this only an entry in the program's initialization file must be changed. In post-processing the same algorithms as for the real-time version are used but reading data from disk files instead of collecting it through the serial port.

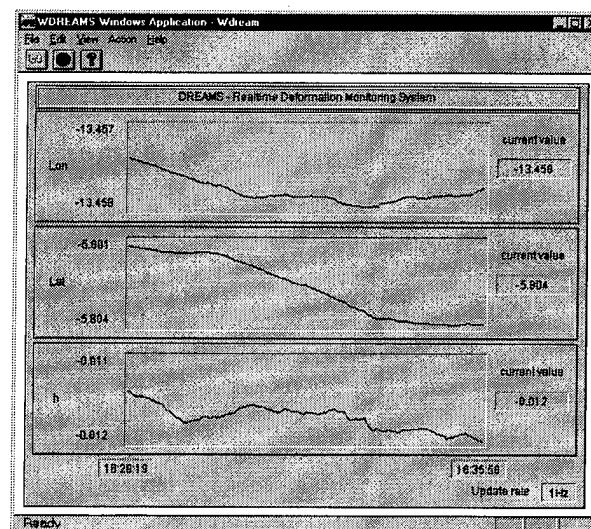


Fig. 6 DREAMS for Windows (Screen shot)

Monitor station

At the monitor stations the necessary software components like the serial-port interface module or the module for computing the carrier phase corrections are designed for MS-DOS. This is due to the fact that the hardware at these stations is based on a slower processor which reduces power consumption. Nevertheless the main architecture can be compared to that of the master station. The biggest difference lies in the module accessing the serial port. In comparison to Windows this process is not based on a device driver.

The monitor station is mainly responsible for

- decoding of received data
- calculation of carrier phase corrections [Blomenhofer-Taveira and Hein, 1993]
- encoding for transmission via the telemetry link.

Fig. 4 illustrates these main tasks among others.

ALGORITHMS

The main computing routine is implemented at the network master station. It is included in the processing module and conducts all computations necessary for the position solution. Furthermore it is responsible for fixing the integer ambiguities and updating the Kalman filter. The computed position is smoothed using a lowpass filter.

Observation Model and Kalman filtering

The applied model incorporated in the Kalman filter is the double difference model using carrier phase observations. The simplified observation equation can be written as

$$\Phi_{AB}^{jk}(t) = \frac{1}{\lambda} \rho_{AB}^{jk}(t) + N_{AB}^{jk} + \varepsilon_{AB}^{jk}(t) \quad (1)$$

- where
- Φ measured carrier phase (cycles)
 - λ L_1 wavelength
 - ρ geometric distance between satellite and receiver
 - N integer ambiguity
 - ε measurement noise, atmospheric influences, multipath
 - AB single difference between receiver A and B
 - jk single difference between satellite j and k

This equation is linearized and included in the equation system used for Kalman filtering.

Since DREAMS is very flexible in its operation the user can choose between two alternatives in the modeling of the Kalman filter. This is done by changing an entry in the program's initialization file. The two choices adapt

the behaviour of the system to the users needs by modifying some parameters in the Kalman filter design. These two different operating modes are

- (1) filtered (smoothed) position data (most of the noise in the higher frequencies is canceled out), but longer reaction times if the position of the receiver changes.
Applications: Observation over longer time spans or objects with small variations in position
- (2) raw (vertical) position data with fast reaction to any movements of the receiver (disadvantage: more noise on the output data).
Applications: Investigations into short-time behaviour (e.g. bridge loading)

Ambiguity fixing

During the initialization of the system the integer ambiguities have to be solved. This is usually done using known approximate coordinates of all positions under investigation. It is sufficient to have these coordinates to an accuracy of a few centimeters. If the coordinates of all stations are unknown, a full initialization process takes place. In order to achieve this, pseudorange observations (and phase-smoothed pseudoranges) are included in the equation system to establish approximate values for the coordinates of the monitor stations. Then the ambiguity space is searched to determine the correct integer ambiguities and the positions of the monitor stations.

In case that the approximate coordinates of all stations are known we can apply equation (2) to solve for the unknown integer ambiguities. The measurement noise ε is set to 0 and we solve the equation system for N instead of p .

$$N_{AB}^{jk} = \Phi_{AB}^{jk}(t) - \frac{1}{\lambda} \rho_{AB}^{jk}(t) \quad (2)$$

This leads to a floating-point solution of the ambiguities. Since we know the positions of the receivers within a few centimeters we can fix the ambiguities to integer values by taking their absolute value. Utilizing this technique we have the full accuracy of the system after the first epoch of collecting data.

There are two ways of checking for cycle slips. Firstly by using the Kalman filter, and secondly, in a process described below, before doing the position update. The second possibility can be applied since we assume that the position of the receiver changes only within a few millimeters or centimeters from epoch to epoch. The main processing module computes the ambiguities for each epoch new, using equation (2) above. So the old ambiguities (for the last epoch) can be compared with the new ones. If the difference between these two values is more than 1/2 cycle, the old value has to be replaced with the new one. The new value is then used to revise the equation system used for the Kalman filter update.

Low-pass filtering

Unfortunately the data collected by the receivers are not free of errors. This is due to various error sources that introduce noise into the data. In order to improve the accuracy of the computed position solutions we have incorporated a low-pass filter in the processing module. In order to find the correct frequency range that contains still measurement information and to define a cutoff frequency over which the higher frequencies (this is the noise) are absorbed, some analysis on the collected data had to be done. For this task a FFT-analysis was performed and showed that most of these oscillations are in the range of „higher“ frequencies, say 10^{-2} to 1 Hz (see Fig. 7). In the test data set no periodicity was found in the noisy part of the unfiltered position deviation

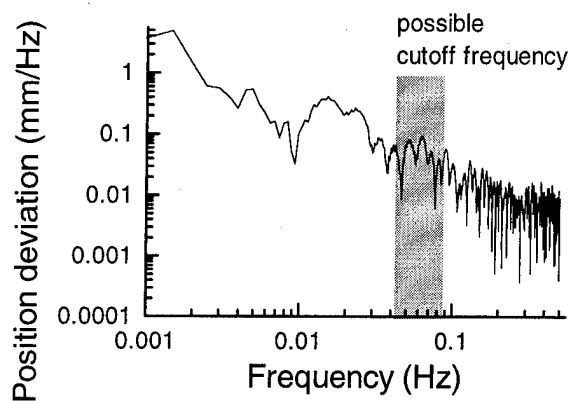


Fig. 7 Spectrum of unfiltered vertical position deviation

Currently we are experimenting with FIR (finite impulse response) low-pass filters using windows of 15 samples and cutoff-frequencies between 10^{-2} and 10^{-1} Hz. Fig. 8 shows the block diagram of such a FIR low-pass.

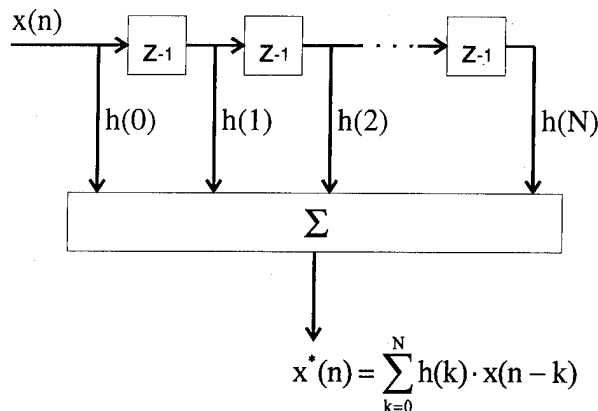


Fig. 8 Low-pass filter design
(Note: h are filter coefficients)

TESTS AND RESULTS

The developed system has been tested under various conditions.

Fig. 9 presents the scenario where all the tests have been done. 6 pillars are available on which the GPS antennae are mounted. This enables us to repeat the measurements at exactly the same positions. The pillars are equipped for center mounting of the antennae. As Fig. 9 shows, the pillars are affected by multipath since they stand close to the institute building and next to the trees in the south and east. Power supply and serial port plugs are available at the pillars. The serial ports of the pillars are available inside the institute building. This gives easy access to the control of the stations mounted on top of the pillars.

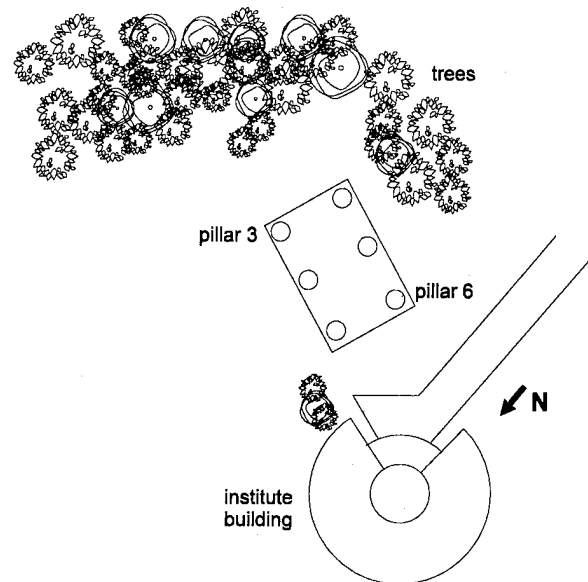


Fig. 9 test scenario

The coordinates of the pillars are known precisely so it is possible to solve the integer ambiguities during the initialisation period of the software within one to two epochs. If a cycle-slip occurs or a new satellite rises and is going to be included in the measurements equation system, the system computes the new integer ambiguities directly without searching the ambiguity space. The algorithm is described above.

All the tests were done using the simplest configuration possible. The setup consisted of the network master station and one monitor station. This was done to test the accuracy and reliability of the algorithms and not to see how many stations the master station and the software is capable of handling.

To verify the accuracy of the hard- and software the stations were put on top of two of the pillars in front of our institute. The master station was on pillar 6 and the monitor station on pillar 3. These two pillars and so therefore the stations, represent the longest possible baseline which is about 14.70 m. The antennae were fixed (static observation). This was in order to show the

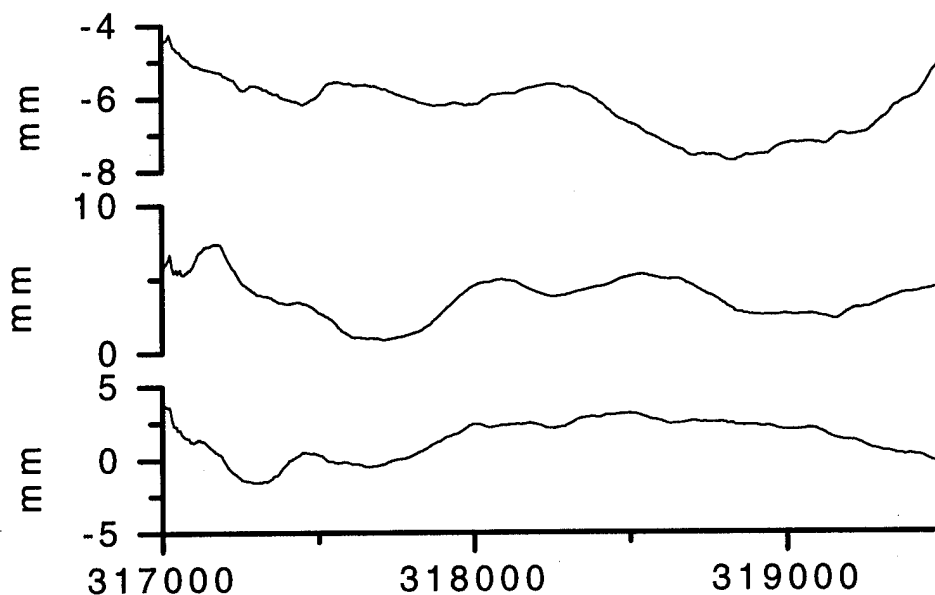


Fig. 10 Measurement noise of static observation (position deviation in Latitude, Longitude, Height)

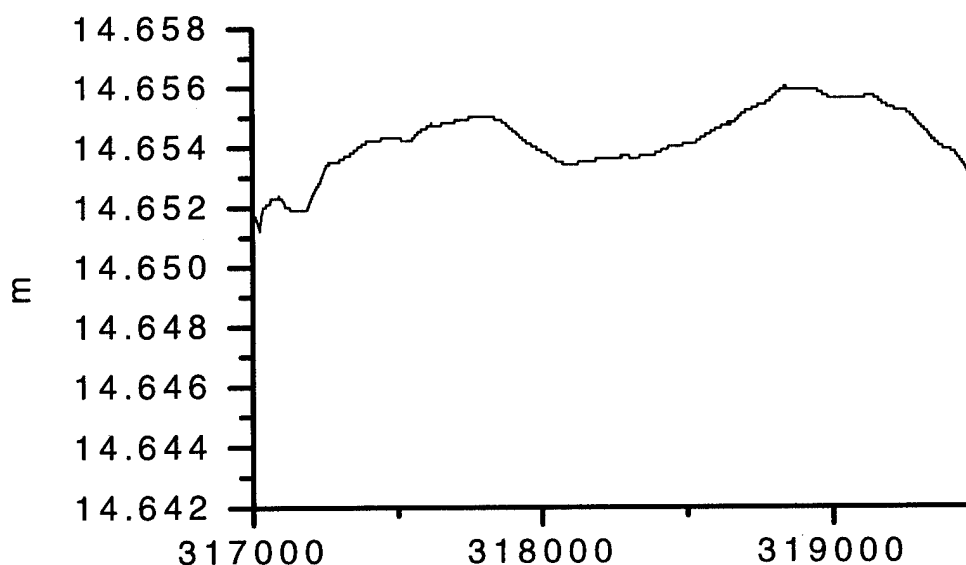


Fig. 11 Measurement noise of static observation (baseline pillar 6 - pillar 3)

noise level of the computed baseline without any movements.

Fig. 10 shows the typical noise level of DGPS derived coordinate components. As Frei reports [Frei *et al*, 1993; Table 1] this noise may be in the range of 1 to 3 mm depending on the quality of the carrier phase observations. Affected by the multipath environment the noise level at our site is quite high. It is expected to be reduced by the factor 2 to 3 if operating in a more open area without buildings or trees around.

To test the main goal of the system, that is to show vertical position changes applied to the monitor station,

the system was also tested in reaction to a generated movement. The master station was fixed on top of pillar 6 as in the static test. The receiver of the monitor station was mounted on a slide allowing us to generate precise three-dimensional movements down to 0.01 mm. Thereby, some insights into the behaviour of the system could be gained, especially with respect to the detection and verification of the correct position change of the receiver at the monitor station.

As you can see in Fig. 12 the observation started at the epoch 568800 on September 2, 1995. The position of the monitor station's antenna was changed at the epoch 569100 for about 5 cm. The software followed this

movement within a few seconds. The time delay of the monitoring system's response to the generated antenna position change is due to the characteristics of the used low-pass filter. After 250 seconds, so at epoch 569350, the antenna was moved back to its startup position. Fig. 12 shows the position of all three coordinates over time. The true position is the shaded line. Fig. 13 shows the observed position change of the baseline in relation to the generated one.

To reduce the before mentioned multipath effects introduced by the difficult placement of the pillars we

have tested the system using choke ring ground planes on both stations.

The update rate for all tests was 1 Hz. In the near future we are planning to test the system with a higher update rate of 10 to 20 Hz (possible applications: oscillations of bridges, etc.). This higher update rate leads to much more data which has to be collected and to a higher computing load at the network master station. Hence it might be necessary to use a faster machine like an Intel Pentium processor at the master station, especially if the network consists of more than a few monitor stations.

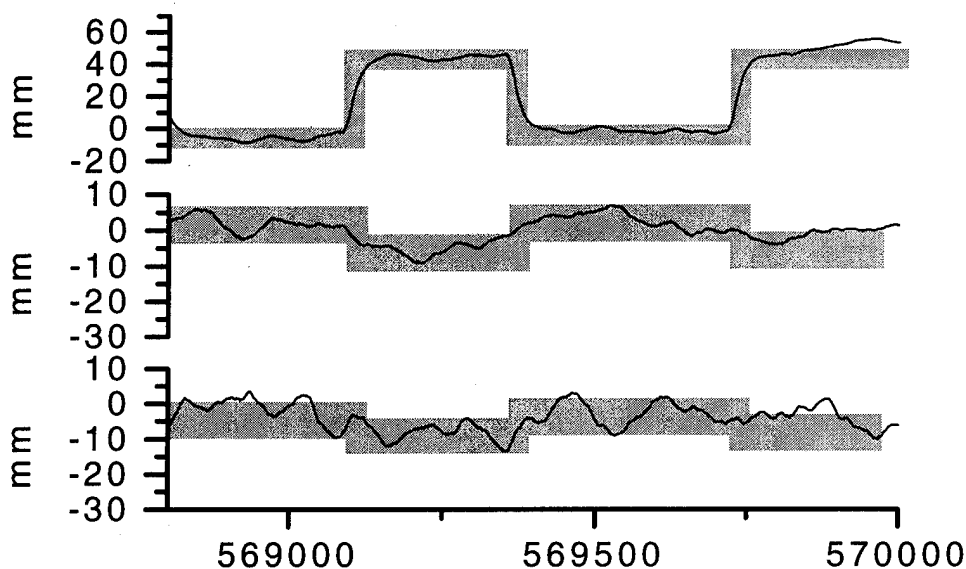


Fig. 12 Observation of generated position change (position deviation in Latitude, Longitude, Height; shaded areas show the true position and indicate the noise level of the measurement)

(Note: This data set is heavily corrupted by multipath of the nearby building wall; for the tests receivers with 3-4 mm phase noise were used (this is fairly bad compared to an excellent receiver with about 1.3 mm phase noise))

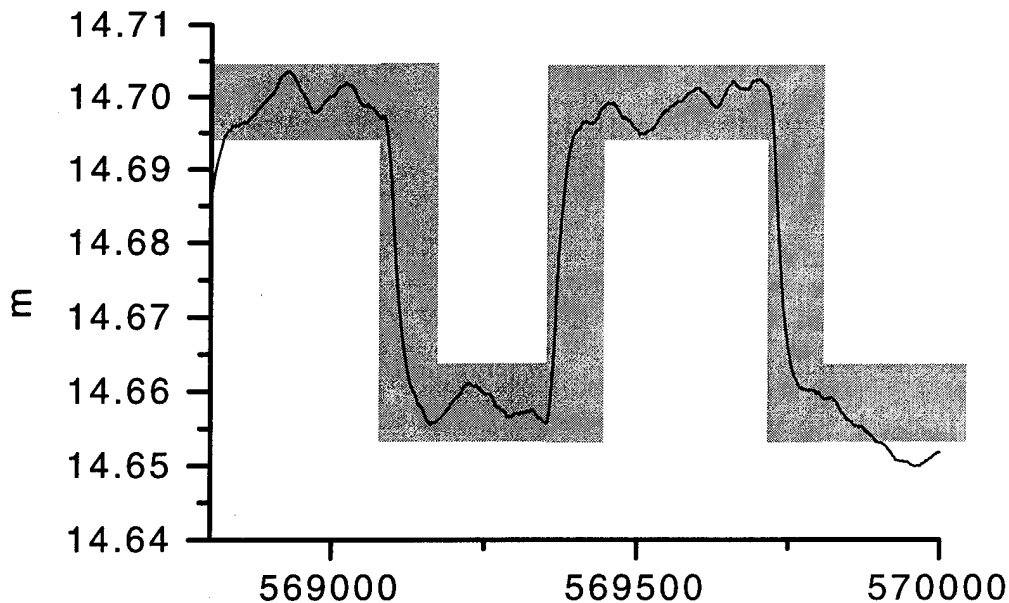


Fig. 13 Observation of generated position change (baseline)

CONCLUSION

At the current point of research we may state that real-time deformation monitoring has several advantages compared to off-line techniques or batch processing. Among these we like to outline the possibility of reacting immediately in cases of danger for man or nature. This would not be possible without continuous monitoring. The deformation monitoring system DREAMS provides these features combined with high accuracy to the user.

ACKNOWLEDGMENT

This project is funded by the German Research Foundation (Deutsche Forschungsgemeinschaft).

REFERENCES

- Frei, E., A. Ryf and R. Scherrer 1993: „Use of the Global Positioning System in Dam Deformation and Engineering Surveys“, SPN Zeitschrift für Satellitengestützte Positionierung, Navigation und Kommunikation 2, 42-48, Wichmann Verlag
- ICOLD 1988: „International Commission for Large Dams Bulletin No. 60: Dam Monitoring - General Considerations“
- Schüssler H. W. 1992: „Digitale Signalverarbeitung“, Springer Verlag Berlin, 3. edition
- Taveira Blumenhofer, E. and G. W. Hein 1993: „Investigations on Carrier Phase Corrections for High-Precision DGPS Navigation“, Proc. ION GPS-93, Sept. 21-23, 1993, Salt Lake City, Utah, pp 1461-1468

Real-Time Precise Marine Navigation: Description and Results

Dr.-Ing. Hans-Jürgen Euler and Craig Hill
Leica AG

Dipl.-Ing. Urs Müller
terra vermessungen ag

BIOGRAPHIES

Dr.-Ing. Hans-Jürgen Euler graduated in geodesy at the Technical University of Darmstadt in 1983. He was awarded a Ph.D. on "Rapid ambiguity resolution techniques for small scale networks" in 1990. He worked with Dr. Clyde Goad at Ohio State University from 1989 to 1990 on precise positioning of highway vehicles. In 1991 he started work on algorithms for real-time applications. In January of 1993 he joined Leica in Switzerland, where he is head of the Data Processing group.

Craig D. Hill graduated from the Royal Melbourne Institute of Technology (RMIT), Australia, with a B.App.Sc. and M.App.Sc. in Surveying in 1990 and 1993 respectively. He has been working in the GPS Design and Applications group and the Data Processing group at Leica in Switzerland since March 1995 and is also enrolled in a Ph.D. program at RMIT.

Dipl.-Ing. Urs Müller graduated with a Federal diploma in surveying engineering at the College of Technology, Basel in 1977. Since graduation he has been actively involved in the surveying industry working in a wide variety of areas which include, geodetic, cadastral, hydrographic and topographic surveying and photogrammetry. He has significant experience in GPS surveying in both post-processed and real-time modes. His current position is Head of Survey Engineering and GIS/LIS Department at terra vermessungen ag, Switzerland.

ABSTRACT

Real-time marine navigation has been available for some time to metre level accuracy, recent advances in GPS technology have allowed centimetre accuracies in real-time. The ability to obtain this order of accuracy in real-time has increased the number of possible applications, and is achieved by processing the GPS carrier phase observable.

presented at ION GPS 95, September 12-15 1995,
Palm Springs.

This paper describes typical marine applications where centimetre accuracy three-dimensional co-ordinates are required in real-time. The Leica System 300 with RT-SKI was deemed as a suitable system to fulfill the requirements of such marine applications. Each of the components of the system are analysed and the results from two different surveys will be presented. The results shown highlight the suitability of the Leica System to provide precise real-time marine navigation.

INTRODUCTION

Real-time GPS surveying to centimetre accuracy has been an important advance in GPS technology. Many advantages can be realised by obtaining position and quality information in the field. No longer is it necessary to wait until post-processed results are computed after the survey has been completed. This is making the technology applicable to many more applications.

Further more, with real-time positioning you can avoid the scenario of expensive re-surveying of points where it was discovered in the office that the required accuracy was not obtained.

Having the functionality to be able to obtain centimetre co-ordinates in real-time makes GPS technology available to an increasing number of applications. Standards such as NMEA (National Marine Electronics Association) for the output of co-ordinates and quality indicators allow GPS to be integrated with a large variety of existing equipment.

REAL-TIME SYSTEM COMPONENTS

Like traditional GPS surveying, real-time requires a reference station and one or many roving stations. The fundamental difference between real-time and post-processed GPS is that data is merged and processed during the survey in the real-time configuration, and in post-processing it is merged and processed after the field work has been completed. The real-time scenario

therefore requires that radio modems are present to transfer GPS observations from the reference station to the roving station. In addition, the roving station requires the software infrastructure to process these reference station and roving station observations to produce co-ordinates with centimetre accuracy and also a realistic assessment of their quality.

The observations from one reference station can be utilised by many rovers who are operating in the vicinity of the reference station's radio transmission range. At each of the roving stations only one person is required to conduct the survey, and can co-ordinate points with high efficiency.

To ensure successful real-time GPS surveying, GPS sensors which provide highly accurate phase and code observations are required. The Leica SR399 sensor is an example of a sensor which has such qualities by providing full wavelength L1 and L2 phase measurements and independent C/A, P1 and P2 code measurements. The data processing scheme used to process these observations has to be highly efficient to satisfy the constraints of real-time applications. In order to provide centimetre accuracy the integer ambiguities introduced by using that phase observable must be resolved. A resolution technique which requires minimal computation time and produces a reliable result is mandatory. Hatch and Euler [1994] describe the efficient technique adopted by Leica AG for the ambiguity resolution task in RT-SKI.

In order to highlight the hardware components necessary to conduct a real-time GPS survey, Figure 1 and Figure 2 are included. Figure 1 shows the reference station configuration, and Figure 2 shows the roving station configuration.

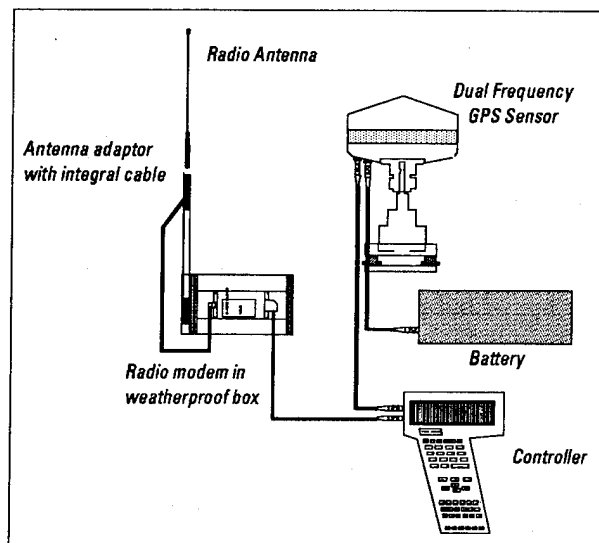


Figure 1 Reference station real-time configuration.

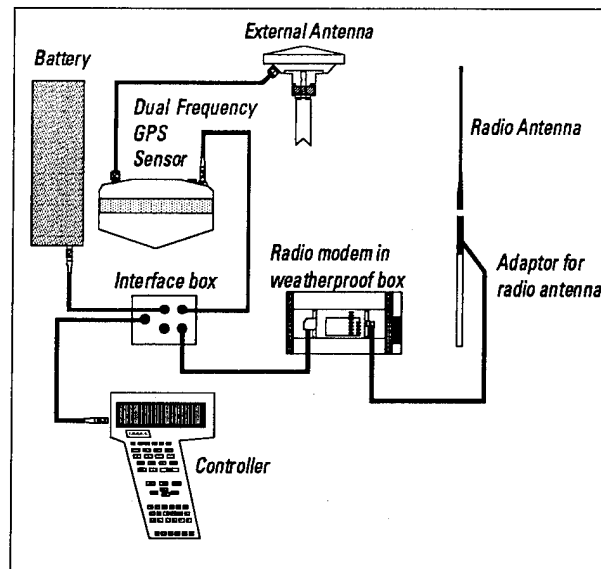


Figure 2 Roving station real-time configuration.

Those familiar with the standard post-processed Leica equipment configuration will notice that the only addition is the inclusion of the radio modem and its associated antenna. Operation of the system is via the familiar controller and operation procedure.

REAL-TIME SYSTEM OPERATION

Conducting a real-time survey is identical to conducting a survey which will be processed after data collection. The measurement techniques available for real-time include:

- Rapid Static,
- Stop and Go and
- Kinematic

Rapid Static: the roving receiver remains stationary at the unknown point until enough data has been collected to solve for the integer ambiguities. Upon successful resolution of the ambiguities, and hence station co-ordinates, the user can move to the next point. Typically just a few minutes is required for ambiguity resolution.

Stop and Go: after an initial Rapid Static initialisation the user can move to unknown points, with continuous tracking to at least four satellites. At each subsequent unknown point the user is required to hold the antenna still over the point for a few seconds and the software will compute the average position of the occupation.

Kinematic: can be achieved by a Rapid Static or Known Point initialisation (SR299/SR399), or with a "on-the-fly" initialisation (SR399) [Leica AG, 1995a]. After initialisation, upon each measurement update the trajectory of the rover is obtained to centimetre accuracy. To record specific points a time-tag can be

used, either as you move past the point or, by occupying it directly.

In all real-time positioning modes the raw data can also be collected at the reference and roving stations and processed at the completion of the survey. Real-time co-ordinates and/or observations can be either stored internally in the controller or on interchangeable memory cards. In addition, if the CR244 or CR344 controllers are used the Leica Open Survey World™ concept which enables the combination of GPS and TPS (Theodolite Positioning Systems) technologies can be used.

The SKI software provides the necessary infrastructure to post-process the GPS observations. SKI provides a seamless platform to import co-ordinates collected from a real-time survey and combine them with results obtained from other real-time or post-processed surveys.

REAL-TIME SURVEY: Lake Constance

A real-time GPS survey was conducted on Tuesday 8th August 1995 on Lake Constance. Lake Constance is located about 20km north-west of Heerbrugg, and has three countries which border its shores, Switzerland, Austria and Germany.

The survey comprised of using two SR399 sensors both equipped with RT-SKI software in their controllers. The radios utilised to transmit measurements between the reference and the roving units were Sateline 2AS which have a transmission power of 1Watt.

Being a maritime application, "on-the-fly" capability was necessary to ensure that the ambiguities could be resolved, if necessary, in a moving environment.

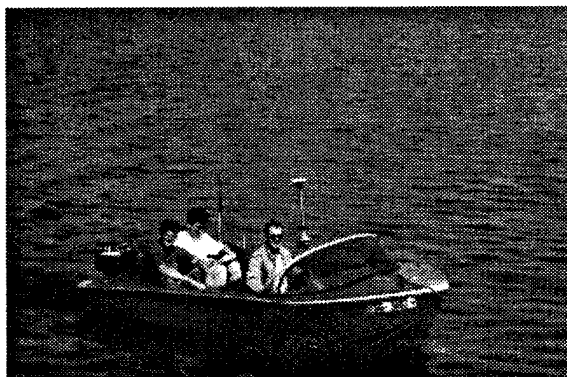


Figure 3 Boat equipped with real-time system.

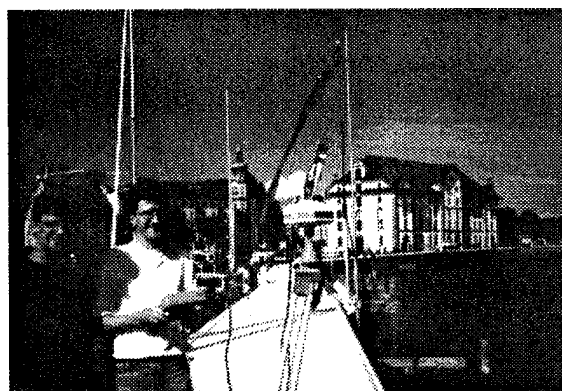


Figure 4 Reference station.

The reference station was located on a boat pier in Rorschach, Switzerland. The rover was first set-up on a fixed point on the pier approximately 240 metres from the reference station. At this control point a Rapid Static occupation was conducted and ambiguities were resolved. A co-ordinate quality of 3cm was set as the threshold before completion of occupation was permitted. The controller provided a message that the required accuracy had been met and the rover was free to move. The roving station equipment was then transferred to the boat and the survey began. A number of loops were traversed in the boat. At the end of each loop the rover was returned to the control point on the pier to allow a comparison of co-ordinates. During the loops a total loss of lock was forced to ensure that a re-initialisation was conducted. Each re-initialisation procedure was conducted whilst "on-the-fly" and each was completed in approximately one minute, after which centimetre accuracy co-ordinates were again available. After each loop the control point on the pier was re-occupied. Due to the forced re-initialisations, each occupation produced independent results. The repeatability between the four occupations of the control point was:

East	North	Height
5mm	17mm	15mm

Table 1 Repeatability of real-time system

During the beginning of the survey the satellite geometry was poor in the North-South direction which is reflected in the larger differences in North when compared to East direction. Figure 5 portrays the satellite geometry during the survey. The Height component is also larger than the East difference, however it still reflects the accepted accuracy which is obtainable.

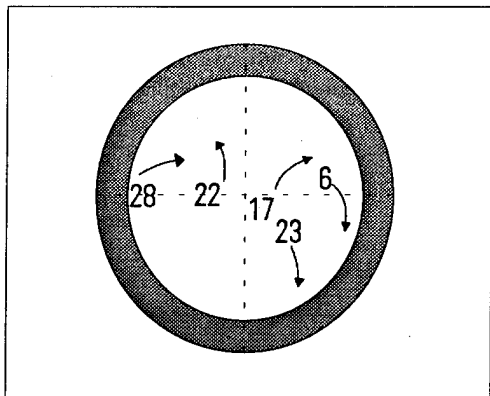


Figure 5 Satellite Geometry during Survey.

Observations were broadcast from the reference station every 2 seconds and hence provided co-ordinates every 2 seconds. Traveling at a velocity of approximately 10 km/h resulted in co-ordinates being obtained every 6 metres along the trajectory of the boat.

The maximum distance, during this survey, between the reference station and roving station was 2.4 kilometres. However, generally separations of up to approximately 10 kilometres can be achieved with real-time GPS to centimetre accuracy, providing a suitable radio/modem configuration is selected and ionospheric conditions are favourable.

During the complete survey the raw GPS measurements were recorded on the PCMCIA memory cards in the CR344 controllers. This allowed the data to be post-processed, and for comparisons to be made with the real-time results.

Figures 6, 7 and 8 are used to highlight the differences obtained after post-processing data and comparing results from a real-time survey.

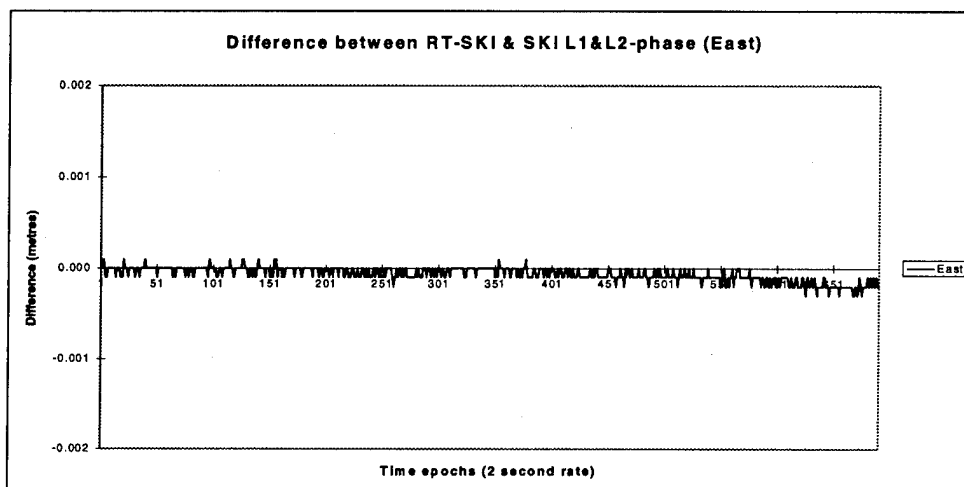


Figure 6 Difference in East RT-SKI and SKI L1&L2-phase

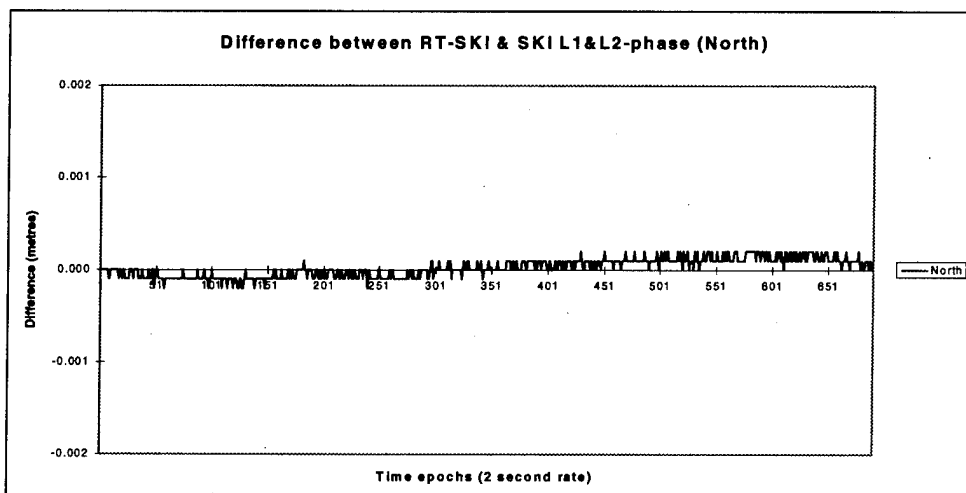


Figure 7 Difference in North RT-SKI and SKI L1&L2-phase

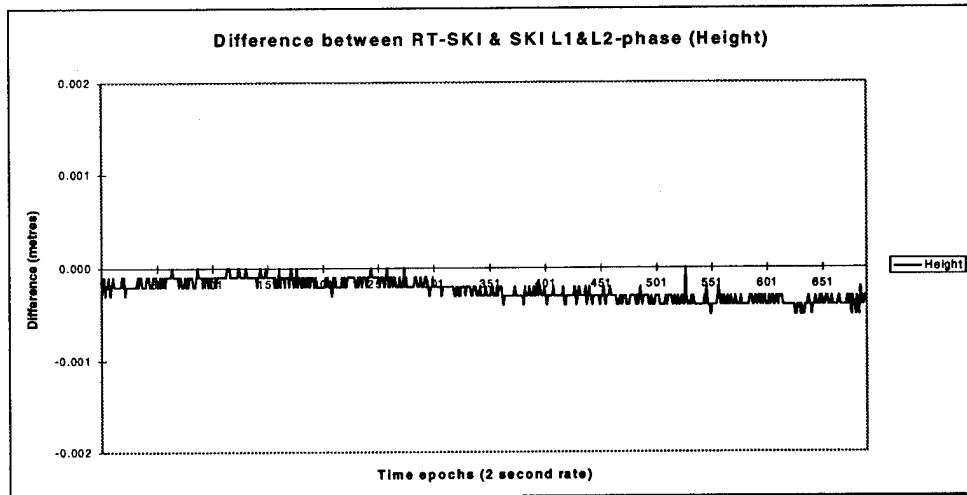


Figure 8 Difference in Height RT-SKI and SKI L1&L2-phase

From Figure 6, 7 and 8 it can be seen that a very good agreement exists between the real-time and post-processed results. One should expect this as the same measurements are used, and providing all measurement biases are handled correctly in both systems then a good agreement should be seen.

It is clear that with using real-time GPS you not only obtain the same results as post-processed, but you also have the results in the field if you need them. A further advantage is you don't have to process the data at the completion of the survey. Once back in the

office the co-ordinates can be loaded directly into your CAD package to create a plan with id's and codes showing which features were surveyed.

As a further example of the possible data processing scenarios the L1 code observations measured by the SR399 sensor were used to compute the position of the boat at each epoch. Figures 9, 10 and 11 show the differences between post-processed L1 code differential positioning and the results derived from the real-time phase processing i.e. "the truth".

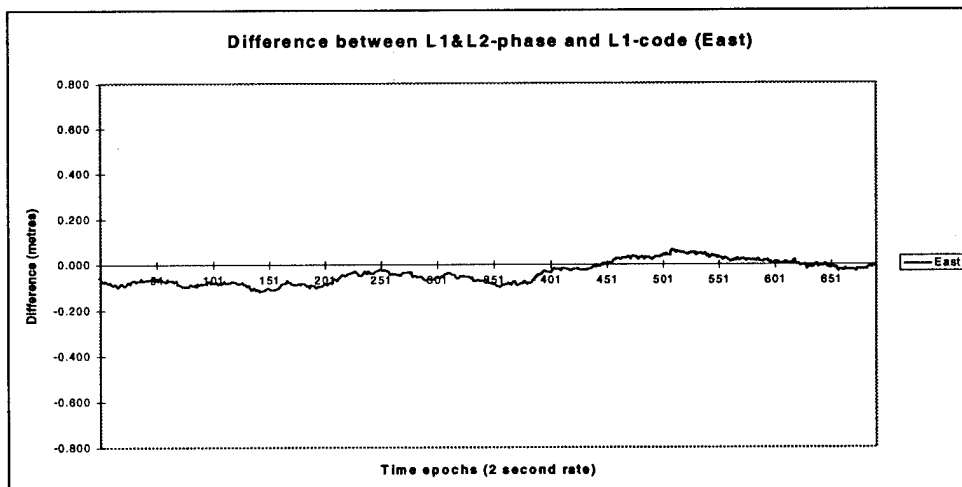


Figure 9 Difference in East L1&L2-phase and L1-code

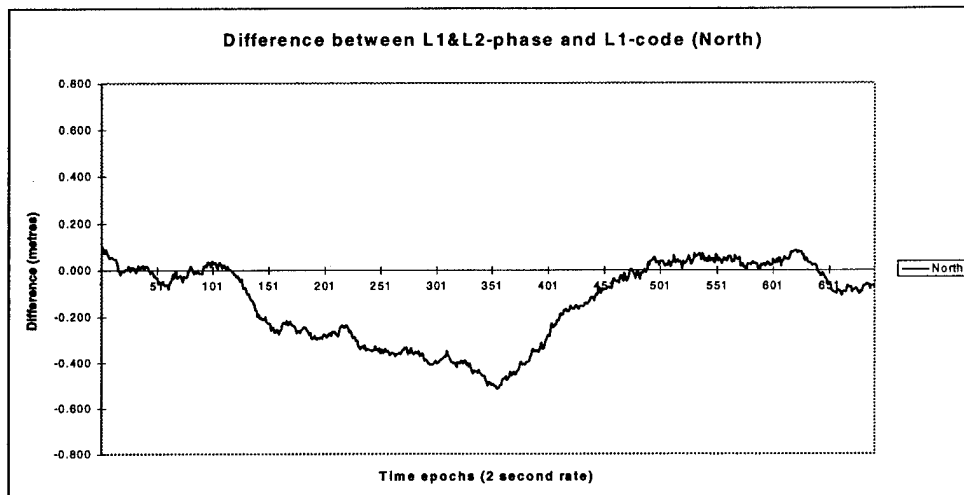


Figure 10 Difference in North L1&L2-phase and L1-code

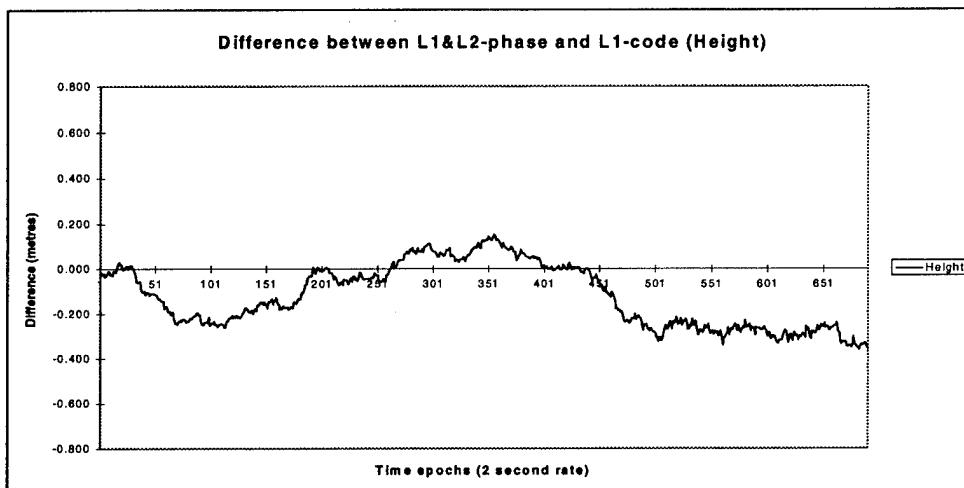


Figure 11 Difference in Height L1&L2-phase and L1-code

The results shown in figures 9, 10 and 11 highlight the achievable accuracies using L1-code observations from "state-of-the-art" receiver technology. During the comparison period the deviation never exceeded 0.5m which agrees with the product specifications for the Leica System 300 which state a differential code accuracy of 50cm (rms) in kinematic mode [Leica AG, 1995b].

It can be seen that better agreement exists in the East component than compared with the North component. This can be attributed to the weaker satellite geometry in the North-South direction. As expected when using GPS the height component will also represent a slightly weaker accuracy.

REAL-TIME SURVEY: Maribor

A further application of using real-time GPS was conducted during the last days of July and the start of August 1995 on the river Drau which extends across Slovenia from the Austrian border to the Croatian border. The survey consisted of measuring 400 river profiles over a 80km section of the river.

A Leica System 300 real-time configuration was used with RT-SKI to provide centimetre accuracy positions. Integrated with the GPS positions which were provided to a central computer via the NMEA format were echo-sounder observations to enable an accurate profile of the river to be captured.

The river Drau is divided into several sections by means of dam walls, which change the water level between 9 and 33 metres. At a number of these dam walls turbines are located to provide hydro-electric

power generation. Figure 12 shows the survey vessel being lifted by crane from one section of the river to another.

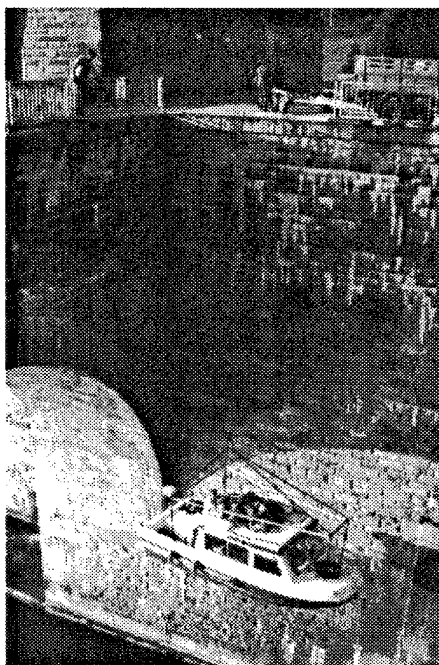


Figure 12 Moving survey vessel by crane.

The length of the 400 river profiles varied from 70 metres to 200 metres, depending on the width of the river at that point. Figure 13 shows a section of the river Drau with its tree lined banks.



Figure 13 View of River Drau and survey vessel.

The GPS positions were transformed to the local datum by using the "one-step" transformation. Points which had known co-ordinates in the local datum are occupied to compute the transformation parameters. This computation of the transformation parameters can be performed prior to the real-time survey using either real-time or post-processed GPS. Upon moving to a new area a new set of transformation parameters must be computed.

The river Drau is controlled at a constant height, this enabled checks to be applied whilst conducting the real-time GPS survey. To ensure the system had been operating correctly and that correct ambiguity resolution had been achieved, the height as computed by the real-time system was compared with the known values. If at any stage the height derived from GPS did not agree to better than 2cm from the known values, the power station authority was contacted to confirm whether a change in the water level had occurred. During the 9 days surveying the 400 profiles there were no occurrences of incorrect ambiguity resolution.

Upon completion of the 400 profiles the combined GPS positions and echo-sounder height measurements were used to produce contour plans and longitudinal section of the river floor. Figure 14 shows a typical longitudinal section.

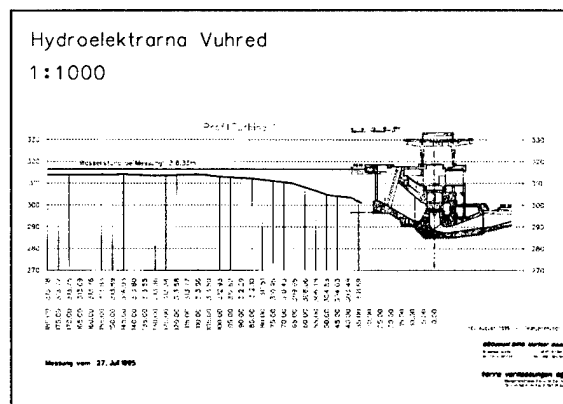


Figure 14 Longitudinal section Drau river.

The final plans could then be used to examine if any sections of the river were suffering from siltation or erosion. An assessment could then be made to determine what action should be taken to ensure the river continues to provide the correct environment for successful power generation.

The real-time GPS system used for this survey was deemed to be far superior to the previous analogue method used. The previous method involved continually moving the shore theodolite station to be located in a suitable position. The fact that GPS does not require line of sight provides a distinct advantage over traditional techniques. Not only was the field work far quicker and less prone to errors, by obtaining the GPS results in the field eliminates any need to post-process the data. In the office all that is required is that the results obtained are introduced into a CAD system and the appropriate plans are created.

SUMMARY

A real-time GPS system has been described in this paper and results have been shown which highlight the agreement between results obtained in the field and those obtained after post-processing the data.

The ability to be able to obtain accurate co-ordinates and an indication of their precision in the field, makes GPS technology applicable to many applications. A marine application is one such application which can benefit from real-time results.

The importance of "on-the-fly" ambiguity resolution is especially important for applications where it is inconvenient to remain stationary whilst ambiguities are being resolved.

A further extremely important feature of a real-time system is that ambiguity resolution is reliable. When the results are being used in real-time, it is critical that these results are correct. Incorrect ambiguity resolution will cause the derived co-ordinates given by the real-time system to be in error and will hence corrupt the survey. It is therefore considered that a system should only resolve ambiguities if it is certain they are the correct set.

A further important feature of a real-time system is that when a co-ordinate is provided to the user that its associated co-ordinate quality is realistic.

ACKNOWLEDGEMENTS

The authors would like to thank the "team" at Leica AG, Heerbrugg for developing the real-time system used in this paper. Further more our thanks are expressed to terra vermessungen ag from Zürich Switzerland and GEOdetski BIRO Maribor from Maribor Slovenia for providing us with the data from the survey of the Drau river.

REFERENCES

- Hatch, R., H.-J. Euler (1994), Comparison of Several AROF Kinematic Techniques, Proceedings of ION-GPS'94, Salt Lake City, Utah.
- Leica AG (1995a), Guidelines to Real Time Surveying using RT-SKI, User documentation, Leica AG, Heerbrugg, CH-9435, Switzerland.
- Leica AG (1995b), GPS Surveying - System 300, Technical Specifications: SR399 and SR399E Sensors, CR333 and CR344 Controllers, Software, Leica AG, Heerbrugg, CH-9435, Switzerland.

Development and Implementation of a Centimeter-Accurate Real-Time-Kinematic Positioning System

Herbert Landau, Christian Pagels, and Ulrich Vollath
terraSat GmbH

BIOGRAPHY

Dr. Herbert Landau is Managing Director of terraSat, a company which actively works in the area of high-precision differential GPS since several years. He has ten years of experience in GPS and has been involved in a large variety of GPS developments for high precision positioning.

Christian Pagels has a degree as physicist. He is currently working as a development engineer on the development of high-precision real-time differential GPS applications.

Dr. Ulrich Vollath has received a Ph.D. in 1993 in Computer Science from the Munich Institute of Technology. Currently he is responsible for the development of real-time GPS applications and ambiguity resolution on-the-fly algorithms.

ABSTRACT

There is no doubt that in the future centimeter-accurate GPS positioning systems will be real-time rather than post-processing systems. Processing algorithms providing these accuracies have been successfully implemented for years. The challenge today is to develop algorithms capable of working in real-time providing sufficient update rates on reasonable processors.

Real-time systems are of interest for different application areas like static surveying, stop&go and on-the-fly positioning. Implementations for the specific applications are presented focusing on the different ambiguity resolution techniques to apply.

The paper discusses the problematic areas with respect to processing speed in such a RTK system like ambiguity initialization, tropospheric modeling, ephemeris computation. Special emphasis is also made on the discussion of Selective Availability aspects related to latency problems in the radio link.

Setting out is a special problem to be considered with respect to the man-machine interface. First it is necessary to provide sufficient updates for a convenient use. Second the position prediction in this

mode has to provide a smooth and reliable user guidance.

Besides the system development aspects the paper presents the real implementation into a survey system and results of system tests, too.

1 AMBIGUITY FILTERING

1.1 Wide-Laning

In the literature many publications on fixing the carrier phase ambiguities using the "Wide-Laning" method are found, see Landau (1993).

$$N_w = \psi_1 - \psi_2 - (\Delta t_1 f_1 + \Delta t_2 f_2) (f_1 - f_2) / (f_1 + f_2)$$

with	N_w	widelane ambiguity
	ψ_1	carrier phase in L1
	ψ_2	carrier phase in L2
	Δt_1	transit time in L1
	Δt_2	transit time in L2
	f_1, f_2	carrier frequencies in L1 and L2

For many applications this has proved a good performance and very short time kinematic ambiguity fixing On-The-Fly.

Nevertheless, revising a huge amount of GPS data from different receivers, antennas, applications, problematic data sets were found. Here, trying to fix the wide lane ambiguities with short time data lead to wrong ambiguities in a number of cases that cannot be tolerated for a real time production quality system.

Further inquiry focused on the multipath problem. Specially for static and low dynamics applications, typical for geodetic users, an amount of error in the code observable was recognized that motivated the development of a different ambiguity fixing process, called ambiguity filtering.

Looking at a dataset influenced by an extreme multipath, the worst case condition can be seen.

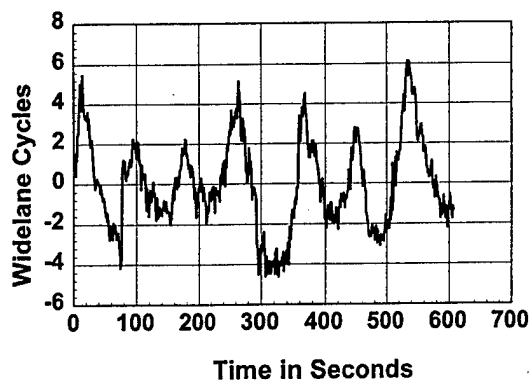


Figure 1: Extreme multipath influence on widelane signal

This plot was taken from a 30° elevation satellite, proving multipath at even medium elevation angles. An important observation is, that even long time averaging of the wide lane doesn't ever produce the correct ambiguity. The mean value is off by one cycle, accompanied by a very small standard deviation from the filter used.

Analyzing many data sets, a standard behavior of the systematic errors in the wide lane was observed.

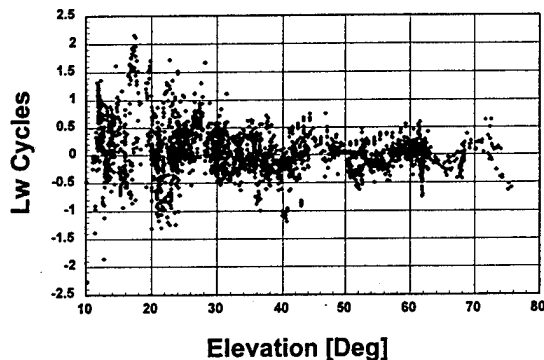


Figure 2: Typical errors in the wide lane with respect to the elevation angle

The error follows a $A/\sin(ele)$ function. The majority of GPS data sets is sufficiently modeled by $A=1.0$.

In bad multipath conditions, static data can go up to $A=3.0$.

The remaining problem was, how to get the best performance out of good-natured data without risking wrong results in worst-case situations.

The solution was to assume the worst without any further knowledge. Then, as the system is running, additional analysis can be done.

Three facts can be used for that.

1) If you are using a receiver producing best quality pseudorange observations, e.g. the GEOTRACER 2200, minimum and maximum of the estimated ambiguities are modeling the real systematic error much better than mean value and standard deviation from classical statistics.

2) The multipath has a kind-of periodic behavior with a period in the range of some minutes.

3) If the ambiguities are fixed, the Wide-Laning estimate can be monitored knowing the absolute error now. This feedback of known ambiguities leads to a closed loop model for the ambiguity fixing process.

1.2 Dual-Frequency Phase Consistency

An additional GPS observable can be exploited to reduce the number of ambiguity combinations

$$\Delta\psi = (\psi_2 + \kappa_2) - f_2 / f_1 (\psi_1 + \kappa_1)$$

with κ_1, κ_2 L1, L2 ambiguities

For each Lw ambiguity derived from the Wide-Laning filter, some (normally 1 or 2) L1 ambiguities can be assigned. These ambiguities can be filtered even more using the above formula.

The following picture show a cross-section of GPS data collected.

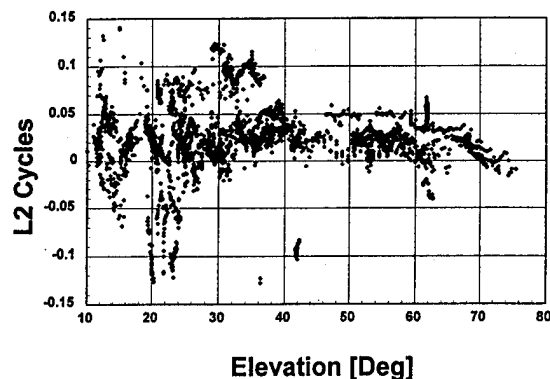


Figure 3: L1/L2 consistency with respect to the elevation angle

1.3 The Geometry Filter

As all Wide-Laning and Dual-Frequency Phase Consistency filtering is not sufficient to leave only one set of carrier ambiguities, a conventional ambiguity search process has to be performed as well. This step is called a geometry filter in this context, because the former two filters are geometry free estimates of the ambiguities.

1.4 Baseline Length Dependencies

Our first assumption was, that the systematic errors should be strongly influenced by the baseline length. Further investigations showed, that in the design range of the RTK system developed (up to 15 km), this is not significant. The biggest source of errors remains multipath.

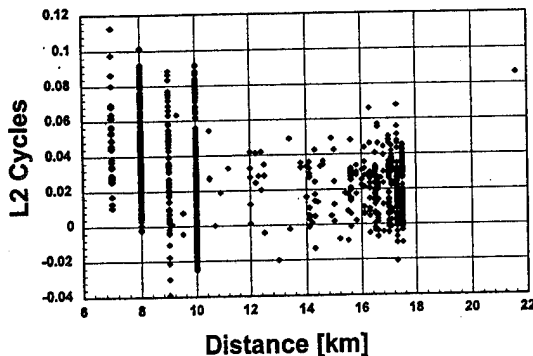


Figure 4: L1/L2 carrier consistency with respect to the baseline length

A significant influence can not be indicated here. Surprisingly, this is even true for the Dual-Frequency Phase Consistency.

The remaining influence of the distance between moving receiver and reference station is mainly on the geometry filter. It is mainly caused by errors in the ephemeris data, model errors in the tropospheric corrections and ionospheric influences.

1.5 The Ambiguity Filtering Model

The presented filters using the Wide-Laning and the Dual-Frequency Consistency are finally combined with the geometry filter.

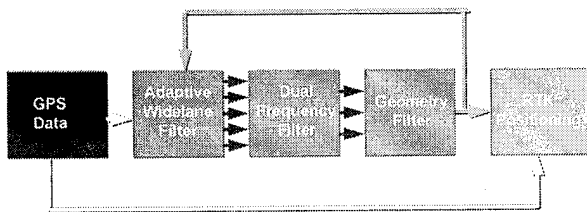


Figure 5: The conceptual design of the ambiguity filter

2 REFERENCE DATA LATENCY

In Real-Time-Kinematic systems with centimeter level accuracy, a new problem comes up. The reference station GPS data is delayed by the telemetry connection.

A trade-off between accuracy of the positions computed and the delay the user of the system sees has to be done.

There are two possibilities:

- 1) Synchronize reference data and roving receiver data. This gives the maximum precision and a substantial delay. Irritations of the user, specially in "Setting Out" operation results.
- 2) Used the latest reference data and extrapolate them to the time of the roving receiver data. A certain additional positioning error is unavoidable.

The former solution is necessary for the carrier phase ambiguity resolution process, as all errors have to be minimized for maximum reliability and performance. It is preferred for all data stored to get optimal precision.

To investigate the effects of the latter alternative, it is appropriate to look at the carrier phase delta differences between two satellites (single receiver), thus eliminating the effects of the receiver clock error and receiver clock error drift.

The errors caused by the satellite clock dithering and broadcast ephemeris errors (SA effects) remain.

The following figure shows a typical situation for selective availability influence on the carrier phase.

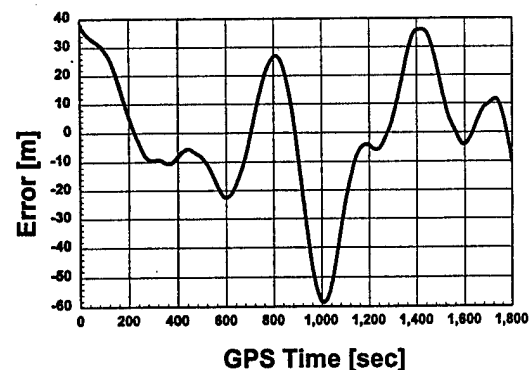


Figure 6: SA effects on delta carrier phase differences

In the differential case we will find that SA effects are completely eliminated if data of both receivers involved are perfectly synchronized. If the data of the two receivers are separated by one second the double differences in carrier phase show the following appearance.

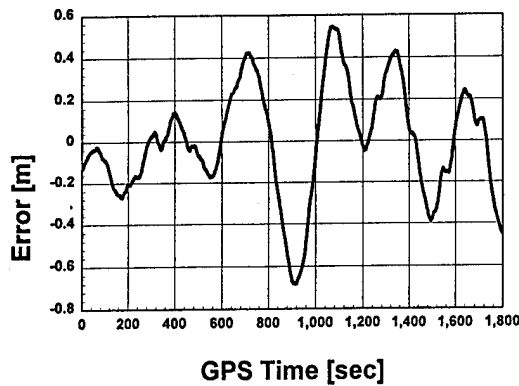


Figure 7: SA effects on double difference carrier phase measurements with 1 second synchronization error

In order to accommodate for latency (synchronization error) effects we can model the error by using the linear Doppler prediction. Errors are reduced dramatically to a typical level of a few centimeters with one second latency (see figure xxxx).

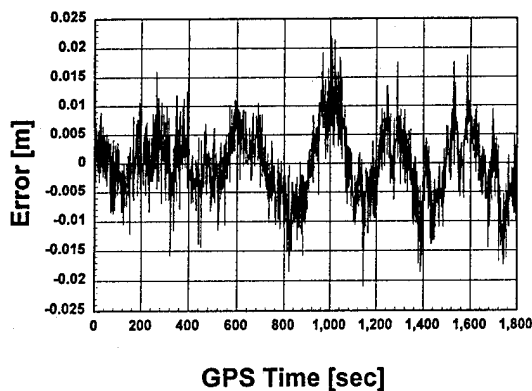


Figure 8: Double difference error for one second latency and linear Doppler prediction

The remaining error will grow quadratically with time difference, i.e. if we have an error of 2 cm with 1 second delay we will find an error of 8 cm with 2 second delay.

In order to minimize the error growth we are using a quadratic extrapolation reducing the remaining error to a quasi-random behavior.

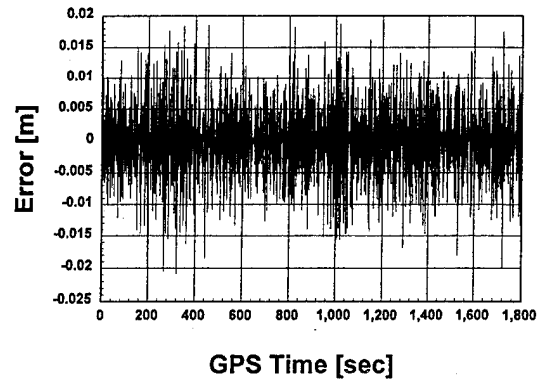


Figure 9: Double difference error for one second latency and quadratic Doppler prediction

Compared to the linear correction the remaining error is now growing linearly and we find an error of 4 cm for a 2 second delay instead of 8 cm in the example above.

3 MINIMIZING PROCESSING TIME

The system has to be implemented on a fairly priced hardware. Also, as much processing power as possible should be used for a comfortable user interface. Thus, the GPS algorithms were tuned for fast computing. Using sophisticated execution time profilers, the main time consuming parts of GPS processing were isolated.

3.1 Tropospheric Modeling

A surprisingly significant amount of time was spent in the computation of the tropospheric delay. As this must be done for each computed position estimate, the number of evaluations can be quite high.

Using the modified Hopfield model (Goad & Goodman, 1974), the first observation was, that much time was spent computing functions with always identical arguments. The reason is, the meteorological data is not available, but accounted for by the algorithm. Partial evaluation of these expressions lead to a first big speedup.

The big acceleration was the development of a table lookup method. A table of tropospheric corrections by elevation angle and receiver height was built. It is optimized for differential GPS applications. This means, the differential error between reference receiver and roving receiver caused by the table interpolation was limited to under a millimeter for a baseline length of 50 km instead of limiting the absolute error.

3.2 Ephemeris Calculation

Another big consumer of processing power was the calculation of the satellite ephemeris from the Kepler orbit elements of the broadcast ephemeris messages. Two simple methods have reduced that.

First, a high order interpolation is used for computation of many satellite positions in a longer time range. As Remondi (1989) has explained, a 17th order polynomial

with time differences of 40 minutes is precise enough for differential carrier phase approximations. Second, the parts of the calculation accounting for earth rotation don't have to be repeated in the estimation process. As long as the ground position doesn't vary by more than about 30 meters, the satellite position stays virtually constant enabling one evaluation from pseudorange processing to final carrier phase positioning.

3.3 Positioning

More fine tuning was done on the position estimators. As the formalism of GPS positioning is extremely good-natured and almost linear, direct matrix inversion and extrapolation of the expected errors reduced processing time.

3.4 Ambiguity Search

The ambiguity search using the filters as described in section 1 does not only enable early fixing of the ambiguities, the reduced number of candidates reduces processing time, too. The Wide-Laning and Dual-Frequency Phase Consistency filters require almost no time. Combined with efficient Geometry Filter implementations (e.g. Martin-Neira et al. (1993), Landau&Vollath (1994), Chen&Lachapelle (1994), Teunissen&Tiberius (1994), even an industry standard handheld computer doesn't let the user wait for the end of processing.

4 THE GEOTRACER RTK 2100/2200 SYSTEM

The carrier phase ambiguity fixing and positioning algorithms presented in this paper and others developed at terraSat were combined with an easy-to-handle user interface.

The result are the GEOTRACER RTK systems 2100/2200 giving the user the choice between a low cost single L1 and an advanced dual frequency system. As the user interface is identical for both systems, the upgrade path and mixed systems are available. This includes combination with GEODIMETER total stations, as data compatibility is guaranteed. Even the proved User Defined Sequences (UDS) of GEODIMETER can be used.

4.1 Design Goals

The central design rule for an accepted geodetic and general purpose positioning tool must always be reliability, a guaranteed precision of the positions computed. Thus, it is better to give no position than a wrong one. This should not be compromised by offering short but unreliable fixing times.

The next logical step is to guide the user of the system to initialize the high precision achieved without introducing operating errors. A good user interface is the right way to support the acceptance of the RTK system. Another advantage designed and implemented into the GEOTRACER RTK system is the availability of a smooth migration path between conventional surveying instruments like total stations and GPS positioning. The idea is to have the best tool for each application without changing data representation. To achieve this, the RTK system was designed for compatibility with total station data. Existing total station software can work on GPS results. Also, collected total station data can be processed by the standard GEOTRONICS postprocessing software GEOTRACER GPS.

This compatibility goes as far as that the "User Defined Sequences" (UDS) known from GEODIMETER total stations, can be used in the RTK providing an efficient and powerful while easy to use method for customizing position display, data storage and real-time output.

The productivity achieved with the RTK system has proved in many tests under operating conditions to be very high, giving as much as 100 centimeter level positions in one hour while having the certainty that phase accurate positioning is available at the time the measurement button is pressed. Much effort was spent to build a balanced frame work fulfilling these design rules, visualized in the following picture.

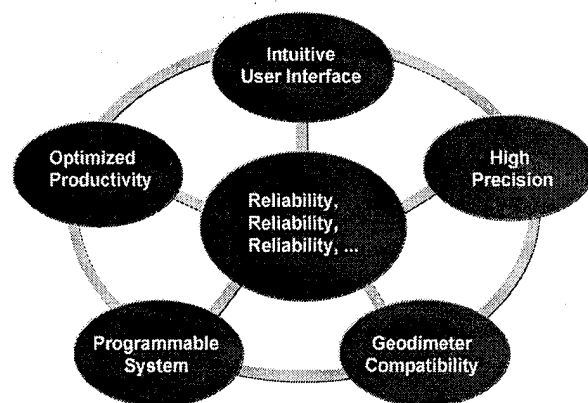


Figure 10: GEOTRACER RTK design rules

4.2 The single frequency RTK system GEOTRACER 2100

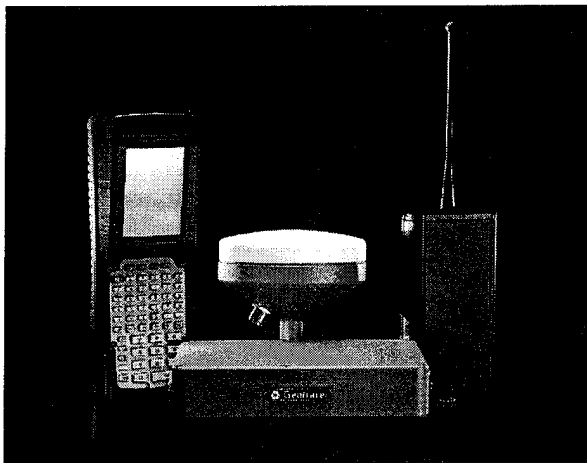


Figure 11: The Geotracer GPS RTK system components

The single frequency L1 RTK system GEOTRACER RTK 2100 is the low cost high productivity solution for geodetic applications. Using initialization techniques like VSFB, Short-Static, Known-Point, a large number of points can be processed in measurement of Setting-Out mode. The update rate of this system is 4 Hz, giving a real dynamic feeling of the kinematic positioning.

VSFB is the acronym for Very Short Fixed Baseline and is a fast initialization method (in our installation 6 seconds). It is based on a given fixed arm length of 25 cm and a given height difference (usually zero). the GEOTRACER VSFB initialization does not require any azimuth information to initialize, it finds the azimuth automatically by itself.

Performance analysis for the L1 RTK system has shown, that real-time short-static positioning is achieved within 4 - 8 minutes in average. A lot of position fixes are made in 2 minutes.

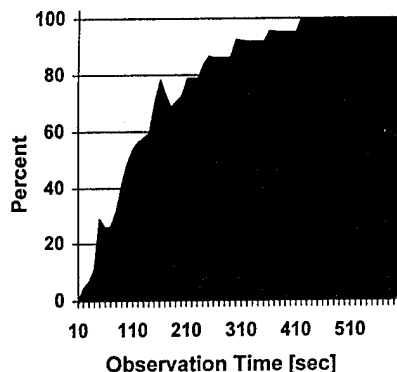


Figure 12: L1 short-static performance

The figure shown above resulted from the analysis of hundreds of datasets with different satellite conditions

with respect to numbers and geometry. The baseline length also varied between 0 and 5 km.

4.3 The dual-frequency RTK system GEOTRACER 2200
Using the advanced Z tracking technology L1/L2 receiver system GEOTRACER RTK 2200, ambiguity resolution On-The-Fly becomes the standard almost instantaneous initialization method. The receiver features robust tracking of satellites even in strongly obstructed areas like trees or near buildings.

The dual-frequency system is usually working with On-the-Fly ambiguity resolution techniques to initialize RTK. Performance analysis of different datasets have shown the performed given in the following figure.

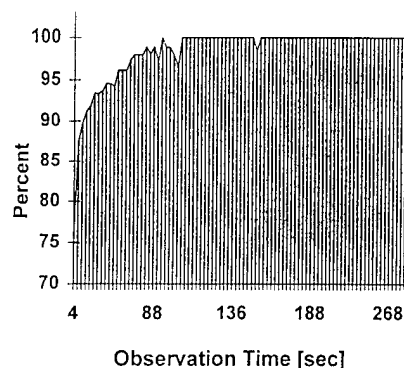


Figure 13: Dual-frequency OTF performance

The GEOTRACER RTK system shows a large amount of OTF fixes in 8 - 14 seconds. In average OTF initialization is performed in one minute. This proves the quality of the developed RTK positioning algorithms.

REFERENCES

Chen,D, G. Lachapelle (1994): A Comparison of the FASF and Least-Squares Search Algorithms for Ambiguity Resolution On the Fly, Proceedings of the International Symposium on Kinematic Systems in Geodesy, Geomatics and Navigation, Banff, Canada, August 30-September 2, 1994, pp. 241-254

Goad, C, L. Goodman (1974): A Modified Hopfield Tropospheric Refraction Correction Model. Paper presented at the Fall Annual Meeting, American Geophysical Union, San Francisco, CA, December 12-17, 1974

Landau (1993) : On-the-Fly Ambiguity Resolution using Differential P-Code Group and Phase Delay Measurements, Proceedings of the DSNS-93 Symposium, Amsterdam, Netherlands, March 1993

Martin-Neira, M., R. Lucas, J. Legido (1993): The Null Space Method for GPS Ambiguity Resolution. Paper distributed by the European Space Agency - ESTEC, G.M.V. Madrid, Spain

Remondi, B. (1989) : Extending the National Geodetic Survey Standard GPS Orbit Formats, NOAA Technical Report NOS 133 NGS-46, Rockville, MD November 1989

Teunissen P.J.G, C.C.J.M Tiberius (1994): Integer Least Squares Estimation of the GPS Phase Ambiguities, Proceedings of the International Symposium on Kinematic Systems in Geodesy, Geomatics and Navigation, Banff, Canada, August 30-September 2, 1994, pp. 221-232

Temporal Characteristics of Multipath Errors

Dr. Ahmed El-Rabbany
Alexandria University

BIOGRAPHY

Dr. El-Rabbany obtained a Ph.D. degree in GPS Surveying from the University of New Brunswick, Canada, in 1994. He has been conducting research in the area of Satellite Surveying and Navigation since 1985. Currently, he is working as an Asst. Professor at the Faculty of Engineering, Alexandria University.

ABSTRACT

Precise (centimeter level) real-time kinematic GPS positioning requires resolving the integer ambiguity parameters on-the-fly. A limiting factor for successful ambiguity resolution is the existing of the unmodelled multipath errors in both the carrier phase and the pseudorange measurements. Multipath errors can be modelled stochastically if the temporal characteristics of these errors are understood. This can be done by analyzing dual frequency data as well as data from short baselines of several meters apart observed under different multipath conditions.

Once the temporal characteristics of the multipath errors are obtained and understood, they can be used to create a covariance model (e.g. first order Gauss-Marcov), which accounts for the multipath errors. In this paper, the multipath errors are analyzed so that their temporal characteristics can be obtained. The way of developing the covariance model is also given.

INTRODUCTION

Multipath is a major error source for real-time kinematic carrier phase and pseudorange applications. The presence of multipath error in the carrier phase and the pseudorange measurements becomes a limiting factor for successful determination of the integer ambiguity parameters. In real-time Differential GPS (DGPS), the existence of multipath errors at the reference station introduces significant errors for the pseudorange corrections. The

new 'tentative' message types 19 and 21 include multipath error estimate at the DGPS reference station (RTCM, 1994).

Multipath error occurs when the GPS signal arrives at the receiver antenna through different paths (Wells et al., 1987). These different paths can be the direct line of sight signal and reflected signals from objects surrounding the receiver antenna. Multipath distorts the original signal through interference with the reflected signals. It affects both the carrier phase and pseudorange measurements, however, its size is much larger in the pseudorange measurements. It is reported by Georgiadou and Kleusberg (1988) that the size of the carrier phase multipath can reach a maximum value of a quarter of a cycle. The pseudorange multipath is reported to be a two order of magnitude larger than the carrier phase multipath (Qiu et al., 1994). However, with the new advances in the receiver technology, e.g. narrow correlator technology, pseudorange multipath is reduced dramatically.

As the satellite-reflector-antenna geometry repeats every sidereal day under the same environment, the presence of multipath errors can be verified using a day-to-day correlation of the adjustment residuals. On the other hand, multipath errors in the undifferenced pseudorange measurements can be identified if dual frequency observations are available. Once the multipath errors are obtained, they can be used to generate series of autocovariance functions which describe the temporal characteristics of multipath errors. These series of autocovariance functions can then be used to develop empirical covariance models to account for multipath effects in a variety of operating conditions. In this paper, the identification of multipath errors in the cases of undifferenced pseudorange and double difference carrier phase measurements are presented. The way of developing the covariance model for the multipath errors in the undifferenced pseudorange measurements is also given. No attempt is made to develop a covariance model for the case of carrier smoothed pseudorange measurements, as the smoothing process introduces an artificial correlation which depends on the amount of smoothing being

performed (see e.g. Nolan et al., 1992). Two GPS experiments were conducted using Trimble SSE receivers.

IDENTIFICATION OF MULTIPATH ERRORS

The carrier phase and pseudorange measurements can be expressed as follows (Wells et al., 1987):

$$\Phi = \rho + c(dt - dT) + \lambda N - d_{ion} + d_{trop} + \eta\Phi + \varepsilon\Phi \quad (1)$$

$$P = \rho + c(dt - dT) + d_{ion} + d_{trop} + \eta P + \varepsilon P \quad (2)$$

where Φ is the observed carrier phase multiplied by the carrier wavelength λ , P is the measured pseudorange, ρ is the geometric range between the receiver and the GPS satellite, c is the speed of light, dt and dT are the offsets of the satellite and the receiver clocks from the GPS time, N is the initial integer ambiguity parameter, d_{ion} and d_{trop} are the ionospheric and tropospheric delays, $\eta\Phi$ and ηP are the carrier phase and the pseudorange multipath errors, $\varepsilon\Phi$ and εP represent the system noise in the carrier phase and the pseudorange measurements respectively.

The identification of multipath error in the pseudorange measurements is based on the analysis of linear combinations of the P1 pseudorange and the L1 and L2 carrier phase measurements. The first combination is formed by subtracting the L1 carrier phase from the P1 pseudorange:

$$P_1 - \Phi_1 = 2 d_{ion1} - \lambda_1 N_1 + (\eta P_1 - \eta \Phi_1) + (\varepsilon P_1 - \varepsilon \Phi_1). \quad (3)$$

The carrier phase multipath and the system noise in the carrier phase and the pseudorange measurements can be neglected as their values are much smaller than the pseudorange multipath. The ionospheric delay on L1 carrier phase measurements, d_{ion1} , can be obtained using a combination of L1 and L2 as follows (Webster and Kleusberg, 1992):

$$d_{ion1} = f_2^2 (\Phi_1 - \Phi_2) / (f_1^2 - f_2^2) + f_2^2 (\lambda_2 N_2 - \lambda_1 N_1) / (f_1^2 - f_2^2) + \varepsilon \quad (4)$$

where f_1 and f_2 are the frequencies of the L1 and L2 signals, respectively. Substituting (4) into (3), an expression for the pseudorange multipath error can be obtained as:

$$\eta P_1 = P_1 - \Phi_1 (f_1^2 + f_2^2) / (f_1^2 - f_2^2) + 2 \Phi_2 f_2^2 / (f_1^2 - f_2^2) - f_2^2 + K \quad (5)$$

where K is a constant given by:

$$K = \lambda_1 N_1 - 2 f_2^2 (\lambda_2 N_2 - \lambda_1 N_1) / (f_1^2 - f_2^2). \quad (6)$$

It should be noted that the value of K can be set to zero without affecting the unbiased autocovariance function of the pseudorange multipath error.

Multipath errors in the double difference carrier phase measurements can be obtained by analyzing the double difference residuals for short baselines of several meters apart. In this case, all errors and biases except multipath error and system noise cancel sufficiently. The data series, however, has to be long enough to avoid the artificial correlation introduced by the adjustment process. It was found that the artificial correlation resulting from the adjustment process is very pronounced for short data sets. However, it is negligible for data series of lengths longer than two hours (El-Rabbany and Kleusberg, 1993).

STOCHASTIC MODELLING OF MULTIPATH ERRORS

As stated earlier, the multipath data series are used to generate series of autocovariance functions which describe the temporal characteristics of multipath errors. Firstly, the linear trend is removed from the data series to avoid distortions in the estimated autocovariance functions. This may result in removing the linear multipath error, if it exists in the data. Assuming that the data represents a stationary random process, an unbiased estimate of the autocovariance function is given by:

$$\hat{C}_{xx}(\tau) = \frac{1}{N - |\tau|} \sum_{i=0}^{N-|\tau|-1} x'(i) x'(i+\tau) \quad (7)$$

where $\tau = -L, \dots, -1, 0, 1, \dots, L$, $x'(j)$, $j = 0, 1, \dots, N-1$ is the data sequence with the mean removed and L is the maximum lag to be considered (Marple, 1987). The normalized autocovariance function at any lag τ is defined as the ratio between the autocovariances at lag τ and zero lag.

The resulting autocovariance function is used to develop an empirical covariance model to account for multipath effect. The exponential function

$$f(\tau) = \exp(-|\tau|/T) \quad (8)$$

is selected to be the empirical covariance model. Where τ is the time shift (lag) in seconds and T is the unknown correlation time (the 1/e point) to be determined using the least squares technique.

RESULTS FOR TEST DATA

Two GPS data sets observed under different multipath conditions were analyzed to develop the empirical covariance model which accounts for the L1 pseudorange multipath error. The first data set was observed in

Norway on 16 February 1994. The receivers were placed in an open sport field covered with the snow. The average temperature was -13°C . The second data set was observed in Cairo, Egypt, on 31 August 1995. The receivers were located close to a large metallic wall with a length of about 30 m and a height of about 10 m. An aluminum table for carrying the equipment was located close to the receiver antenna as well. The average temperature was 30°C . Both data sets were observed with Trimble SSE receivers. The sampling interval was 15 seconds and the cutoff angle was 10 degrees in both cases.

Figures 1 and 2 show two examples of the L1 pseudorange multipath errors, computed according to equation (5), for both data sets. The elevation and azimuth plots are shown in Figures 3 and 4. It can be seen that multipath error is much larger in the second case. This is expected because of the high reflections from the metallic wall.

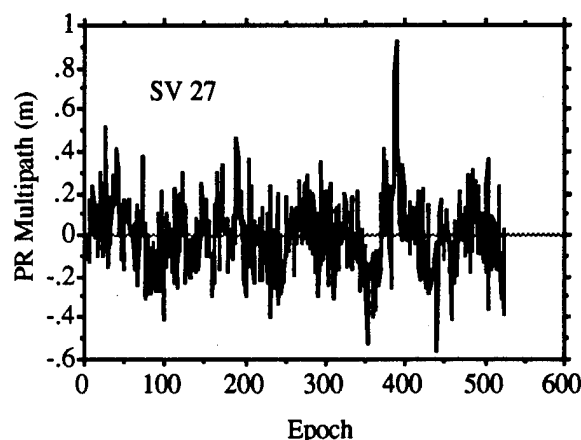


Figure 1. L1 Pseudorange Multipath Errors for SV 27 (Norway Data)

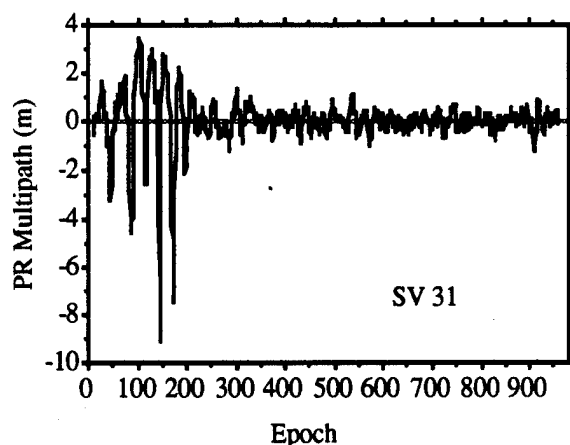


Figure 2. L1 Pseudorange Multipath Errors for SV 31 (Cairo Data)

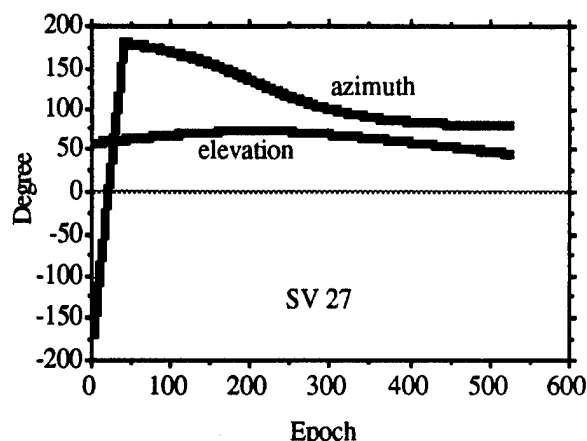


Figure 3. Elevation and Azimuth Plot for SV 27 (Norway Data)

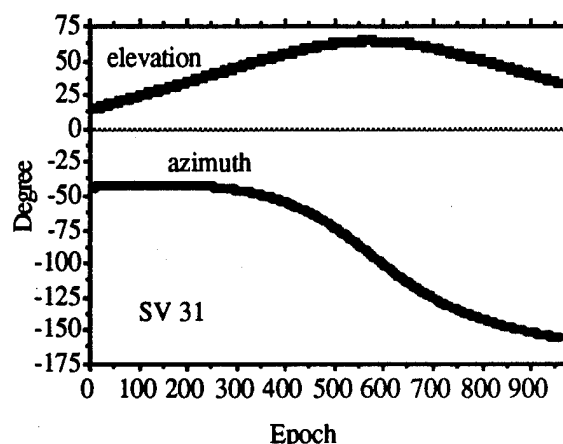


Figure 4. Elevation and Azimuth Plot for SV 31 (Cairo Data)

The autocovariance functions for the multipath errors were estimated according to equation (7). Figures 5 and 6 show the normalized autocovariance functions for the above mentioned examples. It should be pointed out that the finiteness of the data series distorts the estimated covariance function. As the number of lags increases, the number of terms used to estimate the covariance function decreases and the reliability in the estimated covariance function is reduced. To avoid this problem, only the first 25% of the estimated values of the covariance function was considered in the analysis.

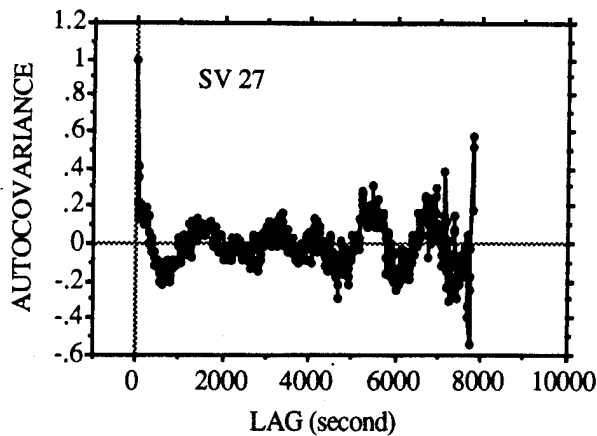


Figure 5. Estimated Autocovariance function for L1 Pseudorange Data (SV 27 - Norway Data)

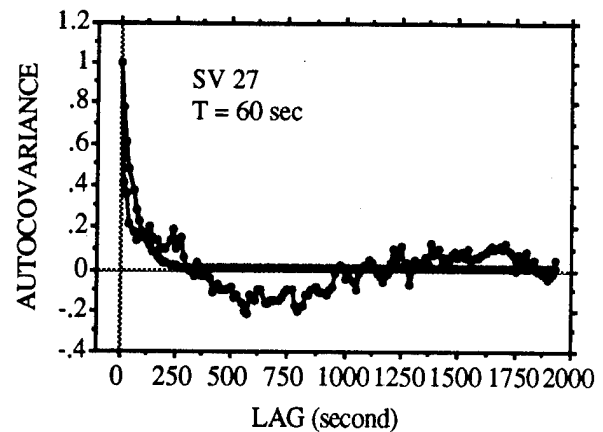


Figure 7. Empirical Autocovariance function for L1 Pseudorange Data (SV 27 - Norway Data)

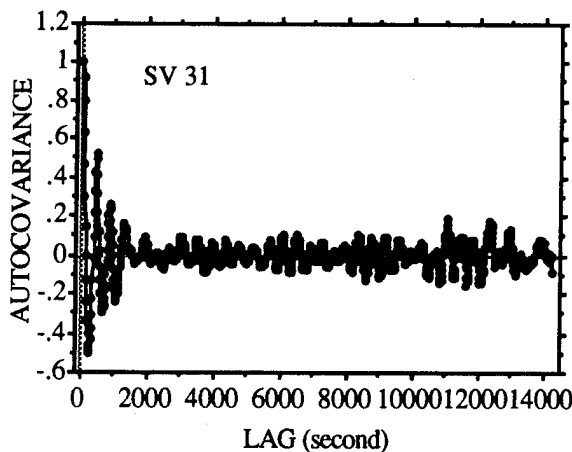


Figure 6. Estimated Autocovariance function for L1 Pseudorange Data (SV 31 - Cairo Data)

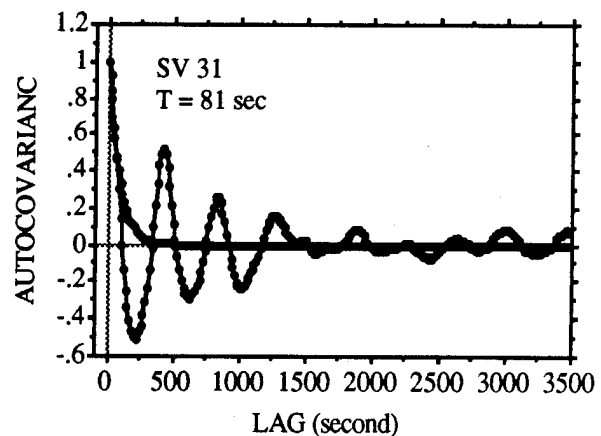


Figure 8. Empirical Autocovariance function for L1 Pseudorange Data (SV 31 - Cairo Data)

The Least Squares technique was applied on the estimated autocovariance functions for the purpose of obtaining the estimated parameters of the empirical covariance model (i.e. the correlation time in the case of the first order Gauss-Marcov). It was found that the correlation times for the different estimated autocovariance functions take the values between 11 and 81 seconds. Figures 7 and 8 show the resulting empirical autocovariance functions for the above mentioned examples. It can be seen in these figures that a better Least Squares fit may be obtained if another empirical model, e.g. exponential cosine model, is applied. This, however, may complicate the adjustment process.

CONCLUSIONS AND FUTURE RESEARCH

An empirical exponential covariance model which describes the temporal correlations of the multipath errors has been developed. The analysis of two different data sets has shown that the correlation time varies between 11 seconds and 81 seconds. It has also been shown that a better fit for the estimated covariance function may be obtained if another empirical covariance model, e.g. exponential cosine, is used.

More data sets will be analyzed in the near future in order to have a better understanding of the behavior of the multipath errors. As the multipath error of each satellite on the so-called cross over point is the same, developing an empirical crosscovariance function which describes the degree of similarity between the different multipath data series will be investigated.

ACKNOWLEDGMENTS

The author expresses his gratitude to Ola Lanola, Norway, for providing the first data set used in this paper, and to Brian Barlow of Trimble Middle East for providing the Trimble equipment used in the second data set. Many thanks goes to Hazem Wageih of the Arab International Optronics for his help during the field measurements of the second data set.

REFERENCES

- El-Rabbany, A. and A. Kleusberg (1993). "Modelling Temporal Correlations in GPS Differential Positioning." *Presented at the European Geophysical Society XVIII General Assembly*, 3-7 May, Wiesbaden, Germany.
- Georgiadou, Y. and A. Kleusberg (1988). "On Carrier Signal Multipath Effects in Relative GPS Positioning." *Manuscripta Geodaetica*, Vol. 13, pp. 172-179.
- Kee, C., and B. Parinkson (1994). "Calibration of Multipath Errors on GPS Pseudorange Measurements." *Proceedings of the ION GPS-94, Seventh International Technical Meeting of the Satellite Division of the Institute of Navigation*, Salt Lake City, Utah, 20-23 September.
- Marple, S. (1987). *Digital Spectral Analysis*. Prentice-Hall, Inc., Englewood Cliffs, New Jersey 07632.
- Nolan, J., S. Gourevitch, and J. Ladd (1992). "Geodetic Processing Using Full Dual Band Observables." *Proceedings of the ION GPS-92, Fifth International Technical Meeting of the Satellite Division of the Institute of Navigation*, Albuquerque, New Mexico, 16-18 September.
- Qui, W., G. Lachapelle, and M.E. Cannon (1994). "Ionospheric Effect Modelling for Single Frequency GPS Users." *Manuscripta Geodaetica*, August.
- RTCM Recommended Standard for Differential NAVSTAR GPS Service. Version 2.1, RTCM Committee No. 104. 1994.
- Webster, I. and A. Kleusberg (1992). "Regional Modelling of the Ionosphere for Single Frequency Users of the Global Positioning System." *Proceedings of the 6th International Geodetic Symposium on Satellite Positioning*, 17-20 March, Columbus, Ohio, USA.
- Wells, D.E., N. Beck, D. Delikaraoglou, A. Kleusberg, E.J. Krakiwsky, G. Lachapelle, R.B. Langley, N. Nakiboglu, K.P. Schwarz, J.M. Tranquilla, and P. Vanicek (1987). *Guide to GPS Positioning*, 2nd corrected printing. Canadian GPS Associates, Fredericton, N.B., Canada.

Utilizing a Low Cost GPS Receiver for Centimeter to Sub-meter Accuracy Real-Time and Post-Processed Applications

Dr. Geraint Ffoulkes-Jones
Navstar Systems Ltd.

Darren Cosandier
Premier GPS Inc.

BIOGRAPHIES

Dr Geraint Ffoulkes-Jones is a Software Engineer with Navstar Systems Ltd, Northampton, England, and specialises in data analysis for navigation and surveying. Dr Ffoulkes-Jones received a PhD in fiducial GPS surveying from the IESSG at the University of Nottingham, England. Before joining Navstar he was a senior research assistant at the IESSG where he co-authored the GAS (GPS Analysis Software) package for fiducial network processing.

Mr Darren Cosandier is completing a PhD in the Department of Geomatics Engineering at the University of Calgary, Canada. His area of research included photogrammetry, GPS, image processing and precise image georeferencing by GPS/INS. He is one of the co-authors of the GPS Post-processing and Real-Time Positioning (RTP) software described in this paper.

ABSTRACT

A high accuracy positioning system has been developed by combining a low cost single frequency C/A code GPS receiver with PC based processing software. The precise pseudorange and carrier phase observations output from a military specified navigation sensor, namely the NavSymm XR5M12, are used to produce results several orders of magnitude more accurate than the internally computed (2-3m CEP) DGPS solutions. The GPS software developed by Premier GPS Inc, offers several types of Kinematic GPS and Ambiguity Search processing algorithms suitable for a variety of applications, in either a real-time or a post-processing mode.

This paper describes the observation techniques, data processing strategies, hardware and

software required, and the results obtained for kinematic positioning in the 2-5cm, 10-30cm and sub-metre accuracy ranges. Results will be presented from both the real-time and post-processing systems.

For example, a common problem in assessing the quality of real-time DGPS algorithms in kinematic trials is finding a more accurate truth. Kinematic GPS surveys performed in a manner to give 2-5cm positions can provide a cheap and convenient solution to this problem. This facility is becoming increasingly important in industry as survey contractors are often asked to provide evidence that the positions and quality indicators output from their systems are actually accurate and reliable.

INTRODUCTION

The differential navigational accuracy of very low cost GPS receivers and OEM sensors is typically of the order of 3-10 m CEP, depending on the quality of the available pseudoranges. Many of these GPS receivers do not attempt to track the phase and hence only able to output measurements of the doppler frequency and pseudorange. Apart from the receiver's internal measurement noise the dominant error source is caused by signal multipath, which can often be in excess of 10 metres.

The next level of GPS receiver is aimed at the precise navigation market offering accuracies of 1-3m CEP and better. These receivers use more sophisticated tracking architectures such as phase lock loops and output more precise doppler frequency and pseudorange measurements. The greatest benefit of this class of receiver is that they also output carrier phase measurements, sometimes with an internal

resolution of better than 1 mm. This level of GPS receiver technology still has a relatively low cost, especially when compared to dedicated geodetic surveying instruments.

Real-Time differential positioning systems which are made up with these higher level receivers usually navigate using pseudorange observations and the RTCM SC-104 Type 1 & 2 differential pseudorange correction formats. The positioning accuracy from such systems tends to be limited by the accuracy of the pseudoranges used and their susceptibility to multipath. Internally the precise carrier phase measurements are only used in the form of delta-range or doppler observations and only contribute towards the velocity states in the Kalman filter.

In order to significantly improve the accuracy of the positioning system the precision of the carrier phase measurements must be used in the position solution. The carrier phase also has the benefit of suffering from negligible (a few centimetres at most) multipath compared to the pseudoranges, and can significantly help to reduce this existing dominant error source.

In order to fully utilise carrier phase in the real-time solutions, the receiver has to do the following:

- Communicate carrier phase information from the base station to the mobile.
- Increase the number of states in the Kalman filter to include the carrier phase ambiguities.
- Detect and allow for carrier phase cycle slips.
- Perform an ambiguity resolution computation for the highest accuracies.
- Have sufficient computing power for the above additional tasks.

In general, all of the above requirements will be beyond the existing memory and processing capabilities of the navigation receiver concerned.

A system has been developed by using the low cost GPS receivers purely as sensors to output raw GPS data. This is then processed by an off-the-shelf PC based platform with external software to produce real-time and post-processing positioning capabilities ranging from sub-metre to 2-3cm, depending on the survey techniques used.

This paper describes the required positioning techniques, data processing strategies, the GPS sensors, the computing hardware and software, and the radio links required for kinematic

positioning in the 2-5cm, 10-30cm and sub-metre accuracy ranges. Results from a high speed real-time trials is used to demonstrate the differences in accuracies obtained with the various techniques.

POSITIONING TECHNIQUES

The accuracies available from the developed system varies from 1-3 m using only the pseudoranges down to a few centimetres by fully utilising the precision of the carrier phase measurements. The operational procedures become more complicated and consequently the system limitations become more severe as the desired accuracy level increases.

The positioning techniques available in the system are as follows

- **Static Surveying.** This mode is capable of geodetic quality carrier phase surveying to an accuracy of $1\text{cm} + 1\text{-}2\text{ppm}$ of the baseline length. The occupation times required vary upwards from 10 minutes, depending on the baseline length, number of satellites tracked and whether ambiguity resolution is to be attempted.
- **Quick Static Surveying.** This technique is best suited for baselines less than 15km and typically requires only about 10 minutes of low PDOP data to produce accuracies of 2-3 cm.
- **Kinematic Positioning with Initialisation.** This is a carrier phase based technique, with the carrier phase ambiguities being set by initialising the mobile receiver at a known point. Usually the position of the known point is computed by an initial Static or Quick Static survey with ambiguity resolution. Accuracies of $2\text{-}5\text{ cm} + 2\text{-}3\text{ ppm}$ are maintained while continuous lock is kept on at least 4 satellites.
- **Continuously Kinematic Positioning.** This is a positioning technique where by the mobile receiver is assumed to never be stationery. The accuracy levels in this mode start at the 1-3 metre accuracy of conventional real-time DGPS, but with time and suitable operating conditions can improve to an accuracy of about 10 cm. Under typical multipath conditions, and if continuous lock is maintained on at least 4 satellites, then sub metre accuracy is obtained within 1-2 minutes, 0.5 metres in about 5 minutes, 30

cm after 10-15 minutes and 10 cm after about 15-20 minutes.

DATA PROCESSING STRATEGIES

Overview of Positioning Filter

The data processing algorithms consist of a Kalman filter to process double differenced (DD) carrier phase, pseudorange and carrier phase based delta-range or doppler measurements. The state vector of unknowns consists of the mobile receivers position and velocity vectors and the DD carrier phase ambiguities.

In this GPS filter architecture the carrier phase and pseudorange measurements tend to only contribute to the receivers position and ambiguity states, whereas the delta-range or doppler measurements tend to only contribute only to the velocity states.

After processing only one epoch of data the carrier phase ambiguities states take values which are equal to the difference between the DD carrier phase and pseudorange measurements. As more data is included over consecutive epochs the ambiguity states become more stable and take values that tend to the least squares optimal mean of the difference between the DD pseudorange and DD carrier phase measurement for the corresponding satellites. In the absence of cycle slips, the ambiguities will also gain successively lower standard deviations with time.

At the start of data processing, the output of the Kalman filter is primarily controlled by the pseudorange measurements, which have an rms noise of between 0.5 to 10 metres, depending on the level of multipath. However, as the DD ambiguity standard deviations reduce, the Kalman filter pays more attention to the range information implied from the combination of an DD ambiguity estimate and carrier phase measurement.

Ambiguity Resolution

If the ambiguities can be resolved to their true integer values, they can then be constrained to this value in the Kalman filter solution. The quality of the range information now dominating the output of the Kalman is simply a function of the carrier phase measurement noise. DD pseudorange measurements which are assigned a standard deviation of say, 7m, are effectively ignored when they are swamped by ambiguity resolved DD carrier phase measurements with a standard deviation of 20 mm.

The DD carrier phase noise is usually in the region of 2 to 20 mm, depending on the baseline length and multipath. These measurements combined with a PDOP of say, 2, will give a relative coordinate precision of 4 to 40 mm. Resolving and constraining the ambiguities in this way will lead to the highest possible accuracies, of only a few centimetres plus 1-2 ppm.

A search technique is used to find the position and integer ambiguity value giving the best fit to the carrier phase data to each satellite throughout the observation period. Before the best trial ambiguity set found is considered as being resolved it must satisfy a set of statistical criteria to ensure that it is in fact the correct set. Two basic types of test are used and the solution must satisfy both to allow ambiguity fixing. They are as follows :

- The degree of fit of the best solution must be sufficiently good that it is believable. ie the implied carrier phase noise is within the 2 to 20 mm that would be expected from such a solution.
- The degree of fit of the best solution is statistically significantly better than its nearest rival.

It is very important that the results of these statistical tests are adhered to strictly. A solution based in incorrectly fixed ambiguities may be up to several metres in error, yet the Kalman filter would be reporting centimetric accuracy. Clearly this is unacceptable.

Real-Time vs Post-Processing

In order to achieve the centimetric accuracies capable with this system, it is necessary to eliminate the errors introduced by SA (Selective Availability) orbit error (epsilon) and satellite clock dither which changes rapidly and at rates of up to 1 metre/second. Post-processing systems overcome this problem by differencing simultaneously (ie within 1 millisecond) observed measurements at two receivers. Unfortunately, there is no way that this error can be computed at a GPS differential base station and propagated forward by, say 1 second for use at the mobile receiver, to an accuracy of a few millimetres.

The only way to maintain < 20mm precision in a real-time differential carrier phase measurement is to process measurements that were observed simultaneously. The consequence of this is that the mobile data has to be buffered until the

corresponding base station data has arrived and thus allow processing to continue.

In essence, a real-time system should alternatively be described as a "near real-time post-processing system", in that the data is actually computed a short time after it was observed and published, say 1 second late. This positioning system does not tell you where you are at the time of publication, but where you were 1 seconds ago.

This short delay does not cause a problem for many survey related applications, such as offshore hydrographic and seismic surveys. In these situations it is often far more important to know in real-time that a survey is producing good results than to know what they actually are. The positions will usually be recorded and combined with other data sources for subsequent analysis.

Since the real-time solution is effectively a post-processed one in the way the algorithm works there is little or no accuracy difference between the two. The main benefit of a post-processing system is the removal of the data link which is often the most troublesome part of the system. Other benefits are that the data can be massaged to remove problem areas and can even be processed backwards in an attempt to overcome catastrophic cycle slips. In addition, many sub-contracted surveys specify that the raw GPS measurements must be recorded during real-time surveys to provide a traceable path to the results to satisfy client quality control procedures.

A LOW COST PRECISE GPS SENSOR

The GPS sensors used in the system described are from the XR5 family of 12 channel L1 C/A code receivers manufactured by Navstar Systems Ltd in the UK and marketed under the NavSymm label. The XR5 contains two proprietary 6 channel digital tracking ASICs running in parallel giving 12 independent tracking channels. This receiver design allows continuous carrier lock to be maintained on the satellites even under high dynamics. Cycle slips only tend to occur when the satellite signal is physically obscured.

The XR5 publishes raw timetag, pseudorange and carrier phase measurements internally at 4Hz, and may be accessed using the Navstar's proprietary Data Monitor interface. This is a request / response utility which allows user software to access and even change many of the internal variables of the XR5 firmware in real-time. A series of pre-defined macros for the raw measurements data have also been defined

which the user can send continuously to one of the data ports.

The XR5 when in DGPS mode publishes positions at 4Hz to an accuracy of 1-3m CEP. These positions are true real-time, ie the velocity states are used to predict the position forward to the instant of publication.

Two different forms of the XR5 may be used with the high accuracy real-time and post-processing systems described in this paper. They are :

- **XR5M-12** (Figure 1)
This is a ruggedised unit which is housed in a die cast aluminium box and is built to MIL-STD-810. A 6 channel multiplexing version of this receiver is used extensively on US-DoD test ranges for DGPS applications in hostile environments such as on land vehicles, helicopters and fighter aircraft. The raw GPS measurements are available at various rates up to 2Hz and at 19,200 baud from an RS232 port.
- **XR5PC-12** (Figure 2)
The XR5-PC is an IBM® AT compatible ISA bussted GPS interface card. It is a half length card, occupies about 1.5 slots and is powered directly from the filtered 5V and 12V on the ISA bus. A major advantage of this card is that the ISA bus can be configured as a standard DOS COM port so that existing software designed for serial ports still works. The ISA bus can also be put into a streaming mode to output the raw GPS measurements at user configurable rates of up to 4Hz. The data transfer across the ISA bus is almost instantaneous making this card ideal for integration into systems requiring high data rates.



**Figure 1 : The NavSymm XR5M-12
Mil Spec GPS Receiver**

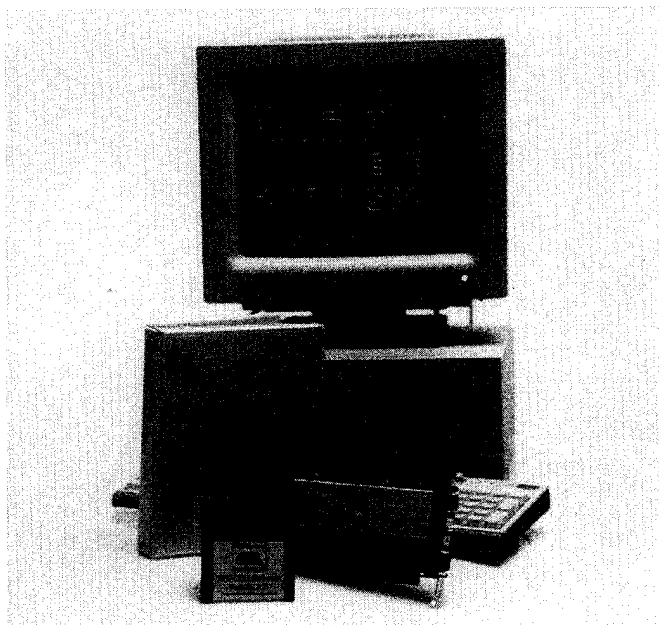


Figure 2 : The NavSymm XR5PC-12 PC GPS Card.

Despite the fact that the XR5 receiver was initially developed for the precise DGPS market, it has proved to produce raw measurements of exceptionally high quality.

The internal measurement noise of the XR5 has been characterised using classical zero baseline bench tests on static receivers, and analysing double differenced measurement residuals. This was done using the GPS Analysis Software (GAS) package developed at Nottingham University [Stewart & Ffoulkes-Jones, 1994]. This particular package was used because it was possible to gain access to the individual a posteriori least squares measurement residuals. The internal measurement resolution of the XR5 12 channel receivers for a data set recorded with an elevation mask of 15° are given in table 1.

	rms noise
pseudorange	10-20 cm
carrier phase	0.7 mm

Table 1: Internal measurement resolution of the XR5 GPS Sensor

The carrier phase resolution of the XR5 family has been improved through firmware compared to the results published at ION GPS'94 [Haddrell, 1994]. It is also worth noting that the low pseudorange noise is achieved using a phase lock loop architecture where the phase rate is fed back into the code tracking loop. There is an initial warming up period of about 50 seconds when the code and carrier loops are aligning themselves with each other. A more detailed description of the XR5PC-12 may be found in [Haddrell, 1995].

DATA PROCESSING SOFTWARE AND COMPUTING PLATFORM

The data processing software used to produce the sub-metre down to 2 cm positioning accuracies has been developed by Premier GPS Inc of Calgary, Canada. The software is designed to run on IBM® AT compatible PCs. Although the Premier software has been designed to operate with a selection of GPS sensors, this paper is only concerned with the systems combining it with the NavSymm XR5M-12 and XR5PC-12 receivers.

The software used varies depending on the processing platform and on whether the system is intended for real-time and / or post-processing applications.

Post-Processing Software.

- NAVBIN. This is the PC based data logging software, which will run on practically any DOS compatible computer. Very small PCs such as HP100 or 200 palmtop computers are adequate for logging at 1Hz.
- GPS_PROC. This is the main GPS Processing engine which can process GPS positioning scenarios described in section 3. It requires a 386DX or better with at least 4MB RAM.
- GRAFNAV. This is the Graphical Navigation interface to GPS_PROC. It allows the user to see the data plotted on the screen, define processing options, manipulate the data, create various output files and display quality information to the screen.

Real-Time Software

- NAVBIN. In addition to data logging NAVBIN acts as a Real-Time Positioning base station and reformats XR5PC streaming data and sends it to the radio link. This task is

performed internally within the XR5M12. 2Hz data can be transmitted at 9600 baud.

- GPS_NAV. This version is designed to run from the hard disk of a standard IBM PC. The user interface is via a standard keyboard and VGA screen.
- RTP_EMB. This version is embedded onto EPROM's which are fitted to OEM PC cards, which do not need a hard disk, keyboard or screen. This software is controlled via a serial link connected to an external CDU.

Full details of this software may be found in [Martell & Cosandier, 1994a, 1994b, 1995].

HARDWARE CONFIGURATIONS

The potential applications of a high accuracy positioning system such as this are almost endless. Each will require its own level of hardware ruggedness, portability, flexibility, power availability, processing speed, user input / output interaction, and overall system cost. The appropriate building blocks can be selected and combined in many different ways to give the most practical and cost-effective solution.

It would be an almost futile task to attempt to list all the possible hardware configurations in this paper. Instead, only the configuration used in the trial survey found in later sections of this paper will be described.

Data Link

The radio data links used were the NavSymm DR5-96S. This is a 2 Watt UHF line of sight 2 packet radio, which is housed in a ruggedised die cast aluminium box (figure 3). These radios will operate in either transmit or receive mode without special configuration.



Figure 3 : The NavSymm DR5-96S UHF Radio

Base Station

An XR5M12 GPS receiver was used, passing 1Hz data to the COM1 serial port of a Toshiba 1900 486SX laptop. The laptop was running NAVBIN which output RTP base station data to the radio via a PCMCIA COM2 serial port. (This trial was conducted before the base station RTP data format was embedded into the XR5M12, hence the requirement for the laptop). The GPS antenna was mounted on a standard surveyors tripod.

Mobile Receiver

An XR5M12 GPS receiver passing 1Hz data to COM1 of a 40 MHz Compaq 486DX running the GPS_NAV Real-Time Positioning (RTP) software. Again the base station data from the radio link was fed to the laptop via a PCMCIA COM2 serial port. A mag-mount patch antenna was mounted in the centre of the roof of a standard saloon car. The RTP software logged the raw data from both the mobile and base station receivers to also allow subsequent post-processing.

SYSTEM TRIALS AND RESULTS

This section presents results from a survey designed to demonstrate the precision of the developed system. The raw measurement data was logged during an RTP (real-time positioning) survey. This data was then subsequently post-processed to show the difference in accuracies that would have been achieved if a different and

less restrictive observational technique had been employed during the real-time survey.

In order to make the tests more realistic, the most precise observation technique was used in real-time to give a vehicle trajectory accurate at the centimetre level. This was achieved using a Quick Start static survey to initialise the ambiguities before going kinematic. Several post-processed solutions were performed on the data in such a way that accuracy of the solutions was reduced by:

- Not attempting to resolve the ambiguities to integers after the static initialisation.
- Assuming that the data from the initialisation period was for a kinematic receiver.
- Removing the initialisation period completely, and starting the processing from the first kinematic epoch of the survey.
- Removing the carrier phase data and basing the entire solution on pseudoranges. Position solutions based on pseudoranges alone will be similar to those obtained from the XR5's internal Kalman filter when operating in DGPS mode.

In order to test the system in truly dynamic scenarios the mobile unit was mounted in a car and driven at speeds of up to 120mph / 200kmh around the Bruntingthorpe test circuit. This is a relatively flat converted airfield site offering a fairly unobstructed view of the sky. Figure 4 shows a horizontal plan of the test circuit. The side road used during the initialisation can also be seen.

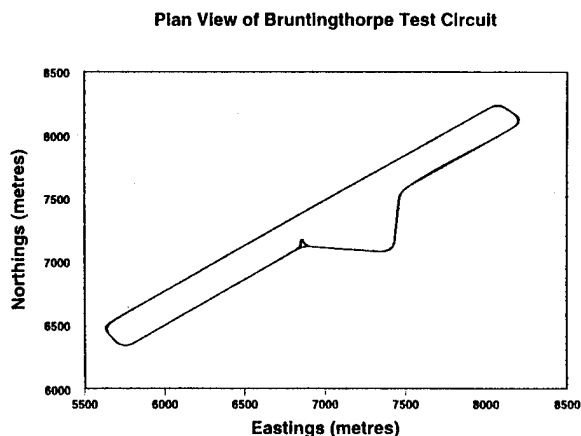


Figure 4 : Plan View of Bruntingthorpe Circuit

We did not have access to a centimetre accuracy truth system or to a person capable of driving to within a centimetre of ground marks at high speed. Therefore, we decided to perform repeat circuits of a relatively flat and marked road surface. Although the horizontal track could only be repeated to say, 1 metre, the height of the road surface could be repeated very accurately. Therefore, the results in this paper demonstrate the precision of the systems by plotting height repeatability against the easting horizontal component. The height scale could be severely exaggerated because of the relatively flat nature of the circuit.

Figure 5 shows the height repeatability of the real-time survey for 6 laps of the circuit, and a close up section where the test car was travelling at around 100 mph is plotted in figure 6. The overall spread of the height results is around 3cm, which implies an rms accuracy of about 1cm. Furthermore, it is well known that GPS accuracy is typically 1 to 2 times worse in height than it is in the horizontal component. The implication of this is that the rms horizontal accuracy of the real-time survey was within 1cm.

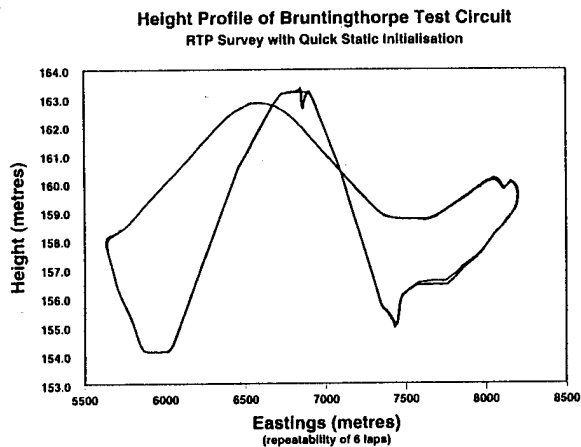


Figure 5

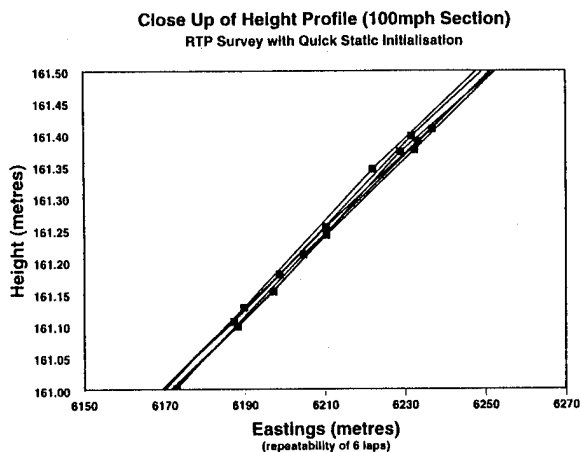


Figure 6

An interesting feature of Figure 5 is where the lines diverge in the bottom right hand section of the circuit. This was caused by the trial car having to change lanes after 3 laps because another user of the circuit had stopped.

The 4 graphs shown in Figures 6 to 9 show the height repeatability of the tracks for the RTP survey (Figure 5) and the various post-processing alternatives described above (Figures 6-9). The increasing thickness of the overlaid lines (ie worse repeatability) in the various plots gives an indication as to their relative quality. As the initialisation information reduces the trajectories take longer to converge. This is roughly half a circuit in figure 8, and 1.5 circuits in figure 9.

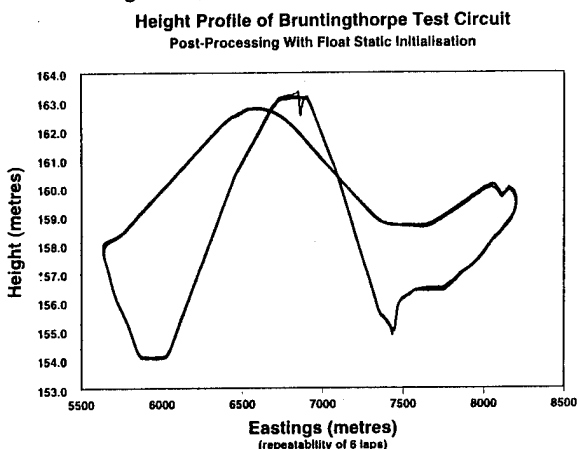


Figure 7

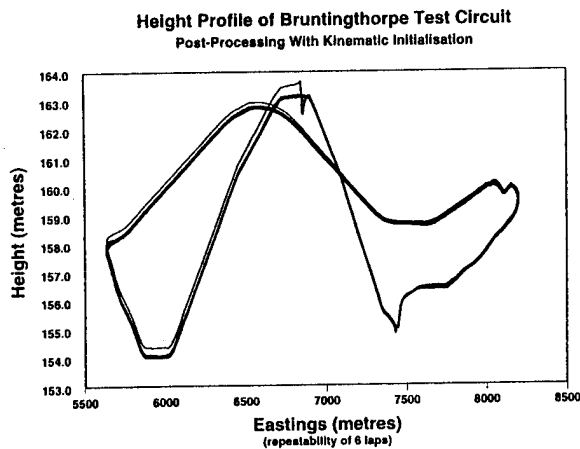


Figure 8

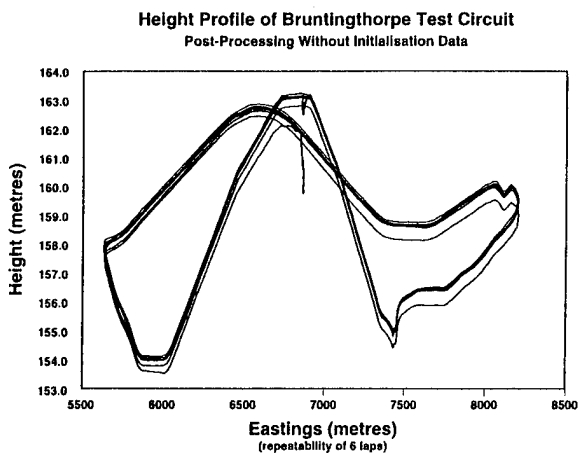


Figure 9

The next 4 graphs in Figures 10 to 13 show the same results but this time as the difference between the less accurate post-processed alternative techniques to the RTP centimetric accuracy solution. It can be clearly seen that the accuracy of each of the carrier phase based techniques is at the 10 cm level after the solution has converged. The only real difference being the successively slower speeds of convergence, caused by not using all of the available information (ie the fact that the ambiguities should be integer; the fact that the receiver was stationary during the initialisation period, or by ignoring the data from the initialisation period completely). The solution took roughly twice as long to converge in kinematic mode, compared to static mode. In essence the difference between the various solutions is purely down to the mode and level of convergence that can be achieved before starting the actual survey.

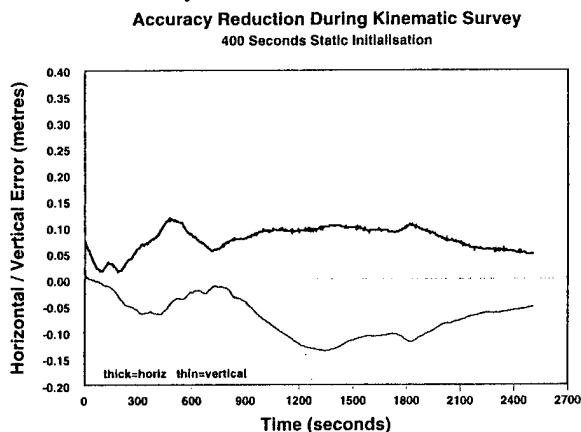


Figure 10

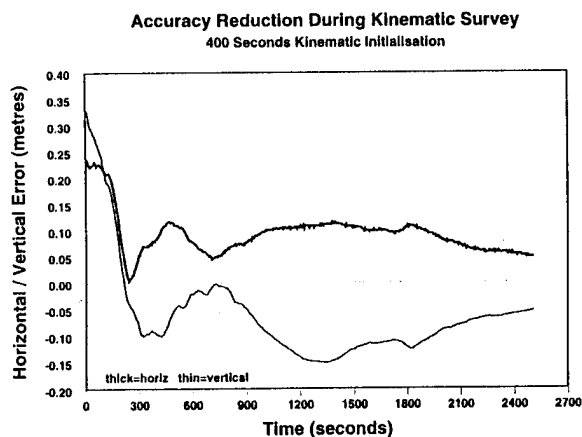


Figure 11

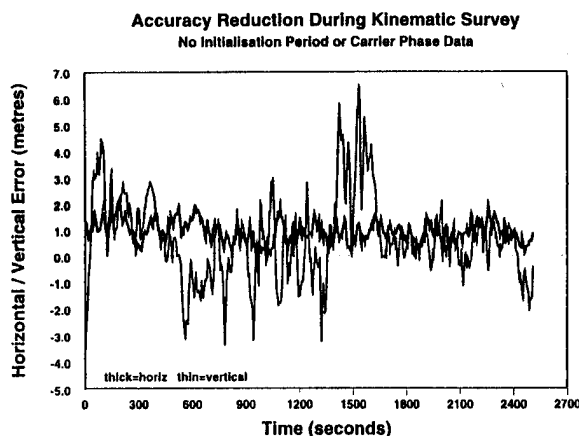


Figure 13

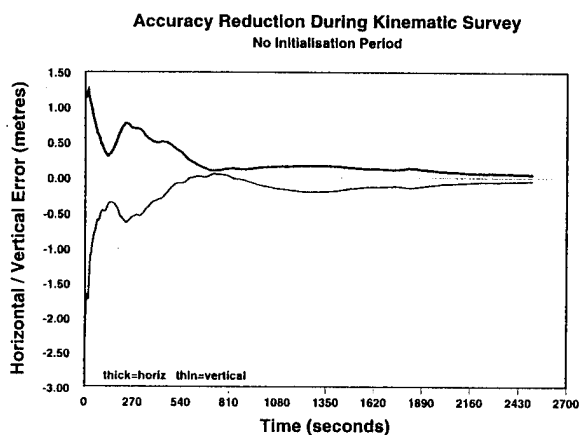


Figure 12

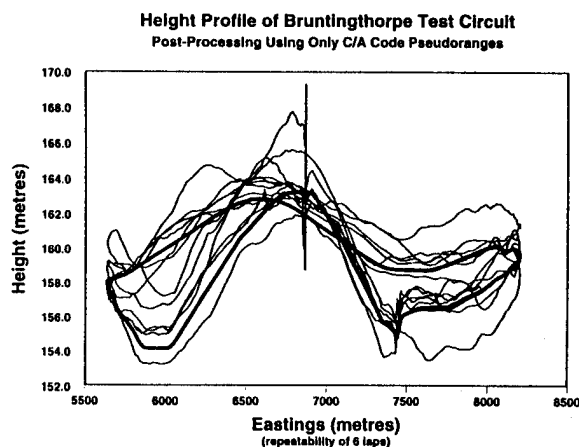


Figure 14

The very noisy solution seen in figures 13 and 14 are the ones obtained from using only the C/A code pseudoranges. This is the level of accuracy expected from a conventional 1-3m DGPS system. There is no evidence of any convergence towards a more accurate solution as is seen when carrier phase measurements are used.

The results obtained during the RTP survey described are exceptionally good. The test circuit used was a low multipath site and caused very few signal blockages which led to cycle slips. Since continuous lock was maintained on at least 4 satellites then had cycle slips occurred on any of the remaining satellites they would not have caused problems. If too many slips had occurred then the solution would tend to the accuracy given from the pseudoranges and the convergence process starts again as the solution re-learns the new carrier phase ambiguity values. If the pseudoranges are corrupted by large multipath errors then the convergence times will be longer.

APPLICATION EXAMPLES

Due to the operational requirement to maintain lock on the satellites as much as possible this technique is best suited to open environments. Nevertheless, the applications of a precise positioning system such as this are almost endless. Some examples of the possible applications include :

- Near shore hydrographic surveys
- Aerial surveys and photogrammetry
- Vehicle tracking on test circuits
- Yield & fertiliser monitoring in agriculture
- Calibration of aircraft landing systems
- Calibration of lower accuracy DGPS systems
- Calibration of any other positioning system
- Engineering surveying control
- Ground profiling
- Positioning of civil engineering plant such as piling rigs
- Setting out & stake out surveys
- etc.

FUTURE DEVELOPMENTS

An obvious improvement to the developed system would be to include the capability to do all the necessary data processing within the XR5 receiver. The current processor used in the XR5 family is the Motorola 68020 which is roughly comparable in performance to a 386SX. We are currently investigating the possibility of upgrading the processor to the recently announced Motorola 5102 whose performance is rated as being somewhere between a 486 and a Pentium. This would provide the required processing power.

CONCLUSIONS

This paper described the observational techniques, processing strategies, hardware and software requirements for a low cost high precision real-time and post-processing positioning system. This is achieved by combining the precise carrier phase and pseudorange measurements from a C/A code GPS sensor with an external PC based processor and software. Several operational techniques and sample trial results were presented to demonstrate positioning performance at the sub-metre, 10-30cm and the 2-5cm accuracy levels.

REFERENCES

- Haddrell, A H, "The XR5 12 Channel Kernel", Proc. *ION GPS'94*, Salt Lake City, September 1994.
- Haddrell, A H, "The XR5-PC12 - Position and Time/Frequency from A single plug-in module", Proc. *ION GPS'95*, Palm Springs, September 1995.
- Martell, H, and Cosandier, D, "Reference Manual for GPS_PROC & Utilities", *Premier GPS Inc*, 1994a.
- Martell, H, and Cosandier, D, "Reference Manual for GRAFNAV GPS Post-Processing Software", *Premier GPS Inc*, 1994b.
- Martell, H, and Cosandier, D, "Premier Surveyor Real-Time Processing RTP", *Premier GPS Inc*, 1995.
- Stuart, M and Ffoulkes-Jones, G, "GAS, GPS Analysis Software Manual Version 2.2", *IESSG, The University of Nottingham*, 1994.



Session B5

GPS User Equipment Technology

Chair:

Dr. Sergei Gourevitch
Ashtech

Co-Chair:

Dr. Durk Van Willigen
Delft University

A Comparison of Three Multipath Mitigation Approaches for GPS Receivers

Armando Montalvo and Alison Brown
NAVSYS Corporation

ABSTRACT:

The presence of multipath components in the received signal of a GPS receiver can adversely affect the ability of the receiver to compute accurate navigational solutions even when differential GPS corrections are available. Thus, for applications that require high accuracy it is important to develop approaches to mitigate the effects of multipath in the received signal. In this conference paper we present the results of a study of three different approaches for multipath mitigation. The first approach uses extended maximum likelihood methods, such as those found in antenna array problems, to estimate the multipath signal parameters during carrier and code acquisition. The second approach uses several narrow band correlators to provide the time-space observations required for maximum likelihood estimation of the multipath signal parameters in order to cancel their effect before code synchronization and tracking is performed in the receiver. The third approach utilizes receiver autonomous integrity monitoring (RAIM) algorithms to detect errors in the navigation solution and, when permitted, correct for such errors. These three approaches are compared with computer simulations. A key figure for comparisons was the multipath cancellation return which is a measure of the amount of multipath cancellation obtained by the approach used. It was found that under both slow and fast fading conditions the first approach obtained slightly higher multipath cancellation than the second approach but at a substantial penalty in computational complexity. The third approach yielded the best results if enough satellites are in view that do not suffer from multipath errors.

1. INTRODUCTION

High accuracy GPS receivers have been developed that can make sub-meter pseudo-range observations on the L₁ and L₂ GPS frequencies. The accuracy of these measurements can be improved further through the use of carrier phase smoothing. One of the most significant error sources in a high accuracy GPS system is caused by multipath. Multipath errors occur on both the pseudo-range and the carrier phase observations in a GPS receiver when reflected signals are received at the antenna. The magnitude of the error is a function of the strength of the reflected signal and the relative phase of the multipath signal.

GPS P-code receivers can discriminate multipath signals delayed by more than 150 nsec. Experimental results have shown that multipath errors typically introduce sinusoidal delay errors of periods 6-10 min and magnitudes of 3 μ sec or less. This would introduce an equivalent error of 1 m in a differential GPS solution. However under some conditions, the error can grow as large as 5.5 nsec (1.6 m). A C/A code receiver is even more severely affected, as the receiver can only discriminate multipath signals delayed by more than 1.5 μ sec.

The dominant error source for both C/A code and P-code differential GPS (DGPS) and kinematic GPS (differential carrier phase processing)

systems is multipath. Under good signal-to-noise ratio conditions (>40 dB-Hz), the receiver noise is less than 0.3 m. This can result in a DGPS accuracy of 0.5 m in good geometry (HDOP <1.7) if multipath errors can be eliminated.

Multipath errors tend to be worst on low elevation satellites. The most common method of minimizing this effect in reference sites has been to use antenna designs that cut off the GPS signals at low elevation. One such antenna design is the choke ring antenna developed by JPL for use with the Rogue receiver. However, this approach has the disadvantage of rejecting signals from low elevation satellites.

Other techniques involve optimizing the receiver estimation techniques with respect to the multipath fading channel. Once the multipath errors are characterized, their effect can be removed from the GPS pseudo-range observations.

1.1 MULTIPATH ESTIMATION

Fundamentally the problem of multipath estimation reduces to identification of the channel through which the transmitted signal passes on its way to the receiver antenna. A good model for multipath propagation is [1]

$$h(\tau; t) = \sum_{k=0}^{M-1} a_k(t) \delta(\tau - \tau_k) \quad (1)$$

where $h(\tau; t)$ is the time-variant impulse response of the channel, with $a_k(t)$ representing the possible time-variant attenuation factors of the M multipath propagation paths. Assuming that a direct-sequence spread-spectrum (DSSS) transmitted signal and additive white Gaussian noise (WGN) is present at the receiver input, the received signal using complex baseband notation is of the form

where w is the carrier frequency, $d(t)$ is the data waveform, $p(t)$ is the chip waveform, and a_k , θ_k , and w_k are respectively the signal phase, amplitude, and relative Doppler of the k th multipath. The term $n(t)$ is complex WGN introduced by the receiver front end.

The typical GPS receiver uses a (noncoherent) delay locked loop (DLL) for code tracking. It is widely acknowledged that the DLL performance degrades in

$$\begin{aligned} (t) &= \text{Re}\{x(t)\} \\ &= \text{Re} \left\{ \sum_{k=0}^{M-1} a_k(t) d(t - \tau_k) p(t - \tau_k) e^{j[(\omega + \omega_k)t + \theta_k]} + n(t) \right\} \end{aligned} \quad (2)$$

multipath unless some sort of multipath suppression can be introduced [2,3,4]. For DSSS ranging applications such as GPS, the problem is to identify the primary or line-of-sight signal delay (τ_0) and phase, (θ_0). Once this has been accomplished, the multipath corrected pseudo-range measurement can then be obtained. It is important to note that the problem at hand is one of multi-parameter estimation. Obtaining τ_0 and θ_0 can only be accomplished by characterizing the entire channel, that is, all the channel parameters.

1.2 MULTIPATH INDUCED ERRORS

IN [5], Van Nee studied the errors induced by multipath in conventional code tracking algorithms based on coherent or non-coherent DLL using narrow correlators with spacing of $d/2$, where $d \ll$ code chip. For the coherent case Van Nee found that for a single multipath reflector and slow fading (when the fading bandwidth is much smaller than the DLL loop bandwidth) the maximum tracking error as a function of the multipath delay error is given by figure 1.0.

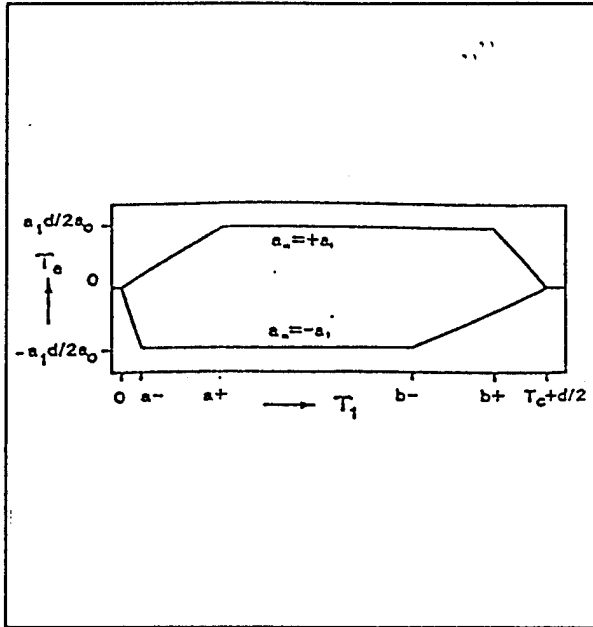


Figure 1.0 Maximum delay errors

The figure is normalized with respect to the signal to multipath ratio $SMR = (a_1/a_0)$, and the early-late spacing d . Notice that when the SMR approaches one we can expect maximum errors of up to $d/2$. Thus for typical receivers where the correlation spacing is a code chip we can expect a maximum error of half a code chip. It is clear from this that narrow correlators will reduce this maximum error substantially as was reported in the literature [6]. For fast fading (when the fading bandwidth is larger than the DLL loop bandwidth and carrier loop bandwidth), VanNee showed that the time average sum of the multipath signals tend to zero and thus multipath components of the code phase signals of the DLL also reduces to zero.

For the noncoherent case, the maximum induced tracking error due to a single multipath is also given by figure 1.0 for the slow fading case. Unfortunately for both cases, slow fading and fast fading, the multipath induced errors develop a positive mean bias due to the non-linearity associated with the squared envelope detection associated with non-coherent DLL. Again the use of narrow correlation spacing will mitigate this bias.

For both cases the problem of synchronizing to a multipath reflected signal rather than the direct line-of-sight signal, when the reflected multipath signal of sufficient amplitude suppresses the direct line-of-sight signal or when the direct line-of-sight signal is shadowed by an object, are by far the worse multipath induced errors that can be encountered. One should realize that conventional DLL and acquisition techniques are the main cause of the problem since they were not designed to deal with multipath reflections. An improved performance should be obtained by replacing conventional DLL and acquisition techniques with other estimation systems designed to operate in multipath fading channels. In the rest of this paper we discuss three such systems. The first system is based in large sample maximum likelihood techniques often found in antenna array problems. Here time-space observation are obtained by using multiple antenna elements. These observations are then used to estimate the multipath complex gain (parameters) and its direction of arrival. The second system uses several narrow band correlators to provide the time-space observations required for maximum likelihood estimation of the multipath signal parameters in order to cancel their effect before conventional code synchronization and tracking is performed in the receiver. The third approach utilizes receiver autonomous integrity monitoring (RAIM) algorithms to detect errors in the navigation solution and, when permitted, correct for such errors. These three approaches are compared with computer simulations and their results are presented.

2.0 THE LARGE SAMPLE MLE

The large sample MLE approach is based in the decouple maximum likelihood estimation algorithm developed by Li, *et. al.*, for angle estimation for signals with known waveforms [7,8]. This algorithm is similar to the ESPIRT algorithm [9] where the shift invariant structure imposed by the antenna elements are exploited. Basically the system uses measurements from several antenna elements to estimate the multipath signal angle of arrival and their corresponding amplitudes and phases.

The output of the antenna elements $x(t)$ can be modeled

as

$$x(t) = A(\theta)s(t) + n(t) \quad (3)$$

where $x(t)$ is the received data vector, $s(t)$ is the incident signal vector to the antenna elements (assumed a $k \times 1$ vector) and $n(t)$ is the additive noise vector term. The matrix $A(\cdot)$ ($M \times k$) is the antenna array manifold describing the array transfer response as a function of the signals parameter vector θ . Each column of $A(\cdot)$ is a steering vector. We make the following assumptions:

- 1) The Array manifold $A(\cdot)$ is unambiguous i.e. the matrix has full rank.
- 2) The noise vector $n(t)$ is circular symmetric zero mean Gaussian with second order moments:

$$E[n(t)n^*(s)] = Q\delta_{t,s} \quad E[n(t)] = 0 \quad (4)$$

- 3) The impinging signals $s(t)$ are scaled versions of a set of known sequences $\{y(t), \dots, y(t)\}$. In other words

$$s(t) = \Gamma Y(t) \quad (5)$$

where $Y(t) = [y(t), \dots, y(t)]$ and Γ is a ($M \times k$) matrix with structure given by

$$\Gamma = \begin{bmatrix} \gamma_{11} & \dots & \gamma_{1d_1} & 0 & \dots & 0 \\ 0 & \dots & 0 & \gamma_{21} & \dots & \gamma_{2d_2} & 0 & \dots & 0 \\ \vdots & & & & & & \vdots & & \\ 0 & \dots & & 0 & \gamma_{c1} & \dots & \gamma_{cd_c} \end{bmatrix}^T$$

where each index k denotes the number of incoming signals corresponding to the k th source signal. Notice that we want to obtain estimates of the elements of the above matrix which represents the complex gain of the multipath signals (amplitude and phase) and the angle of arrival of the multipath signals with relation too the antenna array elements.

It can be shown [10] that the estimate of this parameters is obtain by minimizing the following cost function:

$$L(\theta, \Gamma, Q) = LN(|Q|) + \text{tr}[Q^{-1} + \frac{1}{N} \sum_{t=1}^N [x(t) - BY(t)][x(t) - BY(t)]^H]$$

where $|\cdot|$ denotes the determinant of a matrix and $B = A(\cdot)\Gamma$. It can be shown that the matrix Q that minimizes the above cost function is given by

$$\hat{Q}(B) = \frac{1}{N} \sum_{t=1}^N [x(t) - BY(t)][x(t) - BY(t)]^H \quad (8)$$

Using this in the above cost function we obtain:

$$\begin{aligned} L(\theta, \gamma) &= |\hat{R}_{xx} + B\hat{R}_{yy}B^* - B\hat{R}_{yx} - \hat{R}_{yx}^*B^*| \\ &= |\hat{R}_{xx} - \hat{R}_{yx}\hat{R}_{yy}^{-1}\hat{R}_{yx}^* + (B - \hat{R}_{yx}\hat{R}_{yy}^{-1})\hat{R}_{yy}(B - \hat{R}_{yx}\hat{R}_{yy}^{-1})^*| \\ &= |\hat{Q}| |I + \hat{Q}^{-1}(B - \hat{B})\hat{R}_{yy}(B - \hat{B})^*| \\ &= |\hat{Q}| |I + \hat{R}_{yy}(B - \hat{B})^*\hat{Q}^{-1}(B - \hat{B})| \end{aligned}$$

where

$$R_{yy} = \frac{1}{N} \sum_{t=1}^N Y(t)Y^*(t) \quad (10)$$

and R_{xx} and R_{yx} are similarly defined. It can be shown that the minimization of the above nonlinear cost function can be decomposed into the k independent minimization problems [10] of the form:

$$\hat{\theta}_k, \gamma_k = \arg \min_{\theta_k, \gamma_k} [A(\theta_k)\gamma_k - \hat{b}_k]^* \hat{Q}^{-1} [A(\theta_k)\gamma_k - \hat{b}_k] \quad k=1,2,\dots$$

where \hat{b} denotes the k th column of B and $A(\cdot)$ is the part of $A(\cdot)$ corresponding to the angle

. The minimization with respect to the complex gains of the multipath parameters is

$$\gamma_k(\theta_k) = [\hat{Q}^{-1/2} A(\theta_k)]^+ \hat{Q}^{-1/2} \hat{b}_k \quad (12)$$

where $(\cdot)^+$ is the Moore Penrose of a matrix. Using this in (11) we obtain the following cost function for estimating the arrival angles for the multipath signals:

$$\hat{\theta}_k = \arg \min_{\theta_k} [\hat{\delta}_k^* [\hat{Q}^{-1} - \hat{Q}^{-1} A(\theta_k) (A^*(\theta_k) \hat{Q}^{-1} A(\theta_k))^{-1} A^*(\theta_k) \hat{Q}^{-1}] \hat{\delta}_k]$$

Once the above parameters are found, the complex amplitudes estimates are obtained from (12). It is worth mentioning that the above algorithm is consistent; this follows from the consistency of exact maximum likelihood estimation methods.

3.0 THE MEDLL

A starting point for this algorithm is the work of van Nee [4] on the multipath estimating DLL (MEDLL). The theoretical foundation of the van Nee MEDLL is in a maximum likelihood (ML) based estimation of the channel parameters. Formal application of the ML principle requires that the parameters being estimated are constants. For the multipath channel this assumption is only true for a particular fixed observation interval. Since a recursive solution is the most practical approach to this highly nonlinear, multi-parameter estimation problem, slowly varying channel parameters should not be a problem. Another approach to the estimation problem is that taken by Iltis [2] where a dynamical channel model is assumed, and joint estimation of code delay and multipath channel parameters is obtained using the extended Kalman filter.

Implementation of the ML approach in the presence of WGN reduces to a least-squares problem with cost function of the form

$$J = \int_0^{T_1} |x(t) - \hat{s}(t, \bar{\alpha})|^2 dt \quad (14)$$

where $\hat{s}(t, \bar{\alpha})$ is an estimate of the received multipath signal which is a function of the channel parameters, now grouped into the vector $\bar{\alpha}$. The observation interval T_1 is nominally 1 ms for C/A code tracking. The basic structure of the MEDLL that results from equation (14)

and the conventional DLL is shown in figure 2.0.

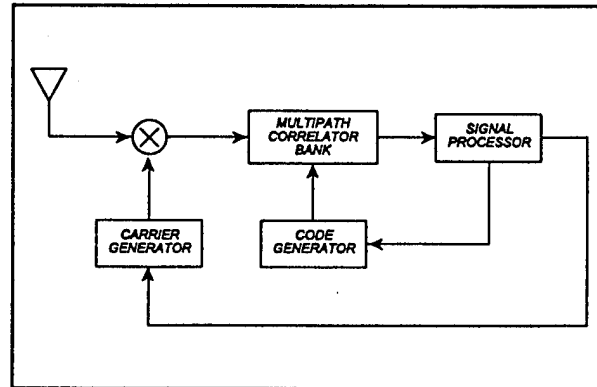


Figure 2.0 MEDLL Block Diagram

A basic operation required in the DLL and an embedded operation in solving (14), is that of code correlation. In a conventional DLL-based GPS receiver, prompt, early, and late correlations of the received signal with the locally generated spreading code are required. In the MEDLL, additional correlations are required to allow estimation of the multipath channel parameters. The multipath spread region of interest is limited to $1.5 T_c$, where T_c is the chip duration. Outside this window multipath components have little influence on the DLL discriminator function (i.e. S-curve).

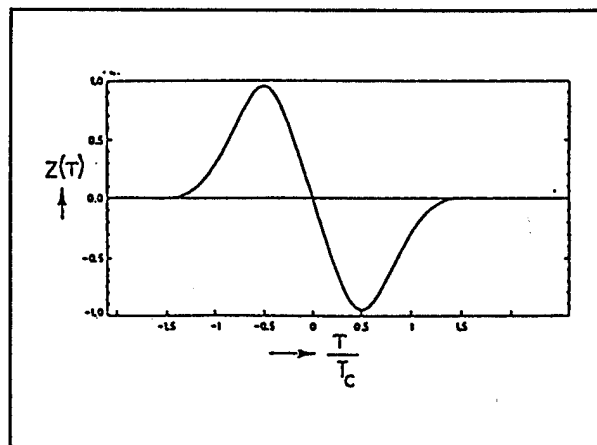


Figure 3.0 Ideal S-Curve of Noncoherent DLL

The S-curve for an ideal situation (no multipath) is shown in figure 3.0. Without multipath there are no reflections and the discriminator output $z(\tau, t)$ has the desired zero crossing solely at τ_0 . Under severe

multipath conditions, the reflection(s) may be 180° out of phase with respect to the direct path signal. This has a dramatic effect on the S-curve, as shown in figure 4.0. The amplitude is greatly reduced and two possible tracking points are present.

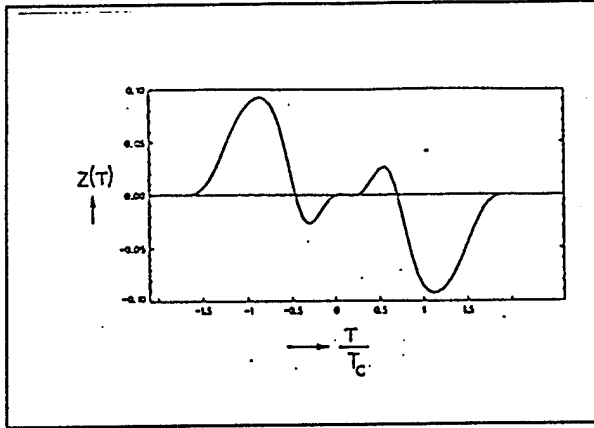


Figure 4.0 Single-Reflection S-Curve

For this research it is proposed that a bank of correlators be effectively placed over the multipath delay spread interval, starting approximately at the location of the line-of-sight delay, as shown in figure 5.0. The correlator spacing will nominally be $\geq T_c/10$. Precise location of the correlator bank in time (code) delay is not required so long as the first 1.5 chips of delay spread is covered.

It can be shown that the minimization of (14) can be reduced k independent (one for each multipath signal present) solution to the following set of equations:

$$\begin{aligned}\hat{\tau}_k &= \max_{\tau_k} [\Re[R_{xk} - \sum_{j \neq k, k=0}^{M_p} a_j R_{kj}]] \\ \hat{a}_k &= \Re[R_{xk} - \sum_{j \neq k, k=0}^{M_p} a_j R_{kj}] \\ \hat{\theta}_k &= \arg(R_{xk} - \sum_{j \neq k, k=0}^{M_p} a_j R_{kj})\end{aligned} \quad (15)$$

where

$$z_{xk} = \int_0^T x(t) p(t - \tau_k) \exp(-j(\omega_{ct} + \hat{\theta}_k)) dt \quad (16)$$

and

$$z_{jk} = \int_0^T p(t - \hat{\tau}_j) p(t - \hat{\tau}_k) \exp(-j(\hat{\theta}_j - \hat{\theta}_k)) dt \quad (17)$$

Essentially, all equations look the same as in the case of a conventional coherent spread-spectrum receiver, where $M = 0$. The only difference is that instead of a simple correlation of the input signal with the local reference code, now the estimated interference correlation functions, due to multipath signals, have to be subtracted. This implies that instead of just estimating the DLOS parameters one simultaneously has to estimate the amplitude and phases associated with all the multipath signals present.

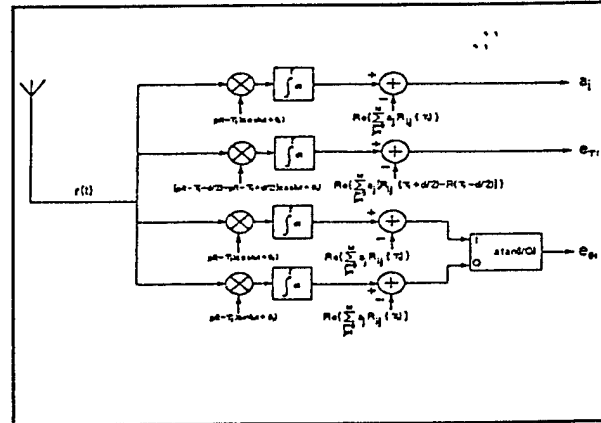


Figure 5.0 Bank of Multipath Correlator Bins

4.0 THE RAIM

There will always be situations in which it will be practically impossible to avoid all multipath reflections. For instance, a strong reflection with a delay $> 1.5\tau_c$ and

destructive phase addition of the reflection with the desired signal can cause the tracking loop to lock onto one of the secondary path signals. If the direct signal is shadowed while the reflection is not, a similar scenario will result. In such situations, it is highly beneficial on a conventional receiver to detect the presence of multipath to warn the user that uncompensatable errors have been detected.

A subsystem that automatically protects GPS receivers from the degrading effects of multipath propagation must have the capability for such autonomous integrity monitoring.

NAVSYS has developed a receiver autonomous integrity monitoring (RAIM) system for the US Coast Guard for use with DGPS. This RAIM system has been extensively researched and tested [11,12,13] and has been shown to reliably flag errors when they occur. The RAIM algorithm makes use of redundant measurements to create a parity or fault vector. Using an innovative application of parity space techniques, any measurement errors are detected, and the system calculates the effect of the error on the navigation airway. The user can set the required integrity levels by specifying the required accuracy, maximum probability of missed detection, and maximum probability of false alarm. Furthermore, if a significant error exists on only one channel, and the other channels are affected only by noise, then the RAIM system not only detects the error, but calculates exactly its effect on the navigation system so the error can be exactly canceled [13]. In tests done by NAVSYS and the USCG, this feature proved very useful in combating multipath caused by the ship's superstructure and affecting only one satellite.

The NAVSYS RAIM uses pseudo range (PR) residuals to compute variance of PR errors. The algorithm will detect biases as they occur, and given enough redundant measurements the detected biases can be removed and a new navigational solution can be recomputed. The algorithm also detects all geometric conditions that might be present when the PR measurements are taken. The algorithm allows the specified navigation accuracy through the settings of: 1) the maximum radial position

error (RPE) allowed, the maximum probability of missed detection (PMD) and maximum probability of false alarm (PFA). A flow diagram of the algorithm is found in figure 6.0. Figure 7.0 shows a general overview of the RAIM for systems using DGPS.

$$z = Hx + n + b \quad (18)$$

The RAIM uses a parity check algorithm with a generalized likelihood test approach for fault detection and isolation (FDI) on a redundant set of PR measurements. The general assumption for this algorithm is that a conventional GPS system will provide a redundant set of N PR measurements, z , which observe the 4×1 state vector, x , through an $N \times 4$ observation matrix, H consisting of the DLOS vectors between the receiver and the satellites being tracked, with the observation corrupted by noise. Parity equations are used to detect biases, b , not induced by random noise in the measurements, since $PH = 0$ we have

$$Pz = P(Hx + n + b) = Pn + Pb = p \quad (19)$$

A detection decision function $DF = p p$ is compared to a threshold set which is controlled by the receiver noise expected, the RPE allowed, the geometry and specified PFA and PMD. Failure isolation can be obtained by selecting the component of the parity vector, p , along the direction of the parity matrix P which is a maximum.

$$DF_j = \frac{(p^T P_j)^2}{P_j^T P_j} \quad (21)$$

If multiple antenna elements are used in the receivers then the RAIM could be used to switch from the antennas once a multipath induced bias is detected. This is discussed in the results section.

5.0 RESULTS

Simulations of the above approaches are based in the following models for the multipath channel. The first

model is a single multipath reflection with a power profile as shown in figure 8.0. The second model is the tap delay model associated with fading channels. In this model the multipath profile is assumed to have a power density that can be written as

$$p(\tau) = \frac{P_0}{md} \exp^{-\tau/md} \quad (21)$$

where P is the total amount of multipath power and md is the mean delay time of the multipath components.

The principal measure of performance considered in this paper was the multipath cancellation achieved by each individual approach. This measure is shown in tables 1.0 and 2.0 for each channel model used.

From this table is easy to see that the amount of cancellation achieved by the large sample MLE approach is superior in the case when multiple reflection signals are present. For the case of a single reflector signal present in one satellite signal the RAIM will outperform all other approaches. It is expected that this will be the case whenever multipath reflections are present in only one or two satellite signals and more than six satellite signals are in view.

For the case of a single reflection in all satellite signals the MEDLL seems to obtain better performance. It achieves the same cancellation than the large sample ML approach but with less computational complexity. In general the issue of performance will be very closely related to computational complexity in any practical implementation of the above algorithms. It seems that in this respect the MEDLL approach will obtain better performance trade off than the large sample ML. But the MEDLL can not by itself deal with the problem of false lock mentioned before. To solve this problem a combination of RAIM with either the large sample ML or MEDLL will be required. Another possible approach is to do more sophisticated acquisition techniques as discussed in [14] where estimates of multipath parameters are taken into consideration.

REFERENCES

- [1] J.G. Proakis, M. Salehi, Communication Systems Engineering, Prentice Hall, 1994.
- [2] Ronald A. Iltis, "Joint Estimation of PN Code Delay and Multipath Using the Extended Kalman Filter," IEEE Trans on Commun, Vol COM-38, Oct 1990.
- [3] R.D.J. van Nee, "Multipath Effects on GPS Code Phase Measurements," ION Sat Div Int'l Tech Mtg, Albuquerque, Sept 1991.
- [4] R.D.J. van Nee, "The Multipath Estimating Delay Lock Loop," ISSTA '92 Conf, Yokohama, Nov-Dec 1992.
- [5] R.D.J. van Nee, "Multipath Effects on GPS Code Phase Measurements," ION Sat Div Int'l Technical Mtg, Albuquerque, Sept 1991.
- [6] A. J. Van Dierendock, P. Fenton, and T. Ford, "Theory and Performance of Narrow Correlator Spacing in GPS Receiver", ION Proceedings, San Diego Jan. 27, 1992.
- [7] J. Li, B. Halder, P. Stoica, M. Viberg, and T. Kailath, "Decouple maximum likelihood Angle estimation for signals with known waveforms," IEEE Transaction on Signal Processing (submitted for publication).
- [8] M. Viberg, P. Stoica, and B. Ottersten, "Maximum Likelihood array processing in Spatially correlated noise fields using parameterized signals," IEEE Trans. On Signal Processing (submitted for publi.)
- [9] R. Roy, A. Paulraj, and T. Kailath, "ESPRIT - a subspace rotation approach to estimation of parameters of cisoids in noise", IEEE trans on Acoustics, Speech And Signal Proc. Vol ASSP-34, Oct 1986.
- [10] GPS Multipath Cancellation and Warning System, NAVSYS Technical Report WP-MP-94100-95-09.
- [11] F. van Diggelen, "Receiver Autonomous Integrity Monitoring Using the NMEA 0183 Message: \$GPGRS," ION Int'l Technical Mtg, Salt Lake City, Sept 1993.

- [12] F. van Diggelen, A. Brown, "Mathematical Aspects of GPS RAIM," IEEE PLANS-94 Sympos, Las Vegas, April 1994.
- [13] "Autonomous Failure Detection for Differential GPS," US Coast Guard SBIR Phase II Final Report, DTRS-57-91-C-0085, NAVSYS Doc #USCG-93-12, April 1993.
- [14] A. Montalvo and A. K. Brown, "ML GPS Receivers for High Dynamic Profiles, Jamming and Multipath Conditions," NAVSYS internal memorandum N95-122.

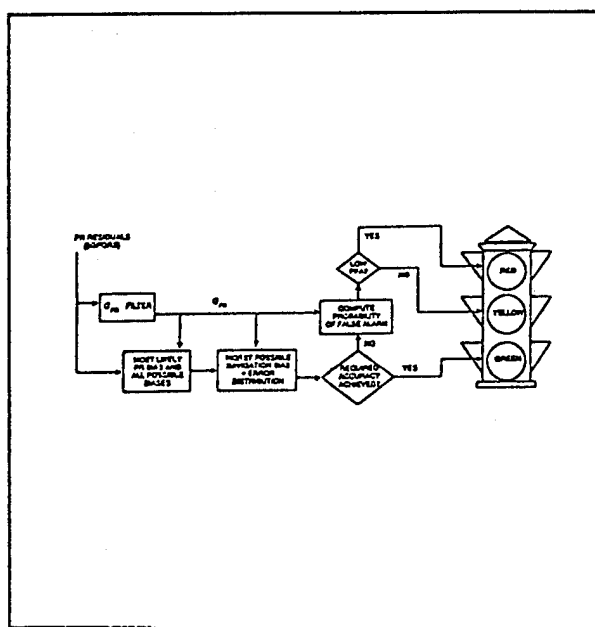


Figure 6.0 RAIM Overview

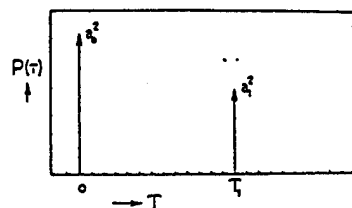


Figure a: Average power-delay profile for one reflector.

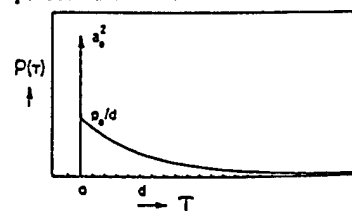


Figure b: Average power-delay profile for many reflectors.

Figure 8.0 Multipath Power Profiles

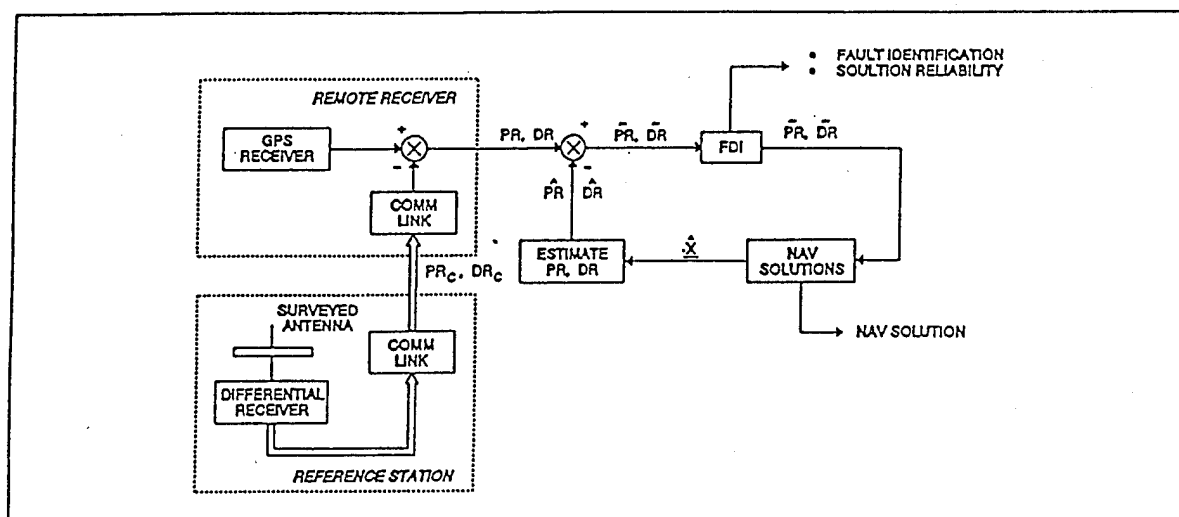


Figure 7.0 Differential GPS System with FDI Capability

Table 1-1 Multipath Cancellation, Inf. = perfect cancellation, M = number of multipath signals, SMR = total DLOS signal power multipath signal power ratio.

Approach	Single channel M=1, SMR =3 dB	M=1 SMR = 5 dB	Multiple Channels M=1, SMR = 3dB	M=1, SMR = 5 dB	Single Channel M = 5 SMR = 0 dB	M = 5 SMR = 3 dB	M = 5 SMR = 5 dB	Multiple Channels M = 5 SMR = 0 dB	M = 5 SMR = 3 dB	M = 5 SMR = 5 dB
LSML	52 dB	60 dB	51.86 dB	59.76 dB	38.72 dB	50.47 dB	58.38 dB	34.26 dB	47.34 dB	54.12 dB
MEDLL	51.6 dB	59.45 dB	51.38 dB	59.24 dB	37.47 dB	49.21 dB	57.12 dB	32.00 dB	45.87 dB	53.89 dB
RAIM	Inf.	Inf.	0	0	Inf.	Inf.	Inf.	0	0	0

Achieving Theoretical Accuracy Limits for Pseudoranging in the Presence of Multipath

Dr. Lawrence Weill
Magellan Systems Corporation
&
California State University at Fullerton

Biography

Dr. Weill received B.S. and M.S. degrees in Electrical Engineering from the California Institute of Technology in 1960 and 1961, respectively. In 1968 he earned a M.S. Degree in Mathematics at San Diego State University, and was awarded the Ph.D. in Mathematics in 1974 at the University of Idaho. He is presently conducting research in applied mathematics as a Professor of Mathematics at California State University, Fullerton, and is a mathematician at Magellan Systems Corporation, specializing in research and development in signal processing and navigation for Magellan GPS Products.

Abstract

In a recent paper by this author [1], it has been shown that modern GPS receiver pseudorange estimation techniques, such as narrow correlator technology, permit pseudoranging accuracy close to the theoretical limit for single-path propagation in the presence of receiver thermal noise. As a result, it is now apparent to receiver designers that in a majority of applications, multipath remains as a dominant source of pseudoranging error.

Although various receiver processing schemes are being developed to combat multipath error, little has been published about the best performance that is theoretically possible when multipath is actually present. The answer to this question would provide the receiver designer with a valuable benchmark. For example, if the performance of a particular pseudoranging algorithm in the presence of multipath were close to a theoretical limit, futile and costly attempts to significantly improve performance could be avoided. On the other hand, if a significant gap exists between algorithm performance and

theoretically optimum performance, the theory often suggests what mathematical signal processing operations would be required to reach the optimal solution.

In this paper, an ultimate limit for pseudorange accuracy in the presence of multipath is developed using results from classical estimation theory. Although the primary focus is on the two-path case encountered in a majority of applications (typified by a direct path and a ground bounce), the theory can be extended to three or more paths. Additionally, the required processing for reaching optimum accuracy is revealed. Subtleties which exist in the case of multipath but not in single-path propagation are also mentioned.

I. BACKGROUND

For many years, the "standard" method of GPS pseudorange measurement has been to correlate the received pseudorandom code with both early and late reference codes having a relative delay of one code chip to form an error signal for a code-tracking loop. Relatively early in the history of this technique it became apparent that large pseudorange errors could occur in the presence of multipath propagation, in which both a direct path signal and a delayed version arrive together at the receiver. Pioneering work by Hagerman [2] revealed that errors as large as 50–100 meters are possible under certain conditions. Recognition of these results spawned a flurry of activity in multipath mitigation techniques that continues today.

Until about 1990, correlation with one-chip code spacing between the early and late reference codes remained an unquestioned *de facto* method of pseudoranging for well over two decades. A

significant breakthrough occurred with the announcement of a substantially more accurate method, commonly referred to as "narrow-correlator technology" [3]. The improvements offered by narrow-correlator technology arise from a wide bandwidth receiver design to sharpen the peak of the code correlation function, combined with the use of early and late reference codes whose relative delay (about 0.1–0.2 chip) is considerably smaller than in previous receiver designs.

The work leading to narrow-correlator designs appeared to be motivated by the quest to reduce measurement errors due to thermal noise rather than those due to multipath. However, it was discovered that substantially better performance was also realized when multipath is present, with typical multipath ranging errors on the order of ten meters. Unfortunately, even this error magnitude is unacceptable in many applications, especially after it is magnified by PDOP. Furthermore, multipath errors are largely systematic (i.e., biases) and therefore are resistant to further reduction by averaging.

This has provided strong motivation to continue research in further reducing multipath errors. Substantial progress has been made in reducing these errors to about the three to four meter level worst-case by signal processing alone [4]. Other methods, including special antenna designs and controlled antenna motions have been developed as well.

II. INTRODUCTION

Philosophy

The work described in this paper results from a problem-solving philosophy which has been proven to be very effective in parameter estimation problems. In the context of multipath error reduction, the central tenet of this philosophy is to apply rigorous apply mathematical estimation theory to achieve pseudorange estimates which are optimal according to a stated criterion. There are several advantages to this approach:

1. A theoretical accuracy limit, which cannot be bettered by *any* processing method, is often obtainable. Such a lower bound is a useful yardstick for evaluating various practical schemes and permits a rational method of setting development goals.
2. A common byproduct is the set of mathematical operations needed to actually reach the theoretical accuracy limit in practice.

3. A much deeper understanding of all aspects of the problem invariably occurs.

The findings presented in subsequent sections will substantiate these claims.

Outline of Paper

In Section III, which follows, a maximum-likelihood (ML-2P) estimator and a minimum-mean-square error (MMSE) estimator of pseudorange are derived for the two-path case. These estimators are compared with the optimal estimator for the single-path case, which is a maximum-likelihood (ML-1P) estimator as described in [1]. Although the ML-1P estimator is optimal in the one-path case, the ML-2P estimator is not optimal in the two-path case. It is then pointed out that the MMSE estimator for the two-path case is optimal according to a meaningful RMS error criterion. The optimality incorporates constraints on the difference of path delays and the amplitude coefficients of the direct-path and delayed-path signals.

A detailed discussion of the results of computer simulations of the ML-1P, ML-2P, and MMSE estimators is presented in Section IV. Implementation of the MMSE estimator is discussed briefly in Section V. A complete summary of results appears in Section VI, and references are listed in Section VII. Section VIII contains the figures referred to in the text.

III. DERIVATION OF PSEUDORANGE ESTIMATORS FOR THE TWO-PATH CASE

Assumptions

The derivations appearing in this section are subject to the following assumptions:

1. Pseudoranging is done with the C/A code only (not with the carrier or P code).
2. Multipath mitigation is to be accomplished only with signal processing in the receiver. No special antennas or spatial processing is used.
3. Only the two-path case is treated for the following reasons: it permits the simplest exposition of optimal multipath processing, it is a dominant scenario because of ground bounce, and once understood, it can be readily generalized to three or more paths.
4. The signal paths are short-term time-stable (on the order of 1 second) with unknown delays and amplitudes.

5. The full bandwidth of the received GPS signal (20 Mhz) is available.

In this section, all integrals with respect to time are over the signal observation interval of length T , and integrals with respect to multipath parameters are taken over all admissible values of the parameters. Expressions involving the summation (Σ) and product (Π) symbols are taken over all samples of the signal in the signal observation interval.

Signal Model

The received GPS signal is modeled by:

$$z(t) = as(t-\tau_1) + bs(t-\tau_2) + n(t) \quad (2-1)$$

where $s(t)$ is the normalized, undelayed GPS signal as transmitted, τ_1 and τ_2 are the respective signal delays of the direct and secondary paths, a and b are the respective received signal amplitudes, and $n(t)$ is zero-mean Gaussian noise having a flat power spectral density N_0 . The structure of $s(t)$ is modeled by:

$$s(t) = c(t)\cos(2\pi ft + \phi) \quad (2-2)$$

where $c(t)$ is the normalized undelayed GPS C/A code waveform as transmitted, f is the L1 carrier frequency (1575.42 Mhz), and ϕ is the carrier phase relative to the code phase.

Except for the effects of bandpass filtering in the transmitter, the values of $c(t)$ swing between -1 and 1 in accordance with the transmitted PN code sequence.

The Likelihood Function for the Multipath Parameters

Since the $s(t)$ has no energy above a certain frequency B , no information is lost if the observed signal $z(t)$ is low-pass filtered with cutoff frequency B . In this case, Shannon's Sampling Theorem states that samples z_i of $z(t)$ taken at time points spaced $1/2B$ apart will contain all information in the signal. Furthermore, the noise components of these samples will be statistically independent. Therefore, the joint probability density function of the samples, given a specific value of the parameter vector $\theta = [\tau_1, \tau_2, a, b]$, is

$$p(z|\theta) = \prod [1/(\sqrt{2\pi}\sigma)] \exp\{-(1/2\sigma^2) \sum [z_i - as_i(\tau_1) - bs_i(\tau_2)]^2\} \quad (2-3)$$

where $\sigma^2 = 2N_0B$, the sample spacing is $1/2B$, and $s_i(\tau_k)$ is the i th sample of $s(t-\tau_k)$.

The summation in the exponent can be replaced with an integral, resulting in:

$$\begin{aligned} p(z|\theta) &= K_1 \exp\{-(1/2N_0) \int [z(t) - as(t-\tau_1) - bs(t-\tau_2)]^2 dt\} \\ &= K_1 \exp\{-(1/2N_0) [\int z^2(t) dt + a^2 R_0 + b^2 R_0 - 2ar_1 - 2br_2 + 2abR]\} \\ &= K_1 K_2 \exp\{-(1/2N_0) [a^2 R_0 + b^2 R_0 - 2ar_1 - 2br_2 + 2abR]\} \end{aligned} \quad (2-4)$$

where $K_1 = \prod [1/(\sqrt{2\pi}\sigma)]$, $K_2 = \exp\{-(1/2N_0) \int z^2(t) dt\}$, $R_0 = \int s^2(t) dt$, $R = \int s(t-\tau_1)s(t-\tau_2) dt$, $r_1 = \int z(t)s(t-\tau_1) dt$, and $r_2 = \int z(t)s(t-\tau_2) dt$. Notice that the argument of the exponential function has no dependence on B . Since $K_1 K_2$ can be determined because, as a probability density, $p(z|\theta)$ must integrate to one, it follows that $p(z|\theta)$ itself has no dependence on B .

Expression (2-4) is called the *likelihood function* for the parameters τ_1 , τ_2 , a , and b . It is regarded as a function of these four variables, with the observed values of the signal $z(t)$ held fixed.

A Sufficient Statistic for the Multipath Parameters

Since the code autocorrelation function $R(\tau_1, \tau_2) = R = \int s(t-\tau_1)s(t-\tau_2) dt$ is a known function of τ_1 and τ_2 , the dependence of $p(z|\theta)$ on the received signal is entirely via r_1 and r_2 . However, these quantities are just evaluations of the cross correlation $\int z(t)s(t-\tau) dt$ at τ_1 and τ_2 . It can be shown that *all* information regarding the true values of the parameters τ_1 , τ_2 , a , and b is contained in this cross-correlation, which is therefore a *sufficient statistic* for the parameters.

The Maximum Likelihood (ML-2P) Estimator For Direct Path Delay

Assuming a two-path model, the *maximum likelihood* (ML-2P) estimate for the direct path delay τ_1 is obtained by maximizing the likelihood function (2-4) over all admissible values of the parameters τ_1 , τ_2 , a , and b and using as the estimate the value of τ_1 at which the maximum occurs. Since the secondary path is always longer than the direct path, the

domain of maximization excludes values where $\tau_1 > \tau_2$.

A Useful Constraint on the ML-2P Estimator

In many two-path situations, it may be safely assumed that the amplitude of the direct path signal is larger than that of the delayed path. In this case, the error in the ML-2P estimator can be significantly reduced by restricting the domain of maximization to that region where $|b| < |a|$. This is in accordance with the estimation-theoretic principle that use of *a priori* knowledge generally results in better estimates. *In the remainder of this paper, it is assumed that this constraint is operative unless specifically stated otherwise, in which case the estimator will be referred to as the unconstrained ML-2P estimator.*

Structural Comparison of the ML-2P Estimator to the Optimal Estimator for the 1-Path Case

It is interesting to compare the ML-2P estimator with the ML estimator derived in [1], which is known to be optimum for the single-path case and is called the ML-1P estimator in this paper. In the ML-1P estimator the likelihood function has the form

$$p(z|\theta) = K_1 K_2 \exp\{-(1/2N_0)[a^2 R_0 - 2ar_1]\} \quad (2-5)$$

where K_1 , K_2 , R_0 , and r_1 are defined as before. Here the maximization would be over the two parameters a and τ_1 , because there is only one propagation path. In this case, however, the location of the maximum with respect to τ_1 does not depend on a , so the ML-1P estimate can be obtained simply by maximizing the cross-correlation r_1 with respect to the single variable τ_1 . This situation does not occur in the case of the multipath model, in which we must maximize over all four parameters, even though we are only interested in an estimate of τ_1 .

The Minimum-Mean-Square Error (MMSE) Estimator

If an *a priori* joint probability density is assumed for all four parameters, another estimator with useful optimality properties can be obtained. The *minimum mean-square-error* (MMSE) estimator for τ_1 minimizes the expected squared τ_1 estimation error, where the expectation is with respect to the joint density of all four parameters. A disadvantage of the MMSE estimator is that, in order to truly achieve the minimum mean-square estimation error, the *a priori* density of the parameters must be known. Although this is seldom the case, it can be shown that the MMSE estimator has another optimality property which does *not* depend on knowing the *a priori*

density; namely, *no other estimator has a uniformly smaller RMS error.*

It is shown in [5, pp. 54-63] that the MMSE estimate for τ_1 is the conditional expectation of τ_1 , given the received signal $z(t)$:

$$E(\tau_1|z) = \int \int \int \tau_1 p(\theta|z) d\theta, \quad (2-6)$$

where $\theta = [\tau_1, \tau_2, a, b]$. Using Bayes' rule, the conditional density $p(\theta|z)$ can be expressed in terms of the known density $p(z|\theta)$ in (2-4), the unconditional density $p(z)$, and the *a priori* parameter vector density $p(\theta)$ to obtain

$$E(\tau_1|z) = [1/p(z)] \int \int \int \tau_1 p(z|\theta) p(\theta) d\theta, \quad (2-7)$$

where

$$p(z) = \int \int \int p(z|\theta) p(\theta) d\theta. \quad (2-8)$$

In this paper, the *a priori* density $p(\theta) = p(\tau_1, \tau_2, a, b)$ is assumed to be uniform. The constraints which are used in the ML-2P estimator can easily be incorporated into the MMSE estimator by simply setting the *a priori* joint density of all four parameters to zero if $|b| \geq |a|$ or $\tau_1 > \tau_2$. *In the remainder of this paper it is assumed that the MMSE estimator uses a uniform density for the parameters which incorporates these constraints.*

IV. DISCUSSION OF RESULTS

An Unbiased Estimator of Direct-Path Range is Undesirable

An estimator of direct-path range τ_1 , which is unbiased (i.e., the expected value of the error is zero), over the full range of path separations in the two-path case has an undesirable property: the standard deviation of the error approaches infinity as the separation of the direct and delayed paths approaches zero. This is readily proved by constructing a 4x4 matrix called the Fisher information matrix. The four diagonal elements of the inverse of this matrix are lower bounds on the variance of any unbiased estimator of the respective four unknown parameters τ_1 , τ_2 , a , and b in the two-path problem. Space does not permit a full discussion of the Fisher information matrix here, but a readable exposition can be found in [5, pp. 79-81].

Figure 1 shows the lower bound on the standard deviation of error in τ_1 (square root of the variance) obtained from the Fisher information matrix as a

function of path separation. Since any unbiased estimator of τ_1 must have an error standard deviation no smaller than the plotted values, we see that even if an unbiased estimator of τ_1 were to exist, its quality would be very poor for small path separations (approximately 0–10 meters). In fact, both the ML-2P and MMSE estimators, which are biased, are significantly superior in this region. It is worth noting that small path separations are a dominant scenario in GPS positioning because they often occur as a result of ground bounce in the vicinity of the GPS antenna.

The standard deviation of a biased estimator is only one component of the estimation error; the other component is the bias. Therefore, root-mean-square (RMS) error is a more meaningful measure of estimation accuracy, because it includes the effects of both standard deviation and bias. *In the remainder of this paper, all errors will be RMS errors.*

Comparison of the ML-2P and MMSE Estimators

Figure 2 shows a performance comparison of the ML-2P and MMSE estimators as a function of path separation $\tau_2 - \tau_1$. The results were obtained by Monte Carlo simulations of both estimators. For the curves shown the direct and secondary path attenuation factors a and b are respectively 1 and 0.5, the direct path C/N_0 is 45 dB-Hz (typical of a moderately strong GPS signal), the signal observation time T is 1 second, and the bandwidth of the signal is 20 MHz (the bandwidth of the signal as actually transmitted from the GPS satellites). The curves above the horizontal axis apply when the carrier phase difference between the two paths is zero (modulo 360) degrees, and those below the axis apply when the phase difference is 180 (modulo 360) degrees. These two cases represent the respective extremes of direct path signal augmentation and partial cancellation depending on the relative phase of the direct and secondary paths.

Also plotted in Figure 2 are curves for the *unconstrained* ML-2P estimator, which gives an idea of how much improvement results from the constraint condition $|b| < |a|$ in the ML-2P and MMSE estimators, as discussed in the previous section.

Figure 2 reveals the following: (1) The MMSE estimator is generally superior to the ML-2P estimator. (2) Accurate estimation of the direct path delay τ_1 is most difficult for small differences between the direct and delayed paths (less than about 20 meters). (3) For larger delay differences, both the ML-2P and MMSE estimators become

unbiased and in fact become minimum-variance unbiased (MVUE) estimators because they reach the Fisher information bound shown in Figure 1. In this case the estimators provide essentially the same performance possible if no multipath were present. (4) For delay differences less than about 20 meters, significantly better performance results when the carrier phase difference between the two paths is an integral multiple of 360 degrees. However, for the larger delays, performance is *independent* of the direct-to-secondary path phase difference.

Because of the superiority of the MMSE estimator, the remaining discussion will focus primarily on this estimator.

Performance of the MMSE Estimator as a Function of SNR

The performance of the MMSE estimator for several values of C/N_0 is shown in Figure 3. Except for the parameterization of C/N_0 , parameter values are the same as in Figure 2.

Note that the RMS error depends linearly on C/N_0 for path separations larger than about 20 meters, but has a nonlinear dependence for smaller separations. In particular, the worst-case errors, which occur at separations below 20 meters, exhibit only about 4–6 dB of variation for a C/N_0 variation of 12 dB.

Performance of the MMSE Estimator as a Function of Secondary Path Amplitude

In Figure 4 the RMS error of the MMSE estimator is plotted with the amplitude of the secondary path as a parameter. The direct path amplitude a is 1, and values of 0, 0.2, 0.5, and 0.8 are used for the amplitude b of the secondary path. As in Figure 2, the direct path C/N_0 is 45 dB-Hz and the signal observation time T is 1 second. For significant secondary path amplitudes and path separations larger than 20 meters, performance is as good as optimal single-path performance. Note, however, that in this case the performance becomes significantly worse as the magnitude of the secondary path amplitude b falls below about 0.2. We are struck with a subtle, not well-known paradox: *When little or no multipath is present ($|b| \cong 0$), the optimal MMSE estimator for two paths will not perform as well as the optimal estimator (ML-1P) designed for one path.*

Comparison of the MMSE and ML-1P Estimators When Two Paths are Present

Figure 5 shows a performance comparison of the MMSE estimator and the optimal single-path estimator (ML-1P estimator) when multipath is

actually present. These curves are an excellent demonstration of the advantage of a MMSE estimator designed for two paths over the use of the ML-1P estimator which is optimal for the single-path case.

Note that for very small path separations (1-2 meters), the ML-1P estimator is actually better than the MSEE estimator, but at a very heavy price. For larger path separations, the ML-1P estimator is *very much* worse. This result is consistent with the fact that no estimator has uniformly smaller RMS error than the MMSE estimator. Attempts to get better results than either estimator alone by selectively using the ML-1P estimator for very small path separations and the MMSE estimator for larger separations are doomed to failure, because it can be proved that it is impossible to determine with sufficient accuracy whether or not the path separation is very small.

V. CONSIDERATIONS IN IMPLEMENTING THE MMSE ESTIMATOR

Implementation of the MMSE estimator imposes a much larger computational load than that required for receivers whose design is based on the assumption of a single-path. As can be seen from expressions (2-7) and (2-8), two 4-fold numerical integrations are required for each estimate of τ_1 , which nominally would occur once per second. However, during the author's development of the simulations for the MMSE estimator, several computational simplifications have been discovered which suggest that the computational load can easily be handled by any of several currently available low-cost microprocessors. Details are beyond the scope of this paper, but additional work is planned to develop an actual hardware design to prove this assertion.

VI. SUMMARY OF RESULTS

In Reference [1] it is shown that a minimum-variance unbiased (MVUE) estimator for pseudorange exists for the single-path case and is, in fact, the one-path maximum-likelihood (ML-1P) estimator. In a code-tracking loop architecture the ML-1P estimator can be implemented by correlating the received code with the *derivative* of a locally generated replica of the received code (including the effects of bandlimiting). While not widely recognized, narrow-correlator designs approximate this derivative with a differential code obtained by subtracting ideal (i.e.) non-bandlimited) early and late reference codes. To the extent that this approximation matches the true

derivative, the performance of a narrow-correlator design will approach the theoretical limit for pseudorange accuracy when multipath is not present. Work by this author suggests that an additional 30% reduction in single-path error variance should be possible if the true derivative of the locally generated code replica were used for correlation.

When multipath is present however, the character of the pseudorange estimation problem changes dramatically:

1. It is not known whether an unbiased estimator of pseudorange exists if multipath is present. It can be shown, however, that if such an estimator exists, the standard deviation of its error approaches infinity as the delay difference between the direct and secondary paths approaches zero. Such poor performance of an unbiased estimator suggests that better estimators might exist that are biased. This turns out to be true. However, the performance of biased estimators is better measured by root-mean-square (RMS) error rather than by standard deviation, which is typically used for unbiased estimators.
2. A reasonable approach to estimating the direct path delay when multipath is present is to use a maximum likelihood estimator based on a multipath model. For the two-path case assumed in this paper, this estimator is called the ML-2P estimator.
3. In the single-path case, the ML-1P estimator requires a maximization with respect to only one parameter — the direct path range — and the maximization algorithm does not have to take into account the received signal amplitude. On the other hand, the ML-2P estimator for the two-path problem involves a maximization over all four parameters mentioned above, even though only the direct path range is of interest.
4. For the two-path case, there are better estimators than the ML-2P estimator! Specifically, an estimator called the minimum-mean-square-error (MMSE) estimator has the following optimality property: *No estimator can have a uniformly smaller RMS error.* The MMSE estimator requires the assumption of an *a priori* probability density function on four unknown parameters: the direct path range,

the secondary path range, and the amplitudes of the signals propagating along each path. Even though this *a priori* density is seldom known, the optimality property mentioned above is retained if a uniform joint density for the four parameters is assumed. Therefore, *the MMSE estimator is generally superior to the ML-2P estimator.*

5. For best performance of either the MMSE or ML-2P estimators, the constraint $|b| < |a|$ should always be used if it is known that the secondary path has greater attenuation than the direct path.
6. Processor loading is a challenge in implementing the MMSE estimator, but appears to be solvable.
7. Although neither the ML-2P nor the MMSE estimator is unbiased over the full range of direct-to-secondary path separation, each becomes a MVUE when the direct and secondary paths are separated by more than about 20 meters and significant secondary path amplitude exists. In this case both estimators behave identically and are as good as the ML-1P estimator when no multipath is present; they actually achieve the theoretical accuracy limit for unbiased estimators. Thus, *the most difficult situation for multipath mitigation occurs at path separations less than about 20 meters.*
8. Regardless of what estimation algorithm is used or whether multipath is present, it can be shown that a *sufficient statistic* for the direct path range is the cross-correlation function of the received signal with a code replica that has been filtered in exactly the same way as the received code. In the single-path case, all information resides in the region near the peak of the cross-correlation function, but when multipath is present the information needed for an optimal estimate of direct path delay is distributed throughout the function.
9. The multipath problem presents subtleties that are not widely recognized, some bordering on the paradoxical. For example, when little or no multipath is present, the ML-1P estimator, designed for the single-path case, actually performs better than the MMSE estimator designed for the two-path case. Another example occurs when significant multipath is

present, but with very small path separation (several meters or less). In this case, the ML-1P estimator is again better than the MMSE estimator. This appears to contradict the claim that the MMSE is optimal in the presence of multipath. However, at larger path separations, the MMSE estimator is *far* better, consistent with the fact that no estimator has *uniformly* smaller RMS error than the MMSE estimator.

10. Both the ML-2P and MMSE estimators for the two-path case can readily be generalized to a greater number of paths.
11. Although the effect of receiver bandwidth is not presented here, it can be shown that optimum performance requires the full bandwidth of the GPS signal as transmitted (20 MHz).

The Bottom Line: *Meter-level, and often submeter-level, C/A code pseudorange accuracy can be achieved at typical GPS signal-to-noise ratios by the MMSE estimator when two-path multipath is present. Further improvements are possible by increasing the signal observation time above 1 second.*

VI. REFERENCES

1. Weill, L. R.; "C/A Code Pseudorange: How Good Can It Get?", *Proceedings of the ION GPS-94 7th International Technical Meeting*, Salt Lake City, Utah, September 1994.
2. Hagerman, L.; "Effects of Multipath on Coherent and Noncoherent PRN Ranging Receiver", Aerospace Report No. TOR-0073(3020-03)-3, Development Planning Division, The Aerospace Corporation, May 15, 1973.
3. Van Dierendonck, A. J., Fenton, P., and Ford, T.; "Theory and Performance of Narrow Correlator Spacing in a GPS Receiver," *Journal of the Institute of Navigation*, USA, Vol. 39, Fall 1993, pp. 265-283.
4. Townsend, B., van Nee, D.J., Fenton, P., and Van Dierendonck, K.; "Performance Evaluation of the Multipath Estimating Delay Lock Loop," *Proceedings of the ION GPS-94 7th International Technical Meeting*, Salt Lake City, Utah, September 1994.
5. Van Trees; H. L., *Detection, Estimation, and Modulation Theory*, Part I, John Wiley and Sons, New York, 1968.

VII. FIGURES

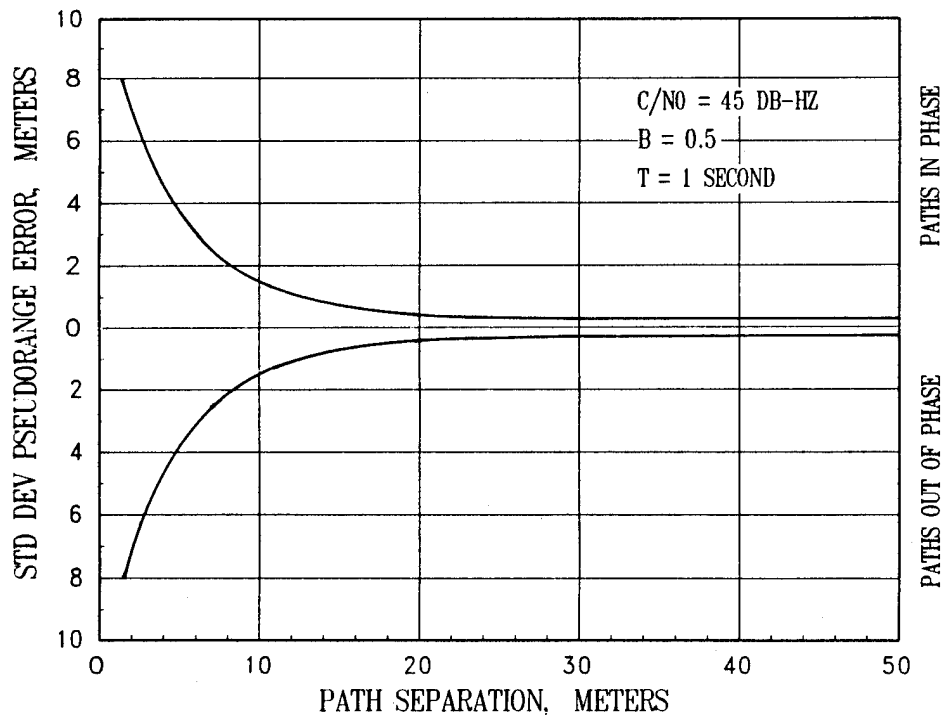


Figure 1. Two- Path Fisher Information Bound for Unbiased Estimator of τ_1

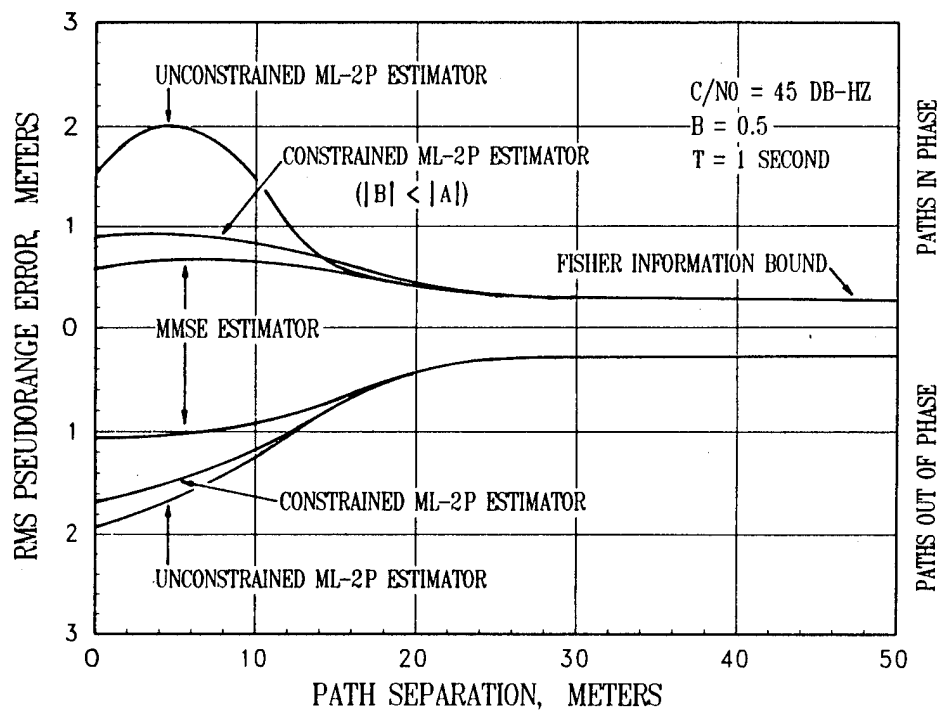


Figure 2. Performance Comparison of Three Estimators

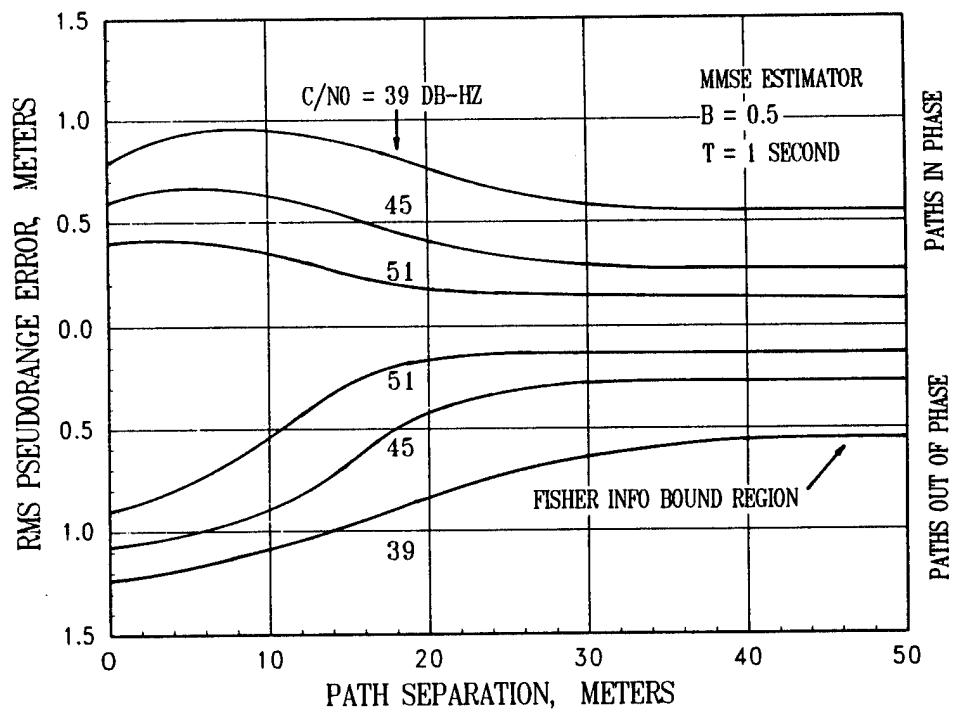


Figure 3. MMSE Estimator Performance Parameterized by Signal-to-Noise Ratio

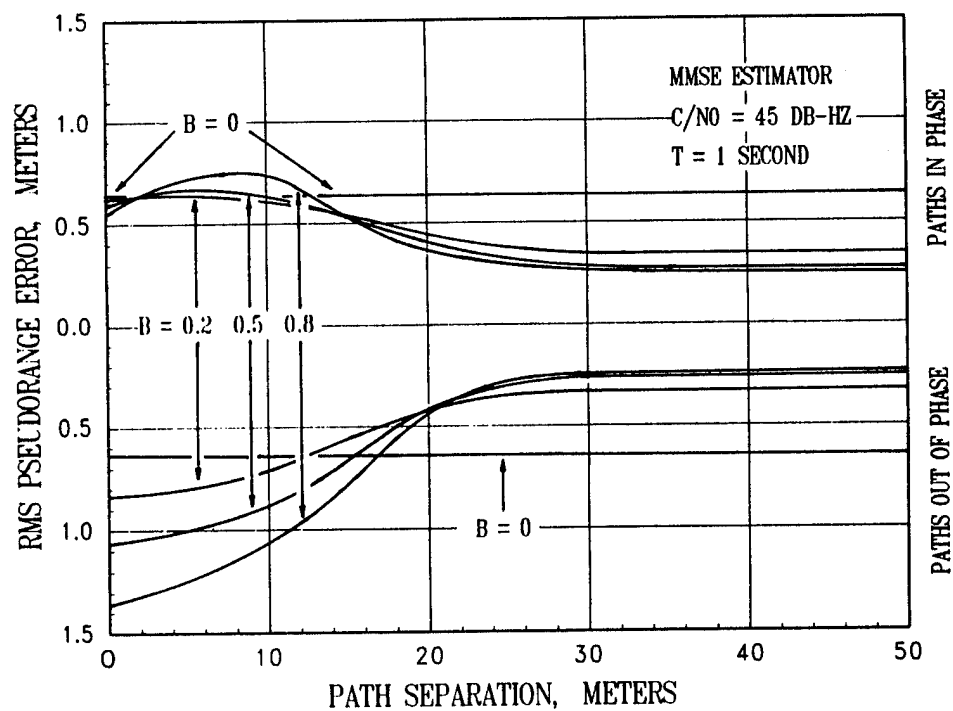


Figure 4. MMSE Estimator Performance Parameterized by Second Path Amplitude

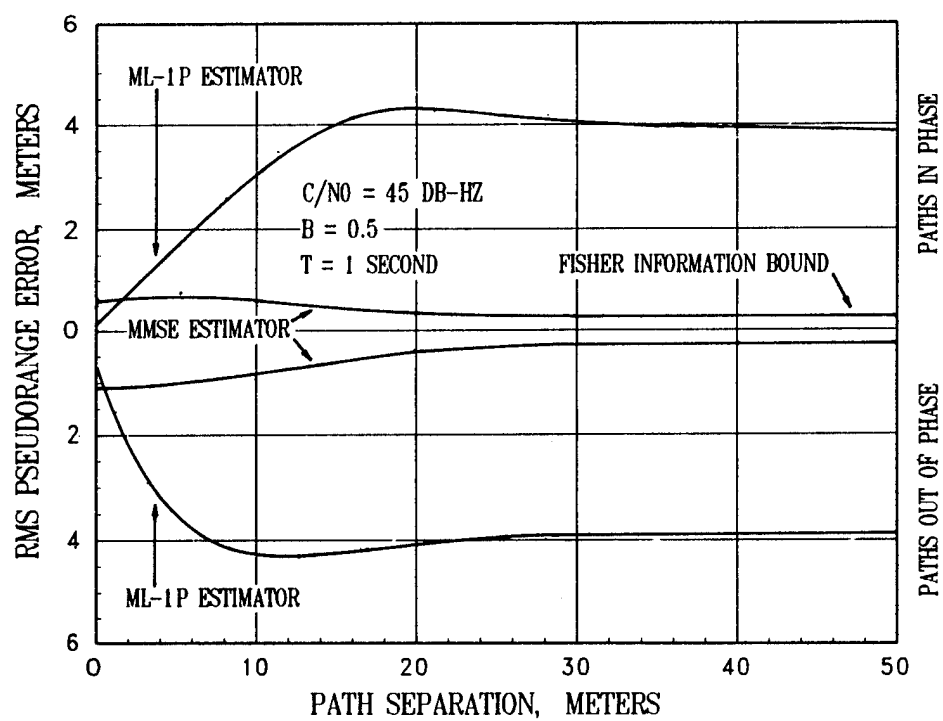


Figure 5. Comparison of MMSE and 1-Path ML Estimators With Two Paths Present

Comparison of Continuity and Integrity Characteristics for Integrated and Decoupled Demodulation/Navigation Receivers

Dr. Jim Sennott and Dave Senffner
Bradley University

BIOGRAPHY

Jim Sennott is Professor of Electrical and Computer Engineering at Bradley University. He received a BSEE from the U. of Delaware, and the MSEE and Ph.D. from Carnegie Mellon University. His areas of interest are optimal estimation, multiple access communications and image processing, as applied to tracking and imaging systems.

Dave Senffner is Instructor of Electrical and Computer Engineering at Bradley University. He received his BSEE and MSEE from Bradley University. His areas of interest are GPS navigation, and electronics.

Abstract

Signal fault events such as momentary blockages on low elevation satellites could jeopardize the continuity and integrity of GPS guidance. Classical receivers are especially vulnerable given their isolated error detectors and loop filters for each channel. By contrast, an integrated receiver's correlator data on all satellites is optimally tested and combined leading to a substantial suppression of cycle slippages during signal faults. The trade between continuity and integrity becomes more favorable with additional satellites/pseudolites. Proving this assertion required the integrated receiver's tracking performance be verified with differing signal geometries since, analogous to RAIM, performance is geometry dependent.

The classical decoupled receiver structure is contrasted with the integrated approach for a variety of geometries and signal faults. A signal fault continuity (SFC) definition is established encompassing accuracy and vertical protection limit (VPL) values to be satisfied during and immediately after signal fault events. Each satellite constellation is scanned to identify times of greatest vulnerability. In blockage testing geometries for which a sequential blockage on the two lowest

elevation satellites could lead to SFC loss are identified. In spoofing tests the disrupted satellite was selected on the basis of VPL maximization.

In both blockage and spoofing tests the conventional receiver consistently loses continuity, whereas a high fraction of the time the integrated design provides seamless tracking, even with the difficult geometries. The impact of faults introduced at random times throughout the day is also ascertained, with substantial improvement for the integrated technique.

Introduction

Differential GPS has scored impressive successes in demonstrations of category III aircraft approach and landing [1-3]. However, signal fault events such as momentary signal blockages could jeopardize the continuity and integrity needed for this stringent landing category. Indeed, instances of momentary losses of low elevation satellites on final approach have been reported [4, 5], suggesting that as more experience is gained with these systems additional safeguards may be desired. Some researchers have suggested inertial reference combining or aiding to offset the impact of reception events on continuity and integrity [6]. A less expensive alternative appears to be improved integration of receiver signal tracking and navigation elements.

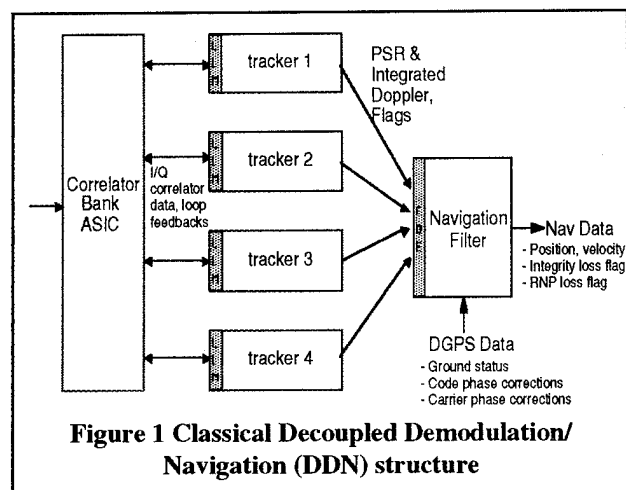
Classical GPS receivers recover their carrier phase and pseudorange parameters from independent satellite tracking channels, with raw correlator data processed in separate error detectors. By contrast, in integrated receivers

correlator data from all satellites is jointly monitored and combined [7-9]. A more complete statistical model as well as high quality differential corrections at an earlier point in the receiver permits rapid response to signal quality conditions, and seamless tracking across faults. With cycle slippages to some degree suppressed during signal fault events, the trade between continuity and integrity becomes more favorable. Unlike the classical structure, as additional satellites/pseudolites become visible the signal tracking performance improves on all satellites .

In order to better understand and evaluate receiver performance in the precision approach regime we first establish a signal fault continuity (SFC) criteria. Following this signal blockage scenarios are developed, and the two architectures are evaluated for periods of poor geometry with low elevation blockages and spoofing. The performance of the two processors is ascertained by a full tracking simulation, including tracking non-linearities. The paper concludes with an analysis of continuity for faults appearing at random times throughout the day.

Performance Criteria

In establishing a useful notion of continuity for short-duration signal fault events the classical DDN GPS avionics structured shown in **Figure 1** was examined. The individual tracking loops responsible for each satellite are protected by local lock monitors (LLM's) where the onset of carrier mistracking is detected by comparing local residuals against a break-lock threshold. These detections are conveyed to the central navigation filter where defective carrier or carrier smoothed code data is blocked prior to navigation. The LLM's are limited in their effectiveness since external data such as differential corrections, navigation state variables and satellite geometry are ignored in their decision making processes. Consequently a second line of defense is needed, the central fault detection and exclusion (FDE) algorithm. While the LLM can respond to signal reception events



such as blockage, attenuation and the like, it is the job of FDE to backstop these decisions, and to detect other errors unrelated to signal blockage and spoofing, such as spacecraft or DGPS ground segment problems. Given an internal alarm condition from either or both LLM and FDE elements the avionics must decide whether a continuation of the approach is warranted. The avionics will primarily consider two factors:

- With the faulty tracking channel excluded is the estimated vertical navigation system error (NSE) be tolerable, and
- With the faulty tracking channel excluded is the computed vertical protection limit (VPL) still adequate.

The receiver's decision is very dependent on available geometry and the required NSE and VPL system specifications. In many circumstances the affected satellite may simply be excluded for the remainder of the final approach, with predicted NSE and VPL values sufficient to meet all landing safety requirements. As will be shown however there are a substantial number of geometries where a signal mistracking detection and channel exclusion event results in a loss of NSE or VPL. Such a circumstance is shown generically in **Figure 2**. Following a reception event and detection/exclusion, estimated NSE and VPL

degrade. While perhaps tolerable for the short period of signal fluctuation the loss of NSE or VPL may persist for an unacceptably long period needed for reliable recovery and repair of the affected channel. Recovery following the event is not instantaneous, and during this interval system continuity is lost. Certainly one solution is to supplement the GPS avionics with IMU inputs, at a cost and complexity unacceptable to many users [6]. Another alternative is to suppress cycle slippage and mistracking for the duration of the signal fault event, thereby reducing the tracking loop recovery and repair time to zero. As one would anticipate the ability to accomplish this seamless tracking depends very much upon the satellite geometry available at the onset of the signal fault event.

The alternative structure is shown in **Figure 3**. The major difference from **Figure 1** is a single central processor for evaluation, weighting and processing of raw I and Q outputs from all

available satellites. This approach has been studied previously [7-9]. The weighting of raw data is varied rapidly in proportion to estimated signal strength and quality. With a full system state model involved in raw data evaluation, phase detection and correlator control, the structure offers a better chance of early fault detection and exclusion of faulty data, without tracking disruption. The internal covariance model carried forward is very useful in predicting performance. However its validity in the difficult reception conditions warrants a full non-linear tracking simulation and/or hardware bench test. In this paper the simulation technique, **Figure 4**, incorporates an analytical model for the correlator bank followed by operational receiver software. Signal fault events of various types are accurately introduced, including blockage, spoofing, and narrow and wide-band interference. We now turn to a comparison of receiver structures.

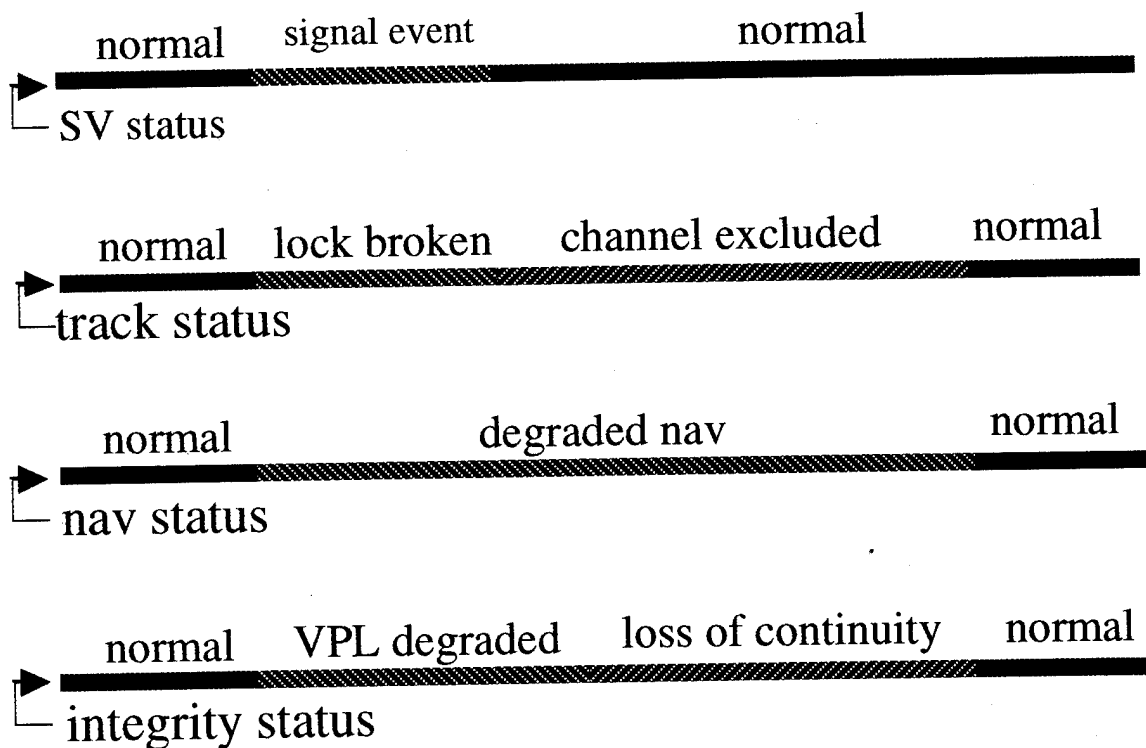
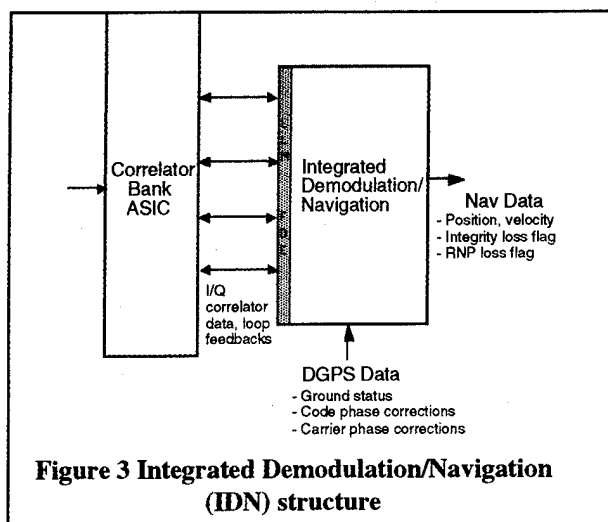


Figure 2 Typical Loss of Continuity Failure Mode

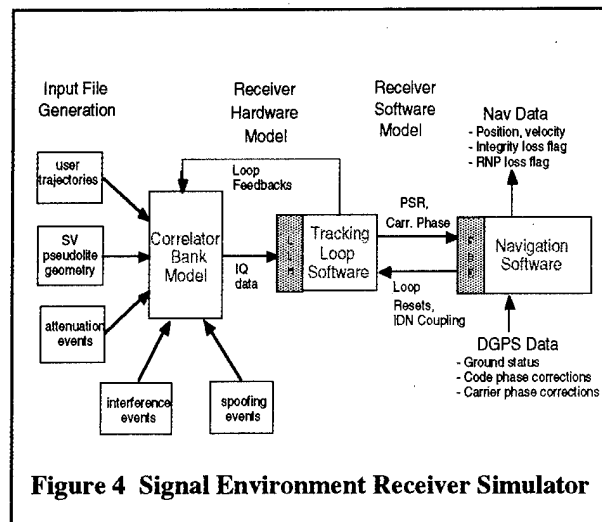


Blockage Tests

While the frequency of occurrence of short attenuation events on final approach due to vehicle blockage or other events has as yet to be carefully studied, it seems that low elevation satellites are most likely to be affected.

Therefore a basic outage scenario consisting of attenuations on the lowest two satellites was introduced. Starting with a converged carrier phase navigation solution good to 0.1 meters, the first satellite was attenuated by 20 dB for a duration of two seconds. Following signal amplitude recovery the second satellite was attenuated by the same duration, followed by recovery. In both cases the amplitude fluctuation rate was 100 dB/sec, demanding responsive amplitude estimation and gain adaptation.

In order to further challenge the receivers a geometry screening was carried out in order to ascertain "poor" geometries, those for which mistracking on both attenuated satellites would result in a VPL value greater than 0.5 meters, 95 percentile. The fault detection false alarm rate was 10^{-5} . VPL computations were carried out using well established techniques [10,11]. Under these difficult reception condition many candidate "poor" geometries were identified for simulation. Those geometries not so identified would not have resulted in excessive VPL, and loss in SFC continuity, unless false alarms occurred in either the LLM or FDE stages of the



receiver. In the present tests these false alarm induced continuity losses were dominated by true outage events and were thus ignored. Three different constellation scenarios were screened: the existing 25 satellite constellation, at 15 and 7.5 degree mask angles, and the 25 satellite constellation at a 7.5 degree mask angle with four satellites removed.

Simulation runs and results were then grouped by number of satellites tracked prior to the signal fault introduction. During receiver simulations continuity was declared lost under the SFC definition if vertical NSE was greater than 0.3 meters following the reception event. The ability to maintain SFC continuity was tabulated for all three constellation assumptions, and averaged to determine overall the continuity versus number of available satellites prior to the reception event. The results are shown in **Figure 5**. It should be noted that in all cases the

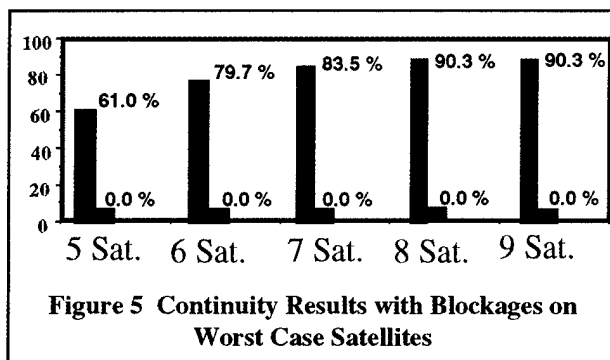


Table 1 Blockage Continuity Results, Averaged over All Sample Times

25 SV 7.5 deg. elev.	IDN	99.7 %
	DDN	98.7 %
25 SV 15 deg. elev.	IDN	92.5 %
	DDN	77.6 %
21 SV 7.5 deg. elev.	IDN	99.1 %
	DDN	93.5 %

DDN structure failed, its success rate with screened geometries being zero. The most common failure mode being a mistracking on both satellites and a subsequent loss after channel exclusion of the 0.5 meter protection limit. By contrast the IDN structure suppressed signal mistracking in many cases, providing continuous service throughout the severe double blockage 79 percent of the time given six satellites. Even with just five satellites prior an event, when any outage immediately results in unbounded VPL and continuity loss, service is continued 62 percent of the time.

In those situations in which IDN fails to suppress mistracking there is a potential for integrity loss. However these false dismissals are protected in two ways. First, the snapshot fault detection available at the start of the event is used upon amplitude recovery at event conclusion to verify whether the fault suppression was successful. Secondly, and more significantly, the central phase error covariance model maintained by IDN reflects the entire signal amplitude history.

Finally, the overall results for each of the three constellations for both good and bad geometries, sampled over 24 hours at five minute intervals, is shown in **Table 1**. Instead of worst case values, these can be interpreted as probabilities of maintaining continuity with the introduction of a signal fault at some random time of day. Perhaps most dramatic in comparing the two receivers is a continuity improvement from 78 percent to 92 percent, for the 25 satellite geometry at a 15 degree mask, and from 93 to 99 percent for the 21 satellite geometry at 7.5 degree mask.

Spoofing Tests

Spoofing presents a somewhat different challenge to the signal processor. By definition the spoofer is able to generate a GPS look alike signal on one or more satellites. With the exception of an extremely sophisticated spoofer able to generate just the right Doppler-delay offset needed to convince the avionics of a valid position, spoofing is easily detectable and excluded. However, this still poses difficulties for continuity. First, the receiver must properly identify the channel damaged by the spoofer. This may require sufficient geometry to support both fault detection and exclusion in the central processor, since the LLM by may fail if the loop is captured. Secondly, assuming the bad channel to be identified, the remaining satellites may be insufficient to support either the accuracy or VPL conditions needed for SFC.

The spoofer in our simulations was tuned to appear in the central delay-Doppler cell of the correlator bank for a two second period, its maximum amplitude equal to the true signal amplitude. Prior to carrying out simulations three constellations were screened. At each time sample point the visible satellites were scanned to find the one which, when removed from the constellation, led to the worst vertical protection limit (VPL). As previously all faulted geometries with a VPL greater than 0.5 meters were flagged for full receiver simulation. Thus, for the selected geometries, once signal mistracking takes place continuity is lost.

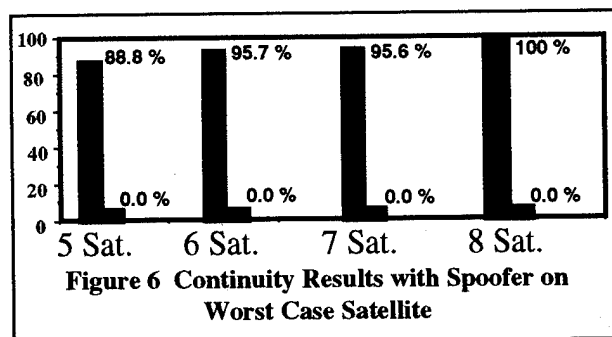


Figure 6 summarizes continuity for the selected "poor" spoofing geometries. In all cases the DDN structure fails to provide continuity. The

IDN however is able to detect and suppress the effects of the spoofer, with full VPL and accuracy recovery upon termination of the spoofing event. With five satellite geometries the success rate is at 89 percent, rising to 96 percent with six satellites.

As for blockage the continuity statistics associated with introduction of a spoofer at a random time of day are also of interest, **Table 2**.

Table 2 Spoofing Continuity Results, Averaged over All Sample Times		
25 SV 7.5 deg. elev.	IDN	99.96 %
	DDN	99.69 %
25 SV 15 deg. elev.	IDN	99.29 %
	DDN	93.73 %
21 SV 7.5 deg. elev.	IDN	99.93 %
	DDN	98.71 %

The most dramatic effects are seen with the 25 satellite constellation, at 15 degree mask, with the SFC increasing from 93.7 to 99.3 percent in switching from DDN to IDN processors. Note that in making this comparison we've made the optimistic assumption in favor of DDN that the LLM and central FDI are sufficient for exclusion of the spoofed satellite. Strictly speaking this may require that DDN have available the stronger geometry needed for fault exclusion, thus further degrading average performance.

Conclusion

As more experience is gained in Cat III approaches under a variety of aircraft and airport environmental conditions, robust techniques for signal tracking may be required. An attractive approach, with respect to both performance and cost, is full integration of the receiver's demodulation and navigation functions. This IDN technology appears to be especially effective in scenarios with rapid signal blockages and spoofing, allowing for near seamless tracking with difficult geometries. Preliminary results also indicate some jamming margin improvement. In summary, the GPS

constellation offers us a great deal of strength in overcoming signal faults without loss of continuity, provided we apply wisely all available information in the signal tracking process.

References

- [1] Wullschleger, V., Swider, R., and Braff, R., Status of FAA Feasibility Investigation of Code-Based DGPS for Category III Precision Approach, ION GPS-95, Palm Springs CA, Sept. 1995.
- [2] van Graas, F., Wullschleger, V., Kuehl, G. FAA/Ohio University/United Parcel Service DGPS Autoland Test Demonstrations, ION GPS-95, Palm Springs CA, Sept. 1995.
- [3] Romrell, G., Brown, R., Johnson, G., et. al., FAA/FEDSIM E-Systems Category IIIB Feasibility Demo Flight Test Preliminary Results, ION GPS-95, Palm Springs CA, Sept. 1995.
- [4] The Card Project: GNSS Landing Trials at Norrkoping/Kungsangen Airport, Luftfartsverket Swedish Civil Aviation Administration Report, June 1994.
- [5] Aebersold, R., Lipp, A., Speckels, J. et. al., Switzerland's Precision Landing Trials, GPS World July 1995, pp. 44-52.
- [6] Meyer-Hilberg, J., Harder, R., Application of INS/GPS System Integration to Increase Performance of Automatic Landing Systems, ION GPS-95, Palm Springs CA, Sept. 1995.
- [7] Sennott, J.W., Senffner, D. "The Use of Satellite Geometry for Prevention of Cycle Slips in a GPS Signal Processor", Journal Institute of Navigation, Vol 39 No. 2, Summer 1992.
- [8] Sennott, J.W., Senffner, D. "A DGPS Signal Processor with Improved Blockage and

Multipath Properties", Proceedings ION GPS-93, Salt Lake City, Utah, September 1993

[9] Sennott, J.W., Senffner, D., "Navigation Receiver with Coupled Signal-Tracking Channels", U.S. Patent 5,343,209, August 1994.

[10] Brown, R., A Baseline GPS RAIM Scheme and a Note on the Equivalence of Three RAIM Methods, *Navigation*, J. of the Inst. of Navigation, Vol. 39, No. 3, Fall 1992, pp. 301-316.

[11] Minimum Operational Performance Standards (MOPS) for GPS/WAAS, Appendices E and K, final draft, July 1995.

L1 Carrier Phase Multipath Error Reduction Using MEDLL Technology

Bryan Townsend, Patrick Fenton, and Keith Van Dierendonck
NovAtel Communications

Richard van Nee
Consultant

BIOGRAPHY

Bryan Townsend received his B.Sc. in 1989 and M.Sc. in 1993 from Geomatics Engineering at The University of Calgary. He is currently doing research in the area of receiver based multipath mitigation techniques at NovAtel Communications Ltd.

Pat Fenton received his B.Sc. in Surveying Engineering from the University of Calgary in 1981. He is currently the Director of Research and Development for the GPS Products Group at NovAtel Communications Ltd.

Keith Van Dierendonck received his B.A. in Mathematics at the University of California, Santa Cruz and is completing his M.Sc. in Geomatics Engineering at the University of Calgary. He is currently Software Test Engineer for the GPS Products Group at NovAtel Communications Ltd.

Richard D.J. van Nee was born in Schoonoord, the Netherlands. He received an M.Sc. in Electrical Engineering Cum Laude from Twente University in Enschede, The Netherlands in 1990. In May 1995, he received his Ph.D. Cum Laude from the Technical University at Delft, The Netherlands. His Ph.D. thesis is on multipath problems in navigation and communication receivers.

ABSTRACT

In single frequency (L1) GPS receivers, multipath is the dominant error source in differential carrier phase and pseudorange measurements. Consequently, it is the dominant error effecting DGPS positioning accuracy.

The Multipath Estimating Delay Lock Loop (MEDLL) is a method for mitigating the effects due to multipath within the receiver tracking loops. The MEDLL does this by separating the incoming signal into its line-of-sight and multipath components. Using the line-of-sight component, the unbiased measurements of code and carrier phase can be made.

In previous papers, the authors have demonstrated MEDLL performance in mitigating the effects of multipath on C/A code pseudorange measurements. Also, they have shown that it is possible to use the MEDLL derived parameters to calculate a multipath error correction for the carrier phase measurements. This carrier phase multipath correction has now been implemented in NovAtel's MEDLL receiver.

Using a GPS signal simulator, the carrier phase performance of the MEDLL receiver for a single multipath and a multiple multipath case was compared to a standard phase lock loop. The results showed the MEDLL receiver was able to substantially reduce the carrier phase multipath errors as compared to a standard NovAtel receiver.

INTRODUCTION

GPS pseudorange and carrier phase measurements suffer from a variety of systematic biases. The satellite orbit, satellite timing, ionospheric, and tropospheric errors are usually handled through DGPS techniques. The measurement bias caused by signal multipath acts differently. Unlike the other error sources, multipath is normally not correlated between antenna locations. Hence, because the base and remote receivers experience different multipath conditions the DGPS techniques are often ineffective and, as a result, multipath is the dominant error source.

The Multipath Estimating Delay Lock Loop (MEDLL) is a method for mitigating the effects due to multipath within the receiver tracking loops. The MEDLL does this by separating the incoming signal into its line-of-sight and multipath components. Using the line-of-sight component, the unbiased measurements of code and carrier phase can be made.

In previous papers, the authors have demonstrated MEDLL performance in mitigating the effects of multipath on C/A code pseudorange measurements.

Also, they have shown that it is possible to use the MEDLL derived parameters to calculate a multipath error correction for the carrier phase measurements. This carrier phase multipath correction has been implemented in NovAtel's MEDLL receiver and the focus of this paper will be evaluating the carrier tracking performance of this receiver.

MULTIPATH CHARACTERISTICS

The term multipath is derived from the fact that a signal transmitted from a GPS satellite can follow a 'multiple' number of propagation 'paths' to the receiving antenna. This is possible because the signal can be reflected back to the antenna off surrounding objects, including the earth's surface. Figure 1 illustrates this phenomena for one reflected signal.

Since GPS is a ranging system, it is desirable to perform measurements on the direct path signal only. The presence of multipath signals corrupts this process because a standard receiver can not distinguish between the signals and tries to correlate with all signals that are present.

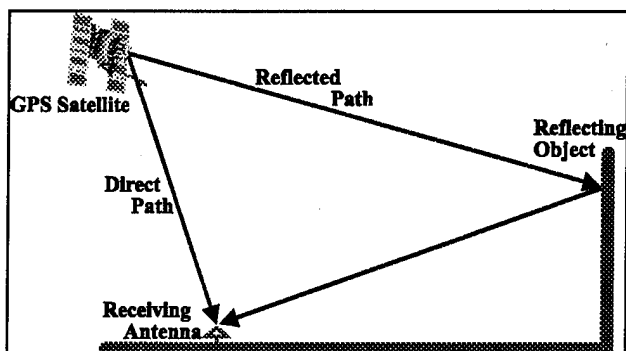


Figure 1: The Direct Path and One Reflected Path (Multipath) Signals

Some important characteristics of multipath are as follows [Townsend and Fenton, 1994]:

- i) The multipath signal will always arrive after the direct path signal because it must travel a longer propagation path.
- ii) The multipath signal will normally be weaker than the direct path signal since some signal power will be lost from the reflection. It can be stronger if the direct path signal is hindered in some way.
- iii) If the delay of the multipath is less than two PRN code chip lengths, the internally generated receiver signal will partially correlate with it. If

the delay is greater than 2 chips, the pseudo-random (PRN) codes are designed so that correlation power will be negligible.

This paper deals with the normal case that the direct path signal is present and is stronger than the multipath signals.

THE EFFECT OF MULTIPATH ON A STANDARD GPS RECEIVER

A standard GPS receiver uses a dot-product or early minus late delay-lock-loop (DLL). This is illustrated in Figure 2. Since a normal DLL is designed to feedback to the hardware in such a way to keep the power at the early and late correlators equal, a correlation function distorted by multipath, biases this process.

The phase tracking is affected in a similar fashion. The phase-lock-loop (PLL) is driven from the punctual correlator. The phase of the composite signal is rarely the same as the direct path signal and therefore a tracking error is introduced.

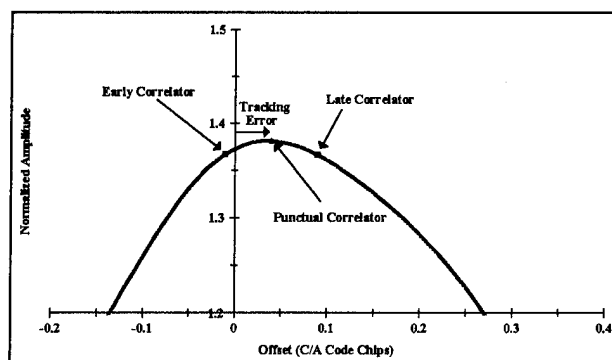


Figure 2: Early-Late DLL Tracking Error Due to Multipath

THE GPS SIGNAL CORRELATION FUNCTION

The received signal at the input of a direct-sequence spread-spectrum receiver can be written as:

$$r(t) = \sum_{m=0}^{M-1} a_m p(t - \tau_m) \cos(\omega t + \theta_m) + n(t) \quad (1)$$

where,

M = number of signals.
t = time.

$p(t)$ = the spread-spectrum code
 $n(t)$ = white Gaussian noise.
 a_m = component signal amplitude.
 τ_m = component signal delay.
 θ_m = component signal phase.

As can be see from this mathematical representation of the GPS signal, the resulting signal correlation function $r(t)$ is really just the linear sum of all signals present. Each signal is defined by a unique amplitude (a_m), phase (θ_m), and delay (τ_m) parameters.

Given the make up of the GPS signal correlation function, it should be possible to measure the correlation function and decompose it into its direct path and multipath components. One method for doing this is using MEDLL technology and this is described in the following section.

THE MULTIPATH ESTIMATING DELAY LOCK LOOP (MEDLL)

For a positioning system like GPS, the parameters of interest are the direct path signal delay and phase. In order to estimate these parameters, the direct path correlation function needs to be determined. The MEDLL approach used here involves the decomposition of the correlation function into its direct and multipath components.

The MEDLL estimates the amplitude, delay, and phase of each multipath component using maximum likelihood criteria. Other criteria such as least squares could be used, but it was found that using maximum likelihood criterion was the most suitable. Each estimated multipath correlation function component is in turn subtracted from the measured correlation function. Once this process is complete an estimate of the direct path correlation function is left. The phase and delay of the direct path is measured and these values are used to correct the carrier phase and pseudorange measurements respectively.

RECEIVER ARCHITECTURE AND DESIGN

The MEDLL algorithms require that the complete correlation function be measured in order to detect distortions caused by multipath. This is achieved by multiple correlator sampling of the correlation function as shown Figure 3.

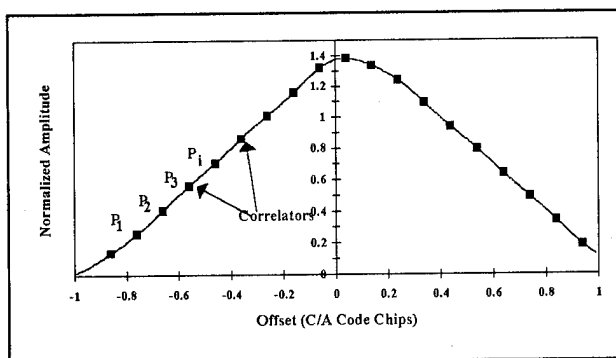


Figure 3: Multiple Correlator Sampling of the Correlation Function

A traditional GPS receiver dedicates only two, possibly three, correlators to each satellite tracking channel. The MEDLL algorithms require many more. Theoretically, the MEDLL only requires three correlators per direct path and multipath signal. In reality more correlators are required in order to obtain the initial estimates of each signal.

The extra correlators require that more hardware be used. This was achieved at NovAtel by grouping some of the standard GPSCards into a multi-card system. The cards are linked to the same RF deck and external OCXO to minimize cross channel biases. The OCXO also gives better clock stability than the TCXO used on the standard GPSCard. The interface to the MEDLL receiver is similar to OEM receiver presently sold by NovAtel. Figure 4 shows a picture of the MEDLL receiver. Its dimensions are 5.5" X 4.5" X 8.5".

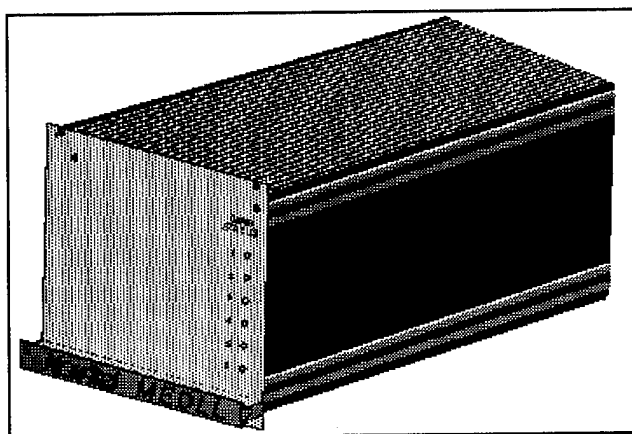


Figure 4: NovAtel MEDLL Receiver

THEORETICAL CARRIER PHASE TRACKING PERFORMANCE

Figure 5 shows a plot of the theoretical phase tracking of MEDLL and a standard PLL in the presence of a 0.5 amplitude multipath signal.

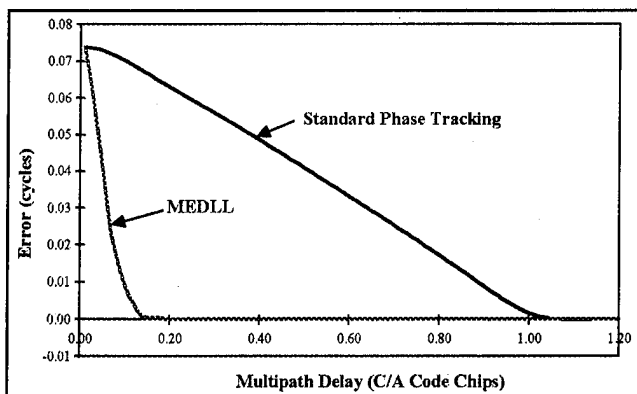


Figure 5: Theoretical MEDLL and Standard Receiver Phase Tracking Performance in the Presence of One Multipath Signal

The multipath signal was varied in delay from 0 to 1.2 chips and the maximum phase error was plotted.

The plot was generated using a simulated correlation function. A precorrelation band width (BW) of 8 MHz was assumed so as to emulate the filtering going on inside the MEDLL receiver.

The plot shows that the MEDLL is significantly better than standard receivers. It virtually eliminates any multipath biases for delays greater than 0.15 chips.

GPS SIMULATOR TEST BED

To evaluate the performance of the MEDLL carrier phase measurements under controlled multipath conditions, a GPS simulator test bed was set as shown in Figure 6. The test bed consists of a Stanford Telecom 7220 GPS signal simulator connected to two NovAtel receivers, the MEDLL and the GPSCard model 3151R using punctual correlator phase tracking. This set up allows us to make a direct comparison in performance between the MEDLL receiver and the GPSCard.

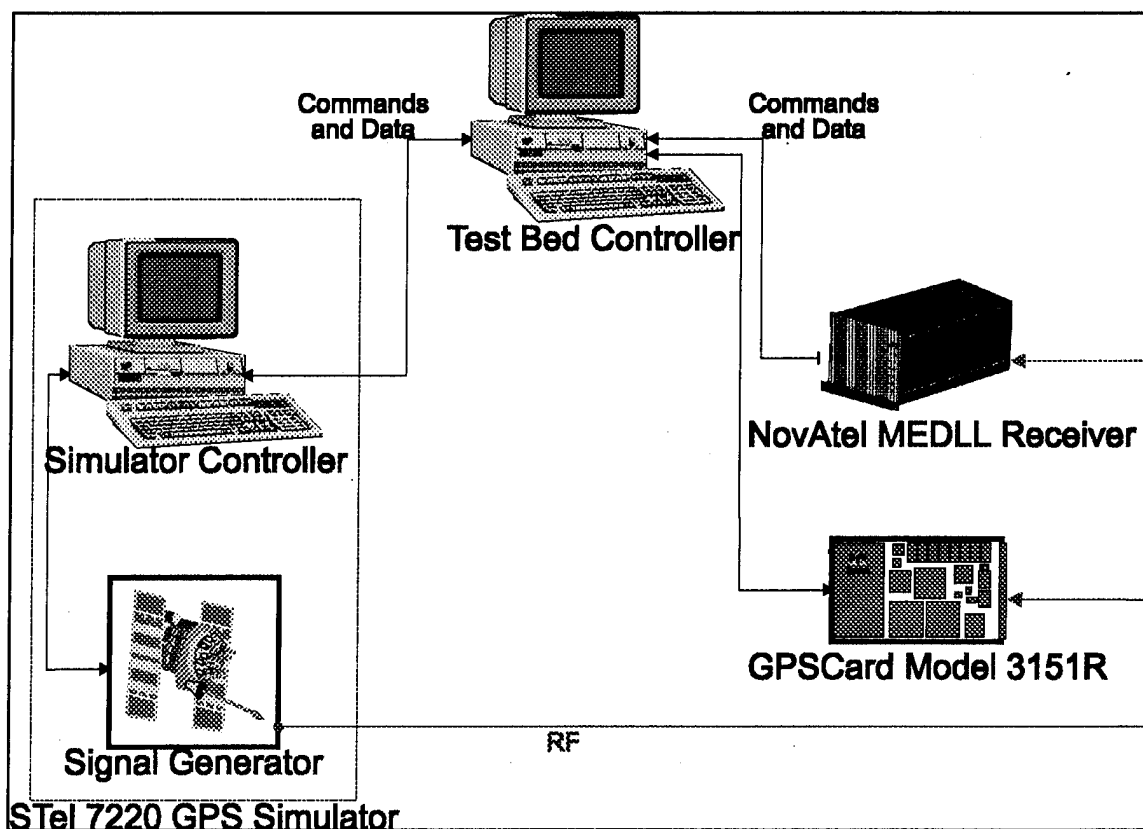


Figure 6: GPS Signal Simulator Test Bed

For each multipath simulation scenario, one channel of the simulator was set up to produce an multipath free signal using PRN 1. The multipath corrupted signal was created by setting 2 or more of the remaining simulator channels to generate a signal using PRN 2. One channel is set to simulate the direct path signal while the other channels generate the multipath signals.

The carrier range error is measured by differencing the PRN 1 measurement with the PRN 2 measurement. The carrier phase ambiguity is subtracted out and the remaining residual is largely due to the multipath error. Figure 7 shows a plot of the residuals.

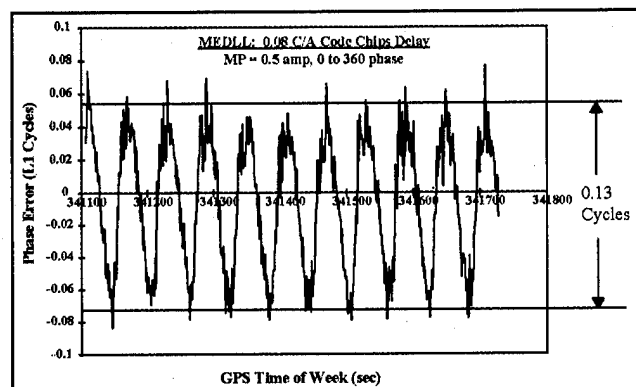


Figure 7: PRN 1 Minus PRN 2 Carrier Phase Residuals

RESULTS - ONE MULTIPATH CASE

For this test, a 0.5 amplitude multipath signal is generated at various delays relative to the direct path. The selected measurement points were 0.02, 0.04, 0.06, 0.08, 0.10, 0.14, 0.20, 0.40, 0.60, 0.80, 1.00, and 1.20 chips delay.

A new simulator scenario was initiated for each measurement point and the GPS receivers were reset at the same time. The simulator channels were configured in the following way:

- Channel 1: PRN 1
- Channel 2: PRN 2 (direct path signal)
- Channel 3: PRN 2 (multipath signal)
- Channels 4 to 10: Idle

The relative doppler between channels 2 and 3 was 1/60 Hz. That is, at the beginning of the scenario, the multipath delay set to the same as the measurement point delay, then it is increased by one carrier cycle every minute. This allows the multipath signal to rotate

through a full 360 degrees of phase relative to the direct path signal. The effects of this can be seen in Figure 7. The period between peak residual points is approximately one minute.

The plot in Figure 8 shows measured phase tracking error versus the theoretical phase tracking error from Figure 5.

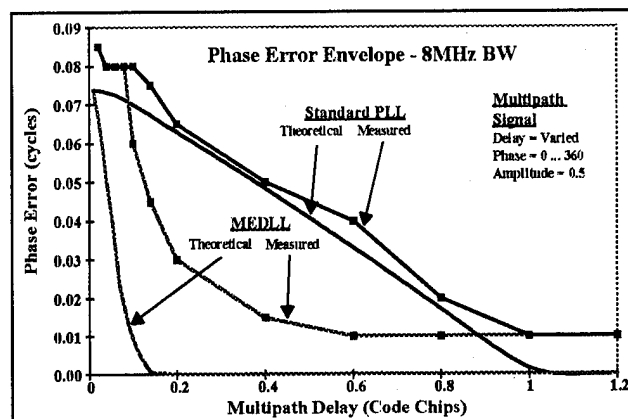


Figure 8: Measured Phase Tracking Error vs. Theoretical Phase Tracking Error

The results show the following:

- Both plots of the MEDLL and GPSCard measured phase errors converge to a value of around 0.013 cycles. The phase noise of the receiver is about this level. This is also shown Figure 7 by the higher noise present on top of the large sinusoidal type trend in the residuals.
- The standard PLL follows closer to the theoretical values then the MEDLL does. The reasons for this are probably errors in the reference correlation function used inside the MEDLL receiver and residual second order effects in applying the carrier phase correction. The MEDLL carrier phase correction is very sensitive to errors in the quadrature of the reference correlation function. This could be improved by measuring the reference function at more points. The residual second effects are caused by the PLL in the MEDLL receiver operating in real time and the correction to the carrier phase being calculated slightly post real-time. This can likely be tuned to improve results.
- The MEDLL shows a marked improvement over the standard PLL.

RESULTS - TWO MULTIPATH CASE

For this test, a 0.5 amplitude multipath signal is generated at various delays relative to the direct path. The selected measurement points were 0.02, 0.10, 0.20, 0.80, and 1.20 chips delay. At the same time a 0.3 amplitude multipath signal is held static at 0.5 chips delay.

As before, a new simulator scenario was initiated for each measurement point and the GPS receivers were reset at the same time. The simulator channels were configured in the following way:

- Channel 1: PRN 1
- Channel 2: PRN 2 (direct path signal)
- Channel 3: PRN 2 (0.5 amp. multipath signal)
- Channel 4: PRN 2 (0.3 amp. multipath signal)

Channels 5 to 10: Idle

The relative doppler between channels 2 and 3 was 1/60 Hz while channel 4 was held at 0 degrees phase relative to channel 2.

The plot in Figure 9 shows the measured phase tracking error for the two multipath case along with the phase tracking error from the single multipath case.

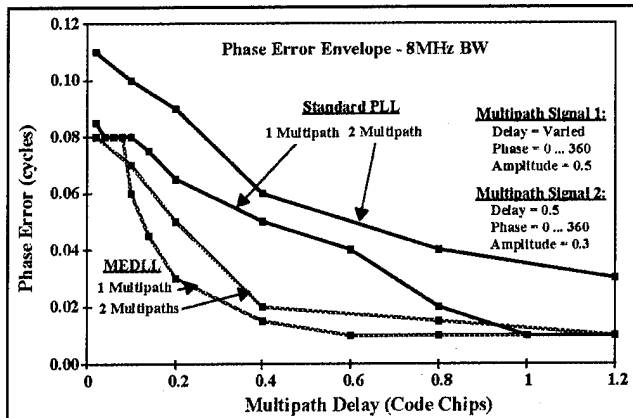


Figure 9: One Multipath Case vs. Two Multipath Case

The results show that the both the MEDLL and the standard PLL suffer a degradation in accuracy due to the addition of one more multipath signal. Relatively speaking, the MEDLL suffers much less than the standard PLL. This indicates that the MEDLL is successfully detecting and removing the additional multipath signal.

CONCLUSIONS

The results show a marked improvement in the MEDLL carrier phase tracking performance over the standard PLL. This shows that MEDLL is able to detect and remove the multipath signal(s). The tracking performance does degrade with the addition of more multipath signals, but the MEDLL suffers much less than the standard PLL.

Still the MEDLL did not perform as well as the simulations indicated it would. This suggests that these results can be improved upon. Some possible areas of improvement are a more accurate reference correlation function and more accurate modeling of second order effects when applying the carrier phase correction.

REFERENCES

Fenton, P., B. Falkenberg, T. Ford, K. Ng, and A. J. Van Dierendonck (1991) **NovAtel's GPS Receiver: The High Performance OEM Sensor of the Future**, Proceedings of the 4th International Technical Meeting of the Institute of Navigation, Albuquerque, NM, USA.

Townsend, B.R., and Fenton, P. (1994), **A Practical Approach to the Reduction of Pseudorange Multipath Errors in a L1 GPS Receiver**, Proceedings of the 7th International Technical Meeting of the Satellite Division of the Institute of Navigation, Salt Lake City, UT, USA.

van Nee, D.J.R., J. Sierveld, P. Fenton, and B. Townsend (1994) **The Multipath Estimating Delay Lock Loop: Approaching Theoretical Accuracy Limits**, Proceedings of the IEEE Position, Location and Navigation Symposium, Las Vegas, NV, USA.

Test Results on Mitigation of SATCOM-Induced Interference to GPS Operation

Triveni Upadhyay, George Dimos, and Wassim Ferzali
Mayflower Communications Company, Inc.

Dennis Weed
Federal Aviation Administration

BIOGRAPHIES

Triveni Upadhyay is President of Mayflower Communications Company, Inc. since 1986. Prior to this Dr. Upadhyay has worked at C. S. Draper Laboratory (1978 - 85) and at Texas Instruments (1973 - 78). Dr. Upadhyay's research interests are advanced GPS signal and data processing concepts with applications to interference mitigation and attitude determination.

George Dimos is a Senior Communications Systems Engineer at Mayflower since 1989. Mr. Dimos has lead the development of GPS anti-jam techniques and evaluation of Aeronautical Mobile Satellite Service (AMSS) for air traffic control applications. Prior to this Mr. Dimos has worked at AT&T Laboratories (1985 - 87).

Wassim Ferzali is Director of Data Link Programs at Mayflower since 1990. Mr. Ferzali specializes in the performance evaluation of AMSS data link and the end-to-end system performance evaluation of AMSS/ATN network for air traffic applications.

Dennis Weed manages the Federal Aviation Administration's Research and Development program for Satellite Communications under the Aeronautical Data Link Program. Mr. Weed has spent the last 10 years (6 years with Stanford Telecommunications Inc., of Reston, Virginia and the past 4 years with the FAA in Washington, D.C.) working on the FAA's Data Link Acquisition Programs.

ABSTRACT

The vulnerability of GPS to intentional or unintentional interference signals has been analyzed and incidence of observed interference has been reported by others [1]. During the past few years both military and commercial organizations have

made investments to develop techniques to mitigate GPS interference concerns. One such technique, namely the Adaptive Transversal Filter (ATF), was developed and patented [8] by Mayflower Communications to mitigate narrowband interference to GPS. An example of a potential narrowband¹ interference to GPS is the AMSS (Aeronautical Mobile Satellite Service) SATCOM-induced intermod interference. This paper discusses the nature of this interference source and the means to mitigate it using the Mayflower ATF technology. The paper also discusses other interference mitigation techniques for narrowband interference and compares it with the ATF technology. The paper summarizes the results of a recent test campaign using RF-simulated SATCOM intermod interference signals with a C/A code GPS receiver incorporating the ATF circuits. These results, performed for FAA SATCOM Program Office, demonstrated that an additional 20 to 30 dB of interference protection can be provided to a commercial GPS receiver using ATF. This additional interference protection provides sufficient margin for any link budget contingencies for simultaneous SATCOM/GPS operation for air transport as well as for General Aviation (GA) applications.

1.0 INTRODUCTION

The radio frequency interference (RFI) or jamming concerns of GPS for military missions have been studied over the past fifteen years by the Department of Defense. It has been postulated that with the introduction of GPS equipped weapon systems new jamming threats will emerge. These future jamming threats will consist of a mix of both narrowband and

¹ An interference signal is defined as *narrowband* if it occupies less than a fraction of 2 MHz bandwidth for C/A code and 20 MHz bandwidth for P code operation.

wideband interference sources. The vulnerability of GPS to jamming was recently highlighted by a Defense Science Board (DSB) Task Force Study (Gilmore and Delaney, 1994 [2]) which identified the need for cost-effective solutions to both wideband and narrowband jamming threats, with particular emphasis on wideband jamming.

Commercial aircraft GPS receivers are also susceptible to unintentional as well as intentional interference (Nisner and Owen, 1995 [3]), (Johnson and Erlandson, 1995 [4]). There are several potential sources of interference to GPS or a GNSS² (Global Navigation Satellite System). These sources can come from RF transmitters, either onboard the aircraft, nearby aircraft, or from ground stations, and include in-band radio frequency interference (RFI), out-of-band RFI, and physical interference. Sources of such interferences, e.g., SATCOM (AMSS) Intermod, VHF Communications Harmonics and Mobile Satellite Service (MSS) have been studied and reported by many organizations and are currently being discussed under the auspices of RTCA SC-159, WG6: *Interference Issues*. The current ARINC specification for interference tolerance in a commercial GPS receiver is defined in terms of interference-to-signal power ratio (I/S) of 24 dB for wideband interference and less than 24 dB for narrowband interference. In other words, if the interference power is more than 24 dB above the GPS signal power level (nominal value -130 dBm) then a commercial C/A code receiver may not be able to maintain signal tracking. With the above level of interference tolerance, a recent Lincoln Laboratory study (Gilmore and Delaney [2]) indicated that a modest 1 W in-band interference source may deny C/A code receiver operation up to a range of about 85 km. Therefore, the need to reduce the interference vulnerability of commercial GPS receivers by providing a low-cost interference cancellation capability is important for safety applications, such as air traffic control.

This paper describes one such low-cost anti-jam technique and demonstrates its efficacy to mitigate SATCOM-induced interference to GPS. Section 2 of the paper discusses potential sources of unintentional interference to commercial aircraft. Section 3 describes the specific ATF anti-jam technique and compares it with other anti-jam signal processing techniques. Section 4 discusses how this anti-jam capability can be provided for inside the receiver,

and Section 5 describes the test configuration used for the demonstration. The test results are summarized in Section 6.

2.0 GPS INTERFERENCE SOURCES IN COMMERCIAL AIRCRAFT APPLICATIONS

Several sources of potential unintentional RFI to GPS receivers onboard commercial aircraft have been identified [3,4]. Such sources range from RF transmitters onboard the aircraft, as well as onboard nearby aircraft and vehicles, to other RF transmitters, such as TV and FM stations in proximity to the aircraft. However, the immediate and highest degree of threat to GPS receivers comes from onboard RF transmitters that are used, or planned to be used, by the aircraft for Aeronautical Operational Control (AOC) and Air Traffic Control (ATC) communications, e.g., VHF radio and the satellite communications (SATCOM) equipment. The potential threat to GPS receivers by such devices must be evaluated and mitigated since future Air Traffic Management (ATM) functions are relying on an integrated COMM/NAV system to meet the civil aviation demands into the next century. In the following, we present an overview of the SATCOM and VHF communication RFI to GPS.

SATCOM Interference

Mobile SATCOM service is currently being standardized by the International Civil Aviation Organization (ICAO). This effort is supported by the civil aviation authorities (CAAs) of several countries, including the US FAA, and national and international consortia, such as Airlines Electronics Engineering Committee (AEEC), RTCA, and Inmarsat. The ICAO Aeronautical Mobile Satellite Services (AMSS) Standards and Recommended Practices (SARPs) were recently approved by ICAO.

AMSS safety service has been assigned the bandwidth 1646.5 to 1656.5 MHz within the entire Mobile Satellite Service (MSS) spectrum of 1626.5 to 1660.5 MHz. SATCOM transmission of multiple carriers has been shown to produce intermodulation (IM) products of 5th order and higher falling in the GPS L1 C/A band (between 1574.42 MHz and 1576.42 MHz). Analysis and test results have shown that the 5th and 7th order IM products have enough power to adversely impact GPS receiver performance on a commercial aircraft. Test data from Boeing, Honeywell, and Ball Aerospace have shown that IM RFI is narrowband interference with bandwidth of about 25 KHz [RTCA, 92]. Figure 1 shows the

² GNSS is defined to include, GPS and GLONASS.

functional diagram of an AES (Aircraft Earth Station) with a high gain antenna and a GPS receiver antenna to illustrate the potential generation of intermods in the GPS frequency band. These intermods are created when the AES uses multi-carriers.

Mayflower Communications has supported the investigation of the SATCOM interference problem to GPS for the FAA under the auspices of RTCA SC 159 and 165. Several solutions to mitigate the interference effect have so far been proposed by RTCA SC 159 WG6 on GNSS interference. The proposed solutions, suggesting to impose constraints on SATCOM in order to completely avoid the generation of IM, would result in operational limitations on SATCOM³. In one of its deliberations on this subject, RTCA suggested to pursue signal processing techniques applicable to the GPS receiver as a solution to mitigate SATCOM interference effect (RTCA, 1994 [5]).

VHF Communications Interference

The VHF channels centered at 121.150, 121.175, and 121.200 MHz, have a 13th harmonic within the GPS bandwidth and, the VHF channels centered at 131.200, 131.250, and 131.300 MHz have a 12th harmonic within the GPS bandwidth. These VHF channels are used for voice and data communications between the airplane and air traffic control centers. The VHF harmonics RFI is also a narrowband interference with bandwidth of about 25 kHz.

Field test on the magnitude of the 13th harmonics, conducted by (Johannessen, Gale, and Asbury, 1990 [6]) confirmed the existence of sufficiently strong interference to impact adversely GPS receiver performance. Field tests to measure the magnitude of the 12th harmonic are currently being conducted by ARINC on a GPS/ACARS testbed.

This activity has caused the RTCA SC 159, dealing with the standardization of GPS receivers for civil aviation, to revise its Terms of Reference to include the preparation of guidelines and the identification of appropriate standards resulting from the identified potential for interference to GPS from the VHF 12th and 13th harmonics.

³ Inmarsat; - the AMSS Service Provider, - has agreed to screen the carrier frequencies in the GES prior to allocation to ensure that 3rd and 5th order intermod are not produced in the GPS band. GLONASS and higher than 5th order intermod in the GPS are still not protected.

3.0 INTERFERENCE MITIGATION TECHNIQUES

Interference mitigation techniques for GPS can be classified in two broad categories: (1) *pre-correlation* signal processing, and (2) *post-correlation* signal/data processing. Pre-correlation signal processing techniques, as the name suggests, do not distinguish between the C/A code and P code. Examples of pre-correlation processing techniques are the well-known adaptive antenna control processing (also referred to as spatial processing) and temporal/spectral processing. The post-correlation signal/data processing refers to primarily data processing techniques inside the GPS receiver that are employed after code correlation and carrier Doppler removal functions. Examples of post-correlation processing are: adaptive aided code and/or carrier tracking loop design, multiple correlator processing for extended tracking, inertial aiding and integrated GPS/INS navigation filter designs. Pre-correlation processing techniques offer between 30 to 50 dB of jammer cancellation (depending on the number and types of jammers) while the post-correlation techniques offer between 10 to 15 dB of jammer power cancellation.

The traditional approach to mitigate jamming in military GPS receivers has been the provision of adaptive antenna to place nulls in the direction of jammers. However, the technology constraints of the existing adaptive antenna systems renders these systems unattractive for many military applications due to their high cost and large size. Adaptive antenna solutions to mitigate GPS interference concerns in commercial applications are also not desirable for the same reasons of high cost and large size. Therefore, alternate GPS interference mitigation approaches have been pursued by the Department of Defense, which either take advantage of special features of the jammer signal prior to code correlation (i.e., pre-correlation processing) or effectively reduce the tracking loop bandwidth (post-correlation processing) [9, 11].

Temporal/Spectral filters are examples of *pre-correlation* GPS signal processing techniques that have been analyzed and successfully implemented to mitigate narrowband interference signals. Depending on the signal domain in which jammer features are sensed and excised (sometimes referred

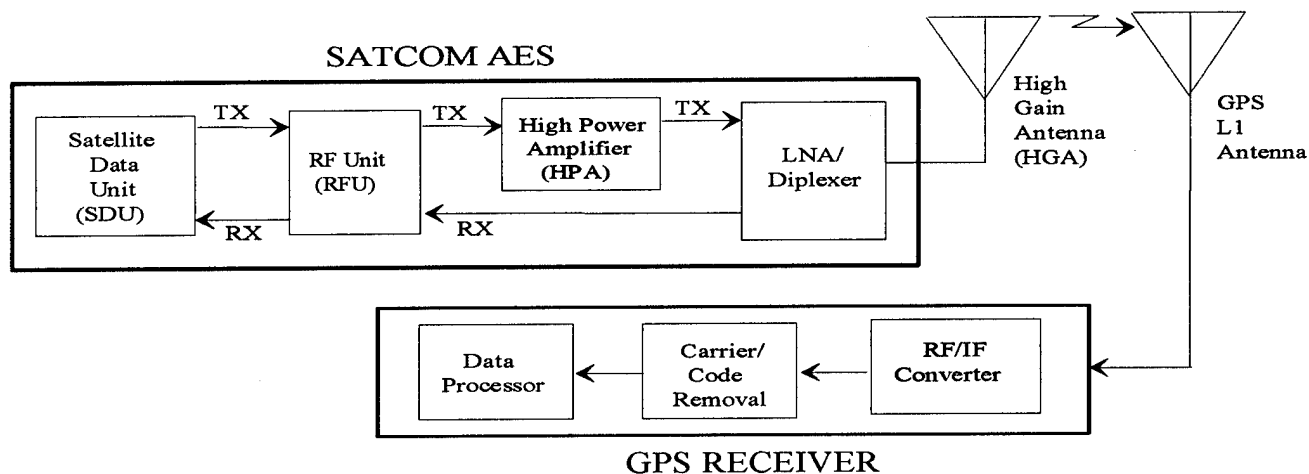


Figure 1. Intermodulation Interference From Multi-Channel SATCOM

to as 'excision' filters), the above pre-correlation techniques are classified as "time domain processing," "frequency domain processing," or "amplitude domain processing."

Time-domain processing requires that the received signal be filtered through an adaptive transversal filter (ATF) or an adaptive lattice filter. The filter weights are updated to minimize the signal power at the filter output (Milstein 1988 [7], Dimos and Upadhyay, 1993 [8]), or to whiten effectively the input spectrum by using correlation information to fit an all-pole model to the input signal. Significant jammer suppression (exceeding 30 dB) is achieved when the ATF spectrum forms spectral notches at the locations of the jammers. Since two real weights (that is, one complex weight consisting of a real and an imaginary component) are required for each ATF spectral notch, this system needs at least twice as many weights (and filter taps) as the maximum number of narrowband jammers to be suppressed. Digital embodiment of ATF processing was demonstrated for the first time by Mayflower Communications under the Air Force Wright Laboratory AGR Program (Dimos, et. al, 1993 [9]) using an 8-bit digital processing. Recently Mayflower demonstrated the operation of the ATF embedded in a GPS receiver using a 10-bit processing under its IR&D program.

Frequency Domain Processing requires that: (1) the received signal be converted into the frequency-domain by a real-time Fourier transform; (2) the spectral peaks be sensed and suppressed through an adaptive threshold power level and an adaptive notch filter; (3) and the signal be converted back to the

time-domain through a real-time inverse Fourier transform (Milstein, 1988 [7]). Technical limitations associated with this method are related to the stability of the input spectral estimate, and issues related to implementation in a small size, power and weight.

Amplitude-domain processing requires that the received signal be subjected to an adaptive nonlinear transformation to suppress peaks in the distribution of the signal amplitude. One simple such method is the adaptive A/D conversion (Amoroso 1983 [10]). This relatively simple technique can achieve processing gains between 5 to 10 dB against CW interference. A more powerful, and more complicated amplitude domain processing technique referred to as "Digital Density Detection", estimates the amplitude distribution [11] in a sequence of the input signal and then provides an optimal amplitude transform to suppress the jammer. The performance of time-domain amplitude diminishes rapidly as the number of jammers increases (even if they are at the same frequency), because of the rapid convergence of the combined amplitude distribution towards the thermal noise, i.e. Gaussian distribution.

With the current state-of-the-art in digital VLSI/VHSIC technology, temporal/spectral filter processing (a pre-correlation anti-jam technique) are typically implemented with digital hardware at the receiver sampling rate, i.e., about 2 MHz for a C/A code receiver and 20 MHz for a P-code receiver. As a result, they are significantly less costly than the antenna anti-jam techniques, which require multiple antenna elements, analog RF processing and digital

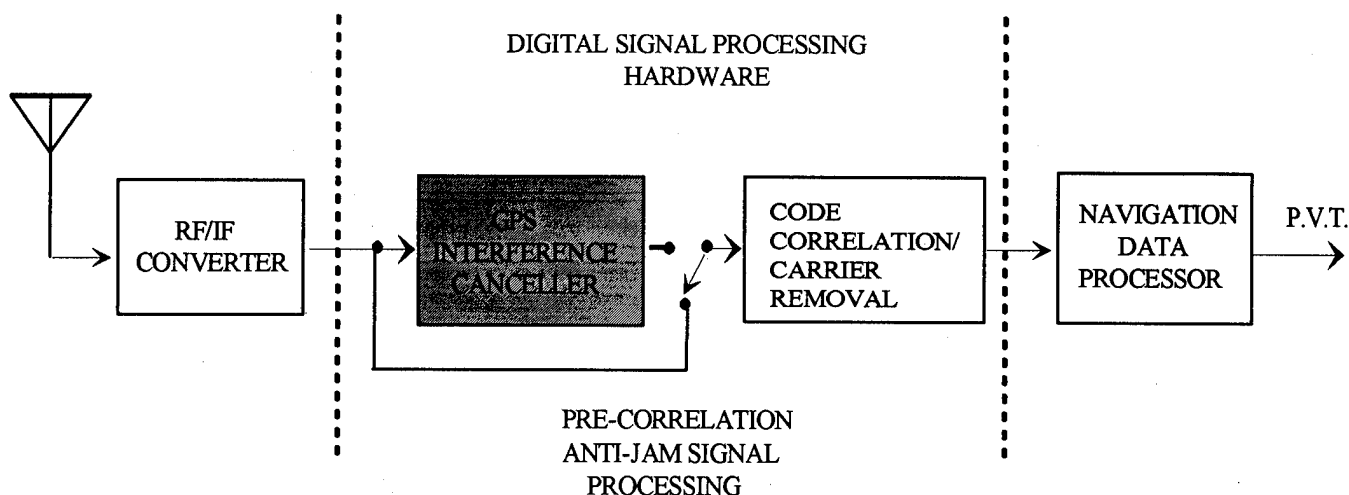


Figure 2. Insertion of Mayflower Interference Canceller* In a GPS Receiver

weight computation. Temporal/spectral anti-jam processing are also applicable to GLONASS interference concerns. It should be noted that GLONASS is potentially more vulnerable to in-band interference than the GPS because of its larger signal bandwidth (i.e., spectrum). Even though not fully discussed in this paper, Mayflower ATF temporal filter can be used to mitigate interference to GLONASS caused by SATCOM intermod, VHF harmonics or any other narrowband interference signal.

While the benefits of a digital temporal anti-jam filter are numerous, it should be noted however, that the temporal/spectral filters are effective only against narrowband interferences while the antenna spatial filter techniques are effective against both narrowband and wideband interference. Temporal filters, in addition to providing excellent jammer power suppression capability for narrowband jammers, are also attractive because of their lower cost and ease of insertion in GPS receivers or antenna electronics. Insertion of temporal filter technology in a GPS receiver is discussed in Section 4.

4.0 INSERTION OF DIGITAL ATF INTERFERENCE MITIGATION TECHNOLOGY IN THE GPS RECEIVER

The adaptive temporal filter (ATF) has been implemented digitally for both the C/A code and P code operation. The C/A code ATF was recently implemented and tested on a chip as a multi-tap weighted delay line in which tap weights are digitally computed in the chip. The ATF is capable of mitigating multiple simultaneous interference signals. Insertion of this interference mitigation technique in a GPS receiver can be accomplished in one of the two ways described below.

In the first method, a GPS receiver analog IF output is digitized in accordance with the ATF chip specification and the output of the ATF chip is provided to the GPS signal processor, shown in Figure 2., for performing standard GPS signal processing functions of code correlation and carrier Doppler.

In this method, the interference canceller chip can be enabled or disabled digitally to evaluate the contribution of this technology. This approach is considered to be the most cost-effective and will offer the best performance. However, it does require some modification to existing GPS receivers. Alternatively, we have considered providing this technique as a stand-alone product where the input to the unit is the L-band antenna signal and the output of the unit is also an L-band signal in which the interference has been mitigated. The functional block diagram of the stand-alone unit, shown in

* PAT NO. 5,268,927, DEC. 1993

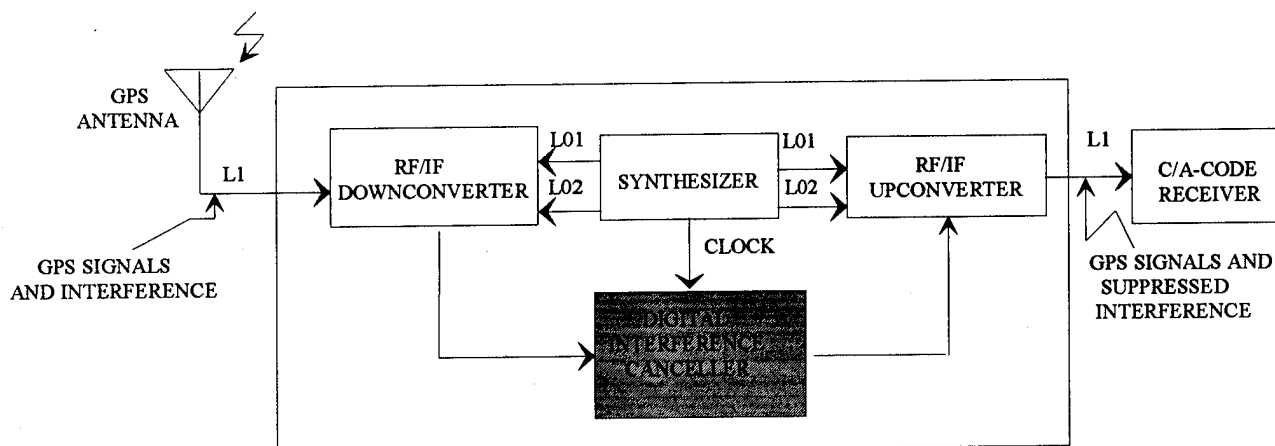


Figure 3. Stand-Alone Interference Canceller Unit

Figure 3, implements downconversion from L-band to IF, digitization of the IF signals which is processed by the ATF and the output of the ATF chip is fed to D/As and upconversion to L_1 frequency.

The standalone interference canceller unit was built and tested. A photograph of the unit is shown in Figure 4. The figure shows the Antenna J1 connector (input), the Receiver J2 connector (output), and a connector for the 28 Volts D.C. power input to the unit. The stand-alone unit, as expected, does not require any modification to existing GPS receivers. It is used as an in-line module between the receiver and the antenna.

In the next section we describe the test configuration. The performance test results with the ATF interference mitigation technique against the SATCOM intermod interference are described in Section 6.

5.0 SATCOM INTERMOD INTERFERENCE TEST CONFIGURATION

The test configuration to test SATCOM interference mitigation to GPS operation was based on a test plan developed jointly in consultation with RTCA, Inmarsat and FAA. The SATCOM intermod was implemented in RF as a narrowband FM with a bandwidth of about 25 KHz. The narrowband intermod signals were generated using a noise generator source whose output was passed to a Low Pass Filter and then modulated using HP FM signal generators (model number HP 8567). Three simultaneous intermod signals were generated at RF and combined together, along with live GPS satellite signal from a roof-top antenna, as shown in Figure 5.

The combined SATCOM intermod interference plus GPS signals were provided to a C/A code GPS receiver, developed earlier by Mayflower for DOT/VNTSC under the MLG/GPS/RNAV program for the FAA.

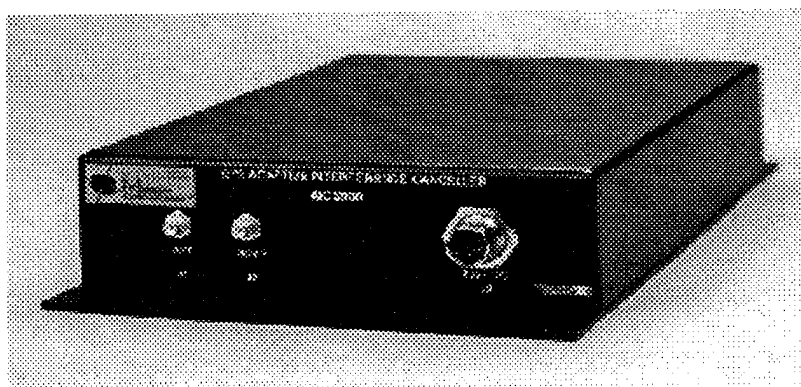


Figure 4. Stand-Alone GPS Adaptive Interference Canceller

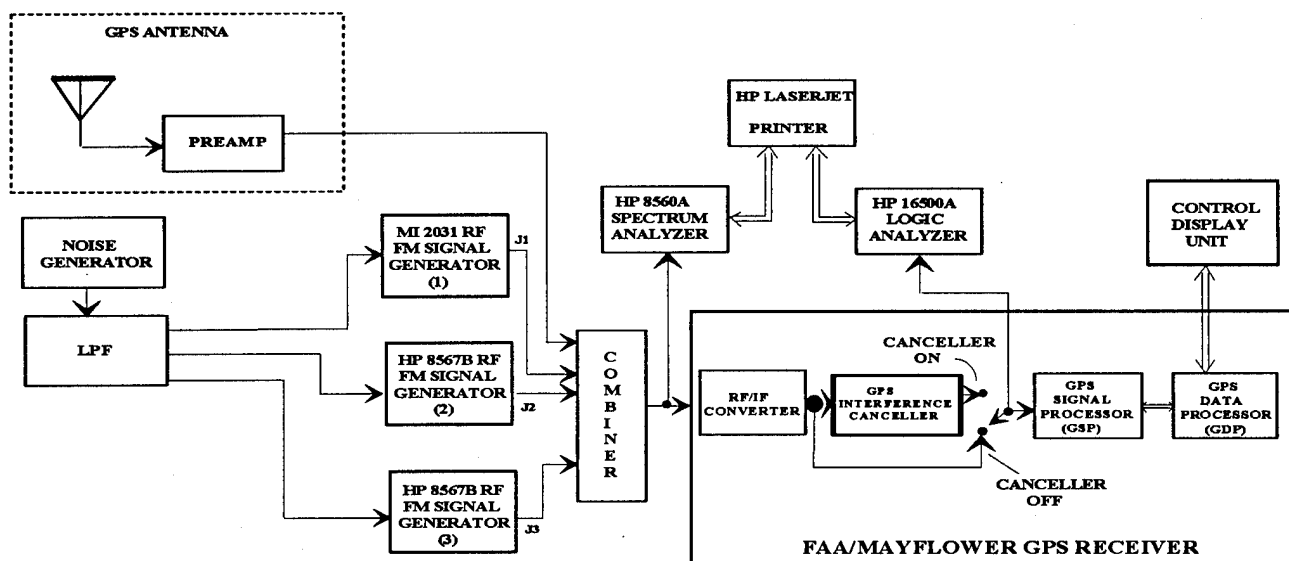


Figure 5. Laboratory Test Set-Up for SATCOM Intermod Interference Mitigation

The DOT/VNTSC receiver was modified to insert the ATF circuits as shown in Figure 5. A HP 8560 Spectrum Analyzer was used to observe and record the input L-band signals to the receiver. The digital signals, before and after the ATF interference canceller, were displayed and recorded on the HP 1650 A Logic Analyzer. Finally, the status of the receiver, e.g., SV number, mode, elevation and azimuth, signal-to-noise power ratio, code and carrier measurements were displayed on a KCU568 CDU and recorded on a PC.

The test configurations consisted of up to three equal power SATCOM narrowband interference signals. In the case of three interference signals, one was centered at L_1 , the second was centered at $L_1+0.5$ MHz, and the third interference signal was centered at $L_1-0.5$ MHz. Other test configurations have also been evaluated, e.g., with CW and with interference signal bandwidth larger than 25 KHz, up to 100 KHz, and the results were consistent with our prediction. However, the test results described in the next section pertain only to the approved test plan for the CW and 25 KHz bandwidth interference signals.

6.0 INTERFERENCE MITIGATION PERFORMANCE: TEST RESULTS

In this section we summarize the performance test results for the test configuration described in the previous section. The interference mitigation performance is measured in terms of additional

interference power a receiver can tolerate when the ATF chip is inserted in the receiver (or equivalently ATF is used as a in-line stand-alone module - see Section 5). The performance was measured both in terms of signal tracking performance and signal acquisition/reacquisition performance. Table 1 summarizes the results for tracking performance with one, two and three CW and 25 KHz narrowband interference signal sources.

Test Number	Interference Type	ATF Gain (dB)		
		Max	Min	Avg
1	1 NB	35	32	33
2	2 NB	32	30	31
3	3 NB	29	22	25
4	1 CW	29	25	27
5	2 CW	32	26	30
6	3 CW	27	23	25

Table 1. Phase I Test Results

The performance results in Table 1 are documented in terms of ATF gain which is defined as additional interference power a commercial receiver can tolerate, before disrupting its operation, using the ATF technology.

The data in Table 1 was collected over many tests that were performed and is presented in terms of maximum, minimum and average interference suppression power in dB. The data indicates

between 25 to 33 dB (average) of additional interference protection that can be afforded to a commercial GPS receiver.

7.0 CONCLUSIONS

The performance test data presented in this paper was collected with a realistic SATCOM intermod interference signal. The data shows about 25 dB of additional interference protection that can be provided inside the receiver for the case of 3 independent interferers and higher level of performance with fewer interference signals. This margin is adequate to mitigate SATCOM interference concerns to GPS operation on the same aircraft. Given the potential sources of unintentional interference to GPS, this level of margin allows FAA and the avionics equipment manufacturers to proceed confidently with the implementation of GPS as a primary navigation and landing system. Additional work is required to test the efficacy of the ATF technology for other potential interference sources, such as VHF, Mobile Satellite Service (MSS) and for other aeronautical navigation signals, such as GLONASS.

ACKNOWLEDGMENT

The authors wish to acknowledge the contributions of Messrs. Larry Chesto (RTCA SC 159 Chairperson), Andy Pickens (RTCA SC 165 Chairperson), Paul Drouilhet (FAA, ASE-12), Ed Spitzer (DOT/VNTSC) and Jose Moraes (Inmarsat) in developing the SATCOM Interference Test Plan and for participation and guidance during the tests.

BIBLIOGRAPHY

1. Aviation Week "Worm Holes in GPS Coverage Raise Interference Concerns", June 5, 1995
2. Gilmore, Sean and William Delaney, "Jamming of GPS Receivers: A Stylized Analysis", Project Report, CMT-174, MIT Lincoln Laboratory, April 1994
3. Nisner, P.D. and J. Owen, "Practical Measurements of Radio Frequency Interference to GPS Receivers and an Assessment of Interference Levels by Flight Trials in the European Region", ION.GPS.95 Proceedings, Palm Springs, CA, September 1995
4. Johnson, M.W. and R.J. Erlandson, "GNSS Receiver Interference - Susceptibility and Civil Aviation Impact", ION.GPS.95 Proceedings, Palm Springs, CA, September 1995
5. RTCA-SC-159 Adhoc Subgroup on GNSS Interference Meeting, Annapolis, MD, August 3-5, 1994.
6. Johannessen R, S. J. Cole, and M. J. Asbury, "Potential Interference Sources to GPS and Solutions Appropriate to Civil Aviation," IEEE AES Magazine, January 1990.
7. Milstein, L.B., "Interference Rejection Techniques in Spread Spectrum Communications", Proceedings of the IEEE, Vol. 76, June 1988.
8. Dimos George and Triveni Upadhyay, "Digital Adaptive Transversal Filter for Spread Spectrum Systems", U.S. Patent No. 5,268,927, December 1993.
9. Dimos George, Steve Cotterill and Triveni Upadhyay, Advanced GPS Receiver (AGR) Technology Demonstration Program, Final Report, WL-TR-93-1051, Mayflower Communications Company, Inc., Reading, MA, January 1993
10. Amoroso, F., "Adaptive A/D Converter to Suppress CW Interference in DSPN Spread Spectrum Communication", IEEE Trans. on Communication, Vol. COM-31, October 1983.
11. Balboni, Ed, et-al, Advanced GPS Receiver Technology Program, Final Report, Volume I, WL-TR-92-1149, C.S. Draper Laboratory Cambridge, MA December 1992.

A Modified Frequency-Locked Loop for Improved WAAS Carrier Tracking

Dr. Gary McGraw* and Dr. Bernard Schnauffer†
Rockwell International

BIOGRAPHIES

Gary McGraw received his B.S. in Electrical Engineering and Mathematics from Iowa State University in 1982, and the M.S. and Ph.D. in Electrical Engineering from UCLA in 1985 and 1989. From 1982-1985, he was employed at Sperry Flight Systems and Hughes Aircraft Co. From 1985-1993 he was employed at The Aerospace Corporation, working in the areas of spacecraft attitude control and adaptive control of flexible structures. In 1993, Dr. McGraw joined the Navigation Technology Section of Rockwell/Collins Commercial Avionics. He works in the areas of GPS receiver technology, RAIM, and aircraft autoland.

Bernard Schnauffer received his B.S., M.S., and Ph.D. degrees in Electrical Engineering from the University of Illinois at Urbana-Champaign. In 1994, he joined the Navigation Technology Section of Rockwell/Collins Commercial Avionics where he is a systems engineer. He works in the areas of GPS receiver analysis and simulation.

ABSTRACT

The proposed Wide Area Augmentation System (WAAS) downlink data consists of 250 bits in each second, 2-to-1 convolutionally encoded, yielding a 500 Hz BPSK symbol rate. This higher symbol rate requires the use of a Viterbi decoder to recover the 250 Hz data and may require modification in receiver carrier tracking loop designs as well. Frequency-locked loops (FLLs) are used in many GPS receivers instead of Costas loops because of the superior dynamic tracking capabilities of FLLs. However, the method of data demodulation commonly used in FLLs has a tendency to yield bursts of data bit errors, negating the coding gain offered by the Viterbi decoder. Loss of the WAAS integrity data, even if only

for a few seconds, is clearly undesirable in many situations. This paper discusses the problems that the WAAS data coding and modulation format present to current carrier loop designs. A modified FLL data demodulation process is proposed and simulation results presented. The WAAS data error and cycle slip performance of this new FLL demodulation scheme is at least as good as a Costas loop, yet retains the other advantages of an FLL.

1. INTRODUCTION

The proposed Wide Area Augmentation System (WAAS) [7] will greatly enhance the utility of GPS as an aircraft navigation aid. WAAS ground stations will monitor the status and accuracy of GPS satellites. GPS satellite integrity and wide-area differential corrections will be broadcast from geostationary satellites. The FAA intends that WAAS will enable sole-means GPS navigation for operations ranging from enroute to Category-I precision approaches.

The WAAS signal structure is similar to that of GPS. The broadcast will be a CDMA spread spectrum signal on GPS-L1, also using length-1023 Gold codes. However instead of 50 Hz BPSK downlink GPS data, the WAAS data will be at 250 bps, 2-1 convolutionally encoded, yielding 500 Hz BPSK symbols [7]. The WAAS signal structure will require some significant changes in GPS receiver design:

- Modified code generators will be needed to produce the Gold codes used by WAAS.
- Receiver carrier tracking loops must be able to demodulate 500 Hz symbols.
- A Viterbi decoder (or similar technique) will be required to recover the convolutionally-encoded data.

The higher WAAS symbol rate implies that the coherent pre-detection integration (PDI) interval for WAAS will be a tenth as long as the PDI interval

*e-mail: gamcgraw@cca.rockwell.com

†e-mail: baschnau@cca.rockwell.com

for GPS, yielding a 10 dB loss in the E_b/N_0 . However the length-7, rate-1/2 convolutional coding yields about 5 dB of coding gain [6]. However this coding gain assumes a random distribution of bit errors. For a rate-1/2 code, a Viterbi decoder with 12 branches can correct any 3 errors in sequences of 24 symbols [6]. Correcting more than three errors is likely beyond the capability of any reasonable decoder. The WAAS signal design protects against burst errors by incorporating 24 cyclic redundancy check (CRC) parity bits into each 250 bit field of data [7]. The CRC will permit the detection of any long bursts of bit errors within a second.

Frequency-locked loops (FLLs) are used in some GPS receivers because they are particularly robust to jamming and host vehicle dynamics as compared to phase-locked or Costas loops. However the method typically used to demodulate BPSK data in a FLL gives rise to blocks of errors, instead of isolated bit errors. While these errors would be detected by the CRC, the coding gain offered by the Viterbi is essentially lost. This loss of downlink data in GPS is not a particular concern, because the signal levels are typically large enough to make the symbol error probability very small and the loss of a subframe of data is not critical.

In this paper we will discuss the two major carrier tracking loop designs used in GPS receivers, FLLs and Costas loops, considering the relative advantages and disadvantages of the two implementations. The data error mechanism described above will be discussed in greater detail. We will then propose an alternative method for demodulating BPSK data in a FLL. Simulation results comparing this new method with a Costas loop will then be presented.

2. GPS CARRIER TRACKING LOOP OVERVIEW

In this section we will compare two carrier tracking loops commonly used in GPS receivers: Costas loops and frequency-locked loops. The Costas loop is discussed in numerous references; see Holmes, [2], for example. FLLs are less commonly discussed in the literature; two references are [1, 3]. Our discussion in this section will be fairly brief. Appendix A provides a more detailed presentation in conjunction with the development of mathematical models for simulation and analysis.

Conceptual block diagrams for the WAAS implementations of the two types of carrier tracking loops are shown in Figs. 1 and 2. A summary of the relative advantages and disadvantages of these two mechanizations is given in Table 1. Our discussion and simulation results assume an ARCTAN detector instead

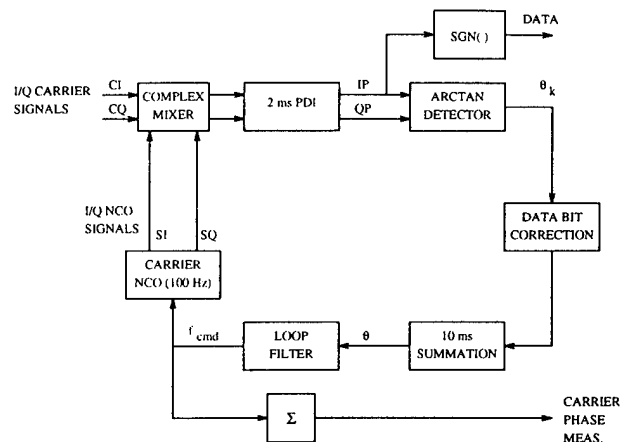


Figure 1: WAAS Costas loop block diagram.

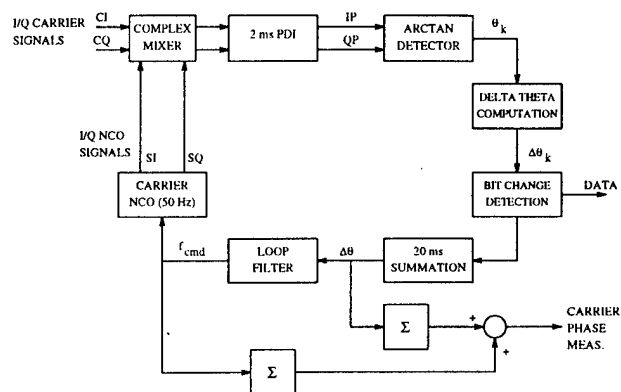


Figure 2: WAAS FLL block diagram.

of the perhaps more standard dot product discriminant for Costas loops or cross product discriminant for FLLs. The results presented here would likely be only slightly affected by use of the other discriminants. Our experience is that the ARCTAN detector slightly outperforms these other discriminants.

Carrier Tracking Method

As discussed in detail in Appendix A, the ARCTAN detector output is proportional to the phase and frequency error between the carrier and the numerically-controlled oscillator (NCO) over the PDI interval. Referring to Fig. 1, we see that the ARCTAN output (corrected for data bits) is the input to the Costas loop filter; therefore the loop will act to null-out both the phase and the frequency error. In the case of the FLL shown in Fig. 2, successive differences of the ARCTAN detector outputs (also corrected for data) are used as the input to the loop filter. Therefore the loop will only act to null-out the frequency error. When a Costas loop is locked, the quadrature component will be small, but in the FLL there will be an

Table 1: Comparison of Costas and FLL carrier tracking loops.

Costas Loop Advantages:

- Tracks carrier phase signal coherently.
- Provides inherent data demodulation.
- Excellent carrier phase measurement accuracy can be obtained in low dynamic environments.

Costas Loop Disadvantages:

- Requires high sampling rate and loop bandwidth for severe dynamic environments.
- Sensitive to clock noise, clock vibration, and jamming.
- Slow pull-in to initial phase and frequency errors.

FLL Advantages:

- Can operate at low sampling rate and loop bandwidth even in severe dynamic environments.
- Rapid pull-in to initial phase and frequency errors.
- Less sensitive to clock noise, clock vibration, and jamming.

FLL Disadvantages:

- Demodulates data by detecting phase transitions.
- Carrier phase measurement processing more complex than Costas.

arbitrary phase offset between the carrier and NCO.

This difference in phase vs. frequency control between the Costas loop and the FLL yields considerable differences in loop response to errors such as line of sight (LOS) dynamics and receiver clock noise. Under extreme loop stress, the FLL can better tolerate cycle slips that occur, whereas the Costas loop is more likely to lose lock completely. For our simulation evaluation, the FLL had a 50 Hz loop update rate, with a third-order, 5 Hz loop filter. This design is able to withstand LOS accelerations of 10 G and LOS jerk of 10 G/s. In contrast, for the Costas loop we used a 100 Hz loop update rate, with a third-order, 10 Hz loop filter, which began to lose lock for an LOS jerk of 4 G/s. To achieve performance comparable to the FLL, a Costas loop update rate on the order of 250 Hz with loop bandwidth of 15 Hz would be required. We chose the Costas loop update rate and bandwidth as a compromise between dynamic tracking and noise. Most applications do not require the high dynamic capability that the FLL offers, and the Costas loop design we used would tolerate the LOS dynamics and clock errors seen in most situations. Note that due to the lower loop update requirements, the FLL design will require a less powerful real-time processor than

the Costas loop, yielding benefits in terms of cost and power.

Carrier Phase Measurements

The measurement of carrier phase in the Costas loop is done by summing and appropriately scaling the NCO commands, as illustrated in Fig. 1. As shown in Appendix B this yields a lowpass filtered measurement of the actual carrier phase.

It is a common misperception that an FLL is unable to measure continuous carrier phase but is only able to measure delta range [5]. It turns out that continuous carrier phase measurements can be made with an FLL, although it is more difficult than with a Costas loop. For the FLL, the NCO sum will always be in error from the true carrier phase, because there will be an arbitrary phase difference between the carrier and the NCO. However, while it is true that the FLL does not *control* the relative phase difference between the carrier and the NCO, this difference is *measured*. As illustrated in Fig. 2 and shown analytically in Appendix B, including the sum of $\Delta\theta$ measurements with the NCO command sum yields a wideband carrier phase measurement. There are a number of subtleties associated with this, the major ones being the offset in time between loop update times and the data epochs, and accounting for the initial phase error. However these issues can be addressed in the receiver software. Rockwell has several receiver designs which produce continuous carrier measurements from an FLL.

Data Demodulation

When the Costas loop is locked, the BPSK data can be determined by looking at the sign of the inphase PDI samples. (This assumes that the initial data polarity has been established using parity checks.) In the FLL the data demodulation process is slightly more involved. As described in [4], when the phase change, $\Delta\theta_k$, is greater than a quarter cycle, a *bit change* is assumed to have occurred and an appropriate half cycle correction is made. Therefore in the FLL, the BPSK data is detected *differentially*. Once the initial data polarity has been established, this process will yield the same results under normal conditions as the Costas loop.

The Costas loop has two primary bit error mechanisms. An isolated bit error occurs if there is an isolated error in demodulation of the 2 ms phase measurements, but the accompanying loop error is small enough that there is no cycle slip or loss of lock. This is illustrated in Fig. 3. In this case, the isolated bit error will be detected and corrected by the Viterbi

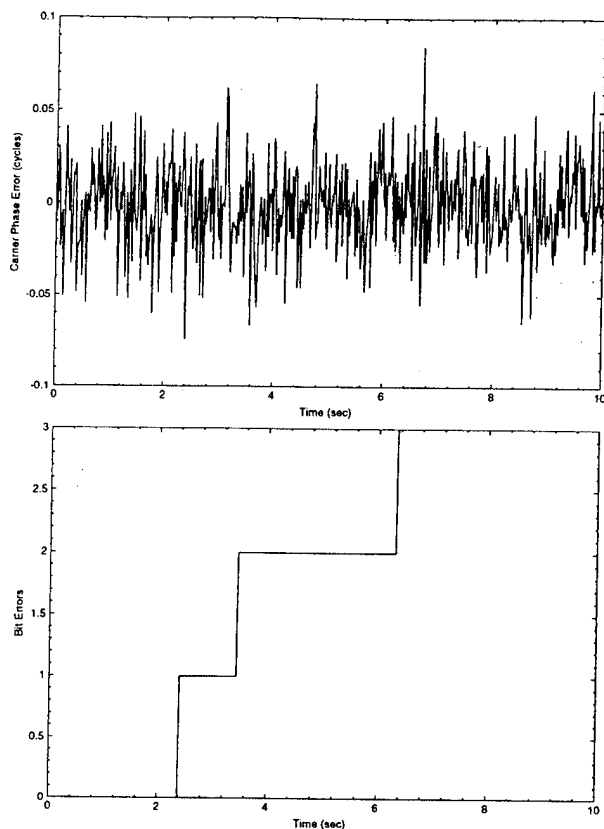


Figure 3: Example of isolated Costas loop bit errors. Top: carrier phase error; bottom: bit error count.

decoder. The other bit error mechanism we refer to as a "phase reference inversion". In this case, there is an error in the loop which induces the loop to settle onto a new lock point which is an odd multiple of half-cycles away from the original lock point. This is illustrated in Fig. 4. It can be seen that all subsequent bits are in error. This will be caught by the parity checks and the data demodulation will be re-initialized.

The FLL has only one bit error mechanism, which is analogous to the phase reference inversion. This is because with the differential data demodulation used, a single demodulation error will lead to all subsequent bits being inverted. When this error occurs there will usually be a cycle slip, since the large $\Delta\theta$ will drive the loop to a new lock point. Isolated bit errors can only occur in a FLL when there are consecutive differential demodulation errors, which is a rare occurrence. Therefore the FLL will typically exhibit bursts of bit errors which negate the coding gain of the Viterbi decoder. The modified FLL which we discuss below addresses this problem.

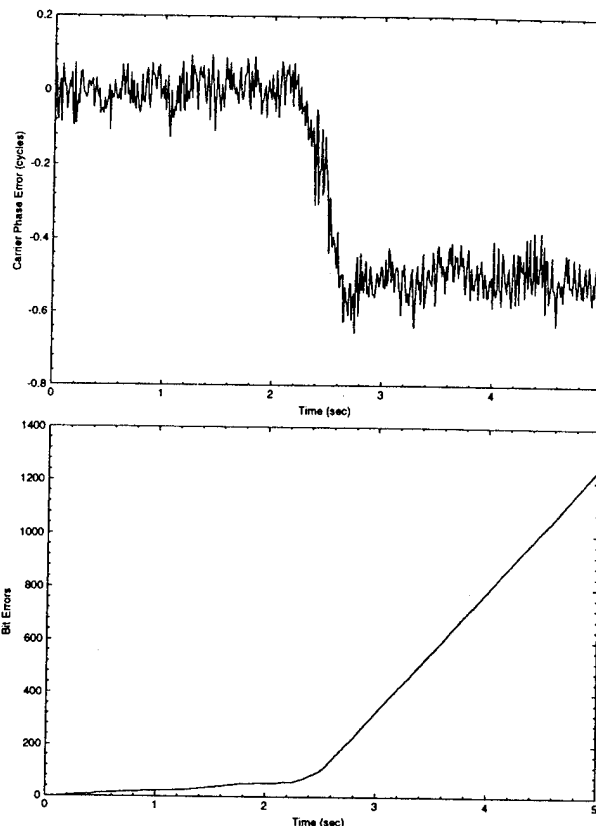


Figure 4: Example of a Costas loop phase reference inversion. Top: carrier phase error; bottom: bit error count.

3. MODIFIED FLL CONCEPT

The block diagram of the Modified FLL (MFLL) is given in Fig. 5. This diagram is substantially similar to that of the FLL of Fig. 2. The two algorithms function identically except for two key differences. First, for the MFLL the data is demodulated by comparing the ARCTAN output with a pre-computed phase reference instead of sensing the magnitude of the $\Delta\theta_k$ signal. Second, the data sense corrections to the $\Delta\theta_k$ samples is based on the new data demodulation method instead of using the magnitude of the individual $\Delta\theta_k$ samples. For the sake of similarity to the original FLL algorithm, the data sense corrections are computed by calculating bit transitions based on the demodulated data stream.

The pre-computed phase reference is calculated by averaging over a finite block of the L most recent I/Q PDI outputs. Since the PDI outputs retain the down-link data modulation, it is necessary to remove this modulation before the averaging is performed. This is accomplished by using the demodulated data stream and is represented in Fig. 5 by the uppermost signal flow line which feeds into the phase reference compu-

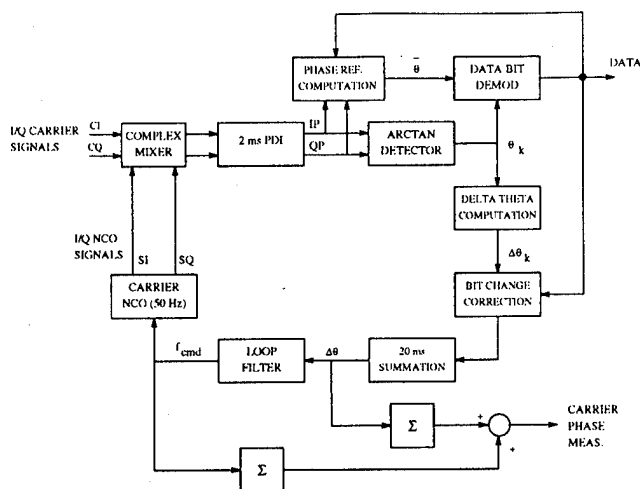


Figure 5: Modified FLL block diagram for WAAS.

tation. The corrected I/Q samples are obtained by multiplying the input I/Q samples by the data polarity determined from the ARCTAN measurement from those samples. The corrected I/Q samples can then be used with the $L - 1$ previous I/Q samples to compute the phase reference for the next iteration. Note that the MFL algorithm requires two length- L delay lines to store the corrected I/Q samples to be used in the phase reference computation.

As might be expected the performance of the MFL algorithm is dependent on the length of the block over which the phase reference is computed. Simulations were performed to determine the best delay line length for the WAAS symbol rate and an FLL with a 50 Hz update rate. The best value of L was found to be 16. This corresponds to a 32 ms averaging window for the phase reference, which is just less than two updates of the FLL.

4. SIMULATION PROCEDURE

Clock Noise and LOS Dynamics

In order to realistically assess and compare the performance of the WAAS Costas loop and FLL, our simulations included a model for VCO clock noise and representative LOS dynamics consistent with an aircraft during precision approach and landing. The clock noise model added to the NCO frequency and consists of two components: white noise to model oscillator frequency jitter, and clock drift. The white noise variance was derived from crystal oscillator Allan variance measurements. An Allan variance of 1 ppb over a 20 ms averaging interval was used. The clock drift component models the divergence of the oscillator frequency due to variations in temperature. A sinusoidal drift profile was used with a worst-case

drift of 0.4 ppm/min, which represents a mediocre crystal oscillator under worse-case temperature variations. Translating this value to L1 yields a frequency ramp of 10.25 Hz/s.

LOS dynamics were incorporated as changes in the carrier frequency. A coordinated aircraft turn model with a twenty degree bank angle was used to generate the LOS dynamics. This model gives rise to a 3.2 m/s^2 sinusoidal acceleration, which is representative of worst-case precision approach dynamics.

Monte Carlo Simulation Procedure

Monte Carlo simulations of the Costas loop and MFL were performed to evaluate their performance. For each tracking loop, the cycle slip and phase reference inversion rate statistics were generated by performing repeated runs of the tracking loop models. Each run was 50 sec in duration. For C/N_0 values of 29 dB-Hz and below, where the number of cycle slips and phase reference inversions in 50 sec are appreciable, 40,000 independent runs were performed. For the higher C/N_0 values, 100,000 independent runs were performed to accumulate significant statistics of the events of interest.

At low C/N_0 values, the loop could lose lock before 50 seconds had elapsed. This would bias the computation of the per second statistics if the length of each run was assumed to be 50 sec. To avoid this difficulty, runs in which lock was lost prior to 50 sec were not used to compute the average number of phase reference inversions and cycle slips in 50 sec. This is described more fully in the next section. However, the number of runs that were initiated before the desired number of full length runs were completed was counted for the sake of computing the Mean Time to Loss of Lock (MTLL).

Computation of the Statistics

The cycle slip statistics were computed by processing the carrier phase error (CPE) signal, i.e., the difference between the true carrier phase and the NCO phase, and counting the number of cycle slips of different magnitudes that occurred in each run. The CPE signal for the Costas loop has 100 points per second since the loop update rate is 100 Hz, and the MFL CPE has 50 points per second. The processing of the CPE for simulation statistics consisted of first filtering it with a block averaging filter and then quantizing the smoothed CPE to half cycle values. The smoothing filter is used to smooth noise which would give rise to false cycle slip counts. The CPE is then scanned point by point and a cycle slip identified when the CPE remained at a new cycle level for

a period of time which was longer than the loop filter dynamics. With this method of counting cycle slips, no cycle slips are missed by the processing procedure. Once the cycle slips of various magnitudes for all the runs are counted, the average number of slips in 50 seconds is computed by dividing by the number of runs. This average number of slips can be converted to a slip rate (per second) by dividing by 50. This, of course, assumes the independence of the different runs, which should be the case.

For a Costas loop and the MFLL, the inversion of the phase reference (which is nominally zero for the Costas loop) results in a long block of consecutive data demodulation errors. Such a block of errors would result in errors in the 250 bit words in the WAAS downlink data which would be detected by the CRC. Hence, the phase reference inversion rate is closely related to the word error rate. In these simulations we flag a phase reference inversion when a block of 18 consecutive data demodulation errors is detected. This number was chosen to ensure that a phase reference inversion actually occurred. For the sake of simplicity and since word boundaries are not imposed in the simulations, a phase reference inversion/word error can be detected only once in any 50 second run of the CTL. Hence, the phase reference inversion simulation data represents an estimated lower bound of the average number of phase reference inversions that occur in 50 sec. As the C/N_0 increases, the probability that more than one phase reference inversion occurs in any 50 sec run decreases and the computed average approaches the actual average rate.

5. RESULTS

The phase reference inversion rates for the Costas loop and the MFLL are plotted in Fig. 6. Below 30 dB-Hz the Costas loop has an advantage over the MFLL. This is not particularly significant since high data demodulation integrity would not be expected at such low signal levels. Above 30 dB-Hz the MFLL out-performs the Costas loop and, in addition, improves at a greater rate than the Costas loop. This means that the MFLL would provide higher data integrity than the Costas loop architecture.

Figure 7 shows the cycle slip rate for the two algorithms. These curves represent the cumulative probability of any size cycle slip. As for the phase reference inversion rate, the two curves cross at a particular signal level and the MFLL improves more rapidly than the Costas loop. In this case the curves cross at just below 29 dB-Hz. This is near the lowest signal level at which GPS receivers will likely be required to operate in a commercial avionics environment without significant cycle slips, and the MFLL has lower cycle

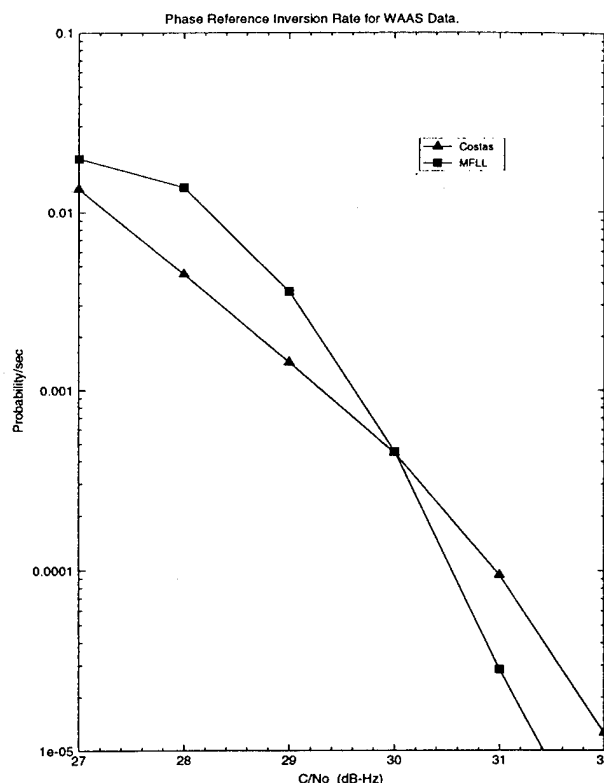


Figure 6: Probability of phase reference inversion for WAAS.

slip rates than the Costas loop.

A final, significant aspect of tracking loop performance is the MTLL. Loss of lock is the ultimate cycle slip catastrophe. Recall that the simulations of the previous two figures ignore this aspect by not including runs that lost lock prior to the 50 sec simulation interval. In order to quantify the MTLL performance measure of the two loops, we assumed a simple Markov model which is discussed in Appendix C. Since the number of runs initiated in each Monte Carlo experiment was recorded, we can use this to determine the probability of loss of lock per second, p , whose reciprocal is the MTLL. A plot of MTLL vs. C/N_0 for the two algorithms is given in Fig. 8. Note that the MFLL is almost an order of magnitude better than the Costas loop in this regard. The superior tracking capability of FLLs is clearly seen here. Increasing the Costas loop update rate and loop bandwidth would help the MTLL, but would adversely affect the phase reference inversion rate.

6. CONCLUSIONS

We have proposed a modified FLL data demodulation scheme which simulation results show will provide excellent WAAS bit error performance, in many cases

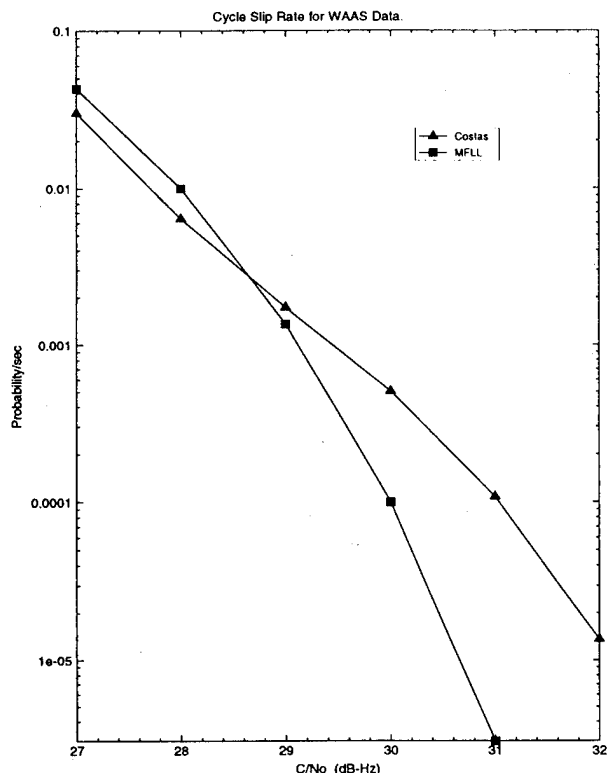


Figure 7: Probability of cycle slip for WAAS.

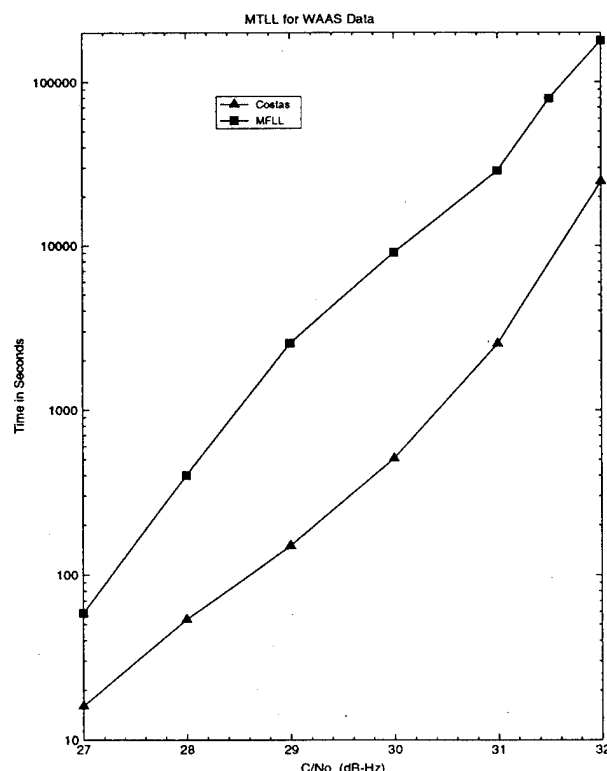


Figure 8: Mean time to loss of lock for WAAS.

better than that offered by a Costas loop. These data demodulation improvements were done without sacrificing the robustness of the FLL to LOS dynamics and clock errors.

ACKNOWLEDGEMENTS

Conversations with Jack Murphy of Rockwell alerted us to the issue of FLL data demodulation for WAAS and provided us with useful background information on FLLs. Juergen Bruckner of Rockwell first proposed the concept of maintaining a phase reference in the FLL for data demodulation.

REFERENCES

- [1] Cahn, C. R., "Improved Frequency Acquisition of a Costas Loop," *IEEE Trans. on Communications*, Vol. COM-25, No. 12, Aug. 1977, pp. 1453-1459.
- [2] Viterbi, A. J. and Omura, J. K., *Principles of Digital Communication and Coding*, NY: McGraw-Hill, 1979.
- [3] Natali, F. D., "AFC Tracking Algorithms," *IEEE Trans. on Communications*, Vol. COM-32, No. 8, Aug. 1984, pp. 935-947.
- [4] Rambo, J. C. "Receiver Processing Software Design of the Rockwell International DoD Standard GPS Receivers," in *Proc. of ION GPS-89, The 2nd International Technical Meeting of the Satellite Division of the Institute of Navigation*, Colorado Springs, CO, Sept 27-29, 1989.
- [5] Van Dierendonck, A. J., "Understanding GPS Receiver Terminology: A Tutorial on What Those Words Mean," *GPS World*, Vol. 6, No. 1, January 1995, pp 34-44.
- [6] Viterbi, A. J. and Omura, J. K., *Principles of Digital Communication and Coding*, NY: McGraw-Hill, 1979.
- [7] "Minimum Operational Performance Standard for Global Positioning System / Wide Area Augmentation System Airborne Equipment, Final Draft," RTCA Paper No. 396-95/SC159-661, July 24, 1995.

Appendix A CARRIER TRACKING LOOP MODELS

This appendix develops mathematical models for carrier tracking loops used in modern digital GPS receivers, such as those illustrated in Figs. 1 and 2. See Holmes [2] for more details, especially for Costas

loops. These models form the basis for the simulations used for the evaluation of the MFLL.

Coherent Integration Models

Over the $T = 2$ ms predetection integration (PDI) period it is assumed that the numerically-controlled oscillator (NCO) frequency and the LOS Doppler of the carrier are constant. The assumption is also made that the NCO commands and the coherent integration are synchronized. In reality this would never be the case since the integration is done synchronous to the data epochs. However this approximation simplifies the simulation modeling considerably. The NCO is modeled as an integrator: the NCO phase is piecewise linear, with a slope given by the commanded NCO frequency.

The in-phase and quadrature carrier signals prior to final down-conversion can be written in complex form as:

$$\begin{aligned} c(t) &= \sqrt{2C}d(t)e^{j(\omega_0 t + \phi_0)} + n(t) \\ C_I(t) &= \text{Re}\{c(t)\} \\ C_Q(t) &= \text{Im}\{c(t)\} \end{aligned}$$

where $t \in [0, T]$, C is the carrier signal power, and $d(t) = \pm 1$ is the data sequence. The complex noise is

$$n(t) = (n_I(t) + jn_Q(t))e^{j(\omega_0 t + \phi_0)}$$

where n_I and n_Q are independent white Gaussian noise (WGN) processes with spectral density N_0 . We assume that the code tracking error is small enough to ignore for the purposes of carrier loop modeling. We also assume that we are perfectly synchronized to the data epoch, so that $d(t)$ is constant over the PDI.

The output of the NCO can be represented in complex form as:

$$s(t) = e^{-j(\omega t + \phi)}$$

These signal representations are true over each PDI; an arbitrary interval of length T can be translated to $[0, T]$ by adjusting the initial phases ϕ_0 and ϕ .

The incoming carrier signals are combined with the NCO signals in a complex mixer, which translates the carrier to baseband without a twice-frequency modulation product. The resulting signal is coherently integrated over $[0, T]$ to obtain the complex prompt sample. Assuming that ω_0 and ω are constant over the integration interval yields:

$$\begin{aligned} P &= \int_0^T c(t)s(t) dt \\ &= Ae^{j(\Delta\omega T/2 + \Delta\phi)} + n_P \\ IP &= \text{Re}(P) \end{aligned} \quad (A1)$$

$$\begin{aligned} &= A \cos(\Delta\omega T/2 + \Delta\phi) + n_{IP} \\ QP &= \text{Im}(P) \\ &= A \sin(\Delta\omega T/2 + \Delta\phi) + n_{QP} \end{aligned}$$

where $A = \sqrt{2CT} \text{sinc}(\Delta\omega T/2)$, $\Delta\omega = \omega_0 - \omega$, and $\Delta\phi = \phi_0 - \phi$.

We now characterize the prompt noise samples n_{IP} and n_{QP} . The complex prompt noise sample is given by

$$\begin{aligned} n_P &= \int_0^T n(t)s(t) dt \\ &= \int_0^T [n_I + jn_Q]e^{j(\Delta\omega t + \Delta\phi)} dt \end{aligned}$$

Defining $\Delta_t = \Delta\omega t + \Delta\phi$, we have

$$\begin{aligned} n_{IP} &= \int_0^T [n_I(t) \cos \Delta_t - n_Q(t) \sin \Delta_t] dt \\ n_{QP} &= \int_0^T [n_I(t) \sin \Delta_t + n_Q(t) \cos \Delta_t] dt \end{aligned}$$

From this we can see that n_{IP} and n_{QP} are Gaussian, zero-mean RVs. The variance of n_{IP} is:

$$\begin{aligned} E\{n_{IP}^2\} &= \int_0^T \int_0^T [E\{n_I(t)n_I(\tau)\} \cos \Delta_t \cos \Delta_\tau \\ &\quad - E\{n_I(t)n_Q(\tau)\} \cos \Delta_t \sin \Delta_\tau \\ &\quad - E\{n_I(\tau)n_Q(t)\} \cos \Delta_\tau \sin \Delta_t \\ &\quad + E\{n_Q(t)n_Q(\tau)\} \sin \Delta_t \sin \Delta_\tau] dt d\tau \end{aligned}$$

The second and third terms are zero by the assumed independence of n_I and n_Q . Using $E\{n_I(t)n_I(\tau)\} = E\{n_Q(t)n_Q(\tau)\} = N_0\delta(t-\tau)$, and the sifting property of the delta function we have

$$\begin{aligned} E\{n_{IP}^2\} &= \int_0^T N_0(\cos^2 \Delta_t + \sin^2 \Delta_t) dt \\ &= N_0 T. \end{aligned} \quad (A2)$$

Using similar arguments it is straightforward to show $E\{n_{QP}^2\} = N_0 T$ and $E\{n_{IP}n_{QP}\} = 0$.

Discriminant and Loop Filter

The ARCTAN detector computes the phase tracking error angle θ_k as a four quadrant arctan(Q_P, I_P), which from (A1) can be seen to be (neglecting noise):

$$\theta_k = \Delta\omega T/2 + \Delta\phi \quad (A3)$$

An approximate implementation of the ARCTAN discriminant suitable for fixed computer word length computation is discussed in [4]. In the classical Costas loop implementation [2], IP and QP are multiplied together to yield a tracking error signal proportional to

$\frac{1}{2} \sin(2\theta_k)$. This form has the advantage of automatically compensating for data parity. The data parity must be eliminated from the ARCTAN discriminant by appropriately adding or subtracting a half cycle from θ_k . The ARCTAN discriminant has a linear response, and signal strength variations are automatically accounted for. In the Costas loop, the 2 ms phase tracking error samples are averaged over the loop update interval (in our case, 10 ms), then passed to the loop filter.

In the FLL, successive differences of the phase tracking error are first computed, i.e., $\Delta\theta_k = \theta_k - \theta_{k-1}$. Assuming that the carrier-NCO frequency difference, $\Delta\omega$, is constant over the successive PDIs we have

$$\begin{aligned}\theta_{k-1} &= \Delta\omega T/2 + \Delta\phi_{k-1} \\ &= \Delta\phi_k - \Delta\omega T/2\end{aligned}$$

so that $\Delta\theta_k \approx \Delta\omega T$. The data changes are detected and removed, and these 2 ms $\Delta\theta_k$ samples are summed over the loop update interval (20 ms for the FLL) to produce a measurement of average frequency error over the update interval, which is input to the loop filter. In older implementations of FLLs [1, 3], a so-called cross-product discriminant of the form: $IP_{k-1}QP_k - QP_{k-1}IP_k$, is used which is proportional to the sine of the frequency error. Again, the ARCTAN detector has the advantage of producing a linear error signal.

The Costas loop filter used in the simulations is based on the third-order "Wiener-optimal" loop filter [2]:

$$\frac{b(s)}{s^2} = \frac{2\omega_n s^2 + 2\omega_n^2 s + \omega_n^3}{s^2}$$

The cut-off frequency is given by $\omega_n = 1.2B_n$, where B_n is the desired noise equivalent bandwidth. The filter is implemented using a backwards-differenced discretization, i.e. $s = (z - 1)/\Delta T$, where ΔT is the loop update interval.

For the FLL, an extra integrator is included to compensate for the $\Delta\theta$ computation:

$$\frac{b(s)}{s^3} = \frac{2\omega_n s^2 + 2\omega_n^2 s + \omega_n^3}{s^3}$$

With this filter, the overall loop transfer function is approximately the same as the Costas loop.

Appendix B LINEARIZED CARRIER TRACKING LOOP MODEL

In this appendix we develop an approximate linear carrier tracking loop model which is suitable for stability and qualitative performance analyses. In particular, we use the linear models to show how carrier

phase measurements are constructed for the Costas loop and FLL.

Linearized Models

Figures 9 and 10 are block diagrams for the linearized carrier tracking models. Comparing with the detailed block diagrams, Fig. 1 and 2, it is seen that we have replaced the I/Q signals with the NCO and carrier phases. The functions of the complex mixer, PDI, and ARCTAN detector are combined into an overall transfer function for the coherent integration process:

$$H_{CI}(s) = \frac{1 - e^{-sT}}{sT} \quad (B1)$$

The loop filter is $b(s)/s^2$ for the Costas loop and $b(s)/s^3$ for the FLL. The $\Delta\theta$ computation in the FLL is approximated by a differentiation. We next demonstrate that the coherent integration model closely approximates the exact model.

Consider the ARCTAN detector output for the case of constant Doppler and no noise shown in Eqn. (A3), i.e.: $\theta = \Delta\omega T/2 + \Delta\phi$. If we assume that the NCO command and carrier frequency are held constant over the PDI interval, $[0, T]$, then the linear model phase signals are:

$$\begin{aligned}\phi_0(t) &= \omega_0 t + \phi_0 \\ \phi(t) &= \omega t + \phi\end{aligned}$$

Filtering $\phi_0(t) - \phi(t)$ through $H_{CI}(s)$, Eqn. (B1) yields $\theta = \Delta\omega T/2 + \Delta\phi$, identical to (A3). Therefore in the case of piece-wise constant Doppler, the linear model and the detailed model yield the same results.

The phase error measurement noise shown in Figs. 9 and 10 is due to the noise in IP and QP when computing the ARCTAN output. Assuming large SNR and making a small angle approximation, it can be shown that the variance of the phase error measurement is

$$\sigma_n^2 = \frac{1}{2(C/N_0)T}$$

Carrier Phase Measurement Transfer Functions

We now discuss the formation of carrier phase measurements in the Costas loop and FLL. To simplify the discussion, we make the approximation that $(1 - e^{-sT})/sT \approx 1$ for frequencies below $1/T$.

Referring to Fig. 9 we see that by integrating the NCO frequency command we can recreate the NCO phase. For the Costas loop, we will have $\phi \approx \phi_0$, if

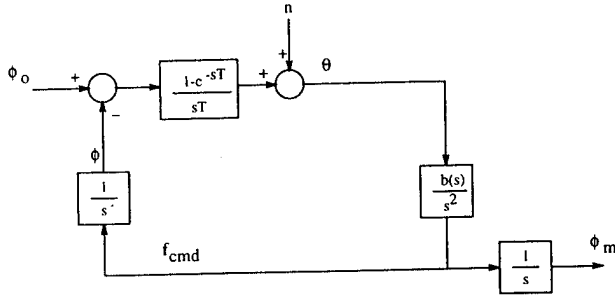


Figure 9: Linearized Costas loop block diagram.

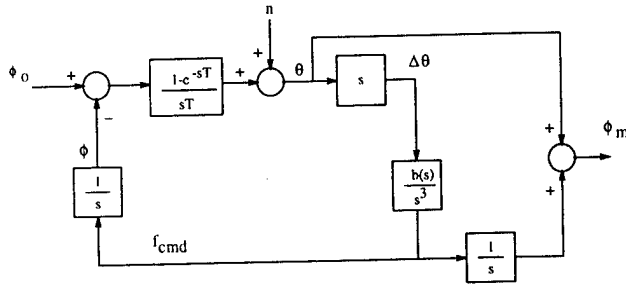


Figure 10: Linearized FLL block diagram.

the loop is locked. This implies $\phi_m \approx \phi_0$. Computing the transfer function from ϕ_0 to ϕ_m in Fig. 9 yields:

$$\frac{\phi_m}{\phi_0} = \frac{b(s)}{s^3 + b(s)}$$

This shows that the carrier phase measurement will be a lowpass filtered version of the true carrier phase.

In the case of the FLL, there may be an arbitrary offset between the NCO phase, ϕ , and the carrier phase, ϕ_0 , because the error signal is differenced prior to being sent to the loop filter. Therefore, the integral of the NCO commands will not be equal to the carrier phase. However, adding the ARCTAN output to the NCO sum accounts for the error between ϕ and ϕ_0 . Computing the transfer function from ϕ_0 to ϕ_m in Fig. 10 yields:

$$\frac{\phi_m}{\phi_0} = \frac{s^3 + b(s)}{s^3 + b(s)} = 1$$

Therefore, the FLL can provide an accurate carrier phase measurement. However, the FLL carrier measurement will include more high frequency noise than the Costas loop measurement for this implementation.

Appendix C MARKOV LOSS-OF-LOCK MODEL

In this appendix we consider a Markov chain model for computing loss-of-lock statistics for carrier tracking loops [2]. We assume that at time step $n = 0$, that

the loop is locked. At each subsequent time there is a probability p that the state of the loop will transition from locked to unlocked in the next second. Then there is a probability of $1 - p$ that the loop will remain locked. Once the loop is unlocked, it remains in that state. Given this model, the probability that the loop will become unlocked at step $n > 0$ is $P_{LL}(n) = p(1 - p)^{n-1}$.

Our simulations were done over 50 sec. If a simulation failed to complete prior to 50 sec, a new one was started for the purposes of the bit error and cycle slip probability computations. Denote the fraction of the total runs which failed prior to 50 sec as P_{50} . Then we have

$$\begin{aligned} P_{50} &= \sum_{n=0}^{49} (1-p)^n p = \frac{p[1 - (1-p)^{50}]}{1 - (1-p)} \\ &= 1 - (1-p)^{50} \end{aligned}$$

This equation gives us a way to compute p based on value P_{50} estimated from our carrier tracking loop simulations.

The mean time to loss-of-lock for the Markov chain model is given by:

$$\begin{aligned} MTLL &= \sum_{n=1}^{\infty} n P_{LL}(n) \\ &= \frac{p}{1-p} \sum_{n=0}^{\infty} n (1-p)^n \\ &= \frac{p}{1-p} \frac{1-p}{p^2} = \frac{1}{p} \end{aligned}$$

Monograph on GPS Antispoofing

Phillip Ward
Navward GPS Consulting

Biography

Phillip W. Ward is President of Navward GPS Consulting, which he founded in 1991, based in Dallas, Texas. From 1960-91, he was a Senior Member of the Technical Staff at Texas Instruments Incorporated (TI) in the Defense Systems & Electronics Group. During a 1967-70 educational leave of absence from TI, he was a Member of the Technical Staff at the Massachusetts Institute of Technology (MIT) Instrumentation Lab (now the Charles Stark Draper Lab). His military service was as a LT(jg) responsible for navigation and communications in the U.S. Coast & Geodetic Survey from 1958-60. From 1953-58 he was a co-op Student Engineer at White Sands Missile Range six months of the year. During that period he earned his B.S.E.E. degree from the University of Texas at El Paso. He earned his M.S.E.E. degree from Southern Methodist University in 1965 as a TI Co-op Student. He took postgraduate courses in Computer Science at MIT.

Mr. Ward has been involved in the field of navigation since 1958 and with GPS receiver design since 1976. He served as the lead systems engineer on several of TI's advanced GPS receiver development programs. He developed five generations of GPS receivers for TI including the TI 4100 NAVSTAR Navigator multiplex receiver, the first commercial GPS receiver. For his pioneering work in the development of the TI 4100, he received the Colonel Thomas L. Thurlow Navigation Award in 1989, the highest award given by the Institute of Navigation (ION). At the MIT Instrumentation Lab, he worked with the Apollo Guidance Computer design team. He is a Past President of the ION and has served in numerous other elected ION offices, including Chair of the Satellite Division. He is also a Senior Member of the Institute of Electrical and Electronics Engineers and is a Registered Professional Engineer in Texas.

Abstract

This paper describes the unclassified characteristics of GPS antispoofing (A-S). First, the paper describes what A-S is and how it is mechanized to deny access to the two-frequency (L1 and L2) precision codes (P codes) of the GPS satellites. Then, the paper describes the protection against enemy spoofing that is provided by A-S, including an explanation of GPS signal spoofing. The primary vulnerability of A-S, which is jamming, is explained and analyzed. The codeless techniques which have been developed to defeat A-S by commercial GPS manufacturers in order to gain access to two frequency measurements are also described. Given this background on A-S, a summary of the advantages and disadvantages of A-S is presented.

Introduction

There was no provision for antispoofing (A-S) or selective availability (SA) in the Block I GPS satellites. The Block I satellites were intended only for concept demonstration. These features were added to the operational GPS satellites starting with the Block II designs. A-S denies access to the precision codes (P-codes) while SA denies full navigation and timing accuracy to unauthorized GPS receivers. Unauthorized GPS receivers are called Standard Positioning Service (SPS) receivers. Authorized GPS receivers are called Precise Positioning Service (PPS) receivers. The basic differences between SPS and PPS receivers are that the SPS receivers contain no GPS crypto keys nor any capability to operate with such keys.

The Control Segment controls the activation of A-S and SA and the level of SA-induced error in the Space Segment. The current Department of Defense (DoD) policy is to activate A-S and SA on all operational GPS satellites. The National Research Council recently recommended immediate removal of SA, the addition of a second civilian user frequency and the continuation of A-S [1]. When the Control Segment activates A-S on a new GPS satellite, the

P-code becomes an encrypted Y-code. The DoD objective for A-S is to prevent an enemy from reproducing the precision codes on L1 (1575.42 MHz primary carrier frequency) and L2 (1227.60 MHz secondary carrier frequency) for the purpose of "spoofing" a DoD GPS receiver. The primary reason for implementing two-frequency operation in the GPS satellites is to provide the User Segment the means for precisely measuring the ionospheric delay (which is proportional to frequency). This is essential for precise navigation accuracy. However, there are parameters broadcast in the GPS satellite navigation message which are used by single frequency receivers to model the ionospheric delay. This, of course, results in reduced navigation accuracy compared with the two-frequency receiver.

Normally, the GPS coarse/acquisition-code (C/A-code), also called the clear/acquisition-code, is absent from the L2 GPS frequency. Therefore, one consequence of A-S is the denial of two-frequency operation for the SPS user segment which has access only to C/A-code. As a result, the conventional SPS receiver becomes a single frequency L1 C/A-code GPS receiver which must model the ionospheric delay. This does not seriously affect the accuracy of the stand-alone SPS user since the navigation error is dominated by SA. However, the A-S denial of conventional two-frequency operation seriously affects the position accuracy for precise differential SPS users. For example, precision geodetic survey and kinematic GPS receivers require two-frequency measurements of the ionospheric delay correction. In the near future, the Federal Aviation Agency's Wide Area Augmentation System (WAAS) will require a precise two-frequency measurement of the ionospheric delay. Because A-S denies two-frequency access by the WAAS airborne GPS users, the precise ionospheric delay will be reconstructed by the WAAS ground segment and an accurate model retransmitted by the WAAS space segment.

The only receivers capable of utilizing the two-frequency capability of GPS with conventional tracking loops are PPS receivers. PPS receivers require classified GPS crypto keys which are loaded into the receiver electronically with a fill device and which must be changed periodically before they expire. In addition to the keys, the PPS receivers have the algorithms and special Y-code hardware per channel, called the Auxiliary Output Chip (AOC), required to gain access to the Y-code. PPS receivers also contain special tamper-resistant hardware to hold the crypto keys, called a Precise Positioning Service - Security Module (PPS-SM). The PPS-SM also performs the classified SA decryption algorithms and part of the A-S function. The AOC and PPS-SM are unclassified hardware, but their manufacture and distribution are carefully controlled by the DoD. Working together, the keys, algorithms and special hardware can accurately replicate the Y-code, remove the SA dither on the L1 and L2 carrier frequencies, and remove

the epsilon error in the broadcast almanac and ephemeris data. The current DoD policy on A-S plus the strong commercial needs for two-frequency differential GPS ionospheric delay measurements has resulted in the development of "codeless" two-frequency SPS receivers. These receivers and their limitations will be described later in this paper.

GPS satellite signal structure

A block diagram which is representative of the GPS space vehicle (SV) signal structure for L1 ($154 f_0$) and L2 ($120 f_0$) is shown in Figure 1. Not shown in this figure is the signal structure for the L3 signal ($135 f_0$) which is normally turned off and is assigned to the nuclear detonation (NUDET) detection system (NDS) payload on the Block II and higher model numbered SVs. The NDS payload on GPS is not affected by A-S and will not be further discussed.

As noted earlier, the precision code is denied to SPS users when the A-S mode is activated. A-S combines the P-code with an encrypted code. The result is called Y-code. The Y-code has the same period and chipping rate as the P-code. Thus, the acronym often used for the precision code is P(Y)-code. As shown in Figure 1, both the C/A-code and the P(Y)-code as well as both carrier frequencies are subjected to the encrypted dither frequency of SA. This SA phase modulation effect creates a pseudo random Doppler error on both the pseudorange and delta pseudorange measurements. This SA error can be removed by the PPS user but cannot be corrected by the SPS user. In addition, SA encrypts an offset error into the satellite's broadcast ephemeris and almanac data. This causes a position error for the SPS user. Differential operation between a reference receiver of known location and a rover receiver removes all Control Segment and Space Segment common mode errors, including the effects of SA. As a result, the conventional SPS differential receivers operate with higher navigation accuracy (1 to 5 meters 1-sigma) than the stand alone PPS receivers (16 meters SEP).

The L1 frequency ($154 f_0$) is modulated by the C/A-code with data and the P(Y)-code with data. The L2 frequency ($120 f_0$) is modulated by only one PRN code at a time, but there are three possible Control Segment selections: P(Y)-code with data modulation, P(Y)-code with no data modulation and C/A code with data modulation. The normal mode is P(Y)-code with data modulation on L2.

The nominal reference frequency, f_0 , as it appears to an observer on the ground is 10.23 MHz. To compensate for relativistic effects, the output of the SV's frequency standard, as it appears from the SV, is 10.23 MHz offset by a $\Delta f/f$ of -4.467×10^{-10} . This results in a Δf of -4.57×10^{-3} Hz and, excluding the effects of selective availability (SA), $f_0 = 10.22999999543$ MHz [2]. To the GPS receiver on the ground, the C/A-code has a chipping rate of 1.023×10^6

chips/second ($f_0/10 = 1.023$ MHz) and the P(Y)-code has a chipping rate of 10.23×10^6 chips/second ($f_0 = 10.23$ MHz). (The term "chip" is used instead of "bit" to convey that no data information is in the PRN codes.) Note in Figure 1 that the 50 bits per second (bps) data is combined with both the C/A-code and the P(Y)-code prior to modulation with the L1 carrier. This combination uses the exclusive-or process, denoted by \oplus . Since the C/A-code \oplus data and P(Y)-code \oplus data is a synchronous operation, the bit transition rate does not alter the chipping rate of the PRN codes. However, the data does cause the phase to change at every bit transition. The exclusive-or process is equivalent to binary multiplication of two one-bit values. Therefore, each exclusive-or process is equivalent to a biphasic shift key (BPSK) modulation process. Also note that BPSK modulation is used to modulate the L1 and L2 carrier signals. There are 204,600 P(Y)-code epochs between data epochs and 20,460 C/A-code epochs between data epochs, so the number of times that the phase could change in the PRN code sequences due to data modulation is relatively infrequent. The P(Y)-code \oplus data is modulated in phase quadrature with the C/A-code \oplus data on L1. Thus, there is a 90-degree phase shift between the C/A-code \oplus

data modulation and the P(Y)-code \oplus data modulation on these two combined L1 carrier frequencies. This is illustrated by the vector phase diagram in Figure 2.

From Figure 1 and the previous signal structure description, the typical GPS two-frequency signal transmitted from SV_i can be described mathematically as follows:

$$S_i(t) = L_1(\omega_1 t) + L_1(\omega_2 t) \quad (1)$$

where:

$$\begin{aligned} i &= \text{PRN number of the SV} \\ \omega_1 &= 2\pi f_{L1} = 2\pi 154 f_0 \text{ (radians/s)} \\ \omega_2 &= 2\pi f_{L2} = 2\pi 120 f_0 \text{ (radians/s)} \\ f_0 &= 10.23 \times 10^6 - 0.00457 + \text{SA dither (Hz)} \end{aligned}$$

and:

$$\begin{aligned} L_1(\omega_1 t) &= A[Y_i(t) \oplus D_i(t)] \cos(\omega_1 t) \\ &\quad + \sqrt{2} A[G_i(t) \oplus D_i(t)] \sin(\omega_1 t) \end{aligned} \quad (2)$$

$$L_1(\omega_2 t) = \frac{\sqrt{2}}{2} A[Y_i(t) \oplus D_i(t)] \cos(\omega_2 t) \quad (3)$$

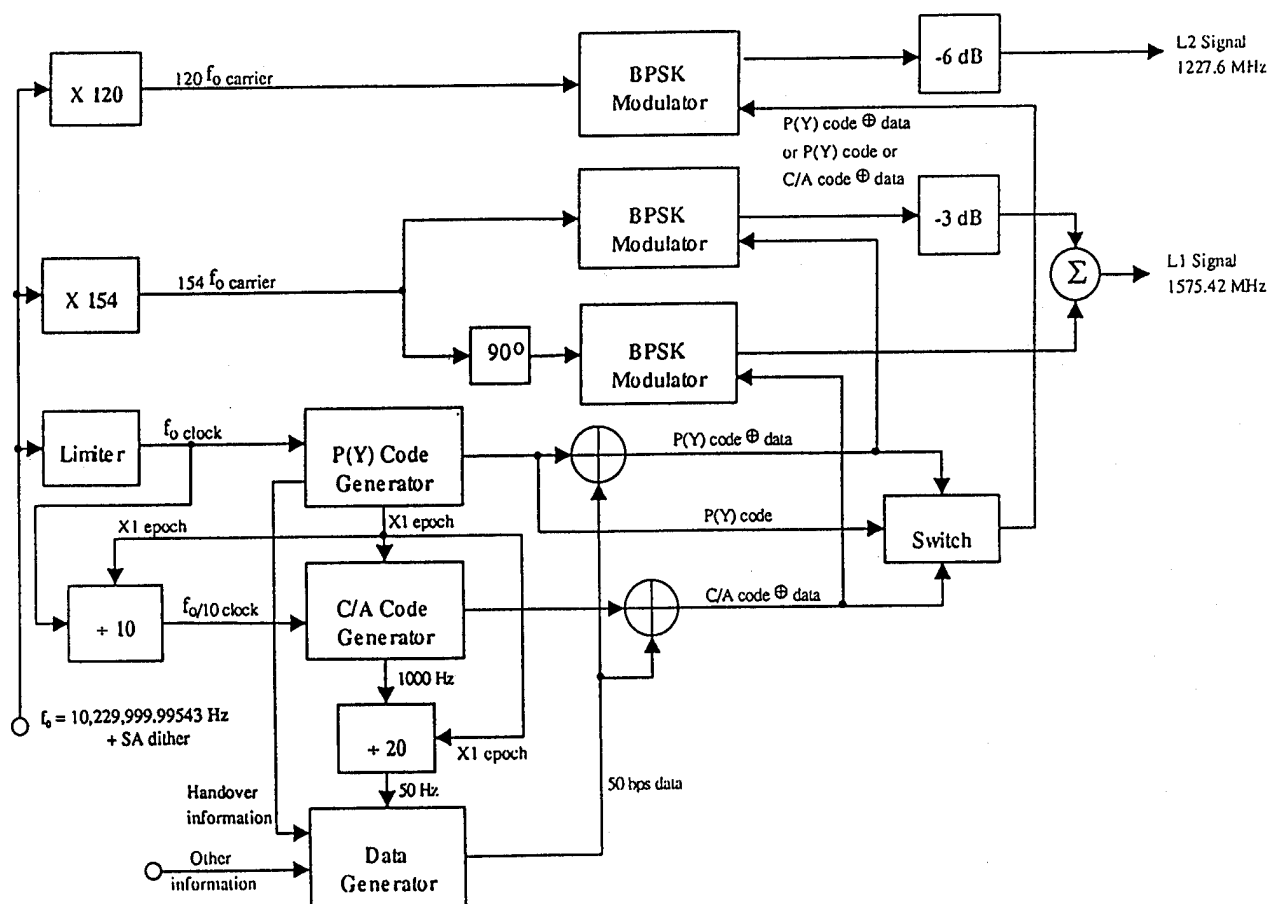


Figure 1. GPS satellite signal structure.

where:

- A = amplitude of the L1 P(Y)-code signal
- $Y_i(t)$ = spread-spectrum Y-code from SV_i with f_0 chipping rate
- $D_i(t)$ = 50 Hz navigation data message from SV_i
- $G_i(t)$ = spread-spectrum C/A-code from SV_i with $0.1f_0$ chipping rate.

Note in Equations 2 and 3 that the Y-code and data modulation on L1 are identical to the Y-code and data modulation on L2. The GPS signal structure as implemented by a two-frequency PPS GPS receiver is summarized in Table 1.

Mechanization of antispoofing

The mechanization of the antispoofing code can be further described as:

$$Y_i(t) = P_i(t) \oplus E_i(t) \quad (4)$$

where:

- $P_i(t)$ = spread-spectrum P-code from SV_i with f_0 chipping rate

$E_i(t)$ = Encrypted code from SV_i

Because the GPS P(Y)-code is periodic, it has a correlation interval which is periodic and its power spectrum is a line spectrum. Figure 3 depicts the autocorrelation function of a maximum length pseudo noise (PN) code and its line spectrum [3]. In this figure:

- $\pm A$ = amplitude of the PN code
- N = total number of chips in one PN code period
- T_c = chip time of the PN code in seconds
- NT_c = correlation period of PN code in seconds
- $\frac{2\pi}{NT_c}$ = line spacing of the power spectrum of the PN code.

The GPS PRN codes have periodic correlation triangles and a line spectrum which closely resemble the characteristics of maximum length shift register PN sequences. However, the GPS PRN codes are not shift register sequences of maximum length. Figure 4 is a plot of the power spectrum of the GPS P(Y)-code and C/A-code (plus 50 Hz data) PSK

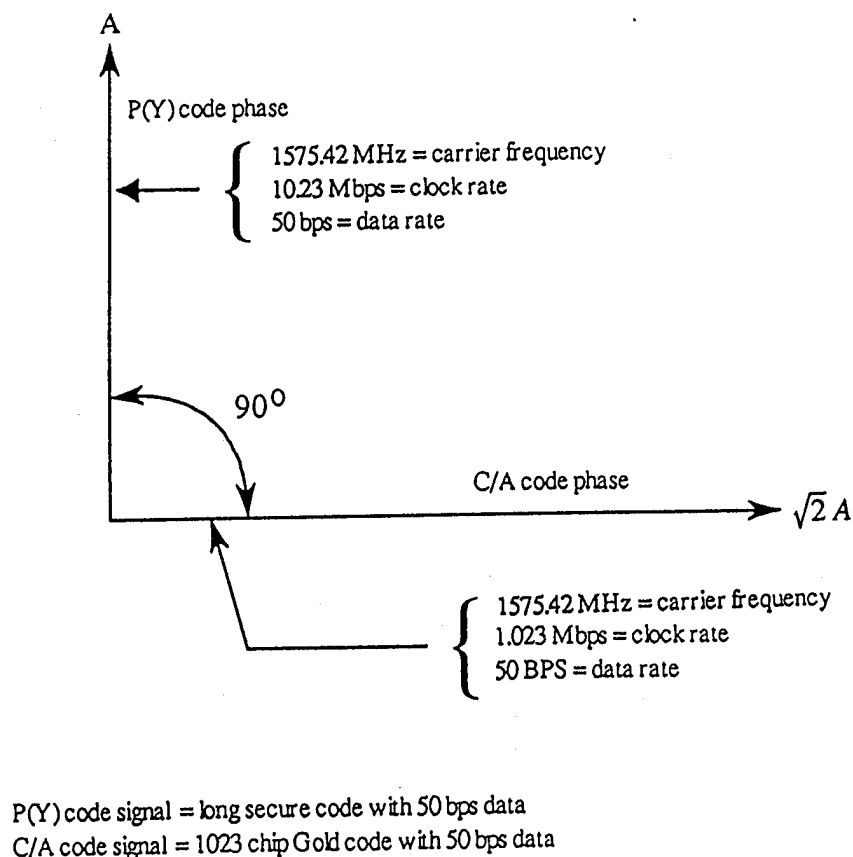


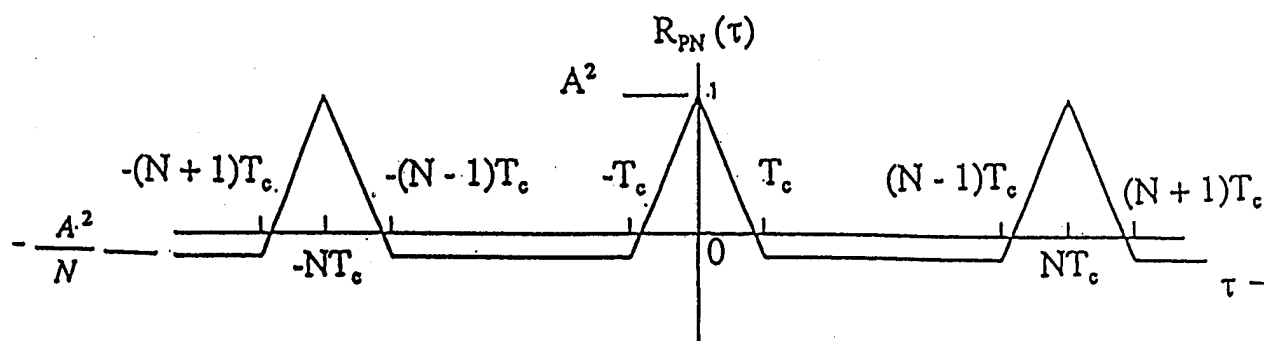
Figure 2. GPS signal structure for L1.

Table 1. GPS receiver signal structure.

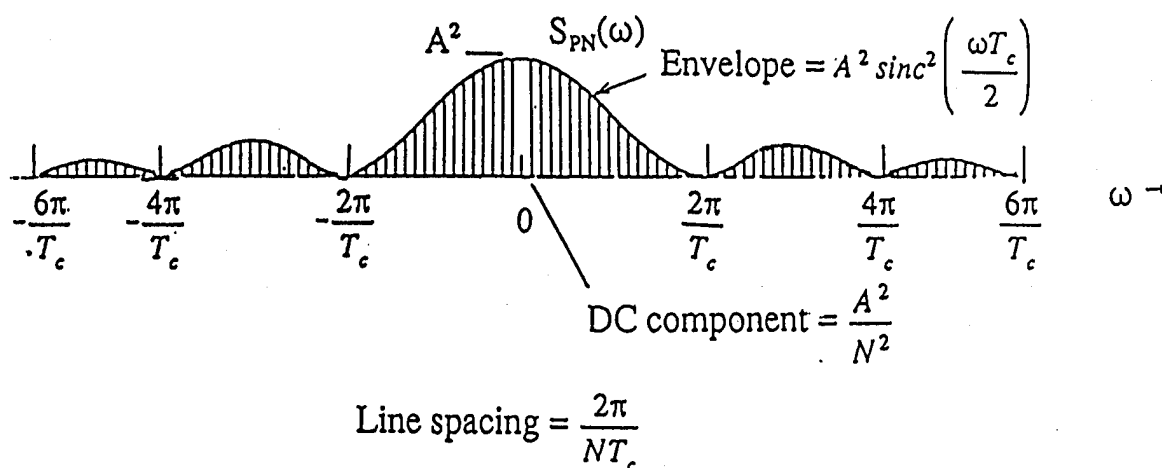
Signal Priority	Primary	Secondary
Signal Designation	L1	L2
Carrier Frequency (Hz)	1575.42×10^6	1227.60×10^6
PRN Codes (chips/s)	$P(Y) = 10.23 \times 10^6$ and $C/A = 1.023 \times 10^6$	$P(Y) = 10.23 \times 10^6$ or $C/A = 1.023 \times 10^6$ (Note 1)
Navigation Message Data Modulation (bps)	50	50 (Note 2)

Note 1: The code usually selected by the Control Segment on L2 is P(Y)-code.

Note 2: The 50 Hz navigation data message is usually modulated on L2 P(Y)-code, but can be turned off by the Control Segment to improve jamming performance. There are three possibilities: P(Y)-code with data, P(Y)-code with no data and C/A-code with data.



(a) Autocorrelation function of PN code with amplitude $\pm A$ and period NT_c .



(b) Line spectrum of PN code

Figure 3. The Autocorrelation function of a maximum length PN code (a) and its line spectrum (b).

modulated onto the L1 carrier. The signal was obtained from a GPS signal generator. The spectrum analyzer performed the plot using a 300 KHz resolution bandwidth. With this level of resolution, it is impossible to observe the line spectrum characteristics of either code. Therefore, the power spectrum **appears** to be continuous, but it is actually a line spectrum. The combined power spectra of C/A-code and P(Y)-codes are centered at the L1 carrier frequency, 1575.42 MHz. The first nulls of the C/A-code power spectrum are at ± 1.023 MHz from the center frequency and the first nulls of the P(Y)-code power spectrum are at ± 10.23 MHz from the center frequency.

Figure 5 is a plot of the power spectrum of the GPS P(Y)-code (plus 50 Hz data) PSK modulated onto the L2 carrier. The plot is similar to Figure 4, except the center frequency is at the L2 carrier frequency, 1227.60 MHz, and the C/A-code modulation is removed. The first nulls of the P(Y)-code are at ± 10.23 MHz from the center frequency.

A-S protection against enemy spoofing

A typical enemy spoofer would attempt to synthesize and transmit a stronger, but false emulation of the actual GPS pseudo random noise (PRN) signals. The ideal spoofing signal would "capture" an in-view GPS receiver's tracking loops by replicating exactly the same but stronger PRN signals at the same code phase and carrier Doppler frequency as the true GPS signals. It would then lead the navigation solution astray after capture with a low probability of detection of the deception. The capability to capture, then smoothly lead the navigation solution to an alternate destination, requires the spoofer to track the GPS receiver in real time. This information must then be used to synthesize the appropriate GPS signals to match the desired alternate trajectory in real time. These requirements result in an unrealistic spoofer system complexity and an impractical real time computational burden. A practical spoofer would be considerably less sophisticated. For example, a spoofer could be developed which can effectively jam the target GPS receiver with its spoofing signals and prevent it from capturing any signals during reacquisition except the stronger spoofing signals. However, the target GPS receiver using the stronger spoofing signals would compute an unrealistic navigation solution. These characteristics are detectable by a well-designed GPS receiver using a jamming-to-noise ratio meter [4] to detect spoofing signals which are above the thermal noise level or using the receiver's C/N_0 meters to detect spoofing signals which are excessively strong in comparison to normal levels. Either of these conditions would lead to further "reasonableness" checking for excessive residuals in the GPS measurements, since the typical unsophisticated spoofer will produce an absurd navigation solution. However, even if the spoofer is caught in the act, it does succeed in effectively jamming the real

GPS signals, even though the spoofer can be prevented from capturing and deceiving the receiver.

Activating A-S theoretically denies an enemy the ability to synthesize a replica of the Y-code signals for spoofing purposes. In theory this prevents enemy spoofing of PPS Y-code receivers. A simple counter-example to this A-S theory is presented later. Since A-S denies access to L1 and L2 Y-code, the enemy is relegated to single frequency L1 C/A-code operation for navigation purposes. This is perhaps the greatest advantage of A-S, because it supports two alternative regional countermeasures against enemy use of L1 C/A-code. First, the L1 C/A-code can be disabled regionally with a 2-MHz spread spectrum jammer that does not disable the L1 Y-code. This permits the PPS receivers to operate in the jamming region using both the L1 and L2 Y-code signals. Second, if a less sophisticated Gaussian (broadband white noise) jammer is used, this might disable the L1 Y-code signals in some areas of the region. In this case, the PPS receivers would revert to single frequency L2 Y-code operation and model the ionospheric delay correction. To support these strategies, the PPS receivers must have initially acquired Y-code with the assistance of L1 C/A-code prior to entering the jamming countermeasures region. Most DoD PPS receivers have direct Y-code acquisition/reacquisition capability after the initial (cold-start) acquisition. There is an ongoing DoD effort to develop PPS receivers capable of direct Y-code acquisition after initial power turn-on. The major problem to solve is the initial time precision.

Vulnerabilities of A-S

The primary vulnerability of A-S is enemy jamming. One purpose of showing the power spectrum plots in Figures 4 and 5 is to illustrate that there is no perceptible difference in the spread spectrum signals if the PN modulation were due to either P-code or Y-code. Since the autocorrelation periods are the same, the line spacings would be identical. Since the chipping rate would be the same, the null points would occur at the same frequencies. As a result, A-S neither increases nor decreases the jamming susceptibility of a PPS receiver. For example, a P-code spread spectrum jammer maps its jamming energy onto any Y-code spectrum just as effectively as it would onto any P-code spectrum.

Although jamming is the expected threat, the DoD should not overlook the obvious A-S vulnerability to enemy spoofing. A determined enemy could track the GPS constellation using an array of high-gain, low noise, dish antennas. Each antenna in the array would track one GPS SV to obtain the Y-code signals. These GPS signals would be amplified and re-broadcast into the spoofing region at a much higher signal-to-noise ratio than the true GPS signals. A PPS receiver could be easily captured by this type of Y-code spoofer. The navigation solution would be the

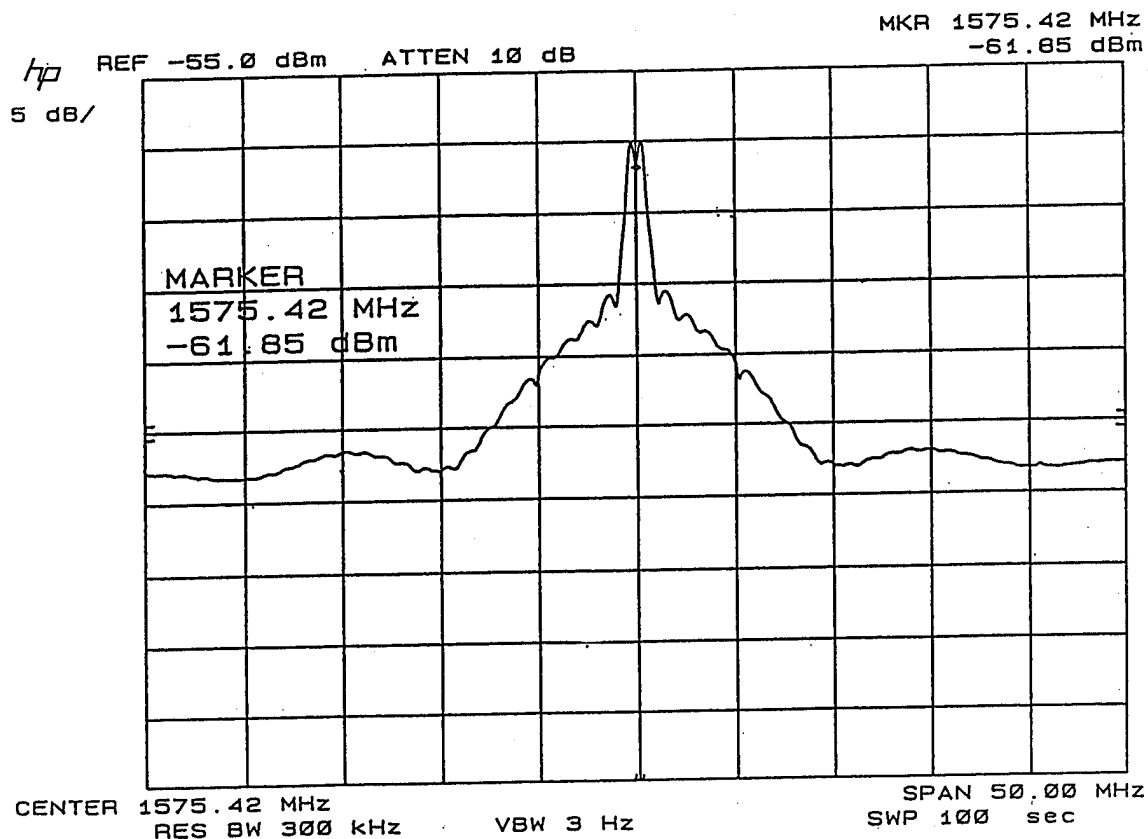


Figure 4. Power spectrum of L1 P(Y)-code and C/A-code from a GPS generator.

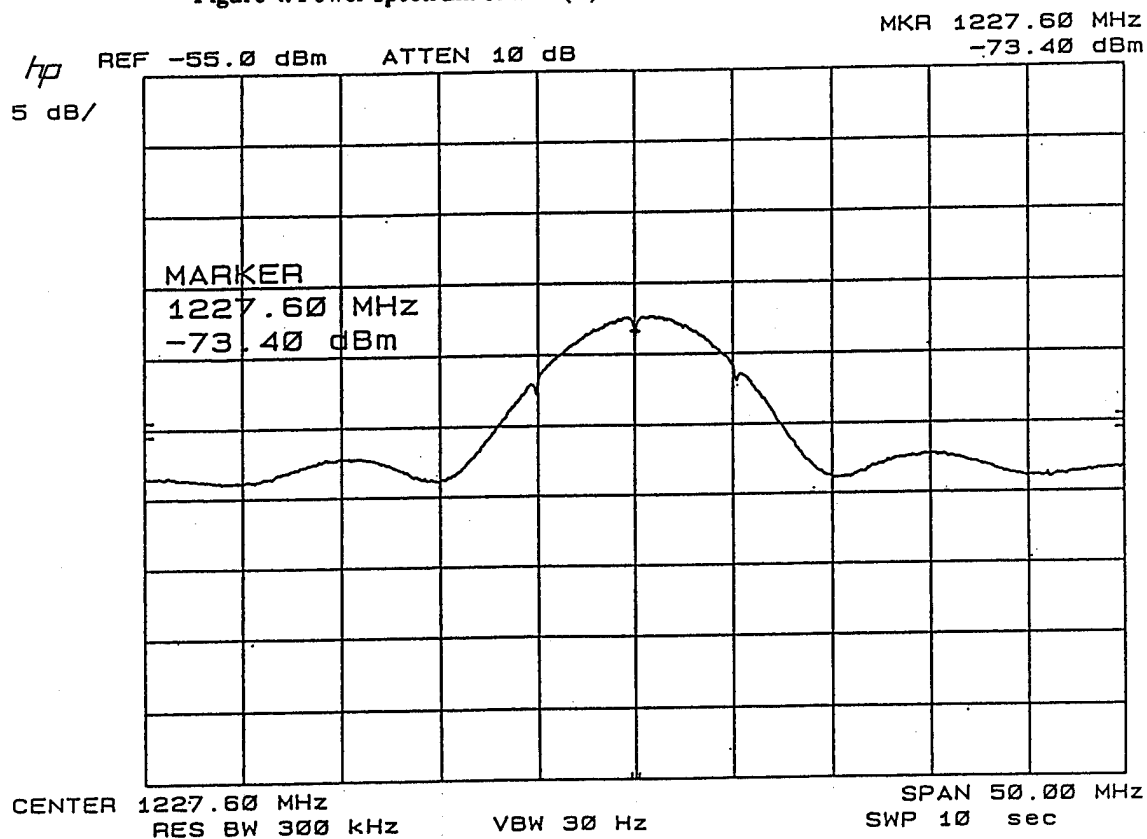


Figure 5. Power spectrum of L2 P(Y)-code from a GPS signal generator.

translated location of the stationary antenna array plus other unbelievable answers. This type of spoofing is easily detected. However, if there is no antispoofing mitigation designed into the PPS receiver, then, when captured by this type of spoofer, the receiver would report very high signal strengths along with an absurd navigation solution. A wideband Gaussian or spread-spectrum jammer would be at least a hundred times less expensive than the least sophisticated spoofer of this type and probably more effective. Therefore, jamming is the expected threat to a PPS receiver.

Codeless GPS receiver techniques

As mentioned earlier, there is a broad class of precise differential SPS users who require two-frequency measurements of the ionospheric delay. As a result of AS, conventional single frequency SPS receivers must model the ionospheric delay instead of measuring it, which is less accurate. However, there are indirect "codeless" means of obtaining the two-frequency ionospheric measurements. The "codeless" designs operate at significantly reduced signal-to-noise ratios (20 dB or more). This greatly increases the "codeless" receiver vulnerability to RF interference (jamming). Successful operation requires the tracking loop bandwidths to be extremely narrow. The processing gain of the narrow tracking loop bandwidths compensates somewhat for the signal loss but this reduces the receiver's ability to operate in a high dynamic environment.

The typical "codeless" receiver design uses a conventional C/A-code receiver to effectively remove the line-of-sight dynamics from the L1 and L2 Y-code signals, then extracts the L1 - L2 differential measurements by some variation of a signal squaring technique which does not require a knowledge of the replica Y-code. The L1-L2 differential signal typically contains low dynamics, except under scintillation conditions. The use of the conventional C/A-code receiver obtains the broadcast navigation message and identifies the SV being tracked in the "codeless" portion of the receiver. The "codeless" tracking cannot extract the message data or identify the SV being tracked. For example, two SVs with the same Doppler will interfere with each other in the "codeless" mode, therefore, the scheme fails for this temporary tracking condition.

One "codeless" technique uses the information learned from its C/A-code tracking loops to steer replicated P-codes so that they partially correlate with the incoming L1 and L2 Y-code signals (see Equation 4). It then integrates and dumps the partially collapsed result to estimate the sign of each encrypted code chip based on the assumption that the encrypted code symbol rate is at the P-code chip rate divided by 20 [5]. This technique results in a reported loss of about 10 dB in the L1 power and about 7 dB in the L2

power for strong received signal-to-noise ratio conditions. These are substantial signal-to-noise ratio degradations, but they are smaller losses than the usual signal squaring techniques. Also, the use of the P-code replica code to partially correlate with the desired SV significantly reduces the interference from other SV signals at the same Doppler.

Summary - Advantages and disadvantages of A-S

The advantages of A-S to the DoD are that it greatly reduces the probability of enemy spoofing of PPS receivers and denies the enemy access to the precision codes of GPS. Limiting the enemy access only to L1 C/A-code is perhaps the greatest benefit of A-S. This permits special regional jamming countermeasures which disable the enemy use of C/A-code for navigation purposes, but permits the continued use of L1 and L2 Y-code. In cases where L1 C/A-code jamming countermeasures also disable L1 Y-code operation in a region, the PPS receiver can revert to single frequency operation in L2 Y-code. If C/A-code jamming is used as a countermeasure, the DoD PPS receivers must have the ability to acquire the Y-code without depending on the C/A-code to perform handover in the jamming region. This countermeasure fails if the PPS receiver enters the C/A-code jamming region without the ability to perform direct Y-code acquisition. From the DoD perspective, the disadvantages of A-S are that it does not improve the PPS receiver susceptibility to jamming (which is the greatest threat), does not totally prevent the possibility of enemy spoofing, and requires the DoD to solve a significant key-management logistics problem which could prevent some of its own PPS receiver resources from gaining access to the precision codes of GPS.

There are disadvantages to the DoD for leaving A-S on continuously instead of only during a military threat. Denying commercial access to the L1 and L2 P-codes in a conventional manner during peacetime prevents advances in P-code technology by commercial GPS receiver developers and keeps the cost of P-code technology high. Continuous A-S also provides an opportunity for a potential enemy to experiment with the encrypted Y-code signals to determine the best countermeasures.

There are no advantages of A-S from the commercial user perspective because it denies access to two-frequency operation. The loss of two-frequency operation is so significant to a large class of commercial differential GPS users that this has prompted manufacturers to develop "codeless" two-frequency receivers. These receivers suffer from serious signal-to-noise ratio losses in comparison with conventional GPS receivers. This increases their vulnerability to both dynamic stress and to RF interference (jamming). This problem would be resolved by the addition of a second civilian C/A-code frequency as recommended by the National Research Council.[1]. Neither the

"codeless" receiver technology nor the second civilian C/A-code frequency pose a threat to the DoD because they are both very susceptible to jamming countermeasures.

Acknowledgments

The author would like to acknowledge that this paper was funded in part by the U.S. Government with the objective of developing greater insight into the vulnerabilities of GPS receivers.

References

- [1] Committee on the Future of the Global Positioning System, *The Global Positioning System - A Shared National Asset - Recommendations for Technical Improvements and Enhancements*, National Research Council, National Academy Press, Washington, D.C., 1995, pp 6-7.
- [2] ICD-GPS-200, *NAVSTAR GPS Space Segment/Navigation User Interfaces (Public Release Version)*, ARINC Research Corporation, 11770 Warner Ave., Suite 210, Fountain Valley CA, 92708, 3 July 1991
- [3] Holmes, J.K., *Coherent Spread Spectrum Systems*, Robert E. Krieger Publishing Company, 1990, pp 379-381.
- [4] Ward, P.W., "GPS Receiver RF Interference Monitoring, Mitigation, and Analysis Techniques," *NAVIGATION, Journal of The Institute of Navigation*, Vol. 41, No. 4, Winter, 1994-95, pp 367-391.
- [5] Gourevitch, S. and Lorenz, R. G., Ashtech, Inc., "The Z-12 Performance Advantage," *Proceedings of the National Technical Meeting of The Institute of Navigation*, January, 1995, pp. 439-444.



Session C5

Airborne Applications

Chair:

Mr. Warren Hundley
Wilcox Electric

Co-Chair:

Ms. Lois Pilley
DSDC

Flight Test Program to Develop a New Terminal Instrument Procedures TERPS for GPS Approaches

John Fagan, Hazem Hejjo, Travis Fox, and Bill Archer
University of Oklahoma

Ralph Sexton
Innovative Solutions International

Gerry McCartor
FAA

Biography

John Fagan is Professor of Electrical Engineering and Computer Science at the University of Oklahoma. Professor Fagan's research is in the area of data acquisition and systems test and has been working with the OU department of aviation in joint research for the past 2 years. John is the OU principle investigator for the flight test project and leads the instrumentation, data acquisition and reduction portion of the current GPS evaluation project.

Ralph Sexton is a supporting engineer for the FAA Satellite Program Office, and serving as a technical advisor on this project. He works with RTCA, Inc. SC-159, GPS Airborne Equipment and SC-181, RNP Specifications. He formerly worked with FAA in TERPS development and testing, where he was also an advisor for the US on the ICAO Obstacle Clearance Panel developing international procedures criteria. He is presently involved in international work for procedures criteria, and GPS implementation.

Bill Archer is chief flight instructor for the OU department of aviation. He leads the pilot evaluation work of the current FAA GPS flight project. He is a long time commercial aviator and has been active in building the aviation program at the University of Oklahoma.

Hazem Hejjo and Travis Fox are graduate students in the Electrical and Computer Engineering program at the University. These students have been responsible for taking all flight test data, and writing the software necessary for data acquisition and data reduction.

Gerry McCartor received his B.S. in Engineering Physics in 1974 from the University of Oklahoma. He was employed as an Electronic Engineer at Tinker AFB developing software for the E-3 AWACS until 1989 when he transferred to the FAA. Gerry is involved in developing and

implementing a mathematical modeling system for computer simulated GPS flights, including GPS signal dynamics and aircraft flight dynamic modeling. He serves as a representative to RTCA SC-159, GPS Airborne Equipment, and works in numerous capacities on a variety of GPS related projects.

Abstract

This paper presents an overview of preliminary flight test results in a program to develop new standards and criteria for GPS terminal instrument procedures. The results presented here are being obtained in an ongoing test program at the University of Oklahoma for the evaluation of non-precision approaches using a GPS navigation system in category A and B aircraft. The OU program is a coordinated partner program with the category C and D programs ongoing at the FAA Technical Center in Atlantic City. This paper will present University of Oklahoma results of flight tests completed to date on the basic "T", straight in, complex and long final non precision GPS approaches. The paper will present preliminary results of isoprobability contours based on the limited data that has been obtained to date. In addition the paper will present initial pilot reactions to the procedures using the GPS navigation systems.

Introduction

Implementation of GPS for instrument approach procedures is one of the final stages in the overall implementation of GPS for air navigation. Standards and criteria for the design of instrument approach procedures is contained in FAA Order 8260.3B, known as TERPS, and several additional orders uniquely applicable to GPS, including Order 8260.38 for civil GPS procedures to runways, and a draft order for civil GPS procedures to heliports. Other documents for procedures standards and criteria and guidance material are underway as are test projects

providing information vital to the design of these criteria. The final stage in the lengthy, involved process leading to the development of the criteria is a series of flight tests, and the analyses of data from the flight tests, conducted with airborne equipment and pilots typical of that used in actual service. That set of flight tests is a kind of "bottom line" or "proof of pudding" step. Extensive research in many disciplines by many institutions - academic, industry, military, US and other governments and countless individuals - has been carried out that has contributed to the design of equipment and implementation methodology in the cockpit. The TERPS flight testing is a final data gathering before designing the instrument procedure criteria.

The discussion here is of the preliminary results of a Category A and Category B project being conducted by the University of Oklahoma departments of Engineering and Aviation, the FAA Satellite Program Office and the FAA Office of Flight Standards. The flight testing is being conducted at Norman Westheimer Field at the University of Oklahoma near the Mike Monroney Aeronautical Center, Oklahoma City, OK. A parallel project for Category C and Category D is being conducted simultaneously at the FAA Technical Center at Atlantic City, NJ. Similar flight tests were conducted using helicopters and the analyses of those data are being conducted at this time for further development of instrument procedures standards and criteria for heliports. In addition, significant flight tests, which supports TERPS development as well as other areas, were conducted by the FAA Technical Center, Canadian Ministry of Transport and the US Air Force. Although these tests were conducted prior to the final development of airborne equipment for civil use, they are a valuable part of the foundation for current testing.

It is also important to mention that the enormous amounts of more basic research leading to the implementation of GPS for air navigation, including TERPS, has resulted in a quantum leap across the board in air navigation capabilities. All areas, including ground equipment, airborne equipment, airborne operations, airspace design, procedures design, air traffic control and any other facet of conducting flight worldwide have the potential of undergoing tremendous change in a compressed time limited only by innovation and economics. The present system is the result of more than fifty years of evolved progress. The

coming system must be the result of careful planning and guided implementation if the technical and economic benefits are to be fully realized. Just as the types of flight testing supporting TERPS combines the results of other research, the results of these tests will feed back into those areas to assist in improvements in each area and the overall implemented system.

Flight Test Program

The procedures being used in this investigation are of four types: basic procedures; complex procedures; extended or long final procedures; and basic "T" procedures. The basic procedures are similar in configuration to conventional procedures that have been in use for VOR and other previously existing nav aids. They have minimal complexity and have collinear initial, intermediate and final segments. The missed approach is a return to the final approach fix (FAF) for holding. The complex procedures are designed to take advantage of the full capabilities of GPS airborne equipment and have complex paths to a final approach segment. These consist of turns at the intermediate waypoint of up to 120° and turns at the final approach waypoint of up to 30°. The missed approach procedure has turns and segments leading to a missed approach holding waypoint not coincident with a waypoint on the approach procedure. The complex procedures exercise the maximum capability of the airborne equipment and investigate the functions of the equipment in maintaining the aircraft on the approach path, particularly in turns and missed approach maneuvers, and the pilot's ability to comply with all required maneuvers and to maintain orientation along the approach path. The extended final approach procedures consist of long (25nm) final approach segments conducted in the approach navigation mode where the full scale sensitivity on the CDI is 0.3nm and the integrity limit is also 0.3nm. This implementation imposes a high workload for an extended time and investigates the use of GPS for parallel approaches to precision final segments, and other accurate terminal navigation applications. The basic "T" approaches are the investigation of a procedures design concept under which two or more initial waypoints are provided to common intermediate, final and missed approach segments. Under this application, aircraft arriving from diverse directions would select the initial waypoint (fix) most advantageous for their arrival direction and thereby fly the most expeditious

path for the approach procedure. The concept is intended to provide the most expeditious and economic route for the maximum number of aircraft arriving and minimize circuitous routing in terminal areas, whether at a controlled or uncontrolled location.

Figure 1, Basic "T", Case 1, illustrates one of the test approaches for the basic T. It shows initial segments originating at CLEAN, requiring a 90 degree turn to the intermediate segment, and at JEAN, which requires a turn of 120 degree (maximum permissible) to the intermediate segment. In the design of an actual procedure, one initial waypoint would be placed on the easterly side of the approach, as CLEAN, with the actual

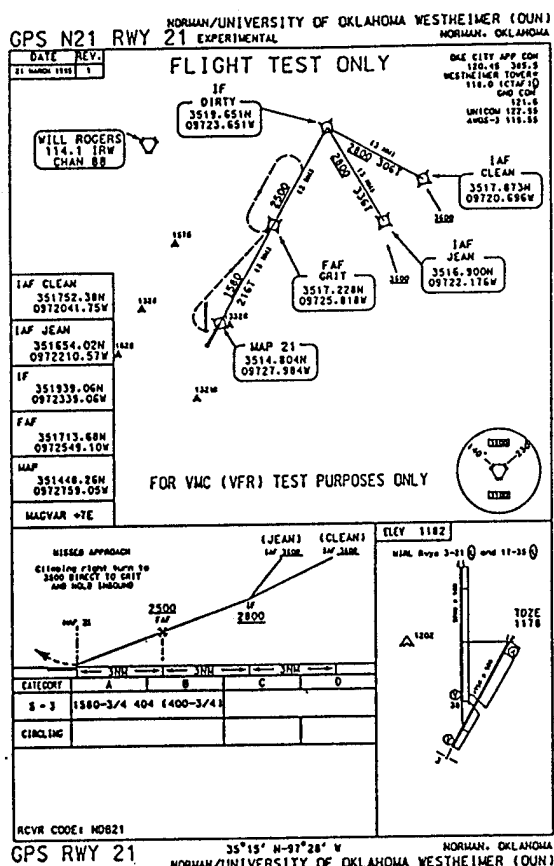


Figure 1. Basic T Case 1

location and turn angle determined by obstacles and/or traffic flow requirements. A counterpart waypoint would be placed on the westerly side of the approach, in the actual location determined by obstacles or traffic flow. Aircraft approaching would select the waypoint most advantageous for the direction of flight, with aircraft approaching from NNE perhaps selecting DIRTY as the first

waypoint in the procedure, once more, if obstacles and traffic flow permit. Thus approach paths are optimized and the need for course reversals by procedure turns or holding patterns is eliminated.

Fig 2, Complex 2, illustrates a procedure of maximum complexity with a turn of 120 degree at the intermediate waypoint and a turn of 30 degree at the final approach waypoint. Also, the missed approach holding waypoint is not coincident with any waypoint on the approach part of the procedure.

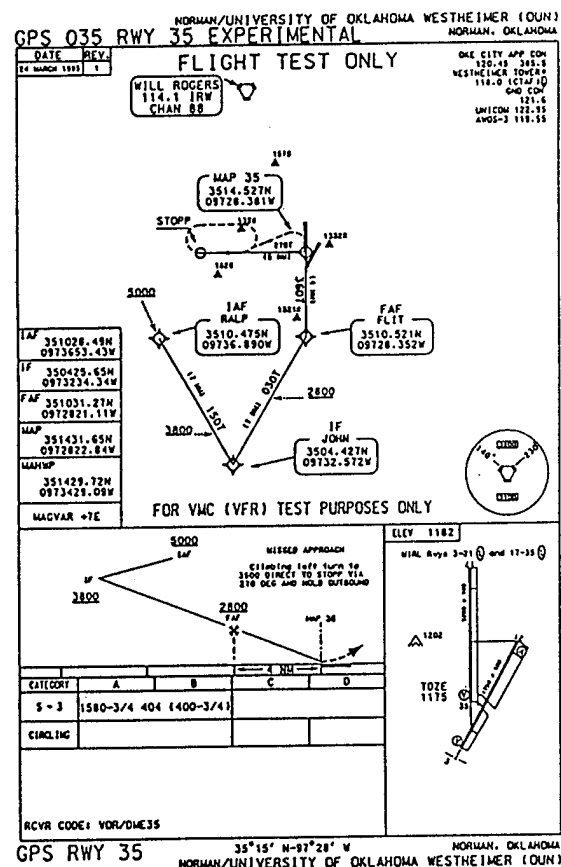


Figure 2. Complex 2

Fig 3, Extended Final 2, illustrates the 25nm final approach. This procedure imposes a high workload for an extended an period since the full scale CDI deflection is 0.3nm. This procedure is in support of development of criteria for parallel approaches and other terminal navigation requiring extremely accurate adherence to the approach path for extended distances.

The results of this testing contribute data for use in development of procedures design standards and criteria. One of the most important factors is

the determination of the requirements for obstacle protection areas. Statistical analyses of data from individual tests, as well as from all tests combined, are used to determine the areas about the approach path which must be free of obstacles. Other design factors include: the required segment lengths vs. aircraft speed category; required segment length vs. turn angle entering and exiting the segment; descent gradients vs. angle of turns and speed of aircraft; effects on size of aircraft and sophistication of other aircraft systems.

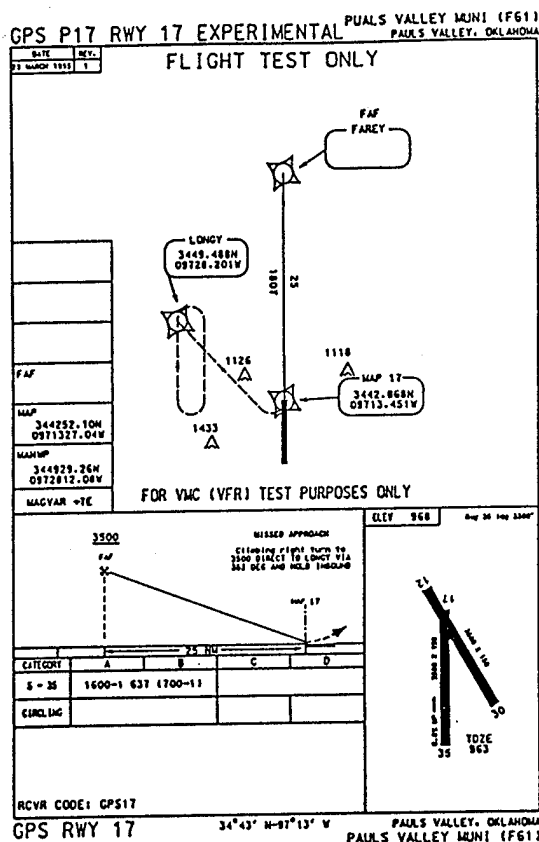


Figure 3. Extended Final

Selected Test Aircraft

In order to conduct the GPS evaluation a pair of test aircraft were chosen for instrumentation. The category A aircraft chosen is a Seneca TA-34-200. The Seneca was chosen for its wide range of category A speeds and could easily typify a large number of category A aircraft and pilot profiles. At the same time, the aircraft would be representative of the upper range of category A aircraft in complexity and speeds. The Aero Commander AC 68 was chosen to represent the

category B aircraft. The AC 68 easily reaches the upper range of the category B and provides complexity typical of the category. In addition, each plane was easily instrumented by the research team and can carry the required instruments and crew during test missions. Both planes are converted from their normal passenger service mission to test aircraft by a set of versatile instrumentation that can be moved on or off the aircraft in order to make maximum use of each aircraft as a research, teaching, or passenger vehicle by The University of Oklahoma. Both planes have worked extremely well and have easily performed test missions at category A through category C speeds.

Each of the aircraft are equipped with two different GPS receivers for purpose of evaluation. The receivers are coupled into the aircraft's pilot instrumentation system by means of the analog outputs of each of the receivers. In each cases the receivers are also coupled to the aircraft's autopilot systems. Both receivers can be operated simultaneously in the aircraft; however, only a single receiver can be selected for the test navigation mission. Each of the receivers is loaded with the University test approaches in addition with the approaches normally accompanying each of the databases for use in normal service in the national airspace system (NAS).

Instrumentation

In order to measure the performance of the category A and B aircraft an instrumentation plan had to be developed. The instrumentation plan was different than that of the FAA technical flight center since the aircraft were to serve both a test mission and a passenger support mission for the University. In order to accomplish this a set of compact, easy to move instrumentation had to be installed in each of the aircraft. The data acquisition system mates to a group of connectors permanently mounted in each of the aircraft.

The aircraft side of the connectors reaches out to the various monitored points in their respective aircraft and brings the monitored data to a central point for data acquisition. The self contained data acquisition system is interfaced to the individual aircraft by the onboard connectors when a flight test mission is ongoing.

The data acquisition system is easily moved on and off each of the test aircraft in about 5 minutes in order to allow the aircraft to easily slip from a test to a passenger mission. The data acquisition is entirely self powered thus making it immune from the normal problems associated with aircraft power.

The data acquisition system is made up of the following group of instrumentation. A modified form of the Fluke Net-Daq data acquisition module is utilized to acquire all analog data, and some digital data generated onboard the aircraft. The modified Fluke module was chosen for a wide variety of reasons. The Fluke system is a highly modular and portable system that easily allows the expansion of the data acquisition system in increments of 21 channels at no hardware or software burden. The sample rates of the Net-Daq are fast enough to collect data for both the non-precision as well as WAAS precision approach applications (Sample rates of 1000 hertz per channel per module can be obtained). The output of the data acquisition system is presented in the form of TCPIP packets on an ethernet which is easily handled by on board 486 computers. The data acquisition system has a 160 dB common mode rejection on all input channels that prevents channel crosstalk and ground loop faults normally associated with common ground data acquisition systems. This particular characteristic was especially useful in the AC-68 due to the presence of power system ground loops and tremendous amounts of electrical noise.

In flight the Net-Daq system is coupled to a 486 laptop via a thin ethernet. The 486 laptop serves as a real time window on all channels of data being taken on the aircraft as well as a logging system for the acquired data.

Some of the analog data that is collected includes but is not limited to, analog outputs of the GPS receivers, the signal that drives the pilot's CDI, roll and pitch. In addition, GPS time, altitude, airspeed, DME data and other parameters are monitored. Flight surfaces are to be monitored in future flights. These parameters are logged in engineering units in a standard CSV format.

In addition to the analog data that is taken, all digital data provided by the individual GPS receivers on the RS 232 outputs are acquired. These include, but are not limited to, GPS position, GPS time, cross track error, ground

speed, and satellite information. The data is taken on a per solution basis and is logged on a separate laptop computer, where the plane's current position and track are also plotted in real time.

Truth System

Each of the test missions is monitored by a position truth system. The system that has been chosen is a modified version of the Ashtech Z12 differential GPS. This system consists of two modified Ashtech Z12 receivers operated in the differential GPS mode. The stationary receiver is placed on a reference position at Westheimer airport. The mobile receiver is placed on the test aircraft. The differential data is mission post processed, and time synchronized with the analog data. The Ashtech Prism software is used to produce differential ground data of each of the flight missions.

The Ashtech Z12 system was chosen because it is a proven differential standard, and has the ability to provide solutions at a faster rate than the test GPS systems. In addition to the use of the Z12 for providing dynamic truth data, the system has been used to provide static survey information for the airfields where procedures are being flown. It was found, early in the testing, that database information did not accurately represent the position of chosen airfield thresholds, with errors as large as 940 feet found. Therefore, the Z12 has been used to accurately define all of the thresholds of the currently used airfields.

Modifications to the Z12 include the change of the solution rate that would be compatible with the WAAS solution rate, and the ability to produce a differential solution that can be conditioned by OU software to a pseudo WAAS correction signal for further testing of the WAAS procedures.

Flight Test Subject Pilot

Each subject pilot is accompanied in the aircraft by a safety pilot, a procedure observer and a data acquisition specialist. The primary duties of the safety pilot are to observe how the pilot performs the procedures, provide the necessary VFR flight safety observer, and to provide some degree of physical relief to the subject pilot between individual approaches. The observer must be familiar with the sortie plan and all of the flight test procedures and provide coordination of the

approach under test and the data acquisition team and act as an additional safety observer. The observer keeps a log of each approach noting the ability of the pilot to operate the equipment, fly the plane, and perform the approach, and to record information on any anomalies that occur during a procedure.

Each subject pilot, prior to making the test approach, spends 2 to 3 hours in simulator familiarization with one of the safety pilots. Here the pilot is acquainted with the GPS receiver and the use of the receiver in conjunction with flying the approach. He will then fly from 1.5 to 3 hours of aircraft familiarization flights using the receiver to make anywhere from 4 to 15 practice approaches.

The individual test pilots are chosen from a voluntary, random pool of category A and B pilots of varying degrees of professional experience and airframe time. An effort was made to accurately reflect the cross section of pilots in each category.

Flight Tests and Results

In June of 1995 a flight test program was initiated by OU after the planes were equipped with data acquisition systems, and data collection/reduction software was developed. The flight test program called for flying the straight, basic "T", complex and long approaches in both the category A and B aircraft. The flight test program called for the use of three GPS navigation systems in the two aircraft to determine the ability of the pilots to make a prescribed non precision approach using a variety of equipment. Approximately 1/2 (one half) of the missions have been completed. A total of 323 approaches and 156 departures have been flown in both the category A and B aircraft. 194 approaches and 90 departures have been flown category A, and 129 approaches and 66 departures have been flown category B. In addition 34 high -speed approaches have been flown simulating category C aircraft for special evaluations.

For each of the approaches and departures flown, data were developed to reflect true path along the approach, flight technical error (FTE) analog (CDI needle position), cross track error, vertical profile of approach, ground speed, total system error, and navigation system error. In addition satellite data, altitude data, airspeed, roll and pitch are logged. A typical set of data for a flight

sortie is shown in figures 4,5,6,7,8,9 and 10. This sortie depicts a representative approach on a single sortie. Figure 4 is a plot of the truth track of the category A aircraft over the intended flight path, as determined by the differential GPS measurement. Figure 5 is a situational plot of the pilots CDI needle. This measurement is analog and is made from the back of the CDI. Figure 6 is the cross track error produced by the GPS receiver and is gathered from the RS-232 port of the unit under test. Both plots 5 and 6 are plotted as cumulative distance along the track. Figure 7 is the ground speed, as measured by the differential truth system (Z12). Figure 8 is a plot of the truth system altitude of the aircraft along the track of figure 4. Figure 9 is a plot of total system error (TSE) and is the measured perpendicular distance from the aircraft's actual track position to the corresponding position on the true track. Finally figure 10 is the Navigational System Error and is the difference between the GPS receivers computed position and the differential truth position at the same GPS time.

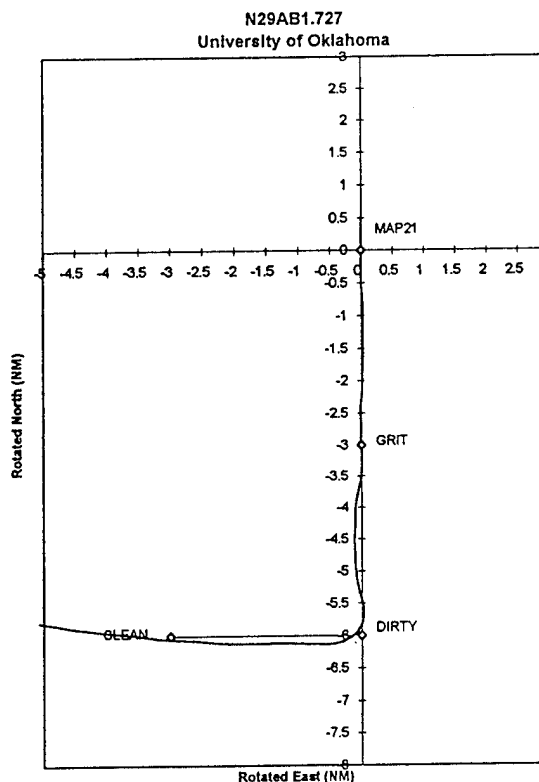


Figure 4. Aircraft Track (z12)

One of the goals of this flight test program is to determine the approach flight space required for each one of the types of basic "T" approaches. In order to determine, or begin to determine, what

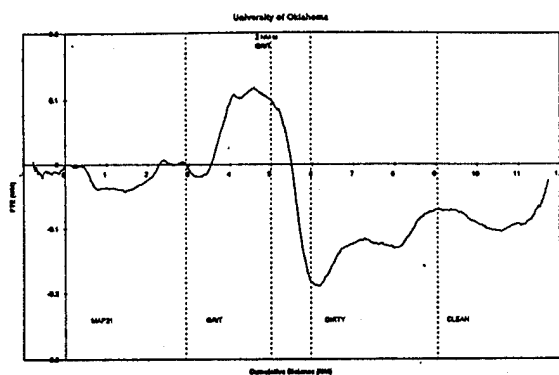


Figure 5. Flight Technical Error (Analog)

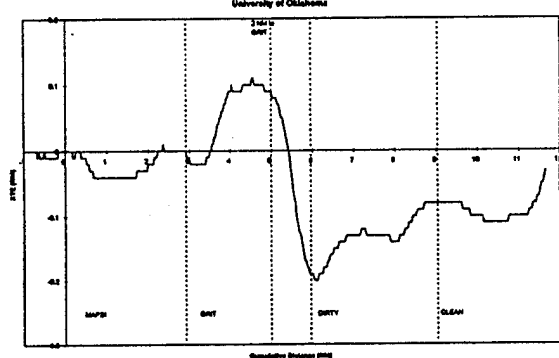


Figure 6. Cross Track Error (Digital)

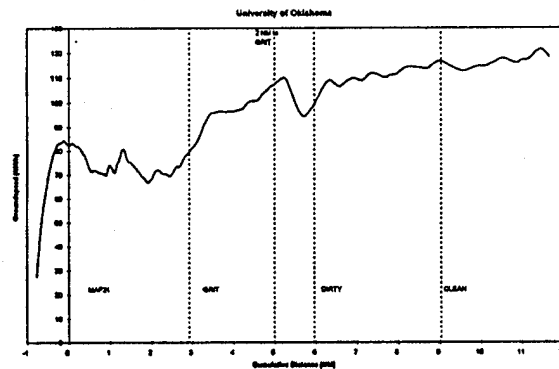


Figure 7. True Ground Speed

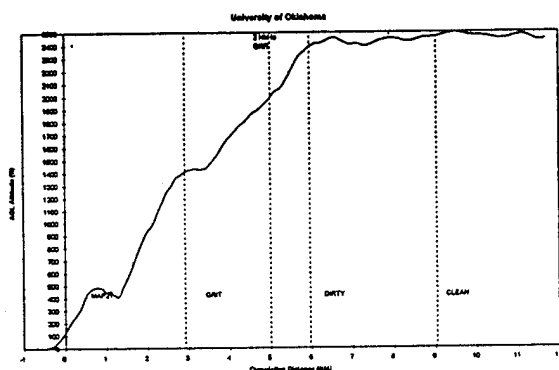


Figure 8. True Altitude Along Track

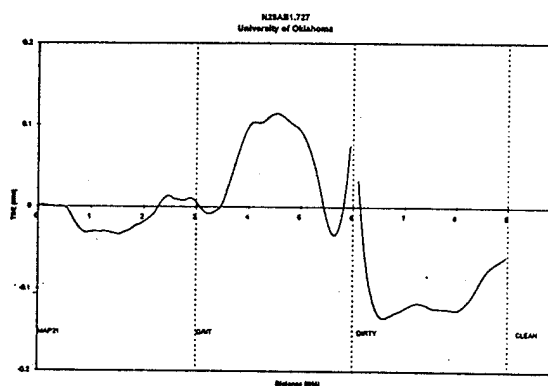


Figure 9. Total System Error

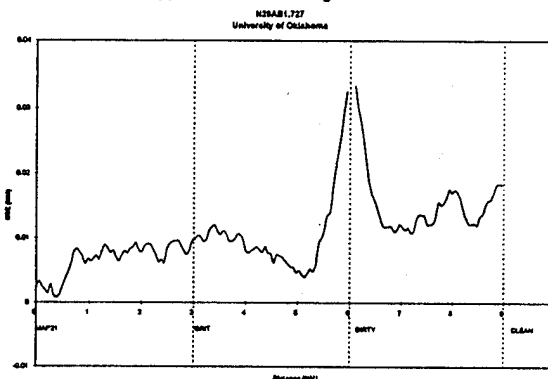


Figure 10. Navigation System Error

the approaches flight space requirements are, the individual sorties can be combined in order to obtain some statistical significance to the collection of individual flight envelopes. With the data that has been gathered to date the following surfaces can begin to be observed. It is important to note that the experiment is only partially finished, and that at this point that only 1/2 of the flight tests have been completed, and not all GPS systems have been fully evaluated, so the data shown here represents only a preview of what the composite approach spaces may be.

In order for the reader to get some idea of what the tests are targeted to, some typical data will be shown. The data shown here only represents a small part of the data that has been taken to date, but is representative of the body of data.

Sample approaches and departures will be shown and both categories A and B. A three mile basic T approach is shown in figure 11 the approach envelopes are shown in figures 12 and 13. Figure 12 shows a 90 degree approach to the intermediate, while figure 13 shows a 120 degree approach to the intermediate. Figure 12a and 13a are category A results, while 12b and 13b are

category B results. The outer envelope represents the 6 sigma envelope, the center envelope is the 2 sigma zone and the line in the center is the mean path for all of the sortie data.

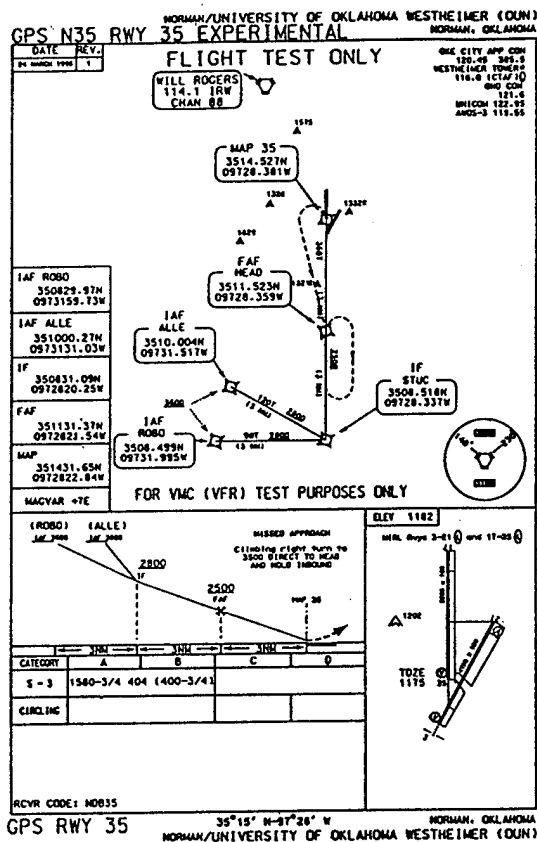


Figure 11. 3 Mile Basic T Approach

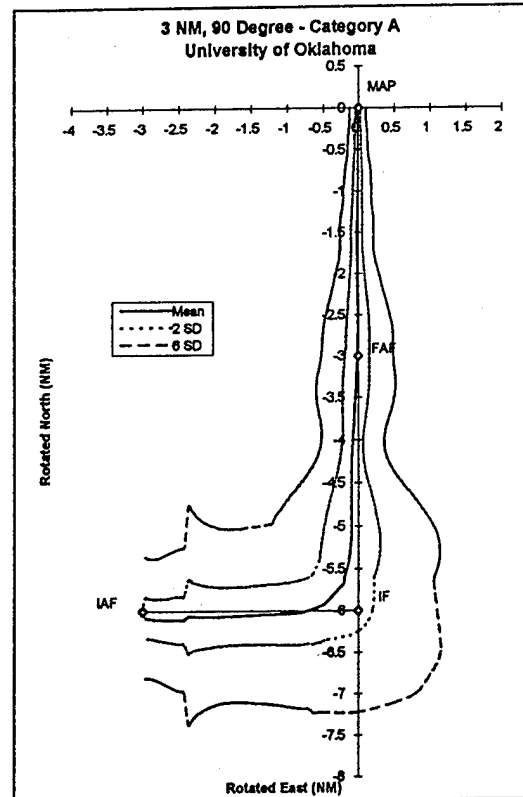


Figure 12a Category A 90 Degree Approach Basic T

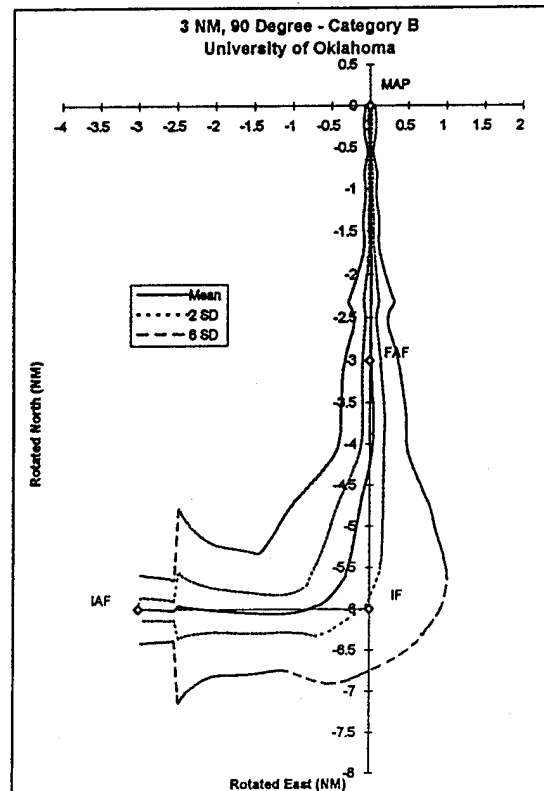


Figure 12b. Category B 90 Degree Approach Basic T

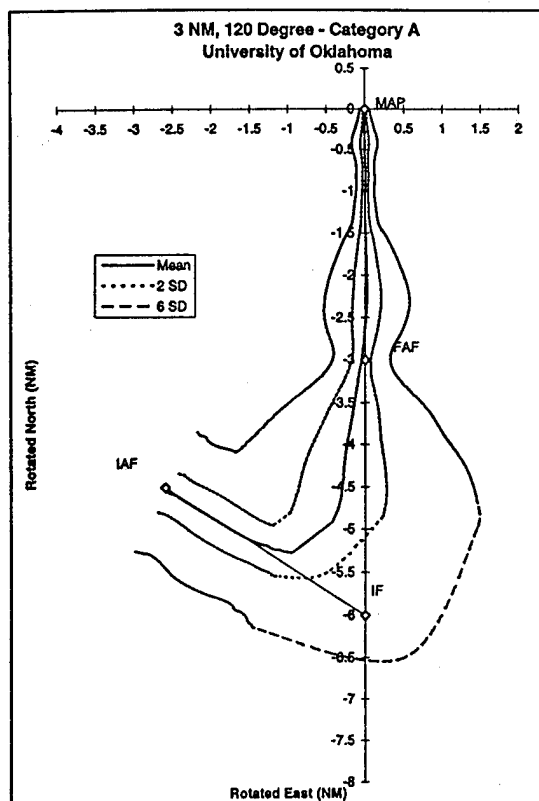


Figure 13a. Category A 120 Degree Approach Basic T

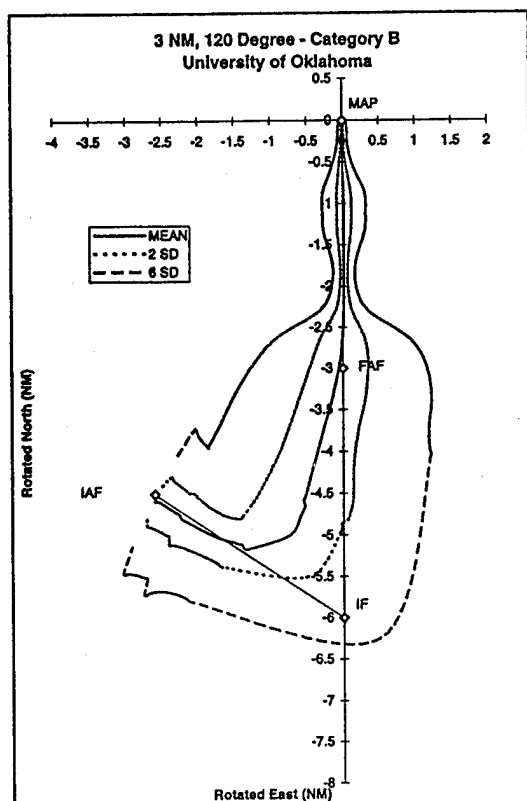


Figure 13b. Category B 120 Degree Approach Basic T

Another approach that was evaluated was the longer 4 mile basic T. This approach was evaluated as were the longer basic Ts. In each case the approach was evaluated for both category A and B aircraft. In addition to the 4 mile basic T the 4 mile straight approach could be evaluated with the pattern.

Figure 14 is the approach plate for the 4 mile basic T and Figures 15 and 16 show flight envelopes for the chosen approach. Figures 15a, and 16a represent category A response, while 15b and 16b are the category B response. Once again the outer envelope is 6 sigma, the inner is 2 sigma and the center path is the mean path.

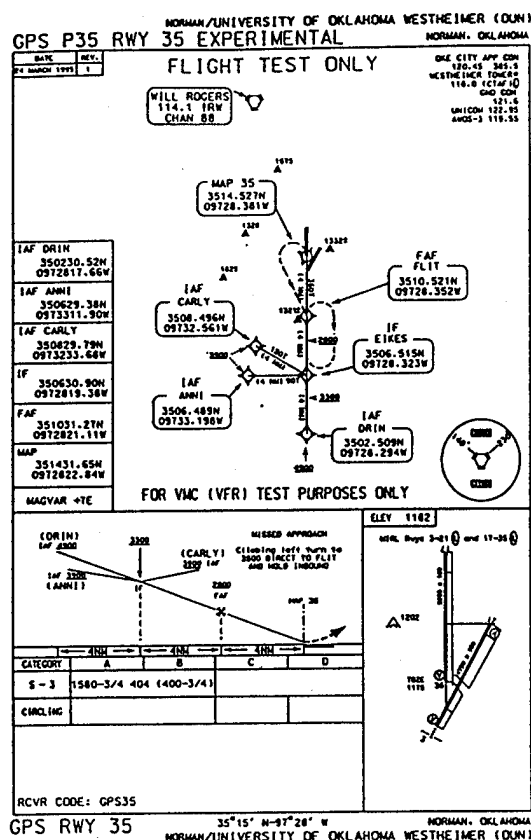


Figure 14. 4 mile Basic T Approach

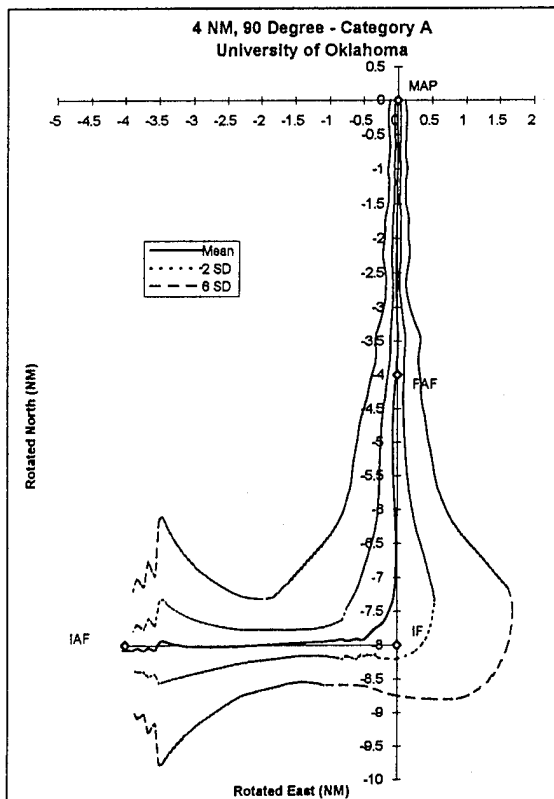


Figure 15a. 4 Mile 90 Degree Approach

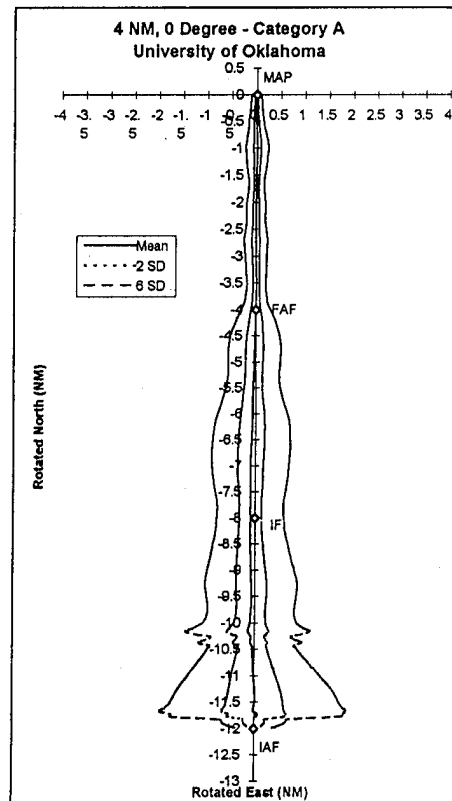


Figure 16a. Category A Straight Approach

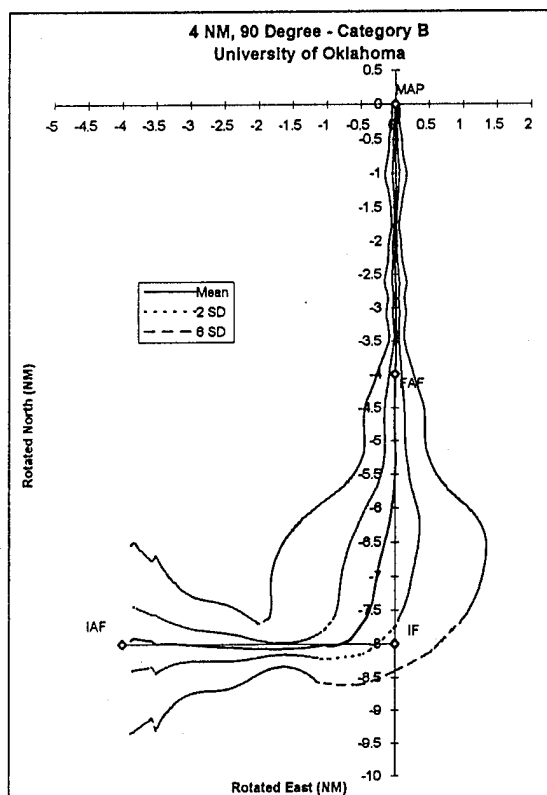


Figure 15b. Category B 4 Mile Basic T

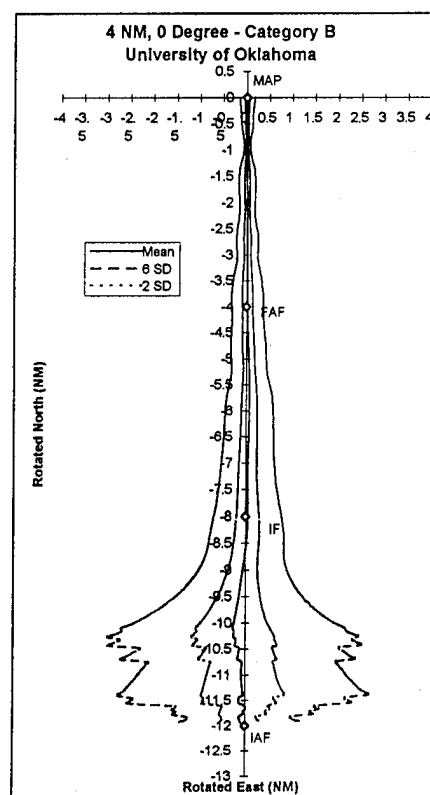


Figure 16b. Category B 4 Mile Straight Approach

In addition to the short basic T approach and the straight in approach, the long approach is being evaluated. The 25 mile straight approach is being evaluated in order to determine the envelope associated with the long final.

Figures 17a and 17b show the preliminary flight envelopes for the 25 mile approach.

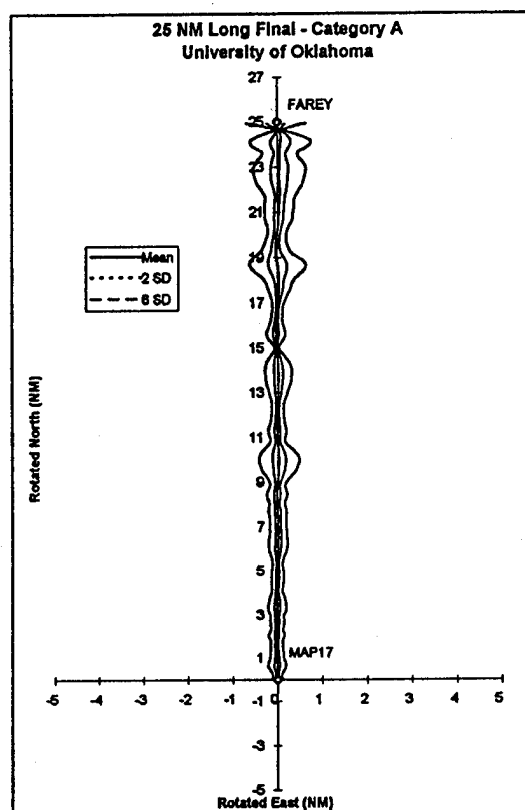


Figure 17a. Category A 25 Mile Approach

In addition to approaches the project test team is also evaluating GPS departures. Again, fewer departures have been completed than approaches so the data presented on departures is only a draft preview of the final test results.

A number of simple and complex departures are being tested. However, unlike the approaches the departures are much more subject to air traffic control and are therefore often interrupted or terminated prior to completion.

Figure 18 depicts the departure plate and figure 19 depicts the statical envelopes associated with the category A and B aircraft for the departure.

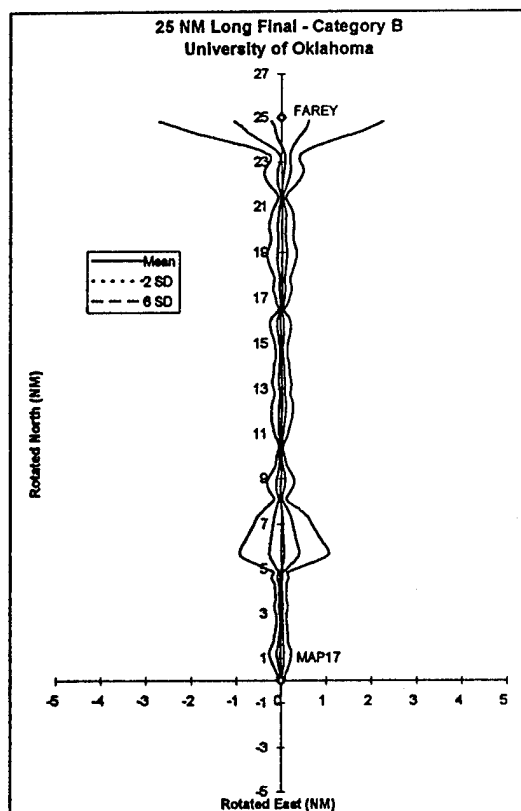


Figure 17b. Category B 25 Mile Straight Approach

Pilot Evaluation

No data analysis or subjective evaluations will be made from these tests which identifies any preferences for one receiver over another, or which identifies any perceived inadequacies in a specific receiver. However, results from this and similar test projects, must identify general operating characteristics of receivers which must be accommodated in procedures design and terminal operations. Features which are considered essential to sole means or primary means equipment of the future must also be identified and provided to those developing performance specifications for such equipment. Therefore, a synopsis of some of the initial pilot reactions is appropriate here.

Using GPS as a primary means of navigation requires that the units be extremely user friendly. Once the particular approach has been selected for the unit, the pilot currently is capable of flying the

Conclusions

Since the major objective of this project is to provide data to support design of GPS criteria and that can only be accomplished after extensive analysis of these data and combinations with other data, it is impossible to conclude the results at this point or to formulate specific recommendations. However, it comes as no surprise at this point in the implementation process for GPS that approach procedures designed generally in conformance with previous RNAV standards and in conformance with the existing criteria for GPS supplemental systems, are fully flyable by general aviation pilots, as well as commercially rated pilots, with short periods of indoctrination and instruction. At this point in the project, the recommendations that are developing are to simplify actions needed to operate equipment, particularly in single pilot use, for aids in maintaining situational awareness and for increased flexibility in terminal navigation. Given the capability of GPS, providing greater flexibility and simplifying equipment operation will be an ambitious objective. The basic operations and procedures configurations seem also to meet the requirements for terminal navigation, and recommendations will likely be for enhancements, not principal changes. The accuracy of GPS, although well established and not part of this test, lives up to full expectations as indicated by the data, and there are, so far, no surprises in the pilot performance in maintaining acceptable FTE. Establishing an operational accuracy figure for GPS for each phase of operation seems to be one of difficulty/cost vs. benefit. The primary consideration, based on initial data from this test, is allowing maximum availability without giving up benefits of increased accuracy. This is indeed the subject of considerable analyses and discussions in industry, special committees and among FAA specialists. Data from this test is also proving to be valuable in investigating possible enhancements for WAAS airborne equipment and in procedures designed to be conducted using that equipment. Data from this project is being supplied to the FAA as the test progresses and will be available in a full report at the completion of the project.

Acknowledgments

The University of Oklahoma research team would like to acknowledge the research conducted by

other organizations, which formed the foundation of this project. We would also especially like to acknowledge the cooperation of the FAA Technical Center, Bob Till, Barry Billman and his staff who simultaneously initiated the parallel test project for category C and D aircraft. Thanks also to Don Pate and Carl Moore of the Oklahoma City FAA Flight Standards "TERPS" Branch, Oklahoma City Approach Control, and last but not least, to David Sandman and David Clemons who have ridden and will continue to ride many hours of rough air in pursuit of the ultimate flight test data. A special thanks also go to all OU graduate students who work on the FAA project whose dedicated slave labor have made the project possible.

Attitude DGPS/INS Based Real-Time Flight Guidance System for Airborne Sensors

Dr. Günter Hein, Dr. Bernd Eissfeller, and Jürgen Pielmeier
Institute of Geodesy and Navigation

BIOGRAPHIES

Dr. Günter W. Hein is full Professor and Director of the Institute of Geodesy and Navigation at the University of Federal Armed Forces Munich. He is responsible for research and teaching in the field of high-precision GPS/GLONASS positioning, navigation, physical geodesy, gravimetry and satellite geodesy. He worked in the field of GPS since 1984 and is the author of numerous papers on static and kinematic positioning. He is lecturer at NavTech seminars in the field of DGPS.

Dr. Bernd Eissfeller is Head of the GPS Laboratory and Vice-Director of the Institute of Geodesy and Navigation at the Federal Armed Forces Munich. He is responsible for the operation of the laboratory, for teaching and research in the field of GPS/GLONASS and inertial technology. Till the end of 1993 he worked in industry as a projectmanager in the development of GPS/INS navigation systems.

Jürgen Pielmeier is Research Associate at the Institute of Geodesy and Navigation at the University of Federal Armed Forces Munich. He studied aerospace engineering at the University of Technology in Berlin. Since 1993 he is doing research on attitude GPS and GPS/GIS integration mainly for a project concerning with GPS aerotriangulation.

ABSTRACT

At the 'Institute of Geodesy and Navigation', an advanced attitude DGPS/INS based guidance system for high precision kinematic airborne sensor positioning and orientation in real-time is under development.

The objective of this airborne system is to support the customer through all phases of flight with a reliable multifunctional navigation system. From take off over enroute navigation to remote sensing and back in real-time with high precision and maximum integrity.

The navigation system has a flexible architecture. The kernel is a 'Intel' based multiprocessor system with scalable performance according the necessary requirements. Through the 'Peripheral Component Interface' up to three colour LC-Displays, a robust memory subsystem and other I/O interfaces as RS232/422, PC-Card and MilStd 1553B are connected to the system. This I/O interfaces enable it to connect nearly every navigation or remote sensor to the system to achieve the desired functionality. The main flight guidance program is responsible of time synchronization and control of the different program threads, parallel executed on the different processors, and the processing of the waypoint based flight plan. The onboard geographic and navigation database is used for optimal visualization of the actual flight situation and decision supporting of the flight crew.

Two main conclusions can be summarized: At first, the integration of attitude, position and velocity information from the different navigation sensors increases precision and integrity for enroute navigation and complete airborne positioning of different remote sensors. Second, the flexible system architecture with it's high performance multiprocessor kernel and open system interfaces enables easy application dependant integration of the desired navigation and/or remote sensors.

The new aspects of this airborne application system can be summarized as follows:

- Scalable performance, open interfaces, easy integration, advanced visualization
- High positioning precision and flight execution integrity
- Complete navigation sensor integration of position, attitude and velocity in realtime
- Easy remote sensor integration, monitoring and control.

INTRODUCTION

The system described on the following pages is only a part of a bigger 'complete production system'. The relationship between the different parts of this

'production cycle' and their logical interaction are shown in Fig.1.

set up new data, to update old data or to combine it with other data inside the database. This database can then be used for data analysis for many applications.

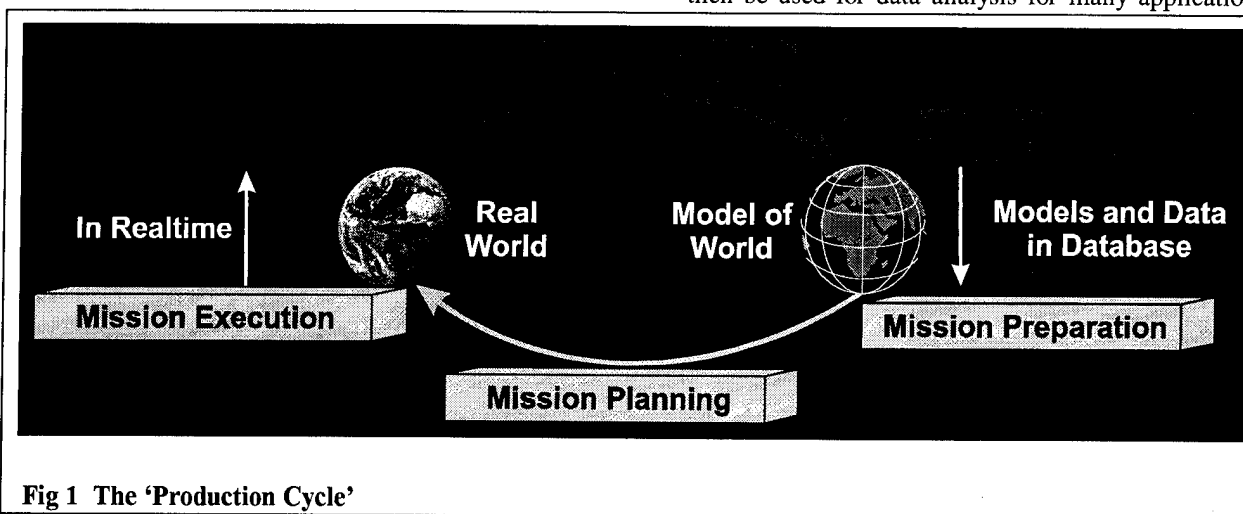


Fig 1 The 'Production Cycle'

This 'production cycle' is divided into two logical sequences and will consist of four parts in the final development stage.

At first a short description of the 'sequence view' of the production cycle.

The first sequence is the 'Mission' sequence. This means the logical steps from 'Mission Preparation' over 'Mission Planning' to 'Mission Execution'. These are the steps necessary to obtain new data. 'Mission Preparation' is the step to decide what kind of data are desired, what accuracies are required and what kind of sensors are necessary to obtain these data. 'Mission Planning' is the planning part of the 'Mission Cycle'. It's responsible to generate a concrete execution plan, usually a flight plan, out of the requirements and restriction from the 'Mission Preparation'. This flight 'execution' plan is then used by the pilot/mission specialist of the airborne sensor platform during 'Mission Execution'. The pilot has to position the aircraft at the waypoints generated in the 'Mission Planning' using the different navigation sensors, while the mission specialist has to control the parameters and the function of the different remote sensors.

The second sequence is the 'Data' sequence. The 'Data' sequence starts with 'Data Acquisition' using the different remote sensors onboard the sensor platform, usually an aircraft. These data are then used during the 'Data Processing' sequence, where the measured raw data of the remote sensors are processed, usually using the logged raw data of the navigation sensors to obtain the desired data outputs. In aerophotogrammetry, this process normally includes bundle block adjustment using aerotriangulation, generating orthophotos and so on. Once these data are processed, they have to be included into the database during 'Data Integration'. These data can be used to

This database is the starting point and the endpoint of the whole production cycle.

The 'Database' is one of the four parts of the 'Development cycle'. This Database includes the two sequence parts 'Data Integration' and 'Mission Preparation'. Mission preparation is only one of many applications of the data in the database. It's a special use of these data, because it's used to obtain new data, to generate a better model and understanding of the real world. Seen the 'production cycle' form a 'time view', this part is the *permanent part*, because the data are stored permanently inside the base and can be used by many different users for many *different applications*. A small database engine was implemented now to test the object-oriented 'data-and-model' approach to a 'Model of the World' database. Investigations of designing a full featured GIS-system are going on.

The mission planning system ('VAMP') is the second part. At the moment, this program is implemented at a Windows 3.1 user-interface. It will be updated to Windows 95 during the next months. Until now it supports planning only for aerial cameras, but it will be upgraded to laser scanners at the end of the year.

The third part of the 'production cycle' is the 'SANC' navigation system. This navigation system includes the two sequences 'Mission Execution' and 'Data Acquisition'. It has the task to guide the sensor platform to the planned remote points and to trigger the remote sensors at these points and to log the time-tags generated at the moment of exposure by the different sensors. The navigation system is based on different navigation sensors like GPS and inertial measurement systems. The actually flown navigation sensors depend on the navigation data, necessary for data post processing (accuracy, position and/or attitude). From the 'time view', this system acts in *real-time* and has only

two tasks, flight guidance and data acquisition. This system is under permanent development at a Windows NT operating system to include new navigation sensors and remote sensors to the system and to enhance position/attitude real-time processing and flight visualization capabilities.

The last part is data processing. Until now, there's no own software development in this area. Instead this work is done by other institutes.

On the following pages, after a short presentation of the planning system 'VAMP', the main topic is the 'SANC' navigation system.

PLANNING PROGRAM 'VAMP'

The mission planning 'VAMP' consists mainly of two working levels, which can be seen in Figure 2.

project. The 'Testflight 1' on the left side consists here of 9 flight tasks, including three photo block areas. On one of these photo blocks, 'Vaihingen' is also shown on the right side of the screenshot. Here the block area is already planned, using the task editor for aerial cameras, which enables the visual selection of a block area for a photo flight on an underlying geographical grid. The user only has to click on the desired edge points of the block area. The system always shows the actual distance and azimuth from the last set point to the actual mouse position. The system can plan block areas, stripes or single point pictures. It has the capability to zoom in and out in a true three-dimensional visualization environment about an order of 10^7 and to rotate in all directions.

In the final system, every task type on the left side will have its own task editor, which enables then planning of starts, landings, enroute navigation and so on. This means that every task planned on the project level starts the dedicated task editor on the task editor level

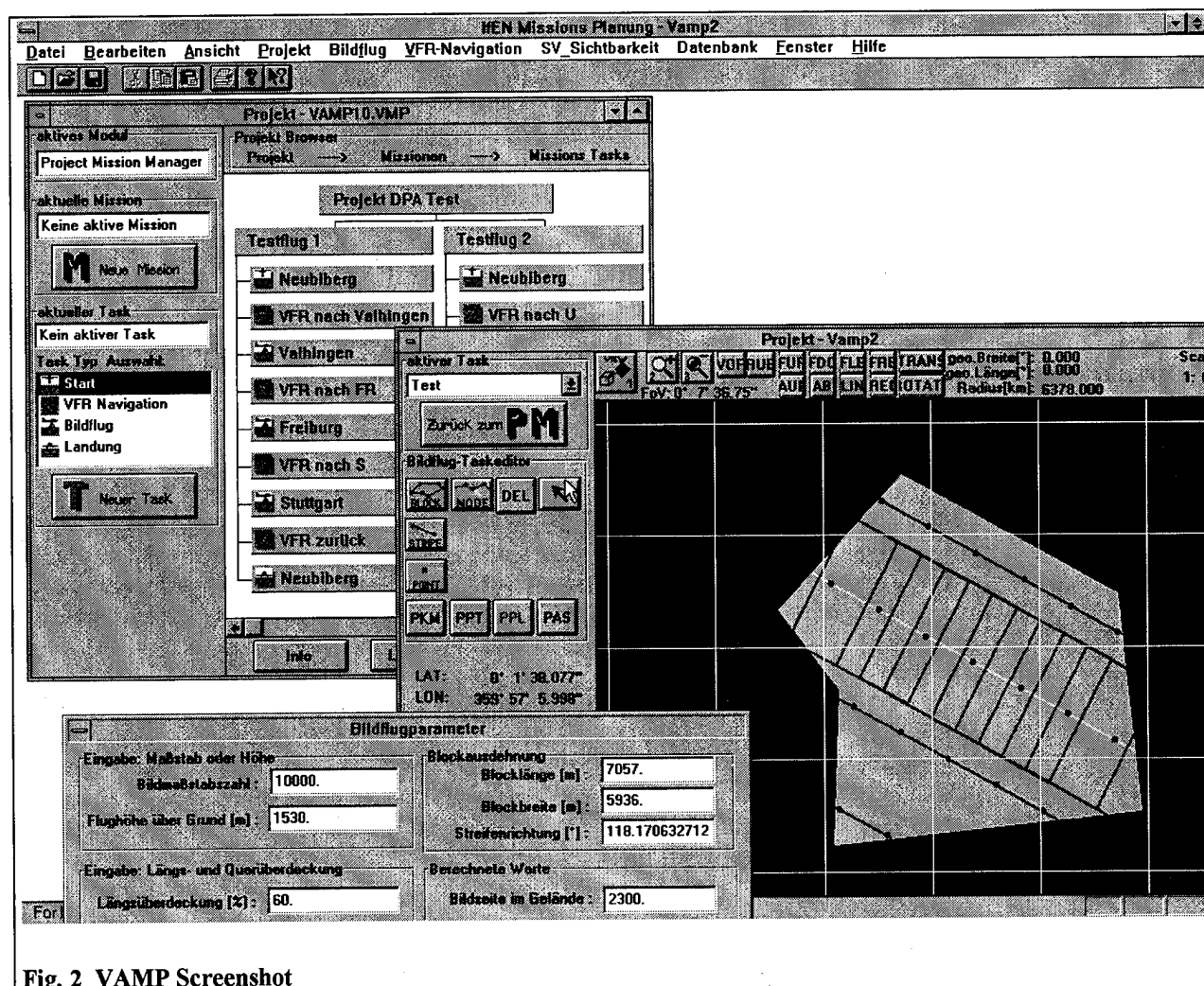


Fig. 2 VAMP Screenshot

On the left side of the screen shot, the 'Project Management Level' shows two planned testflights of one

when it's selected.

To edit a photo block area for an aerial camera, VAMP offers the capability to modify the different photo parameters inside a dialog, see Figure 3, and to

In the next sections, the following topics will be discussed. The SANC overall flight configuration, the hardware system, the system software with deeper focus on navigation sensor handling and remote sensor handling.

Bildflugparameter	
Eingabe: Maßstab oder Höhe	
Bildmaßstabszahl :	10000.
Flughöhe über Grund [m] :	1530.
Blockausdehnung	
Blocklänge [m] :	18371.
Blockbreite [m] :	12315.
Streifenrichtung [°] :	285.318520780
Eingabe: Längs- und Querüberdeckung	
Längsüberdeckung [%] :	60.
Querüberdeckung [%] :	30.
Eingabe: Geschwindigkeit oder Bildzykluszeit	
Aufnahmefolgezeit [s] :	9.2
Geschwindigkeit [m/s] :	100.
Geländehöhe über NN [m] :	
400.	
Berechnete Werte	
Bildseite im Gelände :	2300.
Basislänge [m] :	920.
Streifenabstand [m] :	1610.
Streifenanzahl im Block :	8
Gesamtbilder pro Block :	82
Streifennummer :	4
Streifenlänge [m] :	16218.
Bilder im Streifen :	18

Buttons: OK, Cancel

Fig. 3 Parameter Dialog for Photo Task Editor

view the changes immediately on the screen.

This dialog box contains the usual parameter, necessary to plan a photo block for an aerial camera and the actual block extension, as selected in the task editor. On the left side of the dialog are the input parameters like photo scale/flying height, end lap, side lap, flying speed/exposure interval and flying height above sea level. On the right side are the computed parameters like negative side on the ground, length of base, distance between side laps, number of stripes per block, number of photos in block stripes and the length and photo number of selected stripes.

The camera parameters negative side and focal length are set in a different dialog box.

The computed waypoints and other parameters like flying height and stripe direction are saved together in a 'flight plan' file. Every column in the project level corresponds to one flight mission and therefore to one flight plan.

NAVIGATION SYSTEM 'SANC'

This flight plan is transferred to the SANC navigation system via disk. The SANC system reads the following waypoints including the command to trigger an exposure to the dedicated sensor.

figured according the requirements.

On the low-cost/low-requirements edge this is a cheap dualprocessor flight computer with only one pilot display/interface and the capability to log data from one or two remote sensors and to display the position, delivered from the GPS-processor, on the navigation display. On the high-cost/high-requirements edge this is a true multiprocessor system with multiple displays, remote sensors, navigation sensors and the capability to process DGPS/INS raw data in real-time and to guide the pilot according the flight plan to the desired waypoints using position and attitude data.

SANC always is a combination of kernel components and other external devices, which are added to the kernel system as necessary.

The kernel elements are the flight computer with at least one command and display unit (the blue parts in figure 4). The various hardware interfaces enable it to connect diverse external devices, as described in the 'hardware configuration' section. The capabilities of the kernel system to work together with different sensors are described in the chapters 'navigation sensors' and 'remote sensors'.

In figure 4 there are three navigation sensor types connected to the SANC kernel. Type 1 in figure 4 is usually a Trimble 4000SSE, an Ashtech Z-12 and as soon as available a NovAtel 6000 GPS receiver. Type

Overall Configuration

The real-time navigation system SANC consists of flight computer and the on-board SANC software. It's able to control different remote and navigation sensors in real-time.

A typical system configuration for a flight mission is shown in figure 4.

The system is designed to meet many diverse demands. Therefore it was necessary to develop a flexible hard- and software system, which can be con-

2 is normally a Trimble TANS Vector GPS attitude receiver. Type 3 is an 3-d inertial measurement unit. Normally this is a Motion Pak.

the whole system. As shown in figure 5, the SANC hardware offers four kernel features.

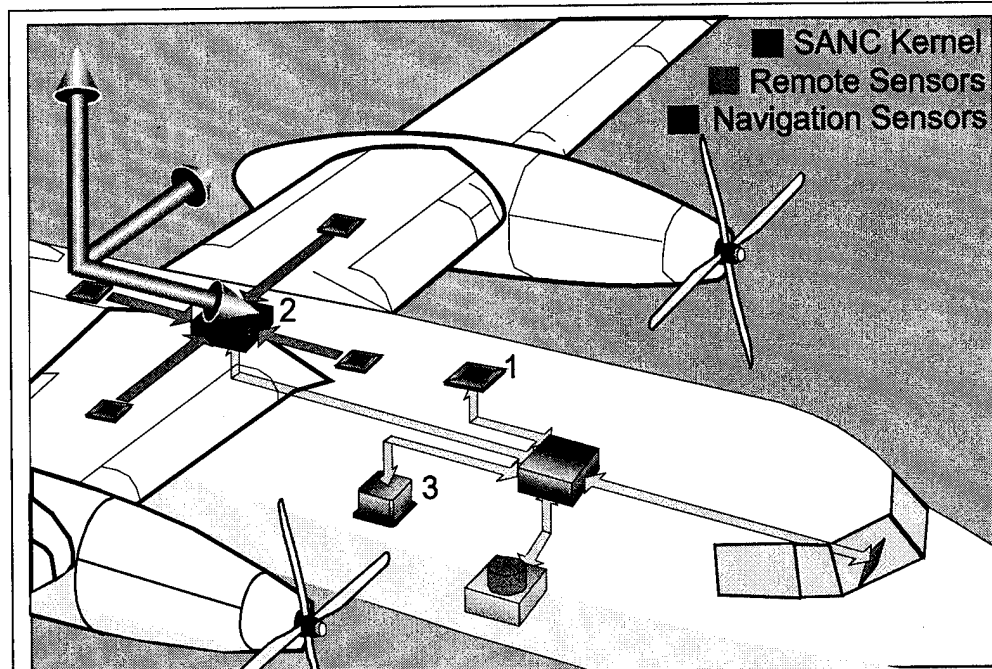


Fig. 4 SANC Overall System

The data of the different sensors can be used by SANC in a precomputed form or it can process the raw data of the different sensors itself in real-time. Further details are described in the 'navigation sensors' chapter.

Hardware configuration

The hardware configuration of SANC is the heart of

First it's multiprocessing capability. SANC can be equipped with up to eight Intel 133 MHz-Pentium processors. The processors are connected together and to the RAM via a 64-bit C-bus II. The minimal configuration are two processors.

The second feature is its multiple 'command and display feature', which enables the system to use three active LC-displays, equipped with a touch screen, simultaneously. Every display has its own graphics card with integrated 3d-hard-ware acceleration capability

with up to 300 000 polygons per second. This enables a 3 dimensional 'highway-in -the -sky' visualization of the flight path if desired.

The third feature are the extended interface capabilities, which are necessary to connect to the different sensors and handle the data streams between sensors, processors and harddisks. Elementary to handle the huge data stream from the GIS/NAV-database two the

graphic cards and from the sensors to the log-data hard-disk are the two completely independant PCI buses with four slots on each bus. The EISA bus is the connection to the different I/O interfaces. At the moment, SANC supports three interface types:

- 8 intelligent serial I/O ports
- 4 PC-Card slots
- Mil-Bus 1553B interface

The fourth kernel feature is a real-time event/counter card. This card is the central element to synchronize SANC to GPS time via the 1pps pulse and provide a highly stable real-time clock to the system.

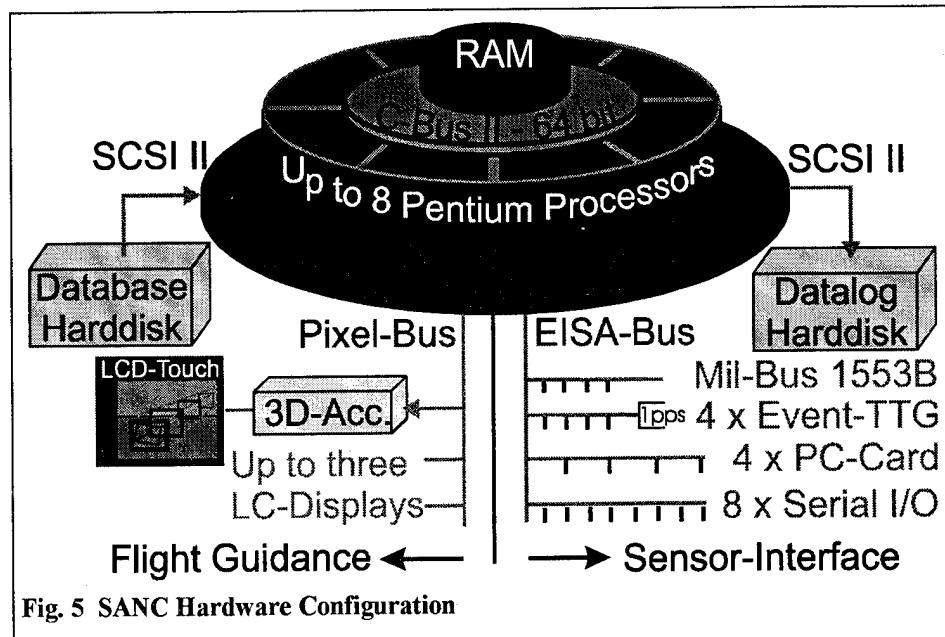


Fig. 5 SANC Hardware Configuration

The advantage of this architecture is the possibility to add sensors as desired and processors as necessary.

The hardware is housed in an EMC 19" case with the capability to bridge a power failure from the 28VDC or 220VAC power supply for at least 6 minutes.

Software architecture

The overall software capabilities of SANC can be divided into three levels. These levels are visualized

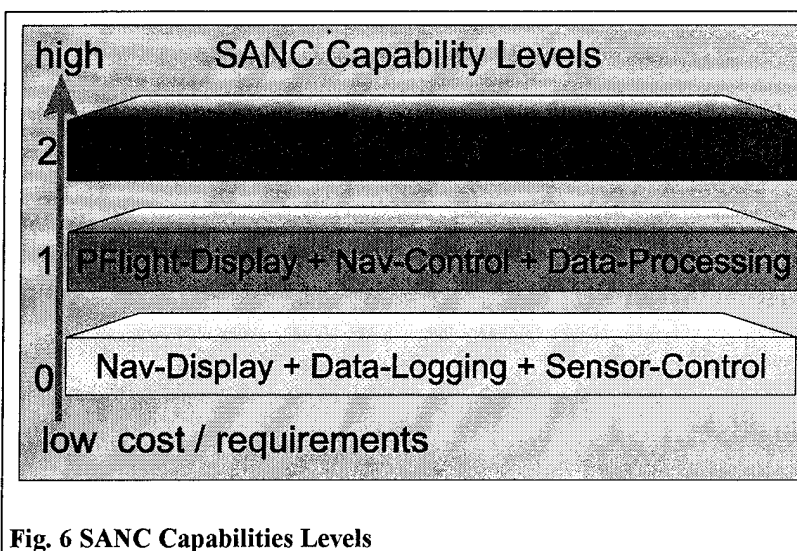


Fig. 6 SANC Capabilities Levels

in figure 6. The base *level 0* represents the minimum configuration and runs with two processors. This level meets the basic requirements to an airborne sensor positioning system. It can control all navigation and remote sensors, e.g. start, stop operating and setting operation parameters. Especially for remote sensors this means that the system is able to synchronize events from the sensor to GPS time. The second capability is to log raw data from the GPS/INS sensors and to log a 'time-log', including the real-time of the different navigation and remote sensors for later postprocessing. This time synchronization is indispensable for post-processing. The precomputed positions (computed by the GPS/INS on-board processors) are displayed on a standard navigation display.

The capability *level 1* requires another two processors. One is necessary for the second screen, where the attitude of the aircraft is displayed on a so called 'Primary-Flight' display. This level adds the capability to compute deviations from the actual flown flight path with a preplanned (with VAMP) flight plan. The deviations are shown on the navigation display. This feature enables the system to automatically start and stop remote sensor operation at the preplanned waypoints (on level 0, remote sensor start/stop must

be entered manually via the user-interface). The second processor is necessary, if a high precision position and/or attitude determination is necessary during the flight in real-time. This processing of navigation raw data depends on the available sensors (GPS-code, L1/L2 phase, availability of attitude GPS raw data, inertial accelerations). Depending on these data and the required accuracy/real-time/update-rate requirements, the appropriate 'Kalman-Filter' processing scheme is selected. It's also possible to run different processing schemes at the same time. Depending on the required processing time, this means to add another processor(s) to the system.

Level 3 is not implemented yet, but it's planned extend SANC's capability to these feature. The first is to add a 3-dimensional 'tunnel-in-the-sky' flight path visualization to the system. The second is to add an interface for direct aircraft navigation control and the third part is a kind of decision support system. This means that SANC proposes the pilot another flight route, if the planned route can't be flown.

The software architecture is based on the multiprocessing capability of the SANC hardware. The software is based on two principal paradigms.

- Message driven user-interface
- Event driven multithreading

The *message driven user-interface* shows the same behaviour as every Windows based programm. The user-interface in figure 7 shows a typical situation.

The soft buttons on the right side are static base options, which the pilot can always select via finger touch. The actual selection is 'SYSTEM' sensors. The sensor soft buttons in the middle column are added dynamically from the SANC program during start up. When the

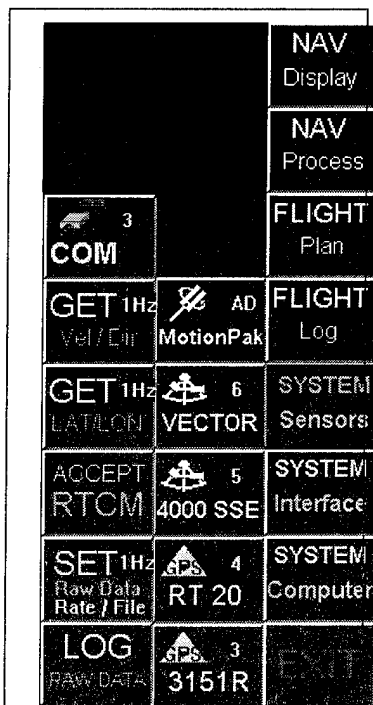


Fig. 7 SANC User-Interface

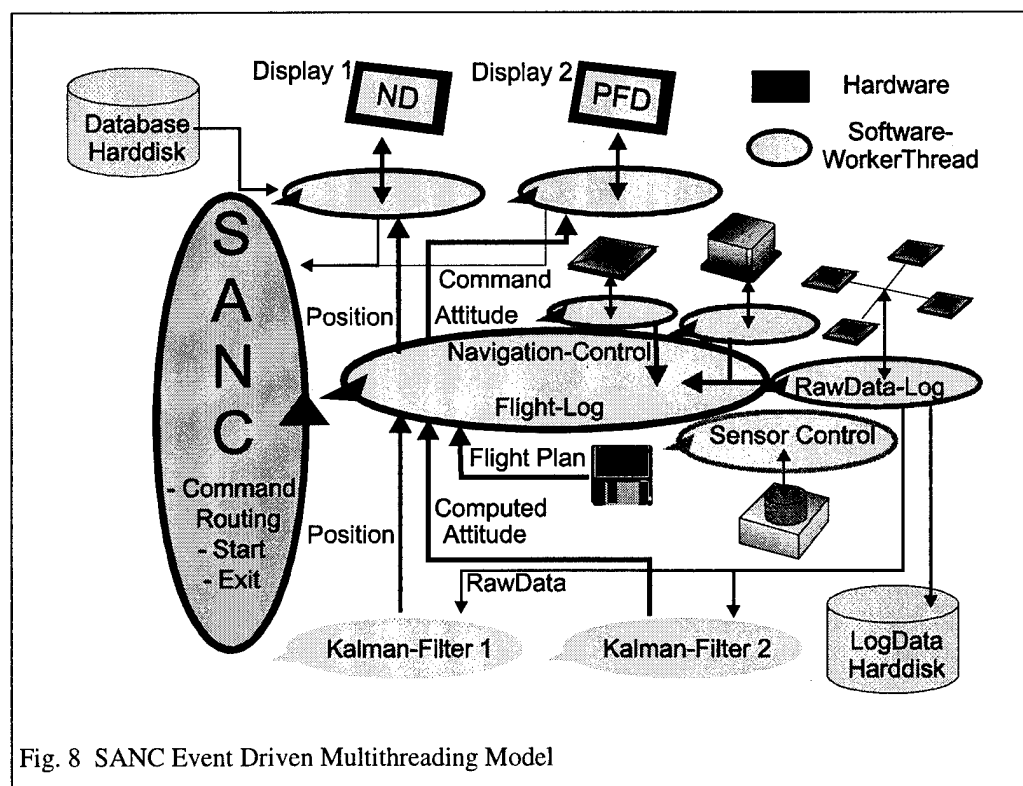
Usually there are at most two button columns visible at the same time, because the rest of the display will be reserved for the navigation display.

This secondary threads are responsible for the complete interaction with the sensors via the interfaces. So, every sensor has it's own thread.

The fourth kind of secondary thread is the 'Display'

The fifth kind of thread is the ‘Data Processing’ thread. This thread receives the raw data from the navigation sensors for computing

The advantage of this event driven model is, that the complete SANC software system can be divided into small independant threads, which only interact through well defined interfaces, the so called events. This enables a clear system design and implementing



The primary thread, the SANC main process is responsible for the detection of all system interfaces and remote or navigation sensors. After this detection process, the primary thread starts the appropriate ‘SensorControl/RawDataLog’ secondary threads.

strategy and avoids the usual complexity problem of big systems. Furthermore this threads only consume processing power if needed. But the biggest advantage is that the system processing power can be upgraded by simply adding new processors to the hardware. Therefore a situation, where a new added sensor overloads the system should never occur.

Navigation Sensors

A typical example for a secondary thread is a 'GPS-Sensor' navigation thread, which is created by SANC after detecting a GPS sensor, for a example on a certain serial port. This worker thread, as all secondary threads, runs in a endless loop. . The activity of this thread is controlled by the so called 'events'. The secondary thread waits for an event to occur. If there's no event set, the thread sleeps and doesn't need any processor time. Than the processor can be used by another thread.

A 'GPS-Sensor' thread typically knows three events. The first event a 'kill event', which causes the thread to exit the endless loop, followed by the automatic destruction of the thread. The second event for this thread is a 'send command' thread. If the thread receives this message, the thread starts and tries to send the command from the serial port command buffer. If the command is sent, the thread resets the event and goes into sleep status waiting for other events to occur. The third and most important event is the 'waitcomm' event. This event is set, if the serial port has received a byte from the sensor. Once again the thread starts and reads the bytes from the serial port input buffer. Then it can start decoding this data or sending this data directly to a kalman-filter based 'data-processing' thread which does the position/attitude calculation. If the 'GPS-sensor' thread has read all bytes from the input buffer, the thread resets he event and the thread sleeps again.

The big advantage with this event driven model is, that it's not necessary to poll the serial port continuously or to implement an interrupt handler. Therefore, if there's no communication from/to the sensor, there's no processing time occupied by the thread.

Remote Sensors

Remote sensor threads are a little different to the navigation sensors, because additional to the navigation sensors, remote sensors also have a direct signal connection to the realtime SANC hardware part. This is necessary, because usual data connections like RS232 have no realtime capability. But this is essential for remote sensors, both for triggering an exposure in

real-time and for getting the moment of exposure with the highest possible time accuracy.

Therefore SANC has a stable (1ppm) real-time clock with 1µsec resolution, which is initialized at the beginning with the actual GPS time and than updated using the 1pps output. Trigger events and time-tags from the remote sensors can be sent or received with 0.4 µsec accuracy. This time accuracy is about two orders better than the usual time accuracy of the exposure event sent from remote sensors. For our 'RMK TOP' aerial camera, this accuracy is about 100 µsec. Therefore the system accuracy does not degrade the exposure signal accuracy.

CONCLUSIONS

Two main conclusions can be summarized: At first, the integration of attitude, position and velocity information from the different navigation sensors increases precision and integrity for enroute navigation and complete airborne positioning of different remote sensors. Second, the flexible system architecture with it's high performance multiprocessor kernel and open system interfaces enables easy application dependant integration of the desired navigation and/or remote sensors.

The new aspects of this airborne application system can be summarized as follows:

- Scalable performance, open interfaces, easy integration, advanced visualization
- High positioning precision and flight execution integrity
- Complete navigation sensor integration of position, attitude and velocity in realtime
- Easy remote sensor integration, monitoring and control

REFERENCES

Hein, G.W. (1993): GPS-Bildflug-navigation. Leipziger BILDMESS-TAGE 1993, Institute of Geodesy and Navigation, FAF Munich.

Hein G.W., G. Baustert, B. Eissfeller, H. Landau (1989): High Precision Kinematic GPS Differential Positioning and Integration of GPS with a Ring Laser Strapdown Inertial System. Navigation, 36, 77-98

Mather P.M. (1993): Geographical Information Handling - Research and Applications. John Wiley & Sons Ltd.

Geometric Correction of Airborne Multispectral Scanner Imagery Using GPS Position and Attitude and Digital Elevation Models

Lawrence Fisher

Lockheed Environmental Systems and Technologies

DISCLAIMER

Notice: The U. S. Environmental Protection Agency (EPA), through its Office of Research and Development (ORD), directed the research described here. It has been subjected to the Agency's peer review and has been approved by EPA for publication. Mention of trade names or commercial products does not constitute endorsement or recommendation for use.

BIOGRAPHY

Lawrence T. Fisher received his ScD degree from New Mexico State University in 1970, following BSEE and MSEE degrees in 1961 and 1963 from the same institution. He has worked in the fields of remote sensing and geographic information systems since 1974 at the University of Wisconsin-Madison, the University of Maine at Orono, and, since 1985, with Lockheed Environmental Systems and Technologies at Las Vegas, Nevada. Since 1990, his interests have focused on the Global Positioning System (GPS) and, in particular, its application to geometric correction of multispectral scanner imagery.

ABSTRACT

Multispectral scanners are valuable for environmental monitoring, but they suffer from severe geometric distortions and errors. We describe an approach to geocorrection of multispectral scanner imagery that uses GPS position and attitude along with digital terrain data. An analysis of contributions of errors from various error sources is presented. Our approach to collection of data for post-processing geocorrection is discussed: We collect GPS attitude and three-dimensional positions (which are later differentially corrected), and derive and store accurate time information for each scan line. The hardware to accomplish this integration is explained. Later, attitude and position, along with digital terrain models, are used to calculate best estimates of pixel

positions. Geocorrection mathematics and processing algorithms are given, and experimental results are shown.

INTRODUCTION

Lockheed Environmental Systems and Technologies Company (LESAT) has maintained and operated a Daedalus Enterprises Model 1260 airborne multispectral scanner (MSS) for the U.S. Environmental Protection Agency (EPA) at its Las Vegas, Nevada laboratory since the 1970s. This instrument uses a rotating mirror to collect radiant energy in 11 spectral bands including ultraviolet, visible, near infrared, and either thermal or mid-infrared. Its instantaneous field of view is 2.5 milliradians, producing a pixel size of 2.5 meters per 1,000 meters of height, and it digitizes its information into 714 pixels per scan line over an 86° field of view. It has been used for a wide variety of environmental monitoring applications including land use, ecological processes, thermal monitoring, and water quality.

Multispectral scanners can sense wavelengths beyond the limits of conventional aerial photography, which gives them advantages for many environmental monitoring applications. However, they have historically suffered from geometric limitations: Any variation in aircraft height or attitude, or any change in surface topography, introduced serious geometric distortions.

In 1990, LESAT designed and installed GPS-based hardware to collect position and height information to accompany the MSS^{[3], [4]}. Software was developed that incorporated this information along with digital elevation model (DEM) data for geocorrection of imagery. The major drawback of this initial GPS integration was inability to account for aircraft attitude. Roll correction was achieved within the MSS by using an internal gyroscope to advance or retard the start of digitizing for each scan line, but headings could only be inferred by interpolating GPS positions. If any cross winds were present, requiring that

the aircraft be crabbed, very significant positional errors occurred. Variations in pitch angle caused lesser, but still serious, errors. Budgetary limitations prevented the use of an inertial navigation system, so other approaches were required. This paper describes the hardware and software system that was developed, and discusses results.

ERROR SOURCES

There are several sources of error which affect geo-correction accuracy:

- Errors in scanner position
- Height error
- Roll error
- Pitch error
- Heading error

To evaluate the contributions of each of these, a typical scenario was selected. Height above terrain was assumed to be 2000 meters. It was assumed that position errors were 3 meters, height errors were 10 meters, and that roll, pitch and heading errors were each 0.1° (1.57 milliradians). The height and position errors are typical of what is possible with C/A code differentially-corrected GPS data. The assumed attitude errors are comparable to those achievable by several technologies.

Height Error. Pixel displacement due to height error (Figure 1) mostly affects the across-scan component of the geometry, and is proportional to height error and the tangent of the scan angle, α . Height error is produced by

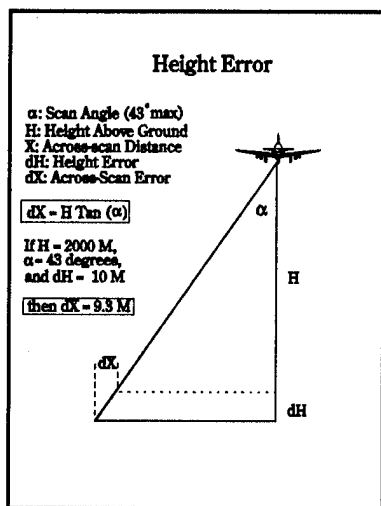


Figure 1: Contributions to Positional Error Due to Height Errors

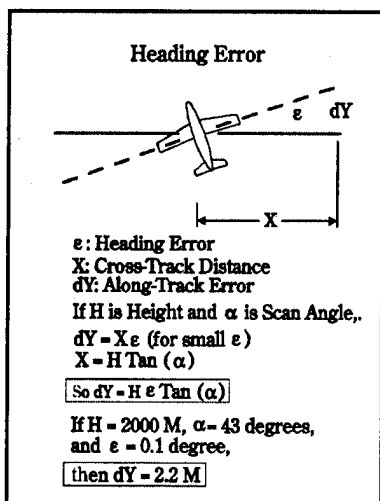


Figure 2: Error Contributions Due to Heading Error

a combination of uncertainties about GPS-measured height and about terrain height above sea level.

Heading Error. Heading errors cause pixel misregistration in a direction that is largely along the direction of flight; pixels are rotated by the heading angle error as illustrated in Figure 2. The error is zero at nadir and increases linearly with the distance across the scan line, which in turn is proportional to the tangent of the scan angle.

Roll Error. Roll is monitored by a mechanical gyro on the MSS, and the system corrects for it by advancing or retarding the mirror angle where digitizing begins. The gyro probably has an error magnitude of about 0.1° , which is the estimate assumed for this analysis. Uncorrected roll error mispositions pixels in the across-scan direction, and it affects all pixels. The amount of the error is proportional to the length of line "L" in Figure 3, and is greatest at scan edges.

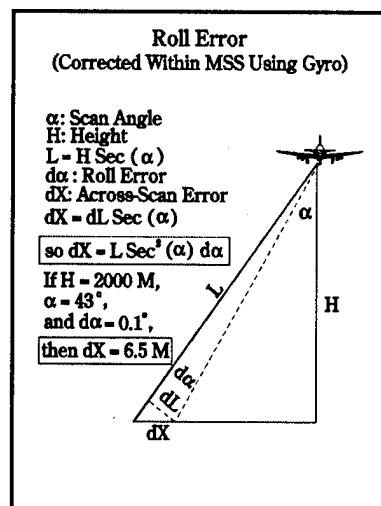


Figure 3: Errors Due to Uncompensated Roll

Pitch Error. Uncorrected pitch (Figure 4) affects all pixels in a scan line equally. If the aircraft is pitched up, the scanner is seeing pixels that are ahead of the instrument; without correction, these would be placed in a geocorrected file too early in the flight line. The opposite is true if the instrument is pitched down.

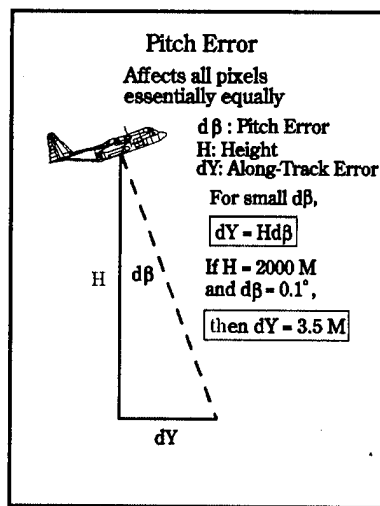


Figure 4: Error Due to Pitch Error

A small second-order effect is also present: If the instrument is not looking straight down at nadir, the "scan ray"

for the center pixel is the dashed diagonal line in Figure 4, not the true nadir line. This line is longer than the true nadir line, and this has the effect of slightly widening the portion of the ground that is viewed, just as if the aircraft was higher. For small pitch angles this is negligible.

Horizontal Positional Error. In addition to height and attitude errors, there will also be errors in the GPS-derived horizontal position. With proper differential correction, we can expect position errors to be about 3 meters using C/A code GPS. Lower errors could be achieved with dual-frequency carrier phase units. Due to differences in signal delay through the troposphere at different heights, there probably would be errors on the order of one meter even with carrier phase units.

Combined Errors. Figure 5 summarizes the effects on pixel position produced by these error sources, showing them as functions of scan angle. Some of the error sources affect pixel positions across the scan line; others predominantly affect along-flight line directions. Since it is unlikely the individual errors would add linearly, the estimate of overall error assumes that they accumulate according to the square root of the sum of the squares of the individual errors. This is referred to in Figure 5 as Root Sum Squares (RSS) error.

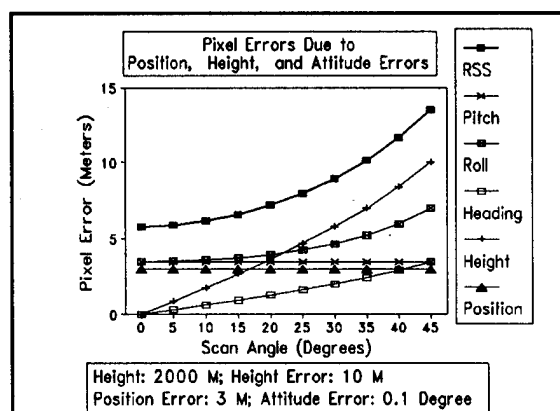


Figure 5: Positional Errors as a Function of Scan Angle

As can be seen from Figure 5, height error becomes the dominant source of positional error as scan angle increases. Uncorrected roll error is the next most significant.

For the scenario, the pixel size would vary from about 5 meters at nadir to about twice that value at the scan edge. Given the assumed height and levels of error, RSS positional errors varied from 6 meters at nadir to about 13 meters at scan edge. Therefore we conclude that it should be possible to geometrically correct MSS imagery to approximately one to two pixels at the 1-sigma level.

HARDWARE

A tightly coupled system combining GPS with a high-quality inertial navigation system would be our first choice, since it can provide accurate attitude information at rapid update rates. However, the budget precluded this approach. Instead, a GPS-only approach was chosen.

The GPS receiver selected for the MSS is an Ashtech 3DF, which is a 24-channel receiver with connections for feedlines from four antennas [1], [6], [11]. In its usual configuration, each antenna is allocated six channels, allowing tracking of L1 carrier phase and C/A code from six satellites. Data from all 24 channels are logged internally in 6 Mbytes of memory and are later downloaded to a laptop computer. The raw data can be corrected with postprocessing DGPS methods. (Real-time corrections are possible but were logistically impractical for this application.) Attitude information is calculated internally, using relative carrier phases of signals arriving at the four antennas from multiple satellites. An accurate survey of the relative locations of the four antennas is necessary before this can be done; this survey is part of the installation procedure for the receiver. The receiver provides a "pulse per second" (PPS) signal that is synchronized within one microsecond to Coordinated Universal Time (UTC). Front panel controls provide access to 12 different control screens. Some of these display system status such as present position and attitude, satellites being tracked, course, distance and time to a destination way point, etc. Other screens allow entry of parameters such as update rate, minimum satellite elevation angle, control of messages, and so on. The 3DF receiver is not used for piloting; a separate GPS receiver is available for that purpose.

The 3DF can operate at a 1/2-second update rate. However, we have used it only at 1-second rates to extend mission endurance before filling memory. At a 1-second rate, it can log data for about 3 hours.

After a flight is completed, receiver data are downloaded into a notebook computer. Carrier and code phase data, time, and some other ancillary information, are placed into a binary "B-File"; a similarly named "E-File" stores satellite ephemeris data. Attitude information, in ASCII format, is placed into a "site file" and includes time, heading, pitch, roll, estimates of errors, and a validity flag.

GPS-MSS Integration. The GPS receiver can record position, height, and attitude information every second, but the MSS scans at a faster rate (6.25 to 100 scans per second). To integrate the two systems, accurate time is placed in the limited space for user-supplied data that the

MSS can record for each scan line. **Figure 6** shows a block diagram of system components. The GPS receiver, with its four antennas, is at the top. Time information and the PPS signal from the receiver control an electronic counter subsystem called the GPS Time Monitor, which counts time in seconds into the week and milliseconds past the second.

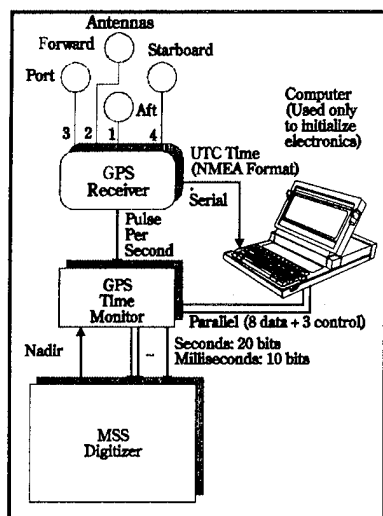


Figure 6: Block Diagram of GPS-MSS Integration Components

A more detailed block diagram of the GPS Time Monitor is shown in **Figure 7**. A 20-bit counter is used to store GPS Seconds of the Week. The seconds begin with 0 at midnight Sunday (GPS Time). The largest time, on Saturday just before midnight, is 604,799. The largest number that can be stored in 20 bits is $2^{20}-1$, or 1,048,575, so 20 bits is both sufficient and necessary.

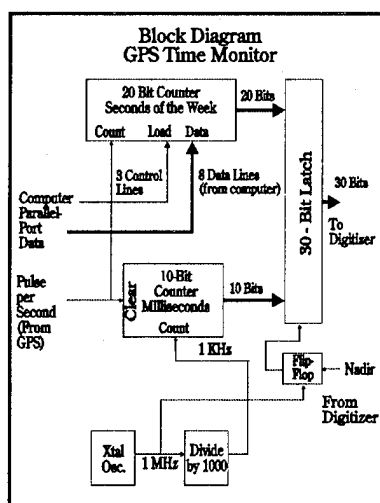


Figure 7: Block Diagram: GPS Time Monitor

The seconds counter must be initialized when power is first applied to the assembly. To accomplish this, the GPS receiver is set up to emit a National Marine Electronics Association (NMEA) time and position message from one of its RS-232 ports once every second, soon after the PPS event occurs. This message is received through the serial port of a computer whose parallel (printer) port is connected to the GPS Time Monitor. Software on the computer decodes the time messages, converts UTC time to GPS time by applying the proper number of "leap seconds" that are occasionally introduced into UTC to keep its time tied closely to the Earth's rotation but that are

ignored by GPS time, and sends information 8, 8, and 4 bits at a time to initialize the counters. The process takes several seconds; when it is completed, the computer can be disconnected and set aside.

A second counter, 10 bits wide, counts milliseconds. It is clocked by a 1 KHz signal derived from a 1 MHz crystal oscillator, and is cleared to zero when PPS occurs. The crystal oscillator is fairly accurate and stable (probably to about one part in 10^5). The count just before PPS may be 998 or 1000 instead of 999, but this difference is negligible.

The final signal that is applied to the integrated system is NADIR, from the MSS digitizer. This is a brief pulse that occurs when the MSS mirror is looking directly down. This signal is used to lock the nadir time into a holding latch until the MSS can record the time information, sometime later in the mirror rotation cycle. Time information is passed to the MSS digitizer, which accepts and records it for each scan line.

GPS Differential Corrections. Differential GPS corrections are needed to achieve the few-meter accuracy positional accuracy levels needed. This requires a suitable source of fixed-position GPS data and appropriate software. An Ashtech M-XII single frequency L1 C/A code and carrier receiver, designed for survey applications, was available for use as a base station. To use it, the 2-person flight crew or cooperators would need to locate suitable control (preferably within 100 km of the flight lines), and set up, tend, and download the base station. Except in special circumstances, the logistics promised to be daunting. Fortunately, we learned of the possibility of post-processing services using the John Chance and Associates "Starfix" wide-area GPS network [7], [8]. Although its emphasis is primarily high-accuracy real time correction, we were able to provide data for individual flight lines in RINEX format, which were subsequently corrected. The base station receiver was therefore used only for special missions where adequate support staff was available to mitigate logistical problems.

There were some opportunities to compare differential corrections from "Starfix" with those using locally obtained base station data. During a 10-minute portion of a test flight over western Las Vegas which involved three 180° turns, aircraft positions were determined using Ashtech's PNAV Kalman filter DGPS software with base station data obtained about 15 km away, and with the "Starfix" system. **Figure 8** shows the differences between the two. Heights agreed within three meters, and horizontal differences were less than two meters. Both systems used L1 C/A code pseudo-ranges and L1 carrier-phase data.

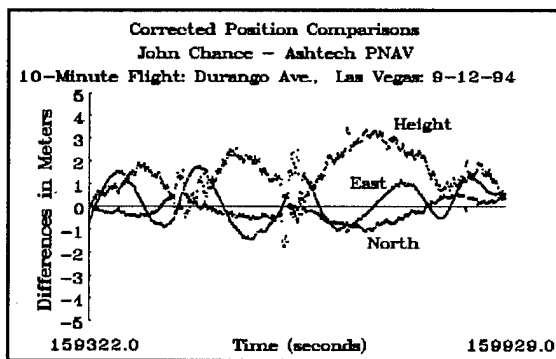


Figure 8: Comparison of John Chance "Starfix" and Ashtech "PNAV" Positions

Coordinate Systems. Geocorrection is a computation-intensive process that is performed on the largest and fastest computer available. Before it is performed, GPS positions must be projected into the required coordinate system and datum. This is typically Universal Transverse Mercator (UTM) based on the North American Datum of 1927 (NAD-27), its counterpart using the newer 1983 datum (NAD-83), or a local State Plane system, usually based on NAD-83. A portable ASCII file called the Flight Line Profile is constructed giving projected positions, attitude, and attitude validity for time periods for data to be geocorrected.

GEOCORRECTION GEOMETRY

Interpolation between infrequent GPS positions and attitudes uses "cubic B-splines" [5]. These are sequences of cubic polynomials in X (easting), Y (northing), and Z (height) that closely approximate "control points" in X, Y, and Z supplied by GPS. Each segment of the polynomials is valid for the interval from one control point to the next, and is defined over four consecutive control points including the points before and after the region of validity. To maintain sufficient smoothness at the point of transition from one polynomial to its successor, they are compelled to be continuous and to have continuous first and second derivatives.

To place this into a well-defined mathematical context, let the sequence of X-Y-Z control points be $P(1), P(2), \dots, P(n)$ where $P(i) = [x(i), y(i), z(i)]$. The interpolating functions are cubics of the form $F_i(t) = [X_i, Y_i, Z_i](t)$ where t is a dimensionless parameter that ranges from 0 to 1. That is,

$$X_i(t) = a_3 t^3 + a_2 t^2 + a_1 t + a_0$$

for suitable a_3, a_2, a_1 , and a_0 . $Y_i(t)$ and $Z_i(t)$ are similar. Each function $F_i(t)$ is valid for an interval in the control point sequence between $P(i)$ and $P(i+1)$.

The continuity constraints, which are called c^0 , c^1 , and c^2 continuity, are expressed in this equation:

$$c^0: F_i(1) = F_{i+1}(0) \quad c^1: \frac{dF_i(1)}{dt} = \frac{dF_{i+1}(0)}{dt} \quad c^2: \frac{d^2 F_i(1)}{dt^2} = \frac{d^2 F_{i+1}(0)}{dt^2}$$

This system of cubics will satisfy the constraints if and only if

$$[X_i, Y_i, Z_i] = k [t^3, t^2, t, 1] \begin{pmatrix} -1 & 3 & -3 & 1 \\ 3 & -6 & 3 & 0 \\ -3 & 0 & 3 & 0 \\ 1 & 4 & 1 & 0 \end{pmatrix} \begin{pmatrix} P(i-1) \\ P(i) \\ P(i+1) \\ P(i+2) \end{pmatrix}$$

where k is a constant. Any value of k is acceptable, but most values have little merit. The case of $k = 0$, for example, leads to constant-zero functions, which are c^i continuous for all i , but are trivial. The particular value $k = 1/6$ leads to the definition of a B-spline, and evaluates to

$$F_i(t) = [X_i(t), Y_i(t), Z_i(t)] = \frac{1}{6} \begin{pmatrix} t^3 [P(i+2) - 3P(i+1) + 3P(i) - P(i-1)] \\ + t^2 [3P(i+1) - 6P(i) + 3P(i-1)] \\ + t [3P(i) - 3P(i-1)] \\ + P(i+1) + 4P(i) + P(i-1) \end{pmatrix}$$

The B-spline function valid for interval i to $i+1$ depends on control points $P(i-1)$ and $P(i+2)$ as well as control points $P(i)$ and $P(i+1)$. Therefore the Flight Line Profile must include at least two points before the beginning of the flight line, and must extend at least two points after the end of the line.

Heading. Attitude information is calculated and recorded by the GPS receiver. Heading and pitch components are included in the Flight Line Profile. Roll information is not included because roll compensation is performed internally in the scanner, using gyro-derived roll angles to advance or retard the start of digitizing for each scan line.

The 3DF attitude data include a "validity flag" that tells whether attitude data are valid. This flag is also included in the Flight Line Profile. If valid attitudes are available, then heading and pitch are interpolated using B-spline methods identical to those used for position and height. If attitudes are invalid for some reason then pitch information is taken from the MSS gyro, recorded on the MSS data tape, and heading is taken from an estimate of the Course Over Ground (COG). This is determined by differentiating the B-spline functions $X_i(t)$ and $Y_i(t)$. The Course Over Ground is the arc tangent of the ratio of these,

$$X_f(t) = \sum_{i=0}^3 a_i t^i \text{ and } Y_f(t) = \sum_{i=0}^3 b_i t^i$$

$$dX_f/dt = \sum_{i=1}^3 i a_i t^{i-1} \text{ and } dY_f/dt = \sum_{i=1}^3 i b_i t^{i-1}$$

$$COG = \tan^{-1} \left(\frac{dX_f/dt}{dY_f/dt} \right) = \tan^{-1} \left(\frac{3a_3 t^2 + 2a_2 t + a_1}{3b_3 t^2 + 2b_2 t + b_1} \right)$$

Determining Scanner Position and Height. GPS accuracies are sufficiently good that separation between the antenna and the scanner must be taken into account. The scan mirror was determined to be about 2.8 meters forward of Antenna 1 and about 1.6 meters below it. Thwartships offsets were negligible. These offsets are used to calculate scanner coordinates,

$$X_{\text{scanner}} = X_{\text{antenna}} + A \sin(\theta)$$

$$Y_{\text{scanner}} = Y_{\text{antenna}} + A \cos(\theta)$$

$$Z_{\text{scanner}} = Z_{\text{antenna}} - D$$

where θ is the heading angle, A is the "Along" offset (2.8 m), and D is the "Down" offset (1.6 m).

Digital Elevation Models. Digital terrain modelling is an important component of the geometric correction process. The DEM coordinate system may be different from the user-chosen coordinates for a project, so a conformal coordinate transformation is defined using two or more match points giving DEM and user coordinates. If more than two match points are supplied, the transformation is calculated using a least squares process.

Many DEMs use NAD-27 UTM coordinates. If a user coordinate system is based on NAD-83, the match points must take conversions between datums into account. This can be done using NADCON software and data sets from the National Geodetic Survey (NGS) [2]. The datum conversion is non-linear, because of distortions and inconsistencies in NAD-27. However, for a local area such as an individual flight line, the non-linearities are small (certainly no worse than a few centimeters), and the linear transformation is completely adequate.

To determine height above terrain (HAT), the sub-aircraft point orthometric height, or height above the geoid, is found from the DEM using coordinates $[X_{\text{scanner}}, Y_{\text{scanner}}]$ after these are transformed to the DEM coordinate system. (If there is no DEM, or if the sub-aircraft point is beyond the DEM bounds, an "Off-DEM" height is used.) The GPS-derived scanner height, however, is a height above the WGS-84 ellipsoid used by GPS. The difference between geoid and ellipsoid is the "geoid height", which varies from place to place, depending on

local gravity. Geoid heights vary slowly in most areas, so the geocorrection software assumes that the value is constant for a given flight line. It can be determined for any point in the United States and its territories using the GEOID93 data set and software from NGS^{[9], [10]}. Typical values are -30 m. The final equation for HAT is

$$HAT = Z_{\text{scanner}} - DEM - GH$$

where Z_{scanner} is the scanner height above ellipsoid, DEM is the orthometric height of the sub-aircraft point, and GH is the geoid height.

Figures 9 and 10 show the basic scanner geometry, assuming, for the moment, flat terrain and ignoring roll angle, which is compensated for within the MSS. In Figure 9, the height above terrain at the sub-aircraft point S is h . If the scanner was not pitched, it would scan vertically at right angles to the heading vector, scanning triangle OPQ . If, however, the aircraft and the instrument are pitched up at angle β (the usual case, due to angle of attack), then the actual scanned area is displaced forward, and the scanned area is the tilted triangle $OP'Q'$. At any pixel, the "scan ray" is the vector from the MSS mirror to the center of the instantaneous field of view. It is located somewhere in triangle $OP'Q'$, depending on scan angle α .

The first part of the geometric correction process seeks to determine the length and angle of vector V (Figures 9 and 10) joining the sub-aircraft point S to the intersection P' of the scan ray and the (flat) surface. The length of V is determined by angles α and β and HAT h . The vector's angle, δ , is determined by angle ϕ , which depends on d and V , and heading angle θ . d , in turn, is a function of β and h . The equations are

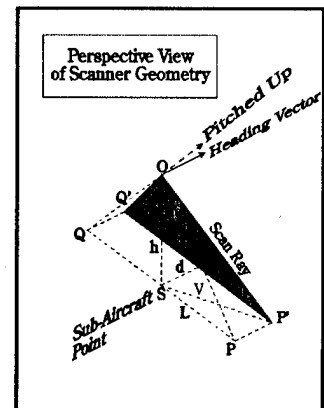


Figure 9: Perspective View of Scanner Geometry

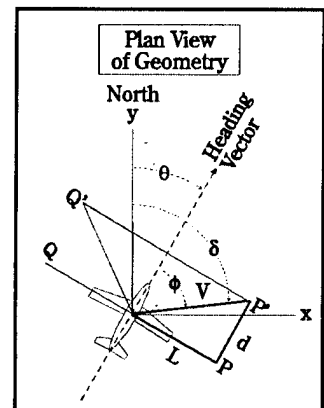


Figure 10: Plan View of Geometry

$$j = h \sec(\beta) = \frac{h}{\cos(\beta)}$$

$$L = j \tan(\alpha)$$

$$d = h \tan(\beta)$$

$$V = \sqrt{L^2 + d^2}$$

$$\phi = \cos^{-1}\left(\frac{d}{V}\right)$$

$$\delta = \phi + \theta$$

Terrain Correction. Corrections for terrain variations are accomplished by forming short "slope models", derived from the DEM, and intersecting them with the scan ray. The process begins with the pixel nearest nadir, and progresses to first the rightmost pixel, and then to the leftmost.

Near nadir, assuming the usual situation of nose-high pitch angle, the initial intersection P' of the scan ray and the sub-aircraft plane will occur some distance forward, and nearly in line with the heading vector. The initial slope model is constructed by starting at the sub-aircraft point whose height has been determined earlier. Then a line is constructed along angle δ in Figure 10 (which, for the moment, is very nearly equal to heading angle θ) with a length equal to the DEM spacing. (This is 30 meters for 7.5 minute DEMs from the U.S. Geological Survey).

The DEM is interrogated at that point to obtain a new height at the end of the line, forming the initial slope model, S to "1" in Figure 11. This line, in plane OSP' (Figures 9 and 10), is intersected with the nadir scan ray, O to P' . If this intersection does not occur in the interior of the slope model, then a new slope model is constructed starting at "1" and extending to "2". This process is repeated until the intersection occurs in the interior of the current slope model. In Figure 11, this occurs with slope model "4" to "5".

The point of intersection defines a new distance V' from the sub-aircraft point S . Together with the angle δ , this, when resolved to rectangular coordinates, determines the best estimate of the position of that pixel.

Once the nadir pixel coordinates are found, other pixels in that scan line are processed. For positive scan angles,

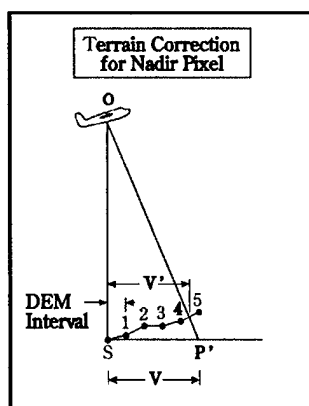


Figure 11: Construction of Slope Models at Nadir

we start with Pixel 357 and work down to pixel 1. Then the process repeats for negative scan angles, starting at pixel 358 and progressing to pixel 714. For each pixel, the current slope model is retained until the scan ray intersection goes beyond the model. In that case, the current slope model end point becomes the new one's beginning, and a new point is calculated along angle δ . δ changes slightly from pixel to pixel, so the plane OSP' changes. Because of this change, the slope model is slightly non-coplanar with plane OSP' from pixel to pixel. The difference, however, is negligibly small.

A Special Case. A special situation can arise if the slope of the slope model is steeper than that of the scan ray, either because of extreme topography or DEM flaws. This situation is illustrated in Figure 12. In this case, Scan Ray "n" intersects slope model "1" to "2" normally, but Scan Ray "n+1" misses. The normal process is to replace the slope model with that from "2" to "3". Because the slope of this slope model is too steep, the intersection of scan ray and slope model occurs at the point marked with a star, closer to nadir than point "2". This is impossible and incorrect. To deal with this case, an adjusted slope model is constructed. Point "1" replaces Point "2", and the slope model becomes "1" to "3". This produces an intersection too far out, so the slope model becomes "3" to "4", and then "4" to "5". At this point, the final intersection is calculated, as shown.

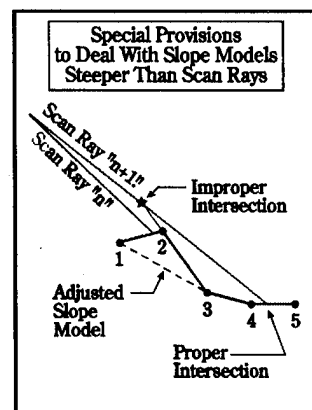


Figure 12: A Special Case: Terrain Steeper Than Scan Ray

A related situation can occur occasionally: The slope model may be parallel (or very close to parallel) to the scan ray. In this case, the intersection subroutine returns a "singular case" flag to say that no intersection can be found. Recovery from the singular case is exactly the same as the "slope too steep" case described.

Operation of the Geocorrection Program During an initial pass through the data, easting and northing coordinates of leftmost and rightmost pixels of all scan lines of interest are calculated and stored, using the scanner and terrain geometry described above. Global extreme positions are used to determine output file dimensions; this file is created and initialized. Although only end pixel coordinates are needed at this stage, coordinates of all pixels are calculated during this process, which is

computationally intensive but which assures that identical geometry is applied during this pass and during the final processing pass.

The processing pass calculates estimated positions of all - pixels and places them in a memory array called the Processing Block that is figuratively moved as needed over the extent of the output file and which is eventually written to disk. This array is 2,048 rows by 2,048 columns in size and has 12 layers, one per MSS channel. A 16-bit halfword is reserved for each 12-bit pixel, so the total size is 96 Mbytes.

The first step in managing the Processing Block is to determine the range of scan lines that can be processed before a geocorrected pixel passes beyond the block's limits. Since flight lines can be oriented in any direction, a "region growing" process is used. Starting at leftmost and rightmost pixels for the earliest desired scan line, minimum and maximum eastings and northings are calculated. This continues for successive scan lines until either the easting or northing differences reach Processing Block limits or until the end of the data of interest is reached. Left, right, top, and bottom coordinates of the Processing Block are then assigned to these limiting coordinates.

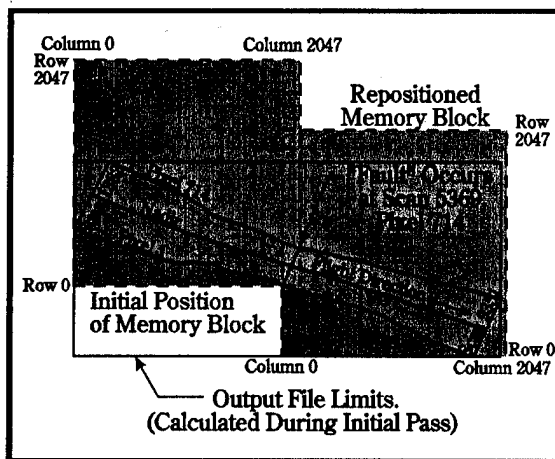


Figure 13: Repositioning the Processing Block

If necessary, the Processing Block is repositioned one or more times to complete processing of a flight line. If this occurs, any "holes", or unfilled pixels, are filled (details are given below), the contents of the Processing Block are written to disk, and the region growing process repeats, starting a few scan lines before the scan that terminated the earlier process. This allows a small amount of overlap to account for unusual geometries. The repositioned Processing Block is filled from disk as necessary. Processing then continues. These steps are repeated as needed until the last scan line of interest has been pro-

cessed. The "hole filling" and file updating processes end the procedure. Figure 13 shows an example with two positionings of the Processing Block.

When filling of the Processing Block is finished, either by a "fault" when a pixel falls outside the Processing Block, or by reaching the last scan line of interest, there may be many pixels into which no data have been deposited. Some of these will be pixels outside the scanned area; it is appropriate that these remain unfilled (at zero values). Others, however, will be in the scanned area. The number and distribution of unfilled pixels depend on many variables, including output pixel size and local terrain variations.

"Hole Filling" is done by locating unfilled pixels which have filled neighbors, and calculating an average value from those neighbors. The process is somewhat complicated, however, because the search for unfilled pixels must be limited to the extent of the scanned area. The scan-end coordinates that were calculated and stored during the initial geometry-setting phase of the program are used to define this.

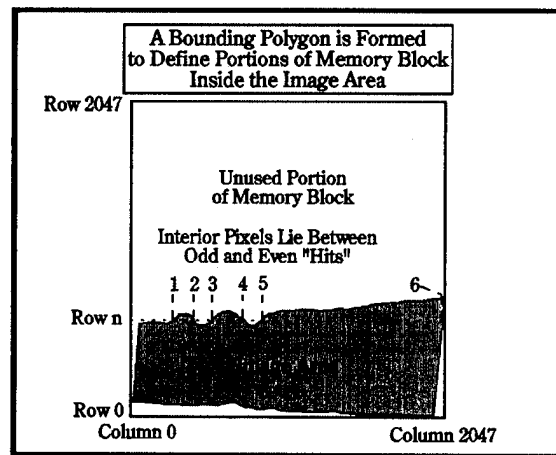


Figure 14: Image Area Polygon in Processing Block for Hole Filling

The coordinates of the Processing Block are row and column numbers ranging from 0 to 2,047. A polygon is constructed by searching the scan-end coordinates for all scan lines involved in the Processing Block and transforming user [easting, northing] coordinates to Processing Block integers. This polygon is built in a clockwise direction, following the leftmost edge from earliest to latest scan line involved in the Processing Block, and then continuing with the rightmost edge from last scan line to first. Care is taken to add vertices to the polygon only if they are "genuine" apexes: Duplicate points are eliminated, and, if a new apex is directly in line with a predecessor, the predecessor is omitted.

A typical polygon is shown in Figure 14. In this case, the polygon begins at the top left corner of the shaded "Image Area", extends to the top right, and continues from lower right to lower left.

With the polygon defined, a search begins for unfilled pixels within the Image Area. During the filling of the Processing Block, bits in a 2,048 by 2,048 bit map were set to 1 whenever pixels were deposited. At this phase, the bit map is searched for cleared (0) bits. If such a bit is found, and if it is in the image area, its nine neighbors are inspected. If the bit map indicates that any of these are filled pixels, an average of all filled neighbors is calculated, that value is placed in the Processing Block, and the appropriate bit in the bit map is set. This process iterates until no further unfilled pixels are located inside the Image Area. Usually two or three iterations are required.

To determine whether pixels are inside the image area, a "polygon hit" procedure is used. For each row in the Processing Block from the lowest to the highest that is involved in the polygon, "hits" are determined where that row intersects the polygon. Often there are only two hits; this would be the case for most rows in the Image Area in Figure 14. However, there may be multiple hits. In the example, at row "n", there are six hits. Points lie inside the Image Area if they lie between odd and even hits.

EXPERIMENTAL RESULTS

Two examples of georeferenced imagery are shown in Figures 15 and 16. The first covers a desert mountain range south of Las Vegas. Height above terrain averages about 2,000 meters; terrain variation exceeds 300 meters across the image. A secondary road crosses the image from southwest to northeast, and another road climbs steeply westward to a radio relay facility. C/A code GPS positions obtained from a surface vehicle overlay the MSS imagery. Georeferenced positions agree to about the width of the road.

Figure 16 shows a portion of a southbound flightline over Durango Avenue in western Las Vegas. Height above terrain was about 800 meters. Terrain variation is minimal, with a general slope trending downward from west to east. "Nibbles" in the east edge of the image show MSS roll compensation at work; there were strong southwest winds that afternoon. GPS positions are also plotted. For unknown reasons, attitude calculations were invalid during part of the flight line (perhaps due to signal blockage due to aircraft roll), but the geocorrection procedures were able to interpolate across these periods with reasonable success.

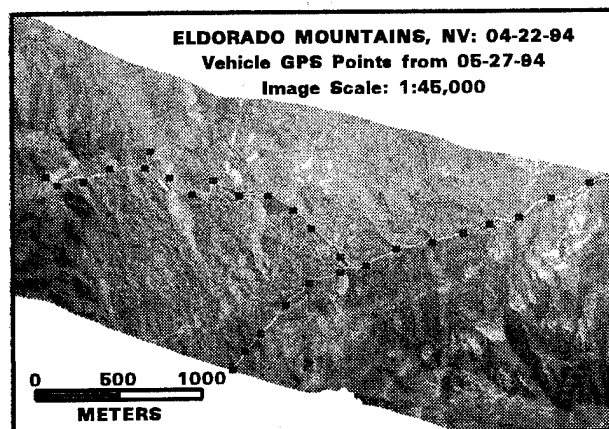


Figure 15: Test Flight in Mountainous Terrain With Surface GPS Points

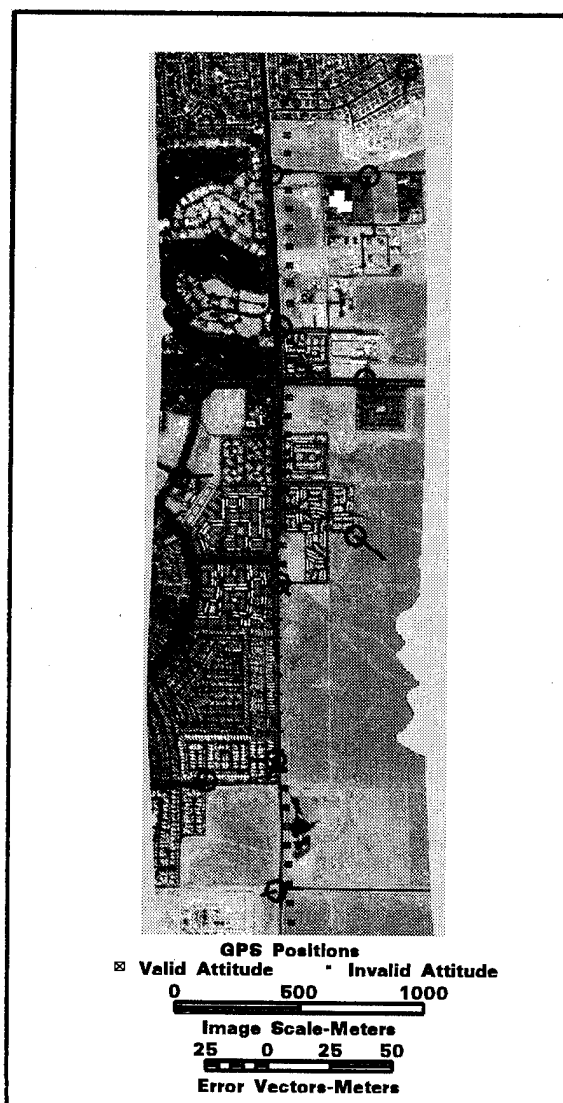


Figure 16: Urban Area Georeferencing Accuracy: Durango Avenue, Las Vegas, NV

Coordinates of 24 selected street intersections were measured using survey-grade GPS, with accuracies estimated to be 50 cm or better, and the corresponding georeferenced image coordinates were interpreted with image processing software to accuracies of one to two meters. These positions and their associated error vectors (exaggerated ten-fold) overlay the image. Positional errors for these 24 control points (12 of which are shown in Figure 16) range from 0 to 21 meters, with standard deviations of 7.4 meters east-west and 4.8 meters north-south.

Some puzzling unanswered questions remain. The same area was flown northbound a few minutes earlier. This time, georeferenced positions for the southern portion of the flightline showed a consistent western offset of 30 meters or more, although errors in the northern part of the line were small. But the GPS positions were differentially corrected by two independent methods (John Chance "Starfix" and Ashtech PNAV) and agreed with each other to within 3 meters. (This period is part of the first half of the plot of Figure 8.)

SUMMARY AND CONCLUSIONS

An approach to geocorrection of multispectral scanner imagery has been shown that uses GPS position and attitude and digital terrain data. An error analysis and mathematical algorithms used for post-processing correction have been discussed. Examples of corrected imagery were included.

Obvious improvements to our system would include more rapid updates of attitude. This would probably be done using an inertial navigation system; recent improvements in laser ring gyros have been significant, and costs are dropping dramatically. Such a system would probably be coupled to GPS. Beyond that, we expect that further increases in georeferencing accuracy would use traditional image transformation and warping using ground control points.

The system that has been developed provides MSS imagery whose geometry is far superior to anything developed earlier for EPA.

REFERENCES

- [1] Ashtech, Inc. "Three-Dimensional Attitude Determination with the Ashtech 3DF 24-Channel GPS Measurement System, (company publication), 1991
- [2] Doyle, D. et al, "NADCON, Version 2.0" (Program Documentation), National Geodetic Survey
- [3] Fisher, L. T., "Aircraft MultiSpectral Scanning with Accurate Geographic Control", Geodetical Info Vol. 5, No. 2, Feb. 1991 pp. 59-62
- [4] Fisher, L. T., "GPS/DTM Method Improves MSS Data", GIS World, Vol. 4, No. 6, Sep. 1991 pp. 38-42
- [5] Foley, J. D. and A. VanDam, Fundamentals of Computer Graphics, Addison-Wesley, 1982
- [6] Kuhl, M., X. Qin and W. Cottrell, "Design Considerations and Operational Results of A GPS Attitude Determination Unit", Proc. ION-GPS, 1994, Salt Lake City, UT
- [7] Lapucha, D. and M. Huff, "Multi-Site Real-Time DGPS System Using Starfix Link; Operational Results", Proc. ION-GPS 1992, Albuquerque, NM pp 581-588
- [8] Lapucha, D. and M. Huff, "Multisite Real-Time DGPS System Using Satellite Data Link: Operational Results", Navigation Vol. 40 No. 3, Fall 1993 pp 283-296
- [9] Milpert, D. G., "GEOID90: A High-Resolution Geoid Height Model for the Conterminous United States", Eos, Trans. of the American Geophysical Union 72(49), Dec. 3, 1991
- [10] Milpert, D. G., "GPS and GEOID90-The New Level Rod", GPS World, Feb. 1992 pp 38-42
- [11] Schwarz, K. P., A. El-Mowafy and M. Wei, "Testing a GPS Attitude System in Kinematic Mode", Proc. ION-GPS 1992, Albuquerque, NM pp 801-809

Interferometric Flight Inspection Systems: Development and Flight Test Results

D. Stratton
Parker Hannifin Corporation

Abstract

New flight inspection systems from Parker Gull use simple but very accurate positioning. The new systems satisfy unique flight inspection requirements using the Global Positioning System (GPS) as a source for interferometry. An airborne inspection console with an autonomous ground unit analyzes a full range of radio navigation systems automatically in flight. Parker Gull validated this new technology in flight tests with Ohio University Avionics Engineering Center. Results of over fifty approaches prove the system achieves Category III capability on a par with automatic systems used by the United States Federal Aviation Administration (FAA). With procedures and software designed especially for flight inspection, robust accuracy is attained even when satellite geometry and supporting measurements are sub-optimal. This latest technology has been integrated with systems and software matured over two decades of FAA support. Gull is producing the first of these systems for FAA certification of GPS helicopter approaches throughout the United States.

Introduction

Flight inspection assures the integrity of radio navigation aids through direct measurement of their signals in space. International Civil Aviation Organization (ICAO) standards mandate flight inspection of navigation aids when commissioned and periodically thereafter [1]. The increased number and types of aids have lead to development of automated flight inspection systems with integrated avionics and high-accuracy tracking. A modern flight inspection system may be classified either as a semi-automatic system using ground tracking equipment, or as an Automatic Flight Inspection System (AFIS) requiring no ground equipment. Over several years, Parker Gull AFIS computers have performed over 300,000 hours of automatic and semi-automatic flight inspection on over fifty FAA and international aircraft [2-6]. As acceptance of Differential GPS (DGPS) as

a tool for aircraft tracking widens [7-11], satellite navigation is finding a number of uses in flight inspection [12-15].

High accuracy is obtained from DGPS by tracking the interference fringes obtained when GPS carriers received at two locations are superimposed. By doing this, Parker Gull's new systems can project an exact azimuth, elevation, and distance outward from a known baseline. This capability was used to develop InterFix™, a unique procedure enabling the baseline to be determined automatically while in flight. The technology is implemented using an autonomous ground unit placed at the facility under inspection. The unit telemeters digitized GPS receptions to a GPS-embedded airborne system where aircraft position is derived (Fig. 1). Over fifty approaches have been flown to confirm that with InterFix™, DGPS technology meets demanding Category III flight inspection requirements, as detailed below. Integration of this technology with established flight inspection systems provides the ultimate in performance and reliability.

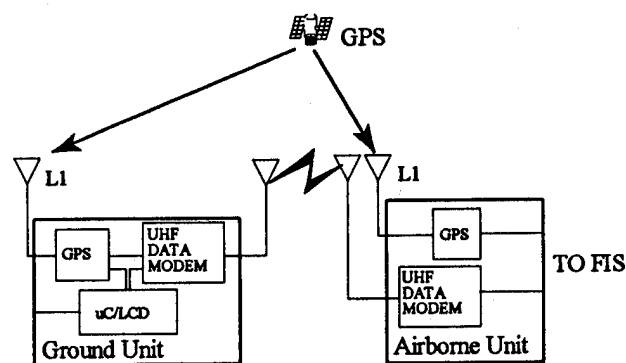


Figure 1. Interferometric Flight Inspection Positioning Components.

Flight Inspection Positioning Requirements

ICAO standards mandate precise aircraft positioning for the measurements of Table 1 (from [1], [16]). The right column of Table 1 contains a single flight inspection positional

accuracy requirement derived for each navigation aid based on the most stringent criterion. These values are derived assuming that the flight inspection system should be at least three times better than the navigation aid acceptance specifications (per [1], Vol. II, Paragraph 6.1.8). Allowances are made for avionics error on a root-sum-squared basis based on [1] for ILS and [16] for MLS. The maximum range (distance from threshold) over which precise positioning is required is also indicated in the right column of Table 1.

The accuracy requirements of Table 1 apply at the threshold for all cases except ILS glide slope, where the required positional accuracy applies from Pt. A (4 nm. from threshold) to Pt. B (3500 ft. from threshold). While MLS accuracy thresholds increase linearly from the threshold to the coverage limit, precise positioning is required to determine PFE, a filtered error metric including alignment bias, to the coverage limit. For ILS, some means of evaluating structure to the coverage limit is required. Because structure as defined by

ICAO [1] is the deviation of course or glide slope from its mean value, structure requirements place a repeatable accuracy or drift requirement on the position reference system. The case is similar for PFN and CMN, which are filtered error metrics quantifying induced flight path variations and induced control motion.

Category III Capability

Three types of positioning technology meet Category III requirements, as summarized in Table 2. Each technology meets the requirements on its own, although integrating multiple systems provides further benefits. Trackers and AFIS have been used for several years, while use of GPS interferometry is just beginning. Each of these technologies is described below.

Navigation Aid	Acceptance Spec.	Location Where Spec. Applied	Derived Positioning System Requirement
ILS Localizer (Category III): Front-Course Alignment Front-Course Structure Back-Course Alignment Back-Course Structure	10 ft 30 uA - 5 uA 200 ft 20 uA	threshold cov. limit - Pt. E 1 nm from threshold 1 nm from threshold	Accuracy: 0.014° Drift: 0.03°/min Range: 1 nm (structure to 20 nm)
ILS Glide Slope (Category III): Alignment Height tolerance Structure	0.12° (3° G/S) 10 ft high, 3 ft low 30 uA - 20 uA	Pt. A to Pt. B Threshold cov. limit - threshold	Accuracy: 0.036° Drift: 0.015°/min Range: 4 nm (structure to 20 nm)
MLS Azimuth: Path-Following Error (PFE) Path-Following Noise (PFN) Control-Motion Noise (CMN)	20 ft, 13.5 ft preferred 0.1° - 0.08° 11.5 ft 0.09° - 0.07° 10.5 ft 0.1° - 0.06°	threshold cov. limit - threshold threshold cov. limit - threshold threshold cov. limit - threshold	Accuracy: 0.019° Drift: 0.05°/min Range: 20 nm (PFE reqt. relaxed beyond 6 nm)
MLS Elevation: PFE PFN CMN	0.16° - 0.133° 0.10° - 0.087° 0.1° - 0.05°	cov. limit - threshold cov. limit - threshold cov. limit - threshold	Accuracy: 0.04° Drift: 0.06°/min Range: 20 nm (PFE reqt. relaxed beyond 6 nm)

Table 1. Summary of Requirements for Category III Flight Inspection Capability.

Technologies Meeting Cat III Requirements	Required Ground Equipment	Range Capability (High Accuracy)
Radio Telemetry Theodolites and Laser Trackers	RTT or tracker and telemetry unit	5 nm (typical conditions) 20 nm (ideal)
AFIS: INS with Precision Update	None	High-precision to 5 nm. (structure to 20 nm)
GPS Interferometry	GPS ground reference/telemetry unit	High-precision to 5 nm (PFE & structure to 20 nm)

Table 2. Summary of Precise Positioning Alternatives for Flight Inspection.

Radio Telemetry Theodolite

Since the early days of ILS, government agencies have used manual optical theodolites for precise aircraft positioning. Manual theodolites require the operator to keep the aircraft centered within the graticule. Visual contact must be maintained at all times, which makes weather an significant operational consideration. With the addition of a data link, the Radio Telemetry Theodolite (RTT) provides azimuth or glide path measurements for real-time comparison with the navigation aid. The RTT must be positioned near each antenna, necessitating re-location for separate localizer and glide slope evaluations. An optional ranging system can be employed to provide distance data to correlate observed features (e.g., structure) over multiple runs.

Although the practical use of RTT is limited to periods of good visibility, it is still considered acceptable as a low cost positioning source. Because of the tight manual tracking required, overall accuracy is highly dependent on operator performance. In practice, a skilled operator can maintain an accuracy within 0.02° . With increasing acceptance of newer technologies, RTT may retain limited utility as a back-up system or for consistency with established procedures.

Laser Trackers

Several varieties of three-dimensional automatic tracking systems have been built based on optical, infra-red, and laser technologies [1]. Auto-tracking provides operational and accuracy benefits over manual tracking. Modern laser-trackers that track an aircraft-mounted reflector are somewhat simpler and more portable than earlier systems. However, automatic trackers still retain many of the limitations of RTT, and they are many times more expensive. For example, weather dependence is still an issue, and localizer and glide slope evaluations are done separately. Dynamic tracking performance involves considerations beyond the laser's static angular accuracy of 0.01° , so achieved accuracy in the field is

difficult to determine. Precise positioning and leveling of the unit is critical to maintain accuracy levels of all measurements. The laser tracker includes an automatic acquisition feature, in which computed aircraft position is telemetered to the ground to steer the unit to acquire the reflector.

AFIS: Inertial Navigation With Precision Update

With requirements to inspect thousands of radio navigation facilities world-wide, the FAA abandoned RTT in 1973 in favor of Automatic Flight Inspection Systems (AFIS). AFIS uses on-board Inertial Navigation Systems (INS) and other airborne sensors for positioning, thereby eliminating weather dependency, visibility limitations, and ground equipment. Integrated GPS/INS is the present standard for automatic flight inspection [17]. Parker Gull AFIS in service with the FAA perform the bulk of all flight inspection in the U.S. today, and Parker Gull AFIS are used by several international governments including the Japan Civil Aviation Bureau. AFIS has several significant operational advantages over RTT, including all-weather 24-hour operations, automated tuning and positioning, analysis and alert logic, long-range navigation and positioning, flight management functions and autopilot interface for en-route guidance. For example, during ILS or MLS evaluations, localizer, glide slope and marker beacon are evaluated simultaneously.

At the present time INS is the only means to meet flight inspection accuracy levels without ground equipment. The error characteristics of ring-laser gyro INS and GPS/INS are quite stable, making in-flight error correction highly accurate. The best INS error estimates are made from position fixes made during low-altitude passes over surveyed runway threshold markings. Two such fixes can be obtained as the aircraft is flown over each end of the runway following an ILS approach. Vertical position bias is determined to an accuracy of one ft using a radio altimeter, while similar accuracy is obtained in the horizontal plane using a camera positioning system (or a manual procedure that provides somewhat less

accuracy) [3]. A second fix enables determination of drift rate to approximately two ft per minute. These corrections are used to provide the measurements of Table 1 out to 5 nm immediately following the approach. Real-time results are uncorrected outside of 5 nm.

Using conservative assumptions, AFIS accuracy is compared to an ideal tracker with 0.02° accuracy (Fig.2-3). AFIS achieves accuracy comparable to automatic trackers. AFIS is routinely used for flight inspection of Category III ILS in the U.S.

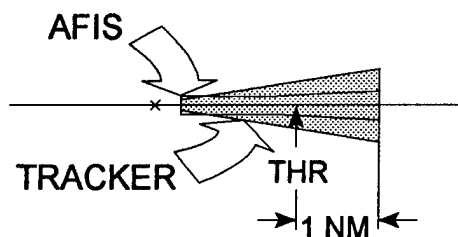


Figure 2. Comparison of AFIS and ideal 0.02° tracker for localizer evaluations. Angles are exaggerated to highlight relative accuracy.

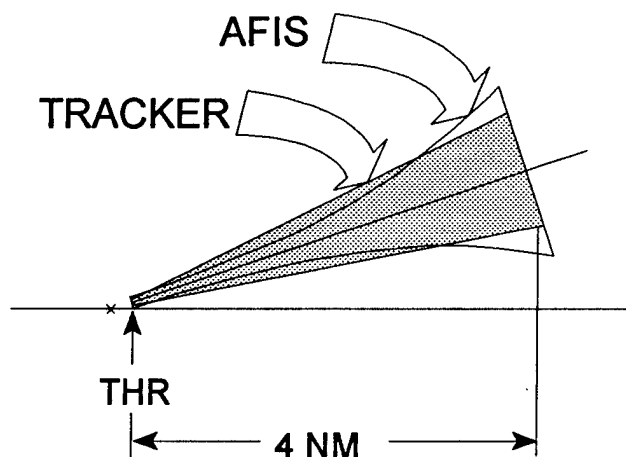


Figure 3. Comparison of AFIS and ideal 0.02° tracker for glide slope evaluations. Angles have been exaggerated to highlight relative accuracy.

GPS Interferometry

GPS interferometry is the latest technology to meet Category III flight inspection accuracy criteria. Parker Gull's new flight inspection approach retains nearly every feature of AFIS (e.g., system automation, simultaneous analysis of localizer and glide slope) while using a simple ground unit in place of the INS. Unlike standard DGPS, GPS interferometry makes use of 1575 MHz carrier transmissions recovered by high-quality commercial receivers. Noise levels on the carriers are a small fraction of the 19-cm carrier wavelength, while residual vertical position biases of 2-5 ft are removed using a custom in-flight procedure. As with a tracker or theodolite, flight inspection is preceded by a landing to set up the ground unit. While the GPS antenna must be carefully positioned relative to facility antennas, there are no critical alignment procedures. Moreover, there is no need to re-locate the unit for separate glide slope and localizer evaluations. Once the unit is operational, it can be left unattended until the inspection is complete.

Use of DGPS begins with real-time navigation at the limit of data link coverage, which is 20 nm. when within line of sight. (GPS is available outside of data link coverage.) Real-time carrier interferometry incorporates filtered GPS Coarse/Acquisition codes used in conventional GPS. Navigation continues in-bound until reaching the threshold, where a single position fix is obtained during threshold overflight. A corrected InterFix™ analysis is generated to produce high-accuracy results as the aircraft heads out-bound for the next run. Corrected results are required only within 5 nm of the threshold since the system's real-time accuracy meets all other requirements (including PFE evaluation out to 20 nm, which is a capability unique to DGPS technology).

The accuracy of this procedure depends on the quality of the position fix itself -- an error in the fix effectively causes a corresponding bias in the corrected solution. Solution drift is negligible over the two-minute period of the corrected analysis. A stand-alone interferometric system uses the real-time DGPS solution to establish horizontal position, and a radio altimeter is used for the vertical. Table 3 presents the overall 2σ RMS accuracy of InterFix™ in a stand-alone system; accuracy is stated as a fixed bias plus a small growth term proportional to the separation of the aircraft from the ground unit (i.e., the "baseline"). These values are based on a flight test verification program described below. In conjunction with a camera positioning system, InterFix™ cross-track accuracy improves to 1 ft + 5 ppm. In fact, because the fix corrections are actually a set of integer values, future versions of the system will determine the exact integers, which will remove the fix biases altogether to achieve centimeter-level accuracy. More detailed descriptions are presented in [12,13]. Figure 4 depicts the relative vertical accuracy of real-time and corrected InterFix™ position.

Position Component	Real-Time Accuracy	Fix Accuracy	InterFix™ Accuracy
Vertical	4 ft + 35 ppm baseline	1 ft (Radio Alt.)	1 ft + 20 ppm baseline
Cross-Track	2 ft + 15 ppm baseline	2 ft (DGPS)	2 ft + 5 ppm baseline
Along-Track	2 ft + 15 ppm baseline	2 ft (DGPS)	2 ft + 5 ppm baseline

Table 3. Summary of DGPS Accuracy.

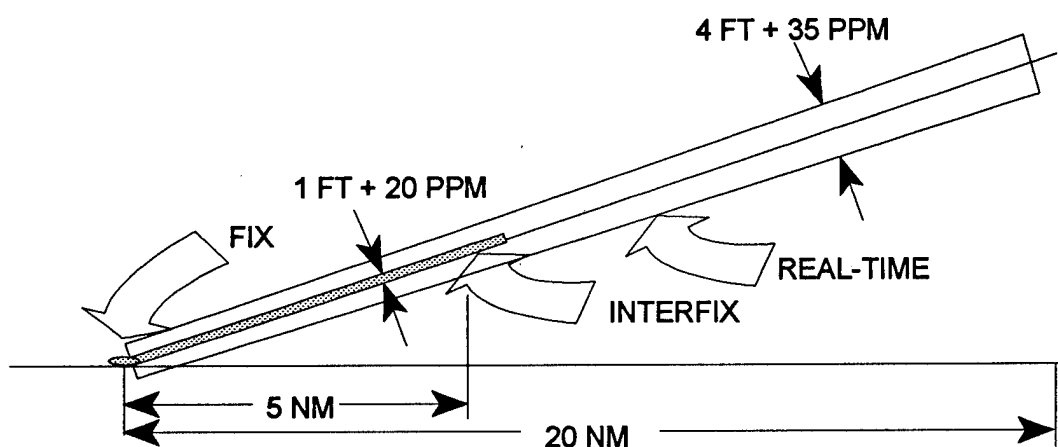


Figure 4. Vertical Accuracy of GPS Interferometry.

Development of Interferometric Flight Inspection

Following flight evaluations of GPS interferometry by several research groups, Parker Gull pursued an independently-funded program to adapt this technology to flight inspection. This program addressed the fact that commercial off-the-shelf DGPS technology will not meet the vertical accuracy required for flight inspection (except marginally under ideal conditions of satellite geometry and multipath). To solve this problem, Parker Gull developed the InterFix™ procedure to provide robust accuracy even under sub-optimal conditions of satellite geometry and multipath [12]. Analysis and laboratory tests showed that Category III capabilities could be achieved without INS, trackers, military GPS signals, or pseudo-lites. A flight test program was initiated to validate the approach.

Flight Test Results

A flight test program was conducted with the assistance of Ohio University Avionics Engineering Center [12,13]. The results below are from the second round of flight tests, which involved over forty approaches with various forms of precision and non-precision guidance. Data link equipment for the prototype was provided by GLB Electronics, Inc., and GPS receivers from NovAtel Communications, Ltd. were used. The Avionics Engineering Center was contracted to provide an aircraft, pilot, truth systems, and technical assistance. The Center has a twenty-year history of research, development, installation, and flight inspection of navigation aids and avionics systems.

Two independent truth systems were used to validate the Parker Gull system, a theodolite tracker with a ranging system, and dual Ashtech Z-12 systems which have achieved accuracy superior to the NASA Wallops Island laser tracker according to NASA researchers [19]. The following results were obtained from Ashtech PNAV post-processing DGPS software. Figure 5 and 6 present the composite residuals of real-time DGPS solutions in cross-track and vertical directions, which verify the real-time accuracy of Table 3.

Sensitivity to Altimeter Performance

Calibrated radio altimeter performance of 1 ft has been verified through several years of operational use by FAA flight inspection, so the flight tests did not include a radio altimeter. Instead, the truth data was used to simulate the radio altimeter for InterFix™ analyses. Previous results showed that with error-free altimeter performance, solution drift is less than 20 ppm baseline [12,13]. To provide a more conservative analysis, a set of ten approaches was randomly selected for a sensitivity analysis. A simulated radio altimeter bias of 1 meter was introduced, and the real-time DGPS solution was used for the horizontal fix component. Cross-track position error of the composite results for 10 approaches is presented as Figure 7, while Figure 8 contains a vertical position error

composite. While the one-meter bias appears in the vertical solutions, the vertical error grows by less than 20 ppm baseline -- this means that the altimeter bias does not affect stability. In fact, the alignment error introduced by this unexpectedly-large altimeter error is only 0.015° -- *still well within Category III requirements*. Horizontal position error remains within the quoted 2σ RMS accuracy of 2 ft plus 5 ppm baseline.

Absence of Cycle Slips

Figure 7 contains an interesting result with regard to cycle-slips -- *there are none*. Cycle slips are a potential error source in GPS interferometry. If one of the GPS receivers temporarily loses lock on a satellite, but does not correctly indicate this, the vertical position error will jump by an integer multiple of 19 cm -- a cycle slip. The smooth degradation of these solutions indicates that no cycle slips were seen on any of the approaches. Loss in carrier lock often does occur while turning onto final approach due to temporary blockage by the wings. This does not present an operational problem for the system, because the InterFix™ solutions actually "begin" at the threshold and propagate backwards in time out the approach. High-quality receivers such as the NovAtel units provide reliable warnings if carrier lock is lost.

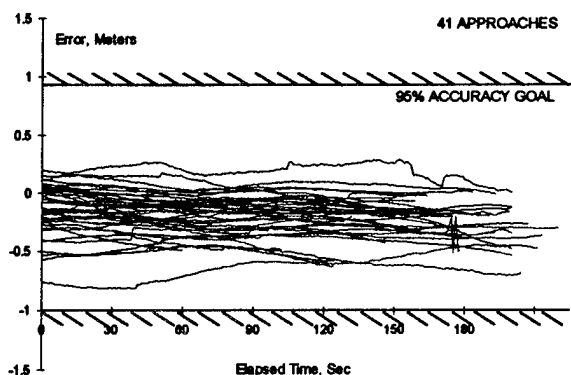


Figure 5. Cross-Track Errors of Real-Time DGPS Solutions.

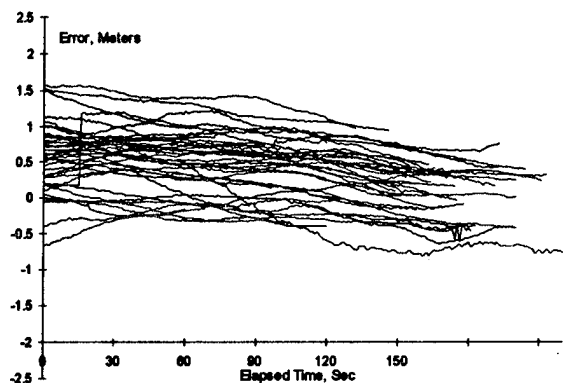


Figure 6. Vertical Errors of Real-Time DGPS Solutions.

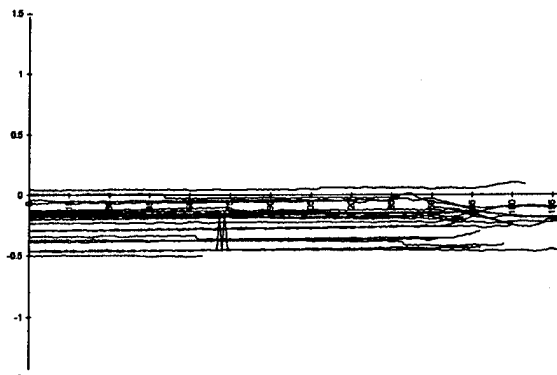


Figure 7. InterFix™ cross-track accuracy including the effect of 1-meter altimeter error.

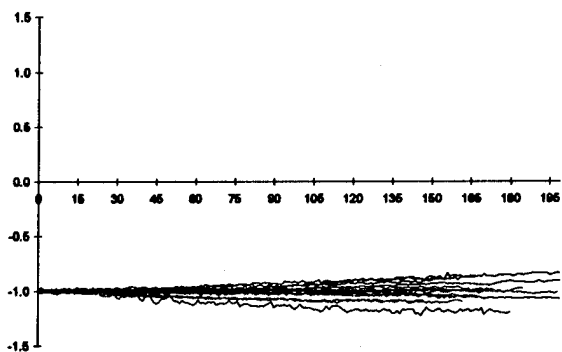


Figure 8. Vertical accuracy of InterFix™ including the effect of a 1-meter altimeter error.

Interferometric Flight Inspection Systems

GPS Flight Inspection System

The Federal Aviation Administration is using the first production version of Gull's DGPS for flight inspection of GPS helicopter approaches. The GPS Flight Inspection System (GFIS) consists of a portable ground unit and an airborne unit designed for temporary installation in a helicopter. The GFIS performs positioning, analysis, and data collection functions similar to the FAA AFIS, which is being used to commission new GPS approaches throughout the United States [18]. GFIS enables the FAA to flight inspect non-precision approaches that would be difficult or impossible to fly with fixed-wing aircraft. Growth capabilities are being provided for precision-approach radar inspection.

Integration with Inertial Navigation

Additional capabilities are provided by integration of INS with DGPS. INS can provide short-term continuity of positioning in case of a brief loss in telemetry. Cycle-slip detection is possible by comparison with stabilized integrated vertical acceleration. When integrated with an existing AFIS, DGPS can be used for dynamic estimation of horizontal drift rate, eliminating the requirement for a second position-fix [14]. This capability becomes somewhat more useful if an existing source of differential corrections is available so that landing of the aircraft is not necessary.

Integration with RTT and Tracker

DGPS can be combined with RTT or laser trackers to support existing semi-automatic operations. Combining DGPS with a tracker provides a complete solution in real time with excellent coverage and accuracy [15]. Figure 9 compares the real-time accuracy and coverage of DGPS and a laser tracker (static tracker accuracy of 0.01° is shown, which is optimistic). Because the tracker accuracy characteristic is primarily angular, the positional accuracy of DGPS is better at long range. As the aircraft passes through the acquisition zone, real-time DGPS and laser-tracker accuracy are equivalent. Upon acquisition by the tracker, positioning and inspection continues based on the tracker until the tracker loses lock on the reflector. Continuity of the inspection results can be used to compare DGPS and laser agreement.

On the other hand, the flight-test results above would raise the question -- *why use the tracker at all?* We expect that field experience with integrated DGPS/tracker systems eventually will settle this question.

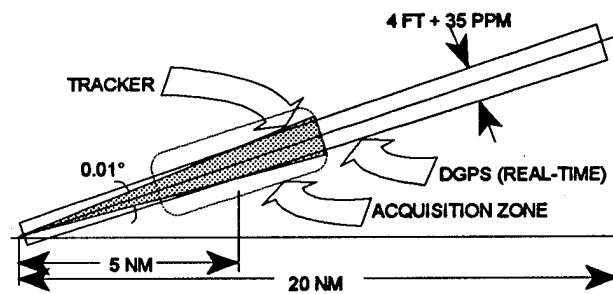


Figure 9. Comparison of Real-Time DGPS and Laser Tracker Accuracy and Coverage. Laser tracker accuracy based on static results.

Conclusions

Flight inspection has traditionally involved a choice between advanced automatic systems with inertial referencing and semi-automatic systems with limited, cumbersome ground positioning. Parker Gull has introduced a new choice: a semi-automatic system with a ground component so simple that it is *virtually* automatic. Now that the robust, high-accuracy of InterFix™ has been verified in flight, operational experience with its stand-alone Category III capability can begin in earnest. The system's compatibility with existing tools and procedures provides a means for a smooth transition from older technologies. Meanwhile, full integration of GPS interferometry into advanced flight inspection systems will elevate the standard for reliability and integrity of flight inspection in the near future.

References

1. **Manual on Testing of Radio Navigation Aids**, Document 8-71, Third Edition, Vol. I-II, International Civil Aviation Organization, Montreal, Canada, April, 1972.
2. Litman, B. "Implementation of Automatic Procedures, for MLS Inspection," **Proceedings of the Seventh International Flight Inspection Symposium**, Vol. 7, p. 11-20, Royal Aeronautical Society, London, WI, June 22-26, 1992.
3. Stratton, D., and Cohen, D., "A Video Camera Position System for Flight Inspection of Aircraft Landing Aids," **Proceedings of the Eighth International Flight Inspection Symposium**, p. 133-140, Denver, CO, June 6-10, 1994.

4. Kwartioff, A., "Flight Inspection of Navigation Aids for Civil Aviation," **Proceedings of the Symposium on World Wide Communications, Navigation, and Surveillance**, p. 333-341, Reston, VA, April 26-29, 1993.
5. R. Gucciardo, "Automatic Flight Inspection -- The 'State of the Art,'" **Proceedings of the IEEE Plans Symposium**, Phoenix, AZ, November, 1994.
6. Kwartioff, A., and Gucciardo, R., "New Generation Displays Increase Flight Inspection Efficiency and Productivity," **Proceedings of the Eighth International Flight Inspection Symposium**, Denver, CO, June 6-10, 1994.
7. Remondi, B., **Using the Global Positioning System (GPS) Phase Observable for Relative Geodesy: Modeling, Processing, and Results**, Ph.D. Dissertation, U.S. Dept. of Commerce, National Geodetic Information Center, National Oceanic and Atmospheric Administration, Rockville, MD, May 1984.
8. van Graas, F., and Diggle, D., "Interferometric GPS Flight Reference/Autoland System: Flight Test Results," **Proceedings of the Sixth International Technical Meeting of the Satellite Division of the Institute of Navigation**, p. 855-870, Salt Lake City, UT, Sept. 22-24, 1993.
9. Qin, X., Gourevitch, S., and Ladd, J., "A High-Precision Dual-Band Solution to Airborne Navigation (Even in the Presence of Spoofing)," **Proceedings of the Sixth International Technical Meeting of the Satellite Division of the Institute of Navigation**, p. 885-891, Salt Lake City, UT, Sept. 22-24, 1993.
10. Cohen, C., Lawrence, D., Pervan, B., Cobb, H.S., Barrows, A., Powel, J.D., and Parkinson, B., "Flight Test Results of Autocoupled Approaches Using GPS and Integrity Beacons," **Proceedings of the Seventh International Technical Meeting of the Satellite Division of the Institute of Navigation**, p. 1145-1153, Salt Lake City, UT, Sept. 20-23, 1994.
11. Blomenhofer, H. Walsh, D., and Hein, G., "On-The-Fly Carrier Phase Ambiguity Resolution for Precise Aircraft Landing," **Proceedings of the Sixth International Technical Meeting of the Satellite Division of the Institute of Navigation**, p. 821-830, Salt Lake City, UT, Sept. 22-24, 1993.
12. Stratton, D., "A Differential Global Positioning System for Flight Inspection of Radio Navigation Aids," **Proceedings of the Seventh International Technical Meeting of the Satellite Division of the Institute of Navigation**, p. 1559-1566, Salt Lake City, UT, Sept. 23-26, 1994.
13. Stratton, D.A., "High-Precision Trajectory Determination Using Satellite Navigation Systems," **Proceedings of the AIAA Guidance, Navigation, and Control Conference**, Baltimore, MD, August, 1995.
14. Feit, C., and Bates, M., "Accurate Positioning in a Flight Inspection System Using Differential Global Navigation Satellite Systems," **Proceedings of the Seventh International Technical Meeting of the Satellite Division of the Institute of Navigation**, p. 955-964, Salt Lake City, UT, Sept. 23-26, 1994.
15. Redeker, A., Haverland, M., and Vieweg, S., "The Impact of Satellite Navigation Technologies on Flight Inspection," **Proceedings of the Eighth International Flight Inspection Symposium**, p. 67-73, Denver, CO, June 6-10, 1994.
16. **Microwave Landing System (MLS) Interoperability and Performance Requirements**, FAA-STD-022d, Dept. of Transportation, Federal Aviation Administration, June 19, 1986.
17. Hartman, R., "Integrated Laser Inertial/GPS Navigation (GPIRS)," **Nav '89 Satellite Navigation Conference**, Royal Institute of Navigation, Oct. 1989.
18. "Four Teams Join Boeing in GPS Approach Tests," **Aviation Week and Space Technology**, McGraw-Hill, p. 47-51, August 21, 1995.
19. Donaldson, G., "Flight Inspection Policy and Standards for the Global Navigation Satellite System (GNSS)," **Proceedings of the Eighth International Flight Inspection Symposium**, p. 58-64, Denver, CO, June 6-10, 1994.

Flight Tests of a 3-D Perspective-View Glass-Cockpit Display for General Aviation Using GPS

Andrew Barrows, Per Enge, Bradford Parkinson, and J. David Powell
Stanford University

BIOGRAPHIES

Andrew K. Barrows is a Ph.D. candidate in the Department of Aeronautics and Astronautics at Stanford University. He is a private pilot and received his S.B. and S.M. degrees from the Massachusetts Institute of Technology, where his Master's thesis focused on realtime flight planning systems for light aircraft.

Per Enge is a Research Professor of Aeronautics and Astronautics at Stanford University. A Ph.D. graduate of the University of Illinois, his research focuses on WAAS aircraft landing applications. He previously taught at Worcester Polytechnic Institute.

Bradford W. Parkinson is a Professor of Aeronautics and Astronautics at Stanford University and is the program manager for the Gravity Probe-B relativity gyro experiment. He served as the first Program Director of the GPS Joint Program Office and was instrumental in the system's development.

J. David Powell is a Professor of Aeronautics and Astronautics at Stanford University, where he has been on the faculty for 24 years. His research deals with land, air, and space vehicle navigation and control. He is a co-author of two control system textbooks.

ABSTRACT

A display that takes advantage of the three-dimensional positioning data available from differential GPS has been flight tested on a general aviation aircraft. This glass-cockpit instrument provides a natural, "out the window" view of the world, making the horizon, runway, and desired flight path visible to the pilot in instrument flight conditions. The flight path is depicted as a series of symbols through which the pilot flies the airplane. Altitude, heading, and airspeed are presented along with lateral and vertical glidepath deviations. Particular attention was given to demonstrating a system satisfying

the budget, power, and form-factor constraints of light aircraft.

Simulator tests and flight trials on a Piper Dakota aircraft showed that the tunnel display allows the pilot to hand fly straight-in approaches with equivalent or better flight technical error than with a typical Instrument Landing System (ILS) needle display. Additionally, the tunnel display provides lateral and vertical guidance on curving missed approach procedures, for which ILS cannot provide positive course guidance. The results demonstrate that GPS-based displays can improve navigation along straight and curving flight paths in light aircraft by enhancing pilot situational awareness. Better path-following accuracy will benefit future Air Traffic Control schemes and a variety of specialized applications.

INTRODUCTION

Today's light aircraft typically fly with cockpit display technology that is 50 years old, in the form of a loosely-integrated set of dials, gauges, and indicators. New opportunities for making flying safer and easier are offered by the accurate 3-D positioning (down to meter and even centimeter accuracy levels) possible with differential GPS. However, even the most accurate information is of no use without a means of displaying it to the pilot. To date, GPS-derived positioning data has typically been displayed in conventional bearing/distance formats, or at best with a small moving map. In this sense, *commercial avionics have barely begun to take advantage of the full 3-D positioning capability offered by GPS.*

To address this need, a display was developed that allows the pilot of a light aircraft to see a three-dimensional (3-D) picture of the outside world, including the desired flight path and runway environment, even in low visibility conditions. This display has been tested in piloted simulations and flight trials, and offers significant benefits over conventional displays.

BACKGROUND

Instrument Landing System

Most light aircraft equipped for instrument flying carry an Instrument Landing System (ILS) receiver and display. The ILS is the most accurate landing system normally used in light aircraft and permits approaches down to decision heights of as little as 200 ft above the runway before the pilot must see the ground or abort the approach [1]. The ILS display shown in Figure 1 consists of two needles that indicate lateral and vertical angular deviations from the straight-in approach path (normally having a slope of 3 deg) down to the runway. If the aircraft is significantly off the glidepath, one or both of the needles will "peg" at full deflection at the edge of the display. Beyond this point, the ILS provides no indication of the magnitude of the lateral or vertical deviation. A significant amount of training and skill is required to smoothly fly an ILS approach by hand. The pilot must integrate information from many sources (artificial horizon, airspeed indicator, altimeter, vertical speed indicator, ILS needles) and mentally differentiate the ILS signal to derive phase lead for the desired damped behavior.

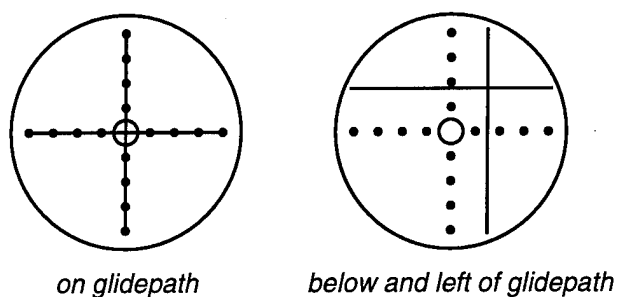


Figure 1: ILS Needle Display

If the pilot cannot see the runway at the decision height or if the approach must be terminated for any other reason, a missed approach is executed. This procedure is designed to maneuver the aircraft back into position to make another approach and therefore typically includes curving segments. Because the missed approach leads the aircraft away from the straight-in approach path, the ILS is of no use during this procedure. *The pilot without positive course guidance during one of the most critical phases of the flight.* Due to varying aircraft performance, pilot performance, and wind conditions, large obstacle-free areas must exist around the approach and missed approach paths [2]. Local terrain determines how much clearance is available, which influences the minimum decision height. This ultimately limits the utility of the instrument approach.

The limitations of the ILS and its cockpit display may be summarized as follows:

1. A high level of pilot skill is required to fly an ILS approach smoothly.
2. The ILS only provides a straight-in approach to a runway. Curving approaches are not possible.
3. If the aircraft is not near the desired glidepath, the ILS needle indicator yields only very coarse information as to where the pilot should fly.
4. The missed approach segment of the ILS approach normally has no positive course guidance.

These characteristics all contribute to a more fundamental problem: that *it is easy to lose situational awareness when using an ILS needle indicator*. Unless the awareness is already nearly on course, it is very difficult to tell from instrument indications where the desired flight path is and how to maneuver to get there. Situational awareness is critical in a demanding phase of flight such as instrument approach, motivating the need for better display technologies.

Tunnel-in-the-Sky

The problems associated with conventional displays has led to work on displays to provide pilots with increased situational awareness. Since flight fundamentally takes place in three dimensions, much of this work has centered on providing a 3-D perspective view of the outside world. Integrating this 3-D view with the many data sources needed for flight results in a single display from which the pilot can obtain all primary flight data. Enhanced vision systems augment the outside view with this 3-D information using a head-up display (HUD) [3]. A common goal of all systems to date has been to give the pilot a natural representation of the outside world.

A logical extension to the perspective-view display concept is an intuitive depiction of the desired flight path. Previous work has used analogies to roads and tunnels familiar to motorists and has used such terminology as "highway-in-the-sky", "pathway-in-the-sky", and "tunnel" [3-5]. With this scheme, the desired flight path is depicted as a tunnel or series of symbols for the aircraft to fly through. The intent is to inform the pilot where the aircraft is relative to the desired flight path and what action needs to be taken to stay on this trajectory.

Most of the work on 3-D perspective displays has centered on laboratory simulation involving large aircraft models [5, 7]. Most previous work has also focused on HUD technology. However, a computer screen in the instrument panel is a more likely candidate for implementation of a perspective display in light aircraft due to the expense and installation requirements of a HUD. The transition from instrument references to visual references may or may not be complicated by using a perspective display in the instrument panel instead of a HUD. These factors indicate a need for flight testing to

assess operational issues involved with perspective displays, especially those related to general aviation.

SYSTEM DESCRIPTION

To satisfy this flight test requirement, a tunnel display system was developed that addresses the budget, power, and form-factor constraints of light aircraft. This was made possible by a number of enabling technologies that could make a production system possible at the low prices demanded by general aviation. Several of these are outlined here.

Enabling Technologies

The advent of the Global Positioning System has made accurate 3-D worldwide navigation data available in light aircraft for the first time. With differential GPS techniques, accuracy can be brought down to meter or even centimeter levels while providing the integrity needed for critical flight operations such as precision approach. Accuracy is good enough that a scene reconstructed from a 3-D database very closely matches the actual view out the cockpit window.

As the personal computer has become a commodity product, prices have dropped and computational power has increased. The personal computer is finding increasing use in embedded and industrial applications and is now available in ruggedized and low-power versions. The rising floating-point math performance of new microprocessors allows these devices to perform the computationally-intensive graphics functions available only in expensive workstations a few years ago. A new generation of rendering chips, developed for the mass multimedia and game-player markets, are making sophisticated 3-D graphics possible at favorable price/performance levels.

Active-matrix liquid crystal display (AMLCD) screens are the leading choice for cockpit computer screens. Without modification, consumer displays are not suitable for use in aircraft due to sunlight-readability considerations. Temperature variations at the surface of the display can also render them unusable. For these reasons, aviation AMLCDs are typically fitted with backlights and heaters to make them practical as primary flight displays. Availability of reasonably-priced flat panel displays has traditionally been a barrier to putting computer displays in light aircraft. Fortunately, the growing popularity of laptop computers is now rapidly bringing down the price of AMLCDs.

Hardware and Software Setup

System hardware consisted of a ruggedized 90 MHz Pentium personal computer with a 64-bit graphics accelerator card. The computer drove a 320x234 pixel 5.5 inch diagonal AMLCD attached to the instrument panel glareshield. The 3-D graphics rendering functions were

based on a low-level library intended for computer game development. The flight hardware communicated through a serial interface with various positioning sources including the Wide Area Differential GPS System [8, 9] and Integrity Beacon Landing System [10], both developed at Stanford University. The display was also interfaced to a simulator for ground-based testing and rapid prototyping.

Tunnel Display

The tunnel display, shown in Figure 2, was kept simple to minimize computational requirements and enhance ease of use. The background consisted of the ground in brown, the sky in blue, and a white horizon line to provide the information found on a standard artificial horizon. The field of view represented was 40 deg vertical by 50 deg horizontal and included the runway and control tower depicted in correct perspective. (Other features could have been added, such as taxiways, roads, and water, but at some computational expense.) The approach path was depicted as a series of green "hoops" and the missed approach path as a series of magenta hoops whose pentagonal shape gave an up/down cue to the pilot. The hoops were 100m wide with a spacing of 500m on straight segments. On curving segments the spacing was reduced to 200m to allow the pilot to better see the tunnel, which curved out the side of the display when the aircraft was in a turn. Superimposed on this 3-D scene were a triangular yellow "own aircraft" symbol at the center of the display, as well as speed, heading, and altitude information. Small tapes at the bottom and right of the display presented the same data shown by standard ILS needles. The sensitivity of these tapes was typically 6 deg full-scale laterally and 1.4 deg full-scale vertically. The 3-D scene could be replaced by a full-screen ILS needle display for comparative testing. Views of the 3-D display on final approach and in a climbing right turn are shown in Figures 3 and 4, respectively.

SIMULATOR TESTS

A high-quality personal IFR procedures simulator was used to evaluate display performance. The simulator ran on an IBM-compatible personal computer and was modified to produce serial output in a packet format identical to that of the GPS equipment used in flight testing. A control yoke and a console with switches and knobs were used to control power, trim, flaps, and landing gear, so that keyboard use was unnecessary. The flight dynamics emulated those of a high-performance single-engine aircraft. The landing gear of the simulator was left down during these tests to closely parallel operation of the fixed-gear Piper Dakota flight test aircraft. Since the runway database used by the simulator was constructed from real-world information in Jeppesen-Sanderson's NavData database, the display looked and functioned exactly as it did in flight using GPS data. The simulator pilot was a 700 hour private pilot with approximately 50 hours flying on instruments.

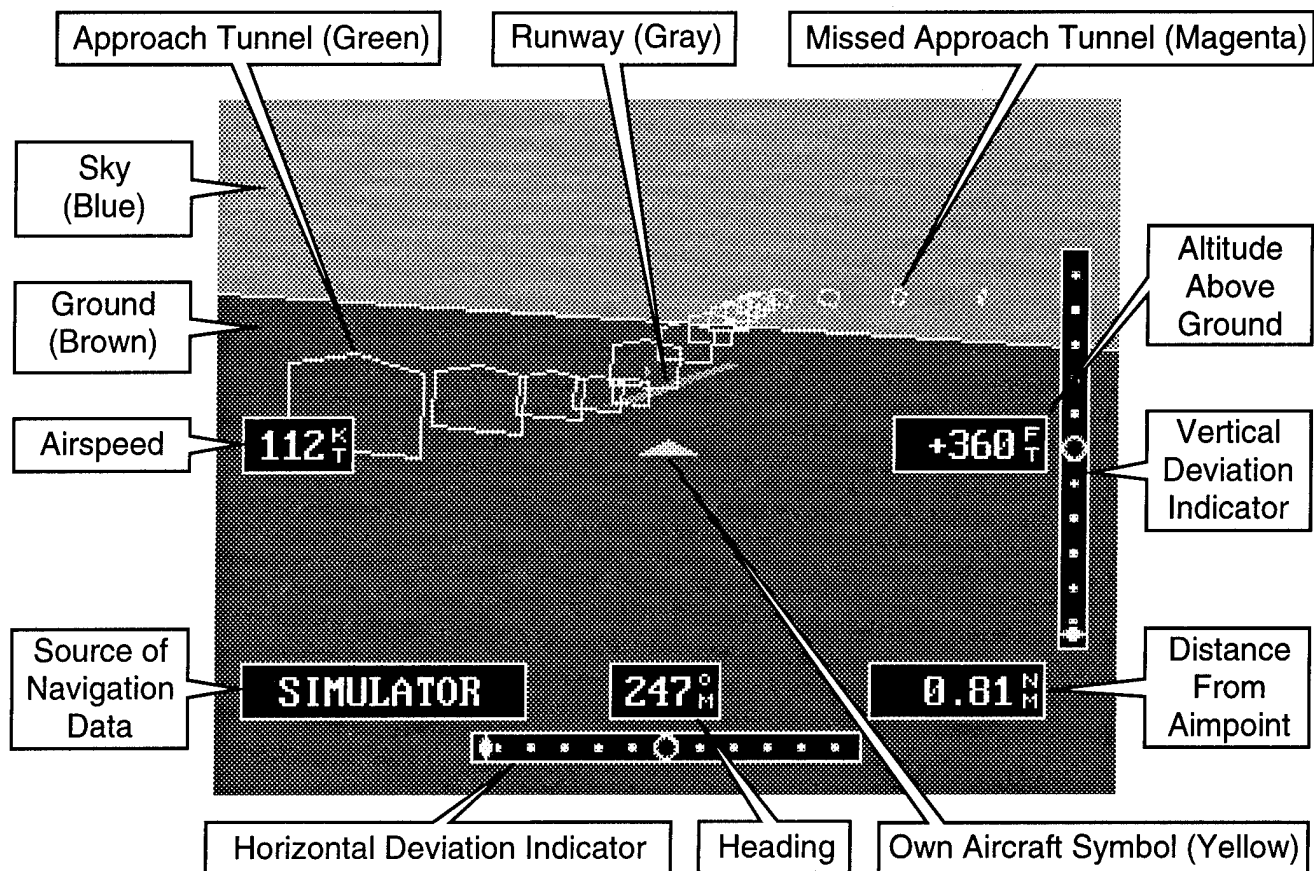


Figure 2: Tunnel Display

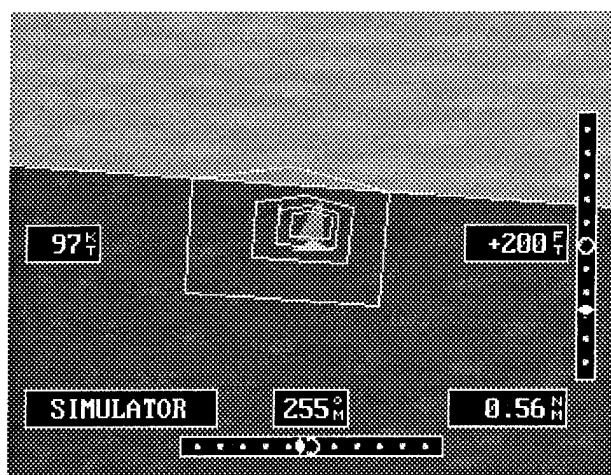


Figure 3: Tunnel Display on Final Approach

Procedure

Simulator tests consisted of approach and missed approach procedures for runway 25R at Livermore, California. The pilot flew six runs using the tunnel display and six using the ILS needle display. A "light"

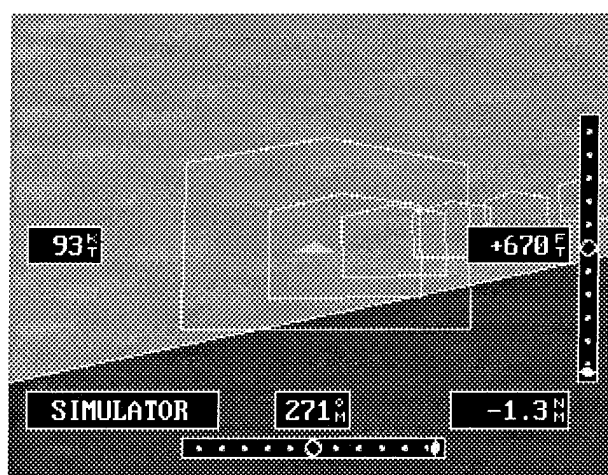


Figure 4: Tunnel Display in Climbing Turn

turbulence setting was selected and six different wind conditions were used as shown in Table 1. The order of display type and wind condition was randomized to mitigate systematic learning effects. A one-hour training session was given on the use of the simulator and displays.

Table 1: Wind Conditions for Simulator Tests

Wind Direction [deg magnetic]	Wind Speed [knots]	Condition
256	0	Calm
166	15	90° Left Crosswind
211	15	45° Left Crosswind
256	15	Wind Down Runway
301	15	45° Right Crosswind
346	15	90° Right Crosswind

A bird's eye view of the procedures conceived for this test is shown in Figure 5. Each run started with the aircraft 11 km from the runway, 2 km to the left of centerline, and below the 2.9 deg glideslope. (This glideslope angle was determined through flight testing at Livermore airport and is expressed relative to local vertical determined from the WGS-84 ellipsoid.) The initial aircraft heading was 285 deg magnetic to make approximately a 30 deg intercept with the runway heading of 256 deg magnetic. The pilot flew straight ahead to intercept the runway centerline and then turned left towards the runway. When the vertical glideslope was intercepted, a descent was commenced to stay on the glideslope. At the decision height of 200 ft above ground level, the pilot was instructed that the runway was not in sight and to execute a missed approach. This consisted of climbing straight ahead to 700 ft, at which point a climbing right turn was initiated. The turn was stopped on a heading of 060 deg magnetic.

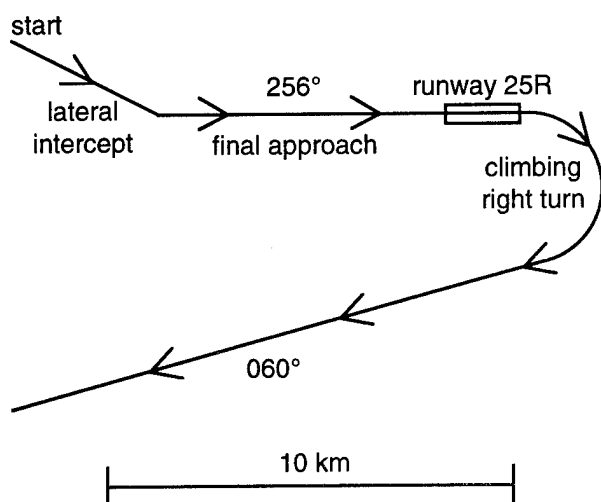


Figure 5: Bird's Eye View of Simulator Test Procedure

Results

Figure 6 shows vertical flight technical error (FTE: the difference between sensed position and desired position) on the straight-in portion of the twelve approaches from 3.5 nautical miles to 1 nautical mile from touchdown. The aircraft moves from left to right on the plot. The tunnel display approaches (represented by solid curves) show generally smaller path following error than the ILS needle display runs (represented by dashed curves). Root-mean-square (RMS) FTE for the tunnel display was 14.2 m compared to 27.5 m for the ILS needle display. At the left side of the plot, the ILS needle runs show a trend towards being low. Since the runs began with the aircraft below the glideslope, this suggests that the pilot was often slow in completing the vertical glideslope intercept.

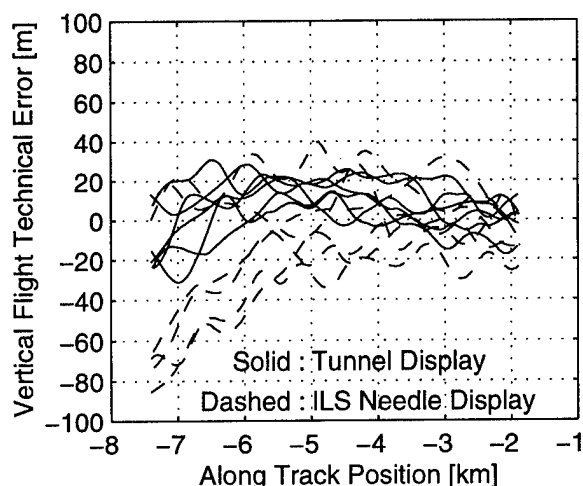


Figure 6: Simulator Test Vertical FTE

Lateral or cross track FTE on final approach is presented in Figure 7. Again, the pilot was able to maintain a smaller lateral RMS FTE during the approach. The tunnel runs had an average of 37.1 m RMS FTE compared with 85.9 m RMS FTE for the ILS needle runs. The ILS needle runs exhibit more oscillation or "hunting" for the correct horizontal path, while the tunnel runs seem to be smoother.

Figure 8 shows a bird's eye view of the lateral intercept made to the runway centerline and reveals some interesting behavior associated with this inbound turn maneuver. The ILS needle runs exhibit overshoot and undershoot as the pilot tried to smoothly intercept the localizer. After intercept, additional hunting for the lateral path is evident. The tunnel runs exhibit less tendency towards overshoot and undershoot, and show that the pilot achieved smoother lateral intercepts when confronted with varying wind conditions.

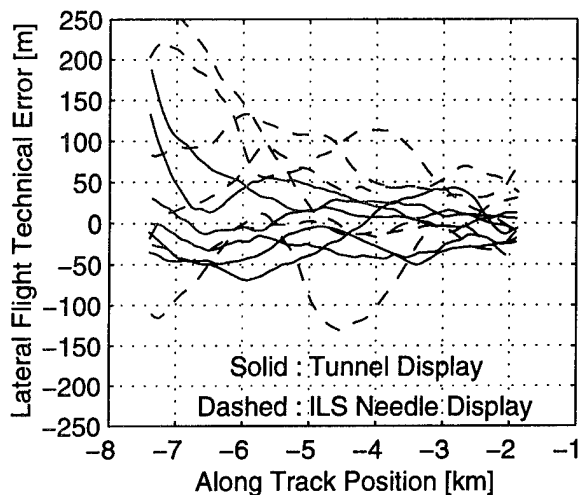


Figure 7: Simulator Test Lateral FTE

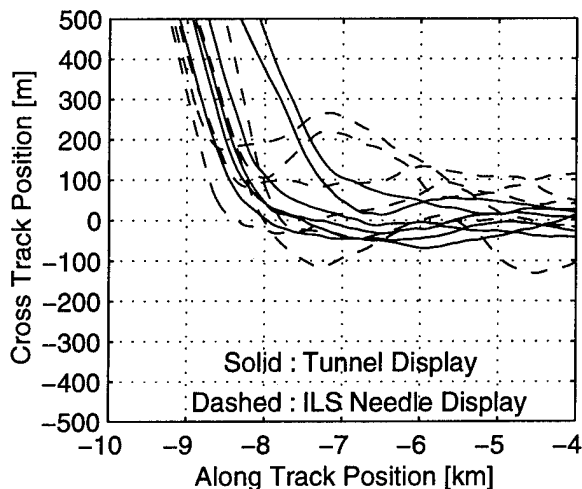


Figure 8: Simulator Test Lateral Flight Path Intercept

A bird's eye view of all twelve approaches is shown in Figure 9. On such a large scale, lateral deviations on the approach are difficult to see; however, the missed approach segments look quite different. The curving missed approaches using the tunnel display collapse onto one thick trace, showing that the pilot was able to repeat the curving flight path with each of the varying wind conditions. The missed approaches flown in the conventional manner show scatter due to different wind conditions. Since the pilot consistently ended the right turn at 060 deg magnetic, the varying winds caused different ground tracks for each run. This illustrates the reason for setting aside large obstacle clearance areas when setting up conventional missed approach procedures [2].

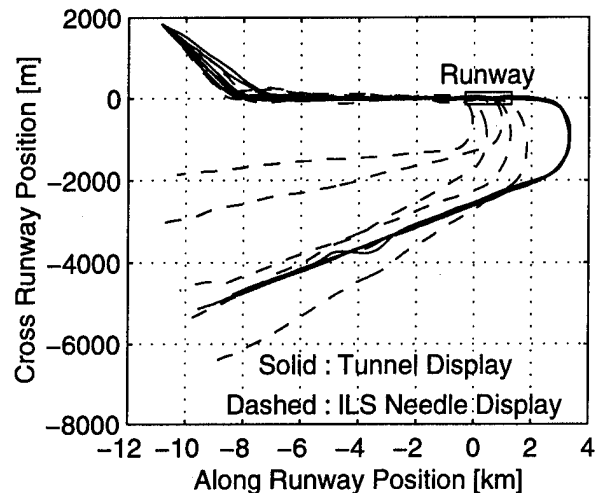


Figure 9: Simulator Test Bird's Eye View

Discussion

On approach, lateral and vertical FTE using the tunnel display were approximately half as large as those using the ILS needle display. When flying with the tunnel display, the pilot commented that he had more difficulty assessing vertical errors than lateral ones. This suggests that a display of raw position error (more prominent than the vertical deviation indicator used) would be desirable.

The tunnel display appeared to allow smoother transitions between flight conditions than the ILS needle display with conventional memorized missed approach instructions. For example, the runway centerline intercept was performed smoothly without overshoot or undershoot. On the curving missed approach, altitude and heading were simultaneously changing, and the pilot was able to easily follow cues on starting and finishing these maneuvers. Climbs and descents were also a good example, where the pilot needed cues on capturing and maintaining an altitude or climb/descent gradient. Of more importance than reducing FTE, it appears that the tunnel display gave the pilot the situational awareness needed to accomplish these tasks accurately and smoothly.

FLIGHT TESTS

Testing was performed in a four-seat Piper Dakota aircraft as an initial flight evaluation of the system. GPS positioning data was provided by the Stanford Wide Area Differential GPS system and had a 2 m 95% vertical accuracy [9]. The test pilot was the same pilot used for the simulator tests.

Procedure

Data was taken on straight-in approaches made to runway 25R at Livermore, California. Primary reference to the glidepath was the GPS-based display with both the

tunnel and ILS needle formats used. The pilot occasionally looked outside the cockpit to spot nearby aircraft called out by the control tower. A safety pilot flew in the right seat, and all testing was done in visual meteorological conditions. Winds at Livermore during the flight tests were reported as being from 240 deg magnetic at 16 knots.

The aircraft began each approach approximately 10 km from the runway, 3 km to the right of centerline, and 2000 ft above ground level. The pilot then turned onto final approach so as to intercept the 2.9 deg glideslope from below. Upon intercepting the glideslope, the pilot began a descent which continued down to, or slightly below, the decision height of 200 ft. Four approaches are documented here, two flown using the tunnel display and two flown with the ILS needle display.

Results

Figure 10 shows vertical FTE on the four approaches from left to right. The vertical RMS FTE has the same order of magnitude for both displays (13.2 m for the tunnel display; 19.4 m for the ILS needle display). One of the ILS needle runs exhibits a vertical deviation of more than 50 m above the glideslope.

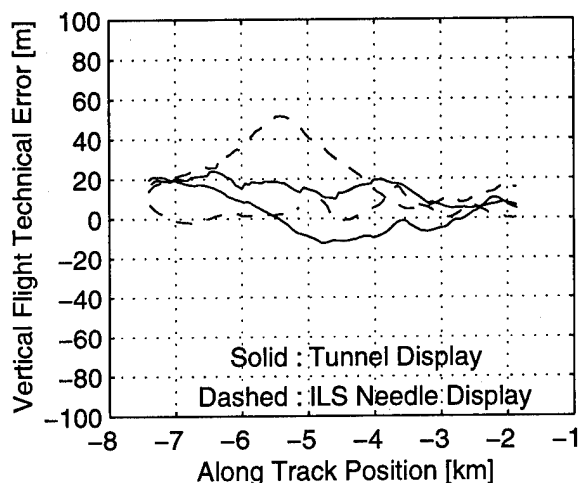


Figure 10: Flight Test Vertical FTE

Lateral FTE is shown in Figure 11. These are similar to the vertical FTE plots, and the RMS FTE has a comparable order of magnitude (28.0 m for the tunnel display; 33.0 m for the ILS needle display).

Figure 12 presents a bird's eye view of part of the approach where runway centerline intercepts were completed. One of the ILS needle runs exhibits an overshoot of the runway centerline of almost 0.5 km. This is noted here because of its relatively large magnitude.

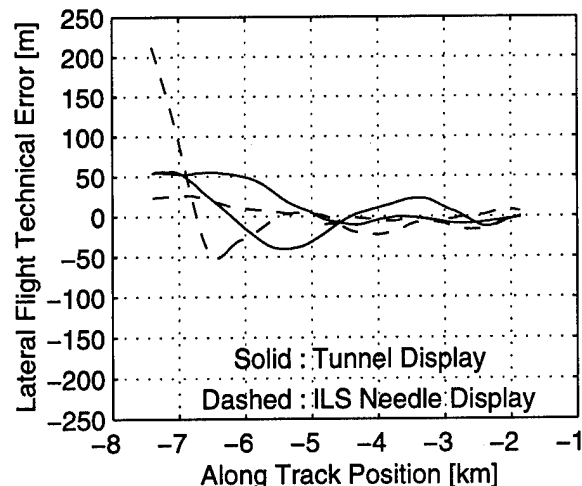


Figure 11: Flight Test Lateral FTE

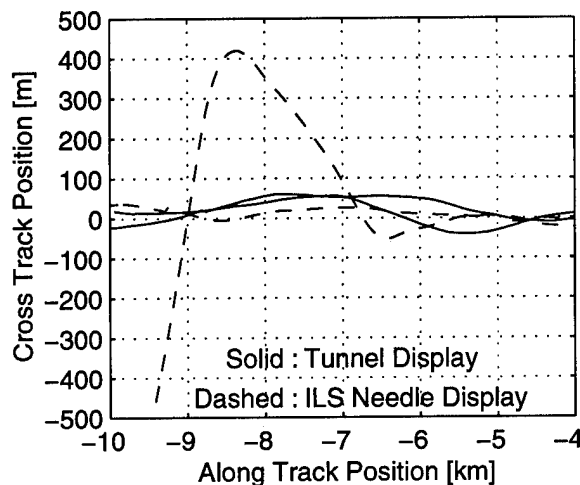


Figure 12: Flight Test Lateral Flight Path Intercept

Discussion

Since there are only two runs per display type, the data is more useful for a qualitative evaluation of the displays than quantitative statistical analysis. The FTE histories do not suggest any reason to believe that path-following performance was markedly different for the two displays. The pilot remarked that vertical deviations were more difficult to assess than lateral ones, a result also seen in the piloted simulations.

It seems that large deviations were more likely to occur with the ILS needle display than with the tunnel display. Examples of this included the vertical FTE deviation and lateral intercept overshoot evident in the data. The tunnel display appeared to allow intuitive recognition of incipient deviations and enabled the pilot to correct for these conditions. As in the simulator tests, the

tunnel display enhanced situational awareness during maneuvers with changing flight conditions.

CONCLUSIONS

The results of piloted simulation and flight testing may be summarized as follows:

1. Piloted simulation indicated that the tunnel display could improve FTE over that provided by an ILS needle display on a straight-in approach, while limited flight data suggested that path-following error characteristics were similar for the two displays.
2. The pilot reported that perception and control was most difficult in the vertical dimension, a result which agrees with [5]. Enhanced depiction of vertical error is necessary to give the pilot better vertical control.
3. Experiments showed that lateral and vertical flight path intercepts could be executed more smoothly with the tunnel display than with the ILS needle display.
4. In piloted simulation, the tunnel display allowed repeatable ground tracks on the curving missed approach, even in the presence of varying wind conditions.
5. Large flight path deviations were more easily recognized with the tunnel display, allowing the pilot to make corrections sooner.

In summary, the natural 3-D display format allowed intuitive recognition of the aircraft's relation to the desired flight path. *These results show that the tunnel display can increase pilot situational awareness and make flying safer and easier.*

The piloted simulations and flight tests demonstrate how GPS-based displays can enable accurate navigation along straight and curving flight paths in light aircraft. Greater VFR and IFR path-following accuracy for all classes of aircraft would result in greater utilization and safety in the National Airspace System. Future Air Traffic Management schemes such as the recently-introduced Free Flight concept [11] will most likely demand such improved accuracy. Additionally, the tunnel display has potential benefits in specialized applications such as aerial fire fighting, agriculture, search and rescue, military operations, flight test, photogrammetry, and medical evacuation.

ACKNOWLEDGMENTS

The authors would like to gratefully acknowledge the support of the FAA Satellite Program Office AND-510 in carrying out this work. The opinions expressed in this paper are the authors' and do not necessarily reflect those of the FAA. The contributions of Awele Ndili and members of the Wide Area Differential GPS and Integrity

Beacon Landing System groups at Stanford are also sincerely appreciated.

REFERENCES

1. Department of Transportation, Federal Aviation Administration, *Airman's Information Manual*, 1990.
2. Department of Transportation, Federal Aviation Administration, *United States Standard for Terminal Instrument Procedures (TERPS)*, Third Edition, U.S. Government Printing Office, Aug., 1993.
3. Yang, L.C. and Hansman, R.J., "A Human Performance Evaluation of Enhanced Vision Systems for Approach and Landing," SPIE Image Sensing, Processing, and Understanding for Control and Guidance of Aerospace Vehicles, Orlando, Florida, USA, April, 1994.
4. Wiener, E.L., and Nagel, D.C., *Human Factors in Aviation*, Academic Press, 1988.
5. Grunwald, A.J., "Tunnel Display for Four-Dimensional Fixed-Wing Approaches," *AIAA Journal of Guidance, Control, and Dynamics*, Vol. 7, No. 3, May-June, 1984, pp. 369-377.
6. Möller, H. and Sachs, G., "Synthetic Vision for Enhancing Poor Visibility Flight Operations," *IEEE Aerospace and Electronic Systems*, Vol. 9, No. 3, March, 1994, pp. 27-33.
7. Bray, R.S., and Scott, B.C., "A Head-up Display for Low Visibility Approach and Landing," AIAA 19th Aerospace Sciences Meeting, St. Louis, Missouri, USA, Jan. 12-15, 1981.
8. Walter, T., Kee, C., Chao, Y.C., et. al., "Flight Trials of the Wide Area Augmentation System (WAAS)," ION GPS-94, Salt Lake City, Utah, USA, Sept. 20-23, 1994.
9. Tsai, Y.J., Enge, P., Chao, Y.C., et. al., "Validation of the RTCA Message Format for WAAS," ION GPS-95, Palm Springs, California, USA, Sept. 12-15, 1995.
10. Cohen, C.E., Lawrence, D.G., Pervan, B.S., Cobb, H.S., et. al., "Flight Test Results of Autocoupled Approaches Using GPS and Integrity Beacons," ION GPS-94, Salt Lake City, Utah, USA, Sept. 20-23, 1994.
11. Nordwall, B.D., "Filter Center," *Aviation Week & Space Technology*, March 20, 1995.

An Evaluation of Precise Kinematic On-The-Fly GPS Positioning with Respect to a Moving Aircraft

Alan Evans, Bruce Hermann, and Christopher Law
Naval Surface Warfare Center

Benjamin Remondi
The XYZ's of GPS, Inc.

Thomas Briggs and Thomas Nelson
Naval Air Warfare Center

BIOGRAPHIES

Alan G. Evans has been working in Global Positioning System (GPS) applications at the Naval Surface Warfare Center, Dahlgren Division since 1981. He received a B.S.E.E. degree from Widener University in 1964 and M.S. and Ph.D. degrees in Electrical Engineering from Drexel University in 1967 and 1972, respectively.

Bruce R. Hermann received his B.S.E.E. degree from Bradley University in 1965, his M.S. in 1966 from Colorado State University, and his Ph.D. in Electrical Engineering from the University of Illinois in 1972. Dr. Hermann has been employed at Naval Surface Warfare Center, Dahlgren Division since 1972 and has been working on various aspects of the Global Positioning System since 1978.

Christopher S. Law received a B.S. degree in Photographic Science from the Rochester Institute of Technology in 1970. He has been employed at Naval Surface Warfare Center, Dahlgren Division as a Photographic Technologist in Range Instrumentation since 1970.

Benjamin W. Remondi earned his B.S.E.E. and M.S. degrees in Mathematics from the University of Delaware and his Ph.D. in Aerospace Engineering from the University of Texas at Austin. He has retired recently from the National Oceanographic and Atmospheric Administration and started a company - The XYZ's of GPS, Incorporated.

Thomas H. Briggs has a B.S. in Aerospace Engineering from Penn State University. He has worked in Air Traffic Control and Landing Systems for the Naval Air Test Center and Naval Air Warfare Center, Aircraft Division for five years, the last three of which have been concerned with Research Development Test and Evaluation of Global Positioning System based landing systems.

Thomas E. Nelson has worked at the Naval Air Warfare Center, Aircraft Division since he received his B.S. in Aerospace and Ocean Engineering from Virginia Tech in 1984. In 1994, he received his M.S. in Mechanical Engineering from the University of Maryland.

ABSTRACT

This paper evaluates the use of the Global Positioning System (GPS) to perform precise kinematic relative positioning when the reference antenna is located on a moving aircraft. This capability can be applied to the precise relative position of a number of vehicles that are within 30 km of each other but far from a land reference site. These applications include aircraft carrier landing, enhanced processing of dual aircraft radar or photogrammetric data, and testing of interceptor and target missiles.

Test results are presented that use the kinematic On-The-Fly relative positioning procedure. The procedure uses L_1 and L_2 frequency pseudorange and phase measurements of the GPS to precisely determine dynamic relative position. This particular algorithm is capable of subdecimeter positioning accuracy with respect to a moving platform.

Positioning is obtained with respect to both a fixed reference and a moving reference. The position of a fixed antenna located next to an aircraft runway is determined relative to an aircraft flying low over the runway. Alternately, the moving aircraft is also positioned with respect to the fixed site. Videometric truth data, obtained from the time-tagged images from two video cameras located near the runway, are used for relative positioning vector comparisons.

INTRODUCTION

Over the past few years, Dr. Remondi [1] and others [2], [3], [4], [5], have proposed, implemented, and documented several precise differential positioning techniques that exploit Global Positioning System (GPS) signals. These include static and dynamic kinematic positioning [6], [7], [8], [9], antenna swapping, and pseudokinematic positioning [10]. Over the past couple of years, the capability of the techniques has steadily improved to the point where the static initialization step for integer cycle ambiguity resolution is no longer necessary. Given at least four satellites in view and a period, typically seconds or minutes, of high-quality uninterrupted data, the integer cycle

ambiguity can be determined automatically over short and medium length baselines to 30 km and beyond. Once found, the integers can be used to obtain precise position solutions to the centimeter level. This technique is designed to determine precisely the position of moving antennas with respect to a static antenna. This advance is called On-The-Fly (OTF) kinematic positioning.

An extension of OTF is presented for the more general case where all sites are in motion with respect to the Earth and to each other - a procedure referred to as OTF kinematic *relative* positioning [11]. There are applications for which precise relative positioning between two sites both in motion and far enough from fixed land based sites that OTF, as described, is not feasible. These applications include: (1) aircraft carrier landing, (2) precise miss distance determination for interceptor missile lethality testing, (3) controlled aircraft refueling and (4) spacecraft rendezvous.

This paper is the result of a joint test between the Naval Surface Warfare Center, Dahlgren Division (NSWCDD), Dahlgren, Virginia, and the Naval Air Warfare Center, Aircraft Division (NAWCAD), Patuxent River, Maryland. Data was collected concurrently during flight test programs sponsored in part by the Federal Aviation Administration (FAA), and the Theater Ballistic Missile Defense program at NSWCDD.

The next section summarizes the relative OTF method. The test equipment and test are described and the results are presented for both the air-to-ground and the ground-to-air positioning. The paper is then summarized.

RELATIVE OTF

The changes necessary to extend the static-reference OTF algorithm into a dynamic-reference OTF algorithm were identified by Dr. Remondi. In the case of the static-reference OTF algorithm, the reference site is fixed and its position is known *a priori*. The reference antenna is normally set up over a geodetic marker. The rover site's approximate dynamic track is determined from a preliminary differential GPS solution. This step is needed to bound the integer cycle possibilities. Trials of integers within an error volume narrows the selection to a set that is consistent with the phase observations throughout the desired time interval. Once the integers are determined, a double difference solution provides the precise kinematic trajectory of the rover with respect to the reference.

The change from a static reference to a dynamic one still requires an absolute position for the reference site at each time step. Instead of being known *a priori*, it must be found by another method. A navigation solution found from smoothed pseudoranges is adequate for most short baseline applications, even when the effects of Selective Availability (SA) are considered. Longer baselines may require Precise Positioning Service (PPS) or differential quality solutions. In this relative mode, the rover is found with respect to the

dynamic reference instead of with respect to a fixed absolute reference. This does not change the rest of the OTF processing nor does it significantly change the final kinematic relative solution. The vector joining the two sites will have centimeter level accuracy. Although possible in principle, real-time processing was not performed during the test evaluations.

TEST EQUIPMENT

An NAWCAD EA-6B Prowler aircraft was instrumented for the test with an Ashtech Z-XII GPS receiver and a laptop personal computer (PC). The aircraft was surveyed for the videometric positioning.

The EA-6B Prowler is a four-seat, twin engine aircraft manufactured by Grumman Aerospace Corporation. The aircraft is used for the carrier-based electronic jamming and counter measures mission. The EA-6B is powered by Pratt and Whitney turbojet engines and is capable of speeds exceeding 500 knots indicated air speed in level flight. The GPS antenna and preamplifier were mounted behind the aft canopy on the top of the fuselage. The GPS receiver and the PC were placed in the port and starboard cheek panels, respectively. The PC was encased in a custom metal container, which included a heating element to maintain the PC above its low-end temperature specification.

Figure 1 shows a picture of a video camera image of the EA-6B as it approached the runway. The GPS antenna is denoted in the picture and can barely be seen above the surface of the aircraft. A black blade communications antenna, located 1.137 m aft of the GPS antenna, is also denoted in the picture. The upper forward point of this black blade antenna was used for the videometric positioning point of the aircraft due to its distinguishability. The height of this videometric positioning point was approximately the same as that of the GPS antenna during the approaches due to the pitch of the aircraft. The videometric positioning point was assumed to fly through the same minimum range point

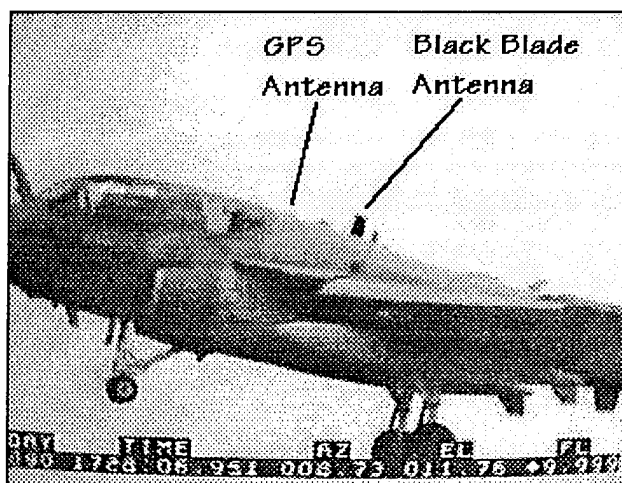


Figure 1. EA-6B Flyby As Seen In A Video Frame From Camera 1.

as the GPS antenna, only slightly later. For the aircraft flying at 140 kn (72 m/s) this delay would be about 0.016 s. Variations in roll, pitch, and yaw and additional lever arm effects are ignored. Consequently, the videometric positioning was approximate.

Two additional Ashtech Z-XII receivers were used during the test. One was located just over 100 ft from the centerline of the runway, as shown in Figure 2, at a temporary ground reference site named PHOTO. The other receiver was located at an absolute ground reference site named GND about 641 m from the PHOTO site.

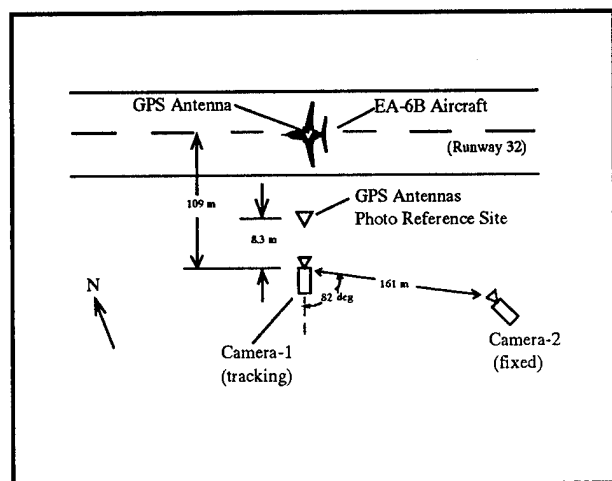


Figure 2. Diagram of Air-to-Ground Test

Also shown in the configuration diagram of Figure 2 are two videometric ground stations placed alongside the aircraft runway. The video cameras produced synchronous and time-tagged frames at 60 frames per second. An independent GPS receiver was used to time tag the video frames. Since all events were recorded with GPS time, receiver latency was not observable. The accuracy of the time tag was about 1 ms.

Camera 1 tracked the approaching aircraft and recorded on each frame the day and time-of-day and the azimuth and elevation of the center of the camera image as shown on the bottom of the image of Figure 1. Camera 1 was located about 8.3 m behind and 0.78 m above the GPS antenna at the PHOTO site, on a line perpendicular to the centerline of the runway as seen in Figure 3. Camera 2 was fixed and located about 161 m away from Camera 1.

TEST DESCRIPTION

Aircraft testing of the relative OTF algorithm was performed at NAWCAD, Patuxent River, Maryland. The test involved establishing the accuracy with which an aircraft's distance and height above the runway could be determined. Data was collected on 31 March 1995 while the EA-6B was conducting 3.5-deg approaches to Naval Air Station,

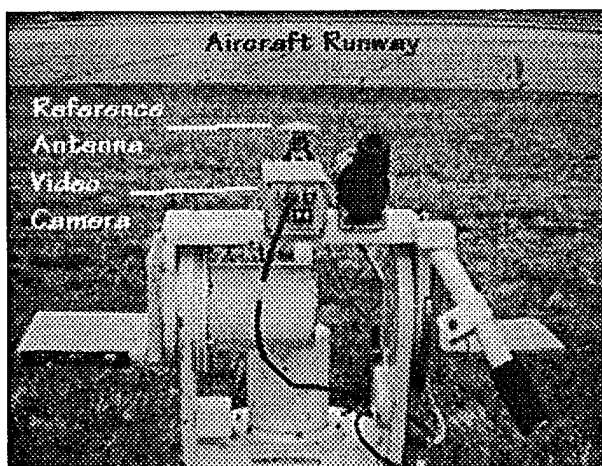


Figure 3. Picture of the Camera 1 Video Equipment and the Reference GPS Antenna Alongside the Runway

Patuxent River's Runway 32 during EA-6B flight technical error characterization tests being conducted by NAWCAD for the FAA.

GPS data was collected both in the aircraft and at the two surveyed ground station locations. The GPS receivers were set up to record L_1 and L_2 pseudorange and phase data each second. The data from the aircraft was downloaded post-flight for processing through the OTF algorithm. Videometric truth data was recorded as the aircraft began its waveoff at the end of each approach.

Both range and height values obtained from videometric measurements were compared to GPS values. In addition, vector differences between the two OTF solutions for differential GPS (fixed PHOTO site reference) and for relative GPS (moving aircraft reference) were determined.

AIR-TO-GROUND POSITIONING

GPS data was recorded for the aircraft takeoff and the subsequent five low passes. The flyby circuit is shown in Figure 4. The OTF solutions allowed the aircraft velocity components and altitude profiles to be accurately determined. These results are illustrated in Figure 5 for the fifth flyby.

For each pass through the view from the PHOTO site, the time of closest approach was determined from the OTF kinematic solutions. Four solutions bracketing this time were used to fit a cubic polynomial to each of the three x, y, z components. An additional polynomial was used for a fit to the ellipsoid height. The polynomials were evaluated each 0.001 s and the minimum range and height determined. Figure 6 shows the cubic fits to the four OTF solutions for the three components. They are nearly straight lines. Figure 7 shows the fit to the ellipsoid height. In this case, the fit is smooth, but probably not representative of the true height outside of the times bracketed by the middle two solutions. The range was computed from the interpolated

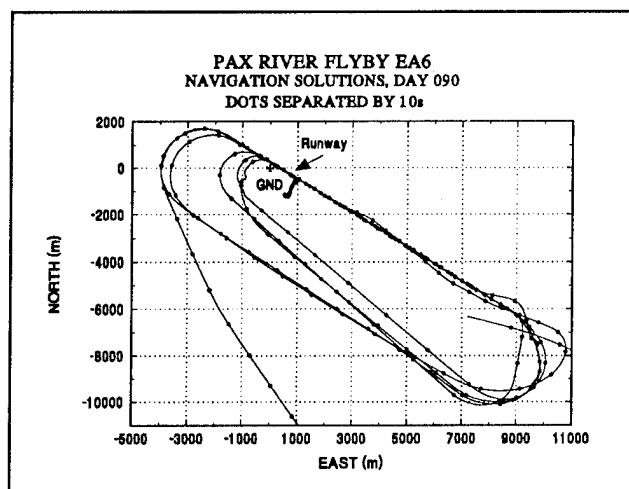


Figure 4. Aircraft Flyby Tracks With Respect to GND

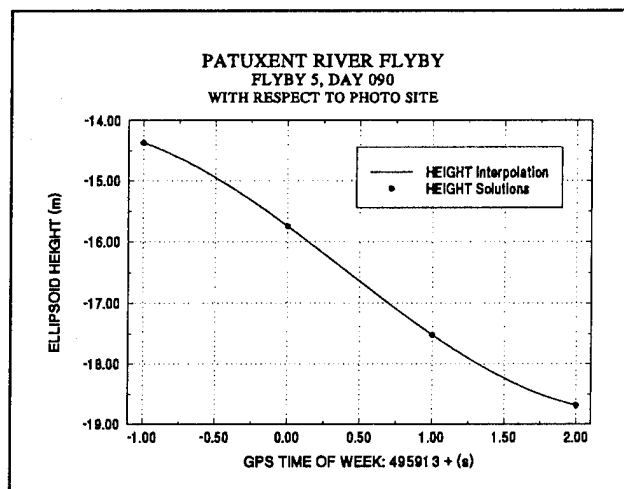


Figure 7. Interpolation Cubic for the Ellipsoid Height

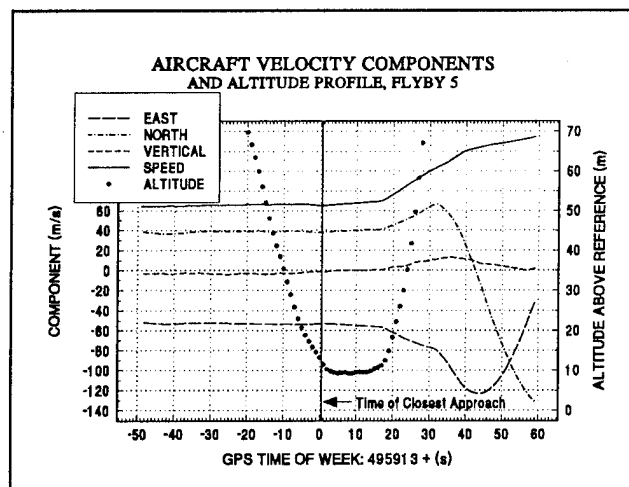


Figure 5. Aircraft Velocity and Altitude Profile for the Fifth Pass

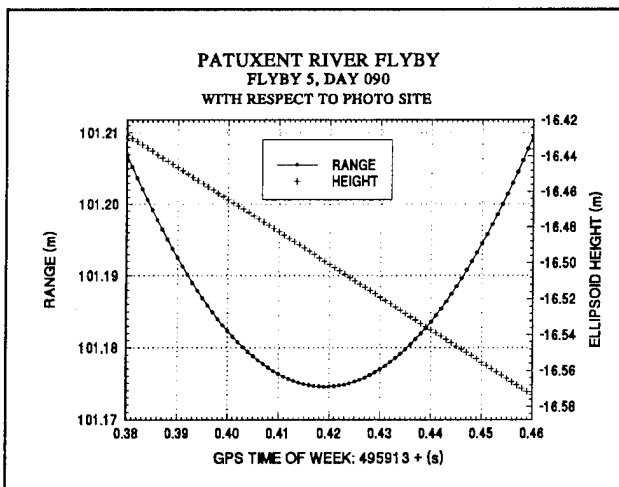


Figure 8. Interpolation Detail at Closest Approach

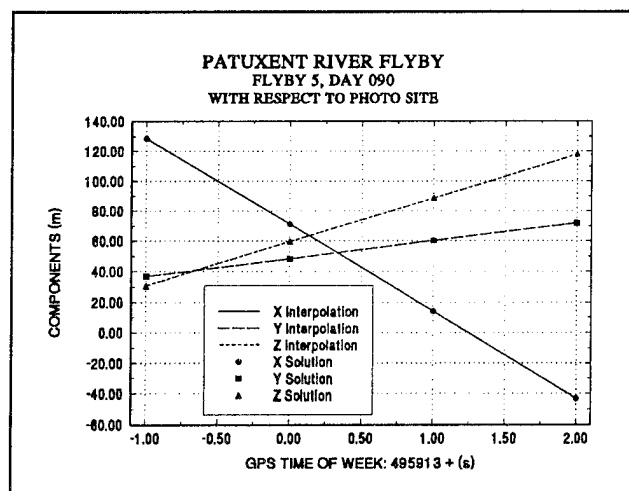


Figure 6. Interpolation Cubics for the Three Components

Table 1. Ranges and Ellipsoid Heights from OTF Interpolated Solutions

Event	GPS Time (s)	Range (m)	Height (m)
Takeoff	494209.901	100.717	-26.267
Flyby 1	494590.848	100.209	-22.667
Flyby 2	494897.299	101.303	-21.307
Flyby 3	495192.343	101.282	-19.693
Flyby 4	495527.999	101.571	-18.932
Flyby 5	495913.419	101.174	-16.499

components and is shown in Figure 8. The ellipsoid height interpolation cubic is also included in this figure. The time of closest approach, the range at closest approach, and the ellipsoid height can be read from the plot. The results from each pass are listed in Table 1.

The truth solutions for these passes were obtained from interpretation of the measurements obtained from the video frames with respect to site PHOTO. Figure 9 presents both the GPS and videometric determined values of range from the aircraft to the PHOTO site for flyby 2. Similarly, Figure 10 is a comparison of GPS and videometric determined heights for the aircraft GPS antenna above the antenna at site photo. GPS/videometric differences were obtained for measurements in a 0.2 s window about the minimum distance time as determined by GPS. These results are listed in Table 2.

GROUND-TO-AIR POSITIONING

The kinematic solutions between the fixed PHOTO site and the EA-6B aircraft were compared with the solutions from the relative algorithm between the same two sites for 1118

Table 2. Ranges and Ellipsoid Height Differences Between OTF and Videometric Truth Measurements

Event	Time Error (s)	Range Error (m)	Height Error (m)
Takeoff	No Video	-	-
Flyby 1	-0.014	-0.289	-0.206
Flyby 2	-0.003	0.006	0.022
Flyby 3	-0.019	0.077	-0.020
Flyby 4	-0.081	0.067	0.139
Flyby 5	0.021	0.104	0.082
Mean	-0.009	-0.007	-0.003
Standard Deviation	0.018	0.145	0.118

noncontinuous seconds. The differences between the solutions are listed in Table 3. The mean difference in range was found to be 1.7 cm. As a further test of the relative OTF algorithm, it was used to position the fixed PHOTO site antenna with respect to the moving aircraft antenna and vice versa. In this case, 1063 noncontinuous seconds were processed. The x, y, and z components of the vector between the PHOTO site and the aircraft were compared with the vector between the aircraft and the PHOTO site to illustrate the dependence of the algorithm on the reference site selection. The mean difference in range was 0.6 cm. A conclusion based upon this experience may not be warranted because the satellite selection and other variables were not controlled. Statistics on these differences are presented in Table 4.

Table 3. Difference Between the Kinematic and Relative OTF Algorithms for 1118 s

	X (m)	Y (m)	Z (m)	Range (m)
Mean	-0.002	-0.002	0.000	0.017
Standard Deviation	0.012	0.015	0.010	0.013
Maximum	0.037	0.050	0.015	0.058

SUMMARY

This paper evaluates the use of GPS to determine precisely the vector difference in position between two antennas in a dynamic environment. Two OTF algorithms, differential positioning with respect to a fixed antenna and relative positioning with respect to a moving antenna, were compared.

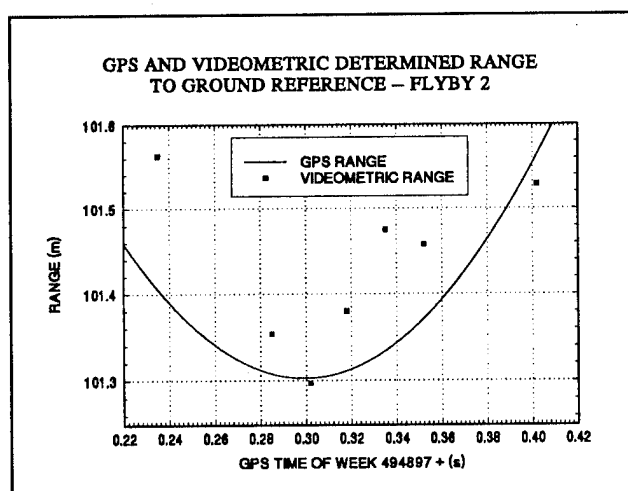


Figure 9. GPS Range and Videometric Truth

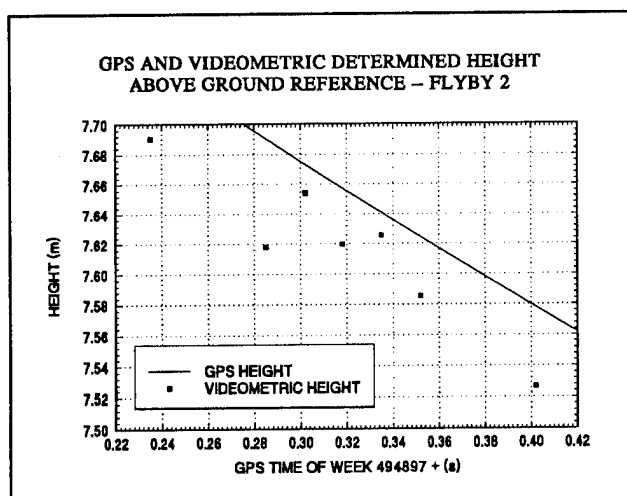


Figure 10. GPS Height and Videometric Truth

Table 4. Relative OTF Algorithm Dependence Upon
Choice of the Reference Site

	X (m)	Y (m)	Z (m)	Range (m)
Mean	-0.003	-0.000	0.003	0.006
Standard Deviation	0.005	0.004	0.004	0.007
Maximum	0.021	0.024	0.047	0.080

Videometric truth data was used to also obtain the three-dimensional difference in position vector. Comparisons were made over a short ± 0.2 s interval as the aircraft approached minimum range. Videometric positioning of the aircraft traveling about 72 m/s as it approached the runway had a standard error of about 10 to 15 cm per component. This is somewhat higher than the expected subdecimeter standard error of the GPS OTF computed position. The test results suggest that both the differential and relative GPS positioning error were within the truth measurement accuracy.

Further testing and demonstrations are anticipated for the relative positioning OTF procedure. Applications include higher velocity missile lethality (precise miss distance evaluation), aiding for aircraft carrier landings, and real-time radar and camera calibrations.

PRODUCT DISCLAIMER

The mention of a commercial company or product does not constitute an endorsement by NSWCD or NAWCAD. The information in this paper is not authorized for use for publicity or advertisements.

ACKNOWLEDGEMENTS

The authors are indebted to a number of people who helped in various ways to produce the results presented in this paper. These include: Mr. Glenn Colby, Mr. Lee Wellons, and Mr. Vernon Pugh of NAWCAD; Mr. Keith Robinson, Mr. John Ellis, Mr. Alvin Lane, and Mr. Gary Sitzman of NSWCD and Mr. Kendall Ferguson, a consultant to XYZ's of GPS, Inc.

REFERENCES

1. Remondi, Benjamin W., *Using the Global Positioning System (GPS) Phase Observable for Relative Geodesy: Modeling, Processing, and Results*, Dissertation: The University of Texas at Austin, May 1984.
2. Euler, H.-J. and Landau, H., *Fast GPS Ambiguity Resolution On-The-Fly For Real-Time Applications*, Proceedings of the Sixth International Geodetic Symposium on Satellite Positioning, Columbus, Ohio, Mar 1992, pp. 650-659.
3. Euler, H.-J. and Goad, C., *On Optimal Filtering of GPS Dual Frequency Observations Without Orbit Information*, Bulletin Géodésique, Vol. 65, No. 2, 1991, pp. 130-143.
4. Hatch, R., *Instantaneous Ambiguity Resolution, Kinematic Systems in Geodesy, Surveying, and Remote Sensing*, IAG Symposium No. 107, Banff, Canada, 1990, pp. 299-308.
5. Teunissen, P. J. G.; de Jonge, P. J.; and Tiberius, C. C. J. M., *A New Way to Fix Carrier-Phase Ambiguities*, GPS World, Vol. 6, No. 2, Apr 1995, pp. 58-61.
6. Remondi, Benjamin W., *Performing Centimeter-Level Surveys in Seconds with GPS Carrier Phase: Initial Results*, Navigation, Vol. 32, No. 4, Winter 1985-86, pp. 386-400.
7. Remondi, Benjamin W., *Global Positioning System Carrier Phase: Description and Use*, Bulletin Géodésique, 59, Jan 1985, pp. 361-377.
8. Remondi, Benjamin W., *Real-Time Centimeter-Accuracy GPS: Initializing While in Motion (Warm Start Versus Cold Start)*, Navigation, Vol. 40, No. 2, Summer 1993, pp. 199-208.
9. Frodge, S.; Remondi, Benjamin W.; and Lapucha, D., *Results of Real-Time Testing and Demonstration of the U. S. Army Corps of Engineers Real-Time On-The-Fly Positioning System*, Proceedings of the ION 1994 National Technical Meeting, 24-26 Jan 1994.
10. Remondi, Benjamin W., *Recent Advances in Pseudo-Kinematic Surveying*, ION GPS-90 Proceedings of the Third International Technical Meeting of the Satellite Division of The Institute of Navigation, Colorado Springs, Co, Sep 1990, pp. 106-114.
11. Hermann, Bruce R., Evans, Alan G., Law, Christopher S., and Remondi, Benjamin W., *Kinematic On-The-Fly GPS Positioning Relative to a Moving Reference*, Proceedings of the ION GPS-94, Salt Lake City, UT., September 1994.

Satellite Based Integrated Navigation and Communication System of the German Air Rescue

Dr. Manfred Haverland and Harry Evers
Aerodata

Dr. Hindemith-Boose and Dr. Roland Kirschenlohr
DRF

Biography

Manfred Haverland studied electrical engineering at the University of Braunschweig. He received his doctors degree in 1988 for a thesis on adaptive flight control. Since 1988 he is working as chief engineer for Aerodata Flugmeßtechnik. His work is focussed on the development of navigation systems, flight inspection systems, and meteorological measurement systems.

Harry Evers Dipl.-Ing. of mechanical engineering (1986) with stress onflight guidance. From 1986 - 1990 he worked as a system engineer at Standard Elektrik Lorenz SEI in Stuttgart in the field of GPS-receiver development. Since 1990 he works as Marketing Manager for Navigation products at the Aerodata Flugmeßtechnik GmbH.

Dr. Hindemith-Boose and Dr. Roland Kirschenlohr are the Project Manager of the Z.E.U.S. Project.

Abstract

The German Air Rescue Service operates more than 20 helicopters and 3 Learjets in order to provide the tasks of primary air rescue services and inter-hospital transportation. An alarm centre is operated for planning and coordination of more than 12.000 worldwide missions per year.

Actually, the alarm centre and all helicopters and aircraft are undergoing an improvement programme in order to optimize the operation of the fleet. After completion of the programme the functions listed below will be realized in the alarm centre:

- display of position and status of each helicopter;
- automatic generation of flight logs and invoices;
- transmission and reporting of health usage monitoring system data (HUMS).

The navigation systems on board the helicopters are based on integrated GPS/inertial navigation systems including a half-duplex data communication based on the INMARSAT satellite system as well as terrestrial mobil phone networks.

Due to the open system concept, the service of the alarm centre are open to other users in the fields of airborne, maritime, and land vehicle applications. All activities for system development and implementation are concentrated within the German Air Rescue under the project title Z.E.U.S.

1 Introduction

Since the introduction of air rescue services in Germany more than 580.000 rescue missions have been flown [1]. Typically, the helicopters providing the helicopter emergency medical service (HEMS) are used for 500 to 1000 missions per year. Two different mission types are accomplished by the rescue helicopters:

- During a **primary mission** the helicopter transports an emergency physician to the scene of accident and provides transportation for the emergency patient to the nearest hospital. Primary missions are normally performed under visual meteorological conditions (VMC) only with a maximum distance of 50 kilometers.
- The transportation of a patient from the initial hospital to a specialized hospital is defined as **transfer or secondary mission**. They may be accomplished both under VMC and instrument meteorological conditions (IMC) for distances up to 150 km.

One of the largest HEMS operators is the German Air Rescue (Deutsche Rettungsflugwacht) owning more than 20 helicopters and 3 Learjets. The German Air Rescue operates an alarm center for planning and coordination of more than 12.000

planning and coordination of more than 12.000 missions per year. The alarm center and the helicopter fleet are actually modernized in order to optimize the organization and the operation of the helicopter and aircraft fleet. The main goals for this program are:

- improvement of the helicopter navigation capabilities,
- provision of two-way data communication between alarm center and helicopter,
- display of helicopter status and position at the alarm center,
- information and position display on board the helicopter,
- automatic flight log and invoice generation,
- transmission and reporting of health usage monitoring system data (HUMS).

2

System Description

The final stage of the overall system is shown in fig. 1. It comprises the alarm center, local alarm centers, rescue helicopter fleet, and the ambulance cars. Data and voice communication on the ground is achieved by the telephone network and mobile phones. For communication with the helicopter fleet, data transmission is accomplished by satellite communication. Depending on the accident, the alarm for the rescue helicopter is either raised by the local or the main alarm center. Helicopter status and position information is transmitted regularly to the main alarm center, which provides these data via phone network to the local centers.

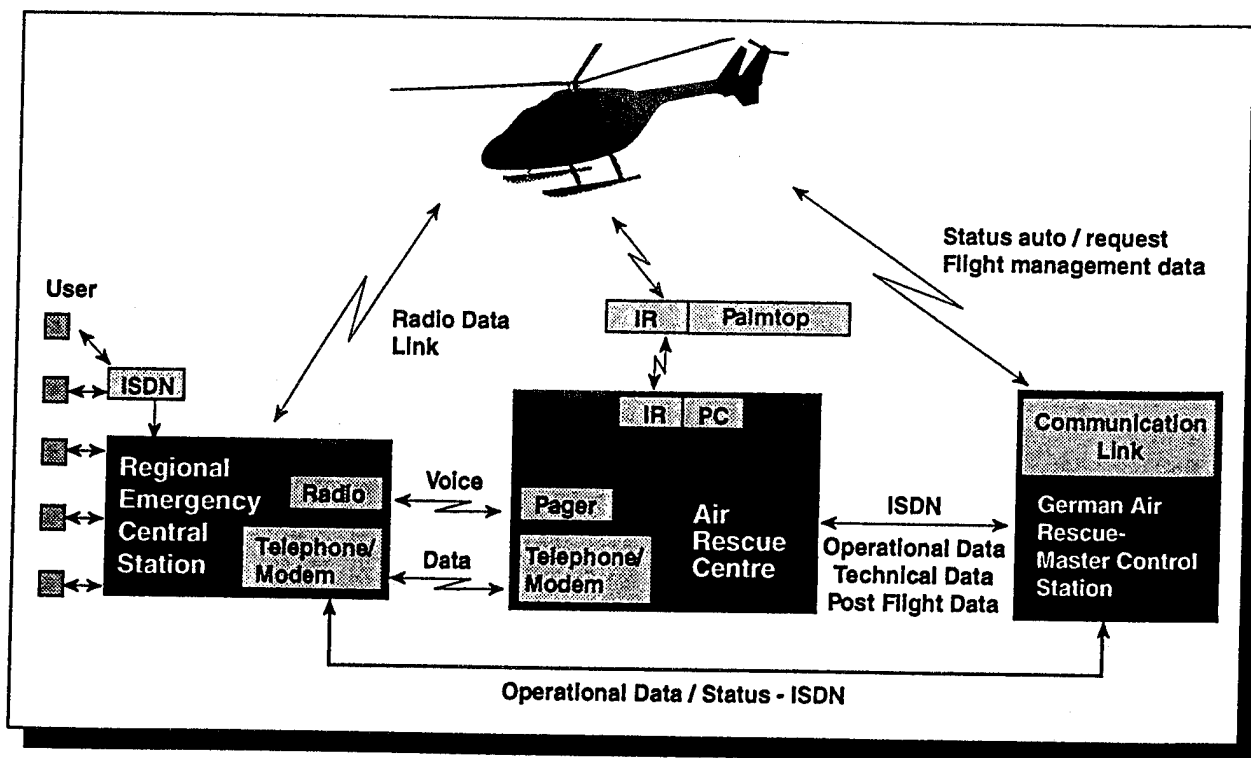


Figure 1 Block diagram of German Air Rescue Service communication system

The kernel of the onboard system is a navigation and communication unit (NCU) [2] providing interfaces to the INMARSAT transceiver, medical devices including chip card reader, health usage monitoring system, digital map display with storage medium, and a printer; see fig. 2. A control and display unit (CDU) is used for pilot operation. One further serial interface is available for data base update, differential GPS correction input, and other data transfer tasks from and to the NCU.

Further navigation sensors are connected to the NCU. With the devices connected to the NCU, the following functions are realized:

- navigation and flight management,
- communication with the alarm center,
- acquisition and storage of medical data as well as health insurance data of the emergency patient,
- acquisition and storage of HUMS,
- generation of print-outs of medical data, HUMS data, flight planning data transmitted from the alarm center.

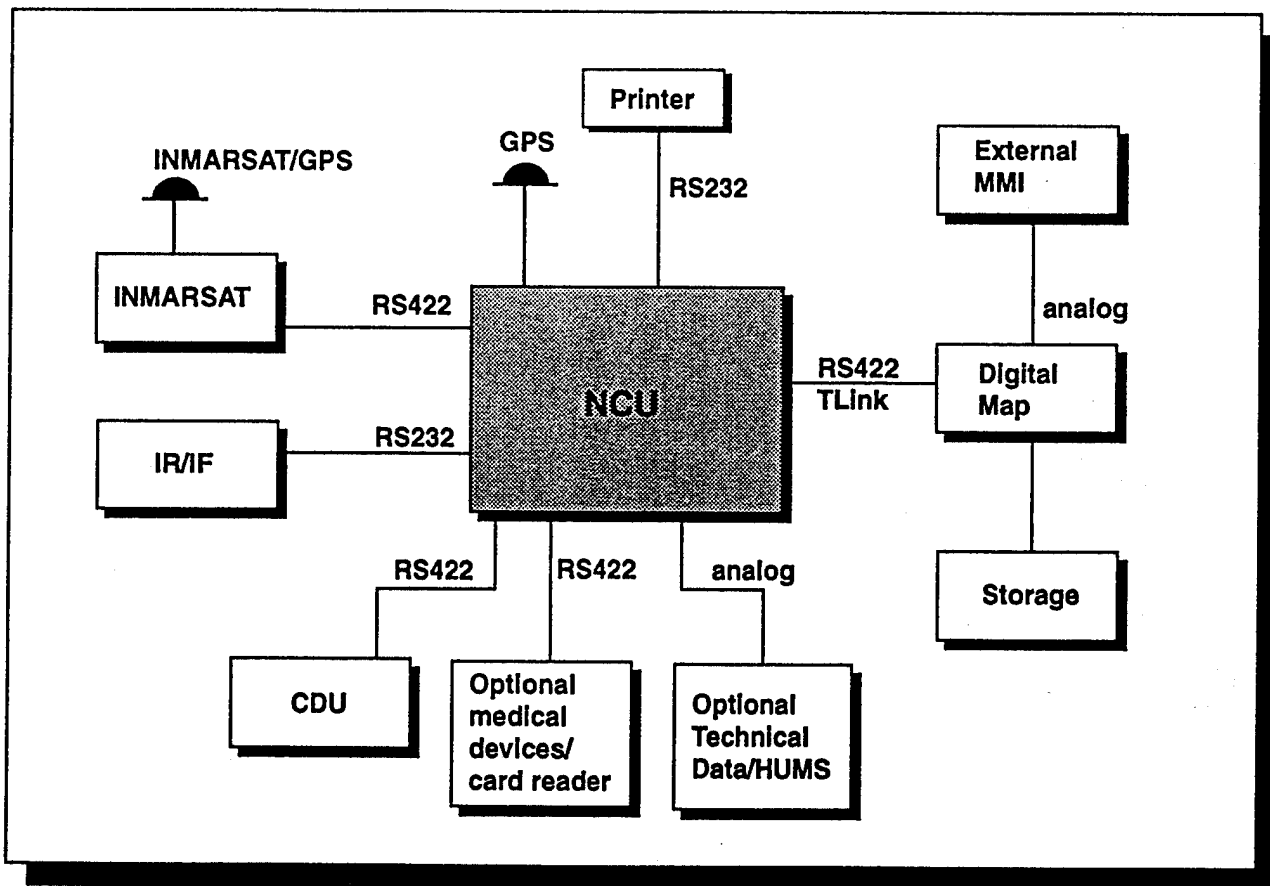


Fig. 2 Block diagram of helicopter navigation and communication system

2.1

Communication and Data Storage

The bidirectional information exchange between the alarm center and the helicopter is a base for the improvement of the helicopter fleet management. As a standard, the helicopter generates periodic position and status reports, which are transmitted to the alarm center by INMARSAT, if the helicopter is airborne or by mobile phone, if the helicopter is on the ground. The data uplink provides alarm information to the helicopter crew; e.g. location and type of accidents. Even the uploading of flight planning information, which may be used directly by the crew, is realized.

In addition to the position and status reporting, the system stores this information with a higher rate in a non-volatile memory. Upon completion of a mission, these data are transferred to the alarm center for the generation of an invoice.

2.2

Navigation and Flight Management

The navigation software of the NCU integrates built-in sensors with complementary characteristics. A GPS receiver provides good long-term stability and accuracy, a 6-DF (degrees of freedom) inertial sensor package provides attitude information and short time accuracy under dynamic conditions. On-line estimation and compensation of the inertial sensor errors using the accurate position information in form of pseudoranges improves the performance of the inertial sensors, see fig. 3. As GPS and inertial measurements are combined in a synergetic manner using a Kalman filter, the navigation package is able to provide position, velocity and attitude information during all phases of flight, even if the reception of GPS signals is disturbed by jamming or shading. A further enhancement of the system integrity is achieved by the integration of barometric altitude and directional gyro information.

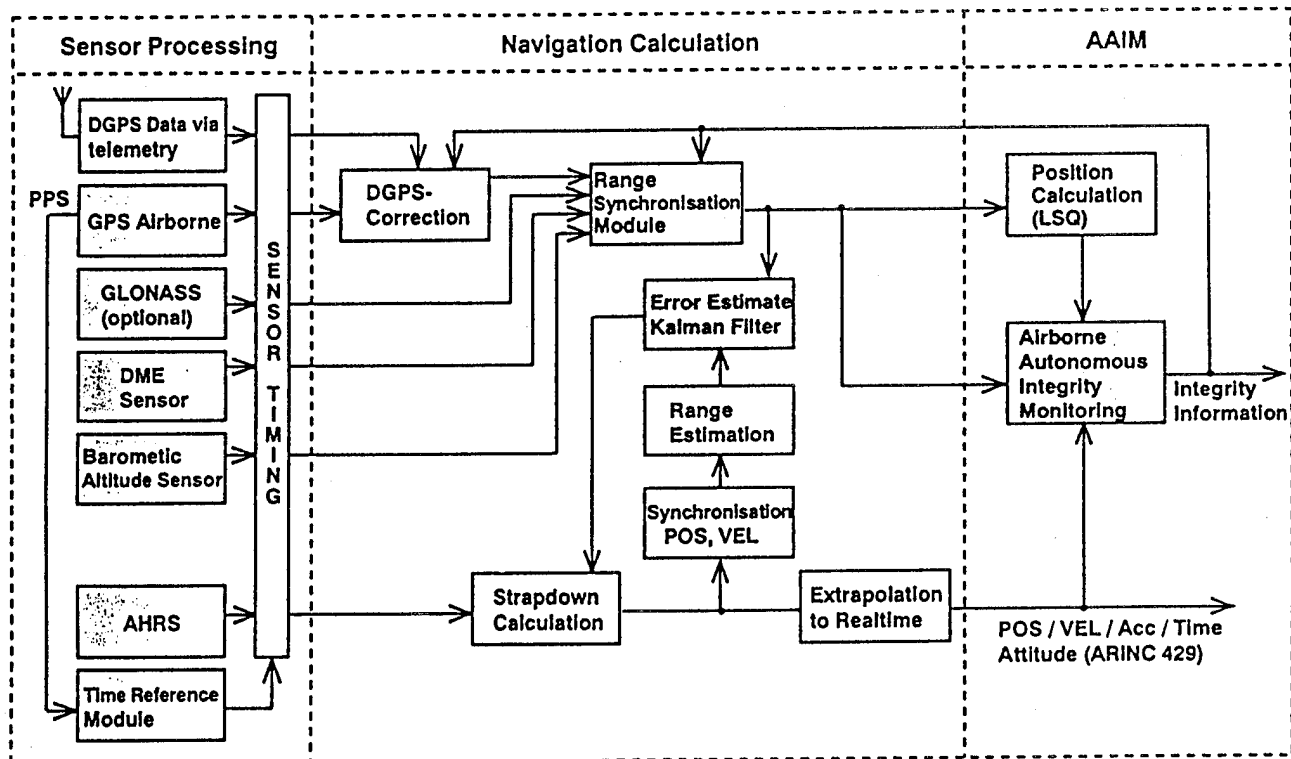


Fig. 3 Navigation Sensor Processing

As the system integrity is dominating airborne navigation tasks, different methods are part of the navigation software. RAIM (receiver autonomous integrity monitoring) techniques allow the identification and isolation of faulty satellite measurements. A further improvement of the failure detection is achieved by AAIM (airborne autonomous integrity monitoring), which uses all available sensor information for failure detection.

Another software package of the NCU provides flight management functions to the cockpit crew very similar to a standard flight management system. This includes steering information, which is displayed on the CDU. One element of the flight management is the data base consisting of fixed data and user-defined waypoints, which form a flight plan. Both data bases may be uploaded or downloaded via a serial data link. Map data, user waypoints and steering information are presented on a digital map display. It includes a planning mode, which allows for the graphical input of flight plans.

2.3 Acquisition and Processing of Medical and Technical Data

Further technical and medical data are acquired by the onboard system. The data from the

onboard medical equipment as well as the patient's health insurance data, stored on a chip card, are read into the system. They are made available to the hospital together with the injured person, thus improving information exchange between the helicopter crew and the surgeons of the hospital. The technical data are usually downloaded with a laptop at the local alarm center.

3 Test Results

The navigation and communication system was integrated into the Dornier 128 turboprop aircraft of the Technical University Braunschweig in order to demonstrate the performance of the navigation package, especially under high dynamic conditions. Severe GPS failures have been simulated. Fig. 4 depicts a typical result, which was produced during an approach to Braunschweig airport. For a period of more than 200 seconds any GPS information was missing resulting in a position drift of about 500 meters. As a reference, a differential GPS solution was used.

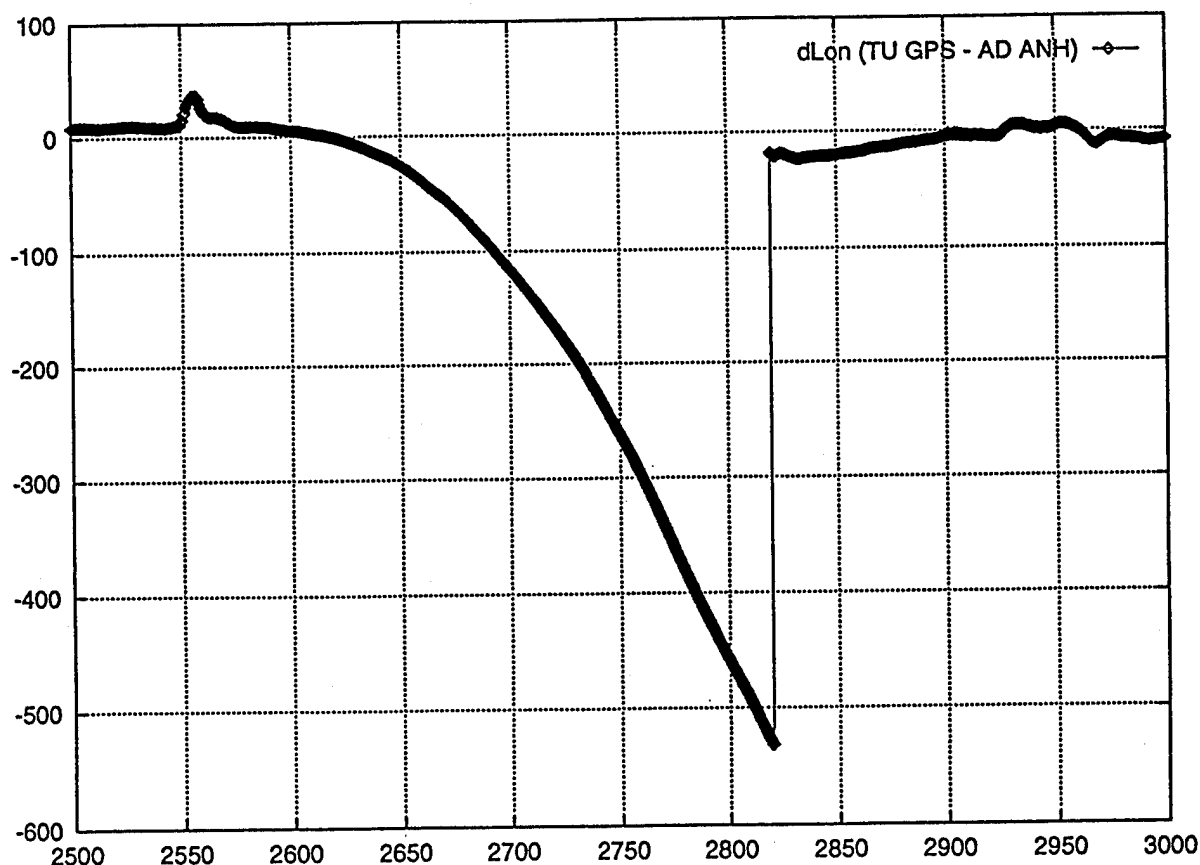


Fig. 4 Position Drift of pure inertial navigation during simulated GPS failure

The development of an integrated navigation and communication system significantly improves the operation of the German Air Rescue helicopter fleet. As the onboard system integrates different navigation sensors, a maximum integrity for the position determination is achieved. The data communication to the alarm centers and the electronic data exchange with the hospitals reduce the workload of the helicopter crew, thus increasing the safety of the helicopter operation. As the system design is flexible, the fleet management and data link service may be provided also to other helicopter operators.

- [1] Schirmeyer: Air Rescue in the Federal Republic of Germany, Organization and Financing. Sheppard Air Rescue Conferences; Berlin, May, 25-26, 1994.
- [2] Jöres, W., Kasties, G., Haverland, M.: Aeronav-H, an Integrated Navigation System for Special Mission Helicopters. International Symposium on Precision Approach and Automatic Landing; Braunschweig, Feb. 21-24, 1995.



Session D5

GPS Reference and Testing

Chair:

Mr. Mike Hadfield
Holloman AFB

Co-Chair:

Mr. Stewart Teasley
Rockwell

Development of High-Rate Differential GPS Reference for Operational Testing

Lt. William Mossle and Andy Chasko
746th Test Squadron, Holloman AFB

BIOGRAPHIES

Lt Chip Mosle was born and raised in Pittsburgh PA. He earned a BS, in Electrical Engineering from Duke University in 1992. Chip continued his studies at the Air Force Institute of Technology, where he earned a M.S.E.E. Currently, Lt Mosle is an avionics integration engineer with the 746th Test Squadron (TS) at Holloman AFB NM, working in support of the Global Positioning System (GPS) Project 2000 initiative.

Mr. Andy Chasko was born on Long Island NY and raised in Fair Oaks CA. He earned a BS, in Physics from Humboldt State University, Arcata CA in 1965, continued graduate studies in Physics at San Diego State University. Andy earned an M.A. in Business Administration from Webster University in 1990. He was a Senior Research Engineer in Advanced Systems avionics and software design with Teledyne Ryan until 1975; was a Senior Engineer with General Dynamics Electronics Division at San Diego where he led the test and integration of the GPS Inverted Range Monitor Station. He continued on with General Dynamics as an Engineering Specialist at Yuma where he supported GPS User Equipment, reference station, and GPS Space Vehicle DT&E and IOT&E testing through 1990. Currently Andy is a GPS analyst with Amcomp in support of the 746th Test Squadron at Holloman AFB NM.

ABSTRACT

In response to increasingly stringent flight test requirements of GPS integrated navigation systems, the 746th Test Squadron (746 TS), also known as the Central Inertial Guidance Test Facility (CIGTF), has developed a high-rate Differential GPS (HR-DGPS) Time-Space-Positioning-Information (TSPI) truth reference system. This system provides high-rate (20 Hz) TSPI without significant platform modifications or implementation of costly range reference trackers. The HR-DGPS reference has been developed for aircraft weapon delivery testing which has a requirement for high-rate, high accuracy TSPI. The HR-DGPS utilizes Space and Control

Segment Observed Range Errors (ORE) produced from the 746 TS Test Support Network (TSN) DGPS ground stations. The HR-DGPS algorithm processes GPS-corrected Inertial Navigation System (INS) data to attain the high-rate. Validation and flight test results demonstrate both the accuracy and independence of the HR-DGPS system. The development of HR-DGPS TSPI is a large step forward in matching the quality and low-cost of differential GPS reference technology to the stringent requirements of military aircraft flight testing.

INTRODUCTION

Modern GPS technology has introduced a new generation of integrated navigation equipment. New avionics systems exploit the benefits of both GPS and INS technology to provide a superior blended navigation solution. The new integrated systems have retained the high-dynamic robust performance of an INS while adding the daunting accuracy of GPS technology. These INS/GPS systems are rapidly redefining the standards for military navigation. Throughout the Air Force, aircraft platforms are moving to upgrade their avionics with this new technology in response to the Congressional mandate to implement GPS by the year 2000, also known as Project 2000.

The improvement in navigation technology has equally affected military test agencies. As the accuracy of INS/GPS systems improves, the accuracy of the reference systems must also improve. Advanced technology has been developed to meet the new test requirements for integrated GPS navigation equipment. These advanced reference systems exploit the precise accuracy of DGPS. The DGPS reference systems are not only extremely accurate, but also require a minimal amount of aircraft test instrumentation.

This paper describes a new advancement in DGPS reference technology made by the 746 TS. The advancement allows DGPS TSPI to be provided at a far higher data rate than previously available. This new technology has been driven by a customer requirement to provide a DGPS TSPI data rate of 20 Hz or greater.

DGPS TSPI had previously been provided at a 1 Hz reference data rate by the 746 TS. The new algorithm exploits the availability of INS data to increase the frequency of the reference TSPI data. This development allows test programs to implement HR-DGPS reference technology in place of Cine-Theodolite (Cine-T) trackers when high-rate reference data is a test requirement. This replacement can greatly reduce the cost of testing without degrading reference data accuracy.

This paper will present background on the 746 TS DGPS TSPI TSN reference system followed by an explanation of the recent HR-DGPS advancements. Following the HR-DGPS algorithm explanation, data is presented which illustrates the position accuracy of the system against Cine-T trackers. The paper finishes with sample flight test data showing HR-DGPS TSPI used to verify the performance of an integrated INS/GPS navigation system.

BACKGROUND

The 746 TS has developed Differential GPS as a cost efficient TSPI reference to evaluate system navigation performance during flight tests. DGPS incorporates information from a ground based differential reference network with on-board information available from the GPS receiver to generate a highly accurate truth reference solution during flight tests.

The process of generating the DGPS reference trajectory is based on two principles. First, the raw GPS measurements collected on-board the aircraft are not affected by the system-under-test (SUT). This allows the airborne GPS receiver to be used as a source of reference data. The raw GPS measurements consist of state 5 pseudoranges (PR) and delta ranges. The second principle is that GPS receivers in a localized area experience common space and control segment errors which are constant or slowly varying. By establishing a stationary reference receiver at a precisely surveyed benchmark, the GPS ORE can be measured. By applying these ground-calculated corrections to the raw PR measurements made aboard the test vehicle, a more accurate DGPS navigation solution (TSPI) is obtained. The errors in the navigation solution of the SUT are then obtained as the difference between the SUT navigation solution and the reference solution produced by DGPS post-processed calculations.

There are three major components to the DGPS reference: aircraft instrumentation, the ground-based TSN satellite reference station (SRS), and post-processing equipment. The aircraft instrumentation

required for DGPS is a GPS receiver and a data collection buffer box. The DGPS data collection systems are currently designed to work with the following military GPS receivers, the Receiver 3A (RCVR-3A) and Miniaturized Airborne GPS Receiver (MAGR). The second system component is the TSN reference network. There are currently six SRSs in the TSN to support continental U.S. (CONUS) flight test operations: China Lake CA, Edwards AFB CA, Holloman AFB NM, Eglin AFB FL, Whiteman AFB MO, and Atlantic City NJ. The TSN reference stations collect the satellite data and generate the differential corrections used in TSPI generation. The third major portion of the system is the post-processing software which creates the highly accurate reference solution.

The standard TSN DGPS TSPI product is a 1 Hz reference trajectory. Table 1 is a listing of the data generated for each TSPI record.

Table 1. TSPI Reference Data Produced by DGPS

UTC Time & PS Time	Velocity (E,N,U)
Position (Lat, Lon)	Acceleration (E,N,U)
Altitude (Absolute, MSL)	ECEF Position (X,Y,Z)
Ground Speed	ECEF Velocity (X,Y,Z)
Flight Path Angle	ECEF Accel. (X,Y,Z)
Roll	Satellite PRN ID's
Ground Track Angle	DOPS (X,Y,Z,T)

The original system verification of the DGPS reference was conducted at the Yuma Proving Grounds (YPG) to benchmark the accuracy of the reference against the Real Time Estimate (RTE) system which uses laser trackers. YPG flight data was processed and analyzed and statistical positioning accuracy estimates were generated for low and moderate levels of vehicle dynamics. Flights were conducted on two aircraft, a T-39 and a C-141. Table 2 is the accuracy of the DGPS reference TSPI based upon the Yuma flight tests and follow-on verification testing. The accuracy of the reference is dependent upon the satellite coverage during the flight test and, even more importantly, the distance between the SUT and the TSN reference station.

Table 2. 1 Hz DGPS TSPI Reference Accuracy

3D RMS Position	2-4 meters
3D RMS Velocity	0.1 meters/second

The 1 Hz DGPS reference has been a highly effective asset used in flight tests across the country. Yet recent flight test programs have levied new test requirements

beyond the capabilities of the 1 Hz DGPS TSPI, which has lead to the development of the HR-DGPS TSPI.

SYSTEM REQUIREMENTS

The fundamental requirement for the new algorithm is an increased data rate of the reference TSPI. Previous DGPS post-processing reference algorithms provided data at 1 Hz. The HR-DGPS TSPI must be available at 20 Hz. There is a secondary requirement to make the HR-DGPS reference TSPI robust with respect to vehicle dynamics. The goal is to "coast" through momentary outages in GPS availability caused by acceleration. Along with the new system requirements, the HR-DGPS TSPI accuracy must not be degraded with respect to the original 1 Hz DGPS.

To fulfill the high-rate data requirements, the post-processing software required additional INS data from the test platform. The required data is the INS aiding data normally transmitted to the GPS MAGR or RCVR-3A receiver. The INS data is available via either the MIL-STD-1553 or RS-422 data bus. Table 3 is the actual information utilized in the high-rate DGPS algorithm.

Table 3. Required INS Data for High-Rate DGPS TSPI

ICD-GPS-059 I-6 (or equivalent) GPS-ICD-150 Block 25 (or equivalent)	
Velocity X	Acceleration X
Velocity Y	Acceleration Y
Velocity Z	Acceleration Z
Platform Azimuth	Time Tag
Cxx, Direction Cosine	HV Roll
Cxy, Direction Cosine	HV Pitch
Cxz, Direction Cosine	HV True Heading

The new requirement does not increase the required instrumentation onboard the test platform. The instrumentation needed to collect the aircraft GPS data can also collect the required INS data. The ability to produce the HR-DGPS TSPI without additional platform instrumentation is perhaps the greatest asset of the HR-DGPS algorithm, as it maintains the low cost of the reference system.

HIGH-RATE DGPS TSPI ALGORITHM

The HR-DGPS processing uses the aircraft INS data in conjunction with 1 Hz DGPS data to estimate position and velocity between the 1 Hz DGPS TSPI points. The process uses the 1 Hz DGPS TSPI data as one of two inputs. The 1 Hz DGPS TSPI exists uncorrupted within

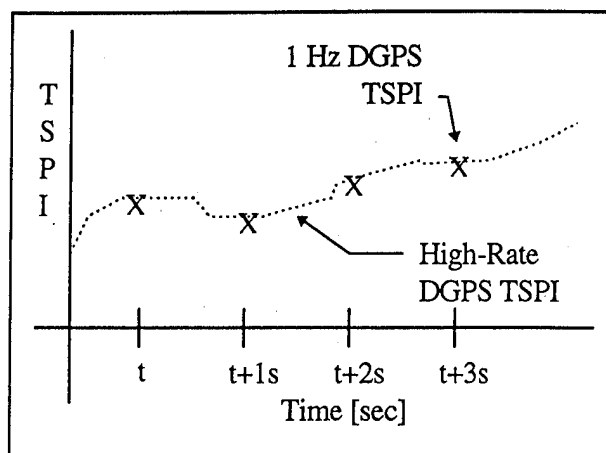


Figure 1. High-Rate/1 Hz DGPS TSPI Relationship

the high-rate TSPI data stream (see Figure 1) and "anchors" the accuracy of the HR-DGPS TSPI. The second input to the HR-DGPS processing is the INS velocity and acceleration data.

The HR-DGPS accuracy between 1 Hz DGPS data points relies on the estimation of INS velocity errors. To maintain the reference accuracy of the HR-DGPS, the INS velocity data error characteristics must be removed. To effectively estimate and remove this error the following INS error model is used.

INS ERROR MODEL

To model and remove the INS velocity error, the INS acceleration is assumed to be correlated over a short interval. A short interval is defined as the length between two 1 Hz DGPS TSPI data points. Over the short interval the estimator can remove the correlated portion of the acceleration error. The uncorrelated portion, induced by large jerk, cannot be removed. The HR-DGPS estimator is not applied to portions of the vehicle trajectory containing significant jerk components.

As an example of slowly varying INS acceleration error, consider the dynamics of the INS attitude reference (tilt) error. The tilt error is modeled between INS resets as

$$-g\phi \quad (1)$$

where

g is the gravity acceleration

ϕ is the error in INS indicated attitude

The acceleration error from Equation (1) varies as a function of tilt error. The tilt error varies from the 84 minute Schuler oscillation of the INS attitude reference

error. Thus the tilt error is seen to change slowly over the intervals we wish to model the INS acceleration error.

To maintain the validity of our assumption concerning INS acceleration error, the interval over which the high-rate algorithm can fill-in data gaps must be small. The algorithm design goal for the interval is 5 seconds. A 5 second interval will allow the high-rate algorithm to fill in DGPS reference drop-outs caused by vehicle dynamics. Normally the interval will only be the 1 second interval between 1 Hz DGPS TSPI data points.

The velocity and acceleration errors for the INS are modeled in a local level East-North-Up (ENU) system. The aircraft INS may be either aided by the receiver or the INS may be in unaided operation. In the aided operation, the INS solution is regularly reset as the INS updates its solution with GPS foreground solution information. The INS velocity error estimation must compensate for the resets without knowledge of the INS reset vector (the reset vector is not available in the standard INS input to the MAGR receiver).

THE HR-DGPS TSPI ESTIMATOR

The HR-DGPS estimator derived below utilizes forward and backward INS acceleration information to fill in the aircraft position, velocity, and time between the 1 Hz DGPS data points. To estimate the reference velocities between 1 Hz DGPS TSPI points, the 1 Hz DGPS velocities of the two end points are defined as,

\bar{V}_a is the 1 Hz DGPS Velocity at time t_a

\bar{V}_b is the 1 Hz DGPS Velocity at time t_b

Figure 2 shows the relationship of the 1 Hz DGPS data and the INS data between times t_a and t_b . For time t_i , between times t_a and t_b , Equation (2) is the derived velocity estimate. Equation (2) uses a forward integral of INS acceleration from time t_a .

$$\bar{V}_i^+ = \bar{V}_a + \int_{t_a}^{t_i} \bar{a} dt \cong \bar{V}_a + (\bar{V}_{INS_i} - \bar{V}_{INS_a}) \quad (2)$$

where

\bar{V}_i^+ is the forward estimate of velocity at time t_i

\bar{V}_a is the DGPS velocity vector at time t_a

\bar{V}_{INS_a} is the INS velocity vector at time t_a

\bar{V}_{INS_i} is the INS velocity vector at time t_i

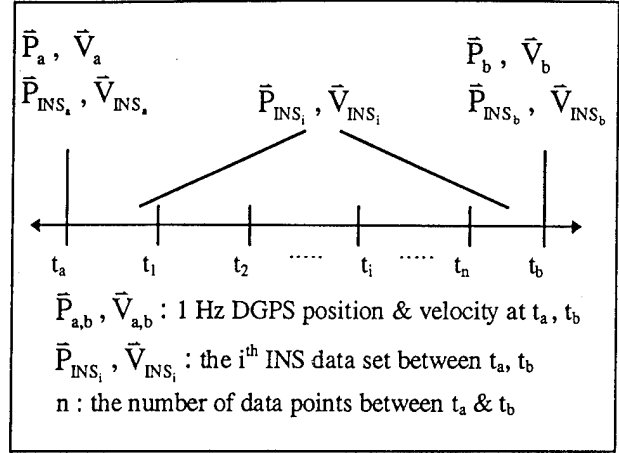


Figure 2. HR-DGPS Data Line between t_a and t_b

A second velocity estimate is similarly computed using a backward integral of the INS accelerations from the DGPS solution at t_b ,

$$\bar{V}_i^- = \bar{V}_b - \int_{t_i}^{t_b} \bar{a} dt \cong \bar{V}_b - (\bar{V}_{INS_b} - \bar{V}_{INS_i}) \quad (3)$$

where

\bar{V}_i^- is the backward estimate of velocity at time t_i

\bar{V}_b is the DGPS velocity vector at time t_b

\bar{V}_{INS_b} is the INS velocity vector at time t_b

\bar{V}_{INS_i} is the INS velocity vector at time t_i

Given our assumption of constant acceleration error over the interval, $t_a < t_i < t_b$, the velocity error of the forward integration is estimated as,

$$\epsilon \bar{V}_i^+ = \int_{t_a}^{t_i} \bar{\epsilon}_{accel} dt \cong \bar{\epsilon}_{accel} (t_i - t_a) \quad (4)$$

Similarly the velocity error of the backward integration is estimated as,

$$\epsilon \bar{V}_i^- = - \int_{t_i}^{t_b} \bar{\epsilon}_{accel} dt \cong -\bar{\epsilon}_{accel} (t_b - t_i) \quad (5)$$

We blend the two solutions of velocity, \bar{V}_i^+ and \bar{V}_i^- , to minimize the error in Equations (4) and (5) in our final velocity estimate for time t_i . Our final velocity estimate is defined as,

$$\hat{\bar{V}}_i = K\bar{V}_i^+ + (1-K)\bar{V}_i^- \quad (6)$$

where $\hat{\bar{V}}_i$ is defined as the HR-DGPS estimate of velocity at time t_i . The blending constant, K , is dependent on t_i , relative to t_a and t_b , and defined as,

$$K = \frac{(t_b - t_i)}{(t_b - t_a)} \quad (7)$$

This gain reduces the effect of slowly varying INS acceleration error, such as INS reference tilt error, on the estimated HR-DGPS velocity at time t_i .

Now we have a time series of HR-DGPS velocity estimates between times t_a and t_b . We use these estimates of velocity to calculate our estimate of HR-DGPS position over the same time interval. The following equation is used to produce the position estimates between times t_a and t_b ,

$$\hat{\bar{P}}_i = \bar{P}_a + \int_{t_a}^{t_i} \hat{\bar{V}}_{int} dt \cong \bar{P}_a + \sum_{j=1}^i \hat{\bar{V}}_j (t_j - t_{j-1}) \quad (8)$$

where

$\hat{\bar{P}}_i$ is the HR-DGPS position estimate at t_i

\bar{P}_a is the 1 Hz DGPS position at t_a

$\hat{\bar{V}}_{int}$ is the theoretical continuous HR-DGPS velocity estimate over the interval $(t_a, t_i]$

$\hat{\bar{V}}_j$ are the HR-DGPS velocity estimates over the interval $(t_a, t_i]$

j is the summation index over the interval $(t_a, t_i]$

i is the time index between t_a and t_b

t_0 is defined as t_a

The position estimate is the position at time t_a varied by our knowledge of velocity over the interval t_a to t_i . This gives a highly accurate HR-DGPS estimate of position. The next section describes the verification of the HR-DGPS algorithm.

REFERENCE VERIFICATION

The best way to verify the accuracy of a reference system is to test it against previously calibrated reference systems. The accuracy was verified against a variety of reference sources. During the development of the system, the 1 Hz DGPS TSPI was utilized as a constant

cross-check for the validity of the HR-DGPS. Once the HR-DGPS processing software was operational, the HR-DGPS TSPI was verified against two independent reference systems: the Holloman Test Track and Cine-T trackers. Since the Cine-T validation data demonstrates the HR-DGPS performance during flight test, this data is presented below.

Both Cine-T reference TSPI and high-rate DGPS TSPI were available for two flight tests. The use of the Cine-T data allows the comparison of the high-rate DGPS against an equally high-rate TSPI source. The Cine-T TSPI was available at 20 Hz. Another benefit of Cine-T data comparison is the independence of the two systems. The error sources of a DGPS reference system are entirely different than those of a Cine-T tracker system. The Cine-T TSPI contains only position information, thus only the position accuracy of the high-rate DGPS TSPI is compared against the Cine-T data.

Five data samples were evaluated from each of the two missions. A sample is defined as an aircraft pass of the Cine-T tracker. Cine-T TSPI is only available during aircraft passes of the tracker field. The two tests were flown on different days to ensure different satellite geometry and GPS OREs. Table 4 provides summary statistics for all ten sample sets from the two flights. The test statistics are calculated from the position differences between the two systems.

The comparison of the two systems shows both the Cine-T and the HR-DGPS position solutions to be extremely stable. The standard deviation of the difference values across all ten samples is on the order of tenths of a meter. The 2DRMS difference is consistent with previous comparisons of DGPS references and Cine-T trackers.

There is an apparent 3.5 meter bias in the vertical difference between DGPS and Cine-T. This difference is not a reference accuracy error, but a mean sea level (MSL) to height above the ellipsoid (HAE) conversion discontinuity in the comparison of the two systems. The DGPS and Cine-T processing use different conversions between the two vertical coordinates, MSL and HAE. This points out the importance in not only using WGS-84 reference datums, but to also ensure the HAE-to-MSL conversion algorithms are identical. The high precision of modern reference systems make seemingly inconsequential processing differences significant with respect to system accuracy.

A data availability anomaly is seen in sample run 4. For this run there is less HR-DGPS data available than

the other nine samples. This is caused by a satellite constellation switch during the ten second sample window. Due to DGPS error transients, HR-DGPS data is momentarily unavailable after a constellation switch. For sample run 4, HR-DGPS data is unavailable for 6 seconds after the constellation switch.

Table 5 shows summary statistics for the 1 Hz DGPS TSPI differenced against the Cine-T TSPI. The table is similar in structure to Table 4. There are two things to note from the comparison of the tables. First, the amount of data from the 1 Hz DGPS is much less than from the HR-DGPS. The increased rate of data is the primary design goal for the HR-DGPS algorithm. The second point to note is the consistency in the mean and standard deviation values of the Table 4 and Table 5. The accuracy and the stability of the HR-DGPS TSPI is unchanged with respect to the original 1 Hz DGPS.

Figure 3 visually shows the HR-DGPS performance for sample run 1. The horizontal and three dimensional (3D) differences between HR-DGPS and Cine-T is

plotted versus time. Figure 4 shows the same difference information for sample run 9.

TEST ITEM PERFORMANCE

The purpose of HR-DGPS TSPI is to test state-of-the-art integrated navigation systems. The following section shows how the HR-DGPS has been used to test system performance. The HR-DGPS reference allows the navigation performance of the aircraft navigation system to be characterized against a proven system.

To analyze navigation system performance, it is required to have the aircraft navigation solution (position and velocity). This solution must be provided with an accurate time tag. For comparison with the HR-DGPS reference, it is best to have integrated system solution time-tagged with either GPS time or Universal Time Coordinated (UTC) time.

Figure 5 shows the position accuracy of a stand-alone GPS receiver against the HR-DGPS TSPI. The

Table 4. High-Rate DGPS, Cine-T Difference Statistics

Run #	Data Points	RMS-2D (m)	RMS-3D (m)	Mean East (m)	Mean North (m)	Mean Up (m)	Std Dev East (m)	Std Dev North (m)	Std Dev Up (m)	Average PDOP
1	193	0.63	5.44	0.52	0.30	5.41	0.06	0.19	0.05	1.90
2	244	1.23	1.33	-0.99	-0.70	-0.50	0.10	0.15	0.08	2.60
3	198	1.24	3.86	1.21	-0.28	3.65	0.08	0.07	0.05	3.40
4	121	0.80	5.53	0.590	-0.03	5.46	0.54	0.03	0.66	3.03
5	193	0.65	4.15	-0.266	-0.55	4.10	0.18	0.10	0.08	2.20
6	191	1.05	2.99	-0.97	-0.39	2.80	0.09	0.09	0.06	2.00
7	185	3.53	4.12	-3.30	1.24	2.12	0.09	0.12	0.08	2.10
8	209	0.46	5.19	-0.36	0.26	5.17	0.06	0.10	0.11	2.20
9	236	1.20	5.03	0.29	-1.16	4.88	0.07	0.08	0.13	4.00
10	231	1.01	5.31	-0.58	0.80	5.22	0.15	0.08	0.04	3.20

Table 5. DGPS (1 Hz), Cine-T Difference Statistics

Run #	Data Points	RMS-2D (m)	RMS-3D (m)	Mean East (m)	Mean North (m)	Mean Up (m)	Std Dev East (m)	Std Dev North (m)	Std Dev Up (m)	Average PDOP
1	10	0.97	5.57	0.48	0.80	5.49	0.10	0.21	0.06	1.90
2	10	1.06	1.12	-1.01	-0.26	-0.36	0.12	0.16	0.09	2.60
3	10	1.19	3.97	1.17	0.17	3.78	0.09	0.09	0.05	3.40
4	6	1.56	5.39	1.03	0.15	4.99	1.07	0.69	1.43	2.85
5	10	0.33	4.21	-0.27	-0.08	4.20	0.17	0.08	0.09	2.20
6	10	.97	3.10	-0.96	-0.03	2.95	0.07	0.10	0.06	2.00
7	10	3.67	4.30	-3.28	1.64	2.23	0.11	0.12	0.08	2.10
8	10	0.72	5.37	-0.31	0.64	5.32	0.06	0.11	0.14	2.20
9	10	0.85	5.08	0.31	-0.77	5.01	0.08	0.09	0.14	4.00
10	10	1.33	5.50	-0.58	1.18	5.33	0.15	0.09	0.05	3.20

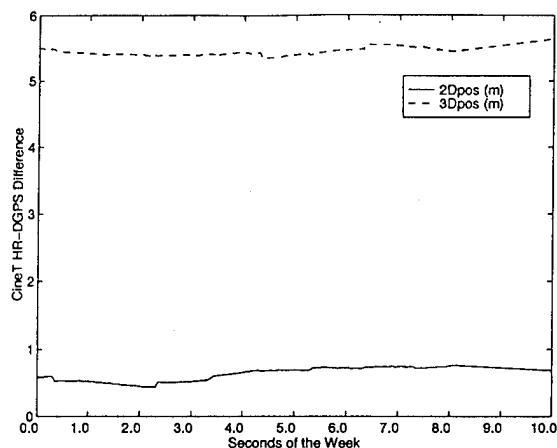


Figure 3. Run 1, HR-DGPS and Cine-T Comparison

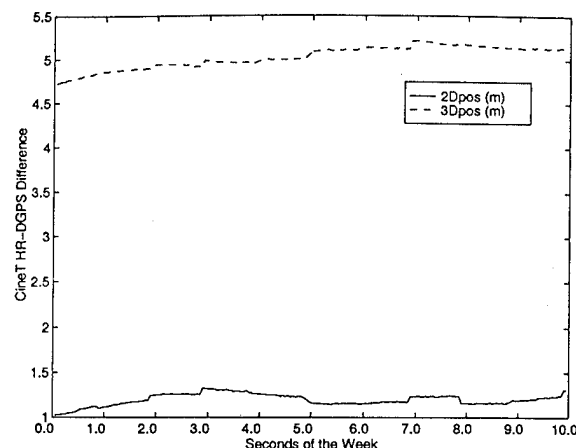


Figure 4. Run 9, HR-DGPS and Cine-T Comparison

GPS receiver is performing well within the requirement for PPS military navigation (16m Spherical Error Probable). Figure 6 displays the velocity performance of the GPS receiver over the complete flight profile.

Figure 7 shows the position performance of the integrated INS/GPS receiver integration. The data displays system performance over a 90 second window during the flight profile. The integrated equipment tested during the flight did not integrate the vertical channel, thus only horizontal position accuracy is presented. Figure 8 displays the velocity performance of the INS/GPS integration. The benefits of INS/GPS integration can be clearly seen in the stability of the INS/GPS velocity performance as compared to the GPS stand-alone performance. Figure 8 shows a velocity error transient. While this transient does occur, the more significant issue is the ability of INS/GPS filter to rapidly recover from the velocity problem. This shows the robust nature of INS/GPS integrations.

The data from the GPS stand-alone and INS/GPS integrated equipment was collected via RS-422 instrumentation port of the GPS receiver. Both the flight data from the SUT and the HR-DGPS data can be collected through this instrumentation port. This allows for a single data collection unit to be used for system navigation accuracy verification.

SUMMARY

The HR-DGPS algorithm is another generation in the development of differential GPS reference technology. The prime purpose of the new algorithm is to increase the data rate without decreasing accuracy. By using INS data in conjunction with the 1 Hz DGPS data, a forward-backward blending filter produces 20 Hz reference TSPI with proven accuracy.

The accuracy of HR-DGPS was tested against its predecessor (1 Hz DGPS), the Holloman Sled Track, and Cine-Theodolite Trackers. The quality performance

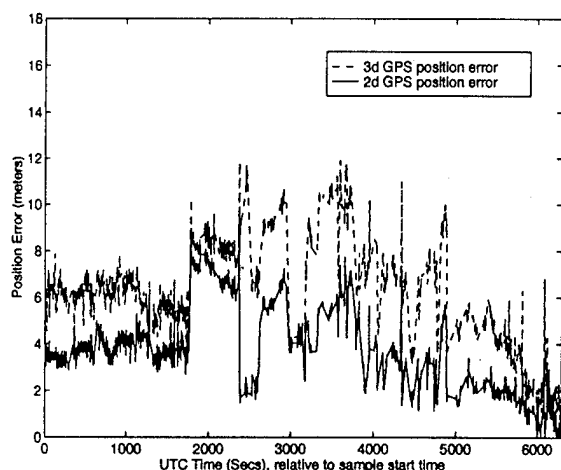


Figure 5. Stand-Alone GPS Position Performance

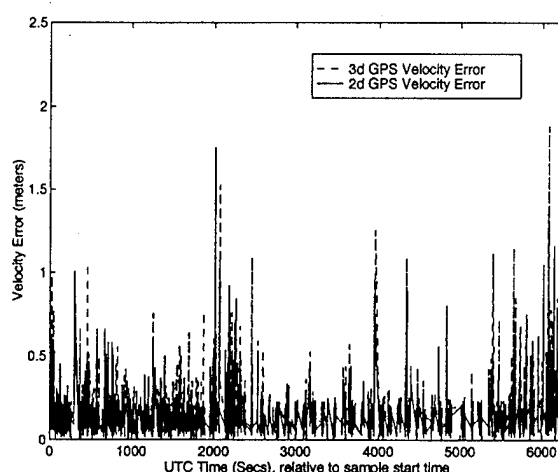


Figure 6. Stand-Alone GPS Velocity Performance

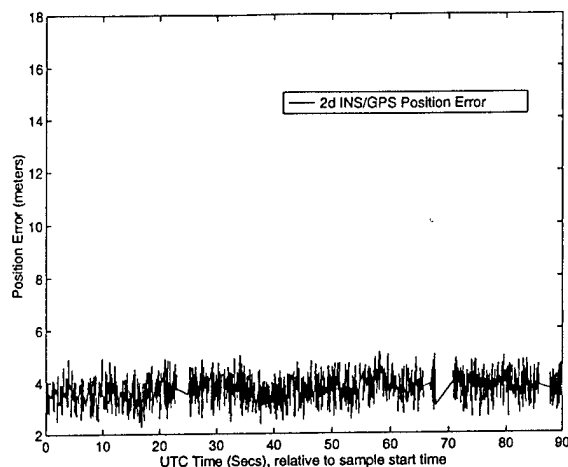


Figure 7. Integrated INS/GPS Position Performance

against all three systems shows HR-DGPS to be stable, precise, and within required TSPI accuracy criteria.

The real benefit of the algorithm is its ability to test high dynamic field aircraft. The implementation of the reference requires minimal onboard instrumentation and the cost of testing is much less than traditional ground tracking systems. The high rate of the data and the low cost make the HR-DGPS algorithm ideal for high dynamic aircraft and weapon delivery testing. HR-DGPS is a proven technology which provides high accuracy/high-rate TSPI reference for flight test.

ACKNOWLEDGEMENTS

We want to thank Lockheed Advanced Development Company (LADC) for making the Cine Theodolite data available to the 746 TS. We would also like to thank the people instrumental in the development of the HR-DGPS filter. Lt Brian Bohenek, Lt Steve Aspey, SSgt Tim Reed, Francisco Ramirez, and Ken Wernle are key members of the 746 TS team which processed and verified the HR-DGPS data. Special thanks goes to Kim Martin of AMCOMP Inc, who helped as key player in the development of the HR-DGPS algorithm. We would also like to thank Don Detorres of Intermetics Inc for his efforts in the development of the HR-DGPS software. As always, we would like to thank the 746 TS community at large for their support in meeting customer requirements with new and exciting technology.

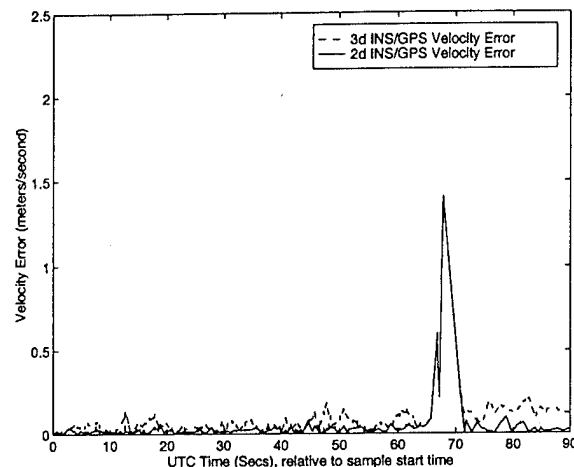


Figure 8. Integrated INS/GPS Velocity Performance

REFERENCES

- Abby, Darwin G., "Verification of a GPS TSPI System," 14th Biennial Guidance Symposium, 1989.
- Hofmann-Wellenhof B., Lichtenegger H., and Collins J., "GPS Theory and Practice," Spring-Verlag Wein 1994.
- Interface Control Document, ICD-GPS-059, Revision C, "GPS User Equipment ICD for MIL-STD-1553 Multiplex Bus Interface," NAVSTAR GPS Joint Program Office, 1993.
- Interface Control Document, ICD-GPS-150, "GPS User Equipment ICD for Instrumentation Port Data Link of the DoD Standard GPS UE Radio Receivers," NAVSTAR GPS Joint Program Office, 1991.
- Maybeck, Peter S., "Performance Analysis of a Particular Simple Kalman Filter," Journal of Guidance & Control, Vol 1, Nov-Dec 1978.

Summary of the Initial GPS Test Standards Document: ION STD-101

Stewart Teasley
Rockwell Telecommunications

James Bybee
Cibola Information Systems

BIOGRAPHY

Stewart P. Teasley is part of the Commercial GPS Receiver team at Rockwell Telecommunications. His experience on GPS began in 1976 as a member of the software design team for one of the concept validation receivers for Phase I GPS User Equipment. He later led a team that pioneered techniques for blending GPS and low cost inertial sensors. On both of these programs, he led the in-plant test phase and the formal field test phase at the US Army's Yuma Proving Ground (YPG) in Arizona. He later led the development and testing of the NavCore V commercial GPS receiver engine at Rockwell.

Mr. Teasley has a Bachelor of Electrical Engineering degree from the Georgia Institute of Technology and a Master of Science degree in Computer Science from Southern Methodist University. He has published a variety of technical papers in symposia of the Institute of Electrical and Electronic Engineers (IEEE) and the Institute of Navigation (ION). He has served as chair of the GPS Test Standards Working group since the inception of the group in 1993.

Jim Bybee is President of Cibola Information Systems Inc. He currently provides GPS consulting services to Intermetrics Inc. at the YPG. While serving in the US Air Force, he was assigned to the GPS Joint Program Office from February 1975 until retirement in 1982. Most of this assignment was with the GPS field test team, testing Phase I GPS receivers at the YPG. Since retiring from the Air Force he has provided consulting services to organizations in the development and test of various GPS equipment. He received a Bachelor of Electrical Engineering degree with a Bio-Medical Electronics Option from the University of Wyoming in 1968 and a Masters degree in Electrical Engineering from the Air Force Institute of Technology in 1970.

ABSTRACT

The GPS Test Standards Working Group (WG) was organized in early 1994 to develop a set of performance test standards applicable to marine, vehicular, and handheld commercial GPS receivers. The need for such a standard arose from the inconsistencies seen in the specifications of various GPS receivers and the confusion among GPS users in comparing the attributes of these products. ION has sponsored the WG through its Satellite Division and has provided meeting facilities at major ION meetings.

This paper summarizes the initial ION STD-101 document produced by the WG. Each of the key tests developed within the document is described along with the rationale for selecting the tests and the methodologies.

An independent validation of the test procedures, data analysis techniques, and data presentation formats of ION STD-101 has been accomplished using the GPS test facilities at the YPG. The results of this validation process are presented along with recommended modifications to the test standard document based on the tests.

Plans to enhance the standard through the addition of specific test limits for marine, vehicular, and handheld applications of GPS are outlined. The future activities of the WG and its relationships with other industry organizations are also discussed.

BACKGROUND AND INTRODUCTION

By 1993 the GPS community recognized the need to develop uniform test standards for GPS equipment. As the GPS system has been used in ever widening commercial markets, the designers of end equipment prod-

ucts tend to have a more user-oriented and less technical GPS knowledge base. In some cases, these users of GPS systems have been confused by conflicting and often inconsistent specifications from the various receiver manufacturers. By infusing GPS users with the tools to execute or judge performance tests using uniform test standards, it was felt that the acceptance of GPS by the general public would be improved.

Although the need was recognized to initiate a test standardization process, the structure and organizational links of such a process were not obvious. A number of organizations such as the IEEE, the Electronic Industries Association (EIA), the Radio Technical Commission for Maritime (RTCM), and the Radio Technical Commission for Aviation (RTCA) have active committee structures and routinely publish specifications and standards.

ION has emerged as the center of expertise on GPS but had no prior experience developing test standards. After some deliberation in 1993, the WG was established by ION to develop a set of test standards for commercial GPS receivers.

The WG is guided by a Terms of Reference Document approved by ION. In this document the responsibilities of the WG are delineated including the marine, land vehicular, and handheld GPS applications that are to be addressed.

The Terms of Reference Document specifically excludes aviation and survey applications of GPS. ION felt that test standards for these applications were adequately addressed in documents produced by other organizations.

The Terms of Reference Document also specifies the desired composition of the WG. The development of any standard necessitates a broad-based membership so the results are not biased to benefit any particular organization. To that end, the Terms of Reference Document states that the WG membership should include representation from the following organizations:

- GPS receiver manufacturers.
- Manufacturers of systems that incorporate GPS receivers.
- GPS test equipment manufacturers.
- Test laboratories or other related groups.
- Others with a special interest in GPS test standards.

The membership of the WG includes representatives from all of the above organizations. A complete list of the WG membership is provided at the end of this paper.

WORKING GROUP ACTIVITIES TO DATE

The WG began its serious technical deliberations in January 1994 during ION's Technical Meeting. The early meetings focused on gathering relevant technical information and determining an appropriate set of tests that could be applied to GPS receivers used in marine, land vehicular, and handheld applications. The WG has been fortunate to have several members from test organizations who have made important contributions in developing the test suite and test methodology.

The set of tests defined for the initial release of ION STD-101 includes the following:

- Initialized Time-To-First-Fix (TTFF).
- Warm start TTFF.
- Reacquisition time.
- Static navigation accuracy.
- Dynamic navigation accuracy.
- Radio Frequency (RF) interference.

These tests were thought to be important to all of the applications that the WG planned to address. Once the set of tests was defined, the WG began to actually write and then review the document at each of the group's meetings. A summary of the early WG activities is contained in the *Initial Report of Activities of GPS Test Standards Working Group* (ref. 1).

In 1994, the *Global Positioning System (GPS) Standard Positioning Service (SPS) Signal Specification* (ref. 2) was released by the Department of Transportation and was found to contain several definitions and methodologies directly relevant to the activities of the WG. Since this publication provided a clear statement of the GPS capabilities that would be made available to the commercial user segment, it was used as both a reference document and a direct source for some definitions and test methodologies.

In 1995, the WG began to perform a detailed review of the completed test standard until the proposed draft was felt to be of adequate quality for circulation outside the WG. At the time of preparation of this paper, copies of the draft standard have been provided to North American GPS receiver manufacturers for their review and comments, and to all members of the Test Standards WG. In addition, there have been notices published in *GPS World Newsletter* and *Global Positioning & Navigation News* stating the availability of the draft standard at ION's national office. Any person or group interested in reviewing the document before its initial publication have been invited to do so through the open press.

The ION Council has the responsibility to approve any document before it can be published under the ION umbrella. The Council has expressed a desire to publish the initial version of ION STD-101 in 1996 subject to review and disposition of comments from all inter-

ested parties. Following publication of the standard, it is hoped that it will be adopted on a voluntary basis by GPS receiver manufacturers.

OUTLINE AND STRUCTURE OF ION STD-101

ION STD-101 has been structured to define a set of six generic tests and to provide a standard presentation format for the results of those tests. It is envisioned that user class appendices will be added to the document in the future. These appendices will define specific aspects of the test conditions and provide limits to be met by equipment validated in each of the categories. The initial draft of ION STD-101 contains no user class appendices, but still provides a framework in which standard tests can be executed and results specified.

Section 1 of ION STD-101 contains a statement of scope and overall intent of the document. Section 2 contains a list of key definitions and other general terms that are used throughout the document. Within this section are the required levels of GPS service that are necessary to support the tests and a description of the requirements to run the tests in Differential GPS (DGPS) mode.

Section 3 is the first of the sections defining the six generic tests that are the primary subject of the standard. The format of Section 3 is explained, but this explanation is not repeated for the other sections since the format is common among them. This format includes the following subsections:

- Test concept.
- Precise definition.
- Test conditions and setup.
- Detailed test methodology.
- Test analysis.
- Test data presentation.

The test concept subsection is a short description of the test written in simple terms. The purpose of this subsection is to convey a basic understanding of the test to a person who has no familiarity with GPS.

The precise definition subsection provides a technical definition of the test and the mathematical basis for interpreting the results. The purpose of this subsection is to provide the technical basis for an informed evaluator to understand and interpret the test results. This subsection also lists those aspects of the test which might be modified by the user class appendices.

In the test conditions and test setup subsection, the environment required to support the test is described. The purpose of this subsection is to give test personnel some organizational flexibility and to specify the conditions under which the test should be conducted.

The detailed methodology subsection provides the test procedure. The test analysis subsection describes the

mathematical basis for analyzing the results of the test. This subsection specifies how the raw recorded data is to be sorted and how the performance measurement parameters are to be computed. The last subsection provides the graphical format in which the test data, as computed using the information in the previous subsection, is to be presented. A specific example is provided to clarify the format.

TEST DESCRIPTIONS

1. Initialized TTFF. This test establishes the time required to obtain GPS navigation data at the specified accuracy after the receiver has been off for several hours. This test can also be thought of as the time required to obtain the first fix after the receiver has been turned off overnight. This test is important to most commercial users of GPS since it quantifies the "dead time" that the user will encounter when the receiver is first turned on.

One of the requirements of this test is that the receiver does not contain currently valid GPS ephemeris data. Therefore, the receiver must collect this data from the satellite signals that it acquires after the start of each test sample. Another requirement of this test is that the samples are spaced randomly so that the acquisition does not line up optimally with the GPS data frame which can make the TTFF appear to be 6 to 12 seconds better than it actually is.

The issue of receiver initialization was considered from two perspectives. Some WG members felt that a deliberate error at initialization should be introduced to eliminate the possibility of the receiver beginning the test with "the correct answer." However, since some receivers do not allow user-supplied initialization data, this requirement was not imposed in the general test definition. If initialization errors are needed to satisfy the requirements of some user classes, the errors can be specified in the user class appendices. This means that if a receiver is certified to a user class that requires initialization errors, the receiver must have provisions for user-supplied initialization data.

The other issue with initialization errors concerns the fact that if a receiver knows the "correct answer" it can echo this value out even if it is not tracking satellites. Specific language was added to Section 2 of the test standard to ensure that a valid navigation data point must be derived from satellite signals being concurrently tracked.

The required minimum number of samples for this test is 20. This number was selected as a compromise between the desire for a large number and the practical limitation of some receivers which requires them to be inoperative for four hours to ensure that they do not contain valid ephemeris data. With a larger sample size the confidence interval associated with the final

data is smaller and the difference between the measured TTFF and the true TTFF is smaller. Collection time for 20 samples by a receiver that does not have a method to "purge" ephemeris data is three days, which was judged to be a practical limit.

2. Warm Start TTFF. This test is similar to the Initialized TTFF test except that the receiver is inoperative for a shorter period of time and still contains valid ephemeris data from its previous navigation session. This test is important for many applications where the receiver may be turned off for short times to conserve battery energy. This parameter is also important for automotive users where the vehicle might be shut down for brief periods and a quick resumption of navigation is desired at power-up.

In both TTFF tests, consideration was given to the quality of navigation data that should be required for the valid navigation point that signals the completion of a TTFF sample. Although some felt that the solution should be required to be within 100 meters of true position, the SPS signal specification (ref. 2) allows the accuracy to be as large as 300 meters 5 percent of the time. Therefore, the value of 300 meters was selected even though any receiver would be expected generally to navigate with much better accuracy.

For this test it was practical to require a higher number of test samples since there is no specific time spacing between tests. Therefore, a minimum number of 50 test samples was chosen. Because of the higher number of samples, the 95 percent confidence level in this test is 0.284 times the sample deviation compared with 0.467 times the sample deviation for the Initialized TTFF test.

3. Reacquisition Time. This test establishes the time required to resume navigation following a short blockage of GPS signals during normal operation. This test is important to all GPS users who operate receivers in areas of signal blockage such as under bridges or around buildings. The test differs from the TTFF tests in that power is maintained to the receiver throughout the test.

There are two independent dimensions to this test: blockage time and the number of satellite signals that are actually blocked. It was decided to structure the generic tests with no specific limits for either of these parameters, but to require that these parameters are stated with the test results. It is expected that as the user class requirements are defined, certain blockage conditions will be developed and specified. Therefore, a receiver would then have to meet these specific requirements to satisfy the general requirements of a particular user class.

A minimum number of 50 samples is required for the Reacquisition Time test. As with other test parameters, the quantity of test samples may be specified differently for any user class.

Unless this test is configured for blockage of all visible signals, it is best accomplished with simulated GPS signals where individual signals may be attenuated to simulate blockage. The test standard allows for tests to be conducted with live or simulated signals, but if simulated signals are used, they must be presented to the receiver at the minimum level specified for the SPS signals in the SPS signal specification (ref. 2).

4. Static Positioning Accuracy. This test establishes the accuracy to which a receiver can determine its position with respect to a known location. This is probably the most frequently asked question among users of GPS receivers and is also the question which is likely to generate the most confusing answers.

Receiver accuracies are currently specified with and without Selective Availability (SA), with varying percentile levels, and with little definition of the test conditions. Yet it is the technical parameter often considered most important by the ultimate user of the receiver.

The SPS signal specification (ref. 2) describes extensive procedures for measuring GPS navigation accuracy and for specifying the GPS signal-in-space conditions necessary to support these measurements. ION STD-101 invokes these procedures and conditions in its definition of the positioning accuracy test. The standard then derives certain additional data items and requires various specific percentile levels to be displayed. This test requires the data to be collected at a surveyed benchmark.

ION STD-101 requires a 24-hour test period as specified in the SPS signal specification (ref. 2). Although this requirement may appear troublesome to some testers, it allows for the receiver to be tested across all satellite visibility conditions and geometric constraints that may exist in a 24-hour period. This requirement also ensures that there is adequate decorrelation of the measured errors so as to give an accurate assessment of receiver performance.

As with other ION STD-101 tests, data may be collected while DGPS corrections are used as long as this condition is noted in the test results. ION STD-101 does not deal with the specific DGPS setup requirements other than to specify the required correction update rate of six seconds. Other issues such as the implementation of Type 2 messages are left to the tester to determine. Failure to deal properly with these issues will likely degrade the measured accuracy of the GPS receiver.

5. Dynamic Navigation Accuracy. This test establishes the accuracy to which a GPS receiver can determine its position in a moving vehicle. Although this parameter is not important to all users, it is critical to such applications as those mapping the position of a moving vehicle. In some cases, poor dynamic accuracy

can make a vehicle appear to be on the wrong street of a map.

A key issue with this test definition was to ensure that the test could be accomplished with a satellite simulator. Very few test facilities have the ability to determine the true trajectory of a test vehicle to the accuracies necessary to determine GPS accuracy. While testing with a simulator is the preferred test mode, the test definition does allow for live tests in a moving vehicle.

Accuracy is determined using the same techniques used in the Static Positioning Accuracy test except that the truth reference is a trajectory file rather than a surveyed position. Obviously, the accuracy of the truth trajectory has a direct effect on the final test results, but no provision is made to reduce the final error based on known errors in the truth source. The final accuracy number must absorb all errors in the testing process.

This test also requires a description of the vehicle dynamics used during the test. Summary parameters are presented with the test results to indicate the general scope of the test conditions. It is expected that certain vehicle dynamics will be specified for the user classes.

6. Radio Frequency Interference. This test establishes the ability of the receiver to operate in the presence of interfering signals that may be received through its antenna. Although there are many commercial GPS applications that aren't concerned with this test, the immunity to signal interference is an important issue for others.

This test specifies the techniques that are used to measure the interfering signal levels at which the receiver first loses a satellite signal and the level at which it completely drops out of navigation mode. As with the other tests, this test may be run with live or simulated signals. Some of the required measurements to support the data analysis, however, make testing with live signals difficult. Clearly, this test is best accomplished with a satellite simulator where signal levels are known precisely.

INDEPENDENT VALIDATION OF ION STD-101

An independent, preliminary evaluation of the test procedures outlined in the draft version of ION STD-101 (5 July 1995) was conducted at the YPG's GPS test facility in Arizona. The purpose of the evaluation was to generate recommended changes to the draft document by exercising the procedures on typical GPS receivers in an operational environment.

YPG's GPS test facility is located on the Cibola test range in a building isolated from other buildings and test structures. A 1x2 meter aluminum platform is located approximately 16 inches above the highest portion of the test facility and was used as a mounting surface for the test receiver antenna as well as the an-

tenna for a reference receiver. The absolute accuracy of this antenna is known to 2 meters.

The antenna cables were routed into the building to a test bench used to hold the GPS receivers and the test equipment during the evaluation. This installation provided an unobstructed view of all satellites above the horizon, and the remote location of the test facility ensured that the evaluation was conducted with a minimum of GPS signal interference.

Three commercial GPS receivers from different manufacturers were used during the evaluation. An additional commercial receiver was used to generate the differential corrections used during some of the tests. Each receiver was delivered with an antenna and this antenna was used whenever the receiver was being tested. The receivers were also delivered with evaluation software that provided a man/machine interface and made it possible to acquire and record data from the system. The evaluation software and laptop computers were used as a data acquisition system when the respective receiver was being used in the evaluation. Because of time constraints, the six procedures outlined in the draft standard were not performed on all three receivers. The Radio Frequency Interference test was not performed on any receiver during this evaluation.

Initialized TTEF. This test was performed for all three test receivers. Each receiver was attached to a laptop computer running the evaluation software for that receiver. Differential corrections were applied to two of the three receivers using an RS-232C connection from the differential receiver processor.

Upon power-up, the power-on time was recorded. Each receiver's output was monitored using the respective manufacturer's evaluation software until the operator was notified by the receiver that the acquisition sequence had been completed and the device was navigating in 3-D mode. Data recording continued subsequent to the report of 3-D navigation until all available satellites were being tracked.

After the specified 20 samples were acquired (8 samples on one receiver), software was generated to determine and record the difference between power-on time recorded at the beginning of each run and the time the set was in 3-D navigation with a total error less than 20 meters as determined from the recorded data.

Spherical Earth assumptions, as delineated in Annex C of the SPS signal specification (ref. 2), were used to assess the navigation error as a function of time. The statistics required by the procedures were also generated. Due to time constraints, the tests were not spread over 24 hours. However, the samples were not synchronized to any UTC boundaries or the GPS 30 second data collection interval and the almanac was current.

Warm Start TTFF (Warm TTFF). The procedures for this test were evaluated on two receivers. One was used to collect only 20 samples. The time that this receiver was turned off before beginning the test varied from 1 minute to 4 hours.

Fifty samples were collected on the other receiver with a fixed two minute interval between test samples during which the receiver power was off. The receiver time was initialized up to five minutes ahead or five minutes behind the actual time that power was restored and the receiver was provided differential corrections throughout the test.

For each test sample, the power-on time was recorded and the receiver navigation output was monitored by the operator and recorded on a laptop computer. The time at which the receiver reported a valid 3-D solution was also noted. After the 50 samples were recorded, the data was processed and the time for which the receiver reported 3-D navigation with a total error of 20 meters or less was determined. This time was compared with the time the acquisition started, and the specified statistics on the time differences were computed.

Forty six samples of the 50 tests conducted were included in the analysis, since the data collection process concluded before the receiver had converged sufficiently to meet the 20-meter error criteria for four of the tests. These four anomalies were due to a significant difference in the receiver performance rather than an inadvertent truncation of the recording time subsequent to the receiver reporting 3-D navigation. The cause of the different receiver performance requires more analysis.

As in the Initialized TTFF evaluation, the Warm TTFF trials were not spread over a 24-hour period. However, the other procedural constraints were followed.

Reacquisition Time (REAO). The definition of this test in the draft standard allows for as few as one signal to be removed from the receiver. However, it was felt that blocking all signals was probably a more severe test and was certainly a very realistic scenario.

The evaluation was performed using three receivers. One of them had an active antenna powered continuously from a regulated laboratory power supply through a bias-T arrangement. Twenty samples were collected from two of the receivers. Fifty samples were collected from the remaining system.

A 0 to 70 dB variable attenuator was connected between each receiver and its corresponding antenna. For each sample, the receiver was allowed to track for a few minutes to ensure a current ephemeris and good navigation. The attenuator was then switched from 0 to 70 dB and left at 70 dB for 3 minutes. Then the at-

tenuator was switched back to 0 and the receiver was allowed to reacquire the signals.

The time at which the attenuator was switched from 70 dB to 0 dB was recorded. Data was recorded on the laptop computer through the 3-minute signal blockage interval, during the reacquisition interval, and for a short period subsequent to the receiver reporting 3-D navigation.

Each of the test samples was analyzed to determine the time between the 70 to 0 dB switchover and 3-D navigation with a total navigation error of 20 meters or less. During this evaluation, there were no significant deviations from the published procedures.

Static Positioning Accuracy. Two receivers were used to evaluate the procedures for this test. The antenna for each receiver was placed at a known location on the antenna platform above the roof of the GPS test facility. Each receiver was allowed to navigate for a 24-hour period with differential corrections applied. The data acquisition system recorded the navigation output of each receiver at the normal receiver output rate. At the conclusion of the 24-hour navigation period, the data was analyzed to provide the statistics required by the procedure.

Dynamic Navigation Accuracy. The evaluation of the procedures for this test was conducted at the YPG dynamometer course. Two receivers were mounted in an Army "Humvee" wheeled vehicle. The antenna for each of the receivers was mounted on the upper surface of the vehicle. No differential data was provided to the receivers for this preliminary dynamic evaluation.

Truth data for the evaluation was provided by one of YPG's laser trackers which tracked an optical reflector also mounted on the upper surface of the "Humvee." An additional truth trajectory was provided by a DGPS-based tracking system mounted in the vehicle.

The "Humvee" was driven around the course at a nearly constant 30 mph. Six 10-minute circuits were completed in the 1-hour test. Preliminary horizontal error data from the receivers for one of the circuits has been compared with the GPS-based vehicle tracking system.

VALIDATION TEST RESULTS

Tables I through V summarize the results of the validation tests. Since the purpose of these tests was to perform a preliminary evaluation of the test procedures, only representative samples are provided here and the identity of the receiver which provided the data is not revealed.

Table I. Initialized TTFF Test Results

MEAN TTFF	MIN TTFF	MAX TTFF	SAMPLE DEV	SIGNAL	NAV MODE	AVAIL ACCY	DGPS
66 sec	59 sec	78 sec	5.03	live	3-D	SPS	Y

Table II. Warm Start TTFF Test Results

MEAN TTFF	MIN TTFF	MAX TTFF	SAMPLE DEV	SIGNAL	NAV MODE	AVAIL ACCY	DGPS
41.4 sec	28 sec	94 sec	12.87	live	3-D	SPS	Y

Table III. Reacquisition Time Test Results

MEAN REAQ	BLOCK-AGE	AVAIL SVs	MIN REAQ	MAX REAQ	SAMPLE DEV	SIGNAL	NAV MODE	AVAIL ACCY	DGPS
6.92 sec	All SVs@ 3 min	***	4 sec	11 sec	1.5	live	3-D	SPS	Y
*** Since live signals were used, this was not a fixed number.									

Table IV. Static Positioning Accuracy Test Results

Accuracy In Meters At Stated Percentile Level							% VALID	SIGNAL	NAV MODE	AVAIL ACCY	DGPS
ACCY MEAS	95%	99.99 %	100%: Max	0%: Min	50%	68%					
ΔHPRE	1.60	3.51	3.82	0	0.67	0.92	100	live	3-D	SPS	Y
ΔUPRE	3.18	5.72	6.09	0	1.21	1.72	100	live	3-D	SPS	Y
ΔPPRE	3.32	5.89	6.25	0	1.54	1.97	100	live	3-D	SPS	Y

Table V. Dynamic Navigation Accuracy Test Results

	TEST TIME (sec):	VELOCITY (m/sec):	ACCELERATION (m/sec ²)	JERK (m/sec ³)
TEST CONDITIONS: MAXIMUM/AVERAGE	3600	13.4	minimal	not available

Accuracy In Meters At Stated Percentile Level				% VALID	SIGNAL	NAV MODE	AVAIL ACCY	DGPS
ACCURACY MEAS	95%	100%: Max	0%: Min					
ΔHPRE	31.4	43.4	0.4	99	live	3-D	SPS	N

CONCLUSIONS FROM VALIDATION TESTING

The ION STD-101 procedures evaluated in this effort are comprehensive and provide good insight into the major performance issues of concern to the commercial GPS community. Potential commercial receiver customers can be assured of the performance integrity of GPS receivers and systems they purchase if they have been subjected to testing according to these procedures. To make the procedures even more comprehensive, the following changes to the draft standards are recommended:

1. Provisions should be made to account for anomalies during testing. For example, during one of the REAQ tests, one of the receivers indicated that it had locked on to all of the satellite signals, but it would not complete the process to 3-D even though the recording continued for many minutes. Also, time was reported as a large negative number during the period. The cause of this is not yet known, but a special case for reporting such an anomaly should be provided. Such performance should not become a part of the 50 samples used to determine typical performance, but neither should such performance go unreported.
2. Some method of reporting the number of satellites available should be devised for tests requiring many samples spread over the course of 24 hours. The number of satellites at a location varies considerably over a 24-hour period.
3. Provisions should be made to require recording differential corrections when they are being used in a test. This will provide a more complete record of the conditions affecting a test and will allow a more complete investigation into any anomalous performance.
4. Differential corrections should be required during dynamic testing in the presence of SA to help separate the effects of SA on navigation performance from navigation errors induced by dynamics.

FUTURE PLANS OF THE WORKING GROUP

The next activity of the WG will be to review all of the comments received from the GPS community regarding the draft ION STD-101 (dated 5 July 1995) currently in circulation. The WG will reach a consensus and present the final document to ION early in 1996. It is anticipated that the test standard will be published essentially in its current form in 1996.

Following publication, the WG will shift its focus to the definition of performance requirements for user classes of GPS. This work will involve cooperative activities with other committees and organizations who are more oriented toward these specific groups. As user

class requirements are defined, they will be released as appendices to ION STD-101 or released as separate standalone documents. The WG will continue to receive and review written comments to ION STD-101 on an ongoing basis.

ACKNOWLEDGMENTS

The WG chair, Stewart Teasley, wishes to acknowledge the work of James Bybee and others at the US Army's YPG who performed the independent validation of the test standards described in this paper.

The work of the following members of the Test Standards WG is also acknowledged. Their support in breaking new ground for developing GPS standards has been essential to the creation of ION STD-101.

Darwin Abby, Consultant
John Anselmo, Hughes Aircraft
Kumar Babu, Consultant
Kevin Barthrup, Stanford Talcum
Dr. Frank Bletzacker, WelNavigate
James Bybee, Cibola Information Systems
Rob Conley, Overlook Technologies
Vincent DiCristofaro, NRaD
Rob Dillingham, NRaD
Per Enge, Stanford University
Don English, ARINC
Ralph Eschenbach, Trimble Navigation
Pat Fenton, Novatel Communications
Robert French, R. L. French & Assoc.
Walter Fried, Consultant
Dick Gibson, CAST
Ed Hallahan, Analytic Systems Engr Corp.
Steven Heppe, Telenergy
Dale Hutchinson, Mitre Corp
Dean Ifune, Welnavigate
Will Johnson, GPS International
Rudy Kalafus, Trimble Navigation
Maj. Karl Kaser, US Air Force
David Kelley, Terrapin Corp.
Len Kruczynski, Trimble Navigation
Marie Lage, Stanford Telecon
Stan Lewantowicz, US Air Force
Tom Logsdon, GPS International
George Lowenstein, NRaD
Harwood McSweeney, Consultant
Bill Moore, EVS Associates
Steve Nagengast, US Coast Guard
Todd Offer, General Motors
Jim Radice, US Coast Guard
James Sennott, Bradley University
Joseph Spalding, US Coast Guard
Stewart Teasley, Rockwell Telecommunications
Ericson Thorbjorn, FFV Aerotech Sweden
Jack Underwood, US Army Proving Ground
Phillip Ward, NavWard Consulting
Bud Wimber, Litton Guidance & Control
Chuck Wiseman, Intermetrics

James Youngberg, Draper Laboratories

REFERENCES

1. Teasley, S. P. and Abby, D. G. *Initial Report of Activities of GPS Test Standards Working Group*, Proceedings of ION GPS-94, page 799.
2. *Global Positioning System (GPS) Standard Positioning Service (SPS) Signal Specification*, 2nd Edition, June 2, 1995.

The 746th Test Squadron: An All-Inclusive GPS Test and Evaluation Facility

Dan Crouch, Lt. Chip Mosle, and Lt. Michael Novy
746th Test Squadron, Holloman AFB

BIOGRAPHIES

Dan Crouch graduated from the University of New Mexico in 1987 with a B.S., in Electrical Engineering. Mr. Crouch has over eight years experience in the development, integration, and testing of GPS/INS navigation systems and is currently the chief integration engineering representative for the 746th Test Squadron at Holloman AFB NM, specializing in the integration and testing of GPS user equipment for all United States Air Force avionics systems.

Lt Chip Mosle was born and raised in Pittsburgh, Pennsylvania. He earned a B.S. in Electrical Engineering from Duke University in 1992. Chip continued his studies at the Air Force Institute of Technology, where he earned a M.S.E.E. Currently, Lt Mosle is an avionics integration engineer with the 746th Test Squadron at Holloman AFB NM, working in support of the GPS Project 2000 initiative.

Lt Michael Novy graduated from Iowa State University in 1993 with a B.S. in Aerospace Engineering. Following his commission into the United States Air Force through the ROTC program, he was assigned to the 746th Test Squadron at Holloman AFB NM. He has been working as an avionics integration engineer, specializing in the integration and testing of GPS user equipment in support of Project 2000.

ABSTRACT

With the Congressional mandate to integrate Global Positioning System (GPS) user equipment into all Department of Defense (DOD) platforms by the year 2000, a significant number of military platforms integrating GPS have entered the laboratory and field test phase for the GPS/avionics upgrade. The number of platforms requiring precise and cost efficient testing and analytical support have yielded an increasing number of integrated GPS test support requirements for the 746th Test Squadron (746 TS). In response to the amount of platforms requiring test support, the 746 TS, also known as the Central Inertial Guidance Test Facility (CIGTF),

has developed the Navigation Test and Evaluation Laboratory (NavTEL), the Test Support Network (TSN), and the Portable Field Jamming System (PFJS) to provide an all-inclusive test and evaluation facility for both military and civilian users integrating GPS. The NavTEL is designed to test integrated GPS architectures in a controlled static or dynamic simulated environment by generating highly accurate time synchronized GPS RF signals, Inertial Navigation System (INS) models, and various navigation aiding sensors to provide a configuration for full integrated navigation performance testing. The TSN, which is used to support field testing and performance evaluation of integrated GPS architectures, consists of a series of six unique Differential GPS (DGPS) ground reference stations that provide continuous Time-Space-Position-Information (TSPI) truth reference data throughout the greater continental United States (CONUS). Finally, to assess interference associated with GPS signals, the 746 TS has developed the PFJS to provide a mobile resource for GPS interference testing. With these unique test capabilities, the 746 TS can provide a "standard" test and evaluation resource for integrated GPS user equipment through the year 2000 and beyond.

INTRODUCTION

The outstanding success of GPS during the Persian Gulf War and its operational effectiveness in the world's commercial surveying and transportation systems has resulted in an extraordinary increase in military and commercial GPS user equipment (UE) development, integration, and test activity. As a result of the outstanding performance provided by well developed, integrated, and tested GPS architectures, Congressional language has specifically stated that all DOD weapon systems must be equipped with GPS UE no later than fiscal year 2000 or risk reduction or elimination of procurement/modification funding. For commercial applications, integration of GPS UE is also moving very rapidly due to the potential decommissioning of existing ground based navigation aids such as TACAN, VOR, DME, ILS, etc. With the proliferation of GPS UE, a substantial increase in integrated GPS system

performance testing has become profoundly evident and as a result has taxed both the military and commercial testing communities significantly. As budgets shrink and as the year 2000 approaches, reducing the effects of integrated systems cost and schedules has become the driving factor for cost efficient and effective system testing.

Recognizing the enormous task of testing and evaluating GPS integrated architectures, the 746th Test Squadron (746 TS), the Responsible Test Organization (RTO) for GPS UE, has strengthened existing and developed new capabilities necessary to properly test and evaluate integrated GPS/avionics systems. With proven resources for laboratory and field testing, the 746 TS has become a "standard" test and evaluation facility for integrated system testing.

In order to mitigate cost, schedule, and installation risks associated with integrated GPS architectures, the 746 TS utilizes several advanced testing resources. For performance risk reduction in a laboratory environment, the Navigation Test and Evaluation Laboratory was developed to accurately simulate integrated UE/avionics mission scenarios to determine functional and performance characteristics for a particular platform. Following laboratory testing, field testing is conducted to further characterize system performance. In support of field testing, CIGTF has developed the Test Support Network and the Portable Field Jamming System. These test assets provide unique resources for truth reference and characterizing system performance in both a "clean" and "challenged" GPS signal environment. With the development of these test resources and over 25 years of proven experience in navigation system test and performance evaluation, the 746 TS can meet the challenges that GPS brings into the world of navigation.

This paper highlights the proven standard resources utilized by the 746 TS in the test and evaluation of integrated GPS/avionics architectures.

NAVIGATION TEST AND EVALUATION LAB

The 746 TS Navigation Test and Evaluation Laboratory (NavTEL) supports GPS integrators working to meet the Project 2000 deadline by evaluating entire integrated navigation systems rather than looking at individual system subcomponents. The integrated system under test consists of multiple subcomponents feeding data to a flight management system or mission computer which processes subsystem data, interfaces with the flight crew, and drives the flight instruments. NavTEL allows

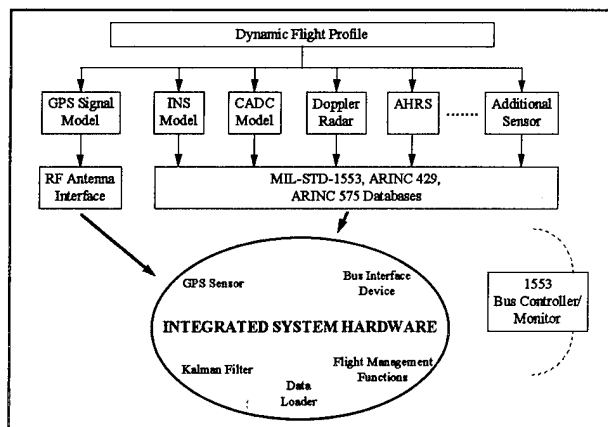


Figure 1. NavTEL Hardware Test Environment

integrators to characterize and troubleshoot integrated systems in a controlled environment.

The NavTEL Concept

The purpose of NavTEL is to "fly" the integrated system in the laboratory. NavTEL stimulates actual system hardware to test both functionality and performance. Precise subsystem modeling is used to recreate navigation hardware components that cannot be dynamically driven in a laboratory environment.

Figure 1 illustrates the NavTEL interfaces with the integration. The flight profile is generated analytically or from actual flight data collected via MIL-STD-1553 or RS-422 data buses. To help in the development of realistic flight profiles, the 746 TS implements aircraft flight models for the F-15 and C-130, as well as a "tunable" generic aircraft profile model. The flight profile is the absolute truth reference used to generate the navigation signals which interface and dynamically drive the hardware integration in the laboratory.

To test the integrated hardware in the laboratory, line replaceable units (LRUs) used in the integration are driven with simulated dynamic signals. These time synchronous signals are created real-time in the laboratory to assist in creating a standard flight profile. NavTEL's benefit to the integrator is its processing power and flexibility to generate all the signals and bus traffic the integrated hardware is designed to receive. The distributed architecture of NavTEL can synchronously create real-time representations of the GPS RF signal and inertial navigation systems (INS), as well as all other expected navigation information: central air data computer (CADC), Doppler-Radar, attitude-heading reference system (AHRS), etc.

The GPS signal is generated by a GPS signal simulator and controlled by NavTEL to maintain accurate time-tagging with the other test elements. Within the GPS simulator, it is possible to vary and control all the GPS Space and Control Segment error sources: ionospheric delay, tropospheric delay, discrete signal errors, and C/N₀ power levels. The simulator also generates "clean" and "challenged" GPS signal environments in order to evaluate the effects of signal interference on the integrated system. This allows the GPS sensor within the integration to be exercised throughout its defined mission flight profile environment.

NavTEL generates precise data traffic models for integrated navigation subcomponents which cannot be dynamically "flown" in the laboratory. The most important of these navigation models is the inertial navigation system. The INS data traffic is generated by combining the flight profile truth data with a highly characterized and verified INS error state model. The 746 TS has verified INS error models for the ENAC-77, SNU-84, and FNU-85 INSs. The NavTEL development staff has also generated a 77-parameter generic INS model that can be modified to represent a myriad of different INSs. The INS data is formatted and transmitted across the data bus which the integrated navigation system is expecting to receive. ARINC-429, ARINC-575, and MIL-STD-1553 are examples of interface buses on which INS data messages are transmitted.

The power of NavTEL lies not in its ability to generate a single error model (like the INS), but to generate all the required models real-time to stimulate the complete navigation system. NavTEL generates and drives the system with all supporting subcomponent data (CADC, Doppler-Radar, AHRS, etc.). This supporting navigation data is formatted into the expected data messages and transmitted on the applicable data bus.

Expandable modeling resources, synchronous parallel processing control, and real-time system interaction make NavTEL a flexible, effective resource for integration test. The overriding goal of NavTEL is to generate a dynamic signal test environment to fully stimulate system hardware in a controlled laboratory setting. The hardware units receive the GPS, INS, CADC, AHRS, and other navigation data as they would during flight test. This ability to dynamically evaluate the complete integrated system allows NavTEL to conduct testing that had previously been the exclusive domain of flight test.

NavTEL Test Capabilities

During integration test programs, NavTEL has shown itself to be invaluable to integrators in two specific test areas: failure identification and performance characterization.

Failure Identification

One of the greatest assets of new integrated systems is their ability to incorporate information from a variety of sensors. The integrated systems blend the sensor data together into a single information source to drive the flight instruments and aircrew displays. Unfortunately, the complexity of the integrated system can make error source isolation difficult when system-level anomalies are detected. System integrations consistently contain subcomponents from different manufacturers with different interfaces, all linked together and expected to work as a single system. NavTEL provides a controlled environment to conduct diagnostics and answer the question: What is causing the problem?

Integrators have utilized NavTEL to identify system-level performance anomalies down to a single error source. This ability to characterize and isolate errors has allowed integrators to correct the problems early in test programs. NavTEL is often used on-the-fly during flight and van testing to characterize errors seen during field testing. If a problem is seen in a van or flight test, the equipment is brought into NavTEL, and the test scenario is recreated in the laboratory. The system analysts can take full advantage of the NavTEL test environment; the controlled nature of laboratory testing, the ability to rerun scenario segments, and the real-time NavTEL test interface to isolate and replicate error sources.

An example of NavTEL's failure identification capability was demonstrated during a MAGR/INS test program conducted at the 746 TS. A problem was seen in the GPS velocity measurements to the integrating Kalman filter. The problem induced a velocity estimate bias from which the filter would not recover. NavTEL was able to recreate the exact velocity error using simulated GPS signals. The problem was identified as a time lag between the occurrence of a subsystem performance degradation and the notification of that degradation. Thus the integrating filter accepted degraded subsystem data with too great of a confidence weighting. By characterizing and documenting the error source in a government laboratory setting, the test program was able to maintain schedule.

While troubleshooting is always a difficult and trying task, NavTEL strives to identify and isolate system failures easily. The point is to give the analyst the support and the tools necessary to answer the questions that arise: What is making the system fail? Is the problem interface cabling or data latency? Is it the GPS figure of merit or the INS gyro drift? Testers can quickly answer these questions using NavTEL and narrow the problem down to a single source. NavTEL becomes the analysis tool to debug the problem and give the integrator the answer needed.

Integration Performance Testing

Like most acquisition programs, GPS integration test programs are being asked to do more with less. The increasing capabilities of the integrated systems call for longer and more extensive test programs. Unfortunately, budget and schedule constraints force integrators toward aggressive test schedules and shorter flight test programs.

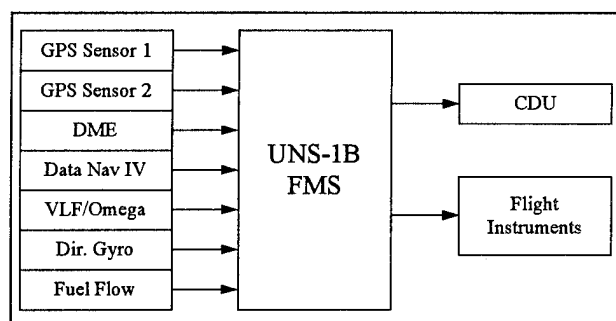


Figure 2. C-21 Proposed Integrated Navigation System

NavTEL, as a standard testbed, is used to mitigate schedule risk and augment the flight test program. NavTEL's ability to recreate flying conditions in the laboratory allows integrators greater flexibility in the design of their test programs. Functional and performance characterization that could previously only be conducted in flight test can now be characterized in the laboratory.

The C-21 integration test program is an example of NavTEL testing used to document system performance. The testing is being conducted on the proposed integration architecture for the C-21 aircraft. The integration consists of a two GPS sensors, a flight management system (FMS), and a variety of other navigation sensors/aids. The FMS integrates all the information together and drives a control display unit and flight instruments (Figure 2).

C-21 NavTEL testing will take place before prototype installation is complete. NavTEL will test the flight management functions, the system interfaces, and the performance of the P(Y) Code GPS sensor proposed for the integration. By completing NavTEL testing before flight test begins, laboratory test results can be used to guide and further define the flight test plan.

NavTEL Architecture and Validation

The NavTEL architecture is modular and object oriented for future expansion. The main processing horsepower is provided by Motorola 68040 processors on VME single board computers. Three SPARCstation 10TM workstations are used for sensor model development, real-time test interface, and data display. Shared data/conflict issues are resolved through the use of a real-time shared memory network. Process synchronization is maintained via the Distributed Ada Real-Time Executive (DARTE). The executive is synchronized with a 1 pulse-per-second signal from the GPS simulator, a Northern Telecom (NT) STR2760. The simulator generates radio frequency (RF) for up to 10 satellites with L1 and L2 signals.

NavTEL, as a GPS Joint Program Office (JPO) developed test and evaluation asset, has taken part in the GPS laboratory validation program. The NT simulator has been certified to the highest level by the Satellite Simulator Control Working Group (SSCWG), which is a GPS JPO sponsored consortium of government agencies. This consortium consists of various government agencies with a wealth of experience in GPS simulation.

NavTEL is a test asset designed to exploit modern simulator technology and parallel computer processing horsepower to aid in the development and test of modern integrated navigation systems. NavTEL is used both as a troubleshooting analysis tool and as a performance characterization testbed. Implemented in conjunction with GPS flight test assets, NavTEL provides a high degree of confidence in the performance of GPS integrated systems.

TEST SUPPORT NETWORK

The primary objective of the TSN is to provide a "wide area," standard, validated Time-Space-Position-Information (TSPI) truth reference resource for field testing (van/flight) GPS architectures throughout the CONUS. Since the major expenses in any field test program include range support, system evaluation, and the costs associated with moving program test resources (hardware and personnel) to an obscure test staging area,

the TSN support capabilities provide a new perspective to the art of system testing. With the TSN, cost effective and efficient testing is available virtually throughout the entire CONUS without the cumbersome logistics of moving or reconfiguring a TSPI resource.

The TSN consists of a series of unique military DGPS ground stations called Satellite Reference Stations (SRS) strategically deployed at military installations throughout the United States. Figure 3 shows the current locations for the network stations. The 500 nautical mile radius circles around each station represent the basic area of coverage for mission operations. With special mission planning, extended coverage can be attained (1). Upon request by the customer, mobile SRS's can be deployed to specific operating locations to support programs in areas not currently covered by an existing TSN station. During a test mission, the SRS collects all-in-view Precise Positioning Service (PPS) GPS data, while a data acquisition system on board the test platform records raw GPS measurements as well as the integrated navigation solution. Once the mission is complete, an on-site team transmits the data via an electronic link or courier services to the 746 TS data processing facility at Holloman AFB. The data processing team processes the raw platform GPS measurements with the SRS data to generate a highly accurate reference TSPI. Accuracy of the TSN is 2-4 m (position) and 0.1m/s (velocity) 3d RMS at 1 Hz. Higher rate data (20 Hz) can be attained

with special on-board INS instrumentation. The test team uses this product plus other recorded GPS, INS, and integrated system data to evaluate the integrated GPS architecture.

Satellite Reference Station (SRS)

The SRS is a self-contained PPS GPS ground reference station designed to support two primary functions. It monitors the GPS Space and Control Segment by tracking all-in-view GPS satellites to detect performance anomalies which affect GPS navigation. This quality control monitoring function is required to isolate space and control segment errors from user equipment errors. Secondly, the SRS tracks all satellites in view and computes pseudorange and deltarange corrections in real time to produce DGPS TSPI in support of test programs. All data is recorded and processed post-mission.

Figure 4 shows the SRS hardware configuration. The GPS receiver is a modified military Collins Receiver (RCVR) 3A; a five channel, two-frequency, P/Y code receiver modified to track all visible satellites. The raw pseudorange and delta range measurements from up to 12 satellites are processed in real time to compute pseudorange and delta range corrections. These corrections are recorded for post processing along with all raw measurements. The antenna is a standard fixed

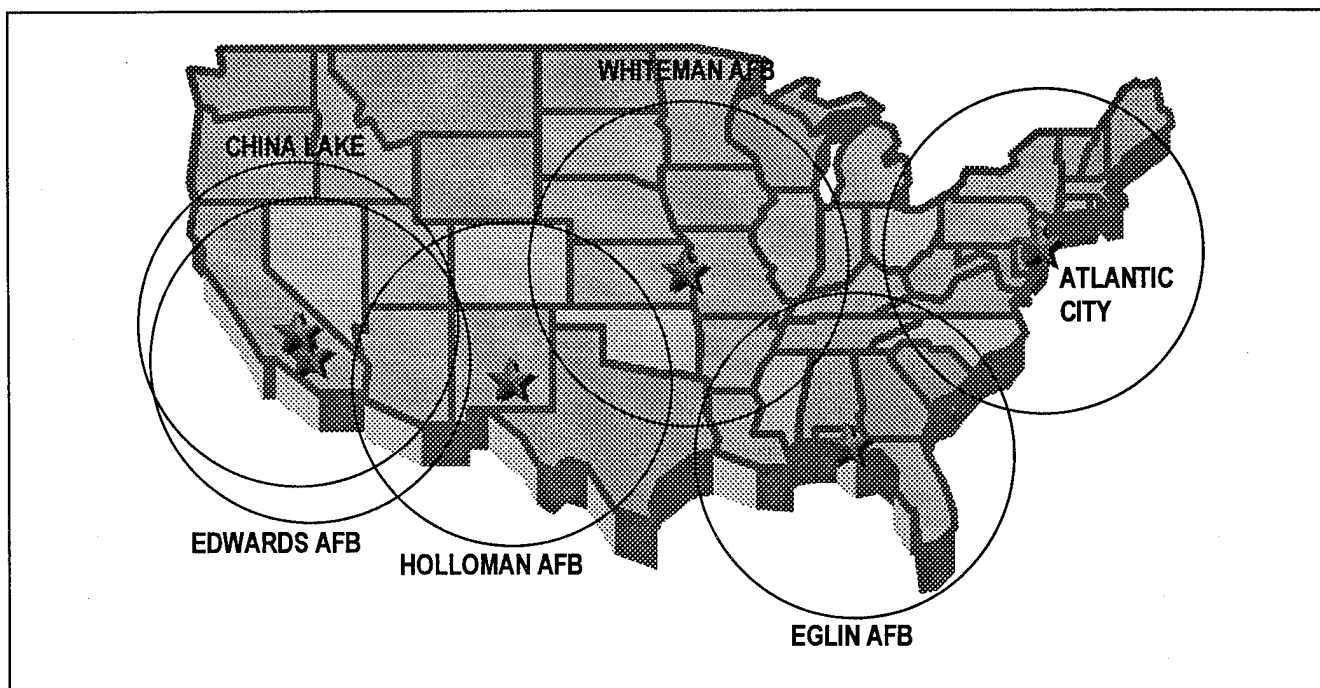


Figure 3. TSN SRS Locations

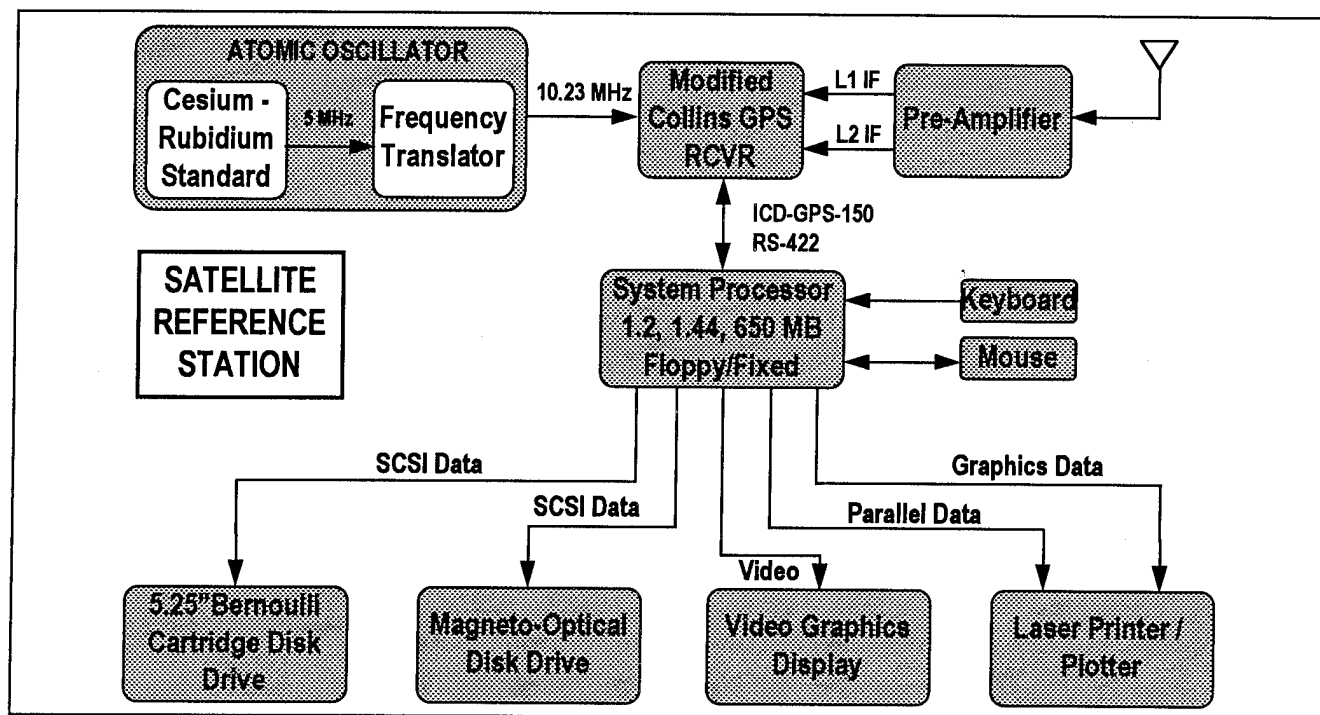


Figure 4. SRS Hardware Configuration

reception pattern antenna (FRPA) which is placed near the receiver to maintain signal integrity. Extreme caution is taken for proper antenna placement in order to eliminate antenna/signal multi-path effects. An external atomic frequency standard provides an extremely stable time source for maintaining system integrity.

Aircraft Instrumentation

The TSN is built around the use of the military Collins RCVR 3A or Miniaturized Airborne GPS Receiver (MAGR) on the test platform. Raw pseudorange and delta-range measurements from the front end of the receiver along with other GPS and sensor data such as INS are recorded on-board the test platform for post-processing. The primary data interface for on-board recording is the RS-422 Instrumentation Port (IP) or MIL-STD-1553B data bus.

Data recording is provided by one of two techniques. Depending on available space, a PC Buffer Box can be interfaced to the IP and digitally recorded in a PC format. If space is limited, RS-422 data can be recorded on one channel of an existing on-board instrumented analog recorder. The analog tape is then replayed through a PCBB on the ground after the mission and recorded. If the platform is not integrated with a Collins 3A or MAGR, or does not have a compatible ICD-GPS-150 interface, a data acquisition instrumentation system can

be installed for raw measurement and navigation data collection.

The test team uses the data products produced by the SRS, test platform, and 746 TS data processing facility to evaluate the integrated GPS navigation solution as well as the GPS and INS sensor data. Data products include an extensive number of table and error plots for any of the recorded parameters. The SRS pseudorange and delta range measurements are processed to generate a "ground truth" which is used as a baseline to compare with the test item and isolate potential anomalies.

Integration Analysis

Table 1 highlights the "basic" evaluation data provided by the data processing facility. Evaluation of the integration is performed using data from four sources when available. These are SRS ground truth, GPS receiver, INS, and integrated navigation solutions. The reference station data helps to isolate any GPS problems or errors. The INS data can be plotted and evaluated to show any INS anomalies. Using all the available data, 746 TS evaluation team analyzes each mission to evaluate the performance of the system, identify problems, and compare the results to the objectives. At the conclusion of the test program, the 746 TS summarizes the results and prepares a final report for submittal to the integrating agency.

The 746 TS DGPS capability has been used for several years to support such programs as the B-2 avionics test program (for both local and wide-area testing), the T-39 Non-Precision and Precision Approach test programs, the B-52G, F-16C, A-10A, C-130 SCNS, AV-8B, F/R-111C, F-111A/E, and F-111F integrated GPS test programs, including a myriad of stand-alone GPS UE test programs. Its use and effectiveness has been very well received and has provided a military standard for system integration testing.

PORTABLE FIELD JAMMING SYSTEM

Following the functional and performance evaluation that NavTEL and the TSN provides, the Portable Field Jamming System (PFJS) is a 746 TS test asset that supports signal interference field testing of GPS receivers and integrated systems. Through the use of portable signal generators, the system provides a known interference environment for integrated systems to pass through. The PFJS allows users to characterize system performance in a challenged signal environment.

The PFJS consists of several vans equipped to transmit interference signals to the system under test (Figure 5). The vans are equipped with an antenna on an extendable mast, a control personal computer (PC), a spectrum analyzer, and a power meter. A trailer-mounted generator provides the power needed to run the system. The system was characterized by the Joint Communications Control Warfare Center (JC2WC), MIT Lincoln Laboratories, and the 46th Test Group Radar Target Scatter Facility (RATSCAT) in March of 1994.

Through strategic placement of the vans, a variable-strength interference environment is produced. The signal generators are controlled through in-house developed software (SkySync) run on the control PC.

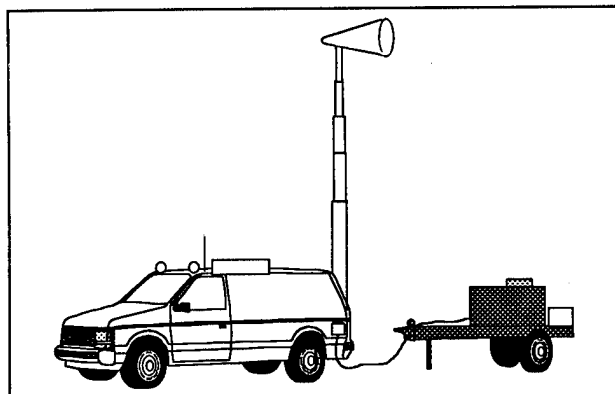


Figure 5. Portable Field Jamming System

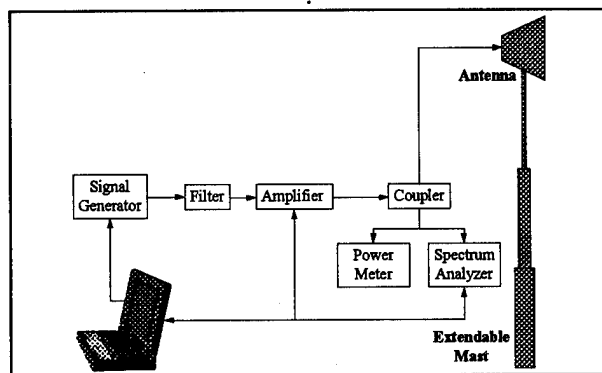


Figure 6. PFJS Block Diagram

The generated signal is filtered and amplified, and finally sent through a coupler to a spectrum analyzer and power meter, and transmitted (Figure 6). Data is collected from the Control PC, the spectrum analyzer and power meter for post-processing. With advanced data processing tools, quick look analysis of the testing is produced in a minimal amount of time.

There are many advantages the PFJS can provide to the test community. Coupled with NavTEL, the PFJS can verify the simulated results with actual field testing. The portability of the system allows testing at a customer desired location. PFJS allows the flexibility to produce a range of interference effects to test a variety of GPS stand-alone and integrated systems.

ANALYSIS

GPS stand-alone and integrated navigation technology has been developed to improve the accuracy and reliability of aircraft navigation systems. The analysis of these systems focuses on characterizing this performance. While any test report will incorporate a variety of variables or test points, three of the most important of these are position estimation performance, velocity estimation performance, and the availability/reliability of these estimates. The 746 TS has developed standard analysis packages that document these variables. Standardization of data representation allows integrators to compare results between programs and increase the cross-flow of information/lessons learned.

Table 1 shows a listing of typical plots generated in a standard data package. The data is represented as difference data between the system-under-test and the truth reference (either the NavTEL simulated flight profile or the TSN DGPS reference TSPI). The data plots show the time history of the system performance over the simulation/flight test as well as summary

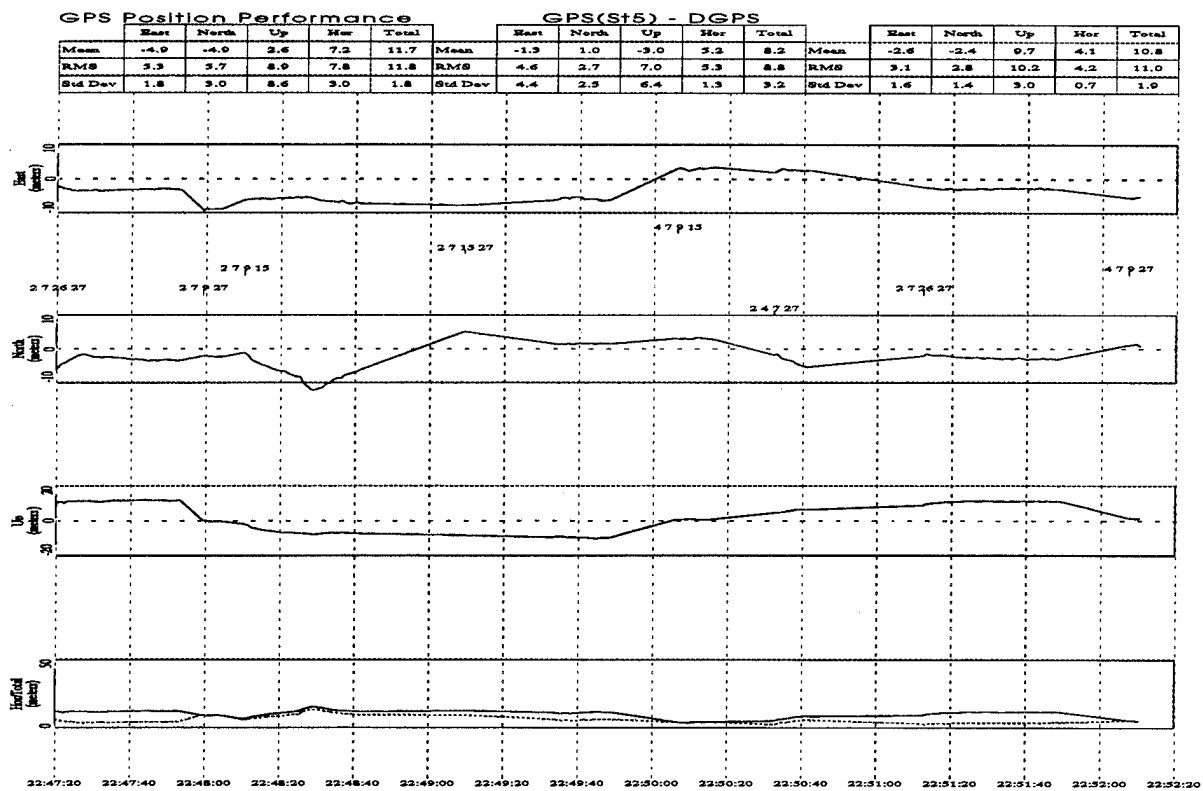


Figure 7. Position Performance Plot

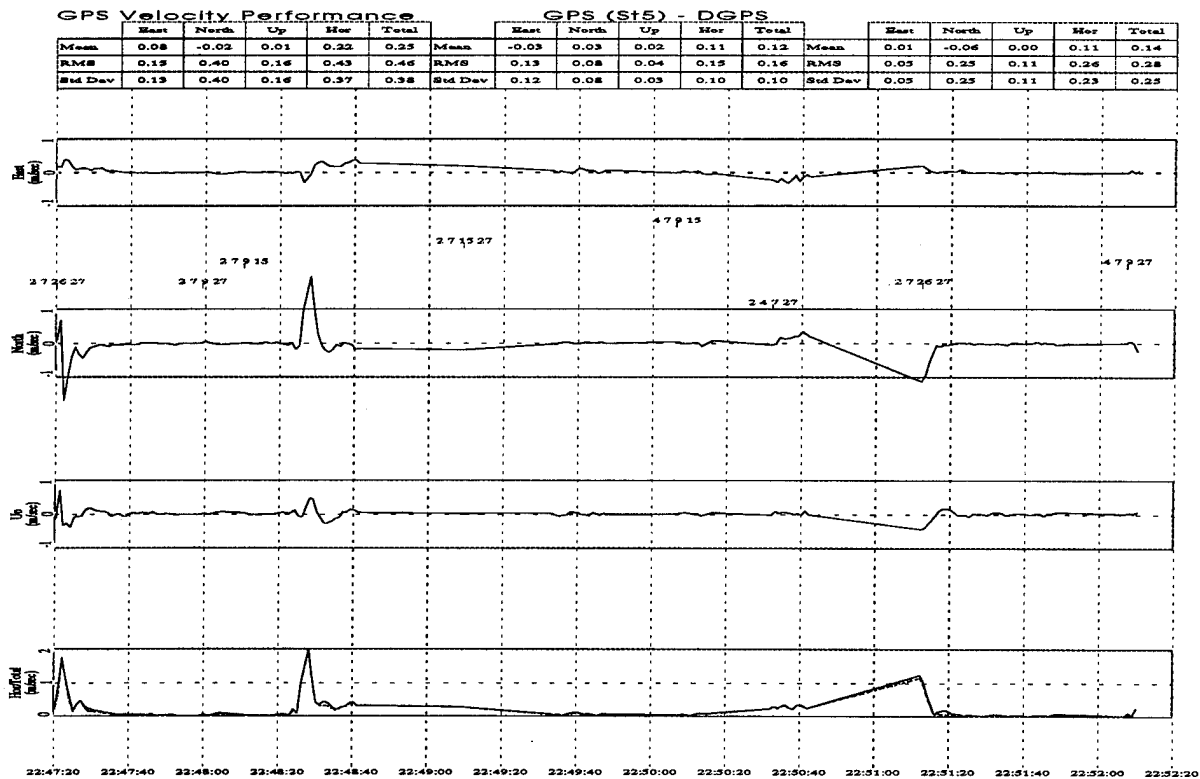


Figure 8. GPS Velocity Performance Plot

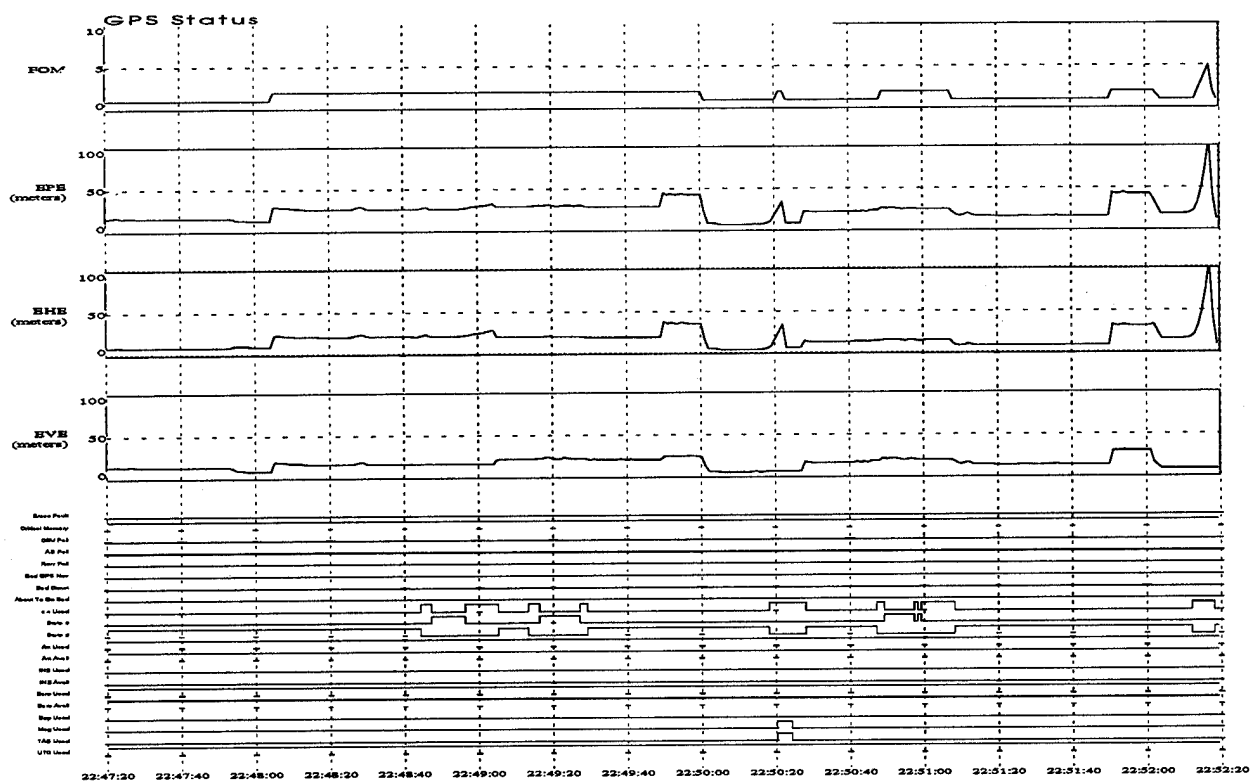


Figure 9. GPS Status Plot

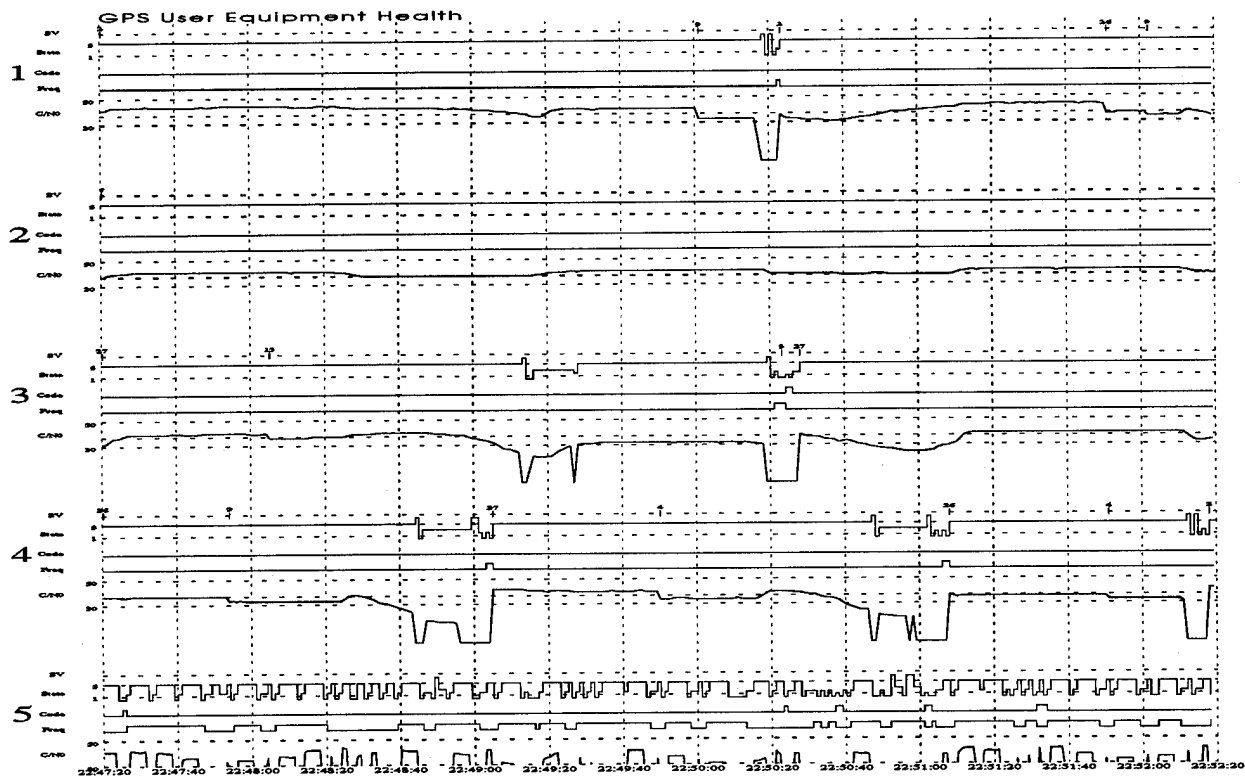


Figure 10. User Equipment Health Plot

Table 1. Standard Performance Plots

PLOT	DESCRIPTION
GPS-DGPS-Ground Truth	Authorized Ground Truth: ORE Fits, Benchmark Difference
ORE Ground Truth	Receiver GPS User Ground Truth from the SRS ORE's
GPS-DGPS Position	Position Error
GPS-DGPS Velocity	Velocity Error
INS-DGPS Position	INS Position Error Plot
INS-DGPS Velocity	INS Velocity Error Plot
GPS Status	GPS Receiver Status (FOM, EPE, EHE, EVE, Status Bits)
UE Health	User Equipment Health (Channel Status)
GPS X vs Y, Z vs Y	Racetrack from GPS Receiver
GPS Position vs Time	GPS Receiver Position
GPS Velocity vs Time	GPS Receiver Velocity
DGPS Quality Assurance	Validation of Post Processed Products

statistics for the mission (mean difference, standard deviation, Root Mean Square Error).

Figures 7 and 8 are standard plots for documenting position and velocity performance. Figure 7 shows the system position performance against DGPS TSPI as produced via the TSN. The plot is divided into four separate horizontally cascaded sections. The top three sections show system performance (system position difference against DGPS TSPI) in its three degrees of freedom in space: East(X), North(Y), and Vertical(Z). The fourth section shows a radial difference in the horizontal plane (2D) and in space (3D). Figure 8 portrays the same information for the system velocity performance. The system velocities V_{North} , V_{East} , and V_{Vertical} are differenced with the DGPS TSPI velocities. Radial velocity performance (2D and 3D) is documented in the same manner as radial system position performance.

Figures 9 and 10 show summary information regarding GPS/system availability and reliability. These plots show system status information collected via the GPS RCVR RS-422 instrumentation port. The data encompasses everything from individual GPS RCVR channel C/N_0 levels to INS data availability. These plots are essential analysis tools in determining the performance of integrated as well as stand-alone GPS systems.

The 746 TS has developed the standardized analysis tools and packages to increase a common test database and cross-flow of information between test programs. By utilizing pre-existing data products, integrators can benefit from the efforts and results of past GPS test programs. The goal is to retain Air Force corporate test knowledge to better support aircraft driving towards the Project 2000 deadline.

SUMMARY

Integrating GPS into over 200 DOD aircraft and completing all laboratory and field testing by the year 2000 is a major undertaking. As the RTO for GPS UE, the 746 TS (CIGTF) has developed the Navigation Test and Evaluation Laboratory, the Test Support Network, and the Portable Field Jamming System as standard, military test resource for integrated GPS test and evaluation. Each test resource was developed with a primary emphasis in mind: provide a test capability that results in tests conducted and reported accurately, efficiently, and cost effectively. While the challenge to integrate GPS into every military system by the year 2000 remains great, the expected laboratory and field test support can be met through the proper planning and utilization of existing proven resources.

ACKNOWLEDGMENTS

Special thanks is given to the following people for their assistance in preparing this paper: Dave Kalkwarf, AMCOMP Inc., for his help with the data analysis and plotting software; James Keith and Lt Scott Jokerst, 746 TS, for information on the intricacies and capabilities of NavTEL; and Lt Dennis Caron, 746 TS, for his insight into the design and use of the PFJS.

REFERENCES

1. Uribe, D., Crouch, D., and Abby, D. "Results of Differential GPS Support for a Coast-to-Coast Flight Test." 746th Test Squadron Seventeenth Biennial Guidance Test Symposium, Ruidoso NM, May 1995.
2. Caron, D. "Supporting Field Tests with the Portable Field Jamming System." 746th Test Squadron Seventeenth Biennial Guidance Test Symposium, Ruidoso NM, May 1995.
3. Payne, K. and Kurtz, R. "Real Time, Multiple Model Simulator Laboratory For GPS Related System Testing." ION-GPS-94, Salt Lake City UT, September 1994.

Time to First Fix: A Definition and Recommended Test Method

Leonard Kruczynski
Trimble Navigation, Ltd.

Stewart Teasley
Rockwell Communications

BIOGRAPHY

Leonard R. Kruczynski

Dr. Kruczynski is the Project Manager for the TANS Vector attitude determination receiver at Trimble Navigation Ltd. Dr. Kruczynski has been involved in GPS since 1974. He earned his Bachelor of Science degree from the United States Air Force Academy, his Master of Science from Purdue University and a Doctor of Philosophy degree from the University of Texas at Austin where he wrote his dissertation on GPS navigation algorithms. Dr. Kruczynski is a retired Air Force officer. He was Commander of the GPS Test Force in Yuma, AZ from 1982 to 1985. He has been employed by Trimble Navigation since 1985.

Stewart Teasley

Stewart P. Teasley is part of the Commercial GPS Receiver team at Rockwell Telecommunications. His experience on GPS began in 1976 as a member of the software design team for one of the concept validation receivers for Phase I GPS User Equipment. He later led a team that pioneered techniques for blending GPS and low cost inertial sensors. He later led the development and testing of the NavCore V commercial GPS receiver engine at Rockwell. Mr. Teasley has a Bachelor of Electrical Engineering degree from the Georgia Institute of Technology and a Master of Science degree in Computer Science from Southern Methodist University. He has served as chair of the GPS Test Standards Working Group since the inception of the group in 1993.

ABSTRACT

Accuracy is the attribute that usually comes to mind when discussing GPS. For navigation using either PPS or SPS, however, accuracy is not often a major distinguishing characteristic for GPS equipment. Users

more often consider physical attributes, cost and availability of features to make buying decisions. Yet one other aspect of GPS is critical: Time to First Fix (TTFF). How long after power-on does it take a GPS receiver to compute a position? This paper discusses the meaning of TTFF and its implications for the user. It describes the limitations of GPS that create lower limits for TTFF. The paper recommends a method to test receivers for TTFF and presents the results of tests conducted using the recommended method.

INTRODUCTION

If a word association game were played and "GPS" was the first word, it's likely that "accuracy" would be the response. The world has been conditioned to believe that GPS equipment provides very accurate answers. Even to those for whom SPS accuracy levels are acceptable, "accuracy" is the knee-jerk response when GPS is mentioned.

Accuracy, however, is only one feature of the performance of a navigation system. There are several items which describe and distinguish the behavior of different navigation systems. The *Federal Radionavigation Plan* [Reference 1] describes navigation system parameters such as coverage (global versus local), availability (24 hours versus part time), fix dimensions (2D versus 3D) and fix rate. Time to First Fix is not specifically included in the FRP's list of system parameters. Yet, in many situations, the time a user must spend waiting for the GPS receiver to obtain its first fix after power-on is the most frustrating part of GPS.

There are different TTFF-type terms to cover different starting conditions for the receiver. Unfortunately, there has been no one-to-one correspondence between a TTFF-term and a set of starting conditions. The consequence is that manufacturers' data sheets and evaluations by

testing agencies provide results that make it difficult to evaluate receiver capabilities.

The GPS Test Standards Working Group was established to put some order to GPS equipment evaluation by creating standard definitions and by recommending test conditions for several performance traits. The Test Standards Working Group document [Reference 2] covers more than TTFF but TTFF is the focus of this paper.

In this paper, we will briefly discuss the confusion surrounding TTFF and describe the scenarios to which TTFF terms apply. We recommend three TTFF related terms and we suggest test procedures to evaluate the INIT TTFF. We close by providing results of INIT TTFF testing of three different GPS receivers.

A RECEIVER SURVEY

The confusion that surrounds TTFF is exemplified in a receiver survey conducted by *GPS World*. *GPS World* tabulated statistics on 275 receivers from 54 manufacturers [Reference 3]. Three TTFF columns were listed. A "Cold Start" TTFF was defined as the case when "ephemeris, almanac, and initial position and time are unknown." For a "Warm Start" TTFF, the receiver has a recent almanac, current time and initial position, but no current ephemeris. And a "Reacquisition" is based on the loss of signal for at least one minute. In some cases, the Cold Start TTFF was shorter than the Warm Start TTFF! Note: The Cold Start and Warm Start columns were switched in the magazine.

Cold Start TTFFs ranged from <35 seconds to 25 minutes. Warm Start TTFF's ranged from 5 seconds to 20 minutes. Reacquisition times ranged from "immediately" and 1 second to 2 minutes. Figures 1 and 2 depict the TTFFs quoted for 121 receivers from 11 different manufacturers. Figure 1 is the Warm Start TTFF and is arranged in order. Figure 2 depicts the Cold Start TTFFs for the corresponding receivers. With such a wide range of values, it would seem that some receivers are very, very good and some are very, very bad. We believe that the wide range of values is caused more by a lack of testing and a lack of a clear definition for the parameter than by any significant receiver deficiency.

THE TESTS STANDARDS EFFORT

Teasley and Abby described the general purpose of the ION Test Standards effort in Reference 4. The Working Group's charter limits the scope of the effort to marine, land and handheld and excludes aviation, military and

survey. There are bodies within the excluded areas that have already established themselves in a role to set standards and/or evaluate equipment. There is no reason why the excluded applications could not use the Working Group's suggestions.

The current draft of the Test Standard [Reference 2] is dated 5 July 1995 and is available for review. Some comments in this paper do not align themselves exactly with the draft. Interested parties should provide comments to the Institute of Navigation.

The Test Standard defines an environment that should exist prior to testing. It requires that GPS coverage exist during the test. Coverage is defined to include a mask angle of 10° and a four satellite PDOP of 6 or less for 3D tests and three satellite HDOP of 4 or less for 2D tests. If GPS coverage does not exist, then there is no test. For the TTFF testing discussed here, the definition of coverage was modified to allow PDOP up to 12. The rationale for this modification is that the first fix need not be the most accurate; simply one to indicate that the receiver has locked onto sufficient satellites to give a reasonably accurate position fix. If applications require more stringent conditions, the test methodology still applies only the numbers change.

TIME TO FIRST FIX

The terminology "Time To First Fix" has had more than one description and more than one explanatory footnote. Rather than discuss the history of the terminology, we propose to focus on a literal definition and how the definition applies to users. The goal is to describe a situation that applies to everyone -- not just to unusual circumstances.

Literally, "Time To First Fix" should mean just what it says: the length of time it takes to get a first fix from the receiver? But this simple definition is complicated by different answers to the "When" and "Where" questions: How long has it been since my last fix? Where was I when I got the fix? :

Of the various combinations of answers to the "When" and "Where" questions, three most common situations occur. The following table lists the different responses to the "When" and "Where" questions and provides a sample situation for each combination of responses. The draft standards document defines three TTFFs to match the three most common situations.

Table 1
Situations Associated with Various "When" and "Where" Responses

	Close to last use	Far away
A few seconds ago	Temporary blockage (passed through a tunnel)	If you are here, you are speeding
About an hour ago	Turned off to go to lunch (to preserve power)	Maybe not quite as fast but you're still moving
Last night	Use GPS daily (relates to the first turn on of the day)	Use GPS daily but just got off an intercontinental flight
A long time ago	Use GPS infrequently and the almanac may be very old	Almanac and position are very old

Table 2
TTFF Definitions Associated with Various "When" and "Where" Responses

	Close to last use	Far away
A few seconds ago	Reacquisition Time (REAQ)	Not an event
About an hour ago	Warm Start Time to First Fix (WARM TTFF)	Not an event
Last night	Initialized Time to First Fix (INIT TTFF)	Rare event
A long time ago	Not covered	Not covered

REAQ, applying to the temporary blockage condition, is identical to "Reacquisition" in the *GPS World* survey. WARM TTFF is not covered in the *GPS World* survey. The INIT TTFF is identical to the "Warm Start" in the survey.

COLD START TTFF AND MEMORY

Many earlier definitions of TTFF used such terms as "Cold Start" and "Warm Start." The terms referred to issues such as the presence of time, last position and an almanac in memory and the stability of an oscillator. Cold Start was created to cover the situation where the receiver had no memory and its oscillator was cold.

Today, virtually all receivers have battery backed-up memory and will save almanac data as well as last position. They also have a real time clock. The result is that, at turn on, the receiver can make an excellent estimate of which satellites are visible. The stability of oscillators has proven to be a minor issue when evaluating TTFF. The Test Standards Working Group did not address "Cold Start TTFF" and we will not discuss Cold Start in this paper. If the receiver under test has no battery backed-up memory, then the test procedure described here can still be used and will clearly show the difficulties related to such a receiver.

GPS DATA STREAM IMPACT ON TTFF

Before moving on to test methods and results, it's important to know what to expect from a receiver. The GPS data stream determines a lower limit to INIT TTFF because INIT TTFF applies to situations when the receiver must collect ephemerides from the satellites. The Working Group did not address the situation where ephemerides could be provided by other sources such as a differential link. Ephemeris and clock information is contained in the first 18 seconds (subframes 1, 2 and 3) of a satellite's 30 second frame of data. If the receiver was turned on at a 30 second boundary and if the receiver could instantaneously lock on to the signal and begin collecting the data, and if the receiver could immediately process the data, then an 18 second TTFF would be achieved.

If a receiver is turned on at any point during the transmission of the 18 seconds of ephemeris data, then it will have to wait until the next 30 second frame to collect the first part of the data. In this case, the minimum TTFF will be greater than 30 seconds. If the receiver is turned on during the 12 seconds when subframes 4 and 5 are being transmitted, then it is possible to get a TTFF between 18 seconds and 30 seconds.

But the lock on and processing requirements require some time. Van Dierendonck [Reference 5] concluded that the shortest achievable INIT TTFF is 21 seconds. Our sample test results support this conclusion and also clearly show the impact of the 30 second data frame length on TTFF.

The impact of the GPS data stream on the test conditions is that the user must collect data without synchronizing within a 30 second interval. A tester can skew the data by turning the receiver on during the broadcast of subframe 5. This would allow the receiver time to lock to the signals prior to transmission of subframe 1 (the first subframe of ephemeris data). There would be no penalty caused by the need to wait for a second transmission of the ephemeris data. Although we could argue that this is not a receiver issue, it certainly is a user concern. The reported TTFF should reflect what the user can expect.

TEST CONDUCT

Equipment tested

Three GPS receivers were tested. The first is a three-channel receiver that must sequence measurements to get a complete fix. The second receiver is a twelve channel receiver which tracks satellites in parallel. The third receiver is a three-channel, handheld receiver.

All receivers use a start-up satellite selection algorithm which assumes that the user has not moved significantly from the last recorded position. All receivers have real-time clocks that keep time when the receiver is off. And all receivers maintain an almanac in memory. These are common characteristics of a majority of GPS receivers including low-cost receivers.

Manual Test Method

The test method used is similar to that described for Initialized Time to First Fix (INIT TTFF) in the 5 July 1995 version of the test standards document [Reference 2]. The INIT TTFF procedure requires that the receiver must not contain current ephemeris data, that the receiver have time to within 5 minutes of truth and position within 15 kilometers horizontal and 1 kilometer vertical. For 2D operation, vertical must be within 50 meters. The 2D requirement is discussed below.

In the manual test method, the Standard specifies that a minimum of 20 samples be collected. With some assumptions (Gaussian distribution, for example), the

mean can be computed with a 95% confidence level. For 20 samples, we can be 95% confident that the mean is within the sample average plus/minus 0.438 times the sample deviation. (Note: the specific value for the confidence interval is subject to revision.) The difficulty with the manual test method is that it requires at least six hours between samples to guarantee that the ephemerides are old. Also, the manual method would lead to a small number of points. With a small number of points, computations of the standard deviation can be significantly distorted by outliers.

Automatic Testing

The Standard allows for automatic testing to facilitate the gathering of a large sample size. For this exercise, we created a program that collects the ephemeris data from the receiver and modifies the recent ephemerides so that the receiver believes that the ephemerides are not current. When the modified ephemerides are loaded into the receiver, a reset command is sent. The reset command is equivalent to a power on. The receiver, recognizing that the stored ephemeris is old, will then collect the ephemeris prior to using the satellite in a position fix.

The data collection program uses the time provided by the receiver to time the position fix events. For the receivers tested, a time message is output within about one second of turn-on (or reset). This starts the data collection timing.

The receiver was allowed to collect either 2D or 3D fixes with PDOP up to 12. The data collection program, however, established events at 2D with a PDOP between 6 and 12; 2D with a PDOP less than 6; 3D with a PDOP between 6 and 12; and 3D with a PDOP less than 6. A receiver did not have to go through each of these events. It could jump straight to the good PDOP, 3D position fix. The "Best TTFF" reported in the following is the earliest time of any of the events

Comments about 2D

The Standard has a tighter requirement for knowledge of altitude for a 2D fix (50 meters versus 1 kilometer). This difference is related to the requirement that a horizontal position be within 300 meters for a navigation data point to be considered valid. GPS is a three-dimensional system. When operating in 2D mode, the user provides an altitude. This is equivalent to providing an additional satellite measurement. An error in the altitude will show up in the horizontal position. It's possible for a one meter altitude error to cause more than one meter of

horizontal error. Thus, if the receiver had an altitude error of one kilometer, the horizontal position in 2D mode could easily be off by more than 300 meters. Yet this is not the fault of the receiver. Hence, the test Standard requires a 50 meter accuracy in altitude.

Because of the impact of an input altitude error on horizontal position accuracy, one might disallow the use of 2D fixes. The Working Group decided, however, that when a user evaluates TTFF, she is more concerned with obtaining a reasonable fix within the shortest time. Hence a TTFF may be quoted based on the provision of a 2D or 3D fix.

TEST RESULTS

Receiver #1

Receiver #1 is a six channel receiver using older acquisition algorithms. Although the receiver has the capability to use overdetermined solutions, it was commanded to use a "Best Four" solution method. This selects the four satellites that provide the lowest PDOP. The receiver will track up to eight satellites by tracking either six in parallel or five in parallel while sequencing the sixth, seventh and eighth satellites on one channel.

Figure 3 displays the TTFF for Receiver #1 in order of the data collection. There were 209 data points collected during the 497 minute data collection period. The average TTFF was 40.28 seconds and the sample standard deviation was 7.65 seconds. TTFFs ranged from 24.64 seconds to 80.14 seconds.

Receiver #2

Receiver #2 is a 12-channel receiver using newer acquisition algorithms. It was commanded to use overdetermined solutions. The use of the overdetermined method will yield lower PDOPs thus allowing the receiver to skip into the 3D, good PDOP event more quickly than with the Best Four method.

Figure 4 displays the TTFF for Receiver #2 in order of the data collection. There were 509 data points collected during the 553 minute data collection period. The average TTFF was 27.31 seconds and the sample standard deviation was 5.96 seconds. TTFFs ranged from 23.25 seconds to 43.25 seconds. This receiver always reached a 3D position fix with a PDOP less than 6 without going through any intermediate position events. The minimum TTFF of 23.25 seconds is close to the

minimum of 21 seconds as described by Van Dierendonck.

Receiver #3

Receiver #3 is a three channel receiver. Although this particular receiver has the capability for overdetermined solutions, the receiver was placed in a Best Four mode to demonstrate the performance that one might expect from lower end handheld receivers. The results clearly identify the receiver as having the slowest TTFF.

Figure 5 displays the TTFF for Receiver #3 in order of the data collection. There were 333 data points collected during the data collection period. The average TTFF was 75.47 seconds and the sample standard deviation was 12.39 seconds. TTFFs ranged from 52.81 seconds to 122.75 seconds.

Summary

The following tables summarize the INIT TTFF performance of the three receivers. The "95% Confidence Mean" row is the range of values within which the population mean is expected to be, with 95% confidence. The "Computed 95%-ile" row is computed by taking the high side of the 95% confidence level mean plus 1.645 times the standard deviation. The 1.645 value represents the number of standard deviations where the upper tail has 5% of the points, assuming a Normal distribution. The "Sample 95%-ile" is the actual 95% point of the samples. Ideally, the "Sample 95%-ile" will be larger than the "Computed 95%-ile" by an amount equal to the confidence interval for the mean. As a matter of interest, the value given in the *GPS World* [Reference 3] survey is also shown.

Table 3 summarizes the results of the first fix, whether 2D or 3D and with a PDOP less than 12. Table 4 requires that the receiver achieve a 3D fix with a PDOP less than 6. The presence of a few long TTFFs for Receiver #1 distorted the computed statistics such that the computed 95%-ile value is significantly different than the actual 95% point. The Test Standards Working Group discussed various ways to handle outliers at its 12 September 1995 meeting. No final decision has been made.

Table 3
INIT TTFF
2D/3D, PDOP<12

	Receiver #1	Receiver #2	Receiver #3
Sample Average	40.28	27.31	75.47
Sample Deviation	7.65	5.96	12.39
Minimum	24.64	23.25	52.81
Maximum	80.14	43.25	122.75
Number of Samples	209	509	333
95% Confidence Mean	40.28±1.04	27.31±0.52	75.47±1.33
Computed 95%-ile	53.89	37.63	97.19
Sample 95%-ile	45.19	42.25	99.22
GPS World quote	1 minute	1 minute	<2 minutes

Note: Units are in seconds.

Table 4
INIT TTFF
3D, PDOP<6

	Receiver #1	Receiver #2	Receiver #3
Sample Average	73.37	27.31	104.94
Sample Deviation	63.75	5.96	38.94
Minimum	24.64	23.25	59.72
Maximum	679.64	43.25	344.66
Number of Samples	209	509	333
95% Confidence Mean	73.37±8.64	27.31±0.52	104.94±4.183
Computed 95%-ile	186.89	37.63	173.19
Sample 95%-ile	76.42	42.25	163.73
GPS World quote	1 minute	1 minute	<2 minutes

Note: Units are in seconds.

RECOMMENDATIONS

As a result of on-going Working Group efforts and the tests conducted for this paper, we offer the following recommendations:

- Manufacturers should use the terminology of INIT TTFF, WARM TTFF or REAQ;
- Use of TTFF without a qualifier is equivalent to INIT TTFF;
- Automated testing is strongly recommended in order to obtain a large sample size; and
- For data sheets, manufacturers should provide computed 95%-ile values when the sample size is small and actual 95%-ile values when the sample size is large.

The current draft version of ION STD 101 does not precisely match these recommendations. In a review of the Standard on 12 September 1995, the reporting table was modified to include the actual sample size. With this modification, there is sufficient data in the table for the evaluator to create confidence levels as required. The Test Standards Working Group is actively soliciting comments to the Standard.

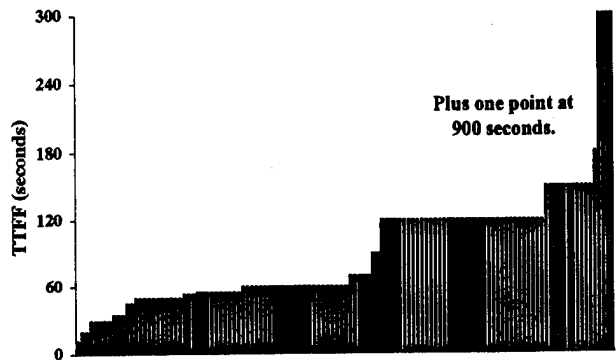
CONCLUSIONS

Any attempt at establishing standards must achieve a balance among good use of the language, applicability to many users and situations, complete test guidelines (although the words "complete" and "guidelines" may be conflicting) and a relatively simple presentation of the results. Time to First Fix fits these criteria. Every user must undergo TTFF. The test guidelines given in the Standard and those utilized by the tests described here are sufficient to provide data so that a meaningful value can be attached to INIT TTFF.

Although the Standard provides guidelines for manual testing, the testing can usually be automated so that a much larger sample size can be provided. If TTFF (or any performance characteristic) is especially important to a particular user, then that user would have to seek more detailed data from the manufacturers or would have to create his or her own set of test conditions. Our tests show that TTFF should be expected to vary from about 30 seconds for a high performance, multi-channel receiver to 2 minutes for receivers with less than four channels.

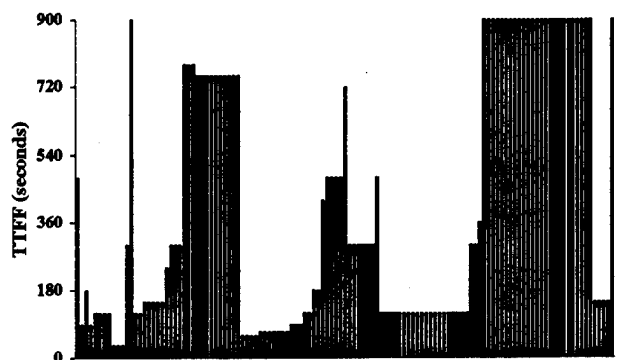
REFERENCES

1. 1992 Federal Radionavigation Plan, Published by Dept. of Transportation and Dept. of Defense, January 1993.
2. ION STD 101, GPS Test Standards, Preliminary Draft Version, 5 July 1995.
3. 1995 GPS World Receiver Survey, GPS World, January 1995, Volume 6, Number 1, pp 46-67.
4. Teasley, Stewart P. and Darwin G. Abby, "Initial Report of Activities of the GPS Test Standardization Working Group," Proceedings of ION GPS-94, Institute of Navigation GPS-94, September 20-23, 1994, pp 799-804.
5. Van Dierendonck, A.J., "Innovation: Understanding GPS Receiver Technology - A Tutorial, GPS World, January 1995, volume 6, number 1, pp34-44.



Source: GPS World, Jan. 1995

Figure 1
Warm Start TTFFs



Source: GPS World, Jan. 1995

Figure 2
Cold Start TTFFs

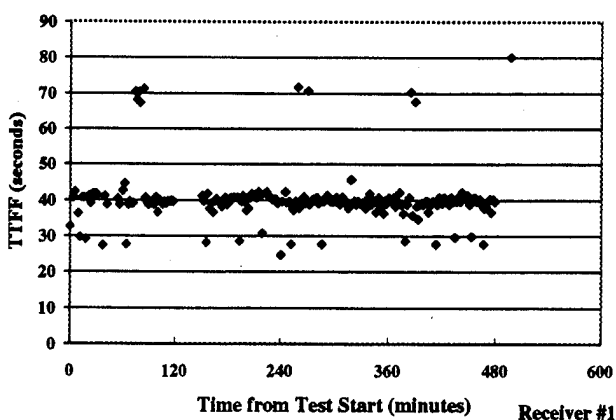


Figure 3
Receiver #1 INIT TTFF (2D/3D, PDOP<12)

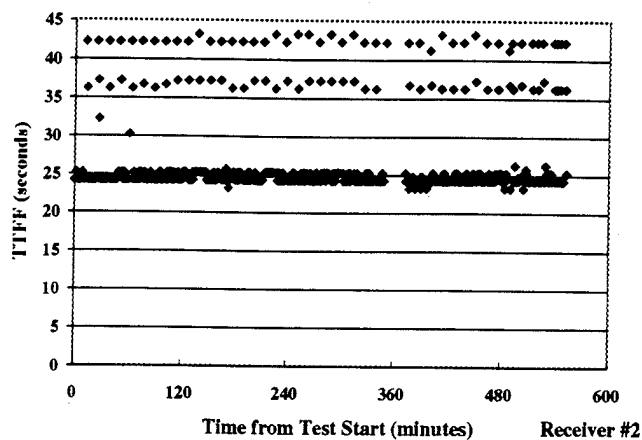


Figure 4
Receiver #2 INIT TTFF (2D/3D, PDOP<12)

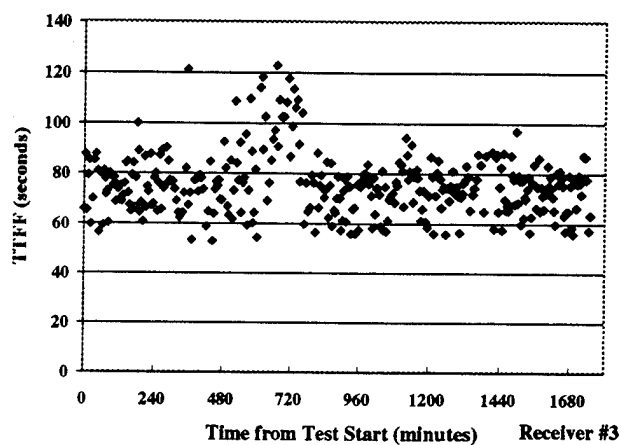


Figure 5
Receiver #3 INIT TTFF (2D/3D, PDOP<12)

Carrier Phase GPS Time, Space, Position Information Demonstration (CAPTIDE)

Gregg Costable
Elgin AFB

BIOGRAPHY

Gregg Costabile began his career as an Aerospace Test Engineer at Eglin AFB, FL in 1985. While completing his Masters of Engineering degree from the University of Florida in 1992, he became the lead test and integration engineer on the Operational Concept Demonstration, the first INS/GPS guided weapon dropped from an aircraft. In June, 1994 the 46th Test Wing appointed him Test Program Manager for the Exploitation of Differential GPS for Guidance Enhancement (EDGE) program.

ABSTRACT

This paper presents a discussion and results of a flight test to obtain Time, Space, Position Information (TSPI) using carrier phase (or kinematic) GPS. A carrier phase capable GPS receiver was installed on board an F-16 aircraft and flown in conjunction with an INS/differential GPS guided weapon test program. The carrier phase TSPI data was compared to the position solution from existing test range TSPI sources, including: four high-dynamic Contraves cinetheodilites operated at 30 frames per second, two FPS-16 radars, the aircraft position system solution, an INS/GPS position measurement pod on board the aircraft, and a post-mission Kalman smoother based software algorithm called "test data optimal processor". The carrier phase and test range solutions were also compared to the INS/DGPS test items. A series of aircraft maneuvers were conducted to collect truth data to compare the carrier phase GPS position with the "truth" position. This was the first experiment known to the authors which utilized the carrier phase observable in an aircraft environment where high accuracy TSPI was available to evaluate the accuracy of the carrier phase technology.

INTRODUCTION

When determining the accuracy performance of any item under test, an analyst desires truth source accuracy an order of magnitude better than the test item to assess its performance. Determining the accuracy of

navigational systems operating in a dynamic environment is becoming more difficult as technology evolves. Current inertial navigation / differential GPS systems are capable of navigating to within one meter of an intended position. A scoring system capable of determining position to within 10 centimeters is therefore required to quantify such a test item's navigational performance. This presents significant challenges for current scoring systems.

To quantify the accuracy of a carrier phase GPS system, truth accuracies an order of magnitude better than the carrier phase system are required. Overall carrier phase position accuracy is on the order of 1 to 4 centimeters¹. This means a truth source capable of determining position to within 1 and 4 millimeters is required to quantify carrier phase position accuracies in high-dynamic applications. Imagine tracking a point on a high performance aircraft performing a high-g turn, or even an airliner on final approach to within 1 and 4 millimeters! Clearly we have approached the state of the art in position determination using existing technologies. The best the CAPTIDE test could hope to do was qualify carrier phase performance to conclude such a system was at least as good as existing position determination technologies. This was the goal of the CAPTIDE program.

BACKGROUND

The Carrier Phase GPS TSPI Demonstration (CAPTIDE) was conducted under the auspices of the Exploitation of Differential GPS for Guidance Enhancement (EDGE) program². As a result, CAPTIDE was not permitted to influence the test method or schedule of EDGE. Aircraft maneuvers or data collection efforts specific to evaluating CAPTIDE were not possible.

The EDGE test program at Eglin AFB, FL provided the means to assess the performance of a carrier phase GPS system employed in a dynamic environment. The EDGE weapon was an inertially guided, differential GPS (INS/DGPS) aided weapon which was employed from an

F-16, Block 50D aircraft. The expected accuracy for this weapon system was between one and three meters. Time-Space-Position Information (TSPI) resources were used on the EDGE program to measure the test item's position accuracy. These resources included four Contraves cinetheodilite cameras, two FPS-16 radars, aircraft INS and aircraft system position solutions, and INS/DGPS TSPI pods which were carried on aircraft stations 2 and 8 (see figure 1). On one of the test missions (captive carry 4), data collected from the four cinetheodilite cameras, two FPS-16 radars, and the aircraft system solution were processed by a Kalman smoother software algorithm called the test data optimal processor (TDOP). The TDOP TSPI solution was the most accurate TSPI solution available at Eglin AFB. Its accuracy was quoted to be between one and three feet³ and was better than any of the TSPI solutions (cinetheodilites, FPS-16 radar, etc.) used independently.

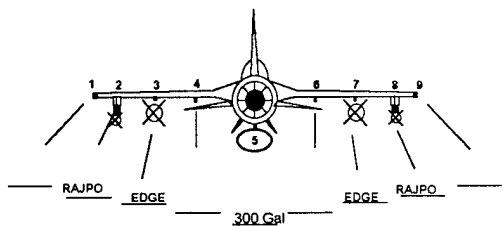


Figure 1 - F-16 Aircraft External Stores Configuration

After successful integration of the system into the F-16 aircraft, the CAPTIDE system was flown on six subsequent EDGE captive carry flight test missions. These captive carry missions were test sorties which did not release the EDGE test item from the aircraft, but were specifically designed to evaluate weapon system performance and function prior to the drop missions. Data analysis efforts for CAPTIDE were focused on three of the six captive carry missions.

TEST ITEM DESCRIPTION

The CAPTIDE system consisted of the carrier F-16 aircraft, an Ashtec Z-12 GPS receiver with 6 megabytes of extended memory with associated antenna, preamp, and cabling, a laptop PC to communicate with the receiver under an autonomous power source and to extract data post-mission, and an Ashtec Z-12 ground reference receiver with associated cabling, power source, and antenna located directly over a surveyed location. The receiver occupied 385 cubic inches of volume and required 800 milliamps of 28 volt dc power.

The CAPTIDE data reduction software consisted of an off-the-shelf Ashtec product, Precise Differential GPS Navigation (PNAV), and various MATLAB routines written by EDGE personnel. The PNAV software was used to resolve the carrier phase integer ambiguities and provided the carrier phase solution. Default PNAV filter values were used for all carrier phase data reduction; forward and backward data smoothing was used for all data reduction.

Carrier Aircraft

The test aircraft used for this program was an F-16D, Block 50 aircraft with block 50D avionics. The carrier phase receiver was installed in the ammo bay just aft of the cockpit. The 30 millimeter gun and ammunition barrel were removed to provide adequate space for test instrumentation. F-16 flight test vibration data were analyzed to choose the most suitable location for the commercial receiver hardware. This commercially available receiver was intended for ground use and not specifically designed for an airborne environment. The ammo bay area was chosen because it provided lower vibration levels throughout most of the aircraft's flight regime with respect to any other suitable location on the aircraft. Additionally, the receiver was mounted in a fixture which in turn was shock mounted to the aircraft fuselage. A bracket mounted on the fixture provided stress relief for the power and communications cabling. A cable was run from the receiver to an access panel under the left leading edge wing strake. This arrangement provided a convenient method to insure the system was functioning properly prior to takeoff, and to extract data after the aircraft landed. A laptop PC was used to interface with the receiver via an RS-232 connector at the access panel. The receiver's antenna was mounted on the turtle deck directly above the ammo bay and directly behind the aircraft canopy.

TEST METHODOLOGY, ANALYSIS, AND RESULTS

The following data analysis methodology was used to assess the performance and accuracy of CAPTIDE. The reported filter values from the CAPTIDE system were qualified via the truth data (TDOP) generated on the fourth captive carry mission. From this baseline, confidence was gained in the CAPTIDE receiver values. CAPTIDE data from the first captive carry mission were used to evaluate the system in a high-dynamic environment. This evaluation investigated filter settling times after the receiver was shielded from the GPS satellite vehicles by the host aircraft (during rolls and wind-up turns), and investigated system performance at extended reference receiver / test receiver baseline

separations. Captive carry six generated the data to evaluate the system in a medium dynamic environment and showed the utility of carrier phase GPS for this particular application. The flight profiles and test resources for these missions provided the data to qualify the performance of the carrier phase GPS system for TSPI applications. Data from the INS/DGPS TSPI pods were not of sufficient accuracy to qualify carrier phase GPS performance.

Captive Carry 1 (CC1)

EDGE captive carry 1 (CC1) was a limited compatibility flight profile mission designed to demonstrate the flight-worthiness of the EDGE weapon system hardware. The test points executed on this test mission are shown in Table 1.

POINT	ALT (ft)	MACH	REMARKS
1	15 K	0.80	3g WUT*, WLSS**, 0g Pushover, 2g L&R 180 deg rolls
2	15 K	0.80	4g WUT, WLSS, - .5g Pushover, 2.5g L&R 180 deg rolls
3	5 K	0.85	Same as Point 2
4	9 K	0.95	Same as Point 2
5	< 1 K	0.90	Speed Soak, 30 minutes

Table 1 - Captive Carry 1 Test Points

* WUT - Wind up turn

** WLSS - Wings level side-slip

This mission was conducted to insure EDGE test item structural and electrical integrity throughout the expected test program flight envelope. The results showed both EDGE weapons and the CAPTIDE system maintained structural and electrical integrity. However, the CAPTIDE receiver's circuit breaker tripped prior to takeoff on all test missions after captive carry six. Subsequently, CAPTIDE data were available for six missions only.

The TDOP position solution was not generated for the first test mission. The aircraft flew over the W151 test range located south of Eglin AFB over the Gulf of Mexico. Filter sigmas, phase residulas, and chi-squared values generated in the receiver were used to investigate

the navigation solution quality of the carrier phase system.

The baseline separation of the receiver on board the aircraft and the reference receiver was 30 to 100 statute miles (26 to 87 nautical miles) for most of the compatibility flight (top plot, Figure 2). Notice just before the 79,000 second time epoch the CAPTIDE radial sigma was less than 2 feet for baseline separation distances approaching 100 miles. The aircraft began a series of roll maneuvers just after the 79,000 time epoch (Figure 3); the receiver lost lock and the radial sigmas increased significantly. The latter segment of figure 2 reveals that separation distances less than 20 miles produced filter sigmas to less than one foot.

The receiver manufacturer recommends baseline separation distances be kept to less than 10km to maintain carrier phase level accuracies. Since no submeter (level of accuracy), independent TSPI resource was available at 30-100 mile baseline sparations, the reported radial sigma values could not be qualified (see conclusions). The sudden decrease in the radial sigma value just after the 82,000 time epoch was a result of the post-mission data processing software fixing the carrier phase integer ambiguities for about three minutes.

The use of dual frequency receivers, to allow for measurement and compensation for ionospheric delays, and the incorporation of higher order terms in the double difference algorithm baseline estimation to account for geometric errors, should allow a carrier phase based scoring system to achieve < 1 foot accuracy at the baseline distances experienced during CC1⁴.

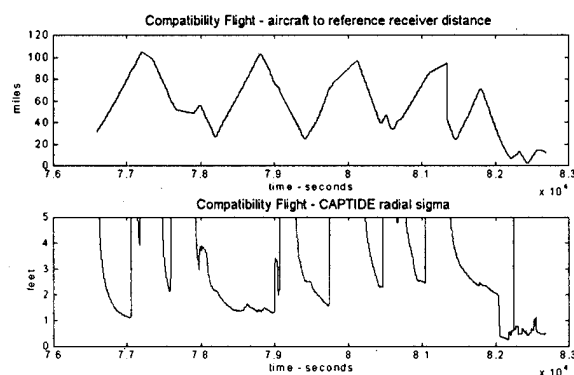


Figure 2 - Compatibility Flight - CAPTIDE separation distance and sigma vs time

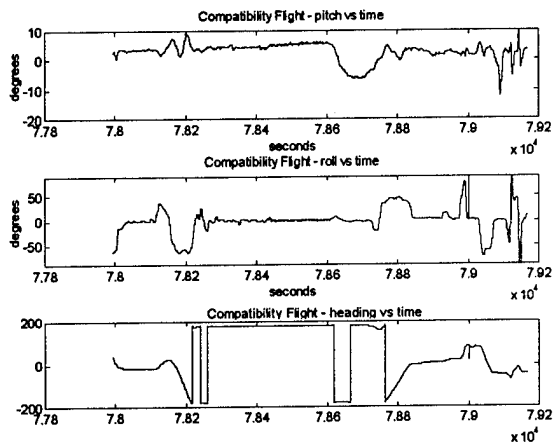


Figure 3 - Compatibility Flight - Aircraft Pitch, Roll, and Heading vs time

Figure 3 is the pitch, roll, and heading dynamics for the aircraft during selected portions of the compatibility flight. Examination of Figure 3, in conjunction with the bottom plot of Figure 2, illustrate the effect of dynamics on the carrier phase solution. The pilot performed a wind-up turn and a 180 degree loaded roll just after the 79,000 time epoch (see the roll and pitch channels of Figure 3). The receiver lost lock at this time due to the aircraft shielding the CAPTIDE antenna from appropriate GPS satellite vehicles. The corresponding time in Figure 2 gives an indication of CAPTIDE filter settling time after the maneuver was completed. The other discontinuities in Figure 2 indicate loaded rolls or wind-up turns and provide additional insight into CAPTIDE filter settling times.

Captive Carry 4 (CC4)

The objective of the fourth captive carry (CC4) mission was to quantify the accuracy of the EDGE weapon system by collecting the most accurate possible TSPI data available from range truth resources (the TDOP solution) and comparing that data with the weapon's navigation solution. Additionally, the TDOP data and the test item data were used to assess the performance of the CAPTIDE system in a low dynamic environment. Twenty-five passes were accomplished. Data reduction and analysis showed twenty passes yielded useful data. The flight path geometry was chosen to optimize the accuracy of the TDOP solution. The test aircraft flew each pass between 260 and 325 knots indicated airspeed (KIAS), straight and level, at approximately 7,000 feet above ground level (AGL).

The aircraft flew a right turn, oval "racetrack" pattern during CC4. Bank angles in the turns were limited to 30 degrees to prevent the CAPTIDE receiver from losing lock on any GPS satellite vehicle. This maneuver

limitation was acceptable to the EDGE test program. A typical CC4 data run is illustrated by Figure 4, which is typical of all runs. The aircraft flew over Eglin test range B70⁵ on a 237 degree heading. The top plot of Figure 4 shows the locations of the Contraves cinetheodolite camera sites (B-141, B-120A, etc.) with respect to the aircraft ground track. The separation distance between adjacent camera sites was about two miles. The bottom plot shows a typical altitude profile. The baseline separation between the ground reference receiver and the aircraft never exceeded 25 miles during this mission.

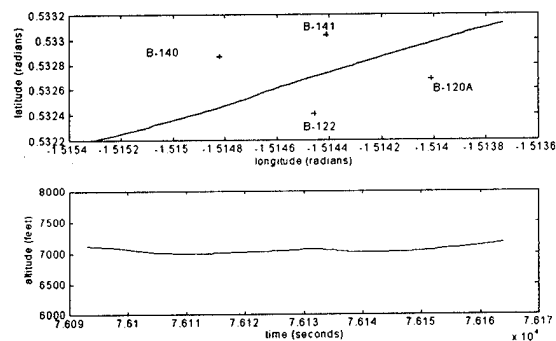


Figure 4: CC4 pass 14 - Ground Track / Altitude vs time

Figure 5 is a comparison of the TDOP and CAPTIDE north, east, and altitude position differences for pass 1. This data is typical of all passes. The upper plot in Figure 5 indicates close agreement in the latitude measurement between TDOP and CAPTIDE. The middle plot shows a periodic oscillation between TDOP and CAPTIDE in the longitude measurement, which is discussed below. The bottom plot shows a bias in the altitude measurement between TDOP and CAPTIDE. The altitude bias changed rather significantly between passes (see Table 2). Based on the collected data, the source of the altitude bias was not conclusively determined.

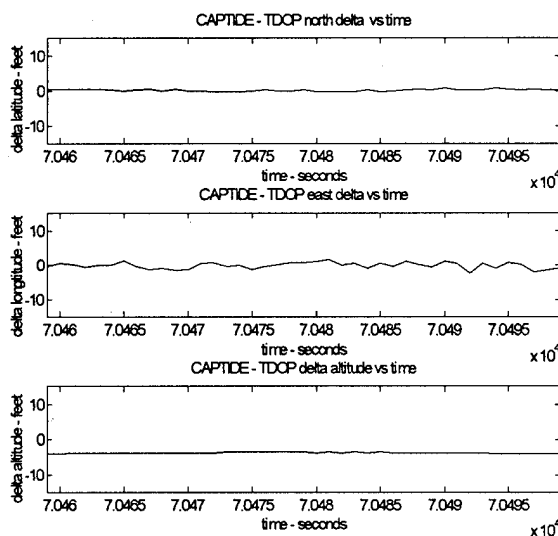


Figure 5 - CC4 TDOP/CAPTIDE Position Differences (pass 1)

Table 2 contains the average position differences between the TDOP and CAPTIDE position solutions for each pass that yielded valid data. The average north position differences were as expected but the variation in east position differences, and the magnitude of the differences in altitude required additional analysis.

Pass #	North	East	Altitude	Radial
1	0.237	-0.177	-3.824	3.836
2	0.107	-0.631	-2.476	2.557
4	0.232	-0.915	-3.607	3.729
6	0.112	-0.925	-3.677	3.793
7	-0.180	-0.968	-3.667	3.797
8	0.422	-0.277	-1.715	1.787
9	-2.790	-0.026	-9.008	9.431
10	-2.350	0.284	-10.060	10.335
14	-0.603	-2.386	-8.664	9.007
15	-0.115	-3.073	-8.534	9.071
16	0.180	-3.594	-8.164	8.922
17	0.441	-0.581	-4.771	4.826
18	0.665	0.085	-4.805	4.852
19	0.226	-0.498	-4.675	4.707
20	0.384	-0.539	-4.125	4.178
21	0.473	-0.601	-4.401	4.467
22	0.340	-0.466	-4.310	4.348
23	0.885	-0.691	-4.339	4.482
24	0.114	-0.893	-4.254	4.348

25	0.045	-0.835	-3.498	3.596
Avg.	-0.059	-0.885	-5.129	5.304

Table 2 - CC4 TDOP/CAPTIDE Average Position Differences (ft)

Figure 6 further illustrates the discrepancy between the TDOP and CAPTIDE longitude measurements. The upper plot in Figure 6 shows the difference in position (in feet) between successive CAPTIDE measurements and the corresponding TDOP measurements. CAPTIDE data was available at a 1 Hz data rate, TDOP was available at 25 Hz. The middle and bottom plots are the first difference in east position ($x[t] - x[t-1]$) for CAPTIDE and TDOP respectively. Notice at time 70491 the top plot indicates agreement between CAPTIDE and TDOP. At the next time epoch, CAPTIDE (middle plot) senses that the magnitude of the first difference in east position changes by about 2 feet. TDOP (bottom plot) does not sense this change and as indicated by the top plot the solutions disagree by about 2 feet. At the next epoch, 70493, TDOP "catches up" and compensates for changes at both epochs, and as indicated by the upper plot the solutions are in close agreement. The data in Figure 6 is typical of all the data generated during CC4.

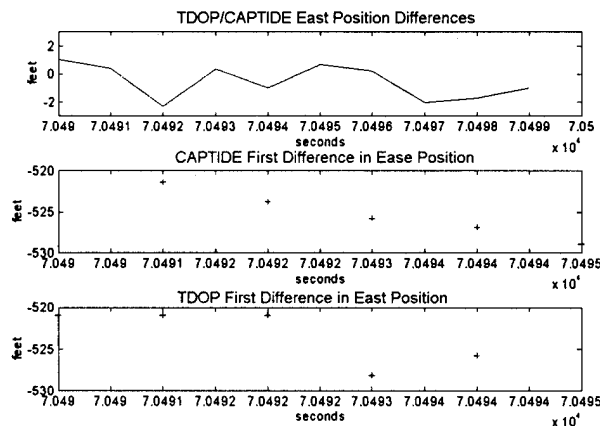


Figure 6 - CC4 pass 1 TDOP/CAPTIDE east position differences / CAPTIDE east 1st difference / TDOP east 1st Difference

Figure 7 illustrates the separation distance, the radial sigma, and the Kalman flag values for pass nine. Notice the radial sigmas reported by the receiver (middle plot) were between .1 and .3 feet for this pass; this was typical data for all passes. The Kalman flag indicated if the receiver solution fixed integer ambiguities. A value of zero indicated an integer-free solution, a value of one indicated an integer-free solution.

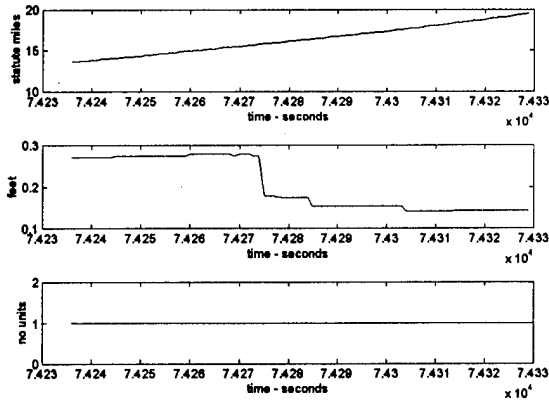


Figure 7 - CC4 Pass 9 - Baseline separation (top plot), Radial sigma (middle plot), and Kalman flag (bottom plot) Vs time

A statistical analysis was conducted on the data to further qualify the CC4 CAPTIDE performance and show biases between TDOP and CAPTIDE. The difference between the CAPTIDE and TDOP position for each data point was determined (for north, east, and altitude). From this data, circular error probable (CEP), CEP RMS, spherical error probable (SEP), and SEP RMS were computed. The CEP shows the 50% data circle centered on the mean of the data set, which in this case is the North-East position deltas between TDOP and CAPTIDE. That is, on the average, 50% of all the data will lie within this circle. The radius of this circle is an indication of randomness in the data set. The CEP RMS is a statistical representation of the data set about the origin, not the mean. The CEP RMS plot is also a 50% circle. That is, on the average, 50% of the data lies within this circle. CEP combined with CEP RMS gives an indication of the biases in the systems. If the system had no biases, the mean of the data set would be zero, and the CEP and CEP RMS circles would be identical. If a system bias exists, then the difference in the CEP and CEP RMS numbers give an indication of the bias. Figure 8 shows the difference in CAPTIDE and TDOP north-east position for the entire CC4 data set and depicts the total CEP and CEP RMS probability circles. The radius of this CEP circle was 1.44 feet with the origin located at -.929 feet east, -.119 feet north. The radius of the CEP RMS circle is 1.61 feet (origin at 0 feet east, 0 feet north). These values, as well as the SEP values, are reflected in the Table 3 totals.

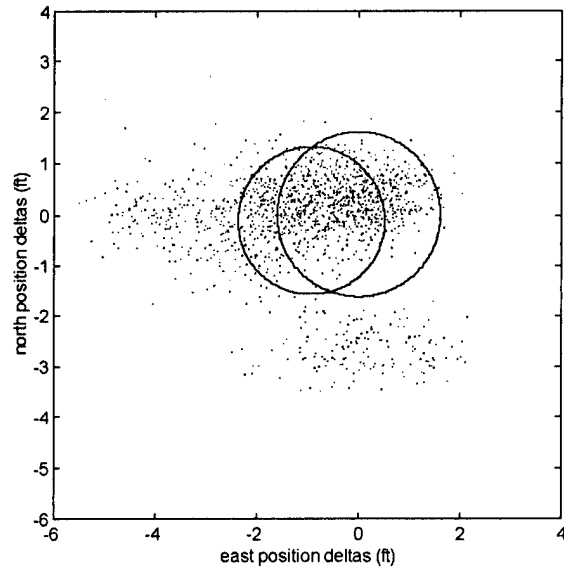


Figure 8 : Total CEP/CEP RMS Statistics

SEP and SEP RMS are similar to CEP and CEP RMS, but include the altitude channel as well. Table 3 contains the circular error probable (CEP) and spherical error probable (SEP) statistics for each of the valid CC4 data passes as well as the total for all data points.

Pass #	CEP	SEP	CEP RMS	SEP RMS
1	0.726	0.713	0.784	2.644
2	0.707	0.750	0.841	2.008
4	0.928	0.999	1.148	2.858
6	0.804	0.900	1.035	2.796
7	0.834	0.883	1.079	2.825
8	0.896	0.871	1.011	1.764
9	0.853	0.868	2.278	6.601
10	0.761	0.748	1.994	6.893
14	0.834	0.818	1.948	6.138
15	0.857	0.846	2.126	6.225
16	0.710	0.691	2.414	6.286
17	1.044	1.099	1.215	3.510
18	0.798	0.773	0.996	3.331
19	1.070	1.133	1.152	3.407
20	0.884	0.953	1.038	3.026
21	0.743	0.906	0.988	3.131
22	0.886	1.009	1.014	3.104
23	0.635	0.649	1.174	3.247
24	1.018	1.182	1.212	3.255
25	1.060	1.200	1.229	2.884
Total	1.442	2.450	1.607	4.292

Table 3 - CC4 TDOP/CAPTIDE Statistics (ft)

Captive Carry 6 (CC6)

The sixth EDGE captive carry mission (CC6) was designed to evaluate the guidance function and assess overall system performance of the EDGE test item. The aircraft flew trajectories on this mission which mimicked the EDGE weapon flight path of an actual weapon free-flight. The weapon impact angle terminal constraint dictated the weapon trajectory. Three different flight profiles were accomplished on this test flight as shown in Table 4.

POINT	ALT (ft)	MACH	REMARKS
1	30 K	0.80	88,000' simulated release, 14 deg at 5.92 nm, 46 deg at 2.30 nm, 15K' target altitude
2	25K	0.80	88,000' simulated release, 14 deg at 8.4 nm, 35 deg at 3.1 nm, 8K' target altitude
3	20 K	0.80	88,000' simulated release, 30 deg at 8.4 nm, then shallow out dive to pass over target at 10 deg, 5K' target altitude

Table 4 - Captive Carry 6 Flight Profiles

The first point was accomplished twice, the second point three times, and the fourth point four times. The first two points were designed to simulate a horizontal attack, or an attack against a bunker type target. For instance, on the first test point the aircraft ingressed at 30,000 feet altitude and 0.80 Mach. At 88,000 feet downrange from the target the EDGE weapon was (simulated) launched, the weapon acquired GPS satellites and began navigating without influence from the host aircraft. At 5.9 nautical miles downrange from the target, the host aircraft pitched over to 14 degrees nose low. At 2.3 nautical miles downrange from the target the host aircraft pitched over to 46 degrees nose low. The pilot then attempted to fly directly "through" the target located at 15,000 feet altitude, which was directly over an actual target on the ground. Similar actions were accomplished on points two and three.

Figure 9 illustrates typical dynamics encountered during this flight in the pitch, roll, and heading axes.

CC6 provided an excellent opportunity to ascertain CAPTIDE performance under the dynamics expected for INS/GPS weapons.

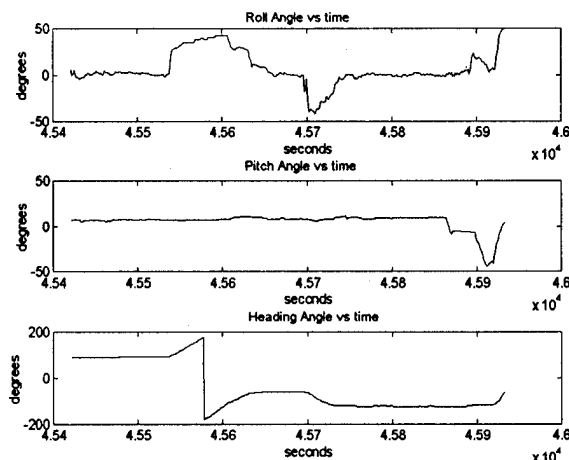


Figure 9 : CC6 pass 1 - Roll, pitch, and heading Vs time

As in the compatibility flight, TDOP data was not generated for comparison with CAPTIDE; therefore, the filter's radial sigma value is presented as an indication of CAPTIDE performance.

Figure 10 presents the radial sigmas and number of tracked satellites for a typical CC6 pass. Comparison of the CC6 (Figure 10, top plot) and CC4 (Figure 7, middle plot) radial sigma values indicates the uncertainty in the radial sigma value is higher for CC6 than it was for CC4. The aircraft banked up to and beyond 60 degrees a number of times during this mission, which resulted in loss of satellite track. The carrier phase integer ambiguities were not fixed at any point during CC6. This is likely the cause of the higher radial sigma values reported in CC6 with respect to CC4.

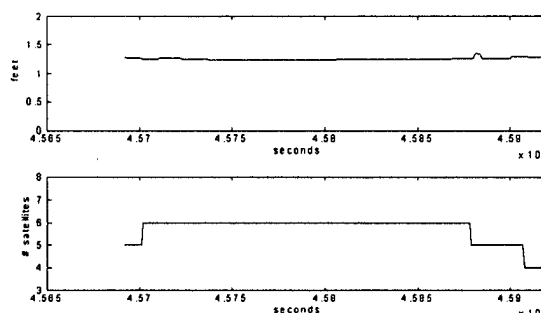


Figure 10 : CC6 pass 1 - Radial sigma (top plot), Number of satellites (bottom plot) Vs time

The position data from the CAPTIDE system helped to uncover a navigational issue in the EDGE test item. Comparison of CAPTIDE and EDGE position solutions helped to reveal a discrepancy in the EDGE navigation solution.

CONCLUSIONS AND RECOMMENDATIONS

The reported radial sigmas in CC1 at long baseline separation ranges could not be qualified. Truth source data of sufficient accuracy was not available to allow a reasonable assessment of the carrier phase position solution. Review of the receiver's filter sigmas and phase residuals, comparison with the available INS/DGPS TSPI pod information, and comparison with the EDGE test item showed the carrier phase solution was not completely erroneous; it agreed with the other navigation sources to within 5 meters. The test aircraft returned to the same location it left; the carrier phase solution showed this was the case. A more specific and controlled experiment is required to better qualify carrier phase performance at baseline separations greater than 15 miles.

CAPTIDE appeared to provide data as good as TDOP in the horizontal (north-east) plane. However, the vertical plane contained unresolved biases. If these vertical biases can be resolved, it appears a CAPTIDE type system can provide TDOP TSPI accuracy levels as long as the test item antenna can maintain line-of-sight to the GPS satellite vehicles.

CAPTIDE presented a viable and useful alternative to classical test range TSPI methods for this program. Position data from CAPTIDE was available within hours after the aircraft landed. The high accuracy TDOP data required the following processing: developed 17,000 feet of film, read each film frame with a data reader, processed the raw cinetheodilite data through a smoothing algorithm, integrated data from the cinetheodilites, FPS-16 radars, and aircraft to provide the final TDOP solution. This process, rushed, took 10 days. Data analysis and comparison of the CAPTIDE solution with other positioning instruments (EDGE weapons, TDOP, INS/DGPS TSPI pods, etc.) indicated the carrier phase data is of sufficient accuracy to score INS/DGPS type weapon systems. The cost of the carrier phase system for this type of application was also attractive.

The advantages of the CAPTIDE system included the following: fast data reduction time, accuracy, all weather capable, and it was not limited by the placement of range TSPI resources. The limitations of the CAPTIDE system included: requires power and space on board the test item, not currently suitable for aircraft control and

vectoring purposes, and not currently suitable for flight safety purposes (flight termination system purposes).

REFERENCES

1. Guide to GPS Positioning, David Wells, Section 9.8, Carrier Phase Beat Ambiguity, Canadian GPS Associates, May 1987
2. AFDTC-TR-95-031, Exploitation of Differential GPS for Guidance Enhancement (EDGE) Test and Evaluation Report, August 1995
3. Freeman Mathematics Briefing, Aug 1994
4. Shi, J., Cannon, M.E.: "High Accuracy Airborne GPS Positioning: Testing, DataProcessing and Results", IEEE Position Location Navigation Symposium (PLANS), Las Vegas, NV, May 1994
5. AFDTC Technical Facilities, Vol II, Land Test Areas, December 1991

Authors:

Gregg Costabile
39 FTS / CAET
601 W. Choctawhatchee Ave., Suite 45
Eglin AFB, FL 32542-5720
E-Mail: COSTABIG@EGLIN.AF.MIL
Phone: (904) 882-2121
FAX: (904) 882-4700

Jesse R. Fowler
Sverdrup Technologies, Inc.

Timothy Elbert
Applied Systems Engineering Inc.
Phone (904) 729-7550

David Reiter III
Sverdrup Technologies, Inc.

The Effect of Tropospheric Propagation Delay Errors in Airborne GPS Precise Positioning

Virgílio Mendes, J. Paul Collins, and Richard Langley
University of New Brunswick

BIOGRAPHIES

Virgílio Mendes received his Diploma in Geographic Engineering from the Faculty of Sciences of the University of Lisbon, Portugal, in 1987. Since then, he has been working as a teaching assistant at this university. In 1990, he completed the Specialization Course in Hydrography at the Hydrographic Institute, Lisbon. In 1991, he enrolled as a Ph. D. student at the University of New Brunswick (UNB). He is involved in tropospheric delay modeling of radio signals and application of the Global Positioning System (GPS) to the monitoring of crustal deformation.

Paul Collins graduated from the University of East London in 1993 with a B.Sc. (Hons) in Surveying and Mapping Sciences. He is currently enrolled in the M.Sc.E. degree program in the Department of Geodesy and Geomatics Engineering at UNB, where he is investigating the effect of the troposphere on kinematic GPS positioning.

Richard Langley is a professor in the Department of Geodesy and Geomatics Engineering at the UNB, where he has been teaching since 1981. He has a B.Sc. in applied physics from the University of Waterloo and a Ph.D. in experimental space science from York University, Toronto. After obtaining his Ph.D., Dr. Langley spent two years with the Department of Earth and Planetary Sciences of the Massachusetts Institute of Technology where he carried out research involving lunar laser ranging and very long baseline interferometry.

Dr. Langley has worked extensively with GPS. He is a co-author of the best-selling Guide to GPS Positioning published by Canadian GPS Associates and is a columnist for GPS World magazine. He has helped develop and present a number of seminar courses on GPS for both Canadian GPS Associates and the American-based Navtech Seminars Inc. Dr. Langley has consulted extensively in the field of GPS with private companies and government agencies both in Canada and abroad.

ABSTRACT

When operating in an airborne environment, test results have shown that ambiguity resolution is particularly sensitive to errors in the tropospheric delay models applied to the carrier phase observations. Since the aircraft is at a higher altitude than the ground-based reference station, the model must accurately represent the relative tropospheric delay caused by the altitude difference. In kinematic applications, the zenith tropospheric delay can be determined with prediction models such as Saastamoinen's using pressure, temperature, and humidity measurements. This zenith delay is then mapped to other elevation angles using mapping functions such as those of Ifadis or Niell.

This paper highlights the performance of several widely used tropospheric delay models, including the model currently proposed for the FAA's WAAS. The accuracy of this model is assessed by (1) comparisons with ray tracing through an extensive set of radiosonde data, covering different latitudes, and (2) analyzing position solutions and the carrier phase observation residuals of GPS flight tests. We conclude that (1) the tropospheric delay error is mainly due to the inaccuracy of the zenith delay determination, and (2) a combination of a zenith delay model with the Niell or Ifadis mapping functions yields improved solutions, as compared to the currently proposed WAAS model.

INTRODUCTION

The need for accurate navigation with GPS lead to the implementation of various differential GPS (DGPS) techniques. In DGPS, corrections are broadcast to a user from a known reference station or stations, in order to eliminate or minimize different range measurement errors. Different implementations of DGPS techniques are mainly conditioned by the area over which the system is intended to cover. Local area differential GPS (LADGPS) and wide area differential GPS (WADGPS) are the two general categories under which most systems fall.

The Wide Area Augmentation System (WAAS), proposed by the Federal Aviation Administration (FAA), is perhaps the most important WADGPS currently planned. It is intended to provide GPS navigation for aircraft across North America and, eventually, worldwide. Recent literature (e.g. Shaw et al., [1995]) indicates that WAAS will be used for in-flight navigation and CAT-I precision approaches. Additionally, a supplemental LADGPS, possibly using carrier phase positioning, will eventually be used for CAT-II and CAT-III precision approaches. The system contract has recently been awarded with the intention of having WAAS fully operational by the year 2001 [Johns, 1995].

Actually WAAS is more than just a GPS differential correction service because of the planned employment of INMARSAT geostationary satellites to not only broadcast differential corrections, but also GPS-like signals on the L1 frequency and integrity data. This augmentation of GPS will help to provide improved positioning accuracy, availability, and integrity.

One important residual error source that will contribute to the overall error budget of WAAS is any mismodeling of the tropospheric delay experienced by the GPS signals propagating through the electrically-neutral atmosphere. In this paper, the accuracy of the proposed WAAS [DeCleene, 1995] tropospheric model is assessed.

TROPOSPHERIC DELAY

A radio signal traveling through the neutral atmosphere suffers a delay (mostly due to the lowest-most region of the atmosphere – the troposphere), which can be defined at the zenith (zenith tropospheric delay) as:

$$d_{\text{trop}}^z = \int_{r_s}^{r_a} [n(r) - 1] dr = 10^{-6} \int_{r_s}^{r_a} N dr,$$

where n is the refractive index, N is the refractivity, r_s is the station geocentric radius and r_a the radius of the top of the neutral atmosphere (for more details, see, for example, Mendes and Langley [1994]). The zenith tropospheric delay is usually divided into two components, designated as hydrostatic (or dry) and wet. The hydrostatic component of the zenith delay can be modeled very accurately provided good station pressure measurements are available. The wet component is spatially and temporally highly variable and poorly predicted by models (see Mendes and Langley [1995]).

The zenith delay can be related to the delay that the signal would experience at other elevation angles through the use of mapping functions. If the mapping functions are determined separately for the hydrostatic and the wet component, the tropospheric delay can be expressed as:

$$d_{\text{trop}} = d_h^z \cdot m_h(\epsilon) + d_w^z \cdot m_w(\epsilon),$$

where d_h^z is the zenith delay due to mostly dry gases, d_w^z is the zenith delay due to water vapor, m_h is the hydrostatic component mapping function, m_w is the wet component mapping function, and ϵ is the non-refracted elevation angle at the ground station. In the early years of space geodesy, the tropospheric delay models had no explicit separation of zenith delay and mapping function. We will designate such models as tropospheric delay models.

The number of available tropospheric delay models, zenith delay models and mapping functions is very large. The performance of fifteen mapping functions was assessed by Mendes and Langley [1994] and the impact on station coordinates of the use of these mapping functions was analyzed by Santerre et al. [1995]. The assessment of four of "the best" zenith wet delay models can be found in Mendes and Langley [1995]. Besides the WAAS tropospheric delay model, we have selected for comparison purposes: (1) two tropospheric delay models widely used in navigation applications, designated Altshuler [Altshuler and Kalaghan, 1974] and NATO [1993]; (2) the Ifadis [1986] global hydrostatic and wet mapping functions; (3) the Niell [1995] hydrostatic and wet mapping functions, also designated as NMF. The Ifadis and NMF mapping functions are both coupled with the Saastamoinen [1973] zenith hydrostatic delay model and the Ifadis [1986] global zenith wet delay model. For the sake of simplicity we hereafter will designate these combinations as Ifadis and NMF, unless stated otherwise.

Both the Altshuler model and the WAAS model, which is derived from Altshuler's [DeCleene, 1995] are driven by the station's height above sea level, station latitude, and day of year. The NATO model uses a reference value for the surface refractivity and the height above sea level for the determination of the zenith total delay. This delay is then mapped using the Chao [1972] dry mapping function. The NMF and Ifadis mapping functions represent different philosophies in modeling the elevation angle dependence of the tropospheric delay. The Ifadis mapping function is parameterized by pressure, temperature and water vapor pressure (both for the hydrostatic and wet mapping functions), whilst the NMF is parameterized by day of year, station latitude and station height (hydrostatic mapping function), and station latitude only (wet mapping function). Despite the different approaches, these mapping functions show comparable accuracy (see Mendes and Langley [1994]). The Saastamoinen zenith hydrostatic delay model is a function of the surface pressure, station height and latitude, and the Ifadis zenith wet delay model is a

function of pressure, temperature and water vapor pressure.

MODEL ASSESSMENT

For the accuracy assessment, we used ray-tracing results as benchmark values, for different sites (for details see Mendes and Langley [1994, 1995]). The results of this comparison are listed in Tables 1 and 2. In general, NMF and Ifadis show a low bias, as compared with the other models, and the scatter about the mean is consistently smaller. The performance of these two models is very similar, as expected. Overall, the WAAS model has a larger bias than the Altshuler model, but a lower scatter. The NATO model performs the worst.

The logical next step in model assessment would be the confirmation of these results in a kinematic environment. The availability of reliable meteorological data is an important issue. If the meteorological data is not available, standard atmospheric profiles to take into account the lapse rate of the meteorological parameters with altitude have to be introduced and may lead to incorrect zenith delay determinations. The models which do not rely on meteorological parameters will apparently have an advantage over the others, unless the modeling of the elevation angle dependence of the delay is poor. From Mendes and Langley [1994] we know that NMF and Ifadis mapping functions have very small biases, and the larger biases seen in the results presented here are nothing other than the amplification of the errors in the zenith delay determination. For the WAAS model, it is difficult to separate the zenith delay error from the mapping function error. Due to the advantage of not relying on meteorological data, we chose NMF as the reference mapping functions for testing against WAAS in the analysis of a set of kinematic GPS data, taken aboard a Convair-580 aircraft. To avoid the propagation of errors in the zenith wet delay determination, due to uncertainties in the measurement of the meteorological parameters, we used the Saastamoinen [1973] zenith wet model, which uses the partial pressure due to water vapor only. In the absence of errors, Ifadis and Saastamoinen zenith wet models have comparable accuracy [Mendes and Langley, 1995].

FLIGHT DATA DESCRIPTION

The flight data processed for our study was part of a data set collected by the National Research Council, Canada, at and around St. John's, Newfoundland, in March 1995. The campaign (denominated *Frizzle '95*) was primarily conducted between the latitudes of 45°N and 52°N and longitudes 57°W to 47°W.

The main objectives of the campaign included:

- studying stratiform drizzle formation, particularly over sea ice;
- studying drizzle formation from frontal lifting;
- measurement of ice accretion and testing of measurement systems;
- testing of a de-icing scheme;
- studying the change in aircraft performance with ice accretion.

The flight paths consisted of repeated horizontal and vertical profiles through cloud layers up to heights of approximately 8 km. Frontal zones and temperature inversions are often associated with potential causes of freezing precipitation and therefore provide highly unpredictable conditions for tropospheric delay modeling.

The GPS data consists of 14 days of dual-frequency pseudorange and carrier phase measurements recorded at two second intervals. Data were simultaneously recorded by an Ashtech Z-12 receiver and NovAtel GPSCard single-frequency receiver, both on the aircraft and at a ground reference station in St. John's. Range corrections were transmitted from the reference station to the aircraft for real-time positioning. The data from each day generally consists of one three-to-five hour flight. Meteorological parameters were recorded at both the ground station and the aircraft. The ground meteorological data is available at one minute intervals and the airborne data every second.

A subset of the data has been analyzed using the Kinematic and Rapid Static (KARS) software developed by Dr. Gerald. Mader at the National Geodetic Survey, NOAA. It uses the ambiguity function method [Mader, 1992] for resolving the carrier phase ambiguities. The generous provision of the source code has allowed the implementation of most of the currently available tropospheric delay models. However, due to the nature of the processing software, which requires dual-frequency GPS observations, we have limited our data analysis thus far to the Ashtech Z-12 receiver observations. It is intended to process the single-frequency data in the future, along with similar data provided as part of the Beaufort Arctic Storms Experiment, undertaken at Inuvik, N.W.T., in October, 1994. Because of the geographic location and nature of these projects it is expected that the data will provide a good test of the currently available tropospheric delay models.

We are using carrier phase data to test the WAAS tropospheric delay model because of the greater accuracy they provide over pseudoranges. The lower noise and multipath components should allow us to more accurately determine any residual tropospheric delay errors induced

STATION	ϵ (°)	AL	NATO	WAAS	IFADIS	NMF
Alert	15	-7	47	-21	-2	-2
	10	-2	69	-21	-3	-4
	5	9	137	81	-6	-10
Denver	15	-35	-50	-51	-2	-2
	10	-43	-72	-64	-3	-3
	5	-74	-117	15	-4	-4
Frobisher	15	11	45	-6	-3	-3
	10	24	66	1	-5	-5
	5	57	132	126	-9	-12
Grand Junction	15	-59	4	-44	4	4
	10	-79	6	-56	6	6
	5	-127	21	-2	11	11
Guam	15	-57	4	-28	1	1
	10	-75	6	-33	1	1
	5	-119	20	45	3	2
Kotzebue	15	2	39	-15	-3	-3
	10	12	58	-11	-4	-4
	5	35	119	105	-8	-8
Nashville	15	-15	-7	-29	-6	-6
	10	-13	-9	-33	-9	-9
	5	-10	-1	70	-16	-18
Oakland	15	3	12	-14	5	5
	10	14	19	-9	8	8
	5	43	51	117	16	15
San Juan	15	-39	-46	-53	-4	-4
	10	-45	-66	-66	-6	-5
	5	-77	-107	13	-10	-9
St. John's	15	2	21	-13	-5	-5
	10	12	31	-9	-7	-7
	5	38	72	112	-12	-14
The Pas	15	-5	26	-14	-3	-3
	10	2	38	-10	-5	-5
	5	19	83	106	-9	-10
Whitehorse	15	-29	28	-16	0	0
	10	-34	42	-14	0	0
	5	-47	87	88	-1	0

Table 1 - Mean tropospheric delay error for 15°, 10° and 5° elevation angle. The values represent the mean differences between the tropospheric delay model predictions and ray-trace results, in centimetres. (Note: AL = Altshuler)

STATION	ϵ (°)	AL	NATO	WAAS	IFADIS	NMF
Alert	15	10	12	9	3	3
	10	14	17	13	5	5
	5	27	28	23	8	10
Denver	15	21	22	21	18	18
	10	31	32	31	26	26
	5	60	60	58	49	48
Frobisher	15	13	16	12	6	6
	10	19	23	18	8	8
	5	33	40	31	15	15
Grand Junction	15	14	17	13	7	7
	10	20	24	19	10	10
	5	38	44	35	20	19
Guam	15	11	13	11	7	7
	10	17	20	16	11	11
	5	31	35	29	20	20
Kotzebue	15	14	17	14	6	6
	10	21	25	20	9	9
	5	39	45	36	16	16
Nashville	15	28	30	27	12	12
	10	41	44	40	18	18
	5	79	81	74	33	33
Oakland	15	13	13	12	10	10
	10	19	19	18	15	15
	5	36	35	34	16	15
San Juan	15	16	16	16	13	13
	10	23	24	23	19	19
	5	45	46	44	35	35
St. John's	15	21	24	21	13	13
	10	31	34	31	19	19
	5	57	62	55	35	35
The Pas	15	11	14	11	7	7
	10	17	21	16	11	10
	5	31	37	28	19	19
Whitehorse	15	11	14	11	5	5
	10	16	21	15	8	8
	5	30	38	27	14	14

Table 2 - Root-mean-square scatter about the mean of the differences between the tropospheric model predictions and the ray-trace results for 15°, 10° and 5° elevation angle, in centimetres. (Note: AL = Altshuler)

by the different models. Our use of carrier phase data is also germane to the idea of extending the WAAS concept to a Local Area Augmentation System (LAAS). This concept requires carrier phase positioning and on-the-fly ambiguity resolution to perform precision CAT-II and CAT-III approaches.

FLIGHT DATA TEST RESULTS

An important consideration in this type of study is that a proper comparison be made between models. Several previous studies have shown that the correlation in meteorological parameters degrades very quickly with height [Brown and van Diggelen, 1994; Qin et al., 1995]. Therefore, only where both air and ground meteorological data are concurrently available are comparisons made, rather than using default meteorological data.

As an example of the kind of data we have processed, we present in Figure 1 the carrier phase double difference residuals for one hour's worth of data, processed with the WAAS model and then the Saastamoinen zenith delay models with the Niell mapping function. As we suspected, using the Saastamoinen wet zenith delay model proved slightly superior than using the Ifadis zenith wet model. The elevation cutoff angle used was 10 degrees. The residuals using the WAAS model appear to be more unstable over a longer period of time. This is partly due to the fact that after two separate cycle slip events at approximately 5 and 45 minutes into the data set, the ambiguities are resolved differently (and incorrectly) than in the Saastamoinen/Niell solution. The difference is only one cycle on both L1 and L2, but it is enough to account for the divergence of the residuals after 30 minutes. A cycle slip also occurs on a low elevation angle satellite at approximately 30 minutes but it drops below the cutoff before its ambiguities can be resolved.

Both these plots show some systematic trends in the residuals and by examining Figure 2 we might suggest a closer correlation with the distance between the two receivers, rather than their relative height difference. Over a distance of nearly 200 kilometres, uncorrelated tropospheric effects and orbit errors should be the predominate errors. Hence, for the residuals presented in Figure 3, which are from exactly the same data and tropospheric model combinations as before but processed with International GPS Service for Geodynamics (IGS) precise orbits, almost all the systematic trends have been removed and the cycle slips are still resolved with a one-cycle difference between the two solutions. However, the biases that remain in the WAAS solution stand out more clearly.

Turning to Figure 4, we consider the effect on the formal errors of the position solutions. This plot represents the height, northings and eastings (respectively reading down the y axes) standard deviation using the broadcast orbits. We can immediately see that the precision of the height component of the WAAS solution is more sensitive compared to the Saastamoinen/Niell solution at all times.

Also in Figure 4, one might note the two jumps in the WAAS height standard deviation. The first, at 30 minutes is also in the Saastamoinen/Niell standard deviation, but the latter at 51 minutes, is not. This would suggest that this is purely a consequence of the use of a different tropospheric delay model, however this is only the case in an indirect way. This jump is actually due to the WAAS model solution solving for the second cycle slip three minutes later than the Saastamoinen/Niell solution.

CONCLUSIONS

The ray trace results indicate that either the Niell or Ifadis mapping functions, coupled with a standard zenith delay model will perform better than the proposed WAAS model. However, reliable meteorological data is advisable, particularly the pressure (one mbar error in the pressure introduces about 2 mm error in the zenith hydrostatic delay determination).

The flight data results indicate that the WAAS model can introduce errors into the ambiguity resolution of the carrier phases even over short distances between the receivers, as compared to the Saastamoinen/Niell model. These errors are small (1 cycle) but significant over long time periods. They were also present even when precise orbits were used to compute the solutions.

The WAAS model solution's precision is degraded slightly with respect to the Saastamoinen/Niell solution and especially in the height component.

Further work at UNB will involve processing more of the flight data using different models and with lower elevation angle cutoffs. The advantages of using a different model at the reference station from that used for the aircraft will also be investigated. Any improvements that can be made to the currently proposed WAAS model will be considered and tested.

Future work will also involve analysis of the NovAtel data set by our partners at NAVSYS Corp., Colorado Springs, CO, using their own on-the-fly software. This phase of the analysis program will look specifically at the effect of tropospheric delay models on aircraft precision approaches.

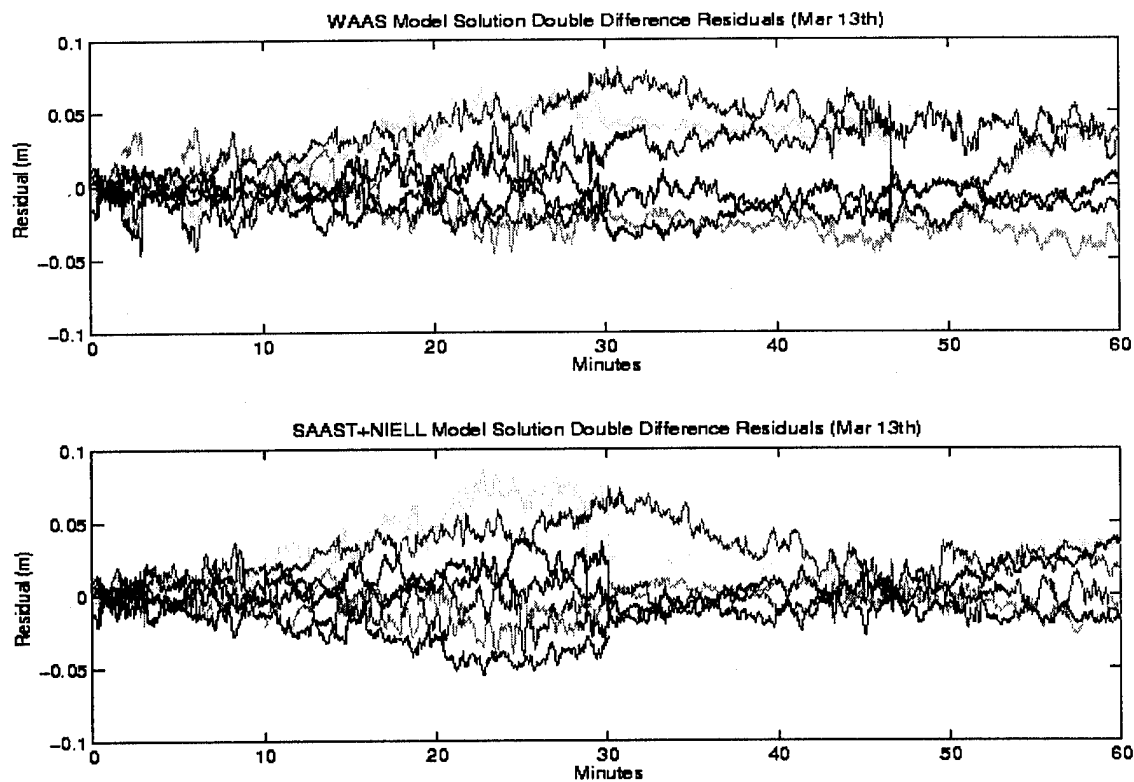


Figure 1. L1 Carrier Phase Double Difference Residuals (Broadcast Orbits).

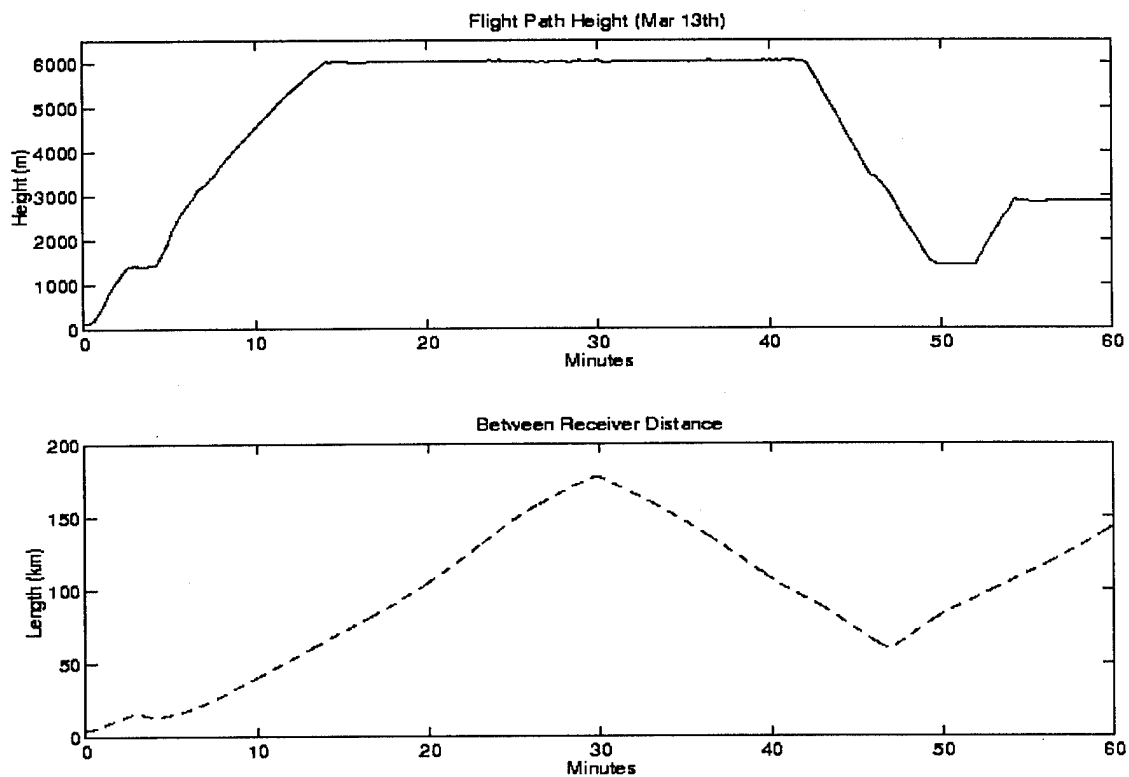


Figure 2. (a) Height of airplane. (b) Distance from reference receiver.

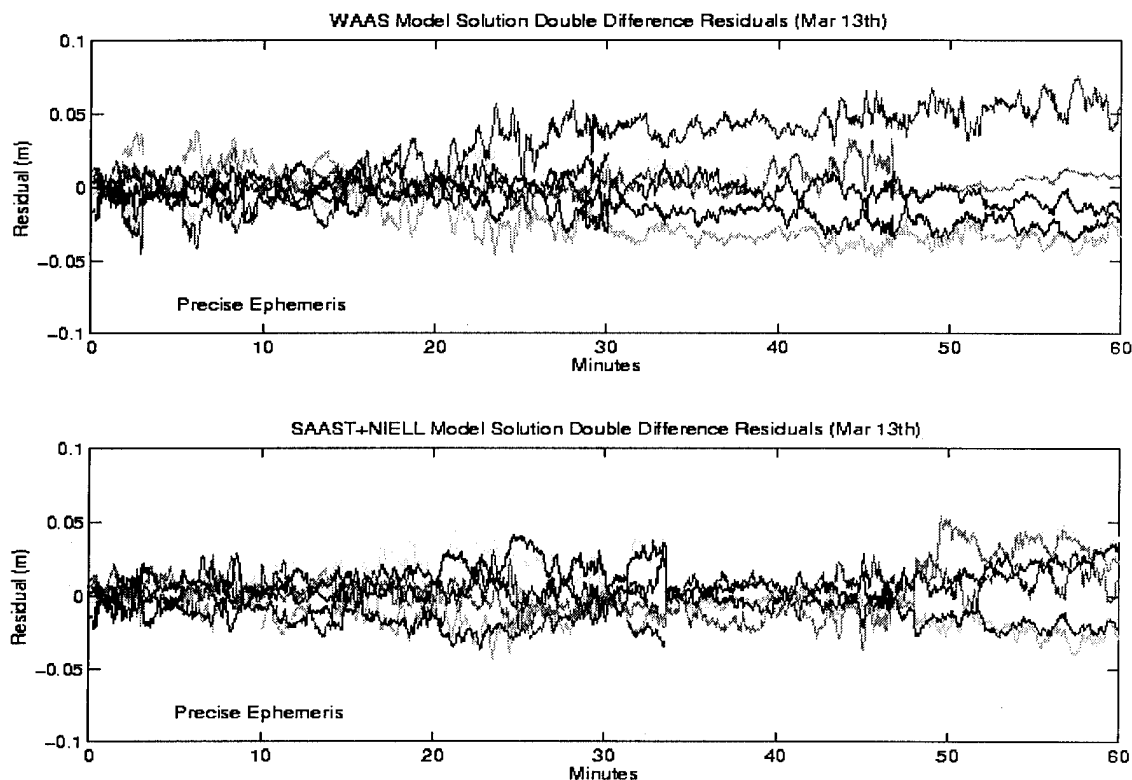


Figure 3. L1 Carrier Phase Double Difference Residuals (Precise Orbits).

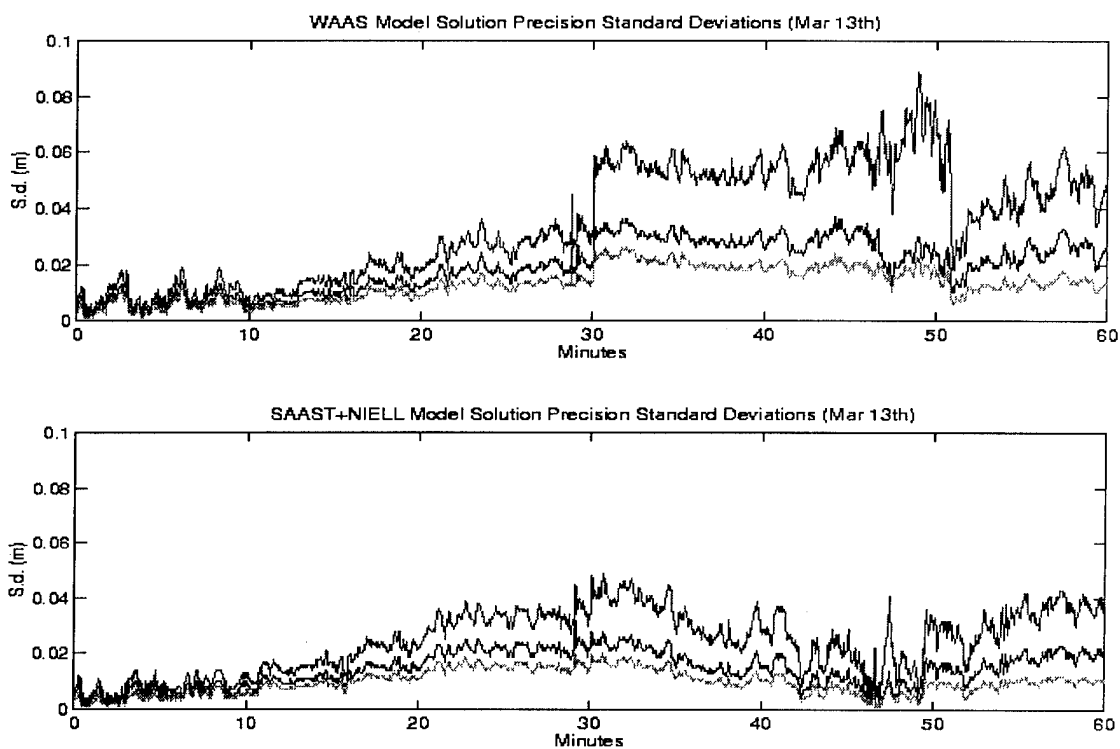


Figure 4. Precision of solutions (standard deviations of height, northings and eastings respectively descending the y axes).

ACKNOWLEDGMENTS

The support of the *PRAXIS XXI/Junta Nacional de Investigação Científica e Tecnológica*, Portugal, and the Natural Sciences and Engineering Research Council of Canada is gratefully acknowledged. The indispensable contributions of the National Research Council of Canada; Transport Canada Aviation and the Federal Aviation Administration are also acknowledged.

REFERENCES

- Altshuler, E.E. and P.M. Kalaghan (1974). "Tropospheric range error corrections for the NAVSTAR system." Interim scientific report Air Force Cambridge Research Laboratories, Bedford, Mass., 16 April, AFCRL-TR-74-0198, 13 pp.
- Brown, A. and F. van Diggelen (1994). "Boundary layer tropospheric effects on airborne on-the-fly ambiguity resolution." Proceedings of KIS94, International Symposium on Kinematic Systems in Geodesy, Geomatics and Navigation, Banff, Canada, 30 August - 2 September, 1994, pp. 99-108.
- Chao, C.C. (1972). "A model for tropospheric calibration from daily surface and radiosonde balloon measurements." JPL Technical Memorandum 391-350, Jet Propulsion Laboratory, Pasadena, CA.
- DeCleene, B. (1995). Personal communication, Federal Aviation Administration, May 1995.
- Johns, J.C. (1995). "FAA awards Wide Area Augmentation System contract." *Satnav News*, Vol. 3, No. 2, pp. 1-2.
- Ifadis, I.I. (1986). "The atmospheric delay of radio waves: modeling the elevation dependence on a global scale." Technical Report 38L, Chalmers University of Technology, Göteborg, Sweden.
- Mader, G.L. (1992). "Rapid Static and Kinematic Global Positioning System Solutions Using the Ambiguity Function Technique." *Journal of Geophysical Research*, 97, (B3), pp. 3271-3283.
- Mendes, V.B. and R.B. Langley (1994). "A comprehensive analysis of mapping functions used in modeling tropospheric propagation delay in space geodetic data." Proceedings of KIS94, International Symposium on Kinematic Systems in Geodesy, Geomatics and Navigation, Banff, Canada, 30 August - 2 September, 1994, pp. 87-98.
- Mendes, V.B. and R.B. Langley (1995). "Zenith wet tropospheric delay determination using prediction models: accuracy analysis." *Cartografia e Cadastro*, Instituto Português de Cartografia e Cadastro, No. 2, pp. 41-47.
- NATO (1993). Standardization Agreement 4294, North Atlantic Treaty Organization, Brussels.
- Niell, A.E. (1995). "Global mapping functions for the atmosphere delay at radio wavelengths." Submitted to the *Journal of Geophysical Research*.
- Qin, X., S. Gourevitch and M. Kuhl (1992). "Very precise differential GPS - Development, status, and test results." Proceedings of ION GPS-92, Albuquerque, NM, 16-18 September 1992, pp. 615-624.
- Saastamoinen, J. (1973). "Contributions to the theory of atmospheric refraction." In three parts. *Bulletin Géodésique*, No. 105, pp. 279-298; No. 106, pp. 383-397; No. 107, pp. 13-34.
- Santerre, R., I. Forgues, V.B. Mendes, and R.B. Langley. (1995). "Comparison of tropospheric mapping functions: their effects on station coordinates." Presented at the IUGG XXI General Assembly, 2-14 July, Boulder, CO.
- Shaw, M., T. Simpson, and K. Sandhoo. (1995). "FAA implementation planning for the use of GPS in air navigation and landing." Proceedings of the ION National Technical Meeting, Anaheim, CA, 18-20 January, pp 11-18.

Measuring User Equipment Errors from Holloman Flight Test Data

Joseph Clifford and Raymond DiEsposti
The Aerospace Corporation

Andrew Chasko
Amcomp Corporation

Kenneth Wernle
CIGTF

Capt. Gregory Fairbanks
GPS JPO, AFSMC, Los Angeles AFB

Biographies

Joseph M. Clifford is a Senior Project Engineer at The Aerospace Corp with over 20 years of experience working in the GPS Joint Program Office (JPO) in user equipment requirements, test, integration, and applications. He obtained his AB from Harvard College and MS and PhD from Lehigh University.

Ray DiEsposti is an engineer at The Aerospace Corp and has been working in the GPS JPO for one year. He has a BS from the University of Pittsburgh, MS from Stanford, and PhD from the University of Southern California.

Mr. Andy Chasko holds a BS in Physics from Humboldt State University, continued graduate studies in Physics at San Diego State University, and earned an MA in Business Administration from Webster University in 1990. He has supported GPS User Equipment, reference station, and GPS Space Vehicle testing since 1975. Andy continues with Amcomp as a GPS analyst, Test Support, with the 746th Test Squadron at Holloman AFB, NM.

Mr. Kenneth R. Wernle holds a BS in Electrical Engineering from UCLA. He continued his studies while on active duty at New Mexico State University, where he earned an MS in 1979. Currently, Mr. Wernle is a Program Manager at the 746th Test

Squadron, also known as the Central Inertial Guidance Test Facility (CIGTF), Holloman AFB. He was the Program Manager for the INU Enhanced Accuracy Honeywell SNU 84-1/E Rev C test program.

Capt. Gregory Fairbanks has been working in User Equipment Test and Evaluation for the GPS JPO, AFMC, Los Angeles AFB for 2½ years. His primary responsibility is Test Manager for GPS airborne receivers. He received a BS from the US Air Force Academy in 1987.

Abstract

A study is being performed to measure GPS UE (user equipment) errors under dynamic conditions by analyzing Holloman AFB flight test data to better characterize the UE contribution to the error budget. Since GPS space and control segment errors will be reduced to two meters or less based on current accuracy enhancement approaches, the errors due to the UE become a much larger relative component of the overall error budget. Techniques to mitigate UE errors thus become of primary importance for a further improvement in navigation accuracy. The objective of this study is to statistically characterize these errors and break them into separate components due to the ionosphere, troposphere, multipath, receiver noise, etc. For the results in

this paper, we were able to estimate the total UE error. However, since ionosphere, troposphere and interchannel bias compensation data were not recorded for the mission studied, a further breakdown of the UE errors was not attempted. Future analyses will include the UE error breakdown to a level limited by truth reference accuracy and availability. Such UE error information is valuable for three reasons: (1) allows verification of GPS error budget, (2) allows planners of UE error reduction techniques to better prioritize their effort, and (3) allows the validation of models for use in error mitigation techniques and navigation filters. A byproduct of this effort is that anomalous conditions will be better understood so that signal processing enhancements, fault detection, isolation, and reconfiguration approaches may be designed. Results are presented for a typical high performance aircraft instrument configuration for two Rockwell Collins user sets, the Miniaturized Airborne GPS Receiver (MAGR) and the 3A.

Introduction

The GPS pseudorange (PR) error budget is separated into three main components [1]: (1) space segment errors, primarily due to the imprecise predictability of space vehicle (SV) clock perturbations and satellite force perturbations, (2) control segment errors, primarily due to satellite tracking errors, imprecise prediction of satellite motion (or latency in the navigation message upload), and suboptimal processing in the Master Control Station, and (3) the user equipment (UE) errors, or errors which are attributed to the GPS user sets, consisting mainly of errors in the ionospheric (iono) and tropospheric (tropo) delay compensation, multipath, interchannel bias and receiver noise. Differential GPS removes or significantly reduces many of the errors which are common to a reference station and a user, such as space and control segment (SS/CS) errors. Also, current enhancements will reduce the SS/CS errors for the stand-alone user to two meters or less [2]. Thus, for the Precise Positioning Service (PPS) user, the UE error will become the dominant error component.

In this study, UE errors are measured in a dynamic environment typical of a high performance aircraft. These errors are expected to be significantly different from those for a slow moving or static user. Some inherent difficulties are: (1) obtaining an accurate enough truth reference for the flight trajectory and a reference whose errors are independent of the GPS solution errors, (2) obtaining truth reference values of ionospheric and tropospheric delay, and (3) separation of the various GPS error sources. We expect this effort to be on-going as additional techniques are developed and implemented to generate more accurate truth references and new UE and instrumentation become available for testing.

Approaches

Approach I - Deriving UE Errors from Nav Domain Errors

In the first approach the UE ranging errors are derived from navigation domain errors. The navigation domain error is computed by subtracting the TSPI (Time, Space, Position Information) state vector from the GPS user set state vector. TSPI is the best estimate of the true trajectory as generated by post processing [3], so that the difference, $GPS - TSPI$, is the best estimate of the total navigation error. To obtain the UE component of the error, the ephemeris errors and SV clock correction errors, as computed by the Holloman reference station, are removed.

The resultant error,

$$\Delta X = X_{GPS} - X_{TSPI} - \Delta X_{eph/clk}$$

is the estimate of the UE error in the navigation domain. The space and control segment error, $\Delta X_{eph/clk}$ is obtained by using the same four SVs as tracked by the user and the SV Observed Range Errors (OREs) computed by the reference station. From the UE navigation error, pseudorange errors may be estimated, for the current set of user SVs, by taking the inverse GPS solution [4],

$$\Delta \vec{P}R = S^{-1} \Delta X$$

where $S = (G^T G)^{-1} G^T$ is the sensitivity matrix, G is the geometry matrix and $\Delta \vec{P}R$ is the vector of SV pseudorange errors. For four satellites, the sensitivity matrix simplifies to $S = G^{-1}$.

Approach II - Measuring PR Errors Directly in the Range Domain

The previous method characterizes the errors based on the output from the user set navigation filter. In order to develop techniques to mitigate errors and develop error models for use in pre-filters and the navigation filter, it is preferable to measure the errors at an earlier point in the data processing. For example, we would like to statistically characterize the errors in the corrected PR and delta range - these are the input observations used by the user set navigation filter. This approach is described next. Other methods of improving filter design involve statistical analysis of the filter measurement residuals.

In this approach, the raw pseudorange measurements and precise ephemeris and SV clock corrections are used to compute PR residuals directly in the range domain.

Data available from Holloman and the Defense Mapping Agency (DMA) which can be used to perform this processing are: (1) Instrumentation Port Data (including PR measurements, broadcast navigation messages, receiver corrections, etc) for the 3A and MAGR [5] for aircraft test flights, (2) TSPI data (truth reference trajectory) for the above tests, (3) OREs, Ground Truth and raw and smoothed iono corrections from the Holloman reference station, and (4) precise ephemeris and SV clock files from DMA for the dates of interest.

The procedure to compute the pseudorange error then proceeds as follows:

1. Let t_i^j be the GPS time of measurement PR_i^j for time index i and SV index j .
2. Using the DMA precise ephemeris/clock (or broadcast ephemeris and SV clock corrections and errors in the broadcast ephemeris and SV clock corrections as calculated by the Holloman reference station) and Holloman TSPI, compute the "precise" range:

$$\hat{\rho}_i^j = | \vec{R}_s(t_i^j) - \tau - \vec{R}_u(t_i^j) |$$

where \vec{R}_u is the "true" user location given by TSPI, $\tau = \frac{r}{c}$ is the signal transit time and $\hat{\rho}$ is computed in the Earth Centered Inertial (ECI) coordinate frame.

3. The uncorrected pseudorange (not corrected for iono, tropo, SV clock, relativity, SA, etc)

is of the form [4]:

$$PR(t) = \rho(t) + I(t) + T(t) - B_s(t) + B_u(t) + SA(t) + n(t)$$

where

$PR(t)$ is the measured pseudorange without iono, tropo, SV clock, etc, receiver corrections

$\rho(t)$ is the true range at time t

$I(t)$ is the true iono delay

$T(t)$ is the true tropo delay

$B_s(t)$ is the true SV clock time offset plus relativity effect

$B_u(t)$ is the user clock bias

$SA(t)$ is the Selective Availability error

$n(t)$ is the random error (receiver noise, multipath, etc)

4. Pseudorange residuals can be formed by subtracting precise range from step 2, DMA precise SV clock correction, SA, and receiver corrections for iono and tropo:

$$\begin{aligned} \Delta PR_i^j &= PR_i^j - \hat{\rho}_i^j - [\hat{I}(t_i^j) + \hat{T}(t_i^j) - B_s(t_i^j) + SA(t_i^j)] \\ &= (\Delta R_s + \Delta B_s) + \Delta R_u + \Delta I_i^j + \Delta T_i^j + B_u(t_i^j) + n(t_i^j) \end{aligned}$$

The terms within parentheses are the error component in the precise ephemeris along the LOS (Line-of-Sight direction from user to SV) and the precise SV clock correction error, ΔR_u is the TSPI error along the LOS, ΔI and ΔT are the receiver iono and tropo delay compensation errors. When computing residuals this way, the simplest way to remove the unknown user clock bias $B_u(t_i^j)$ is to subtract off the average residual of the four SVs which are currently being tracked. (For a single point navigation solution calculation, the average value of the PR residual is interpreted as a user clock error and thus does not affect navigation error. However, part of the average residual may be due to error components other than the user clock bias.)

In addition to characterizing the total UE error, we would like to further separate this error into components of iono, tropo, multipath, noise, etc.

Assuming sufficiently accurate TSPI and precise ephemeris/SV clock, successful characterization of component errors requires obtaining accurate values of the true iono and tropo delay and separating multipath from noise and any tracking loop lag errors. Techniques such as, "pseudorange minus accumulated delta range" [6] to identify and separate multipath, may also be applied.

Other UE errors may be present in one approach but not the other. For example, errors introduced by the navigation filter will be present in Approach I but not Approach II. Conversely, the navigation filter should provide some smoothing benefit that reduces random errors. UE clock instability compensation will be different for the two approaches. For example, Approach II can remove UE clock offset by subtracting the mean PR residual, as described above, while in Approach I, the UE clock bias is one of the states estimated in the navigation filter. Also, other non-traditional type errors may be present in both approaches. One such example would be bit errors in the navigation message. The UE channel management software also affects performance [7].

The following discussion summarizes the tasks required to process errors in the range domain. Holloman supplies user set instrumentation port data and TSPI data in binary format and OREs and Ground Truth in ASCII format. DMA precise ephemeris, consisting of ECEF position and velocity, is available in 15 minute steps. To interpolate this data, error functions were formed by subtracting the broadcast ephemeris, evaluated at the DMA 15 minute epoch times, from the DMA data. These are smooth functions, which when added to broadcast ephemeris states, evaluated at any intermediate time, obtain almost the same accuracy as the DMA ephemeris. Other analysts have accurately interpolated the 15 minute DMA ephemeris using eight order polynomials [8]. DMA precise SV clock data is available in one hour steps. The SA corrections need to be obtained, which involves classified processing. Other receiver PR corrections, such as ionospheric, tropospheric, SV clock corrections, relativity, interchannel bias, etc, have to be recorded (or recomputed exactly as in the UE) so that they may be added to form the receiver's corrected pseudorange. The receiver corrections may also be compared to reference values, such as the reference station smoothed iono, to form estimates of the errors in the corrections. The GPS data time tags and the TSPI times have

to be adjusted to account for any time tagging biases relative to GPS time. In addition, the ephemeris computation requires that signal transit time be included. Finally, TSPI data, PR correction data, DMA precise ephemeris and SV clock correction data need to be interpolated with negligible interpolation error to the GPS time of PR measurement reception.

Mission Profile

Results are provided for the test flight of 5 Jan 1995. This flight originated at Holloman AFB, flew south to about the NM state line, then approximately west through San Simon and Stanford waypoints, north to Drake, then east to Albuquerque, and finally south back to Holloman.

GPS Satellite Reference Station

The Holloman Satellite Reference Station (SRS) provides an independent monitoring of Space and Control Segment (SS/CS) errors. This capability was developed by the JPO to support GPS receiver testing, GPS/INS aircraft integration, and DGPS TSPI generation. The SRS provides monitor station accuracy in the determination of the ionospheric error and the satellite ephemeris and clock error contributions to navigation error (Ground Truth). This Ground Truth error model provides support for field testing user equipment for the DoD.

The SRS includes the modified Collins 3A based Data Analysis Station (DAS) and the new GPS Reference System (GRS) in development. The DAS Collins 3A is clock aided with a high performance Cesium atomic clock reference and includes PC based receiver control, tracking scheduling and data acquisition. The DAS functions as a monitor station and was qualified against the Inverted Range Monitor Station (IRMS) by the JPO at Yuma. The DAS is the existing standard for reference station support of DoD receivers and in integrity monitoring of GPS performance and anomalies for the JPO and Air Force Operational Test and Evaluation Center (AFOTEC). The SRS capability will be upgraded later in 1995 with the addition of a new eight channel GRS to

provide increased satellite coverage, simultaneous eight satellite track of the L1/L2 P codes and C/A codes, and to support the civilian receiver test and application in an SA and A-S environment.

The SRS fills three distinct requirements in the field testing of GPS receivers and GPS integrations at Holloman. First, the SRS provides monitoring of SS/CS performance and anomalies during testing. Next, the SRS provides the Observed Range Errors (OREs) used to determine the Ground Truth. The Ground Truth is the SS/CS error contribution to a GPS receiver. The Ground Truth is used in calculating the URE portion contributed by the GPS User Equipment and is used to verify the UE against its specifications. Lastly, the SRS provides the DGPS TSPI with accuracy comparable to the laser tracking systems with the FAA and DoD. The DGPS TSPI is highly sought by a number of test agencies who require the reduced cost and high precision of this reference along with the Ground Truth and satellite monitoring capability.

Aircraft Data Acquisition

Two Enhanced Accuracy USAF Standard Inertial Navigation Units (SNUs) [9] were interfaced to a Kontron IP Lite 386 DX airworthy personal computer and Honeywell's Configurable Data Acquisition Test Software (CDATS), which performs 1553 bus controller functions, data display system bus control, initialization, data display and high speed 1553 data bus recording.

Differential GPS TSPI

The DGPS reference system generates highly accurate postflight time, space, and position information (TSPI) data using the Holloman SRS and government furnished user equipment (GFE) aboard the mobile van or flight test bed. The SRS uses a modified Collins 3A GPS receiver to track all visible GPS satellites. The GFE on the flight test platform was a Collins 3A GPS receiver for the reference and a MAGR from the integrated systems. The MAGR was inertially aided by the SNU, while the 3A reference receiver was not inertially aided but was aided by an atomic clock. The JPO developed standard control and display unit (CDU), fixed reception pattern antenna (FRPA)

50% Pos Error (m)			Rms Vel Error (m/s)			
Hor	Ver	3D	E	N	UP	3D
2.0	2.0	2.5	0.02	0.04	0.02	0.05

Table 1: DGPS TSPI Accuracies

and antenna electronics (AE-4) are used with the Collins 3A receiver. DGPS accuracies have been verified to a distance of 500 miles from the reference station. The SRS and UE data are processed post-test to remove errors introduced by the GPS space and control segments, ionosphere and troposphere.

The DGPS navigational accuracies are dependent on the position dilution of precision (PDOP) and on the accuracy of the fitted ionospheric and observed range errors. The test window can be chosen to minimize each of these errors. The operational constellation will have four or more satellites more than five degrees above the horizon, providing PDOP < 6 coverage, 99 % of the time. Typical accuracies displayed in Table 1 were verified on the 746th Test Group's High Speed Test Track and documented in report number AFDTC-TR-94-48.

Results

Data was analyzed for a flight test occurring on 5 Jan 1995. Since both the 3A and the MAGR were included in the aircraft's instrumentation pallet, a comparison of the two for the same flight can be made.

From the 1 Hz flight test and post processed TSPI "truth" navigation data, UE position and velocity errors were computed for analysis. Representative time histories for the 3A errors are shown in Figures 1 through 3 for GPS time from 407500 (or about 17^h11^m40^s Universal Coordinated Time, UTC) to 409300 sec. The aircraft was initially climbing and heading approximately west at speeds of 60 to 70 m/s. After about eight minutes, the aircraft leveled off, followed three minutes later by an abrupt heading change to northwest and speed increase to about 105 m/s, then another abrupt heading change to southwest at about 26 minutes. Spikes in the time histories seem to coincide with the heading changes. The 3A, which was not INS aided, shows an interrup-

tion in track and SV switching at the time of the first heading change, while the MAGR does not.

Figure 1 shows the navigation error due to the GPS user equipment (GPS - TSPI - Eph/clock - see Approach I). From the data in Figure 1, PR errors for the four satellites being tracked were computed at each time point as described in Approach I. For example, Figure 3 shows the UE PR error for the SV tracked by the first channel. The time shown on the x-axis is measured relative to the initial GPS time shown in the top of each plot. The mean and standard deviation of the errors are displayed at the upper left of each plot and the four SV PRN numbers are shown at the top right of the position and velocity error plots. The occurrences of receiver channel SV switching are shown as vertical dashed lines. The omission of position error data from 500 to 560 sec was due to the unavailability of SS/CS corrections (Holloman Ground Truth).

Similar MAGR time histories are shown in Figures 4 through 6. Notice that the 3A and MAGR often do not track the same SVs and that SV switching between the two is not consistent. The MAGR velocity errors tend to be much smaller. This is probably due to the MAGR being velocity aided by the SNU, while the 3A was not. A strange sinusoidal characteristic appears in the MAGR vertical velocity. This may be due to an incorrectly measured lever arm or baro altimeter error into the SNU which was aiding the MAGR.

The errors computed by Approach I may be summed to form cumulative error distributions. These were computed for the 3A over the entire mission time span of 403975 to 417500 sec. Figures 7, 8 and 9 show the UE x-y-z position, velocity and 2D/3D error cumulative distributions, respectively, for the 3A. Notice that the Up position and velocity errors tend to be larger than the East and North errors and that the Up position error has a rather large bias. Similar plots for the MAGR errors are shown in Figures 10 through 12.

From the data in Figures 7 and 10, the UE PR errors were calculated and arranged into histogram bins for each SV that was tracked during the mission. These consisted of PRNs 1, 5, 14, 15, 18, 20, 21, 22, 23, 25, 28, 29 and 31, and each of their cumulative distribution curve is shown in Figure 13 for the 3A and Figure 14 for the MAGR. Some of the SV PR curves show significant biases. These may be due to errors in the Holloman Ground

Truth, biases in the receiver PR corrections, or multipath. The aggregate cumulative PR error distributions for the entire set of the 13 satellites are shown in Figures 15 for both 3A and MAGR.

The PDOP parameter time history for the 3A and MAGR are shown in Figure 16. This is a useful parameter for relating navigation domain errors to PR errors.

Pseudorange residual errors, calculated as described in Approach II with average residual subtracted out at each time, were computed for a 450 sec span of data for the 3A starting at GPS time 407520. These are shown in Figure 17 for data sampled every 30 sec. DMA precise ephemeris was used to compute the precise range, and SA, DMA SV clock corrections and relativity corrections were removed from the pseudorange measurements, but the iono, tropo and interchannel bias corrections were not recorded and were thus not included. This may explain why the PR residuals are somewhat larger than expected. The transient like effect is due to an incorrect initial guess of the receiver clock bias, which is quickly updated using the mean PR residual.

PR error statistics are tabulated for each of the satellites for the 3A for the time interval 403975 - 417500, in Table 2 and for the MAGR for the time interval 404568 - 417480, in Table 3. Aggregate PR statistics for the 13 SVs are $\bar{x} = 0$, $\sigma = 1.56$ meters, for the 3A, and $\bar{x} = 0$, $\sigma = 1.25$ meters, for the MAGR. The aggregate means are zero since the PR bias, common to the four SVs being tracked, is removed at each time point. These values compare with the total user equipment error budget of 3.6 meters rms for Precise Positioning Service (PPS) user sets [1].

Conclusions and Future Work

The analysis and results presented in this paper are very preliminary. However, some general conclusions and recommendations for future study may be presented. Much more effort, consisting of both analysis of test data and TSPI enhancement will be required to realize the objectives of this study, the statistical characterization of user set errors and a breakdown of overall UE error into separate error components.

Unexplained biases and anomalies occurred in the

SV	\bar{x}	σ	rms
1	0.04	1.35	1.35
5	-0.52	1.40	1.49
14	-1.39	0.78	1.60
15	1.04	1.40	1.74
18	1.64	0.82	1.83
20	0.42	0.91	1.00
21	0.87	1.67	1.88
22	0.43	1.20	1.27
23	-1.02	0.39	1.09
25	-0.87	1.95	2.14
28	-0.01	1.64	1.64
29	0.34	0.88	0.95
31	-0.04	0.82	0.82

Table 2: 3A PR Error Statistics

SV	\bar{x}	σ	rms
1	-0.50	0.98	1.10
5	0.34	1.20	1.24
14	-1.07	0.88	1.39
15	0.66	1.30	1.46
18	0.89	0.52	1.03
20	-0.09	0.91	0.91
21	0.46	0.44	0.64
22	-0.27	0.66	0.72
23	-1.33	0.91	1.61
25	0.65	1.52	1.66
28	0.22	1.42	1.44
29	-0.18	1.04	1.06
31	0.35	1.47	1.51

Table 3: MAGR PR Error Statistics

UE errors. Mitigation of these errors will require further understanding of the causal effects. The aggregate rms PR error for the 3A and MAGR were measured at 1.56 and 1.25 meters, respectively, being substantially less than the UE specification value of 3.6 meters. TSPI accuracy was stated as being about 2.5 meters in 3D. The mission PDOP ranged from about 2.0 to slightly over 3.0. This implies that PR errors should be measurable to an accuracy of about one meter. Thus the UE errors are approaching the same size as the TSPI truth reference accuracy.

The 3A velocity errors in the Up direction were significantly larger than the East and North errors. The INS-aided MAGR velocity errors were substantially smaller than the unaided 3A velocity errors. A further refinement in measuring the

velocity errors will be available with the use of Holloman High Rate TSPI (HRO) at 20 Hz.

Some ideas for future study are presented next.

- Data from several additional missions will have to be considered to provide a statistically meaningful characterization of UE errors. Separate statistics should be compiled for variable conditions, such as time of day, type of instruments, instrument configuration, trajectories and maneuvers, etc, in order to study the effects on accuracy of different instruments, geometries, dynamics, atmospheric and ionospheric conditions. Different levels of GPS accuracy may need to be reported for different mission characteristics, for example, high dynamics vs low dynamics flights.
- Approach II should be further studied. The PR residuals, after including the receiver corrections, can be compared to the PR errors estimated using Approach I. Any differences need to be explained. The separation of the UE error into the constituent components will continue in future effort. For example, recorded receiver correction data such as iono compensation, can be compared to the smoothed iono available from the Holloman SRS. UE component errors will be characterized statistically when feasible. Error statistics can be compared with current UE error models and these models and error budgets will be revised.
- Velocity errors should be further analyzed. An attempt should be made to extend Approach II for the computation of delta range residuals using delta range measurements and precise range rate.
- The relationship between motion, masking, and motion dependent errors may be studied by cross correlating the UE errors with aircraft translation and rotation, using the direction of the LOS, aircraft size and shape information.
- Biases in the UE errors should be further explored. Theoretically, biases attributable to imprecise modeling can be reduced.
- The accuracy of TSPI is critical to the objectives of this study. Accuracies of better

than one meter are required in order to measure a user set error component of one meter. Also, any correlation between TSPI errors and GPS errors are important. For example, if TSPI and the GPS solution have a common bias, the subtraction **GPS - TSPI** will give an overly optimistic GPS accuracy calculation. Further tests should be performed to verify TSPI position and velocity accuracy, to measure any correlation between TSPI errors and GPS errors, and to assess any significant degradation of TSPI at maximum test distances from the Holloman SRS. The use of independent truth reference measuring devices may be necessary.

- Further development and implementation of techniques to improve TSPI accuracy, continuity and reliability are required. Currently, TSPI is not computed when less than four satellites are tracked (or less than three SVs with atomic clock aiding), or when DGPS corrections or SRS Ground Truth is unavailable. Potential TSPI enhancement approaches are differencing techniques using carrier phase measurements and carrier cycle ambiguity resolution, and TSPI based on optimally fused data: inertial instrument measurements, DGPS corrections [10], and any other external data.
- Reference stations should be enhanced to provide more accurate space and control segment (SS/CS) error data (OREs) and reference values of iono and possibly tropo compensation. For example, an Allen Osborne TurboRogue user set is scheduled to be installed at the Holloman SRS. This receiver, which uses carrier smoothing techniques to reduce multipath effects, will enable a more accurate calculation of SS/CS errors.

Acknowledgements

The authors would like to thank Kathy Chan, R. T. Bow and Bob Wong for their assistance in decoding the Holloman data and Bill Feess for providing consultation and his computer program which computes pseudorange residuals. Thanks also to John Clark, Bill Feess and Barry Siegel for reviewing the manuscript and constructive

feedback. Thanks to the DMA for supplying the precise ephemeris and SV clock data. Special thanks go to Capt Lynn Anderson and Rita Lollock, who had the insight to recognize the importance of this work, for providing their support.

References

- [1] NAVSTAR GPS User Equipment Introduction, GPS Joint Program Office, Los Angeles AFB, Feb 1991.
- [2] Jim Butts, Capt Chris Shank, "Navigation Message Correction Tables: A Proposal," *ION Proc of National Tech Meeting*, Jan 1995.
- [3] J. E. Robbins, "Reference Trajectories from GPS Measurements," *Proc of Institute of Navigation*, Sept 1987.
- [4] "Differential GPS (Part I)," Navtech Tutorial Notes, Dr Bradford Parkinson, 1994.
- [5] GPS User Equipment Interface Control Document for Instrumentation Port Data Link of the DoD Standard GPS UE Radio Receivers, ICD-GPS-150, GPS JPO, 9 Aug 1991.
- [6] Michael S. Braasch, "Isolation of GPS Multipath and Receiver Tracking Errors," *ION Journal*, Vol 41, No 4, Winter 1994-1995.
- [7] GPS User Equipment Software Technical Description, Receiver-Manager, Synetics Corp, 12 Oct 1986.
- [8] Personal discussion with Bill Feess of The Aerospace Corp, August 1995.
- [9] Specification for the USAF Standard F³ Enhanced Accuracy Inertial Navigation Unit, SNU 84-1 Rev C, AFMC, Wright-Patterson AFB, 4 Oct 1993.
- [10] DGPS/IRG System Description Document, Differential GPS/Inertial Reference Generator (Aided TSPI), Intermetrics, Inc, 29 April 1993.

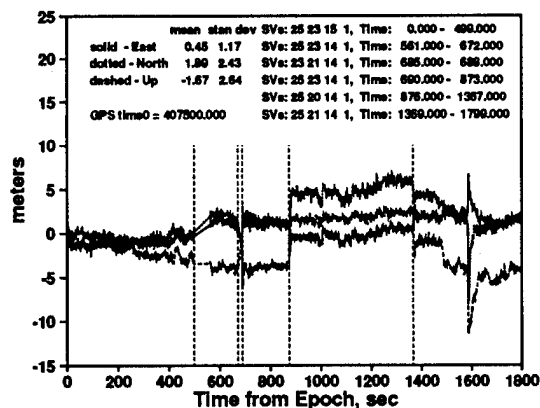


Figure 1: UE Position Error for 3A

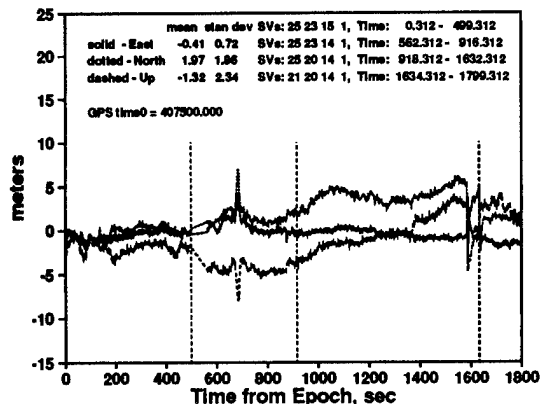


Figure 4: UE Position Error for MAGR

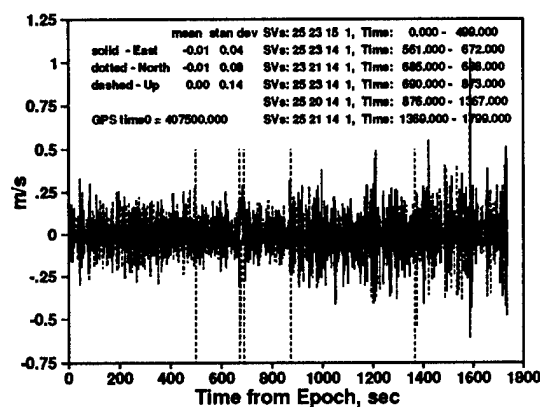


Figure 2: GPS Velocity Error for 3A

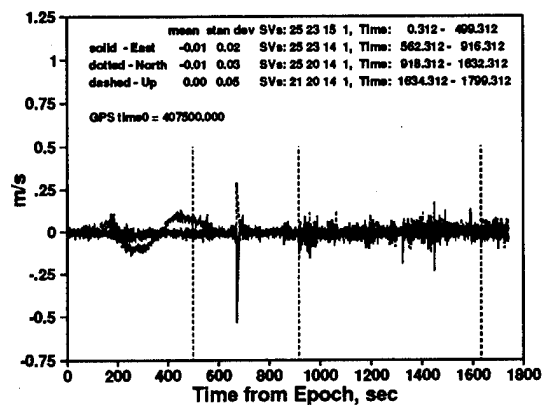


Figure 5: GPS Velocity Error for MAGR

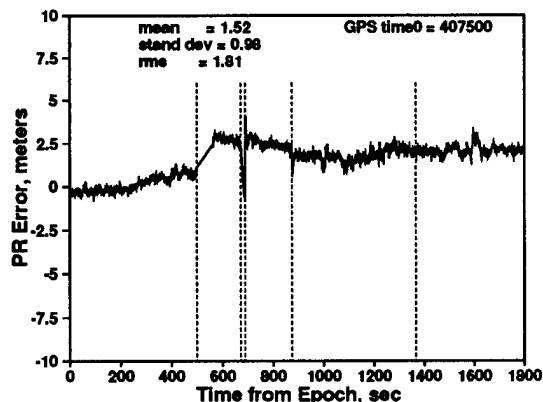


Figure 3: 3A UE PR Errors for First SV

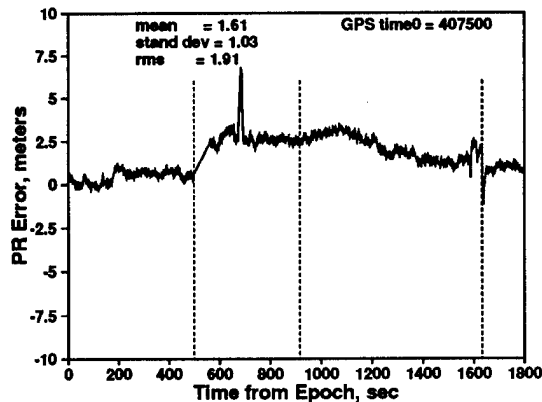


Figure 6: MAGR UE PR Errors for First SV

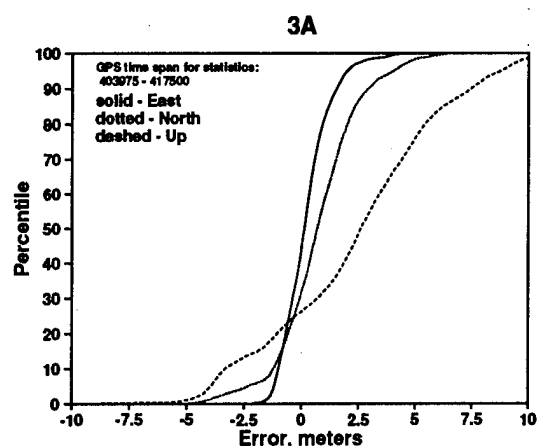


Figure 7: UE Position Error Cumulative Distribution

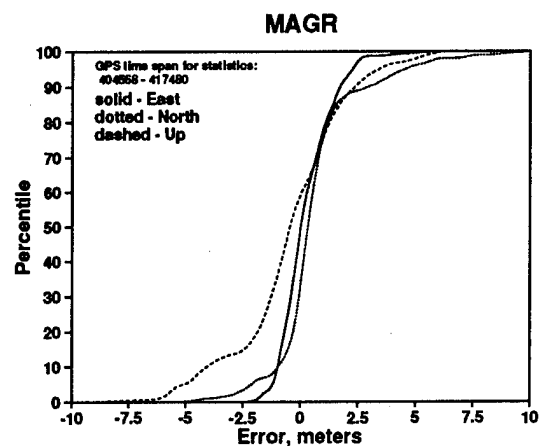


Figure 10: UE Position Error Cumulative Distribution

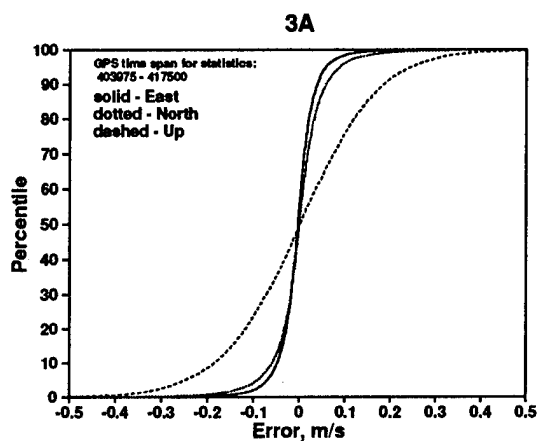


Figure 8: Velocity Error Cumulative Distribution

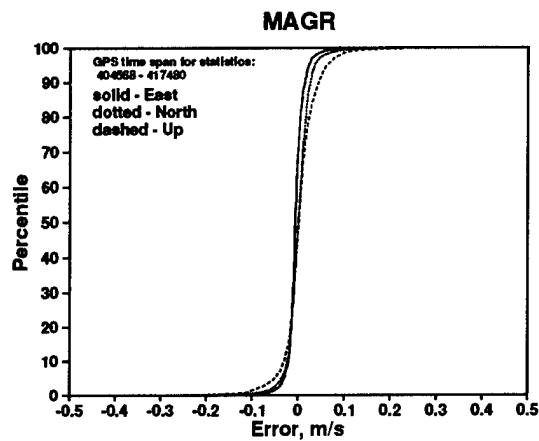


Figure 11: Velocity Error Cumulative Distribution

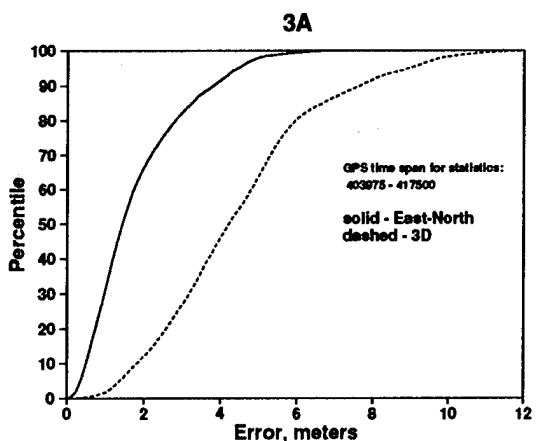


Figure 9: UE 2D & 3D Error Cumulative Distribution

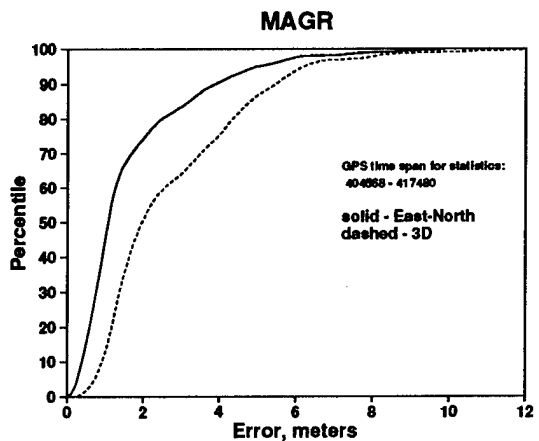


Figure 12: UE 2D & 3D Error Cumulative Distribution

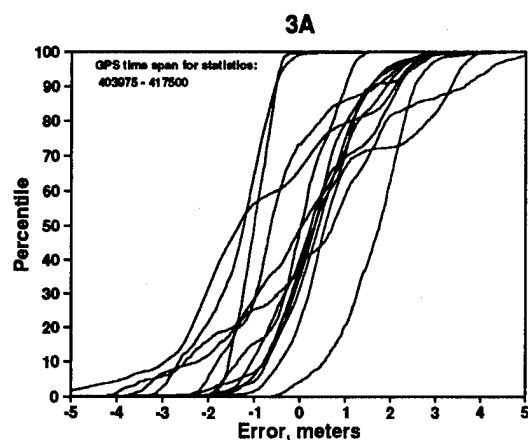


Figure 13: PR Error Cumulative Distributions

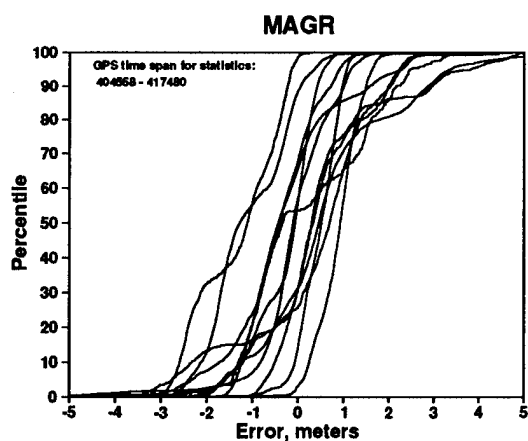


Figure 14: PR Error Cumulative Distributions

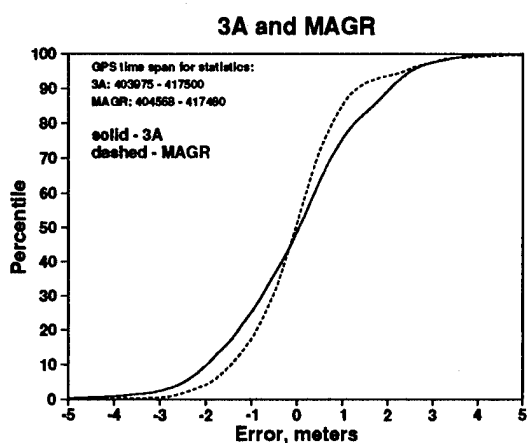


Figure 15: Aggregate PR Error Cumulative Distributions

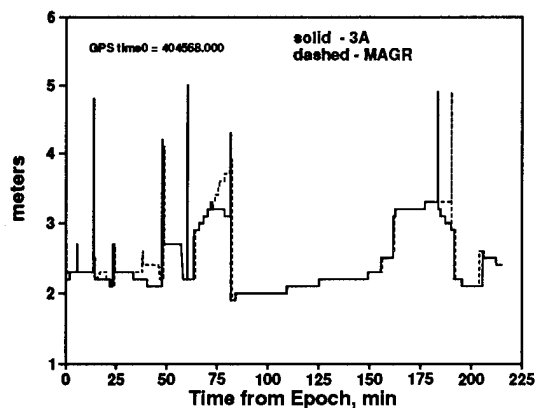


Figure 16: PDOP Time History

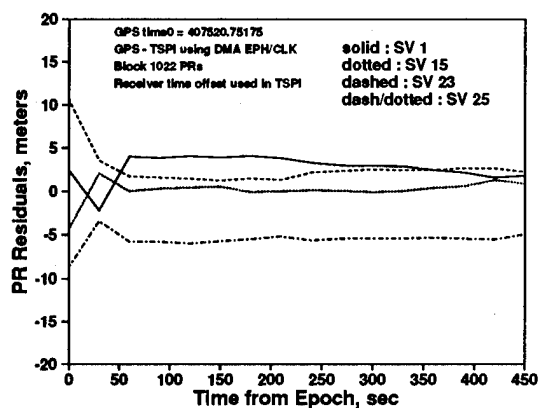


Figure 17: 3A PR Residuals

Mobile Inertial Test System: A Dynamic Testbed for the EDGE Flight Tests

Theodore Herrera and Brian Taylor
Elgin AFB

BIOGRAPHY

Theodore D. Herrera has been Chief of the Inertial Technology Test Team at the Wright Laboratory Armament Directorate, Eglin AFB since 1992. He planned, developed, and conducted dynamic ground tests for the Operational Concept Demonstration (OCD), and the Exploitation of Differential GPS for Guidance Enhancement (EDGE) High Gear programs.

Brian Keith Taylor has been the lead systems integration engineer on the Inertial Technology Test Team since 1990. He developed the architecture for Mobile Inertial Test System's real-time operating system and coded the MIL-STD-1553 bus interface for both OCD and EDGE weapons.

ABSTRACT

The Mobile Inertial Test System (MITS) is a truck-mounted testbed used by engineers at Wright Laboratory Armament Directorate, Eglin Air Force Base, to conduct dynamic tests of developmental tactical grade navigation systems. MITS hosts aircraft avionics to provide a truth reference system for evaluating and characterizing navigation performance. Recently, MITS was used to support Aeronautical Systems Center technology demonstration programs by emulating the MIL-STD-1553 inertial GPS interface between an aircraft platform and a developmental GPS-aided inertial munition for pre-flight ground tests. These tests included functional verification of the MIL-STD-1553 interface, transfer of alignment of the inertial measurement unit, and fast acquisition aspects of the GPS receiver.

This paper discusses the MITS test configuration and test procedures to conduct the pre-flight tests in accordance with the aircraft Operational Flight Program. The data presented are results from dynamic ground test support of a HIGH GEAR Joint Direct Attack Munition

Product Improvement Program called the Exploitation of Differential GPS for Guidance Enhancement (EDGE) program. In this program, wide area differential corrections were applied to the GPS-inertial navigation system of the air-to-surface munition. The EDGE guidance unit consists of a Honeywell Integrated Flight Management Unit incorporating Honeywell's HG1700 Ring Laser Gyro Inertial Measurement Unit and Interstate Electronics Corporation's SEM-E GPS receiver cards. The wide-area differential corrections are processed by SRI International's 1000 mile baseline reference receiver network which used four Ashtech 12-channel receivers.

INTRODUCTION

The challenge in designing future autonomous, standoff precise munitions is the development of tactical navigation, guidance and control systems that yield the most accuracy within cost, size, weight and power constraints. This is the goal of the Armament Directorate of Wright Laboratory, which leads the research and development of advanced munitions for the Department of Defense. One approach the Armament Directorate undertakes to meet this goal is developing and demonstrating innovative navigation technologies such as silicon inertial sensors, micromachined inertial measurement units, tightly-coupled GPS-aided navigation systems and anti-jam GPS antenna electronics. In addition, studies and demonstrations of inertial transfer alignment methods between the aircraft and the weapon are being pursued to accelerate transfer alignment, and improve the accuracy of the weapon's initial conditions before launch.

Within the Directorate, an in-house research and test capability exists to independently characterize and validate the performance of the advanced navigation technologies. A key asset of this in-house test capability is the Mobile Inertial Test System (MITS), a truck-mounted testbed that was developed to test munition navigation

performance in a moderately dynamic environment. In past years, the Directorate has used MITS to support three Precision Guided Munition (PGM) flight test demonstrations for the Joint Direct Attack Munition program office. Through these programs, MITS has evolved into a practical and versatile dynamic Hardware-In-the-Loop (HIL) testbed for munition flight test programs. This paper discusses the MITS hardware configuration, capabilities and support role for the Exploitation of Differential GPS for Guidance Enhancement (EDGE) program flight tests.

MOBILE INERTIAL TEST SYSTEM

MITS is an in-house testbed developed to evaluate and analyze the inertial, GPS-aiding, and antijam GPS performance of weapon-grade navigation systems. To achieve these objectives, MITS uses modern aircraft avionics to produce a position and velocity truth reference system. Truth reference data is calculated by updating a high-quality Inertial Navigation System (INS) with GPS measurements. Figure 1 is a picture of the MITS interior, showing the operator stations and racks housing the computer systems, power supplies, avionics equipment, and fixture for the IMU/GPS test hardware (bottom right).



Figure 1. MITS Interior

Illustrated in Figure 2 is a schematic showing the organization of the principle MITS subsystems. At the core of the MITS lie two ruggedized PC's. The first PC is a ruggedized 486 DX 66 Mhz Personal Computer (PC) with 32 MB RAM, Removable 105 MB Syquest hard drive, and DDC-65515 MIL-STD-1553 bus card. It acts as the MIL-STD-1553 Bus Controller (BC), overseeing basic communications between the avionics and the guidance unit, including GPS position updates to the H-423 to create the Truth Reference System (TRS). In addition, it is used to develop software in Pascal and C.

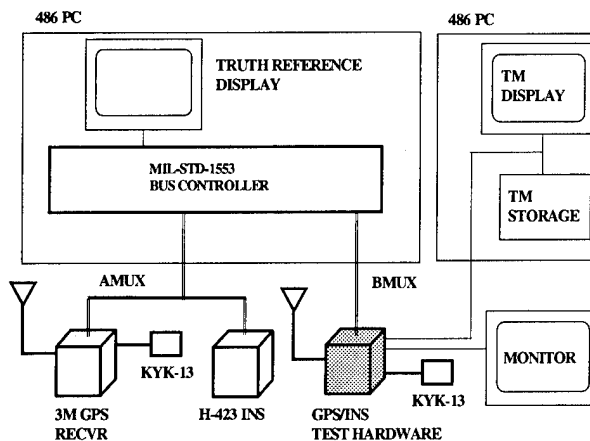


Figure 2. Schematic of MITS Subsystems

The second PC collects and displays telemetry data via a high speed (up to 1000 Kbaud) RS422 serial interface. It is a ruggedized 486 DX 66 Mhz Personal Computer with 20 MB RAM, removable 150 MB Bernoulli hard drive and a removable 88 MB Syquest hard drive. Data are saved to disk cartridges for post-test processing. The MITS can operate in classified environments up to SECRET level.

Avionics

Aircraft avionics consist of a Honeywell H-423 0.8 nm/hr INS and Rockwell-Collins 3M Miniaturized Airborne GPS Receiver (MAGR) linked to the 1553 bus as remote terminals. The BC uses P-code GPS position information from the 3M MAGR to update the H-423 to create a position and velocity truth reference system with 8 - 10 m position and 0.5 fps velocity accuracy. This accuracy is adequate to evaluate tactical grade inertial measurement units with drift rates of 1 - 10 degrees/hr. The MITS GPS antenna is a Rockwell International Controlled Radiation Pattern Antenna (CRPA-2) while the antenna for the IMU/GPS test hardware is the weapon antenna supplied by the customer.

The H-423 adheres to the "Specification for USAF Standard Form, Fit, and Function Medium Accuracy Inertial Navigation Unit," (SNU-84). The SNU-84 establishes the requirements (including performance) of form, fit, and function for an Inertial Navigation Unit (INU) applicable to a broad spectrum of vehicles. It is the intent of this specification to define the INU requirements such that multiple contractor designed and produced hardware can be used interchangeably at the Line Replaceable Unit (LRU) level in any given vehicle.

This ICD affords the INU, or INS, to operate in one of several reference frames; Earth Centered Earth Fix (ECEF), Local Geodetic, Navigation, Sensor, Gyroscope,

Accelerometer, Chassis, and Aircraft Body. The Direction Cosines Matrices (DCMs) for coordinate frame transformations are included in the MIL-STD-1553 messages. A dedicated high speed vector, in which the navigation data is updated up to 200 times per second, is available as is a correction vector used to update the INS using external sensors, i.e., a GPS receiver.

The 3M MAGR receiver follows the "GPS User Equipment Interface Control Document for MIL-STD-1553 Multiplex Bus Interface," (ICD-GPS-059). ICD-GPS-059 defines the 3 M MAGR MIL-STD-1553 interface. Data available from this ICD include ephemeris, navigation, covariance, waypoint, satellite almanac and Precise Time and Time Interval (PTTI) outputs. It is important to note that no classified data is permitted to transmit on the 1553 bus. As a result, the corrected pseudorange data is not available via 1553.

The 3M MAGR also offers an RS-422 instrumentation port (IP) defined by the "GPS User Equipment Interface Control Document for Instrumentation Port Data Link of the DoD Standard GPS UE Radio Receivers" (ICD-GPS-150). ICD-GPS-150 defines the Instrumentation Port Data Link (IPDL) interface. The IPDL provides an interface to transfer data and commands between an external device (in this case, a PC) and a GPS receiver. It has its own protocol and offers virtually the same messages as the ICD-GPS-059, but in greater detail. In the case of the 3M MAGR, raw GPS measurements, classified included, are available.

MITS Power Distribution

Figure 3 depicts the MITS power generation and distribution system. Main power is provided from either two 6.5 Kwatt generators or external building power. One 6.5 KW generator feeds power to the MITS power supplies and computers, while the other 6.5 KW generator is used to run the air-conditioning units. 28V, +/- 15V, +5V DC and 115V AC 400 Hz 3 phase power are furnished by two power supplies. The power distribution system is also designed to run off either generator or completely on external building power.

Test Range

Eglin AFB has at its disposal a vast expanse of ranges. Deserted airfields are prime candidates for testing since they provide clear views of the sky for satellite tracking and wide runways for maneuverability. Several of the runways have surveyed waypoints to intermittently gauge the performance of the test unit. In the near fu-

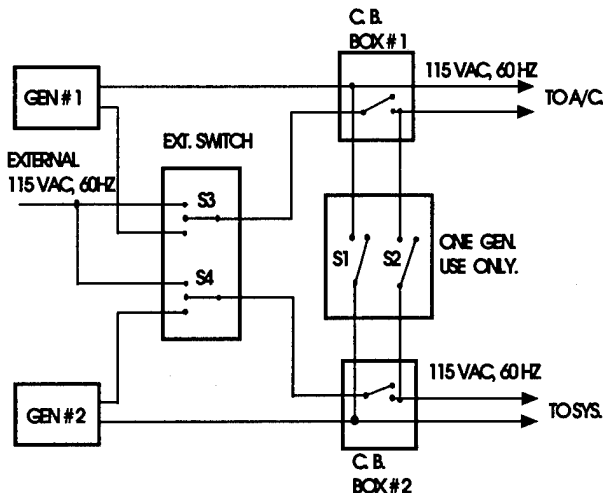


Figure 3. MITS Power Distribution System

ture, WL/MNAG will be able to quickly survey new waypoints according to the test organization's specifications.

Evolution to Dynamic HIL Testbed

Although developed to test advanced tactical navigation systems, these capabilities have positioned MITS as a viable and practical testbed for munition flight test programs. In 1993, the Aeronautical System Center (ASC) initiated the Operational Concept Demonstration (OCD), an Eglin AFB in-house flight test demonstration of an IMU/GPS guided weapon. MITS was recruited to test the guidance hardware and software under dynamic conditions while emulating the 1553 communications interface between the aircraft and the guidance unit. The OCD dynamic ground tests characterized critical software deficiencies and established the value of conducting pre-flight HIL mobile tests with MITS.

Consequently, MITS has evolved into a premier risk-reduction test asset for munition flight test programs. Recently, ASC requested using MITS to conduct similar pre-flight ground dynamic tests for a developmental PGM program entitled Exploitation of Differential GPS for Guidance Enhancement (EDGE). What follows is a discussion of the EDGE program and the pre-flight ground test support using MITS.

EXPLOITATION OF DIFFERENTIAL GPS FOR GUIDANCE ENHANCEMENT

The Exploitation of Differential GPS for Guidance Enhancement (EDGE) program is part of a Product Improvement Program for the Joint Direct Attack Munition

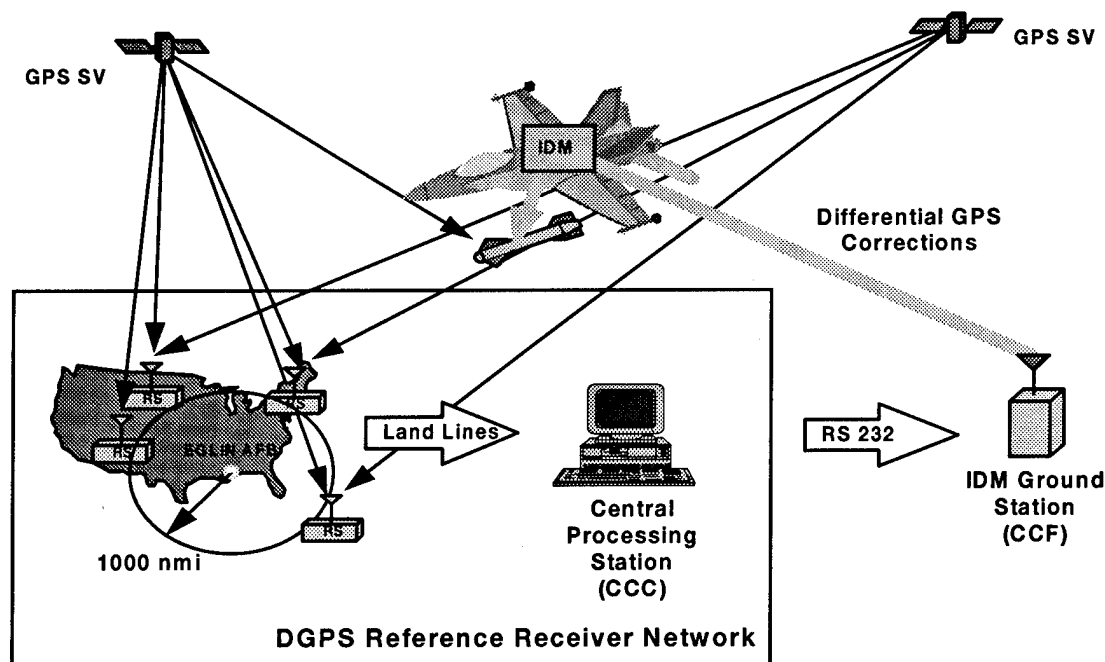


Figure 4. EDGE System Concept

(JDAM) program. System concept of the program is illustrated in Figure 4. Wide-area differential GPS using reference receivers in a network with over 1000 nautical miles separation was identified as a key element in a DGPS JDAM guidance upgrade concept. The objective of EDGE was to demonstrate weapon navigation accuracy improvement through the use of Wide-Area Differential GPS. SRI International developed the Wide-Area Reference Receiver Network by incorporating four reference receiver stations, each hosting a P(Y) code 12-channel Ashtech receiver at sites approximately 1000 nautical miles radius from the Eglin AFB Florida test range. These sites are at Ellsworth AFB, South Dakota; Holloman AFB, New Mexico; Hanscom AFB, Massachusetts; and Roosevelt Roads NS, Puerto Rico.

The EDGE weapon is a 2000 pound bomb with a modified Guided Bomb Unit tail kit known as the GBU-15. The front section normally houses a guidance seeker, but is now replaced with a Honeywell Integrated Flight Management Unit (IFMU). Cardinal components of the IFMU include the 1 degree/hr HG 1700 Inertial Measurement Module and Interstate Electronics Corporation (IEC) SEM-E Fast Acquisition GPS Receiver. GPS time and ephemeris are sent from the aircraft GPS receiver to the IFMU via the 1553 bus, and used to aid in the fast acquisition of GPS signals. The IFMU is responsible for

implementing the tightly-coupled IMU/GPS filter, transfer alignment algorithm, incorporation of differential corrections, and autopilot outputs.

Referring to Figure 4, the EDGE operation begins with the transmission of uncorrected GPS pseudoranges from the reference receivers via land lines to a Central Processing facility at Eglin AFB. Using these pseudoranges, the Central Processor derives and merges a composite set of DGPS corrections for all satellites in view. A subset of the DGPS corrections for the satellites in the local area are transmitted via encrypted UHF to the aircraft's (F-16 BLK 50) Improved Data Modem (IDM), then sent to the weapon through the MIL-STD-1553 bus. After the aircraft executes a transfer alignment and weapon inertial sensor calibration sequence, the EDGE weapon is then released from the F-16 at altitudes and velocities sufficient to permit acquisition and tracking of GPS signals for high-altitude air-to-surface trajectories.

After launch, the weapon acquires GPS and Time-To-First-Fix is achieved in 15-20 secs. During the 120 second flight, the IFMU calculates ionospheric errors and applies differential corrections to the GPS measurements. The IMU/GPS Kalman filter is updated by the corrected

measurements and the Inertial Measurement Module generates velocity and attitude estimates for the autopilot.

EDGE DYNAMIC GROUND TESTS

To reduce program risk, the EDGE program office conducted ground tests to validate the weapon system performance requirements before flight testing. The primary component of the ground tests was using MITS to perform dynamic HIL tests. These MITS HIL tests provided the first dynamic environment for testing the use of differential corrections to aid navigation performance in a fully built-up weapon guidance system. The objectives of the mobile tests were to:

- Verify the MIL-STD-1553 communications interface between the actual aircraft avionics, and differential corrections transmission and the IFMU
- Validate the Transfer Alignment process between the aircraft INS and munition IFMU
- Perform Aircraft/Weapon Mechanization to simulate weapon launch
- Validate GPS fast acquisition and TFFF
- Perform acceptance testing of six guidance kits prior to flight tests

MITS EDGE CONFIGURATION

The MITS operating software was modified to emulate a subset of the F-16 BLK 50 MIL-STD-1553 bus traffic in accordance with the Operational Flight Program (OFP) developed for EDGE. The modification includes sending GPS time and ephemeris from the aircraft GPS receiver, and embedding the differential corrections into the 1553 bus bit stream. In addition, a 3A GPS receiver was acquired to imitate the GPS receiver in the actual aircraft. A PC controlled the MIL-STD-1553 communications bus between MITS and the weapon to duplicate the wing station interface between the aircraft and the weapon. As shown in Figure 5, a Cellular Secure Telephone Unit (STU-III) is used to transmit the differential correction data from the Commahd Control Facility (CCF) to the MITS platform. The corrections are then passed to the 486 PC bus controller and sent to the IFMU. Telemetry from the IFMU is sent through a RS-422 interface to the 486 PC telemetry receiver.

The IFMU's navigation performance was driven by differential GPS accuracies--hence, the MITS truth reference system was not capable of providing truth to effectively evaluate the IFMU. Instead, a series of waypoints were surveyed to provide truth data. These waypoints, and the overall trajectory of the MITS testing, is shown in Figure 6.

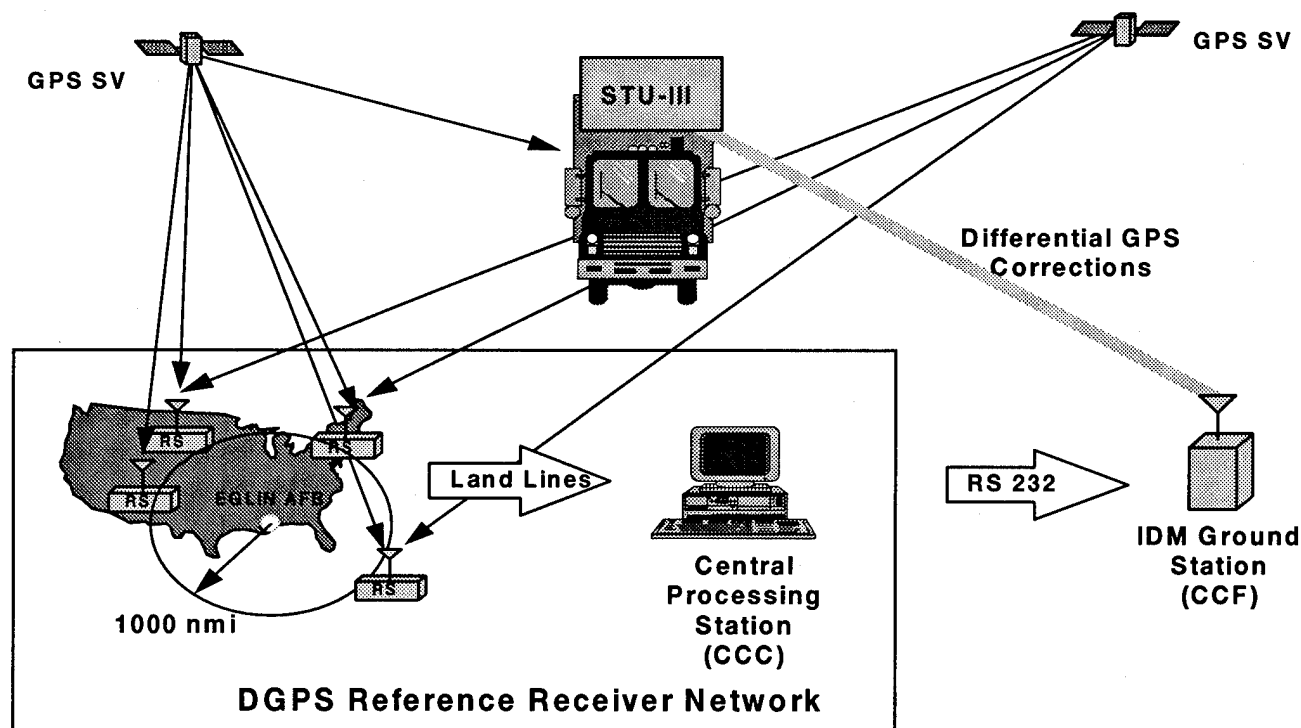


Figure 5. MITS EDGE Dynamic Ground Test Concept

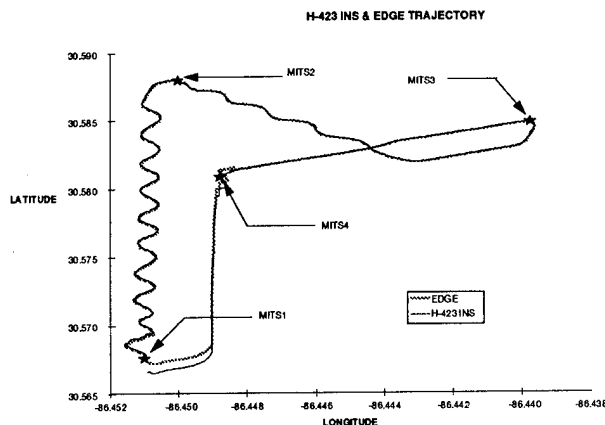


Figure 6. EDGE Ground Test Trajectory

PROCEDURE

As mentioned earlier, the primary role of MITS for the EDGE project was to provide a ground based platform to validate the basic operations of the guidance system. To this end, the mobile test begins by gyrocompassing the H-423 INS situated at a survey point. This assures the most accurate INS data for the remainder of the test. The three basic stages of the PGM are Transfer of Alignment (T/A) initialization, launch and flight. Each of these phases is initiated and monitored by MITS. Figure 7 is a schematic of the MITS EDGE configuration.

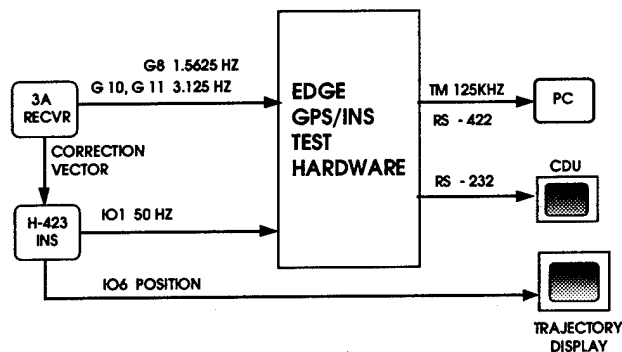


Figure 7. MITS EDGE Signal Configuration

During the T/A phase, the control system is sending the EDGE unit, via MIL-STD-1553, inertial data at a 50 Hz rate. The primary data are extracted from the INS IO1 message block and include position, velocities, accelerations and tilts. The EDGE unit uses these data to determine its orientation within the ECEF reference and to characterize its Kalman filter parameters and biases. Once the item has completed the T/A phase, it should know where it is, how it is oriented, and how to weight its sensor inputs to calculate a valid navigation solution.

Also during this phase, GPS information is being sent at 3.125 Hz (the ephemeris data) and 1.5625 Hz (the position and time data). With this information, the test item GPS receiver can determine the current constellation and position and, at launch time, will be able to quickly and reliably acquire and track enough satellites to begin aiding the IMU. At launch, there is typically about 10 to 15 sec of unaided navigation while the GPS receiver readies itself. At about 10 sec before impact, the GPS aiding is disabled, allowing the weapon to terminate its flight in free inertial mode. This is to prevent any possible "glitches" to the autopilot, and hence any last second control adjustments that may jerk the weapon off its intended course. Therefore, for a 120 sec time of flight, there is approximately 100 seconds of GPS aiding.

Progress of the T/A stage is constantly monitored using the telemetry collect and display capability of the MITS. The primary data of interest include Kalman filter parameters, biases, position, velocities, tilts and error estimates. With these displays, engineers observe the guidance system's progress and performance. More detailed examination is possible by "replaying" the data at a later time. Data presentation and analysis is available through standard PC tools such as Microsoft Excel and custom designed programs.

Timing

Timing is perhaps the most crucial of issues with EDGE. To achieve GPS fast acquisition, the IEC receiver must know time within 10 msec of GPS time. The high dynamics of the aircraft also require that timing be well synchronized among the avionics to assure that inertial data is accurate.

Each device on the MIL-STD-1553 bus, including the BC, has an internal 16 bit clock with a 64 msec resolution. If one of these clocks were to start at zero, it would rollover to zero again 4.194304 seconds later. For the system to operate smoothly, these clocks must be synchronized to within one or two bit times, 64 or 128 msec. The BC is responsible for time synchronization and does so using the MIL-STD-1553 synchronize with data word mode code. The data word associated with this mode code is the time to which the clock is to be set. For EDGE, synchronization occurs every 3.84 sec.

Data from the aircraft INS and GPS receiver contain a time of validity word, indicating when the data can be considered valid. The internal 64 msec clocks are the source for these time tags. Given this with the time of reception, the guidance unit can easily determine the age of the data by simple subtraction.

There is, however, a potential problem at the clock synchronization point. It is entirely possible that a data set from the INS be tagged with a pre-synchronization clock value, and synchronization occur before the guidance unit receives the data. In this case, the guidance unit receives its data at t_1 with a time tag of t_0 , with $t_0 > t_1$, indicating that the data sample is valid sometime in the future. This is not possible.

To circumvent this problem, the PGM must know when synchronization occurred. This is accomplished by yet another MIL-STD-1553 message. Therefore, given the synchronization time, t_s , the age of the data at or near synchronization can be determined by:

$$\text{age} = (t_s + t_1) - t_0$$

The age should never be over 20 msec for the INS and 1 sec for the GPS data.

The GPS receiver must have a time solution within 10 msec of the actual GPS time to achieve fast acquisition. Universal Time Coordinate (UTC) time is passed in the 1.5625 Hz data as is the time of validity for that UTC time. After calculating the age of the data, the PGM can easily determine within 10 msec the actual UTC time.

Differential Corrections

The source of GPS differential corrections is the CCF at Eglin AFB. Data from the four remote GPS stations converge here, providing information for all satellites in view. The CCF is responsible for determining the optimum satellite constellation and calculating corrections for the EDGE unit.

In the operational scenario, the corrections are transmitted to the aircraft through the IDM and then to the weapon over the communications bus. For MITS testing, the STU-III cellular phone is used. Both links are certified secure. The numbers are recorded from the STU-III, entered in the PC and transmitted directly to the weapon in another MIL-STD-1553 message.

INS Altitude Data

Altitude data is necessary for proper INS operation. For the F16, altitude is available using the baroaltimeter. During MITS ground tests, the altitude changes stay well within the advertised accuracy of the baroaltimeter, ± 50 ft. As a result, the controlling PC can easily simulate the baroaltimeter's data, given an initial value close to field elevation.

RESULTS

The following results represent data from typical mobile ground tests of the EDGE guidance hardware. The intent here is to show what data is collected and analyzed to validate the aircraft-weapon interface, transfer alignment, and navigation performance. Figures 8 - 10 show the inertial misalignment estimates and variances of the estimates from the IFMU transfer alignment Kalman filter. In all three axis, a transition exists between initial estimates and relatively smaller estimates of axis misalignment. Prior to this point, the variances are converging up to the transition point where they expand and then settle to a relatively constant value. This transition point signifies when an artificial "Transfer Align

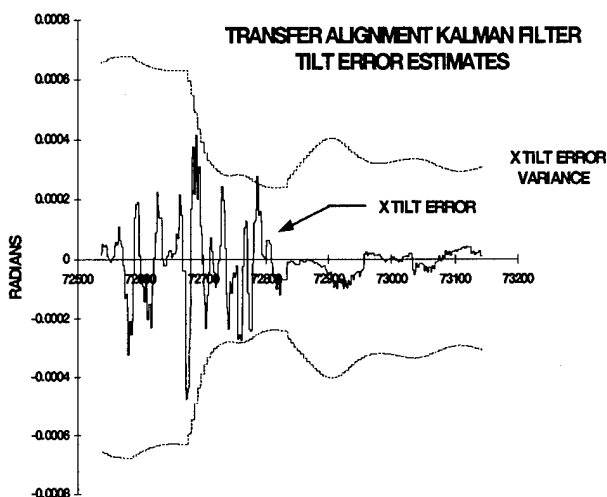


Figure 8. Transfer Alignment filter X axis tilt error estimates

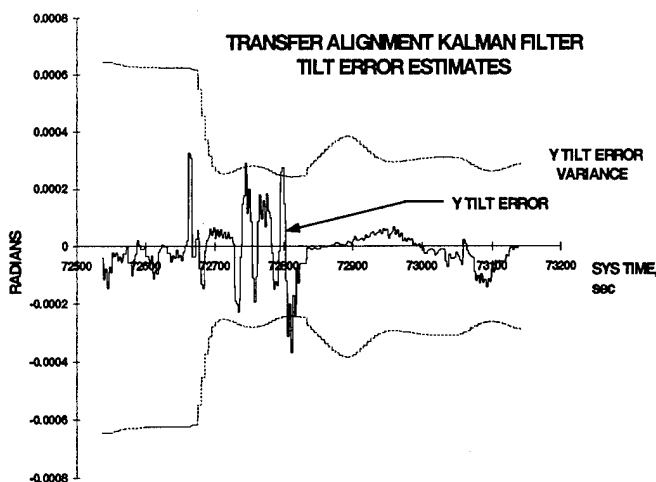


Figure 9. Transfer Alignment filter Y axis tilt error estimates

Complete" discrete is sent by MITS. The signal is artificially induced because MITS dynamics do not approach the aircraft's dynamic environment. However, this test is

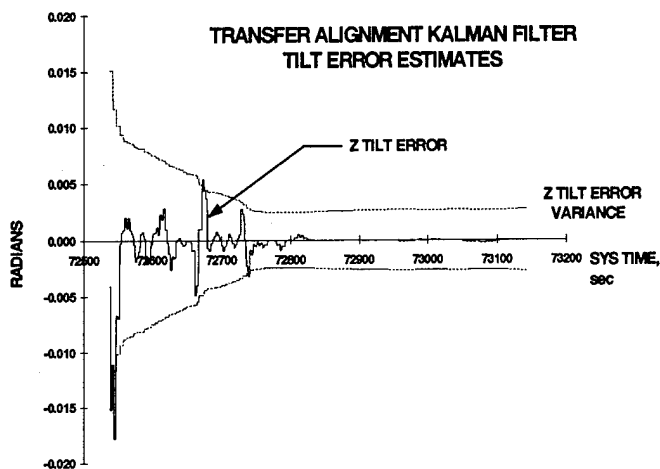


Figure 10. Transfer Alignment filter Z axis tilt error estimates

a notable event since it signifies successful MIL-STD-1553 interface with the aircraft avionics and validates the functionality of the Transfer Alignment filter. Note how well the Z axis misalignment estimates and variances perform. This is due to the observability of heading (or azimuth) errors when performing S-turns (refer to the test trajectory in Figure 6).

Figures 10 and 11 show position latitude and longitude GPS errors of three systems, respectively: a) the aircraft P-code 3A GPS Receiver, b) the EDGE GPS-aided navigation solution with wide area differential corrections and c) the weapon P-code IEC SEM-E GPS Receiver. The data in these plots represent MITS moving toward and stopping at the MITS1 waypoint. As seen in both figures, the non-corrected 3A GPS receiver position exhibit favorable behavior in latitude, but has initial diver-

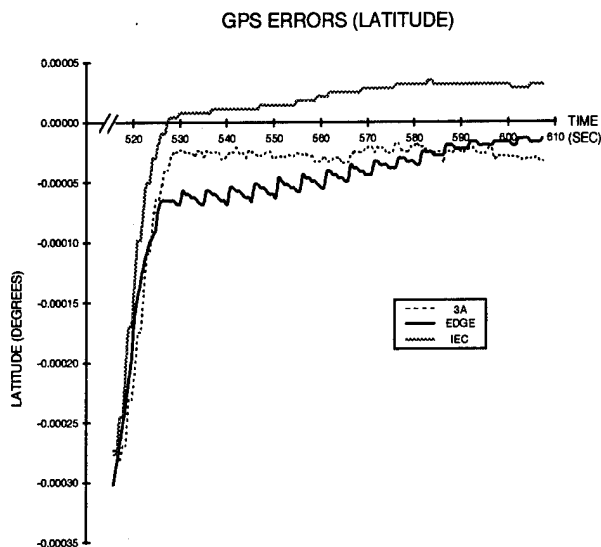


Figure 11. EDGE Latitude GPS Errors

gent behavior in longitude, indicating a bias in that direction. In comparison, the EDGE Differential GPS-aided position solution converges in latitude and is well-behaved in the longitudinal direction. The performance seen here of the EDGE GPS-aided navigation attests the accuracy enhancement gained by using wide area differential corrections.

SUMMARY

This paper describes the instrumentation and capabilities of the Mobile Inertial Test System (MITS), and discusses its application as an in-house test asset for advanced tactical grade navigation systems and, lately, a dynamic HIL testbed for PGM flight demonstration programs. For EDGE, engineers at Wright Laboratory Armament Directorate have modified the MITS operating

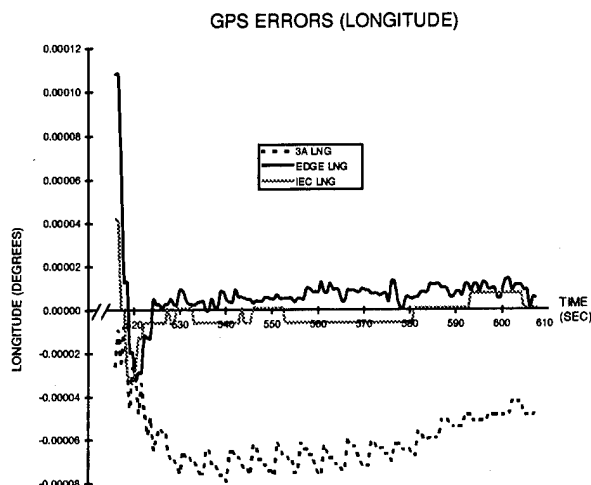


Figure 12. EDGE Longitude GPS Errors

software to emulate a subset of the F-16 BLK 50 MIL-STD-1553 bus traffic in accordance with the OFF. As a result, MITS was used to validate the transfer alignment function, GPS fast acquisition, wide area differential correction accuracies, and GPS-aided navigation performance of each EDGE guidance unit prior to flight tests. Experience with EDGE and other PGM flight demonstration programs has given Armament Directorate engineers the flexibility to use MITS to emulate the aircraft-weapon interface of any DOD aircraft with a MIL-STD-1553 bus in accordance to an established OFF.

REFERENCES

1. Specification for USAF Standard Form, Fit, and Function Medium Accuracy Inertial Navigation Unit, (SNU-84).

2. GPS User Equipment Interface Control Document for MIL-STD-1553 Multiplex Bus Interface, (ICD-GPS-059).
3. GPS User Equipment Interface Control Document for Instrumentation Port Data Link of the DoD Standard GPS UE Radio Receivers (ICD-GPS-150).

HIL Testing of the Navy LEAP GPS/INS Package

George Stupp and David Lehnus
The Johns Hopkins Applied Physics Laboratory

BIOGRAPHY

George B. Stupp is a Senior Engineer in the Guidance, Control and Navigation Systems Group at The Johns Hopkins Applied Physics Laboratory (JHU/APL). He received his B.S. in Electrical Engineering in 1969 and M.S. in Electrical Engineering in 1971 from the University of Illinois. Mr. Stupp joined JHU/APL in 1973 and has worked extensively with all-digital and hardware-in-the-loop simulation of missile systems. He was principal developer and is currently the lead engineer and manager of JHU/APL's Navigation and Guidance System Integration Laboratory (NAVSIL).

David S. Lehnus is a Senior Engineer in the RF Missile Systems Group at JHU/APL. He received his B.S. in Electrical Engineering at Virginia Tech University in 1984, and an M.S. in Electrical Engineering from Johns Hopkins University in 1991. Mr. Lehnus joined JHU/APL in 1986 and was responsible for the development of an ECM signal simulator for the NAVSIL. Since 1992, he has led the performance evaluations of various GPS guidance systems in the NAVSIL.

ABSTRACT

As part of the Navy Lightweight Exo-Atmospheric Projectile (LEAP) Technology Demonstration program, a new interceptor based on STANDARD Missile and a shipboard weapon system was built to demonstrate the potential of integrating the required technologies to defend against tactical ballistic missiles. Incoming tactical missiles would be engaged in outer space (prior to atmospheric reentry) with a Kinetic Kill Vehicle (KKV). Accurate knowledge of interceptor attitude as well as position and velocity is critical to pointing the KKV at the target. The LEAP system used an integrated GPS/INS package to provide this data. The mission contained both high acceleration and high velocity while demanding high accuracy attitude estimates at the end of the short flight.

The paper describes hardware-in-the-loop (HIL) testing done on the LEAP GPS/INS package using JHU/APL's NAVSIL laboratory. The test configuration presented a detailed simulated flight environment to the GPS/INS through both

simulated GPS RF and simulated inertial sensor signals. Multiple flight trajectories were generated by a high fidelity 6-DOF all-digital interceptor simulation. Detailed effects in the HIL simulation included inertial instrument errors, GPS antenna pattern signal level effects, and acceleration induced GPS receiver reference oscillator shift. The resulting high fidelity HIL testing capability provided important support to development of the GPS/INS package and an independent assessment of expected GPS/INS performance. Overall mission success was predicted by inserting measured HIL GPS/INS errors into the 6-DOF LEAP mission simulation.

INTRODUCTION

In support of the Navy Lightweight Exo-Atmospheric Projectile (LEAP) program, The Johns Hopkins University Applied Physics Laboratory (JHU/APL) tested and evaluated the LEAP demonstration vehicle's GPS/INS navigation system. The goal of JHU/APL was to provide the Navy with a high confidence assessment that the LEAP GPS-Aided Inertial Navigation System (GAINS) would perform according to the requirements in the LEAP mission environment. The performance assessment of the GAINS was conducted in the JHU/APL Navigation and Guidance System Integration Laboratory (NAVSIL).

The Navy LEAP was a technology demonstration program for a tactical ballistic missile intercept system based on the Terrier Standard Missile (SM-2). The three-stage missile carries a kinetic kill vehicle (KKV) with an infra-red seeker system. The KKV is ejected by the missile third stage at a point where its seeker has a high-probability of acquiring the target. The KKV then autonomously guides and intercepts the target with a direct impact.

The third stage guidance system in the LEAP missile is the GAINS, an inertial navigation system consisting of a navigation and Kalman filter processor developed by Hughes Aircraft Company, a preselected AMRAAM inertial measurement unit, and a Rockwell-Collins GEM-I GPS receiver. The GAINS relies on position and velocity updates from the GEM-I receiver to estimate and correct the errors in

the inertial sensor. The addition of GPS allows the GAINS to achieve the required level of accuracy with a medium quality inertial sensor.

LEAP Mission

The LEAP mission presented a challenging environment for GPS receiver technology. The mission contains extreme dynamics in not only acceleration and velocity but also in the missile body attitude. The GPS receiver must be able to reacquire lost satellites quickly and to navigate accurately at high Mach number velocities. Figure 1 shows the velocity, acceleration, and body angles versus time for a nominal LEAP mission. The nominal mission characteristics include boost, second and third stage motors at nominal temperature, a nominal intercept range, and 90° of roll during boost.

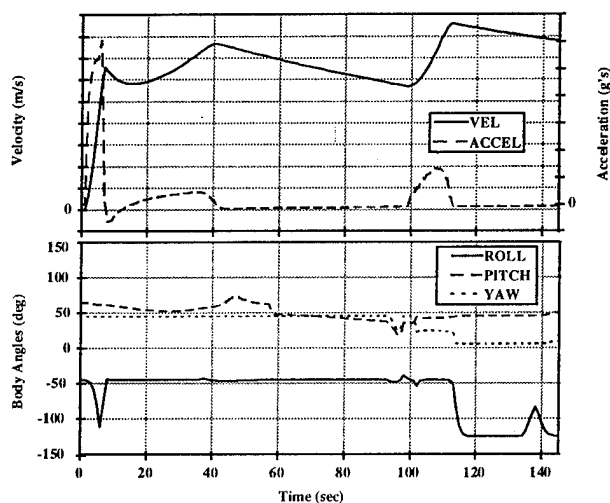


Figure 1 Nominal Mission Acceleration, Velocity and Body Angles versus Time

Figure 2 illustrates the body angles for a simulated stressing mission (discussed later). The principal stressing feature is the large, high angular rate roll excursion of 2000° during boost. The angular motion is due to an assumed maximum booster fin misalignment.

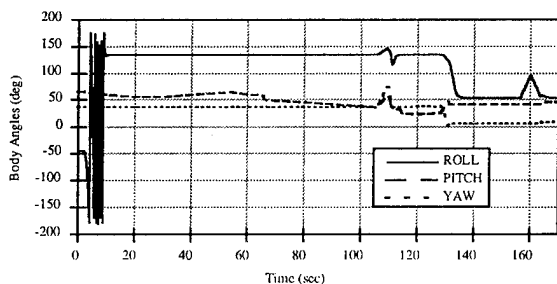


Figure 2 Stressing Mission Body Angles versus Time

Prior to the LEAP launch, power is provided to the GAINS so that the GEM-I receiver can be initialized and perform satellite acquisition. Sufficient time is allotted to allow the

receiver to acquire four satellites and begin navigating, acquire the additional visible satellites, and to update its almanac. At approximately 5 minutes before the launch, the GAINS navigation processor and Kalman filter are initialized and begin to process both inertial sensor data and GPS solutions.

At launch the missile enters the boost phase during which the missile longitudinal acceleration exceeds 25 g's and the receiver loses lock on the satellite signals that were tracked. The missile second stage follows boost and burns for approximately 30 seconds in a nominal mission as shown in Figure 1. Simulated missile velocity exceeds Mach 3. The receiver should reacquire the lost GPS signals and provide solutions to the GAINS navigator during the second stage burn, so that the errors in the attitude estimates can be corrected as soon as possible.

After the second stage and a coast period, the remaining third stage undergoes a rapid pitch and yaw maneuver shown in Figure 1 at approximately 95 seconds. This 'pitch to ditch' maneuver is performed so that the nose cone over the KKV can be ejected away from the missile. A tracked satellite can potentially be lost during this maneuver, as the deep nose null in the GPS antenna pattern sweeps through an arc of approximately 25° .

Maintaining tracking of four satellites at the beginning and during third stage rocket motor burn is important to maintaining position, velocity and pointing accuracy. The third stage, with a maximum acceleration of >6 g's, can also cause a loss of lock on one or more of the satellites being tracked. The accuracy of the GAINS position and velocity solutions are critical at this point in the mission to maintain pointing of the third stage in the correct direction for the KKV intercept. Following the third stage and a short coast, the KKV is provided with inertial alignment and is ejected. The pitch, roll, and yaw estimates provided by the GAINS must be sufficiently accurate to allow the KKV seeker to place its field of view over the target with minimal searching.

In summary, the LEAP mission is characterized by high dynamics and a short duration which impose demanding requirements on the GPS receiver and the GAINS system. The LEAP GPS receiver must have the capability to reacquire quickly and to rapidly substitute for satellites lost due to antenna pattern nulls. The challenges of the LEAP application for the GAINS were a compelling motivation for extensively utilizing hardware-in-the-loop testing during the design and development phases.

GAINS Package

The HIL simulation capability in NAVSIL was specifically enhanced to support HIL testing of the GAINS. Both general and special purpose simulations and signal generation systems

were developed for the GAINS tests. As background for the description of the NAVSIL simulation, a brief discussion of the GAINS design, operation, and requirements is presented here.

The GAINS is an inertial navigation system with an integrated GPS receiver that provides the guidance for the LEAP third stage. As shown in Figure 3, the GAINS package contains a navigation and Kalman filter processor card, and input/output (I/O) card and the Rockwell-Collins GEM-I receiver in a SEM-E form. The GEM-I receiver is a 5-channel, L1-only GPS receiver. The additional position accuracy provided by a dual-frequency GPS receiver was not required for the GAINS to meet the position accuracy specifications. Inertial aiding is provided to the GEM-I to allow the receiver to reacquire following boost and to assist the receiver in tracking through the missile dynamics.

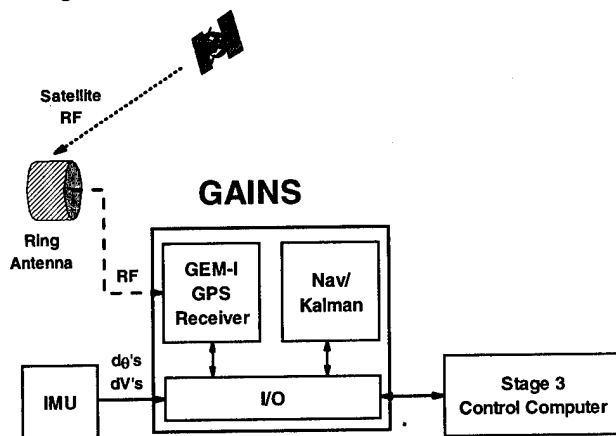


Figure 3 GAINS Functional Configuration

External to the GAINS package are the inertial measurement unit (IMU) and the GPS antenna. A set of AMRAAM IMU's manufactured by GEC were preselected for the LEAP program. The AMRAAM IMU is a medium-quality (30° /hour) inertial sensor. For the LEAP mission, specific units were preselected at the factory to have 10° /hour drift characteristics. Error characteristics of the IMU such as sensor misalignments and g and g^2 sensitivities cause the inertial system to develop large errors during the boost phase.

The GPS antenna is a wrap-around design that is located on the third stage behind the KKV nose cone. The antenna consists of individual patches and a feed line structure. The resulting pattern has a lobe and null pattern in the azimuth plane in addition to the deep nulls in the nose and tail aspects. The various nulls in the pattern introduced potential risk of loss of satellites during many phases in the mission.

The GAINS navigator processes inertial measurements (ΔV 's and $\Delta \theta$'s) from the IMU that are generated at a 100 Hz rate. GPS solutions are transmitted from the receiver to the navigation processor. Velocity updates are done at 1 Hz while position updates occur at 50 second intervals. The position update rate is lower to avoid potential correlation problems

between the receiver and INS Kalman filters.

The GAINS is initialized through the Stage 3 Control Computer (S3CC) while on the launcher rail and provides position, velocity, and attitude data to the S3CC throughout the missile flight.

The LEAP Mission Requirements Definition (MRD) placed the following performance requirements on the GAINS. During the third stage burn, the position and velocity errors in each axis must not exceed 61 meters and 5 meters per second respectively. At KKV release, the GAINS pointing, or attitude, error limits were 7.5 milliradians in pitch and yaw and 15.0 milliradians in roll.

CHARACTERISTICS OF NAVSIL

NAVSIL consists of various subsystems that provide control of the HIL simulation, signals to the GPS navigation system under test, monitoring of the simulation, and the recording of output data and simulation parameters. A functional diagram of the principal NAVSIL subsystems utilized in the GAINS HIL testing is shown in Figure 4.

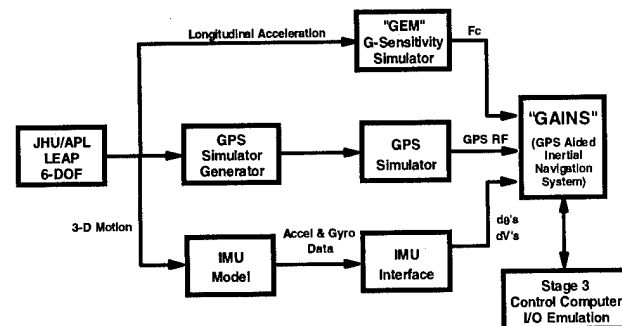


Figure 4 NAVSIL GAINS Testing Configuration

The LEAP 6-DOF trajectory description is produced in an off-line simulation. The trajectory data drives the satellite generator, IMU data generator and interface, and the receiver reference generator, or g -sensitivity simulator. These devices then independently transmit to the GAINS the corresponding signals precisely synchronized to the simulation time.

Initialization of the GAINS, consisting of initial estimates of position, velocity, and attitude, are provided through the Stage 3 Control Computer simulator. Following initialization, the Stage 3 simulator provides data recording capability.

GPS Satellite Signal Simulator

The GPS satellite simulator in NAVSIL is a 10-channel Stanford Telecommunications Model 7200. The satellite simulator can accept any GPS almanac and simulate the visible satellites at any location for any date and time. The simulator accurately reproduces both the carrier and code effects that are induced due to satellite and missile motion and

propagation effects. In the GAINS testing, trajectory and satellite power updates were provided to the satellite simulator at 20 Hz and 4 Hz respectively. The simulator is capable of simulating L1 and L2 with C/A and P codes. GPS space segment errors were approximated with the addition of biases to the simulator's pseudorange calibration values. The set of bias values was selected from a normal distribution with a standard deviation of 4.3 meters.

IMU Signal Generator

A VME-based, IMU Signal Generator was developed at JHU/APL to provide the real-time IMU data (delta-velocity and delta-angle values) to the LEAP GAINS. The IMU Signal Generator was tightly synchronized to the simulation time so that the IMU data at 100 Hz would precisely correspond to the simulated missile trajectory. The simulated IMU data was generated in an off-line IMU model developed at JHU/APL. This digital IMU simulation allows control of the IMU characteristics, e.g. accelerometer bias, misalignment, scale factor errors, and noise; gyro drift, misalignment, scale factor errors, g and g^2 sensitivity, and noise.

Receiver External Reference Generator

An external reference signal for the GPS receiver was provided in the NAVSIL GAINS testing. The frequency of this reference was varied in real-time to simulate the g -effects on the crystal reference in the receiver. The GEM-I internal reference has a specified g sensitivity of 0.002 ppm/ g and a nominal frequency of approximately 10.9 MHz. A time-tagged file of 20-Hz g -sensitivity data was produced in an off-line computation for each LEAP trajectory used in GAINS tests. A PC-based controller with a high-speed D/A card was used to provide the required analog control of an RF signal generator with a DC FM capability.

LEAP 6-DOF Trajectory Simulation

The LEAP 6-DOF simulation is a digital simulation of the SM-2/LEAP missile that provides high-fidelity trajectory data for NAVSIL HIL tests. The LEAP 6-DOF simulation accurately models the thrust/velocity profiles and the attitude maneuvers during the SM-2/LEAP flight. The LEAP mission trajectories began with the missile on the launch rail and ended with the KKV release. A minimum of 7 minutes was simulated on the launch rail followed by the missile flight of 145 to 165 seconds. The GAINS tests were conducted with various trajectories that represented cold, nominal and hot thrust profiles for the boost, second stage, and third stage motors.

GAINS GPS Antenna Pattern

The effects of the GAINS GPS antenna pattern were simulated in all of the NAVSIL GAINS testing. An antenna simulation

was necessary in order to accurately predict the reacquisition performance of the GAINS GPS receiver following boost, as well as to assess the receiver tracking performance during the remaining flight. The LEAP GPS antenna was a ring design consisting of eight patches. This design produced a lobe and null pattern in the azimuth plane in addition to the deep nulls toward the missile's nose and tail. Using data from antenna pattern measurements conducted in an anechoic chamber, the antenna gain effects were simulated on each individual satellite signal in real-time.

Stage 3 Control Computer

A PC-based system was used in GAINS testing to simulate the Stage 3 Control Computer (S3CC) in the LEAP vehicle. The S3CC system provided the primary method for the initialization of the GAINS and the data extraction of GAINS output messages. The S3CC system provided the capability to record the telemetry and autopilot messages from the GAINS. The GAINS was normally initialized with zero initial velocity and position error. Initial misalignment errors, representing launcher pointing errors, were introduced into the initial values of roll, pitch, and heading transmitted to the GAINS.

Other NAVSIL Subsystems

Two additional NAVSIL subsystems, not shown in the figure, were utilized during the GAINS testing. Control of the simulation was provided by the Real-Time Computer System (RTCS), a Concurrent Model 8500 digital computer with six R-3000 CPU's. This system has real-time processing capabilities and provides real-time I/O through a VME backplane. The RTCS commands the GPS simulator to produce the GPS RF signals that correspond to the desired missile trajectory and also commands the signal levels of the individual simulated satellites. The RTCS also controls the establishment of the simulation time, so that the operation of all of the subsystems in the facility can be synchronized. Finally, the RTCS provides a data extraction capability in many test situations.

A NAVSIL GPS ECM Signal Simulator was developed at JHU/APL specifically for the performance evaluation of missile navigation systems that utilize GPS. The ECM simulator was used in the GAINS testing to assess the susceptibility of the system to possible L-band radio frequency interference (RFI).

NAVSIL HIL GAINS TESTING RESULTS

Numerous test series were performed on the GAINS package throughout its development. Numerous tests of GAINS and GEM-I software versions were done. Other studies included pre-launch drift effects, misalignment sensitivities, and satellite visibility and trackability in the antenna pattern. Only

example results will be shown here using the final as-flown GAINS design. For each test GAINS package output data was recorded and compared with "truth", as defined by the HIL simulation, to calculate errors. In addition to examining position, velocity and attitude estimate errors from the INS function in the GAINS, other parameters typically analyzed following each test were Kalman filter Figure-of-Merit, Kalman filter position and velocity residuals, GEM-I receiver position and velocity errors, GEM-I receiver constellation change flag, number of receiver channels in State 5 tracking, and GEM-I receiver Figure-of-Merit. Other parameters recorded in each test that were available for examination to support more thorough analysis included GEM-I receiver covariance matrix, GEM-I receiver C/N₀, tracking states, and satellite ID's, Kalman filter correction matrix, Kalman filter U & D matrices, and GAINS and GEM-I error diagnostics.

Table 1 lists the conditions used for two types of missions, a nominal mission and a stressing mission. Other near nominal and stressing missions were tested, but are not discussed here. The stressing mission shown was one of several used to expose the limits of GAINS performance. It contained maximal roll attitude change early in the flight combined with long rocket motor burn time (cold motors) and a long mission flight time. In the results shown below, cases were run using picks from various distributions as shown in Table 1. For example, 10 stressing cases were run. IMU errors were used from 10 picks from a normal distribution with 1 sigma values set to 1/3 of the LEAP IMU specification for each IMU error variable, e.g. 10 sets of IMU errors. The stressing sets were the 10 worst cases from the 20 nominal sets. The expected launch window was divided into seven intervals. Each case was run starting at the beginning of one of these intervals, using intervals again as needed to cover the number of cases.

Mission Conditions	Nominal (20 cases) - nominal motors - nom. intercept range - 90 deg boost roll	Stressing (10 cases) - cold motors - max. intercept range - 2000 deg boost roll
IMU Errors	20 Sets selected from a normal distribution (1σ = 1/3 spec)	10 Sets selected from a normal distribution (1σ = 1/3 spec)
INS Initialization Errors	20 Sets selected from a uniform dist. (max = 1.5 deg)	10 Sets selected from a uniform dist. (max = 1.5 deg)
Launch Times (launch times repeated)	7 Times at regular intervals over the launch window	6 Times from original set of 7 during the launch window

Table 1 Example Test Mission Conditions

Figures 5 through 9 show the GAINS performance results. Each figure contains an overplot of all the cases for that mission. This illustrates the envelope of performance encountered in the HIL testing. The LEAP specification for each parameter of interest is shown on each figure. Note the specified performance applies only at or over certain times. For example, the position error requirements are specified from the beginning of third stage rocket motor burn, whereas attitude requirements apply at KKV release. Figures 5 and 6

contain overplots of the ECEF X, Y and Z position and velocity errors. Reacquisition following loss of lock during boost varies with the cases, with the latest being about 60 seconds for the nominal mission. Third stage rocket motor acceleration combined with attitude errors causes loss of lock in several cases. In several cases the resulting position and velocity errors exceeded specification over a short period for the stressing mission. Note the velocity scales are different for the stressing mission. An off-line 6-DOF simulation study of KKV intercept performance showed insignificant degradation in miss distance resulting from these errors.

The angular specifications for the GAINS were considered the most difficult to meet. The accuracy of the angular initialization of the GAINS was dependent on the tracking accuracy of the missile launcher. In addition missile roll attitude was more difficult for the GAINS to measure after initialization and prior to launch because of the 65° launcher rail elevation. During boost the large g and g² gyro errors induced large angle estimate errors. The stressing mission produced very large roll errors which are off scale in Figure 7 until near the end of third stage rocket motor burn. The simulated third stage separation at about 65 seconds in the stressing mission caused sufficient angular motion to increase the angular errors. These angle errors must then be corrected before KKV release. As can be seen in the figures, the third stage acceleration allowed adequate correction of angular estimate errors to meet specifications in all cases.

CONCLUSIONS

Throughout the development of the GAINS package, interactive HIL testing proved highly valuable in surfacing problems early, thus allowing easier solutions. The mission realistic fidelity, explicit knowledge of "truth" and repeatability of the HIL simulation revealed subtle details of GAINS response and sensitivities to parameter variation that would be difficult or impossible to detect in flight tests. The ability to examine a large number of trials under highly stressing conditions demonstrated robustness. In support of post-flight analysis, the NAVSIL HIL simulation confirmed the cause of behaviors seen in the flight.

The NAVSIL HIL testing demonstrated the GAINS would meet the performance requirements under nominal LEAP mission conditions. The mission risk was thus reduced through the utilization of extensive HIL testing. The successful performance of the GAINS in the FTV-4 test flight confirmed the NAVSIL HIL performance predictions.

ACKNOWLEDGEMENTS

The authors would like to acknowledge Todd Moore and Frank Ziolkowski of Hughes Aircraft Company for their assistance during the NAVSIL facility development and the subsequent testing and analysis.

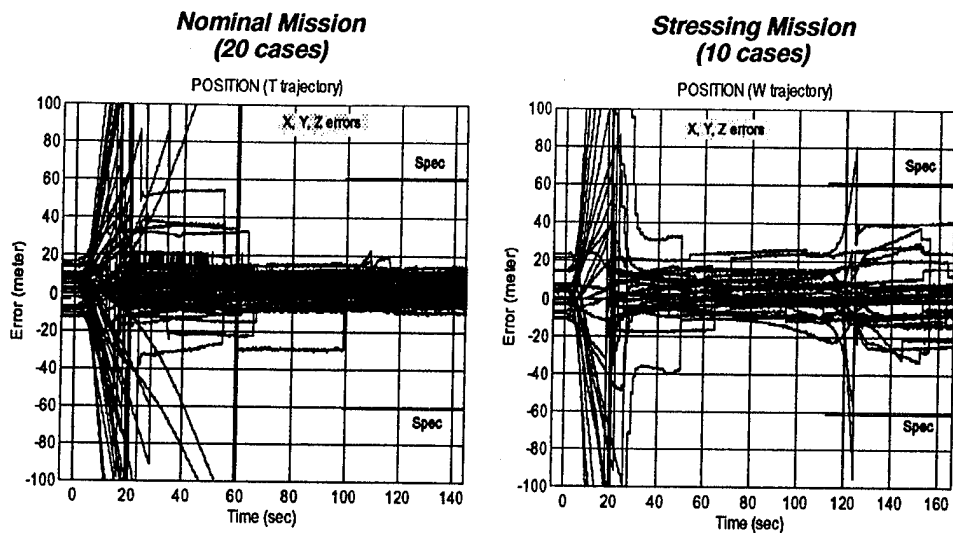


Figure 5 Position Errors versus Time

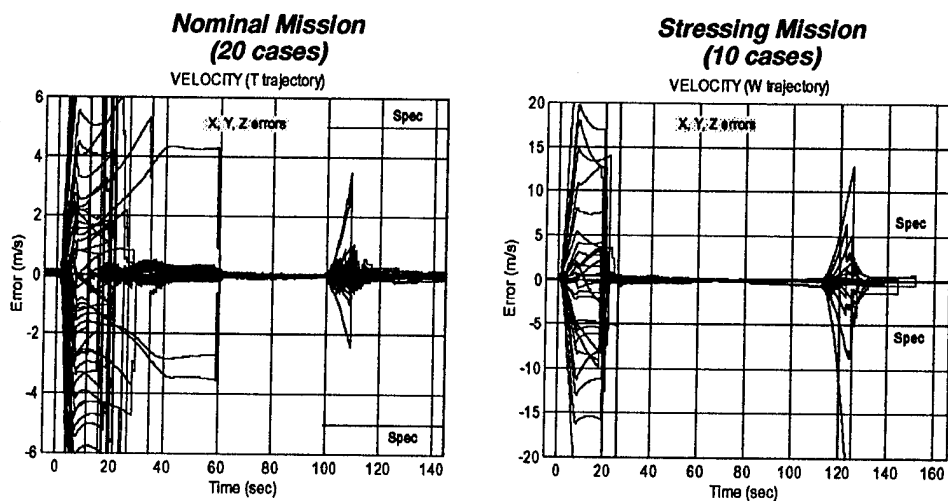


Figure 6 Velocity Errors versus Time

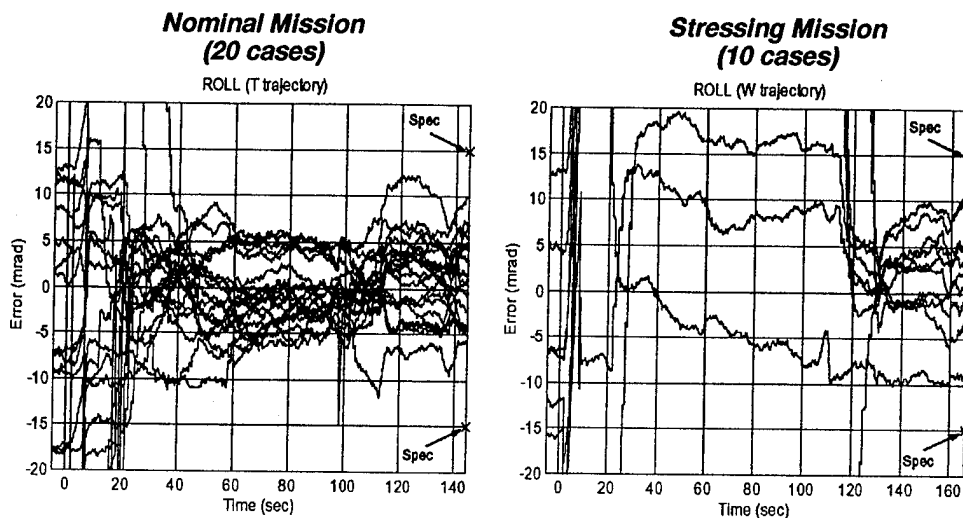


Figure 7 Roll Errors versus Time

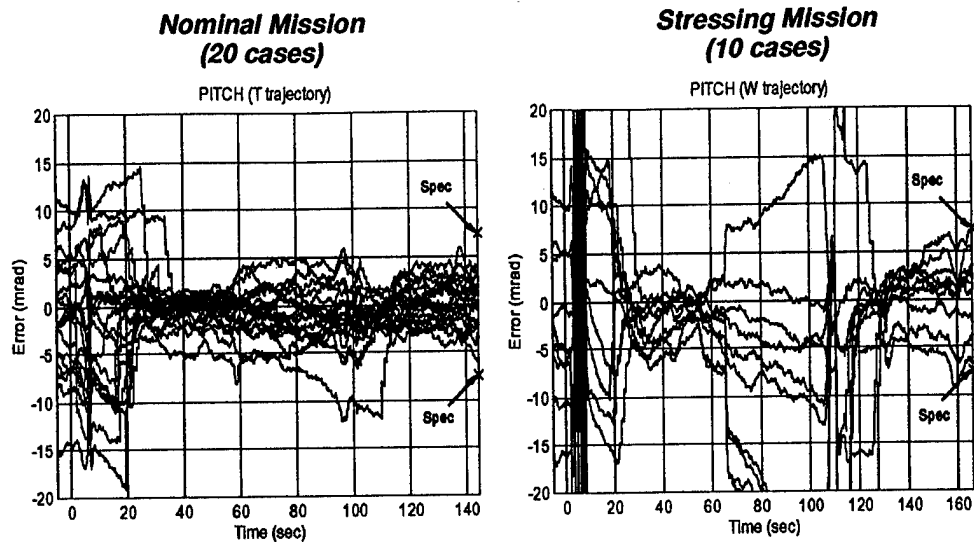


Figure 8 Pitch Errors versus Time

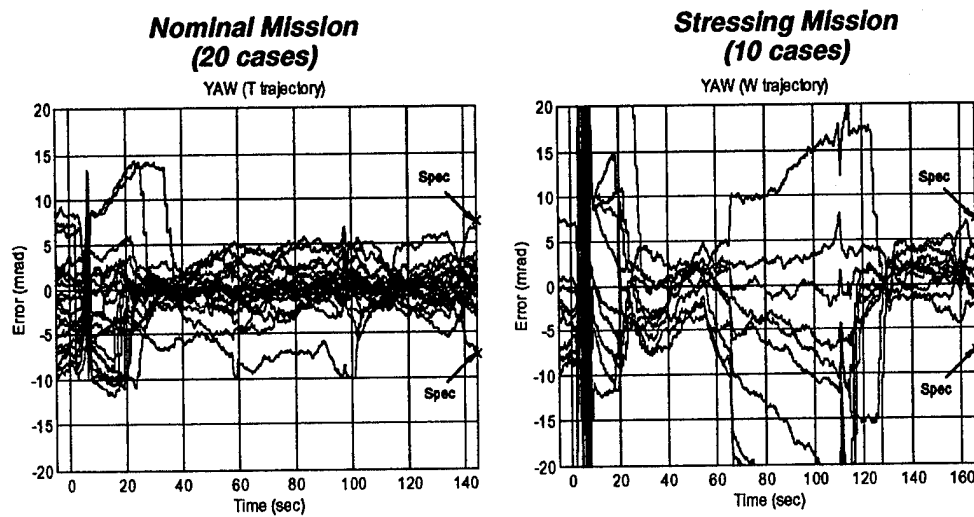


Figure 9 Yaw Errors versus Time



Session A6

Attitude Determination

Chair:

Dr. Penina Axelrad
University of Colorado

Co-Chair:

Mr. Ron Brown
E-Systems

A Single-Baseline Attitude Measurement System Using Low-Cost C/A-Code Receivers

James Gilkey, David Richardson, and Christopher Terndrup
SRI International

BIBLIOGRAPHY

James Y. Gilkey, a Senior Research Engineer at SRI International, specializes in analyzing training range requirements and applying GPS to meet those requirements. His recent project assignments have included development of a GPS attitude measurement system for use on an Army National Guard training range (the subject of this paper), analysis of carrier phase tracking for automated highway systems (the subject of an ION '94 paper), analysis and comparison of seeker alternatives for the Joint Direct Attack Munition (JDAM), and development of differential correction software for and accuracy analysis of a GPS tracking system. Jim received both a B.S.E.E. and M.S.E.E. from Stanford University. He has been with SRI since 1966.

David Y. Richardson, also a Senior Research Engineer at SRI, specializes in systems engineering, applied mathematics, simulation, and software development. In addition to being involved in developing this GPS-based attitude measurement system, he was a major participant in the development of a family of GPS equipment for test and training range applications, and he acted as a test director during testing of GPS equipment at the U.S. Army Kwajalein Atoll. A recent assignment required him to provide GPS test support during prototype testing of the Arrow missile. Dave, who has been with SRI since 1973, holds a B.S. in mathematics from the University of Michigan and an M.S. in industrial and systems engineering from Ohio State University.

Christopher W. Terndrup is a Senior Research Engineer at SRI and has been with SRI since 1978. He specializes in analyzing the requirements for, and then developing, instrumentation for test and training ranges. He is currently project leader for the training system for which this attitude measurement system was developed. He has designed and developed both hardware and software for numerous military training ranges across the United

States, and recently investigated the feasibility of using the Miniaturized Airborne GPS Receiver (MAGR) on the F/A-18 and AV-8B as a source of tracking data for tactical training range instrumentation. Chris received his B.S. in electrical engineering and computer science from the University of California at Santa Barbara.

ABSTRACT

This paper describes a single-axis, dual-antenna, GPS attitude measurement system developed by SRI International to determine the azimuth and elevation angles of military weapons, such as the 120-mm gun on the Abrams tank, during training exercises. The pointing angle is used to pair the weapon with the intended target.

The system uses low-cost, six-channel, commercially available, single-frequency, C/A-code GPS receivers. No attempt is made to synchronize the receivers' clocks. Antenna separation is approximately six wavelengths.

Ambiguity resolution is achieved using a modified Hatch integer search algorithm. Resolution is facilitated by a clinometer that provides approximate elevation angle information when the vehicle and weapon are stationary; angular motion limits the search sector when the weapon is moving. With six satellites in track, ambiguities are almost always resolved in less than 100 seconds and are typically resolved in less than 10 seconds. Once angular "track" has been achieved, the validity of the integer set is revalidated each epoch by monitoring the residuals, the computed baseline length, and the elevation or azimuth sector limits that can be inferred from the clinometer and from relative antenna motion.

At the end of the paper, the results of this constrained design are compared with results achieved using longer baselines, better receivers, and better multipath conditions.

INTRODUCTION

The objective of this effort has been to develop a low-cost attitude measurement technique that will perform satisfactorily on the gun barrel of an M1A1 tank or an M2/M3 Bradley during training exercises. In most cases, the vehicle will be operating in an arena devoid of buildings and foliage that would mask GPS satellite signals. The measurement technique is being incorporated into a multi-vehicle tracking system that will support force-on-force training for the Idaho National Guard. The system, called DFIRST (Deployable Force-on-Force Instrumented Range System), will accommodate up to 42 combatant and 18 non-combatant vehicles, all of which will be linked to a base monitoring station through high-data-rate radio modems. GPS differential corrections will be uplinked from the base station to the participants; vehicle position, gun angle, and status will be downlinked from the participants to the base station. During an exercise, when a simulated "shot" is fired by a combatant, the gun attitude measurement will be used to "pair" the shooter with the intended target. Figure 1 shows the major components of the system.

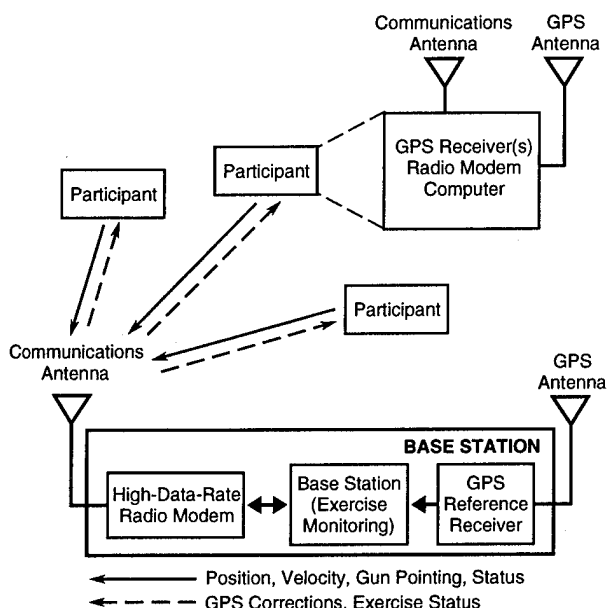


FIGURE 1 DFIRST SYSTEM DIAGRAM

One of the major challenges in implementing a GPS-based interferometric angle measuring system is the resolution of whole-cycle phase ambiguities. Figure 2 illustrates the problem for a single-baseline, two-antenna configuration. The relative positions of the antennas (and, hence, the angle between them) can be computed if the difference in range to each of four or more satellites can be

determined. Each receiver provides the phase of the carrier signal and integrates this phase over time, but the starting point of the integration is arbitrary within a whole number of cycles. Hence, just subtracting the carrier phase values is not sufficient. The difference in starting points must be determined.

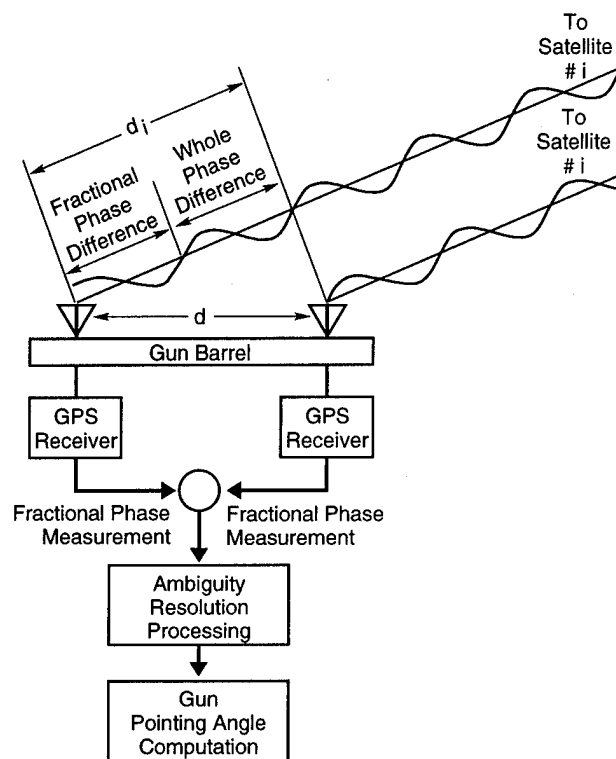


FIGURE 2 ESTIMATING GUN POINTING ANGLES

The way to resolve ambiguities depends on the application. *A priori* knowledge of the pointing angle is helpful: in this case, we know there are constraints on the gun elevation angle. Possible auxiliary measurements are discussed in the following section. A search approach can be used when more than the minimum number of satellites are tracked. Search algorithms [Hatch] use redundant data to eliminate whole-cycle values that yield non-coincident solutions. Motion-based methods [Cohen and Parkinson] can be applied during intervals when the direction of the baseline is changing. Our application is a hybrid approach that draws upon each of these possibilities.

A second implementation challenge is to achieve adequate angle measurement accuracy. Three factors determine the angular error: receiver phase noise, multipath, and baseline length. In the tank environment,

multipath very often exceeds the receiver noise and is, therefore, the dominant source of phase measurement error. For a given *phase* error, the *angle* error is inversely proportional to the length of the baseline, and thus, in principle, can be made arbitrarily small by increasing the separation between antennas. However, in this application, the length of the gun barrel established a practical limit.

The collective characteristics of using low-cost (noisier) receivers, short antenna baselines, and an uncontrolled multipath environment (as encountered with tank installations) result in attitude performance below that typically achieved under more favorable design conditions. To illustrate this performance contrast, some of our results obtained using better receivers, longer baselines, and a more benign multipath environment are provided at the end of this paper.

APPROACH

Several issues were addressed to determine the best way to meet the above requirements. These issues, listed below, are discussed in the following narrative.

- The specific receiver and antenna types to be used.
- The antenna and baseline configuration (number of baselines, number of antennas and independent receivers, etc.).
- Possible auxiliary measurements (such as compass or clinometer) to simplify the ambiguity resolution process.
- The methodology for cycle ambiguity resolution.

Hardware

When the investigation began, only two vendors offered off-the-shelf, C/A-code receivers that provided phase measurements and were sufficiently inexpensive for our application. We selected the Leica GPS Engine, a 6-channel receiver, because our measurements indicated that it had lower phase noise than the other candidate.

In selecting the antenna, our primary concern was to choose a unit that would provide reasonable performance in the potentially challenging multipath environment found on a tank. Of the three models evaluated, the Motorola Oncore and the Micropulse 90LL13700 offered comparable overall performance.

The issue of whether to use a single clock rather than a separate clock for each receiver was briefly examined. Use

of a single clock would offer two advantages: lower noise when the receiver-to-receiver phase differences are calculated, and possible reduction (by one) of the number of satellites needed to produce the attitude measurements. However, this option was rejected because it would have required significant and potentially costly hardware modifications.

Baseline Configuration

From the beginning of this effort, we anticipated a single-baseline system, inasmuch as it would be the least costly to implement and would conform to the linear geometry of the gun barrel. Moreover, the single baseline would provide both azimuth and elevation of the barrel; roll angle was not required.

Several variations were considered to facilitate ambiguity resolution. For example, one configuration employed three receivers and three colinear antennas, as suggested in Figure 3. The two antennas on the left (A and B) are sufficiently close together that there are few or no ambiguities to be resolved. The pointing angle can be computed approximately using the phase differences from the close pair alone; under most circumstances, this angle is sufficiently accurate to allow direct computation of the whole cycle values over the full baseline length (from Antenna A to Antenna C). We rejected this approach in favor of a two-receiver system because of the cost of the additional receiver and the increased complexity of the software and hardware interfaces to the participant computer.

Sector Limits

The ambiguity resolution process can also be simplified by limiting the angular sector over which one searches. One possibility is to restrict potential solutions based on *a priori* knowledge. For example, in our case it was reasonable to assume that the elevation of the gun barrel would be limited by the allowable vertical movement of the gun relative to the hull and by the minimum and maximum pitch angle that the hull might assume as it moves across the terrain.

Another option, under static* conditions, would be to measure the elevation angle of the barrel with a clinometer, thereby constraining elevation sector limits to a few degrees. We also considered using an electronic

*A clinometer, being gravity-sensitive, will not provide an accurate estimate of the elevation angle if the baseline is vibrating or accelerating.

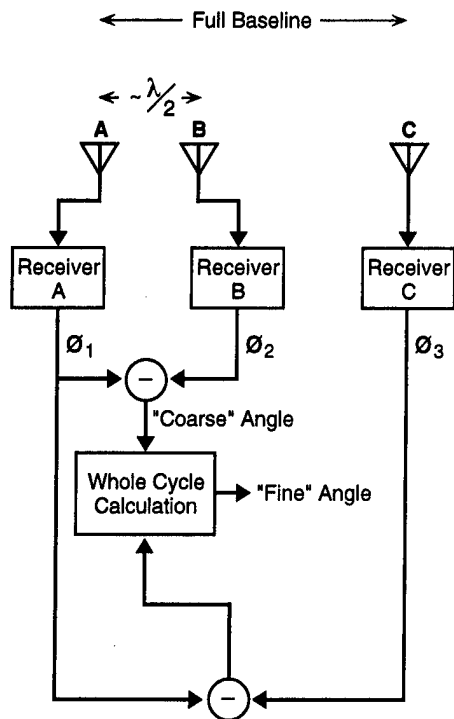


FIGURE 3 THREE-RECEIVER/THREE-ANTENNA CONFIGURATION

compass to limit the azimuth sector. However, compasses that will operate satisfactorily inside a tank were expensive and (at the time this project began) had uncertain performance.

Relative motion between the antennas can also be used to bound the solution and help reject invalid solutions. For example, false solutions tend to exhibit changes in baseline length when the direction of the baseline changes. Consequently, if the baseline is rotating and the length of the baseline appears to be changing, the ambiguities have been incorrectly resolved.

Figure 4 shows the actual hardware configuration. The software is described in the following subsection.

Resolution Algorithm

The ambiguity resolution algorithm can be divided into five steps, as shown in Figure 5:

- "Order" tracked satellites.
- Calculate double differences.
- Determine sector limits from baseline motion and clinometer.

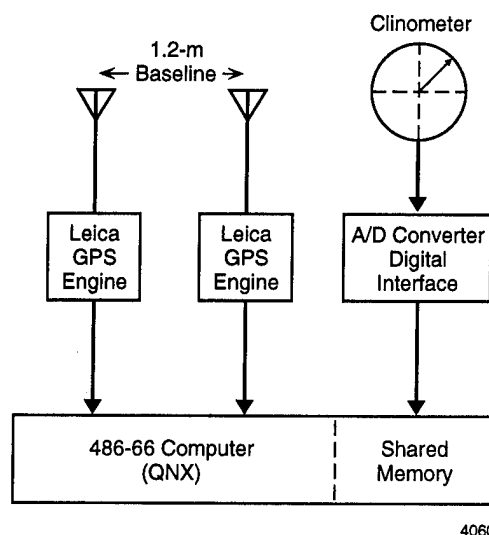


FIGURE 4 HARDWARE CONFIGURATION USED

- Search allowable integer volume.
- Check perspective solutions against known constraints.

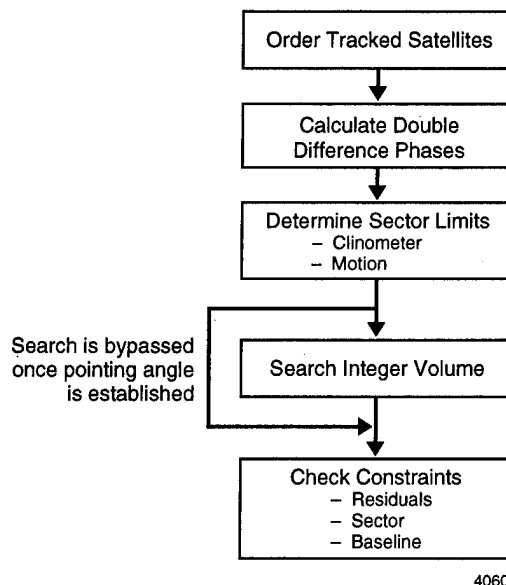


FIGURE 5 SOFTWARE DIAGRAM

Ordering the satellites involves selecting from the tracked satellites the four that provide the best position dilution of precision (PDOP). These "primary" satellites are placed at the top of the list, with the highest elevation

satellite first. The remaining "secondary" satellites are placed at the bottom of the list.

The double-differencing step includes calculating the receiver-to-receiver phase differences, then subtracting the phase of the first satellite from each of the others. To minimize the chance that the first satellite has excessive multipath, the highest of the first four satellites is used.

Any relative motion between the antennas can be detected by examining the epoch-to-epoch change in carrier phase, which is equivalent to calculating the differential velocity between the two. This is accomplished in the same way that one would compute the velocity of a remote receiver relative to the reference station in a differential GPS system. Once determined, the motion can be used to help eliminate invalid solutions.

The ambiguity search method we have used is similar to one proposed by Hatch. A search volume is established to accommodate the length of the baseline and the pseudorange measurement accuracy of the receivers. In our case, because the baseline is ~6 wavelengths and the pseudorange measurement error of the receivers is much larger, the search volume is based on baseline length only. The "primary" satellites are used to step through this volume, one integer set at a time. For each set, the integer that yields the minimum residual can then be calculated directly for each of the secondary satellites. In this application, because the length of the baseline is known, the integer for the fourth satellite in the primary set can often be directly calculated as well.

For each set of integers determined in the previous step, the corresponding pointing solution is then checked against a variety of constraints, including: the known distance between antennas; any sector limits established by the clinometer, the relative motion, or the extremes of allowable gun barrel position; and the residuals.

PERFORMANCE SUMMARY

Copious data collected with stationary antennas indicate that the random portion of the measurement error varies from about 0.12 deg to as high as 0.5 deg (1- σ). The larger errors occur in high multipath environments. Figure 6 shows a sample of data collected in a relatively benign rooftop environment (standard deviation: 0.13 deg). Figure 7 shows a sample of data collected with the antennas mounted on the barrel of an M1A1 tank (standard deviation: 0.23 deg). The next section presents a detailed accuracy analysis comparing GPS azimuth data with an independent reference.

When six satellites are in track, the system can resolve ambiguities and produce a valid pointing angle measurement in 5-10 s nominal (after the receivers are tracking and putting out integrated carrier phase). If the pointing angle is changing, rapid resolution is virtually always achieved; in static situations, however, it sometimes takes longer. Currently, the acceptance parameters are set for a very low probability of locking onto an incorrect pointing solution. With these settings, static resolution is achieved in less than 10 s about 75% of the time and in less than 100 s about 95% of the time.

In our experience, erroneous angle solutions are rarely produced and generally are maintained for only 30-60 s. Such solutions can occur in extreme multipath situations—for example, when the vehicle is within a few feet of buildings or other vehicles.

Our implementation requires at least five satellites for ambiguity resolution. Once resolution is achieved, four satellites must be in track to maintain the solution. (Theoretically, because the length of the baseline is known, only three satellites would be required; however, we have not attempted to implement this capability.)

Masking of the antennas by foliage or buildings, which occurs frequently in urban environments, can lead to loss of phase lock on multiple satellites and, therefore, to loss of pointing angle. However, in open areas such as the Idaho training range, masking of satellites is infrequent. Pointing angle will also be lost if a cycle slip occurs. This seldom happens in static situations, but we have observed cycle slips when the tank's turret was slewing rapidly (approximately 50 deg/s). With an overdetermined solution, cycle slips can be detected and repaired as they occur, without the necessity of re-initiating the ambiguity resolution process. We are currently developing software routines to correct such slips.

Table 1 summarizes the performance parameters.

Table 1: Performance Parameters

Azimuth Error (4-ft baseline)	0.19 deg, 1- σ (rooftop tests) 0.2-0.5 deg, 1- σ (on M1A1 tank, very limited data)
Time to Resolve Ambiguities	<10 s (dynamic) <10 s 75% of time (static) <100 s 95% of time
Track Continuity	Rare single epoch dropouts (static) Occasional cycle slips (high dynamics)
Erroneous Solutions	Can occur in extreme multipath situations; maintained for 30 to 60 s, typically

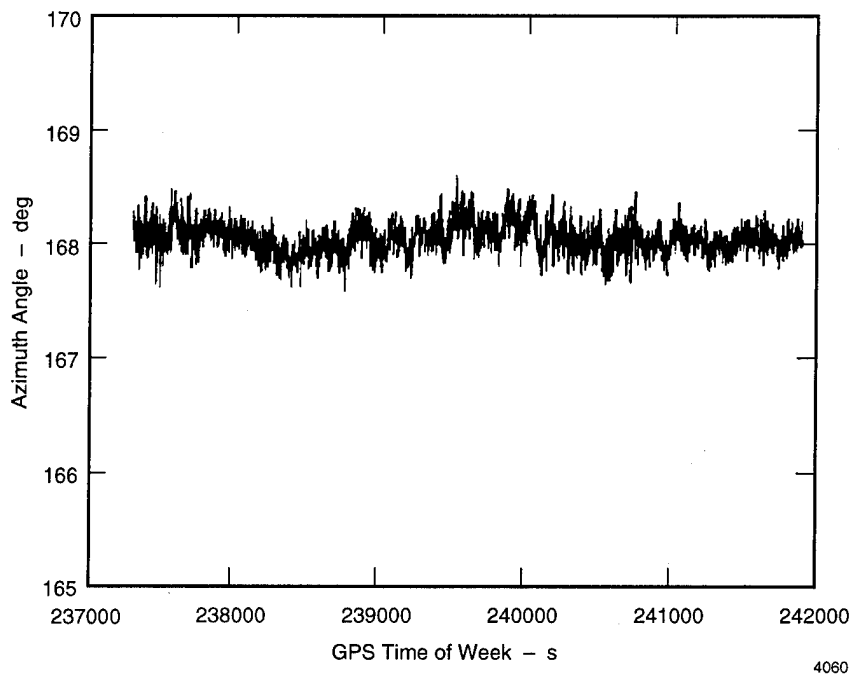


FIGURE 6 STATIC AZIMUTH MEASUREMENT – ROOFTOP

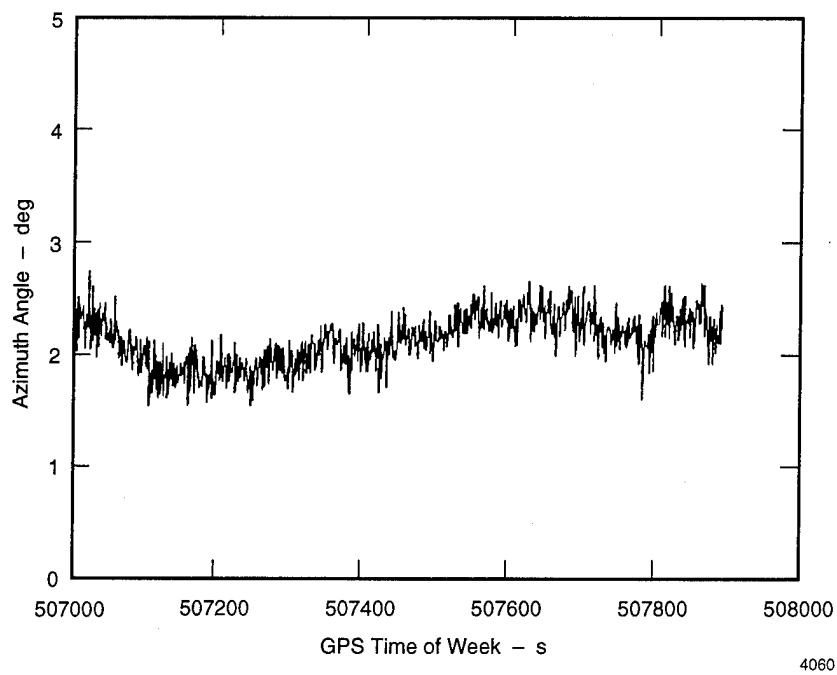


FIGURE 7 STATIC AZIMUTH MEASUREMENT – M1A1 TANK

ACCURACY ANALYSIS

Truth Reference for Determining Pointing Accuracy

Extensive testing has been done to determine the pointing accuracy of the system. To measure pointing errors of a few tenths of a degree, special techniques are required; currently, we have established a methodology only for static and low angular rate (~15 deg/hr) conditions. On a rooftop at SRI International in Menlo Park, CA, we installed an optical testbed for mounting antenna fixtures. The testbed includes a motor-driven, computer-controlled, 10-in. Cassegrain telescope (Meade LX200) for tracking stars, and a smaller, refracting telescope attached to the Meade for pointing at surveyed landmarks. A wooden bracket is used to mount the antenna fixtures to the main telescope, and counterbalancing is provided to neutralize torque on the telescope mechanism.

Tests were conducted with the telescope pointed at a variety of stars and terrestrial landmarks. We estimate that the star pointing was accurate to within 1 arc minute, and the terrestrial pointing to within 2 arc minutes. These values are well below the anticipated accuracy of the GPS system and are therefore negligible.

Objectives of Tests

The accuracy tests had three major objectives. First, we wanted to compare the performance of three different antenna mounting configurations: choke rings, ground planes, and direct attachment to the antenna fixture (or "barrel jig"). Second, we wanted to assess the pointing error that would remain following a maximum 30-min calibration session to remove bias errors. Third, we wanted to assess the random error in pointing angle resulting from receiver noise and multipath.

Results

The results of the testing done in pursuit of the first objective are given in Table 2. Azimuth accuracy is shown because it is the primary pairing determinant in the DFIRST application. Elevation angle error is about twice as large, due primarily to vertical DOP.

Table 2: Accuracy Performance

	Antenna Mounting Configuration		
	Choke Rings	Ground Planes	Direct to Fixture
Number of 5-min runs	27	18	18
Range of mean azimuth errors	0.95 deg	0.39 deg	0.48 deg
Aggregate sample size	7154	5136	4488
Aggregate azimuth standard deviation	0.26 deg	0.19 deg	0.24 deg

For each of the three configurations, multiple 5-min data collection runs were made with the testbed pointed at various stellar and terrestrial reference points. The ground plane configuration had the lowest noise level (0.19 deg) and also showed the smallest range of average differences between the reference azimuth and the sets of measured azimuths (0.39 deg). The range of mean azimuth errors was used as a measure of calibration accuracy. This strongly suggests that the ground plane configuration will provide better performance than the two alternatives. Therefore, the ground planes were chosen for the remainder of the testing.

Because the 5-min runs showed a relatively large range of mean azimuth errors, we experimented to see how long a calibration run would have to be to yield reasonably low biases. Two different data sets* (one 24-hour and one 18-hour), using only terrestrial landmarks, were analyzed for this purpose. The results are shown in Table 3, which lists the range of mean azimuth errors for 10- to 90-min subsets of the two runs. These results suggest that 30- to 40-min runs provide better calibration than 10-min runs. Calibration intervals longer than this would be unacceptable in the training application for which the equipment is being designed. Based on these results, we conclude that, following a 30-min calibration period, there will be a residual bias error of no greater than approximately ± 0.15 deg.

Numerous 30-min runs taken with the ground plane configuration on the rooftop testbed and with two different antennas (Motorolas and Micropulses) yielded standard deviations of 0.15-0.20 deg, depending on antenna type and pointing direction. Table 4 summarizes the results. For the Motorola antenna, which (for cost and availability reasons) was selected for the system, the 1- σ error is 0.19 deg.

*Taken using Micropulse antennas.

Table 3: Range of Average Azimuths (deg)

Interval Duration (min)	Data Set C	Data Set D
10	0.45	0.72
20	0.33	0.41
30	0.28	0.42
40	0.24	0.29
50	0.25	0.29
60	0.23	0.23
70	0.14	0.28
80	0.16	0.21
90	0.16	0.18

Quantification of Multipath

In an attempt to quantify the multipath contribution, a 48-hour run was conducted in which the testbed was pointed continuously at the same landmark. The first 24-hour segment (technically, 23 hours and 56 minutes) was then compared to the second, when the directions to the satellites and all other conditions were the same. Table 5 shows that the standard deviation for each of the 24-hour intervals was 0.15 deg. But when the two data sets were subtracted, point by point, the standard deviation of the differences (adjusted by $\sqrt{2}$ for two noise sources) dropped to 0.09 deg.

Further tests showed that, as expected, the multipath is spatially dependent. When the testbed is moved a few feet between consecutive 24-hour runs, the multipath cancellation in the difference is significantly decreased.

One curious, and as yet unexplained, situation arose during the multipath evaluation. When the power spectral density was computed for the two 24-hour subsets of the 48-hour run, each of the spectra showed a distinct spike at about 10^{-4} seconds, indicating a strong 3-hour component to the multipath. This spike did not occur in the 18-hour run when the telescope was pointed at an alternative landmark.

Table 4: Results for 30-Minute Runs

Data Set	Antenna	Parameter type	Results
A 5/30-6/2/95	Motorola	Number of 30-min runs	7
		Range of mean azimuths	0.12 deg*
		Aggregate sample size	12027
		Aggregate azimuth standard deviation	0.19 deg
B 6/9-6/13/95	Micropulse	Number of 30-min runs	12
		Range of mean azimuths	0.23 deg
		Aggregate sample size	22355
		Aggregate azimuth standard deviation	0.16 deg
C 6/23-6/24/95 (24-hr run)	Micropulse	Number of 30-min runs	47
		Range of mean azimuths	0.28 deg
		Aggregate sample size	85018
		Aggregate azimuth standard deviation	0.15 deg
D 6/29-6/30/95 (18-hr run)	Micropulse	Number of 30-min runs	30
		Range of mean azimuths	0.42 deg
		Aggregate sample size	55084
		Aggregate azimuth standard deviation	0.20 deg

*This value alone implies that the Motorola calibrates more accurately than the Micropulse but the number of 30-min runs is small. Other data, not included here, indicate that the value is larger.

Table 5: 24-Hour Multipath Consistency

	First 24 Hours	Second 24 Hours	Differences
Sample size	85018	91524	84509
Azimuth mean error (deg)	0.69	0.70	0.01
Azimuth standard deviation (deg)	0.15	0.15	0.09

Testing on M1A1 Tank

To date, only limited testing on tanks has been completed and no "truth" reference points have been available. Therefore, only the random component of the error can be assessed. Static data have been collected with the gun barrel in three different positions, relative to the hull: forward, rear, and side. The gun was at an elevation angle of approximately 5 deg. Results of these tests are shown in Table 6. Note that the random error is significantly greater than for the rooftop tests. For the June 21 tests, the antennas were mounted close to the turret; for the July 7 tests, in an attempt to reduce reflections from the hull, they were mounted near the end of the barrel. The results to date are inconclusive regarding where the antennas should be placed on the barrel.

**Table 6: M1A1 Tank Test Results
(Standard Deviation)**

Antenna Type	Date	Barrel Position		
		Front, 5-deg Elevation	Right, 5-deg Elevation	Rear, 5-deg Elevation
Micropulse	6/21	0.36 deg	0.17 deg	0.55 deg
Motorola	6/21	0.28 deg	0.20 deg	0.35 deg
Motorola	7/7	0.23 deg	0.46 deg	0.26 deg

The data set collected on June 21, using Micropulse antennas with the gun pointed over the rear of the tank, exhibited a particularly large standard deviation. During this run, the measured azimuth angle changed by 2 deg in about 400 seconds (even though the gun barrel was

stationary). Further analysis showed that one satellite had about 4 cm of multipath error. When this satellite was removed from the solution, the standard deviation dropped to about 0.30 deg.

Techniques for reducing multipath effects are currently under investigation with the expectation that pointing errors on the tank can be reduced.

Results in Low-Multipath Environment Using High-Performance Receivers

For comparative purposes, angle measurement data have been collected in a relatively benign multipath environment, using NovAtel receivers and a 2.4-m baseline (as opposed to a 1.2-m baseline on the tank). The two antennas were placed directly on a flat roof, with few nearby vertical surfaces. Figure 8 shows typical results, with an azimuth error of about 0.04 deg.

Acknowledgement

The authors wish to acknowledge the generous support of Dr. James W. Sinko (SRI International) for his assistance in designing the accuracy experiments and developing the telescope testbed.

References

1. Hatch, R., "Instantaneous Ambiguity Resolution," *Proceedings of the KIS Symposium*, Banff, Canada, September 1990.
2. Cohen, Clark E., and Bradford W. Parkinson, "Expanding the Performance Envelope of GPS-Based Attitude Determination," ION GPS, Albuquerque, NM, September 1991.

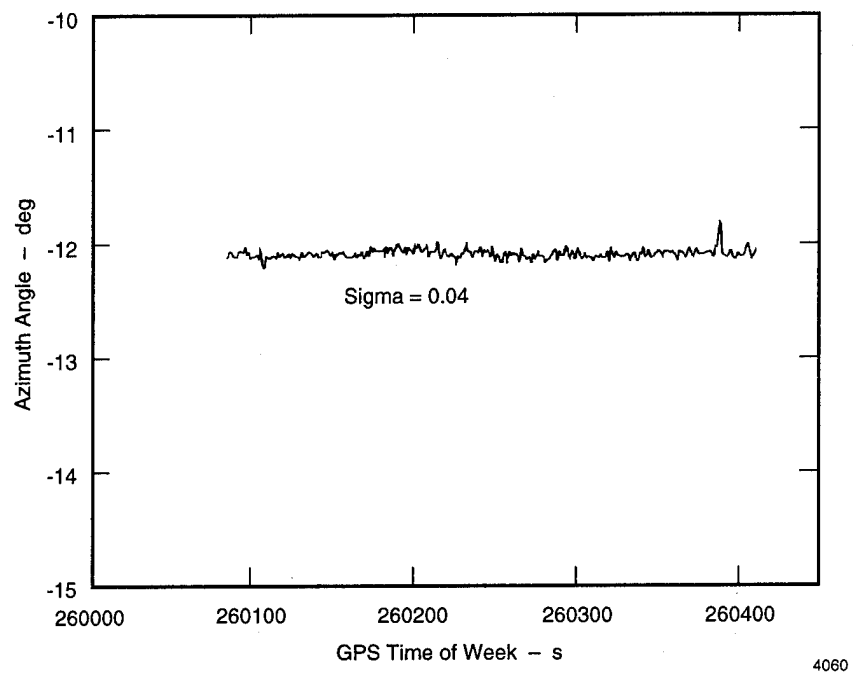


FIGURE 8 AZIMUTH ANGLE – NOVATEL RECEIVERS, 8-ft BASELINE

Accurate Azimuth from a Single PLGR+GLS DoD GPS Receiver Using Time Relative Positioning

Karl Ulmer, Patrick Hwang, Brent Disselkoen, and Mark Wagner
Rockwell

BIOGRAPHIES

Karl W. Ulmer is a GPS Project Engineer for GPS Surface Mobility Products at Rockwell International. He received his B.S. in Electrical Engineering from South Dakota State University, Brookings SD, and his M.S. in Electrical Engineering from Iowa State University. Since joining Rockwell in January of 1993, he has been involved in the design and analysis of enhanced measurement techniques and the development of software improvements for the DoD PLGR products.

Patrick Y. C. Hwang is a Senior Systems Analyst for Advanced Technology & Engineering. He received his Ph.D. in Electrical Engineering from Iowa State University. He is involved in high accuracy GPS development where he gets to apply his Kalman filtering and signal processing expertise.

Brent A. Disselkoen is a Software Design Engineer for Standard Airborne GPS Products. He received his B.S. in Electrical Engineering and Computer Science from Dordt College, Sioux Center IA, and his M.S. in Electrical Engineering from Arizona State University. Since joining Rockwell in September of 1993, he has been involved in the digital signal processing design and analysis for the handheld and airborne GPS products.

Mark R. Wagner received his B.S.S. in Mathematics and Computer Science from Cornell College, Mt. Vernon IA, and his M.S. in Applied Mathematics from Northwestern University, Evanston IL. He has been involved in the design and development of Navigation and Time-related software for CACD GPS receivers since 1988 and the PLGR receiver in particular since 1990. He is currently working on the Video Data Link upgrade to the Tomahawk cruise missile.

ABSTRACT

A new application of the Precision Lightweight GPS Receiver (PLGR) incorporates a proprietary technique called Time Relative Positioning to obtain highly accurate azimuth and pitch information. This technique is currently employed in the PLGR+GLS (Gun Laying System) to determine the 3-dimensional vector representing the relative horizontal and vertical displacement between two points marked by the receiver. In addition to providing a cost-efficient method for deriving a precision gun sighting vector, the PLGR+GLS demonstrates one to three mil accuracy on the resulting azimuth measurement.

The Time Relative Positioning technique relies on kinematic based measurements and the careful calibration of known error sources to derive its azimuth and elevation measurements. Contrary to many kinematic applications, this result is derived completely internal to a single receiver. This paper addresses the application to gun laying methodology, kinematic survey and attitude determination requirements, known error sources and integration issues and presents an analysis of actual field test results.

The incorporation of Time Relative Positioning into the PLGR product offers significant performance improvements in certain military gun laying environments. In addition, the autonomous nature of this attitude determination technique implies a broad range of future applications.

I. Introduction

PLGR+GLS is designed to focus on the unique requirements of indirect fire and other azimuth dependent applications (see Figure 1). It provides pointing and gun-laying applications with accurate weapon position along with precision azimuth and pitch information from a single Rockwell PLGR (Precision Lightweight GPS Receiver), the standard U.S. Department of Defense

portable, handheld and vehicle-mounted GPS receiver. The PLGR+GLS requires minimal setup and measurement time and has demonstrated better than three mils (rms) accuracy in azimuth as reported in the results section of this paper. See Figure 2 for the relationship between degrees, mils, and milliradians.

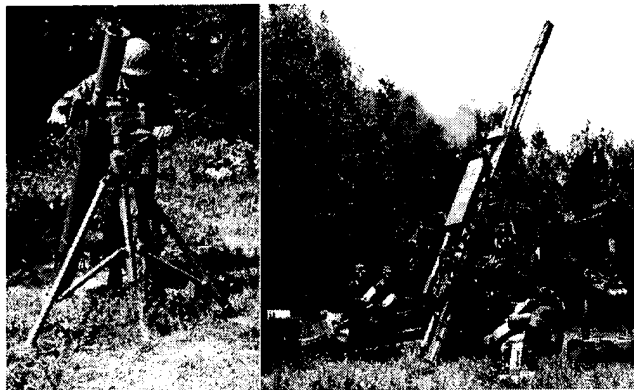


Figure 1. Indirect Fire Weapons

Unlike differential GPS techniques, which rely on multiple GPS receivers and equipment for a data link, the Time Relative Positioning technique generates an accurate real-time relative positioning vector using a single autonomous receiver. The PLGR+GLS employs this cost effective technique to provide gun laying applications with an accurate azimuth reference.

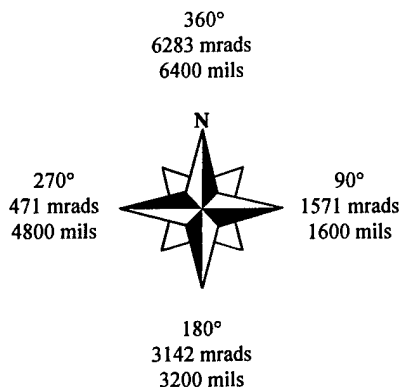


Figure 2. Relationship between degrees, mils, and milliradians.

Indirect fire is achieved by calculating the distance and direction of the target from the gun position, selecting the appropriate charge and inclination angle for the desired range and accurately deflecting the weapon into the desired firing direction. Traditionally, personnel using indirect fire weapons, such as 60 mm and 81 mm mortars, rely on coarse maps for weapon position and a magnetic

compass for azimuth reference information. After obtaining accurate target location information, an indirect fire application relies on both a gun position and azimuth reference to align the weapon's firing direction into the desired target. Traditional position and azimuth inaccuracies result in the need to fire several registration rounds before calibrating for the errors introduced by the coarse position and azimuth reference data.

On rare occasions, usually in a defensive position, the personnel may rely on the availability of a survey team to provide azimuth references to within one mil azimuth accuracy. This process employs expensive equipment such as theodolites with north-finding gyros found in Position and Azimuth Determination Systems (PADS).

More often than not, this equipment is not available and the mortar crews rely on magnetic compass measurements for azimuth information. Compass measurements provide less than desirable accuracy, on the order of 10 to 30 mils, due to magnetic variations and unreliable equipment, thus requiring the fire direction center to fire several rounds before engaging the target and firing for effect. The PLGR+GLS system can provide decreased return fire vulnerability and increased weapon efficiency through accurate position and azimuth measurements.

II. Gun Laying Application Overview

The Time Relative Positioning technique employs integrated Doppler measurements from a single frequency five channel PPS PLGR. A multipath resistant external antenna is attached to a portable antenna mounting assembly to provide quick disconnect mating with the tripod assemblies. Section VI shows the equipment used for the system performance testing.

The PLGR+GLS system requires a setup and a measurement operation. The setup involves the placement of tripods to construct a reference sighting vector for the weapon. After the tripods have been placed such that they align with the weapon's sight, the measurement operation is performed. The PLGR+GLS measurement operation is controlled by the user with the PLGR keyboard. Performing the pointing measurement requires distinct actions from the user as requested via the PLGR's display interface. The measurement operation is depicted in Figure 3.

First the operator obtains a good position fix with the PLGR unit. Then the antenna mounting assembly is placed on one of the tripods and a key entry is made to signify start of the time relative positioning procedure. The operator then removes the mounting assembly and begins to traverse to the other tripod. During the

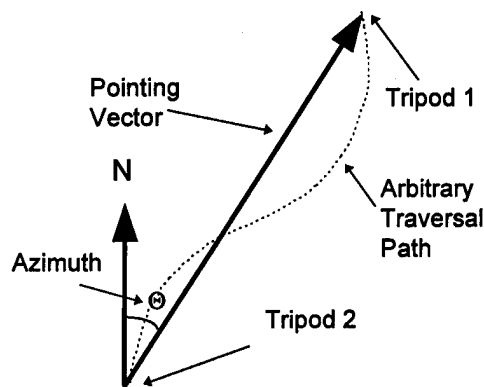


Figure 3. Pictorial representation of the Time Relative Positioning measurement.

traversal, the operator needs to ensure that the signals from the primary satellites in track are not obscured. The operator makes another key entry upon arrival at the second tripod to end the relative positioning operation. At this point, the PLGR unit will process a vector solution that represents the vector adjoining the two tripods that had been occupied. Any functional anomalies (i.e. cycle slips, parity errors, etc.) occurring during the traversal between tripods will cause the PLGR to estimate the vector solution using less accurate measurement information. Additionally, a quality factor representing accuracy of the solution is calculated and posted with the solution.

The azimuth of the vector connecting the two points is then communicated to the user via the display. Using this reference line, determined by two tripods, the user then accurately deflects the weapon's firing direction into the target identified by the forward observer. The data displayed includes range, azimuth of the vector (referenced to north), elevation angle or pitch of the vector, and estimated position, azimuth, and pitch error. Azimuth accuracy is dependent on distance between measurement locations, satellite geometry, signal strength, receiver and satellite clock stability, time elapsed during the measurement interval, and user errors associated with the alignment.

General applications of Time Relative Positioning

The flexibility and autonomy of the Time Relative Positioning technique implies an ideal solution for numerous applications. Variations of the PLGR operator interface can be used to generate systems customized to suit the needs of many other applications including but not limited to:

- Providing an azimuth reference for vehicle mounted weapons.

- Providing highly accurate heading information for vehicles traveling at low speeds (± 10 mils at 7 mph) where standard GPS based velocity measurements are not adequate.
- Providing accurate real-time, autonomous, relative positioning information over short baselines (typical errors of less than 30 cm horizontal relative positioning accuracy per minute).
- Surveying in the length, direction, and location of remote airstrips.
- Calibrating the azimuth and range of survey and related equipment (i.e. laser range finder, compass, etc.).
- Providing accurate real-time relative positioning and contour data for short-baseline survey applications.

III. Theory of Time Relative Positioning

Relative Positioning Concept

When surveying a line connecting two points for gun sighting purposes, the location of one point must be determined very accurately with respect to the other. This is a relative positioning type of problem. The concept of differential GPS, in its conventional sense, exploits the fact that the system errors that corrupt the range measurement made at location A are highly correlated with the errors that corrupt the range measurement at location B (Figure 4). The system errors β can then be eliminated by taking the difference in range measured nearly simultaneously at the two locations, the result of which will account, through the geometric relationship of Eq. 1, for the spatial separation between the locations.

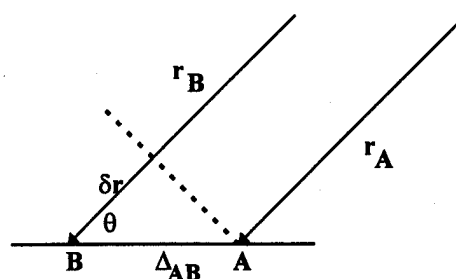


Figure 4. Relative positioning concept.

$$[r_B(t_1) - \beta(t_1)] - [r_A(t_1) - \beta(t_1)] =$$

$$[r_B(t_1) - r_A(t_1)] = \delta r = \cos \theta \Delta_{AB} \quad (\text{Eq. 1})$$

Now consider the one-dimensional relative positioning situation in Figure 4 where a range measurement is made at location A at time t_1 and at location B at time t_2 . Suppose for now that any changes in the satellite

The solution for $[x(t_k) - x(t_0)]$ is given by:

$$\begin{bmatrix} x(t_k) - x(t_0) \\ y(t_k) - y(t_0) \\ z(t_k) - z(t_0) \\ t(t_k) - t(t_0) \end{bmatrix} = \begin{bmatrix} h_1(t_k) \\ h_2(t_k) \\ h_3(t_k) \\ h_4(t_k) \end{bmatrix}^{-1} \cdot \begin{bmatrix} \Phi_1(t_k) - \Phi_1(t_0) \\ \Phi_2(t_k) - \Phi_2(t_0) \\ \Phi_3(t_k) - \Phi_3(t_0) \\ \Phi_4(t_k) - \Phi_4(t_0) \end{bmatrix}$$

The above is a least-squares solution with little need for filtering because the measurement noise of the carrier phase data is already very small in relation to other errors. The major error sources and their contributions are discussed in the following section.

IV. Error Budget Analysis

The error sources associated with the Time Relative Positioning technique were assessed to identify the major contributor to relative positioning error. The error in the user's assumed position has the most impact. The largest change in the satellite geometry, occurring when a satellite is overhead of the observer who is in the plane of the satellite orbit, is about 0.00019/s. From that, a more reasonable value to use in the error budget is 0.0001 per second. If the assumed position error $[x(t_0) - x^*]$ is 16 meters, then the error contribution of $[h(t_k) - h(t_0)] \cdot [x(t_0) - x^*]$ from Eq. 4 over 30 seconds is $0.0001/s \times 30s \times 16m = 0.048m$. Table 1 gives the error budget that corresponds to the accuracy of this method for a 30-second time interval.

Based on the error budget and a 50 meter baseline, a 0.25 m horizontal error distributed equally along the baseline and perpendicular to the baseline would result in a 3.6 mil azimuth error (95%). (i.e. $0.25m \div \sqrt{2} = 0.1777m$ perpendicular to the baseline.) This assumes the entire operation is completed in 30 seconds. The error budget assumes a typical position error (16 m) for the position error contribution. It also uses a nominal satellite Doppler change that is considered to be the same for all satellites in the solution.

V. Field Testing of Time Relative Positioning

Field Test Overview

Live field testing was performed on the PLGR+GLS system to characterize the system's accuracy under a variety of conditions. Over several weeks, 166 measurement samples were collected. Many different satellite constellations were chosen to provided HDOP values that varied between 1.0 and 5.0, with an average HDOP of 2.5.

Table 1. Time Relative Positioning Error Budget.

ERROR SOURCE	RMS RANGE ERROR (30-second time interval)
Satellite frequency error	$10^{-12} \text{ s/s} \times 3(10^8)\text{m/s} \times 30\text{s}$ = 0.009 m
Selective Availability [†]	≈ 0
Iono delay changes	≈ 0
Tropo delay changes	≈ 0
Assumed position error ^{††} (typical satellite geometry)	$0.0001 /s \times 16 \text{ m} \times 30 \text{ s} =$ 0.048m
Multipath error* (typical)	0.01 m
Carrier tracking noise* (dependent on C/N ₀)	0.004-0.006 m
Root sum square of errors	0.050 m
Horizontal Dilution Of Precision (from field tests)	2.5
Horizontal relative position error (rms)	0.125 m
Horizontal relative position error (95 %)	0.25 m
Azimuth error (95%)	3.6 mils

[†] The effects of Selective Availability are removed with the appropriate authorized Crypto-Variables in the PPS PLGR.

^{††} This results from the term on the right hand side of Eq. 4 which depends on the size of the assumed position error $[x(t_0) - x^*]$.

* These errors components are not dependent on the length of the time interval.

Test Site Description

PLGR+GLS performance testing was performed on Rockwell's Geodetic Reference Network Demonstration (GRND) Test Facility. The GRND facility consists of three (3) highly-precise surveyed geodetic points located near the Rockwell GPS development center complex. The locations are relatively accurate within the GRND to $< \pm 8 \text{ mm}$ and are referenced within the NAD83/WGS84 and NAVD88 geodetic datums to better than second order class I horizontal and better than second order class II vertical control closures. The GRND will be tied into the local Iowa High Accuracy Reference Network (HARN) overseen by the National Geodetic Service.

Test Setup

The PLGR+GLS measurements were collected on a 50 meter baseline. The time to perform the traversing portion of the measurement varied between 25 and 35 seconds. The equipment shown in Figure 5 was used to ensure

geometry is insignificant, i.e. θ is constant between t_1 and t_2 . Then the range difference between measurements made at the two locations at different times will be equivalent to the range difference made simultaneously if the system errors β do not change between t_1 and t_2 (Eq. 2).

If $\beta(t_1) = \beta(t_2)$,

$$[r_B(t_2) - \beta(t_2)] - [r_A(t_1) - \beta(t_1)] =$$

$$[r_B(t_2) - r_A(t_1)] = \delta r = \cos \theta \Delta_{AB} \quad (\text{Eq. 2})$$

If this condition can be satisfied, then a single receiver can perform the task of occupying one location first, and then moving on to the other to measure the range difference between the two locations. This is the basic concept of *time relative positioning*. In the discussions that follow, it will be obvious that the satellite geometry change over the observation interval $[t_1, t_2]$ though small must be considered and it has an indirect impact on the error budget. The assumption here that the system errors do not change appreciably over the short observation interval involved in the operation is valid provided that Selective Availability is not a system error component.

Observation Constraints

The concept of *range measurement* used in the discussion above is a general one. What then is a suitable measurement to use for obtaining ranging information? Code phase measurements directly yield ranging information once the receiver is able to track the satellite signal. However, code tracking errors can significantly reduce the ranging accuracy, particularly as a result of multipath effects. On the other hand, carrier phase measurements encounter much lower tracking errors. The carrier phase does not directly yield ranging information but by maintaining continuity of tracking over the observation interval between occupation of the two locations, the desired range difference can be extracted. The requirement of continuous carrier tracking increases the operational complexity but is justified by the accuracy performance it provides.

Time Relative Positioning

Time Relative Positioning relies on tracking the continuous carrier phase (i.e. integrated Doppler) to determine relative change in position, the accuracy of which depends on the stability of the GPS carrier signal over the time interval involved. The measurement equation for each satellite is simply:

$$\phi(t_k) - \phi(t_0) = [r_k + N] - [r_0 + N]$$

or

$$[\phi(t_k) - \phi(t_0)] - [d(x^*, t_k) - d(x^*, t_0)] = h(t_k) \cdot [x(t_k) - x^*] - h(t_0) \cdot [x(t_0) - x^*] \quad (\text{Eq. 3})$$

where

- $\phi(t_k)$ = carrier phase at t_k (end point)
- $\phi(t_0)$ = carrier phase at t_0 (beginning point)
- r_k = range plus range biases at t_k
- r_0 = range plus range biases at t_0
- N = integer cycle ambiguity
- $h(t_k)$ = direction cosines at t_k
- $h(t_0)$ = direction cosines at t_0
- $x(t_k)$ = antenna position at t_k
- $x(t_0)$ = antenna position at t_0
- x^* = assumed antenna location at t_0
- $d(x^*, t_k)$ = geometric range from x^* to satellite plus deterministic biases at t_k
- $d(x^*, t_0)$ = geometric range from x^* to satellite plus deterministic biases at t_0 .

Written in a different way, Eq. 3 becomes

$$[\phi(t_k) - \phi(t_0)] - [d(x^*, t_k) - d(x^*, t_0)] = h(t_k) \cdot [x(t_k) - x(t_0)] + [h(t_k) - h(t_0)] \cdot [x(t_0) - x^*] \quad (\text{Eq. 4})$$

The ultimate solution simply consists of the term $[x(t_k) - x(t_0)]$. We can ignore the second term on the right hand side due to the assumed position error $[x(t_0) - x^*]$ because this term is not observable over a short time interval. In addition, $[h(t_k) - h(t_0)]$ is very nearly zero so its contribution is small over a short time interval.

If we combine the carrier phase observation and deterministic biases into the term $\Phi(t)$ where

$$\Phi(t) = \phi(t) - d(x^*, t),$$

then the final equation we need to work with is:

$$\Phi(t_k) - \Phi(t_0) = h(t_k) \cdot [x(t_k) - x(t_0)] \quad (\text{Eq. 5})$$

The solution for $[x(t_k) - x(t_0)]$ is then obtained by solving Eq. 5 simultaneously, from at least four satellites:

$$\begin{bmatrix} \Phi_1(t_k) - \Phi_1(t_0) \\ \Phi_2(t_k) - \Phi_2(t_0) \\ \Phi_3(t_k) - \Phi_3(t_0) \\ \Phi_4(t_k) - \Phi_4(t_0) \end{bmatrix} = \begin{bmatrix} h_{11}(t_k) \\ h_{21}(t_k) \\ h_{31}(t_k) \\ h_{41}(t_k) \end{bmatrix} \cdot \begin{bmatrix} x(t_k) - x(t_0) \\ y(t_k) - y(t_0) \\ z(t_k) - z(t_0) \\ t(t_k) - t(t_0) \end{bmatrix}$$

consistent results and minimize the error in positioning the equipment over the truth positions.

measurements was 0.42 and 1.6 per second, respectively. The data from the plot is summarized below.

Field Test Data

The data collected during the field tests included satellite vehicle IDs, HDOP, VDOP, measurement start and end times, measurement start and end positions, and local level east, north, and up components of the Time Relative Positioning vector. A comprehensive analysis of the resulting azimuth solution is given in the following section. A separate analysis of the easting, northing, and vertical error components of the Time Relative Positioning vector is also provided.

VI. Azimuth Performance Results

The azimuth error is plotted for each of the 166 measurements in Figure 6. Of the 166 azimuth measurements, 3 were considered outliers. The cause of outlier 1 corresponding to sample 136 could not be identified from the information that was collected during the measurement. However, the rapidly degrading satellite geometry is suspected to have introduced an unusually large position error for the measurements identified by outliers 2 and 3. HDOP and VDOP for the measurements were 4.8 and 16.7, respectively and the rate of change in HDOP and VDOP at the time of the



Figure 5. Gun Laying System Test Equipment.

PLGR+GLS Field Test Results

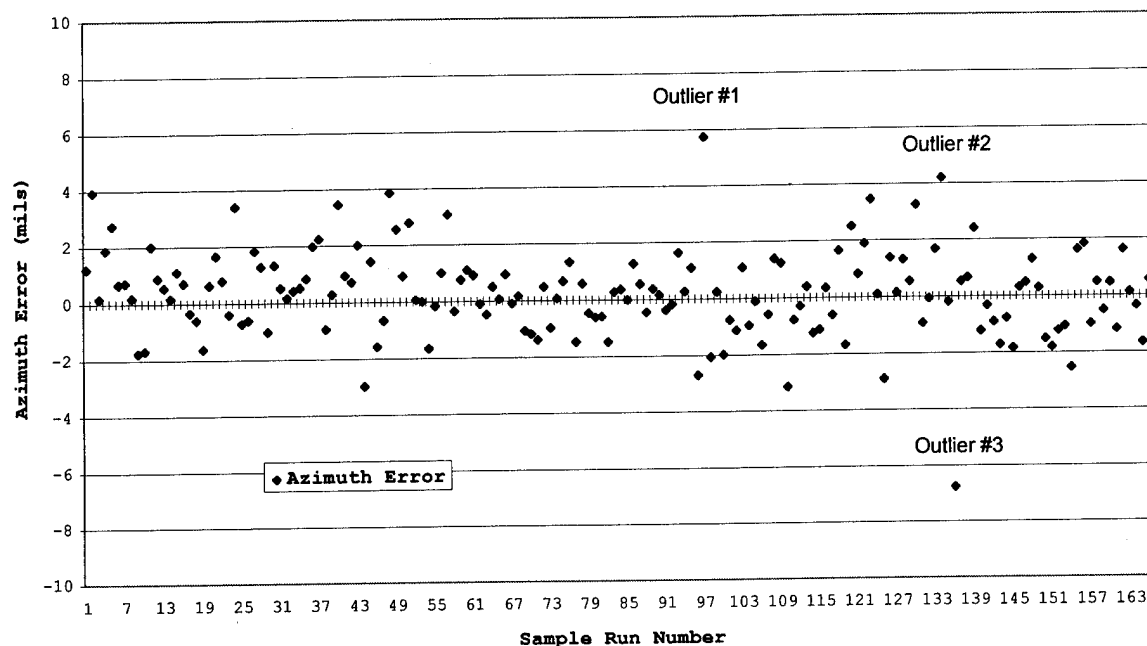


Figure 6. Performance demonstrated in the rigorous testing performed on Rockwell's Geodetic Reference Network and Demonstration test site.

Summary of Azimuth Test Results

The theoretical performance goals and error contributions were reasonably well represented in the measurement data collected from these field tests. The Azimuth Error Probable (50%) for the test data collected was 1.0 mil. The rms azimuth error observed in the data was 1.64 mils, and the 95% azimuth error was 3.2 mils. The disagreement between the field test results (3.2 mils) and the theoretical performance estimate (3.6 mils) is 11%. This disagreement is due in part to the special considerations taken in the software implementation of the algorithm to calibrate out other deterministic system induced errors. These error sources and the estimation techniques applied to reduce them are not discussed here due to their proprietary nature.

As the error budget shows, the error in the assumed position is the dominant source of error. Thus, HDOP plays a significant role in obtaining an accurate azimuth measurement. The data in Table 2 shows the correlation between HDOP and azimuth error observed in this data. The basis for the correlation is founded in the primary error contributor listed in the error budget table, the assumed position error.

Table 2. Correlation between HDOP and Azimuth error.

HDOP	Azimuth Error (RMS)	# of Samples
1.0-2.0	±1.08 mils	59
2.0-3.0	±1.63 mils	50
3.0-4.0	±1.78 mils	43
4.0-5.0	±2.54 mils	14

Azimuth errors less than ±1.0 mil are represented by 89 of the 166 trials (53%); 142 of the 166 trials (85%) have an azimuth error of less than ±2.0 mils and only 12 trials (7%) have an azimuth error of greater than ±3.0 mils.

VII. Relative Positioning Performance Analysis

The east, north, and vertical error components were also calculated from the 166 measurement samples. The distributions for these errors are plotted below and commented on in the following sections. The horizontal and vertical error components normalized by the appropriate DOP to remove satellite geometry contributions are also presented.

Individual Error Component Distributions

The individual easting and northing error components are reasonably well represented by Gaussian distributions as shown in Figure 7. The basic statistics associated with these error components are listed in Table 3 below. The maximum errors in the easting and the northing components correspond to outliers 2 and 3 in Figure 6. These data points are not represented in Figure 7. The vertical error statistics are also included in the table, but not plotted.

Table 3. Individual Error Component Statistics.

	Relative Error Statistics (cm)		
	Easting	Northing	Vertical
Minimum	-24.1	-20.2	-34.1
Maximum	36.4	35.6	225.1 [†]
Average	-0.3	-0.2	0.8
Std. Dev.	7.7	7.1	26.8

[†] This measurement corresponds to outlier 2 in Figure 5. The unusually large relative vertical positioning error was due in part to the excessively large VDOP of 16.

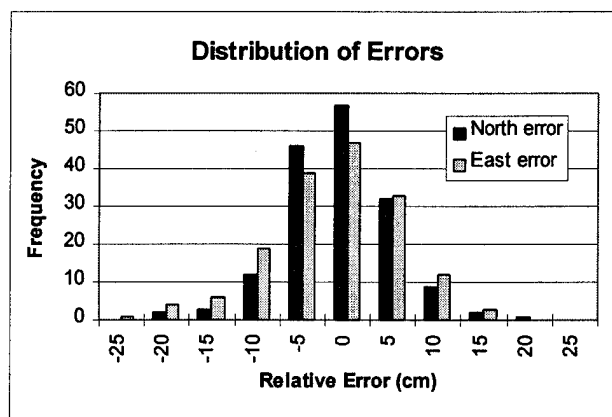


Figure 7. Distribution of northing and easting errors.

Magnitude of Horizontal and Vertical Errors

Additional analysis was performed on the individual components to form the error distributions for the magnitude of the horizontal and vertical errors in the Time Relative Positioning vector measurements. This analysis also involved normalizing the two error components by HDOP and VDOP, respectively.

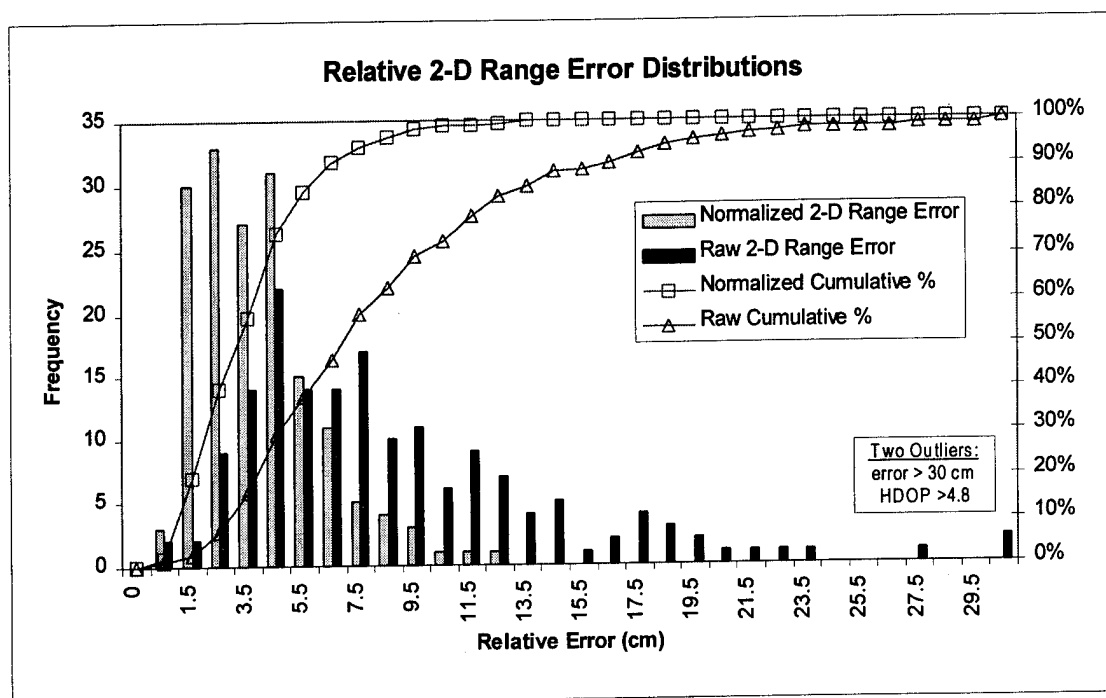


Figure 8. Distributions for both raw and normalized (with respect to HDOP) relative 2-D range error.

Figure 8 shows the horizontal (i.e. 2-D range) error distribution for both raw and normalized data. The corresponding cumulative distribution plots indicate an estimated relative horizontal positioning error of 19.0 cm and 8.0 cm (2 sigma) for raw and normalized data, respectively. The distributions take the form of a Rayleigh distribution as expected. Table 4 shows the basic statistics for the magnitude of the raw and normalized horizontal errors. Two outliers are identified in the lower right corner of the plot. Again, these

Table 4. Relative Horizontal Error Statistics.

	Relative Horizontal Error Statistics (cm)*	
	Raw	Normalized
Minimum	0.6	0.15
Maximum	46.5	12.5
Average	8.3	3.5
Std. Dev.	6.4	2.3

* The error statistics shown here represent the magnitude of the relative horizontal positioning error.

correspond to outliers 2 and 3 in Figure 6. It should be noted that after the relative horizontal errors are normalized with respect to HDOP, the distribution contains no extreme data points that could be identified as outliers. This reinforces the strong correlation between low HDOP and accurate relative horizontal position or azimuth.

The raw and normalized relative vertical positioning error distributions are shown in Figures 9 and 10, respectively. The data was not combined as in Figure 8, due to the large variation in the two data sets as the statistics in Table 5 show. After normalizing the vertical error with respect to VDOP, it results in a distribution very similar to the horizontal error (e.g. compare the statistics for the normalized errors in Tables 4 and 5). This indicates that the Time Relative Positioning technique can provide the relative positioning accuracy desired in the horizontal and vertical components by selecting the satellite constellation that provides the appropriate HDOP and VDOP values. If relative horizontal accuracy is of the utmost importance, as in the PLGR+GLS application, then the constellation can be selected to optimize HDOP over VDOP. An obvious tradeoff exists when horizontal and vertical accuracy are equally important as in most applications.

Table 5. Relative Vertical Error Statistics.

	Relative Vertical Error Statistics (cm)*	
	Raw	Normalized
Minimum	0.05	0.02
Maximum	225.1 [†]	16.2
Average	15.8	3.4
Std. Dev.	21.7	2.6

* The error statistics shown here represent the magnitude of the relative vertical positioning error.

[†] See note on Table 2.

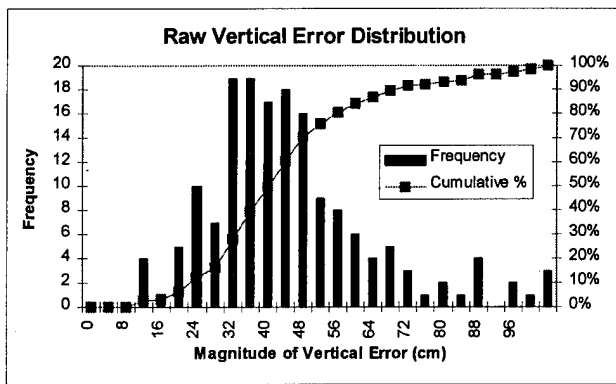


Figure 9. Distribution of the vertical positioning errors.

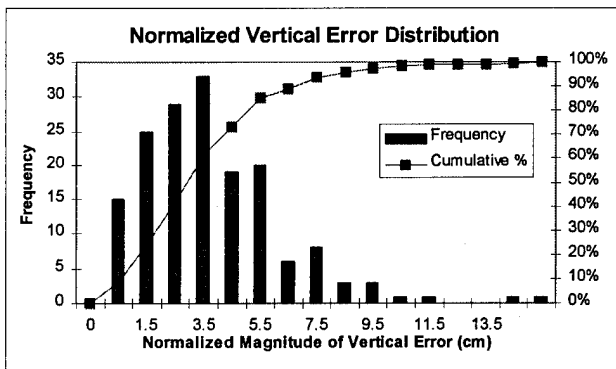


Figure 10. Distribution of the normalized vertical positioning errors.

VIII. Independent Testing Results

The Norwegian Army Materiel Command performed additional testing of the PLGR+GLS during the month of August 1995. The testing was performed to assess the azimuth performance over various baseline lengths and to assess the system's performance during live round testing compared to the traditional gun laying method.

The PLGR+GLS system was tested in various terrain and masking environments along baselines that varied between 30 m and 90 m. The test results were comparable to those described above. Since true azimuth was not available, the repeatability of the solution over a specific baseline was used to assess the systems performance. The results from a selected series of tests over a 30 m and 65 m baseline are tabulated in Table 6. The table provides measurement statistics including the standard deviation of the sample azimuth measurements, the average HDOP, the average traversal speed between tripods, and the number of sample measurements collected on the baseline. The last column of data in the table was collected by walking very slowly during the traversal and shows the negative impact of longer measurement intervals.

Table 6. Norwegian Army Test Statistics

	Norwegian Army Test Results		
	30 m Baseline	65 m Baseline	30 m Baseline
Std. Dev. (mils)	1.40	1.89	3.74
Avg. HDOP	1.8	2.2	2.3
Avg. Speed (mph)	2.8	3.3	1.4
# of Samples	18	6	10

The testing performed thus far was used to characterize the system's performance and identify the operational steps that are critical to achieving the full accuracy. After achieving a level of comfort in performing the operation, the PLGR+GLS was used to align mortars in live firing exercises. The exercises proved the PLGR+GLS to be successful in improving the weapon's effectiveness over traditional methods. Further testing is planned.

IX. Summary and Future Investigation

Although the Time Relative Positioning concept may not be new, its application to several real world relative positioning needs is new and exciting. The quick-and-easy measurement technique used here has demonstrated less than 20 cm of relative horizontal positioning error (2-sigma) and 3.2 mil azimuth error (2-sigma) in both the field data presented here and in independent testing.

The application of this technology to short baseline survey needs such as those in the Soil Conservation Agency, USGS, and USDA will result in affordable product solutions.

Future work in this area will involve a more thorough error budget assessment and better modeling of the known error sources to improve the system's performance.

ACKNOWLEDGMENTS

The authors want to acknowledge the Norwegian Army Materiel Command for their assistance in the design of the operational interface and for their contributions of system performance results from their field test evaluations. The authors would also like to acknowledge the Iowa and Illinois Marine Corp. reserve units that provided valuable input in developing the operational procedure for the system. Special thanks goes to the individuals in the Surface Mobility Products Department at Rockwell who put forth great effort to make this a success.

Results of DC-10 Tests Using GPS Attitude Determination

Leonard Kruczynski and John Delucchi
Trimble Navigation Ltd.

Timothy Iacobacci
United Airlines

BIOGRAPHY

Leonard R. Kruczynski

Dr. Kruczynski is the Project Manager for the TANS Vector at Trimble Navigation Ltd. Dr. Kruczynski has been involved in GPS since 1974. He earned his PhD from the University of Texas at Austin where he wrote his dissertation on GPS navigation algorithms. Dr. Kruczynski is a retired Air Force officer. He was Commander of the GPS Test Force in Yuma, AZ from 1982 to 1985. He has been employed by Trimble Navigation since 1985.

John Delucchi

Mr. Delucchi is a Senior Staff Software Engineer at Trimble Navigation. He is responsible for the firmware in the TANS Vector and for the supporting software for the product. Prior to his arrival at Trimble, he was a software engineer at ARGOSystems and at Kaiser Aerospace. Mr. Delucchi received his BS in Electrical Engineering from California State University at San Jose.

Timothy R. Iacobacci

Mr. Iacobacci is a Senior Engineer for United Airlines. His current responsibilities include DC-10 Navigation Systems and support for the DC-10 Electrical Power and Instruments. He has worked in the Shuttle Avionics Integration Laboratory at NASA Johnson Space Center and in flight test for Northrop's B-2 Division. Mr. Iacobacci received his MS in Electrical Engineering from California State University at Fresno at Edwards Air Force Base.

ABSTRACT

A TANS Vector GPS Attitude Determination System has been installed on a DC-10 as part of an ongoing effort to evaluate the benefits of GPS to commercial aircraft operations. The DC-10 flies in revenue service and, in addition to the Vector, has two TNL-8100s and two inertial navigation systems to support SATCOM antenna pointing. This paper presents the results of flight tests of the Vector. The results show that the Vector maintained solutions during aircraft maneuvers, that it provided accuracy well within the beam width of the antenna, and

that its integer resolution methods were fast and accurate. The tests showed that GPS-based attitude determination has the potential to provide primary attitude information for aircraft.

INTRODUCTION

Commercial aircraft are being outfitted with satellite communications systems to provide additional support for air crews and more services to passengers. Among these are real-time flight data, additional communications channels, access to premium television channels, fax and data transmission capability and air phone availability world-wide. [Reference 1] Such operations require a high-gain directional antenna that must be kept pointed at the communications satellite.

SATCOM antennas are typically electrically steered in elevation and either electrically or mechanically steered in azimuth. Proper antenna pointing requires knowledge of aircraft position, satellite position and aircraft attitude. The communications satellites are in well-defined geosynchronous orbits. GPS has established itself as the best source of aircraft position. With the availability of GPS-based attitude, it is now possible to get three-axis orientation from GPS equipment.

In summer of 1994, United Airlines approached Trimble Navigation with the offer to test GPS-based attitude for the SATCOM application. United had already committed to using Trimble 8100 GPS receivers in the test aircraft. Attitude information for SATCOM antenna pointing was obtained from the INS, gyros or compass on the aircraft. The attitude information was then passed to the SATCOM equipment to point the SATCOM antenna. United engineers believed that a GPS-based attitude solution would be a better solution and they were willing to fly a Vector to evaluate the performance of the system.

On 10 December 1994, a test flight of Vector on board a DC-10 demonstrated the potential of Vector to fulfill the need for SATCOM antenna pointing. This paper reviews the results of the test flight and describes what must be done next to fulfill the needs of this application.

DESCRIPTION OF TANS VECTOR

General

The Trimble TANS Vector is a GPS receiver dedicated to providing three axis orientation as well as position, velocity and time (PVT). Vector consists of four antennas mounted on the host platform, a Receiver/Processor Unit (RPU) and associated cables. Software provided with the Vector system (PCVector) controls Vector operation, displays attitude and PVT solutions either graphically or in text form and records data for later processing. Users typically integrate Vector into their own systems.

Vector is a Standard Positioning Service (SPS) receiver with the capability for differential GPS (DGPS). In autonomous SPS operation, Vector provides 100 meters, 2dRMS (95%) horizontal position accuracy. Vertical accuracy is 156 meters (95%). The U.S. government does not specify a velocity accuracy for the corrupted SPS signal. Vector has demonstrated a horizontal velocity accuracy of 1 meter per second (2 kts) horizontal at the 95% level and a vertical velocity accuracy of 1 m/s (2 kts) 95%. [Reference 2]

In differential mode, horizontal accuracy is on the order of 2 to 5 meters. Differential GPS performance is dependent on standard GPS environmental parameters such as multipath and geometry and is also strongly influenced by base station parameters such as distance to the base station and update rate.

Attitude Determination

Vector is a six-channel receiver with a signal processor that creates differential phase measurements on up to six satellites. A differential phase measurement is the difference in the arrival time of a GPS signal from a satellite at one antenna compared to the signal arrival time at a second antenna. The Vector fast multiplexes among the three baselines, creating up to 18 measurements. The signal processor maintains track of integer cycles.

The TANS Vector is a dedicated attitude determination receiver. A key feature is the use of a single oscillator. Using a common local oscillator results in double difference measurements that are free of the noise that is introduced by differencing measurements created using separate oscillators. The end result of the quieter measurements is quieter attitude solutions.

Integrity checks are used to validate that there have been no cycle slips. If the integrity check fails, the integers are re-evaluated. If the integrity checks are passed, Vector will compute and output the attitude over an RS422 serial port.

The accuracy of a Vector attitude fix is influenced by satellite geometry, multipath and array size and geometry. For one meter baselines, angular accuracy has a standard deviation on the order of 0.3° . Accuracy improves inversely with baseline length. Integer resolution time, however, increases with baseline length. In addition, larger arrays cannot be maintained as rigid as a short array. Most arrays use three meter or shorter baselines.

Vector Modes

The TANS Vector has two basic modes: calibration and normal operations.

Calibration

Calibration is required after installation on the host platform. Vector has two calibration methods: Self Survey and Line Bias Calibration (LBC). Self Survey determines the physical distances between all antennas and the differential electrical path lengths that the signals travel through the cables and the electronics. If the user can accurately measure the antenna distances, the LBC mode computes only the line biases.

Normal Operation

In normal operation, the Vector will use a search algorithm to determine the integer portions of the differential phase measurements at power up and will begin computing attitude solutions. As long as signals are continuously available, the signal processor will keep track of integer changes without requiring execution of the integer resolution algorithm. If a new satellite is tracked while attitude solutions are available, there is no need to execute the integer resolution search.

Integer Resolution

The integer resolution algorithm is a search algorithm that uses a maximum likelihood approach [Reference 3]. To reduce the search volume, there is a restriction on the pitch and roll of the platform (not the array itself). The limits are user selectable. Increasing the limits will increase the search time.

An unaided search examines the range of integers associated with a platform at any azimuth within user specified pitch/roll limits. An aided search capability is available. There are several approaches to the aiding but the best method for aircraft applications is the velocity aided search. In velocity aiding, there is an assumption that the orientation of the array with respect to the host platform is fixed and that the direction of the velocity vector is fixed (or nearly so) in the host platform's coordinates. Based on this assumption, the search algorithm examines integer solutions for a cone around the velocity vector which is provided by Vector's normal PVT solution. If the platform is not moving or is moving slowly, the velocity aided search defaults to unaided.

Attitude solutions

The signal processor in the Vector computes differential phase measurements twice per second. About 80% of the time, the attitude processor requires more than 0.5 seconds to compute an attitude fix. The result is the loss of a set of measurements and a 1Hz output. When the attitudes are computed within the 0.5 second measurement interval, the customer sees a 2Hz output rate.

The new 10Hz Vector uses a faster processor. Measurements are created every 0.1 second and the attitude processor computes a solution within the 0.1 second interval before the next set of measurements is made available.

During a short loss of signal on all satellites, the integer resolution algorithm is not automatically executed. Instead, the integers "fly-wheel" through the signal loss. If there is no significant change in direction, attitude solutions restart immediately on signal recovery.

The attitude algorithm in the Vector requires only six differential phase measurements to compute an answer. The six measurements must be available from at least two of the three baselines. A complete blockage of any single antenna, except the master antenna, will not stop the computation of attitude fixes.

AIRCRAFT EQUIPMENT

The designated test aircraft was United Airlines DC-10, tail number N1828U. The aircraft flies in revenue service between San Francisco and Hawaii.

Satellite Communications Equipment

The aircraft uses a Honeywell SATCOM system with a Canadian Marconi high-gain, beam-steering antenna and a Collins control panel. The antenna pattern has a 3° beam width. It is a phased array antenna mounted in a shell nearly 67 inches long, 18.5 inches wide and 4.75 inches high. The antenna is mounted on the top center of the fuselage.

Inertial Navigation Systems

The DC-10 has two Delco Carousel IV Inertial Navigation Systems (INS). The Carousel is a free-azimuth INU which contains a four-gimbal Inertial Reference Unit (IRU) using single-degree-of-freedom, floated gyros. In addition, the aircraft is equipped with a vertical gyro and a compass.

GPS Equipment

In addition to the Vector, the aircraft was equipped with two modified TNL-8100 GPS receivers. The 8100s

accepted data from the INS or the gyro/compass to provide flight information to the autopilot and to provide real-time pointing of the SATCOM antenna.

Data recording

Data was recorded from the two IRUs onto an optical disk. ARINC 429 labels are recorded at 10Hz. The information contained time, position, ground speed, attitude and attitude rate.

VECTOR INSTALLATION

Array Size and Location

A Vector with one meter baselines is specified at 0.3° RMS accuracy in a given axis – an order of magnitude smaller than the antenna's beam width. The Vector antenna array installed on the DC-10 has a 1.5 meter baseline between the master antenna and antenna #2. The master antenna and antenna #2 are located on the top of the aircraft along the longitudinal axis of the airframe. Antennas #1 and #3 are separated by 1.2 meters and are located on a line perpendicular to the master-#2 line and about 1 meter forward of the master antenna. This diamond shaped array (See Figure 1 and the photo in Figure 2) results in antennas #1 and #3 about 9 cm below the master-#2 line (assuming the master-#2 line is level). The curvature of the fuselage creates about a 10° tilt for the normal to antennas #1 and #3. This tilt was considered to be acceptable and the data supports this assumption. The array was calibrated using Self Survey.

Platform to Vector Rotation

No attempt was made to align the Vector with the inertial reference. Alignment of the INS with the aircraft is accomplished to within 0.1°. Given the mounting of the Vector antennas, any heading misalignment with the aircraft's longitudinal axis is assumed to be on the order of 0.1°.

The reference for pitch and roll is related to the aircraft's orientation at the time of calibration. A formal alignment would adjust for the INS indicated pitch and roll. Any biases in the pitch and roll differences between Vector and INS are most likely caused by misalignment.

Vector allows the user to input information to rotate the Vector computed attitude into the platform's coordinate system. This option was not exercised for the DC-10 installation. Instead, it was assumed that the Vector coordinates were aligned with the aircraft body coordinates.

Because of the mechanical installation of the array, the azimuth reported by Vector will be close to the INS reported heading. Pitch is affected by the difference between the pitch of the Vector array and the pitch of the

aircraft during the self survey. The mechanical installation of the cross antennas (antennas #1 and #3) should keep any roll misalignment limited to second order effects caused by the small pitch difference.

TEST FLIGHT

Flight Profile

On Friday, 9 December 1994, (Saturday, 10 December UTC), the DC-10 was flown on a test flight from San Francisco International Airport (SFO). The flight time was about three hours. Most of the time was spent over the Pacific just off the coast of California. Three landing approaches were conducted at Oakland International Airport prior to returning to SFO (See Figure 3).

Vector Tests Performed

To take maximum advantage of the test flight, Vector was placed in several different modes. Tests included a continuous series of integer resolutions using the unaided mode, a continuous series of integer resolutions with the aided mode, on-the-fly calibration, VHF interference and normal operation.

Integer Resolution Tests

If one were to depend on the loss of signals to cause an integer resolution cycle, then no data would have been collected to evaluate the integer resolution. Even with roll angles over 30°, the attitude computations were solid with no need to execute the integer resolution. To exercise integer resolution, the Vector was placed in a mode which continually forced the integer resolution.

During the unaided mode, the average time to determine integers was 8.7 seconds and the maximum time was 26.5 seconds. During the velocity aided mode, the average time was 3.5 seconds and the maximum time was 7.5 seconds. One aided integer test was accomplished during a landing approach to Oakland airport. No erroneous solutions were provided by the search method.

In Flight Line Bias Calibration

A short portion of the flight was used to evaluate LBC performance while in flight. LBC requires that the platform be pointed in a specified direction with some variation allowed. There was insufficient data to make any detailed conclusions about the in-flight LBC. The calibration values were not significantly changed as a result of this test. After the test, the Vector continued to provide good attitude solutions.

RF Interference Tests

Certain VHF frequencies have been identified as causing difficulties for GPS receivers. In this installation, the aftmost Vector antenna was located about 2.54 meters forward of the VHF antenna (See Figure B). The VHF

radio has a power output of 25 watts. For the VHF interference tests, Vector was placed in a normal operating mode and the PCVector program was executed. PCVector provides visibility to the signal strengths from all tracked satellites on all four antennas. The co-pilot keyed the VHF transmitter for about 20 seconds at each of the frequencies of interest. The PCVector program showed no noticeable drop in signal strengths nor any loss of signals. During the entire test period, Vector continued to provide attitude solutions. Post processing of the data validated the real-time conclusion that there were no noticeable adverse effects on Vector operation.

It should also be noted that the master Vector antenna is located 0.5 meters forward of the TCAS antenna and 1.5 meters forward of the mode S antenna. The TCAS directional antenna output power is between 160-400 watts and the Mode S antenna output is 250-550 watts. The frequency for both systems is between 1060 and 1090 MHz.

Accuracy Evaluation

For this flight test, accuracy of Vector was a secondary concern. The major issues were solution availability and the integrity of the solutions.

Reference System Accuracy

The accuracy of the reference was evaluated by differencing the solutions reported by the two IRUs. The differences were larger than the specified accuracy for the Vector array. The unusual behavior of the IRU references is starkly evident in the plot of the difference between the IRUs in turns. During one segment of the flight (designated as Segment H), the pilot executed a counter-clockwise, 30° bank turn followed by a clockwise turn. Figures 4 and 5 show the azimuth, pitch and roll during this flight segment. Figures 6, 7 and 8 show the azimuth, pitch and roll differences between the IRU's during this segment of flight. The behavior of the reference data pervades the entire flight making it difficult to evaluate accuracy of Vector to better than about 0.25°. Also, the recorded IRU data sometime came from the gyro/compass combination, further degrading the accuracy of the reference.

Incorrect Truth Data

An error was discovered in the processing of magnetic variation with the reference equipment. When the cockpit commanded magnetic heading, the magnetic variation was implemented twice. The result was an approximate 16° error in the recorded data. The error was observed when differencing the two IRUs as well as when comparing IRU data to Vector. Those points with this error were removed.

Difference between Vector and IRU

The entire flight time is not available to evaluate the accuracy of the Vector solutions. Much of the time was used for stress tests such as the integer resolution tests.

The magnetic variation error further reduced the amount of time during which a reference solution is available for comparison. Regardless, there were 4791 Vector solutions which could have statistics computed. Some solutions could not be evaluated because of the absence of a valid reference solution.

The following table summarizes the statistics of the differences between Vector solutions and IRU solutions. Points where the reference was deemed incorrect are not included in the statistical computation. Because of the inaccuracy of the reference, the mean and RMS values are not representative of Vector performance. Since there were no large differences, one can conclude that the Vector solution integrity was good.

Statistics of Differences between
Vector and IRU-1

	Azimuth	Pitch	Roll
Mean	-0.089°	-0.602°	0.835°
RMS	0.415°	0.111°	0.395°
Minimum	-1.835°	-1.254°	-0.146°
Maximum	1.556°	0.158°	2.363°

Figures 9, 10 and 11 show the difference in azimuth, pitch and roll between Vector and the reference identified as IRU-1 for the entire flight. Figure 9 does not display those points during which the reference was deemed incorrect. Figures 10 and 11 include those points resulting in noisy plots during that time. The noisy results at the end of the mission are likely due to multipath. At that time, the aircraft had parked next to the hangar. Figures 12, 13 and 14 show the attitude differences during Segment H.

CONCLUSIONS

The TANS Vector exhibited solid performance during the test flight including during the times of VHF operation. In normal operating mode, the Vector provided continuous solutions with no breaks and no incorrect solutions. When stressed by external commands to force a loss of integer lock, the Vector responded by finding a correct set of integers, quickly and accurately.

The accuracy of the reference source was unsuitable to quantify the accuracy of Vector. The RMS of the difference between Vector and IRU was on the order of the RMS of the difference between the IRUs, after eliminating clearly erroneous IRU solutions. When the IRU solution was validated, Vector never differed by more than 2.4°.

With a higher output rate, the Vector can be used to actively control the pointing of the SATCOM antenna. Considering the dynamics of commercial aircraft and the

requirement that the SATCOM antenna have sky visibility, an installation similar to that tested on the DC-10 has the accuracy and robustness to satisfy the SATCOM antenna pointing application.

RECOMMENDATIONS

Several actions should be taken before Vector can be legitimately used in this application. A higher output rate is required; an ARINC interface must be available; and a backup attitude source should be available. A Vector using a faster processor on the attitude board is being released in the fourth quarter of 1995 and will satisfy the output rate requirement. The new Vector is capable of output rates beyond 10Hz and resolves integer ambiguities more than ten times faster. The ARINC interface remains to be defined but the interface is not a state-of-the-art issue. To provide backup, the Vector can be integrated with inexpensive gyros or other attitude sensors. The gyros can be kept calibrated when Vector is operating. Since the backup would be needed only during only short GPS outages, the accuracy of the system would be more than adequate to satisfy the SATCOM application.

ACKNOWLEDGEMENTS

The authors would like to acknowledge the support provided by United Airlines Oakland Maintenance Base (OAKOV/OAKEG), San Francisco Maintenance Base (SFOOV/SFOEG), and McDonnell Douglas.

REFERENCES

1. "Cabin Management Market Growing", Aviation Week and Space Technology, August 15, 1994, pp 48-49.
2. Global Positioning System Standard Positioning System Signal Specification, 5 November 1993.
3. Knight, Don, "A New Method of Instantaneous Ambiguity Resolution," in Proceedings of ION GPS-94, Salt Lake City, Utah, 20-23 September 1994, by the Institute of Navigation, pp. 707-716.

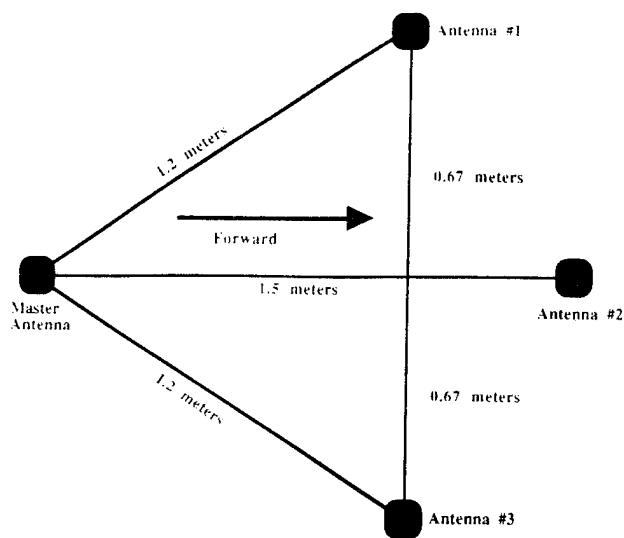


Figure 1
Array Dimensions

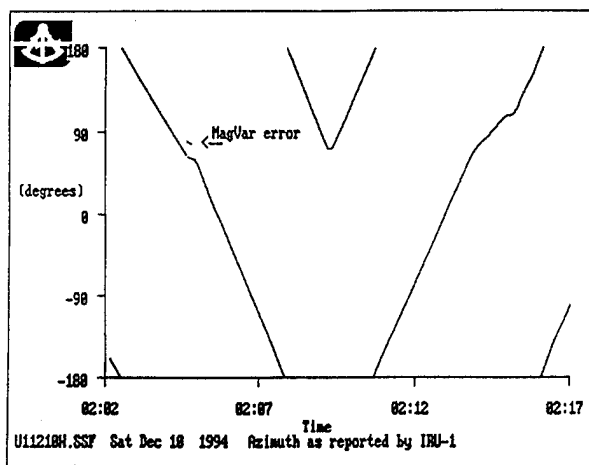


Figure 4
Azimuth Reported by IRU-1
(Segment H)

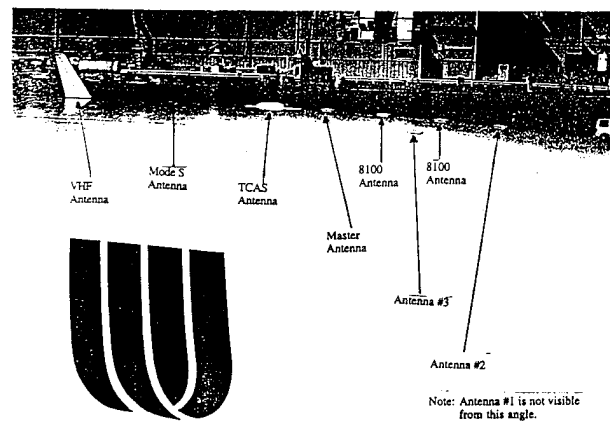


Figure 2
Aircraft Antenna Photograph

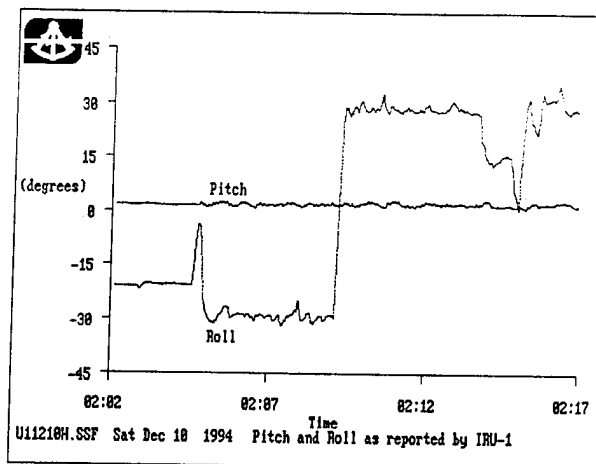


Figure 5
Pitch and Roll Reported by IRU-1
(Segment H)

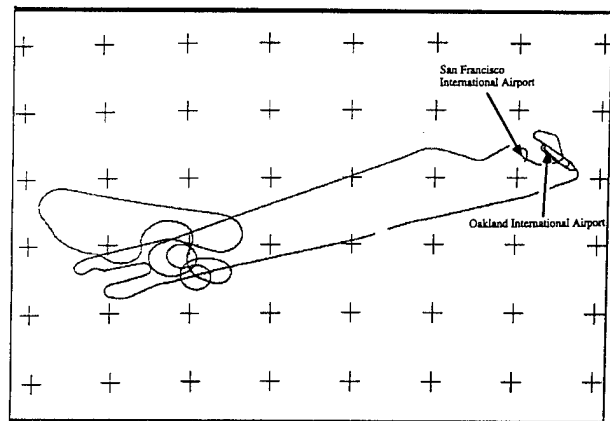


Figure 3
Ground Track
(50 km tick marks)

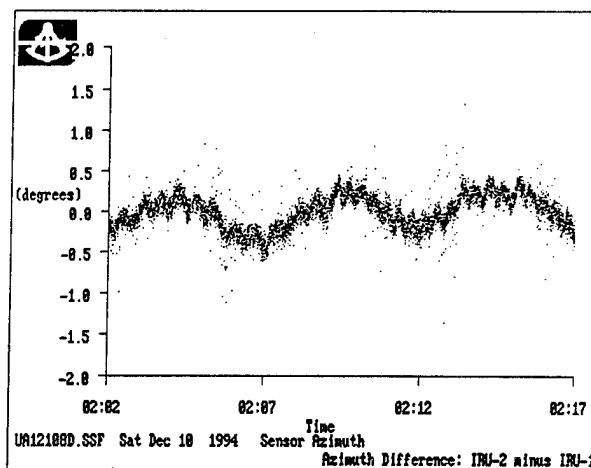


Figure 6
Azimuth Difference - IRU-2 minus IRU-1
(Segment H)

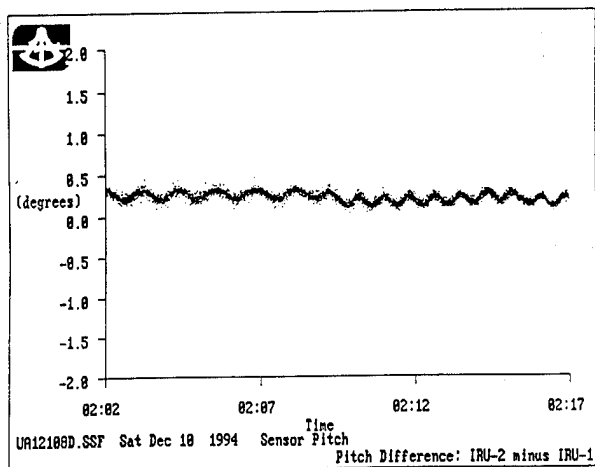


Figure 7
Pitch Difference - IRU-2 minus IRU-1
(Segment H)

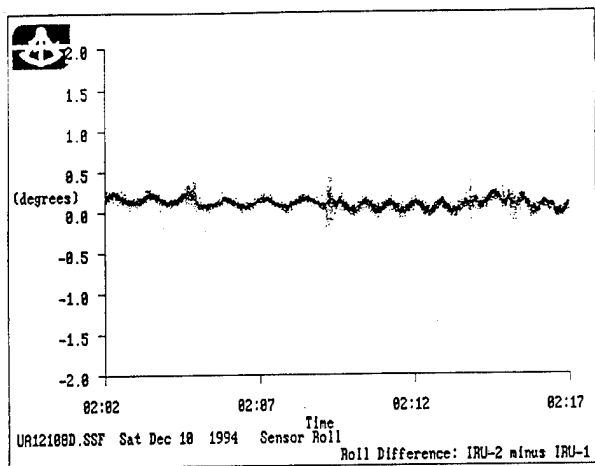


Figure 8
Roll Difference - IRU-2 minus IRU-1
(Segment H)

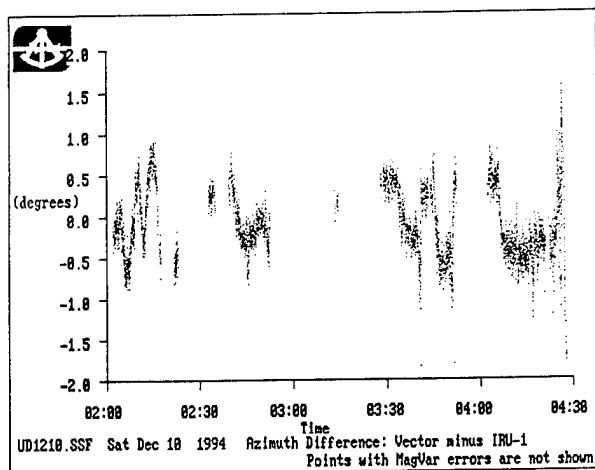


Figure 9
Azimuth Difference - Vector minus IRU-1
(Entire flight excluding invalid reference points)

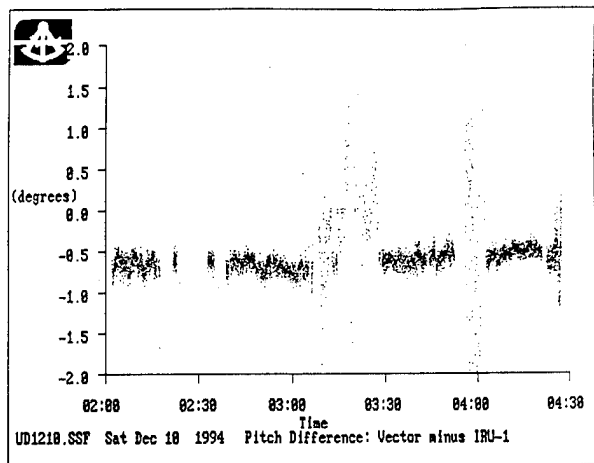


Figure 10
Pitch Difference - Vector minus IRU-1
(Entire flight including invalid reference points)

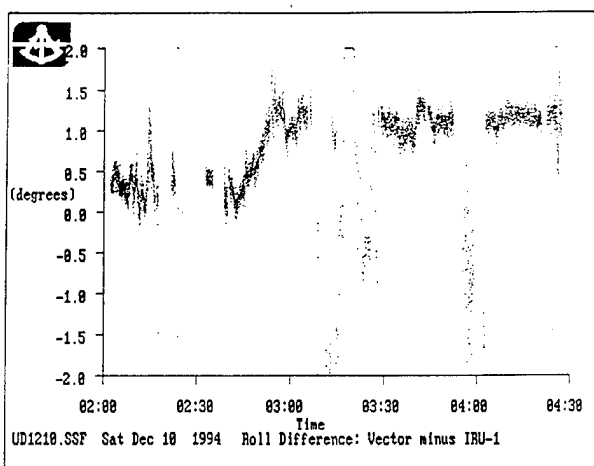


Figure 11
Roll Difference - Vector minus IRU-1
(Entire flight including invalid reference points)

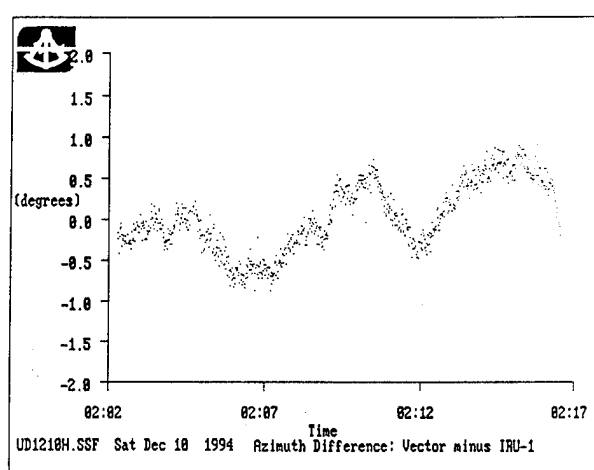


Figure 12
Azimuth Difference - Vector minus IRU-1
(Segment H with Valid Reference Points)

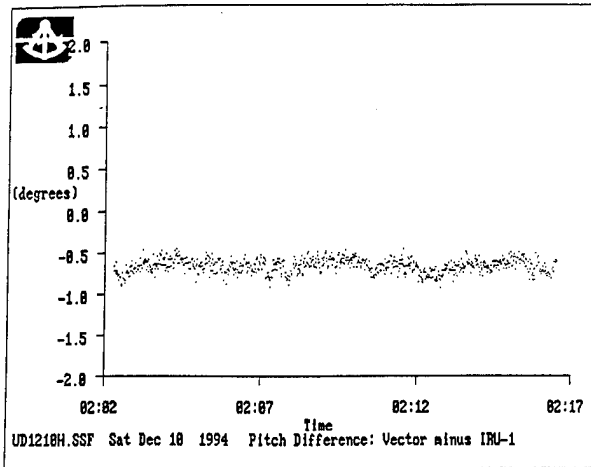


Figure 13
Pitch Difference - Vector minus IRU-1
(Segment H with Valid Reference Points)

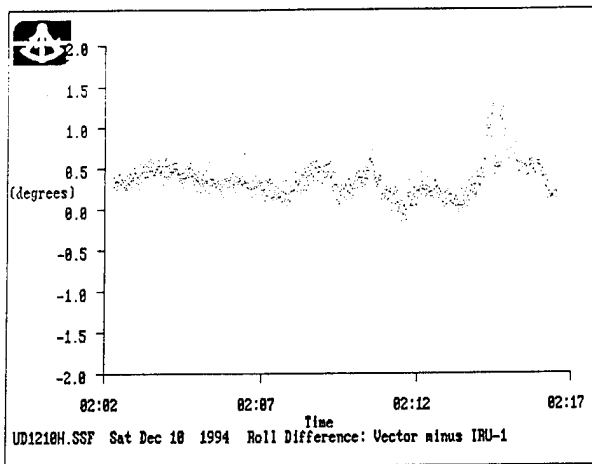


Figure 14
Roll Difference - Vector minus IRU-1
(Segment H with Valid Reference Points)

Attitude Determination: Exploiting all Information for Optimal Ambiguity Resolution

Dr.-Ing. Hans-Jürgen Euler and Craig Hill
Leica AG

BIOGRAPHIES

Dr.-Ing. Hans-Jürgen Euler graduated in geodesy at the Technical University of Darmstadt in 1983. He was awarded a Ph.D. on "Rapid ambiguity resolution techniques for small scale networks" in 1990. He worked with Dr. Clyde Goad at Ohio State University from 1989 to 1990 on precise positioning of highway vehicles. In 1991 he started work on algorithms for real-time applications. In January of 1993 he joined Leica in Switzerland, where he is head of the Data Processing group.

Craig D. Hill graduated from the Royal Melbourne Institute of Technology (RMIT), Australia, with a B.App.Sc. and M.App.Sc. in Surveying in 1990 and 1993 respectively. He has been working in the GPS Design and Applications group and the Data Processing group at Leica in Switzerland since March 1995 and is also enrolled in a Ph.D. program at RMIT.

ABSTRACT

It is possible to significantly aid integer ambiguity resolution by exploiting redundant information. Attitude determination using multiple GPS sensors provides such additional information to allow instantaneous ambiguity resolution and hence the necessary information to achieve accurate attitude determination. Optimal use of all information provides not only ambiguity resolution, but the necessary constraints to provide confident resolution.

This paper describes a number of different scenarios where additional information about the baseline(s) is provided to the processing algorithm to allow enhanced resolution times and confidence. Results using a minimal number of GPS sensors, perpendicularly located are shown. It is highlighted that instantaneous ambiguity resolution is possible, in addition, the introduction of redundant information reduces the possibility of measurement biases causing incorrect resolution.

INTRODUCTION

Traditional baseline computations are used very often for attitude determination. Since the baseline lengths are in general relatively short, a special computation scheme for attitude determination may be used. Many similarities exist between traditional and attitude determination computation schemes. The most important similarity is that the so-called integer ambiguities have to be resolved to obtain the required accuracy. The significant differences when comparing traditional relative coordinate determination and attitude determination are:

1. the baseline length is limited to a few meters;
2. the length can be surveyed beforehand;
3. in most cases the orientation is not completely unknown;
4. the absolute position of both ends of the baseline are unknown.

Since in attitude determination the baseline lengths are fairly short, the atmospheric corrections are negligible. Knowledge of the baseline lengths and approximate orientation reduces the number of possible solutions required in the search for the correct set of ambiguities. Furthermore, when using an antenna array additional plausibility checks are available. For instance, the angle between two baselines can be measured and incorporated in the processing scheme to assist in identifying the correct integer ambiguity values.

The issue of the absolute position of the antenna is important, however a high level of accuracy is not required. In situations where the accuracy of a navigation solution is inadequate, the position can be determined with the aid of RTCM corrections. An accuracy of a few meters should introduce no biases in the result.

Like in normal baseline computations, ambiguity resolution is a critical component of the processing scheme. The focus of this paper is to highlight how to correctly identify the correct set of ambiguities using apriori knowledge of the antenna configuration. The constraints, which can be introduced because of the apriori knowledge of the antenna configuration, help to make the identification easier than in traditional relative coordinate determination. Most of the possible integer ambiguity candidates will not satisfy the constraints and therefore the integer ambiguity identification should need less time than in a computation of a traditional baseline. Depending on the baseline length, instantaneous resolution of the integer ambiguities are reported by El-Mowafy and Schwarz (1994). The baseline lengths are in this case less than 1 cycle of the carrier phase, for example, for L1 carrier phase observations the baseline length must not exceed their wavelength of approximately 0.19 meter. With this restriction no ambiguities are needed in the observation equations. The baseline can be determined directly. However, short baselines produce orientations with reduced accuracy. The orientation parameters are derived from cartesian baseline components. Longer baseline components produce a better relative accuracy than shorter components, since the accuracy is not dependent on the baseline length. Therefore, El-Mowafy and Schwarz (1994) use collinear antennas for higher accuracy. The baseline with a length of less than 1 cycle is used to determine the approximate orientation and to limit the search space for the longer lines. Schade and Cramer (1994) need 5-50 consecutive data epochs for solving the integers on longer baselines.

The scope of this paper is the investigation of advantages when combining all information. It could be possible to resolve the ambiguities instantaneously if the available information is used in a suitable way.

THE TRADITIONAL BASELINE APPROACH

The equations of a relative coordinate determination are not too different from the equations of a navigation solution. One may write the model in a single or double difference notation. The following linearised equations are given for single differences:

$$\begin{aligned}\Delta\phi_{12}^1 &= dt + (x_1^1 dx_1 + x_2^1 dx_2 + x_3^1 dx_3) / \lambda + N^1 \\ \Delta\phi_{12}^2 &= dt + (x_1^2 dx_1 + x_2^2 dx_2 + x_3^2 dx_3) / \lambda + N^2 \\ \Delta\phi_{12}^3 &= dt + (x_1^3 dx_1 + x_2^3 dx_2 + x_3^3 dx_3) / \lambda + N^3 \\ \Delta\phi_{12}^4 &= dt + (x_1^4 dx_1 + x_2^4 dx_2 + x_3^4 dx_3) / \lambda + N^4\end{aligned}$$

where:

$\Delta\phi_{12}^i$ is the single difference observation of stations 1, 2 to satellite i ,

dt is the receiver clock difference,

x_j^i is the component j of the unit vector pointing to satellite i ,

λ is the wavelength of the carrier phase,

dx_j is the component j of the unknown position vector of the second receiver, and

N^i is the single difference integer ambiguity associated with satellite i .

As is well-known, the set of 4 equations provide, with known integer ambiguities, the relative position of 2 antenna phase centers. The cartesian baseline components have to be transformed to the required orientation parameters.

The number of equations can be reduced by building double differences. Alternatively, one of the integer ambiguities can be chosen freely, since the forth ambiguity cannot be distinguished from a receiver clock offset (Goad 1985, Euler and Goad, 1990). Any integer ambiguity combination delivering a relative coordinate solution within a sphere with the radius of the baseline length is a possible candidate for the correct result. In addition the combination should reproduce the baseline's length to within a few millimeters.

More than four available single difference phase observations allow a least squares adjustment and the application of an integer search strategy. Different search strategies are reviewed in Hatch and Euler (1994). These techniques have to be changed in order to give direct access to the restrictions of baseline length and the pre-defined orientation limits. In addition, where the number of single difference phase observations is limited to 3 satellites, a separate model has to be applied. This model makes use of the known baseline length to reduce the degree of freedom to 3. It is quite clear that nobody would force the use of only 3 satellites (due to the reduction of redundancy), but the solution for very short baselines is feasible and it might be a requirement where the coverage is limited in urban areas.

A DIFFERENT APPROACH

Based on Euler (1995) the following section shows a model which incorporates the baseline components from the beginning.

The reference system for the baseline, whose attitude should be determined, might be any suitable reference system. The orientation of the vector is probably needed in a topocentric system and therefore it might be desirable to use also a topocentric system for the definition of the vector. Moreover, a topocentric reference system provides, as we see later, a convenient way to incorporate tilt limitations. The baseline vector is given with:

$$\vec{b} = (b_1; b_2; b_3)$$

$$b = \sqrt{b_1^2 + b_2^2 + b_3^2}$$

where, due to the topocentric reference system,

b_1 northing,
 b_2 easting, and
 b_3 height.

The single difference observations to 3 different satellites measured on the baseline are:

$$\lambda\phi^{S1} = b \cos\beta^{S1} + \lambda N^{S1} + t_c$$

$$\lambda\phi^{S2} = b \cos\beta^{S2} + \lambda N^{S2} + t_c$$

$$\lambda\phi^{S3} = b \cos\beta^{S3} + \lambda N^{S3} + t_c$$

where:

$\phi^{S1}, \phi^{S2}, \phi^{S3}$ single difference carrier phase observations to satellite $S1, S2$, or $S3$, respectively,

N^{S1}, N^{S2}, N^{S3} the so-called integer ambiguities of the single differences,

t_c the difference of receiver clocks,

λ the wavelength of the carrier phase, and

$\beta^{S1}, \beta^{S2}, \beta^{S3}$ are the angles between baseline and the associated satellite.

The cosines of the angles between the satellites and baseline are given by the well-known vector relation:

$$\cos\beta^{S1} = \frac{\vec{b} \cdot \vec{x}^{S1}}{b} = \frac{b_1x_1^{S1} + b_2x_2^{S1} + b_3x_3^{S1}}{b}$$

$$\cos\beta^{S2} = \frac{\vec{b} \cdot \vec{x}^{S2}}{b} = \frac{b_1x_1^{S2} + b_2x_2^{S2} + b_3x_3^{S2}}{b}$$

$$\cos\beta^{S3} = \frac{\vec{b} \cdot \vec{x}^{S3}}{b} = \frac{b_1x_1^{S3} + b_2x_2^{S3} + b_3x_3^{S3}}{b}$$

The combination of these equations provides the double difference equations:

$$\lambda(\phi^{S2} - \phi^{S1}) =$$

$$b_1(x_1^{S2} - x_1^{S1}) + b_2(x_2^{S2} - x_2^{S1}) + b_3(x_3^{S2} - x_3^{S1}) + \lambda(N^{S2} - N^{S1})$$

$$\lambda(\phi^{S3} - \phi^{S1}) =$$

$$b_1(x_1^{S3} - x_1^{S1}) + b_2(x_2^{S3} - x_2^{S1}) + b_3(x_3^{S3} - x_3^{S1}) + \lambda(N^{S3} - N^{S1})$$

Substituting

$$C^{i1} = \lambda(\phi^{Si} - \phi^{S1})$$

$$N^{i1} = (N^{Si} - N^{S1})$$

$$\Delta x_1^{i1} = (x_1^{Si} - x_1^{S1})$$

$$\Delta x_2^{i1} = (x_2^{Si} - x_2^{S1})$$

$$\Delta x_3^{i1} = (x_3^{Si} - x_3^{S1})$$

and

$$b_3 = \sqrt{b^2 - b_1^2 - b_2^2}$$

we get:

$$C^{21} = b_1\Delta x_1^{21} + b_2\Delta x_2^{21} \pm \sqrt{b^2 - b_1^2 - b_2^2} \Delta x_3^{21} + \lambda N^{21}$$

$$C^{31} = b_1\Delta x_1^{31} + b_2\Delta x_2^{31} \pm \sqrt{b^2 - b_1^2 - b_2^2} \Delta x_3^{31} + \lambda N^{31}$$

These two equations give the baseline components of a baseline with known length. The square root, as the substitute for the third baseline component, offers two possible results. But in most cases these results will be distinguishable. If however 4 or more satellites are available all three components of the baseline can be computed directly.

$$C^{21} = b_1 \Delta x_1^{21} + b_2 \Delta x_2^{21} + b_3 \Delta x_3^{21} + \lambda N^{21}$$

$$C^{31} = b_1 \Delta x_1^{31} + b_2 \Delta x_2^{31} + b_3 \Delta x_3^{31} + \lambda N^{31}$$

$$C^{41} = b_1 \Delta x_1^{41} + b_2 \Delta x_2^{41} + b_3 \Delta x_3^{41} + \lambda N^{41}$$

....

$$C^{n1} = b_1 \Delta x_1^{n1} + b_2 \Delta x_2^{n1} + b_3 \Delta x_3^{n1} + \lambda N^{n1}$$

In comparison to traditional baseline computations, the known information provides a significant advantage. The number of possible combinations is reduced considerably if one uses the baseline length restriction. Moreover, in many cases the baseline's orientation is not totally arbitrary. For instance, two antennas mounted on the roof of a land vehicle will tilt only up to a certain amount. From this limited tilt, an additional restriction can be formulated.

The height component is defined with the inequality

$$b_3 = \sqrt{b^2 - b_1^2 - b_2^2} \leq b \cdot \sin(\text{tilt}_{\max})$$

and the horizontal base is defined with the inequality

$$b \geq \sqrt{b_1^2 + b_2^2} \geq b \cdot \cos(\text{tilt}_{\max})$$

For example, for a maximum tilt of 15 degrees, one gets the following constraints

$$b_3 = \sqrt{b^2 - b_1^2 - b_2^2} \leq b \cdot \sin(15 \text{ deg}) \approx b \cdot 0.2588$$

and

$$b \geq \sqrt{b_1^2 + b_2^2} \geq b \cdot \cos(15 \text{ deg}) \approx b \cdot 0.9659$$

The inequalities can be used to overcome the problem with the computational inconveniences caused by the square roots in the equation system. Only integer combinations providing an horizontal baseline result supporting both inequalities need to be tested. Favorably, these initial tests will use satellites in a good geometrical position. Remaining satellites might be used to prove whether the current orientation is valid. Since probably only a few data epochs or just one will be used to identify the proper set of ambiguities, a test procedure as described by Hatch (1990, Hatch and Euler, 1994) "least-squares-search" seems to be suitable.

The processing procedure can be split into the following steps:

- Measure baseline lengths and angles in antenna array

- Select reasonable tilt limits and a maximum uncertainty for the baseline lengths
- Identify a set of satellites with favorable geometry
- Compute all possible integer ambiguity candidates
- Test and reject baseline candidates which don't satisfy slope, horizontal and height baseline length constraints
- Choose a maximum variance for all residuals
- Test with remaining observations for large residuals
- Reject combinations with large residuals for any satellite
- Test baselines in antenna array with known angles

At the conclusion of these tests only one baseline per antenna pair should remain as suitable candidates, and hence allow accurate attitude determination.

DATA PROCESSING EXAMPLES

The scheme described in the previous section should be thorough enough for a complete understanding of the method. Figure 1 shows the three examples which have been selected to show the performance of the technique. Data was collected with the antenna array remaining static for the duration of the data collection period.

In all scenarios it could be assumed that:

- the distances between the antennas are known, and
- the angle formed by the antennae is also known.

This allowed constraints to be applied during data processing, to exploit this known information.

The instrumentation used for attitude determination normally comprises of single frequency receivers as dual frequency receivers are not needed. However, in each configuration shown in Figure 1 a dual frequency receiver providing L1 and L2 phase and pseudo range observations was connected to each antenna. However during data processing only the L1 phase data was used.

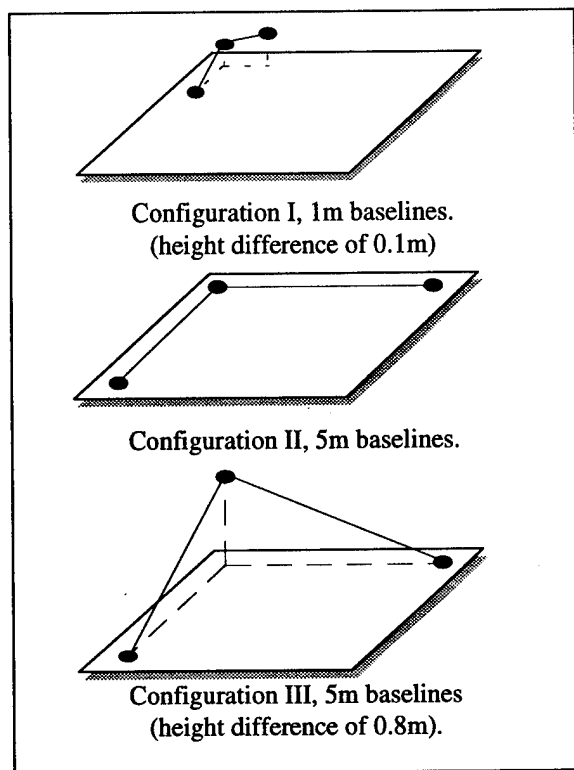


Figure 1 Antenna configurations

Parameters set during data processing were:

- a maximum uncertainty of 0.02 meter was adopted for the baseline length. All computational results delivering a length outside the limits of ± 0.02 meter were rejected directly.
- the baseline was tested to see if its tilt exceeded 20 degrees, by applying the constraints on the horizontal and height components of the baseline

Whenever these criteria are satisfied a variance test was conducted, where the observations were used in conjunction with the phase ambiguities in a least squares adjustment.

- whenever, the adjusted variance was less than 0.0001 square meters, the selection of integer ambiguities is considered as a possible set.

Once all test been applied to both baselines, the baselines can be combined to test the final constraint. The baselines will be accepted, providing:

- they satisfy the condition of the know angle between the two baselines, if the difference between the computed angle and the known angle is within 2° (1m baseline) and 0.3° (5m baseline) the baselines are accepted.

In addition, if more than one set of integer ambiguities remain for each baseline then this test will reject the baselines which should not be considered.

The rigorous tests that each set of ambiguities needs to satisfy ensures that a high degree of confidence can be achieved that ambiguity resolution was successful, and measurement biases have not caused a selection of the incorrect set of ambiguities.

Using this technique every search is totally independent from the previous searches as it is based only on the data of the current epoch. Therefore, if there would have been cycle slips on one or even all channels, it could not affect the result.

In Euler (1995), the initial tests indicated that a instantaneous ambiguity resolution was feasible most of the time on a 1.5 m baseline. The tests here extend that test by showing tilted baselines and baselines with longer lengths.

The data on the short baselines, Configuration I, was collected on tilted baselines. Figure 2 shows the number of possible solution candidates and the number of satellites available for that specific observation interval.

It can be seen from Figure 2 that on many occasions more than one candidate passed all rejection criteria. However, when applying the angular constraint introduced by the second baseline, these incorrect candidates can easily be exclude. Of the nearly 2000 epochs processed on nine occasions after applying this final angular constraint two possible baselines pairs still remained. However, an inspection of the variances allowed the correct baseline pair to be selected. At each of these nine epochs only five satellites were available.

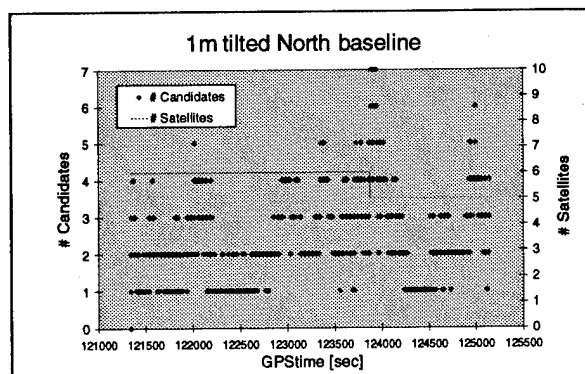


Figure 2 Number of candidates and satellites

The further two data sets were measured on longer baselines of 5 meters, Configurations II & III. When inspecting the formulas involved and the geometry of the ambiguity search space, one can easily imagine

that probably more integer candidates are available on the longer line, because the total range for the search will be larger. Furthermore, one might expect that more candidate solutions will pass the rejection criteria.

Figure 3 shows the analysis of the number of candidates and the number of available satellites for the north baseline in Configuration III. As expected, the number of accepted candidates increased significantly. It can also be seen that a correlation exists between the number of satellites available and the number of possible candidates. It can therefore be said that the number of candidates accepted is inversely proportional to number of satellites available.

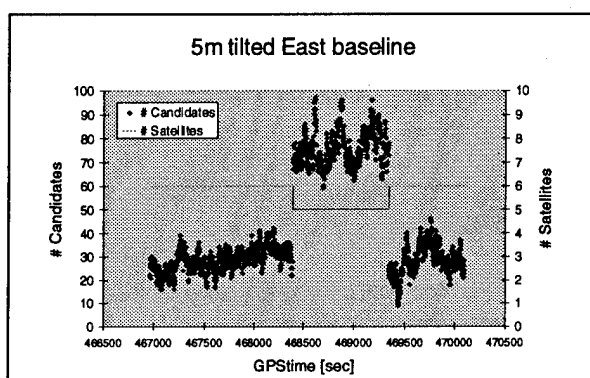


Figure 3 Number of candidates and satellites

However, after combining the candidates from the two baselines and applying the angular constraint and minimum variance if more than one baseline pair remained, the correct baseline pair was identified 80% of the time. Similar results were obtained for Configuration II.

The assumption of requiring independent ambiguity resolution at each epoch is not in reality necessary. If at an epoch the correct baseline pair could not be identified then the ambiguity values from the previous epoch could be used to "bridge the gap".

In addition, in these tests only the L1 carrier phase information was used. Current receiver technology delivers L1 pseudo range measurements with an accuracy significantly better than a meter (Jackson et al. 1995). The incorporation of this high accurate range observations may even further improve the scheme.

SUMMARY AND CONCLUSIONS

The results of these different processing scenarios show that instantaneous ambiguity resolution is feasible on baseline length of several phase cycles. However, a reduced performance was observed on the

longer baselines. It is suggested that extra information is required to improve the performance on these baselines.

The major problem for high accuracy in baseline orientation and also for the resolution of the integer ambiguities is multi-path. It is likely that some of the incorrect results in the 5m baseline tests, described above, is due to multi-path. In a static environment multi-path changes only very slow. On a moving vehicle the multi-path will be more random as long as it is not introduced by the platform itself.

The independent solution on every epoch is not a requirement of such applications. It is considered an advantageous feature. It can be used to verify that the previous solutions were correct, because the algorithm will reproduce the same sets of ambiguities from epoch to epoch. The change of geometry between the antennas and the satellites, while moving will also help to eliminate potential candidate ambiguity sets.

REFERENCES

- El-Mowafy, A., K.P. Schwarz (1994), Epoch by Epoch Attitude Determination Using a GPS Multi-Antenna System in Kinematic Mode, Proceedings of KIS'94, Banff, Canada.
- Euler, H-J (1995), GPS Attitude Determination: Utilizing Auxiliary Information to Obtain Improved Results, Proceedings of the 3rd International Workshop on High Precision Navigation, University of Stuttgart, Germany.
- Euler, H.-J., C.C. Goad (1991), On Optimal Filtering of GPS Dual Frequency Observations Without Orbit Information, Bulletin Geodesique, 65, 2, pp 130-143.
- Goad, C.C. (1985), Precise Relative Position Determination Using Global Positioning System Carrier Phase Measurements in a Nondifference Mode, Proceedings of the First International Symposium On Precise Positioning with the Global Positioning System, Rockville, Maryland.
- Hatch, R. (1990) Instantaneous Ambiguity Resolution, Proceedings of KIS'90, Banff, Canada.
- Hatch, R., H.-J. Euler (1994), Comparison of Several AROF Kinematic Techniques, Proceedings of ION-GPS'94, Salt Lake City, Utah.
- Jackson, P., J. Schwarz, R. Keegan, B. Jalali (1995), GPS Surveying-System 300: A new Range of

GPS Sensors, GPS Controllers and Software,
Leica AG, Heerbrugg, Switzerland.

Schade, H., M. Cramer (1994), Airborne Kinematic
Attitude Determination with GPS for
Photogrammetry and Remote Sensing,
Proceeding of KIS'94, Banff, Canada.

Tightly Coupled Attitude Determination Using GPS Carrier Phase Observables

Gene Howell and Dr. Wang Tang
ARINC

BIOGRAPHIES

Gene Howell is a Senior Principal Engineer at ARINC. He has worked in the field of aided navigation systems for 15 years. He holds B.S. and M.S. degrees in mathematics from Southern Illinois University in Carbondale.

Wang Tang is Technical Director of the Systems Integration Department at ARINC. He has 16 years experience in the field of navigation and guidance systems. He is the recipient of the 1994 ARINC Technical Excellence Award. He received a B.S. degree from National Cheng Kung University, Taiwan, an M.S. degree from University of Texas at El Paso, and a Ph.D. degree from Iowa State University, all in electrical engineering. He is a registered Professional Engineer in the Commonwealth of Massachusetts.

ABSTRACT

The synergism of integrating an inertial navigation system (INS) with the Global Positioning System (GPS) is well known. The GPS provides position and velocity information to the INS to enhance the INS navigation accuracy, while the INS aids the GPS with velocity information to increase its anti-jamming capability by narrowing the tracking loop bandwidth. The standard GPS/INS integration approach is to implement a Kalman filter to process measurements and estimate errors in both systems. The integration can be "tightly coupled", whereby the GPS pseudoranges are the measurements to the filter, or "loosely coupled", where 3-dimensional position is first found by the GPS receiver, then used as measurements to the filter.

Although GPS was designed primarily as a positioning and timing system, recent signal processing advances have allowed the phase of the GPS carrier to be measured very accurately. Using the carrier phase observable, the distance between two receivers can be

determined precisely, as can the orientation of the baseline. A number of techniques have been proposed for attitude determination using the carrier phase observable, and simulation and test results have been obtained.

The attitude determination algorithms typically find the three Euler angles of yaw, pitch, and roll. The subsequent integration is similar in nature to the loosely coupled filter using 3-dimensional position as measurements since the GPS observables are pre-processed before being used by the integrating filter. However, by using the carrier phase directly, the integrating filter becomes tightly coupled in attitude.

Two major benefits are gained by integrating GPS with the INS in this way:

- 1) the need to perform gyrocompassing, which normally takes from 5 to 30 minutes, is eliminated;
- 2) the need to excite heading error by maneuvering to cause level accelerations (s-turn) for in-flight alignment is eliminated.

This paper describes an INS/GPS Kalman filter tightly coupled in attitude. An overview of the algorithms is described and the measurement equation is given. Simulation results are presented. Questions relating to initialization of the system and observability of attitude errors are addressed.

1. INTRODUCTION

The integration of GPS with an INS has been extensively studied. The benefits to both systems when integrated together is well understood. The INS is calibrated using GPS position and/or velocity measurements while the GPS receiver is aided with velocity from the INS to improve the receiver's tracking performance in a jamming environment.

The INS typically processes the GPS position and velocity information in a Kalman filter. These quantities may be pre-processed by the GPS receiver to produce three dimensional position, either a geocentric position vector or latitude, longitude, and altitude. The INS then uses these positions to drive its Kalman filter. An alternative is for the INS to use the GPS measurements of pseudorange and deltarange directly. In this case the GPS receiver is essentially a sensor producing measurements only. Employing 3-D position or pseudoranges as measurements is referred to as "loosely coupled" or "tightly coupled" respectively. These filter designs have been documented since the advent of GPS.

More recent advances in signal processing capability has led to the use of the GPS carrier phase as an observable. The carrier phase has been widely used in surveying and kinematic positioning systems for a number of years. In a multiple antenna configuration, the carrier phase also allows relatively accurate determination of the orientation of the antennas with respect to each other, or attitude.

Most of the attitude determination systems have concentrated on independent and complete calculation of attitude [1-5]. Similar to position and velocity, the carrier phase from a GPS receiver may also be integrated with an INS, in this case to provide attitude information. Also similar to position and velocity, the carrier phase, or attitude information, may be loosely coupled with the INS. That is, if the three Euler angles are found first, then used as measurements to an integrating INS/GPS Kalman filter, the system is loosely coupled in attitude. If the carrier phase measurements are used directly as measurements to the filter, then the GPS and INS are tightly coupled in attitude.

After power on, an INS needs to be aligned, either on the ground or in air. For ground alignments, level is quickly found by processing the accelerometer outputs. The heading of the platform is determined by gyrocompassing. The degree to which heading can be found is limited by the east gyro drift. Depending on the magnitude of the east gyro drift, the heading limit can be reached in anywhere from 5 to 30 minutes.

For in-air alignments, the orientation of the INS with respect to level is also quickly found. The time required to estimate heading is usually decreased by performing a maneuver that excites the heading error, making it observable. This requires some kind of horizontal acceleration, typically obtained by some type of level turn; eg, the famous s-turn or half s-turn. If the vehicle

does not accelerate, then the time required to estimate heading is the same as for the ground alignment.

By processing carrier phase measurements, the attitude is observed directly. For the ground alignment, heading is found almost as quickly as level. For in-air alignments, the need to perform some type of maneuver is removed.

This paper is organized into five following sections. The next section provides the measurement equation for the carrier phase observable, which expands [6]. Then the integer ambiguity resolution and initialization procedures are discussed. The following section considers observability. Simulation results are presented next, ending with a summary.

2. MEASUREMENT EQUATION

For an attitude tightly coupled Kalman filter, the measurements to the filter are carrier phase measurements. In order to eliminate receiver bias errors, the double differenced carrier phase measurements are formed. It is assumed that the integer ambiguities have been resolved before the double difference phase measurements are processed. The resolution of the integer ambiguities is addressed in section 3.

In what follows, vectors are in bold faced type with the superscript denoting the coordinate frame and the subscripts defining the initial and end points of the vector. For example, \mathbf{r}_{jk}^i is a vector from j to k coordinatized in the i frame.

Denote the GPS antennas by A and B . The double differenced carrier phase measurement for antennas A and B and satellites i and j is given by

$$\begin{aligned}\Phi_{AB}^{ij} &= \Phi_B^j - \Phi_A^j - \Phi_B^i + \Phi_A^i \\ &= (\rho_B^j - \rho_A^j - \rho_B^i + \rho_A^i)/\lambda + N_{AB}^{ij}\end{aligned}$$

Here ρ is the distance from the receiver's antenna to the satellite and found from

$$\rho_A^i = |\mathbf{r}_{Ai}^e| = |\mathbf{r}_{ei}^e - \mathbf{r}_{eA}^e|$$

N_{AB}^{ij} is the double difference integer ambiguity for satellites i and j . The term \mathbf{r}_{ei}^e is the geocentric position vector of the GPS satellite which can be determined from the satellite ephemeris.

Perturbing this equation gives

$$\delta \rho = -(\mathbf{u}_{Ai}^e)^T \delta \mathbf{r}_{eA}^e$$

The vector \mathbf{u}_{Ai}^e represents the unit vector from receiver A to satellite i .

Taking the first order perturbation of the double difference phase equation, and assuming that the integer ambiguities have been resolved correctly yields

$$\delta \phi_{AB}^{ij} = \frac{1}{\lambda} (-\mathbf{u}_{Bj}^e + \mathbf{u}_{Bi}^e)^T \delta \mathbf{r}_{AB}^e$$

The antennas are assumed to be relatively close so that $\mathbf{u}_{Ai}^e \approx \mathbf{u}_{Bi}^e$.

In addition to resolution of the integer ambiguities, the initialization procedure, discussed in section 3, includes determination of the orientation of antenna B with respect to antenna A in the body frame. Thus the vector \mathbf{r}_{AB}^b is assumed known. With q_b^e denoting the quaternion transforming the body frame to the earth-centered-earth-fixed (ECEF) frame,

$$\mathbf{r}_{AB}^e = q_b^e \mathbf{r}_{AB}^b q_b^b$$

Once again taking a first order perturbation of this equation, and using $\delta q_b^e = \frac{1}{2} q_b^e \epsilon_{eb}^b$ leads to

$$\delta \mathbf{r}_{AB}^e = C_n^e (\mathbf{r}_{AB}^n \times (\epsilon_{np}^n - \epsilon_{ne}^n))$$

The term ϵ_{eb}^b is a vector of misalignments and can be viewed as a quaternion with zero scalar part so that this equation involves quaternion multiplication.

The quantity C_n^e is the direction cosine matrix relating the navigation frame to the ECEF frame. It was assumed in deriving this equation that the inertial measurement unit (IMU) is a strapdown platform coincident with the body frame. Thus the indices "p" and "b" are interchangeable. The vectors ϵ_{np}^n and ϵ_{ne}^n are misalignments between the platform and navigation frames (the standard platform tilt vector) and the computer and true frames respectively.

Finally, substituting the expression for the error in \mathbf{r}_{AB}^e into the equation for the double difference error gives the measurement equation

$$\begin{aligned} \delta \phi_{AB}^{ij} &= \frac{1}{\lambda} (\mathbf{u}_{Bi}^e - \mathbf{u}_{Bj}^e)^T [C_n^e (\mathbf{r}_{AB}^n \times (\epsilon_{np}^n - \epsilon_{ne}^n))] \\ &= \frac{1}{\lambda} (\mathbf{r}_{AB}^n \times (\mathbf{u}_{Bj}^n - \mathbf{u}_{Bi}^n))^T (\epsilon_{np}^n - \epsilon_{ne}^n) \end{aligned}$$

It can be seen that the sensitivity of the platform tilts to the carrier phase measurements is directly proportional to the length of the antenna baseline.

3. INITIALIZATION

Two problems associated with the initialization of the integrated INS/GPS filter for processing double differenced carrier phase measurements are the definition of the orientation of the antennas with respect to each other and the resolution of the integer ambiguities.

The basis of study in this paper is that there are only two antennas mounted on the top of the fuselage of an aircraft, or along the x-body axis of any vehicle, nominally coplanar with the longitudinal body axis. Since even a low accuracy INS (eg, 1°/hr gyro drifts) can generally provide relatively accurate measurements of level, the benefit of the GPS is to provide heading. Standard ground alignment will give almost immediately the orientation of the platform with respect to level (pitch and roll) but the determination of heading is much slower and is limited by the east gyro drift rate. The double difference measurements from two GPS antennas mounted along the longitudinal axis will quickly provide accurate heading information.

The derivation of the measurement equations above assume that the antenna baseline length and orientation with respect to the body is known. The length of the baseline can be measured with a tape measure at installation, assuming that the antenna phase center is stable and located near the physical center of the antenna. Procedures exist for aligning an INS to the aircraft body axes [7,8]. The antennas may then be mechanically aligned in azimuth to the aircraft longitudinal axis. However, the azimuth alignment using these procedures may be relatively coarse. The preferred method would be to perform a carrier phase based survey after antenna installation while gyrocompassing. This would give the accurate antenna baseline length and the orientation of the baseline with respect to the INS platform axes. The azimuth orientation may be more accurately determined from a mechanical alignment than a gyrocompass if the IMU

has poor quality gyros. Residual azimuth error will manifest itself as an east gyro drift. After this initialization process, the angular offsets of the antenna baseline from the INS platform axes can be stored for later use when estimating the double difference measurements from the INS data.

The problem of integer ambiguity resolution has been studied extensively [9-13]. The preceding developments assume that the ambiguities have been resolved correctly before any measurements are processed by the Kalman filter. In this application, the INS provides relatively accurate information that defines level. The length of the baseline vector is also known. Thus the integer ambiguity resolution becomes a constrained search through possible headings. An algorithm has been formulated that takes advantages of the constraints, then determines the ambiguities and estimates heading with one epoch of phase measurements by minimizing a cost function. Only an initial gross estimate of heading is needed. The algorithm will find the correct ambiguities with an initial uncertainty interval as large as 90° , given enough visible satellites (it is assumed that the receiver is all-in-view).

As an example of the performance of this algorithm, phase data was collected at the ARINC facility in San Diego, California, in June, 1995 using two NovAtel 3951R GPSCard receivers. The antenna baseline was approximately 13.3 meters. Seven satellites were tracked, yielding six double differences. The cost function over the 90° heading search interval is shown in Figure 1. The true heading, found by performing a static survey, was 15.176° . The estimated heading was found to be 15.200° , and the ambiguities were all estimated correctly.

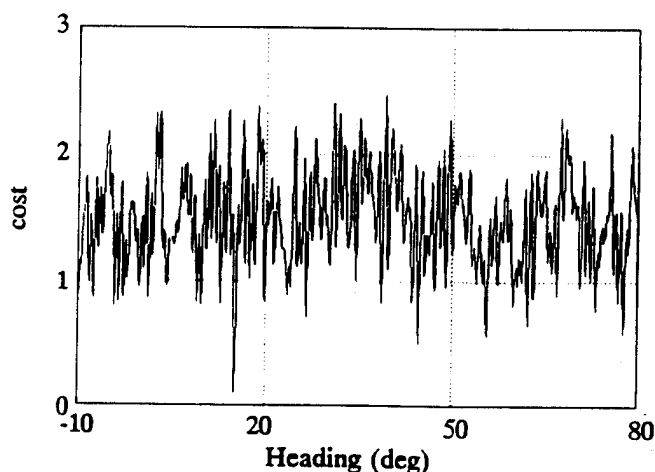


Figure 1. Heading Search Cost Function.

Note that there is a tradeoff between the estimation of platform tilts and integer ambiguity resolution. Larger antenna baseline increases the ability to estimate platform tilts. However, it decreases the ability to initialize the ambiguities correctly using the search algorithm since smaller changes in heading yield larger changes in estimated ambiguities.

4. OBSERVABILITY

As noted in Section 3, the configuration considered consists of two antennas mounted nominally along the vehicle longitudinal axis. Using only two antennas prohibits independent determination of the three Euler axis angles. In fact, the misalignment around the antenna baseline is unobservable. Consequently, if the baseline were aligned with the body x-axis, then roll error would be unobservable in this configuration. This is clear when considering the measurement equation coordinatized in the body frame instead of the navigation frame. Then the only non-zero element of the vector r_{AB}^b is the first component, giving a zero entry for the x-body, or roll, measurement sensitivity. Note that this configuration does not preclude observation of the level tilts since they are defined in navigation axes.

For aircraft, an advantage of using only two antennas mounted on the fuselage would be less impact of structural deformations. For three or more antennas with at least one on a wing tip, loading on the wings causes a change in the body frame relative locations of the antennas, forcing an estimation of the wing flexure [2,5]. While not free from deformations, the fuselage is typically more rigid, especially when considering that the antennas do not need to be mounted as far apart as possible on the fuselage. The utility of only two antennas mounted along the longitudinal axis emphasizes once again the synergy between the INS and GPS. Pseudorange and delfarange measurements from the GPS receiver to the integrating filter allows level tilt error to be kept low, while the GPS double difference measurements allow azimuth tilt to be measured without the need for maneuvering. Complete determination of attitude by GPS is not needed.

5. PERFORMANCE

A number of covariance results have been presented in [6] showing the advantages of double differenced carrier phase measurements for integrated INS/GPS performance. Results emphasizing certain aspects only of the benefits of direct carrier phase updating are given here.

The primary advantage of using the double differenced carrier phase measurements in the configuration described above is the fast and accurate determination of heading. A covariance analysis was performed, comparing heading error for standard gyrocompassing with carrier phase measurement processing.

A low cost IMU was simulated, with $1^\circ/\text{hr}$ gyro biases, $1000 \mu\text{g}$ accelerometer biases, and $0.01^\circ/\sqrt{\text{hr}}$ random walk on attitude. Four measurement scenarios were considered:

- 1) velocity updates once every 10 seconds, 0.01 meters/sec measurement noise standard deviation (ground alignment);
- 2) all-in-view double difference carrier phase measurements once every 10 seconds, 0.1 cycles measurement noise standard deviation;
- 3) one double difference carrier phase measurement every 10 seconds, 0.1 cycles measurement noise;
- 4) velocity and all-in-view double difference carrier phase measurements, alternating every 10 seconds, measurement noises as in (1) and (2).

Each scenario lasted 10 minutes.

A plot comparing the azimuth error in each case is illustrated in Figure 2. The plots are labeled by the measurement case number described above. Note that the vertical axis is logarithmic in this plot. The improvement in reducing azimuth error by using carrier phase measurements is clear from the graph. When gyrocompassing, the azimuth error is limited to 248 arc minutes by the large east gyro drift. When using carrier phases from all satellites in view to form double differences, the azimuth error is reduced to 1.25 arc minutes after 10 minutes. Even when using only one double difference measurement, the azimuth error is estimated down to 5 arc minutes, one sigma. Although not shown, the best overall performance for reducing velocity and platform tilts is by using a combination of velocity and carrier phase measurements.

To illustrate more dramatically the time benefit of using double differenced carrier phase measurements over traditional gyrocompassing, the above scenario was repeated but with a better quality IMU. For this case, the gyro drifts were set to $0.01^\circ/\text{hr}$ and the accelerometer biases to $100 \mu\text{g}$'s. No random walk on attitude was modeled. Figure 3 compares the behaviors

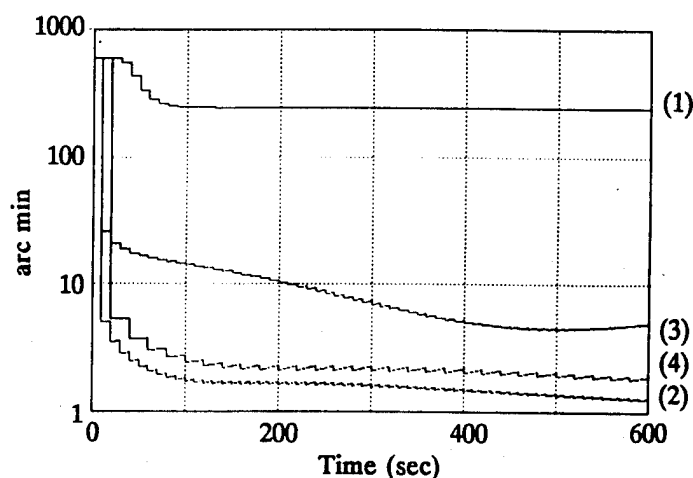


Figure 2. Z Platform Tilt Uncertainty:
 $1^\circ/\text{hr}$ Gyro Drifts

of the four cases. The differences in the speed with which azimuth error is reduced is readily apparent.

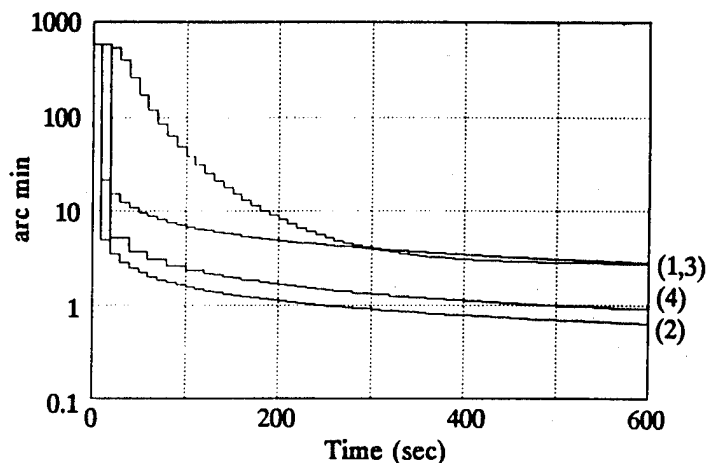


Figure 3. Z Platform Tilt Uncertainty:
 $0.01^\circ/\text{hr}$ Gyro Drifts

Another advantage of the integrated INS/GPS is the ability to reinitialize the integer ambiguities after loss of lock. Use of double difference measurements increases calibration of the IMU gyro errors, permitting decreased free inertial error growth rates when the GPS signal is lost.

To investigate the reinitialization of the integer ambiguities, the conditions of (4) above served as a starting point. After the 10 minutes of velocity and carrier phase measurements while static, the aircraft accelerated to 100 meters/sec and climbed to low altitude, flying the ground track depicted in Figure 4.

The total time to traverse the track shown was 13.5 minutes. During this time, pseudorange and deltarange measurements, corrupted by SA, and carrier phase measurements were performed at 30 second intervals, offset from each other by 10 seconds; i.e., one type of measurement was performed every 10 seconds, but each type was repeated only once every 30 seconds. Pseudorange measurements were done first, followed by deltarange measurements 10 seconds later, then double difference carrier phase measurements at the next 10 second mark. The sequence was then repeated for the duration of the trajectory. Shadowing of the GPS signal by the aircraft body was also simulated, assuming top mounted antennas.

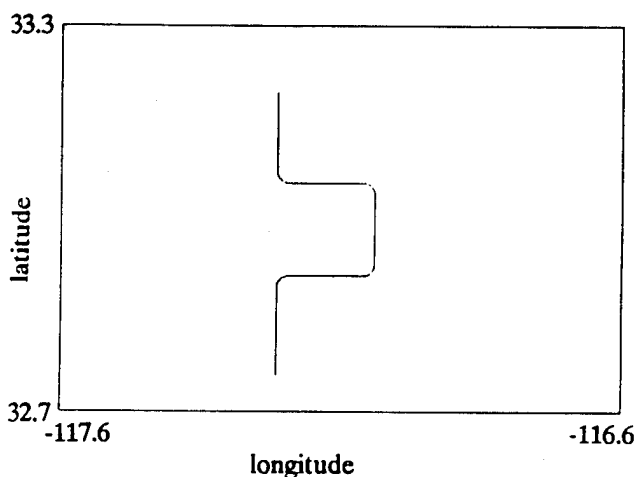


Figure 4. Simulated Vehicle Ground Track

At 13.5 minutes, a loss of the GPS signal was simulated. The vehicle continued flying straight north free inertially. Since the position errors remain small enough so that the errors in line-of-sight vectors to the satellites are negligible, the determining factor for correct reinitialization of the integer ambiguities is the platform tilt error. The tilt growth rate is dominated in this case by the azimuth gyro drift. At the beginning of the free inertial propagation, the z-gyro bias is $0.1^\circ/\text{hr}$, one sigma. The time history of the azimuth error standard deviation is shown in Figure 5.

Various methods for initializing the integer ambiguities while in motion (on-the-fly) have been proposed. They generally involve some type of search with the use of dual frequency receivers reducing the search time through the wide lane approach. With an integrated INS/GPS system, it may be possible to obtain the ambiguities directly in certain cases.

The sensitivity of integer ambiguity errors to a direct computation given absolute position of the INS and

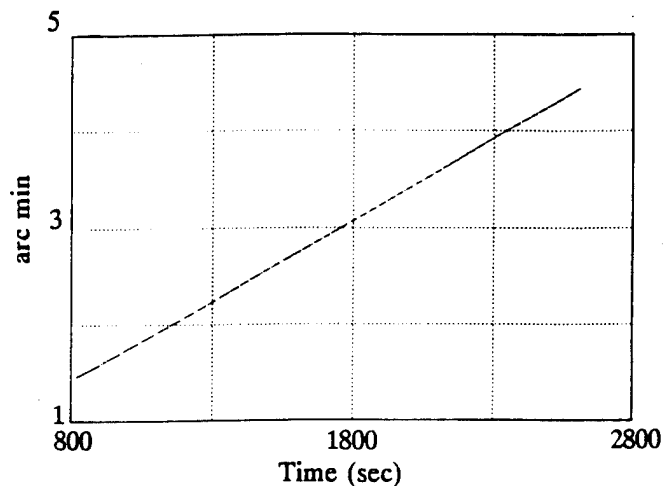


Figure 5. Free Inertial Z Platform Tilt

relative positions of the two antennas is similar to the double difference measurement error and is given by (ignoring the position error term)

$$\delta N_{AB}^{ij} = -\frac{1}{\lambda} [(u_{Bj}^n - u_{Bi}^n)^T (r_{AB}^n \times e_{np}^n)] + \epsilon$$

The ϵ term encompasses all phase measurement noise.

This equation gives limits on the maximum allowable platform tilt to correctly compute the integer ambiguity. As an example, consider only azimuth error. For an INS heading north with the navigation axes defined as east, north, up (ENU), and a 10 meter antenna baseline, the worst case geometry would have the base satellite for double differences at the horizon directly east or west while the second satellite in the double difference would be 180° from the first (due west or east). If the phase measurement errors are independent between channels and equal in magnitude to 0.05 cycles, one sigma, and if $1/3$ cycle is the limit for determining the integer ambiguity correctly with 0.9 probability, then the tilt error can contribute no more than 0.27 cycles to the total ambiguity error. This means that the azimuth error must be no more than $0.138 \lambda_1 / 20 \text{ rad} \approx 4.5$ arc minutes. In the case analyzed here, the ambiguities could be computed directly from the INS data for up to 20 minutes after the loss of GPS. No search algorithms or dual frequency receivers are required. Thus reinitialization of the integer ambiguities is greatly simplified.

Note that straightforward use of double difference carrier phase measurements yields correlated

measurements. Strategies have been proposed in [6] to create independent measurements. Independent measurements are desirable for real time systems since they can be processed sequentially by the Kalman filter as scalar measurements, obviating the need to invert a matrix of dimension equal to the number of measurements. An alternative strategy is to decorrelate the measurements by a rotation in the usual way. This procedure involves computing the inverse of a symmetric matrix similarly to what is done in using a measurement vector. When the phase measurement errors are independent between channels and have equal variances, the inverses for various expected measurement dimensions can be pre-computed and stored. In this case, the noise matrix is given by

$$R = \sigma^2 \begin{pmatrix} 4 & 2 & \dots & 2 \\ 2 & 4 & \dots & 2 \\ \vdots & \vdots & & \vdots \\ 2 & 2 & \dots & 4 \end{pmatrix}$$

The inverse of the square root of R can be computed and used to rotate the measurements and measurement matrix, giving uncorrelated measurements with unity variance; i.e, compute S^{-1} such that

$$R = \sigma^2 S S^T$$

then rotate the measurements and observation matrix by

$$z' = \frac{1}{\sigma} S^{-1} z$$

$$H' = \frac{1}{\sigma} S^{-1} H$$

6. SUMMARY

Measurement equations have been presented for performing direct double difference carrier phase measurements in an integrated INS/GPS Kalman filter. There is a symbiosis in this tightly coupled integration as there is for typical position/velocity tight coupling. The INS benefits by quick and accurate estimation of heading and increased calibration of gyro errors from the GPS while the reinitialization of integer ambiguities due to loss of lock for the GPS is greatly facilitated by the INS information. As a result, the need for extended time periods to gyrocompass during static alignments or

the requirement to perform maneuvers during transfer alignments is eliminated.

Initialization of the integer ambiguities has been addressed as well as defining the orientation of the GPS antenna baseline with respect to the INS platform axes. Further refinements of the procedure for determining the orientation of the two systems can be made.

Covariance results have been presented. The next step is to implement the integrating Kalman filter with actual GPS receivers and an INS to study the performance. Although it appears that much of the emphasis on GPS attitude determination is pointing to an ultimate goal of replacing inertial instruments with a pure GPS system, the advantages of an integrated system, even with a low cost IMU, should not be dismissed.

REFERENCES

- [1] Van Graas, F., Braasch, M., *GPS Interferometric Attitude and Heading Determination: Initial Flight Test Results*, Papers Published in Navigation, Vol IV, 1993, pp.359-378.
- [2] Cohen, C., Parkinson, B., McNally, B. *Flight Tests of Attitude Determination Using GPS Compared Against an Inertial Navigation Unit*, Navigation, The Journal of the Institute of Navigation, Vol. 41, No. 1, Spring 1994, pp.83-98.
- [3] Weill, L., *Optimal GPS Attitude Determination without Ambiguity Resolution*, Proceedings of the 1994 National Technical Meeting, Institute of Navigation, San Diego, California, 1994, pp.433-439.
- [4] Juang, J., *A Fast Algorithm for GPS Attitude Determination*, Proceedings of the First GPS Technical Seminar, Taiwan, March 1994, pp.327-336.
- [5] Cannon, E., Sun, H., Owen, T., Meindl, M., *Assessment of a Non-Dedicated GPS Receiver System for Precise Airborne Attitude Determination*, Proceedings of ION GPS-94, Seventh International Technical Meeting, Salt Lake City, Utah, September 1994, pp.645-654.
- [6] Miller, B., Phillips, C., Evans, A., Bibel, J., *A Kalman Filter Implementation for a Dual-Antenna GPS Receiver and an Inertial Navigation System*, Proceedings of ION GPS-93, Sixth International Technical Meeting, Salt Lake City, Utah, September 1993, pp.593-602.

[7] *LTN-72 Inertial Navigation System and LTN-72R Area Navigation System, Installation Instructions*, Revision 8, Litton Aero Products, September 1993.

[8] *LTN-92 Inertial Navigation System, Installation/Line Maintenance*, Revision 12, Litton Aero Products, August 1994.

[9] Hatch, R., *Ambiguity Resolution While Moving - Experimental Results*, Proceedings of ION GPS-91, Fourth International Technical Meeting, Albuquerque, New Mexico, September 1991, pp.707-713.

[10] Landau, H., Euler, H., *On-the-Fly Ambiguity Resolution for Precise Differential Positioning*, Proceedings of ION GPS-92, Fifth International Technical Meeting, Albuquerque, New Mexico, September 1992, pp.607-613.

[11] Brown, R., *Instantaneous GPS Attitude Determination*, Proceedings of the IEEE Position, Location, and Navigation Symposium (PLANS), 1992, pp.113-120.

[12] Sauermann, K., Becker, M., Mathes, A., *Ambiguity Resolution "On-the-Fly" Using the Latest Generation of GPS Receivers*, Proceedings of ION GPS-93, Sixth International Technical Meeting, Salt Lake City, Utah, September 1993, pp.1107-1114.

[13] Knight, D., *A New Method of Instantaneous Ambiguity Resolution*, Proceedings of ION GPS-94, Seventh International Technical Meeting, Salt Lake City, Utah, September 1994, pp.707-716.

GPS Modeling in the Attitude Determination Error Analysis System: Development and Application to TRACE

Eleanor Ketchum and Joseph Garrick
NASA Goddard Space Flight Center

Mohammad Rokni
Computer Science Corporation

BIOGRAPHIES

Eleanor Ketchum has been an engineer at the Goddard Space Flight Center for the last nine years. She is currently in the Attitude Control and Stabilization branch of the Special Payloads Division, and has also worked in the attitude analysis section of the Flight Dynamics Division. Ms. Ketchum received her BA in Mathematics from the College of William and Mary in 1986 and MS in Applied Mathematics from the Johns Hopkins University in 1989. She is currently a doctoral candidate in Mechanical Engineering/ Astronautics at the George Washington University's Joint Institute for the Advancement of Flight Sciences. Her research interests are in low Earth orbit attitude sensors and attitude determination.

Joe Garrick has been an aerospace engineer in the attitude analysis section of the Flight Dynamics Support Branch for the past seven years and a software engineer in the Software Development Branch for the first five years of his work experience at the Goddard Space Flight Center. Mr. Garrick received his BS in mathematics from the University of Missouri in 1982 and an MS in Electrical Engineering, with emphasis in control and estimation theory, from the Johns Hopkins University in 1992.

Mohammad Rokni has been in the Attitude Analysis Department of the Computer Sciences Corporation for the past 6 years. He received his BS in 1979 in Mechanical Engineering from West Virginia University, and an MS and Ph.D., in 1981 and 1986 respectively, from the University of Maryland, also in Mechanical Engineering.

ABSTRACT

The technology of GPS attitude determination for spacecraft is young but growing rapidly. The developments in the field have traditionally drawn from a single measurement model and evolved from there. Those most closely involved in the process have not necessarily had experience in spacecraft attitude sensor modeling and performing in-flight calibration, but have been more hardware or even navigation specialists. In the process of modeling GPS for use in the Goddard Space Flight Center's existing spacecraft Attitude Determination Error Analysis System (ADEAS), some shortcomings in current measurement modeling approaches surfaced.

This paper presents an improved measurement model for GPS attitude determination of the form used for other traditional spacecraft attitude sensors. Similar models are presented for three axis magnetometers and star trackers for comparison. Attitude error analysis for the Transition Region And Coronal Explorer (TRACE) using ADEAS is presented. TRACE will be launched in September 1997 with a three axis gyro pack, a magnetometer, and GPS. Interestingly, the GPS antennas will be on separate deployable solar panels, rendering pre-launch self-survey nearly useless. Analysis is presented which explores the ability to solve for attitude, baseline misalignment, baseline length uncertainty, and baseline bias in either a single filter or a combination of batch least squares and a sequential filter using measurements from various combinations of the TRACE attitude hardware including GPS only.

NOMENCLATURE

A_{IB} Attitude matrix from body to inertial

a_i	Amplitude of orbit-related or other unknown periodic error source
b_I	Sensor bias in inertial space
b_i	Bias of the i th sensor
B_{est_I}	Estimate of the magnetic field in inertial space
B_S	Measured magnetic field in sensor coordinates
C_{SQ}	Torquer coupling matrix
\bar{D}_Q	Commanded dipole
h_i	Alignment error of the i th measurement
k_{ij}	Integer for baseline i , GPS SV j
M_{BS}	Alignment matrix between body and sensor
Δr_{ij}	Measured differential carrier phase for baseline i , SV j
S	Scale factor
\hat{s}_j	Line of sight unit vector to SV j
\tilde{S}_{ref_I}	Reference star direction in inertial space
\tilde{S}_S	Measured star in sensor coordinates
sf_i	Scale factor error in i th measurement
\bar{x}_i	i th baseline vector
δx_i	i th baseline length error
v	Noise (considered white)
ω_i	Frequency of periodic error in i th measurement
ψ_i	Phase angle of periodic error in i th measurement

INTRODUCTION

This paper explores the GPS measurement model, comparing it to other attitude sensor measurement models. The addition of this GPS model to an existing attitude error analysis program is discussed. In order to both demonstrate the GPS model in the attitude error analysis program and perform necessary system attitude error analysis for a mission, the Transition Region And Corona Explorer (TRACE) spacecraft example is studied and recommendations are offered.

TRACE BACKGROUND

TRACE is the fourth in the Small Explorer (SMEX) program at the Goddard Space Flight Center, and the first to use a GPS receiver. The solar observing spacecraft will be launched in September, 1997 into a 600 km, 6am 6pm

sun synchronous orbit. The spacecraft will be without shadow for several months at a time; during the eclipse season no science data will be collected, and the spacecraft will be essentially shut down.

The main telescope, aligned with the spacecraft +Y axis, will be pointing at the sun throughout the mission. A guide telescope mounted on the main one will be responsible for fine attitude determination of Pitch and Yaw (rotations about the spacecraft +X and +Z axes), in order to keep the science telescope pointing at specific areas of the sun to within arc seconds. While more coarse at $0.8^\circ 1\sigma$ onboard and 0.1° post-processed, the determination of Roll (rotation about the spacecraft +Y axis) falls on the spacecraft Attitude Control System (ACS) and ground post processing using measurements from the roll gyro, Three Axis Magnetometer (TAM), and GPS. The analysis presented in this paper focuses on the Roll determination.

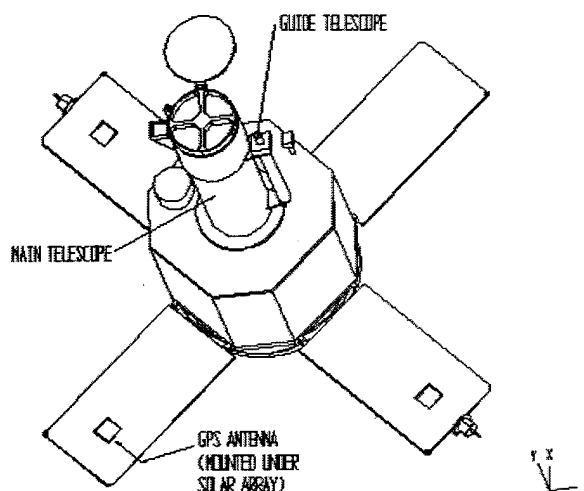


Figure 1 Fully Deployed TRACE Spacecraft

As currently planned, the GPS receiver will provide position, velocity, time, carrier phase, and house keeping information. Although the receiver's primary function is to provide position and time to the spacecraft, since there will be three antennas viewing in approximately the same direction, it can provide measurements for attitude as well. There are several interesting "features" associated with the attitude determination function on TRACE specifically related to GPS. The three GPS antennas will be located on the back sides of separate deployable solar

panels with their normals in the spacecraft -Y direction. The uncertainties in the baseline lengths and alignments could be large as a result of being mounted on deployables that may not deploy nominally, in addition to the motion of the phase center inherent in the patch antennas themselves. The spacecraft is sun pointing, not nadir pointing, so that GPS Space Vehicle (SV) viewing may be degraded periodically. Finally, while the thermal environment should be constant during times of operation, studies have shown that biases in cable length must be determined in flight¹⁻³.

As the spacecraft will also have a TAM and gyro pack onboard, the study of the attitude determination error analysis of the system, not just the GPS alone, becomes necessary. These other sensors are often onboard even small spacecraft, particularly the TAM for momentum management. Including these coarse measurements with GPS, if properly modeled, according to general sequential filtering theory should improve the attitude solution over GPS alone. A comparative study of the attitude determination errors expected in the GPS/TAM/gyroscope system as compared to GPS alone, and the system without GPS, will be presented, as will a discussion of the sensor measurement models used and various errors that could be included and determined.

THE ATTITUDE DETERMINATION ERROR ANALYSIS SYSTEM (ADEAS)

Background

ADEAS provides a general-purpose linear error analysis capability for various attitude determination geometries and processes. ADEAS does not process sensor data but simulates the attitude determination logic and computes the resulting attitude determination and sensor calibration accuracies.

The scenarios that ADEAS can analyze include the following:

- Low earth to earth-sun libration point orbit profiles
- Three-axis or spin stabilized attitude profiles
- Sequential filter or batch weighted least squares attitude determination methods
- Sensor complements which include sun sensors, earth sensors, star trackers, three-axis magnetometers, gyroscopes, and now GPS.

The output from this system includes, among other things, the following:

- Requested uncertainties and correlation information over the specified times
- Sensor viewing (for GPS, the specific SV's in view are listed, but the statistics for the span of the run are not yet included)
- Sun, earth, moon, and magnetic field vectors in the body (and others where appropriate) coordinate system. GPS SV vectors in the body coordinate system will be included in a later version of the program.

Given that the attitude determination process involves errors of various behavior, such as measurement noise, misalignments, and drifting, among others, it is important to understand how these errors affect the system's overall attitude determination accuracy. ADEAS allows an analyst to specify the initial uncertainty estimate of these types of errors and computes the resulting uncertainties in a user specified subset of measurement and dynamic parameters. These errors can be either "solved for" states or "considered" error contributions. This flexibility allows the user to assess the merits of including states operationally, or to "solve for" some errors with a separate batch or filter and include (uplink) these errors in an operational filter.

Measurement Models

Adding the GPS model to ADEAS not only provides a method of determining attitude errors as driven by mission unique error sources, but also allows the user to assess overall attitude uncertainties for spacecraft with other attitude sensors available. Fortunately, GPS observations can be modeled in ADEAS exactly like the other sensors are modeled.

Much of the literature up to this point has been drawn from the following model⁴⁻⁷:

$$\Delta r_{ij} = \hat{s}_j^T \bar{x}_i - k_{ij} - b_i + v$$

The changes made for the ADEAS model expand the types of errors that can be examined while making the GPS observation behave like the other sensors in ADEAS. If the model relating the baseline to the carrier difference is instead:

$$\Delta r_{ij} = \hat{s}_j^T M_{BS} \bar{x}_i \left(1 + \frac{\delta x_i}{|\bar{x}_i|}\right) - k_{ij} - b_i + v$$

the baseline can have some error associated with its physical length, or scale factor, as well as some misalignment. Although sensing the magnetic field as

opposed to interferometry, a magnetometer can be modeled similarly as follows:

$$\vec{B}_{est_i} = A_{IB} M_{BS} S(\vec{B}_S + \delta\vec{B}_S) - \vec{b}_I + v$$

where often: $\delta\vec{B}_S = C_{SQ} \vec{D}_Q$

although in ADEAS, no specific assumptions are made about $\delta\vec{B}_S$.

As a final example, a star tracker can also be modeled in a comparable fashion:

$$\vec{S}_{ref_i} = A_{IB} M_{BS} (\vec{S}_S + \delta\vec{S}_S) - \vec{b}_I + v$$

As evident from the measurement models above, in ADEAS all sensors have a misalignment, scale factor, and bias that can each have uncertainties associated with them, as well as noise and periodic errors. Since ADEAS works only with uncertainties, its general sensor model is actually the model of the residual between the i th actual and computed measurement:

$$resid_i = (1 + sf_i)h_i + b_i + a_i(\sin(\omega_i t + \psi_i)) + v$$

The errors in each of misalignment, scale factor, bias, as well as the measurement noise and any periodic errors for each of the sensors can be clearly mapped from the above sensor measurement models and those like them for Earth and Sun sensors. Note that while not included in the above magnetometer measurement model, errors between the reference and true magnetic field can be modeled in ADEAS as periodic errors with a twice per orbit frequency and 1° amplitude. The contributions of each error source to the system and the associated partial derivatives are described in reference 8.

TRACE ATTITUDE ERROR ANALYSIS STUDY

General Assumptions

Although all three axes can be determined by either the magnetometer or GPS, only the spacecraft roll errors are examined in this study as they are the main concern of the spacecraft and ground attitude determination systems.

Throughout the study, a minimum variance weighted sequential filter is assumed, mimicking the ground post processing system. Due to science control requirements

in jitter and drift, the onboard attitude filter cannot be tuned in the same way, keeping the roll determination accuracy at its onboard upper limit of 0.85° 1 σ . Where noted, batch least squares solutions were used to “solve for” calibration errors, when filter convergence was not achieved for those same parameters as filter states. This is not uncommon operationally, as sensor errors that do not change over time, such as TAM bias, are similarly solved for in batches and uplinked to the spacecraft.

The one calibration parameter that is routinely included in the state is the gyro bias. Including this state normally improves convergence of the filter and the accuracy of the attitude solution. For this reason, the default states for this study include the attitude and gyro bias, unless otherwise noted.

The spacecraft orbit and attitude profile was defined to match that for TRACE as described above. The initial uncertainty in the spacecraft roll was 0.5°. The ADEAS runs in this study are four orbits, totaling approximately 6 hours, unless otherwise noted. Finally, the uncertainties given are 1 σ values, so that the results should also be thought of as 1 σ .

Sensor Uncertainty Assumptions

For this TRACE roll study, a TAM and GPS antennas were modeled. In ADEAS, the gyroscope is not modeled as a sensor, but in terms of dynamic errors to the system. With this in mind, a true GPS only system, without a gyroscope, can be assumed to behave like the GPS/gyro study except with larger errors in the dynamics; for the filter to work without a rate measurement, the dynamics instead must be modeled, introducing higher errors.

Gyro/Dynamics

As described above, the gyro bias was routinely a filter state, or “solve for” ADEAS parameter. The short term drift, or noise, was set at 3 °/hour. The long term drift, an effect seen over about 12 hours, was assumed to be 1°/hour. These values were derived from studies of a duplicate gyro assembly’s behavior in recent ground testing. The uncertainty in the scale factor used was 4E-04.

The misalignment in the gyro in the truest sense only contributes to inaccurate slewing; when a spacecraft is fixed, the misalignment will be zero. Therefore, as the spacecraft will be essentially still, gyro misalignment is not a factor in the TRACE mission.

TAM

The TAM is aligned with the spacecraft body axes. Roll truth data (better than 0.1°) derived from the science data, will be available on a very limited basis; this data can then be used to calibrate the TAM. The uncertainty in the TAM alignment was "considered" to be 0.1° , a conservative estimate of the post calibrated TAM misalignment. The TAM bias was set at $2.0\text{E-}08$ Tesla. The scale factor error used was 0.1% . The uncertainty in the measurement itself, or noise, was $7\text{E-}08$ Tesla.

As mentioned above, periodic errors were modeled for the TAM to emulate errors in the magnetic field reference model as 1° errors with twice per orbit frequency. As one might expect, these errors tend to average out over an orbit; this fact has actually been shown with flight data from the Upper Atmospheric Research Satellite (UARS) as well as the Extreme Ultra Violet Explorer (EUVE)⁹. These periodic errors were "considered" in ADEAS for completeness.

GPS

For GPS, ADEAS asks for assumed antenna locations in body coordinates, then asks which antennas form which baselines. TRACE is planning to use 3 antennas, placed on the back sides of the solar arrays. Antenna 1 is on the $-X/+Z$ panel, antenna 2 on the $-X/-Z$ array, and antenna 3 on the $+X/-Z$ array. The 2 baselines chosen include antennas 1 and 2 for a baseline length of 172.7 cm and 1 and 3 for a length of 244.23 cm. The nominal antenna normals were all assumed to be in the spacecraft $-Y$ direction. A mask angle of 60° (measured from the antenna normal) was chosen in order to err on the conservative side in terms of SV viewing.

The starting values for baseline length (in ADEAS, this is scale factor uncertainty, computed as $\delta x / |\vec{x}|$) and alignment uncertainties were computed assuming the arrays deploy with an uncertainty of 1° (the hinge configuration is such that there should be no effective roll contribution)¹⁰ and the phase center of the antennas is unknown to 1.0 cm. The line bias uncertainty was chosen to be 2.0 cm. Finally, the measurement uncertainty, or noise, was chosen as 0.1 of a wavelength, or 1.9 cm.

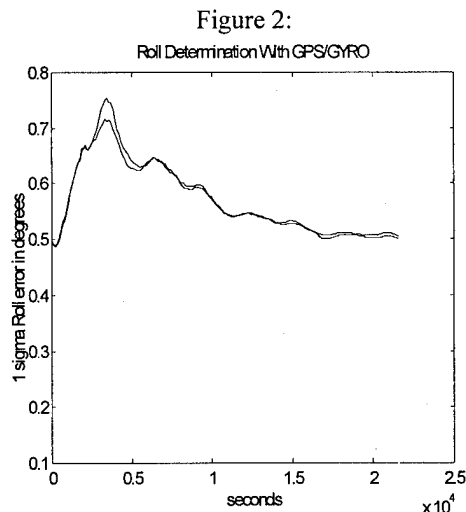
As ADEAS performs a covariance analysis, not attitude determination, GPS integer ambiguity is not a factor; being an entire integer off would obviously radically out weigh the errors taken into account in this study.

Similarly, multipath errors were not modeled here. For the TRACE configuration, there will be no reflective surfaces interfering with the signals received in the patch antennas. However, if the antennas are elevated at all from the solar array without additional ground plane, the considerable back lobes will cause large multipath errors that will act like systematic errors and overwhelm the error budget to the extent that all other errors will be rendered insignificant.

Results

GPS/GYRO

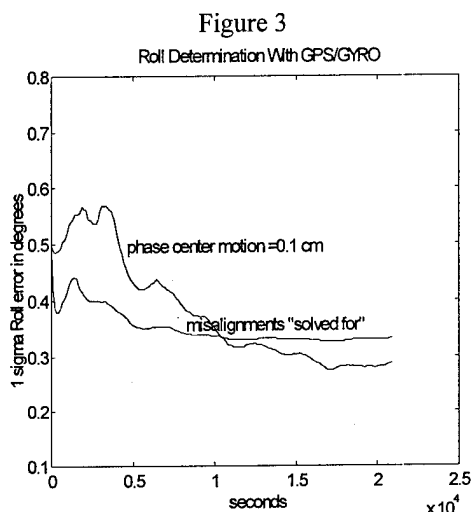
The results for roll uncertainty for the initial GPS/gyro only system are seen in Figure 2. The converged uncertainty for roll was close to 0.51° .



There are actually two cases plotted in Figure 2, the second, very slight improved, case assumed the solar panels were deployed with only 0.5° uncertainty, the baseline length was "solved for" in a batch therefore improving the scale factor by an order of magnitude, and the line bias was known to 0.5 cm. Here, the improvement in the baseline length knowledge trimmed the peaks some, as one might expect with a scale factor improvement. Due to the long baseline, the baseline length error that is observable in the roll direction is quite small to start with, so the improvements are not dramatic. The same is true for the effect of deployment errors, unless they get very large. Finally, improved knowledge of the line bias does not improve the determination of roll much either.

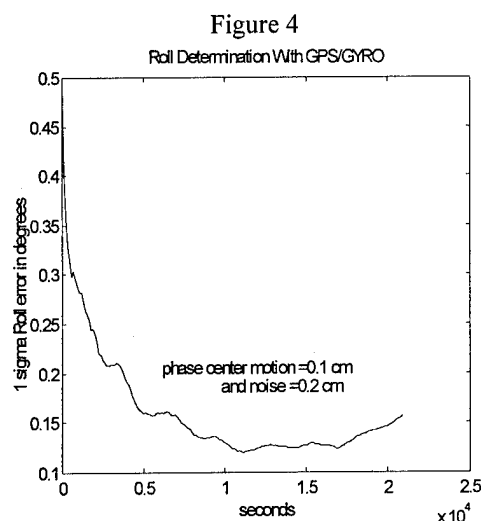
Perhaps more interesting for roll determination is knowing the exact phase center of the antennas, as that

contributes the largest effect to baseline misalignment and scale factor errors in the spacecraft roll direction. The effect of knowing the phase center location to 0.1 cm is shown in Figure 3, improving the roll accuracy to approximately 0.3° .



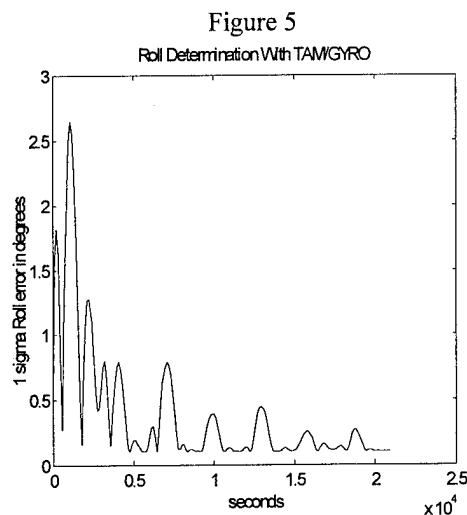
While “solving for” all the uncertainties as states would seem to imply the best possible accuracy, in reality, this results in large sparse matrices which cause mathematical problems. It is therefore important to choose one’s states carefully and sparingly. The results in Figure 1 showed that the scale factor is relatively well known since the baselines are large. Therefore, the baseline misalignments in the spacecraft roll direction are the errors primarily affected by the phase center uncertainty. Therefore, including only those misalignments in the state, along with the gyro bias, should improve the solution. This is shown in the second line in Figure 3, which assumed the same baseline misalignments as the plots in Figure 2, but “solved for” the misalignment for each baseline corresponding to the spacecraft roll direction. The solution is improved to 0.33° , nearly the same result as for lowering the phase center uncertainty by an order of magnitude.

The final parameter to think about is the measurement error itself. If the noise can be decreased from 0.1 of a wavelength to 0.01 with the more stable phase center, the roll accuracy achieved is approximately 0.15° , as seen in Figure 4. The noise seen on the EUVE spacecraft, which used a Motorola demonstration receiver, was on the order of 0.01 wavelength, or approximately 0.2 cm^{11} .



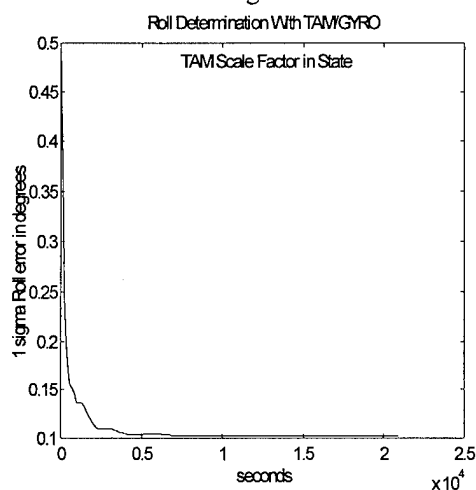
TAM/GYRO

The results for the TAM/gyro system are shown in Figure 5. The twice per orbit periodic errors to emulate the reference magnetic field errors are averaged out over the 4 orbit span as expected. The oscillations due to the scale factor errors decrease in amplitude over time. The converged solution is approximately 0.12° .



Similar to “solving for” the misalignment in the GPS case, improvements occur if the TAM scale factor is “solved for”. The results of “solving for” the TAM scale factor along with the gyro bias and roll are shown in Figure 6. The improvement in convergence is remarkable, while the final attitude accuracy, albeit more stable, is only slightly better at 0.102° .

Figure 6

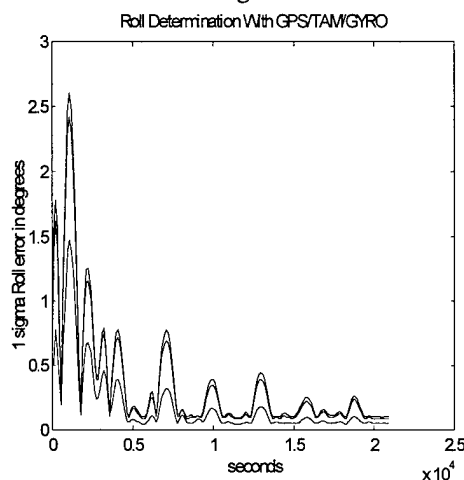


TAM/GPS/GYRO

As one might expect, including GPS in the filter, while not harmful to the roll solution accuracy of the system, will not result in much improvement over the TAM/Gyro scenario, as its errors in the best cases above are not better than those for the TAM/gyro alone. This was in fact the case, the difference in the results shown in Figure 6 were not observable with the naked eye, and the resulting uncertainty only differing in the thousandths.

For illustrative purposes, the case where the TAM scale factor was not "solved for" was then examined. The three lines in Figure 7 represent GPS noise values of 0.19 cm, 0.019 cm, and 0.0019 cm, respectively. It clearly takes an unreasonably low noise of 0.0001 of a wavelength (0.0019 cm) to achieve noticeable improvement in convergence or attitude accuracy.

Figure 7



CONCLUSIONS/RECOMMENDATIONS

This paper presented a new measurement model for GPS which classifies errors as misalignments, scale factors, biases, and noise. This characterization is common for spacecraft attitude sensors. Therefore, although the interferometric process used for GPS attitude observations seems quite different than measuring the magnetic field or viewing a star, with a little thought, GPS could be added to ADEAS easily.

The roll determination for the TRACE spacecraft was then examined with the new ADEAS. Since it is not practical to include every uncertainty as a "solve for" state, determining which states to include, as well as the achievable roll accuracy were examined.

The post processing goal of 0.1° can nearly be met with GPS and gyro alone. It is necessary, however, to have a measurement error on the order of 0.01 wavelength, and either a stable phase center (to 0.19 cm) or include the baseline misalignments in the spacecraft roll direction as filter states.

The roll determination goal can be met much more convincingly by including the TAM in the system. "Solving for" the TAM scale factor improves the convergence dramatically and the final accuracy slightly.

While leaving GPS out of the system does not hamper the ability to meet the post processing goal on the ground, including GPS could allow the post processed type accuracy to be achieved onboard, completely separately from the existing filter used in the control system. Of course, including an *additional* filter onboard the spacecraft tuned for attitude determination accuracy and using only the TAM and gyro could also accomplish this. However, in keeping with NASA's goals to force down costs, TRACE's software and computer electronics are heritage systems from past SMEX missions; adding extensive software is prohibitively expensive. One way to achieve the post processed roll determination goal onboard TRACE is to use the GPS processor and measurements.

ACKNOWLEDGMENTS

The authors would like to thank Rick Harman of the Flight Dynamics Division at Goddard for his good will in allowing ADEAS to be updated, and Mark Nicholson, of CSC, for his remarkable willingness and ability to make the updates. The authors would also like to thank Dave Olney and Tom Budney of the Special Payloads Division,

and Dr. Richard Freeman of the Engineering Directorate, for their reviews of this paper.

REFERENCES

- ¹Ward, L., and Axelrad, P., "Spacecraft Attitude Estimation Using GPS: Methodology and Results for RADCAL," *Proceedings from the ION National Technical Meeting*, Anaheim, California, Jan., 1995.
- ²Rodgers, C., Gardner, A., and Stroup, D., "Testing and Analysis of Baseline Length as a Performance Factor in GPS Attitude Determining Systems," *Proceedings from the ION National Technical Meeting*, Jan. 1994.
- ³Gomez, S., "Analysis of Effect of Baseline Motion and Multipath on GPS Attitude Determination Accuracy," Presentation to the GPS Algorithms Synthesis Team, Dec., 1994.
- ⁴Cohen, E., and Parkinson, B., "Expanding the Performance Envelope of GPS-Based Attitude Determination," *Proceedings from the ION GPS-93*, Albuquerque, NM, Sept., 1991.
- ⁵Cohen, E., and Parkinson, B., "Mitigating Multipath Error in GPS Based Attitude Determination," AAS 91-024, Feb., 1991.
- ⁶Axelrad, P., and Ward, L., "On-Orbit GPS Based Attitude and Antenna Baseline Estimation," *Proceedings from the ION GPS-94*, Salt Lake City, Utah, Sept., 1994.
- ⁷Brock, K., Fuller, R., Hur-Diaz, S., and Rodden, J., "GPS Attitude and Orbit Determination for Space," *Proceedings from the ION GPS-94*, Salt Lake City, Utah, Sept., 1994.
- ⁸Nicholson, M., Markley, F., and Seidewitz, E., "Attitude Determination Error Analysis System Mathematical Specifications Document," Document number CSC/TM-88/6001, Oct., 1988.
- ⁹Hashmall, J., Rokni, M., and Liu, K., "Accurate Spacecraft Attitudes from Magnetometer Data," *Proceedings from the CNES International Symposium on Space Dynamics*, Toulouse, France, June, 1995.
- ¹⁰Communications with TRACE lead mechanical engineer
- ¹¹Ketchum, E., and Hart, R., "Attitude Determination of the Extreme UltraViolet Explorer Using GPS," *Proceedings from the ION National Technical Meeting*, Anaheim, California, Jan., 1995.

A GNSS-based Attitude Determination System for Low-Earth Observation Satellites

Jesús Serrano, Pelayo Bernedo, and Pablo González
GMV S.A.

Pierluigi Silvestrin
ESA/ESTEC

BIOGRAPHIES

Jesús B. Serrano (e-mail: jbserrano@gmv.es) is the head of the Flight Dynamics and Avionics Division of GMV (Spain). He received his M.S. degree in Aeronautical Engineering in 1983 from the Polytechnic University of Madrid (Spain). He was visiting scientist of the Mission Analysis Section at ESOC in 1984. He joined GMV in 1985. At present his major areas of involvement are satellite guidance, navigation and control, including GPS applicability and operational issues.

Pelayo Bernedo received his M.S. degree in Aeronautical Engineering from the Polytechnical University of Madrid, Spain in 1988. He worked for McDonnell Douglas in the MD-80 twinjet series within the structures group. Since 1991 he works in the Simulation Division in GMV, where he specializes in GPS based navigation for airborne applications and tracking systems for fleets of ground vehicles.

Pablo González received his M.S. degree in Aeronautical Engineering from the Polytechnical University of Madrid, Spain in 1989. He awarded research fellowships at NASA Lewis Research Centre, INTA and CSIC. In September 1990 he joined the Flight Dynamics and Avionics in GMV, where he has worked in spacecraft attitude determination including GPS applicability.

Pierluigi Silvestrin is a Senior Systems Engineer in the Earth Observation Preparatory Programme Division (EOPP) of ESTEC in Noordwijk (The Netherlands). He graduated in Electronic Engineering at the University of Padova (Italy) in 1985, specialising in control systems design. After working for one year at the Joint European Torus in Abingdon (UK), he joined in 1987 the Attitude and Orbit Control Systems Section of ESTEC. In 1989 he joined the EOPP, where he is presently responsible for studies of space systems and supporting technologies for future Earth observation missions of the European Space Agency.

ABSTRACT

This paper presents the design of an attitude determination concept based on differential carrier phase measurements. The results of the investigations are illustrated with the example of an application to MetOp, the European Polar Meteorological Satellite, developed by ESA for EUMETSAT. Both nominal and safe modes of operation of the attitude control system are addressed. The paper analyses the drivers of the concept and possible differential multipath mitigation techniques and presents a detailed analysis of the selected technique based on a Kalman filter with solved-for differential multipath parameters. This is compared to the classical scheme in which no estimation of the differential multipath parameters is done. For the safe mode, a suitable approach using the attitude point solution is developed. The null space method (NSM) is selected for solving the integer ambiguity resolution problem (OFAR). Improvements of such a method for speeding up the algorithm are presented. A performance analysis is presented for the three concepts under investigation.

The performances of the concept with differential multipath estimation is assessed through a sensitivity analysis with respect to the multipath characteristics, angular rate disturbances, receiver, antenna characteristics and filter update frequency. Furthermore, different configuration of antennas are analyzed. The performance of the selected OFAR technique is assessed in terms of convergence, CPU time, and sensitivity to the initial attitude knowledge error, initial angular velocity, receiver characteristics and multipath effects. Finally, the performance for the safe mode is presented, including the sensitivity to the initial attitude which is the most critical parameter.

The study shows that the MetOp nominal pointing mode accuracy requirements can be fulfilled using a Kalman filter which estimates also the differential multipath. The preferred configuration has four antennae located in the vertices of a 0.5 m square. This

allows to mount the antennas in a dedicated carbon fibre reinforced structure in order to improve structural stability. The use of narrow FOV antennas is proposed to minimise differential multipath effects. For the OFAR technique, the study shows that the NSM algorithm is very robust giving no failures, even without any attitude knowledge. CPU time for the OFAR depends strongly on the number of satellites considered: starting the computation with a small set of satellites leads to important time savings. For the safe mode, the study shows that a baseline length of 0.2 m is preferable in order to avoid the complexity of OFAR techniques: this would provide a worst case performance of 8°. On the other hand and for an antenna baseline of 0.5 m, the attitude determination accuracy is always better than 3°.

1. INTRODUCTION

The European Space Agency (ESA) is currently investigating the use of the information provided by the GPS/GLONASS receivers for performing attitude determination of low Earth observation satellites, using the MetOp mission as a study case. The MetOp system is a European satellite series for operational meteorology and climate monitoring from a sunsynchronous 820 Km altitude orbit which will complement the NOAA Polar Orbiting Environmental Satellite System.

The application of GPS for attitude determination has been studied since the early stage of the GPS system. In fact, the development of a GPS-based integrated navigation and attitude determination system has evident benefits as it reduces the physical requirements of power and weight on board the user platform as compared to current multi-sensor approaches. Those advantages become of first importance when platform resources are scarce.

Interferometers can be used to derive attitude information by measuring a line-of-sight angle between a spacecraft axis, as defined by an antenna array, and a RF emitter whose position is accurately known. The angle is measured by detecting the phase difference of the signal arriving at a pair of receiving antennae (Figure 1). Angular information can be derived from knowledge of the phase difference through the equation:

$$\phi = \frac{2\pi L}{\lambda} \cos \theta$$

where L is the distance between the antennae, λ is the signal wavelength, θ is the angle formed by the incoming signal direction and the antenna baseline vector and ϕ is the phase difference.

Hence, the phase of the carrier is the basic observable to be processed for this application.

This differential carrier phase concept is selected for being investigated in detail for low Earth observation satellites due to the high accuracy expected thanks to the accuracy of the carrier phase measurements. Alternative AD concepts have been also investigated¹ but provide worse performances and do not meet the imposed requirements.

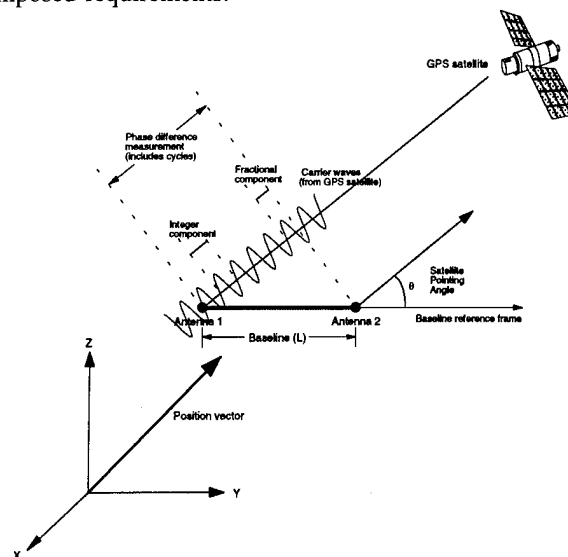


Figure 1: Interferometry concept, GPS measurement geometry and integer ambiguity.

2. PROBLEM CHARACTERIZATION

2.1. MetOp reference case

The MetOp-1 will operate in a 7198 Km mean semi-major axis sun synchronous near circular orbit. This orbit has a repetitive ground track pattern with a repeat cycle of 5 days comprising 71 orbits. The orbit is chosen to be slightly elliptical (0.001165 mean eccentricity) with a mean argument of perigee of 90° in order to minimize the orbit perturbations due to the Earth non-sphericity. The node time (9 h local solar time of the descending node) is chosen to reduce Sun glint and to provide sufficient Earth illumination for the optical instruments.

It is a three-axes stabilized satellite with its nominal orientation being nadir pointing. During the operational phase, a yaw steering strategy has been developed for Earth rotation compensation. The imposed attitude estimation and control requirements for the corresponding attitude control mode (namely, Yaw Steering Mode) are quite stringent: 0.15° (3σ) absolute pointing error, 0.10° (3σ) absolute measurement error and 0.005°/s (3σ) absolute rate error.

For such operational mode, the actual attitude is assumed to be close (< 1°) to the nominal one. This implies the availability of an a-priori rough estimate of

the spacecraft attitude equal to the nominal attitude orientation.

For the requirements and operations of the safe mode some hypothesis have been made. It is assumed that the spacecraft will enter into safe mode once some (failure related) entry conditions are reached. The safe mode is in charge of managing the spacecraft state starting from such anomalous situations, of achieving the safe mode reference pointing (in this case Sun pointing³) and of maintaining the spacecraft attitude *close* to the reference one such that the corresponding pointing accuracy and the attitude estimation accuracy requirements (taken as 8° and 1° respectively³) are satisfied.

Finally, it is assumed that the deviation of the actual attitude from the nominal one is bounded (e.g., < 15°) since the safe mode will be initialized once some given conditions (e.g., exit of an attitude window around the nominal orientation) are reached. This implies the availability of an a-priori very crude estimate of the spacecraft attitude. In any case, an attempt has been made to identify whether the selected concepts might be used in case of no attitude knowledge at all and for any spacecraft attitude (namely, the applicability of the concept for the initial acquisition modes). Angular rates up to 3°/s where also assumed.

2.2. Basic observables

It is assumed that all the antennas are connected to a single GPS receiver with a common oscillator and with very high symmetry and stability between different signal paths.

Single differences (SD_i) which are formed by subtracting the carrier phase of the two signals received by the antennas for the *i*-GPS satellite. It carries the basic attitude information and has the advantage of cancelling some bias errors in the GPS system itself (e.g., GPS satellite ephemerides, Selective Availability and clock errors, signal propagation perturbations) as well as the bias errors of the receiver (clock biases and clock drifts) which are common to the antenna,

$$SD_i = \phi_i^{An1} - \phi_i^{An2}$$

This is a quasi-bias-free phase measurement with a low random noise added. However, the ambiguity of an integer number of carrier wavelengths (19 cm for the GPS L1) exists in this observable (see section 2.4). Such ambiguity might be removed by forming the double difference in time which is basically a *Doppler Frequency Measurement (DMi(t))*. The observable is constructed as follows,

$$DM_i(t) = SD_i(t) - SD_i(t - \Delta t)$$

where $SD_i(t)$ is the single difference carrier phase

obtained between two GPS antennas with respect to GPS satellite *i* at time *t*. However, this is a time-difference measurement, hence it is only suitable for measuring changes in attitude (i.e., angular rates).

2.3. Assumptions and constraints

We assume the availability on-board of a single multi-channel parallel receiver and an appropriate set of antennas designed and accommodated in such a way to provide 160° field of view, with the antenna boresights coinciding with the zenith direction. The GPS constellation is assumed to be composed of 24 satellites. The GPS receiver is assumed to be an all-in-view receiver with 1 mm tracking loop noise standard deviation, negligible interchannel biases and 0.5 mm antenna position error.

In general, the largest impediment to accuracy of carrier phase measurements is multipath. Experimental studies⁴ indicate that a value of about 5 mm rms is an appropriate figure for difficult multipath environments. Thermal noise in the carrier tracking loops can be limited to 1 mm rms, whereas the variations in the antenna phase centre and the electrical path length differences can be made smaller than 0.1 mm.

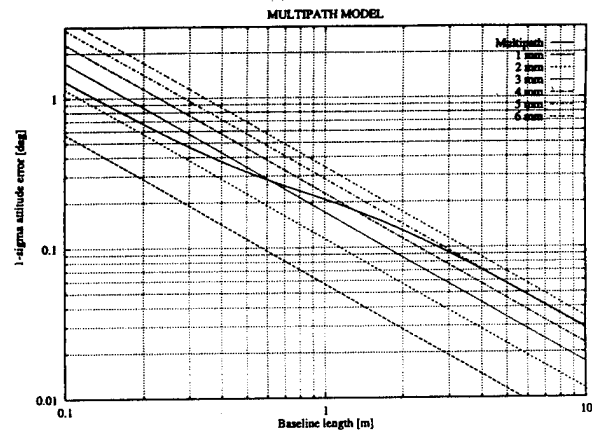


Figure 2: Attitude error (1σ), for one baseline, as function of the antenna separation².

No information on the multipath effects for the MetOp configuration are available for the time being. A model has then been constructed for use in the analyses. Taking into account the results presented in the literature⁶, a first order Gauss-Markov process has been selected for modelling such effect. The time constant has been taken as 20 seconds, whereas the corresponding standard deviation has been constructed (Figure 2) by taking the following into account: first, some experimental results⁷ suggest that relative multipath phase error could increase slightly with the baseline length, second, it can be expected that differential multipath will be very low when the antennas are near enough ($L \sim 0.1$ m), whereas it will

be independent of the distance for large baseline lengths ($L > 4$ m).

The spacecraft attitude evolution has been simulated using an initial attitude deviation (w.r.t. the nominal one) of $\pm 0.05^\circ$ for each Euler angle. The deviation of the actual angular rate from the nominal one has been assumed, according to the analysis of the control and perturbing torques carried-out, to be also a first-order Gauss-Markov process with a time constant of 10 seconds and with a standard deviation of $0.0003^\circ/\text{s}$.

3. ANTENNA CONFIGURATIONS

A preliminary analysis of the most promising antennae layouts has been performed using the dimensionless attitude dilution of precision concept which is defined as⁸

$$ATDOP = L \cdot \sqrt{\text{trace}[(H^T H)^{-1}]} \\ = \sqrt{EDOP^2 + RDOP^2 + AZDOP^2}$$

where H is the observation matrix, L is the characteristic baseline length of the antenna configuration, $EDOP$, $RDOP$ and $AZDOP$ are the elevation, roll and azimuth dilutions of precision which depend on the antenna configuration (number and location of the antennas and considered baselines) and number and position of the visible GPS satellites. When the attitude of the user satellite is less than few degrees off the nominal one, which occurs for most of the space applications, the observation matrix can be written as

$$\delta r_{ij}^k = \Delta r_{ij}^k - \underline{b}_{ij}^T [T_I^B]_n \underline{s}^k = H \begin{bmatrix} \theta \\ \phi \\ \psi \end{bmatrix} \quad H = \begin{bmatrix} \dots \\ \underline{b}_{ij}^T [T_I^B]_n \underline{s}^k \\ \dots \end{bmatrix}$$

where δr_{ij}^k is the measured relative ranging for the ij baseline and the k GPS satellite, Δr_{ij}^k is the differential range between antennas i and j , \underline{b}_{ij} is the baseline vector between antennae i and j (expressed in body axes, i.e., in spacecraft fixed axes), $[T_I^B]_n$ is the nominal rotation matrix an inertial frame to the body frame, \underline{s}^k is the line of sight (LOS) unitary vector of the k GPS satellite from the user spacecraft (expressed in an inertial frame), ψ, ϕ and θ are the 3-2-1 Euler angles from nominal frame to actual body frame, and S_k^x is the skew symmetric matrix associated to the line-of-sight unitary vector for the k GPS satellite.

The attitude estimation accuracy can be related to the differential carrier phase measurement accuracy (relative ranging error, σ_r) by means of the DOP concept:

$$\sigma_{Pitch} = EDOP \frac{\sigma_r}{L} \\ \sigma_{Roll} = RDOP \frac{\sigma_r}{L} \\ \sigma_{Yaw} = AZDOP \frac{\sigma_r}{L}$$

The effect of the GPS antennae layout has been analyzed when using three and four antennas in planar and three dimensional configurations. The results, averaged over one orbit (leading to a mean number of 7.033 visible GPS satellites), appear in Figure 3. With only two antennae, 3-axes attitude determination is not achievable, independently of the number of visible satellites, because there is a single baseline and there remains the uncertainty of the S/C attitude rotation about it. For a three antennae configuration, a large DOP reduction (accuracy improvement) is achieved when using the measurements of the three possible baselines instead of two. The geometry of the antennae layout (equilateral or right-angled triangle) has not a large importance. Finally, for a four antennae configuration, the results are similar: the geometrical configuration is not so relevant, whereas the number of baselines plays an important role on DOP reduction. Three dimensional configurations (like the inverted orthogonal triad tested) are discarded because of their manufacturing complexity, and the low accuracy improvement that can be obtained. A coplanar GPS antennae configuration can be easily integrated in the zenith face of the satellite, improving the rigidity of the mounting baseplane structure w.r.t a three dimensional one.








No. of antennas	No. of baselines	Configuration	ATDOP	E&R-DOP	AZDOP
3	2		1.014	0.618	0.531
	3		0.792	0.502	0.367
	3		0.831	0.512	0.425
4	4		0.715	0.435	0.377
	6		0.512	0.309	0.261
	3		0.850	0.493	0.493
	6		0.483	0.280	0.261

Figure 3: Influence of the number and configuration of the antennas and number of considered baselines in ATDOP values.

For a fixed antenna configuration, the observation matrix and the DOP values are time-varying, as a consequence of changes in number and positions of the visible satellites. For example, and for the 4-antennas

and six baselines configuration and for the MetOp orbit, the ATDOP varies from 0.5 (for 9 visible satellites) up to 0.68 (for 3 visible satellites).

An antennae layout consisting of 4 antennas in a square configuration and processing the information from 6 baselines is being used in the following.

4. NOMINAL POINTING MODE

4.1. On-board attitude determination algorithms

The on-board attitude determination algorithms for the yaw steering mode have been selected taking into account the imposed accuracy requirements as well as the specific constraints. In particular, it is of major importance the fact that the deviation from the nominal attitude will be always smaller than 1° .

Taking this into account, relative deviations from the reference values will be first estimated by the attitude determination algorithms and, finally, the absolute attitude will be computed. Following this approach, both the system and the measurement equation are linear and then a simple discrete Kalman filter can be used as estimation algorithm. The output of the filter is the relative attitude, in terms of multiplicative quaternion representation with a forced normalization of the updated quotient quaternion, and the relative angular velocity.

In addition, an alternative attitude determination scheme has been constructed by augmenting the filter state vector with some parameters associated to the differential multipath. The parameters are associated to the independent differential multipath values, hence, the number of independent values is, for each GPS satellite, equal to the number of antennas minus one.

4.2. Nominal performances

Two concepts have been introduced, i.e. on-board algorithms with and without the capability to estimate the differential multipath between two antennas. The performance of those two concepts has been assessed for different values of the parameters of the multipath model. Multipath model time constant have been assumed to take the values of 0.001, 2, 20 and 100 seconds.

For the no-multipath estimation scheme the following results have been obtained. First, for a 0.001 sec multipath time constant (practically a white noise for the integration step of 0.1 sec), the estimation error is less than 0.02 deg for roll, pitch and yaw angles. A small estimation bias appears in the roll and yaw angles due to the errors in antenna position due to structural deformations (0.5 mm). On the other hand, when

increasing the time constant, the estimation error increases while maintaining appropriate behaviour in the Kalman filter (namely, consistency between the estimation error and the error estimate): for a 2 sec multipath time constant, the estimation error rises to 0.035° for roll and pitch angles and 0.025° for yaw angle, whereas for a 20 sec multipath time constant, the pitch and roll angle estimation errors reach maximum values of 0.07° level and yaw angle error is under 0.05° . Finally, for a 100 sec time constant, the differential multipath behaves approximately as a bias, giving a drifted attitude estimate (steps in the drift appear due to changes in the visible satellites, causing changes in the measurement multipath pseudo-biases): the estimation accuracy is less than 0.1° in pitch and roll angles whereas it is under 0.07° for the yaw angle, however, some problems in the filter performances were found: unreasonable values on the uncertainty associated to the differential carrier phase observable should be used.

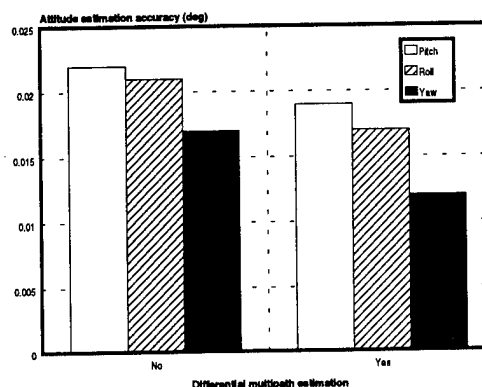


Figure 4: Comparison of the AD performance for the no-multipath estimation and multipath estimation schemes (rms values, deg).

For the multipath estimation scheme, the behaviour of the filter is very good with reasonable values in the on-board model for all the uncertainties under consideration (associated to the propagation or the measurement models). Maximum estimation errors are, for roll and pitch angles, 0.041° , 0.045° and 0.064° for the 2, 20 and 100 seconds time constants respectively, whereas for the yaw angle they are 0.034° for all the cases. The improvement in the performance when using this scheme is more significant when the time constant increases: the improvements obtained are between 20% and 40%. The multipath estimation scheme should be retained as a time constant of 20 seconds for the differential multipath model looks realistic.

4.3. Sensitivity analyses

The multipath estimation scheme has been selected for investigating the effect of different error sources identified in section 2.3. Additional work was made in

order to define the antenna configuration for the MetOp satellite. These two points are summarized in the following.

First, analysis with respect to the standard deviation associated with the differential multipath model was performed: values of 1.5 mm and 6 mm were assumed in addition to the 3 mm nominal one. Results are summarized in Figure 5. The AD algorithms work properly and the effect of doubling the multipath standard deviation is an increment of less than 30% in the attitude estimation error.

The sensitivity of the selected AD scheme with respect to the receiver characteristics has been investigated considering different values of the carrier tracking loop noise (0.5 mm and 2 mm) and of the electrical path length bias (1 mm and 2 mm). Since the carrier tracking loop noise is simulated as a white noise, the filter handles properly this type of errors and, consequently, the influence on the final estimation accuracy is quite negligible: an increment of less than 10% (rms) in the attitude estimation error appears when doubling the standard deviation of the noise.

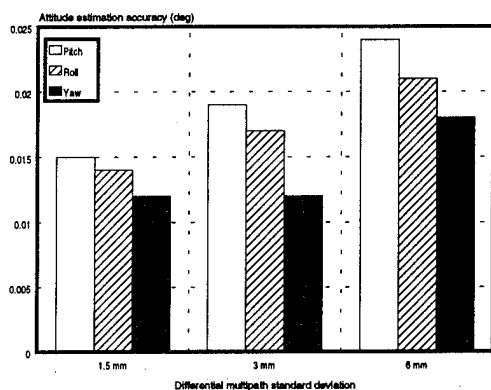


Figure 5: Sensitivity with respect to the differential multipath standard deviation (rms, deg).

Electrical path length differences have been simulated as a bias in the differential carrier phase measurement. The results show that a part of the bias is compensated because it is estimated as a multipath error. Nevertheless, an attitude bias remains and is the cause of an increment in the mean of the estimation error. For a 1 mm bias the rms values of the attitude estimation error are about 0.055° in pitch, 0.077° in roll and 0.015° in yaw whereas the corresponding mean values are about 0.051°, 0.068° and 0.005°. Electrical path length differences in both the receiver and the connections between the different antennae and the receiver must be minimized, possibly by on-ground and in-flight calibration.

The sensitivity has also been analyzed with respect to

the antenna configuration as well as antenna beamwidth. Three configurations have been considered: a 0.2 m triangular configuration (for which a 2 mm differential multipath has been assumed), a 1 m square configuration (with a 3 mm differential multipath error assumption) and the nominal 2 m square configuration. The results obtained (Figure 6) show that in two square configurations, the achieved attitude determination accuracy meets the requirements whereas for the simplest configuration (an equilateral triangle of 0.2 m side) the estimation errors are almost two times worse than the 1 m square configuration.

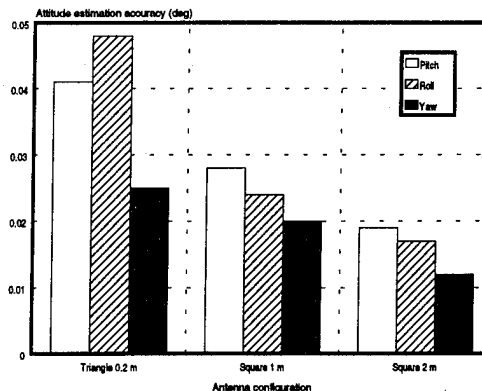


Figure 6: AD accuracy (rms, deg) for the three antenna configurations under consideration.

Concerning the antenna beamwidth, three different values have been considered: 120° (with a 1 mm differential multipath error assumption), 140° (with 2 mm multipath) and 160° nominal value. Apart from the reduction on the expected differential multipath, narrow FOV antennae result in the reduction in the number of visible GPS satellites. At least 2 visible satellites are required for a full observability of the user spacecraft attitude and this might imposed a strong constraint on the reduction of the antenna beamwidth. For a 120 beamwidth, only 2 satellites are visible during an orbit arc. Narrow field of views can not be considered except when using both GPS and GLONASS satellites: then the minimum number of visible satellites increases up to 5 with a 120° antenna FOV.

The attitude determination results for the different antenna beamwidths are presented in Figure 7: the improvement when using a 120° antenna instead of the nominal 160° one is about 20% in the yaw angle and about 40% for the pitch and roll angles.

From the obtained results, it appears feasible to reduce the baseline length to values under 1 meter without much compromising the attitude determination accuracy. A configuration of four antennae, located in the vertices of a 0.5 m square appears as a very attractive configuration, because it is possible to mount it on a dedicated CFRP structure in order to improve structural stability. The use of 120° field of view

antennas in combination with a GNSS receiver looks promising. For such baseline concept (and assuming a 1 mm differential multipath) the following results have been obtained (rms): 0.015° in pitch, 0.018° in roll and 0.020° in yaw.

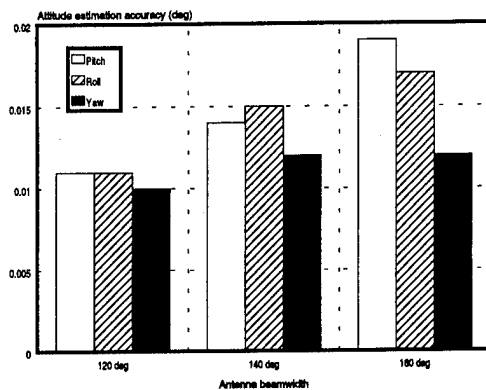


Figure 7: AD accuracy (rms, deg) for the three antenna beamwidths under consideration.

5. SAFE MODE

5.1. On-board OFAR scheme and performances

Cycle ambiguity arises from the inability of the receiver carrier tracking loop to measure whole carrier cycles. The receiver can only measure the fractional part of the carrier phase at the antenna. The phase difference measured between two antennas can also be incorrect by an unknown number of wavelengths if the baselines (L) are longer than $\lambda/\sin\theta$ where θ is the antenna half beamwidth (Figure 1). Then, the problem of cycle ambiguity is obviously more severe for longer baselines.

On-the-fly ambiguity resolution (OFAR) process should be carried-out during initialisation (in case no a-priori attitude information is available) and once solved, the cycle counts can be maintained up to date as long as there is no loss of signal lock or cycle slips in the receiver (note that cycle slips are very fast events whereas attitude changes are not, and also that OFAR is needed only if cycle slips occur on more than one carrier).

The integer ambiguity problem can be resolved directly, if the spacecraft orbit position and attitude knowledge are sufficiently good. In fact, as can be observed from figure 1, for a given knowledge of the spacecraft orbit and attitude, the angle θ_i to any visible GPS satellite is known to a certain degree of accuracy. In these conditions, one can be easily derived how accurate the knowledge of θ_i must be so that the integer ambiguity resolution problem does not appear. As shown in figure 8, this is a function of both the angle θ_i and the baseline length L . Since in our application the angle θ_i

can take any value between 10 and 170 degrees (assuming the antennas beamwidth of 160 degrees and the antenna boresight perpendicular to the baseline), then one must take the minimum of plot 8 to identify which is the required orbit and attitude knowledge accuracy below which the integer ambiguity problem does not appear.

Very different methods might be used for solving the integer ambiguity, including stationary methods, dual-baseline approach, precise pseudo-ranges approach, dedicated antenna motion methods, motion based approach and search methods².

An investigation of the Null Space Method (NSM)⁹ has been carried-out, resulting in the development and performance testing of the so-called Improved NSM². The NSM falls into the category of search methods where the residuals for all possible integer candidates falling within the search domain are computed and those which are bigger than a certain threshold are rejected. The integer solution selected is that which produces the smallest of the sum of residuals during a certain time interval. The original NSM⁹ represent a 'brute force' approach for space applications since it lacks the ability of limiting the number of integer combinations to be scanned as a function of the (known) baseline length and, in case it is available, of the initial attitude knowledge error. The improvement of the NSM has consisted mainly in an enhanced search strategy and the reduction of the search grid on the basis of an improved initialisation mechanism, of the knowledge of the baselines lengths and of the initial attitude knowledge error.

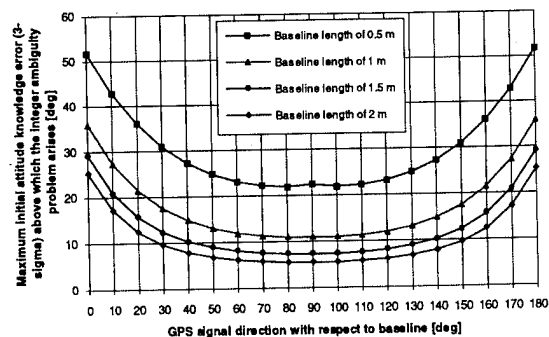


Figure 8: Required initial attitude knowledge below which the integer ambiguity problem can be resolved for directly.

The Improved NSM has proven to work with a remarkable reliability (no failure has been recorded in thousands of simulations performed) for any baselines configuration and baselines length, and, more important, for any initial attitude knowledge error, which makes that this method suitable not only for its primary purpose of resolving the integer ambiguity problem at

initialisation (in case not sufficiently accurate initial attitude knowledge is available) but also as a bootstrap in the safe mode where the spacecraft attitude may be completely unknown.

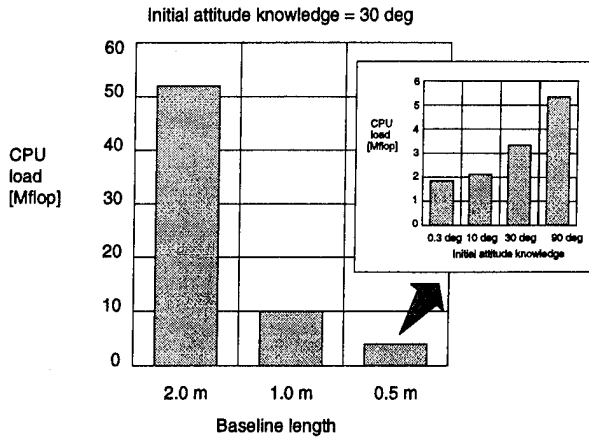


Figure 9: CPU demands of the Improved NSM.

The CPU load, as shown in figure 9, is mainly a function of the number of baselines, of the baseline length and of the initial attitude knowledge error. The computational demands are acceptable and 10 times lower than the conventional NSM.

The attitude determination accuracy provided by the Improved NSM is also remarkable, of less than 0.2 degrees, in all the cases examined (see figure 10).

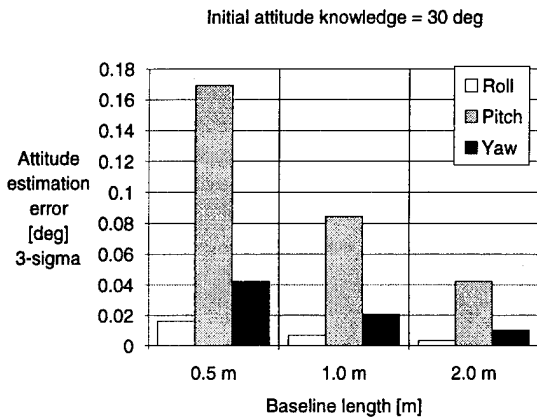


Figure 10: Attitude estimation accuracy provided by the Improved NSM.

5.2. On-board attitude determination scheme and performances

The requirements which are imposed on the safe mode are quite different (see section 2.1) from those of the nominal pointing mode, hence, a new on-board attitude determination scheme has been studied. Furthermore, the corresponding attitude determination concept should

be simple, robust and reliable (due to all the range of possible situations which should be managed) and requiring small processing resources in order to allow a possible hardware implementation.

The use of an attitude estimation scheme requiring an on-board propagation model (which is the case for the Kalman filters, the linear observers, minimum variance reduced order filters, ...) does not seem to be appropriate due to the fact that, depending on the safe mode conditions, the on-board propagation model might deviate quite significantly from the actual spacecraft state evolution: this might be due to anomalous conditions such as continuously activated actuators, ...

In addition, the use of a Kalman filter is not appropriate because of the intrinsic complexity of the algorithms and the possible problems which might appear during the initialization and during its operation, such as divergences, ...

Taking this into account, a simple algorithm trying to estimate the "point solution" of the spacecraft attitude seems a better solution. Hence, a least squares type scheme is selected for the attitude estimation in the safe mode. Following this rationale, an optimum attitude solution for a given set of range measurements $\Delta r_{ij,k}^B$ (differential range between antennae i and j and for the GPS satellite k , see section 3), taken at a single epoch is obtained by minimizing the quadratic cost function

$$F([\hat{T}_I^B]) = \sum_{ij} \sum_k w_{ij,k} (\Delta r_{ij,k}^B - (\hat{b}_{ij}^B)^T [\hat{T}_I^B] \hat{s}_k^I)^2$$

where the differential range is obtained by processing the carrier phase measurements as already shown in chapter 3. The parameters $w_{ij,k}$ represent optional measurement weights for generality.

Then, the problem is to minimize the previously stated cost function with respect to the rotation matrix estimate. Different schemes might be used for solve this problem (including the Wahba's problem solvers¹, in case the problem is posed in an appropriate way⁵). The performance of the various schemes will differ in efficiency (mainly in terms of processing time) and, in some cases, in robustness to uncertainties. A simple scheme based on the linearized cost function is selected: assuming unity weighting factors, the performance of the attitude determination (in terms of attitude estimation accuracy, σ_θ) is assessed as function of the antenna pointing for a given antenna configuration and baseline length using the following expression

$$\sigma_\theta = ATDOP \frac{\sigma_r(L, \delta_{GPS}(\delta))}{L}$$

where the relative ranging error (σ_r) is assumed to be

a function of not only the baseline length (L , to account for the variation of the differential multipath) but also of the declination of the GPS satellite with respect to the local horizontal plane (δ_{GPS} , to account for the ionospheric effects) which will depend (for the analyses under consideration) on the antenna boresight pointing (δ).

The performances of the attitude determination concept selected have been evaluated for different antenna pointing orientations. The full range of antenna boresight declination and azimuth angles (defined with respect to the local vertical local horizontal frame) has been investigated: declination (δ) varying between -90° and 90° and azimuth (ϕ) varying from 0° and 360° . Different antenna configurations (triangular and square for various baseline lengths) have been investigated. Major conclusions are summarized in the following.

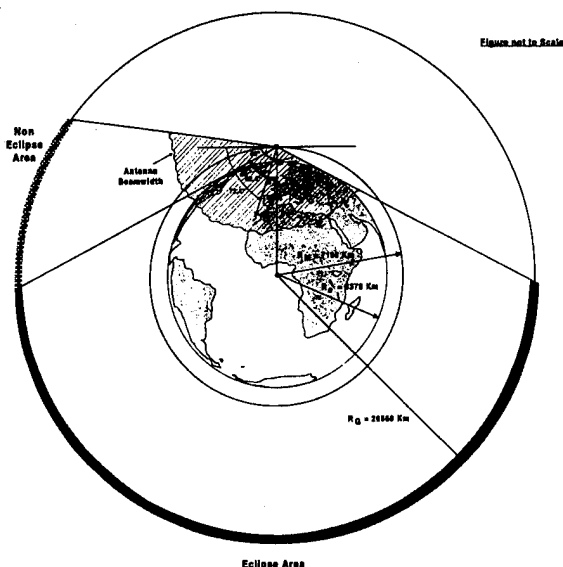


Figure 11: Worst case antenna pointing declination (160° antenna beamwidth, no atmosphere).

The minimum number of visible satellites for the complete range of declinations is always equal or higher than two (assuming a radius of 6378 Km or 6478 Km to take into account the atmospheric effects) for the checking of the Earth eclipse condition and an antenna beamwidth of 160° . The spacecraft attitude is then fully observable for the whole range of declinations if at least two baselines are available. The worst conditions appear for a declination of about -72° (-74° if atmospheric effects are taken into account) since for such a case, GPS satellites can only be visible in one side of the Earth due to the fact that the 6378 Km eclipse radius corresponds to an angle of about 62° (64° if atmospheric effects are taken into account) from the MetOp orbit (Figure 11). This minimum number of visible satellites is applicable both for the 24 satellites

and for the 21 satellites constellations: the number of satellites in the constellation has some effect on the maximum number of visible satellites as well as the mean number of visible satellites but, on the other hand, it has no influence on the minimum number of visible satellites due to the fact that the probability of occurring both event is very small for the GPS constellation.

For the triangle configuration, the attitude of the spacecraft can be estimated with an accuracy better than about 3° (24 GPS satellites) or 5° (21 GPS satellites) (99.7% confidence level) for baseline lengths equal or larger than 0.2 m and for antenna boresight pointings with positive declination (i.e., above the local horizontal plane). On the other hand, the attitude estimation accuracy can be degraded up to about 12° or 18° (99.7% confidence level) for antenna boresight pointings with negative declinations.

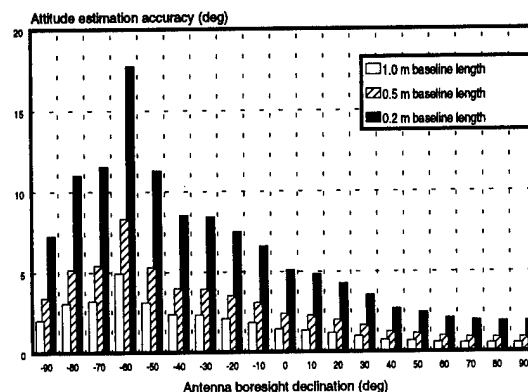


Figure 12: Influence of the declination angle on the attitude determination accuracy (99.7% confidence level) for the triangular configuration

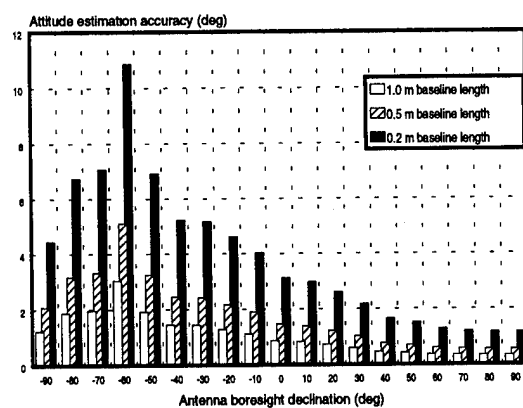


Figure 13: Influence of the declination angle on the attitude determination accuracy (99.7% confidence level) for the square configuration.

For the square configuration, the attitude of the spacecraft can be estimated with an accuracy better than

2° (24 GPS satellites) or 3° (21 GPS satellites) (99.7% confidence level) for baseline lengths equal or larger than 0.2 m and for antenna boresight pointings with positive declination (i.e., above the local horizontal plane). The attitude estimation accuracy can be degraded to about 7.5° or 11° (99.7% confidence level) for antenna boresight pointings with negative declinations. For an antenna baseline length of 0.5 m the attitude estimation accuracy is always better than 3.5° or 5° (99.7% confidence level).

Finally, accounting for the atmosphere can play some role on the attitude estimation accuracy for the nadir pointing orientation due to the satellites which are visible and their geometry. For the 24 GPSS constellation and for nadir pointing orientations the attitude estimation accuracy can be degraded to 10° (99.7% confidence level) and to 6° for the 0.2 m triangular and square antenna configurations respectively when no atmospheric effects are taken into account, whereas such degradation is up to 12° (99.7% confidence level) and 7.5° for the same antenna configurations when atmospheric effects are taken into account. For the 0.5 m baseline and square antenna configuration, the attitude estimation accuracy is always better than 3° (99.7% confidence level) when no atmosphere is taken into account and better than 3.5° when it is considered.

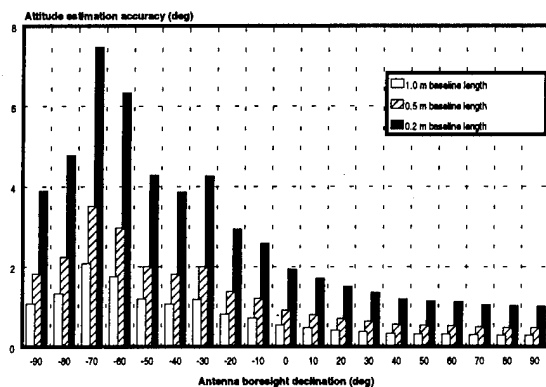


Figure 14: Influence of the declination angle on the attitude determination accuracy (99.7% confidence level) for the square configuration (24 GPS satellites, atmospheric effects).

6. REFERENCES

- [1] Serrano-Martínez, J.B.; Potti, J.; Silvestrin, P. and Martínez, M.A.: *A new Spacecraft Attitude Determination Scheme based on the use of GPS Line-Of-Sight Vectors*. ION GPS-95. Eighth International Technical Meeting of the Satellite Division of the Institute of Navigation, Palm Springs, California, September 12-15, 1995.
- [2] Serrano-Martínez, J.B.; Potti, J.; González, P.; Peláez, A.: *Study of Autonomous Orbit and Attitude Determination Techniques For Low Earth Observation Systems*. ESTEC Contract No. 10976/94/NL/CN. TR-3 Autonomous Attitude Determination using GPS. GMV/ATLEOS/TN/TR3. Issue 3. July 11, 1995.
- [3] Leibrandt W.: *ATLEOS, Attitude Determination Accuracy in SAFE Mode*. Personal communication. February 10, 1995.
- [4] Cohen, C.E. and Parkinson, B.W.: *Mitigating Multipath Errors in GPS based Attitude Determination*. AAS Paper 91-024. Presented at the AAS Guidance and Control Conference, Keystone, CO, February 1991.
- [5] Cohen, C.E.; Cobb, H.S. and Parkinson, B.W.: *Two Studies of High Performance Attitude Determination Using GPS: Generalizing Wahba's Problem for High Output Rates and Evaluation of Static Accuracy Using a Theodolite*. ION GPS-92. Fifth International Technical Meeting of the Satellite Division of the Institute of Navigation, Albuquerque, NM, September 16-18, 1992.
- [6] Cohen, C.E.: *Attitude Determination using GPS. Development of an all solid-state guidance, navigation and control sensor for air and space vehicles based on the Global Positioning System*. PhD Thesis. Stanford University, December 1992.
- [7] Rodgers, C.E.; Gardner, A.R. and Stroup, D.: *Testing and Analysis of Baseline Length as a Performance Factor in GPS Attitude Determining Systems (ADS)*. 1994 National Technical Meeting of the Satellite Division of the Institute of Navigation, January 24-26, 1994.
- [8] Jurgens, R.D; Fan, L.; Diefes, D. and Rodgers, C.: *Measurement of Errors in GPS Attitude Determining Systems*. ION GPS-92. Fifth International Technical Meeting of the Satellite Division of the Institute of Navigation, Albuquerque, NM, September 16-18, 1992.
- [9] Martin-Neira, M., Toledo, M. and Peláez, A.: *The Null Space Method for GPS Integer Ambiguity Resolution*. DSNS 95.

A Comparison of GPS-based Attitude Estimation Techniques for Spinning Satellite

Penina Axelrad and Charles Behre
University of Colorado

Biography

Penina Axelrad is an assistant professor at the University of Colorado. Her research and teaching are focused on GPS technology and applications. Previously she was a Member of the Technical Staff with Stanford Telecommunications, working on GPS receiver development. Dr. Axelrad received her Ph.D. in Aeronautics and Astronautics from Stanford University and her M.S. and S.B. from M.I.T.

Charles Behre is a Ph.D. student at the University of Colorado. His research focuses on GPS based attitude determination for spinning satellites. Mr. Behre received his M.S. in Aerospace Engineering from the University of Southern California, and his B.S. from the University of Virginia.

Abstract

This paper describes several techniques for the determination of the attitude of a spinning satellite using GPS. Because both spinning satellites and GPS receivers have the potential to provide high reliability at low cost, the combination of the two is quite promising. Furthermore, the kinematics of spinning satellites provide unique advantages for GPS-based attitude estimation. GPS antennas mounted on the satellite's rim are constantly undergoing large displacements, and phase difference measurements can be used to determine the oscillating displacement vector between the two antennas. Previously, Martin-Niera and Lucas [5] showed that by analyzing these measurements in the frequency domain, one can determine vehicle attitude, nutation angle, body nutation rate, and inertial nutation rate. The spin frequencies appear as spikes in the frequency domain and the attitude is related to the amplitude of the spikes. Alternative time domain techniques can be used to estimate the instantaneous angular velocity which is related to the principle spin frequencies. The spacecraft attitude can then be derived by averaging the vector perpendicular to the antenna displacement.

A comparison is made between the performance of these techniques when applied to a simulated spinning satellite. Analysis focuses on the effect of nutation angle

magnitude on the accuracy of the different algorithms and their relative advantages and disadvantages. Simulation results indicated that frequency domain techniques perform quite well with large nutation angles; whereas a Kalman Filter approach is superior for small nutation angles.

1.0 Introduction

Low cost satellite missions such as the Student Nitric Oxide Explorer [1] are designed to spin about the spacecraft major axis for both attitude stabilization and instrument scanning of the Earth. This type of spacecraft typically does not have very stringent onboard attitude control requirements; however, both position and attitude knowledge to better than 1 km and 1 degree, respectively are needed for post mission analysis of the science data. GPS has the potential to provide this information cost effectively in terms of dollars, weight, and power.

The use of GPS for spacecraft attitude determination onboard an Earth pointing spacecraft has been already demonstrated on the USAF RADCAL satellite [2,3] and the Crista Spas missions [4]. In general, a minimum of two antenna baselines comprising three antennas are required for full attitude estimation. Phase difference measurements to two or more satellites form the basis for the attitude estimation algorithms.

The application of GPS specifically to spinning satellites was suggested by Martin-Neira and Lucas in 1992 [5]. They described an FFT based method for using a single GPS antenna baseline to determine spacecraft spin and nutation rates as well as nutation angles and orientation of the angular momentum vector. Their approach uses triple differenced phase measurements as the basic observable.

Attitude determination of a spinning vehicle with GPS is particularly attractive because of the inherent baseline motion. This regular motion permits direct three axis attitude estimation with a single baseline, i.e. two antennas or in some cases even a single GPS antenna. This may result in a reduction in onboard hardware or improved redundancy with existing hardware. Furthermore, the baseline motion permits highly accurate solutions to be obtained from time differenced observations, thus elimi-

nating the need for ambiguity resolution and minimizing the effect of cycle slips.

This paper discusses and compares several algorithms for estimation of the spinning spacecraft angular rates and orientation of the angular momentum vector based on GPS data. We begin with a description of the GPS observables to be used in section 2.0 plus a description of the satellite motion in section 3.0. Section 4.0 describes a simple method for determining the orientation of the spacecraft's angular momentum vector. In section 5.0, two frequency domain approaches are investigated - the FFT method and an alternative Auto-Regressive method (AR). Sections 6.0 and 7.0 present two time domain approaches - an averaging method and a Kalman Filtering approach to the same problem. Section 8.0 describes the computer simulation used to test the algorithms and the results obtained. The paper concludes with a comparison of the various approaches, a description of an upcoming experiment to validate these results, and suggestions for future work.

2.0 Displacement Vectors

Time differenced GPS phase observations have been used in surveying to establish an initial estimate for long antenna baselines [7] and in attitude determination as a means for initial ambiguity resolution [9]. In general, they do not produce high accuracy estimates because the measurement noise is higher and the geometry is weaker than a single difference (between antennas) or double difference (between antennas and satellites) observable. The latter problem is not the case for a spinning satellite, where the rapid antenna motion produces a strong geometry for time differenced observations. The time difference observations are used to solve for what we will call antenna displacement vectors, which form the basis for the attitude solution methods described subsequently.

The basic equation for the $\Delta\phi$ measurement for one baseline and from one satellite is

$$\Delta\phi = \hat{e} \cdot \mathbf{r} - j + \beta + v \quad (1)$$

where \hat{e} is the line of sight unit vector to the GPS satellite, \mathbf{r} is the baseline vector, j is an integer ambiguity, β is a line bias, and v is noise. The symbol Δ will subsequently be used to denote a difference between two antennas. By time differencing two $\Delta\phi$ measurements and assuming no cycle slips, an equation for the antenna displacement vector, $\vec{\delta r}$, at each measurement time, t_i , can be formed as

$$\delta\Delta\phi(t_i) = \hat{e}(t_i) \cdot \vec{\delta r}(t_i) + (v_{i+1} - v_i) \quad (2)$$

where the symbol δ will be used to denote time differences

and

$$\delta\Delta\phi(t_i) \equiv \Delta\phi(t_{i+1}) - \Delta\phi(t_i) \quad (3)$$

Because of the effects of noise, it might be desirable to increase the size of the displacement vectors. Figure 1 shows two different sizes of displacement vectors. In equation (2) two consecutive $\Delta\phi$ measurements are differenced to compute $\vec{\delta r}_1$. Larger displacements, designated as $\vec{\delta r}_k$, can be computed by differencing two $\Delta\phi$ measurements taken more than one measurement interval apart as in equation (4)

$$\delta\Delta\phi_k(t_i) = \hat{e}(t_i) \cdot \vec{\delta r}_k(t_i) + (v_{i+k} - v_i) \quad (4)$$

where

$$\delta\Delta\phi_k(t_i) \equiv \Delta\phi(t_{i+k}) - \Delta\phi(t_i) \quad (5)$$

k is a constant integer equal to the number of measurement intervals between two differenced $\Delta\phi$ values, and i is a changing index for each measurement time. Neglecting changes in the line of sight vector plus errors in the measurements, $\vec{\delta r}_k$ is exactly equal to the sum of single interval displacement vectors as in equation (6).

$$\vec{\delta r}_k(t_i) = \sum_{n=1}^{k-1} \vec{\delta r}_1(t_{i+n}) \quad (6)$$

It should be noted that while the time interval between antenna position is increased, the measurements are still accumulated at every sample time. Therefore, there is no loss in the amount of observational data.

To solve (4) for $\vec{\delta r}_k$, measurements from at least three GPS satellites must be available and the line of sight vectors must be approximately constant over the interval t_i to t_{i+k} . If we assume that the noise is uncorrelated and unbiased, then the least squares solution is

$$\vec{\delta r}_k(t_i) = (H^T H)^{-1} H^T \begin{bmatrix} \delta\Delta\phi^1(t_i) \\ \delta\Delta\phi^2(t_i) \\ \vdots \\ \delta\Delta\phi^M(t_i) \end{bmatrix} \quad (7)$$

where

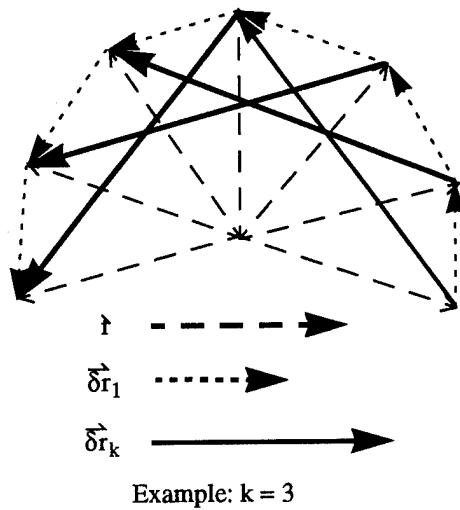
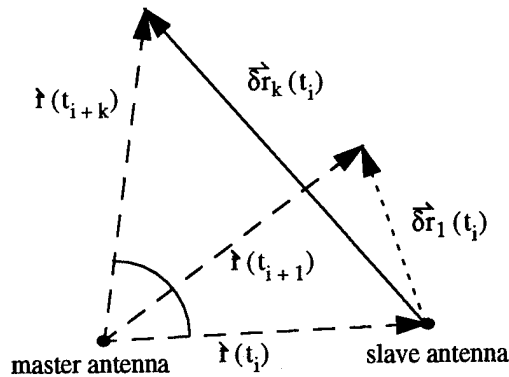


Figure 1. Antenna displacement vectors.

$$H = [\hat{e}^1 \hat{e}^2 \dots \hat{e}^M]^T, \quad (8)$$

the superscript refers to each satellite, and M is the number of satellites.

3.0 Satellite Kinematic Model

Figure 2 illustrates the antenna configuration on the spinning satellite and defines the key vectors and angular rates. For simplicity, the vehicle is assumed to be axisymmetric about the z^B axis. The master antenna is located at the center with the master-slave baseline perpendicular to the axis of symmetry. The body x -axis is defined by the position of the slave antenna. I_s is defined to be the spin axis moment of inertia and I_t is the transverse moment of inertia. The angular velocities are defined in [8] as follows: ω is the inertial spin rate about the instantaneous rotation axis; ω_p is the body nutation rate; and ω_l is the inertial nutation rate. The nutation angle is θ . The relationships

between ω , ω_p , ω_l , θ , and the inertias are

$$\omega_p = \frac{I_t - I_s}{I_s} \omega_l \cos \theta \quad (9)$$

and

$$\omega^2 = \omega_p^2 + \omega_l^2 + 2\omega_p \omega_l \cos \theta. \quad (10)$$

The body frame is fixed to the rotating satellite and is denoted with a superscript B . The angular momentum frame, denoted by the superscript H , is defined with the z axis along the spacecraft's angular momentum vector. The orbit local frame is designated by the superscript L .

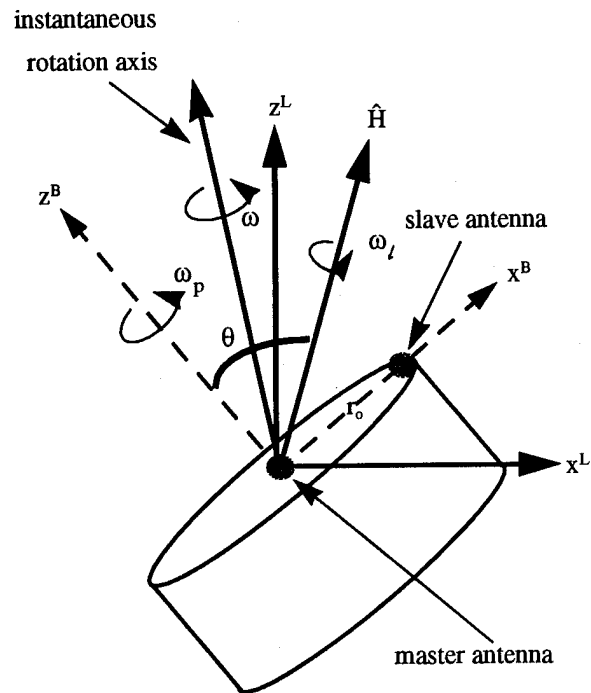


Figure 2. Kinematic model.

3.1 Antenna Motion

In the absence of external torques a GPS antenna on the rim of a spinning satellite will move according to the kinematic model described in equations (9) and (10). In the body fixed system, the antenna position remains constant. In the local system, however, the position is dependent on satellite rotations and the orientation of the angular momentum vector in this system.

The position of the antenna in these two coordinate systems can be related with two separate rotation matrices given by

$$\mathbf{r}^L = \mathbf{L}_C^{HH} \mathbf{C}_r^B \mathbf{r}^B \quad (11)$$

where

$$\mathbf{r}^B = \begin{bmatrix} r_o \\ 0 \\ 0 \end{bmatrix}$$

is the position of the antenna in the body frame, and

$$\mathbf{H}_C^B = \begin{bmatrix} c\psi c\phi - c\theta s\psi s\phi & -s\psi c\phi - c\theta c\psi s\phi & s\theta s\phi \\ c\psi s\phi + c\theta s\psi c\phi & -s\psi s\phi + c\theta c\psi c\phi & s\theta c\phi \\ \sin\theta \sin\psi & s\theta c\psi & c\theta \end{bmatrix} \quad (12)$$

is the rotation matrix from the body fixed system to the angular momentum system. The angles ψ and ϕ are time dependent angles related to the kinematic frequencies by

$$\psi = \omega_p t + \psi_o \quad (13)$$

and

$$\phi = \omega_l t + \phi_o \quad (14)$$

The matrix \mathbf{L}_C^{HH} rotates from the angular momentum system to the local system. If equation (11) is differenced in time an expression relating the displacement vectors to the satellite kinematics can be formulated. For a constant orientation of a satellite's angular momentum vector, this relationship at time t_i is

$$\delta \mathbf{r}^L(t_i) = \mathbf{L}_C^{HH} [\mathbf{H}_C^B(t_{i+k}) - \mathbf{H}_C^B(t_i)] \begin{bmatrix} r_o \\ 0 \\ 0 \end{bmatrix} \quad (15)$$

The displacement vectors in the local frame were computed from the GPS phase differences by equation (7). Equation (15) describes how these components are related to the spacecraft attitude. In particular, the \mathbf{L}_C^{HH} matrix is a function of the orientation of the angular momentum vector, and \mathbf{H}_C^B is a function of the nutation angle, as well as the body and inertial nutation rates.

The following section discusses a simple method to estimate the elements of \mathbf{L}_C^{HH} from the cross products of the $\delta \mathbf{r}^L(t_i)$ values. Section 5.0 describes a frequency domain technique that determines the frequencies in (15) as well as the nutation angle and \mathbf{L}_C^{HH} . Section 7.0 shows a time domain method to compute ω_p and θ .

4.0 Orientation of the Angular Momentum Axis from Displacement Vector Cross Products

Ideally, a spinning satellite is rotating perfectly about its rotation axis (i.e. no nutation) which will also be its angular momentum axis. A GPS antenna located on one face of the satellite will rotate in a plane perpendicular to this axis. The displacement vector of the moving antenna will be in this plane. Taking the cross products of two of these vectors will yield a vector with the same orientation as the angular momentum axis given by

$$\hat{\mathbf{H}} = \frac{\delta \mathbf{r}^L(t_i) \times \delta \mathbf{r}^L(t_{i+k})}{|\delta \mathbf{r}^L(t_i) \times \delta \mathbf{r}^L(t_{i+k})|} \quad (16)$$

Because the GPS measurements are taken in the local frame, $\hat{\mathbf{H}}$, will be computed in the local frame. As a result, $\hat{\mathbf{H}}$, defines the orientation of the satellite in the local frame.

When nutation is introduced, the cross product of two successive displacement vectors is not the orientation of $\hat{\mathbf{H}}$. However, as the satellite's instantaneous spin axis rotates about $\hat{\mathbf{H}}$, the average of all the vectors formed from these cross products will tend towards the actual orientation $\hat{\mathbf{H}}$. This is given by

$$\hat{\mathbf{H}} = \frac{1}{N} \sum_{i=1}^N \frac{\delta \mathbf{r}^L(t_i) \times \delta \mathbf{r}^L(t_{i+k})}{|\delta \mathbf{r}^L(t_i) \times \delta \mathbf{r}^L(t_{i+k})|} \quad (17)$$

where N is the number of measurements.

5.0 Modal Analysis Techniques

From equations (12), (13), and (14) we see that the displacement vector is comprised of terms containing the sines and cosines of ψ and ϕ . From equation (15) it can be seen that only the first column of \mathbf{H}_C^B is required. Since the angle ψ rotates at ω_p and ϕ rotates at ω_l , the sine and cosine products will cause oscillations at $\omega_l \pm \omega_p$. The $\sin\psi$ term in the last row will cause an oscillation at ω_p . Thus, three frequencies can be determined from the displacement vector components. Two methods for extracting the desired frequencies are described in this section.

5.1 FFT Method

To determine the modal frequencies and modal amplitudes of a signal the following steps are applied:

- 1) Apply an FFT algorithm to the sampled signal data.
- 2) Compute the power spectral density (PSD) of the trans-

formed data in step 1.

- 3) Identify the peaks of the PSD.
- 4) Determine the frequency at which each peak occurs.
- 5) Relate these frequencies back to a kinematic model.

Using only the PSD values, the frequencies found in step 4 are the most likely estimate (MLE) of each signal mode. Ideally, they are the exact frequencies of the modes. However, the sampling properties of the signal can lead to errors.

Ideally, the signal should be sampled so that the modal frequencies are integer multiples of the frequency bin. The frequency bin size is determined from dividing the sample frequency by the number of data points.

In reality, however, the peaks of the PSD occur in the frequency bins that are closest to the correct modes. The signal power of each mode is spread over a range of frequency bins surrounding the correct frequency. In order to determine a better estimate, the frequency center of the bins are computed by weighting them according to their power. Additionally, increasing the sample size increases the resolution of each bin.

Another problem that degrades the determination of the modal frequencies is noise in the signal. For the ideal sampling case, this is not a problem if the signal power is significantly larger than the noise level. The frequency of each mode still occurs exactly at one bin. For the non-ideal sampling case, there are some additional effects. When bin weighting is used, extra power due to noise contained in these surrounding bins causes the estimation of the frequency center to be less accurate.

One way to decrease the effect of noise is to use a window function on the data. Ideally, the most accurate FFT would be of an infinite length of data, however, in reality a finite set of data has to be used. Mathematically, this appears as an abrupt change from some sampled data value to an infinite number of zeros. This has the effect of amplifying the noise. If a window function is applied to the data, this abrupt change is smoothed and the effect of noise is decreased.

In the implementation of an FFT algorithm there are no assumptions about the structure of the signal. In other words, the FFT can be applied to any type of signal. There are other frequency estimation methods which can take advantage of the knowledge of the signal's structure. The next section discusses one of these methods called the autoregressive or AR method.

5.2 AR Method

In general, a discrete-time process can be well approximated by a time series or rational transfer function model [6]. If it is modeled as an AR process of order p , the sampled data can be represented by the recursive difference relation

$$x[n] = - \sum_{k=1}^p a[k] x[n-k] + u[n] \quad (18)$$

where the coefficients $a[k]$ are estimated from the sampled data. Taking the Z-transform of (18) yields the transfer function

$$\frac{X(z)}{U(z)} = \frac{1}{P(z)} \quad (19)$$

where

$$z = \exp(j2\pi fn) \quad (20)$$

and

$$P(z) = 1 + \sum_{k=1}^p a[k] z^{-k} \quad (21)$$

From the estimated $a[k]$ in (18) the roots of $P(z)$ are found from (21). The roots occur in complex conjugate pairs and lie on a unit circle at angles corresponding to the sinusoidal frequencies f_k , where

$$f_k = \frac{f_k}{f_s} \text{ are the normalized sinusoidal frequencies}$$

and

f_s is the sample frequency in Hertz.

This is illustrated in Figure 3. It should be noted that this

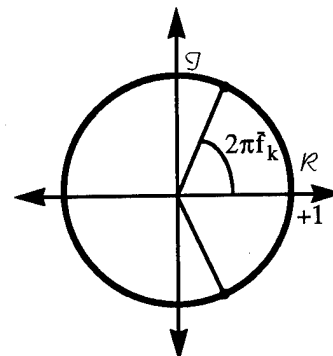


Figure 3. Relationship between signal frequency and transfer function poles.

technique directly estimates the frequencies f_k , therefore it does not depend on the modal frequencies being multi-

ples of the frequency bins.

Ideally for the case where there is no noise and the signal is perfectly modeled by (21), the signal is assumed to be composed of exactly $2p$ sinusoids. This means that each pole of (19) lies exactly on the unit circle at the exact angle of $2\pi f_k$.

For the non-ideal case, however, there is noise and the signal can not be perfectly modeled by (21). To take into account the noise, a higher order model than $2p$ is used. This allows for the power contained in the noise to be spread among the non-modal frequencies. The poles of (19) corresponding to the modes now lie near the unit circle, while the poles corresponding to the noise lie farther away. The angles of the poles are only approximately equal to $2\pi f_k$. As the model order is increased, there are more frequencies available for the noise. As a result, the poles for the modal frequencies get closer to the unit circle and the angles get closer to $2\pi f_k$. If the model order is too high spurious frequencies might become dominant. This is illustrated in Figure 4.

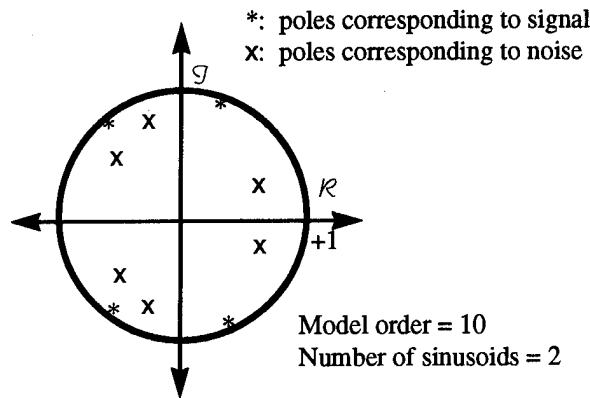


Figure 4. The Pole - Frequency relationship for a noisy sampled signal.

5.3 Application of Modal Analysis to Spinning Satellites

The modal analysis methods as described in the last section can be used to determine the frequencies associated with a spinning satellite and to determine its attitude. The components of the antenna displacement vectors oscillate according to the kinematic model illustrated in Figure 2. The frequency estimation techniques can be applied to the antenna displacements. The dominant frequencies as found from the FFT or AR methods correspond to the frequencies contained in the model. After the frequencies are

computed, other techniques can be used to determine the elements of the attitude matrix. The next section describes the application of the frequency and amplitude estimation methods.

5.4 Application of Frequency Estimation Techniques to the Spinning Satellite Model

There are three frequencies contained in (15):

$$1) \quad f_d = f_l - f_p,$$

$$\text{where } f_l = \frac{\omega_l}{2\pi} \text{ and } f_p = \frac{\omega_p}{2\pi},$$

$$3) \quad f_p,$$

and

$$4) \quad f_t = f_l + f_p.$$

Applying an FFT algorithm to observations computed by (7) yields a PSD with spikes at these three frequencies. Applying the AR method to (7) yields three pairs of complex roots of (19). The positive angles on the unit circle are

$$\frac{2\pi f_d}{f_s}, \frac{2\pi f_p}{f_s}, \text{ and } \frac{2\pi f_t}{f_s}.$$

5.5 Attitude and Nutation Angle Estimation

The technique for attitude estimation involves first reformulating the right hand side of equation (15) into the product of a constant element matrix, an oscillatory one, and the constant r_o .

$$\delta \vec{r}(t_i) = AB(t_i)r_o \quad (22)$$

where A is 3 x 5 matrix given by

$$A = \begin{bmatrix} a_{11} & -a_{11}c\theta & a_{12} & a_{12}c\theta & a_{13}s\theta \\ a_{21} & -a_{21}c\theta & a_{22} & a_{22}c\theta & a_{23}s\theta \\ a_{31} & -a_{31}c\theta & a_{32} & a_{32}c\theta & a_{33}s\theta \end{bmatrix} \quad (23)$$

and a_{ij} are the nine elements of ${}^L C^H$. Matrix B is a 5 x 1 matrix composed of the sines and cosines of ψ and ϕ given by

$$B(t_i) = \begin{bmatrix} c\psi(t_{i+k})c\phi(t_{i+k}) - c\psi(t_i)c\phi(t_i) \\ s\psi(t_{i+k})s\phi(t_{i+k}) - s\psi(t_i)s\phi(t_i) \\ c\psi(t_{i+k})s\phi(t_{i+k}) - c\psi(t_i)s\phi(t_i) \\ s\psi(t_{i+k})c\phi(t_{i+k}) - s\psi(t_i)c\phi(t_i) \\ s\psi(t_{i+k}) - s\psi(t_i) \end{bmatrix} \quad (24)$$

where ψ and ϕ are found by equations (13) and (14) respectively.

The elements of A can be estimated using the following steps:

- 1) Collect a batch of data and apply (7) to get $\delta \vec{r}(t_i)$ at time $i = 1, 2, 3, \dots, N$, where N is the number of measurement times;
- 2) Estimate the three frequencies using either the FFT or AR method;
- 3) Using these estimated frequencies accumulate the $5 \times N$ matrix

$$\beta = [B(t_1) \ B(t_2) \ \dots \ B(t_N)]; \quad (25)$$

- 4) Form the $3 \times N$ matrix

$$\Lambda = [\delta \vec{r}(t_1) \ \delta \vec{r}(t_2) \ \dots \ \delta \vec{r}(t_N)] \quad (26)$$

- 5) Solve for A by

$$A = \Lambda \beta^T (\beta \beta^T)^{-1}. \quad (27)$$

6.0 Approximation of Instantaneous Angular Velocity

As an alternative to determining the angular rates based on frequency domain techniques, we can develop a model based on the approximation of the instantaneous angular velocity. Every two successive positions of a rotating antenna creates an angle with the spin axis that can be used for this approximation. This angle shown in Figure 5 can be computed by

$$\alpha = 2 \arcsin \left(\frac{\frac{1}{2} |\delta \vec{r}|}{r_o} \right) \quad (28)$$

where $r_o = |\vec{r}|$. If we define the mean angular rate ω^* by

$$\omega^* = \frac{\alpha(t_i)}{\Delta t} \quad (29)$$

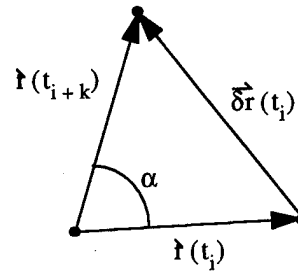


Figure 5. Angular displacement.

where $\Delta t = t_{i+k} - t_i$ and define the rate of change of the antenna position with respect to the local frame expressed in the local frame by

$$\left(\frac{L}{\vec{r}} \right)^L \equiv \frac{d\vec{r}}{dt}, \quad (30)$$

then as $\Delta t \rightarrow 0$ we can say

$$\omega^* \approx \frac{1}{r_o} \left| \frac{d\vec{r}}{dt} \right|. \quad (31)$$

In general

$$\frac{L}{\vec{r}} = \frac{B}{\vec{r}} + \frac{B}{\omega} \times \vec{r} \quad (32)$$

and if (32) is expressed in the body frame then $\frac{B}{\vec{r}} = 0$ and

$$\left(\frac{L}{\vec{r}} \right)^B = [\times^B \omega^L] \vec{r}^B. \quad (33)$$

Taking the magnitude of the right hand side of (33) and using (31) we get

$$\omega^* = \frac{1}{r_o} \left| \begin{bmatrix} 0 & -\omega_3 & \omega_2 \\ \omega_3 & 0 & -\omega_1 \\ -\omega_2 & \omega_1 & 0 \end{bmatrix} \vec{r}^B \right| \quad (34)$$

where ω_1 , ω_2 , and ω_3 are the angular rates about the body axis and

$$\omega = \sqrt{\omega_1^2(t_i) + \omega_2^2(t_i) + \omega_3^2}. \quad (35)$$

Since

$$\vec{r}^B = \begin{bmatrix} r_o \\ 0 \\ 0 \end{bmatrix},$$

the equation for ω^* can be reduced to

$$\omega^* = \sqrt{\omega_2^2 + \omega_3^2}. \quad (36)$$

The equations of motion for the spinning satellite written in terms of ω_1 , ω_2 , and ω_3 are

$$\dot{\omega}_1 = \left(1 - \frac{I_s}{I_t}\right) \omega_2 \omega_3, \quad (37)$$

$$\dot{\omega}_2 = -\left(1 - \frac{I_s}{I_t}\right) \omega_1 \omega_3, \quad (38)$$

and

$$\dot{\omega}_3 = 0. \quad (39)$$

The solution to this set of differential equations is

$$\omega_1(t_i) = \omega_T \cos \omega_p(t_i - t_0), \quad (40)$$

$$\omega_2(t_i) = -\omega_T \sin \omega_p(t_i - t_0), \quad (41)$$

and

$$\omega_3 = \frac{\omega_p}{\left(1 - \frac{I_s}{I_t}\right)} \quad (42)$$

where $\omega_T = \sqrt{\omega_1^2(t_i) + \omega_2^2(t_i)}$.

Looking at (36) and (41), it can be seen that ω^* oscillates according to ω_p . Its minimum value is ω_3 and its maximum value is ω . For a nutation angle of zero, equations (9), (10), and (42) can be combined to show that $\omega = \omega_3 = \omega^*$. As a result, for small nutation angles, ω can be approximated by the average of the ω^* computed from the displacement vectors. Furthermore, if an accurate value of the satellite's inertia ratio is known, an estimate of ω_p and ω_l can also be found.

7.0 Nutation Angle Filter

The nutation angle filter is a Kalman filter that uses the GPS antenna displacement vectors to estimate the nutation angle θ , the angular rate of the antenna about the body z^B -axis, ω_p , and the initial phase about the z^B -axis, ψ_0 . A graphical representation of these states is shown in Figure 6.

7.1 Equations of motion

In the absence of external torques and nutation damping, the rate of change for each of the states is zero. The case involving passive nutation damping has been examined, but for typical damping time constants of hours the rate of

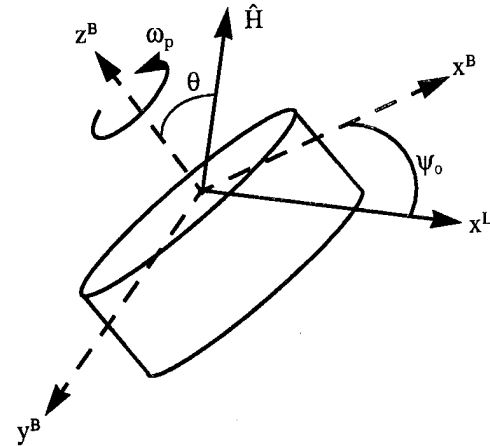


Figure 6. Filter states.

change can still be considered zero for short time spans.

7.2 Observation Equation

The observation for the nutation angle filter is derived by rotating the displacement vector into the angular moment frame, scaling it by the radius of the satellite, and taking the third component.

$$(\delta \vec{r}')^H = \begin{bmatrix} \delta x' \\ \delta y' \\ \delta z' \end{bmatrix}^H = \frac{H_{CL}(\delta \vec{r})^L}{r_0} \quad (43)$$

Expanding the $\delta z'$ component of $\delta \vec{r}'$ yields

$$\delta z' = s\theta(t_{i+k})c\psi(t_{i+k}) - s\theta(t_i)c\psi(t_i) \quad (44)$$

where

$$\psi(t) = \omega_p(t)t + \psi_0. \quad (45)$$

8.0 Simulation

A computer simulation was set up to generate GPS measurements for a comparison by these various methods. The program simulated $\Delta\phi$ measurements from two antennas on a spinning satellite. Gaussian noise with a mean of zero and a standard deviation of 5 mm was added to each $\Delta\phi$ measurement. Two nutation angle cases were examined. Table 1 shows the parameters used for the simulation.

Table 1. Simulation parameters.

Satellite radius	0.381 m
Nominal spin rate (ω)	5 rpm
Inertia ratio $\left(\frac{I_s}{I_t}\right)$	1.3
Nutation angles	5 and 25 degrees
Batch lengths	30, 100, and 400 seconds
Sample frequency	2 Hz
Differencing Interval	5 seconds (i.e. $k = 10$)

8.1 Frequency Estimation

The body and inertial nutation rates were estimated using the FFT and AR frequency domain techniques, using the averaging of ω^* , and using the nutation filter. The nutation filter, however, was only used to estimate ω_p . The results for each nutation angle are shown in Tables 2 and 3. The estimated frequencies are given to four decimal places. This degree of precision is required in the next section for adequate attitude estimation when using the batch least squares technique.

The frequency domain techniques performed better with the large nutation angle. For the large angle case, the AR method performs very well with only a small batch size. The error is less 0.1% after 30 seconds. The FFT

method, however, requires a larger batch size for comparable performance. The nutation angle filter also works well, but also requires more time to equal the performance of the AR method.

For smaller nutation angles, the accuracy of the frequency domain techniques gets worse. This is expected because the third term in the first column of (12), containing the ω_p frequency, approaches zero as the nutation angle goes to zero. Both the AR and FFT methods require a larger batch size to match the results shown for the large angle. A 100 second batch is needed before the AR errors are under one percent. The FFT does not produce meaningful results with a 30 second batch and it achieves errors less than one percent with the 400 second batch. The nutation filter, however, shows only a small drop in performance for the small angle case.

The approximation involved in computing the value of ω^* is worse for larger nutation angles. This shows up in the results in determining frequencies for large and small nutation. For small angles, the estimations are comparable to the other methods. For large angles, they are much worse. The 100 second batch produced errors around five percent for the 25 degree nutation angle, while the errors were less than one percent for the 5 degree angle. It should also be noted that this technique is dependent on an accurate knowledge of the satellite's inertia values.

Table 2. Frequency estimation for $\theta = 25$ deg.

Method	30 second batch		100 second batch		400 second batch	
	ω_l (rad/s)	ω_p (rad/s)	ω_l (rad/s)	ω_p (rad/s)	ω_l (rad/s)	ω_p (rad/s)
True Value	0.6423	-0.1343	0.6423	-0.1343	0.6423	-0.1343
AR	0.6424	-0.1344	0.6422	-0.1343	0.6424	-0.1344
FFT	0.5821	-0.0748	0.6416	-0.1331	0.6424	-0.1340
Average ω^*	0.6088	-0.1405	0.6071	-0.1401	0.6073	-0.1403
Nutation filter		-0.1415		-0.1342		-0.1343

Table 3. Frequency estimation for $\theta = 5$ deg.

Method	30 second batch		100 second batch		400 second batch	
	ω_l (rad/s)	ω_p (rad/s)	ω_l (rad/s)	ω_p (rad/s)	ω_l (rad/s)	ω_p (rad/s)
True Value	0.6789	-0.1561	0.6789	-0.1561	0.6789	-0.1561
AR	0.6760	-0.1530	0.6779	-0.1550	0.6794	-0.1565
FFT	no solution	no solution	0.6473	-0.1226	0.6795	-0.1562
Average ω^*	0.6780	-0.1565	0.6748	-0.1557	0.6759	-0.1560
Nutation filter		-0.1488		-0.1605		-0.1556

8.2 Attitude Estimation

The orientation of the angular momentum axis was estimated using the batch least squares method in section 5.5 and using the averaging of the displacement vector cross products described in section 4.0. Tables 4 and 5 show results for each nutation angle. Figures 7 and 8 show a time history for the cross product method of estimation.

Table 4. Angular mom. axis estimation for $\theta = 25$ deg.

Method	\hat{H} pointing error (deg)		
	30 s	100 s	400 s
Batch least squares	0.42	0.26	0.13
\vec{dr} cross products	0.98	0.35	0.17

Table 5. Angular mom. axis estimation for $\theta = 5$ deg.

Method	\hat{H} pointing error (deg)		
	30 s	100 s	400 s
Batch least squares	0.53	0.31	0.16
\vec{dr} cross products	0.13	0.13	0.11

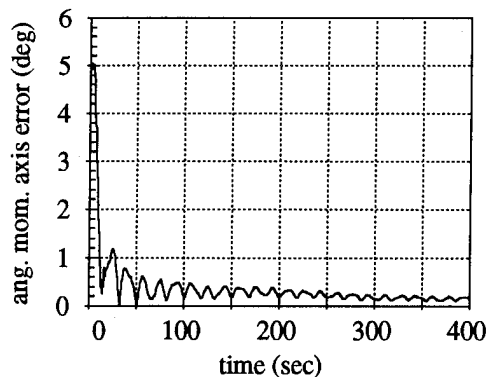


Figure 7. Cross product axis estimation for $\theta = 25$ deg.

The batch least squares method shows its best performance for the larger nutation angle. Results improve with a larger batch size. This is most likely due to the increased accuracy of the frequency estimation as the batch size grows larger.

The cross product method does better for small angles. As the nutation angle becomes larger, the approximation that equation (16) is correct gets worse. As more cross products are added to the average in equation (17), the estimate improves. For small angles the approximation improves very quickly. This is demonstrated in Fig-

ures 7 and 8. The frequency of the bumps in the graphs is approximately equal to $\frac{\omega_l - \omega_p}{2}$.

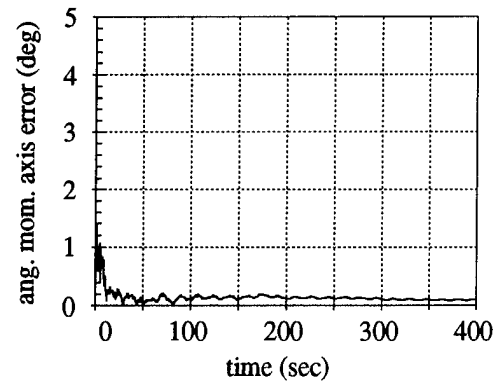


Figure 8. Cross product axis estimation for $\theta = 5$ deg.

8.3 Nutation Angle Estimation

The nutation angle θ was estimated using the method of batch least squares and the nutation angle filter. Tables 6 and 7 show results for each nutation angle. Figures 9 and 10 show a time history of the nutation angle estimation from the nutation angle filter.

Table 6. Nutation angle estimation for $\theta = 25$ deg.

Method	θ (deg)		
	30 s	100 s	400 s
True value	25.00	25.00	25.00
Batch least squares	27.94	25.43	27.48
Nutation filter	20.98	24.38	24.91

Table 7. Nutation angle estimation for $\theta = 5$ deg.

Method	θ (deg)		
	30 s	100 s	400 s
True value	5.00	5.00	5.00
Batch least squares	no sol.	2.02	6.65
Nutation filter	4.23	4.79	5.04

As with the angular momentum axis determination, the batch least squares technique for determining the nutation angle worked best with large angles. However, large batch sizes did not show an increase in accuracy. Several other cases with batch sizes between 30 and 400 seconds showed about a 10% fluctuation in the error. For small angles the batch size did make a significant difference. The small batch case failed to provide a meaningful result.

The 100 second size batch still had a 3 degree error. Even with the largest batch the error was still 1.6 degrees.

The nutation filter, on the other hand, worked well with both nutation angles. In both cases the error was under ten percent in about 40 seconds and steadily improved afterwards.

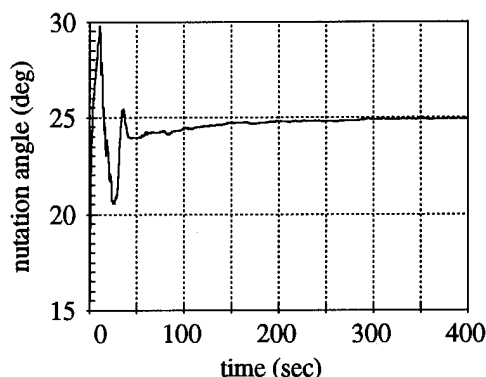


Figure 9. Nutation filter estimation for $\theta = 25$ deg.

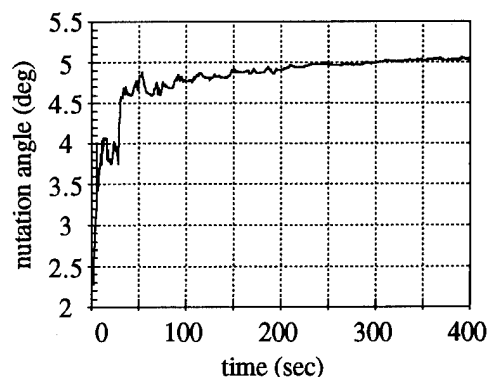


Figure 10. Nutation filter estimation for $\theta = 5$ deg.

9.0 Conclusions

A comparison of several methods for GPS based attitude determination of a spinning satellite has been presented. For large nutation angles the frequency domain techniques, especially the AR method, offer a way to estimate the spin frequencies with a high degree of accuracy. The computationally simpler method of averaging ω^* is not that accurate. The accuracy of the nutation filter is comparable only after a long period of time.

For small nutation angles, on the other hand, the frequency domain techniques require a much greater batch size to achieve a certain level of accuracy. The averaging of ω^* works much better and quickly gets a high level of accuracy but it requires knowledge of the inertias. The

nutation filter still requires a longer time than the AR method to achieve a certain level of accuracy.

For large nutation angles both the batch least squares and cross product methods have comparable accuracy in estimation of attitude. The batch least squares is better with small batch sizes. The cross product method, however, is much simpler and its accuracy quickly improves. For small angles, the cross product method is very accurate with only a small amount of data.

The nutation filter is the only one of the two methods to give a very accurate estimation of the nutation angle. For both small and large angles, the percentage error is about the same for a given length of time.

The performance of these methods appears more than adequate to meet the requirements of an inexpensive satellite mission. The SNOE satellite has a pointing requirement of ± 5 deg and spin rate requirement of ± 1 rpm [1]. This level of precision is well with the levels shown in this paper. For the typical time scales of hours, the techniques have more than enough performance for an accurate estimation of the satellite's parameters. After only one minute of data collection and processing, the pointing error is below one degree and the angular rate errors are below one percent.

10.0 Future plans

To further assess the usefulness of these methods, experimental data is required. Future test plans include mounting a GPS receiver on a spinning platform. The platform will have the ability to simulate the kinematics of a spinning satellite for a range of frequencies and nutation angles. Another area for further investigation includes the development of a more robust method to determine the correct frequencies from the AR method. We hope to implement the proposed approaches on a future satellite mission. The ultimate goal is closed loop attitude control based on GPS data from an antenna on a spinning spacecraft.

Acknowledgments

This research is sponsored by the Department of the Navy, Office of the Chief of Naval Research. The content does not necessarily reflect the position or the policy of the Government, and no official endorsement should be inferred.

References

- [1] Barth, C. A., S.C. Solomon, D.W. Rusch, and T. N. Woods, "Student Nitric Oxide Explorer", Investigation

and Technical Plan - Proposal to the Universities Space Research Association Student Explorer Demonstration Initiative, from the Laboratory for Atmospheric and Space Physics, University of Colorado, 1994.

[2] Ward, L.M. and P. Axelrad, "Spacecraft Attitude Estimation Using GPS: Methodology and Results for RADCAL," ION National Technical Meeting, Anaheim, CA, 813-825, January 1995.

[3] Lightsey, E.G., C.E. Cohen, W.A. Fees, B.W. Parkinson, "Analysis for Spacecraft Attitude Measurements Using Onboard GPS," AAS Guidance and Control Conference, Keystone, CO, Feb. 1994, pp. 521-532.

[4] Brock, J. K., R. Fuller, B. Kemper, D. Mleczko, J. Rodden, and A. Tadros, "GPS Attitude Determination and Navigation Flight Experiment," To Be Given at Proceedings of ION GPS-95, Palm Springs, California, Sept 12-15 1995.

[5] Martin-Niera, M. and R. Lucas, "GPS Attitude Determination of Spin Stabilized Satellites," Proceedings of ION GPS-92, Albuquerque, New Mexico, Sept 16-18, 1992.

[6] Kay, Steven M., *Modern Spectral Estimation Theory & Application*, Prentice Hall, 1988.

[7] Hofmann-Wellenhof, B., H. Lichtenegger, and J. Collins, *GPS Theory and Practice*, Springer-Verlag Wien, 1992.

[8] Wertz, James R., ed., *Spacecraft Attitude Determination and Control*, D. Reidel Publishing Company Library in Astrophysics and Space Science, 1978.

[9] Cohen, Clark E., *Attitude Determination Using GPS*, Phd. Dissertation, Department of Aeronautics and Astronautics, Stanford University, Dec. 1992.

A New Spacecraft Attitude Determination Scheme Based on the Use of GPS Line-Of-Sight Vectors

Jesús Serrano, Jorge Potti, and Pelayo Bernedo
GMV S.A.

Pierluigi Silvestrin
ESA/ESTEC

BIOGRAPHIES

Jesús B. Serrano (e-mail: jbserrano@gmv.es) is the head of the Flight Dynamics and Avionics Division of GMV (Spain). He received his M.S. degree in Aeronautical Engineering in 1983 from the Polytechnic University of Madrid (Spain). He was visiting scientist of the Mission Analysis Section at ESOC in 1984. He joined GMV in 1985. At present his major areas of involvement are satellite guidance, navigation and control, including GPS applicability and operational issues.

Jorge Potti is Project Manager at GMV. He received his M.S. degree in Aeronautical Engineering in 1986 from the Polytechnic University of Madrid (Spain) where he gained the third national award of university studies. Since that time he is working at GMV in the research and development group of the Flight Dynamics and Avionics Division. At present his major areas of research are satellite guidance, navigation and control, including GPS applicability and operational issues.

Pelayo Bernedo received his M.S. degree in Aeronautical Engineering from the Polytechnical University of Madrid, Spain in 1988. He worked for McDonnell Douglas in the MD-80 twinjet series within the structures group. Since 1991 he works in the Simulation Division in GMV, where he specializes in GPS based navigation for airborne applications and tracking systems for fleets of ground vehicles.

Pierluigi Silvestrin is a Senior Systems Engineer in the Earth Observation Preparatory Programme Division (EOPP) of ESTEC in Noordwijk (The Netherlands). He graduated in Electronic Engineering at the University of Padova (Italy) in 1985, specialising in control systems design. After working for one year at the Joint European Torus in Abingdon (UK), he joined in 1987 the Attitude and Orbit Control Systems Section of ESTEC. In 1989 he joined the EOPP, where he is presently responsible for studies of space systems and supporting technologies for future Earth observation

missions of the European Space Agency.

ABSTRACT

This paper presents the design and performances of a simple, fast, robust and reliable low-accuracy attitude determination concept based on the information provided by a GPS receiver without using the carrier phase. The paper reviews different alternatives including GPS satellites visibility checking and signal level (in terms of signal to noise ratio, SNR) measurements. A detailed presentation of the selected concept is included: this uses two canted antennas and processes the SNR information provided by both antennas for the commonly tracked GPS satellites. This concept provides full attitude observability when at least two common satellites are tracked by the antennas, hence, the concept does not rely on some a-priori knowledge.

The attitude determination scheme consists of a simple estimation algorithm which processes some GPS line-of-sight (LOS) vectors constructed by using the signal level measurements from the common GPS satellites tracked by two GPS antenna with a separation angle of about 10° to 20° and with a nominal orientation such that one of the antennas is pointing to the zenith in the nominal Earth pointing spacecraft attitude. The processing resources required by the designed attitude determination concept based on GPS LOS vectors are very small: the selected algorithm is very fast and the memory load is very small. The designed scheme based on GPS LOS vectors provides an estimate of the full spacecraft attitude even if the a-priori knowledge is very poor. The accuracy of the estimate mainly depends on the signal level mismodelling error level: few degrees accuracy is obtained when tenths of dB (3σ) SNR mismodelling errors are assumed and better than 18° accuracy is obtained for the worst case considered, namely, 3 dB SNR mismodelling error.

Depending on the intended application, the concept might be improved (without increasing the complexity of the processing algorithm) with respect to the

sensitivity to the SNR mismodelling errors. This can be performed by using a third antenna: with three sources of information one would be able to determine the two angles of the GPS LOS vector as well as determine the common SNR mismodelling term.

1. INTRODUCTION

The European Space Research and Technology Centre (ESTEC) is currently investigating the use of the information provided by the GNSS receivers for performing the attitude determination of Low Earth Observation Satellites using the MetOp mission as a study case. The MetOp system is a European satellite series for operational meteorology and climate monitoring from a sunsynchronous 820 Km altitude orbit which will complement the NOAA Polar Orbiting Environmental Satellite System.

The use of the differential carrier phase from various antennas connected to a single receiver is the most promising concept for obtaining highly accurate performances. However, the use of such a concept has some drawbacks such as the need of an OFAR technique in case the baseline lengths are higher than the wavelength of the carrier, as well as the need of additional schemes

- for the initialization of the attitude determination (in case the OFAR algorithm is not fast enough or just to improve the OFAR with some a-priori spacecraft attitude knowledge),
- for the validation of the integer ambiguity computed by the OFAR and
- for ensuring appropriate robustness of the complete on-board attitude determination function.

Hence, an investigation was carried out in order to construct an attitude determination concept which is simple, robust, reliable and requires small processing resources, even at the expense of accuracy.

2. CANDIDATE CONCEPTS

2.1. Concept based on visibility checkings

An estimate of the user spacecraft position vector and of the GPS satellite position vector is provided by the GPS receiver. Such information can be used as follows: from the estimated position vectors, one can deduce if a satellite should be visible or not, taking into account either the nominal spacecraft attitude or the a-priori estimate of the spacecraft attitude. On the other hand, from an all-in-view receiver output, the satellites which are actually visible are known. Some improvement on the spacecraft attitude knowledge is then possible by

processing such information.

A method for computing a low accuracy estimate of the attitude of a GPS antenna using as the only available information the presence of GPS satellites within a GPS receiver antenna field may be sketched as follows. Let's denote \underline{u}_A the normal unit vector of the antenna aligned with the antenna boresight and β the antenna field of view (beamwidth). The set of GPS satellites S_{GPS} can be subdivided into (Figure 1) three disjoint subsets: S_{VIS} is the class of GPS satellites which are inside the GPS antenna field of view, S_{INV} is the set of GPS satellites which are invisible from the current position of the user satellite because they are eclipsed by the Earth, and finally S_{POT} is the set of GPS satellite which are potentially visible by the GPS receiver antenna (i.e., they would be visible for some attitude of the user satellite).

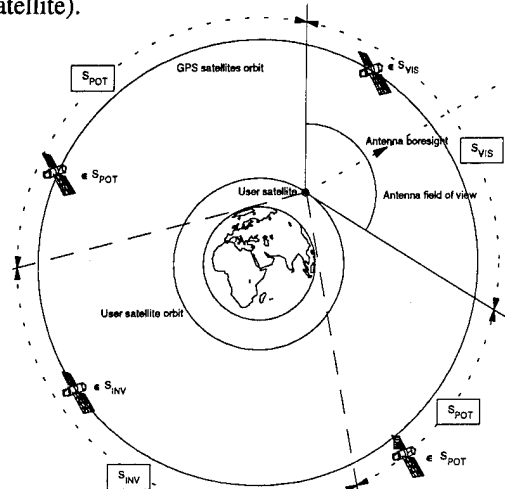


Figure 1: Definition of visible, invisible and potentially visible GPS satellites.

Clearly the contents of the three subsets varies with time and is a function of both the user satellite's attitude (which affects the relative split between S_{VIS} and S_{POT}) and the user satellite's position on the orbit (which determines S_{INV}). At any given time the user knows the contents of all three subsets: S_{VIS} is directly given by the receiver, S_{INV} can be computed on the basis of the current user satellite's position (which is also given by the receiver) and S_{POT} can be derived by difference with S_{GPS} . The users can moreover compute (in an inertial frame) the relative directions to the GPS satellites. These direction will be indicated by the vectors $\underline{u}_{A,GPSi}$ which will be defined as the unit vector along the line joining the host satellite to GPS satellite i .

The knowledge of the subsets of S_{GPS} induces the following constraints on the direction of \underline{u}_A :

$$\begin{aligned} \underline{u}_A^T \underline{u}_{A,GPSi} &> \cos(\beta/2) && \text{for } i \text{ belonging to } S_{VIS} \\ \underline{u}_A^T (-\underline{u}_{A,GPSi}) &> -\cos(\beta/2) && \text{for } i \text{ belonging to } S_{POT} \end{aligned}$$

The problem of estimating the direction of the GPS antenna can therefore be stated as follows: *find the set of vectors \underline{u}_A of unit length which satisfy the above constraints.*

The above method, which is low demanding in terms of computing power required, has been simulated so as to derive the expected attitude determination accuracy. Simulations under realistic conditions for the MetOp platform show that under worst case conditions the achieved accuracy is always better than 18° . Such an accuracy would be sufficient to completely remove the integer ambiguity problem for short baselines (less than 0.61 m). For longer baselines, it can be used to initialise a more accurate search method or to validate its output.

The knowledge of the receiver antenna pointing allows to derive an estimate of the attitude of the spacecraft, except for the rotation of the spacecraft about the antenna boresight. 3-axis attitude of the spacecraft can be obtained by having at least two GPS receiver antennas suitably canted.

2.2. Concepts based on SNR information

In addition to the pseudorange and the integrated carrier phase, receivers can provide the signal level associated with the tracked satellites. This signal level is a measure of the signal to noise ratio (SNR) and contains some information on the spacecraft attitude because it depends on the angle between the GPS satellite LOS vector from the user spacecraft and the antenna boresight. Hence, a possible concept would consist in using a single antenna and processing the SNR measurements.

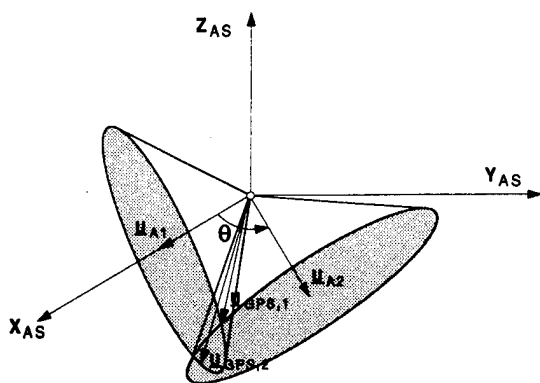


Figure 2: Construction of line-of-sight vectors using two canted antennas.

It has been assumed here that typical a typical antenna is used, with a pattern symmetric around the antenna boresight. The signal level observable contains information only on the angle between the GPS LOS vector and the antenna boresight and it does not contain any information on the azimuth angle. The concept of

a single antenna would then provide some information on the spacecraft attitude but it will not full observability.

This disadvantage can be overcome by using two canted antennas (Figure 2) and processing the SNR information provided by both antennas for the commonly tracked GPS satellites: this will provide full attitude observability when at least two common satellites are tracked. There will then be no need to rely on some a-priori attitude knowledge. The drawback is the need for a second antenna with a certain cant angle with respect to the first antenna.

This is the concept selected for further analysis in detail in the following sections.

3. ANALYSIS OF THE SIGNAL-TO-NOISE RATIO OBSERVABLE

The basic observable is the SNR level at the output of the receiver, which can be expressed as follows

$$SNR = EIRP + L_t + L_s + L_b + G_r + L_a - 10 \log_{10} T_s + 228.6$$

EIRP is the effective isotropic radiated power by the emitting GPS satellites in the maximum gain direction. Based on actual GPS signal levels, which are around 5 dB higher than specifications². One should be aware that these levels are not guaranteed by the U.S. Government. Such power could decrease to the specified level by the end-of-life of the GPS satellite. *EIRP* (in dB) is,

$$EIRP = P_t + L_t + (G_t)_{\max}$$

where P_t is the transmitter power. It is unclear if the GPS satellites transmitter power is commandable or not, and in case it is, the operational error margins. Therefore this term may contain some important uncertainties. L_t is the transmitter to antenna gain loss. $(G_t)_{\max}$ is the transmit antenna gain in the maximum gain direction.

L_t is the transmitter antenna gain loss with respect to the maximum gain direction. This term accounts for the antenna gain pattern of the GPS satellites³. L_s is the free-space loss, given by

$$L_s = 20 \log_{10} \frac{\lambda_0}{4\pi d}$$

where λ_0 is the wavelength (19 cm at L1 frequency) and d is the distance between the GPS-satellite and the GPS receiver. There is negligible uncertainty associated with this magnitude (at any time, it is possible to know on-board the spacecraft the ephemeris of the GPS satellites with a degree of accuracy mainly governed by

the disturbing effect of SA). Finally, L_b encompasses other system losses like polarization mismatch, etc.

On the user side, G_r is the receiver antenna gain in the maximum gain direction. L_a is the attenuation of the signal when received from a direction different from the antenna maximum gain: this is a function of the deviation of the incoming signal from the maximum gain direction (zenith). A typical pattern⁴ is used in the following. Finally, T_s is the system noise temperature which is composed of a number of individual contributions from various sources: those originating ahead of the antenna output terminal (e.g. in the atmosphere) usually referred to as the antenna noise temperature (including galactic noise, solar noise, presence of the Earth, ...) and these noise sources between the antenna terminal and the receiver output which are lumped together and called receiver noise temperature.

Multipath effects might have an important effect: if direct and reflected signals are present, the signal power can be up to 3 dB higher than the only direct signal. The present concept has therefore to be restricted to benign multipath environments.

4. ON-BOARD ATTITUDE DETERMINATION ALGORITHMS

4.1. Attitude determination using vector observations

The problem of attitude determination from vector observations consists in finding the proper orthogonal matrix $[L_{B,I}]$ that minimizes the following non-negative loss function

$$F([L_{B,I}]) \equiv \frac{1}{2} \sum_{i=1}^{i=n} a_i \| \underline{b}_i^B - [L_{B,I}] \underline{r}_i^I \|^2$$

where the unit vectors \underline{r}_i^I are representations in a reference frame (here the inertial reference frame, I, is used) of the directions to some observed objects, the \underline{b}_i^B are the unit vector representations of the corresponding observations in the spacecraft body frame, the a_i are positive weights, and n is the number of observations. The motivation for this loss function is that if the vectors are error-free and the true attitude matrix $[L_{B,I}]_{true}$ is assumed to be the same for all the measurements, then \underline{b}_i^B is equal to \underline{r}_i^I for all i and the loss function is equal to zero for $[L_{B,I}]_{opt}$ equal to $[L_{B,I}]_{true}$.

Attitude determination algorithms based on minimizing this loss function have been used for many years. The original solution to Wahba's problem solved for the spacecraft attitude matrix directly, but most practical applications have been based on Davenport's q-method which solves for the quaternion representing the attitude

matrix. More efficient algorithms for solving the Wahba's problem have been developed recently. Those algorithms are more efficient in terms of speed as well as in terms of robustness in approaching the true solution in presence of uncertainties and measurement errors. Some examples are the iterative orthogonalization algorithm⁵, the singular value decomposition (SVD) algorithm⁶, the polar decomposition (PD) algorithm⁷, the QUEST algorithm⁸ and the Fast Optimal Attitude Matrix (FOAM) and Slower Optimal Attitude Matrix (SOAM) algorithms by Markley⁹.

In the following the SVD algorithm is used for solving the posed Wahba's problem. It has been shown that this method is not very efficient in terms of speed but it is very robust for computing the optimal estimate of the attitude matrix. Since the purpose of the present work is to assess the feasibility of determining the spacecraft attitude using GPS related vector observations and that the computation time required by the SVD algorithm is quite small, this algorithm is used in the following. Once the feasibility of the concept has been assessed, a second step might be to try to optimize the concept by using more efficient algorithms: for example, the FOAM or PD algorithms which are about ten times faster than the SVD one.

In the following the SVD decomposition used by Markley is applied⁶. It consists of decomposing the matrix B as follows

$$B \equiv \sum_{i=1}^{i=n} a_i \underline{b}_i^B (\underline{r}_i^I)^T$$

$$B = U_+ \text{diag}[S_1, S_2, S_3] V_+^T$$

where U_+ and V_+ are proper orthogonal matrices; $\text{diag}[\dots]$ denotes a matrix with the indicated elements on the main diagonal and zeros elsewhere; and S_1 , S_2 and $|S_3|$, the singular values of B , obey the inequalities

$$S_1 \geq S_2 \geq |S_3|$$

The optimal attitude estimate is given in terms of these matrices by

$$[L_{B,I}]_{opt} = U_+ V_+^T$$

4.2 On-board SNR observable model

The on-board system will predict, for each tracked satellite, the value of the SNR measured in the receiver. In order to do that, the predicted spacecraft state (including both position and attitude) and the predicted location of the GPS satellite will be used together with an on-board model of the SNR. The SNR on-board model which is used in the next sections for the satellite tracked in the channel i is as follows

$$\begin{aligned} \hat{SNR} = & \hat{P}_t + \hat{L}_t + (\hat{G}_t)_{\max} + \hat{L}_t(\delta_t) + \hat{L}_s(\hat{d}) + \hat{L}_b + \\ & \hat{G}_r + \hat{L}_a(\delta) - 10\log_{10}\hat{T}_s + 228.6 + w_t + w_r, \end{aligned}$$

where the hat means on-board models or values (to distinguish those from the actual or real ones discussed in section 3).

The different terms have the same meaning as indicated in section 3. The new terms are defined in the following: δ_t is the angle between the spacecraft user LOS (from the antenna of the GPS satellite) and the transmitter antenna boresight, δ is the angle between the GPS satellite LOS (from the antenna of the user spacecraft) and the user antenna boresight.

Estimated values for the position vectors and antenna pointing of the user and GPS satellites will be used in the on-board SNR model. This will introduce some discrepancies between this model and the actual SNR. Furthermore, some mismodeling will exist either due to lack of information on some models (such as those related to the GPS signal characteristics) or due to the limited knowledge of some parameters (such as those related to the user dependent parameters). Dedicated calibration campaigns might improve the consistency between the SNR models however a perfect matching can not be attempted. Two other terms have therefore been included in the above equation: w_t to account for the discrepancy between the on-board and the actual values of the common SNR terms for the various user spacecraft antennas (i.e., P_t , L_t , G_t , L_r , L_s , L_b), and w_r to account for the discrepancies between the on-board and the actual values of the user antenna dependent SNR terms (i.e., G_r , L_a , T_s , multipath effects).

4.3. Pseudomeasurement on the GPS LOS vector

The vector which will be processed in order to estimate the attitude of the spacecraft will be the line-of-sight (LOS) vector from the antenna of the user spacecraft to the antenna of the GPS satellite (\underline{u}_{AAGPS}). As the receiver does not provide such information, a pseudomeasurement will be constructed from the available information: the SNR measurements as indicated in section 2.2. The \underline{u}_{AAGPS}^B -pseudo-measurement (vector expressed in the user satellite body frame, B) is computed after constructing the corresponding pseudomeasurements on δ and on the user antenna to GPS satellite antenna LOS vector expressed in an antenna compound frame ($\underline{u}_{AAGPS}^{AS}$). The process is detailed in the following.

First, the pseudomeasurement of the angle formed by the GPS LOS vector and the user antenna boresight (δ_{pm}) is computed from the SNR measurement (SNR_m) taking into account the on-board model of the SNR observable detailed in section 4.2

$$\begin{aligned} \hat{L}_a(\delta_{pm}) = & SNR_m - \hat{P}_t - \hat{L}_t - (\hat{G}_t)_{\max} - \hat{L}_t(\delta_t) - \\ & \hat{L}_s(\hat{d}) - \hat{L}_b - \hat{G}_r + 10\log_{10}\hat{T}_s - 228.6 \end{aligned}$$

where the position vector of the user spacecraft and of the GPS satellites are assumed to be known on-board because they are provided by the receiver. In addition to that, an estimate of the rotation matrix between the body frame and the inertial frame is constructed with a priori estimate of the spacecraft attitude (it will be shown in the following that very rough estimate is sufficient depending upon the accuracy of the SNR observable). From that value, the pseudomeasurement on the angle formed by the GPS LOS vector and the user antenna boresight can be computed using the on-board model of the attenuation of the GPS signal when received from an off-boresight direction.

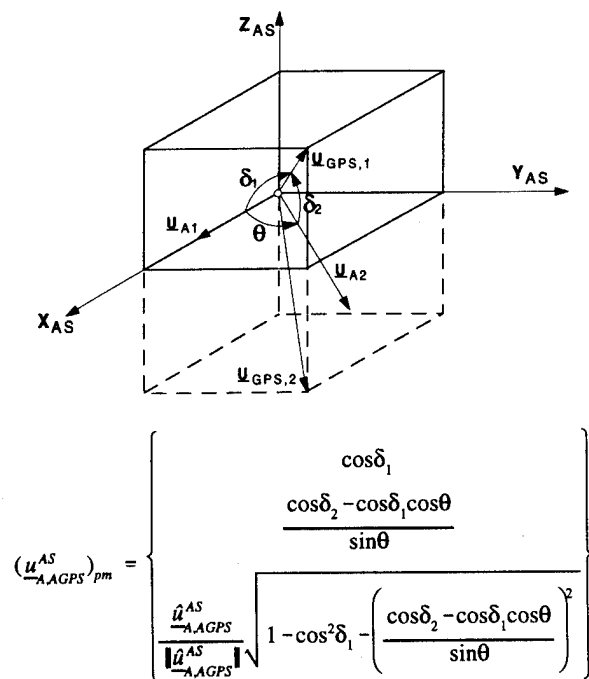


Figure 3: Computation of the pseudomeasurement on the LOS vector to a GPS satellite.

As indicated in section 2.2, two antennas are used in order to construct the GPS LOS vector. Once the pseudomeasurements in the angles formed by the GPS LOS vector and the user antenna boresights ($\delta_{pm,1}$) ($\delta_{pm,2}$) are computed, the pseudomeasurement on the GPS LOS vector in the "2 antenna sensor" reference frame (AS) is computed as indicated in Figure 3. Because of the lack of information in the azimuth angle around each of the antenna boresights, there are two possible solutions for the GPS LOS vector under computation, which are the two intersecting lines between the two antenna cones (Figure 3): the sign discrimination is performed by using the a-priori estimate of the GPS LOS vector computed by processing the on-board values of the user spacecraft

and GPS satellite position vectors and the a-priori estimate of the spacecraft attitude (Figure 3). The sign could be discriminated with a third antenna. However, it has been demonstrated (see section 5) that the concept of 2 antennas work properly, so a third antenna seems not needed (see section 6 for further considerations on a 3 antenna concept).

Finally, the pseudomeasurement on the GPS LOS vector expressed in the body-frame (\underline{u}_{AAGPS}^B) is computed by using the vector computed in the previous bullet and the rotation matrix between the "2 antenna sensor" reference frame and the body reference frame as follows

$$(\underline{u}_{AAGPS}^B)_{pm} = [L_{BAS}] (\underline{u}_{AAGPS}^{AS})_{pm}$$

This pseudomeasurement will be used for the estimation of the spacecraft attitude using the algorithm indicated in section 4.4.

4.4. Attitude estimation algorithm

The algorithm which used in the following for estimating the MetOp spacecraft attitude using GPS LOS vectors has been constructed on the basis of the attitude determination using vector observations stated in section 4.1 and the GPS LOS vector pseudomeasurement detailed in section 4.3. Details are provided in the following.

First, the rotation matrix between the body fixed frame and the inertial frame ($[L_{B,I}]$) is computed such that the following non-negative loss function is minimized

$$F([L_{B,I}]) \equiv \frac{1}{2} \sum_{i=1}^{i=n} a_i \| ((\underline{u}_{AAGPS}^B)_{pm})_i - [L_{B,I}] (\hat{\underline{u}}_{AAGPS}^I)_i \|^2$$

where, for each observable (i) a_i is the positive weights used for the loss function. Two values have been used: one which is common to all the observations

$$a_i = \frac{\lambda_0}{n}$$

n being the number of common satellites which are visible for both antennas, and an other value which depends on the geometry of the LOS vector and the boresights of both antennas as follows

$$a_i = \frac{\lambda_0 \sin^2 \left(\frac{\delta_1 + \delta_2}{2} \right)}{\sum_{i=1}^{i=n} a_i}$$

where δ_1 and δ_2 are defined in Figure 3. Moreover, $((\underline{u}_{AAGPS}^B)_{pm})_i$ is the pseudomeasurement on the LOS vector from the user spacecraft to the GPS satellite expressed in the body frame and $(\hat{\underline{u}}_{AAGPS}^I)_i$ is the foreseen value of the LOS vector from the user

spacecraft to the GPS satellite expressed in the inertial frame.

Then, the rotation matrix between the body fixed frame and the inertial frame is computed using the SVD as follows

$$[\hat{L}_{B,I}] \equiv [L_{B,I}]_{opt} = U_+ V_+^T$$

where U_+ and V_+ are proper orthogonal matrices (see section 4.1) of the SVD of the B matrix which is constructed as follows

$$B \equiv \sum_{i=1}^{i=n} a_i ((\underline{u}_{AAGPS}^B)_{pm})_i ((\hat{\underline{u}}_{AAGPS}^I)_i)^T$$

This is the simple scheme to obtain an estimate of the user spacecraft attitude. However, it has been found (see section 5.1) that, in case the initial knowledge on the spacecraft attitude is very poor, an iterative scheme is required. A-priori value of the rotation matrix is required for constructing the pseudomeasurement on the GPS LOS vector, hence, the iterated rotation matrix is computed by applying the scheme detailed in the previous paragraph a certain number of times (see section 5.1): the first iteration is performed with the a-priori knowledge of the spacecraft attitude, whereas the subsequent iterations are performed using the optimum rotation matrix obtained during the previous iteration.

5. PERFORMANCE ANALYSIS

5.1. Error sources contribution

In order to assess the performances of this SNR based attitude determination concept, first the effect of various error sources which might have an effect on the performances of this concept was assessed. The error sources which have been investigated are as follows: initial knowledge of the spacecraft attitude (30° 3σ in each Euler angle has been taken as typical value), antenna misalignment errors ($30 \mu\text{rad}$ 3σ knowledge error in each of the two angles have been taken as typical values), spacecraft position knowledge errors (an error of 300 m 3σ in each of the three components of the spacecraft position vector has been assumed) and SNR mismodelling errors (it has been assumed that the total SNR mismodelling error lumping together the common and the user antenna dependent terms comes from a gaussian distribution of 0.09 dB 3σ). Further analyses for different, more realistic, figures are presented in section 5.3.

Results show that this scheme based on GPS LOS vectors is able to estimate very accurately the attitude of the spacecraft even if the a-priori knowledge is very poor: for a-priori attitude knowledge errors of 30° (3σ) the concept estimates (in case no other errors are present) the spacecraft attitude with an accuracy of few microrad (less than $4 \mu\text{rad}$ at 3σ , Figure 4). Such good

performances are obtained using very small resources (in terms of CPU and memory load) even taking into account that a certain number of iterations are required for the large a-priori attitude knowledge errors under consideration:

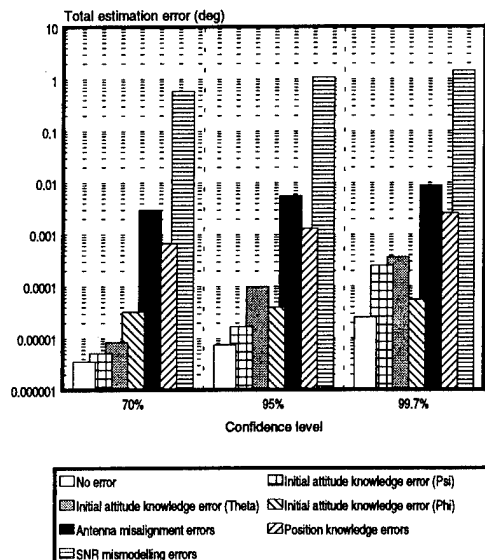


Figure 4: One-by-one error sources contribution to the total estimation error.

- For the single Euler angle performance analysis (maximum total a-priori attitude knowledge errors of up to 39° (3σ) are handled by the attitude determination scheme) only two iterations are required for convergence of the algorithm (further iterations do not vary the attitude estimate).
- However, when errors in the three Euler angles (each of them of 30° 3σ) are simultaneous, the attitude determination scheme should manage maximum total a-priori attitude knowledge errors of up to 49° . Three iterations are required. The effect of the number of iterations on the performance of the attitude determination concept based on GPS LOS vectors is shown in Figure 5: the improvement when going from one to three iterations is clear. No further improvement is obtained for a higher number of iterations.

The effect of the number of iterations is only important when taking into account a-priori attitude knowledge errors. The effect is negligible for the other error sources. In the following, three iterations have been chosen for the baseline attitude determination concept.

Antenna misalignment errors are obviously directly reflected in the performances of the attitude determination concept (Figure 4). On the other hand, the effect of the spacecraft position knowledge errors on the performances of the scheme is very small.

The performance driver for this attitude determination scheme is the SNR mismodelling error, as already said: the concept accuracy is of 1.449° (3σ) for a SNR mismodelling error of 0.09 dB (3σ). The influence of this error source is much higher than the others, hence, realistic figures for this SNR mismodelling error should be used. Little information is available without dedicated experiments, hence a sensitivity analysis has been performed (see section 5.3).

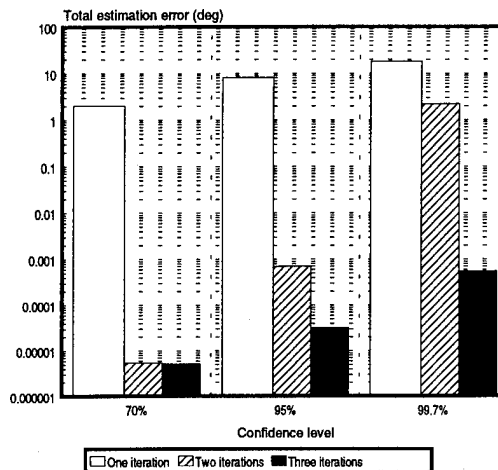


Figure 5: Effect of iterations on the concept performances.

The error in computing the angle between the GPS LOS vector and the antenna boresight is proportional to the error in the SNR with a coefficient which is a function of the inverse of the sine of such angle. Therefore SNR mismodelling errors are amplified for GPS LOS vectors close to the antenna boresight. Two different sets of weighting factor have been used: a constant weighting factor and a varying one (see section 4.4). Such factor is very important when SNR mismodelling errors are present: a 30% improvement has been obtained for the varying weighting scheme (for a 0.30 dB 99.7% confidence level SNR mismodelling error). In the following a varying weighting factor is used.

5.2. Sensitivity to antenna configuration

The influence of the antenna configuration, in terms of antennas orientation and angle between them, on the performances of the attitude determination concept based on GPS LOS vectors has been investigated for the typical values of the errors stated in previous section except for the SNR mismodelling error: 0.30 dB at 3σ has been assumed. Furthermore, the baseline concept previously selected and consisting of three iterations and varying weighting factors is used.

Different antenna configurations have been analyzed including: configurations in the vertical plane with

(configurations 1 to 7) and without (configurations 8 to 11) one antenna along the vertical and for different angles between antennas (10° , 20° , 30° , 45° , 60° , 90° , 10° , 20° , 30° and 90° for the eleven configurations respectively).

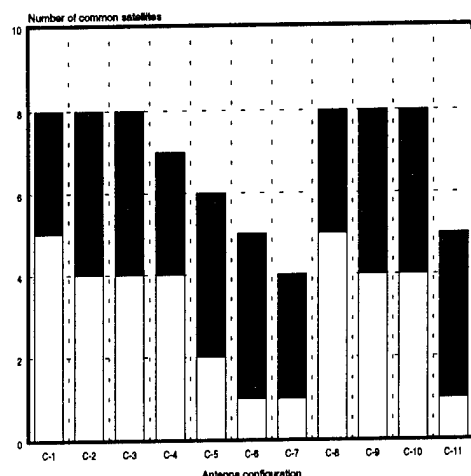


Figure 6: Influence of antenna configuration in the number of common visible satellites.

A minimum of two common visible GPS satellites to the two antennas is required in order to have full observability of the spacecraft attitude. The two antennas should form an angle lower than about 60° : for bigger separations the number of common GPS satellites is lower than two (Figure 6).

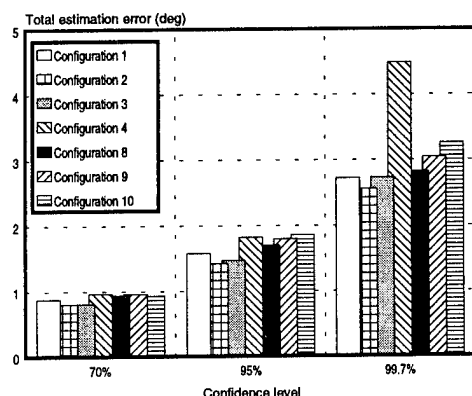


Figure 7: Performances of the attitude determination based on GPS LOS vectors for different antenna configurations.

The optimum antenna separation angle seems to be about 20° . However, the concept performances are not very sensitive to the antenna separation angle for small and moderate separation angles (i.e., for angles around 10° and 30°), whereas they are quite sensitive for large separation angles (e.g., bigger than 30°): the estimation error increases by about 6% when going from 20° to 30° separation angle and by about 60% when going

from 20° to 45° (Figure 7).

The optimum antenna orientation is with one antenna pointing to the zenith and the other in the plane perpendicular to the orbital plane, probably because this configuration is able to track a common set of GPS satellites which are more separated from the antenna boresights, so improving the performance as indicated above. The performance will be degraded when the spacecraft is far away from the nominal Earth pointing attitude: about a 20% performance degradation (99.7% confidence level) is found for a spacecraft attitude deviation of 10° from the Earth pointing orientation.

5.3. Nominal performance

The performance of the attitude determination concept based on GPS LOS vectors for the baseline concept selected in section 5.1, namely, three iterations and varying weighting factors is presented in Figure 8 for the nominal values for all the error sources: initial knowledge of the spacecraft attitude: 30° (3σ) in each Euler angle, antenna misalignment errors: $30\mu\text{rad}$ (3σ) knowledge error in each of the two angles, spacecraft position knowledge errors: 300 m (3σ) in each of the three components of the spacecraft position vector and SNR mismodelling error: 0.30 dB (3σ).

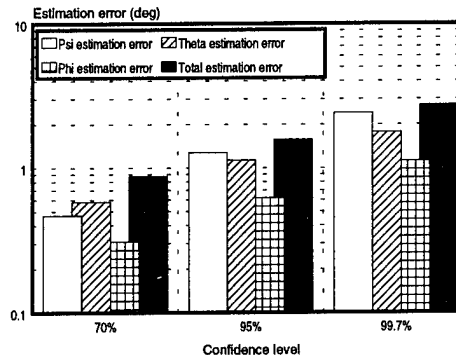


Figure 8: Nominal performances for the typical values of the errors under consideration.

For such a case the total estimation error is less than 3° (3σ) which should be compared to the about 38° (3σ) initial uncertainty assumed.

The antenna misalignment errors might be higher than those specified above due to the difficulty of aligning the canted antennas. A $300\mu\text{rad}$ (3σ) value might be more realistic.

A nominal value of 0.30 dB (3σ) has been used for SNR mismodelling. This figure is too optimistic taking into account that there are quite important uncertainties on the GPS transmitter power, GPS transmit antenna

gain pattern, ... i.e. on the mismodelling sources (values and stability over extended periods) common to the various antennas. In principle, one can solve this problem using the improved concept of three antennas outlined in section 6. On the other hand, further discrepancies might occur between the on-board and the actual values of the user antenna dependent terms, namely, G_r , L_a and T_s (see sections 4). For instance: the calibration of the antennas might be worst than assumed (about 0.5 dB for each antenna is realistic), in case the Earth gets into the FOV of one antenna important noise terms can appear, and finally the multipath might cause large mismatches between the expected SNR and the received one.

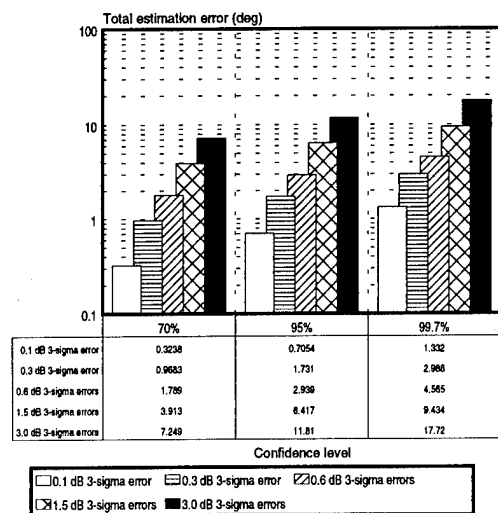


Figure 9: Sensitivity with respect to the SNR mismodelling errors (all other error sources included).

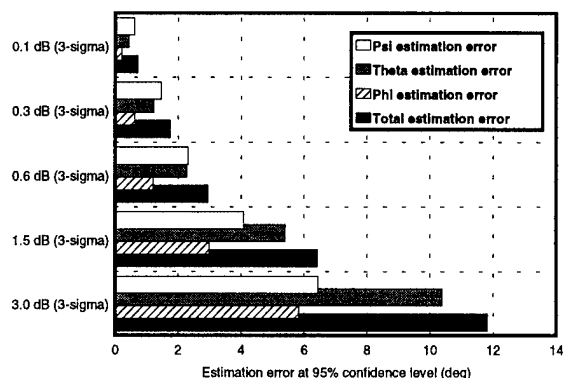


Figure 10: Sensitivity with respect to the SNR mismodelling errors (all other error sources included): estimation error components at a 95% confidence level.

Therefore, such an analysis is presented in the following where an antenna misalignment of 300 μ rad (3σ) and SNR mismodelling errors of 0.1 dB, 0.3 dB,

0.6 dB, 1.5 dB and 3.0 dB (3σ) have been used. As expected, the SNR mismodelling has a very important effect on the performance of this attitude determination scheme: the total angular estimation accuracy varies from 1.3° for a 0.1 dB 3σ SNR mismodelling up to 17.7° for the 3 dB mismodelling. Nevertheless, even in the worst SNR mismodelling case a quite important improvement is obtained from the initial 38° 3σ initial angular error assumed (Figure 10).

6. CONCLUSIONS

A simple, robust and reliable attitude determination scheme has been designed consisting of a simple estimation algorithm which processes some GPS line-of-sight (LOS) vectors constructed by using the SNR measurements from the common GPS satellites tracked by two GPS antennas with a separation angle of about 10° to 20° and with a nominal orientation such that one of the antennas is pointing to the zenith in the nominal Earth pointing spacecraft attitude. However, the SNR mismodelling is the critical driver for this concept.

The processing resources required by the designed attitude determination concept based on GPS LOS vectors are small: the selected algorithm is very fast and the memory load is very small. Using the SVD, the required FLOP are about 28000. This simple scheme might be further improved in terms of speed on memory load by using other algorithms for solving the Wahba's problem such as the Fast Optimal Attitude Matrix (FOAM) algorithm or the Polar Decomposition (PD) algorithm (see section 4.1), as about 60% of the total number of operations is spent in the singular value decomposition.

The designed scheme based on GPS LOS vectors provides an estimate of the full spacecraft attitude even if the a-priori knowledge is poor.

This simple scheme might be used for different purposes: as a stand-alone scheme for attitude determination during safe mode, as a complementary scheme for validation of the differential phase attitude determination during the safe mode (in case OFAR is required), as a complementary scheme for the initialization of the differential phase attitude determination in any attitude mode or as a complementary scheme for supporting the failure detection and identification.

Depending on the intended application, the concept might be improved (without increasing the complexity of the processing algorithm) with respect to SNR mismodelling errors by using a third antenna in two different ways. First, the influence of the common SNR mismodelling term could be cancelled by processing the information from the third antenna: with three sources

of information one would be able to determine the two angles of the GPS LOS vector (as above) as well as the common SNR mismodelling term. Second, the influence of the user antenna dependent SNR mismodelling term can be reduced by constructing the pseudomeasurement on the GPS LOS vector using the information from the three antennas: the accuracy of the LOS vector pseudomeasurement would be improved by weighting properly the redundant information from the three antennas.

7. REFERENCES

- [1] Serrano Martínez, J.B.: *Spacecraft Attitude Rate Measurement Systems without Gyros. Critical Review of gyroless ARMS Algorithms and Sensors (WP-31)*. ESTEC Contract No. 9982/92/NL/JG (Work Order No. 6). GARMS-TN-GMV-02, GMVSA 2032/94. Issue 1. March 24, 1994.
- [2] Legido, J.M. and Martínez-Olague, M.A.: *Tracking of Geostationary Satellites with GPS, GPS-GEOTRACK, Phases 1 & 2 Final Report*. Doc. No. GMVSA 2070/94. Issue 1. July 1994.
- [3] Czopek, F.M. and Shollenberger, S.: *Description and Performance of the GPS Block I and II L-Band Antenna and Link Budget*. Proceedings of the ION GPS-92, Fifth International Technical Meeting of the Satellite Division of the Institute of Navigation, Albuquerque, New Mexico, USA, September 1992.
- [4] Micro Pulse GPS antennas specification (commercial information).
- [5] Bar-Itzhack, I.Y. and Oshman, Y.: *Attitude Determination from Vector Observations: Quaternion Estimation*. IEEE Transactions on Aerospace and Electronic Systems, Vol. AES-21, January 1985, pp. 128-135.
- [6] Markley, F.L.: *Attitude Determination Using Vector Observations and the Singular Value Decomposition*. The Journal of the Astronautical Sciences, Vol. 36, No. 3, July-September 1988, pp. 245-258.
- [7] Bar-Itzhack, I.Y.: *Polar Decomposition for Attitude Determination from Vector Observations*. Flight Mechanics/Estimation Theory Symposium 1992. NASA Conference Publication 3186, pp. 243-258, 1993.
- [8] Shuster, M.D. and Oh, S.D.: *Three-Axis Attitude Determination from Vector Observations*. Journal of Guidance and Control, Vol. 4, No. 1, January-February 1981, pp 70-77.
- [9] Markley, F.L.: *Attitude Determination Using Vector Observations: A fast Optimal Matrix Algorithm*. The Journal of the Astronautical Sciences, Vol. 41, No. 2, April-June 1993, pp. 261-280.



Session B6

Integrated Systems

Chair:

Mr. Jeff Geier

Motorola

Co-Chair:

Dr. Manfred Haverland

Aerodata

An Artificially Intelligent Vehicle Highway System

Vidal Ashkenazi, Terry Moore, Mark Dumville, David Lowe, and Maria Tsakiri
The University of Nottingham

BIOGRAPHIES

Vidal Ashkenazi, Director of the IESSG at the University of Nottingham, has a DPhil and a DSc in Physical Sciences from Oxford University. He has supervised over 40 doctorate students, and acted as a Consultant to many government, commercial and manufacturing companies. He is a Fellow of the Royal Institute of Navigation.

Terry Moore is a Lecturer of the IESSG at the University of Nottingham. He holds a BSc degree in Civil Engineering and a PhD in Space Geodesy, both from the University of Nottingham, and is a Fellow of the Royal Institute of Navigation. He is currently the Secretary of the United Kingdom Civil Satellite Navigation Group of the RIN.

Mark Dumville is a Research Assistant of the IESSG at the University of Nottingham. He holds a BEng in Civil Engineering and a PhD in Space Geodesy. He is software manager at the IESSG.

David Lowe is a Senior Research Assistant at the IESSG specialising in sensor integration. He has worked on numerous projects involving sensor integration. Most notably are those projects involving the monitoring of mean sea level using bouys and GPS-assisted helicopter photogrammetry.

Miss Maria Tsakiri graduated from the National Technical University of Athens, Greece, with a BEng in Surveying Engineering. She is currently studying for a PhD at the IESSG in the field of GPS applications for vehicle navigation. She is a Student Member of the Royal Institute of Navigation.

ABSTRACT

Conditions for land navigation are among the most severe in the urban environment, where there is no low cost positioning system capable of continuously providing the necessary high accuracy positional information. The Global Positioning System (GPS) is

having a profound impact on the development of automatic vehicle location systems but suffers from a number of problems. A hybrid and robust GPS-based system is required to offer continuous and accurate positioning. This study has investigated the integration of differential GPS measurements with a digital odometer, a flux-gate compass and tilt sensors to give a low cost 3-dimensional positional system for the vehicle navigation.

In contrast to the traditional method of sensor integration using Kalman Filtering techniques, a novel approach has been adopted in the use of artificial intelligence, and in particular, neural computing techniques. The integrated neural architecture consists of a stand-alone neural network processing model augmented with a dead reckoning (DR) position fix algorithm. The neural network model accepts sensor measurements as input from which it computes an optimised position fix, subsequently used to calibrate the sensors for systematic drifts.

Studies have been performed to investigate this novel approach, the results of the study are compared against those achieved using the conventional kalman filtering techniques of sensor integration.

INTRODUCTION

GPS and its use in the worldwide IVHS movement is at the centre of an expanding mobile information society. Automatic Vehicle Location (AVL) systems that incorporate GPS technology are more robust and cost-competitive with the purely land-based systems, such as beacons or INS. A limitation of a GPS only AVL system is that satellite signals may be temporarily blocked while a vehicle is in 'urban canyons', tree-covered areas and tunnels. In order to operate with a higher degree of reliability the GPS component must be integrated with other sensors. In this research and AVL system integrating GPS with dead-reckoning (DR) sensors has been investigated.

Integration of GPS with DR has a major potential in AVL systems, because such a system can alleviate most of the shortcomings of each technology. Both systems use complementary techniques and are capable of providing accurate and continuous information by using relatively low cost hardware. In this project, a DR system comprising of an in-house built odometer, a fluxgate compass and tilt sensors was integrated with GPS using neural computing techniques.

FIELD TRIALS

The vehicle tests involved the testing of the integrated GPS/DR system performance in the urban environment. The route to the city centre of Nottingham consisted of a mix of residential, secondary and major freeway roads, whereas in the city centre the routes included clear routes, tree covered segments and built-up regions.

In all tests the differential GPS concept was used. The main reference receiver was positioned over a known geodetic point at the University campus and the second roving antenna was mounted on a roof rack, specifically made for the trials, on top of the van (Figure 1). Prior to all tests, an initialisation was performed whereby the roving antenna was set up on a tripod for approximately 10 minutes, in order to facilitate the use of the 'on-the-fly' software algorithms, that provided the truth. During the tests, no attention was paid to the satellite geometry, as this is not the situation in real vehicle navigation conditions. Therefore the DOP values varied between low (2) and high (7) values, where only 4 satellites were observed. The number of satellites observed in the city centre area varied from 9 to none. Furthermore, the environment that the receivers were situated, was not 'multipath-free'. The reference antenna was placed on a roof around which there were some surfaces that were likely to cause multipath effects. The roving antenna during the tests on the runway was still affected by multipath caused from nearby low structures, and in the city centre multipath was caused by buildings, trees, and high sided vehicles.

SENSOR INTEGRATION

The auxiliary sensors for the DR system consisted of two Lucas Schaevitz tilt sensors orthogonally mounted, a Burmarc fluxgate compass and an odometer, designed and built *in-house* and controlled using a modified 486 based PC. The schematic for the integration is given in Figure 2.



Figure 1
Sensor Configuration

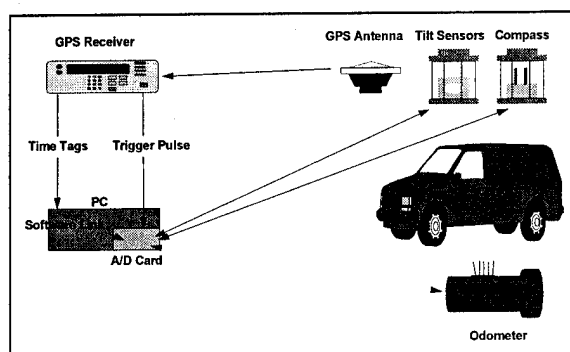


Figure 2
Sensor Integration

The centre of the GPS/DR integration was a 486 computer, it contained a 16 channel 12 bit Analogue to Digital (A/D) card. The tilt sensors and fluxgate compass all provided analogue output which enabled direct connection to the A/D card. Auxiliary ports on the A/D card allowed the connection of the odometer to a built in pulse counter, with a resolution of 65535 pulses per second. The calibration of the tilt sensors and fluxgate compass was carried out prior to delivery, and the constants supplied by the manufacturer were used in the logging software. The calibration of the odometer was a little more problematical, and involved the deduction of all the different gear ratios between the rear drive wheels and the speedometer drive bush. Once these constants had been obtained, together with the effective circumference of the rear wheels, the conversion constant for the odometer could be calculated and incorporated into the logging software.

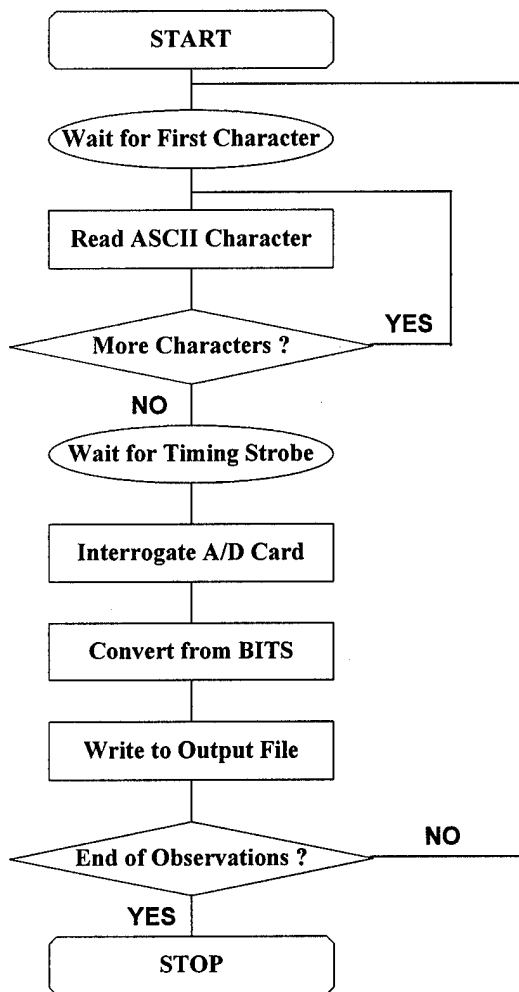


Figure 3
Measurement Integration

To control the timing of the auxiliary data, a 1 PPS (Pulse Per Second) timing strobe was connected between the GPS receiver and a digital input trigger on the A/D card. This enabled the logging software to wait until the exact time that the GPS data was logged before interrogating the auxiliary sensors. The GPS receiver also provided the UTC (Universal Time Coordinated) time tags in an ASCII format, these time tags described the next arriving timing strobe pulse. The process can be shown in a simple flow diagram (Figure 3).

The logging software was written in ANSI standard C to enable quick and easy communications with the GPS receiver and updating. Current communications protocols only enable data transfer at 4800 baud which results in only the time tags being logged by the PC. Updates in the near future will allow faster communications which should enable the PC to log the actual GPS observations in addition to the time tags and remove the restriction of the on-board memory of the GPS receiver. Once this is achieved it is a small step to insert a radio link, at either end of the system, to enable data transfer. This could result in near real time vehicle

location for the vehicle or near real time vehicle tracking at a base location.

KALMAN FILTER APPROACH

Kalman filtering is a *time-variant* filtering process (i.e., it can process parameters that change with time). It can deduce the minimum error estimate of the *state* (the vector of the quantities that have to be solved) of a linear system in real time, by using the previous and current measurements at the time of interest. This technique has to take into account the:

- knowledge of the system dynamics and the measurement dynamics,
- assumed statistics of system noise and measurement errors, and
- initial conditions of the system.

The Kalman filter is based on the *a-priori* knowledge of the system state vector and as in any *recursive* procedure, it utilises all the measurements sequentially, as they become available. In a recursive processing scheme, therefore, the results of the previous step are utilised to obtain the desired results for the current step. The system state vector for a dynamic system is composed of any set of quantities that are sufficient to describe completely the unforced motion of that system.

The filter processes the measurement data given knowledge of a system model and any measurement that possesses the same behaviour (for example, linear behaviour) as the statistical models which characterises the system, the measurement errors and initial condition information.

Therefore, at an initial epoch $k = 0$, the quantities that must be known before estimation can begin are:

- the *system model*, which describes how the system state vector varies with time,
- the *measurement model*, which relates the observables with the unknown states of the system, as well as, some noise errors due to measurement uncertainties, and
- the *initial* conditions of the system state vector.

Centralised Filter

This type of architecture uses one central main filter, as can be seen in Figure 4. In the centralised filter the states of the entire system are defined in a single global state vector with a corresponding global model of the system error state. Therefore, only a one-step procedure is followed where a global optimal estimate

is computed utilising all the available data from all the individual local sensors.

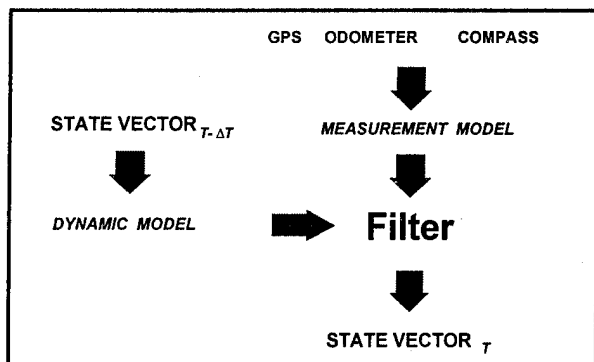


Figure 4
Centralised Kalman Filter

The GPS raw measurements and the measurements from the other sensors are direct input to the main filter. For this reason the filter can directly update the measurements and model both the GPS and the DR sensors. When GPS fails, the sensors can still provide full navigation capability by using the latest calibration. Furthermore, this filter can use incomplete GPS measurements (e.g. less than four satellites), by constraining parameters, such as the height.

A centralised filter, in general, is optimal in the sense that it uses all the available information in a collective manner considering the global dynamics of the system. There is, however, a lack of robustness in that if one of the DR system's sensors fails and there is no GPS information, the navigation capability is degraded. In this research, a centralised filter has been used to integrate GPS and DR sensors.

The centralised kalman filter was used to obtain optimised position fixes for the moving vehicle. The positions were used as the *truth* for assessing the performance of the neural and hybrid networks in their role as adaptive integration filters.

ADAPTIVE NEURAL NETWORKS

Neural networks are powerful computing devices. They can process information more readily than traditional computer systems. This is due to their highly parallel architecture inspired by the structure of the brain. Applications and research into the use of neural networks have evolved from their ability to understand complex relationships and hidden patterns within large data sets. Neural networks are now becoming an accepted tool for signal and image processing in the scientific communities of engineering and medicine (Lippman, 1987).

Unlike expert systems, which are computer structures based on sets of rules, neural networks,

- do not require rules to learn
- do not require large amounts of memory
- possess no database.

In contrast to expert systems, they are adaptive processing models that are trained to perform a specific task and to provide a specific response. Neural networks are robust computational structures, tolerant of faults and have the advantage over traditional computer systems in that they can respond to incomplete and/or noisy data sets (Stonham, 1994). This is in contrast to conventional software which requires careful and correct programming rules and a specified input format (Powell, 1994).

Neural network structures will typically incorporate a large number of small processing *units*, termed *neurons*. A network will be subjected to example data and will adjust its internal structure, between neurons, in accordance to the problem presented. On some occasions *supervised training* may be used. In such a case the network will produce an output when presented with some form of input data. According to the discrepancy between the network's output value(s) and the desired target output value(s), the network will internally adjust the processing structure. This adjustment ensures that when facing the same problem, the network error will be reduced. *Unsupervised learning* involves presenting only input data to a network. The neural network is used to identify patterns within the data sets and form colonies (classes) containing input sets possessing common features. Unsupervised learning is typically used in classification problems.

An Artificial Neural Network (ANN) behaves in similar a manner to its natural counterpart, the biological neural network. ANNs are required to perform tasks and depending on the outcome of the task they adjust their internal weighting structure, according to success or failure. This constitutes a basic form of learning (i.e., trial and error). Using this approach, when a problem, which has previously been shown to the network is encountered again, the network will show an improvement. They are extremely useful in detecting trends within data sets that are not immediately apparent even to the most experienced analysts.

Neural Network Architecture

Figure 5 shows the *topology* of a Multi-Layer Perceptron (MLP). This neural network is a *connectionist* model - where all units on all layers are fully connected. It consists of two processing layers; a hidden layer and an output layer plus input. The input nodes are not considered as active processing units, they are used as a starting point for the distribution of

the input signals to the hidden layer via the internal weighted connections.

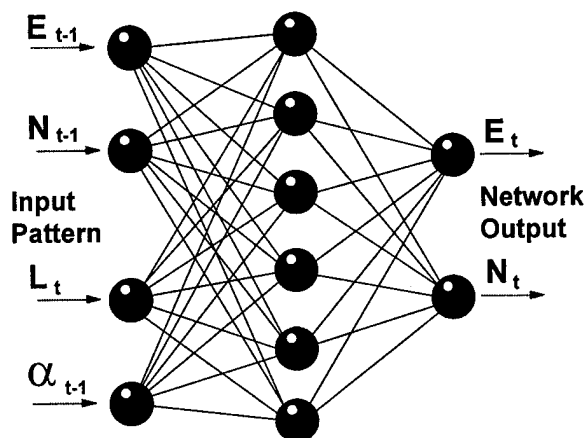


Figure 5
The Multi-Layer Perceptron

Units within the hidden layer act as feature detectors, finding common patterns that exist within the data. The output layer is also an active layer and is used to link features within the hidden layer thereby forming the overall network response.

Feed-Forward Back-Error Propagation

A neural network differs from conventional computational algorithms in that the connectionist architecture between the processing units provides the ability for the network to adapt and learn. A neural network is not programmable it is trained through example. It does not require a knowledge of relationships between the input variables, any logical associations that exist are learnt through repetitive training.

The network is trained using example patterns selected from within the larger data set where the input and corresponding output is known to a predefined level of precision. An example pattern, from the set, is presented at input where it is then fanned-out and propagated through the network via the internal connections. All connections within the network are assigned a weight (*connection strength*). The input signal on a connection is modified according to the strength of that connection and passed onto the hidden layer of processing units. The units gather the weighted signals, apply a transfer function and are subsequently fanned-out and propagated along the hidden-output weighted connections leading onto the output layer. The output from the network is compared with the corresponding known output of the training pattern. The discrepancy between the two values is termed the network error. This value is used to correct the weighted connections within the network in a manner as to reduce the discrepancy the next time that input pattern is presented. This routine is repeated for every pattern within the training data set and is then repeated

continuously until the network has shown to learn the function. This is an iterative process and often takes many thousands of iterations until a stable solution is achieved.

The network error can be seen to be directly associated with the learning of the system. Another variable present in the learning process is the learning term. This controls the rate of learning. The term has no specific value, it is generally in the range 0.001 to 0.999 and can only be determined through rigorous experimentation. To assist the system converge to a stable global minima the network learning process can benefit from the incorporation of a momentum rate. This behaves as a low pass filter effectively smoothing the learning process. It further increases the speed of convergence helping avoid the occurrence of the solution being lodged in a local false solution.

Neural Network Design

In order to decide upon the best neural network topology for the integration task, several design tests were required. They included tests for the number of hidden layer processing units, tests for determining the correct learning term and tests for deciding upon the correct choice for the momentum rate. The results of the tests produced a 2-layer network with a learning term of 0.4 and a momentum rate of 0.6. This network is regarded as the *optimised* neural network for the training data.

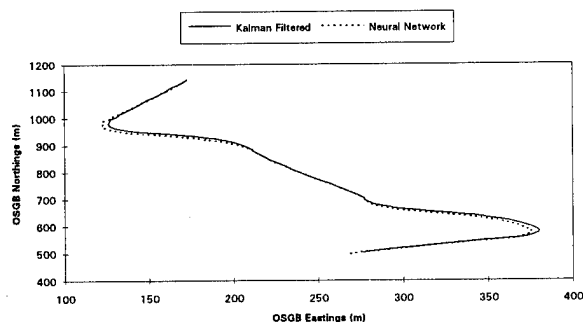


Figure 6
Neural Network Trajectory

The trained neural network produced the integrated trajectory as shown in figure 6. Also shown within the figure is the trajectory produced using the centralised kalman filter. The two paths are closely related. The vehicle's path starts at the top of the graph and winds itself to the bottom. Apparent within the figure, particularly at the bends, are the large differences between the two trajectories. As a means of investigating this further, figures 7 and 8 present the component differences in the Easting and Northing directions.

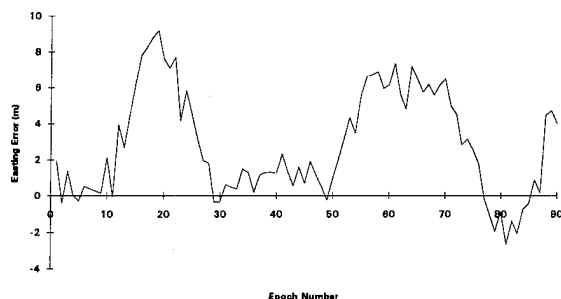


Figure 7
Neural Network Eastings Error

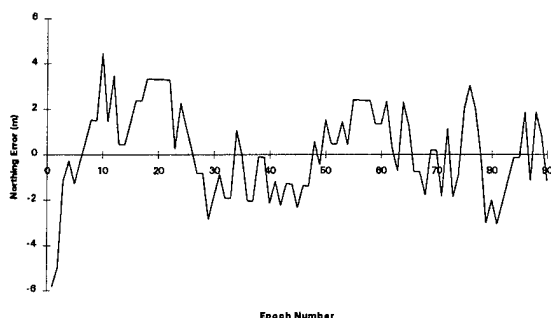


Figure 8
Neural Network Northings Error

The systematic nature of the offsets is clear when examining the individual graphs, with the Easting direction being more prone to the effects of periodic fluctuating drifts. Similar patterns were observed by *Dumville and Tsakiri (1994)* using an independent data set. Their study indicated the differences between a neural network's predicted position and the true GPS position increase with a periodic pattern as the length of integration period increases.

This is a clear problem with the use of neural networks for integration filters. They have been shown to be capable of performing the integration of the GPS and DR measurements but for limited periods only. Some factors which hamper their ability are listed below.

Problems associated with Neural Networks

Rumelhart et al. (1986) state the aim of the learning procedure "is to find a set of weights to ensure that for each input vector the output vector produced by the network is the same (or sufficiently close to) the desired output vector". To find the correct set of weights involves searching many hypotheses in an iterative manner. It is not possible to search the entire range due to constraints and many may lead to false solutions. This is just one of many problems associated with using neural networks as universal function approximations.

i) False Minima

A major factor affecting the correct use of a neural network is the problem associated with the *false well*

syndrome (Dayhoff, 1990). This is a local minima of the solution space. The network is trained, as previously mentioned, with a set of training patterns. The network adjusts the weights to minimise the difference between the desired target value and the network output. This is achieved through the use of a learning rule. However, there are occurrences when a neural network minimises the error for only a limited local region instead of for the general global case resulting in the solution being lodged in a false minima.

ii) Typical Data

Having a neural network trained to be a function approximator or an interpolator can only provide as good a result as the data which is presented in the training set. The training data must be typical of the values to be expected in the general scenario, and must cover the complete range of values to be expected.

iii) Learning Time

With computer technology advancing at such a rapid rate the problem of computational time is decreasing. The network must, nevertheless, learn the function through experimentation. There are no correct values for how many layers, how many units per layer, the learning term etc. The architecture of the network is left to trial and error and the overall decision is made by the operator.

To be taught to approximate a function requires each pattern within the training set to be presented to the network. The network feeds the input patterns through the network to produce the output pattern. This value is compared to the target value. Any differences between the output and the desired output is distributed through the network by adjusting the weight values in order to reduce the error. The process is repeated for each input pattern within the training set and the whole procedure is continually repeated until the network is producing a sufficiently small error. Therefore the network design stage, the stage when various combinations of number of layers, units/layer and different learning terms are being tested, is computer intensive and, hence, very time consuming.

iv) Hard Learning

A further problem can arise when continuously presenting the network with the training data in that the network can *hard learn* the function (*Minsky and Papert, 1969*). When a neural network *hard learns* a function it provides the correct output for the training data but cannot be used for a more general, larger population of data patterns.

v) Correct Input Terms

To find a relationship within the data there must be a relationship in existence. The neural network must be presented with the correct input signals to generate the desired output. If the input vector does not contain all of

the possible input variables for the function, an imperfect approximation will result. If there are no patterns due to incorrect input terms the network will be unable to find any relationships.

vi) Hidden Function

When a relationship has been established through rigorous experimentation, the network can be used to generate output for any given input that was not contained within the training data. The relationship learnt by the network is nevertheless hidden within the weight matrix. The only indication of what the function may consist of is through examining the weights of the connections and the state of the processing units. From this information the major contributing input signals and combinations of signals can be deduced but it is difficult to convert them into logical terms suitable for implementation as a series of pure mathematical expressions.

HYBRID NETWORKS

A hybrid network is a network whose architecture consists of two or more separate processing structures. Hybrid neural networks consist of a neural network augmented with another processing structure which can be included within the system running parallel to, or in series with, the neural network.

The use of a hybrid network for sensor integration allows the process to benefit from the advantages of the individual processes, and to a certain extent become tolerant of their drawbacks. In addition to providing a more precise integration system, the hybrid architecture is *highly parallel* and ideally suited to parallel processing producing a highly effective and computationally efficient system (Burniston, 1994).

Algorithms have been developed that combine programmed rules (similar to an expert system) with iterative learning in neural networks. *Growth algorithms* have been developed which dynamically allocate additional hidden layers depending upon the complexity of the problem. This approach is an example of a hybrid network that adapts its topology based on decision rules used in conjunction with the network learning process. This algorithm has been shown to be useful in generalising the function to be learnt (Nadal, 1989).

Pre-processing techniques (e.g., data sorting, sampling and filtering) can also be classified as components of a hybrid system; i.e., two or more processes working sequentially to produce the desired result. These techniques have been employed in studies to partly classify patterns prior to the neural network (Kozoto and De Wilde, 1991). The main advantage is reducing the time taken to train the network. Within this kind of

hybrid network, the input patterns have been pre-processed, thus, the neural network is provided with filtered data. This reduces the number of tasks the network is required to perform and results in reduced training times. A reduction in the time taken to train the network is, nonetheless, at the expense of additional pre-processing filtering algorithms.

Function Approximation using Hybrid Networks

The technique adopted for the integration process is similar to that presented by Bengio *et al.* (1992). Hidden Markov Models have a proven success in the modelling of the temporal structure of speech, whereas the artificial neural network (and in particular the multi-layer perceptron) has a proven success in continuous function approximation. The system used by Bengio *et al.* (*ibid*) combines the advantages of the two independent techniques. A similar approach was used by Burniston (1994), consisting of a simple *rule-based* model to approximate the speech pattern. The multi-layer perceptron neural network was then used to identify and model the peculiarities and fine detail of the speech. This form of network construction removes the requirement for the network to learn the complete function. This allows the neural network module to focus its ability on recognising the patterns which exist in the difference between the rule-based estimate and the true GPS coordinates of the training patterns. This is achieved in a learning process similar to that used in conventional neural network training algorithms (e.g. Back-error propagation).

Hybrid Network Design

The hybrid network is required to learn a different function to that learnt by the stand-alone neural network. From the exterior of the hybrid network there is no evident change of architecture. The input and output patterns are the same as those used for the stand-alone neural network. However, internally the architecture of the two differ significantly. The neural network module of the hybrid network is used to provide corrections to the estimated coordinates produced from the rule-base that operates in parallel to the neural network module. The neural network performs a different task to that previously studied, a different integration function is required, and therefore a new topology is required. The new architecture is illustrated in figure 9.

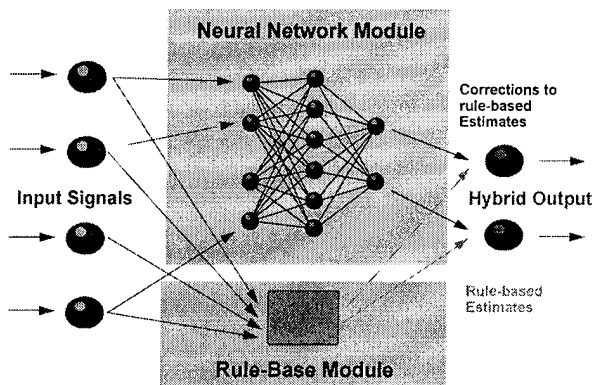


Figure 9
Hybrid Network Configuration

Tests were performed to decide upon the new topology and values for the new network parameters within the neural network module of the hybrid model. This included tests for the number of hidden layer units, the learning term and the momentum rate.

The first test was to decide on the topology of the processing model. The neural network module has the same four inputs as the stand-alone model, namely the GPS E,N coordinates, a compass bearing and an odometer distance measurement (figure 9). The output layer consists of the same two outputs. However, for this network, the output units do not provide the predicted coordinates, rather because of the hybrid structure, they provide *corrections* to the rule-base estimated coordinates.

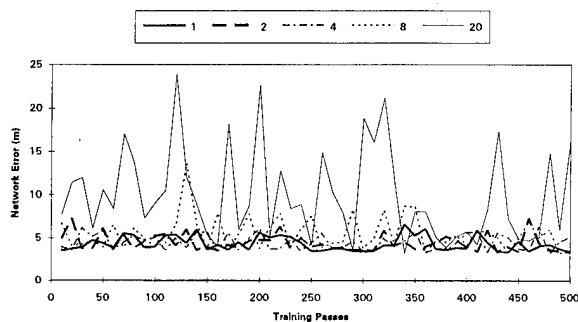


Figure 10
Hidden Layer Size Test Results

Figure 10 shows the effect of altering the number of the hidden layer processing units. From the figure it is evident that four out of the five curves are highly correlated, possessing very similar characteristics (apart from the noisy curve possessing 20 hidden units). What is apparent from the figure is that the final result is approximately the same for all curves *independent* of the number of hidden layer units. Therefore, the test shows that a hybrid network, used in this case for sensor integration, requires fewer processing units than a stand-alone network. This property of hybrid networks was also concluded by *Burniston (1994)*, for the use of hybrid networks in speech approximation.

Hybrid Network Learning

The learning characteristics of a hybrid network are significantly different to those of a stand-alone neural network. Three learning curves are presented in Figure 11 of which two are from neural networks and the third from a hybrid network. The hybrid network curve, because of the inclusion of the rule-base estimates, never has the presence of large errors. The rule-base produces estimates for the position close to the truth so that the hybrid training process is fast and smooth to reach an acceptable level of precision. The second curve, that of a neural network, starts with a network error off the displayed scale (approximately 320 m) but is soon to reduce to a stable value of around 30 m. The topology associated with this network is the same as that used in the previous hybrid test. This demonstrates that different topologies of network are required whether the problem is modelled using a stand-alone network or a hybrid network. Finally, the third curve is associated with a stand-alone neural network whose topology has been optimised for the integration task (ie the results of the design tests outlined earlier, 6 hidden units, 0.4 learning term and 0.6 momentum rate). The curve achieves the same the level of precision as the hybrid network, however, it does take 1200 training passes to do so as compared to only a few for the hybrid network.

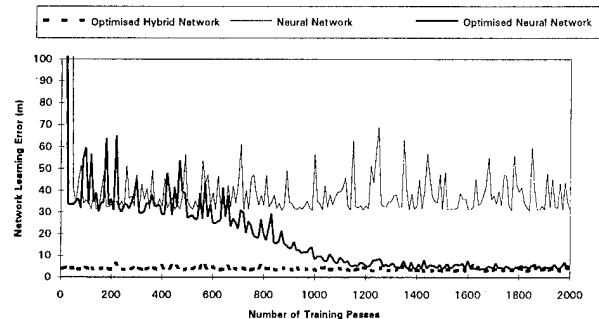


Figure 11
Hybrid Network Learning

Hybrid Network Performance

The results of the design tests for the hybrid network yielded a topology consisting of only a single processing unit in hidden layer, a learning term of 0.1 and a momentum term of 0.9. This set of values is not as critical as those of the stand-alone neural network. The design tests revealed that any number of hidden layer units, ranging from 1 to 10 will produce the same integration results.

The trained hybrid network behaving as the integration function produced the trajectory shown in figure 12. The two paths (ie the kalman filtered positions and the hybrid network positions) have stronger correlation than the previous neural network results.

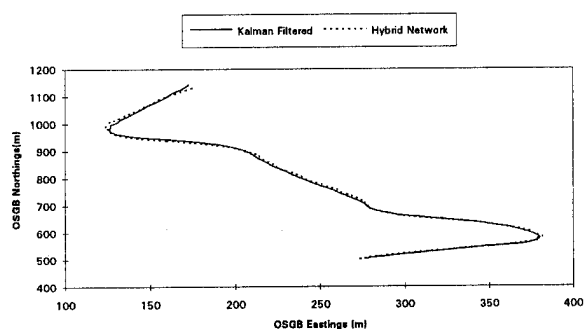


Figure 12
Hybrid Network Trajectory

There are slight discrepancies between the two curves during the initial epochs of positional data. This can be attributed to the initialisation of the sensors onboard the vehicle. What is evident is that as the test continues the paths approach one another. Again the two components, namely the Easting and Northing components, have been separated and presented in figures 11 and 12. In contrast to figures 7 and 8 the graphs begin with quite large errors but as the length of trajectory increases the differences between the kalman filtered positions and the hybrid network positions reduce until after 90 epochs their differences are at the 2 m level.

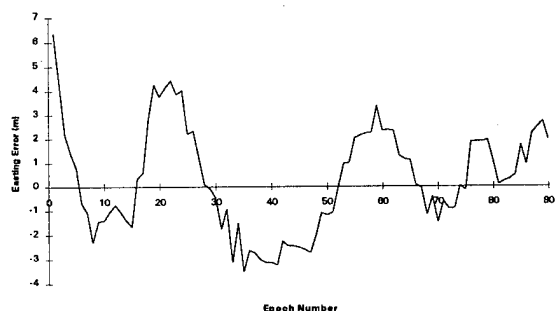


Figure 14
Hybrid Network Eastings Error

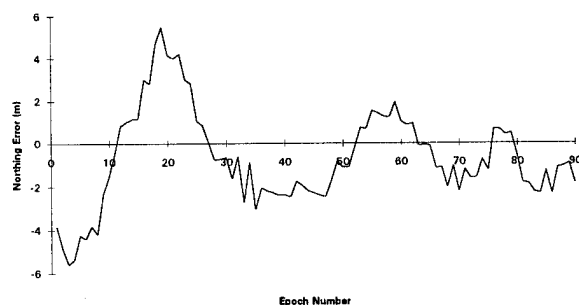


Figure 15
Hybrid Network Northings Error

Robustness of Hybrid and Neural networks

Considering the hardware implementation of neural/hybrid networks one feature cannot be surpassed

by the conventional kalman filtering algorithms, that is the high parallelism of the neural structure. As an example of the tolerance of a hybrid network to faults a simple test was performed. A trained hybrid network consisting of 8 hidden layer processing units had its weights altered and the effects on the positions were noted. On each occasion a connection was selected at random and its weight was set to zero. Thus simulating a broken connection. The results are presented in Table 1.

Number of Broken Connections	Kalman - Hybrid RMSE (m)
1	3.4
2	3.4
3	3.5
4	20.7

Table 1
Robustness of Hybrid Networks

The results in Table 1 conclude the ability of neural/hybrid networks to perform on faulty data or even with a faulty hardware system. Both of which ought to be considered when examining suitable filters for the real-time integration of navigation sensors.

CONCLUSIONS

The hybrid network architecture has been shown capable of integrating the GPS observations with the DR measurements to a level of precision comparable to the conventional method of kalman filtering.

In contrast to the stand-alone neural network integration filter, the performance of the hybrid network is far less dependent upon the network's topology and choice of its learning term and momentum rate. The network learning curve is also far smoother than those obtained using neural networks and the desired level of precision is achieved much faster (10's of passes as opposed to 1000's of passes with a neural network).

Overall, the hybrid network offers faster training speeds and processing speeds than a neural network. However, this enhanced learning performance is at the expense of having to perform additional rule-based computations. As long as the rule-base is kept to simple operations to provide the estimates then the advantages gained from the use of a hybrid network far outweighs the slight additional computational demand of the network.

ACKNOWLEDGEMENTS

Thanks are due to numerous staff members and researchers at both the IESSG and the Parallel

Processing Specialist Group (PPSG) for their ideas and inputs into this study.

REFERENCES

Bengio, Y, De Mori, R, Flammia, G and Kompe, R, *Global Optimisation of a Neural Network-Hidden Markov Model Hybrid*, IEEE Transactions on Neural Networks, Vol 3, No 2, March 1992.

Burniston, J D, Integrated Neural Network/Rule-Based Architecture for Continuous Function Approximation, PhD Thesis, Department of Electrical and Electronic Engineering, The University of Nottingham, 1994.

Dumville M and Tsakiri M, *An Adaptive Filter for Land Navigation using Neural Computing*, Proc. of ION GPS-94, Salt Lake City, USA, September 1994.

Kozato, F and De Wilde, P H, *A Probablistic Rule-based System in Artificial Neural Networks*, Proc of 2nd Int. Conf. on Artificial Neural Networks, pp153-157, 1991.

Lippman, R. P., *An Introduction to Computing with Neural Networks.*, IEEE ASSP Magazine, April 1987.

Nadal, J, *Study of a Growth Algorithm for a Feed-Forward Network*, Int. Journal of Neural Systems, Vol. 1, No. 1, pp55-60, 1989.

Powell, J. A., *Preface*, Proceedings of Neural Networks, Neuro-fuzzy and other Learning Systems for Engineering Applications and Research, London, United Kingdom, May 1994

Rumelhart, D. E., Hinton, G. E., and Williams, R. J., *Learning Representations by Back Propagating Errors.*, Nature Vol 323, 9 October 1986.

Stonham T J, *Neural Networks - How they Work - Their Strengths and Weaknesses*, Proc. of Neural Networks, Neuro-Fuzzy and Other Learning Systems for Engineering Application and Research, Information Technology Awareness in Engineering, EPSRC, April 1994.

Widrow, B., and Hoff, M., 1960. *Adaptive switching circuits*, 1960 IRE WESCON Convention Record, New York: Institute of Radio Engineers.

Making the Best with GPS in Car Applications

Ralph Moussa
Renault

BIOGRAPHY

R. Moussa is working as a project manager for RENAULT Research Division, since October 1992. He has an electronic engineer degree. His experience in GPS began in 1988, as he was working on the lack of integrity of the GPS in aeronautical applications. Now he is involved in the integration of car applications.

ABSTRACT

Since several years, European car manufacturers have done common work in order to improve safety and efficiency of transports. This was the goal of the PROMETHEUS program (PROgram for an European Traffic with Highest Efficiency and Unprecedented Safety). Among necessary technologies, the statement was made that a lot of systems were relying on the ability to localize vehicles correctly, it means with sufficient precision and availability for the aimed application.

First steps consisted in examining existing localization systems like Loran-C, Syledis and map-matching technique. As GPS became reasonable for car applications from the economic point of view, some projects have been launched to evaluate the ability to satisfy the technical requirements.

RENAULT and PSA have been involved in two studies with French electronic suppliers, with the following goals:

- to develop the algorithms taking the best advantage of GPS (natural or differential), hybridized with low cost dead-reckoning sensors (magnetic heading or gyrometer), in order to meet the levels of precision and fix availability required by car applications, like guidance systems or fleet management
- to realize prototypes and the measurement methodology to analyze the performances in various environments (city center, urban area, etc.) and to perform experiments on the Paris area.

The results of these experiments show a significant improvement of the precision and the fix availability, compared to stand-alone GPS or DGPS. Hence the fix

availability may be permanent and the fix precision may reach the few meters level, even in a very difficult environment.

1 The context of the study

1.1 The appearance of navigation needs on the automobile industry area.

Since 1986, the European automobile industry has been cooperating with partners from the Electronics and Automotive Supply industry in order to aim significant improvements in European road transport. Two particular domains of this program which were investigated are the route guidance and the fleet management. Different strategies and systems were developed. All of these need localization means. This may be an embedded function or a remote function, depending of the type of application. But this function may also be of different levels of performance. Some requirements may be quite loose, some other very precise. Indeed, we do not necessarily need to have continuous and very precise positioning of the vehicle; for instance, when representing it on a map, in order to indicate roughly to the user where he lies and, for instance, where are the traffic problems located, or when looking for the management of a truck fleet. On the contrary, in the case of route guidance aid in a very dense urban area, with a lot of decision points between whom the user has to make a safe choice, it cannot be tolerated to give the information too imprecisely. The user must be aided continuously and precisely. On these examples, we see extreme case of performances level requirements. The aim of this article and the related work is to show the way toward the best solutions for the most demanding applications.

1.2 Investigated solutions.

One of the first steps of this Prometheus study was to examine the state of the art of the localization technologies. As the Prometheus program began, GPS was far away from the European automobile industry. Among the available localization systems, we could find the Loran-C, the Syledis, two examples of radio localization systems. On the other hand, and a quite

different system, was the map-matching technique. The French car manufacturers worked together with their suppliers in order to determine which performances could be reached with these systems. Different configurations and prototypes were tested. So Loran-C was studied as stand-alone system or coupled with dead-reckoning means; the results were not sufficient for the route guidance requirements and the future of the system itself was not enough encouraging us to continue our efforts. On the contrary, the Syledis allowed to achieve very high precision and availability performances; but this system is more dedicated to a local and professional use. The map-matching technique, using low cost dead-reckoning sensors, is one of the actually implemented solutions. This technique requires a complete and precise digital map. More, it is not really an absolute localization system, since it requires an initialization procedure. So absolute localization aid seems to be necessary.

2 The GPS in car applications.

2.1 The interest of the GPS.

Two aspects made the GPS more accessible for the automobile world. First of all, the increasing use of GPS in civilian applications, especially in the yachting domain, led to a more and more democratic use of this new localization technology. Prices began to decrease, in such a way that they were considered as probably soon acceptable for the automotive industry. The second important point was the deeper integration of the GPS receivers, and the appearance of better performances. This concerns the receivers themselves and their antennas. This made it possible to meet both following requirements:

- a sufficient integration in order to find the room onboard the car;
- an adequate level of performances in accordance with the use in car applications.

The GPS system provides a rather good precision throughout the world. And this without the need of a geographic data base. This is undoubtedly an advantage over the above mentioned systems.

But the GPS has not only advantages.

2.2 The GPS limitations.

Our experience of the use of GPS let us see a few limitations, which make the use of GPS on a car not so easy as it could appear to other users, like for instance maritime or geodetic applications.

Let us take some examples. Why does the system calculate our position on the wrong side of the Seine, which is more than 100 meters wide? Why is it so difficult to have some fix information through the Bois de Boulogne, in summer as it worked so well last winter? Why are these small streets of the old quarter of Victor Hugo so difficult for the brand new satellite system? All these questions may be asked by stand-alone GPS receiver users, while making car

navigation with it. Let us analyze what happens by these different cases.

2.2.1 Signal availability.

The signal availability is the ability of the GPS antenna to be provided with some satellite signal. In some difficult situations, the signal cannot reach the antenna. That is particularly the case in tunnels, in urban canyons, or under a thick tree foliage. This aspect will depend on the environment and the generated masks. But on a car, this will also depend on the position of the antenna on the car. An antenna on the roof penalizes not so much the signal availability as an antenna on the rear parcel shelf. The tendency of the car design choices are rather to try to put the antenna on an as not intruding as possible place in order to save the tooling investments costs. Second the cars should avoid to demonstrate that they are equipped with a navigation system and so a discrete antenna integration would be preferable. This is an important point, since it will certainly increase the difficulty of a good signal reception.

2.2.2 Measurement availability.

Once the signal arrives to the receiver, it may be processed in order to produce the individual raw measurements (for instance the Pseudo-Ranges). This is the job of the acquisition process, constituted by an RF stage, followed by the digital signal processing stage. As a car drives often through masked area and has only short time windows where signal are available, this process is often too slow for providing some qualified measurements.

2.2.3 Measurement precision.

The measurement precision may be affected by different noise terms. Some are very short-lived and may be suppressed by integrating several consecutive measurements. Other are more permanent like the multi-path effect. The multi-path may degrade the precision in a detrimental manner, in particular in areas with reflecting buildings. Its influence on the user error may reach a level of a few hundred meters.

2.2.4 Fix availability and precision

The fix availability will depend on two factors. One is purely mechanical and lays on the preceding processes (enough signals and measurements are available for calculating a fix). But the fix resulting of the process of these measurements may be of different levels of precision. So a fix will be considered as available if its precision is better than a given threshold.

The fix precision will depend on the precision of the different measurements and on the quality of the satellite constellation relatively to the user position. The latter is represented by the GDOP (Geometric Dilution Of Precision). Typically, in nominal reception conditions, the estimation of the user fix error may be obtained by the product of the multiplication of the pseudo-range error (affected by

propagation errors and the projection of the satellite position and clock errors) and the GDOP (HDOP for horizontal error). In this way, the estimation of the expected user error with the GDOP assumes that the errors are of the same value on the different pseudo-ranges and is based on a mean value of the multi-path error. So the DOP's could appear as a representation of the user position error. But the GDOP does not guarantee that the precision is below the given threshold. Indeed in some difficult situations, the multi-path effect may dramatically increase the measurement error and lead to an increased user position error.

Concerning the DOP value itself, it will depend on two factors. One is the environment where the car drives. As soon as it lets some signals reach the GPS antenna, these signals will often come from satellites with a poor geometry (satellites above the car in the axis of the road) presenting a high DOP value.

Another important point is the influence of the choice made for the integration of the GPS antenna. As we saw in part 2.2.1, the latter has to meet some requirements, which are not necessary the best for the GPS use.

The fix precision is also altered by the SA (Selective Availability), even if this degradation should stay in a finite range.

We see that availability and precision are very close concepts and that a compromise must be made, depending on the needs of the given application.

An application which only needs to represent the position on a rough map may tolerate a high GDOP mask, and thus allows a higher fix availability. On the contrary, some applications require very precise position information with only time to time updating, allowing a lower availability level (for instance in the case of a map-matching system as primary means, with some repositioning when the map-matching algorithms are less confident).

But more requiring applications will need precise positioning, and this permanently.

Tests were made through Paris and show the rate of fix availability and also the actual precision of natural GPS (« natural » means « not differential »).

2.2.5 Fix behavior

Even with a good reception, the behavior of the different processed fixes may be difficult to manage directly in a navigation system. For instance, the fixes may move even if the car stays.

Another point is the receiver strategy for the choice of the satellites leading to the fix processing, in particular for not all-in-view receivers. This may lead to a lot of constellation switches, and an erratic behavior at the user level.

A lot of improvements were made on the GPS receivers themselves, correcting by the way some of the cited limitations. But some of these cannot be managed by the receiver in a stand-alone

configuration (SA, better and guaranteed precision, permanent availability). One possibility is the use of the differential GPS technique. This will reduce the measurement errors and the SA effect, and so improve the precision of the fixes. It will also allow to work with higher GDOP thresholds and thereby increase the availability. But it will have no influence on the availability in some areas where no sufficient GPS signal is available.

That is why the way to follow is the adding of external information to the GPS receiver, like dead-reckoning information. The latter have properties, which are complementary to the GPS ones.

3 The hybridization.

The choice was made to realize the coupling with dead-reckoning sensors, which become accessible for the car industry.

Different types of hybridization were developed and evaluated. First step was simply to couple the GPS fix with dead-reckoning, in a loose hybridization. In order to improve the precision, a second step was to use DGPS. The third technique was to make a tight integration by the hybridization of the GPS raw measurements and the dead-reckoning measurements.

3.1 GPS fixes and Dead-Reckoning.

This is the simplest use of the different sensors. The principle is the propagation of the estimated user position by the dead-reckoning measurements. As a qualified GPS measurement is processed, it allows to update the estimated user position and to update the dead-reckoning sensors transfer gains. By construction, this leads to a continuous positioning. However, it will be considered as a continuous service only if the precision level of all the processed position estimations is sufficient.

3.2 DGPS fixes and Dead-Reckoning.

In order to improve the precision of the resulting user position estimation, the differential technique was also tested. The filter is also a loose coupling, this time of the DGPS fixes with the dead-reckoning information..

3.3 GPS raw measurements and Dead-Reckoning.

In order to take advantage of the most of GPS signals, which are often available, but do not allow to process GPS fixes solutions, the goal of this Kalman filter is to calculate a fix solution with the different raw measurements by a tight coupling.

This technique allows to work with less than 3 satellites. For instance, if only 2 satellite measurements could be done, the dead-reckoning measurements help to propagate the acquired measurements until the third satellite information could be acquired in order to process a new fix solution. In this filter, the dead-reckoning information may also help to reacquire the GPS satellite signals, improving the acquisition delay and thereby the measurement availability.

These different ways were explored in the frame of Prometheus studies with the French electronic systems suppliers Sercel and Sagem.

Sercel worked on the loose coupling, testing the performances with natural and differential GPS.

Sagem worked on different filters using only natural GPS information, from a simple GPS updating filter until a tight coupling.

Both studies led to prototypes allowing to demonstrate the interest of the developed algorithms through real experiments.

4 Experiments

4.1 The measurement methodology

One of the problems by evaluating the precision performances of a localization module is the ability to have a reference; that means to have a much better localization module available for this use. In both studies, the reference was an high precision inertial system. This could allow to measure the precision of GPS or hybrid fixes.

Other parameters were measured like the global fixes availability, the distances without GPS fixes, the number of satellite signals.

Concerning the DGPS technique, it was not possible to work with real-time information over Paris, because no DGPS channel is actually available. So the measurements were recorded and post-processed. However, the results could be verified on Nantes, where Sercel could make real-time DGPS experiments.

4.2 Implementation aspects

As we could see in part 2, the receiver itself makes an important part of the performance of the localization module, independently of the algorithm used for the hybridization. This was experienced by Sagem making a comparison of three different receivers, running simultaneously on the same drive. So we could see a reception of 3 or more satellites varying from 49% to 82% of the traveled distance. The mask distances along this drive, corresponding to the distances where the receivers were not able to process fixes, were below 350 meters (95%) for the most dynamic receiver, below 600 meters (95%) for the less dynamic receiver.

This means that the different results should be considered in respect to the used receiver. No results will be compared between different algorithms running on different receivers.

In both studies, the dead-reckoning sensors were a car odometer and a low cost Murata gyrometer.

4.3 Characterization of the test sites.

Paris is an interesting test site. There we find the conditions of difficulties for using GPS for localization. In order to characterize the nature of these difficulties, an evaluation of the GPS availability was realized by Sercel on the 5 test drives.

The « Périphérique » is a 35 km urban ring circling Paris. There we may find a lot of underground portions and tunnels. This allows to study the reacquisition of the receivers, and the behavior of the hybridization during GPS outage. The measured availability is of 44% on the East part and 16% on the West part of the Périphérique.

The « Bois de Boulogne » is a wooded area; there we may see the impact of the tree foliage on GPS reception (GPS availability: 54%).

On the Seine banks, we have something like a one-side mask (GPS availability: 37%).

« Le Marais » is constituted by little houses, but very close each together. This may be considered as a « urban canyon » (GPS availability: 23%).

« La Défense » is a business and commercial area. There we may find some skyscrapers and tunnels (GPS availability: 17%).

5 Results

5.1 Loose coupling with GPS/DGPS fixes.

In both cases, the availability increases to the 100% level. The precision is also improved by the filtering of the GPS fixes during the non dilution period of the dead-reckoning sensors. This allows to achieve a 50 to 60 meters precision level in urban areas, whereas a 20 to 30 meters precision level could be achieved in sub-urban areas.

Concerning the filter which used the differential GPS fixes, the availability is also 100%. The precision level is much better, since it reaches the 20 meters level in urban areas, and 6 meters in sub-urban areas.

5.2 Tight coupling with raw measurements.

Here also, a 100% availability is achieved. The measured precision is 50 meters on the Paris area, with a highest error of 65 meters. This should be compared with the performances obtained with the loose coupling developed by Sagem, giving 75 meters precision (95%), but a worst case of 230 meters. The improvement is clearly demonstrated.

5.3 Comment of the results.

The related performances seem to lead to the conclusion that both filters, loose and tight are equivalent. But we have to keep in mind that they were achieved with different receivers. So it is not possible to compare the absolute values of the achieved performances. On the contrary, it is possible to compare the improvement rates in both cases from a loose coupling with natural GPS to a loose coupling with DGPS and to a tight filter of the raw measurements, without the DGPS technique. For instance in the case of the urban area conditions, 55 to 20 meters (95%) for the loose coupling, 75 to 50 meters for the tight coupling (worst case from 230 to 65 meters).

CONCLUSION

These studies have proven that, functionally, good levels of performances are achievable for the localization of a vehicle, which is the first element of a navigation system. The best performances, which are necessary for the most demanding applications like the route guidance, seem to require the use of the DGPS. This service is not always available. Second it will represent a supplementary cost for the user.

However these studies should be considered as a first step, since these results were obtained with first prototypes, which were not fully optimized. The improvement of some cited GPS parameters, like for instance the acquisition delay, could certainly lead to better performances, even without the need of DGPS.

Now the question is to know when and at which price this precise localization function will be available, in order to provide soon the user with innovative systems, which will meet his quality and cost requirements .

GPS/Inertial Mapping (GIM) System for Real Time Mapping of Roadways Using WADGPS

Tim Ash, Randy Silva, Alison Brown, and James LaMance
NAVSYS Corporation

BIOGRAPHIES

Timothy Ash

Timothy Ash is a Systems Engineer at NAVSYS Corporation where his responsibilities include the development of navigation instrumentation. He has more than five years of experience in the design, development, and testing of complex hardware and software systems. Mr. Ash received his Masters in Electrical Engineering from San Diego State University.

Randy Silva

Mr. Silva is a Software Engineer at NAVSYS Corporation. He has worked for the last several years developing software for many GPS applications. Mr. Silva received his Bachelors Degree from the University of Colorado.

Alison Brown

Alison Brown is the President of NAVSYS Corporation, which specializes in developing GPS customized products and services. Dr. Brown has more than 15 years experience in GPS receiver design and has seven GPS related patents. She has published numerous papers on GPS applications and is on the editorial board for GPS World and GIS World magazines. She is currently the Space Representative for the ION Council. Dr. Brown received her BA in Engineering from Cambridge University, a MS from MIT, and a PhD from UCLA.

James LaMance

James LaMance is a Senior Engineer at NAVSYS Corporation, in Colorado Springs, CO, where he is involved with GPS navigation systems design and analysis. Dr. LaMance has worked in the areas of GPS, remote sensing, and orbit determination for the past six years. Dr. LaMance holds a PhD and MS in Aerospace Engineering from the University of Colorado at Boulder, and a BS in Aerospace Engineering from Auburn University, Auburn, AL.

ABSTRACT

Geographic Information Systems (GIS) constitute a multi-billion dollar market for geographic data, and GPS offers a quick and accurate method to meet the demand for this data. A significant problem in the gathering of mapping information using GPS is the gaps in the base map data base caused by satellite shadowing, which may not be discovered until after the survey is complete. Gaps may also exist in the GIS attribute data base because items were missed during the survey. These are costly problems that usually require new surveys to remedy. To address this problem a low-cost, miniaturized GPS/Inertial Mapping (GIM) system has been developed that can deliver 1-2 meter accuracies in real time even in the event of temporary GPS signal loss. The GIM system combines inertial aided GPS navigation, position synchronized video, and automatic roadway attribute entry, to provide a powerful tool for generating precise, high quality GIS databases.

This paper will describe GIS mapping sessions conducted with the GIM system on the roadways of El Paso County, CO. El Paso County offers an ideal geography to test the capabilities of the NAVSYS GIM system because it offers both urban and rural sections where the GPS signals can be blocked by obstructions that vary from buildings to mountain canyons. The paper will include the test data collected during the mapping sessions, and will demonstrate why inertial aiding is an important component for mapping instrumentation.

The NAVSYS GIM system incorporates an innovative optimal processing algorithm that enhances the performance of the inertial/GPS system enabling a low cost Inertial Measurement Unit (IMU) to be employed in combination with a GPS receiver, and the John E. Chance Omnistar wide area

accurate, real time position and attitude reference. The overall process is controlled by an intelligent data management system capable of recording feature and attribute information in real time, with associated time tagging for exact location tagging, in both video and electronic formats. The GIM system is packaged into a portable, modular architecture that is suited for various vehicles such as cars, four wheel drives, watercraft, or railroad cars, allowing quick and accurate surveys to be performed in a wide variety of geographies.

INTRODUCTION

A large emphasis has been placed recently on GPS as an aid to collecting data for Geographic Information Systems (GIS). Using GPS it is possible to automatically "tag" locations of interest during the survey process. Use of GPS becomes especially advantageous for cases where data is collected in digital form. These cases include mapping of roadways with vehicles, digitizing the path of a pipeline or utility transmission line from helicopters, collecting a database of road features, and mapping environmental areas such as forests or supersite boundaries. In all cases, it is imperative to generate a complete data base that includes the base map, and the related GIS attribute information.

GPS systems require line of sight to at least four satellites to achieve full precision. This is a significant problem in many geographical areas where satellite view is often obscured by foliage, buildings or other features. To solve this problem, it is necessary to provide 'dead-reckoning' capability during the satellite dropout period. Obtaining the performance accuracy required during these dropout periods has previously involved the use of expensive Inertial Navigation Systems (INS) systems. Several less expensive solutions have been implemented using devices such as a vehicle wheel counter. However, this solution does not provide the accuracy of an INS, and can be cumbersome to install and maintain.

Another problem that can occur while collecting information for a GIS database is the omission of important attributes. This can occur for many reasons, the most simple being the attribute was missed by the surveyor. This problem is easily addressed by using a video camera, so that all attributes are collected and then recorded in post process. However the attribute information is useless to the GIS database unless the video image is related to the GPS location.

To address these problems, a low cost GPS/Inertial Mapping (GIM) System has been developed that combines GPS and INS navigation with video imaging into a system that can collect base map and attribute information in real time with position accuracies of 1-2 meters.

This paper describes how the GIM system can be utilized as a complete GIS database acquisition system, and the importance of using INS aided navigation to ensure quality, precise, and complete results.

GIM SYSTEM DESCRIPTION

The GIM system is designed to serve as a complete GIS database acquisition system. The system consists of a geo-referencing unit, the operator console, and the video collection system. The geo-referencing unit generates the position solution that is used by the rest of the system, the operator console is the user interface to the GIM system, and the video collection system creates a visual record of survey attribute information.

The geo-referencing unit utilizes an optimal processing algorithm developed by the NAVSYS Corporation [1,2,3] to compute the position solution. The algorithm combines measurements from a GPS receiver, an inertial measurement unit, and the John E. Chance Omnistar wide area differential correction service in order to compute a navigation solution in real time. The Omnistar system allows the system to operate anywhere in the continental United States, as well as most of Canada, Alaska, and Central America. The unit is portable, modular, and operates from a single 12 volt power source. A picture of the geo-referencing unit integrated into a mapping vehicle is shown in Figure 1.



Figure 1 GIM System Geo-Referencing Unit

The operator console is the user interface for the GIM system. The console provides the important system information such as navigation solution, solution accuracy, system health, and other important status messages. All necessary commands to operate the system can be issued by the console from the menu driven user interface. GIS attribute information can also be automatically entered into a relational database from the console. The console is implemented with a laptop computer that can be remotely located from the geo-referencing unit.

The video collection system includes a CCD camera, a video encoder/decoder (VED), video recorder, and a monitor. A picture of the GIM camera is shown in Figure 2. The signal from the camera is passed to the VED. The VED operates in two modes. During recording the VED receives navigation information from the geo-referencing unit and combines this information with the signal from the camera for output to the video recorder. In addition to the view from the camera, the recorded image now has a text bar showing the GPS time when the frame was recorded. The time is also digitally encoded onto the video.

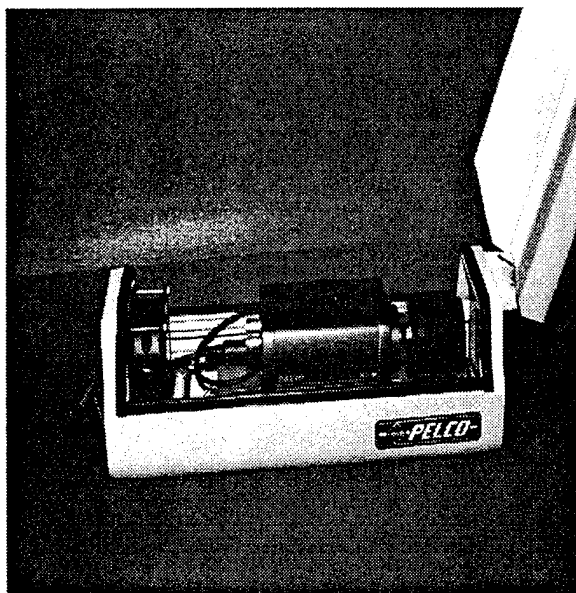


Figure 2 GIM System Video Camera

During playback, the signal from the recorder is passed to the VED. The VED decodes the GPS time from the video signal, and outputs the information to a GIS workstation. This allows for automated generation of a GIS attribute database from the video tape. A picture of the GIM video system is shown in Figure 3. The entire GIM system integrated into a mapping vehicle is shown in Figure 4.

GIM NAVIGATION PERFORMANCE

The GIM system is capable of maintaining a position accuracy of 1 -2 meters even in the case of GPS loss of up to 100 seconds [3]. In order to test this feature of the system a road survey was conducted with the

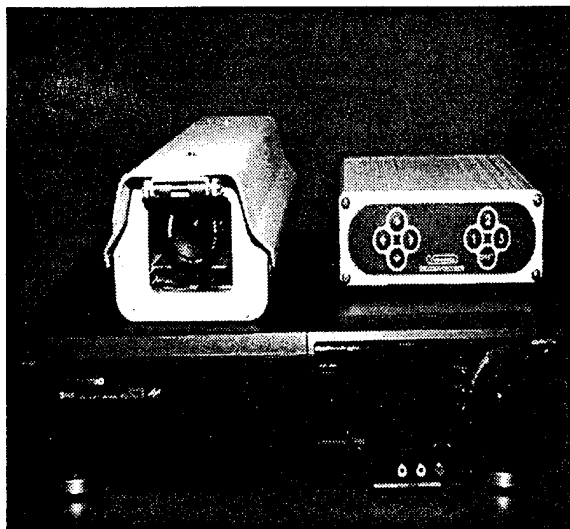


Figure 3 GIM Video System

GIM system in a region with adequate GPS coverage so that a post process kinematic solution of the survey



Figure 4 Integrated GIM System

could be computed. Then the data from the survey was played through the GIM system in post process, with a 100 second dropout introduced into the data stream during a section with several turns. The results of the GIM system position solution were then compared to the kinematic solution. Figure 5 is a plot of navigation solution computed by the GIM system in post process. The importance of INS aided

navigation is clearly demonstrated by this figure from the dotted line which indicates the solution that would be generated by a GPS-only system.

Figure 6 is a graph comparing the GIM system post process navigation solution to the kinematic solution for the North axis, during the dropout period. This figure demonstrates that the system maintained better than one meter accuracy as compared to the kinematic reference for the entire dropout period. The results for the east and down axes demonstrated similar results.

GIM SURVEY RESULTS

Another survey was conducted on the roadways of El Paso County, Colorado for the purpose of demonstrating the value of INS aided navigation. The survey was conducted in urban, rural, and mountainous regions during the month of September. The surveys in the mountain region demonstrated the expected results where many periods of dropouts were noticed. The most surprising results, however, were the surveys conducted in the urban areas. Most of the survey for this region was conducted on residential roadways with mature foliage. These roadways were a representative sample of those found in most of the residential areas in the county. Table 1 shows the results of the percentage of satellites visible during the survey. This table clearly demonstrates that fewer than four satellites were visible for more than 15% of the survey. This is a clear indication of the value of INS aided navigation.

CONCLUSIONS

NAVSYS Corporation has developed an accurate, reliable GIS data accession system. The GIM system incorporates differentially corrected GPS and INS data in a geo-referencing unit that computes navigation solutions in real time with 1-2 meter accuracy in real time. The system integrates the geo-referencing unit with a powerful user interface, and an integrated video attribute collection system. The GIM system has been used to clearly demonstrate the importance of using INS aided navigation to ensure accurate and complete GIS databases.

Table 1 Satellite Coverage

# SVs	Percentage
0	.44%
1	.89%
2	3.77%
3	8.66%
4	14.87%
5	20.87%
6	14.43%
7	32.30%
8	3.77%

ACKNOWLEDGMENTS

The authors would like to acknowledge the support of NASA for this work under contract NASW-4919.

REFERENCES

- 1) J. Coetsee, A. Brown, "The NAVSYS GPS/Inertial Mapping (GIM) System," ION 50th Annual Meeting, June 1994.
- 2) J. Coetsee, A. Brown, and J. Bossler, "GIS Data Collection Using the GPS Van Supported by a GPS/Inertial Mapping (GIM) System," ION Satellite Division International Technical Meeting, September 1994.
- 3) T. Ash, J. Coetsee, R. Silva, and A. Brown, "Test Results of the NAVSYS GPS/Inertial Mapping (GIM) System," ION 51st Annual Meeting, June 1995.

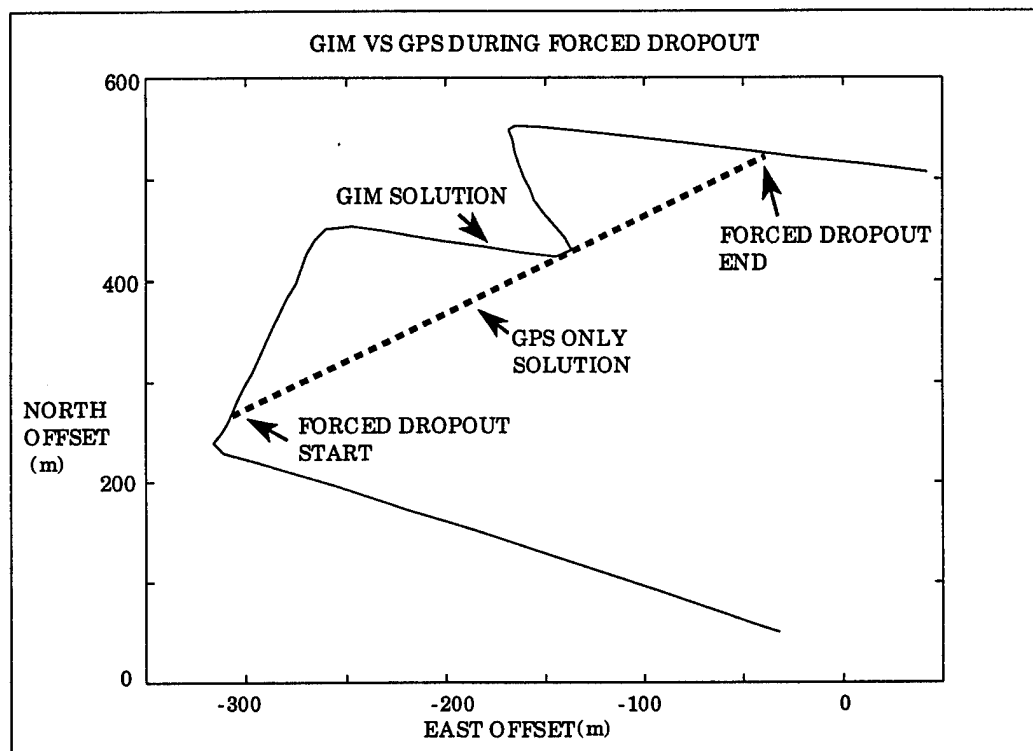


Figure 5 GIM System Post Process Survey Results with Forced Dropout

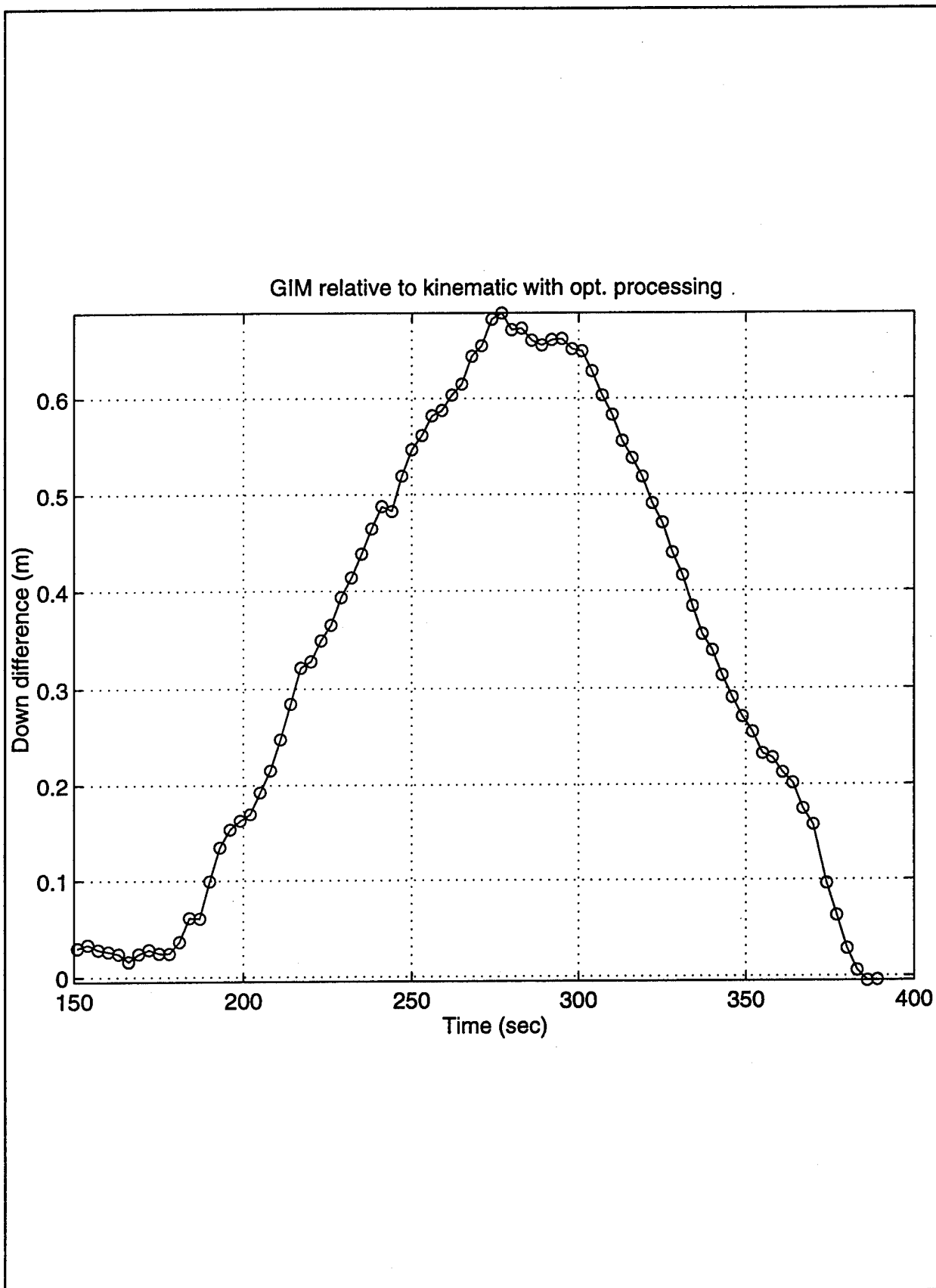


Figure 6 GIM Relative to Kinematic - With Optimal Processing (North Difference)

Twenty-Centimeter Kinematic DGPS Positioning With Digital Barometry

John Schleppe, James McLellan, Jill Battie, and J. Scott McCarron
Pulsearch Navigation

BIOGRAPHY

John B. Schleppe is the Manager of Geomatics Engineering for Pulsearch Navigation Systems Inc. He holds his B.Sc. in Surveying Engineering from The University of Calgary and is currently pursuing an M.Eng. degree. Mr. Schleppe has over 14 years experience in operations and systems development for land and marine exploration surveys.

James F. McLellan is the Vice President and General Manager of Pulsearch. He has a B.Sc. and M.Eng. in Surveying Engineering from The University of New Brunswick and The University of Calgary respectively. Mr. McLellan has over 18 years experience in the design of geodetic software, establishment of geodetic control networks, and the design and development of integrated navigation and fleet tracking systems.

Jill Battie is a Geomatics Engineer at Pulsearch with a B.Sc. in Surveying Engineering from The University of Calgary and is currently pursuing a M.Eng. degree. She has over 4 years experience in survey operations and software development with her focus for the last two years being modeling and software development for barometric leveling.

J. Scott McCarron is the Pulsearch Product Line Representative for NavSEIS. He holds a diploma in Land Surveying and a B.Sc. in Electrical Engineering. Mr. McCarron has 4 years experience in exploration surveying and navigation and 7 years experience in electrical project engineering, design and manufacturing. Mr. McCarron is responsible for the mechanical design and manufacturing of the NaviGATOR system.

ABSTRACT

Use of GPS in land geophysical surveys has increased significantly over the last few years, with dual frequency

Real Time Kinematic (RTK) systems dominating the market. While effective in open areas, GPS signal attenuation and multipath limit its use in tree covered terrain. Conventional surveys remain the primary means of layout and survey of seismic points in tree covered areas. Pressures on oil and geophysical companies to limit tree cutting have made them look for alternate methods for surveying under tree canopies. An integrated system developed by Pulsearch Navigation Systems Inc. provides a solution to this problem, offering satisfactory vertical accuracies in both open and tree covered areas. A description of the system is given, along with a review of barometric leveling techniques. A series of controlled and field tests were performed to assess the achievable accuracies of the system and to help identify main error sources. Tests demonstrating the achievable accuracy of the integrated system are described and results are discussed.

INTRODUCTION

GPS has been used in exploration surveys since the first viable commercial receivers were introduced in the early 1980s. The marine and land geophysical communities quickly made use of this new tool to aid their integrated marine radio navigation systems and provide highly accurate geodetic control for the conventional land geophysical surveys. As DGPS systems with viable radio links became available and satellite coverage improved, marine geophysical operators began to rely more on GPS and less on medium and low frequency radio navigation systems.

Today DGPS systems are used for the majority of marine geophysical positioning tasks ranging from vessel navigation and positioning to gun and cable buoy positioning. On the other hand the land geophysical community has been slower to adopt GPS systems for general point layout and positioning. Up until the early 1990's, GPS was still only being used for establishing

control with conventional survey techniques being used for the actual station layout and coordinate determination. There were several reasons for this, including: high DGPS system costs; the inability of early pseudorange based DGPS systems to determine accurate elevations; an incomplete satellite constellation; high power consumption and system weight making backpacking difficult; and resistance to change techniques which had provided satisfactory results for years. Things started to change with the introduction of the dual frequency RTK systems. These systems provided elevation accuracies better than 1 metre when used in open terrain; could be backpacked; and though their cost was significantly higher than a conventional total station, their increased production capability made them economically viable.

Currently we are seeing GPS crews replacing conventional crews in open areas, with the conventional crews being shifted to forested and swamp areas. The GPS signal attenuation caused by the forest makes accurate DGPS positioning difficult [Lachapelle et al 1994] in these areas without significantly increased occupation times, clearing trees or somehow raising the GPS antenna above the canopy. Conventional techniques, while being able to provide the vertical accuracies required by the geophysicists, also require line clearing in forested areas. Moreover oil and geophysical companies are encountering increased pressures to reduce tree cutting for a number of compelling reasons: less cutting exposes personnel to fewer of the risks inherent in tree falling; fees to forestry companies owning timber rights over seismic prospects can be significant; decreased impact opens up increased opportunities to conduct surveys in environmentally sensitive areas.

As a solution to these issues, barometric leveling was investigated by Shell Canada Ltd. in 1991 and Pulsesearch was approached in 1992 to develop an integrated DGPS / Barometry system for use during Shell's heli-portable surveys in the Rocky Mountains of Alberta and British Columbia [McLintock et al. 1994].

Research continued on barometric leveling and the first commercial systems featuring the NovAtel 10 channel 2151R narrow correlator L1, C/A code receiver and the AIR SB barometer were available in 1994. These systems were used to conduct seismic surveys in Canada, United States and Venezuela. The 10 channel 2151R board provided satisfactory horizontal positioning for most applications, but lacked the necessary accuracy to achieve in real-time 1 metre vertical accuracy at a 95% confidence level. The barometry was relied upon to provide the vertical component for the seismic programs under taken by Pulsesearch's clients, with the vertical control being provided by static GPS surveys. The first systems used by Pulsesearch's clients were subjected to

conditions radically different from any the systems had previously been used in. In previous years, prototypes had been used by Shell and contractors in mountain and winter conditions. Now the systems were being used in near tropical climates along coastal regions. This identified a number of problems with the first systems and engineers participating in the survey projects took note of the problems and made a successful case for new packaging.

Late in the fall of 1994, the RT-20™ OEM board was made available by NovAtel. It was based on the 12 channel 3151R board, and allowed the surveyors to perform real-time phase double differencing using one frequency. This system proved itself to be capable of providing vertical accuracy's below the 1 metre at 95% level. Companies that switched from the 2151R to the RT20s reported excellent results with resurvey percentages being reduced and the need for barometry in open areas eliminated. This still left barometry in the tree covered areas and Pulsesearch continued refinement of the barometry system, introducing in 1995 a repackaged backpack system, a new barometer and a new suite of Windows™ based processing software.

BAROMETRIC LEVELING

Barometric leveling is used primarily for reconnaissance, mapping and resource exploration surveys. It was widely used to provide vertical control throughout many of the developing countries during their initial mapping programs. Below we will describe the physical principles behind barometric leveling and some of the error sources. In the other sections we will discuss the hardware and software in Pulsesearch's barometric leveling system, along with the survey methodology.

The primary observable in barometric leveling is air pressure. Air pressure is the weight of a column of air on a unit area. A basic property of air pressure on Earth is that it decreases with increasing elevation. That is, as we move uphill, the air pressure decreases. The reduction in pressure is not constant with each metre of elevation increase. At sea level a reduction in 1 mb of pressure is equal to approximately 8.5 metres increase in elevation. At 1000 metres elevation, the same 1 mb decrease in pressure is equal to approximately 9.6 metres increase in elevation. The air pressure observed is not only dependent on elevation, it is also dependent on air temperature and to a lesser extent on humidity, gravity and geographic region. The equation we use must account for all of these factors. When leveling with barometers the relationship between elevation difference and change in air pressure are of the most interest, so other effects on air pressure are modeled out. Temperature is measured along with

latitude (gravity changes with latitude) while humidity is estimated and these parameters are placed in the barometric height difference equation allowing us to solve for elevation differences by inserting two pressures.

The barometric leveling equation used gives elevation differences as a function of pressure at two stations, average temperature, average elevation, and average partial pressure of water vapour in air. It does make several assumptions: the first is that the two points are assumed to lie on the same pressure gradient plumb line, or the isobaric surfaces at the two points are parallel; the second is that temperature is considered constant (isothermal) and that it changes uniformly between stations; the third is that the humidity is the same at both stations [Kahmen, 1988].

Air pressure is measured by comparison with an opposing pressure. Mercury barometers use a mercury column for this. You still commonly see these barometers at airports. They are cumbersome and most have to be read manually. The aneroid barometer uses the tension of a spring connected to a vacuum box to measure air pressure. Many of the handheld altimeters commonly used by hikers and foresters come from this class of barometers. Several different techniques are employed by digital barometers to measure air pressure. One technique used in military and commercial aircraft engine pressure sensors and recently applied to the barometric market by Weston Solartron relies on a vibrating cylinder surrounded by a vacuum. As the differential pressure changes, it changes the resonant frequency of the hoop mode of vibration in a predictable fashion [Copley, 1994]. The Weston barometer has good drift characteristics at 0.1 mbar and a very good short term noise of 0.035 mbar. Another manufacturer, Paroscientific, employs transducers that use a vibrating quartz beam with an output frequency that varies with applied pressure. These also have good drift rates at 0.1 mbar per year and excellent short term noise characteristics at 0.015 to 0.020 mbar. Atmospheric Instrumentation Research produces a lower cost digital barometer, but short term noise increases to 0.06 mbar.

Observation techniques always involve the use of two or more barometers. Typically base barometers are deployed in the area we are working in. They measure the change in pressure from one epoch to another and allow us to estimate how much the regional pressure has changed in the time it has taken the surveyor to move from one station to the next. With barometric leveling then we do not obtain absolute elevations from the pressure measurements, rather we obtain elevation differences between stations.

Error Sources

A number of error sources can affect the accuracy of the height determined using barometric leveling techniques. The major sources of error are: barometer reading errors, temperature measuring errors, localized pressure and temperature anomalies, and wind.

Performing calibrations or observations with a barometer undergoing rapid heating or cooling can be another source of error. Pulsesearch has performed tests with two barometers attached to the same pressure source, one undergoing rapid temperature changes and the other in a stable temperature environment. The tests revealed a 0.04 to 0.08 mbar bias between the two barometers due to the 1 degree Celsius per minute temperature shock. Once temperatures stabilized the bias disappeared.

The measurement of temperature is an integral portion of barometric leveling since the temperature of an air column affects its weight and hence the pressure read by the barometers in that air column. In the field, the air temperature can at best be obtained to $\pm 1^\circ\text{C}$. In elevations up to 1000m, a temperature error of $\pm 1^\circ\text{C}$ corresponds to a height error of about $\pm 0.0037 \Delta H$. Table 1 shows the effect of a 1°C temperature error for a range of height differences.

Table 1 - Effect of 1°C Temperature Error on Computed Height Difference

Height Difference (m)	Height Error (m)
10	0.04
20	0.07
50	0.18
100	0.37
200	0.74
500	1.85
1,000	3.7

It is important for field operators to be aware of the effect temperature can have on computed height differences. The temperature probe must be isolated from body and equipment heat and be kept in a shaded spot. The temperature probe should also be situated as high as possible, and be at least 1.5 metres above the ground.

Weather systems can often increase a region's ambient pressure by 1 to 10 mb equating to roughly 9 to 90 metres in elevation change. These weather systems are regional in nature and their effect can be reduced if simultaneous measurements are made at several base barometers spread throughout the region. The barometric base station allows us to measure the pressure change and remove it at the remote station.

Wind is a major source of error that is difficult to eliminate. It can produce random effects, such as when the wind gusts, or systematic effects as are evident when a strong steady wind blows. Longer observation times and air probe design can help eliminate some of the random effects of wind.

SYSTEM DESCRIPTION

The NavSEIS integrated GPS / Barometry system consists of field hardware, a field collection software system and post-mission processing software. The NaviGATOR field pack worn by surveyor is comprised of a number of major components integrated into a rugged, waterproof survey system as illustrated in Figure 1.

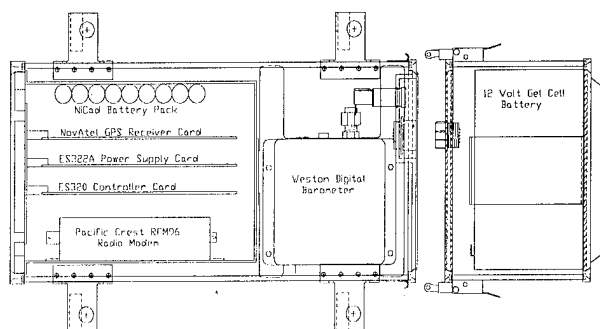


Figure 1: NaviGATOR Components

The instrument enclosure is a heavy duty aluminum extrusion powder painted while the face plate and bottom plate are machined from solid aluminum stock to ensure exact fit and strength. The end plates are finished with a durable anodizing process to prevent fading and protect the finish of the plates. The face plate features a recessed lexan panel to facilitate viewing the diagnostic LEDs and labeling the functionality of the various connectors. The bottom panel has a recessed power connector and fuse holder. The recess protects the connector and allows the unit to stand upright. The instrument enclosure also features four quick-release brackets that allow the instrument to be attached quickly and securely to either the backpack or vehicle mounting plate.

A custom power management board distributes power to the radio datalink, the controller board, the NovAtel GPS board and the barometer. A custom controller board acts as a data distribution centre, combining data from the radio datalink, the GPS board, the barometer and temperature sensor and communicating with the Corvallis PC-5L datalogger which controls the various components and stores the survey data for post mission processing.

All NaviGATOR units include a 2 watt, UHF or VHF radio modem for transmission (from Base units) and reception (at Rover units) of GPS differential correction messages. Base units can also be equipped with 15 or 35 watt power amplifiers to increase range. A UHF or VHF waterproof repeater is also available in a 2, 15 or 35 watt configuration. This option allows the surveyor to easily extend radio coverage into areas not accessible from the main base station. Lightweight flexible whip antennas attach directly to the NaviGATOR face plate, thereby eliminating an external cable. Base stations typically use a high-gain antenna mounted on 10 to 20 metres of tower.

The barometer in the NaviGATOR unit receives its external air supply by means of a specially designed probe which attaches to the front panel of the NaviGATOR. This sensor shelters the air supply from the elements and filters out wind disturbances. The air supply is then piped through the instrument to the integral air dryer chamber that uses a desiccant pack to keep the air dry.

The NaviGATOR uses a digital temperature sensor that is built into a connector shell which simply attaches the mating connector on the face plate of the instrument.

The system has a NiCad battery pack to allow the unit to keep running while changing main battery modules. This feature is designed to minimize downtime due to battery changes.

The battery modules are packaged in the same heavy duty aluminum extrusion as the electronics with t

he end plates machined from solid aluminum stock and anodized to match the instrument plates. The top of the battery module mates to the bottom of the instrument to eliminate interconnecting cables. The mating components have an interlocking tongue and groove feature to provide additional lateral rigidity and the battery module fastens to the electronics package by two stainless steel spring loaded clamps which have a safely lock to prevent accidental disconnection.

A backpack is supplied for surveying on foot. The pack is built around a high quality mountaineering backpack suspension with an adjustable shoulder harness, lumbar support, vertical and horizontal stabilizers, contoured shoulder straps, reflective stripes and three large pockets for storing gear.

NovAtel RT-20™ Receiver

The NovAtel RT-20™ receiver used onboard the NaviGATOR is a 12 channel L1, C/A code receiver capable of real-time double differencing providing accuracies at 20 cm (1 sigma) [Ford et al. 1994]. It

features a robust floating ambiguity filter capable of providing positions at 10 Hz and incorporates NovAtel's MET (Multipath Elimination Technology) [Townsend, 1994]. The base station transmits a RTCM type 59 proprietary message every 2 seconds, a RTCM type 1 pseudorange correction message every 5 seconds and a RTCM type 3 position message every 15 seconds. A choke ring antenna is normally used at the base and a standard NovAtel 501 geodetic antenna used by the rover. During layout and positioning operations, the field system uses position data from the RT-20™ at a 2 Hz rate.

Software

There are several steps to take in order to obtain results from NavSEIS. Figure 2 illustrates the data flow diagram for the NavSEIS system, followed by a description of the software packages and their role relative to seismic surveying.

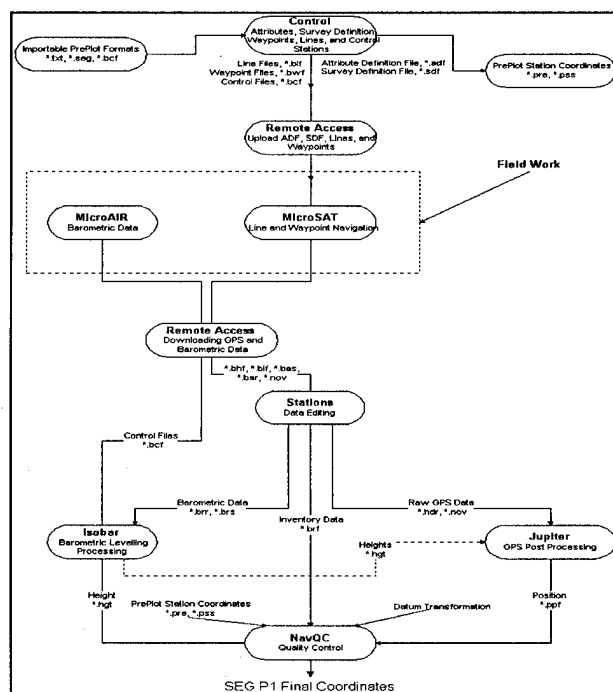


Figure 2 - Data Flow Diagram

The first step is to import any preplot information which may exist on a project. This is done using Control which sets up the point attributes, survey parameters, lines, waypoints, and control points used on the project. The data are then uploaded to the dataloggers. Next the field work is conducted. This includes the use of both the NaviGATOR backpack units as well as the barometric base station units.

The post-mission processing procedures come next in the data flow. Data are first downloaded from the dataloggers and placed on a PC in an appropriate directory. The data files are then "cleaned" using Stations which ensures consistency in individual data files and between the different types of data.

Isobar is used to process the barometric leveling data. The remote and base barometric data are loaded into Isobar and processed with the output containing a height file of all the stations which have been surveyed.

The raw GPS data can be processed using Jupiter and the height file from Isobar can be used to aid in processing if required.

Finally the real time inventory files, height files, post processed files, and preplot files are loaded into NavQC. Here they are combined into a database and analyzed for quality control. The user sets tolerance levels and the program runs a series of tests on the database. The preplot information is used to find missing stations and gaps in the data, as well as determining offsets and skids from lines in the project. The output from NavQC is a SEG P1 file containing the "best" results from NavQC's analysis.

FIELD TESTS

In order to assess critical GPS and barometry errors and quantify achievable position accuracy, a series of controlled tests were performed in Calgary at varying baseline lengths. In addition the completed systems were taken to an active seismic survey site in Louisiana and tested under actual field conditions.

Calgary Tests

A series of controlled tests at varying baseline lengths were conducted in Calgary during the summer of 1995. Weather conditions were unsettled allowing the engineers the opportunity of investigating the use of base barometers in improving barometric leveling performance. The first test performed measured the RT-20™ lock on time and static position accuracy. A MicroSAT field collection software was modified to reset the RT-20™ every 10 minutes. Position data was collected at a 15 second epoch for approximately 12 hours at each of four locations. At the same time, phase data was collected and later processed using Semikin [Cannon, 1990] to provide antenna locations accurate to 1 centimetre for comparison purposes. The four locations chosen included a zero baseline, and sites located at 4.2 km, 8.8 km and 15.2 km from the base station. Figures 3 to 6 show the RT-20™ position error plotted against the time since the RT-20™ was reset. This provides us with

both an illustration of the time required for the RT-20™ to achieve lock-on and the overall static accuracy of the receiver after 10 minutes.

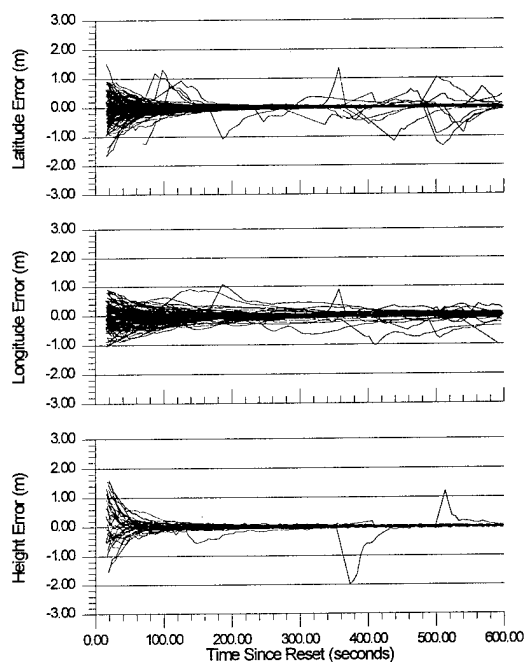


Figure 3 - Zero Baseline - RT-20™ Position Error

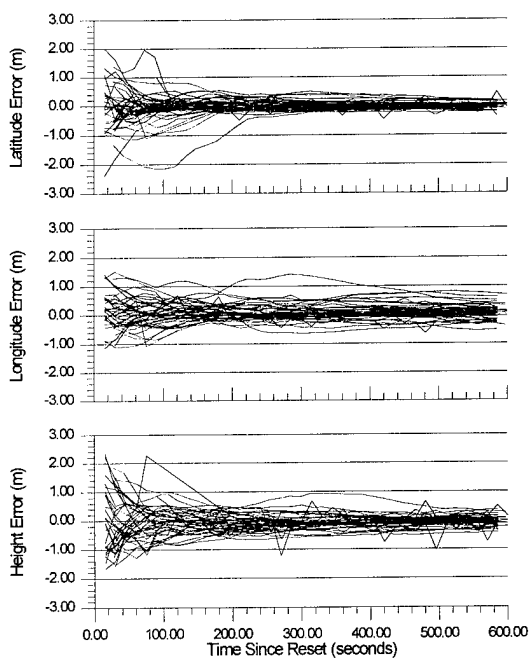


Figure 4 - 4.2 Km Baseline - RT-20™ Position Error

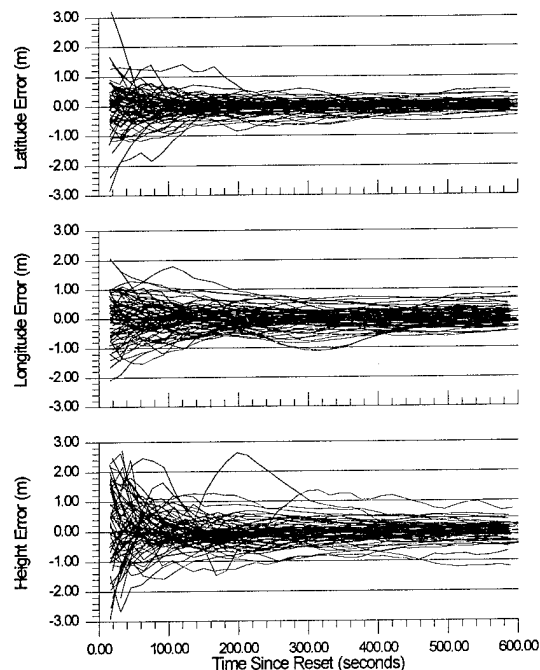


Figure 5 - 8.8 Km Baseline - RT-20™ Position Error

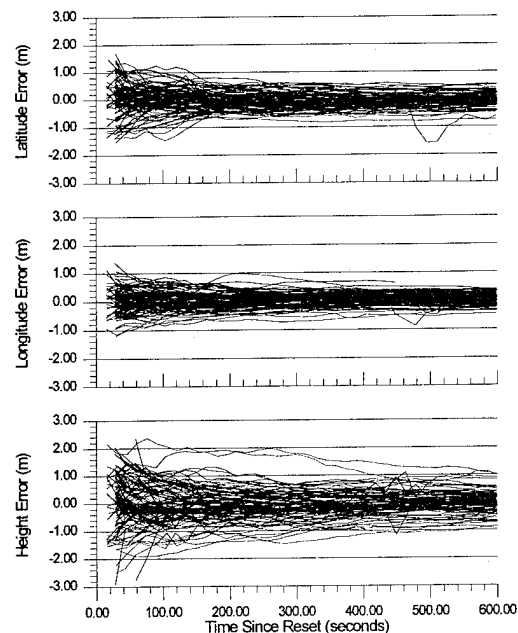


Figure 6 - 15.2 Km Baseline - RT-20™ Position Error

The results of the static - reset tests are tabulated in Table 2. The approximate position stabilization (lock on) times were estimated from the graphs. The rms estimates for the positions were computed for the data following lock-on. Generally better accuracies were achieved over shorter baselines, but the differences are not significant

with accuracies approaching 20cm horizontally and 30 cm vertically.

Table 2 - Calgary RT-20™ Static Baseline Results

Baseline Length (km)	Lock On Time (s)	Latitude Error (m RMS)	Longitude Error (m RMS)	Height Error (m RMS)
0	60 - 80	0.063	0.080	0.070
4.2	80 - 90	0.167	0.233	0.329
8.8	80 - 90	0.157	0.238	0.276
15.2	100 - 120	0.210	0.177	0.353

Barometric results were also determined over varying baseline lengths. The field collection software was modified to create a new station every 15 seconds and log barometric data for periods ranging from 10 to 20 hours. Two series of tests were performed with the data collected at each of the four stations. The first test included processing the remote data along with the data collected at the broadcast base station's barometer. Since no local base barometer was used, the results should deteriorate as baseline length increases. The results are plotted in Figure 7. As was expected, the best results were obtained for the zero baseline and the worse for the 15.2 km baseline. The poor results are a result of not adequately modeling the change in atmospheric pressure at the remote station between station readings.

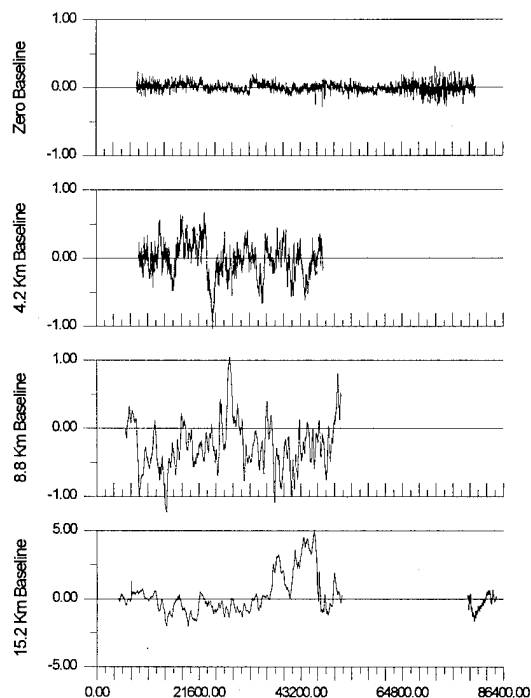


Figure 7 - Barometric Leveling Without Local Base Barometer

The second test used both the data from the broadcast base station and a local base station while processing the remote stations data. The local base stations helps model the changes in local atmospheric pressures. No appreciable deterioration in the results should be seen, since the local base station was in close proximity to the remote station during the test. Figure 8 shows the results of the multibase processing.

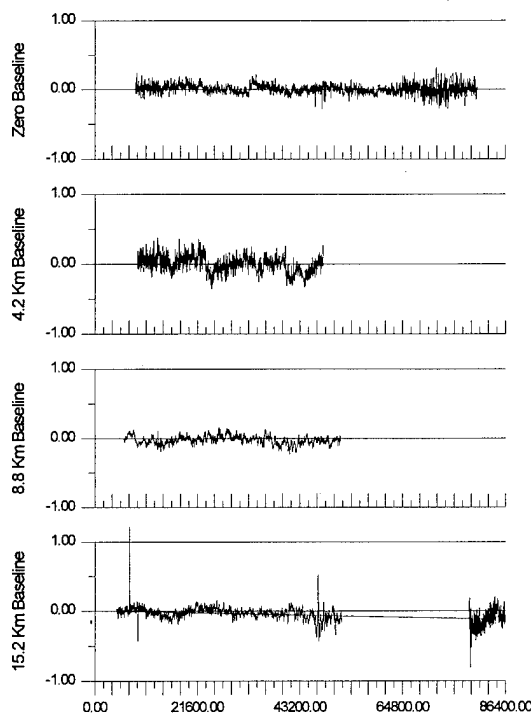


Figure 8 - Barometric Leveling With Local Base Barometer

The results for the processing with a local base station are significantly better than those without. Table 3 summarizes the results for the tests and shows that as baseline length increases, the barometric leveling accuracy deteriorates when a local base barometer is not used to model local atmospheric pressure changes. In the case of the 15.2 km baseline, the accuracy is 1.4 metres RMS without a local base, and improves to 0.113 metres RMS when a local base barometer is used. Several spikes are evident in Figure 9 on the plot for the 15.2 km data. These could be due to the gusty wind conditions at the station during the evening and early morning hours.

Table 3 - Barometric Leveling Results With and Without Local Base Barometer

Baseline Length (km)	With Local Base Barometer (m RMS)	Without Local Base Barometer (m RMS)
0	NA	0.063
4.2	0.116	0.252
8.8	0.060	0.358
15.2	0.112	1.391

Louisiana Tests

During June 1995 a test of Pulsesearch's new NavSEIS 3D system was carried out at Egan, Louisiana. The purpose of the test was to perform rigorous field testing of Pulsesearch's new seismic navigation system concentrating on the hardware, field acquisition software and pre-mission and post-mission processing software. The primary goal of the testing was to identify the primary problems preventing the system from achieving full operational status. Secondary goals included proving the performance of the barometry and identifying areas where further development on the NavSEIS system was necessary.

While at Egan two series of tests were performed on the NavSEIS systems. The first was the seismic survey tests where the new systems and software were introduced gradually into a crew doing production seismic surveys. Various surveyors operating under varying conditions used the systems.

Seismic Survey Tests

On days 168, 170, 172 and 173 surveyors used the beta NavSEIS systems during production surveys. During the various partial and full days of surveying approximately 101 stations were placed using the NaviGATOR.

Figure 9 compares the GPS heights derived from the RT-20™ with the barometric heights from Isobar. The vertical axis gives the difference between the two methods of height determination, while the horizontal axis gives the reported RT-20™ vertical standard deviation. As the standard deviation of the RT-20™ height increases so should the difference between the RT-20™ GPS and barometric heights since the higher standard deviation indicates a degradation of quality in the GPS height. Comparisons below 0.5 metres of GPS standard deviation are all below 0.95 metres with the majority below the 0.5

metre range. Above a standard deviation of 0.5 metres the comparisons are randomly distributed across a wider height difference range. Typical survey practice on the GPS crews dictates that a 0.5 metre standard deviation cutoff be used.

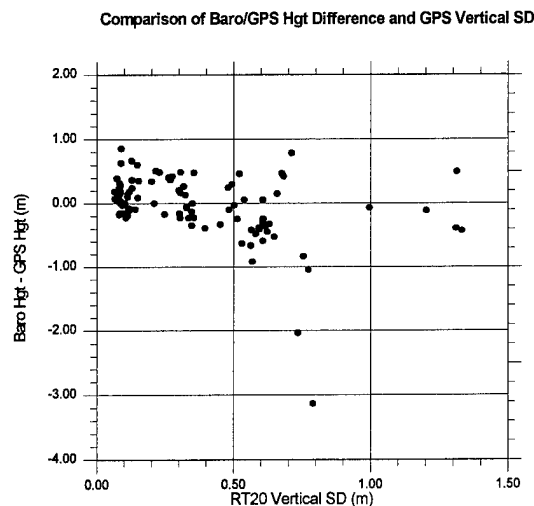


Figure 9 - Barometric Height Compared to Real-time RT-20™ Height During Seismic Survey

A comparison of the height profiles from GPS RT-20™ and barometry is given in Figure 10. Visible differences between the two profiles include several spikes present in the GPS heights but not the barometric. These spikes occurred when the GPS standard deviation exceeded 0.5 m indicating poor geometry or a recent loss of lock.

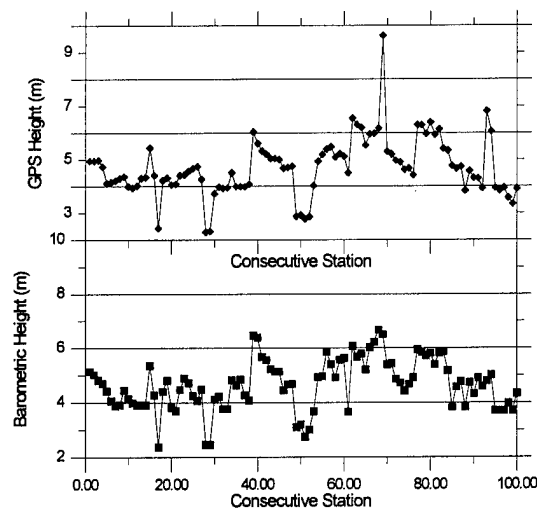


Figure 10 - Comparison of GPS and Barometric Height Profiles for Seismic Survey

Tree Testing

The repeatability of the barometric height determination system was tested on Day 171 in a treed area outside of

Egan, Louisiana. Weather was clear, with slight wind and temperatures in the 32 degree Celsius range. Nine stations were located along a truck trail through the heavily treed area as shown in Figure 11. The deciduous trees were oak with heavy foliage. The stations were spaced at 15 metre intervals along the trail. The first two stations were placed beside a rice field with the first station having a clear view above 10 degrees elevation. Stations 3 through 7 are each beside large trees. Station 9 has a clear view of satellites above 20 degrees elevation.

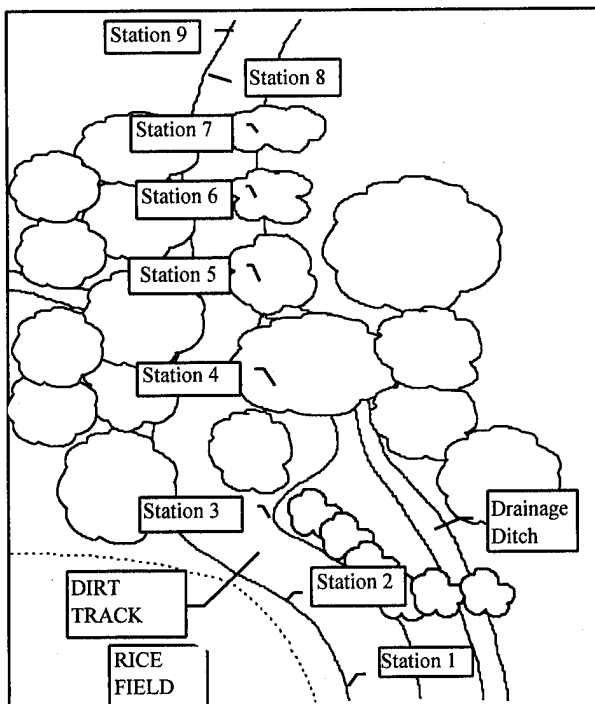


Figure 11 - Egan Test Area

A total of 6 occupations of station 1 to 9 were performed with two packs to give 108 station occupations. Figure 12 compares the barometric height given by Isobar with the GPS heights output from the RT-20™ receiver. The differences between the two methods of height determination are larger than for the production surveys. This is due to the increased multi-path and signal attenuation experienced by the RT-20™ under the heavy tree cover. Height differences in the 1 to 2 metre range were obtained when the RT-20™ vertical standard deviation was less than 0.5 metres as compared to 0.5 to 1 metres difference for open areas.

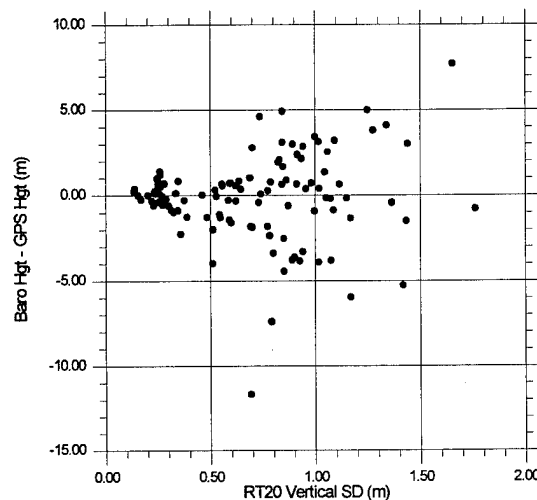


Figure 12 - Barometric Height Compared to Real-time RT-20™ Height During Tree Testing

Figure 13 shows the vertical standard deviations reported by the RT-20™ for each station occupation. In addition to the standard deviations, the mean deviation (thick crosses) along with the associated standard deviation is also plotted (thin crosses).

Plotting the RT-20™ vertical standard deviations recorded at each station occupation shows that the standard deviations increase with tree cover as would be expected. It is interesting to note that in some cases standard deviations below 0.4 metres are achieved in heavily treed areas. It is doubtful that the absolute accuracy in these cases was comparable given the tree canopy and probable GPS signal attenuation resulting from it.

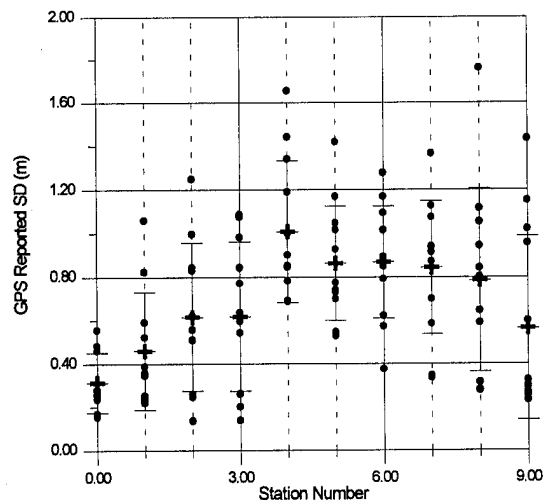


Figure 13 - Reported GPS Standard Deviations During Tree Testing

The height profiles for stations 1 through 9 are plotted in Figure 14. Separate profiles for GPS and barometry were

made. The repeatability of the GPS height profiles is in the order of 0.5 to 1 metre for the GPS in open areas and 5 metres in treed areas. The repeatability of the barometry is in the order of 0.3 to 0.5 metres at all stations. Since Stations 1 and 9 were used as control in the barometric processing their heights remain the same on all runs.

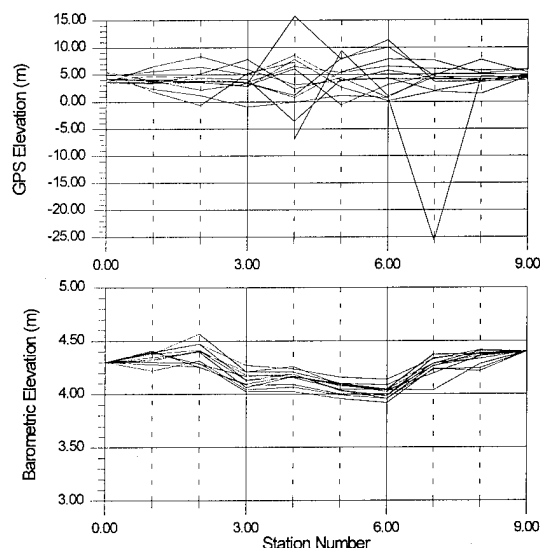


Figure 14 - Comparison of GPS Height Profile With Barometric Height Profile During Tree Testing

CONCLUSIONS

Results show that seismic point layout and positioning are possible with a single frequency L1 C/A code GPS receiver and barometry system. In this case the NovAtel RT-20™ integrated within the Pulsesearch NaviGATOR provides a cost effective positioning system which is accurate and reliable. The RT-20™ receiver provides positions and control in open areas, while the barometry is an effective tool in tree covered terrain.

Static tests show that the RT-20™ requires from 60 to 120 seconds to achieve stable positioning results below 1 metre following a loss of lock on all satellites. Accuracies of 20 cm horizontally and 30 cm vertically are achievable on short baselines of up to 8 km, while accuracies of 25 cm horizontally and 35 cm vertically were achieved on a longer baseline of 15 km.

Tests during production surveys and tests in treed areas showed the new barometry system to be consistent regardless of tree cover. The synergism between the GPS and barometry is an important factor in the accuracy of the barometry. The barometric heights are only as accurate as the GPS heights providing control, so it is important to ensure that adequate and accurate GPS

heights are gathered during the course of the working day to be used for barometric control. With the new barometers, drift between barometers is not as large a factor as external effects such as temperature fluctuations on slopes and the effect of weather systems. Tests performed in Calgary showed that by utilizing local base barometers, the effect of local pressure systems on barometric leveling can be reduced.

ACKNOWLEDGMENTS

We would like to thank Shell Canada Ltd. for introducing Pulsesearch to barometric leveling and encouraging our continued research. We would like to thank Eagle Surveys International Ltd. for their assistance in testing the NavSEIS system at their prospect in Louisiana.

REFERENCES

- Cannon, M.E. (1990), High-Accuracy GPS Semikinematic Positioning: Modeling and Results, *Navigation*, Journal of the Institute of Navigation, Vol. 37, No. 1, pp.53-64.
- Copley, D.W. (1994), The Application of Vibrating Cylinder Pressure Transducers to Non-Military Applications, Weston Aerospace Limited, Farnborough, Hampshire, UK.
- Ford, T.J., J. Neumann (1994), NovAtel's RT-20 - A Real Time Floating Ambiguity Positioning System, *Proceedings of ION GPS-94*, Institute of Navigation, Alexandria, VA.
- Kahmen, H., W. Faig (1988), *Surveying*, de Gruyter, New York.
- Lachapelle, G., J. Henriksen, and T. Melgard (1994), Seasonal Effect of Tree Foliage on GPS Signal Availability and Multipath for Vehicular Navigation, *Proceedings of ION GPS-94*, Institute of Navigation, Alexandria, VA.
- McLintock, D., G. Deren, E.J. Krakiwsky (1994), Environment - Sensitive: DGPS and Barometry for Seismic Surveys, *GPS World*, February 1994, pp. 20 - 26.
- Townsend, B., P. Fenton (1994), A Practical Approach to the Reduction of Pseudorange Multipath Errors in a L1 GPS Receiver, *Proceedings of ION GPS-94*, Institute of Navigation, Alexandria, VA.

H-764G GPS/INS High Dynamics GPS Tracking Tests Using a Roller Coaster

Al Hasselbring
Honeywell, Inc.

BIOGRAPHY

Al Hasselbring is presently the Manager of Land Navigation Engineering at Honeywell's Guidance and Navigation Operation in St. Petersburg, Florida. In the early 1990s Mr. Hasselbring served as the Technical Director for Honeywell's H-764G Embedded GPS/INS — EGI — development effort and has been involved in the development of numerous navigation systems over the past ten years. Prior to that, he worked at McDonnell Douglas developing Flight Control and Mission Computer systems.

ABSTRACT

The purpose of this paper is to document a new method of performing cost-effective testing of GPS/INS systems in fighter-like environments. In addition to cost savings, this method also has other advantages over actual flight testing of Global Positioning Systems/Inertial Navigation Systems (GPS/INSs). (See Figure 1).

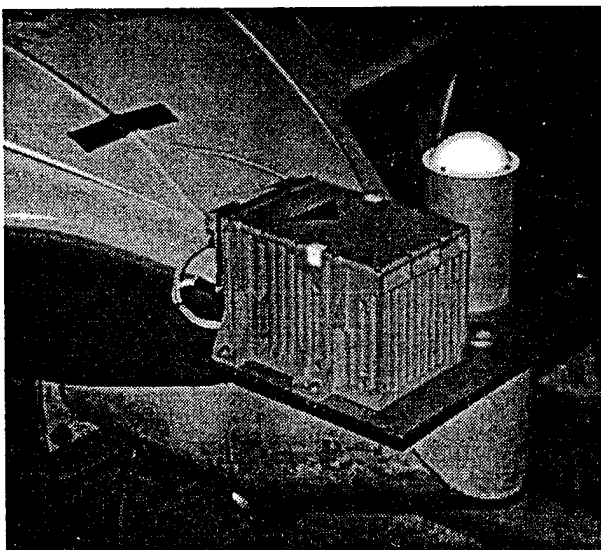


Figure 1. The H-764G and its GPS Antenna on the nose of the KUMBA roller coaster.

The Problem

In the late 1980s, I was at Holloman Air Force Base's Central Inertial Guidance Test Facility (CIGTF) and found myself brainstorming with a CIGTF engineer about better ways to test tightly coupled GPS/INS systems in highly dynamic (fighter-like) conditions. There were many problems to overcome.

One problem was that the accuracy of tightly coupled GPS/INSs was nearly equal to the accuracies of even the most advanced test-range telemetry and position determination systems. This made it difficult to determine if errors recorded during flight tests were coming from the GPS/INS being tested or from the range's "test equipment."

Another problem was that, while simulating inertial inputs to an INS had been done for years and simulating satellite signals to a GPS was not overly difficult, successfully simulating both strap-down-INS and GPS inputs in a manner that didn't confuse the blending Kalman filter of a tightly coupled GPS/INS was extremely difficult.

Also, while simulating highly dynamic profiles can uncover some anomalies, it doesn't simulate the effects of g-loading of, for instance, the GPS's oscillator. These "real" forces on the hardware can create error combinations which can cause acquisition and re-acquisition performance characteristics in "real" flight tests which differ greatly from "identical" flight profiles which are merely simulated.

The fourth problem was that flight testing is extremely expensive. Turn-around time is also a problem. For instance, testing the dynamic performance of five different types of aiding or Kalman filter parameter settings could require five flights spread over an entire week (and a flight test bill of \$100,000 or more).

And the final problem was that, while testing a GPS/INS on a rocket sled simulates the g levels of a flight test, it can't accurately simulate the GPS outages created due to antenna shading during loops, rolls, etc.

The CIGTF engineer and I brainstormed for hours over better ways to cheaply and accurately test GPS/INS systems in highly dynamic environments. At the end of the night, our "best" idea was for CIGTF to build a fully instrumented rocket sled that did loops and rolls. Obviously, even back in the big-budget-'80s, this idea never got funded.

As we developed the H-764G GPS/INS at Honeywell in the late '80s and early '90s, I often re-played that CIGTF discussion in my mind. There had to be a better option.

The Answer

And then it happened. The Busch Gardens theme park, across the bay from us in Tampa, built "*KUMBA*" — a state-of-the-art, seven-loop, 60-mph roller coaster. As soon as the H-764G design team saw it, we knew that our "looping rocket sled" had arrived.

The *KUMBA* simulates fairly well the g-loading (3.5-4.5 g's), angular rate dynamics (nearly 200°/sec), and GPS antenna shading characteristics of a fighter aircraft. It provides an excellent, highly repeatable test-bed for verifying the H-764G's ability to quickly re-acquire satellites in high-g, fighter-like dynamic environments at a fraction of the cost of a fully instrumented fighter flight test over a desert test range.

Plots of a few kinematic parameters are shown in Figure numbers 2 through 4.

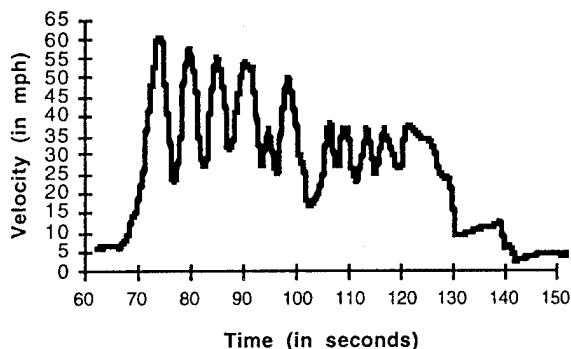


Figure 2. Velocity for a single run.

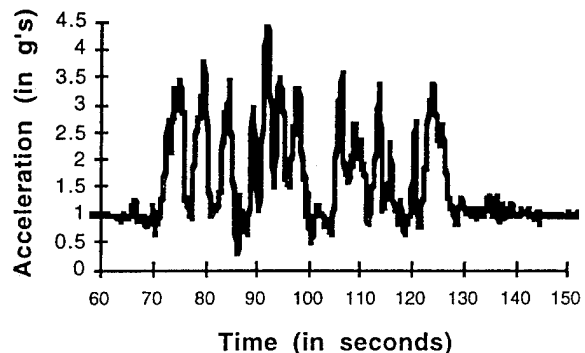


Figure 3. Total Acceleration (RSS of all three axes).

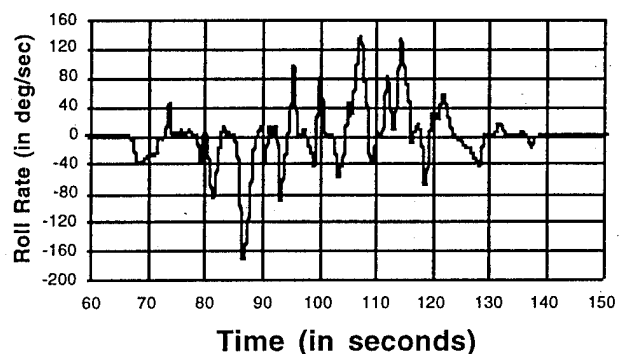


Figure 4. Roll rate plot for a single run.

A map of the *KUMBA* track (generated from H-764 data) is shown in Figure 5.

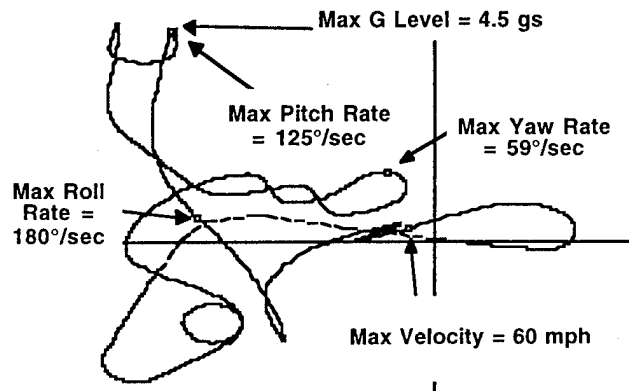


Figure 5. The *KUMBA* offers an exciting ride. Map of the *KUMBA* track, looking down.

A major advantage over flight testing was the *KUMBA*'s five-minute "turn-around time" which allowed us to quickly test performance with a variety of aiding methods, Kalman filter settings, etc. A test series which would require a week of flight tests at Edwards Air Force Base can be completed in only an hour or two of *KUMBA* testing.

The cost of roller coaster testing is minuscule compared to a fighter-based flight test. Busch Gardens only charged us for overtime labor and the electricity required to operate the roller coaster (a standard per-hour rate).

Safety concerns, however, approached those of a real flight test. Drawings and test plans had to be approved by Busch Gardens engineers and the engineering firm in Switzerland that originally designed and built the *KUMBA*. Safety wires, locking fasteners and large design margins were required throughout. This process took several months. It was also stipulated that no one would be allowed to ride on the coaster during the test.

The System

The H-764G is an 18-pound GPS/INS that Honeywell is producing at a rate of approximately 60 per month in a number of variants for approximately two dozen different applications (fixed wing aircraft, helicopters, missiles, land vehicles, and portable "back-pack" applications).

The H-764G creates a precision navigation solution and high bandwidth kinematic data outputs using information from three sets of sensors:

- Three Honeywell GG1320 digital laser gyros (DLGs)
- Three AlliedSignal QA2000 accelerometers
- A Rockwell Collins GEM™ III P/Y Code GPS module.

The H-764G uses a Bierman Upper Diagonal (UD) Kalman filter to blend 1536 Hz inertial data with GPS pseudo-range and delta-range data to create a highly accurate, high-rate, low-lag solution for sensor stabilization, flight control, pointing, and general navigation applications. An H-764G system is shown in Figure 6, a disassembled system is shown in Figure 7 and a block diagram of the H-764G is shown in Figure 8.

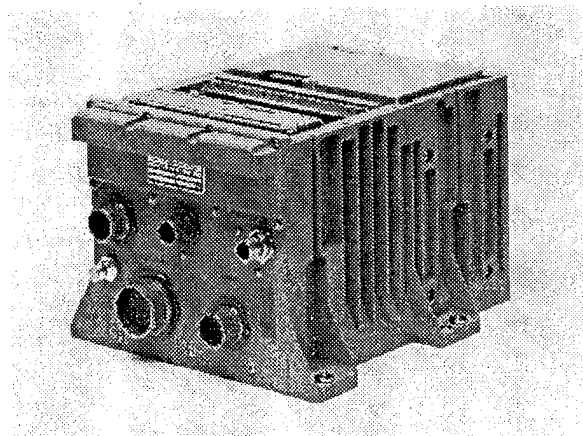


Figure 6. H-764G GPS/INS.

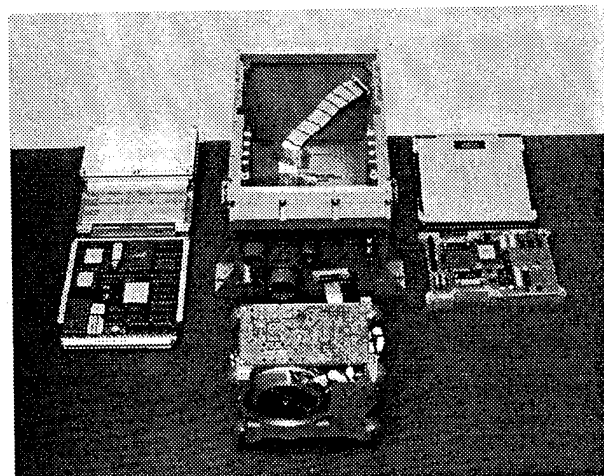


Figure 7. H-764G Exploded View.

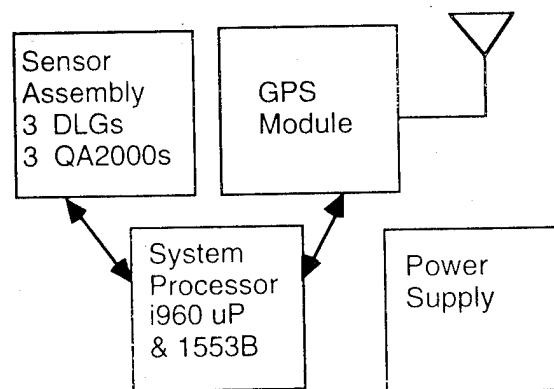


Figure 8. H-764G Block Diagram.

The Test

Once all the approvals were in place, we were ready to test the system. Testing was performed at night after the park had closed. Engineers from Busch Gardens installed a camera mount on the nose of the lead car of the coaster. This mount normally holds a Beta-Cam and is used in the making of promotional videos.

For this test, Honeywell fabricated an adapter plate which allowed us to mount the H-764G system and GPS antenna on the camera mount (Figures 9 and 10). A 24 Vdc battery was mounted in *KUMBA's* front seat along with a PC-based 1553 bus controller (for gathering data). A video camera went along for a few of the rides as well.

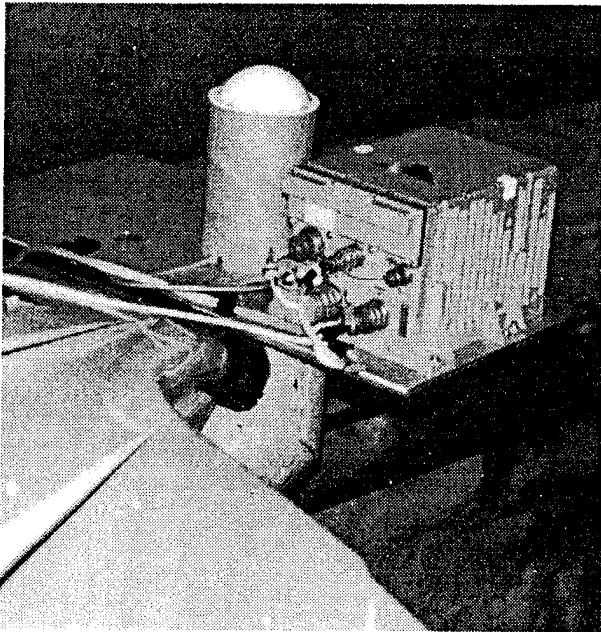


Figure 9. H-764G mounted on the *KUMBA's* camera mount.

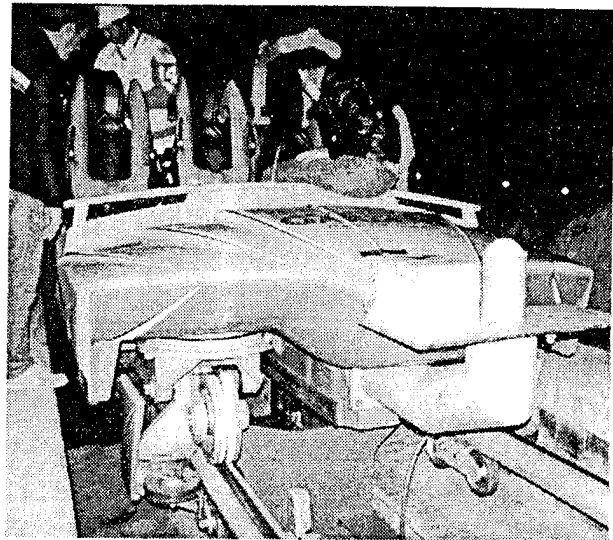


Figure 10. View of the H-764 & GPS antenna on *KUMBA's* front (nose) camera mount.

The ruggedized PC (Figure 11) gathered approximately a dozen 32-word 1553 messages at rates as high as 256 Hz. We used a PC featuring a removable hard drive. After every circuit of the course, we removed the hard drive and replaced it with a new hard drive so that the data from one run could be analyzed while the next run was in progress.

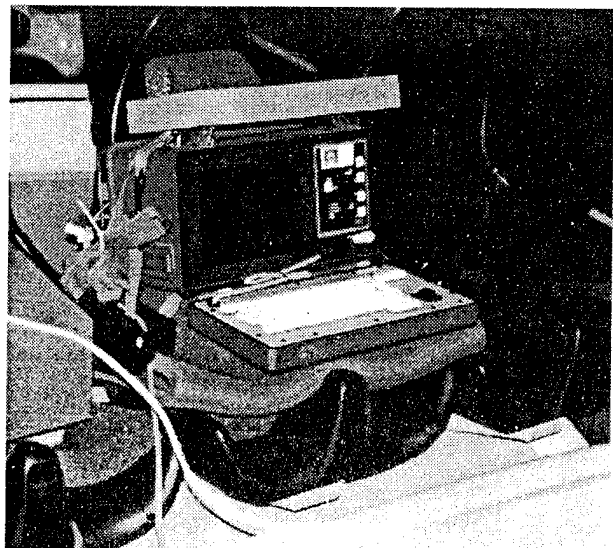


Figure 11. Ruggedized PC in front seat.

We are presently working on a test set-up in which a cellular phone mounted on the roller coaster and connected to the on-board-PC's modem will be able to modem data back to the base station in real time. This set-up could also be used to send commands to the H-764G in real time (mode commands for instance) while it is "in flight."

Results And Observations

Test results for the H-764G were generally very good. Some of the results were expected:

- The test again brought to light the advantages of using corrected line of sight (pseudo-range and delta-range) Satellite Vehicle (SV) data over position, velocity, and time (PVT) data to aid the inertial solution. As the *KUMBA* flipped and twisted, satellites were seldom in view for more than a couple of seconds. The ability of the H-764's Kalman filter to aid the inertial solution with data from only one or two SVs at any one time was crucial.

- The advantages of aiding the GPS tracking loops with high quality inertial data was shown. Without inertial aiding, it was virtually impossible for the GPS to re-acquire in high-gs after it had flipped upside down and lost all SVs (it had no idea where to start looking in either the areas of frequency or code tracking). With inertial aiding, the GPS was able to quickly re-acquire SVs, even in high-g environments.

Other results, however, were a little more subtle:

- High-dynamic environments greatly accentuate time-tagging errors. Small timing errors in either the GPS aiding of the inertial solution or inertial aiding of the GPS tracking loops will cause little or no degradation in "normal" conditions. But in "*KUMBA*-like" conditions, a data timing error of a few milliseconds can be the difference between tracking and not tracking SVs.

- Proper processing of lever-arm information (the distance from the center of the GPS antenna to the inertial system's center of computation) must only be "close" for most situations, but in high dynamic situations, it must be exact. The lever arm data must be processed and time tagged flawlessly for the integrated GPS/INS system to perform well in high dynamics.

What's Next?

"What is the relationship between the accuracy of inertial sensors and the ability of a GPS to track (and re-acquire) SVs in high dynamics?"

Honeywell's latest generation of inertial systems is unique in that the interface between the system mother board and the Inertial Sensor Assembly (ISA) is standardized, and totally digital. The H-764G, for instance, (produced by Honeywell's Guidance and Navigation Operation

in St. Petersburg, Florida) is designed so that its GG1320 DLG sensor assembly can be easily removed and replaced with a Fiber Optic Gyro sensor assembly (produced by Honeywell's operation in Phoenix) or with a lower cost, lower performance GG1308 ring-laser-gyro-based sensor assembly (produced by Honeywell's operation in Minneapolis). It is this digital interface that makes "swapping ISAs" practical.

Later in 1995 or early 1996, Honeywell plans to run tests on *KUMBA* to determine the effects of these various classes of inertial sensors on GPS tracking quality in high dynamics. A single H-764G could be tested multiple times, placing a new type of sensor assembly in the system following each run. Or, three H-764Gs, each with a different class of inertial sensor, could be "flown" on *KUMBA* simultaneously. Either way, it should be a good test in that everything, except the inertial sensors, will be held constant.

Conclusion

Testing the H-764G GPS/INS on a roller coaster was a very cost-effective method of gathering some excellent test data. It gave us great confidence prior to actual high performance fighter flight tests. Other avionics may also benefit from this test method, Forward Looking Infra Red (FLIR) imaging systems come to mind immediately. The test was truly a win-win situation as Busch Gardens engineers found the 256 Hz kinematic data useful in analyzing the performance of their roller coaster.

In any case, it sure beat spending another night in the lab!



Figure 12. Navigation engineers "simulating" a ride on the *KUMBA*. (For safety reasons, no one actually rode with the system during testing).

ACKNOWLEDGMENTS

Busch Gardens, Tampa, Florida: It was the great support and patience the of the folks at Busch Gardens that made this test possible. Special thanks to their engineering, marketing, and legal departments. Doug Schmidt's assistance in acquiring all of the approvals required for this test was invaluable.

DESCO, Tampa, Florida: DESCO is the engineering firm that operates and maintains *KUMBA*. It was the DESCO engineers and technicians who actually supported us on the day of the test (and late into the night as well).

Bolliger and Mabillard Inc., Monthey Switzerland: This is the engineering firm that originally designed and built the *KUMBA* roller coaster. As such, they had final review and approval authority for all test plans and all test fixturing.

Honeywell Military Avionics Division, Guidance & Navigation Operation, St. Petersburg, Florida: Dozens of people, mostly members of the H-764G development team, contributed to this test and the writing of this paper. This included engineers, machinists and tech-pubs personnel to name only a few. Their contributions are greatly appreciated.

Integration of a Fibre Optical Gyro Attitude and Heading Reference System with Differential GPS

Manfred Bäumker
FH Bochum

Manfred Hüllenkremer and Axel Lehmann
LITEF GmbH

BIOGRAPHY

Dr. Manfred Bäumker is Professor for Geodesy at the Fachhochschule Bochum. He worked for 8 years at LITEF as head of the system analysis group. During this time he analysed and designed several inertial systems. His main interest today is the integration of GPS and INS for geodetic applications.

Manfred Hüllenkremer received his M.S. in Geodesy at the University of Bonn in 1980. Since 1985 he works as system analyst and software engineer at the engineering department at LITEF. His main activities concern the development of AHRS and Inertial Navigation Systems for airborne and maritime applications including the implementation of real time software for embedded systems.

Axel Lehmann received his M.S. in Electronics at the Technical University of Berlin. He now has fifteen years of experience in the design, test and application of inertial systems. His expertise goes from low accuracy AHRS to very high precision marine laser navigation systems. He presently serves as the project manager of the FOG-AHRS/ GPS development at LITEF.

ABSTRACT

LITEF produces the FOG-AHRS LCR-92 (with bubble levels). This system is presently the only AHRS in the world with Fibre Optical Gyros, and is certified by the German authorities and the FAA. The next generation FOG-AHRS with micromechanic accelerometers is under development. As an interim solution an AHRS using conventional accelerometers has been built for integration with (D)GPS/ GLONASS.

Presently, this prototype system uses an external

processor to perform the full AHRS/DGPS calculations. Further studies are focussed on different integration approaches of the DGPS measurements: the cascaded and integrated Kalman filter approach. The next step is to implement the algorithms we are evaluating into a second processor of the AHRS.

The paper will give an overview of the project and its present status, including test results of the prototype system using a cascaded and an integrated Kalman filter approach.

1 INTRODUCTION

LITEF is producing and developing a family of highly integrated attitude and heading reference systems (AHRS) using new technology for application in the general aviation (GA) market. The family started with the LCR-92, a vertical / directional gyro compass system with fibre optic gyros (FOG) and bubble levels. This system has been certified by German and US authorities and is meanwhile well established in the market.

The more accurate successors LCR-93 and LCR-94 presently under development are using micro-mechanical accelerometers and are equipped with a powerful computer for the integration of GPS. The systems are based as its predecessor on fibre optical gyros. Fibre optical gyro systems are expected to have a higher MTBF than the last generation (DTG) systems because they have no moving parts, and are therefore well suited for the application in today's guidance and approach systems, where highest reliability is expected. The systems will have the capability for autonomous navigation and are designed to meet the upcoming requirements for precision approaches according to the new tunnel concept.

The new tunnel concept for precision approaches [1] defines the Required Navigation Performance (RNP) in terms of a Total System Error (TSE) and does not distinguish as in the older requirements between the Navigation System Error (NSE) and the Flight Technical Errors (FTE), i.e. errors of the autopilot. This makes it easier to distribute the accuracy between different components of a complete system, but the requirements on integrity, continuity and availability are very demanding.

The development of the new systems is separated into two major steps. Because the development of a flight critical avionics system is very costly and the process of certification is quite time consuming, it was decided to explore in a first step the feasibility of the new concept and alternate concepts in a prototype system. In a second step the final concept is transferred to the target system.

The prototype system described below is developed to meet all standards, which are used to certify airworthiness. It is an experimental system only in that sense, that the computer used for the integration of the AHRS and (D)GPS is a stand-alone unit.

2 HARDWARE

As already mentioned the prototype system built and tested had to fulfill all standards of airworthiness. On the other hand - to examine different concepts - it has to be as flexible as possible with respect to the interfaces and to easy modification and adaption.

Therefore, it was decided to distribute the system into an AHRS with a dedicated interface and a general purpose computer, which can be adapted to different needs and can also incorporate a GPS receiver. This configuration is shown in Fig. 1. Additionally, a separate computer (ruggedized PC) is used to record the data of the different units of the system.

FOG-AHRS

The basis of the prototype system is the already mentioned LCR-92. The LCR-92 was broadened to get additional space for the three accelerometers. At the time the development of this prototype system was started, the micromechanical accelerometers were not yet available. Therefore, LITEF's standard accelerometers B-280 were used. This prototype system is shown in Fig. 2. It is expected, that the performance of the old and new technology accelerometers will not differ largely. The keyrole in such

AHRS systems are the gyros and its errors especially the gyro drift and the random walk of the FOG's. The parameters of the FOG's used in the prototype system are:

bias repeatability	< 0.5	°/h (1 σ)
random walk	< 0.1	°/h (1 σ)
scale factor error	< 300	ppm (1 σ).

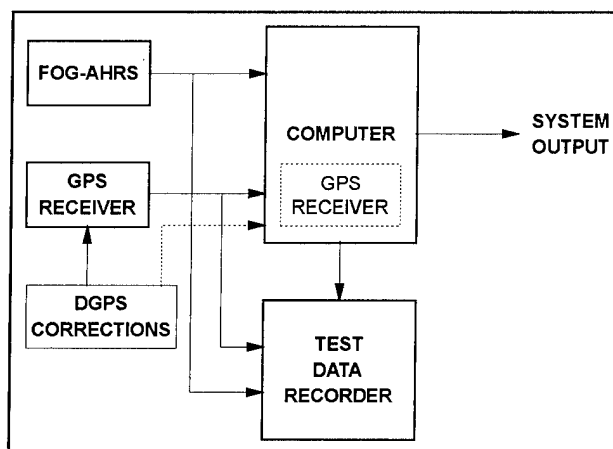


Fig. 1 AHRS/DGPS Test System

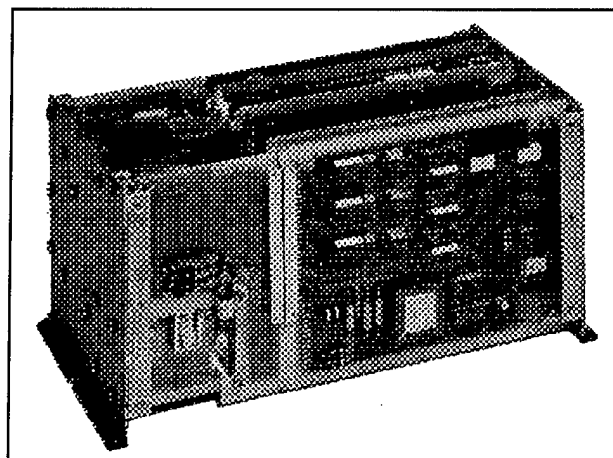


Fig. 2 FOG-AHRS with B-280

INTEGRATION COMPUTER AND GPS RECEIVER

The integration computer for the combination of AHRS and GPS data was built using LITEF's ruggedized VME-Bus modules. The main CPU uses a Motorola 68030 and a math co-processor. Two multi-purpose I/O boards contain each a processor 68302 and can handle a variety of I/O:

- RS-232 and RS-422 buses including high speed HDLC protocols
- ARINC-429 high speed serial buses
- dual port RAM interface

The completed computer including an internal GPS receiver is shown in Fig. 3.

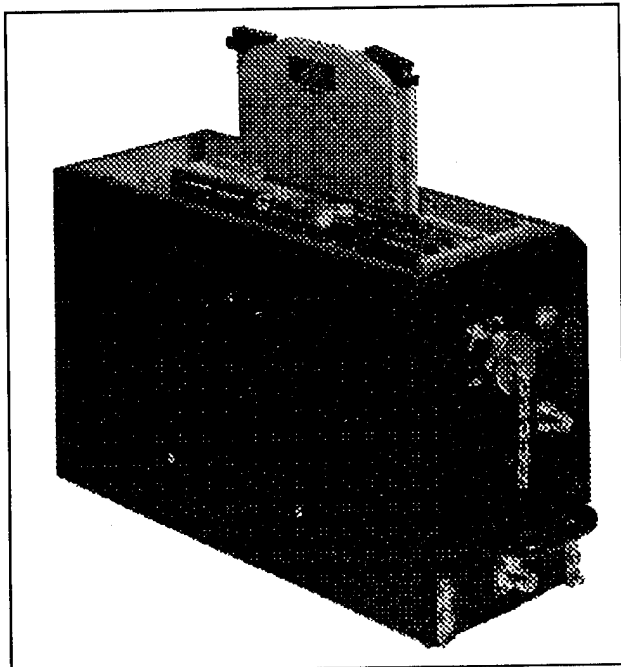


Fig. 3 Integration Computer with GPS-RX

The system was planned as an open architecture system. Any kind of GPS receiver can be connected to the computer, as long as the interface uses either RS-232, RS-422 or ARINC-429.

Presently a Collins GEM-I GPS receiver is used. To achieve fast data access and to minimize data latencies, the GPS unit is mounted in the computer housing and communicates with the main CPU via a dual port RAM interface to get the original GPS raw data (pseudoranges, deltaranges and ephemerides). For the synchronization of the GPS data and the AHRS data the 1PPS signal is essential. Provisions are made for internal or external input of this signal.

3 SOFTWARE

The software for the main CPU, mainly the Kalman filter, was written in Ada. It was developed and tested on a VAX as host and then loaded into the target computer. This transition was remarkably easy and fast. New methods in developing the algorithms of this software were introduced by using real time data collected by a special test system already described in [4]. This considerably accelerated the development process. The interface software was written in C.

The use of Ada will enable LITEF to re-use large parts of this code in the final design. The certification

of software written in a high-level language for flight critical applications is usually laborious and complicate. The use of Ada and certified compilers takes a lot of pain out of this work.

3.1 REDUNDANCY CONCEPT

To achieve the required extremely high integrity of an autonomous landing system, a sophisticated redundancy concept is necessary. Besides the integrity, the availability and continuity criteria are also regarded in this concept.

Integrity is the probability to detect errors in an appropriate time interval (alarm time) after their occurrence. *Continuity* is the probability that the required system functions are further available with the specified accuracy to successfully terminate the approach procedure. *Availability* is the probability that the functions are available when starting the approach.

Numerous examinations have shown that a GPS based navigation system alone cannot fulfill the requirements with respect to integrity, availability and continuity. Therefore, several concepts have been developed to ensure the integrity. The concepts are based on the combination of GPS measurements with inertial measurements or other sensors and specific algorithms for failure detection and isolation, i.e. receiver autonomous integrity monitoring (RAIM) and aircraft autonomous integrity monitoring (AAIM) [2], [3].

In the following, a new integrity concept based on the combination of a FOG-AHRS with differential GPS for failure detection and isolation is presented. This concept is based on several features. These are

- individual failure detection on the level of GPS measurements (pseudoranges and delta ranges) based on a new RAIM algorithm,
- failure detection by testing the measurements for plausibility with respect to vehicle capabilities,
- failure detection on the level of Kalman filter observations (divergence problem) using delayed Kalman filter updates,
- failure detection by sophisticated built-in tests (BIT) for the digital control loops of the fibre optical gyros and the interfaces used for data transmission and

- failure detection by comparison of two independent platform and navigation computations (conventional AHRS compared with AHRS/DGPS). This concept is called "brickwall" concept.

Details of the algorithms are described in the following.

3.2 PROCESSING OF DGPS DATA AND RAIM

To achieve the required stringent integrity of a flight critical Attitude and Heading Reference System a sophisticated redundancy concept for the total system and for the external sensors used is necessary. This is especially important for an AHRS/DGPS combination, because an AHRS does not have the long term stability of an INS and therefore the position and velocities mainly depend on the DGPS data. For these reasons the cascaded filter concept (based on the PVT solution of the GPS receiver) and not the integrated filter concept (based on the PR/DR measurements) was chosen for the final system.

The cascaded filter concept comprises

- the calculation of DGPS positions and velocities from the corrected pseudoranges (PR) and deltaranges (DR),
- the monitoring of the DGPS position and velocities using a new powerful receiver autonomous integrity monitoring algorithm (RAIM),
- and the derivation of corrections for the AHRS parameters from the DGPS positions and velocities used as measurements in the AHRS/DGPS 16 state Kalman filter.

The DGPS positions and velocities are derived by the least squares method using the corrected carrier smoothed pseudoranges and deltaranges of all satellites. The pseudoranges and deltaranges have to pass a RAIM test shown below.

$$\mathbf{X} = \mathbf{X}_0 + (\mathbf{H}^T \cdot \mathbf{H})^{-1} \cdot \mathbf{H}^T \cdot (\mathbf{PR} - \mathbf{PR}_0) \quad (1)$$

with

- \mathbf{X} : position vector including the clock bias
- \mathbf{X}_0 : approximate position and clock bias vector
- \mathbf{H} : measurement matrix
- \mathbf{PR} : vector containing the pseudoranges of all satellites
- \mathbf{PR}_0 : approximate vector of the pseudoranges

Using the same measurement matrix \mathbf{H} , the velocities of the antenna and the clock rate can be calculated from the deltarange measurements:

$$\mathbf{V} = \mathbf{V}_0 + (\mathbf{H}^T \cdot \mathbf{H})^{-1} \cdot \mathbf{H}^T \cdot (\mathbf{DR} - \mathbf{DR}_0 - \mathbf{DR}_{Sat}) \quad (2)$$

with

- \mathbf{V} : velocity vector including the clock rate
- \mathbf{V}_0 : approximate velocity and clock rate vector
- \mathbf{DR} : vector containing the deltaranges of all satellites
- \mathbf{DR}_0 : approximate vector of the pseudoranges
- \mathbf{DR}_{Sat} : vector containing the deltarange part due to the velocity of the satellites

To ensure the integrity of the DGPS positions and velocities these data have to be monitored by an appropriate redundancy concept. In case of more than 4 satellites are tracked, redundant measurements exist which can be used for receiver autonomous integrity monitoring (RAIM).

Many RAIM concepts are based on the residuals calculated from the least squares solution shown before (e.g. see [6]). These concepts normally cannot detect more than one error once. In the following a new RAIM algorithm to detect and to isolate erroneous pseudorange and deltarange measurements is described.

The vectors \mathbf{X} in (1) and \mathbf{V} in (2) contain four unknowns. Thus for solving the unknowns four GPS measurements (pseudorange and deltaranges) are required. But in case of more than four GPS measurements (pseudoranges and deltaranges) a failure detection is possible. An unambiguous failure isolation is only possible, if the following relationship is fulfilled:

$$n_e < m - u - 1 \quad (3)$$

- with n_e : number of errors
- m : number of measurements
- u : number of unknowns (here: $u = 4$).

The following method is designed to minimize the occurrence of ambiguous results in the error detection and isolation solution. The method is applied independently to the pseudorange and deltarange measurements and is based on the following equations.

$$\mathbf{Y} = \mathbf{F} \cdot \mathbf{X} + \mathbf{e} \quad (4)$$

with

- Y:** measurement vector, consisting of the pseudoranges or the delta ranges (m rows)
F: linearized measurement matrix (m rows, u columns)
X: vector of unknowns (coordinates and clock bias in case of pseudoranges or velocities and clock rate in case of delta ranges), (u rows)
e: error vector (m rows)

It should be mentioned that the matrix **F** is the same for processing the pseudoranges and delta ranges and is equivalent to the matrix to be used in the least squares algorithms when calculating the vector **X** and the vector of the residuals **v**:

$$\hat{\mathbf{X}} = (\mathbf{F}^T \cdot \mathbf{F})^{-1} \cdot \mathbf{F}^T \cdot \mathbf{Y} \quad (5)(a,b)$$

$$\mathbf{v} = \mathbf{F} \cdot \hat{\mathbf{X}} - \mathbf{Y}$$

The magnitude of the residuals is in general not an unambiguous indicator for an error. A solution of this problem is to form a discrepancy vector, **w**, which depends only on the measurements, but not on the unknown itself. This leads to the following equation:

$$\mathbf{w} = \mathbf{B} \cdot \mathbf{Y} = \mathbf{B} \cdot \mathbf{F} \cdot \mathbf{X} + \mathbf{B} \cdot \mathbf{e} \quad (6)$$

Obviously the independence of **w** from the vector **X** is guaranteed if the new condition matrix **B** fulfils the following condition:

$$\mathbf{B} \cdot \mathbf{F} = \mathbf{0} \quad (7)$$

The required condition matrix **B** can be found as shown in the following example. The first step is to calculate the vector of unknown **X₁₄** by using only the first four GPS measurements:

$$\mathbf{X}_{14} = \mathbf{F}_{14}^{-1} \cdot \mathbf{Y}_{14} \quad (8)$$

Taking any of the remaining GPS measurements **Y_i**, one can form the following equation for each measurement not used in the calculation of **X₁₄**:

$$\mathbf{Y}_i = \mathbf{f}_i \cdot \mathbf{X}_{14} = \mathbf{f}_i \cdot \mathbf{F}_{14}^{-1} \cdot \mathbf{Y}_{14} \quad (9)(a,$$

$$\text{or} \quad \mathbf{0} = \mathbf{f}_i \cdot \mathbf{F}_{14}^{-1} \cdot \mathbf{Y}_{14} - \mathbf{Y}_i = \mathbf{b}_{i4i} \cdot \mathbf{Y}_{14i} \quad b)$$

The equation is only valid if no measurement errors occur or if the error vector **e** is **0**. But if one or more measurements are erroneous a discrepancy **w_{14i}** can

be calculated. To get discrepancies with equivalent variances it is evident to normalize each row vector **b**.

$$\mathbf{w}_{14i} = \frac{\mathbf{b}_{14i}}{|\mathbf{b}_{14i}|} \cdot \mathbf{Y}_{14i} \quad (10)$$

If more than 5 measurements are available, this procedure has to be extended in such a way that all combinations of 5 measurements have to be established, resulting in the discrepancy vector **w**:

$$\mathbf{w} = \mathbf{B} \cdot \mathbf{Y} \quad (11)$$

The number of discrepancy equations n_w can be calculated by

$$n_w = \frac{m!}{(n-(u+1))! \cdot (u+1)!} \quad (12)$$

In case of 6 satellites tracked, 6 discrepancy equations (of which two are linearly independent) can be found and ordered in the following way:

$$\begin{bmatrix} \mathbf{w}_1 \\ \mathbf{w}_2 \\ \mathbf{w}_3 \\ \mathbf{w}_4 \\ \mathbf{w}_5 \\ \mathbf{w}_6 \end{bmatrix} = \begin{bmatrix} 0 & \mathbf{b}_{12} & \mathbf{b}_{13} & \mathbf{b}_{14} & \mathbf{b}_{15} & \mathbf{b}_{16} \\ \mathbf{b}_{21} & 0 & \mathbf{b}_{23} & \mathbf{b}_{24} & \mathbf{b}_{25} & \mathbf{b}_{26} \\ \mathbf{b}_{31} & \mathbf{b}_{32} & 0 & \mathbf{b}_{34} & \mathbf{b}_{35} & \mathbf{b}_{36} \\ \mathbf{b}_{41} & \mathbf{b}_{42} & \mathbf{b}_{43} & 0 & \mathbf{b}_{45} & \mathbf{b}_{46} \\ \mathbf{b}_{51} & \mathbf{b}_{52} & \mathbf{b}_{53} & \mathbf{b}_{54} & 0 & \mathbf{b}_{56} \\ \mathbf{b}_{61} & \mathbf{b}_{62} & \mathbf{b}_{63} & \mathbf{b}_{64} & \mathbf{b}_{65} & 0 \end{bmatrix} \cdot \begin{bmatrix} \mathbf{Y}_1 \\ \mathbf{Y}_2 \\ \mathbf{Y}_3 \\ \mathbf{Y}_4 \\ \mathbf{Y}_5 \\ \mathbf{Y}_6 \end{bmatrix} \quad (13)$$

For example, assuming only one error in measurement **Y₁**, results in 5 discrepancies (**w₂** to **w₆**) while the discrepancy **w₁** is not affected. Thus the error of **Y₁** can be detected and isolated. Generally a non affected discrepancy **w_i** indicates an erroneous measurement **Y_i**. This scheme and strategy can be extended if more than 6 satellites are available. Generally $(m-u-1)$ errors can be detected and at most $(m-u-2)$ errors can be isolated but the number of equations increases with the number of measurements m . In case of 7 satellites the number is 21 and in case of 9 satellites the number is already 126. Because of the slowly varying line of sight vectors to the satellites the coefficients \mathbf{b}_{ij} are varying slowly too. Thus the coefficients need not to be calculated every second in contrast to those coefficients to be used in the least squares solution. To minimize the amount of equations in case of more than 6 satellites, subsets using different groups of satellites can be formed and examined individually.

If all discrepancies are less than a predefined threshold all measurements are used in the least squares solution delivering the GPS positions and velocities. Otherwise only the measurements or groups of measurements are used which have passed the test.

In the following, an example of the RAIM algorithm applied to the DGPS-corrected deltaranges of 6 satellites tracked is shown. The original measurements of the 6 PRN's and the corresponding measurement matrix H needed for the least squares solution and to calculate the condition matrix is shown. The measurements are already reduced by the velocity of the satellites. Thus the measurements only contain the clock rate of the receiver and the velocity of the antenna which was not moved during this example. The results are shown below:

GPS time: 223244, 6 Satellites tracked on both stations; the measurements are the DR's from which the satellite motion is removed.

PRN meas.	Measurement Matrix H					
5	194.4728	-0.465228	-0.382469	-0.798298	1.000000	
1	194.4711	-0.537353	0.701787	-0.467704	1.000000	
9	194.4694	-0.767881	-0.637048	-0.067298	1.000000	
6	194.4642	-0.982342	0.178837	0.054962	1.000000	
24	194.4688	-0.272917	-0.916207	-0.293396	1.000000	
20	194.4751	-0.591787	0.356686	-0.722885	1.000000	

The normalized condition matrix **B** is calculated with the formulas shown before. The first row does not use the satellite with PRN 5, the second satellite PRN 1, and so on. Due to the normalization the root summed square of each row is 1 resulting in discrepancies with same variances.

Condition matrix B normalized						
0.000000	0.409344	0.649115	-0.501541	-0.325703	-0.231216	
-0.492437	0.000000	0.544888	-0.465943	-0.074333	0.487826	
0.528793	0.368985	0.000000	0.048250	-0.213769	-0.732259	
0.508917	0.393017	0.060101	0.000000	-0.235890	-0.726144	
0.542350	0.102892	-0.436957	0.387104	0.000000	-0.595389	
-0.179143	0.314185	0.696441	-0.554454	-0.277029	0.000000	

The 6 discrepancies calculated from the original deltarange measurements are shown in the following first row. The threshold to indicate an erroneous discrepancy is set to 0.01 m. In the first row all discrepancies are below this threshold. Thus the measurements of all satellites pass the test. Then, an error of only 0.5 m was added to the deltarange of the first satellite (PRN 5) and the discrepancies were calculated again (see row 2). The asterisk behind the discrepancies indicate an error. In this case only the first discrepancy does not indicate an error. Thus the satellite with PRN 5 must be faulty. The same procedure is repeated with the other satellites. In all cases the faulty satellite is recognized correctly.

discrepancies w1 to w6

no faults:	0.0023	0.0036	-0.0018	-0.0016	-0.0034	0.0030
PRN 5:	0.0023	-0.2426*	0.2626*	0.2529*	0.2678*	-0.0865*
PRN 1:	0.2069*	0.0036	0.1827*	0.1950*	0.0481*	0.1601*
PRN 9:	0.3268*	0.2760*	-0.0018	0.0285*	-0.2219*	0.3513*
PRN 6:	-0.2485*	-0.2294*	0.0223*	-0.0016	0.1902*	-0.2742*
PRN 24:	-0.1606*	-0.0336*	-0.1087*	-0.1195*	-0.0034	-0.1355*
PRN 20:	-0.1134*	0.2475*	-0.3680*	-0.3646*	-0.3011*	0.0030

3.3 BRICKWALL CONCEPT

A latent danger using *closed loop Kalman filters* to integrate GPS or other measurements in inertial navigation systems are the non detected errors of the augmentation sensors which can corrupt all system parameters. A way out is the *open loop Kalman filter*.

Another novel concept is to calculate the AHRS functions twice, the so called "brickwall" concept.

The AHRS processor performs the conventional AHRS computations of the output parameters specified in ARINC-705 [5]. The computations include the augmentation by means of a True Airspeed Sensor (TAS), a static pressure sensor (Baro Altitude) and a magnetic heading device. The magnetic heading device is used to initialize magnetic heading and to compensate for earth rate and drift of the vertical gyro. This is shown in the upper part of Fig. 4.

The lower part shows the redundant and more accurate computations of the AHRS output parameters according to ARINC-704 using the (D)GPS measurements in a Kalman Filter. These computations performed by the integration computer use the same gyro and accelerometer data as the conventional computation but the analytical platform and the navigation parameters are now augmented by the (D)GPS positions and velocities already checked by the RAIM test. Thus true heading is also available.

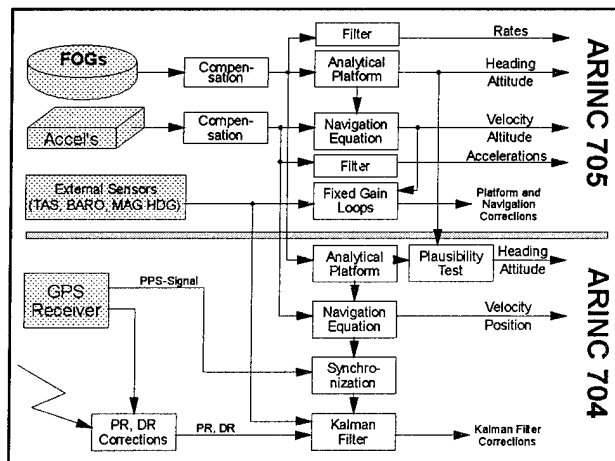


Fig. 4 Brickwall Concept

Although the RAIM applied to the DGPS positions and velocities already cancels the most significant errors, slowly varying errors, i.e. slight ramp errors, are difficult to detect. Due to the AHRS/DGPS Kalman filter, besides the inertial positions and velocities, all the other states (i.e. the platform angles and the sensor error estimations) are additionally affected by such non-detected errors. On the other hand, due to the complexity of the Kalman filter computations these computations are critical with respect to certification purposes, i.e. the failure mode and error analysis (FMEA). For these reasons the standard AHRS functions are calculated twice using different processors and augmentation sources. The parameters of both calculations are fed into a plausibility test to detect inconsistencies between the two independent computations and to increase the capability of the system to detect errors.

This capability is further improved by additional tests and processing concepts.

3.4 ADDITIONAL PRECAUTIONS

CASCADED KALMAN FILTER APPROACH

The cascaded Kalman Filter approach instead of a integrated Kalman filter is used in this concept to ensure the integrity of the overall system. As already proven in [4] the integrated Kalman filter has no advantage if at least 4 satellites are available. If less than 4 satellites are available the GPS measurements should be neglected because its gain is very poor and the synchronization of the GPS data to the PPS signal is degraded rapidly with the clock rate. On the other hand RAIM can only be applied if measurements of more than four satellites are available.

VEHICLE CAPABILITIES AND DELAYED UPDATES

Before the unfiltered GPS positions and velocities are used as measurements in the AHRS/DGPS Kalman filter, position and velocity changes are checked against actual speed for plausibility with respect to the vehicle capabilities. If the check fails, the measurements are rejected.

Because of the time needed to validate the GPS measurements, delayed Kalman filter updates are performed, giving an additional benefit. As the modeling of the vehicle motion dependent noise in the Kalman filter has a great impact on the filter performance, delayed updates give the possibility to

separate accurately periods of high and low vehicle dynamics.

KALMAN FILTER DIVERGENCE TEST

Before entering the Kalman filter a second statistical test is performed comparing the differences between the inertially and the GPS derived parameters, i.e. the observations. The Kalman filter itself gives the possibility of testing the observations for reasonableness. The filter's estimated observation variance is evaluated by:

$$\mathbf{D} = \mathbf{H} \cdot \mathbf{C} \cdot \mathbf{H}^T + \mathbf{R} \quad (14)$$

\mathbf{H} = measurement matrix

\mathbf{C} = error covariance matrix

\mathbf{R} = measurement noise matrix

The square root of \mathbf{D} is compared to the corresponding value extracted from the observations. Only if both values are similar, the observation is accepted and the update performed. The thresholds for accepting or rejecting the observations must be set very carefully, because of the consequences to filter performance.

BUILT IN TEST (BIT)

Besides the plausibility tests, which are applied to the external data, the internal sensor data processing must be monitored and augmented by a sophisticated BIT of the inertial sensors. FOG's, as developed by LITEF, have the advantage that BIT functions can be easily implemented due to the closed loop control of the FOG's. Therefore, test signals are applied continuously without disturbing the measurements or the accuracy. Thus, the function of the gyros is monitored and the data processing is verified.

This concept is not feasible with so called "low cost" sensors.

4 TEST RESULTS

The first prototype of the LCR-94 has been tested in July 1995 in the LITEF test van. During the trials two C/A-Code GPS receivers from MAGNAVOX were used (a 12 channel receiver for the reference station and a 6 channel receiver in the truck). The tests show the accuracy of the prototype system in the DGPS augmented navigation mode and in the free inertial navigation mode when not enough satellites are available. Although the system is designed to meet the AHRS requirements according to

ARINC-705 based on an additional magnetic heading input, the system is able to perform an autonomous alignment by estimating heading from the earth rate components. The initial heading errors are about 2° , but after some manoeuvres in DGPS augmented mode the heading error decreases to 0.1° . It should be mentioned that heading has not to be confused with track, which is calculated from the north and east velocity components. The difference between the both is the drift angle which can reach 10° and more in aircrafts.

The following plots show the positions measured by the DGPS only and by the navigation system during the trials performed in a country region with small villages. The distance to the reference station was about 10 km. One can see gaps of several minutes in the DGPS positions (Fig. 5) caused by obstacles near the test route. The navigation system is able to bridge these outages (Fig. 6). A continuous GPS position was not available for longer than 1 min, thus the OTF-method to calculate reference positions in post-processing could not be applied. The accuracy was estimated by comparing the same positions at different times. The comparisons led to a position accuracy in the DGPS augmented mode of 0.5 m to 1.5 m. This accuracy can be preserved in the free inertial mode only during the first ten seconds after GPS outages. The position accuracy decreases to 10 m after one minute and about 50 m after a 3 min GPS outage. The results show that an AHRS is only able to bridge GPS outages up to 1 minute. This is normally enough for avionics applications. Improvements are only possible with sensors used in inertial navigation systems (INS).

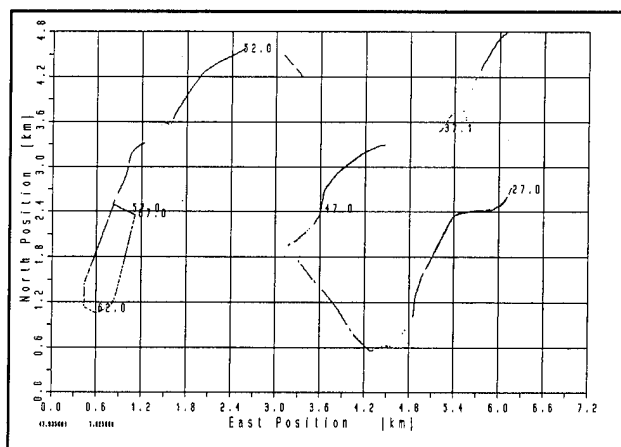


Fig. 5 Position Plot, DGPS only

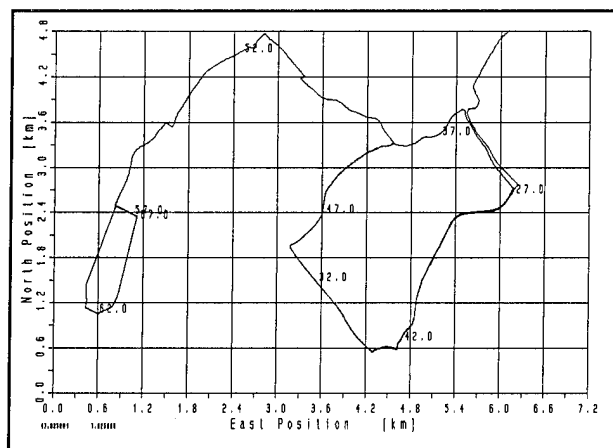


Fig. 6 Position Plot, AHRS/DGPS

Further examinations are focussed on the accuracy of the heading angle. Fig. 7 shows the heading angle when driving the same road four times. One can see the variation of the heading angle driving a lane in southern direction (see lower left part of the position plots). The heading angles are plotted with respect to the distance of an arbitrarily chosen reference point at the starting corner. The distance is calculated from the position of the hybrid navigation system. Thus the plots are showing the accuracy of the heading and the positions. The random variations of the heading angles are caused by the steering manoeuvres of the driver. Comparing the mean values of the four trials, the heading differences are below 0.1° . Further results derived from the truck tests are:

accuracy of roll and pitch angle:	0.02°
velocity (with DGPS):	0.01 m/s
gyro bias repeatability:	$0.32^\circ/\text{h}$
accelerometer bias repeatability:	0.323 mg

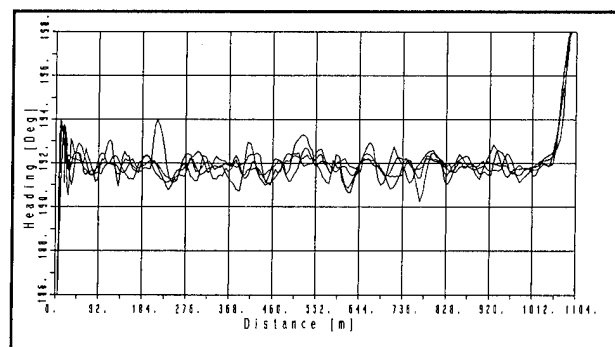


Fig. 7 Heading Accuracy

5 CONCLUSIONS

A new AHRS/DGPS system designed for flight critical applications has been described. The system is based on the newest inertial sensor technology: fibre optical gyros and micromechanical accelerometers. Attitude, heading, velocities and position are available with a data rate of 64 Hz. A new sophisticated redundancy concept for the GPS measurements and the integrated system shall guarantee the stringent integrity requirements. This concept is based on a specific RAIM algorithm to monitor the GPS measurements, and a dual calculation of the flight critical parameters using the "brickall" concept.

The algorithms were developed and analyzed in a prototype system. The first tests with the described system have shown that a position accuracy of ± 0.5 m to ± 3.0 m can be achieved even during GPS outages of up to 10 seconds. During longer outages the position accuracy decreases between 5 m to 20 m per minute depending on the manoeuvres. The accuracy achievable is limited by the quality of the GPS receiver. The 1 m level or better is only achievable if provision against multipath effects is applied.

The new generation of C/A-Code GPS receivers (narrow correlator receivers or the L1-receivers using the P-Code even under AS) will be able to offer this accuracy without the necessity of using ambiguity resolution techniques not suitable for flight critical applications. Thus outages from 10 s to 20 s can be bridged to fulfill the requirements for precision approach up to CAT III.

6 REFERENCES

- [1] Davis, J. and Kelly, R.:
RNP Tunnel Concept for Precision Approach with GNSS Application.
Proceedings of the Institute of Navigation Annual Meeting, 21-23 June 1993.
- [2] Cohen, F., Pervan, B., Cobb, H.S., Lawrance, D., Powell, J.D., Parkinson, B.B.:
Real-Time Cycle Ambiguity Resolution using a Pseudolite for Precision Landing of Aircraft with GPS.
Second International Symposium on Differential Satellite Navigation Systems. 30.3.-2.4.1993, Amsterdam, The Netherlands.
- [3] Meyer-Hilberg, T. Jacob:
High Accuracy Navigation and Landing System using GPS/IMU System Integration.
IEEE PLANS, 1994.
- [4] Bäumker, M., M. Hüllenkremer, A: Lehmann:
Integration of a FOG-AHRS with (D)GPS.
DGON Symposium on Gyro Technology, Stuttgart 1994.
- [5] ARINC: Attitude and Heading Reference System
ARINC Characteristic 705-5
Annapolis, April 30, 1985
- [6] Vieweg, S.:
Aircraft Autonomous Integrity Monitoring for an Integrated Satellite / Inertial-Navigation System.
Proceedings ION GPS-93, Satellite Division of the Institute of Navigation, Salt Lake City, Sept. 1993.

A Proposed GPS Block IIF Satellite Design with Civilian Dual Frequency and WAAS Signals

Mohan Ananda, Prem Munjal, and K.T. Woo
The Aerospace Corporation

Rich Cole
Innovative Solutions International, Inc.

Capt. Steve Steiner
US Air Force

BIOGRAPHY

Dr. Mohan Ananda is a consultant to The Aerospace Corporation. He has been involved with GPS since 1980 and previously worked for the Jet Propulsion Laboratory and The Aerospace Corporation. He obtained his M.S. from the California Institute of Technology and his Ph.D. from the University of California, Los Angeles.

Dr. Prem Munjal is a Senior Project Engineer at The Aerospace Corporation working in the GPS Joint Program Office. He is currently Manager of the FAA Satellite Navigation Program support activities. He obtained his M.S. and Ph.D. from the University of California, Berkeley.

Dr. K.T. Woo is an engineering specialist in the Communication System Engineering Department of The Aerospace Corporation. He obtained his B.S., M.S., and Ph.D. from the University of California, Los Angeles.

Mr. Richard Cole is Director of Washington Operations with Innovative Solutions International, Inc. He is an operational expert on the implementation of satellite-based navigation and WAAS. He has an M.S. from Embry-Riddle Aeronautical University.

Capt. Stephen Steiner is Chief of Advanced GPS Navigation Systems in Advanced Projects Division of the GPS Joint Program Office. He obtained his BSEE from the United States Air Force Academy.

ABSTRACT

The United States Air Force and, in particular, the GPS Joint Program Office (JPO) is acquiring the GPS follow-on satellites known as Block IIF. It is estimated that about 33 Block IIF satellites will be procured. This paper presents a Strawman design for integration of the Global Positioning System (GPS) and the Wide Area Augmentation System (WAAS) into a seamless architecture to provide the highest level of system performance to both DOD and the civilian community. This architecture consists of three basic features: 1) incorporation of the transmission of the WAAS signal

from GPS satellites, 2) transmission of dual frequency civil signals to facilitate ionospheric delay estimation by civil users, and 3) uplink of WAAS data from WAAS ground stations to Block IIF satellites. The proposed design retains all Block IIR satellite features such as crosslink ranging and autonomous navigation, and adds new capabilities to uplink WAAS data from the WAAS ground station to any Block IIF satellite. This uplink data would be crosslinked to all Block IIF satellites so that updated data could be downlinked on the WAAS signal within six seconds to meet the WAAS integrity and availability requirements. This use of Block IIF satellites could eliminate the need for additional geostationary satellites beyond the three necessary for the initial state WAAS.

This paper presents two designs for crosslinking WAAS data. One design consists of a Frequency Division Multiplexing (FDM) scheme using a UHF frequency band between 286 and 286.3 MHz and the second design utilizes a 60-GHz frequency crosslink. A cost benefit tradeoff should facilitate selection of the approach that should be implemented. This paper also presents a system architecture of WAAS with Block IIF satellites to supplement the geostationary satellites which already exist in the initial WAAS design to transmit the WAAS signal.

1. Introduction

It is important for the operational GPS to maintain a constellation of 24 satellites to provide the required navigation service to its users. Since the satellites have a specific expected design life, additional satellites must be procured to maintain the required constellation size. Currently operational satellites are identified as Block II and IIA; additional Block IIR satellites are in production. It is expected that, in late 1996 or early 1997, Block IIR satellites will begin to be placed in operation. There will be 21 Block IIR satellites available and these satellites will be launched over a 6- to 8-year period. Although the Block IIR satellites have been designed to maintain backward compatibility to GPS signal characteristics, these satellites have additional design features such as

autonomous navigation and reprogrammable software. Because DOD procurement lead time for satellites from the time of request for proposal to delivery is about six to seven years, the GPS Joint Program Office (JPO) is currently procuring the GPS follow-on satellites known as Block IIF. It is expected that about 33 Block IIF satellites will be procured. Based on expected design life and possible launch and/or on-orbit failures, this number will be sufficient for about an additional ten years.

The 33 satellites will be designed in three groups. The initial design consists of six satellites. The second and third designs consist of 15 and 12 satellites each. New options can be incorporated in the second and third designs to be defined by the Government. The Wide Area Augmentation System (WAAS) crosslinks can be incorporated in the second and third designs for satellites 7 through 33 if desired. Because of schedule constraints, incorporation of WAAS crosslinks in the first six Block IIF satellites may be difficult. However, dual frequency signals for civil ionospheric correction can be incorporated in the first six Block IIF satellites and may be as early as some of the later Block IIR satellites. Opportunities for design changes to incorporate WAAS functions on Block IIF are available. The time windows are critical however; appropriate and timely decisions will be necessary to ensure success.

Although GPS was primarily designed for navigation service to military systems, civilian applications are increasing significantly. It is clear that without augmentation the current 24-satellite GPS constellation will be unable to meet the required performance for many of these desired civil uses, particularly aviation. To ensure aviation needs are met, the United States Federal Aviation Administration (FAA) is augmenting the GPS with WAAS. Ultimately, GPS/WAAS will become the primary navigation system for the National Airspace (NAS) as civil and military aviation transition from land-based to space-based navigation service.

The primary purpose of WAAS is to achieve enhancement to aviation system capacity, efficiency, and flight safety. To achieve these goals, WAAS is being implemented specifically for performance improvements in increased availability, accuracy, integrity, and continuity of service for civil aviation.

WAAS architecture is described in the WAAS specifications¹. As currently planned, WAAS depends on geostationary satellites (initially through Inmarsat) to broadcast GPS integrity and correction parameters to civil aviation users to provide additional ranging signals and to improve navigation accuracy, enabling precision approach landing for civil aviation. WAAS signal specifications are described in detail by Van Dierendonck and Enge². The WAAS signal will be generated from the ground at Wide-area Master Stations (WMS) by processing data collected

from Wide-area Reference Stations (WRS) located over the service area and by uplinking via Ground Earth Stations (GES) to the geostationary satellites for retransmission.

In conjunction with the FAA, the GPS JPO has been studying the possibility of developing a communication satellite augmented GPS (CAG) payload which would be deployed on a number of existing Defense Satellite Communication System (DSCS) satellites to be launched over the next ten years. The FAA was also interested in the possible development of CAG to supplement Inmarsat satellites for broadcasting WAAS signals. The CAG concept was to meet the needs of both DOD and WAAS and is discussed in a paper by Siegel et al³. The payload description is provided in a paper by Ananda et al⁴. The signal structure is discussed in a paper by Ananda et al⁵. The data format accommodating the needs of both military users and civil aviation users is described in another paper by Ananda et al⁶. CAG payload architecture has been studied in detail by the GPS Block IIR satellite contractor, results of which are presented in a paper by Aparicio et al⁷. Further, the JPO also considered the possibility of developing an independent geostationary satellite identified as Augmented GPS (AGPS) instead of a payload on the Defense Satellite Communications System. This system architecture is presented in a paper by Ananda et al⁸.

Development of AGPS would be highly desirable; however, concurrent development of AGPS and procurement of Block IIF satellites would be extremely difficult due to existing cost constraints. Therefore, studies have been performed to evaluate whether Block IIF satellites could be modified to meet WAAS operational performance requirements while retaining all other GPS mission capabilities. Analysis has shown that without impacting the GPS satellite system architecture, the satellite design could be modified to accommodate an independent WAAS signal on the Block IIF satellite.

This paper presents a satellite design for Block IIF that would meet all GPS mission and WAAS requirements. This paper provides a system architecture, describes signal structure, provides a description of the required satellite design changes, describes operational scenarios, and provides a summary and conclusions.

The proposed concept can be considered as an extension of, and would not affect, the initial WAAS system to be deployed in the 1998–2000 time frame. As an extension of the end-state WAAS system planned for the 2000–2002 time frame, Block IIF with dual frequency civil signals and WAAS data relay crosslinks would, however, provide the possibilities of reducing the number of WAAS reference stations required for ionospheric measurements and the number of geostationary satellites required for availability and continuity of service. This paper does not discuss the phase-in time line for such

incorporation. However, the possibility of such improvement is discussed.

2. System Architecture

As stated earlier, the primary requirements for WAAS are to achieve increased availability, accuracy, integrity, and continuity of service for civil aviation. The WAAS space segment should be deployed such that the satellites, in conjunction with the WAAS ground system, are able to meet specified requirements. Initial WAAS architecture requires three Inmarsat satellites. End-state WAAS would require three to five additional geostationary satellites¹. Because availability requirements are extremely stringent, any WAAS subsystem failure will cause the system to be less available. Since every GPS satellite could transmit the WAAS integrity and correction signals, system availability will increase significantly and any single satellite failure will have minimal impact on system availability.

One advantage of the geostationary satellite is that a single ground station can keep a continuous communication link with the satellite. However, a GPS satellite with a 12-hour orbit cannot keep a continuous communication link with the ground station. If, however, a crosslink communication system is built into the satellite architecture, a ground station communicating via any GPS satellite in the constellation could keep a nearly continuous communication link with all GPS satellites in the constellation. Further, if the communication link exists primarily to update data and not to transmit a ranging signal, then a nearly continuous communication link is sufficient. Moreover, onboard ranging code and carrier generation is preferable to ground generation to minimize errors of time synchronization and carrier and code coherence.

Like the currently planned WAAS operations, an independent communication link between the WAAS ground system and the Block IIF satellite through the GES is required. The WAAS ground system will generate WAAS data and uplink to the satellite in a nearly continuous mode, with stringent requirements on lag time between observation and transmission time. A system architecture meeting all WAAS constraints and specifications has been generated and is depicted in Figure 1. GPS satellites will be interconnected by an independent, dedicated, cross-communication link to transmit WAAS data between satellites. In addition to the S-band uplink available for GPS to uplink data for the DOD mission via the GPS Operational Control Segment (OCS), there will be another S-band uplink dedicated to WAAS for uplinking WAAS data by the WAAS ground system through GES.

GES operation will be independent of OCS, and both ground stations can uplink to the same satellite simultaneously without interference. Although the GES

cannot continuously track any particular GPS satellite, nearly continuous communication with all satellites will be achieved by the ground station communicating with any visible satellite and then periodically switching to another visible satellite and repeating this process. GPS ranging signals on an additional frequency will also be generated onboard the satellite to facilitate ionospheric calibration. Aviation users with properly equipped receivers will be able to track the conventional GPS signal and the WAAS signal.

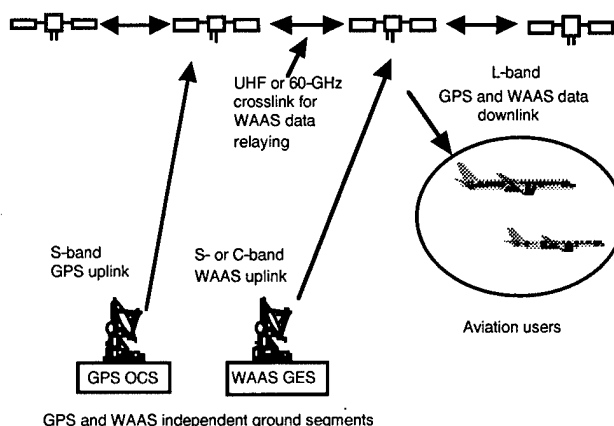


Figure 1. Block IIF crosslink to relay WAAS data: system architecture.

3. L-band Signal Structure

The GPS is an operational system; it is thus imperative that backward compatibility with the GPS signal be completely maintained. However, it is permissible to augment the signal without impacting the conventional GPS signal. Concepts for the GPS Block IIF satellite procurement have been presented by Decou⁹.

The signal structure as proposed for the Block IIF satellite is shown in Figure 2. The inphase channel (I) of the L1 frequency will contain a conventional C/A code, modulated with the navigation message identified as D1 at a rate of 50 bps. The conventional Y-code, modulated with the same D1 data, is on the quadrature phase channel of the L1 frequency. In addition to the Y-code, a new WAAS C/A code identified as C/A' and modulated with WAAS data (identified as D3 at a rate of 250 bps) will also be transmitted on the quadrature phase channel.

On the L2 frequency, the quadrature channel will contain the Y-code modulated with D1 data. Additional signals and data may appear on the inphase channel as well. Further, on a new frequency identified here as L5, about 20 MHz offset from the L2 frequency, the C/A code will again be transmitted to provide dual frequency measurements to civil aviation users to enable ionospheric calibration. The frequency identified here as L5 has been referred to as L4 by NRC and NAPA reports^{10,11}. With minimal modifications, the navigation message identified

as D1 could be modulated as the C/A code on the L5 frequency also.

Modulation of the L1 signal structure can be accomplished with an Interplex modulator as shown in Figure 3, using one common high power amplifier (HPA). Another alternative is to use separate modulators and HPAs for GPS and WAAS signals. A power budget of the L1 signals is given in Table 1.

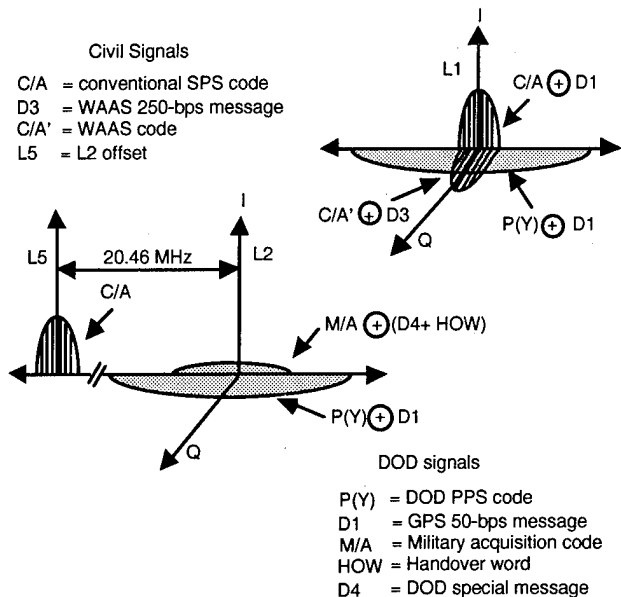


Figure 2. Proposed Block IIF L-band downlink signal structure.

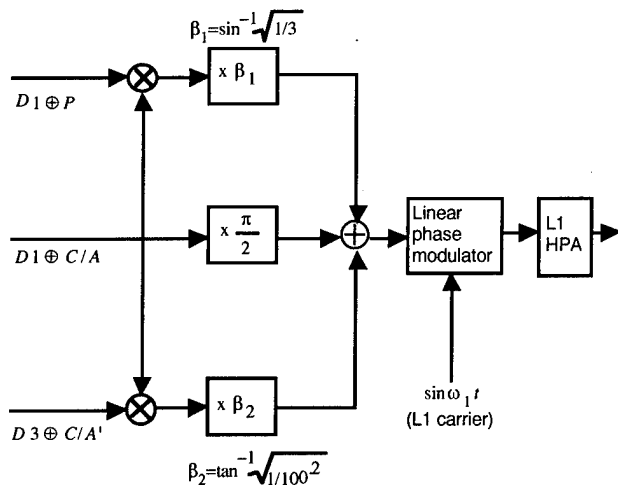


Figure 3. L1 interplex modulator.

With regard to user receiver performance, analysis has shown that there will be practically no interference between the C/A and C/A' codes on quadrature channels of L1 since the codes are nearly orthogonal to each other. Mutual interference is less than 0.1 dB as the Gold code cross-correlation is less than 65/1023 and assuming the orthogonal phase alignment

error is less than 6 degrees. Analysis has also shown that the C/A' code does not interfere with P or Y code since the P(Y) code receiver spreads the C/A' signal in code correlation and the C/A' code appears as a wideband noise input. It has been calculated that degradation on P(Y) code C/No is less than 0.02 dB when nominal P(Y) channel C/No and C/A' code power twice that of the P(Y) power are assumed. Analysis also has shown that the P(Y) channel will not interfere with C/A' code receptions because the P(Y) signal appears as wideband noise to the C/A' code receiver. It has been calculated that degradation on C/A' code C/No is less than 0.01 dB for a nominal C/A' channel C/No.

Table 1. L1 Downlink Power Split

	C/A Code Nav Data	C/A' code WAAS Data	P(Y) Nav Data	Intermodulation Product Loss
HPA power (dBW)	14.35	12.35	11.35	9.35
Circuit loss (dB)	-1.25	-1.25	-1.25	-1.25
Antenna gain (dBi)	13.0	13.0	13.0	13.0
EIRP (dBW)	26.1	24.1	23.1	21.1
Path loss (dB)	-184.4	-184.4	-184.4	-184.4
Polariz. loss (dB)	-3.7	-3.7	-3.7	-3.7
Atm. loss* (dB)	-1.0	-1.0	-1.0	-1.0
User antenna gain (dBi linear)	3.0	3.0	3.0	3.0
User rec'd power	-160.0	-162.0	-163.0	-165.0
Total L1 RF power required = 67 W				

* Atmospheric loss is customarily assumed to be 2 dB in GPS budgets, which includes both atmospheric and multipath losses. In this calculation we did not budget for multipath loss.

Therefore, the proposed signal structure for the Block IIF satellite will be backward-compatible and will meet signal requirements for WAAS without causing any potential interference problems. Further, two frequency measurements for achieving ionospheric calibration by civil aviation users can be accomplished without impacting DOD missions. The signal structure can also accommodate any needed additional data and code modulation for any specific DOD applications.

4. Block IIF Satellite Design

Since most system requirements for the Block IIF satellite are the same as for Block IIR, basic satellite design would be similar to Block IIR. However, certain key modifications are necessary to implement the additional requirements. Required new features are: an independent WAAS data uplink, independent crosslink to update WAAS data between all GPS satellites, new signal structure with backward compatibility, onboard processing to combine multiple WAAS uplink data to properly modulate data on the C/A' code to downlink according to the satellite location, and additional health and status monitoring subsystem elements.

A block diagram of major subsystem elements of the Block IIF satellite is shown in Figure 4. Certain

existing modules can be modified and others developed. The existing S-band antenna could be used for receiving both the GPS and the WAAS uplinks. However, there must be an additional S-band receiver for receiving WAAS uplink data. The existing architecture of the mission computer unit can be suitably modified to accommodate data routing processor function for storing, combining, and forwarding WAAS update data on the crosslink. The reference frequency system and the synthesizer assembly need not be modified at all. The dithered reference frequency will be the input frequency for generating all carriers and codes onboard the satellite.

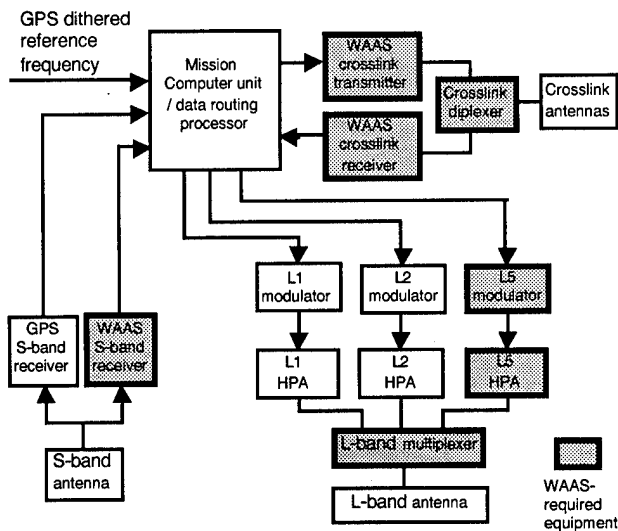


Figure 4. Block IIF design to accommodate WAAS data crosslink and downlink.

The current existing crosslink on the Block IIR satellite is based on a Time Division Multiple Access (TDMA) scheme on a UHF frequency band taking 36 seconds to complete a single crosslink frame in which all satellites have an opportunity to transmit. This will not be suitable for WAAS data update because the update lag time required by WAAS is significantly less than 36 seconds. Further, the existing crosslink supports other priority functions and may not always be available for WAAS. Therefore, a new dedicated crosslink for WAAS data is necessary and two potential schemes have been proposed in this paper. Depending on the complexity of implementation and associated cost, after a detailed tradeoff analysis, one proposed scheme can be selected.

For the dedicated crosslink, a crosslink transmitter, receiver, and diplexer must be added to the satellite. However, it is possible to use the existing crosslink antenna if the new crosslink frequency is in the UHF band. Otherwise, new crosslink antennas must also be added to the design. Regarding the L-band systems, a new L5 modulator and an L5 high power amplifier must be designed to transmit the C/A code on L5. All other subsystems can be used. Some modification to incorporate

the WAAS signal on L1 will be required, such as L1 power increase and the interplex modulator as discussed in Section 3.

There would be measurable, but small, impact on the total satellite weight and power and if the new features are built into the early design of the total satellite, weight and power impacts can be further reduced. However, if these new features are added as improvements after the design of the conventional GPS satellite, the weight and power impact would be considerably higher.

5. UHF Crosslink Option for WAAS Data Relay

Two crosslink options have been considered in the study to relay WAAS data through the Block IIF constellation: 1) a UHF option, and 2) a 60-GHz option. The UHF crosslink option is the baseline approach because it has the least payload impact and schedule risk between the two approaches. By sharing the same crosslink transmit/receive antennas with the current GPS crosslink system, the payload cost and weight/power increase for WAAS data relay can be minimized. This and the following section describe the UHF and 60-GHz options and give preliminary weight and power impact on the Block IIF payload for each option.

The system concept of using Block IIF crosslinks to relay WAAS data is illustrated in Figure 1. The basis of this concept is packet communication with crosslink relaying. The WAAS GES, which uplinks WAAS data in the current WAAS design to a geostationary satellite, is modified to transmit to Block IIF satellites within its field of view via S-band gimbaled antennas. A single Block IIF satellite is selected as the designated network entry satellite at any particular time. Satellite selection is achieved by ground-to-space antenna selectivity and by associating the uplink message packet with the identity of the selected satellite in a packet header added on the WAAS message structure during uplink transmission. Since the GPS satellites have 12-hour orbits, different network entry satellites, depending on satellite geometry, will be selected during each day. Two S-band uplink antennas will be used during network entry satellite transition, and a make-before-break strategy should be used in transition from one network entry satellite to another to avoid loss of uplink signal during this transition.

The network entry satellite, after receiving an uplinked WAAS message, will broadcast the message across the Block IIF constellation through the UHF crosslinks using a flood routing or combined flood and directed routing protocol. Each satellite in the constellation that receives this message for the first time will rebroadcast the same message to its neighboring satellites. This is performed until each satellite has seen the message at least once, at which time the satellites will cease relaying that message within the constellation. They

are then ready to relay another WAAS message when it arrives on the uplink.

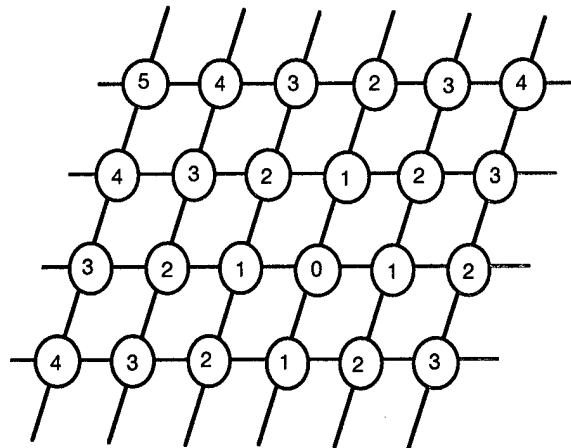
To facilitate message routing through the crosslink and to control crosslink transmission error, a new packet header (denoted here as the network routing header) will be added to the WAAS message during uplink and crosslink transmission. This header will contain the identity of the designated network entry satellite that receives the uplink transmission, a message count or a message ID number giving the order of the uplink messages during the day, and parity bits of a Cyclic Redundancy Code (CRC), which is used to verify that the message is correctly received over the crosslink. Only messages verified to be correctly received by the CRC will be retransmitted over the crosslink. This will minimize the throughput requirement of the network. The message ID can be given either by the time of day at which this message is generated at the WMS, or by numbering the uplinked messages within a convenient time period, such as a 24-hour day. The identity of the designated network entry satellite, as mentioned above, is used to select the appropriate Block IIF satellite for uplink message reception. The message ID will allow the satellites to determine whether they have received the message already, and cease relaying that message if they have seen it before. The network routing header length, including the network entry satellite ID, message ID, and CRC parity, is estimated to be 50 bits.

In addition to crosslink relaying, the Block IIF satellite is also responsible for transmitting on L1 the received WAAS message to aviation users as discussed in Section 3. The WAAS message received from the crosslink packet is reformatted before downlink transmission by deleting the network routing header and properly reordering message packets to form a continuous data stream of 250 bps, as currently planned, to be broadcast from the geostationary satellite. The 250 bps data is modulated with a satellite-generated Gold code (C/A') and transmitted to aviation users with GPS C/A and $P(Y)$ code navigation signals. The C/A and C/A' codes will be different members of Gold codes belonging to the same Pseudo-Random-Noise (PRN) family, and are unique for each satellite. By choosing C/A' codes, the user can elect to receive the WAAS message from a number of visible Block IIF satellites. Availability of WAAS signals should be significantly improved over the current WAAS design with a maximum of only two visible geostationary satellites for CONUS users. This is especially true over high latitude regions where geostationary coverage is poor.

A stored-and-forward mode is used for both GES uplink and satellite crosslink message transmission. To absorb the overhead of the network routing header used for uplink and crosslink transmission, and to reduce latency associated with crosslink relaying, the uplink and crosslink burst data transmission rate will necessarily be

increased above the current WAAS downlink data rate of 250 bps. A 2.4-Kbps uplink burst data rate is considered in the study, and preliminary analysis results indicate that the WAAS time-to-alarm requirement of 6 seconds can be met with sufficient margin including other WAAS data delays with this burst data rate.

A scheme for crosslink message relaying is illustrated in Figure 5, in which a 6-plane 24-satellite constellation is shown. The numbers within each circle denote the order in which the uplink message was received from uplinks and crosslinks. The number 0 is used to denote the network entry satellite (i.e., satellite-0) which receives the uplink message from the GES, which in turn receives the 250-bit message from the WMS. The GES transmits the WAAS message to satellite-0 via S-band at a 2.4-Kbps burst rate after appending a network routing header to the WAAS message. Assume the network routing header is 50 bits in length as described above. The resultant packet with the network routing header is 300 bits. Transmission time of this packet is $1/8$ -second at the 2.4-Kbps burst rate. The propagation delay is < 0.1 seconds for GPS with a radial distance of 26,570 km. The combined delay is 0.23 seconds before satellite 0 receives the uplinked message from GES. After receiving this 300-bit packet, satellite-0 will retransmit it via the UHF crosslink to its neighboring satellites, again at a 2.4-Kbps burst rate.



Numbers indicate how many hops are required to propagate through the constellation

Figure 5. UHF/FDM crosslink latency.

In Figure 5 we assume two satellites on the same plane, ahead of and behind satellite 0, and the two closest satellites on two adjacent planes to satellite 0 will tune to the transmit frequency of satellite 0 and receive its messages. These satellites are denoted by the number 1 and will receive satellite 0's retransmission of the uplinked message in the first hop of the crosslink network. The distance from one GPS satellite to adjacent satellites on the same plane and to the closest satellite on two adjacent

planes is < 38,000 km, resulting in a propagation delay of < 0.13 seconds. The combined delay due to propagation and transmission times in the first hop is < 0.26 seconds. The satellites labeled with the number 1 will retransmit their received messages to their in-plane and cross-plane neighbors and, in this way, the uplinked message is propagated throughout the constellation. The maximum number of retransmissions before the uplinked message reaches all satellites in the constellation is five, as indicated in Figure 5. The satellites keep a record of the IDs of all messages received. The received message packets are reformatted as described previously and sent to aviation users on L1. The downlink propagation delay is < 0.1 seconds, and the message transmission time is 1 second at the downlink rate of 250 bps. The maximum delay between the time the message is transmitted on the GES uplink and the time that the user receives the WAAS message on L1 is less than 2.6 seconds, as indicated below:

$$\begin{aligned}
 & \text{uplink delay} \quad \text{max crosslink delay} \quad \text{downlink delay} \\
 T \quad & \text{UHF Crosslink Delay} \leq (0.1+0.125) + 5(0.13+0.125) + (0.1+1.0) \\
 & = 2.6 \text{ sec.}
 \end{aligned}$$

Note that the delay shown above is the absolute worst case delay because the message must propagate throughout the GPS constellation. For regional WAAS, the nominal delays are smaller. For example, only GPS satellites in view of the North American Continent are needed to relay the WAAS message to CONUS users, and satellites over Europe or Asia will not be required to broadcast the same WAAS message generated from a CONUS GES. The number of crosslink hops required to propagate the WAAS message among the satellites in view of the North American Continent is only one or two and not as many as five. Maximum crosslink delay for a regional WAAS such as the CONUS WAAS is thus < 2.0 seconds. In addition, it should be noted also that the 2.4-Kbps uplink and crosslink burst data rate sized in this study, while necessary to minimize latency in message relay throughout the network, is eight times higher than the information throughput requirement of the WAAS data (250 bps). This implies that this crosslink network is capable of accepting and relaying uplink data from other regional WAAS in addition to the CONUS WAAS, providing a future growth potential for international expansion of the current WAAS.

The proposed frequency plan for UHF crosslink relay of WAAS messages is illustrated in Figure 6. This frequency plan is chosen to avoid conflict with current Block IIR crosslink frequencies used for GPS Autonomous Navigation and NDS Data Relay. Twenty-four frequencies in the band from 286 to 286.3 MHz are selected, producing a dedicated transmission channel for each Block IIF satellite. The minimum channel separation

is 12.5 KHz. Since each Block IIF satellite has knowledge of its own position and that of its neighboring satellites, it can tune to three or four of its closest neighbors to receive the crosslink messages. The FDM concept requires implementation of a UHF receiver that receives three to four FDM channels simultaneously. This deviates from the current Block IIR Autonomous Navigation UHF crosslink, which uses a band of random frequencies and a Time Division Multiplexing (TDM) format with a 36-second minimum TDM cycle and 1.5-second transmission slot for each satellite. The advantage of the FDM format is that each satellite can retransmit its received message as soon as the message is received, and avoid the inherent latency of the TDM format.

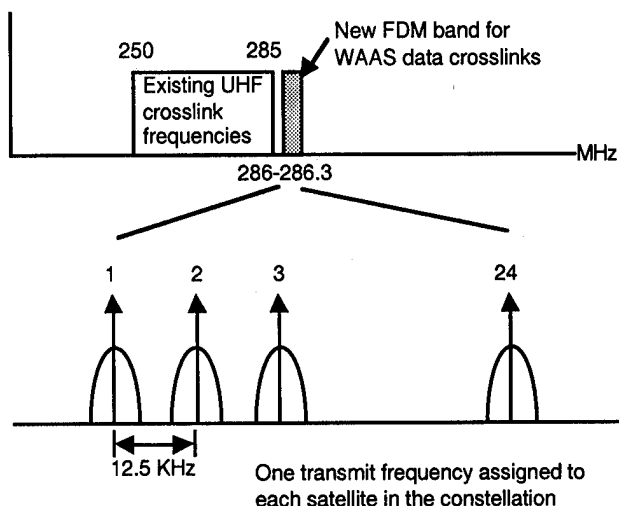


Figure 6. Proposed UHF crosslink FDM frequency plan.

Table 2 gives a link budget for the UHF crosslinks. The UHF transmit power is estimated to be around 85 W for the UHF FDM crosslink with a 2.4-Kbps data rate. The WAAS data and the GPS data crosslinks will share the same UHF transmit and receive antennas, which are broad beam antennas that do not require pointing.

The equipment to be added to the basic Block IIF payload for receiving the WAAS data from WAAS GES, relaying it through the Block IIF crosslinks, and sending it down to the users at L1 are the following:

- S-band receiver to receive WAAS uplink
- UHF transmitter for WAAS crosslink
- UHF receiver for WAAS crosslink
- crosslink multiplexer
- L5 modulator
- L5 high power amplifier

Table 3 details the weight and power impact of the WAAS crosslink and up/downlink equipment on the Block IIF payload. A weight increase of approximately 60 lbs and a power increase of approximately 275 W is estimated. An estimate of the total weight increase of the launch due to these added weight and power requirements is also given in Table 3. The total increase in launch vehicle weight is estimated to be about 360 lbs for the UHF crosslink option. In this estimate, redundancy is only assumed to be internal, and there is no provision for cross-strapping redundancy. However, both the UHF and 60-GHz crosslink option discussed in this paper are very tolerant to satellite failures and link outages. Since there are multiple paths by which a message can propagate through the constellation, ground communication to different Block IIF satellites is assured even in the presence of link outages. This, combined with the fact that the WAAS signal can be received by the user from several Block IIF satellites in his field and that in practice he would only require to receive the WAAS signal from one of these satellites, indicates that the WAAS performance on availability and continuity of service would be improved over the initial WAAS design and would not be affected by crosslink outages and would, in fact, not require an excessive redundancy design on the WAAS crosslink equipment.

Table 2. UHF FDM Crosslink - Link Budget
(RHCP antenna, circular coverage,
85 W transmitter)

Link Design Parameters			Link Budget		
Frequency	GHz	0.29	Transmit power	dBW	19.29
Burst data rate	Kbps	2.40	TX ckt loss	dB	-0.50
TX to RX dist	Km	38000.00	TX ant gain	dBi	-1.00
TX RF power	W	85.00	EIRP	dBW	17.79
TX ckt loss	dB	0.50	TX point loss	dB	0.00
TX point error	deg	0.00	Space loss	dB	-173.29
RX point error	deg	0.00	Polariz loss	dB	-0.20
Polariz loss	dB	0.20	RX ant gain	dBi	-1.00
RX ant temp	K	100.00	RX point loss	dB	0.00
RX ckt loss	dB	0.50	Rain loss	dB	0.00
Recv NF	dB	1.00	Rec'd sig power	dBW	-156.69
Req'd BER E (-5)		1.00	RX ant temp	K	100.00
Req'd rain marg	dB	0.00	Temp due to WG	K	35.39
Req'd Eb/No	dB	9.60	Temp due to RX NF	K	84.25
Implem loss	dB	2.00	Syst noise temp	K	219.64
WF ovhd loss	dB	0.00	Syst noise PSD	dBW/Hz	-205.18
			Rec'd P/No	dB-Hz	48.49
			Implem loss	dB	-2.00
			Rec'd Eb/No	dB	12.69
			Req'd Eb/No	dB	9.60
			Margin	dB	3.09

6. The 60-GHz Crosslink Option

In addition to UHF, other frequencies can also be considered for Block IIF crosslink to relay WAAS data. The final selection will depend on system cost and risk, as well as impact on the existing crosslink system and Block IIF payload. While final recommendations cannot be

made now, a 60-GHz alternative has been considered and the study result is summarized here.

One advantage of the 60-GHz crosslink option is antenna size. Small aperture antennas can be used to provide a substantial gain (e.g., more than 30 dBi with a 4-inch slotted array). This results in a much smaller RF power requirement for the crosslink transmitter (e.g., 2 W for 2 Kbps) than that required by the UHF crosslink (85 W) with broad-beam, low-gain antennas. However, the antennas must be gimbaled because of the relative orbital motion of GPS satellites and satellite motion required to point the solar panels toward the sun. Furthermore, the DC/RF efficiency of current 60-GHz solid state power amplifiers (SSPA) is still very low (10 percent maximum), resulting in a high DC power requirement although the RF power requirement is small.

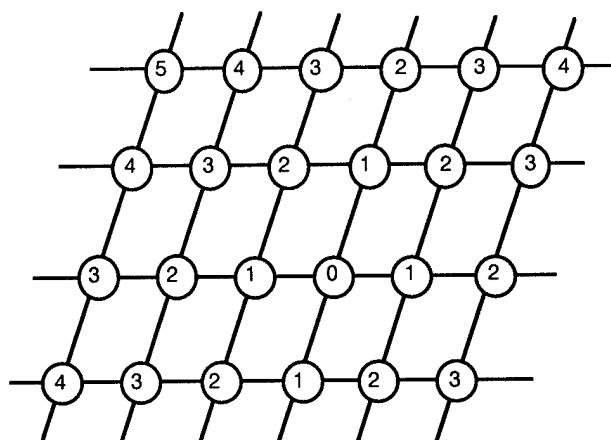
Table 3. Preliminary Estimate of WAAS Payload
Impact on Block IIF (UHF Crosslink
Option)

Unit	Weight (lbs)	Power (W)	Comments
S-band SGLS recv	80	80	to receive WAAS uplink
Processor	10.0	80	data routing, network mgmt.
FDM modulator, U/C	25	25	
UHF HPA	50	142.0	85 W RF, 70% efficient
UHF diplexer	50	00	
UHF D/C	15	25	
FDM multichannel recv	80	100	
Frequency synthesizer	15	20	
L1 modulator increase	20	15	for add'l WAAS signal
L1 HPA increase	50	75.0	30 W RF, 40% efficient
L5 modulator, U/C	25	25	
L5 HPA, DC/DC converter	110	22.5	9 W RF, 40% efficient
Total payload	620	276.5	
Power subsystem, AKM structure	299.5		
Total launch weight increase	361.5		
Block IIF Increase due to WAAS:			
Block IIF	4619.0	1152	
Block IIF with WAAS	4980.5	1429	
% increase	7.8	24	

The same packet communication concept as described in the UHF crosslink option can be used in the 60-GHz option. The WAAS data is packet reformatted by adding a network routing header of approximately 50 bits in length to the 250-bits WAAS message and transmitted to the Block IIF network entry satellite by the WAAS GES via S-band at the 2.4 Kbps burst rate. The network entry satellite retransmits this message to its closest neighbors after the message is received and verified to be correct. The neighboring satellites retransmit this message to their closest neighbors. This process repeats until all satellites have seen this message, when network routing of

this message will cease. The main differences between the UHF and 60-GHz options are the antennas and the HPAs, and that signal multiplexing in the crosslink network is provided by FDM alone in the UHF option, while it is provided by both frequency division and antenna directivity in the 60-GHz option.

Figure 7 illustrates a 60-GHz crosslink network with full connectivity between each satellite to two adjacent satellites on the same orbital plane, and one satellite each on the two adjacent planes. This will require four gimbaled antennas on each satellite, and each antenna will be required to transmit and receive simultaneously (full duplex). The network entry satellite that receives the WAAS S-band uplink is labeled with the number 0. The received message is retransmitted by satellite-0 to its four closest neighbors, labeled with the number 1. These satellites, after they have received the message correctly from satellite-0 as verified by the CRC check, will again retransmit this message to their respective closest neighbors. The process repeats until the message is propagated throughout the constellation. The maximum number of retransmissions required to propagate a message throughout the 24-satellite constellation is five, as illustrated in Figure 7. Thus, the maximum end-to-end latency from the GES uplink transmission to the aviation user for this 4-antenna-per-satellite configuration is the same as for the UHF option described earlier, which is < 2.6 seconds for global relaying, and < 2.0 seconds for the regional WAAS for CONUS.

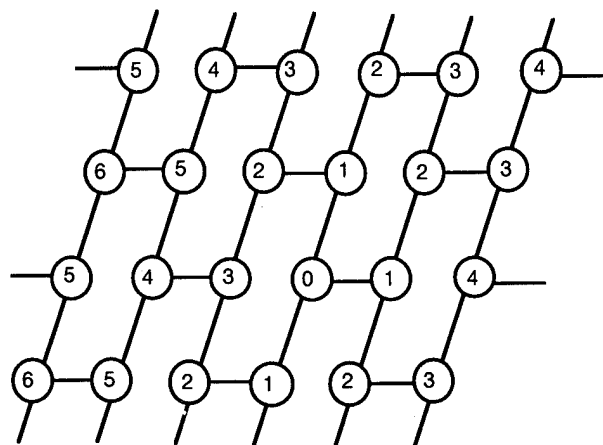


Numbers indicate how many hops are required to propagate signal from ground earth station through the constellation

Figure 7. 60-GHz crosslink connectivity with four antennas on each satellite.

To reduce system cost, a 3-antenna-per-satellite option is also considered. Network connectivity for this option is illustrated in Figure 8. Each satellite is connected to three of its closest neighbors: two on the same plane, and one on an adjacent plane. The message latency is slightly degraded with this option because connectivity

between network elements is reduced. However, the penalty is only one more retransmission, as illustrated in Figure 8. Instead of five, the 3-antenna-per-satellite option requires six retransmissions before a message can propagate throughout the constellation. The end-to-end latency for the 3-antenna-per-satellite option is < 2.9 seconds for global relay, and < 2.0 seconds for regional relay for the CONUS WAAS. Both options will meet the 6-second time to alarm requirement of WAAS.



Numbers indicate how many hops are required to propagate signal from ground earth station through the constellation

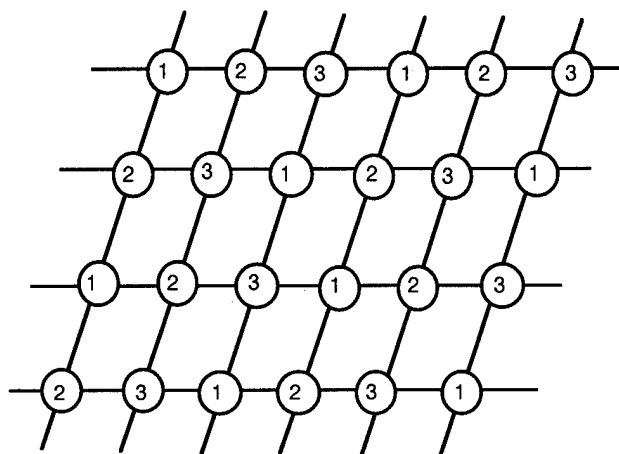
Figure 8. 60-GHz crosslink connectivity with three antennas on each satellite.

Since the crosslink antennas have to operate in full duplex mode, separate 60-GHz frequencies must be selected for neighboring satellites in order to avoid transmit/receive conflict. To solve this problem, it is possible to select three different 60-GHz frequencies and assign them appropriately to satellites in the constellation to be used as their transmission frequencies. This 3-frequency plan will avoid transmit/receive conflicts on each satellite, since each satellite will be receiving four crosslink signals with frequencies other than its own transmission frequency, as illustrated in Figure 9.

With the 3-frequency scheme discussed above, crosslink signals from different satellites can still be received on the same frequency even though transmit/receive conflict is completely avoided. Since the 60-GHz antennas have narrow beams, separation can be provided by antenna discrimination alone. However, more separation between crosslink reception, if necessary can be provided by assigning more frequencies in the constellation to be used for satellite transmission. Figure 10 illustrates a 6-frequency scheme in which a total of six different 60-GHz frequencies are used. This scheme is capable of providing frequency separation between the four crosslinks on which messages are received from each satellite's closest neighbors, in addition to eliminating transmit/receive conflicts for every

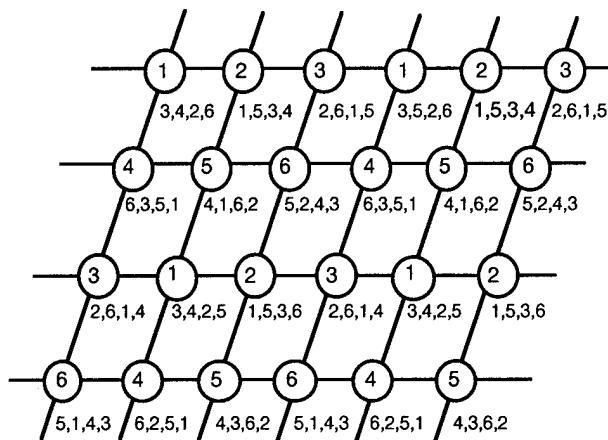
satellite in the constellation. A 3- to 6-multiplexer is required in the antenna compartment for the 60-GHz crosslink implementation.

A crosslink RF power requirement estimate is given in the link budget as shown in Table 4. For the 2.4-Kbps burst rate, the required RF power is estimated to be < 2.5 W with the proposed 4-inch slotted-array antenna.



- Numbers indicate frequencies assigned to each satellite for its transmission
- Channelization in V-band crosslinks provided by FDM and spatial division

Figure 9. 60-GHz crosslink transmit frequency plan using three frequencies.



- Numbers inside the circle indicate frequencies assigned to each satellite for its transmission
- Numbers adjacent to the circles indicate receive frequencies for each satellite from its neighboring satellites

Figure 10. 60-GHz crosslink transmit frequency plan using six frequencies.

The weight and power impact of the 60-GHz crosslink on the Block IIF payload is estimated and given in Table 5 to be approximately 80 lbs and 260 W for the 4-antenna-per-satellite configuration, and can be slightly

reduced with the 3-antenna-per-satellite option. An estimate of the total weight increase of the launch due to these added weight and power requirements is also given in Table 5. The total increase in launch vehicle weight is estimated to be approximately 390 lbs for the 60-GHz crosslink option.

Table 4. 60 GHz Crosslink - Link Budget
(4-inch gimbaled slotted array antennas,
2.4 W transmitter)

Link Design Parameters			Link Budget		
Frequency	GHz	60.00	Transmit power	dBW	3.80
Burst data rate	Kbps	2.40	TX ckt loss	dB	-1.50
TX to RX dist	Km	38000.00	TX ant gain	dBi	34.09
TX RF power	W	2.40	EIRP	dBW	36.39
TX array diam	m	0.10	TX point loss	dB	-0.16
TX ant eff		0.65	Space loss	dB	-219.60
TX ckt loss	dB	1.50	Polariz loss	dB	-0.20
TX 3-dB beam w	deg	3.50	RX ant gain	dBi	34.09
TX point error	deg	0.40	RX point loss	dB	-0.16
RX array diam	m	0.10	Rain loss	dB	0.00
RX ant eff		0.65	Rec'd sig power	dBW	-149.63
RX 3-dB beam w	deg	3.50	RX ant temp	K	100.00
RX point error	deg	0.40	Temp due to WG	K	119.64
Polariz loss	dB	0.20	Temp due to RX NF	K	885.75
RX ant temp	K	100.00	Syst noise temp	K	1105.38
RX ckt loss	dB	1.50	Syst noise PSD	dBW/Hz	-198.16
Recv NF	dB	5.00	Rec'd P/No	dB-Hz	48.54
Req'd BER E (-5)		1.00	Implem loss	dB	-2.00
Req'd Eb/No	dB	9.60	Rec'd Eb/No	dB	12.74
Implem loss	dB	2.00	Req'd Eb/No	dB	9.60
			Margin	dB	3.14

In selecting crosslink design, the constellation build-up phase must also be considered. This phase can span several years before a full operational capability is achieved. During this phase, a mix of Block IIR and IIF satellites will coexist. Block IIR satellites will be replaced gradually by Block IIF satellites until the entire constellation is composed of Block IIF satellites. A detailed constellation build-up study is underway and the effect on the WAAS data relay capability using Block IIF crosslinks is being evaluated in detail. A simple analysis, given below, shows that an 8-satellite buildup could be adequate to relay WAAS data over the CONUS. Assume the Block IIF satellites are uniformly distributed among the 24-satellite constellation. There will be an average of four satellites over the Northern Hemisphere, and from one to three satellites will be visible over the CONUS. Either GES, located in Los Angeles or Boston, can uplink the WAAS message to one of these visible Block IIF satellites, which will then attempt to relay the message to the other seven Block IIF satellites in the mixed constellation. In the build-up phase, the Block IIF satellites will complement the geostationary satellites. However, the initial study indicates that, in the fully built-

up Block IIF constellation, the primary means availability requirements for WAAS signals can be met worldwide without geostationary satellites.

Table 5. Preliminary Estimate of WAAS Payload Impact on Block IIF (60-GHz Option)

Unit	Weight (lbs)	Power (W)	Comments
S-band SGLS recv	8.0	8.0	to receive WAAS uplink
Processor	10.0	8.0	data routing, packet mgmt.
FDM modulator, U/C	2.5	2.5	
60-GHz SSPA (4)	2.0	96.0	2.4 W RF each at 10% DC/RF efficiency
60-GHz multiplexer/switch (4)	6.0	12.0	
60-GHz D/C (4)	4.0	10.0	
Crosslink recv (4)	4.0	10.0	
Crosslink antenna w GDA (4)	20.0	16.0	
Frequency synthesizer	1.5	2.0	
L1 modulator increase	2.0	1.5	for additional WAAS signal
L1 HPA increase	5.0	75.0	30 W RF power at 40% efficiency
L5 modulator, U/C	2.5	2.5	
L5 HPA, DC/DC conv	11.0	22.5	9 W RF power at 40% efficiency
Total payload	78.5	266.0	
Power subsystem, AKM structure	310.7		
Total launch weight increase	389.2		
Block IIF Increase due to WAAS:			
Block IIF	4619.0	1152	
Block IIF with WAAS	5008.2	1418	
% increase	8.4	23.1	

7. WAAS Operations With Block IIF

Unlike a geostationary satellite, which serves only one region, a Block IIF satellite provides global service. Therefore, failure of a single Block IIF satellite in the constellation will have an insignificant impact on integrity and availability of WAAS to users. Since C/A code measurements are also available on two frequencies, maintenance and operation of a large network of ground stations to model the ionosphere, as currently planned in conjunction with Inmarsat satellites, can be significantly reduced. Similarly, concerns of time synchronization between the WAAS signal and GPS time are eliminated since all signals are generated with reference to GPS time. This also will eliminate the need to create and maintain an independent WAAS network time.

WAAS operation would become much simpler with Block IIF satellites. However, the WAAS ground system would be independently managing the WAAS uplink. Further, WAAS data processing will be done independently by the WAAS ground system. Such independent data processing would provide independent integrity verification to enhance system safety.

As currently planned and similar to the case of geostationary satellites, a network of ground stations (WRS) would be tracking Block IIF satellites and the

measurements sent to master stations (WMS) where data processing will be done to compute the WAAS update data. Such data will be uplinked to the satellite via GES. GES will be tracking a particular Block IIF satellite during its viewing period. Before the satellite goes out of view, the GES will switch to another satellite and this process will be repeated. This guarantees continuous connectivity between the GES and any Block IIF satellite. Uplinked data will be crosslinked to all other Block IIF satellites in the constellation and the crosslink process occurs automatically without control by the ground system.

It is expected that there will be adequate redundant ground system elements to support WAAS operations. Although a particular GES would be the prime ground station assigned for uplink to the satellite, there would be another GES in a hot standby mode, prepared to assume the uplink function in the case of any failure in the prime GES. Similarly, there would be a backup WMS that would be prepared to generate update data in the event of a failure in the prime WMS. This would be coordinated to guarantee continuity of operations.

Until the constellation consists of only Block IIF satellites, for a considerable period of time the constellation will consist of both Block IIR and Block IIF satellites. During this period, Block IIF satellites could function to supplement the geostationary satellites to provide the WAAS signal. Crosslink design has been carried out to maximize crosslink communication between all Block IIF satellites even when there are only a few Block IIF satellites in the mixed constellation.

Prior to deployment of Block IIF satellites, WAAS signals are only available via geostationary satellites. Over the CONUS region, it is expected that there will be initially three geostationary satellites which will provide dual coverage over the coastal regions and single coverage over the central region. Unless additional geostationary satellites are placed in orbit the availability requirements will not be met. Moreover, WAAS signals will not be available from geostationary satellites in the high latitude regions, whereas the Block IIF satellites have no such limitations. Further, when Block IIF satellites are deployed, their number increases in the constellation and eventually when the constellation consists of only Block IIF satellites, there will be as many WAAS signals as GPS signals, eliminating the need for additional geostationary satellites beyond the initial three Inmarsat satellites. Further study may show that a full Block IIF constellation alone is adequate to meet the WAAS signal in space requirements.

The Block IIF satellites are designed such that multiple ground systems from different regional WAAS could uplink to the satellites simultaneously and the satellites could downlink WAAS data to respective

regions as a dedicated geostationary satellite would be able to transmit data to a particular corresponding region. This feature allows interconnection to the various regional WAAS operations to provide a seamless navigational service to the global civil aviation user.

8. Summary and Conclusions

A system architecture incorporating the WAAS operational system with Block IIF satellites has been presented. A GPS signal structure consisting of backward-compatible conventional GPS signals and WAAS signals has been suggested and analysis has been performed to show that almost no interference would occur between the various signals. Further, it also shows that two frequency measurements to calibrate the ionosphere for the civil aviation users can be implemented without affecting backward compatibility.

A preliminary design of the Block IIF satellite that meets the requirements of both GPS and WAAS has been presented. The design modifications were based on Block IIR architecture and have minimum cost and weight impact to the satellite. The new features include an independent uplink, an independent crosslink, new signal structure, improved onboard processing to facilitate data routing and related subsystems. A preliminary estimate of the weight and power impact of the Block IIF satellite has been presented and the increase in weight and power could be minimized by incorporating the design changes in the early design stage.

Two alternate schemes for implementation of the crosslink have been proposed. The first scheme is based on an FDM access method on a UHF frequency band. The second scheme is also an FDM method, but on a 60-GHz frequency band. These schemes have distinct advantages and limitations. Further detailed tradeoff analysis would be required to select the method based on weight, power, and cost impact.

A brief discussion regarding the operation of WAAS with Block IIF satellites was also presented. However, further studies are required to evaluate how the operations could be improved during the buildup phase of the Block IIF satellites.

This study has shown that incorporation of dual frequency civil signals for ionospheric delay calibration by civil aviation and WAAS signals meeting WAAS operational performance requirements on the Block IIF satellite is not only feasible but also achievable with minimum impact to the satellite.

ACKNOWLEDGMENTS

The authors acknowledge the funding support by the Federal Aviation Administration and United States Air Force for conducting this study.

REFERENCES

1. "Wide Area Augmentation System (WAAS) Specification," U.S. Department of Transportation, Federal Aviation Administration, FAA-E-2829, May 9, 1994
2. Van Dierendonck, A.J. and Per Enge, "The Wide Area Augmentation System (WAAS) Signal Specification," Proceedings of ION GPS-94, 7th International Technical Meeting of the ION, Salt Lake City, Utah, September 1994
3. Siegel, B., P. Munjal, R. Sung, and M. Ananda, "Communication Satellite Augmented GPS (CAG)," 45th Annual Meeting of the ION, Cambridge, Massachusetts, June 1993
4. Ananda, M., P. Munjal, B. Siegel, R. Sung, and K.T. Woo, "Proposed GPS Integrity and Navigation Payload on DSCS," 1993 IEEE Military Communication Conference, Boston, Massachusetts, October 1993
5. Ananda, M., P. Munjal, R. Sung, and K.T. Woo, "Combined Transmission of DOD-FAA Signal Structure from CAG," ION 1994, National Technical Meeting, San Diego, California, January 1994
6. Ananda, M., P. Munjal, R. Sung, and K.T. Woo, "CAG Signal Structure to Accommodate Wide Area Differential GPS (WADGPS) Data," Third International Conference on Differential Satellite Navigation Systems, Canary Wharf, London, April 1994
7. Aparicio, M., P. Brodie, J. Rajan, and R. Sung, "Communication Satellite Augmented GPS Payload Architecture," ION GPS-94 Seventh International Technical Meeting of the Satellite Division of ION, Salt Lake City, Utah, September 1994
8. Ananda, M., P. Munjal, and K.T. Woo, "Augmented Global Positioning System (AGPS)-An Extended WAAS," 1995 National Technical Meeting of the Institute of Navigation, Anaheim, California, January 1995
9. Decou, S., "Advanced Planning for GPS Block IIF Satellites," 49th Annual Meeting of the ION, Cambridge, Massachusetts, June 1993
10. "The Global Positioning System, A Shared National Asset," National Research Council, National Academy Press, Washington, D.C., 1995
11. "The Global Positioning System, Charting the Future," National Academy of Public Administration and National Research Council, May 1995

New Approach to Kalman Time Propagation for GPS/INS Integrated Systems

Dr. Leonid Schimelevich and Dr. Rahel Naor
Israel Aircraft Industries Ltd.

BIOGRAPHY

Dr. Leonid Schimelevich is a Member of the System Analysis Group of the Navigation Dept. at TAMAM (Precision Instruments Industries), a Subsidiary of the Israel Aircraft Industries. Its areas of interest are filter design with emphasis in non-linear filtering application. He holds a Ph.D. from the Technical University of St. Petersburg.

Dr. Rahel Naor is the Head of the System Analysis Group of the Navigation Dept. at TAMAM (Precision Instruments Industries), a Subsidiary of the Israel Aircraft Industries. Its areas of interest are Navigation System Analysis and filter design. She holds a Ph.D. from the Weizman Institute of Science at Rehovot, Israel.

ABSTRACT

According to the current approach to Kalman time propagation based on truncated Taylor expansion of matrix exponent one must choose a propagation interval such that the dynamic matrix will be approximately constant within it. For vehicles submitted to drastic dynamic behavior this method implies the use of extremely short propagation interval. Consequently heavy recursive computations of the covariance matrix has to be done at high frequency.

In this paper a new approach to Kalman time propagation for GPS/INS integrated systems is proposed. This new method allows a considerable saving of computational load while keeping the required accuracy of the propagation.

The proposed propagation algorithm consist of two phases: a) auxiliary computations carried out at the high frequency during the interval between GPS - measurements reception; b) recursive computations of

the covariance matrix carried out only at the time of GPS - measurements reception (before Kalman updates). The required accuracy is kept due to the fact that the propagation is based on the approximate solution of INS - error differential equations up to the given order of small parameter, which is inherent in INS - error dynamic matrix.

INTRODUCTION

Kalman filter for GPS/INS integrated systems includes Kalman time propagation - recursive computations of the covariance matrix according to INS - error dynamic model, which is the system of linear differential equations. The coefficient matrix of these equations (the dynamic matrix) depends on vehicle's velocity and acceleration, consequently it varies as a function of time. To carry out Kalman time propagation INS - error differential equations must be approximately solved on the interval (~ 1 sec) between GPS - measurements reception. However since the most known approximate solution method based on truncated Taylor expansion of matrix exponent suits only the case of the constant dynamic matrix one presets a propagation interval so that vehicle's velocity and acceleration will be approximately constant within it. For vehicle's with drastic dynamic behaviour this approach forces to carry out heavy matrix computations at a high frequency.

Our purpose is to obtain an approximate solution of INS - error differential equations with the time-varying dynamic matrix during the interval between GPS - measurements receptions in order to utilize this interval as a propagation of the covariance matrix only at the time of GPS - measurements reception (before Kalman updates). The desired solution must have an approximation order selection which allows to keep the required accuracy of the propagation.

STEP-BY-STEP METHOD

Let INS - error dynamic model be described by the system of linear differential equations

$$\dot{\bar{X}}(t) = A(t) \bar{X}(t) \quad (1)$$

where $\bar{X}(t)$ is the vector of INS - errors and $A(t)$ is the dynamic matrix. Consider an interval $[t_{k-1}, t_k]$ between times t_{k-1} , t_k of GPS - measurements reception.

$$T = t_k - t_{k-1}.$$

For Kalman time propagation of the covariance matrix from t_{k-1} to t_k we need a matrix B_k which connect $\bar{X}(t_{k-1})$ and $\bar{X}(t_k)$ i.e.

$$\bar{X}(t_k) = B_k \bar{X}(t_{k-1}) \quad (2)$$

To obtain B_k the equation (1) must be solved in the interval $[t_{k-1}, t_k]$ given the initial condition $\bar{X}(t_{k-1})$. Since the accurate solution of (1) cannot be computed our purpose is to find an approximate solution and consequently an approximation to B_k . In case of the constant dynamic matrix $A(t) \equiv A_k$ for $t \in [t_{k-1}, t_k]$ such an approximation is well known - truncated Taylor expansion of $B_k = \exp \{TA_k\}$, i.e.

$$B_k \cong B_k^{(n)} = I + TA_k + \frac{T^2}{2} A_k^2 + \dots + \frac{T^n}{n!} A_k^n \quad (3)$$

where I is the unit matrix.

The dynamic matrix is a function of time due to its dependence on vehicle's velocity and acceleration. For a vehicle submitted to drastic dynamic behaviour the assumption that its velocity and acceleration are constant on an interval ~ 1 sec is often wrong. For this reason the interval $[t_{k-1}, t_k]$ is divided in several subintervals

$$[t_{k-1} + (i-1)\Delta, t_{k-1} + i\Delta], \quad i=1, \dots, J, \quad J=T/\Delta \quad (4)$$

so that $A(t) \cong A_{ki}$ for $t \in [t_{k-1} + (i-1)\Delta, t_{k-1} + i\Delta]$.

These subintervals are utilized as propagation intervals for recursive computations of the covariance matrix based on the approximations

$$B_{ki} \cong B_{ki}^{(n)} = I + \Delta A_{ki} + \frac{\Delta^2}{2} A_{ki}^2 + \dots + \frac{\Delta^n}{n!} A_{ki}^n \quad (5)$$

This approach results in heavy computational load even for powerful processors.

To develop a different concept let us obtain an approximate solution of (1) free of any assumptions regarding dynamic matrix variability on the interval $[t_{k-1}, t_k]$. It will be noted that matrix exponent method is not applicable to the case of time - varying dynamic matrix

$$\text{since } B_k \neq \exp \left\{ \int_{t_{k-1}}^{t_k} A(\tau) d\tau \right\}.$$

The equivalent integral form of the differential equation (1) is

$$\bar{X}(t) = \bar{X}(t_{k-1}) + \int_{t_{k-1}}^t A(\tau) \bar{X}(\tau) d\tau \quad (6)$$

The approximate solution can be obtained based on a recursion formula

$$\tilde{\bar{X}}^{(n)}(t) = \bar{X}(t_{k-1}) + \int_{t_{k-1}}^t A(\tau) \tilde{\bar{X}}^{(n-1)}(\tau) d\tau \quad (7)$$

given the initial approximation $\tilde{\bar{X}}^{(0)}(t) \equiv \bar{X}(t_{k-1})$. This step-by-step method yields

$$B_k \cong B_k^{(n)} = I + \int_{t_{k-1}}^{t_k} A(\tau) d\tau + \int_{t_{k-1}}^{t_k} A(\tau_1) \int_{t_{k-1}}^{\tau_1} A(\tau_2) d\tau_2 d\tau_1 + \dots \\ \dots + \int_{t_{k-1}}^{t_k} A(\tau_1) \int_{t_{k-1}}^{\tau_1} A(\tau_2) \dots \int_{t_{k-1}}^{\tau_{n-1}} A(\tau_n) d\tau_n \dots d\tau_2 d\tau_1 \quad (8)$$

The obtained approximation generalizes the matrix exponent method for the case of time - varying dynamic matrix. Indeed, by substitution of $A(t) \equiv A_k$ into (8) we get equation (3) given that

$$\int_{t_{k-1}}^{t_k} \int_{t_{k-1}}^{\tau_1} \dots \int_{t_{k-1}}^{\tau_{m-1}} d\tau_m \dots d\tau_1 = \frac{T^m}{m!}, \quad m=1, \dots, n$$

However for a general case of time-varying dynamic matrix the integrals in (8) cannot be computed analytically. To evaluate these integrals approximately we must utilize the subintervals (4) and replace the integrals in (8) with the corresponding sums. It yields

$$B_k \cong B_k^{(n)} = I + S_1 + S_2 + \dots + S_n \quad (9)$$

where the sums

$$S_1 = \Delta \sum_{i=1}^J A_{ki}, \quad S_2 = \Delta^2 \sum_{i_1=1}^J \sum_{i_2=1}^{i_1} A_{ki1} A_{ki2}, \dots, \\ S_n = \Delta^n \sum_{i_1=1}^J \sum_{i_2=1}^{i_1} \sum_{i_3=1}^{i_2} \dots \sum_{i_n=1}^{i_{n-1}} A_{ki1} A_{ki2} \dots A_{kin} \quad (10)$$

can be obtained by means of recursion formulas

$$S_1^{(i)} = S_1^{(i-1)} + \Delta A_{ki}, \\ S_2^{(i)} = S_2^{(i-1)} + \Delta A_{ki} S_1^{(i)}, \\ \dots \\ S_n^{(i)} = S_n^{(i-1)} + \Delta A_{ki} S_{n-1}^{(i)} \quad (11)$$

where $i=1, \dots, J$ and the initial conditions are $S_1^{(0)} = 0$, $S_2^{(0)} = 0, \dots, S_n^{(0)} = 0$. At the moment t_k we obtain $S_1^{(J)} = S_1$, $S_2^{(J)} = S_2, \dots, S_n^{(J)} = S_n$ which must be substituted into (9). Therefore the proposed propagation algorithm can be divided in two phases: a) auxiliary computations (11) carried out at the high frequency throughout the propagation interval $[t_{k-1}, t_k]$; b) Kalman time propagation of the covariance matrix from t_{k-1} to t_k carried out only at the time t_k and based on the approximation (9).

ACCURACY ANALYSIS

To keep the required accuracy of the propagation we must select n in the approximation (8) such that the approximation error

$$\xi_n = \sum_{m=n+1}^{\infty} \int_{t_{k-1}}^{t_k} A(\tau_1) \int_{t_{k-1}}^{\tau_1} A(\tau_2) \dots \int_{t_{k-1}}^{\tau_{n-1}} A(\tau_m) d\tau_m \dots d\tau_2 d\tau_1 \quad (12)$$

will be sufficiently small according to some criteria. Let μ be some given small parameter (unitless positive number much smaller than 1). Let us specify that the approximation error is sufficiently small if $\xi_n \sim o(\mu^l)$, i.e. all the elements of the matrix ξ_n have an infinitesimal order with respect to μ less than μ^l , where l is predefined according to the required accuracy. The validity of this criteria will be demonstrated by the natural existence of the small parameter which is inherent in the INS - error dynamic matrix. Let us specify the state vector of INS - errors:

$$\bar{X} = \begin{bmatrix} \delta P \\ \delta V \\ \delta \epsilon \end{bmatrix}; \quad \delta P = \begin{bmatrix} \delta \lambda \\ \delta L \\ \delta h \end{bmatrix}; \quad \delta V = \begin{bmatrix} \delta V_e \\ R \\ \delta V_N \\ R \\ \delta V_Z \\ R \end{bmatrix}; \quad \delta \epsilon = \begin{bmatrix} \delta \epsilon_e \\ \delta \epsilon_N \\ \delta \epsilon_Z \end{bmatrix}$$

where $\delta \lambda$, δL , δh are the errors in vehicle's longitude λ , latitude L and altitude h ; δV_e , δV_N , δV_Z are the errors in vehicle's east velocity V_e , north velocity V_N and vertical velocity V_Z ; $\delta \epsilon_e$, $\delta \epsilon_N$, $\delta \epsilon_Z$ are the vehicle's attitude errors; R is the earth radius. Let a_e , a_N , a_Z be the Vehicle's acceleration; Ω be the earth rotation rate. Now let us describe the dynamic matrix of INS - error model:

$$A = \begin{bmatrix} A_{PP} & A_{PV} & 0 \\ A_{VP} & A_{VV} & A_{V\epsilon} \\ A_{\epsilon P} & A_{\epsilon V} & A_{\epsilon\epsilon} \end{bmatrix} \quad (13)$$

The submatrices of A are shown in figure 1.

To estimate the approximation error ξ_n let us substitute into (12) such a matrix A that its elements are upper bounds for the corresponding elements of the dynamic matrix (13). It yields

$$\xi_n \sim \begin{bmatrix} o(\mu^n) & o(\mu^{n-1}) & o(\mu^n) \\ o(\mu^n) & o(\mu^n) & o(\mu^n) \\ o(\mu^n) & o(\mu^{n-1}) & o(\mu^n) \end{bmatrix} \quad (14)$$

where

$$\mu = T \max \left\{ \Omega + \frac{V_{\max}}{R} + \left(\frac{g + a_{\max}}{R^{1/2}} \right)^{1/2} \right\}, \quad (15)$$

V_{\max} , a_{\max} are the maximal vehicle's velocity and acceleration. For reasonable values of V_{\max} , a_{\max} the unitless positive number μ is much smaller than 1 ($\mu \sim 10^{-3} \div 10^{-2}$) and can be considered as a given small parameter.

As follows from (14), to ensure that $\xi_n \sim o(\mu^l)$ for a given l we must select $n = l + 1$. However the last

summand of $B_k^{(l+1)}$ is

$$\int_{t_{k-1}}^{t_k} A(\tau_1) \int_{t_{k-1}}^{\tau_1} A(\tau_2) \dots \int_{t_{k-1}}^{\tau_{l+1}} A(\tau_{l+1}) d\tau_{l+1} \dots d\tau_2 d\tau_1 =$$

$$= \begin{bmatrix} 0 & C_{PV}^{(l+1)} & 0 \\ 0 & 0 & 0 \\ 0 & C_{eV}^{(l+1)} & 0 \end{bmatrix} + o(\mu^l) \quad (16)$$

where the submatrices $C_{PV}^{(l+1)}$, $C_{eV}^{(l+1)}$ have the infinitesimal order μ^l . We may omit in (16) all the terms with infinitesimal order less than μ^l , i.e. we may use

instead $B_k^{(l+1)}$ an approximation

$$\tilde{B}_k^{(l+1)} = \tilde{B}_k^{(l)} + \begin{bmatrix} 0 & C_{PV}^{(l+1)} & 0 \\ 0 & 0 & 0 \\ 0 & C_{eV}^{(l+1)} & 0 \end{bmatrix} \quad (17)$$

An example ($l=1$) is shown in figure 2.

CONCLUSIONS

The proposed propagation algorithm is based on the approximate solution of INS - error differential equations with the time - varying dynamic matrix on the interval between GPS - measurements reception. This interval is utilized as a propagation interval, i.e. Kalman propagation of the covariance matrix is carried out only at the time of GPS - measurements reception.

The approximate solution of INS - error differential equations obtained by means of step-by-step method includes some integrals of dynamic matrix elements. To compute these integrals the propagation interval is divided in several subintervals so that the dynamic matrix will be approximately constant within each of them and the integrals can be replaced by the corresponding sums. Thus the proposed propagation algorithm includes auxiliary computations carried out at the high frequency, but the overall computational load has been significantly decreased.

Step-by-Step method allows to obtain the sequence of approximations. To keep the required accuracy of the propagation the approximation is selected to have the given infinitesimal order with respect to some small parameter which is inherent in INS - error dynamic matrix.

FIGURE 1

$$A_{PP} = \begin{bmatrix} 0 & \frac{V_e \tan L}{R \cos L} & -\frac{V_e}{R \cos L} \\ 0 & 0 & -\frac{V_N}{R} \\ 0 & 0 & 0 \end{bmatrix}, \quad A_{PV} = \begin{bmatrix} \frac{1}{\cos L} & 0 & 0 \\ 0 & 1 & 0 \\ 0 & 0 & 1 \end{bmatrix}$$

$$A_{VP} = \begin{bmatrix} 0 & \frac{2V_N}{R} \Omega \cos L + \frac{2V_Z}{R} \Omega \sin L + \frac{V_e V_N}{R^2 \cos L} & \frac{V_e V_Z}{R^2} - \frac{V_e V_N \tan L}{R^2} \\ 0 & -\frac{2V_e}{R} \Omega \cos L - \frac{V_e^2}{R^2 \cos^2 L} & \frac{V_e^2 \tan L}{R^2} + \frac{V_N V_Z}{R^2} \\ 0 & -\frac{V_e}{R} \Omega \sin L & \frac{2g}{R} - \frac{V_e^2 + V_N^2}{R^2} \end{bmatrix}$$

$$A_{VV} = \begin{bmatrix} \frac{V_N \tan L}{R} - \frac{V_Z}{R} & 2\Omega \sin L + \frac{V_e \tan L}{R} & -2\Omega \cos L - \frac{V_e}{R} \\ -2\Omega \sin L - \frac{2V_e \tan L}{R} & -\frac{V_Z}{R} & -\frac{V_N}{R} \\ 2\Omega \cos L + \frac{2V_e}{R} & \frac{2V_N}{R} & 0 \end{bmatrix}$$

$$A_{V\epsilon} = \begin{bmatrix} 0 & -\frac{a_z + g}{R} & \frac{a_N}{R} \\ \frac{a_z + g}{R} & 0 & -\frac{a_e}{R} \\ -\frac{a_N}{R} & \frac{a_e}{R} & 0 \end{bmatrix}, \quad A_{\epsilon P} = \begin{bmatrix} 0 & 0 & \frac{V_N}{R} \\ 0 & -\Omega \sin L & -\frac{V_e}{R} \\ 0 & \Omega \cos L + \frac{V_e}{R^2 \cos L} & -\frac{V_e \tan L}{R} \end{bmatrix}$$

$$A_{\epsilon V} = \begin{bmatrix} 0 & -1 & 0 \\ 1 & 0 & 0 \\ \tan L & 0 & 0 \end{bmatrix}$$

$$A_{\epsilon\epsilon} = \begin{bmatrix} 0 & \Omega \sin L + \frac{V_e \tan L}{R} & \Omega \cos L + \frac{V_e}{R} \\ -2\Omega \sin L - \frac{2V_e \tan L}{R} & 0 & -\frac{V_N}{R} \\ \Omega \cos L + \frac{V_e}{R} & \frac{V_N}{R} & 0 \end{bmatrix}$$

FIGURE 2

$$B_k^{(1+)} = \begin{bmatrix} I + \int_{t_{k-1}}^{t_k} A_{PP}(\tau) d\tau & \int_{t_{k-1}}^{t_k} A_{PV}(\tau) d\tau + C_{PV}^{(2)} & 0 \\ \int_{t_{k-1}}^{t_k} A_{VP}(\tau) d\tau & I + \int_{t_{k-1}}^{t_k} A_{VV}(\tau) d\tau & \int_{t_{k-1}}^{t_k} A_{Ve}(\tau) d\tau \\ \int_{t_{k-1}}^{t_k} A_{eP}(\tau) d\tau & \int_{t_{k-1}}^{t_k} A_{eV}(\tau) d\tau + C_{PV}^{(2)} & I + \int_{t_{k-1}}^{t_k} A_{ee}(\tau) d\tau \end{bmatrix}$$

$$C_{PV}^{(2)} = \int_{t_{k-1}}^{t_k} A_{PP}(\tau_1) \int_{t_{k-1}}^{\tau_1} A_{PV}(\tau_2) d\tau_2 d\tau_1 + \int_{t_{k-1}}^{t_k} A_{PV}(\tau_1) \int_{t_{k-1}}^{\tau_1} A_{VV}(\tau_2) d\tau_2 d\tau_1 ,$$

$$C_{eV}^{(2)} = \int_{t_{k-1}}^{t_k} A_{eP}(\tau_1) \int_{t_{k-1}}^{\tau_1} A_{PV}(\tau_2) d\tau_2 d\tau_1 + \int_{t_{k-1}}^{t_k} A_{eV}(\tau_1) \int_{t_{k-1}}^{\tau_1} A_{VV}(\tau_2) d\tau_2 d\tau_1 + \int_{t_{k-1}}^{t_k} A_{ee}(\tau_1) \int_{t_{k-1}}^{\tau_1} A_{eV}(\tau_2) d\tau_2 d\tau_1$$



Session C6

Emerging Applications

Chair:

Mr. Glen Gibbons
GPS World

Co-Chair:

Dr. David Tyler
Springhill Engineering

Real-time Landslide Detection System Using Precise Carrier Phase GPS

Hitoshi Kondo
Furuno Electric Co., Ltd.

M. Elizabeth Cannon
The University of Calgary

Biographies

Hitoshi Kondo is an assistant chief in Development Section 1 of System Products Development & Marketing Headquarters at Furuno Electric Co., Ltd., where he conducts development of systems using GPS. He holds a B.Eg. and M.Eg. in Electronics Engineering.

M. Elizabeth Cannon is an Associate Professor in the Department of Geomatics Engineering at The University of Calgary where she conducts research and teaching into precise GPS static and kinematic positioning. She holds a B.Sc. in Math as well as a B.Sc., M.Sc. and Ph.D. in Surveying Engineering.

Abstract

It is very important to monitor the mechanical behaviour of an extensive area in geotechnical engineering such as high cut slopes, landslides and subsidences. It is very expensive to continuously measure many points to monitor the behaviour.

Since GPS is available in all weather, day and night, and can monitor a large measurement network, it is very useful tool for measuring displacement vectors over an extensive area.

Recently, some applications of GPS to subsidence and landslide measurement have been studied. A real-time system to measure the positions of up to 10 points and to detect displacement of these points, however, has not yet been developed.

The authors have developed a system using precise carrier phase GPS techniques to detect displacement for monitoring the mechanical behavior of an extensive area at the level of a few centimeters. In this paper, the system concepts are described and results of the field experiments to prove the applicability of the system are given. Field tests show that displacements on the order of 2 cm can be detected.

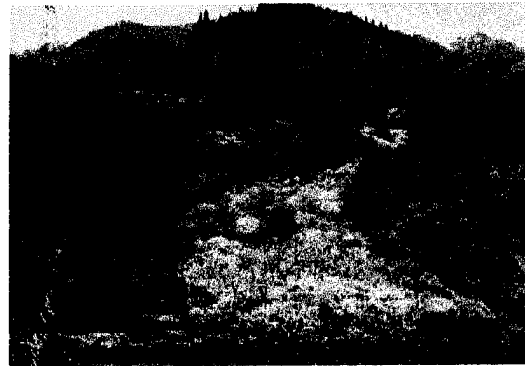


Figure 1: A Landslide Area

INTRODUCTION

Since Japan is a small and mountainous country with a large population, many people live in or around areas with potential risk of landslides. Statistics show that the number of areas with potential risk of disaster from landslides in Japan is more than ten thousand. In order to avoid these disasters, it is important to accurately monitor the mechanical behaviour for movements.

Figure 1 shows a typical landslide area which can measure a few hundred meters long and a few hundred meters wide. These landslide areas tend to move in blocks such that many points in the area must be monitored so that a complete picture of the displacement can be formed. By knowing the direction and distance of displacements within the various blocks, a decision can be made as to whether an area is dangerous or not, so that countermeasures can be taken to avoid disasters.

Displacement measurements have conventionally been done using extensometers or electro-optical distance measuring instruments. While an extensometer is able to measure to an accuracy of a millimeter, it can only measure in one direction. Electro-optical distance measuring instruments are widely used in the surveying field, however, they do not work well in poor visibility. In addition, when

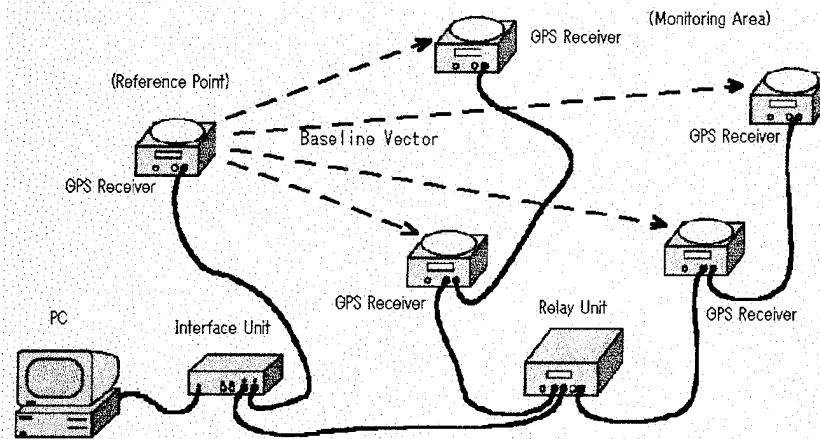


Figure 2: Real-time Landslide Detection System

using both these instruments, the measurement of a large number of points on a continuous basis is very expensive.

Recently, the application of GPS to measure subsidence and landslides has been undertaken [1] [2]. When using GPS precise positioning techniques based on carrier phase data, the resulting accuracy can rival conventional surveying methods. GPS is also available in all-weather, day and night and offers the capability to automatically process data on a small computer to generate positions in an autonomous mode. For these reasons, GPS was selected as the tool to measure displacement vectors over a large area.

Traditionally, most static and kinematic GPS surveys require post-processing in order to generate accurate position information. Recently, Real-Time Kinematic (RTK) systems have been developed which accurately locate a user with respect to a fixed reference system in real-time [3]. A real-time system which continuously determines the position of several receiver locations simultaneously to determine if displacements occur over time, has not yet been developed. Such a system has been developed by the authors and is capable of providing accuracies on the order of 2 cm in real-time. System concepts and test results form the basis of this paper.

SYSTEM OVERVIEW

A system for monitoring a landslide is required to have the following functions:

- to be able to simultaneously determine the positions of several points (up to 10)
- to measure these points automatically in real-time

- to measure the points with a high accuracy (1-2 cm)
- to detect displacement accurately and reliably
- to be capable of operating over a long period of time (weeks to months)

In order to satisfy these requirements, the system was developed according to Figure 2. All data from the GPS receivers are collected at the PC via the communication network. The baseline vectors between each receiver and the reference are then calculated in real-time using the carrier phase data. In order to detect displacement, these estimated positions are compared to an initial position determined at the start of the test. If significant displacement is detected, it is reported to users through warning messages displayed on the PC screen. This procedure of position estimation and displacement detection is performed repeatedly.

The GPS receiver used for the reference station as well as in the monitoring area is shown in Figure 3. It is a C/A code, 8 channel unit, capable of outputting raw GPS data such as pseudorange and carrier phase at a 0.5 Hz rate.

The communication network consists of a Relay Unit, Interface Unit and some cables. In Figures 4 and 5, the Relay and Interface Units are shown, respectively. The Relay Unit passes data from the GPS receivers to the Interface Unit and also supplies power to each receiver. The Interface Unit passes data from the GPS reference receiver and the Relay Unit to the PC, as well as supplies power to the reference receiver. Since the GPS receiver and Relay Unit are waterproof, they can be placed in the monitoring area during inclement weather.

The monitoring area which can be covered by the receivers is within a diameter of 800 m centered by the Relay Unit. The maximum distance

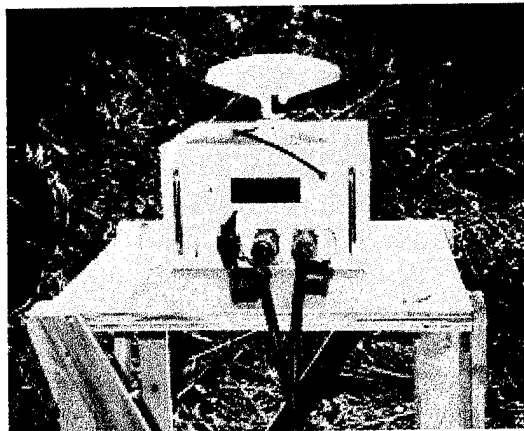


Figure 3: Receiver and Antenna

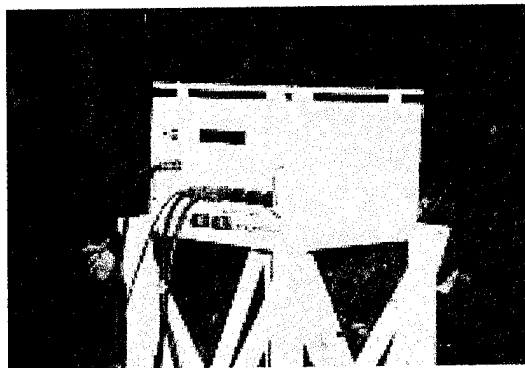


Figure 4: Relay Unit

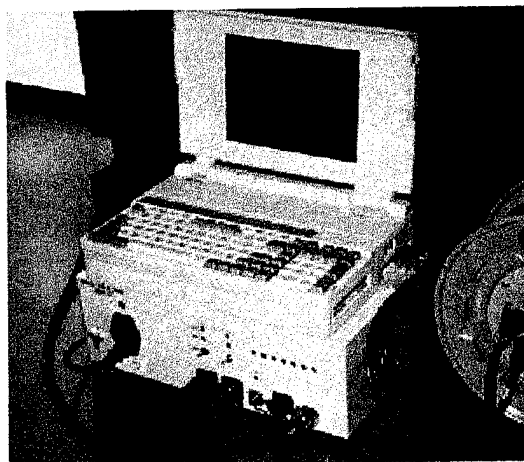


Figure 5: Interface Unit and PC

between the reference GPS receiver and each remote receiver is 1200 m. Since the power source of the each receiver is supplied from either the Relay Unit or Interface unit via some cables, only these two units are actually powered from external sources.

Figure 6 shows an example of some of the graphics that can be displayed on the PC screen during normal operations. This figure shows the location of all receivers as well as numeric results of the baseline analysis and detection tests. Plots of latitude (or longitude) versus time and baseline separation versus time can also be displayed.

Some specifications of the system are as follows:

- the number of reference receivers is one
- the maximum number of measurement points is ten
- the monitoring area must be within a circle of 800 m centered by the Relay Unit
- the maximum distance between the reference point and each measurement point is 1,200 m.
- measurement interval is 1 minute.
- power consumption is less than 160 VA with one reference receiver and ten receivers placed on the monitoring area.

System Behaviour

The system has two modes, namely *Initialization Mode* and *Monitoring Mode*. A flowchart of the two modes is shown in Figure 7 and each is discussed below.

Initialization Mode

The goals of the initialization mode are to 1) accurately determine the initial coordinates of the receivers in the monitoring area with respect to the reference receiver, and 2) determine the double difference integer ambiguities for each of the baselines.

In order to fulfil goal (1) above, approximately 30-60 minutes of data are collected at each receiver location. Each baseline is then computed using a standard least squares adjustment which ultimately results in a double difference fixed-integer ambiguity solution [4]. Once the position of each receiver is determined using this process, the coordinates are stored in a database so that they can be recalled during monitoring mode for movement detection purposes. It is clearly important that the receivers in the monitoring area be stable during initialization mode.

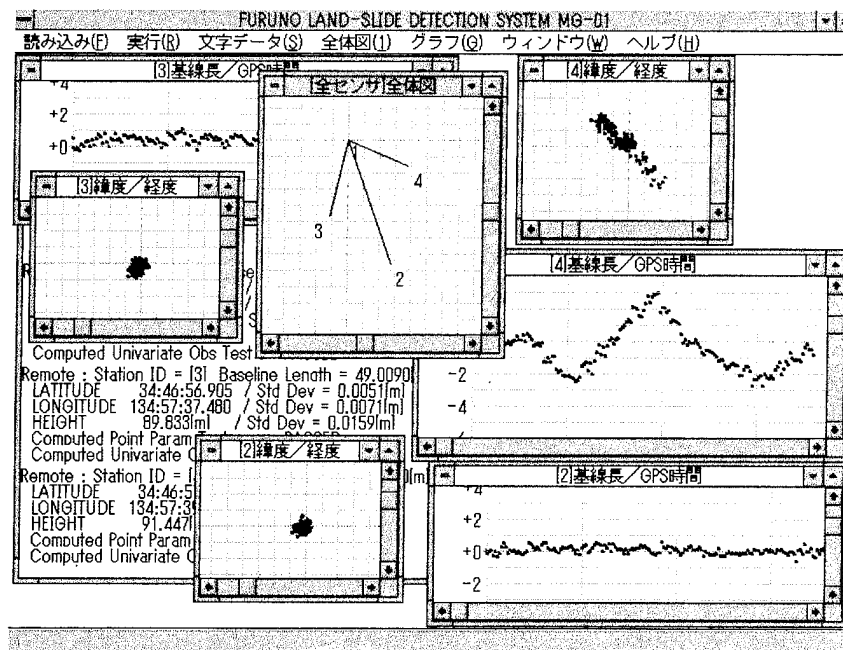


Figure 6: An Example of Display

Monitoring Mode

This mode is the method by which the position of each receiver is tracked to determine if movement has occurred. This entails the processing of distinct epochs of data which are then compared to the database of the positions generated in the initialization mode.

Since integer ambiguities are held fixed during monitoring mode (using the values obtained from the initialization mode), only ten seconds of data are used to estimate each receiver's position. This ten second span is considered one epoch. The spacing between measurement epochs is one minute if ten receivers are deployed in the monitoring area. If the number of receivers is reduced to four, then the epoch interval is increased to every 20 seconds.

Displacement Detection

Two statistical tests have been implemented in order to detect displacement in each of the reference-receiver pairs. The first test is to assess whether the computed distance between the reference and receiver falls within a normal (Gaussian) distribution. The estimated baseline length is compared against the mean distance such that if the deviation is too large, a flag is set and the user is warned.

The second statistical test which is implemented is a Chi-squared test on the difference between the estimated position of a particular receiver versus the true value as stored in the database from initialization. Again, if this test fails, a second flag is set and the user is warned.

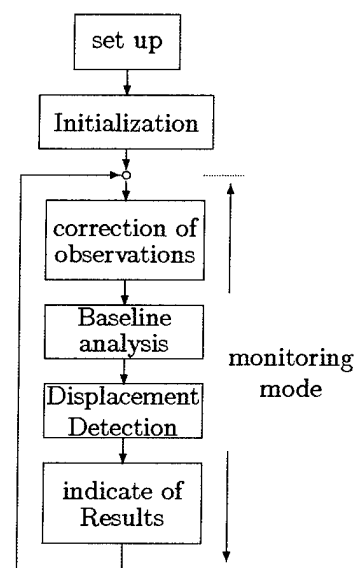


Figure 7: flow-chart

In order to generate reliable results, a statistical probability level of 99% is used for both tests.

EXPERIMENTAL RESULTS

Fundamental Tests

Two tests were made to check the fundamental function and performance of the system. Both tests were conducted in an open field shown in Figure 8.

Test 1

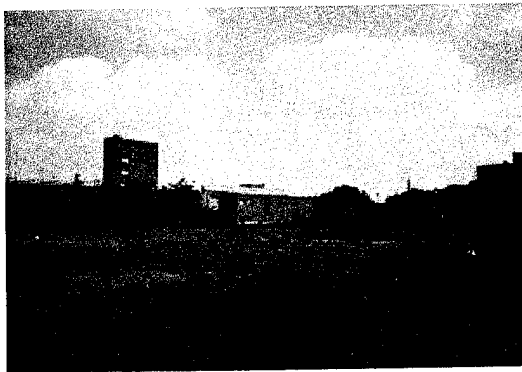


Figure 8: An Open Field

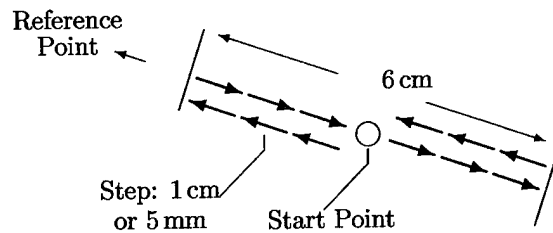


Figure 10: Movement of Receiver No.4

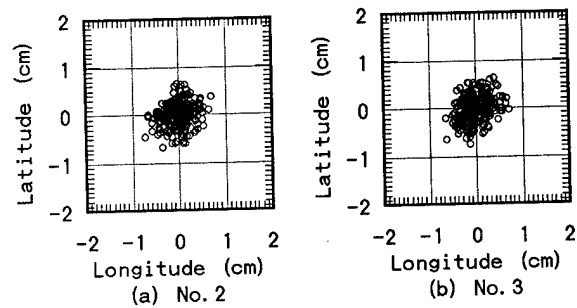


Figure 11: lat-lon about Receiver No.2 and No.3

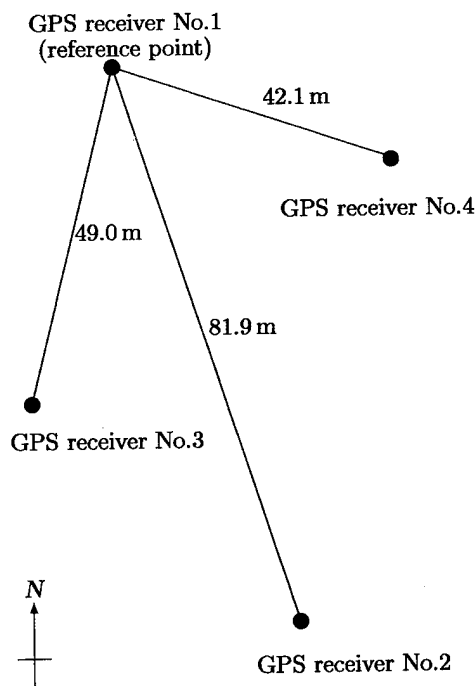


Figure 9: Receiver Placement for Test1

In this test, four receivers numbered 1 to 4 were deployed as shown in Figure 9. The reference GPS receiver was No. 1 while the other three receivers were considered measurement points. The distances between the measurement points and the reference receiver ranged from about 40 to 80 m. Approximately 20 minutes of data was used to initialize the baselines, and then the positions of the measurement points were computed every 20 seconds thereafter.

In order to test the performance of the system, receiver Nos. 2 and 3 were held stationary during the 84 minute test while Receiver No. 4 was moved 1 cm or 5 mm every 2 minutes as shown in Figure 10.

Figure 11 illustrates the horizontal position of receiver Nos. 2 and 3 during the test and shows that the precision of the position estimates is at the level of 5 mm. Alternatively, Figure 12 shows the estimated baseline length between receiver No. 4 and the reference receiver. In this case, the black dots show epochs where the statistical test has detected that motion has occurred. The white dots indicate that the system considers the point stationary, i.e. no movement has been detected. In this case, it is clear that movements on the order of ± 1 cm can be detected. Figure 13 shows a similar plot, but in this case, differences between the horizontal coordinates from the epoch results and the true coordinates from the database are shown. Again, once there is movement of ± 1 cm, it can be

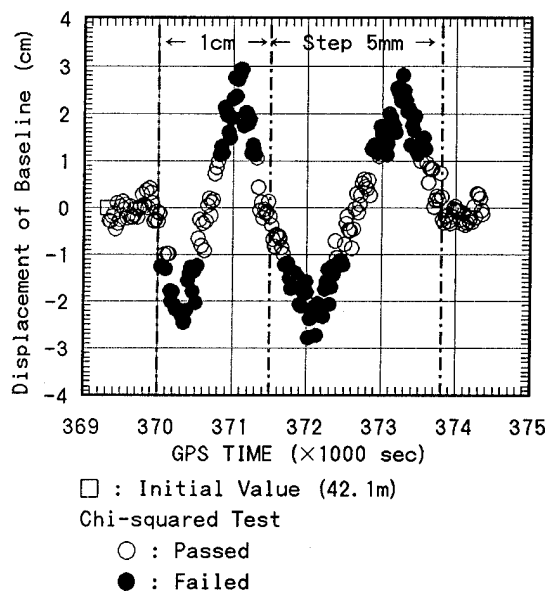


Figure 12: Baseline Length about Receiver No.4

detected.

Test 2

In the second test, three receivers were deployed as shown in Figure 14. Receiver Nos. 2 and 4 were alternatively considered the reference receivers as will be discussed below. Receiver No. 3 was moved in 1 cm increments every 2 minutes as shown in Figure 15. The distances between the measurement points and the reference receiver ranged about 20 m. Approximately 15 minutes of data was used to initialize the baselines, and then the positions of the measurement points were computed every 20 seconds thereafter.

Figure 16 gives the horizontal position errors of Receiver No. 3 when Receiver No. 4 is considered the reference receiver. Also shown on the figure are the results of the Chi-squared test on the position differences. Again, the block dots indicate when the statistical test fails, i.e. motion is detected. Figure 17 shows similar results for the baseline test (i.e. for normal distribution). The graphs show that in some cases, one test may pass while the other fails.

The use of more than one statistical test is useful in maintaining a high system reliability since each statistical test has difference character and each estimated value of coordinates or a baseline length has different deviations. For example, Chi-squared test can detect displacements of all directions, but the baseline test can not detect displacements along a circumference centered by the reference point.

Figure 18 give an analogous result to Figure 16 and 17 when receiver No. 2 is considered as the ref-

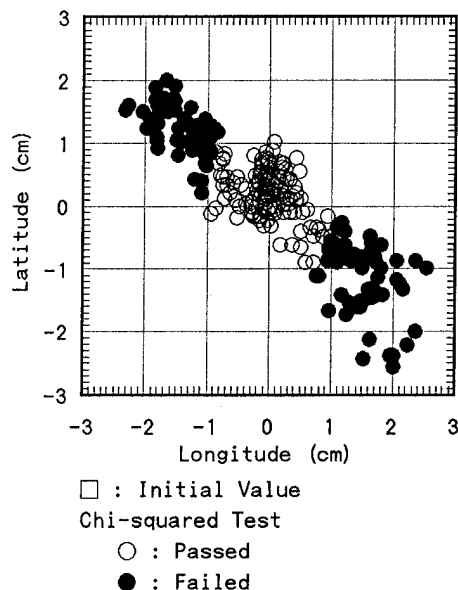


Figure 13: lat-lon about Receiver No.4

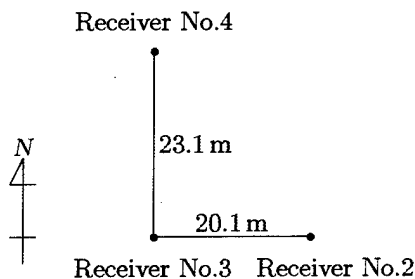


Figure 14: Receiver Placement for Test2

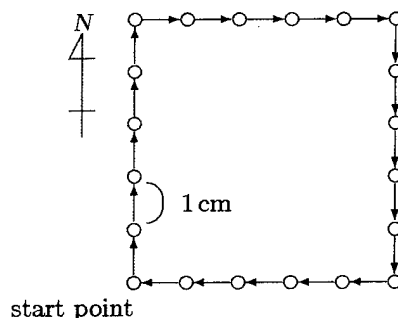


Figure 15: movement of antenna

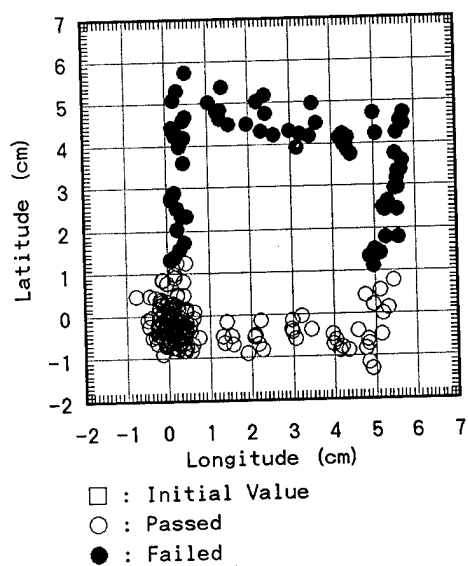


Figure 16: Chi-squared test for baseline No.4 to No.3

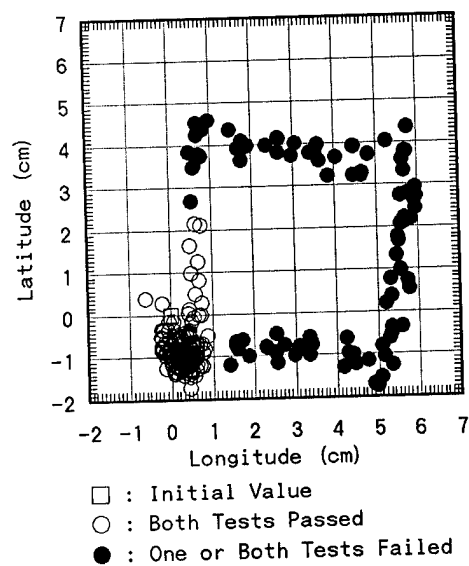


Figure 18: The statistical test for baseline No.2 to No.3

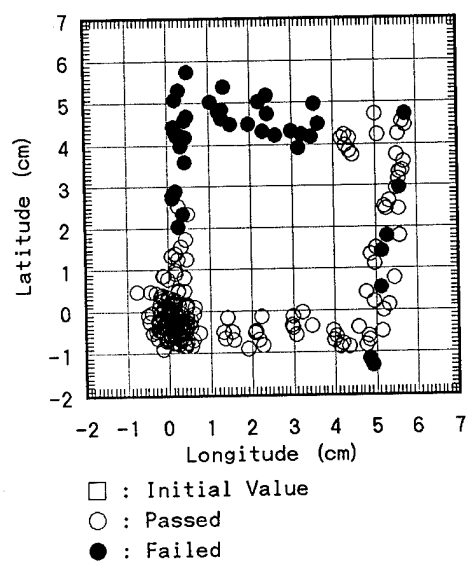


Figure 17: Baseline test for baseline No.4 to No.3

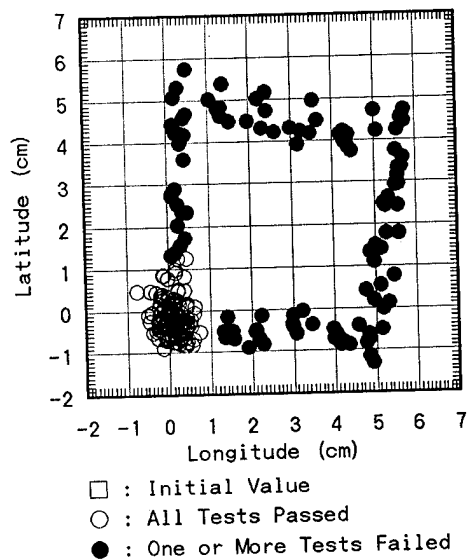


Figure 19: Statistical test for baselines No.4 to No.3 and No.2 to No.3

erence receiver except that the block dots indicate when at least one of the two statistical tests fails. The results are similar to those discussed above except that the statistical tests pass along a different axis of motion.

It is shown in Figure 19 that the dots in Figure 16 were made the block dots corresponding to the block dots in Figure 18. This result shows that displacements of order of 1-2 cm can be detected by measuring two baselines.

One of the conclusions of this test is that redundancy in the baseline analysis is important. For example, the interstation vectors between the various measurement points should be computed in addition to the vectors between the reference and measurement points. This is particularly important if blocks within the monitoring area are moving at different directions and speeds. This feature is also available in the current system.

Field Test

A field test is on going in the real landslide area shown Figure 1. Five receivers are used in this test. One is on the reference point and others are on measurement points. It seems that there are some blocks moving at different speeds in this area. It is expected that the movement of each block is cleared by using this system.

CONCLUSIONS

A system has been developed to continuously determine the positions in real-time of up to ten locations for potential displacement using precise GPS carrier phase processing techniques. This system has advantages over conventional systems in that it works in all-weather, day and night and is autonomous. It can be used to measure displacements in an area such as landslides, high cut slopes and subsidences.

Results of fundamental experiments show that the order of 2 cm of displacements can be detected by statistical tests. The use of more than one statistical test is useful in maintaining a high system reliability and the redundancy in the baseline analysis is important. This system has the advantage of high system reliability because of its redundancy of baseline analysis.

In the future, the availability of this system in a real field will be evaluated by some results of field tests. And because of more feasibility of placement of receivers, the system using radio links instead of some cables will be developed.

References

- [1] N. Shimizu and S. Sakurai: *Application of the Global Positioning System (GPS) for monitoring a high cut slope*, Proc. the 6th Int. FIG-Symposium on Displacement Measurements, Hanover, session 8, p.8, 1992.2.
- [2] S. Sakurai and N. Shimizu: *Monitoring of cut slopes by using the Global Positioning System (GPS)* Journal of Mining Research, 1(3), pp.19-29, 1992.12.
- [3] P. Griffioen, T. Allison and S. Dreier: *Real Time Kinematic: The Next Surveying Tool*, Proceedings of the 1993 ION Technical Meeting, 1993.1.
- [4] A. Leick: *GPS Satellite Surveying*, John Wiley & Sons, New York, 1990.

GPS-Based Launch Vehicle Tracking Using a Common Multi-Patch Antenna Configuration

M. Santina, J. Leung, G. Smit, J. Tekawy, and G. T. Seng
The Aerospace Corporation

J. McKay and S. Bandel
Hughes Aircraft Co.

ABSTRACT

A GPS-based launch vehicle tracking architecture is under serious consideration by the Air Force to replace or augment the current radar-based tracking system. Due to the unique launch vehicle configuration, demanding operational environments, and stringent timing and reliability requirements, the application of GPS to launch vehicles presents special implementation and integration challenges different from both earth-surface and satellite navigation. Standardization of GPS antenna configuration and implementation for different launch vehicles is a critical element in AF's acquisition strategy. Finding such a standardized configuration is the objective of this paper.

The paper presents a brief review of the antenna configuration trades including the trade between ring and patch antennas and the trade study on patch size and number. A 1/4-wave patch, which is commercially available, has a broad beam width but is more sensitive to edge diffraction effects caused by the neighboring structural elements. Aerospace has developed a prototype 1/2-wave patch, which can reduce the edge diffraction effects with a reduced beam width. Results of the trade studies indicate that either three 1/4-wave patches or four 1/2-wave patches should provide adequate GPS satellites coverage. A four 1/2-wave patch configuration, which is less sensitive to peculiar neighboring structural elements of different vehicles, is a better choice for standardization.

The first phase of development of a modularized simulation program is completed and has been used to evaluate the system tracking performance. The simulation includes the following key modules: vehicle trajectory and attitude motion, experimentally verified patch antenna models (with user's choice of patch number, size, location on vehicle, and signal combining scheme), GPS constellation and visibility, antenna switching logic, and an integrated receiver/IMU. Using the actual flight trajectory and geometry of several vehicles, the same four 1/2-wave patch antenna

configuration was simulated. The results confirmed the preliminary finding of the trade studies that the four patch configuration can satisfy the stringent launch vehicle requirements. Therefore, a common patch antenna configuration is feasible for standardized applications.

1. Introduction

The USAF Space and Missile Systems Center and The Aerospace Corporation have recently concluded several top level studies [Ref.1] investigating the use of the GPS for primary tracking and metric data processing for space launch activities at the Eastern Range (ER) and Western Range (WR). The study results indicated that a GPS-based tracking system would enjoy significant cost and performance advantages over the current radar-based tracking system. Due to the unique launch vehicle configuration, demanding operational environment, and stringent timing and reliability requirements, the application of GPS to launch vehicles presents new challenges different from both earth-surface and satellite navigation.

The range safety requirements are documented in References 2 and 3. Several important ones of interest here are described below. First of all, two totally independent trajectory measurement sources that meet Instantaneous Impact Point (IIP) accuracy are needed [Ref.2] with the reliability of each trajectory measurement source to be 0.999 at a 95% confidence level for a one hour duration. ER and WR have different IIP accuracy requirements [Ref.2] for real time tracking. For instance, ER has a 100-ft accuracy requirement for the Launch Area (LA) while WR's LA requirement is 1000 ft. On the post flight trajectory reconstruction [Ref.3], a 3-m position accuracy, a 0.003-m/s velocity accuracy, and a 100-nanoseconds timing accuracy are required for the guidance evaluation. Considering the high level dynamics that many launch vehicles and ballistic missiles will experience, these requirements are very stringent indeed.

The vehicles under consideration are Titan, Delta, Atlas, Taurus, Pegasus, and Minuteman. These vehicles vary greatly in physical size, geometric configuration, and flight profile. A major government acquisition objective is to be able to buy a common GPS User Equipment (GUE) configuration for standardized applications to all vehicles. As the first step of establishing the feasibility of achieving such an objective, The Aerospace Corporation has developed a database regarding the dynamics envelope, GUE placement constraints, and launch phase environments (e.g., thermal, vibration, shock, humidity) of these vehicles. The launch phase environments are highly dependent on where the GPS antennas and receiver are located. In the current study, it is assumed that they would be placed at the same locations as those of the C-Band antennas and transponder, respectively. In the presence of significant structurally transmitted and acoustically induced disturbances, the vibration and shock environments are extremely stressing. However, means are available to achieve adequate vibro-acoustic attenuation. Thermal and humidity environments, although still demanding, pose less a challenge to the GPS hardware. The rotational rates of these vehicles fall into two distinct categories; a few degrees per second for both large (e.g., Titan) and small (e.g., Pegasus) launch vehicles and an order of magnitude or higher for ballistic vehicles (e.g., Minuteman). This suggests that the vehicle dynamics should be fully accounted for in evaluating the system level tracking performance.

Despite the enormous size of some of the launch vehicles (e.g., Titan, Delta), the placement of the GUE components is subject to severe constraints. Using Delta II as an example, the GPS antenna is limited to be placed on the so-called "mini-skirt" (Figure 1) for range safety operations. The mini-skirt is about 8 feet in diameter but only 11-inch wide. A ring antenna is not practical because of the existence of other critical components on the skirt as well as the prohibitive weight and cost penalties for vehicles of this size. Same conclusion was also arrived for Titan II, Titan IV, and Atlas. For Taurus, Pegasus, and Minuteman vehicles, it is possible to find adequate space for a ring antenna. However, the associated weight and cost penalties could still be unacceptable. A patch antenna configuration was therefore selected because of its universal applicability and its apparent cost and weight advantages.

2. Antenna system

For launch vehicles, the GPS antennas are subjected to very restrictive requirements above and beyond those for most other navigation users. The configuration and structure of launch vehicles dictate that the mounting space for GPS antennas are allocated very small sections of the cylindrical surface. For example, on Delta II, the

real estate available is a "miniskirt" on the second stage, merely 11" wide.

The requirements for light weight, low profile, and ease of integration very much point to micro strip patch antennas as candidates for launch vehicle applications. While many of the GPS antennas flown in past experiments with launch vehicles were rings, ring antenna is not a viable option for most large launch vehicles. A large ring antenna of a few meter diameter weights hundreds of pounds; there will also be structural obstructions on the vehicle surface to prevent the mounting of a complete ring.

Figure 2 plots the gain pattern of patch antennas of different sizes, computed with the 2 slot approximation [Ref.4]. The sizes of antennas are expressed as fractions of the wavelength, λ . It can be seen that for patch sizes above 0.5λ , the antenna patterns contain large nodes and sidelobes. These patterns are clearly undesirable because of the large gain variation leading to coverage holes at 20-60° zenith angles.

The dominant multipath contribution for patch antennas mounted on a narrow cylindrical ground plane originates from the diffraction from the edges of the ground plane. An antenna pattern with a null at and around 90° zenith angle tends to be more immune to multipath effect. This is an argument against a 0.25λ antenna, which offers no rejection of multipath interference. The 0.5λ patch, on the other hand, offers an optimal balance between gain variation and multipath rejection. The physical sizes of the different patches for the 1.5754 GHz L1 is listed Table 1.

Because of the relatively severe rotational dynamics, a major concern of the launch vehicle antenna system is GPS coverage. A simulation documented in [2] has shown that with 4 65°-half-beamwidth patches, a Delta II has an average visibility of more than 10 GPS satellites over the launch trajectory. According to the gain pattern shown in Figure 2, 0.5λ patches provide adequate coverage for this vehicle.

3. GPS-Based Tracking Simulation

Members of the Technical Staff at the Aerospace Corp. are developing a modularized GPS Tracking Simulation program (GTSIM) to study the application of GPS to launch and space vehicles. In particular, GTSIM will be used to perform trade studies in order to satisfy the stringent launch vehicle requirements. The program is written in FORTRAN and hosted on the SUN workstation.

Figure 3 shows the major modules of GTSIM that are related to launch vehicle applications. The vehicle trajectory parameters that are required to perform the simulation are read into GTSIM as data files. These parameters include the vehicle position, velocity, acceleration, body rate, thrust, weight, elements of the inertial to body transformation matrix etc.. Figures 4 and 5 show the velocity (in ECI frame) and rates (about body axes), respectively, of the delta II vehicle which was considered for the simulation. From the figures, it is shown that the solid rocket burnout occurs at about 1 and 2 minutes, the main engine cutoff at about 4.5 minutes, and the second stage cutoff at about 11.3 and 20 minutes. The vehicle performs two attitude maneuvers; one between 11.5 and 12 minutes and the second between 16 and 18 minutes into the flight.

GTSIM also includes experimentally verified models for multiple patch antennas (with user's choice of patch number) that can be mounted on desired locations on the launch vehicle. The antenna model requires azimuth and elevation angles of a line-of-sight vector from an antenna to a GPS satellite and produces antenna gain and phase.

A broadcast GPS ephemeris file which includes the navigation message is used to propagate each GPS satellite motion. That is, the position and velocity vectors of each satellite in the constellation are updated using the broadcast orbital elements and the correction terms of the orbital elements. Knowing the position vectors of the launch vehicle and the GPS satellites, it can be determined, based on the usable beamwidth of the individual antenna, which GPS satellite falls within the field of view of each of the antennas mounted on the vehicle. Furthermore, because of the earth's finite dimensions, many GPS satellites are occulted from the launch vehicle by the earth. This condition on visibility is also included in GTSIM.

Coverage of the GPS satellites with patch antennas is demonstrated by the simulation of the Delta II mission. Figure 6 shows the number of GPS satellites tracked by 4 patches of 85 degrees half-beamwidth antennas evenly spaced on the skirt of the second stage. At liftoff, where the antennas are looking sideways (horizontally), there are 7 satellites visible but more come into the view as the vehicle gains altitude and pitches over. After 3.5 minutes from liftoff, the number of GPS satellites in the view varies between 11 and 12. The histogram in Figure 7 shows the percentage of time (from liftoff until the end of the flight) that N satellites are visible ($6 \leq N \leq 12$). It is seen that 11 satellites are visible 45% of the time, 12 satellites are visible 38% of the time and so on. Figure 8 shows the prn's of the visible satellites. GPS measurement geometry is good throughout the whole time.

Similar simulation results for 4 patches of 65 degrees half-beamwidth antennas were reported in [Ref. 1]. Of particular interest is the situation shown in Figure 9 where the tracking history of prn 19 by the 4 antennas is displayed. The abscissa is the boresight angle of the satellite in the coordinates of the individual antennas. During the vehicle maneuver (Figure 5), this satellite comes in and out of the field of view of one tracking antenna and then in the field of view of a neighboring one. This phenomena calls for a receiver control module with cooperative tracking capability between channels to maintain continuous lock and to acquire uninterrupted carrier phase measurement without incurring undetected cycle slips. When a satellite appears in the field of view of two neighboring antennas simultaneously, it is desirable to track the phase difference between the signals from these two antennas in anticipation of the transfer of the tracking task from one channel to the other. An integrated IMU/GPS systems dedicated to range safety bridge the gap during temporary GPS loss of track, and facilitate fast GPS reacquisition.

4. GPS Augmentation Using Low Cost IMUs

Due to the possibility of short duration GPS drop-out (typically due to inadequate antenna coverage) and subsequent loss of navigation data, it is desirable to augment the GPS receiver. This can be done with a low-cost inertial measurement unit (IMU - a combination of a three axis gyro and a three axis accelerometer). The idea is that the GPS receiver plus augmenting IMU would cost less than a navigation grade IMU. The recent emergence of micro machining techniques, in which integrated circuit technology is used to make mechanical as well as electronic components, has made possible the fabrication of very small, very low cost IMUs [Ref. 5]. Such micro-electromechanical systems (MEMS) including inertial measurement devices and interface electronics are currently under manufacture for various terrestrial applications (e.g. air-bag triggers). Moderate performance levels have been reported. For example, [Ref. 6] cites a gyro drift rate of about 30 degrees/hour. We now look at the kinds of performance requirements which must be levied on the augmenting IMU for a GPS system for a launch vehicle.

The GPS drop out periods (e.g. during fairing separation) would be of the order of few seconds. The basic performance requirement on the augmenting IMU must be that it adequately "fill in the gap", and that it also permit the GPS receiver to efficiently reacquire lock on its input signal as soon as that signal again becomes available. Without the presence of the IMU to fill in the periods of GPS outage, vehicle course changes could go undetected for the duration of the outage times, possibly incurring a

safety problem. With an IMU, any sudden course deviations would be immediately detected. For this purpose, a relatively low performance IMU will be adequate. For example, during a few second GPS outage, even a 30 degree per hour gyro will detect if large enough course deviations have occurred to have an impact on range safety.

To evaluate the trade between IMU performance and system performance, we need to take into account a number of factors, including the duration of the expected GPS drop-outs, and the GPS reacquisition time as a function of error when reacquisition is started.

Assume that the drop-outs are due to the loss of signal from individual satellites (i.e. not due to the loss of the whole constellation) and that these losses are due to geometric effects (antenna pointing due to launch vehicle maneuvers, satellites going over the horizon, etc.). Under these circumstances, drop-outs are typically a few seconds. Exceptions would be if the launch vehicle only has, for example, an antenna on top, and it rolls so that the antenna faces the earth and loses contact with all GPS signals until it rolls back again. We must now look at the build-up of errors as a function of IMU presence and quality. Figure 10 illustrates the error build-up as a function of IMU drift.

Another question which arises concerns whether the more accurate tracking afforded by the IMU during GPS drop-outs would result in improved GPS reacquisition times. To translate the accuracy numbers into reacquisition times, we note that this will depend on algorithms being used in the GPS receiver.

In order to provide a multi-access, low power (i.e. very low signal to noise ratio) signal, the GPS satellite outputs use pseudo random noise coding. The receiver generates a similar code, the phase of which must be varied until the correlation between the two signals is optimized. The amount of searching required to achieve this depends on the accuracy of the initial guess, and on the search algorithm used. Typically, the search time for reacquisition on C/A code will range from several seconds for an initial error of hundreds of kilometers down to practically instantaneous for errors under a kilometer. Even at a 10 g acceleration for a 10 second drop out, the error will only be 5 kilometers, so the impact of an IMU on reacquisition time should be small.

As indicated above, the main advantage of the IMU is that it could warn of an anomaly without having to wait for the end of the drop-out period. Another advantage of the IMU is that it improves the performance of the Kalman filter.

5. GPS Measurement Equation and Kalman Filtering

Presently, the GPS receiver measurement equations used in GTSIM is pseudo range. The pseudo range measurement Z_i to the i^{th} satellite is given by

$$Z_i = [(S_{xi} - P_x)^2 + (S_{yi} - P_y)^2 + (S_{zi} - P_z)^2]^{1/2} - C \cdot Br - C \cdot Dr \cdot \text{time} + V_r$$

where

$S_i = (S_{xi}, S_{yi}, S_{zi})$ is the i^{th} GPS position vector (ECI)

$P = (P_x, P_y, P_z)$ is the launch vehicle position vector (ECI)

C = speed of light

Br = Receiver clock bias minus satellite clock bias

Dr = Receiver clock drift minus satellite clock drift

V_r = random noise.

The random noise V_r includes the pseudo range noise, range quantization, range mechanization, ionospheric dual frequency error, and tropospheric residual. Values and characteristics of these error sources are presented in Table 2. The GPS ephemeris error and GPS satellite clock bias error are combined as one bias error source of 3 meters, 1σ . As shown in the table, the error sources are modeled either as white noises or random biases and are added to generate the receiver measurements that drive the Kalman filter.

Currently, an 8-state Kalman filter is used in GTSIM to estimate the launch vehicle position, velocity, receiver clock bias and receiver clock drift.

The system is described by the state equations

$$\dot{\mathbf{x}}(t) = \mathbf{F}\mathbf{x}(t) + \mathbf{L}\mathbf{w}(t)$$

where $\mathbf{w}(t)$ is a white noise process with covariance matrix given by

$$E\{\mathbf{w}(t)\mathbf{w}^{\dagger}(t + \tau)\} = \mathbf{Q}_c\delta(\tau)$$

where E denotes expected value and the superscript \dagger means transpose of the quantity. The elements of the process noise covariance matrix \mathbf{Q}_c represent unmodeled acceleration effects and receiver clock uncertainties.

It can easily be shown that the discretized state equations are

$$\mathbf{x}(k+1) = \Phi \mathbf{x}(k) + \mathbf{w}(k)$$

where

$$\Phi = e^{\mathbf{F}T}$$

and

$$E\{\mathbf{w}(k)\mathbf{w}^T(k)\} = \mathbf{Q}_d = \int_0^T \Phi(\gamma) \mathbf{L} \mathbf{Q}_c \mathbf{L}^T \Phi^T(\gamma) d\gamma$$

The Kalman filter corrector equations are:

$$\mathbf{K}(k) = \mathbf{P}(k/k-1) \mathbf{H}^T(k) [\mathbf{H}(k) \mathbf{P}(k/k-1) \mathbf{H}^T(k) + \mathbf{R}(k)]^{-1}$$

$$\hat{\mathbf{X}}(k/k) = \hat{\mathbf{X}}(k/k-1) + \mathbf{K}(k) [\mathbf{Z}(k) - \mathbf{H}(k) \hat{\mathbf{X}}(k/k-1)]$$

$$\mathbf{P}(k/k) = [\mathbf{I} - \mathbf{K}(k) \mathbf{H}(k)] \mathbf{P}(k/k-1)$$

and the Kalman filter predictor equations are:

$$\hat{\mathbf{X}}(k+1/k) = \Phi \hat{\mathbf{X}}(k/k)$$

$$\mathbf{P}(k+1/k) = \Phi \mathbf{P}(k/k) \Phi^T + \mathbf{Q}(k)$$

In these equations, boldface letters indicate vector and matrix quantities. The hat over a quantity means an estimate of the quantity, and the superscript T means transpose of the quantity.

In a single sample interval of 1 second, the Kalman filter corrector equations are processed sequentially for all GPS satellites in view, while the predictor equations are used once after all corrections are made. Other processing schemes and other Kalman filter implementations are of course possible.

The measurement Jacobian matrix $\mathbf{H}(k)$ used in the above equations is given by

$$\mathbf{H}(k) = \frac{\partial \mathbf{g}(\mathbf{x})}{\partial \mathbf{x}} \bigg|_{\mathbf{x} = \hat{\mathbf{x}}(k/k-1)}$$

$$= [-u_x \ -u_y \ -u_z \ -C \ 0 \ 0 \ 0 \ 0] \bigg|_{\mathbf{x} = \hat{\mathbf{x}}(k/k-1)}$$

where $\mathbf{g}(\mathbf{x})$ is the noise free term of the measurement equation, and (u_x, u_y, u_z) is the LOS unit vector given by

$$u_x = (S_x - P_x)/|\mathbf{R}|$$

$$u_y = (S_y - P_y)/|\mathbf{R}|$$

$$u_z = (S_z - P_z)/|\mathbf{R}|$$

and

$$|\mathbf{R}| = [(S_x - P_x)^2 + (S_y - P_y)^2 + (S_z - P_z)^2]^{1/2}$$

Figures 11, 12 and 13 show the preliminary simulation results of the above 8-state filter. In all these figures, the error is defined as the difference between the filter estimated state and the true state of the vehicle and the receiver. The launch vehicle RSS position error shown in Figure 11 is well under 100 meters during the mission except at the indicated spikes. The cause of these spikes is that the Kalman filter uses an oversimplified model of the acceleration during solid rocket burnout and main engine cutoff. Similar comments apply to the pseudo range residual error shown in Figure 12 and the receiver clock bias error shown in Figure 13. It can be shown from this figure that the position error due to receiver clock bias is about 4.5 meters. Recall that the receiver clock bias error also includes the receiver clock drift.

6. Concluding Remarks

The first phase of development of a simulation program designed for tracking and range safety applications is completed. Preliminary results show that vehicle position errors well under 100 meters are achievable. Effort is continuing at The Aerospace Corporation to simulate an integrated GPS/IMU system as outlined in Figure 3. As stated in Section 4, for brief drop-outs (of the order of a few seconds), the quality of the IMU will not be very important. Accelerometer bias stabilities of the order of 0.01 g's and gyro drift rates of the order of a degree per minute will yield acceptable performance. Thus MEMS units can be used to great advantage in this application.

Acknowledgments

The authors would like to thank William Emanuelson, Steven Johns, and William Smit of the Aerospace Corporation for their contributions in preparing this paper.

References

- [1]. Leung, Jurn, G. L. Schipper, G. T. Tseng, P.C. Wildhagen, and D. W. Wingard, "GPS Applications to Launch Vehicles," presented at the 51st ION Annual Meeting, Colorado Springs, Colorado, 5-7 June 1995. (Proceedings of the 51st ION Annual Meeting, to be published.)
- [2]. USAF EWRR 127-1, 31 March 1995.
- [3]. USAF Range Standardization and Automation (RSA) Technical Requirements Document (TRD), 11 May 1995.
- [4]. Balanis, C A, *Antenna Theory, Analysis and Design*, John Wiley & Sons, Inc., 1982.
- [5]. B.E. Boser, R.T. Howe, A.P. Pisano, course notes from UCB short course on *Monolithic Surface-Micromachined Inertial Sensors*, May 1995.
- [6]. R. Hulsing, D. MacGugan: "Miniature IMU based on micromachined Coriolis Sensors, ION 1993 National Technical Meeting.

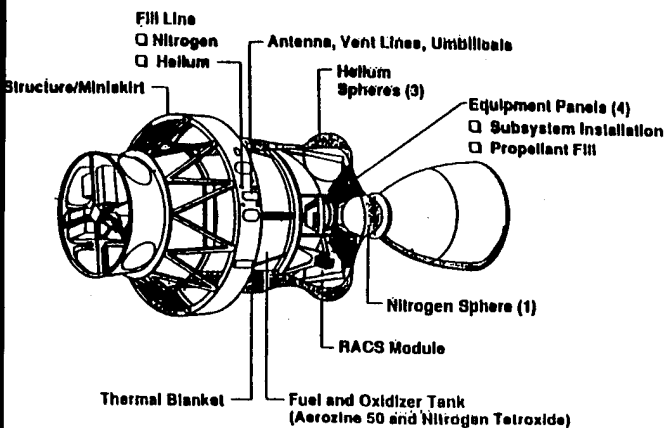


Figure 1. Delta II second stage

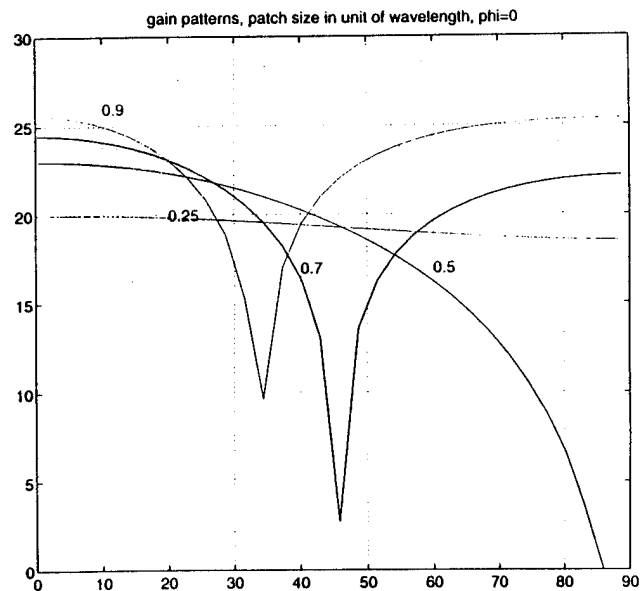


Figure 2. Gain pattern of patch antennas of different sizes

Table 1. Antenna sizes

fraction of λ (L1)	0.9	0.7	0.5	0.25
dimension (cm)	17.12	13.32	9.51	4.76

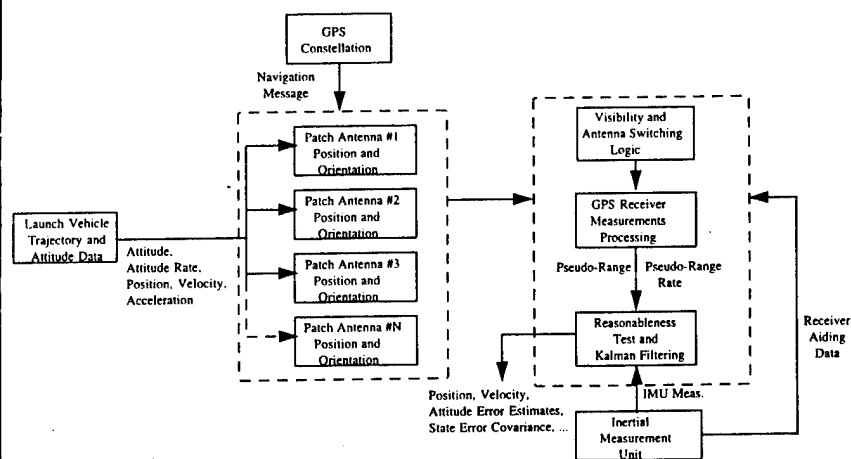


Figure 3. GPS-based launch vehicle tracking simulation block diagram

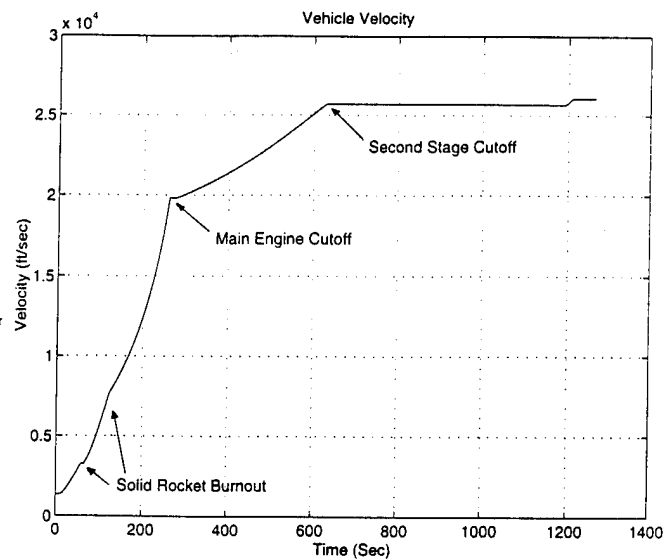


Figure 4. Magnitude of Delta II velocity vector

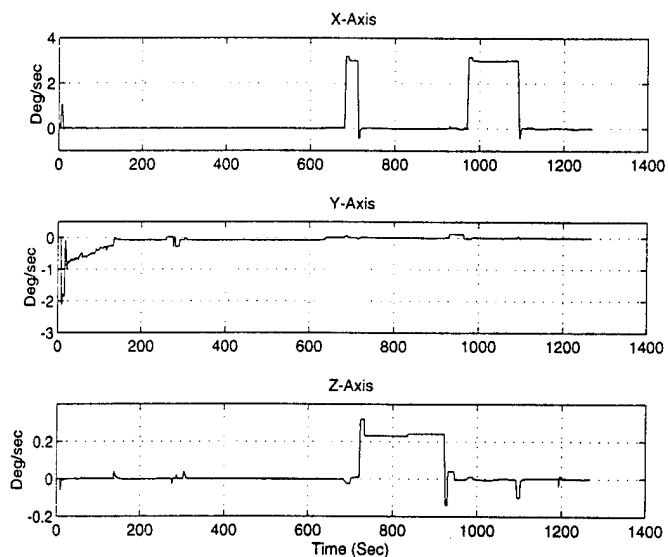


Figure 5. Attitude maneuver of Delta II vehicle

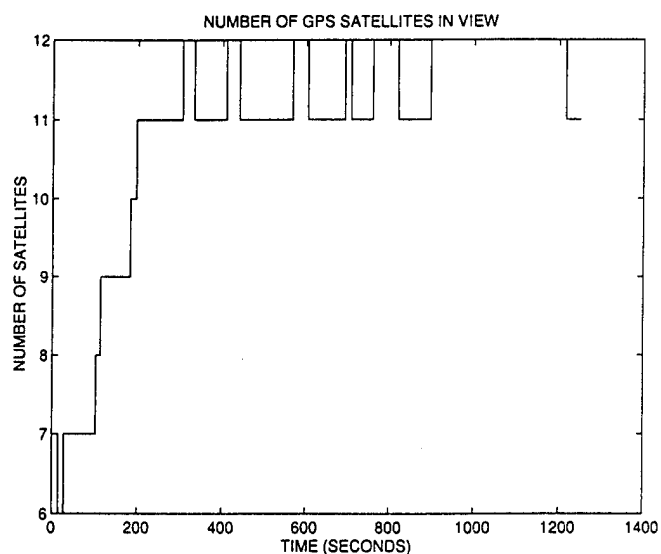


Figure 6. Number of GPS satellites visible with 4 patches

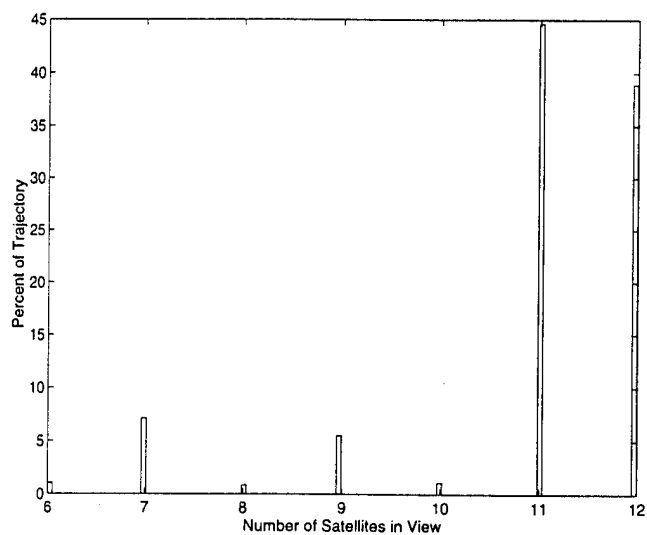


Figure 7. Histogram of GPS satellites tracked during mission

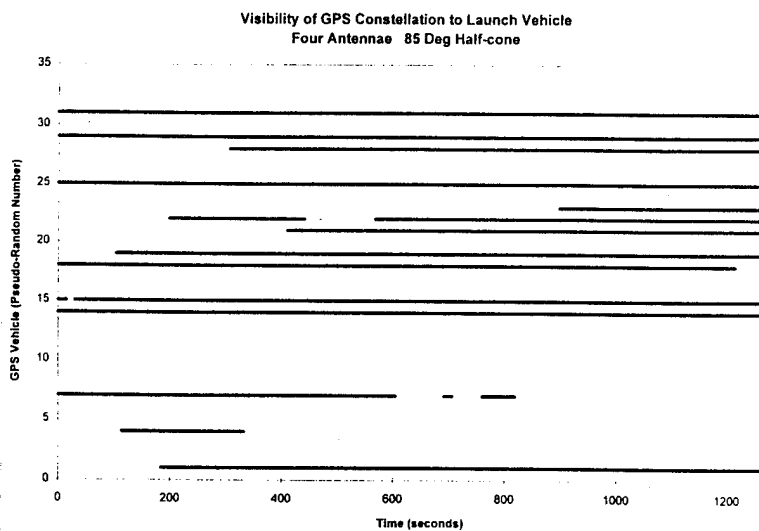


Figure 8. 4 antenna (85 deg) visibility

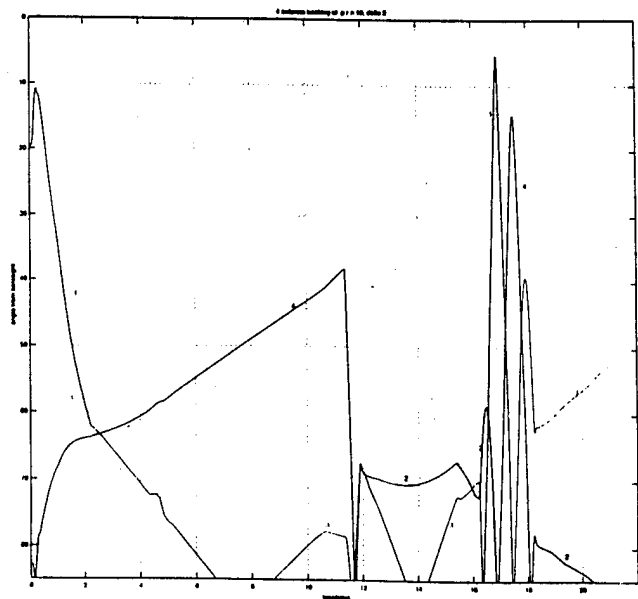


Figure 9. 4 antenna tracking of prn 19.

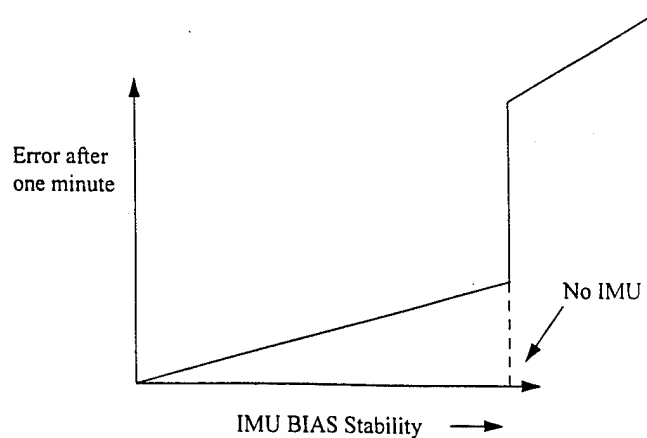


Figure 10. Effects of GPS dropouts vs IMU performance.

Table 2. MEASUREMENT MATRIX (1σ)

Error Contributor	Pseudorange(meters)	Statistics
GPS Satellite Segment		
Satellite Ephemeris	2.12	Bias
Satellite Group & Clock	2.12	Bias
GPS User Segment		
Pseudorange Noise	1.0	White Noise
Range Quantization	0.3	White Noise
Range Mechanization Error	1.0	White Noise
Propagation Link		
Ionospheric Dual Frequency Error	1.5	White Noise
Tropospheric Residual	1.0	White Noise

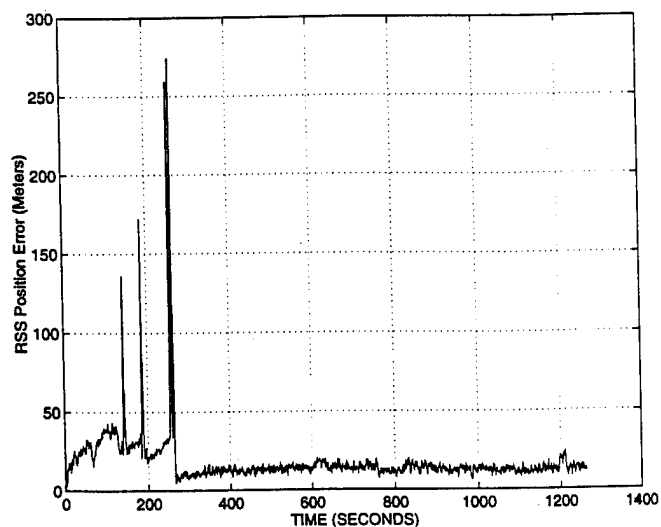


Figure 11. Launch vehicle RSS position error (Meters)

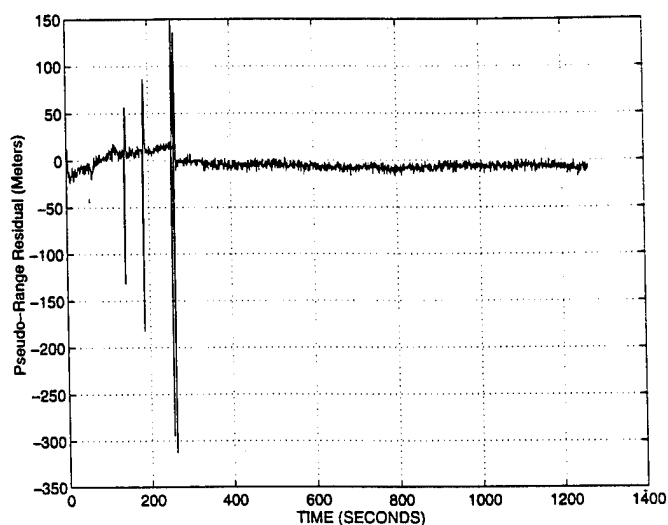


Figure 12. Kalman filter pseudo range residual error (Meters)

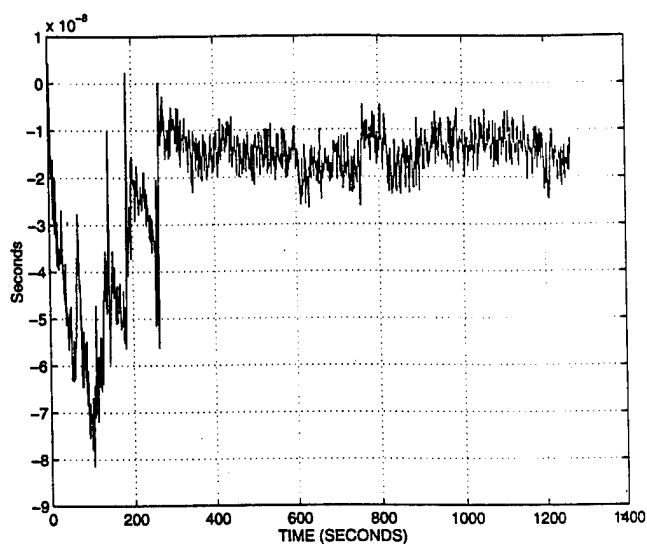


Figure 13. Receiver clock bias error (Seconds)

GPS Goes 'Beyond the Gate'

Samuel Shaw
California Maritime Academy

Jack Hunter
California DOT

BIOGRAPHY

Samuel G. Shaw is a Professor of Maritime Management at the California Maritime Academy, Vallejo, CA. He holds a US Coast Guard license of Unlimited Master of Steam or Motor Vessels as well as a Limited Master of Sail Vessels. He also holds a Master's Degree in Geography from the University of Washington.

Jack Hunter is a California State archaeologist assigned to the CALTRANS Central Coast District, headquartered in San Luis Obispo. A major interest for Jack has been the application of remote sensing techniques to the investigation of underwater archaeological resources.

ABSTRACT

The integration of GPS positions with external sensors for use in a GIS database has been described many times. It is rare, however, for the description to be of sufficient detail to serve as a guide for a reader interested in adopting the technique. Many important details are usually glossed over in an effort to focus on the eventual success of the project. This paper focuses on the experience gained in trying to realize the dream of seamless GPS integration. The reader is guided experientially through the techniques of making integrated measurements during a time sensitive research project. All equipment was 'off the shelf' and was selected for reasons of economy as well as capability. The reader will learn about NMEA strings, connectors, power and battery problems, dataports, datalinks and antennae to name a few topics.

INTRODUCTION

'Beyond the Gate' is the name of a collaborative underwater archaeological field school project involving the Los Angeles Maritime Museum, Sonoma State University and the California Maritime Academy (a California State University). The goal of the work is to create a better understanding of the role of the Central California riverine highway in the development of the California Gold Rush. The project name comes from the direction of travel that a gold miner would have pursued

in 1849. When approached from seaward, the gold fields lay approximately 100 miles *beyond the Golden Gate* entrance to San Francisco harbor. This area is very flat, covers several thousand square miles and is crisscrossed with numerous waterways. In most areas, the elevation is only a few meters above sea level. The region is popularly known as the California Delta. The first phase of the research effort was to conduct an inventory of the submerged cultural resources that were suspected to exist in a portion of the delta. Legal permission to investigate underwater features in this region was granted by the California State Lands Commission.

The Research Objectives

The 'field school' (as the project became known) selected the wreck of the sailing vessel *Chesapeake* as one of the first resources to be inventoried. The vessel's trade was typical of the area, and the specifics of the wreck made it likely that artifacts could be located. This decision focused attention on a narrow waterway called Steamboat Slough.

The Steamboat Slough Shortcut

The water transit from San Francisco to Sacramento now benefits from a very well defined and maintained ship channel. In the middle part of the nineteenth century, however, this was not the case. There were many different ways to make the transit. Different routes also offered different trading opportunities with the many farms that were located between the waterways. The advantage offered by the Steamboat Slough route was that it was shorter than most others. A disadvantage, however, was that it was more narrow and winding than the longer routes. In the early 1850s the *Chesapeake* was making its way down the slough from Sacramento toward San Francisco. The holds contained mining equipment that had not been claimed by the consignee, and was being returned to San Francisco. The vessel is reported to have grounded on a sandbar and foundered at a point in the slough called 'the Hogback'. Newspaper and other reports from that era indicate that neither the vessel nor the cargo were ever successfully salvaged.

THE REMOTE SENSING PLAN

The delta is considered a 'black water' area due to a high suspended sediment load. This means that even under good conditions the visibility for divers is extremely poor. At some points the visibility is near zero at a depth of only a few feet below the surface. These conditions made it necessary to first search the target area with remote sensing tools. Promising locations would then be 'ground-truthed' by divers employing non-visual search techniques. Since visibility was such a limiting factor, it was necessary to attach the remotely sensed data to a highly accurate (and re-occupiable) location. Differential GPS (DGPS) was selected as the primary positioning tool because it offers the necessary accuracy, and is easier to accomplish, than the terrestrial methods that were also considered (e.g., survey poles or laser stations).

In its new role as a California State University, the California Maritime Academy assumed the task of coordinating the equipment, personnel and expertise needed to accomplish the integration of various remote sensors with DGPS position information. The Academy also provided the marine vessels that would be needed as both remote sensing platforms and diving platforms.

Economic and Time Constraints

Nearly all the equipment available to the field school was 'off the shelf'. This term is usually applied to equipment that can be purchased without any special modifications being necessary. For this project, however, it also meant that nearly all of the equipment had to be already owned by the participating institutions. This is because the budget for the project was extremely tight. Every effort was made to avoid spending money on equipment that could be found without a cash outlay. For this reason, most of the equipment was not of the latest model or enhancement. The magnetometer was leased, however, and included all the common features.

Once the field school assembled, everything had to happen within a two week period. The task list included the provision of room and board for the staff and students, the assembly and testing of the sensing equipment, and the training of the students. Field school staff were also busy with the operation of the remote sensing tools, the execution of the academic program, the post-processing of data, the selection of dive sites and the conducting of the dive operations.

The Tools

Magnetometer

Since the shipwreck is believed to have been carrying a cargo of mining equipment, the usefulness of a magnetometer became self-evident. The model employed was of the proton-precession type. A magnetometer is capable of detecting local disturbances to the earth's magnetic field caused by concentrations of ferrous material. As the sensor closely approaches a local

magnetic disturbance (such as that produced by a mining equipment debris field) the instrument registers this variation and thus reveals the existence of the object causing the disturbance.

Sidescan Sonar

A sidescan sonar is an acoustic device that is capable of returning a record of the existence of objects on both sides of a vessel. This is accomplished by directing sound signals away from the survey platform as the sensor is moved across the area of interest. The sonar echo causes a trace on a recorder that reveals physical structures under the water. As the name implies, the area directly beneath the survey platform is not recorded. The interpretation of the printout requires a certain amount of experience. With practice, however, an observer can make some educated guesses as to the size and nature of objects that are detected with a sidescan sonar.

GPS Tools

The use of GPS was divided into two tasks. The first task addressed the need to archive the data from the other tools in such a way that the locations of objects of interest could be readily determined. The second task was to return the divers to any site that was selected by the project archaeologists. For both of these tasks, there would be scant opportunity to occupy the site except instantaneously as the vessel transited the desired position.

Differential techniques were necessary to achieve an adequate level of positional accuracy. Both real-time and post-mission corrections were applied as appropriate to achieve final accuracies of two to-five meters. A higher accuracy would have been desirable, but was not possible given the budget constraints.

The first task was accomplished through the use of a GIS grade receiver. The magnetometer data was integrated automatically with the GPS position data using a commercially available software package. The software writes the GPS positions and external sensor data to the same GIS attribute record in a database. Since the sidescan sonar data is graphical instead of tabular, it was necessary to also log event positions that could later be used to ensure that features on the sidescan printout could be linked to GPS positions. The event marks were logged at two minute intervals.

The second task was accomplished by using a marine navigation receiver. The change in receivers was beneficial because the navigation receiver readily lent itself to displaying real-time differentially corrected position information in a way that was useful to a person who was actually operating the vessel. The GIS receiver did offer some utilities for this task, and would probably have been adequate if the need had been pressing.

A SUCCESSFUL OUTCOME

The focus of this paper is to discuss some of the difficulties associated with the integration of GPS positions with other sensors during a field application. Before moving in that direction, however, it is useful to first review the techniques that produced a successful outcome for the project under review.

Locating a Submerged Cultural Resource

The search for archaeological artifacts, whether submerged or not, is not a random one. Long before the start of the field school, staff archaeologists had been studying the delta area. Thus, the target area was selected because there was good reason to believe that the site was not only relevant but also promising.

The most useful piece of information when searching for the shipwreck was provided by the sidescan sonar. A portion of the printout is shown below in Figure 1. The figure shows an area of white near the bottom of the display. This area represents a likely debris field on the bottom of the slough. The debris field is also close to the location where it is suspected that the shipwreck exists. A distance scale is provided with the sonar trace, so distance measurements can later be made with a ruler. Figure 2 shows the trace of the magnetometer at the time the sensor passed near the debris field evident in Figure 1. The large dip located near the middle of the chart matches the location of the debris field shown in Figure 1.

The Role of GPS

The displays shown in Figures 1 and 2 represent only a tiny fraction of the total data collected. It was not known

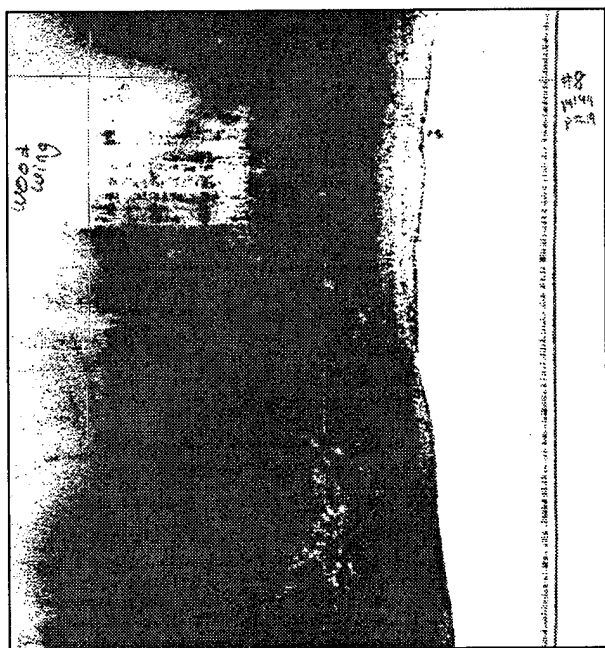


Figure 2: A Sidescan Sonar Printout

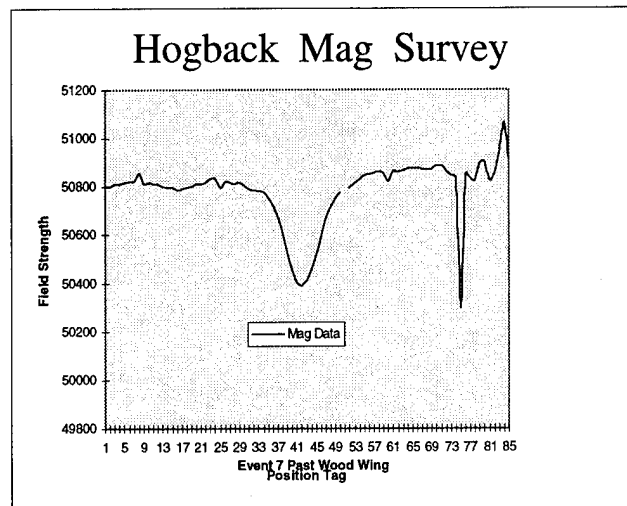


Figure 1: A Magnetometer Hit. The Plot Is Adjusted For The Distance Of The Sensor To The GPS Antenna.

with any certainty which particular two minute interval of data would draw the interest of the archaeologists. GPS was used to ensure that the entire data set was linked to accurately determined locations. Event marks matching those linked to the GPS positions were physically logged on the sidescan trace in the field. In Figure 1, one of the event marks (event #8) can be seen in the upper right hand corner of the trace. The magnetometer data was fed to a laptop that was also linked to the GPS positions and the event marks. The resulting data was then post-processed to produce differentially corrected positions. The magnetometer data was also printed as a graphic in real-time on a dot matrix printer. Event marks were manually marked on this trace as well.

Figures 3 and 4 on the following page provide examples of how the data was logged with a laptop. Figure 3 shows the track of the survey platform with the event marks. At the top of the screen is the notation 'at wreck site'. This is a special event mark. It constitutes a note by the navigator that the vessel was occupying the suspected site of the wreck at that particular time. A notation such as 'at target location' would have been a somewhat better logging practice.

Figure 4 shows the magnetometer data as it was read to the software. The data was logged automatically every two seconds.

Making The Dive Happen

Determining The Location (Ashore)

Once the area of interest was located on the sidescan sonar trace, distance measurements were made from the nearest event marker (event #8 in this case). These measurements were made directly on the paper trace using the built in distance scale. Since great care had gone into steering the boat in as straight a line as possible, the

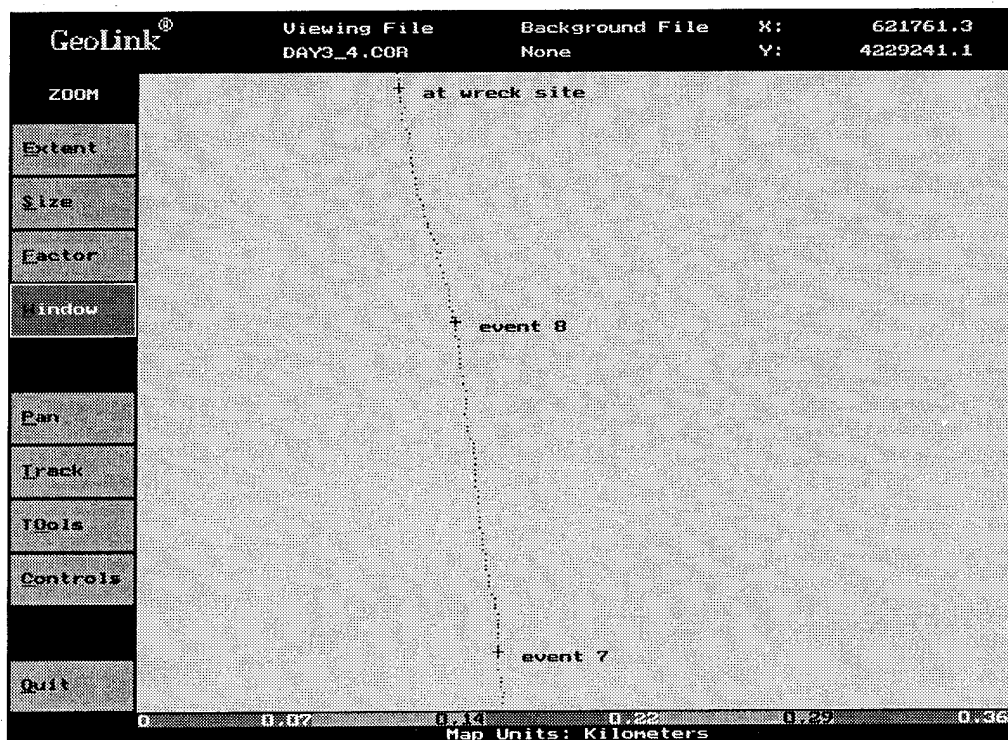


Figure 3: Event Marks Logged As Attributes.

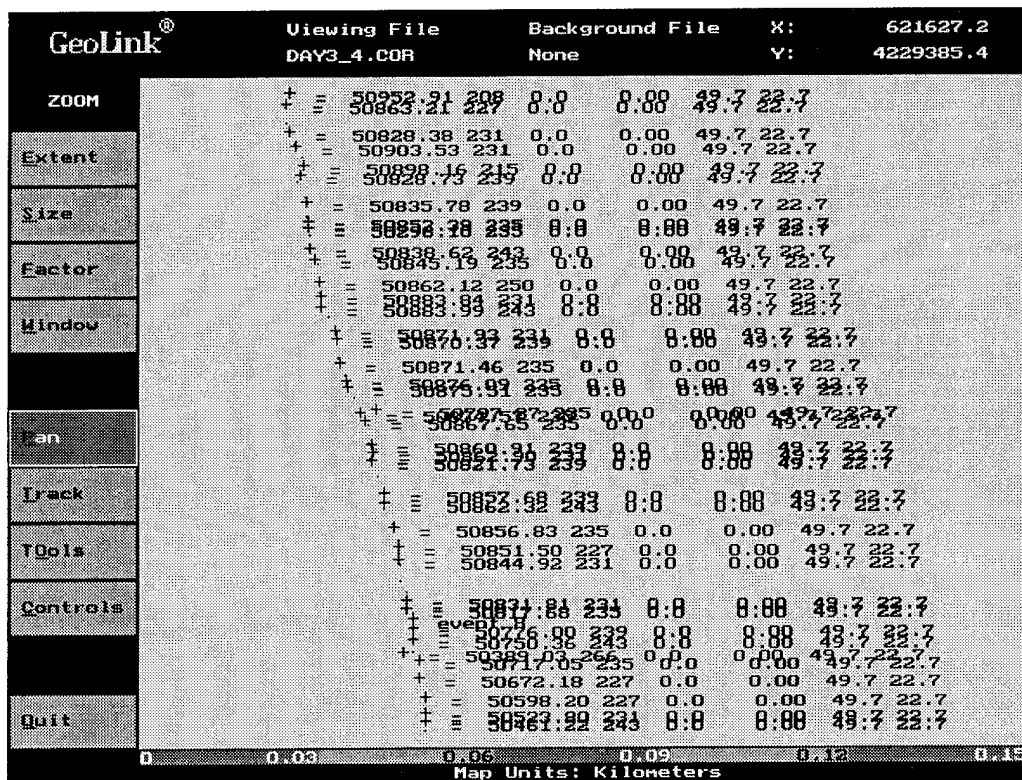


Figure 4: Magnetometer Data and Event Marks Logged As Attributes

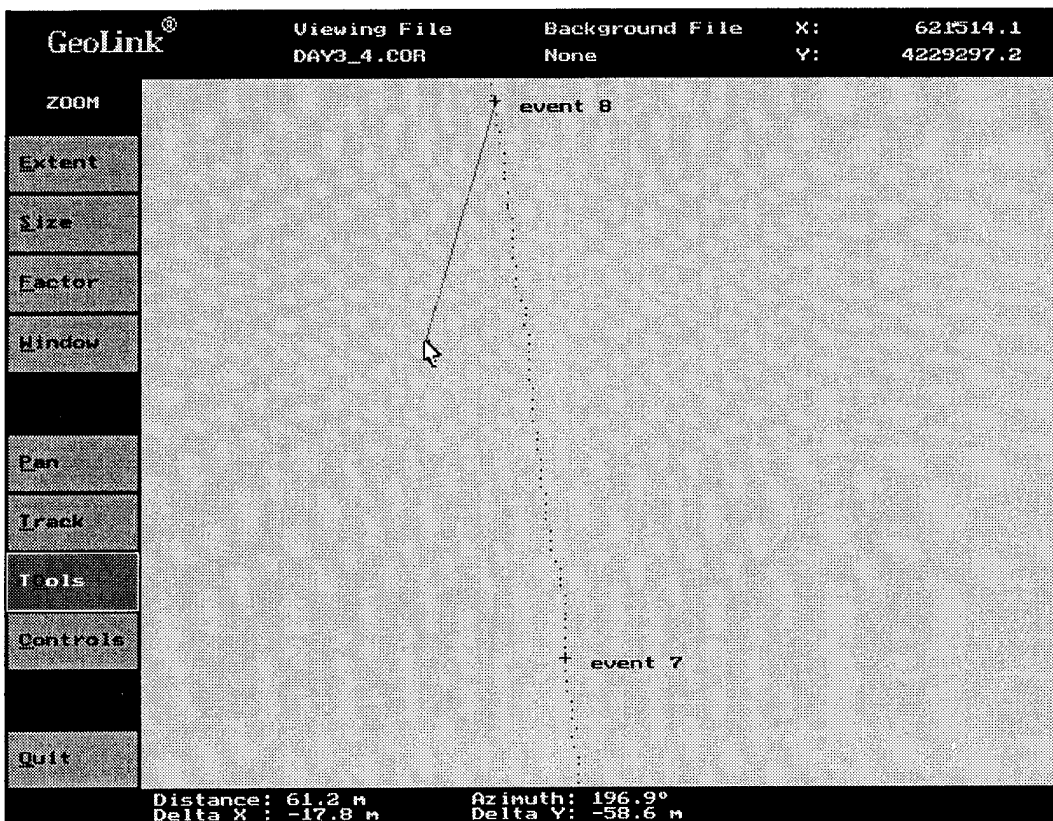


Figure 5: Measuring Distance From An Event Mark

measurements could be considered to be in terms of so many meters between events and so many meters over from the event to event line. As a cross-check, the distance back from event 8 was also computed as a percentage of the total distance between events 7 and 8. The difference between this calculation and the one described above was a fraction of a meter. Since this is well below the measurement capability of both the sidescan sonar and the GPS receiver, it was subsequently ignored.

Once the location was referenced as a distance from event 8, that distance could be transferred to the laptop where the events had been logged as attributes. This process is shown in Figure 5. Since the track of the vessel is shown, the distance between events can be applied in the correct direction. The distance 'over' was applied by moving the cursor in a direction 90 degrees from that which represented the distance back. The coordinates of a position resulting from applying these offsets can be viewed on the computer screen (the top right corner of Figure 5 shows an example).

Determining The Location (Afloat)

The coordinates (in latitude and longitude) of the desired location were transferred to the marine receiver as a waypoint. Three persons checked the numbers to make sure that the waypoint had been entered properly. The position was also plotted on a nautical chart to make sure

that no gross errors had been made in deriving the position from the computer. Real-time differential corrections were fed to the receiver (using a commercial FM subcarrier service) and the survey vessel was navigated to the correct position. The navigation utilities provided with the marine receiver made it a much more suitable choice than the GIS receiver. The site was marked by placing a buoy at the correct location.

To achieve maximum accuracy, the GPS antenna offset from the edge of the boat was taken into account. It was also necessary for the boat to be moving at a speed that would allow the operator to maintain control of the boat, but not so fast that a small delay in actually dropping the buoy would cause an important position error.

Since the location was near land, several evaluation passes were made before dropping the buoy. During this time, terrestrial bearings were taken and checked on each pass. This helped make sure that the same location was being occupied each time the GPS receiver indicated that the proper site was being passed.

When the navigator was satisfied in all respects, the buoy was released. The boat then made several more passes at the location of the buoy in order to detect any possible errors

The Dive Site

When the divers made their first descent, the visibility was nearly zero. Thus it was necessary for them to adopt a physical search pattern. The search located a debris field a few feet from the buoy anchor within a few minutes. Subsequent investigation over the next two days showed the debris to consist of wood and iron objects. This kind of material is consistent with the type that would be associated with the wreck. No conclusive evidence of the origin of the objects has yet been recovered, however. The site is so promising, though, that future dives have been scheduled.

DIFFICULTIES AND WORKAROUNDS

A time and budget sensitive collaborative project to be conducted on the water is probably the surest way to experience equipment problems. The field school had its share. Some of these problems were just bothersome; others were somewhat more serious. The paragraphs below will describe some of the problems that might be expected, and also offer some advice as to how to keep problems from developing.

The Three Golden Rules

No project should be expected to be problem free. Problems can be reduced or mitigated, however, if three simple rules are always kept in mind:

- 1) Always have more than one way to do whatever it is you are trying to do.
- 2) Keep it simple.
- 3) Test all equipment configuration changes - no matter how small.

A near golden rule would be:

- 4) Involve field personnel in the installation of equipment on the survey platform.

These rules are probably universally known and also universally broken. Discipline in this area, though, is certain to have its payoffs.

The NMEA 0183 Standard

This standard data format has become fairly popular in recent years because it allows the machines of different manufacturers to communicate with each other without a protocol arrangement between the manufacturers. A well-known problem with the standard, however, is that it can be interpreted by different manufacturers in different ways. The GPS receivers used for this project were capable of outputting a position to the sidescan sonar but the sonar was unable to recognize what the receiver was sending. The problem was that the same NMEA 0183 sentence was formatted differently by the two manufacturers. The workaround for this standoff was to use manual event markers in the field. The magnetometer software did accept the NMEA sentences as output by the receiver.

Gender Changers and Adapters

It is highly recommended that every conceivable serial cable adapter be taken into the field. Gender changers for 9-pin and 25-pin connectors will be needed. It may also be useful to have 9-pin to 25-pin adapters and vice versa. Serial cables that have a connector at one end and are loose wired at the other end (9- and 25-pin models, of course) were needed to route the differential corrections to the navigation receiver. Standard spare serial cables should also be on hand. RS-232 splitter boxes may prove invaluable. These can be made from printer data switch boxes. A Volt-Ohm Meter (VOM) will prove useful but make sure to have an assortment of leads. Pin-out documentation for every piece of equipment should be available to be taken into the field. A 9-pin and a 25-pin null modem adapter may also be necessary.

Once all of the pieces that might be needed are identified, be sure to have at least two of all of them. Electrical tape and contact cleaner are both useful as well.

Data Format Problems

The data set had to be corrected, mapped, identified, converted, and exported or imported. It seemed to be a function of Murphy's Law that each one of these steps required a different format for the data in one respect or another. The idea of collecting the data in a GIS format proved to be a good one indeed. The GIS format allowed both the position data and the magnetometer data to be output into an ASCII file. The format of this file could be tailored for the specific use of the data.

If an ASCII file is not exactly in the desired form it can be manipulated by both Microsoft Word and Microsoft Excel. Between these two readily available packages, it is possible to accept an ASCII file in almost any form and export it in almost any desired form. Microsoft Word is especially good at searching for unwanted formatting and replacing it with desired formatting. Microsoft Excel is especially good at dealing with delimiting characters, charting data and adding or removing feature counters or indices.

Accomplishing the Differential Corrections

To integrate the magnetometer readings with the GPS positions, it was necessary for the positions to be fed to the computer. Since this used the receiver's only dataport, it was no longer possible to use the real-time differential signals that were available in the area. Thus it became necessary to post-process differential corrections in the field. This procedure involved downloading base files by way of a modem. Since a land line was not readily available, a cellular telephone was used to make the connection. The reader is cautioned that most cell phones are not able to download data reliably. In the case of the field school, a special adapter for the cell phone was required. The cell phone was then used to access a US

Forest Service base station that was located about 30 miles distant.

It developed that the cellular coverage in the delta area was rather poor. This caused a loss of data when downloading a base file. After some experimentation, it was discovered that occupying the highest point in the region (a hill with an elevation of about 50 feet) made all the difference. From this vantage point the base files were downloaded easily.

The base files were provided free of charge to anyone who could access them. This does not mean that the service was guaranteed, however. One very important base file was found to simply not contain a full set of corrections! Luckily, another base station at about 60 miles distant was available and provided a base file that would work. The extra distance probably slightly decreased position accuracy for that hour, but the alternative would have been to use uncorrected data.

Both of the available base stations had begun logging their files in a new format. A user of older equipment would have found that the correction process no longer worked unless the base files were converted from the new format to the old one. The process is simple and the converter software is distributed free of charge *but it is not distributed automatically*. A user who had not learned of the change would receive error messages that would lead troubleshooting efforts in a fruitless direction.

A real-time FM subcarrier differential service was available in the area and worked very well. The service was received via a common FM automobile antenna. It should be remembered that this technique offers different levels of position accuracy at different prices. Thus, differentially corrected positions acquired this way may have accuracies that vary from very good to very mediocre depending on the terms of a subscription. To the uninformed user, the two outcomes are produced by equipment that looks identical.

Some receivers are capable of accepting differential corrections and simultaneously outputting NMEA 0183 sentences on a single dataport. The user is cautioned that the differential modem will probably have to be configured for a 4800 baud rate in order for this to work.

Software Compatibility Problems

The integration software advertises that it is completely compatible with the receivers that were to be used on the project. In fact, the GIS attribute data is stored in a format that is not completely compatible with the post-processing software that comes with the receiver. Thus, features cannot be viewed or edited from within the software shipped with the receiver.

The only substantive problem encountered in using the integration software was that it did not support data collection in a space-delimited format. This (of course) was the only format that could be output by the

magnetometer. The advertising for the software leads one to believe that the software itself can handle up to dozens of external sensors. In reality, an extra piece of hardware is needed between the software and the external sensors. Also, the user has no control over which field in the GIS database the information will be logged.

Computer Considerations and Power Supplies

One thing to be considered ahead of time is how the data will flow from one machine to another. When operating more than one sensor (GPS plus another) it is likely that two physical serial ports will be required on the field computer; most laptops only provide one. In the field, it may be necessary to disconnect the mouse and recover a serial port in this way. This causes little trouble in practice because a mouse is nearly useless on a moving platform such as a small boat or an automobile. In these cases, it is much more efficient to use keystrokes to implement the logging process.

A second serial port might be added via a PC Card (formerly PCMCIA Card). These devices sell for under \$150. The same PC Card slot can also be used for a PC Card modem. It has become popular for laptops to offer two PC Card slots along with the regular serial port. This can be useful, but when operating more than two peripheral devices, the computer must be specially configured to avoid memory conflicts. Modems and PC Cards also consume conventional memory. This can cause logging and mapping software to be unable to run.

Electrical power management can be a critical issue. Be sure to carefully flowchart the requirements for batteries, generators (and the appropriate fuel), extension cords and inverters. As might be expected, the need to pre-plan the way the machines connect to the power supplies is paramount. If a power system is to be built in the field, it will prove very useful to have voltage and amperage meters handy.

The Check Off List

Table 1 on the following page provides a check off list that may be useful before going into the field. The format is self-explanatory. This list is not product specific, so it can be used in conjunction with the check off lists that are provided by most manufacturers of GPS equipment.

SUMMARY

This paper focuses on the experience gained in trying to realize the dream of seamless sensor integration. The specific application involved a survey of the underwater archaeological resources located in a specific area of interest. Sonar and magnetometer data was integrated with GPS positions in such a way that a site of interest could be re-occupied within a very short amount of time. Differential techniques (both real-time and post-processed) were employed to achieve the accuracy level required by the application.

Further comments, questions or advice concerning the topics raised in this paper are invited. Please Email to tobias@ix.netcom.com.

ACKNOWLEDGMENTS

The staff of the 1995 Delta Underwater Field School, besides the authors, were Sheli O. Smith, Margaret Purser, Richard Swete, Monica Hunter, Michael Jablonowski, and John Muir. Additional support was received from John W. Foster of the California Department of Parks and Recreation, Donald Newman of California State University at Long Beach, Robert Orlins of the California Department of Water Resources, Carl McClain of the California Department of Transportation, Ross Johnson of Geometrics, Inc. (Sunnyvale, CA) and David Wolf of the California Maritime Academy. Special recognition should also go to the very capable and willing students who attended the field school.

Table 1 : Sample Check Off List

INTEGRATED MARINE SURVEY CHECK OFF LIST

Project

Date

GPS TOOLS:

Power Supply	Mask Angle	Mode
--------------	------------	------

Cable Check Completed:

☐

Data Format Correct

☐

DIFFERENTIAL CORRECTIONS:

Source	Expected Accuracy	Cable Check Completed:
--------	-------------------	------------------------

☐

REMOTE SENSOR #1:

Power Supply	Sensor Type	Sensor Offset
--------------	-------------	---------------

Cable Check Completed:

☐

Data Stream Format

NOTES:

REMOTE SENSOR #2:

Power Supply	Sensor Type	Sensor Offset
--------------	-------------	---------------

Cable Check Completed:

☐

Data Stream Format

NOTES:

Experimental Demonstration of GPS for Rendezvous Between Two Prototype Space Vehicles

Kurt Zimmerman and Dr. Robert Cannon, Jr.
Stanford University

Abstract

The objective of this research is to demonstrate that Differential Carrier Phase GPS techniques can be employed as the primary means of sensing both the relative position and the relative attitude of two space vehicles in order to perform complex maneuvers such as multi-vehicle rendezvous and station-keeping in Low Earth Orbit. An experimental hardware system, consisting of a prototype space robot, target vehicle, and GPS system, has been devised to closely emulate real spacecraft. Since the experiments take place indoors where GPS satellite signals cannot be received, several GPS pseudolite transmitters have been built and installed around the perimeter of the laboratory to provide the GPS signals. The indoor GPS environment created by the close-range pseudolite transmitters poses additional constraints on the algorithms used to extract relative position and relative attitude from the carrier phase measurements. Therefore, a secondary objective of this research is to develop GPS for indoor sensing, where it has the potential to be applied to indoor mobile robots and to automated manufacturing systems. This paper presents the theoretical formulation and results of a rendezvous experiment between a prototype space robot vehicle and a passive target vehicle. An mpeg movie of this experiment can be viewed at <http://sunvalley.stanford.edu/movies/movies.html>.

1 Introduction

This work is motivated by the need to increase the efficiency and safety of assembly, maintenance, inspection, and repair tasks in the high-risk environment of Low Earth Orbit. Examples of such tasks include satellite retrieval, Orbital Replacement Unit (ORU) change-outs on satellites and the proposed space station, and assembly of modules and truss structures for advanced space missions. Currently these tasks are performed by astronauts through hundreds of hours of Extra-Vehicular Activity (EVA). Highly au-

tonomous robot systems – managed at the *task level* by a ground or space-based supervisor – can make these tasks more routine and lower risk.

Communication bandwidth limitations and data delay between the robot and the human supervisor force the need for a highly autonomous robot that can react to unpredictable situations. The degree of autonomy required for such a robotic system can only be achieved through reliable, high-bandwidth on-board sensors that enable dynamic control loops to be closed at the local level. Specifically, in order to perform a rendezvous task or multi-vehicle station-keeping, it is necessary to sense the relative position and orientation between both vehicles. This research project takes advantage of Differential Carrier Phase GPS technology to perform a precise intercept and capture of a free-floating target by an autonomous free-flying space robot. This paper presents:

- The fundamental research issues involved in developing an indoor testbed for GPS-based rendezvous.
- A description of the hardware system that has been developed.
- The theoretical analysis for using GPS to sense two non-stationary vehicles.
- Practical implementation issues, results and conclusions from this experiment.

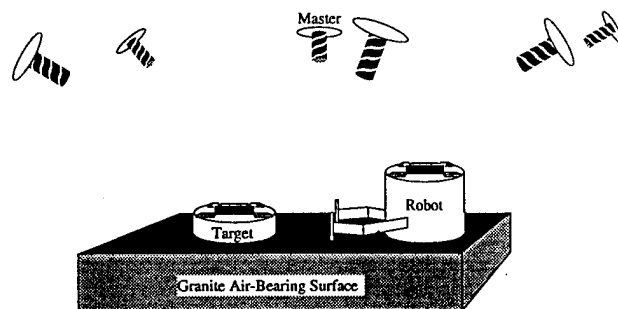


Figure 1: Rendezvous Experiment Configuration

2 Research Issues

There are several fundamental research issues that had to be addressed prior to the successful completion of this project, and prior to the use of GPS technology in a true space rendezvous mission. The issues addressed by this research are listed below. Related research issues have been studied by [1], [2] and [3]

The use of GPS as a sensor in real-time feedback control – GPS sensing is susceptible to both predictable and unpredictable loss of sensor data due to occlusion, vehicle configuration, and multipath. Partial loss of signal information can be compensated for with measurements from several satellites together with proper prediction using vehicle dynamics.

The use of GPS for indoor sensing – The prospect of using GPS indoors presents several fundamental problems, such as those initially discussed in [4]:

- *Spherical wavefronts* – Since the transmitters are very close to the workspace, the wavefront will be spherical rather than planar. This leads to non-linear phase measurement equations from which the position and attitudes must be derived.
- *Lack of pseudorange* – Pseudorange (time-of-flight measurements) cannot be used indoors due to the relatively low accuracies available. The pseudolites are therefore not even designed to broadcast the data needed to calculate pseudorange. This resulted in the need to reformulate attitude and integer-resolution algorithms to meet this constraint [5].
- *High multipath environment* – Signal reflections off of walls can result in a much greater occurrence of multipath indoors than outdoors. This problem is being alleviated through the use of custom-designed helical antennas with conical-shaped beam patterns.
- *Near-far problem* – The close proximity of the transmitting sources to the receivers leads to very large variations in the power of the signal received as the vehicle traverses the workspace. The signal power of each of the pseudolites must be carefully adjusted so that the receiver does not cross-correlate signals (jam) at one extreme of the workspace and yet is still able to receive the signal at the other extreme of the workspace.
- *Calibration of a pseudolite positions and antenna baselines* – The locations of the phase centers of

the pseudolite transmitter antennas and the vehicle receiver antennas need to be precisely determined before the necessary tolerances to perform rendezvous can be met.

Coordinated control of a multi-arm space robot – The Stanford Aerospace Robotics Lab (ARL) has already demonstrated the coordinated control of a multi-arm free-flying space robot for target rendezvous and capture [6]. These pioneering experiments were successfully demonstrated through the use of an overhead vision sensing system which was employed to provide the relative vehicle/satellite position and orientation. A constraint of this vision system is that it operates in only two dimensions and requires an overhead, perpendicular view of illuminated target points on each object in the workspace. The GPS system replaces the overhead vision system as the source of relative position and attitude information. Data from the vision system is still used as a means for evaluating the performance of the GPS system.

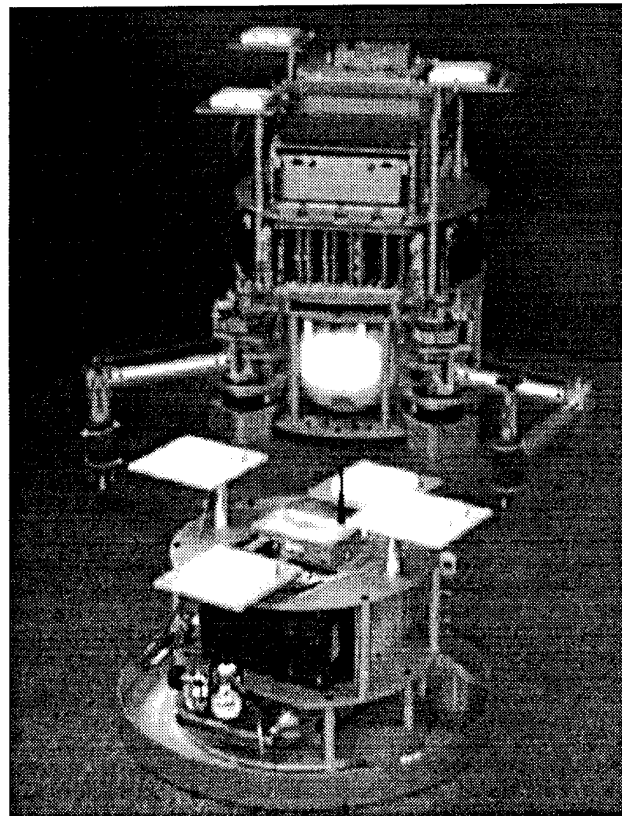


Figure 2: ARL Free-Flying Space Robot and Target Vehicle

3 System Description

Experiment Configuration – The experiment configuration is shown in Figure 1. GPS signals are generated by six pseudolites distributed around the laboratory above the workspace of the vehicle. The robot is commanded at an intuitive, task level through a graphical user interface to rendezvous and capture the moving target. The robot combines its phase measurements with the target's phase measurements to estimate the relative position and attitude and plan an intercept trajectory in real time. Once it is within capture range, the robot can grasp the target using its manipulators.

Robot and Target Vehicles – The robot and target vehicles are each equipped with a six-channel GPS receiver that is capable of multiplexing between four antennas, i.e. up to 24 carrier phase measurements on each vehicle, prior to taking differences. The receivers are off-the-shelf TANS Quadrex receivers from Trimble Navigation, with customized internal software. Carrier phase measurements from the target vehicle's GPS receiver are time-tagged and broadcast out through a 19.2k baud modem. The robot receives the measurements and combines them with its own measurements and processes them to derive position and orientation relative to the target vehicle. Specifically, the target broadcasts 18 differential carrier phase measurements and 6 raw carrier phase measurements at 10Hz (see Figure 6).

The robot, depicted in Figure 2, uses an air-cushion support system to achieve the drag-free, zero-g characteristics of space in two dimensions. It is a self-contained autonomous vehicle, complete with on-board VME-bus computers, radio-link Ethernet transceiver, batteries, cold-gas propulsion system with eight on-off thrusters, and dual cooperating manipulators. The control software is written in "C" and "C++" and is being developed using *ControlShell*TM [7] and the *VxWorks*TM Operating System.

The target vehicle, also depicted in Figure 2 is equipped with its own power, communication, and flotation devices.

Pseudolite Constellation – Each pseudolite produces its own L1 (1.575GHz) carrier phase signal modulated by its own unique C/A code. In order to perform differential carrier phase measurements between the robot and the target vehicle, the receivers on both vehicles must be synchronized to within one millisecond, so that the carrier phase measurements from each are tagged to the same millisecond epoch. Syn-

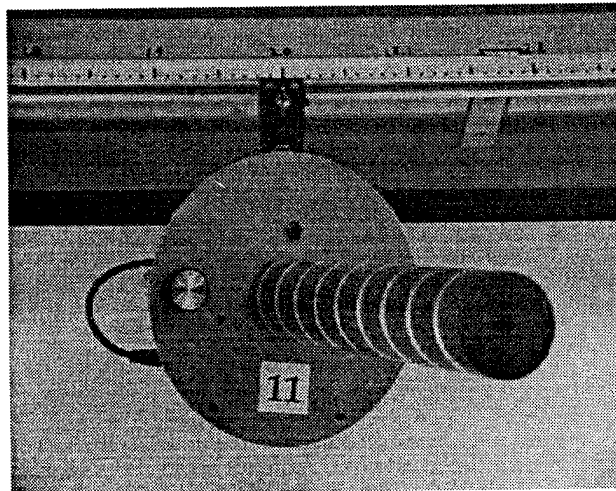


Figure 3: Mounted Pseudolite

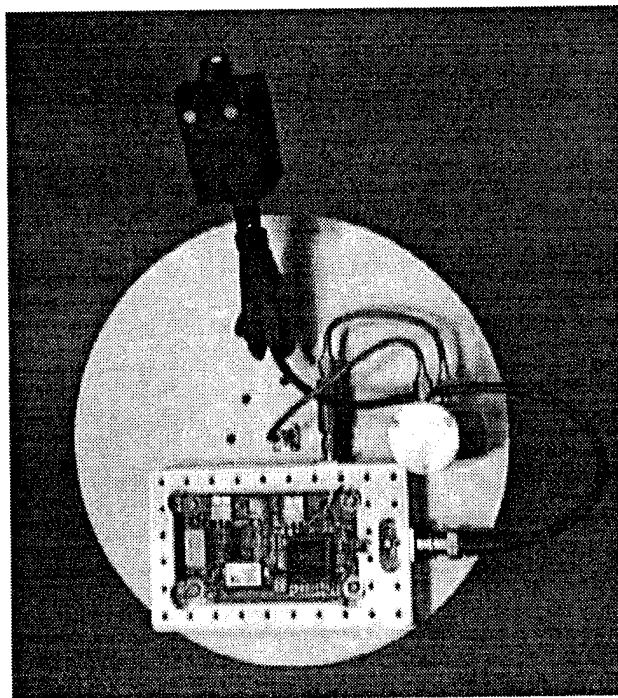


Figure 4: Pseudolite Transmitter

chronization is achieved through a "Master Pseudolite" which broadcasts a 50bps GPS data signal modulated on top of the C/A code. This 50bps data signal contains valid timing information from which the two receivers can automatically synchronize, enabling differential carrier phase measurements between the two receivers. Figure 3 shows a mounted pseudolite (broadcasting as PRN 11). The pseudolite is completely self-contained, and can be mounted anywhere around the room on a standard track-lighting fixture

which supplies power at 12V. Figure 4 shows the internals of a GPS pseudolite transmitter box as it is mounted on the back of the helical antenna. For size reference, the ground plate of the antenna is 8.5" in diameter. The transmitter electronics board was designed by the Stanford GPS Laboratory for use on their automated landing system for aircraft [8]. The antenna is designed to broadcast L1 in the normal mode with a conical beam pattern.

Overhead Global Vision System – An overhead vision system (not shown) that is capable of tracking the robot and target vehicles also exists for evaluation of the GPS system performance. The vision system can track the vehicles at 60Hz, with an absolute accuracy estimated at better than 2cm over the entire workspace and static noise of less than 1mm.

4 Theoretical Analysis

The rendezvous and station-keeping experiments require the estimation of the attitudes and positions of both vehicles. This section provides the derivation of the equations needed to compute the states of the vehicles from the GPS carrier phase measurements. Figure 5 shows the method in which the phase differences are taken and Figure 6 shows the variable definitions. The following assumptions and conventions are made in the derivation:

Assumptions

- The initial position of each vehicle is known. This means that as long as the pseudolites stay in lock after initialization, the integer ambiguity problem can be ignored¹.
- Pseudorange cannot be used in the formulation. The pseudolites do not provide the information required to perform pseudorange measurements since the accuracy of these measurements would be useless at very close range.
- The receivers provide measurements synchronized to within one millisecond. These measurements are further refined to effectively achieve much better than millisecond synchronization, as described in **Time Bias Corrections** below.
- The positions of the pseudolite transmitters are known and fixed.

Conventions

- Subscript i is always a *vehicle* index, j is an *antenna* index, and k is a *pseudolite* index; Subscript $j = m$ refers to the *master antenna* of a vehicle and $k = M$ refers to the *master pseudolite*.
- A plain-text Δ refers to the first-difference between antennas on the *same* vehicle; a **boldface** Δ refers to the first-difference *between the master antennas of the two vehicles*.
- The attitude is alternatively represented as a rotation matrix, R_i , and also as an equivalent angle-axis vector, V_i . These representations are related to the quaternion state as shown below:

$$R_i = \begin{bmatrix} 1 - 2\epsilon_2\epsilon_2 - 2\epsilon_3\epsilon_3 & 2(\epsilon_1\epsilon_2 - \epsilon_3\epsilon_4) & 2(\epsilon_1\epsilon_3 + \epsilon_2\epsilon_4) \\ 2(\epsilon_1\epsilon_2 + \epsilon_3\epsilon_4) & 1 - 2\epsilon_1\epsilon_1 - 2\epsilon_3\epsilon_3 & 2(\epsilon_2\epsilon_3 - \epsilon_1\epsilon_4) \\ 2(\epsilon_1\epsilon_3 - \epsilon_2\epsilon_4) & 2(\epsilon_2\epsilon_3 + \epsilon_1\epsilon_4) & 1 - 2\epsilon_1\epsilon_1 - 2\epsilon_2\epsilon_2 \end{bmatrix}$$

$$V_i = \begin{bmatrix} \frac{2\epsilon_{i1} \cos^{-1}(\epsilon_{i4})}{\sin(\cos^{-1}(\epsilon_{i4})/2)} \\ \frac{2\epsilon_{i2} \cos^{-1}(\epsilon_{i4})}{\sin(\cos^{-1}(\epsilon_{i4})/2)} \\ \frac{2\epsilon_{i3} \cos^{-1}(\epsilon_{i4})}{\sin(\cos^{-1}(\epsilon_{i4})/2)} \end{bmatrix}$$

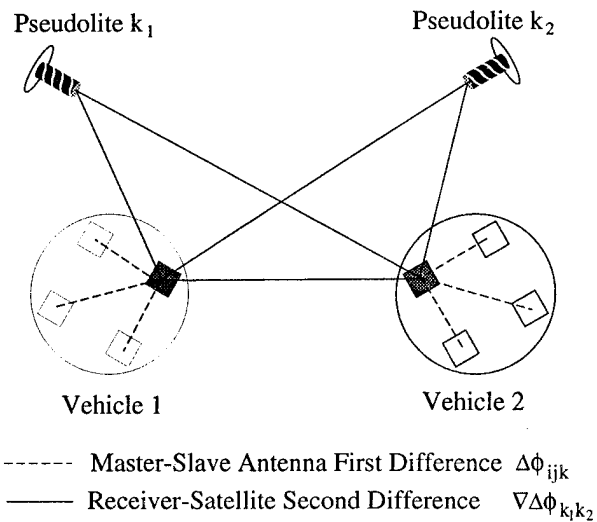


Figure 5: Phase Difference Method

¹In the actual implementation, knowledge of the state and dynamics of the vehicles is used to recompute the integer values when pseudolite signals are lost or gained

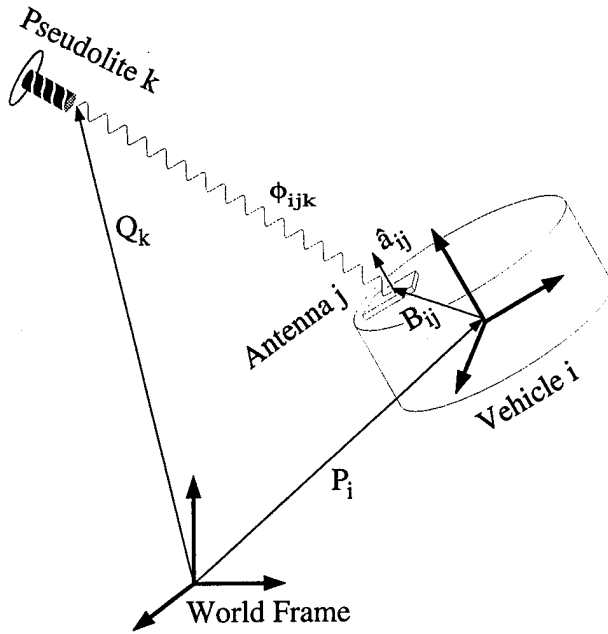


Figure 6: Variable Definitions

- P_i Position of vehicle i , in world frame
- R_i Attitude of vehicle i , in world frame (as rotation matrix)
- B_{ij} Baseline from vehicle center to antenna position, in vehicle frame
- c Speed of light
- τ_{vi} Receiver clock drift for vehicle i
- τ_{pk} Transmitter clock drift for pseudolite k
- λ GPS L1 carrier wavelength
- K_{ijk} Integer ambiguity between antenna j of vehicle i and pseudolite k
- V_i Attitude of vehicle i , in world frame (as equivalent angle-axis vector)
- \hat{a}_{ij} Antenna bore site vector of antenna j of vehicle i , in vehicle frame

The Unknown State

The state of each vehicle is represented as a 7x1 vector:

$$X_i = \begin{bmatrix} P_i \\ E_i \end{bmatrix} = \begin{bmatrix} p_{ix} \\ p_{iy} \\ p_{iz} \\ \epsilon_{i1} \\ \epsilon_{i2} \\ \epsilon_{i3} \\ \epsilon_{i4} \end{bmatrix} \quad (1)$$

where $\epsilon_{i1}, \epsilon_{i2}, \epsilon_{i3}$, and ϵ_{i4} are the four quaternion parameters that describe the attitude of the vehicle.

The fourth quaternion ϵ_{i4} is constrained by the equation:

$$\epsilon_{i1}^2 + \epsilon_{i2}^2 + \epsilon_{i3}^2 + \epsilon_{i4}^2 = 1 \quad (2)$$

Measurement Equations

The measured carrier phase for vehicle i , antenna j , from pseudolite k is:

$$\phi_{ijk} = |(P_i + R_i B_{ij}) - Q_k| + c\tau_{vi} + c\tau_{pk} + \lambda K_{ijk} - V_i \cdot \hat{a}_{ij} \quad (3)$$

The term $V_i \cdot \hat{a}_{ij}$ represents the change in the phase measurement due to antenna rotation in the circularly polarized field. If all the antenna bore sites are aligned on the vehicle, this term cancels after taking phase differences.

Master-Slave Antenna First Differences (for each vehicle):

The master-slave antenna first differences are used to determine the attitude of each vehicle. These are derived by taking the differences between the master antenna ($j = m$) and each of the slave antennas j of vehicle i for measurement from pseudolite k :

$$\Delta\phi_{ijk} = |(P_i + R_i B_{im}) - Q_k| - |(P_i + R_i B_{ij}) - Q_k| + \lambda M_{ijk} - V_i \cdot (\hat{a}_{im} - \hat{a}_{ij}) \quad (4)$$

where $M_{ijk} = K_{imk} - K_{ijk}$.

Receiver-Satellite Second Differences (between vehicles):

The receiver-satellite second differences are used to determine the relative positions between each vehicle. Starting with first differences between master antennas of each vehicle ($i \in \{1, 2\}$):

$$\Delta\phi_k = |(P_1 + R_1 B_{1m}) - Q_k| - |(P_2 + R_2 B_{2m}) - Q_k| + c(\tau_{v1} - \tau_{v2}) + \lambda(K_{1mk} - K_{2mk}) + V_1 \cdot \hat{a}_{1m} - V_2 \cdot \hat{a}_{2m} \quad (5)$$

Given N pseudolites, there are N unique second differences between pseudolite k_1 and k_2 ($k_1 \neq k_2$). These differences are taken to eliminate the remaining effects due to clock errors $c(\tau_{v1} - \tau_{v2})$

$$\begin{aligned} \nabla \Delta \phi_{k_1 k_2} = & |(P_1 + R_1 B_{1m}) - Q_{k_1}| - \\ & |(P_2 + R_2 B_{2m}) - Q_{k_1}| - \\ & |(P_1 + R_1 B_{1m}) - Q_{k_2}| + \\ & |(P_2 + R_2 B_{2m}) - Q_{k_2}| + \\ & \lambda N_{k_1 k_2} \end{aligned} \quad (6)$$

where $N_{k_1 k_2} = K_{1m k_1} - K_{2m k_1} - K_{1m k_2} + K_{2m k_2}$.

Combining the Measurements

All of the measurements are coupled to the states of both vehicles, so all of the measurements must be combined to resolve these states. From equations (4), (6), and constraints (2) the complete set of measurements can be related to the vehicle states:

$$\begin{bmatrix} \Delta \phi_{1jk} \\ 0 \\ \Delta \phi_{2jk} \\ 0 \\ \nabla \Delta \phi_{k_1 k_2} \end{bmatrix} = \begin{bmatrix} h_1(X_1) \\ 1 - (\epsilon_{11}^2 + \epsilon_{12}^2 + \epsilon_{13}^2 + \epsilon_{14}^2) \\ h_2(X_2) \\ 1 - (\epsilon_{21}^2 + \epsilon_{22}^2 + \epsilon_{23}^2 + \epsilon_{24}^2) \\ h_{12}(X_1, X_2) \end{bmatrix} \quad (7)$$

where h_1 is a set of nonlinear functions of X_1 , h_2 is a set of nonlinear functions of X_2 , and h_{12} is a set of nonlinear functions of both X_1 and X_2 . The optimal estimate of X_1 and X_2 can be solved using a Newton-Raphson algorithm as described in [9].

Note that for the case in which all pseudolites are in view by all antennas of both vehicles, the dimension of h_1 and h_2 is 18×1 , and the dimension of h_{12} is 6×1 . Adding the two constraints, there are a total of 44 measurements. This is far more than necessary to resolve the 14 state variables. The fewest number of pseudolites that can be in view and yet still resolve the states is three, so long as all three are in common between both vehicles. Since time is synchronized by a single master pseudolite, a fourth pseudolite is not needed to solve for time.

Time Bias Corrections

The equations derived thus far assume that the phase measurements $\phi_{ijk}(t)$ are taken at the same instant for both vehicles. In reality, this is not true. Each of $\phi_{ijk}(t)$ can be thought of as a "snapshot" of the carrier wave at time t . Since the receivers are only synchronized to within a millisecond by the data message that is broadcast by the master pseudolite [10], the error can be as large as the maximum observed carrier phase rate (Doppler ≈ 1 kHz) times the receiver time bias (≈ 1 msec) times the wavelength (0.19m),

which can be several centimeters. It is therefore necessary to estimate the measurement at time t , given only measurements at times t_k . This is done with a simple first-order expansion:

$$\begin{aligned} \phi_{ijk}(t) &= \phi_{ijk}(t_k) + \int_{t_k}^t \dot{\phi}_{ijk}(t) dt \\ &\approx \phi_{ijk}(t_k) + \\ &\quad \frac{\phi_{ijk}(t_k) - \phi_{ijk}(t_{k-1})}{t_k - t_{k-1}} (t - t_k) \end{aligned} \quad (8)$$

If the master pseudolite clock is assumed to be "true time", then the C/A code phase of the master pseudolite $\psi_M(t_k)$ is directly proportional to the time bias error $(t - t_k)$ and this can be used to compute the phase correction factor: (note here that the M subscript indicates that this is the code phase for the master pseudolite, $k = M$, and that the corrections are only applied to the phases used in the difference equations between the vehicles, where $j = m$).

$$\begin{aligned} \phi_{imk} &\approx \phi_{ijk}(t_k) + \\ &\quad \frac{\phi_{imk}(t_k) - \phi_{imk}(t_{k-1})}{t_k - t_{k-1}} K_\psi \psi_M(t_k) \end{aligned} \quad (9)$$

If ψ is measured in chips, then $K_\psi = 1/1.023 \times 10^6$ sec/chip. All of the phases used in (6) are adjusted for receiver time bias using (9).

5 Implementation Issues

Several issues needed to be resolved before practical experiment implementation was possible. These were dealt with as follows:

Mitigation of Multipath Errors - The effects of multipath measurement errors are reduced by comparing the actual phase measurements with predicted phase measurements. Knowledge of vehicle dynamics and the current state are used to predict the next set of phase measurements through a Kalman filter. The new phase measurements are then compared with the predicted phases, and the difference between the two is bounded to produce an estimated phase that is used in the next computation of the vehicle state. Figure 7 is a diagram of how this is done. The signal ϕ_{err} is bounded by passing it through a sigmoid function, with linear gain and an adjustable cutoff level. The phase that is used in the next state computation ϕ_{est} is then the sum of the bounded error and the predicted phase. Note that for small values of ϕ_{err} , the value of ϕ_{est} is ϕ_{meas} , while for large values of

ϕ_{err} , the value of ϕ_{est} is $\phi_{pred} + cutoff_{level}$. If the value of ϕ_{err} is greater than one full integer wavelength, then it is assumed that an integer slip has occurred and ϕ_{meas} is adjusted accordingly. The cutoff level of the sigmoid function was experimentally set to be 2.5cm for these experiments. Setting the cutoff level too high will miss the multipath errors; setting it too low is essentially running the control system "open-loop". This technique is a simple work-around to implementing a full extended Kalman filter that would incorporate both the dynamics of the vehicle and the nonlinear transformation from carrier phase measurements to the vehicle states.

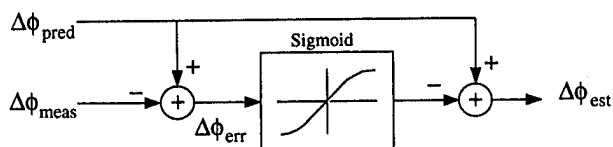


Figure 7: Multipath Error Mitigation

Near-far Problem and Occlusion – The near-far problem and occlusion of antennas by other antennas or vehicles results in a weak, unreliable measurement or complete loss of a signal. These problems are managed by having many more measurements available than necessary to solve the state estimate equations, and then reducing the set of valid signals for the solution. The method used to reduce multipath, as described above, can also reduce errors introduced by partially occluded signals. In order to deal with complete loss of signals, the algorithms that solve equation (7) were implemented to handle any combination of pseudolites in view by the two vehicles. The equations in (7) can be solved for any set of measurements, as long as at least three pseudolites are in common between both vehicles. For example, if vehicle 1 is locked on to five pseudolites, and vehicle 2 is locked on to four pseudolites, with three in common between them, then h_1 will be of dimension 15×1 , h_2 will be of dimension 12×1 , and h_{12} will be of dimension 3×1 , and all available information is used in the solution.

Calibration of pseudolite positions and antenna baselines – A method to simultaneously calibrate the antenna baselines and pseudolite positions was implemented by considering equation (7) to be a function of unknown states B_{ij} and Q_k , with X_i known. The X_i were obtained from the global vision system, and data was collected for over one hundred vehicle locations over the workspace. This data was then used to obtain a least squares fit for the antenna baselines and pseudolite positions.

Integer ambiguity resolution – A motion-based algorithm has been developed and tested in simulation, but has not been implemented. The algorithm relies on spherical wavefront properties for resolving the integers and would be greatly enhanced in practice by incorporating other sensors, such as accelerometers, to increase the rate of convergence. For this experiment the integers were initialized by observing the vehicle locations with the overhead global vision system.

6 Results

Several experiments were carried out to demonstrate the functionality of the integrated GPS-controlled robot system. The most visual of these was the rendezvous experiment shown in the snapshot sequence on the following page. In this sequence, the target vehicle was given an initial velocity and the robot was commanded to follow a trajectory to close-in on the target. Once the target vehicle was within grasp range, the robot arms were commanded to track the gripper ports on the target. This was done using the relative position and orientation to infer the port locations on the target. Once the gripper ports were tracked, the robot lowered its grippers into the ports to grasp the target vehicle. Except for initialization, GPS was the only sensor used to complete this experiment. It has been shown that the robot can consistently grasp inside the the 9cm diameter gripper ports of the moving target vehicle.

Another experiment that was performed was autonomous station-keeping, in which the robot was commanded to hold station a fixed distance from the target and to follow the orientation of the target. The target vehicle was then manually perturbed in position and orientation and the robot followed. In order to get a sense for how well the robot can track the target, the vehicle's response to step inputs in position and orientation are shown in Figures 9 and 10. These plots also show a comparison between the GPS system and the global vision system. The static noise levels of the GPS system are summarized in the table of Figure 11. It is important to note that these are *static* noise levels, i.e. the RMS values of the noise observed when the vehicles remained in a fixed position and orientation. These do not reflect the effects of more serious error sources such as pseudolite and antenna baseline calibration errors, antenna phase-center stability, and multipath. These sources can create a "steady state" error of the vehicle position and attitude.

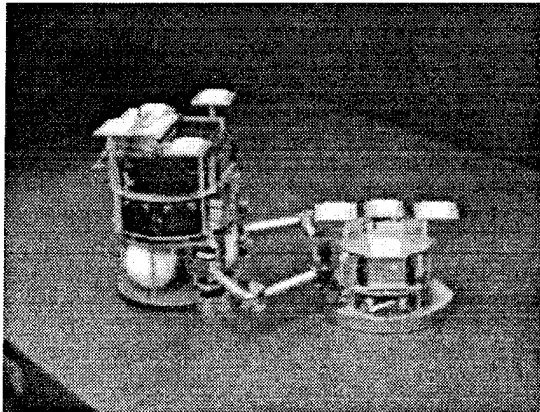
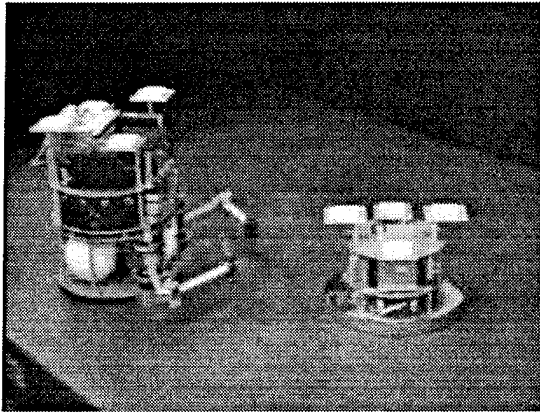
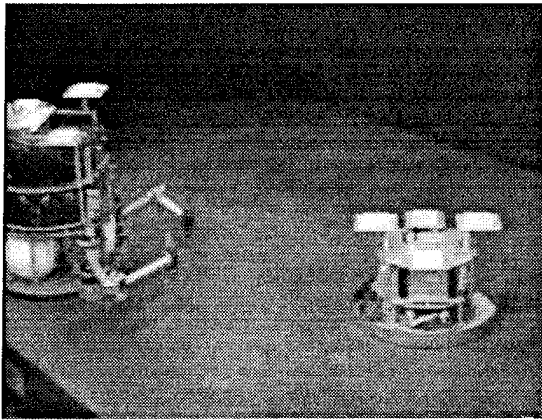


Figure 8: Rendezvous Sequence

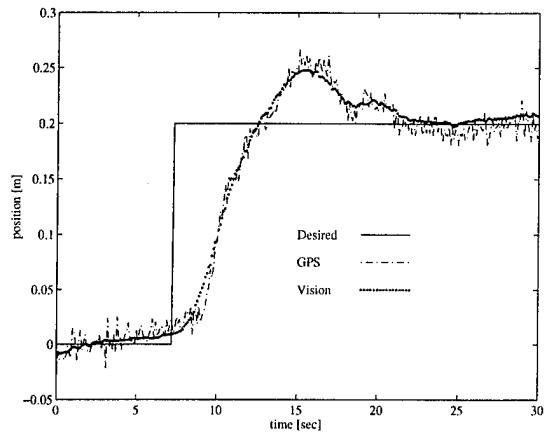


Figure 9: Position Step Response

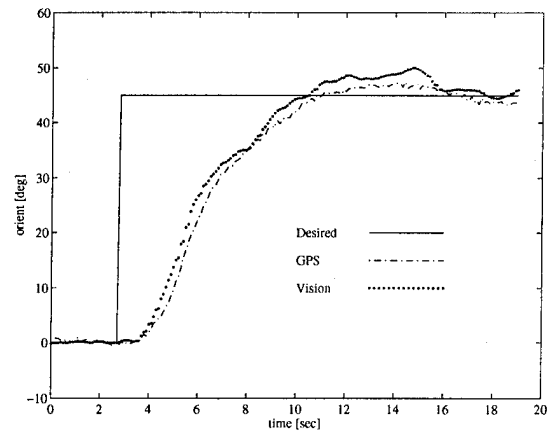


Figure 10: Orientation Step Response

Differential Position	0.5 cm
Absolute Position	6.0 cm
Differential Orientation	0.09°
Absolute Orientation	0.24°

Figure 11: Static Noise Characteristics

The comparison between the GPS and vision systems in the step response plots provide some sense of typical "steady state" errors in the GPS measurements (e.g. the orientation error appears to be approximately 3° around time $t = 15$ sec). The worst consequence of these errors is that when a pseudolite signal is acquired or lost, the recomputed integers for the new system configuration may be incorrect if the absolute position of either of the vehicles is off by more than half a wavelength (9.5cm), and the system needs to be re-initialized using the vision system.

7 Conclusions

The research presented in this paper has demonstrated a broad range of objectives:

- Established feasibility of performing rendezvous and station keeping using GPS as the primary means of sensing.
- Demonstrated an innovative use of GPS for indoor systems.
- Introduced a method for potentially testing GPS-based space systems end-to-end in lab prior to flight.
- Identified limitations and areas for improvement as GPS is developed for future space systems.

8 Acknowledgments

This research is supported under NASA Cooperative Contract NCC 2-333. The authors thank the members of the Stanford GPS Lab for their help and suggestions, and Trimble Navigation for not only supplying receiver hardware, but also offering the freedom to modify it for this research.

References

- [1] Frank Bauer, E. Glenn Lightsey, et. al. Pre-Flight Testing of the SPARTAN GADACS Experiment. In *Proceedings of the Institute of Navigation GPS-94 Conference*, Salt Lake City UT, September 1994.
- [2] A. Wayne Deaton Jorge I. Galdos, Triveni N. Upadhyay and James J. Lomas. GPS Relative Navigation for Automatic Spacecraft Rendezvous and Capture. In *Proceedings of the National Telesystems Conference*, Atlanta GA, June 1993.
- [3] Lubomyr V. Zyla and Moises N. Montez. Use of two gps receivers in order to perform space vehicle rendezvous. In *Proceedings of the Institute of Navigation GPS-93 Conference*, Salt Lake City UT, September 1993.
- [4] K. R. Zimmerman and R. H. Cannon Jr. GPS-Based Control for Space Vehicle Rendezvous. In *Proceedings of the ASCE: Robotics for Challenging Environments*, Albuquerque NM, February 28 - March 3 1994.
- [5] Clark Emerson Cohen. *Attitude Determination Using GPS*. PhD thesis, Stanford University, Department of Aeronautics and Astronautics, Stanford, CA 94305, December 1992.
- [6] M. A. Ullman. *Experiments in Autonomous Navigation and Control of Multi-Manipulator Free-Flying Space Robots*. PhD thesis, Stanford University, Stanford, CA 94305, March 1993. Also published as SUDAAR 630.
- [7] S. A. Schneider, V. W. Chen, and G. Pardo-Castellote. ControlShell: A Real-Time Software Framework. In *Proceedings of the AIAA/NASA Conference on Intelligent Robots in Field, Factory, Service and Space*, volume II, pages 870-7, Houston, TX, March 1994. AIAA, AIAA.
- [8] Clark E. Cohen, B. Pervan, et. al. Real-Time Flight Test Evaluation of the GPS Marker Beacon Concept for Category III Kinematic GPS Precision Landing. In *Proceedings of the Institute of Navigation GPS-93 Conference*, Salt Lake City UT, September 1993.
- [9] Arthur E. Bryson, Jr. and Yu-Chi Ho. *Applied Optimal Control: Optimization, Estimation, and Control*. Hemisphere Publishing Corporation, 1025 Vermont Ave., N.W., Washington, D.C., 1975. Revised Printing.
- [10] K. R. Zimmerman and R. H. Cannon Jr. GPS-Based Control for Space Vehicle Rendezvous. In *Proceedings of the Institute of Navigation GPS-94 Conference*, Salt Lake City UT, September 1994.

Application of GPS Technology to Part 141 Flight Training

Dr. James Lyall
Embry-Riddle Aeronautical University

BIOGRAPHY

Dr. James R. Lyall was born and raised in Milwaukee, Wisconsin. He earned a Bachelor of Electrical Engineering degree from General Motors Institute, and a MSEE from the University of Colorado. After graduation, he worked as Design Engineer, Project Engineer, and Advanced Development Engineer at King Radio Corporation (now Bendix/King Division of Allied Signal) from 1976 to 1986, during which time he earned the Doctor of Engineering degree from the University of Kansas. He accepted the position of Director of Engineering at Smiths Industries Aerospace and Defense Systems in Malvern Pa. in 1986. In the Fall of 1988 he joined the faculty of Embry Riddle Aeronautical University, Prescott Arizona, as Chair of Electrical Engineering and Computer Science. The Electrical Engineering Program received initial ABET Accreditation in 1994, at which time he left the chair to assume full time teaching and research responsibilities. He holds the Private Pilot Certificate.

ABSTRACT

The Flight Technology Department and the Electrical Engineering Department at Embry Riddle Aeronautical University's Prescott Arizona Campus have embarked upon a joint program to apply GPS technology in a major upgrade of their Part 141 Flight Training Program. Recorded GPS position data will be used as an additional tool in the evaluation of both students and instructors. Position data (latitude, longitude, altitude) is recorded at ten second intervals throughout each training, solo and check flight. This data may be used to replay the flight and objectively evaluate the proficiency of the student pilot.

This paper describes the development of the experimental Mission Recorder Units (MRU's). The availability of actual mission data provided by these units will allow the data distribution, debrief and evaluation infrastructures to be designed and

implemented within the context of the existing Part 141 pilot training environment at Embry Riddle Aeronautical University.

OVERVIEW

Embry Riddle Aeronautical University operates its flight training curriculum under FAR Part 141 rules. Certification under Part 141 provides for "self examination authority", whereby the recommended exposure (or hours) at a particular training stage may be waived on the basis of "demonstrated proficiency." The objective of the current program is to more clearly and objectively specify levels of proficiency appropriate to progressive training stages, and also to provide a mechanism for objectively demonstrating student proficiency during solo operation. The knowledge on the part of the student that his solo operations will be scrutinized will certainly discourage the abuse of solo time, with obvious benefits to both the students training progress and safety.

Integration of recorded flight position data into the pilot training program is progressing on several fronts. A computer network has been installed at the flight training facility which will provide the archiving and secure distribution of student flight data. It will also provide for the availability of secure and well maintained evaluation tools, both for debrief and research.

The requirements for the debrief tools will evolve as experience with prototype tools accumulates, the needs of instructors and students come into clearer focus, and evaluation metrics are integrated into the curriculum.

It is imperative that use of the data collection equipment does not adversely affect the flight training environment during the initial phases of the program. In addition, it is important that use of the equipment not effect the STC of the aircraft. Thus, the following

set of requirements present themselves in the definition of the MRUs:

- 1) Self contained, portable, easy to handle, rugged.
- 2) Not dependent upon aircraft power (internal battery required).
- 3) Secure and unobtrusive, no operator controls, unambiguous status indication, autonomous operation.
- 4) Sufficient battery and data capacity for 12 hours of operation between charges.
- 5) Data extraction process is straightforward and secure.
- 6) Dispatch from the charging environment. (Charge while awaiting dispatch)
- 7) Functional flexibility (software based design).

OPERATIONAL INFRASTRUCTURE: Software

Deployment of the MRUs in the training environment requires a suite of four integrated software modules:

- 1) MRU control/data acquisition program (AIVLOGxx). This is the program which resides within the MRU and provides all of the operational functionality of the unit, including control of the GPS Sensor, determination of flight conditions, logging data, and provision for download of flight data as well as upload or download of system operational or initialization data (almanac, time/date, initial fix, etc.)
- 2) Ground Support Equipment test and initialization program (AIVGSExx). This program is the primary maintenance, test, debug, and validation tool. Running on a host PC, it exercises all interface functions of the MRU.
- 3) Dispatch, Download, and Network Data Distribution Program (DDNDDxx). This program runs on a host PC in the dispatch environment and provides for the downloading of recorded flight data files from the MRUs after a mission. It performs some preprocessing functions (such as error

correction and/ or detection, flight leg concatenation, differential correction, etc.) and archives the mission flight file on the flight line network server with the appropriate access security.

- 4) Data Evaluation and Debrief program (FLT_TRAX). This program is resident on the debrief cubicle PC. It accesses mission data files archived on the server and is used to display all pertinent aspects of the flight using a graphical interface. It is within this program that performance metrics will be applied to the flight data to provide objective evaluation of student performance as a basis for both grading and advancement decisions.

MRU CHARACTERISTICS

The MRU consists of an AIV-10 GPS sensor manufactured by Magellan Inc., a KS3-B single board computer manufactured by Kila Systems Inc., a 6.3 volt sealed lead acid storage battery, and a three terminal voltage regulator. Internal communication between modules as well as communication between the MRU and the host computer are accomplished using the Magellan/AIV-10 message protocol shown in figure 1.

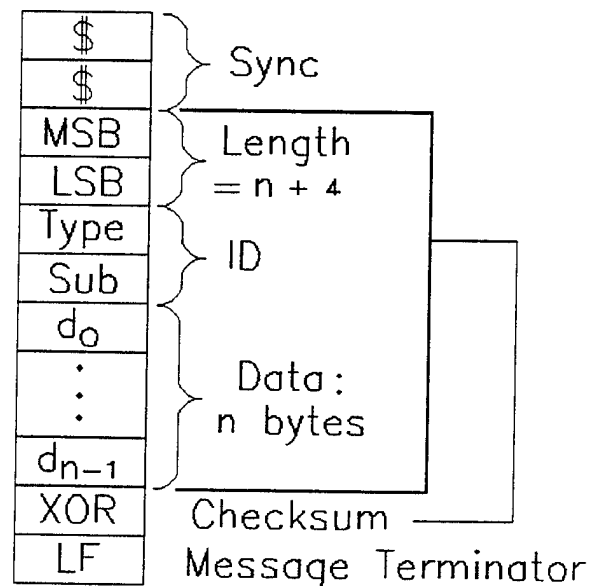


Figure 1: Message Format

AIV-10. The AIV-10 sensor contains a ten channel GPS receiver and operates on +5 VDC. Communication with a controller is provided via a serial link having timing characteristics identical to RS-232, but using voltage levels of 0 and +5 VDC.

Several messages not defined in the Magellan protocol were created to serve host related functions required by the application. Table 1 lists all messages used by the application, including newly created ones.

Message ID Typ/Sub	Description
01/00	General Setup Data
01/10*	MRU Mode Change
01/11*	Download Specified Data File
01/12*	Kill Specified Data File
02/00	Message Request
03/01	Initial Position
04/00	Initial Time/Date
06/00	Simulate Power Cycle
06/01	Erase RAM
06/02	Erase All Memory
08/00	Initial Almanac
81/22	Fix Data
82/01	GPS System Time (UTC)
84/00	Receiver Status
86/00	Current Almanac Data
88/00*	Download Fix Record
88/01*	Download Terminator/Checksum
88/02*	Data Filename (Download Header)
88/03*	Data Filename (Name List)
88/10*	Text: Response Message
88/11*	Text: Status Message

* Indicates new message defined for this application.

Table 1: Message Definitions

Table 2 shows which messages are passed between the GPS Sensor, the KS3-B, and the host PC.

Message ID Typ/Sub	AIV-10 <>	KS3-B <>	Host
01/00	<		
01/10*		<	
01/11*		<	
01/12*		<	
02/00	<	<	
03/01	<	<	
04/00	<	<	
06/00	<	<	
06/01	<	<	
06/02	<	<	
08/00	<	<	
81/22	>		
82/01	>	>	
84/00	>		
86/00	>	>	
88/00*		>	
88/01*		>	
88/02*		>	
88/03*		>	
88/10*		>	
88/11*		>	

Table 2: Message Interface

KS3-B. The KS3-B computer is a DOS based single board PC, which operates on +5 VDC. It contains three directories. **A:** is a ROM directory which contains the DOS system operating software as well as utilities for up/downloading, control of the clock, etc. **D:** is a ROM directory which contains the application module and the run-time module. **C:** is a battery backed static RAM directory in which initialization data and flight data files are held. Application modules may be downloaded and run from this directory during development and test. The **B:** directory is reserved for a floppy disk drive, which is not used in this application. It contains three RS-232 compatible serial ports: system console, **COM1** and **COM2**. The fact that console I/O is a serial link precludes the use of screen based programming environments such as QuickBASIC on the KS3-B as host. A dumb terminal (or emulator) is used as a console for the KS3-B.

Communication between KS3-B and the AIV-10 is accomplished via the **COM1**: port. The **COM1**: output circuitry had to be modified to provide compatibility with the voltage levels required for serial communication with the AIV-10.

Communication between the MRU and its external host is conducted over **COM2**:, which is connected

directly to the external data connector, as shown in figure 2.

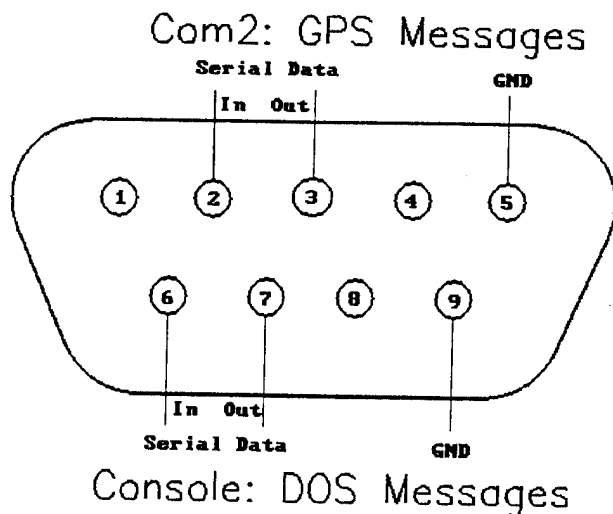


Figure 2: Data I/O Connector

Note that console I/O is also available at the output data connector using pins normally associated with hardware handshake signals. Since the AIV-10 protocol does not include hardware handshaking, only Tx and Rx lines are provided. A standard two wire (plus ground) null modem (reversing) cable is used for host communication, and an adapter may be used for console communication with the MRU.

Mechanical. The unit is housed in an aluminum case measuring 8 x 5 x 3.5 inches with a fixed carrying handle. The unit weighs 2.5 Kg, including the battery. The only external operator control is an on/off switch, and the only indicator is a green status LED.

There are three connectors on the rear of the unit: a power connector for charging the battery, a 9-pin subminiature D connector (figure 2), and a BNC connector for the GPS antenna.

The 9-pin subminiature D connector is used in conjunction with a null modem cable to connect the unit to a lap top PC or other host. This connection is for data download, unit initialization, and/or test.

The center pin of the BNC connector provides a +5 VDC bias supply for an active antenna. If a passive antenna is to be used, this bias supply can be disabled by cutting a wire inside the box; however

tracking performance can be severely degraded if a passive antenna is used, therefore this is not recommended. The BNC form factor was used rather than the preferred TNC to facilitate the frequent connect/disconnect cycles which the application demands.

The power connector has been positioned such that a mating connector in the storage rack will provide charging current while the unit is not in use. A charge status indication is also provided by the charging circuitry in the rack.

The battery is a nominal 6.3 VDC sealed lead acid type with a 10 hour discharge rate of 6.5 Amp-Hours. This provides an endurance of approximately 12 hours of continuous operation on a fully charged battery. Recharging should be accomplished using practices compatible with maximum life of a lead acid battery with the above described characteristics. A recharging station for the ten units in service has been designed, but will not be discussed here.

UNIT OPERATION

Installation. The aircraft should be equipped with an installation position which provides that the unit be secured with a strap which passes through the handle (velcro works great) and an antenna connection via a male BNC connector on a cable with sufficient service loop to preclude any sharp bends or kinks occurring. After the unit has been secured and the antenna connection made, the power switch is switched to the "ON" position.

Initialization. Upon application of power the KS3-B, operating under PC-DOS, executes **A:\AUTOEXEC.BAT** which initializes system time from the battery backed calendar/clock. It then transfers control to the file **USER.BAT** in the **C:** (static RAM) directory. This is another batch file which transfers control to the **AIVLOGxx** application module. Recall that the **A:** directory, hence the **AUTOEXEC.BAT** file, is in ROM. The **C:\USER.BAT** file is used so that execution may be redirected in the development environment, since it is a static RAM file and can be easily modified from the DOS command prompt.

The application program (**AIVLOGxx.EXE**) utilizes data contained in files on the **C:** directory which were resident within the unit when it was last turned off, along with KS3_B system time and date (ZULU) to initialize the GPS sensor. During the initialization process, the green LED indicator flashes at a one

second rate. Assuming current initialization data and a good satellite geometry in view, an initial fix is usually available within 60 seconds. The LED indicator will remain on steady as long as a continuous fix is maintained, and flash if the continuous fix condition is interrupted.

If the unit has not been used for several months, the stored almanac information may not be valid. If the unit has been moved a substantial distance (say, 100 Km) since it was turned off, the initialization position may not be sufficiently accurate to allow a fast first fix. These are the most likely causes for poor first fix performance; however if any initialization data is severely corrupted, the unit may revert to the "I'm lost" mode, in which case it may take up to 30 minutes to achieve a first fix. If such conditions occur, one can update the initialization data using the **AIVGSExx** utility on a lap top or other host computer if a long wait for self initialization cannot be tolerated.

Flight Data Logging. After a continuous fix has been achieved, the unit monitors and filters ground speed as determined by the GPS sensor. When filtered ground speed exceeds 45 knots, a data file is opened and given a name which encodes time and date. The data file is closed when filtered ground speed falls below 15 knots. In this way each flight leg is assigned its own unique data file and filename. After the data file has been closed, current almanac data and position information is saved on the C:\ directory in anticipation of the next initialization sequence.

Internal static memory capacity provides for approximately 15 hours of flight data. Each data record contains latitude, longitude, altitude, and a fix timetag. The final record of a data file contains a vertical checksum of all data records. All data items are stored as binary long integers (4 bytes per value).

Removal and Data Download. After completion of the flight, the unit is turned off, the antenna cable disconnected, and the unit removed from its secured position. It is carried to the download station, turned on, and connected to the 9-pin subminiature D connector of the host download cable. Both the host computer and the MRU should be **ON** when the connection is made to prevent on/off transients from generating error conditions on the RS-232 medium. Host download software initiates the data download process in response to a menu command initiated by the user. The normal download sequence is initiated when the host requests message 88/00 (download data record) from the MRU using message 02/00

(message request), whereupon all files are transmitted to the host and deleted from the unit memory. If greater fault protection is required, files may be downloaded and deleted individually by the following sequence:

- 1) Request message 88/03 using message request 02/00. The MRU will respond by transmitting 88/03 messages containing one data file name for each data file (flight leg) currently in memory.
- 2) Command Download of each file individually using message 01/11.
- 3) Kill each file individually using message 01/12 after successful download has been verified.

Each data record (message 88/00) is transmitted as a GPS message consistent with the defined AIV-10 message protocol. Presence of a checksum byte with each record, and the final vertical checksum record (message 88/01) allows correction of single bit errors and detection of multiple bit errors.

Soft flow control (XON/XOFF) has been implemented to protect the host from input buffer overflow during download.

ALTERNATE OPERATIONAL MODES

Three alternate operational modes have been provided, and are initialized by dedicated commands issued by a host via the download connection.

Bench Test. This command bypasses the velocity dependent data logging capability. A data file is immediately opened, logging of position data begins and continues independent of ground speed, until the bench test mode is exited. At this time the data file is closed and velocity dependent data logging is reestablished.

Direct Mode. This command provides a direct link between the host and the GPS sensor. The KS3-B acts simply as a data conduit between its two serial ports. It examines incoming messages, and terminates direct mode when the command to cancel direct mode is detected. In addition, it continuously monitors position changes and updates the initialization position data accordingly.

Quit. This command provides for an orderly exit from the application module and a return to the DOS

command level of the KS3-B operating system.

DEVELOPMENT ENVIRONMENT

Application and ground support software for the MRU is developed on the Imbedded Application Development System for GPS, or IADS-GPS.

A functional schematic for this environment appears in figure 3. IADS operates in three fundamental modes, which are defined by the routing of the serial I/O lines between the various components and their ports. This routing is accomplished by a rotary switch assembly. Each communication line shown on figure 3 represents both transmit and receive serial lines.

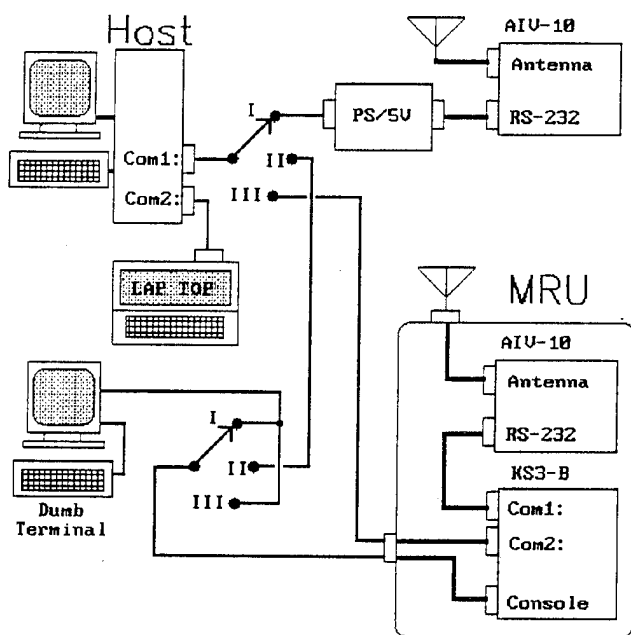


Figure 3: IADS-GPS Schematic

Mode I: Code Development. In this mode the host PC plays the role of the embedded controller (KS3-B). The host **COM1**: port is connected to an AIV-10 GPS receiver which is an integral part of the IADS system. Since the serial I/O of the AIV-10 board operates at 0-5 volt logic levels rather than standard RS-232 levels, a PS/5V interface adapter provided by Magellan must be placed between the AIV-10 and the host PC to provide signal level compatibility with the host **COM** port. The **COM1**: port of a lap top PC is connected to the host **COM2**: port to monitor the status and download information which the MRU would ordinarily provide at its output connector. Both the host PC and the lap top may be operating in the QuickBasic (or other high level language)

development environment to facilitate debugging. In this mode, the dumb terminal is connected to the console port of the KS3-B to provide a functional access to the controller, although it is not an active participant of the development process in this mode. Once a module has been developed and debugged in the language development environment, it can be compiled and linked into an .EXE file and run on the host or lap top. It is thus possible to debug and integrate **AIVLOGxx** (on the host) and **AIVGSExx** (on the lap top) simultaneously.

Mode II: Download. The only functional connection in this mode is between the **COM1**: port of the host and the console port of the KS3-B. This mode is used to download executable code compiled on the host to the **C:** (static RAM) directory of the KS3-B for integration testing. Test data files can also be transferred between host and KS3-B.

Mode III: Monitor. This mode is used to monitor and verify operation of the functioning MRU once the application module has been downloaded to the **C:** (static RAM) directory or burned into the **D:** (ROM) directory. The **COM2**: port of the KS3-B is connected to the **COM1**: port of the host, which may be running AIVGSExx or some other compatible test/debug or download program. The console port of the KS3-B is connected to the dumb terminal for monitoring messages and control at the DOS level.

The IADS system has shown itself to be quite flexible and adaptable to configuration changes as the MRU design matured. For example, the original configuration provided for the sharing of the IADS GPS sensor between the host in **Mode I** and an isolated KS3-B board in **Mode III**. As completed units having their own GPS sensor became available, this feature was no longer necessary. A simple change of interconnect cables allows use of the IADS system with either completed units or separate subsystem boards.

OPERATIONAL STATUS

Ten units have been constructed, tested, and placed on operational status. The charging station has been designed and is currently under construction. Several test missions have been flown and the units performed as required.

Three MRUs were use extensively during June of 1995 for collection of simultaneous fixed and mobile ground data. Ten ground missions were executed over the same 50 mile closed route. Fixed MRU's

located at the origin and extreme point on the route recorded fixed position data as the ground route was traversed. These data will be analyzed and the results incorporated in an upgrade to the download software for providing differential correction to flight data as it is being downloaded. The units performed admirably over more than 100 hours of combined data collection time.

The inherent flexibility of the MRUs was demonstrated through the ease by which the logging criteria could be reprogrammed from a velocity dependency to a fixed schedule of missions over a three week period. This was necessary since one of the units was pre-positioned at a remote site and was left running continuously during the entire experiment.

STAY TUNED

Regular service of the ten MRUs in the recording of large numbers of training flight missions is scheduled to commence in the Fall 1995 semester at the Prescott Campus of Embry Riddle Aeronautical University, and should be underway as this paper is delivered. The data will initially be used solely for student debrief. As data and experience accumulates, a well focussed set of requirements will evolve for the design of a seamless and well integrated infrastructure utilizing recorded GPS position data as an integral component of flight training in a Part 141 training environment.

The long term vision of this program is to install commercially available GPS avionics in the fleet and utilize this sensor as the data source. A data storage unit will be designed for permanent installation concurrent with the installation of the commercial GPS systems. The data storage unit in the aircraft will be linked to the operations network in a manner which has yet to be determined. The timing of this phase of the program is strongly dependent upon any changes in Part 141 rules addressing the use of GPS navigation sensors in pilot training curricula; or unilateral decisions regarding this issue as made by the Embry Riddle Flight Technology Department.

ACKNOWLEDGEMENTS

I would like to express my appreciation to Dan Carrell and Dave Roy of the ERAU Flight Technology Department for their enthusiastic support of this project. In addition, all of the engineering documentation required for the production of these units, as well as documentation of the application software and ground support software was compiled by Karsten Fels as a part of his Masters Thesis.

REFERENCES

Fels, Karsten; **The Design and Construction of a GPS Flight Tracker Unit for General Aviation Flight Training.** (Masters Thesis); Embry Riddle Aeronautical University; April 1995

Users Guide for the Magellan AIV-10 OEM GPS Modules; Magellan Systems Corporation; 1994

KS3 Technical Manual; Kila Systems Inc.; March 1992

A GPS Based Nuclear Radiation Detection Device Training System

Edward Groeber

US Army Chemical and Biochemical Defense Command

BIOGRAPHY

Mr. Groeber was born 28 June 1946 in Hempstead, NY. He graduated in 1968 from New York University with a BS in Nuclear Engineering. He was commissioned as a Second Lieutenant in the USAF in 1968 and was stationed at the Air Force Weapons Laboratory, Kirtland AFB, NM where he worked in the development of Nuclear Radiation Detectors. He left the Air Force in 1972 and went to work for the US Army as a Project Engineer in Radiac Research and Development at Ft Monmouth, NJ. He received an MS in Electronics Engineering from Fairleigh Dickinson University in 1980. He is currently the Radiac Product Manager for the Project Manager for Nuclear, Biological and Chemical Defense, US Army Chemical and Biological Defense Command, Edgewood, MD.

ABSTRACT

The US Army has a requirement to train soldiers in the use of nuclear radiation detection devices (Radiacs) to help them survive on a modern battlefield in the event nuclear weapons are employed. A Radiac Training System is also required to train for health and safety tasks such as response to nuclear weapons accidents and the monitoring of depleted uranium after a war is over.

The currently fielded training system uses a radio-frequency (RF) transmitter and a simulated doserate meter that functions like a radiac but is, in fact, a radio frequency signal strength meter. The system simulates operation in a typical nuclear fallout field. The readings on the simulated ratemeter are inversely proportional to the distance from the transmitter and the resulting "fallout pattern" can be changed in shape by changing the antenna design. With this approach, however, it is difficult to get reproducible results because of multi-path reflections from power lines, fences, vehicles and the soldier's body. Receiver antenna orientation and position with respect to the body must be constant to obtain consistent readings. Changing the

fallout pattern becomes difficult after certain limits are reached because of power and antenna design considerations.

The development of GPS and the continuing reductions in size, weight, power consumption and cost made it possible to consider integrating a position location receiver into a simulated radiacmeter to provide an alternate approach to using RF transmitters and receivers. A prototype system was developed using a commercial GPS receiver and a palm-top computer. Software was written to input latitude and longitude from the GPS and to calculate a simulated doserate reading for that position based on a previously input latitude and longitude for "ground zero" (GZ). The prototype was tested by setting GZ to be a known road intersection, mounting the GPS antenna on the roof of car and driving to GZ. The test was successful and the resulting "fallout pattern" was a fair representation of the real situation.

This technique has great promise for use in military training for operation on the nuclear battlefield, for operation in peacetime for nuclear weapons accidents and in civilian training for nuclear reactor accidents.

DESCRIPTION OF NEED

The US Army recognized the need for training devices for nuclear radiation detection instruments (commonly referred to as radiac instruments) in the 1960s. Radiac instruments are used on the battlefield to help soldiers survive if nuclear weapons are used. They are used in peacetime to monitor maintenance areas where equipment containing radioactive materials are repaired and for response to nuclear weapons accidents. Most recently, they have been used to safely recover damaged armored vehicles that contain depleted Uranium in the ammunition or the armor plate. It is not feasible to use radioactive materials in training soldiers on the use of radiacs because of personnel safety and environmental considerations.

DESCRIPTION OF EXISTING HARDWARE

A radiofrequency training system was developed and fielded during the 1970s. It consists of a 1/4 watt transmitter for small area training and hotspot simulation, a 20 watt transmitter for large area training and simulated receivers that look like the Army's tactical radiacmeter. The receiver is basically a signal strength meter that registers higher readings when either the transmitter power is increased or the operator moves closer to the antenna. While the system provides fairly realistic training, it also suffers from some problems that limit the usefulness of the data obtained. Signal reflections from buildings, power lines, vehicles and people cause inconsistencies and a lack of reproducibility in the obtained data. Training scenarios are also limited by receiver sensitivity, antenna size and design and transmitter power. The maximum effective range for the fielded system is approximately 12 miles. Because of the age of the system, spare parts are no longer available and a new system is required to replace it. A modern radiofrequency system could be easily developed using standard military and/or commercial transmitters and antennas. The operational and technical drawbacks, however, would not be overcome.

DESCRIPTION OF PROPOSED SYSTEM

Attempts have been made in the past to utilize a GPS receiver and a computer to simulate a radioactive fallout field on the ground. Limited success was obtained. The main problem was to develop a way to generate a large fallout pattern using portable computers with limited memory. Until recently, this technique could only be considered for large equipment simulators of relatively low fielded density, such as helicopter mounted survey systems. The trend of size reduction in GPS engines and continually dropping prices has made this technique usable in almost any simulated radiac instrument. In the case of radiacsets with detachable probes, the GPS engine and a microcomputer would be built into the probe. In smaller instruments without probes, the GPS and the microcomputer would be built into a simulated instrument. In either case, the programed scenario would be downloaded into the simulated radiacset via an external PC using the serial port.

DESCRIPTION OF PROTOTYPE

A technique was devised to simply generate data for simulated fallout patterns using a few algorithms. This eliminated the need for large lookup tables and large memory requirements. A program was written in GWBASIC to input position data from a GPS receiver and, based on a previously input location for the simulated GZ, calculate a simulated radiation doserate for the

operator's current position. A prototype was assembled using a Garmin GPS 75 receiver and a Hewlett Packard 95 palmtop computer.

DESCRIPTION OF SOFTWARE

A technique was required to convert latitude and longitude to simulated radiation doserate readings. Typical nuclear fallout patterns are elliptical in nature. Fallout is radioactive dirt and debris that is formed when large quantities of ground material are sucked up and into the fireball and results in the familiar mushroom shaped cloud. This cloud is then wind driven and the contaminated debris falls out along the path of travel. An idealized pattern would be elliptical with ground zero forming the point of highest contamination. Lines of equal contamination concentration, on which the doserate readings are identical, called isopleths, are ellipses starting at GZ with the major axis oriented with the wind direction.

The major axis for the simulation was picked as the line of latitude passing through GZ which, in the simulation, is picked by the user and becomes the X-axis. GZ becomes the origin for the coordinate system and the Y-axis is the line of longitude passing through GZ. Since prevailing winds are normally from the west, the pattern for the simulation was chosen as starting at GZ and oriented from west to east. The users position, as determined by the GPS receiver, is used by subtracting the coordinates for GZ and the results then become the XY coordinates for the simulation.

A technique was required to generate the required "fallout" pattern without using a lookup table. A lookup table could be used but requires a large amount of memory for even relatively small patterns. Since a fallout pattern is relatively continuous, resolution with a lookup table would be very crude and interpolation would be required to adequately describe patterns of tens to hundreds of square miles. An ellipse can be described algebraically. All that is required, therefore, is a way to assign simulated doserate readings to a family of ellipses that will result in a simulation that will adequately resemble a fallout pattern.

The formula for an ellipse is as follows:

$$(X-C)^2 / A^2 + (Y-D)^2 / B^2 = 1 \quad \text{eq. 1}$$

where X and Y are the XY coordinates, C and D are the X and Y coordinates respectively for the center of the ellipse and A is the major radius and B is the minor radius. Since the ellipses are to lie on the X-axis with the western most points of the major radii to go through the origin (GZ), $C = A$ and $D = 0$. Since fallout patterns are elongated in the direction of the wind, A was chosen to be equal to 2B.

This is arbitrary, however, and other ratios can be used. Substituting the values for A, C and D and solving eq. 1 for B, the following equation results:

$$B = (4 Y^2 + X^2) / 4X \quad \text{eq. 2}$$

For any position obtained from the GPS receiver, therefore, a unique ellipse can be obtained that lies on the X-axis, passes through the position and GZ, and has the characteristic $A = 2B$. The easiest way to assign "doserate" values to the ellipses is where they cross the X-axis. These points are obtained by the following equation:

$$L = 2A \quad \text{eq. 3}$$

Since fallout patterns are not linear but tend to increase in doserate faster as GZ is approached, a non-linear function was selected to assign values. $1 / L^2$ was picked as a starting point and gave a good representation of historically mapped patterns. The instrument being simulated, the AN/VDR-2, is a microprocessor based digital ratemeter (see Fig. 1) that covers a range from background, which is approximately .1 uGy/hr, to a maximum rate of approximately 230 Gy/hr (A Gy is a Gray, a unit of measure for absorbed nuclear radiation dose).

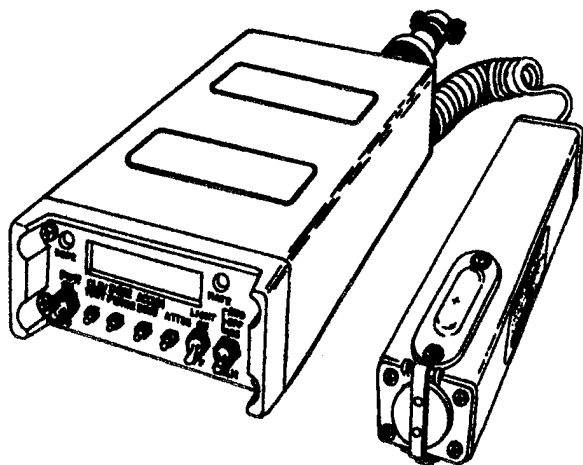


Fig. 1

The values for L are calculated in seconds of longitude and the displayed "doserate" values were desired to be at the maximum value of 230 Gy/hr at or very close to GZ. The initial value required to give the expected results was 1080000. The equation to convert to doserate is:

$$DR = 1080000 / L^2 \quad \text{eq. 4}$$

Some typical values for the simulated fallout patterns are shown at Fig. 2.

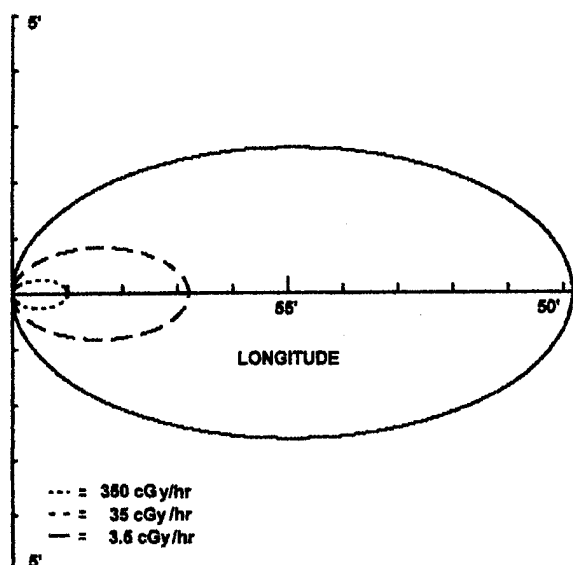


Fig. 2

This method only generated patterns that were oriented from west to east. In order to make the system more flexible, a method was needed to select other wind directions. It was decided that the simplest way to do this was to rotate each pattern back to the base case since the XY coordinate system was defined using latitude and longitude. Once this is done, all of the methods used to calculate the simulated doserates are still valid. The formulae for rotating coordinates are as follows:

$$X_n = X \cos(\theta) - Y \sin(\theta) \quad \text{eq. 5}$$

$$Y_n = X \sin(\theta) + Y \cos(\theta) \quad \text{eq. 6}$$

where X_n and Y_n are the new coordinates in the rotated system and θ is the angle between the original X-axis and the new X-axis. Since this technique requires rotation back to the original coordinate system, the expressions for X and Y in terms of X_n and Y_n were required. Equations 5 and 6 were solved for X and Y and are as follows:

$$X = X_n \cos(\theta) + Y_n \sin(\theta) \quad \text{eq. 7}$$

$$Y = Y_n \cos(\theta) - X_n \sin(\theta) \quad \text{eq. 8}$$

Wind directions are input by the user and the angle, θ , is calculated by the software. Once this is done, each position obtained from the GPS is converted to an XY coordinate and then rotated into the base case (elliptical patterns with the major axis on the positive X axis) where

the formulae are applied to calculate the simulated doserate.

A real fallout pattern has a relatively small circular pattern around GZ caused by the initial explosion. This causes a backlobe that extends in the opposite direction from the main elliptical pattern. This was simulated using the equation for a circle to get the X-axis crossover and using the formula :

$$DR = 1080000 / L^5 \quad \text{eq. 9}$$

to give a backlobe of much smaller dimensions than the main ellipse pattern. This same technique will be used to introduce "hotspots". These are caused by bomb debris and highly concentrated areas of contamination caused by rain water runoff. The circular pattern will be used but the exponent in the denominator of eq. 5 will be increased to give an even smaller pattern and the number in the numerator will be decreased to reduce the overall intensity. A "GZ" for each hotspot will be used so that they can be placed anywhere in the simulated area.

If a relatively new event is to be simulated, a rise and subsequent fall of the doserate at a given location is necessary to accurately depict the arrival and following decay of the fallout intensity. This will be done by increasing the initial value (the numerator in eq.4) from 0 to the maximum value in the first hour of the simulation and then applying the formula $T^{-1.2}$, where T is the time in hours after the maximum value is reached. The equation for this scenario would be:

$$DR = (T^{-1.2}) (1080000 / L^2) \quad \text{eq. 10}$$

Because the display on the palmtop computer is small, it was difficult to read the simulated doserate while operating the prototype. The numbers and letters required were developed in the software using graphics commands and were placed in a lookup table. As each new reading is obtained, the lookup table is used and the appropriate characters are displayed in the appropriate position on the display.

TEST RESULTS

The prototype was tested by mounting the GPS receiver antenna on the roof of a car using a lab built magnetic mount. "GZ" was obtained from a map and was selected by picking a major intersection of two roads, one of which was generally in an east/west orientation. The simulated readings increased as predicted as the vehicle travelled west toward "GZ". The readings reached the maximum value just before reaching "GZ" and then dropped to "background" just past the intersection (the backlobe was not implemented for this demonstration). The results were reproduced on the return trip.

FUTURE PLANS

The long term goal is to develop simulated radiac instruments that contain the GPS receiver and microcomputer in a configuration that looks and operates like the actual instruments. The microcomputer would contain the firmware with the fallout pattern generating algorithms and the necessary data inputs for "GZ", wind direction, pattern size, etc. would be via an RS-232 serial port and an external PC. This technique is also applicable to biological and chemical detectors and methods are being developed to simulate moving chemical clouds.



Session D6

Integrity

Chair:

Dr. John Diesel
Litton Aero Products

Co-Chair:

Ms. Marie Lage
Stanford Telecom

New Techniques Relating Fault Detection and Exclusion Performance to GPS Primary Means Integrity Requirements¹

Young Lee
The MITRE Corporation

BIOGRAPHY

Young C. Lee is a Lead Engineer in the Center for Advanced Aviation System Development at The MITRE Corporation in McLean, VA. He has been working in the areas of GPS integrity and aviation applications of GPS for the last 10 years and has published over a dozen papers in these areas. For the past few years he has been providing technical support to the FAA Satellite Operational Implementation Team (SOIT) in their development of TSO C-129 and a position paper on use of GPS as a primary means of navigation in oceanic and remote airspace. He has also been actively participating in RTCA SC-159, especially in its Fault Detection and Isolation Working Group and Wide-Area Augmentation System Working Group, and is currently serving as the secretary of the committee. He received his B.S. from Seoul National University and Ph.D. from the University of Virginia, both in electrical engineering.

ABSTRACT

In the use of GPS, receiver autonomous fault detection and exclusion (FDE) often plays a major role in assuring integrity of the user navigation solution. For use of GPS as a supplemental means of navigation, simple detection of the presence of a fault was considered sufficient since the aircraft can immediately revert to an alternate means of navigation. In the case for the use of GPS as a primary means of navigation, however, detection would not be sufficient; upon detection of a fault, the avionics should try to exclude the bad satellite and continue navigation whenever possible since no other normal means of navigation is available. Such use of FDE for primary means of navigation is currently being proposed to provide integrity for oceanic airspace and even in conjunction with the Wide-Area Augmentation System

(WAAS), namely outside WAAS signal coverage area or as a backup in the unlikely event of a WAAS outage.

While the basic FDE techniques have been well established, the relation between the FDE algorithm performance and the primary means integrity requirements has not been well established. This paper proposes and analyzes new methods of correctly calculating two quantities that must be properly calculated to ensure meeting the primary means integrity requirements. The first one is a proposed method of calculating the horizontal protection level (HPL), based on which the probability of missed detection (P_{md}) is determined. It will be shown that this new method consistently meets the integrity requirements while the existing method does not, and yet it has minimal impact on FDE availability. The second is a method of calculating probability of incorrect identification/exclusion, which has not been investigated before.

1.0 INTRODUCTION

Fault detection and exclusion (FDE) is a receiver processing function that autonomously provides integrity monitoring for the position solution, using redundant range measurements. FDE consists of two distinct parts: fault detection and fault exclusion. The fault detection part detects the presence of an unacceptably large position error for a given phase of flight. Upon detection of an error, fault exclusion follows and excludes the source of the unacceptably large position error (without always necessarily identifying it), thereby allowing navigation to continue using GPS without interruption.

An FAA document, Technical Standard Order (TSO) C-129, described avionics requirements for the use of the Global Positioning System (GPS) as a supplemental means of navigation for civil aviation in December 1992 [1, 2]. Since the TSO was intended for use of GPS as a

¹ This paper is based on navigation system research and development studies performed by The MITRE Corporation for the FAA Satellite Program Office (AND-510). The contents of this paper reflect the views of the author, who is solely responsible for the accuracy, analyses, and suggestions presented herein.

supplemental means of navigation, safety was the primary concern so it specified use of only the fault detection function under the name of receiver autonomous integrity monitoring (RAIM). Recently, an FAA notice on use of GPS as a primary means of navigation in oceanic and remote airspace has been issued, which calls for an improved version of the FDE function beyond that specified in the TSO, including use of a fault exclusion function [3, 4].² Currently, the Radio Technical Commission for Aeronautics (RTCA) Special Committee (SC)-159 is wrapping up its efforts developing FDE requirements to include in the WAAS Minimum Operational Performance Standards (MOPS) [5]. According to the MOPS, the FDE capabilities may be used for primary means navigation when and where WAAS is unavailable for en route through nonprecision approach phases of flight. The study contained in this paper applies to these phases of flight.

Integrity requirements are defined by two parameters: a false alert rate and probability of missed alert (P_{ma}). A false alert is a false annunciation that the position error has exceeded some specified limit when it has not. For supplemental use of GPS, the maximum allowable false alert rate requirement is once every 500 hrs or equivalently, $1/15,000$ samples [6]; for primary means use of GPS, it is much tighter (10^{-5} per hr) since no other normal means of navigation is available [7]. A missed alert is defined to be a failure to annunciate to the pilot (or externally outside the sensor in case of a sensor only equipment) within the time-to-alert when the position error exceeds a certain specified limit (or level). (Note: An alert refers only to those pilot-observable indications that are provided by the equipment while detection refers to an internal processing condition associated with the FDE algorithm.) The integrity requirement for missed alert is set at a conditional probability of 0.001.

With regard to the limit that the position error shall not exceed, two limits are used in the definition of P_{ma} to serve different purposes: one is horizontal alert limit (HAL) and the other is horizontal protection level (HPL). HAL is a limit that the position error shall not exceed for a safe operation in a given phase of flight (e.g., 0.3 nmi for nonprecision approach phase of flight). HPL is a limit (or level) that a receiver guarantees that the horizontal position error would not exceed without being detected. Therefore, while P_{ma} with respect to HAL is an operational requirement, performance of a receiver FDE algorithm is tested for P_{ma} with respect to HPL. It is the latter definition of P_{ma} that is of concern in this paper.

A simplified state flow diagram in Figure 1 shows what events lead to a missed alert, which is of ultimate concern for integrity. Upon occurrence of a satellite failure, a missed detection may occur, which results in a missed alert. If the satellite failure is detected,

identification/exclusion will follow. If the exclusion is a correct one, it will go back to a normal state. However, if it is an incorrect exclusion, it will go to a transient state, from which missed detection may again occur. Therefore, a missed alert may occur not only from the initial missed detection but also from a missed detection that follows an incorrect identification/exclusion. Because these two sequences of events are mutually exclusive, P_{ma} is a sum of the two probabilities (neglecting probability of a missed detection following a second or later incorrect exclusion). Therefore, in order to have a sufficiently small P_{ma} meeting the requirement, it is important to assure ourselves of sufficiently small P_{md} and probability of incorrect identification/exclusion. In order to do that, that is, in order to ensure meeting the primary means integrity requirements, it is necessary to be able to correctly calculate HPL, based on which P_{md} is determined, and probability of incorrect identification/exclusion.

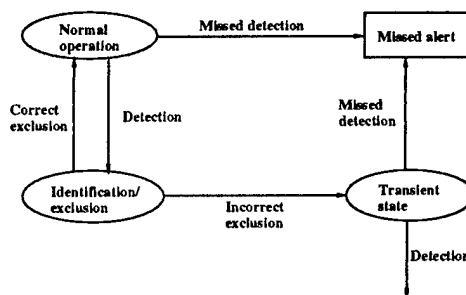


Figure 1
Simplified State Flow Diagram

Currently existing FDE techniques can be classified into two groups: one is called the least squared residual (LSR) scheme, and the other is called the parity space scheme [8, 9, 10]. These two schemes have been shown mathematically identical [11, 12]. While basic detection and isolation techniques have been well established, performance of these techniques and the primary means integrity requirements have not been well related. Specifically, no method exists to correctly calculate HPL and $\Pr\{\text{incorrect identification/exclusion}\}$. For this reason, this paper proposes and analyzes new methods of correctly calculating these two quantities.

² A primary means of navigation refers to the airborne navigation equipment that meets the requirements of radionavigation for the intended phase of flight (route to be flown). These requirements include satisfying the necessary level of accuracy, integrity, continuity, and availability for a particular area, route, procedure, or operation. [5]

The next section develops a new formula for calculating horizontal protection level (HPL) and compares it with the existing method. The subsequent section derives a formula for calculating probability of incorrect/exclusion upon detection of a fault. The last section summarizes the paper.

2. NEW METHOD OF CALCULATING HORIZONTAL PROTECTION LEVEL (HPL)

In the following, the basic relationship between the position error and the test statistic is examined along with the P_{md} performance for a growing bias error on the failed satellite. This is followed by a review of the existing HPL calculation methods, and then a new method is proposed. Finally, the proposed method is compared with the existing method(s) in terms of FDE performance and availability.

2.1 Position Error vs. Test Statistic

Detection performance may perhaps be best explained with a plot shown in Figure 2. It plots position error that we want to protect against vs. test statistic, i.e., observed quantity (e.g., RSS of range residuals or parity vector magnitude). The decision threshold is set on the basis of the maximum allowable false alert rate in a normal condition. Upon selection of two parameters, decision threshold and HPL, the whole region is divided into four sub-regions: normal region, timely detection region, early detection region, and missed detection region. Among these, the missed detection region is the most critical. That is, when we select the HPL, we have to make sure that upon occurrence of a satellite failure, the missed detection region is not reached with a probability greater than 0.001

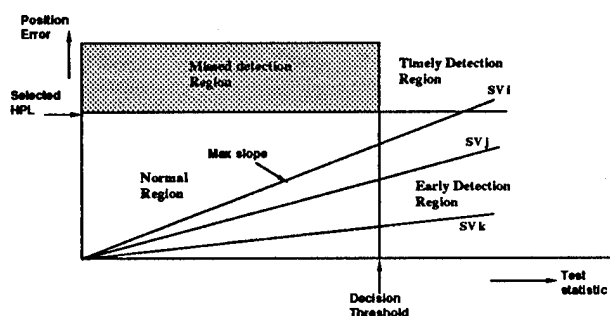


Figure 2
Position Error vs. Test Statistic
- Deterministic Error Trajectory

(Note: Strictly speaking, in order to meet P_{ma} of 0.001, P_{md} should be slightly smaller. This is because as stated

earlier, a missed alert results not only from the initial missed detection but also from a missed detection that follows an incorrect identification/exclusion. Because the small deviation does not alter our discussion, P_{md} requirement of 0.001 is assumed in our analysis.) The fundamental problem of FDE is that there is no direct measurement. However, if one considers only the bias error on one of the satellites at a time and neglects the range errors on all the other satellites, then the position estimation error and the test statistic become linearly proportional to each other, and the slope varies depending on which satellite has the bias error. The satellite that is the most difficult to detect is the one with the maximum slope because for the same observed test statistic, the probability of missed detection is the highest for the failure of that satellite.

Figure 3 again plots the position error vs. test statistic. As the bias error grows, the center of the distribution remains on the slope, but the realizations of the position error-test statistic pair are scattered around the center. One can observe how this P_{md} per sample basis might vary as the bias error magnitude varies as follows. If the bias error magnitude is very small, the probability of position error exceeding HPL is small so that P_{md} is also small. At the other extreme, if the bias error magnitude becomes very large, the probability of position error exceeding HPL is very large but the probability of the alarm going off is also large so that P_{md} is again small. It is somewhere in between where P_{md} is the maximum. It will be shown later how this P_{md} per sample varies as a function of the bias error.

As discussed above, the detection requirement is that any occurrence of a satellite failure shall be detected with a probability of 0.999 or greater. However, as was observed above and as will be further discussed later, P_{md} varies depending on the bias error magnitude, which the receiver has no knowledge of and which may continuously vary. For this reason, the off-line simulation tests for P_{md} verification specified in the WAAS MOPS [5] have been designed as follows (The same test scenario was also specified in RTCA DO-208 [6], which later became a part of TSO C-129 [1, 2]). First, the effect of SA with a correlation time constant of 2 min is simulated on all satellites. A ramp-type failure with a range error growing at a rate of 5 m/sec is then introduced into the most difficult-to-detect satellite with the ramp error allowed to continue to grow until either detection or missed detection occurs in each test. Many of these tests are performed, in each of which a condition in which the HPL is exceeded, but the alarm is not triggered within the specified time-to-alarm, is counted as a miss. P_{md} is then obtained as the average of the occurrence of this event. The question is how this P_{md} observed in the tests is related to the P_{md} per sample basis.

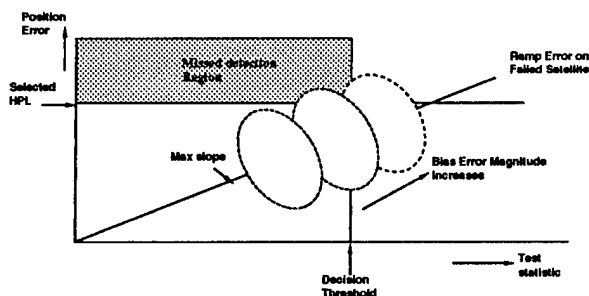


Figure 3
Pr{missed detection} vs. Bias Error

In order to relate the P_{md} calculated on a per sample basis and P_{md} observed in the tests, it is important to recognize that even if P_{md} per sample is small for a given value of bias error, the probability of having one or more missed detections in the test will be increasingly large as the duration of the test gets larger. This is because as the duration of the test gets longer, the number of independent samples during the course of the test increases. The same would be true if the bias error grows very slowly, such that many independent sample realizations occur while the bias error grows. It will be shown later (Figure 7), the P_{md} values are negligible except for some small range of bias error values. With a bias error growing at the rate of 5 m/sec and a correlation time constant of 2 min for the random errors, practically only one independent set of samples is realized during the time the bias error passes through this small region. For this reason, the P_{md} that results in the tests specified in the WAAS MOPS [5] and the TSO [1, 2] is governed by the maximum of the P_{md} calculated on a per sample basis.

Having established that the P_{md} observed in the tests can be approximated by the maximum of the P_{md} that varies as a function of the bias error, the following questions are asked:

1. How does P_{md} vary as a function of the bias error magnitude?
2. When does the maximum P_{md} occur?
3. How to choose HPL such that maximum $P_{md} \leq 0.001$?

The analytic approach to be proposed later answers these questions.

2.2 Existing HPL Calculation Methods

Two HPL calculation methods exist. As shown in Figure 4, the first method, which was proposed by Prof. G. Brown a few years ago, determines HPL as a scalar

multiple of a quantity called Approximate-Radial-Protected (ARP), which is the product of the decision threshold and the maximum slope [13]. Via extensive Monte-Carlo simulation, it was determined that HPL should be approximately 1.7 times the ARP to meet the P_{md} requirement of 0.001 (Note: More precise values are obtained as a function of the number of satellites used as ranging sources [13].) Remember that the decision threshold is determined by the maximum allowable false alert rate, which is set differently depending on whether it is for supplemental means or primary means of navigation. The scale factor of 1.7 was determined for the maximum allowable false alert rate requirement for supplemental use of GPS. For primary means use of GPS, this requirement becomes much tighter (10^{-5} per hr), and thus, the scale factor of 1.7 no longer applies.

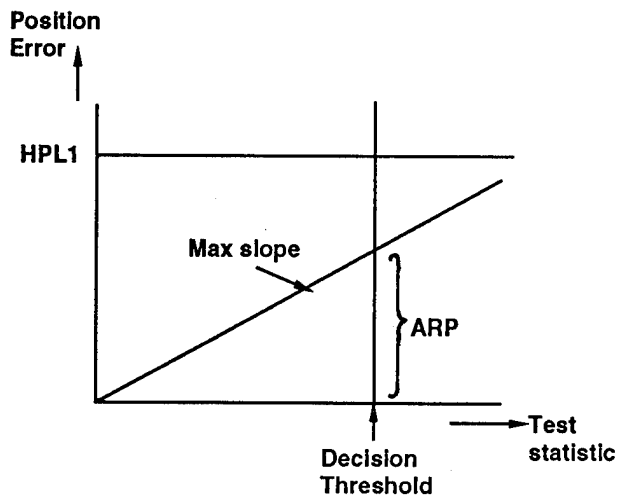
The second method was proposed by people advocating the parity space RAIM scheme [10, 12]. In this method, one first determines how large the bias error has to be in order that the probability of the test statistic being less than the decision threshold becomes equal to 0.001. Then the position error due to the bias error is taken as the HPL. This HPL can be expressed in a simple analytic form. However, what they did not recognize was that P_{md} varies as a function of the bias error magnitude, and this HPL applies only to the bias error of the chosen magnitude in a snapshot mode. This method is not sufficiently accurate as discussed below.

It was first reported by VOLPE National Transportation Systems Center (VNTSC) that HPL calculated using the second method often fails to meet the P_{md} requirement when the tests are performed according to the off-line dynamic simulation test scenario described earlier [14]. This has also been confirmed by MITRE as shown in Figure 10. In the dynamic simulation test scenario, as the range error for the failed satellite increases, the maximum P_{md} occurs before the bias error reaches the value that determines the HPL in the second method. This, which was observed in Figure 3, explains why HPL calculated using this method often fails to meet the P_{md} requirement.

(Note: P_{md} appears to become smaller than the requirement if one counts a miss as a missed detection only if the position estimation error exceeds the HPL for longer than the time-to-alert, which is 10 sec for the case of the nonprecision approach phase of flight and longer for the en route and terminal phases of flight. However, the discussion and analysis at hand is important because one should correctly design the HPL calculation algorithm and cannot simply rely on the time-to-alert in its design.)

Now, with the second method not usable, we could redo the Monte-Carlo simulations to derive a similar expression that applies to the primary means use of GPS.

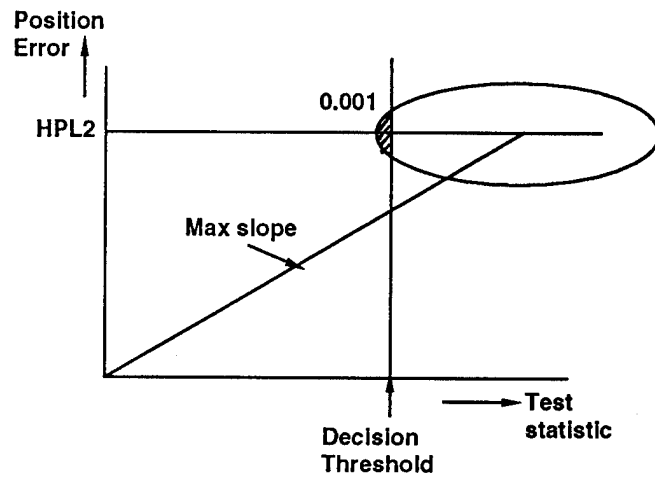
Method #1



$$HPL1 \cong 1.7 \times ARP$$

1.7 obtained via Monte-Carlo simulation
for $\Pr\{\text{false alert}\} = 1/15,000$ samples

Method #2



$$HPL2$$

Analytically derived
Not sufficiently accurate

Figure 4. Existing Calculation Methods of Horizontal Protection Level (HPL)

However, this is tedious and time consuming and gives no insight, which an analytic approach often gives. An analytic method is proposed below that is sufficiently accurate without requiring a Monte-Carlo simulation.

2.3 Proposed HPL Calculation Method

The basis of proposed analytic approach is illustrated in Figure 5, showing two separate spaces to work with: parity space (or observation space) and the horizontal position domain. It is first assumed that a bias error of a given magnitude is on the satellite that is the most difficult to detect. The parity vector and position error due to this bias error determine the center of statistical distributions in the two spaces, respectively. The distances of these centers from the origins of their respective domains are denoted as $d1$ and $d2$, respectively, as shown in Figure 5, where $d1 = c1 \times \text{Bias}$, $d2 = c2 \times \text{Bias}$, and $c1$ and $c2$ are scalars determined solely by the geometry.

An advantage of working with parity space is that the components of a parity vector due to random errors have a

joint normal distribution of dimension $(N-4)$ (assuming a normal distribution for the random range errors), where N is the number of satellites used as ranging sources, with an equal variance in all directions. (The variance is identical with that for the pseudorange error in a normal condition.) With this observation, the probability of a parity vector not exceeding the decision threshold circle (a sphere of dimension $(N-4)$, in general) is approximated as a cumulative Gaussian distribution of the following form:

$$\Pr\{\text{no alarm}\} = \text{erf}\left(\frac{\text{Threshold} - c1 \cdot \text{Bias}}{\sigma_{SV}}\right)$$

where

$$\text{erf}(x) = \int_{-\infty}^x \frac{1}{\sqrt{2\pi}} e^{-\frac{t^2}{2}} dt$$

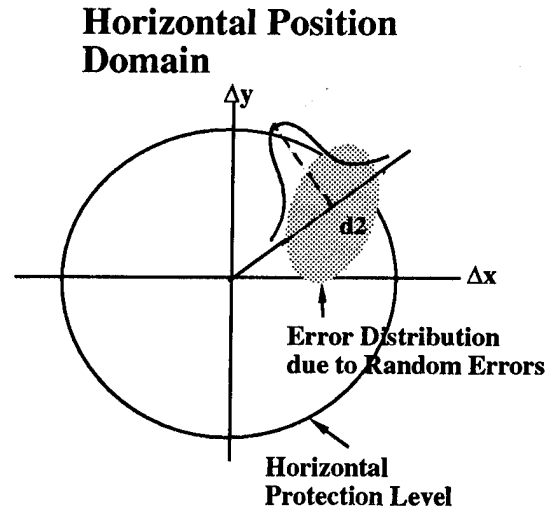
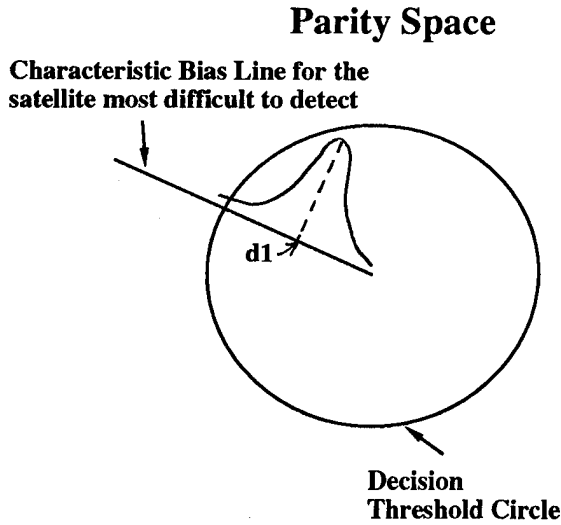


Figure 5
Basis of the Proposed Analytic Approach

In the horizontal position domain, a similar approximation can be made. In this case, one first obtains the standard deviation of the Δx and Δy position errors (having a non-zero correlation coefficient, in general) along the axis defined by the origin and the position error vector due to the bias error on the satellite that is the most difficult to detect. This can be done as follows.

Step 1: Determine the angle θ between the Δx axis and the axis defined by the origin and the position error vector due to the bias on the satellite whose error is the most difficult to detect.

Step 2: Construct a matrix rotating the Δx - Δy axes of the solution vector by angle θ on the Δx - Δy plane as follows:

$$Q_\theta = \begin{bmatrix} \cos \theta & -\sin \theta & 0 & 0 \\ \sin \theta & \cos \theta & 0 & 0 \\ 0 & 0 & 1 & 0 \\ 0 & 0 & 0 & 1 \end{bmatrix}$$

Step 3: Obtain the covariance matrix for the user position and user time with respect to the rotated reference frame

$(\Delta x' - \Delta y' - \Delta z - \Delta t)$, assuming an equal variance for the pseudorange errors.

$$DOP = \text{cov}[\Delta \underline{x}'] = \left[(H Q_\theta)^T (H Q_\theta) \right]^{-1}$$

Step 4: Obtain the standard deviation σ_m along the $\Delta x'$ axis, as given by

$$(\sigma_m)^2 = DOP[1,1]$$

The probability of a position error exceeding a selected HPL radius is then approximated as another cumulative Gaussian distribution of the following form:

$$\begin{aligned} & \Pr\{\text{position error} > HPL\} \\ &= 1 - \text{erf}\left(\frac{HPL - c2 \cdot \text{Bias}}{\sigma_m}\right) \end{aligned}$$

Figure 6 shows results of numerical evaluation of $\Pr\{\text{no alarm}\}$ and $\Pr\{\text{position error exceeding HPL}\}$, using the above formula as a function of bias error. Then, the joint probability of position error exceeding HPL and no alarm, which is P_{md} , is approximated as the product of those

two probabilities. This is an approximation because in general, the two events are not uncorrelated. Later simulation results, however, show that it is a good approximation.

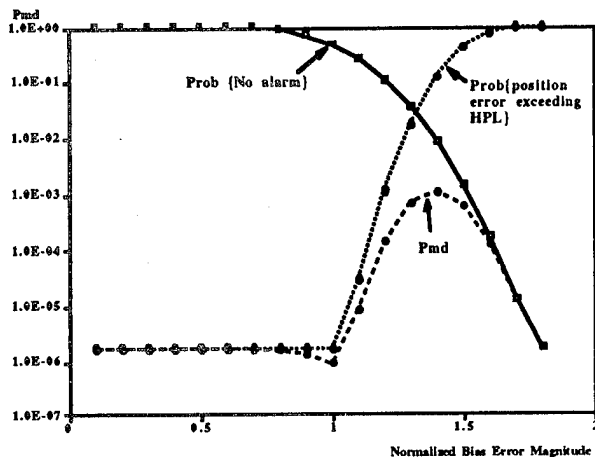


Figure 6
Example Pr{missed detection} vs. Bias Error

For derivation of an HPL formula, we start with a formula for HPL of the following form:

$$\text{HPL} = (\text{ARP ratio}) \times (\text{ARP})$$

Figure 7 shows how P_{md} approximated as above varies as a function of bias error magnitude for a given geometry for different values of ARP ratios. It is observed that different peak P_{md} values are obtained depending on the ARP ratio used. From the figure, one can determine what ARP ratio one has to use as a minimum in order to have maximum P_{md} no greater than 0.001. For the case shown in Figure 7, the minimum ARP ratio is 1.53.

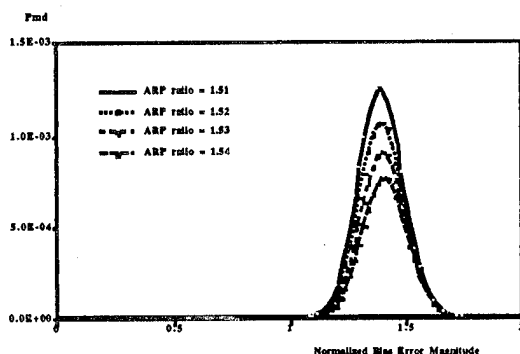


Figure 7
Pr{missed detection} for Different ARP Ratios
(HPL = (ARP Ratio) x ARP; ARP = 218.5 m)

The ARP ratios giving P_{md} no greater than 0.001 are plotted in Figure 8 for 30 different geometries. The plot shows a clear pattern on how the critical ARP ratio varies as a function of ARP. Based on this observation, the following formula is proposed for the ARP ratio:

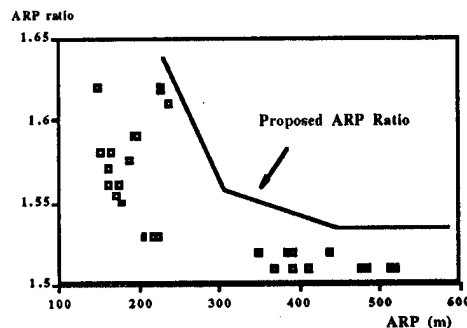


Figure 8
ARP Ratio Providing Maximum $P_{md} \leq 0.001$
 $\text{HPL} = (\text{ARP Ratio}) \times \text{ARP}$

For $\text{ARP} \leq 300$ m,

$$\text{ARP ratio} = 1.62 - \frac{0.07}{70}(x - 230)$$

For $300 \text{ m} < \text{ARP} < 440$ m,

$$\text{ARP ratio} = 1.55 - \frac{0.03}{140}(x - 300)$$

For $\text{ARP} \geq 440$, $\text{ARP ratio} = 1.52$

HPL is then given by

$$\text{HPL} = (\text{ARP ratio}) \times (\text{ARP}) + 8 \text{ (m)}$$

Note that a somewhat arbitrary value of 8 m is added as a "fudge factor" in the formula for HPL.

Figure 9 shows the comparison of HPL values calculated using the existing method (the second method in Section 2.2) and the proposed method for an identical set of 40 different geometries. It is shown that HPL calculated using the proposed method is larger than HPL using the existing method typically by 40 m or so. It is noted that the increase is significantly smaller for geometries with a large HPL.

2.4 Comparison of the Existing and Proposed Methods in terms of P_{md} Performance

Figure 10 shows $\Pr\{\text{missed detection}\}$ obtained via Monte-Carlo simulation for the proposed method and the existing method. It is shown that while the existing method fails to meet the P_{md} requirement of 0.001 in most cases, the proposed method consistently meets the requirement.

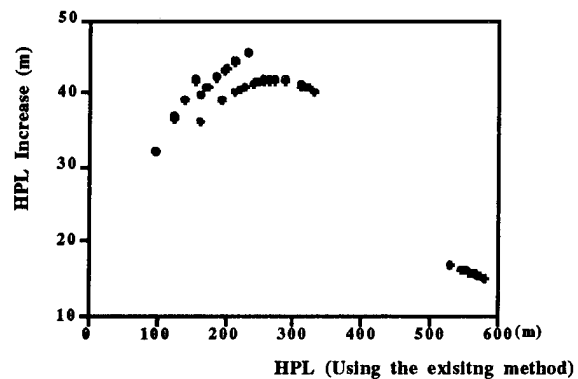


Figure 9
Increase in HPL with the Proposed Method Compared with the Existing Method

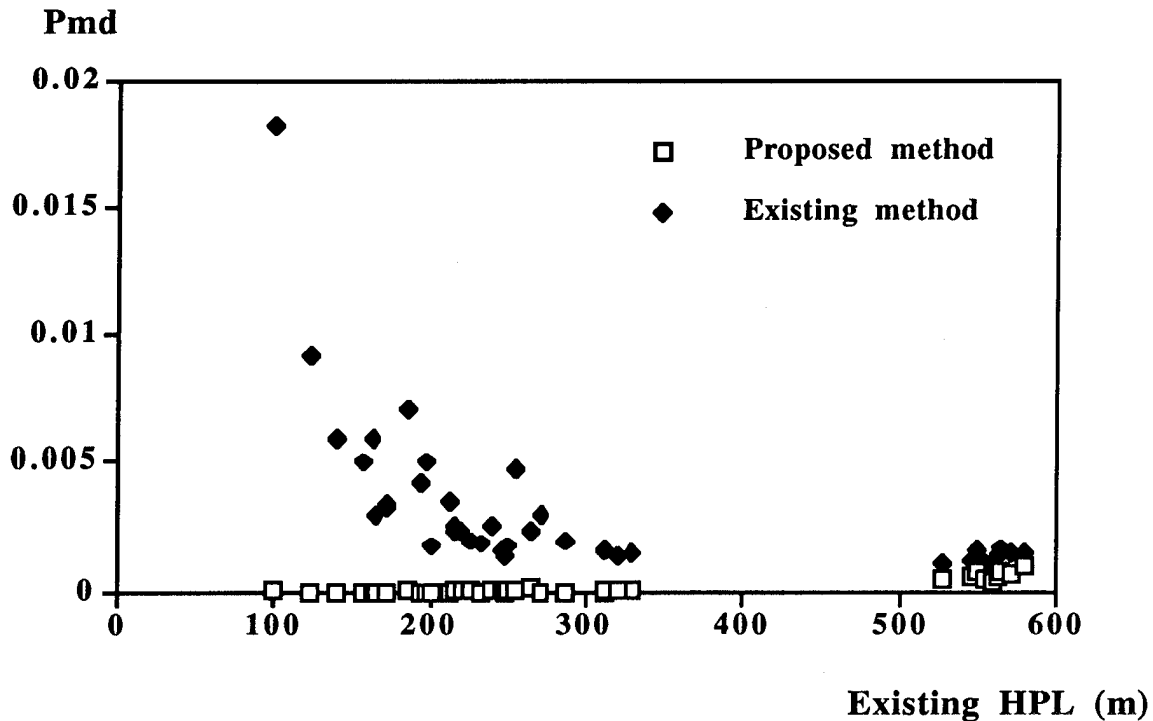


Figure 10
Comparison of $\Pr\{\text{missed detection}\}$ between the Existing and Proposed Methods

2.5 Comparison of the Existing and Proposed Methods in terms of FDE Availability

Figures 11 and 12 compare FDE availability between the proposed method and the existing method. The FDE availability is evaluated at five airport locations in CONUS, assuming the optimized 24 constellation with all satellites operating and a mask angle of 5 deg.

Figure 11 compares the detection availability for the two methods for the nonprecision approach and terminal phases of flight. For the terminal phase, there is no difference. For the nonprecision approach phase of flight, detection availability is reduced less than half a percent on the average. Maximum reduction was about 1.6 percent.

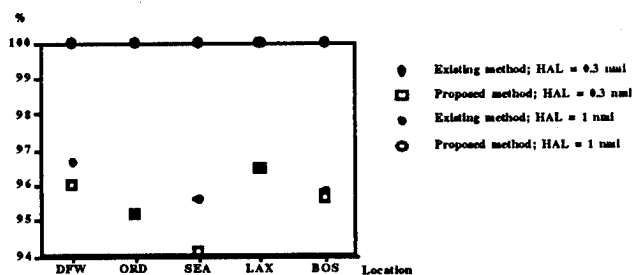


Figure 11
Comparison of Detection Availability
(Optimized 24 Constellation with all SVs Operating;
5 deg mask angle)

Figure 12 compares the exclusion availability. For the terminal phase, there is no appreciable difference between the two methods. For the nonprecision approach phase of flight, exclusion availability is reduced by less than 1 percent on the average and by 2 or 3 percent maximum.

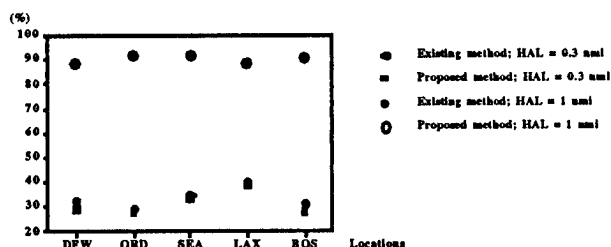


Figure 12
Comparison of Exclusion Availability
(Optimized 24 Constellation with all SVs Operating;
5 deg mask angle)

3.0 A Method of Calculating Probability of Incorrect Identification/Exclusion Upon a Fault Detection

As was stated earlier, while there exist different FDE schemes, they are basically equivalent. An FDE scheme used in our analysis is illustrated in Figure 13. This figure shows an example case of a two-dimensional parity space for a set of six satellites (A parity space has dimension $(N-4)$, in general, where N is the number of satellites used as ranging sources). Each of the six characteristic bias lines shown in Figure 13 represents the trace of a parity vector with increasing bias error on the corresponding satellite and with no errors on the others. Note that for any error monotonically increasing for a failed satellite, the trace of the parity vector is likely to remain close to the characteristic line corresponding to the failed satellite. Therefore, the characteristic bias line that is the closest to the observed parity vector is determined as the one associated with the failed satellite.

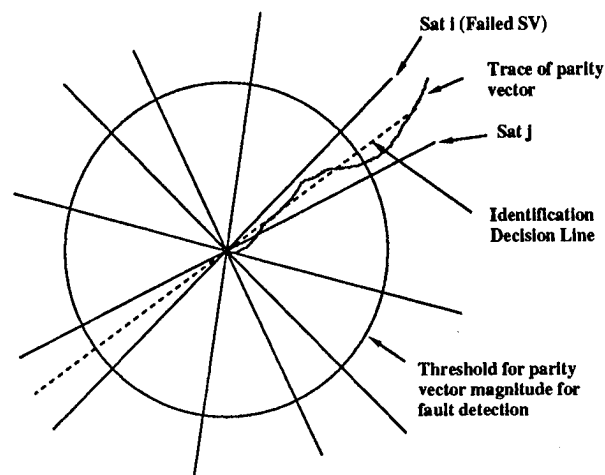


Figure 13
Parity Space for a 6-Satellite Case
(Failure of Satellite i assumed)

As was discussed earlier, the components of a parity vector in parity space due to random errors have a joint normal distribution of dimension $(N-4)$ (assuming a normal distribution for the random range errors) with an equal variance in all directions with the center of the distribution determined by the parity vector components due to the bias error on the failed satellite. Figure 14 again illustrates a two-dimensional parity space as an example. With the parity vector magnitude used as the test statistic for detection, upon detection of a fault, the parity vector due to a combination of the bias and random errors lies on the threshold circle (or sphere of dimension $(N-4)$, in general). Since the satellite associated with the characteristic bias line closest to the parity vector is identified as being faulty, a wrong exclusion would occur if the parity vector happens to be closer to an adjacent bias line.

For the center of the distribution lying somewhere along the characteristic bias line for the failed satellite, one may draw an x axis perpendicular to the bias line at its center of the distribution at C in Figure 14. Then, the arc segment between A and B can be approximated as a straight line parallel to the x-axis if the two bias lines are close to each other, which is the case of primary interest. In this case, the conditional probability along the arc is approximately the same as the distribution along the x-axis. Therefore,

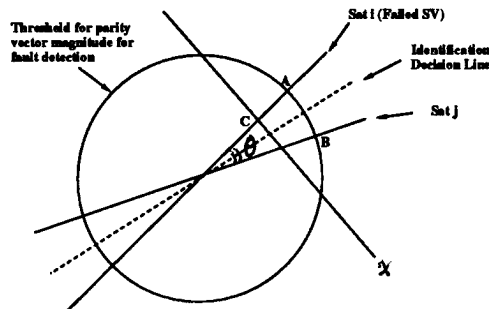


Figure 14
Calculation of $\Pr\{\text{Incorrect Identification/Exclusion}\}$
in Parity Space
(A 6-Satellite Example Case; Failure of Satellite i assumed)

$$\Pr\{\text{wrong exclusion}\} = \Pr\left\{x > \frac{d}{2}\right\} \quad (3-1)$$

$$= \frac{1}{\sigma\sqrt{2\pi}} \int_{d/2}^{\infty} \exp\left(-\frac{x^2}{2\sigma^2}\right) dx$$

where x is the distance between the parity vector and the bias line associated with the failed satellite and d is the distance between the two bias lines, that is, between point A and point B in Figure 14. Therefore,

In order to have $\Pr\{\text{wrong exclusion}\} \leq 0.001$,

$$d/2 \geq 3.08 \sigma \quad (3-2)$$

On the other hand, note that

$$d/2 = \text{threshold radius} \times \sin(\theta/2) \quad (3-3)$$

where θ is the angle between the two adjacent bias lines. This can be easily calculated from the matrix defining the characteristic bias lines.

In general, more than one bias line may lie close to the bias line at hand. In this case,

$$\Pr\{\text{wrong exclusion}\} = \sum_{i=1}^m \Pr\left\{x > \frac{d_i}{2}\right\} \quad (3-4)$$

Eq. (3-4) should be evaluated using Eq. (3-2) only for bias lines close to the bias line at hand on the decision radius circle (on the sphere of dimension (N-4), in general) since the approximation used in Eq. (3-1) holds only for such cases.

While $\Pr\{\text{wrong exclusion}\}$ can be calculated as above for a given satellite failure, there are three different ways to calculate $\Pr\{\text{wrong exclusion}\}$ for a given geometry:

1. Calculate $\Pr\{\text{wrong exclusion}\}$ assuming the failure of every satellite used and take the largest.
2. Take $\Pr\{\text{wrong exclusion}\}$ assuming the failure of the satellite that is the most difficult to detect.
3. Calculate $\Pr\{\text{wrong exclusion}\}$ assuming the failure of every satellite used and take the average assuming that failures are equally likely among the satellites.

While criterion #1 would guarantee $\Pr\{\text{wrong exclusion}\}$ no greater than a specified value regardless of which satellite fails, its requirement on geometry is the most stringent. It should be noted that a failure is assumed always on the satellite that is the most difficult to detect in fault detection performance evaluations and that this most-difficult-to-detect satellite is, in general, not the same as the satellite that is the most difficult to exclude. Therefore, criterion #1 may be too conservative to represent most cases encountered in real operations. A final choice among the different criteria would depend on the operational requirements, which have not been fully resolved at this time.

4.0 SUMMARY

While the basic fault detection and exclusion (FDE) techniques have been well established, the relation between the FDE algorithm performance and the primary means integrity requirements has not been well established. Specifically, no method has existed to correctly calculate horizontal protection level (HPL), based on which the probability of missed detection (P_{md}) is determined, and the probability of incorrect identification/exclusion. Correct calculation of these is essential in meeting the primary means integrity requirements. For this reason, this paper proposes and analyzes new methods of correctly calculating these two quantities.

A method to calculate P_{md} for a given HPL was derived analytically. From this derivation, a formula was also developed that obtains an HPL that meets the P_{md} requirement, without using Monte-Carlo simulation. It is shown that while no existing HPL calculation method meets the P_{md} requirement consistently, the proposed method does. On the other hand, the new HPL calculation method brings a minimal impact on FDE availability. Proper calculations of the two quantities derived in this paper will ensure meeting the overall missed alert probability requirement for primary means operations.

ACKNOWLEDGMENTS

The author would like to thank Ms. Karen van Dyke of VNTSC for her cooperation in performing an independent evaluation of the probability of missed detection performance based on the HPL calculation method proposed in this paper and Prof. Grover Brown for reviewing the paper and giving good comments. He would also like to thank Joe Dorfler of the FAA Satellite Program Office (AND-510) for his support and his colleagues at MITRE, Curt Shively, Ron Braff, J. P. Fernow, Mel Zeltser, and Bakry El-Arini for reviewing the draft and giving the author many helpful suggestions.

REFERENCES

1. Technical Standard Order (TSO) C-129, Airborne Supplemental Navigation Equipment Using the Global Positioning System (GPS), FAA Aircraft Certification Service, Washington, D. C., 10 December 1992.
2. Technical Standard Order (TSO) C-129a: Draft 6, Airborne Supplemental Navigation Equipment Using the Global Positioning System (GPS), FAA Aircraft Certification Service, Washington, D. C.
3. GPS As a Primary Means of Navigation for Oceanic/Remote Operations, Satellite Operational Implementation Team (SOIT) Position Paper, FAA, Washington, D. C., December 5, 1994.
4. GPS As a Primary Means of Navigation for Oceanic/Remote Operations, FAA Notice N8110.57, FAA Aircraft Certification Service, Washington, D. C., July 1995.
5. Minimum Operational Performance Standard for Global Positioning System / Wide Area Augmentation System Airborne Equipment, Final Draft, RTCA Paper No. 498-95/SC159-672, RTCA Inc., Washington D.C., September 1, 1995.
6. Minimum Operational Performance Standards for Airborne Supplemental Navigation Equipment Using Global Positioning System, RTCA/DO-208, RTCA Inc., Washington D.C., July 1991.
7. DeCleene, B., "Derivation of FDE Requirements," Presented at RTCA SC-159, FDI Working Group, April 17, 1995.
8. Parkinson, B.W. and Axelrad, P. A., "Autonomous GPS Integrity Monitoring Using the Pseudorange Residual," NAVIGATION, Journal of The Institute of Navigation, Vol. 35, No. 2, Summer 1988, pp. 255-74.
9. Brenner, M., "Implementation of a RAIM Monitor in a GPS Receiver and an Integrated GPS-IRS," Proceedings of the Third International Technical Meeting of the Satellite Division of The Institute of Navigation (ION GPS-90), Colorado, Springs, CO, September, 19-21, 1990, pp. 397-406.
10. Farrell, J. and van Graas, F., "Receiver Autonomous Integrity Monitoring (RAIM): Techniques, Performance & Potential," Proceedings of the Annual Meeting of The Institute of Navigation, Williamsburg, VA, June 1991.
11. Brown, R. G., "A Baseline GPS RAIM Scheme and a Note on the Equivalence of Three RAIM Methods," NAVIGATION, Journal of The Institute of Navigation, Vol. 39, No. 3, Fall 1992, pp. 301-16.
12. Brown, R. G., "GPS RAIM: Calculation of Thresholds and Protection Radius Using Chi-square Methods - A Geometric Approach," RTCA Paper No. 491-94/SC159-584, RTCA Inc., Washington D.C., November 1994.
13. R. G. Brown, et al., "Comparison of FDE and FDI RAIM Algorithms for GPS," Proceedings of the National Technical Meeting, Institute of Navigation, 24-26 January 1994, San Diego, CA.
14. K. Van Dyke and J. Kraemer, Written Comments Presented to RTCA SC-159 on Minimum Operational Performance Standard for Global Positioning System / Wide Area Augmentation System Airborne Equipment, Draft 6, RTCA Paper No. 396-95/SC159-661, August 23, 1995.

A General RAIM Algorithm Based on Receiver Clock*

P. Misra, M. Pratt, R. Muchnik, and B. Manganis
Massachusetts Institute of Technology

ABSTRACT

A new approach to receiver autonomous integrity monitoring (RAIM) is proposed. The basic idea is simple and intuitive: A measurement anomaly affecting position estimate will affect clock bias estimate too. A clock with predictable behavior can, therefore, provide a basis for detecting faulty measurements. A test would consist of (i) prediction of clock bias on the basis of past measurements, and (ii) comparison of the predicted value with the estimate obtained from the current snapshot of measurements. A discrepancy beyond that which can be accounted for would signal a measurement anomaly. That's fault detection, without requiring redundant measurements. This approach offers 100% availability of the fault detection function for nonprecision approaches with the 24-satellite GPS constellation; availability of fault detection and exclusion exceeds 95%.

Practicality of the proposed clock-based RAIM currently rests on our ability to model the receiver clock behavior accurately using GPS measurements. The basic requirement is that there be no significant, unpredictable change in the clock frequency, and the period of such stability be long enough to allow for the clock parameters to be estimated accurately. Laboratory and flight tests have shown the approach to be practical.

1. INTRODUCTION

The basic objective of receiver autonomous integrity monitoring (RAIM) is to ensure that error in a position estimate based on satellite measurements is not so large as to compromise the user's safety. As is well known, the quality of a position estimate may be degraded by several

factors: system malfunction, receiver malfunction, environmental anomalies, electromagnetic interference, poor satellite geometry, and unfavorable combination of measurement errors. For user requirements no more stringent than those for a non-precision approach, RAIM is essentially equivalent to ensuring that there are no measurement anomalies. Faulty measurements are to be detected and excluded from position estimation. This function is referred to as fault detection and exclusion (FDE). The FDE schemes proposed to date are based on the following premise: If the measurements are verified to be consistent, the user can rule out measurement anomalies, and accept the position estimate as conforming to prior experience with similar satellite geometry and measurement data quality, typically characterized by dilution of precision (DOP) and rms user range error (URE), respectively.

Two of the better known consistency checks deal with the least-squares residuals, and, the more intuitive, scatter of the position estimates obtained from subsets of measurements. These schemes require a redundant set of measurements. One redundant measurement is required at a minimum to detect an anomaly. Two redundant measurements are required at a minimum to identify an anomalous measurement. The performance of a consistency-checking algorithm depends essentially upon the number of redundant measurements available to the user, which, in turn, depends upon the size of the satellite constellation. With the current algorithms, the availability of fault detection (FD) function for nonprecision approaches over CONUS for the 24-satellite GPS constellation is reported to be 95% [1]; availability of the FDE function is reported to be 67-88% [2-4].

We propose a RAIM algorithm which is more economical in its use of the measurements, effectively freeing an additional measurement for

* This work is sponsored by the Federal Aviation Administration. Opinions, interpretations, conclusions, and recommendations are those of the authors and are not necessarily endorsed by the FAA.

the purpose of consistency check. As expected, with each user effectively gaining an additional measurement for RAIM, the benefits are significant: 100% availability of FD function for nonprecision approaches, and better than 95% availability of FDE with the 24-satellite GPS constellation. This benefit is available at a modest price in terms of stability of the receiver clock.

As is well known, clocks are at the heart of satellite navigation. The satellites carry very precise and ultra stable clocks costing several tens of thousands of dollars. What makes satellite navigation practical, however, is the fact that most users can get by with an inexpensive clock (\$50-200) in their receivers. In general, the stability requirements on a receiver clock are modest, and relate to short term, that phase noise not be so large as to lose track of the satellites. There is no serious requirement on frequency stability over seconds and minutes. It turns out that if the receiver clock were stable in the looser sense that its frequency did not change unpredictably, it could provide a basis for FDE. Actually, such a clock can do more for a user. The clock stability can be exploited to improve the vertical navigation accuracy substantially, an important benefit for precision approaches. The clock can also support the RAIM function for precision approaches where FDE is effectively done by a ground reference station. A discussion of clock-aided navigation and RAIM for precision approaches is given in [5]. In this report, we'll focus on FDE with an unaugmented GPS.

The next section lays out the basis for a clock-based FDE algorithm. Section 3 provides a background in the requisite clock stability and clock modeling. The focus is on empirical data from laboratory and field tests. Section 4 discusses an FDE algorithm based on the receiver clock and its performance vis-à-vis the requirements of nonprecision approach.

2. FDE BASED ON RECEIVER CLOCK

The basic idea of RAIM based on receiver clock is as follows: From each snapshot of measurements, we can estimate three coordinates of user position and the instantaneous receiver clock bias. In general, any anomaly in the measurements that affects the quality of position estimates would affect the clock bias estimate too. If somehow we knew the 'right' answer for clock bias, we could compare it with the

estimate obtained from the current measurements. A discrepancy beyond that which is to be expected would be reason to conclude that the current measurement snapshot is anomalous. That's fault detection. Having concluded that a measurement set is anomalous, we could check if there exists a subset of four or more measurements which gives a clock bias estimate 'close' to the 'right' answer. If so, we can trust the corresponding position estimate too. That's fault detection and exclusion.

How can we know the right answer for receiver clock bias? Obviously if the frequency of the receiver clock were stable, its bias relative to GPS time would be stable and known once and for all. A requirement of such stability, however, is both unrealistic and unnecessary. We can estimate the right answer for the bias if the receiver clock behavior were merely predictable, given data on its recent trend. The premise of this approach is that we can model the receiver clock behavior accurately over time using the GPS measurements, and use this model to predict the value of clock bias. The minimum requirement for such modeling appears to be that there be no significant, unpredictable change in the clock frequency, or that the frequency drift rate be stable. The period of such stability has to be long enough to allow for the clock parameters to be estimated from the GPS measurements. If the receiver clock behavior is stable over 60 minutes, (i.e., the frequency drift rate is constant), the receiver clock bias can be predicted for, say, 15 minutes with an rms error of 100 ns (or, 30 m), which is adequate for our purpose.

It's easily seen that use of a receiver clock in this manner is tantamount to 'freeing up' or gaining a GPS pseudorange measurement. As we'll see, this additional degree of freedom improves the availability of fault detection and exclusion. But, first, we have to address several questions: How can we model receiver clock behavior so as to predict its bias? How do we verify in real-time that a model actually holds? And, what's the price of the required stability in a receiver clock? We deal with these questions in the next section.

3. RECEIVER CLOCK MODELING

It is well known that the rms error in the clock bias estimate (in units of length) based upon a single snapshot of pseudorange measurements is [6]:

$$\sigma_b = \sigma_{URE} \cdot TDOP,$$

where σ_{URE} is the rms error in the GPS range measurements, and TDOP is the time dilation of precision parameter reflecting the satellite geometry. The measurement error in GPS pseudoranges is generally modeled as Gaussian with zero mean and standard deviation σ_{URE} , denoted compactly as $N(0, \sigma_{URE})$. In the presence of Selective Availability (SA), σ_{URE} has been estimated conservatively as 33 m (observed value: 25 m). For the constellations of interest, TDOP typically ranges between 0.75 and 1.5. Taking a typical value of 1 for TDOP in our simple calculations below, the rms error in clock bias estimated from a single snapshot of the range measurements, $\sigma_b \approx \sigma_{URE} \approx 33$ m.

Our focus in this report is on unaugmented GPS, but note that in differential mode σ_{URE} is greatly reduced; the correlation time of the measurements is reduced too. As a result, the clock model parameters can be estimated both more accurately and more quickly, as discussed in the companion paper [5].

If we had available GPS measurements over a time period (t_0, t) during which the receiver clock frequency drift rate was stable, we could model the clock bias at time t simply as a quadratic function

$$b(t) = b_0 + b_1 (t - t_0) + b_2 (t - t_0)^2,$$

and estimate parameters b_0 , b_1 , and b_2 from the available measurements. The quality of these estimates, and of the prediction, would depend upon the number of statistically independent measurement samples available in time period (t_0, t) . Given k statistically independent measurement snapshots, the rms error in the clock bias estimate will be $\sigma_b \approx \sigma_{URE} / \sqrt{k-3}$. The dominant error in the measurements is due to SA, which has been observed to have a correlation time of about 3-4 minutes. If the frequency drift rate of the receiver clock were known to be stable over, say, 60 minutes, we could fit a quadratic model to the clock bias estimates over the previous 45 minutes, and retain a prediction capability for the next 15 minutes with an rms error of about $33/\sqrt{8}$ m ≈ 12 m. As we'll see, this is more than adequate to support FDE for nonprecision approaches.

Figure 1 shows the behavior of several receiver clocks as observed in our laboratory over a 12-hour period. Included are a cesium standard, a rubidium oscillator, an oven-controlled crystal oscillator (OCXO) and a temperature-compensated crystal oscillator (TCXO). The figure shows clock bias estimates in units of meters for each clock computed 3 s apart from GPS measurements snapshot by snapshot. The plots are intended as typical examples for each of the clocks, and our purpose is only to draw attention to certain qualitative features.

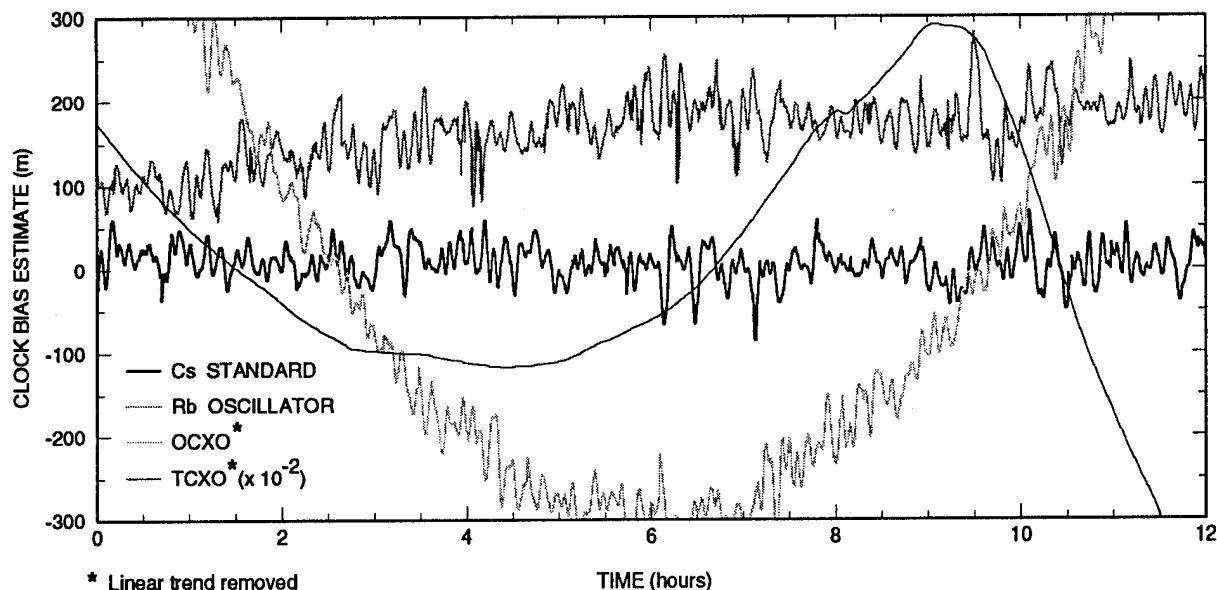


Figure 1.

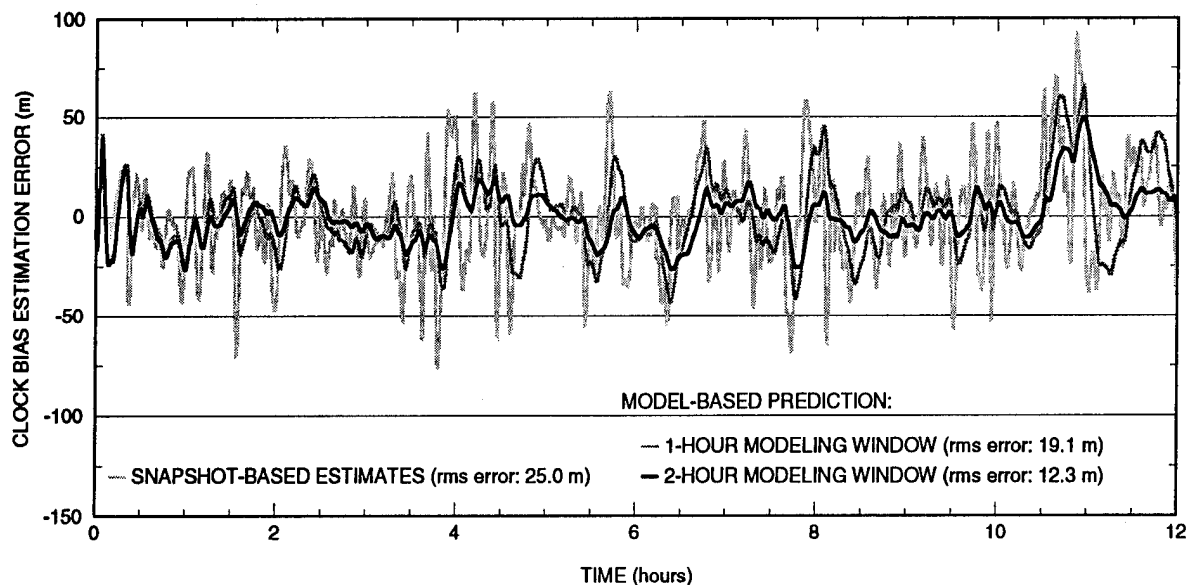


Figure 2.

The clock bias estimates shown in Figure 1 appear noisy, but are consistent with our model for SA. Stability of the cesium standard (FTS 4040, price > \$10K) is obvious: no frequency offset or drift is apparent. The rubidium oscillator (Ball Efratom FRS-C, \$2-4K) also shows no significant frequency offset, but signs of slight drift are clear. Such drift, however, appears constant over 30-60 minutes. The OCXO (HP 10811E, \$1K) has accumulated a small frequency offset (about 1 part in 10^8) so that the clock bias actually changes by about 2 m/s on average. We have taken out the effect of this offset via a linear regression, and have plotted the residuals, which show a clear quadratic trend. The behavior of both atomic clocks and the OCXO appears consistent with the proposed model: clock bias is indeed predictable, given recent data on its trend. The actual quality of such prediction is discussed below.

The TCXO (price \approx \$100) has accumulated a frequency offset of about 1 part in 10^6 , and changes by about 200 m/s on average. Again, the residuals from linear regression are plotted. These residuals, however, are two orders of magnitude larger than those for the OCXO, and swing widely. It's clear that the TCXO does not exhibit the requisite stability of frequency drift rate for the time period required, and the proposed model does not fit. Experience with other TCXOs was similar.

How well does the proposed clock model fit our measurements for the atomic clocks and the OCXO? For the OCXO, the answer is given in Figure 2; the atomic clocks did better. Figure 2 gives the post-fit residuals for the OCXO bias estimates shown in Figure 1. At each point, a quadratic model is fitted to data over the previous hour and two hours separately, and clock parameters b_0 , b_1 , and b_2 estimated in each case. The residual at each point is defined as the discrepancy between the predicted value of clock bias based on the fitted model, and the actual measurement. The parameter estimation process begins in each case at $t = 0$ with no prior knowledge assumed, and for the first 15-30 minutes, there aren't enough measurements on which to base a model, and the discrepancy between the predicted and actual values tends to be large. The rms error in the snapshot-based clock bias estimates is 25 m; the rms error in model-based clock bias predictions is 19.1 m and 12.3 m for the one-hour and the two-hour modeling windows, respectively. These rms values are generally consistent with the results of our simple calculations earlier in this Section. The model, clearly, fits the data.

The measurements shown in Figure 1 were taken under typical laboratory conditions. The clocks did not have to contend with any serious temperature gradients or vibrations, which would be

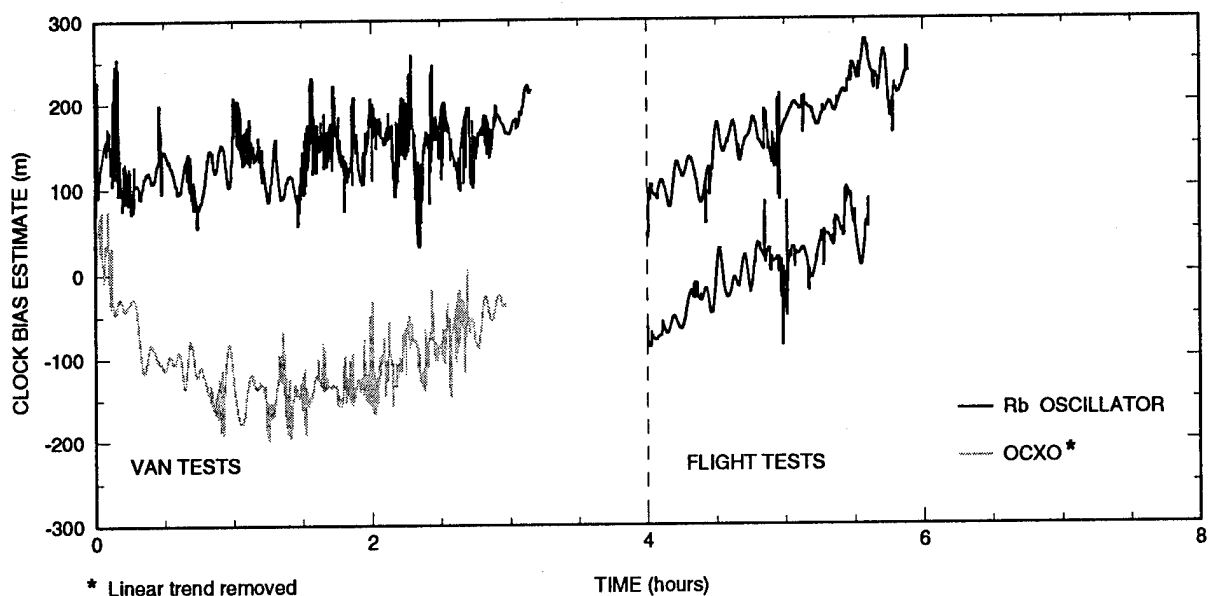


Figure 3.

encountered by a receiver installed in an aircraft. Representative data from several field tests are shown in Figure 3 for the rubidium oscillator and the OCXO. These tests consisted of data collection using a mobile GPS receiver (a NovAtel GPS Card installed in a PC, with provision for external clock input). This demonstration unit was driven in a utility van and flown in an aircraft. No attempt was made to coddle the clock with a special shock mounting or temperature regulation. The results (Figure 3), show no significant change in clock behavior from that observed in the laboratory: for both clocks tested, the clock bias remains predictable, given recent data. The main purpose of the field tests was to see if the requirements of the proposed clock model could be met reasonably under real-world conditions. The clocks appear robust, but more tests are needed to observe their behavior in carefully controlled environments, as specified in RTCA DO-160C [7].

4. FDE ALGORITHM

The basic idea of the algorithm can be restated as follows: (i) a measurement anomaly affecting position estimate will affect the receiver clock bias estimate too, and (ii) if the clock bias could somehow be predicted reliably, the discrepancy between the predicted value and the estimate based on the current measurements can serve as

a basis for FDE. In this section, we discuss an algorithm and its performance.

Let b be the least-squares estimate of the instantaneous receiver clock bias based on a snapshot of measurements modeled as $N(0, \sigma_{URE})$. The distribution of b is $N(0, TDOP \cdot \sigma_{URE})$. Let b_p be the corresponding predicted value based on adaptive modeling of the clock, distributed as $N(0, \sigma_{CPE})$, where CPE stands for clock prediction error. We define the clock bias discrepancy as

$$b_d = b - b_p$$

If the measurements in the current snapshot conform to their model, the rms value of such discrepancy is easily seen to be:

$$\sigma_d = \text{rss} (TDOP \cdot \sigma_{URE} + \sigma_{CPE}),$$

Therefore, if the observed discrepancy conforms to distribution $N(0, \sigma_d)$, we may conclude that the current measurements conform to the model $N(0, \sigma_{URE})$. If not, the measurements are anomalous.

The next question is if there exists a subset of the measurements that conforms to this model on which to base the position estimate. Clearly, there have to be at least four 'good' measurements available, and the algorithm has to be able to find them.

In practice, both σ_{URE} and σ_{CPE} will be estimated adaptively from the measurements. any change in clock behavior beyond that predicted by the model will be seen as larger-than-expected residuals. The statistics of the residuals will provide an ongoing check to determine how well the models fits the data, and if RAIM can continue to be based on the receiver clock. There are at least two complications to be dealt with. First, with certain geometries, an anomaly in a particular satellite might manifest itself as a large position error, but with little impact to clock bias estimate, and vice versa. These geometries, however, are recognized easily, and have to be treated appropriately. The second complication deals with ensuring that clock modeling is not corrupted by anomalous measurements. A reasonable approach is to maintain an appropriate time lag to allow for screening of the measurements by the GPS Ground Segment and by onboard FDE. A one-hour modeling window that doesn't include measurements from the past 15-20 minutes may be enough to assure that clock bias prediction is free of anomalies.

Figure 4 is a scatter plot of position error vs. clock bias discrepancy from a simulation for the 24-satellite GPS constellation with $\sigma_{URE} = 33\text{m}$, $\sigma_{CPE} = 20\text{ m}$, and elevation angle mask = 5° . Results are shown in different gray levels for 0, 1, and 2 anomalies in a snapshot of measurements. As expected, without any measurement anomalies, the distribution of errors in position and clock bias estimates is quite compact: the position error rarely exceeds 300 m, and the clock bias error generally remains below 200 m. The two errors are clearly correlated; given one, the other can be estimated.

With an anomalous measurement, both errors grow, depending upon the size of the anomaly and the satellite geometry. The correlation between the two errors is less strong than in the case without anomalies. Note also the complication pointed out earlier that with certain geometries an anomaly can affect one estimate and not the other. In general though, a large clock bias error implies a large position error. With two anomalous measurements, the band of scatter grows wider, but without any qualitative change in the relationship between position error and clock bias error.

An outline of the FDE algorithm based on receiver clock is given in Figure 5. The basic elements

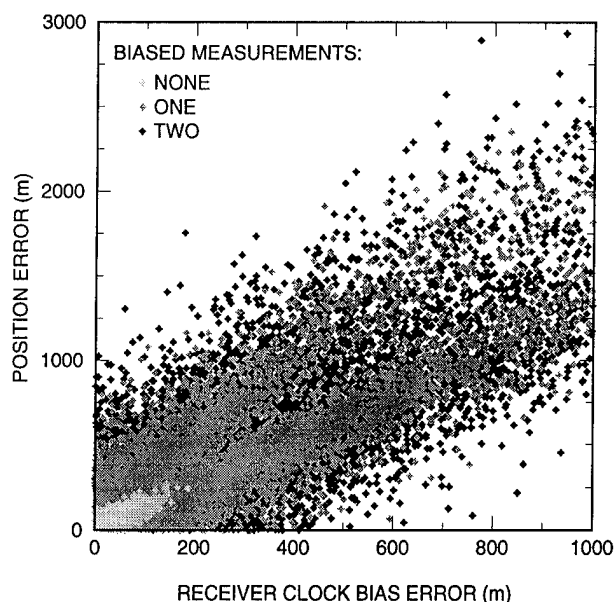


Figure 4.

have been discussed earlier and illustrated in Figure 4. Steps consist of determining thresholds accounting for (i) the satellite geometry in the form of horizontal-error-to-clock error magnification factor, and (ii) the statistical variability in terms of TDOP, σ_{URE} , and σ_{CPE} . Note that FD is possible with four satellites; FDE requires five at a minimum. If the geometry is seen as hiding perils, or if the clock bias discrepancy is seen as high, a consistency check is executed by computing estimates of position and clock bias (4-D estimation) leaving out one measurement at a time. Size of the scatter of these estimates serves as a consistency statistic. Once the hidden perils have been ruled out and a (sub)set of measurements (≥ 4) has been found with acceptable clock bias discrepancy, the predicted clock bias is accepted as the clock bias estimate. A final consistency check is executed in 3-D estimation mode. With clock bias no longer an unknown, 3-D position estimates are computed leaving out one measurement at a time. Size of the scatter, again, serves as a consistency statistic.

5. CONCLUSIONS

We have analyzed an approach to RAIM based on receiver clock modeling to predict its bias. Such modeling requires that frequency drift rate of the clock be stable for long enough to allow accurate estimation of its parameters from GPS measurements. This approach, referred to as clock-aided RAIM, has been found to offer a

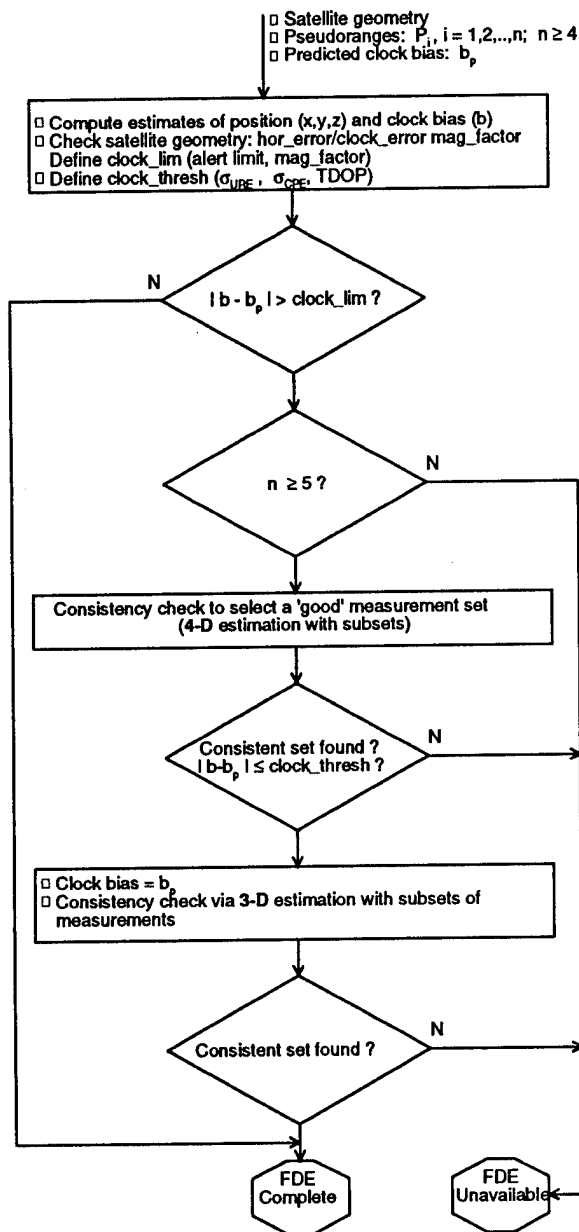


Figure 5.

significant improvement in availability of fault detection and exclusion functions. With the 24-satellite GPS constellation, the availability of clock-aided fault detection for nonprecision approaches is 100%; availability of fault detection and exclusion exceeds 95%.

Laboratory and flight tests have shown the approach to be practical. Several commercial receiver clocks have been found to offer the requisite stability. In order for clock aiding to be practical for general aviation, however, robust

clocks have to be available at lower prices. It's noteworthy that there are encouraging developments in the time reference industry with a trend toward higher stability at lower prices.

ACKNOWLEDGMENTS

This work was sponsored by the Federal Aviation Administration under Interagency Agreement DTFA01-95-Z-02046. The authors are grateful to Joseph F. Dorfler, Program Manager, FAA Satellite Program, for his support. A debt of gratitude is owed to Simon Newby and Pat Fenton of NovAtel for being responsive to our unique requirements.. Thanks are also due to James Hungerford, GFI Technologies; Dr. Tom McLelland, Frequency Electronics, Inc.; and Andrew Snow, Frequency and Time Systems, Inc., for loaning us promising candidates for GPS receiver clocks for testing.

REFERENCES

- [1] K. Van Dyke, "RAIM Availability for Supplemental GPS Navigation," *NAVIGATION*, Journal of the Institute of Navigation, Vol. 39, No. 4, Winter 1992-1993, pp. 429-443.
- [2] F. Van Graas and J. L. Farrell, "Baseline Fault Detection and Exclusion Algorithm," *Proc. ION 49th Annual Meeting*, Cambridge, MA, June 21-24, 1993, pp. 413-420.
- [3] K. Van Dyke, "Fault Detection and Exclusion Performance using GPA and GLONASS," *Proc. ION National Technical Meeting*, Anaheim, CA, January 18-20, 1995, pp. 241-251.
- [4] R. G. Brown, J. H. Kraemer, and G. C. Nim, "A Partial Identification RAIM Algorithm for GPS Sole Means Navigation," *Proc. ION GPS-94*, Salt Lake City, UT, September 20-23, 1994.
- [5] P. Misra, M. Pratt, B. Burke, and R. Ferranti, "Adaptive Modeling of Receiver Clock for Meter-level DGPS Vertical Positioning," *Proc. ION GPS-95*, Palm Springs, CA, 12-15 September 1995.
- [6] R. J. Milliken and C. J. Zoller, "Principle of Operation of NAVSTAR and System Characteristics," *Global Positioning System*, Papers published in *NAVIGATION*, Vol. I, The Institute of Navigation, Washington, DC, 1980, pp. 3-14.

- [7] *Environmental Conditions and Test Procedures for Airborne Equipment*, RTCA/DO-160C, RTCA, Washington, D. C., December 1989.

Integrated GPS/Inertial Fault Detection Availability

Mats Brenner
Honeywell CAS-SPO

BIOGRAPHY

Mats Brenner graduated from the Royal Institute of Technology in Stockholm Sweden in 1974 with a degree corresponding to a master of science in applied Mathematics. From 1975 to 1984 Mats worked with various Kalman filter applications at SAAB in Sweden. Since 1984 Mats has been developing algorithm and architectures for autonomous GPS, differential GPS and hybrid GPS/inertial systems at Honeywell CAS-SPO in Minneapolis.

ABSTRACT

GPS systems possess a high availability of accurate horizontal positioning but detection and exclusion techniques based on satellite redundancy do not provide the integrity availability sufficient for primary means navigation in the terminal and non precision phases of flight. To achieve primary means integrity availability different types of augmentations such as WAAS, Loran, baro aiding, atomic clock and inertial aiding are under consideration. Different techniques have been proposed to combine GPS and inertial sensor information and recent published findings seem to indicate that primary means integrity availability is achievable with standard 2 nmi/h inertial sensor performance. This paper investigates and quantifies what different inertial effects that contribute to enhanced integrity of the integrated GPS/inertial system such as coasting, Schuler feedback etc. A Kalman filter based integration scheme that preserves the integrity information in an optimal fashion is presented and used to quantify integrity performance. The availability of fault detection and exclusion will depend on the geometry of the satellites used for positioning. The availability of satellites in good geometry is in turn a function of the status of the GPS constellation (failures, maintenance etc.). Methods for availability calculations have been developed and adopted by the RTCA SC-159. The availability of fault detection and exclusion over a specified region can be calculated for most augmentations but corresponding

estimates (conforming with RTCA SC-159 guidelines) of the FDE availability provided by GPS/inertial integration techniques have not yet been published. This paper proposes an approximate model, incorporating the main inertial effects contributing to integrity, that can be used to calculate the achievable integrity (horizontal integrity limit) at any geographical location and time. This model is used to estimate the availability of fault detection (FD) for an integrated GPS/inertial system. The availability of fault detection for the GPS/inertial system is compared to the availability of FD for other augmentations to provide trade off information.

INTRODUCTION

As affordable computing capacity in embedded applications is steadily increasing a renewed interest in integrated GPS/inertial systems has emerged for meeting the anticipated RTCA/FAA requirements for primary means GPS based navigation. Integrity requirements and associated test procedures that meet future needs have been developed for autonomous GPS receivers. Due to the complexity of hybrid GPS/inertial systems, clear requirements and appropriate test procedures have not yet been developed. This paper describes one possible implementation and demonstrates how the availability of integrity monitoring, which is a major certification issue, can be determined.

FDE REQUIREMENTS AND ASSUMPTIONS

The RAIM requirements that were published in RTCA DO-208 are used throughout this paper. The false detection rate (p_{fd}) is set to 0.002/h and the missed detection probability (p_{md}) is 0.001. Alert limits are 0.3 nmi for non precision approach, 1 nmi for terminal and 2 nmi for enroute and (deviating from DO-208) 5 – 10 nmi for oceanic.

A failure in a satellite that causes the horizontal error to exceed the alert limit for the phase of flight at hand must be announced to the pilot. The probability that the position error exceeds the alert limit at annunciation

must be smaller than or equal to p_{md} . Although multiple satellite failures most likely will be announced, praxis mandate that only single satellite failures need to be considered when the integrity performance is evaluated. The false detection rate is internal to the algorithm and only false detections indicating failures that can not be contained within the alert limit, will cause false alerts.

No assumptions can be made regarding the dynamics of the satellite failure i.e. whether it is a ramp, oscillation, random walk etc. This ground rule is crucial in the described implementation.

The dominating measurement error is the selective availability noise (SA). For test purposes the total system error is modelled as a second order markov process (see reference 1) and a bias. The second order process has the following characteristics. The time constant is 118 s, the damping factor is $\frac{1}{\sqrt{2}}$ and the pseudorange rate sigma σ_{pv} is $0.1217 \times \sigma_{pr}$. The pseudorange sigma σ_{pr} varies depending on the bias such that $\sqrt{\sigma_{pr}^2 + \sigma_{bias}^2} \leq 33.3$ m. The ratio of bias to dither is not known. However, SA bias components are rarely observed. The analysis in this paper is mostly directed towards the impact of dithered SA but bias components are also briefly discussed. This SA model has been established for certification testing by the RTCA. The details of the true SA model are not known.

The satellite constellation used is the optimized 24 satellite constellation. The constellation weights, taken from reference 4, and the representative average cases (reference 7) used are included in Table 1 below.

number of satellites	weight	excluded satellites
24	0.703	N/A
23	0.227	A3
22	0.055	A1,F3
21	0.015	A2,E3,F2

Table 1

The weights for 21 and less satellites are accumulated in the 21 satellite case.

An essential error component in a hybrid system is the local variations of gravity. Deviations in the vertical direction (Δg_z) from the nominal vertical g are characterized as gravity anomalies and measured in parts per million (ppm). Deviations in the horizontal directions ($\Delta v_x, \Delta v_y$) are characterized as gravity deflections and measured in arcseconds. The following numbers are used in this paper:

gravity component	1-sigma	correlation distance
anomaly	25 ppm	20 nmi
deflections	5 arcsec	20 nmi

Table 2

A SOLUTION SEPARATION BASED RAIM ALGORITHM

Most snap shot RAIM algorithms are derivable from parity space theory. In such algorithms the monitoring either takes place in the measurement domain or in the parity space. The impact of a failure is calculated by projecting the estimated worst case offset into the horizontal plane. It is demonstrated here that it is possible to create a RAIM algorithm that is purely based on solution separation in the horizontal plane. The approach presented is somewhat different from the approach presented in reference 2 and incorporates derivations of threshold setting and calculation of horizontal integrity limit. The integrity limit derived this way has been shown to be almost identical to the integrity limit calculated by the Honeywell parity space algorithm which is a refined version of the algorithm presented in reference 3. The algorithm presented in reference 3 has been further refined to properly account for the SA noise in all involved satellites and not only the satellite in which a possible failure is considered.

The solution separation algorithm proposed in this paper is derived as follows. Let S_0 be the least square solution matrix for a full set of N measurements. Let S_n be the solution matrix for the subset were satellite n is excluded. Construct S_n so that it operates on the full set of measurements by extending the 4 by $N-1$ subsolution matrix with an n^{th} zeroed column.

The full solution is

$$\Delta x_0 = S_0 \Delta p \quad (1)$$

The subsolutions are

$$\Delta x_n = S_n \Delta p \quad (n=1, N) \quad (2)$$

Δx denotes the position correction to the initial estimate in a local geographic north-east-down (NED) coordinate system. The fourth component is the receiver time correction times the speed of light. Δp is the N dimensional measurement vector relative to the initial estimate. The discriminator d_n is defined as.

$$d_n = \sqrt{(\Delta x_0(1) - \Delta x_n(1))^2 + (\Delta x_0(2) - \Delta x_n(2))^2} \quad (3)$$

The impact of the SA noise in the full solution is

$$\delta x_0 = \Delta x_0 - \tilde{\Delta x} = S_0 w \quad (4)$$

The SA noise impact in the subsolutions are

$$\delta x_n = \Delta x_n - \tilde{\Delta x} = S_n w \quad (n=1, N) \quad (5)$$

δx denotes the position error relative to the actual position offset $\tilde{\Delta x}$. w is the N dimensional measurement noise vector. $E[w w^T] = I \sigma_p^2$

The covariance matrix describing the statistics of the separation between the full filter and the sub filter is defined as

$$dP_n = E [(\Delta x_0 - \Delta x_n) (\Delta x_0 - \Delta x_n)^T] \quad (6)$$

and can be calculated as follows

$$dP_n = (S_0 - S_n) \sigma_{pr}^2 (S_0 - S_n)^T \quad (7)$$

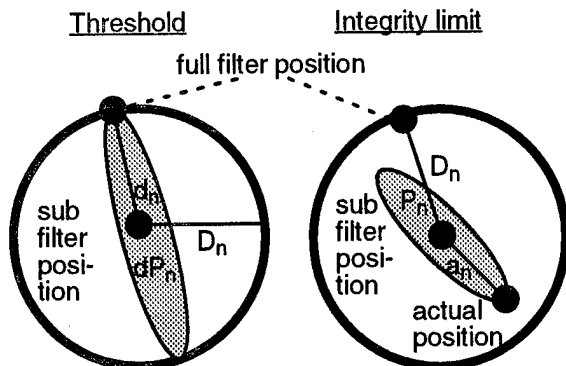


Figure 1

Due to the directional character of this distribution one eigenvalue will dominate and a stringent upper bound of the discriminator variance is the maximum eigenvalue λ^{dP_n} of the horizontal position separation distribution. This eigenvalue can be calculated from the covariance matrix elements $dp_n(1,1)$, $dp_n(1,2)$ and $dp_n(2,2)$.

Considering both sides of the distribution and the fact that any of the N filters may cause a false detection, the threshold D_n (Figure 1) is calculated as

$$D_n = \sqrt{\lambda^{dP_n}} Q^{-1} \left(\frac{p_{fd}}{2N} \right) \quad (8)$$

where Q^{-1} is the inverse of

$$Q(x) = \frac{1}{\sqrt{2\pi}} \int_x^\infty e^{-\frac{t^2}{2}} dt \quad (9)$$

The covariance matrices P_n describing the error in the sub filters, defined as

$$P_n = E [\delta x_n \delta x_n^T] \quad (n=1, N) \quad (10)$$

is calculated as

$$P_n = S_n \sigma_{pr}^2 S_n^T \quad (n=1, N) \quad (11)$$

At detection (see Figure 1) the separation between the full filter and the sub filter is D_n . The distribution of the actual horizontal position versus the subfilter position is described by P_n . A stringent upper bound of the error variance along the direction of the separation D_n is given by the maximum eigenvalue λ^{P_n} . The error bound a_n corresponding to the missed detection probability p_{md} is

$$a_n = \sqrt{\lambda^{P_n}} Q^{-1}(p_{md}) \quad (12)$$

a_n and D may act in different directions (see Figure 1) but an upper limit on the full filter position error at detection is given by $D + a_n$.

The horizontal integrity limit (also referred to as the horizontal protection limit HPL) is then

$$HIL_{cov} = \max \{ D_n + a_n \} \text{ over } n=1, N \quad (13)$$

The horizontal integrity limit HIL_{par} calculated using the current Honeywell parity space algorithm and the covariance based horizontal integrity limit HIL_{cov} are both plotted in Figure 2.

meters

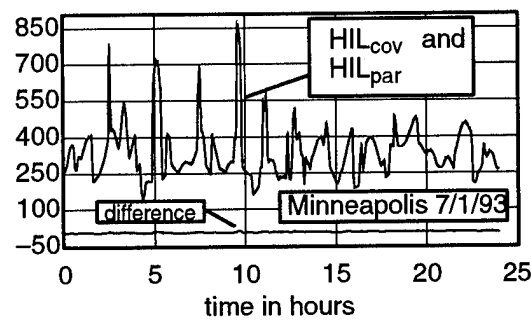


Figure 2

It is an important finding that these HIL's although calculated by fundamentally different algorithms employing seemingly different upper bound approximations are nearly identical.

GENERALIZATION TO BANK OF KALMAN FILTERS

When integrating inertial systems with GPS the complexity of the inertial dynamics suggests Kalman filter based implementations. The major difference between the covariance based RAIM algorithm and the parity space algorithm is that it is possible to generalize the former to Kalman filter based GPS implementations. As pointed out in reference 5 and 6 the integrity assurance will require a separate sub Kalman filter for each satellite. In order to rigorously incorporate the basic FD requirements this paper proposes that a sub filter and a covariance propagator are assigned to each tracked satellite. The sub filter is a straight forward Kalman filter producing a position solution with one satellite excluded. The covariance propagator calculates the statistics of the separations between the full filter and the subfilters.

The rationale for this is as follows. Assume that the state vector (see Appendix 1) for the full solution is $\Delta x_0(t)$ and the corresponding covariance matrix is $P_0(t)$. Usually the dimension of the state vector will be at least 18 so P_n is at a minimum an 18×18 matrix. The dependence of time is included to emphasize that the (positioning) filtering occurs over time as opposed to the least square snap shot solution discussed in the previous section. N sub Kalman filters with covariance matrices $P_n(t)$ excluding satellite n and providing solutions $\Delta x_n(t)$ are generated. The N solution separations $\delta x_n(t)$ are calculated

$$\underline{dx}_n(t) = \underline{\Delta x}_0(t) - \underline{\Delta x}_n(t) \quad (14)$$

The covariance propagator calculates the covariance matrix $dP_n(t)$ describing the statistics of the separations between the full filter and the sub filters .

$$dP_n(t) = E[(\underline{\Delta x}_0(t) - \underline{\Delta x}_n(t)) (\underline{\Delta x}_0(t) - \underline{\Delta x}_n(t))^T] \quad (15)$$

For each satellite measurement that is processed this calculation utilizes the Kalman gain vector g_n from the n^{th} subfilter and the gain vector g_0 from the full filter to create the $2N \times 2N$ covariance matrix $P_n^{\text{dual}}(t)$. This is further described in Appendix 2. The covariance matrix $P_n^{\text{dual}}(t)$ can be partitioned as

$$P_n^{\text{dual}}(t) = \begin{bmatrix} P_0(t) & \text{cross corr} \\ \text{cross corr} & dP_n(t) \end{bmatrix} \quad (16)$$

The separation statistics are described by $dP_n(t)$.

THRESHOLD SETTING AND HORIZONTAL INTEGRITY LIMIT

The matrix elements of interest are the elements representing the horizontal position separation and error statistics. The error state vector (see Appendix 1) will carry these in position 7 and 8. Using the results from the previous section the two maximum eigenvalues are determined. $\lambda^{dP_n}(t)$ is calculated from the covariance matrix elements $dp_n(7,7)$, $dp_n(7,8)$, $dp_n(8,8)$ describing the statistics of the filter separations in the horizontal plane. $\lambda^{P_n}(t)$ is calculated from the covariance matrix elements $p_n(7,7)$, $p_n(7,8)$, $p_n(8,8)$ describing the statistics of the sub filter position error.

For each subfilter a discriminator is defined as

$$d_n = \sqrt{(\Delta x_0(7) - \Delta x_n(7))^2 + (\Delta x_0(8) - \Delta x_n(8))^2} \quad (17)$$

and a variable threshold $D_n(t)$ is set based on the current subfilter versus full filter separation statistics represented by the upper bound variance $\lambda^{dP_n}(t)$ in full correspondence with equation 8 .

$$D_n(t) = \sqrt{\lambda^{dP_n}(t)} Q^{-1}\left(\frac{p_{id}}{2N}\right) \quad (18)$$

Likewise an upper bound on the subfilter error, commensurate with the missed detection probability, is calculated as

$$a_n(t) = \sqrt{\lambda^{P_n}(t)} Q^{-1}(p_{md}) \quad (19)$$

In analogy with equation 13 it now follows that the horizontal integrity limit for the GPS/inertial hybrid system is

$$HIL_{hyb} = \max \{ D_n(t) + a_n(t) \} \text{ over } n=1,N \quad (20)$$

The simulated HIL_{hyb} for a 2nmi/h inertial system is plotted in Figure 3 versus the snap shot based HIL_{par} . The time step is 120 s between each set of satellite measurement updates. The HIL_{hyb} grows between the Kalman filter measurement updates due

to the uncertainty in the estimated error states. This will cause a saw-tooth appearance.

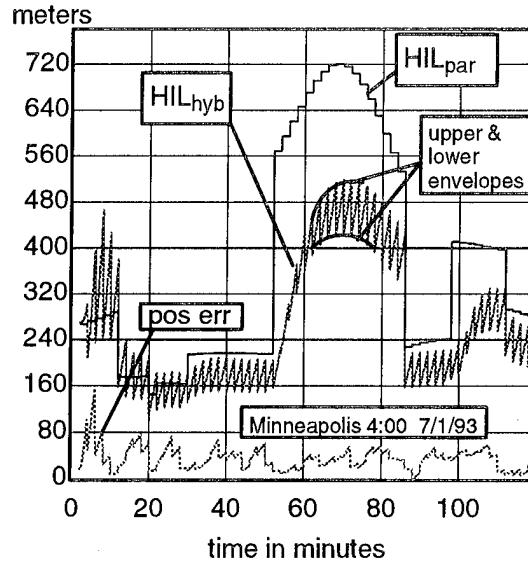


Figure 3

Just after 50 min (4:50) a 0.3 nmi integrity hole occurs and the snap shot RAIM HIL_{par} goes up to 560 m. The subfilters (in particular the subfilter representing the worst case satellite impact as shown in Figure 3) will be unaffected by any failure in this excluded satellite and will make use of the optimal estimates of the inertial error states in combination with additional measurements from satellites now in a less favorable geometry, to carry the truth reference through this integrity hole. In this particular case the hybrid integrity limit will stay below the 550 m required for non precision approach (NPA). The approach suggested in this paper for determining the availability of the hybrid integrity is to demonstrate first, that HIL_{hyb} (lower envelope) is always less than HIL_{par} and second, (as demonstrated in Figure 3) determine for each RAIM integrity hole if the hybrid integrity will meet the alert limit for the particular phase of flight under consideration.

The growth in HIL_{hyb} between Kalman corrections causes a variation in the corrected and uncorrected HIL of up to 80 m (width of saw-tooth pattern). The reason measurements are taken 2 min apart is that such SA samples can be assumed to be uncorrelated. The 2 min sample time is also related to the capacity of the on board hybrid computer and results in an acceptable CPU load. Theoretically though, since GPS measurements are available every second, nothing would prevent a series of independent banks of filters, shifted in time , all using a 2 min time step, that provided fully Kalman corrected error states every 5 seconds. Availability results will therefore be provided both for the upper envelope and for the lower envelope. If further SA modelling details in addition to the 2 min decorrelation assumption, such as the second order characteristics of the dither, are pursued the sub filters in this approach can be extended with

additional SA states which would allow the update time to be shortened to seconds. However, to ensure compliance with available SA information the results in this investigation are based on the the 2 min SA decorrelation only i.e. no further assumptions regarding the dynamics of the SA dither are utilized.

The simulation program that produced the result in Figure 3 containing the bank of the hybrid sub filters and covariance propagators used for detection and HIL calculations is modelling the airplane dynamics and runs with a 0.1 s time step. The number of integrity holes with a 5° mask angle ranges from 5349 for 24 satellites to 23687 for 21 satellites. Due to time constraints it is currently not possible to run this high fidelity simulation for all integrity holes. One major result of this paper is the characterization of the basic effects responsible for the hybrid integrity and the creation of a simplified model that approximately predicts the coasting performance demonstrated in Figure 3. This simplified model will use a 2 min time step and will run fast enough to be used for the availability determination.

Typical sensor errors for a 2 nmi/h inertial system are summarized in Table 3.

gyro random walk	0.003 °/h ^{1/2}
gyro bias	0.008 °/h
gyro scale factor	5 ppm
gyro misalignment	17 arcsec
accel bias	80 µg
accel scale factor	300 ppm
accel misalignment	17 arcsec

Table 3

SCHULER FEEDBACK, GRAVITY FEEDBACK AND COASTING

In order to create a simplified model the basic effects that provide the hybrid integrity enhancements were determined. An extensive simulation effort has rank-ordered the effects as follows.

1	Inertial coasting
2	Vertical gravity/Schuler feedback coupling
3	Vertical gravity feedback/clock coupling
4	Schuler feedback/clock coupling

Note that the effect responsible for the estimation of SA biases in a Kalman filter using separate bias states for each satellite is due to the satellite motion and is not related to any inertial effect. Such bias estimation requires long term stability of the SA biases. There is currently no DOD or FAA endorsed SA bias specification available.

Inertial Coasting

Inertial coasting is the main contributor to integrity. For any single satellite failure there is always at least one subfilter that has been calibrated for a long time with measurements that are completely unaffected by this satellite failure. Even if the failure has been in progress over a long time the subfilter is still providing a true reference for integrity monitoring. Inertial coasting was illustrated in Figure 3.

Schuler Feedback/clock coupling

Any horizontal position error will induce a velocity error which in turn will reduce the position error and subsequently reverse the sign of the initial error. A clock phase error will have different dynamic characteristics. The hybrid sub Kalman filters can use such characteristics to reduce the position error over time even if only 3 satellites in good geometry are available in each sub filter. Due to the gyro drift and the unfavorable correlations created during alignment the integrity limit that can be obtained based on this effect by a 2 nmi/ h system using only 4 satellites, is about 56,000 m (30 nmi).

Vertical Gravity Feedback/clock coupling

An inertial system incorporates a gravity model. The accuracy of this model is reflected in the gravity anomaly and deflection first order processes in Table 2. The gravity model includes a height (h) dependence based on the familiar inverse square law. An offset in altitude will cause a residual z-acceleration. The relation between the residual acceleration and the height offset is (see Appendix 1)

$$dg = -2/R g(0) dh \quad (21)$$

In a stationary application the height can be measured by processing the z-accelerometer outputs. In a dynamic application the vertical channel is inherently unstable. If the vertical channel is combined with a receiver clock model using a 0.1 m/s/√s random walk in clock frequency (6 state model) and measurements are performed that observe the sum of vertical position and clock phase error, the different characteristics of the clock and the gravity feedback allows the Kalman filter to pull in the vertical position and clock phase error to about 2500 m (1σ). This limit depends strongly on the clock performance but not much on z-accelerometer accuracy in the interval 40 – 300 µg.

Vertical Gravity/Schuler feedback coupling

To demonstrate this coupling effect the vertical channel using a 40 µg z-accelerometer and the clock (6 states) are combined with the Schuler dynamics of one of the horizontal channels (6 states) in a 12 state Kalman filter. Measurements that are the sum of the vertical position and the clock phase error combined with measurements that are the sum of the lateral position and the same clock phase error, are performed. The vertical position error will be pulled in to about 300 m (1σ). This result is not sensitive to the clock performance but is strongly related to the z-accelerometer accuracy. The Kalman filter was able

to eliminate the clock phase error due to the radically different dynamics of the vertical and horizontal channels. The hybrid Kalman filter will automatically incorporate this type of information. This means that integrity below 1 nmi can be established with only 4 satellites (in good geometry) in view and no altitude aiding. It can be demonstrated that an accurate z-accelerometer is approximately equivalent to an altitude measurement. The z-accelerometer versus altitude (1σ) accuracy relation is summarized in the table below.

accel	300 μ g	100 μ g	40 μ g	20 μ g
altitude	920 m	420 m	300 m	280 m

ALTITUDE AIDING

Further benefits are provided by baro corrected altitude (50 m 1σ accuracy) and calibrated pressure altitude (150 – 250 m 1σ). The bank of Kalman filters and covariance propagators automatically incorporates pressure altitude aiding. This is required in order to assure stability of the solution if satellites are temporary lost. Since every subfilter has its own private pressure altitude bias unaffected by the excluded satellite the integrity of the bias correction is automatically protected. For a 2 nmi/h system the benefit of altitude aiding (calibrated or baro corrected) will exceed any of the inertial coupling effects described except in special circumstances when pressure altitude calibration has not yet been performed and baro corrections are not available.

SIMPLIFIED MODEL

Availability is calculated by using a world wide grid of test points combined with time sampling over 24 hours. The grid elements are 180 nmi \times 180 nmi in size and the time step used is 5 min. The total number of time-space points N_{tot} is 681,120. For each of the 4 constellations, indexed by $i = 0,3$, in Table 1, the integrity limit calculated at each time-space point is compared to the alert limit. The number of time-space points where the integrity limit is less than the alert limit is N_i . The weights in Table 1 are denoted w_i ($i=0,3$). The availability A is calculated as

$$A = \sum_{i=0}^3 w_i \frac{N_i}{N_{tot}} \quad (22)$$

The location, time and duration of all contiguous integrity holes are stored on disc for each of the 4 constellations. To investigate the availability of augmentations involving calibration such as pressure altitude aiding, atomic clock aiding and hybrid GPS/Inertial filtering, only the holes are run with allowance for sufficient calibration time before the hole

starts. The number of holes is considerable and a simplified HIL_{hyb} model as described below has been developed for this purpose.

It is a known fact that GPS/Inertial Kalman filters can be designed either to process pseudo ranges or position information from a GPS receiver. Even if the latter methods is not theoretically correct since position errors in the north and east directions sometimes are correlated, it usually works. In the simplified approach equations 1 and 2 are used to create the full least square solution Δx_0 and the sub least square solutions Δx_n (one for each excluded satellite n). The subsolution covariance matrix P_n (equation 10) and associated worst case variance λ^{Pn} as well as the separation covariance matrix dP_n (equation 7) and the associated worst case variance λ^{dPn} are calculated. A bank of 6 state Kalman filters and 6 state covariance propagators are used to model the inertial dynamics in the (horizontal) direction of the worst case variances as provided by the least square sub solutions and least square separations. The 6 state vector is chosen as (see Appendix 1).

$$\Delta x^T = (\psi_y^L, \Delta v_x^L, \Delta r_x^L, \Delta \omega_{oy}^B, \Delta a_{ox}^B, \Delta v_x) \quad (23)$$

The Kalman filter measurement is defined by

$$h^T = (0,0,1,0,0,0) \quad (24)$$

The covariance matrix generated by the 6 state sub filter is $P_n^a(k)$. At the beginning of the availability run $P_n^a(k)$ is initialized with a 300 m position sigma, 0.1 m/s velocity sigma and a 0.1 mrad attitude sigma and sensor errors (1σ) are initialized according to Table 3. The element $P_n^a(3,3)$ approximates the worst case variance λ^{Pn} of the hybrid sub filter. The covariance matrix generated by the covariance propagator is $dP_n^a(k)$. This matrix is initialized to 0 and $dP_n^a(3,3)$ corresponds to the worst case variance λ^{dPn} of the hybrid covariance propagator. The horizontal integrity limit HIL_{hybavl} is calculated (following equations 8–13) as

$$HIL_{hybavl} = \max \{ D_n + a_n \} \text{ over } n=1,N \quad (25)$$

Where

$$D_n = \sqrt{dP_n^a(3,3)} Q^{-1} \left(\frac{P_{td}}{2N} \right) \quad (26)$$

$$a_n = \sqrt{P_n^a(3,3)} Q^{-1}(p_{md}) \quad (27)$$

The logic used for initializing and releasing these 6 state filters and covariance propagators as satellites are lost and gained, is the same as for the complete hybrid integrity filters and propagators (see Appendix 2). The performance of the simplified model is demonstrated in Figure 4 without pressure altitude aiding active.

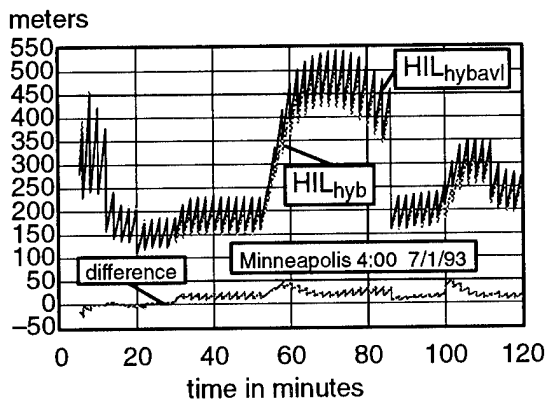


Figure 4

The simplified model accurately reflects the essential dynamics of the hybrid horizontal integrity limit. This demonstrates that the basic effects involved are understood.

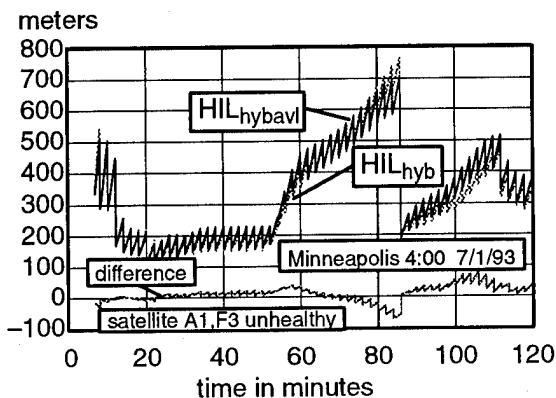


Figure 5

In Figure 5 two satellites are set unhealthy and pressure altitude aiding is incorporated in the simplified model. In each subfilter this is done by including an altitude measurement with an associated sigma σ_{altb} that is calibrated to $\sigma_{altb} = \text{VDOP}(\text{pure GPS}) \times \sigma_{pr} \times \text{fac}$ when the condition

$$\text{VDOP}(\text{pure GPS}) \times \sigma_{pr} \times \text{fac} < \sigma_{altb}$$

is met. σ_{altb} is propagated in compliance with FAA TSO-C129. The factor fac (= 4), compensating for the non white character of the calibrated bias, is determined by matching HIL_{hybavl} with HIL_{hyb} . In this case the NPA integrity hole was of a type that can not be overcome by pressure altitude aiding and coasting in combination.

Although the complete model can incorporate bias states the simplified model has not yet been refined to do so. The availability results presented assumes that the SA noise is dithered.

AVAILABILITY RESULTS

The simplified model has been used to determine the availability of the hybrid integrity. The simplified model is run through each registered integrity hole and allowed 1 hour of calibration. Credit is given for any 2 min interval with HIL_{hybavl} below the alert limit. The results without pressure altitude aiding are given in Table 4.1 and 4.2.

When using the lower envelope and a 2° mask angle the results are:

constellation	0.3 nmi	0.6 nmi	1 nmi	2 nmi
24	0.99992	1.00000	1.00000	1.00000
23	0.99809	0.99993	1.00000	1.00000
22	0.99481	0.99966	1.00000	1.00000
21	0.96900	0.99535	0.99920	0.99998
weighted	0.99876	0.99990	0.99999	1.00000

Table 4.1

For the remaining combinations the weighted averages are:

mask,type	0.3 nmi	0.6 nmi	1 nmi	2 nmi
2°,upper	0.99729	0.99981	0.99998	1.00000
5°,lower	0.99524	0.99945	0.99995	1.00000
5°,upper	0.99015	0.99898	0.99989	1.00000

Table 4.2

The impact of calibrated pressure altitude aiding in combination with coasting are presented in Table 5.

mask,type	0.3 nmi	0.6 nmi	1 nmi	2 nmi
2°,lower	0.99966	0.99998	1.00000	1.00000
2°,upper	0.99896	0.99997	1.00000	1.00000
5°,lower	0.99831	0.99989	0.99998	1.00000
5°,upper	0.99557	0.99982	0.99998	1.00000

Table 5

The results for baro corrected pressure altitude aiding in combination with coasting are presented in Table 6. $\sigma_{altb} = 50$ m as recommended in FAA TSO-C129.

mask,type	0.3 nmi	0.6 nmi	1 nmi	2 nmi
2°,lower	0.99992	1.00000	1.00000	1.00000
2°,upper	0.99980	1.00000	1.00000	1.00000
5°,lower	0.99962	0.99997	1.00000	1.00000
5°,upper	0.99910	0.99995	0.99999	1.00000

Table 6

The following augmentations are included to provide trade off reference data.

Basic GPS:

This is the availability averaged over the constellations in Table 1 with no augmentation.

mask	0.3 nmi	1 nmi	2 nmi	5 nmi	10 nmi
2°	0.98849	0.99932	0.99978	0.99992	0.99996
5°	0.96686	0.99702	0.99882	0.99954	0.99972

Calibrated pressure altitude:

Calibration of the pressure altitude bias only occurs when the vertical integrity limit VIL satisfies

$$VIL/3 < \sigma_{altb}$$

where σ_{altb} is the current predicted pressure altitude bias error 1σ . The time propagation of σ_{altb} adheres to the requirements in FAA TSO-C129. An Integrity based calibration of this type is currently mandated by the RTCA SC-159.

mask	0.3 nmi	1 nmi	2 nmi	5 nmi	10 nmi
2°	0.99416	0.99990	0.99998	0.99999	1.00000
5°	0.97968	0.99940	0.99986	0.99996	0.99998

Exact and fault free altitude:

The altitude is known without noise or faults and can therefore be eliminated in the RAIM algorithm. This provides an upper availability bound for any altitude aiding augmentation.

mask	0.3 nmi	1 nmi	2 nmi	5 nmi	10 nmi
2°	0.99928	0.99999	1.00000	1.00000	1.00000
5°	0.99672	0.99987	0.99996	0.99999	0.99999

Calibrated atomic clock:

Calibration of the atomic clock phase only occurs when the time integrity limit TIL satisfies

$$TIL/3 < \sigma_{phase}$$

where σ_{phase} is the current predicted clock phase error 1-sigma . The time propagation of σ_{phase} corresponds to a 10^{-11} frequency stability.

mask	0.3 nmi	1 nmi	2 nmi	5 nmi	10 nmi
2°	0.99866	0.99996	0.99999	1.00000	1.00000
5°	0.99306	0.99976	0.99992	0.99998	0.99999

Exact and fault free clock:

The clock phase is known without noise or faults and can therefore be eliminated in the RAIM algorithm. This provides an upper availability bound for any clock aiding augmentation.

mask	0.3 nmi	1 nmi	2 nmi	5 nmi	10 nmi
2°	0.99965	0.99999	1.00000	1.00000	1.00000
5°	0.99771	0.99988	0.99996	0.99999	0.99999

Pressure altitude aiding and inertial HIL coasting:

A reference solution that has been assured by pressure altitude aided RAIM is propagated based on uncalibrated inertial information. The HIL is propagated through the integrity holes based on a predetermined Schuler based drift profile that reflects

the 2 nmi/h performance. This type of inertial augmentation is currently the subject of RTCA SC-159 WG 3.

mask	0.3 nmi	1 nmi	2 nmi	5 nmi	10 nmi
2°	0.99416	0.99990	0.99998	1.00000	1.00000
5°	0.97968	0.99940	0.99986	0.99998	1.00000

TESTING AND CERTIFICATION

The following off line tests in combination with formal verification of simulation model versus actual system are proposed for the hybrid integrity approach presented in this paper.

1/

Verify the missed detection probability by simulating 5000 failures (see RTCA DO-208). If no assumptions about the dynamics of the failure have been used in the derivation of the horizontal integrity limit or in the Kalman filters, as was the case for the algorithm presented, it is sufficient to use ramp failures. If the calculation of the integrity limit is based on the assumption that the failure growth is a ramp (linear) other types such as parabolas etc. must be included in the test. The missed detection probability for the presented algorithm has been verified in 1000 ramp tests.

2/

Verify the false detection rate by lowering the internal detection threshold and perform 5000 runs to assure that the false detection rate corresponds to the predicted value based on this modified threshold and assumptions about the simulated SA noise. This was done for the presented algorithm and it was verified using 33.3 m (1σ) white noise SA that the false detection rate was correctly predicted. With the 2 state SA dither model the false detection rate was about 8 times too high. This indicates that the FAA/RTCA SC-159 assumption that SA samples taken 2 min apart can be considered uncorrelated is not met for the recommended test model (see reference 1). However, the RTCA assumption that real SA samples taken 2 min apart are uncorrelated is used throughout this paper.

3/

Show by analysis and simulation that the hybrid integrity limit (lower envelope) always will be better than the normal parity space based RAIM algorithm. This was done by demonstrating that the hybrid integrity limit is obtained by providing the snap shot based separation and positioning variances as the measurement variances used by the simplified 6 state covariance propagators and Kalman filters. Any Kalman filter with calibration capability will reduce the variance of the white noise measurement variance.

4/

Use the parity space based RAIM algorithm to identify integrity holes. Record the location, time and duration

of these holes. Demonstrate the claimed availability by using either a high fidelity model of the complete hybrid bank or a verified simplified model to show that the outage time accumulated over all holes corresponds to the claimed availability.

5/

Demonstrate by simulation that the impact of airplane dynamics such as holding patters are properly incorporated when calculating the horizontal integrity limit.

It is also recommended that the inertial performance is constantly monitored based on GPS for a system in service and that any observed significant statistical deviation from the model used for the integrity calculations is flagged as a fault.

CONCLUSIONS

It was demonstrated that inertial effects such as coasting can be used to enhance the integrity provided by receiver autonomous integrity monitoring (RAIM). Primary means detection capability is achievable for the enroute and oceanic phases of flight. By using an accurate z-accelerometer or altitude aiding, primary means detection capability can most likely be achieved in the terminal phase as well. Depending on the mask angle used and the capacity of the embedded CPU an availability of failure detection in the range 0.995 – 0.9996 is expected for 0.3 nmi and 0.9998 – 0.99998 for 0.6 nmi when calibrated pressure altitude aiding is used. The availability is 0.9991 – 0.99992 for 0.3 nmi and 0.99995 – 1.00000 for 0.6 nmi when baro corrected altitude is used. The 0.99999 availability proposed for sole means GPS non precision approach (0.3 nmi) is not readily obtainable. These results assume that SA is dithered and that the 2 min SA decorrelation time is valid. Similar results can be obtained with SA biases present but if there are slower frequency components not meeting the 2 min decorrelation time nor the constant bias characteristics, more investigations and further information about SA are needed. Primary means capability also requires exclusion. Although the bank of Kalman filters and covariance propagators presented can be extended to perform exclusion for favorable geometries a rigorous investigation of exclusion availability is not yet available.

APPENDIX 1 : INERTIAL MODELING

The inertial error model used is summarized below. All errors are referenced to the local vertical coordinate frame L.

$$\begin{aligned}\dot{\psi}^L &= \hat{C}_B^L \Delta\omega_{IB}^B + \psi^L \times (\hat{\omega}_{IE}^L + \hat{\omega}_{EL}^L) \\ \dot{\Delta v}^L &= \psi^L \times \hat{C}_B^L a_{raw} + \hat{C}_B^L \Delta a_{IB}^B + (2 \hat{\omega}_{IE}^L + \hat{\omega}_{EL}^L) \times \Delta v^L +\end{aligned}\quad (28)$$

$$+ \begin{bmatrix} -g(0)/R^{[1]} & 0 & 0 \\ 0 & -g(0)/R^{[1]} & 0 \\ 0 & 0 & 2g(0)/R^{[2]} \end{bmatrix} \Delta r^L + \Delta g^L \quad (29)$$

$$\dot{\Delta r}^L = \Delta v^L + \hat{\omega}_{EL}^L \times \Delta r^L \quad (30)$$

Where

$\Delta\omega_{IB}^B = \Delta\omega_0^B$ + scale factor and misalignment errors

$\Delta a_{IB}^B = \Delta a_0^B$ + scale factor and misalignment errors

ψ^L Attitude error in local vertical frame L.

Δv^L Velocity error in L frame.

$\hat{\omega}_{IE}^L$ Estimated rotation of earth fixed frame E versus inertial frame I transformed to L frame.

$\hat{\omega}_{EL}^L$ Estimated rotation of local vertical frame L versus earth fixed frame E transformed to L frame.

$\Delta\omega_0^B$ Gyro biases modelled as first order Markov processes with a 100 h time constant.

Δa_0^B Accelerometer biases modelled as first order Markov processes (100 h)

a_{raw} Measured raw acceleration in body frame B.

ω_{raw}^L Measured raw angular velocity in body frame B.

\hat{C}_B^L Transformation matrix from body frame B to local vertical frame L.

Δg^L Gravity deflections and anomaly ($v_x g$, $v_y g$, Δg_z)

R Earth radius.

$g(0)$ Gravity at zero height.

In addition since the vertical channel needs pressure altitude support for stability the pressure altitude bias $\Delta altb$ is included. This bias is modelled as a first order Markov process with a 10,000 s time constant. Since pseudorange is measured, the receiver clock also needs to be included. The two states used are the clock phase error Δrtc expressed as a distance and the clock frequency error Δvfc expressed as a velocity. The terms that affect integrity are marked in the error model. [1] indicates the two terms that are responsible for the Schuler feedback. [2] indicates the term responsible for the vertical gravity feedback. The error state vector used in the basic hybrid filters has the following 18 states.

$$\Delta x^T = (\psi^L, \Delta v^L, \Delta r^L, \Delta rtc, \Delta vfc, \Delta\omega_0^B, \Delta a_0^B, \Delta altb) \quad (31)$$

The coasting capability is provided by the continuous estimation of these error states. If SA biases are considered this state vector can be extended with up to 12 additional states Δp_{SA} that represent the bias part of SA yielding a total of 30 states.

APPENDIX 2 : THE HYBRID INTEGRITY KALMAN FILTERS AND COVARIANCE PROPAGATORS

The inertial model is linearized and the time propagation of the error states of the full filter ($n=0$) and subfilters ($n=1, N$) can be expressed in time discrete form ($T=2$ minutes) as

$$\Delta \underline{x}_n(k+1) = \Phi(k) \Delta \underline{x}_n(k) \quad (32)$$

The error $\delta \underline{x}_n(k)$ in the propagated estimate versus the actual inertial offset $\underline{\tilde{x}}(k)$ ($\delta \underline{x}_n(k) = \Delta \underline{x}_n(k) - \underline{\tilde{x}}(k)$) is propagated as

$$\delta \underline{x}_n(k+1) = \Phi(k) \delta \underline{x}_n(k) + \underline{v}(k) \quad (33)$$

Here $\underline{v}(k)$ is the process noise, $Q(k) = E[\underline{v}(k) \underline{v}(k)^T]$. The full filter and the subfilter covariances are propagated and updated according to the standard Kalman recipe.

The covariance time propagation is

$$P_n(k+1) = \Phi(k) P_n(k) \Phi(k)^T + Q(k) \quad (34)$$

For each GPS measurement except the n^{th} do the following

$$\underline{g}_n = P_n(k) \underline{h} / (\underline{h}^T P_n(k) \underline{h} + r) \quad (35)$$

$$P_n(k) = P_n(k) - \underline{g}_n \underline{h}^T P_n(k) \quad (36)$$

\underline{h} defines what error states that are involved in the GPS measurement. r is the measurement noise variance $r = E[w^2] = \sigma_{pr}^2$.

$$\underline{h}^T = (0, 0, -\underline{\text{los}}^L, 1, 0, 0, 0, 0) \quad (37)$$

$\underline{\text{los}}^L$ is the line of sight vector to the satellite. The covariance propagator keeps track of the statistics of the separation $\underline{dx}_n(k) = \Delta \underline{x}_0(k) - \Delta \underline{x}_n(k)$ by forming a state vector

$$\underline{\delta X}(k) = \begin{bmatrix} \delta \underline{x}_0(k) \\ \underline{dx}_n(k) \end{bmatrix} \quad (38)$$

This vector is time propagated as

$$\begin{bmatrix} \delta \underline{x}_0(k) \\ \underline{dx}_n(k) \end{bmatrix} = \begin{bmatrix} \Phi(k) & 0 \\ 0 & \Phi(k) \end{bmatrix} \begin{bmatrix} \delta \underline{x}_0(k) \\ \underline{dx}_n(k) \end{bmatrix} + \begin{bmatrix} \underline{v}(k) \\ 0 \end{bmatrix} \quad (39)$$

resulting in a covariance propagation

$$P_n^{\text{dual}}(k+1) = \begin{bmatrix} \Phi(k) & 0 \\ 0 & \Phi(k) \end{bmatrix} P_n^{\text{dual}}(k) \begin{bmatrix} \Phi(k)^T & 0 \\ 0 & \Phi(k)^T \end{bmatrix} + \begin{bmatrix} Q(k) & 0 \\ 0 & 0 \end{bmatrix} \quad (40)$$

For each satellite measurement except the n^{th} the covariance vector is updated based on

$$\begin{bmatrix} \delta \underline{x}_0(k) \\ \underline{dx}_n(k) \end{bmatrix} = \Phi \begin{bmatrix} \delta \underline{x}_0(k) \\ \underline{dx}_n(k) \end{bmatrix} + \Gamma w \quad (41)$$

with

$$\Phi = \begin{bmatrix} I - \underline{g}_0 \underline{h}^T & 0 \\ (\underline{g}_n - \underline{g}_0) \underline{h}^T & I - \underline{g}_n \underline{h}^T \end{bmatrix} \quad \text{and} \quad \Gamma = \begin{bmatrix} \underline{g}_0 \\ \underline{g}_n - \underline{g}_0 \end{bmatrix}$$

Resulting in a covariance update yielding

$$P_n^{\text{dual}}(k) = \Phi P_n^{\text{dual}}(k) \Phi^T + \Gamma r \Gamma^T \quad (42)$$

P_n and dP_n contain all information about the 2 dimensional elliptical distributions in the horizontal plane.

Special rules apply to the initialization and release of the sub filters and propagators to assure that a satellite failure in the excluded satellite can never affect the subfilter associated with this satellite and that at least one subfilter is kept that is always unaffected by any satellite failure. When a new satellite is providing measurements a new subfilter is initialized with the full filter solution which is unaffected by any failure in this new satellite. When the pseudo range measurements from a satellite are lost and the corresponding sub filter is to be released, special logic will assure that the impact of a failure in this satellite is not propagated in the remaining subfilters. This is done by delaying the release of any subfilter until the HDOPs of all subfilters are below a predetermined threshold for at least 5 minutes.

ACKNOWLEDGMENTS

The assistance of Randy Reuter for compiling the availability numbers was crucial to the timely completion of this paper.

REFERENCES

1. RTCA paper no. 148-93/SC159
2. R. Grover Brown and Paul W. McBurney, Self-Contained GPS Integrity Check Using maximum Solution Separation, Navigation: Journal of The Institute of Navigation Vol. 35 No 1. Spring 1988.
3. Mats A. Brenner, Implementation of a RAIM Monitor in a GPS Receiver and an integrated GPS/IRS, Proceedings of the ION Third International Technical Meeting, Colorado Springs 1990.
4. J-M Durand GPS availability- Part I, Proceedings of the ION third International Meeting, Colorado springs 1990.
5. R. G. Brown and P. Y. C. Hwang, GPS Failure Detection by Autonomous Means Within the Cockpit, Navigation: Journal of The Institute of Navigation Vol. 33 No 4. Winter 1986-1987.
6. Dr. John Diesel, A New Approach to GPS Integrity/Availability, Proceedings of the ION Seventh International Technical Meeting, Salt Lake City 1994.
7. RTCA paper no. 308-94/SC159-544 (Results from Aerospace Corp. JPO study)

GPS/IRS AIME: Calculation of Thresholds and Protection Radius Using Chi-Square Methods

Dr. John Diesel and Sherry Luu
Litton Aero Products

BIOGRAPHY

Dr. John Diesel is presently a scientist at Litton Aero Products. He holds several patents, and has published several technical papers on navigation and control systems. He received the PhD. in E. E. and Mathematics from Washington University in St. Louis in 1959, and is a member of Sigma Xi.

Ms. Sherry Luu is a senior engineer at Litton Aero Products. She is currently working on IRS/GPS integration, and has been responsible for much of the C language programming in Litton's latest IRS software mechanizations. She received a B. S. in Computer Science from California State University at Northridge.

ABSTRACT

A mathematical justification for AIME is developed, and it is compared with the mathematical justification for RAIM. It is seen that the mathematical bases for the two approaches is essentially the same. The test statistic for AIME is based on the residuals in the innovations process of the Kalman filter, rather than the residuals from the instantaneous "snapshot" least squares solution used in RAIM. This is logical since the Kalman filter residual is the difference between measured Pseudo Range to each satellite and the predicted Pseudo Range from the estimated solution, which is the least squares solution based on all past measurements.

Rather than the parity transformation used in RAIM, AIME transforms the residuals to the principal axes (eigenvectors) of the ellipsoid for the n dimensional normal distribution of the residuals. It is shown that any deterministic failure of a satellite leads to a non-central chi square distribution. This makes it possible to determine the exact probabilities for failure detection and exclusion on a single covariance run, which corresponds to an infinite number of Monte Carlo runs.

INTRODUCTION

Autonomous Integrity Monitored Extrapolation (AIME) is a software mechanization for integrating GPS with IRS to solve the GPS integrity/availability problem (References 1, 2). AIME can be used to achieve primary means of navigation for en-route, terminal area, and non-precision approach, without WAAS.

Using Kalman filter principles, AIME generates a least-squares solution based on the entire history of GPS measurements. There are 24 parameters estimated in each of the many parallel Kalman filters used in AIME, in addition to four parameters estimated separately. These include all of the significant user clock bias states, baro error states, and inertial error states. Also included are DC bias error states for each satellite. This means that once the integrity of a new satellite is established, only changes in the DC bias over 2.5 minute averaging intervals need be monitored to detect satellite failures.

At the request of RTCA Special Committee 159, Working Group 3A (GPS/INS), a mathematical basis for the AIME failure detection and exclusion (FDE) algorithm was developed. It is comparable to that used for the RAIM FDE, as developed by R. Grover Brown in Reference 3. The mathematical basis for RAIM is first reviewed in this paper. The corresponding mathematical basis for AIME is then presented, with corresponding equation numbers so that they can be compared step by step.

In RAIM, the instantaneous "snapshot" least squares residual vector is used to compute the test statistic. In AIME, the Kalman filter innovations process residual vector is used to compute the test statistic. In both cases, the test statistic is chi-square distributed, which is the basis for computing the failure detection and exclusion (FDE) probabilities.

RAIM FDE

(This review is a summary of the methods described by R. Grover Brown in Reference 3).

1. RAIM uses n satellite measurements y ($n \times 1$) to obtain a least squares estimate of four parameters x (4×1).

The four estimated parameters x are the errors in the three position coordinates, and the aircraft receiver clock bias, which have been obtained from previous estimates. The measurements y are the differences between measured pseudoranges and predicted ones, based on the previous estimates. The linearized relationship between y and x is:

$$y = G \cdot x + \epsilon \quad (R1)$$

where G ($n \times 4$) is a linear observation matrix, depending on satellite geometry. Its first three columns are the direction cosines to each of the satellites, and a column of ones corresponding to the receiver clock bias error. The measurement error ϵ ($n \times 1$) may have both random and deterministic parts.

Assuming $n > 4$, the least squares estimate is obtained as:

$$x_{LS} = (G^T G)^{-1} G^T y \quad (R2)$$

2. RAIM determines integrity from the range residual vector w ($n \times 1$).

The range residual vector is defined by first determining the measurement change y_{LS} ($n \times 1$) which results from the least squares fit solution:

$$y_{LS} = G \cdot x_{LS} \quad (R3)$$

The range residual vector w ($n \times 1$) is then the measurement difference:

$$w = y - y_{LS} = y - G \cdot x_{LS} \quad (R4)$$

3. Satellite failures are detected by using the magnitude of the parity vector p ($(n-4) \times 1$) as the test statistic.

The range residual vector is first transformed by the parity transformation P ($((n-4) \times (n))$):

$$p = P \cdot w \quad (R5)$$

The sum-squared residuals are then given by:

$$p^2 = p^T \cdot p = w^T \cdot w \quad (R6)$$

where p is the magnitude of the parity vector.

If there are no satellite failures, it is assumed that the random part of the measurement error ϵ is normally distributed with zero mean. The sum-squared residual p^2 (1×1) is chi-square distributed with $n-4$ degrees of freedom (DOF). The threshold p_D for detecting failures is selected from this distribution to result in the false alarm rate $P_{FA} = 10^{-5}$ /hour, assuming no satellite failures.

4. The effect of a deterministic range bias error b in the i th satellite is determined.

The parity vector resulting from this range bias error is given by:

$$dp_i = P \cdot b_i \quad (R7)$$

where vector b_i ($n \times 1$) has a b in row i , and zero elements elsewhere. The magnitude of this parity vector is denoted dp_i .

From Equation (R2) for the least squares solution, the effect of this same error b_i on the solution is given by:

$$dx_i = (G^T G)^{-1} G^T \cdot b_i \quad (R8)$$

The horizontal (radial) position error is obtained from the first two components, dx_{i1} , and dx_{i2} , of dx_i . The horizontal error dR_i is:

$$dR_i = (dx_{i1}^2 + dx_{i2}^2)^{1/2} \quad (R9)$$

The linear relationship between the horizontal error and the test statistic is given by the characteristic slope:

$$\text{SLOPE}(i) = dR_i / dp_i \quad (R10)$$

In this relationship, the assumed magnitude b of the original range bias error has cancelled out.

5. The test statistic p^2 resulting from both the random noise with zero mean and the deterministic bias error b is next considered.

This statistic has a non-central chi square distribution. When the corresponding horizontal error exceeds a specified protection level HPL, it is desired that this statistic exceed the threshold p_D so that the satellite failure is detected.

The critical bias p_{bias} is defined as the deterministic value of the test statistic which exceeds the detection threshold by a sufficient margin that the probability

P_{miss} of not exceeding the threshold is less than 0.001, when the random noise is added. The probability P_{miss} is also called the probability of missed detection.

6. The horizontal protection level (HPL) is determined.

The satellite whose failure is most difficult to detect is the one with the smallest test statistic when the horizontal limit exceeds the protection level. This is the satellite with the maximum slope, $\text{SLOPE}_{\text{max}}$, as computed in Equation (R10). The HPL is then computed as:

$$\text{HPL} = \text{SLOPE}_{\text{max}} \cdot P_{\text{bias}} \quad (\text{R11})$$

The value of p_{bias} is determined from the non-central chi-square distribution with $n-4$ degrees of freedom. It is the non-centrality parameter which results in a probability less than P_{miss} of p being less than the detection threshold p_D .

7. If a fault is detected, using 3 above, the faulty satellite is excluded.

This is done by selecting the j th subset of $n-1$ satellites with the smallest normalized test statistic. (Reference 4, Appendix K). However, for navigation to continue, the test statistic must be less than a 99.9% decision threshold. Also, the HPL_j based on this threshold must be less than the horizontal alert limit (HAL) for that phase of flight.

The reason the decision threshold can be temporarily reduced to the 99.9% level is that the false alarm rate is determined by the original fault detection threshold in 3 above. Once a fault is detected, the probability of failed exclusion is less than 0.001, using the reduced threshold, regardless of which satellite is faulty.

AIME FDE

Both the step numbers and the equation numbers in the following correspond to the respective numbers for RAIM above. By comparing the two approaches, it can be seen that the mathematical justification for them is essentially the same. In both cases, the probabilities for detection and exclusion are based on both the central and the non-central chi square distributions.

1. AIME uses (n_{xt}) satellite measurements $z(t)$ (n_{xt}) to obtain a least squares estimate of 24 parameters x (24×1)

The 24 estimated parameters are the error states $x(t)$ in a Kalman filter. The measurements $z(t)$ are the differences, at 1 Hz., between the measured pseudoranges and

predicted ones, based on the previous estimates. These measurements are pre-filtered by averaging over the Kalman filter cycle time ($t_k - t_{k-1}$) = 150 seconds (2.5 minutes). The linearized relationship between the averaged measurements z and the residual errors x is:

$$z(k) = H(k) \cdot x(k) + v(k) \quad (\text{A1})$$

where $H(k)$ ($n \times 24$) is an averaged observation matrix. The averaged measurement error $v(k)$ ($n \times 1$) may have both random and deterministic parts.

For any number of satellites $n > 0$, the least squares estimate is obtained as:

$$x^+(k) = x^-(k) + K(k) \cdot [z(k) - H(k) \cdot x^-(k)] \quad (\text{A2})$$

where $x^-(k)$ is the previous least square estimate.

2. AIME determines integrity from the residuals $r(k)$ ($n \times 1$) in the Kalman filter innovations process.

If $x^-(k)$ is the estimate of the error state before the updates at cycle k , the predicted measurement is

$$z^-(k) = H(k) \cdot x^-(k) \quad (\text{A3})$$

The Kalman filter residual (denoted Greek letter "nu" in the literature) is:

$$\begin{aligned} r(k) &= z(k) - z^-(k) \\ &= z(k) - H(k) \cdot x^-(k) \end{aligned} \quad (\text{A4})$$

The components of $r(k)$ have an n dimensional normal distribution with zero mean and known covariance:

$$\begin{aligned} E[r(k)] &= 0 \\ E[r(k) \cdot r^T(k)] &= V(k) \end{aligned}$$

where the covariance is:

$$V(k) = H(k) \cdot P^-(k) \cdot H^T(k) + R(k)$$

If there are no satellite failures and the Kalman filter model is correct, the residual vectors are independent for different k (the "innovations property", Reference 5). The innovations property can be expressed as:

$$E[r(j) \cdot r^T(k)] = 0, \text{ if } j \neq k$$

3. Satellite failures are detected by using the magnitude of the normalized residual vector s ($nx1$) as the test statistic.

Since the covariance matrix V is symmetric and positive definite, its eigenvectors l_j ($nx1$) are orthogonal, and its eigenvalues $d_j = \sigma_j^2$ are positive (Reference 6). Denoting the modal matrix by L (nxn), and the diagonal matrix of eigenvalues by D (nxn), the residuals are transformed by:

$$\begin{aligned} r &= L \cdot q \\ q &= D^{1/2} \cdot s \end{aligned} \quad (A5)$$

The test statistic is the normalized sum square of the normalized transformed residual s ($nx1$). In Appendix A it is shown that:

$$s^2 = s^T \cdot s = r^T \cdot V^{-1} \cdot r \quad (A6)$$

If there are no satellite failures, it is shown in Appendix A that s^2 is chi square distributed with n degrees of freedom (DOF). The threshold s_D for detecting failures is selected to result in the false alarm rate $P_{FA} = 10^{-5}$ /hour, assuming no satellite failures.

The innovations property makes it possible to detect very slow satellite drifts. This is done by estimating the mean of the residuals over a long time interval, to determine the averaged residual. To avoid contaminating the Kalman filter, both the measurements and residuals are stored in buffers for periods of 30 minutes or more.

Batch processing is used to determine the averages. Using the alternative form of the Kalman filter, the inverse covariance of the final estimate is obtained first:

$$V_{avg}^{-1} = \Sigma_k V^{-1}(k)$$

The estimate of the mean is then obtained as:

$$r_{avg} = (V_{avg}^{-1})^{-1} \cdot \Sigma_k V^{-1}(k) \cdot r(k)$$

The normalized sum-squared estimated mean residual is:

$$s_{avg}^2 = (r_{avg}^T \cdot (V_{avg}^{-1}) \cdot r_{avg})$$

As shown in Appendix A, this statistic has a central chi-square distribution if there is no failure. As shown in Appendix B, the distribution is non-central chi-square if there is a failure. By taking a long averaging interval, the covariance of the averaged residual becomes small. If there is a failure, the averaged residual does not become

small, so that the statistic becomes large. This makes it possible to detect very slow satellite failures.

4. The effect of a range bias error b in the i th satellite is determined.

The transformed residual ds_i ($nx1$) resulting from this range bias error is given by:

$$ds_i = D^{-1/2} \cdot L^T \cdot b_i \quad (A7)$$

where vector b_i ($nx1$) has a b in row i , and zero elements elsewhere. The magnitude of this transformed residual vector is denoted ds_i .

From equation (A2), the effect of this same error on the solution is given by:

$$dx_i^+(k) = K(k) \cdot b_i \quad (A8)$$

The horizontal (radial) position error is obtained from the first two components of dx_i . The horizontal error is:

$$dR_i = (dx_{i1}^2 + dx_{i2}^2)^{1/2} \quad (A9)$$

The linear relationship between the horizontal error and the test statistic is given by the characteristic slope:

$$\text{SLOPE}(i) = dR_i/ds_i \quad (A10)$$

In this relationship, the assumed magnitude b of the original range bias error has cancelled out.

5. The test statistic s^2 resulting from both the random noise with zero mean and the deterministic bias error b is next considered.

It is shown in Appendix B that this statistic has a non-central chi square distribution. The critical bias $ds = s_{bias}$ is defined as the deterministic value of the test statistic which exceeds the detection threshold by a sufficient margin that the probability P_{miss} of the total statistic not exceeding the threshold is less than 0.001, when random noise is added.

6. The horizontal protection level is determined.

The satellite whose failure is most difficult to detect is the satellite with maximum slope, SLOPE_{max} , as computed in Equation (A10). The HPL is:

$$\text{HPL} = \text{SLOPE}_{max} \cdot s_{bias} \quad (A11)$$

The value of s_{bias} is determined from the non-central chi-square distribution to give a probability less than P_{miss} of s being less than the detection threshold s_D .

7. If a fault is detected, using 3 above, the faulty satellite is excluded.

This is done by running a bank of n test Kalman filters in parallel with the least squares Kalman filter. Each of these test Kalman filters excludes a different satellite and uses a subset of $n-1$ satellites. If a failure is detected by the least squares filter, which uses all n satellites, the test Kalman filter with the smallest test statistic s_j is assumed to exclude the bad satellite.

For navigation to continue, this test statistic must be less than the 99.9% decision threshold. Also, the HPL_j for this threshold must be less than the HAL for that phase of flight.

CONCLUSIONS

Unlike RAIM, which only uses present measurements in a "snapshot" approach, AIME uses all present and past measurements to determine a least squares solution in a Kalman filter. This means that failure detection and exclusion does not require a minimum number of satellites in view. As a result, AIME can be used for primary navigation for all flight phases with a high availability.

To isolate and exclude failures, AIME uses parallel Kalman filters, each of which excludes different satellites. An additional filter is used to exclude baro or inertial failure modes. If a failure is detected using all satellites in view, the failure is isolated by comparing averaged residuals from each of the parallel Kalman filters.

REFERENCES

1. Diesel, J. W., "A New Approach to GPS Integrity/Availability: Immediate Global Sole Means Without WAAS", Proceedings of the ION GPS-94, Salt Lake City, Utah, September 20-23, 1994.
2. Diesel, J. W., and King, J., "Integration of Navigation Systems for Fault Detection, Exclusion, and Integrity Determination - Without WAAS", Proceedings of the ION National Technical Meeting, Anaheim, California, January 18-20, 1995.
3. Brown, R. Grover, "GPS RAIM: Calculation of Thresholds and Protection Radius Using Chi-Square Methods - A Geometric Approach", RTCA Paper No. 491-94/SC159-584, November 7, 1994.
4. "Minimal Operational Performance Standard for Global Positioning System/Wide Area Augmentation System Airborne Equipment", Final Draft (Draft 6), July 24, 1995. (RTCA Paper No. 396-95/SC159-661).
5. Gelb, A., ED., "Applied Optimal Estimation", The Analytical Sciences Corp., M.I.T. Press, Cambridge, Mass., 1974.
6. Guillemin, E. A., "The Mathematics of Circuit Analysis", The Technology Press, M.I.T., John Wiley & Sons, Inc., New York, N. Y., 1949.

APPENDIX A. WHY THE TRANSFORMED TEST STATISTIC IS CHI SQUARE DISTRIBUTED

The modal transformation L transforms the residual vector r to a transformed residual q , whose components q_i are uncorrelated:

$$r = L \cdot q \quad (AA1)$$

The covariance matrix V is transformed to diagonal form:

$$D = L^{-1} \cdot V \cdot L \quad (AA2)$$

where

$$\begin{aligned} d_{ij} &= 0, \text{ if } i \neq j, \\ d_{ii} &= \sigma_i^2 \end{aligned} \quad (AA3)$$

Since V is symmetric, the eigenvectors are orthogonal. The modal matrix L is then an orthogonal transformation, so that $L^{-1} = L^T$. This transformation rotates the axes to the eigenvectors, which are the principal axes of the ellipsoid representing the n dimensional normal distribution.

The inverse V^{-1} is obtained from (AA2):

$$\begin{aligned} D^{-1} &= L^{-1} \cdot V^{-1} \cdot L = L^T \cdot V^{-1} \cdot L \\ V^{-1} &= L \cdot D^{-1} \cdot L^{-1} = L \cdot D^{-1} \cdot L^T \end{aligned} \quad (AA4)$$

The transformation Equation (AA1) and Equation (AA4) are then substituted into the definition of the transformed test statistic:

$$s^2 = r^T \cdot V^{-1} \cdot r$$

The substitution gives:

$$\begin{aligned}
 s^2 &= \mathbf{q}^T \cdot \mathbf{L}^T \cdot \mathbf{L} \cdot \mathbf{D}^{-1} \cdot \mathbf{L}^T \cdot \mathbf{L} \cdot \mathbf{q} \\
 &= \mathbf{q}^T \cdot \mathbf{D}^{-1} \cdot \mathbf{q} \\
 &= \sum_i q_i^2 / \sigma_i^2 \\
 &= \sum_i s_i^2
 \end{aligned}$$

Since the q_i are independent with variance σ_i^2 , the s_i are independent, and are $N(0,1)$. By definition, s^2 is chi square distributed with n DOF.

APPENDIX B. WHY THE TRANSFORMED STATISTIC WITH SATELLITE FAILURE IS NON-CENTRAL CHI SQUARE

If there is a failure in satellite i , resulting in range bias error b_i , the corresponding residual is denoted $\mathbf{dr} = b_i$. More generally, \mathbf{dr} could represent any satellite failure, such as a ramp. Also, the components of \mathbf{dr} could be correlated if the failure extended over more than one Kalman filter cycle.

Since the Kalman filter is a time-varying linear system, the total residual due to a failure is determined by superposition as:

$$\mathbf{r}_F = \mathbf{r} + \mathbf{dr}$$

where \mathbf{r} is the residual with no satellite failure, and \mathbf{dr} is the system response due to the failure alone.

The total residual with the satellite failure included is transformed into the total test statistic by:

$$\begin{aligned}
 s_F &= \mathbf{D}^{-1/2} \cdot \mathbf{L}^T \cdot (\mathbf{r} + \mathbf{dr}) \\
 &= \mathbf{s} + \mathbf{ds}
 \end{aligned}$$

where

$$\begin{aligned}
 \mathbf{s} &= \mathbf{D}^{-1/2} \cdot \mathbf{L}^T \cdot \mathbf{r} \\
 \mathbf{ds} &= \mathbf{D}^{-1/2} \cdot \mathbf{L}^T \cdot \mathbf{dr}
 \end{aligned}$$

Since \mathbf{s} has an n dimensional spherical normal distribution, the axes can be rotated so that \mathbf{ds} lies along one of the axes. This proves that

$$s_F^2 = \mathbf{s}_F^T \cdot \mathbf{s}_F$$

has a non-central chi square distribution with non-centrality parameter \mathbf{ds}^2 .

USDRAIM:

An Innovative Approach to Increasing RAIM Availability

Jonathan Bernick and William Michalson
Worcester Polytechnic Institute

Biographies

Jonathan P. Bernick is a Master's candidate in the Department of Electrical and Computer Engineering at Worcester Polytechnic Institute. He holds a Bachelor of Science in Electrical Engineering from Illinois Institute of Technology, a Master of Science in Physics from The University of Akron, and a Master of Science in Mathematics from Rensselaer Polytechnic Institute. Mr. Bernick's thesis research is on error propagation and latency reduction in WAAS. He is a member of IEEE, Eta Kappa Nu, and Sigma Pi Sigma.

Dr. Michalson is an Assistant Professor in the Electrical and Computer Engineering Department at Worcester Polytechnic Institute, where he also directs the Satellite Navigation Laboratory. The majority of his research focuses on the development, test, and evaluation of GPS integrity monitoring algorithms, with an emphasis on integrity monitoring for sole-means navigation and precision approach. He is also involved with the development of GPS systems for specialized applications. Previously he was with Raytheon Company where he developed computer system architectures for space-based data and signal processors.

Abstract

In order to use GPS as a sole-means navigation aid for non-precision approach it is necessary to insure that the system can produce navigation solutions, with integrity, reliably 24 hours a day. In this context, integrity refers to the ability of user equipment to determine if a computed navigation solution is accurate to within 555m radially, the RTCA tolerance for non-precision approach. Unfortunately, all previous RAIM methods only provide such protection when 5 or more satellites are in view. Should ground masking or satellite failure reduce the

number of usable satellites to less than 5, no integrity checking is available.

Underdetermined Systems RAIM (UDSRAIM) allows solutions with integrity to be obtained when 4 satellites are in view. Three methods are detailed: The first two obtain integrity information by assuming one coordinate of the user position 4-vector to be constant, creating redundancy with only 4 satellites in view; the third works by using the pseudoinverse for underdetermined matrices to find 3-dimensional positions in space, with clock bias, using subgroups of 3 satellites.

Introduction

All previous RAIM methods require at least 5 satellites to be in view, reducing RAIM availability compared to navigation availability. This is no longer the case: We will derive several methods of performing RAIM when exactly 4 satellites are in view.

Two general approaches to performing RAIM when exactly 4 satellites are in view are presented: The first approach fixes at a constant value one coordinate of the 4-vector of user position and clock bias, resulting in redundant positioning information; the second performs RAIM by direct evaluation of position by underdetermined subgroups of 3 satellites. The second approach presents a possible problem as there is a potential that excessive vertical and temporal errors can be projected into the horizontal solution. We examine the effects of clock bias and clock drift on positions obtained with groups of 3 satellites, using quartz, temperature-controlled quartz, and rubidium clocks. From these alternatives, an algorithm for performing integrity checking with 4 visible satellites is developed. This algorithm, called UDSRAIM, is detailed, and algorithm performance, based on simulated results for non-precision approach, is presented.

Theory - Overdetermined Systems

The Navigation Equation.

It is well known that GPS positioning, given $n \geq 4$ satellites in view, is accomplished by solving the navigation equation $\mathbf{y} = \mathbf{H}\mathbf{x} + \mathbf{\epsilon}$, where \mathbf{y} is the n -vector of satellite pseudoranges, \mathbf{H} the $n \times 4$ cosine matrix, $\mathbf{\epsilon}$ the n -vector of pseudorange errors, and $\mathbf{x} = (x, y, z, b)$ the 4-vector of user position and clock bias. When $n > 4$, the system is *overdetermined*; such a system may be solved by means of the *overdetermined pseudoinverse*, which yields the least-squares solution

$$\mathbf{x} = (\mathbf{H}^T \mathbf{H})^{-1} \mathbf{H}^T \mathbf{y} \Big|_{n \geq 4}.$$

In this case, \mathbf{H} contains redundant information about the user position, and can thus be directly used to obtain integrity for the solution.

Now let us consider the case where some arbitrary coordinate k of $\mathbf{x} = (a, b, c, k)$ is assumed equal to some initial value k_0 and allowed to drift with time. For such a system $\mathbf{x} = (a, b, c)$; accordingly, the direction cosine matrix \mathbf{H} is a $n \times 3$ matrix, and the condition for overdetermination $n > 3$. \mathbf{H} can be constructed for such a system by assuming $k = k_0$ for purposes of calculating the pseudorange, and treating any drift in k as pseudorange noise. Given that \mathbf{H} is a $n \times 3$ matrix, such a system is exactly determined for 3 satellites in view, and overdetermined for 4 or more satellites in view. In the next section we demonstrate how this technique can be used to obtain positions with integrity when exactly 4 satellites are in view.

Positioning and Integrity.

As we discussed in the last section, if one of the coordinates of the 4-vector $\mathbf{x} = (x, y, z, b)$ is given some initial value and thereafter allowed to float, \mathbf{x} becomes a 3-vector and \mathbf{H} a $n \times 3$ matrix. If we do this when exactly 4 satellites are in view, \mathbf{H} becomes an overdetermined 4×3 matrix. Also, 4 positions can be obtained by forming exactly determined direction cosine matrices from the 4 possible subgroups containing 3 satellites. Therefore, we have both the 4-in-view position and redundant information about that position, and can thus determine integrity for the 4-in-view position. Since non-precision approach is a 2-dimensional specification we will examine the cases where z is allowed to coast, giving $\mathbf{x} = (x, y, b)$, and where b is allowed to coast, giving $\mathbf{x} = (x, y, z)$, respectively. In either case, allowing a coordinate to coast raises some concerns about positioning accuracy; we will address these concerns in subsequent sections.

Since we are solely concerned with positioning in two dimensions, it should be understood that all values of user radial error (*URE*) in this paper are in x and y only.

Positioning in $\mathbf{x} = (x, y, b)$.

When the positioning method using $\mathbf{x} = (x, y, b)$ is used, error in estimating the value of the z -coordinate will generally result in increases in *URE*. Fortunately, any aircraft will have a check on z in the form of an altimeter. Previous research [5] states that the $\sigma = 49\text{m}$ for the altitudes measured by an altimeter at 1500 ft; this error is incorporated into our simulations.

When positioning in $\mathbf{x} = (x, y, b)$, a potential problem arises in assuming $z_{4\text{-in-view}} = z_{\text{real}}$. Since the z -coordinate is not being updated as position is calculated, all solutions in (x, y, b) will have a greater or lesser error in z , and it is possible that this error will project onto the horizontal plane, increasing *URE*. The tolerance of algorithms using $\mathbf{x} = (x, y, b)$ to such perturbations is examined later in this paper.

Positioning in $\mathbf{x} = (x, y, z)$.

If the clock is allowed to coast with the initial bias b known and a precise clock available to the user [2], \mathbf{x} is transformed into the 3-vector $\mathbf{x} = (x, y, z)$.

It should be noted that solutions obtained by this method will degrade with time; i.e., $\text{URE}(t)$ will be an increasing function. From [2] it has been shown that for a known clock bias b the user position can be obtained by solving the exactly determined 3 satellite system

$$\mathbf{y} = \mathbf{H}\mathbf{x} + b\mathbf{1},$$

where $\mathbf{1} = [1 \ 1 \ 1]^T$. Accordingly, if $b = b(t)$, successive solutions of the equation as t increases will allow us to measure the degradation of \mathbf{x} .

From [3] we know that, for a coasting clock, the time-averaged rms variance σ_b^2 of the clock drift is given by

$$\sigma_b^2(\Delta t) = \sqrt{\frac{S_f}{\Delta t} + \frac{S_g \Delta t}{3}},$$

where S_f and S_g are white noise spectral amplitudes that are dependent on the type of clock used (see Table 1) and Δt the sampling interval, with Δt and σ_b^2 in seconds.

Table 1 - White noise parameters.

Clock Type	S_f	S_g
Crystal	$4.0(10^{-19})$	$1.6\pi^2(10^{-19})$
Ovenized Crystal	$1.6(10^{-19})$	$3.2\pi^2(10^{-22})$
Rubidium	$4.0(10^{-20})$	$3.2\pi^2(10^{-28})$

After t seconds the expected clock-drift induced pseudorange error is

$$b(t) = c \cdot \sigma_b^2 (\Delta t) \cdot t,$$

where c is the speed of light. Thus, if we assume our GPS receiver to be using a sampling interval of 1 second, when the receiver clock is allowed to drift we may expect the clock-drift induced pseudorange ramp error to increase at the rates given in Table 2.

Table 2 - Expected rates of increase of clock-coasting induced pseudorange ramp error.

Clock Type	σ_b^2 (meters/sec.)
Crystal	0.2885
Ovenized Crystal	0.1203
Rubidium	0.0600

Theory - Underdetermined Systems

The overdetermined pseudoinverse cannot be used to solve a system of 3 satellites for $\mathbf{x} = (x, y, z, b)$. Such a system, consisting of 3 equations and 4 variables, is said to be *underdetermined*. For any system of $n < 4$ satellites, if a solution is desired for $\mathbf{x} = (x, y, z, b)$, the navigation equation must be solved by means of the *underdetermined pseudoinverse*, which yields the solution

$$\mathbf{x} = \mathbf{H}^T (\mathbf{H}\mathbf{H}^T)^{-1} \mathbf{y} \Big|_{n < 4}.$$

If we form the direction cosine matrix \mathbf{H} for the 4-in-view case with user position $\mathbf{x} = (x, y, z, b)$, \mathbf{H} is a 4×4 matrix, and as such cannot alone provide a solution with integrity. In examining the 4 possible 3 satellite subgroups of the 4 satellites in view, we note that each one is an underdetermined system. If we solve each in turn we obtain 4 estimates of the user position, and thus have the redundant information necessary to provide integrity for the 4-in-view solution.

It should be noted that, since we have a greater number of unknowns than of equations, a solution to an underdetermined system is not unique. This has lead to some concern that, when the underdetermined system is being solved iteratively, different initial estimates of \mathbf{x} may lead to different final values. Due to this non-uniqueness of solution, this technique is not currently recommended for operational use. The results presented are intended as informational and may be the subject of future study.

Integrity Monitoring

Overdetermined Systems.

For all methods of solving exactly determined and overdetermined satellite systems, covariance analysis [1] shows that

$$\text{cov } \mathbf{x} = (\mathbf{H}^T \mathbf{H})^{-1},$$

where \mathbf{x} is the optimum user position. Therefore, DOP is available as an admissibility criterion. The availability of HDOP and the fact that \mathbf{H} is overdetermined imply that both the δH_{MAX} and Approximate Radial Error Protected (ARP) admissibility criteria are available to us, and we make use of both of them.

In [12] Brown describes the δH_{MAX} and Approximate Radial Error Protected (ARP) admissibility criteria. For both measures a value is calculated based on geometry and compared to an allowable threshold. If the threshold is exceeded, the system is eliminated from further consideration [6]. Simulations were performed to determine these thresholds for solutions obtained by both $\mathbf{x} = (x, y, b)$ and $\mathbf{x} = (x, y, z)$ positioning.

Given the existence of HDOP, the use of δH_{MAX} as an admissibility criterion follows logically. When 4 satellites are in view, if $i = 1, \dots, 4$ denotes the i th subset containing 3 satellites, then

$$\delta H_{\text{MAX}} = \text{Max}_i \sqrt{\text{HDOP}_i^2 - \text{HDOP}^2}.$$

UDSRAIM is available for a system if $\delta H_{\text{MAX}} \cdot T_A < 555\text{m}$, where T_A is the appropriate admissibility threshold. δH_{MAX} has been demonstrated to be more discriminating than the older HDOP_{MAX} criterion [4], and will be used in preference to it.

Brown has demonstrated that δH_{MAX} is linearly proportionate to ARP [12]; therefore, the availability of the former implies the availability of the latter. To calculate ARP we must first calculate a quantity called $\text{SLOPE}_{\text{max}}$. Let us define the quantity $\text{SLOPE}(i)$ of the i th visible satellite as

$$\text{SLOPE}(i) \Big|_{i=1, \dots, 4} = \sqrt{\frac{A_{1i}^2 + A_{2i}^2}{1 - B_{ii}}},$$

where \mathbf{H} is the direction cosine matrix, $\mathbf{A} = (\mathbf{H}^T \mathbf{H})^{-1} \mathbf{H}^T$, and $\mathbf{B} = \mathbf{H}(\mathbf{H}^T \mathbf{H})^{-1} \mathbf{H}^T$. Then

$$\text{SLOPE}_{\text{max}} = \text{max}[\text{SLOPE}(i)] \Big|_{i=1, \dots, 4}$$

and

$$\text{ARP} = \text{SLOPE}_{\text{max}} \times T_A$$

where T_A is the appropriate admissibility threshold. If $ARP < 555\text{m}$, the point is admissible for non-precision approach. It should be noted that in [12] Brown expresses ARP as

$$ARP = SLOPE_{\max} \times T_D \times k,$$

where T_D is the detection threshold and k a scaling factor; in our work, $T_A = k \cdot T_D$.

Detection is accomplished by means of the comparison of a test statistic γ to some detection threshold T_D , with an alarm being sounded if $\gamma > T_D$. Two such test statistics were used: the square root of Sum of Squares Error (SSE), and Maximum Separation of Solutions (Δx_{\max}).

We will now demonstrate the availability of SSE as a detection criterion. Let \mathbf{H} denote the overdetermined direction cosine matrix created by Taylor expansion about the nominal user position. It is well known that the optimal solution \mathbf{x} to the navigation equation $\mathbf{y} = \mathbf{H}\mathbf{x} + \boldsymbol{\varepsilon}$ for such \mathbf{H} is the least-squares solution, and is given by [12]

$$\mathbf{x} = (\mathbf{H}^T \mathbf{H})^{-1} \mathbf{H}^T \mathbf{y}.$$

We use this result to calculate the nominal pseudorange vector $\mathbf{y}_{\text{nom}} = \mathbf{H}\mathbf{x}$. Let \mathbf{y} denote the vector difference between the measured and nominal pseudorange vectors; i.e., the error vector $\boldsymbol{\varepsilon}$. We may then obtain the pseudorange residual vector

$$\mathbf{w} = (\mathbf{I} - \mathbf{H}(\mathbf{H}^T \mathbf{H})^{-1} \mathbf{H}^T) \mathbf{y},$$

which yields the sum of squares error

$$SSE = \mathbf{w}^T \mathbf{w}.$$

For the sake of convenience we use the test statistic $\gamma = \sqrt{SSE}$. If $\gamma > T_D$ an integrity alarm is sounded.

To compute our detection statistic using Maximum Separation of Solutions (Δx_{\max}), we note that from the 4 satellites in view we may form 4 subgroups of 3 satellites. We obtain the test statistic $\gamma = \max |\mathbf{x}_i - \mathbf{x}_j|$, $i, j = \{1, \dots, 4\}$, where \mathbf{x}_i and \mathbf{x}_j are the user's position in x and y as calculated from the i th and j th subgroups respectively. Again, if $\gamma > \Delta x_{\max}$, an integrity alarm is sounded.

Underdetermined Systems.

No equivalent to DOP can be said to exist for the solution to the underdetermined system. Since an infinite number of optimal solutions exist, it is meaningless to speak of a standard deviation from one. As we empirically

demonstrate in Figure 1, an inverse relationship between URE and V exists, where V is the volume of the pyramid whose vertices are at the locations of the 3 satellites being used for positioning and the user location. Based on this observation, we have elected to use the admissibility statistic

$$\alpha = (V_{\min})^{-1},$$

where

$$V_{\min} = \min V_i \big|_{i=1, \dots, 4},$$

and V_i is V of the i th 3 satellite subgroup of the 4 satellites in view. Detection is accomplished using maximum separation of solutions, with \mathbf{x}_i and \mathbf{x}_j being calculated using the underdetermined pseudoinverse.

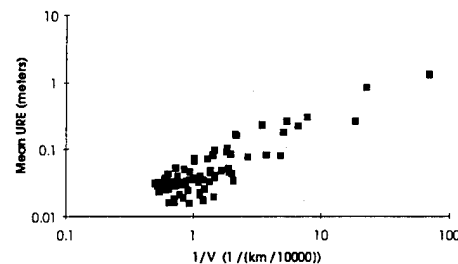


Figure 1 - Empirical demonstration of the correlation between the volume of the pyramid whose vertices are at the locations of the 3 satellites being used for positioning and the user location, and mean URE of 1000 positions obtained with that 3 satellite group under SA and receiver noise.

UDSRAIM Algorithm

The UDSRAIM algorithm consists of the following steps:

1. Collect the GPS observables (number of satellites, ephemeris data, and pseudoranges to each satellite) as per Figure 2.
2. Determine the number of satellites in view.
 - a) If 5 or more satellites are in view, conduct standard RAIM.
 - b) If 3 or fewer satellites are in view, report navigation failure and terminate algorithm.
3. Calculate the admissibility test statistic α .
 - a) If $\alpha \times T_A < 555\text{m}$ the geometry is admissible; proceed to step 4.
 - b) If $\alpha \times T_A \geq 555\text{m}$ the geometry is inadmissible. Algorithm terminates.
4. Calculate the detection test statistic γ .
 - a) If $\gamma < T_D$, then it is assumed that there is no integrity failure.

- b) If $\gamma \geq T_D$, then a detection has occurred and an integrity alarm is sounded.

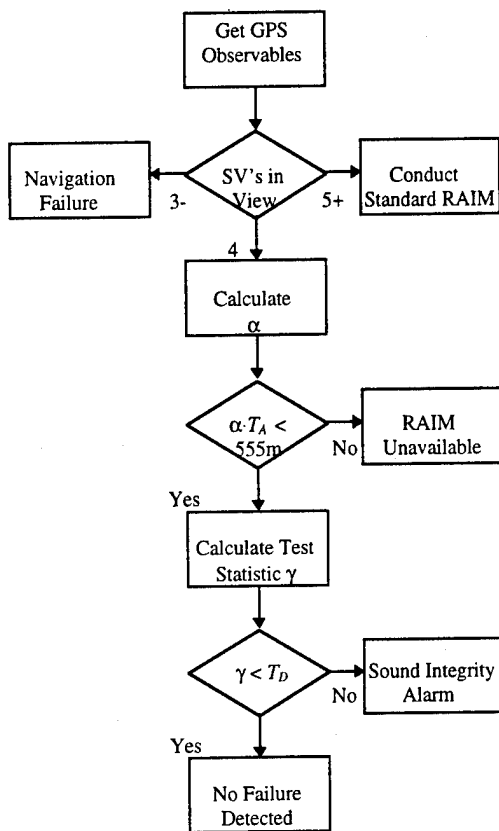


Figure 2 - UDSRAIM algorithm.

Data and Results

Test Parameters.

All threshold determination simulations conformed to the RTCA Supplemental MOPS [13] for non-precision approach; i.e.,

1. Maximum alarm rate: 0.002/hr.
2. Maximum Time to Alarm: 10 sec.
3. Min. Detection Probability: 0.999
4. Alarm Limit: 555 meters.

Data was gathered on a 5° grid over the surface of the earth at 30 minute intervals over the course of 1 day. The Optimal 21 constellation was used.

All admissibility and detection thresholds were calculated with the following algorithm:

1. For each space-time point (STP) on the grid, as illustrated in Figure 3, examine number of satellites (SV's) visible.
 - a) If 5 SV's are visible, group SV's as 5 STP's with 4 SV's each.

- b) If exactly 4 SV's are visible, keep STP.

- c) If fewer than 4 or more than 5 SV's are visible, discard STP.

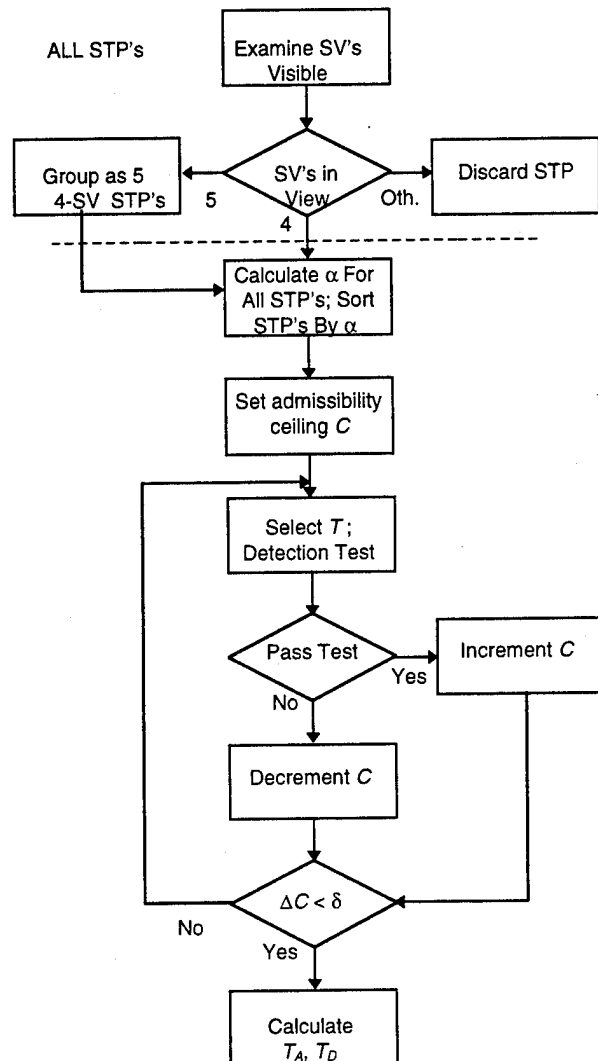


Figure 3 - Threshold determination algorithm.

2. Calculate the admissibility criterion α for each STP.
3. Sort STP's by α in ascending order.
4. Establish a ceiling cutoff C such that 80% of all STP's are admissible.
5. At each admissible point generate 10 values of receiver noise and SA, and calculate the detection criterion for each. Based on these numbers, select a threshold T such that $P_A < 0.001$.
6. A ramp error test [13] is performed on the 10 worst admissible STP's, with 10000 runs executed per STP and T used as the detection threshold.
 - a) If the test is passed, increase C in a binary search pattern.

- b) If the test is failed, decrease C in a binary search pattern.
7. If the change in C is greater than some minimum δ , go to 4.
8. Calculate T_A .
 - a) Let α_0 equal α for the worst admissible STP.
 - b) $T_A = (555\text{m} / \alpha_0)$.
9. Calculate T_D .
 - a) Let T_0 equal the current T ; let T_1 and T_2 equal the values of T from the previous iteration and the one preceding it, respectively.
 - b) $T_D = \max T_i \mid i = \{0,1,2\}$.

For our implementation of this algorithm:

1. Step 1 resulted in a test space of 34980 STP's.
2. For all simulations in $\mathbf{x} = (x,y,b)$ altimeter error was modeled as a $N(0,49.0)$ meter random variable added to the z term of the measured pseudoranges.
3. All simulations in $\mathbf{x} = (x,y,z)$ were considered to be taking place immediately after the number of satellites visible has dropped from 5 to 4. The receiver clock had thus not had time to drift, and the only clock-induced error was that resulting from the difference between the user and satellite clocks. In accordance with the 1994 Federal Radionavigation Plan specification [14] that the distribution of differences between the user and satellite clocks have a 2σ level of 340 nanoseconds the initial clock difference for all simulations in $\mathbf{x} = (x,y,z)$ was modeled as a $N(0,170)$ nanosecond random variable.

The thresholds obtained with the UDSRAIM algorithm are listed in Tables 3 to 5. A "-" indicates that the final admissible set was fewer than 10 STP's, rendering the algorithm unable to calculate either threshold.

Table 3 - Admissibility thresholds (meters) for UDSRAIM using overdetermined systems.

Positioning Method	$\mathbf{x} = (x,y,b)$	$\mathbf{x} = (x,y,z)$
$SSE(\delta H_{MAX})$	349	280
$\Delta \mathbf{x}_{max}(\delta H_{MAX})$	-	309
$SSE(ARP)$	115	607
$\Delta \mathbf{x}_{max}(ARP)$	219	-

Table 4 - Detection thresholds (meters) for UDSRAIM using overdetermined systems.

Positioning Method	$\mathbf{x} = (x,y,b)$	$\mathbf{x} = (x,y,z)$
$SSE(\delta H_{MAX})$	138	232
$\Delta \mathbf{x}_{max}(\delta H_{MAX})$	-	505
$SSE(ARP)$	174	199
$\Delta \mathbf{x}_{max}(ARP)$	600	-

Table 5 - Admissibility and detection statistics for UDSRAIM using underdetermined systems.

V_{min} ($[10^4 \text{ km}]^3$) ⁻¹	$\Delta \mathbf{x}_{max}$ (meters)
1.222	334

Effects of z-error on Integrity Monitoring for Positioning in $\mathbf{x} = (x,y,b)$.

UDSRAIM in $\mathbf{x} = (x,y,b)$ assumes that z is constant; that is, the user is maintaining the altitude he or she was at when UDSRAIM use began. If this assumption is rendered untrue through altitude change or altimeter error a shift in z is created. Since we have no way to know z with integrity, we must determine how change in z affects positioning in (x,y,b) .

To determine the effects of a change in z on positioning in (x,y,b) , a test was run on the 10 worst admissible STP's for each UDSRAIM method: At each STP a z -bias of 1 meter/second was applied to the measured pseudoranges of all 4 satellites. The z -bias was allowed to increase until URE exceeded 555m or a detection occurred, at which point the total z -bias was recorded. This was done 1000 times per STP, with different values of receiver noise and SA used each time. When all 10000 tests were completed, the mean of the recorded z -biases was taken; this quantity represents an estimate of the mean maximum allowable shift in z when using UDSRAIM in $\mathbf{x} = (x,y,b)$.

The mean values of maximum allowable shift in z estimated by this process are given in Table 6. Given that these times are means it is possible that they are somewhat optimistic, and the reader is cautioned accordingly.

Table 6 - Mean maximum shift in z coordinate allowable during use of UDSRAIM in $\mathbf{x} = (x, y, b)$.

Integrity Method	Maximum z-shift (meters)
$SSE(\delta H_{MAX})$	414
$\Delta x_{max}(\delta H_{MAX})$	-
$SSE(ARP)$	690
$\Delta x_{max}(ARP)$	995

Since T_A and T_D could not be determined when detection by Δx_{max} and admissibility by δH_{MAX} were used, no simulations were performed for this combination. Note that the non-precision phase of flight occurs at altitudes between 1000 and 200 feet. Since 414 meters is about 1360 feet, this implies that any aircraft operating in the non-precision phase of flight will not exceed the allowable shift in z for any UDSRAIM method in $\mathbf{x} = (x, y, b)$.

Effects of Clock Bias on Integrity Monitoring for Positioning in $\mathbf{x} = (x, y, z)$.

When the number of satellites in view drops from 5 to 4 and UDSRAIM in $\mathbf{x} = (x, y, z)$ begins, the receiver clock offset is no longer known with integrity. Since there is no longer a mechanism to update the clock, the effects of clock drift become more pronounced, and increase with the passage of time. Since we have no way to correct for such effects, we must determine how long it takes before they degrade our positioning to the point of unsuitability. If this period is shorter than the length of time UDSRAIM may be in use a potential problem occurs in that positioning with integrity may be lost. To determine whether this problem may occur we must also know the maximum length of time exactly 4 satellites are in view from any point.

To determine the maximum period any given spot on the earth can expect to have exactly 4 satellites in view, simulations of GPS availability were performed over a 24 hour interval on a 5° grid, using a 10 second time increment. Since the United States Air Force guarantees that at least 21 satellites will be operational at least 98% of the time [11], we assumed 21 functioning satellites as a worst-case scenario; accordingly, we executed the simulations using the Primary 21 constellation with satellites #18, #19, and #20 failed, and the Optimal 21 constellation. The simulations were accomplished by performing the following algorithm on each grid point:

1. Using the information from the satellite ephemeris database, calculate the positions of all satellites in the constellation as illustrated in Figure 4.

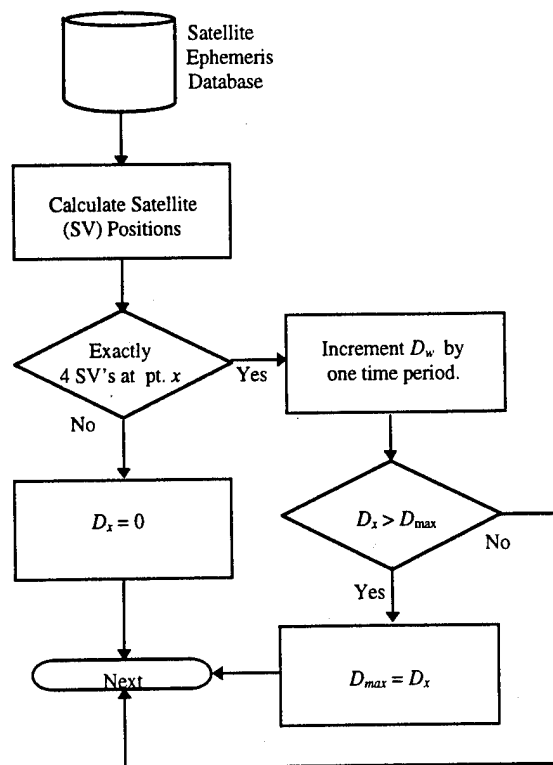


Figure 4 - Algorithm for determination of probable maximum UDSRAIM duration. D_x is the duration of the current period of UDSRAIM use at point x ; D_{max} is longest period of UDSRAIM use of any point in the simulation.

2. Count the number of satellites in view at grid point x .
 - a) If the number of satellites visible is not equal to 4,
 - i) Set D_x equal to zero, and
 - ii) proceed to step 3.
 - b) Increase D_x by one time increment.
 - c) If $D_x > D_{max}$, then $D_{max} = D_x$.
3. Increase simulation time by one time increment.
 - a) If simulation time exceeds time interval, end simulation.
 - b) Else, go to 1.

The D_{max} values obtained with this algorithm are given in Table 7. These values represent the worst-case intervals of UDSRAIM use.

Table 7 - Global maximum interval (seconds) of exactly 4 satellites in view.

Mask Angle	Optimal 21	Primary 21- 3 satellites failed
5.0°	3300	3750
7.5°	4650	4750
10.0°	6900	8160

To estimate the probable duration of usability for UDSRAIM in $\mathbf{x} = (x, y, z)$ a test was run wherein a clock bias increasing linearly with time was applied equally to the measured pseudorange of each satellite, with the rate of increase of the bias corresponding to the clock type used (Table 2). Each test was allowed to continue until a detection occurred or until URE exceeded 555m, at which point the elapsed time was recorded. In each case the ten worst admissible STP's were used, and 1000 tests were made at each point, with different values of receiver noise, SA, and initial clock difference for each test. When all 10000 tests were completed the mean of the recorded elapsed times was taken; this quantity represents an estimate of the mean period of UDSRAIM usability.

The UDSRAIM usability durations estimated by this process are given in Table 8. Given that these times are means it is possible that they are somewhat optimistic, and the reader is cautioned accordingly. Since T_A and T_D could not be determined when detection by Δx_{max} and admissibility by ARP were used, no simulations were performed for this combination.

Table 8 - Maximum duration of use (seconds) for UDSRAIM in $\mathbf{x} = (x, y, z)$.

Integrity Method	Crystal	Ovenized Crystal	Rubidium
$SSE(\delta H_{MAX})$	1445	3476	5953
$\Delta x_{max}(\delta H_{MAX})$	2634	6330	10914
$SSE(ARP)$	1278	3071	5269
$\Delta x_{max}(ARP)$	-	-	-

A comparison of the numbers in Table 7 with those in Table 8 leads us to conclude that it is possible that UDSRAIM use could continue long enough for the accuracy of UDSRAIM in $\mathbf{x} = (x, y, z)$ to degrade beyond usability. However, since UDSRAIM is a purely mathematical technique, there is no reason that a receiver using a $\mathbf{x} = (x, y, z)$ algorithm could not also be programmed with a $\mathbf{x} = (x, y, b)$ algorithm and switch between them as the situation demands. It would be of considerable interest to obtain data on the lengths and distribution of the actual intervals during which exactly 4 satellites are in view, and thereby determine to what

extent clock-coasting-related problems may be expected to occur.

It should be noted that, if clock coasting is allowed, UDSRAIM is no longer strictly receiver autonomous, and relies on a functioning receiver clock. In light of the fact that a receiver failure effectively results in GPS unavailability, we do not regard this as a significant problem.

Summary and Conclusions

This paper has presented a new RAIM algorithm called UDSRAIM that makes it possible to have GPS service with integrity monitoring when only 4 satellites are in view. The three new methods of positioning that made this algorithm possible were presented, and the limitations of each discussed. Admissibility and detection thresholds were calculated for several different criteria in accordance with the RTCA specifications for non-precision approach. Since all previous RAIM methods require at 5 satellites to be visible, it is reasonable to surmise that UDSRAIM, when used in conjunction with some standard RAIM method, will increase RAIM availability.

A large number of unanswered questions remain regarding UDSRAIM. As of now only empirical evidence exists for the use of V_{min} as an admissibility criterion for UDSRAIM in $\mathbf{x} = (x, y, z, b)$; a mathematical justification for this result must be found both to ensure confidence and to allow the development of improved admissibility criteria. Our current means of selecting detection thresholds is somewhat crude, and requires refinement. Finally, it is of pressing interest whether UDSRAIM can augment the availability of some other RAIM method to the point where sole-means non-precision approach becomes possible; both simulations and experimental data are desirable in answering this question.

It appears that, with further investigation, UDSRAIM will prove a useful augmentation to standard RAIM methods. In addition, it is possible that UDSRAIM, when used in such a capacity, may increase RAIM availability to the point where sole-means non-precision approach becomes possible. It is apparent that much work remains to be done to explore the possibilities of UDSRAIM, but such exploration appears justified.

Acknowledgment

This work was sponsored by the FAA Satellite Program Office through the FAA Office of Research and Technology Applications under Grant Number 92-G-013.

References

1. Strang, G., *Linear Algebra and Its Applications*, Academic Press, Inc., New York, 1980.
2. Sturza, M., "GPS Navigation Using Three Satellites and a Precise Clock," in *Global Positioning System*, Vol. 2, Institute of Navigation, Alexandria, 1984.
3. Hwang, P., and Brown, R. G., *Introduction to Random Signals and Applied Kalman Filtering*, John Wiley & Sons, Inc., New York, 1992.
4. Brown, R. G., "Receiver Autonomous Integrity Monitoring (RAIM)," to appear in *AIAA Book on GPS*.
5. Lee, Y., "RAIM Availability for GPS Augmented with Barometric Altimeter Aiding and Clock Coasting," to appear in *AIAA Book on GPS*.
6. Michalson, W., and Easton, C., "Experiences Implementing the Supplemental Off-Line Test Procedures," *Proceedings of the Sixth International Technical Meeting of the Satellite Division of the Institute of Navigation (ION GPS-93)*.
7. Durand, J-M., and Caseau, A., "GPS Availability, Part II: Evaluation of State Probabilities for 21 and 24 Satellite Constellations," *Navigation: Journal of the Institute of Navigation*, Vol. 37, No. 3, Fall 1990, pp. 285-297.
8. Durand, J-M., Michal, T., and Bouchard, J., "GPS Availability, Part II: Availability of Service Achievable for Different Categories of Civil Users," *Navigation: Journal of the Institute of Navigation*, Vol. 37, No. 2, Summer 1990, pp. 123-139.
9. Michalson, W., Bernick, J., Levin, P., and Enge, P., "RAIM Availability for Augmented GPS-Based Navigation Systems," *Proceedings of the Seventh International Technical Meeting of the Satellite Division of the Institute of Navigation (ION GPS-94)*.
10. Markin, K., Wroblewski, P., Hsiao, T., and Poor, W., "Availability Assessment of Alternative Category I Approach and Landing System Architectures," *Navigation: Journal of the Institute of Navigation*, Vol. 41, No. 4, Fall 1994, pp. 353-364.
11. *Introduction to NAVSTAR GPS User Equipment*, The NATO Team, NAVSTAR GPS Joint Program Office, June 1987.
12. Brown, R. G., "A Baseline GPS RAIM Scheme and a Note on the Equivalence of Three RAIM Methods," *Navigation: Journal of the Institute of Navigation*, Vol. 39, No. 3, Fall 1992, pp. 301-316.
13. "Minimum Operational Performance Specification for Airborne Supplemental Navigation Using Global Positioning System (GPS)," RTCA Document RTCA/DO-208, July 1991.
14. *1994 Federal Radionavigation Plan*, National Technical Information Service, Springfield, 1995.

GPS Carrier-Phase RAIM

William Michalson and Hua Hua
Worcester Polytechnic Institute

Duncan Cox, Jr.
DBC Communications, Inc.

BIOGRAPHIES

Dr. Michalson is an Assistant Professor in the Electrical and Computer Engineering Department at Worcester Polytechnic Institute, where he also directs the Satellite Navigation Laboratory. The majority of his research focuses on the development, test, and evaluation of GPS integrity monitoring algorithms, with an emphasis on integrity monitoring for sole-means navigation and precision approach. He is also involved with the development of GPS systems for specialized applications. Previously he was with Raytheon Company where he developed computer system architectures for space-based data and signal processors.

Dr. Cox is President of DBC Communications, Inc., in Manchester, MA. His technical experience has been primarily in the development of new technology relating to inertial and radio navigation systems, with a strong focus on GPS systems. Currently, he is developing techniques and algorithms employing GPS carrier phase measurements for accurate relative navigation of satellites, for range instrumentation, and for enhancing navigation integrity. He is also developing image processing techniques, algorithms, and software. He was previously a cofounder and chairman of Mayflower Communications Company and a division leader at the C.S. Draper Laboratory. He received a D. Eng. degree from Yale University in 1964.

Hua Hua is a Ph.D. candidate in the Department of Electrical and Computer Engineering at Worcester Polytechnic Institute. She holds a Bachelor of Science in Physics from The University of Science and Technology of China, a Master of Science in Physics from Western Illinois University, and a Master of Science in Electrical Engineering from Rose-Hulman Institute of Technology. Her primary research interests are GPS RAIM algorithms and precision positioning using receiver carrier phase.

ABSTRACT

Carrier phase data from four or more GPS satellites can be used to determine the evolution of the trajectory of a

vehicle from an arbitrary initial position with great precision and high update rate. The accuracy is limited primarily by incremental errors in satellite position and time, ionospheric and tropospheric delay, multipath, and SA. If estimates of the primary components of satellite and propagation errors are provided through LAAS or WAAS correction messages, then phase-based techniques can allow a user to accurately determine their trajectory evolution at the correction epochs.

Carrier phase data from five or more GPS satellites can be used to determine the initial position associated with the above trajectory. The sensitivity of the position estimation errors to the measurement errors decreases as changes in satellite geometry evolve. Increasing the number of satellites generally improves the rate of sensitivity reduction (seven or more satellites results in rapid convergence). Once the initial position has been determined to a certain level of accuracy, the accuracy is essentially preserved as long as four or more satellites are available with suitable geometry.

Carrier phase data from five or more GPS satellites can be used to provide redundant estimates of trajectory evolution and, hence, can be used to detect new (incremental, since the start of the trajectory) violations of integrity criteria. We call this "incremental RAIM." [1]

Carrier phase data from six or more GPS satellites can be used to provide redundant estimates of the trajectory's initial position and, hence, can be used in conjunction with incremental RAIM to provide absolute RAIM alarms. Once the initial integrity is established, absolute RAIM can be continued with incremental RAIM, requiring five or more satellites (not necessarily the same ones) with suitable geometry.

Because of the enhanced resolution of the phase data, in comparison with that of pseudorange data, the carrier-phase RAIM system can be used to enhance the performance of conventional RAIM. The amount of improvement depends upon the availability of suitable error-correction data from whatever augmentation system is being utilized.

The correction data from a WAAS that is designed for only pseudorange data may be sufficient for carrier-phase RAIM to be a useful augmentation. In this case, the carrier-phase-RAIM algorithm would incorporate accumulated incremental changes in the WAAS corrections, with the changes in ionospheric delay reversed in sign to account for the ionospheric phase advances corresponding to the ionospheric group delays. However, modifying the WAAS or LAAS corrections may allow further improvements in carrier-phase RAIM performance.

This paper is an extension of the discussion presented in [1]. In contrast to this earlier discussion, here we assume that suitable corrections are received from either a WAAS or LAAS augmentation. In the following sections we present a description of the underlying theory for a carrier-phase RAIM system that is under development. In addition, some preliminary results obtained using the carrier-phase algorithm in the presence of satellite failures is presented. These results suggest that carrier-phase RAIM is possible for Category I approach. This concept is expected to be important for the successful evolution of future GPS WAAS and LAAS systems.

BACKGROUND

Receiver Autonomous Integrity Monitoring is a process for identifying inconsistencies in received GPS data early enough to avoid including erroneous data in a receiver's navigation solution. Although such errors occur infrequently, they are important to detect due to their potential impact on safety.

Errors can enter the GPS system in a wide variety of ways. Most commonly, errors occur due to excessive clock drift, incorrect upload of navigation message data or corrections, or component failure. Within RTCA special committee 159, the typically assumed probability of a satellite failure is approximately 10^{-4} per hour. This is close to the value of 1.64×10^{-4} per hour previously determined by Durand using a simulation of system failure probabilities and outage duration[2].

In general, failures fall into two distinct classes: large step failures and ramp failures. Of the two, step failures are considered most common, occurring an order of magnitude more frequently than ramp errors. Loosely defined, a step error is an anomaly which causes a substantial, virtually instant shift in calculated user position. Such step errors are generally considered easy to detect, since they imply unrealistic vehicle dynamics.

Ramp errors are more difficult to detect since the dynamics associated with a ramp error may be more similar in magnitude to normal aircraft dynamics. In this case, a user is slowly dragged off to an erroneous position.

For non-precision approach, an integrity monitoring system must ensure that any satellite error causing the user position to deviate more than 0.3 nautical miles (555m) is detectable with high probability. This is easily achievable using a variety of widely publicized snapshot RAIM algorithms [3-6]. Practically, this means that the differentiation between step and ramp errors is unimportant for non-precision approach since the snapshot-type integrity algorithms are sensitive to the relative magnitude of satellite error, not the rate at which it accumulates.

This situation changes somewhat as the required level of integrity protection approaches Category I precision approach. In this case, much higher navigation accuracy is required. Assuming an RNP tunnel concept is implemented in the National Airspace (NAS), the required levels of positioning accuracy might be:

Level of Precision	Inner Tunnel		Outer Tunnel	
	Horz	Vert	Horz	Vert
Category I	33	9.7	130	33
Category II	23	4.6	100	20
Category III	16	na	75	na

In the above, the inner tunnel numbers indicate the 95% accuracy requirements while the outer tunnel values indicate 99.99999% accuracy requirements. While integrity monitoring requirements for the RNP tunnel have not been formally stated, it seems reasonable to assume that the integrity protection limit must be well within the outer tunnel limits¹.

The more stringent accuracy requirements for precision approach present a difficulty for conventional RAIM algorithms since most are based on the use of the pseudorange residual as a test statistic[7]. While this test statistic is excellent at non-precision levels, it becomes a very noisy measure at precision levels. Figure 1 presents simulation data which illustrates the behavior of the pseudorange residual when there are no satellite failures and no signal degradation due to Selective Availability. In this figure, it is clear that at URE levels below about 30 meters, the pseudorange residual is poorly correlated

¹ It should be noted that the RNP numbers reflect total system error which is a function of sensor error and flight technical error. This will impact the selection of an integrity protection limit. See [1].

with URE. This makes it difficult to apply effectively to protect even a Category I outer tunnel limit.

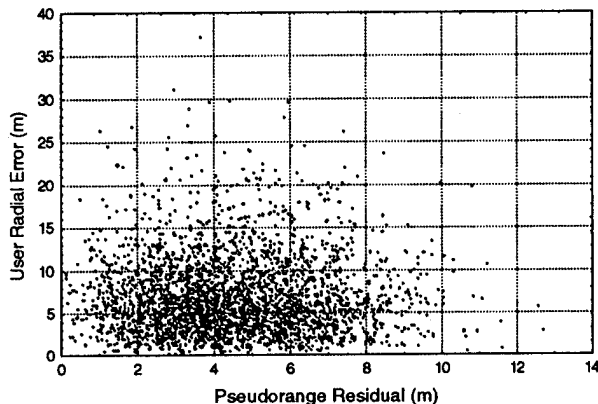


Figure 1: Typical Residual vs. URE Without SA

WAAS/LAAS INTEGRITY MONITORING

It is well-known that the effects of selective availability limit the use of GPS in the NAS to supplemental navigation for enroute, terminal, and non-precision phases of flight. Sole-means use of GPS in these applications is limited largely by the availability of integrity monitoring. In an attempt to expand the role of GPS in the NAS, a Wide Area Augmentation System (WAAS) is being developed [8] to facilitate sole-means aircraft navigation down to the Category I precision approach phase of flight.

An example of a WAAS integrity monitoring structure is illustrated in figure 2. In this system, the reference stations collect measurements from the GPS satellites and pass the data to the WAAS Control Station. This Control Station, in turn, determines vector and scalar corrections which are passed to users using geostationary communications satellites.

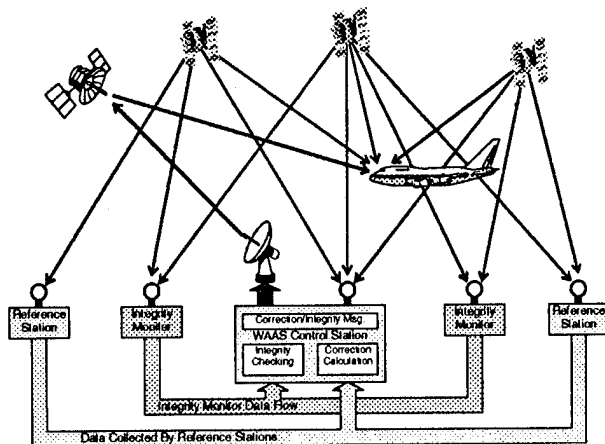


Figure 2: WAAS Integrity Monitoring

As shown in the figure, integrity monitors receive both the raw GPS observables and the correction messages from the WAAS. Using this information, each integrity monitor can compute its position using WAAS corrections and compare it to its surveyed location. In the event that the calculated integrity monitor position exceeds the WAAS system specifications, the integrity monitor can alert the WAAS Control Station that an integrity failure has occurred.

This WAAS-based integrity architecture helps solve several problems associated with integrity availability since integrity is constantly monitored over the coverage area. For non-precision approach, the WAAS provides substantial improvement over unaugmented RAIM since the latencies associated with the WAAS are low enough to fall within the required time to alarm specifications. For Category I approach, however, the latency within the WAAS is approximately equal to the time to alarm specification, making WAAS-based integrity monitoring for this phase of flight marginal[1]. In addition, it may be desirable for the user to retain the ability to locally monitor system status during precision operations. Thus, there is still a need for RAIM during Category I and higher operations.

PSEUDORANGE RAIM

Most published schemes for performing Integrity monitoring base their integrity checks on pseudorange measurements. While figure 1 illustrates that this will not be sufficient for Category I operations, it is important to understand the operation of a typical RAIM algorithm to form a basis for subsequent discussions.

When performing RAIM, it is assumed that the integrity monitoring function is performed based solely on the signals available at the user receiver. Strictly speaking, true RAIM would use only the signals received from GPS to perform integrity monitoring. However, research suggests that in order to meet the availability requirements for sole means flight, (availability = 0.99999) some form of augmentation is necessary[9,10]. Possible augmentations include altimeter aiding, clock aiding, or the use of additional ranging sources (such as Inmarsat satellites with navigation payloads), or WAAS.

While there are many different approaches to performing RAIM, all are roughly equivalent in function. The basic algorithm, illustrated in figure 3, is fairly straightforward. First, an all-in-view position is computed using signals from the n visible satellites. In order to maintain sufficient redundancy for decision making, n must be greater than or equal to 5. Next, the visible constellation is checked for admissibility. This

requires determining if each of the n subsets consisting of $n-1$ satellites has a sufficiently robust geometry. This selection ensures that each subset can provide a navigation solution that is reliable. This is important since, in the event of a satellite failure, all but one subset of satellites will be dragged off of the correct position. If the geometry of the remaining good subset was questionable, it may not provide a sufficiently reliable navigation solution to form a basis for comparison. Even worse, it is possible that a precarious geometry could degrade user position faster than a good geometry which includes a failed satellite.

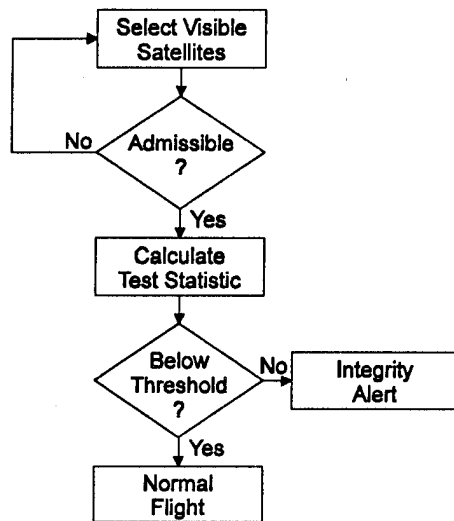


Figure 3: General RAIM Algorithm

CARRIER-PHASE BASED POSITIONING

Instead of performing RAIM based on pseudorange, it is possible to use carrier phase for both positioning and integrity monitoring. Using phase measurements is similar to using pseudorange measurements except that phase measurements: 1) have much less multipath and front end noise, 2) include an ionospheric advance instead of an ionospheric delay, and 3) include an arbitrary additive constant (the cycle count). When four accumulated phase measurements are available to an aircraft navigator over a period of time from satellites exhibiting a suitable PDOP, and if suitable corrections for SA and other errors are supplied, the flight path of the aircraft can be determined with extreme precision [11]; however, the starting point remains unknown, being associated with the unknown cycle counts.

In order to understand carrier phase-based positioning, it is useful to explore the basic process of ranging based on carrier phase information. In essence, the phase pseudorange is the distance between a user and a visible

satellite measured in units of carrier wavelength. Ignoring tropospheric and ionospheric errors, this can be calculated as:

$$\Phi^i = \frac{1}{\lambda} \rho^i + \frac{c}{\lambda} \delta t \quad (1)$$

where ρ^i is the geometric distance between the user and satellite i , and λ is the wavelength at the frequency of interest (at the L1 frequency of 1575.42 MHz $\lambda \approx 19$ cm). The δt term characterizes the user and satellite time offsets from GPS system time.

Unfortunately, there is no way to directly measure Φ^i in a GPS receiver. Rather, the GPS receiver generates an internal copy of the GPS signal and measures the phase difference between the received signal and the internal copy. Thus, from some arbitrarily selected initial starting point, the receiver measures the fractional portion of a cycle and can keep track of the number of cycles that have passed since the count was started. We call this measurement the accumulated phase, Φ_A^i . This measurement process is illustrated in figure 4.

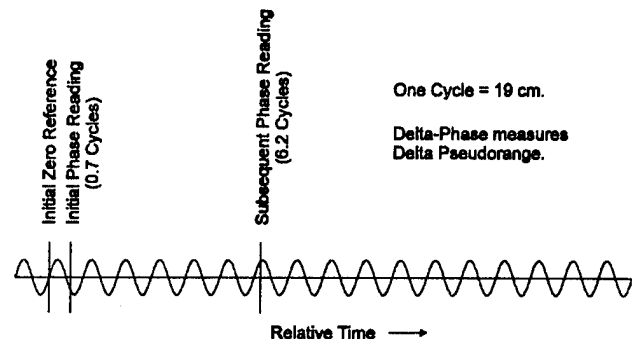


Figure 4: Accumulated Phase Measurement

Since we cannot know the actual number of cycles between the user and the satellite, we must modify equation 1 slightly to yield:

$$\Phi_A^i = \frac{1}{\lambda} \rho^i + \frac{c}{\lambda} \delta t + N^i + \epsilon \quad (2)$$

where N^i is referred to as the integer ambiguity and ϵ represents other system errors (SA, ionospheric, tropospheric, and ephemeris). Although this ambiguity is initially unknown, it remains constant as long as the receiver maintains phase lock on the GPS signal. Throughout this discussion, we will drop the physical constants and error term to simplify the equations and improve clarity.

Incremental Positioning for a Static User

Given this understanding of the carrier phase measurement, it appears that the main difference between

carrier and code based navigation lies in the handling of the ambiguity terms. Since, at one level, these terms merely represent additional unknowns, given a sufficient number of satellites, it seems reasonable to formulate a carrier phase solution in a manner analogous to that used to formulate a code-based solution. The problem is that the number of unknowns is large enough to prohibit forming a solution in a single epoch. Thus, a solution must be formed incrementally.

To explain how an incremental position is determined, we will first discuss the case of a static user.

In principle, a static user can perform point positioning by observing satellites at different points in time. In the carrier phase domain, each observation carries with it an integer ambiguity. Further, the user's position is considered static, but unknown, and the user's clock bias may change between observation epochs. Suppose a user sees five satellites. How many epochs are necessary to solve for position and ambiguity? Consider the following:

Epoch	New Variables	New Measurements
1	$x, y, z, N^1, N^2, N^3, N^4, N^5, t_1$	5
2	t_2	5

We can see from the above that for a static user seeing five satellites, two epochs seemingly provide a sufficient number of equations to solve for all of the unknown variables.

Following the presentation in [12] we can develop a system of equations to perform point positioning of this static user that are analogous to the navigation equations used for point positioning using pseudorange. In this case:

$$\delta U = H^{-1} \delta \Phi_A$$

where δU is the change in the user state vector which is defined as:

$$\delta U = [\delta x \mid \delta N \mid \delta t]$$

and

- δx is a 1×3 vector denoting the change in user x , y , and z position,
- δN is a $1 \times \text{Number of Satellites}$ vector of change in ambiguity,
- δt is a $1 \times \text{Number of Epochs}$ vector of changes in clock bias,
- H is a sensitivity matrix consisting of the direction cosine matrix, augmented with additional columns to include the integer ambiguities and the user clock biases, and

Φ_A is the change in incremental carrier phase.

Since the satellite positions will change between epochs, the sensitivity matrix must contain information for multiple epochs. For example, for n visible satellites, we define

$$H_x(t) = \begin{bmatrix} h_x^1(t) & h_y^1(t) & h_z^1(t) \\ \vdots & \vdots & \vdots \\ h_x^n(t) & \dots & h_z^n(t) \end{bmatrix}$$

where $h_j^i(t)$ is the direction cosine between the user and satellite i at time t . We also define the $n \times n$ matrix

$$\lambda = \begin{bmatrix} -\lambda & 0 & \dots & 0 \\ 0 & -\lambda & 0 & \vdots \\ \vdots & 0 & \ddots & 0 \\ 0 & \dots & 0 & -\lambda \end{bmatrix}$$

to yield the complete sensitivity matrix

$$H = \left[\begin{array}{c|c|c|c} H_x(t_1) & \lambda & 1 & 0 \\ \hline H_x(t_2) & \lambda & 0 & 1 \end{array} \right] \quad (3)$$

Once cast into this form, a final solution to the point positioning equation could be sought. There is a subtle problem, however, with this straightforward approach. Close inspection reveals that the last column is a linear combination of the prior columns which contain λ and time terms. An intuitive interpretation of this result is that since both the ambiguity terms and the user clock error result in the same effect on the solution, it is impossible to resolve all of the terms in this manner without additional information. Thus the formulation given in equation 3 leads to an underdetermined set of equations.

We can manipulate the equations so as to eliminate these unobservable unknowns. Consider equation 2 for some particular point in time, t_k :

$$\Phi_A^j(t_k) = \frac{1}{\lambda} \rho^j(t_k) + \frac{c}{\lambda} \delta t_k + N^j(t_k) \quad (4)$$

For each of the n visible satellites, the measurement contains unique information about the range and integer ambiguity for each satellite and the time offset with respect to GPS system time. It is useful to note that this time offset is the same for each of the satellite measurements taken at a given epoch.

We can eliminate the time offset from the positioning equations by computing the differences between measurements from different satellites. Suppose we have n satellites in view. In this case there are $n-1$ differences

that may be calculated (assuming no cycle slip, the ambiguities are not a function of time).

By defining $\Delta\Phi_{t_k}^i = \Phi_{t_k}^i - \Phi_{t_k}^n$, substituting into equation 4, and rearranging, we obtain:

$$\lambda \begin{bmatrix} \Delta\Phi_{t_k}^1 \\ \Delta\Phi_{t_k}^2 \\ \vdots \\ \Delta\Phi_{t_k}^{n-1} \end{bmatrix} = \begin{bmatrix} \rho_{t_k}^1 \\ \rho_{t_k}^2 \\ \vdots \\ \rho_{t_k}^{n-1} \end{bmatrix} - \begin{bmatrix} \rho_{t_k}^n \\ \rho_{t_k}^n \\ \vdots \\ \rho_{t_k}^n \end{bmatrix} + \lambda \begin{bmatrix} N^1 - N^n \\ N^2 - N^n \\ \vdots \\ N^{n-1} - N^n \end{bmatrix} \quad (5)$$

which is a system of $n - 1$ equations in $n + 2$ unknowns ($n - 1$ ambiguity differences and x, y, z position) that are purely a function of position and differential ambiguity.

To solve for user position, we must derive a new sensitivity matrix that can be used with $\Delta\Phi_{t_k}^i$. For this we must linearize equation 5.

Given that

$$\Delta\Phi_{t_k}^i(U) = \Phi_{t_k}^i(x, y, z, N^i, b_{t_k}) - \Phi_{t_k}^n(x, y, z, N^n, b_{t_k}) \quad (6)$$

where b_{t_k} is the unknown user clock bias. We can linearize the equation by taking its Taylor series expansion about some estimated $(n+2) \times 1$ user state vector

$$\hat{U}^T = [\hat{x} \quad \hat{y} \quad \hat{z} \quad \hat{N}^1 \quad \hat{N}^2 \quad \dots \quad \hat{N}^{n-1}].$$

Resulting in:

$$\begin{aligned} \Delta\Phi_{t_k}^i(U) &= \Delta\Phi_{t_k}^i(\hat{U}) + (\hat{N}^i - \hat{N}^n) \\ &\quad + [(h_x^n(t_k) - h_x^i(t_k))(x - \hat{x}) \\ &\quad + (h_y^n(t_k) - h_y^i(t_k))(y - \hat{y}) \\ &\quad + (h_z^n(t_k) - h_z^i(t_k))(z - \hat{z})] \end{aligned}$$

which, as expected is purely a function of user position and integer ambiguities.

Now, we define

$$\delta\Phi_A = \begin{bmatrix} \Delta\Phi_{t_k}^1(U) - \Delta\Phi_{t_k}^1(\hat{U}) \\ \vdots \\ \Delta\Phi_{t_k}^{n-1}(U) - \Delta\Phi_{t_k}^{n-1}(\hat{U}) \end{bmatrix}$$

and

$$h_{t_k}^i = [h_x^i(t_k) - h_x^n(t_k) \quad h_y^i(t_k) - h_y^n(t_k) \quad h_z^i(t_k) - h_z^n(t_k)]$$

Thus, in a manner similar to that presented in equation 3, we have the sensitivity matrix for accumulated phase-based positioning for n satellites viewed over k epochs defined as

$$H_A = \begin{bmatrix} h_{t_k}^1 & & & \\ \vdots & & & \\ h_{t_k}^{n-1} & & & \\ & \lambda_{(n-1) \times (n-1)} & & \\ & & \ddots & \\ & & & \lambda_{(n-1) \times (n-1)} \\ h_{t_k}^{n-1} & & & \end{bmatrix}_{k(n-1) \times (n+2)}$$

Now, collecting terms into a matrix expression yields the following phase-based navigation equation:

$$\delta\Phi_A = H_A \delta U. \quad (7)$$

Figure 5 shows the general approach to using equation 7 in a navigation algorithm. First, phase measurements are taken from each visible satellite. If enough common satellites have been observed over a sufficient number of epochs, then a position solution is available. If not, additional measurements must be made at a future epoch.

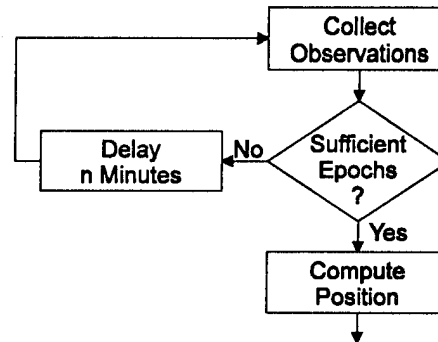


Figure 5: General Incremental Navigation Algorithm

Based on equation 7, we can use the matrix pseudoinverse to obtain a least mean squares solution for δU at a given measurement epoch as follows

$$\delta U_A = (H_A^T H_A)^{-1} H_A^T \delta\Phi_A.$$

This equation can be used to solve for user position in a manner analogous to that presented in [13].

Figure 6 shows the simulated position accuracy results obtained for a static user. In this case there were four satellites visible at two epochs yielding six equations in six unknowns (four satellites were selected to illustrate a worst-case situation, a larger number of satellites would

yield better results). In this experiment, 2mm of phase noise was added to represent receiver frontend noise and multipath. It is assumed that other system errors are eliminated through LAAS/WAAS corrections. Root mean squared position errors were averaged over 100 iterations. From the figure we see that user error becomes sub-meter when the amount of time that elapses between epochs is greater than 4 minutes.

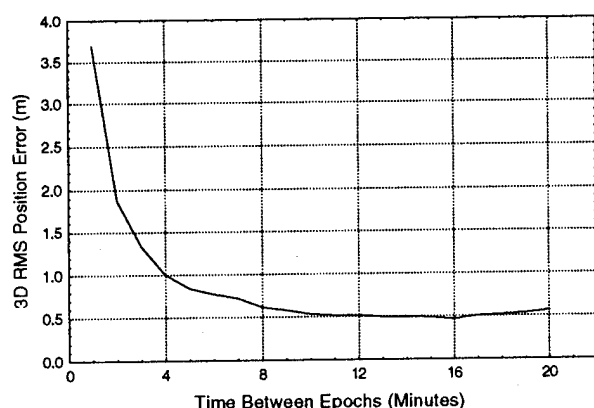


Figure 6: Static User Incremental Positioning Accuracy

Incremental Positioning for a Moving User

The next step is to extend the solution for a static user into the case where the user moves. In this case, the equations are similar to the static user case where for the first time measurement there are $n-1$ equations in $n+2$ unknowns (3 position components plus $n-1$ ambiguity integer differences). At each measurement epoch $n-1$ new equations are obtained. The difference for the moving user case is that user position is a function of time, meaning that three new unknown user positions are added at each measurement epoch. Thus, U for the moving user becomes a function of time

$$U_M^T(t_k) = [x(t_k) \ y(t_k) \ z(t_k) \ N^1 \ N^2 \ \dots \ N^{n-1}]$$

Given the increase in the number of unknowns, additional measurement epochs are needed to obtain a sufficient number of equations. The following table illustrates case for five satellites:

Epoch	New Variables	New Measurements
1	$x(t_1), y(t_1), z(t_1), \delta N^1, \dots, \delta N^4$	4
2	$x(t_2), y(t_2), z(t_2)$	4
3	$x(t_3), y(t_3), z(t_3)$	4
4	$x(t_4), y(t_4), z(t_4)$	4

Thus, after four epochs, sufficient variables are available to solve 16 equations in 16 unknowns. Generally, for k

epochs and n satellites, there are $k(n-1)$ equations with $(n+2)+3(k-1)$ unknowns. The following table illustrates the number of measurement epochs necessary for a given number of visible satellites.

Number Of Common Satellites	Required Number of Measurement Epochs
≤ 4	No Positioning
5	4
6	3
≥ 7	2

It can be seen from the table that there must be at least five satellites visible in four epochs to perform carrier phase positioning for a moving user.

Forming the actual navigation equations is similar to the static user case, the primary difference being the need to account for the evolution of the user position. The basic navigation equation is

$$\delta \Phi_M = H_M \delta U_M \quad (8)$$

where

$$\delta \Phi_M = \begin{bmatrix} \Delta \Phi_{t_1}^1(U_M(t_1)) - \Delta \Phi_{t_1}^1(\hat{U}_M(t_1)) \\ \vdots \\ \Delta \Phi_{t_1}^{n-1}(U_M(t_1)) - \Delta \Phi_{t_1}^{n-1}(\hat{U}_M(t_1)) \\ \vdots \\ \Delta \Phi_{t_k}^1(U_M(t_k)) - \Delta \Phi_{t_k}^1(\hat{U}_M(t_k)) \\ \vdots \\ \Delta \Phi_{t_k}^{n-1}(U_M(t_k)) - \Delta \Phi_{t_k}^{n-1}(\hat{U}_M(t_k)) \end{bmatrix}$$

and

$$\delta U_M = \begin{bmatrix} U(t_1) - \hat{U}(t_1) \\ \vdots \\ U(t_k) - \hat{U}(t_k) \end{bmatrix}$$

Since the user now has a trajectory, the sensitivity matrix becomes

$$H_M = \begin{bmatrix} H(t_1) & 0 & \dots & 0 & \lambda \\ 0 & H(t_2) & 0 & \vdots & \lambda \\ \vdots & 0 & \ddots & 0 & \vdots \\ 0 & \dots & 0 & H(t_k) & \lambda \end{bmatrix}$$

where each $H(t_i)$ is defined as

$$H(t_i) = \begin{bmatrix} h_x^1(t_i) - h_x^n(t_i) & h_y^1(t_i) - h_y^n(t_i) & h_z^1(t_i) - h_z^n(t_i) \\ h_x^2(t_i) - h_x^n(t_i) & h_y^2(t_i) - h_y^n(t_i) & h_z^2(t_i) - h_z^n(t_i) \\ \vdots & \vdots & \vdots \\ h_x^{n-1}(t_i) - h_x^n(t_i) & h_y^{n-1}(t_i) - h_y^n(t_i) & h_z^{n-1}(t_i) - h_z^n(t_i) \end{bmatrix}$$

Figure 7 shows the results obtained using equation 8 as the basis for a moving user positioning algorithm. As before, the simulation includes phase noise and each data point represents a rms position error averaged over 100 positions. Different simulations were run for various numbers of satellites and measurement epochs.

In general, increasing the number of visible satellites reduces the time required to achieve a desired level of accuracy.

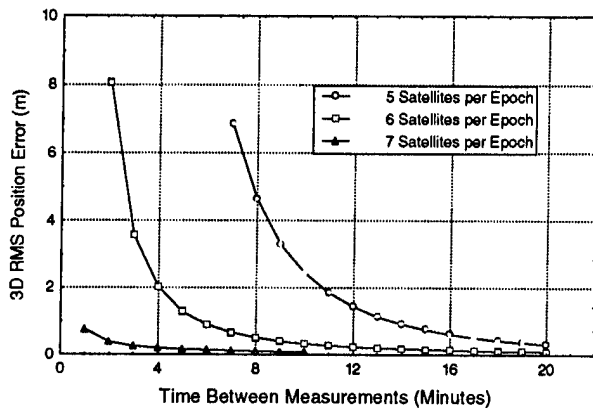


Figure 7: Moving User Positioning Accuracy

DOP-Related Issues

In the conventional GPS model, dilution of precision is used to predict the user error that might result as a consequence of satellite geometry. For the usual navigation equation for n visible satellites

$$\begin{bmatrix} h_x^1 & h_y^1 & h_z^1 & 1 \\ h_x^2 & h_y^2 & h_z^2 & 1 \\ \vdots & \vdots & \vdots & \vdots \\ h_x^n & h_y^n & h_z^n & 1 \end{bmatrix} \begin{bmatrix} \delta x \\ \delta y \\ \delta z \\ \delta b \end{bmatrix} = \begin{bmatrix} \delta \rho^1 \\ \delta \rho^2 \\ \vdots \\ \delta \rho^n \end{bmatrix}$$

or,

$$H\delta U = \delta \rho.$$

Performing a covariance analysis shows that

$$\text{Cov}(H) = (H^T H)^{-1} = \begin{bmatrix} \sigma_{xx}^2 & \sigma_{yx} & \sigma_{zx} & \sigma_{bx} \\ \sigma_{xy} & \sigma_{yy}^2 & \sigma_{zy} & \sigma_{by} \\ \sigma_{xz} & \sigma_{yz} & \sigma_{zz}^2 & \sigma_{bz} \\ \sigma_{xb} & \sigma_{yb} & \sigma_{zb} & \sigma_{bb}^2 \end{bmatrix}.$$

For three dimensional positioning the geometric measure of interest is referred to a PDOP, which is defined by

$$\text{PDOP} = \sqrt{\sigma_{xx}^2 + \sigma_{yy}^2 + \sigma_{zz}^2}.$$

Extending this concept into the carrier phase GPS model, requires substituting the H matrix defined in equations 7 or 8 into the covariance calculation outlined above. For the moving user, this results in

$$\text{Cov}(H_M) = \begin{bmatrix} \sigma_{xx}^2(t_1) & \sigma_{yx} & \sigma_{zx} & 0 & 0 \\ \sigma_{xy} & \sigma_{yy}^2(t_1) & \sigma_{zy} & 0 & 0 \\ \sigma_{xz} & \sigma_{yz} & \sigma_{zz}^2(t_1) & 0 & 0 \\ 0 & 0 & 0 & \ddots & 0 \\ 0 & 0 & 0 & 0 & \sigma \end{bmatrix} \begin{matrix} \\ \\ \\ \sigma_N \\ \sigma_{NN}^2 \end{matrix}$$

where, for simplicity, only the covariance terms of interest for a single epoch are expanded.

Thus, for a given epoch along the user's trajectory a phase-PDOP term is calculated as

$$\text{PDOP}(t_k) = \sqrt{\sigma_{xx}^2(t_k) + \sigma_{yy}^2(t_k) + \sigma_{zz}^2(t_k)}.$$

Like the normal pseudorange PDOP, since carrier phase PDOP is purely determined by satellite geometry, we can know in advance whether or not a position result is reliable by performing a carrier phase PDOP calculation. This can be seen figure 8 where user error and phase-PDOP are calculated for a simulated user traveling east at 200m/s for 24 hours. In this simulation the time between epochs was 10 minutes and each data point represents rms user error averaged over 100 positions. Other simulation parameters are identical to the static and moving user cases.

It is important to note that since the simulation ran continuously, the number of satellites visible to the user could change. Thus, the positioning algorithm used had to store the history of four epochs (the current epoch and three previous epochs). In the event that the number of visible satellites changed, the algorithm could select an appropriate set of visible satellites from the historical data.

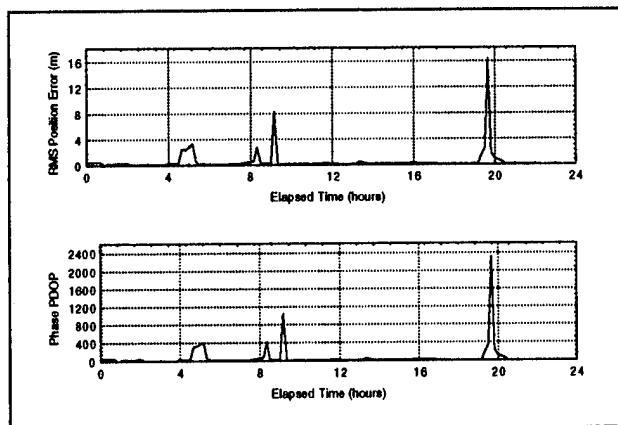


Figure 8: DOP Vs. Positioning Accuracy

Figure 9 provides a scatterplot of the same data presented in figure 8. The dashed line represents the best fit to the data points. As can be seen in the figure, the phase-PDOP is very well correlated to user position error.

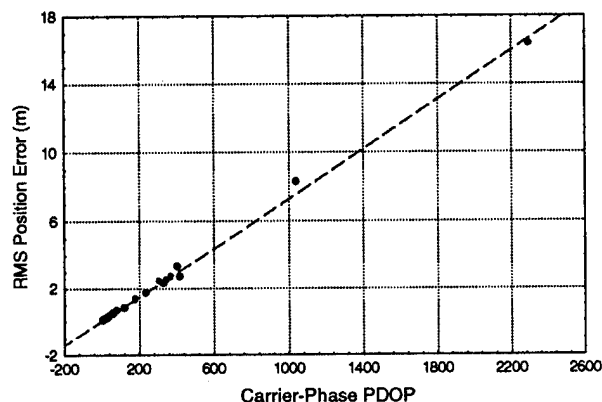


Figure 9: Correlation Between URE and Phase DOP

ACCUMULATED-PHASE RAIM

Performing RAIM using differential carrier phase is analogous to using pseudorange. For the current experiments, we defined an accumulated phase test statistic in a manner analogous the usual pseudorange residual[7]. In our case, the accumulated phase test statistic is the root sum of squares of the accumulated phase measurement residuals

$$r(t_k) = \sqrt{\delta\Phi^T(t_k)\delta\Phi(t_k)}.$$

Using this scalar as a test statistic requires it to be well correlated with the actual user position error that results from a satellite bias. Figure 10 illustrates this correlation for a static user. The constellation contained 6 satellites at 2 measurement epochs, each epoch being separated by 10 minutes. As before, random phase noise is added to each measurement. A range bias from 0 to 10 meters is applied to each satellite.

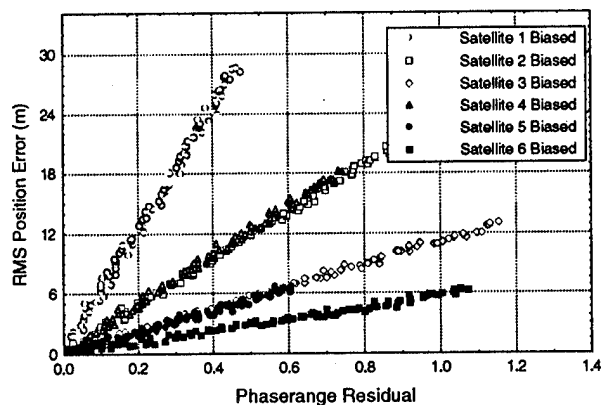


Figure 10: Accumulated Phase Test Statistic Behavior

As we can see in the figure, the differential accumulated phase test statistic is very well correlated with the actual user position error. The measurement noises are sufficiently well behaved that user position errors in the range required for Category I approach are detectable.

CONCLUSIONS

The work presented here is a first step towards performing integrity monitoring using carrier phase. Thus far, it appears that the differential accumulated phase test statistic derived here is much more sensitive to satellite biases than the pseudorange residual. In addition, for the 2mm random measurement errors assumed in the simulations, the test statistic appears sufficiently well correlated to user position error to be useful for Category I approach.

There are, however, many additional issues which are currently under investigation. First, a complete phase-RAIM algorithm is under development and will require additional work to complete and characterize. Second, this work assumes that errors in carrier phase are a proper indicator of satellite failure. Last, it is of interest to determine the viability of the phase-based approach in the presence of anticipated LAAS/WAAS errors.

ACKNOWLEDGMENT

This work was sponsored by the FAA Satellite Program Office through the FAA Office of Research and Technology Applications under Grant Number 92-G-013.

REFERENCES

- [1] D. B. Cox Jr. and W. R. Michelson, "Use of Uncorrected GPS Carrier Phase Measurements for Incremental RAIM with WAAS," *Proceedings of*

- ION 51st Annual Meeting*, Colorado Springs, CO, 5-7 June 1995; pp. 515-520.
- [2] J. M. Durand and T. M. Carlier, "GPS Continuity: Initial Findings," *Proceedings of ION GPS-91*, Albuquerque, NM, 11-13 Sept. 1991; pp. 971-980.
 - [3] "Minimum Operational Performance Specification for Airborne Supplemental Navigation Using Global Positioning System (GPS)," RTCA Document RTCA/DO-208, July 1991.
 - [4] M. A. Sturza and A. K. Brown, "Comparison of Fixed and Variable Threshold RAIM Algorithms," *Proceedings of the Third International Technical Meeting of the Satellite Division of the Institute of Navigation (ION-GPS90)*, Colorado Springs, CO, September 19-21, 1990, pp. 437-443.
 - [5] Brown, R. G., "A Baseline GPS RAIM Scheme and a Note on the Equivalence of Three RAIM Methods," *NAVIGATION, Journal of the Institute of Navigation*, Vol. 39, No. 3, Fall 1992, pp. 301-316.
 - [6] "Appendix F. Baseline Fault Detection and Exclusion Algorithm," F. van Graas, 1993-12-05 WG5/RTCA SC-159.
 - [7] Parkinson and P. Axelrad, "Autonomous GPS Integrity Monitoring Using the Pseudorange Residual," *Navigation: Journal of the Institute of Navigation*, pp. 255-274, vol. 35, no. 2, Summer 1988.
 - [8] "Wide Area Augmentation System", U.S. Department of Transportation, Federal Aviation Administration, Request for Proposal DTFA01-94-R-21474, 8 June 1994. (Commonly referred to as "WAAS RFP".)
 - [9] W. R. Michalson, J. Bernick, et. al., "RAIM Availability for Augmented GPS-Based Navigation Systems," *Proceedings of the 7th International Technical Meeting of the Satellite Division of the Institute of Navigation, ION GPS-94*, pp. 587-595, Salt Lake City, UT, Sep 20-23, 1994.
 - [10] V. G. Virball, P. Enge, W. R. Michalson, and P. Levin, "A GPS Integrity Channel Based Fault Detection and Exclusion Algorithm Using Maximum Solution Separation," *Proceedings of the IEEE 1994 Position, Location, and Navigation Symposium PLANS-94*, pp. 747-754, Las Vegas, NV, Apr 11-15, 1994.
 - [11] R. G. Brown and P. Y. C. Hwang, *Introduction to Random Signals and Applied Kalman Filtering*, John Wiley & Sons, NY, 2nd Ed., 1992; pp. 432-436.
 - [12] Hofmann-Wellenhof, H. Lichtenegger, and J. Collins, "Global Positioning System Theory and Practice," Springer-Verlag, 1993.
 - [13] Noe, K.A. Meyers, and T.K. Wu, "A Navigation Algorithm for the Low-Cost GPS Receiver," *ION Redbooks Volume 1*, pp. 166-172.

An Analysis of Using Carrier Phase to Fulfill Cat III Required Navigation Performance

Dr. David Walsh and Prof. Peter Daly
The University of Leeds

Mr. Tim Rowe
UK National Air Traffic Services

BIOGRAPHIES

Dr. Walsh is a Senior Research and Development Engineer at the Civil Aviation Authority (CAA) Institute of Satellite Navigation (ISN) at the University of Leeds. He obtained a PhD from the University of Nottingham in 1994. He has previously worked as a Research Assistant at the Federal Armed Forces University, Munich and at the Centre for Nuclear Research (CERN) in Geneva.

Prof. Daly is Director of the CAA Institute of Satellite Navigation at the University of Leeds and has been involved with GPS/GLONASS satellite navigation issues since 1982.

Mr. Tim Rowe is a Software Systems Engineer in the Satellite Navigation Sub-Department Division, Directorate of Infrastructure Services at the UK National Air Traffic Services. He is responsible for assessing and investigating the safety issues concerned with future navigation systems.

ABSTRACT

This paper describes an analysis of whether on-the-fly (OTF) carrier phase ambiguity techniques can fulfil the very strict required navigation performance (RNP) of Category III precision approach and landing. While carrier phase techniques have been shown to fulfil the accuracy requirements once the unknown carrier phase ambiguities have been resolved, the integrity, continuity and availability requirements are more difficult to meet because of the ambiguous and less robust nature of carrier phase compared to code phase. It is essential that rigorous techniques are developed to fulfil all these requirements, especially integrity, to determine if carrier phase can be used for Cat III.

A critical analysis of OTF techniques is described in this paper. The impact on integrity of each stage of the ambiguity resolution process is examined. In particular, the final 'resolution' of the ambiguities, which is often loosely defined without reference to associated confidence levels, is addressed in this paper.

The paper also describes the effects on the RNP when using ambiguity resolution techniques in practice due to the unmodelled errors encountered (eg multipath) and varying conditions (eg number of satellites).

A brief analysis of the potential when combining GLONASS and GPS is also given.

INTRODUCTION

Differential positioning using GPS code phase routinely provides accuracies at the metre level. By simultaneously measuring ranges to at least 4 satellites from a GPS receiver on a vehicle, and from a receiver at a reference station of known coordinates, the differential position of the moving vehicle from the reference station can be determined. For centimetre level accuracy it is necessary to use the carrier phase observable. The advantage of using GPS carrier phase measurements is that they are precise to a few millimetres. However, they are ambiguous because the whole number of wavelengths between the satellite and receiver (the integer ambiguity) is unknown. Therefore, in order to use the carrier phase these ambiguities must be resolved. The problem is further complicated by the need to re-determine the ambiguities every time lock is lost on the ranging signal from the satellite (a cycle slip).

This paper assesses the viability of achieving the Required Navigation Performance (RNP) for Category III Precision Approach and Landing using GPS carrier phase observables. Each aspect of RNP is addressed, namely accuracy, integrity, continuity and availability. The effect of ambiguity resolution techniques on these aspects of RNP is described. Particular emphasis is given to ambiguity search techniques. Two elements of search techniques are studied in more detail,

- (i) the integrity of the criteria and tests used to resolve the ambiguities,
- (ii) the time required to resolve the ambiguities under varying conditions.

Finally, a brief analysis of the potential of combining GPS with GLONASS is given.

CAT III REQUIREMENTS

ICAO [1] defines the Required Navigation performance (RNP) of an aircraft positioning system according to four parameters: accuracy, integrity, continuity and availability where:

- **Accuracy** is the ability of the total system to maintain the aircraft position within the total system error (TSE) limit with a 95% probability.
- **Integrity** is that quality which relates to the trust which can be placed in the correctness of the information supplied by the total system. The integrity risk is the probability of an undetected failure of the system to provide the specified accuracy. Integrity includes the ability of a system to provide timely valid warnings to the user when the system must not be used for the intended operation.
- **Continuity** is the ability of the total system to perform its function without interruption during the intended operation. The continuity risk is the probability that the system will be interrupted and not provide the required guidance information during the intended operation.
- **Availability** is the ability of the total system to provide the required guidance at the initiation of the intended operation. Availability risk is the probability that the required guidance will not be present at the initiation of the intended operation.

These RNP requirements proposed in [1] for Cat. III precision approach and landing are given in table 1. The decision heights are given in brackets for the lateral and vertical accuracies. The integrity warning time is shown in brackets and the time of operation for the continuity requirement. The integrity and continuity are per hour.

CARRIER PHASE AMBIGUITY RESOLUTION TECHNIQUES FOR CAT III PRECISION APPROACH AND LANDING

For any Cat. III precision approach and landing system which uses carrier phase, which is either wholly a GPS system, or if GPS forms only part of the system, the performance of the ambiguity resolution algorithm will affect the RNP parameters as follows:

- **Accuracy.** It is necessary to resolve the integer ambiguities in order to be able to use the GPS carrier phase observable to obtain unambiguous ranges for precise positioning. Until the ambiguities are resolved centimetre level positioning will not be achieved. The ambiguities must be resolved within a specified time to obtain the required accuracy early enough on the approach for efficient aircraft traffic management.
- **Integrity.** The ambiguity resolution technique must correctly specify the level of confidence in the position solution. Additionally, after the ambiguities have been

initially resolved the integrity of the resolution can be continuously monitored not only by continuing the initial resolution algorithm, but also by continually re-initialising the resolution algorithm (which requires ambiguity resolution in short periods to be most effective).

- **Continuity.** Once ambiguity resolution is achieved it must be maintained throughout the operation to ensure centimetre level positioning. If cycle slips occur then the ambiguities for the ranges where the cycle slip has occurred must be re-resolved. In the worst case this might apply to enough satellite ranges such that 3D positioning is not available until the ambiguities are resolved. If they can be resolved very quickly then the operation may be able to continue, otherwise a missed approach would have to be initiated. The exact time periods must come from an analysis of RNP. At the very least, unresolved cycle slips reduce the number of satellite ranges available, thus reducing the RAIM capability.

- **Availability.** Centimetre level positioning will only be available when conditions are such that the ambiguities can be resolved.

Clearly, therefore, performance requirements for Cat III precision approach and landing when using an ambiguity resolution technique must include a time element. For example, a definition of the time available to resolve the ambiguities with the required confidence and availability (including details such as the distances from the threshold). The same will be true for any positioning system which may not achieve the accuracy required instantaneously.

The rest of this paper concentrates on the following particular aspects of using satellite navigation systems for Cat III Precision Approach and Landing:

- the integrity of ambiguity resolution techniques (including an analysis of the integrity of the criteria and tests used to resolve the ambiguities in a search technique),
- the variation of the time taken to resolve the ambiguities.

Firstly, a description of the essential steps in a search algorithm is given, followed by a description of an example search technique implemented for this analysis. The steps in the search algorithm are then analysed in more detail.

Ambiguity Resolution using Search Techniques

The ambiguity search technique is the one most often used in on-the-fly applications [2,3,4]. The reasons for using a search technique are as follows:

- it is not affected by numerical instability. A solution is not necessarily dependent on more than

Phase	Lateral Accuracy	Vertical Accuracy	Integrity	Continuity	Availability
Cat III	± 6.0 m (ht = 15 m)	± 0.6 m (ht = 15 m)	3.3×10^{-9} (2 secs)	4.0×10^{-6} (15 secs)	1.0×10^{-3}

Table 1 RNP requirements for Cat III precision approach and landing

one epoch of data if no significant unmodelled errors are present. Therefore, a significant change in satellite geometry is not required for stability. Furthermore, the integers are held fixed so there is greater redundancy.

- Pseudorange observations are only used for the initial estimate of position so the effect of pseudorange multipath is less.

There are many different algorithms for search techniques. However, all search techniques are made up of two basic essential steps which have to be considered in an integrity analysis:

- (i) **Define a Search Volume.** The search volume defines the space in which the correct ambiguity combination will lie, and which contains all possible candidate ambiguity combinations.
- (ii) **Test Ambiguity Combinations.** Two tests must be satisfied if the best ambiguity combination is to be resolved as the correct one,
 - (i) **an acceptance test**, to determine if the best solution fits the data as well as would be expected if it was the correct solution,
 - (ii) **a discrimination test**, to determine if the best solution is significantly better than the rest.

Both these tests are extremely important and directly affect both the time it takes to resolve the ambiguities, and the integrity of the solution. The probability of the final position solution from an ambiguity search technique being correct depends on the probability of the search volume containing the correct solution **and** the probability that the acceptance and discrimination tests have resolved the correct solution.

Example Search Technique

The ambiguity search technique which was implemented to obtain the results given in this paper is described below. This search technique is not optimal and where improvements have been suggested these are noted. However, it should be noted that whatever technique is used the integrity of each stage must be demonstrated to satisfy the Cat III requirements.

The position of the search volume is determined from the position estimate from a differential phase

smoothed pseudorange solution [5], and the size is determined by the standard error of the pseudoranges derived from a least squares adjustment. The search volume is defined in observation space (eg a search window for each range of $\pm 3\sigma$). If the pseudoranges were only affected by white noise this should define a search volume which has a 99.7% probability of containing the correct ambiguity combination. However, the search volume is subject to unmodelled errors in the pseudoranges, particularly multipath. To avoid the correct solution being outside the search volume, and so causing the search to fail, a search window of $\pm 4\sigma$ or $\pm 5\sigma$ is often used. This is usually a subjective decision based on experience. It is also possible to include the code and carrier phase observations in a weighted least squares solution to define the search volume.

Any ambiguity search technique which is used for Cat III precision approach and landing must rigorously define this stage of the process to obtain strict confidence levels for the search volume to contain the correct solution.

All the ambiguity combinations which lie in the search volume are formed. The potential ambiguity combinations are formed using a set of 4 primary satellites which form 3 double difference observations which uniquely define a point in the search volume [2]. The number of ambiguity combinations is defined by the search windows for the 4 primary satellites. Any extra satellites reduce the number of ambiguity combinations because some of the primary ambiguity combinations may be outside the search window from the new satellites. A number of algorithms have been developed [4] which determine the number of ambiguity combinations in an optimised manner and reduce the computation time for the search. Two other methods are the null space method [6] and the LAMBDA method [8]. Whichever method is used, a total number of ambiguity combinations must be formed with the required confidence level of not rejecting the correct solution.

Each remaining ambiguity combination is tested to determine the best one. The test variable is the sum of squares of least squares residuals, including observations from all satellites. The ambiguity

combination with the lowest sum of squares of residuals (or accumulated sum of squares of least squares residuals over time) is the best one. Figure 1 shows the sum of squares of residuals for the correct solution and second best solution for a 30 minute period. Even though initially the second best solution is better or as good as the correct one, eventually the satellite geometry change ensures that the correct one has the lowest residuals.

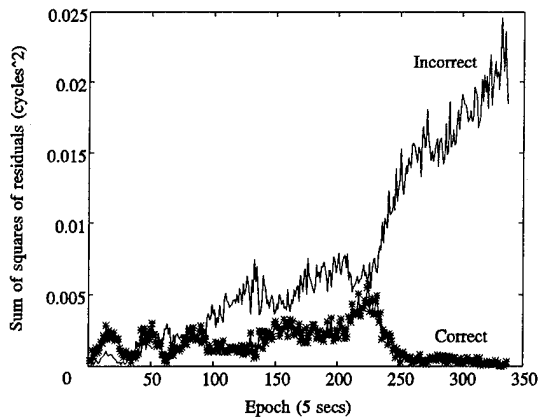


Figure 1 Sum of Squares of residuals for correct and second best ambiguity combinations (cycles²)

Two tests must be satisfied if the best ambiguity combination is the correct one (the acceptance and discrimination tests),

- (i) the variance of the correct solution is below a specified threshold,
- (ii) the variance of the correct solution must be significantly better than the rest of the ambiguity combinations.

In this example the specified threshold could be set from experience and must take account of the effect of unmodelled errors to give a margin of safety. If it is set too low then there is a risk of never resolving the correct ambiguities. However, if it is set too high then there is a risk of resolving the wrong ambiguities.

The second test is usually done by a form of ratio testing using the variances of the ambiguity combinations. The simplest way is to use a fixed ratio, eg 2 or 3. While this might be sufficient if the test is performed after a long period of data has been processed, it is clearly unsatisfactory when there is only a short period of data as it takes no account of the changing degrees of freedom at each epoch and is not statistically rigorous.

In this analysis the Fisher (F) test was used. The F test compares the ratio of the variances against an F ratio which is calculated at the required significance level (99.7%) and which decreases with added observations. If the actual ratio is greater than the F ratio then the variance of the best ambiguity combination is significantly different and it can be resolved. This is dealt with in more detail below.

STATISTICAL TESTS TO RESOLVE AMBIGUITIES

In this section the criteria for resolving the ambiguities using a search algorithm will be examined in more detail.

Definition of Ambiguity Resolution for Search Techniques

Two statements can be made about the correct solution and the incorrect solution.

The least squares residuals of the correct solution will be normally distributed with zero mean and with variance σ_v^2 , where σ_v^2 is the variance due to the measurement noise alone (given no unmodelled errors).

The least squares residuals of the incorrect solution will not be normally distributed and will not have a zero mean and the variance will be greater than σ_v^2 , where σ_v^2 is the variance due to the measurement noise alone (given no unmodelled errors).

The acceptance and discrimination tests devised to resolve the ambiguities are likely to be based on the above statements.

Effect of Unmodelled Errors

Before discussing the statistical tests used it is worthwhile to mention the effects of unmodelled errors. If significant coloured noise effects are present over the period of observations (ie from multipath or the troposphere) then this could have an effect on:

- the distribution of the residuals of the correct and incorrect solutions
- the correlation between the residuals of the correct and incorrect solutions

Therefore, when any statistical tests are analyzed it is necessary to consider the effects of unmodelled errors. If possible, it might be necessary to quantify these effects to determine whether they are significant.

ACCEPTANCE TEST

A number of acceptance tests are described below.

Acceptance test based on Variance

In the algorithm described above the acceptance test determines whether the variance of the best solution (σ_{Best}^2) is better than or equal to the expected variance of the correct solution. An *a priori* value (σ_{ap}) was used to set the threshold. If the variance was greater than the threshold then the best solution was not accepted. In other words the null hypothesis, H_0 , is

$\sigma_{\text{Best}}^2 \leq \sigma_{\text{ap}}^2$ and the alternative hypothesis is $\sigma_{\text{Best}}^2 > \sigma_{\text{ap}}^2$. The value of σ_{ap} is often set from experience. It would also be possible to obtain an *a priori* value from the receiver carrier phase tracking loop which would include a multipath contribution. However, in any situation where an *a priori* value is used uncertainty exists as to whether it is appropriate for the particular conditions (ie unmodelled errors as stated above).

An alternative is to use information from actual observations. In [8] and in the FARA technique for static surveying [9] a float solution is determined and the variance of the candidate integer solution is compared to the variance of the float solution ($H_0: \sigma_{\text{Best}}^2 \leq \sigma_{\text{float}}^2$, $H_1: \sigma_{\text{Best}}^2 > \sigma_{\text{float}}^2$). The test statistic is given by

$$D = \frac{\frac{\sigma_{\text{Best}}^2}{n-m}}{\frac{\sigma_{\text{Float}}^2}{n-m-a}}$$

where D is assumed to have an F distribution, m is the number of position and clock unknowns, a is the number of ambiguity unknowns and n is the number of observations. The test statistic D could then be compared with an appropriate threshold, T. T would be determined from the standard F distribution according to the required significance level. This test is making the assumption that the distributions of the variances of the best solution and the float solution are normal and that they are independent.

The disadvantage of using a float solution in a precision landing application is that there will only be a limited period of time to obtain data. The problem is that there are an increased number of unknowns because the ambiguities have to be estimated. Therefore, a significant satellite geometry change is required to give a numerically stable solution. In a short period the satellite geometry change might not be sufficient to ensure numerical stability. This would affect the variance of the float solution. If it was too large then there is a greater chance of accepting an incorrect solution. If it is too small then there would be a greater chance of rejecting the correct solution.

The stability of the float solution could be increased either by:

- (i) taking a longer period of data,
- (ii) using pseudolite observations,
- (iii) using the pseudorange measurements in a weighted least squares solution.

In a Cat III situation there will be a limited amount of time to take more data. Any ambiguity technique must demonstrate that the probability of obtaining a useable float solution in the time available is sufficiently high.

If not, the probability of having to abort a landing would be too high.

Using pseudolite observations, which give a greater geometry change because of the aircraft overflight, would increase the numerical stability of the least squares solution in a shorter period of time. The third option significantly increases the stability of the least squares solution if precise pseudoranges are available.

Clearly, if the float solution is used as a comparison then some criteria must be used to assess whether the variance of the float solution can be used, and with what level of confidence. The ability to obtain good data within this period may also be constrained because of cycle slips, or atmospheric effects at distances of over 10 km. Therefore, the effect on the float solution residuals of unmodelled errors need to be taken into account. It must be determined if this would be significant. In addition unmodelled errors would mean that the distribution of the residuals would not be normal with zero mean.

Whichever method is used for the acceptance test it is perfectly possible for incorrect ambiguity combinations to pass the acceptance test for limited periods of data before the satellite geometry takes effect. Equally, given significant unmodelled errors, it is possible for the correct solution to have residuals which do not satisfy the acceptance test for a short period unless the threshold is set to take account of these unmodelled errors.

In summary, if an *a priori* value is used for an acceptance test it must be ensured that this is representative, and if a value is used from a float solution then it must be ensured that this is a sufficiently good estimate.

Acceptance Test based on the Distribution of Residuals

As stated above the residuals for the correct solution should be normally distributed and the residuals for the incorrect will not be normally distributed. Therefore, it would be possible to test the normality of the distribution of the best solution.

One test which could be used is the chi-square test of goodness of fit. The null hypothesis is $H_0: N(\mu, \sigma)$ and the alternative hypothesis is $H_1: \neq N(\mu, \sigma)$. No assumptions are made about μ and σ at this stage so they are determined from the sample. The range of the distribution is divided into p mutually exclusive and exhaustive intervals. If O_i is the number of variates in the *i*th interval and E_i is the number expected in a normal distribution then it can be shown that the statistic

$$\chi^2 = \sum_{i=1}^p \frac{(O_i - E_i)^2}{E_i}$$

has the chi-square distribution with $p-1-q$ degrees of freedom where q is the number of statistics drawn from the sample. Given the required level of significance the chi-square percentile can be determined and if it is greater than the χ^2 statistic then the null hypothesis is accepted. The problem with using this test is that a significant sample size is required (>50 [10]) and the class intervals must be carefully chosen because E_i must be greater than about 5 [10] for all i ; this is a problem towards the tails of the pdf where E_i becomes very small. Otherwise there is a chance that a small variation in O_i would bias the result. In practice this test has been shown to be very sensitive to the choice of class size with a limited sample size, ie 200 epochs of data. This suggests that this test would be of limited use in a real time application like Cat III precision approach and landing.

A further problem is that due to unmodelled errors (particularly multipath and atmospheric errors) there is a significant chance that the distribution of the residuals of the correct solution will not be normal. Clearly, any test of normality must have a margin of error to avoid rejecting the correct solution. If it is possible to quantify the unmodelled errors present then this would allow a margin of error to be quantified.

One of the main issues identified at the beginning of this section was the question of whether the distributions of the variables used in the statistical tests are correct. Therefore, while a test for normal distributions may not be used as a test of acceptance, such a test is required for monitoring the distributions of variables used in other tests, eg the F test.

DISCRIMINATION TESTS

The main problem with a discrimination test is that the tests include incorrect solutions and it is difficult to make assumptions about the distributions of the residuals of incorrect solutions. This is because incorrect solutions by their definition will have, most probably, more than one incorrect range due to wrong values for the ambiguities. This, in turn, means that the residuals will not be normally distributed with zero mean. For example, a standard RAIM algorithm will not be appropriate because it assumes that only one range is in error. It is also possible that for a limited period of time the residuals of an incorrect solution will appear to be normally distributed, because of measurement noise and unmodelled errors, before the effect of geometry is seen. This could be a factor in any statistical tests used.

Further effects of unmodelled errors need to be borne

in mind at this point. Unmodelled errors will increase the residuals of the correct solution. However, they could increase or decrease the residuals if incorrect solutions. Therefore, this could cause a discrimination test to be either optimistic or pessimistic.

Discrimination Test of Variances

In the algorithm described above the discrimination test was carried out using a Fisher (F) test which compared the variances of the best two solutions. If the variance of the best solution was significantly better than the second best then the best solution was chosen as the correct one, providing that they had passed the acceptance test. Therefore, the null hypothesis H_0 is $\sigma_1^2 = \sigma_2^2$ and the alternative hypothesis H_1 is $\sigma_1^2 \neq \sigma_2^2$. The test procedure is similar to the acceptance test using the float solution described above. Firstly, the ratio of variances is calculated for all the data over the required period. Then the F ratio is calculated at the level of significance required for the correct degree of freedom. If the determined ratio is greater than the F ratio then the variances of the two solutions are considered to be significantly different.

The problem with using the F test is that it requires both variances to come from samples with zero mean and with a normal distribution. This is not the case for any incorrect ambiguity combination as described above. This is an important fact which poses a problem when using comparative tests in search techniques. The performance of the F test is good in practice but it must be determined if such a technique will fulfil the integrity requirements for Cat III precision approach and landing.

Discrimination Test comparing Different Means

Just as it is possible to compare the variances of two samples so it is possible to compare the means of two samples ($H_0: \mu_1 = \mu_2$ and $H_1: \mu_1 \neq \mu_2$). The test statistic when testing normal means of two samples with unknown variances is

$$\frac{\mu_1 - \mu_2}{\sqrt{\frac{s_1^2}{n} + \frac{s_2^2}{m}}}$$

(n is the number of residuals in sample 1, and m is the number of residuals in sample 2). However, it does not have a t-distribution when H_0 is true. Its distribution is the Behrens-Fisher distribution. Even though in this case $n=m$, because the redundancy for both samples is the same, there is no exact single stage solution [10]. However, this test still requires that the distribution of the residuals of both solutions is normal and that they are independent, which is untrue on both counts for the incorrect solution.

An alternative test would be to, in effect, repeat the acceptance test for the mean of the second best solution, ie resolve the ambiguities if $\mu_2 \neq 0$, given $\mu_1 = 0$ from the original acceptance test. Again the fact that the residuals for the second best solution are not normally distributed will cause problems.

Discrimination Test using Pair Tests

A possible discrimination test which would avoid the problem of non-normal distributions is a pair test. The test statistic D is given by

$$D^k = r_1^k - r_2^k$$

where r_1^k is the residual for satellite k for the best solution and r_2^k is the residual for satellite k for the second best solution (for the same measurement z^k). The central limit theorem states that for small sample sizes D^k will be normally distributed even though r_2^k is not. Therefore, the problem of the non-normal distribution for incorrect solutions is avoided. Clearly, however, it must be ensured that the central limit theorem holds for the sample size in question. A multivariate test could be set up for a combined test statistic ΣD^2 to include data from all satellites. Initial analysis suggests that the fact that the residuals from the two solutions are not independent affects only the derivative of the D^k statistic with time which is not a problem. Further analysis is required to determine whether the test performs as expected and produces reliable statistics.

An important point about the distributions used in the statistical test should be noted. It is not necessary to be able to exactly describe the distributions used if it can be shown that the probabilities derived from the distributions will be pessimistic. Therefore, if any statistical tests, and assumed distributions of the variables used in the tests, are found not to be as required then further analysis is required to determine if,

- (i) the difference is not significant,
- (ii) the result can only be pessimistic which produces a safer system than required.

VARIATION OF THE TIME TO RESOLVE THE AMBIGUITIES

A series of tests has been carried out to look at the variation of the time taken to resolve the ambiguities in varying conditions [5]. A summary of the results of two tests is shown in this section.

The effect of unmodelled errors (eg multipath, ionospheric and tropospheric effects) is determined by processing a number of consecutive short periods of static differential carrier phase data during which all conditions are the same (eg 6 satellites, similar satellite geometry). The widelane (L1-L2) observable was used

and the distance was approximately 1 km. Any variation in the results is most likely due to varying unmodelled errors. The results are shown in Table 2.

Period	Time Found (secs)	Time Resolved (secs)	Ratio
1	1	5	7.5
2	5	-	1.1
3	1	5	7.3
4	55	65	2.3
5	60	-	1.1
6	1	15	6.3
7	1	10	4.5
8	10	15	4.9

Table 2 Time ambiguities are found and resolved for different periods (secs)

The second column gives the time at which the correct ambiguity combination became the best one, the third column gives the time the correct ambiguities were resolved (ie passed the acceptance and discrimination tests). The fourth column gives the ratio of the accumulated sum of squares of residuals of the best and second best ambiguity combination at the end of the period.

The correct ambiguities are not resolved in two of the eight periods, whereas they are resolved after 5 seconds in two others. In the periods where they are resolved the time varies considerably in one case. The ratio further demonstrates the variation. The greater the ratio the more confidence there is that the correct ambiguities have been resolved. Clearly the confidence level varies. These results were obtained in a high multipath environment with an algorithm which can be further optimised and were chosen to demonstrate the variation which is possible. However, any ambiguity resolution algorithms proposed for Cat III precision approach and landing must demonstrate the required consistency.

The time taken to resolve the ambiguities using different numbers of satellites is given in Table 3. The baseline distance is just over 10 km and the widelane observable was used. ('1' means resolved instantaneously, '-' means not resolved).

Clearly, the ambiguities are generally resolved more quickly with more satellites. This is not always the case which is probably due to poor pseudoranges from

Period	Number of Satellites		
	8	7	6
1	15	40	-
2	20	20	40
3	10	15	15
4	5	10	30
5	20	15	60
6	5	30	95
7	70	80	100
8	10	1	-
9	15	25	15
10	5	20	45

Table 3 Time to resolve the ambiguities for different numbers of satellites (secs)

new satellites at low elevations. When 8 satellites are available the ambiguity resolution times are more consistent. As would be expected these results suggest that a greater number of satellites is more likely to satisfy Cat III precision approach and landing requirements. The availability of the required conditions for ambiguity resolution (eg number of satellites, satellite geometry) will determine the overall availability for Cat III applications.

Two things should be noted at this point. Firstly, these results are only isolated examples to illustrate a point and will not be representative of more optimised systems; particularly those which use combinations of systems, eg pseudolites. Secondly, the actual time available for ambiguity resolution must be defined to determine if various techniques can resolve the ambiguities quickly enough.

GPS/GLONASS COMBINED INTEGRITY AND AVAILABILITY

For Cat III precision approach and landing a number of issues will affect the satellite availability required.

- The high accuracy and integrity requirements.
- The choice of method to be used. The possible methods to be used to achieve Cat III have yet to be fully specified or analyzed. If an ambiguity resolution system is used, without pseudolites, then this may require 7 satellite availability. If pseudolites are used then this reduces the number of satellites required, although exactly how many

are needed to fulfil the total RNP needs to be determined.

- The time available to perform Cat III precision approach and landing. For example, if a long time period is available then perhaps only 6 satellites will be required for ambiguity resolution using a search technique.

Using GLONASS as well as GPS obviously increases the number of satellites and, therefore, improves the redundancy and the satellite geometry. It also provides an independent positioning system. Sturza and Brown [12] state that simulation results have shown that a combined GPS/GLONASS constellation would provide continuous, world-wide RAIM coverage even in the event of six satellite failures (3 GPS and 3 GLONASS).

It should be noted that no attempt is made to use the results in this paper to prove that specific integrity requirements can be fulfilled, such a decision cannot be made from limited data sets or landing experiments. Instead the main aim of the results is to compare the performance of GPS alone and GNSS.

The minimum number of satellites available using GPS and GLONASS, and GPS alone for a section of the earth's surface are shown in the figures 2 and 3. The results are shown for an area of the earth's surface bounded by the equator and 80° line of latitude, and the 30° West and 40° East lines of longitude. The number of satellites is calculated for a 2°x2° grid square. The number of satellites were calculated over a single 24 hour period. At that time there were 25 GPS satellites available (including 1 Block I satellite) and 22 GLONASS satellites. The number of satellites are calculated for a 10° elevation mask.

The fact that no attempt to model possible masking due to objects above the nominal elevation mask should be noted when interpreting the results. Equally, it has been assumed that all the available satellites are healthy for the whole period. This will obviously not be the case in reality and a model for satellite outages should be used.

The improvement of GNSS satellite availability over GPS can be seen. There are always more than 8 satellites with GPS/GLONASS. Importantly, this demonstrates that, in this region, using both GPS and GLONASS has a better chance of providing the satellite availability for demanding applications.

CONCLUSIONS

A number of issues require further analysis if search techniques for ambiguity resolution are to be used for Cat III landing using the carrier phase observable.

- The precise method of ambiguity resolution needs

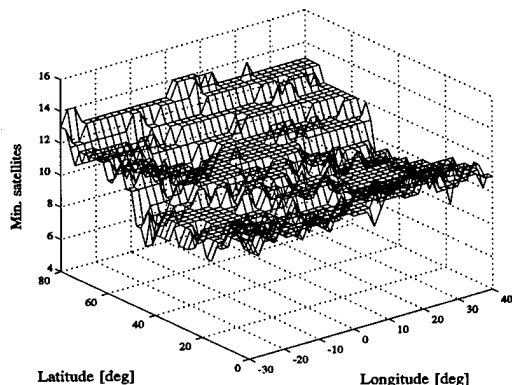


Figure 2 Minimum number of GPS/GLONASS satellites with a 10° elevation mask

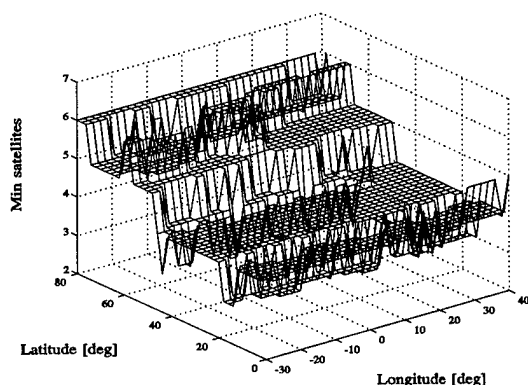


Figure 3 Minimum number of GPS satellites with a 10° elevation mask

to be further defined, including the acceptance and discrimination tests used.

- The distributions of the statistical variables used in any tests must conform to the correct distribution (ie if a chi-square distribution is required then the variable used (eg the variance of the incorrect solution) must be chi-square).
- A test is required to determine if sufficient data has been taken to have the required confidence in any decision about the distributions and the acceptance and discrimination tests.
- The tests must account for the fact that the residuals of any two potential solutions are not independent.
- The effects of unmodelled errors on the statistical tests must be determined.
- It must be possible to derive statistics from the ambiguity resolution tests which conform to the integrity requirements for Cat III (eg probability of missed detection).

- Combining GPS and GLONASS has a lot of potential for increased RNP.

ACKNOWLEDGEMENTS

The authors are grateful to Dr Stuart Riley and other members of the ISN for their help with this work.

DISCLAIMER

The opinions expressed in this paper are the authors own and not necessarily those of the organisations concerned.

REFERENCES

- [1] ICAO, 'International Standards, Recommended Practices and Procedures for Air Navigation Services - Annex 10', ICAO, April 1985
- [2] Hatch, R, "Instantaneous Ambiguity Resolution", Proc. of KIS Symposium, Banff, Canada, 1990.
- [3] Remondi, B, "Real Time Positioning Using GPS: Initialising While in Motion (Warm Start vs Cold Start)", ION GPS-92, ION Satellite Division, 5th International Technical Meeting, Albuquerque, New Mexico, September 16-18, 1992.
- [4] Landau, L, and H-J Euler, "On-The-Fly Ambiguity Resolution for Precise Differential Positioning", ION GPS-92, ION Satellite Division, 5th International Technical Meeting, Albuquerque, New Mexico, September 16-18, 1992.
- [5] Walsh, D, "A Feasibility Study of Category III Precision Approach and Landing using GPS, GLONASS and Pseudolites", Report submitted to UK CAA, June 1995.
- [6] Martin-Neira, M et al, "The Null Space Method for GPS Integer Ambiguity Resolution", DSNS95, Bergen, Norway, April 1995.
- [7] Hatch, R, "Instantaneous Ambiguity Resolution", Proc. of KIS Symposium, Banff, Canada, 1990.
- [8] Tiberius, C, et al, "Fast positioning using the Lambda Method", DSNS95, Bergen, Norway, April 1995.
- [9] Frei, E, and G Beutler, "Rapid Ambiguity Resolution based on the Fast Ambiguity Resolution Approach 'FARA': Theory and First Results", Manuscripta Geodetica 1990, 15:pp 325-356.
- [10] Parsons, R, "Statistical Analysis: A Decision Making Approach", Harper and Row.
- [11] Dudewicz, J, and Mishra, S, "Modern Mathematical Statistics", Wiley.
- [12] Sturza, M and A Brown, "Comparison of Fixed and Variable Threshold RAIM Algorithms", Proc of ION GPS-90, Colorado Springs, Colorado, September 19-21, pp437-443.

Weighted RAIM for Precision Approach

Todd Walter and Per Enge
Stanford University

Abstract

The use of differential GPS is becoming increasingly popular for real-time navigation systems. As these systems migrate to safety-of-life applications (e.g. precision approach and landing), their integrity becomes more important than their accuracy. One method for increasing both accuracy and integrity is the use of weighting in the navigation solution. This method uses *a priori* information to weight certain satellites (e.g. those at higher elevation) over other satellites. The accuracy increases because we better use the information available. The integrity increases because satellites that are more likely to introduce error contribute less to the solution.

A weighted position solution by itself does not provide sufficient integrity to support precision approach. However, this method can be combined with a weighted form of Receiver Autonomous Integrity Monitoring (RAIM) to increase the level of integrity. RAIM uses redundant measurements to check the consistency of an overdetermined solution. This check is crucial because only a user can detect certain error types (e.g. severe airframe multipath or local interference). A differential reference station can detect many types of errors. However, it is only at the user where all the information is combined. The use of RAIM (or some form of integrity at the user) must be combined together with integrity checking at the reference station to provide the overall safety of the system.

Weighted RAIM is investigated for application to Category I precision approach as supported by a Wide Area Augmentation System (WAAS). This paper details how to implement weighted RAIM and how to use geometry selection to guarantee a certain level of protection. Also, we provide information on the availability of these geometries. The results are based upon analysis, Monte Carlo simulation and actual data

collected from Stanford University's wide-area differential GPS network.

1.0 Introduction

The use of differential GPS in a safety-of-life application, such as precision approach, requires that the system provide accurate navigational information with a high degree of integrity. Any potentially hazardous or misleading piece of information must be flagged as such, *before* it leads to a positioning error. The most robust way to ensure that the information is valid is to have a multi-layer series of checks with as much independence between the layers as possible. Ideally the validity of the corrections would be verified both on the ground and in the air. Receiver Autonomous Integrity Monitoring (RAIM) is one possible method to check the validity of the corrections in the air.

RAIM is a simple yet powerful technique to check the consistency of the navigation solution. This paper presents the weighted form of RAIM and how it can be applied to precision approach. Specifically, we will concentrate on Category I precision approach as will be supported by the Wide-Area Augmentation System (WAAS). WAAS is the FAA's implementation of Wide-Area Differential GPS (WADGPS) coupled with ground integrity monitoring and supplemental ranging signals.

Although the availability results presented in this paper are specific to WAAS, the application of weighted RAIM can readily accommodate many different systems. This method can be applied to local-area differential GPS and it can also be applied to the use of additional augmentations such as GLONASS satellites, barometric altimeters or precise user clocks, to name a few. The main reason to use the weighted form of RAIM is that some satellites (chiefly those nearer to the horizon) are more likely to suffer from greater errors than other

satellites. Instead of treating all satellites equally, we can reduce the contribution from satellites likely to be "noisier" by reducing their weighting. Which satellites should be de-weighted can be determined through *a priori* information or through use of weights broadcast from the source of the differential corrections. The GPS satellites currently broadcast weighting information in the User Ranging Accuracy (URA) parameters.

This paper begins with a brief overview of WAAS and of the integrity that will be provided by its ground network. Next we will discuss using weighting information to improve the position solution and how to implement RAIM in its weighted form. Finally, we will present the results of our analysis and of our Monte Carlo simulations followed by our conclusions.

2.0 WAAS Ground Network Integrity

The Federal Aviation Administration (FAA) of the United States is rapidly developing a system to incorporate WADGPS [1] with other augmentations to create a system that is capable of providing navigation information with sufficient accuracy, integrity, availability and continuity to be used to support Category I precision landings. This Wide Area Augmentation System (WAAS) will initially be available as a supplemental means of navigation by the end of 1997.

The WAAS ground network contains three components: Wide Area Reference Stations (WRSs), Wide Area Master Stations (WMSs) and Ground Earth uplink Stations (GESs). The reference stations consist of dual frequency GPS receivers with antennae located at surveyed sites which also have clear visibility to the horizon. Also attached to each WRS receiver is an atomic clock, a meteorological station and a datalink to the master station. The WRS sends back to the WMS the raw GPS observables, the meteorological measurements and the broadcast ephemeris and GPS data.

The master station uses the information to separate the observed pseudorange errors into contributions from satellite clock error (including SA), satellite ephemeris error, ionospheric delay and tropospheric delay. The first three components are broadcast to the user. This information will be incorporated with a standard model of tropospheric delay to construct the scalar pseudorange correction valid at the user location.

The data is broadcast to the user via the GES and a geostationary satellite. The geostationary satellite will broadcast the WAAS data together with a ranging signal. This satellite signal will appear very similar to a GPS

satellite signal except that it will from a geostationary source and it will send information at a 250 rather than 50 bit per second rate. All of the WADGPS corrections in addition to integrity information will be contained in these 250 bps messages.

This system has been described in more detail elsewhere [1-3] [11][12]. Previous attention has been paid principally to the accuracy achievable with WADGPS. This paper instead concentrates on the integrity aspects of WAAS and will focus primarily on user algorithms. The following subsections will describe how integrity is built into the ground network of WAAS to insure the quality of the broadcast messages. In addition, they will outline how an independent set of ground monitors can be used to augment integrity in local areas.

2.1 Reference Station Integrity

Each WRS can separate its measurements satellite by satellite because each WRS antenna is at a surveyed location and because we are using very stable atomic clocks. Each measurement of pseudorange, from the WRS to a satellite, is almost entirely independent of all of the other satellites. Therefore it is possible to detect errors in the pseudorange nearly instantly. However, the WRS does not necessarily have enough information to separate correctable errors (such as SA or small ephemeris offsets) from uncorrectable errors (large satellite clock or ephemeris errors outside of the field of the 250 bit correction message). Additionally, a single receiver may not be able to distinguish between errors originating at the satellite and errors originating at the receiver (channel bias or excessive multipath). Therefore the best location to make integrity decisions is at the WMS.

2.2 Master Station Integrity

Each WMS concentrates the information from multiple WRSs. Here it can perform a consistency check to determine the likelihood of an error. Each WRS has redundant receivers and each satellite is often observed by multiple WRSs. Therefore, in the event of an error, the WMS should be able to isolate the faulty component and take appropriate actions. If one receiver's measurements do not agree with several others (including one or two others at the same location) then the receiver can be declared failed and removed from the solution. If, on the other hand, all of the receiver measurements are consistent but there is a problem with the estimated satellite clock or ephemeris errors, then the WMS would broadcast a message not to use that satellite (or at least to give it a lower weighting). Examples of observable problems would include: errors beyond the maximum range permitted by the 250 bit messages, a lack of consistency between current and previous estimates or a disagreement between new measurements and the derived model.

As a further measure of integrity the WMS can compute an expected user accuracy model for its service region. This model would combine information about the confidences of the measurements, the locations of the measurements and reasonable uncertainties in the models used to form the corrections. Thus, the WMS could determine whether certain geographical locations might suffer from inaccurate corrections due to poor observing conditions.

The final check of the corrections can be performed either at the WMS or at the GES. This check compares the broadcast corrections (and warnings) generated at one WMS to those generated by another. These WMSs could share all of the same WRSs or use different subsets. This comparison would help to mitigate undetected errors in any one WMS. This check is different from the pseudorange comparison because it compares the final calculations. Errors introduced by the WMS itself in addition to measurement errors propagated through the system may be found in this manner.

To guard against data corruption, the WMS 250 bit message includes 24 bits of Cyclic Redundancy Checks (CRCs). The 24 CRC parity bits provide protection against both burst and random errors with a probability of undetected error being less than 6×10^{-8} [4]. This measure reduces the likelihood that valid WMS data would be wrongly interpreted by the user resulting in an erroneous correction.

2.3 Monitor Station Integrity

While the above integrity algorithms should protect against a wide variety of error modes, it is still conceivable that some error modes might pass undetected through the system. Most notably, local disturbances in the ionosphere or troposphere may not be detected by distant reference stations, and yet, through some extremely unlikely combination, create a significant positioning error.

One possibility to detect such effects is to co-locate WAAS capable receivers at the local Air Traffic Control (ATC) centers. Because these receivers would have their antennae positions at known pre-surveyed locations it would be possible to determine if the position solution obtained is of sufficient accuracy to support Category I precision approach. A pilot desiring to make such an approach must contact ATC, who would then check if their local WAAS monitor indicates sufficient system accuracy. Because the WAAS Monitor is close to the region of operation of the airplane a great many possible errors should be common to the monitor and the airplane.

This is a powerful cross-check of the WAAS because the monitors are independent of the WAAS ground network. It is feasible (although extremely unlikely) that some form of common-mode error could propagate through the WAAS ground network undetected, due to its interconnectedness. However, these independent ground stations should be able to detect any significant error of this kind, in addition to flagging errors caused by local ionospheric or tropospheric disturbances.

A very attractive feature is that the monitor station directly measures any error in the positioning domain (as opposed to the pseudorange or ionospheric delay domain). Therefore, if the error is not detected by the monitor station, it is unlikely to lead to a positioning error at the user (provided the same set of satellites is used both on the ground and in the air). Additionally this receiver need not be expensive. A single frequency receiver of the similar to those used in the airplanes would suffice. The main differences would be in the software and the surveying of the antenna.

The best method to protect against potential errors (both foreseen and unforeseen) is to have multiple, independent, redundant systems. The level of redundancy built into the WAAS ground network provides a high degree of integrity. The addition of a "shadow" set of independent monitor stations offers an even greater level of protection against a wider class of possible failure modes.

3.0 Weighted Position Solution and RAIM

For stand alone GPS, the dominant error is caused by Selective Availability (SA). Consequently, there is little advantage in weighting one satellite over another. Errors are separated into geometrical factors (DOPs) and User Ranging Accuracies (URAs). However, with differential GPS, some satellites may have predictably larger errors than others. As an example, it may be desirable to give higher elevation satellites more weighting when performing a position solution. Low elevation satellites suffer from greater multipath effects, increased tropospheric delay uncertainty and usually have a lower Signal-to-Noise Ratio (SNR).

There are several advantages to weighted position solutions: the position fix is more accurate; it is more robust because satellites that are more likely to have errors contribute less to the solution; and the discontinuities in the position fix caused by rising and setting satellites are greatly reduced. While many readers may be familiar with

DOPs and URAs, there is less familiarity with the weighted position solution. This section presents a brief derivation of the weighted form of the Receiver Autonomous Integrity Monitoring (RAIM). We begin by first showing the weighted least-squares navigation solution. Next we show how the consistency of the redundant measurements may be used to generate a test statistic. Finally, we present necessary conditions for this consistency check to gauge the accuracy of the solution.

It is important to have integrity checking at the user because this is the only place where all information used to form the position solution is present. There are many possible error modes that may only affect the user. These include: excessive multipath, receiver error, poor differential corrections resulting from data drop-out and localized ionospheric or tropospheric effects. While these error modes are extremely unlikely, they may not be detectable by either the WAAS ground network or the local monitor station. Therefore, some form of integrity checking must take place within the user's equipment. RAIM is easily implemented, requires no additional hardware and is capable of providing this final layer of integrity.

3.1 Weighted Position Solution

The basic linearized GPS measurement equation is

$$y = G \cdot x + \varepsilon$$

where x is the four dimensional position vector (north, east, up and clock) about which the linearization has been made, y is an N dimensional vector containing the raw pseudorange measurements minus the expected ranging values based on the location of the satellites and the location of the user (x), G is the observation matrix and ε is an N dimensional vector containing the errors in y .

The weighted least squares solution for x can be found by

$$\hat{x} = (G^T \cdot W \cdot G)^{-1} \cdot G^T \cdot W \cdot y \equiv K \cdot y$$

where the definition has been made for K (the weighted pseudo-inverse of G) and where W is the inverse of the covariance matrix. For simplification we will assume that the error sources for each satellite are uncorrelated with the error sources for any other satellite. Therefore, all off-diagonal elements are set to zero. The diagonal elements are the inverses of the variances (σ^2 s) corresponding to each satellite. While this assumption may not be strictly true, it should be a reasonably good approximation. The equations subsequently derived do not

depend on this assumption. It only makes them easier to implement in practice.

Because the satellites are weighted unequally, we can no longer separate the expected positioning errors into a geometrical factor (DOP) and a user ranging accuracy (URA, or σ , common to all satellites). Instead these values are combined into expected positioning confidences. Instead of VDOP given by

$$VDOP \equiv \sqrt{[(G^T \cdot G)^{-1}]_{33}}$$

we now have σ_v given by

$$\sigma_v \equiv \sqrt{[(G^T \cdot W \cdot G)^{-1}]_{33}}$$

as a measure of the confidence of the vertical accuracy. In a similar manner the horizontal confidence HRMS can be given by

$$HRMS \equiv \sqrt{[(G^T \cdot W \cdot G)^{-1}]_{11} + [(G^T \cdot W \cdot G)^{-1}]_{22}}$$

These measures give the 1-sigma expected accuracy in the vertical dimension and the 2-dimensional RMS expected accuracy in the horizontal dimensions respectively. The accuracies of these measures depend on the accuracies of the satellite covariances in the W matrix.

3.2 Weighted RAIM

So far we have only presented the weighted position solution. Now we wish to assess the accuracy of the least squares fit to the data. The quantity we are most interested in is the positioning error ($\hat{x} - x$). Unfortunately it is not possible to obtain a direct measurement of this quantity, unless we were to have access to an independent, more accurate positioning system. Instead, we can examine the overall consistency of the solution. Provided we have more than four measurements, the system is overdetermined and cannot be solved exactly. This is why a least squares solution is performed in the first place. Since all of the conditions realistically cannot be met exactly, there is a remaining error residual to the fit. By quantifying how closely we were able to make all the observations agree, we can get an estimate of the goodness of the fit. Then we make the assumption that if the fit was good, the error in position is most likely small. This is the foundation for RAIM.

We can get an estimate of the ranging errors from the least squares fit and the basic measurement equation

$$\hat{\varepsilon} = y - G \cdot \hat{x} = (I - G \cdot K) \cdot y \equiv (I - P) \cdot y$$

where the definition has been made

$$P \equiv G \cdot K = G \cdot (G^T \cdot W \cdot G)^{-1} \cdot G^T \cdot W$$

From these error estimates we can define a scalar measure defined as the Weighted Sum of the Squared Errors

$$WSSE = \hat{\varepsilon}^T \cdot W \cdot \hat{\varepsilon} = [(I - P) \cdot y]^T \cdot W \cdot [(I - P) \cdot y]$$

which is equivalent to

$$WSSE = y^T \cdot W \cdot (I - P) \cdot y$$

We use \sqrt{WSSE} as our test statistic in order to judge the goodness of the least squares fit. This statistic is observable whereas the positioning error of the least squares solution ($\hat{x} - x$) is not. Therefore, for integrity purposes we want to use the statistic to flag bad position solutions. Typically, a certain threshold is selected. If the statistic exceeds that threshold the position fix is assumed to be unsafe. However if the statistic is below the threshold, then the position fix is assumed to be valid. Thus, the statistic-vertical error plane is broken up into four regions consisting of: normal operation points, missed detections, successful detections and false alarms (See Figure 1). Ideally, there would never be any missed detections or false alarms.

The threshold T , is chosen such that the probability of false alarm is commensurate with the continuity requirement for precision approach. Under normal conditions, if we assume ε_i is a normally distributed zero mean random variable with a standard deviation of σ_i for all N satellites in view, then the statistic is a chi-square distributed variable with $N-4$ degrees of freedom. Therefore the threshold T can be selected analytically. $T(N, P_{FA})$ will only be a function of the number of satellites (N) and the desired probability

of false alarms (P_{FA}). By examining the distribution it is possible to find the value $T(N, P_{FA})$ such that, for normal conditions, the statistic only has a probability of P_{FA} of exceeding it. Given the probability of false alarms, the threshold is found by inverting the incomplete gamma function [5] [9] [10]

$$1 - P_{FA} = \frac{1}{\Gamma(a)} \int_0^{T^2} e^{-s} s^{a-1} ds$$

where a is the number of degrees of freedom divided by two, or in terms of the number of measurements N

$$a = \frac{N-4}{2}$$

The best way to find the values for $T(N, P_{FA})$ is through an iterative root finding process. Note that these values can be easily computed beforehand and stored for use later in a RAIM algorithm. For convenience several such values are listed in Table 1.

3.3 Protection Levels

Unfortunately, the N errors in the vector ε are mapped into two orthogonal spaces; one of dimension 4 corresponding to the position solution error and one of dimension $N-4$ corresponding to our statistic. Thus, in the most general case, the statistic cannot be used absolutely to indicate a bad or a good position solution. However, in the case of a single satellite failure, it is possible to restrict the satellite geometries such that a large bias that is mapped into a position error is also mapped into the statistic with certainty. Thus, for this failure mode we can guarantee that the position error will not grow too large without a corresponding growth in the statistic.

This restriction is not necessarily unreasonable because it is assumed that ground monitoring will pick up and isolate any faulty satellite within a relatively short period of time. Thus the likelihood of multiple satellite errors not detected by the ground monitoring network are

$N \setminus P_{FA}$	10^{-2}	10^{-3}	10^{-4}	10^{-5}	10^{-6}	10^{-7}	10^{-8}	10^{-9}
5	2.576	3.291	3.891	4.417	4.892	5.327	5.731	6.109
6	3.035	3.717	4.292	4.798	5.257	5.678	6.070	6.438
7	3.368	4.033	4.594	5.089	5.538	5.950	6.335	6.694
8	3.644	4.297	4.849	5.336	5.777	6.184	6.563	6.920
9	3.884	4.529	5.074	5.555	5.991	6.392	6.767	7.120
10	4.100	4.739	5.278	5.754	6.185	6.583	6.954	7.304
11	4.298	4.932	5.466	5.938	6.366	6.760	7.128	7.475
12	4.482	5.111	5.612	6.110	6.535	6.926	7.292	7.636

Table 1. Values of Threshold (T) for given probabilities of false alarm and number of satellites.

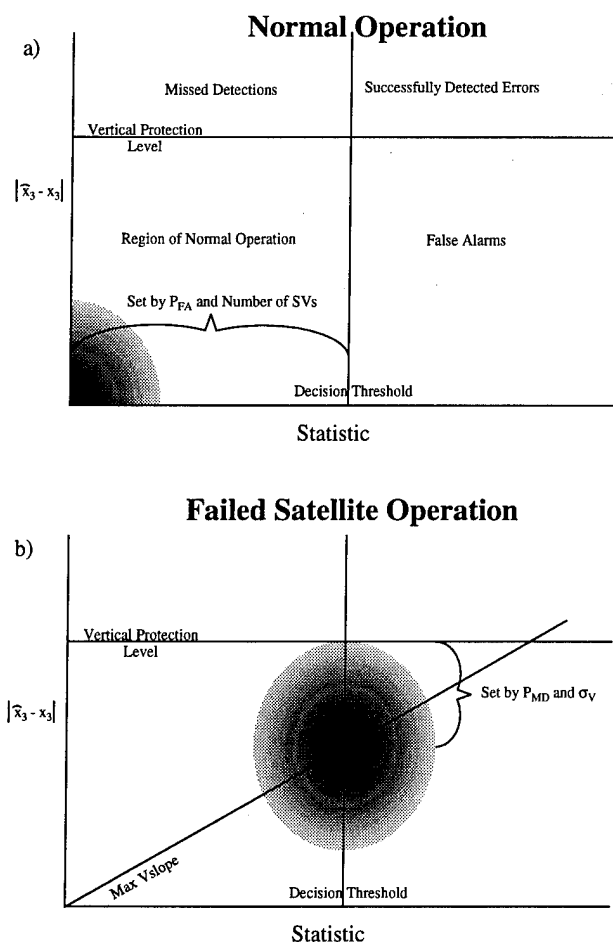


Figure 1. The distribution of vertical errors and the RAIM statistic are shown here for both normal operation and in the case of a failed satellite.

expected to be exceedingly small.

We can use the method developed by Brown [5] to guarantee integrity by only accepting geometries which provide adequate redundancy to determine if there is an error on any one channel of the receiver. This method trades availability for integrity. In the vertical dimension, this method requires that the vertical slope for each satellite (i), given by [6]

$$Vslope_i \equiv \frac{|K_{3i}| \sigma_i}{\sqrt{1 - P_{ii}}}$$

be less than some maximum allowable slope.

If there is a failure of a single satellite, the expected distribution of operation points in the statistic-vertical error plane is still an ellipse with roughly the same contours as in the absence of failures. The difference is that now the ellipse is no longer centered near the origin. Instead, its center has moved out along the line

with the corresponding Vslope for the failed satellite (see Figure 1b). How far it moves along the line depends on the magnitude of the bias. A valid integrity algorithm should alert the pilot to this failure before the vertical error exceeds the desired vertical integrity limit (VIL), thus keeping all points in this ellipse out of region of missed detections.

From Figure 1b we can see that the maximum allowable slope is a function of the desired probability of false alarms, the acceptable probability of missed detection, the vertical error we are trying to protect and σ_v [6]. Integrity is only declared available if each Vslope is less than

$$\frac{VIL - k(P_{MD})\sigma_v}{T(N, P_{FA})}$$

where $k(P_{MD})$ is the number of standard deviations corresponding to the specified P_{MD} .

Another point of view is to assume the WAAS ground network will provide a sufficient level of integrity. Instead we now wish to determine how much additional integrity RAIM can provide. The equation above can be rearranged to give the vertical protection level that the fault detection algorithm is capable of protecting (VPL_{FD} or HPL_{FD} in the horizontal plane). These values are given by

$$VPL_{FD} \equiv \max[Vslope]T(N, P_{FA}) + k(P_{MD})\sigma_v$$

$$HPL_{FD} \equiv \max[Hslope]T(N, P_{FA}) + k(P_{MD})HRMS$$

While this analysis determines the capability of RAIM in the presence of a single satellite failure, this form of RAIM cannot be made robust against any type of multiple satellite error. One can always conceive of a satellite pair failure that would yield zero contribution to the statistic and yet result in a large positioning error. However, RAIM is one layer of a multi-layer integrity structure. It cannot guarantee catching all errors, but no system can. Despite these limitations, RAIM would very likely detect a random multi-satellite failure. In addition, the probability of this failure mode occurring and escaping the detection of both the WAAS ground network and the local monitor is extremely remote.

Results

In order to investigate the availability of RAIM, we ran simulations which made assumptions about the expected satellite variances, protected vertical error and

probabilities of missed detection and false alarms. The probabilities that we used were: a probability of false alarms no greater than 10^{-5} per approach (5 independent samples per approach) and a probability of missed detections less than 10^{-3} per independent sample. The overall probability of hazardous or misleading navigation information is required to be below 10^{-7} per approach. This last requirement adds a restriction on σ_v . Even if there were no errors, normal operating conditions might not sufficiently protect the desired vertical error. For a true Gaussian distribution, 10^{-7} corresponds to a 5.33σ error (see Table 1). Realistic distributions usually have broader tails than a true Gaussian distribution. However the WAAS ground network is designed to prevent long tails. The moderately conservative approach taken here is to require that the $5.5 \sigma_v$ error be within the desired protected vertical error. As the actual distribution of errors becomes better characterized over time this value will be subject to change. For a vertical integrity limit of 19 meters, this requirement is equivalent to restricting σ_v to ~ 3.5 meters or below. If that condition is not met, the landing may not safely proceed, regardless of the integrity conditions of the WAAS ground network and/or the local WAAS monitor.

The variances that are assumed for each satellite depend strongly upon elevation angle and take the following form [6]

$$\sigma_i^2 = \sigma_{UDRE i}^2 + F^2(E_{l_i}) \sigma_{UIVE i}^2 + \sigma_{SNR i}^2 + \frac{\sigma_{m45}^2}{\tan^2 E_{l_i}} + \frac{\sigma_{trv}^2}{\sin^2 E_{l_i}}$$

The following definitions have been made: σ_i^2 is the total variance of the i^{th} satellite, $\sigma_{UDRE i}^2$ is the variance of the supplied tropo-free iono-free pseudorange correction, $\sigma_{UIVE i}^2$ is the variance of the vertical ionosphere correction, $F(E_{l_i})$ is the obliquity factor converting vertical

measurements into slant, $\sigma_{SNR i}^2$ is the receiver noise variance and can be related to signal-to-noise ratio (C/N_0), σ_{m45}^2 is the variance of the multipath contribution at 45 degrees and σ_{trv}^2 is the variance of the vertical tropospheric delay estimate. The values used in our simulation are based on values we observe regularly with the Stanford WAAS network[1] and are given by:

$$\begin{aligned}\sigma_{UDRE} &= 0.5\text{m} \\ \sigma_{UIVE} &= 0.5\text{m} \\ \sigma_{SNR} &= 0.22\text{m} \\ \sigma_{m45} &= 0.22\text{m} \\ \sigma_{trv} &= 0.15\text{m}\end{aligned}$$

Figure 2. shows the weighting curve that results from this model and these values.

In order to calculate availability we combined these error variances with realistic failure models for the GPS satellites and for geostationary satellites [7] [8] to calculate the percentage of the time the accuracy would be sufficient to support Category I or near Category I landings and the percentage of time that the geometry (and variances) would support RAIM.

The Monte Carlo results presented here are based on 10^7 simulated geometries. We computed the results for three different satellite constellations. For reference we calculated a GPS only case, although in reality geostationary satellites are required in order to transmit the differential corrections. The other two cases augment the GPS constellation with INMARSAT and with INMARSAT plus four additional geostationary satellites selected to provide good coverage over the continental United States (CONUS). In all cases the user mask angle was set to 5° . Figure 2 demonstrates that the results should not depend too strongly on user mask angle as satellites are heavily de-weighted below $\sim 10^\circ$.

All cases were computed over the CONUS region. For the cases using geostationary satellites, we assumed that these satellites provided additional ranging signals with accuracies equivalent to the differential GPS values. The three visible INMARSAT satellites in the CONUS region are; the Atlantic Ocean Region East and West (18.5° W and 55° W) and the Pacific Ocean Region (180°). The four additional geostationary satellites were located at 85° W, 110° W, 140° W and 165° W.

Six different availabilities were investigated and summarized in Table 2. At least four satellites are required in order to obtain navigation solutions. In addition, a minimum of five satellites must be in view to be able to implement RAIM. These raw availabilities are listed in the first two columns of Table 2. The next two

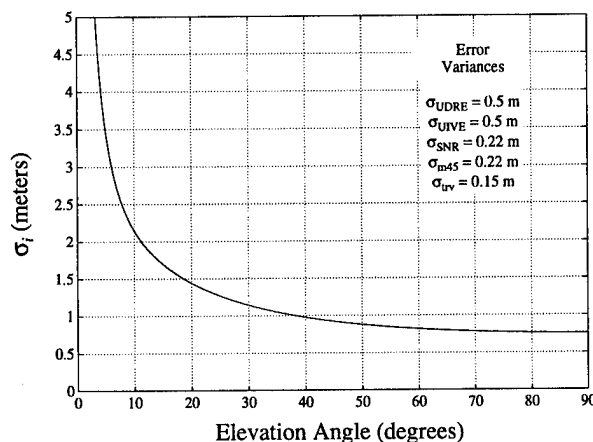


Figure 2. Here pseudorange uncertainty is plotted as a function of elevation angle.

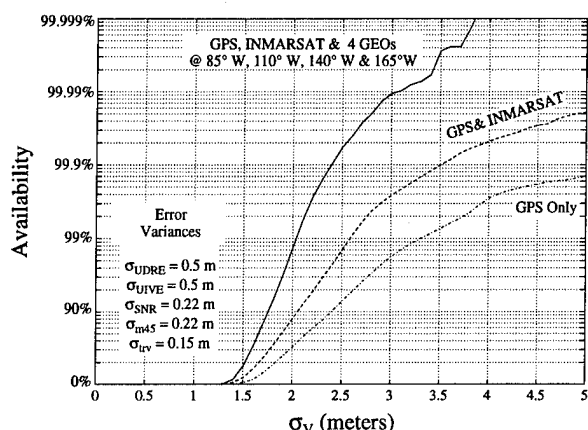


Figure 3. This graph shows the availability of σ_v for three different satellite constellations.

columns show the availabilities of σ_v and of RAIM that would meet the Category I requirements (for a 200 foot decision height the vertical integrity limit is 19 meters). While the availability of the system is good, particularly with augmentations, the availability of RAIM is low. The last two columns show the availability of near Category I approaches (using a decision height of 400 feet, the vertical integrity limit is ~26 meters which corresponds to an upper bound on σ_v of ~ 4.7 meters). The availability of RAIM markedly improves.

Figures 3 and 4 show the overall availability of σ_v and of the vertical protection limit provided by RAIM respectively. These results clearly show the benefit of having additional ranging signals. GPS with just INMARSAT can very nearly meet the desired availability for Category I landings of 99.9% if RAIM were not a requirement. Unfortunately none of the augmentations tried for this paper can provide RAIM to that same degree of availability.

If the accuracy of the WAAS were to improve there would be a corresponding increase in availability. Smaller values of σ_i lead to smaller values for σ_v and VPL_{FD} . This in turn will increase both the availabilities of the system and of RAIM. Figure 4 clearly shows that only the case with GPS, INMARSAT and the 4 Geos has any chance of making RAIM available 99.9% of the time. Unfortunately it would take a 40% reduction in the values of σ_i in this fully augmented case to make RAIM

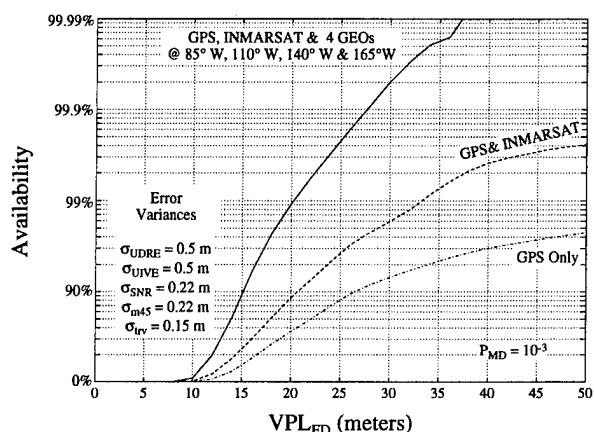


Figure 4. This plot shows the availability of specific vertical protection levels provided by the fault detection algorithm.

available to the desired level. This reduction may be overly optimistic, but a modest improvement coupled with alternate augmentations or with higher decision thresholds could sufficiently increase the availability of RAIM.

It should be noted that RAIM should be applied even if the vertical protection level exceeds the desired vertical integrity limit. RAIM would still catch large errors and errors on satellites whose Vslopes were below the maximum allowable slope. The only drawback is that there is no guarantee that RAIM would catch the error with the specified probability of missed detections. As long as RAIM is one part of an overall integrity scheme then it should be applied regardless of the vertical protection level.

Figure 5 shows the distribution of the RAIM statistic for some data collected at Stanford's WAAS network [1][11]. This data represents over 14,000 points in which seven satellites were in view of a statically surveyed passive user. For reference the expected chi-square distribution is also shown. Although the sample size is not large enough to draw any definitive conclusions, it does appear that our estimates of the satellite covariances are too conservative. A reduction of all the sigma values by roughly 30% would bring the actual data more in line with the theoretical curve. We need to perform a more careful evaluation of how we

	$N \geq 4$	$N \geq 5$	$\sigma_v < 3.45$	$VPL_{FD} < 19m$	$\sigma_v < 4.7$	$VPL_{FD} < 26m$
GPS Only	99.996%	99.95%	99.2%	67.6%	99.8%	89.0%
GPS & INMARSAT	> 99.999%	> 99.999%	99.89%	85.0%	99.97%	96.9%
GPS, INMRST & Geos	> 99.999%	> 99.999%	99.996%	98.4%	> 99.999%	99.8%

Table 2. Availabilities for three satellite constellations.

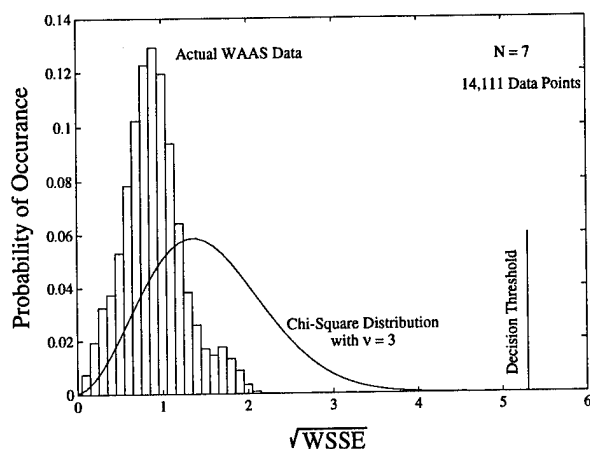


Figure 5. The distribution of the RAIM statistic from actual WAAS data is compared to theoretical expectations.

generate the covariances, and collect much more data before we can safely begin to adjust these values.

Conclusions

We have presented the equations for the weighted form of GPS positioning and for RAIM. These equations are simple extensions of the familiar unweighted methods. We argue that correct weighting will improve both the accuracy and the integrity of the navigation solution. As the use of differential GPS (as well as additional augmentations) become more common, weighted position fixes should replace non-weighted positioning as the standard.

We feel that a multiple layer approach, with three independent checks (WAAS ground network, WAAS ground monitors and RAIM) is capable of providing sufficient integrity to support precision approach. RAIM is an important element in providing complete system integrity. Only at the airplane is all of the information present and only at the airplane can certain errors be detected. It is therefore extremely important to verify the integrity of the corrections at the airplane. RAIM can provide this integrity check. RAIM can be implemented without any hardware modifications to the airplane. It can be easily performed using information already available in the receiver. It should be implemented whenever redundant measurements are available.

It seems quite likely that WAAS will be capable of supporting Category I (or near Cat I) precision approaches with availabilities of 99.9%. RAIM should be applied in order to catch errors larger than the VPL_{FD} (RAIM still has a lesser chance than P_{MD} to catch errors below this level). The probability of encountering errors

which can escape all ground monitoring and not lead to a large RAIM statistic is likely to be well below 10^{-7} .

In the early stages of WAAS it may be necessary to rely primarily on the WAAS ground network and the monitor stations to provide integrity when RAIM cannot meet the desired protection level. However this should be viewed as a temporary solution. As the accuracies improve and as additional measurements become available, so will the protection level of RAIM improve.

Our results show that the WAAS will provide sufficient accuracy to support near Category I landing requirements. Our experience with our own test-bed supports these results. WAAS will become an invaluable navigation provider for Category I precision approaches.

Acknowledgments

The Authors would like to thank Boris Pervan and Sam Pullen for numerous discussions about integrity. We also gratefully acknowledge the support and assistance of AND-510 (FAA satellite program office).

References

- [1] *Flight Trials of the Wide Area Augmentation System (WAAS)*. T. Walter, C. Kee, Y. C. Chao, Y. J. Tsai, U. Peled, J. Ceva, A. K. Barrows, E. Abbott, D. Powell, P. Enge and B. Parkinson, Proceedings of ION-GPS 94, Salt Lake City, Sept 22-24, 1994, pp. 1245-54.
- [2] *Evaluation of Orbit and Clock Models for Real Time WAAS*. Y. J. Tsai, Y. C. Chao, T. Walter, C. Kee, D. Powell, P. Enge and B. Parkinson. Proceedings of the National Technical Meeting, Anaheim, Jan 18-20 1995.
- [3] *Ionospheric Delay Model Improvement for Stanford WAAS Network*. Y. C. Chao, Y. J. Tsai, T. Walter, C. Kee, D. Powell, P. Enge and B. Parkinson. Proceedings of the National Technical Meeting, Anaheim, Jan 18-20 1995.
- [4] *Wide Area Augmentation System Signal Specification*. A. J. Van Dierendonck, RTCA Publication, January 1994.
- [5] *A Baseline GPS RAIM Scheme and a Note on the Equivalence of Three RAIM Methods*. R. G. Brown, *Navigation*, Vol. 39, No. 3, Fall 1992, pp. 301-316.
- [6] *Baseline Weighted Navigation Solution, Navigation Sensor Error and Total System Error Algorithms for*

Precision Approach. T. Walter, P. Enge and A. J. Van Dierendonck, Appendix E to Draft RTCA WAAS MOPS August 1995.

[7] *GPS Availability, Part II: Evaluation of State Probabilities for 21 and 24 Satellite Constellations.* J. M. Durand and A. Caseeau, **Navigation**, Vol. 37, No. 3, Fall 1990, pp. 285-96.

[8] *Availability Characteristics of GPS and Augmentation Alternatives.* W. S. Phlong and B. D. Elrod, **Navigation**, Vol. 40, No. 4, Winter 1993-4, pp. 409-28.

[9] *Autonomous GPS Integrity Monitoring Using the Pseudorange Residual.* Parkinson, B. W. and Axelrad, P., **Navigation**, Vol. 35, No. 2, 1988, pp 255-74.

[10] **Handbook of Mathematical Functions.** Abramowitz, M. and Stegun, I. A., New York, Dover Pub. Inc., 1972.

[11] *An Algorithm for Inter-frequency Bias Calibration and Application to WAAS Ionosphere Modeling.* Y. C. Chao, Y. J. Tsai, T. Walter, C. Kee, P. Enge and B. Parkinson, Proceedings of ION GPS 95, PALm Springs, Sept. 12-15, 1995.

[12] *Validation of the RTCA Message Format for WAAS.* Y. J. Tsai, P. Enge, Y. C. Chao, T. Walter, C. Kee, J. Evans, A. K. Barrows, D. Powell and B. Parkinson, Proceedings of ION GPS 95, PALm Springs, Sept. 12-15, 1995.

Solving Integrity Insufficiencies of Sat Nav Systems with Complementary Navigation Information

Stefan Vieweg
Institute of Flight Guidance and Control

Carsten Butzmuehlen
Technical University Braunschweig

Biography

Stefan Vieweg's academic background includes an diploma in mechanical engineering in the field of aerospace and aeronautics (1990) and an additional diploma in economics and business administration (1992), both TU Braunschweig. Since 1990 he has been member of the Institute of Flight Guidance and Control (TU Braunschweig). His responsibilities have been project management of different navigation programs incl. GPS, GLONASS, LORAN-C, integrated GNSS and inertial navigation. He has more than 50 publications during the last 2 1/2 years on his account.

Carsten Butzmuehlen studied aerospace and aeronautics at the Technical University Braunschweig and got his diploma in mechanical engineering in 1994. He works at the Institute of Flight Guidance and Control in the field of satellite and inertial navigation.

Abstract

In order to comply with the required navigation performance (RNP) parameters and the integrity, a continuous monitoring of the GNSS status is essentially needed. The certification process for satellite navigation as "sole means", primary navigation system is difficult extremely unlikely for high precision / safety critical procedures in aviation applications, due to insufficiencies in the dynamic environment of the vehicle (satellite masking, multipath, cycle slips, etc.).

A combination of satellite information with inertial sensors, which have dissimilar characteristics to satellite navigation, is proposed in this paper. The inertial sensors are an ideal complement to GNSS due to their good dynamic properties, although they can be characterized by a longterm drift.

A complementary satellite/inertial navigation system enables the estimation and compensation of different sensor errors of the inertial as well as the satellite subsystem within the Airborne Autonomous Integrity Monitoring (AAIM). Some concepts for onboard

integrity monitoring, which have shown the potential to compensate the insufficiencies of RAIM, are discussed in this paper.

1 Introduction

Without doubts the accuracy performance of satellite navigation (GNSS) provides a broad variety of applications of incomparable precision. Nevertheless for safety-critical issues and certification reasons all required navigation performance (RNP) parameters, i.e. accuracy, availability, reliability (continuity of service) as well as integrity, have to be fulfilled, but can hardly be complied with GNSS for itself. Thus the certification process for satellite navigation as "sole means", primary system is difficult and extremely unlikely for high precision / highly safety-critical procedures like CAT II/III approaches. For system integrity checks, i.e. failure detection and identification, a variety of approaches like Receiver Autonomous Integrity Monitoring (RAIM), pseudolite-aiding or ground based overlay techniques (e.g. within the Wide Area Augmentation System, WAAS) with different advantages and shortcomings are in discussion and tested. But still these techniques are not able to compensate GNSS insufficiencies concerning the dynamic environment in the local vicinity of the vehicle like satellite masking, multipath, cycle slips, dynamic influences on the receiver, electro-magnetic disturbances etc. which degrade the quality (i.e. accuracy as well as integrity).

Therefore a combination of satellite information with inertial sensors suggests itself, because the latter are an ideal complement to GNSS due to their good dynamic behaviour, although they are characterized by longterm drift as a result of misalignment, accelerometer and gyro errors. Furthermore they are absolutely selfsupporting, hence the critical RNP-limits can mostly be met with redundancy techniques.

A complementary GNSS / inertial navigation system enables the estimation and compensation of different sensor errors of the inertial as well as the satellite

subsystem within the Airborne Autonomous Integrity Monitoring (AAIM). Some concepts for onboard integrity monitoring, which have shown the potential to compensate the insufficiencies of RAIM, are discussed in this paper.

2 System Requirements

Navigation systems used as primary means for aviation in safety critical applications are subject to stringent requirements. Therefore, the system capability, i.e. accuracy in the case of navigation, is not necessarily the limiting factor: all requirements towards certification are of utmost importance. Hence, the required performance of navigation systems can be subdivided into

- Requirements toward certifiability: Accuracy, Integrity, Availability and Reliability / Continuity of Service
- Economical requirements: Independence, adequate acquisition and running costs.

2.1 Aspects Relevant for Certification

2.1.1 Accuracy

Depending on the phase of flight, the required accuracy of navigation solution can be expressed by the Total System Error TSE and the Sensor Error SE. The Total System Error is the difference between the actual aircraft position and its nominal position on a specified flight path. Additional to Sensor Errors, the Total System Error covers other error sources such as coordinate errors and errors that arise from the data transmission from a differential reference station of the aircraft. The table 1 lists the maximum allowable

Total System Error for the different phases of flight (see [2], [7]).

Since GNSS (in differential mode) has the capability even to meet the highest accuracy requirements listed in table 1, the overall accuracy performance of an integrated GNSS /inertial system is determined by GNSS, not by the inertial sensors. Since the inertial subsystem can be calibrated by an accurate GNSS information and as long as the inertial error characteristic can sufficiently be modelled, the integrated system can keep the GNSS accuracy performance in a short term sense even during GNSS-outages.

2.1.2 Integrity

For safety-critical applications the integrity of the navigation system must be extremely high: For precision approaches the overall probability of a fatal accident due to an error (resulting in the total loss of the aircraft) should be in the range of 10^{-7} to 10^{-9} (see table 2).

Hence the integrity requirements for the onboard-subsystems, those on ground and for the data link in between are obviously higher. The most critical subsystem is the onboard segment with integrity requirements of approx. 10^{-8} . Summarizing, the following aspects can be concluded:

- Onboard integrity is essentially needed (like in „traditional“ navigation systems).
- GNSS can scarcely meet the integrity requirements for CAT II/III.
- The combination of GNSS and inertial systems presents itself as an adequate solution, since inertial sensors (a) are self-supporting, so that their failure behaviour is sufficiently known and (b) can be arranged in redundant configuration in order to meet the integrity requirements.

Phase of Flight	Tolerable Horizontal Error [m]	Tolerable Vertical Error [m]
Enroute	2200	-
Terminal	1100	-
Non Precision Approach	550	-
S-CAT I ([3])	33.5	9.7
CAT III ([1])	5 ¹	0.6 ¹
Airfield:		
Traffic Flow Control	15 ... 1	-
Docking	0.1	-

Table 1: Maximum total system error of GNSS for different phases of flight

¹ valid for short runways, larger values for longer runways

Subsystem	Instrument Approach	
	CAT I	CAT III (X: still unknown)
Airborne Segment	$3 * 10^{-8}$	$X * 10^{-10}$
Data Link Ground \Leftrightarrow Board	$1 * 10^{-8}$	$X * 10^{-10}$
Ground Segment	$6 * 10^{-8}$	$X * 10^{-10}$
Total Integrity	$1 * 10^{-7}$	$1 * 10^{-9}$
D-GPS Experiences	10^{-2}	

Table 2: Tolerances of integrity risk

2.1.3 Availability

Regarding the current and planned availability of GPS and/or GLONASS, the use of these existing satellite navigation systems as "sole means" seems to be difficult. For example, the performance of the "Standard Positioning Service" of GPS has an guaranteed availability of 95%, although for airborne navigation systems figures around 99.999% are in discussion (see [7]). Thus, the combination of GNSS/inertial systems might help to overcome at least short-term GNSS-outages.

2.1.4 Continuity of Service

Although the continuity for precision approaches with ILS-localizer is better than $1 - 2 * 10^{-6}$ during the critical approach phase of 15 sec (see [1]), the experiences with Differential-GPS is about four orders of magnitude worse ($1 - 2 * 10^{-2}$). Obviously those GNSS insufficiencies might be compensated by inertial information within an integrated navigation solution.

2.2 Economical Aspects

2.2.1 Independence

Due to the fact that inertial sensors are self-supporting, their combination with GNSS can maintain the advantages of global operationability of satellite navigation systems and the infrastructure on ground is kept at a minimum level.

2.2.2 Acquisition and Running Costs

Apart from the aspect of cost effectiveness of the essential infrastructure, the combination GNSS / inertial systems provides the following economical advantage: Inertial information of reduced accuracy

might be suitable for the purpose of integration with GNSS - even for high precision applications -, since the overall accuracy performance is determined by GNSS, not by the inertial subsystem.

3 Onboard Integrity Monitoring

The majority of integrity monitoring concepts used on the onboard-side exclusively make use of satellite measurements, therefore they are known as RAIM: Receiver Autonomous Integrity Monitoring. Additional information from other sensors onboard are neglected.

3.1 Snapshot vs. Time-Averaging

Concerning the kind of information, in general two different types of approaches can be used for integrity monitoring: The first are snapshot methods which exclusively use the actual measurements, whereas the second type, time-averaging methods, use the whole history of data (or part of it). From that, the following characteristics can be summarized:

- Snapshot methods are not dependent on the consistency of the tracking and the consistency of geometry (constellation changes)
- Time-averaging methods can identify smaller trends and drifts better, since they are evaluating the data in the context of its history (with the assumption that significant changes are very unlikely)

3.2 Different RAIM Approaches

Position comparison methods are based on the position solution of the navigation process. These are the earlier RAIM-approaches which concern themselves with the result (the horizontal position error) the user is interested in.

Range comparison methods are based on the evaluation of individual pseudorange-residuals. With these methods, the probability distribution of range-residuals can be described more efficiently. Thus, the mathematical treatment (with regard to statistical questions) is better. Most of the range-comparison methods are now parity-space algorithms, where the vector of range-residuals is transformed into a parity-vector by an orthogonal transformation. Thus, the information of the range-residuals is divided into two parts: the LSQ-information (position solution) and the redundant information that can be used for integrity monitoring purposes.

3.3 Hypothesis Testing

All the integrity monitoring algorithms are based on the concept of hypothesis testing: a decision variable D (computed from the measured data) is compared with threshold T (that is calculated using required limits, see chapter 2.1). Since there always exists the risk of making a faulty decision, two types of wrong decisions have to be distinguished:

- Raising an alarm when the decision variable indicates so, although everything is actually within specification (FALSE ALARM).
- Accepting the null-hypothesis when the decision variable indicates so, although there is actually an SV-failure (MISSED DETECTION).

The obvious aim would be to minimize both the probabilities of making an error. But minimizing the probability of false alarm increases the probability of missed detection (and vice versa). Some authors treat the false alarms only as a nuisance and concentrate only on minimizing the probability of missed detection, without doubts an absolutely essential issue for safety-critical applications. But on the other side low false alarm rates are an economical issue of the system design and therefore cannot be neglected. There are thus two approaches to RAIM algorithms (CFAR and CPOD):

- Setting the probability of false alarm to a constant value, calculating the probability of missed detection and checking whether it is below the integrity requirements (CFAR).
- Setting the probability of missed detection to a constant value, calculating the probability of false alarm and checking whether it is below the integrity requirements (CPOD) - this monitoring is not necessary, according to some authors, although it is worth thinking about it.

3.4 Summarized RAIM Characteristics

There are several disadvantages to all RAIM algorithms that lead to a poor performance under worst-case scenarios:

- The measurement matrix must be known exactly (i.e. the user position as well). This assumption can not be met if the navigation solution is already contaminated with errors that are to be detected via the RAIM algorithms
- The satellite geometry, S/A and errors influence the position solution significantly (and therefore the RAIM performance as well)
- By theory, there is only ONE satellite failure assumed.
- The user needs a minimum of 5 satellites for a failure detection, 6 satellites for a failure exclusion.
- The time-averaging methods are additionally handicapped in a sense that they need to monitor the system beforehand (in some approaches at least for 30 minutes) to predict the system performance adequately. In consequence this will lead to problems at the beginning of the flight where a landing due to aircraft failures should be considered. And what about short distance flights?
- Time-averaging methods are depending on a fairly constant geometry to be able to predict the system performance (at least no one has mentioned yet the effect of significant system changes, e.g. constellation changes, manoeuvring etc.).
- Time-averaging methods that depend on the prediction of the receiver clock bias state are influenced significantly by the stability characteristics of the receiver clock. This leads to more-sophisticated receiver oscillators (maybe with a higher price). And the influence of user dynamics (accelerations, curves, etc.) has scarcely been investigated so far.

4 Hybrid Residuals

Due to the problems discussed in the previous section, several approaches of integrity monitoring have been investigated in the simulation as well as real flight environment at the Institute of Flight Guidance and Control.

This concept (figure 1) utilizes satellite measurements in combination with informations from other onboard sensors like inertial systems and altimeter. The decisive advantage towards RAIM is to use hybrid residuals, i.e. the difference between GNSS-ranges (GNSS-range rates) and calculated ranges (or range

rates, respectively), based on the dissimilarly onboard sensors.

Further discussions on the fundamental performance will be given on ranges, the additional information will be obtained by a navigation solution using inertial sensors. The situation using range rates would be quite similar.

4.1 Hybrid Range Calculation

The measured GNSS ranges can be divided into a correct part and an error (regardless of the measurements and of how this error might look like):

$$R_i^{GNSS} = R + DR_i^{GNSS}$$

From the external navigation solution (achieved from the additional sensors) ranges to each satellite that is received can be calculated. Again, these calculated ranges can be divided into a correct part and an error:

$$R_i^{calculated} = R + DR_i^{calculated}$$

The method uses three difference operations:

- The first difference is to correct the measured pseudoranges with differential corrections.

- The second difference operation eliminates the correct range by subtracting the calculated range from the GNSS range. The result is a difference which exclusively contains the error budgets of the ranges.

$$\delta R_i = R_i^{calculated} - R_i^{GNSS} = DR_i^{calculated} - DR_i^{GNSS}$$

- The third difference operation eliminates the errors in the calculated range by subtracting the result from above, for two different satellites. The result is a difference only including the error parts of the GNSS-ranges.

$$\begin{aligned} \Delta R_{ij} &= \delta R_i - \delta R_j \\ &= (DR_i^{calculated} - DR_i^{GNSS}) - (DR_j^{calculated} - DR_j^{GNSS}) \\ &\Rightarrow \Delta R_{ij} \approx DR_i^{GNSS} - DR_j^{GNSS} \end{aligned}$$

This approach incorporates the assumption that the calculated range errors for two different satellites are almost equal in size. Clearly, the performance of this algorithm depends on the assumption stated above. Since in reality the error budgets $DR_i^{calculated}$ and $DR_j^{calculated}$ depend on the satellite geometry, a worst-case investigation can show the maximum impair: The obtained error in the hybrid ranges are maximum, if the position error of the aiding system (e.g. inertial) lies within the plane of the satellites - a two-dimensional scene.

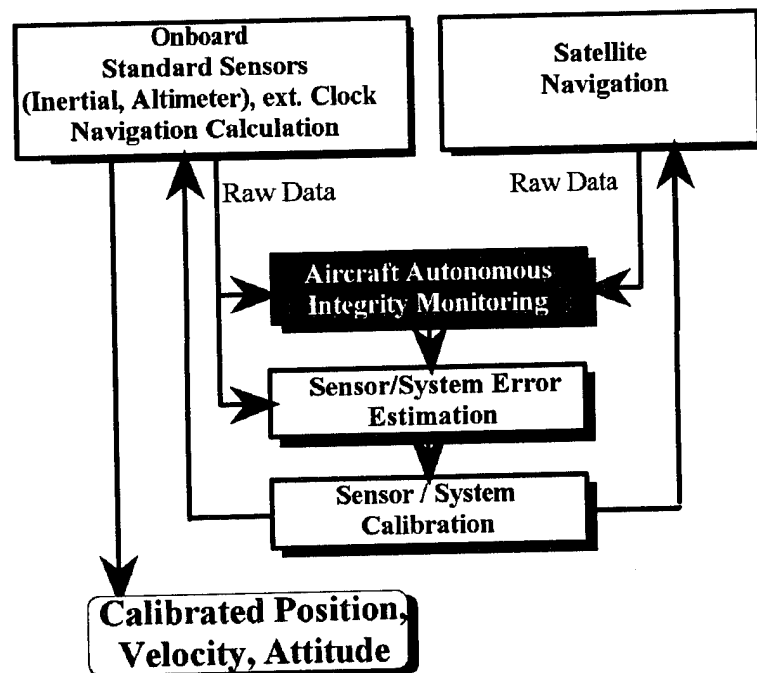


Figure 1: Concept of GNSS integrity monitoring with additional information from dissimilar onboard sensors

By varying the angles to the base-line of the two satellites independently, it can be seen that the resulting error in the hybrid residuals are below (or equal to) twice the assumed position error of the aiding navigation solution (figure 2).

This limit can be used to estimate the minimum GNSS-range error that can be detected in the presence of an aiding system position error. Vice versa, via the required error in the GNSS-ranges that has to be detected in order to guarantee the integrity requirements for a particular phase of flight, the acceptable position error in the aiding system can be estimated.

Since the inertial position error increases with time (due to gyro drifts and accelerometer errors), the minimum performance of an uncalibrated inertial navigation solution can be derived for the individual phase of flight. For example, in the critical phase (10 sec) of a CAT III approach (horizontal) under worst case conditions, an uncalibrated gyro drift of $0.1^\circ/\text{sec}$ would be sufficient to fulfill the GNSS integrity monitoring function. Typical AHRS or INS gyro drifts are about three or four orders of magnitude smaller.

4.2 Hybrid Ranges versus Double Differencing Residuals

At a first glance, the approach to use hybrid residuals seems to be similar to (or even equal to) the well-known double differencing technique that is used to compute the pure phase navigation. Nevertheless these approaches basically differ concerning the following aspects:

- The major difference between both techniques is a different methodology. The pure phase solution

uses a "master satellite". Therefore only double differences of this master satellite with base satellites are calculated, since there is no further information in any difference between base satellites for the purpose of phase solution. The hybrid residuals aim is a relative statement concerning the error of two satellites. Thus, the difference operations have to be done for each satellite, using all other satellite in view.

- The purpose of pure phase navigation solution is to obtain a precise user position, but by differencing hybrid ranges a statement about the "relative" error of exclusively two satellites is investigated.
- For a pure phase solution, the user needs a minimum of 4 - 6 satellites in view (for statistical calculations even more). To use the hybrid residuals, a minimum of just 3 satellites in view is needed.
- The first difference operation for both algorithms is the differential correction (D-GNSS). The pure phase solution needs it to find the phase solution space (where the search for the correct ambiguities can continue). The hybrid residuals algorithm needs it to eliminate all errors due to the satellites. In principle this step is not necessary if GNSS errors like S/A etc. can be tolerated.
- The second difference operation in the pure phase solution eliminates the errors due to the satellites, whereas in the hybrid residual approach the correct pseudoranges are eliminated, so that only an error budget is left.
- The third difference operation eliminates in the pure phase solution all errors due to the receiver, whereas in the hybrid residuals the errors due to the aiding source (e.g. inertial system) are to be eliminated.

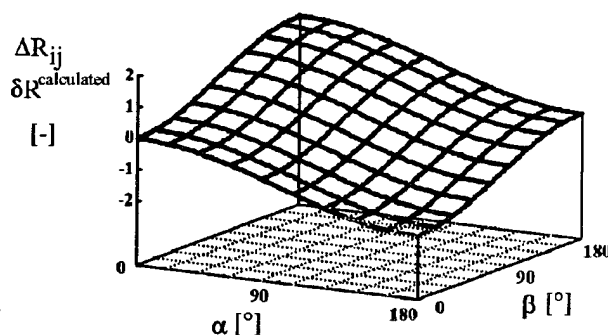
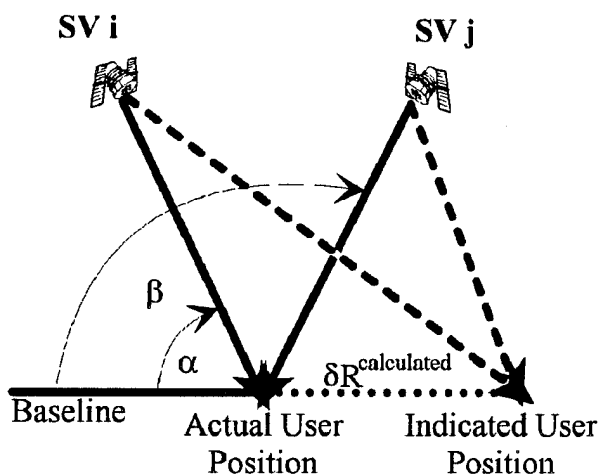


Figure 2: Error influence of the calculated position, depending on the satellite geometry

Number of Satellites	Max. Allowable No. of Failures	No. of Actual Failures Identifiable	Decision
3	≤ 1	✓	Detection
4	≤ 2	✓	Exculsion (1 failure)
4	≤ 2	✓	Detection (2 failures)
5	≤ 3	✓	Exculsion
6	≤ 3	✓	Exculsion (≤ 2 failures)
6	≤ 3	✓	Detection (3 failures)
7	≤ 3	✓	Exculsion
8	≤ 4	✓	Exculsion (≤ 3 failures)
8	≤ 4	✓	Detection (4 failures)
9	≤ 4	✓	Exculsion

Table 3: Performance of the hybrid range AAIM-approach

- The result of these three difference operations is in the pure phase solution still range- and error-dependent, whereas it is in the hybrid residuals only error-dependent.

4.3 Characteristics of AAIM compared with RAIM

All combinations of hybrid range (range rate) informations are used for the detection and exclusion process, which utilize the given statistical quantities shown in chapter 2.1. The improvements towards RAIM have already been demonstrated, e.g. in [9]. At this point the major performance criteria of the AAIM-approach using hybrid range information are summarized in table 3.

Even under multi-error scenarios failure detection and (with few restrictions) exclusion is possible. Furthermore it can be derived that with AAIM and hybrid residuals, only a minimum of three satellites in view is necessary. With RAIM, a minimum of 5 satellites in view is necessary for detection and a minimum of 6 satellites in view for identification under the assumption of just one failure.

5 AAIM versus RAIM

To demonstrate the ability of the proposed AAIM algorithm to detect and identify two simultaneous failures (and the inability of the RAIM approaches to do this), a horizontal phase of a flight with the research aircraft DO 128 of the Institute is chosen. In the time between 381850 sec and 381900 sec (GPS

time of week), where 9 space vehicles were in view, a ramp failure of 1 m/s was programmed on SV 17 (elevation 13 degrees, azimuth 175 degrees) and SV 25 (elevation 25 degrees, azimuth 270 degrees). The figure 3 depicts the pseudorange residuals of the RAIM CFAR algorithm of [8].

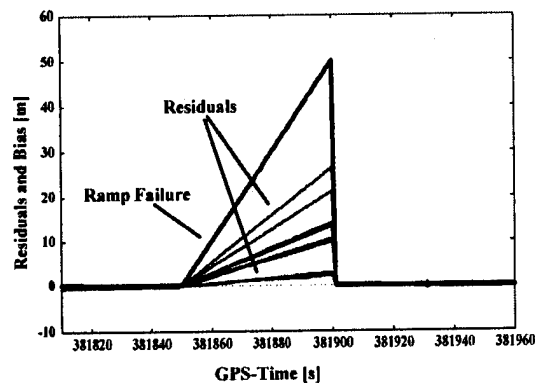


Figure 3: RAIM - Decision Variables and Bias

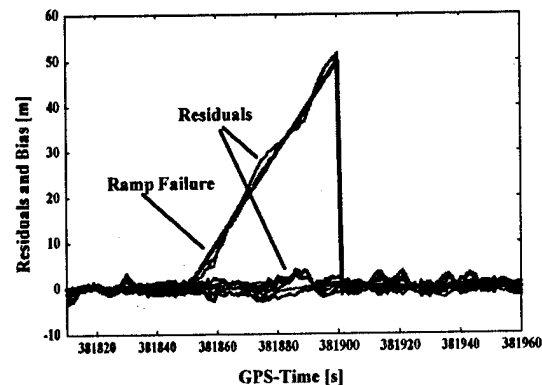


Figure 4: AAIM - Decision Variables and Bias

It is obvious that the residuals are correlated due to the use of the least squares estimation. Not only the corrupted residuals, but as well others, show a significant rise, leading to a possibility of false identification. The figure 4 shows the hybrid residuals obtained via the second difference operation of the proposed AAIM algorithm. Only the two corrupted residuals exhibit a significant rise due to the modelled failure.

The figure 5 summarizes the comparison of the proposed AAIM algorithm with two selected RAIM approaches: the CFAR algorithm of [8] and the ORTHO-algorithm of [3]. Whereas the AAIM algorithm detects and identifies the two simultaneous failures after 10 seconds (ramp height 10 m), both RAIM approaches do not identify the second failure. The detection time of the RAIM algorithms is slightly higher (12 seconds and 13 seconds, respectively) than that of the AAIM algorithm and the RAIM ORTHO-approach identifies the first modelled failure incorrectly at first.

6 Conclusion

In order to comply with the accuracy as well as the safety requirements for safety critical application, a continuous monitoring of the system status in its dynamic environment is essentially needed, in particular with GNSS. The evaluation of RAIM approaches and the investigations to compensate for their insufficiencies leads to the concept of using additional

(Non-GNSS) information onboard, which has dissimilar characteristics to satellite navigation. The combination of GNSS with self-supporting inertial information presents itself as an adequate solution. Differencing hybrid ranges from these measurement sources lead to major improvements in comparison to RAIM. Using inertial measurements as an example for such additional information source showed quite positive results:

- The performance of the hybrid range algorithms does not depend very much on the geometry of the satellites, since the position information is obtained from the aiding source.
- Multi-error scenarios can be dealt with, as long as the assumed number of failures is less or equal to half the number of received satellites.
- Only a minimum of three satellites in view are needed, whereas with RAIM at least five satellites are necessary.
- The number of failures in the received set of satellites can always be determined (as long as the assumption above holds: failures are smaller than half the number of the received satellites).
- Even if this assumption is violated, there exists a qualitative statement about the actual false decision in that very moment (with RAIM, there is no such statement available).
- Failure exclusion is inherently possible, not so with RAIM.

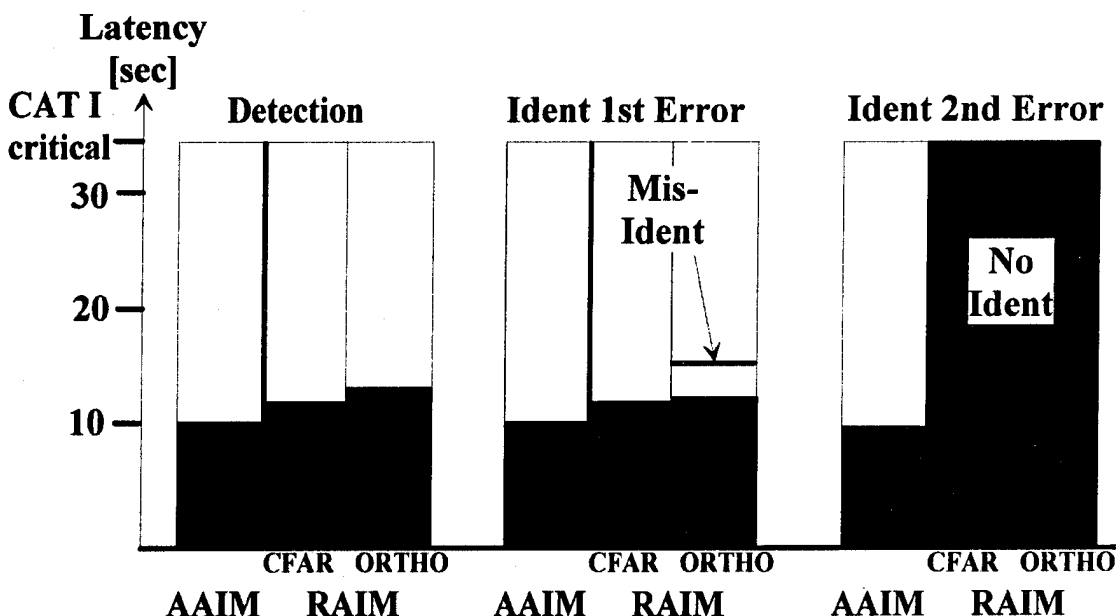


Figure 5: Comparison of RAIM and AAIM - Failure Detection and Identification Latency with an artificial error ramp on two satellites simultaneously

Currently a refinement of certain aspects of the AAIM-approach is investigated as well as car and flight tests are ongoing at the Institute of Flight Guidance and Control.

References

- [1] - : ICAO ANNEX 10' Aeronautical Telecommunications'. Vol. I, Part I and II, 1985
- [2] - : Minimum Aviation System Performance Standards - DGNSS Instrument Approach System: Special Category I (SCAT-I) RTCA/DO-217, Aug. 1993
- [3] **Brenner, M.** : Implementation of a RAIM Monitor in a GPS Receiver and an Integrated GPS/IRS, ION GPS-90, Colorado Springs, USA, Sep. 1990
- [4] **Brenner Hartman, R.G., Brenner, M.A., Kant, N., Fowler, B.** : Results from GPS / GLONASS Flight and Static Tests. DGPS '91, Braunschweig, Sept. 1991
- [5] **Brown, R.G., Kraemer, J.H., Nim, G.C.** : A Partial Identification RAIM Algorithm for GPS Sole Means Navigation. ION-GPS '94, Salt Lake City, Sept. 1994
- [6] **Diesel, J.W.** : A New Approach to GPS Integrity/Availability: Immediate Global Sole Means Without WAAS. ION-GPS '94, Salt Lake City, Sept. 1994
- [7] **Loh, R.** : FAA Wide Area Integrity and Differential GPS Program. DSNS '93, Amsterdam, 1993
- [8] **Sturza, M. A.** : Navigation System Integrity Monitoring Using Redundant Measurements. NAVIGATION, Journal of The Institute of Navigation, Vol. 35, No. 4, Winter 1988-89, pp. 483-501.
- [9] **Vieweg, S.** : Integrity Monitoring and Failure Identification within an Integrated Satellite-/ Inertial Navigation System. PLANS '94 Las Vegas, April 1994

Effects of Worst Case Geometries on RAIM Testing

Christine Easton
Rockwell Defense Electronics

William Michalson
Worcester Polytechnic Institute

BIOGRAPHY

Christine A. Easton is a GPS Engineer at Collins Avionics & Communications Division, Rockwell Defense Electronics currently working on implementing RAIM for standard stand alone GPS products. She was previously a Research Assistant in the Satellite Navigation Research Group at Worcester Polytechnic Institute focusing on GPS integrity.* Prior to attending WPI she worked in Aerospace Ground Equipment systems at General Electric.

Dr. Michalson is an Assistant Professor in the Electrical and Computer Engineering Department at Worcester Polytechnic Institute, where he also directs the Satellite Navigation Laboratory. His research focuses on the development, test, and evaluation of GPS integrity monitoring algorithms, with an emphasis on integrity monitoring for sole-means navigation and precision approach. He is also involved with the development of GPS systems for specialized applications. Previously he was with Raytheon Company where he developed computer system architectures for space-based data and signal processors.

ABSTRACT

This paper describes using different sets of user locations for the off-line MOPS test to identify any condition where the current procedure could result in overestimating a RAIM algorithm's performance. The supplemental Minimum Operation Performance Standard (MOPS), RTCA DO-208 document [1], specifies the worldwide geographic user locations to use for off-line testing of RAIM algorithms. These locations are used to verify that a RAIM algorithm meets the MOPS detection

probability and alarm rate requirements for any global location at all times.

If the MOPS test locations contain true worst case geometries, then the detection probability should be satisfied globally. To determine if the MOPS off-line RAIM test includes true worst case geometries, a test scenario at the maximum probability of missed detection and the maximum allowable alarm rate using the MOPS specified locations is established.

Under the same test scenario, replacing the MOPS locations with a grid of locations should not cause an increase in the missed detection probability. The detection and alarm tests are run with a 5 degree grid over the Northern Hemisphere to generate globally distributed geometries. The results of this experiment are presented in this paper.

INTRODUCTION

The MOPS off-line test, hereafter referred to as the MOPS test, describes two test requirements that must be met. One requirement is the maximum alarm rate. This is the total alarm rate with the equipment in normal operation and no satellite failures, which must not exceed 0.002/hr. The other requirement, maximum probability of missed detection, is the total undetected failure rate when a satellite failure exists. The probability of missed detection is not to exceed 0.001.

The missed detection probability requirement is to be met globally at all times for a single satellite failure. To test if this requirement is satisfied, a worst case test condition is needed. The worst case test condition requires the use of worst case satellite geometries due to their influence on the position accuracy. When selecting geometries from a small set of locations, these locations may not contain the worst case admissible geometries. This condition can inaccurately test a RAIM algorithm's

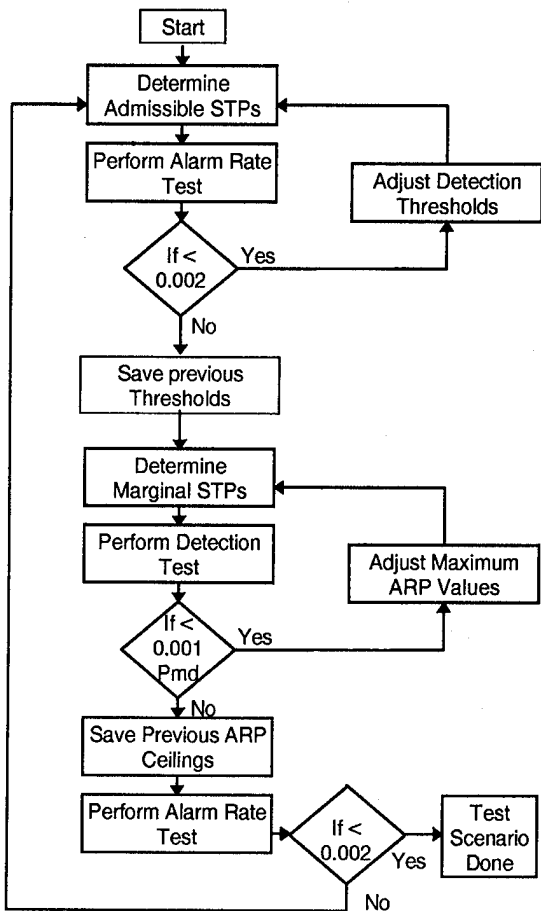
* The majority of this work was performed before joining Rockwell while at Worcester Polytechnic Institute.

performance, therefore, the 24 worldwide user locations, listed in the MOPS, need to contain the worst case admissible geometries. This paper describes experiments performed to examine if true worst case geometries are included in the set of marginal geometries as obtained following the MOPS test procedures.

MAXIMUM REQUIREMENT TEST SCENARIO PROCEDURE

The experiment requires the determination of a test scenario at the maximum requirements of missed detection and alarm rate. This is accomplished through several steps shown in Figure 1.

Figure 1: Maximum Requirements Test Scenario Procedure



First, the alarm rate test is executed as an iterative process to obtain detection thresholds that result in the maximum number of allowable alarms. The set of admissible space time points (STPs) determined by a geometric criteria are used as input to the alarm rate test.

An STP has a particular set of satellites visible at the user location at a specific point in time and the visible satellites form a geometric volume in space. A geometric criteria is used to determine if the satellite geometry for the STP is admissible for RAIM testing. The Approximate Radial-Error Protected (ARP) method is used as a measure of the satellite geometry for this experiment. An STP with an ARP value below a selected ARP ceiling is admissible. The set of admissible STPs changes with each change in the threshold values.

To determine the detection thresholds that result in the maximum number of allowable alarms for the MOPS locations, the STP sorting and the alarm test were executed while decreasing the threshold values until the alarm rate specification was met. The thresholds were decreased at 1 meter increments from the initial values listed in Table 1. The detection thresholds obtained at the maximum number of alarms are then used in the detection test.

Table 1: Initial ARP Ceilings and Thresholds for Non-Precision Approach.

Visible Satellites	ARP Ceiling (m)	Threshold (m)
5	328	124
6	339	96
7	352	84
8	352	77
9+	352	64

The detection test uses the marginal STPs, which are the 10 STPs of the admissible set with the largest ARP values. The largest ARP values of the admissible set yields the marginal geometries. The detection test is repeated for each change in the geometric admissible cutoff point, ARP ceiling, until the probability of missed detection of 0.001 is reached. The detection test was run using the MOPS marginal geometries while decreasing the ARP ceilings by 1 meter increments from the initial ARP ceilings listed in Table 1. The STP sorting is performed at each change in ARP ceiling. When 5 misses occur the ARP ceilings are recorded. The alarm test must now be performed with the new ARP ceilings.

This process was iterated until both the alarm and detection test are at specification. At this point the thresholds and ARP ceilings are saved to be used with the grid set of locations. The final thresholds and ARP ceilings obtained at the maximum allowable alarm rate and probability of missed detection are listed in Table 2.

The threshold and ARP ceiling values are now used to perform the alarm rate and detection test for the grid

locations. At this point the test scenario at maximum test requirements is determined.

Table 2: ARP Ceilings and Thresholds for Maximum Requirements Test Scenario

Visible Satellites	ARP Ceiling (m)	Threshold (m)
5	471	120
6	482	92
7	495	80
8	495	73
9+	495	60

Data describing the 10 marginal MOPS geometries for this maximum requirements test scenario are collected. This data includes the maximum slope, ARP, Horizontal Dilution of Precision (HDOP), and subset HDOPs. The 10 marginal geometries should now contain the 10 worst case geometries for testing following the MOPS test.

Alternate User Locations

If the MOPS set of geographic user locations is replaced with a different set of locations, the probability of missed detection and alarm rate must not increase. The set of points used to test this conjecture is a grid of points covering the contiguous US states, longitude of 65° to 125° West and latitude 25° to 50° North, and a set covering the Northern Hemisphere to a latitude of 85°. The alarm rate and missed detection tests are run with the previously set parameters, thresholds and admissibility cutoffs, from the maximum test scenario. The same data, maximum slope, ARP, HDOP, and subset HDOPs, for the 10 marginal geometries of the US and Northern Hemisphere grids are collected for comparison. This is done to look for similarities in marginal geometries derived from different user location sets.

Testing with Alternate Locations

If the detection test fails with the grid locations, then there must be points that are true worst case geometries not contained in the MOPS set of points. This allows a RAIM algorithm to pass the missed detection test but fail the requirement of meeting the missed detection conditions globally at all times, thereby overestimating a RAIM algorithm's performance.

If the set of grid marginal geometries passes the alarm and detection tests, the MOPS test points seem to sufficiently test a RAIM algorithm's performance. This applies only to the algorithm used for this experiment and may have varying results with different algorithms.

RAIM ALGORITHM DESCRIPTION

A generic RAIM algorithm consists of the following steps:

1. Collect GPS ephemeris data and pseudorange measurements.
2. Determine if RAIM is available based on satellite geometry and number of visible satellites. If RAIM is not available send appropriate signal to the user.
3. If RAIM is available, calculate a test statistic to use for fault detection.
4. Determine if the test statistic, that gives a measure of error, is less than the protection threshold for the current phase of flight.
5. If the test statistic is greater than the protection threshold, the algorithm is to notify the user of a failure otherwise it continues with normal operation.

The primary differences in algorithms are how the admissibility criteria and the test statistic are calculated. For this experiment, the ARP method [2] is used to determine admissibility and uses the normalized Sum of the Squares of the range residual Errors (SSE) test statistic [4].

ARP Criteria

The ARP provides an approximation of the level of radial error in the users horizontal position which can be detected. In an ideal case, this would be the protection limit or alarm limit which is determined by the user's phase of flight. A failure exists when the horizontal position radial error is outside the alarm limit for the phase of flight in progress. An ARP ceiling is used to account for the effects of noise and Selective Availability (SA) to limit the number of missed detections [6]. When the calculated ARP, for a user location at a particular time, is below the ARP ceiling then the geometry at hand is considered admissible.

For detection purposes, ARP requires at least 5 visible satellites. The ARP criteria details are described in several publications by Brown [2,3,5,6], along with experimental results using the ARP method for simulations similar to the one described in this paper. For these reasons, the ARP criteria was selected for this experiment and is calculated by the following equations [5].

$$\text{ARP} = \text{Slope}_{\max} \times \text{Threshold}_n$$

$$\text{Slope}_{\max} = \text{Max}_i [\text{Slope}(i)]$$

$$\text{where, Slope}(i) = \sqrt{\frac{(A_{1i}^2 + A_{2i}^2)(n-4)}{1 - B_{ii}}} \text{ for } i = 1 \dots n.$$

$$\text{and } \mathbf{A} = (\mathbf{H}^T \mathbf{H})^{-1} \mathbf{H}^T$$

$$\mathbf{B} = \mathbf{H}(\mathbf{H}^T \mathbf{H})^{-1} \mathbf{H}^T$$

\mathbf{H} = Direction Cosine Matrix

The slope is calculated for each satellite in view and n is the total number of visible satellites.

Test Statistic

The SSE in the all-in-view least squares solution is given by:

$$\text{SSE} = \mathbf{w}^T \mathbf{w}$$

where \mathbf{w} denotes the range residual error. The normalized test statistic, with $(n-4)$ degrees of freedom, chosen for this paper is:

$$\text{Test Statistic} = \sqrt{\frac{\text{SSE}}{n-4}}$$

The normalized SSE has a chi-square distribution with $(n-4)$ degrees of freedom where n is the number of visible satellites [4]. The test statistic is compared to a threshold as a way to detect inconsistent measurements.

The detection thresholds are calculated based on a constant alarm rate of 1/15,000 samples for independent samples [2]. Chi-square tables can be used to obtain the applicable chi square variate for the $(n-4)$ degrees of freedom and an upper tail probability of 0.000067 [3].

SIMULATION DESCRIPTION

The software simulation consists of four modules. A space segment simulator which generates the STPs, an STP sorting program, the detection and alarm test programs.

STP Database

The space segment simulator generates a file for each user location that contains the user and satellite position vectors, location name, and time reference. For this simulation only the "Optimal 21" satellite constellation is considered. The constellation orbital parameters and epoch are taken from Appendix I of the MOPS. The satellite information is retained for those satellites above a 7.5 degree mask angle. The simulation time is 24

hours with output data generated at 30 minute time steps. This generates 48 time points per user location. The user location data files are used for the STP sorting module. An STP database is generated for the 24 MOPS locations and the 5 degree grid locations.

STP Admissibility

The STP sorting module generates an admissible STP data set and a marginal STP data set. The admissible set contains the points in time for each user location with an ARP value below the ARP ceiling and at least 5 visible satellites. The 10 marginal STPs are the points with the largest ARP values of the admissible set and referred to as the marginal geometries.

Error Sources

The SA model for this experiment is based on the MOPS change 1 description, which is a second order Markov process and a random constant. The receiver noise is modeled as a uniform random variable plus a Gaussian random variable at the minimum sigma of 5 meters. At each user point in time, the true satellite and user locations are known within the space segment simulation data and the true range can be calculated. The receiver and SA noises are combined and added to the true ranges to yield an equivalent of the measured pseudorange.

Satellite failure is simulated by a ramp-type failure at the minimum rate of 5 meters per second, as stated in the MOPS. The ramp error is added to the pseudorange of the hardest to detect satellite. This is the satellite with the maximum slope value and determined during the ARP calculation.

Alarm Test

The alarm test uses the admissible set of STPs. For each admissible STP, 100 data samples of the position error are collected with no satellite failure but with the effects of receiver and SA noise present. The data samples are taken at two minute intervals to have independent samples [1]. The number of alarms are recorded. To pass the alarm test the MOPS specifies the total number of alarms is not to exceed:

$$\frac{\text{number of admissible space time points}}{1152(\text{Total STPs})} \times 14$$

Also, the number of alarms for any single space time point cannot be greater than 1.

Detection Test

The detection test follows the MOPS test procedure where 500 ramp type failures are performed for each marginal geometry to detect a satellite failure. The satellite failure is simulated by a ramp error of 5 meters per second and reset to zero after each detection event. The results are recorded according to four events.

1. The detection alarm is set and protection limit is not exceeded. This is an *early* detection.
2. The protection limit is exceeded and the detection alarm is set. This is a *timely* detection.
3. The protection limit is exceeded and the detection alarm is not set. This is a *missed* detection.
4. The protection limit is not exceeded and the detection alarm is not set within 400 seconds after initiating the ramp failure. This is an *inconclusive* run.

The total number of misses shall be less than or equal to 5 to pass the detection probability simulation test. The protection limit is set for non-precision approach, 555 meters.

EXPERIMENTAL RESULTS

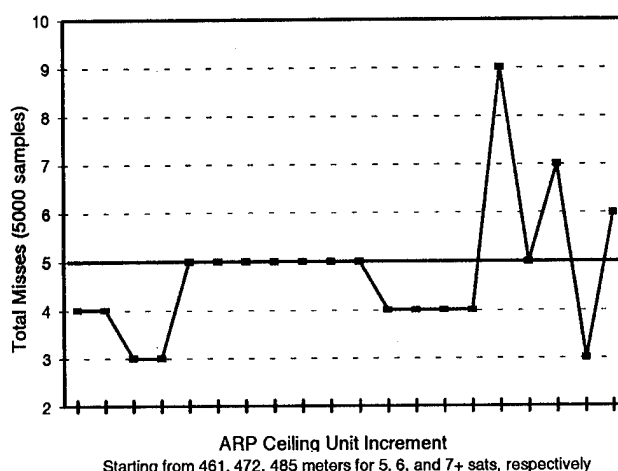
Maximum Requirements Test Scenario Procedure

The missed detections did not increase linearly as the ARP ceilings were increased as shown in Figure 2. The number of misses is the total misses for 10 marginal geometries with 500 samples each. The non-linearity allowed the selection of a maximum requirements test scenario past the first point were both the maximum alarm rate and missed detections are obtained.

The step size used to iterate the detection thresholds and ARP ceilings started with a 10 meter increment until the alarm and detection limits were exceeded. Next, with a step size of 1 meter the detection thresholds and ARP ceilings were decreased from the values where the 10 meter step failed the alarm and detection test. The process had to be changed to start at the beginning of the 10 meter interval due to the erratic behavior of the number of missed detections.

A change in the set of marginal geometries did not always correspond to a change in the number of misses. The plateau of 5 misses was sustained even though the set of marginal geometries changed 3 times.

Figure 2: Total Misses for MOPS Marginal STPs



STP Data

The marginal STPs for each of the user locations are listed in Tables 3, 4, and 5. The 10 marginal geometries for the Northern Hemisphere have ARP values that span only 1 meter from the smallest marginal ARP value to the largest ARP value. The MOPS range is 17 meters from the smallest to largest ARP value. The 1 meter range of the Northern Hemisphere makes it less likely that another admissible geometry would fall between the ARP values listed, therefore, assuring other more marginal geometries do not exist. At the same time these locations are more dispersed than the MOPS STPs. Several of the MOPS marginal geometries occur at the same location but at different times.

The largest ARP value for the MOPS geometries is greater than the largest value of the US grid but less than the Northern Hemisphere grid. This may be attributed to the MOPS and Northern Hemisphere grids consisting primarily of 7 satellite geometries compared to the 6 satellite geometries typical for the US grid.

Table 3: MOPS Marginal Geometries

Location	Visible Sats	ARP (m)	Slope _{max}	HDOP
Liberia	7	492.729	6.175	1.945
Singapore	8	489.313	6.740	1.796
Marshall Is.	7	488.322	6.119	2.371
London	7	487.780	6.113	1.580
Singapore	7	487.178	6.105	1.911
Indian Ocean	7	482.512	6.047	1.574
Ecuador	7	482.349	6.045	2.313
Liberia	7	479.915	6.014	2.339
So. Atlantic	6	476.026	5.174	2.985
Easter Is.	8	475.665	6.552	1.785

Table 4: US Marginal Geometries

Location Lat. Long.		Visible Sats	ARP (m)	Slope _{max}	HDOP
25	-105	7	485.827	6.088	1.866
30	-70	6	481.690	5.236	2.487
50	-110	6	481.650	5.235	2.478
25	-100	6	481.556	5.234	2.956
35	-85	6	481.090	5.229	2.653
50	-125	6	480.337	5.221	2.854
30	-85	6	480.221	5.220	2.656
30	-95	6	480.001	5.217	2.193
35	-115	6	479.498	5.212	2.792
45	-120	6	479.156	5.208	2.821

Table 5: Northern Hemisphere Geometries

Location Lat. Long.		Visible Sats	ARP (m)	Slope _{max}	HDOP
0	-180	8	494.978	6.818	1.793
40	15	7	494.966	6.203	2.061
55	-180	7	494.941	6.202	2.277
5	-5	7	494.807	6.201	2.281
10	-175	8	494.698	6.814	1.792
85	-50	7	494.693	6.199	1.576
50	-130	7	494.653	6.199	1.460
65	115	7	494.471	6.196	1.149
85	-115	7	494.454	6.196	1.056
80	20	7	494.349	6.195	1.838

Maximum Pmd Test

As shown in Table 6, the MOPS marginal geometries pass the missed detection test by having less than or equal to 10 misses, but the misses per individual STPs increased. This increase in missed detections for single STPs is also prevalent in the grid locations.

The US grid passes the missed detection test and the Northern Hemisphere grid does not as shown in Table 7 and 8. The number of misses did not increase significantly, but the number of misses increased more for individual STPs. Each set of marginal geometries had 5 or less of the STPs contribute to the missed detection probability with 500 samples.

The MOPS test makes no requirement on individual STP missed detection probabilities. The missed detection requirement as stated in the MOPS averages the missed detection over the 10 marginal geometries. This means that one STP of the 10 marginal geometries could contain 5 misses and still pass the MOPS detection test. Testing with 500 samples, the missed detection probability of 0.001 is less than one miss for a single

STP. The detection test was run with 1000 samples per STP to show more clearly the individual STP missed detection.

Table 6: MOPS Misses per Marginal Geometry

Location		Misses 500 Samples	Misses 1000 Samples	Visible Satellites
Liberia		0	0	7
Singapore		1	5	8
Marshall Is.		0	0	7
London		1	4	7
Singapore		1	0	7
Indian Ocean		0	1	7
Ecuador		0	0	7
Liberia		0	0	7
So. Atlantic		1	0	6
Easter Is.		1	0	8
Totals		5	10	

Table 7: US Misses per Marginal Geometry

Location Lat. Long.		Misses 500 Samples	Misses 1000 Samples	Visible Satellites
25	-105	0	0	7
30	-70	2	4	6
50	-110	0	0	6
25	-100	1	0	6
35	-85	0	1	6
50	-125	0	0	6
30	-85	0	0	6
30	-95	1	1	6
35	-115	0	0	6
45	-120	1	1	6
Totals		5	6	

Table 8: Northern Hemisphere Misses per Marginal Geometry

Location Lat. Long.		Misses 500 Samples	Misses 1000 Samples	Visible Satellites
0	-180	0	1	8
40	15	0	0	7
55	-180	2	2	7
5	-5	2	8	7
10	-175	1	2	8
85	-50	3	4	7
50	-130	1	1	7
65	115	0	0	7
85	-115	0	1	7
80	20	0	0	7
Totals		9	19	

If testing is to be with the worst case geometries, then results are consistent with the ARP values of the marginal geometries. That is, the US grid marginal geometries have lower ARP values than the MOPS set and are better geometries. The Northern Hemisphere marginal geometries have higher ARP values making them more- "worse case" than the MOPS marginal geometries.

Maximum Alarm Rate Test

The US grid passes the alarm test as is expected since none of the marginal geometries of the US was of a higher ARP value than the MOPS geometries. The number of admissible grid geometries for the Northern Hemisphere is over 50,000 and would require excessive processing time for the alarm rate test, therefore the alarm test was not performed on the Northern Hemisphere grid.

CONCLUSIONS

Changing the set of locations used to perform the MOPS off-line test, made it possible to overestimate a RAIM algorithm's performance. Replacing the test locations from those listed in the MOPS to a grid covering the Northern Hemisphere did not significantly increase the missed detection probability, but was enough to cause the RAIM algorithm for this experiment to fail after it had successfully passed with the MOPS set of marginal geometries.

The grid covering the US passes the detection and alarm test using a maximum test requirements scenario. Thus, the MOPS procedure appears to sufficiently test a RAIM algorithm for operation over the contiguous US states. When the grid is expanded to cover the Northern Hemisphere, the RAIM algorithm fails the detection test under the same conditions where it had previously passed with the MOPS set of locations.

In all test cases that passed the MOPS missed detection test, some of the individual marginal geometries failed while the total misses allowed for the 10 marginal geometries was not exceeded. This conflicts with the requirement for the detection probability and alarm rate to be met globally at all times.

Doubling the samples per marginal geometry has a dramatic change in the number and distribution of misses. The MOPS recognizes that the sampling is statistically small and results shown in this paper confirm this. The MOPS allows tests to be continued with a larger number of samples if an algorithm fails. Increasing the number of samples would not help in this

situation. The geometric criteria needs to be set below the maximum requirements to avoid overestimating the algorithm's performance due to the MOPS locations not having true worst case geometries and the small number of samples used for detection probability tests.

Results presented in this paper, are presumed accurate for other RAIM algorithms and phases of flight. However, further tests are being conducted to verify this assumption.

ACKNOWLEDGMENTS

This work was sponsored by the FAA Satellite Program Office through the FAA Office of Research and Technology Applications under Grant Number 92-G-013.

REFERENCES

- [1] "Minimum Operational Performance Standards for Airborne Supplemental Navigation Using Global Positioning System (GPS)," RTCA Document RTCA/DO-208, July 1991.
- [2] Brown, R. G., Chin, G. Y., and Kraemer, J. H., "Update on GPS Integrity Requirements of the RTCA MOPS," Proceedings of the Fourth International Technical Meeting of the Satellite Division of the Institute of Navigation (ION GPS-91), Albuquerque, NM, September 11-13, 1991, pp. 761-772.
- [3] Brown, R. G., Chin, G. Y., and Kraemer, J. H., "RAIM: Will it Meet The RTCA GPS Minimum Operational Performance Standards?," Proceedings of the National Technical Meeting of the Institute of Navigation, Phoenix, AZ, January 22-24, 1991, pp. 103-111.
- [4] Parkinson, B. W., and Axelrad, P., "Autonomous GPS Integrity Monitoring Using the Pseudorange Residual," NAVIGATION, Journal of the Institute of Navigation, Vol. 35, No. 2, Summer 1988, pp. 255-274.
- [5] Brown, R. G., "A Baseline GPS RAIM Scheme and a Note on the Equivalence of Three RAIM Methods," NAVIGATION, Journal of the Institute of Navigation, Vol. 39, No. 3, Fall 1992, pp. 301-316.
- [6] Chin, G. Y., Kraemer, J. H., and Brown, R. G., "GPS RAIM: Screening Out Bad Geometries Under Worst-Case Bias Conditions," NAVIGATION, Journal of the Institute of Navigation, Vol. 39, No. 4, Winter 1992-93, pp. 407-427.

- [7] Sturza, M. A., and Brown, A. K., "Comparison of Fixed and Variable Threshold RAIM Algorithms," Proceedings of the Third International Technical Meeting of the Satellite Division of the Institute of Navigation (ION GPS-90), Colorado Springs, CO, September 19-21, 1990, pp. 437-443.

Worst Case GPS Integrity Monitoring

Donald Benson, Jr.
Dynamics Research Corporation

BIOGRAPHY

Don Benson is a project engineer at Dynamics Research Corporation, Andover, MA., developing and evaluating system concepts that use inertial technologies, GPS, gravity gradiometers, gravimeters and other navigation equipment. He has fifteen papers in the open literature, most are related to Kalman filtering and navigation technology. His previous work experiences include TASC and AC Electronics Division of GM. Mr. Benson has a BS in Physics and MS in Aeronautics and Astronautics both from the Massachusetts Institute of Technology. E-mail dbenson@s1.drc.com

ABSTRACT

A technique is developed in this paper to set thresholds and evaluate integrity monitoring performance based on worst case analysis. The worst case methods described here assume that the healthy satellites can have errors over a finite range, and then solves the following problems. What are the smallest and largest error magnitudes a satellite in question can have to cause the threshold to just be equaled (set off an alarm)? In this framework, setting thresholds and evaluating performance of integrity monitoring do not depend upon probability distributions.

Based on likelihood functions or least squares a quadratic decision function is used. With this decision function, the paper shows estimation residuals or raw data yield identical results. Integrity monitoring thresholds and performance evaluation can be based on noise models; thus the measurements and state vector do not have to be simulated.

INTRODUCTION

With aircraft and ship safety a major concern when using GPS or any other navigation aid, this paper develops an

integrity monitoring algorithm based on worst case methodology. The worst case techniques are used to set thresholds and to evaluate monitoring performance. Worst case analysis for integrity monitoring asks the following question. If healthy satellites have errors in a normal but finite range, what are the maximum and minimum error magnitudes an unhealthy satellite can have that will just cause the threshold to be equaled? If the minimum value is small then there will be many false alarms since the threshold can be equaled when the error of the satellite in question is close to or within the range of normal values. Conversely, if the maximum error is large then there will be many missed detections since large errors just below the maximum, which we would like to detect, will not cause an alarm to be set.

The worst case methodology offers an alternative to setting thresholds and evaluating performance without relying on probability distributions, although the quadratic decision function that this paper uses has its foundation in the gaussian probability density function [1,2,3]. Using the worst case technique does not depend upon a quadratic decision function, and other functions can be used. Other than quadratic decision functions are in use [4], but [5,6] show that for gaussian probability density functions the likelihood ratio or equivalently the log likelihood ratio (which yields quadratic functions) are optimal. By optimal, [5,6] show that the probability of error is minimized, or for a given probability of false alarm, the probability of missed detection is minimized (Neyman-Pearson theorem).

Integrity monitoring based on probability places strong reliance on good knowledge of the tails of the distribution which is the least known about a distribution. The distribution function or even the a priori probability for failed or unhealthy satellites are not well known since the system was not designed to be unhealthy. The above items can be significant drawbacks of probability based

threshold setting and performance evaluation for integrity monitoring.

The paper is organized as follows. After a brief review of the principles of integrity monitoring, including methods and models that are needed to perform integrity monitoring, a heuristic description of the worst case methodology follows. Threshold setting and performance evaluation results are then discussed. Finally conclusions are drawn and recommendations made. Since this paper is based on work in progress some of the suggestions are noted as speculative, and they would have to be verified with further work. Most of the mathematical details are left for the appendices.

REVIEW OF PRINCIPLES

The basic principles of integrity monitoring are illustrated in a two dimensional example shown in Figures 1a-1d, where, for simplicity, no clock errors are assumed. The satellite measurement is basically the distance from the satellite to the user. A distance measurement, r_1 , from one satellite measurement places the user anywhere on a circle of radius, r_1 , from satellite 1. A second distance measurement from another satellite also places the user anywhere on another circle of radius, r_2 , from satellite 2. The user position is the intersection of the two circles as shown in Fig. 1a. The circles intersect at two points but these points are generally so far apart that there is no question as to the correct intersection. Note that only two satellites are needed (with no clock errors) for a two dimensional fix, and if one satellite is unhealthy the user will obtain a bad fix unbeknownst to him. A redundant third satellite measurement will confirm a good fix if the intersection of the three arcs of circles are clustered close together as in Fig. 1b. If one of the satellites is unhealthy then the three circle arcs will not be clustered together but will intersect as in Fig. 1c, and the residual errors will be large. Thus we can determine that a satellite is bad, but we cannot deduce which one. With a fourth satellite measurement we now can determine which satellite is unhealthy and exclude it from the fix as shown in Fig. 1d.

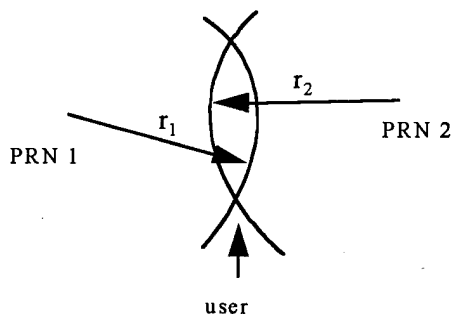


Figure 1a. Two Satellite Fix

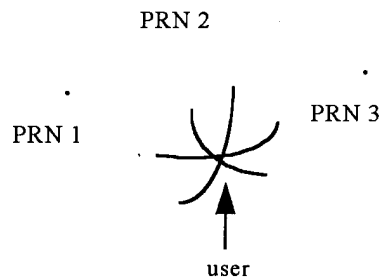


Figure 1b. Redundant Confirmation

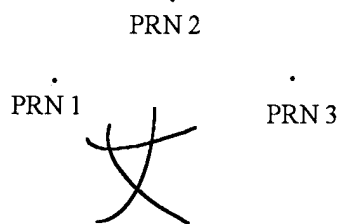


Figure 1c. Detection of Unhealthy Satellite

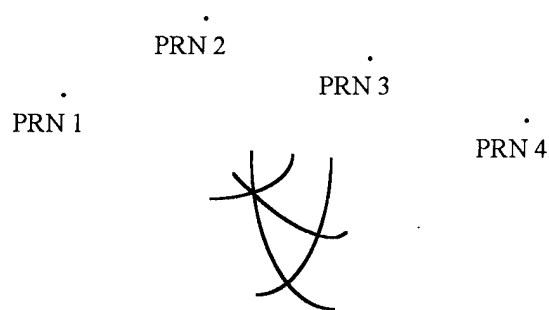


Figure 1d. Identification of Unhealthy Satellite PRN 1

The reasoning from the two dimensional example can be generalized to a three dimensional fix with a clock bias error. In this situation, with four unknowns, five satellites would be required to determine if a satellite or channel is unhealthy. Six satellites then would be necessary to isolate the unhealthy satellite or channel.

METHODS AND MODELS NEEDED

The above example shows that if the GPS data does not look like what we expect (i.e. large residuals) then issue an alarm. Thus we need:

1. A model of "what we expect" the GPS measurements to look like.
2. A decision function to accept the GPS data and output a number.
3. A threshold value to compare with the output of the decision function.
4. A method to evaluate performance of the integrity monitoring algorithm so that the threshold and/or the decision function can be modified if necessary.

The model of what we expect from GPS is commonplace but we will briefly repeat it here for completeness and also since we will also be referring to this model. The GPS fix is basically determined by equating the range from time difference to the range from position difference. For one satellite the equation is:

$$C(T_R - T_{T1}) = \sqrt{(X_{S1} - X_R)^2 + (Y_{S1} - Y_R)^2 + (Z_{S1} - Z_R)^2} \quad (1)$$

where T_R is the time the receiver receives the signal

T_{T1} is the time satellite 1 transmits the signal

X_{S1}, Y_{S1}, Z_{S1} is the position of the satellite at T_{T1}

X_R, Y_R, Z_R is the position of the receiver at T_R

C is the speed of electromagnetic propagation

Since there are four unknowns T_R, X_R, Y_R, Z_R at least four satellite measurements are needed. Usually the user knows his position accurately enough that these equations can be linearized about a nominal, and the linearized equations for m satellite measurements are:

$$\begin{bmatrix} Z_1 \\ \vdots \\ Z_m \end{bmatrix} = \begin{bmatrix} \alpha_{1X} & \alpha_{1Y} & \alpha_{1Z} & 1 \\ \vdots & \vdots & \vdots & \vdots \\ \alpha_{mX} & \alpha_{mY} & \alpha_{mZ} & 1 \end{bmatrix} \begin{bmatrix} \delta X \\ \delta Y \\ \delta Z \\ \Delta T \end{bmatrix} + \begin{bmatrix} V_1 \\ \vdots \\ V_m \end{bmatrix}$$

$$\text{or } Z = Hx + V \quad (2)$$

Where in (2) the α s in each row of H are the direction cosines from the user's nominal position to the corresponding satellite. The measurement vector Z is the difference between the time range and the position range

computed from (1) but evaluated at the known nominal user position and time.

As discussed in the introduction, we will use a quadratic decision function. In addition to the optimal properties a quadratic decision function also has the properties that a constant value represents contours of constant probability or, in the case of least squares, constant weighting. As shown in Appendix A, the function is an ellipsoid given by:

$$J = Z^T [I - H(H^T H)^{-1} H^T] Z \quad (3)$$

The threshold is determined by setting a value for J so that if J is exceeded an alarm is set. The value selected depends upon the performance desired. In a probability formulation performance is evaluated by the false alarm and missed detection probabilities. For the worst case methodology, performance is determined by minimum and maximum values at the threshold.

WORST CASE METHODOLOGY

The concepts of worst case methodology will be illustrated with a two dimensional example. The measurement noise for each healthy satellite is assumed to lie in the interval $|V_2| \leq 2\sigma$. If the threshold is set at J_{T1} as shown in Fig. 2, and we presume that satellite 2 is healthy, what values of V_1 can cause an alarm? As seen in Fig. 2 all values $|V_1| > V_{1MAX}$ will set alarms. $V_1 = 0$ can cause alarms over a small range of V_2 . This is highly undesirable since there would be many false alarms. Thus the threshold should be set higher. In Fig. 3 the threshold is now increased to J_{T2} as evidenced by the larger ellipse. As seen in the figure $V_1 = 0$ will never set an alarm, and other values such that $|V_1| < V_{1MIN}$ will never set an alarm. Now values of V_1 whose magnitude is slightly less than V_{1MAX} will go undetected. Thus, with the increased threshold setting, missed detections will increase but at the expense of fewer false alarms. The same procedure can be performed but with the roles of V_1 and V_2 interchanged. The principles illustrated in this two dimensional example are extended in the next section to a six dimensional case where thresholds are chosen and performance is evaluated. The necessary mathematics are described in Appendix B.

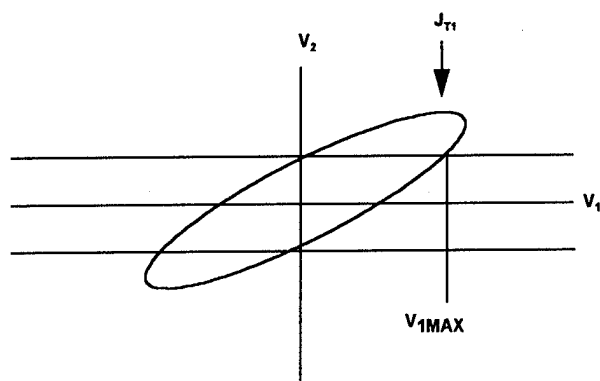


Figure 2. Example Ellipse with Threshold J_{T1}

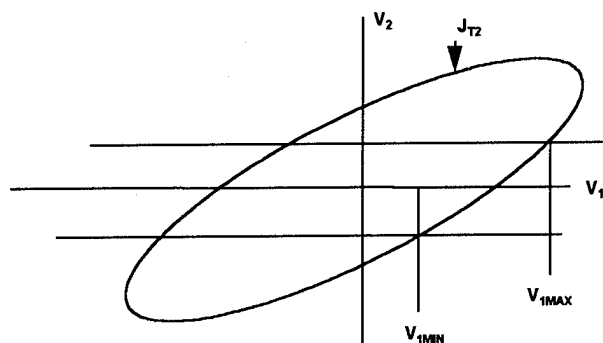


Figure 3. Example Ellipse with Threshold Increased to J_{T2}

SETTING THRESHOLDS AND EVALUATING PERFORMANCE

A GPS simulation program was used to determine satellites and their direction cosines for the H matrix. Table 1 shows the user location and the time of the fix. For this fix, minimum GDOP was used to choose 6 out of the 8 satellites visible with a mask angle of 10° during a 15 minute window (-5 to +10) about the time of the fix. Minimum GDOP for this selection was 2.34.

Table 1 Location and Time of GPS Fix

LOCATION	LAT	LONG	HEIGHT
	42°	78°	0 METERS
TIME	YEAR	DAY	SECONDS
	1994	67	3600

To see how worst case methodology can be used to determine a threshold and evaluate performance, we first chose a threshold value $J=9$. Rather than a random guess for J , the method we used to choose the initial value of 9 for J is based on Chi-square. The six satellite

measurements and the four unknowns leaves two degrees of freedom, and a probability of alarm of 0.01 gives $J=9.21$ from Chi-square tables. We will use a maximum error for healthy satellites of $V_{MAX}=2.0$, where all results in the tables are normalized by UERE (User Equivalent Range Error) of $\sigma=6$ meters. Appendix B shows that satellite errors can be used to evaluate performance rather than the satellite measurement or the measurement residual.

Table 2 shows the maximum satellite errors required to just equal the threshold of 9. Satellite 3, if it was unhealthy, could have an error as large as $22.69 \times$ UERE=136 meters before an alarm would be set. Table 3 shows the minimum satellite errors required to equal the threshold. For satellite 3 and 6 a zero error can set an alarm, and the other satellite errors are not even at their extrema. The row of other satellite errors is not filled since there are many values or errors that will allow satellite 3 or 6 to have zero error at the threshold. Thus we would likely have too many false alarms. Consequently the threshold should be set higher. Table 4 and 5 show the maximum and minimum errors required to equal a threshold of 25. The maximum errors have increased over using the threshold of 9 but not significantly. However we have achieved a significant increase in the minimum error, and thus there would be a significant decrease in the false alarm rate.

If the alarm is set with six satellites then one of the satellites is unhealthy, and, as discussed previously, we know that it can be eliminated and the remaining five can be used for the position fix. A procedure to effect this is to evaluate six different quadratic decision functions. Each function has five measurements with a different one of the six satellites not included. Pick, as the healthy five, the function with the minimum value.

Table 2 Maximum Satellite Error to Achieve a Threshold of 9

SATELLITE IN QUESTION	MAXIMUM ERROR	OTHER SATELLITE ERRORS TO ACHIEVE MAXIMUM, $V_{MAX}=2.0$					
		1	2	3	4	5	6
1	7.77		2.0	-2.0	2.0	1.63	2.0
2	7.28	2.0		2.0	-2.0	0.74	-2.0
3	22.69	-2.0	2.0		-2.0	2.0	2.0
4	9.14	-0.02	-2.0	-2.0		2.0	2.0
5	8.38	2.0	2.0	2.0	2.0		-2.0
6	19.39	2.0	1.99	2.0	2.0	-2.0	

Table 3 Minimum Satellite Error to Achieve a Threshold of 9

SATELLITE IN QUESTION	MINIMUM ERROR	OTHER SATELLITE ERRORS TO ACHIEVE MINIMUM, $V_{MAX}=2.0$					
		1	2	3	4	5	6
1	0.602		-2.0	2.0	2.0	-2.0	2.0
2	0.137	-2.0		-2.0	-2.0	2.0	-2.0
3	0.000						
4	0.294	2.0	2.0	2.0		-2.0	-2.0
5	0.500	-2.0	-2.0	-2.0	-2.0		2.0
6	0.000						

Table 4 Maximum Satellite Error To Achieve a Threshold of 25

SATELLITE IN QUESTION	MAXIMUM ERROR	OTHER SATELLITE ERRORS TO ACHIEVE MAXIMUM, $V_{MAX}=2.0$					
		1	2	3	4	5	6
1	10.78		2.0	-2.0	2.0	2.0	2.0
2	10.14	2.0		2.0	-2.0	0.94	-2.0
3	29.13	-2.0	2.0		-2.0	2.0	2.0
4	12.35	0.23	-2.0	-2.0		2.0	2.0
5	11.33	2.0	2.0	2.0	2.0		-2.0
6	25.50	2.0	2.0	2.0	2.0	-2.0	

Table 5 Minimum Satellite Error To Achieve a Threshold of 25

SATELLITE IN QUESTION	MINIMUM ERROR	OTHER SATELLITE ERRORS TO ACHIEVE MINIMUM, $V_{MAX}=2.0$					
		1	2	3	4	5	6
1	2.47		-2.0	2.0	2.0	-2.0	-2.0
2	2.59	-2.0		-2.0	-2.0	2.0	2.0
3	2.75	2.0	-2.0		2.0	-2.0	-2.0
4	2.58	2.0	-2.0	2.0		-2.0	-2.0
5	2.43	-2.0	2.0	-2.0	-2.0		2.0
6	2.86	-2.0	2.0	-2.0	-2.0	2.0	

CONCLUSIONS AND RECOMMENDATIONS

The worst case methodology developed in this paper provides an alternative method to set thresholds and evaluate integrity monitoring performance without relying on probability distributions. Especially difficult to quantify are knowledge of and confidence in the tails of the distributions and the probability density functions (pdf) of unhealthy satellites. With worst case methodology, the minimum error and the maximum error a satellite in question can have to just equal the threshold determines performance. With the quadratic decision function, a threshold of 9 could cause an undesirable number of false alarms. Setting the threshold higher to 25 to eliminate the false alarm problem provides good performance. Other GPS fix locations and times should be evaluated to ensure that the threshold has acceptable performance. The methodology can be easily extended to include other types of measurements, such as altitude, depth, or accurate clocks.

Tables 2-5 and Figs. 2-3 imply that if the minimum and maximum errors could be closer, then performance could be improved. For a fixed minimum, the missed detection rate would be lower because the maximum error at the threshold would be smaller. We speculate that this could be achieved with a higher order decision function. Use of parity vectors is probably the easiest way to implement higher order decision functions. Such a function would more heavily penalize large residuals or large noise values.

ACKNOWLEDGMENTS

This author wishes to express his appreciation for the thoughtful review of this paper by his colleagues at DRC, especially Alan Zorn, Dr. George Koehler, and Dr. Vis Sankaran.

REFERENCES

- [1] E. Gai, J.V. Harrison, and K.C. Daly, *FDI Performance of Two Redundant Sensor Configurations*, IEEE Trans. on Aerospace and Elec. Systems, Vol. AES-15, No. 3, May 1979.
- [2] B. W. Parkinson and P. Axelrad, *Autonomous GPS Integrity Monitoring Using the Pseudorange Residual*, NAVIGATION: Journal of The Institute of Navigation, Vol. 35, No. 2, Summer 1988.
- [3] M. A. Sturza, *Navigation System Integrity Monitoring Using Redundant Measurements*, NAVIGATION: Journal of The Institute of Navigation, Vol. 35, No. 4, Winter 1988-89.
- [4] *Global Positioning System Receiver Applications Module (GRAM) Standard (Final Draft)*, NAVSTAR Global Positioning System Joint Program Office, Los Angeles, CA 90245, 24 Jan. 1995.
- [5] F. C. Schweppe, *Uncertain Dynamic Systems*, Prentice-Hall, Inc. Englewood Cliffs, NJ. 1973.
- [6] R. V. Hogg and A. T. Craig, *Introduction to Mathematical Statistics*, 3rd. Ed. Macmillan Co., Inc. New York, N.Y., 1970.

APPENDIX A:

QUADRATIC DECISION FUNCTION WITH A COMPLETELY UNKNOWN STATE VECTOR

With a measurement vector Z , and completely known state vector, x , and noise, v ,

$$Z = Hx + v \quad (A-1)$$

the quadratic term of the gaussian probability density function of Z , $P(Z)$ is

$$J_1 = (Z - Hx)^T R^{-1} (Z - Hx) \quad (A-2)$$

where R is the covariance of the measurement noise, v . J_1 cannot be used as a decision function since x is completely unknown. However, if we use \hat{x} for x then we have a quadratic decision function that can be used:

$$J = (Z - H\hat{x})^T R^{-1} (Z - H\hat{x}) \quad (A-3)$$

$$\text{where } \hat{x} = (H^T R^{-1} H)^{-1} H^T R^{-1} Z \quad (A-4)$$

We can assume without loss of generality that $R = I$ [5, page 274]. Substituting (A-4) into (A-3) gives:

$$J = Z^T (I - H(H^T H)^{-1} H^T) (I - H(H^T H)^{-1} H^T) Z = Z^T (I - H(H^T H)^{-1} H^T) Z \quad (A-5)$$

since

$$(I - H(H^T H)^{-1} H^T) (I - H(H^T H)^{-1} H^T) = I - H(H^T H)^{-1} H^T = B \text{ (definition of } B) \quad (A-6)$$

We note that B is not invertible since if dimension $Z = m$ and $\dim x = n$, we can pick n parameters, a , and write

$$Z = H a \quad (A-7)$$

substitute (A-7) into (A-5) gives $J = 0$ for $Z \neq 0$. Thus, B is not invertible. If we decompose Z into two parts, Z_1 and Z_2 so

$$Z_1 = (I - H(H^T H)^{-1} H^T) Z \text{ and} \quad (A-8)$$

$$Z_2 = H(H^T H)^{-1} H^T Z \quad (A-9)$$

Then $Z = Z_1 + Z_2$ and $Z_1^T Z_2 = 0$, and this means that Z_1 and Z_2 are orthogonal and all vectors, Z , can be made from Z_1 and Z_2 . It can be shown that the rank of $H(H^T H)^{-1} H^T$ is n . Because $Z = Z_1 + Z_2$, the rank of $(I - H(H^T H)^{-1} H^T)$ is $m - n$, and this is the number of degrees of freedom. Z_1 is called the fault vector and is related to the parity vector [3].

If the residuals $Z - H\hat{x}$ are used instead of Z in (A-5) we get:

$$J_1 = (Z - H\hat{x})^T [I - H(H^T H)^{-1} H^T] (Z - H\hat{x}) = J \quad (A-10)$$

Also if we substitute $Z = Hx + v$ into (A-5) we get:

$$J = (Hx + v)^T [I - H(H^T H)^{-1} H^T] (Hx + v) = v^T [I - H(H^T H)^{-1} H^T] v \quad (A-11)$$

Eq. (A-5), (A-10) and (A-11) are very useful because of their properties. Eq. (A-5) and (A-10) imply we can use either the raw measurements or the residuals with the same weighting $[I - H(H^T H)^{-1} H^T]$ and get the same answer. Eq. (A-11) says that the decision function depends only on the noise. This is extremely useful to evaluate performance since we only have to use noise properties and we don't have to use or simulate the properties of the actual measurements. If the parity vector is used in a quadratic decision function which is the square of the magnitude of the parity vector, then it is

easy to show that the same properties hold. That is, performance depends upon the noise, and the residuals yield the same value for the decision function as the raw data.

APPENDIX B:

DETERMINING MAXIMUM AND MINIMUM ERRORS

In this appendix we will describe a method to obtain the maximum and minimum errors a satellite can have so that the threshold is just reached.

If (A-1) is substituted into (A-5) we get:

$$J = v^T (I - H(H^T H)^{-1} H^T) v = v^T B v \quad (\text{definition of } B) \quad (B-1)$$

and performance depends only on the noise v . Eq. (B-1) is the same as Eq. (A-11). We will first assume that B is invertible and then use these results for the case where B is not invertible. The question that we are asking is: What is the largest noise value the satellite in question can have such that the threshold is just reached? Since we are on the threshold we must have

$$dJ = 0 = 2 v^T B dv \quad (B-2)$$

$$0 = dJ = v^T \begin{bmatrix} \uparrow & \uparrow & \uparrow & \uparrow \\ \underline{b}_1 & \underline{b}_2 & \dots & \underline{b}_j & \dots & \underline{b}_m \\ \downarrow & \downarrow & \downarrow & \downarrow \end{bmatrix} \begin{bmatrix} dv_1 \\ dv_2 \\ \vdots \\ dv_i \\ \vdots \\ dv_m \end{bmatrix} = v^T [\underline{b}_i] dv_i + \dots + \underline{b}_m dv_m \quad (B-3)$$

where \underline{b}_i is the i th column of B

If the satellite error that we want to maximize is satellite i then:

$$v^T \underline{b}_j = 0 \quad \text{for all } j \neq i \quad (B-4)$$

since the coefficients of all the independent variables must be zero or, equivalently,

$$\frac{dv_i}{dv_j} = 0 \quad \text{for } i \neq j \quad \text{since we are maximizing } v_i.$$

Substituting (B-4) into (B-1) gives:

$$J = [0 \dots v^T \underline{b}_i 0 \dots 0] \begin{bmatrix} v_1 \\ \vdots \\ v_m \end{bmatrix} = v^T \underline{b}_i v_i = [v^T] \underline{b}'_i + v_i \underline{b}_i] v_i \quad (B-5)$$

where $v = v$ without element v_i

$$\underline{b}'_i = \underline{b}_i \text{ without element } b_i$$

From (B-4) we can write

$$0 = v^T [\underline{b}_1 \underline{b}_2 \dots \underline{b}_m] = v'^T B' + v_i \underline{b}'_i{}^T \quad (B-6)$$

for all \underline{b}_j but \underline{b}_i is not included and where B' is B without row and column i .

Since B is invertible because it is a positive definite matrix so is B' .

$$\text{Thus from (B-6)} \quad v'^T = -v_i \underline{b}'_i{}^T B'^{-1} \quad (B-7)$$

Substitute (B-7) into (B-5) gives

$$J = [-\underline{b}'_i{}^T B'^{-1} \underline{b}'_i + \underline{b}_i] v_i^2 \quad (B-8)$$

Eq. (B-8) is a solution for the maximum noise v_i satellite i can have to reach the threshold J . The values for the noise of the other satellites at the maximum is determined by substituting v_i into the transpose of (B-7), viz.,

$$v' = -B'^{-1} \underline{b}'_i v_i \quad (B-9)$$

Now we will discuss the case where B in (B-1) is not invertible. We will eliminate n dependent variables from (A-5) to end up with the same form as (B-1) with $m-n$ variables and an invertible B . Then (B-8) and (B-9) apply to this case as well.

Pick $m-n$ measurements that we want to keep to perform the maximization, resulting in n measurements that are to be eliminated. Rearrange the measurement vector to put the n Zs to be eliminated on top. Call the rearranged vector Z and the corresponding measurement matrix H . Now partition H into two parts, an $n \times n$ top part called H_1 and remaining part called H_2 .

$$H = \begin{bmatrix} H_1 \\ \dots \\ H_2 \end{bmatrix} \quad (B10)$$

$n \times n$ H_1 matrix is always invertible no matter which n Zs we chose to eliminate provided rank H is n . This is true provided the measurement geometry is good ($\text{GDOP} < \infty$). Now define a vector Y ,

$$Y = [I - H(H_1^{-1} \vdots 0)]Z \quad (B-11)$$

where

0 is a $n \times m-n$ matrix of zeros

Notice that:

$$J = Z^T (I - H (H^T H)^{-1} H^T) Z = Z^T (I - H (H_1^{-1} \vdots 0))^T (I - H (H_1^{-1} \vdots 0) (I - H (H_1^{-1} \vdots 0))^T) Z \quad (B-12)$$

Substituting (B-11) into (B-12) gives:

$$J = Y^T (I - H (H^T H)^{-1} H) Y = Y^T B Y \quad (B-13)$$

With (B-10) into (B-11) gives:

$$Y = \begin{bmatrix} I_1 & 0 \\ 0 & I_2 \end{bmatrix} - \begin{bmatrix} H_1 \\ \vdots \\ H_2 \end{bmatrix} \begin{bmatrix} H_1^{-1} \vdots 0 \end{bmatrix} Z = \begin{bmatrix} 0 & 0 \\ -H_2 H_1^{-1} & I_2 \end{bmatrix} \begin{bmatrix} Z_1 \\ \vdots \\ Z_2 \end{bmatrix}$$

$$= \begin{bmatrix} 0 \\ \vdots \\ -H_2 H_1^{-1} Z_1 + Z_2 \end{bmatrix} = \begin{bmatrix} Y_1 \\ \vdots \\ Y_2 \end{bmatrix} \quad (B-14)$$

where from (B-14) Y_1 is n dimensional zero vector and Y_2 is m-n

Substituting (B-14) into (B-13) gives:

$$J = (0^T \vdots Y_2^T) \begin{bmatrix} B_{11} & B_{12} \\ B_{12}^T & B_{22} \end{bmatrix} \begin{bmatrix} 0 \\ \vdots \\ Y_2 \end{bmatrix} = Y_2^T B_{22} Y_2 \quad (B-15)$$

Eq. (B-15) is the form we want and everything leading to the solution (B-8) and (B-9) applies but with Y_2 of dimension (m-n) in place of v and B_{22} in place of B . To evaluate the performance of the decision function and threshold J we can use v in place of Z (see B-1), thus from (B-14),

$$v_2 = Y_2 + H_2 H_1^{-1} v_1 \quad (B-16)$$

If we maximize the first element of the vector Y_2 call it $Y_{2(1)}$ in (B-15), then we can find the maximum error that the satellite in question (the first element in $v_2, v_{2(1)}$) can have using (B-16). If the noise on good satellites can have values $-v_{MAX} \leq v \leq v_{MAX}$ then $v_{2(1)MAX}$ is obtained by making the product of the first row of $H_2 H_1^{-1}$ and v_1 a maximum. This will occur with each element of v_1 either $+v_{MAX}$ or $-v_{MAX}$ depending upon the sign of the corresponding element in the first row of $H_2 H_1^{-1}$. Thus we have determined v_1 and the first element of v_2 . The rest of v_2 is known from (B-16) since we know the elements of Y_2 which are the independent variables from the maximization and all of v_1 . Some of the elements of v_2 (other than $v_{2(1)}$) may be larger than v_{MAX} . This is not allowed since $|v| \leq v_{MAX}$ and in this situation $v_{2(1)}$ is then maximized when each element of v is either

$+v_{MAX}$ or $-v_{MAX}$. We must go through this procedure for all combinations of satellites (except the satellite in question) as independent variables. For example, suppose there are 7 satellites. We eliminate 4 measurements because the state vector is dim 4 i.e. $(\Delta X, \Delta Y, \Delta Z, \Delta T)^T$. One of the remaining 3 is the satellite in question and the other 2 are the dependent variables. We can choose 2 dependent variables from 6 satellites in $6! / (2!4!) = 15$ ways.

The following summarizes the procedure for finding the maximum satellite error. Recall that we are determining the maximum error a satellite in question can have at the threshold while all other satellites have errors within their normal ranges, $-v_{MAX} \leq v \leq v_{MAX}$.

Procedure for Determining Maximum Satellite Error

1. Chose the satellite whose maximum error we want to determine.
 2. Pick a group of 4 satellite measurements that we want to eliminate. (Assuming the state vector is dim 4) and rearrange the measurement vector so these are the first 4.
 3. Compute B matrix (B-13) and get B_{22} (B-15).
 4. Compute maximum value for Y_2 that corresponds to satellite in question (B-8).
 5. Compute the other Y_2 s (B-9).
 6. From the Y_2 vector, compute the maximum error the satellite in question can have and the error values for the dependent variables. (B-16)
- Determine if the error values for the dependent variables are within the range $\pm v_{MAX}$.
- If yes then the solution is a candidate for a maximum, and go to 2. for the next group of satellites to eliminate.
- If no then the solution is not a candidate for maximum and go to 2. for next group of satellites to eliminate..
7. If the result for each group is no, then the maximum for the satellite in question occurs when the error for each of the other satellites is either $\pm v_{MAX}$. A solution can be found by searching over all values of $\pm v_{MAX}$ using (B-1).

Procedure for Determining the Minimum Satellite Error

The procedure for determining the minimum error that the satellite in question can have at the threshold is much simpler than for the maximum. Since differentiating the quadratic will find a maximum but not a minimum, the

minimum is either zero or it occurs at the extrema ($\pm v_{MAX}$) for all the other satellite errors.

1. Determine if zero error is possible by putting zero v for the satellite in question in $v^T B v$ of Eq. (B-1) and then find the maximum value for $v^T B v$ for $\pm v_{MAX}$ errors for the other satellites. If $(v^T B v)_{MAX} \geq J$ then zero is a solution.
2. If zero is not a solution, then the minimum error for the satellite in question occurs at the extrema ($\pm v_{MAX}$) for the other satellites. A solution can be found by trying all values of $\pm v_{MAX}$ and solving the quadratic $v^T B v = J$ for v of the satellite in question.

Analysis of Risk Affecting Integrity and Continuity

Jizhang Sang, Kurt Kubik, and Yanming Feng
SCSN, Queensland University of Technology

BIOGRAPHY

Jizhang Sang is a PhD student at Queensland University of Technology, Australia. He received his Master degree in Satellite Geodesy from Wuhan Technical University of Surveying and Mapping in 1986. He now works at GPS integrity monitoring, GPS aircraft application and Wide Area Augmentation System(WAAS).

ABSTRACT

In [1], integrity, continuity and accuracy of the system are defined to meet the requirement that the probability of any part of the aircraft leaving the tunnel without warning shall be less than 1 in 10^7 approaches. This requires an integrity risk of 6×10^{-8} and continuity risk of 2×10^{-5} per approach in the aircraft component.

The parameters influencing the airborne subsystem risk probability are tunnel dimension, the flight technical error(FTE) and the navigation system error(NSE). This study is directed in particular toward a first critical examination of treatment of above parameters. A new approach is proposed in this paper to compute the airborne subsystem risk probabilities of integrity and continuity in a rigorous way based on the joint probability distribution of NSE and FTE. This approach gives significantly different results from [1]. It is also shown that the probability of exceeding an alarm limit is significantly different from the probability of being outside the alarm limit. Thus, the computation of the SCAT-I risk probability as given in [1] should be reviewed.

1. INTRODUCTION

Tomorrow's civil aviation requires increased capability for aircraft equipment. GPS and WAAS are being researched to enhance the aircraft navigation performance. These enhancement must maintain or further improve the current safety level. The Required Navigation Performance(RNP) concept has been

proposed and used to solve the more complex airspace management problem[1][2].

The central RNP notion is the aircraft containment surface, called the tunnel, which partitions the airspace and defines the obstacle clearance surface. RNP is simply the requirement necessary to keep the aircraft inside the tunnel. The requirements are defined by four RNP parameters--accuracy, integrity, continuity and availability. RNP is an airspace system function and not a navigation sensor function. This means that airspace requirements can be satisfied independently of the methods by which they are achieved. In summary, RNP manages and defines the airspace so that user operational and economic benefits are realised without compromising safety.

Risk analysis, which is one of two activities used to keep the aircraft within the tunnel, allocates a risk to each design element of the aircraft and its navigation system. To meet the requirement that the probability of any part of the aircraft leaving the tunnel without warning shall be less than 1 in 10^7 approaches, it requires an integrity risk of 6×10^{-8} and continuity risk of 2×10^{-5} per approach in the aircraft component[1].

For the airborne subsystem risk analysis studied here, the parameters influencing the integrity and continuity risk probabilities are tunnel dimension, the Flight Technical Error(FTE) and the Navigation System Error(NSE). This paper is intended to have a critical examination of the treatment of these parameters. With the assumption of the independence of FTE and NSE and assuming the tunnel incident warning algorithm as in [1], the rigorous computations of integrity and continuity risk probabilities are carried out based on the joint probability distribution of NSE and FTE. This treatment of NSE and FTE is different from that in the [1],[3] and [4], where NSE and FTE are treated separately. These two approaches give significantly different results.

This paper also discusses the tunnel incident alarm problem. Following the theoretical derivation of FTE value rising through a given alarm limit and computation of

alarm probabilities, it is shown that the probability of exceeding an alarm limit is significantly different from the probability of being outside the alarm limit as given in [1].

2. THE TUNNEL CONCEPT AND RISK ALLOCATION

The tunnel concept is synonymous with RNP, which is defined by four parameters--accuracy, integrity, continuity and availability.

A tunnel is an aircraft containment surface with the assigned flight path as the central line. The dimensions of the tunnel determine the separation standard between the terrain, ground obstacles or other aircraft flying inside their assigned tunnels. A tunnel incident occurs only when the aircraft leaves its tunnel unintentionally

Because the events that cause a tunnel incident are uncertain, the best way to analyse tunnel event is probability analysis which allocates a portion of the tunnel incident risk to each RNP parameter.

Total System Error(TSE) excess that leads to a tunnel incident is associated with a risk that is specified by the accuracy parameter. The risk associated with unscheduled navigation function interruption is specified by the

continuity parameter, while the risk of latent equipment or design failures is specified by the integrity parameter. Availability ensures that the navigation function is available as aircraft enters the tunnel.

A tunnel incident has the possibility of leading to a loss-of-aircraft accident; this possibility is expressed by the accident-to-incident ratio which describes the conditional probability of an accident caused by tunnel incident. The calculated risk of an accident is compared with a safety goal called the target level of safety(TLS) which is defined by the community to determine an acceptable level of safety. In this paper, TLS is defined by the equation $TLS = (\text{accident-to-incident ratio}) \times (\text{tunnel incident risk})$.

For example, the realisation of TLS and allocation of RNP risks for SCAT I approach is shown in Figure 1 as in[1][2]. It is seen that the tunnel incident risk is equally allocated to three RNP parameters--accuracy, continuity and integrity. The loss of continuity and the loss of integrity per approach are required less than 1×10^{-4} and 1.3×10^{-7} , respectively, that require loss of the continuity and loss of the integrity of aircraft component less than 2×10^{-5} and 6×10^{-8} , respectively. These two figures are used as the target in the following computation results analysis.

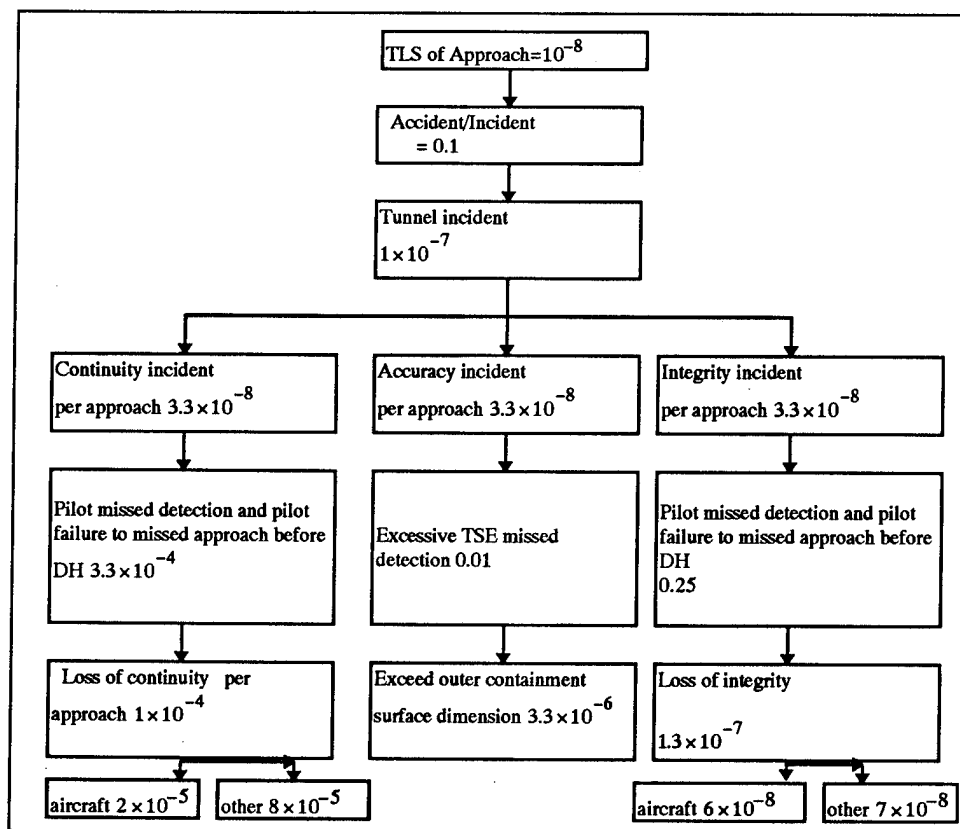


Figure 1: Example of RNP Tunnel Incident Risk Allocation for SCAT I Approach

3. RIGOROUS INTEGRITY AND CONTINUITY RISK COMPUTATION

3.1 Tunnel Incident Warning

As mentioned above, a tunnel is an aircraft containment surface which the aircraft can unintentionally leave with the probability of 10^{-7} over the specified phase of flight. For the SCAT I precision approach of 150 seconds, assuming there are 10 independent events, this defines that the half-dimension of the outer tunnel is the sum of $5.73\sigma_{TSE}$ and lateral or vertical aircraft semi-dimensions, and $2\sigma_{TSE}$ gives the half-dimension of the inner tunnel, if the fault-free total system error follows a normal $N(0, \sigma_{TSE}^2)$ distribution.

The total system error(TSE) is the incorporation of FTE and NSE. Assuming $TSE = |FTE| + NSE$, then there will be a tunnel penetration warning if

$$|FTE| + NSE > T-M \quad (1)$$

where

T is the half-width or half-height of the tunnel.

M is the margin required to protect aircraft extremities from penetrating the tunnel, that is, M is the semi-wing span for lateral tunnel, and 20 feet wheel height for the vertical tunnel.

NSE is taken as multiple of σ_{NAV} , where σ_{NAV} is one-sigma of the navigation solution, ie., $NSE = k\sigma_{NAV}$.

The loss of integrity of aircraft occurs only when the aircraft leaves the tunnel without warning. The loss of continuity of aircraft occurs only when the true or false alarm of tunnel penetration occurs. The following discussion of this section follows these definitions and the warning equation (1).

3.2 The Probability Expression of Integrity and Continuity of Airborne Navigation System

For the airborne subsystem, according to the tunnel penetration warning equation (1), we can express different tunnel events by a two-dimensional graph, as in Figure 2. From this figure, we have four possible tunnel events:

- P1: aircraft within tunnel and $|FTE| + NSE < T-M$: permissible
- P2: aircraft outside tunnel but $|FTE| + NSE < T-M$: integrity risk
- P3: aircraft within tunnel but $|FTE| + NSE > T-M$: false alarm
- P4: aircraft outside tunnel and $|FTE| + NSE > T-M$: true alarm

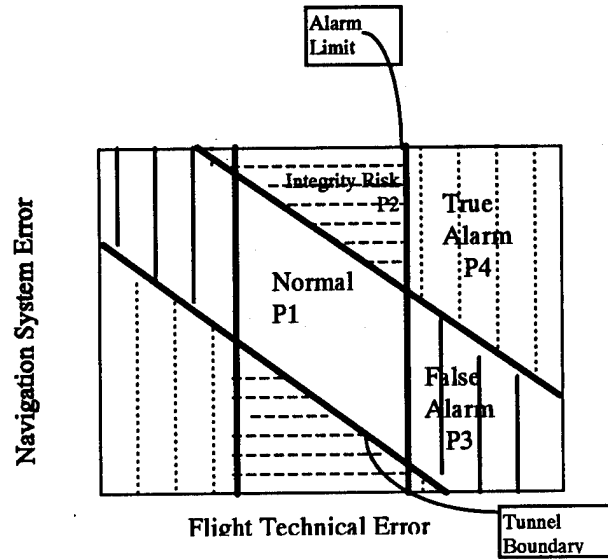


Figure 2: Illustration of Four Possible Tunnel Events

If we assume that FTE and NSE are independent Gaussian variables, we have the probability density functions of FTE and NSE:

$$f(FTE) = \frac{1}{\sqrt{2\pi}\sigma_{FTE}} e^{-\frac{FTE^2}{2\sigma_{FTE}^2}}$$

$$f(NSE) = \frac{1}{\sqrt{2\pi}\sigma_{NSE}} e^{-\frac{NSE^2}{2\sigma_{NSE}^2}}$$

and the joint probability density function of FTE and NSE:

$$f(FTE, NSE) = \frac{1}{2\pi\sigma_{FTE}\sigma_{NSE}} e^{-\left(\frac{FTE^2}{2\sigma_{FTE}^2} + \frac{NSE^2}{2\sigma_{NSE}^2}\right)}$$

From the inspection of Figure 2 and assumption of σ_{FTE} , σ_{NSE} , the probabilities P1 to P4 are obtained as follows:

$$P_1 = \frac{1}{2\pi\sigma_{FTE}\sigma_{NSE}} \int_{-s}^s e^{-\frac{FTE^2}{2\sigma_{FTE}^2}} dFTE \int_{-(T-M+FTE)}^{T-M-FTE} e^{-\frac{NSE^2}{2\sigma_{NSE}^2}} dNSE \quad (2)$$

$$P_2 = \frac{2}{2\pi\sigma_{FTE}\sigma_{NSE}} \int_{-s}^s e^{-\frac{FTE^2}{2\sigma_{FTE}^2}} dFTE \int_{T-M-FTE}^{\infty} e^{-\frac{NSE^2}{2\sigma_{NSE}^2}} dNSE \quad (3)$$

$$P_3 = \frac{4}{2\pi\sigma_{FTE}\sigma_{NSE}} \int_s^{\infty} e^{-\frac{FTE^2}{2\sigma_{FTE}^2}} dFTE \int_0^{T-M-FTE} e^{-\frac{NSE^2}{2\sigma_{NSE}^2}} dNSE \quad (4)$$

$$P_4 = \frac{4}{2\pi\sigma_{FTE}\sigma_{NSE}} \int_s^{\infty} e^{-\frac{FTE^2}{2\sigma_{FTE}^2}} dFTE \int_{(T-M-FTE)}^{\infty} e^{-\frac{NSE^2}{2\sigma_{NSE}^2}} dNSE \quad (5)$$

The probabilities are valid for each independent event. For the duration of the SCAT I precision approach, consisting of 10 independent events, the probabilities have to be multiplied by 10.

It can be seen that these computations are more complete than those of SCAT I, Appendix J-8/J-9 in [1] as they allow the computation of both true and false alarm risk.

3.3 Computation Results of Integrity and Continuity Risks

It is known from Eqs.(2) to (5) that the probabilities P1 to P4 are determined by the tunnel dimension(T and M), the alarm limit S and two probability density function

Table 1: Alarm Risk Computation Results

T-M (m)	S (m)	σ_{NSE} (m)	σ_{FTE} (m)	P3	P4	P3+P4
30	24	2	2	2.15E-32	1.11E-35	2.15E-32
30	26	2	2	7.92E-38	9.23E-40	8.01E-38
30	28	2	2	9.81E-44	1.12E-44	1.09E-43
30	30	2	2	0.00E+00	0.00E+00	0.00E+00
30	24	2	4	3.85E-09	6.57E-12	3.86E-09
30	26	2	4	1.61E-10	3.22E-12	1.64E-10
30	28	2	4	4.77E-12	7.06E-13	5.48E-12
30	30	2	4	8.08E-14	6.19E-14	1.43E-13
30	24	2	6	8.67E-05	1.37E-06	8.81E-05
30	26	2	6	1.96E-05	1.29E-06	2.09E-05
30	28	2	6	3.50E-06	9.57E-07	4.46E-06
30	30	2	6	4.06E-07	4.49E-07	8.55E-07
30	24	2	8	3.07E-03	2.15E-04	3.29E-03
30	26	2	8	1.21E-03	2.12E-04	1.42E-03
30	28	2	8	3.89E-04	1.93E-04	5.82E-04
30	30	2	8	8.49E-05	1.39E-04	2.24E-04
30	18	4	2	1.04E-18	9.09E-22	1.04E-18
30	22	4	2	2.09E-27	3.53E-29	2.13E-27
30	26	4	2	6.97E-38	1.04E-38	8.01E-38
30	30	4	2	0.00E+00	0.00E+00	0.00E+00
30	18	4	4	1.15E-05	1.83E-08	1.15E-05
30	22	4	4	6.94E-08	1.52E-09	7.09E-08
30	26	4	4	1.41E-10	2.37E-11	1.64E-10
30	30	4	4	7.61E-14	6.67E-14	1.43E-13
30	18	4	6	3.48E-03	2.11E-05	3.50E-03
30	22	4	6	3.21E-04	1.34E-05	3.34E-04
30	26	4	6	1.70E-05	3.95E-06	2.09E-05
30	30	4	6	4.13E-07	4.43E-07	8.55E-07
30	18	4	8	2.80E-02	6.36E-04	2.86E-02
30	22	4	8	6.59E-03	5.74E-04	7.16E-03
30	26	4	8	1.06E-03	3.67E-04	1.42E-03
30	30	4	8	9.40E-05	1.30E-04	2.24E-03
30	12	6	2	6.35E-09	6.65E-12	6.35E-09
30	18	6	2	1.02E-18	1.93E-20	1.04E-18
30	24	6	2	1.85E-32	2.99E-33	2.15E-32
30	30	6	2	0.00E+00	0.00E+00	0.00E+00
30	12	6	4	3.94E-03	7.24E-06	3.95E-03
30	18	6	4	1.13E-05	2.64E-07	1.15E-05
30	24	6	4	3.28E-09	5.80E-10	3.86E-09
30	30	6	4	7.45E-14	6.82E-14	1.43E-13
30	12	6	6	5.47E-02	2.74E-04	5.50E-02
30	18	6	6	3.37E-03	1.26E-04	3.50E-03
30	24	6	6	7.21E-05	1.60E-05	8.81E-05
30	30	6	6	4.17E-07	4.38E-07	8.55E-07

Table 2: Integrity Risk Computation Results

T-M(m)	S(m)	σ_{NSE} (m)	σ_{FTE} (m)	P2	T-M(m)	S(m)	σ_{NSE} (m)	σ_{FTE} (m)	P2
30	24	2	2	3.33E-26	30	18	4	4	9.61E-08
30	26	2	2	3.33E-26	30	22	4	4	1.18E-07
30	28	2	2	3.33E-26	30	26	4	4	1.19E-07
30	30	2	2	3.33E-26	30	30	4	4	1.19E-07
30	24	2	4	8.30E-12	30	18	4	6	4.34E-06
30	26	2	4	1.67E-11	30	22	4	6	1.69E-05
30	28	2	4	2.06E-11	30	26	4	6	2.89E-05
30	30	2	4	2.12E-11	30	30	4	6	3.24E-05
30	24	2	6	5.30E-08	30	12	6	2	5.91E-08
30	26	2	6	3.55E-07	30	18	6	2	2.18E-06
30	28	2	6	1.07E-06	30	24	6	2	2.18E-06
30	30	2	6	1.78E-06	30	30	6	2	2.18E-06
30	18	4	2	2.13E-11	30	12	6	4	1.60E-05
30	22	4	2	2.13E-11	30	18	6	4	3.25E-05
30	26	4	2	2.13E-11	30	24	6	4	3.28E-05
30	30	4	2	2.13E-11	30	30	6	4	3.28E-05

parameters σ_{FTE} , σ_{NSE} . We assume use of DGPS with accuracy of $\sigma_{NAV}=2m$ to $16m$ and a Flight Technical Error with accuracy of $\sigma_{FTE}=2m$ to $16m$. We also assume the tunnel dimension as T-M=30m, 60m and 90m, respectively. The Navigation System Error(NSE) is assumed as σ_{NAV} , $2\sigma_{NAV}$, $3\sigma_{NAV}$. So the alarm limit S is

$$S = T-M - \sigma_{NAV}, \text{ or } S = T-M - 2\sigma_{NAV}, \\ \text{or } S = T-M - 3\sigma_{NAV}$$

Some of the computed probabilities are listed in Tables 1 and 2. These probabilities are valid for one single event of 15 seconds duration. They have to be multiplied by a factor of 10 in order to cover the total approach duration of 15 seconds.

The probability of $|FTE| > S$ depends purely on the relationship between S and σ_{FTE} . For a normal distribution it holds:

Table 3: Relationship between S/σ_{FTE} and

S/σ_{FTE}	$P(FTE \geq S)$
2	4.5E-02
3	2.7E-03
4	6.3E-04
5	7.0E-06
6	1.0E-09
7	1.5E-10

Thus, the alarm limit can be selected as an appropriate multiple of σ_{FTE} in order to meet the continuity risk specification. Note, in particular, that the risk probability is very sensitive to the alarm limit.

The ratio between the false alarms and the true alarms can be studied through P3/P4. This ratio depends on the

distance between tunnel boundary and alarm limit. For the proposed distance of $3\sigma_{NAV}$, this ratio is between 10 and 100, that means, there are some 10 to 100 false alarms to every true alarm. For the distance of $2\sigma_{NAV}$, there will be less than 10 false alarms to each true alarm.

Overall, the following parameter combinations (Tables 4,5 and 6) are permissible in order to meet the specifications of continuity risk and integrity risk if NSE is taken as $2\sigma_{NAV}$. For the alarm limit $S = T-M - 2\sigma_{NAV}$, we have the following permissible parameter combinations of $(\sigma_{NSE}, \sigma_{FTE})$ which satisfy the RNP specification shown in Figure 1, and keep the false alarm rate small (less than 10 for each true alarm):

For T-M=30 m:

Table 4: Admissible Combinations of σ_{NSE} (m) and

σ_{FTE} (m) for T-M = 30 m	
σ_{NSE} (m)	σ_{FTE} (m)
≤ 4	≤ 4

For T-M=60 m:

Table 5: Admissible Combinations of σ_{NSE} (m) and

σ_{FTE} (m) for T-M = 60 m	
σ_{NSE} (m)	σ_{FTE} (m)
≤ 4	≤ 10
≤ 8	≤ 8
≤ 10	≤ 4

For T-M=90 m:

Table 6: Admissible Combinations of $\sigma_{NSE}(m)$ and

$\sigma_{FTE}(m)$ for T-M = 90 m	
$\sigma_{NSE}(m)$	$\sigma_{FTE}(m)$
≤ 6	≤ 16
≤ 12	≤ 12
≤ 14	≤ 6

Particularly, from the above we learnt that the results are very sensitive to alarm limit S if the tunnel incident warning Eq.(1) is used. If the navigation accuracy indicator σ_{NAV} is estimated online from the navigation data and use this estimated value for warning, this will change the risk probabilities significantly.

4. FURTHER DISCUSSION ON ALARM

To determine the alarm rate, the probability that FTE exceeds the alarm limit, as well as the frequency of this occurrence, must be computed.

We can illustrate simply how this probability is significantly different from the value obtained for the probability of FTE exceeding the alarm limit, following the computation procedure shown in Appendix J.4.3 of [1], namely:

$$Pr_{warning} = Pr(|FTE| \geq 12.54) = 1.25 \times 10^{-6} \quad (6)$$

Assuming two sine functions of equal amplitude but with different frequencies (for example, see Figure 3). Over a sufficiently long interval, the proportional area above the nominal alarm limit (the probability of a value exceeding the nominal value) will be equal for both curves. However, the alarm condition (approach and penetration of the nominal limit) will occur much more frequently for the high frequency curve (by a factor which is equal to the ratio of the higher to the lower frequency).

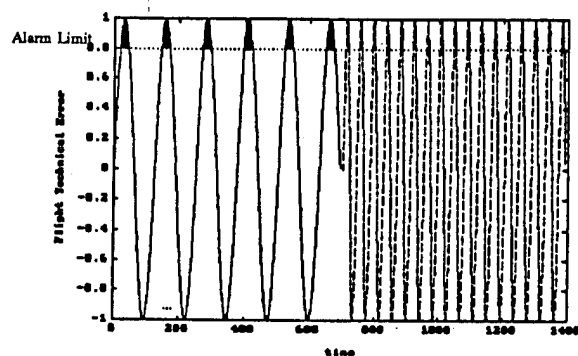


Figure 3: Sine-function-like Flight Technical Error

Once the alarm limit is passed, the (auto-)pilot will initiate a missed approach procedure. Therefore, only the probability of an occurrence when FTE passes the alarm limit S is relevant, while the probability $Pr(|FTE| > S)$

has no meaning here as it has little predictive significance. The quantity that must be determined is the probability of the first occurrence of $|FTE|$ exceeding the set limit and the spectral composition of $|FTE|$ bears directly on this probability.

The theory underlying more rigorous alarm computations and some numerical results are given below.

Consider the stationary random function $FTE(t)$ and its time derivative $DFTE(t)$. Let the joint probability density function of $FTE(t)$ and $DFTE(t)$ be $p(S, V)[5]$. The probability that $FTE(t)$ at time t lies between S and $S+dS$ and at the same time, $DFTE(t)$ lies between V and $V+dV$, is given by $p(S, V)dSdV$. On the other hand, this expression also represents the time interval which, during unit time, is being spent by FTE within the strip dS while moving with speed V . Now, the duration of single crossing of the strip is given by $dS/|V|$, where the absolute sign has to be taken since it is immaterial whether the speed V is positive (going upwards) or negative (going downwards). Dividing the total time being spent within the strip by the duration of one crossing, we obtain the mean number of crossings of the line $FTE=S$ per unit time for the speed V as below:

$$n_{S,V} = |V|p(S, V)dV \quad (7)$$

The total number of crossing (with arbitrary speed) per unit time is, therefore:

$$n_S = \int_{-\infty}^{\infty} |V|p(S, V)dV \quad (8)$$

In particular, the number of passages through zero is obtained as:

$$n_0 = \int_{-\infty}^{\infty} |V|p(0, V)dV \quad (9)$$

Since, in the mean, the number of upward and downward crossings of the line $FTE=S$ will be equal, we conclude that, in the mean, the frequency for $FTE(t)$ to exceed a given value S will be $n_S / 2$.

If $FTE(t)$ and $DFTE(t)$ are independent and $DFTE(t)$ is normal $N(0, \tau^2)$, then

$$p(S, V) = p(S) \frac{1}{\tau \sqrt{2\pi}} e^{-\frac{V^2}{2\tau^2}}$$

It follows that:

$$n_S = \sqrt{\frac{2}{\pi}} \tau p(S) \quad (10)$$

If $FTE(t)$ is normal $N(0, \sigma^2)$ too, then:

$$n_s = \frac{1}{\pi} \frac{\tau}{\sigma} e^{-\frac{s^2}{2\sigma^2}} \quad (11)$$

and in particular,

$$n_0 = \frac{1}{\pi} \frac{\tau}{\sigma} \quad (12)$$

For our particular tunnel penetration alarm warning, we have:

$$n_s = \frac{1}{2\pi} \frac{\sigma_{DFTE}}{\sigma_{FTE}} e^{-\frac{FTE^2}{2\sigma_{FTE}^2}} \quad (13)$$

$$n_0 = \frac{1}{2\pi} \frac{\sigma_{DFTE}}{\sigma_{FTE}} \quad (14)$$

Here, n_s denote the number of upward crossing of alarm limit and n_0 denoting the number of zero crossings of FTE per unit time. σ_{DFTE} can be derived from σ_{FTE} and following expression:

$$DFTE = \frac{\Delta FTE}{\Delta t} \quad (15)$$

The duration of one independent event of 15 seconds during the approach is analogous to the time interval between two zero crossing. This relationship is used in this paper to derive the change rate $DFTE$ for a given σ_{FTE} value.

The alarm risk probabilities for a 1 second interval were computed and listed in Table 7. In this Table, the first column lists σ_{FTE} , while the first row lists the alarm limit S . For the SCAT I approach of 150 seconds, these probability values have to be multiplied by a factor of 150.

We note that these probabilities are significantly different from the probability $\Pr(|FTE| \geq S)$.

In overall, it may be noted that the alarm risks are larger than computed conventionally, increasing alarm probabilities by a factor of 10. For the example of $\sigma_{FTE} = 2.59$ and frequency = 1/15 seconds, the probability of FTE crossing the alarm limit of 12.5 meters is 3×10^{-7} . For the approach duration of 150 seconds this probability is 4.5×10^{-5} which is significantly different from the value 1.25×10^{-6} .

Thus, it appears that further studies into the theoretical behaviour of the continuity and integrity risks are particularly important. There is a need to take into account the actual probability distribution of the aircraft/autopilot control systems which are certainly non-Gaussian.

5. CONCLUSIONS

From above discussions and results, we can conclude:

- The computations in this study are based on the joint probability distribution of NSE and FTE and are thus more rigorous than those in [1], [3] and [4]. These two approaches give significantly different results. It is shown that there exists a reasonable number of combinations of $(\sigma_{NSE}, \sigma_{FTE})$ which satisfy the RNP specifications of integrity and continuity for precision approach and keep the false alarm rate small.
- It is shown that the probability of exceeding an alarm limit is significantly different from the probability of being outside the alarm limit. Thus, the computation of continuity risk probability in [1] should be reviewed.

The further study on aircraft navigation integrity and continuity risk considering σ_{NAV}^2 as the function of a chi-square variable is currently being carried out by the authors. It is believed it will provide more rigorous results.

REFERENCES

1. RTCA SC-159, Minimum Aviation System Performance Standards, DGNSS Instrument Approach System Special Category I (SCAT-I), Proposed Final Draft, RTCA Paper No. 272-93/SC159-443, June 25, 1993.
2. Kelly, R.J. and Davis, J.M, Required Navigation Performance(RNP) for Precision Approach and Landing with GNSS Application, Navigation: Journal of The Institute of Navigation, Vol. 41, No. 1, Spring 1994.
3. AWOP-WP/644, RNP Tunnel Concept for Precision Approach and Landing, January 25, 1993.
4. AWOP/14-WP/659, Report on Agenda Item, February 3, 1993..
5. Grandall, S.H, Zero Crossings, Peaks and Other Statistical Measures of Random Response, J. Acoust. Soc. Am, Vol.37, 1963.

Table 7: Alarm Probability n_S for one Record

	0	10	20	30	40	50	60	70	80	90	100
2	3E-02	1E-03	6E-24	0E+00	0E+00	0E+00	0E+00	0E+00	0E+00	0E+00	0E+00
4	3E-02	8E-03	1E-07	2E-14	6E-24	4E-36	0E+00	0E+00	0E+00	0E+00	0E+00
6	3E-02	8E-03	1E-04	1E-07	7E-12	3E-17	6E-24	9E-32	8E-41	0E+00	0E+00
8	3E-02	2E-02	1E-03	3E-05	1E-07	1E-10	2E-14	8E-19	6E-24	1E-29	4E-36
10	3E-02	2E-02	5E-03	4E-04	1E-05	1E-07	5E-10	8E-13	4E-16	9E-20	6E-24
12	3E-02	2E-02	8E-03	1E-03	1E-04	6E-06	1E-07	1E-09	7E-12	2E-14	3E-17
14	3E-02	3E-02	1E-02	3E-03	6E-04	6E-05	3E-06	1E-07	3E-09	4E-11	3E-13
16	3E-02	3E-02	2E-02	6E-03	1E-03	3E-04	3E-05	2E-06	1E-07	4E-09	1E-10
18	3E-02	3E-02	2E-02	8E-03	3E-03	7E-04	1E-04	2E-05	2E-06	1E-07	7E-09
20	3E-02	3E-02	2E-02	1E-02	5E-03	1E-03	4E-04	7E-05	1E-05	1E-06	1E-07
22	3E-02	3E-02	2E-02	1E-02	6E-03	3E-03	8E-04	2E-04	4E-05	8E-06	1E-06
24	3E-02	3E-02	2E-02	2E-02	8E-03	4E-03	1E-03	5E-04	1E-04	3E-05	6E-06
26	3E-02	3E-02	2E-02	2E-02	1E-02	5E-03	2E-03	9E-04	3E-04	8E-05	2E-05
28	3E-02	3E-02	3E-02	2E-02	1E-02	7E-03	3E-03	1E-03	6E-04	2E-04	6E-05
30	3E-02	3E-02	3E-02	2E-02	1E-02	8E-03	5E-03	2E-03	1E-03	4E-04	1E-04

AUTHORS INDEX

Aardoom, Eric	835	Caldwell, John	7
Abbott, Eric	1269	Campan, Genevieve	257
Abousalem, Mohamed	25	Cannon, M. Elizabeth	899, 1111, 1877
Abusali, P.A.M.	229, 613	Cannon, Robert	1905
Adams, Larry	7, 1341	Cannon, Stewart	925
Albertson, Thomas	629, 1247	Canny, Joseph	7
Allison, Timo	1461	Cardoza, Miguel	423
Ananda, Mohan	1857	Carmona, Juan Carlos	173
Archer, Bill	1575	Carpenter, Russell	229
Ash, Tim	1825	Cashin, Tim	247
Ashbury, Michael	1383	Casotto, Stefano	619
Ashkenazi, Vidal	463, 1809	Chao, Yi-Chung	793, 661, 639
Axelrad, Penina	1785	Chasko, Andrew	1691, 1637
Balendra, Anushia	507	Chen, Wu	463
Bandel, S.	1885	Chistyakov, Valery	1013
Bar-Sever, Yoaz	599	Christie, Jock	793, 1451
Barker, Richard	1443	Christophe, B.	797
Barnes, Timothy	533	Cislaghi, Massimo	269
Baron, Luc	1417	Clifford, Joseph	1691
Barré, Hubert	269	Cobb, Stewart	793, 827, 1451
Barrows, Andrew	661, 1615	Cohen, Clark	827, 1451
Battie, Jill	1831	Cole, Rich	1857
Bauer, Frank	555	Collins, J. Paul	1681
Bäumker, Manfred	1847	Combs, Nick	229
Behre, Charles	1785	Conker, Robert	1247
Beisner, Henry	685	Conley, Rob	1363
Belton, David	853	Cooke, Michael	229
Benoist, R.	715	Cooper, John	499
Benson, Donald	677, 2023	Corcoran, Wendy	133
Bernedo, Pelayo	173, 589, 1775, 1797	Cosandier, Darren	1433, 1499
Bernick, Jonathan	1965	Costable, Greg	1673
Bertiger, Willy	183, 647, 1167, 1175	Courtney, G.	715
Beser, Jacques	507, 1041	Cox, Duncan B.	1975
Bishop, Gregory	1091, 1209	Cox, Duncan B.	217, 1655
Blackwell, Earl	399	Da, Ren	1285
Bobb, L.	443	Daly, Peter	499, 835, 1021, 1985
Bock, Yehuda	105	Dargen, John	413
Bogdanov, Pytor	1013	de Cevins, Julie	763
Bondarenco, Nicholas	619	de Jong, Cees	1071
Brading, John D.W.	217	Dedes, George	1081, 1285
Braff, Ron	773	Delucchi, John	1743
Brenner, Mats	1949	Denisov, Vladimir	971
Briggs, Thomas	1623	DePersia, D.	443
Brock, J. Kurt	141, 545	Diesel, John	1959
Brown, Alison	381, 907, 1175, 1317, 1511, 1825	DiEsposti, Raymond	1691
Brown, James L.	481	Diggle, David	727
Brown, John	93	Dimeo, Mark	727
Brown, Ron	739	Dimos, George	1545
Bullock, Blake	319	Disselkoen, Brent	1733
Burke, B.	1127	Doherty, Patricia	1247
Burkhardt, Laura	449	Donahue, Arnold	1351
Butzmuehlen, Carsten	2005	Dorsey, Arthur	685
Bybee, James	1645	Dow, John	619

Dowd, Marylouise	889	Gourevitch, Sergei	167
Duginov, Sergey	93	Grewal, Harkirat	1333
Dumville, Mark	1809	Groeber, Edward	1923
Duncan, Courtney	229	Guarino, R.	373
Dunn, Charles	229	Haddrell, Tony	161
Durand, Jean-Claude	257	Haines, Bruce	1175
Easton, Christine	2015	Hajj, George	1167
Eckert, Chuck	413	Hammada, Youcef	339
Eissfeller, Bernd	1589	Hamry, Bob	1237
El-Arini, Bakry	1247	Han, Shaowei	349, 1145
El-Rabbany, Ahmed	1493	Hansen, Paul	291
El-Sheimy, Naser	1307	Harder, Harald	755
Elkaim, Gabriel	1261	Harding, Brent	247
Enge, Per	639, 661, 773, 1403, 1615, 1995	Hardwick, C. Douglas	491, 1393
Engler, Evelin	1183	Harms, Pamela	413
English, Don	517	Hart, Roger	555
Erlandson, Robert	781	Hartman, David	391
Erpelding, Eric	507	Hartman, Kate	555
Euler, Hans-Jürgen	1477, 1751	Hartnett, Richard	1323
Evans, Alan	1623	Hasselbring, Al	1841
Evans, Jennifer	661	Haunschild, Martin	1061
Evers, Harry	1629	Haverland, Manfred	1629
Exner, Michael	229	Hein, Günter	1137, 1467, 1589
Fagan, John	1575	Hejjo, Hazem	1575
Fairbanks, Gregory	1691	Hekmat, Taymoor	845
Farnworth, Richard	473, 671	Hermann, Bruce	431, 1623
Fee, Joseph	1425	Herrera, Theodore	1703
Feltens, Joachim	619	Hilb, Robert	727
Feng, Yanming	705, 2033	Hill, C. J.	463
Fenton, Patrick	817, 1539	Hill, Craig	1477, 1751
Ferrage, Pascale	257	Hill, Lori	807
Ferranti, R.	1127	Hindemith-Boose, Dr.	1629
Ferzali, Wassim	1545	Holden, Tom	817
Ffoulkes-Jones, Geraint	853, 869, 1499	Holland, Elizabeth	1091, 1209
Filatchenkov, Sergey	1013	Howard, Neil	835
Fisher, Lawrence	1597	Howell, Gene	517
Flament, D.	797	Howell, Gene	1759
Fox, Travis	1575	Hua, Hua	1975
Fraile-Ordóñez, José	1193	Hüllenkremer, Manfred	1847
Frezet, Michael	269	Hundley, W.	715
Fryt, Mark	1363	Hunter, Jack	1895
Fuller, Rich	545	Hwang, Patrick	1733
Ganin, Alexander	959, 1049	Iacobacci, Timothy	1743
Ganther, Ken	807	Ichikawa, Tsutomu	573
Gao, Yang	25	Ikeda, Ray	1295
Garrick, Joseph	1767	Isben, Paul	373
Gazit, Ran	281	Ishikawa, S.	1301
Gecan, Anton	861	Issler, Jean-Luc	257
Gelatka, W.	443	Ito, T.	1301
Gevorkyan, Arvid	1013	Ivanov, Nicolay	991
Giacomini, Stefano	205	Jehl, Jean-François	1417
Gilkey, James	1723	Johannessen, Rolf	1383
Godwin, Paul	93	Johnson, Andrew	1237
Goguen, J.P. Thomas	1461	Johnson, Bruce	381
Gomez, Susan	195	Johnson, Greg	739
González, Pablo	1775	Johnson, Mark	695, 781
Gorev, Victor	959	Jolley, Stuart	671

Jonquiere, J. L.	797	Lorenz, Mark	247
Joy, Chris	291	Lovett, Andrew	671
Juan Ceva	647	Lowe, David	1809
Jungstand, Arne	1031	Lu, Ba	195
Kammeyer, Peter	73	Lu, Gang	1111
Kaufmann, Dave	739, 773	Luckau, Alfred	363
Kazantsev, V.	985	Lunday, Mark	889, 941
Kee, Changdon	639, 661	Luu, Sherry	1959
Kelly, Donald	413	Lyall, James	1915
Kemper, Brian	545	Macabiau, Christophe	299
Ketchum, Eleanor	1767	Macgregor, John	17
Khimulin, Vladlen	1013	Mackin, C.	773
Kim, Sonia	507	Mader, Gerald	1041
Kirschenlohr, Roland	1629	Mallett, Angela	1081
Klähn, Dietmar	1031, 1183	Malys, Stephen	431
Klinger, Gil	7	Manganis, B.	1941
Klobuchar, John	1247	Mannucci, Anthony	1199
Kondo, Hitoshi	1877	Marchel, N.	797
Krabill, W.	1117	Marcille, Herve	269
Kraus, Donna	247	Marquez, Shelley	105
Kruczynski, Leonard	1665, 1743	Marradi, Livio	205
Kubik, Kurt	705, 2033	Martell, Hugh	1433
Kuehl, Greg	727	Martín Mur, Tomás	619
Kuhl, Mark	167	Martin, C.	1117
Kulnev, Victor	959	Martinelli, Vincent	143, 1295
Kumagai, Susumu	573	Martinez, Carlos Garcia	619
Kursinski, Rob	1167	Mattos, Philip	123
Lachapelle, Gerard	817, 899, 1111	Maurer, Martin	845, 1061
Lala, Jaynarayan	449	Mazzella, Andrew	1091, 1209
LaMance, James	907, 1175, 1317, 1825	McCarron, J. Scott	1831
Lamb, Dave	727	McCartor, Gerry	1575
Lan, H.	899	McCloskey, Rick	229
Landau, Herbert	1485	McCullough, Jon	555
Langley, Richard	1681	McDonald, Keith	7, 1341
Lapucha, Dariusz	1443	McDonald, Samantha	229
Last, David	1229	McGraw, Gary	1553
Lavigne, Martin	1307	McKa, J.	1885
Lavrakas, John	157	McLellan, James	25, 1831
Law, Christopher	1623	Meehan, Tom	229
Lawrence, David	793, 827, 1451	Meldrum, David	935
Leake, Stephen	555	Melgård, Tor Egil	1229
Lebedev, Michael	959	Mendes, Virgílio	1681
Lee, Young	1929	Merrigan, Michael	45
Lehmann, Axel	1847	Meyer-Hilberg, Jochen	755
Lehnus, David	1713	Michaelson, William	1965, 1975, 2015
Leick, Alfred	1041	Misra, P.	1127, 1941
Leisten, Oliver	853, 869	Mistry, Hemant	473
Leroy, Stephen	1167	Mistutake, Masaki	573
Leung, J.	1885	Mieczko, Dave	545
Li, Jinye	1041	Moeglein, Mark	399
Li, Zuofa	331	Montalvo, Armando	381, 1511
Lichten, Stephen	183	Moore, T.	463
Lightsey, E. Glenn	237, 555	Moore, Terry	1809
Lindqwister, Ulf	183	Moore, Todd	363
Liu, Jeffrey	491, 1393	Mosle, Chip	1655
Liu, Jingnan	705	Mosle, William	1637
Liu, Ziwen	1443	Moussa, Ralph	1819

Muchnik, R.	1941	Riley, Stuart	499, 835
Mueller, Tysen	1237	Rim, H.	63, 613
Muellerschoen, Ron	183, 647	Rizos, Chris	1145
Müller, Urs	1477	Robertson, Glen	913
Munjal, Prem	1857	Rodden, J.	545
Murakami, Y.	1301	Rokni, Mohammad	1767
Murdock, Kelly	247	Romans, Larry	1167
Nakahara, N.	1301	Romrell, Glyn	739
Nakayama, David	399	Rowe, Tim	1985
Naor, Rahel	1869	Rowson, S.	715
Nash, Anthony	817	Rudolph, Kevin	363
Nelson, Shane	1155	Ryan, S.	899
Nelson, Thomas	1623	Salik, A.	443
Newby, Simon	133	Salischev, Vadim	991
Niklasch, Norbert	845, 1061	Sandlin, Allison	1341
Ninomiya, Keiken	573	Sang, Jizhang	705, 2033
Nisner, Paul	1373	Sankaran, Vis	677
Novy, Michael	1655	Santina, M.	1885
O'Connor, Michael	1261	Sardon, Esther	1031, 1183
O'Donnell, James	555	Saunders, Jimmy	423
O'Donnell, P.	715, 773	Saunders, Penny	195
O'Keefe, William	879	Schimelevich, Leonid	1869
O'Toole, James	45	Schleppe, John	1831
Ochieng, W. Y.	463	Schlesinger, James	3
Ottman, Geoffrey	1323	Schnauffer, Bernard	1553
Owen, John	1373	Schofield, Tim	1167
Pace, Scott	7	Schroeder, Christine	229
Pagels, Christian	1485	Schutz, Bob	63, 229, 613
Pairot, Jean Michael	269	Schwarz, Klaus-Peter	1101, 1307
Panneton, Robert	195	Scott, Sean	1363
Parkinson, Brad	237, 639, 647, 661, 793, 827, 1261, 1403, 1451, 1615	Senffner, Dave	1531
Pascal, Virginie	269	Seng, G.T.	1885
Pasetti, Alessandro	589	Sennott, Jim	1531
Pelletier, C.	817	Serfling, Steve	147
Pervan, Boris	827	Serrano, Jesús	1775, 1797
Peterson, Benjamin	1323	Sexton, Ralph	1575
Petway, Jon	563	Shaw, Samuel	1895
Pielmeier, Jürgen	1589	Silva, Randy	1825
Pilley, Lois	525	Silvestrin, Pierluigi	173, 835, 1775, 1797
Pilley, Robert	525	Simpson, Theodore	1425
Pogorelc, Scott	247	Singh, Daljit	1333
Ponsot, Pascal	763	Sinko, James	35
Poor, Walter	629	Skidmore, Trent	695
Potti, Jorge	173, 589	Sledzinski, Janusz	83
Powell, David	661, 793, 827, 1269, 1451, 1615	Smit, G.	1885
Pratt, M.	1127, 1941	Smith, Jeff	925
Pujara, Neeraj	391	Smuk, Jeff	437
Pullen, Samuel	1403	Sonntag, J.	1117
Qin, Xinhua	167	Spalding, Joseph	889, 907, 941
Qiu, Weigen	817	Sperry, Roger	1351
Racquet, John	817	Steiner, Steve	1857
Reid, Robert	919	Stratton, D.	1607
Remondi, Benjamin	1623	Stull, Craig	1219
Rhode, James	73	Stupp, George	1713
Richardson, David	1723	Suwa, Y.	1301
Richert, Walter	1061	Sweeting, Martin	579
Riedl, Bernhard	1467	Swider, R.	773

Swyers, S.	443	Yen, Pauline	629
Tabsh, Adel	1433	Yoshida, Bob	143
Tadros, Alfred	545	Youhanaie, Mark	391
Tang, C.	899	Young, William	105
Tang, Wang	517, 1759	Yuan, Dah-Ning	1199
Tapley, Byron	63, 229, 613	Yunck, Thomas	647
Taylor, Brian	1703	Zarraoa, Nestor	1031
Teasley, Stewart	1645, 1665	Zimmerman, Kurt	1905
Tekawy, J.	1885	Ziolkowski, Frank	363, 391
Terndrup, Christopher	1723	Zoltowski, Michael	861
Thérout, Yves	117		
Thomas, Bernard	1229		
Thomas, M. H. G.	949		
Thomas, Ulrich	269		
Tighe, Moira	17		
Townsend, Bryan	1539		
Trimble, Charles	7		
Tsai, Yeou-Jyh	639, 661		
Tsakiri, Maria	1809		
Turner, Dave	1341		
Uematsu, Hirohiko	237		
Uijt, Maarten	727		
Ulmer, Karl	1733		
Unwin, Martin	579		
Upadhyay, Triveni	1545		
Van Dierendonck, A. J.	1219		
Van Dierendonck, Keith	1539		
van der Marel, Hans	1071		
van Diggelen, Frank	167		
van Graas, Frank	727, 773		
van Nee, Richard	1539		
Velez, R.	715, 773		
Vieweg, Stefan	2005		
Vinogradov, Alexander	991		
Vollath, Ulrich	1485		
Wagner, Mark	1733		
Walsh, David	499, 1985		
Walter, Todd	639, 661, 793, 1995		
Wanninger, Lambert	55		
Ward, Phillip	1563		
Webster, John	913		
Wee, S.	899		
Weed, Dennis	1545		
Wei, Ming	1101, 1307		
Weill, Lawrence	1521		
Werner, Wolfgang	1137		
Wernle, Kenneth	1691		
Whitworth, Gerald	853, 935		
Wiles, George	437		
Wilson, Brian	1199		
Woo, K.T.	1857		
Wu, Sien	1175		
Wullschleger, Victor	715, 773		
Xin-Xiang	1071		
Xu, Benlin	309		
Yamamoto, T.	1301		
Yasuda, T.	1301		

ION GPS-95

The Satellite Division of The Institute of Navigation 8th International Technical Meeting
September 12-15, 1995 • Palm Springs Convention Center • Palm Springs, California

Conference Registrants

AASE, OIVIND
ABAUNZA, JOHN
ABBASSI, POURIA
ABBOTT, ANTHONY
ABBOTT, ERIC
ABBY, DARWIN
ADACHI, SUSUMU
ADAMS, ALAN
ADAMS, CHARLES
ADAMS, DANIEL
ADAMS, GREG
ADAMS, JOHN
ADAMS, NELLIS
ADAMS, W.T.
ADCOCK, JOHN
ADDIE, GORDON
ADELI, AMAN
ADEYEMI, BOLANIE
ADKINS, MICHAEL
AGEE, WILLIAM
AIKENS, JOHNNY
AIRTH, WALTER
AKITA, RICHARD
AKRIGG, STEVE
ALBA, JOE
ALBINGER, RICHARD
ALBRECHT, UWE
ALEXANDER, MICHAEL
ALEXANDROV, SEMEN
ALLAN, DAVID
ALMAAS, FRANK
ALNAJJAR, ASAAD
ALSLEBEN, WALTER
ANDERSON, A.J.
ANDERSON, BRADFORD
ANDERSON, LEE
ANDERSSON, LEIF
ANDRADA MARQUEZ, LUIS
ANDREWS, KEN
ANTON, JOHN
ANTRUM, GEOFF
ARAKAWA, YOSHI
ARCHER, BILL
ARCHIBALD, JIM
ARMACAST, SHAWN
ARMENDAREZ, JOHN
ARMSTRONG, WOODIE
ARNDT, PHIL
ARNOLD, JAMES
ARNOLD, RICHARD
ARNOLD, ROBERT
ARNOTT, GEORGE
ARRINGTON, ADAM
ARRIOLA, JOSE

FOTONOR AS
WARRENTON TRAINING CENTER
L.A. BUREAU OF SANITATION
NORTHROP GRUMMAN
STANFORD UNIVERSITY
GPSTSS
ROCKWELL TELECOMMUNICATIONS
BD SYSTEMS, INC.
HEWLETT PACKARD
USAF
VIZ
LOCKHEED MARTINE MISSILES & SP
JET PROPULSION LABORATORY
RTCM
AGMC/MLEE
NEVILLE CROSBY INC.
AFFILIATION UNKNWN
SHELL PETROLEUM PDC/XTDE
TOPCON
US ARMY WHITE SANDS MISSILE RA
USAF DET 4 AFOTEC/GPS
MAGNAVOX ELECTRONIC SYSTEMS CO
ACCURATE AUTOMATION CORPORATIO
HMGCC
MINISTRY OF DEFENCE PMSP16(1)
ROCKWELL
MANNESMANN PILOTENTWILUNG
ROCKWELL
NESTRO c/o ROMONA
ALLAN'S TIME
SIEMENS A/S
L.A. BUREAU OF STREET LIGHTING
AMCOMP
KELVIN HUGHES LTD.
INTERSTATE ELECTRONICS
GEOTRONICS
SWEDISH AIR FORCE
AENA
M/A-COM
USAF HQAFSPC/XPXS
COMPUTING DEVICES CANADA
AISIN WORLD CORP. OF AMERICA
THE UNIVERSITY OF OKLAHOMA
ALLIEDSIGNAL AEROSPACE COMPANY
LOCKHEED MARTIN
SMITHS INDUSTRIES
746 TS/TGGML
ASTER PUBLISHING/GPS WORLD MAG
FEDERAL HIGHWAY ADMINISTRATION
FAA GPS-NAV
HONEYWELL
ROCKWELL INTERNATIONAL
EARL DUDLEY ASSOCIATES, INC.
ROCKWELL INTERNATIONAL

NORWAY
WARRENTON,VA
LOS ANGELES,CA
HAWTHORNE,CA
STANFORD,CA
ALAMOGORDO,NM
JAPAN
TORRANCE,CA
SANTA CLARA,CA
PALMDALE,CA
PHILADELPHIA,PA
PALO ALTO,CA
PASADENA,CA
WASHINGTON,DC
NEWARK AFB,OH
CANADA
SIERRA VISTA,AZ
NIGERIA
PARAMUS,NJ
WHITE SANDS MISSILE RANGE,NM
PETERSON AFB,CO
TORRANCE,CA
CARLSBAD,CA
ENGLAND
GT BRITAIN
ARLINGTON,VA
GERMANY
ANAHEIM,CA
RUSSIA
FOUNTAIN GREEN,UT
NORWAY
LOS ANGELES,CA
HOLLOMAN AFB,NM
ENGLAND
ANAHEIM,CA
ITASCA,IL
SWEDEN
SPAIN
LOWELL,MA
PETERSON AFB,CO
CANADA
DOWNERS GROVE,IL
NORMAN,OK
TETERBORO,NJ
PITTSFIELD,MA
GRAND RAPIDS,MI
HOLLOMAN AFB,NM
METUCHEN,NJ
MCLEAN,VA
WASHINGTON,DC
IRVINE,CA
NEWPORT BEACH,CA
BIRMINGHAM,AL
ANAHEIM,CA

ASCHE, CLARENCE
 ASH, RICHARD
 ASHJAE, JAVAD
 ASHKENAZI, VIDAL
 ASPEY, STEVE
 ATKINSON, DOUGLAS
 AUGUST JONES, SHARON
 AUSEMS, MICHEL
 AVEY, JOEL
 AXELRAD, PENINA
 AYANSINA, YEMI
 BABU, KUMAR
 BADEWITZ, RICHARD
 BAEDER, BRIAN
 BAGLEY, LARRY
 BAHDER, TOM
 BAILEY, JONATHAN
 BAILEY, MICHAEL
 BAILEY, SCOTT
 BAKER, DOUGLAS
 BAKER, JEFF
 BAKER, ROBERT L.
 BALDWIN, TERRY
 BALKMAN, DOUG
 BALODIS, MIKE
 BANELA, RICHARD
 BANH, NAM
 BAR-SEVER, YOAZ
 BARBER, R.E.
 BARBOSA, OSCAR
 BARBOUX, JEAN-PIERRE
 BARKER, CLEON
 BARKER, RICHARD
 BARNES, CHARLES
 BARNES, MICHAEL
 BARNES, TIMOTHY
 BARRON, BRUCE
 BARROWS, ANDREW
 BARRY, JOHN
 BARRY, EDWARD
 BARTHOLOMEW, TOM
 BARTON, GREGG
 BARTON, HUGH
 BARTON, MICHAEL
 BARTONE, CHRIS
 BASKER, SALLY
 BASSETT, WAYNE
 BATCHELOR, ANDREW
 BAUER, FRANK
 BAUGHMAN, DAVID
 BAUMBACH, JASON
 BAUMKER, MANFRED
 BAXTER, TERRY
 BAZAK,
 BEAL, ROBERT
 BEAMISH, MICHAEL
 BEANBRIER, GREG
 BEARD, RONALD
 BEATTIE, HUGH
 BECK, JIM

HONEYWELL, INC.
 CORVALLIS MICROTECHNOLOGY INC.
 ASHTECH, INC.
 UNIV OF NOTTINGHAM, IESSG
 746 TS/TGGPI
 ASC/XRSS
 LEICA, INC.
 SURVEY DEPT, RIJWSWATERSTAAT
 TRIMBLE NAVIGATION
 UNIVERSITY OF COLORADO
 SHELL PDC NIGERIA LTD/XTDW TOP
 DEL NORTE TECHNOLOGY INC.
 CUBIC DEFENSE SYSTEMS
 U.S. ARMY MISSILE COMMAND
 STA, INC.
 U.S. ARMY RESEARCH LAB
 US DEPT OF COMMERCE/NOAA
 NAWC
 CATERPILLAR INC.
 A.E.T.E.
 KOHLMAN SYSTEMS RESEARCH
 ITT FEDERAL SERVICES CORP.
 TECHNOLOGY SYSTEMS, INC.
 3M DSD
 LEICA, INC.
 DEPT OF ARMY (WSMR)
 ROCKWELL
 JET PROPULSION LAB/CALTECH
 SERCO CONSULTANTS LTD
 THE AEROSPACE CORPORATION
 SERCEL
 746 TS/TGGPP
 JOHN E. CHANCE & ASSOCIATES
 WILCOX ELECTRIC, INC.
 RACAL SURVEY USA
 ZETA ASSOCIATES
 MCDONNELL DOUGLAS HELICOPTER
 STANFORD UNIVERSITY
 HQ AFOTEC/TKB
 ROCKWELL INTERNATIONAL
 TASC
 C.S. DRAPER LABORATORY, INC.
 GEC MARCONI
 CATERPILLAR, INC.
 OHIO UNIVERSITY
 RACAL RESEARCH LTD.
 WR-ALC/LKNE
 RACAL RESEARCH LTD.
 NASA GSFC
 TRW
 AFIWC/SAV
 FH BOCHUM/LITEF
 2SOPS/DOAN
 HUGHES SPACE & COMMUNICATIONS
 OO-ALC/TISFA
 PELORUS NAVIGATION SYSTEMS INC
 US ARMY YUMA PROVING GROUND
 NAVAL RESEARCH LABORATORY
 EXPLORATION GEODESY, INC.
 CAST, INC.

MINNEAPOLIS,MN
 CORVALLIS,OR
 SUNNYVALE,CA
 UK
 HOLLOMAN AFB,NM
 WPAFB,OH
 TORRANCE,CA
 HOLLAND
 SUNNYVALE,CA
 BOULDER,CO
 NIGERIA
 EULESS,TX
 SAN DIEGO,CA
 REDSTONE ARSENAL,AL
 COLORADO SPRINGS,CO
 ADELPHI,MD
 SILVER SPRING,MD
 CHINA LAKE,CA
 PEORIA,IL
 CANADA
 LAWRENCE,KS
 VANDENBERG AFB,CA
 WISCASSET,ME
 AUSTIN,TX
 NORCROSS,GA
 LAS CRUCES,NM
 CEDAR RAPIDS,IA
 PASADENA,CA
 UK
 WALNUT,CA
 FRANCE
 HOLLOMAN AFB,NM
 LAYFAYETTE,LA
 KANSAS CITY,MO
 HOUSTON,TX
 ALEXANDRIA,VA
 MESA,AZ
 PALO ALTO,CA
 KIRTLAND AFB,NM
 ANAHEIM,CA
 LINTHICUM,MD
 CAMBRIDGE,MA
 ENGLAND
 PEORIA,IL
 ATHENS,OH
 ENGLAND
 WARNER ROBINS AFB,GA
 ENGLAND
 GREENBELT,MD
 ALBUQUERQUE,NM
 SAN ANTONIO,TX
 GERMANY
 FALCON AFB,CO
 LOS ANGELES,CA
 HILL AFB,UT
 CANADA
 YUMA,AZ
 ALEXANDRIA,VA
 HOUSTON,TX
 LOS ALAMITOS,CA

BECKMANN, MARTIN
 BEDELL, COLE
 BEHMER, DAVID
 BEHRE, CHARLES
 BEHRNS, ANN MARIE
 BEISEL, KATHY
 BEISNER, HENRY
 BELL, JAMES
 BELL, DONNA
 BELLO, ERIK
 BELTON, JACK
 BENGLSDORF, CURT
 BENITEZ, JESUS
 BENNETT, NEIL
 BENNETT, SID
 BENNETT, VERNE
 BENSON, JOHN
 BERG-JOHANSEN, ROAR
 BERGENE, OYVIND
 BERGESON, JOHN
 BERGLJUNG, PETER
 BERKEL, STEVE
 BERNEDO, PELAYO
 BERNICK, JONATHAN
 BERRY, MARTIN
 BERRY, MICHAEL
 BERTIGER, WILLY
 BESER, JACQUES
 BETTENCOURT, STEVE
 BETTS, WILLIAM
 BEVERLY, EDGAR
 BIACS, ZOLTAN
 BIBAUT, ALAIN
 BIEDERMAN, ARTHUR
 BIENSTOCK, BERNARD
 BILLINGS, CHARLES
 BINEGAR, KIMBERLY
 BINGHAM, PETER
 BINNING, PATRICK
 BISHOP, GREGORY
 BLACKBURN, ALBERT
 BLACKWELL, EARL
 BLAIR, JOHN
 BLAIR, RONALD
 BLANKENHORN, JANICE
 BLAETH, GARY
 BLETZACKER, FRANK
 BLOMENHOFER, HELMUT
 BLOUNT, CLIVE
 BOCOVICH, PAUL
 BOEN, HAKIN
 BOESENBERG, CHARLES
 BOHENEK, BRIAN
 BOLAND, THOMAS
 BOLAND, LISA
 BOMBARD, TRACY
 BONE, A.
 BOONE, CHUCK
 BOOTH, JANET
 BORRE, KAI

TRIMBLE NAVIGATION, LTD.
 HONEYWELL MAV
 ROCKWELL INTERNATIONAL/CACD
 UNIVERSITY OF COLORADO
 HQ AFFSA/X01A
 TRIMBLE
 PARADEIGMA, INC.
 NORTHROP-GRUMMAN
 MOTOROLA
 ROCKWELL INTERNATIONAL
 AMERICAN NUCLEONICS CORPORATIO
 PHILLIPS BUSINESS INFORMATION
 WHITE SANDS MISSILE RANGE
 NATIONAL SYSTEMS & RESEARCH
 ANDREW CORP
 MAGELLAN SYSTEMS CORPORATION
 COMANT INDUSTRIES
 II MORROW, INC.
 NORWEGIAN ARMY MATERIAL CMD
 BOEING DEFENSE & SPACE
 SAAB DYNAMICS
 NAWCWPNS
 GMV
 WORCESTER POLYTECHNIC INSTITUT
 RACAL SURVEY USA
 HUGHES EOS
 JET PROPULSION LABORATORY
 3S NAVIGATION
 BATTELLE MEMORIAL INSTITUTE
 DFAS HQ USAFA
 US ARMY (PM-GPS)
 TRIMBLE NAVIGATION
 DASSAULT ELECTRONICS
 HUGHES AIRCRAFT COMPANY
 HUGHES SPACE CO.
 NORTHERN TELECOM INC.
 ROCKWELL INTERNATIONAL
 GEC PLESSEY SEMICONDUCTORS LTD
 NRL
 USAF/PHILLIPS LABORATORY/GPIA
 NAVSAT INTERNATIONAL, INC.
 SRI INTERNATIONAL
 INTERNATIONAL GEOMATICS SERVICE
 MOBIL RESEARCH & DEVELOPMENT C
 MAGELLAN SYSTEMS CORP
 GEC-MARCONI ELECTRONIC SYSTEMS
 WELNAVIGATE, INC.
 DAIMLER-BENZ AEROSPACE AG
 ROYAL AIR FORCE
 NAWCWPNS
 SEATEX AS
 ASHTECH INC.
 746TH TS/TGGDC
 ARINC RESEARCH CORP.
 2SOPS/DOAN
 BOOZ-ALLEN & HAMILTON, INC.
 UK MOD, MAIN BUILDING
 SMC/CZG
 BOEING COMMERCIAL FLIGHT TEST
 AALBORG UNIVERSITY

SUNNYVALE, CA
 CLEARWATER, FL
 CEDAR RAPIDS, IA
 BOULDER, CO
 ANDREWS AFB, MD
 SUNNYVALE, CA
 ROCKVILLE, MD
 GLENDALE, CA
 NORTHBROOK, IL
 NEWPORT BEACH, CA
 WESTLAKE VILLAGE, CA
 POTOMAC, MD
 WSMR, NM
 COLORADO SPRINGS, CO
 ORLANDO PARK, IL
 REDMOND, WA
 SANT AFE SPRINGS, CA
 SALEM, OR
 NORWAY
 BELLEVUE, WA
 SWEDEN
 POINT MUGU, CA
 SPAIN
 WORCESTER, MA
 HOUSTON, TX
 CAMBRIDGE, MA
 PASADENA, CA
 LAGUNA HILLS, CA
 COLUMBUS, OH
 COLORADO SPRINGS, CO
 LOS ANGELES AFB, CA
 SUNNYVALE, CA
 FRANCE
 LOS ANGELES, CA
 LOS ANGELES, CA
 SCHAUMBURG, IL
 ANAHEIM, CA
 ENGLAND
 WASHINGTON, DC
 HANSCOM AFB, MA
 MCLEAN, VA
 MENLO PARK, CA
 CANADA
 DALLAS, TX
 SAN DIMAS, CA
 GLEN RIDGE, NJ
 OXNARD, CA
 GERMANY
 UK
 PT. MUGU, CA
 NORWAY
 SUNNYVALE, CA
 HOLLOMAN AFB, NM
 SAN DIEGO, CA
 FALCON AFB, CO
 BEDFORD, MA
 GT BRITAIN
 COLORADO SPRINGS, CO
 SEATTLE, WA
 DENMARK

BOSACK, LEN
 BOTTENSEK, DALE
 BOTTOMS, BILL
 BOUCHARD, PAUL
 BOULTON, PETER
 BOUSHELL, SCOTT
 BOWEN, STUART
 BOWER, DOUGLAS
 BOWYER, DEAN
 BOYD, DAVID A.
 BOYD, STEVE
 BOYLE, DAVID
 BOYNTON, FRANCK
 BRAASCH, MICHAEL
 BRADING, JOHN
 BRAFF, RONALD
 BRAISTED, PAUL
 BRAND, TIMOTHY
 BRATLAND, ORVILLE
 BRAUN, RALPH
 BRAUNSTEIN, DAVID
 BRENN, VITO
 BRENNER, CHARLES
 BRENNER, MATS
 BREWER, MIKE
 BRICE, C. EDWARD
 BRIENZA, DOMENICO
 BRISBOIS, LAWRENCE
 BROCK, JOHN
 BROCKMAN, RANDY
 BROCKSTEIN, ALLAN
 BRODIE, KEITH
 BRODIE, PETE
 BROOKIN, JONATHAN
 BROHAUGH, TERRY
 BROKLOFF, NED
 BROOKS, LAWRENCE
 BROTTLAND, BRIAN
 BROWN, DONALD
 BROWN, ALISON
 BROWN, R. GROVER
 BROWN, BRUCE
 BROWN, JAMES
 BROWN, KARL
 BROWN, LARRY
 BROWN, ROBERT
 BROWN, RONALD
 BRUCE, RONALD
 BRUMLEY, FRANKIE
 BRUNER, PHIL
 BRUNO, ANTHONY
 BRYANT, MARK
 BUCHER, CHARLIE
 BUCHLER, ROBERT
 BUISSON, JAMES
 BULGHERONI, PETER
 BULLOCK, BLAKE
 BULLOCK, SCOTT
 BUNNELL, WILLIAM
 BUREAU, JERI

XKL SYSTEMS CORP.
 WESTERN GEOPHYSICAL
 ASHTECH
 TRAKMOBILE/ACCUCOM WSI
 NORTHERN TELECOM EUROPE LTD.
 2SOPS/DOAN
 SAN JOSE STATE UNIVERSITY
 NAESU
 LOCKHEED MARTIN
 E-SYSTEMS, ECI DIVISION
 NASA, JFK SPACE CENTER
 LEICA
 NAVTECH SEMINARS
 OHIO UNIVERSITY
 BRADING SYSTEMS & TECHNOLOGY
 THE MITRE CORPORATION
 TRIMBLE NAVIGATION
 C.S. DRAPER LABORATORY, INC.
 HONEYWELL AVIONICS
 LEICA AG
 STANFORD TELECOM
 MAGNAVOX ELECTRONIC SYSTEMS CO
 MOTOROLA
 HONEYWELL INC
 DIFFERENTIAL CORRECTIONS, INC.
 SONY ELECTRONICS INC.
 NAVAL AIR WARFARE CENTER
 JRC INTERNATIONAL INC.
 SPACE SYSTEMS/LORAL
 USSPACECOM/J330S
 LITTON SYSTEMS, INC.
 ROCKWELL INTERNATIONAL
 ITT A/CD
 COMPUTING DEVICES CANADA
 NORTHROP GRUMMAN
 JHU/APL
 JHU/APL
 NATIONAL SYSTEMS & RESEARCH
 OVERLOOK SYSTEMS TECHNOLOGY
 NAVSYS CORPORATION
 IOWA STATE UNIVERSITY
 TMI COMMUNICATIONS
 AYDIN CORPORATION EAST
 U.S. DEPARTMENT OF INTERIOR
 MOTOROLA, GSTG
 TRIMBLE
 E-SYSTEMS
 AMCOMP CORP.
 U.S. BUREAU OF RECLAMATION
 LITTON SYSTEMS, INC.
 TRIMBLE NAVIGATION
 TRIMBLE NAVIGATION
 MOTOROLA
 LITTON SYSTEMS, INC.
 NRL/SFA
 HANI-PROLECTRON AG
 MOTOROLA
 E-SYSTEMS, MONTEK DIVISION
 RRD
 MAGELLAN SYSTEMS

REDMOND, WA
 HOUSTON, TX
 PALO ALTO, CA
 SAN DIEGO, CA
 ENGLAND
 FALCON AFB, CO
 PALO ALTO, CA
 PHILADELPHIA, PA
 ORLANDO, FL
 ST. PETERSBURG, FL
 KENNEDY SPACE CENTER, FL
 TORRANCE, CA
 ARLINGTON, VA
 ATHENS, OH
 EXETER, NH
 MCLEAN, VA
 SUNNYVALE, CA
 CAMBRIDGE, MA
 MINNEAPOLIS, MN
 SWITZERLAND
 SUNNYVALE, CA
 TORRANCE, CA
 SCOTTSDALE, AZ
 COON RAPIDS, MN
 CUPERTINO, CA
 PARK RIDGE, NJ
 INDIANAPOLIS, IN
 FORT WORTH, TX
 PALO ALTO, CA
 PETERSON AFB, CO
 WOODLAND HILLS, CA
 LAKEWOOD, CA
 CLIFTON, NJ
 CANADA
 HAWTHORNE, CA
 LAUREL, MD
 PHOENIX, MD
 COLORADO SPRINGS, CO
 COLORADO SPRINGS, CO
 COLORADO SPRINGS, CO
 CLEAR LAKE, IA
 CANADA
 HORSHAM, PA
 DENVER, CO
 SCOTTSDALE, AZ
 SUNNYVALE, CA
 SEMINOLE, FL
 FOUNTAIN VALLEY, CA
 PHOENIX, AZ
 WOODLAND HILLS, CA
 SUNNYVALE, CA
 SPRINGFIELD, VA
 CHANDLER, AZ
 WOODLAND HILLS, CA
 SPRINGFIELD, VA
 SWITZERLAND
 NORTHBROOK, IL
 SALT LAKE CITY, UT
 COLUMBUS, GA
 SAN DIMAS, CA

BURKE, BRIAN
 BURTON, JIM
 BUSCHUR, DON
 BUTLER, BRUCE
 BUTLER, DENNIS
 BUTTS, JIM
 BYBEE, JIM
 BYRNE, JEFFERY
 CAFFERY, DENNIS
 CAFFEY, IDA
 CAIN, GARY
 CAIN, WILLIAM
 CAISSY, MARK
 CALABRESE, KAREN
 CALBI, VITO
 CALDWELL, JIM
 CALICCHIA, LUIGI
 CALISE, CARLO
 CALLAGHAN, STEVEN
 CALLENDER, DAVID
 CAMBERLEIN, LOIC
 CAMPAGNE, PASCAL
 CAMPBELL, CHARLES
 CANNON, M. ELIZABETH
 CANNON, STEWART
 CANTIN, NORMAN
 CAPOZZOLI, MARTIN
 CARBERT, ART
 CARDOZA, MIKE
 CAREY, RICHARD
 CARLILE, G.
 CARLSON, RODNEY
 CARLSON, LESLIE
 CARPENTER, ELISABETH
 CARR, ERIC
 CARRIGAN, ANGELA
 CARROLL, ROBERT
 CARTER, CARL
 CASIANO, RAY
 CASKEY, RANDY
 CASLOW, SCOTT
 CASSIDY, DAN
 CASSWELL, REBECCA
 CASTALANELLI, CASS
 CASTLEMAN, WAYNE
 CEVA, JUAN
 CHA, Y.K. JIM
 CHADHA, KANWAR
 CHADWICK, J. BROOKS
 CHAFFEE, JAMES
 CHAN, LING
 CHAN, YAT
 CHANG, CHIN-FENG
 CHANG, MIN-I
 CHANNEL, T.R.
 CHAO, YI-CHUNG
 CHAO, YU XING
 CHAPLIN, A.J.
 CHAPMAN, E.
 CHARLTON, GERRY

MIT LINCOLN LABORATORY
 4D SOLUTIONS
 U.S. AIR FORCE
 TRIMBLE NAVIGATION
 ROCKWELL SPACE OPERATIONS
 BD SYSTEMS, INC.
 CIBOLA INFORMATION SYSTEMS
 AUTECH
 NAWC WPN
 SAIC
 SPECTRA-PHYSICS LASERPLANE
 MACA
 GEOMATICS CANADA
 HONEYWELL, INC.
 MAGNAVOX ELECTRONIC SYSTEMS CO
 NAVSYMM POSITIONING SYSTEMS
 TRW
 AAAVTAG'
 OVERLOOK SYSTEMS TECHNOLOGIES
 GEC MARCONI DEFENCE SYSTEMS
 SAGEM
 FRANCE DEFENSE COUNSEIL
 NASA/GSFC
 UNIV OF CALGARY/GEOMATICS ENG
 PELAGOS CORPORATION
 NORTHSTAR TECHNOLOGIES
 ALLIED SIGNAL
 HONEYWELL, INC.
 ARL/UNIVERSITY OF TEXAS
 NCCOSC NRaD
 U.S. ARMY
 SYSTEM TECHNOLOGY ASSOC., INC.
 STANFORD TELECOM
 US DOT/RSPA/VNTSC
 HARRIS CORPORATION
 DET 4 AFOTEC/GSS
 THE MITRE CORPORATION
 ALLEN OSBORNE ASSOCIATES, INC
 USCG, GPS INFORMATION CENTER
 WESTERN AIR MAPS
 COMANT INDUSTRIES
 TOPCON
 U.S. COAST GUARD NAVCEN
 FUGRO SURVEY
 HONEYWELL INC.
 STANFORD UNIVERSTIY
 FAA
 SIRF TECHNOLOGY INC.
 CONSULTANT
 J. CHAFFEE & ASSOCIATES
 ASTER PUBLISHING/GPS WORLD
 THE AEROSPACE CORPORATION
 LEICA
 SVERDRUP
 MCDONNELL DOUGLAS
 STANFORD UNIVERSITY
 TRIMBLE NAVIGATION LTD
 RACAL AVIONICS LTD.
 DERA/CES/BCDE DIV
 U.S. COAST GUARD

LEXINGTON,MA
 JACKSONVILLE,FL
 FAYETTEVILLE,NC
 UK
 HOUSTON,TX
 TORRANCE,CA
 YUMA,AZ
 WEST PALM BEACH,FL
 LOS ANGELES,CA
 TORRANCE,CA
 DAYTON,OH
 OKLAHOMA CITY,OK
 CANADA
 GLENDALE,AZ
 TORRANCE,CA
 SAN JOSE,CA
 SAN BERNARDINO,CA
 ITALY
 GARDEN GROVE,CA
 SCOTLAND
 FRANCE
 FRANCE
 GREENBELT,MD
 CANADA
 SAN DIEGO,CA
 ACTON,MA
 BALTIMORE,MD
 CLEARWATER,FL
 AUSTIN,TX
 SAN DIEGO,CA
 COLORADO SPRINGS,CO
 COLORADO SPRINGS,CO
 SUNNYVALE,CA
 CAMBRIDGE,MA
 MELBOURNE,FL
 COLORADO SPRINGS,CO
 BEDFORD,MA
 WESTLAKE VILLAGE,CA
 ALEXANDRIA,VA
 LENEXA,
 SANTA FE SPRINGS,CA
 PARAMUS,NJ
 CLINTON,MD
 AUSTRALIA
 CLEARWATER,FL
 STANFORD,CA
 WASHINGTON,DC
 SANTA CLARA,CA
 BELLFLOWER,CA
 AUSTIN,TX
 METUCHEN,NJ
 LOS ANGELES,CA
 TORRANCE,CA
 EGLIN AFB,FL
 HAZELWOOD,MO
 STANFORD,CA
 CHINA
 UK
 ENGLAND
 PETALUMA,CA

CHARRON, LAURA
CHASKO, ANDREW
CHEN, DINGSHENG
CHEN, MINGWHEI
CHEN, AN
CHERRY, WILLIAM
CHESEBROUGH, MICHAEL
CHESTO, LAWRENCE
CHHANG, KEN
CHIBA, TAKAHIDE
CHISHOLM, JOE
CHOI, WON
CHONG, DAVID
CHRISTENSEN, RONALD
CHRISTIE, JOCK
CHRISTMAN, MARSHALL
CHRISTMAN, WARREN
CHRISTOFF, CORKY
CHRISTOPHE,
CHU, ALBERT
CHU, PAUL
CHUN, DENISE
CIMA FONTE, MICHAEL
CITRON,
CLANTON, ROBERT
CLARK, MARK
CLARK, BILL
CLARK, JOHN
CLARK, JOHN E.
CLARK, JOHN M.
CLARK, JON
CLARK, REX
CLARK, RICHARD
CLARKE, KENNETH
CLIFFORD, JOSEPH
CLISE, WILLIAM
CLYNCH, JAMES
CNOSSEN, RICHARD
COBB, KEVIN
COBB, STEWART
CODIK,
COHEN, CLARK
COHEN, ABRAHAM
COLEMAN, LEONARD
COLEMAN, RONALD
COLEMAN, CAROLYN
COLESTOCK, ANNABELLE
COLLEY, JAIME
COLMER, KEITH
CONGER, PAULA
CONKER, ROBERT
CONLEY, ROB
CONLON, THOMAS
CONNOLLY, PETER
CONNORS, MARK
COOK, GERALD
COONS, BRUCE
COOPER, DALE
COOPER, EDWARD
COOPER, JOHN

U.S. NAVAL OBSERVATORY/TSO
AMCOMP
AFFILIATION UNKNOWN
GALAXY SCIENTIFIC CORPORATION
SAIC
KEYSTONE COMPUTER ASSOCIATES,
413 TS, USAF
ARINC
NAWC WPNS
NTT MOBILE COMMUNICATIONS NETW
GEOTRONICS
HITCOM CORPORATION
LITTON GCS
HUGHES
STANFORD UNIVERSITY
4113 EW
RMS TECHNOLOGY/VISTA
LOCKHEED MARTIN
ONERA
MOTOROLA
TOPPER ENTERPRISES CO LTD
PACIFIC MISSILE RANGE FACILITY
HQ AFSPC/DRFN
HUGHES SPACE & COMMUNICATIONS
TRW
PRC (USAF)
TAMSCO
CAST, INC.
THE AEROSPACE CORPORATION
DEFENSE MAPPING SCHOOL
SOKKIA CORPORATION
UNIVERSITY OF GEORGIA
NAIC/TASS (USAF)
NAWC
THE AEROSPACE CORPORATION
SENTINEL COMMUNICATIONS
NPS
MAGNAVOX ELECTRONIC SYSTEMS CO
SATLOC
HANSEN LABS GP-B MC: 4085
HUGHES SPACE & COMMUNICATIONS
STANFORD UNIVERSITY
MTC
SMC/CZF
DCS CORPORATION
46 TW/TSWW
ARL/UNIVERSITY OF TEXAS
ROCKWELL INTERNATIONAL
GEO
WR-ALC/LKNE
THE MITRE CORPORATION
OVERLOOK SYSTEMS TECHNOLOGIES
LOCKHEED MARTIN
MICRO-PULSE INC.
USAF 746TH TEST GROUP/TGGSG
SEQUOIA RESEARCH CORPORATION
DEPARTMENT OF THE ARMY
SANDIA NATIONAL LABS
SVERDRUP TECHNOLOGY INC
UNIVERSITY OF LEEDS

WASHINGTON,DC
HOLLOMAN AFB,NM
CANADA
WARMINSTER,PA
SAN DIEGO,CA
LEXINGTON PARK,MD
LAS VEGAS,NV
ANNAPOLIS,MD
POINT MUGU,CA
JAPAN
ITASCA,IL
SAN DIEGO,CA
WOODLAND HILLS,CA
PLACENTIA,CA
MOUNTAIN VIEW,CA
LAS VEGAS,NV
MOLALLA,OR
ROSWELL,GA
FRANCE
NORTHBROOK,IL
TAIWAN
KEKAHA,HI
PETERSON AFB,CO
LOS ANGELES,CA
MANHATTAN BEACH,CA
REDONDO BEACH,CA
EVANS,GA
LOS ALAMITOS,CA
LOS ANGELES,CA
FT. BELVOIR,VA
OVERLAND PARK,KS
ATHENS,GA
WPAFB,OH
PATUXENT RIVER,MD
LOS ANGELES,CA
SEATTLE,WA
MONTEREY,CA
TORRANCE,CA
TEMPE,AZ
STANFORD,CA
LOS ANGELES,CA
STANFORD,CA
SHREWSBURY,NJ
LOS ANGELES AFB,CA
ARLINGTON,VA
EGLIN AFB,FL
AUSTIN,TX
NEWPORT BEACH,CA
DENVER,CO
ROBINS AFB,GA
MCLEAN,VA
COLORADO SPRINGS,CO
CUPERTINO,CA
CAMARILLO,CA
HOLLOMAN AFB,NM
TORRANCE,CA
SALINAS,CA
ALBUQUERQUE,NM
EGLIN AFB,FL
UK

COPROS, ERIC
 COPSEY, ROBERT
 CORCORAN, TIMOTHY
 CORCORAN, WENDY
 CORRADI, MIKE
 CORRIE, LEE
 COSANDIER, DARREN
 COSENTINO, BARBARA
 COSTABILE, GREGG
 COULSON, ROBERT
 COUVERCHEL, FRANCOIS
 COX, DUNCAN B.
 COX, PAUL
 CRAMPTON, PAUL
 CRANE, DEL
 CRAWLEY, MATT
 CROOK, CHERYL
 CROSBY, GRAEME
 CROSS, PAUL
 CROUCH, DAN
 CRUM, JEFF
 CRUTCHLOW, MICHAEL
 CUAVE, DALE
 CUNNINGHAM, SARAH
 CURRY, JOHN
 CUTHBERTSON, JOHN
 CYR, KEN
 CZAPEK, FRANK
 DA, REN
 DA SILVA FERRAO, GILBERTO
 DAERR, AXEL
 DAFESH, PHILIP
 DAILEY, LYDIA
 DALGLEISH, SHAWN
 DALME, LINDA
 DALY, PETER
 DAMIANI, THOMAS
 DANA, PETER
 DANAHER, JAMES
 DANIELS, JIM
 DANO, PAUL
 DANTE JOAQUIN, JOSE
 DARDEN, WILLIAM
 DARNELL, SHARON
 DARWIN, JIM
 DAVID, GUY
 DAVIDSON, ALAN
 DAVIS, PATRICK
 DAVIS, SETH
 DAWSON, TERRY
 DAYTON, RONALD
 DE CEVINS, JULIE
 DE LA FUENTE, CLIVE
 DE MAIO, DORIAN
 DE TEMPLE, TOM
 DEAL, DAVID
 DECK, PHIL
 DECLEENE, BRUCE
 DEGRANDCOURT, ROBERT
 DELLBY, BENGT

MATRA MARCONI SPACE FRANCE
 SMC/CZN
 NAWCWPNS
 NOVATEL COMMUNICAITONS LTD
 EMBRY-RIDDLE AERONAUTICAL UNIV
 SSSG/CZG/GPS JPO
 PREMIER GPS, INC.
 746 TS/TGGPP
 DEPARTMENT OF THE AIR FORCE
 HARRIS CORPORATION
 AEROSPATIALE
 DBC COMMUNICATIONS, INC.
 CHRYSLER TECHNOLOGIES AIRBORNE
 BNR EUROPE LTD
 NAVSTAR GPS JPO
 TRIMBLE NAVIGATION
 NAWC-WD
 AIRSERVICES AUSTRALIA
 UNIVERSITY NEWCASTLE UPON TYNE
 746 TS/CIGTF
 2SOPS/DOAN
 CANADIAN HYDROGRAPHIC SERVICE
 DEFENSE MAPPING SCHOOL
 KELVIN HUGHES LIMITED
 US ARMY YUMA PROVING GROUND
 EFRATOM, TIME & FREQUENCY
 CUBIC DEFENSE SYSTEMS INC.
 ROCKWELL INTERNATIONAL
 CENTER FOR MAPPING/OSU
 PETROLEO BRASILEIRO S.A.-PETRO
 GPS GMBH
 THE AEROSPACE CORPORATION
 NAVAL OCEANOGRAPHIC OFFICE
 MOTOROLA
 SAF/IADM
 UNIVERSITY OF LEEDS
 ROCKWELL INTERNATIONAL
 CONSULTANT
 3S NAVIGATION
 ROCKWELL INTERNATIONAL
 DEL NORTE TECHNOLOGY, INC.
 ARINC
 NAVAL AIR WARFARE CENTER
 FEDERAL AVIATION ADMIN.
 LORAL SPACE & RANGE SYSTEM
 AMCOMP
 CONCEPT SYSTEMS, LTD.
 NAVSYMM POSITIONING SYSTEMS
 DRAPER LABORATORY
 ROCKWELL INTERNATIONAL
 BOEING COMPANY
 AIRBUS INDUSTRIE
 NAVSTAR SYSTEMS LTD
 SAIC
 ITT FSC
 ROCKWELL INTERNATIONAL CORP.
 LEICA
 FAA
 ROCKWELL INTERNATIONAL
 FMV

FRANCE
 LOS ANGELES AFB,CA
 RIDGECREST,CA
 CANADA
 PRESCOTT,AZ
 PETERSON AFB,CO
 CANADA
 HOLLOMAN AFB,NM
 NICEVILLE,FL
 MELBOURNE,FL
 FRANCE
 MANCHESTER,MA
 WACO,TX
 UK
 LA AFB,CA
 SUNNYVALE,CA
 CHINA LAKE,CA
 AUSTRALIA
 UK
 HOLLOMAN AFB,NM
 FALCON AFB,CO
 CANADA
 STAFFORD,VA
 UK
 YUMA,AZ
 IRVINE,CA
 SAN DIEGO,CA
 CEDAR RAPIDS,IA
 COLUMBUS,OH
 BRAZIL
 GERMANY
 LOS ANGELES,CA
 STENNIS SPACE CENTER,MS
 NORTHBROOK,IL
 WASHINGTON,DC
 UK
 NEWPORT BEACH,CA
 GEORGETOWN,TX
 LAGUNA HILLS,CA
 RICHARDSON,TX
 EULESS,TX
 EL SEGUNDO,CA
 PATUXENT RIVER,MD
 FPO AP,
 SUNNYVALE,CA
 REDONDO BEACH,CA
 SCOTLAND
 SAN JOSE,CA
 CAMBRIDGE,MA
 NEWPORT BEACH,CA
 WOODINVILLE,WA
 FRANCE
 ENGLAND
 TORRANCE,CA
 VANDENBERG AFB,CA
 CEDAR RAPIDS,IA
 TORRANCE,CA
 WASHINGTON,DC
 ARLINGTON,VA
 SWEDEN

DELICKER, SCOTT
 DELMAJ, JEAN-JACQUES
 DENARO, ROBERT
 DENIGAN, THOMAS
 DENISOV, VLADIMIR
 DENNEHY, KEVIN
 DENNIS, ARTHUR
 DENNIS, JAMES
 DENTINGER, MICHAEL
 DENTON, JACK
 DEPERIA, DINA
 DEREN, GARY
 DES GROSEILLIERS, GARY
 DETOMA, EDOARDO
 DEVEREUX, WILLIAM
 DEVILBISS, STEWART
 DEVINE, TOM
 DEVINEY, CHARLES
 DIAZ, JOSE
 DICKSON, DICK H.
 DICKSON, WILLIAM
 DICRISTOFARO, VINCENT
 DIEDERICH, PIERRE
 DIEFES, DEBRA
 DIELMAN, RICK
 DIESEL, JOHN
 DIESPOSTI, RAYMOND
 DIETER, GARY
 DIGGLE, DAVID
 DILL, JIM
 DIMUZIO, KEVIN
 DINTER, EDWARD
 DIREN, GOKHAN
 DIXON, CHARLES
 DIXON, WILLIAM
 DO, JAMES
 DOBELMAN, JOHN
 DODDS, LARRY
 DODDS, MARIE
 DOHLMAN, WAYNE
 DOIZI, JEAN MARIE
 DOLCE, DAVID
 DOMEY, DANIEL
 DONAHUE, ARNOLD
 DONOVAN, ANDY
 DORPINGHAUS, TERRI
 DOUGUINOV, SERGUEI
 DOWNES, M.
 DRANE, LANCE
 DRAPE, THOMAS
 DREWETT, ADRIAN
 DREWETT, NICOLA
 DRISCOLL, BOB
 DRISCOLL, CLEM
 DROUILHET, PAUL
 DUBOIS, J.
 DUBROWSKI, JOHN
 DUCKHAM, MICHAEL
 DUDLEY, DONALD
 DUDLEY, JOHN

US ARMY YUMA PROVING GROUND
 TELEDIFFUSION DE FRANCE
 MOTOROLA INC. - PNSB
 ARINC
 INTERNAVIGATION RES & TECH CTR
 PHILLIPS BUSINESS INFORMATION
 ASTRODETTICS, INC.
 USAF/AFIWC/SAV
 TRIMBLE NAVIGATION
 WAG CORPORATION
 NAWC
 SHELL CANADA, LTD.
 DAIMLER BENZ RTNA, INC.
 ALLIED SIGNAL
 JHU/APL
 U.S. AIR FORCE
 LORAL FEDERAL SYSTEMS
 MACA
 746 TS/TGGDA
 NAWC
 DICKSON CONSULTING
 NRaD, WARMINSTER
 RACAL RESEARCH LTD
 DCS CORPORATION
 TRUETIME, INC.
 LITTON AERO PRODUCTS
 THE AEROSPACE CORPORATION
 2SOPS/DOAN
 OHIO UNIVERSITY
 ITT A/CD
 NCCOSC, RDT&E DIV DET
 ALLIEDSIGNAL AEROSPACE COMPANY
 EBI
 BNR EUROPE LTD.
 DOT/FAA/ALM-60
 LEICA
 DOT/FAA
 C.S. DRAPER LABORATORY, INC.
 C.S. DRAPER LABORATORY, INC.
 WILCOX ELCTRIC INC.
 CGG
 M/A-COM
 CANADIAN MARCONI COMPANY
 NAPA
 GEOTRONICS
 BD SYSTEMS, INC.
 ROMONA LTD
 DEFENCE RESEARCH AGENCY
 C.S. DRAPER LABS
 SMC/CZTS
 PETROLEUM DEVELOPMENT OMAN
 UNIV OF NEWCASTLE UPON TYNE
 SCTS
 BOBIT PUBLISHING
 FEDERAL AVIATION ADMIN.
 CGG
 TASK
 NAVSTAR SYSTEMS LTD.
 AUTEC RANGE SERVICES
 EARL DUDLEY ASSOC., INC.

YUMA,AZ
 FRANCE
 NORTHBROOK,IL
 EL SEGUNDO,CA
 RUSSIA
 POTOMAC,MD
 LEAGUE CITY,TX
 SAN ANTONIO,TX
 SUNNYVALE,CA
 TUPELO,MS
 WARMINSTER,PA
 CANADA
 CAMBRIDGE,MA
 ITALY
 LAUREL,MD
 WPAFB,OH
 MONUMENT,CO
 OKLAHOMA CITY,OK
 HOLLOMAN AFB,NM
 CHINA LAKE,CA
 CANADA
 RICHBORO,PA
 ENGLAND
 ALEXANDRIA,VA
 SANTA ROSA,CA
 WOODLAND HILLS,CA
 LOS ANGELES,CA
 FALCON AFB,CO
 ATHENS,OH
 CLIFTON,NJ
 ROBINS AFB,GA
 TETERBORO,NJ
 TURKEY
 ENGLAND
 WASHINGTON,DC
 TORRANCE,CA
 FORT WORTH,TX
 CAMBRIDGE,MA
 CAMBRIDGE,MA
 KANSAS CITY,MO
 FRANCE
 AMESBURY,MA
 CANADA
 WASHINGTON,DC
 ITASCA,IL
 TORRANCE,CA
 RUSSIA
 UK
 CAMBRIDGE,MA
 EL SEGUNDO,CA
 SULTANATE OF OMAN
 SULTANATE OF OMAN
 WOODLAND HILLS,CA
 PALOS VERDES ESTATES,CA
 WASHINGTON,DC
 HOUSTON,TX
 RESTON,VA
 ENGLAND
 FPO AA,
 BIRMINGHAM,AL

DUGAS, HUEY
DUMAINE, M.
DUNCAN, WILLIAM
DUNCOMBE, STEVE
DUREN, RON
DUTTON, LYN
DWYER, REX
EASTON, CHRISTINE
EASTWOOD, RAY
EBERLE, LAURA
ECKERT, CHARLES
EDGAR, CLYDE
EDSALL, DONALD
EIDULBERGER,
EISSFELLER, B.
EL-ARINI, M. BAKRY
EL-RABBANY, AHMED
EL-SHEIMY, NASER
ELCHYNSKI, JOE
ELDESSOUKI, MASSOUD
ELLERBE, GAIL
ELLIS, ADRIAN
ELROD, BRYANT
ELSAWY, AMR
ELWELL, JOHN
ELWOOD, JOHN
EMILE, EDDY
ENDO, TOKI
ENGE, PER
ENGLER, MAURICE
ENGLISH, DON
ERDOGAN, TEMEL
ERICSCON, THORBJORN
ERICSON, PETER
ERLANDSON, ROBERT
ESCHENBACH, RALPH
ESCOBEDO, RICHARD
ESTEP, GENE
ESTRADA, EDWARD
ETHERINGTON, MICHAEL
ETIENNE, JEAN-DANIEL
EUCHNER, BILL
EULER, HANS-JUERGEN
EVANS, ALAN
EVANS, CHARLIE
EVANS, CURTIS
EVANS, GEORGE
EVANS, STEVE
EVANS, JENNIFER
EWING, ROBERT
EXNER, MICHAEL
EYRING, DANIEL
FAGAN, JOHN
FAIL, WALLACE
FALKENBERG, WILLIAM
FARAG, RAOUF
FARINE, PIERRE-ANDRE
FARRAR, RICHARD
FARRELL, JAMES
FASSLER, CRAIG

CAPITAL REGION PLANNING COMM.
CANADIAN MARCONI COMPANY
DEFENCE MAPPING AGENCY
LEICA, INC.
TELECOM SOLUTIONS
ROYAL AIR FORCE
ASHTECH, INC.
ROCKWELL CACD
MAGNAVOX ELECTRONIC SYSTEMS CO
LOCKHEED-MARTIN
HONEYWELL
THE AEROSPACE CORPORATION
HQ AFOTEC/TSN
LOCKHEED-MARTIN
UNIVERSITY FAF MUNICH
THE MITRE CORPORATION
UNIVERSITY OF NEW BRUNSWICK
UNIV OF CALGARY/DEPT GEOM ENG
HONEYWELL MAVD
TRANSPORT CANADA
LITTON GCS
ROCKWELL TELECOMMUNICATIONS
STANFORD TELECOMMUNICATIONS
THE MITRE CORPORATION
C.S. DRAPER LABORATORY, INC.
FREQUENCY ELECTRONICS INC.
SMC/CZUP
NORTHROP-GRUMMAN
STANFORD UNIVERSITY
COMMUNICATION SYSTEMS INT'L
ARINC
I-NET, INC.
FFV AEROTECH AB
TERACOM SVENSK RUNDRAIO AB
ROCKWELL
TRIMBLE NAVIGATION LTD.
746 TS/CIGTF
46 TW/TSWGI
USAF
LEICA
ASULAB SA
ALLEN OSBORNE ASSOCIATES INC
LEICA AG
NAVAL SURFACE WARFARE CENTER
LITTON GCS
WL/AAAI-3
TRINITY HOUSE
SOUTH CAROLINA ELEC & GAS CO
STANFORD UNIVERSITY
ROCKWELL TELECOMMUNICATIONS
UCAR, GPS/MET PROGRAM
C.S. DRAPER LABORATORY, INC.
UNIV OF OKLAHOMA/ELEC ENGIN
SVERDRUP/TEAS
SATLOC INC.
LITTON GCS
ASULAB SA
THE AEROSPACE CORPORATION
NaVIGIL
RADIX TECHNOLOGIES, INC.

BATON ROUGE, LA
CANADA
ST. LOUIS, MO
TORRANCE, CA
SAN JOSE, CA
UK
SUNNYVALE, CA
CEDAR RAPIDS, IA
TORRANCE, CA
PRINCETON, NJ
MINNEAPOLIS, MN
LOS ANGELES, CA
KIRTLAND AFB, NM
PRINCETON, NJ
GERMANY
MCLEAN, VA
CANADA
CANADA
ST. PETERSBURG, FL
CANADA
SIMI VALLEY, CA
ENGLAND
RESTON, VA
MCLEAN, VA
CAMBRIDGE, MA
MITCHEL FIELD, NY
LOS ANGELES AFB, CA
YORBA LINDA, CA
STANFORD, CA
CANADA
SAN DIEGO, CA
KENNEDY SPACE CENTER, FL
SWEDEN
SWEDEN
CEDAR RAPIDS, IA
SUNNYVALE, CA
WSMR, NM
EGLIN AFB, FL
LOS ANGELES, CA
TORRANCE, CA
SWITZERLAND
WESTLAKE VILLAGE, CA
SWITZERLAND
LA PLATA, MD
WOODLAND HILLS, CA
BEAVERCREEK, OH
ENGLAND
COLUMBIA, SC
MENLO PARK, CA
NEWPORT BEACH, CA
BOULDER, CO
CAMBRIDGE, MA
NORMAN, OK
NICEVILLE, FL
TEMPE, AZ
NORTHRIDGE, CA
SWITZERLAND
LOS ANGELES, CA
SEVERNA PARK, MD
MOUNTAIN VIEW, CA

FAVRE, DOMINIQUE
 FAY, CHARLES
 FEAIRHELLER, SCOTT
 FEDERICI, LUCI
 FEENEY, SHAWN
 FEERER, PATTY
 FEESS, WILLIAM
 FEIT, CECELIA
 FELLER, WALTER
 FELTES, DOUGLAS
 FENG, YANMING
 FENTON, MIKE
 FENTON, PATRICK
 FERER, HARVEY
 FERGUSON, RONALD
 FERRANTI, RICHARD
 FERRE, GERARD
 FESNAK, ALAN
 FETTER, ROBERT
 FFOULKES-JONES, GERAINT
 FIEDLER, RALF
 FIELDS, JERRY
 FILATCHENKOV, SERGEI
 FINLEY, RICHARD
 FISCHER, CURTIS
 FISCHER, NORMAN
 FISH, MARK
 FISHER, RICHARD
 FISHER, LAWRENCE
 FISHER, ROBERT
 FISHER, STEVEN
 FITZPATRICK, SEAN
 FJELLSTAD, OLA-ERIK
 FLAMENT, DIDIER
 FLANAGAN, ROBERT
 FLANIGAN, JOHN
 FLEENOR, MIKE
 FLEMATE, JAVIER
 FLETCHER, ROBERT
 FLIEGEL, HENRY
 FLOYD, THOMAS
 FONTAINE, WALT
 FORBES, FRED
 FORD, THOMAS
 FORGY, JAMES
 FORSETH, DAN
 FORSSELL, BORJE
 FOWLER, WALT
 FOX, TRAVIS
 FRAILE-ORDONEZ, JOSE
 FRAMPTON, J.
 FRANCISCO, SHERMAN
 FRANK, DANIEL
 FRANKO, ROBIN
 FREESTONE, TODD
 FREI, ERWIN
 FRENCH, ROBERT
 FRIED, WALTER
 FRISHEN, CLARK
 FRISKMAN, HAKAN

ROCKWELL
 NORTHERN TELECOM EUROPE LTD.
 USAF/FASTC/TASS
 NRaD
 2SOPS/DOAN
 SMC/CZN
 AEROSPACE CORPORATION
 SIERRA TECHNOLOGIES
 COMPUTING DEVICES
 ROCKWELL - CACD
 QUT SPACE CENTRE FOR SAT NAV
 STANFORD TELECOM
 NOVATEL COMMUNICATIONS, LTD.
 H. FERER & ASSOCIATES
 DEPT OF NATIONAL DEFENCE
 MIT LINCOLN LABORATORY
 DASSAULT ELECTRONIQUE
 GHOSTECH INC.
 ARINC RESEARCH CORP
 NAVSTAR SYSTEMS LTD
 UNIVERSITY OF ROSTOCK
 ZETA ASSOCIATES, INC.
 RIRNT
 TRW
 USAF 746TS (CIGTF)
 BATTELLE
 SMC/CZUI
 USAF
 LOCKHEED ENV SYS & TECH
 NOAA/MGR FAA PROG N/CG23
 ROCKWELL INTERNATIONAL
 TOPCON
 SEATEX
 THOMSON-CSF
 AMERICAN NUCLEONICS CORPORATIO
 ITT/ACD
 ARINC
 TRW
 CAMBRIDGE GPS
 AEROSPACE CORPORATION
 US ARMY, HQ, CECOM
 U.S. COAST GUARD NAVCEN
 CANADIAN COAST GUARD
 NOVATEL COMMUNICATIONS
 SAIC
 ROCKWELL - CACD
 UNIVERSITY OF TRONDHEIM
 STARLINK, INC.
 UNIVERSITY OF OKLAHOMA
 KAYSER-THREDE GMBH
 DERA/CES/CBDE DIV
 LORAL FEDERAL SYSTEMS COMPANY
 LEIGH FISHER ASSOCIATES
 LEICA
 NASA MSFC
 LEICA LTD., HEERBRUGG
 R.L. FRENCH & ASSOCIATES
 CONSULTANT
 SEATEX AS
 TELUB AB

FRANCE
 SCHAUMBURG, IL
 KETTERING, OH
 WARMINSTER, PA
 FALCON AFB, CO
 LOS ANGELES AFB, CA
 EL SEGUNDO, CA
 BUFFALO, NY
 CANADA
 CEDAR RAPIDS, IA
 AUSTRALIA
 SUNNYVALE, CA
 CANADA
 MARINA DEL REY, CA
 CANADA
 LEXINGTON, MA
 FRANCE
 LANSDALE, PA
 COLORADO SPRINGS, CO
 ENGLAND
 GERMANY
 RESTON, VA
 RUSSIA
 FAIRBORN, OH
 HOLLOMAN AFB, NM
 COLUMBUS, OH
 SAN PEDRO, CA
 LOS ANGELES AFB, CA
 LAS VEGAS, NV
 SILVER SPRING, MD
 DOWNEY, CA
 HACKENSACK, NJ
 NORWAY
 FRANCE
 WESTLAKE VILLAGE, CA
 FORT WAYNE, IN
 SAN PEDRO, CA
 REDONDO BEACH, CA
 WARREN, VT
 EL SEGUNDO, CA
 FORT MONMOUTH, NJ
 ALEXANDRIA, VA
 CANADA
 CANADA
 SAN DIEGO, CA
 CEDAR RAPIDS, IA
 NORWAY
 AUSTIN, TX
 NORMAN, OK
 GERMANY
 ENGLAND
 GAITHERSBURG, MD
 SAN FRANCISCO, CA
 TORRANCE, CA
 HUNTSVILLE, AL
 SWITZERLAND
 FORT WORTH, TX
 SANTA ANA, CA
 NORWAY
 SWEDEN

FRITZ-NEMETH, PAUL
 FRODGE, SALLY
 FROMHERTZ, PAM
 FROMM, KRIS
 FROST, GERALD
 FRY, GEORGE
 FUERSTEIN, DAVID
 FURZE, JOHN
 FYFE, PETER
 GAAB, SCOTT
 GADD, DONALD
 GALDOS, JORGE
 GALVIN, DENNIS
 GALYEAN, JEAN
 GAMBINO, JOEL
 GANIEUX, DANIEL
 GANIN, ALEXANDER
 GANTHER, KEN
 GAO, YANG
 GARCIA, JOHAN
 GARCIA, JOHN
 GARIN, LIONEL
 GARNAAT, JOHN
 GAROUTTE, JAMES
 GARRETT, DALE
 GARRISON, JAMES
 GAST, DICK
 GATES, DALE
 GAZIT, RAN
 GAZLAY, LEE
 GEIER, JEFFREY
 GEISER, PAUL
 GEITNER, KARL
 GELATKA, WILLIAM
 GELLEE, ERIC
 GELSTER, GARTH
 GEMMER, MICHAEL
 GEORGE, KINGSTON
 GEROCK, DONALD
 GETTING, IVAN
 GEYER, MICHAEL
 GIBBONS, GLEN
 GIBBS, EDDIE
 GIBSON, DICK
 GILKEY, JAMES
 GILLET, JOEL
 GILLIGAN, TONY
 GILLOTTI, ANTHONY
 GIRTS, DAVE
 GITT, TONY
 GIULIANELLI, LISA
 GLOWACKI, JOHN
 GLUCH, MICHAEL
 GODICKE, SILENO
 GODWIN, PAUL
 GOGUEN, TOM
 GOKHALE, VINAY
 GOLD, KENN
 GOLDSTEIN, SAM
 GOLETZ, JAY

DEPT OF NATIONAL DEFENCE
 DOT HQ
 NATIONAL GEODETIC SURVEY
 EPG, USARMY
 RAND
 AVISO MICRO TECHNOLOGY
 APPLIED RESEARCH LABORATORIES
 C.S. DRAPER LABORATORY, INC.
 ROCKWELL INTERNATIONAL
 SMC/CZUI
 NAVSURFWARCENDIV COASTSYSTA
 COMPUTATIONAL SOLUTIONS
 ROCKWELL INTERNATIONAL
 ACCQPOINT COMMUNICATIONS CO.
 NASA/GSFC
 TECHMATION SA
 GLONASS COORDINATION
 WILCOX ELECTRIC
 PULSEARCH NAVIGATION SYSTEMS,
 SWEDISH ARMY
 SAIC
 ASHTECH, INC.
 LORAL DEFENSE SYSTEMS
 FAA FLIGHT STANDARDS
 CDSI/WTC
 NASA LANGLEY
 TRAK SYSTEMS
 MICRO SYSTEMS INC.
 STANFORD UNIVERSITY
 U.S. COAST GUARD NAVCEN
 MOTOROLA
 ARINC
 LOCKHEED-MARTIN E&M
 NAWC
 FRANCE DEFENSE CONSEIL
 HEWLETT-PACKARD CO.
 U.S AIR FORCE
 ACTA, INC.
 WHITE SANDS MISSILE RANGE
 THE AEROSPACE CORPORATION
 TASC
 ADVANSTAR/GPS WORLD MAGAZINE
 WL/MNAG
 CAST, INC.
 SRI INTERNATIONAL
 BENG S.C.
 SVERDRUP TECHNOLOGY
 SAIC
 HONEYWELL, INC.
 LITTON AERO PRODUCTS
 AFFILIATION UNKNOWN
 JSOC J-8R
 UNIVERSITY OF ROSTOCK
 AAAVTAG
 MOBIL OIL CO.
 TRIMBLE NAVIGATION
 ROCKWELL INTNL
 UNIVERSITY OF COLORADO
 SAIC
 AGMC/MLEE

CANADA
 ALEXANDRIA,VA
 SILVER SPRING,MD
 FT. HUACHUCA,AZ
 SANTA MONICA,CA
 PHOENIX,AZ
 AUSTIN,TX
 CAMBRIDGE,MA
 IRVINE,CA
 LAAFB,CA
 PANAMA CITY,FL
 READING,MA
 ORANGE,CA
 IRVINE,CA
 GREENBELT,MD
 FRANCE
 RUSSIA
 KANSAS CITY,MO
 CANADA
 SWEDEN
 SAN DIEGO,CA
 SUNNYVALE,CA
 LITCHFIELD PARK,AZ
 ANCHORAGE,AK
 WARRENTON,VA
 HAMPTON,VA
 TAMPA,FL
 FT. WALTON BEACH,FL
 STANFORD,CA
 ALEXANDRIA,VA
 SCOTTSDALE,AZ
 SAN DIEGO,CA
 ALTAMONTE SPRINGS,FL
 WARMINSTER,PA
 FRANCE
 SANTA CLARA,CA
 RANDOLPH AFB,TX
 VANDENBERG AFB,CA
 WSMR,NM
 LOS ANGELES,CA
 READING,MA
 EUGENE,OR
 EGLIN AFB,FL
 LOS ALAMITOS,CA
 MENLO PARK,CA
 HOUSTON,TX
 EGLIN AFB,FL
 TORRANCE,CA
 PHOENIX,AZ
 WOODLAND HILLS,CA
 AUSTIN,TX
 FORT BRAGG,NC
 GERMANY
 ITALY
 GARLAND,TX
 SUNNYVALE,CA
 NEWPORT BEACH,CA
 BOULDER,CO
 TORRANCE,CA
 NEWARK AFB,OH

GOMEZ, SUSAN
GONIN, IRENE
GONZALES, V.
GONZALEZ, ROGER
GONZALEZ, ADALBERTO
GONZALEZ, GUILLERMO
GORDON, MICHAEL
GOTTSCHALK, STEVE
GOTZLER, RON
GOUGH, RICHARD
GOUNON, RENE
GOUREVITCH, SERGEI
GOUSSAK, KENNETH
GOWER, ARTHUR
GRABER, RON
GRACE, JAMES
GRAF, JAMES
GRAHAM, ANDREW
GRAHAM, GREG
GREEN, GAYLORD
GREEN, JOE
GREENSPAN, RICHARD
GREGERS-WARG, TAGE
GREGORY, GEORGE
GRIFFITH, BUD
GRIMES, DAVID
GROEBER, EDWARD
GROENNEVIK, LEIF
GRONEMEYER, STEVEN
GRUBER, BERNARD
GUARINO, ROBERT
GUDAT, ADAM
GUGGENBUEHL, PAUL
GUILFORD, DON
GUNDERSEN, BREDE
GUNNARSSON, TORSTEN
GUNTHER, THOMAS
GURKOWSKI, KEVIN
GURLEY, STEVE
GUTHEIM, GEORGE
GUY, ADRIANA
HAAG, JONATHAN
HAAS, STEVEN
HADDEN, DAVID
HADDRELL, ANTHONY
HADFIELD, MICHAEL
HAGENAS, PER
HAHN, PAUL
HAJJ, GEORGE
HALEK, MILAN
HALEY, RONALD
HALL, GENE
HALL, MARTIN
HAMANN, FRANK
HAMEL, STEVEN
HAMMADA, YOWCEF
HAMMOND, NEAL
HAN, HO
HAN, SHOAWEI
HANSARD, DERWIN

NASA - JSC
U.S. DEPARTMENT OF TRANSPORTAT
AMCOMP CORPORATION
USAF/SMC/CZU
WHITE SANDS MISSILE RANGE
DET 4 AFOTEC
MAGNAVOX ELECTRONIC SYSTEMS CO
ZSOPS/DOAN
EWA
LEICA, INC.
SERCEL
ASHTECH INC.
ARINC
LORAL FEDERAL SYSTEMS
CLIFFS MINING SERVICE
INTERSTATE ELECTRONICS
LOCKHEED MARTIN
TRANSPORT CANADA
US ARMY MICOM
NAVASTRO COMPANY
ALLIED SIGNAL CORPORATION
C.S. DRAPER LABORATORY, INC.
AFFILIATION UNKNOWN
746TH TEST SQUADRON (CIGTF)
II MORROW INC.
GRIMES SURVEYING & MAPPING
US ARMY CBDCOM
NORWEGIAN MAPPING AUTHORITY
ROCKWELL INTERNATIONAL
USAF, SMC/CZU
WESTINGHOUSE NORDEN SYSTEMS
CATERPILLAR INC.
NAVAL AIR WARFARE CENTER
PALISADES GEOPHYSICAL INSTITUT
NORWEGIAN MAPPING AUTHORITY
TELUB TEKNIK AB
USCG R&D CENTER
MACA
HUBER & SUHNER, INC.
CAST, INC.
AMTECH
U.S. AIR FORCE
LOCKHEED MARTIN
GEOTRONICS
NAVSTAR SYSTEMS LTD
746 TS/CA
KTH
GEOTRONICS
JET PROPULSION LABORATORY
AQUILA AVIATION
DIFFERENTIAL CORRECTIONS INC.
U.S. COAST GUARD NAVCEN
NAVSTAR SYSTEMS LTD
ROCKWELL
WHITNEY, BRADLEY & BROWN INC
THE UNIVERSITY OF CALGARY
ROCKWELL SPACE OPERATIONS COMP
NAVAL AIR WARFARE CENTER
UNIV OF NEW SOUTH WALES
NAWC-WD

HOUSTON, TX
WASHINGTON, DC
HOLLOMAN AFB, NM
LOS ANGELES AFB, CA
WSMR, NM
COLORADO SPRINGS, CO
TORRANCE, CA
FALCON AFB, CO
RIDGECREST, CA
TORRANCE, CA
FRANCE
SUNNYVALE, CA
EL SEGUNDO, CA
GAITHERSBURG, MD
ISHPEMING, MI
ANAHEIM, CA
PHILADELPHIA, PA
CANADA
REDSTONE ARSENAL, AL
LOS ALTOS, CA
PASADENA, CA
CAMBRIDGE, MA
SWEDEN
HOLLOMAN AFB, NM
SALEM, OR
LOS ANGELES, CA
FT. MONMOUTH, NJ
NORWAY
NEWPORT BEACH, CA
LOS ANGELES AFB, CA
NORWALK, CT
EDELSTEIN, IL
RIDGECREST, CA
CAPE CANAVERAL, FL
NORWAY
SWEDEN
GROTON, CT
OKLAHOMA CITY, OK
ESSEX, VT
LOS ALAMITOS, CA
WASHINGTON, DC
LOS ANGELES AFB, CA
PHILADELPHIA, PA
ITASCA, IL
ENGLAND
HOLLOMAN AFB, NM
SWEDEN
ITASCA, IL
PASADENA, CA
BERTHOUD, CO
CUPERTINO, CA
ALEXANDRIA, VA
ENGLAND
GARDEN GROVE, CA
VIENNA, VA
CANADA
HOUSTON, TX
POINT MUGU, CA
AUSTRALIA
CHINA LAKE, CA

HANSEN, NEIL
 HANSEN, PAUL
 HANSEN, RUSSELL
 HANSEN, RUNE
 HARDEE, MONA
 HARDMAN, GORDON
 HARDWICK, DOUG
 HARLOW, RAY
 HARLOW, MELINDA
 HARP, ELAINE
 HARPER, PAUL
 HARRI, FERDINAND
 HARRINGTON, KRISTINA
 HARRIS, CLYDE
 HARRIS, DAVID
 HARRISON, A.J.
 HARROD, GREGORY
 HART, AL
 HART, DAMON
 HARTER, MARK
 HARTMAN, RANDY
 HARTO, DEBRA
 HARVEY, EDWIN
 HARVEY, ROBERT
 HASIK, JIM
 HASS, ARIE
 HASSELBRING, ALAN
 HASTINGS, KIM
 HATANAKA, YUKI
 HATCH, RONALD
 HAUGEN, OLAV
 HAUNSCHILD, MARTIN
 HAVENS, WALTER
 HAVENS, SANDI
 HAVERLAND, MANFRED
 HAZLEHURST, ROBERT
 HEADRICK, HOWARD
 HECKATHORN, DONALD
 HEDGECOCK, JERRY
 HEDLING, GUNNAR
 HEIN, GUNTER
 HEINEMANN, PETER
 HEINS, ROBERT
 HEJJO, HAZEM
 HEKMAT, TAYMOOR
 HELMEY, BRIAN
 HENDERSON, DANIEL
 HENDERSON, DAVE
 HENDRICKSON, CLARK
 HENDRY, DOUG
 HENDY, MARTIN
 HERMANN, BRUCE
 HERMES, DOUG
 HERRERA, THEODORE
 HERRERA, HECTOR
 HERRING, TOM
 HERRON, ROGER
 HILDE, TORE
 HILL, CRAIG
 HILL, FRED

46TH GTS/TGGXR
 UNIV OF NOTTINGHAM/ENG SURVEY
 NORTHROP GRUMMAN
 NORWEGIAN MAPPING AUTHORITY
 NAVSURFWARCE DIV COASTSYSTA
 CROSSLINK, INC.
 NATIONAL RESEARCH COUNCIL
 ARBITER SYSTEMS
 ROCKWELL DEFENSE ELECTRONICS
 ROCKWELL INTERNATIONAL
 COORS CERAMICS COMPANY
 SWISS FOCA
 THE AEROSPACE CORPORATION
 MOTOROLA INC. - IVHS
 MCDONNELL DOUGLAS
 RACAL SURVEY USA
 CATERPILLAR INC.
 PM GPS
 CNS OUTLOOK
 2SOPS/DOAN
 HONEYWELL INC.
 USAF
 OAO CORPORATION
 ARMY TEXCOM
 ANSER
 IAI LTD
 HONEYWELL, INC.
 VITRO
 GEOGRAPHICAL SURVEY INSTITUTE
 NAVCOM TECHNOLOGY, LLC
 NORWEGIAN MAPPING AUTHORITY
 MAN TECHNOLOGIE AG
 THE BOEING COMPANY
 PACIFIC CREST CORPORATION
 AERODATA FLUGMESSTECHNIK GMBH
 IBM FEDERAL SYSTEMS CO.
 TELE-WARE SERVICES INC.
 NORTHROP GRUMMAN CORP.
 TRIMBLE NAVIGATION
 NATIONAL LAND SURVEY OF SWEDEN
 IAPG, UNIVERSITY FAF MUNICH
 TRIMBLE NAVIGATION
 JHU/APL
 UNIVERSITY OF OKLAHOMA
 VICON ENGINEERING GMBH
 LORAL FEDERAL SYSTEMS COMPANY
 CATERPILLAR INC.
 TOPCON
 NCCOSC RDTE DIV
 MOTOROLA
 AUSLIG
 NAVAL SURFACE WARFARE CENTER
 2SOPS/DOAN
 WL/MNAG
 HQ AFOTEC/TKB
 MIT
 LOCKHEED MARTIN
 FUGRO STARFIX
 LEICA AG
 M/A-COM

HOLLOMAN AFB, NM
 UK
 HAWTHORNE, CA
 NORWAY
 PANAMA CITY, FL
 BOULDER, CO
 CANADA
 PASO ROBLES, CA
 CEDAR RAPIDS, IA
 CEDAR RAPIDS,
 POMONA, CA
 SWITZERLAND
 LOS ANGELES, CA
 NORTHBROOK, IL
 HUNTINGTON BEACH, CA
 HOUSTON, TX
 PEORIA, IL
 FORT MONMOUTH, NJ
 BETHESDA, MD
 FALCON AFB, CO
 COON RAPIDS, MN
 EGLIN AFB, FL
 SPRINGFIELD, VA
 FT. HOOD, TX
 ARLINGTON, VA
 ISRAEL
 ST. PETERSBURG, FL
 EGLIN AFB, FL
 JAPAN
 WILMINGTON, CA
 NORWAY
 GERMANY
 BELLEVUE, WA
 SANTA CLARA, CA
 GERMANY
 COLORADO SPRINGS, CO
 PLANO, TX
 NORWOOD, MA
 SUNNYVALE, CA
 SWEDEN
 GERMANY
 POMPANO BEACH, FL
 LAUREL, MD
 NORMAN, OK
 GERMANY
 GAITHERSBURG, MD
 PEORIA, IL
 PARAMUS, NJ
 SAN DIEGO, CA
 NORTHBROOK, IL
 AUSTRALIA
 DAHLGREN, VA
 FALCON AFB, CO
 EGLIN AFB, FL
 KIRTLAND AFB, NM
 CAMBRIDGE, MA
 MARIETTA, GA
 NORWAY
 SWITZERLAND
 AMESBURY, MA

HILL, PHILLIP
HILL, STEVE
HINCK, MARC
HINKLE, JOHN
HIORTH, DONALD
HIROE, NOBUO
HIRSCH, DAVID
HOFFMAN, RANDY
HOFFMAN, RANDY
HOGAN, RUSS
HOJO, HARUMASA
HOKEUN, LEE
HOL, R.
HOLDEN, TOM
HOLLADAY, GARY
HOLLAND, KENNETH
HOLLOMAN, DAVID
HOLSAPPLE, BOYD
HOLTERHAUS, BRIAN
HOLTON, PATRICK
HOME, MICHAEL JOHN
HOOPER, GRAEME
HOOSER, MICHAEL
HOPE, ALAN
HOPE, CLINTON
HOPKINS, JIM
HOPKINS, JOHN
HORNBY, JOHN
HOWARD, BOB
HOWELL, DANA
HOWELL, GENE
HOWELL, JAMES
HOWINGTON, KEITH
HOWLAND, CHARLES
HOYLE, DIXON
HSIUNG, JACOB
HUA, HUA
HUDSON, CRAIG
HUFF, MAX
HUFFMAN, LARRY
HUGHES, DENNIS
HUGHES, HAROLD
HUGO, MIKE
HUME, JAMES R.
HUNDLEY, WARREN
HUNTER, ROGER
HUNTER, TOM
HURLEY, ANDREW
HVIZD, JAMES
IBIS, MIKE
IBSEN, PAUL
ICHIKAWA, TSUTOMU
IFUNE, DEAN
IGLI, DAVID
IKEDA, RAY
IKETANI, TAKESHI
IMRICH, TOM
INCARDONA, RUBEN
INGOLD, JEFF
INOUE, ANDY

THE AEROSPACE CORPORATION
CMT, LTD.
INNOVATIVE SOLUTIONS INT'L, IN
LEICA, INC.
ER, INC.
NEC CORPORATION
STARLINK, INC.
MAGELLAN
NTIA US DEPT OF COMMERCE
MINISTRY OF TRANSPORTATION
JAPAN RADIO CO. LTD
KOREA GPS ENGINEERING
TNO-FEL
STANFORD TELECOMMUNICATIONS
TECHSONIC INDUSTRIES
46TH TEST GROUP/CA
MCDONNELL DOUGLAS
WRIGHT LABORATORY (USAF)
ROCKWELL CACD
ACQPOINT COMMUNICATIONS
ROYAL AIR FORCE
GPSat SYSTEMS
U.S. AIR FORCE
NAVAL RESEARCH LABORATORY
WALT DISNEY IMAGINEERING
LORAL DEFENSE SYSTEMS
NAVIGATION DEVELOPMENT SERVICE
SIKORSKY AIRCRAFT
AROMAT CORPORATION
WL/AAAI-1
ARINC RESEARCH, INC.
RAYTHEON COMPANY
INTERSTATE ELECTRONICS
HQ AFSPC
NATIONAL GEODETIC SURVEY/NOAA
CAST/ITRI
WORCESTER POLYTECHNIC INSTITUT
II MORROW INC.
JOHN E. CHANCE & ASSOCIATES
E-SYSTEMS, MONTEK DIV
SAIC
ROCKWELL INTERNATIONAL
NAWC
GREENFIELD ASSOCIATES
WILCOX ELECTRIC, INC.
2SOPS/DOAN
ASHTECH, INC.
LEICA, INC.
MARTIN MARIETTA
HONEYWELL, INC.
NORDEN SYSTEMS
INSTITUTE OF SPACE & ASTRO SCI
WELNAVIGATE, INC.
LOCKHEED MARTIN ASTRONAUTICS
HITACHI CABLE AMERICA
FURUNO ELECTRIC
U.S. AIR FORCE/WRIGHT LABORATO
FROMERAVIA
ALLIED SIGNAL TECH SERVICES
AROMAT CORPORATION

LOS ANGELES, CA
ENGLAND
EDMOND, OK
TORRANCE, CA
FAIRFIELD, NJ
JAPAN
AUSTIN, TX
SAN DIMAS, CA
BOULDER, CO
CANADA
JAPAN
KOREA
THE NETHERLANDS
SUNNYVALE, CA
EUFULA, AL
HOLLOMAN AFB, NM
O'FALLON, MO
YELLOW SPRINGS, OH
CEDAR RAPIDS, IA
IRVINE, CA
UK
AUSTRALIA
WASHINGTON, DC
WASHINGTON, DC
WAINSCOTT, NY
LITCHFIELD PARK, AZ
NORTHRIDGE, CA
STRATFORD, CT
EL SEGUNDO, CA
WPAFB, OH
SAN DIEGO, CA
MARLBORO, MA
ANAHEIM, CA
PETERSON AFB, CO
ST. PAUL, MN
TAIWAN
WORCESTER, MA
SALEM, OR
HOUSTON, TX
SALT LAKE CITY, UT
CLINTON, MD
ANAHEIM, CA
CHINA LAKE, CA
ROLLING HILLS, CA
KANSAS CITY, MO
FALCON AFB, CO
SUNNYVALE, CA
ENGLEWOOD, CO
SAN DIEGO, CA
COON RAPIDS, MN
NORWALK, CT
JAPAN
OXNARD, CA
DENVER, CO
WHITE PLAINS, NY
JAPAN
WPAFB, OH
ITALY
COLUMBIA, MD
EL SEGUNDO, CA

IRDEM, ENVER
 IRECKI, VIC
 IRWIN, BARRY
 ISHIKAWA, SEIJI
 ISMAGIL, RAWIL
 ISON, MARILYN
 ISSLER, JEAN-LUC
 ITANI, KENJI
 ITO, TORU
 IWASKI, PAUL
 IYEMURA, RON
 JACKSON, DAVID
 JACKSON, EDWARD
 JACKSON, KEN
 JACOBS, ROGER
 JACOBS, DENICE
 JACOBSON, LEN
 JACOBSON, RALPH
 JAKOBSSON, LARS
 JALALI, BIJAN
 JAMES, CALVIN
 JANNIERE, J.
 JARRY, LLOYD
 JAYME, ERNIE
 JEHL, JEAN-FRANCOIS
 JENSEN, MICHAEL H.B.
 JETT, ROBERT
 JIN, HAIPING
 JIN, X.
 JOB, ANDRE
 JOHANNESSEN, ROLF
 JOHANSEN, GORM
 JOHNSON, BRUCE
 JOHNSON, BEN
 JOHNSON, DAR
 JOHNSON, DONALD B.
 JOHNSON, GREG
 JOHNSON, JEFFREY
 JOHNSON, JEFFREY S.
 JOHNSON, KELLEY
 JOHNSON, MARK
 JOHNSON, MICHAEL
 JOHNSON, PATRICK
 JOHNSON, R.H. BUD
 JOHNSON, RUSSELL
 JOHNSON, TED
 JOHNSON, WALLY
 JOHNSTON, GORDON
 JOHNSTON, HUGH
 JOKERST, SCOTT
 JOLY, PASCAL
 JONES, EDWARD J.
 JONES, GREG
 JONES, KEITH
 JONQUIERE, JEAN-LOUIS
 JONSSON, BO
 JORGEN VASE, NIELS
 JOWANOWITCH, THOMAS
 JOY, CHRIS
 JUAREZ, ARMANDO

EBI AS
 NEW ZEALAND DEFENCE FORCE
 US GEOLOGICAL SURVEY
 AISIN SEIKI CO., LTD.
 DEPARTMENT OF TRANSPORTATION
 USAF SMC/CZ
 CNES
 FURUNO ELECTRIC CO
 TOYOTA MOTOR CORPORATION
 TOPCON
 PACIFIC CREST CORPORATION
 USSPACECOM/J330S
 AMCOMP CORPORATION
 ASHTECH TELESIS
 M/A-COM
 WL/AAAI-1
 INTERMETRICS/GSAM
 C.S. DRAPER LABORATORY, INC.
 NATIONAL MARITIME ADMIN.
 LEICA, INC.
 ALLIEDSIGNAL TECH SERVICES
 ALCATEL ESPACE
 WHITE SANDS MISSILE RANGE
 AFFILIATION UNKNOWN
 SEXTANT AVIONIQUE
 SHELL INT'L PETROLEUM (EPX/25)
 ETA TECHNOLOGIES CORP.
 SPACE SYSTEMS LORAL
 DELFT UNIV OF TECHNOLOGY
 CNES
 LAMBOURNE NAVIGATION LTD.
 SEATEX AS
 NAVSYS
 SENSIS CORPORATION
 BD SYSTEMS, INC.
 HQ ESC/TGM
 E-SYSTEMS, MONTEK DIVISION
 OVERLOOK SYSTEMS TECHNOLOGIES
 U.S. AIR FORCE
 TRIMBLE
 ROCKWELL INTERNATIONAL
 VITRO SERVICES CORP.
 INTEL CORPORATION
 MOTOROLA, GED
 RADIX TECHNOLOGIES
 CATERPILLAR INC.
 COORS CERAMICS COMPANY
 RACAL SURVEY
 TRIMBLE NAVIGATION LTD.
 746 TS (CIGTF)
 AEROSPATIALE AVIONS
 NAVAL RESEARCH LABORATORY
 U.S. ARMY TOPO ENG CENTER
 LOCKHEED MARTIN
 FRENCH CAA/STNA/3
 NATIONAL LAND SURVEY OF SWEDEN
 EIVA A/S
 LOCKHEED MARTIN
 IESSG/UNIVERSITY OF NOTTINGHAM
 NATIONAL RANGE OPERATIONS DIR

TURKEY
 NEW ZEALAND
 FALMOUTH,MA
 JAPAN
 LOS ANGELES,CA
 LOS ANGELES AFB,CA
 FRANCE
 JAPAN
 JAPAN
 PARAMUS,NJ
 SANTA CLARA,CA
 PETERSON AFB,CO
 HOLLOMAN AFB,NM
 SUNNYVALE,CA
 AMESBURY,MA
 WPAFB,OH
 LONG BEACH,CA
 CAMBRIDGE,MA
 SWEDEN
 TORRANCE,CA
 COLUMBIA,MD
 FRANCE
 LAS CRUCES,NM
 ALBUQUERQUE,NM
 FRANCE
 THE NETHERLANDS
 COLORADO SPRINGS,CO
 PALO ALTO,CA
 THE NETHERLANDS
 FRANCE
 ENGLAND
 NORWAY
 COLORADO SPRINGS,CO
 DEWITT,NY
 TORRANCE,CA
 HANSCOM AFB,MA
 SALT LAKE CITY,UT
 COLORADO SPRINGS,CO
 EDWARDS AFB,CA
 SUNNYVALE,CA
 CEDAR RAPIDS,IA
 SIERRA VISTA,AZ
 CHANDLER,AZ
 SCOTTSDALE,AZ
 MOUNTAIN VIEW,CA
 PEORIA,IL
 SAN DIEGO,CA
 ENGLAND
 LYNNWOOD,WA
 HOLLOMAN AFB,NM
 FRANCE
 WASHINGTON,DC
 ALEXANDRIA,VA
 MOUNTAIN VIEW,CA
 FRANCE
 SWEDEN
 DENMARK
 ONTARIO,CA
 UK
 WSMR,NM

JUBIN, JOHN
JUDGE, KEVIN
KAHLE, LARS-IVAR
KAHN, MIKE
KAISER, GORDON
KAKUTANI,
KALAFUS, RUDOLPH
KAMMEYER, PETER
KAPLAN, ELLIOT
KARELS, STEVEN
KARKLINS, ALDIS
KARUZA, CHARLES
KASER, KARL
KASHIWAGI,
KAZANTSEV, VICTOR
KEAGAN, KATHLEEN
KEE, CHANGDON
KEE, D. SCOTT
KEEGAN, RICHARD
KEEN, DANNY
KEEPERS, WILLIAM
KELLY, DONALD
KELLY, JOHN
KELLY, ROBERT
KELTON, PHILLIP
KENNEDY, HOWARD
KENNEDY, LARRY
KERWIN, RAYMOND
KETCHUM, ELEANOR
KEY, JOHN
KEYS, ERIC
KFIR, ADAM
KIAZAND, BAHMAN
KIBLER, JEFFREY
KILMER, CHARLES
KIM, ILSUN
KIMURA, KOICHI
KIMURA, KOICHI
KING, DENNIS
KING, KERRY
KINSELLA, MARK
KIRIAZES, JOHN
KIRK, JOHN
KIRSHMAN, JOEL
KITCHING, IAN
KIZHNER, SEMION
KLAHN, DIETMAR
KLEIN, JOE
KLEINHAUS,
KLINE, MICHAEL A.
KLINE, PAUL
KLINE, PAUL
KLINGER, DENNIS
KLOBUCHAR, JOHN
KLOTZ, ROB
KNIGHT, DON
KNITT, BRIAN
KNOX, MICHAEL
KO, PING-YA
KOCH, ROBERT

ROCKWELL INTERNATIONAL
GREENFIELD ASSOCIATES
SWEDISH ARMED FORCES HQ
GARMIN INTERNATIONAL
ACCQPOINT COMMUNICATIONS
FURUNO ELECTRIC CO., LTD.
TRIMBLE NAVIGATION, LTD.
US NAVAL OBSERVATORY
MITRE CORPORATION
TASC
ACCQPOINT COMMUNICATIONS CO
THE AEROSPACE CORPORATION
SMC/CZTU (JPO)
FURUNO ELECTRIC CO., LTD.
RESEARCH & PRODUCTION ASSOC
AFFILIATION UNKNOWN
STANFORD UNIVERSITY
NRaD, WARMINSTER
LEICA, INC.
U.S. AIR FORCE
PANAMA CANAL COMMISSION
SVERDRUP TECHNOLOGY, INC.
ROCKWELL
ORBCOMM
ROCKWELL INTERNATIONAL
MOTOROLA INC.
LORAL FEDERAL SYSTEMS
TOPCON
NASA GSFC
FAA/MMAC/AOS-240
N/SPJ2FS NORAD/USSPACECOM
AZIMUTH LTD
ALLIED SIGNAL INC
ARINC
GLOBAL SYSTEMS & MARKETING
SEOUL NATIONAL UNIVERSITY
AERO ASAHI CORPORATION
CONSULTANT
E-SYSTEMS, MONTEK DIVISION
746 TS/TGGPI
QUT SPACE CENTRE FOR SAT NAV
NASA/KENNEDY SPACE CENTER
GPS JPO
THE AEROSPACE CORPORATION
GEC PLESSEY SEMICONDUCTORS
NASA GSFC
GERMAN AEROSPACE RESEARCH EST
AERO ANTENNA TECHNOLOGY, INC.
BOOZ-ALLEN & HAMILTON
746 TS/TGGML
OHIO UNIVERSITY
VIRGINIA TECH
NRaD
AF PHILLIPS LAB/GEOPHYSICS DIR
DOD
KNIGHT SYSTEMS
SMC/CZTU
DIGICON
STANFORD UNIVERSITY
LITTON G&CS

RICHARDSON, TX
TORRANCE, CA
SWEDEN
LENEXA, KS
IRVINE, CA
JAPAN
SUNNYVALE, CA
BETHESDA, MD
BEDFORD, MA
READING, MA
IRVINE, CA
EL SEGUNDO, CA
LOS ANGELES AFB, CA
JAPAN
RUSSIA
MCLEAN, VA
MOUNTAIN VIEW, CA
GLENSIDE, PA
TORRANCE, CA
DAYTON, OH
APO AA,
NICEVILLE, FL
CEDAR RAPIDS, IA
DULLES, VA
COVINA, CA
PHOENIX, AZ
GAITHERSBURG, MD
PARAMUS, NJ
GREENBELT, MD
OKLAHOMA CITY, OK
PETERSON AFB, CO
ISRAEL
BARSTOW, CA
EL SEGUNDO, CA
ANAHEIM HILLS, CA
KOREA
JAPAN
JAPAN
SALT LAKE CITY, UT
HOLLOMAN AFB, NM
AUSTRALIA
KENNEDY SPACE CENTER, FL
LOS ANGELES AFB, CA
LOS ANGELES, CA
UK
GREENBELT, MD
GERMANY
CHATSWORTH, CA
MCLEAN, VA
HOLLOMAN AFB, NM
ATHENS, OH
BLACKSBURG, VA
WARMINSTER, PA
HANSCOM AFB, MA
OLNEY, MD
PALOS VERDES, CA
LOS ANGELES AFB, CA
HOUSTON, TX
STANFORD, CA
WOODLAND HILLS, CA

KOIKE, YOSHIFUMI
 KOLB, ERIC
 KOLLIPOPOULOS, DANIEL
 KOLMAN, LEONARD
 KONDO, HITOSHI
 KONIK, EDWARD
 KOON, RICKY
 KOOREY, ALFRED
 KOPCHA, DAMIAN
 KOREMURA, KAZUNOBU
 KORNOUKHOV, BORIS
 KOSMOS, GEORGE
 KOVACH, JOHN
 KOVACH, KARL
 KOVARIK, L.
 KOZAKI, TOSHIYA
 KRABILL, WILLIAM
 KRAEMER, JOHN
 KRAKIWSKY, EDWARD
 KRAKIWSKY, SEAN
 KRAMER, GORDON
 KRASNJANSKI, DAVID
 KRISHNAMURTI, GIDDU
 KRONMAN, JAMES
 KRUCZYNSKI, LEONARD
 KUCAR, ANDY
 KUHL, MARK
 KULSHRESHTHA, AMIT
 KULYESHIE, EDWARD
 KUNZE, HANS-JUERGEN
 KURTIN, DUANE
 KUSSEROW, TODD
 KUSTERS, JACK
 KWANGSIK, KIM
 KYLE, ARTHUR M.J.
 LACHAPPELLE, GERARD
 LAGE, MARIE
 LAHAV, TZVI
 LAI, KEN
 LALA, JAY
 LAMANCE, JAMES
 LAMM, KENNETH
 LAMOND, JIM
 LANCASTER, FRED
 LANDA, STEVEN
 LANDIS, BRUCE
 LANE, JAMES
 LANGELIER, DANIEL
 LANGER, JOHN
 LANGLEY, RICHARD
 LANGSHAW, DUANE
 LAPINE, LEWIS
 LAPUCHA, DARIUSZ
 LARGAY, MARIE
 LARKIN, THOMAS
 LARKINS, WALLIS
 LARSON, PAUL
 LARSSON, FRANK
 LASHLEE, ROBERT
 LASKEY, ANGELA

NEC CORPORATION
 PL/VT-B
 NAWC AIRCRAFT DIVISION
 NAVAL AIR WARFARE CENTER
 FURUNO ELECTRIC CO, LTD
 LITTON SYSTEMS, ICN.
 HQ AFSPC/DRF
 SAIC
 DEFENSE MAPPING AGENCY
 ENRI
 ROMONA LTD
 NCCOSC RDT&E DIVISION
 SOKKIA TECHNOLOGY, INC.
 ARINC
 AMCOMP CORP
 PIONEER ELECTRONIC CORPORATION
 NASA/WALLOPS FLIGHT FACILITY
 DOT/VOLPE CENTER
 THE UNIVERSITY OF CALGARY
 UNIVERSITY OF CALGARY
 HUGHES AIRCRAFT CO
 NR&D WAR DET
 ROCKWELL INTERNATIONAL
 TRW
 TRIMBLE NAVIGATION LTD
 4U COMM. RESEARCH, INC.
 ASHTECH, INC.
 LEAR ASTRONICS CORP
 HUGHES AIRCRAFT
 ALLEN OSBORNE INC
 APPLIED RESEARCH LAB
 SMC/CZZ
 HEWLETT PACKARD
 MARINE ELECTRONICS CORP.
 NASA/GSFC
 UNIV OF CALGARY/GEOMATICS ENG
 STANFORD TELECOM
 EMBASSY OF ISRAEL
 SMC/CZS - USAF
 C.S. DRAPER LABORATORY
 NAVSYS CORPORATION
 U.S. DEPARTMENT OF TRANSPORTAT
 BRUNEI SHELL PETROLEUM COMPANY
 U.S. NAVY
 SAIC
 LOCKHEED MARTIN CORP.
 DYNAMICS RESEARCH CORPORATION
 CANADIAN HYDROGRAPHIC SERVICE
 THE AEROSPACE CORPORATION
 UNIVERSITY OF NEW BRUNSWICK
 JOHN E. CHANCE & ASSOCIATES
 NGS/NOAA/N/NGS, SSMC3, 8657
 JOHN E. CHANCE & ASSOCIATES
 NAVAL RESEARCH LABORATORY
 AMCOMP CORP
 TRANDES CORP.
 U.S. COAST GUARD EECEN (NG)
 GEOTRONICS
 WL/AAAS-3
 U.S. AIR FORCE

JAPAN
 KIRTLAND AFB,NM
 PATUXENT RIVER,MD
 PATUXENT RIVER,MD
 JAPAN
 WOODLAND HILLS,CA
 PETERSON AFB,CO
 CORONADO,CA
 ST. LOUIS,MO
 JAPAN
 RUSSIA
 SAN DIEGO,CA
 OVERLAND PARK,KS
 WHITTIER,CA
 HOLLOMAN AFB,NM
 JAPAN
 WALLOPS ISLAND,VA
 CAMBRIDGE,MA
 CANADA
 CANADA
 EL SEGUNDO,CA
 PHILADELPHIA,PA
 CEDAR RAPIDS,IA
 LOS ANGELES,CA
 LOS ALTOS,CA
 CANADA
 SUNNYVALE,CA
 CHATSWORTH,CA
 EL SEGUNDO,CA
 WESTLAKE VILLAGE,CA
 AUSTIN,TX
 LOS ANGELES AFB,CA
 SANTA CLARA,CA
 KOREA
 GREENBELT,MD
 CANADA
 RESTON,VA
 WASHINGTON,DC
 LOS ANGELES AFB,CA
 CAMBRIDGE,MA
 COLORADO SPRINGS,CO
 WASHINGTON,DC
 BRUNEI
 COLUMBIA,MD
 CARLSBAD,CA
 PHILADELPHIA,PA
 WEST NEWTON,MA
 CANADA
 LOS ANGELES,CA
 CANADA
 LAYFAYETTE,LA
 SILVER SPRING,MD
 LAYFAYETTE,LA
 FALLS CHURCH,VA
 REDONDO BEACH,CA
 SAN DIEGO,CA
 WILDWOOD,NJ
 ITASCA,IL
 WPAFB,OH
 TINKER AFB,OK

LATTA, THOMAS
 LATTERMAN, DONALD
 LAU, KENNETH
 LAVRAKAS, JOHN
 LAW, JULIUS
 LAWRENCE, DAVID
 LAWRENCE, TIMOTHY
 LAZAR, STEVEN
 LEACH, MARK
 LEAKE, STEPHEN
 LEAL, JULIO
 LEARY, TONY
 LEAVITT, PAUL
 LEBEDEV, MIKHAIL
 LEE, YOUNG
 LEE, DON
 LEE, SAMUEL
 LEE, TOM
 LEE, SANG JEONG
 LEHNUS, DAVID
 LEICK, ALFRED
 LEIGHTY, ROBERT
 LEININGER, BRIAN
 LEISTEN, OLIVER
 LEITTEN, MICHAEL
 LEMIEUX, CLIFFORD
 LEMMON, JOHN
 LEMOINE, ROBERT
 LENNEN, GARY
 LEONG, ALBERT
 LESSING, PETER
 LESTER, MARK
 LEUNG, JURN
 LEVI, ROBERT
 LEVY, LARRY
 LEW, YON
 LEWANDOWSKI, W.
 LEWANTOWICZ, ZDZISLAW
 LEWIN, ANDY
 LEWIS, CEDRIC
 LI, KEN
 LI, ZUOFA
 LICHTEN, STEPHEN
 LICU, FRANK
 LIEBER, STEVEN
 LIEFFRIG, PETER
 LINSBALL, DAVID
 LIPPS, DALE
 LISICA, CHRIS
 LITTLE, ANDREW
 LITTLE, CHUCK
 LITTON, JAMES
 LIU, JEFFREY
 LIU, ZIWEN
 LLOYD, DOUG
 LOCHHEAD, KIM
 LODATO, GERI
 LOEGERING, GREG
 LOH, ROBERT
 LOKSHIN, ANOTOLE

TYCHO ASSOCIATES
 SMC/CZJ
 JPL
 ADVANCED RESEARCH CORPORATION
 JET PROPULSION LABORATORY
 STANFORD UNIVERSITY
 SHELL UK EXPRO (UEX/51)
 THE AEROSPACE CORPORATION
 APL/UNIVERSITY OF TEXAS
 NASA/GSFC
 MARAVEN S.A.
 SUBSEA OFFSHORE LTD.
 LORAL DEFENSE SYSTEMS
 GLONASS COORDINATION
 THE MITRE CORPORATION
 NIPPANDENSO AMERICA
 ROCKWELL INTERNATIONAL
 UNIVERSITY OF SOUTHERN CALIFOR
 CHUNGNAM NATIONAL UNIVERSITY
 JHU/APL
 UNIVERSITY OF MAINE
 LEIGHTY & ASSOC., INC.
 LORAL DEFENSE SYSTEMS
 NAVSTAR SYSTEMS LTD
 COORS CERAMICS COMPANY
 NAVAL AIR WARFARE CENTER
 U.S. DEPT OF COMMERCE
 COUNTY OF ORANGE, CA
 TRIMBLE NAVIGATION, LTD.
 THE AEROSPACE CORPORATION
 NATIONAL DATA BUOY CENTER
 USAF
 THE AEROSPACE CORPORATION
 POINT RESEARCH CORP.
 JOHNS HOPKINS UNIVERSITY APL
 ANTARCTIC SUPPORT ASSOCIATES
 BIPM
 USAF, WL/AA
 ORBITAL SCIENCES CORP.
 NAVAIR
 LEAR ASTRONICS CORPORATION
 UNIV OF CALGARY/GEOMATICS ENG
 JET PROPULSION LABORATORY
 M/A-COM
 STEVE LIEBER & ASSOC., INC.
 TRANSOCEANIC CABLESHIP CO.
 RACAL SURVEY
 RACAL SURVEY USA
 US NAVY (SMC/CZN)
 NORTHERN TELECOM INC.
 HEWLETT-PACKARD CO.
 LITTON CONSULTING GROUP, INC.
 NATIONAL RESEARCH COUNCIL
 JOHN E. CHANCE & ASSOCIATES IN
 MAGELLAN GPS SYSTEMS
 GEODETIC SURVEY OF CANADA
 E-SYSTEMS
 TELEDYNE RYAN AERONAUTICAL
 INNOVATIVE SOLUTIONS INT'L INC
 MAGELLAN

DEERFIELD BEACH, FL
 LOS ANGELES AFB, CA
 PASADENA, CA
 COLORADO SPRINGS, CO
 PASADENA, CA
 MOUNTAIN VIEW, CA
 ENGLAND
 LOS ANGELES, CA
 AUSTIN, TX
 GREENBELT, MD
 VENEZUELA
 SCOTLAND
 MINNETONKA, MN
 RUSSIA
 FAIRFAX, VA
 SOUTHFIELD, MI
 DOWNEY, CA
 PALOS VERDES ESTATES, CA
 KOREA
 LAUREL, MD
 ORONO, ME
 VIENNA, VA
 WOODBURY, MA
 UK
 GOLDEN, CO
 POINT MUGU, CA
 BOULDER, CO
 HUNTINGTON BEACH, CA
 SUNNYVALE, CA
 LOS ANGELES, CA
 STENNIS SPACE CENTER, MS
 FALCON AFB, CO
 LOS ANGELES, CA
 SANTA ANA, CA
 LAUREL, MD
 ENGLEWOOD, CO
 FRANCE
 WP AFB, OH
 DULLES, VA
 ANNAPOLIS, MD
 SANTA MONICA, CA
 CANADA
 PASADENA, CA
 LOWELL, MA
 WEBSTER, TX
 BALTIMORE, MD
 HOUSTON, TX
 HOUSTON, TX
 SAN PEDRO, CA
 SCHAUMBURG, IL
 SANTA CLARA, CA
 WOODLAND HILLS, CA
 CANADA
 LAFAYETTE, LA
 AUSTRALIA
 CANADA
 ST. PETERSBURG, FL
 SAN DIEGO, CA
 VIENNA, VA
 SAN DIMAS, CA

LOLLOCK, RITA
 LONG, PETER
 LONGAKER, HAROLD
 LONGWORTH, DAVID
 LOOSE, JOHN
 LOPEZ, MARTIN
 LOPEZ, PETE
 LOVEMAN, BRAD
 LOWENSTEIN, GEORGE
 LOY, GEORGE
 LU, GANG
 LUBBES, ARIS
 LUCE, JENNIFER
 LUENGO, HUMBERTO
 LUKAC, CARL
 LUNDAY, MARK
 LUPASH, LAWRENCE
 LUSE, WILL
 LYALL, JAMES
 LYLES, FRED
 MACABIAU, CHRISTOPHE
 MACFARLANE, MEG
 MACGREGOR, JOHN
 MACHNIAK, MARTIN
 MACK, GILES
 MAEDA, HIROAKI
 MAENPA, JON
 MAETHER, PASCALE
 MAGGARD, WILLIAM
 MAGNUSON, R. GARY
 MAGNUSSON, LARS
 MAHMOOD, SULTAN
 MAIDA, JAMES
 MALAPIT, JEFFREY
 MALLETT, IAN
 MALYS, STEPHEN
 MANDIBLES, ED
 MANFREDI, PHILIP
 MANISCALCO, CHARLES
 MANNUCCI, ANTHONY
 MANTEUFEL, SUZANN
 MARCEAU, GUY
 MARCHESELLO, TOM
 MARCILLE, HERVE
 MARCK, BILL
 MARCOUX, MICHAEL
 MARDER, ED
 MARDER, CAROL
 MARKOWSKI, ROMAN
 MARRADI, LIVIO
 MARSH, C.
 MARTELL, HUGH
 MARTENS, DAN
 MARTIN, EDWARD
 MARTIN, MICHAEL
 MARTIN-MUR, TOMAS
 MARTINO, ROBERT
 MARTINSSON, JONNY
 MASON, ALLEN
 MASSON, ARNAUD

AEROSPACE CORPORATION
 RAYTHEON MARINE COMPANY
 TRIMBLE NAVIGATION, LTD.
 NAWC AD
 LEAR ASTRONICS
 OVERLOOK SYSTEMS TECHNOLOGIES
 TRAK SYSTEMS
 TRW
 NRAD DET WARMINSTER
 OCEONICS, INC.
 TRIMBLE
 FUGRO NV
 USAF
 VIASA AIRLINES
 U.S. NAVAL OBSERVATORY/TSSP
 USCG R&D CENTER
 AMCOMP
 LORAL DEFENSE SYSTEMS
 EMBRY RIDDLE AERONAUTICAL UNIV
 USAF SMC/CZPU
 LTST
 MOTOROLA
 SHELL UK, UEX/S12
 NISE WEST
 RACAL SURVEY
 TOSHIBA CORPORATION
 LEICA
 AEROSPATIALE
 NICHOLS RESEARCH CORP
 NATIONAL OCEAN SERVICE
 SWEDISH DEFENCE MA
 SVERDRUP TECHNOLOGY INC (TEAS)
 ADVANCED ANTENNA TECHNOLOGY, I
 NAVSTAR GPS JPO
 AIRSERVICES AUSTRALIA
 DEFENSE MAPPING AGENCY
 ITT FSC
 DCS CORPORATION
 TRIMBLE NAVIGATION LTD
 JPL/CALTECH
 TRIMBLE NAVIGATION
 CANADIAN COAST GUARD
 2 SOPS/DOAN
 MATRA MARCONI SPACE FRANCE
 NAWCAD
 USAF/SMC/CZU
 ITT/ACD
 ITT/ACD
 UNIVERSITY OF CALGARY
 LABEN S.P.A.
 MINISTRY OF DEFENCE MOD(PE)
 PREMIER GPS INC.
 SAIC
 ROCKWELL INTERNATIONAL
 ROCKWELL
 ESOC/ESA
 TRW
 SAAB MILITARY AIRCRAFT
 SMC/CZE
 LRBA-DGA

EL SEGUNDO, CA
 MANCHESTER, NH
 THE WOODLANDS, TX
 INDIANAPOLIS, IN
 SANTA MONICA, CA
 REDONDO BEACH, CA
 TAMPA, FL
 TORRANCE, CA
 DOYLESTOWN, PA
 HOUSTON, TX
 CANADA
 THE NETHERLANDS
 RANCHO PALOS VERDES, CA
 MIAMI, FL
 WASHINGTON, DC
 GROTON, CT
 ALAMOGORDO, NM
 LITCHFIELD PARK, AZ
 PRESCOTT, AZ
 LOS ANGELES AFB, CA
 FRANCE
 NORTHBROOK, IL
 SCOTLAND
 SAN DIEGO, CA
 HOUSTON, TX
 JAPAN
 TORRANCE, CA
 FRANCE
 DOVER, FL
 SILVER SPRING, MD
 SWEDEN
 NICEVILLE, FL
 ESCONDIDO, CA
 LOS ANGELES AFB, CA
 AUSTRALIA
 MONROVIA, MD
 VANDENBERG AFB, CA
 ARLINGTON, VA
 SUNNYVALE, CA
 PASADENA, CA
 SUNNYVALE, CA
 CANADA
 FALCON AFB, CO
 FRANCE
 MARLTOW, NJ
 LOS ANGELES AFB, CA
 FORT WAYNE, IN
 FORT WAYNE, IN
 CANADA
 ITALY
 ENGLAND
 CANADA
 TORRANCE, CA
 ANAHEIM, CA
 ANAHEIM, CA
 GERMANY
 REDONDO BEACH, CA
 SWEDEN
 LA AFB, CA
 FRANCE

MATHIES, MAX
 MATHIS, CLARENCE
 MATHIS, JON
 MATSUDA, ATSUSHI
 MATTHEWS, JAMES
 MATTISSEK, ANDREAS
 MATTOS, PHILLIP
 MAURER, MARTIN
 MAURER, JAMES
 MAZZONI, JANE
 MCCALL, EDWARD
 MCCALL, TIMOTHY
 MCCALLON, LARRY
 MCCARTOR, GERRY
 MCCONNELL, JOHN
 MCCUTCHEON, SAM
 MCDANIEL, MICKEY
 MCDONALD, KEITH
 MCDONALD, CAROLYN
 MCDONOUGH, LARRY
 MCEWEN, GLEN
 MCFADDEN, JOHN
 MCGANN, EDWARD
 MCGEE, MICHAEL
 MCGIBNEY, DANIEL
 MCGRAW, GARY
 MCGREGOR, LLOYD
 MCGURN, TERENCE
 MCILWAIN, TED
 MCINERNEY, JOHN
 MCINTOSH, DAVE
 MCLELLAN, JAMES
 MCLENNAN, MYRA
 MCLOUGHLIN, FRANK
 MCMAHAN, MICHAEL
 MCMILLAN, STANTON
 MCNALLY, DAVID
 MCNAMEE, STUART
 MCWARD, RAYMOND
 MEDEIROS, MARC
 MEE, BRIAN
 MEEKER, BRENT
 MEIER, STEVE
 MEIGS, MICHAEL
 MEINDL, MARK
 MELESKI, JERRY
 MELGARD, TOR EGIL
 MEMERY, PHILIPPE
 MENDOZA, PATRICIA
 MERRILL, DAN
 MES, MARIUS
 MESSIER, JOHN
 MEYER, MAURICE
 MEYER-HILBERG, JOCHEN
 MICHALI, PETER
 MICHALSON, WILLIAM
 MICHEL, P.
 MIELE, NIEL
 MIER, FRANCISCO
 MILLAR, DAVID

LEICA
 SMC/CZEM
 BD SYSTEMS, INC.
 SONY CORPORATION
 C.S. DRAPER LABORATORY INC.
 DAIMLER BENZ AEROSPACE
 SGS-THOMSON MICROELECTRONICS
 MAN TECHNOLOGIE AG
 LITTON G&CS
 LEICA
 USAF
 DYNAMIC SATELLITE SURVEYS
 NORTHROP GRUMMAN
 FAA
 30 SW/XPE - USAF
 AUTEX SYSTEMS CORPORATION
 NAWC AD
 SAT TECH SYSTEMS, INC.
 NAVTECH SEMINARS & BOOKSTORE
 NATIONAL SYSTEMS & RESEARCH CO
 MCEWEN CONSULTING
 AVIATION WEEK GROUP/MCGRAW-HIL
 MEGAPULSE
 MCGEE SURVEYING CONSULTING
 USAF SMC/CZE
 ROCKWELL INTL, COLLINS
 LOCKHEED MARTIN
 US GOVERNMENT
 FAA
 ROCKWELL
 STANFORD TELECOM
 PULSEARCH NAVIGATION SYSTEMS
 DTIC
 SEAGULL TECHNOLOGY, INC.
 NAVSTAR SYSTEM LTD
 BALL CORPORATION
 NASA AMES RESEARCH CENTER
 412 TW/TSPE
 DATA AUTOMATION SYSTEMS
 RIVERSIDE COUNTY FLOOD CONTROL
 ENSCO, INC.
 NAWC
 STEVE LIEBER & ASSOC., INC.
 FAA
 SANDIA NATIONAL LABS
 LORAL
 AFFILIATION UNKNOWN
 DGA/DCAE/STTE
 ARINC
 FAA
 PHILLIPS PETROLEUM COMPANY
 HONEYWELL
 MEYER ASSOCIATES
 DAIMLER-BENZ AERISPACE
 LEICA
 WORCESTER POLYTECHNIC INST.
 EUROPEAN SPACE AGENCY
 TELEPHONICS CORPORATION
 GRAFINTA SA
 PELAGOS CORPORATION

REDONDO BEACH, CA
 LA AFB, CA
 TORRANCE, CA
 JAPAN
 WAYLAND, MA
 GERMANY
 UK
 GERMANY
 WOODLAND HILLS, CA
 TORRANCE, CA
 EGLIN AFB, FL
 AUSTRALIA
 HAWTHORNE, CA
 OKLAHOMA CITY, OK
 VANDENBERG AFB, CA
 SAN DIEGO, CA
 INDIANAPOLIS, IN
 ARLINGTON, VA
 ARLINGTON, VA
 COLORADO SPRINGS, CO
 PEORIA, AZ
 NEW YORK, NY
 BEDFORD, MA
 SANTA BARBARA, CA
 LOS ANGELES AFB, CA
 CEDAR RAPIDS, IA
 STENNIS, MS
 RESTON, VA
 OKLAHOMA CITY, OK
 ARLINGTON, VA
 SUNNYVALE, CA
 CANADA
 FORT BELVOIR, VA
 CUPERTINO, CA
 ENGLAND
 BROOMFIELD, CO
 MOFFETT FIELD, CA
 LANCASTER, CA
 SANTA CLARA, CA
 RIVERSIDE, CA
 SPRINGFIELD, VA
 POINT MUGU, CA
 WEBSTER, TX
 SEATTLE, WA
 ALBUQUERQUE, NM
 MANASSA, VA
 NORWAY
 FRANCE
 SAN DIEGO, CA
 OKLAHOMA CITY, OK
 NORWAY
 MINNEAPOLIS, MN
 NATICK, MA
 GERMANY
 TORRANCE, CA
 CHARLTON, MA
 THE NETHERLANDS
 FARMINGDALE, NY
 SPAIN
 SAN DIEGO, CA

MILLER, DOUGLAS
 MILLER, JAMES
 MILLER, JAMES
 MILLER, MATTHEW
 MIOLA, JOE
 MIRANIAN, MIHRAN
 MIRDAS, JOANNE
 MISRA, PRATAP
 MITCHELL, ADOLPH
 MITCHELL, BRIAN
 MITCHELL, ROBERT
 MJAALAND, STEIN
 MOBARAKI, HOSSEIN
 MOBBS, SHAWN
 MOEGLEIN, MARK
 MOHLER, CHARLES
 MONTALVIO, ARMANDO
 MONTGOMERY, HALE
 MOORE, TERRY
 MOORE, GERALD
 MOORE, JAMES
 MOORE, KEITH
 MOORE, MARK
 MOORE, TODD
 MOORE, LINDA
 MORENO, MIGUEL
 MORGAN, JAMES
 MORRIS, BARRY
 MORRIS, JEFF
 MORRISON, ALLEN
 MORRISSEY, THOMAS
 MOSLE, CHIP
 MOSLEY, DEVIN
 MOUSSA, RALPH
 MOYA, DAVID C.
 MOYER, CAROLINE
 MRSTIK, PAUL
 MUELLER, CONRAD
 MUELLER, TYSEN
 MUELLERSCHOEN, RONALD
 MUKUND, MIKE
 MULDER, F.
 MULLER, KARL-FRANZ
 MUNJAL, PREM
 MURAKAMI, AKIRA
 MURFIN, TONY
 MURPHY, DAN
 MURPHY, JOE
 MURPHY, JOHN
 MURPHY, TIMOTHY
 MUSKAT, DAVE
 MYERS, STEVEN
 NADEAU, FRED
 NAGANO, SUKETOSHI
 NAGENGAST, STEVEN
 NAGLE, JIM
 NAJARIAN, RICHARD
 NAKAMURA, RUSSELL
 NAKAYAMA, DAVID
 NAOR, RAHEL

JOHN E. CHANCE & ASSOCIATES
 NCCOSC, RDT&E DIV DET
 QUT SPACE CENTRE FOR SAT NAV
 COMOPTEVFOR US NAVY
 C.S. DRAPER LABORATORY
 U.S. NAVAL OBSERVATORY
 ARINC
 MIT LINCOLN LABORATORY
 NAVAL AIR WARFARE CENTER
 C2SID U.S. ARMY
 MCDONNELL DOUGLAS HELICOPTER
 FOTONOR AS
 ALLIED SIGNAL AEROSPACE
 2SOPS/DOAN
 SRI INTERNATIONAL
 HUGHES
 NAVSYS CORPORATION
 GPS WORLD MAGAZINE
 UNIVERSITY OF NOTTINGHAM
 MOTOROLA - GED
 USAF
 LOCKHEED MARTIN ASTRO SPACE
 US GOV
 HUGHES AIRCRAFT COMPANY
 SPECTRA-PHYSICS LASERPLANE
 AIR FORCE INFORMATION WARFARE
 CHEVRON PETROLEUM TECH CO.
 GPSAT SYSTEMS AUSTRALIA
 NORTHSTAR TECHNOLOGIES
 SAIC
 U.S. GOVERNMENT
 746 TS/TGGPI
 TASC
 RENAULT
 HONEYWELL, INC.
 EFRATOM, TIME & FREQUENCY
 GEOSURV, INC.
 CEM CONSULTANTS
 SEAGULL TECHNOLOGY, INC.
 JET PROPULSION LABORATORY
 ROCKWELL INTERNATIONAL
 US GOVERNMENT
 INST. OF GEODESY AND NAVIGATION
 THE AEROSPACE CORPORATION
 GPS HAND-SET DESIGN SHOP
 NOVATEL COMMUNICATIONS LTD
 HONEYWELL, INC.
 NOVATEL COMMUNICATIONS
 WESTINGHOUSE ELECTRIC CORP.
 THE BOEING COMPANY
 US NAVY
 ARBITER SYSTEMS
 USAF 746TH TEST SQUADRON
 TOSHIBA CORPORATION
 US COAST GUARD
 INMARSAT
 ROCKWELL INTERNATIONAL
 LORAL FEDERAL SYSTEMS
 SRI INTERNATIONAL
 TAMAN IAI

HOUSTON, TX
 ROBINS AFB, GA
 AUSTRALIA
 NORFOLK, VA
 CAMBRIDGE, MA
 WASHINGTON, DC
 SAN DIEGO, CA
 LEXINGTON, MA
 POINT MUGU, CA
 POINT PLEASANT BEACH, NJ
 MESA, AZ
 NORWAY
 PASADENA, CA
 FALCON AFB, CO
 MENLO PARK, CA
 LOS ANGELES, CA
 COLORADO SPRINGS, CO
 WASHINGTON, DC
 UK
 SCOTTSDALE, AZ
 EGLIN AFB, FL
 PHILADELPHIA, PA
 MCLEAN, VA
 WEST HILLS, CA
 DAYTON, OH
 SAN ANTONIO, TX
 HOUSTON, TX
 AUSTRALIA
 ACTION, MA
 SAN DIEGO, CA
 SPRINGFIELD, VA
 HOLLOMAN AFB, NM
 FORT WALTON BEACH, FL
 FRANCE
 ST. PETERSBURG, FL
 IRVINE, CA
 CANADA
 INVER GROVE HEIGHTS, MN
 CUPERTINO, CA
 PASADENA, CA
 NEWPORT BEACH, CA
 WASHINGTON, DC
 GERMANY
 LOS ANGELES, CA
 W. COVINA, CA
 CANADA
 GLENDALE, AZ
 CANADA
 PITTSBURG, PA
 SEATTLE, WA
 CAMARILLO, CA
 PASO ROBLES, CA
 HOLLOMAN AFB, NM
 JAPAN
 CAPE MAY, NJ
 ENGLAND
 NEWPORT BEACH, CA
 GAITHERSBURG, MD
 MENLO PARK, CA
 ISRAEL

NASH, ANTHONY
 NAVARRO, RICARDO
 NAVE, KYLE
 NAVONI, FRANCO
 NAVONI, FRANCO
 NDILI, AWELE
 NEDIMALA, EDWARD
 NEGAST, WILLIAM
 NEIL, WILLIAM
 NEILAN, RUTH
 NELSON, DAVID
 NELSON, GREG
 NELSON, MARK
 NELSON, SHANE
 NELSON, NANCY
 NEUMANN, JANET
 NEUPERGER, FRANK
 NGUYEN, HOA
 NICHOLAS, JAMES
 NICHOLS, MITCH
 NICHOLSON, GRADY
 NIKLASCH, NORBERT
 NIKOLAO, RUDY
 NILSSON, GUNNAR
 NISHIGUCHI, HIROSHI
 NISNER, PAUL
 NIX, RICHARD
 NOEL, BRUCE
 NOERBECK, TORBJOERN
 NOLAN, RICHARD
 NORDWALL, BRUCE
 NORLING, BRIAN
 NORRIS, JIM
 NOVAK, KYLE
 NOVY, MICHAEL
 NOWICKI, RICHARD
 NWANGANGA, CHUKWUMA JEASON
 O'BRYANT, CARVEL
 O'CONNOR, MICHAEL
 O'GRADY, CRAIG
 O'GRADY, TIM
 O'HARA, MARK
 O'KEEFE, WILLIAM
 O'LOUGHLIN, CARL
 O'NEIL, T. GREG
 O'TOOLE, JAMES
 OAKS, JAY
 OBERG, MAGNUS
 OCVIRK, THOMAS
 ODDEN, VANJA
 OFER, RAN
 OFSTAD, ARNE
 OIWA, DAVE
 OLAFSEN, KNUT
 OLIVER, ROBERT
 OLSEN, DAVE
 OLSON, TOM
 OLSON, RUTH
 OMORI, TAKESHI
 OSBORN, CHARLES

746 TS/TGGDC
 NAWC-WD
 SPACE VECTOR CORP.
 LASER
 LASER
 STANFORD UNIVERSITY
 FAA
 METRIC SYSTEMS CORPORATION
 RMS TECHNOLOGY/VISTA
 JET PROPULSION LABORATORY
 THE AEROSPACE CORPORATION
 ROCKWELL INTERNATIONAL
 US ARMY YUMA PROVING GROUND
 ARL/UNIVERSITY OF TEXAS
 TRIMBLE NAVIGATION
 NOVATEL COMMUNICATIONS, LTD.
 SATLOC INC.
 EFRATOM
 NAVSTAR SYSTEMS
 II MORROW INC.
 COMPUTER SCIENCES CORPORATION
 VICON ENGINEERING GMBH
 SPO
 TELUB AB
 JAPAN GPS COUNCIL
 CAA-NAT'L AIR TRAFFIC SERVICES
 US ARMY YUMA PROVING GROUND
 DIFFERENTIAL CORRECTIONS, INC.
 NORWEGIAN MAPPING AUTHORITY
 SMC/CZK - USAF
 AVIATION WEEK & SPACE TECH
 LITTON GCS
 ROCKWELL INTERNATIONAL
 PL/VT-B
 746 TS/TGGPI
 SYNETICS
 GEODETIC POSITIONING SERVICES
 NAVAIR/AIR 4513
 STANFORD UNIVERSITY
 ROCKWELL TELECOMMUNICATIONS
 ARINC
 LORAL FEDERAL SYSTEMS
 NEWCOMB COMMUNICATIONS INC
 COLORADO DOT
 U.S. AIR FORCE
 NSWCDD
 NAVAL RESEARCH LABORATORY
 FFV AEROTECH AB
 OVERLOOK SYSTEMS TECHNOLOGY
 NORWEGIAN HYDROGRAPHIC SERVICE
 TEL-AVIV UNIVERSITY
 NORWEGIAN HYDROGRAPHIC SERVICE
 KBK INC
 NORWEGIAN ARMY MATERIAL COMMAN
 REO MENAGEMENT CORPORATION
 FEDERAL AVIATION ADMIN/ASD-120
 PRINCE CORPORATION
 STUDENT
 PIONEER NAVICOM INC.
 COLSA CORPORATION

HOLLOMAN AFB,NM
 POINT MUGU,CA
 CHATSWORTH,CA
 ITALY
 ITALY
 STANFORD,CA
 WASHINGTON,DC
 FORT WALTON BEACH,FL
 MOLALLA,OR
 PASADENA,CA
 LOS ANGELES,CA
 CEDAR RAPIDS,IA
 YUMA,AZ
 AUSTIN,TX
 SUNNYVALE,CA
 CANADA
 GILBERT,AZ
 IRVINE,CA
 WOODLAND HILLS,CA
 SALEM,OR
 HOLLOMAN AFB,NM
 GERMANY
 ALEXANDRIA,VA
 SWEDEN
 JAPAN
 ENGLAND
 YUMA,AZ
 CUPERTINO,CA
 NORWAY
 LOS ANGELES AFB,CA
 WASHINGTON,DC
 SALT LAKE CITY,UT
 ANAHEIM,CA
 KIRTLAND AFB,NM
 HOLLOMAN AFB,NM
 LAGUNA HILLS,CA
 NIGERIA
 ARLINGTON,VA
 PALO ALTO,CA
 NEWPORT BEACH,CA
 CHESAPEAKE BEACH,MD
 GAITHERSBURG,MS
 MANCHESTER,NH
 DENVER,CO
 EL SEGUNDO,CA
 DAHLGREN,VA
 WASHINGTON,DC
 SWEDEN
 COLORADO SPRINGS,CO
 NORWAY
 ISRAEL
 NORWAY
 CEDAR RAPIDS,IA
 NORWAY
 MONTECITO,CA
 WASHINGTON,DC
 HOLLAND,MI
 HEALDSBURG,CA
 JAPAN
 HUNTSVILLE,AL

OSBORNE, MICHAEL
 OSBORNE, SKIP
 OSKOWSKY, MARK
 OSTER, ALLAN
 OTT, LEE
 OTTERMAN, KEVIN
 QUELLETTE, JOSEPH
 OUTLAW, DAVID
 OVSTEDAL, OLA
 OW, STEVE
 OWEN, J.I.R.
 OWEN, TODD
 OZAWA, RYUICHI
 PACHER, MEIR
 PALOMINO, ANTONIO
 PANEFIEU, BERNARD
 PAOLUCCI, DON
 PARIKH, VIJAY
 PARK, CHANSIK
 PARKER, DEWEY
 PARKINSON, BRADFORD
 PARSONS, STEPHEN
 PATTERSON, GLENN
 PAULSON, GARY
 PAVLOFF, MICHAEL
 PECK, R. STEVE
 PEDERSEN, BRUVE
 PEETZ, BRUCE
 PELET, PHILIPPE
 PELOSI, LOUIS
 PENDER, RICHARD
 PENG, MEI-HO
 PENG, SHENG
 PENNO, GARY
 PEREZ, ALBERTO
 PERKINS, B.
 PERLETTI, PAUL
 PERRETT, MICHAEL
 PERSAUD, RUDY
 PERVAN, BORIS
 PESTOOR, RICK
 PETERS, STEPHEN
 PETERSEN, UWE
 PETERSON, BENJAMIN
 PETWAY, JON
 PHAN, HUAN
 PHILLIPS, ROBERT
 PIETERSEN, OTTO
 PILLEY, LOIS
 PILLSBURY, CHARLES
 PINKER, ARON
 PLATE, KENNETH
 PLATO, JOHN
 PLUNK, DORSEY
 POGOREIC, SCOTT
 POIZNER, STEVE
 POLLOCK, DAVID
 POMIJE, BILL
 PON, RAYMAN
 PONSOT, PASCAL

LOCKHEED MARTIN
 ALLEN OSBORNE ASSOCIATES, INC.
 ROCKWELL TELECOMMUNICATIONS
 SMC/CZJ
 JOHN E. CHANCE & ASSOC., INC.
 GARMIN INTERNATIONAL
 SMC/CZU (PRC)
 USAF HQ AFSC
 DEPT OF SURVEYING NLH
 MICRO-PULSE INC.
 DEFENSE RESEARCH AGENCY
 SANDIA NATIONAL LABS
 NTT DATA COMMUNICATIONS SYSTEM
 AFIT/ENG
 DEPT OF ARMY/WSMR
 LRBA
 CANADIAN MARCONI
 ROCKWELL INTERNATIONAL
 SEOUL NATIONAL UNIVERSITY
 U.S. AIR FORCE
 STANFORD UNIV-GRAVITY PROBE B
 CANADIAN HYDROGRAPHIC SERVICE
 NAVSTAR SYSTEMS LTD
 II MORROW INC.
 HUGHES SPACE & COMMUNICATIONS
 ROCKWELL INTERNATIONAL
 ALLEN OSBORNE ASSOC.
 TRIMBLE NAVIGATION
 SAGEM
 SYNETICS CORPORATION
 NCS INTERNATIONAL
 AAT
 AAT
 SATLOC
 ROCKWELL INTERNATIONAL
 AMCOMP CORPORATION
 MT. HOOD COMMUNITY COLLEGE
 HUGHES MISSILE SYSTEMS CO.
 SOUTH DAKOTA DOT
 STANFORD UNIVERSITY
 ROCKWELL INTERNATIONAL
 WL/AAA
 AFFILIATION UNKNOWN
 U.S. COAST GUARD ACADEMY
 ROCKWELL
 ROCKWELL
 ARIZONA DOT
 NATIONAL AEROSPACE LAB NLR
 DSDC
 OVERLOOK SYSTEMS TECHNOLOGIES
 ANSER
 DORNE & MARGOLIN INC.
 BELLCORE
 USDA-NRCS
 STANFORD TELECOM
 STRATEGIC MAPPING, INC.
 NAVSTAR SYSTEMS INC
 ROCKWELL INTERNATIONAL
 TRIMBLE NAVIGATION
 AEROSPATIALE AVIONS

MORRISON, CO
 WESTLAKE VILLAGE, CA
 NEWPORT BEACH, CA
 LOS ANGELES AFB, CA
 HOUSTON, TX
 LENEXA, KS
 LOS ANGELES AFB, CA
 COLORADO SPRINGS, CO
 NORWAY
 CAMARILLO, CA
 ENGLAND
 ALBUQUERQUE, NM
 JAPAN
 WPAFB, OH
 EL PASO, TX
 FRANCE
 CANADA
 NEWPORT BEACH, CA
 KOREA
 MONUMENT, CO
 LOS ALTOS, CA
 CANADA
 ENGLAND
 SALEM, OR
 REDONDO BEACH, CA
 CARSON, CA
 WESTLAKE VILLAGE,
 SUNNYVALE, CA
 FRANCE
 WARMINSTER, PA
 HOUSTON, TX
 ESCONDIDO, CA
 ESCONDIDO, CA
 TEMPE, AZ
 DOWNEY, CA
 HOLLOMAN AFB, NM
 GRESHAM, OR
 TUCSON, AZ
 PIERRE, SD
 MOUNTAIN VIEW, CA
 YORBA LINDA, CA
 WPAFB, OH
 GERMANY
 WATERFORD, CT
 DOWNEY, CA
 NEWPORT BEACH, CA
 PHOENIX, AZ
 THE NETHERLANDS
 DEERING, NH
 LA HABRA, CA
 ARLINGTON, VA
 BOHEMIA, NY
 RED BANK, NJ
 FORT WORTH, TX
 RESTON, VA
 SANTA CLARA, CA
 WOODLAND HILLS, CA
 CEDAR RAPIDS, IA
 SUNNYVALE, CA
 FRANCE

POOR, WALTER
 PORTER, WADE
 PORTSMOUTH, JACKIE
 POSTEMA, LARRY
 POURAHMADI, FRANK
 POWELL, J. DAVID
 POWELL, STEVEN
 PREISS, GEORGE
 PRESTWOOD, MALCOLM
 PRINDIVILLE, DENISE
 PROSUCH, SCOTT
 PUJARA, NEERAJ
 PULLEN, SAMUEL
 PUPO, DANIEL
 PURVIS, JAY
 QIN, XINHUA
 QIU, WEIGEN
 QUIN, JEFF
 QUIST, SCOTT
 RABOURN, CHRIS
 RADICE, JIM
 RADZYMSKI, J.
 RAFFERTY, SHAUN
 RAGSDALE, ROB
 RAIDER, MICHAEL
 RAIMONDO, NAT
 RAKOWSKY, PETER
 RALSTON, CHRIS
 RAMBO, JEFFREY
 RAQUET, JOHN
 RASBERRY, JEFF
 RASHER, MICHAEL
 RASHWAN, ADEL
 RASMUSSEN, BOB
 RAUHUT, ANGELA
 RAY, DOUG
 RAYMOND, MICHAEL
 READ, ARNOLD
 REDSHAW, MARY
 REHMERT, HEINRICH
 REICHEL, JACK
 REICHERT, OLIVIER
 REID, ROBERT
 REIL, WOLFGANG
 REINERS, STEVEN
 REINES, PATRICK
 REINHARDT, GREG
 REINHARDT, VICTOR
 RETA, MARIA
 REUSSER, LARRY
 REYES, ROLANDO
 REYNARD, VINCE
 REYNOLDS, JON
 REYNOLDS, GARY
 RHEA, JEFF
 RICH, RICHARD
 RIGGINS, ROBERT
 RILEY, STUART
 RIM, HYUNG JIN
 RIN, GERLACH

THE MITRE CORPORATION
 US ARMY YUMA PROVING GROUND
 MOBILE TECHNOLOGY CENTER
 SMITHS INDUSTRIES
 ROCKWELL
 STANFORD UNIVERSITY
 CORNELL UNIVERSITY
 OLSEN NORGE AS
 RACAL SURVEY LTD
 USAF/SMC/CZE
 DESA
 WL/AAAI-3
 STANFORD UNIVERSITY
 SVERDRUP TECHNOLOGY
 PURVIS TECHNOLOGIES
 ASHTECH INC.
 UNIV OF CALGARY/GEOMATICS ENGI
 LITTON AERO PRODUCTS
 HITACHI CABLE AMERICA
 U.S AIR FORCE
 U.S. COAST GUARD NAVCEN
 AMCOMP CORPORATION
 HONEYWELL LTD.
 GEOTRONICS
 NAWCWPNSDIV
 RAIMONDO CONSULTING SERVICES
 DEFENSE MAPPING AGENCY
 TRIMBLE NAVIGATION
 ROCKWELL INTERNATIONAL
 UNIV OF CALGARY/GEOMATICS ENGI
 JOHN E. CHANCE & ASSOCIATES
 USDA-NRCS
 BAPETCO
 HONEYWELL, INC.
 GEODYNAMICS CORPORATION
 WARRENTON TRAINING CENTER
 TRIMBLE
 NORTHERN TELECOM EUROPE LTD.
 SPACE APPLICATIONS CORP.
 ELSAT GMBH
 REICHEL TECHNOLOGY
 SAGEM
 NUWC
 GECO-PRAKLA (SCHLUMBERGER)
 SAIC
 HONEYWELL INC.
 NOVATEL CONNUMUNICATIONS LTD
 HUGHES AIRCRAFT CO.
 746 TS/TGGPM
 FAA
 I-NET, INC.
 746 TS
 HUGHES SPACE & COMMUNICATIONS
 SATLOC
 COLSA CORPORATION
 FALCON RECONNAISSANCE SYSTEMS
 USAF AFIT/ENG
 UNIVERSITY OF LEEDS
 CENTER FOR SPACE RESEARCH
 3S NAVIGATION

MCLEAN,VA
 YUMA,AZ
 DALLAS,TX
 GRAND RAPIDS,MI
 CEDAR RAPIDS,IA
 MENLO PARK,CA
 ITHACA,NY
 NORWAY
 HOUSTON,TX
 LA AFB,CA
 ALBUQUERQUE,NM
 WPAFB,OH
 STANFORD,CA
 EGLIN AFB,FL
 DAYTON,OH
 SUNNYVALE,CA
 CANADA
 WOODLAND HILLS,CA
 WHITE PLAINS,NY
 EGLIN AFB,FL
 ALEXANDRIA,VA
 HOLLOMAN AFB,NM
 ALBUQUERQUE,NM
 ITASCA,IL
 POINT MUGU,CA
 TORRANCE,CA
 COCOA BEACH,FL
 SUNNYVALE,CA
 CEDAR RAPIDS,IA
 CANADA
 HOUSTON,TX
 BURLESON,TX
 EGYPT
 GLENDALE,AZ
 SANTA BARBARA,CA
 WARRENTON,VA
 SUNNYVALE,CA
 SCHAUMBURG,IL
 ARLINGTON,VA
 GERMANY
 CONCORD,CA
 FRANCE
 NEWPORT,RI
 GERMANY
 ALBUQUERQUE,NM
 MCLEAN,VA
 CANADA
 LOS ANGELES,CA
 HOLLOMAN AFB,NM
 OKLAHOMA CITY,OK
 KENNEDY SPACE CENTER,FL
 HOLLOMAN AFB,NM
 HUNTINGTON BEACH,CA
 TEMPE,AZ
 HUNTSVILLE,AL
 FRIDAY HARBOR,WA
 WPAFB,OH
 UK
 AUSTIN,TX
 LAGUNA HILLS,CA

RISINGER, PAUL
 RITTER, WILLIAM
 ROBB, DAVID
 ROBB, WILLIAM
 ROBBINS, JAMES
 ROBERTS, QUINTON
 ROBERTSON, GLEN
 ROCKWELL, DONALD
 RODDEN, JACK
 RODGERS, CHARLES
 ROE, GENE
 ROJAS, PETER
 ROLLINS, HOLLY
 ROMANOWSKI, PATRICIA
 ROMBERG, JAMES
 ROMRELL, GLYN
 RON, DANNY
 ROONEY, FRANK
 ROONEY, TOM
 ROSENBERG, MAGNUS
 ROSENTHAL, ALEX
 ROTH, STEVE
 ROTT, MILLIE
 ROUDEBUSH, EMILY
 ROY, EDITH
 RUDMAN, MICHAEL
 RUDOLPH, KEVIN
 RULAND, MATHEW
 RUSSELL, ANTHONY
 RUSSELL, WILLIAM
 RUSSO, NICHOLAS
 RUSSO, ANTHONY
 RUSTON, BRUCE
 RYAN, KAY
 RYDERGREN, BERTIL
 SACCO, STEPHEN
 SAGE, DAN
 SAJOVIC, ZORAN
 SAKRAN, CHARLIE
 SALISCHEV, VADIM
 SALVAGE, DEREK
 SALVAY, STEVEN
 SALZMANN, BONNIE
 SANCHEZ, JERRY
 SANDHOO, KAN
 SANDLIN, ALLISON
 SANTERRE, ROCK
 SANTINA, MOHAMMED
 SAPANKEVYCH, BILL
 SATKUNANATHAN, LINGAN
 SATO, ERIC
 SATOH, KEN
 SAUNDERS, JIMMY
 SAVARD, MICHAEL
 SAVILL, MIKE
 SCAPERDAS, BASIL
 SCHAFFER, DANIEL
 SCHAFFERT, LOWELL
 SCHAUER, GEORGE
 SCHEERER, JOHN

NAVSTAR SYSTEMS LTD
 746 TS/CA
 AVIONICS MAGAZINE
 HQ, DEPT OF ARMY
 TRIMBLE NAVIGATION
 U.S. AIR FORCE
 MINI-SYSTEMS, INC.
 C.S. DRAPER LABORATORY
 SPACE SYSTEMS/LORAL
 OPTIMUS CORPORATION
 BLUE MARBLE GEOGRAPHICS
 USAF/SMG/CZUD
 BOOZ-ALLEN & HAMILTON
 ALLEN OSBORNE ASSOCIATES INC.
 MCDONNELL DOUGLAS
 E-SYSTEMS
 ROKAR INTERNATIONAL, LTD.
 ROCKWELL INTERNATIONAL
 SATLOC
 TERACOM SVENSK RUNDRADIO AB
 IAI
 II MORROW INC.
 ROCKWELL INTERNATIONAL
 NAVTECH SEMINARS
 UNIVERSITY LAVAL
 ARINC
 HUGHES AIRCRAFT
 SAF/IAW
 WR, INC.
 AIR TRANSPORT ASSOC OF AMERICA
 U.S. COAST GUARD EECEN (NG)
 PARKER/GULL ELECTRONICS
 NAWCWPNS
 KENNECOTT UTAH COPPER
 SILVA SWEDEN AB
 C.S. DRAPER LABORATORY
 FAA
 NAVSTAR GPS JOINT PROGRAM OFFI
 NAWC
 ISDE
 EXXON EXPLORATION
 NORAND CORPORATION
 GEOTRONICS
 746 TG/CIGTF
 THE MITRE CORPORATION
 NATIONAL RESEARCH COUNCIL
 LAVAL UNIVERSITY
 THE AEROSPACE CORPORATION
 MAYFLOWER COMMUNICATIONS
 ALLIED SIGNAL
 SUMITOMO CORP AMERICA
 AMTECHS CORP
 ARL/UNIVERSITY OF TEXAS
 NDHQ DGAEM DASP 7-3-2
 NORTHERN LIGHTHOUSE BOARD
 ASTER PUBLISHING/GPS WORLD MAG
 RAYTHEON COMPANY
 ITT FSC
 MOTOROLA, INC.
 SPACE SYSTEMS/LORAL

ENGLAND
 HOLLOMAN AFB,NM
 POTOMAC,MD
 WASHINGTON,DC
 SUNNYVAL,CA
 COLORADO SPRINGS,CO
 ATTLEBORO,MA
 CAMBRIDGE,MA
 PALO ALTO,CA
 ST. LEONARD,MD
 GARDNER,ME
 LA AFB,CA
 MCLEAN,VA
 WESTLAKE VILLAGE,CA
 ST. CHARLES,MO
 SALT LAKE CITY,UT
 ISRAEL
 ANAHEIM,CA
 TEMPE,AZ
 SWEDEN
 ISRAEL
 SALEM,OR
 CEDAR RAPIDS,
 ARLINGTON,VA
 CANADA
 SAN DIEGO,CA
 SIMI VALLEY,CA
 WASHINGTON,DC
 SAN JOSE,CA
 WASHINGTON,DC
 WILDWOOD,NJ
 SMITHTOWN,NY
 POINT MUGU,CA
 BINGHAM CANYON,UT
 SWEDEN
 CAMBRIDGE,MA
 RENTON,WA
 LOS ANGELES AFB,CA
 MECHANICSVILLE,MD
 RUSSIA
 HOUSTON,TX
 CEDAR RAPIDS,IA
 ITASCA,IL
 ALAMOGORDO,NM
 MCLEAN,VA
 WASHINGTON,DC
 CANADA
 EL SEGUNDO,CA
 READING,MA
 POMPANO BEACH,FL
 LOS ANGELES,CA
 JAPAN
 AUSTIN,TX
 CANADA
 SCOTLAND
 METUCHEN,NJ
 PORTSMOUTH,RI
 VANDENBERG AFB,CA
 SCOTTSDALE,AZ
 LOS ALTOS,CA

SCHEIDKER, ERIC
 SCHENK, GARY
 SCHIPPER, BRIAN
 SCHLEPPE, JOHN
 SCHMIDT, FRANK
 SCHMIDT, MICHAEL
 SCHMIDT, RICH
 SCHNAUFER, BERNARD
 SCHNEIDER, THOMAS
 SCHNITZIUS, MICHAEL
 SCHOSTAK, BRIAN
 SCHULTZ, STEVE
 SCHUTZ, BOB
 SCHWARTZ, JACK
 SCHWARTZ, WILLIAM
 SCHWARZ, JOHANNES
 SCHWEITZER, BERNARD
 SCHWENT, DEL
 SCHWINN, DAN
 SCOGGINS, DARRELL
 SCOTT, BENGE
 SCOTT, DOUGLAS
 SCOTT, GEORGE
 SCOTT, STEVE
 SCOTT, W.H.
 SCRIBNER, COY
 SEAVOY, THOMAS
 SEERY, SAM
 SEGALL, ILANA
 SENECHAL, CALVIN
 SENFFNER, DAVE
 SENNOTT, JAMES
 SENOUR, ERIC
 SENTER, STEVEN
 SENUS, WALTER
 SERFLING, STEVE
 SETH, AJAY
 SETTERLUND, ROY
 SEVERINO, ROBERT
 SEXTON, RALPH
 SHAMBERGER, RICHARD
 SHAVE, NICK
 SHAW, MICHAEL
 SHAW, SAMUEL
 SHAY, PATRICK
 SHECKELLS,
 SHEYNBLAT, LEONID
 SHIMELEVICH, LEONID
 SHIMIZU, TAKAO
 SHIRER, HEYWOOD
 SHRADER-FRECHETTE, MAURICE
 SHRESTHA, RAMESH
 SIANO, DICK
 SIFFERLEN, STEPHEN
 SIKORSKI, ROY
 SILVERMAN, GEORGE
 SILVERMAN, JONATHAN
 SIMBURGER, EDWARD
 SIMMONS, JESSE
 SIMON, MARY

ROCKWELL INTERNATIONAL
 U.S. COAST GUARD
 HONEYWELL
 PULSESEARCH NAVIGATION SYSTEMS,
 SYSTEM TECHNOLOGY ASSOCIATES
 GEOLOGICAL SURVEY OF CANADA
 ROCKWELL
 ROCKWELL COLLINS AVIONICS
 HQ AFFSA/XO1P
 USAF/SMC/CZGE
 SHELL OFFSHORE INC.
 STUDENT
 UNIV OF TEXAS/CTR FOR SPACE RE
 GPS JPO (NAVY)
 CTA
 LEICA AG
 RAND
 MCDONNELL DOUGLAS
 AVIDYNE
 RESOURCE MANAGEMENT SYSTEMS
 NAWCWPNS
 GEOMATICS CANADA
 U.S. NAVY
 ROCKWELL
 LORAL FEDERAL SYSTEMS COMPANY
 METRIC SYSTEMS CORPORATION
 THE BOEING COMPANY
 II MORROW INC.
 ELBIT LTD.
 HONEYWELL, INC.
 BRADLEY UNIVERSITY
 BRADLEY UNIVERSITY
 NAWCWPNS
 NORTHERN TELECOM INC.
 DEFENSE MAPPING AGENCY
 HONEYWELL INC.
 LEICA, INC.
 C.S. DRAPER LABORATORY, INC.
 CLAREMONT GRADUATE SCHOOL
 UNIVERSITY OF OKLAHOMA
 FEDERAL RAILROAD ADMINISTRATIO
 DEFENCE RESEARCH AGENCY
 FAA
 CALIFORNIA MARITIME ACADEMY
 MOTOROLA, INC. - IVHS
 HUGHES SPACE & COMMUNICATIONS
 TRIMBLE NAVIGATION
 ISRAEL AIRCRAFT INDUSTRIES
 NTT DATA COMMUNICATIONS SYSTEM
 DEPARTMENT OF TRANSPORTATION
 HONEYWELL, INC.
 UNIVERSITY OF FLORIDA
 TWA
 C.S. DRAPER LABORATORY, INC.
 MOTOROLA GST GROUP
 ELECTRO-RADIATION
 AVIATION WEEK GROUP/MCGRAW-HIL
 THE AEROSPACE CORP
 ASC/VXG
 ARINC RESEARCH CORPORATION

CEDAR RAPIDS, IA
 ALEXANDRIA, VA
 MINNEAPOLIS, MN
 CANADA
 COLORADO SPRINGS, CO
 CANADA
 FULLERTON, CA
 CEDAR RAPIDS, IA
 ANDREWS AFB, MD
 PETERSON AFB, CO
 NEW ORLEANS, LA
 HEALDSBURG, CA
 AUSTIN, TX
 FOUNTAIN VALLEY, CA
 CALIFORNIA CITY, CA
 SWITZERLAND
 SANTA MONICA, CA
 FLORISSANT, MO
 LEXINGTON, MA
 OAK RIDGE, TN
 CHINA LAKE, CA
 CANADA
 ALEXANDRIA, VA
 DOWNEY, CA
 GAITHERSBURG, MD
 FORT WALTON BEACH, FL
 SEATTLE, WA
 SALEM, OR
 ISRAEL
 MINNEAPOLIS, MN
 PEORIA, IL
 PEORIA, IL
 POINT MUGU, CA
 SCHAUMBURG, IL
 FAIRFAX, VA
 MINNEAPOLIS, MN
 TORRANCE, CA
 CAMBRIDGE, MA
 IRVINE, CA
 NORMAN, OK
 WASHINGTON, DC
 UK
 WASHINGTON, DC
 VALLEJO, CA
 NORTHBROOK, IL
 LOS ANGELES, CA
 SUNNYVALE, CA
 ISRAEL
 JAPAN
 WASHINGTON, DC
 ST. PETERSBURG, FL
 GAINESVILLE, FL
 FLEMINGTON, NJ
 CAMBRIDGE, MA
 SCOTSDALE, AZ
 FAIRFIELD, NJ
 NEW YORK, NY
 LOS ANGELES, CA
 EGLIN AFB, FL
 COLORADO SPRINGS, CO

SINKO, JAMES
SIPPEL, JUERGEN
SIVES, CARLA
SKALSKI, HANK
SKIDMORE, TRENT
SLEDZINSKI, JANUSZ
SLINGLAND, WILLIAM
SLIVINSKY, SANDRA
SMITH, ROBERT
SMITH, BERNALD
SMITH, BLANCHARD
SMITH, BRUCE
SMITH, DAVE
SMITH, DEREK
SMITH, DONALD
SMITH, ERIC
SMITH, JEFFREY
SMITH, RANDALL
SMITH, RANDY
SMITH, RONALD
SMITH, SCOTT
SMITH, WAYNE
SMUK, JEFF
SNEAD, DONALD
SNOW, JIMMY
SNOW, ROBERT
SNYDER, ARTHUR
SOBOL, DIANA
SOEHNGEN, HENRY
SOLARI, PAUL
SOLCO, KELVIN
SOLOMON, JOSEPH
SONG, INSEONG
SONG, HO JUN
SONNTAG, JOHN
SORDEN, JAMES
SORRENTINO, MICHAEL
SOYKA, MARK
SPALDING, JAY
SPEELMAN, LARRY
SPERRY, ROGER
SPILKER, JAMES
SPITZER, ALLAN
SPOFFORD, PAUL
SPOHNHEIMER, NELSON
SPRICK, THOMAS
SPRONG, ANDRE
SPYROPULOS, CHARLES
SRIDHARAN, GUROSAMI
SRINIVASAN, JEFFREY
STACH, BRUCE
STAFFORD, DARRELL
STANDERSKI, JEFFREY
STANGL, JOHN
STANLEY, DAVID
STANSELL, THOMAS
STARR, STANLEY
STASTKA, RONALD
STEELE, KEN
STENER, STEPHEN

SRI INTERNATIONAL
VDO-STRABE 1
GALAXY SCIENTIFIC CORPORATION
DOT HQ AFSPC/DRFN
OHIO UNIVERSITY
INST OF GEODESY & GOEDETIC WUT
SPACE SYSTEMS LORAL
U.S. AIR FORCE
THE AEROSPACE CORPORATION
SOARING SOCIETY OF AMERICA
ST RESEARCH CORPORATION
LITTON LASER SYSTEMS
IEC
TRIMBLE
CO-OPERATIVE ENGR SVCS, INC.
LOCKHEED MARTIN
APPLIED REMOTE TECHNOLOGY
DEFENSE MAPPING AGENCY
TRUE TIME, INC.
US NAVY
TRIMBLE NAVIGATION
DEERE & COMPANY
HITTITE
NAVAL AVIATION ENGINEERING SER
FAA/AVN-5
ALLEN OSBORNE ASSOCIATES, INC.
THE MITRE CORPORATION
ARINC
SIDNEY B. BOWNE & SON
MINI-SYSTEMS, INC.
DOT/FAA
SVERDRUP, TEAS GROUP
SAMSUNG DATA SYSSYSTEMS CO., L
CHUNGNAM NATIONAL UNIVERSITY
EG&G WASC, INC.
TRIMBLE NAVIGATION LTD
OVERLOOK SYSTEMS TECHNOLOGIES
NAVAL RESEARCH LAB
USCG R&D CENTER
II MORROW INC.
NAPA
STANFORD TELECOMMUNICATIONS
FUTROM CORP
NATIONAL GEODETIC SURVEY, NOAA
FAA
GDE SYSTEMS INC.
ODETICS, INC.
THE MITRE CORPORATION
ROCKWELL INTERNATIONAL
JET PROPULSION LABORATORY
ITT A/CD
CATERPILLAR INC
ROCKWELL INTERNATIONAL
GEC-MARCONI ELECTRONICS SYSTEM
JCAIR INC.
LEICA, INC.
I-NET, INC.
LOCKHEED MARTIN
ROCKWELL
USAF

MENLO PARK, CA
GERMANY
WARMINISTER, PA
PETERSON AFB, CO
ATHENS, OH
POLAND
PLEASANTON, CA
KIRTLAND AFB, NM
HOUSTON, TX
FREMONT, CA
NEWINGTON, VA
APOPKA, FL
ANAHEIM, CA
SUNNYVALE, CA
SPRING VALLEY, OH
DENVER, CO
SAN DIEGO, CA
MT. AIRY, MD
SANTA ROSA, CA
OXNARD, CA
SUNNYVALE, CA
EAST MOLINE, IL
WOBBURN, MA
PHILADELPHIA, PA
OKLAHOMA CITY, OK
WESTLAKE VILLAGE, CA
MCLEAN, VA
EL SEGUNDO, CA
MINEOLA, NY
ATTLEBORO, MA
FORT WORTH, TX
MARY ESTHER, FL
KOREA
KOREA
ROCKVILLE, MD
SUNNYVALE, CA
VIENNA, VA
WASHINGTON, DC
GROTON, CT
SALEM, OR
WASHINGTON, DC
SUNNYVALE, CA
GREENBELT, MD
IJAMSVILLE, MD
RENTON, WA
SAN DIEGO, CA
ANAHEIM, CA
BEDFORD, MA
NEWPORT BEACH, CA
PASADENA, CA
FORT WAYNE, IN
DUNLAP, IL
CEDAR RAPIDS, IA
ROLLING HILLS EST, CA
NEW CENTURY, KS
TORRANCE, CA
KENNEDY SPACE CENTER, FL
FREMONT, CA
ANAHEIM, CA
LOS ANGELES AFB, CA

STEPP, TIM
 STEUMARK, J.
 STEVENS, CHRISTOPHER
 STEVENS, TOM
 STEVENSON, JOHN
 STEWART, DOC
 STILES, PAUL
 STILLWAGEN, FREDERIC
 STINNETT, GARY
 STITES, JOHN
 STOCKER, HAROLD
 STONE, MITCH
 STOWELL, JAMES
 STRACHAN, RUSSELL
 STRAKA, ALEXANDER
 STRANGE, WILLIAM
 STRANGELAND, ROD
 STRATTON, ALEX
 STUCHY, OLIVER
 STUDENNY, JOHN
 STULL, CRAIG
 STURGES, MATT
 STUTEVILLE, STEVEN
 SUDHARMO, FRANKISCUS
 SUGERMAN, LEONARD
 SUN, HUANGQI
 SUNNER, RICK
 SUTHERLAND, BRUCE
 SUTTON, STEPHEN
 SUTYARJOKO, MEIDITOMO
 SUZUKI, DAVID
 SWANSON, KYLE
 SWIDER, RAYMOND
 SWIEK, F. MICHAEL
 SWIFT, DAVID
 SYNSTELIEN, LARRY
 TABACO, A.
 TABSH, ADEL
 TADROS, ALFRED
 TAGGART, DOUGLAS
 TAGLIAFERRO, WILLIAM
 TALBOT, NICHOLAS
 TALLMAN, BRIAN
 TALMI, DORON
 TANG, WANG
 TANG, CHUANYA
 TANIGUCHI, TAKASHI
 TANJU, BEREKET
 TAYLOR, ALEX
 TAYLOR, BRIAN
 TAYLOR, RICHARD
 TAZARTES, DANIEL
 TEASLEY, STEWART
 TEMPLES, SUE
 TERRAMEO, ANTHONY
 TETESKY, AVRAM
 THEBEAU, JIM
 THEODOROU, DIMITRI
 THEROUX, Y.
 THIEL, KARL-HEINZ

LEAR ASTRONICS CORPORATION
 LEICA, INC.
 NAVAL AIR WARFARE CENTER
 TOPCON
 RAF & GPS JPO/SMC/CZJU
 NEW ZEALAND DEFENCE FORCE
 PREMIER GPS INC.
 LOCKHEED MARTIN
 MCDONNELL DOUGLAS
 COMANT INDUSTRIES, INC.
 PSI ENERGY
 ODETICS PRECISION TIME DIV.
 ASHTECH INC.
 ROCKWELL SPACE OPERATION
 UNIVERSITY OF CALGARY
 NATIONAL GEODETIC SURVEY, NOAA
 HONEYWELL
 PARKER GULL ELECTRONICS
 DASA NFS GMBH
 CANADIAN MARCONI COMPANY
 WILCOX ELECTRIC
 U.S. NAVY
 LOCKHEED MARTIN
 INDONESIAN AEROSPACE INC.
 PHYSICAL SCIENCE LAB/NMSU
 UNIV OF CALGARY/GEOMATICS ENGI
 DET 4 AFOTEC/GSS
 746 TEST SQUADRON
 NAVAIRWARCENWPNDIV
 USC
 AF PHILLIPS LABORATORY/VT-B
 AEROVIRONMENT, INC.
 FEDERAL AVIATION ADMIN/AND-510
 US GPS INDUSTRY COUNCIL
 COSSOR ELECTRONICS
 ROCKWELL/AVIONICS & COMMUNIC.
 HUBER & SUHNER, INC.
 PREMIER GPS INC.
 SPACE SYSTEMS/LORAL
 U.S. COAST GUARD
 COMPUTER SCIENCES CORPORATION
 TRIMBLE NAVIGATION
 DMA AEROSPACE CENTER
 DORAMI INTERNATIONAL LTD
 ARINC RESEARCH CORPORATION
 UNIV OF CALGARY/GEOMATICS ENGI
 TOPCON CORPORATION
 NRaD
 WOODSIDE OFFSHORE PETROLEUM
 WL/MNAG
 THE BOEING COMPANY
 LITTON SYSTEMS, INC.
 ROCKWELL INTERNATIONAL
 PRC
 NAWCWPNS
 C.S. DRAPER LABORATORY
 ROCKWELL INTERNATIONAL
 HUGHES AIRCRAFT COMPANY
 CANADIAN MARCONI COMPANY
 UNIVERSITAT STUTTGART/NAVIG.

SANTA MONICA, CA
 NORCROSS, GA
 LEXINGTON PARK, MD
 PARAMUS, NJ
 LOS ANGELES, CA
 NEW ZEALAND
 CANADA
 HAMPTON, VA
 HUNTINGTON BEACH, CA
 SANTA FE SPRINGS, CA
 BROWNSBURG, IN
 ANAHEIM, CA
 SUNNYVALE, CA
 HOUSTON, TX
 CANADA
 CHARLES TOWN, WV
 COON RAPIDS, MN
 SMITHTOWN, NY
 GERMANY
 CANADA
 KANSAS CITY, MO
 SPRINGFIELD, VA
 FORT WORTH, TX
 INDONESIA
 LAS CRUCES, NM
 CANADA
 PETERSON AFB, CO
 HOLLOMAN AFB, NM
 POINT MUGU, CA
 EL SEGUNDO, CA
 KIRTLAND AFB, NM
 SIMI VALLEY, CA
 WASHINGTON, DC
 WASHINGTON, DC
 UK
 CEDAR RAPIDS, IA
 ESSEX, VT
 CANADA
 PALO ALTO, CA
 WASHINGTON, DC
 EDWARDS, CA
 SUNNYVALE, CA
 ST. LOUIS, MO
 ISRAEL
 SAN DIEGO, CA
 CANADA
 JAPAN
 LAMBERVILLE, NJ
 AUSTRALIA
 EGLIN AFB, FL
 SEATTLE, WA
 WOODLAND HILLS, CA
 NEWPORT BEACH, CA
 SOLAMA BEACH, CA
 POINT MUGU, CA
 CAMBRIDGE, MA
 CEDAR RAPIDS, IA
 EL SEGUNDO, CA
 CANADA
 GERMANY

THIESSEN, MARK
 THOMAS, JEFFREY
 THOMAS, HUBERT
 THOMIS, JAN
 THOMPSON, DAVID
 THOMPSON, SCOT
 THOMPSON, TIMOTHY
 THORNTON, M.J.
 TIESSEN, TIM
 TIGHE, MOIRA
 TIQUI, EMILIO
 TOLLE, CINDY
 TOLMAN, S.
 TONG, TOMMY
 TONNEMACHER, JEFF
 TORIMOTO, HIDEYUKI
 TORRIONE, PETER
 TOSH, GEORGE
 TOWNSEND, BRYAN
 TOWNSEND, TODD
 TRAN, HUNG
 TRANKOVICH, LAWRENCE
 TRANS, FRANCOIS
 TRASK, CRAIG
 TRAWEEK, DUNSTAN
 TRETHEWEY, MICHAEL
 TRICKEY, TYLER
 TSAI, TIM
 TSAI, YEOU-JYH
 TSAI, NANCY
 TSENG, G.T.
 TSUJIMURA, SHIGERU
 TUCKER, ARNOLD
 TUCKER, JACK W.
 TUCKER, CAMILLE
 TURNER, DAVID
 TURNER, JEAN
 TURNEY, PAUL
 TYLER, DAVID
 UCHIYAMA, MASAYUKI
 UELAMO, GARD
 UEMATSU, HIROHIKO
 UENO, MAMI
 UIJT DE HAAG, MAARTEN
 ULGEN, SUHA
 ULMER, KARL
 UNTERNAEHRER, BILL
 UNWIN, MARTIN
 UPADHYAY, TRIVENI
 UPLINGER, SHANNON
 UPTON, PETER
 URDA, TED
 VACHERLON, JAMES
 VAN DE KOP, FRANZ
 VAN DE VELDE, VALERIE
 VAN DEE, JOSEPH
 VAN DER MAST, A.
 VAN DIERENDONCK, A.J.
 VAN DIGGELEN, FRANK
 VAN DIJK, JAN

SPECTRA-PHYSICS LASERPLANE, IN
 U.S. COAST GUARD NAVCEN
 A.C.S.A.
 LITTON SYSTEMS, INC.
 TEXACO
 ANDREW CORP
 NAWC/AD
 FILTRONIC COMPONENTS LTD
 COMPUTING DEVICES COMPANY
 SHELL UK EXPRO
 WHITE SANDS MISSILE RANGE
 GEORESEARCH
 LEICA, INC.
 TRW
 TRIMBLE NAVIGATION
 DX ANTENNA CO LTD
 ITT A/CD
 COSSOR ELECTRONICS LTD
 NOVATEL COMMUNICATIONS LTD
 ASHTECH INC.
 ROCKWELL AEROSPACE
 U.S. AIR FORCE
 UDLP/SIL
 JRC INTERNATIONAL INC.
 FEDERAL AVIATION ADMIN.
 SIGNAL COMPUTING LTD
 ROCKWELL INTERNATIONAL
 WAG CORPORATION
 STANFORD UNIVERSITY
 ARINC
 THE AEROSPACE CORPORATION
 PIONEER ELECTRONIC CORPORATION
 ARL/UNIVERSITY OF TEXAS
 SAIC
 ARL:UT
 NATIONAL RESEARCH COUNCIL
 ACCQPOINT COMMUNICATIONS CO.
 TRIMBLE NAVIGATION
 ASHTECH
 LEICA, INC.
 SEATEX AS
 STANFORD UNIVERSITY
 LAVAL UNIVERSITY
 OHIO UNIV/AVIONICS ENGIN CTR
 IMAGINS
 ROCKWELL INTERNATIONAL
 HONEYWELL
 UNIVERSITY OF SURREY
 MAYFLOWER COMMUNICATIONS, INC.
 UPLINGER TRANSLATION SERVICES
 SIGNAL COMPUTING, LTD
 SPAWAR (PMA 177-1)
 ROCKWELL INTERNATIONAL
 NAVOCEANO
 ALCATEL ESPACE
 GEOGRAPHIC POSITIONING
 ROYAL NETHERLANDS ARMY
 AJ SYSTEMS
 ASHTECH INC.
 ROYAL NETHERLANDS ARMY

DAYTON, OH
 ALEXANDRIA, VA
 FRANCE
 WOODLAND HILLS, CA
 BELLAIRE, TX
 ORLAND PARK, IL
 LEXINGTON PARK, MD
 ENGLAND
 CANADA
 ENGLAND
 WSMR, NM
 BILLINGS, MT
 NORCROSS, GA
 REDONDO BEACH, CA
 SUNNYVALE, CA
 JAPAN
 CLIFTON, NJ
 ENGLAND
 CANADA
 SUNNYVALE, CA
 DOWNEY, CA
 LANCASTER, CA
 SAN JOSE, CA
 CANADA
 N. RICHLAND HILLS, TX
 ENGLAND
 CEDAR RAPIDS, IA
 TUPELO, MS
 STANFORD, CA
 EL SEGUNDO, CA
 LOS ANGELES, CA
 JAPAN
 AUSTIN, TX
 MOORPARK, CA
 AUSTIN, TX
 WASHINGTON, DC
 IRVINE, CA
 SUNNYVALE, CA
 BELGRADE, MT
 NORCROSS, GA
 NORWAY
 STANFORD, CA
 CANADA
 ATHENS, OH
 OXNARD, CA
 CEDAR RAPIDS, IA
 GLENDALE, AZ
 UK
 READING, MA
 ALEXANDRIA, VA
 UK
 ARLINGTON, VA
 CEDAR RAPIDS, IA
 DIAMONDHEAD, MS
 FRANCE
 MONTICELLO, AR
 THE NETHERLANDS
 LOS ALTOS, CA
 SUNNYVALE, CA
 THE NETHERLANDS

VAN DYKE, KAREN
 VAN GRAAS, FRANK
 VAN HYNING, DON
 VAN WILLIGEN, DURK
 VANDEN-HEUVEL, MICHAEL
 VARONEN, JUKKA
 VASHON, D.
 VASSALOTTI, MARK
 VENABLES, MICHAEL
 VENTRESCA, RICHARD
 VENTRONE, FREDERICK
 VETH, MICHAEL
 VETTORI, SANDRO
 VIGEN, ERIK
 VIGNONE, EDWARD
 VILES, ROAMEY
 VITO, R.E.
 VO, NHO HONG
 VOGT, GENE
 VOIT, FRANK
 VON BRAUN, CURT
 VORHOEFF, STEPHEN
 VU, QUANG
 WAHID, IRWIN
 WAIBEL, REINHARD
 WAID, JAMES
 WAITE, STEVE
 WAITS, JOHN
 WALKER, DAVID
 WALKER, EDWARD
 WALKER, ROD
 WALLIS, SCOTT
 WALSH, DAVID
 WALTER, TODD
 WALTERS, BILL
 WALTON, RICK
 WANNINGER, LAMBERT
 WARD, PHILLIP
 WARD, RONALD
 WARDRIIP, S. CLARK
 WARREN, ROBERT
 WASINGER, WILLIAM
 WASSERMAN, MARK
 WATKINS, MICHAEL
 WATSON, STEVE
 WAYNE, ERNEST
 WEATHERFORD, TOM
 WEBER, LYNN
 WEBSTER, JOHN
 WEI, MING
 WEIDMAN, JOHN
 WEILER, EARL
 WEILL, LAWRENCE
 WEINMAN, NEIL
 WEISZ, DANIEL
 WELDON, ROGER
 WELLS, MICHAEL
 WELSHE, ROBERT
 WEN, WILLIAM
 WENZEL, ROBERT

DOT/RSPA/VOLPE CENTER
 OHIO UNIVERSITY
 TRW
 DELFT UNIVERSITY OF TECHNOLOGY
 USAF
 FINNISH MARITIME ADMINISTRATIO
 METRIC SYSTEMS CORPORATION
 U.S. COAST GUARD EECEN (NG)
 STELLAR NAVIGATION SYSTEMS INC
 DYNAMICS RESEARCH CORPORATION
 NAWC
 419 FLTS US AIR FORCE
 AT SYSTEM
 GECO-PRAKLA
 ROCKWELL
 DOT/FAA/ALM-60
 FREQUENCY ELECTRONICS, INC.
 LITTON AERO PRODUCTS
 US COAST GUARD
 THE AEROSPACE CORPORATION
 MIT LINCOLN LABORATORY
 COMMUNICATIONS SYSTEMS INT'L
 SMC/CZUD
 P.T. IPTN
 LEICA, AG
 BATTELLE
 WR, INC.
 JOHN E. CHANCE & ASSOC.
 QUANTUM TECHNOLOGY INC.
 NAWC-AD
 QUT SPACE CENTRE FOR SAT NAV
 AUSTRALIAN DEFENCE FORCE
 INSTITUTE OF SATELLITE NAVIG
 STANFORD UNIVERSITY
 TRIMBLE NAVIGATION
 COMSAT
 TU DRESDEN
 NAVWARD GPS CONSULTING
 LOGICON SYSCON
 ALLIED SIGNAL AEROSPACE
 SUMMIT COUNTY ENGINEER
 MOTOROLA, GSTG
 CANADIAN MARCONI COMPANY
 JPL
 NEW ZEALAND DEFENCE FORCE
 ARIZONA DOT
 NAWC-WD
 DIFFERENTIAL CORRECTIONS, INC.
 MINI-SYSTEMS, INC.
 UNIV OF CALGARY/GEOMATICS ENG
 MOTOROLA
 INTERSTATE ELECTRONICS CORP.
 MAGELLEN SYSTEMS
 NRaD WARMINSTER
 LEIGH AEROSYSTEMS CORP.
 HQ AFOTEC/TSN
 U.S. AIR FORCE SMC/CZL
 WESTERN GEOPHYSICAL
 SNT INC.
 U.S. COAST GUARD NAVCEN

CAMBRIDGE, MA
 ATHENS, OH
 REDLANDS, CA
 THE NETHERLANDS
 FT. WALTON BEACH, FL
 FINLAND
 FORT WALTON BEACH, FL
 WILDWOOD, NJ
 OGDENSBURG, NY
 WEST NEWTON, MA
 PATUXENT RIVER, MD
 EDWARDS AFB, CA
 ITALY
 NORWAY
 SAN CLEMENTE, CA
 WASHINGTON, DC
 MITCHELL FIELD, NY
 WOODLAND HILLS, CA
 MIDDLETOWN, CA
 LOS ANGELES, CA
 LEXINGTON, MA
 CANADA
 LOS ANGELES AFB, CA
 INDONESIA
 SWITZERLAND
 COLUMBUS, OH
 SAN JOSE, CA
 HOUSTON, TX
 SMYRNA, GA
 ST. INIGOES, MD
 AUSTRALIA
 PALOS VERDES ESTATES, CA
 ENGLAND
 STANFORD, CA
 SUNNYVALE, CA
 CLARKSBURG, MD
 GERMANY
 DALLAS, TX
 ARLINGTON, VA
 SANTA MARIA, CA
 AKRON, OH
 SCOTTSDALE, AZ
 CANADA
 PASADENA, CA
 NEW ZEALAND
 PHOENIX, AZ
 POINT MUGU, CA
 CUPERTINO, CA
 HUNTSVILLE, AL
 CANADA
 SCOTTSDALE, AZ
 ANAHEIM, CA
 SEAL BEACH, CA
 CHALFONT, PA
 CARLSBAD, CA
 KIRTLAND AFB, NM
 LOS ANGELES AFB, CA
 HOUSTON, TX
 SEATTLE, WA
 ALEXANDRIA, VA

WESTFALL, BRIAN
 WESTON, EDWARD
 WETHERBEE, LISA
 WETZEL, STEPHEN
 WEXLER, HERBERT
 WEYRAUCH, JOHN
 WHEATON, BOBBIE
 WHITAKER, ROBERT
 WHITAKER, CECILIA
 WHITE, GAYLE
 WHITE, JOHN
 WHITE, W.B.
 WHITMORE, GUY
 WHITWORTH, GERALD
 WICHNIENCHAROER, CHUGIAT
 WIGGERS, GEORGE
 WIGGINS, MARK
 WILBUR, LEE
 WILES, GEORGE
 WILFONG, RON
 WILLIAMS, RODNEY
 WILLIAMS, W. PETER
 WILLIAMS, CONNIE
 WILLIFORD, JIM
 WILSON, DONALD
 WILSON, KRIS
 WILSON, MARK
 WILSON, MIKE
 WILSON, ROBERT R.
 WILSON, RON
 WILSON, RON
 WILSON, STEVE
 WILSON, DAWN
 WISE, PETE
 WLAKA, MICHAEL
 WOLCOTT, D.
 WOLF, PETER
 WONG, RICHARD
 WOO, KAI
 WOOD, TONY
 WOODEN, WILLIAM
 WOODWORTH, STEWART
 WOOLARD, DANNY
 WRIGHT, DAVID
 WU, THOMAS
 WULLSCHLEGER, VICTOR
 WYSS, LINDA
 XU, BENLIN
 YAKOS, MICHAEL
 YAMA, SHIGERU
 YAMAZAKI, TAKAYUKI
 YANG, CHUN
 YANG, JIAN
 YATSU, NOBUYUKI
 YAU, JOAN
 YEE, PATRICK
 YOUHANAIE, MARK
 YOUNG, SAMMIE
 YOUNG, DAVID
 YOUNG, WILLIAM H.

TRIMBLE NAVIGATION LTD
 COMPUTER SCIENCES CORPORATION
 TRIMBLE NAVIGATION
 INGALLS SHIPBUILDING/LITTON
 GEODYNAMICS CORP.
 HONEYWELL TECHNOLOGY CENTER
 AFOTEC/BI
 LOS ALAMOS NATIONAL LAB
 METROPOLITAN WATER DISTRICT
 ROCKWELL SPACE OPERATIONS
 DEFENSE MAPPING AGENCY
 ROYAL AIR FORCE
 RACAL SURVEY LTD
 NAVSTAR SYSTEMS LTD
 CHULALONGKORN UNIVERSITY
 U.S. DEPT OF TRANSPORTATION
 USCG R&D CENTER
 ROCKWELL INTERNATIONAL, SW81
 ARMY RESEARCH LAB/AMSRL-SE-EA
 USAF
 US ARMY
 MAGELLAN
 NASA AMES - SSSUF
 ROCKWELL-AESD
 ENSCO, INC.
 TASC
 FAA
 HEWLETT-PACKARD
 HARRIS CORPORATION
 GLB ELECTRONICS, INC.
 GLB ELECTRONICS
 LEICA, INC.
 NAWCAD
 U.S. AIR FORCE
 DAIMLER-BENZ AEROSPACE/DORNIER
 METRIC SYSTEMS CORPORATION
 GERMAN LIAISON OFFICE
 WESTERN GEOPHYSICAL
 THE AEROSPACE CORPORATION
 JOHN E. CHANCE & ASSOCIATES
 9950 CHERRY TREE LANE
 BIZER COROPORATION
 CMT, LTD.
 UK CAA NATS
 MLRS PROJECT OFFICE
 FAA TECHNICAL CENTER
 ITT AEROSPACE/COMMUNICATIONS
 UNIVERSITY OF NEW BRUNSWICK
 ROCKWELL INTERNATIONAL
 TRIMBLE JAPAN K.K.
 TOPCON
 SIGNAL & SYSTEM TECHNOLOGIES
 CHIAN TIAN SURVEY MAPPING & MA
 MITSUI & CO., LTD.
 LEICA CANADA
 COMPUTER SCIENCES CORP.
 HUGHES AIRCRAFT CO.
 ATTN: SFAE-C3S-GPS
 TRIMBLE NAVIGATION
 RIVERSIDE COUNTY FLOOD CONTROL

SUNNYVALE, CA
 TEHACHAPI, CA
 SUNNYVALE, CA
 PASCAGOULA, MS
 FAIRFAX, VA
 PLYMOUTH, MN
 EDWARDS AFB, CA
 LOS ALAMOS, NM
 SAN DIMAS, CA
 COLORADO SPRINGS, CO
 HOLLOMAN AFB, NM
 UK
 ENGLAND
 UK
 THAILAND
 WASHINGTON, DC
 GROTON, CT
 SEAL BEACH, CA
 ADELPHI, MD
 TINKER AFB, OK
 YUMA, AZ
 SAN DIMAS, CA
 MOFFETT FIELD, CA
 ANAHEIM, CA
 COLORADO SPRINGS, CO
 FT. WALTON BEACH, FL
 MIDWEST CITY, OK
 DAYTON, OH
 MELBOURNE, FL
 BUFFALO, NY
 BUFFALO, NY
 TORRANCE, CA
 PATUXENT RIVER, MD
 EGLIN AFB, FL
 GERMANY
 FORT WALTON BEACH, FL
 RESTON, VA
 HOUSTON, TX
 ORANGE, CA
 HOUSTON, TX
 SILVER SPRING, MD
 WESTON, MA
 ENGLAND
 UK
 REDSTONE ARSENAL, AL
 ATLANTIC CITY, NJ
 FORT WAYNE, IN
 CANADA
 CEDAR RAPIDS, IA
 JAPAN
 PARAMUS, NJ
 HATFIELD, PA
 CHINA
 JAPAN
 CANADA
 JOLON, CA
 PLAYA DEL REY, CA
 FORT MONMOUTH, NJ
 SANTA CRUZ, CA
 RIVERSIDE, CA

YOUNGBERG, JAMES
YU, JIMMY
ZACHERY, RANDY
ZADZORA, TIM
ZEBAL, KEN
ZEIJLMAKER, L.
ZELON, BARBARA
ZELTSER, MELVIN
ZGIRSKI, PIERRE
ZIMMER, MICHAEL
ZIMMERMAN, KURT
ZINN, NOEL
ZORN, ALAN
ZWAAN, HENK

C.S. DRAPER LABORATORY
ALLIED SIGNAL INC. GAA
USAF, WL/MNAG
U.S. AIR FORCE/WRIGHT LABORATO
SMC/CZU (PRC)
NAM
ROCKWELL INTERNATIONAL
THE MITRE CORPORATION
AEROSPATIALE
U.S. NAVY
STANFORD UNIVERSITY
WESTERN GEOPHYSICAL
DYNAMICS RESEARCH CORPORATION
OCEONICS (UK) LTD

TYNGSBOROUGH,MA
OLATHE,KS
EGLIN AFB,FL
WPAFB,OH
TORRANCE,CA
THE NETHERLANDS
CEDAR RAPIDS,IA
MCLEAN,VA
FRANCE
CROFTON,MD
STANFORD,CA
HOUSTON,TX
ANDOVER,MA
UK